



Dr. Ambedkar Institute of Technology for Handicapped UP



Kanpur

on the
Occasion of



Collection of
75

Faculty Research Papers

16 August, 2022

List of 75 Research Papers Published by the AITH Faculty Members

Sr. No	Details of the Research Paper	Indexed In
1.	Asthana, Rachna , Y. N. Singh, "Distributed Protocol for Removal of Loop Backs and Optimum Allocation of p-Cycles to Minimize the Restored Path Lengths," IEEE Journal of Lightwave Technology, 26: 5, 616-627, 2008.	SCIE
2.	Asthana, Rachna , Y. N. Singh, "Protection and Restoration in Optical Networks," IETE Journal of Research, 50: 5, 319-329, 2004.	SCIE
3.	Asthana, Rachna , Y.N. Singh, "Second Phase Reconfiguration of Restored Path for Removal of Loop Back in p-Cycle Protection," IEEE Communication Letters, 11:2, 201 – 203, 2007.	SCIE
4.	Asthana, Rachna , Y.N. Singh, and Wayne D. Grover, "p-Cycles: An Overview," IEEE Communications Surveys and Tutorials, 12: 1, 97-111, 2010.	SCIE
5.	Dixit, Shobhit , and Vijay Laxmi Yadav, "Comparative study of polystyrene/ chemically modified wheat straw composite for green packaging application," Polymer Bulletin, 77:3, 1307-1326, 2019.	SCIE
6.	Dixit, Shobhit , Binita Joshi, Pawan Kumar, and Vijay Laxmi Yadav. "Novel hybrid structural biocomposites from alkali treated-date palm and coir fibers: morphology, thermal and mechanical properties." Journal of Polymers and the Environment, 28: 9, 2386-2392, 2020.	SCIE
7.	Hari O. , and Upadhyay S. K., Rhannolipid–metal ions (Cr ^{VI} and Pb ^{II}) complexes: Spectrophotometric, conductometric, and surface tension measurement studies. Journal of Surfactants and Detergents, 24:2, 281-288, 2021.	SCIE
8.	Katiyar, Kalpana , et al. "Cryptosporidiosis, a public health challenge: A combined 3D shape-based virtual screening, docking study, and molecular dynamics simulation approach to identify inhibitors with novel scaffolds for the treatment of cryptosporidiosis." Indian Journal of Biochemistry and Biophysics (IJBB) 59:3, 296-310, 2022.	SCIE
9.	Kumar M., A. Seth, A. K. Singh, M. S. Rajput , and M Sikandar, "Remediation strategies for heavy metals contaminated ecosystem: A review," Environmental and Sustainability Indicators, 12, 100155, 2021.	SCIE
10.	Kumar, Ankit , R Singh, A.S.K. Sinha, "Catalyst modification strategies to enhance the catalyst activity and stability during steam reforming of acetic acid for hydrogen production" International Journal of Hydrogen Energy 44:26, 12983-13010, 2019.	SCIE
11.	Kumar, Ankit et al. , "A state of the art overview of carbon-based composites applications for detecting and eliminating pharmaceuticals containing wastewater," Chemosphere, 288, 1-23, 2022.	SCIE
12.	Kumar, Ankit , and A. S. K. Sinha, "Comparative study of hydrogen production from steam reforming of acetic acid over synthesized catalysts via MOF and wet impregnation methods," International Journal of Hydrogen Energy, 45:20, 11512-11526, 2020.	SCIE
13.	Kumar, Ankit , and A. S. K. Sinha, "Hydrogen production from acetic acid steam reforming over nickel-based catalyst synthesized via MOF process," International Journal of Hydrogen Energy, 45:46, 24397-24411, 2020.	SCIE
14.	Kumar, Ankit , Hsiao-Chun Su, Yong-Song Chen, and Amornchai Arpornwichanop. "Effect of catalyst layer with zeolite on the performance of a proton exchange membrane fuel cell operated under low-humidity conditions." International Journal of Hydrogen Energy, 46:29, 15878-15886, 2021.	SCIE

15.	Kumar, Ankit , J. P. Chakraborty, and Rupesh Singh. "Bio-oil: the future of hydrogen generation." <i>Biofuels</i> , 8:6, 663-674, 2017.	SCIE
16.	Kumar, Ankit , K Sahoo, J P Chakraborty, "A comparative study on valuable products: bio-oil, biochar, non-condensable gases from pyrolysis of agricultural residues," <i>Journal of Material Cycles and Waste Management</i> , 23:1, 186-204, 2020.	SCIE
17.	Kumar, Indrajeet, Vikash Sachan , Ravi Shankar, and Ritesh Kumar Mishra. "An investigation of wireless S-DF hybrid satellite terrestrial relaying network over time selective fading channel." <i>Traitement du Signal</i> , 35:2, 103, 2018.	SCIE
18.	Kumar, Pawan, Shobhit Dixit , and Vijay Laxmi Yadav. "Effect of hydrophilic bentonite nano particle on the performance of polyvinylchloride membrane." <i>Materials Research Express</i> , 6:12, 126415, 2019.	SCIE
19.	Mishra, Ashutosh , and R.K. Trivedi, "A comparative study of biosurfactant preparation by <i>Pseudomonas aeruginosa</i> MTCC 424 using rice bran oil and soybean oil substrates, <i>J. Indian Chem. Soc.</i> , 97(B): 87-100, 2501-2515, 2020.	SCIE
20.	Mishra, Ashutosh , et al. "Optimization of process inputs for the synthesis of waste rice bran oil isolated <i>Pseudomonas aeruginosa</i> MTCC 424 biosurfactant using response surface methodology for oil recovery applications." <i>Bioresource Technology Reports</i> , 14, 100653, 2021.	SCIE
21.	Nigam, Ravi , and Sachin K. Singh. "Crack detection in a beam using wavelet transform and photographic measurements." In <i>Structures Elsevier</i> , 25, 436 - 447, 2020.	SCIE
22.	Rajput, M. S. , M Singh, SK Singh, "Dairy Effluent Biodegradation by Endogenous Fungal Isolates in the Integrated Wastewater Treatment System," <i>Journal of Water Chemistry and Technology</i> 44:1, 48-55, 2022.	SCIE
23.	Rajput, M. S. , V Dwivedi, SK Awasthi, "Biodegradation of pyridine raffinate by microbial laccase isolated from <i>Pseudomonas monteilii</i> & <i>Gamma proteobacterium</i> present in woody soil," <i>Biocatalysis and Agricultural Biotechnology</i> , 26, 101650, 2020.	SCIE
24.	Rajput, M. S. , V Dwivedi, SK Awasthi, "Enzymatic degradation of pyridine raffinate using response surface and artificial neural network simulation," <i>Indian Journal of Experimental Biology (IJEb)</i> , 58:8, 584-592, 2020.	SCIE
25.	Sachan, Vikash , Indrajeet Kumar, Ravi Shankar, and Ritesh Kumar Mishra. "Analysis of transmit antenna selection based selective decode forward cooperative communication protocol." <i>Traitement du Signal</i> , 35: 1, 2018.	SCIE
26.	Sachan, Vikash. , Mishra, R.K. Uplink sum rate and capacity of hybrid precoding mmWave massive MIMO system. <i>Traitement du Signal</i> , 36: 2, 155-160, 2019.	SCIE
27.	Sahoo, Kedar, Ankit Kumar , and Jyoti Prasad Chakraborty. "A comparative study on valuable products: bio-oil, biochar, non-condensable gases from pyrolysis of agricultural residues." <i>Journal of Material Cycles and Waste Management</i> , 23:1, 186-204, 2021.	SCIE
28.	Sawood, Ghazi Mohd , and S. K. Gupta. "Arsenate adsorption from aqueous solution using iron-loaded <i>Azadirachta indica</i> roots: batch and fixed-bed column study." <i>Desalin. Water Treat</i> , 203, 292-308, 2020.	SCIE
29.	Sawood, Ghazi Mohd , and S. K. Gupta. "Kinetic equilibrium and thermodynamic analyses of As (V) removal from aqueous solution using iron-impregnated <i>Azadirachta indica</i> carbon." <i>Applied Water Science</i> 10: 6, 1-18, 2020.	SCIE
30.	Sawood, Ghazi Mohd , Ashutosh Mishra, and S. K. Gupta. "Optimization of arsenate adsorption over aluminum-impregnated tea waste biochar using rsm–central composite design and adsorption mechanism." <i>Journal of Hazardous, Toxic, and Radioactive Waste</i> , 25:2, 2021.	SCIE

31.	Sawood, Ghazi Mohd , Shobhit Dixit, Gaurav Mishra, and S. K. Gupta. "Selective As (v) capture by a novel magnetic green Fe-biochar composite in a packed column: an application of central composite design." <i>Environmental Science: Water Research & Technology</i> , 7:11, 2129-2144, 2021.	SCIE
32.	Sengupta A, Ghosh S, Basant A, Malusare S, Johri P , Pathak S, Sharma S, Sonawat HM. Global host metabolic response to Plasmodium vivax infection: a 1H NMR based urinary metabonomic study. <i>Malaria journal</i> , 10:1, 1-3, 2011.	SCIE
33.	Sharma, Rohit , and Raghuraj Singh. "A Highly Reliable and Cost-effective Service Model for Finite Population Clouds: Analysis and Implementation." <i>Arabian Journal for Science and Engineering</i> , 47:2, 1181-1196, 2022.	SCIE
34.	Sharma, Rohit , and Raghuraj Singh. "Performance evaluation and reliability analysis of predictive hardware failure models in cloud platform using ReliaCloud-NS." <i>International Journal of Cloud Computing</i> 10:3, 207-224, 2021.	SCIE
35.	Sharma, Rohit , and Raghuraj Singh. "Resource provisioning optimization for cloud computing systems serving multi-class requests, <i>International Journal of Adhoc and Ubiquitous computing</i> , 40:4, 239-249, 2022.	SCIE
36.	Sharma, Rohit , Prateek Gupta, and Raghuraj Singh. "Hypergeometrically Represented Responsive and Reliable Cloud Service Model for Personal and Private Clouds." <i>Wireless Personal Communications</i> , 125, 1501-1522, 2022.	SCIE
37.	Singh, Sushil Kumar , Robinka Khajuria, and Loveleen Kaur. "Biodegradation of ciprofloxacin by white rot fungus Pleurotus ostreatus." <i>3 Biotech</i> , 7:1, 1-8, 2017.	SCIE
38.	Tripathi P, Siddiqui S44S, Sharma A, Johri P , Singh A. Molecular docking studies of Curcuma Longa and aloe vera for their potential anticancer effects. <i>Asian Journal of Pharmaceutical and Clinical Research</i> , 11:4, 314-318, 2018.	SCIE
39.	Upadhyay S. K., Hari O . Spectrophotometric and conductometric study of the interaction of saponin with chromium (VI) and lead (II). <i>International Journal of Environmental Science and Technology</i> ; 16:12, 7997-8004, 2019.	SCIE
40.	Khan, Mohd Kaif, Mukund Mohan, Pradyumn Jaiswal, Prashant Kumar, and Purna Srivastava . "A Review Paper on Rice Quality Analysis Using Image Processing Technique." 10:5, 292-294, 2022.	Scimago
41.	Chandra, Gaurav , Manjari Chakraborty, and A. K. Sinha. "Framework for Assessing Efficient Water Consumption Attributes and Their Relative Importance in Office Complexes." <i>Asian Journal of Water, Environment and Pollution</i> 14:3, 65-74, 2017.	SCOPUS
42.	Chandra, Gaurav , Manjari Chakraborty, and A. K. Sinha. "WSI OC: The Water Sustainability Index for Office Complexes." <i>Asian Journal of Water, Environment and Pollution</i> 15:2, 223-238, 2018.	SCOPUS
43.	Dixit, Shobhit , and Vijay Laxmi Yadav. "Optimization of polyethylene/polypropylene/alkali modified wheat straw composites for packaging application using RSM." <i>Journal of Cleaner Production</i> , 240, 118228, 2019.	SCOPUS
44.	Dwivedi, Sri Nath , Harish Karnick, and Renu Jain. "Relation Classification: How Well Do Neural Network Approaches Work?." <i>Iberoamerican Knowledge Graphs and Semantic Web Conference</i> . Springer, Cham, 2020.	SCOPUS
45.	Johri, Parul , Mala Trivedi, Drishti Srivastava, Aman Kumar Singh, and Mohammed Haris Siddiqui. "Protein Characterization at atomic level: A Novel approach for sequence analysis." <i>Current Trends in Biotechnology & Pharmacy</i> 12:4, 2018.	SCOPUS
46.	Katiyar, Kalpana , Ramesh Kumar Srivastava, and Ravindra Nath. "Comparative Genomics Analysis of Cryptosporidium Parvum and Repurposing of Triazole Derivative	SCOPUS

	as Anti-Cryptosporidial Agents." Biomedical & Pharmacology Journal, 13:1, 127-137, 2020.	
47.	Katiyar, Kalpana , Ramesh Kumar Srivastava, and Ravindra Nath. "Identification of novel anti-cryptosporidial inhibitors through a combined approach of pharmacophore modeling, virtual screening, and molecular docking." Informatics in Medicine Unlocked 24, 100583-93, 2021.	SCOPUS
48.	Kumar Rakesh, and ShivKishan Dubey , "Simulation of language competition by bilingual agents," Int. J. Knowledge and Learning, 12:4, 362-378, 2018.	SCOPUS
49.	Mishra, Ashutosh and Rakesh Kumar Trivedi. "Deinking of old used papers using crude rhamnolipid biosurfactant." Poll. Res. 40, no. may Suppl. Issue S250-S256, 2021.	SCOPUS
50.	Mishra, Ashutosh , and Rakesh Kumar Trivedi. "Synthesis and characterization of biosurfactant using waste from oil processing industry as substrate by Pseudomonas aeruginosa (MTCC 424)." Rasayan J. Chem., 12: 2, 1011-1021, 2019.	SCOPUS
51.	Parul Johri et.al. "Toxicity Mitigation of Textile Dye Reactive Blue 4 by Hairy Roots of Helianthus annuus and Testing Its Effect in In Vivo Model Systems" BioMed Research International, 13, 2022	SCOPUS
52.	Prabhakar, Abhishek , Amod Tiwari, and Vinay Kumar Pathak. "Hello Messaging based Aodv Routing Protocol and Its Simulation." International Journal of Applied Engineering Research, 12:18, 7321-7328, 2017.	SCOPUS
53.	Rajput M. S. , B N Mishra, "Biodegradation of pyridine raffinate using bacterial laccase isolated from garden soil," Biocatalysis and Agricultural Biotechnology, 17, 32-35, 2019.	SCOPUS
54.	Schan Shweta, Parul Johri , Mala Trivedi and Aditi singh, " Sequencing and In silico annotation of a novel Pseudomonas strain," Asian Journal of Microbiology, Biotechnology and Environmental Science, 19:4, 148 – 151, 2017.	SCOPUS
55.	Ramnivas Kumar, Ravi Nigam , Sachin K Singh "Selection of suitable mother wavelet along with vanishing moment for the effective detection of crack in a beam", Mechanical Systems and Signal Processing, 163, 108136, 2022	SCOPUS
56.	Singh, Devendra Pratap. , Rakesh Kumar Trivedi, " Biofule from wastes an economic and environmentally feasible resource, Energy Procedia, 54, 634-641, 2014.	SCOPUS
57.	Srivastava N. K., R. S. Rajput, and M. Singh , "Evaluation of Dairy Effluent Detoxification and Removal Efficiency in an Integrated Wastewater Treatment System Using Low-cost Adsorbent," Rasayan Journal of Chemistry, 15:1, 593-599, 2022.	SCOPUS
58.	Srivastava, Anuj et al., "Analytical Study of A Two-Phase Model For Steady Flow of Blood in A Circular Tube," International journal of Engineering Research and Applications, 102-112, 2020.	SCOPUS
59.	Tripathi Shweta , and Garima Saini, "A Literature review on Ultra –Wide band Circular Polarization Antenna," Pensee, 15:3, 1934-1945, 2021.	SCOPUS
60.	Varma, Chandra Prakash , and Singh Yaduvir, "A review of sizing, system, security and reliability controller design and system stability of integrated renewable energy source," Wulfenia journal, 26:8, 2019.	SCOPUS
61.	Varma, Chandra Prakash , and Singh Yaduvir, "Optimum scheduling techniques for integrated renewable energy source," Wulfenia journal, 26:8, 2019.	SCOPUS
62.	Varma, Chandra Prakash , Mishra S. K., and Jaisal Amit, "Multi junction cells and their utility for power generation," IETET, 333-337, 2013.	SCOPUS
63.	Verma, S. R., and Anuj Srivastava , "Effect of magnetic field on steady blood flow through an inclined circular tube." International Journal of Engineering Research and Applications, 3:4, 428-432, 2013.	SCOPUS

64.	Agnihotri, Abhishek , Vikash Yadav, and Vandana Dixit Kaushik. "Role of data mining and machine learning techniques in medical imaging." International Journal of Advanced Intelligence Paradigms, 15: 3, 340-351, 2020.	UGC
65.	Gaur S. K. Singh , "Sustainable use of recycled construction and demolished concrete/masonry Aggregates in India," International Journal of Engineering and Technology, 7:7, 5001-5010, 2020.	UGC
66.	Gaur S. K. Singh , and Sunil Kumar, "Performance of Concrete with Demolished Concrete as Coarse Aggregate on Strength, Durability and Fire Resistance," Journal of Construction Management, 37:2, 46-55, 2022.	UGC
67.	Gaur S. K. Singh , and Sunil Kumar. "Mathematical models for performance of concrete by replacing natural sand with stone dust." ADBU Journal of Engineering Technology, 10, 1-5, 2021.	UGC
68.	Kanaujia, Ravi Kumar , "Palm print recognition based on pca and its variants," Current trends in signal processing, 5: 3, 7-14, 2015.	UGC
69.	Prabhakara, Abhishek , Amod Tiwarib, and V. K. Pathak. "Study of various generation and bandwidth sharing issues in mobile network." Adv Wireless Mobile Commun., 10:5, 913-924, 2017.	UGC
70.	Singh, B. R. , Sushil K. Agarwal, and Garima Singh, "Design of floating point vedic multiplier using VHDL," IJIESM Journal, 4:2, 13-16, 2016.	UGC
71.	Singh, Devendra Pratap , and Ashish Narain Dubey, "Production of Biofuel (Biodiesel and Bioethanol): An Economical and Environmentally Feasible way to the Society," Journal of Energy, Environment & Carbon Credits, 11:2, 1-10, 2021	UGC
72.	Singh, Devendra Pratap , and Hemant Kumar, "Production of Biodiesel using Immobilized Pseudomonas Fluorescence," International Journal of Research and development in Engineering, 2, 17-23, 2013.	UGC
73.	Singh, Devendra Pratap , and Rakesh Kumar Trivedi. "Acid and Alkaline pretreatment of lignocellulosic biomass to produce ethanol as biofuel." International Journal of Chem. Tech Research, 5: 2, 727-734, 2013.	UGC
74.	Srivastava, Divya, Rohit Sharma and Anuj Srivastava , "Reliability Analysis of Cloud Computing Systems Serving Multi-Class Requests," Journal of Scientific Research of BHU, 65:5, 286-292, 2021.	UGC
75.	Verma, S. R., and Anuj Srivastava , "Analytical Study of A Two-Phase Model For Steady Flow of Blood in A Circular Tube." International Journal of Engineering Research and Applications, 4:12, 1-10, 2014.	UGC

Distributed Protocol for Removal of Loop Backs and Optimum Allocation of p-Cycles to Minimize the Restored Path Lengths

Rachna Asthana, *Student Member, IEEE*, and Yatindra Nath Singh, *Senior Member, IEEE*

Abstract—p-Cycle-based protection is one of the most promising techniques of span protection in optical networks because of mesh-like efficiency and ring-like speed. We have presented a modified distributed cycle preconfiguration protocol (MDCPC) which reduces the computational complexities, by finding all the copies of the same p-cycle in single iteration. All the copies of the same p-cycle are aggregated together to reduce the number of switching fabrics and the amount of signalling traffic. Further, the restoration paths provided by the p-cycles are usually many hops long, as longer p-cycles provide better efficiency. Obviously, with longer p-cycles, the nodes in the working path may be repeated in the restoration path provided by the p-cycle. They will give rise to loop backs in the restored path. The restored path lengths will unnecessarily be longer due to these loop backs. If these loop backs can be removed, the restored path length will be reduced significantly, and redundant capacity will also be released. In the present work, a distributed protocol has been presented for the implementation of removal of loop back (RLB) algorithm to reconfigure the restored path. The reduction in the restored path length also depends on the fact that which p-cycle is being used to protect a particular path. The problem has been formulated as optimum p-cycle allocation (OPA) problem and solved with the Hungarian algorithm. The average lengths of the restored paths with and without RLB for the networks with 2.0 average nodal degree have also been derived.

Index Terms—Capacity saving, distributed cycle preconfiguration (DCPC), p-cycles, path restoration, reconfiguration of restored path.

I. INTRODUCTION

THE research on p-cycle (pre-configured cycle) based span protection technique has gained tremendous momentum in recent years, due to their ability to provide ring-like speed, mesh-like efficiency, and flexibility for survivability of wavelength division multiplexed (WDM) optical networks [1]–[6]. The main difference between any ring-based scheme and the p-cycle scheme is the protection of straddling spans by the p-cycles [1] (Fig. 1). The mesh-like efficiency can be achieved due to the shared protection provided by the p-cycle to all the on-cycle spans as well as straddling spans. The spare capacity of the network is preconnected to form the p-cycles. Hence, only two switching actions (as in rings), at the end nodes of the failed

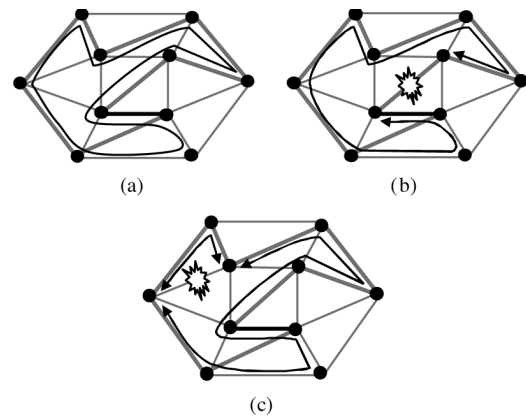


Fig. 1. (a) p-cycle, (b) on-cycle failure, and (c) straddling span failure.

span, are needed in the event of failure, to switch the traffic to the protection path provided by the pre-configured cycle.

In recent years, lot of work has been reported in literature [6] on various issues in p-cycles. To achieve the theoretical efficiency of mesh networks, extensive work has been done with Hamiltonian p-cycles [7], [8]. Strategies have been proposed to provide dual [9] or multifailure network survivability [10] with reconfigurable or shared p-cycles. Recently, the span protection technique of p-cycle has also been extended to provide node and path segment protection [11]. To obtain the optimal solution for the configuration of p-cycles, many heuristics have been developed [12]–[15]. To limit the protection path length of the p-cycle, “hop limit” and “circumference limit” designs of the p-cycles have been proposed [16]. The joint optimization strategies for working path and required capacity for the formation of p-cycles have also been reported in [17] and [18].

The concept of protected working capacity envelope (PWCE) has been used in [18] and [19] for dynamic traffic environments.

All of the above algorithms can be placed under the centralized techniques of p-cycle formation. In the distributed techniques, distributed cycle pre-configuration (DCPC) protocol [1] is the basic method. The p-cycles are searched and preconfigured in the spare capacity using DCPC protocol or its variants [20]. This protocol can be implemented in any real network to enable the deployment of p-cycles. However, only one p-cycle is obtained in one iteration of the algorithm. Hence, when multiple copies of same p-cycles exist, the algorithm’s efficiency reduces. With slight modifications, we can reduce the computational complexities of DCPC protocol. At the same time, the number of switching fabrics required for deployment of p-cycles will also be reduced significantly.

Manuscript received July 20, 2007; revised October 29, 2007.

R. Asthana is with the Harcourt Butler Technological Institute, Kanpur, UP, 208002, India (e-mail: rachnas@iitk.ac.in).

Y. N. Singh is with the Electrical Engineering Department, Indian Institute of Technology Kanpur, UP, 208016, India (e-mail: ynsingh@iitk.ac.in).

Color versions of one or more of the figures in this paper are available online at <http://ieeexplore.ieee.org>.

Digital Object Identifier 10.1109/JLT.2007.915277

A lot has been said in the literature about the formation of p-cycles. However, there are various issues related with restoration after the failure event. One such issue is the length of the restored path. In [16], successful efforts have been made to reduce the restored path length at the cost of increased initial spare capacity with smaller hop limits. When hop limit exceeds a certain threshold, the total spare capacity requirement matches with that of the other methods and the restored paths length also increases. Due to the large restored paths length, the following problems may arise, mainly in case of long-haul networks.

- Excessive signal degradation.
- Excessive signal delay.
- More resources are consumed for restoration in the event of failure.
- Due to larger number of hops in the restored path, the probability of surviving in the event of second failure will be less.
- Usually after the restoration of traffic in the event of failure, reconfiguration of the network takes place to survive the second failure. Fewer resources are available with distributed protocols for reconfiguration.

In the networks under consideration, the failure rate is one fiber cut in four days [6], and single fiber can carry more than 160 wavelengths using the dense wavelength division multiplexing (DWDM) technique [2]. Therefore, above problems cannot be ignored in case of optical networks. The problems can be minimized if the length of the restored path could be shortened.

In this paper, we have discussed the proposed modified DCPC algorithm, and the distributed algorithm for second phase reconfiguration [21]–[23] to reduce the restored path length along with optimum p-cycle allocation. In Section II, we have presented the distributed protocol MDCPC for formation of p-cycles. In Section III, we have presented the distributed protocol to implement RLB (removal of loop back) along with DCPC. Also, the model (from [23]) has been used to evaluate the performance of RLB. In Section IV, the optimum p-cycle allocation (OPA) problem has been discussed along with its solution using the Hungarian algorithm. Simulations and results are given in Section V, and finally, conclusions are presented in Section VI.

II. MODIFICATIONS IN DCPC PROTOCOL

The p-cycle can be used in MPLS layer [24], [25] where label switched paths can be provided protection. In WDM or DWDM optical networks, the technique can be used to provide protection to wavelength paths [6], [15], [26] and [27]. In case of optical WDM or DWDM network, one p-cycle can protect one wavelength on any of its on cycle span and two wavelengths on any of its straddling spans. With DCPC, in single iteration, only one copy of a p-cycle can be found. If more spare capacity is available for more copies of the same p-cycle, to find all of them, the number of iterations required by the DCPC will be equal to the number of copies of the p-cycle. The problem becomes more severe in case of heavily loaded or large size networks where a large number of p-cycles are required to provide protection. This will also increase the number of copies of a p-cycle and hence, more iterations of DCPC and more signaling traffic for p-cycle management will be required.

To reduce the complexity, the concept of capacity of p-cycles is introduced for WDM and DWDM networks. The total number of copies, which can be aggregated together, of the same p-cycle, is called “capacity” of the p-cycle in the present work. We have modified the DCPC protocol such that all the copies of the same p-cycle can be found in single iteration.

A. Modified DCPC (MDCPC) With Capacity Field

In the statelets used in basic DCPC algorithm [1], an additional field “capacity” is added by the Cyclor nodes. This capacity field stores the number of working wavelengths which can be protected by the p-cycle among all its on-cycle spans and half of the working wavelengths which can be protected on straddling spans. When statelet reaches to a Tandem node, the capacity field is also modified. The Tandem node compares the following capacity field value in the statelet.

- Spare capacity on the span, to which the statelet is to be broadcast.
- Working capacity of on-cycle span, to which the statelet is to be broadcast.
- Half of the working capacity on spans with straddling relationships at the current Tandem node.

Then Tandem node puts the minimum value in the capacity field.

When the Cyclor node receives any incoming statelet within sampling duration, then a p-cycle is formed. The score and capacity of the p-cycle are stored. When another p-cycle is formed at the Cyclor node then the score of newly arrived p-cycle is compared with present score, and the p-cycle with better score is retained. If both have the same score, then the capacity of the two is compared, and better one is retained. In case, both the parameters are the same, then the p-cycle is chosen randomly.

As in DCPC, one by one each node acts as Cyclor node and finds the best p-cycle based on the above modification. The cycle with highest score is selected as the p-cycle of choice. If there are two or more p-cycles with the same score, then the p-cycle with better capacity is selected, and if capacity is also the same then, selection is based on the ordinal rank of the nodes involved as in [1]. It should be noted that due to the use of the capacity field in the p-cycle selection, the set of p-cycles formed by MDCPC may not be the same as formed by DCPC. For the deployment, management and maintenance of p-cycles, the Cyclor node of the selected p-cycle is responsible. As all the copies of the same p-cycle can now be found in single iteration, the computational complexity is expected to reduce significantly. Otherwise, with DCPC, the complete process is repeated for every copy of the p-cycle.

In short, we have aggregated all the copies of the same p-cycle together to have one p-cycle with capacity equal to the number of copies. Another advantage with this aggregation is that protection can be provided with coarser granularity in fully convertible¹ optical networks, reducing switching complexity of the optical switches. The advantage of aggregation can be explained as follows. In case of DCPC, to deploy the p-cycle, one cross-connection is required at every node of the p-cycle between the incoming and outgoing spare wavelength. Thus,

¹In a fully convertible network, any incoming wavelength at a switch in the network can be converted into any one of the free wavelengths at the output.

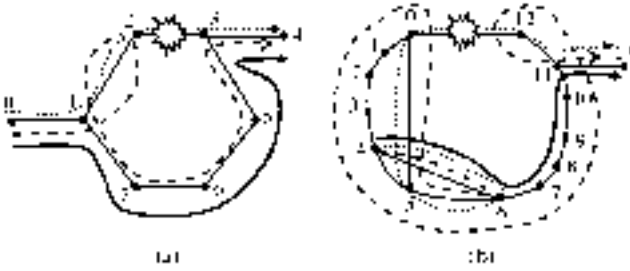


Fig. 2. Working path (dotted line), restored path (dashed line), and final path after removal of loop back (thick line).

the number of cross-connections for all the copies of the same p-cycle will be equal to the number of cross-connections of one p-cycle multiplied by the number of copies of the p-cycle. Obviously, switching complexity will be more. The switching complexity can be reduced with waveband switching of the aggregated p-cycle. The advantages of waveband switching have been given in [28]–[32]. With waveband switching, all the copies of the p-cycle can be deployed together, with only one waveband cross-connection between incoming wavelengths and outgoing wavelengths. Thus, the number of cross-connections required by all the copies together will be same as required by a single p-cycle.² Up to 20 wavelengths per waveband have been reported for switching [30]. It should be mentioned here that as given in [31] and [32], waveband switching can be realized without requiring any changes in the hardware of the network, provided the waveband signals fit within the allowable optical pass-bands. As all the p-cycles form the waveband, the working paths through the span are also supposed to be in the wavebands. During failures, the working paths can also be restored using waveband switching. The complexity and cost of optical switches are expected to reduce significantly due to waveband switching with the proposed algorithm. Here, for simplicity, we have assumed that the network is fully convertible. As the number of p-cycles reduces, management of p-cycles at nodes will also get simplified. All this can be done without compromising on any advantages of DCPC; only a capacity field is added in the statelets.

III. LOOP BACK IN THE RESTORED PATH

Consider the networks shown in Fig. 2. We are assuming that the networks are fully convertible (we are showing the network connections in one direction, and assuming that corresponding symmetrical network will exist for reverse direction also). Let 2,1,7,6,5,3,2 be a p-cycle formed in spare capacity [Fig. 2(a)]. Let us consider the working path 0,1,2,3,4 and failure of the on-cycle span 2,3. The working path 0,1,2,3,4 which is passing through the failed span, will now be routed via the remaining portion of the p-cycle as shown by the dotted line. If any node is common between the working path and the p-cycle, except the end nodes of the failed span, then the restored path will pass through that node twice. This is called loop back. The node 1 is visited twice in the restored path; hence, there is a loop back

²However, a single p-cycle with capacity “n” can provide protection to “n” wavelengths on every on-cycle span and “2n” wavelengths to every straddling span of the p-cycle.

at node 1. If the number of common nodes in the working path and the restoration path provided by the p-cycle are higher, then there will be more loop backs as shown in Fig. 2(b). These loop backs can be removed with RLB to reduce the restored path length significantly. The RLB algorithm [23], does not interfere with the routing of working paths as well as with the formation of p-cycles. After the occurrence of a failure, to retain the “ring-like speed” of the p-cycle, the working paths are restored in the first phase by the end nodes of the failed span [1]. In the second phase, the loop backs are removed by reconfiguration of the restored paths using RLB.

The loop backs can also be removed with the concept of path segment with flow p-cycles [11]. The removal of loop backs can be viewed as the protection of the complete path segment (intersecting the flow p-cycle), instead of only the failed link. However, the speed of protection is compromised in this scenario, and more complexity is involved in finding the flow p-cycles which protects the path segments [11].

To release the loop back capacity, the loop with the longest path length should be removed during reconfiguration of the restored path. The loop with the longest path length is identified both at source and destination ends, and then the switching action is performed at the corresponding common nodes. This reconfigures the restored path. All the other nodes which are part of the loop back paths modify the state information about the capacity involved with loop backs, as released. In Fig. 2(a), the switching action will be performed at 1, and states at 2 and 1 for the capacities used by the loop back path between 1,2,1, are set as unused to release the loop back. Now, the final path will be 0,1,7,6,5,3,4.

A. Mathematical Model

The detailed mathematical model of the algorithm can be found in [23]. The symbols and notations used to define the performance parameter of RLB are as follows.

- W_i Set of working paths passing through failed span i indexed by r .
- S Set of spans, indexed by i (failed) or j (surviving).
- $[]$ Ordered set of nodes.
- $[R]$ Nodes of the working path from source to destination.
- $[F]$ The failed span (F_1 , the upstream node, and F_2 , the downstream node).
- $[C]$ The p-cycle with the nodes organized in such a way that F_1 is the first node and F_2 is the last node in $[C]$.
- $[O]$ The portion of the working path from source node to the upstream node of the failed link.
- $[D]$ The portion of the working path from downstream node of the failed link to the destination node.
- $[FP]$ Restored path before RLB.
- $[FR]$ Restored path after RLB.
- L_U The length of $[U]$; defined as the total number of nodes in the set minus one.

It is obvious that $[FP] = [O] + [C] + [D]$. The $[FR] = [O1] + [C1] + [D1]$, where $[O1]$, $[C1]$ and $[D1]$ are the subsets of $[O]$, $[C]$ and $[D]$, respectively. $[O1]$, $[C1]$ and $[D1]$ are the sets representing segments of restored path after the removal of loop backs.

Thus, the length of the restored path before the RLB, will be $L_{FP} = L_O + L_C + L_D$, and after the RLB it will be $L_{FR} = L_{O1} + L_{C1} + L_{D1}$. The average length of the restored paths without RLB is

$$\begin{aligned} L_{\text{WRLB}} &= \frac{\sum_{\forall i \in S, \forall r \in W_i} (L_{FP})_{r,i}}{\sum_{\forall i \in S, \forall r \in W_i} 1} \\ &= \frac{\sum_{\forall i \in S, \forall r \in W_i} (L_{FP})_{r,i}}{\sum_{\forall i \in S} |W_i|} \end{aligned} \quad (1)$$

and with RLB, it is

$$\begin{aligned} L_{\text{RLB}} &= \frac{\sum_{\forall i \in S, \forall r \in W_i} (L_{FR})_{r,i}}{\sum_{\forall i \in S, \forall r \in W_i} 1} \\ &= \frac{\sum_{\forall i \in S, \forall r \in W_i} (L_{FR})_{r,i}}{\sum_{\forall i \in S} |W_i|}. \end{aligned} \quad (2)$$

Here, $|W_i|$ is the cardinality of set W_i .

It is expected that restored path lengths with and without RLB, also depends upon the average node degree (\bar{d}) [23]. For any network, the minimum \bar{d} can be two for all the nodes to be dual connected. The maximum \bar{d} can be $(n - 1)$, where n is the total number of nodes in the network. For \bar{d} equal to two, the network topology will be ring. In this case, the average restored path length without RLB and with RLB will be given by (assuming a lightpath for every node pair)

$$\begin{aligned} L_{\text{WRLB}} &= \frac{2(n-1)(2n-1)}{3n}; \quad n \text{ is even,} \\ &= \frac{2(2n-3)}{3}, \quad n \text{ is odd} \end{aligned} \quad (3)$$

and

$$\begin{aligned} L_{\text{RLB}} &= \frac{2(n^2-1)}{3n}, \quad n \text{ is even,} \\ &= \frac{2n}{3}, \quad n \text{ is odd} \end{aligned} \quad (4)$$

respectively.

The derivation for the above result is given in the Appendix. Further, in case of $\bar{d} = n - 1$, all the nodes are connected to each other. Hence, length of the working paths will be one hop count. Therefore, when paths are restored with p-cycles, there will not be any loop backs. Hence, L_{FP} and L_{FR} will be same and will depend upon the length of the p-cycles protecting the paths. With Hamiltonian p-cycles, these lengths will be $n - 1$ for on cycle link failure and $n/2$ on an average for straddling link failures.

B. Distributed Protocol for Removal of Loop Backs (DRLBs)

In this protocol [33], we have assumed that each node maintains a status table, consisting of previous node, next node, wavelength/fiber in previous span, wavelength/fiber in the next span for every lightpath passing through it. All the nodes are also maintaining status tables for all the configured p-cycles in the form of mapping from previous node and wavelength/fiber to next node and wavelength/fiber. For second phase reconfiguration, each light path has been identified with its PathId at the setup time. Three types of packets, ‘‘Probe,’’ ‘‘Switch,’’ and ‘‘Release’’ have been used to collect the information about the working and the p-cycle path, to send instructions to perform the switching action and to release the capacity respectively. The ‘‘Probe’’ and ‘‘Switch’’ packets are generated by the end nodes of the failed span, and ‘‘Release’’ packet is generated by the common node identified by the end nodes. All the packets will have first and second fields as follows.

- PacketId: This field will contain the information about the type of the packet, i.e., it identifies whether packets is ‘‘Probe,’’ ‘‘Switch,’’ or ‘‘Release.’’
- PathId: This field will contain the identification number of the path for which second phase reconfiguration is taking place.

The *Probe packets* will have additional third field as

- Route: In this field, the Ids of the nodes, through which ‘‘Probe’’ packet will pass, are added.

The *Switch packet* will have following additional fields.

- FirstNodeId: This field contains the Id of the node to which, the light path is going from the destination of the ‘‘Switch’’ packet.
- SecondNodeId: This will contain the Id of the node to which, the light path is to be switched for removal of loop back.

The *Release packet* will have the following additional fields.

- ReleaseCap: When this field is set, the node through which the packet is passing will release the capacity (wavelength).
- NodeId: This field contains the Id of the common node which has generated this packet.
- DirectionFlag: Upstream or downstream forwarding.

The distributed protocol will be initiated at both the upstream and downstream nodes of the failed spans. Consider the network shown in Fig. 2(a). Let us call the upstream node 2, and the downstream node 3 of the failed span 2, 3, as F_1 and F_2 , respectively. The algorithm will work as follows.

Step 1 is to collect the information about the route of the working path and the p-cycle path with ‘‘Probe’’ packets by end nodes of the failed span. The $F_1(F_2)$ node will send ‘‘Probe’’ packets to the source (destination) node via the upstream (downstream) nodes of the light path and to the $F_2(F_1)$ node through the restoration path provided by the p-cycle. Thus, for each light path, two Probe packets will be sent by $F_1(F_2)$ node of the failed span.

Every node will enter its Id in the route field of the ‘‘Probe’’ packet. When the packet reaches the source node (destination node) of the light path, then it is sent back to the $F_1(F_2)$ node of the failed span. This packet contains the route information of the working path from the source to

the F_1 (F_2 to the destination) node. The F_1 (F_2) node will also receive the Probe packet sent by the F_2 (F_1) node. This packet will contain the information of the restoration path provided by the p-cycle.

Step 2 is the identification of the common nodes with longest loop back lengths by end nodes of the failed span. As the F_1 (F_2) node will have the complete information of the working path from source to the F_1 (F_2 to the destination) node, and the restoration path of the p-cycle, it can identify the common nodes in the working path and the restoration path. Then, F_1 (F_2) will calculate the length of the loop backs for each of the common nodes and identify the loop back path having maximum length. The corresponding common node $N1$ ($N2$) is identified by F_1 (F_2).

Step 3 is to send the “Switch” packets to the common nodes by end nodes of the failed span. The F_1 (F_2) node will send “Switch” packet, to the identified common node $N1$ ($N2$).

Step 4 is to perform the switching action for removal of loop backs by the common node. The common node will identify the lightpath with its PathId and perform the switching action to switch the lightpath from the node identified by the FirstNodeId to the node identified by the SecondNodeId. This will remove the loop back from the restored path.

Step 5 is to send the “Release” packet to the nodes involved in loop back for releasing the loop back capacity. The common node $N1$ ($N2$) will send the “Release” packet to FirstNodeId. The FirstNodeId will release the capacity corresponding to the PathId and send a similar request to next node in the downstream (upstream) direction. This chain of messages ultimately will arrive back at the common node $N1$ ($N2$) completing the release process.

IV. OPTIMUM P-CYCLE ALLOCATION TO THE PATHS IN THE FAILED SPAN (OPA)

To protect a span, through which a number of light paths are passing, there are number of p-cycles. Some of them may be copies of each other while others may be different. The restored path length after removal of loop backs will depend upon allocation of a p-cycle to a particular path. This is illustrated in Fig. 3. There are two working paths; Path A (1,0,8,6,5) and Path B (1,0,12) [Fig. 3(a)] passing through the failed span 1,0. There are two p-cycles (found with ILP model) to protect 1,0 as straddling span (the nomenclature of paths provided by p-cycles for on-cycle and straddling spans are shown in Fig. 4). These two p-cycles provide four protection paths, LP1, RP1 provided by p-cycle 1 and LP2, RP2 provided by p-cycle 2 [Fig. 3(a)]. Let the Path A be protected by LP2, and Path B be protected by RP1. The restored paths with RLB are 1,9,12,10,11,0,8,6,5 and 1,2,10,3,4,5,6,7,8,11,0,12 of Path A and Path B, respectively [Fig. 3(b)]. In this case, the total restored path length is $19(8 + 11)$. Now, let the Path A be protected by RP2 and Path B protected by LP1. The restored paths with RLB are 1,2,3,4,5 and 1,9,12 of Path A and Path B, respectively [Fig. 3(b)]. The total restored path length is now $6(4 + 2)$. Thus, it is clear that restored path lengths depend upon the allocation of the p-cycles to the paths. There will be C_2^4 , i.e., 12 such combinations

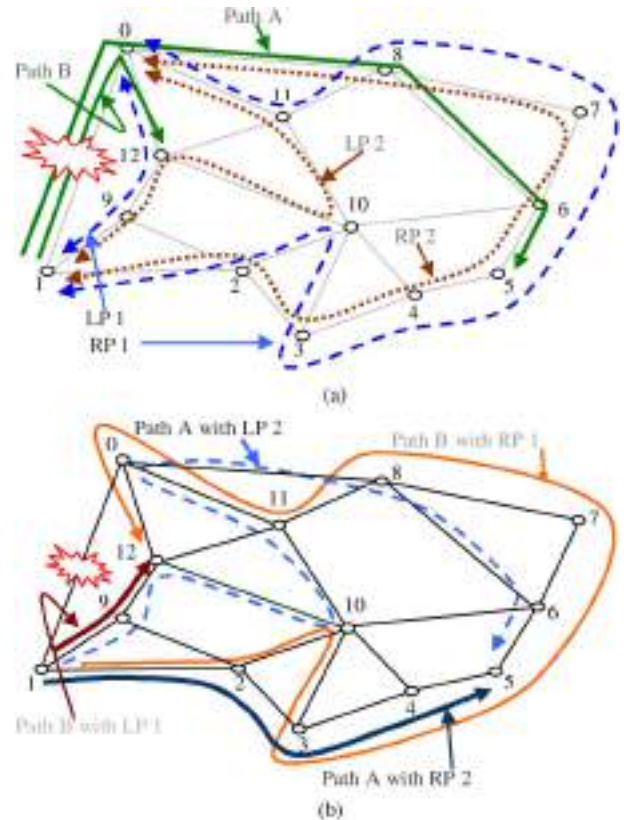


Fig. 3. Illustration of the fact that restored path lengths depends upon the allocation of p-cycle to the paths.

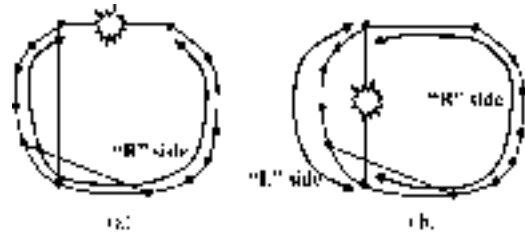


Fig. 4. Left (shorter) and right (longer or equal) path definitions for (a) on-cycle spans and (b) straddling spans as per [16].

in the above example and one of them is to be selected. Thus, the problem is to allocate the left or right paths of the p-cycles to the paths passing through the failed span in such a way that the total restored path lengths with RLB will be minimized. If the total paths and the total p-cycles segments are equal, then this is minimum-cost (or maximum-weight) maximum cardinality matching on a bipartite graph. It has the complexity of $n!$ combinations (n is the dimension of the square matrix) with brute-force approach. However, the problem can be solved with the Hungarian algorithm with the complexity of $O(N^3)$ [34], [35]. The Hungarian algorithm has been used for OPA in the present work. In the input matrix, the element $C_{i,j}$ for the Hungarian algorithm will be given by $C_{i,j} = L_{FR}$ when the i th path is protected by the j th p-cycle. Here, L_{FR} is length of the restored path after removal of loop back.

The OPA based p-cycle assignment to different paths can be computed in advance for all the spans at the end nodes having knowledge of complete topology, working path, and p-cycles.

V. SIMULATIONS AND RESULTS

In this section, first of all, we have evaluated the performance of MDCPC for various networks. Then we have evaluated the effectiveness of RLB with OPA (RLBOPA) for DCPC,³ ILP [3] and hop count limited (H-L) [16] models of p-cycle formation for different test networks. Next, the effect of \bar{d} on the restored path length has been found with RLBOPA for DCPC, ILP, and H-L. Finally, we have tested RLBOPA for dual-failure survivability.

The working traffic assuming unit traffic matrix is routed with shortest path Dijkstra's algorithm using hop count as the metric for all the evaluations to generate the working capacity on each span. A simulator, developed by us in Java, has been used to evaluate the performance. The ILP models have been solved with CPLEX 9.0 using data files generated by us with Java-based simulator.

The H-L model given in [16] is joint optimization, used to optimize both the working path lengths and the capacity used for the formation of p-cycles with the hop count limit constraint. In the present work, we want to judge the performance of RLBOPA; hence, instead of joint optimization, spare capacity required by the p-cycles have been optimized. The modified version of the model of [16] is given below.

Parameters used by us are as follows.

- Δ A large positive constant (in our case it was 10000; however, any value which is much larger in comparison with maximum working capacity on any span is good enough).
- $x_i^{p,L}$ Equal to 1 if the L side of cycle p offers an acceptable protection path for failure of span i , otherwise 0.
- $x_i^{p,R}$ Equal to 1 if the R side of cycle p offers an acceptable protection path for failure of span i , otherwise 0.
- π_j^p Equal to 1 if cycle p crosses span j , otherwise 0.
- w_j Working capacity on span j .

Variables used are as follows.

- T_{sp} Total spare capacity required for the formation of p-cycles
- sp_j Spare capacity required on span j .
- n^p Number of unit-capacity copies of cycle p in the solution.
- n_i^p Number of copies of cycle p used to protect span i .
- $n_i^{p,L}$ Number of copies of cycle p required for protection of span i , when the L side of the cycle is used.
- $n_i^{p,R}$ Number of copies of cycle p required for protection of span i , when the R side of the cycle is used.

The objective is to minimize

$$T_{sp} = \sum_{\forall j \in S} sp_j. \quad (5)$$

³RLB can be used with MDCPC only when a group of similar working paths are protected by aggregated p-cycle. Presently, we are assuming one working path between each source destination pair.

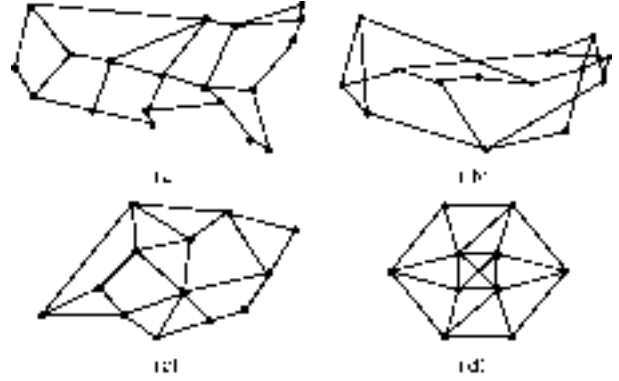


Fig. 5. Test networks (a) Net1, 19 nodes, 28 span, $\bar{d} = 2.94$. (b) Net2, 14 nodes, 22 span, $\bar{d} = 3.0$. (c) Net3, 13 nodes, 23 span, $\bar{d} = 3.5$. (d) Net4, 10 nodes, 22 span, $\bar{d} = 4.4$.

Subject to:

$$\sum_{\forall p \in P} \left(x_i^{p,L} \cdot n_i^{p,L} + x_i^{p,R} \cdot n_i^{p,R} \right) \geq w_i \quad \forall i \in S \quad (6)$$

$$\sum_{\forall p \in P} \pi_j^p \cdot n^p = sp_j \quad \forall j \in S \quad (7)$$

$$n_i^p \geq n_i^{p,L} \quad \forall i \in S \quad \forall p \in P \quad (8)$$

$$n_i^p \geq n_i^{p,R} \quad \forall i \in S \quad \forall p \in P \quad (9)$$

$$n^p \geq n_i^p \quad \forall i \in S \quad \forall p \in P \quad (10)$$

$$n_i^{p,L} \leq \Delta \cdot x_i^{p,L} \quad \forall i \in S \quad \forall p \in P \quad (11)$$

$$n_i^{p,R} \leq \Delta \cdot x_i^{p,R} \quad \forall i \in S \quad \forall p \in P. \quad (12)$$

The objective function (5) minimizes the total spare capacity required to form the p-cycles. Equation (6) ensures that all the working capacity will be protected either by L or R paths of the p-cycles. Equation (7) ensures enough spare capacity on every span to form all the p-cycles. Equations (8)–(10) make sure that copies of cycle p should be equal to or greater than the number of copies required by any single span failure. Equations (11) and (12) are “backup” constraints to ensure that, if cycle p is not eligible to restore span i using either the L or R side, then it will not be considered for protection of that span.

In the above model, we have eliminated the parameters, variables and constraints which are related to routing of working paths in [16]. We have used shortest path Dijkstra's algorithm with hop count as metric for routing of working paths. Obviously, $\sum_j w_j$ will be minimum; however, the total spare capacity required to form the p-cycles will be more than required with joint optimization. Since, there is hop count constraint for restored path lengths, the length of the path provided by p-cycle for protection will not be affected, and we can safely analyze the results of RLBOPA with H-L model.

A. Performance of MDCPC

The MDCPC has been tested with various networks, shown in Fig. 5. The test networks—Net1, Net3, and Net4 are taken from [7], [36], and [1], respectively; Net2 is NSFNET. In the first case, the spare capacity provided on each span is same as required for link disjoint path protection (LDPP), and in the second case, the spare capacity on each span is provided as

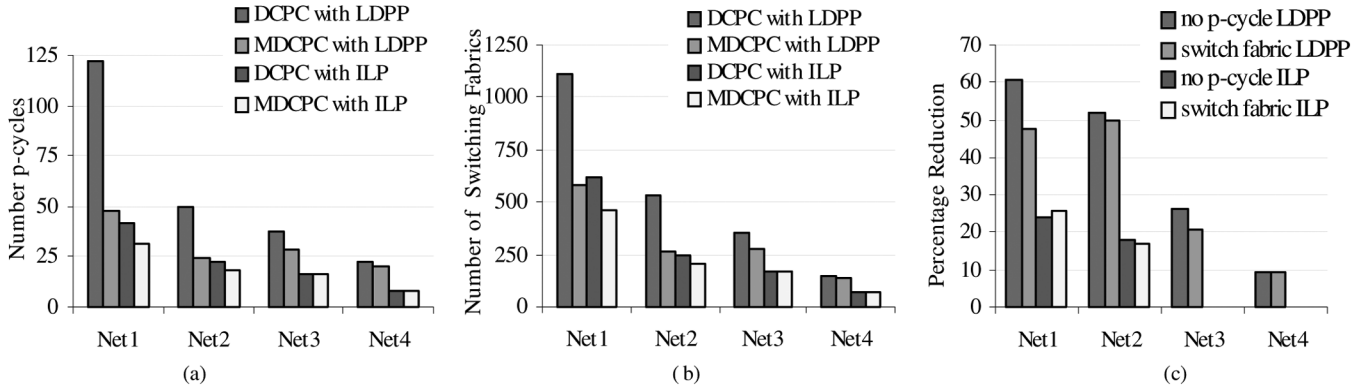


Fig. 6. Effect of MDCPC on number of p-cycles and switching fabrics with spare capacities provided as required in link disjoint path protection (LDPP) and ILP (a) Total number of p-cycles, (b) Number of switching fabrics, and (c) percentage reduction in number of p-cycles and switching fabrics.

per the ILP. First, the p-cycles in the network have been found with DCPC as given in [1]. Then p-cycles have been found with MDCPC. With aggregation of p-cycles in MDCPC, the total number of p-cycles is now much less as compared to total number of p-cycles in DCPC [Fig. 6(a)]. MDCPC reduces the computational complexity, as in single-iteration DCPC finds only one p-cycle, while MDCPC find all the copies of the same p-cycle. The reduction in the computational complexity will be same as the reduction in the number of p-cycles as shown in Fig. 6(a).

Further, with aggregation, there is significant amount of saving in the total number of switching fabrics required by p-cycles. We have assumed that every copy of p-cycle requires one switching fabric at every node in its path in DCPC; while in MDCPC, the aggregated p-cycle requires one switching fabric at every node. This reduction is shown in Fig. 6(b). The percentage of reduction in number of p-cycles and switching fabric is shown in Fig. 6(c). It is clear that with network having more nodes (Net1), the reduction is more significant. This is due to the fact, that in larger network, the traffic will be more. Hence, large number of p-cycles will be required having many copies of a p-cycle. Thus, with aggregation in MDCPC, the reduction in the number of p-cycles will be more.

The reduction is also more with LDPP as compared to ILP. As the spare capacity required with LDPP is much more than with ILP. The maximum reduction is for Net1, as many copies of the same p-cycle exist in the network. For Net3 and Net4, the difference between DCPC and MDCPC with LDPP, is small and there is no difference with ILP. These two networks are relatively smaller networks and all the p-cycles found with DCPC are single. Hence, there is no effect of aggregation. This is to be mentioned, that with spare capacity provided as in ILP, 100% protection with DCPC is not guaranteed. (100% protection is achieved only for Net4).

B. Removal of Loop Back With DCPC, ILP, and H-L

It is obvious that the RLB algorithm will almost always reduce the restored path length. To verify, the algorithm has been tested for various methods of p-cycle formation, i.e., for DCPC, ILP, and H-L models.

1) *The Following Method is Used for DCPC:* To start with, the spare capacity in each span is assumed to be the same as

required by the ILP model, and the p-cycles are formed with DCPC in our simulator. To protect all the paths of the failed span, sufficient number of p-cycles are required. In case all the paths could not be protected with the formed p-cycles, then a sufficient number of copies are added to the p-cycle which can protect maximum number of unprotected paths. This is repeated until all the working paths are protected.

2) *The Following Method is Used With ILP Model:* The set of optimal p-cycles to protect all the working capacities on each span has been found with ILP model given in [3]. For the H-L model, the set of optimum p-cycles has been found with hop count limit equal to the number of nodes in the network. The results by varying hop count limit are discussed later.

Further, the length of the restored path will also depend upon the allocation of p-cycles as shown in Section IV. To consider this effect, the results with sequential allocation (SA) of p-cycles to the paths and with OPA, have been compared. Finally, for all the cases, the L_{WRLB} and L_{RLB} are calculated and results are shown in Fig. 7.

The effectiveness of OPA with DCPC, ILP, and H-L is clearly evident in Fig. 7. The minimum L_{RLB} is obtained with the OPA method. The reduction in the average restored path lengths or the difference in L_{WRLB} and L_{RLB} is also shown by numeric values (Fig. 7). The reduction increases from 3.3 (about 32%) with SA to 5.2 (more than 51%) with OPA for Net2 with the ILP model [Fig. 7(b)]. It increases with the H-L model also from 2.6 (about 26%) to 5.1 (about 52%). The amount of reduction depends on the number of nodes in the network and \bar{d} .

C. Effectiveness With Hop Count Limited Model

In the previous case, we have taken fixed hop count limit for the purpose of comparison with other methods of p-cycle formation. To study the effect of hop count limit, L_{WRLB} and L_{RLB} are calculated for different values of hop count limits. The results are shown in Fig. 8. For smaller values of hop count, the restored path lengths are small, and reduction in the restored path length with RLB is very small. This is due to the fact that with smaller hop count limits, there is almost no loop backs. However, for these cases, the initial spare capacity required for the formation of the set of p-cycles is quite large (Fig. 9). Therefore, to achieve the smaller restored path lengths, initially more spare capacity is to be provisioned. For higher hop count limits

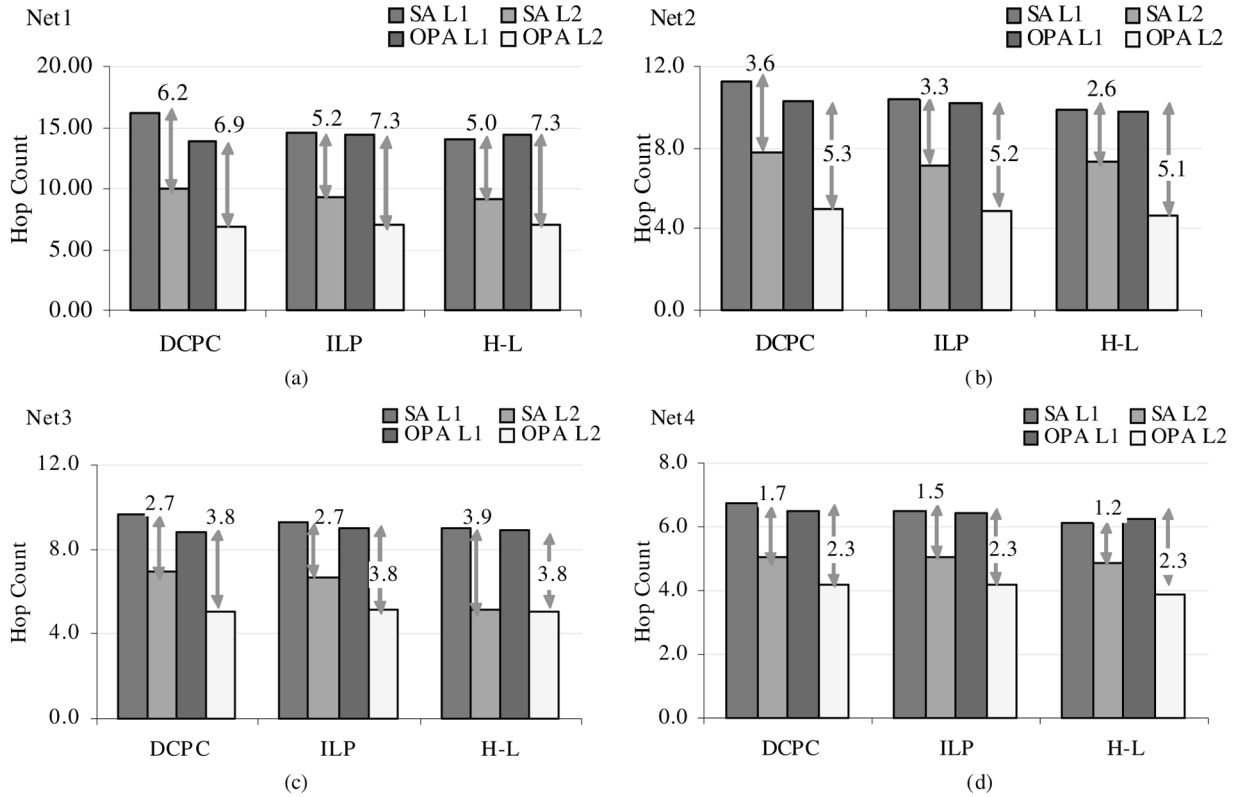


Fig. 7. Effect of RLB with sequential allocation (SA) and optimum path allocation (OPA) method for different test networks, and for DCPC, ILP, and Hop Count Limited models ($L1 = L_{WRLB}$ and $L2 = L_{RLB}$).

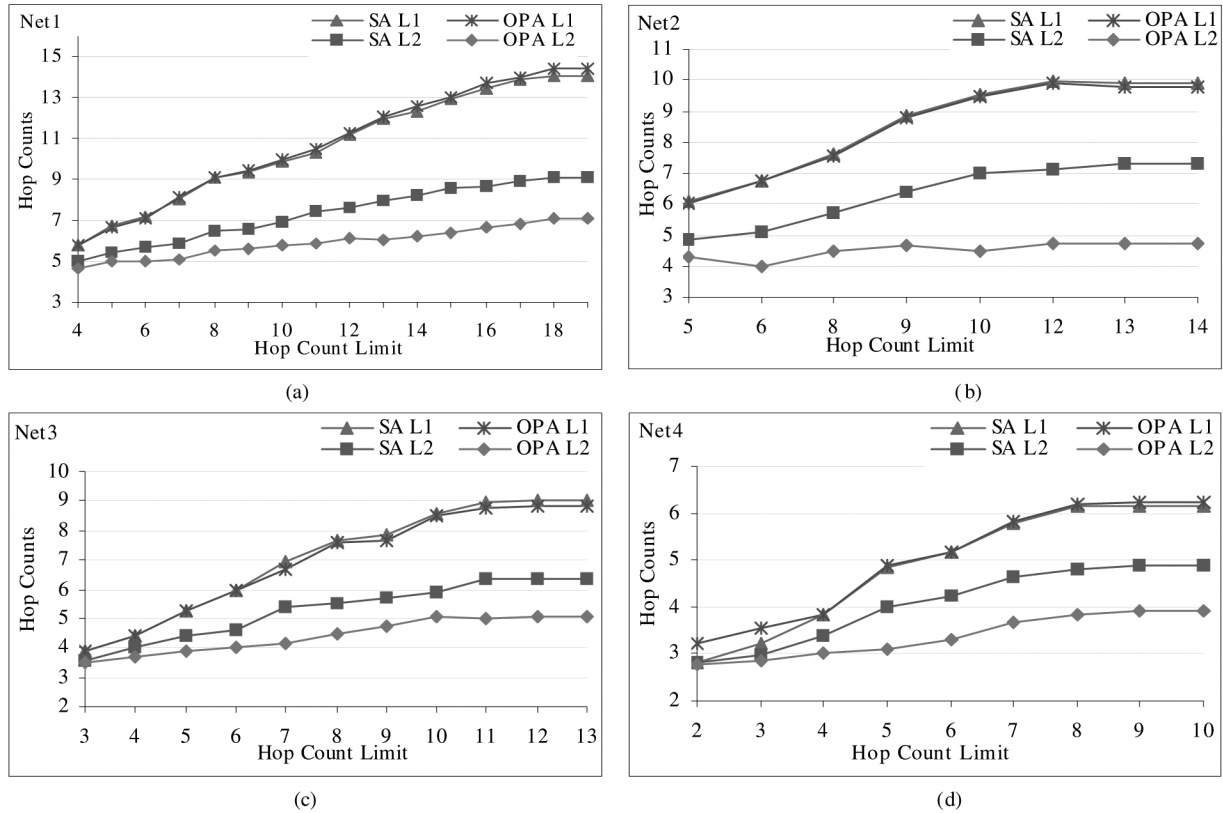


Fig. 8. Effect of RLBOPA with varying hop count limit in different test networks ($L1 = L_{WRLB}$ and $L2 = L_{RLB}$).

approaching to the number of nodes in the network, the spare capacity required for the formation of the set of p-cycles ap-

proaches to that of the ILP model. With increase in the hop count limit, the values of L_{WRLB} and L_{RLB} also increases and

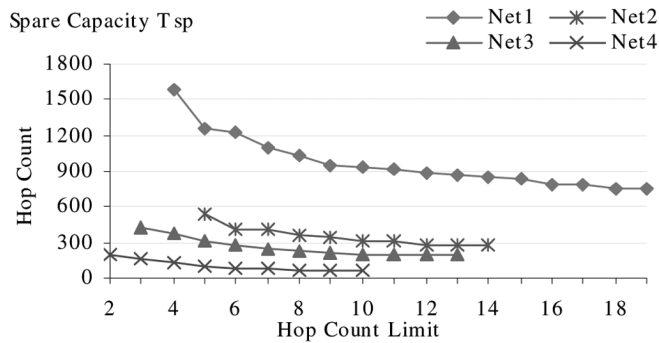


Fig. 9. Requirement of initial spare capacity T_{sp} with different hop count limits.

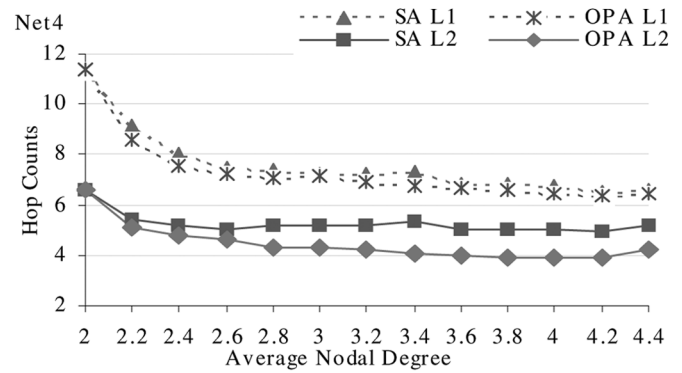
matches with that of the ILP model. This further strengthens our argument of loop backs and longer restored path lengths, the price paid for mesh-like efficiency of the p-cycles. Thus, with efficient p-cycles, restored paths will be longer resulting in more loop backs, and making RLB with OPA more effective. If smaller p-cycles are used, obviously, restored paths will be shorter with less loop backs, but with more initial spare capacity, whereas smaller restored path lengths can be obtained with RLBOPA, with optimum initial spare capacity.

D. Effectiveness of Removal of Loop Back With Average Nodal Degree and Number of Nodes in the Network

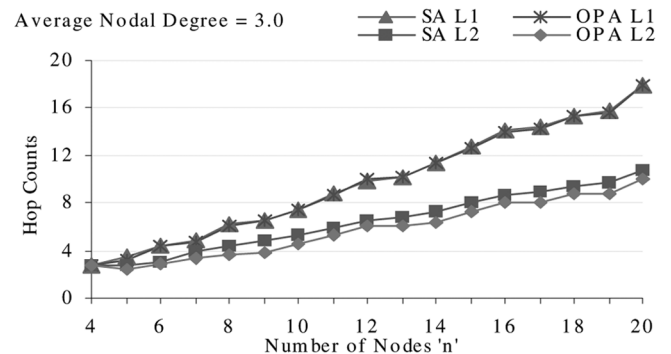
To consider the effect of \bar{d} on the amount of released capacity, we have tested the algorithm with decreasing \bar{d} for Net4 for the ILP model. To decrease the \bar{d} , spans are removed randomly. The simulations were done many times with different random seeds, and average is taken for all the simulations [Fig. 10(a)]. Similarly, the simulations are carried out for constant \bar{d} and increasing “ n ” [Fig. 10(b)]. Again, the smallest values of L_{RLB} are obtained with OPA [Fig. 10(a)]. The results with H-L will be similar to the results with ILP, for hop count limit more than a threshold value. The reduction in the restored path length is maximum for $\bar{d} = 2.0$, then it initially reduces faster with increase in \bar{d} , and thereafter the rate of reduction is much smaller. The reduction will become equal to zero for $\bar{d} = n - 1$ which is a limiting case, when there will be no loop backs and L_{RLB} remains equal to L_{WRLB} . The theoretical values for $\bar{d} = 2.0$, can be obtained with (3) and (4). The simulated values come out to be the same as calculated values. This also validates our simulator.

E. RLB With Various Traffic Distributions

We have further considered the general case of traffic matrix for Net4 when the traffic from one node is generated with probability “ p ” for every other node in the network and values of “ p ” are taken as 0.1, 0.2, ..., 1.0. With each value of “ p ” the traffic matrix is generated and p-cycles are found with the ILP model. The L_{WRLB} and L_{RLB} are calculated with SA and OPA. The results are shown in Fig. 11. As expected, the L_{RLB} values for OPA are less for more traffic in the network. For a smaller amount of traffic, the L_{RLB} for SA and OPA differs only by very small amount. This is due to the fact that with less traffic in the network, the spare capacity required to form the p-cycle



(a)



(b)

Fig. 10. Effect of RLBOPA (a) for varying \bar{d} in Net4, (b) for $\bar{d} = 3.0$ and varying the number of nodes in the network ($L1 = L_{WRLB}$ and $L2 = L_{RLB}$).

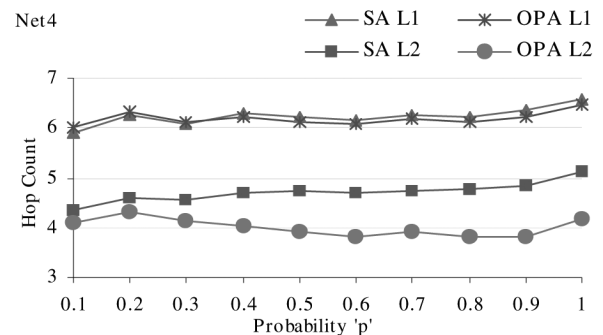


Fig. 11. Effect of RLBOPA for ILP model with various traffic distributions in Net4 (“ p ” is the probability of one unit traffic to every other node in the network, $L1 = L_{WRLB}$ and $L2 = L_{RLB}$).

is small, and in many cases just one p-cycle is sufficient to provide protection. Hence, OPA has a very limited choice between the left and the right paths of the p-cycle for straddling spans. Therefore, the effect of OPA is not visible for smaller amounts of traffic. The difference between L_{WRLB} and L_{RLB} remains almost constant and is more with OPA (approximately 2.3). The amount is the same as obtained with the H-L case for hop count limit more than the threshold value and with DCPC [Fig. 7(d)]. This suggests that reduction is almost independent of the traffic load.

F. Effectiveness in Case of Dual-Failure Survivability

The released capacity with RLBOPA can be used for providing protection in the event of a second failure. The effect

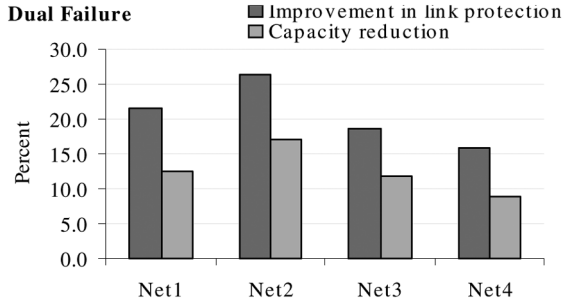


Fig. 12. Results for dual-failure restorability with RLBOPA.

has been investigated in two ways. First, the effect on the total number of links which could be restored during second failure with and without RLBOPA has been found. Next, the total amount of capacity has been found using ILP for 100% dual-failure restorability with and without RLBOPA for p-cycle based protection. The results (Fig. 12) show the improvement in the number of links restored with RLBOPA in the event of a second failure. Further, for 100% dual-failure restorability, the percentage reduction in the amount of initial capacity to be provisioned with RLBOPA, has also been shown. For all the networks, with RLBOPA, more links could be restored during a second failure with the same amount of capacity, and for 100% restorability the amount of initial capacity to be provisioned is smaller. For Net2, 26.4% more links could be restored in the event of second failure and 17% less capacity is required to provide dual failure restorability.

Dual-failure restorability has also been reported in [37] and [38]. However, the schemes proposed in these papers are basically path-based protection schemes. In [39], dual-failure protection based on the span protection technique has been presented. Our scheme can be compared with that of [39] in terms of capacity requirements. We have compared the spare to working capacity ratio in both the schemes. The minimum ratio is 1.89 for the National network given in [39], for the other two networks of [39], the above ratio is even higher for dual-failure restorability for all possible failure combinations, whereas in our case, the maximum value of this ratio is 1.62 with RLBOPA and 2.01 without RLBOPA, for the test network Net1. Therefore, the capacity efficiency obtained with RLBOPA is better.

VI. CONCLUSION

The p-cycle is a very promising technique of optical layer protection. In this paper, we have presented MDCPC, which will reduce the computational complexities and the number of switching fabrics significantly. It is achieved by adding a “capacity” field in the statelets used for the formation of p-cycles in the DCPC. The MDCPC can be implemented even in operational networks employing DCPC, to get the advantages of waveband switching.

The proposed DRLB algorithm can be implemented in any real network designed with p-cycle-based protection. It can be implemented with DCPC protocol of p-cycle formation with all the advantages of distributed protocols. The DRLB starts operation after the paths passing through the failed span are restored with switching actions at the end nodes of the failed

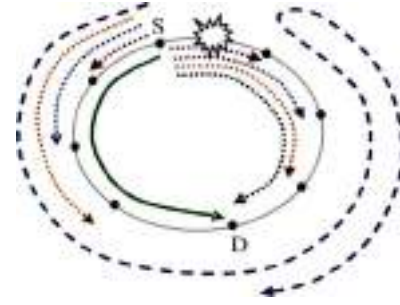


Fig. 13. Working paths (dotted lines), restored path without RLB (dashed line), restored path with RLB (thick line).

span, thereby retaining the ring-like speed of the p-cycles. Then DRLB finds out the loop backs and reconfigures the restored path by one switching action at the common node. In the meantime, lightpath remains functional. Hence, ring-like speed is retained in DRLB.

The OPA minimizes the sum of restored path lengths of all the paths passing through a span after removal of loop backs. Hence, for all the test cases, minimum restored path lengths are obtained with RLBOPA. With the ILP model, the reduction in the path lengths has been increased from about 32% with RLB, to 51% with RLBOPA for Net2. Even the minimum reduction for Net4 (with the ILP model) with RLBOPA is about 35%. The reduction is also independent of the traffic load. The amount of reduction in the average path length is always significant for all the networks. Thus, without compromising on any feature of the p-cycle, restoration can be provided with smaller restored path lengths using our RLBOPA schemes with second phase reconfiguration.

The reduction in the restored path length reduces the propagation delay, excessive signal degradation, and increases the reliability of the restored path in the event of second failure. At the same time, the released capacity will be helpful in the dual-failure survivability.

The relationship between number of nodes, L_{WRLB} and L_{RLB} has also been derived for the network with average nodal degree of 2.0.

APPENDIX AVERAGE RESTORED PATH LENGTH FOR RING TOPOLOGY NETWORK

Let us consider the $\bar{d} = 2$ network (Fig. 13). Let the total number of nodes in the network be n . The working paths (shown by dotted lines in Fig. 13) are shortest path based on hop count, for unit traffic matrix. There will be two cases, corresponding to n odd, and n even. If n is even, then there will be two paths, each with hop counts H , where H is from 1 to $n/2 - 1$, and one path with hop count $n/2$. For odd n , there will be two paths, each with hop counts H , where H is from 1 to $(n - 1)/2$. The length of the p-cycle path, protecting working paths, will be $n - 1$. Hence, the restored path length without RLB (shown by dashed line)

$$\begin{aligned}
 L_{FP} &= n - 1 + H - 1 \\
 &= n + H - 2.
 \end{aligned}$$

The restored path length with RLB

$$L_{FR} = n - H.$$

For all the paths originating from a node, when n is even

$$\begin{aligned} \sum_{\forall i \in S, \forall r \in W_i} (L_{FR})_{r,i} &= \left[\sum_{H=1}^{H=(n/2)-1} 2\{H(n+H-2)\} \right] \\ &+ \frac{n}{2} \left(\frac{3n-4}{2} \right) \\ &= \frac{n}{6}(n-1)(2n-1). \end{aligned}$$

Here, the left-hand side is the sum of lengths of the restored paths, over all the spans if they fail (one at a time) and for all the paths passing through that span. On the right-hand side, the order of summation has been changed, and the total number of spans in a path is summed over all the paths. Similarly,

$$\begin{aligned} \sum_{\forall i \in S, \forall r \in W_i} r_i &= \left(\sum_{H=1}^{H=(n/2)-1} 2H \right) + \frac{n}{2} \\ &= \frac{n^2}{4} \\ \sum_{\forall i \in S, \forall r \in W_i} (L_{FR})_{r,i} &= \left[\sum_{H=1}^{H=(n/2)-1} 2\{H(n-H)\} \right] + \frac{n^2}{4} \\ &= \frac{n}{6}(n^2-1). \end{aligned}$$

Hence, from (1) and (2) of Section III-A

$$\begin{aligned} L_{WRLB} &= \frac{2(n-1)(2n-1)}{3n}, \text{ without RLB} \\ &\text{and} \\ L_{RLB} &= \frac{2(n^2-1)}{3n}, \text{ with RLB.} \end{aligned}$$

Similarly, when n is odd

$$\begin{aligned} L_{WRLB} &= \frac{2(2n-3)}{3}, \text{ without RLB} \\ &\text{and} \\ L_{RLB} &= \frac{2n}{3}, \text{ with RLB.} \end{aligned}$$

ACKNOWLEDGMENT

The authors would like to thank Mr. S. Chinthalapudi for the discussions on the optimum path allocation (OPA) problem, the help related to the Hungarian algorithm, and contributions in the implementation of Java modules to simulate OPA, during his M.Tech. thesis work. They would also like to thank the anonymous reviewers whose feedback helped them in improving the manuscript.

REFERENCES

- [1] W. D. Grover and D. Stamatelakis, "Cycle-oriented distributed pre-configuration: Ring like speed with mesh-like capacity for self-planning network restoration," in *Proc. IEEE ICC 1998*, Atlanta, GA, Jun. 1998, pp. 537–543.
- [2] D. Colle *et al.*, "Data-centric optical networks and their survivability," *IEEE J. Sel. Areas Commun.*, vol. 20, pp. 6–20, Jan. 2002.

- [3] W. D. Grover and D. Stamatelakis, "Bridging the ring-mesh dichotomy with p-cycles," *Proc. DRCN'00*, pp. 92–104, 2000.
- [4] R. Asthana and Y. N. Singh, "Protection and restoration in optical networks," *IETE J. Research*, vol. 50, no. 5, pp. 319–329, Sep.–Oct. 2004.
- [5] W. Grover, J. Doucette, M. Clouqueur, D. Leung, and D. Stamatelakis, "New options and insights for survivable transport networks," *IEEE Comm. Mag.*, vol. 40, no. 1, pp. 34–41, Jan. 2002.
- [6] W. D. Grover, "p-cycles," in *Mesh-Based Survivable Networks: Options for Optical, MPLS, SONET and ATM Networking*. Upper Saddle River, NJ: Prentice-Hall, 2003, ch. 10.
- [7] A. Sack and W. D. Grover, "Hamiltonian p-cycles for fiber-level protection in homogeneous and semi-homogeneous optical networks," *IEEE Netw.*, vol. 18, no. 2, pp. 49–56, Mar.–Apr. 2004.
- [8] H. Huang and J. A. Copeland, "A series of Hamiltonian cycle-based solutions to provide simple and scalable mesh optical network resilience," *IEEE Commun. Mag.*, vol. 40, no. 11, pp. 46–51, Nov. 2002.
- [9] D. A. Schupke, W. D. Grover, and M. Clouqueur, "Strategies for enhanced dual failure restorability with static or reconfigurable p-cycle networks," in *Proc. IEEE Int. Conf. Commun. (ICC'04)*, Paris, France, Jun. 20–24, 2004, pp. 1628–1633.
- [10] H. Wang and H. T. Mouftah, "P-cycles in multi-failure network survivability," in *Proc. ICTON'05*, Jul. 3–7, 2005, pp. 381–384.
- [11] G. Shen and W. D. Grover, "Extending the p-cycle concept to path segment protection for span and node failure recovery," *IEEE J. Sel. Areas Commun.*, vol. 21, no. 8, pp. 1306–1319, Oct. 2003.
- [12] Z. Zhang, W.-D. Zhong, and B. Mukherjee, "A heuristic method for design of survivable WDM networks with p-cycles," *IEEE Commun. Lett.*, vol. 8, no. 7, pp. 467–469, Jul. 2004.
- [13] A. Kodian and W. D. Grover, "Failure-independent path-protecting p-cycles: Efficient and simple fully preconnected optimal-path protection," *J. Lightw. Technol.*, vol. 23, no. 10, pp. 3241–3259, Oct. 2005.
- [14] J. Doucette, D. He, W. D. Grover, and O. Yang, "Algorithmic approaches for efficient enumeration of candidate p-cycles and capacitated p-cycle network design," in *Proc. DRCN'03*, Banff, AB, Canada, Oct. 2003, pp. 212–220.
- [15] H. Zhang and O. Yang, "Finding protection cycles in DWDM networks," in *Proc. IEEE Int. Conf. Commun. (ICC'02)*, New York, May 28, 2002, vol. 5, pp. 2756–2760.
- [16] A. Kodian, A. Sack, and W. D. Grover, "p-Cycle network design with hop limits and circumference limits," in *Proc. 1st Int. Conf. Broadband Netw.*, 2004, pp. 244–253.
- [17] W. D. Grover and J. Doucette, "Advances in optical network design with p-cycles: Joint optimization and pre-selection of candidate p-cycles," *Proc. IEEE/Leos Summer Topicals*, pp. 49–50, Jul. 2002.
- [18] Z. Zhang, W. D. Zhong, and S. K. Bose, "Dynamically survivable WDM network design with p-cycle based PWCE," *IEEE Commun. Lett.*, vol. 9, no. 8, pp. 756–758, Aug. 2005.
- [19] W. He, J. Fang, and A. K. Somani, "A new p-cycle based survivable design for dynamic traffic in WDM networks," in *Proc. IEEE Globecom'05*, Nov. 2005, pp. 1–5.
- [20] R. Asthana, T. Garg, and Y. N. Singh, "Critical span protection with pre-configured p-cycles," in *Proc. Int. Conf. Photon.*, Cochin, Dec. 9, 2004, NET 1.4.
- [21] R. Asthana, "Second phase reconfiguration of restored path for removal of loop back in p-cycle based protection in optical networks," ACES/EE Departmental Library, IIT, Kanpur, India, 2006, Tech. Rep. 2006/2294/TR.
- [22] R. Asthana and Y. N. Singh, "Removal of loop back in p-cycle protection: Second phase reconfiguration," in *Proc. IEEE Int. Conf. Commun. Syst.*, Oct.–Nov. 2006, pp. 1–5.
- [23] R. Asthana and Y. N. Singh, "Second phase reconfiguration of restored path for removal of loop back in p-cycle protection," *IEEE Commun. Lett.*, vol. 11, no. 2, pp. 201–203, Feb. 2007.
- [24] D. Stamatelakis and W. D. Grover, "IP layer restoration and network planning based on virtual protection cycles," *IEEE J. Sel. Areas Commun.*, vol. 18, no. 10, pp. 1938–1949, Oct. 2000.
- [25] J. Kang and M. J. Reed, "Bandwidth protection in MPLS networks using p-cycle structure," in *Proc. 4th Int. Workshop Design of Reliable Communication Networks (DRCN'03)*, Oct. 2003, pp. 356–362.
- [26] D. A. Schupke, "Fast and efficient WDM network protection using p-cycles," in *Proc. IEEE/LEOS Summer Topicals 2002*, Jul. 2002, pp. WA1–47–WA1–48.
- [27] C. Mauz, "p-Cycle protection in wavelength routed networks," in *Proc. 7th Working Conf. Opt. Network Design and Modelling (ONDM'03)*, Feb. 2003 [Online]. Available: <http://www.nari.ee.ethz.ch/wireless/pubs/p/ondm03>

- [28] X. Cao, V. Anand, and C. Qiao, "Waveband switching in optical networks," *IEEE Commun. Mag.*, vol. 41, pp. 105–112, Apr. 2003.
- [29] X. Cao, V. Anand, Y. Xiong, and C. Qiao, "A study of waveband switching with multilayer multigranular optical cross-connects," *IEEE J. Sel. Areas Commun.*, vol. 21, no. 7, pp. 1081–1095, Sep. 2003.
- [30] X. Cao, V. Anand, and C. Qiao, "Multi-layer versus single-layer optical cross-connect architectures for waveband switching," in *Proc. IEEE INFOCOM'04* [Online]. Available: http://www.ieee-infocom.org/2004/Papers/38_2.PDF
- [31] A. Kolarov, T. Wang, B. Sengupta, and M. Cvijetic, "Impact of waveband switching on dimensioning multi-granular hybrid optical networks," in *Proc. Conf. Opt. Netw. Design Modeling*, Feb. 7–9, 2005, pp. 371–381.
- [32] P. Toliver, R. Runser, J. Young, and J. Jackel, "Experimental field trial of waveband switching and transmission in a transparent reconfigurable optical network," in *Proc. Opt. Fiber Commun. Conf. OFC'03*, Mar. 23–28, 2003, vol. 2, pp. 783–784.
- [33] R. Asthana, "A distributed protocol for second phase reconfiguration and p-cycle allocation to minimize the restored path lengths in p-cycle protected networks," ACES/EE Departmental Library, IIT, Kanpur, India, 2007, Tech. Rep. 2007/2295/TR.
- [34] J. Munkres, "Algorithms for assignment and transportation problems," *J. Soc. Industrial Appl. Math.*, vol. 5, no. 1, pp. 32–38, Mar. 1957.
- [35] F. Burgeois and J. C. Lasalle, "An extension of the Munkres algorithm for the assignment problem to rectangular matrices," in *Proc. Commun. ACM*, 142302–806, 1971, vol. 14, no. 12, pp. 802–804.
- [36] R. Ramaswami and K. N. Sivarajan, *Optical Networks: A Practical Perspective*, 2nd ed. San Francisco, CA: Morgan Kaufmann, 2002, pp. 667–710.
- [37] W. He and A. Somani, "Path-based protection for surviving double-link failures in mesh-restorable optical networks," in *Proc. IEEE GLOBECOM'03*, Dec. 1–5, 2003, pp. 2558–2563.
- [38] L. Guo *et al.*, "On finding feasible solutions with shared backup resources for surviving double-link failures in path protected WDM mesh networks," *J. Lightw. Technol.*, vol. 25, no. 1, pp. 287–296, Jan. 2007.
- [39] H. Choi, S. Subramaniam, and H. A. Choi, "Loopback methods for double-link failure recovery in optical networks," *IEEE/ACM Trans. Netw.*, vol. 12, no. 6, pp. 1119–1130, Dec. 2004.



Rachna Asthana (S'05) was born in Lucknow, India. She received the M.Tech. degree in electronics and communication engineering from the Indian Institute of Technology, Roorkee (then UOR) Roorkee, India, in 1990. She is currently pursuing the Ph.D. degree from the Indian Institute of Technology, Kanpur.

She joined HBTI, Kanpur, India, in 1991 as a Lecturer in the Electronics Engineering Department. Currently, she is working as an Assistant Professor. Her current research interests are in the field of

all-optical networks, survivability, and network management.

Ms. Asthana is a corporate member of the Institution of Electronics and Telecommunication Engineers (IETE), India.



Yatindra Nath Singh (M'99–SM'03) was born in Delhi, India, in 1969. He received the B.Tech. degree (honors) in electrical engineering from Regional Engineering College, Hamirpur, Himachal Pradesh, India, in July 1991, the M.Tech. degree in optoelectronics and optical communications from the Indian Institute of Technology, Delhi, in December 1992, and the Ph.D. degree from the Department of Electrical Engineering, Indian Institute of Technology, Delhi, in 1997.

He was with the Department of Electronics and Computer Engineering, IIT Roorkee, India, as a Member of Faculty from February 1997 to July 1997. He is currently working as a Member of Faculty in the Department of Electrical Engineering, Indian Institute of Technology, Kanpur. He is involved in development of Open Source E-learning platform tools code named Brihaspati (<http://brihaspati.sourceforge.net/>).

Dr. Singh is a Fellow of the IETE. He received the AICTE Young Teacher Award in 2002.



Protection and Restoration in Optical Networks

Rachna Asthana MIETE & Yatindra Nath Singh MIETE

To cite this article: Rachna Asthana MIETE & Yatindra Nath Singh MIETE (2004) Protection and Restoration in Optical Networks, IETE Journal of Research, 50:5, 319-329, DOI: [10.1080/03772063.2004.11665521](https://doi.org/10.1080/03772063.2004.11665521)

To link to this article: <http://dx.doi.org/10.1080/03772063.2004.11665521>



Published online: 04 Jan 2004.



Submit your article to this journal 



View related articles 

Protection and Restoration in Optical Networks

RACHNA ASTHANA, MIEE

Harcourt Butler Technological Institute, Kanpur 208 002, India.
email: rachnas@utk.ac.in

AND

YATINDRA NATH SINGH, MIEE

Electrical Engineering Department, Indian Institute of Technology, Kanpur 208 016, India.

Various protection and restoration techniques for IP over optical network framework have been surveyed in this paper. These schemes are based on different concepts. They have been classified according to the concepts used. An attempt has been made to identify mechanism to evaluate their relative performance. Further subjective comparison of various approaches of mixing, protection and restoration technique in various layers of networks has been presented.

Indexing terms: Survivability, Protection, Restoration, Optical networks.

1. INTRODUCTION

RAPID developments are taking place in the communication networks. Traditional PSTN (Public Switched Telephone Networks) systems were circuit switched, optimized for voice traffic, totally based on copper cables to carry the voice traffic. With the advances in optical fiber technology revolution came in the transport technology. Optical fibers offer much higher bandwidths than copper cables and are less susceptible to various kinds of electromagnetic interference and other undesirable effects. This led to replacement of copper cables in the core networks by optical fibers. Still in the present systems the incredible bandwidth offered by the optical fibers has only been used as a very high-speed channel, replacing copper cables. Optical fibers are acting just as point-to-point links. Voice traffic is carried on these fiber links using SONET (Synchronous Optical Network)/SDH (Synchronous Digital Hierarchy).

The wide spread use of Internet and World Wide Web in recent years has led to an exponential growth in the data traffic to be carried by core communication networks. Data traffic has even started dominating voice traffic [1,2]. To accommodate and also to profit from this new service demand, the PSTN operators have started their new Internet Service Provider (ISP) business by running IP (Internet Protocol) network in parallel with voice networks. The same infrastructure is used for this new service [3]. The data traffic is bursty in nature and IP packets are used to carry data traffic in the form of bursts. ATM (Asynchronous Transfer Mode) layer may be used as service integration layer on top of SONET/SDH. ATM provides a powerful set of capabilities in terms of traffic engineering. Further, ATM is

advantageous because of availability of faster ATM switches and its ability to provide quality of service guarantees, such as bandwidths and delays [4]. These parameters are missing in the IP layer. ATM standards also provide interfaces with IP and SONET/SDH so that it acts as lower layer of IP and upper layer of SONET/SDH.

These networks, which utilize optical fibers to carry traffic between point-to-point links, are called first generation optical networks. These networks are bit rate, protocol and format dependent i.e. opaque at all switching nodes. In these networks, at each node, all the data (data intended for that node and the data, which is being passed through that node) have to go through O-E-O (optical-electronic-optical) conversions.

Significant advances in optical component technologies e.g., optical add-drop multiplexers (OADMs), optical cross-connects (OXCs), erbium doped fiber amplifiers (EDFAs) etc., have made possible routing of optical signals based on wavelengths [5, 6].

The networks with this feature are known as second-generation optical networks. They can also be thought of as an abstraction of optical layer that offers services to higher layer [7]. For example, optical layer may provide lightpath services to IP networks. A lightpath is a connection between two nodes in the network and it is set up by assigning a dedicated wavelength to it, on each link in its path. The entire bandwidth of the light path can be given to higher layer as in circuit switched networks or the bandwidth may be shared between many demands as in the case of virtual circuit services. For the latter case, higher layer must incorporate some form of time division multiplexing to combine multiple virtual circuits onto a single wavelength in WDM links. A major feature of second-generation networks is the

transparency of the circuit switched lightpath. Once a lightpath is set up, a certain maximum bit rate or bandwidth might be specified and it may accept the data at any bit rate, modulation, protocol, format, and form i.e., analog or digital, conditioned that transported signal bandwidth does not exceed the maximum allowed in the lightpath.

In the multi-layer approach for using optical networks, the layered structure of IP/ATM/SONET/WDM (wavelength division multiplexing) is natural extension. But there is significant functional overlap between various layers. This was justified approach with first generation of optical networks where at each node data has to undergo optical-electronic-optical (O-E-O) conversions. This multi-layer approach has some significant disadvantages also. It reduces efficiency and poses increased management cost due to functional overlap and O-E-O conversions at each intermediate node.

The popularity of internet which is based on TCP/IP and the use of TCP/IP in almost all forms of end user application, have made it clear that common traffic convergence layer is going to be IP. WDM has emerged as the only practical solution to exploit the huge bandwidth of fibers. Therefore if IP layer can be transported using WDM, significant cost reduction and efficiency enhancement can be achieved. In fact this trend is already evident today with the emergence of IP routers with tunable WDM laser interfaces [5].

Future optical networks are emerging as optical networks providing services to the IP layer (Fig 1). A consensus is emerging in Optical Internetworking Forum (OIF) for using GMPLS (Generalized Multi-Protocol Label Switching) in the control plane of optical layer and thus

providing necessary bridge between IP and optical layer [8]. The optical layer provides lightpaths between IP networks. Lightpath is a wavelength channel from source to destination without any O-E-O conversion. Each fiber can have many lightpaths passing through it on different wavelengths using WDM. Since fiber has large bandwidth a large number of lightpaths in a single fiber can exist. Up to 160 lightpaths each with capacity of 10 Gbps have been reported in literature [3,9]. Henceforth, incredibly large traffic volumes can be supported by a single fiber. In this scenario a single fiber failure (single fiber cut) can lead to simultaneous failure of all the light paths in the fiber. This will result in failure of thousand of higher layer paths and loss of significant amount of traffic and hence the revenue. Therefore network survivability issue is very critical in optical networks. In the traditional multi-layer IP/ATM/SONET/WDM approach the survivability is provided by Automatic Protection Switching (APS) in SONET layer, which is quite robust. It has the capacity of providing recovery within 50 ms in the event of any failure [5]. Therefore, for the success of IP over WDM networks, survivability and fast recovery in optical networks should be as good as what SONET provides. Researchers have been working on various schemes to provide efficient and fast protection and restoration in IP over WDM networks.

2. FAILURE RECOVERY SCHEMES

The network failure recovery schemes can be broadly classified into two categories viz., (a) Protection and (b) Restoration, as shown in Fig 2. Protection is defined as pre provisioned failure recovery [3,5,8,10]. The back up path (secondary path or alternate path) which is link disjoint

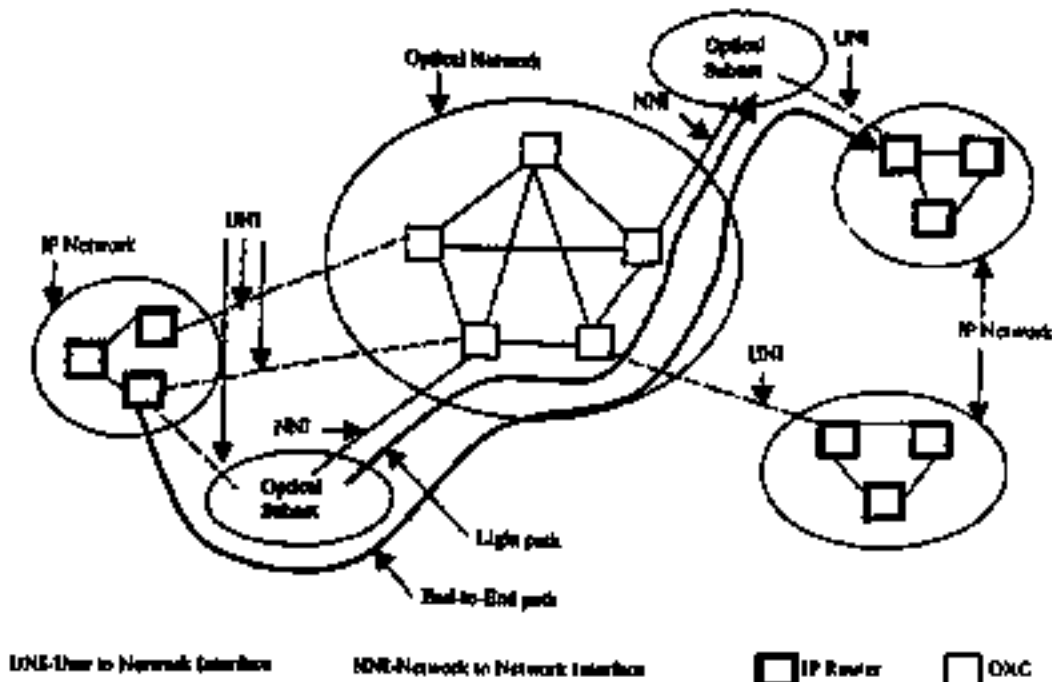


Fig 1 An IP over optical network

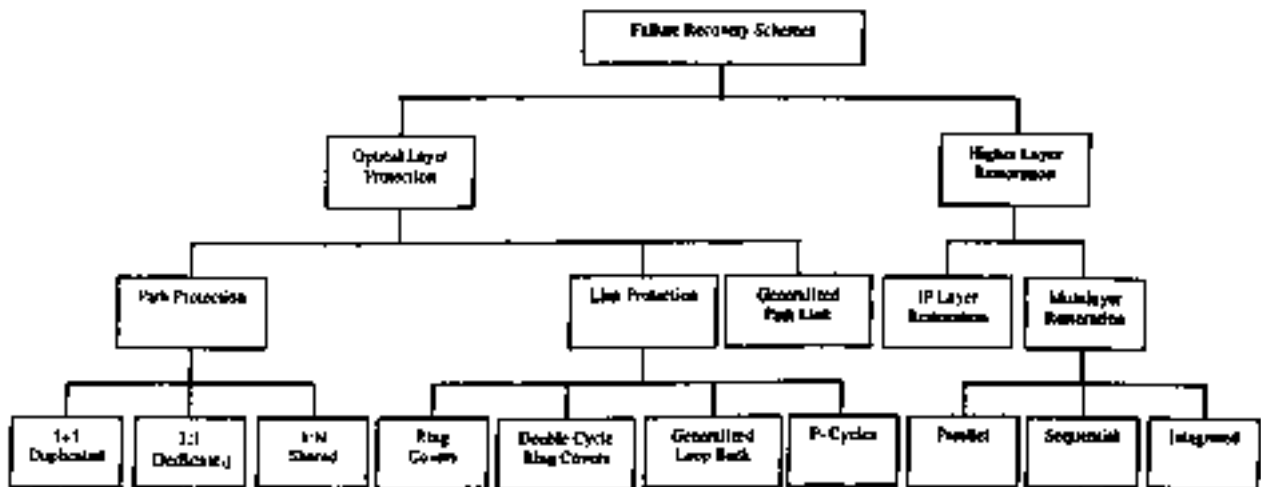


Fig. 2. Survivability schemes

and may be node disjoint also with the primary path, is set up along with the primary path. Usually, the same routing protocol is used after eliminating the links used for setting up the primary path to determine the link disjoint back up path. Similarly, if the nodes in the primary path (except source and destination) are also eliminated while computing back up path, the back up path will be link and node disjoint. The primary path is used to transmit the data and back up path is reserved for use in the event of failure. After the detection of failure the switches are re-configured to use the back up path. These schemes can provide guaranteed protection since the demand set up completes only if the secondary path is also available. Secondly, these schemes can provide fast recovery because the back up path computation is already done and in the event of failure, only the failure detection and switch reconfiguration has to be done. However resource utilization is not efficient due to reservation of resources for back up paths.

Restoration schemes refer to dynamic recovery after the onset of failure [3, 5, 8, 10]. The restoration involves detection of a failure, new path computations for the failed connections and reconfiguration of switches for the restoration path. These schemes provide efficient utilization of resources. However, successful recovery cannot be guaranteed since enough resources may not be available at the time of failure. Further time required for recovery is more [11]. Usually optical layer can provide fast protection while higher layers can be used for intelligent restoration.

In section 3 various optical layer protection schemes are discussed and section 4 gives merits and demerits of protection in optical domain. Section 5 presents different restoration schemes.

3. OPTICAL LAYER PROTECTION

The optical layer protection schemes can be divided into path protection, link protection and generalized path-link protection schemes.

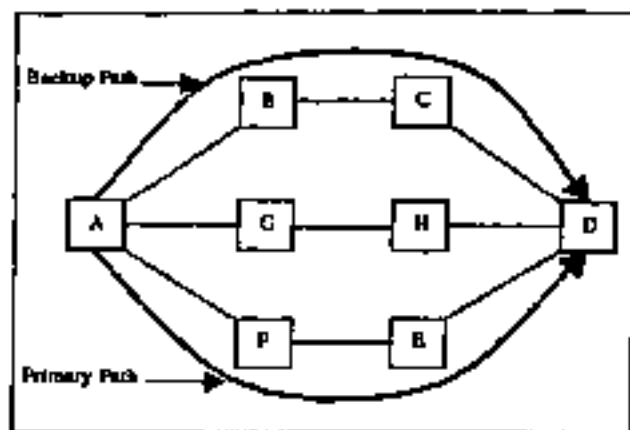
3.1. Path Protection

The entire light path from source to destination is protected in these schemes. In the event of failure, fault localization is not required, instead traffic is switched over to link and node disjoint backup path. Various path protection schemes are shown in Fig 3. These optical layer path protection schemes are 1 + 1 (duplicated), 1 : 1 (dedicated), and 1 : N (shared). In 1 + 1 duplicated path protection (Fig 3a), the sender transmits on both primary and backup paths. In the event of failure the receiver simply switches to the alternate backup path. This approach is very simple and very fast. However in this approach, the network resource utilization is very poor [11].

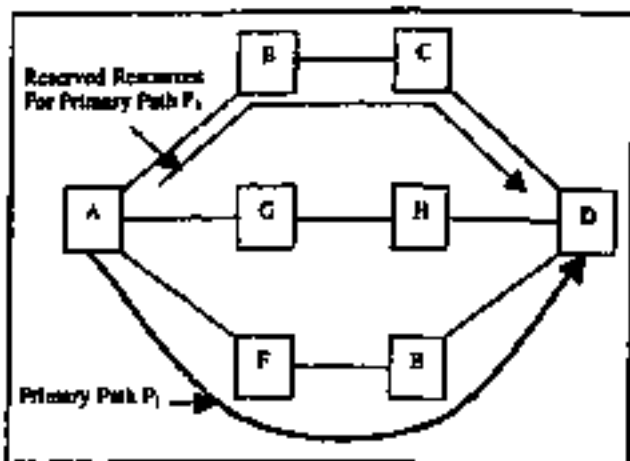
The 1:1 protection is also known as dedicated path protection (Fig 3b). Here the resources for the backup paths are reserved at the time of connection set up. The resources are reserved as backup for respective primary lightpath only. They cannot be shared as back up path for some other primary lightpaths. However these can be used to carry some low priority (preemptable) traffic. In the event of failure the low priority traffic through back up path is dropped and traffic to be protected is directed through backup path.

The 1 + 1 and 1 : 1 protection schemes have been compared in [12] for resource utilization. In this study, the primary and backup paths and the resources such as total number of fibers, OXCs etc. have been selected optimally to minimize the total facility cost. The total facility cost includes the cost of fibers and cost of OXCs. It has been found that to minimize the total cost, the ratio of fiber length in the 1 + 1 & 1 : 1 schemes is approximately 1.6. Almost the same ratio of 1.6 comes out for OXCs. The total lightpath length has been found to be more in both the schemes in the above study as the number of wavelengths per fiber increases. This is due to the fact that to minimize the total cost, longer light paths may have to be selected.

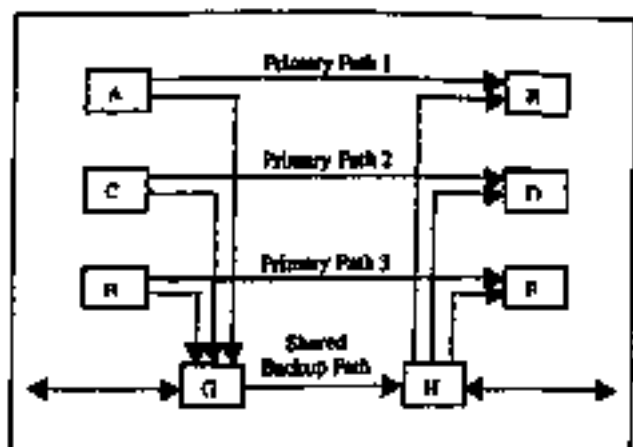
The 1 : N protection is shared path protection (Fig 3c).



(a)



(b)



(c)

Fig 3 Path protection schemes. (a) 1 + 1 Duplicated path protection, (b) 1 : 1 Dedicated path protection, (c) 1 : N Shared path protection

and at the time of connection setup backup path resources are also computed and reserved. The reserved resources can also be used to provide protection to some other primary path. However, the primary paths sharing the backup should be link and node disjoint. Hence a single failure cannot affect more than one primary lightpath [8,13,14]. To ensure this condition Shared Risk Link Group (SRLG) concept can also be used [15,16]. An SRLG is a group of lightpaths having a common element whose failure can lead to failure of all the light paths in the group. For example, if a single fiber is cut then all the light paths through that fiber will be affected. Hence all the lightpath using this fiber belongs to one SRLG. Similarly the conduit carrying multiple fibers may define another SRLG. Therefore primary paths not having any common SRLG may share the backup path. The 1 : N protection implies that up to N primary paths, share a backup path. The 1 : N protection schemes provide most efficient use of resources and thus most preferred form of protection. One of the important performance issues in this scheme is finding of new backup paths if protection is activated for some failed primary path.

3.2. Link Protection

Another mechanism of protection is called link protection. These schemes are designed basically to provide Automatic Protection Switching (APS) of rings in the optical mesh networks. The protection mechanism for these schemes is fast, distributed and autonomous [17].

Any lightpath can be considered as different links being put together end-to-end. Each of these links can be provided individual protection. In case of a link failure, a backup path replaces only the faulty link, other links in the lightpath remain same. Due to smaller scale of link and localization of fault, link protection schemes are faster in response. However, due to local recovery (Fig 4) the total number of hops may be more and resource utilization may be less efficient. Another very important feature of link protection is that it can be preplanned once and for all, since it is not dependent upon specific demand patterns [18]. With increased speed, the issue of identification and localization of faults and hence switchover to protection link become important. One needs to look into how this will be implemented efficiently. Some link protection schemes are as follows.

(i) Ring Covers

The mesh network is presented as graph in which node represents a vertex and each link is represented as edge. The entire network is divided into smaller cycles (rings) in such a way that each edge comes under at least one cycle. Having another protection fiber along the cycle protects the whole cycle. In this approach, an edge may be covered by more than one cycle. With fiber based protection every cycle is a four-fiber ring (two fibers for bi-directional working paths and two for bi-directional backup paths). Therefore an edge covered by two rings requires eight fibers, and an edge

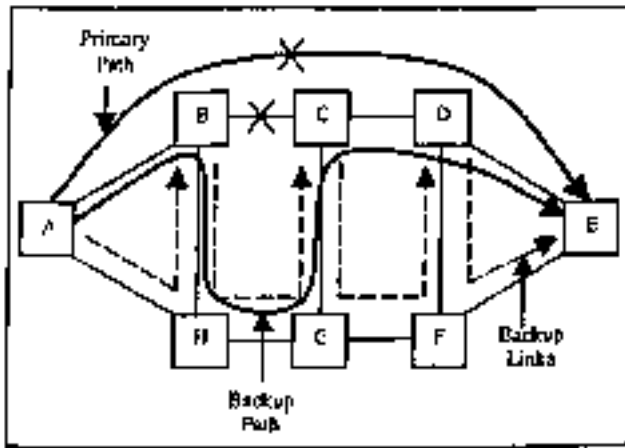


Fig 4 Link protection

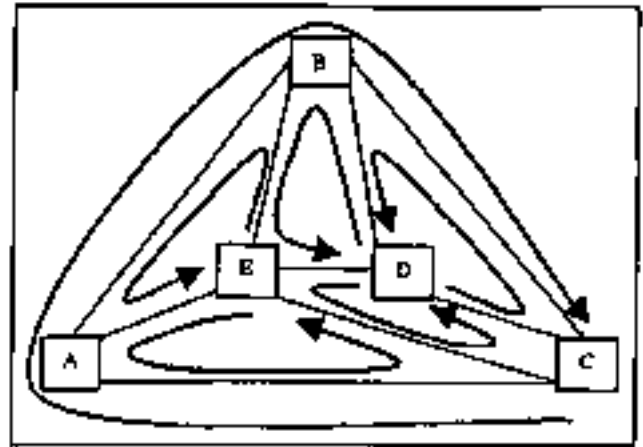


Fig 5 Double cycle ring covers

covered by n rings requires $4n$ fibers. Thus the problem is formulated in such a way so as to minimize the redundancy of protection fibers. However, in most cases the redundancy required is more than 100% [18, 19].

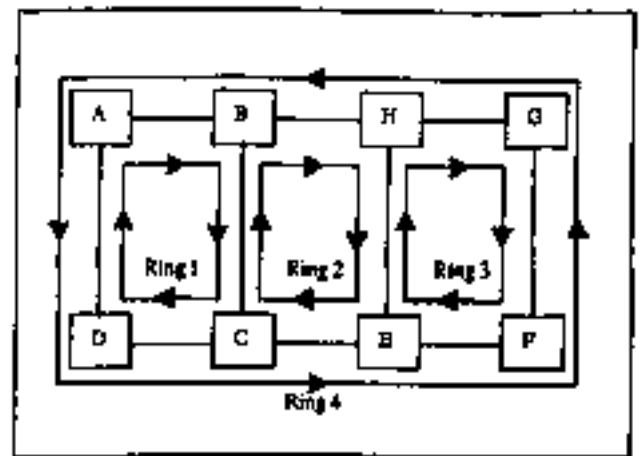
(ii) Double Cycle Ring Covers

The mesh networks are represented as directed graphs (diagrams). Each edge of the diagram has a pair of unidirectional working fiber (bi-directional working link) and a pair of unidirectional back up fiber (bi-directional protection link). Thus each edge is covered by exactly two rings. This method reduces redundancy to exactly 100%. All these digraphs are established at the time of setup of network. For planar graph (if it can be drawn on a plane in such a way that no two edges intersect each other, then the graph is planar) having N vertices ($N \geq 3$) and M edges; the total no of faces will be $F = 2 + M - N$. This includes $F - 1$ inner faces and one outer face. Thus the required set of protection cycles can be obtained as in [17] by identifying all the faces of planar graph. All the inner faces are covered in a certain direction (say anti-clockwise). The outer face is covered in the opposite direction (i.e., clockwise) as shown in Fig 5.

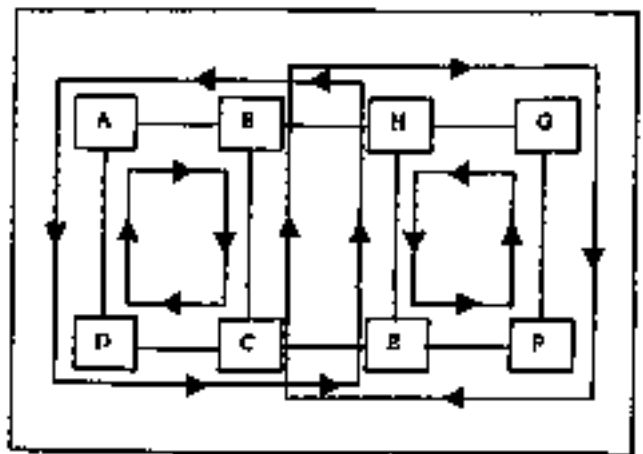
In non-planar graphs, heuristics are used to find the double cycle ring covers. These cycles can then be used as rings to recover traffic. In Fig 6 for another fiber topology, two possible double cycle ring covers are shown [18]. In all these cases four fibers are used and recovery is fiber-based recovery i.e., all the traffic on one fiber is transferred to another as such in the event of failure. Protection granularity is at the level of fiber. With double cycle ring covers, to recover a failure on link AB (Fig 6), the traffic which is going from A to B may be recovered by Ring 4 through ADCEFGHB, and the traffic in the reverse direction i.e. from B to A is recovered through Ring 1 i.e., BCDA. The two directions on a link will, therefore, have different delays in their restoration times and may cause different timing jitters.

(ii) Generalized Loop Back Recovery

Application of ring recovery schemes (ring covers and



(a)



(b)

Fig 6 Double cycle ring covers for another fiber topology (a) Ring 1, Ring 2, Ring 3 are in clockwise direction, Ring 4 is an anti-clockwise direction (b) another possible double cycle ring cover

double cycle covers) in mesh based networks, requires more hardware, and hence it is more expensive. Further, as nodes are added or networks are interconnected, ring based structures may be difficult to preserve, thus limiting their scalability. Therefore, another approach more suitable to mesh networks has evolved [18, 20] and is known as Generalized loop back recovery. This method is applicable to arbitrary two-link-redundant and two-node-redundant networks to restore services after the failure of a link or a node respectively. A two-link (node) redundant network remains connected after the failure of a link (node). As in Ring cover schemes, network is represented by graphs and failure of a link (node) is mapped to the disappearance of an edge (vertex) in the corresponding graph. In generalized loop back, pair of conjugate diagrams are used for routing primary path and reservation of protection path respectively. Traffic flows in the primary diagrams and protection is provided through the use of its conjugate, the backup diagrams. These diagrams are calculated once for the network before the network is put on line for the first time. The heuristic algorithms are used [18] to calculate the recovery loops. In the event of failure, nodes adjacent to the failure, simply flood the pre-established backup diagrams with traffic of the failed link.

Consider Fig 7, for simplicity, only unidirectional conjugate diagram is shown. The primary diagram is shown in solid lines and secondary diagram is shown in dashed lines. Let's say there is failure in link BC. The traffic is switched over to back up diagram. The back up diagram is flooded with the back up traffic by node B and the back up traffic finds its way to node C. There can be two possible paths for the back up traffic (B A E D C) and (B A E F C). This is ensured by the protocol used that only the traffic, which arrives at a node first, is forwarded to the output ports. Traffic, which arrives subsequently, is simply discarded and the node that sends out this traffic is notified by means of a negative acknowledgement message (NACK). After receiving a NACK, the node stops forwarding traffic to the corresponding out put port. Therefore only one of the two possible paths is actually established.

In generalized loop back recovery, the protection is fiber based i.e., the entire traffic carried by a fiber is backed by another fiber. For bi-directional traffic flow, fiber based restoration requires four fibers as shown in Fig 8. Here fiber 1 and fiber 2 carry primary traffic. Backup is provided by fiber 3 for fiber 1 and by fiber 4 for fiber 2. Loop back recovery schema is further extended to WDM based loop back recovery. In this protection, paths are reserved at wavelength level. It requires only two fibers. Figure 9 illustrates WDM based recovery. Primary traffic is carried by fiber 1 on λ_1 and by fiber 2 on λ_2 . Back up is provided by λ_1 on fiber 2 (for λ_1 on fiber 1) and by λ_2 on fiber 1 (for λ_2 on fiber 2). The main advantage of WDM based loop back recovery system over fiber based system is that only two fibers are essential in former whereas at least four fibers are required in the latter

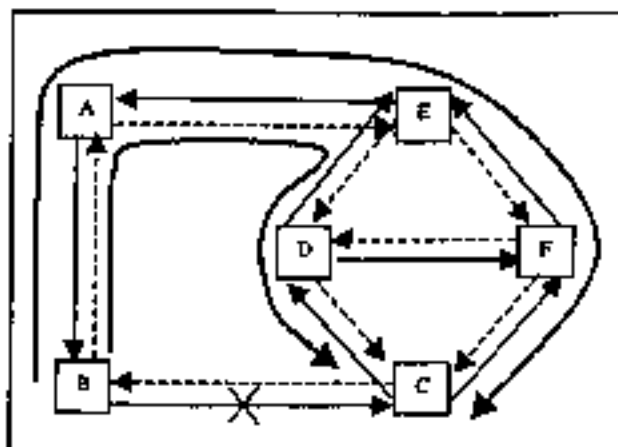


Fig 7 Generalized loop back recovery

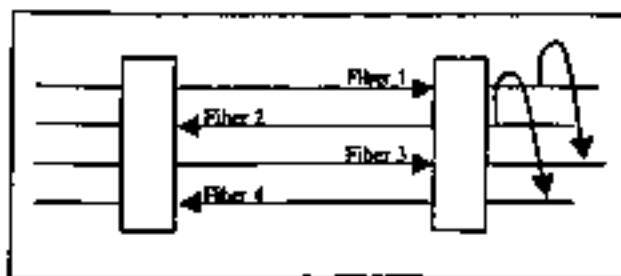


Fig 8 Fiber 3 provides protection to fiber 1 and fiber 4 provides protection in fiber 2

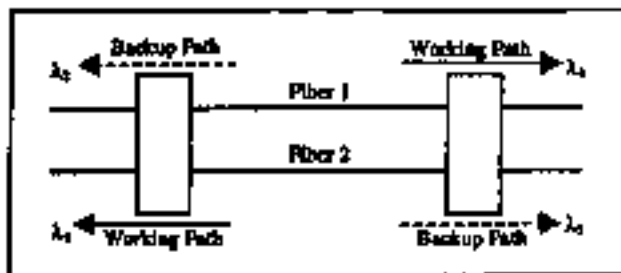


Fig 9 WDM based recovery Back up for λ_1 in fiber 1 is on λ_2 in fiber 2 and back up for λ_2 in fiber 2 is on λ_1 in fiber 1

(iv) P-cycles

The recovery is very fast (50 ms for SONET rings) in ring-based networks. However, these networks are inefficient and inflexible [21] as compared to mesh-based networks. P-cycles are the result of efforts to obtain ring like speed and mesh like capacities and flexibility. P-cycles are fully connected structures of spare capacity of mesh networks. In fact all spare capacity of the network is pre-connected and only two switching actions (as in rings) are needed in the event of failure to switch the traffic on the back up path. Figure 10a shows an example of p-cycle. Solid lines represent the p-cycle. This is pre-connected cycle of spare resources in the links. Figure 10b shows the failure on the cycle. In this type of failure, the p-cycle recovery acts as ring recovery and the traffic of the failed link is switched to the

other side of the cycle. Figure 10c shows the recovery in case of straddling link failure. A straddling link is one that has its end nodes on the p -cycle, but is not itself part of the p -cycle. In case of straddling link failure 'AJ', two protection paths are available viz., 'ABJ' and 'AFHGDCJ'. The key difference between p -cycles and any ring or cycle cover is

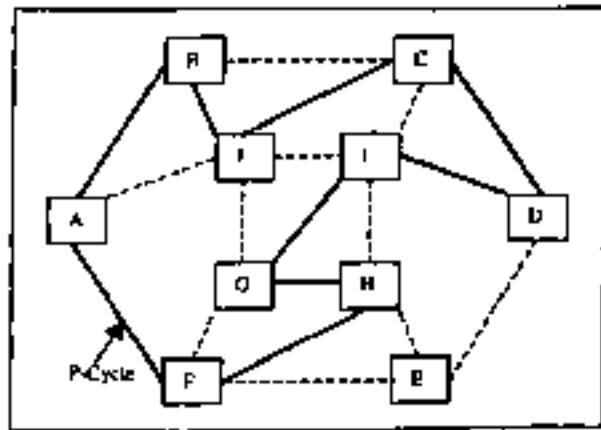
the protection of straddling link failures. These links are having zero spare capacity and efficiency of covering these failures is double that of on cycle failure because two back up paths are available from each side of p -cycle. It has been found [21] that sets of p -cycles can cover all span failures with three to six times less capacity than required with ring covers. Hence it offers mesh like capacity efficiencies. Another advantage is due to the fact that p -cycles are formed in the spare capacity only, and can be logically rearranged to adapt to changing traffic patterns as needed. In short, p -cycles will not affect the flexibility of mesh networks. However, several p -cycles may be required to cover an entire network, hence management among p -cycles becomes necessary. Even finding p -cycles, which cover a large number of nodes, may be difficult [18].

3.3. Generalized Path and Link Protection

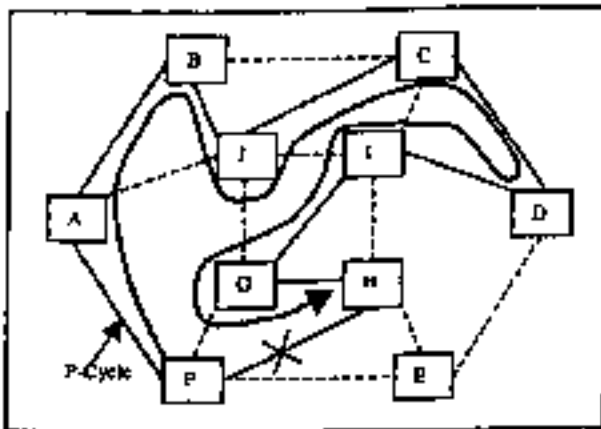
This scheme has been evolved to combine the advantages (merits) of path and link protection schemes. The working path is divided into several overlapping protection domains of equal length; each of which contains a working and protection path pair. This scheme is also called Short Leap Shared Protection (SLSP) [16]. In this scheme, once a primary path is selected and divided into protection domain (p -domain) then each p -domain is assigned a p -domain ID by the source node. The overlapping in p -domain is used to provide protection for the node failures along the primary path. A link disjoint protection path is searched for each working path segment in a p -domain. The node, which switches traffic to secondary path, is called Path Switch Label Switched Router (PSL) and the node, at which the traffic merges with the primary path, is known as Path Merge Label Switched Router (PML). The diameter of a p -domain is defined as the hop count of the shortest path between the PSL and PML of the p -domain. Link and path based shared protection schemes can be categorized as two extreme cases of SLSP with domain diameters of 1 and H respectively, where H is the hop count of the primary path.

The working of this scheme is shown in Fig 11. Node A is the source node and N is the destination node. The p -domains 1, 2, 3 and 4 are from A-E, D-H, G-K and J-N respectively. (A, E), (D, H), (G, K) and (J, N) are the corresponding PSL, PML pair of each domain. The overlap of two nodes and a link in p -domain ensures that any single link failure or node failure along the primary path can be recovered by at least one p -domain. For example, a fault on F-G link or node F is localized by the downstream node G. Node G sends a notification message to its PSL node 'D'. The PSL 'D' then activates the traffic switchover to corresponding protection path in that domain. If a failure occurs to a link or node covered by two p -domains (GH link) the node localizing the fault i.e., node 'H' will notify the closest upstream PSL 'G'. Tell and go mechanism is used to switchover the traffic to the protection path.

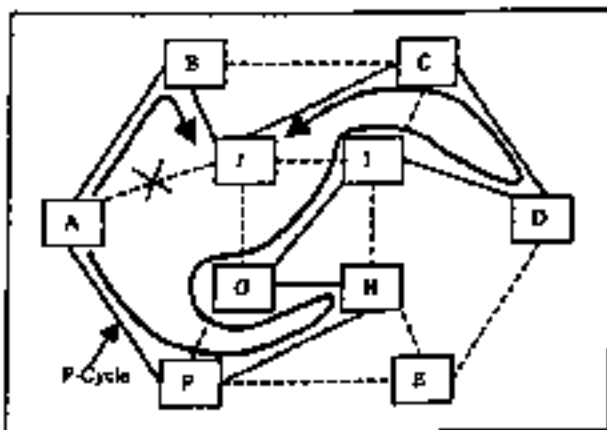
The advantages of this scheme are fully distributed



(a)



(b)



(c)

Fig10 P-cycles, (a) Pre-connected spare resources (P-cycle), (b) Failure on p-cycle, traffic is switched over to other side of p-cycle, (c) Failure on straddling link AJ, two protection paths are available, ABJ and AFHGDCJ

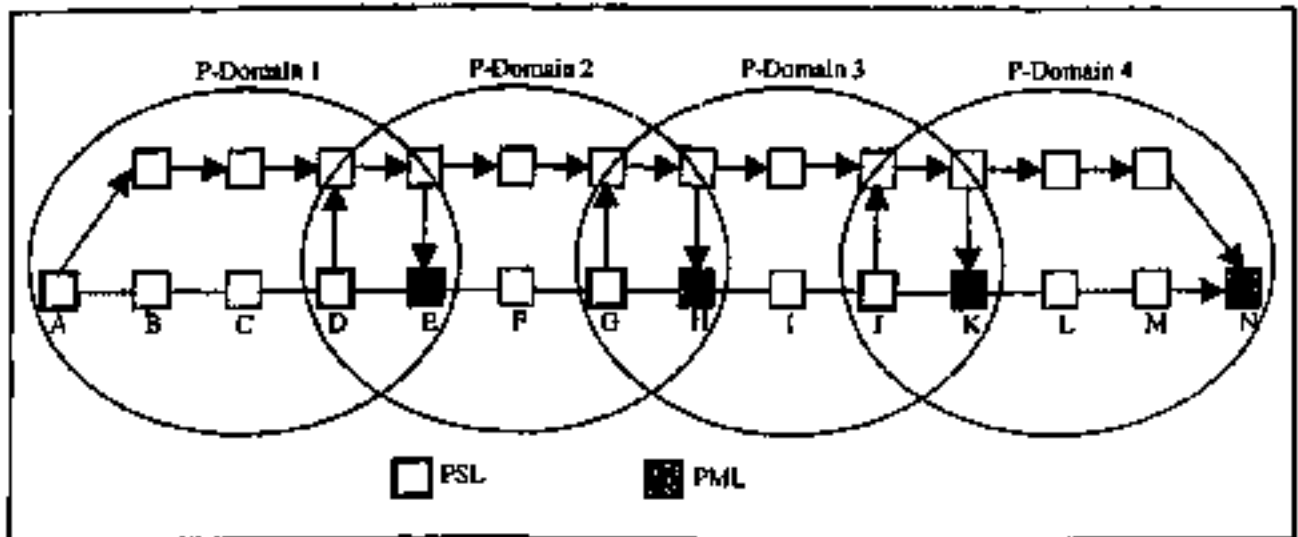


Fig. 11 Recovery in the P-domain, short leap shared protection (SLSP)

computing process, service recovery time guarantee by limiting the size of p -domains, capacity efficiency, and scalability. However a major disadvantage is the increase in signaling complexity.

4. MERITS AND DEMERITS OF PROTECTION IN THE OPTICAL DOMAIN

Various protection mechanisms, performed in the optical domain have been discussed in the previous sections. These schemes offer several advantages as well as disadvantages. In the following sections their merits and demerits are presented.

4.1. Merits

- (i) Optical layer is relatively closer to most of the usual faults that occur such as cable cuts. The detection of failure is fast for this layer. The amount of signaling required to perform protection is less. Hence failure recovery in optical domain is expected to be faster, compared to those provided by higher layers.
- (ii) Optical layer failure recovery can protect many services, which do not have built-in recovery mechanism or whose recovery mechanism is slow (e.g., IP services).
- (iii) The optical layer provides lightpath to higher layers. A single lightpath may be used to carry a large number of higher layer connections and an optical fiber may carry several such lightpaths. Hence even a single failure (e.g. link, node or fiber cut) may affect a very large number of higher layer connections [22]. However, protection in the optical domain may involve just a 2×2 switch to switch over to another fiber in case of fiber cut or by passing the link (node) in case of link (node) failure. Hence, protection can be done with coarser granularity in the optical domain reducing the switching cost significantly.

(iv) The additional resources required for protection in the optical domain are shared among multiple higher layer connections and hence, the resources can be better optimized by optical layer protection schemes.

(v) Optical layer failure recovery schemes allow building the virtual topologies, which may be resilient to single fiber failures [23-25].

4.2. Demerits

- (i) The optical layer protection schemes cannot handle the failure of higher layer electronic equipment or nodes.
- (ii) It cannot monitor higher bit error rates hence in this case protection switching cannot be done in the optical layer [19].
- (iii) Due to coarser granularity it is very difficult to provide different levels of protection to different classes of traffic.
- (iv) The alternate paths are not optimized and hence may be very large.

5. RESTORATION SCHEMES

In optical layer protection schemes, in the event of a failure, the fault is detected and simple switching is used to divert the traffic through an alternate pre-computed backup path for which resources are already reserved. However, these schemes cannot protect the faults occurring at higher layers e.g., network interface card failures and IP router (node) failures. There are also network-operating scenarios in which optical layer protection is not an option technically or economically. There may be an ISP operator having a logical network, which is based on leased line services from facilities based operators (i.e., physical layer service providers). Such an operator will require failure recovery schemes, which are in his own control i.e., in the logical network plane. This is either because control of (or may be

even knowledge of) the physical layer is not available to him or the optical layer service provider may charge more to provide failure recovery in the optical layer.

At a higher layer an alternate path can be worked out on the basis of an algorithm after the failure. Higher layer can also take 'priorities' into consideration. Thus the process can be more intelligent. This is known as restoration. However, if no new path was discovered for a failed working path, the traffic carried by that path would be lost. Therefore, restoration schemes cannot be used for guaranteed survivability. Further, this process is more time consuming than protection. Hence this mechanism is not used alone. Usually this works along with the optical layer protection. In the following sections some higher layer restoration schemes are presented.

5.1. IP Layer Restoration

Conventional IP is connectionless protocol. In IP layer, restorations are best effort in nature. In this layer to restore the services the traffic (IP packets) is rerouted by updating routing tables at the nodes. This is done automatically using OSPF (open shortest path first) and BGP (border gateway protocol) with the help of link state and route advertisement messages. However, these are relatively slow processes. For rapid IP restoration an interesting idea is proposed in [26]. Here the concept of pre-configured protection cycles (p -cycles) (already explained in section 3.2 (iv)) is used at the IP layer to protect node (IP router) or logical link failures. If there is failure of any logical link, then the router ports, which terminate the failed link, will be marked as dead, and the usual link state advertisement update process will be triggered. During the time in which global routing update is affected in conventional IP, the packets to be directed to the dead ports, according to their destination address, are deflected into a p -cycle, which has been assigned to protect the link. Deflection onto a p -cycle is done by encapsulating packet as a " p -cycle packet". This packet contains the address of pre-assigned p -cycle and the packet travels through the p -cycle. When the packet comes at the other end of the failed link, the original IP packet is removed from the encapsulating packet and forwarded on its route towards final destination.

This scheme can be used to restore failure of a single logical IP link between a pair of adjacent routers. For fiber cuts or physical layer failures, which can cause fault multiplication from one fiber cut to several logical link failures in the IP layer, the optical layer protection schemes are best suited. Therefore for effective failure recovery scheme, IP layer restoration using p -cycles should be used on top of the optical layer protection schemes.

5.2. Multi-layer Restoration

Even the simplified IP over WDM network typically consists of multiple layers. Different protection and restoration mechanism may be present in different network layers. Therefore, two main issues arise with multi-layer

survivability

(i) All the layers try to rectify the same fault causing 'chaos'.

(ii) During faults, spare resources have to be present for being used by each layer.

Multi-layer recovery can combine the merits of optical layer and the higher layer schemes. In order to do this, inter-working between different layers is required. The inter-working between different layers is called "escalation" [3, 5, 27, 28]. Escalation strategies deal with issues such as when to start, stop and how to coordinate activities of different layer protection and restoration mechanisms. There are three types of escalation strategies

(a) Parallel strategies

(b) Sequential strategies

(c) Integrated strategies

(i) Parallel Strategies

In this escalation strategy, different protection and restoration schemes are activated simultaneously in the event of a single failure. When one scheme recovers the failure, all other schemes stop. This is fast and no communication or coordination is required between different protection and restoration schemes. However, they may contend for the same spare resources and may obstruct each other. Therefore efficient spare capacity sharing mechanisms are required. Such resource sharing schemes are given in [28, 29].

(ii) Sequential Strategies

In these strategies the protection and restoration schemes in different layers can be activated sequentially in an order. Either they can be activated from top-to-bottom i.e., top-down strategies or from bottom-to-top i.e., bottom-up strategies. In the top-down approach, the recovery actions are activated in the top (highest possible) layer, and the lower layer schemes are activated only if higher layer cannot restore the traffic. An advantage is that it can differentiate traffic with respect to the service types. Thus high priority traffic may restore first. However, this is more time consuming approach. In the bottom-up approach, the recovery starts at the bottom (lowest) layer where the failure is detected. Higher layer restoration is activated for the traffic, which cannot be restored by lower layer. This can achieve fast recovery at much coarser granularity. Timers are used to activate different layer protection and restoration schemes.

(iii) Integrated Strategy

The integrated strategy is based on a single integrated multi-layer recovery scheme. This recovery scheme has a full knowledge of all the network layers and it can decide about the recovery action i.e., when and which layer (or

layers) is activated to start the recovery process. A good example of this scheme is given in reference [8]. In this integrated scheme, GMPLS (Generalized Multi-Protocol Label Switching) control plane is used to combine the network state information from both IP and WDM layers. This scheme dynamically allocates restorable bandwidth guaranteed paths in IP over WDM networks against optical link/node failures. It has been shown that integrated schemes improved the network performance. The integrated approach is most flexible one but at the cost of increased complexity due to requirement of intelligence in the network.

6. CONCLUSION

Several protection and restoration schemes have been reviewed. In optical layer protection schemes, the path protection schemes provide better resource utilization at the cost of more computational complexity, whereas link protection can be provided once and for all. However, resource utilization will be the issue in link protection schemes. *P*-cycles have addressed this issue and tried to improve the resource utilization using protection for straddling link failures also. Protection domain concept came as a result of combining best of path and link protection schemes.

Optical layer protection schemes provide protection at the fiber level i.e., coarser granularity. All the light paths (thousands of connections at higher layers) in a single fiber can be protected simultaneously in fiber level protection schemes. However higher layer node (IP router) failures cannot be recovered in optical level protection. Higher layer restoration schemes take care of failure in IP and higher layers. To recover failures, because of fiber cuts, at higher layer is not advisable due to fault multiplication problem i.e. a single fiber cut result in the failure of thousands of connections at higher layer.

The integrated schemes can be used to combine the best of optical layer and higher layer protection and restoration schemes. The physical level failures are to be recovered in the optical layer schemes to avoid the severe problem of fault multiplication in the higher layer. On top of this, higher layer schemes can be used to recover higher layer node (IP router) failures or single link failure in the higher layers.

REFERENCES

- Marco Listanti *et al.*, Architectural and Technological Issues for Future Optical Internet Networks, *IEEE Comm Mag.*, vol. 38, pp 82-92, Sept 2000.
- Murari Sridhan *et al.*, A practical Approach to Operating Survivable WDM Networks, *IEEE J Selected Areas in Communication*, vol. 20, pp 34-46, Jan 2002.
- Didier Colle *et al.*, Data-Centric Optical Networks and Their Survivability, *IEEE J Selected Areas in Communications*, vol. 20, pp 6-20, Jan 2002.
- Yinghua Ye *et al.*, On Joint Protection/Restoration in IP-Centric DWDM-based Optical Transport Networks, *IEEE Comm Mag.*, vol. 38, pp 174-183, June 2000.
- Nasir Ghani *et al.*, On IP over WDM Integration, *IEEE Comm Mag.*, vol. 38, pp 72-84, March 2000.
- Rud C. Alfness *et al.*, The Evolution of Optical Systems, *Optics Everywhere, Bell Labs Tech Jour.*, vol. 5, pp 188-202, Jan-March 2000.
- Rajiv Ramaswami & Kumar N Sivarajan, *Optical Networks: A Practical Perspective*, pp 2-22, Morgan Kaufmann.
- Yinghua Ye *et al.*, A simple Dynamic Integrated Provisioning Protection Scheme in IP over WDM Networks, *IEEE Comm Mag.*, vol. 39, pp 174-182, Nov 2001.
- Alastair M Glass *et al.*, *Advances in Fiber Optics*, Bell Labs Tech Jour, vol. 5, pp 168-187, Jan-March 2000.
- Cheli Aww *et al.*, Optical Networking and Real Time Provisioning: An Integrated vision for the Next Generation Internet, *IEEE Network*, vol. 15, pp 36-45, July-August 2001.
- Gokhan Sahin & Murat Azizoglu, Optical Layer Survivability for Single and Multiple Services Classes, *J High Speed Networks*, vol. 10, no 2, pp 91-108, 2001.
- Yasuhiko Miyao & Hiroaki Saito, Optimal Design and Evaluation of Survivable WDM Transport Networks, *IEEE J Selected Areas in Communications*, vol. 16, no 7, pp 1190-1198, Sep 1998.
- Bharan T Doshi *et al.*, Optical Network Design and Restoration, *Bell Labs Tech Jour*, vol. 4, pp 58-84, Jan-March 1999.
- Laxman Sahasrabudhe, S Ramamunthy & B Mukherjee, Fault Management in IP over WDM Networks; WDM Protection Versus IP Restoration, *IEEE J Selected Areas in Communications*, vol. 20, pp 21-33, Jan 2002.
- Bala Rajgopalan *et al.*, IP over Optical Networks: Architectural Aspects, *IEEE Comm Mag.*, vol. 38, pp 94-102, Sept 2000.
- Pin Han Jia & T Moutath, A Frame work for Service Guaranteed Shared Protection in WDM Mesh Networks, *IEEE Comm Mag.*, vol. 40, pp 97-103, Feb 2002.
- Georgios Ellinas *et al.*, Protection Cycles in Mesh WDM Networks, *IEEE J Selected Areas in Communication*, vol. 18, pp 1924-1937, Oct 2000.
- Muriel Medard *et al.*, Generalized Loop-Back Recovery in Optical Mesh Networks, *IEEE ACM Trans Networking*, vol. 10, pp 153-164, Feb 2002.
- Kulathumani Vinodkrishnan *et al.*, Survivability in IP over WDM Networks, *J High Speed Networks*, vol. 10, no 2, pp 79-90, 2001.
- Son-il Kim & S Lumetta, Addressing Node Failures in All Optical Networks, *J Optical Networking*, vol. 1, pp 154-163, April 2002.
- Wayne Grover *et al.*, New Options and Insights for Survivable Transport Networks, *IEEE Comm Mag.*, vol. 40, pp 34-41, Jan 2002.

22. Vincent W S Chin *et al.*, Architecture and Technologies for High-Speed Optical Data Networks, *IEEE/OSA Lightwave Technology*, vol 16, pp 2144-2168, Dec 1998.
23. Olivier Crochat *et al.*, Protection Interoperability for WDM Optical Networks, *IEEE ACM Trans on Networking*, vol 8, pp 384-395, June 2000.
24. Olivier Crochat & Jean-Yves Le Boudec, Design Protection for WDM Optical Networks, *IEEE JSAC*, vol 16, pp 1158-1165, Sept 1998.
25. Eytan Modiano & Aradhana Narula-Tam, Survivable Light Path Routing: A New Approach to the Design of WDM Based Networks, *IEEE JSAC*, vol 20, pp 800-809, May 2002.
26. Demetrios Stamatidakis & Wayne D Grover, IP Layer Restoration and Network Planning Based on Virtual Protection Cycles, *IEEE JSAC*, vol 18, pp 1938-1949, Oct 2000.
27. Ornan Gerstel & Rajiv Ramaswami, Optical Layer Survivability-An Implementation Perspective, *IEEE JSAC*, vol 18, pp 1885-1899, Oct 2000.
28. Keping Long *et al.*, A New Approach to Multi-layer Network Survivability: Strategic Model and Algorithm, *J High Speed Networks*, vol 10, No 2, pp 127-134, (2001).
29. Suprie De Maesschalek *et al.*, Intelligent Optical Networking for Multi-layer survivability, *IEEE Commun. Mag* vol 40, pp 42-49, Jan 2002.

AUTHORS



Rachna Asthana received her M Tech degree in Electronics & Communication from Indian Institute of Technology, Roorkee (then UPR) Roorkee in year 1990. She joined HBTI (Harcourt Butler Technological Institute) in 1991 as Lecturer in Electronics Engineering Department.

Currently she is working as Assistant Professor and Head of the Department. She is also pursuing her Ph D degree from Indian Institute of Technology, Kanpur. Her current research interests are in the field of all optical networks, survivability and network management. She is actively involved in activities of IETE Kanpur local center and is member of executive body. She had also been Faculty Advisor of IETE Student Forum, HBTI for many years.



Yatindra Nath Singh was born in Delhi in 1969. He obtained BTech. in Electrical Engineering with honours from Regional Engineering College, Hamirpur, Himachal Pradesh in July 1991, MTech in Optoelectronics & Optical Communications from Indian Institute of Technology, Delhi in December 1992 and PhD from department of electrical engineering,

Indian Institute of Technology, Delhi in 1997. He was with the department of electronics and computer engineering, IIT Roorkee, India as faculty from Feb '97 to July '97. He is currently working as faculty in the department of electrical engineering, Indian Institute of Technology, Kanpur. He is a member of Institution of Electronics and Telecommunication Engineers (IETE), India and senior member of The Institution of Electrical and Electronics Engineers, Inc., (IEEE) USA. His academic interests include Optical Networks, Photonic packet Switching, Optical Communications, telecom networks, Network management, E-learning systems, Opensource software development. He is actively involved in development of Open Source E-learning platform named Smtaspati.

Second Phase Reconfiguration of Restored Path for Removal of Loop Back in P-Cycle Protection

Rachna Asthana, *Student Member, IEEE*, and Y. N. Singh, *Senior Member, IEEE*

Abstract—P-Cycles are one of the most promising techniques used for span protection in optical networks. However when p-cycle is used to provide protection to any failed span, there may be overlapping of some nodes in the working path and in the restoration path provided by the p-cycle. These nodes are repeated in the restored path, hence redundant link capacity is used. These repetitions will form loops at the overlapping nodes. To remove these loops and release the redundant capacity, an algorithm is developed to reconfigure the restored path. This aspect of the p-cycle has not been discussed so far in the literature. The capacities required without reconfiguration and after reconfiguration have been compared. It has been found that with reconfiguration, considerable amount of capacity can be released, and the restored path length can also be reduced significantly.

Index Terms—P-Cycles, path restoration, reconfiguration of restored path, capacity saving.

I. INTRODUCTION

IN the field of optical network protection and restoration, p-cycles have gained tremendous momentum in recent years, due to their ability to provide ring like speed and mesh like efficiency and flexibility [1]-[2]. P-Cycles, a technique for span protection, are preplanned and fully pre-connected closed loop structures of spare capacity; hence real-time switching actions are required only at the two end nodes of the failed span. P-Cycles provide protection to on-cycle spans and unlike rings, they provide protection to straddling spans (chords of the p-cycle) also. Hence, their efficiency can be as good as the efficiency of mesh networks [2]. Since p-cycles are formed only in the spare capacity, routing of primary paths is not affected. Therefore the flexibility of mesh networks is retained with p-cycles.

In recent years, a lot of work has been reported in literature [3] on various issues in p-cycles. To achieve the theoretical efficiency of mesh networks, extensive work has been done with Hamiltonian p-cycles [4]. Strategies have been proposed to provide dual or multi failure network survivability [5] with re-configurable or shared p-cycles. To obtain the optimal solution for the configuration of p-cycle, many heuristics have been developed [6]-[7]. Recently the span protection technique of p-cycle has been extended to provide node [8] and path protection [9] also.

Manuscript received October 7, 2006. The associate editor coordinating the review of this letter and approving it for publication was Prof. Maode Ma. This work was supported in part by the Department of Science and Technology, Govt. of India under Fast Track Scheme for Young Scientist vide Grant No SR/FTP/ETA-31/2003.

R. Asthana is with Harcourt Butler Technological Institute, Kanpur, UP, 208002 India (email: rachnas@iitk.ac.in).

Y. N. Singh is with the Electrical Engineering Department, Indian Institute of Technology Kanpur, UP 208016 India (email: ynsingh@iitk.ac.in).

Digital Object Identifier 10.1109/LCOMM.2007.061635.

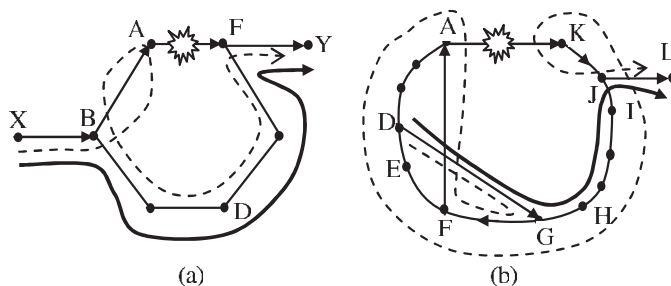


Fig. 1. Primary path (sequence of arrows), restored path (dashed line), and final path after removal of loop back (thick line).

However, the loop back in the restored path of p-cycle has not been discussed so far in the literature. In the next section, we explain the issue and in Section III, the mathematical model [10] and technique to remove the loop back is given [11]. Section IV discusses the simulations and results and finally, conclusions are given in Section V.

II. LOOP BACK IN RESTORED PATH

Consider the hypothetical networks shown in Fig. 1. AB..D..FA is a p-cycle formed in spare capacity in Fig. 1(a). (Although we are showing the network connections in one direction, in reality, the same will exist for reverse direction also.) Let us consider the failure of on-cycle span AF. A working path XBAFY (shown by sequence of arrows), from source 'X' to destination 'Y' and passing through the failed span, will now be restored by the p-cycle AB..D..F. The restored path will now be XBA-B..D..F-Y (shown by dashed line). If any node is common between working path and the p-cycle, except the end nodes of the failed link, then the restored path will pass through that node twice. This is called loop back in the present work. In the restored path of Fig. 1(a) the node B is visited twice; hence there is a loop back at node B. If the number of common nodes in working path and the path provided by p-cycle is more, then there will be more loop backs. Refer to Fig. 1(b), the working path is DGF..AK..JL. In the event of failure of AK, the restoration path, provided by the p-cycle (A..DEF..GHI..JKL), is DGFA-DEF..GHI..JKL (shown by dashed line), and common nodes are D, F, G, and J (A, and K are the end nodes of the failed link). There are loop backs at all the common nodes. Due to the loop backs in the restored path, extra capacity will be used. If these loop backs can be removed from the restored path then all the redundant capacity will be released. The released capacity can be used for routing of other working paths or for protection. The removal of loop backs will also reduce the number of hops and the restored path length. Hence propagation delay and signal degradation

will also be reduced. The reliability of the restored path will now be more due to the reduced number of hops.

To release the loop back capacity, the loop with the largest path length is to be removed, i.e. the restored path is to be reconfigured. It is obvious that removal of the largest loop will release the maximum number of links.

In the first phase, the traffic is switched over to the path provided by the p-cycle in the traditional manner [1] to retain the ‘ring like speed’ of the p-cycle. In the second phase, the restored path is reconfigured by identifying the loop with the largest path length and performing one switching action at the loop back node to release the redundant capacity. This reconfiguration is done at each end of the failed link. Thus all the capacity, engaged at the intermediate nodes of the loop back path, would now be released. In Fig. 1(a), the switching action will be performed at B to release the loop back in the restored path, and to have the final path XB..EFY (thick line).

III. THE ALGORITHM

Let $[R]$, $[P]$, $[M]$, $[S]$, and $[D]$ be the ordered sets consisting of nodes of the working path, the p-cycle, the failed link (M1, the upstream and M2, the downstream node), a portion of the working path, from source node to the upstream node of the failed link, and another portion of the working path, from downstream node of the failed link to the destination node, respectively. The nodes in $[P]$ are organized such that M1 is the first node and M2 is the last node in $[P]$. Let L_U be the length of $[U]$, defined as the total number of nodes in the set minus one. Let J_{UX} represent the index of element X in the set $[U]$. The index starts from 0 and ends at L_U . Addition and subtraction operations for ordered sets are defined as follows. $[U]=[V]+[W]$, where operation ‘+’ adds all the elements of $[W]$, except the first one, to the elements of $[V]$ in the ordered form to get $[U]$; the last element of $[V]$ and first element of $[W]$ should be the same for ‘+’ operation. Thus $[R]=[S]+[M]+[D]$. $[V]=[U]-[W]$, where operation ‘-’ eliminates the elements of $[W]$ from $[U]$ again in the ordered form except the first (last) element of $[W]$ when last (first) elements of $[W]$ and $[U]$ are same. $[W]$ has to be the subset of $[U]$, such that either the start nodes or the end nodes are same in both $[W]$ and $[U]$.

First Step: Finding the common nodes in $[S]$ and $[P]$: Let $[N1]$ be the set having common nodes of $[S]$ and $[P]$, excluding end nodes of the failed link i.e. M1.

Hence, $[N1]=([S]\cap[P])-([S]\cap[P]\cap[M])$; the second term excludes the end node of failed link. Note that $[S]\cap[P]$ is not an ordered set, hence normal subtraction operation is used.

Second Step: Finding the largest length of the loop back paths: The length of the loop back path for node N, $L_N=L_S-J_{SN}+J_{PN}$;

Among all elements of $[N1]$, take the element, X1, having the largest loop back length, L_{X1} .

Now $[R1]=[S]-[S1]$, where $[S1]$ =set of nodes from node at index J_{SX1} to M1 in $[S]$.

At destination end of the failed link;

First Step: Finding $[N2]=([D]\cap[P])-([D]\cap[P]\cap[F])$;

Second Step: The length of the loop back path, $L_N=L_P-J_{PN}+J_{DN}$.

Among all elements of $[N2]$, take the element, X2, having the

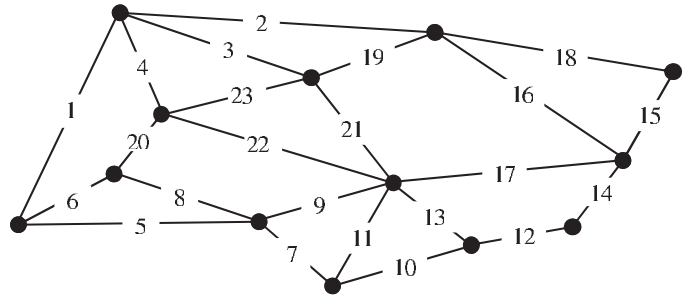


Fig. 2. Test network: Net1.

largest loop back length, L_{X2} .

Then $[R2]=[D]-[D1]$, where $[D1]$ is the set of nodes from M2 to node at index J_{DX2} in $[D]$.

Third Step: Removing the loop back path: The resultant final path is $[FP]=[R1]+(([P]-[P1])-[P2])+[R2]$, where $[P1]$ =set of nodes from M1 to the node at index J_{PX1} in $[P]$, and $[P2]$ is the set of nodes from node at index J_{PX2} to M2 in $[P]$;

The mathematical model is illustrated using network shown in Fig.1 (a) as follows.

Here $[R]=[X, B, A, F, Y]$; $[P]=[A, B, C, D, E, F]$; $[M]=[A, F]$; $[S]=[X, B, A]$; $[D]=[F, Y]$; M1=A; M2=F.

Hence $[R]=[X, B, A]+[A, F]+[F, Y]=[X, B, A, F, Y]$

Then, $[S]\cap[P]=[A, B]$; $[S]\cap[P]\cap[M]=[A]$; and $[N1]=[B]$.

$L_B=2$; Then $[S1]=[B, A]$; $[R1]=[X, B, A]-[B, A]=[X, B]$.

At destination end, $[N2]=[]$, $L_{X2}=0$, and $[R2]=[F, Y]-[]$.

hence $[P1]=[A, B]$; $[P2]=[]$; $[FP]=[X, B]+(([A, B, C, D, E, F]-[A, B])-[])+[F, Y]=[X, B]+[B, C, D, E, F]+[F, Y]$.

Thus $[FP]=[X, B, C, D, E, F, Y]$.

IV. SIMULATIONS AND RESULTS

It is obvious that the algorithm will almost always release the capacity. The test network (Fig. 2) Net1 [4], with 13 nodes, 23 spans (span numbers are shown) and 3.54 average node degree (A.N.D.), has been simulated to find the amount of capacity released. The primary paths for unit traffic matrix are routed using shortest path Dijkstra’s algorithm with hop count as metric. The set of optimal p-cycles, to protect all the working capacities on each span, has been found with Integer Linear Programming (ILP) model given in [2].

All the paths, passing through the failed span, and the p-cycles, protecting the failed span, are identified. One p-cycle can protect one path if the failed span is on-cycle and two paths if the failed span is straddling span of the p-cycle. The total capacity used for restoration is calculated for all the paths passing through the failed span (one unit of capacity stands for one link between two nodes). With our algorithm, the loop backs in the restored paths are removed, and the amount of released capacity is calculated. This process is repeated for each span considering it as failed one. Then the average is taken for all the spans of the network. The results are shown in Table I.

To determine the effect of amount of traffic in the network on the released capacity, we have further considered the general traffic distribution when the traffic from one node is generated with probability ‘p’ for every other node in the network. The values of ‘p’ are taken as 0.1, 0.2, ..., 1.0. With

TABLE I

Link no.	Total no. of paths	Capacity used without reconfiguration	Capacity released with reconfiguration	Percentage of released capacity
1	12	206	34	16.5
2	11	202	66	32.7
3	4	104	42	40.4
4	3	54	24	44.4
5	7	156	38	24.4
6	3	78	40	51.3
7	9	164	50	30.5
8	8	130	40	30.8
9	8	148	50	33.8
10	7	154	48	31.2
11	6	130	44	33.8
12	10	206	60	29.1
13	7	128	32	25.0
14	8	186	56	30.1
15	8	188	82	43.6
16	10	130	38	29.2
17	12	160	20	12.5
18	4	74	12	16.2
19	3	54	4	7.4
20	3	76	12	15.8
21	7	118	42	35.6
22	6	98	32	32.7
23	2	28	0	0.0
Avg.	6.9	129.2	37.7	29.1

each value of 'p', the traffic matrix is generated fifty times and each time, p-cycles are found with ILP model [2]. The mean value of released capacity for each value of 'p' is calculated. Fig. 3 shows mean savings in the capacity with respect to probability 'p' of one unit traffic from one node to every other node in the network.

V. CONCLUSION

It is clear from Table I that as large as 51.3% and on an average 29.1% of capacity savings can be achieved with our algorithm. Fig. 3 shows that this saving remains around 29% for various traffic distributions. This suggests that saving is almost independent of the traffic load. The algorithm has been further verified with 19 node, 28 span, 2.95 A.N.D. network [12], 14 node, 21 span, 3.0 A.N.D., NSFNET and 10 node, 22 span, 4.4 A.N.D., network [1], the amount of capacity saving is 35.5%, 31.7%, and 22.0% respectively for these networks. The capacity saving is 29.1% with Net1, 3.54 A.N.D. This suggests that the effectiveness of algorithm will be network topology dependent. Thus it is hypothesized that effectiveness will initially reduce faster with increase in average node degree and thereafter the rate of reduction will be much smaller. A possible explanation is that as the A.N.D. increases, there will be more straddling spans. To protect a straddling span only a portion of the p-cycle is used, hence the length of the restored path will be less. Therefore loop backs will also be less. However this needs to be further investigated.

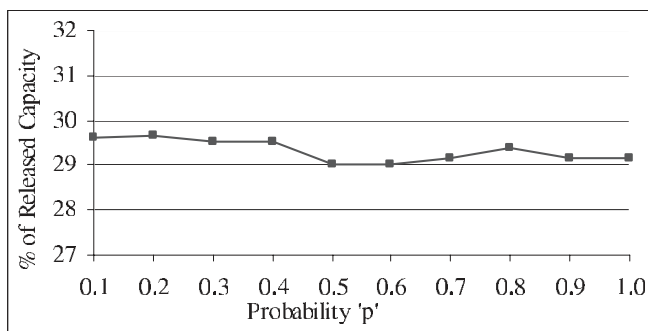


Fig. 3. Variation in capacity saving with various traffic distributions ('p' is the probability of one unit traffic to every other node in the network).

With our simple but effective algorithm, significant amount of saving can be achieved in the resources used for restoration without affecting the 'ring like speed' of p-cycles. Our algorithm will also reduce the restored path length. The data shown in Table I also provides the information about reduction in the restored path length. As one unit of capacity represents one hop of a path, the reduction in the restored path length, due to second phase reconfiguration, will be equal to the amount of released capacity. The reduction in the restored path length reduces the propagation delay, excessive signal degradation and increases the reliability of the restored path in the event of second failure.

REFERENCES

- [1] W. D. Grover and D. Stamatelakis, "Cycle-oriented distributed preconfiguration: ring like speed with mesh-like capacity for self-planning network restoration," in *Proc. IEEE ICC 1998*, pp. 537-543.
- [2] W. D. Grover and D. Stamatelakis, "Bridging the ring-mesh dichotomy with p-cycles," in *Proc. DRCN 2000*, pp. 92-104.
- [3] W. D. Grover, "p-Cycles," chapter 10 in *Mesh-Based Survivable Networks: Options for Optical, MPLS, SONET and ATM Networking*. Prentice-Hall, 2003.
- [4] A. Sack and W. D. Grover, "Hamiltonian p-cycles for fiber-level protection in homogeneous and semi-homogeneous optical networks," *IEEE Network*, vol. 18, no. 2, pp. 49-56, Mar. 2004.
- [5] H. Wang and H. T. Mouftah, "P-cycles in multi-failure network survivability," in *Proc. ICTON 2005*, pp. 381-384, 2005.
- [6] Z. Zhang, W.-D. Zhong, and B. Mukherjee, "A heuristic method for design of survivable WDM networks with p-cycles," *IEEE Commun. Lett.*, vol. 8, no. 7, pp. 467-469, July 2004.
- [7] D. A. Schupke, C. G. Gruber, and A. Autenrieth, "Optimal configuration of p-cycles in WDM networks," in *Proc. IEEE ICC 2002*, pp. 2761-2765.
- [8] G. Shen and W. D. Grover, "Extending the p-Cycle concept to path segment protection for span and node failure recovery," *IEEE J. Sel. Areas in Commun.*, vol. 21, no. 8, pp. 1306-1319, Oct. 2003.
- [9] A. Kodian and W. D. Grover, "Failure-independent path-protecting p-cycles: efficient and simple fully preconnected optimal-path protection," *J. Lightwave Technol.*, vol. 23, no. 10, pp. 3241-3259, Oct. 2005.
- [10] R. Asthana, "Second phase reconfiguration of restored path for removal of loop back in p-cycle based protection in optical networks," *ACES/EE Dept. Lib.*, IIT Kanpur, Tech. Rep. 2006/2294/TR, March 2006.
- [11] R. Asthana and Y. N. Singh, "Removal of loop back in p-cycle protection: second phase reconfiguration," in *Proc. IEEE ICCS 2006*.
- [12] R. Ramaswami and K. N. Sivarajan, *Optical Networks: A Practical Perspective, Second Edition*. Morgan Kaufmann, 2002, pp. 667-710.

p -Cycles: An Overview

Rachna Asthana, *Member, IEEE*, Y.N. Singh, *Senior Member, IEEE*, and Wayne D. Grover, *Fellow, IEEE*

Abstract—One of the most promising techniques of network protection i.e. p -Cycles (pre-planned, preconfigured-cycles) is reviewed in this paper. In this paper we provide a survey of the main work on p -cycles to date. The characteristics of p -cycles and various types of protection provided by them are discussed. Finally, some possible extensions or enhancements of the p -cycle concept are discussed.

Index Terms— p -Cycles, network protection design, centralized protection, distributed protection, optical networks.

I. INTRODUCTION

VARIOUS network protection schemes can be evaluated on the basis of their speed and capacity efficiency. Generally, mesh based protection schemes are capacity efficient whereas the ring based protection schemes are fast. Similarly, among the various mesh protection schemes, path based protection schemes are generally more efficient whereas span or link based schemes are faster [1], [2]. One of the most efficient path protection based schemes is shared backup path protection (SBPP) [3]. The p -cycle based protection schemes, first reported by Grover, Stamatelakis et al. [4], have combined ring like speed with mesh-like capacity efficiency, close to that of SBPP [3]. The spare capacity of the network is pre-connected to form the ring-like structures called p -cycles. Consequently only two switching actions (as in rings), at the end nodes of the failed span, are needed in the event of failure, to switch the traffic to the protection path provided by the pre-configured cycle. The main difference between any ring-based scheme and the p -cycle scheme is the protection of straddling spans by the p -cycles as shown in Fig. 1 [4]. (Another important but often overlooked additional efficiency of p -cycles over rings, is that working paths may be freely routed over the network graph, and are not required to follow ring-constrained routings in order to be protected). The SBPP-like efficiency is achieved due to the shared protection provided by the p -cycle to all the on-cycle as well as straddling spans. Thus, we can say that p -cycles are a form of shared span protection. p -Cycles have become one of the most promising protection schemes due to the above features. The research on p -cycle based techniques has gained momentum in recent years. Considerable literature has covered many different aspects of p -cycles. The various p -cycles discussed in the literature have been named on the basis of their structural relationship with the network and the type

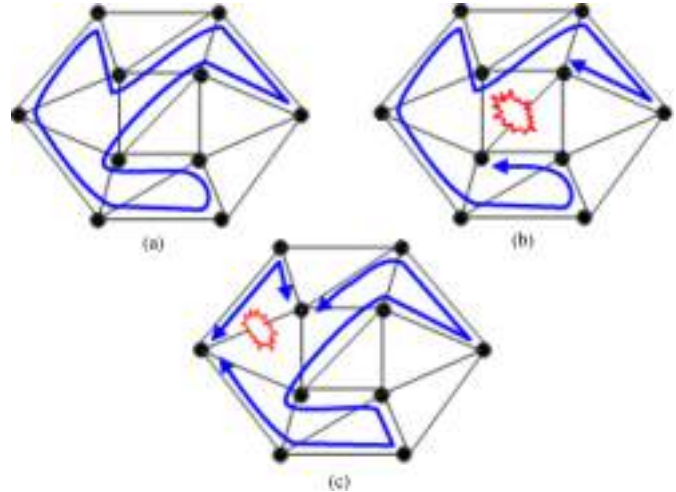


Fig. 1. (a) p -cycle, (b) On-cycle failure, (c) Straddling span failure (adapted from [4]).

of protection provided by them. Hamiltonian, simple and non-simple p -cycles are named as per their structural relationships as follows.

Hamiltonian p -cycle: The p -cycle which passes through all the nodes of the network only once is called a Hamiltonian cycle.

Simple p -cycle: The p -cycle which does not pass through any node or span more than once is called simple p -cycle.

Non-simple p -cycle: The p -cycle which passes through a node or a span more than once is known as non-simple p -cycle. The following p -cycles are named after the type of protection provided by them.

Span p -cycle: The simple p -cycle which provides protection to spans is called span p -cycle. The p -cycle shown in Fig. 1 is an example of Hamiltonian, simple and span p -cycle.

Node encircling p -cycle: The traffic passing through the failed node can be restored in case of node failure with this type of p -cycle. This p -cycle passes through the adjacent nodes of the failed node but not through the failed node itself.

Path protecting p -cycle: The complete path, having source and destination node lying on the p -cycle can be protected by path protecting p -cycle.

Flow p -cycle: It provides protection to complete path segment lying on the p -cycle. The details of the above are given in concerned sub-sections.

In the next section, various methods of p -cycle network design are discussed. Section III deals with the capacity-efficiency of p -cycles. The various types of protection which can be provided by p -cycles are discussed in section IV. The implementation of p -cycles, in the form of preconfigured structures, is treated in section V. A few variations

Manuscript received September 9, 2008; revised May 21, 2009.

Rachna Asthana is with Harcourt Butler Technological Institute, Kanpur, UP, 208002 India (e-mail: rachnaasthana@rediffmail.com).

Y.N. Singh is with Electrical Engineering Department, Indian Institute of Technology Kanpur, UP 208016 India (e-mail: ynsingh@iitk.ac.in).

Wayne D. Grover is with Department of Electrical and Computer Science, University of Alberta, Canada (e-mail: grover@trilabs.ca).

Digital Object Identifier 10.1109/SURV.2010.1001xx.

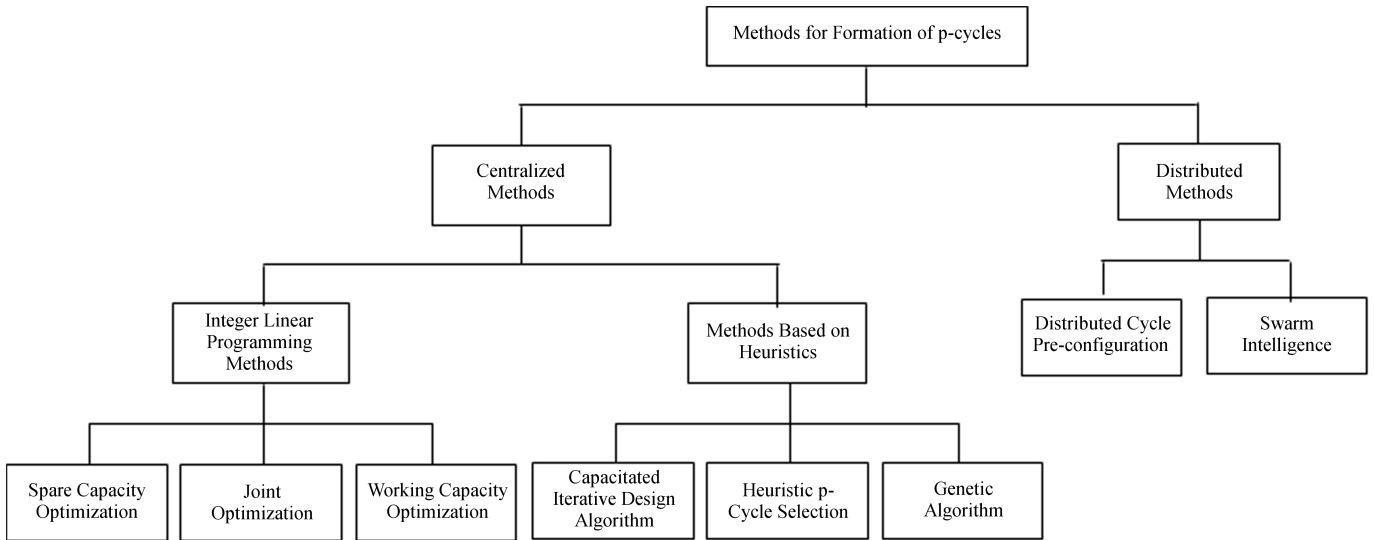


Fig. 2. p -Cycle Network Design or Configuration Methods.

and enhancements are discussed in section VI and finally, conclusions are given in Section VII.

II. p -CYCLE NETWORK DESIGN METHODS

On the basis of the work reported in literature, methods for the formation of p -cycles can be categorized in several ways. One basis for categorization can be the computation method. The problem of p -cycle network design or network configuration can be approached in either a centralized or distributed manner. Another categorization can be based on the order of p -cycle formation and routing of working demands. In one case, the p -cycles can be formed after routing of working demands or jointly with the working demands. It is also possible that first p -cycles are formed (or existing p -cycles are present in a network) and then demands are routed as per the available envelope of protection capacity that these p -cycles provide [5]. Still another basis for classification can be the method used for optimization. For optimization of network designs, ILP, genetic algorithms, Swarm Intelligence or custom heuristics can be used. An overall classification based on the above aspects is shown in Fig. 2 and discussed below.

A. Centralized Methods

In this method, p -cycles are chosen either from the set of all distinct cycles of the network graph, or alternatively from a suitably large set of eligible candidate cycles for the design, to protect all the working capacities on the spans. Various methods to do this computation are discussed below.

1) *Integer Linear Programming Models*: In literature, three different models have been used for optimization. In the first, only spare capacity is optimized. The second model is for joint capacity optimization where working and spare capacities are optimized jointly. In the third model, concept of protected working capacity envelope (PWCE) [5] has been used. Here, the protection capacity in the form of p -cycles is found and

then the demands are routed in such a way that they are protected.

a) *Spare Capacity Optimization (SCO)*: In this approach, also called the SCP class of design problems for Spare Capacity Placement [3], all the cycles of the network graph, or a large candidate subset of cycles, are found in advance using any one of several possible search techniques [3]. The working paths are also separately routed with any suitable algorithm as per the traffic matrix. Then from the set of all the cycles of the network, a set of p -cycles is selected using an optimization model, to protect all the working capacities on the spans of the network. Being based on ILP, this approach strictly-speaking is in the class of NP-hard problems [6]. However, with modern solver engines quite large problem instances can actually be solved to optimality in reasonable times. The optimization objective is to minimize the capacity required for the formation of p -cycles [7]. The p -cycles obtained by this model are span-protecting p -cycles [8]. Most of the studies of p -cycles are based on this method. The basic model as given in [7], is given below.

Sets:

- S : Set of spans, indexed by j .
- P : Set of p -cycles indexed by p .

Parameters:

- c_j : Cost of span j .
- w_j : Working capacity on span j .
- π_j^p : Equal to 1 if p -cycle p crosses span j , otherwise it will be equal to 0.
- x_j^p : Equal to 1 if the p -cycle p protects span j as on cycle span, equal to 2 if p -cycle p protects span j as straddling span and 0 otherwise.

Variables:

- a_j : Spare capacity required on span j .
- n^p : Number of unit-capacity copies of p -cycle p in the solution.

The objective of ILP is to minimize:

$$\sum_{\forall j \in S} c_j \cdot a_j \quad (1)$$

Subject to:

$$w_j \leq \sum_{\forall p \in P} x_j^p \cdot n^p \quad \forall j \in S, \quad (2)$$

$$a_j = \sum_{\forall p \in P} \pi_j^p \cdot n^p \quad \forall j \in S, \quad (3)$$

and

$$n^p \geq 0 \quad \forall p \in P. \quad (4)$$

Equation (1), the objective function, minimizes the total spare capacity used to form the p -cycles. In general, this is a surrogate for total cost, which in practice can be the actual objective, but has the same mathematical form as Equation (1). Equation (2) ensures that all the working capacity of every span is protected for 100% protection for single failures. Equation (3) provides sufficient spare capacity on every span to form p -cycles.

This model gives a set of p -cycles that provide 100% protection against any single complete span-failure. To select p -cycles with specific further objectives in mind, various authors have defined additional constraints. The flow p -cycles have been found to protect the path segments of contiguous working flows and also for transiting working flows passing through a failed node [8]. With flow p -cycles, the capacity efficiency has been further increased from that of the span protecting p -cycles. The flow p -cycle concept has been further extended to protect dynamic flows in [9]. The complete path protection with p -cycles has also been determined using ILP models [10], [11]. This has been done to achieve the capacity efficiency of shared backup path protection (SBPP) with pre-connected backup path property of p -cycles.

In a transparent optical network, there is usually a limit on the length of the lightpaths. Beyond this limit transmission quality may be affected. To sustain adequate transmission quality, regeneration may be a solution but increases the overall cost of the network. Therefore for these networks, to restrict the restored path length, hop limited and circumference limited p -cycles have also been studied with an ILP model [12]. In this case, there is an additional constraint which restricts the protection path length by the hop limit, or more subtly, restricts the maximum length of any used protection path segment from a p -cycle, regardless of the p -cycles own entire circumference. Because of this constraint, the minimum capacity required for the formation of p -cycles may be relatively higher compared to the basic model. In the basic model and other models discussed above, each selected p -cycle requires spare capacity separately on each on-cycle span for its formation. The concept of shared p -cycles has also been reported for the protection of WDM networks [13]. The authors claim that it will increase the capacity efficiency of p -cycle protection. However, this needs to be analyzed. In this model, all the p -cycles passing through a common span share the capacity on that span for their formation. Obviously the capacity efficiency come out to be more as compared to other methods, but the property of pre-connection of protection

path will be lost with this model and hence the ring like speed. There is, however, a logical conundrum or intellectual degeneracy with the concept of shared capacity p -cycles, because to obtain this added efficiency, they forego the pre-connectedness property. But once this is done, the intellectual exercise has then gone full circle and one is simply back to considering mesh span restoration scheme, in which, shared protection is provided for single failure scenario. Previous published work on the concept does not point this out. In other words, with the concept of shared capacity, the pre-configuration of p -cycles is lost and it no longer remains p -cycle protection. The added efficiency from shared capacity in p -cycles, is obtained only by actually departing from the p -cycles concept, adding control complexity, and ruining the speed of p -cycle-based restoration schemes, although retaining the p -cycle name. Another point to be noted is that probability of restoration in case of second failure will reduce, as all the so called p -cycles which share even a single link with the p -cycle being used for restoration of first failure, will break. While in proper p -cycles, only the p -cycles having the failed span on cycle, or which are used to restore the traffic of failed span being straddling link, are consumed.

In [14], with the help of ILP model, p -cycles have been found to provide protection against single SRLG (shared risk link groups) failure. The ILP model has also been used to find the p -cycles such that end to end unavailability of the restored path remains within the unavailability bound required by the user [15].

The total number of cycles in a large network with high degree of connectivity, will be quite large. Various heuristic algorithms are available [16]-[19] for pre-selection of appropriate p -cycles from all possible cycles of the network to reduce the size of the set of candidate p -cycles. This reduces the solution time of ILP.

b) Joint Capacity Optimization (JCO): In the first model, only the spare capacity is optimized with the constraints of protecting all the working capacity of every span. The JCO model (also called JCP for Joint Capacity Placement in some of the papers) provides for the optimization of total capacity i.e. spare plus working together. The demands are not routed in advance to find the working capacity, instead the set of eligible working route options are found for each source-destination pair. From the set, the working paths for each source-destination pair are selected along with the placement of spare capacity to optimize the total capacity [3], [20]. The JCO model (as in [3]) is given below. The additional variables and parameters over and above the ones used in SCO, are as follows.

Sets:

D : Set of demand pairs having non-zero demand indexed by t .

E^t : Set of eligible working routes for demand pair t , indexed by e .

Parameters:

d^t : The values of demand for each demand pair t (integer).

$f^{t,e}$: Number of demand units (integer) for t^{th} demand assigned to the e^{th} eligible route in E^t .

$\lambda_j^{t,e}$: Equal to 1 if the $e(th)$ working route for the $t(th)$ demand passes through span j , 0 otherwise.

Variables:

w_j : Working capacity on span j .

Minimize:

$$\sum_{\forall j \in S} c_j(w_j + a_j) \quad (5)$$

Subject to:

$$d^t = \sum_{\forall e \in E^t} f^{t,e} \quad \forall t \in D, \quad (6)$$

$$w_j = \sum_{\forall t \in D} \sum_{\forall e \in E^t} f^{t,e} \cdot \lambda_j^{t,e} \quad \forall j \in S, \quad (7)$$

$$a_j = \sum_{\forall p \in P} \pi_j^p \cdot n^p \quad \forall j \in S, \quad (8)$$

$$w_j \leq \sum_{\forall p \in P} x_j^p \cdot n^p \quad \forall j \in S, \quad (9)$$

$$n^p \geq 0 \quad \forall p \in P, \quad (10)$$

and

$$a_j \geq 0, \quad w_j \geq 0 \quad \forall j \in S. \quad (11)$$

Equation (5), the objective function minimizes the cost weighted total capacity required for routing of working paths and for providing protection. Constraint (6) ensures that all the demands are routed, and constraint (7) gives the amount of working capacity on a span. Equation (8) provides sufficient spare capacity on a span required by all the p -cycles of the solution set. Constraint (9) ensures that the protection provided by all the p -cycles of the solution set is sufficient to protect all the working capacity of the span. The results of SCO and JCO have been compared in [20]. The comparison clearly establishes the superiority of JCO with respect to capacity requirement. However, the solution time is much more in case of JCO as compared to the spare capacity optimization.

JCO has also been used to optimize the capacity without using all possible cycles of the network [21]. It can select only from the fundamental cycles that have no straddling links. Non-simple cycles have also been considered in the solution. However, this approach is suitable only for planar networks. Not surprisingly, if non-simple p -cycles are allowed, the ILP solution exhibits better capacity-efficiency than the simple cycle ILP models. The advantage of non-simple p -cycles in terms of capacity, over simple p -cycles has also been shown in [22]. This problem has also been formulated as JCO. It must be said however, that p -cycle network design with non-simple cycles is probably at best a research curiosity. It seems highly unlikely in practice that a network operator would be comfortable, from a network management and operations standpoint, with operating a network where protection structures could loop through nodes more than once in a “figure-8 like” manner.

c) *Protected Working Capacity Envelope Optimization:*

In this model, the p -cycles for protection are found first, with certain notions of maximizing an entire general volume of working channels that are structurally protected, and then

the working paths are routed within the resulting protection domain or envelope. The concept is known as protected working capacity envelope (PWCE) [5]. The objective (in general-there are variations) is to maximize the total volume of working capacity which is protected with the set of p -cycles found in the ILP model. There can be many problem formulations depending upon the type of inputs given. The total capacity of each span may be given, or only the spare capacity of each span may be given. These cases have been extensively explored in [23]. The model for the case in which spare capacity of each span is given to begin with, is given below.

Maximize:

$$\sum_{\forall j \in S} w_j \quad (12)$$

Subject to:

$$w_j \leq \sum_{\forall p \in P} x_j^p \cdot n^p \quad \forall j \in S, \quad (13)$$

$$a_j \geq \sum_{\forall p \in P} \pi_j^p \cdot n^p \quad \forall j \in S. \quad (14)$$

If total capacity of the spans is given, then following constraint is also added.

$$T_j \geq w_j + a_j \quad \forall j \in S, \quad (15)$$

where T_j is the total capacity of span j .

The PWCE concept has also been used for dynamic traffic. The incoming requests are routed in the available capacity which is protected [24], [25]. The nature of dynamic traffic is random. The connection requests arrive and depart randomly. To provide optimization to the dynamic traffic scenario, the adaptive PWCE (APWCE) has been proposed in [26]. The APWCE slowly adapts to the changing traffic scenario with re-optimization process using ILP based on the previous envelope. The objective is to provide protection to as many demands as possible within the available capacity constraints.

Considerable other work to optimize the spare or working or both capacities, based on ILP methods, is also available in the literature. Solutions are available for static as well as dynamic traffic scenarios. They can be solved quickly with ILP models for small networks and are very useful to perform in depth studies and to gain insight in the p -cycle techniques. Thus, ILP based models fundamentally have a place in network research. But the fact that ILP in general is in a class of “NP-hard” problems, is often over-stated as to how usable the ILP method can be in practice. Detailed network problems involving 50 to 100 nodes can often be solved to optimality within hours of solution time these days in practice. In addition strictly, only the solution of an ILP to provable optimality (full termination) is NP-hard. In practice, extremely good large-scale design solutions may be obtained without having to reach full termination with an ILP solver. Nevertheless, p -cycle design problems can also be approached with many heuristics algorithms.

2) *Methods Based on Heuristics*: Generally, heuristic algorithms provide solutions in a significantly smaller time, but at the cost of reduced capacity efficiency as compared to ILP models. Depending on the specific heuristic and problem details, the solutions may be very close to optimum, although in production use, one reality is that one never actually knows precisely how close to the best possible solution quality one is obtaining.

a) *Capacitated Iterative Design Algorithm (CIDA)*: The basic CIDA procedure was first outlined in [3] and consists of iteratively assessing the efficiency of candidate cycles in context of the remaining uncovered working capacity on the network, and placing one top-ranked cycle per iteration, until no unprotected working capacity remains. The basic CIDA algorithm can use the set of all possible cycles, or any pre-selected subset of cycles of particular interest or eligible qualities. One use of CIDA [27] begins with the straddling link algorithm (SLA) [16] to find a small initial set of candidate p -cycles with a single straddling link and then large cycles are formed by ‘add’, ‘join’, ‘expand’ and ‘grow’ operations. The details of the operations are available in [27]. Then, the set of p -cycles to protect all the working capacities of the spans are found using CIDA. The working capacities become available as input to algorithm as the working paths are setup as per the traffic matrix and some suitable routing algorithm e.g. shortest path. The demand-weighted or actual efficiency (DWE) of a p -cycle in a specific environment of remaining unprotected working capacity is defined as

$$DWE(p) = \frac{\sum_{\forall j \in S} \min(x_j^p, w_j)}{\sum_{\forall j \in S | \pi_j^p = 1} c_j}. \quad (16)$$

Here, w_j is the unprotected working capacity left on the span j at the time of calculation of actual efficiency. A p -cycle can protect two units of capacity on a straddling span, however, it may be possible that only one unit of working capacity is left unprotected on that span. Then, the numerator in the right hand side will have one unit instead of two. Thus, the numerator working capacity may be less than the protection capability of the p -cycle. The term in the denominator of the right hand side gives the total cost of the p -cycle ($\pi_j^p = 1$ if j is an on-cycle span). If all $c_j = 1$ then this term will simply give the hop counts of the p -cycle. The actual efficiency of every p -cycle in the set of candidate p -cycles is calculated. The copy of the p -cycle having best actual efficiency is selected and the traffic protected by this p -cycle is subtracted from the existing values of the working capacity. The process is repeated until all the working capacity is protected. The CIDA-grow algorithm performs best and requires just 5.9% more capacity than the ILP model [27].

The work in [28] is almost similar to the heuristic discussed above. However, for finding the set of candidate p -cycles, the algorithm given in [29] has been used, after that CIDA is used to select the final set of p -cycles.

b) *Heuristic p -Cycle Selection (HPS) and Refine Selected Cycles (RSC)*: The set of candidate p -cycles is selected using modified version of SLA in the method given in [30]. With the

modified version, all the cycles of the network are selected by finding K shortest path between two nodes of all the spans. By joining two such paths, a cycle is formed and then by increasing the number K , all the cycles of the network can be found.

The HPS selects the p -cycle on the basis of cycle weight, the waste capacity, the effective straddling span factor, and the actual protection capacity. The cycles which are passing through the spans having zero spare capacity are removed before every search. The cycle weight is defined as the ratio of the total actual protected capacity with the power n (a control parameter) to the total spare capacity required.

If a cycle is passing through a span with zero working capacity, then the cycle is not protecting any on-cycle capacity and the capacity used by the cycle is considered as ‘waste’. The waste capacity of the cycle is found by adding the waste capacity of all the spans of the cycle. Thus a cycle with a lower value of waste capacity is better.

Similarly, the effective straddling span factor is calculated by finding the actual capacity protected by the cycle on all of its straddling spans.

The cycles are compared on the basis of the above four factors and the best cycle is selected. The search is repeated till all the working capacity is protected.

The set of selected cycles is again refined using RSC. Two or more p -cycles are replaced with a single p -cycle if the total protection capacity remains the same with smaller amount of spare capacity used by the new p -cycle.

c) *Genetic Algorithm*: In [31] a genetic algorithm has been used with general heuristic search technique. In this work, the a priori efficiency $AE(p)$ of a p -cycle is defined (same as in [3]) as

$$AE(p) = \frac{\sum_{\forall j \in S} x_j^p}{\sum_{\forall j \in S | \pi_j^p = 1} c_j}. \quad (17)$$

The actual network protection efficiency ANPE is defined as the ratio of total working capacity of the network to the total spare capacity used by the p -cycles to protect all the working capacity in the network. (In most previous other work this ratio would be identified simply as the reciprocal of network redundancy.)

The ANPE is used as the goal function. A set of ‘top-ranked’ p -cycles are selected from the set of all the cycles of the network based on their a priori efficiency. With the optimization process of the genetic algorithm, the optimization variable n^p (number of copies of p -cycle p , it may be 0 also) for top-ranked p -cycles is calculated (for more details the reader is referred to [31]). This will give the required spare capacity in the network and then goal function can be calculated. The quality of a given solution is obtained by the goal function which directs the process of searching optimal solutions. However, the results of genetic algorithm have not been compared with ILP or any other heuristic in literature.

B. Distributed Methods

The above approaches for network design are centralized techniques. However, in the second category i.e. distributed algorithms, only two methods are available - DCPC (Distributed cycle Pre-Configuration) and Swarm Intelligence based on ant like agents. One of the major difference between study of centralized and distributed methods is the assumption in centralized method that the required capacities on each link for all the required p -cycles and working path can always be provided. This implies that 100% protection of working paths using p -cycles can be provisioned. In other words the distributed methods we cover now are actually dealing with the problem of optimal logical configuration and allocation of already in-place physical capacities. Thus, distributed methods are more oriented towards the operational short-term real life situation where the total link capacities are already given and essentially fixed, but the logical distinction and use of channels as working and spare can still be decided. Obviously, in this context, 100% protection to working paths cannot be achieved beyond a certain working capacities, as the leftover capacities which are needed for setting p -cycle reduces with setting of more working paths.

1) *DCPC*: In this method, p -cycles are spontaneously self-organized in the spare capacity with DCPC (Distributed cycle Pre-Configuration) protocol [4]. Again, the working paths are established with a suitable algorithm as per the traffic matrix, then the p -cycles are formed in totally distributed manner using DCPC in the remaining capacity of the network. As shown in [4], this method is very near to optimum solution. In this method, a self-organizing strategy for the autonomous deployment of p -cycles has been developed. With the DCPC approach, the set of the p -cycles can be allowed to re-adapt continuously to modify themselves in response to changes in the working capacities, to remain near-optimum. This arises rather easily just by letting the DCPC protocol re-run itself periodically in the background. It only alters connections between spare channels, so it is quite feasible to consider this mode of operation. In light of more recent concepts related to the PWCE approach for handling uncertain dynamic demand, it is also apparent that the DCPC protocol could be run less often, but arranged to configure or adapt the current protected working envelope, rather than a specific individual single demand pattern. By its nature DCPC has all the usual advantages of distributed protocols but in addition, being statelet-based it operated in the very robust and primitive level of signaling, equivalent to SONET APS K-byte signaling, as opposed to Internet style packet-message based distributed interaction. It is in this regard that DCPC is especially strong in the sense of being a low-level self-organizing mechanism. There are no separate network databases at all. The network state itself, as recorded locally in each node only, is inherently the database which guides the DCPC outcome.

This protocol can be implemented in any real network for the deployment of p -cycles with optimality. The DCPC protocol builds up on the statelet broadcasting. The statelets¹ are information-bearing packets with some defined fields. The

broadcast rules of the statelets are based on the self-healing network (SHN) protocol given in [32]. The algorithm runs in the background without affecting the routing of working paths and p -cycles are formed in advance of any failure. As initially described in the literature [4], only one p -cycle is obtained per iteration of the algorithm. This is the most general basic way to describe and understand the protocol. Obviously, however, the basic protocol can be adapted to also identify and construct multiple unit-channel p -cycles in any case where several p -cycles having the identical cycle in common are indicated within the remaining environment of unprotected working capacity during DCPC execution. (It is only a matter of an internal fully local update to the nodal score-assignment rules, to also identify and assemble multiple identical p -cycles, in other words p -cycles with more than a unit capacity depth).

2) *Swarm Intelligence System*: Swarm intelligence [33], helps in enabling the distributed, adaptable and self organized network management operations. These systems are based on 'emergent behavior' and are inspired by biological systems. The system consists of simple and similar autonomous mobile or ant like agents which communicates with each other asynchronously. The management information is disseminated through these agents whose behavior is similar to those of ants. The operation of these agents is almost independent. The p -cycle ant system used in [33] is based on cross entropy Ants (CE-Ants). The details on cross entropy are available in [34]. The communication between agents took place with the messages they leave or gather at nodes they visit. The aggregation of messages forms the basis for the formation of p -cycles. The p -cycle search and the traffic switch over to a p -cycle may be performed online in a fully distributed manner.

The swarm intelligence systems are also fully distributed with high redundancy and adaptability. They can be used to find near optimal solutions to NP hard problems. Details of these systems can be found in [35].

We have discussed the various methods available for the formation of p -cycles. Broadly the methods have been characterized as centralized and distributed methods. Further, centralized schemes have been classified as ILP based and heuristics based schemes. Many available variants of these schemes have been introduced. The optimum methods based on ILP formulations have been discussed in more details as these methods provides the base line for other heuristics and distributed methods.

III. CAPACITY EFFICIENCY OF p -CYCLES

A number of studies have focused on the capacity efficiency, or conversely, the redundancy of network designs using p -cycles [3], [7], [36], [37]. The redundancy is defined as the ratio of spare to working capacity and capacity efficiency is reciprocal of redundancy. It has been proved in [36] that in the limiting case when p -cycle passes through all the nodes of the network (i.e., Hamiltonian p -cycles), the efficiency of p -cycle has the same well known lower limit of $1/(\bar{d} - 1)$ as that for a span restorable mesh network (where, $\bar{d} = 2S/n$, S and n are total number of spans and nodes respectively in the network). It is now understood that Hamiltonian p -cycles can be extremely good as individual p -cycles in terms of efficiency [3], [6] in circumstances where the remaining unprotected

¹The readers are referred to [4] for details of statelets and other concepts of DCPC.

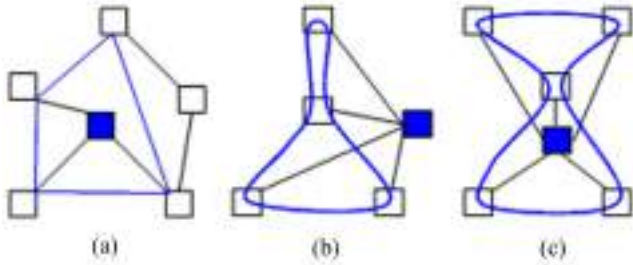


Fig. 3. Node encircling p -cycles, (a) Simple p -cycle, (b)-(c) Non-simple p -cycles (adapted from [39]).

working capacity is sufficient to employ all the protection relationships that a full Hamiltonian cycle provides, but that at the same time, complete network designs will generally require a mixture of both some Hamiltonians and other non-Hamiltonians to achieve optimal capacity-efficiency.

In [6], [38], it has been shown that the best p -cycle efficiency can be obtained with ‘flat mesh networks’ where the capacities of all the spans are identical. In [6], the efficiency for the homogeneous network (where all the spans have equal working capacity) is shown to be $2/\bar{d}$. This is not quite as tight as the lower bound shown in [36]. This is due to the fact that in homogeneous networks the total protection capacity of a p -cycle could not be exploited. The unique feature of straddling span protection of p -cycles is lost. The double protection on straddling spans could not be utilized as on every span the working capacity is the same. With this understanding, the concept of semi-homogeneous networks was put forward in [3] where the working capacities can be made double on straddling spans as compared to on-cycle spans. Then the lower limit of $1/(\bar{d} - 1)$ can actually be achieved by construction (not just a lower limit reached asymptotically) in such a network with Hamiltonian p -cycles. ILP solutions have also shown that often the p -cycles of the solution set are Hamiltonian or near Hamiltonian (just a node or two less than the total number of nodes in the network) and yet in an optimal design, other required p -cycles will be smaller and far from visiting every node. The selection of small cycle in the optimum solution is due to the local concentration of the traffic. The traffic density between the nodes of a small p -cycle is more as compared to the nodes of a large p -cycle [37]. In fact, it is important to stress this general nature of the cycles used as p -cycles in optimal designs, because in some of the literature relating to Hamiltonian p -cycles a quite misrepresentative and oversimplified view became extant for a few years to the effect that p -cycles only used Hamiltonians and therefore tended to be “too large” in practice. This is not correct and especially misleading because any given length of cycle can be set as a limit in practical network designs. Moreover, the designs can be limited also in terms simply of the total number of protection relationships any p -cycle is allowed to sustain [39].

Thus, the theoretical efficiency of $1/(\bar{d}-1)$ can be achieved with Hamiltonian p -cycles in the semi-homogeneous networks. However, this may not lead to optimum solutions always. In real networks, the situation may be quite different and the optimal solution usually contain other p -cycles (which

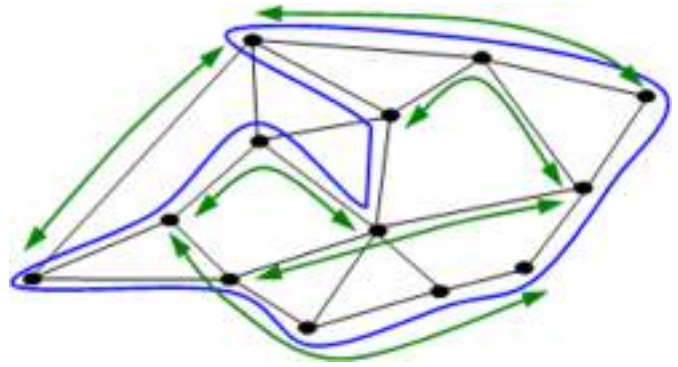


Fig. 4. A FIPP p -cycle protecting a set of six mutually disjoint working paths having their end nodes on the FIPP p -cycle.

are not Hamiltonian) as well.

IV. TYPES OF PROTECTION WITH p -CYCLES

Initially p -cycles were invented and used for link or span protection. In the sense that with respect to on-cycle working paths, a p -cycle operated like a BLSR ring, it was recognized that the same node-failure survivability that a BLSR ring has, is also inherent in p -cycles for on-cycle paths (but not inherently for straddling paths through a failed node). With recognition of the attractive features of p -cycles for span failure protection, however, it became natural to consider other types of protection, such as node failure protection, as well. Accordingly p -cycles have now also been extended or adapted and studied for use at various network layers with varying granularity and even for multiple failures. This section surveys these various other types of failure protection with p -cycles. It is worth mentioning here that the protection cycles discussed in [40] also provides ring like protection. They provide ring covers at the level of fibers. All the traffic flowing in one fiber is transferred to another as such in the event of failure. The straddling span protection, key feature of p -cycles, is missing in the protection cycles. To form the ring covers, extra fibers are used. Thus, the protection cycles are different from p -cycles.

A. Node, Path and Path-Segment Protection

Apart from providing span protection, p -cycles can also provide node protection with the node encircling p -cycles (NEPC) concept [41], [42]. The idea was proposed in [41]. To define an NEPC protecting the flows through a given node, the p -cycle has to pass all the nodes adjacent to the failed node but not the failed node itself. This defines a perimeter fence notion which is able to intercept, and hence to protect, all the flows which are passing through the failed node. The traffic originating or terminating at the failed node cannot be recovered with these p -cycles. The node encircling p -cycles may not always be simple cycles i.e., they may also be non-simple (Fig. 3). A network with n number of nodes requires n p -cycles to protect all the nodes with node encircling p -cycles. An algorithm to find the node encircling p -cycles is given in [42]. The algorithm is called node-encircling p -cycles mining algorithm (NCMA).

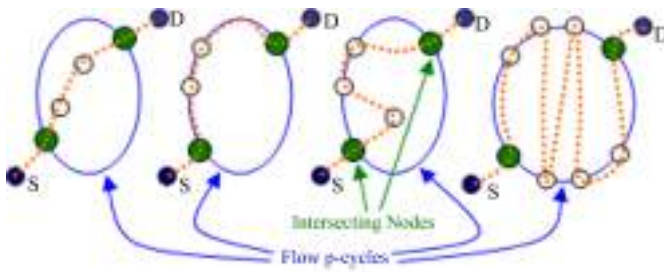


Fig. 5. The flow p -cycle protecting various types of flows or path segments (adapted from [8]).

The above network model with one p -cycle to protect a node is not capacity efficient as shown in [43]. Two more network models have been developed with the help of ILP and shared node-encircling p -cycles (NEPC). In one model, any one side of the NEPCs can be used to route the protection path, whereas in the other model, the side of the NEPC, to which the protection path is routed, for each light path being affected is also determined making it even more capacity efficient.

The p -cycle technique has also proved to be successful for complete path protection with failure-independent path-protecting (FIPP) p -cycles [10]. The idea is to have a common p -cycle for all the paths which are mutually disjoint and having end nodes on the p -cycle (Fig. 4). Path protecting p -cycles offer all the advantages of SBPP and in addition the protection path is pre-configured also. Real time switching is only required at the end nodes of the failed path. However, some signaling is required between the end nodes to perform the switching as in any other path protecting scheme except 1+1 APS. In case of span p -cycles, if there is a failure on a span, then both the end nodes of the span will know about it independently by the loss of light at the later node of the span. However in case of FIPP, the failure information is to be conveyed to the source and destination nodes of the path as both source and destination of a path may not be on the end nodes of a span. The signaling mechanism will be required specifically for this purpose. If the working paths are also node disjoint then node protection is also provided with path protecting p -cycles. A fast method to design the FIPP network based on disjoint route set using ILP and a heuristic to reduce the set of candidate p -cycles for the final set is given in [11].

Flow p -cycles have been used to protect path segments or flows [8]. The flow or the path segment is the portion of the working path which lies between two intersecting nodes of the path and the p -cycle (Fig. 5). The p -cycle which can protect the flows is called flow p -cycle. Flow p -cycles can also provide path protection (if the source and destination nodes are on the p -cycle), node protection (for any intermediate node between two intersecting nodes) and the usual span protection. It has been shown that only a very small additional capacity is required to provide 100% node and span failure [8].

However, the speed of the p -cycle may be compromised in these scenarios as some signaling is required between the nodes which lie on the p -cycle as well as on the flow path. More complexity is involved in finding the node-encircling, FIPP, and flow p -cycles as compared to span protecting p -cycles. Further, methods of finding these p -cycles falls under

the centralized category, whereas span protecting p -cycles can also be found in distributed manners [4], [33].

B. Protection at Various Layers

Theoretically p -cycles can be used to provide protection at any connection-oriented transport layer like SONET and WDM applications [7]. They can also be used to provide protection in connectionless environments such as ATM or IP layer [7], [41]. In MPLS networks also, p -cycles can be used to provide protection with higher bandwidth efficiency [44].

However, most of the work on p -cycles is related to WDM or DWDM optical network protection [9], [13], [16], [24], [25], [28], [37], [42], [45]-[49]. In these networks, usually the protection is provided at the level of a wavelength path, or an OC-n management signal unit, where one unit corresponds to one wavelength. If the same wavelength is used by a path on all the links, then the path is said to be a wavelength path (WP) and the corresponding constraint is called wavelength continuity constraint. On the other hand if wavelength converters are available at every node of a path and the path can have any free wavelength on any link then the path is called virtual wavelength path (VWP) and the network is known to be fully convertible.

The ILP formulation for WP case is given in [46]. One more dimension of wavelength is added to the spare capacity optimization case discussed in centralized methods. The ILP for VWP case is similar to spare capacity optimization case. The wavelength assignment is an important aspect in these networks. A heuristic has been given for wavelength assignment and p -cycle search (PCS) in [47]. The WP and VWP are the two extreme cases, one without any wavelength converter and other fully wavelength convertible nodes, i.e. at every node any wavelength can be converted to any other wavelength. The networks with a few wavelength converters have been discussed in [48], [49]. It has been shown in [48] that with a small increase in spare capacity, number of wavelength converters can be reduced significantly. The wavelength converters are placed at the points where WP p -cycles are accessed. It shall be noted that for on-cycle protection, p -cycle and working path (which is wavelength path) need to use different wavelengths. Hence, during restoration using p -cycle, wavelength conversion is needed at two nodes where switching actions take place.

C. Protection to Multiple Failures

Many strategies have been proposed in literature to provide dual or multi failure network survivability. Survivability to dual failures with static ² p -cycles has been provided with ILP formulation in [50]. Survivability to multiple failures is again provided with static p -cycles in [51], assuming that only one failure occurs on one p -cycle, and in [52], multi failure survivability (MFS) scheme has been used to provide survivability while handling one failure at a time. The results show that networks with higher \bar{d} has higher survival chances to second failure as compared to networks with lower \bar{d} .

²The same set of p -cycles which are used for single failure protection, has also been used for dual protection.

The study in [39] shows that with reconfigurable p -cycles, the dual failure restorability enhances. In this study, after the restoration of the first failure, the p -cycles are reconfigured either a) completely or b) incrementally. In the complete reconfiguration, the p -cycles are reconfigured in the spare capacity dynamically, and a new set of optimum p -cycles is found to protect second failure. While in case of incremental configuration, the old p -cycles are retained and some new p -cycles are deployed to protect second failure. The study in [53] compares the reconfiguration method of p -cycle with two step dynamic repair of p -cycle. Two effects are observed on the p -cycle, first the failed span and second the path provided to protect the working traffic. In the dynamic repair method, to repair the effected p -cycle, either an alternate path (which is alternative to working path being protected) is found to free the capacity used by protection path provided by p -cycle or another alternate path is found to replace the failed span. The dynamic repair method has been found to be more efficient in terms of spare capacity utilization as compared to incremental configuration method. However, complete reconfiguration of p -cycles after the first failure is the most efficient method.

Differentiated services has been provided with p -cycles using ILP formulation in [54]. Here again, the dual failure survivability is provided to the platinum traffic. It has also been shown that within the same resources of single failure survivability, p -cycles can provide dual protection to as much as 30% of all demands in the test cases.

D. Protection to Dynamic Traffic

Initially the p -cycles have been proposed to be formed in the spare capacity, after routing of the working paths. However, p -cycles can also be used to provide restoration in the dynamic traffic environments. The p -cycles are formed in advance and then as per the demands, working paths are routed in such a way that protection is available to the working paths. The issue is how to form the p -cycles in advance and how to allocate protection capacity.

In [25], the set of p -cycles has been found in such a way that protection could be provided to all the spans, either as on-cycle or straddling span. For on-cycle spans half of the capacity is allocated for protection. The set of p -cycles has been found again using ILP model. As the demands arrive, the working paths have been found using some preferred routing scheme. The results show that the p -cycle based approach provides better restoration than SBPP for networks with higher values of \bar{d} for smaller values of \bar{d} , reverse is true.

In another approach [55], for every link of the network one p -cycle is found using either SLA [16] or Grow [27] algorithm to form the set of candidate p -cycles. Initially no p -cycle is selected. As per the traffic demand, links of the working path are found using shortest path algorithm. The path is protected by providing protection to each of its link separately. For protecting each link of the path one or more p -cycles are selected from the set of candidate p -cycles. On the arrival of new demands, the priority is given to links having available protected capacity through previously selected p -cycles, during the routing of working paths. If any link(s) in the path remains unprotected then more p -cycle(s) from the candidate set are selected to protect the link(s).

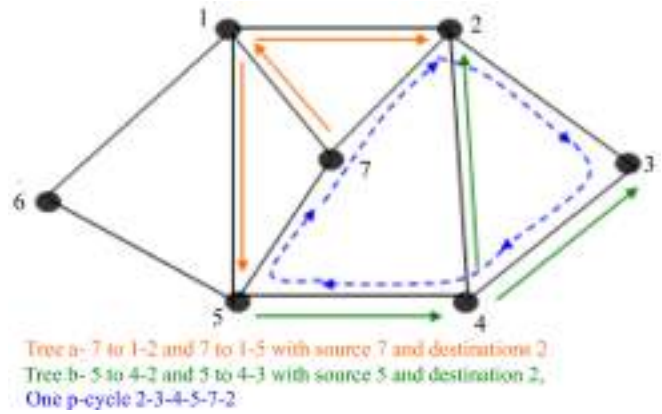


Fig. 6. The source and destinations nodes of tree a and tree b are on-cycle. Tree a and tree b are mutually link disjoint with each other and are also directed link disjoint with the p -cycle. In case of failure of link 1-7, the traffic to destinations node 2 and 5 is protected by the protection path 7-2-3-4-5.

Another approach has been used in [56], [57] for the protection of dynamic traffic. In this approach, a traffic demand can be accepted if it is possible to find a new p -cycle set in the available capacity to protect the total working capacity including the working capacity of the current demand.

The concept of PWCE and APWCE have also been used in [23], [24], [26] for dynamic traffic environments.

E. p -Cycles in Multicasting

All the p -cycle network design methods and types of protections (section II and section IV) discussed are used for unicast traffic. Recently, p -cycles have also been used to protect multicast traffic [58]-[60]. In case of multicasting, the traffic is mostly asymmetric. Therefore, the trees and the p -cycles used for multicasting are usually unidirectional or directed.

A p -cycle can be used to protect all the link disjoint trees used for multicast traffic (Fig. 6). The methods used to form the p -cycle for protection of multicast trees are based on the methods discussed in section II. In [58], SOPT (spare capacity optimization design of p -cycle based tree protection), SOPS (spare capacity optimization design of p -cycle based segment protection), JOPL (joint capacity optimization design of p -cycle based link protection), and NJOPL (non-joint design of p -cycle based link protection) based on ILP methods have been compared. These design methods are based on SCO and JCO (discussed in section II.A.i.a and b). It has been found that the JOPL method performs best in terms of capacity efficiency and SOPL is the fastest in terms of solution time. ERH (efficiency ratio based unity p -cycle heuristic algorithm) which is multicast version of the CIDA (section II.A.ii.a), has also been evaluated and its performance has been found to be close with that of SOPL [58]. The details are out of the scope of this paper, interested readers are referred to [58] for details.

ERH algorithm has been extended to provide combined link and node failure recovery [59]. Like FIPP p -cycles, tree protecting p -cycles protect trees on end-to-end basis. They have been used to provide combined link and node failure recovery. The PWCE scheme has been used to protect dynamic

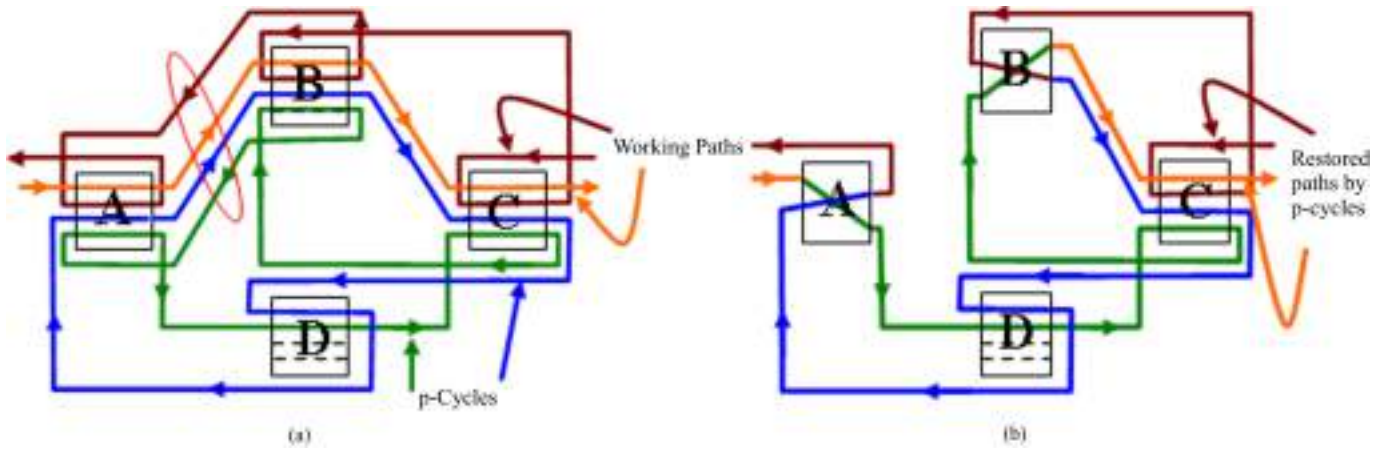


Fig. 7. Implementation of p -cycles (one pair of working paths can be restored by a pair of p -cycles).

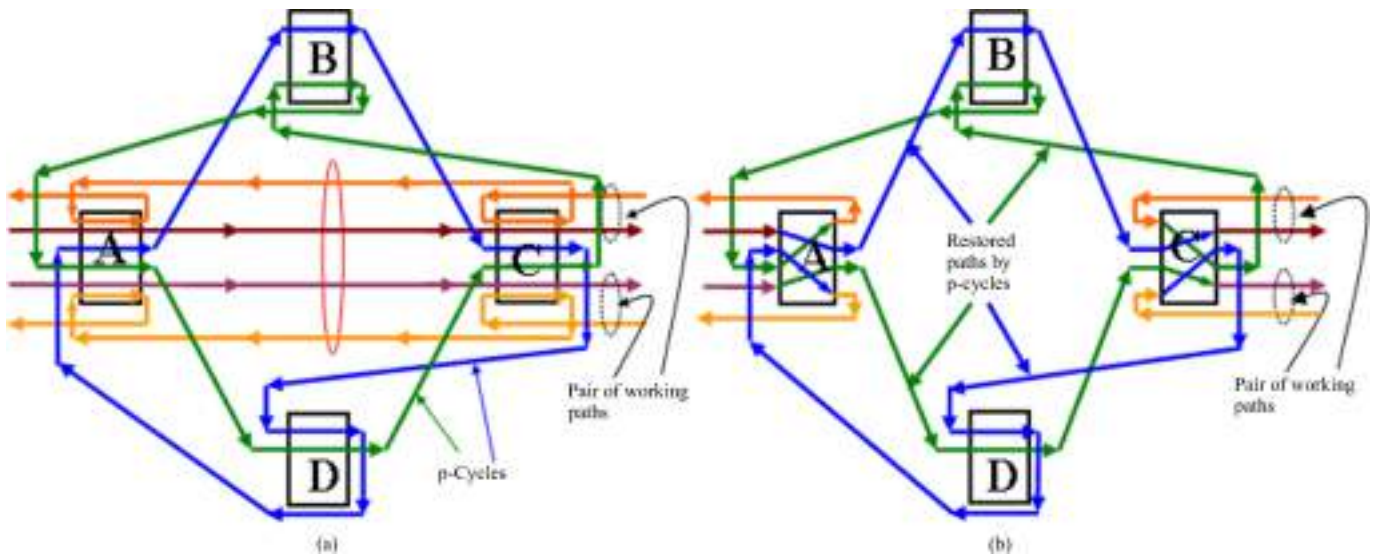


Fig. 8. Implementation of p -cycles for straddling span (pair of two working paths can be restored with one pair of p -cycles for straddling span).

multicast sessions [60]. The trees of the multicast sessions are routed within the configured PWCE. It has been shown that the PWCE scheme has outperformed the other schemes in terms of blocking probability and computation time [60].

In this section, we have seen the versatile nature of p -cycles. They can be used to provide span, node, path, and path segment protections. With p -cycles, protection can be provided at various network layers. Multiple failures can also be protected with p -cycles. They can also be used in dynamic traffic environments. The p -cycles have shown their superiority in multicast traffic protection also.

V. IMPLEMENTATION OF p -CYCLES

Some details of how to implement p -cycles in a network are shown in Fig. 7. A working path through ABC (shown in brown and orange colour) is set up from a source node to a destination node. Since we are assuming the network to be bidirectional and symmetric, hence, a reverse path through CBA also exists. Similarly the p -cycles-ADCBA (shown in

green color) and ABCDA (shown in blue colour) also forms a pair of p -cycles. These are pre-configured with the spare capacity to protect the bidirectional working paths (Fig. 7(a)). Here, we are assuming that the nodal elements are optical or electrical cross-connect devices, or add-drop multiplexer type elements capable of having the same set of connections to establish and use the p -cycles.

To illustrate the use of p -cycles for protection, let us consider the failure of span AB. The working paths will now be restored with the protection path provided by the p -cycles. The working path through ABC and CBA will now be restored through the protection paths ADCB of p -cycle ADCBA and BCDA of p -cycle ABCDA respectively (Fig. 7(b)).

The ring like speed of p -cycle can now be appreciated. In the event of failure of span AB, two switching actions are performed, simultaneously and automatically (because the switching actions are fully pre-planned at each node for each failure); node A, switches the affected working path signal from the working path to the p -cycle independently; at the same time node B switches the traffic from p -cycle to the

remaining portion of the working path. Similarly, path CBA will also be restored.

The straddling span failures can also be restored in the similar manner (Fig. 8). In case of straddling spans, p -cycles provide two paths. Therefore, two pair of working paths can be restored with one pair of p -cycles as shown in Fig. 8(b).

VI. A FEW ENHANCEMENTS

A lot has been said in the literature about the formation of p -cycles. In the distributed method of p -cycle formation, DCPC protocol is the basic method. The p -cycles are searched and pre-configured in the spare capacity using DCPC protocol. This protocol can be implemented in any real network to enable the deployment of p -cycles. However, as mentioned, it has so far been explained only in terms where one p -cycle is obtained per iteration of the algorithm. Hence, at present, when multiple copies of the same p -cycle exist, the algorithm has to run for every copy of the p -cycle. As the p -cycles are formed before the occurrence of failure, the calculation time to find all the cycles, is not so important. It shall be possible to reduce the number of times, the algorithm runs, if multiple copies are found in single run.

With slight modifications in DCPC all the copies of a p -cycle can be found in single run using MDCPC (modified DCPC). The switch implementation can also be simplified in case of transparent optical networks [61], [62] by implementing all the copies of a p -cycle together.

The reliability (strictly the path availability) of p -cycles has not been discussed much in the literature. However, it has been shown [63] that, the all terminal availability (all the nodes of the network are connected for a given period of time), of p -cycle is inferior to four fiber bidirectional line switched rings (BLSR) and unidirectional path switched rings (UPSR). This is not very surprising, as p -cycles provide straddling span protections also in addition to on-cycle protections provided by BLSR. Obviously therefore, we are asking for more protection combinations from the same investment in spare capacity, and so if not designed accordingly, the availability would be lower. The all terminal availability decreases with increase in the number of straddling spans. The values of two terminal availability (the connectivity between a source destination pair), for on-cycle spans, are better for BLSR and UPSR. However, for straddling spans, the performance of p -cycles is superior over both BLSR and UPSR. This is due to the fact that with straddling spans, two protection paths are available. Further study [64] shows that the mean time to failure (MTTF) is low for p -cycles and the expected loss of traffic (ELT) over a year due to failures is high as compared to shared link protection (SLP). The study also shows that considering both- capacity efficiency of the p -cycles and its availability, p -cycles have been found better for metropolitan area networks (MAN) as compared to SLP. However, for long haul networks it is not always true. It has been found in [63], [64], that p -cycles are more suitable to MAN than to long haul networks as far as availability values are concerned. However, the issue can be resolved with the enhanced availability design model presented in [65]. To obtain higher values of availability smaller p -cycles can be used at the expense of capacity

efficiency. Another thing to understand about p -cycles, that is especially pertinent to availability issues, is the unique attribute of p -cycles in providing inherent dual-failure protection for any priority paths that are routed over straddling spans. For instance recent work such as in [65] explains how designated service paths through p -cycle networks can inherently obtain ultra-high availability, by guaranteed survival to dual failures. In practice, to a network operator, the ability to define a differentiated special priority service offering is far more valuable and is a quantum difference in availability compared to small multiplicative factors on theoretical availability over all paths of the network as a whole.

In p -cycles, after restoration, a loop back can form. This is the same effect as has always existed with BLSR rings. It is an inherent aspect of BLSR rings, that was accepted in very widespread deployment of rings. These loop backs do not serve any purpose but whether or not they are undesirable is debatable and depends on the network circumstances. In any case where the overall end-to-end length of a restored path remains technically acceptable, then there can be no real objection to the existence of a loop back, other than on purely aesthetic grounds. Especially as the loop back that may exist is associated or arising from meeting the overriding goal of the fastest possible (ring-like) switching speed. It has been shown in [66] that even with loop back elimination there is very small (about 1%) or no saving in the initial spare capacity in most of the test cases.

On the other hand, conceivably in transparent optical networks, where the greatest capacity efficiency is still desired, the overall path length in the restored state may by implication exceed some transmission length limit. Thus, there may be interest in adapting p -cycles for use wherein after the initial switching, any loop backs, or loop backs exceeding a desired limit, are identified and removed from the respective end-to-end paths (with obvious implications for the overall speed of restoration). Fig. 9 illustrates the formation of loop back, removal of loop back and reduction in the length of the restored path. The loop backs can be removed thereby reducing the restored path length and hence signal degradation as well as signal delay. The loop back removal also releases some resources which can be used for reconfiguration of network protection against second failure. Also, due to reduction in the restored path length, the probability of occurrence of second failure in the restored path will reduce. Thus with same spare capacity, higher reliability can be obtained [62], [67].

An algorithm for removal of loop backs from the restored paths is given in [68], [69]; to retain the speed of p -cycles, second phase reconfiguration has been used for removal of loop backs. It has been found that reduction in the restored path length also depends upon the allocation of p -cycles to the failed paths (Fig. 10). It has been shown in [61], [62] that with optimum allocation of p -cycles to the failed paths, the length of the restored paths can be reduced significantly. With removal of loop backs the dual failure restorability has also been improved [61]. The reliability of the restored paths also increases after removal of loop backs [67].

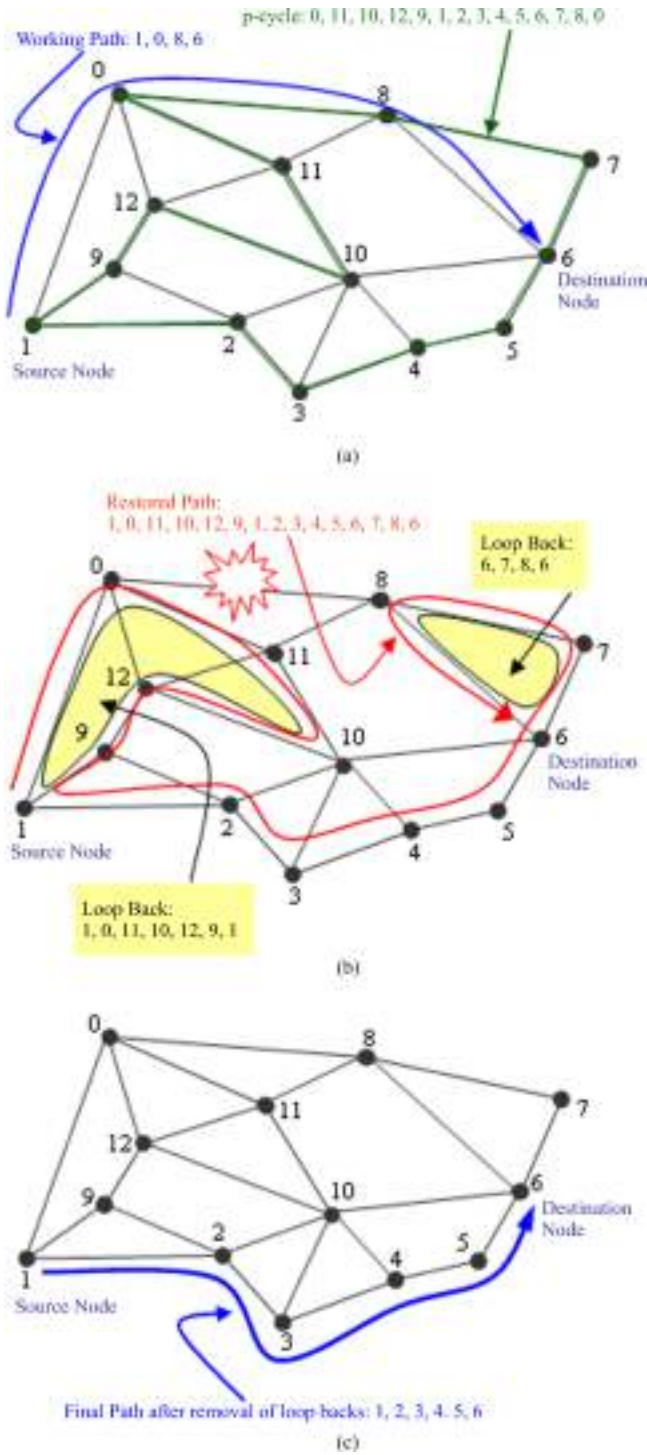


Fig. 9. One typical case of loop back. (a) There is a working path 1,0,8,6 between source-1 and destination-6. Links 1-0 and 8-6 of the working path can be protected as straddling links and the link 0-8 can be protected as on-cycle link of the given Hamiltonian p -cycle 0, 11, 10, 12, 9, 1, 2, 3, 4, 5, 6, 7, 8, 0. (b) The restored path after failure of on-cycle link 0-8. It contains two loop backs 6,7,8,6 and 1, 0, 11, 10, 12, 9, 1 and its length is 14 hops. (c) The final path after removal of loop backs. Its length is 5 hops. The reduction in the length of the restored path is 9 hops in this particular example.

VII. CONCLUSION

The versatility of p -cycles is beyond any doubt. They are attracting a lot of attention of the research community [70]. They can provide the advantage of fast restoration of rings

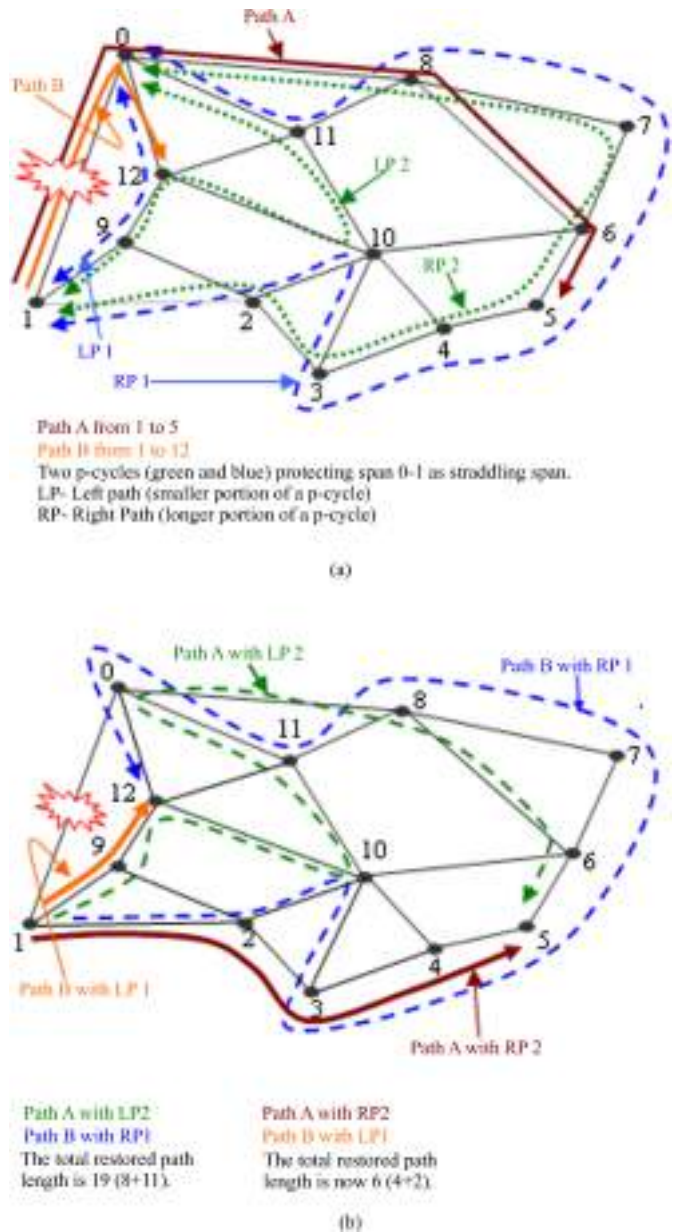


Fig. 10. Removal of loop back with illustration of the fact that restored path lengths depends upon the allocation of p -cycle to the paths. There will be 12 such combinations in the above example and one of them is to be selected. This selection can be done with optimum allocation of p -cycle based on Hungarian algorithm presented in [61].

along with the capacity efficiency of mesh networks. The reason behind the ring like speed is pre-connection of spare capacity of the network to form the p -cycles. The theoretical limit of capacity efficiency of span restorable mesh networks, and almost that of SBPP, can be achieved with p -cycles because protection to all the on-cycle and straddling spans is provided by a p -cycle on shared basis.

Various methods are available to design the networks with p -cycle protection. The p -cycles can be formed either by distributed method in any real network in real time or they can be computed centrally and implemented in a network. Many tradeoffs are available for designing the p -cycles e.g. spare capacity vs. length of the restored path, computation time vs. heuristics etc.. They can be implemented at various network

layers with varying granularity. Almost all types of protection like span, path segment, path and node can be provided with p -cycles. p -Cycles can also be used to protect multicast traffic trees.

With a slightly modified DCPC protocol, all the copies of a p -cycle can be found in single run of the algorithm and all the copies of the p -cycles can be implemented together with coarser granularity in transparent optical networks. With optimum allocation of p -cycles to the working paths through a failed span and removal of loop back during second phase reconfiguration, the restored path lengths can be reduced significantly without compromising on the capacity efficiency of the basic model of p -cycle formation and the ring like speed of the p -cycles. The reliability of the restored paths will be more after removal of loop backs than the reliability of the restored paths without removal of loop backs.

REFERENCES

- [1] R. Asthana and Y.N. Singh, "Protection and restoration in optical networks," *IETE J. Research*, vol. 50, no. 5, pp. 319-329, Sept.-Oct. 2004.
- [2] R. Asthana and Y.N. Singh, "Survivability in all optical networks," in *Proc. Int. Conf. on Optical Communication Networks*, Bangalore, India, 20-22 Oct., 2003, Paper no. 2038.
- [3] W.D. Grover, *Mesh-based Survivable Networks: Options for Optical, MPLS, SONET and ATM Networking*, Prentice-Hall, Aug. 2003.
- [4] W.D. Grover, and D. Stamatelakis, "Cycle-oriented distributed pre-configuration: ring-like speed with mesh-like capacity for self-planning network restoration," in *Proc. IEEE International Conference on Communications*, Atlanta, Georgia, USA, June 7-11, 1998, pp. 537-543.
- [5] W.D. Grover, "The protected working capacity envelope concept: An alternate paradigm for automated service provisioning," *IEEE Commun. Mag.*, vol. 42, no. 1, pp. 62-69, January 2004.
- [6] A. Sack, and W.D. Grover, "Hamiltonian p -cycles for fiber-level protection in homogeneous and semi-homogeneous optical networks," *IEEE Network*, vol. 18, no. 2, pp. 49-56, Mar-Apr 2004.
- [7] W.D. Grover, and D. Stamatelakis, "Bridging the ring-mesh dichotomy with p -cycles," in *Proc. of 2nd Int. Workshop on the Design of Reliable Communication Networks*, Munich, Germany, October 16-19, 2000, pp. 92-104.
- [8] G. Shen, and W.D. Grover, "Extending the p -cycle concept to path segment protection for span and node failure recovery," *IEEE J. Sel. Areas Commun.*, vol. 21, pp. 1306-1319, Oct. 2003.
- [9] C. Liu, and L. Ruan, "Dynamic provisioning of survivable services using path-segment protecting p -cycles in WDM networks," in *Proc. of 15th Int. Conf. on Computer Communications and Networks*, Arlington, Virginia, USA, Oct. 9-11, 2006, pp. 275-280.
- [10] A. Kodian, and W.D. Grover, "Failure-independent path-protecting p -cycles: efficient and simple fully preconnected optimal-path protection," *IEEE J. Lightwave Technol.*, vol. 23, no. 10, pp. 3241-3259, Oct. 2005.
- [11] A. Kodian, W.D. Grover, and J. Doucette, "A disjoint route-sets approach to design of path-protecting p -cycle networks," in *Proc. of 5th Int. Workshop on the Design of Reliable Communication Networks*, Ischia Island, Italy, Oct. 16 - 19, 2005, pp. 231-238.
- [12] A. Kodian, A. Sack, and W.D. Grover, " p -Cycle network design with hop limits and circumference limits," in *Proc. First Int. Conf. on Broadband Networks*, San Jose, CA, USA, Oct. 25-29, 2004, pp. 244-253.
- [13] W.D. Zhong, and Z.R. Zhang, "Design of survivable WDM networks with shared- p -cycles," in *Proc. Optical Fiber Communication Conference*, Anaheim, California, USA, Feb. 24-26, 2004, vol. 1.
- [14] C. Liu, and L. Ruan, " p -Cycle design in survivable WDM networks with shared risk link groups (SRLGs)," in *Proc. of 5th Int. Workshop on the Design of Reliable Communication Networks*, Ischia Island, Italy, Oct. 16-19, 2005, pages: 6 pp.
- [15] D.S. Mukherjee, C. Assi, and A. Agarwal, "An alternative approach for enhanced availability analysis and design methods in p -cycle-based networks," *IEEE J. Sel. Areas Commun.*, vol. 24, no. 12, pp. 23-34, Dec. 2006.
- [16] H. Zhang and O. Yang, "Finding protection cycles in DWDM networks," in *Proc. IEEE Int. Conf. on Communications*, New York City, April 28-May 2, 2002, vol.5, pp. 2756-2760.
- [17] C. Liu, and L. Ruan, "Finding good candidate cycles for efficient p -cycle network design," in *Proc. of 13th Int. Conf. On Computer Communications and Networks*, Chicago, Illinois, Oct. 11-13, 2004, pp. 321-326.
- [18] W. Mardini, O. Yang, and Y. Zhai, "Using MCG to find PP-cycles in planar graphs," *Technical Digest. 1st Combined Optical Fiber Communication Conference and the National Fiber Optics Engineers Conference*, Anaheim, CA, March 6-11, 2005, vol. 3, pages: 3 pp.
- [19] K. Lo, D. Habibi, A. Rasan, Q. V. Phung, H. N. Nguyen, and B. Kang, "A hybrid p -cycle search algorithm for protection in WDM mesh networks," in *Proc. of 14th IEEE Int. Conf. on Networks*, Singapore, Sept. 13-15, 2006, vol. 2, pp. 1-6.
- [20] W.D. Grover, and J. Doucette, "Advances in optical network design with p -cycles: Joint optimization and pre-selection of candidate p -cycles," in *Proc. IEEE/Leos Summer Topicals*, Quebec, Canada, July, 15-17, 2002, pp. 49-50.
- [21] H.N. Nguyen, D. Habibi, Q.V. Phung, L. Stefan, K. Lo, B. Kang, "Joint optimization in capacity design of networks with p -cycle using the fundamental cycle set," *IEEE Global Telecommunications Conference*, San Francisco, California, USA, Nov. 27-Dec. 1, 2006, pp. 1-5.
- [22] C.G. Gruber, "Resilient networks with non-simple p -cycles," in *Proc. 10th Int. Conf. Telecommunications*, Tahiti, Papeete, French Polynesia, Feb. 23-March 1, 2003, vol. 2, pp. 1027-1032.
- [23] G. Shen, *Design and performance of protected working capacity envelopes based on p -cycles: an alternative framework for dynamic survivable network service provisioning*. PhD Thesis, University of Alberta, Edmonton, 2006.
- [24] Z. Zhang, W.D. Zhong, and S.K. Bose, "Dynamically survivable WDM network design with p -cycle based PWCE," *IEEE Commun. Lett.*, vol. 9, pp. 756-758, Aug. 2005.
- [25] W. He, J. Fang, and A.K. Somani, "A new p -cycle based survivable design for dynamic traffic in WDM networks," in *Proc. IEEE Global Telecommunications Conference*, St. Louis, Missouri, Nov. 28-Dec. 2, 2005, pages: 5 pp.
- [26] G. Shen, W.D. Grover, "Automatic lightpath service provisioning with an adaptive protected working capacity envelope based on p -cycles," in *Proc. of 5th Int. Workshop on the Design of Reliable Communication Networks*, Ischia Island, Italy, Oct. 16-19, 2005, pages: 9 pp.
- [27] J. Doucette, D. He, W.D. Grover, and O. Yang, "Algorithmic approaches for efficient enumeration of candidate p -cycles and capacitated p -cycle network design," in *Proc. of 4th Int. Workshop on the Design of Reliable Communication Networks*, Banff, Canada, Oct. 2003, pp. 212-220.
- [28] Z. Zhang, W-D. Zhong, and B. Mukherjee, "A Heuristic method for design of survivable WDM networks with p -cycles," *IEEE Commun. Lett.*, vol. 8, No. 7, pp.467-469, July 2004.
- [29] H. Hwang, S.Y. Ahn, Y.H. Yoo, and S.K. Chong, "Multiple shared backup cycles for survivable optical mesh networks," in *Proc. of 10th Int. Conf. on Computer Communications and Networks*, Scottsdale, Arizona, Oct. 15-17, 2001, pp. 284-289.
- [30] K. Lo, D. Habibi, Q.V. Phung, A. Rasan, and H.N. Nguyen, "Efficient p -cycles design by heuristic p -cycle selection and refinement for survivable WDM mesh network," in *Proc. IEEE Global Telecommunications Conference*, San Francisco, CA, USA, Nov. 27-Dec. 1, 2006, pp. 1-5.
- [31] R. Inkret, M. Lackovic, and B. Mikac, "Applying p -cycles to multi-service photonic network," in *Proc. of 7th Int. Conf. on Transparent Optical Networks*, Barcelona, Spain, July 3-7, 2005, vol. 1, pp. 71-76.
- [32] W.D. Grover, "Self organizing broadband transport network," in *Proc. IEEE*, vol. 85, no. 10, pp.1582-1611, Oct.1997.
- [33] O. Wittner, B.E. Helvik, and V. Nicola, "Internet failure protection using Hamiltonian p -cycles found by ant-like agents," in *Proc. of 5th Int. Workshop on the Design of Reliable Communication Networks*, Ischia Island, Italy, Oct. 16-19, 2005, pp. 437-444.
- [34] R.Y. Rubinstein, "The cross-entropy method for combinatorial and continuous optimization," *Methodology and Computing in Applied Probability*, vol. 1 no. 2, pp.127-190, 1999.
- [35] O. Wittner, *Emergent behavior based implements for distributed network management*. PhD thesis, Norwegian University of Science and Technology, NTNU, Department of Telematics, Nov. 2003.
- [36] D. Stamatelakis, and W.D. Grover, "Theoretical underpinnings for the efficiency of restorable networks using preconfigured cycles (p -cycles)," in *IEEE Trans. Commun.*, vol. 48, no.8, pp. 1262-1265, Aug. 2000.
- [37] D.A. Schupke, "Analysis of p -cycle capacity in WDM networks," *Photonic Network Commun.*, vol. 12, no. 1, pp. 41-51, July 2006.
- [38] S. Shah-Heydari, W. Mardini, and O. Yang, "Theoretical analysis of restorability of Hamiltonian protection cycles in random mesh networks," in *Proc. of 9th IEEE Symposium on Computers and Communications*, Alexandria, Egypt, June 28-1 July, 2004, vol. 2, pp. 921-926.

- [39] D.A. Schupke, W.D. Grover, and M. Clouqueur, "Strategies for enhanced dual failure restorability with static or reconfigurable p -cycle networks" in *Proc. IEEE Int. Conf. on Communications*, Paris, France, Jun. 20-24, 2004, pp. 1628-1633.
- [40] G. Ellinas, A.G. Hailemariam, and T.E. Stern, "Protection Cycles in Mesh WDM Networks," *IEEE J. Sel. Areas Commun.*, vol. 18, pp. 1924-1937, Oct. 2000.
- [41] D. Stamatlakis, and W.D. Grover, "IP layer restoration and network planning based on virtual protection cycles," *IEEE J. Sel. Areas Commun.*, vol. 18, pp. 1938-1949, Oct 2000.
- [42] Z. Taifei, L. Lemin, and Y. Hongfang, "Finding good candidate node-encircling pre-configuration cycles in survivable WDM mesh networks," in *Proc. Int. Conf. on Communications, Circuits and Systems*, Guilin, China, June 25-28, 2006, vol. 3, pp. 1877-1881.
- [43] J. Doucette, A.P. Giese, and W.D. Grover, "Combined node and span protection strategies with node-encircling p -cycles," in *Proc. of 5th Int. Workshop on the Design of Reliable Communication Networks*, Ischia Island, Italy, Oct. 16-19, 2005, pages: 9 pp.
- [44] J. Kang, and M.J. Reed, "Bandwidth protection in MPLS networks using p -cycle structure," in *Proc. of 4th Int. Workshop on the Design of Reliable Communication Networks*, Banff, Canada, Oct. 19-22, 2003, pp. 356-362.
- [45] D.A. Schupke, "Fast and efficient WDM network protection using p -cycles," in *Proc. IEEE/Leos Summer Topicals*, Quebec, Canada, July, 15-17, 2002, pp. WA1-47-WA1-48.
- [46] D.A. Schupke, C.G. Gruber, and A. Autenrieth, "Optimal configuration of p -cycles in WDM networks," in *Proc. IEEE Int. Conf. on Communications*, New York City, April 28-May 2, 2002, pp.2761-2765.
- [47] C. Mauz, " p -Cycle protection in wavelength routed networks," in *Proc. the 7th Working Conference on Optical Network Design and Modeling*, Budapest, Hungary, Feb. 3-5, 2003.
- [48] D.A. Schupke, M.C. Scheffel, and W.D. Grover, "An efficient strategy for wavelength conversion in WDM p -cycle networks," in *Proc. 4th Int. Workshop on the Design of Reliable Communication Networks*, Banff, Canada, Oct. 19-22, 2003, pp. 221-227.
- [49] T. Li, and B. Wang, "Optimal configuration of p -cycles in WDM optical networks with sparse wavelength conversion," in *Proc. IEEE Global Telecommunications Conference*, Dallas, Texas, USA, Nov. 29-Dec. 3, 2004, vol. 3, pp. 2024-2028.
- [50] D. A. Schupke, "The tradeoff between the number of deployed p -cycles and the survivability to dual fiber duct failures," in *Proc. IEEE Int. Conf. on Communications*, Anchorage, Alaska, USA, May 11-15, 2003, vol. 2, pp. 1428-1432.
- [51] D. A. Schupke, "Multiple failure survivability in WDM networks with p -cycles," in *Proc. Int. Symposium on ISCAS '03*, vol. 3, pp. III-866-III-869, 25-28 May 2003.
- [52] H. Wang, and H.T. Mouftah, " P -cycles in multi-failure network survivability," in *Proc. of 7th Int. Conf. on Transparent Optical Networks*, Barcelona, Spain, July 3-7, 2005, pp.381-384.
- [53] D.S. Mukherjee, C. Assi, and A. Agarwal, "Alternate strategies for dual failure restoration using p -cycles," *IEEE Int. Conf. on Communications*, Istanbul, Turkey, June 11-15, 2006, vol. 6, pp. 2477-2482.
- [54] A. Kodian, and W.D. Grover, "Multiple-quality of protection classes including dual-failure survivable services in p -cycle networks," in *Proc. of 2nd Int. Conf. on Broadband Networks*, Boston, Massachusetts, USA, Oct. 3-7, 2005, vol. 1, pp. 231-240.
- [55] L. Ruan, and F. Tang, "Dynamic establishment of restorable connections using p -cycle protection in WDM networks," in *Proc. 2nd Int. Conf. on Broadband Networks*, Boston, Massachusetts, USA, Oct. 3-7, 2005, vol. 1, pp. 137-144.
- [56] D.A. Schupke, M. Jager, and R. Hulsermann, "Comparison of resilience mechanisms for dynamic services in intelligent optical networks," in *Proc. 4th Int. Workshop on the Design of Reliable Communication Networks*, Banff, Canada, Oct. 19-22, 2003, pp. 106-113.
- [57] D.A. Schupke, "Comparison of p -cycle configuration methods for dynamic networks," *IFIP Optical Networks and Technologies Conference (OpNeTec)*, Pisa, Italy, October 18-22, 2004.
- [58] F. Zhang, W. D. Zhong, and Y. H. Jin, "Optimizations of p -cycle based protection of optical multicast sessions," *IEEE J. Lightwave Technol.*, vol. 26, no. 19, pp. 3298-3306, Oct. 2008.
- [59] F. Zhang, and W. D. Zhong, " p -Cycle based tree protection of optical multicast traffic for combined link and node failure recovery in WDM mesh networks," *IEEE Commun. Lett.*, vol. 13, no. 1, pp. 40-42, Jan 2009.
- [60] F. Zhang, and W. D. Zhong, "Applying p -cycles in dynamic provisioning of survivable multicast sessions in optical WDM networks," in *Proc. OFC 2007*, Anaheim, California, USA, March 25-29, 2007.
- [61] R. Asthana, and Y.N. Singh, "Distributed protocol for removal of loop backs and optimum allocation of p -cycles to minimize the restored path lengths," *IEEE J. Lightwave Technol.*, vol. 26, no. 5, pp. 616-627, March 2008.
- [62] R. Asthana, *Study of p -cycle based protection in optical networks and removal of its shortcomings*. PhD Thesis, Indian Institute of Technology, Kanpur, Kanpur, April 2008.
- [63] P. Cholda, and A. Jajszczyk, "Reliability assessment of rings and p -cycles in DWDM networks," *Next Generation Internet Networks 2005*, pp. 364-371, 18-20 April 2005.
- [64] P. Cholda, and A. Jajszczyk, "Reliability assessment of p -cycles," *IEEE Global Telecommunications Conference*, St. Louis, Missouri, Nov. 28-Dec. 2, 2005, vol. 1, pp. 5 pages.
- [65] M. Clouqueur, and W.D. Grover, "Availability analysis and enhanced availability design in p -cycle-based networks," *Photonic Network Communications*, Springer Science, 10:1, pp. 55-71, July 2005.
- [66] W.D. Grover, and M. Scheffel, "Resolving a question about span restoration: Do loop backs involve a capacity penalty?," in *Proc. of 6th Int. Workshop on the Design of Reliable Communication Networks*, La Rochelle, France, October 7-10, 2007.
- [67] R. Asthana, and Y.N. Singh, "The effect of removal of loop back on the reliability of the restored paths provided by p -cycles," *IEEE Int. Conf. TENCON 2008*, Hyderabad, India, 18-21 Nov., 2008, Paper no. 1569125570.
- [68] R. Asthana, and Y.N. Singh, "Removal of loop back in p -cycle protection: Second phase reconfiguration," in *Proc. IEEE Int. Conf. on Communication Systems*, Singapore, Oct. 30-Nov. 1, 2006, pp. 1-5.
- [69] R. Asthana, and Y.N. Singh, "Second phase reconfiguration of restored path for removal of loop back in p -cycle protection," *IEEE Commun. Lett.*, vol. 11, no. 2, pp. 201-203, Feb. 2007.
- [70] M.S. Kiaei, C. Assi, and B. Jaumard, "A Survey on the p -Cycle Protection Method," *IEEE Commun. Surveys Tutorials*, vol. 11, no. 3, pp. 53-70, July 2009.



Rachna Asthana Rachna Asthana was born in Lucknow, India. She received M. Tech degree in Electronics and Communication Engineering from Indian Institute of Technology, Roorkee (then UOR) Roorkee in year 1990 and PhD from Department of Electrical Engineering, Indian Institute of Technology, Kanpur in 2008.

She joined HBTI (Harcourt Butler Technological Institute), Kanpur, India, state Engineering College in 1991 as Lecturer in Electronics Engineering Department. Currently she is working as Assistant

Professor. Her current research interests are in the field of all optical networks, survivability and network management.

Ms Asthana is a corporate member of Institution of Electronics and Telecommunication Engineers (IETE), India and member of The Institution of Electrical and Electronics Engineers, Inc., (IEEE) USA.



Y.N. Singh Yatindra Nath Singh was born in Delhi in 1969. He obtained B.Tech. in Electrical Engineering with honours from Regional Engineering College, Hamirpur, Himachal Pradesh in July 1991, M.Tech. in Optoelectronics and Optical Communications from Indian Institute of Technology, Delhi in December 1992 and Ph.D. from department of Electrical Engineering, Indian Institute of Technology, Delhi in 1997.

He was with the department of Electronics and Computer Engineering, IIT Roorkee, India as faculty from Feb'97 to July'97. He is currently working as faculty in the department of Electrical Engineering, Indian Institute of Technology, Kanpur. His academic interests include Optical Networks, Photonic packet Switching, Optical Communications, Telecom Networks, Network Management, E-learning systems, Open source software development. He is involved in development of Open Source E-learning platform tools codenamed Brihaspati (<http://brihaspati.sourceforge.net/>).

Dr. Singh is a fellow of Institution of Electronics and Telecommunication Engineers (IETE), India and senior member of The Institution of Electrical and Electronics Engineers, Inc., (IEEE) USA. He has been given AICTE young teacher award in 2002.



Wayne D. Grover Wayne D. Grover received the B.Eng. degree from Carleton University, Canada, the M.Sc. degree from the University of Essex, U.K., and the Ph.D. degree from the University of Alberta, Canada, all in electrical engineering. He had 10 years of experience as scientific staff and manager at BNR (Nortel Networks) working on fiber optics, switching systems, digital radio, and other areas before joining TRILabs as its founding Technical VP in 1986. He now functions as Chief Scientist Network Systems, TRILabs, and as Professor, Electrical and

Computer Engineering, at the University of Alberta.

He has 32 patented inventions, and amid his nearly 200 peer reviewed publications are highly cited papers in clock distribution, error-correction coding for fiber optics, digital subscriber loops, and transport network design and survivability, including origination of the p-cycles concept and the protected working capacity envelope (PWCE) concept for dynamic survivable service provisioning.

He is a Fellow of the Royal Society of Canada, a Fellow of the Engineering Institute of Canada and a recipient of the IEEE Baker Prize Paper Award and IEEE Fellow. Among other awards are the APEGGA Ingenuity Fund Research Award, IEEE Canada Outstanding Engineer Award, the Alberta Science and Technology Leadership Award, and an NSERC Steacie Fellowship. He has received TRILabs Technology Commercialization Awards for the licensing of restoration and network design-related technologies. He is also author of Mesh-based Survivable Networks, Prentice-Hall PTR, 2004 and a co-author of Next Generation Transport Networks, Springer Science, 2005. Current research interests focus on network design optimization, new survivability architectures including p-cycles, and new approaches to operation and ongoing re-optimization of dynamic transport networks.



Comparative study of polystyrene/chemically modified wheat straw composite for green packaging application

Shobhit Dixit¹ · Vijay Laxmi Yadav¹

Received: 20 December 2018 / Revised: 25 April 2019 / Accepted: 2 May 2019
© Springer-Verlag GmbH Germany, part of Springer Nature 2019

Abstract

The recalcitrant nature of native wheat straw (WS) biomass results from cellulose, lignin, hemicellulose and some amount of protein embedded together in a composite structure causing poor adhesion to a polymer matrix composite. Adequate pre-treatment can curtail the recalcitrance structure of WS and enhance the susceptible cellulose area to synthesize a green composite. This paper examined the effect of various chemical pre-treatment procedures in improving surface morphology of wheat straw. Moreover, polystyrene (PS), PS (60 wt%)/native WS (40 wt%), PS (60 wt%)/NaOH-treated WS (40 wt%), PS (60 wt%)/HCl-treated WS (40 wt%), and PS (60 wt%)/H₂SO₄-treated WS (40 wt%) composite films were prepared using solution casting method. The changes in crystalline structure, hydrophobicity, water vapor migration rate, and thermal and mechanical stabilities of synthesized bio-composites were examined. From the results it can be concluded that the alkali-treated WS is highly compatible with the PS and can be used to synthesize a biodegradable composite film for various industrial green packaging applications.

Keywords Wheat straw · Chemical pre-treatment · Polystyrene · Green composite

Introduction

At present juncture, massive use of polymeric products is a potential threat to a sustainable environment. Worldwide production and consumption of polymers have increased globally from 1.5 million ton in 1950 to more than 311 million ton in the present decade [1–3]. However, this fact is correlated with a significant amount of waste disposal problems; most of them are non-biodegradable [4–7]. In order to reduce the contribution of polymeric non-biodegradable products on a global level, we need to promote the use of green materials as a substitute for polymer [8–14]. On

✉ Vijay Laxmi Yadav
vlyadaviitbhu2014@gmail.com

¹ Department of Chemical Engineering and Technology, IIT BHU, Varanasi, Uttar Pradesh 221005, India

the other hand, India faces a huge production of crop residue. Nearly 500–550 tons agro-waste is generated every year [15]. Despite using agro-waste as a substitute for polymer, many farmers burn agro-waste such as straws, leaves, wood, and grasses, which releases polycyclic aromatic hydrocarbons, carbon dioxide, carbon monoxide, and particulate matter (PM) into the environment, which is not an environmentally acceptable form of agro-waste management. So understanding the proper utilization of lignocellulosic waste is very important. It will boost the agriculture sector's economy and provide farmers some extra income from agro-waste. Abundantly available agro-waste is composed of holocellulose (cellulose, hemicellulose), lignin, and other components (proteins, lipids, and inorganic materials, for example) embedded together in a complex structure having biodegradable and renewable characteristics and thus can be used for reinforcement of a polymer matrix [16, 17]. Due to its recalcitrance structure, the agro-waste plant cell is rigid in nature which is not suitable for polymer adhesion. So pre-treatment is a stimulating step to overcome the recalcitrance property of biomass [18, 19].

In modern era pre-treatment is one of the most promising techniques for changing the physicochemical characteristics of an agro-waste. Pre-treatment involves enhancing numerous properties of agro-waste such as increased energy density, hydrophobicity, and improved grindability, and it also creates porosity [20]. A review of the available literature shows that the pre-treatment can be classified into chemical pre-treatment, physical treatment, and biological treatment. Many researchers have shown that chemical pre-treatment including acid treatment and alkaline treatment could be used for making biomass more accessible for cellulose region. The main virtues of chemical treatment are to significantly remove hemicellulose and lignin from agro-waste, thus enhancing digestible cellulose area by increasing void openings at the surface of biomass [21, 22]. Pre-treatment of agro-waste with acid has two main steps as follows: Firstly, it removes the ester bonds between the hemicellulose and lignin. Subsequently, hydrolysis of hemicellulose and partially decomposition of lignin takes place [23]. But in alkali pre-treatment, strong delignification process occurs after breaking the ester bonds between cellulose, hemicellulose, and lignin [24]. Both treatments could be correlated to the increase in cellulose digestibility region for the synthesis of the green composite [25].

Polystyrene is a styrene-based polymer which is used for insulation material, housewares, furniture, electrical goods, and a wide variety of packaging applications. It has remarkable water-resistant property. It can be easily fabricated, and it is hard and colorless. On the other hand, abundantly available natural straw especially straw bales may be considered as novel cellulose-based material. This cereal straw, including wheat, rice, and barley, offers a sustainable and renewable resource for different kinds of reinforcement applications such as building products and packaging film.

da Silva et al. [26] prepared different volume fractions of curaua/polyester composites and observed the significant changes in mechanical property of resultant composites. Borges et al. [27] synthesized hollow glass microspheres/piassava fiber-reinforced homo- and *co*-polypropylene composites and examined the surface and mechanical properties of synthesized composites. Pigatto et al. [28] studied the properties of polypropylene/ethylene propylene diene monomer/alkali-treated sisal

fibers composite film. The reinforcement incorporation with alkali-treated sisal fiber in the polymer matrix exhibited higher mechanical stability of the resultant composite film. In this paper, alkali-treated sisal and curaua fibers were blended with polyester resin and the short beam strength of hybrid composites was examined [29]. Almeida Jr. et al. [30] observed the effect of curaua/glass fiber ratio on mechanical properties of synthesized polyester hybrid composites. Zegaoui et al. [31] prepared the cyanate ester/benzoxazine/alkali-treated hemp fiber and evaluated the mechanical behavior, surface morphology, and water uptake properties of the synthesized composites. Zehetmeyer et al. [32] prepared polypropylene/montmorillonite composites for food packaging application by melt blending method using twin-screw extruder. Hadj-Hamou et al. [33] synthesized the polycaprolactam/nanoclay packaging film and examined the thermal decomposition kinetics of synthesized film. Gutiérrez et al. [34] reviewed the natural fibers used in starch-based matrix film for food packaging application. Zehetmeyer et al. [35] synthesized film of poly(butylene adipate-*co*-terephthalate) incorporated with peptide nisin using electrospinning technique and examined the mechanical stability and crystalline changes in synthesized composite film for food packaging industry. Berthet et al. [36] synthesized a polyhydroxy-*co*-3-butyrates-*co*-3-valerate (PHBV)-based wheat straw green composites and improved its water vapor transfer rate for sustainable food packaging. Asgher et al. [37] synthesized a PVA-based de-lignified and bacterially treated wheat straw green composite for enzymatic treatment using glycerol as a plasticizer. Stelte et al. [38] prepared wheat straw-based porous polymer sustainable composites for fabrication of green fiber board. Till today no literature work has been carried out on the comparison of various chemical pre-treatments on wheat straw used for reinforcement of a polymer composite.

Current trends stride toward the use of green composites for reinforcement applications. The authors of this paper investigated the effect of chemical pre-treatments at the surface of wheat straw. In this paper, the biomass, i.e., wheat straw, has been pre-treated with dilute hydrochloric acid (HCl), dilute sulfuric acid (H₂SO₄), and dilute sodium hydroxide (NaOH). Subsequently, all treated wheat straws are blended with polystyrene (PS) for preparing composite films that can be used for industrial applications such as automotive industry, packaging goods, and furniture applications.

Materials and methods

Materials

Wheat straw lignocellulosic biomass was collected from a local farmer near Banaras Hindu University, Varanasi, Uttar Pradesh, India. The biomass was washed with distilled water and dried in an oven overnight at 70 °C. The dried wheat straw was ground and sieved. The average particle size of wheat straw is in between 74 and 44 μm. All pre-treatment chemicals (hydrochloric acid, sulfuric acid, and sodium hydroxide) and solvent (toluene) were procured from Fisher Scientific, USA.

Polymer (polystyrene) and plasticizer (polybutene) were procured from Sigma-Aldrich, USA.

Pre-treatment

Pre-treatment is a method which is generally applied to a sample in order to make it more effective for composite synthesis.

Chemical pre-treatment

In this method different types of acid and alkali are used for making our feed more effective for composite preparation.

Acid treatment

In this treatment, the ground wheat straw was treated with HCl (1.4 V/V%) at a temperature of 120 °C for 90 min. The solid loading of biomass was 5 g in 100 ml of HCl. The free liquid was drained out through the filtration process using a vacuum pump, and the resultant residue was washed with distilled water until it attains pH 7.0. Then biomass was dried out in an oven, kept in an air-sealed container, and used for reinforcement of a polymer matrix.

The sieved wheat straw was also treated with H₂SO₄ (0.8 V/V%) at a temperature of 120 °C for 90 min, and the similar procedure was adopted to obtain the biomass for further experiments [39].

Alkali treatment

Alkali treatment of native and milled wheat straw was carried out at a temperature of 60 °C for 1 h. The optimum concentration of NaOH was 4.5 W/V%. The solid loading of biomass was 5 g in 100 ml of NaOH. The free liquid was pulled out through a vacuum pump filtration process, and the residue was washed with distilled water until it attains pH 7.0. Then biomass was dried out in an oven, preserved in an air-sealed container, and was used for the formation of polymer composite [40].

Synthesis of bio-composites

A solution casting method was used to synthesize bio-composites in which firstly polystyrene was dispersed in toluene at 70 °C. Subsequently, a 40 wt% of native and pre-treated biomass was added. Polybutene plasticizer (0.5 ml) was also added in the composite for enhancing flexibility, and the mixture was maintained at 90 °C for 4 h. The mixture was cast in a petri dish and kept at room temperature for 24 h.

Analytical methods

XRD analysis

The XRD analysis gives the idea of crystallinity of a material. Hence, the crystallinity of the native, pre-treated wheat straw, pure polystyrene film (PS), polystyrene composite film reinforced by native wheat straw (PS/native WS), polystyrene composite film reinforced by NaOH-treated wheat straw (PS/NaOH-treated WS), polystyrene composite film reinforced by HCl-treated wheat straw (PS/HCl-treated WS), polystyrene composite film reinforced by H₂SO₄-treated wheat straw (PS/H₂SO₄-treated WS) was investigated using X-ray diffractometer (XRD, model Miniflux II, Rigaku, Japan). In this test, copper was used as target material with known wavelength of 1.5481 Å to produce monochromatic X-rays. These X-rays were directed on the sample, and the reflected X-rays by the sample were recorded. The scanning rate for films was 5° per minute in the range of 5°–75° (2θ) with 0.02° step size.

The crystallinity values of all untreated and treated wheat straws were calculated using Segal's method, according to Eq. 1.

$$\text{CrI (\%)} = \frac{I_{200} - I_{\text{am}}}{I_{200}} \times 100 \quad (1)$$

CrI (%) represents percentage crystallinity index and I_{200} and I_{am} are the maximum and minimum intensities, respectively [41].

SEM analysis

To study the surface morphology of a polymeric composite film, structure analysis of native wheat straw, chemically treated wheat straw, PS film, PS/untreated WS film, and PS/treated WS film was performed using scanning electron microscopy (SEM, model JEOL JSM5410, Japan).

Mechanical testing

To investigate the tensile strength of a sample, the mechanical testing of all treated and untreated polymeric composite films was done by INSTRON 5982 Floor Model System, USA, according to the ASTM D882 using a testing speed of 30 mm/min. ASTM D882 test method is generally used for film having thickness < 1 mm. This test method is used to determine the tensile strength and elongation at break (%) of the film. The thickness of all the prepared films was around ±0.30 mm, and gauge length was 5 mm.

Contact angle measurement

Contact angle measurement gives the idea of hydrophobicity of a film. In this case water contact angle values of PS, PS/native WS, PS/NaOH-treated WS, PS/HCl-treated WS, and PS/H₂SO₄-treated WS film were measured using water contact angle measurement (DSA25 Series, Germany). DI water was used as a probe liquid.

TGA

TGAs provide information about the thermal stability of a film over time as temperature changes. Thermal analysis of PS, PS/native WS, PS/NaOH-treated WS, PS/HCl-treated WS, and PS/H₂SO₄-treated WS film was investigated by using PerkinElmer instrument, Waltham, MA, USA. In this analysis, sample was heated up to from 30 to 700 °C at a heating rate of 10 °C/min. Nitrogen gas was also employed to create an inert environment at a flow rate of 20 ml/min in TGA.

Water absorption test

In this test, water uptake analysis of PS, PS/native WS, PS/NaOH-treated WS, PS/HCl-treated WS, and PS/H₂SO₄-treated WS film was performed. For this, the film (20 × 20 × 0.30 mm) was completely immersed into distilled water at a temperature of 30 ± 2 °C for 24 h. The relative humidity of the room was around 20–25%. The weight of films was measured at a regular time interval of 2 h. Each film was gently cleaned to remove the excess amount of water present at the surface of a film before weighing using tissue paper. The dry samples were weighed and immersed into distilled water. Based on the change in weight of the film, the water absorption of the films was determined using the following Eq. 2 [42].

$$\text{WA} = \frac{(M_t - M_o)}{M_o} \times 100 \quad (2)$$

where WA represents the water absorption (%), M_o is the weight of the samples before testing (g), and M_t is the weight of the samples at a certain time (g).

Soil burial test

Soil burial test was carried out at ambient temperature under moisture-controlled conditions. All composite films were kept in wooden perforated boxes which were filled by moisturized soil. The perforated box (30 × 10 mm) was buried 100 mm beneath the surface of the soil which was regularly sprayed with water. The samples were taken out from the soil surface at soil burial period of 30, 60, 90, and 120 days. After that, all samples were washed with double-distilled water to remove all the

impurity, dried in an oven at 50 °C, and then stored in desiccator until they attained a constant weight. Based on the changes in weight, degradation behavior of all composite films was observed using the following Eq. 3 [43].

$$\text{weight loss (\%)} = \frac{(W_i - W_t) \times 100}{W_i} \quad (3)$$

where W_i represents initial mass (g) and W_t represents remaining mass at any given time (g) of a film.

Water vapor transmission rate test

In water vaporization transmission rate (WVTR) test, a weighed wet chamber covered with airtight film is kept in a glass jar and placed it in an incubation chamber. The chamber was kept at 23 °C with 50–60% relative humidity. The weight of the wet chamber was measured regularly at a period of 1 day [44, 45]. Change in the weight of a wet chamber fixed with the polymeric composite film signified the water vapor passing through the film. Water vaporization rate through a film is calculated using Eq. 4.

$$\text{WVTR} = \frac{\text{WC1} - \text{WC2}}{\text{WC1} \times A \times \text{day}} \quad (4)$$

where WC1 represents the initial weight of the wet chamber, WC2 represents the final weight of the wet chamber, and 'A' represents the exposing area of a wet chamber.

Results and discussion

XRD analysis

Comparative XRD analysis of native WS, NaOH-treated WS, HCl-treated WS, H₂SO₄-treated WS, PS film, PS (60 wt%)/native WS (40 wt%) film, PS (60 wt%)/NaOH-treated WS (40 wt%) film, PS (60 wt%)/HCl-treated WS (40 wt%) film, PS (60 wt%)/H₂SO₄-treated WS (40 wt%) film is shown in Fig. 1.

From Fig. 1, it is clear that the crystalline peaks are observed at 2θ around 16° and 22° revealing a cellulosic material present in all types of treated and untreated biomass. The broad peaks were found at 21.37° in native WS (Fig. 1a), 21.81° in NaOH-treated WS (Fig. 1b), 22.36° in HCl-treated WS (Fig. 1c), and 22.08° in H₂SO₄-treated WS (Fig. 1d). On the other hand, the higher intensity of peaks was observed at 19.89° in PS, 20.01° in PS (60 wt%)/native WS (40 wt%) film (Fig. 1a), 21.02° in PS (60 wt%)/NaOH-treated WS (40 wt%) film (Fig. 1b), 20.98° in PS (60 wt%)/HCl-treated WS (40 wt%) film (Fig. 1c), and 20.89° in PS (60 wt%)/H₂SO₄-treated WS (40 wt%) film (Fig. 1d).

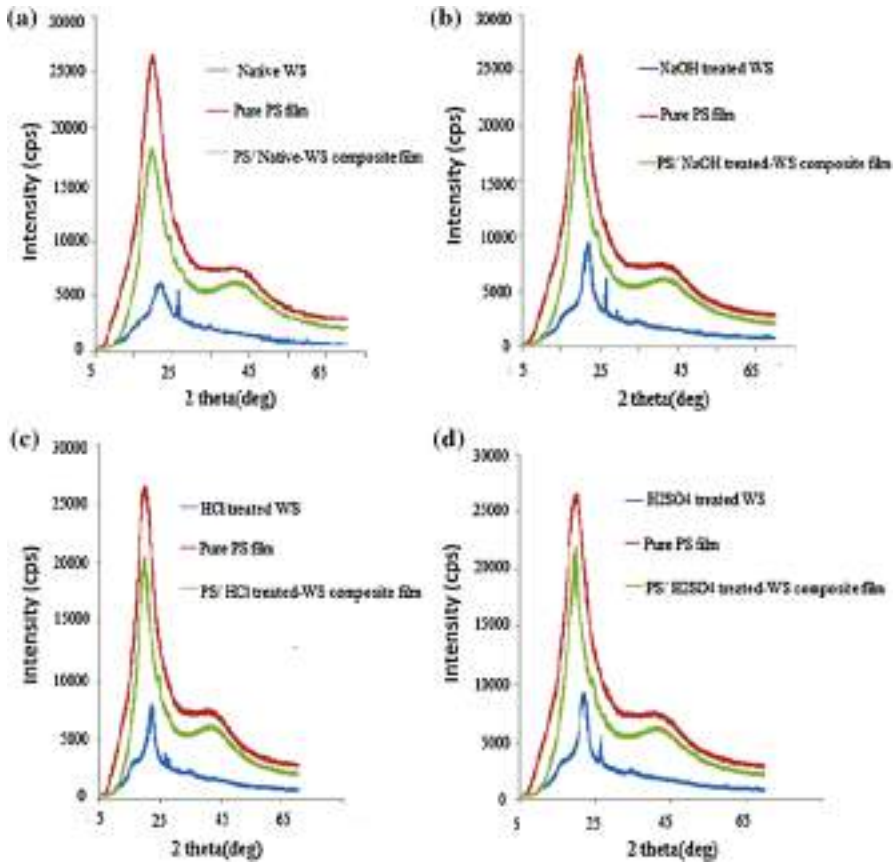


Fig. 1 X-ray diffraction pattern of native WS, chemically treated WS, and polymeric composite films. **a** Native WS, PS film, and PS/native WS film; **b** NaOH-treated WS, PS film, and PS/NaOH-treated WS film; **c** HCl-treated WS, PS film, and PS/HCl-treated WS film; **d** H₂SO₄-treated WS, PS film, and PS/H₂SO₄-treated WS film

After pre-treatments with acid and alkali, the graphs showed higher peak intensity as compared to native wheat straw and shifting of the peak toward the higher Bragg angle 2θ represented the decreasing lattice parameter magnitude according to Bragg’s law. The higher intensity peak represents higher crystallinity value of cellulose material in a chemically treated wheat straw showing removal of amorphous

Table 1 Crystalline values of untreated and treated wheat straws

Biomass	CrI (%)
Raw	50
Wheat straw treated with HCl	65
Wheat straw treated with H ₂ SO ₄	71
Wheat straw treated with NaOH	73

hemicellulose and lignin from the biomass and thus an enhancement in a crystalline region of cellulose in pre-treated wheat straw. The XRD peak at 21.81° in NaOH-treated wheat straw has higher peak intensity which assures that it has a higher crystalline value of cellulose as compared to untreated and acid-treated wheat straw (Fig. 1b). The percentage values of the crystallinity index of WS, NaOH-treated WS, HCl-treated WS, and H_2SO_4 -treated WS are 50, 73, 65, and 71, respectively (Table 1) [46].

After adding a native and treated WS biomass in a PS, PS film based on NaOH-treated WS shows higher intensity peak as compared to the PS film based on native and acid-treated WS which are also visualized in Fig. 1 [47, 48]. If we compared all the graphs, it may be concluded that PS/NaOH-treated WS composite film has comparable thermal stability with the pure PS film which is also confirmed by TGA (Fig. 6).

SEM analysis

In order to elucidate the surface topography of biomass, all kinds of untreated and treated WS were examined using scanning electron microscopy (SEM). SEM analysis of raw, acid-treated, and alkali-treated WS is shown in Fig. 2. After

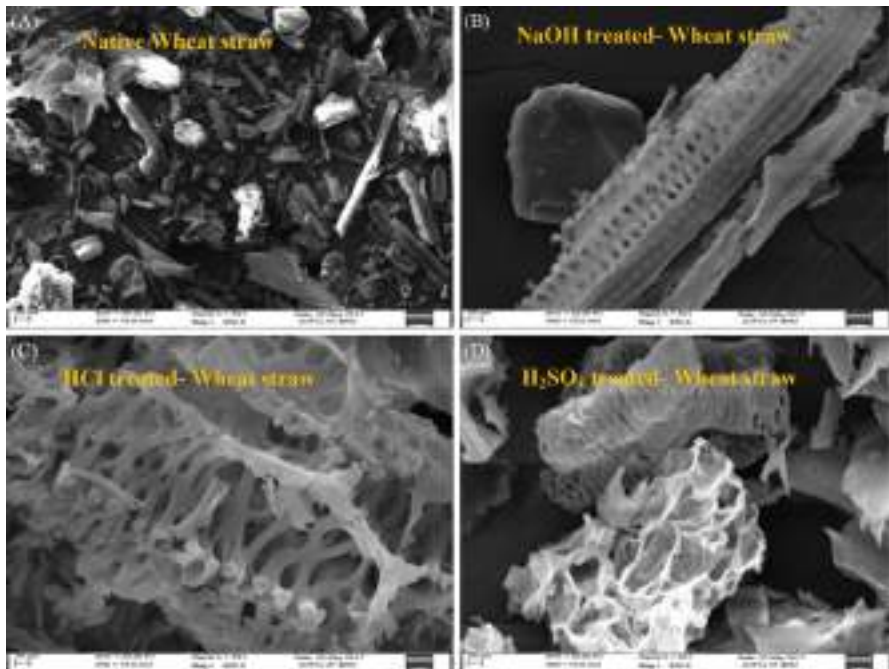


Fig. 2 Scanning electron microscopy micrographs of native wheat straw and all pre-treated wheat straw biomass: **a** native wheat straw, **b** NaOH-treated wheat straw, **c** HCl-treated wheat straw, **d** H_2SO_4 -treated wheat straw

pre-treatments with acid and base, the change in surface morphology of WS was analyzed by SEM to obtain the structural modification of the surface. Figure 2 reveals the cellular structure of the WS. In the native wheat straw, the surface might have contained some impurities such as residual lignin (Fig. 2a). After applying the HCl and H₂SO₄ pre-treatments on WS, a destruction of plant cells resulted in irregular shape observed in SEM images (Fig. 2c, d). Also, some porosity was found at the surface of pre-treated biomass [49]. For the biomass pre-treated with NaOH, SEM images are showing the surface of WS in a cylindrical shape having many filaments, cells, and pores [50] (Fig. 2b). Voids present at the surface of biomass confirmed that the sample morphology was very suitable for adhesion between WS and polymer matrix which is also proven by the result for PS blended with treated WS composite film. It also indicates that for pre-treated WS with acid/base, there is a decrease in resistant nature of WS by increasing the cellulose digestibility.

Further adding a native and chemically treated wheat straw in a polystyrene matrix, SEM images of PS, PS (60 wt%)/native WS (40 wt%), PS (60 wt%)/NaOH-treated WS (40 wt%), PS (60 wt%)/HCl-treated WS (40 wt%), PS (60 wt%)/H₂SO₄-treated WS (40 wt%) films are shown in Fig. 3. Figure 3a shows that the surface is clean and pure in the case of pure PS film. However, SEM analysis of PS/native WS composite film is elucidating the debonding between untreated wheat straw and polystyrene matrix (Fig. 3b). Figure 3d, e shows that the surface morphology of PS/HCl-treated WS and PS/H₂SO₄-treated WS composite films revealed better fiber bonding matrix as compared to PS/native WS composite film. But in the case of PS/NaOH-treated WS composite film, SEM image is showing better interface locking in between the NaOH-treated wheat straw and the polystyrene matrix as shown in Fig. 3c. Moreover, it represents the highest tensile strength as compared to all other composite films [51].

Mechanical testing

To examine the mechanical strength of the composite, the parameters such as tensile strength and elongation at break (%) of PS, PS (60 wt%)/native WS (40 wt%), PS (60 wt%)/NaOH-treated WS (40 wt%), PS (60 wt%)/HCl-treated WS (40 wt%), and PS (60 wt%)/H₂SO₄-treated WS (40 wt%) films were also investigated and are given in Figs. 4 and 5. Figure 4 shows that the tensile strength of PS/treated WS composite film was higher as compared to PS/native WS composite film. Tensile strengths of pure PS, PS/native WS, PS/NaOH-treated WS, PS/HCl-treated WS, and PS/H₂SO₄-treated WS composite films were 3 MPa, 2.3 MPa, 3.56 MPa, 3.14 MPa, and 3.10 MPa, respectively. On the other hand, elongation at break (%) of pure PS film was 210%. After 40 wt% replacement of PS by untreated and treated fibers, the flexibility of the green composite films was decreased. As is clear from Fig. 5, the elongation at break (%) of PS/native WS, PS/NaOH-treated WS, PS/HCl-treated WS, and PS/H₂SO₄-treated WS composite films can be seen as 110%, 140%, 132%, and 127%, respectively.

Borges et al. [27] used piassava fiber as reinforcing agent in polypropylene matrix and observed 15 wt% loading of piassava fiber in the polymer matrix exhibiting

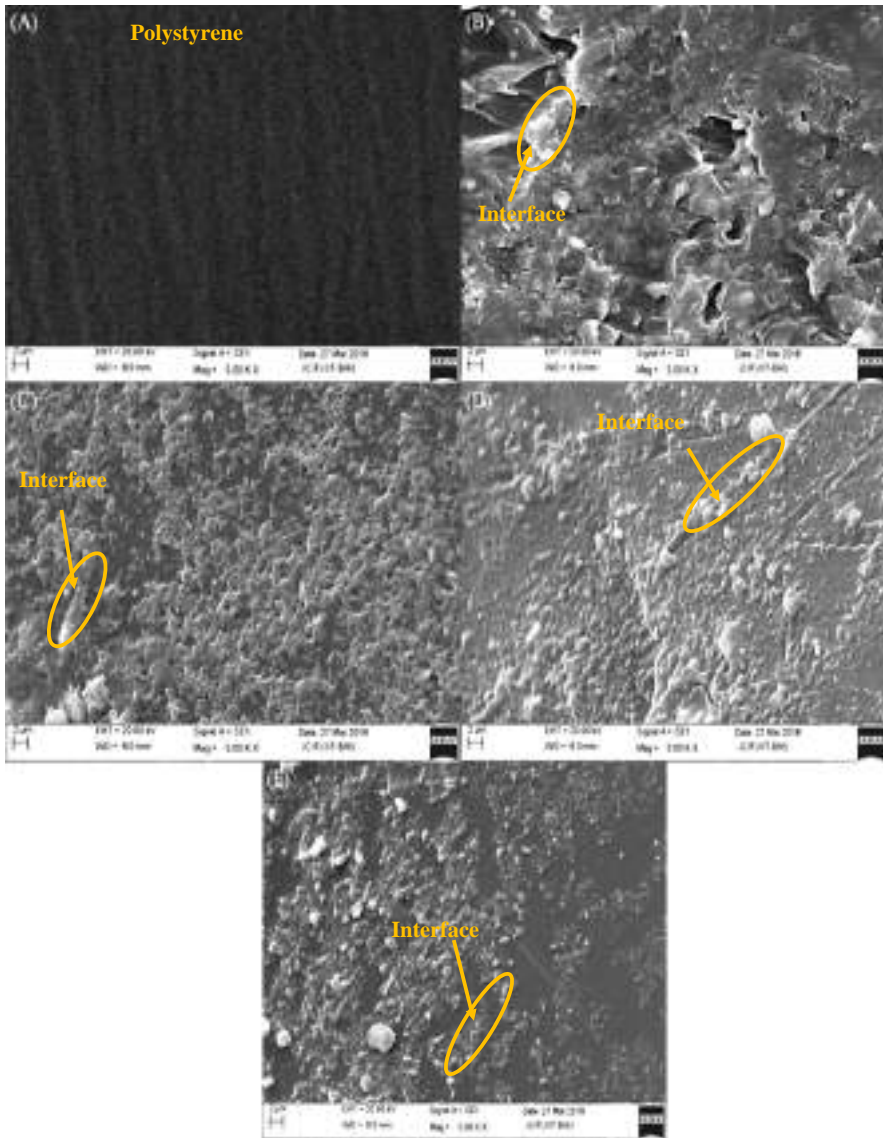


Fig. 3 Scanning electron microscopy micrographs of PS, PS/native WS, and PS/treated WS composite films: **a** PS, **b** PS/native WS, **c** PS/NaOH-treated WS, **d** PS/HCl-treated WS, **e** PS/H₂SO₄-treated WS composite films

higher tensile strength which was 25 MPa with 2.5% elongation limit. Pigatto et al. [28] reported polypropylene/ethylene propylene diene monomer blended with 15 wt%. Alkali-treated sisal fibers represent significant improvement in the tensile strength of composite film, which was 19 MPa. da Silva et al. [29] explained curaua fiber was a best substitution for glass in polymer matrix. According to the literature,

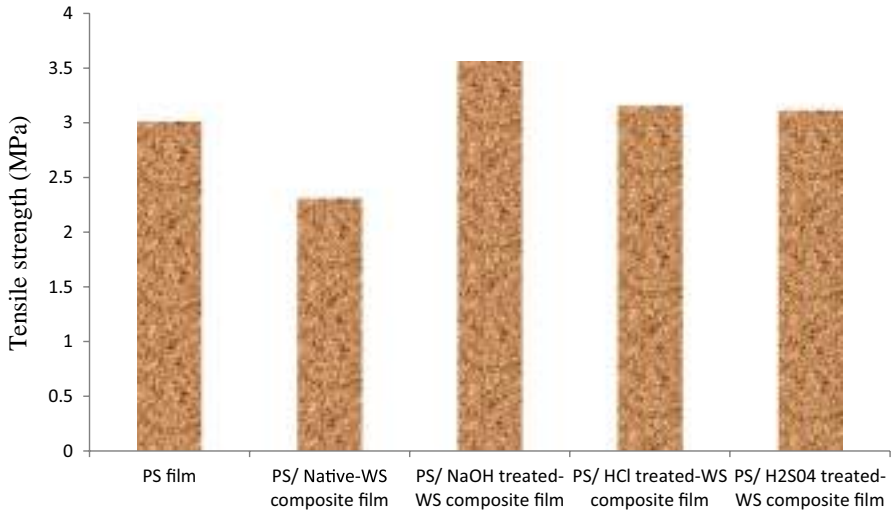


Fig. 4 Tensile strength of polystyrene (PS), PS/native WS, and PS/treated WS composite films

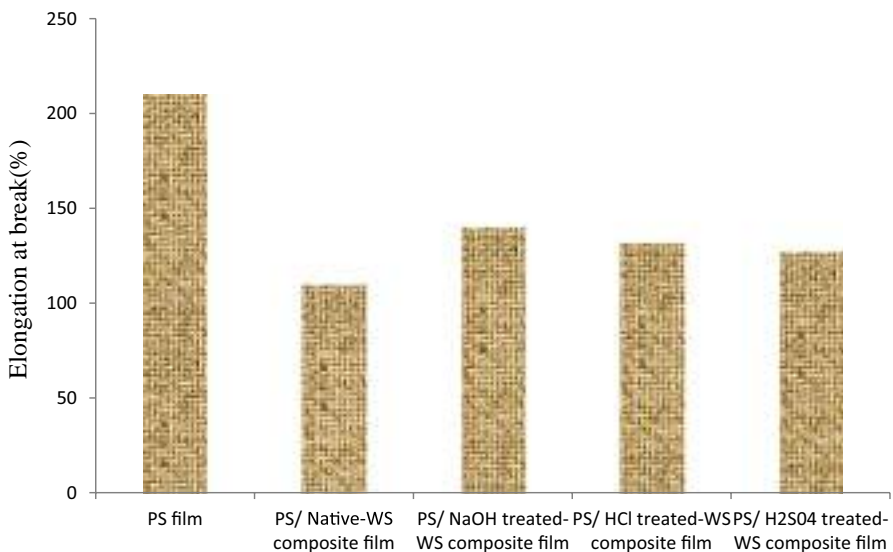


Fig. 5 Elongation at break (%) of polystyrene (PS), PS/native WS, and PS/treated WS composite films

30 wt% substitution of glass with curaua fiber was possible without losing its tensile strength [30]. Certain pre-treatment of fiber was also applied for reinforcement of curaua-based composites. The tensile strength of treated curaua fiber-based polyester composites was 85 MPA, and the composite showed higher mechanical stability as compared to other bio-composites [26]. This signified the improvement in the

adhesion between the polymer and treated fibers due to pre-treatment of cellulosic fibers.

The higher tensile strength and moderate elongation limit as compared to pure PS film signify the polymeric film based on alkali-treated biomass and assure the successful application of these composites for green packaging application.

Contact angle measurement

Water contact angle values of PS, PS (60 wt%)/native WS (40 wt%), PS (60 wt%)/NaOH-treated WS (40 wt%), PS (60 wt%)/HCl-treated WS (40 wt%), and PS (60 wt%)/H₂SO₄-treated WS (40 wt%) composite films are shown in Table 2.

Water contact angle values of PS, PS/native WS, PS/NaOH-treated WS, PS/HCl-treated WS, and PS/H₂SO₄-treated WS composite films are 101°, 86°, 98°, 91°, 90°, respectively. The contact angle value is increased by 12° after dispersing an alkali-treated WS in the polymer matrix exhibiting its water-resistant nature. Generally, contact angles greater than 90° exhibit low tension force between film and water as compared to the surface tension of the water. Thus, the inclusion of alkali-treated wheat straw in the polymer matrix renders the film hydrophobic and makes it suitable for green packaging applications [52, 53].

TGA

In order to elucidate the thermal stability of a composite film, TGA graphs of PS, PS (60 wt%)/native WS (40 wt%), PS (60 wt%)/NaOH-treated WS (40 wt%), PS (60 wt%)/HCl-treated WS (40 wt%), and PS (60 wt%)/H₂SO₄-treated WS (40 wt%) composite films were recorded and are shown in Fig. 6. A small wt loss of PS/native WS is observed at 120–160 °C. It can be concluded that there may be debonding present between the PS and native WS. These results are equivalent to the results published by Seggiani et al. [54] in his research article. TGA graph also showed that the major degradation of all polymer composite films started around 220 °C and ended at around 450 °C, which is attributed to the degradation of polymer composite chain. Furthermore, the addition of HCl-, H₂SO₄- and NaOH-treated WS has a remarkable impact on the thermal stability of PS composite film as compared to the PS/native WS composite film. The degradation temperature shifts toward higher

Table 2 Contact angle and water vapor transmission rate of PS, PS/native WS, PS/NaOH-treated WS, PS/HCl-treated WS, and PS/H₂SO₄-treated WS composite films

Film	Contact angle (°)	WVTR (g/m ² day ⁻¹)
Pure polystyrene film (PS)	101	55
Polystyrene (PS)/untreated wheat straw (WS) composite	86	210
Polystyrene (PS)/NaOH-treated wheat straw (WS) composite	98	71
Polystyrene (PS)/HCl-treated wheat straw (WS) composite	91	99
Polystyrene (PS)/H ₂ SO ₄ -treated wheat straw (WS) composite	90	106

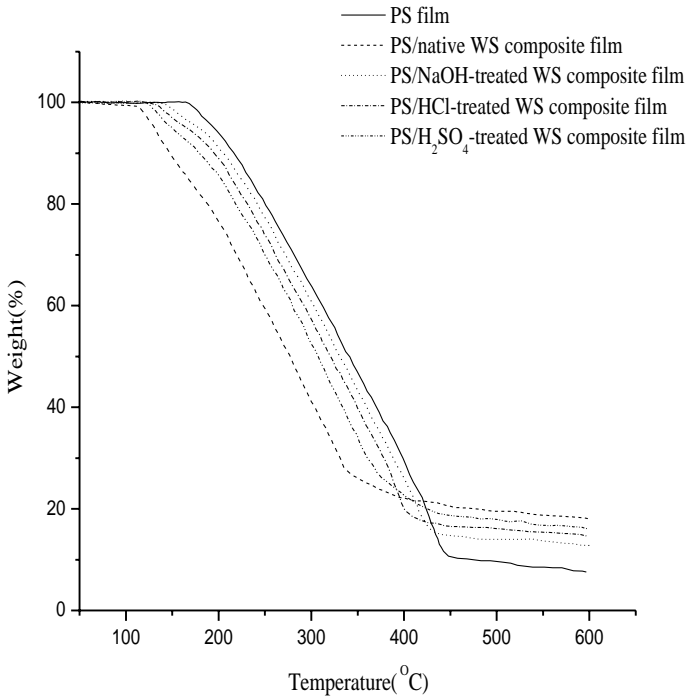


Fig. 6 TGA analysis of PS, PS/native WS, PS/NaOH-treated WS, PS/HCl-treated WS and PS/H₂SO₄-treated WS composite films

temperatures as polymer matrix interacted with the chemically treated wheat straw [55]. This exhibits that the pre-treatment results in better interfacial interaction between the polymer matrix and treated wheat straw [56]. Perumal et al. [57] have also reported the similar results in their research article. The thermal stability of PS/NaOH-treated WS is found to be higher in a TGA thermogram which is comparable with the pure polymeric film [58].

Water absorption test

The water absorptions of PS, PS (60 wt%)/native WS (40 wt%), PS (60 wt%)/NaOH-treated WS (40 wt%), PS (60 wt%)/HCl-treated WS (40 wt%), PS (60 wt%)/H₂SO₄-treated WS (40 wt%) composite films are shown in Fig. 7. In the graph, water absorption of all bio-composite films is continuously increasing with increasing soaking time. The water absorption curves of all bio-composite films linearly increase at the initial stage, then slow down, and reach the equilibrium. The water absorptions of PS, PS/native WS, PS/NaOH-treated WS, PS/HCl-treated WS, and PS/H₂SO₄-treated WS films bio-composite films are 0%, 17%, 5%, 10%, and 9%, respectively.

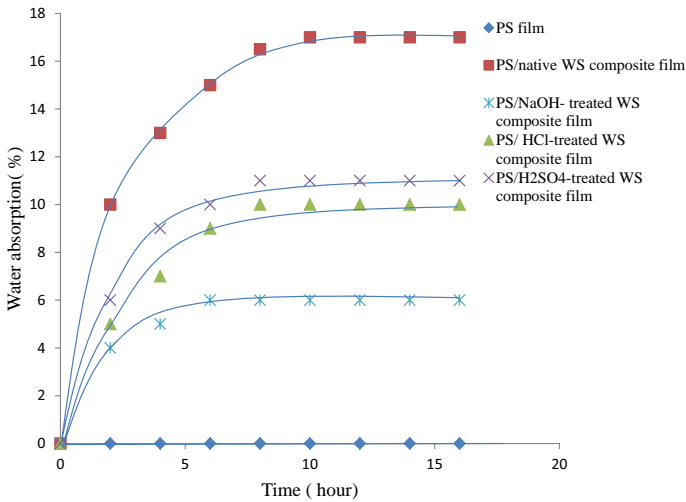


Fig. 7 Water absorption test of PS, PS/native WS, PS/NaOH-treated WS, PS/HCl-treated WS and PS/H₂SO₄-treated WS composite films

PS/NaOH-treated WS absorbed less water as compared to all other native and acid-treated WS-based composite films. The water absorption of PS/NaOH-treated WS composite film was comparable with the pure PS film. This result may be correlated with the strong adhesion established between the polymer and alkali-treated WS. Water-resistant quality of PS/NaOH-treated WS film is assuring the successful application of this composite for packaging application.

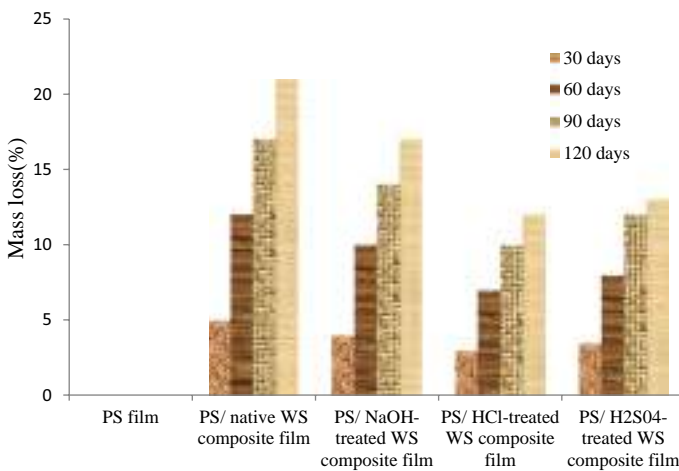


Fig. 8 Soil burial test of PS, PS/native WS, PS/NaOH-treated WS, PS/HCl-treated WS and PS/H₂SO₄-treated WS composite films

Soil burial test

In this test, soil degradation behavior of PS, PS (60 wt%)/native WS (40 wt%), PS (60 wt%)/NaOH-treated WS (40 wt%), PS (60 wt%)/HCl-treated WS (40 wt%), and PS (60 wt%)/H₂SO₄-treated WS (40 wt%) composite films was investigated and the results are comprehensively given in Fig. 8. The composite film was washed with distilled water and dried in an oven at the end of each soil burial time (30, 60, 90, and 120 days). Furthermore, all composite films were stored in a desiccator until they attain a constant weight. Soil degradation graph of the composite film based on biomass is showing the same nature. All bio-composite films are biodegradable in nature. Mass degradation in all composite films increases with increasing soil burial period [59–61]. The mass loss observed in PS, PS/native WS, PS/NaOH-treated WS, PS/HCl-treated WS, and PS/H₂SO₄-treated WS composite films is 0%, 21%, 17%, 12%, and 13%, respectively, at the end of 120 days of soil burial test.

During the first 30 days, soil degradation of bio-composite films was high due to the microbial attack as compared to pure PS film. So probably, fibers present in the polymer matrix seem to be good for biodegradation. This result was in good agreement with the results reported by the Alvarez et al. [62]. The mass loss obtained in a PS/native WS composite film after 120 days of soil burial test was 21%. It seems that WS favors biodegradation process [63, 64].

Water vapor transmission rate test

Water vapor transmission rate test was prepared for all polystyrene-based composite films, and the results are depicted in Table 2. WVTR of PS, PS (60 wt%)/native WS (40 wt%), PS (60 wt%)/NaOH-treated WS (40 wt%), PS (60 wt%)/HCl-treated WS (40 wt%), and PS (60 wt%)/H₂SO₄-treated WS (40 wt%) composite films is 55, 210, 71, 99, and 106 g/m² day⁻¹, respectively.

Polymer matrix blended with native wheat straw exhibits a higher WVTR due to fractured surface of the film. This film provides the better affinity of CH which permitted water molecules migrate through the film. Similar result was reported by Sánchez-Safont et al. [65] in research article. WVTR of PS/NaOH-treated WS is showing a moisture-resistant nature. WVTR is not high because of the existence of strong interface between treated biomass and polymer matrix. So probably, PS/NaOH-treated WS can be a better substitution for a polymeric film for water-resistant packaging application [66, 67].

Conclusions

In this work, comparison of the effects of various chemical treatments on wheat straw for enhancing the suitability of biomass in the polymer matrix followed by preparation of wheat straw-reinforced polystyrene composite was studied. SEM and XRD analyses of the treated biomass-based composite film explore a better adhesion

of treated WS with the polymer matrix. Mechanical stability of chemically treated biomass-based polymeric composite films had also extensively increased as compared to those prepared with pure polymeric or untreated biomass with benchmark elongation limit. Alkali treated-biomass based composite film has lower affinity of CH results in less WVTR and excellent interfacial interaction causes higher thermal stability as compared to other bio-composites. Low contact angle value of PS/NaOH-treated WS film signified the existence of low tension force between film and water. The films resulting from PS/alkali-treated WS render the resulting bio-composite more hydrophobic, mechanically stable, and impervious to the movement of water vapor. Hence, it can be concluded that alkali treatment of biomass is admirable for sustainable environment development via green packaging applications.

References

1. Díaz S, Ortega Z, McCourt M, Kearns MP, Benítez AN (2018) Recycling of polymeric fraction of cable waste by rotational moulding. *Waste Manag* 76:199–206
2. Bajracharya RM, Manalo AC, Karunasena W, Lau K (2016) Characterisation of recycled mixed plastic solid wastes: coupon and full-scale investigation. *Waste Manag* 48:72–80
3. Fazeli M, Keley M, Biazar E (2018) Preparation and characterization of starch-based composite films reinforced by cellulose nanofibers. *Int J Biol Macromol* 116:272–280
4. Gaurh P, Pramanik H (2018) A novel approach of solid waste management via aromatization using multiphase catalytic pyrolysis of waste polyethylene. *Waste Manag* 71:86–96
5. Imam S, Cinelli P, Gordon S, Chiellini E (2005) Characterization of biodegradable composite films prepared from blends of poly (vinyl alcohol), cornstarch, and lignocellulosic fiber. *J Polym Environ* 13:47–55
6. Kyrikou I, Briassoulis D (2007) Biodegradation of agricultural plastic films: a critical review. *J Polym Environ* 15:125–150
7. Briassoulis D, Dejean C (2010) Critical review of norms and standards for biodegradable agricultural plastics part I. Biodegradation in soil. *J Polym Environ* 18:384–400
8. Bourmaud A, Baley C (2007) Investigations on the recycling of hemp and sisal fibre reinforced polypropylene composites. *Polym Degrad Stab* 92:1034–1045
9. Bourmaud A, Baley C (2009) Rigidity analysis of polypropylene/vegetal fibre composites after recycling. *Polym Degrad Stab* 94:297–305
10. Abrial H, Anugrah AS, Hafizulhaq F, Handayani D, Sugiarti E, Muslimin AN (2018) Effect of nanofibers fraction on properties of the starch based biocomposite prepared in various ultrasonic powers. *Int J Biol Macromol* 116:1214–1221
11. Jia N, Li S-M, Ma M-G, Sun R-C, Zhu J-F (2012) Hydrothermal fabrication, characterization, and biological activity of cellulose/CaCO₃ bionanocomposites. *Carbohydr Polym* 88:179–184
12. Garlotta D (2001) A literature review of poly (lactic acid). *J Polym Environ* 9:63–84
13. Mohanty AK, Misra M, Drzal L (2002) Sustainable bio-composites from renewable resources: opportunities and challenges in the green materials world. *J Polym Environ* 10:19–26
14. Luckachan GE, Pillai C (2011) Biodegradable polymers—a review on recent trends and emerging perspectives. *J Polym Environ* 19:637–676
15. Devi S, Gupta C, Jat S, Parmar M (2017) Crop residue recycling for economic and environmental sustainability: the case of India. *Open Agric* 2:486–494
16. Castro DO, Ruvolo-Filho A, Frollini E (2012) Materials prepared from biopolyethylene and curaua fibers: composites from biomass. *Polym Test* 31:880–888
17. MacMilan JD (1994) Pretreatment of lignocellulosic biomass, ACS symposium series, America, pp 292–324
18. Alvira P, Tomás-Pejó E, Ballesteros M, Negro MJ (2010) Pretreatment technologies for an efficient bioethanol production process based on enzymatic hydrolysis: a review. *Bioresour Technol* 101:4851–4861

19. Taherzadeh MJ, Karimi K (2008) Pretreatment of lignocellulosic wastes to improve ethanol and biogas production: a review. *Int J Mole Sci* 9:1621–1651
20. Somani A, Nandi TK, Pal SK, Majumder AK (2017) Pre-treatment of rocks prior to comminution— a critical review of present practices. *Int J Min Sci Technol* 27:339–348
21. Mirmohamadsadeghi S, Chen Z, Wan C (2016) Reducing biomass recalcitrance via mild sodium carbonate pretreatment. *Bioresour Technol* 209:386–390
22. Kim JS, Lee YY, Kim TH (2016) A review on alkaline pretreatment technology for bioconversion of lignocellulosic biomass. *Bioresour Technol* 199:42–48
23. Yan X, Wang Z, Zhang K, Si M, Liu M, Chai L, Liu X, Shi Y (2017) Bacteria-enhanced dilute acid pretreatment of lignocellulosic biomass. *Bioresour Technol* 245:419–425
24. Salehian P, Karimi K, Zilouei H, Jeyhanipour A (2013) Improvement of biogas production from pine wood by alkali pretreatment. *Fuel* 106:484–489
25. Agbor VB, Cicek N, Sparling R, Berlin A, Levin DB (2011) Biomass pretreatment: fundamentals toward application. *Biotechnol Adv* 29:675–685
26. da Silva HSP, Ornaghi Júnior HL, Santos Almeida Júnior JH, Zattera AJ, Campos Amico S (2014) Mechanical behavior and correlation between dynamic fragility and dynamic mechanical properties of curaua fiber composites. *Polym Compos* 35:1078–1086
27. Borges TE, Almeida JHS, Amico SC, Amado FDR (2017) Hollow glass microspheres/piassava fiber-reinforced homo- and *co*-polypropylene composites: preparation and properties. *Polym Bull* 74:1979–1993
28. Pigatto C, Santos Almeida Júnior JH, Luiz Ornaghi Júnior H, Rodríguez AL, Mählmann CM, Amico SC (2012) Study of polypropylene/ethylene-propylene-diene monomer blends reinforced with sisal fibers. *Polym Compos* 33:2262–2270
29. da Silva LV, Júnior JHSA, Angrizani CC, Amico SC (2013) Short beam strength of curaua, sisal, glass and hybrid composites. *J Reinf Plast Compos* 32:197–206
30. Almeida JHS, Amico SC, Botelho EC, Amado FDR (2013) Hybridization effect on the mechanical properties of curaua/glass fiber composites. *Compos Part B Eng* 55:492–497
31. Zegaoui A, Derradji M, Ma R, Cai W, Medjahed A, Liu W, Dayo AQ, Wang J, Wang G (2018) Influence of fiber volume fractions on the performances of alkali modified hemp fibers reinforced cyanate ester/benzoxazine blend composites. *Mater Chem Phys* 213:146–156
32. Zehetmeyer G, Soares RM, Brandelli A, Mauler RS, Oliveira RV (2012) Evaluation of polypropylene/montmorillonite nanocomposites as food packaging material. *Polym Bull* 68:2199–2217
33. Hadj-Hamou AS, Metref F, Yahiaoui F (2017) Thermal stability and decomposition kinetic studies of antimicrobial PCL/nanoclay packaging films. *Polym Bull* 74:3833–3853
34. Gutiérrez TJ, Alvarez VA (2017) Cellulosic materials as natural fillers in starch-containing matrix-based films: a review. *Polym Bull* 74:2401–2430
35. Zehetmeyer G, Meira SMM, Scheibel JM, da Silva CB, Rodembusch FS, Brandelli A, Soares RMD (2017) Biodegradable and antimicrobial films based on poly (butylene adipate-*co*-terephthalate) electrospun fibers. *Polym Bull* 74:3243–3268
36. Berthet MA, Angellier-Coussy H, Chea V, Guillard V, Gastaldi E, Gontard N (2015) Sustainable food packaging: valorising wheat straw fibres for tuning PHBV-based composites properties. *Compos Part A Appl Sci Manuf* 72:139–147
37. Asgher M, Ahmad Z, Iqbal HMN (2017) Bacterial cellulose-assisted de-lignified wheat straw-PVA based bio-composites with novel characteristics. *Carbohydr Polym* 161:244–252
38. Stelte W, Clemons C, Holm JK, Ahrenfeldt J, Henriksen UB, Sanadi AR (2011) Thermal transitions of the amorphous polymers in wheat straw. *Ind Crops Prod* 34:1053–1056
39. Mussatto SI (2016) Chapter 8—biomass pretreatment with acids. In: Mussatto SI (ed) *Biomass fractionation technologies for a lignocellulosic feedstock based biorefinery*. Elsevier, Amsterdam, pp 169–185
40. Nargotra P, Sharma V, Gupta M, Kour S, Bajaj BK (2018) Application of ionic liquid and alkali pretreatment for enhancing saccharification of sunflower stalk biomass for potential biofuel-ethanol production. *Bioresour Technol* 267:560–568
41. Caliarí ÍP, Barbosa MHP, Ferreira SO, Teófilo RF (2017) Estimation of cellulose crystallinity of sugarcane biomass using near infrared spectroscopy and multivariate analysis methods. *Carbohydr Polym* 158:20–28
42. Poormohammadian SJ, Darvishi P, Dezfúli AMG (2018) Investigating the structural effect of electrospun nano-fibrous polymeric films on water vapor transmission. *Chin J Chem Eng* 27:100–109

43. Phua YJ, Lau NS, Sudesh K, Chow WS, Mohd Ishak ZA (2012) Biodegradability studies of poly(butylene succinate)/organo-montmorillonite nanocomposites under controlled compost soil conditions: effects of clay loading and compatibiliser. *Polym Degrad Stab* 97:1345–1354
44. Sirviö JA, Kolehmainen A, Liimatainen H, Niinimäki J, Hormi OEO (2014) Biocomposite cellulose-alginate films: promising packaging materials. *Food Chem* 151:343–351
45. Răpă M, Miteluț AC, Tănase EE, Grosu E, Popescu P, Popa ME, Rosnes JT, Sivertsvik M, Darieniță RN, Vasile C (2016) Influence of chitosan on mechanical, thermal, barrier and antimicrobial properties of PLA-biocomposites for food packaging. *Compos Part B Eng* 102:112–121
46. Nitsos CK, Matis KA, Triantafyllidis KS (2013) Optimization of hydrothermal pretreatment of lignocellulosic biomass in the bioethanol production process. *Chem Sus Chem* 6:110–122 (**Epub 2012/11/28**)
47. Lila MK, Singhal A, Banwait SS, Singh I (2018) A recyclability study of bagasse fiber reinforced polypropylene composites. *Polym Degrad Stab* 152:272–279
48. Guerrica-Echevarría G, Eguiazabal JI, Nazabal J (1996) Effects of reprocessing conditions on the properties of unfilled and talc-filled polypropylene. *Polym Degrad Stab* 53:1–8
49. Goshadrou A, Karimi K, Lefsrud M (2013) Characterization of ionic liquid pretreated aspen wood using semi-quantitative methods for ethanol production. *Carbohydr Polym* 96:440–449
50. Karimi K, Shafiei M, Kumar R (2013) Progress in physical and chemical pretreatment of lignocellulosic biomass. In: Gupta VK, Tuohy MG (eds) *Biofuel technologies: recent developments*. Springer, Berlin, pp 53–96
51. Rashid B, Leman Z, Jawaid M, Ghazali MJ, Ishak MR, Abdelgnei MA (2017) Dry sliding wear behavior of untreated and treated sugar palm fiber filled phenolic composites using factorial technique. *Wear* 380–381:26–35
52. Tang CY, Kwon Y-N, Leckie JO (2009) Effect of membrane chemistry and coating layer on physicochemical properties of thin film composite polyamide RO and NF membranes: II. Membrane physicochemical properties and their dependence on polyamide and coating layers. *Desalination* 242:168–182
53. Baek Y, Kang J, Theato P, Yoon J (2012) Measuring hydrophilicity of RO membranes by contact angles via sessile drop and captive bubble method: a comparative study. *Desalination* 303:23–28
54. Seggiani M, Cinelli P, Mallegni N, Balestri E, Puccini M, Vitolo S, Lardicci C, Lazzeri A (2017) New bio-composites based on polyhydroxyalkanoates and *Posidonia oceanica* fibres for applications in a marine environment. *Materials* 10:326
55. Saravanan S, Akshay Gowda KM, Arul Varman K, Ramamurthy PC, Madras G (2015) In-situ synthesized poly(vinyl butyral)/MMT-clay nanocomposites: the role of degree of acetalization and clay content on thermal, mechanical and permeability properties of PVB matrix. *Compos Sci Technol* 117:417–427
56. Johar N, Ahmad I, Dufresne A (2012) Extraction, preparation and characterization of cellulose fibres and nanocrystals from rice husk. *Ind Crops Prod* 37:93–99
57. Perumal AB, Sellamuthu PS, Nambiar RB, Sadiku ER (2018) Development of polyvinyl alcohol/chitosan bio-nanocomposite films reinforced with cellulose nanocrystals isolated from rice straw. *Appl Surf Sci* 449:591–602
58. Dias AB, Müller CMO, Larotonda FDS, Laurindo JB (2011) Mechanical and barrier properties of composite films based on rice flour and cellulose fibers. *LWT Food Sci Technol* 44:535–542
59. Kapanen A, Schettini E, Vox G, Itävaara M (2008) Performance and environmental impact of biodegradable films in agriculture: a field study on protected cultivation. *J Polym Environ* 16:109–122
60. Briassoulis D (2006) Mechanical behaviour of biodegradable agricultural films under real field conditions. *Polym Degrad Stab* 91:1256–1272
61. Briassoulis D (2004) An overview on the mechanical behaviour of biodegradable agricultural films. *J Polym Environ* 12:65–81
62. Alvarez VA, Ruseckaite R, Vazquez A (2006) Degradation of sisal fibre/mater Bi-Y biocomposites buried in soil. *Polym Degrad Stab* 91:3156–3162
63. Amano Y, Nozaki K, Araki T, Shibasaki H, Kuga S, Kanda T (2001) Reactivities of cellulases from fungi towards ribbon-type bacterial cellulose and band-shaped bacterial cellulose. *Cellulose* 8:267–274
64. Żuchowska D, Steller R, Meissner W (1998) Structure and properties of degradable polyolefin-starch blends. *Polym Degrad Stab* 60:471–480

65. Sánchez-Safont EL, Aldureid A, Lagarón JM, Gámez-Pérez J, Cabedo L (2018) Biocomposites of different lignocellulosic wastes for sustainable food packaging applications. *Compos Part B Eng* 145:215–225
66. Laadila MA, Hegde K, Rouissi T, Brar SK, Galvez R, Sorelli L, Cheikh RB, Paiva M, Abokitse K (2017) Green synthesis of novel biocomposites from treated cellulosic fibers and recycled bioplastic polylactic acid. *J Clean Prod* 164:575–586
67. Tănase EE, Popa ME, Râpă M, Popa O (2015) PHB/cellulose fibers based materials: physical, mechanical and barrier properties. *Agric Agric Sci Proc* 6:608–615

Publisher's Note Springer Nature remains neutral with regard to jurisdictional claims in published maps and institutional affiliations.



Novel Hybrid Structural Biocomposites from Alkali Treated-Date Palm and Coir Fibers: Morphology, Thermal and Mechanical Properties

Shobhit Dixit¹ · Binita Joshi¹ · Pawan Kumar¹ · Vijay Laxmi Yadav¹

© Springer Science+Business Media, LLC, part of Springer Nature 2020

Abstract

In this concern study, the surging demands for regulating the environmental aspects associated with controlling a massive generated synthetic wastes in the field of structural applications, has motivated researchers to synthesize green products using agricultural wastes. Therefore, in this work, a novel hybrid epoxy composites based on alkali treated-date palm fiber and native coir fiber at different weight fractions were prepared using hand layup technique and investigated the hybridization effect of the resultant composites. Hybrid composites were characterized using several analytical techniques i.e. X-ray diffraction analysis, thermogravimetric analysis, contact angle measurement, dart impact test and tensile test. Reported results explored that the alkali treatment on date palm fiber had a reliable impact on the experimentally evaluated mechanical, hydrophobic and thermal properties of the resultant hybrid composites. The required structural properties for 50 wt% coir fiber incorporated in 50 wt% treated-date palm fiber based epoxy composites are 76.51 MPa tensile strength, 2.77% elongation limit, 832.2 J/m impact strength, and 100.2° contact angle, respectively possess highest value as compared to all other hybrid composites. Hence, the incorporation of 50 wt% treated-date palm fiber in 50 wt% coir fiber based epoxy composite has the best structural properties in terms of mechanical, water resistant and thermal properties for green rigid applications.

Keywords Composites · Agricultural wastes · Epoxy · Hand layup

Introduction

The extensive concerns to regulate the environmental aspects and controlled the pollution created by non-biodegradable materials have triggered the scientists to fabricate more convincing biodegradable novel hybrid green materials in order to meet the growing demands in various ranges of sectors. Therefore, ecological aspects have motivated researchers to synthesize hybrid biodegradable green composites products having synergetic characteristics i.e. biodegradable in nature, low-cost, easy to fabricate, light-weight, good as a thermal insulator and having high hygroscopic for various industrial sectors like automotive and structural applications [1]. So, this is the eye opener for the industrialist to fabricate agro-waste fiber based hybrid structural composites due to their providing high mechanical stability with remarkable stiffness that is comparable with synthetic

structural composites. Hybrid composites, as an imperative class in the field of composites, represent those composites in which one kind of reinforcing material is blended in the combination of different matrix [2, 3]. The idea of hybrid composites with impressive combination of characteristics i.e. high specific properties, low density and excellent thermal stability is fulfilling the requirements of medium density fiberboards, insulation boards and other automotive applications while understanding the needs of cost reduction and waste minimization. Therefore, the perfect use of plenty available natural fibers like a banana [4], cotton [5], coir [6], sisal [7], date palm [8] and jute [9, 10] for structural applications is the need of the hour.

Agricultural wastes like date palm, coir etc. fibers are mainly composed of cellulose (33–45%), hemicellulose (59.5–74.8%) and lignin (14–27%) and cotton coir is composed of cellulose (36–43%), hemicellulose (0.15–0.25%) and lignin (41–45%) [11, 12]. Due to the recalcitrance nature of biomass, the existence of undesirable materials (hemicellulose and lignin) cause weak compatibility found between natural fibers and polymer matrix [13]. Many authors have adopted reliable pre-treatment techniques in order to

✉ Vijay Laxmi Yadav
vlyadaviitbhu2014@gmail.com

¹ Department of Chemical Engineering and Technology, IIT BHU, Varanasi, Uttar Pradesh 221005, India

improve the suitability of biomass for blending in polymer matrix. Many researchers have used chemical pre-treatment for making biomass more promising for polymer adhesion. The main purpose of using chemical pre-treatment is to destruct the biomass body and create some voids opening at the surface. Generally, in alkali treatment, a significant delignification process followed by the removal of a small branched chain of carbohydrate that is hemicellulose from natural fiber [14–16]. It has been found that the alkali treatments enhanced the suitability of agricultural wastes for polymer adhesion [17].

Mochane et al. reviewed the various natural fibers such as jute, flax, sisal, banana, hemp based polymer composites for structural applications [18]. Otto et al. synthesized chemically modified based lignocellulosic fibers reinforced polyurethane composites and observed benchmark elastic property showing higher potential applications for padding material and shock absorption [19]. Sanjay et al. studied mechanical and physical characteristics of natural fiber incorporated glass fiber based polymer composites using hand layup technique for engineering applications [20]. Alavudeen et al. synthesized chemically modified banana and kenaf fibers reinforced polyester composites using hand layup technique and studied the mechanical stability of resultant composites for structural applications [21]. The authors investigated the mechanical behavior of unidirectional flax/synthetic fibers hybrid composites [22]. AL-Oqla et al. confirmed the reliable use of date palm fiber based polymer composites for automotive applications on the basis of mechanical stability [23]. In this study, the authors fabricated a new composite material based on sisal-jute fiber and demonstrated the perfect replacement of synthetic glass fiber reinforced polymer composites with bio composites [24]. Sanjay et al. [16] reviewed various techniques for improving suitability of natural fibers in polymer composites. Asim et al. [25] compared the mechanical properties of the silane modified pine leaf fiber/phenolic composites with silane treated-kenaf fiber/phenolic composites for green applications. The author of this study investigated the dynamic mechanical properties of the bamboo/woven kenaf fiber based composites for building applications [26]. Ozben et al. [27] studied drop weight technique for analyzing the impact behavior of hybrid composites for structural applications. This study demonstrated the impact of date palm fiber at different loading in epoxy composites on the basis of mechanical and thermal properties for engineering applications [28]. Safri et al. [29] reviewed the impact behavior for various hybrid composites synthesized from natural fibers for structural applications. Muhammad et al. [30] demonstrated the effect of kenaf fiber in glass fiber based composites and found highest impact strength in the resultant hybrid composites. However, till today no research work has been published on the combination of alkali treated natural fiber with native fiber in epoxy

matrix in order to understand their hybridization effects for the structural properties of polymer composite.

In this research work, different combinations of natural fibers i.e. alkali treated-date palm fiber and native coir fiber based epoxy novel composites were prepared using hand layup method. Further, authors of this paper have demonstrated the characteristics of all synthesized hybrid composites in terms of Physico-chemical stability using various kinds of analytical techniques like X-ray diffraction, Thermogravimetric analysis, tensile test, impact test and Contact angle measurement for green reinforcement applications.

Materials and Methods

Materials

The coir and jute fibers are procured from a local farmer near BHU, Varanasi, Uttar Pradesh. Fibers are washed with distilled water and kept in an oven at a temperature of 70 °C for 8 h. Further, fibers are ground in a powder form. The epoxy resin (LY 556) and the hardener HY-951 are acquired from Green products Pvt. Ltd. Epoxy LY556 of density 1.15–1.20 g/cm³, mixed with hardener HY951 of density 0.97–0.99 g/cm³ was used to synthesize the composite laminate. The epoxy and hardener were mixed in the ratio 2:1 on a weight basis. Sodium hydroxide pellets were purchased from Green products Pvt. Ltd. It is highly soluble in water and was used for natural fiber surface pretreatment to enhance bonding between fibers and polymer.

Alkali Pretreatment

The external sheath of lignin and to some extent hemicelluloses restricts the cellulose to make the effective interfacial bond with the polymers. Thus to overcome poor adhesion, several pretreatment methods are to be incorporated to improve the bonding between the hydrophilic fiber and hydrophobic matrix [31]. In order to get improved mechanical and thermal characteristics of the composites, date palm fiber was subjected to the NaOH treatment process. Alkali treatment provides porous structure of fiber that is increase the interfacial bonding between treated and non-treated fibers. A 5 g weight of sieved agricultural waste was treated with 9.1% (W/V) NaOH aqueous solution for 24 h at room temperature followed by drying in an oven at 70 °C for 12 h [16, 32].

Synthesis of Green Composites

Initially, a mold of dimension 220 mm × 220 mm × 3 mm was cleaned and dried before the fabrication process. The releasing wax was also applied to mold releasing sheet and

Table 1 Compositional analysis for synthesized green composites

Composites	Chemical pretreatment	Date palm fiber (wt%)	Coir fiber (wt%)
E1	–	–	100
E2	Date palm fiber treated with NaOH	50	50
E3	Date palm fiber treated with NaOH	25	75
E4	Date palm fiber treated with NaOH	75	25
E5	Date palm fiber treated with NaOH	100	0
E6	–	50	50
E7	–	100	0
E8	–	25	75
E9	–	75	25

fibers were mixed with the resin inside the mold using hand layup technique. Further, the mixture was allowed to set inside the mold for a period of 24 h at room temperature. In this work, different combinations of treated-date palm/coir/epoxy are prepared which are shown in Table 1. The specimens were finally cut into the appropriate dimensions for characterization.

Characterizations for Treated-Date Palm/Coir Based Epoxy Composites

XRD analysis was used to analyze the crystalline changes after incorporation of natural fibers in epoxy polymer using X-ray diffractometer (model Minifux II, Rigaku). The crystallinity index (CI) of the composite samples was calculated by using the formula:

$$CI = \frac{I_{max} - I_{am}}{I_{max}} \times 100 \quad (1)$$

where I_{max} is the maximum intensity of diffraction on the crystallographic plane at a 2θ angle and I_{am} is the intensity of diffraction of the amorphous material taken at a 2θ angle from where the peak originates.

In order to visualize the thermal stability for all green composites, TGA analysis is performed from 30 to 800 °C temperature at a scan rate of 10 °C/min in an inert atmosphere using Perkin Elmer instrument, USA and weight changes is recorded as a function of temperature. The sessile drop method (KRUSS DSA25 Series, Germany) was used to check water repelling characteristics for all green composites. The tensile test of the composites was conducted in INSTRON 1195 testing machine as per the ASTM D3039 standards. This property is determined in accordance with the ASTM D3039. The specimen was cut in the required dimension 50 mm × 20 mm × 3 mm. Further, the test was conducted at a constant strain rate of 2 mm/min and

demonstrated the mechanical stability of the material. Dart impact strength for all hybrid composites was analyzed using Dart impact tester (Asian Test Equipments, Hapur, India). In this test, a dart was free fell on the surface (220 mm × 220 mm × 3 mm) with 13.2 m/s striking velocity and calculated impact strength using following equation.

$$\text{Impact energy}(KE) = \frac{1}{2}mv^2 \quad (2)$$

$$\text{Impact Force} = \frac{KE}{d} \quad (3)$$

where d (m) is the thickness of hybrid composite and m (g) is dart impact failure weight.

Results and Discussions

XRD Analyses for Hybrid Composites

XRD analysis was used to estimate crystalline changes in the hybrid composites. In this test, XRD analysis for E1, E2, E3, E4, E5, E6, E7, E8 and E9 was conducted and shown in Fig. 1. There is one major peak found in XRD spectra of all composites which are 20.68° for E1, 20.52° for E2, 20.74° for E3, 20.46° for E4, 20.86° for E5, 20.07° for E6, 20.19° for E7, 19.83° for E8 and 19.59° for E9, respectively. The higher intensity peak observes in E2 hybrid composite at 20.52° 2 theta. The crystallinity index value is 84.48% for E1, 88.37% for E2, 84.32% for E3, 85.92% for E4, 85.74% for E5, 85.61% for E6, 85.82% for E7, 84.61% for E8 and 84.76% for E9, respectively.

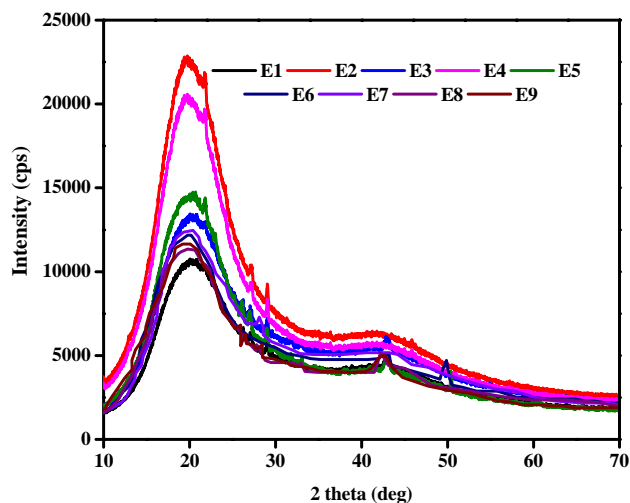


Fig. 1 XRD analyses for E1, E2, E3, E4, E5, E6, E7, E8, and E9 hybrid composites

Some shifting of 2 theta peaks observes due to biomass addition in epoxy matrix. The presence of effective peak at around $21^{\circ} 2$ theta in XRD spectra attributes to the crystalline structure of cellulose that is present in the hybrid composite. The higher intensity peak observes in the E2 hybrid composite shows better compatibility of fibers with epoxy matrix assuring remarkable mechanical and thermal stabilities which confirms in mechanical and thermal tests. A similar result that is higher intensity peak concept in composites is also explained by Laadila et al. [33] in their published article.

Thus it can be concluded that 50% treated date palm fiber/50% coir fiber based epoxy composite has a higher crystalline stable structure as compared to other hybrid composites showing its suitability for green applications.

TGA Analyses for Hybrid Composites

Thermal stability analyses for coir fiber incorporated treated-date palm fiber/epoxy composites have been studied using TGA analysis. In this analysis, thermal stability tests for E1, E2, E3, E4, E5, E6, E7, E8 and E9 were performed in a programmed temperature range of 30–800 °C (Fig. 2). The primary, main and final degradation temperature ranges for hybrid composites have been determined in this analysis. Small degradation is mainly observed in E1, E3, E6, E7, E8 and E9 from 100 to 250 °C temperature range. The main degradation starts from 250 °C around at 14% weight loss for E1, 5.13% weight loss for E2, 4.71% weight loss for E3, 4.86% weight loss for E4, 4.87% weight loss for E5, 7.31% weight loss for E6, 5.51% weight loss for E7, 8.41% weight loss for E8 and 9.97% weight loss for E9, respectively. In addition, degradation ends at around 522 °C with 92%

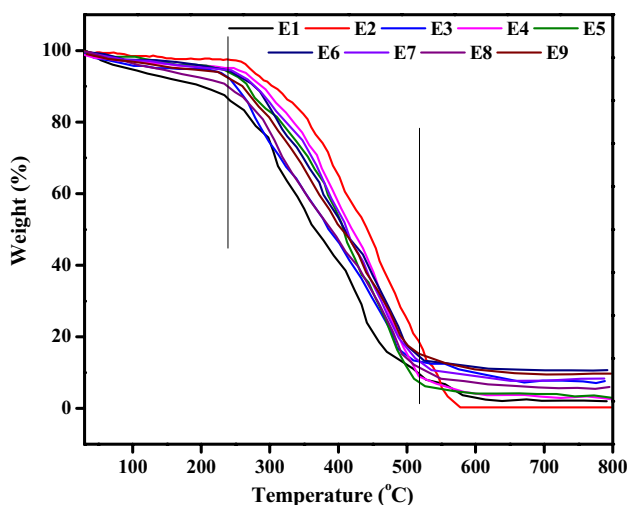


Fig. 2 TGA analyses for E1, E2, E3, E4, E5, E6, E7, E8, and E9 hybrid composites

weight loss for E1, 560 °C with 95% weight loss for E2, 511 °C with 86% weight loss for E3, 517 °C with 93% weight loss for E4, 526 °C with 94% weight loss for E5, 515 °C with 86.44% weight loss for E6, 518 °C with 87.81% weight loss for E7, 519 °C with 89.29% weight loss for E8, 521 °C with 89.79% weight loss for E9, respectively.

The earlier degradation is observed in E1, E3, E6, E7, E8 and E9 composites. This may be lot of lesser amounts of some impurities like hemicellulose, pectin and wax present in treated-date palm fiber. Gheith et al. [28] synthesized 50% date palm fiber based epoxy composites and observed similar initial degradation corresponds to water molecules and impurities. This characteristic associated with poor interfacial bonding between the fiber and polymer ascribe to less mechanical stability of natural fiber based composites. Nair et al. [34] also observed similar result sisal fiber based polystyrene composites for reinforcement applications. Puglia et al. [35] demonstrated the effect of alkali and silane treatments on phormium tenax fiber and observed initial degradation in native fiber based composites due to wax and pectin present in the material. In addition, it shows lower thermal stability than the higher cellulose containing composites. The main degradation starts from 250 to 550 °C due to the degradation of cellulose and lignin in the composites. The thermal stability of E2 seems higher as compared to all other composites. This is the main effect of hybrid composites synthesized from equal amounts of native coir fiber and treated-date palm fiber based epoxy composites. Gheith et al. [28] prepared date palm fiber at different weight fractions based epoxy composites and found highest thermal stability in 50% date palm fiber based epoxy composites. Chee et al. [26] prepared 50% bamboo fiber incorporated 50% kenaf fiber based epoxy hybrid composites and observed highest dimensional stability of the resultant composite. Boopalan et al. [36] used equal percentages of jute and banana fibers in epoxy matrix and observed higher thermal stability as compared to other hybrid composites. This behavior reveals the strong adhesion present in treated fiber incorporated native fiber based epoxy composites and assuring E2 composite suitability for structural applications.

Wettability of Hybrid Composites

The wettability of hybrid composites was evaluated using the sessile drop method as shown in Fig. 5. The sessile drop method is based on the surface tension between liquid-solid interfaces. In this analysis, the sessile drop is permitted to fall on the surface of hybrid composites and observe the wettability of the surface with time. Higher contact angle (greater than 90°) represents the less wettability of the surface and confirms the hydrophobic characteristics of the synthesized hybrid composites. Generally, fibers are hydrophilic in nature and have higher wettability characteristics. Authors

of this paper have prepared different combinations of treated and untreated fibers in epoxy matrix and observed its contact angle in order to attain the higher hydrophobic quality among all synthesized hybrid composites. The contact angle value is measured progressively with time as shown in Fig. 3. The averaged contact angle value is 29.09° for E1, 101.78° for E2, 54.50° for E3, 73.56° for E4, 61.88° for E5, 42.16° for E6, 38.99° for E7, 33.07° for E8, and 40.43° for E9, respectively. It is clear from the graph that the contact angle decreases as a function of time. So, the length of the interface between liquid drop and epoxy hybrid composites increases as time elapsed. This surface characteristic explores mainly due to liquid spreading over the hybrid composite surface. The sessile drop volume decreases due to liquid penetrate into the surface of date palm/coir fiber based epoxy composites. Zhang et al. [37] explained the

wettability behavior of rice straw/coir fiber based composite and observed similar results in their published article.

The contact angle value is higher for E2 hybrid composite. This may be due to strong adhesion present between treated-date palm fiber and untreated- coir fiber. Generally, contact angle greater than 90° explores between the sessile drop and hybrid composite surface is very weak. This characteristic is enabling E2 composite for hydrophobic structural applications.

Tensile Test for Hybrid Composites

The mechanical stability test is playing a pivotal role in visualizing the ability of hybrid composites to withstand force. The tensile test for E1, E2, E3, E4, E5, E6, E7, E8, E9 and E10 hybrid composites were performed in this analysis (Fig. 4). Tensile strength, elongation limit and young modulus have been summarized in Table 2. The mechanical stability of hybrid composites depends on fiber-polymer interaction, fiber percentage and distribution of fiber in the matrix. Stress represents the maximum stability of composites to withstand force and strain represents the change in length of material with respect to original length of the material. The stress vs. strain curve is depicted in Fig. 5c. The tensile strength is 54.03 MPa for E1, 76.51 MPa for E2, 55.65 MPa for E3, 61.04 MPa for E4, 59.89 MPa for E5, 49.02 MPa for E6, 50.01 MPa for E7, 45.85 MPa for E8, 46.75 MPa for E9 and 48.84 MPa for E10, respectively. The tensile strength is higher for E2 (50% treated date palm fiber/50% untreated coir fiber/epoxy composite) hybrid composites due to strong interfacial bonding present between fibers and polymer. Further addition of fiber causes a decrement in the mechanical stability of the resultant hybrid composites. Boopaln et al. [36] explained similar results in jute/banana fiber based epoxy composites in their published literature. Asim et al. [25] compared the mechanical property of treated-fibers based composites and observed highest tensile strength

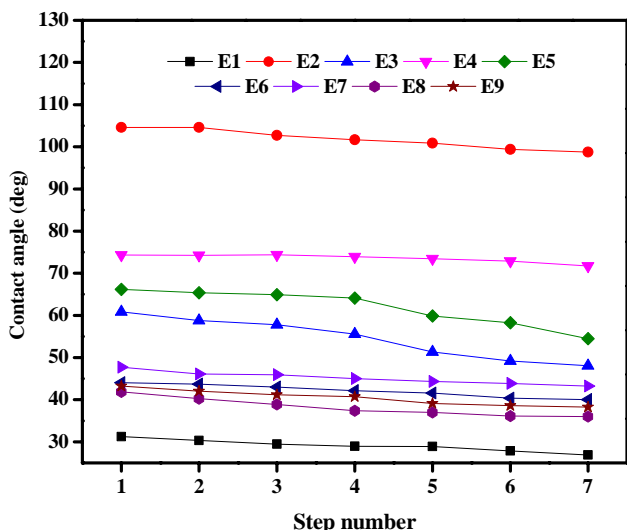


Fig. 3 Wettability analyses for E1, E2, E3, E4, E5, E6, E7, E8, and E9 hybrid composites

Table 2 Dart impact velocity, dart impact height, dart impact strength, dart impact failure weight, tensile strength, elongation at break (%), tensile modulus for E1, E2, E3, E4, E5, and E6 hybrid composites

Hybrid composite	Dart Impact velocity before strike (m/s)	Dart impact height (m)	Dart impact failure weight (g)	Dart impact strength (J/m)	Tensile strength (MPa)	Elongation at break (%)	Tensile modulus (MPa)
E1	3.63	0.66	310	709.56	45.85	1.34	3421
E2	3.63	0.66	380	832.2	76.51	2.77	2762
E3	3.63	0.66	335	733.65	55.65	2.53	2199
E4	3.63	0.66	360	788.4	61.04	2.61	2388
E5	3.63	0.66	350	766.5	59.89	2.34	2599
E6	3.63	0.66	325	711.75	49.02	0.75	6535
E7	3.63	0.66	330	722.70	50.01	0.49	10206
E8	3.63	0.66	315	689.85	46.75	0.62	7540
E9	3.63	0.66	320	700.8	48.84	0.55	8880

(≈ 46 MPa) in 50% kenaf fiber based phenolic composites for engineering applications. Chee et al. [26] also observed highest mechanical stability in 50% bamboo/50% kenaf fibers based epoxy composites.

The elongation limit is 2.25% for E1, 2.77% for E2, 2.53% for E3, 2.61% for E4, 2.34% for E5, 0.75% for E6, 0.49% for E7, 1.34% for E8, 0.62% for E9 and 0.55% for E10, respectively. The higher percentage of flexible limit is observed in the case of E2 hybrid composite due to strong adhesion present between the fibers and polymer. Authors also observed similar result in 50% pineapple leaf based composites for green applications [25].

The tensile modulus is the ratio of stress and strain. The tensile modulus is 2401 MPa for E1, 2762 MPa for E2, 2199 MPa for E3, 2388 MPa for E4, 2599 MPa for E5, 6235 MPa for E6, 10206 for E7, 3421 for E8, 7540 MPa for E9 and 8880 MPa for E10, respectively (Table 2).

The mechanical stability of E2 hybrid composite is higher as compared to other hybrid composites. This signifies the better adhesion exists between fibers and polymer assuring E2 composite suitability for green structural applications (Fig. 4).

Dart Impact Test

Dart impact strength is a valuable property in terms of structural applications. Dart impact strength explores a material ability to withstand a sudden force applied on the surface of hybrid composites and demonstrated the quality of the sample for structural industries. In this dart test, the impact strength is calculated for all hybrid composites using the free fall method. This is a reliable technique to understand the behavior of composite's impact resistance according to ASTM D1709. The thickness of the hybrid composite is 3 ± 0.05 mm. Initially, a 75 g dart is free-fell at 66 cm impact height to the surface of the hybrid composite and observed hybrid composite is partially fractured or not. The impact strength is calculated at dart impact failure weight. All characteristics such as dart impact strength, Dart impact energy, dart failure weight, and striking velocity before impact for E1, E2, E3, E4, E5, E6, E7, E8, E9 and E10 are shown in Table 2. The dart impact strength is 709.56 J/m for E1, 832.2 J/m for E2, 733.65 J/m for E3, 788.4 J/m for E4, 766.5 J/m for E5, 711.75 J/m for E6, 722.70 J/m for E7, 678.9 J/m for E8, 689.85 J/m for E9 and 700.8 J/m for E10, respectively (Fig. 5).

The impact strength depends on fiber-matrix interaction behavior and was observed highest in the case of 50% coir incorporated 50% treated-date palm fiber based hybrid composites (E2). Asim et al. [25] synthesized pine apple leaf based phenolic composites and observed similar result in 50% treated-pine apple leaf reinforced composites for green applications. So increase in impact strength was ascribed to

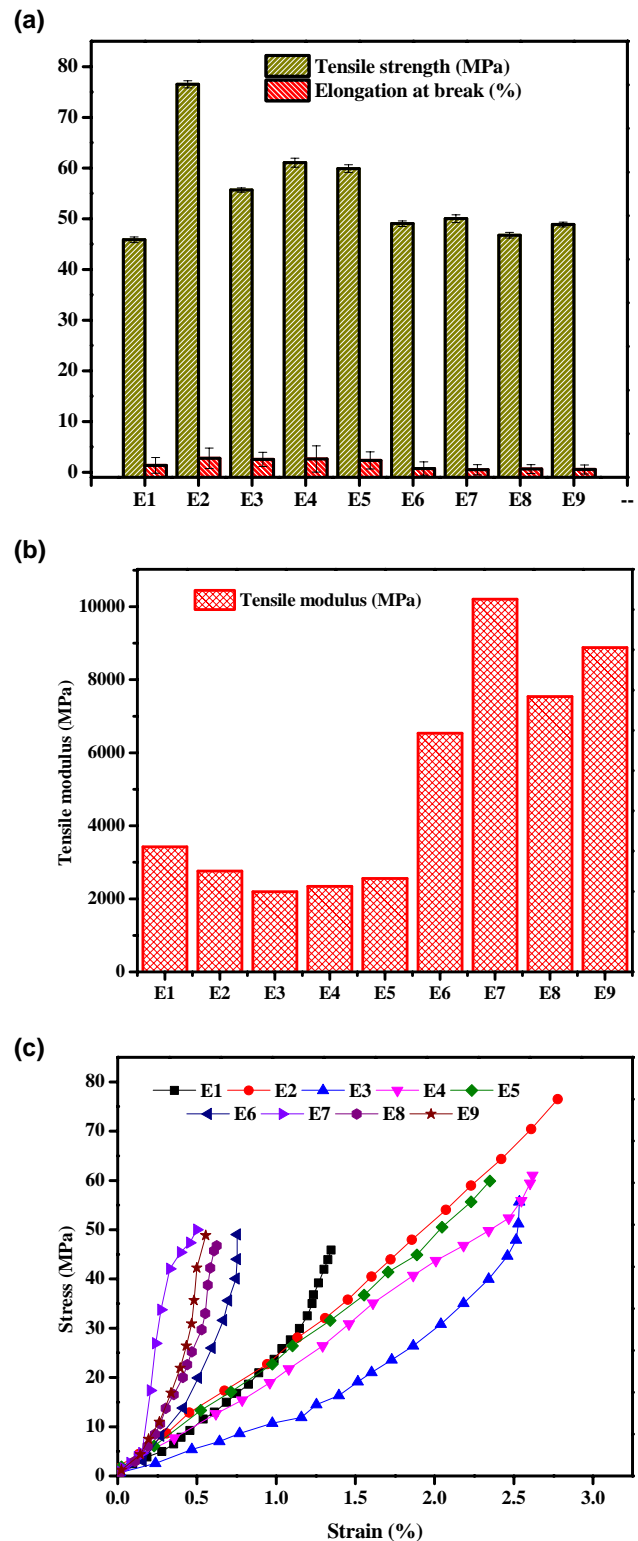


Fig. 4 **a** Tensile strength and elongation at break tests for E1, E2, E3, E4, E5, E6, E7, E8, and E9 hybrid composites. **b** Tensile modulus for E1, E2, E3, E4 and E5 hybrid composites. **c** Stress vs., strain curve for E1, E2, E3, E4, E5, E6, E7, E8, and E9 hybrid composites

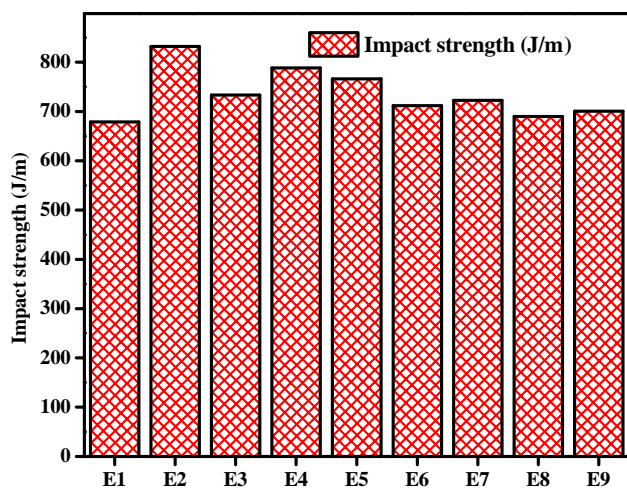


Fig. 5 Impact strengths for E1, E2, E3, E4, E5, E6, E7, E8, and E9 hybrid composites

homogeneous distributions of fibers in epoxy matrix resulting in remarkable impact strength. So, this excellent interfacial interaction presented between fibers and polymer which was proved in a stress test for green structural applications.

Conclusions

The impacts of fiber type and their different combinations on surface morphology, mechanical, thermal, crystalline and wettability characteristics were studied in this paper. The hybrid composite synthesized from treated-date palm fiber incorporated coir fiber based epoxy composite has proven as an inexpensive novel material for structural applications. The coir fiber has a remarkable impact on the thermal and mechanical properties of E2 hybrid composite, especially the wettability, load bearing ability and tensile strength. The E2 hybrid composite consists of equal weight fraction of treated-date palm fiber and coir fiber has represented the highest tensile and impact strengths with reliable elongation limit as compared to other hybrid composites at different weight fractions of fibers. The higher thermal stability with suitable less wettability of E2 hybrid composite has also managed to perform excellently for thermal stable hydrophobic structural applications. So it can be concluded that E2 had the ability to be used in structural applications which might be a possible solution of agricultural wastes.

References

- Pickering KL, Efendy MGA, Le TM (2016) *Compos Part A: Appl Sci Manufact* 83:98
- Le TM, Pickering KL (2015) *Compos Part A: Appl Sci Manufact* 76:44
- Dixit S, Yadav VL (2019) *Indian J Chem Technol* 26:494

- Kenned JJ, Sankaranarayanan K, Binoj JS, Chelliah SK (2020) *Compos Sci Technol* 185:107890
- Jiang L, Zhang X, Chen Y, Qiao L, Lu X, Tian X (2018) *Mater Chem Phys* 219:368
- Santos JCD O, LÁd G, Vieira LM, Mano V, Freire RTS, Panzera TH (2019) *Constr Build Mater* 211:427
- Sun Z, Mingming W (2019) *Ind Crops Prod* 137:89
- Chennouf N, Agoudjil B, Boudenne A, Benzarti K, Bouras F (2018) *Constr Build Mater* 192:348
- Ozawa M, Subedi Parajuli S, Uchida Y, Zhou B (2019) *Constr Build Mater* 206:219
- Kundu SP, Chakraborty S, Chakraborty S (2018) *Constr Build Mater* 191:554
- Dungani R, Karina M, Subyakto AS, Hermawan D, Hadiyane A (2016) *Asian J Plant Sci* 15:42
- Khiari R, Mhenni MF, Belgacem MN, Mauret E (2010) *Biores Technol* 101:775
- Mirmohamadsadeghi S, Chen Z, Wan C (2016) *Bioresour Technol* 209:386
- Salehian P, Karimi K, Zilouei H, Jeihanipour A (2013) *Fuel* 106:484
- Agbor VB, Cicek N, Sparling R, Berlin A, Levin DB (2011) *Biotechnol Adv* 29:675
- Siengchin MRS, Parameswaranpillai S, Jawaid J, Pruncu M, Khan CI A (2019) *Carbohydr Polym* 207:108
- da Silva LV, Júnior JHSA, Angrizani CC, Amico SC (2013) *J Reinf Plast Compos* 32:197
- Mochane M, Mokhena TC, Mokhothu T, Mtibe A, Sadiku E, Ray SS, Ibrahim I, Daramola O (2019) *Express Polym Lett* 13:159
- Otto GP, Moisés MP, Carvalho G, Rinaldi AW, Garcia JC, Radovanovic E, Fávoro SL (2017) *Compos Part B: Eng* 110:459
- Sanjay MR, Yogesha B (2017) *Mater Today* 4:2739
- Alavudeen A, Rajini N, Karthikeyan S, Thiruchitrabalam M, Venkateshwareen N (2015) *Mater Des* (1980–2015) 66:246
- Zhang Y, Li Y, Ma H, Yu T (2013) *Compos Sci Technol* 88:172
- Al-Oqla FM, Sapuan SM (2014) *J Clean Prod* 66:347
- Ramesh M, Palanikumar K, Reddy KH (2013) *Compos Part B* 48:1
- Asim M, Jawaid M, Abdan K, Ishak MR (2018) *J Polym Environ* 26:1520
- Chee SS, Jawaid M, Sultan M, Alothman OY, Abdullah LC (2019) *Compos Part B: Eng* 163:165
- Özben T (2016) *Mater Test* 58:442
- Gheith MH, Aziz MA, Ghori W, Saba N, Asim M, Jawaid M, Alothman OY (2019) *J Mater Res Technol* 8:853
- Safri SNA, Sultan MTH, Jawaid M, Jayakrishna K (2018) *Compos Part B: Eng* 133:112
- Muhammad YH, Ahmad S, Abu Bakar MA, Mamun AA, Heim HP (2015) *J Reinf Plast Compos* 34:896
- Dixit S, Yadav VL (2020) *Polym Bull* 77:1307
- Dixit S, Yadav VL (2019) *J Clean Prod* 240:118228
- Laadila MA, Hegde K, Rouissi T, Brar SK, Galvez R, Sorelli L, Cheikh RB, Paiva M, Abokitse K (2017) *J Clean Prod* 164:575
- Nair KM, Thomas S, Groeninckx G (2001) *Compos Sci Technol* 61:2519
- Puglia D, Monti M, Santulli C, Sarasini F, De Rosa IM, Kenny JM (2013) *Fibers Polym* 14:423
- Boopalan M, Niranjana M, Umapathy M (2013) *Compos Part B: Eng* 51:54
- Zhang L, Hu Y (2014) *Mater Des* 55:19

Publisher's Note Springer Nature remains neutral with regard to jurisdictional claims in published maps and institutional affiliations.

Rhamnolipid–Metal Ions (Cr^{VI} and Pb^{II}) Complexes: Spectrophotometric, Conductometric, and Surface Tension Measurement Studies

Om Hari¹ · Santosh K. Upadhyay¹ 

Received: 6 March 2020 / Revised: 12 November 2020 / Accepted: 18 November 2020
© 2020 AOCS

Abstract The formation of rhamnolipid complexes with metal ions of chromium (VI) and lead (II) has been studied spectrophotometrically, conductometrically, and by surface tension measurement. The values of the critical micelle concentration (CMC) of rhamnolipid, obtained by spectroscopic, conductometric, and surface tension measurements, were 5.2×10^5 , 5.0×10^5 , and 5.3×10^5 mol.dm⁻³, respectively, which are in close agreement. An increase in CMC on increasing metal ion content in the rhamnolipid solution and a shift in λ_{max} in the spectra of rhamnolipid indicated the formation of a complex between rhamnolipid and both the metal ions, namely, chromium (VI) and lead (II). The values of stability constants for the {rhamnolipid–chromium (VI)} and {rhamnolipid–lead (II)} complexes have been determined by spectroscopic data and were as 0.58×10^4 and 0.50×10^4 at 308 K, respectively.

The thermodynamic parameters for micellization, namely, free energy change (ΔG_{mic}), entropy change (ΔS_{mic}), and heat enthalpy change (ΔH_{mic}), have been determined by conductivity measurements. An increase in the negative value of ΔG_{mic} and a decrease in the value of ΔS_{mic} on increasing metal ion content in the surfactant solution indicated lower micellization of rhamnolipid in the presence of metal ions. The electrostatic attractions and entrapment of chromium (VI) in the micelles of the biosurfactants were found to be responsible for {rhamnolipid–lead (II)} and {rhamnolipid–chromium (VI)} complexes, respectively.

Keywords Rhamnolipid · Chromium (VI) · Lead (II) · Biosurfactant complexes

J Surfact Deterg (2020).

Introduction

The recovery of heavy metals from contaminated soil and water using biosurfactants have been a subject of major interest in recent years. The formations of biosurfactant heavy metal complexes have been observed by researchers (Ayangbenro and Babalola, 2018; Dan et al., 2017; Herman et al., 1995; Juwarkar et al., 2007; Miller, 1995; Mulligan, 2005; Neilson et al., 2003; Stacey et al., 2008; Tan 1994; Wang and Mulligan, 2009) during the remediation/recovery of heavy metals from soil/water. It has been observed (Kim and Vipulanandan, 2006; Lang, 2002; Maier and Soberon-Chavez, 2000; Ochoa-Loza et al., 2001; Slizovskiy et al., 2011) that the carboxyl or hydroxyl group of the biosurfactant forms a strong bond with heavy metals. However, not much information is available on the nature and thermodynamic parameters of these biosurfactant metal complexes.

Recently, the stability constant and thermodynamic parameters for the formation of the complexes of saponin with metal ions, namely, chromium (VI) and lead (II), have been reported by Upadhyay and Hari (2019). The complex formation was reported as the formation of a bond between metal ions and the carbonyl group of saponin. The formation of complexes by forming a bond between the hydroxyl and carbonyl groups of biosurfactants and metals have also been reported by other researchers (Hong et al., 2000; Mulligan et al., 1999; Tang et al., 2017). The stability

✉ Santosh K. Upadhyay
upadhyay_s_k@rediffmail.com

¹ Department of Applied Sciences, Dr. Ambedkar Institute of Technology for Handicapped, Awadhपुरi, Kanpur, Uttar Pradesh 208024, India

constant for the complex between saponin and chromium (VI) was higher than that for the complex between saponin and lead (II). In order to understand the nature of metal ion biosurfactant complexes, it was thought to be worthwhile to conduct further studies with other biosurfactants.

Rhamnolipids are microbial biosurfactants and act as a natural surface-active agent. They consist of one or two (L)-rhamnose with a glycoside linkage to the hydrophilic group having one or two β -hydroxy fatty acids. Depending on the number of rhamnose molecules, rhamnolipids are classified as either mono- or di-rhamnolipid. Rhamnolipids have widely been used in various fields (Fazaalipoor et al., 2010; Khoshdast et al., 2011; Ochoa-Loza et al., 2007; Sandrin et al., 2000; Torrens et al., 1998).

It has been observed that rhamnolipids act as ligands and have a very strong affinity for metals (Maier and Soberon-Chavez, 2000; Mulligan, 2005). Rhamnolipids are weak acids, and due to the presence of carboxylic acid moieties, they undergo aggregation in solutions (Herman et al., 1995; Tan et al., 1994). Therefore, it was worthwhile to perform a detailed investigation on the rhamnolipid–metal ion complexes in order to understand the nature of these complexes and to determine the thermodynamic parameters for the complex's formation.

Chromium (VI) and lead (II) are major problems in industrial effluents, and removal of these metal ions from effluents must be considered seriously in order to ensure environmental protection. Therefore, the formation of rhamnolipid complexes with two metal ions, namely, chromium (VI) and lead (II), in aqueous medium are investigated. The complex formation has been studied spectrophotometrically, conductometrically, and by surface tension measurement, and the results obtained by these three methods were compared.

Experimental Procedures

Materials

R-90 Rhamnolipid (Lot number AGA031918b; Sigma-Aldrich (St. Louis, MO, USA)) was purchased from AGAE Technologies, Corvallis, OR, USA. It was a light brown, granular solid consisting a mixture of RhaRhaC₁₀C₁₀ (C₃₂H₅₈O₁₃, $m/z = 649$) and RhaC₁₀C₁₀ (C₂₆H₄₈O₉, $m/z = 503$). The average molecular weight of the rhamnolipid, i.e., 578, was considered in the present investigation. The supplied rhamnolipid was used, and purity was checked with infrared spectroscopy (IR) spectra and compared with previously reported literature. The rhamnolipid solutions were prepared in double-distilled water. The critical micelle concentration (CMC) of rhamnolipid was determined by

surface tension measurement and was found to be 5.3×10^{-5} mol dm⁻³ at room temperature of 310 K. Aşçı et al. (2008) reported the CMC of rhamnolipids to be 50 mg L⁻¹ or 8.6×10^{-5} mol dm⁻³. It is also reported that biosurfactants have low CMC within the range of 1–200 mg L⁻¹ (Lang and Wagner, 1987).

Analytical-grade chemicals K₂Cr₂O₇ (purity 99.9%, Thomas Baker, Maharashtra, New Delhi, India) and Pb(NO₃)₂ (purity 99.5%, Rankem, India) were used for the preparation of the solutions. All experiments were performed with double-distilled water.

Spectroscopic Study

A UV–visible spectrophotometer (BT-UVS-DB8-E, Benchtop Lab System, India) for absorbance measurement was used for spectroscopic studies. Square quartz cells of a thickness of 10 mm with a silt width of 1 nm were used. Aqueous solutions of rhamnolipid in the absence and presence of metal ions, namely, chromium (VI) and lead (II), were prepared and were maintained at 310 K to establish the equilibrium. The spectra of these solutions were reported. The experiments were repeated thrice. The reported results were reproducible within $\pm 2\%$.

The stability constants for rhamnolipid–metal ion complexes have been determined by differential spectroscopy as reported in our earlier study (Upadhyay and Hari, 2019). Kawamura et al. (1989) used the following equation to calculate the partition coefficient (K_x) for metal–surfactant interaction:

$$\frac{1}{\Delta A} = \frac{1}{K_c \Delta A_\infty (C_a + C_s^m)} + \frac{1}{\Delta A_\infty} \quad (1)$$

where ΔA is the difference of absorbance, i.e., (absorbance of rhamnolipid + metal-ions) – (absorbance of metal-ions only), and K_c and K_x are the stability constant and partition coefficient, respectively, and are related as follows:

$$K_x = K_c X n_w \quad (2)$$

where n_w is moles of water per dm⁻³.

ΔA_∞ is the difference in absorbance (i.e., ΔA) at infinite dilution; C_a is the concentration of additive (metal ions) and $C_s^m = C_s - \text{CMC}_o$, where C_s is concentration of rhamnolipid and CMC_o represents the CMC of the surfactant in water. According to Eq. (1), the value of K_c can be determined with the help of intercept ($1/\Delta A$) and slope ($1/K_c \cdot \Delta A K_\infty$) of the plot between ($1/\Delta A$) and $1/[\text{Rhamnolipid}]$.

The standard free energy change of the partition was calculated using the plot of Younas et al. (2017) following the relationship,

$$\Delta G_p = -RT \ln K_x \quad (3)$$

Conductometric Study

A digital conductivity meter (model EI-641, EISCO, Ambala, India) was used for the conductivity measurement. The conductivity meter can measure specific conductivity in the range of 0.01–199.9 μS . The instrument was calibrated with aqueous KCl solution. The data were reproducible within a ± 0.05 error. For conductivity, CMC, and the thermodynamic parameter measurements, solutions were maintained at 310 K for 30 min to achieve the equilibrium conditions. Then, the specific conductivity of these solutions was measured. The experiments were repeated thrice. The values of CMC were reproducible within $\pm 2\%$.

The following equations (Usman and Siddiq, 2013; Usman et al., 2010, 2013) have been used for determining thermodynamic parameters, namely, free energy change (ΔG_m), enthalpy change (ΔH_m), and entropy change (ΔS_m) for micellization process;

$$\Delta G_m = (2 - \beta) RT \ln X_{cmc} \quad (4)$$

$$\Delta H_m = -2.303 (2 - \beta) RT^2 \left[\frac{\partial \log X_{cmc}}{\partial T} \right] \quad (5)$$

$$\Delta G_m = \Delta H_m - T \Delta S_m \quad (6)$$

where R is the universal gas constant ($8.314 \text{ J mol}^{-1} \text{ K}^{-1}$), X_{cmc} is the mole fraction of surfactant, and β is the degree of dissociation ($\beta = \frac{S_2}{S_1}$, where S_1 and S_2 are slopes of straight lines before and after micellization, respectively).

Surface Tension Study

Surface tension was measured by a straight graduated stalagmometer (model 694 A, PERFIT, India) using the drop weight technique by measuring the weight of drops of a fluid falling from a capillary glass tube. The experiments were repeated until the surface tension was reproducible within $\pm 0.5 \text{ mN m}^{-1}$.

Results and Discussion

Spectroscopic Studies

The spectra of the rhamnolipid in the absence and in the presence of chromium (VI) and lead (II) were recorded at 310 K. The maximum absorbance of the aqueous solution of rhamnolipid was observed at 255 nm. In the presence of chromium (VI), the wavelength of maximum absorbance (λ_{max}) was shifted to 321 nm. In the presence of lead (II), the maximum absorbance peaks were obtained at 321, 334,

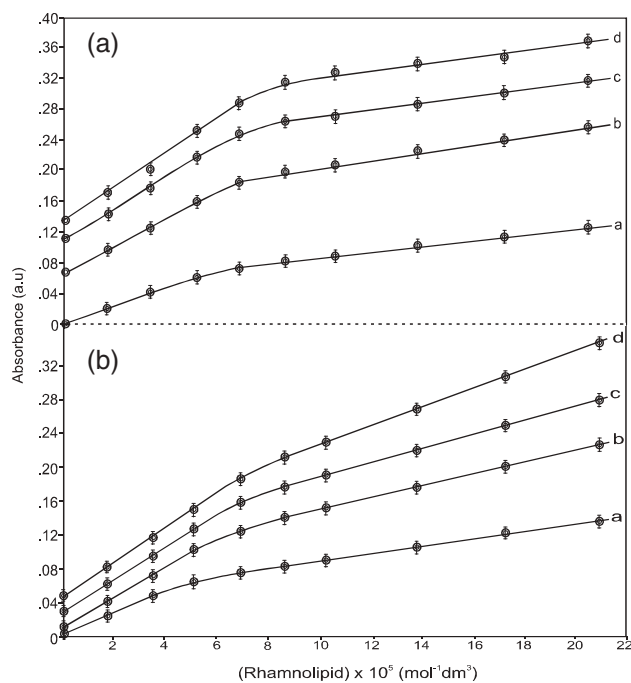


Fig 1 Plots of absorbance (A) versus [Rhamnolipid] at 310 K in absence and presence of metal ions. (A) a, b, c, and d rhamnolipid in presence of nil, 9.6×10^{-5} , 19.2×10^{-5} , and $28.8 \times 10^{-5} \text{ mol dm}^{-3} \text{ Cr}^{\text{VI}}$, respectively. (B) a, b, c, and d rhamnolipid in presence of nil, 4.8×10^{-5} , 9.6×10^{-5} , and $14.4 \times 10^{-5} \text{ mol dm}^{-3} \text{ Pb}^{\text{II}}$, respectively

and 376 nm. The interaction of rhamnolipid with metal ions is indicated by the shifting of λ_{max} of rhamnolipid in the presence of metal ions. The shift in λ_{max} toward a longer wavelength (red shift) is due to the complexation of rhamnolipid with metal ions.

The CMC of rhamnolipid in the absence and the presence of metal ions have been determined by plotting the absorbance against the concentration of rhamnolipid and by the point of interaction of two straight lines at lower and higher concentrations of rhamnolipid. Figure 1 represents (Absorbance) versus [Rhamnolipid] in the presence of different amounts of chromium (VI) and lead (II).

An increase in the absorbance with an increase in rhamnolipid concentration at λ_{max} (Fig. 1) in each case indicates the incorporation of metal ions within the micelles. The CMC in each case, obtained from Fig. 1, are given in Table 1. The CMC of rhamnolipid increases with an increase in metal ion concentration (Table 1).

The CMC of rhamnolipid in the presence of metal ions have also been determined by considering the difference in absorbance, i.e., ΔA . The plots of ΔA versus [Rhamnolipid] in the presence of different concentrations of chromium (VI) and lead (II) are represented in Fig. 2. The CMC of rhamnolipid in the presence of metal ions obtained from Fig. 2 are also given in Table 1. The CMC of rhamnolipid in the presence of metal ions obtained from Figs. 1 and 2 are found to be in good agreement.

Table 1 CMC, stability constant, and partition parameters determined by spectroscopic data

$10^5 [\text{Cr}^{\text{VI}}]$ (mol. dm ⁻³)	$10^5 [\text{Pb}^{\text{II}}]$ (mol. dm ⁻³)	10^5CMC (mol. dm ⁻³)		$10^4 K_c$	$10^5 K_x$	$\Delta G_p \pm 0.10$ (kJ mol ⁻¹)
		From Fig. 1	From Fig. 2			
9.60	—	6.4	6.4	0.60	3.33	-32.77
19.20	—	7.0	6.9	0.57	3.16	-32.63
28.80	—	8.4	8.0	0.56	3.11	-32.59
—	4.80	6.0	5.8	0.52	2.89	-32.40
—	9.60	7.2	6.9	0.50	2.77	-32.29
—	14.40	7.9	7.8	0.50	2.77	-32.29

CMC of rhamnolipid in absence of metal ions = 5.2×10^5 mol. dm⁻³; The CMC values were reproducible within $\pm 2\%$ in replicate runs.

The plots of $(1/\Delta A)$ versus $1/[\text{Rhamnolipid}]$ in the presence of different initial concentrations of chromium (VI) and lead (II) are given in Fig. 3. The values of K_c and K_x evaluated from the slopes and intercepts of these plots are given in Table 1. The higher average values of K_c (0.58×10^4) and K_x (3.20×10^5) in the presence of chromium (VI) than those in the presence of lead (II) (0.50×10^4) and K_x (2.81×10^5) indicate that chromium

(VI) partitioned more in rhamnolipid micelles than lead (II).

ΔG_p , the standard free energy change, was calculated in each case and is given in Table 1. The more negative value of ΔG_p in the case of chromium (VI) also indicates more spontaneity in the partition phenomena and stability in the case of chromium (VI) in comparison to lead (II). This is also supported by the Hofmeister series in proteins (Hofmeister, 1888), according to which an anion has a larger effect than a cation on the solubility of proteins and stability of their structure. A negative ion has a strong

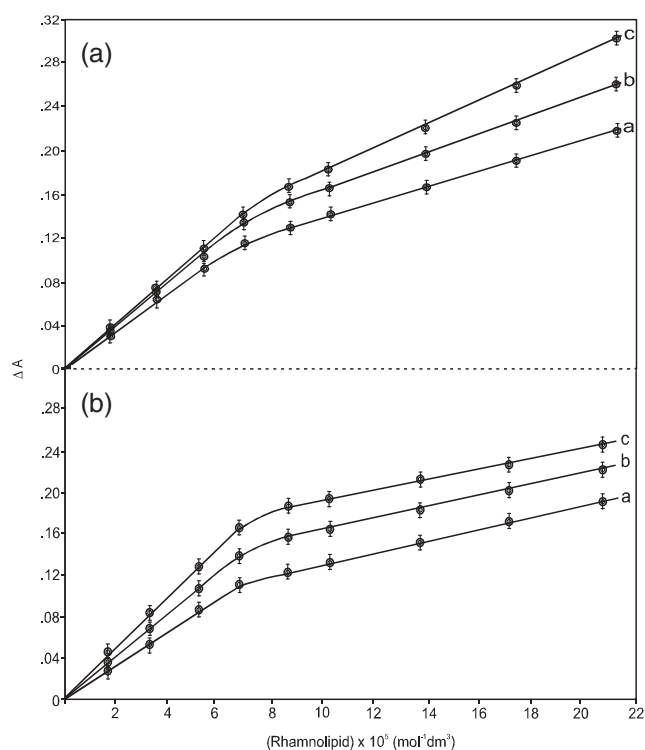


Fig 2 Plots of (ΔA) versus $[\text{Rhamnolipid}]$ at 310 K in presence of metal ions, where ΔA is (absorbance of solution consisting rhamnolipid and metal ions) - (absorbance of metal ions). (A) a, b, and c rhamnolipid in presence of 9.6×10^{-5} , 19.2×10^{-5} , and 28.8×10^{-5} mol dm⁻³ Cr^{VI}, respectively. (B) a, b, and c rhamnolipid in presence of 4.8×10^{-5} , 9.6×10^{-5} , and 14.4×10^{-5} mol dm⁻³ Pb^{II}, respectively

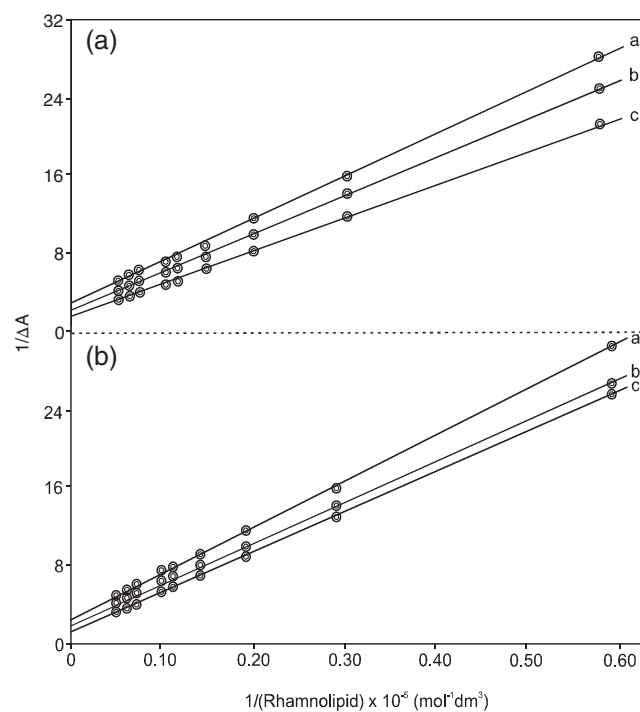


Fig 3 Plots of $(1/\Delta A)$ versus $1/[\text{rhamnolipid}]$ at 310 K in presence of metal ions. (A) a, b, and c rhamnolipid in presence of 9.6×10^{-5} , 19.2×10^{-5} , and 28.8×10^{-5} mol dm⁻³ Cr^{VI}, respectively. (B) a, b, and c rhamnolipid in presence of 4.8×10^{-5} , 9.6×10^{-5} , and 14.4×10^{-5} mol dm⁻³ Pb^{II}, respectively.

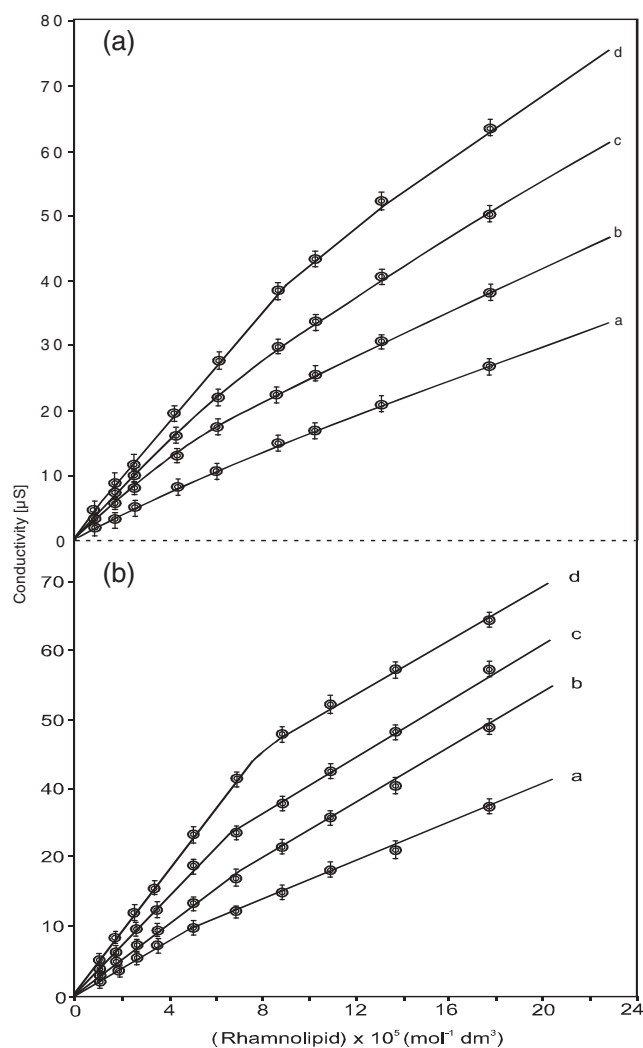


Fig 4 Plots of conductivity *versus* [Rhamnolipid] at 310 K in absence and presence of metal ions. (A) a, b, c, and d rhamnolipid in presence of nil, 4.8×10^{-5} , 9.6×10^{-5} , and 14.4×10^{-5} mol dm $^{-3}$ Cr VI , respectively. (B) a, b, c, and d rhamnolipid in presence of nil, 2.4×10^{-5} , 4.8×10^{-5} , and 7.2×10^{-5} mol dm $^{-3}$ of Pb II , respectively

“salting in” effect and may interact much more strongly in comparison to a cation, which has a “salting out” effect.

Specific Conductivity and Thermodynamic Parameters

The plots of specific conductivity *versus* rhamnolipid in the absence of metal ions and in the presence of three different initial concentrations of chromium (VI) and lead (II) are given in Fig. 4. It is observed that conductivity increases on increasing surfactant concentration, and a plot of specific conductivity *versus* rhamnolipid showed two straight lines at lower and higher rhamnolipid concentrations (Fig. 4). Furthermore, an increase in specific conductivity was observed on increasing metal ion concentration of the

solution. The CMC value in each case was evaluated by the intersection point of two straight lines.

The values of CMC of rhamnolipid in the absence and the presence of different initial concentrations of both metal ions, i.e., chromium (VI) and lead (II), are reported in Table 2. It is observed from Table 2 that the CMC of rhamnolipid was found to increase with an increased metal ion in the solution of rhamnolipid. On increasing the metal ion in rhamnolipid, the micellization increases due to the structure-breaking effect on adsorption of the metal ion, which results in an increase in CMC.

The CMC of rhamnolipid were also determined at different temperatures, namely, at 310, 315, and 320 K, and were found to be 5.0×10^{-4} , 5.5×10^{-4} , and 6.0×10^{-4} mol dm $^{-3}$, respectively. With the help of CMC values at different temperatures, the value of $\left[\frac{\partial \log X_{\text{cmc}}}{\partial T}\right]$ was calculated and was found to be 0.56×10^{-4} .

The values β , ΔG_{mic} , ΔS_{mic} , and ΔH_{mic} of aqueous rhamnolipid solution in the absence and presence of metal ions are given in Table 2. The negative magnitude of ΔG_{mic} indicates the spontaneity of micellization. The lower rise in entropy, ΔH_{mic} , and less-negative value of ΔG_{mic} on increasing metal ion content in the solution also indicate that micellization becomes less favorable on increasing metal ion content in the solution.

Surface Tension Method

CMC of rhamnolipid in the absence and the presence of both metal ions have also been determined by measuring the surface tension of solutions. The plots of surface tension *versus* log rhamnolipid in the presence of chromium (VI) and lead (II) are given in Fig. 5. The CMC evaluated from the intersection point of two straight lines (at lower and lighter concentrations of rhamnolipid) of these plots are summarized in Table 3. It was also observed that the values of CMC evaluated spectrophotometrically (Table 1), by specific conductivity (Table 2), and by the surface tension method (Table 3) in each case are in close agreement within the experimental error.

Complex between Rhamnolipid and Metal Ions

Biosurfactant–metal binding may involve ion exchange, counterion association, precipitation–dissolution, and electrostatic interactions (Rufino et al., 2012), although removal of metal ions by rhamnolipid depends on various factors, including the concentration of rhamnolipid. At very low concentrations of rhamnolipid, the monomers start complexation with metal ions, while at concentrations above CMC, the complexation efficiency is influenced by the rhamnolipid micelles (Dan et al., 2017).

Table 2 CMC and thermodynamic parameters for micellization of rhamnolipid determined from conductivity data

$10^5 [\text{Cr}^{\text{VI}}]$ (mol. dm ⁻³)	$10^5 [\text{Pb}^{\text{II}}]$ (mol. dm ⁻³)	10^5CMC (mol. dm ⁻³)	β	$-\Delta G_m \pm 0.10$ (kJ mol ⁻¹)	$-\Delta H_m \pm 0.05$ (kJ mol ⁻¹)	$\Delta S_m \pm 0.50$ (J K ⁻¹)
—	—	5.0	0.60	35.74	14.58	68.26
9.60	—	6.0	0.63	34.33	14.26	64.74
19.20	—	7.5	0.66	33.05	14.06	61.25
28.80	—	8.2	0.69	31.77	13.64	58.48
—	4.80	6.2	0.62	34.46	14.32	65.00
—	9.60	6.6	0.65	33.55	14.06	62.87
—	14.40	7.2	0.67	32.70	13.85	60.80

CMC of rhamnolipid in absence of metal ions = 5.0×10^5 mol. dm⁻³; the CMC values were reproducible within $\pm 2\%$ in replicate runs.

As the carboxyl group of rhamnolipid has a strong affinity with metal ions, the complex between rhamnolipid and Pb (II) may be proposed by forming a bond between the

carboxyl group of rhamnolipid and Pb (II). The complex between aescin (anionic biosurfactant) and divalent metal ions and the ionic bond character in the complex have also been confirmed by IR spectra (Hong et al., 1998).

In the present investigations, chromium (VI) and surfactants both are anionic, and therefore, the possibility of counter ion association and electrostatic attractions is negligible. The removal of chromium (VI) by a biosurfactant has been studied by Gnanamani et al. (2010), and chromium (VI) was observed to reduce to chromium (III) in the presence of the biosurfactant. Chromium (III) then was entrapped in the micelles of the biosurfactant. In the present investigation, the conversion of chromium (VI) to chromium (III) by rhamnolipid in aqueous solution was tested, and no chromium (III) was present in the reaction mixture. In addition, no precipitation of chromium (III) was observed during the experiments. Therefore, the possibility of precipitation–dissolution and conversion of chromium (VI) to chromium (III) may be ruled out.

Avramovic et al. (2013), with regard to the effect of chromium (VI) on mono- and di-rhamnolipids in aqueous medium, indicated significant proof for a possible coordination of CrO_4^{2-} with protonated rhamnolipid by IR spectra.

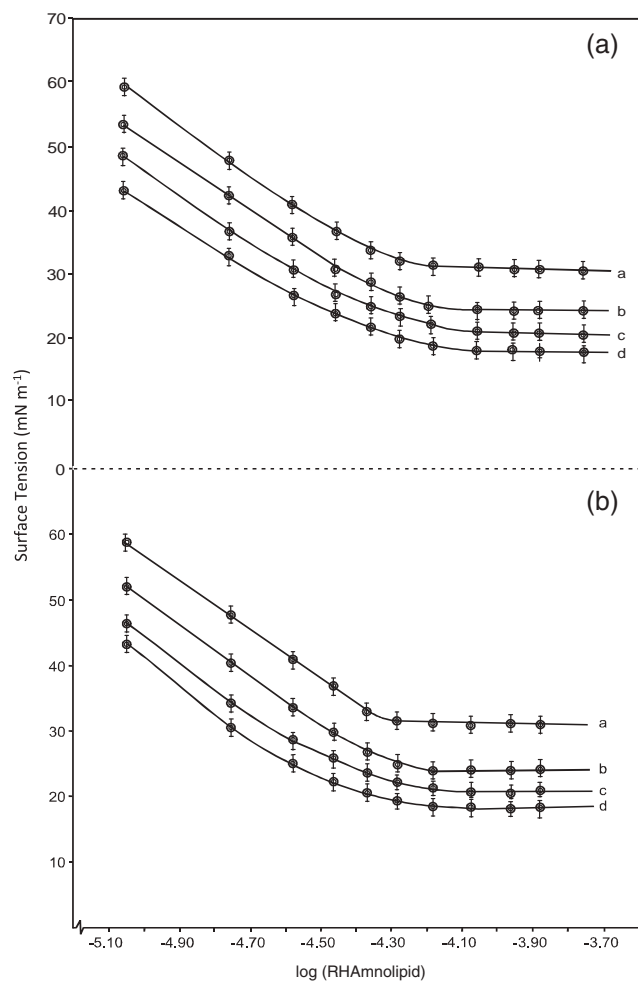


Fig 5 Plots of surface tension *versus* [Rhamnolipid] at 310 K in absence and presence of metal ions. (A) a, b, c, and d rhamnolipid in presence of nil, 4.8×10^{-5} , 9.6×10^{-5} , and 14.4×10^{-5} mol dm⁻³ Cr^{VI}, respectively. (B) a, b, c, and d rhamnolipid in presence of nil, 2.4×10^{-5} , 4.8×10^{-5} , and 7.2×10^{-5} mol dm⁻³ of Pb^{II}, respectively

Table 3 CMC of rhamnolipid in absence and presence of metal ions by surface tension method

$10^5 [\text{Cr}^{\text{VI}}]$ (mol dm ⁻³)	$10^5 [\text{Pb}^{\text{II}}]$ (mol dm ⁻³)	10^5CMC from Fig. 5 (mol dm ⁻³)
9.60	—	6.4
19.20	—	7.6
28.80	—	8.6
—	4.80	5.2
—	9.60	6.6
—	14.40	7.6

CMC of rhamnolipid in absence of metal ions = 5.3×10^5 mol. dm⁻³; the CMC values were reproducible within $\pm 2\%$ in replicate runs.

The present study has been carried out in neutral aqueous medium in which protonated rhamnolipid does not exist.

The ion-exchange mechanism for binding between anionic surfactants and chromate ions has been proposed by Sabatini et al. (1997). In the present case, the ion-exchange mechanism, i.e., exchange of carboxylate ion by chromate ion, is not possible as the carboxylate ion is a part of the structure of the rhamnolipid. Based on the above facts and experimental results, it may be considered that, in the case of rhamnolipid and chromium (VI), the complex formation is due to the entrapment of chromium (VI) in the micelles of the rhamnolipid.

Conclusion

The partition parameters for rhamnolipid–metal ion complexes and the thermodynamic parameters for the micellization of rhamnolipid in the presence of chromium (VI) and lead (II) have been determined by spectrophotometric and conductometric methods, respectively. The experimental results indicated the formation of a rhamnolipid–metal ion complex. The rhamnolipid–lead (II) complex is proposed by forming a bond between the carboxyl group of rhamnolipid and lead (II). In case of chromium (VI), the results indicated entrapment of chromium (VI) in the micelles of the rhamnolipid.

Acknowledgement The authors are thankful to Prof. Rachna Asthana, Director, AIITH, Kanpur, for her keen interest and providing necessary facilities for the work.

Conflict of Interest The authors declare that they have no conflict of interest.

References

- Aşçı, Y., Nurbaş, M., & Sağ-Açikel, Y. (2008) A comparative study for the saponin of Cd (II) by soil with different clay contents and mineralogy and the recovery of Cd (II) using rhamnolipid. *Journal of Hazardous Materials*, **154**:663–673.
- Avramovic, N., Nikolic-Mandic, S., & Karadzic, I. (2013) Influence of rhamnolipids, produced by *Pseudomonas aeruginosa* NCAIM(P), B001380 on Cr (VI) removal capacity in liquid medium. *Journal of the Serbian Chemical Society*, **78**:639–651.
- Ayangbenro, A., & Babalola, O. (2018) Metal(loid) bioremediation: Strategies employed by microbial polymers. *Sustainability*, **10**:3028–3042.
- Dan, Z., Zhenzhen, L., Xianping, L., & Jia, S. (2017) Leaching of rare earth elements from contaminated soils using saponin and rhamnolipid bio-surfactant. *Journal of Rare Earth*, **35**:911–919.
- Fazaalipoor, M. H., Koshdast, H., & Ranjbar, M. (2010) Coal flotation using a biosurfactant from *Pseudomonas aeruginosa* as a frother. *Korean Journal of Chemical Engineering*, **27**:1527–1531.
- Gnanamani, A., Kavitha, V., Radhakrishnan, N., Suseela, R. G., Sekaran, G., & Mandal, A. B. (2010) Microbial products (biosurfactant and extracellular chromate reductase) of marine

microorganism are the potential agents reduce the oxidative stress induced by toxic heavy metals. *Colloids and Surfaces B: Bio-interfaces*, **79**:334–339.

- Herman, D. C., Artiola, J. F., & Miller, R. N. (1995) Removal of cadmium, lead, and zinc from soil by a rhamnolipid biosurfactant. *Environmental Science & Technology*, **29**:2280–2285.
- Hofmeister, F. (1888) Zur Lehre von der Wirkung der Salze. *Arch Exp Pathol Pharmacol.*, **24**:247–260.
- Hong, K. -J., Choi, Y. -K., Tokunaga, S., Ishigami, Y., & Kajiuchi, T. (1998) Removal of cadmium and lead from soil using aescin as a biosurfactant. *Journal of Surfactants and Detergents*, **1**:247–250.
- Hong, K.-J., Tokunaga, S., & Ishigami, Y. (2000) Extraction of heavy metals from MSW incinerator fly ash using saponin. *Chemosphere*, **41**:345–352.
- Juwarkar, A. A., Nair, A., Dubey, K. V., Singh, S., & Devotta, S. (2007) Biosurfactant technology for remediation of cadmium and lead contaminated soils. *Chemosphere*, **68**:1996–2002.
- Kawamura, H., Manabe, M., Miyamoto, Y., Fuzita, Y., & Tokunaga, S. (1989) Partition coefficients of homologous omega-phenylalkanols between water and sodium dodecyl sulfate micelles. *The Journal of Physical Chemistry*, **93**:5536–5540.
- Khoshdast, H., Sam, A., Vali, H., & Akbari-Noghabi, K. (2011) Effect of rhamnolipid biosurfactants on performance of coal and mineral flotation. *International Biodeterioration & Biodegradation*, **65**:1238–1243.
- Kim, J., & Vipulanandan, C. (2006) Removal of lead from contaminated water and clay soil using a biosurfactant. *Journal of Environmental Engineering*, **132**:777–786.
- Lang, S., & Wagner, F. (1987) Structure and properties of biosurfactants. In N. Kosaric, W. L. Cairns, & N. C. C. Gray (Eds.), *Biosurfactants and biotechnology* (Vol. **25**, pp. 21–47). New York, NY: Marcel Dekker.
- Lang, S. (2002) Biological amphiphiles (microbial biosurfactants). *Current opinion in Colloid & Interface Science*, **7**:12–20.
- Maier, R. M., & Soberón-Chávez, G. (2000) *Pseudomonas aeruginosa* rhamnolipids: Biosynthesis and potential applications. *Applied Microbiology and Biotechnology*, **54**:625–633.
- Miller, R. M. (1995) Biosurfactant-facilitated remediation of metal-contaminated soils. *Environmental Health Perspectives*, **103**:59–62.
- Mulligan, C. N. (2005) Environmental applications for biosurfactants. *Environmental Pollution*, **133**:183–198.
- Mulligan, C. N., Yong, R. N., & Gibbs, B. F. (1999) Heavy metal removal from sediments by biosurfactants. *Journal of Hazardous Materials*, **85**:111–125.
- Neilson, J. W., Artiola, J. F., & Maier, R. M. (2003) Characterization of lead removal from contaminated soils by nontoxic soil-washing agents. *Journal of Environment Quality*, **32**:899–908.
- Ochoa-Loza, F. J., Artiola, J. F., & Maier, R. M. (2001) Stability constants for the complexation of various metals with a rhamnolipid biosurfactant. *Journal of Environmental Quality*, **30**:479–485.
- Ochoa-Loza, F. J., Noordman, W. H., Janssen, D. B., Brusseau, M. L., & Maier, R. M. (2007) Effect of clays, metal oxides, and organic matter on rhamnolipid biosurfactant sorption by soil. *Chemosphere*, **66**:1634–1642.
- Rufino, R. D., Luna, J. M., Campos-Takaki, G. M., Ferreira, S. R. M., & Sarubbo, L. A. (2012) Application of the biosurfactant produced by *Candida lipolytica* in the remediation of heavy metals. *Chemical Engineering Transactions*, **27**:61–66.
- Sabatini, D. A., Knox, R. C., Tucker, E. E., & Puls, R. W. (1997) Innovative measures for surface chromium remediation: Source zone, concentrated plume, and diluted plume (report no. EPA-R-820736). Environmental research brief, United States Retrieved from United States Environmental Protection Agency. <https://clu-in.org/download/toolkit/epa600s97005.pdf>.

- Sandrin, T. R., Chech, A. M., & Maier, R. M. (2000) A rhamnolipid biosurfactant reduces cadmium toxicity during naphthalene biodegradation. *Applied and Environmental Microbiology*, **66**:4585–4588.
- Slizovskiy, I. B., Kelsey, J. W., & Hatzinger, P. B. (2011) Surfactant facilitated remediation of metal contaminated soils efficacy and toxicological consequences to earthworms. *Environmental Toxicology and Chemistry*, **30**:112–123.
- Stacey, S. P., McLaughlin, M. J., Çakmak, I., Hettiarachchi, G. M., Scheckel, K. G., & Karkkainen, M. (2008) Root uptake of lipophilic zinc–rhamnolipid complexes. *Journal of Agricultural and Food Chemistry*, **56**:2112–2117.
- Tan, H., Champion, J. T., Artiola, J. F., Brusseau, M. L., & Miller, R. M. (1994) Complexation of cadmium by a rhamnolipid biosurfactant. *Environmental Science & Technology*, **28**:2402–2406.
- Tang, J., He, J., Liu, T., Xin, X., & Hu, H. (2017) Removal of heavy metal from sludge by the combined application of a biodegradable biosurfactant and complexing agent in enhanced electrokinetic treatment. *Chemosphere*, **189**:599–608.
- Torrens, J. L., Herman, D. C., & Miller-Maier, R. M. (1998) Biosurfactant (rhamnolipid) sorption and the impact on rhamnolipid facilitated removal of cadmium from various soils under saturated flow condition. *Environmental Science and Technology*, **32**:776–781.
- Upadhyay, S. K., & Hari, O. (2019) Spectrophotometric and conductometric study of the interaction of saponin with chromium (VI) and lead (II). *International Journal of Environmental Science and Technology*, **16**:7997–7805.
- Usman, M., Cheema, M. A., Khan, A., Farooki, Z. H., Mosquera, V., & Siddiq, M. (2013) A comparative study of thermodynamic properties of structurally related phenothiazine drugs in aqueous solution. *Journal of the Chilean Chemical Society*, **58**:1842–1845.
- Usman, M., Khan, A., & Siddiq, M. (2010) Thermodynamic properties of amphiphilic antidepressant drug citalopram HBr. *Journal of the Chemical Society of Pakistan*, **32**:1–6.
- Usman, M., & Siddiq, M. (2013) Surface and micellar properties of chloroquine diphosphate and its interactions with surfactants and human serum albumin. *The Journal of Chemical Thermodynamic*, **58**:182–190.
- Wang, S., & Mulligan, C. N. (2009) Rhamnolipid biosurfactant enhanced soil flushing for the removal of arsenic and heavy metals from mine tailings. *Process Biochemistry*, **44**:296–301.
- Younas, N., Rashid, M. A., Nazir, S., Usman, M., Sarfraz, R. A., Jamil, A., & Whitwood, A. C. (2017) Spectroscopic and conductometric study of interaction of anionic surfactants with [co(phen)₃]F₂ · 2H₂O complex. *Journal of Molecular Lipids*, **240**:351–360.



Cryptosporidiosis, a public health challenge: A combined 3D shape-based virtual screening, docking study, and molecular dynamics simulation approach to identify inhibitors with novel scaffolds for the treatment of cryptosporidiosis

Kalpana Katiyar^{1*}, Ramesh Kumar Srivastava², Ravindra Nath³ & Gagandeep Singh^{4,5}

¹Department of Biotechnology, Dr. Ambedkar Institute of Technology for Handicapped, Kanpur-208 024, Uttar Pradesh, India

²Technology & Business Development Division, Central Institute of Medicinal & Aromatic Plants (CSIR-CIMAP), Lucknow-226 015, Uttar Pradesh, India

³University Institute of Engineering & Technology, CSJM University, Kanpur-208 012, Uttar Pradesh, India

⁴Section of Microbiology, Central Ayurveda Research Institute, Jhansi-284 003, Uttar Pradesh, India

⁵Kusuma School of Biological Sciences, Indian Institute of Technology, New Delhi-110 016, Delhi, India

Received 08 June 2021; revised 15 February 2022

Cryptosporidiosis is a neglected tropical disease caused by the protozoan parasite *Cryptosporidium parvum*. Limited therapeutic options, limitation in *in vitro* parasite culture, and lack of a reliable animal model of parasite for replication of *in vivo* life cycle and drug testing demand alternative methods for drug development. The *in silico* methods of drug discovery prove a crucial process in such conditions. Recent research reported a limited number of small molecules for drug development. Purine nucleotide biosynthesis in *Cryptosporidium* species is dependent on the IMPDH (CpIMPDH) enzyme, so distortion of parasite IMPDH has been pursued as a compelling strategy for curbing *Cryptosporidium* infection due to its different kinetics from the host enzyme. Our study's primary aim was to discover novel ligand molecules with noticeable activity against *Cryptosporidium parvum* IMPDH. For this purpose, we selected 18 previously discovered ligands to understand the interaction feature between ligand and receptor, and their shape and electronic features are employed as a template for shape-based virtual screening of the ZINC database (drug-like subset) search approach via Schrodinger-2019 (Maestro 11.9). The obtained hits were subsequently subjected to structure-based screening, quantum polarized ligand docking (QPLD), and molecular dynamics simulations to fetch potential small molecules with the highest binding affinity for CpIMPDH protein. Further ligand binding energy and pharmacokinetic analysis were also taken into consideration as filtering criteria for selecting the most promising drug-like compounds.

On this experimentation analysis, three top-ranked (ZINC24855054, ZINC58171263, and ZINC08000072) molecules were found to have appropriate pharmacokinetic properties along with surpassing *in silico* inhibitory potential towards the CpIMPDH compared to known inhibitors. The molecular docking and molecular dynamics simulation analysis results satisfactorily confirmed the inhibitory action. Therefore, these new scaffolds deduced by the presented computational methodology could recommend lead molecules for designing promising anti-cryptosporidial drugs targeting CpIMPDH protein.

Keywords: *Cryptosporidium parvum*, Inosine 5'-monophosphate dehydrogenase (IMPDH), MM/GBSA, Molecular Docking, Molecular Dynamics Simulations, Virtual Screening

The novel coronavirus disease 2019 (COVID-19) is one of the most trounced pandemics of the twentieth century who tried to grapple humanity worldwide. COVID-19 is engendered by the severe acute respiratory syndrome coronavirus 2 (SARS-CoV-2). The rapid transmission drive of SARS-CoV-2, high mortality and morbidity, and unavailability of treatment options are chief factors responsible for the pandemic dispersal. The COVID-19 has conquered

the year's headlines and geared all significant research attention. The everyday cost of common parasitic diseases has been disoriented under the shadow of COVID-19. The parasitic diseases are considered as a considerable reckoning on local communities. Hitherto, because most of these parasitic diseases are no longer endemic to developed nations, the projects underlying research and development of parasitic diseases are not funded at levels that are proportional to their global morbidity and mortality. The scientific and public health communities' energy and attention concern the COVID-19, but though managing this, it

*Correspondence:
E-mail: kalpna@aith.ac.in

will be essential to show steadfast resolution toward interpretation and combating the parasitic diseases¹. The COVID-19 pandemic has turned the clock back by years in the fight against other parasitic diseases, and it has interrupted research, trials, and other efforts to ease the public health burden.

Tyzzler first recognized *Cryptosporidium* species (spp.) in 1907, but it remained undercover until the 1980s when AIDS became endemic in humans. The parasitic possessions are considered primary etiological agents responsible for various clinical complications associated with gastrointestinal epithelium among infants and immunocompromised persons. Specific medical and symptomatic complications led by *Cryptosporidium* spp. infection include watery diarrhea, nausea, fever, and in extreme cases, neuro-development disorders. Such medical situations are categorized as cryptosporidiosis disease². The cryptosporidiosis disease burden varies geographically. A recent systematic review on epidemiological analysis of human *Cryptosporidium* infection in China (1987-2018) asseverated average prevalence of *Cryptosporidium* was 2.97% in reported areas. Among these, 1.77-12.87%infection prevalence is found in rural areas compared to 0-3.70% prevalence in urban areas. The nationwide prevalence of *Cryptosporidium* in humans is 0.1-14.1% in Asian countries,2.6-21.3% in African countries,0.1-14.1% in Europe,3.2-31.5% in central and south American countries, and 0.3-4.3% in North America³. A meta-analysis study on the prevalence of the *Cryptosporidium* in HIV-positive patients reported 11.2% prevalence and 14.4% globally. The low number of CD4⁺ cells in AIDS patients is one primary reason for the high infection rate⁴. The most prominent epidemiological studies like MAL-ED (Etiology, Risk Factors, and Interactions of Enteric Infections and Malnutrition and the Consequences for child health and development), GEMS (Global Enteric Multicenter Study), and GBD (Global Burden of Disease) reported that *Cryptosporidium* spp. was among the most critical pathogens for diarrheal infections in children under 12-month-old and community clinics. The *Cryptosporidium parvum* (*C. parvum*) infection is associated with a long duration of diarrhea and 2-3 fold higher mortality rates in malnourished young children than healthy ones⁵. *Cryptosporidium* spp. induced pediatric diarrhea accounts for 9% of global child mortality and 50% of water-borne infections in the United States due to *Cryptosporidium*⁶. The primary infectious species of the parasite associated with human and animal infections are *C. parvum*, *C. hominis*, *C. meleagridis*, *C. andersoni*,

C. felis, *C. suis*, and *C. canis*. However, more than 39 species and 30 genotypes of *Cryptosporidium* spp. are identified *C. parvum* and *C. hominis* are associated with 90% of cases of human infection. The small subunit (SSU) rRNA gene and glycoprotein 60 (gp60) gene are validated genetic markers for phylogenomic analysis of the parasite. The genome identity between *C. hominis* and *C. parvum* Iowa II is 96.85%. The subtle variation in the genome of *C. hominis* and *C. parvum* are responsible for phenotypic differences in host-parasite interface proteins⁷. The parasite stuck a monogenous life cycle with both the asexual and sexual phases. The life cycle begins with the ingestion of sporulated oocysts. The oocysts are resistant to the environment and generalized sterilization methods. After ingestion, oocyst excystation occurs in the upper intestine releasing four sporozoites. The sporozoites penetrate nearby intestinal epithelium cells and settle in the parasitophorous vacuole. It is intracellular but extra-cytoplasmic. A feeder organelle made a channel between the parasitophorous vacuole and host cell cytoplasm.

From 2004 up to the recent five-year period, scientists have failed to design a fully effective therapeutic agent to resist parasite invasion. Parasite contaminated dietary and other products act as a way forward for its transmission to reach the gastrointestinal tract, where the parasite utilizes host cellular metabolites via pedestal and feeder organelle⁸.

Taxonomically, *C. parvum* (genome size approx 9 Mbp), *C. hominis*, and *C. fragile* are placed in the same Phylum (Apicomplexa) as *Plasmodium* spp. and *Toxoplasma* spp. Intriguingly, in comparison to *Plasmodium* spp. and *Toxoplasma* spp. significant gene loss was reported in *C. parvum* encoding 3,500 genes⁹. Metabolic interventions following *C. Parvum* synthetic machinery apicoplast and mitochondrial genome loss proved insufficient to overcome parasite pathogenicity⁹. Parasite persistent pathogenicity indicates the existing knowledge gap to understand unexpressed glycolytic enzymes responsible for the unusual microbial energy generation mechanism¹⁰.

Similarly, *C. parvum*'s intracellular metabolic mechanism matched obligate parasites like *Rickettsia* spp. and *Chlamydia* spp, which command over host synthetic machinery for survival. Parasite's unique anabolic mechanism indicates possible therapeutic targets to inhibit parasitic growth¹¹. Following CRISPR/Cas9, a gene disruption technology, scientists unveiled Dihydrofolate Reductase-Thymidylate Synthase (DHFR-TS) and Inosine Monophosphate

Dehydrogenase (IMPDH) enzymes as a suitable target for drug designing to overcome *C. Parvum* pathogenicity. Both enzymes are integral in marinating parasite energy via importing host purines¹². Targeting IMPDH and DHFR-TS enzymes with specific drug molecules were of great importance to inhibit the parasitic life cycle^{13,14}. Scientific efforts regarding drug designing and Nitazoxanide's discovery, Paromomycin made significant contributions regulating *C. parvum* growth among infants and adults with the compromised immune system. However, it failed to kill *C. parvum* completely. The underlying reason for the in effectiveness of Nitazoxanide and Paromomycin is still debatable^{15,16}. Recent progress made by scientists identifying IMPDH structural characteristics, inhibition, potent inhibitors' selection, and potential lead molecules' identification indicated encouraging results over the model organisms. *C. parvum* IMPDH (CpIMPDH) protein has distinct genomic and structural characteristics compared to mammalian IMPDHs¹⁷.

Cryptosporidium parvum lacks adenine and guanine synthesis; as usual, most parasite siblings synthesize and rely upon the host nucleosides via the CpIMPDH pathway to convert IMP (inosine 5'-monophosphate) into xanthosine 5'-monophosphate¹⁸. Medical applications of benzoxaborole derivatives activity inhibiting aminoacyl-tRNA synthetases activity during fungal and bacterial protein synthesis led to the development of FDA-approved effective therapeutic ligands against gram-negative bacteria¹⁹. However, the development of effective therapeutic molecules against CpIMPDH is questionable after significant scientific progress.

Virtual screening is an essential aspect of the modern drug discovery process. It reduces resources, cost, and overall time in the drug development process. It also dispenses novel chemical species with desirable activities from diverse chemical databases. The output of virtual screening candidates has been proven to be an appropriate starting point for further exploration and development in the drug discovery process. The ligand and structure-based virtual screening are routinely practiced in most successful drug discovery projects²⁰. Despite much research in the last decades, only a few inhibitors against CpIMPDH with good pharmacokinetic properties have been uncovered. Thus, there is room to develop novel and potent chemotypes or optimize existing inhibitors against CpIMPDH to curb *Cryptosporidiosis*.

Structure-less ligand prioritization approaches were followed by many scientists covering minimal future drug development aspects treating *Cryptosporidiosis*. Molecular modeling prioritizing existing ligand molecules via computational analytical tools, including virtual screening and ligand enzyme structure-activity relationship, seems revolutionary for drug discovery and development. While prioritizing ligand molecules based on enzyme-ligand compatible molecular characteristics in the availability of thousands of an average efficacy ligand, it seems an excellent challenge for pharmacologists to shortlist the most effective ligand molecule against *Cryptosporidium*²¹.

Currently, molecular dynamics is the best available protein-ligand interaction approach to cross high energy barriers within the feasible time duration to achieve protein-ligand interaction at unusual temperatures²². Molecular dynamics calculations from multiple ligand positions are routinely adopted to estimate protein-ligand compatibility and energy gap minimization²³. Ranking and evaluating ligand domains and predicting binding domains is vital for the virtual screening structure²⁴. Calculation of reliable protein-ligand complexes scoring requires excellent expertise to distinguish between active and inactive protein-ligand complexes²⁵.

About retrospective therapeutic challenges, our study aims to discover amino-methyl benzoxaborole based novel ligand molecules with visible activity against *Cryptosporidium parvum*. At the same time, the significant objectives include standardization of treatment strategies following *Cryptosporidiosis*, virtual screening of potential ligand molecules, comparative structural activity relationship, preparation of 3D ligand molecules, and identification of effective therapeutic agents among immune-compromised patients.

This work predicted the 3D structure of the inosine monophosphate dehydrogenase receptor from its amino acid sequence deploying various tools. The 3D structure was predicted using a threading approach that relies on the observation that all naturally occurring proteins have limited fold, so relatively distant homologous proteins have a similar structure, and predicted 3D model quality is checked thoroughly at various levels.

The present investigation aims to identify novel inhibitors of *C. parvum* IMPDH enzyme using a combination of various *in silico* approaches like

shape-based screening (SBS), ADMET, molecular docking, and molecular dynamics studies. The present study can be used as a pilot for the rational drug design for other pathogenic microbes and cancer treatment.

Materials and Methods

Hardware and software specifications

In this study, Schrodinger's Drug Discovery Suite 2015 (evaluation/trial version) with Module Maestro 11.9, Shape Screening Module, Merge Duplicates Module, Virtual screening workflow Module, Protein Preparation Wizard Module, LigPrep Module, QikProp Module, Prime/MM-GBSA Module installed on Intel® core(TM) i3-8100 CPU @3.60 GHz, 64 GB RAM with a 2GB graphics card exploited for all computations in this research.

Shape-based molecular similarity screening

The shape-based molecular similarity is a new strategy for discovering new chemical scaffolds. It relies on the principle that if two molecules are structurally similar, they frequently have a similar biological function and physical properties. This similarity approach is an advanced tool for the virtual screening of an extensive database of compounds. Molecular similarity analysis between two molecules can be performed through (i) structural representations and (ii) quantitative similarity measurement among the two entities.

We followed the shape screening approach via Schrodinger-2019 (Maestro 11.9), a molecular shape screening computational tool²⁶. Similarly, pharmacophore models, also called quantitative 3D tools for novel inhibitor validation tools, were also used in virtual screening protocols²⁷. Before following quantitative pharmacophore modeling analysis, the feature mapping module was adopted for each presented molecule. The primary aim was to shortlist the universal potent ligand molecule. Outcomes in terms of hydrogen bond acceptor, hydrogen bond donor, hydrophobic, and aromatic ring ligands were effectively mapped with molecules under consideration, and calculated features were considered to generate hypotheses and identify potential ligands. Simultaneously, uncertainty in the pharmacophore model was the critical parameter to care about while determining agonist. The preferred value set for uncertainty was about a 2-3 magnitude level²⁸. The ZINC database (drug-like subset) is a free, commercial database of over 10 million

purchasable compounds supported by the Department of Pharmaceutical Chemistry at the University of California, San Francisco (UCSF)²⁹. The 3D structures of 18 previously reported CpIMPDPH inhibitors were taken on board to find similar drug-like compounds with a threshold limit of 80% similarity. The output of 2000 hits was saved in a suitable file format.

Before proceeding towards the structure-based virtual screening (VS), ligand preparation is essential for generating three-dimensional (3D) geometries, bond order correction, and generation of accurate tautomer and ionization steps. LigPrep module generates the most appropriate ionization state (pH=7.0) for each ligand molecule. The OPLS-AA_2005 force field was used to generate the lowest energy conformers of ligands³⁰.

Toxicity and ADME studies

It is desirable that candidate ligand molecules passed through VS protocol must have good ADMET profiles. Nowadays, various *in silico* tools are available to investigate the pharmacokinetics, toxicity, bioavailability, and safety. QikProp (rapid ADME predictions of drug candidates) module in Schrodinger drug discovery suite was used to predict MDCK and Caco-2 cell permeability, overall CNS activity, octanol/water, and water/gas log Ps, log S, and log BB like pharmaceutically relevant properties³¹.

Target protein preparation

The primary structure of the target protein sequence (Accession number AF426177) was retrieved from GeneBank (<https://www.ncbi.nlm.nih.gov/genbank/>)³². The homolog structure was identified through BLAST using the PDB database. The highest homology was pragmatic (PDB ID:4IXH), having 95% similarity with 95% query coverage. The enzyme structure (PDB ID:4IXH) was chosen for the reference receptor protein structure. It is the catalytic domain crystal structure of CpIMPDPH (resolution- 2.105 Å) with (2S)-2-(naphthalen-1-yloxy)-N-[2-(pyridin-4-yl)-1,3-benzoxazol-5-yl] propenamide inhibitor along with substrate submitted in protein data bank (<https://www.rcsb.org/>)³³.

The successful outcome of molecular docking protocol relies on the optimized three-dimensional (3D) structure of protein and ligand for the precise binding affinity prediction. Therefore, the modeled 3D structure of the protein is evaluated for any structural quality distortion. The central aspect is to scrutinize unusual conformation, residue packing

anomaly, sequence-structure mapping, residue-shift error, and errors due to incorrect side-chain residue. The PROCHECK tool was deployed for structure validation of the protein³⁴.

Receptor protein was prepared using the protein preparation wizard by involving the parameters like assigning bond orders to hydrogen's, zero-order bonds created to metal atoms, creating disulfide bonds, and de-solvation out by deleting the crystallized free water molecules beyond 5Å³⁰. The protein 3D structure integrity was checked, and appropriate modification was done. The tautomeric and protonation states of Glu, Arg, His, Lys, and Asp were adjusted, and also the orientation of Gln and Asn residues generated. Finally, the protein hydrogen bonds were optimized and minimized using the force field OPLS3e³⁵. With the receptor generation program from the Glide module, the active pocket in the protein was fixed for docking³⁶.

Structure-based virtual screening

The hits (1595) retrieved through the similarity search approach were passed through the structure-based virtual screening module against the active-site of the prepared CpIMPDH target protein. It is a multi-step screening procedure with Lipinski's Rule of 5 (ROS) and reactive group filter placed at the appropriate position to remove hits with chemically active functional groups and undesirable drug-likeness properties. The extracted hits were passed through docking by Glide docking protocol which consists of High-throughput Virtual screening (HTVS), Standard Precision (SP), Extra Precision (XP) and docking protocol. Docking calculations were first performed in HTVS mode, and the top 50% best-docked hits (999 compounds) were passed through the subsequent SP docking calculations. Finally, the top 30% (299 compounds) of the SP docking protocol were passed through the XP docking screening protocol. XP Glide scores were used to sort the best-docked ligands^{36,37}.

Most of the docking protocols are molecular mathematical calculations in which the polarization effect of a ligand is not considered. It is now well characterized that the electrostatic charge on molecules has a paramount role in ligand-receptor protein interaction in docking. As a result, in order to reduce the false positive hits, QPLD protocols were applied to the screened compounds from the previous filter. In the QPLD protocol, the ligand atoms are contemplated at the quantum mechanical level. In the

execution of this protocol same grid-level parameters were used that had already been set in virtual screening docking calculations³⁸. Docking calculations were carried out in two steps, initially Glide Standard precision protocol (SP) docking protocol. In the subsequent step, the protein field-induced polarization effect on ligands was calculated which is conjoined with Jaguar quantum mechanics. Density Functional Theory (DFT) method was applied in scoring ligands docked in target protein and elucidated by the OPLS-2005 force field. In the end, ligands were strained based on lower values of XP Glide Score and interacting amino acid residues^{39,40}.

To further enhance the virtual screening protocol's productivity and remove the pitfall of the scoring function of Glide Score, the best ligand-protein complex picked from QPLD studies was subjected to an MM-GBSA analysis⁴¹. It prioritized ligands based on the relative binding free energy Δ (G) between ligand and receptor molecule.

$$\begin{aligned} \Delta G_{bind} &= G_{complex} - (G_{protein} + G_{ligand}) \\ &= \Delta EMM + \Delta GSOL \\ \Delta GSOL &= \Delta GGB + \Delta GSA \end{aligned}$$

Where: ΔEMM -minimized energy difference between protein-ligand complex and the total energy of protein and unbound ligand, $\Delta GSOL$ -solvation free energy difference obtained by the polar (ΔGGB) and non-polar (ΔGSA) solvation energy.

Molecular dynamics simulation

The best-ranked ligands from the MM-GBSA study were further scrutinized in molecular dynamics simulation protocol to evaluate ligand stability of binding mode and thermodynamic performance in the receptor protein (CpIMPDH) active-site⁴². Molecular dynamics (MD) simulation of docked complexes was done by GROMACS package 5.1 to unveil the docked ligands' structural behavior⁴³. The simulation was done using a GROMOS 43a1 force field and systems solvation by using a water model, single point charge (SPC) cubic box apart 1.0 nm from the surface of the protein box. Both systems were neutralized by their corresponding ions. The existing energy gap in docked complexes was processed *via* the steepest descent algorithm by following about 50,000 steps used for each simulation to meet the complex's stability.

Similarly, equilibration of both systems was achieved by using NVT and NPT ensembles for 100ps each. The V-rescale thermostat was used for equilibration with a reference temperature of 310.15 K

for 1 ns. Finally, the production MD run was performed with 100 ns time duration. GROMACS in-built tools were used to compute protein RMSD and RMSF^{44,45}.

Results and Discussion

This study's main objective is to identify novel and promising lead molecules that interfere with CpIMPDH and are deployed as potential anti-cryptosporidial agents. An integrative and highly superior virtual screening protocol incorporating various *in silico* approaches (shape-based virtual screening) is deployed in a stepwise riddler approach to fulfill this objective. Beneath the result of various computational approaches applied for the efficient identification of inhibitors against CpIMPDH are presented and discussed.

Target protein preparation and binding mode analysis

The Protein preparation wizard was used for receptor protein preparation by polar hydrogen atom addition, crystallographic water molecule removal, disulfide bond creation, missing side chains, and loops correction. The parameters like assigning bond orders to hydrogen, zero-order bonds creation to metal atoms, creating disulfide bonds, and desolvation were carried out by deleting the crystallized free water molecules beyond 5Å. The protein 3D structure integrity was checked, and appropriate modification was done. The tautomeric and protonation states of Glu, Arg, His, Lys, and Asp were adjusted, and also the orientation of Gln and Asn residues generated. Finally, the protein hydrogen bonds were optimized and minimized using the force field OPLS3. With the receptor generation program from the Glide module, the active pocket in the protein was fixed for docking. The coordinates of the co-factor NADH were transferred into the enzyme

structure at its binding domain, and the coordination pose was compared with other reported structures of CpIMPDH. In the native conformation of the protein, each atom is in equilibrium and thermal stable, but as temperature increases or protein interacts with the ligand or solvent creates oscillation of atom around the equilibrium position. The B-factor profile of an atom in a protein describes the displacement of the atom from the lowest energy or equilibrium position. For this receptor protein, a normalized B-factor graph is shown in (Fig. 1). It is in the permissible range as most of the amino acid residues have a negative value that indicates a more stable position of that residue.

Furthermore, protein is also checked for any atomic disorder. For this, a plot of the probability of disorder (on the y-axis) for each numbered residue (on the x-axis) is generated. All the residues above the threshold (shown as a dashed line on the plot) could be considered disordered and below as mostly ordered and shown in (Fig. 2).

Again OPLS-2005 force field was used for energy minimization of receptor protein with RMSD cut-off up to 0.90 Å. The receptor grid box was generated around the center of the receptor protein active site with a cubic volume of $50 \times 50 \times 50 \text{ \AA}^3$ with a grid point spacing of 0.974 Å. The induced-fit docking protocol was employed, the maximum number of energy evaluations was set as 20,00,000 per run.

Shape-based molecular similarity screening

Huston CD *et al*, 2015 performed a structure-activity relationship (SAR) testing benzimidazole activity against *C. parvum* IMPDH and explained its significant possibility as a potential inhibitor to overcome Cryptosporidiosis. Another similar SAR-based study focusing on phthalazine reported benzofuranamide derivatives' role in inhibiting minute concentration of *C. parvum* IMPDH protein. They

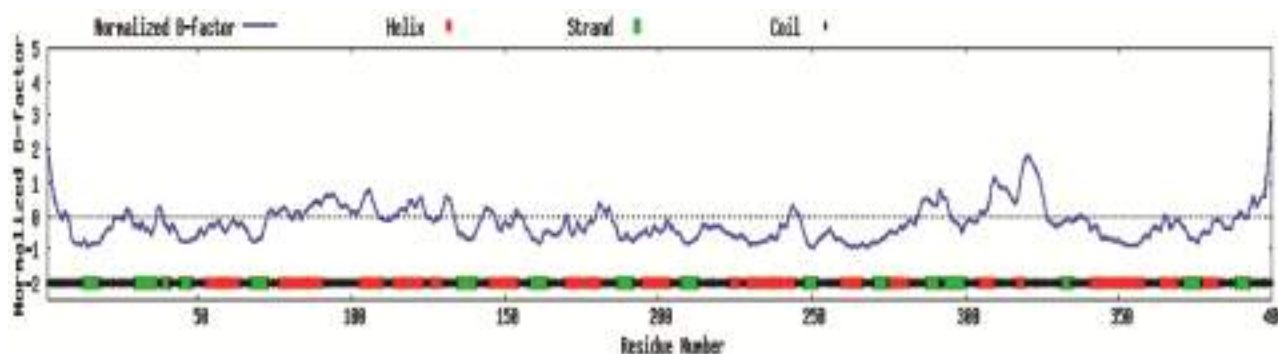


Fig. 1 — The normalized B-factor graph of receptor protein showing each amino acid residues' stability in native conformation

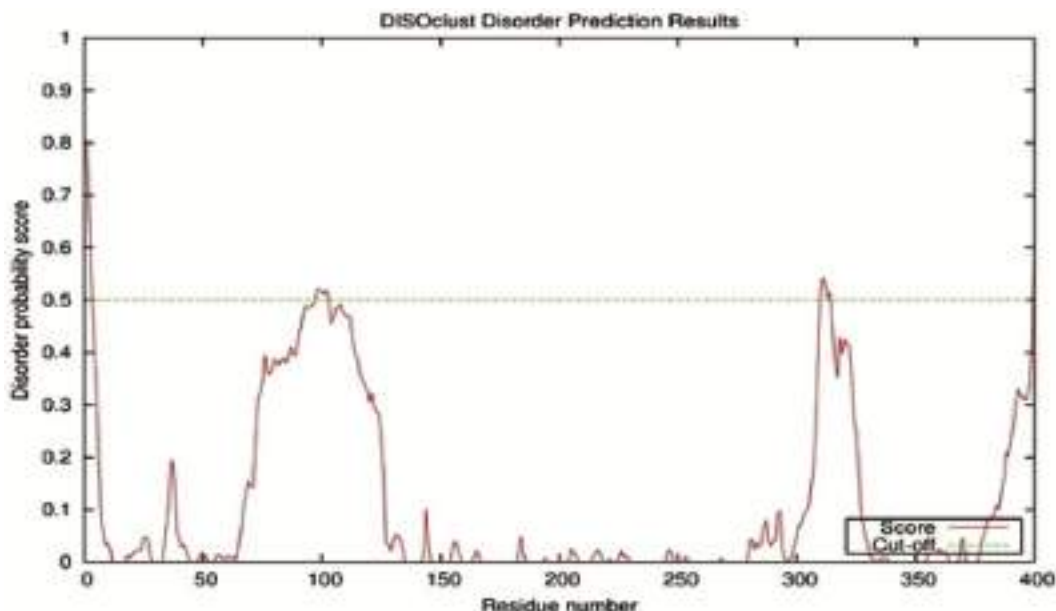


Fig. 2 — A plot of the probability of disorder (on the y-axis) for each numbered residue (on the x-axis) of the receptor protein

highlighted that these scaffolds have an impact on inhibiting CpIMPDH activity. While another approach led by Teotia *et al.*, 2018 screening 38 benzoxazole derivatives docking four compounds revealed adverse outcomes over the model organisms. The most competent outcome introducing heterophilic pyridine substituents at benzoxazole 2-position highlighted enhanced CpIMPDH inhibitory action with super antiparasitic sensitivity. Literature reported 4-oxo-benzopyrano[4,3-c] pyrazole derivative in literature as an average potent inhibitor following CpIMPDH in comparison to urea-based selective inhibitors with leading potency and stability^{46,47}. To extract all essential features of previously designed active ligands, the most active representatives of benzoxazole series, phthalazinone derivative series, and urea-based inhibitor series were used for shape-based screening (SBS) in order to screen the database and shown in (Fig. 3). The 3D shape-based screening was run with default parameters, search type pharmacophore types, and the maximum number of conformers was set as 100. This analysis was performed by overlaying and superpositioning of generated conformer in a way that allows maximum volume overlap. The underlying algorithm calculates atomic overlap mathematically. Approximately 1800 new molecules were identified. Following its merge module, 1500 duplicate records were removed with the identification of 18 *Cryptosporidium parvum* IMPDH potential inhibitors, as shown in (Fig. 3A).

These 18 ligands CpIMPDH inhibitor molecules were selected as a training ligand data set for a similarity search in a ligand-based virtual screening experiment. The ZINC database was screened for retrieving compounds with 80% structural similarity concerning the training ligand set dataset, and VS workflow is shown in (Fig. 4).

Merged 1595 ligand molecules were tested and prepared by the LigPrep module. After ligand preparation, 488 new conformations of ligands were generated. The 2D structures of all ligands were converted to 3D using LigPrep using the default settings. According to the user manual, (i) hydrogens were added, (ii) salts were removed, (iii) stereoisomers were generated, (iv) probable ionization states were calculated at pH value of 7.0 ± 2.0 using the module specified chirality was retained, and energy minimization of each structure was carried out using OPLS3e force field. Lipinski's filter-based rule of five, a standard criterion for differentiating compounds from drug molecules including $MW < 500$, Partition coefficient $\log P < 5$, donor HB < 5 , acceptor HB < 10 , was applied to focus all ligands, only 1999 ligands passed Lipinski's rules. These 2083 ligands' ADME properties were calculated by the QikProp module.

Molecular docking studies

QPLD docking studies were performed for 2000 compounds having satisfactory predicted activities for the best binding confirmation into the active site of

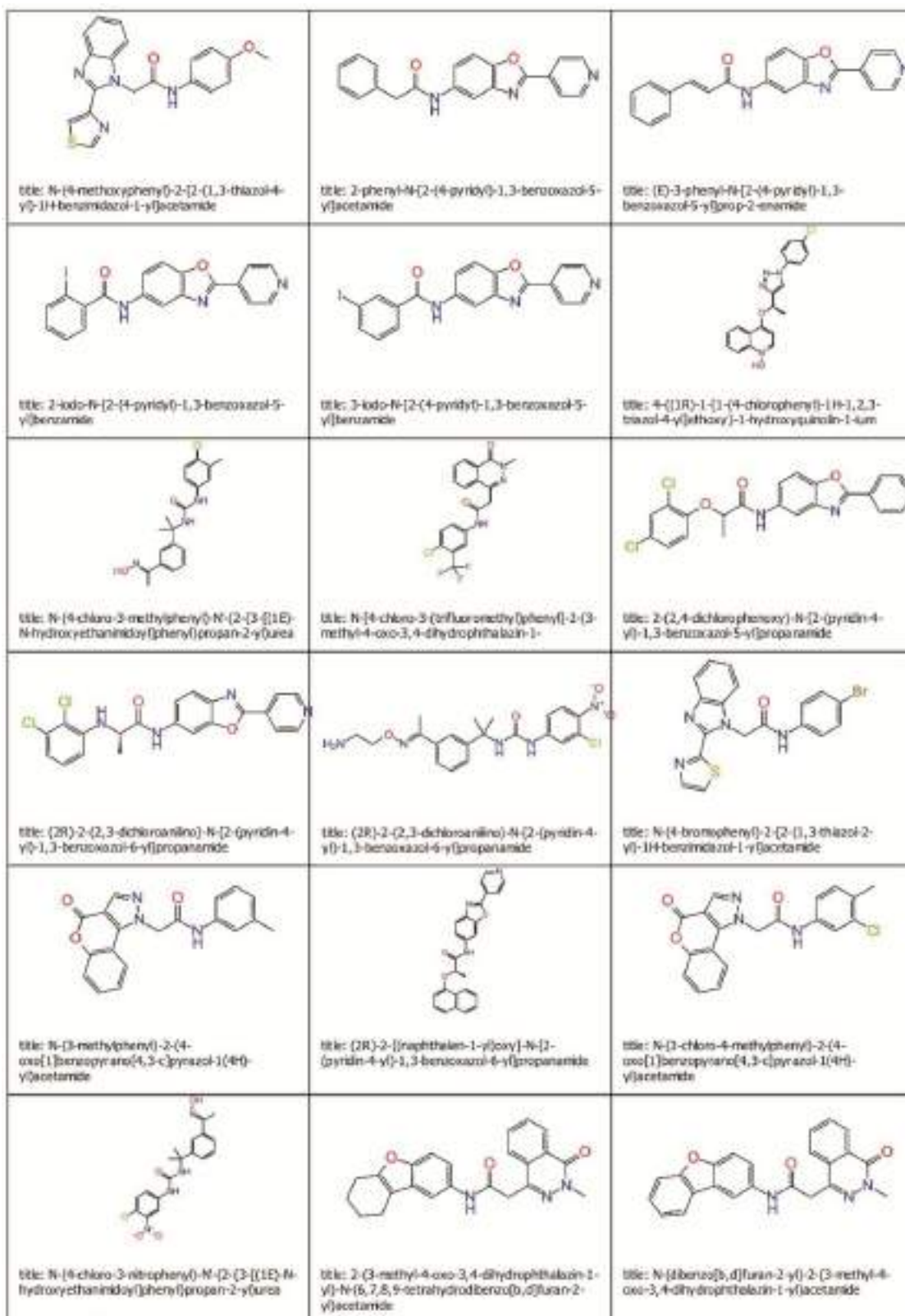


Fig. 3 — The benzoxazole series, phthalazinone derivative series, and urea-based inhibitor series ligands molecules deployed for shape-based screening process implemented in this study

CpIMPDPH, subjected to QPLD molecular docking studies⁴². The crystal structure of CpIMPDPH (PDB ID: 4IXH) after relevant modifications was exploited for docking calculations. Phthalazinone and Benzimidazole were docked as a reference compound to validate docking protocol. A flow diagram of the

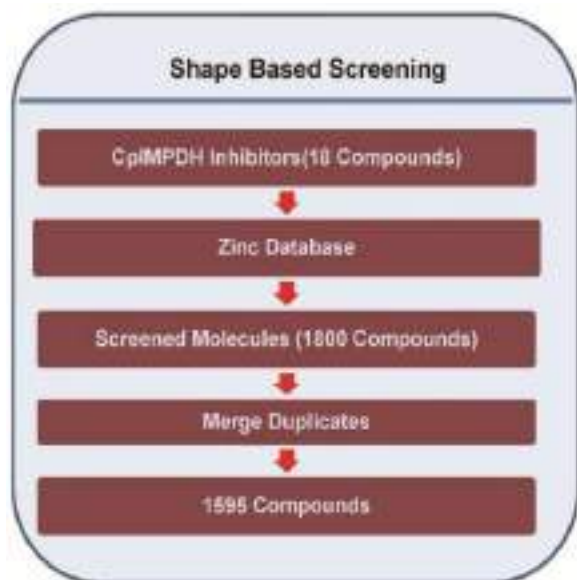


Fig. 4 — Schematic representation of the shape-based screening

molecular docking process employed in this study is shown in (Fig. 5).

The biologically active form of CpIMPDPH exists as a tetramer, and each monomer consists of 400 amino acid residues. The residues Ser48, Ser217, SER276, Gly303, Met302, Tyr299, Gly275, Asp252, and Gly254 of each chain are active sites and located near the interface region. Among these are mobile catalytic strings (residues 302-330) to help cofactor detachment during the enzymatic reaction. IMPDPH catalyzed reaction completes in two-phase. In the first phase, catalytic Cys219 makes a nucleophilic attack on the IMP and forms a covalent intermediate E-XMP* (transition state) and NADH. In the second phase, mobile catalytic Cys residue and a putative water molecule hydrolyze E-XMP* to Enzyme and XMP.

Literature survey revealed that previously discovered CpIMPDPH inhibitors consist of two aromatic moieties. One aromatic ring makes π -stacking interactions with the purine base of IMP while the other aromatic ring interacts with adjacent chain Tyr358 amino acid residue. This interaction changes the inhibitor's conformation and allows the formation of a hydrogen bond with Glu329 amino acid residue.



Fig. 5 — Schematic representation of the molecular docking process employed for structure-based virtual screening

The 1999 ligands with satisfactory docking scores from the first phase of docking carried out to filter similar compounds from the ZINC database were subjected to QPLD calculations for a more accurate determination of binding mode. Reference compound docking score (-6.174 to -7.768 Kcal/mol) was used as filtering criteria, and compounds having lower docking scores were ranked based on the XP Glide score.

The Molecular Mechanics and Poisson-Boltzmann or Generalized Born and Surface area continuum Solvation (MM-GBSA) post docking calculations have been performed to the best-docked pose of each ligand. The MM-GBSA estimates binding free energy between molecules based on electrostatic, vander Waals interactions, polar solvation, and non-polar solvation energy. The final rankings of the ligands were carried out based on the obtained free energy of binding (ΔG_{bind}). All the ligands having lower free

energy (against reference ligands) were arranged in decreasing order of free binding energy.

A total of 29 ligand molecules flaunted acceptable binding free energies (ΔG_{bind}) together with prerequisites non-covalent bonding interactions with active siteGly275, Ser276, and ser217 residues shown in (Table 1).

The selected ligands have shown lower binding free-energy values than known inhibitors docked to the same pocket of CpIMPDH. Moreover, the detailed inspection of docking results has revealed that the van der Waals (Glide evdw (Kcal/mol) and the Coulomb energy (Glide ecol (Kcal/mol)) are the most critical energy determinant contributing towards ligands binding energy. Among the 29 ligands, three ligands (ZINC 24855054, ZINC 58171263, and ZINC08000072) molecules have -7.764 kcal/mol, -7.752 Kcal/mol, and -7.438 Kcal/mol. The XP glide score was (-80.944) Kcal/mol, (-83.157)

Table 1 — Binding energy result of the finally selected compounds from the ZINC database screened by successive shape-based screening, ADMET filter, and Molecular docking filter

S.No.	Ligand ID	SP Glide Score Binding Energy (Kcal/mol)	XP Glide Score Binding Energy (Kcal/mol)	ΔG_{SolGB} (Kcal/mol)	ΔG_{vdW} (Kcal/mol)	$\Delta G_{\text{Coulomb}}$ (Kcal/mol)	ΔG_{Lipo} (Kcal/mol)	$\Delta G_{\text{covalent}}$ (Kcal/mol)	ΔG_{HBond} (Kcal/mol)	ΔG_{bind} (Kcal/mol)
1	ZINC24855054	-7.764	-7.768	-7.768	-48.229	-7.382	-55.611	6.706	-1.745	-86.543
2	ZINC58171263	-7.752	-7.752	-7.752	-42.296	-11.548	-53.844	0.527	-1.57	-85.046
3	ZINC08000072	-7.438	-7.438	-7.438	-34.293	-7.252	-41.545	0.645	-0.403	-83.157
4	ZINC71375394	-7.413	-7.413	-7.413	-52.565	-5.663	-58.229	3.647	-0.35	-82.166
5	ZINC00205921	-7.335	-7.336	-7.336	-50.034	-5.998	-56.031	2.304	-1.143	-81.835
6	ZINC44685020	-6.941	-6.941	-6.941	-40.636	-10.363	-50.999	-1.934	0	-81.756
7	ZINC44192084	-6.874	-6.874	-6.874	-41.849	-6.969	-48.818	5.3	-0.469	-80.944
8	ZINC14200809	-6.784	-6.784	-6.784	-45.882	-6.808	-52.691	3.132	-1.33	-78.413
9	ZINC02978189	-6.762	-6.762	-6.762	-40.656	-8.596	-49.252	11.975	-1.544	-77.252
10	ZINC86189966	-6.749	-6.749	-6.749	-39.461	-8.547	-48.008	1.648	-1.4	-76.763
11	ZINC75162825	-6.724	-6.724	-6.724	-37.535	-10.712	-48.247	2.781	-0.762	-75.073
12	ZINC77878093	-6.602	-6.669	-6.669	-42.469	-6.276	-48.745	4.306	-0.7	-74.636
13	ZINC58417699	-6.597	-6.637	-6.637	-38.698	-3.631	-42.329	4.434	-0.175	-73.886
14	ZINC79689858	-6.624	-6.624	-6.624	-46.827	-9.797	-56.624	1.639	-1.208	-73.586
15	ZINC03608608	-6.594	-6.594	-6.594	-38.693	-8.919	-47.612	3.552	-0.156	-73.027
16	ZINC12539837	-6.576	-6.581	-6.581	-48.866	-7.407	-56.274	-7.574	-0.351	-72.883
17	ZINC63450248	-6.532	-6.532	-6.532	-45.412	-6.093	-51.506	0	0	-71.776
18	ZINC75162691	-6.518	-6.518	-6.518	-38.52	-9.565	-48.085	1.885	-0.425	-70.225
19	ZINC45755764	-6.51	-6.51	-6.51	-43.956	-8.503	-52.458	4.304	-0.908	-69.799
20	ZINC79689842	-6.483	-6.483	-6.483	-46.011	-8.78	-54.792	0.991	-1.17	-69.606
21	ZINC79689787	-6.421	-6.421	-6.421	-47.04	-10.071	-57.111	5.019	-1.166	-69.176
22	ZINC38550569	-6.345	-6.377	-6.377	-41.745	-7.904	-49.648	5.148	-0.791	-67.744
23	ZINC40307723	-6.283	-6.365	-6.365	-50.282	-8.432	-58.714	8.375	-0.7	-67.369
24	ZINC69875817	-6.338	-6.344	-6.344	-42.94	-9.309	-52.249	6.364	-0.744	-66.646
25	ZINC78773873	-6.245	-6.245	-6.245	-36.891	-6.359	-43.25	2.04	-0.228	-60.918
26	ZINC83979447	-6.228	-6.228	-6.228	-37.729	-10.974	-48.704	3.42	-0.35	-59.736
27	ZINC19085672	-6.209	-6.209	-6.209	-50.482	-1.848	-52.33	23.644	-0.224	-58.207
28	ZINC40307848	-6.201	-6.206	-6.206	-47.316	-8.567	-55.883	7.962	-0.854	-57.243
29	ZINC06801372	-6.174	-6.174	-6.174	-47.261	-8.178	-55.44	4.873	-1.25	-56.773

Kcal/mol, and (-58.207) Kcal/mol binding energy (ΔG_{bind}) values. When a rigorous examination on binding residues was performed, it was observed that although the three top selected ligands (ZINC 24855054, ZINC58171263, and ZINC08000072) have the lowest binding energy than reference ligand, the binding residues are different. The ZINC 24855054 ligand was perfectly lodged in the binding pocket making Hydrogen bond interaction with SER217, SER276, and Gly275 key residues and shown in (Figs 6 and 7). The obtained docking results justify that ZINC24855054 has better binding stability than the ZINC58171263 and ZINC08000072 ligand in the same binding pocket. So, the binding mode stability of the ZINC24855054, ZINC58171263, and ZINC08000072 ligands on the CpIMPDPH active site is further validated by performing an MD run.

Molecular dynamics simulations

MD simulation analysis of docked complexes offers a valuable insight into the thermodynamic and dynamic stability of the biological system. The conformational changes of ligands and protein complex on time scales provide dynamic

behavior analysis. Thus, the best-docked pose of top 3 ligands (ZINC24855054, ZINC58171263, and ZINC08000072) along with reference docked complex (CpIMPDPH-4IXH) with lowest binding free energy in the CpIMPDPH binding site were subjected to 100 nanoseconds (ns) MD study to validate the stability of the proposed intermolecular interactions of the ligand and active site residues during a time frame. The MD analysis data was represented in root mean square deviations (RMSD) and root-mean-square fluctuations (RMSF) plots from the trajectories. The RMSD graph was generated for all backbone atoms and ligands. The RMSF graph was generated for individual amino acid residues. The RMSD value represents the average distance between the backbone atom of receptor protein when interacting with the ligand. The RMSF value measures the average deviation of each receptor protein's residue during the interaction with the ligand. The RMSD and RMSF analysis results for each complex are shown in (Figs 8 and 9), respectively. The RMSD fluctuations of all four complexes, as seen in (Fig. 8), attained the equilibrium

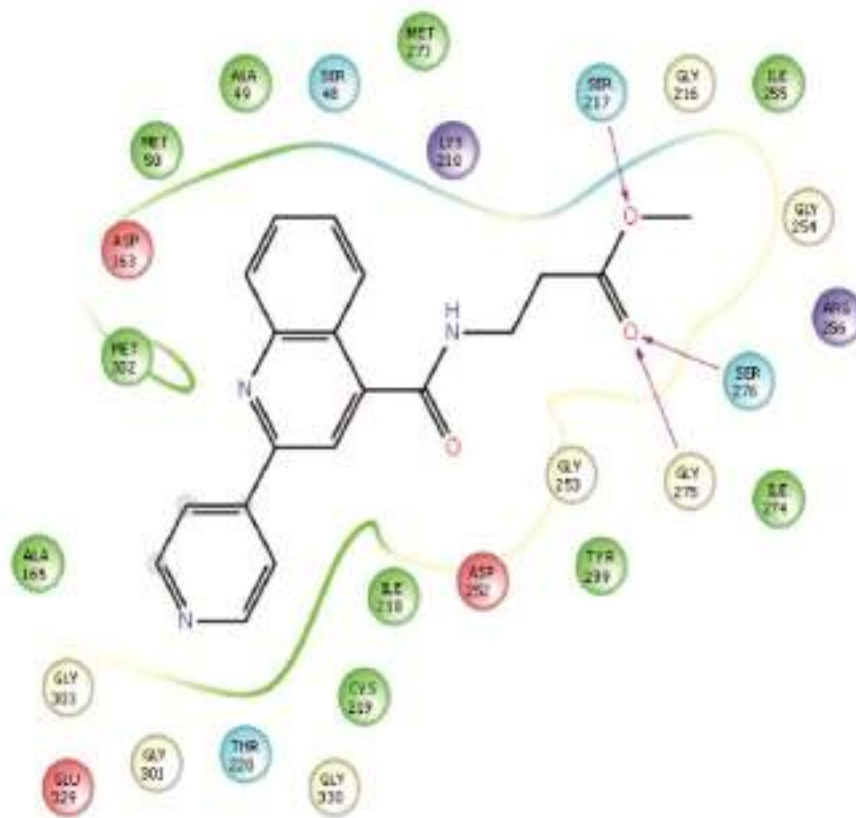


Fig. 6 — The representation of the 2D interaction diagram of the ZINC24855054 ligand with the critical amino acid residues in the CpIMPDPH binding pockets

position and remained stable throughout the simulation period where 4IXH-ZINC24855054 complex attained the stable state early on within 10 ns of the timescale. In these protein-ligand complexes, the RMSF values from the trajectories (Fig. 9) show that residual backbone fluctuations were not much different from each other at various residues of the native protein (4IXH) except at the terminal residues and regions mapped by the residues 90-120 and 310-330 which showed significant fluctuations. The observed dynamic stability of the simulated complex

reinforced the reliability of the docking results and supported the compound behavior as CpIMPDPH inhibitors. As concluded from these studies, shape-based screening (SBS) using known active ligands identified ligands (ZINC24855054, ZINC58171263, and ZINC08000072) having new scaffolds with good binding energies and binding poses. One limitation of this work is that all analysis was performed in *in silico* mode, but a key strength of this research lies in its design and methods for screening new potent ligands.

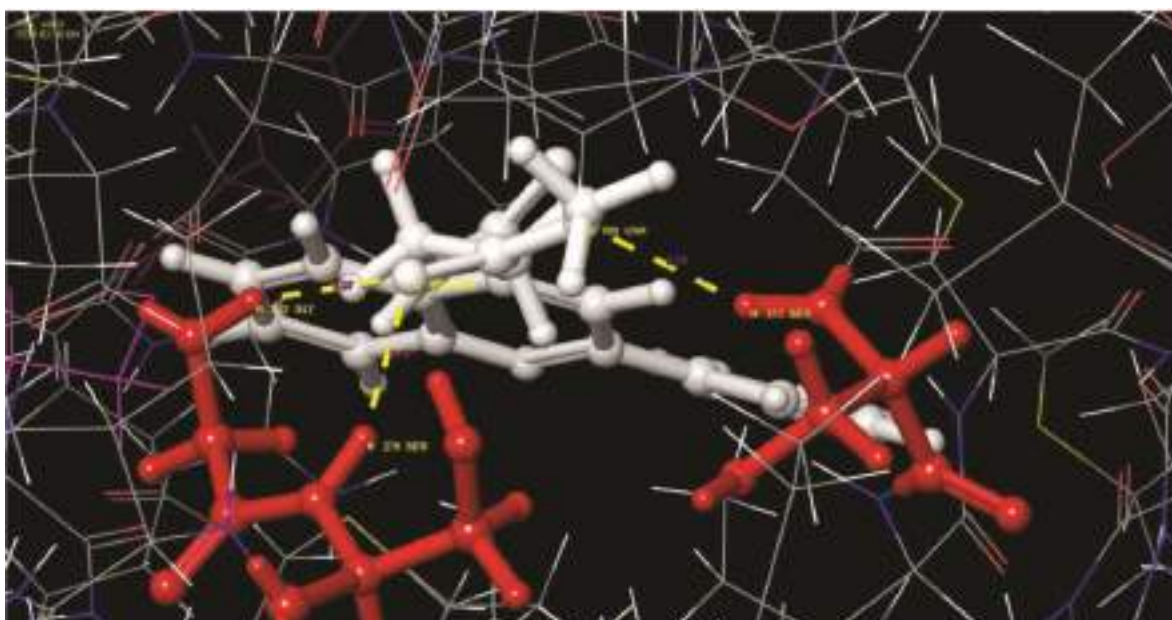


Fig. 7 — Detailed view of ZINC24855054 ligand interaction within CpIMPDPH binding pocket

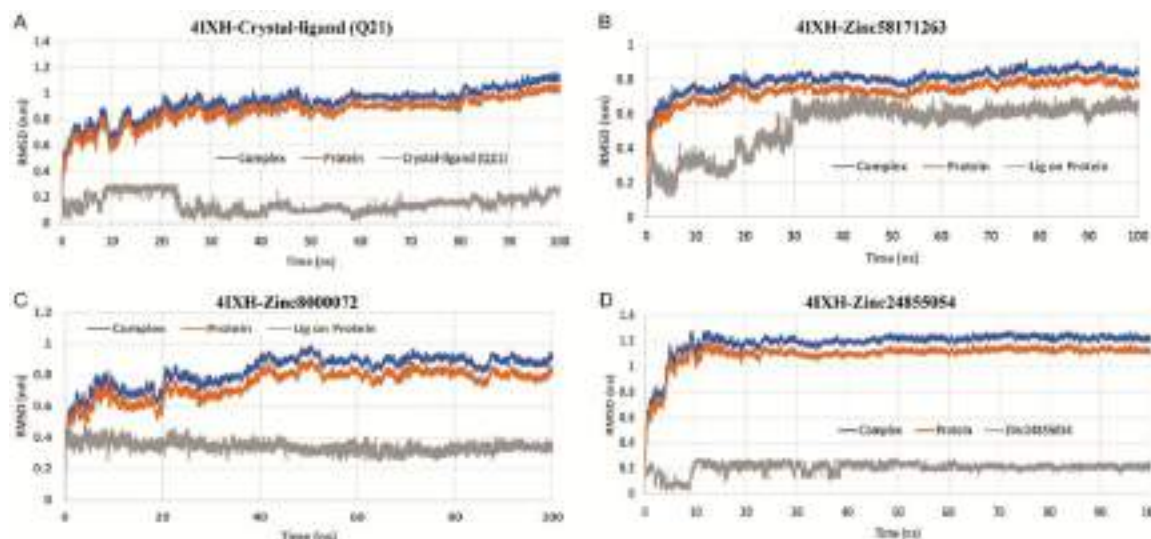


Fig. 8 — Backbone RMSD plot of free and bound form of CpIMPDPH complexed with (A) reference ligand Q21; (B) ZINC58171263; (C) ZINC08000072; and (D) ZINC24855054

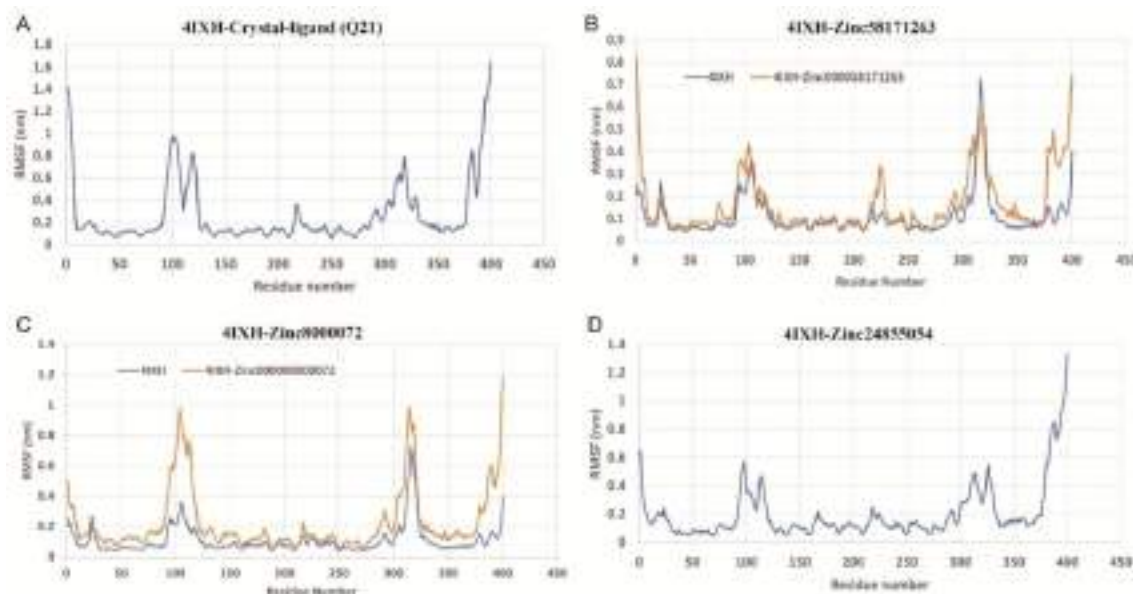


Fig. 9— Backbone RMSF plot of CpIMPDH complexed with (A) reference ligand Q21; (B) ZINC58171263; (C) ZINC08000072; and (D) ZINC24855054

Table 2 — Interaction profile of ligand (ZINC24855054) with receptor protein and interacting amino acids and bond length

Ligand (ZINC24855054) part	Protein (PDB ID:4IXH) Part	Bond Length (Ångström)
Ligand Atom	Atom Amino acid	
O	H GLY 275	2.07
O	H SER 276	2.18
O	H SER 217	2.14

Conclusion

This study carried out an integrated shape-based and structure-based virtual screening, ADME analysis, molecular docking, and molecular dynamics studies to identify potent novel small-molecule inhibitors of IMPDH of *C. parvum*.

Cryptosporidium parvum IMPDH (PDB ID: 4IXH) protein was selected as a receptor template. The target protein was prepared by the protein preparation wizard, and the receptor grid was generated by Glide Module. Initially, the Q21 ((2S)-2-(naphthalene-1-yloxy)-N-[2-(pyridine-4-yl)-1,3-benzoxazol-5-yl] propanamide) was docked into the prepared receptor protein for binding mode analysis. In this respect, computational evaluation of a library of 10,000 compounds attained by the similarity search approach deploying previously reported 18 ligands against CpIMPDH in a stepwise manner. About 1595 Ligands molecules were prepared by the LigPrep module. In successive steps, 2083 ligands were generated, and ADMET analysis of these ligands was performed by the QikProp module, and Lipinski's rules were applied

for all ligands to filter it. Only 1999 ligands were passed Lipinski's rules. These strained ligands from SBS analysis possess a similar functional group as carried by previously identified ligands but possess different scaffolds. All 1999 ligands were docked with the receptor (PDB ID:4IXH) protein by using the Glide High-Throughput Virtual Screening (HTVS) docking method. After this docking, 50%, the best compounds (999 compounds) were processed for the next steps. The HTVS selected ligands were docked with 4IXH protein by using Glide Standard Precision (SP) docking method (47-48). After this docking, 30% best compounds (299 compounds) were processed for the next steps. The SP-selected Ligands were docked with 4IXH protein by using Glide Extra Precision (XP) docking method. After docking, 10%, best compounds (29 compounds) were processed for further analysis. The 29 principal compounds docking results were further processed based on the lowest Glide Score values and the desirable interaction pattern with the key amino acid residues of the CpIMPDH active site obtained from QPLD calculations (Table 2). The effectiveness of docking molecules estimation is considered of vital importance in the availability of a variety of virtual screening ligand complexes. All three protein-ligand complexes' binding free energy was calculated by the Prime/MM-GBSA module. Approximately -80.944 Kcal/mol is the binding free energy of the 4IXH - ZINC24855054 complex. CpIMPDH-ZINC24855054

complex interaction profiles were analyzed, and stability was evaluated using molecular dynamics simulation studies.

On this basis, the top three ligands binding free energy values were computed using Prime/MM-GBSA simulations. The above-discussed filtering approach resulted in three small lead molecules. These small molecules displayed satisfactory ADMET Properties, binding and thermodynamic stability in the complex stage compared with the reference molecule. Among these three ligands, the ZINC24855054 ligand has maximum binding interaction with the active-site residue of the receptor protein. This ligand carries one pyridine ring and one quinolone ring scaffold required for the binding of CpIMPDPH. The best-docked pose of ZINC24855054, ZINC58171263, and ZINC08000072 remained stable in the 100ns MD run. The RMSD and RMSF values obtained during MD simulations were also permissible. In view of all these examinations, the experimental exploration of these compounds as anti-CpIMPDPH molecules will enable to dispensing of explicit indications for the design and development of CpIMPDPH inhibitor molecules with an improved pharmacological outline.

Acknowledgement

I acknowledge and extend my thanks to Dr. Ambedkar Institute of Technology for Handicapped for support to conduct this work smoothly. The authors acknowledge HPC facility of IIT, Delhi for providing computational resources and also the authors would like to thank Prof. Tapan K. Chaudhuri for his insightful suggestions for the work.

Conflict of interest

All authors declare no conflict of interest.

References

- Hillyer JF, Parasites and parasitology in this SARS-CoV-2, COVID-19 world: An American Society of Parasitologists presidential address. *J Parasitol*, 106 (2020) 859.
- Bhalchandra S, Cardenas D & Ward HD, Recent breakthroughs and ongoing limitations in *Cryptosporidium* research. *F1000 Res*, (2018).
- Liu A, Gong B, Liu X, Shen Y, Wu Y, Zhang W & Cao J, A retrospective epidemiological analysis of human *Cryptosporidium* infection in China during the past three decades (1987-2018). *PLoS Negl Trop Dis*, 14 (2020) e0008146.
- Ahmadpour E, Safarpour H, Xiao L, Zarean M, Hatam-Nahavandi K, Barac A, Picot S, Rahimi MT, Rubino S & Mahami-Oskouei M, Cryptosporidiosis in HIV-positive patients and related risk factors: A systematic review and meta-analysis. *Parasite*, 27 (2020).
- Madadi S, Mahami-Oskouei M, Rafeey M, Spotin A, Aminisani N, Mahami-Oskouei L, Ghoyouchi R & Berahmat R, Comparative evaluation of *Cryptosporidium* infection in malnourished and well-nourished children: parasitic infections are affected by the interaction of nutritional status and socio-demographic characteristics. *Comp Immunol Microbiol Infect Dis*, 68 (2020) 101406.
- Tandel J, English ED, Sateriale A, Gullicksrud JA, Beiting DP, Sullivan MC, Pinkston B & Striepen B, Life cycle progression and sexual development of the apicomplexan parasite *Cryptosporidium parvum*. *Nat Microbiol*, 4 (2019) 2226.
- Arias-Agudelo LM, Garcia-Montoya G, Cabarcas F, Galvan-Diaz AL & Alzate JF, Comparative genomic analysis of the principal *Cryptosporidium* species that infect humans. *Peer J*, 8 (2020) e10478.
- Bamaiyi PH & Redhuan NEM, Prevalence and risk factors for cryptosporidiosis: A global, emerging, neglected zoonosis. *Asian Biomed*, 10 (2016) 309.
- Swapna LS & Parkinson J, Genomics of apicomplexan parasites. *Crit Rev Biochem Mol Biol*, 52 (2017) 254.
- Ryan U & Hijjawi N, New developments in *Cryptosporidium* research. *Int J Parasitol* 45 (2015) 367.
- Vinayak S, Pawlowic MC, Sateriale A, Brooks CF, Studstill CJ, Bar-Peled Y, Cipriano MJ & Striepen B, Genetic modification of the diarrhoeal pathogen *Cryptosporidium parvum*. *Nature*, 523 (2015) 477.
- Branda S, Courtney CM, Sinha A, Poorey K, Schoeniger JS, LaBauve AE & Williams KP, Elucidation & manipulation of host-pathogen interactions for development of countermeasures against intracellular bacterial pathogen *Burkholderia pseudomallei*. (2018).
- Beverley SM, CRISPR for *Cryptosporidium*. *Nature*, 523 (2015) 413.
- Mukerjee A, Iyidogan P, Castellanos-Gonzalez A, Cisneros JA, Czyzyk D, Ranjan AP, Jorgensen WL, White AC, Vishwanatha JK & Anderson KS, A nanotherapy strategy significantly enhances anticryptosporidial activity of an inhibitor of bifunctional thymidylate synthase-dihydrofolate reductase from *Cryptosporidium*. *Bioorg Med Chem Lett*, 25 (2015) 2065.
- Cabada MM & White AC, Treatment of cryptosporidiosis: Do we know what we think we know? *Curr Opin Infect Dis*, 23 (2010) 494.
- Manjunatha UH, Chao AT, Leong FJ & Diagana TT, Cryptosporidiosis Drug Discovery: Opportunities and Challenges. *ACS Infect Dis*, 2 (2016) 530.
- Li RJ, Wang YL, Wang QH, Huang WX, Wang J & Cheng MS, Binding mode of inhibitors and *Cryptosporidium parvum* IMP dehydrogenase: A combined ligand- and receptor-based study. *SAR QSAR Environ Res*, 26 (2015) 421.
- Gollapalli DR, MacPherson IS, Liechti G, Gorla SK, Goldberg JB & Hedstrom L, Structural determinants of inhibitor selectivity in prokaryotic IMP dehydrogenases. *Chem Biol*, 17 (2010) 1084.
- Hedstrom L, Liechti G, Goldberg JB & Gollapalli DR, The Antibiotic Potential of Prokaryotic IMP Dehydrogenase Inhibitors. *Curr Med Chem*, 18 (2011) 1909.
- Leelananda SP & Lindert S, Computational methods in drug discovery. *Beilstein J Org Chem*, 12 (2016) 2694.

- 21 Ferreira LG, Dos Santos RN, Oliva G & Andricopulo AD, Molecular docking and structure-based drug design strategies. *Molecules*, 20 (2015) 13384.
- 22 Choudhury M, Sharma D, Das M & Dutta K, Molecular docking studies of natural and synthetic compounds against human secretory PLA2 in therapeutic intervention of inflammatory diseases and analysis of their pharmacokinetic properties. *Indian J Biochem Biophys*, 59 (2022) 33.
- 23 Liu X, Shi D, Zhou S, Liu H, Liu H & Yao X, Molecular dynamics simulations and novel drug discovery. *Expert Opin Drug Discov*, 13 (2018) 23.
- 24 Toppo AL, Yadav M, Dhagat S, Ayothiraman S & Jujjavarapu SE, Molecular docking and ADMET analysis of synthetic statins for HMG-CoA reductase inhibition activity. *Indian J Biochem Biophys*, 58 (2021) 127.
- 25 De Vivo M, Masetti M, Bottegoni G & Cavalli A, Role of molecular dynamics and related methods in drug discovery. *J Med Chem*, 59 (2016) 4035.
- 26 Sastry GM, Dixon SL & Sherman W, Rapid shape-based ligand alignment and virtual screening method based on atom/feature-pair similarities and volume overlap scoring. *J Chem Inf Model*, 51 (2011) 2455.
- 27 Gimeno A, Ojeda-Montes MJ, Tomás-Hernández S, Cereto-Massagué A, Beltrán-Debón R, Mulero M, Pujadas G & Garcia-Vallvé S, The Light and Dark Sides of Virtual Screening: What Is There to Know? *Int J Mol Sci*, 20 (2019) 1375.
- 28 Bao G, Zhou L, Wang T, He L & Liu T, A Combined Pharmacophore-Based Virtual Screening, Docking Study and Molecular Dynamics (MD) Simulation Approach to Identify Inhibitors with Novel Scaffolds for Myeloid cell leukemia (Mcl-1). *Bull Korean Chem Soc*, 35 (2014) 2097.
- 29 Sterling T & Irwin JJ, ZINC 15 - Ligand Discovery for Everyone. *J Chem Inf Model*, 55 (2015) 2324.
- 30 Schrodinger LLC, Schrodinger Suite 2012 Protein Preparation Wizard; Epik version 2.3, Impact version 5.8, Prime version 3.1. (*New York Schrodinger*), 2012.
- 31 Ioakimidis L, Thoukydidis L, Mirza A, Naeem S & Reynisson J, Benchmarking the reliability of QikProp. Correlation between experimental and predicted values. *QSAR Comb Sci*, 27 (2008) 445.
- 32 Striepen B, White MW, Li C, Guerini MN, Malik S-B, Logsdon JM, Liu C & Abrahamsen MS, Genetic complementation in apicomplexan parasites. *Proc Natl Acad Sci U S A*, 99 (2002) 6304.
- 33 Kim Y, Maltseva N, Mulligan R, Makowska-Grzyska M, Gu M & Gollapalli D, Crystal Structure of the Catalytic Domain of the Inosine Monophosphate Dehydrogenase from *Bacillus anthracis* in the complex with IMP and the inhibitor P200. (2017).
- 34 Laskowski RA, Rullmann JAC, MacArthur MW, Kaptein R & Thornton JM, AQUA and PROCHECK-NMR: programs for checking the quality of protein structures solved by NMR. *J Biomol NMR*, 8 (1996) 477.
- 35 Harder E, Damm W, Maple J, Wu C, Reboul M, Xiang JY, Wang L, Lupyan D, Dahlgren MK & Knight JL, OPLS3: A force field providing broad coverage of drug-like small molecules and proteins. *J Chem Theory Comput*, 12 (2016) 281.
- 36 Halgren TA, Murphy RB, Friesner RA, Beard HS, Frye LL, Pollard WT & Banks JL, Glide: A new approach for rapid, accurate docking and scoring. 2. Enrichment factors in database screening. *J Med Chem*, 47 (2004) 1750.
- 37 Friesner RA, Murphy RB, Repasky MP, Frye LL, Greenwood JR, Halgren TA, Sanschagrin PC & Mainz DT, Extra precision glide: Docking and scoring incorporating a model of hydrophobic enclosure for protein-ligand complexes. *J Med Chem*, 49 (2006) 6177.
- 38 Cho AE, Guallar V, Berne BJ & Friesner R, Importance of accurate charges in molecular docking: quantum mechanical/molecular mechanical (QM/MM) approach. *J Comput Chem*, 26 (2005) 915.
- 39 Bochevarov AD, Watson MA, Greenwood JR & Philipp DM, Multiconformation, density functional theory-based p K a prediction in application to large, flexible organic molecules with diverse functional groups. *J Chem Theory Comput*, 12 (2016) 6001.
- 40 Yu HS, Watson MA & Bochevarov AD, Weighted Averaging Scheme and Local Atomic Descriptor for p K a Prediction Based on Density Functional Theory. *J Chem Inf Model*, 58 (2018) 271.
- 41 Genheden S & Ryde U, The MM/PBSA and MM/GBSA methods to estimate ligand-binding affinities. *Expert Opin Drug Discov*, 10 (2015) 449.
- 42 Siroos H, Chemi G, Campiani G & Brogi S, An integrated in silico screening strategy for identifying promising disruptors of p53-MDM2 interaction. *Comput Biol Chem*, 83 (2019) 107105.
- 43 Kumari R, Kumar R, Consortium OSDD & Lynn A, g_mmpbsa-A GROMACS tool for high-throughput MM-PBSA calculations. *J Chem Inf Model*, 54 (2014) 1951.
- 44 Lindahl E, Bjelkmar P, Larsson P, Cuendet MA & Hess B, Implementation of the charmm force field in GROMACS: Analysis of protein stability effects from correction maps, virtual interaction sites, and water models. *J Chem Theory Comput*, 6 (2010) 459.
- 45 Bernardi A, Faller R, Reith D & Kirschner KN, ACPYPE update for nonuniform 1–4 scale factors: Conversion of the GLYCAM06 force field from AMBER to GROMACS. *Software X*, 10 (2019) 100241.
- 46 Huston CD, Spangenberg T, Burrows J, Willis P, Wells TNC & van Voorhis W, A proposed target product profile and developmental cascade for new cryptosporidiosis treatments. *PLoS Negl Trop Dis*, (2015).
- 47 Kirubakaran S, Gorla SK, Sharling L, Zhang M, Liu X, Ray SS, MacPherson IS, Striepen B, Hedstrom L & Cuny GD, Structure-activity relationship study of selective benzimidazole-based inhibitors of *Cryptosporidium parvum* IMPDH. *Bioorganic Med Chem Lett*, (2012).



Remediation strategies for heavy metals contaminated ecosystem: A review

Mahendra Kumar^{a,*}, Aparna Seth^b, Alak Kumar Singh^a, Manish Singh Rajput^b, Mohd Sikandar^c

^a School of Chemical Technology, Harcourt Butler Technical University, Kanpur, 208002, India

^b Department of Biotechnology, Dr AITH, Kanpur, 208024, India

^c Uttar Pradesh Pollution Control Board, Kanpur, India

ARTICLE INFO

Keywords:

Adsorption
Heavy metals
Biosorption
Adsorption capacity

ABSTRACT

Industries and anthropogenic activities around us engender our natural resources with their noxious discharge, untreated waste water or sludge containing variety of heavy metals. These toxic metals in turn are emerging health risks for living beings triggering allergies, infection, defects and diseases. Consequently, there is evolving needs for ecologically safe, systematic and novel approach to remediate these toxic heavy metals. Physical, chemical and biological methods have not been much effective in dealing of contaminated ecosystem. These conventional approaches have limitation in terms of higher cost, energy consumption and less efficiency. Overcoming their drawbacks, adsorption, a physico-chemical surface phenomenon came to light which is a way cheaper, effective, flexible, reactive and efficient technique for eliminating heavy metals like cobalt, chromium, lead, nickel, mercury, arsenic, uranium, cadmium, copper etc. Modulating chemical and physical characteristics of microbes, lignocellulosic material, industrial waste biomass, nanotubes, metal organic frameworks (MOFs) and nanocomposite material, escorts in fabricating a magnificent adsorbent. This review critically evaluates various type of adsorbents, their application and adsorption efficiency. It also analysed the parameters affecting the adsorption processes.

1. Introduction

Since a long time, the anthropogenic activities are directing towards environmental contamination caused due to the accumulation of heavy metals (naturally occurring element) into water bodies, land and air. These are directly or indirectly deteriorating ecological system and living resources thus, accelerating health risks (Masindi and Muedi, 2018). Discharged wastewater from commercial industries of leather tanning, textile, electroplating, non-ferrous metal refineries, printing, pigmenting and nuclear power plants, include traces of heavy metal pollutants like cobalt, chromium, lead, nickel, mercury, arsenic, uranium, cadmium, copper etc. Some of these elements in the form of pesticides, insecticides and fertilizers are also required to carry out the biological metabolism, but due to their high dosage, it enters into the food chain and so are manifested highly toxic to the flora and fauna (Lakherwal, 2014). Exposure of heavy metals to a human body causes defect to organs, like kidney, lungs, liver and eyes and biological entities such as nervous system, immune system, reproductive system and respiratory system further heading towards diseases like anaemia, cancer, nausea, organ failure, loss in bone mineral, tumour induction etc

(ZeraatkarAmin et al., 2016a).

There are many methods discovered till now, that comes under the category of either physical, chemical or biological methods. Also, several techniques for its removal from the environment has been adopted that also work towards diminishing the problem of water scarcity with its reuse. The physical methods involved are drying, crushing, ball milling, sedimentation, filtration, sieving and absorption of metal ions from sludge to eliminate toxic metals (Sharma et al., 2016). Though this is a cheap method but efficiency (~50%) and its operation at large scale is matter of concern (Khoei Javanshires et al., 2018). Chemical precipitation, electroplating, ion-exchange, and reverse osmosis are some chemical remediation strategies discovered till now, to eliminate these pollutants from industrial and domestic sludge (Bordoloi et al., 2017). The efficiency of chemical methods is impressive (~98–99%) but production of secondary wastes and the use of expensive and toxic chemicals make it a less of priority (Renu and Singh, 2017). Besides using physical and chemical strategies, biological methods have also paved its way in the remediation technique, known as bio-absorption (Kumar et al., 2019). Bio-absorption is a physicochemical process by which living tissues are capable of binding chemically with

* Corresponding author.

E-mail address: mahendra.bbt@gmail.com (M. Kumar).

the contaminants and resulting in their elimination. It involves plant residue, lignocellulosic material, aquatic plants and microorganisms such as yeasts, bacteria, fungi and algae. Microalgae has a greater potential to sorb toxic metals from wastewater (Li et al., 2020). Its efficiency mainly depends on the concentration of metal ions, pH, temperature, chemical oxygen demand and chemical composition of aqueous solution (Kumar et al., 2014). *Anabaena*, *cyanobacteria*, *Callitriche lusitanica* and *Azolla caroliniana* are some of the biological agents utilized for extracting Ar, Cu, Mt and Dz from sewage and sludge (Jasrotia et al., 2017; Real et al., 2007). Although being a cheapest technique yet its dependence on such physiological parameters to sustain in environment, is the only drawback to use biological methods for metal extraction. All these methods need some modifications on their physical and chemical parameters so as to attain maximum efficiency.

Other than these techniques, adsorption is a wide physiochemical phenomenon by which a solid substance, known as adsorbent, is used to attract other solute particles such as atoms, ions and molecules on its surface mainly due to the property of adhesion, electrostatic attraction and ion exchange and thus, is used for such remediation purposes in order to attach all contaminants on its surface and purify the sample being place. Adsorbents are classified into microbial, lignocellulosic, waste biomass, industrial waste and more advance like hybrid adsorbents, nano adsorbents and metal organic frames etc. (Ndimele et al., 2018; Ma et al., 2015a). This review critically analyses the advances in various adsorbents from its infant stage to till date and simultaneously compare its removal efficiency and adsorption capacity.

2. Toxicity of heavy metals to ecosystem

Heavy metals are naturally occurring elements present as sulphide and ores comprising of high density as well as high relative atomic mass those are poisonous even at the exposure of low concentration. Natural sources of these include leaching, soil erosion, metal erosion and volcanic eruption while the others sources are like agriculture, pharmaceutical, geogenic and industry. The toxicity of heavy metals is considered on basis of many factors like dose, way of exposure and medium. Arsenic, cadmium, chromium, lead, and mercury are among the priority metals that are of public health concern due to their high toxicity. These metals are considered systemically hazardous.

3. Copper

Copper is an essential element for growth and development of both plants and animals but its high concentration in the environment may have adverse effects in all living resources. It exists in different forms like metal, ion, mineral, and chemical that can be released into the surroundings along with domestic wastewater, mining, fertilizer, sludge, decaying vegetation, natural sources etc (Kumar et al., 2020). Due to its ability of getting attached with soil and air as well as its solubility in water, it can enter into the body and increase health risks including hypotension, melena, hematemesis, coma, jaundice, gastrointestinal distress, vomiting, nausea, respiratory problems, abdominal pain, liver and kidney failure. Cu(II) not only degrades human health but also have toxicity on marine dinoflagellate e.g. *Amphidinium carterae* (Lage et al., 1996) World Health Organization (WHO) has set limit of 2 mg/L copper ion concentration in water while United States Environmental Protection Agency (USEPA) has defined 1.3 mg/l of copper ion concentration in industrial discharge (Kumar et al., 2020). Remediation techniques of removing copper ion include membrane filtration, electrodialysis, electrocoagulation, electrofloatation, physical adhesion, chemical precipitation, co-precipitation, ion-exchange, nanofiltration and adsorption (Arbabi and Golshani, 2016).

4. Cadmium

Cadmium is a naturally occurring element present as dietary

component in vegetables, nuts, cereals, starch items and meat products (Abernethy et al., 2010). But its high concentration turns into toxicity of food products and water. Main sources of cadmium toxicity are paint industry, electroplating industry, batteries, electronic wastes and nuclear power plants. Exposure of such wastes or its byproducts into air, water, soil and land contaminates it on another level. The utmost limit of cadmium existence in water set by Environmental Protection agency (EPA) is 0.003mg/dm³ but distressing human activities led to an upsurge in this level. However, cadmium(II) is being regarded as Group B1 carcinogen by USEPA (Environmental Protec, 1999). Inhalation, intake as well as ingestion of these highly polluted components leads its accumulation in body parts causing organ failure and variety diseases. After being absorbed and then transported into the body, the deposited cadmium traces are found in kidney and respiratory tracts that adversely effects their metabolism (Argonne National Laborato, 2001). The amount of oxidative stress and oxidative damage caused due to the ill effects of cadmium, induces tissue injury and apoptosis of tubular cells, respectively (Cuypers et al., 2010; Fujiwara et al., 2012). Other than these it also engender emphysema, sensory alteration, mutation, osteoporosis, hypochromic, bone denegeration, anaemia and osteomalacia. (Hubicki and Kolodyńska, 2012). Cadmium is one of the component present in cigarettes whose intake while smoking results in lung insufficiency. Certain technologies like biosurfactant, chemical precipitation, floatation, Micellar Enhanced Ultrafiltration (MEUF) and adsorption are being employed for the treatment of waste water discharge (Renu and Singh, 2017).

5. Arsenic

Arsenic is ubiquitous and a natural component present in groundwater that is highly toxic in its inorganic form (Das et al., 1995; Mandal and Suzuki, 2002). According to World Health Organisation (WHO), intake of this water as a purpose for drinking is of great concern as no treatment has still been made for the removal of accumulated arsenic from body. Provenances of inorganic arsenic integrant are industries of pigment, paper, textile, metal, glass, tanning, pharmaceuticals and ammunition. Wastewater from industries and groundwater contaminated with excessive levels of arsenic are the cause of polluting irrigated agricultural land, drinking water, organic food, dairy product, seafood and poultry. Toxicity caused is the greatest threat to public health. Tobacco plant has the greatest potential for naturally absorbing arsenic from soil water and so its exposure to human body is the cause of damage. Short-term revelation to arsenic traces is indicated by the symptoms of vomiting, numbness, diarrhoea, muscle cramping, skin disorder and long-term by are skin cancer, hyperkeratosis, change in pigmentation, bladder cancer and lung cancer. Many other adverse effects of arsenic can be seen in pregnant females with outcomes of infant mortality and health damage of child (Quansah et al., 2015). Hence, embracing activated carbon, immobilization, coagulation, filtration, phytoremediation and precipitation (Mahimairaja et al., 2005).

6. Mercury

Food chain and food web is the vital provenience of mercury circulation among humans, animals, marine animals, fishes and microbes due to the contaminated soil and water (Davidson et al., 2004). As per laws of United States Environmental Protection Agency, its toxicity to human body depends upon the mercury concentration, its chemical composition, exposure to the body, time of contact and its susceptibility. It exists as liquid state but can vaporise at room temperature because of its low latent heat of vaporisation which is the main cause of various respiratory problems. Electrical equipments, medial appliances, barometers, mercury amalgams, paper industry and paint industry are some current origins for mercury redistribution in the form of municipal and industrial waste (Guzzi and Caterina, 2008). A compound of mercury known as methylmercury, inorganic contaminant, is a neurotoxin present in

every body but its presence in high concentration have adverse effects to human health (Rice et al., 2014). While dimethylmercury is a highly toxic compound that causes immediate death of a person even if he is exposed to its lowest concentration, i.e. in microliters (Joshi et al., 2012). Bioaccumulation of mercury in body have repercussions like tremors, insomnia, headache, blindness, mental retardation, nervousness and many other nervous system damages (Guzzi and Caterina, 2008). Hence, mercury has been ranked as the 3rd most poisonous component by the US Government Agency for Toxic Substances (CliftonJack, 2007).

7. Chromium

Although chromium is an essential element for human growth and development chromium with hexavalent valency has been ranked as the most toxic element polluting the earth's crust (Altaf et al., 2008). Waste generated by industry, agriculture, mining and transportation containing chromium metal are poisonous to all natural resources. Chromium salts are considered to be the most extensively used compound for tanning purpose but a large percentage of used chromium renders into sludge. Thus, tanning industry induces several environmental problems and death-traps (Wionczyk et al., 2006). Other industries of metal cleaning, galvanization, cement, leather, paint and pharmaceuticals involve chromium usage, hence, its release into the environment in different physical and chemical states ends into metal accumulation in plants, clams, crabs and fishes (Belay, 2010). Intake of these lethal products is carcinogenic, mutation causing, organ damaging. Immediate measures are necessary to be taken for its removal and recovery from our surroundings. This include chemical precipitation, electro-coagulation, reverse osmosis, nanofiltration, ion exchange, biosorbent, adsorption and membrane filtration. These are some versatile techniques applied for the remediation purpose in order to enhance the recovering and recycling efficiency of toxic chromium metal from effluents. Among all, biosorbent treatment is regarded as the cheapest as well as the most effective way of removing chromium from sludge. Composite used for biosorption is made up of acid treated palm shell charcoal coated with chitosan, component comprising paramount capacity of sorption (Akunwa et al., 2014). Throughout the procedure, temperature, pH, agitation, dose of adsorbent, effluent quantity and time of contact are some necessary parameters that must be taken into consideration (Casano et al., 2007).

8. Accessible techniques for heavy metal elimination

Variety of techniques have been employed for the remediation of soil, water and air that are categorised into physical, chemical and biological technologies (Fig. 1). Assessment of sample, strategy, chemical and physical properties is a necessary requirement to carry out the procedure.

Physical remediation techniques – Electrokinetic remediation, thermal desorption, sorting, vapour stripping soil washing, vetrification, encapsulation and permeable barrier are some methodologies used for the elimination of contaminants and pollution prevention (Hamby, 1996; Bradl and Xenidis, 2005; Peters and Shem, 1993). Moreover, due to their fewer efficiency and effectiveness of such techniques needed a replacement (Lindgren et al., 1994; Cabrera-Guzman et al., 1990).

Chemical remediation techniques – Chemical precipitation, coagulation-flocculation, ion-exchange, floatation, complexation, distillation, membrane filtration, electrodialysis and reverse osmosis are some cases employed for extraction of heavy metals (Benfield et al., 1982a, 1982b; Hubicki and Kołodryska, 2012; Environmental Protec, 1981; Srivastava et al., 1980). Chemical precipitation is further classified into five basic techniques – chelating precipitation, hydroxide precipitation, sulphide precipitation, carbonate precipitation and xanthate precipitation (Peters and Shem, 1993; Esmaeili and Vazirinejad, 2005). Engineers are successful in designing an Ion Exchange Treatment Plant (IETP) for the ministration of Acid Mine Drainage wastewater (AMD) in regards of copper ion that is basically based upon Indion 730 (14 BSS) and indion 236 (Ion Exchange of Indian Limited) (Gaikwad et al., 2010; Kumar et al., 2018). In spite of efficient technique, it is not preferred because of high cost and chemical sludge accumulation (Barakat, 2011; Peters, 1997)

Biological remediation techniques – Living organisms such as algae, fungi, bacteria, protozoa, worms, insects and enzymes are responsible to carry out the process of bioremediation. It involves methods like biosorption, biotransformation, activated sludge, anaerobic digestion and biofiltration (Dhokpande and Kaware, 2013; Mane et al., 2011). Biosorption is phenomenon by which active, inactive, dead or microbial biomass cells, dependent on metabolic or non-metabolic pathways, are capable to affix contaminants on their cell surface, intracellular or extracellular portion (Ahalya et al., Kanamadi 2; Galun et al., 1987). Activated sludge process, carried out to treat the wastewater, has the COD removal efficiency of about

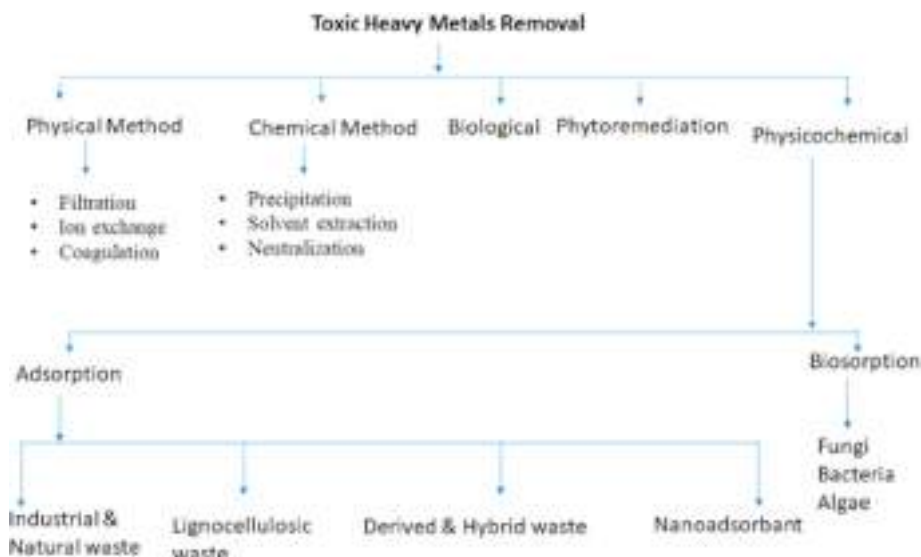


Fig. 1. Scheme of various methods involved in heavy metal remediation with special emphasis on bio-sorption and adsorption.

95–98% (Medhat Moustafa and Gaber Idris, 2003; Pagnanelli et al., 2009). Extracellular polymeric substances extracted from the activated sludge, by accomplishing the centrifugation technique, plays crucial role in this procedure (HassaniHossenzadeh and Torabifar, 2010; Rossin et al., 1982; Liu et al., 2001).

Phytoremediation techniques:

Phytoremediation evolves as a technology that involves use of specific and bioengineered plants like *Pistia stratiotes*, *Alysum lesbia-cum*, *Brassica juncea* and many more to detoxify nasty substances like toxic heavy metals. It is not only eco-friendly, systematic and coherent but cost effective too. It helps the ecosystem in preventing soil erosion and metal leaching with added benefits.

9. Adsorption: A robust physico-chemical approach for the elimination of toxic heavy metals

Adsorption is a physico-chemical phenomenon for adhesion of substances on the surface of solid adsorbent with the help of chemical bondage and physical attraction between adsorbent and contaminant, thus, creating a thin film of adsorbate ("Glossary". The Brownfiel, 2008). The physical adsorption involves vander wall forces and other different forces of attraction assisted by controlling temperature at considerably low rate while chemical adsorption involves chemical forces, activation energy, ion swapping and chemical bonds assisted by high temperature (Singh and Gupta, 2016). It is basically an exothermic process and surface phenomenon by which substances such as heavy metal contaminants, condensed gases, organic and inorganic components are removed or separated from waste water, sludge, municipal waste or industrial waste along with heat liberation in order to immaculate the region. Successive processes of adsorption and desorption aid in collecting the adsorbate (atom, ion or molecule) in a solution for their further processing (Mishra, 2014). Factors affecting adsorption are nature of adsorbate and adsorbent, reversibility of adsorption and desorption, the surface area of adsorbent, activation of adsorbent and experimental conditions such as temperature, pH, pressure etc. Among all physical, chemical and biological remediation techniques, adsorption has been proved one of the best methods for removal of noxious heavy metal components from discharged effluents. Its low cost, good efficiency, easy operation, high reactivity with adsorbate, flexible design and regeneration or reuse has proved it to be the most prevailing one (Fu and Wang, 2011). Some types of adsorbents utilized for adsorption are fabricated of microbes, lignocellulosic material, industrial waste biomass, nanotubes, metal organic frameworks (MOFs) and nanocomposite materials.

10. Microbes as adsorbents

Adsorption through microorganisms is a dynamic, efficacious and economical approach for potential removal of heavy metal contaminants from polluted water bodies or effluents. Microbes being fungi, bacteria and algae are exploited for this purpose because of their easy growth, high yielding and reusable characteristics (Apiratikul and Pavasant, 2008). A large amount of biomass can also be obtained from various fermentation industries present as a by-product there which would be cheap enough to be called as best out of waste (Han et al., 2006). This adsorption technique through microbial adsorbent is also known as biosorption. Both living or dead cell biomass are opted to carry out this remediation technique depending upon either metabolic processes or non-metabolic processes respectively. Nevertheless, dead or inactive cells are more favoured due its modulated physical and chemical state, no dependency on culture media and negligible possibilities of promoting toxicity. Generally, formula $R = ((C_i - C_f) * 100) / C_i$ is implied to calculate the percentage of adsorbate where, R is the percentage of adsorbate adsorbed by adsorbent, C_i is the initial concentration of metal ion in mg/l and C_f is the final concentration in mg/l. (Gksungur et al., 2005b) However the equation derived for calculating the adsorption capacities of metal adsorbed to the biomass is $Q = ((C_i - C_f) * V) / m$ where,

V is the metal ion solution volume (ml), C_i and C_f is the initial and final metal ion concentration respectively in equilibrium (mg/l) and m is the weight of biomass (Dhal and Pandey, 2018). For the biosorption study by microorganisms at different parameters several methods or models were opted that includes Langmuir and freundlich isotherm and adsorption kinetics.

11. Fungi

Fungal hyphae have proved to be a good source of bioremoval of toxic metals whose exposure causes variety of health hazardous. Significance of implementation of fungus as an adsorbent is its capability of easy growing in way too large proportion and accompanying easy genetic modification. Besides that, yeast of kingdom fungi and domain eukaryota is a multi-cellular organism consisting of distinct membrane bound nucleus plus cytoplasm, elevates the metal binding property of it (Wang and Chen, 2009). Till date, variety of experiments have been constructed employing contrasting categories of fungus, for instance *Aspergillus niger*, *Rhizopus arrhizus* *Saccharomyces cerevisia*, *Lentinused-odes* etc. in combination with compounds or reagents improves uptake assimilation, thus making its surface more permeable to adhesion of atoms, ions and molecules (Burakov et al., 2018). It was predicted that the adsorption capacity mainly depends upon fungal strain, physical and chemical pre-treatment methods, exposure of metal binding sites, pH of solution, pregnable functional groups on the surface of strain and elimination ability of biomass surface impurities (Kapoor and Viraraghavan, 1997, 1998).

The fungus *Aspergillus niger* is one of the important species usually spotted in fermentation industries. It has been exercised to acquire analytical patterns and optimizing biosorption of numerous destructive ions or atoms (Amini et al., 2009). Fungal biomass was grown in a culture medium, deactivated by heating, washed with deionized water, dried at 50C, grinded and then pre-treated with NaOH followed by further washing with deionized water, drying and grinding (Gksungur et al., 2005a). Application of scanning electron microscopy determined microporosity as well as pore size of pre-treated *A.niger* whereas central composite design and response surface methodology helped to study the optimum condition (Kunamneni and Singh, 2005; Song et al., 2016). Biosorption experiments were conducted in accordance with various methods at several time intervals in order to study maximum adsorption capacity and maximum efficiency of adsorbent to remove adsorbate (Wang et al., 2014; Huang and Huang, 1996; Ruthven, 1984). *Aspergillus niger* is being applied for the withdrawal of metal ions of cadmium, copper, uranium, lead, cobalt, europium etc. with maximum adsorption capacities given on the table below (Mukhopadhyay et al., 2008; Yang et al., 2019; Dang et al., 2018).

Rhizopus arrhizus is a filamentous fungus basically used in alcohol fermentation industry due to the production of lactic acid and cortisone from it. Furthermore, it is an excellent agent for bioremediation purpose consequently removing heavy metals from circumambient ("Journal of Scientific &, 2005). The biomass is collected, washed with deionized water, dried at 60C, grinded, sieved and then was prepared to carry out the experimental procedures (Fourest et al., 1994). This microbial community has the potential of eliminating uranium and thorium ion at a much higher rate, i.e. around 2.3 and 20 times more than ion exchange resin method, respectively (Tsezos and Volesky, 1981). Its maximum affinity towards biosorption of metal ions at a particular pH, with or without its pretreatment with a substrate is revealed below in the table.

Saccharomyces cerevisiae is a species of yeast majorly used in fermentation, baking and brewing industries and is sometimes called as top-fermenting yeast. Easily available and non-expensive nature makes it a good adsorbing agents for removing metallic ions of copper, cadmium, lead, uranium, arsenic etc. Certain parameters responsible for modulating the adsorption capacities of dead microbes are pH, contact time, metal ion concentration, function groups present on the surface of biomass and quantity of biomass used. (Can and Wang, 2010; Hadiani

et al., 2019). Comparison of maximum adsorption capacity and efficiency of metal ions eliminated by the use of different fungal species with or without their treatment are summarized in Table 1.

12. Bacteria

Bacterial exclusive cell wall plays a critical role in the biosorption process due to the presence of different functional groups on its surface (Abdi and Kazemi, 2015a). The aforementioned was correspondingly noted to be the first biosorbent for heavy metal accumulation as well as deduction since most of them have the capability to accommodate themselves in all adverse surroundings in addition they are the most diverse creature to be seen till date (Vijayaraghavan, 2008; Norberg and Persson., 1984; Abbas et al., 2014; Urrutia, 1997; Vasudevan et al., 2001). According to gram cataloguing, bacteria are broadly characterised into gram positive and gram negative. Experimental procedures determined gram positive as a better adsorbent as compared to gram negative, because of the presence of glycoprotein responsible for metal binding along with its uptake (Abdi and Kazemi, 2015b; Gourdon et al., 1990). Bacterial species in charge of eradicating metals, such as arsenic, cadmium, chromium, cobalt, copper, gold, lead, mercury, nickel, selenium, silver and zinc, from waste water and soil are *Bacillus*, *Pseudomonas*, *Escherichia* etc. (Kinoshita et al., 2013)

Bacillus subtilis offers a potential detoxification and elimination of metal ions as a conventional water treatment source. In accordance with the studies, the two bacterial strains, i.e., C-13 and C-16, showed high tolerance and adsorption capacity against noxious waste, like Cd, Cr, Mn and Pb, present in activated sludge. The two strains of *bacillus sp.* were pretreated with either acid or alkali for augmenting metal uptake aptitude. Alkali treatment showed much better results at pH between 7 and 10 (García et al., 2016; Zhai et al., 2011; Velásquez and Jenny, 2009; Volesky, 2003). Alternative experiments were conducted concerning the metabolic activities of *bacillus subtilis* with the aim of comparing the adsorption efficiencies of pretreated or untreated living biomass. It was known, that the biomass pretreated with supercritical CO₂ (SC-CO₂) or steam autoclaved were more efficient biosorbents than the untreated or living biomass. Maximum biosorption capacity was shown in order of super critical CO₂ pretreatment > steam autoclave pretreatment > living biomass with efficiency of 98.54, 99.2 and 96.3 respectively (Al-Gheethi et al., 2017).

Pseudomonas aeruginosa is ubiquitous and the most resourceful bacteria showing resistance against chemicals, metals, antibiotics and organic solvents. Thus it has been recorded to have the highest metal

removal efficiency. This microbial community is used in bioremediation of toxic metals with application of different uptake mechanisms (Pardo et al., 2003; Haritash and Kaushik, 2009; Orhan et al., 2006; Abdelbary et al., 2019). While metals eliminated after pretreatment of biomass with immobilized activated carbon are mercury, copper, nickel, chromium and zinc (Orhan et al., 2006; Abdelbary et al., 2019). Henceforth *pseudomonas* would be deliberated as a promising bioadsorbing agent once being genetically modified.

Escherichia coli is the most common microbe to be extensively used and perform as a prototype for research, experimental and laboratory purposes. Dynamics that brand it of such commercial use include-thrive on extreme conditions, has fast growing rate, cheap, easily genetically modified, most studied and ensures biosafety (Idalia and NaurúFranco, 2017). Active, inactive, living, dead and physically and chemically pretreated bacteria are utilized for metal removal from aqueous solution having varied accumulation capacities. Surface modifications attained on reaction of chemicals with the biomass marks it a superior adsorbing mediator (Huang et al., 2001). Dependency of pH, temperature, chemical pretreatment reagents and equilibration time affects the adsorption efficiency of biomass (Huang et al., 2001; Strandberg et al., 1981; Marqués et al., 1991; Tsezos and Volesky, 1981). Metal ions eliminated by the use of different bacterial species are summarized in Table 2.

13. Algae

By far algae has always been opted as a promising representative in variety of remediation purposes with the intention of eliminating pollution or contaminants from our surroundings (Keskinan et al., 2003). Industrially used algae is later cast off for implementing biosorption technique of heavy metal exclusion, proves to be a productive, cost-effective, environmental friendly and efficient scheme (Udaiyappan Farhan Mohdet et al., 2017; ZeraatkarAmin et al., 2016b). Different strains of algae comprises of different adsorption capacities attributable to different toxic levels of heavy metal ion. Accumulation of metal would either dependent or independent on cellular metabolism, i.e. occur in cell surface or cytoplasm respectively (Ahmad et al., 2013; Wilde et al., 2006; Perales-Vela et al., 2006). Experimental factors affecting the adsorption capacities of micro as well as macro algae includes pH, contact time, biomass concentration, temperature, shaking rate, alginate content and others (Mata et al., 2008; Mehta and Prakash Gaur, 2001; Gokhale et al., 2008; Cruz et al., 2004). Pretreatment of biomass with certain chemical reagents also enhance the rate of metal uptake.

Table 1

Comparison of maximum adsorption capacity and efficiency of metal ions eliminated by the use of different fungal species with or without their treatment.

Fungus	Metal eliminated	Treatment	pH	Adsorption capacity(mg/g)	Efficiency (%)	References
<i>Aspergillus niger</i>	Cd(II)	NaOH	5.96	10.14	82.2	Amini et al. (2009)
	Cu(II)	HCl	5	13.38	83.96	Mukhopadhyay et al. (2008)
	U(VI)	Polydopamine	5	257.7	87.41	Yang et al. (2019)
	Pb(II)	With EPS	5	20.7	77.6	Dang et al. (2018)
	Pb(II)	Without EPS	5	291.6	97.6	Dang et al. (2018)
	Co(II)	6	76.41	79.34	Song et al. (2016)
	Eu(III)	6	135	85.79	Song et al. (2016)
<i>Rhizopus arrhizus</i>	Cr(VI)	NaCl	2	114.9	49.89	(Aksu and Balibek, 2007; Preetha and Viruthagiri, 2007)
	Cu(II)	5.5	59.66	97	Subudhi and Kar (2008)
	Ni(II)	5.5	59.78	80	Subudhi and Kar (2008)
	Fe(III)	13	612.2	Aksu et al. (1999)
	Pb(II)	7	200	Fourest et al. (1994)
	Zn(II)	5.8	16	Fourest et al. (1994)
	U(VI)	4	180	Tsezos and Volesky (1981)
<i>Saccharomyces cerevisiae</i>	Cu(II)	5	4.73	76	NascimentoJéssica et al. (2019)
	Pb(II)	7	34.9	81	(Ma et al., 2015b; Can and Wang, 2010)
	Cd(II)	7	16.65	(Ma et al., 2015b; Hadiani et al., 2019)
	Pb(II)	Ca(OH) ₂	7	116.69	85.2	Ma et al. (2015b)
	Cd(II)	Ca(OH) ₂	7	42.63	92.5	Ma et al. (2015b)
	Ag(I)	4	41.542	58	Can and Wang (2010)

Table 2

Comparison of maximum adsorption capacity and efficiency of metal ions eliminated by the use of different bacterial species.

Bacteria	Metal eliminated	Pretreatment	pH	Adsorption capacity(mg/g)	Removal Efficiency (%)	References	
<i>Bacillus subtilis</i>	Cd(II)	SC-CO2	6	98.54	Al-Gheethi et al. (2017)	
	Cd(II)	Autoclaved	6	99.2	Al-Gheethi et al. (2017)	
	Hg(II)	6.5	78.5	Schut et al. (2011)	
	Cr(VI)	NaOH	6	0.120	García et al. (2016)	
	Mn(II)	NaOH	5.5	0.465	García et al. (2016)	
	Cu(II)	NaOH	6.5	0.528	67.36	García et al. (2016)	
	Cu(II)	Immobilized	5.5	69.34	Rani et al. (2010)	
	Pb(II)	dead	5.5	16.25	44.73	Schut et al. (2011)	
	<i>Pseudomonas aeruginosa</i>	CD(II)	Immobilized	6	0.140	42	(Pardo et al., 2003; Orhan et al., 2006)
		Hg(II)	Immobilized	6	0.425	99.3	(Orhan et al., 2006; Abdelbary et al., 2019)
Cr(VI)		Immobilized	6	0.625	84	(Orhan et al., 2006; Abdelbary et al., 2019)	
Ni(II)		Immobilized	5.5	80	(Orhan et al., 2006; Abdelbary et al., 2019)	
Cu(II)		Immobilized	6	79	(Orhan et al., 2006; Marqués et al., 1991)	
<i>Escherichia coli</i>		Pb(II)	5.5	0.340	68.51	Huang et al. (2001)
	Cd(II)	6	0.725	63.39	Huang et al. (2001)	
	Cr(II)	5.5	0.615	60.26	Huang et al. (2001)	
	Pb(II)	NaOH	6	0.432	81	Huang et al. (2001)	
	Cd(II)	NaOH	6.5	78	Huang et al. (2001)	
	Cr(II)	NaOH	5.5	0.52	72	Huang et al. (2001)	

Chemical reagents intricate NaOH, CaCl₂, HNO₃, formaldehyde etc. that plays an important role in causing physico-chemical modification to the biomass thus, expanding the surface area along with activating and exposing several functional groups present of its surface for effecting binding with adsorbate (Errasquin and Vazquez, 2003; Rincón et al., 2005; Dabbagh et al., 2008). Besides surface property, modifications carried out at genetic level, protein engineering and biological mechanisms also results in accumulative metal uptake thus increasing tolerance capacity of cell biomass (Rosen, 2002; Ghosh et al., 1999).

A wide variety of algae are used for industrial purpose as food supplements, B-carotene production, biofuel etc. (Sharma and Sharma, 2017) After achieving the product, the algal byproduct can be obtained as a biomass for waste water treatment. Microbial community counted in are *Chlorella vulgaris*, *Cladophora* sp., *Spirulina* sp., *Spirogyra insignis*, *Sargassum* sp. etc. All these species have different adsorption capacities and adsorption efficiencies towards variety of metals at its optimum pH.

Spirulina is a biomass of cyanobacteria usually with high protein

content and is being used as nutrient-rich dietary supplement. Moreover it also has the ability to adsorb toxic metal ions such as chromium, cadmium etc. at certain pH and temperature. By means of it we could achieve an eco-friendly, cheap, reliable and active method of remediation (Al-HomaidanAli et al., 2015).

Chlorella vulgaris is an algae grown for using it as a nutrient supplement agent. It is basically applicable in pharmaceutical industries because of its high medicinal properties to fight against numerous deficiencies, defects and diseases. It is similarly being utilized to carry out biosorption procedure mainly depending upon its metabolic and surface properties. Surface functional groups like carboxyl and amine are modified to improve its adsorption efficiency, that plays a major role in coordination of different metal ions given below on its surface (Vogel et al., 2010; Cho et al., 1994). In Table 3 observed values of maximum adsorption capacity and efficiency of metal ions eliminated by the use of different algal species are recorded.

Table 3

Comparison of maximum adsorption capacity and efficiency of metal ions eliminated by the use of different algal species.

Algae	Metal adsorption	Pretreatment	pH	Adsorption capacity(mg/g)	Efficiency (%)	References
<i>Cladophora glomerata</i>	Cr(VI)	HCl	2.5	63.2	66.6	Al-HomaidanAli et al. (2018)
	Pb(II)	HCl	3.5	46.51	Lee and Chang (2011)
	Cu(II)	5	14.71	Lee and Chang (2011)
	Se(IV)	5	74.9	Tuzen and Sari (2010)
<i>Chlorella vulgaris</i>	Ni(II)	HCl	5.5	20.23	93	Mehta and Prakash Gaur (2001)
	Cu(II)	HCl	3.5	14.48	96	Mehta and Prakash Gaur (2001)
	Cu(II)	HCl	3.5	714.892	Volesky (2007)
	Ni(II)	HCl	4.5	437.84	Volesky (2007)
	Cr(VI)	1.5	163.93	Gokhale et al. (2008)
	Cd(II)	4	111	Cruz et al. (2004)
	U(VI)	4.4	27	90	Vogel et al. (2010)
<i>Spirulina plantensis</i>	Cr(VI)	B-carotene extract	1.5	188.68	73.6	Gokhale et al. (2008)
	Cr(VI)	1.5	212.76	86.2	Gokhale et al. (2008)
	Cd(II)	8	87.6	Al-HomaidanAli et al. (2015)
<i>Spirogyra</i> spp.	Cu(II)	6	38.61	Lee and Chang (2011)
	<i>Spirogyra insignis</i>	Pb(II)	5	140
Cr(III)		CaCl ₂	5	30.21	81.02	Bishnoi et al. (2007)
Cr(VI)		HNO ₃	4	265	Yaqub et al. (2012)
Zn(II)		6	21.1	Romera et al. (2007)
<i>Cystoseira indica</i>		Cs(II)	Formaldehyde	5	63.5
<i>Laminaria japonica</i>	Al(III)	CaCl ₂	4.5	75.27	Lee et al. (2004)
	Cr(II)	CaCl ₂	4.5	94.103	Lee et al. (2004)
	Pb(II)	CaCl ₂	4.5	348.09	Lee et al. (2004)
	Zn(II)	CaCl ₂	4.5	56.88	Lee et al. (2004)
	Cd(II)	CaCl ₂	4.5	136.1	Lee et al. (2004)

14. Lignocellulosic material as adsorbent

Desiccated or dried out stuff of plants or trees predominantly composed of cellulose, hemicellulose, lignin and extractives is known as lignocellulosic biomass. This comprise sawdust, bark, needles, straw, soyabean hulls, sugarcane bagasse, fruit and vegetable peels, corn stover, forestry and agriculture residues, woodchips and many more (Zhou et al., 2014; Lin et al., 2019; Sukumaran et al., 2009). It is basically present in copiousness amount on earth and so is easily available to the industries in order to accomplish the biorefining process. Chemical or physical pretreatment of lignocellulosic material for the production of biofuel, biogas, biopolymer, biofibres, bio-based chemicals, bio-based thermostat, renewable energy, pulp and paper, cosmetics, fertilizers, emulsifiers, phenolic compounds, lubricants etc. has somewhere concluded into the upsurge of our bioeconomy (de Jong et al., 2012; Mussatto and Dragone, 2016; Dotan, 2014; Fortunati and KennyLuigi, 2019). Attaining the unsurpassed items for consumption out of such massive volume of surplus remainders has been a great achievement till date. And now these lignocellulosic constituents are being employed for the adsorption of deadly metals commencing from industrial and environmental seepages. Being an alternative approach of costly conventional methods, it is cost effective, easily available, sustainable and renewable method (Ramamoorthy et al., 2019; Aksu and Isoglu, 2005). Biosorption through lignocellulosic biomass first steps into the process of pre-treatment with physical or chemical agents to achieve operational and biochemical modifications. These modifications increase the adsorption capacity and its efficiency by attaching functional groups such as carboxyl, amine, phosphate, nitrile, cyanide, sulphonate, oxalate etc. to the biomass surface to which the metal ions get attached as well as shows effective binding. All these procedures are carried out in either of the reactors - stirred tank reactor, fluidized bed reactor, packed bed reactor or airlift reactors taking certain variable parameters into account

(Volesky, 2007; Lindholm-Lehto and Camilla, 2019). The adsorption efficiency similarly depends upon experimental factors for example pH, temperature, initial metal ion concentration, biomass concentration and agitation speed (Park et al., 2010; Basso et al., 2002). Detection of the interactions, characterisation of composite properties, morphological analysis and calculation of experimental values is done by scanning electron microscopy, x-ray diffraction data, transmission electron microscopy, thermogravimetric analysis or Fourier transform infrared spectroscopy while the explanation is done by Freundlich, Temkin or Langmuir isotherm model (Vvu and Argyropoulos, 2003; Nair et al., 2014; Song et al., 2015; Kwak et al., 2018). Moreover, biosorbents used must also comprehend the property of regeneration or desorption making it an excellent mediators for industrial use (Bishnoi, 2005; Saman et al., 2018). One such recent research activities directed fabrication of biochar, porous carbonaceous material, manufactured through thermochemical decomposition of biomass feedstock in negligible amount of oxygen (Rangabhashiyam and Balasubramanian, 2019; Fang et al., 2018). It was further engineered by means of supplementary chemical, physical or biological pre and post treatments in order to intensify the surface area, adsorption capacity and superficial functional groups (Xiang et al., 2020; Wang et al., 2017). Thermal carbonization technologies was categorised into pyrolysis, microwave assisted pyrolysis, hydrothermal carbonization, gasification and torrefaction those possess dissimilar effects on adsorption and desorption (Zhang et al., 2017a; Mutsengerere et al., 2019). The above mentioned advanced biosorbent attested potential in eliminating heavy metals, dyes, organic and inorganic contaminants and so is used in soil remediation, enhancing crop productivity and waste water treatment (Palansooriya et al., 2020; Zhang et al., 2017b). It is a cost-effective, environment friendly and highly efficient adsorbent that can also be easily utilized for large scale remediation purpose. Table 4 summarized the maximum adsorption capacity and efficiency of metal ions eliminated by the use of

Table 4

Comparison of maximum adsorption capacity and efficiency of metal ions eliminated by the use of different lignocellulosic constituents with or without their treatment.

Lignocellulosic material	Pretreatment	Metals adsorbed	Adsorption capacity(mg/g)	Efficiency (%)	References
Peach stone particle	Mechanical treatment	Cu(II)	69%	Lopičić et al. (2017)
Apricot shells	All by alkali (NaOH)	Fe(II)	97%	Šostarić et al. (2018)
		Cu(II)	87.1%	
		Pb(II)	81.23%	
		Cr(VI)	80.4%	
		Zn(II)	14.97%	
		Ni(II)	33.2%	
Olive stones	Coated by iron and magnetite nanoparticle	Cr(VI)	67.0%	Vilardi et al. (2018)
Chili seeds (<i>Capsicum annum</i>)	Cd(II)	56%	Medellin-Castillo et al. (2017)
	Pb(II)	62.5%	
Butternut (<i>Cucurbita moschata</i>)	Cu(II)	59.2%	Khan and Ali Khan Rao (2017)
	Ni(II)	76%	
Pine bark (<i>Pinus radiata</i>)	Acid	Pb(II)	98.1%	Montes-Atenas and Schroeder (2015)
Cone biomass (<i>P. sylvestris</i>)	Cr(VI)	84%	Ucun et al. (2002)
	Cu(II)	98%	Nuhoglu and Oguz (2003)
Brazil nutshell	Cd(II)	>90	Basso et al. (2002)
	Ni(II)	19.4	Basso et al. (2002)
Lignocellulosic biomass	Homogenous succinoylation	Pb(II)	381.7 mg/g	Zhong et al. (2012)
		Cd(II)	278.6 mg/g	Zhong et al. (2012)
Lignin	Cr(III)	17.97	Vvu and Argyropoulos (2003)
Lignin	Chitosan-alkali	Cr(VI)	95	Nair et al. (2014)
Lignin	Diethylenetriami	Cr(VI)	56	(Song et al., 2015; Chauke et al., 2015)
Lignin-based resin	glutaraldehyde	Cr(VI)	350.87	(Kwak et al., 2018; Liang et al., 2013)
	sodium				
Lignosulfonate	Graphene oxide	Pb(II)	13.08	Li et al. (2016)
Coconut pith	Aminopropyltriethoxysilane	Au(III)	261.36	Saman et al. (2018)
Lignocellulosic waste	Carbonization + KOH	Hg(II)	137.4	Saman et al. (2015)
Pomelo peel	H3PO4	Ag(I)	88.7	Zhao et al. (2018)
	H3PO4	Pb(II)	79.3	Zhao et al. (2018)

different lignocellulosic materials.

15. Industrial wastes as adsorbents

Trashes coming out of industries of food, beverage, pharmaceutical, fermentation, sugar and power plants face a major deposition problem in current scenario causing unwanted circumstances. Around 30% of it is being utilized by the refineries as a constituent but the other 70% is passed out along with other effluents triggering contamination to the environment (Ahmaruzzaman, 2010; Gamage et al., 2011). The complications in disposing waste and eliminating heavy metals can be overcome by the process of adsorption in which both of them would complement each other to resolve the environmental issues. Transforming large quantity of debris attained from industries such as vegetable and fruit peels, sugar bagasse, microbial wastes, biomass waste, food processing waste, poultry litters, flyash, lignin, pharmaceutical wastes etc. as well as municipal solid waste and sewage sludge into a highly effective and low-cost adsorbent would be a potential technique in replacing all the expensive conventional methods. Some processing practices are opted for treating the components chemically so as to enhance its adsorption capacity, porosity and surface functionalities which would favour easy trapping of toxic metals to its surface (Ahmaruzzaman, 2011).

Fly-ash is one such adsorbent produced by incinerating wastes, biomass, fossil fuels or pulverized coal and is entitled accordingly like bagasse fly ash, biomass fly ash and coal fly ash depending on different chemical composition and physical properties (Ahmaruzzaman, 2010; Gamage et al., 2011). Although it is being used as pozzolan in Portland cement concrete, grouts, road based stabilization and asphalt filler yet its presence in high amount leads to an expensive as well as precarious deposition (Rossow, 2003). And so the notion of consuming it as an adsorbent for removing heavy metals is an excellent approach towards environmental protection (Mishra and Tripathi, 2008). Metals like chromium, nickel, copper, cadmium, lead, zinc, mercury, cobalt and arsenic were investigated to experimentally calculate the adsorption capacity of fly ash in their respect and also determine the varying parameters like pH, contact time, diffusion, temperature, particle size, adsorbate concentration and fly ash dosage affecting its capacity (Sharma et al., 2008; Kitchainukul, 2010; Nawar et al., 2013; Dasmahapatra et al., 1996). It has also been scrutinised that coal fly ash acts as an remarkable adsorbent for radionuclides of caesium as well as strontium (Shawabkeh et al., 2004). Other than heavy metals, application of fly ash as an adsorbent in eliminating toxic components like dyes, phenolic compounds and pesticides from effluents in being extremely appreciated (Mohan et al., 2002; Daifullah and Gad, 1998; Gupta and Imran, 2001; Gupta et al., 2002).

Sewage sludge when undergoes a physical, chemical or biological treatment at the time of sewage treatment can be further reprocessed and fabricated into an adsorbent for eradicating in addition to purifying all those metals causing toxicity in our surroundings (Rozada et al., 2008). Generating valuable products like activated carbon and carbonaceous char with the use of chemical agents on such discarded, unwanted and leftover material would be considered as of much economical worth (Martins et al., 2007). Mainly ZnCl₂ and H₂SO₄ are being used as a chemical reagent for activating sludge that would lead to the production of different types of activated carbon depending upon their chemical composition (Rozada et al., 2005a, 2005b). An experiment was conducted taking both sludge and reagent at a ratio of 1:1 with the aim of determining the adsorption capacity of activated carbon. It was found that the maximum adsorption capacity of activated carbon was about 1358.5 mg/g for iodine and 139.4 mg/g for the dye, methylene blue (Rozada et al., 2005a). Besides these, it has also been observed as an incredible agent in metal eradication including Hg(II), Pb(II), Cu(II), Cr(II) etc.

16. Natural waste adsorbent

There are a lot of naturally occurring substances or their composites as well involved in the remediation technique. Due to their abundance around us, these are also considered as an inexpensive agent for controlling contaminants. These include clay, zeolite, chitosan, peat and siliceous material used for carrying out adsorption with the aim of eliminating metals.

17. Clay

It is a naturally occurring substance having a great impact on metal elimination by the process of adsorption. Since a very long time, clay has been considered as an excellent adsorbent, both in its natural and modified state because of its easy availability, non-toxicity, inexpensive nature and large surface area (Uddin, 2017; Crini and Badot, 2011; Srinivasan, 2011). Investigations conducted so far revealed an effective adsorption of Cu(II), As(V), Cd(II), Pb(II) and Cr(VI) by natural clay and Cr(VI), Fe(III), Hg and Mn(II) by modified clay with simultaneously varying the dependency parameters like pH and temperature (Zacaroni Mendonça et al., 2015; Khan and Singh., 2010; Bentahar et al., 2016; Bhattacharyya and Gupta., 2006; Shen et al., 2015).

18. Zeolite

Are crystal-like hydrated aluminosilicate natural substance demonstrating properties of surface sorption, pore geometry, high cation exchange capacity, hydration-dehydration, ion selectivity and molecular sieve that promotes adsorption of heavy metals in addition to their separation and purification (Wang and Peng, 2010; Caputo and Pepe, 2007; Hong et al., 2019). The presence of variety of zeolites in environment depicts diverse impacts in their adsorption mechanisms. This involve clinoptilolite zeolite, FAU zeolite, MLTA-P zeolite, Jordanian zeolite, natrolite zeolite any many other that have been detected widely functional in toxic metal removal- (Yuna, 2016; GholikandiGagiket al., 2010). Also many waste products are now used for achieving a zeolite material with the same property (Yuna, 2016).

19. Chitosan

It is a representative of biosorbents that displays biocompatible, biodegradable and non-toxic attributes while being serviceable within the environment. Being the second most plentiful natural biopolymer, it is highly available to be exploited in any form (Ahmad et al., 2015). Chitosan in its original form or when modified with zeolite, fly ash, nanoparticles, ceramic alumina etc. have been observed as an effective flocculants and adsorbing agent in eliminating heavy metals, dyes, organic pollutants and other noxious substances present in industrial effluents and municipal sludge (El Mouzdahir et al., 2010; Abd-Elha-keemMohamed and Alkhulaqi, 2014; Ngah et al., 2011; Nechita, 2017).

20. Peat

It is a brown deposit obtained after the decomposition of large number of organic substances in presence of wet acidic condition. Its character of ion exchange facilitates removal of heavy metals from aqueous solution with the application of adsorption procedure. Investigations were done to find out the metal adsorption capacity of peat samples named Sphagnum and Carex against the metal copper and zinc (Ringqvist et al., 2002). While the adsorptive performance of alkali treated peat was also determined which showed high removal efficiency of Pb(II), Co(II) and Ni(II) with 23.07%, 23.53% and 26.19% respectively.

21. Siliceous material

It comprises of SiO₂ as the principal constituent in it. Sedimentary rocks, sand, stone, pozzolan, diatomite etc. are some examples of this category (Agarwal, 2006; Manevich et al., 2012). These substances are treated mechanically or chemically to make them good for adsorbing heavy metals. For example-mesoporous silica materials obtained is versatile adsorbent for eliminating Pb(II), Cu(II) and Cd(II) with maximum adsorption capacity of 58.5 mg/g, 36.3 mg/g and 32.3 mg/g respectively (Zhu et al., 2017). Besides these, siliceous materials are mainly used for fabricating hybrid adsorbents that would aid in maintaining pore size of the adsorbent and enhance trapping efficiency.

22. Derived and hybrid adsorbents

Researchers and analysts have now combined two or three components together to enhance the structural and chemical properties of the formed hybrid adsorbent that in return would exhibit much higher rate of accumulation, excision and exceptional selectivity of heavy metals. The interaction of organic and inorganic substances were made possible by encompassing sol-gel method, interpenetrating networks, hierarchical structures and self-assembly process (Samiey et al., 2014). All these techniques initiate polymerization and grafting for the creation of different composites (Mori, 2012). Basically precursors involved for fabrication and synthesis of hybrid tends to be environment friendly that have shown its extensive applications in all fields. Models assigned for the determination of adsorption isotherm are Langmuir, Freundlich and Dubinin-Radushkevich (Yang et al., 2017b; Li et al., 2018b). While the structural properties, synergy effects and changes in moieties of composites are known by implementation of various analytical techniques as of x-ray diffraction data, Fourier transform infrared spectroscopy, scanning electron microscopy and many others (Li et al., 2018b). Factors effecting its metal adsorption capacity are pH, concentration of adsorbent, initial concentration of adsorbate and temperature (Tighadouini et al., 2017). The need for this is to enhance the metal uptake capacity and recyclability with little time consumption. Hybrids designed under the category of zwitterionic hybrid polymers and imprinted ionic polymers are utilitarian for the adsorption of heavy metals (Liu et al., 2010;

Table 5

Comparison of maximum adsorption capacity of metal ions eliminated by utilizing different hybrid metal adsorbents.

Hybrid Metal Adsorbent	Metals	Adsorption capacity (mg/g)	References
SiNPz-Fn	Pb(II)	87.71	Tighadouini et al. (2018)
	Zn(II)	54.64	
	Cu(II)	28.81	
	Cd(II)	10.77	
Poly-GPTS/Ti-Tyr-hydrolyzate	Pb(II)	270.3	Kayan et al. (2014)
	Ni(II)	204.1	
	Cu(II)	188.7	
	Zn(II)	131.6	
Poly-GPTS/Ti-hydrolyzate	Pb(II)	181.2	Bozbas et al. (2013)
	Cu(II)	44.6	
	Cd(II)	35.8	
P(A-O)/AT Al-GPTS-NaOSiMe ₃ -H	Pb(II)	109	Jin et al. (2011) Cerrahoglu et al. (2017)
	Pb(II)	83.3	
	Fe(III)	75.3	
	Cu(II)	73.9	
	Zn(II)	68.3	
Fe ₃ O ₄ (SiO ₂ /Schiff base)	Ni(II)	81.6	Moradinasab and Behzad (2016)
	Cu(II)	97.2	
	Zn(II)	87.0	
AAH-Si	Pb(II)	36.64	Passos et al. (2008)
	Pb(II)	30.27	
Superadsorbent composite	Pb(II)	1666.67	Bulut et al. (2009)
	Ni(II)	270.27	
	Cd(II)	416.67	
	Hg(II)	769	
UiO-66-NHC(S)NHMe	Hg(II)	769	Saleem et al. (2016)

Wu and Yi, 2013). Examples are given in the table shown below. Table 5 summarized the metal ions eliminated by utilizing different hybrid metal adsorbents.

It is worth mentioning some of the adsorbent and their characteristics here. Biochar is the product of thermochemical decomposition of biomass feedstock such as organic waste from industries, corn grits, peels and shells, lignocellulose residues etc. in absence of oxygen so as to increase its porosity, surface area and adsorption capacity (Beery and Ladisch, 2001; Colantoni et al., 2016; X, 2016). Switch-grass biochar and magnetic switch-grass biochar are the two examples that effectively eliminates organic contaminants (fertilizers) at low pH.

23. Nano material adsorbents

Nanomaterial adsorbents which include metal organic frameworks (MOFs) and organofunctionalized magnetic graphene oxide nanocomposites have emerged as efficient candidates to remove toxic metals from ecosystem. On the other hand, inorganic compounds such as zeolite, TiO₂, SiO₂ in addition to biomass form nanocomposites, are also used to increase its potential to remove toxins from the aqueous solution. Metal organic frameworks (MOFs) molecular sieves, activated charcoal, activated alumina, silica gel and lithium chloride are some of the examples of inorganic adsorbents employed for industrial uses of extraction and conversion (Huang et al., 2010). Among these, metal organic framework is a microporous crystalline compound consisting of organic and inorganic linker molecules connected through co-ordination bond on its surface to which the metal traces get easily attached (Li et al., 1999). Its recyclability, stability, selectivity, adsorbing capacity, functionality, hydrophilicity, surface area and pore size makes it an amazing inorganic adsorbing agent (Li et al., 2018a). MOFs like GO-COOH/UiO-66, MOF-76, Co-SLUG-5 etc. are some modified compound mainly used to remove radioactive metal ions like uranium, chromium, zirconium, etc. from the solution (Yang et al., 2017a).

24. Conclusion

This review article presented about all poles apart techniques adopted so far, aimed at removing toxic metal ions or compounds like lead, chromium, nickel, zinc, arsenic etc. Out of various techniques adsorption has been successful in vanquishing the shortcomings perceived in service of physical, chemical and biological techniques. Advanced water treatment technologies are critically needed under the current circumstances to ensure high-quality water, decrease chemical and biological impurities, and boost in industrial production processes. Until far, the majority of published findings have been based on laboratory experiments. The biggest disadvantage of employing cost-effect analysis is the lack of information regarding pilot-scale systems. Low-cost, easy availability, tranquil operation, high reactivity, selectivity and reusability are some imperative facts renowned while implementing the process of adsorption. On the other hand, this technique has also been impressively co-operative in making the use of left-over, unwanted or discarded entities such as microorganisms, lignocellulosic materials, flyash, sludge, agricultural waste and industrial waste by pre-treating them physically or chemically and fabricating it into an adsorbent intended for eliminating toxic components from waste water. Production of hybrid adsorbents in presence of environment friendly precursors are also of pronounced significance. Several nanomaterials have been developed, and sewage treatment research has been completed successfully. Nano adsorbents (based on the oxides Fe, MnO, ZnO, MgO, CNT), photocatalysts, electrocatalysts (Pt, Pd), MOFs and nanofilms are only a few examples. With further valid alterations, it is still conceivable to achieve an adsorbent of superior adsorption capacity.

Declaration of competing interest

We wish to confirm that there are no known conflicts of interest

associated with this publication and there has been no significant financial support for this work that could have influenced its outcome.

Acknowledgement

The authors thank Department of Biochemical Engineering and Food Technology, HBTU Kanpur and Dr Ambedkar Institute of Technology of Handicapped, Kanpur for providing the necessary facilities to write this review manuscript.

References

- Glossary". The Brownfields and Land Revitalization Technology Support Center. Archived from the Original on 2008-02-18. Retrieved 2009-12-21. *J. Sci. Ind. Res.* 64, February 2005, 93–100 (Fungus — An alternative for bioremediation of heavy metal containing wastewater: A review").
- Abbas, Salman H., et al., 2014. Biosorption of heavy metals: a review. *Journal of chemical science and technology* 3 (4), 74–102.
- Abd-Elhakeem, Mohamed, A., Alkhulaqi, Taher A., 2014. Simple, Rapid and Efficient Water Purification by Chitosan Coated Magnetite Nanoparticles.
- Abdelbary, Salah, Elgamel, Mamdouh S., Farrag, Ayman, 2019. Trends in heavy metals tolerance and uptake by *Pseudomonas aeruginosa*. In: *Pseudomonas Aeruginosa-An Armory within*. IntechOpen.
- Abdi, Omran, Kazemi, Mosstafa, 2015a. A review study of biosorption of heavy metals and comparison between different biosorbents. *J. Mater. Environ. Sci.* 6 (5), 1386–1399.
- Abdi, Omran, Kazemi, Mosstafa, 2015b. A review study of biosorption of heavy metals and comparison between different biosorbents. *J. Mater. Environ. Sci.* 6 (5), 1386–1399.
- Abernethy, Darrell R., et al., 2010. Metal impurities in food and drugs. *Pharmaceut. Res.* 27 (5), 750–755.
- Agarwal, S.K., 2006. Pozzolanic activity of various siliceous materials. *Cement Concr. Res.* 36 (9), 1735–1739.
- N. Ahalya, T.V. Ramachandra* 1 and R.D. Kanamadi 2N. Ahalya, T.V. Ramachandra* 1 and R.D. Kanamadi 2.
- TALEBI, Ahmad, Farhad, et al., 2013. Comparative salt stress study on intracellular ion concentration in marine and salt-adapted freshwater strains of microalgae. *Not. Sci. Biol.* 5 (3), 309–315.
- Ahmad, Mudasir, et al., 2015. Adsorption of heavy metal ions: role of chitosan and cellulose for water treatment. *Langmuir* 79, 109–155.
- Ahmaruzzaman, M., 2010. A review on the utilization of fly ash. *Prog. Energy Combust. Sci.* 36 (3), 327–363.
- Ahmaruzzaman, M., 2011. Industrial wastes as low-cost potential adsorbents for the treatment of wastewater laden with heavy metals. *Adv. Colloid Interface Sci.* 166 (1–2), 36–59.
- Aksu, Z., Balibek, E., 2007. Chromium (VI) biosorption by dried *Rhizopus arrhizus*: effect of salt (NaCl) concentration on equilibrium and kinetic parameters. *J. Hazard Mater.* 145 (1–2), 210–220.
- Aksu, Z., Isoglu, I.A., 2005. "Removal of copper(II) ions from aqueous solution by biosorption onto agricultural waste sugar beet pulp,". *Process Biochem.* 40 (9), 3031–3044. <https://doi.org/10.1016/j.procbio.2005.02.004>.
- Aksu, Z., et al., 1999. Biosorption of iron (III)-cyanide complex anions to *Rhizopus arrhizus*: application of adsorption isotherms. *Process Biochem.* 34 (5), 483–491.
- Akunwa, N.K., Muhammad, M.N., Akunna, Joseph C., 2014. Treatment of metal-contaminated wastewater: a comparison of low-cost biosorbents. *J. Environ. Manag.* 146, 517–523.
- Al-Homaidan, Ali, A., et al., 2015. Adsorptive removal of cadmium ions by *Spirulina platensis* dry biomass. *Saudi J. Biol. Sci.* 22 (6), 795–800.
- Al-Homaidan, Ali, A., et al., 2018. Potential use of green algae as a biosorbent for hexavalent chromium removal from aqueous solutions. *Saudi J. Biol. Sci.* 25 (8), 1733–1738.
- Altaf, M.M., Masood, F., Malik, A., 2008. Impact of long-term application of treated tannery effluents on the emergence of resistance traits in *Rhizobium sp.* isolated from *trifolium alexandrinum*. *Turkish J. Biol.* 32, 1–8.
- Al-Gheethi, Adel, et al., 2017. Removal of heavy metal ions from aqueous solutions using *Bacillus subtilis* biomass pre-treated by supercritical carbon dioxide. *Clean* 45 (10), 1700356.
- Amini, Malihe, Younesi, Habibollah, Bahramifar, Nader, 2009. Statistical modeling and optimization of the cadmium biosorption process in an aqueous solution using *Aspergillus Niger*. *Colloid. Surface. Physicochem. Eng. Aspect.* 337 (1–3), 67–73.
- Apiratikul, R., Pavasant, P., 2008. Batch and column studies of biosorption of heavy metals by *Caulerpa lentillifera*. *Bioresour. Technol.* 99, 2766–2777.
- Apiratikul, R., Pavasant, P., 2008. Batch and column studies of biosorption of heavy metals by *Caulerpa lentillifera*. *Bioresour. Technol.* 99, 2766–2777.
- Arbabi, Mohsen, Golshani, Nazila, 2016. Removal of copper ions Cu (II) from industrial wastewater. *International Journal of Epidemiologic Research* 3 (3), 283–293.
- Argonne national laboratories, Cadmium, Human Health Fact Sheet, 2001. Argonne National Laboratories, Lemont, Ill, USA.
- Barakat, M.A., 2011. New trends in removing heavy metals from industrial wastewater. *Arabian journal of chemistry* 4 (4), 361–377.
- Basso, M.C., Cerrella, E.G., Cukierman, A.L., 2002. Lignocellulosic materials as potential biosorbents of trace toxic metals from wastewater. *Ind. Eng. Chem. Res.* 41 (15), 3580–3585.
- Beery, Kyle E., Ladisch, Michael R., 2001. Chemistry and properties of starch based desiccants. *Enzym. Microb. Technol.* 28 (7–8), 573–581.
- Belay, Alebel Abebe, 2010. Impacts of chromium from tannery effluent and evaluation of alternative treatment options. *J. Environ. Protect.* 1 (1), 53.
- Benfield, Larry D., Judkins, Joseph F., Weand, Barron L., 1982a. *Process Chemistry for Water and Wastewater Treatment*. Prentice Hall.
- Benfield, Larry D., Judkins, Joseph F., Weand, Barron L., 1982b. *Process Chemistry for Water and Wastewater Treatment*. Prentice Hall.
- Bentahar, Yassine, et al., 2016. Adsorptive properties of Moroccan clays for the removal of arsenic (V) from aqueous solution. *Appl. Clay Sci.* 119, 385–392.
- Bhattacharyya, Krishna G., Gupta, Susmita Sen, 2006. Adsorption of Fe (III) from water by natural and acid activated clays: studies on equilibrium isotherm, kinetics and thermodynamics of interactions. *Adsorption* 12 (3), 185–204.
- Bishnoi, Narsi R., 2005. Fungus-an Alternative for Bioremediation of Heavy Metal Containing Wastewater: a Review.
- Bishnoi, Narsi R., et al., 2007. Biosorption of Cr (III) from aqueous solution using algal biomass *spirogyra spp.* *J. Hazard Mater.* 145 (1–2), 142–147.
- Bordoloi, Neonjyoti, et al., 2017. Biosorption of Co (II) from aqueous solution using algal biochar: kinetics and isotherm studies. *Bioresour. Technol.* 244, 1465–1469.
- Bozbas, Karayunlu, Seda, Ay, Umit, Kayan, Asgar, 2013. Novel inorganic-organic hybrid polymers to remove heavy metals from aqueous solution. *Desalination and Water Treatment* 51 (37–39), 7208–7215.
- Brad, H., Xenidis, A., 2005. Remediation techniques. In: *Interface Science and Technology*, vol. 6. Elsevier, pp. 165–261.
- Bulut, Yasemin, et al., 2009. Synthesis of clay-based superabsorbent composite and its sorption capability. *J. Hazard Mater.* 171 (1–3), 717–723.
- Burakov, Alexander E., et al., 2018. Adsorption of heavy metals on conventional and nanostructured materials for wastewater treatment purposes: a review. *Ecotoxicol. Environ. Saf.* 148, 702–712.
- Cabrera-Guzman, Diana, Swartzbaugh, Joseph T., Weisman, Andrew W., 1990. The use of electrokinetics for hazardous waste site remediation. *J. Air Waste Manag. Assoc.* 40 (12), 1670–1676.
- Can, Chen, Wang, Jianlong, 2010. Removal of heavy metal ions by waste biomass of *Saccharomyces cerevisiae*. *J. Environ. Eng.* 136 (1), 95–102.
- Caputo, Domenico, Pepe, Francesco, 2007. Experiments and data processing of ion exchange equilibria involving Italian natural zeolites: a review. *Microporous Mesoporous Mater.* 105 (3), 222–231.
- Cassano, A., Pietra, L.D., Dioli, E., 2007. *Integrated Membrane Process for the Recovery of Chromium Salts from Tannery Effluents*, vol. 26. Industrial & Engineering Chemistry Research, American Chemical Society, Washington, DC, pp. 6825–6830. No. 21.
- Cerrahoglu, Elif, Kayan, Asgar, Bingöl, Deniz, 2017. New inorganic-organic hybrid materials and their oxides for removal of heavy metal ions: response surface methodology approach. *J. Inorg. Organomet. Polym. Mater.* 27 (2), 427–435.
- Chauke, Vongani P., Arjun, Maity, Avashnee, Chetty, 2015. High-performance towards removal of toxic hexavalent chromium from aqueous solution using graphene oxide-alpha cyclodextrin-polyppyrrrole nanocomposites. *J. Mol. Liq.* 211, 71–77.
- Cho, Dae-Yeon, et al., 1994. Studies on the biosorption of heavy metals onto *Chlorella vulgaris*. *Journal of Environmental Science & Health Part A* 29 (2), 389–409.
- Clifton II, Jack, C., 2007. Mercury exposure and public health. *Pediatr. Clin.* 54 (2), 237–el.
- Colantoni et al., 2016; Xiong et al., 2019.
- Crini, Grégorio, Badot, Pierre-Marie (Eds.), 2011. *Sorption Processes and Pollution: Conventional and Non-conventional Sorbents for Pollutant Removal from Wastemasters*. Presses Univ. Franche-Comté.
- Cruz, Claudio CV., et al., 2004. Kinetic modeling and equilibrium studies during cadmium biosorption by dead *Sargassum sp.* biomass. *Bioresour. Technol.* 91 (3), 249–257.
- Cuyper, Ann, et al., 2010. Cadmium stress: an oxidative challenge. *Biomaterials* 23 (5), 927–940.
- Dabbagh, R., et al., 2008. Biosorption of stable cesium by chemically modified biomass of *Sargassum glaucescens* and *Cytospora indica* in a continuous flow system. *J. Hazard Mater.* 159 (2–3), 354–357.
- Daifullah, Abd El-Hakim, Gad, Hamdy, 1998. Sorption of semi-volatile organic compounds by bottom and fly ashes using HPLC. *Adsorpt. Sci. Technol.* 16 (4), 273–283.
- Dang, Chenyuan, et al., 2018. Role of extracellular polymeric substances in biosorption of Pb²⁺ by a high metal ion tolerant fungal strain *Aspergillus Niger* PTN31. *Journal of Environmental Chemical Engineering* 6 (2), 2733–2742.
- Das, D., Chatterjee, A., Mandal, B.K., Samanta, G., Chakraborty, D., Chanda, B., 1995. Arsenic in groundwater in six districts of West Bengal, India: the biggest arsenic calamity in the world. Part 2. Arsenic concentration in drinking water, hair, nails, urine, skin-scales and liver tissues (biopsy) of the affected people. *Analyst* 120, 917–924.
- Dasmahapatra, G.P., et al., 1996. Studies on separation characteristics of hexavalent chromium from aqueous solution by fly ash. *Separ. Sci. Technol.* 31 (14), 2001–2009.
- Davidson, P.W., Myers, G.J., Weiss, B., 2004. Mercury exposure and child development outcomes. *Pediatrics* 113 (4 Suppl. 1), 1023–1029.
- de Jong, Ed, et al., 2012. Bio-based chemicals value added products from biorefineries. IEA Bioenergy, Task42 Biorefinery 34.

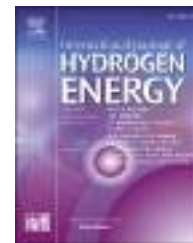
- Dhal, Biswaranjan, Pandey, Banshi Dhar, 2018. Mechanism elucidation and adsorbent characterization for removal of Cr (VI) by native fungal adsorbent. *Sustainable Environment Research* 28 (6), 289–297.
- Dhokpande, Sonali R., Kaware, Jayant P., 2013. Biological methods for heavy metal removal—A review. *International Journal of Engineering Science and Innovative Technology* 2 (5), 304–309.
- Dotan, Ana, 2014. Biobased thermosets. In: *Handbook of Thermoset Plastics*. William Andrew Publishing, pp. 577–622.
- El Mouzdahir, Y., et al., 2010. Equilibrium modeling for the adsorption of methylene blue from aqueous solutions on activated clay minerals. *Desalination* 250 (1), 335–338.
- U.S. Environmental Protection Agency, 1981. Summary Report: Control and Treatment Technology for the Metal Finishing Industry; Ion Exchange, EPA 625/8-81-007.
- U.S. Environmental Protection Agency (USEPA), 1999. Integrated Risk Information System (IRIS) on Cadmium. National Center for Environmental Assessment, Office of Research and Development, Washington, DC.
- Errasquin, E. López, Vazquez, C., 2003. Tolerance and uptake of heavy metals by *Trichoderma atroviride* isolated from sludge. *Chemosphere* 50 (1), 137–143.
- Esmaeili, Abass, Vazirinejad, Reza, 2005. Chromium (III) Removal and Recovery from Tannery Wastewater by Precipitation Process.
- Fang, June, et al., 2018. Minireview of potential applications of hydrochar derived from hydrothermal carbonization of biomass. *J. Ind. Eng. Chem.* 57, 15–21.
- Fortunati, Elena, Kenny, José M., Luigi, Torre, 2019. Lignocellulosic materials as reinforcements in sustainable packaging systems: processing, properties, and applications. In: *Biomass, Biopolymer-Based Materials, and Bioenergy*. Woodhead Publishing, pp. 87–102.
- Fourest, Eric, Canal, Catherine, Roux, Jean-Claude, 1994. Improvement of heavy metal biosorption by mycelial dead biomasses (*Rhizopus arrhizus*, *Mucor miehei* and *Penicillium chrysogenum*): pH control and cationic activation. *FEMS (Fed. Eur. Microbiol. Soc.) Microbiol. Rev.* 14 (4), 325–332.
- Fu, F., Wang, Q., 2011. Removal of heavy metal ions from wastewaters: a review. *J. Environ. Manag.* 92, 407–418.
- Fujiwara, Yasuyuki, et al., 2012. Cadmium renal toxicity via apoptotic pathways. *Biol. Pharm. Bull.* 35 (11), 1892–1897.
- Gaikwad, R.W., Sapkal, V.S., Sapkal, R.S., 2010. Ion exchange system design for removal of heavy metals from acid mine drainage wastewater. *Acta Montan. Slovaca* 15 (4), 298.
- Galun, M., Galun, E., Siegel, B.Z., Keller, P., Lehr, H., Siegel, S.M., 1987. *Water. Air Soil Pollut* 33, 359–37.
- Gamage, N., et al., 2011. Overview of Different Types of Fly Ash and Their Use as a Building and Construction Material.
- García, Rocío, et al., 2016. Biosorption of Cd, Cr, Mn, and Pb from aqueous solutions by *Bacillus* sp strains isolated from industrial waste activate sludge. *TIP* 19 (1), 5–14.
- Gholikandi, Badalians, Gagik, et al., 2010. Natural zeolites application as sustainable adsorbent for heavy metals removal from drinking water. *Iranian Journal of toxicology* 4 (3), 302–310.
- Ghosh, Mallika, Shen, Jian, Rosen, Barry P., 1999. Pathways of as (III) detoxification in *Saccharomyces cerevisiae*. *Proc. Natl. Acad. Sci. Unit. States Am.* 96 (9), 5001–5006.
- Gksungur, Y., ren, S., Güvenç, U., 2005a. Biosorption of cadmium and lead ions by ethanol treated waste baker's yeast biomass. *Bioresour. Technol.* 96, 103–109.
- Gksungur, Y., ren, S., Güvenç, U., 2005b. Biosorption of cadmium and lead ions by ethanol treated waste baker's yeast biomass. *Bioresour. Technol.* 96, 103–109.
- Gokhale, S.V., Jyoti, K.K., Lele, S.S., 2008. Kinetic and equilibrium modeling of chromium (VI) biosorption on fresh and spent *Spirulina platensis*/*Chlorella vulgaris* biomass. *Bioresour. Technol.* 99 (9), 3600–3608.
- Gourdon, Rémy, et al., 1990. Comparison of cadmium biosorption by Gram-positive and Gram-negative bacteria from activated sludge. *Biotechnol. Lett.* 12 (11), 839–842.
- Gupta, Vinod K., Imran, Ali, 2001. Removal of DDD and DDE from wastewater using bagasse fly ash, a sugar industry waste. *Water Res.* 35 (1), 33–40.
- Gupta, V.K., Rastogi, A., 2008. Biosorption of lead from aqueous solutions by green algae *Spirogyra* species: kinetics and equilibrium studies. *J. Hazard Mater.* 152 (1), 407–414.
- Gupta, Vinod K., et al., 2002. Removal of lindane and malathion from wastewater using bagasse fly ash—a sugar industry waste. *Water Res.* 36 (10), 2483–2490.
- Guzzi, GianPaolo, Caterina, AM La Porta, 2008. Molecular mechanisms triggered by mercury. *Toxicology* 244 (1), 1–12.
- Hadiani, Rasoul, Mohammad, Khosravi-Darani, Kianoush, Rahimifard, Nahid, 2019. Optimization of as (III) and as (V) removal by *Saccharomyces cerevisiae* biomass for biosorption of critical levels in the food and water resources. *Journal of Environmental Chemical Engineering* 7 (2), 102949.
- Hamby, D.M., 1996. Site remediation techniques supporting environmental restoration activities—a review. *Sci. Total Environ.* 191 (3), 203–224.
- Han, R., Li, H., Li, Y., Zhang, J., Xiao, H., Shi, J., 2006. Biosorption of copper and lead ions by waste beer yeast. *J. Hazard Mater.* 137 (3), 1569–1576.
- Haritash, A.K., Kaushik, C.P., 2009. Biodegradation aspects of polycyclic aromatic hydrocarbons (PAHs): a review. *J. Hazard Mater.* 169 (1–3), 1–15.
- Hassani, A.H., Hosseinzadeh, Torabifar, B., 2010. Investigation of using fixed activated sludge system for removing heavy metals (Cr, Ni and ph) from industrial wastewater. *J. Environ. Stud.* 36, 22 to 24.
- Hong, Mei, et al., 2019. Heavy metal adsorption with zeolites: the role of hierarchical pore architecture. *Chem. Eng. J.* 359, 363–372.
- Huang, C., Huang, C.P., 1996. Proton competition in Cu(II) adsorption by fungal mycelia. *Water Res.* 30, 1985.
- Huang, Min-sheng, Pan, Jing, Zheng, Le-ping, 2001. Removal of heavy metals from aqueous solutions using bacteria. *J. Shanghai Univ. (Engl. Ed.)* 5 (3), 253–259.
- Huang, H.-J., et al., 2010. Separation and Purification processes for lignocellulose-to-bioalcohol production. In: *Bioalcohol Production*. Woodhead Publishing, pp. 246–277.
- Hubicki, Zbigniew, Kolodyńska, Dorota, 2012. Selective Removal of Heavy Metal Ions from Waters and Waste Waters Using Ion Exchange Methods. *Ion Exchange Technologies*, pp. 193–240.
- Idalia, Naurá, Vargas-Maya, Franco, Bernardo, 2017. *Escherichia coli* as a model organism and its application in biotechnology." recent advances on physiology, pathogenesis and biotechnological applications. In: *Tech Open, Rijeka, Croatia*, pp. 253–274.
- Jasrotia, Shivakshi, Kansal, Arun, Mehra, Aradhana, 2017. Performance of aquatic plant species for phytoremediation of arsenic-contaminated water. *Applied Water Science* 7 (2), 889–896.
- Jin, Xinliang, et al., 2011. Synthesis of novel inorganic-organic hybrid materials for simultaneous adsorption of metal ions and organic molecules in aqueous solution. *J. Hazard Mater.* 198, 247–256.
- Joshi, Deepmala, et al., 2012. Therapeutic potential of N-acetyl cysteine with antioxidants (Zn and Se) supplementation against dimethylmercury toxicity in male albino rats. *Exp. Toxicol. Pathol.* 64 (1–2), 103–108.
- Kapoor, A., Viraraghavan, T., 1997. Heavy metal biosorption sites in *Aspergillus Niger*. *Bioresour. Technol.* 61, 221–227.
- Kapoor, A., Viraraghavan, T., 1998. Biosorption of heavy metals on *Aspergillus Niger*: effect of pretreatment. *Bioresour. Technol.* 63, 109–113.
- Kayan, Asgar, et al., 2014. Novel tyrosine-containing inorganic-organic hybrid adsorbent in removal of heavy metal ions. *Journal of Environmental Chemical Engineering* 2 (2), 935–942.
- Keskinkan, O., et al., 2003. Heavy metal adsorption characteristics of a submerged aquatic plant (*Myriophyllum spicatum*). *Process Biochem.* 39 (2), 179–183.
- Keskinkan, O., et al., "Heavy metal adsorption characteristics of a submerged aquatic plant (*Myriophyllum spicatum*)." *Process Biochemistry* 39.2 (2003): 179-183.
- Khan, Umra, Ali Khan Rao, Rifaqat, 2017. A high activity adsorbent of chemically modified *Cucurbita moschata* (a novel adsorbent) for the removal of Cu (II) and Ni (II) from aqueous solution: synthesis, characterization and metal removal efficiency. *Process Saf. Environ. Protect.* 107, 238–258.
- Khan, Tabrez A., Singh, Ved Vati, 2010. Removal of cadmium (II), lead (II), and chromium (VI) ions from aqueous solution using clay. *Toxicological and environ chemistry* 92 (8), 1435–1446.
- Khoei, Javanshir, Arash, et al., 2018. Application of physical and biological methods to remove heavy metal, arsenic and pesticides, malathion and diazinon from water. *Turk. J. Fish. Aquat. Sci.* vol. 19, 21–28, 1.
- Kinoshita, Hideki, et al., 2013. Biosorption of heavy metals by lactic acid bacteria and identification of mercury binding protein. *Res. Microbiol.* 164 (7), 701–709.
- Kitchainukul, Waraporn, 2010. The Use of Fly Ash to Stabilise Low Concentrations of Mercury in the Environment. *Diss. University of Southampton*.
- Kumar, M., Kumar, D., Singh, B., 2014. Utilization of agro residue corncob for production of acetone-butanol using *Clostridium acetobutylicum* and process optimization through RSM. *J. Microb. Biochem. Technol.* S. 8 (2).
- Kumar, M., Singh, A.K., Sikandar, M., 2018 Dec 1. Study of sorption and desorption of Cd (II) from aqueous solution using isolated green algae *Chlorella vulgaris*. *Applied Water Science* 8 (8), 225.
- Kumar, M., Goswami, L., Singh, A.K., Sikandar, M., 2019 Oct 1. Valorization of coal fired-fly ash for potential heavy metal removal from the single and multi-contaminated system. *Heliyon* 5 (10), e02562.
- Kumar, M., Singh, A.K., Sikandar, M., 2020 Jan 1. Biosorption of Hg (II) from aqueous solution using algal biomass: kinetics and isotherm studies. *Heliyon* 6 (1), e03321.
- Kunamneni, A., Singh, S., 2005. Response surface optimization of enzymatic hydrolysis of maize starch for higher glucose production. *Biochem. Eng. J.* 27, 179–190.
- Kwak, Hyo Won, et al., 2018. Water-resistant lignin/poly (vinyl alcohol) blend fibers for removal of hexavalent chromium. *Fibers Polym.* 19 (6), 1175–1183.
- Lage, O.M., et al., 1996. Toxicity effects of copper (II) on the marine dinoflagellate *Amphidinium carterae*: influence of metal speciation. *Eur. J. Phycol.* 31 (4), 341–348.
- Lakherwal, Dimple, 2014. Adsorption of heavy metals: a review. *Int. J. Environ. Res. Dev.* vol. 4, 41–48, 1.
- Lee, Yi-Chao, Chang, Shui-Ping, 2011. The biosorption of heavy metals from aqueous solution by *Spirogyra* and *Cladophora* filamentous macroalgae. *Bioresour. Technol.* 102 (9), 5297–5304.
- Lee, H.S., et al., 2004. Effect of aluminum in two-metal biosorption by an algal biosorbent. *Miner. Eng.* 17 (4), 487–493.
- Li, Hailian, et al., 1999. Design and synthesis of an exceptionally stable and highly porous metal-organic framework. *Nature* 402 (6759), 276–279.
- Li, Fengfeng, et al., 2016. A lignosulfonate-modified graphene hydrogel with ultrahigh adsorption capacity for Pb (II) removal. *J. Mater. Chem.* 4 (30), 11888–11896. Li, Fengfeng, et al. "A lignosulfonate-modified graphene hydrogel with ultrahigh adsorption capacity for Pb (II) removal." *Journal of Materials Chemistry A* 4.30 (2016): 11888-11896.
- Li, Jie, et al., 2018a. Metal-organic framework-based materials: superior adsorbents for the capture of toxic and radioactive metal ions. *Chem. Soc. Rev.* 47 (7), 2322–2356.
- Li, Jie, et al., 2018b. Metal-organic framework-based materials: superior adsorbents for the capture of toxic and radioactive metal ions. *Chem. Soc. Rev.* 47 (7), 2322–2356.
- Rongguo Li, Tingting Zhang, Haifeng Zhong, Weikang Song, You Zhou, Xueqiong Yin. (2020).
- Liang, Feng-Bing, et al., 2013. Adsorption of hexavalent chromium on a lignin-based resin: equilibrium, thermodynamics, and kinetics. *Journal of Environmental Chemical Engineering* 1 (4), 1301–1308.

- Lin, Long, et al., 2019. Biological treatment of organic materials for energy and nutrients production—anaerobic digestion and composting. In: *Advances in Bioenergy*, vol. 4. Elsevier, pp. 121–181.
- Lindgren, E.R., Mattson, E.D., Kozak, M.W., 1994. Electrokinetic remediation of unsaturated soils. In: *Emerging Technologies in Hazardous Waste Management IV*. American Chemical Society, Washington, DC.
- Lindholm-Lehto, Camilla, Petra, 2019. Biosorption of heavy metals by lignocellulosic biomass and chemical analysis. *BioResources* 14 (2), 4952–4995.
- Liu, Y., Lam, M.C., Fang, H.H.P., 2001. Adsorption of heavy metals by EPS of activated sludge. *Water Sci. Technol.* 43 (6), 59–66.
- Liu, Junsheng, et al., 2010. Preparation of zwitterionic hybrid polymer and its application for the removal of heavy metal ions from water. *J. Hazard Mater.* 178 (1–3), 1021–1029.
- Lopičić, Zorica R., et al., 2017. Optimization of the process of Cu (II) sorption by mechanically treated *Prunus persica* L.—Contribution to sustainability in food processing industry. *J. Clean. Prod.* 156, 95–105.
- Ma, Wei, et al., 2015a. Synthesis of macroporous silica biomass nanocomposite based on XG/MgSiO₃ for the removal of toxic ions. *Bioresour. Technol.* 186, 356–359.
- Ma, Xiaoming, et al., 2015b. Efficient biosorption of lead (II) and cadmium (II) ions from aqueous solutions by functionalized cell with intracellular CaCO₃ mineral scaffolds. *Bioresour. Technol.* 185, 70–78.
- Mahimairaja, S., et al., 2005. Arsenic contamination and its risk management in complex environmental settings. *Adv. Agron.* 86, 1–82.
- Mandal, B.K., Suzuki, K.T., 2002. Arsenic round the world: a review. *Talanta* 58, 201–235.
- Mane, P.C., Bhosle, A.B., Jangam, C.M., Vishwakarma, C.V., 2011. Bioadsorption of selenium by pretreated algal biomass. *Adv. Appl. Sci. Res.* 2, 207–211.
- Manevich, V.E., et al., 2012. Diatomite—siliceous material for the glass industry. *Glass Ceram.* 69 (5–6), 168–172.
- Marqués, Ana M., et al., 1991. Uranium accumulation by *Pseudomonas* sp. EPS-5028. *Appl. Microbiol. Biotechnol.* 35 (3), 406–410.
- Martins, Ayrton F., et al., 2007. Low temperature conversion of rice husks, eucalyptus sawdust and peach stones for the production of carbon-like adsorbent. *Bioresour. Technol.* 98 (5), 1095–1100.
- Masindi, Vhahangwele, Muedi, Khathutshelo L., 2018. Environmental contamination by heavy metals. *Heavy Metals* 19, 2019.
- Mata, Y.N., et al., 2008. Characterization of the biosorption of cadmium, lead and copper with the brown alga *Fucus vesiculosus*. *J. Hazard Mater.* 158 (2–3), 316–323.
- Medellin-Castillo, Nahum A., et al., 2017. Single and competitive adsorption of Cd (II) and Pb (II) ions from aqueous solutions onto industrial chili seeds (*Capsicum annum*) waste. *Sustainable Environment Research* 27 (2), 61–69.
- Medhat Moustafa, a, Gaber Idris, b, 2003. Biological removal of heavy metals from wastewater. *Alexandria Engineering Journal* 42, 767–771.
- Mehta, Surya Kant, Prakash Gaur, Jai, 2001. Characterization and optimization of Ni and Cu sorption from aqueous solution by *Chlorella vulgaris*. *Ecol. Eng.* 18 (1), 1–13.
- Mishra, S.P., 2014. Adsorption-desorption of heavy metal ions. *Curr. Sci. India* 107 (4), 601–612.
- Mishra, Archana, Tripathi, Brahma D., 2008. Utilization of fly ash in adsorption of heavy metals from wastewater. *Toxicol. Environ. Chem.* 90 (6), 1091–1097.
- Mohan, Dinesh, et al., 2002. Removal of dyes from wastewater using flyash, a low-cost adsorbent. *Ind. Eng. Chem. Res.* 41 (15), 3688–3695.
- Montes-Atenas, G., Schroeder, S.L.M., 2015. Sustainable natural adsorbents for heavy metal removal from wastewater: lead sorption on pine bark (*Pinus radiata* D.Don). *Surf. Interface Anal.* 47 (10), 996–1000. <https://doi.org/10.1002/sia.5807>.
- Moradinab, Sheida, Behzad, Mahdi, 2016. Removal of heavy metals from aqueous solution using Fe₃O₄ nanoparticles coated with Schiff base ligand. *Desalination and Water Treatment* 57 (9), 4028–4036.
- Mori, Hideharu, 2012. Design and synthesis of functional silsesquioxane-based hybrids by hydrolytic condensation of bulky triethoxysilanes. *International Journal of Polymer Science* 2012.
- Mukhopadhyay, Mausumi, Noronha, S.B., Suraishkumar, G.K., 2008. Copper biosorption in a column of pretreated *Aspergillus Niger* biomass. *Chem. Eng. J.* 144 (3), 386–390.
- Mussatto, Solange Ines, Dragone, G.M., 2016. Biomass pretreatment, biorefineries, and potential products for a bioeconomy development. In: *Biomass Fractionation Technologies for a Lignocellulosic Feedstock Based Biorefinery*. Elsevier, pp. 1–22.
- Mutsengerere, S., et al., 2019. A review of operating parameters affecting bio-oil yield in microwave pyrolysis of lignocellulosic biomass. *Renew. Sustain. Energy Rev.* 104, 328–336.
- Nair, Vaishakh, Panigrahy, Ajitesh, Vinu, R., 2014. Development of novel chitosan–lignin composites for adsorption of dyes and metal ions from wastewater. *Chem. Eng. J.* 254, 491–502.
- Nascimento, do, Jéssica, M., et al., 2019. Biosorption Cu (II) by the yeast *Saccharomyces cerevisiae*. *Biotechnology Reports* 21, e00315.
- Nawar, Nagwa, Mohamed Ebrahim, Sami, Eslam, 2013. Removal of heavy metals Fe³⁺, Mn²⁺, Zn²⁺, Pb²⁺ and Cd²⁺ from wastewater by using rice straw as low cost adsorbent. *Academic Journal of Interdisciplinary Studies* 2 (6), 85.
- Ndimele, Prince Emeka, et al., 2018. Remediation of crude oil spillage. In: *The Political Ecology of Oil and Gas Activities in the Nigerian Aquatic Ecosystem*. Academic Press, pp. 369–384.
- Nechita, Petronela, 2017. Applications of chitosan in wastewater treatment. *Biological activities and application of marine polysaccharides* 209–228.
- Ngh, WS Wan, Teong, L.C., Hanafiah, M.A.K.M., 2011. Adsorption of dyes and heavy metal ions by chitosan composites: a review. *Carbohydr. Polym.* 83 (4), 1446–1456.
- Norberg, Anders B., Persson, Hans, 1984. Accumulation of heavy-metal ions by *Zoogloea ramigera*. *Biotechnol. Bioeng.* 26 (3), 239–246.
- Nuhoglu, Y., Oguz, E., 2003. Removal of copper (II) from aqueous solutions by biosorption on the cone biomass of *Thuja orientalis*. *Process Biochem.* 38 (11), 1627–1631. [https://doi.org/10.1016/S0032-9592\(03\)00055-4](https://doi.org/10.1016/S0032-9592(03)00055-4).
- Orhan, Yuksek, Hrenović, J., Büyükgüngör, Hanife, 2006. Biosorption of heavy metals from wastewater by biosolids. *Eng. Life Sci.* 6 (4), 399–402.
- Pagnanelli, F., Mainelli, S., Bornoroni, L., Dionisi, D., Toro, L., 2009. Mechanisms of heavy-metal removal by activated sludge. *Chemosphere* 75, 1028–1034.
- Palansooriya, Kumuduni Niroshika, et al., 2020. Occurrence of contaminants in drinking water sources and the potential of biochar for water quality improvement: a review. *Crit. Rev. Environ. Sci. Technol.* 50 (6), 549–611.
- Pardo, Rafael, et al., 2003. Biosorption of cadmium, copper, lead and zinc by inactive biomass of *Pseudomonas putida*. *Anal. Bioanal. Chem.* 376 (1), 26–32.
- Park, D., Yun, Y.-S., Park, J.M., 2010. The past, present, and future trends of bio-sorption. *Biotechnol. Bioproc. Eng.* 15 (1), 86–102. <https://doi.org/10.1007/s12257-009-0199-4>.
- Passos, Camila G., et al., 2008. Use of 7-amine-4-azapeptilsilica and 10-amine-4-azadecylsilica xerogels as adsorbent for Pb (II): kinetic and equilibrium study. *Colloid. Surface. Physicochem. Eng. Aspect.* 316 (1–3), 297–306.
- Perales-Vela, Virgilio, Hugo, Pena-Castro, Julián Mario, Canizares-Villanueva, Rosa Olivia, 2006. Heavy metal detoxification in eukaryotic microalgae. *Chemosphere* 64 (1), 1–10.
- Peters, Robert W., 1997. Treatment of copper-laden waste streams. *Handbook of Copper Compounds and Applications* 265.
- Peters, Robert William, Shem, Linda, 1993. *Separation Of Heavy Metals: Removal from Industrial Wastewaters and Contaminated Soil*. No. ANL/ES/CP-78514; CONF-9303107-1. Argonne National Lab., IL (United States). Energy Systems Div.
- Preetha, B., Viruthagiri, T., 2007. Batch and continuous biosorption of chromium (VI) by *Rhizopus arrhizus*. *Separ. Purif. Technol.* 57 (1), 126–133.
- Quansah, R., Armah, F.A., Essumang, D.K., Luginaah, I., Clarke, E., Marfoh, K., et al., 2015. Association of arsenic with adverse pregnancy outcomes/infant mortality: a systematic review and meta-analysis. *Environ. Health Perspect.* 123 (5), 412–421.
- Ramamoorthy, Sunil Kumar, et al., 2019. Mechanical performance of biofibers and their corresponding composites. In: *Mechanical and Physical Testing of Biocomposites, Fibre-Reinforced Composites and Hybrid Composites*. Woodhead Publishing, pp. 259–292.
- Rangabhashiyam, S., Balasubramanian, P., 2019. The potential of lignocellulosic biomass precursors for biochar production: performance, mechanism and wastewater application—a review. *Ind. Crop. Prod.* 128, 405–423.
- Rani, M. Johnny, et al., 2010. Comparative assessment of heavy metal removal by immobilized and dead bacterial cells: a biosorption approach. *Afr. J. Environ. Sci. Technol.* 4 (2).
- Real, Francisco J., et al., 2007. Removal of diazinon by various advanced oxidation processes. *J. Appl. Chem. Biotechnol.: International Research in Process, Environmental & Clean Technology* 82 (6), 566–574.
- Renu, Madhu Agarwal, Singh, Kailash, 2017. Methodologies for removal of heavy metal ions from wastewater: an overview. *Interdiscip. Environ. Rev.* vol. 18, 124–142, 2.
- Rice, Kevin M., et al., 2014. Environmental mercury and its toxic effects. *Journal of preventive medicine and public health* 47 (2), 74.
- Rincón, J., et al., 2005. Biosorption of heavy metals by chemically-activated alga *Fucus vesiculosus*. *J. Appl. Chem. Biotechnol.: International Research in Process, Environmental & Clean Technology* 80 (12), 1403–1407.
- Ringqvist, L., Holmgren, Allan, Öborn, L., 2002. Poorly humified peat as an adsorbent for metals in wastewater. *Water Res.* 36 (9), 2394–2404.
- Romera, E., et al., 2007. Comparative study of biosorption of heavy metals using different types of algae. *Bioresour. Technol.* 98 (17), 3344–3353.
- Rosen, Barry P., 2002. Transport and detoxification systems for transition metals, heavy metals and metalloids in eukaryotic and prokaryotic microbes. *Comp. Biochem. Physiol. Mol. Integr. Physiol.* 133 (3), 689–693.
- Rossin, A.C., Sterritt, R.M., Lester, J.N., 1982. The influence of process parameters on the removal of heavy metals in activated sludge process. *Water Air Soil Pollut.* 17, 185–198.
- Rossow, Mark, 2003. *Fly Ash Facts for Highway Engineers*. Continuing Education and Development, New York, NY.
- Rozada, F., et al., 2005a. Activated carbons from sewage sludge and discarded tyres: production and optimization. *J. Hazard Mater.* 124 (1–3), 181–191.
- Rozada, F., et al., 2005b. Producing adsorbents from sewage sludge and discarded tyres: characterization and utilization for the removal of pollutants from water. *Chem. Eng. J.* 114 (1–3), 161–169.
- Rozada, F., et al., 2008. Adsorption of heavy metals onto sewage sludge-derived materials. *Bioresour. Technol.* 99 (14), 6332–6338.
- Ruthven, D.M., 1984. *Principles of Adsorption and Adsorption Processes*. Wiley, New York, p. 278, 86.
- Saleem, Hira, Rafique, Uzaira, Robert, P., Davies, 2016. Investigations on post-synthetically modified UiO-66-NH₂ for the adsorptive removal of heavy metal ions from aqueous solution. *Microporous Mesoporous Mater.* 221, 238–244.
- Saman, Norasikin, et al., 2015. Adsorptive efficacy analysis of lignocellulosic waste carbonaceous adsorbents toward different mercury species. *Process Saf. Environ. Protect.* 96, 33–42.
- Saman, Norasikin, et al., 2018. Recovery of Au (III) from an aqueous solution by aminopropyltriethoxysilane-functionalized lignocellulosic based adsorbents. *React. Funct. Polym.* 123, 106–114.
- Samiey, Babak, Cheng, Chil-Hung, Wu, Jiangning, 2014. Organic-inorganic hybrid polymers as adsorbents for removal of heavy metal ions from solutions: a review. *Materials* 7 (2), 673–726.
- Schut, Sina, et al., 2011. Biosorption of copper by wine-relevant lactobacilli. *Int. J. Food Microbiol.* 145 (1), 126–131.

- Sharma, Poonam, Sharma, Nivedita, 2017. Industrial and biotechnological applications of algae: a review. *Journal of Advances in Plant Biology* 1 (1), 1.
- Sharma, Y.C., Upadhyay, S.N., Weng, C.H., 2008. Studies on an economically viable remediation of chromium rich waters and wastewaters by PTPS fly ash. *Colloid. Surface. Physicochem. Eng. Aspect.* 317 (1–3), 222–228.
- Sharma, S., et al., 2016. Physical, chemical and phytoremediation technique for removal of heavy metals. *Journal of Heavy Metal Toxicity and Diseases* vol. 1, 1–15, 2.
- Shawabkeh, Reyad, et al., 2004. Conversion of oil shale ash into zeolite for cadmium and lead removal from wastewater. *Fuel* 83 (7–8), 981–985.
- Shen, Boxiong, Chen, Jianhong, Yue, Shiji, 2015. Removal of elemental mercury by titanium pillared clay impregnated with potassium iodine. *Microporous Mesoporous Mater.* 203, 216–223.
- Singh, N., Gupta, S.K., 2016. Adsorption of heavy metals: a review. *Int. J. Innov. Res. Sci. Eng. Technol.* 5 (2), 2267–2281.
- Song, Zhanxin, et al., 2015. Novel magnetic lignin composite sorbent for chromium (VI) adsorption. *RSC Adv.* 5 (17), 13028–13035.
- Song, Wencheng, et al., 2016. Accumulation of Co (II) and Eu (III) by the mycelia of *Aspergillus Niger* isolated from radionuclide-contaminated soils. *Chem. Eng. J.* 304, 186–193.
- Šostarić, Tatjana D., et al., 2018. Study of heavy metals biosorption on native and alkali-treated apricot shells and its application in wastewater treatment. *J. Mol. Liq.* 259, 340–349.
- Srinivasan, Rajani, 2011. Advances in application of natural clay and its composites in removal of biological, organic, and inorganic contaminants from drinking water. *Advances in Materials Science and Engineering* 2011.
- Srivastava, S.K., Bhattacharjee, G., Sharma, A.K., Oberoi, C.K., 1980. Studies on the use of inorganic gels in the removal of heavy metals. *Water Res.* 14, 113–115.
- Strandberg, Gerald W., Shumate, Starling E., Parrott, John R., 1981. Microbial cells as biosorbents for heavy metals: accumulation of uranium by *Saccharomyces cerevisiae* and *Pseudomonas aeruginosa*. *Appl. Environ. Microbiol.* 41 (1), 237–245.
- Subudhi, E., Kar, R.N., 2008. *Rhizopus arrhizus*—An efficient fungus for copper effluent treatment. *Int. J. Integr. Biol.* 2 (3), 166–171.
- Sukumaran, Rajeev K., et al., 2009. Cellulose production using biomass feed stock and its application in lignocellulose saccharification for bio-ethanol production. *Renew. Energy* 34 (2), 421–424.
- Tighadouini, Said, et al., 2017. Removal efficiency of Pb (II), Zn (II), Cd (II) and Cu (II) from aqueous solution and natural water by ketoenol-pyrazole receptor functionalized silica hybrid adsorbent. *Separ. Sci. Technol.* 52 (4), 608–621.
- Tighadouini, Said, et al., 2018. Engineering β -ketoenol structure functionality in hybrid silica as excellent adsorbent material for removal of heavy metals from water. *New J. Chem.* 42 (16), 13229–13240.
- Tsezos, Marios, Volesky, Bohumil, 1981. Biosorption of uranium and thorium. *Biotechnol. Bioeng.* 23 (3), 583–604.
- Tuzen, Mustafa, Sari, Ahmet, 2010. Biosorption of selenium from aqueous solution by green algae (*Cladophora hutchinsiae*) biomass: equilibrium, thermodynamic and kinetic studies. *Chem. Eng. J.* 158 (2), 200–206.
- Ucun, H., Bayhan, Y.K., Kaya, Y., Cakici, A., Algur, O.F., 2002. Biosorption of chromium (VI) from aqueous solution by cone biomass of *Pinus sylvestris*. *Bioresour. Technol.* 85 (2), 155–158. [https://doi.org/10.1016/S0960-8524\(02\)00086-X](https://doi.org/10.1016/S0960-8524(02)00086-X).
- Udaiyappan, Farhan Mohd, Anil, et al., 2017. A review of the potentials, challenges and current status of microalgae biomass applications in industrial wastewater treatment. *Journal of Water Process Engineering* 20, 8–21.
- Uddin, Mohammad Kashif, 2017. A review on the adsorption of heavy metals by clay minerals, with special focus on the past decade. *Chem. Eng. J.* 308, 438–462.
- Urrutia, M.M., 1997. General Bacterial Sorption Processes. *Biosorbents for metal ions*, pp. 39–66.
- Vasudevan, P., et al., 2001. Biosorption of Heavy Metal Ions.
- Velásquez, Lina, Jenny, Dussan, 2009. Biosorption and bioaccumulation of heavy metals on dead and living biomass of *Bacillus sphaericus*. *J. Hazard Mater.* 167 (1–3), 713–716.
- Vijayaraghavan, K., 2008. A Yeoung-Sang YUN. *Bacterial biosorbents and biosorption*. *Biotechnol. Adv.* 266–291.
- Vilardi, Giorgio, et al., 2018. On the removal of hexavalent chromium by olive stones coated by iron-based nanoparticles: equilibrium study and chromium recovery. *J. Clean. Prod.* 190, 200–210.
- Vogel, M., et al., 2010. Biosorption of U (VI) by the green algae *Chlorella vulgaris* in dependence of pH value and cell activity. *Sci. Total Environ.* 409 (2), 384–395.
- Volesky, Bohumil, 2003. Sorption and Biosorption. *BV Sorbex*.
- Volesky, Bohumil, 2007. Biosorption and me. *Water Res.* 41 (18), 4017–4029.
- Vvu, S., Argyropoulos, D., 2003. An improved method for isolating lignin in high yield and purity. *J. Pulp Pap. Sci.* 29 (7), 235–240.
- Wang, J., Chen, C., 2009. Biosorbents for heavy metals removal and their future. *Biotechnol. Adv.* 27 (2), 195–226.
- Wang, Shaobin, Peng, Yuelian, 2010. Natural zeolites as effective adsorbents in water and wastewater treatment. *Chem. Eng. J.* 156 (1), 11–24.
- Wang, J., Li, Q., Li, M.M., Chen, T.H., Zhou, Y.F., Yue, Z.B., 2014. Competitive adsorption of heavy metal by extracellular polymeric substances (EPS) extracted from sulfate reducing bacteria. *Bioresour. Technol.* 163, 374–376.
- Wang, Shengsen, et al., 2017. The sorptive and reductive capacities of biochar supported nanoscaled zero-valent iron (nZVI) in relation to its crystallite size. *Chemosphere* 186, 495–500.
- Wilde, Karyn L., et al., 2006. The effect of pH on the uptake and toxicity of copper and zinc in a tropical freshwater alga (*Chlorella* sp.). *Arch. Environ. Contam. Toxicol.* 51 (2), 174.
- Wionczyk, B., Apostoluk, W., Charewicz, W.A., 2006. Sol-vent extraction of chromium (III) from spent tanning liquors with Aliquat 336. *Journal of Hydrometallurgy* 82 (No. 1–2), 83–92.
- Wu, Jin-Bao, Yi, Yan-Li, 2013. Removal of cadmium from aqueous solution by organic-inorganic hybrid sorbent combining sol-gel processing and imprinting technique. *Kor. J. Chem. Eng.* 30 (5), 1111–1118.
- Xiang, Wei, et al., 2020. Biochar technology in wastewater treatment: a critical review. *Chemosphere* 126539.
- Yang, Peipei, et al., 2017a. Interfacial growth of a metal-organic framework (UiO-66) on functionalized graphene oxide (GO) as a suitable seawater adsorbent for extraction of uranium (VI). *J. Mater. Chem.* vol. 5, 17933–17942, 34.
- Yang, Peipei, et al., 2017b. Interfacial growth of a metal-organic framework (UiO-66) on functionalized graphene oxide (GO) as a suitable seawater adsorbent for extraction of uranium (VI). *J. Mater. Chem.* 5 (34), 17933–17942.
- Yang, Hao, et al., 2019. Immobilization of dopamine on *Aspergillus Niger* microspheres (AM/PDA) and its effect on the U (VI) adsorption capacity in aqueous solutions. *Colloid. Surface. Physicochem. Eng. Aspect.* 583, 123914.
- Yaqub, A., et al., 2012. Biosorption of hexavalent chromium by *Spirogyra* spp.: equilibrium, kinetics and thermodynamics. *The Journal of Animal and Plant Sciences* 22 (2), 408–415.
- Yuna, Zhao, 2016. Review of the natural, modified, and synthetic zeolites for heavy metals removal from wastewater. *Environ. Eng. Sci.* 33 (7), 443–454.
- Zacaroni, Mendonça, Lidiary, et al., 2015. Natural clay and commercial activated charcoal: properties and application for the removal of copper from cachaça. *Food Control* 47, 536–544.
- Zeraatkar, Amin, Keyvan, et al., 2016a. Potential use of algae for heavy metal bioremediation, a critical review. *J. Environ. Manag.* 181, 817–831.
- Zeraatkar, Amin, Keyvan, et al., 2016b. Potential use of algae for heavy metal bioremediation, a critical review. *J. Environ. Manag.* 181, 817–831.
- Zhai, YunBo, et al., 2011. Removal of copper and lead ions from aqueous solutions by adsorbent derived from sewage sludge. *Int. J. Environ. Waste Manag.* 8 (3–4), 229–240.
- Zhang, Yaning, et al., 2017a. Effects of feedstock characteristics on microwave-assisted pyrolysis—a review. *Bioresour. Technol.* 230, 143–151.
- Zhang, Xueyang, et al., 2017b. Adsorption of VOCs onto engineered carbon materials: a review. *J. Hazard Mater.* 338, 102–123.
- Zhao, Tuo, et al., 2018. Facile low-temperature one-step synthesis of po,melo peel biochar under air atmosphere and its adsorption behaviors for Ag (I) and Pb (II). *Sci. Total Environ.* 640, 73–79.
- Zhong, Lin-xin, et al., 2012. Adsorption of heavy metals by a porous bioadsorbent from lignocellulosic biomass reconstructed in an ionic liquid. *J. Agric. Food Chem.* 60 (22), 5621–5628.
- Zhou, Minghua, et al., 2014. Bioelectrochemistry of microbial fuel cells and their potential applications in bioenergy. In: *Bioenergy Research: Advances and Applications*. Elsevier, pp. 131–152.
- Zhu, Wenjie, et al., 2017. Investigating the heavy metal adsorption of mesoporous silica materials prepared by microwave synthesis. *Nanoscale research letters* 12 (1), 1–9.

Available online at www.sciencedirect.com

ScienceDirect

journal homepage: www.elsevier.com/locate/he

Review Article

Catalyst modification strategies to enhance the catalyst activity and stability during steam reforming of acetic acid for hydrogen production

Ankit Kumar ^{a,*}, Rupesh Singh ^b, A.S.K. Sinha ^a^a Department of Chemical Engineering & Technology, Indian Institute of Technology (BHU), Varanasi -221005 UP, India^b Verdeen Chemicals Private Limited, D-11 UPSIDC Industrial Area, Phase-I, Masoori-Gulawathi Road, Dist. Hapur, Uttar Pradesh, 201015 India

ARTICLE INFO

Article history:

Received 6 December 2018

Received in revised form

8 March 2019

Accepted 17 March 2019

Available online 25 April 2019

Keywords:

Acetic acid

Hydrogen production

Steam reforming

Coke deposition

Catalyst

Bio oil

ABSTRACT

A high energy content (~122 MJ/kg H₂) and presence of hydrogen-bearing compounds abundance in nature make hydrogen forth runner candidate to fulfill future energy requirements. Biomass being abundant and carbon neutral is one of the promising source of hydrogen production. In addition, it also addresses agricultural waste disposal problems and will bring down our dependency on fossil fuel for energy requirements. Biomass-derived bio-oil can be an efficient way for hydrogen production. Acetic acid is the major component of bio-oil and has been extensively studied by the researchers round the globe as a test component of bio-oil for hydrogen generation. Hydrogen can be generated from acetic acid via catalytic steam reforming process which is thermodynamically feasible. A number of nickel-based catalysts have been reported. However, the coke deposition during reforming remains a major challenge. In this review, we have investigated all possible reactions during acetic acid steam reforming (AASR), which can cause coke deposition over the catalyst surface. Different operating parameters such as temperature and steam to carbon feed ratio affect not only the product distribution but also the carbon formation during the reaction. Present review elaborates effects of preparation methods, active metal catalyst including bimetallic catalysts, type of support and microstructure of catalysts on coke resistance behavior and catalyst stability during reforming reactions. The present study also focuses on the effects of a combination of a variety of alkali and alkaline earth metals (AAEM) promoters on coke deposition. Effect of specially designed reactors and the addition of oxygen on carbon deposition during AASR have also been analyzed. This review based on the available literature focuses mainly on the catalyst deactivation because of coke deposition, and possible strategies to minimize catalyst deactivation during AASR.

© 2019 Hydrogen Energy Publications LLC. Published by Elsevier Ltd. All rights reserved.

Abbreviations: AAEM, Alkali and alkaline earth metal; AASR, Acetic acid steam reforming; SEAASR, Sorption enhanced acetic acid steam reforming; AcOH, acetic acid; X_{AcOH}, acetic acid conversion %; S/C, steam to carbon molar ratio; WHSV, weight hour space velocity; LHSV, liquid hour space velocity; GHSV, gas hour space velocity; SCMNPs, size control metal nanoparticles; MA, mesoporous alumina; TOS, time on stream; M(TOA), M = Rh or Ru and TOA = Trioctylamine; ZDA, zhun dong ash; PG, palygorskite.

* Corresponding author.

E-mail address: ankit.rs.che14@iitbhu.ac.in (A. Kumar).<https://doi.org/10.1016/j.ijhydene.2019.03.136>

0360-3199/© 2019 Hydrogen Energy Publications LLC. Published by Elsevier Ltd. All rights reserved.

Contents

Introduction	12984
Coke formation mechanism during AASR	12986
Nature of carbon deposit (AASR)	12988
Effect of operating conditions on reforming reaction	12990
Effect of type of reactors	12991
Effect of Co-feeding of oxygen	12991
Effect of catalyst preparation methods	12992
Modification of catalyst	12993
Active metal	12993
Cobalt	12993
Nickel	12994
Copper	12994
Bimetallic catalyst	12994
Trimetallic catalyst	12996
Active metal sintering	12996
Support effect (doping with other metals)	12996
Alumina	12997
ZrO ₂	12997
CeO ₂	12998
La ₂ O ₃	12998
Mixed oxide	12999
Effect of alkali and alkaline earth metals	12999
Conclusions	13003
Acknowledgments	13004
References	13004

Introduction

Economic growth of any country depends strongly on its energy infrastructure. Because of global industrialization, energy requirement round the world has experienced a steady increase in demand. Till date, fossil fuels have been used primarily to fulfill this demand. However, the use of these fossil fuels raises severe environmental concern when effluent gases are released into the atmosphere [1–3]. Also, depletion of these fossil fuel reserves has raised alarms to develop an alternative sustainable energy source to meet future energy requirement [4,5].

Hydrogen, as a clean fuel, is recognized as the most promising future energy alternative for transportation due to its high energy density ~122 MJ/kg and environmental friendly nature [6–14]. Fig. 1 shows the different sources of hydrogen generation. It is mostly produced by steam reforming (SR) of natural gas, naphtha, and coal gasification [7] which are not renewable energy sources. These processes also release a large amount of CO₂, which is one of the major cause of climate change and global warming [15]. Biomass is considered a carbon-neutral renewable fuel resource, and fuels derived from it have been widely accepted as promising alternatives to fossil fuels [16,17]. Biomass-derived bio-fuel obtained from thermo-chemical processes such as fast pyrolysis of biomass has been projected as a renewable source to

produce hydrogen by steam reforming [18]. Hydrogen production via steam reforming of bio-oil is still a difficult task because of the complex composition of bio-oil [19]. The complex composition of bio-oil significantly depends on the pyrolytic conditions and type of biomass [20]. In general, bio-oil is a dark brown color and smoky odor liquid consisting of many groups of oxygenated hydrocarbons such as carboxylic acids, aldehydes, ketones, alcohols, phenols and guaiacols [21,22]. Acetic acid is one of the major fractions (concentration up to range 12–19% by wt.) of bio-oil [23–26]. Acetic acid may be used safely for hydrogen production as it is non-flammable

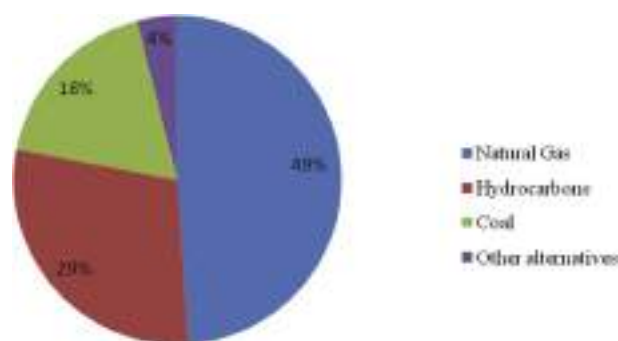
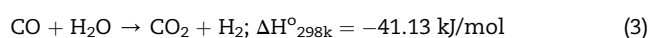
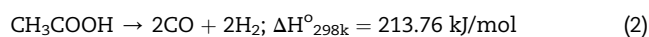


Fig. 1 – Different sources of hydrogen generation adapted from Parthasarthy et al. [235].

and can be easily obtained via fermentation process [24,27]. For this reason, acetic acid is often selected as a model compound for bio-oil for studying hydrogen production via steam reforming [24,28–38]. Fig. 2 shows the detailed schematic representation of H₂ generation from biomass-derived bio-oil via steam reforming reaction.

AASR for H₂ generation (Eq. (1)) can take place via acetic acid decomposition (Eq. (2)) followed by water gas shift reaction (Eqn. (3)) respectively [39].



Due to the complex composition of bio-oil and severe operating conditions of reforming reaction catalyst used are subjected to deactivation because of sintering, coking and metallic phase oxidation and thus lowering the H₂ yield [27,40,41]. Various types of catalysts have been reported in the literature. It includes noble metals (Pt, Pd, Rh, Ru, Ir) [26,34,42–46], transition metals (Cu, Co, Fe, and Ni) [24,27,32,47] and also a combination of both transition metals and noble metals [39,48–52]. However, noble metal catalysts are not economically viable [53]. Among transition metal catalysts, Ni, Co and Cu are found to be the most active metals for AASR. Consequently, these metals have been extensively examined using various supports such as Al₂O₃, ZrO₂, La₂O₃ and CeO₂ [25,54,55]. However, deposition of carbonaceous species as coke over catalyst surface and sintering of particles during a hydrothermal environment of steam reforming remain a severe operational challenge for researchers. In the past two decades, the primary focus of the research has been on the catalyst modification strategies to reduce the coke deposition during AASR. It has been reported that the addition of oxygen in the feed stream can eliminate coke deposition [56].

Steam reforming of the oxygenated compound is more complicated compared to hydrocarbons due to the presence of CO bonds that cause a large number of side reactions. Oxygenated compounds, especially acetic acid, show a

tendency of thermal vulnerability to decompose into carbonaceous deposition which is perceived as an obstruction to commercial implementation [57]. Takanabe et al. discovered that for Pt supported on ZrO₂, tested for AASR conditions, the active sites of Pt present on catalyst surface immediately deactivate by oligomers derived from acetic acid/acetone via oligomerization/condensation reactions [58,59]. Lemonidou et al. discovered that both high steam to carbon ratio and high oxygen mobility were necessary for stable catalyst execution of AASR [57]. Thus for acetic acid steam reforming, development of more stable catalyst capable of providing high H₂ yield has ever been a research subject. Catalyst development includes a selection of active metals and support. Valle et al. investigated that the effect of calcinations/reduction temperature over Ni/La–Al catalyst and explained that the catalyst calcined at 550 °C and reduced at 700 °C showed the best catalytic activity and stability [60]. Hu et al. studied acetic acid steam reforming over different transition metal catalysts supported over alumina and concluded that Ni and Co catalysts exhibited much better activity and stability in comparison to Fe and Cu catalysts. Besides, Ni and Co also showed different reaction network and product distribution. Moreover, the Ni catalyst showed the lowest coke deposition, metal sintering, and active metal oxidation rates which ensured its stability [27].

Coke deposition and metallic phase oxidation cause rapid catalyst deactivation. The growth of carbon species over the catalyst surface is dictated by the intermediate hydrocarbons formed [61]. AASR by-products such as ethylene, CO, and acetone are the primary sources of coke formation [62]. Hence, the intermediate products along with the catalyst composition play a major role in determining the rate of carbon generation and its control. Carbon deposition also relies on active metal and suitable support composition. Other than the support surface and active metal, the metal support interface is the major site for coke deposition and development [63]. The rate of carbon generation accelerates at high temperature [64]. Coke deposition over the catalyst surface can be limited by hindering the surface reaction either by preventing its formation or by facilitating the oxidation reaction using the presence of particular metals/support [27,57] and also by the utilization of specially

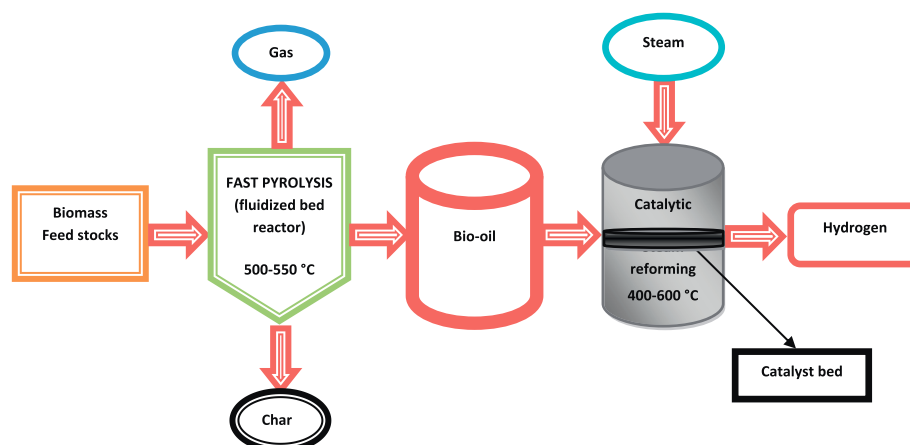


Fig. 2 – A possible route of hydrogen generation from biomass via steam reforming [236].

designed reactors [65]. Recently, published reviews on hydrogen production from acetic acid and bio-oil derivatives via catalytic steam reforming, a concise review of catalyst deactivation has been reported [4,66]. The thermodynamic analysis showed that the coke deposition over the catalysts surface is suppressed by increasing S/C ratio. High S/C ratio supports the adsorption and activation of steam which favours the water gas shift reaction along with CH_4 steam reforming. Both the intermediates products CO and CH_4 are the main coke precursor which are removed by excess steam [67]. Hu et al. also published a critical review to analyze the effect of different catalysts, reforming process and type of reactors in the development of AASR and only a brief discussion related to coke deposition on catalyst surface have been presented [67]. However, there is no critical review available which is exclusively dedicated to noble metal or transition metal catalysts dealing on modification strategies to control coke deposition and sintering of active metal over catalyst surfaces during AASR. The present review focuses mainly on the catalyst deactivation caused by carbon deposition and discusses the possible strategies to minimize catalyst deactivation during AASR based on the published researched work. An endeavor has been made to abridge sustainable catalysts modification strategies for their stability, along with the efficiency of AASR for renewable hydrogen production highlighting transition metal catalysts which are cost-effective catalysts.

Coke formation mechanism during AASR

The reaction pathways of acetic acid steam reforming (AASR) generally involve a complex reaction network due to some secondary intermediates and products formed. For better identification of reaction mechanism of AASR, whole reaction mechanism distinguishes into two parts including main reactions as mentioned in (Eqs. (1)–(3)) [39,68]. Few of these reactions lead towards the generation of undesired products [4]. Furthermore, acetic acid is unstable in the temperature range from 500 C–800 °C, where coke formation easily occurs because of thermal decomposition and the interaction between formed intermediate and catalyst surface which are likely to take place at operating conditions (Eqs. (4)–(6)). There

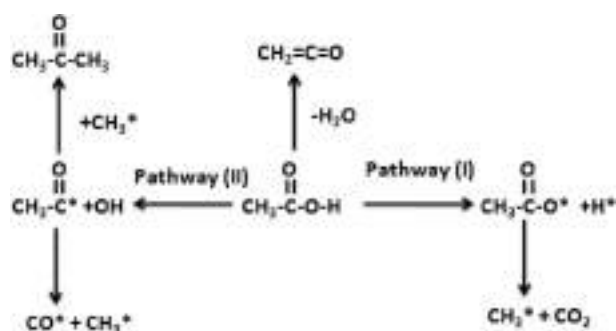


Fig. 4 – Assumed reaction pathways and carbon deposition mechanism from intermediate methyl group during AcOH during reforming. Reprinted with permission from Ref. [85].

also exist pathways for dehydration reaction Eq. (7) as well as ketonization reaction of acetic acid on acidic sites over catalyst surface for which the produced acetone is a carbon precursor. Ketonization is a common reaction taking place at low temperature and especially when support is solely used without active metals (Eq. (8)) [59,66]. These carbon precursors such as ketene, ethylene or acetone, eventually generate coke through condensation reactions [52]. However, above 400 °C, acetone and ketene are also steam reformed [Eqs (9) and (10)] [69]. In addition, the acute hydrothermal conditions during steam reforming reactions are favorable for active metal sintering as well as coke deposition. As a result, the catalyst loses its activity easily as time on stream [68,69]. A simple reaction mechanism of AASR proposed in several studies [42,58,59] is shown in Fig. 3 and Fig. 4. The dissociation of acetic acid over the catalyst surface is shown along with the proposed bi-functional mechanism. Dissociation of acetic acid over active metal phase takes place by cleavage of C–O and O–H bonds, resulting in the formation of acyl and acetate species respectively. Acetate further decomposes to form adsorbed CO_2 and methyl species. Whereas the formed species combine with $^*\text{OH}$ species forming H_2 and CO_2 . The CH_x species would then react with adsorbed hydrogen to generate methane. On the other hand, formed acyl species can further dissociate to form methyl and CO^* , which can further react with methyl group to form acetone. Meanwhile interaction with acidic

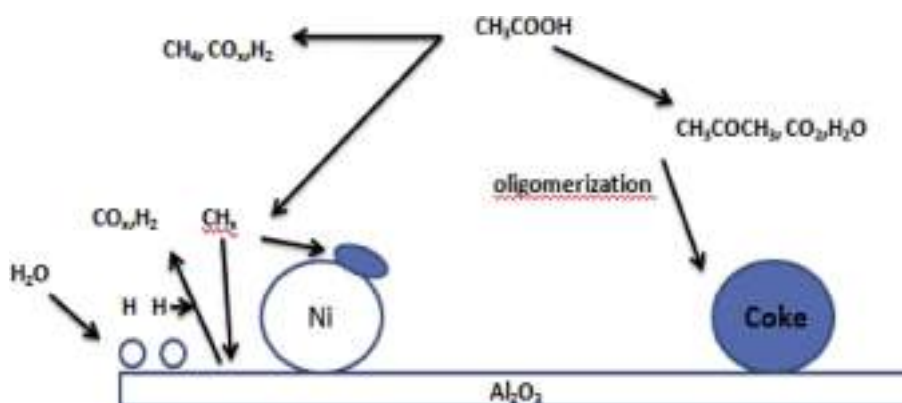


Fig. 3 – Schematic representation of reaction mechanism for acetic acid steam reforming [108].

support site, ketonization reaction might occur, that is followed by oligomerization of acetone resulting in coke formation not only over the support but also over metal/support interface [70]. Several workers have worked on the design of stable catalyst for steam reforming reactions [54,55] by improving the surface oxygen mobility that prevents the interfacial carbon formation and improves the catalyst activity and stability.

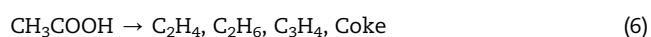
Decomposition-1



Decomposition-2



Decomposition-3



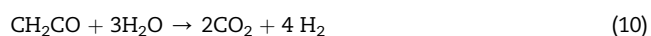
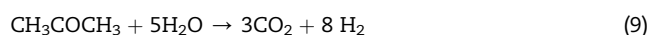
Dehydration reaction



Ketonization reaction

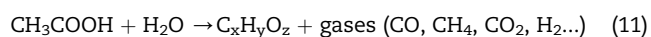


Reforming reaction of by-products



During AASR several undesired by-products are generated, which lowers hydrogen yield. CO is one of the main intermediates during the steam reforming process. Steam reforming efficiency is low at low temperature, and consequently favors the decomposition of the acetic acid [Eq. (11)] giving a high CO yield. However, high temperatures favor the reverse water gas shift reaction [Eq. (12)], which also promotes the production of CO. On the other hand, the water gas shift reaction [Eq. (3)] and the CO methanation [Eq. 14 and 15] give rise to the removal of CO in mild temperature conditions [71,72]. CH₄ formation, which significantly lowers hydrogen yield, is another main by-product in AASR. Firstly methane comes directly from the thermal decomposition of the acetic acid (Eq. (11), since acetic acid is thermally unstable, it may decompose before reaching the catalyst bed [73], and secondly, methane may come from the methanation of CO [Eqs. 14 and 15]. Primarily these are two possible ways for the methane formation, which are favored at high temperature [27,42,74]. Due to high concentrations of H₂ and CO in product gases and the high efficiency of Ni catalyst for methanation of CO favor these two reactions in AASR [75,76]. Therefore, steam reforming of methane may result in the removal of methane at high temperatures [Eqs. 16 and 17].

Thermal decomposition



Reverse water gas shift reaction



Water shift gas reaction



Methanation



Methane steam reforming



Boudouard reaction

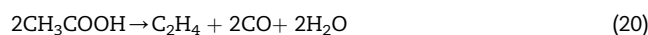


Thermal decomposition of CH₄



Along with active metal and support material properties, coke formation also depends upon the operating conditions especially reaction temperature [77]. Temperature below 400 °C can facilitate carbon deposition via the “Boudouard” reaction [Eq. (18)]. Carbon deposition can also occur via thermal decomposition of CH₄ [Eq. (19)] at higher reaction temperatures (above 600 °C) [78] and irreversible decomposition of acetic acid to coke precursors such as ethylene or other olefins. These intermediates may lead to carbon deposition after polymerization [Eqs. (20) and (21)] [78]. Verykios et al. [33] observed that for γ-Al₂O₃ supported catalysts, the reaction temperatures ≤400 °C triggers ketonization reactions (Eq. (8)), which results in the formation of CO₂ and acetone. Furthermore, acetone undergoes oligomerization reactions resulting in the formation of intermediates such as mesityl oxide, ketene, etc. which is one of the major routes for coke formation. The formation of ketene and mesityl oxide act as coke precursor via CH₃COCH₃ intermediate oligomerization (Eqs. 22–24 [59].

Thermal decomposition of acetic acid to ethylene and subsequent coke

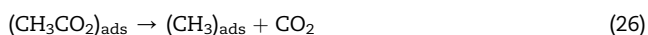


Acetone oligomerization





Several researchers also explained the coke generation routes [55,79] and proposed that in case of Pt/ZrO₂ catalyst, ketonization reaction readily occurs over the ZrO₂ surface, forming acetone which acts as a coke precursor leading towards the coke formation as shown in Fig. 3. Different studies conducted over Ni-based catalysts suggest that mixture of acetic acid and steam in the presence of Ni catalyst triggers catalytic cracking reactions (Eqs. (25)–(27) resulting in the formation of CO, CO₂, CH₄, and H₂ along with intermediate (CH₁₋₃)_{ads}. To avoid coke deposition over catalyst surface, formed (CH₁₋₃)_{ads} needs to be quickly gasified by H₂O to prevent further oligomerization which can form coke over catalyst surface (Eq. (28)) [40,80].



Hoang et al. [26] have concluded that coke formation is caused by decomposition of acetic acid and acetone produced during AASR. Presently, understanding of coke formation during AASR is typically limited to experimental observations. Researchers also presented theoretical considerations to understand the coke deposition mechanism during AASR by implementing density functional theory (DFT) [81–83]. Wang et al. [82] reported the dissociation mechanism of acetic acid over Co(1 1 1) and observed that $\text{CH}_3\text{COOH} \rightarrow \text{CH}_3\text{COO}^* \rightarrow \text{CH}_3\text{CO}^* \rightarrow \text{CH}_3^* + \text{CO}^*$ was the minimal energy pathway. Whereas Li et al. [79] proposed that $\text{CH}_3\text{COOH}^* \rightarrow \text{CH}_3\text{CO}^* \rightarrow \text{CH}_2\text{CO}^* \rightarrow \text{CH}_2^* \rightarrow \text{CH}^*$ was the most favorable pathways and dehydrogenation of CHCO^* is the rate determining step (RDS). The density functional theory over Ni (1 1 1) surface were investigated by Ran et al. [83] and based on DFT calculation the activation energy (E_a) for the formation of CH_3COO^* was found 45.6 kJ/mol, while activation energy for the formation of CH_3CO^* was 89.5 kJ/mol. Evidently, The formation of CH_3COO^* from the decomposition of acetic acid is the preferred route due to low E_a . Further, CH_3COO^* formed CH_3CO^* by losing one O*, E_a for which was found 84.8 kJ/mol. In another pathway CH_3COO^* formed CH_3^* by losing a CO₂ molecule. The E_a for this reaction was found 194.8 kJ/mol which is very high compared to the previous reaction. Thus CH_3CO^* formation was preferred intermediate. After losing CO* radical, CH_3CO^* formed CH_3^* radical [82]. Similar DFT calculation over Ni (111) surface of decomposition of acetic acid was reported by Wang et al. and proposed that CH_3COO^* formation is the preferred route in comparison to CH_3CO^* formation [84]. Furthermore, CH_3^* dissociation by losing H* step by step to form CH*. In the steam reforming process both the CH_3^* and CH* are the major sources for coking and play a crucial role in coke deposition. For instance, methyl combines with H* to form the by-product CH₄. It could also dehydrogenate step by step to form C* species, which would further form coke and deactivate the catalyst and its stability. C* species could also combine with the

OH* and gasify to form carbon die oxide and hydrogen, H₂ was not only produced from the recombination of dissociatively adsorbed species of acetic acid and steam but CH_3^* and CH* also dissociative to lose H* and could integrate to form H₂ and coke. Furthermore, to suppress the by-products like CO and CH₄ and gasify the carbon precursor-like CH_x (x = 0–3) species, catalyst surface must have enough *OH species on the vicinity of CH_3^* [85].

Nature of carbon deposit (AASR)

Several researchers investigated the development of carbon formation and its nature during reforming of hydrocarbons such as methane [86,87] and propane [88]. They concluded that there are two types of coke formation mainly (i) Ni-encapsulating amorphous coke and (ii) structured (filamentous coke) which also classified as carbon nanotubes (CNT) under certain specific conditions. The mechanism of CNTs generation suggested by Lattore et al. [89–91], assumes that methane resides as a metastable carbide form, which eventually leads to the generation of carbon atoms diffusing through the interphase of metallic nanoparticles and forming nanotubes after nucleation stage. Two major types of coke formation were also observed during reforming of oxygenated compounds such as acetic acid [24,92], ethanol [93–96] and bio-oil [97]. Carbon deposition behavior is significantly different for different catalysts. Iwasa et al. [36], reported that after AASR, amorphous type of carbon was formed on the surface of Pt/Al₂O₃ catalyst. On the other hand, fiber-like structures were observed over Pt/smectite. Whereas on Pt/CeO₂ catalyst, acetone acts as a coke precursor produced from acetic acid condensation/dehydration and further converts to oligomeric coke species. Condensation of oxygenated reaction intermediates plays a significant role in the evolution of amorphous and encapsulating coke while structured coke generation was due to dehydrogenation of CH₄ along with Boudouard reaction. Three types of surface carbonaceous species (amorphous, filamentous and graphitic) are generated during CH₄ decomposition. The first one, highly reactive carbidic species which act as an intermediate for filamentous carbon formation (hydrogenable at temperature ≈ 323 K) is formed via dissociation of methane forms graphitic carbon at high temperature and it is favoured over Ni catalyst [61,98]. The spectroscopic studies suggest that carbon formation over Ni (100) requires a lower decomposition temperature in comparison to Ni (111) surface during hydrogenation of carbidic carbon. The difference in surface energies at different Ni surfaces (100) and (111) affects the local CH_x species growth which causes an observed difference in thermal stability over the Ni surface [99]. On the other hand, nickel carbide readily decomposes into metallic form as well as graphitic carbon form at temperature >873 K [100]. The second one is amorphous carbon which is developed via polymerization of carbidic carbon promotes the formation of carbon whiskers. The third one the graphitic carbon that is hydrogenable at temperature ~673 K and shows variable reactivity for oxidation and hydrogenation reaction [100]. Nogueira et al. [101] through TGA and DTA analysis, investigated the oxidation behavior of different carbonaceous species formed during AASR reaction over 15NiAl and 15NiMg/Al

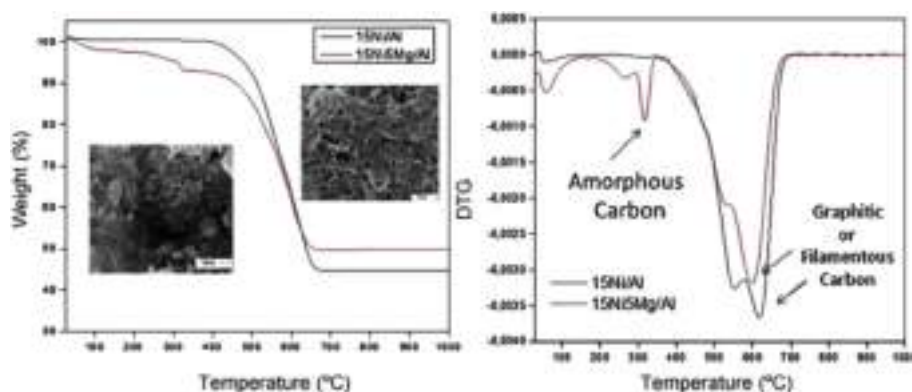


Fig. 5 – (a) TGA of used 15Ni/Al (inset, SEM micrographs of 15Ni/Al catalyst after reaction) and 15Ni5Mg/Al (inset, SEM micrographs of 15Ni5Mg/Al catalyst after reaction) catalysts performed under airflow and (b) derivative thermograms for used 15Ni/Al and 15Ni5Mg/Al catalysts. Reprinted with permission from Ref. [101].

catalysts, respectively (Fig. 5). They reported that for 15Ni/Al catalyst, oxidation of carbon started at 400 °C and continued till at 670 °C. On the other hand for 15Ni5Mg/Al catalyst, oxidation of carbon started at 100 °C and ended at 670 °C. For both the samples, most of the deposited carbon remained over the catalyst surface at 500 °C. The peak at 350 °C was due to the removal of readily oxidizable carbon species and desorption of H₂O and CO₂ from the catalyst surface. Whereas the peak at temperature >500 °C was assigned to oxidation of graphitic and filamentous carbon species.

Generally, amorphous and filamentous type of coke were formed over Cu based catalysts. However, Ni-based catalysts deactivated by the formation of filamentous and graphitic carbon [24,92]. For Ni/ γ -Al₂O₃ catalyst, increase in Ni loading resulted in promotion of catalytic cracking reaction at the cost of ketonization reaction. Increase in Ni loading also resulted in an increase in deposition of the graphitic form of carbon deposition over catalyst surface at the expense of amorphous carbon. A DTA analysis (Fig. 6) of spent catalysts (Ni and Cu supported on mesoporous support) was carried out to find out the characteristics of coke formed during AASR. Three types of carbon formation (amorphous, filamentous and graphitic) on the catalyst surface observed. At low temperature around 400 °C DTA peak corresponded to the amorphous carbon. The filamentous type carbon is generally oxidized around 550 °C. Moreover, higher temperature oxidation peaks over 700 °C correspond to the graphitic type carbon [24]. The nonfilamentous carbon blocks nickel active sites [95,102]. On the other hand, the filamentous carbon formed via CO and CO₂ resulted in the separation of support and the active nickel sites. The amorphous coke formed during the process could cover catalytically active sites, resulting in deactivation of the catalyst species. The filamentous coke grown over metallic species shows relatively less effect compared to amorphous coke on catalytic activity [102].

De Bokx et al. investigated the formation of filamentous carbon from CO and CH₄ in the temperature range of 600–1000 K over nickel and iron catalysts. They observed that initially carbon is deposited in the form of a metastable carbon intermediate which thermally decomposes to form filamentous carbon [103]. The relatively high mechanical strength of filamentous carbon makes it compatible enough to

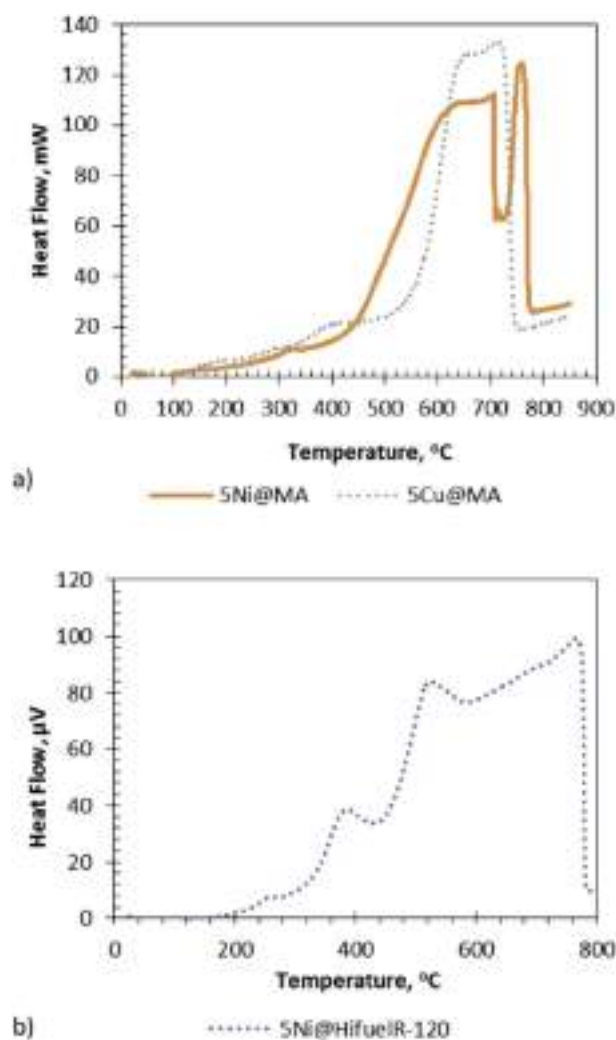


Fig. 6 – DTA analysis of used catalysts (a) 5Ni/MA, 5Cu/MA (b) 5Ni/HifuelR-120. Reprinted with permission from Ref. [24].

disintegrate active metal from catalyst support completely [104]. Reports suggest that amorphous carbon resulted in severe deactivation in comparison to filamentous carbon [105].

The graphitic form of carbon is formed not only by direct deposition of carbon in the vapor phase but also via heat treatment of amorphous carbon [106]. At lower temperature, coke formation occurs mainly due to the catalytic cracking reactions whereas at high-temperature CO disproportionation reaction is responsible for the coke formation [92]. The typical SEM of graphitic like carbon formed on the deactivated Ni/CeO₂-ZrO₂ catalyst is shown in Fig. 7. [107] Cheng et al. also have reported two different carbonaceous sites for coke deposition over the catalyst surface. The lower temperature peak at 330 °C in TPO was attributed to the carbon deposition on the active metal, whereas higher temperature peaks [550 °C] the (significant one) was attributed to carbon deposition over the support surface.

It has been concluded by many workers that the lower temperature peak represents polyaromatic compounds whereas higher temperature peak represents a pseudo graphitic structure [108–110]. Francisco et al. have also described that carbon deposits over catalyst surface during AASR was of two types: one is easily oxidizable carbon (300 °C) amorphous carbon, another oxidized at higher than 500 °C is assigned to the graphitic or filamentous carbon [111,112].

Effect of operating conditions on reforming reaction

Different studies in the literature showed that operating parameters such as temperature, water to the acetic acid ratio (S/C) and catalyst to acetic acid flow rate (space velocity)

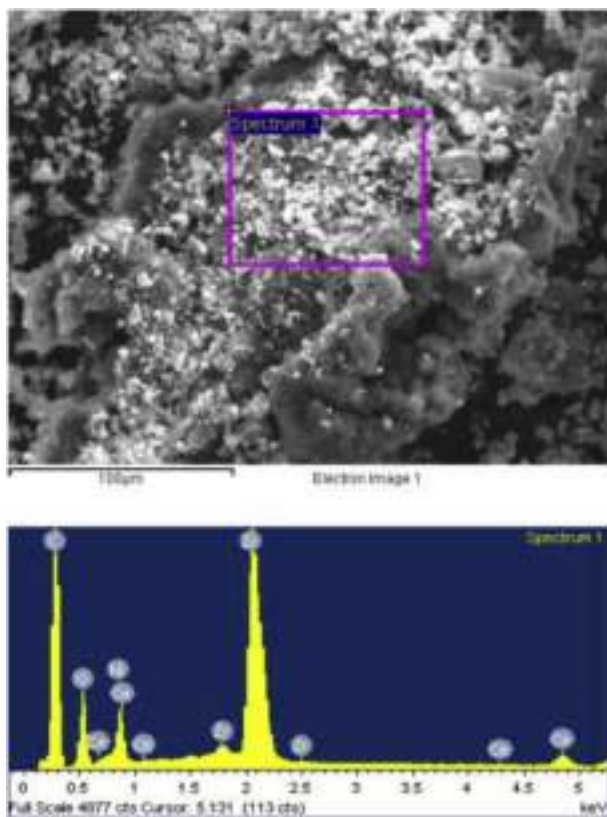


Fig. 7 – Scanning electron microscopy and EDX scan of the used 12%Ni/CeO₂-ZrO₂ catalyst. Reprinted with permission from Ref. [107].

affected not only the product distribution but also the carbonaceous deposition during steam reforming reaction. Studies have shown that molar ratio of acetic acid and water has a significant effect on hydrogen production and mitigation of coke deposition in AASR [31,32]. Steam is required during AASR for the gasification of secondary reaction intermediate generated during the reaction. Thermodynamic analysis has exhibited that S/C ratio greater than 2 to 1 in AASR is viable. Furthermore, mol% of CO increases in gaseous product with temperature beyond 700 °C [72]. This is mainly because of the exothermic nature of the water gas shift reaction. Operating parameters such as high steam to carbon ratio and temperature promote the removal of by-products and carbonaceous deposition and also favor the hydrogen generation both in AASR and in sorption enhanced acetic acid steam reforming (SEAASR) [113–115]. These parameters also play a crucial role in formation of intermediate products (CO, CH₄, C₂H₄, CH₃COCH₃), which are responsible for coke deposition via different reactions as shown in Eq. ((18)–(24)). Hoang et al. investigated the AASR on Ni/HT catalyst in the temperature range of 600–700 °C. They have reported that conversion of acetic acid and yield of H₂ strongly depended on the reaction temperature. They showed that the activity of catalyst drastically decreased due to deactivation by coke deposition. They concluded that at lower temperature, the initial deactivation of catalyst was strongly influenced by the formation of acetone [25]. It's well reported in the literature that during steam reforming process reaction temperature and S/C ratio both significantly affects the coke deposition over catalyst surface [33]. Hoang et al. have also reported that the steam/carbon ratio had a strong impact on conversion and deactivation of the catalyst. They reported that conversion of acetic acid dropped from 100 to 76% When the S/C ratio lowered down from 14 to 5. Higher S/C ratio enhanced WGS reaction. During the steam reforming reaction, both feedstock and steam compete for active sites over catalyst surface [116]. High steam to carbon ratio promoted the adsorption of steam on the active sites and consequently suppressed the decomposition or degradation of the feedstock. High steam partial pressure also promotes water gas shift reaction to remove CO intermediate resulting in a higher hydrogen selectivity [62]. A typical results showing the effect of S/C ratio given in Table 1. Results show that relatively low carbon balance is obtained at lower S/C ratio. Low steam ratio favors decomposition of feedstocks that results in the formation of a large number of by-products which act as a precursors during coke deposition. On the other hand high, S/C ratio promotes gasification of carbon deposits and suppresses formation of carbon precursors (i.e., CO and CH₄), resulting in a higher carbon balance [62]. Carbon depositions are also regulated by different types of reactions that occur at different temperatures. Verykios et al. have reported that during AASR, nature of carbonaceous species formed over catalyst surface was different at the different reaction temperatures. They explained that at a lower temperature (500 °C), CH_x type of carbonaceous species formed via acetone intermediate whereas at high temperature (700 °C) only carbon exists on the catalyst surface [34]. Thermodynamically, the Boudouard reaction and hydrogenation of CO are the governing reactions favored at lower temperatures which favor the coke formation. Whereas at high-

Table 1 – . Effects of S/C ratio on acetic acid conversion and selectivities of gaseous product at T = 673 K; T = 973 K LHSV = 10.1 h⁻¹; P = 1 atm [62].

S/C	Conversion (%)	Product selectivity (%)					Carbon Balance %
		H ₂	CO ₂	CH ₄	CO	Others	
1	57.3	42.6	40.3	21.4	9.5	12.1	88.8
3	70.9	61.6	54.2	17.2	8.6	10.2	90.6
6	85.4	79.1	79.7	11.7	1.1	4.6	94.3
9	100	90.5	91.8	1.6	0.9	0.5	99.2

S/C- steam to carbon ratio.

temperature Boudouard reaction reverses, and the coke deposition occurs via decomposition and polymerization of hydrocarbons (Eqs. (9), (11), (12) (20) (21)) [33,117]. Cheng et al. described that below 650 °C reaction temperature; a huge amount of coke deposition occurs on the reactor wall generated via the Boudouard reaction. Increasing the temperature to 650 °C or above carbon deposited on the wall of the reactor was removed [108]. Coke deposition behavior on Rh/La₂O₃/CeO₂–ZrO₂ catalyst was studied during AASR by Lemonidou et al. at different operating parameters such as S/C ratio, co-feeding of oxygen (oxidative steam reforming) and time on stream. A result of their studies of coke generated is presented in Table 2 as mole% of carbon in a reactant converted to coke. It is clearly seen that the rate of coke deposition over Rh/La₂O₃/CeO₂–ZrO₂ catalyst is meager. At S/C ratio 3, the average coke formed per mole of C of acetic acid over the catalyst surface after 3 h of time on stream (TOS) were measured at 0.009%. The increase of the S/C ratio from 1.5 to 6 results in a reduction in coke deposition ~4 times, indicating the significance of excess steam is preventing coke deposition. While, after 15 h TOS, 0.010 mol of coke was deposited per mole of carbon present in acetic acid which is equivalent to 2.95 wt% coke deposited on catalyst [57].

Effect of type of reactors

Generation of carbonaceous species is one of the major operational challenges that result in catalyst deactivation, especially for nickel-based catalysts used in steam reforming. During the reforming process of bio-oil and any of its model compounds, there always exists a high possibility of coke

formation which not only deactivates the catalyst but also fouls reactors. For the same reason, it is imperative to use specially designed reactors to avoid reactor fouling because of coke formation [65].

Combination of a proper reactor design along with appropriate catalyst formulation can minimize carbon formation during reforming reaction [39]. In case of fluidized bed reactors, it is comparatively easy to gasify the coke deposited over the catalyst surface. For the same reason, fluidized beds are found to perform better than fixed ones for a continuous process of AASR [118]. Some authors have also successfully studied the concept of sequential cracking and coke burn off as an alternative heat integrated process for bio-oil processing [119,120]. Davidson et al. investigated a modified dual-bed (2-bed) system in series for AASR as illustrated in Fig. 8. They reported that bare catalyst supports show activity only towards acetic acid ketonization reaction and form comparatively low coke deposition during AASR. Once the Co was impregnated into supports, coke deposition increases significantly. On the other hand, in case of dual bed (2-bed) configuration utilized for AASR, wherein the first bed acetic acid converts to acetone via ketonization reaction which further undergoes steam reforming in the second bed. The modified system demonstrated ~4 times improved stability to overall coke deposition in comparison to conventional single bed reactor. The improved stability of the catalyst system could be because the steam reforming of acetone resulting in less coke deposition in contrast to acetic acid and also there was an increase in S/C feed ratio via ketonization reaction which produces one molecule of H₂O and converts one carbon molecule to CO₂ [121].

Effect of Co-feeding of oxygen

During the steam reforming reaction, coke deposition depends on the nature of feed [122]. A small amount of oxygen during reforming reaction can minimize not only the coking but also promotes endothermicity of the reactions. Garcia et al. studied the effect of oxygen addition during AASR and reported that without addition of oxygen, conversion of acetic acid decreased with time on stream while the addition of small amount of oxygen (~4%) had a beneficial effect on acetic acid conversion with less coke deposition and remained constant up to a value 100% over 6 h TOS (time on stream). On the other hand, the yield of hydrogen moderately decreased because some amount of hydrogen react with oxygen and give water [124]. Lemonidou et al. showed that H₂ yield declined by approx 19% in comparison to proposed thermodynamic

Table 2 – . Coke deposition over Rh/La₂O₃/CeO₂–ZrO₂ after acetic acid steam reforming under various conditions [57].

Conditions	Mole C (coke) per mole C in acetic acid, %
S/C = 1.5 (T = 750 °C)	0.025
S/C = 3.0 (T = 750 °C)	0.009
S/C = 6.0 (T = 750 °C)	0.006
Auto thermal steam reforming (T = 750 °C, O ₂ /steam/carbon = 0.15/3/1)	0.007
Steam reforming, time on stream (T = 650 °C, 15 h, S/C = 3.0)	0.010

S/C- steam to carbon ratio.



Fig. 8 – Graphical representation of single-bed (1-bed) catalyst system consisting of Co-supported catalyst (e.g., Co/CeO₂), and dual-bed (2-bed) catalyst system with ketonization catalyst (e.g., CeO₂) placed in sequence with a Co-supported steam reforming catalyst [121].

calculations on autothermal steam reforming of acetic acid while keeping the same operating conditions, i.e., 700 °C and the O₂/AcOH ratio was 0.4 [123]. The surface morphology of Ni/Al catalyst after 6 h reactions without and with oxygen by scanning electron microscopy (Fig. 9a and b) showed a clear difference on the catalyst surface. Without oxygen, the major presence of filamentous carbon was observed while the clean surface was observed with the addition of oxygen on the catalyst surface [124]. To resolve the deactivation problem, Guell et al. reported that activity and stability of Pt/CeO₂ and Pt/ZrO₂ could be improved during AASR with the addition of 1% O₂ to the reaction mixture. The coke deposition could be minimized during the reaction by in-situ gasification of coke in the presence of oxygen [55].

Effect of catalyst preparation methods

Wang et al. studied the effect of catalyst preparation method on the catalytic steam reforming of acetic acid. They

synthesized Ni/ATC (attapulgite clay) via precipitation, impregnation and mechanical blending methods. They observed that strong interaction between Ni species and ATC support could be attained through a precipitation method which further enhanced the activity and stability of Ni/ATC catalyst [125]. Porous silica coated Ni/CeO₂-ZrO₂ catalyst indicated a notably improved activity (93% AcOH conversion) compared to Ni/CeO₂-ZrO₂. The coating of porous silica shell altered the electronic dispersion of Ni surface and enhanced the intrinsic activity of nickel. The under-coordinated Ni active site also showed different selectivity of products. The coated catalysts also showed better stability and no noticeable deactivation was observed at 600 °C for 30 h. It was reported that the porous silica coated Ni/CeO₂-ZrO₂ catalyst showed not only excellent resistance to Ni sintering but also exhibited significant inhibition of coke formation and enhanced stability during AASR, which showed that the presence of a porous silica layer over Ni metal resists coke deposition [126]. Catalyst preparation methods regulate the effective dispersion of

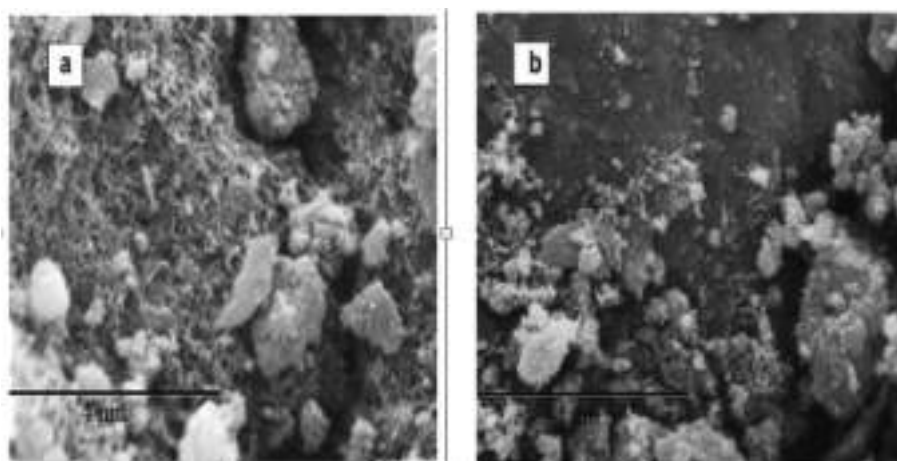


Fig. 9 – SEM images of Ni/Al catalyst after 6 h reaction: (a) with no oxygen addition and (b) with 4% oxygen addition. Reprinted with permission from Ref. [124].

active phase and metal support interaction. It impedes the carbonaceous formation during AASR. Wang et al. compared the effect of type of support (γ -Al₂O₃ and nano γ -Al₂O₃) during AASR and inferred that nano γ -Al₂O₃ provides more active sites for the reforming reaction which helps to attain high conversion and resistance to coke deposition [127]. Huang and co-worker compared AASR activity and stability over Ni–Co/MgO catalyst prepared by two different methods, i.e. co-precipitation and impregnation methods. They observed that H₂ yield decreased over the time for the catalyst prepared by impregnation method due to the formation of acetone via ketonization reaction, which caused the coke deposition over catalyst surface and resulted in catalyst deactivation. They also carried out XPS analysis and reported that despite having more reducible property, the catalyst prepared via impregnation method showed lesser stability in comparison to catalyst prepared using the co-precipitation method during AASR [48]. Santo et al. reported that coke deposition was not dependent on the nature of the metal, but on the preparation method. They developed Rh and Ru supported on mixed MgAl(O) catalyst via a new preparation methodology named size controlled metal nanoparticles deposition (SCMNPs) for AASR. The prepared Ru SCMNPs derived catalysts showed high coke resistance and enhanced activity in comparison to traditionally used impregnation method [44].

Modification of catalyst

Groups of researchers have adopted various strategies to reduce coke formation during AASR. These include increasing steam to carbon ratio; auto-thermal steam reforming, co-feeding of O₂, Co-feeding of H₂ and catalyst modification (both active metal and support modification). Increase in steam to carbon ratio demands a high consumption of energy for the conversion of water to facilitate the reaction. Auto-thermal steam reforming is an exothermic reaction thus requires less energy in comparison to steam reforming; however, overall hydrogen yield gets reduced. A small amount of oxygen addition is beneficial to minimize coke deposition but moderately decreases H₂ yield. The co-feeding of hydrogen during reaction reduces deposited carbon, but it enhances the hydrocarbon yield regardless of H₂. Therefore, modification of catalyst is a better option for limiting the coke deactivation of catalysts during AASR without affecting yield as well as cost. Formulation of effective catalyst necessitates information about metals activity, support and synergistic interaction between metals and their support during AASR for the carbon generation and deposition.

Active metal

Chemical nature of an active metal plays a major role in defining the catalytic activity and stability of the catalyst. A strong basic characteristic of active metal assists in CO₂ adsorption (molecule with acidic characteristics) and helps in gasification of the formed carbon deposits over catalyst surface. However, those active metals which possess acidic nature assist in coke deposition [128]. Nabgan et al. estimated basicity of a catalyst via CO₂-TPD based peak area and

reported that strong basic sites present in active metals become an active oxygen source species with high activity and act as the inhibitor for coke deposition on catalyst surface [129]. Furthermore, the acidic behavior of the catalysts varies with the nature and the proportion of active metal.

Hu et al. studied acetic acid steam reforming over different transition metal catalysts supported over alumina and concluded that Ni and Co catalysts exhibited much better activity and stability in comparison to Fe and Cu catalysts. Besides, Ni and Co also showed different reaction network and selectivity. Moreover, the Ni/Al₂O₃ catalyst exhibited the lowest coke deposition, metal sintering, and active metal oxidation rates in comparison to all tested catalysts [27]. Guell et al. [54] have investigated Ni/ZrO₂ catalyst and found quick deactivation, but activity of the Ni catalysts got enhanced by the incorporation of basic La₂O₃ and CeO₂ in ZrO₂ support [25,54,55]. Noble metals showed more resistance to coke deposition in contrast to nonnoble metals. Verykios et al. [30] compared nickel with noble metals; they conclude that noble metals showed lower activity but more stable behavior towards coke deposition. They also proved that among noble metals Rh was the most active noble metal in comparison to Ru, Pt, and Pd. Among noble metals, Rh had the capacity of scission both C–C and C–H bond [46,128].

Cobalt

Cobalt-based catalysts had relatively high activities towards water gas shift reactions at low temperatures [129,130]. Cobalt catalysts are also low-cost catalysts in comparison to noble metal catalysts and have the capacity of breaking of C–C bonds at lower temperatures. Nonetheless, the performance of metallic cobalt-based catalyst suffers severe deactivation due to carbon deposition [32]. Deactivation also occurs because of metal oxidation [27,38,39]. Mizuno et al. reported that Co catalyst remained oxidized and inactive at a lower temperature. A lower carbon deposition was observed when Co was combined with Ni catalyst due to a higher rate of oxidation of C* by O and OH, as well as the presence of CoO on metal cores of Co and CoNi catalysts [131]. The DFT calculation was carried out to investigate the decomposition mechanism of AcOH steam reforming over cobalt [81,82]. The Co (111) surface, was shown to follow minimal energy pathway with the formation of acetate (CH₃COO) intermediate, which adsorbed on the surface to form a bridge configuration connecting two O atoms bonded on the top site of catalyst surface [82]. Li et al. thoroughly investigated the acetic acid decomposition mechanism and proposed that the formation of acyl species (CH₃CO) and dehydrogenation is the rate-determining step (RDS) [81]. However, Xun et al. showed that Co/Al₂O₃ catalyst was more active in the thermal decomposition of acetic acid and higher amounts of CO was formed in comparison to Ni/Al₂O₃ [6]. Metallic cobalt phase is an active phase for the steam reforming reaction. Oxidation of these species causes catalyst deactivation, which further leads to coke formation reaction [69]. It is in order to mentioned that Co supported on alumina showed strong interaction with the support and resulted in the formation of cobalt aluminate, which was difficult to reduce. As a result, it exhibited low activity during the reforming reaction [132].

Nickel

Nickel is the most extensively used metal catalyst for steam reforming of acetic acid due to its excellent ability in facilitating cleavage of C–C, O–H and C–H bond and dehydrogenation reactions [126,133,134]. Similar to cobalt, nickel-based catalysts require lower reaction temperature and exhibit high activity. Activity of the base metal decreases in the order Ni > Co > Fe > Cu [27]. The main advantage of Ni-based catalysts compared with those of noble metals is their high activity towards C–C bond cleavage and high selectivity for the H₂ generation at a substantially lower cost [40,115,118,124,135–138]. However, Ni-based catalysts are more vulnerable to coke formation [29]. Hence the development of Ni-based catalysts, having more resilience towards coke deposition and remains a major challenge [24,139].

Coke formation depends not only on the properties of the reactants but also on the oxidation state of nickel species present over the support surface. Ni in its metallic form is considered to be an active state for steam reforming reaction; on the other hand, the oxide form of the Ni (NiO) does not catalyze the reaction [140]. Hence, the catalytic activity of Ni/Al₂O₃ catalyst is mainly determined by the characteristic of metallic Ni species over Al₂O₃. Amount of Ni loading over Ni/γ-Al₂O₃ catalyst affects the carbon deposition species and coke formation. With an increase in Ni loading 10 to 20 wt% stability is enhanced due to the resistance of catalyst towards coke formation [102]. The increase of Ni loading did not increase the activity of catalyst while it only alters the properties and structures of the coke formed as confirmed by the TPO and TEM result of catalysts shown in Fig. 10 and Fig. 11 (a) & (b). Fibrous kind of structures was formed over the 20% Ni/Al₂O₃ while 10% Ni/Al₂O₃ catalysts showed the amorphous type of coke on catalytic sites. Moreover, 20 wt% Ni/γ-Al₂O₃ catalyst had more aromatic and carbon nanotube structured coke species which, however, was not noticeable over 5 wt% Ni/γ-Al₂O₃ catalyst [102,106]. Hu et al. observed an increase in graphitic like species when Ni loading was increased from 9 to 15% [76,98]. The coke formation study of steam reforming reaction over Ni-based catalysts showed (Fig. 12) that catalyst deactivation was because of encapsulation by nonfilamentous carbon, which blocked the active catalyst sites [41]. Filamentous carbon formed from CO and CO₂ does not lead to catalyst

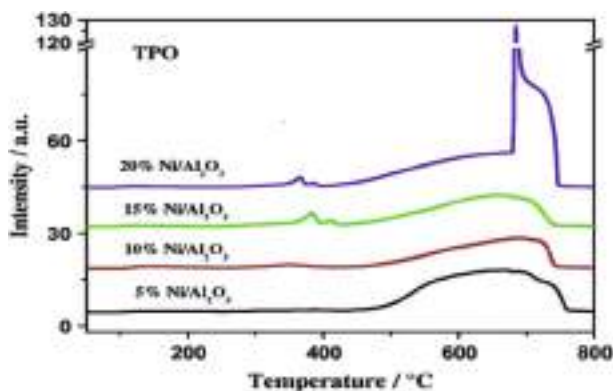


Fig. 10 – TPO analysis of catalysts. Reprinted with permission from Ref. [141].

deactivation but results in detachment of active nickel sites from the support [95,140]. Medrano et al. [124] investigated the influence of calcination temperatures (750, 850 and 900 °C) on Ni/Al catalyst and observed an increase in spinel phase formation (NiAl₂O₄) at high calcinations temperature, which was difficult to reduce. Hence, 900 °C calcined catalyst showed a lower activity in comparison to catalyst calcined at 750 °C and 800 °C. Calcination temperature affects the interaction of metal and support it has been investigated by Hu et al. who reported that catalyst calcined at high temperature could improve the catalytic stability due to enlarged mean pore size, which enhanced the mass transfer efficiency [141]. Goyal et al. observed that 12 wt% Ni–Al monolithic catalyst was more stable than 12 wt% Ni–Al pelletized catalyst [142]. Stability of Ni-based catalyst against carbon deposition can be enhanced by increase water adsorption over the support to gasify coke precursor or by modification of active metal surface via the presence of other metals [46,143,144].

Copper

Cu based catalysts have better activities in case of low-temperature reactions. For example, Cu–ZnO catalyst showed excellent performance for methanol steam reforming. However, in case of acetic acid reforming, Cu–ZnO and Cu supported γ-Al₂O₃ catalysts showed poor activity [27,145]. Addition of Cu into Ni/Al catalyst resulted into a poor catalytic activity in comparison to conventional Ni/Al catalyst Bimbela et al. found that when copper was used as a promoter, it improved the stability of Ni/Al co-precipitated catalyst with a slight decrease in initial reforming activity because of a reduction of Ni sites concentration. Consequently, it acted as a resistance for the encapsulation of coke formation. However, the formation of filamentous type carbon increased due to the presence of copper [146]. Addition of Cu also exhibited a better activity towards methane decomposition and also facilitated the gasification of carbonaceous species deposited during thermal decomposition of methane [147,148]. Comparison of the catalytic performance of Cu and Ni-based catalysts showed that Cu/γ-Al₂O₃ activates the decomposition of AcOH giving mainly CH₄ and CO₂ and exhibits better stability towards coke formation [24].

Hu et al. studied AASR for hydrogen generation utilizing transition metal catalysts (Ni, Fe, Co or Cu)/Al₂O₃. They found that Ni and Co had higher activities for C–C and C–H bonds cleavage. As discussed above, the copper-based catalyst showed lower activity and selectivity of hydrogen during steam reforming of acetic acid. For the same reason, bimetallic catalysts (e.g., Fe–Co, Ni–Co, and Ni–Pd) have been widely studied [125,149,150].

Bimetallic catalyst

Monometallic catalysts showed a significant amount of coke deposition while in the case of a bimetallic catalyst, synergistic interaction between the two metals may have a beneficial effect to prevent carbon deactivation and increased H₂ selectivity during AASR [24,129–131,151,152]. Therefore, extensive research is being carried out in recent past to investigate the synergistic effect of bimetallic catalysts such

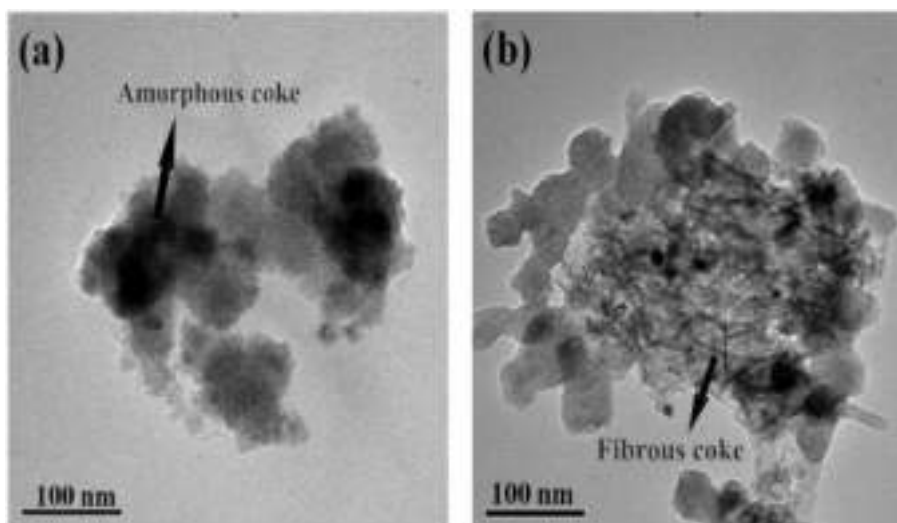


Fig. 11 – Typical structure of coke species formed on (a) 10% Ni/Al₂O₃ (b) 20% Ni/Al₂O₃ during AASR. Reprinted with permission from Ref. [102].

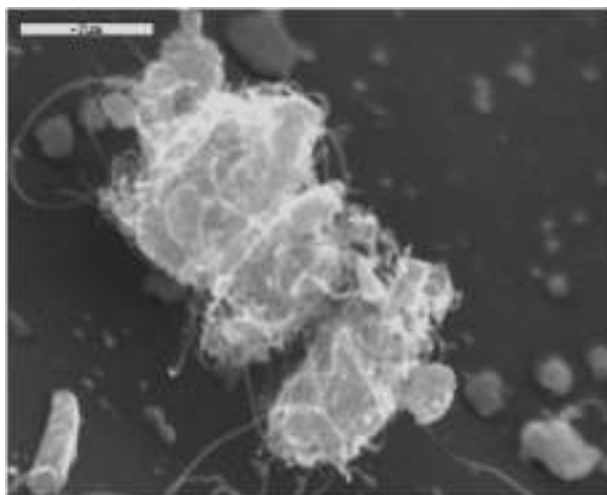


Fig. 12 – Scanning electron microscopy of 5% Ni/CeO₂–ZrO₂ catalyst after reaction. Reprinted with permission from Ref. [26].

as Ni–Co during steam reforming to minimize deactivation by coke deposition. In comparison to bimetallic solely Ni or Co catalyst showed higher coke deposition [153,154]. The study showed that bimetallic catalysts had better activities and stabilities and excellent coke resistance during the steam reforming reactions [155,156]. Besides, Ni–Cu bimetallic catalyst also promoted capability of carbonaceous species gasification during reforming reaction [155]. Hu et al. has also reported an increase in catalyst activity and stability of bimetallic catalysts during AASR [130,151]. They found that mixed Co–Ni and Co–Fe catalysts exhibited high activity and stability during AASR. However, they did not explain the reasons for high activity and stability. Wang et al. reported detailed studies over Co–Fe unsupported catalysts with different Co/Fe ratios. They found that increasing amount of Fe decreased the activity and stability due to unstable

adsorption of H₂O on Fe surface, it obstructed the steam reforming and WGS reaction [82]. Pant et al. reported that high hydrogen yield (~80%) and less coke deposition on catalyst surface occurred over bimetallic Cu–Zn/Ca–Al catalysts. The incorporation of Zn not only improved the H₂ yield but also reduced deactivation of active catalyst sites [47]. In addition, Liu et al. Described that Few active sites of Cu and Zn over the catalyst surface were deactivated by carbon deposition during acetic acid steam reforming [157]. When successive layers of coke deposition begin to develop on various site of active metals, the adsorbed carbonaceous atomic groups nearby the active sites of catalyst generated from the hydrocarbon (like ketones) get deposited on the catalyst surface, which may remain on catalyst surface for a longer span and obstruct the activity of Cu. At that crisis, active sites of Zn particle break the inter-cohesive force between catalyst active sites and carbide, as the carbide begins to develop [47].

Pant et al. synthesized bi-functional Ni–Co catalysts which showed better performance in comparison to conventional catalysts because of inhibition of methanation or reverse water gas shift reactions [39]. Bimetallic Co–Ni catalysts prepared by impregnation method supported over MgAl₂O₄ with different Co/Ni ratio for acetic acid steam reforming have been studied. The study reported that the use of Co–Ni catalyst inhibited the CH₄ formation and carbon accumulation. The authors reported that active Ni catalyst favored the C–C bond cleavage and promoted the formation of CH_x species and further CH_x converted to CH₄ combining with produced H₂ at low temperature and thus resulting in low H₂ yield. At high temperatures, CH_x species gets decomposed into C* and H* on active Co surface at high temperature [131]. Because of the synergistic effect use of Ni–W bimetallic catalyst shows high stability with the minimal CH₄ formation. Addition of W into Ni-based catalyst improves the coke resistivity of the catalyst, improving the stability of the catalyst during AASR reaction [158]. Use of small loading of noble metals, e.g., Rh, Ru, Ir, Pt comparatively exhibited more activity and less coke generation during AASR, but because of the higher cost issue, these

types of catalysts are difficult to commercialize. Assaf et al. observed that bimetallic Ni–Co/ γ -Al₂O₃ showed comparatively better performance at a lower temperature (500 °C) during acetic acid steam reforming in comparison to monometallic Ni/ γ -Al₂O₃. Presence of cobalt in the bimetallic catalyst inhibits coke formation over catalyst surface [38]. It is apparent that Co addition has a significant effect on suppression of coke formation. Xun et al. [130] proved that the addition of Co in Nickel catalyst exhibited the long-term stability up to 70 h. Huang et al. investigated steam reforming of acetic acid as a representative compound of bio-oil over Ni–Co bimetallic catalysts supported on MgO. They reported that bimetallic catalysts showed better resistance to coke deposition than monometallic. The characterization results of catalyst indicate that higher activity of catalyst ascribed to 1) high intrinsic activity of metal, 2) resistance to coke formation, and 3) stability of structures and electronics properties in AASR [48]. In the case of Bimetallic Ni–Cu catalyst, the formation of the alloy of these metals was observed and performance of this catalyst was reported to be better than a monometallic Ni-based catalyst, yielding less CH₄. Addition of Cu suppressed the coke formation and enhanced the stability of Ni-based catalyst during the steam reforming [159]. Both sole Ni and Cu based catalysts showed severe coke formation on the catalyst surface compared to Ni–Cu alloy-based catalyst [24].

Trimetallic catalyst

Hu et al. demonstrated that due to synergistic effect, trimetallic Cu, Zn, and Co had better resistivity towards coke formation in comparison to bi-metallic and monometallic catalysts. During AASR Cu species are active for removal of CO generated during reaction while Co shows activity for CH₄ and acetone reforming and Zn acts as a significant promoter to enhance the catalytic activity at low temperature [145].

Active metal sintering

In addition to coke deposition, sintering is another important cause for catalyst deactivation during steam reforming reaction [160]. The cause of sintering is the minimization of the surface energy, subsequent to the reduction of the surface area resulted into agglomeration of small particles size which lead to increase average particle size. Its effect is pronounced in case of supported nickel catalysts during steam reforming [161]. German also suggested sintering geometry and concluded that bond developed during sintering become apparent as the contact area between the particles increases [162]. Assaf et al. described above phenomenon over 15Ni/Al catalyst by high-resolution transmission electron microscopy, in which sintering of nickel particles was observed Fig. 13 [101]. Sintering of nickel catalysts during steam reforming has been investigated extensively in H₂O/H₂ model atmosphere [41,163–165], which is quite appropriate for steam reforming reaction. It has been observed in the reforming process that partial pressures of steam and hydrogen are exceedingly important and most likely control the rate of sintering [161]. Sehested et al. reported that Ni/Al₂O₃ catalysts

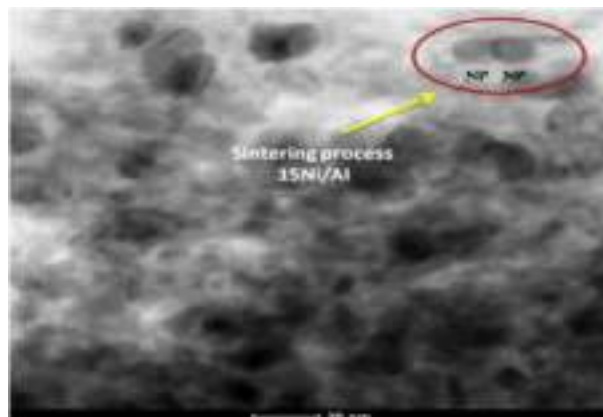


Fig. 13 – HRTEM image of 15 Ni/Al catalyst (sintering process). Reprinted with permission from Ref. [101].

typically sintered in a severe hydrothermal environment because of the large amount of loading of Ni and formation of NiAl₂O₄. While the addition of a small amount of magnesium and potassium resulted in formation of MgAl₂O₄ and K₂Al₂O₄, which suppressed the nickel segregation on the support surface and formation of NiAl₂O₄ and consequently prevented the sintering [166]. Qian et al. investigated a fresh and a spent catalyst by XRD analysis and concluded that after the AASR, crystallite sizes of the Ni^o estimated by Scherrer equation increased due to the sintering of nickel crystallites [152]. Addition of Mg [167], Ce [168] and La [169,170] were able to disperse the active metal efficiently and prevent the formation of less active NiAl₂O₄ and inhibit sintering also. A series of nickel core-shell catalysts with different shell species SiO₂, Al₂O₃, CeO₂, and TiO₂ were synthesized. All core-shell catalysts showed superior resistance towards Ni sintering at high reaction temperatures. Fig. 14 explains the schematic representations of the inhibition of nickel sintering in core-shell catalysts [68]. It was reported that the porous silica coated Ni/CeO₂–ZrO₂ catalyst exhibited an excellent resistance towards Ni sintering [126].

Support effect (doping with other metals)

Besides active metals, support materials also affect catalytic activity and coke formation during steam reforming reaction. As mentioned in the literature, supports take part in steam reforming reactions by dissociating H₂O into ions [42,171,172]. Goicoechea et al. investigated and reported that catalytic performance and stability are strongly dependent not only on the support surface but also on chemistry and strength of metal support interaction [32]. Al₂O₃ supported metal catalysts exhibited high selectivity towards hydrogen generation during steam reforming of acetic acid. On the other hand, the acidic property of Al₂O₃ also catalyzes dehydration reaction which subsequently leads to the deactivation of the catalyst due to coke formation. Basic supports such as MgO and ZnO are used to avoid dehydration reactions, but they also catalyze secondary reactions such as ketonization and oligomerization which deactivate catalyst due to coke formation [131]. Redox ability and basicity of the support materials are the major

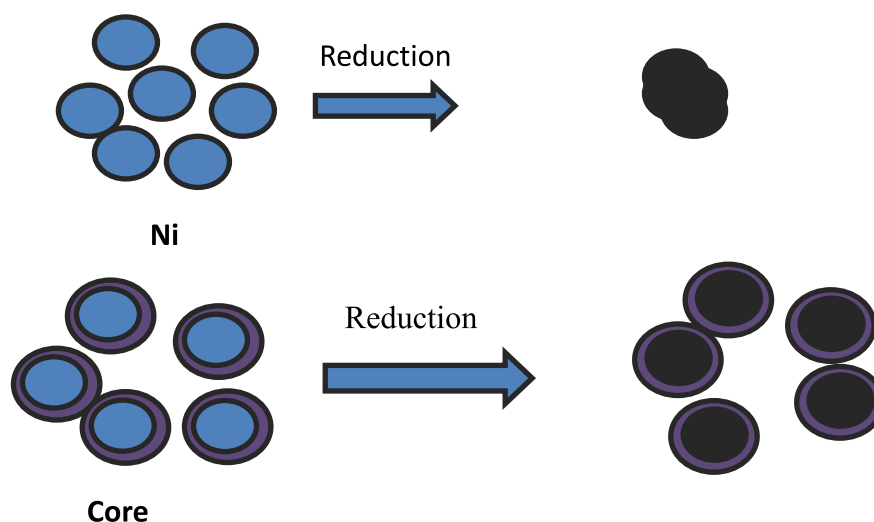


Fig. 14 – Schematic illustrations of the Ni sintering inhibition of the core-shell catalysts [68].

factors that influence the coke resistance during acetic acid steam reforming. Catalyst support composition also affects the coke resistivity of catalysts [173]. Wang et al. carried out steam reforming of acetic acid over Ni/nano- Al_2O_3 catalyst and observed that nano-size Al_2O_3 support exhibits excellent activity and stability (more than 10 h) in comparison to commercial $\gamma\text{-Al}_2\text{O}_3$ due to a high surface area which results in a better dispersion of active metals [127]. Development of silicate organized mesoporous materials, such as MCM-41 and SBA-15, have opened new opportunities in the area of catalysis synthesis. These materials, having ordered pore structures, are less vulnerable to carbon deposition as compared to traditional microporous catalyst supports. Also, they offer less diffusional resistance during the movement of reactants to the active sites [174–178]. However, in the presence of water vapor, some of the silicates organized mesoporous materials exhibit low hydrothermal stability [158].

Alumina

Among the different supports available, alumina is extensively used as a support in steam reforming reaction due to high surface area for active metal dispersion, and also it exhibits high chemical and thermal stability [32,152,171,179]. Water adsorption capability of support decides the steam reforming reaction pathway involved. It promotes product selectivity followed by coke gasification. Presence of acidic sites over catalyst surface results in adsorption of a higher number of CO species and the promotes the water gas shift reaction [180]. Chen et al. investigated the influence of the crystalline phase of Al_2O_3 over Ni-based catalyst during AASR and concluded that coke deposition was different on all four phases (α , β , γ , θ) of alumina. They inferred by the TGA analysis that Ni/ $\alpha\text{-Al}_2\text{O}_3$ showed better stability compared to other Ni/ $x\text{-Al}_2\text{O}_3$ catalysts ($x = \alpha, \beta, \gamma, \theta$) [92]. The presence of Lewis acid sites over alumina support causes catalysts deactivation due to coke formation over the catalyst surface. Verykios et al. compared carbon deposition behavior over Al_2O_3 support and concluded that Al_2O_3 being acidic favors decomposition and

subsequent polymerization reactions which resulted in the generation of a considerable amount of graphitic carbon deposition over support during the AASR, [33]. Addition of basic metal oxides (i.e., MgO , CeO_2 , and ZrO_2) in Al_2O_3 helps in lowering down the coke formation [181].

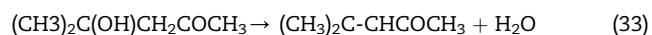
ZrO_2

ZrO_2 is an amphoteric oxide, where both acidic/basic sites co-exist. This property not only assists in the adsorption of steam and carbon oxides onto the catalyst surface but also promotes dissociation of water over the catalyst surface. This helps in improving H_2 yield and catalyst stability [149,182]. During reforming reactions, ZrO_2 (without any catalyst) decomposes acetic acid into acetone, carbon dioxide and methane as primary products with no hydrogen [58,149]. Consequently, the active phase particularly Pt and Ni were explored for high conversion and selectivity towards hydrogen from acetic acid. ZrO_2 was utilized as support by Takanabe and co-worker for the Pt-based catalyst during steam reforming reactions [58,59]. They reported severe deactivation of the catalyst due to blockage of the active site even in the presence of higher steam to carbon ratio via formation of coke/oligomers. The main drawback, when ZrO_2 was solely used as a support, is its low surface area and mechanical stability which make ZrO_2 unsuitable as support for AASR, [183]. Li et al. described that Ni (16 wt %) ZrO_2 catalyst can inhibit coke formation efficiently in comparison to other metallic catalysts over ZrO_2 support. Nickel particle size did not change with nickel loading up to 16 wt%. A further increase in Ni loading resulted in an increase in particle size which adversely affected the conversion of the catalyst [149]. Reports suggest that modification of Ni/ ZrO_2 catalyst with CeO_2 makes catalyst more resilient towards coke formation [184–186]. Ni/ $\text{CeO}_2\text{-ZrO}_2$ catalysts provide 83.4% of the maximum hydrogen selectivity and 0.39% of minimum methane selectivity at 650 °C, which is much better in comparison to commercial catalysts [187]. Observing pulse experiments with acetic acid over ZrO_2

support, Takanbe et al. have observed the formation of ketene (CH_3CO) and CH_4 in a small amount by the decomposition of acetone (Eq. (29)) and by dehydration of AcOH . Because of the presence of excess steam during steam reforming, decomposition reaction was the most favorable pathway for Ketene formation via AcOH [58].



Acetone formed on ZrO_2 can also further go aldol condensation reaction:



Ketene and mesityl oxide both can undergo oligomerization reaction to form carbon deposits, which block the catalytically active sites and in process deactivate the catalyst [58]. Porous silica coated $\text{Ni/CeO}_2\text{-ZrO}_2$ catalyst showed a significantly enhanced activity (93% AcOH conversion) than $\text{Ni/CeO}_2\text{-ZrO}_2$, the coated catalysts exhibit excellent stability, and no apparent deactivation was detected at 550 °C and 600 °C within 30 h [126].

CeO_2

It has been observed that the incorporation of CeO_2 increases the activity as well as the stability of the catalyst by increasing the active metal dispersion and oxidation of carbon deposited over the catalyst surface [188]. The redox properties of CeO_2 , due to the presence of oxygen vacancies on its surface or metal-ceria interface and high oxygen storage capabilities qualifies CeO_2 as active support during AASR [189,190]. The CeO_2 when used as catalyst support significantly promotes the elimination of coke deposition formed over catalyst surface owing to high oxygen storage capabilities and facile redox properties, but it is unstable at higher temperature [80,86]. Fig. 15 displays that a sufficient amount of oxygen vacancies are present on the surface of CeO_2 or the metal-ceria interfaces. Therefore, the water gas shift reaction gets promoted by the addition of CeO_2 [Eq. (2)] [191]. The main drawback of

the CeO_2 is its low surface area. One of the possible routes may be that it is incorporated with high surface area support like $\gamma\text{-Al}_2\text{O}_3$ [152]. It is well known that the incorporation of CeO_2 enhances catalyst activity by improving the Ni dispersion over catalyst surface [87] also that of noble metal catalyst [145]. Besides, the generation of CeAlO_3 species under reducing conditions at high temperatures, the reducing environment also favors elimination coke precursor and thus prevents coke deposition over catalyst surface [192,193]. Jianglong et al. have reported that the coke deposition is significantly reduced by the addition of ceria in case of bimetallic $\text{Ni-Ru/Al}_2\text{O}_3$ catalyst because of oxygen storage and the oxygen release property of ceria as explained by the following reaction-



where O_x represents the mobile lattice oxygen present over the CeO_2 surface.

The mobile oxygen present in the CeO_2 lattice can be transferred from the oxygen vacancies to the surface of the catalyst, and the oxygen is further transferred to the metallic surface and accelerates mitigation of coke precursor oxidation by following reactions:



where C_xH_y represents the coke species on the catalyst surface.

Therefore, coke generation is reduced by bringing down the growth of coke precursor [152]. CeO_2 also act as an oxygen buffer by reversible redox oxidation state ($\text{Ce}^{4+}/\text{Ce}^{3+}$) ability that can exchange oxygen efficiently [191,194]. The presence of Ce^{3+} ions over the CeO_2 surface affects coke generation over the catalyst surface due to the presence of mobile lattice oxygen [152]. Moreover, the existence of migrated oxygen over the metal surface improves coke precursor oxidation, which is represented by the reaction below [195].



Where $\text{C}_{(s)}$ is the coke species on the catalyst.

La_2O_3

Acetic acid steam reforming was carried out over $\text{Ni/La}_2\text{O}_3$, $\text{Co/La}_2\text{O}_3$, and $\text{Ni-Co/La}_2\text{O}_3$ catalyst by Walid et al.. They observed

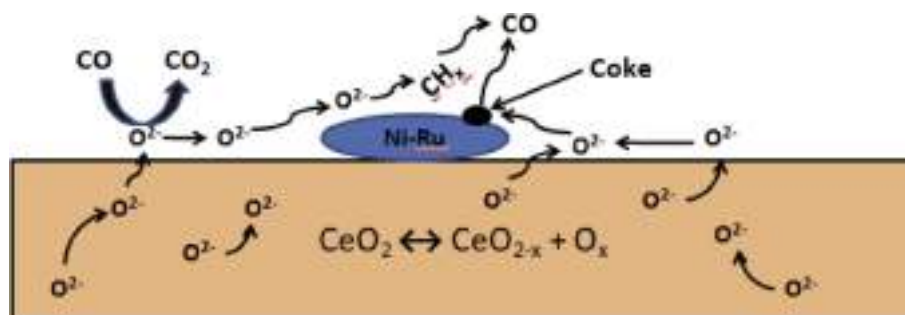


Fig. 15 – The oxidation of CO, coke and coke precursor via migrated oxygen vacancies in the lattice of CeO_2 during the steam reforming of acetic acid [152].

that at all the investigated temperature ranges lanthanum supported Ni catalyst exhibited excellent performance in terms of both high hydrogen yield and stability by reducing carbon deposition over the catalyst surface [129]. Generally, γ - Al_2O_3 is used as catalyst support in the different thermochemical process because of its low cost and excellent thermal stability as well as the high surface area. However, high acidic nature makes it susceptible to coke deposition on its surface and consequently catalyst activity and stability by deactivation of catalyst is lowered [80]. Hence, the addition of basic promoters e.g. alkali metal and alkaline earth metal has been proposed to neutralize the acidic sites of γ - Al_2O_3 [196,197]. One more approach is the incorporation of rare earth metals La_2O_3 , which extensively enhance the performance and prevent carbon formation over the metallic surface due to the basic characteristics and CO_2 absorption features in comparison to the γ - Al_2O_3 during AASR [31,198,199]. Lanthanum modified Ni/ZrO₂ catalyst was investigated by Guell et al. They reported that the addition of La_2O_3 not only enhanced the conversion and hydrogen yield but also increased catalyst stability during AASR [54]. La_2O_3 forms oxygen-containing species ($\text{La}_2\text{O}_2\text{CO}_3$) during the reaction and finally hindered the coke deposition over the catalyst surface. The excellent characteristic of prevention of coke deposition of La_2O_3 is due to the reactions given below Eqs. (37) and (38) [85].



Garbarino et al. reported that addition of La_2O_3 lowers the acidity of the support by associating with acidic sites present on the Al_2O_3 surface and thus enhancing the hydrogen selectivity and catalyst stability [198]. Reports suggest that the incorporation of La_2O_3 in nickel-based catalysts causes the interaction between Ni and La atoms which prevents the formation of NiAl_2O_4 [169]. Sanchez-Sanchez et al. experimented Ni/x% La_2O_3 - Al_2O_3 ($x = 3, 6, 15$) catalyst with a different La_2O_3 loading over γ - Al_2O_3 surface and reported that incorporation of lanthanum not only decreased the acidity but also increased the dispersion and stability of nickel metal by inhibiting the coke formation. It also influenced the interaction of support and Nickel metallic phase, with high interaction of Ni and La atoms resulting in the formation of nickel aluminates (NiAl_2O_4) [200]. On the other hand, Hernandez et al. have reported the opposite results. They showed that, following addition of La_2O_3 , increased the proportion of NiO species and weak interaction between support and metal phase [201]. Moreover, La_2O_3 is also known to prevent sintering of oxides and metal particles at severe reaction conditions [164]. Therefore, for preparation of the highly active and stable catalyst, the addition of La_2O_3 is widely used as an additive over γ - Al_2O_3 [60,118,137,169,198,200].

Mixed oxide

Various studies have been reported which aim at a better selectivity towards hydrogen generation and minimization of coke formation over catalyst surface [30,57,59,80,202,203]. Use

of mixed oxide supports such as CeO_2 - ZrO_2 and La_2O_3 / CeO_2 - ZrO_2 helps in lowering down the coke formation [26,57]. Lemonidou et al. investigated steam reforming of acetic acid over $\text{Rh}/\text{La}_2\text{O}_3/\text{CeO}_2$ - ZrO_2 and reported that coke formation was inhibited because of CeO_2 - ZrO_2 support which acted as a reducible support. The reducible property of CeO_2 - ZrO_2 support assists in removing the deposited coke over active sites efficiently in the form of CO and CO_2 .

Effect of alkali and alkaline earth metals

The coke formed covers the active catalytic sites and does not allow reactant molecules to reach to the sites responsible for steam reforming reaction [204,205]. Use of acidic supports (e.g., Al_2O_3) also promotes coke formation over active metal during steam reforming reaction. In order to neutralize acidic sites and enhance the performance of catalyst by inhibiting the coke formation over catalyst surface, the incorporation of basic alkali metals such as (Li, Na, K, and Cs) and alkaline earth metals (Ca, Mg and Sr) has been reported [29,30,66,100,206]. Furthermore, modification with alkaline earth oxides (CaO, MgO) is extensively used in reforming reactions to neutralize the acidic sites of γ - Al_2O_3 and enhance stability [196,197,207]. Moreover, adding alkali and alkaline earth metals favours adsorption of H_2O and OH^- mobility over catalyst surface significantly, which facilitate carbon oxidation and subsequently inhibit coke formation over catalysts surface [47,208,209]. Pant et al. reported that coke generation over the support ($\text{Ca}_{.12}/\text{Al}_{.7}$) surfaces was insignificant because of excess oxygen present in the $12\text{CaO} \cdot 7\text{Al}_2\text{O}_3$ phase [47]. Lu et al. reported that addition of K to cobalt supported catalyst significantly enhanced the hydrogen production via effectively diminishing the methane formation during AASR as well as high catalytic stability by resisting the coke formation [69]. Potassium also suppresses the CH_4 dehydrogenation and slow down the coke formation over nickel-supported catalyst [210]. Incorporation of CaO and MgO to support material not only results in diminishing the quantity of coke deposition but also changes the nature of coke [211,212]. The initial coke formation rate over the catalyst surface gets accelerated with the incorporated promoters (Mg and Ca) with the catalyst. After a long time on stream (TOS) reaction, the amount of the coke deposited over catalyst surface with promoter was less in comparison with the catalyst without promoter [213]. Basic oxides help in lowering down the coke deposition over catalyst surface. Alkaline earth support increases the concentration of basic sites and strengthens the adsorption of CO_2 on the catalyst. This adsorbed CO_2 reacts with carbon species, resulting in suppression of deposited carbon by the following reaction:



Where $\text{C}_{(A)}$ represent the amorphous carbon. ($\Delta G^\circ_{600^\circ\text{C}} = -4.4 \text{ kJ mol}^{-1}$) [214].

Passos et al. reported that among basic earth metals, the addition of Ca and Mg to Ni/ α - Al_2O_3 improved the overall activity and stability of the catalyst. However, Mg only was accounted for the reduction of Ni ensembles particles size due to the attachment of nickel particles with Mg. Mg obstructs

Table 3 – Conversion, selectivity of H₂, carbon deposition and stability analysis during AASR over different type of catalyst.

Catalyst (Active Metal)	Support	Steam/AcOH (S/C)	Temp (°C)	Conversion of AcOH (%)	Yield/Selectivity (%)	Carbon Deposition	Stability (h)	Space Velocity (h ⁻¹)	Ref.
12 Ni	CeO ₂ –ZrO ₂	3	700	100	~80	–	15	–	[108]
12 Ni	7.5CeO ₂ –ZrO ₂	3	650	100	83.4	–	25	2.8 (LHSV)	[187]
10Ni	7.8CeO ₂ –ZrO ₂	3	600	85	85	0.092mmoleC/h.g _{AcOH} (TOS 15 h)	15	0.45 (WHSV)	[126]
Silica-coated Ni	CeO ₂ –ZrO ₂ @P–SiO ₂	3	600	~95	~94	0.048mmoleC/h.g _{AcOH}	30	0.45 (WHSV)	[126]
15Ni	La ₂ O ₃ –ZrO ₂	3	600	~100	89.27	0.23 mmoleC/h.g _{AcOH}	20	0.789 (WHSV)	[226]
15Ni	5MgO–Al ₂ O ₃	2	600	96	69~	0.057mmoleC/h.g _{AcOH} (TOS 6 h)	24	1.14 (WHSV)	[101]
15Ni	10MgO–Al ₂ O ₃	2	600	93	~48	0.050mmoleC/h.g _{AcOH} (TOS 6 h)	60	1.14 (WHSV)	[101]
15Ni	1MgO–Al ₂ O ₃	2	600	97	~47	0.088050mmoleC/h.g _{AcOH} (TOS 6 h)	60	1.14 (WHSV)	[101]
17Ni	La ₂ O ₃ –Al ₂ O ₃	5.7	600	78	0.53moleH ₂ /moleAcOH	–	~2	53.33 (W/F _{A0})	[39]
17Ni	La ₂ O ₃ –Al ₂ O ₃	3	750	97	–	0.22 (TOS 4 h)	4	–	[30]
17 Ni	La ₂ O ₃ –Al ₂ O ₃	3	700	62	98	0.43 mmoleC/h.g _{AcOH} (TOS 2.10 h)	2.1 (TOS)	0.005 g s/cm ³	[33]
10Ni	La–3Al ₂ O ₃	2.5	700	100	83	–	20	10 (WHSV)	[227]
10Ni	Ca.2Al	3	750	100	~83	14.8% or 0.28 mmoleC/h.g _{AcOH} (TOS 3 h)	3	34500 (GHSV)	[128]
5Ni	Ca.2Al	3	750	100	~89	5.4% or 0.10 mmoleC/h.g _{AcOH} (TOS 3 h)	3	34500 (GHSV)	[128]
5Ni	12Ca.7Al	3	750	100	~31	9.4% or 0.18 mmoleC/h.g _{AcOH} (TOS 3 h)	3	34500 (GHSV)	[128]
3Ni	1Ce-Olivine	5	750	90.9	59.3	2.5% (TOS 2 h)	2	2987 (GHSV)	[217]
6Ni	1Ce-Olivine	5	750	91.5	59.5	0.5% (TOS 2 h)	2	2987 (GHSV)	[217]
3Ni	1Ce–1Mg/Olivine	5	750	97.3	60.9	7.7%	70	2987 (GHSV)	[217]
6Ni	1Ce–1Mg/Olivine	5	750	97.9	61.1	4.1%	70	2987 (GHSV)	[217]
6Ni	3Ce–1Mg/Olivine	5	750	99.7	61.5	0.2%	70	2987 (GHSV)	[217]
Co	La ₂ O ₃ –Al ₂ O ₃	1	400	100	93.8	5% C	20	10.1 (LHSV)	[228]
Co	La ₂ O ₃ –CeO ₂	1	400	87.4	86.3	6%	20	10.1 (LHSV)	[228]
15Ni	Al ₂ O ₃	2	600	93	~57	0.079 mmoleC/h.g _{AcOH} (TOS 6 h)	6	1.14 (WHSV)	[101]
15Ni	Nano-Al ₂ O ₃	9.2	700	~98	~85	–	13	3	[127]
16Ni	ZrO ₂	1	500	100	90	–	~6	10.1 (LHSV)	[149]
10Ni	Al ₂ O ₃	3	600	95	1.8moleH ₂ /moleAcOH	1.09 mmoleC/h.g _{AcOH} (TOS 6 h)	6	–	[38]
20Ni	Al ₂ O ₃	3	600	98	2.4moleH ₂ /moleAcOH	1.23 mmoleC/h.g _{AcOH} (TOS 6 h)	6	–	[38]
30Ni	Al ₂ O ₃	3	600	100	2.4moleH ₂ /moleAcOH	1.45 mmoleC/h.g _{AcOH} (TOS 6 h)	6	–	[38]
15Ni	La ₂ O ₃	2.5	700	100	80.9	–	20	10 (WHSV)	[31]
17Ni	Al ₂ O ₃	3	750	~80	~99	0.24% (TOS 4 h)	4	–	[30]
15Ni	γ-Al ₂ O ₃	2	600	~100	79	6.5% (TOS 1 h)	1	–	[92]
15Ni	θ-Al ₂ O ₃	2	600	~100	33	5% (TOS 1 h)	1	–	[92]
15Ni	δ-Al ₂ O ₃	2	600	~100	53	4.5% (TOS 1 h)	1	–	[92]

15Ni	α -Al ₂ O ₃	2	600	~100	90	1.7% (TOS 1 h)	1	–	[92]
25Ni	Al ₂ O ₃	3	550	~93	~84	0.041gC/gcat.h	24	20.6 (LHSV)	[140]
Ni	@Al ₂ O ₃ @core shell	3.18	750	98.8	~69	42.0% (TOS 10 h)	10	21 (WHSV)	[68]
Ni	@Al ₂ O ₃ -i i-improved	3.18	750	~100	~90	15.2% (TOS 10 h)	10	21 (WHSV)	[68]
Ni	@Al ₂ O ₃ -10Ce	3.18	650	97	~73	14.8% (TOS 10 h)	10	21 (WHSV)	[229]
5Ni	Mesoporous Al ₂ O ₃ (MA)	2.5	750	100	68	37.8% (TOS 3 h)	3	–	[24]
15Ni	Ash	9.2	700	98.4	85.6	–	11	4 (WHSV)	[230]
30Ni	Al ₂ O ₃	6	600	100	90	12% (TOS 20 h)	20	10.1 (LHSV)	[62]
3Ni	Olivine	5	750	57.2	54.8	5.8% (TOS 1 h)	1	2987 (GHSV)	[217]
6Ni	Olivine	5	750	59.2	54.0	5.4% (TOS 2 h)	2	2987 (GHSV)	[217]
5Ni	Zr-SBA-15	2.5	750	100	57.8	39% (TOS 3 h)	3	–	[158]
5Ni	SBA-15	2.5	750	100	70.3	8% C (TOS 3 h)	3	–	[158]
15Ni	MgO-m m-mesoporous	6	600	~100	3.1 mol H ₂ /mole AcOH	4% C	20	–	[218]
10Ni	Al ₂ O ₃	1.5	600	95–72	68–50	–	30	12.1 (LHSV)	[221]
5Ni	50W-Zr-SBA-15	2.5	750	93	45	10% C (TOS 3 h)	3	–	[158]
10Ni	K-Al ₂ O ₃	1.5	600	95–92	75–72	–	30	12.1 (LHSV)	[221]
5 Cu	(MA)	2.5	750	66	10	25.3% (TOS 3 h)	3	–	[24]
15 Co	ZnO	3.5	500	100	98	43.35% C or 1.0×10 ⁻² gC/g AcOH (TOS 3.8 h)	3.8	190000 (GHSV)	[121]
15Co	3CeO ₂	3.5	500	96	34	33.99% or 7.03×10 ⁻³ gC/gAcOH (TOS 1.6 h)	1.6	880000 (GHSV)	[121]
30Co	Al ₂ O ₃	1.2	400	~83.5	~83.5	~28%	30	15.1 (LHSV)	[69]
30Co	Mg-Al ₂ O ₃	1.2	400	~70	~71	~48%	30	15.1 (LHSV)	[69]
30Co	K-Al ₂ O ₃	1.2	400	~100	~92	~15%	30	15.1 (LHSV)	[69]
17Ni	Al ₂ O ₃ -La ₂ O ₃	3	750	97	100	0.24% (TOS 4 h)	100	45.67 (WHSV)	[30]
17 Ni	MgO-Al ₂ O ₃	3	750	100	100	0.22 (TOS 4 h)	45	45.67 (WHSV)	[30]
5Ni	CeO ₂ -ZrO ₂	3	750	100	92	1.5% or 0.029 molC/mol C in AcOH (TOS 3 h)	3	34500 (GHSV)	[26]
0.5 Pt	ZrO ₂	5	600	100	87.0	>15% C (TOS 3 h)	3	40000 (GHSV)	[59]
0.84 Pt	ZrO ₂	5	352	46.2	8.2	3.7 μmol/g.s (TOS 5 min pulse)	–	320000 (GHSV)	[42]
0.5Rh	La ₂ O ₃ -CeO ₂ -ZrO ₂	3	750	100	98	0.009% C (TOS 3 h)	3	34500 (GHSV)	[57]
0.5Rh	Ca.2Al ₂ O ₃	3	750	86.5	~69	1.6% or 0.03mmoleC/ mole AcOH (TOS 3 h)	3	34500 (GHSV)	[128]
0.5Rh	12Ca.7Al ₂ O ₃	3	700	100	~78	3.3% or 0.06mmoleC/ mole AcOH (TOS 3 h)	3	34500 (GHSV)	[128]
0.5Rh	CeO ₂ -ZrO ₂	3	750	100	90	1.71% or 0.007 molC/mol C in AcOH (TOS 15 h)	15	34500 (GHSV)	[26]
5Ru	Al ₂ O ₃	3	700	18	95	8.4% (TOS 2 h)	2	45.67 (WHSV)	[34]
5Ru	MgO-Al ₂ O ₃	3	750	100	99	0.11% (TOS 4 h)	30	45.67 (WHSV)	[30]
5Ru	CeO ₂ -Al ₂ O ₃	3	750	93	94	0.61% (TOS 4 h)	4	45.67 (WHSV)	[30]
5Ru	La ₂ O ₃ -Al ₂ O ₃	3	750	100	98	0.26% (TOS 4 h)	50	45.67 (WHSV)	[30]
0.5Rh	Al ₂ O ₃	3	750	~56	~91	0.39% (TOS 4 h)	4	45.67 (WHSV)	[30]
1 Pt	Al ₂ O ₃	3	750	~9	~12	0.37% (TOS 4 h)	4	45.67 (WHSV)	[30]
1Pd	Al ₂ O ₃	3	750	~13	~81	1.37% (TOS 4 h)	4	45.67 (WHSV)	[30]
1Ru	Al ₂ O ₃	3	750	~15	~81	0.43% (TOS 4 h)	4	45.67 (WHSV)	[30]
5Ru	Al ₂ O ₃	3	750	~35	~92	0.32% (TOS 4 h)	4	45.67 (WHSV)	[30]

(continued on next page)

Table 3 – (continued)

Catalyst (Active Metal)	Support	Steam/AcOH (S/C)	Temp (°C)	Conversion of AcOH (%)	Yield/Selectivity (%)	Carbon Deposition	Stability (h)	Space Velocity (h^{-1})	Ref.
5Pd	HZSM-5	9.2	600	95.7	60	–	–	345 (GHSV)	[146]
5Ni–5Co	La ₂ O ₃	–	550	89.2	0.59 mol %	9.6% (TOS 6 h)	6	0.1134 (WHSV)	[129]
Ni0.2-C00.8	6MgO	8	600	~100	3.1moleH ₂ /mole AcOH	7.1% (TOS 20)	20	–	[48]
5 Cu-28 Ni	Al ₂ O ₃ –MgO	5.6	650	94.3	3.0 moleH ₂ /mole AcOH	–	10	1.0gcat.min/g.AcOH	[231]
15Ni–60Co	La ₂ O ₃ –Al ₂ O ₃	5.7	600	92	1.05 moleH ₂ /mole AcOH	–	~2	53.33gcat.h/mole	[39]
20Ni–80Co	–	5.7	600	96	2.6 moleH ₂ /mole AcOH	–	4	53.33gcat.h/mole	[39]
Cu–Zn–Co (Cu/Zn/Co = 1:1:1)	–	7.5	500	100	90	3.5% (TOS 100 h)	100	5.1 (WHSV)	[145]
15Ni–2Ru	10CeO ₂ –Al ₂ O ₃	3.18	750	~100	~74.6	–	~2	21 (WHSV)	[152]
20Ni–10Co	Al ₂ O ₃	3	600	100	1.4 moleH ₂ /mole AcOH	1.83mmoleC/h (TOS 6 h)	6	–	[38]
25Ni–5Co	Al ₂ O ₃	3	600	100	2.1 moleH ₂ /mole AcOH	1.83mmoleC/h (TOS 6 h)	6	–	[38]
10Ni-9.9Fe	ZDA	9.2	700	100	90	–	11	4 (WHSV)	[29]
5.5Ni-2.5Co	MgAl ₂ O ₄	4	500	~100	~62	8.2mgC/gcat.h (TOS 6 h)	6	–	[131]
4Co–4Ni	MgAl ₂ O ₄	4	500	~100	~63	8.9mgC/gcat.h (TOS 6 h)	6	–	[131]
2.5Cu-2.5Ni	Mesoporous alumina (MA)	2.5	750	100	67	33.1 (TOS 3 h)	3	–	[24]
Ni–Fe (Ni/Fe = 1:1)	PG	3	600	80	52	12.5mgC/gcat.h (TOS 4 h)	4	14427 (GHSV)	[232]
Ni–Fe (Ni/Fe = 1:1)	Ce _{0.4} -PG	3	600	95	87	9.6mgC/gcat.h (TOS 4 h)	4	14427 (GHSV)	[232]
8Ni	MgAl ₂ O ₄	4	500	~100	~63	22.7mgC/gcat.h (TOS 6 h)	6	–	[131]
8Co	MgAl ₂ O ₄	4	500	~100	~62	5.4mgC/gcat.h (TOS 6 h)	6	–	[131]
0.4Ni	Mg–Al	3	600	70	1.89 moleH ₂ /mole AcOH	3.51% (TOS 12 h)	12	–	[233]
0.5Ni	Mg–Al (hydrotalcite precursor)	3	600	70	1.81 moleH ₂ /mole AcOH	4.07% (TOS 12 h)	12	–	[233]
0.51Rh	MgAlO (Mg70)	6	700	~100	~65–70	3.4mgC/gcat.h (TOS 20 h)	20	6 (WHSV)	[44]
0.37Rh	M(TOA)/Mg70 (SCMNPs method)	6	700	100	~65–70	1.9mgC/gcat.h (TOS 20 h)	20	6 (WHSV)	[44]
0.59Ru	(Mg70)	6	700	60	40	4.9mgC/gcat.h (TOS 20 h)	20	6 (WHSV)	[44]
0.38Ru	M(TOA)/Mg70 (SCMNPs method)	6	700	100	70	2.0mgC/gcat.h (TOS 20 h)	20	6 (WHSV)	[44]
Perovskite La _{0.9} Ce _{0.1} NiO ₃	Perovskite	3	750	95	90	11.8% (TOS 30 h)	30	2.1 (WHSV)	[234]

graphene nucleation pathway and, in the process, helped in less reactive coke formation. While addition of Ca, showed advance characteristics and have been recommended because of its capacity to gasify adsorbed carbon species [211,215]. It was observed that the integration of MgO to Ru/Al₂O₃ exhibits beneficial effect towards coke deposition, which was attributed due to the formation of magnesium aluminate spinel structure, which enhances O and –OH anion overflow from the carrier onto the Ru particles and hence improves the carbon gasification rate and thus increasing the catalyst life [78,143]. Incorporation of MgO as an additive in Ni/Al₂O₃ catalyst, resulted in improved catalytic performance for both H₂ yield and carbon conversion [216]. Xu et al. have reported that the addition of MgO in Ni–CeO₂/olivine promoted the steam adsorption capability and improved the activity and lowered down the coke deposition [217]. Yang et al. investigated acetic acid steam reforming over Ni/MgO-m (mesoporous MgO) and observed that MgO as support showed the highest catalytic activity and stability [218]. Ni–Co bi-metallic MgO based catalyst was tested in AASR for hydrogen production. Ni_{0.2}Co_{0.8}Mg₅O_{7±δ} catalyst showed high resistance towards coke formation [48]. NiO forms a solid solution into the MgO matrix and helps in inhibiting the growth of Ni particles over the surface of Ni-based catalysts [218]. Addition of promoters may also prevent the coke formation on Ni-based catalysts. During steam reforming of methane, incorporation of alkali and alkaline earth metals, K, Na, Ca and Mg, to the support improved catalytic activity and stability of Ni catalysts [219,220]. Recently, Medrano et al. [202] investigated that addition of Mg to Ni/Al catalysts enhanced the catalytic activity and stability during AASR. Mg incorporation in Ni/Al catalyst with a Mg/Ni molar proportion of 0.26 gave an excellent performance during steam reforming without deactivation. Hu et al. [221] reported the effect of the addition of alkali metals like Li, Na, K, and Mg in Ni/Al₂O₃ catalysts during AASR. They observed that alkali metals modified catalysts restrained the formation of methane, especially with Ni–K/Al₂O₃ catalyst.

Moreover, the presence of K also enhances the stability of the Ni catalyst through inhibition of carbon formation. Many researchers have reported different promoters for the steam reforming process [137,143,211,222]. Among them, calcium has been utilized as a promoter for nickel supported alumina catalysts for dry reforming of CH₄ [210,223,224] and some researchers explained its utilization in steam reforming reaction, enhancing the stability of nickel phases in hydrocarbon cracking processes [128,211]. Mg modified nickel-alumina catalysts enhances the catalyst strength and improve the adsorption of steam; improving carbonaceous species gasification and also stabilizes active nickel sites because of preventing their sintering [143,225]. Hence, both (Mg and Ca) enhance the stability of the catalyst by reducing its acidity and also lower down the cracking and polymerization reactions [211].

Table 3 presents the comparative study of conversion, H₂ selectivity, amount of carbon deposition and stability analysis during AASR reported by previous researchers over different types of catalysts and supports. The table demonstrates the correlation among different kind of active metals (noble and the non-noble), the interaction of bimetallic catalysts,

supports, modified and mixed oxide supports regarding conversion H₂ yield, stability and the amount of coke deposition during AASR. The amount of coke deposition over different temperatures and with different time on streams have also been compared during the reaction. The steam to carbon feed ratio was also taken arbitrarily or to the requisite stoichiometric basis by various researchers. Therefore, a significant part of catalyst deactivation is dependent on different operating parameters. Overall, among noble metal Rh showed minimum coke deposition. Ni and Co or their bimetallic interactions with mixed oxide or spinel structure catalyst have indicated significant abilities to minimize the carbon deposition during AASR. Individual synthesized support like size controlled metal nanoparticles and silica-coated catalyst have also shown lower coke deposition even in long-term duration TOS.

Conclusions

Prevention of the coke deposition over the catalyst surface during acetic acid steam reforming is a big challenge for the AASR process. Encapsulation of catalyst surface with the coke results in severe catalyst deactivation. There are different techniques practiced by industries in order to control the coke formation among which coke gasification to convert into CO and CO₂ is the most practiced one. Present review summarizes a broad analysis for the reduction of carbon formation using suitable catalysts and supports, types of reactors etc., to increase catalyst life. Reduction in the rate of carbon formation during reforming reaction is also a technique to improve the catalyst life but not a permanent solution. Modification of active metal and support or both is the best approach to prevent carbon formation. Present review also discusses the potential reaction pathways, mechanism of carbonaceous deposition over catalyst surface and different intermediate reactions involved during AASR. Which are the major deactivation routes during the AASR process. Different types of active metal facilitate a defined reactions pathway, which may or may not produce carbonaceous species. There are significant advantages to study hydrogen generation from acetic acid, and so far, a number of catalysts have been formulated for AASR. Among available catalysts, Rh and Pt-based catalysts were reported to exhibit excellent catalytic activity, long-term stability and lower coke formation. However, their high cost prevents the utilization of noble metals in an industrial scale. Among different transition metals, nickel-based catalysts are cheaper and exhibit high performance towards hydrogen generation. However, deactivation due to coke formation over the nickel-based catalyst is the major issue. Traditionally, oxide support such as Al₂O₃, CaO and MgO are used for steam reforming reaction, but all supports suffer severe coke deactivation problem. Therefore, for longer stability CeO₂, ZrO₂ are identified as oxide supports because of their high redox property and basic character on the catalyst surface. Rare earth metal oxide La₂O₃ also exhibits excellent coke resistance nature by forming La₂O₂CO₃. Utilization of mixed oxide support and the addition of alkali and alkaline earth metals such as Mg and K over Ni/Al₂O₃ catalyst promotes oxygen mobility and easy coke gasification by

increasing the reaction between steam and coke deposited over the catalyst surface and in the process reduces the carbon polymerization. Hence, nickel-based catalysts supported over $ZrO_2/CeO_2/LaO_2$ kind of oxide support might be a promising catalyst. Incorporation of small amounts of oxygen during reforming reaction also helps to minimize the coking by gasifying the carbon deposited over the catalyst surface. Combination of proper reactor design along with suitable catalyst formulation also plays a significant role in minimization of carbon formation. Fluidized bed reactor and dual bed system in series during AASR showed lesser coke deposition compared to fixed bed reactor.

However, not only coke deposition but catalyst sintering is also a primary objective to minimize catalyst deactivation. So, with all the useful information in the literature, it is still a challenge to design and develop an active, stable and high hydrogen-selective catalyst for AASR.

Acknowledgments

The authors are grateful to the Institute to provide financial support (T.A.) for this work to Mr. Ankit Kumar.

REFERENCES

- [1] Singh R, Kunzru D, Sivakumar S. Monodispersed ultrasmall NiMo metal oxide nanoclusters as hydrodesulfurization catalyst. *Appl Catal, B* 2016;185:163–73.
- [2] Singh R, Kunzru D. Hydrodesulfurization of dibenzothiophene on NiMo/ γ - Al_2O_3 washcoated monoliths. *Fuel* 2016;163:180–8.
- [3] Singh R, Kunzru D, Sivakumar S. Co-promoted MoO_3 nanoclusters for hydrodesulfurization. *Catal Sci Technol* 2016;6:5949–60.
- [4] Nabgan W, Abdullah TAT, Mat R, Nabgan B, Gambo Y, Ibrahim M, et al. Renewable hydrogen production from bio-oil derivative via catalytic steam reforming: an overview. *Renew Sustain Energy Rev* 2017;79:347–57.
- [5] Nabgan W, Abdullah TAT, Mat R, Nabgan B, Gambo Y, Moghadamian K. Acetic acid-phenol steam reforming for hydrogen production: effect of different composition of $La_2O_3-Al_2O_3$ support for bimetallic Ni-Co catalyst. *J Environ Chem Eng* 2016;4:2765–73.
- [6] Hou T, Yuan L, Ye T, Gong L, Tu J, Yamamoto M, et al. Hydrogen production by low-temperature reforming of organic compounds in bio-oil over a CNT-promoting Ni catalyst. *Int J Hydrogen Energy* 2009;34:9095–107.
- [7] Kirillov V, Meshcheryakov V, Sobyenin V, Belyaev V, Amosov YI, Kuzin N, et al. Bioethanol as a promising fuel for fuel cell power plants. *Theor Found Chem Eng* 2008;42:1–11.
- [8] Momirlan M, Veziroglu TN. The properties of hydrogen as fuel tomorrow in sustainable energy system for a cleaner planet. *Int J Hydrogen Energy* 2005;30:795–802.
- [9] Haryanto A, Fernando S, Murali N, Adhikari S. Current status of hydrogen production techniques by steam reforming of ethanol: a review. *Energy Fuels* 2005;19:2098–106.
- [10] de Bruijn F. The current status of fuel cell technology for mobile and stationary applications. *Green Chem* 2005;7:132–50.
- [11] Thanomjit C, Patcharavorachot Y, Ponpesh P, Arpornwichanop A. Thermodynamic analysis of solid oxide fuel cell system using different ethanol reforming processes. *Int J Hydrogen Energy* 2015;40:6950–8.
- [12] Dodds PE, Staffell I, Hawkes AD, Li F, Grünewald P, McDowall W, et al. Hydrogen and fuel cell technologies for heating: a review. *Int J Hydrogen Energy* 2015;40:2065–83.
- [13] Barbora L, Acharya S, Singh R, Scott K, Verma A. A novel composite Nafion membrane for direct alcohol fuel cells. *J Membr Sci* 2009;326:721–6.
- [14] Barbora L, Singh R, Shrotri N, Verma A. Synthesis and characterization of neodymium oxide modified nafion membrane for direct alcohol fuel cells. *Mater Chem Phys* 2010;122:211–6.
- [15] Winter C-J. Hydrogen energy—abundant, efficient, clean: a debate over the energy-system-of-change. *Int J Hydrogen Energy* 2009;34:S1–52.
- [16] Huber GW, Iborra S, Corma A. Synthesis of transportation fuels from biomass: chemistry, catalysts, and engineering. *Chem Rev* 2006;106:4044–98.
- [17] Shen D, Jin W, Hu J, Xiao R, Luo K. An overview on fast pyrolysis of the main constituents in lignocellulosic biomass to valued-added chemicals: structures, pathways and interactions. *Renew Sustain Energy Rev* 2015;51:761–74.
- [18] Chattanathan SA, Adhikari S, Abdoulmoumine N. A review on current status of hydrogen production from bio-oil. *Renew Sustain Energy Rev* 2012;16:2366–72.
- [19] Kumar A, Chakraborty J, Singh R. Bio-oil: the future of hydrogen generation. *Biofuels* 2017;8:663–74.
- [20] Bridgwater A, Cottam M. Opportunities for biomass pyrolysis liquids production and upgrading. *Energy Fuels* 1992;6:113–20.
- [21] Stas M, Kubicka D, Chudoba J, Pospisil M. Overview of analytical methods used for chemical characterization of pyrolysis bio-oil. *Energy Fuels* 2014;28:385–402.
- [22] Quitete CP, Tavares RP, Bittencourt RCP, Souza MM. Coking study of nickel catalysts using model compounds. *Catal Lett* 2016;146:1435–44.
- [23] Demirbaş A. Partly chemical analysis of liquid fraction of flash pyrolysis products from biomass in the presence of sodium carbonate. *Energy Convers Manag* 2002;43:1801–9.
- [24] Karaman BP, Cakiryilmaz N, Arbag H, Oktar N, Dogu G, Dogu T. Performance comparison of mesoporous alumina supported Cu & Ni based catalysts in acetic acid reforming. *Int J Hydrogen Energy* 2017;42:26257–69.
- [25] Hoang T, Geerdink B, Sturm J, Lefferts L, Seshan K. Steam reforming of acetic acid—A major component in the volatiles formed during gasification of humin. *Appl Catal, B* 2015;163:74–82.
- [26] Vagia EC, Lemonidou AA. Investigations on the properties of ceria–zirconia-supported Ni and Rh catalysts and their performance in acetic acid steam reforming. *J Catal* 2010;269:388–96.
- [27] Hu X, Lu G. Comparative study of alumina-supported transition metal catalysts for hydrogen generation by steam reforming of acetic acid. *Appl Catal, B* 2010;99:289–97.
- [28] Lemonidou A, Kechagiopoulos P, Heracleous E, Voutetakis S. Steam reforming of bio-oils to hydrogen. The role of catalysis for the sustainable production of bio-fuels and bio-chemicals. Elsevier; 2013. p. 467–93.
- [29] Wang S, Zhang F, Cai Q, Zhu L, Luo Z. Steam reforming of acetic acid over coal ash supported Fe and Ni catalysts. *Int J Hydrogen Energy* 2015;40:11406–13.
- [30] Basagiannis A, Verykios X. Catalytic steam reforming of acetic acid for hydrogen production. *Int J Hydrogen Energy* 2007;32:3343–55.

- [31] Zhang F, Wang M, Zhu L, Wang S, Zhou J, Luo Z. A comparative research on the catalytic activity of La_2O_3 and $\gamma\text{-Al}_2\text{O}_3$ supported catalysts for acetic acid steam reforming. *Int J Hydrogen Energy* 2017;42:3667–75.
- [32] Goicoechea S, Kraveva E, Sokolov S, Schneider M, Pohl M-M, Kockmann N, et al. Support effect on structure and performance of Co and Ni catalysts for steam reforming of acetic acid. *Appl Catal, A* 2016;514:182–91.
- [33] Basagiannis A, Verykios X. Reforming reactions of acetic acid on nickel catalysts over a wide temperature range. *Appl Catal, A* 2006;308:182–93.
- [34] Basagiannis AC, Verykios XE. Influence of the carrier on steam reforming of acetic acid over Ru-based catalysts. *Appl Catal, B* 2008;82:77–88.
- [35] Kirtay E. Recent advances in production of hydrogen from biomass. *Energy Convers Manag* 2011;52:1778–89.
- [36] Iwasa N, Yamane T, Takei M, Ozaki J-i, Arai M. Hydrogen production by steam reforming of acetic acid: comparison of conventional supported metal catalysts and metal-incorporated mesoporous smectite-like catalysts. *Int J Hydrogen Energy* 2010;35:110–7.
- [37] Trane R, Dahl S, Skjøth-Rasmussen M, Jensen A. Catalytic steam reforming of bio-oil. *Int J Hydrogen Energy* 2012;37:6447–72.
- [38] Assaf PG, Nogueira FGE, Assaf EM. Ni and Co catalysts supported on alumina applied to steam reforming of acetic acid: representative compound for the aqueous phase of bio-oil derived from biomass. *Catal Today* 2013;213:2–8.
- [39] Pant KK, Mohanty P, Agarwal S, Dalai AK. Steam reforming of acetic acid for hydrogen production over bifunctional Ni–Co catalysts. *Catal Today* 2013;207:36–43.
- [40] Wang D, Montane D, Chornet E. Catalytic steam reforming of biomass-derived oxygenates: acetic acid and hydroxyacetaldehyde. *Appl Catal, A* 1996;143:245–70.
- [41] Sehested J. Sintering of nickel steam-reforming catalysts. *J Catal* 2003;217:417–26.
- [42] Takanabe K, Aika K-i, Inazu K, Baba T, Seshan K, Lefferts L. Steam reforming of acetic acid as a biomass derived oxygenate: bifunctional pathway for hydrogen formation over Pt/ZrO₂ catalysts. *J Catal* 2006;243:263–9.
- [43] Basile A, Gallucci F, Iulianelli A, Borgognoni F, Tosti S. Acetic acid steam reforming in a Pd–Ag membrane reactor: the effect of the catalytic bed pattern. *J Membr Sci* 2008;311:46–52.
- [44] Bossola F, Evangelisti C, Allieta M, Psaro R, Recchia S, Dal Santo V. Well-formed, size-controlled ruthenium nanoparticles active and stable for acetic acid steam reforming. *Appl Catal, B* 2016;181:599–611.
- [45] Gil MV, Feroso J, Pevida C, Chen D, Rubiera F. Production of fuel-cell grade H₂ by sorption enhanced steam reforming of acetic acid as a model compound of biomass-derived bio-oil. *Appl Catal, B* 2016;184:64–76.
- [46] Rioche C, Kulkarni S, Meunier FC, Breen JP, Burch R. Steam reforming of model compounds and fast pyrolysis bio-oil on supported noble metal catalysts. *Appl Catal, B* 2005;61:130–9.
- [47] Mohanty P, Patel M, Pant KK. Hydrogen production from steam reforming of acetic acid over Cu–Zn supported calcium aluminate. *Bioresour Technol* 2012;123:558–65.
- [48] Zhang F, Wang N, Yang L, Li M, Huang L. Ni–Co bimetallic MgO-based catalysts for hydrogen production via steam reforming of acetic acid from bio-oil. *Int J Hydrogen Energy* 2014;39:18688–94.
- [49] Koike M, Li D, Watanabe H, Nakagawa Y, Tomishige K. Comparative study on steam reforming of model aromatic compounds of biomass tar over Ni and Ni–Fe alloy nanoparticles. *Appl Catal, A* 2015;506:151–62.
- [50] Lytkina AA, Zhilyaeva NA, Ermilova MM, Orekhova NV, Yaroslavtsev AB. Influence of the support structure and composition of Ni–Cu-based catalysts on hydrogen production by methanol steam reforming. *Int J Hydrogen Energy* 2015;40:9677–84.
- [51] Ma Z, Xiao R, Zhang H. Catalytic steam reforming of bio-oil model compounds for hydrogen-rich gas production using bio-char as catalyst. *Int J Hydrogen Energy* 2017;42:3579–85.
- [52] Yue Y, Liu F, Zhao L, Zhang L, Liu Y. Loading oxide nano sheet supported Ni–Co alloy nanoparticles on the macroporous walls of monolithic alumina and their catalytic performance for ethanol steam reforming. *Int J Hydrogen Energy* 2015;40:7052–63.
- [53] Song H, Ozkan US. Changing the oxygen mobility in Co/Ceria catalysts by Ca incorporation: implications for ethanol steam reforming. *J Phys Chem A* 2009;114:3796–801.
- [54] Güell BM, da Silva IT, Seshan K, Lefferts L. Sustainable route to hydrogen—Design of stable catalysts for the steam gasification of biomass related oxygenates. *Appl Catal, B* 2009;88:59–65.
- [55] Güell BM, Babich I, Nichols K, Gardeniers J, Lefferts L, Seshan K. Design of a stable steam reforming catalyst—a promising route to sustainable hydrogen from biomass oxygenates. *Appl Catal, B* 2009;90:38–44.
- [56] Grace JR, Li X, Lim CJ. Equilibrium modelling of catalytic steam reforming of methane in membrane reactors with oxygen addition. *Catal Today* 2001;64:141–9.
- [57] Lemonidou AA, Vagia EC, Lercher JA. Acetic acid reforming over Rh supported on La₂O₃/CeO₂–ZrO₂: catalytic performance and reaction pathway analysis. *ACS Catal* 2013;3:1919–28.
- [58] Takanabe K, Aika K-i, Seshan K, Lefferts L. Sustainable hydrogen from bio-oil—steam reforming of acetic acid as a model oxygenate. *J Catal* 2004;227:101–8.
- [59] Takanabe K, Aika K-i, Seshan K, Lefferts L. Catalyst deactivation during steam reforming of acetic acid over Pt/ZrO₂. *Chem Eng J* 2006;120:133–7.
- [60] Valle B, Aramburu B, Remiro A, Bilbao J, Gayubo AG. Effect of calcination/reduction conditions of Ni/La₂O₃– α -Al₂O₃ catalyst on its activity and stability for hydrogen production by steam reforming of raw bio-oil/ethanol. *Appl Catal, B* 2014;147:402–10.
- [61] Djaidja A, Libs S, Kiennemann A, Barama A. Characterization and activity in dry reforming of methane on NiMg/Al and Ni/MgO catalysts. *Catal Today* 2006;113:194–200.
- [62] Hu X, Lu G. Investigation of the steam reforming of a series of model compounds derived from bio-oil for hydrogen production. *Appl Catal, B* 2009;88:376–85.
- [63] Rossetti I, Biffi C, Bianchi CL, Nichele V, Signoretto M, Menegazzo F, et al. Ni/SiO₂ and Ni/ZrO₂ catalysts for the steam reforming of ethanol. *Appl Catal, B* 2012;117–118:384–96.
- [64] Shaikjee A, Coville NJ. The role of the hydrocarbon source on the growth of carbon materials. *Carbon* 2012;50:3376–98.
- [65] Kechagiopoulos PN, Voutetakis SS, Lemonidou AA, Vasalos IA. Sustainable hydrogen production via reforming of ethylene glycol using a novel spouted bed reactor. *Catal Today* 2007;127:246–55.
- [66] Chen G, Tao J, Liu C, Yan B, Li W, Li X. Hydrogen production via acetic acid steam reforming: a critical review on catalysts. *Renew Sustain Energy Rev* 2017;79:1091–8.
- [67] Zhang L, Hu X, Hu K, Hu C, Zhang Z, Liu Q, et al. Progress in the reforming of bio-oil derived carboxylic acids for hydrogen generation. *J Power Sources* 2018;403:137–56.
- [68] Pu J, Nishikado K, Wang N, Nguyen TT, Maki T, Qian EW. Core-shell nickel catalysts for the steam reforming of acetic acid. *Appl Catal, B* 2018;224:69–79.

- [69] Hu X, Dong D, Shao X, Zhang L, Lu G. Steam reforming of acetic acid over cobalt catalysts: effects of Zr, Mg and K addition. *Int J Hydrogen Energy* 2017;42:4793–803.
- [70] Zhang Q, Chang J, Wang T, Xu Y. Review of biomass pyrolysis oil properties and upgrading research. *Energy Convers Manag* 2007;48:87–92.
- [71] Aasberg-Petersen K, Hansen J-HB, Christensen T, Dybkjaer I, Christensen PS, Nielsen CS, et al. Technologies for large-scale gas conversion. *Appl Catal, A* 2001;221:379–87.
- [72] Goicoechea S, Ehrich H, Arias PL, Kockmann N. Thermodynamic analysis of acetic acid steam reforming for hydrogen production. *J Power Sources* 2015;279:312–22.
- [73] Mackie J, Doolan K. High-temperature kinetics of thermal decomposition of acetic acid and its products. *Int J Chem Kinet* 1984;16:525–41.
- [74] Suleman F, Dincer I, Agelin-Chaab M. Comparative impact assessment study of various hydrogen production methods in terms of emissions. *Int J Hydrogen Energy* 2016;41:8364–75.
- [75] Czekaj I, Loviat F, Raimondi F, Wambach J, Biollaz S, Wokaun A. Characterization of surface processes at the Ni-based catalyst during the methanation of biomass-derived synthesis gas: X-ray photoelectron spectroscopy (XPS). *Appl Catal, A* 2007;329:68–78.
- [76] Hu C-W, Yao J, Yang H-Q, Chen Y, Tian A-M. On the inhomogeneity of low nickel loading methanation catalyst. *J Catal* 1997;166:1–7.
- [77] Hou T, Zhang S, Chen Y, Wang D, Cai W. Hydrogen production from ethanol reforming: catalysts and reaction mechanism. *Renew Sustain Energy Rev* 2015;44:132–48.
- [78] Trane-Restrup R, Jensen AD. Steam reforming of cyclic model compounds of bio-oil over Ni-based catalysts: product distribution and carbon formation. *Appl Catal, B* 2015;165:117–27.
- [79] Sá S, Silva H, Brandão L, Sousa JM, Mendes A. Catalysts for methanol steam reforming—a review. *Appl Catal, B* 2010;99:43–57.
- [80] An L, Dong C, Yang Y, Zhang J, He L. The influence of Ni loading on coke formation in steam reforming of acetic acid. *Renew Energy* 2011;36:930–5.
- [81] Li X, Wang S, Zhu Y, Yang G, Zheng P. DFT study of bio-oil decomposition mechanism on a Co stepped surface: acetic acid as a model compound. *Int J Hydrogen Energy* 2015;40:330–9.
- [82] Wang S, Li X, Guo L, Luo Z. Experimental research on acetic acid steam reforming over Co–Fe catalysts and subsequent density functional theory studies. *Int J Hydrogen Energy* 2012;37:11122–31.
- [83] Ran Y-X, Du Z-Y, Guo Y-P, Feng J, Li W-Y. Density functional theory study of acetic acid steam reforming on Ni (111). *Appl Surf Sci* 2017;400:97–109.
- [84] Wang S, Li X, Zhang F, Cai Q, Wang Y, Luo Z. Bio-oil catalytic reforming without steam addition: application to hydrogen production and studies on its mechanism. *Int J Hydrogen Energy* 2013;38:16038–47.
- [85] Li Z, Hu X, Zhang L, Lu G. Renewable hydrogen production by a mild-temperature steam reforming of the model compound acetic acid derived from bio-oil. *J Mol Catal A Chem* 2012;355:123–33.
- [86] Parizotto N, Rocha K, Damyanova S, Passos F, Zanchet D, Marques C, et al. Alumina-supported Ni catalysts modified with silver for the steam reforming of methane: effect of Ag on the control of coke formation. *Appl Catal, A* 2007;330:12–22.
- [87] Koo KY, Lee S-h, Jung UH, Roh H-S, Yoon WL. Syngas production via combined steam and carbon dioxide reforming of methane over Ni–Ce/MgAl₂O₄ catalysts with enhanced coke resistance. *Fuel Process Technol* 2014;119:151–7.
- [88] Alenazey F, Cooper C, Dave C, Elnashaie S, Susu A, Adesina A. Coke removal from deactivated Co–Ni steam reforming catalyst using different gasifying agents: an analysis of the gas–solid reaction kinetics. *Catal Commun* 2009;10:406–11.
- [89] Latorre N, Romeo E, Cazana F, Ubieto T, Royo C, Villacampa J, et al. Carbon nanotube growth by catalytic chemical vapor deposition: a phenomenological kinetic model. *J Phys Chem C* 2010;114:4773–82.
- [90] Latorre N, Romeo E, Villacampa J, Cazaña F, Royo C, Monzón A. Kinetics of carbon nanotubes growth on a Ni–Mg–Al catalyst by CCVD of methane: influence of catalyst deactivation. *Catal Today* 2010;154:217–23.
- [91] Latorre N, Cazana F, Martínez-Hansen V, Royo C, Romeo E, Monzón A. Ni–Co–Mg–Al catalysts for hydrogen and carbonaceous nanomaterials production by CCVD of methane. *Catal Today* 2011;172:143–51.
- [92] Chen G, Tao J, Liu C, Yan B, Li W, Li X. Steam reforming of acetic acid using Ni/Al₂O₃ catalyst: influence of crystalline phase of Al₂O₃ support. *Int J Hydrogen Energy* 2017;42:20729–38.
- [93] Vicente J, Ereña J, Montero C, Azkoiti MJ, Bilbao J, Gayubo AG. Reaction pathway for ethanol steam reforming on a Ni/SiO₂ catalyst including coke formation. *Int J Hydrogen Energy* 2014;39:18820–34.
- [94] Vicente J, Montero C, Ereña J, Azkoiti MJ, Bilbao J, Gayubo AG. Coke deactivation of Ni and Co catalysts in ethanol steam reforming at mild temperatures in a fluidized bed reactor. *Int J Hydrogen Energy* 2014;39:12586–96.
- [95] Montero C, Ochoa A, Castaño P, Bilbao J, Gayubo AG. Monitoring NiO and coke evolution during the deactivation of a Ni/La₂O₃– α Al₂O₃ catalyst in ethanol steam reforming in a fluidized bed. *J Catal* 2015;331:181–92.
- [96] Słowik G, Greluk M, Machocki A. Microscopic characterization of changes in the structure of KCo/CeO₂ catalyst used in the steam reforming of ethanol. *Mater Chem Phys* 2016;173:219–37.
- [97] Remiro A, Valle B, Aguayo A, Bilbao J, Gayubo AG. Steam reforming of raw bio-oil in a fluidized bed reactor with prior separation of pyrolytic lignin. *Energy Fuels* 2013;27:7549–59.
- [98] de la Piscina PR, Homs N. Use of biofuels to produce hydrogen (reformation processes). *Chem Soc Rev* 2008;37:2459–67.
- [99] He H, Nakamura J, Tanaka K-i. Spectroscopic evidence for the formation of CH_x species in the hydrogenation of carbidic carbon on Ni (100). *Catal Lett* 1992;16:407–12.
- [100] Sharma YC, Kumar A, Prasad R, Upadhyay SN. Ethanol steam reforming for hydrogen production: latest and effective catalyst modification strategies to minimize carbonaceous deactivation. *Renew Sustain Energy Rev* 2017;74:89–103.
- [101] Nogueira FGE, Assaf PGM, Carvalho HWP, Assaf EM. Catalytic steam reforming of acetic acid as a model compound of bio-oil. *Appl Catal, B* 2014;160–161:188–99.
- [102] Zhang C, Hu X, Zhang Z, Zhang L, Dong D, Gao G, et al. Steam reforming of acetic acid over Ni/Al₂O₃ catalyst: correlation of calcination temperature with the interaction of nickel and alumina. *Fuel* 2018;227:307–24.
- [103] De Bokx P, Kock AJH, Boellaard E, Klop W, Geus JW. The formation of filamentous carbon on iron and nickel catalysts: I. Thermodynamics. *J Catal* 1985;96:454–67.
- [104] Anderson J, Boudart M. *Catalysis science and technology* vol. 6; 1984.
- [105] Liu F, Qu Y, Yue Y, Liu G, Liu Y. Nano bimetallic alloy of Ni–Co obtained from LaCo_xNi_{1-x}O₃ and its catalytic

- performance for steam reforming of ethanol. *RSC Adv* 2015;5:16837–46.
- [106] Iijima S. Helical microtubules of graphitic carbon. *Nature* 1991;354:56.
- [107] Hu R-r, Yan C-f, Zheng X-x, Liu H, Zhou Z-y. Carbon deposition on Ni/ZrO₂-CeO₂ catalyst during steam reforming of acetic acid. *Int J Hydrogen Energy* 2013;38:6033–8.
- [108] Cheng F, Dupont V. Nickel catalyst auto-reduction during steam reforming of bio-oil model compound acetic acid. *Int J Hydrogen Energy* 2013;38:15160–72.
- [109] Park C, Keane MA. Catalyst support effects in the growth of structured carbon from the decomposition of ethylene over nickel. *J Catal* 2004;221:386–99.
- [110] Chen J, Yang X, Li Y. Investigation on the structure and the oxidation activity of the solid carbon produced from catalytic decomposition of methane. *Fuel* 2010;89:943–8.
- [111] Guo J, Lou H, Zhao H, Chai D, Zheng X. Dry reforming of methane over nickel catalysts supported on magnesium aluminate spinels. *Appl Catal, A* 2004;273:75–82.
- [112] Perez-Lopez OW, Senger A, Marcilio NR, Lansarin MA. Effect of composition and thermal pretreatment on properties of Ni–Mg–Al catalysts for CO₂ reforming of methane. *Appl Catal, A* 2006;303:234–44.
- [113] Tian X, Wang S, Zhou J, Xiang Y, Zhang F, Lin B, et al. Simulation and exergetic evaluation of hydrogen production from sorption enhanced and conventional steam reforming of acetic acid. *Int J Hydrogen Energy* 2016;41:21099–108.
- [114] Vagia EC, Lemonidou AA. Thermodynamic analysis of hydrogen production via steam reforming of selected components of aqueous bio-oil fraction. *Int J Hydrogen Energy* 2007;32:212–23.
- [115] Wang D, Czernik S, Montane D, Mann M, Chornet E. Biomass to hydrogen via fast pyrolysis and catalytic steam reforming of the pyrolysis oil or its fractions. *Ind Eng Chem Res* 1997;36:1507–18.
- [116] Marquevich M, Medina F, Montané D. Hydrogen production via steam reforming of sunflower oil over Ni/Al catalysts from hydrotalcite materials. *Catal Commun* 2001;2:119–24.
- [117] Trimm DL. Catalysts for the control of coking during steam reforming. *Catal Today* 1999;49:3–10.
- [118] Galdámez JR, García L, Bilbao R. Hydrogen production by steam reforming of bio-oil using coprecipitated Ni–Al catalysts. Acetic acid as a model compound. *Energy Fuels* 2005;19:1133–42.
- [119] Davidian T, Guilhaume N, Daniel C, Mirodatos C. Continuous hydrogen production by sequential catalytic cracking of acetic acid: part I. Investigation of reaction conditions and application to two parallel reactors operated cyclically. *Appl Catal, A* 2008;335:64–73.
- [120] Davidian T, Guilhaume N, Provendier H, Mirodatos C. Continuous hydrogen production by sequential catalytic cracking of acetic acid: Part II. Mechanistic features and characterisation of catalysts under redox cycling. *Appl Catal, A* 2008;337:111–20.
- [121] Davidson SD, Spies KA, Mei D, Kovarik L, Kutnyakov I, Li XS, et al. Steam reforming of acetic acid over Co-supported catalysts: coupling ketonization for greater stability. *ACS Sustainable Chem Eng* 2017;5:9136–49.
- [122] Trimm DL. Coke formation and minimisation during steam reforming reactions. *Catal Today* 1997;37:233–8.
- [123] Vagia EC, Lemonidou AA. Thermodynamic analysis of hydrogen production via autothermal steam reforming of selected components of aqueous bio-oil fraction. *Int J Hydrogen Energy* 2008;33:2489–500.
- [124] Medrano J, Oliva M, Ruiz J, Garcia L, Arauzo J. Catalytic steam reforming of acetic acid in a fluidized bed reactor with oxygen addition. *Int J Hydrogen Energy* 2008;33:4387–96.
- [125] Wang Y, Chen M, Liang T, Yang Z, Yang J, Liu S. Hydrogen generation from catalytic steam reforming of acetic acid by Ni/attapulgitic catalysts. *Catalysts* 2016;6:172.
- [126] Zhao X, Xue Y, Yan C, Huang Y, Lu Z, Wang Z, et al. Promoted activity of porous silica coated Ni/CeO₂ZrO₂ catalyst for steam reforming of acetic acid. *Int J Hydrogen Energy* 2017;42:21677–85.
- [127] Wang S, Cai Q, Zhang F, Li X, Zhang L, Luo Z. Hydrogen production via catalytic reforming of the bio-oil model compounds: acetic acid, phenol and hydroxyacetone. *Int J Hydrogen Energy* 2014;39:18675–87.
- [128] Vagia EC, Lemonidou AA. Hydrogen production via steam reforming of bio-oil components over calcium aluminate supported nickel and noble metal catalysts. *Appl Catal, A* 2008;351:111–21.
- [129] Nabgan W, Abdullah TAT, Mat R, Nabgan B, Jalil AA, Firmansyah L, et al. Production of hydrogen via steam reforming of acetic acid over Ni and Co supported on La₂O₃ catalyst. *Int J Hydrogen Energy* 2017;42:8975–85.
- [130] Hu X, Lu G. Investigation of steam reforming of acetic acid to hydrogen over Ni–Co metal catalyst. *J Mol Catal A Chem* 2007;261:43–8.
- [131] Mizuno SCM, Braga AH, Hori CE, Santos JBO, Bueno JMC. Steam reforming of acetic acid over MgAl₂O₄-supported Co and Ni catalysts: effect of the composition of Ni/Co and reactants on reaction pathways. *Catal Today* 2017;296:144–53.
- [132] Arbag H, Yasyerli S, Yasyerli N, Dogu G, Dogu T. Enhancement of catalytic performance of Ni based mesoporous alumina by Co incorporation in conversion of biogas to synthesis gas. *Appl Catal, B* 2016;198:254–65.
- [133] Pieterse J, Boon J, Van Delft Y, Dijkstra J, Van den Brink R. On the potential of nickel catalysts for steam reforming in membrane reactors. *Catal Today* 2010;156:153–64.
- [134] Wu G, Li S, Zhang C, Wang T, Gong J. Glycerol steam reforming over perovskite-derived nickel-based catalysts. *Appl Catal, B* 2014;144:277–85.
- [135] Wang D, Czernik S, Chornet E. Production of hydrogen from biomass by catalytic steam reforming of fast pyrolysis oils. *Energy Fuels* 1998;12:19–24.
- [136] Bimbela F, Oliva M, Ruiz J, García L, Arauzo J. Hydrogen production by catalytic steam reforming of acetic acid, a model compound of biomass pyrolysis liquids. *J Anal Appl Pyrolysis* 2007;79:112–20.
- [137] Ramos MC, Navascués AI, García L, Bilbao R. Hydrogen production by catalytic steam reforming of acetol, a model compound of bio-oil. *Ind Eng Chem Res* 2007;46:2399–406.
- [138] Medrano J, Oliva M, Ruiz J, García L, Arauzo J. Hydrogen from aqueous fraction of biomass pyrolysis liquids by catalytic steam reforming in fluidized bed. *Energy* 2011;36:2215–24.
- [139] Bimbela F, Ábrego J, Puerta R, García L, Arauzo J. Catalytic steam reforming of the aqueous fraction of bio-oil using Ni–Ce/Mg–Al catalysts. *Appl Catal, B* 2017;209:346–57.
- [140] Hu X, Zhang L, Lu G. Pruning of the surface species on Ni/Al₂O₃ catalyst to selective production of hydrogen via acetone and acetic acid steam reforming. *Appl Catal, A* 2012;427–428:49–57.
- [141] Zhang Z, Hu X, Li J, Gao G, Dong D, Westerhof R, et al. Steam reforming of acetic acid over Ni/Al₂O₃ catalysts: correlation of nickel loading with properties and catalytic behaviors of the catalysts. *Fuel* 2018;217:389–403.
- [142] Goyal N, Pant K, Gupta R. Hydrogen production by steam reforming of model bio-oil using structured Ni/Al₂O₃ catalysts. *Int J Hydrogen Energy* 2013;38:921–33.

- [143] Garcia La, French R, Czernik S, Chornet E. Catalytic steam reforming of bio-oils for the production of hydrogen: effects of catalyst composition. *Appl Catal, A* 2000;201:225–39.
- [144] Kechagiopoulos PN, Voutetakis SS, Lemonidou AA, Vasalos IA. Hydrogen production via steam reforming of the aqueous phase of bio-oil in a fixed bed reactor. *Energy Fuels* 2006;20:2155–63.
- [145] Hu X, Zhang L, Lu G. Steam reforming of acetic acid over CuZnCo catalyst for hydrogen generation: synergistic effects of the metal species. *Int J Hydrogen Energy* 2016;41:13960–9.
- [146] Bimbela F, Chen D, Ruiz J, García L, Arauzo J. Ni/Al coprecipitated catalysts modified with magnesium and copper for the catalytic steam reforming of model compounds from biomass pyrolysis liquids. *Appl Catal, B* 2012;119–120:1–12.
- [147] Li Y, Chen J, Chang L, Qin Y. The doping effect of copper on the catalytic growth of carbon fibers from methane over a Ni/Al₂O₃ catalyst prepared from feitknecht compound precursor. *J Catal* 1998;178:76–83.
- [148] Chen J, Li Y, Li Z, Zhang X. Production of CO_x-free hydrogen and nanocarbon by direct decomposition of undiluted methane on Ni–Cu–alumina catalysts. *Appl Catal, A* 2004;269:179–86.
- [149] Li Z, Hu X, Zhang L, Liu S, Lu G. Steam reforming of acetic acid over Ni/ZrO₂ catalysts: effects of nickel loading and particle size on product distribution and coke formation. *Appl Catal, A* 2012;417:281–9.
- [150] Ma H, Zeng L, Tian H, Li D, Wang X, Li X, et al. Efficient hydrogen production from ethanol steam reforming over La-modified ordered mesoporous Ni-based catalysts. *Appl Catal, B* 2016;181:321–31.
- [151] Hu X, Lu G. Steam reforming of acetic acid to hydrogen over Fe–Co catalyst. *Chem Lett* 2006;35:452–3.
- [152] Pu J, Ikegami F, Nishikado K, Qian EW. Effect of ceria addition on NiRu/CeO₂/Al₂O₃ catalysts in steam reforming of acetic acid. *Int J Hydrogen Energy* 2017;42:19733–43.
- [153] Papageridis KN, Siakavelas G, Charisiou ND, Avraam DG, Tzounis L, Kousi K, et al. Comparative study of Ni, Co, Cu supported on γ -alumina catalysts for hydrogen production via the glycerol steam reforming reaction. *Fuel Process Technol* 2016;152:156–75.
- [154] Braga AH, Sodr  ER, Santos JBO, de Paula Marques CM, Bueno JMC. Steam reforming of acetone over Ni- and Co-based catalysts: effect of the composition of reactants and catalysts on reaction pathways. *Appl Catal, B* 2016;195:16–28.
- [155] Li D, Lu M, Aragaki K, Koike M, Nakagawa Y, Tomishige K. Characterization and catalytic performance of hydrotalcite-derived Ni–Cu alloy nanoparticles catalysts for steam reforming of 1-methylnaphthalene. *Appl Catal, B* 2016;192:171–81.
- [156] Ishihara A, Qian EW, Finahari IN, Sutrisna IP, Kabe T. Addition effect of ruthenium on nickel steam reforming catalysts. *Fuel* 2005;84:1462–8.
- [157] Chen T, Wu C, Liu R. Steam reforming of bio-oil from rice husks fast pyrolysis for hydrogen production. *Bioresour Technol* 2011;102:9236–40.
- [158] Cakiryilmaz N, Arbag H, Oktar N, Dogu G, Dogu T. Effect of W incorporation on the product distribution in steam reforming of bio-oil derived acetic acid over Ni based Zr-SBA-15 catalyst. *Int J Hydrogen Energy* 2018;43:3629–42.
- [159] Khzouz M, Wood J, Pollet B, Bujalski W. Characterization and activity test of commercial Ni/Al₂O₃, Cu/ZnO/Al₂O₃ and prepared Ni–Cu/Al₂O₃ catalysts for hydrogen production from methane and methanol fuels. *Int J Hydrogen Energy* 2013;38:1664–75.
- [160] Horiuchi T, Sakuma K, Fukui T, Kubo Y, Osaki T, Mori T. Suppression of carbon deposition in the CO₂-reforming of CH₄ by adding basic metal oxides to a Ni/Al₂O₃ catalyst. *Appl Catal, A* 1996;144:111–20.
- [161] Sehested J, Larsen NW, Falsig H, Hinnemann B. Sintering of nickel steam reforming catalysts: effective mass diffusion constant for Ni-OH at nickel surfaces. *Catal Today* 2014;228:22–31.
- [162] German RM. Sintering theory and practice. *Solar-terrestrial physics. Solnechno-zemnaya fizika*; 1996. p. 568.
- [163] Sehested J, Carlsson A, Janssens T, Hansen P, Datye A. Sintering of nickel steam-reforming catalysts on MgAl₂O₄ spinel supports. *J Catal* 2001;197:200–9.
- [164] Sehested J, Gelten JA, Remediakis IN, Bengaard H, N rskov JK. Sintering of nickel steam-reforming catalysts: effects of temperature and steam and hydrogen pressures. *J Catal* 2004;223:432–43.
- [165] Sehested J. Four challenges for nickel steam-reforming catalysts. *Catal Today* 2006;111:103–10.
- [166] Sehested J, Gelten JA, Helveg S. Sintering of nickel catalysts: effects of time, atmosphere, temperature, nickel-carrier interactions, and dopants. *Appl Catal, A* 2006;309:237–46.
- [167] Iriondo A, Barrio V, Cambra J, Arias P, G mez M, Navarro R, et al. Hydrogen production from glycerol over nickel catalysts supported on Al₂O₃ modified by Mg, Zr, Ce or La. *Top Catal* 2008;49:46.
- [168] Cui Y, Galvita V, Rihko-Struckmann L, Lorenz H, Sundmacher K. Steam reforming of glycerol: the experimental activity of La_{1-x}Ce_xNiO₃ catalyst in comparison to the thermodynamic reaction equilibrium. *Appl Catal, B* 2009;90:29–37.
- [169] Profeti LP, Dias JA, Assaf JM, Assaf EM. Hydrogen production by steam reforming of ethanol over Ni-based catalysts promoted with noble metals. *J Power Sources* 2009;190:525–33.
- [170] Dehkhoda AM, West AH, Ellis N. Biochar based solid acid catalyst for biodiesel production. *Appl Catal, A* 2010;382:197–204.
- [171] Rem n J, Medrano J, Bimbela F, Garc a L, Arauzo J. Ni/Al–Mg–O solids modified with Co or Cu for the catalytic steam reforming of bio-oil. *Appl Catal, B* 2013;132:433–44.
- [172] Thacharonsutcharittham S, Meeyoo V, Kitiyanan B, Rangsunvigit P, Rirksomboon T. Hydrogen production by steam reforming of acetic acid over Ni-based catalysts. *Catal Today* 2011;164:257–61.
- [173] Sugisawa M, Takanabe K, Harada M, Kubota J, Domen K. Effects of La addition to Ni/Al₂O₃ catalysts on rates and carbon deposition during steam reforming of n-dodecane. *Fuel Process Technol* 2011;92:21–5.
- [174] Mustu H, Yasyerli S, Yasyerli N, Dogu G, Dogu T, Djinovi  P, et al. Effect of synthesis route of mesoporous zirconia based Ni catalysts on coke minimization in conversion of biogas to synthesis gas. *Int J Hydrogen Energy* 2015;40:3217–28.
- [175] Gunduz S, Dogu T. Sorption-enhanced reforming of ethanol over Ni- and Co-incorporated MCM-41 type catalysts. *Ind Eng Chem Res* 2011;51:8796–805.
- [176] Mel ndez-Ortiz HI, Puente-Urbina B, Castruita-de Leon G, Mata-Padilla JM, Garc a-Uriostegui L. Synthesis of spherical SBA-15 mesoporous silica. Influence of reaction conditions on the structural order and stability. *Ceram Int* 2016;42:7564–70.
- [177] Fuxiang L, Feng Y, Yongli L, Ruifeng L, Kechang X. Direct synthesis of Zr-SBA-15 mesoporous molecular sieves with high zirconium loading: characterization and catalytic performance after sulfated. *Microporous Mesoporous Mater* 2007;101:250–5.
- [178] Arbag H, Yasyerli S, Yasyerli N, Dogu G. Activity and stability enhancement of Ni-MCM-41 catalysts by Rh

- incorporation for hydrogen from dry reforming of methane. *Int J Hydrogen Energy* 2010;35:2296–304.
- [179] Kamonsuangkasem K, Therdthianwong S, Therdthianwong A, Thammajak N. Remarkable activity and stability of Ni catalyst supported on CeO₂-Al₂O₃ via CeAlO₃ perovskite towards glycerol steam reforming for hydrogen production. *Appl Catal, B* 2017;218:650–63.
- [180] Djinović P, Levec J, Pintar A. Effect of structural and acidity/basicity changes of CuO–CeO₂ catalysts on their activity for water–gas shift reaction. *Catal Today* 2008;138:222–7.
- [181] Goicoechea S, Kraveva E, Ehrich H. Effect of Al₂O₃/ZnO ratio on Ni (Co)–AlZnOx catalysts for syngas production by steam reforming of acetic acid. *Catal Lett* 2017;147:1403–10.
- [182] Fisher IA, Woo HC, Bell AT. Effects of zirconia promotion on the activity of Cu/SiO₂ for methanol synthesis from CO/H₂ and CO₂/H₂. *Catal Lett* 1997;44:11–7.
- [183] Silveira E, Rabelo-Neto R, Noronha F. Steam reforming of toluene, methane and mixtures over Ni/ZrO₂ catalysts. *Catal Today* 2017;289:289–301.
- [184] Passos FB, de Oliveira ER, Mattos LV, Noronha FB. Partial oxidation of methane to synthesis gas on Pt/Ce_xZr_{1-x}O₂ catalysts: the effect of the support reducibility and of the metal dispersion on the stability of the catalysts. *Catal Today* 2005;101:23–30.
- [185] Kim DK, Stöwe K, Müller F, Maier WF. Mechanistic study of the unusual catalytic properties of a new NiCe mixed oxide for the CO₂ reforming of methane. *J Catal* 2007;247:101–11.
- [186] Ferreira-Aparicio P, Benito M, Kouachi K, Menad S. Catalysis in membrane reformers: a high-performance catalytic system for hydrogen production from methane. *J Catal* 2005;231:331–43.
- [187] Zheng X-x, Yan C-f, Hu R-r, Li J, Hai H, Luo W-m, et al. Hydrogen from acetic acid as the model compound of biomass fast-paralysis oil over Ni catalyst supported on ceria–zirconia. *Int J Hydrogen Energy* 2012;37:12987–93.
- [188] Gonzalez-DelaCruz VM, Holgado JP, Pereñíguez R, Caballero A. Morphology changes induced by strong metal–support interaction on a Ni–ceria catalytic system. *J Catal* 2008;257:307–14.
- [189] Toyoda T, Nishihara Y, Qian EW. CO hydrogenation on group VI metal–ceria catalysts. *Fuel Process Technol* 2014;125:86–93.
- [190] Mohamed M, Salama T, Othman A, El-Shobaky G. Low temperature water–gas shift reaction on cerium containing mordenite prepared by different methods. *Appl Catal, A* 2005;279:23–33.
- [191] Kašpar J, Fornasiero P, Graziani M. Use of CeO₂-based oxides in the three-way catalysis. *Catal Today* 1999;50:285–98.
- [192] Kim TY, Kim SM, Lee WS, Woo SI. Effect and behavior of cerium oxide in Ni/γ-Al₂O₃ catalysts on autothermal reforming of methane: CeAlO₃ formation and its role on activity. *Int J Hydrogen Energy* 2013;38:6027–32.
- [193] Chen W, Zhao G, Xue Q, Chen L, Lu Y. High carbon-resistance Ni/CeAlO₃-Al₂O₃ catalyst for CH₄/CO₂ reforming. *Appl Catal, B* 2013;136:260–8.
- [194] Schmitz P, Usmen R, Peters C, Graham G, McCabe R. Effect of calcination temperature on Al₂O₃-supported CeO₂: complementary results from XRD and XPS. *Appl Surf Sci* 1993;72:181–7.
- [195] Tomishige K, Kimura T, Nishikawa J, Miyazawa T, Kunimori K. Promoting effect of the interaction between Ni and CeO₂ on steam gasification of biomass. *Catal Commun* 2007;8:1074–9.
- [196] Li M, Wang X, Li S, Wang S, Ma X. Hydrogen production from ethanol steam reforming over nickel based catalyst derived from Ni/Mg/Al hydrotalcite-like compounds. *Int J Hydrogen Energy* 2010;35:6699–708.
- [197] Elias KF, Lucrédio AF, Assaf EM. Effect of CaO addition on acid properties of Ni–Ca/Al₂O₃ catalysts applied to ethanol steam reforming. *Int J Hydrogen Energy* 2013;38:4407–17.
- [198] Garbarino G, Wang C, Valsamakis I, Chitsazan S, Riani P, Finocchio E, et al. A study of Ni/Al₂O₃ and Ni–La/Al₂O₃ catalysts for the steam reforming of ethanol and phenol. *Appl Catal, B* 2015;174:21–34.
- [199] Iriondo A, Barrio V, Cambra J, Arias P, Güemez M, Navarro R, et al. Influence of La₂O₃ modified support and Ni and Pt active phases on glycerol steam reforming to produce hydrogen. *Catal Commun* 2009;10:1275–8.
- [200] Sánchez-Sánchez M, Navarro R, Fierro J. Ethanol steam reforming over Ni/La–Al₂O₃ catalysts: influence of lanthanum loading. *Catal Today* 2007;129:336–45.
- [201] Melchor-Hernández C, Gómez-Cortés A, Díaz G. Hydrogen production by steam reforming of ethanol over nickel supported on La-modified alumina catalysts prepared by sol–gel. *Fuel* 2013;107:828–35.
- [202] Medrano J, Oliva M, Ruiz J, García L, Arauzo J. Catalytic steam reforming of model compounds of biomass pyrolysis liquids in fluidized bed reactor with modified Ni/Al catalysts. *J Anal Appl Pyrolysis* 2009;85:214–25.
- [203] Li C, Yu C, Shen S. Studies on the transformation of carbon species from CH₄ decomposition over a Ni/Al₂O₃ catalyst. *Acta Chim Sin* 2000;58:1188–90.
- [204] Bermúdez J, Fidalgo B, Arenillas A, Menéndez J. CO₂ reforming of coke oven gas over a Ni/γ-Al₂O₃ catalyst to produce syngas for methanol synthesis. *Fuel* 2012;94:197–203.
- [205] Chen D, Lødeng R, Anundskås A, Olsvik O, Holmen A. Deactivation during carbon dioxide reforming of methane over Ni catalyst: microkinetic analysis. *Chem Eng Sci* 2001;56:1371–9.
- [206] Chen S, Wang H, Liu Y. Perovskite La–St–Fe–O (St= Ca, Sr) supported nickel catalysts for steam reforming of ethanol: the effect of the A site substitution. *Int J Hydrogen Energy* 2009;34:7995–8005.
- [207] Vizcaíno A, Lindo M, Carrero A, Calles J. Hydrogen production by steam reforming of ethanol using Ni catalysts based on ternary mixed oxides prepared by coprecipitation. *Int J Hydrogen Energy* 2012;37:1985–92.
- [208] Choong CK, Zhong Z, Huang L, Wang Z, Ang TP, Borgna A, et al. Effect of calcium addition on catalytic ethanol steam reforming of Ni/Al₂O₃: I. Catalytic stability, electronic properties and coking mechanism. *Appl Catal, A* 2011;407:145–54.
- [209] Sánchez-Sánchez M, Navarro R, Fierro J. Ethanol steam reforming over Ni/M_xO_y-Al₂O₃ (M= Ce, La, Zr and Mg) catalysts: influence of support on the hydrogen production. *Int J Hydrogen Energy* 2007;32:1462–71.
- [210] Hou Z, Yokota O, Tanaka T, Yashima T. A novel KCaNi/α-Al₂O₃ catalyst for CH₄ reforming with CO₂. *Catal Lett* 2003;87:37–42.
- [211] Lisboa JdS, Santos DC, Passos FB, Noronha FB. Influence of the addition of promoters to steam reforming catalysts. *Catal Today* 2005;101:15–21.
- [212] Lin J, Chen L, Choong CKS, Zhong Z, Huang L. Molecular catalysis for the steam reforming of ethanol. *Sci China Chem* 2015;58:60–78.
- [213] Lødeng R, Barre-Chassonnery M, Fathi M, Rokstad O, Holmen A. Carbon formation from decomposition of CH₄ on supported Ni catalysts. *Studies in surface science and catalysis*. Elsevier; 1997. p. 561–6.
- [214] Barroso MN, Galetti AE, Abello MC. Ni catalysts supported over MgAl₂O₄ modified with Pr for hydrogen production from ethanol steam reforming. *Appl Catal, A* 2011;394:124–31.

- [215] Zhang Z, Verykios X. Carbon dioxide reforming of methane to synthesis gas over supported Ni catalysts. *Catal Today* 1994;21:589–95.
- [216] Salehi E, Azad FS, Harding T, Abedi J. Production of hydrogen by steam reforming of bio-oil over Ni/Al₂O₃ catalysts: effect of addition of promoter and preparation procedure. *Fuel Process Technol* 2011;92:2203–10.
- [217] Xu X, Zhang C, Liu Y, Zhai Y, Zhang R, Tang X. Catalytic reforming of acetic acid as a model compound of bio-oil for hydrogen production over Ni-CeO₂-MgO/olivine catalysts. *Environ Prog Sustain Energy* 2015;34:915–22.
- [218] Yang X, Wang Y, Li M, Sun B, Li Y, Wang Y. Enhanced hydrogen production by steam reforming of acetic acid over a Ni catalyst supported on mesoporous MgO. *Energy Fuels* 2016;30:2198–203.
- [219] Barroso-Quiroga MM, Castro-Luna AE. Catalytic activity and effect of modifiers on Ni-based catalysts for the dry reforming of methane. *Int J Hydrogen Energy* 2010;35:6052–6.
- [220] Frusteri F, Arena F, Calogero G, Torre T, Parmaliana A. Potassium-enhanced stability of Ni/MgO catalysts in the dry-reforming of methane. *Catal Commun* 2001;2:49–56.
- [221] Hu X, Lu G. Inhibition of methane formation in steam reforming reactions through modification of Ni catalyst and the reactants. *Green Chem* 2009;11:724–32.
- [222] Bengaard HS, Nørskov J, Sehested J, Clausen B, Nielsen L, Molenbroek A, et al. Steam reforming and graphite formation on Ni catalysts. *J Catal* 2002;209:365–84.
- [223] Hou Z, Yokota O, Tanaka T, Yashima T. Characterization of Ca-promoted Ni/ α -Al₂O₃ catalyst for CH₄ reforming with CO₂. *Appl Catal, A* 2003;253:381–7.
- [224] Lemonidou AA, Vasalos IA. Carbon dioxide reforming of methane over 5 wt.% Ni/CaO-Al₂O₃ catalyst. *Appl Catal, A* 2002;228:227–35.
- [225] Arauzo J, Radlein D, Piskorz J, Scott DS. Catalytic pyrogasification of biomass. Evaluation of modified nickel catalysts. *Ind Eng Chem Res* 1997;36:67–75.
- [226] Xue Y-p, Yan C-f, Zhao X-y, Huang S-l, Guo C-q. Ni/La₂O₃-ZrO₂ catalyst for hydrogen production from steam reforming of acetic acid as a model compound of bio-oil. *Kor J Chem Eng* 2017;34:305–13.
- [227] Wang M, Zhang F, Wang S. Effect of La₂O₃ replacement on γ -Al₂O₃ supported nickel catalysts for acetic acid steam reforming. *Int J Hydrogen Energy* 2017;42:20540–8.
- [228] Hu X, Lu G. Acetic acid steam reforming to hydrogen over Co-Ce/Al₂O₃ and Co-La/Al₂O₃ catalysts—the promotion effect of Ce and La addition. *Catal Commun* 2010;12:50–3.
- [229] Pu J, Luo Y, Wang N, Bao H, Wang X, Qian EW. Ceria-promoted Ni@Al₂O₃ core-shell catalyst for steam reforming of acetic acid with enhanced activity and coke resistance. *Int J Hydrogen Energy* 2018;43:3142–53.
- [230] Wang S, Zhang F, Cai Q, Li X, Zhu L, Wang Q, et al. Catalytic steam reforming of bio-oil model compounds for hydrogen production over coal ash supported Ni catalyst. *Int J Hydrogen Energy* 2014;39:2018–25.
- [231] Wang Q, Wang S, Li X, Guo L. Hydrogen production via acetic acid steam reforming over HZSM-5 and Pd/HZSM-5 catalysts and subsequent mechanism studies. *BioResources* 2013;8:2897–909.
- [232] Wang Y, Chen M, Yang J, Liu S, Yang Z, Wang J, et al. Hydrogen production from steam reforming of acetic acid over Ni-Fe/palygorskite modified with cerium. *BioResources* 2017;12:4830–53.
- [233] Borges R, Ferreira R, Rabelo-Neto R, Noronha F, Hori C. Hydrogen production by steam reforming of acetic acid using hydrotalcite type precursors. *Int J Hydrogen Energy* 2018;43:7881–92.
- [234] Li L, Jiang B, Tang D, Zhang Q, Zheng Z. Hydrogen generation by acetic acid steam reforming over Ni-based catalysts derived from La_{1-x}Ce_xNiO₃ perovskite. *Int J Hydrogen Energy* 2018;43:6795–803.
- [235] Parthasarathy P, Narayanan KS. Hydrogen production from steam gasification of biomass: influence of process parameters on hydrogen yield – a review. *Renew Energy* 2014;66:570–9.
- [236] Peres APG, Lunelli B, Fllho R. Application of biomass to hydrogen and syngas production. *Chemical Engineering Transactions* 2013;32:589–94.



A state of the art overview of carbon-based composites applications for detecting and eliminating pharmaceuticals containing wastewater

Walid Nabgan, PhD^{a,b}, Aishah Abdul Jalil^{a,b,*}, Bahador Nabgan^a, Muhammad Ikram^{c,**}, Mohamad Wijayanuddin Ali^{a,b}, Ankit kumar^d, Parashuram Lakshminarayana^e

^a School of Chemical and Energy Engineering, Faculty of Engineering, Universiti Teknologi Malaysia, 81310, Skudai, Johor, Malaysia

^b Centre of Hydrogen Energy, Institute of Future Energy, Universiti Teknologi Malaysia, 81310, Skudai, Johor, Malaysia

^c Solar Cell Applications Research Lab, Department of Physics, Government College University Lahore, 54000, Punjab, Pakistan

^d Department of Chemical Engineering and Technology, Indian Institute of Technology (BHU), Varanasi, UP, 221005, India

^e Department of Chemistry, New Horizon College of Engineering Affiliated to VTU, Bangalore, 560087, India

HIGHLIGHTS

- A review of carbon nanomaterials for removing pharmaceuticals was conducted.
- Exponential increase in the (bio)sensors using carbon black was identified.
- Several analytical methods to detect pharmaceuticals were reviewed.
- This study offered scientific data to generate new systematic breakthroughs.

GRAPHICAL ABSTRACT



ARTICLE INFO

Handling Editor: Derek Muir

Keywords:
Removal
Sensors
Nano-materials
Systematic
Bibliometric

ABSTRACT

The growing prevalence of new toxins in the environment continues to cause widespread concerns. Pharmaceuticals, organic pollutants, heavy metal ions, endocrine-disrupting substances, microorganisms, and others are examples of persistent organic chemicals whose effects are unknown because they have recently entered the environment and are displaying up in wastewater treatment facilities. Pharmaceutical pollutants in discharged wastewater have become a danger to animals, marine species, humans, and the environment. Although their presence in drinking water has generated significant concerns, little is known about their destiny and environmental effects. As a result, there is a rising need for selective, sensitive, quick, easy-to-handle, and low-cost early monitoring detection systems. This study aims to deliver an overview of a low-cost carbon-based composite to detect and remove pharmaceutical components from wastewater using the literature reviews and bibliometric analysis technique from 1970 to 2021 based on the web of science (WoS) database. Various pollutants in water and soil were reviewed, and different methods were introduced to detect pharmaceutical pollutants. The advantages and drawbacks of varying carbon-based materials for sensing and removing pharmaceutical wastes were also introduced. Finally, the available techniques for wastewater treatment, challenges and future perspectives on the recent progress were highlighted. The suggestions in this article will facilitate the development

* Corresponding author. School of Chemical and Energy Engineering, Faculty of Engineering, Universiti Teknologi Malaysia, 81310, Skudai, Johor, Malaysia.

** Corresponding author.

E-mail addresses: wnabgan@gmail.com (W. Nabgan), aishahaj@utm.my (A.A. Jalil), dr.muhammadikram@gcu.edu.pk (M. Ikram).

<https://doi.org/10.1016/j.chemosphere.2021.132535>

Received 12 August 2021; Received in revised form 16 September 2021; Accepted 8 October 2021

Available online 11 October 2021

0045-6535/© 2021 Elsevier Ltd. All rights reserved.

of novel on-site methods for removing emerging pollutants from pharmaceutical effluents and commercial enterprises.

Abbreviations

Al(III)	Aluminum(III)	LLE	Liquid-liquid extraction
AOPs	Advanced oxidation processes	MGAC	Micro-grain activated carbon
As(III)	Arsenic	MIP-SPME	Molecularly imprinted polymer aided solid-phase microextraction
CB	Carbon black	MLRA	Multiple linear regression analysis
Cd(II)	Cadmium(II) ion	Mn(II)	Manganese (II) ion
CE	Capillary electrophoresis	MOFs	Metal-organic frameworks
CNFs	Carbon nanofibers	MRS	Magnetic resonance spectroscopy
CNTs	Carbon nanotubes	MS	Mass spectrometry
Co(II)	Cobaltous cation	MWNTs	Multi-walled carbon nanotubes
CSO	Combined sewage overflow	Ni(II)	Nickel (II) ion
Cu(II)	Cupric ion	NIR	Near-infrared spectroscopy
D	Dimensions	nm	Nanometers
1D	One-dimensional	NMR	Nuclear magnetic resonance
2D	Two-dimensional	NSAIDs	Non-steroidal anti-inflammatory drugs
3D	Three-dimensional	Pb(II)	Lead(II) ion
Ecs	Emerging contaminants	PCA	Principal component analysis
Eg	Gap energy	PFASs	Polyfluoroalkyl substances
ERA	Environmental risk assessment	PhACs	Pharmaceutically-active compounds
FT	Fourier transform	PLSR	Partial least squares regression
GAC	granulated activated carbon	ppm	Parts per million
GC	Gas chromatography	RO	Reverse osmosis
GO	Graphene oxide	SP ²	Mixing of 1 s and two p atomic orbitals
Graphene	Rolled-up single-layer carbon atom sheets	SPE	Solid-phase extraction
Hg(II)	Mercury(II) ion	SPME	Solid-phase microextraction
¹ H NMR	Proton nuclear magnetic resonance	SWNTs	Single-walled carbon nanotubes
HPLC	High-performance liquid chromatography	TiO ₂	Titanium dioxide
LC	Liquid chromatography	TLC	Thin-layer chromatography
LC-MS/MS	Liquid chromatography-tandem mass spectrometry	WoS	Web of Science
LC-MS	Liquid chromatography coupled to mass spectrometry	WTW	Wastewater treatment works
		Zn(II)	Zinc ion

1. Introduction

The existence of pharmaceutical chemicals and their metabolites in the aquatic environment, which are regarded as emergent organic micropollutants, is now a significant issue globally (Couto et al., 2019; Pereira et al., 2020). The development in the health care system's ability to manage and prevent illnesses has resulted in a rapid increase in pharmaceutical use. Emerging contaminants (ECs) are substances that enter water systems from a variety of sources, including human excretion (sewage), improper disposal, landfill leachate, drain water, and industry (Archer et al., 2017). Human medicines' potential for harmful ecotoxicological consequences in the aquatic environment, especially in sublethal quantities, has been a source of worry since the problem was first brought to light in 1985 (Richardson and Bowron, 1985). Environmental risk assessment (ERA) for pharmaceuticals is widely acknowledged as critical for implementing measures to reduce their potential environmental effect (Meisel et al., 2009). However, new difficulties in pharmaceutical pollutant detection and removal are posed by the need to detect pollution with new materials and treat wastewaters with the latest technology.

Numerous techniques have been stated to evaluate pharmaceuticals in various matrices containing liquid and gas chromatography (Frink et al., 2014; Yilmaz and Ciltas, 2015; Ge et al., 2020), colorimetry (Bridgeman et al., 2014; Lantam et al., 2020), surface plasmon resonance (Bridgeman et al., 2014; El-Zahry, 2018), fluorescence (Zhu et al.,

2018), ion mobility spectrometry (Masár et al., 2020), capillary electrophoresis (Pollap et al., 2020) and etc. On the other hand, the detection device must be immersed directly into the sample or subjected to a flow-through method to monitor the illegal production continuously. The chromatographic techniques, including capillary electrophoresis (CE), gas chromatography (GC) and liquid chromatography (LC), are the furthestmost typical methods for the determination of pharmaceutical compounds, which are capable of identifying and quantifying a wide variety of pharmaceutical compounds from different groups at trace levels with great accuracy. A traditional analytical technique, for example, depends primarily on high-performance liquid chromatography-mass spectrometry, which has high selectivity, sensitivity, and stability (Gao et al., 2017). This approach needs sample pre-treatment before analysis, such as purifying raw wastewater using solid-phase extraction and reconstituting it in an organic solvent for analysis. Several research works dealing with electrochemical methods for pharmaceutical detection have been proposed (Simioni et al., 2017; Razmi et al., 2019; Camargo et al., 2020). Electrochemical techniques are an intriguing alternative to previously stated methods due to many benefits that characterise them, such as cheap cost, simplicity, no sample preparation need, and quick analysis time. Therefore, the development and amendment of electrode surface with nano-structured constituents offers rapid, simple, and inexpensive analytical methods to determine pharmaceuticals in wastewater.

Carbon-based compounds such as single-walled carbon nanotubes, multi-walled carbon nanotubes, fullerenes, and graphene have been

used as electrode surface modifiers. These materials have many applications, such as nanoelectronic devices, catalyst carriers, electrode materials, hydrogen storage materials and composite materials. Those materials are generated structurally by one or more hexagonal layers. Each carbon atom with sp^2 hybridization is linked to three other atoms that rearrange in various dimensions (D) to generate distinct allotropic configurations (Beluomini et al., 2019). Nano-onions and fullerenes could be found in 2-D graphene and nanowalls, 1-D nanotubes, 0-D, and 3-D graphene and nanoflowers (Aslam et al., 2018). By modifying electrodes with metal nano-sized particles, the surface area-to-volume ratio will be increased (Campbell and Compton, 2010; Maringa et al., 2014), and electrochemical activity will be improved (Etesami et al., 2011; Hu et al., 2011; Maringa et al., 2014). This enhancement is because of the faster electron-transfer kinetics and a reduction in the necessary over-potential for the electrochemical reaction (Huang et al., 2008; Maringa et al., 2014). High chemical stability, permeability toward water adsorption capacity, physical resilience, excellent adhesion on conventional electrochemical surfaces, and cheap cost were among the advantages of electrochemical sensors with a metal composite sheet (Paz Zanini et al., 2015; Hwang et al., 2019b, 2019c). For the identification of the molecule of interest, these sensors showed a low detection limit (about $nmol L^{-1}$), excellent stability, repeatability, and a decent imprinting influence.

Few review papers have been issued on nanomaterial-based electrochemical sensors to detect pharmaceutical pollutants in wastewater (Torriinha et al., 2020; Wang et al., 2020b; Qian et al., 2021). Sajid and coworkers (Sajid et al., 2018) critically evaluated the elimination of heavy metals and organic contaminants from wastewater using adsorbents based on dendrimers polymer. Ruhma and co-authors (Rashid et al., 2021) looked at the effectiveness of the adsorption method to eradicate various water contaminants. Ankita and co-authors (Ojha et al., 2021) delivered an insight into all kinds of nanocomposites and their conventional application methods to remove toxic organic pollutants from aqueous systems. Despite much research on carbon materials application to detect and remove developing contaminants during the last few years, their practical applications remain restricted. With the help of bibliometric analysis, this paper offers performance assessment, impacts of process parameters, and methods for eradicating pharmaceuticals via carbon composites aided the physical, chemical and biological process. This study seeks to give an overview of current information about the different treatment techniques available for removing pharmaceuticals and personal care products from industrial wastewaters in order to provide a baseline understanding of their efficacy. This information may assist pharmaceutical manufacturing facilities in being prepared to take preventive steps before law requires them to do so.

2. Pollutants in water and soil

Pollution is described as the release of harmful chemicals into the environment. Several industrial processes have released biodegradable and non-biodegradable organic and inorganic contaminants into the air, land, and water since the industrial revolution (Trujillo-Reyes et al., 2014). Water and soil pollutants are two of the most common types of pollution in the environment (Lipczynska-Kochany, 2018). Human-made wastes, such as domestic and food trash, industrial and agricultural wastes, fertilizers used by farmers, oil spills, pharmaceuticals, and radioactive materials, are often responsible for water and soil pollution. According to the Waste Index Report 2021, the 931 million tonnes of food wastes produced in 2019 accounted for about 17% of all food accessible to customers (Forbes et al., 2021). Crop residues are described as undesired waste generated by agricultural operations (i.e., horticultural plastics and veterinary medicines, wastes from a slaughterhouse, poultry houses, and farms, herbicides, pesticides, fertilizer, silage plastics, oil, and manure). Soil contamination inputs include natural nutrient (fertilizer) and pesticide inputs, sewage sludge and

manure application, air deposition of exhaust fumes and particles from cars and industries, and sedimentation of diffuse particles from waste water discharges in surface waterways. The physical characteristics of soil may be affected by oil contamination in which the pore gaps of soil's molecules may get blocked, reducing soil freshening and water diffusion while also increasing bulk density, limiting plant development. Oil spills may suffocate fish, tangle birds and animals' plumage, and block light from photosynthetic plants in the water. Drugs from humans and animals end up in rivers, lakes, and even drinking water, presenting a significant danger to aquatic and human health. Radioactive waste is a kind of hazardous waste that contains radioactive materials. Many activities generate radioactive waste, including nuclear medicine, nuclear research, nuclear power generation, rare-earth mining, and nuclear weapons reprocessing. These pollutants originated from different sources and are illustrated in Fig. 1; in this study, the pharmaceutical wastes in wastewater and soil will be discussed and elaborated.

2.1. Water pollution basics

Water pollution is the discharge of chemicals into oceans, estuaries, rivers, lakes, and underground water to the point that the pollutants inhibit clean water use for environmental purposes. In addition to releasing chemicals or microorganisms, water pollution may contain the energy release, such as heat or radiation, into water bodies. Various types of water pollution are illustrated in Fig. 2. When research focuses on the planet's water resources, concerns emphasize oceans, lakes, rivers, or the surface waters that are first impacted by pollution processes (an oil spill produces a hydrophobic oil layer that may influence a large region of an ocean/watercourse). It is known that not all of the water on the planet is found on the surface; a significant portion is located in underground rock formations known as aquifers or subsurface waters. Rivers are fed by aquifers, which provide most of the drinking water. Wastewater released into surface waterways may provide a potentially dependable water supply, but it can also transport chemical and microbiological contaminants downstream to towns and drinking water intakes (Wang et al., 2017). Pharmaceuticals, a vast and varied category of developing organic micropollutants, have sparked growing apprehension concerning their ecological occurrence and effect in the past thirty years. Many medicines have been found in wastewater treatment works (WTW) discharges, groundwater and surface water throughout the globe (Perkins et al., 2021). Only a few individual examples have surfaced too far, demonstrating the severe effect medicines may have on wildlife due to a lack of data on drug residue bioaccumulation in animals (Fent et al., 2006). Pharmaceuticals have varied and frequently inadequate removal effectiveness throughout wastewater treatment, resulting in their ongoing release into the marine environment (Verlicchi et al., 2012) and devastating effects on aquatic and human health. For example, a mixture of pharmaceutical components prevents the growth of embryonic kidney cells in humans (Pomati et al., 2006). Those compounds have a feminizing effect on male fish and cause to alter female-to-male ratios, leading to abnormal change or disruption of growth and reproduction in fish and aquatic wildlife (Srivastava and P-B., 2020). Treatment systems are bypassed in some circumstances, such as when combined sewage overflow (CSO) events occur, resulting in the discharge of untreated sewage, further increasing the amounts of some wastewater pollutants present (Kay et al., 2017). Most medicines, on the other hand, are only partially eliminated during wastewater treatment. Sanderson and coworkers (Sanderson et al., 2004) indicated that antiviral medications are among the anticipated most dangerous treatment groups in toxicity against algae, daphnids, and fish, based on (Q)SAR modelling of nearly 3000 different chemicals. Besides, there has been a lot of worry about the possible environmental impacts of anti-influenza medicines, which have seasonal fluctuations and peak emissions during influenza outbreaks (Nannou et al., 2019). According to Dougherty and co-authors (Dougherty et al., 2010), about 25% of the US population utilizes a decentralized system to treat and

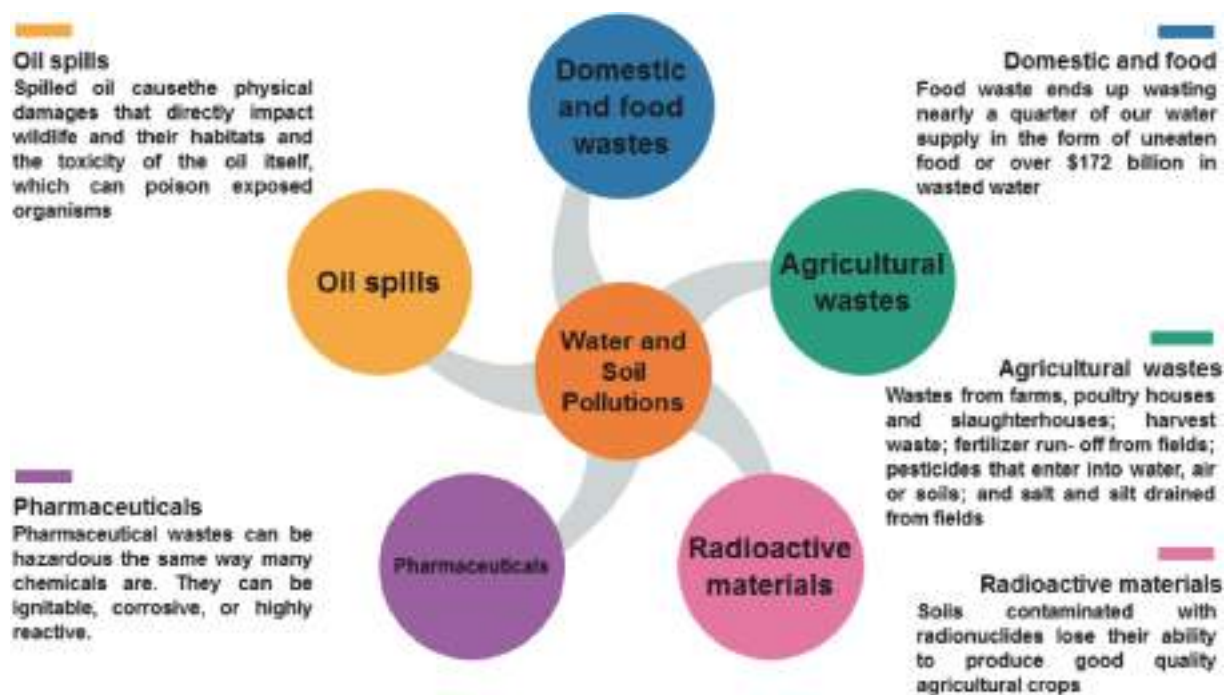


Fig. 1. Examples of various common sources of pollution in water and soil.



Fig. 2. Various sources of pollutants in water.

dispose of household wastewater, while the other 75% is linked to municipal sewers. Consequently, calculating medicines' steady-state concentrations or understanding their destiny and mobility in the environment may be challenging, making it difficult to develop an effective management plan. These findings point to the necessity to assess these chemicals in centralized sewers and beyond to comprehend their dispersion patterns completely.

Pharmaceutical pollution research is partly growing due to increasing concern about possible side effects and advances in the analytical methods to identify such chemicals in low quantities (Tijani et al., 2016). Antibiotics are among the most prescribed medications worldwide (Khataee et al., 2018). However, despite a relatively high degree of research in pharmaceutical waste, minimal effort has been made to remove antibiotics and medicines. The number of studies

performed remains hugely modest compared to other chemical groups. By employing the keyword such as “water”, “pollution”, “food” and “pharmaceutical” at the range of 1970–2021, 145 published works were detected at the WoS database, and the network visualization map is shown Fig. 3. The highest total link strength in the discovered items was pharmaceuticals (86), waste-water (55), personal care products (43), aquatic environments (36), surface-water (27) and removal (26). However, very low attentions were given to the “removal”, “toxicity”, and “fish” keywords. There is no word found in even detection or sensing of food and pharmaceutical waste in these searches, which revealed the lack of studies in this area. To detect these compounds in environmental matrices, highly sensitive and selective analytical methods, such as liquid chromatography-tandem mass spectrometry (LC-MS/MS), are essential. Effective sample treatment is practiced to deliberately remove matrix interferences from the analytes of interest (Dimpe and Nomngongo, 2016).

2.2. Soil pollution basics

The soil is the earth’s skin, a mantle riddled with scars, thousand-year-old wrinkles, and more recent wounds inflicted by both man and nature. Although many studies (Chapman et al., 2019; Smith, 2019; Gupta Pankaj, 2020; Fonseca et al., 2021) emphasize the potential impact of pollutants deposited in floodplains on surface water quality, considerably less consideration is paid to measuring metal flux with groundwater demanding contaminated alluvial soils. Soil health is critical to ecosystem services, providing food, fibre, fuel production and regulatory, cultural, and supporting components. Because soil is a universal sink, it bears the brunt of environmental contamination. In many parts of the world, the rapid growth of urbanization and industrialization has resulted in severe soil pollution (Yaylali-Abanuz, 2011). It is growing more contaminated and is becoming more polluted in various

ways; thus, controlling soil pollution is urgently needed to maintain soil fertility and improve production. Pollution is described as an alteration in the biological, chemical, or physical features of air, water, or soil that negatively affects human life, the lives of other critical living animals and plants, industrial development, living situations, and cultural possessions (Ashraf et al., 2014). There are a variety of compounds that may contaminate soils, ranging from simple inorganic ions to complex organic molecules, and they can be separated into two groups: inorganic and organic. The greatest significant inorganic pollutants in soil are heavy metals such as zinc, arsenic, mercury, cadmium, chromium, and copper. Organic wastes found in soil could include herbicides, carbamate and organophosphorus insecticides, polycyclic aromatic hydrocarbons, polychlorinated dibenzofurans, polybrominated biphenyls, polychlorinated biphenyls, organic fuels, especially gasoline and diesel. Fig. 4 summarizes the major sources of developing organic pollutants pollution in the environment, including examining important sources, routes, and fates of emerging organic contaminants in the subsurface that may contribute to soil and groundwater contamination. Point providers to the soil zone and water resources include sewage treatment plants, hospital effluent, industrial effluent, and septic tanks, to name a few. On the other hand, diffuse pollution is difficult to identify as a particular place over a wide range of geographical scales.

Pharmaceuticals, detergent metabolites, perfumes, antimicrobials, pesticides, and industrial chemicals are among the organic pollutants discovered in soil. Pharmaceuticals and personal care products, one of the growing biological impurities, has recently been recognized as a chemical of increasing environmental significance. It’s been extensively utilized in human medicine to cure or prevent illnesses and agriculture as veterinary medicines and growth boosters. As seen in Fig. 5, previous research focused on soil, pharmaceutical, and personal care products. Still, very little attention was given to techniques to remove toxicity and detect hazardous materials between 1970 and 2021. Thus, it is crucial to

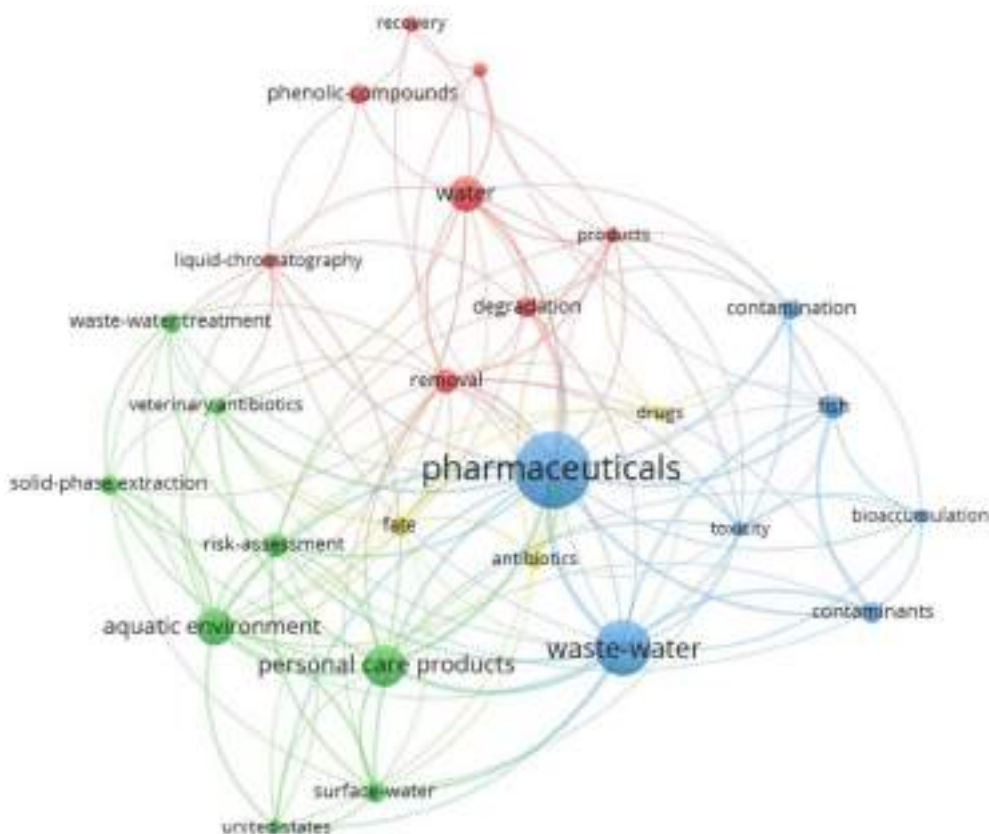


Fig. 3. Network visualization curves for the link between the 145 detected studies of “water”, “pollution”, “food” and “pharmaceutical”, matching to the complete record of publication, reflecting the period of 1970–2021, four clusters with minimum keywords of 5.

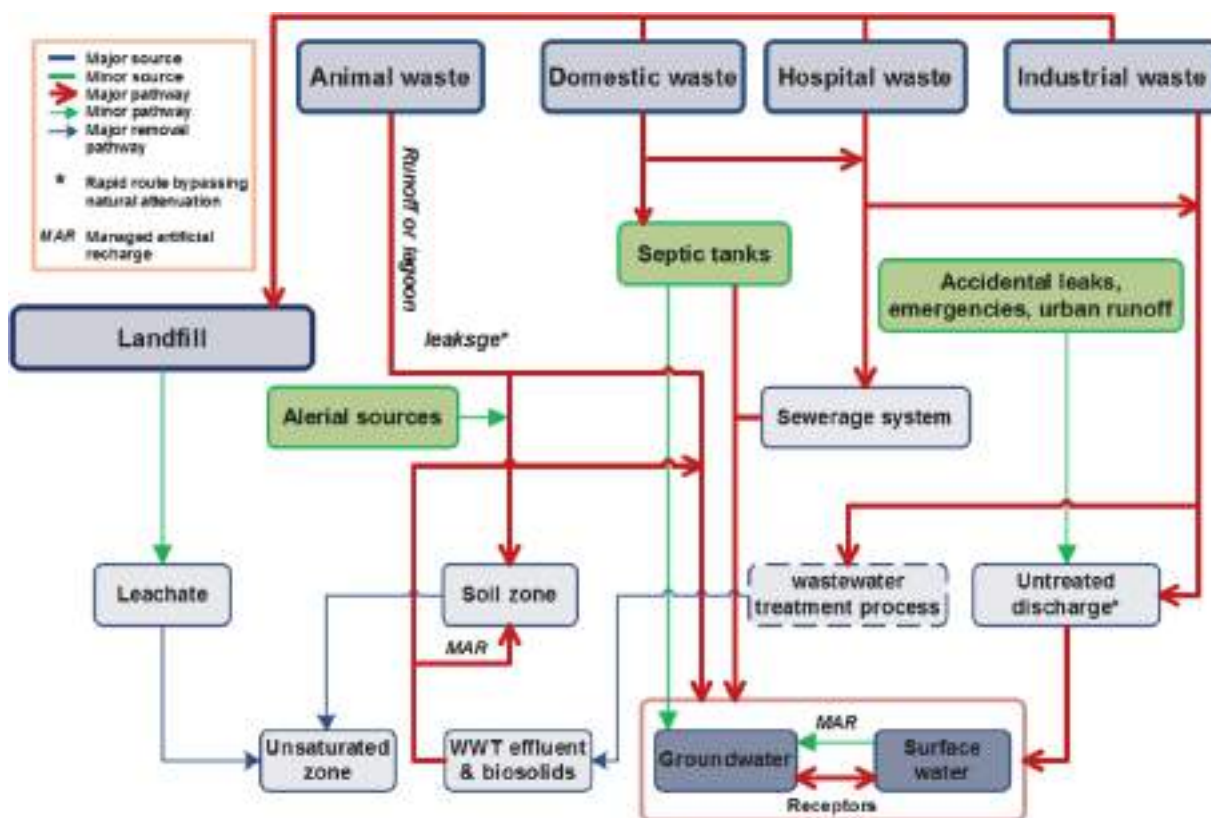


Fig. 4. Graphic drawing, utilizing the source-pathway-receptor method, emphasizing prospective pathways and sources for groundwater effluence by emergent organic pollutants (Lapworth et al., 2012).

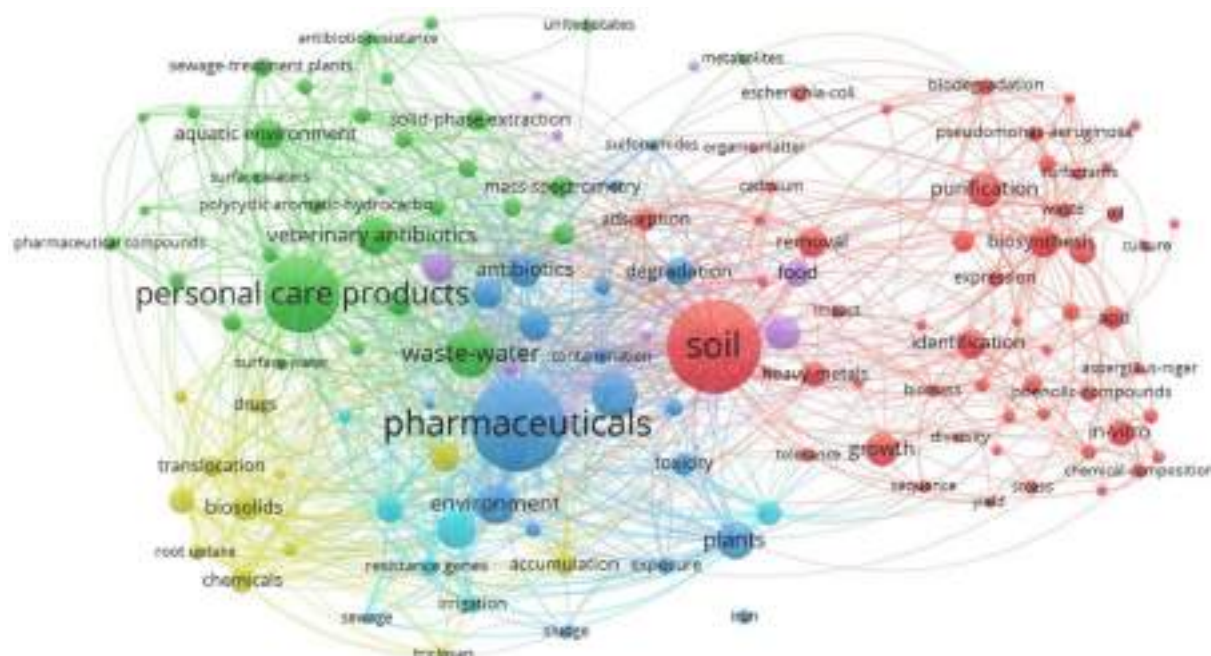


Fig. 5. Network visualization map for the link among the 515 detected studies of “soil”, “food”, and “pharmaceutical”, rendering to the complete record of journals, reflecting the time-span 1970–2021, four clusters with minimum keywords of 5.

understand which methods and characteristics may be utilized to determine if pollutant concentrations are potentially degradative to soil, soil organisms, and plants (He et al., 2018). As a result, the ability to detect and monitor these wastes are critical to our health.

3. Methods for sensing pharmaceutical pollutants

Many analytical techniques are needed to detect polar and non-polar organic molecules in the dissolved and suspended phases, detecting

pharmaceutical drugs and affecting water quality.

3.1. Spectroscopic methods

Spectroscopic methods have sparked substantial interest in the biotechnology field in recent years. In forensic labs, spectroscopic methods are often employed for quantitative and qualitative analysis. The technical development and improvements in spectroscopic techniques to examine complicated materials have recently been assigned significant significance. The following subsections will describe two types of spectroscopic techniques, nuclear magnetic resonance and near-infrared spectroscopy.

3.1.1. Nuclear magnetic resonance (NMR)

The spectroscopic method of nuclear magnetic resonance spectroscopy, often known as NMR spectroscopy or magnetic resonance spectroscopy (MRS), is used to detect local magnetic fields surrounding atomic nuclei. This sensor was discovered in the context of substantial prior research into fast nutrition monitoring, which primarily resulted in techniques based on electric conductivity measurements (Moral et al., 2005; Provolo and Martínez-Suller, 2007; Yagüe and Quílez, 2012). NMR is a vital technique for determining interactions, dynamics, and molecular structures in basic to complex systems and molecules and in different physical phases (gas, liquid, gel, and solid) (Alves Filho et al., 2015). NMR spectroscopy offers some advantages; To begin with, NMR is a quick method that is ideal for identifying unstable chemicals. Second, two-dimensional (2D) and one-dimensional (1D) spectra may be used for compound identification. Third, NMR spectroscopy is quantitative and qualitative, allowing concentrations to be determined without the necessity of commercial or synthetic standards. Fourth, NMR does not demand any sample preparation, and finally, NMR is a nondestructive technology. Due to the poor sensitivity of the technique (sensing limit of $\sim 1 \mu\text{M}$), the findings should be verified using more competitive analysis tools like mass spectrometry (Singh and Mehta, 2020). As a result, NMR has undergone several enhancements for directional and multifunctional analysis. The effective use of solid-state ^{13}C cross polarisation magic angle spinning nuclear magnetic resonance (^{13}C CP MAS NMR) to identify humic and fulvic components of soil, peat (Preston et al., 1987) and sludge (Aldmour et al., 2019; Hatcher et al., 2019; Mayans et al., 2019), showed its utility in evaluating soil and solid waste environments. Working with highly tiny quantities of adsorbent (45 mg) and slight mixture ratios (350 μl) was possible with the suggested technique. On-site NMR in industrial applications have also been developed (Sørensen et al., 2014; Trujillo-Reyes et al., 2014). However, cyanide can only be identified at high concentrations owing to its limited natural loads and low magnetogyric volumes of nitrogen-15 and nuclei carbon-13 (Mazumder et al., 2013). The NMR spectroscopy of derivatives may be utilized to detect and identify analytes retrospectively (Mazumder et al., 2012). This method can provide NMR analysis the sensitivity and selectivity it requires. Proton nuclear magnetic resonance (^1H NMR) spectroscopy was used by Achim and coworkers (Preiß et al., 1997) to analyse explosives and associated chemicals in ground-water samples. This technique has the benefit of allowing the analysis of polar nitroaromatic compounds, such as nitrophenols and nitrobenzoic acids, to be carried without derivatization.

3.1.2. Near-infrared spectroscopy (NIR)

The near-infrared analysis is a precise and quick technique for determining the main components in a wide range of foods and agricultural goods. There are four kinds of NIR systems: functional, frequency domain, time domain, and continuous, as well as many commercially available instruments. The employment of various technological components to generate continuous NIR readings distinguishes those instruments. Their resultant values aren't always interchangeable, and just a few researchers have attempted to compare them (Denault et al., 2018). NIR has many benefits for agricultural and

food product analysis, including speed (1 min or less per sample), appropriate in solid, liquid or gaseous samples, environmental acceptability and suitable for at-line and on-line uses, non-invasivity, non-destructivity, nearly universal application (any particle comprising O–H, S–H, N–H, or C–H bonds), and the absence of sample preparation (Ciurczak and Igne, 2014). Because of this method's speed, simplicity, and excellent accuracy when combined with chemometrics, it is feasible to anticipate the chemical compounds contained in any material. The major drawback of NIR measurements is that the outcomes (reported as absorbance) are not directly equivalent to those achieved using traditional analytical techniques. As a result, since NIR spectra are often wide absorbing and overlapping (Manley, 2014), analysing the target analyte from complex matrices, such as pharmaceutical wastewater, without any separation processes (Fu et al., 2012). Chemometric methods such as partial least squares regression (PLSR), principal component analysis (PCA), and multiple linear regression analysis (MLRA) should be used to measure the findings of NIR spectroscopy and then followed by chemometric modellings (Beć et al., 2021). The advances in chemometrics have enabled researchers to overcome the challenges posed by the spectra's inherent complexity. As a result, the combination of fourier transform (FT)-NIR and chemometrics is now regarded as a promising technology capable of quantifying a wide range of organic compounds (Quintelas et al., 2019).

3.2. Chromatographic methods

Mikhail Semyonovich Tswett from Russia, working as a plant scientist at the University of Warsaw in Poland (Tswett, 1906), developed chromatography in 1903. Initially, organic compounds were separated and determined primarily using liquid chromatography (LC), thin-layer chromatography (TLC), and gas chromatography (GC). At both the preparative and analytical phases, chromatographic techniques were employed. The complex processes and lengthy analysis periods are, yet, the drawbacks of chromatographic techniques. The resolution of the two valent forms may be weak in certain instances.

3.2.1. Gas chromatography

Gas chromatography (GC) is an analysis method for splitting chemical compounds in a test sample and then sensing them to classify their absence or presence and how much each constituent is there. A thorough examination of analytical techniques has been carried out (Boulard et al., 2018). Nevertheless, environmental science commonly obtains evidence on the distribution of contaminants over time (Zhong et al., 2021). Therefore previous study (Manasfi et al., 2021) focused on developing an analytical methodology that allows for the simultaneous determination of Salbutamol, Propranolol hydrochloride, Paracetamol, Mefenamic acid, and Ibuprofen at low concentrations in waters and wastewaters using a combination of methods. Regrettably, carboxylic acid and hydroxyl moieties' derivatization of a less polar group is often required for GC–MS analysis of pharmaceutical and personal-care goods. After chemical derivatization with diazomethane, several GC–MS techniques for recognizing polar pharmaceuticals in wastewater samples have been developed (Nosek et al., 2014). The existence of functional groups with “active” but weakly reactive hydrogens (e.g., amides, amines, aliphatic –OH clusters, and certain phenols), for which forceful derivatization substances are needed, is another difficulty in the study of medicines by GC.

3.2.2. HPLC, liquid chromatography

The development of analytical equipment, particularly the maturing of liquid chromatography coupled to mass spectrometry (LC–MS), has aided the fast growth of these new pollutants during the past 10–15 years. Because many of these compounds are non-volatile and include polar functional groups, LC–MS benefits direct injection (Deventer et al., 2014), while gas chromatography (GC) may need a derivatization step and is frequently inappropriate for higher molecular weight and polar

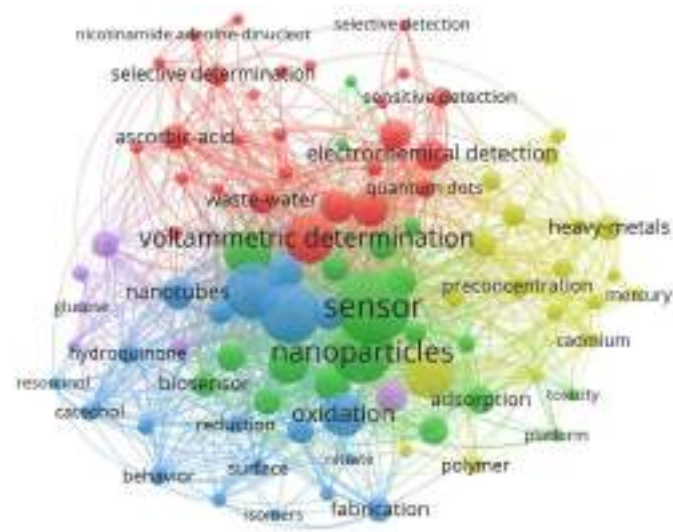


Fig. 7. Co-occurrence network map of keywords about research on “electrochemical”, “sensor”, “carbon” and “wastewater”.

Fig. 7) to illustrate the causing concept map to picture the relationship associations among category and main keywords. In this figure, five diverse clusters were recognized and marked with different colors. The colour indicates the cluster in which the keyword is included based on the number of co-appearances, and the size of the circle represents the number of articles in which each term occurs. The more often the essential term appears, the bigger the circle becomes. A short distance between them represents a high number of co-occurrences of two words. The figure comprises four significant keywords with the highest total link strengths detected for sensor (235), nanoparticles (197), glassy-carbon electrode (185) and electrochemical sensor (164). Each of these keywords is the cluster’s most related keyword. The clusters are interconnected, demonstrating the complimentary features of various research topics in carbon-based electrochemical sensors. The red colour cluster indicated wastewater and carbo; the blue cluster represented medicines, and the green cluster represented toxicity. The wastewater cluster was the most tightly connected, having the most connections, followed by pharmaceuticals and toxicity. Carbon compounds, effluent, medicines, and toxicity, on the other hand, were discovered on the outskirts, suggesting a lower frequency and connection with other nodes. Based on the above analysis results, there is a lack of research hotspots in carbon-based materials for detecting pharmaceuticals present in wastewater.

3.4. Spectrophotometry

Spectrophotometry is the quantitative measurement of a material’s absorbance or transmission properties as a function of wavelength. The basic principle is that most molecules absorb light over a specific range of wavelengths in the ultraviolet and visible regions of the spectrum. This technique is a standard and low-cost method to measure light absorption or the number of chemicals in a solution. Besides, spectrophotometry may be used to determine the trace levels of drugs in wastewater, especially in combination with extraction to separate special-purpose components from the primary admixture. The choice of reagents is essential with spectrophotometric methods as the proper reagent could increase the sensitivity and selectivity of a particular element in wastewater. The spectrophotometric determination of dapsone, flutamide, dopamine hydrochloride, isoniazid, and catechol derivatives with various reagents was reported in the previous study (Nagaraja et al., 2002). For instant, Ardeshir and coworkers (Shokrollahi et al., 2008) stated that the eriochrome cyanine R is a suitable reagent for the determination of Al(III) that has high sensitivity ($\epsilon = 6.5 \times 10^4$ L

$\text{mol}^{-1} \text{cm}^{-1}$). After using three keywords of “spectrophotometry”, “pharmaceutical”, and “wastewater” in the topic search of the WoS database, only 33 published works were detected. For example, Snawar and co-authors (Hussain et al., 2020) developed precise, accurate, and reliable spectrophotometric methods to detect venlafaxine in highly polluted wastewater. The noticeable features of their approach include minimum processing steps, the absence of secondary extraction steps or the use of carcinogenic solvents, and its robustness against excipients usually present in the aquatic environmental samples. Nevertheless the reported method was not sensitive enough to test the ultra-trace-level pharmaceutical concentrations in the vast surface waters. Another study focused on detection of veterinary pharmaceuticals (ractopamine, sulfamethoxazole, oxytetracycline, and enrofloxacin) in pig farm wastewater by fluorescence spectrophotometry (León-Aguirre et al., 2019). The detection of these pharmaceuticals in the effluents of treated wastewater from the biodigesters of the pig farms suggests the need to optimize the system and prevent the entry of these compounds into the environment. Thus, an accurate reagent and proper development are required for the spectrophotometry method for detecting pharmaceutical components in the wastewater.

4. Carbon nano-materials for pollutant sensing

Adsorption, filtration, advanced oxidation processes (AOPs), photocatalysis, and other techniques may be used to remove organic contaminants and pharmaceutically active substances using nanomaterials (Cai et al., 2018; Gholami et al., 2020; Nazal, 2020; Yousef Tizhoosh et al., 2020). Carbonaceous nanoparticles as adsorbents can remove per- and polyfluoroalkyl substances (PFASs) pollutants from aqueous environments; electrostatic and hydrophobic interactions, hydrogen bonding, and ligand exchange are the primary processes for perfluorooctane sulfonate and perfluorooctanoate adsorption (Saleh et al., 2019; Liu et al., 2020). Carbon nanotubes and silicon nanowires are examples of nanomaterials that can be easily functionalized and used as nanosensors or nanodevices for ultrasensitive pollution monitoring. Carbon’s relative abundance has been calculated to be between 180 and 270 parts per million (Allègre et al., 1995). In this respect, newly designed nanomaterials with large surface areas and exceptional reactivities are highly promising for sensing and eliminating these dangerous pollutants (Zhang et al., 2019b). For example, carbon nanotubes and graphene have high electrical conductivity and are used to make field-effect transistor sensors to detect heavy metal ions (Su et al., 2012). Numerous studies have demonstrated that nanoparticles have a lot of promise and capacity in water and wastewater treatment, especially in the fields of disinfection and sensing (Das et al., 2015), catalytic oxidation (Ayati et al., 2014), membrane process (Pendergast and Hoek, 2011), and adsorption (Ali, 2012). Carbon-based (nano) materials offer an unusually high surface-to-area ratio, excellent chemical stability, cheap cost, and a minimal chemical effect on the environment. These advantages make them ideal for treatment and suitable adsorbents for organic pollutants in aqueous solutions (Yang et al., 2011; Wei et al., 2013). Graphene, fullerenes, multi-walled carbon nanotubes (MWNTs), and single-walled carbon nanotubes (SWNTs) and are only a few examples of nano-scale carbon-based materials (Wanekaya, 2011), as shown in Fig. 8. The processing techniques for making carbon-based magnetic nanomaterials seek to utilize carbonaceous material as a substrate and add magnetic characteristics to the matrix by including magnetically active components. Hydrothermal carbonization, chemical co-precipitation, pyrolysis, and ultrasonication are all low-cost and time-effective ways to make magnetic nanomaterials. Each technique alters the final result in a unique way and has its own set of limits and drawbacks. Fig. 9 shows how structural cooperation of diverse magnetic and carbon constituents may lead to the creation of numerous morphological magnetic carbon nano-materials generated by these techniques.

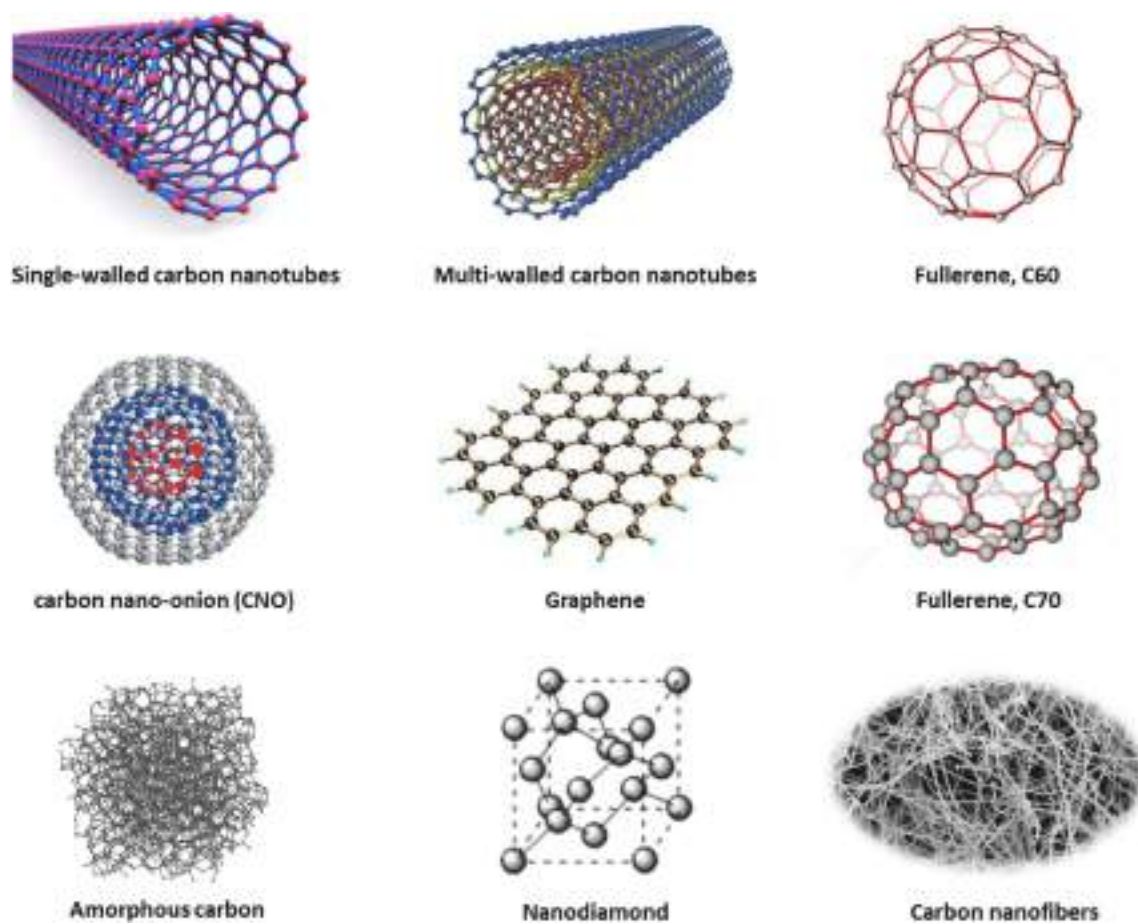


Fig. 8. Some examples of nano-scale carbon-based materials.

4.1. Carbon black

Carbon black is a significant genus of industrial carbons produced from petrochemicals and utilized mainly as strengthening means in rubber and as black pigments in inks, plastics, and coatings. Carbon black (CB) is a carbonaceous nanostructured material with appealing electrochemical characteristics, including high conductivity, chemical stability, a large specific surface area, and the ability to create a stable dispersion without the necessity of complex processes (Silva et al., 2017; Deroco et al., 2018). Due to its unmatched advantages, such as low price, high specific surface area, good conductivity, and interface performance, CB has been used as catalysts and modifiers for fuel cells, lithium batteries, and sodium batteries (Tran et al., 2011). Environmental friendliness, cheap pricing, low electrical resistance, a stable structure, good conductivity, and strong interface performance are all crucial features of conductive carbon black. It is a modifier with unrivalled benefits (Gupta and Tai, 2019). Doping conductive carbon black into an electroplating deposition solution increases the solution's conductivity and ion transfer rate, resulting in improved conductivity of the produced electrode (Song et al., 2019a). These techniques are often used for sterilization, disinfection, deodorization, and related microbiological applications (Savariraj et al., 2020). The electrochemical method is one of the standard techniques for wastewater treatments. Since 2007, CB has been acknowledged as a trustworthy nanomaterial for the construction of electrochemical sensors (Hocevar and Ogorevc, 2007), and a growing number of (bio)sensing configurations have been suggested, as emphasised by relevant research groups (Lo et al., 2012; Vicentini et al., 2015). CB's excellent electrochemical performances have boosted the usage of this cost-effective and sustainable nanomaterial in building electrochemical (bio)sensors as a result of these early attempts. Fig. 10

shows how this carbon-based material is becoming more important in the design of electrochemical (bio)sensors. Previous investigations (Arduini et al., 2010, 2012; Cinti et al., 2015, 2017; Talarico et al., 2015) used the electrochemical properties of CB to create a number of miniaturised and low-cost sensors for the detection of a variety of chemicals, including hydrogen peroxide, thiocholine, cysteine, and nicotinamide adenine dinucleotide. Furthermore, other research groups, such as Compton's and Fatibello-Filho's, have produced CB modified-glassy carbon electrodes to measure uric acid, dopamine, ascorbic acid, nicotine, and paracetamol, to mention a few (Lo et al., 2012; Hou et al., 2014; Batista Deroco et al., 2015; Shamagsumova et al., 2015; Wu et al., 2015; Vicentini et al., 2016). After title searching in the WoS database using "carbon", "black", and "wastewater" keywords, there are only 11 papers detected, which are listed in Table 1. It was found that carbon black (CB) presence as catalysts, support, or conductive materials could significantly enhance wastewater remediation.

4.2. Carbon nanotubes

Carbon nanotubes (CNTs) are particles with cylindrical shapes made up of rolled-up single-layer carbon atom sheets (graphene) that were discovered in 1991 (Iijima, 1991). Single-walled nanotubes have a diameter of fewer than 2 nm (nm). In contrast, multi-walled nanotubes have a diameter of more than 25 nm and are composed of numerous concentrically linked nanotubes that form an array of concentric cylinders. Their length may range from a few micrometres to millimetres. Because of the low friction of water on their smooth inner surfaces, which resemble biological water channels, carbon nanotubes are one of the most promising scaffold architectures for artificial water channels. Because of their exceptional mechanical, electrical, thermal, and

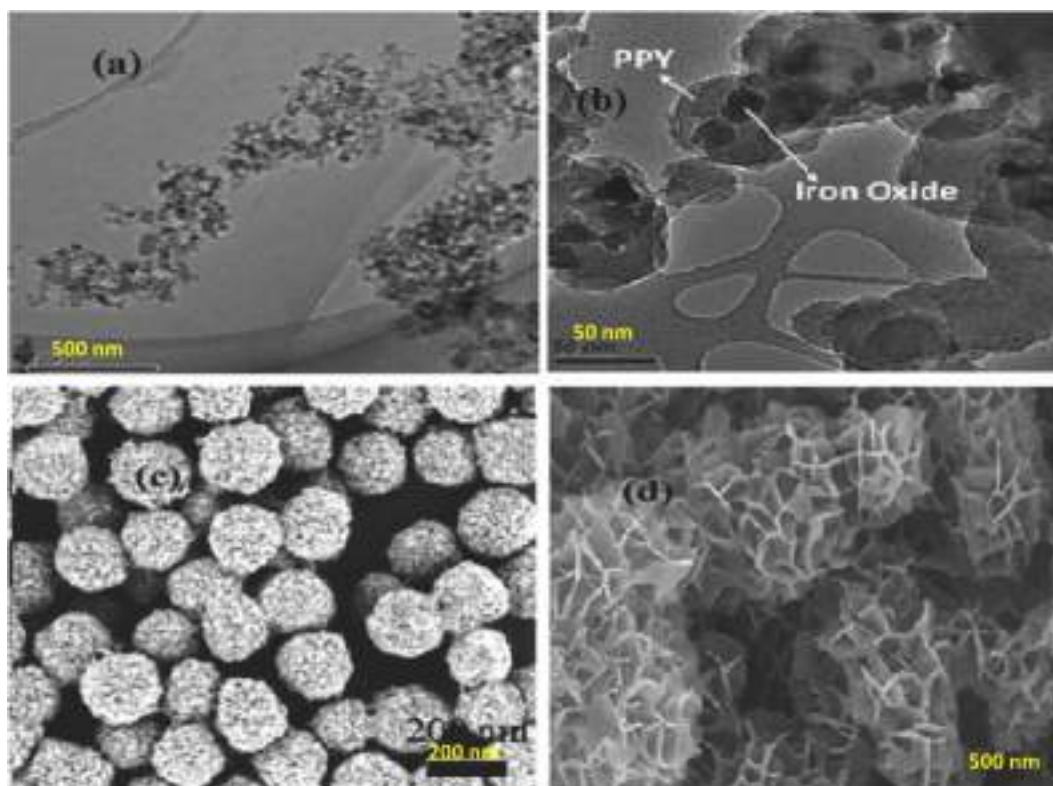


Fig. 9. TEM pictures of several magnetic nano-materials; a) magnetic carbon nano-composite, b) magnetic polypyrrole nano-composite c) magnetic carbon nano-clusters d) magnetic carbon nano-flowers (Siddiqui et al., 2019).

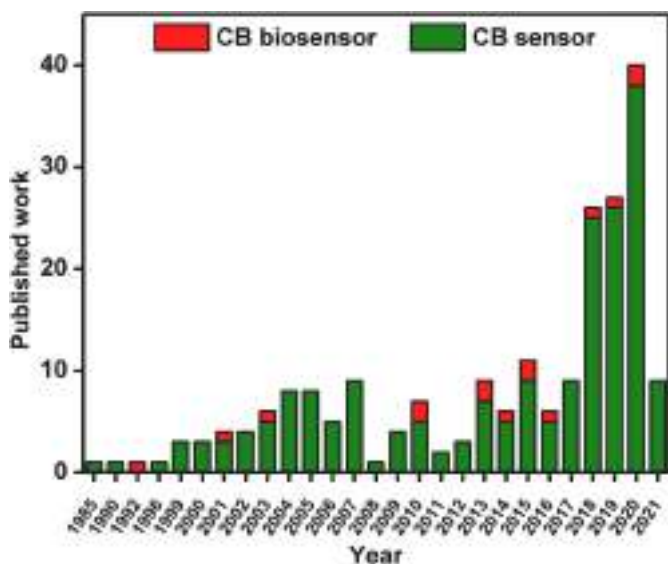


Fig. 10. Available studies linked to utilizing CB as nanomaterials for electrochemical (bio)sensor and their spreading amongst biosensors and sensors.

structural characteristics, carbon nanotubes have shown tremendous promise in applications as composite reinforcements, field emitters for flat panel displays, sensors, energy storage and energy conversion devices, and catalytic support sites (Li et al., 2007; Tehrani and Khanbolouki, 2018). Because of its unique structural, mechanical, electrical, optoelectronic, semiconductor, chemical, and physical characteristics, CNTs have driven research into new areas in several studies (Gupta et al., 2016; Kumar et al., 2018). CNTs are practical adsorbents for heavy metal removal due to their chemical stability, huge specific surface area

(150–1500 m²/g, which is several times more than fullerenes), and obtainability of well-developed mesopores (Gupta et al., 2011; Wang et al., 2012). Electrostatic attraction, sorption–precipitation, and chemical interaction between metal ions and the surface functional groups of CNTs seem to be the processes by which metal ions are sorbed onto CNTs (Anitha et al., 2015). After employing the keywords such as “carbon”, “nanotube”, and “wastewater”, 197 published works have been detected so far, and the network visualization plots are shown in Fig. 11. A significant contribution was given to adsorption, aqueous-solution, and removal research areas; however, shallow intentions were given to pharmaceuticals, toxicity, dye, etc. Pharmaceutical wastewaters are the primary source of pharmaceuticals in the environment (Gadipelly et al., 2014). Because the quantities are modest and various products are generated from the same battery of separators and reactors, a unique treatment is not tried because the wastewater flowing out of pharmaceutical units varies in content and concentration. Non-steroidal anti-inflammatory drugs (NSAIDs) are typical pharmaceuticals found in wastewater (El-Sheikh et al., 2019). Pharmaceutically-active compounds (PhACs) pollution of the aquatic environment has sparked widespread worldwide concern (Zhan et al., 2019). There are different methods for using CNTs in the treatment of pharmaceutical wastewater, such as photocatalysis and adsorption. According to Min-Quan and co-authors (Yang et al., 2014), adding CNT to TiO₂ improves its adsorptive capabilities while cause decreasing nanocomposites’ band gap energy (E_g). Some studies investigated the influence of CNT geometrical dimensions on its removal performance toward (Vijayan et al., 2019); adsorption and SPE of nitro-phenols and chloro-phenol from water (El-Sheikh et al., 2012), adsorption and SPE of Hg(II) (El-Sheikh et al., 2011) and simultaneous solid-phase extraction of different metal ions (Cd(II), Mn(II), Pb(II), Zn(II), Cu(II), Ni(II), Co (II)) (Djerahov et al., 2016). The three potential methods of photocatalysis improvement in CNT–TiO₂ compounds were reported in the previous studies (Woan et al., 2009; Leary and Westwood, 2011). According to the original hypothesis, the metal nanoparticles doped TiO₂

Table 1

Published work in the WoS database using “carbon”, “black”, and “wastewater” keyword for title search.

No.	Title	Remarks	Ref.
1	“removal of an ionic surfactant from wastewater by carbon blacks adsorption”	The porosity of the samples has a significant impact on adsorption in sodium dodecyl sulphate.	González-García et al. (2002)
2	“Functionalized carbon black nanoparticles used for separation of emulsified oil from oily wastewater”	A new demulsifier is given for the demulsification of emulsified oily effluent.	Wang et al. (2018)
3	“Activated carbon supported iron-nickel bimetallic nanoparticles for decolorization of Reactive Black 5 wastewater”	The nFeNi-GAC compound proved successful in decolorizing RB5 effluent.	Shu et al. (2015)
4	“Removal of phenol and chlorine from wastewater using steam activated biomass soot and tyre carbon black”	For wastewater treatment, steam activated biomass soot and tyre carbon black are potential options.	Trubetskaya et al. (2019)
5	“Photocatalytic degradation of real textile wastewater using carbon black-Nb ₂ O ₅ composite catalyst under UV/Vis irradiation”	The enhanced photocatalytic activity of the Nb ₂ O ₅ over carbon black (CB) catalyst was ascribed to an increase in adsorption capacity and the bandgap narrowing caused by CB impregnation, which redshifted the absorption edge wavelength to the visible range.	Domingues et al. (2021)
6	“Adsorption application of activated carbon from ripe black locust seed pods for wastewater taken from Ergene River, Turkey”	In the Ergene River sample, activated carbon derived from mature black locust seed pods performed well in removing most elements, unpleasant odours, and colour.	Üner et al. (2021)
7	“Application of carbon black and iron phthalocyanine composites in bioelectricity production at a brewery wastewater fed microbial fuel cell”	The usage of FePc and carbon black in combination resulted in higher power densities.	Mshoperi et al. (2014)
8	“Enhancement of the electrocatalytic oxidation of antibiotic wastewater over the conductive black carbon-PbO ₂ electrode prepared using novel green approach”	The addition of conductive carbon black may boost efficiency, encourage the production of hydroxyl radicals, and speed up the oxidation of metronidazole.	Wang et al. (2019)
9	“Photoelectrocatalytic performance of conductive carbon black-modified Ti/F-PbO ₂ anode for degradation of dye wastewater (reactive brilliant blue KN-R)”	The incorporation of conductive carbon black into the PbO ₂ coating inhibited the growth and aggregation of PbO ₂ crystal grains, resulting in the formation of porous structure and the preferential development of the (101) and (301) planes of the PbO ₂ crystal, as well as increased oxygen evolution over	Zhou et al. (2018)

Table 1 (continued)

No.	Title	Remarks	Ref.
10	“Enhancing oxygen reduction reaction by using metal-free nitrogen-doped carbon black as cathode catalysts in microbial fuel cells treating wastewater”	potential and carrier density. Carbon powder was treated with sulfuric acid and nitrogen-doped to improve a slow oxygen reduction process activity.	Wang et al. (2020a)
11	“Effect of black carbon on the migration and biodegradation of pentabromodiphenyl ether (BDE-99) during natural groundwater recharge with treated municipal wastewater”	The residual BDE-99 levels in the black carbon amendment column were significantly greater than in the silty clay column at various depths.	Ma et al. (2016)

can play an efficient role ([Orooji et al., 2021](#)) and a high-energy photon excites an electron from the valence band to the conduction band of anatase TiO₂. According to Wang’s second concept, CNTs are sensitizers that transfer electrons to TiO₂. On the other hand, the mechanism may be more complicated since it is the result of two variables. The first is related to the increased light absorption that occurs when the C–O–Ti link is present (carbon doping). The last component is linked to a higher number of faults causing mid-band-gap phases ([Leary and Westwood, 2011](#)).

CNTs may be used in various waste water treatment applications and can play a vital role in removing organic salts, poisonous dyes, and heavy metals from water. For an instant, it can be used either as a direct filter or as a filler to improve the membrane performance. The immobilization of carbon nanotubes in the pores of a hydrophobic membrane is shown to positively modify water membrane interactions, promoting vapour permeability while limiting liquid entry into the membrane pores. Gethard and coworkers ([Gethard et al., 2011](#)) showed that CNTs might act as a sorbent in CNT-polyvinylidene fluoride membranes to offer an alternative route for solute transport, as illustrated in [Fig. 12](#).

4.3. Activated carbon

Because of its vast surface area, polymodal (but basically microporous) porous structure, high adsorption capacity, and changeable surface chemical composition, activated carbon is the major flexible adsorbent ([Saleem et al., 2019](#)). Activated carbon is generated from high-carbon substance trash in the environment. For the production of activated carbons, lignocellulosic and coal materials have been utilized as raw constituents. Activated carbon is produced from various carbonaceous materials that have been treated to improve its adsorptive characteristics. Wood, wastewater treatment sludge, sugar, pulp mill black ash, petroleum-based wastes, pecan shells, peat, lignite, coconut shells, bones, and bituminous coal are the main materials used to produce activated carbon. Chemical and physical activations are the two methods for making activated carbon utilized in water purification operations. There are two types of activated carbon that have been stimulated: The H-type and the L-type ([Ahmad and Azam, 2019](#)). The L-type carbon is a more powerful solid acid than the H-type carbon, which has a negative charge in water and can neutralize strong bases while remaining hydrophilic. When put into water or treated with strong acids, H-type carbon takes on positive charges and is classified as hydrophobic. Only a few research studies on removing pharmaceuticals from aqueous media by activated carbons have been published to our knowledge. Most of the time, commercially available carbons were used ([Calisto et al., 2015](#); [Li et al., 2018](#)). Furthermore, because of its adsorption capability and ability to be recovered, granulate activated carbon is often used in various treatment facilities throughout multiple nations. If granulated activated carbon (GAC) is utilized instead, the

sensors, wastewater, personal care products and aqueous solutions.

4.5. Graphene

Graphene is a new wonder material that has piqued scientists' interest in recent years. It's a carbon allotrope composed of a single layer of atoms organised in a honeycomb lattice in two dimensions. Like other carbon-based materials, Graphene has a large surface area, better charge mobility and thermal conductivity, flexibility, and chemical stability, and has been utilized as a quick adsorbent for a variety of contaminants (Zhang et al., 2019a; Pan et al., 2020; Wu et al., 2020; Sadeghi Rad et al., 2022). At the moment, the most popular method for making graphene is to use graphene oxide (GO) as a precursor. The excellent properties associated with a defect-free and single-layer 2D graphene sheet have yet to be fully realized in the reported graphene-based materials (Yang et al., 2014) due to irreversible aggregation or restacking of graphene sheets during the wet chemistry preparation and the lower electronic conductivity of the prepared GO-derived graphene (i.e., reduced graphene oxide, rGO) (Loh et al., 2010; Zhang et al., 2011). Despite its higher cost than conventional adsorbents, several factors may contribute to graphene adsorption becoming a competitive technology in the future, including (i) lower effluent toxicity, (ii) high expected process efficiency (resulting in a lower regeneration frequency), and (iii) higher specific surface area of graphene (resulting in a lower volume for water treatment), (iv) stricter regulation on urban wastewater disposal, and (v) more technological development (with anticipated lower costs) (Rizzo et al., 2015). The adsorption ability of graphene for the removal of heavy metal ions (Cr^{6+} , Cd^{2+} , Pb^{2+} , etc.) (Deng et al., 2010), dyes (Ramesha et al., 2011), and bisphenol A (Xu et al., 2012) from aqueous solutions has been described in the literature. Al-Khateeb and coworkers (Al-Khateeb et al., 2014) researched pharmaceuticals adsorption onto graphene material which revealed high proficiency when employed for the aspirin, caffeine, and acetaminophen removal from actual ecological

samples such as red sea water, waste water, and TAP water. The benefit of graphene over other carbonaceous materials is its ability to selectively adsorb aromatic molecules with benzene rings via strong π - π interactions (Cai et al., 2011). Ramin and coauthors (Hassandoost et al., 2019) stated that the unbounded π electrons of graphene deliver a remarkable capacity for adsorbing pollutant molecules via π - π interactions and a stage for even diffusion of particles. As a result, graphene is anticipated to be a viable adsorbent in water treatment to eliminate aromatic compounds. Fig. 15 shows the adsorption flow diagram of pharmaceutical pollutants on graphene-based constituents. 13 papers have been detected when applying "graphene", "wastewater", and "pharmaceutical" in the title search of the WoS database and are reported in Table 2. However, the application of porous graphene as a tertiary treatment filter for the subtraction of widely consumed pharmaceutical pollutants has not been fully explored yet. As a result, there is a need to create new, stable, and readily separable composite materials for the pharmaceutical and personal care items removal from water and wastewater and a better understanding of the process' mechanism.

4.6. Other carbon nano-sized materials

Carbon-based adsorbents are often employed to eradicate heavy metals from an aqueous solution. Other carbon nanomaterials such as mesoporous carbon (Kalate Bojdi et al., 2015; Pollap et al., 2018) and biochar (Dong et al., 2018) have also been used in the development of (bio)sensors for emerging pollutants in waterways. Thuan and coworkers (Van Tran et al.; Tran et al., 2019a; Tran et al., 2019b) produced hierarchically mesoporous carbon by pyrolyzing the Fe-MOF precursor to quickly and effectively remove antibiotics such as ibuprofen (206.5 mg/g), ciprofloxacin (90.0 mg/g), chloramphenicol (96.3 mg/g), and tetracycline (224 mg/g). The transformation of different kinds of metal-organic frameworks into new mesoporous carbons for antibiotic treatment was described by Sung and co-authors (Ahmed et al., 2018; An

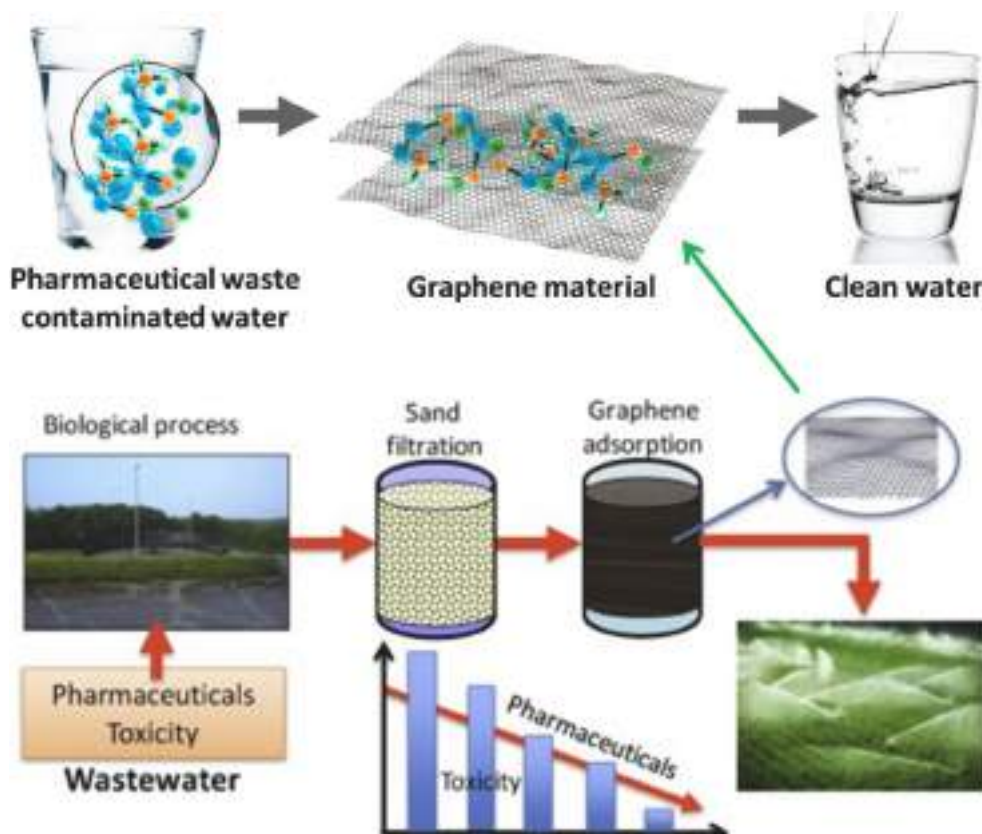


Fig. 15. Pharmaceutical waste adsorption on graphene-based constituents (Rizzo et al., 2015; Carmalin Sophia et al., 2016).

Table 2

Published work in the WoS database using “graphene”, “wastewater”, and “pharmaceutical” keyword for title search.

No.	Title	Remarks	Ref.
1	“Performance evaluation of porous graphene as filter media for the removal of pharmaceutical/emerging contaminants from water and wastewater”	An adsorption column filter with porous graphene packing of optimized design and operation parameters could potentially be used as a highly efficient tertiary treatment unit for the removal of pharmaceutical contaminants	Khalil et al. (2021)
2	“Performance and reaction mechanism of MgO/ZnO/Graphene ternary nanocomposite in coupling with LED and ultrasound waves for the degradation of sulfamethoxazole and pharmaceutical wastewater”	The combination of graphene nanosheets, UV-A, and US waves may be used to treat actual pharmaceutical wastewaters in practical applications in a new and efficient way.	Moradi et al. (2020)
3	“Modeling the mineralization kinetics of visible led graphene oxide/titania photocatalytic ozonation of an urban wastewater containing pharmaceutical compounds”	From a kinetics standpoint, the influence of photochemical processes within the first 10 min is minimal; thus medicines may be regarded solely consumed with ozone.	Beltrán et al. (2020)
4	“Designing AgFeO ₂ -graphene/Cu ₂ (BTC) ₃ MOF heterojunction photocatalysts for enhanced treatment of pharmaceutical wastewater under sunlight”	The photogenerated electrons in AgFeO ₂ 's conduction band interacted with O ₂ molecules to produce O ₂ anion (as the main oxidative species), accelerating the degradation/mineralization of adsorbed drug molecules on the catalyst surfaces.	El-Fawal et al. (2020)
5	“On the role of a graphene oxide/titania catalyst, visible LED and ozone in removing mixtures of pharmaceutical contaminants from water and wastewater”	The kinetic regime of ozone reactions and the relative significance of mass transfer and chemical reactions may be evaluated using gas-liquid absorption kinetics.	Checa et al. (2020)
6	“The residual tetracycline in pharmaceutical wastewater was effectively removed by using MnO ₂ /graphene nanocomposite”	The significant adsorption process that led to the complexation of Mn (IV) and π-π contacts of the benzene ring structure on treated graphene sheets with tetracycline molecules was the interaction of the benzene ring structure with tetracycline molecules.	Song et al. (2019b)

Table 2 (continued)

No.	Title	Remarks	Ref.
7	“Facile solvothermal fabrication of cubic-like reduced graphene oxide/AgIn ₅ S ₈ nanocomposites with anti-photocorrosion and high visible-light photocatalytic performance for highly-efficient treatment of nitrophenols and real pharmaceutical wastewater”	With the help of 1 mL H ₂ O ₂ , 40 mg of 1% reduced graphene oxide/AgIn ₅ S ₈ can successfully deal with actual pharmaceutical wastewater, removing 89% of the chemical oxygen requirement, showing excellent practicability in actual pharmaceutical wastewater treatment.	Che et al. (2018)
8	“Application of graphene based materials for adsorption of pharmaceutical traces from water and wastewater- a review”	Graphene compounds are effective against a broad range of water contaminants and may be utilized in water treatment as photocatalysts, adsorbents, and disinfectants.	Carmalin Sophia et al. (2016)
9	“Removal of phthalates and pharmaceuticals from municipal wastewater by graphene adsorption process”	In preliminary research, the optimum operating parameters for emerging pollutants of concern in model solutions were determined to be a graphene dose of 0.1 g/L and adsorption duration of 12 h.	Yang and Tang (2016)
10	“Graphene oxide-polyaniline nanocomposite as a potential sorbent for dispersive solid-phase extraction and determination of pharmaceutical and personal care products in wastewater samples using HPLC with a diode-array detector”	Considering the complexity of the analytical issue, the proposed technique was effectively used to determine most of the chosen contaminants in wastewater samples with acceptable recovery and accuracy.	Rashvand and Vosough (2016)
11	“Advanced treatment of urban wastewater by sand filtration and graphene adsorption for wastewater reuse: Effect on a mixture of pharmaceuticals and toxicity”	When graphene adsorption reactors were compared to traditional (granular activated carbon) adsorption processes, the best performance in the removal of pharmaceutical mixtures was very low (62% in terms of UV absorbance) (96%)	Rizzo et al. (2015)
12	“Magnetic solid phase extraction of gemfibrozil from human serum and pharmaceutical wastewater samples utilizing a beta-cyclodextrin grafted graphene oxide-	Simple, high kinetic sorption of the target analyte, low detection limit (3 pg mL ⁻¹), good precision (Relative standard deviation = 1.09%), great accuracy, and high	Abdolmohammad-Zadeh and Talleb (2015)

(continued on next page)

Table 2 (continued)

No.	Title	Remarks	Ref.
13	"Application of graphene for the analysis of pharmaceuticals and personal care products in wastewater"	sorption capacity (49.8 mg/g) are some of the benefits of the proposed technique. For examining pharmaceuticals and personal care items in wastewater samples, a 20% graphene/silica gel derivatized with MTBSTFA followed by the GC-MS analysis technique may be utilized successfully.	Yu and Wu (2013)

et al., 2018; Sarker et al., 2018). Biochar, which is defined as carbonaceous by-products and is a carbon-rich solid produced from biomass (organic matter from plants) cooked in a low-oxygen atmosphere, is an alternative to activated carbons. Biochar has been used to enhance the adsorption characteristics of developing pharmaceutical pollutants and their metabolites (Essandoh et al., 2015; Karunanayake et al., 2017; Peiris et al., 2017). Biochar and activated carbon were evaluated as catalysts in an ultrasonic process to degrade acetaminophen and naproxen, and Jong-Kwon and coworkers (Im et al., 2014) discovered that biochar was more effective than activated carbon in degrading

pharmaceutically active chemicals under ultrasonic radiation. More study is needed to bridge the gap in understanding the biological processes of biochar's ability to reduce membrane fouling.

5. Methods for removing pharmaceutical pollutants

The pharmaceutical compounds are strong, physiologically active substances, and little is known about their ecological impacts (Santos et al., 2010; Boxall Alistair et al., 2012). This is due to abundant information regarding their pharmacological and toxicological effects at high concentrations. Most pharmaceutical wastewaters have high chemical oxygen demand concentrations, which may vary depending on manufacturing industry activities (Cetecioglu et al., 2015). Chemical oxygen demand values ranged from 4410 to 40,000 mg L⁻¹ in most pharmaceutical wastewaters. On the other hand, pharmaceuticals have been demonstrated in many studies to reach rivers, mainly via treated wastewater effluent, and to stay biochemically active in aquatic systems (Hughes et al., 2013; Loos et al., 2013). Removal of pharmaceuticals from wastewater was done using various treatment methods such as physical, chemical, and biological processes summarized in Fig. 16. Physical treatment methods involve adsorption, electro dialysis, reverse osmosis (RO), evaporation, filtration, sedimentation, and flocculation. Various chemical technologies are adopted to eliminate pharmaceuticals from wastewater, such as oxidation, flocculation/coagulation, electrochemical oxidation, ozone, Fenton, ultrasonication, heterogeneous, and homogeneous photocatalytic reactions. Biological treatment processes through aerobic and anaerobic methods include constructed wetlands process, membrane bioreactors, biodegradation, and activated sludge

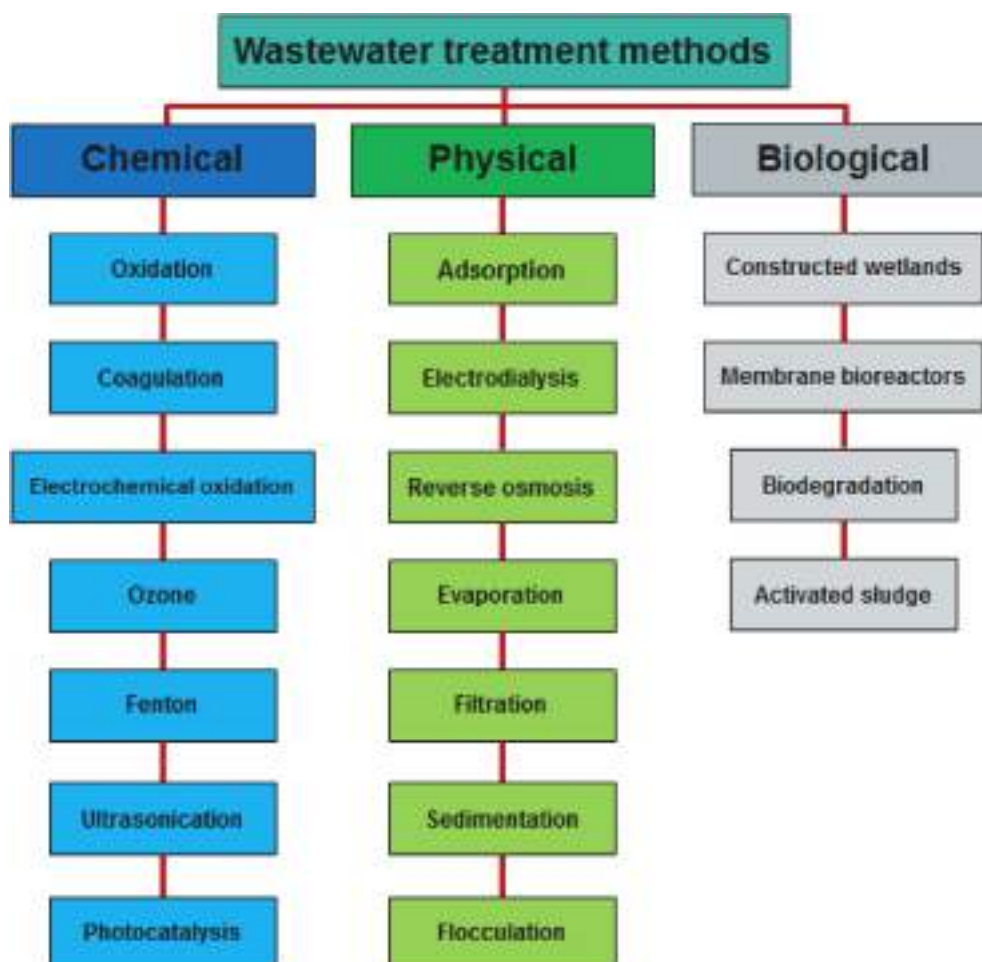


Fig. 16. Treatment methods for the pharmaceutical removal from wastewater effluent.

process for the pollutant elimination from wastewater. A concept for improving the performance of wastewater treatment facilities in terms of pharmaceutical removal may be provided, typically by adding additional processes intended to remove such pollutants more effectively. Despite this, many wastewater treatment facilities throughout the globe only have two treatment stages (physical and biological), and just a few employ tertiary or advanced treatment steps (e.g. osmosis, advanced oxidation, ozonation, flocculation, or ultrafiltration) (Amor et al., 2019). As people become more aware of the inefficiencies of individual treatment methods for removing dangerous chemicals from pharmaceutical wastewater, the integration and combination of treatment technologies may become a more effective, although more costly, option in the future.

6. Challenges and perspectives

Pharmaceutical industrial effluent may be a potential source for value-added product recovery, and treated wastewater can also be utilized in agriculture. Despite advancements in optical sensors, there are still certain limits that must be overcome. Susceptibility to environmental changes, such as pH, turbidity, temperature, flow rate, and so on, affects optical equipment. Improvements in measuring comparability and reliability, for example, are required. Water quality factors must also be clearly defined and validated consistently. The robustness, simplicity, speed, and cost factors of a system will determine its success and economic feasibility. Before they can be utilized commercially in wastewater plants, sensor research should follow the development of state-of-the-art hardware sensors, including their reliability, practicality, and cost, as well as the usual measures used for process management. In this respect, adding efficient recognition components (such as entire microbes or biomolecules) may enhance the applicability of sensors by allowing them to detect smaller quantities of analytes, especially in murky samples like wastewaters. It's also been proposed that a new method to wastewater monitoring, namely the use of specifically built carbon-based sensors, may lead to the successful creation of an improved platform capable of offering better sensitivity in real-time water content detection. For example, the proposed Fe-Chitosan-coated carbon electrode sensor could provide high sensitivity and good selectivity for As(III) in a complex water matrix, demonstrating a dependable As(III) monitoring capability applicable in actual wastewater. More pilot and large-scale studies to evaluate the remediation effectiveness of different carbon compounds and their cost-effective synthesis from renewable resources may enhance the commercial acceptability of carbon-based materials in the environmental remediation sector.

Furthermore, electrochemical cells may be used in conjunction with other small-molecule detection methods such as fluorescence spectroscopy, nuclear magnetic resonance spectroscopy, and mass spectrometry. Significant progress has been made in this area, and routine analytical instruments may be replaced shortly by the reported nano and biosensors based on carbon materials, which provided fast, simple, sensitive, and selective detection of pharmaceutical-containing wastewater. As a result of continuing sensor technology advances, creating more advanced detection methods for biomolecules analysis in the near future is anticipated.

For the treatment of refractory organic wastewater, more attention should be given to the fundamental concepts and degradation processes of adsorption, filtering, AOPs, and photocatalysis techniques. It is suggested that researchers concentrate on the degrading treatment process of real industrial wastewater and encourage the large-scale implementation of the methods described in industrial wastewater treatment. Reducing the cost of the treatment process and resolving the reaction facility corrosion issue are both essential aspects in encouraging the industrial use of those techniques. Additionally, in removing pharmaceutical pollutants from the environment, combined modes of membrane filtration and electrochemical oxidation, developing electrode

materials and catalytic materials with better antibiotic treatment effects, and exploring the best external conditions for the reaction are all critical. MOFs, for example, with the intrinsic surface area of $1000 \text{ m}^2 \text{ g}^{-1}$ to $10,000 \text{ m}^2 \text{ g}^{-1}$ (Doustkhah et al., 2021a), have been shown to be effective in the treatment of industrial wastewater. Pellets, spherical, mold, nanorods, beads, and other forms of adsorbents and photocatalysts are among the most common. As a result, MOF composites have shown a number of benefits, especially in photocatalysis, where a narrow bandgap is needed and they tend to exhibit pores having diameters comparable in length-scale to the molecular size of solute compounds (Doustkhah et al., 2021b). The use of MOFs in wastewater treatment, on the other hand, requires excellent structural stability under working circumstances, which may be achieved by introducing and mixing transition metals such as Fe, Cu, Cd, and Fe.

Although there is a large body of literature supporting the usage of carbon-based nanomaterials, researchers should thoroughly evaluate their characteristics before claiming extraordinary behavior. Furthermore, although the use of carbon nanotubes has been the focus of previous studies, the authors believe that this trend will shift as researchers create new kinds of carbon-based materials. Carbon-based materials are an excellent substrate for energy and the environment, regardless of wastewater treatment applications. There is considerable space for scientific research to enhance their performance in a wide variety of applications. More multidisciplinary research is needed to progress new and sustainable carbon-based heterostructured materials for energy and environmental applications. It is suggested that analytical applications of carbon-based nanomaterials will continue to grow and become a mature and autonomous area in the near future.

7. Concluding remarks

This article delivered an overview of how carbon-based nanomaterials may be used to detect and remove pharmaceutical contaminants in wastewater. In recent years, there has been an exponential increase in WoS articles in (bio)sensor fabrication using carbon black as nanomaterials, indicating the possibility of developing products and technologies using carbon-based nanomaterials. Even though carbon-based composites offer many benefits over presently available carbon and organic resins for pollution sensing and removal, they have yet to be widely marketed. Carbon-based nanomaterials are desirable electrode modification and fabrication elements because of their outstanding electrochemical stability, conductivity, fast electron transfer, and broad electrochemical windows. Carbon-based materials such as carbon black, carbon nanotubes, activated carbon, carbon nanofibers, graphene mesoporous carbon, and biochar sorbents are reviewed, with each having potential characteristics as well as drawbacks for the adsorption of pharmaceutical wastes. Several analytical techniques, such as electrochemical, chromatographic, and spectroscopic methods, were studied to detect the pharmaceutical materials and impact water quality. Electrochemical sensors were thought of as the most applicable detecting approach in clinics for their advantages, including cheapness, simplicity, and the fact that they are highly selective, sensitive, and easy to miniaturize. Significant progress has been made in treating and managing pharmaceutical wastewater, which can be treated using biological, physical, or chemical methods. The biological or advanced eco-friendly techniques appear to be the most appropriate because they offer the potential for resource recovery (in the form of energy or chemicals). The optimum treatment technique combines traditional treatment methods, membrane reactors, and sophisticated post-treatment procedures. It is expected that this review will inspire the rapid development of novel fluorescent investigations for the application of carbon-based nanomaterials to detect and remove pharmaceutical pollutants in wastewater.

Author contributions

W. Nabgan: First author who carried out the writing sections. A.A. Jalil: Owner of the project. B. Nabgan: Take care on the bibliometric parts. M. Ikram: Took the English revision. M.W. Ali: Supervisor who read and comments on the paper. A. kumar: Took the response to reviewer tasks. P. Lakshminarayana: Help to draw the Figures and English editing.

Declaration of competing interest

The authors declare that they have no known competing financial interests or personal relationships that could have appeared to influence the work reported in this paper.

Acknowledgments

The principal author, Walid Nabgan, is thankful for Universiti Teknologi Malaysia's support in the form of the Post-Doctoral Fellowship Scheme "Simultaneous heavy metals ions and organic pollutants photoredox reactions over SiO₂/ZrO₂ based catalysts under solar-light irradiation (PDRU Grant number: 05E49).

References

- Abdolmohammad-Zadeh, H., Talleb, Z., 2015. Magnetic solid phase extraction of gemfibrozil from human serum and pharmaceutical wastewater samples utilizing a β -cyclodextrin grafted graphene oxide-magnetite nano-hybrid. *Talanta* 134, 387–393.
- Akhshami, A., Kafrahi, F., Ahmadi, M., Madrakian, T., 2015. A new chiral electrochemical sensor for the enantioselective recognition of naproxen enantiomers using L-cysteine self-assembled over gold nanoparticles on a gold electrode. *RSC Adv.* 5, 58609–58615.
- Ahmad, A., Azam, T., 2019. 4 - water purification technologies. In: Grumezescu, A.M., Holban, A.M. (Eds.), *Bottled and Packaged Water*. Woodhead Publishing, pp. 83–120.
- Ahmadzadeh, S., Rezayi, M., Faghih-Mirzaei, E., Yoosefian, M., Kassim, A., 2015. Highly selective detection of titanium (III) in industrial waste water samples using meso-octamethylcalix[4]pyrrole-doped PVC membrane ion-selective electrode. *Electrochim. Acta* 178, 580–589.
- Ahmed, I., Bhadra, B.N., Lee, H.J., Jhung, S.H., 2018. Metal-organic framework-derived carbons: preparation from ZIF-8 and application in the adsorptive removal of sulfamethoxazole from water. *Catal. Today* 301, 90–97.
- Al-Khateeb, L.A., Almotiry, S., Salam, M.A., 2014. Adsorption of pharmaceutical pollutants onto graphene nanoplatelets. *Chem. Eng. J.* 248, 191–199.
- Aldmour, S.T., Burke, I.T., Bray, A.W., Baker, D.L., Ross, A.B., Gill, F.L., Gibin, G., Ries, M.E., Stewart, D.L., 2019. Abiotic reduction of Cr(VI) by humic acids derived from peat and lignite: kinetics and removal mechanism. *Environ. Sci. Pollut. Control Ser.* 26, 4717–4729.
- Ali, I., 2012. New generation adsorbents for water treatment. *Chem. Rev.* 112, 5073–5091.
- Allègre, C.J., Poirier, J.-P., Humler, E., Hofmann, A.W., 1995. The chemical composition of the Earth. *Earth Planet. Sci. Lett.* 134, 515–526.
- Álvarez-Torrellas, S., Peres, J.A., Gil-Álvarez, V., Ovejero, G., García, J., 2017. Effective adsorption of non-biodegradable pharmaceuticals from hospital wastewater with different carbon materials. *Chem. Eng. J.* 320, 319–329.
- Alves Filho, E.G., Alexandre e Silva, L.M., Ferreira, A.G., 2015. Advancements in waste water characterization through NMR spectroscopy: review. *Magn. Reson. Chem.* 53, 648–657.
- Alves, T.C., Cabrera-Codony, A., Barceló, D., Rodríguez-Mozaz, S., Pinheiro, A., Gonzalez-Olmos, R., 2018. Influencing factors on the removal of pharmaceuticals from water with micro-grain activated carbon. *Water Res.* 144, 402–412.
- Amor, C., Marchão, L., Lucas, M.S., Peres, J.A., 2019. Application of Advanced Oxidation Processes for the Treatment of Recalcitrant Agro-Industrial Wastewater: A Review. *Water* 11.
- An, H.J., Bhadra, B.N., Khan, N.A., Jhung, S.H., 2018. Adsorptive removal of wide range of pharmaceutical and personal care products from water by using metal azolate framework-6-derived porous carbon. *Chem. Eng. J.* 343, 447–454.
- Anitha, K., Namsani, S., Singh, J.K., 2015. Removal of heavy metal ions using a functionalized single-walled carbon nanotube: a molecular dynamics study. *J. Phys. Chem.* 119, 8349–8358.
- Archer, E., Petrie, B., Kasprzyk-Hordern, B., Wolfaardt, G.M., 2017. The fate of pharmaceuticals and personal care products (PPCPs), endocrine disrupting contaminants (EDCs), metabolites and illicit drugs in a WWTW and environmental waters. *Chemosphere* 174, 437–446.
- Arduini, F., Amine, A., Majorani, C., Di Giorgio, F., De Felicis, D., Cataldo, F., Moscone, D., Palleschi, G., 2010. High performance electrochemical sensor based on modified screen-printed electrodes with cost-effective dispersion of nanostructured carbon black. *Electrochem. Commun.* 12, 346–350.
- Arduini, F., DiNardo, F., Amine, A., Micheli, L., Palleschi, G., Moscone, D., 2012. Carbon black -ModifiedScreen -PrintedElectrodes as electroanalytical tools. *Electroanalysis* 24, 743–751.
- Ashraf, M.A., Maah, M.J., Yusoff, I., 2014. Soil contamination, risk assessment and remediation. *Environ. Risk Assessment Contamination* 1, 3–56.
- Aslam, M., Kalyar, M.A., Raza, Z.A., 2018. Polyvinyl alcohol: a review of research status and use of polyvinyl alcohol based nanocomposites. *Polym. Eng. Sci.* 58, 2119–2132.
- Ayati, A., Ahmadvpour, A., Bamoharram, F.F., Tanhaei, B., Mänttari, M., Sillanpää, M., 2014. A review on catalytic applications of Au/TiO₂ nanoparticles in the removal of water pollutant. *Chemosphere* 107, 163–174.
- Baj-Rossi, C., Rezzonico Jost, T., Cavallini, A., Grassi, F., De Micheli, G., Carrara, S., 2014. Continuous monitoring of Naproxen by a cytochrome P450-based electrochemical sensor. *Biosens. Bioelectron.* 53, 283–287.
- BatistaDeroco, P., Campanhã Vicentini, F., Fatibello-Filho, O., 2015. An electrochemical sensor for the simultaneous determination of paracetamol and codeine using a glassy carbon electrode modified with nickel oxide nanoparticles and carbon black. *Electroanalysis* 27, 2214–2220.
- Beć, K.B., Grabska, J., Huck, C.W., 2021. NIR spectroscopy of natural medicines supported by novel instrumentation and methods for data analysis and interpretation. *J. Pharmaceut. Biomed. Anal.* 193, 113686.
- Beltrán, F.J., Checa, M., Rivas, J., García-Araya, J.F., 2020. Modeling the mineralization kinetics of visible led graphene oxide/titania photocatalytic ozonation of an urban wastewater containing pharmaceutical compounds. *Catalysts* 10.
- Beluomini, M.A., da Silva, J.L., de Sá, A.C., Buffon, E., Pereira, T.C., Stradiotto, N.R., 2019. Electrochemical sensors based on molecularly imprinted polymer on nanostructured carbon materials: a review. *J. Electroanal. Chem.* 840, 343–366.
- Benstoem, F., Nahrstedt, A., Boehler, M., Knopp, G., Montag, D., Siegrist, H., Pinnekamp, J., 2017. Performance of granular activated carbon to remove micropollutants from municipal wastewater—a meta-analysis of pilot- and large-scale studies. *Chemosphere* 185, 105–118.
- Boulard, L., Dierkes, G., Ternes, T., 2018. Utilization of large volume zwitterionic hydrophilic interaction liquid chromatography for the analysis of polar pharmaceuticals in aqueous environmental samples: benefits and limitations. *J. Chromatogr. A* 1535, 27–43.
- Boxall Alistair, B.A., Rudd Murray, A., Brooks Bryan, W., Caldwell Daniel, J., Choi, K., Hickmann, S., Innes, E., Ostapik, K., Staveley Jane, P., Verslycke, T., Ankley Gerald, T., Beazley Karen, F., Belanger Scott, E., Berninger Jason, P., Carriquiriborde, P., Coors, A., DeLeo Paul, C., Dyer Scott, D., Ericson Jon, F., Gagné, F., Giesy John, P., Gouin, T., Hallstrom, L., Karlsson Maja, V., Larsson, D.G.J., Lazorchak James, M., Mastrocco, F., McLaughlin, A., McMaster Mark, E., Meyerhoff Roger, D., Moore, R., Parrott Joanne, L., Snape Jason, R., Murray-Smith, R., Servos Mark, R., Sibley Paul, K., Straub Jürg, O., Szabo Nora, D., Topp, E., Tetreault Gerald, R., Trudeau Vance, L., Van Der Kraak, G., 2012. Pharmaceuticals and personal care products in the environment: what are the big questions? *Environ. Health Perspect.* 120, 1221–1229.
- Bridgeman, D., Corral, J., Quach, A., Xian, X., Forzani, E., 2014. Colorimetric humidity sensor based on liquid composite materials for the monitoring of food and pharmaceuticals. *Langmuir* 30, 10785–10791.
- Cai, X., Tan, S., Lin, M., Xie, A., Mai, W., Zhang, X., Lin, Z., Wu, T., Liu, Y., 2011. Synergistic antibacterial brilliant blue/reduced graphene oxide/quaternary phosphonium salt composite with excellent water solubility and specific targeting capability. *Langmuir* 27, 7828–7835.
- Cai, Z., Dwivedi, A.D., Lee, W.-N., Zhao, X., Liu, W., Sillanpää, M., Zhao, D., Huang, C.-H., Fu, J., 2018. Application of nanotechnologies for removing pharmaceutically active compounds from water: development and future trends. *Environ. Sci.: Nano* 5, 27–47.
- Calisto, V., Ferreira, C.I.A., Oliveira, J.A.B.P., Otero, M., Esteves, V.I., 2015. Adsorptive removal of pharmaceuticals from water by commercial and waste-based carbons. *J. Environ. Manag.* 152, 83–90.
- Camargo, J.R., Andreotti, I.A.A., Kalinke, C., Henrique, J.M., Bonacin, J.A., Janegitz, B. C., 2020. Waterproof paper as a new substrate to construct a disposable sensor for the electrochemical determination of paracetamol and melatonin. *Talanta* 208, 120458.
- Campbell, F.W., Compton, R.G., 2010. The use of nanoparticles in electroanalysis: an updated review. *Anal. Bioanal. Chem.* 396, 241–259.
- Carmalin Sophia, A., Lima, E.C., Allauende, N., Rajan, S., 2016. Application of graphene based materials for adsorption of pharmaceutical traces from water and wastewater—a review. *Desalination and Water Treatment* 57, 27573–27586.
- Cernat, A., Tertiş, M., Săndulescu, R., Bedioui, F., Cristea, A., Cristea, C., 2015. Electrochemical sensors based on carbon nanomaterials for acetaminophen detection: a review. *Anal. Chim. Acta* 886, 16–28.
- Cetecioglu, Z., Ince, B., Gros, M., Rodríguez-Mozaz, S., Barceló, D., Ince, O., Orhon, D., 2015. Biodegradation and reversible inhibitory impact of sulfamethoxazole on the utilization of volatile fatty acids during anaerobic treatment of pharmaceutical industry wastewater. *Sci. Total Environ.* 536, 667–674.
- Chapman, P.J., Kay, P., Mitchell, G., Pitts, C.S., 2019. *Surface Water Quality. Water Resources: an Integrated Approach*.
- Che, W., Luo, Y., Deng, F., Zhang, A., Zhao, L., Luo, X., Ruan, Q., 2018. Facile solvothermal fabrication of cubic-like reduced graphene oxide/AgIn₅S₈ nanocomposites with anti-photocorrosion and high visible-light photocatalytic performance for highly-efficient treatment of nitrophenols and real pharmaceutical wastewater. *Appl. Catal. Gen.* 565, 170–180.
- Checa, M., Beltrán, F.J., Rivas, F.J., Cordero, E., 2020. On the role of a graphene oxide/titania catalyst, visible LED and ozone in removing mixtures of pharmaceutical

- contaminants from water and wastewater. *Environ. Sci.: Water Res. Technol.* 6, 2352–2364.
- Chu, N., Liang, Q., Hao, W., Jiang, Y., Liang, P., Zeng, R.J., 2021. Microbial electrochemical sensor for water biotoxicity monitoring. *Chem. Eng. J.* 404, 127053.
- Cinti, S., Arduini, F., Carbone, M., Sansone, L., Cacciotti, I., Moscone, D., Palleschi, G., 2015. Screen-printed electrodes modified with carbon nanomaterials: a comparison among carbon black, carbon nanotubes and graphene. *Electroanalysis* 27, 2230–2238.
- Cinti, S., Mazzaracchio, V., Cacciotti, I., Moscone, D., Arduini, F., 2017. Carbon black-modified electrodes screen-printed onto paper towel, waxed paper and parafilm M. *Sensors* 17.
- Ciurczak, E.W., Igne, B., 2014. *Pharmaceutical and Medical Applications of Near-Infrared Spectroscopy*. CRC Press.
- Couto, C.F., Lange, L.C., Amaral, M.C.S., 2019. Occurrence, fate and removal of pharmaceutical active compounds (PhACs) in water and wastewater treatment plants—a review. *J. Water Process Eng.* 32, 100927.
- Das, S., Sen, B., Debnath, N., 2015. Recent trends in nanomaterials applications in environmental monitoring and remediation. *Environ. Sci. Pollut. Control Ser.* 22, 18333–18344.
- Denault, A.Y., Shaaban-Ali, M., Cournoyer, A., Benkreira, A., Mailhot, T., 2018. Chapter 7 - near-infrared spectroscopy. In: Prabhakar, H. (Ed.), *Neuromonitoring Techniques*. Academic Press, pp. 179–233.
- Deng, X., Lü, L., Li, H., Luo, F., 2010. The adsorption properties of Pb(II) and Cd(II) on functionalized graphene prepared by electrolysis method. *J. Hazard Mater.* 183, 923–930.
- Deroco, P.B., Melo, I.G., Silva, L.S.R., Eguiluz, K.I.B., Salazar-Banda, G.R., Fatibello-Filho, O., 2018. Carbon black supported Au–Pd core-shell nanoparticles within a dihexadecylphosphane film for the development of hydrazine electrochemical sensor. *Sensor. Actuator. B Chem.* 256, 535–542.
- Deventer, K., Pozo, O.J., Verstraete, A.G., Van Eenoo, P., 2014. Dilute-and-shoot-liquid chromatography-mass spectrometry for urine analysis in doping control and analytical toxicology. *Trac. Trends Anal. Chem.* 55, 1–13.
- Díaz-Cruz, M.S., García-Galán, M.J., Guerra, P., Jelic, A., Postigo, C., Eljarrat, E., Farré, M., López de Alda, M.J., Petrovic, M., Barceló, D., 2009. Analysis of selected emerging contaminants in sewage sludge. *Trac. Trends Anal. Chem.* 28, 1263–1275.
- Dimpe, K.M., Nomngongo, P.N., 2016. Current sample preparation methodologies for analysis of emerging pollutants in different environmental matrices. *Trac. Trends Anal. Chem.* 82, 199–207.
- Din, I.U., Shaharun, M.S., Naeem, A., Alotaibi, M.A., Alharthi, A.I., Bakht, M.A., Nasir, Q., 2020. Carbon nanofibers as potential materials for catalysts support, a mini-review on recent advances and future perspective. *Ceram. Int.* 46, 18446–18452.
- Djerahov, L., Vasileva, P., Karadjova, I., Kurakalva, R.M., Aradhi, K.K., 2016. Chitosan film loaded with silver nanoparticles—sorbent for solid phase extraction of Al(III), Cd(II), Cu(II), Co(II), Fe(III), Ni(II), Pb(II) and Zn(II). *Carbohydr. Polym.* 147, 45–52.
- Domingues, F.S., Geraldino, H.C.L., Freitas, T.K.F.d.S., de Almeida, C.A., Figueiredo, F.F.d., Garcia, J.C., 2021. Photocatalytic degradation of real textile wastewater using carbon black-Nb2O5 composite catalyst under UV/Vis irradiation. *Environ. Technol.* 42, 2335–2349.
- Dong, X., He, L., Liu, Y., Piao, Y., 2018. Preparation of highly conductive biochar nanoparticles for rapid and sensitive detection of 17 β -estradiol in water. *Electrochim. Acta* 292, 55–62.
- Dougherty, J.A., Swarzenski, P.W., Dinicola, R.S., Reinhard, M., 2010. Occurrence of herbicides and pharmaceutical and personal care products in surface water and groundwater around Liberty Bay, puget sound, Washington. *J. Environ. Qual.* 39, 1173–1180.
- Doustkhah, E., Hassandoost, R., Khataee, A., Luque, R., Assadi, M.H.N., 2021a. Hard-templated metal–organic frameworks for advanced applications. *Chem. Soc. Rev.* 50, 2927–2953.
- Doustkhah, E., Tahawy, R., Simon, U., Tsunoji, N., Ide, Y., Hanaor, D.A.H., Assadi, M.H.N., 2021b. Bispropylurea bridged polysilsesquioxane: a microporous MOF-like material for molecular recognition. *Chemosphere* 276, 130181.
- Durán-Alvarez, J.C., Becerril-Bravo, E., Castro, V.S., Jiménez, B., Gibson, R., 2009. The analysis of a group of acidic pharmaceuticals, carbamazepine, and potential endocrine disrupting compounds in wastewater irrigated soils by gas chromatography–mass spectrometry. *Talanta* 78, 1159–1166.
- Ejeian, F., Etedali, P., Mansouri-Tehrani, H.-A., Soozanipour, A., Low, Z.-X., Asadnia, M., Taheri-Kafrani, A., Razmjou, A., 2018. Biosensors for wastewater monitoring: a review. *Biosens. Bioelectron.* 118, 66–79.
- Ek, M., Baresel, C., Magnér, J., Bergström, R., Harding, M., 2014. Activated carbon for the removal of pharmaceutical residues from treated wastewater. *Water Sci. Technol.* 69, 2372–2380.
- El-Fawal, E.M., Younis, S.A., Zaki, T., 2020. Designing AgFeO₂-graphene/Cu₂(BTC)₃ MOF heterojunction photocatalysts for enhanced treatment of pharmaceutical wastewater under sunlight. *J. Photochem. Photobiol. Chem.* 401, 112746.
- El-Sheikh, A.H., Al-Degs, Y.S., Al-As'ad, R.M., Sweileh, J.A., 2011. Effect of oxidation and geometrical dimensions of carbon nanotubes on Hg(II) sorption and preconcentration from real waters. *Desalination* 270, 214–220.
- El-Sheikh, A.H., Al-Jafari, M.K., Sweileh, J.A., 2012. Solid phase extraction and uptake properties of multi-walled carbon nanotubes of different dimensions towards some nitro-phenols and chloro-phenols from water. *Int. J. Environ. Anal. Chem.* 92, 190–209.
- El-Sheikh, A.H., Qawariq, R.F., Abdelghani, J.I., 2019. Adsorption and magnetic solid-phase extraction of NSAIDs from pharmaceutical wastewater using magnetic carbon nanotubes: effect of sorbent dimensions, magnetite loading and competitive adsorption study. *Environ. Technol. Innovat.* 16, 100496.
- El-Zahry, M.R., 2018. A localized surface plasmon resonance sensing method for simultaneous determination of atenolol and amiloride in pharmaceutical dosage forms and urine samples. *J. Analytical Method. Chem.* 9065249, 2018.
- Essandoh, M., Kunwar, B., Pittman, C.U., Mohan, D., Mlsna, T., 2015. Sorptive removal of salicylic acid and ibuprofen from aqueous solutions using pine wood fast pyrolysis biochar. *Chem. Eng. J.* 265, 219–227.
- Etessami, M., Karoonian, F.S., Mohamed, N., 2011. Electrochemical deposition of gold nanoparticles on pencil graphite by fast scan cyclic voltammetry. *J. Chin. Chem. Soc.* 58, 688–693.
- Farré, M., Petrovic, M., Barceló, D., 2007. Recently developed GC/MS and LC/MS methods for determining NSAIDs in water samples. *Anal. Bioanal. Chem.* 387, 1203–1214.
- Femina Carolin, C., Senthil Kumar, P., Janet Joshiba, G., Vinoth Kumar, V., 2021. Analysis and removal of pharmaceutical residues from wastewater using membrane bioreactors: a review. *Environ. Chem. Lett.* 19, 329–343.
- Fent, K., Weston, A.A., Caminada, D., 2006. Ecotoxicology of human pharmaceuticals. *Aquat. Toxicol.* 76, 122–159.
- Fonseca, R., Pinho, C., Albuquerque, T., Araújo, J., 2021. Environmental factors and metal mobilisation in alluvial sediments—minas Gerais, Brazil. *Geosciences* 11.
- Forbes, H., Quested, T., O'Connor, C., 2021. *Food Waste Index Report 2021*. United Nations Environment Programme, Nairobi, Kenya.
- Frink, L.A., Weatherly, C.A., Armstrong, D.W., 2014. Water determination in active pharmaceutical ingredients using ionic liquid headspace gas chromatography and two different detection protocols. *J. Pharmaceut. Biomed. Anal.* 94, 111–117.
- Fu, Q., He, X., Lin, G., Suo, H., Zhao, C., 2012. On-line analysis of sulfonamides in pharmaceutical wastewater based on magnetic molecularly imprinted polymer extraction and near infrared spectroscopy. *Anal. Method.* 4, 1813–1819.
- Gadipelly, C., Pérez-González, A., Yadav, G.D., Ortiz, I., Ibáñez, R., Rathod, V.K., Marathe, K.V., 2014. Pharmaceutical industry wastewater: review of the technologies for water treatment and reuse. *Ind. Eng. Chem. Res.* 53, 11571–11592.
- Gao, T., Du, P., Xu, Z., Li, X., 2017. Occurrence of new psychoactive substances in wastewater of major Chinese cities. *Sci. Total Environ.* 575, 963–969.
- Ge, L., Li, S.-P., Lisak, G., 2020. Advanced sensing technologies of phenolic compounds for pharmaceutical and biomedical analysis. *J. Pharmaceut. Biomed. Anal.* 179, 112913.
- Gethard, K., Sae-Khow, O., Mitra, S., 2011. Water desalination using carbon-nanotube-enhanced membrane distillation. *ACS Appl. Mater. Interfaces* 3, 110–114.
- Gholami, P., Khataee, A., Soltani, R.D.C., Dinpazhoh, L., Bhatnagar, A., 2020. Photocatalytic degradation of gemifloxacin antibiotic using Zn-Co-LDH/biochar nanocomposite. *J. Hazard Mater.* 382, 121070.
- Gong, X., Zhang, D., Embile, I.B., She, Y., Shi, S., Gamez, G., 2020. Low-temperature plasma probe mass spectrometry for analytes separated on thin-layer chromatography plates: direct vs laser assisted desorption. *J. Am. Soc. Mass Spectrom.* 31, 1981–1993.
- González-García, C.M., González-Martín, M.L., Gallardo-Moreno, A.M., Gómez-Serrano, V., Labajos-Broncano, L., Bruque, J.M., 2002. Removal of an ionic surfactant from wastewater by carbon blacks adsorption. *Separ. Sci. Technol.* 37, 2823–2837.
- Gupta Pankaj, K., 2020. Pollution load on Indian soil-water systems and associated health hazards: a review. *J. Environ. Eng.* 146, 03120004.
- Gupta, S., Tai, N.-H., 2019. Carbon materials and their composites for electromagnetic interference shielding effectiveness in X-band. *Carbon* 152, 159–187.
- Gupta, V.K., Agarwal, S., Saleh, T.A., 2011. Chromium removal by combining the magnetic properties of iron oxide with adsorption properties of carbon nanotubes. *Water Res.* 45, 2207–2212.
- Gupta, V.K., Moradi, O., Tyagi, I., Agarwal, S., Sadeq, H., Shahryari-Ghoshekandi, R., Makhlof, A.S.H., Goodarzi, M., Garshabi, A., 2016. Study on the removal of heavy metal ions from industry waste by carbon nanotubes: effect of the surface modification: a review. *Crit. Rev. Environ. Sci. Technol.* 46, 93–118.
- Hao, C., Zhao, X., Yang, P., 2007. GC-MS and HPLC-MS analysis of bioactive pharmaceuticals and personal-care products in environmental matrices. *Trac. Trends Anal. Chem.* 26, 569–580.
- Hassandoost, R., Pouran, S.R., Khataee, A., Orojji, Y., Joo, S.W., 2019. Hierarchically structured ternary heterojunctions based on Ce³⁺/Ce⁴⁺ modified Fe₃O₄ nanoparticles anchored onto graphene oxide sheets as magnetic visible-light-active photocatalysts for decontamination of oxytetracycline. *J. Hazard Mater.* 376, 200–211.
- Hatcher, P.G., Waggoner, D.C., Chen, H., 2019. Evidence for the existence of humic acids in peat soils based on solid-state ¹³C NMR. *J. Environ. Qual.* 48, 1571–1577.
- He, D., Luo, Y., Lu, S., Liu, M., Song, Y., Lei, L., 2018. Microplastics in soils: analytical methods, pollution characteristics and ecological risks. *Trac. Trends Anal. Chem.* 109, 163–172.
- Hendawy, H.A.M., Salem, W.M., Abd-Elmonem, M.S., Khaled, E., 2019. Nanomaterial-based carbon paste electrodes for voltammetric determination of naproxen in presence of its degradation products. *J. Analytical Method. Chem.* 2019, 5381031.
- Hočevar, S.B., Ogorevc, B., 2007. Preparation and characterization of carbon paste micro-electrode based on carbon nano-particles. *Talanta* 74, 405–411.
- Hou, C., Tang, W., Zhang, C., Wang, Y., Zhu, N., 2014. A novel and sensitive electrochemical sensor for bisphenol A determination based on carbon black supporting ferroferric oxide nanoparticles. *Electrochim. Acta* 144, 324–331.
- Hu, Y., Song, Y., Wang, Y., Di, J., 2011. Electrochemical synthesis of gold nanoparticles onto indium tin oxide glass and application in biosensors. *Thin Solid Films* 519, 6605–6609.
- Huang, X., Li, Y., Chen, Y., Wang, L., 2008. Electrochemical determination of nitrite and iodate by use of gold nanoparticles/poly(3-methylthiophene) composites coated glassy carbon electrode. *Sensor. Actuator. B Chem.* 134, 780–786.

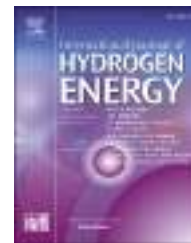
- Hughes, S.R., Kay, P., Brown, L.E., 2013. Global synthesis and critical evaluation of pharmaceutical data sets collected from river systems. *Environ. Sci. Technol.* 47, 661–677.
- Hussain, S., Ramnarayanan, C., Roopashree, T.S., Anwer, M.K., Sreeharsha, N., Nair, A.B., 2020. Rapid, precise and affordable estimation of venlafaxine and its metabolites in highly polluted effluent waters: proof-of-concept for methodology. *Molecules* 25.
- Hwang, J.-H., Pathak, P., Wang, X., Rodriguez, K.L., Park, J., Cho, H.J., Lee, W.H., 2019a. A novel Fe-Chitosan-coated carbon electrode sensor for in situ As(III) detection in mining wastewater and soil leachate. *Sensor. Actuator. B Chem.* 294, 89–97.
- Hwang, J.-H., Wang, X., Zhao, D., Rex, M.M., Cho, H.J., Lee, W.H., 2019b. A novel nanoporous bismuth electrode sensor for in situ heavy metal detection. *Electrochim. Acta* 298, 440–448.
- Hwang, J., Wang, X., Pathak, P., Rex, M.M., Cho, H.J., Lee, W.H., 2019c. Enhanced electrochemical detection of multiheavy metal ions using a biopolymer-coated planar carbon electrode. *IEEE Trans. Instrument. Measure.* 68, 2387–2393.
- Iijima, S., 1991. Helical microtubules of graphitic carbon. *Nature* 354, 56–58.
- Im, J.-K., Boateng, L.K., Flora, J.R.V., Her, N., Zoh, K.-D., Son, A., Yoon, Y., 2014. Enhanced ultrasonic degradation of acetaminophen and naproxen in the presence of powdered activated carbon and biochar adsorbents. *Separ. Purif. Technol.* 123, 96–105.
- Jelić, A., Petrović, M., Barceló, D., 2009. Multi-residue method for trace level determination of pharmaceuticals in solid samples using pressurized liquid extraction followed by liquid chromatography/quadrupole-linear ion trap mass spectrometry. *Talanta* 80, 363–371.
- Kaale, E., Risha, P., Layloff, T., 2011. TLC for pharmaceutical analysis in resource limited countries. *J. Chromatogr. A* 1218, 2732–2736.
- Kalate Bojdi, M., Behbahani, M., Mashhadizadeh, M.H., Bagheri, A., Hosseiny Davarani, S.S., Farahani, A., 2015. Mercapto-ordered carbohydrate-derived porous carbon electrode as a novel electrochemical sensor for simple and sensitive ultra-trace detection of omeprazole in biological samples. *Mater. Sci. Eng. C* 48, 213–219.
- Karunanayake, A.G., Todd, O.A., Crowley, M.L., Ricchetti, L.B., Pittman, C.U., Anderson, R., Mlsna, T.E., 2017. Rapid removal of salicylic acid, 4-nitroaniline, benzoic acid and phthalic acid from wastewater using magnetized fast pyrolysis biochar from waste Douglas fir. *Chem. Eng. J.* 319, 75–88.
- Kassim, A., Rezayi, M., Ahmadzadeh, S., Rounaghi, G., Mohajeri, M., Yusof, N.A., Tee, T.W., Heng, L.Y., Abdullah, A.H., 2011. A novel ion – selective polymeric membrane sensor for determining thallium(I) with high selectivity. *IOP Conf. Ser. Mater. Sci. Eng.* 17, 012010.
- Kay, P., Hughes, S.R., Ault, J.R., Ashcroft, A.E., Brown, L.E., 2017. Widespread, routine occurrence of pharmaceuticals in sewage effluent, combined sewer overflows and receiving waters. *Environ. Pollut.* 220, 1447–1455.
- Khalil, A.M.E., Memon, F.A., Tabish, T.A., Fenton, B., Salmon, D., Zhang, S., Butler, D., 2021. Performance evaluation of porous graphene as filter media for the removal of pharmaceutical/emerging contaminants from water and wastewater. *Nanomaterials* 11.
- Khare, P., Talreja, N., Deva, D., Sharma, A., Verma, N., 2013. Carbon nanofibers containing metal-doped porous carbon beads for environmental remediation applications. *Chem. Eng. J.* 229, 72–81.
- Khataee, A., Hassandoost, R., Rahim Pouran, S., 2018. Cerium-substituted magnetite: fabrication, characterization and sonocatalytic activity assessment. *Ultrason. Sonochem.* 41, 626–640.
- Kumar, S., Nehra, M., Kedia, D., Dilbaghi, N., Tankeshwar, K., Kim, K.-H., 2018. Carbon nanotubes: a potential material for energy conversion and storage. *Prog. Energy Combust. Sci.* 64, 219–253.
- Lantam, A., Limbut, W., Thiagchanya, A., Phonchai, A., 2020. A portable optical colorimetric sensor for the determination of promethazine in lean cocktail and pharmaceutical doses. *Microchem. J.* 159, 105519.
- Lapworth, D.J., Baran, N., Stuart, M.E., Ward, R.S., 2012. Emerging organic contaminants in groundwater: a review of sources, fate and occurrence. *Environ. Pollut.* 163, 287–303.
- Leary, R., Westwood, A., 2011. Carbonaceous nanomaterials for the enhancement of TiO₂ photocatalysis. *Carbon* 49, 741–772.
- León-Aguirre, K., Hernández-Núñez, E., González-Sánchez, A., Méndez-Novelo, R., Ponce-Caballero, C., Giacomán-Vallejos, G., 2019. A rapid and green method for the determination of veterinary pharmaceuticals in swine wastewater by fluorescence spectrophotometry. *Bull. Environ. Contam. Toxicol.* 103, 610–616.
- Li, H., He, Y., Hu, Y., Wang, X., 2018. Commercially available activated carbon fiber felt enables efficient solar steam generation. *ACS Appl. Mater. Interfaces* 10, 9362–9368.
- Li, X., Huang, A., Liao, X., Chen, J., Xiao, Y., 2020. Restricted access supramolecular solvent based magnetic solvent bar liquid-phase microextraction for determination of non-steroidal anti-inflammatory drugs in human serum coupled with high performance liquid chromatography-tandem mass spectrometry. *J. Chromatogr. A* 1634, 461700.
- Li, Y.H., Zhao, Y.M., Hu, W.B., Ahmad, I., Zhu, Y.Q., Peng, X.J., Luan, Z.K., 2007. Carbon nanotubes - the promising adsorbent in wastewater treatment. *J. Phys. Conf. Ser.* 61, 698–702.
- Lipczynska-Kochany, E., 2018. Humic substances, their microbial interactions and effects on biological transformations of organic pollutants in water and soil: a review. *Chemosphere* 202, 420–437.
- Liu, L., Liu, Y., Gao, B., Ji, R., Li, C., Wang, S., 2020. Removal of perfluorooctanoic acid (PFOA) and perfluorooctane sulfonate (PFOS) from water by carbonaceous nanomaterials: a review. *Crit. Rev. Environ. Sci. Technol.* 50, 2379–2414.
- Lo, T.W.B., Aldous, L., Compton, R.G., 2012. The use of nano-carbon as an alternative to multi-walled carbon nanotubes in modified electrodes for adsorptive stripping voltammetry. *Sensor. Actuator. B Chem.* 162, 361–368.
- Logan, B.E., Rossi, R., Ragab, A.a., Saikaly, P.E., 2019. Electroactive microorganisms in bioelectrochemical systems. *Nat. Rev. Microbiol.* 17, 307–319.
- Loh, K.P., Bao, Q., Eda, G., Chhowalla, M., 2010. Graphene oxide as a chemically tunable platform for optical applications. *Nat. Chem.* 2, 1015–1024.
- Loos, R., Carvalho, R., António, D.C., Comero, S., Locoro, G., Tavazzi, S., Paracchini, B., Ghiani, M., Lettieri, T., Blaha, L., Jarosova, B., Voorspoels, S., Servaes, K., Haglund, P., Fick, J., Lindberg, R.H., Schwesig, D., Gawlik, B.M., 2013. EU-wide monitoring survey on emerging polar organic contaminants in wastewater treatment plant effluents. *Water Res.* 47, 6475–6487.
- Ma, W., Yan, Y., Ma, M., Su, F., Zhang, Y., 2016. Effect of black carbon on the migration and biodegradation of pentabromodiphenyl ether (BDE-99) during natural groundwater recharge with treated municipal wastewater. *Int. Biodeterior. Biodegrad.* 113, 177–186.
- Mailler, R., Gasperi, J., Coquet, Y., Buleté, A., Vulliet, E., Deshayes, S., Zedek, S., Mirande-Bret, C., Eudes, V., Bressy, A., Caupos, E., Moilleron, R., Chebbo, G., Rocher, V., 2016. Removal of a wide range of emerging pollutants from wastewater treatment plant discharges by micro-grain activated carbon in fluidized bed as tertiary treatment at large pilot scale. *Sci. Total Environ.* 542, 983–996.
- Manasfi, R., Labad, F., Montemurro, N., 2021. Development of methods for the determination of PhACs in soil/earthworm/crop system irrigated with reclaimed water. In: Pérez Solsona, S., Montemurro, N., Chiron, S., Barceló, D. (Eds.), *Interaction and Fate of Pharmaceuticals in Soil-Crop Systems: The Impact of Reclaimed Wastewater*. Springer International Publishing, Cham, pp. 417–491.
- Manley, M., 2014. Near-infrared spectroscopy and hyperspectral imaging: non-destructive analysis of biological materials. *Chem. Soc. Rev.* 43, 8200–8214.
- Maringa, A., Antunes, E., Nyokong, T., 2014. Electrochemical behaviour of gold nanoparticles and Co tetraaminophthalocyanine on glassy carbon electrode. *Electrochim. Acta* 121, 93–101.
- Masár, M., Hradskí, J., Nováková, M., Szucs, R., Sabo, M., Matejčík, Š., 2020. Online coupling of microchip electrophoresis with ion mobility spectrometry for direct analysis of complex liquid samples. *Sensor. Actuator. B Chem.* 302, 127183.
- Mayans, B., Pérez-Esteban, J., Escolástico, C., Eymar, E., Masaguer, A., 2019. Evaluation of Commercial Humic Substances and Other Organic Amendments for the Immobilization of Copper through ¹³C CP/MAS NMR, FT-IR, and DSC Analyses, vol. 9. *Agronomy*.
- Mazumder, A., Kumar, A., Dubey, D.K., 2013. High resolution ¹⁹F(1H) nuclear magnetic resonance spectroscopy and liquid chromatography–solid phase extraction–offline ¹H nuclear magnetic resonance spectroscopy for conclusive detection and identification of cyanide in water samples. *J. Chromatogr. A* 1284, 88–99.
- Mazumder, A., Kumar, A., Purohit, A.K., Dubey, D.K., 2012. A high-resolution phosphorus-31 nuclear magnetic resonance (NMR) spectroscopic method for the non-phosphorus markers of chemical warfare agents. *Anal. Bioanal. Chem.* 402, 1643–1652.
- Meisel, M.L., do Céu Costa, M., Pena, A., 2009. Regulatory approach on environmental risk assessment. Risk management recommendations, reasonable and prudent alternatives. *Ecotoxicology* 18, 1176–1181.
- Moradi, S., Sobhgol, S.A., Hayati, F., Isari, A.A., Kakavandi, B., Bashardoust, P., Anvaripour, B., 2020. Performance and reaction mechanism of MgO/ZnO/Graphene ternary nanocomposite in coupling with LED and ultrasound waves for the degradation of sulfamethoxazole and pharmaceutical wastewater. *Separ. Purif. Technol.* 251, 117373.
- Moral, R., Perez-Murcia, M.D., Perez-Espinosa, A., MorenoCaselles, J., Paredes, C., 2005. Estimation of nutrient values of pig slurries in Southeast Spain using easily determined properties. *Waste Manag.* 25, 719–725.
- Mshoperi, E., Fogel, R., Limson, J., 2014. Application of carbon black and iron phthalocyanine composites in bioelectricity production at a brewery wastewater fed microbial fuel cell. *Electrochim. Acta* 128, 311–317.
- Nagaraja, P., Yathirajan, H.S., Sunitha, K.R., Vasantha, R.A., 2002. A new, sensitive, and rapid spectrophotometric method for the determination of sulfa drugs. *J. AOAC Int.* 85, 869–874.
- Nannou, C., Ofrydopoulou, A., Evgenidou, E., Heath, D., Heath, E., Lambropoulou, D., 2019. Analytical strategies for the determination of antiviral drugs in the aquatic environment. *Trends Environ. Anal. Chem.* 24, e00071.
- Nazal, M.K., 2020. An Overview of Carbon-Based Materials for the Removal of Pharmaceutical Active Compounds. *Carbon-Based Material for Environmental Protection and Remediation*.
- Nie, Y., Qiang, Z., Zhang, H., Adams, C., 2009. Determination of endocrine-disrupting chemicals in the liquid and solid phases of activated sludge by solid phase extraction and gas chromatography–mass spectrometry. *J. Chromatogr. A* 1216, 7071–7080.
- Nosek, K., Styszko, K., Golas, J., 2014. Combined method of solid-phase extraction and GC-MS for determination of acidic, neutral, and basic emerging contaminants in wastewater (Poland). *Int. J. Environ. Anal. Chem.* 94, 961–974.
- Ojha, A., Tiwary, D., Oraon, R., Singh, P., 2021. Degradations of endocrine-disrupting chemicals and pharmaceutical compounds in wastewater with carbon-based nanomaterials: a critical review. *Environ. Sci. Pollut. Control Ser.* 28, 30573–30594.
- Omar, F.S., Duraisamy, N., Ramesh, K., Ramesh, S., 2016. Conducting polymer and its composite materials based electrochemical sensor for Nicotinamide Adenine Dinucleotide (NADH). *Biosens. Bioelectron.* 79, 763–775.
- Orooji, Y., Tanhaei, B., Ayati, A., Tabrizi, S.H., Alizadeh, M., Bamoharram, F.F., Karimi, F., Salmanpour, S., Rouhi, J., Afshar, S., Sillanpää, M., Darabi, R., Karimi-Maleh, H., 2021. Heterogeneous UV-Switchable Au nanoparticles decorated tungstophosphoric acid/TiO₂ for efficient photocatalytic degradation process. *Chemosphere* 281, 130795.
- Palmeri, M.J., Putz, K.W., Ramanathan, T., Brinson, L.C., 2011. Multi-scale reinforcement of CFRPs using carbon nanofibers. *Compos. Sci. Technol.* 71, 79–86.

- Pan, X., Ji, J., Zhang, N., Xing, M., 2020. Research progress of graphene-based nanomaterials for the environmental remediation. *Chin. Chem. Lett.* 31, 1462–1473.
- Pardakhti, A., Ahmadzadeh, S., Avazpour, S., Gupta, V.K., 2016. Highly sensitive and efficient voltammetric determination of ascorbic acid in food and pharmaceutical samples from aqueous solutions based on nanostructure carbon paste electrode as a sensor. *J. Mol. Liq.* 216, 387–391.
- Paredes, L., Fernandez-Fontaina, E., Lema, J.M., Omil, F., Carballa, M., 2016. Understanding the fate of organic micropollutants in sand and granular activated carbon biofiltration systems. *Sci. Total Environ.* 551–552, 640–648.
- Paz Zanini, V.I., Giménez, R.E., Linares Pérez, O.E., López de Mishima, B.A., Borsarelli, C.D., 2015. Enhancement of amperometric response to tryptophan by proton relay effect of chitosan adsorbed on glassy carbon electrode. *Sensor. Actuator. B Chem.* 209, 391–398.
- Pazdro, K., Borecka, M., Siedlewicz, G., Biak-Bieliska, A., Stepnowski, P., 2016. Analysis of the residues of pharmaceuticals in marine environment: state-of-the-art, analytical problems and challenges. *Curr. Anal. Chem.* 12, 202–226.
- Peiris, C., Gunatilake, S.R., Mlnsa, T.E., Mohan, D., Vithanage, M., 2017. Biochar based removal of antibiotic sulfonamides and tetracyclines in aquatic environments: a critical review. *Bioresour. Technol.* 246, 150–159.
- Pendergast, M.M., Hoek, E.M.V., 2011. A review of water treatment membrane nanotechnologies. *Energy Environ. Sci.* 4, 1946–1971.
- Pereira, A., Silva, L., Laranjeiro, C., Lino, C., Pena, A., 2020. Selected pharmaceuticals in different aquatic compartments: Part II—toxicity and environmental risk assessment. *Molecules* 25.
- Perkins, R., Whitehead, M., Goulson, D., 2021. Dead in the water: comment on “Development of an aquatic exposure assessment model for imidacloprid in sewage treatment plant discharges arising from use of veterinary medicinal products”. *Environ. Sci. Eur.* 33, 88.
- Pollap, A., Baran, K., Kuszewska, N., Kochana, J., 2020. Electrochemical sensing of ciprofloxacin and paracetamol in environmental water using titanium sol based sensor. *J. Electroanal. Chem.* 878, 114574.
- Pollap, A., Knihnicki, P., Kuśtrowski, P., Kozak, J., Golda-Cępa, M., Kotarba, A., Kochana, J., 2018. Sensitive voltammetric amoxicillin sensor based on TiO₂ sol modified by CMK-3-type mesoporous carbon and gold nanoparticles. *Electroanalysis* 30, 2386–2396.
- Pomati, F., Castiglioni, S., Zuccato, E., Fanelli, R., Vigetti, D., Rossetti, C., Calamari, D., 2006. Effects of a complex mixture of therapeutic drugs at environmental levels on human embryonic cells. *Environ. Sci. Technol.* 40, 2442–2447.
- Preiß, A., Lewin, U., Wennrich, L., Findeisen, M., Efer, J., 1997. Analysis of nitrophenols and other polar nitroaromatic compounds in ammunition wastewater by high-field proton nuclear magnetic resonance (1H-NMR) spectroscopy and chromatographic methods. *Fresen. J. Anal. Chem.* 357, 676–683.
- Preston, C.M., Shiptalo, S.E., Dudley, R.L., Fyfe, C.A., Mathur, S.P., Levesque, M., 1987. Comparison OF 13C CPMAS NMR and chemical techniques for measuring the degree OF decomposition IN virgin and cultivated peat profiles. *Can. J. Soil Sci.* 67, 187–198.
- Provolto, G., Martínez-Suller, L., 2007. In situ determination of slurry nutrient content by electrical conductivity. *Bioresour. Technol.* 98, 3235–3242.
- Qian, L., Durairaj, S., Prins, S., Chen, A., 2021. Nanomaterial-based electrochemical sensors and biosensors for the detection of pharmaceutical compounds. *Biosens. Bioelectron.* 175, 112836.
- Quintelas, C., Mesquita, D.P., Ferreira, E.C., Amaral, A.L., 2019. Quantification of pharmaceutical compounds in wastewater samples by near infrared spectroscopy (NIR). *Talanta* 194, 507–513.
- Radjenović, J., Jelić, A., Petrović, M., Barceló, D., 2009. Determination of pharmaceuticals in sewage sludge by pressurized liquid extraction (PLE) coupled to liquid chromatography-tandem mass spectrometry (LC-MS/MS). *Anal. Bioanal. Chem.* 393, 1685–1695.
- Ramesha, G.K., Vijaya Kumara, A., Muralidhara, H.B., Sampath, S., 2011. Graphene and graphene oxide as effective adsorbents toward anionic and cationic dyes. *J. Colloid Interface Sci.* 361, 270–277.
- Rashid, R., Shafiq, I., Akhter, P., Iqbal, M.J., Hussain, M., 2021. A state-of-the-art review on wastewater treatment techniques: the effectiveness of adsorption method. *Environ. Sci. Pollut. Control Ser.* 28, 9050–9066.
- Rashvand, M., Vosough, M., 2016. Graphene oxide–polyaniline nanocomposite as a potential sorbent for dispersive solid-phase extraction and determination of selected pharmaceutical and personal care products in wastewater samples using HPLC with a diode-array detector. *Anal. Method.* 8, 1898–1907.
- Razmi, H., Ezzati, L., Khorablou, Z., 2019. Direct electrochemical synthesis of graphene oxide/cobalt oxide nanocomposite on pencil graphite electrode for highly sensitive and selective detection of insulin in pharmaceutical samples. *J. Electrochem. Soc.* 166, B961–B968.
- Rezayi, M., Heng, L.Y., Kassim, A., Ahmadzadeh, S., Abdollahi, Y., Jahangirian, H., 2012. Immobilization of ionophore and surface characterization studies of the titanium(III) ion in a PVC-membrane sensor. *Sensors* 12.
- Richardson, M.L., Bowron, J.M., 1985. The fate of pharmaceutical chemicals in the aquatic environment. *J. Pharm. Pharmacol.* 37, 1–12.
- Rizzo, L., Fiorentino, A., Grassi, M., Attanasio, D., Guida, M., 2015. Advanced treatment of urban wastewater by sand filtration and graphene adsorption for wastewater reuse: effect on a mixture of pharmaceuticals and toxicity. *J. Environ. Chem. Eng.* 3, 122–128.
- Sadeghi Rad, T., Khataee, A., Arefi-Oskoui, S., Sadeghi Rad, S., Orooji, Y., Gengec, E., Kobya, M., 2022. Graphene-based ZnCr layered double hydroxide nanocomposites as bactericidal agents with high sonophotocatalytic performances for degradation of rifampicin. *Chemosphere* 286, 131740.
- Sajid, M., Nazal, M.K., Ihsanullah, Baig, N., Osman, A.M., 2018. Removal of heavy metals and organic pollutants from water using dendritic polymers based adsorbents: a critical review. *Separ. Purif. Technol.* 191, 400–423.
- Saleem, J., Shahid, U.B., Hijab, M., Mackey, H., McKay, G., 2019. Production and applications of activated carbons as adsorbents from olive stones. *Biomass Conversion and Biorefinery* 9, 775–802.
- Saleh, N.B., Khalid, A., Tian, Y., Ayres, C., Sabaaraya, I.V., Pietari, J., Hanigan, D., Chowdhury, I., Apul, O.G., 2019. Removal of poly- and per-fluoroalkyl substances from aqueous systems by nano-enabled water treatment strategies. *Environ. Sci.: Water Res. Technol.* 5, 198–208.
- Sanderson, H., Johnson, D.J., Reitsma, T., Brain, R.A., Wilson, C.J., Solomon, K.R., 2004. Ranking and prioritization of environmental risks of pharmaceuticals in surface waters. *Regul. Toxicol. Pharmacol.* 39, 158–183.
- Santos, L.H.M.L.M., Araújo, A.N., Fachini, A., Pena, A., Delerue-Matos, C., Montenegro, M.C.B.S.M., 2010. Ecotoxicological aspects related to the presence of pharmaceuticals in the aquatic environment. *J. Hazard Mater.* 175, 45–95.
- Saraswat, R., Talreja, N., Deva, D., Sankaramakrishnan, N., Sharma, A., Verma, N., 2012. Development of novel in situ nickel-doped, phenolic resin-based micro-nano-activated carbon adsorbents for the removal of vitamin B-12. *Chem. Eng. J.* 197, 250–260.
- Sarker, M., Song, J.Y., Jhung, S.H., 2018. Adsorptive removal of anti-inflammatory drugs from water using graphene oxide/metal-organic framework composites. *Chem. Eng. J.* 335, 74–81.
- Savariraj, A.D., Mangalaraja, R.V., Prabakar, K., Viswanathan, C., 2020. Electrochemical aspects for wastewater treatment. In: Naushad, M., Rajendran, S., Lichtfouse, E. (Eds.), *Green Methods for Wastewater Treatment*. Springer International Publishing, Cham, pp. 121–149.
- Sebastián, D., Ruiz, A.G., Suelves, I., Moliner, R., Lázaro, M.J., 2013. On the importance of the structure in the electrical conductivity of fishbone carbon nanofibers. *J. Mater. Sci.* 48, 1423–1435.
- Sebastián, D., Suelves, I., Lázaro, M.J., Moliner, R., 2009. Carbon nanofibers as electrocatalyst support for fuel cells: effect of hydrogen on their properties in CH₄ decomposition. *J. Power Sources* 192, 51–56.
- Shamagsumova, R.V., Shurpik, D.N., Padnya, P.L., Stoikov, I.I., Evtugyn, G.A., 2015. Acetylcholinesterase biosensor for inhibitor measurements based on glassy carbon electrode modified with carbon black and pillar[5]arene. *Talanta* 144, 559–568.
- Shokrollahi, A., Ghaedi, M., Niband, M.S., Rajabi, H.R., 2008. Selective and sensitive spectrophotometric method for determination of sub-micro-molar amounts of aluminium ion. *J. Hazard Mater.* 151, 642–648.
- Shu, H.-Y., Chang, M.-C., Hsu, H.-W., 2015. Activated carbon supported iron-nickel bimetallic nanoparticles for decolorization of Reactive Black 5 wastewater. *Desalination and Water Treatment* 54, 1184–1193.
- Siddiqui, M.T.H., Nizamuddin, S., Baloch, H.A., Mubarak, N.M., Al-Ali, M., Mazari, S.A., Bhattu, A.W., Abro, R., Srinivasan, M., Griffin, G., 2019. Fabrication of advance magnetic carbon nano-materials and their potential applications: a review. *J. Environ. Chem. Eng.* 7, 102812.
- Silva, T.A., Moraes, F.C., Janegitz, B.C., Fatibello-Filho, O., 2017. Electrochemical biosensors based on nanostructured carbon black: a review. *J. Nanomater.* 2017, 4571614.
- Simioni, N.B., Oliveira, G.G., Vicentini, F.C., Lanza, M.R.V., Janegitz, B.C., Fatibello-Filho, O., 2017. Nanodiamonds stabilized in dihexadecyl phosphate film for electrochemical study and quantification of codeine in biological and pharmaceutical samples. *Diam. Relat. Mater.* 74, 191–196.
- Singh, J., Mehta, A., 2020. Rapid and sensitive detection of mycotoxins by advanced and emerging analytical methods: a review. *Food Sci. Nutr.* 8, 2183–2204.
- Smith, R., 2019. *Groundwater-surface Water Connectivity of Heavily Modified Rivers*. Durham University, County Durham, UK.
- Song, X., Jiang, Q., Liu, J., Shao, Y., Feng, Y., 2019a. Enhanced electricity generation and water pressure tolerance using carbon black-based sintered filtration air-cathodes in microbial fuel cells. *Chem. Eng. J.* 369, 652–659.
- Song, Z., Ma, Y.-L., Li, C.-E., 2019b. The residual tetracycline in pharmaceutical wastewater was effectively removed by using MnO₂/graphene nanocomposite. *Sci. Total Environ.* 651, 580–590.
- Sørensen, M.K., Vinding, M.S., Bakharev, O.N., Nesgaard, T., Jensen, O., Nielsen, N.C., 2014. NMR sensor for onboard ship detection of catalytic fines in marine fuel oils. *Anal. Chem.* 86, 7205–7208.
- Srivastava, B., R, P.B., 2020. Impacts of drugs in the surface waters on fish health. In: *Internal Medicine: Open Access*, vol. 10.
- Su, S., Wu, W., Gao, J., Lu, J., Fan, C., 2012. Nanomaterials-based sensors for applications in environmental monitoring. *J. Mater. Chem.* 22, 18101–18110.
- Talarico, D., Arduini, F., Amine, A., Moscone, D., Palleschi, G., 2015. Screen-printed electrode modified with carbon black nanoparticles for phosphate detection by measuring the electroactive phosphomolybdate complex. *Talanta* 141, 267–272.
- Talreja, N., Kumar, D., Verma, N., 2014. Removal of hexavalent chromium from water using Fe-grown carbon nanofibers containing porous chromium microbeads. *J. Water Process Eng.* 3, 34–45.
- Tehrani, M., Khanbolouki, P., 2018. Carbon nanotubes: synthesis, characterization, and applications. In: Balasubramanian, G. (Ed.), *Advances in Nanomaterials: Fundamentals, Properties and Applications*. Springer International Publishing, Cham, pp. 3–35.
- Tijani, J.O., Fatoba, O.O., Babajide, O.O., Petrik, L.F., 2016. Pharmaceuticals, endocrine disruptors, personal care products, nanomaterials and perfluorinated pollutants: a review. *Environ. Chem. Lett.* 14, 27–49.
- Torrinha, Á., Oliveira, T.M.B.F., Ribeiro, F.W.P., Correia, A.N., Lima-Neto, P., Morais, S., 2020. Application of nanostructured carbon-based electrochemical (Bio)Sensors for

- screening of emerging pharmaceutical pollutants in waters and aquatic species: a review. *Nanomaterials* 10.
- Tran, C., Kafle, J., Yang, X.-Q., Qu, D., 2011. Increased discharge capacity of a Li-air activated carbon cathode produced by preventing carbon surface passivation. *Carbon* 49, 1266–1271.
- Tran, T.V., Nguyen, D.T., Le, H.T.N., Bach, L.G., Vo, D.-V.N., Lim, K.T., Nong, L.X., Nguyen, T.D., 2019a. Combined minimum-run resolution IV and central composite design for optimized removal of the tetracycline drug over metal-organic framework-templated porous carbon. *Molecules* 24.
- Tran, T.V., Nguyen, D.T.C., Le, H.T.N., Ho, H.L., Nguyen, T.T., Doan, V.-D., Nguyen, T.D., Bach, L.G., 2019b. Response surface methodology-optimized removal of chloramphenicol pharmaceutical from wastewater using Cu₃(BTC)₂-derived porous carbon as an efficient adsorbent. *Compt. Rendus Chem.* 220, 487–503.
- Trubetskaya, A., Kling, J., Ershag, O., Attard, T.M., Schröder, E., 2019. Removal of phenol and chlorine from wastewater using steam activated biomass soot and tire carbon black. *J. Hazard Mater.* 365, 846–856.
- Trujillo-Reyes, J., Peralta-Videa, J.R., Gardea-Torresdey, J.L., 2014. Supported and unsupported nanomaterials for water and soil remediation: are they a useful solution for worldwide pollution? *J. Hazard Mater.* 280, 487–503.
- Tswett, M., 1906. Physikalisch-chemische Studien über das Chlorophyll. *Ber. Dtsch. Bot. Ges.* 24, 316–323.
- Üner, O., Körükçü, B.C., Özcan, C., 2021. Adsorption application of activated carbon from ripe black locust seed pods for wastewater taken from Ergene River, Turkey. *Int. J. Environ. Anal. Chem.* 1–16.
- Van Tran, T., Cam Nguyen, D.T., Le, H.T.N., Nguyen, O.T.K., Nguyen, V.H., Nguyen, T.T., Bach, L.G., Nguyen, T.D., A Hollow Mesoporous Carbon from Metal-Organic Framework for Robust Adsorbability of Ibuprofen Drug in Water. *Royal Society Open Science* vol. 6, 190058.
- Verlicchi, P., Al Aukidy, M., Zambello, E., 2012. Occurrence of pharmaceutical compounds in urban wastewater: removal, mass load and environmental risk after a secondary treatment—a review. *Sci. Total Environ.* 429, 123–155.
- Vicentini, F.C., Ravanini, A.E., Figueiredo-Filho, L.C.S., Iniesta, J., Banks, C.E., Fatibello-Filho, O., 2015. Imparting improvements in electrochemical sensors: evaluation of different carbon blacks that give rise to significant improvement in the performance of electroanalytical sensing platforms. *Electrochim. Acta* 157, 125–133.
- Vicentini, F.C., Raymundo-Pereira, P.A., Janegitz, B.C., Machado, S.A.S., Fatibello-Filho, O., 2016. Nanostructured carbon black for simultaneous sensing in biological fluids. *Sensor. Actuator. B Chem.* 227, 610–618.
- Vijayan, R., Ghazinezami, A., Taklimi, S.R., Khan, M.Y., Askari, D., 2019. The geometrical advantages of helical carbon nanotubes for high-performance multifunctional polymeric nanocomposites. *Compos. B Eng.* 156, 28–42.
- Wanekaya, A.K., 2011. Applications of nanoscale carbon-based materials in heavy metal sensing and detection. *Analyst* 136, 4383–4391.
- Wang, H., Xu, H., Jia, W., Ren, S., 2018. Functionalized carbon black nanoparticles used for separation of emulsified oil from oily wastewater. *J. Dispersion Sci. Technol.* 39, 497–506.
- Wang, G., Guo, Y., Yang, L., Han, M., Zhao, J., Cheng, X., 2012. Nanomaterials as sorbents to remove heavy metal ions in wastewater treatment. *J. Environ. Anal. Toxicol.* 2, 154.
- Wang, X., Xie, Y., Yang, G., Hao, J., Ma, J., Ning, P., 2019. Enhancement of the electrocatalytic oxidation of antibiotic wastewater over the conductive black carbon-PbO₂ electrode prepared using novel green approach. *Front. Environ. Sci. Eng.* 14, 22.
- Wang, X., Yuan, C., Shao, C., Zhuang, S., Ye, J., Li, B., 2020a. Enhancing oxygen reduction reaction by using metal-free nitrogen-doped carbon black as cathode catalysts in microbial fuel cells treating wastewater. *Environ. Res.* 182, 109011.
- Wang, Y.-f., Pan, M.-m., Yu, X., Xu, L., 2020b. The recent advances of fluorescent sensors based on molecularly imprinted fluorescent nanoparticles for pharmaceutical analysis. *Curr. Med. Sci.* 40, 407–421.
- Wang, Z., Shao, D., Westerhoff, P., 2017. Wastewater discharge impact on drinking water sources along the Yangtze River (China). *Sci. Total Environ.* 599–600, 1399–1407.
- Wei, H., Deng, S., Huang, Q., Nie, Y., Wang, B., Huang, J., Yu, G., 2013. Regenerable granular carbon nanotubes/alumina hybrid adsorbents for diclofenac sodium and carbamazepine removal from aqueous solution. *Water Res.* 47, 4139–4147.
- Woon, K., Pyrgiotakis, G., Sigmund, W., 2009. Photocatalytic carbon-nanotube-TiO₂ composites. *Adv. Mater.* 21, 2233–2239.
- Wu, L.-N., Tan, Y.-L., Wang, L., Sun, S.-N., Qu, Z.-Y., Zhang, J.-M., Fan, Y.-J., 2015. Dopamine sensor based on a hybrid material composed of cuprous oxide hollow microspheres and carbon black. *Microchimica Acta* 182, 1361–1369.
- Wu, X., Hu, J., Qi, J., Hou, Y., Wei, X., 2020. Graphene-supported ordered mesoporous composites used for environmental remediation: a review. *Separ. Purif. Technol.* 239, 116511.
- Xu, J., Wang, L., Zhu, Y., 2012. Decontamination of bisphenol A from aqueous solution by graphene adsorption. *Langmuir* 28, 8418–8425.
- Yagüe, M.R., Quílez, D., 2012. On-farm measurement of electrical conductivity for the estimation of ammonium nitrogen concentration in pig slurry. *J. Environ. Qual.* 41, 893–900.
- Yang, G.C.C., Tang, P.-L., 2016. Removal of phthalates and pharmaceuticals from municipal wastewater by graphene adsorption process. *Water Sci. Technol.* 73, 2268–2274.
- Yang, M.-Q., Zhang, N., Pagliaro, M., Xu, Y.-J., 2014. Artificial photosynthesis over graphene-semiconductor composites. Are we getting better? *Chem. Soc. Rev.* 43, 8240–8254.
- Yang, M., Yang, Y., Liu, Y., Shen, G., Yu, R., 2006. Platinum nanoparticles-doped sol-gel/carbon nanotubes composite electrochemical sensors and biosensors. *Biosens. Bioelectron.* 21, 1125–1131.
- Yang, S., Hu, J., Chen, C., Shao, D., Wang, X., 2011. Mutual effects of Pb(II) and humic acid adsorption on multiwalled carbon nanotubes/polyacrylamide composites from aqueous solutions. *Environ. Sci. Technol.* 45, 3621–3627.
- Yaripour, S., Mohammadi, A., Mousavi, S., Esfanjani, I., Arabzadeh, N., Mozaffari, S., 2019. Simultaneous determination of 2-nitrophenol and 4-nitrophenol in pharmaceutical industrial wastewater by electromembrane extraction coupled with HPLC-UV analysis. *Pharmaceut. Sci.* 25, 57–64.
- Yaylali-Abanuz, G., 2011. Heavy metal contamination of surface soil around Gebze industrial area, Turkey. *Microchem. J.* 99, 82–92.
- Yilmaz, B., Ciltas, U., 2015. Determination of diclofenac in pharmaceutical preparations by voltammetry and gas chromatography methods. *J. Pharmaceut. Analysis* 5, 153–160.
- Yousef Tizhoosh, N., Khataee, A., Hassandoost, R., Darvishi Cheshmeh Soltani, R., Doustkhah, E., 2020. Ultrasound-engineered synthesis of WS₂@CeO₂ heterostructure for sonocatalytic degradation of tylosin. *Ultrason. Sonochem.* 67, 105114.
- Yu, Y., Wu, L., 2013. Application of graphene for the analysis of pharmaceuticals and personal care products in wastewater. *Anal. Bioanal. Chem.* 405, 4913–4919.
- Zhan, J., Li, Z., Yu, G., Pan, X., Wang, J., Zhu, W., Han, X., Wang, Y., 2019. Enhanced treatment of pharmaceutical wastewater by combining three-dimensional electrochemical process with ozonation to in situ regenerate granular activated carbon particle electrodes. *Separ. Purif. Technol.* 208, 12–18.
- Zhang, F., Li, Y.-H., Li, J.-Y., Tang, Z.-R., Xu, Y.-J., 2019a. 3D graphene-based gel photocatalysts for environmental pollutants degradation. *Environ. Pollut.* 253, 365–376.
- Zhang, W., Zhang, D., Liang, Y., 2019b. Nanotechnology in remediation of water contaminated by poly- and perfluoroalkyl substances: a review. *Environ. Pollut.* 247, 266–276.
- Zhang, Y., Wu, X., Nsabimana, A., Munyentwali, A., Han, C., Li, M., Guo, L., 2015. Green and facile synthesis of an Au nanoparticles@polyoxometalate/ordered mesoporous carbon tri-component nanocomposite and its electrochemical applications. *Biosens. Bioelectron.* 66, 191–197.
- Zhang, Y., Tang, Z.-R., Fu, X., Xu, Y.-J., 2011. Engineering the unique 2D mat of graphene to achieve graphene-TiO₂ nanocomposite for photocatalytic selective transformation: what advantage does graphene have over its forebear carbon nanotube? *ACS Nano* 5, 7426–7435.
- Zhong, R., Zou, H., Gao, J., Wang, T., Bu, Q., Wang, Z.-L., Hu, M., Wang, Z., 2021. A critical review on the distribution and ecological risk assessment of steroid hormones in the environment in China. *Sci. Total Environ.* 786, 147452.
- Zhou, K., Tian, Y., Ma, H., Ma, C., Fu, Y., Dong, X., Zhang, X., 2018. Photoelectrocatalytic performance of conductive carbon black-modified Ti/F-PbO₂ anode for degradation of dye wastewater (reactive brilliant blue KN-R). *J. Solid State Electrochem.* 22, 1131–1141.
- Zhu, J., Zhang, Q., Chen, H., Zhang, R., Liu, L., Yu, J., 2020. Setaria viridis-inspired electrode with polyaniline decorated on porous heteroatom-doped carbon nanofibers for flexible supercapacitors. *ACS Appl. Mater. Interfaces* 12, 43634–43645.
- Zhu, X.-D., Zhang, K., Wang, Y., Long, W.-W., Sa, R.-J., Liu, T.-F., Lü, J., 2018. Fluorescent metal-organic framework (MOF) as a highly sensitive and quickly responsive chemical sensor for the detection of antibiotics in simulated wastewater. *Inorg. Chem.* 57, 1060–1065.

Available online at www.sciencedirect.com

ScienceDirect

journal homepage: www.elsevier.com/locate/he

Comparative study of hydrogen production from steam reforming of acetic acid over synthesized catalysts via MOF and wet impregnation methods

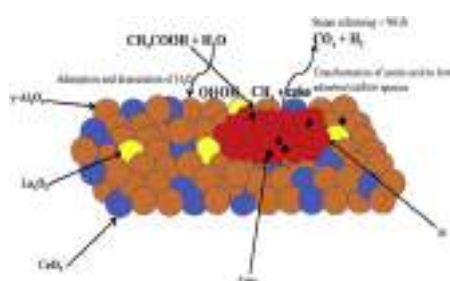
Ankit Kumar*, A.S.K. Sinha

Department of Chemical Engineering & Technology, Indian Institute of Technology (BHU), Varanasi-221005, India

HIGHLIGHTS

- Catalysts were prepared with MOF and wet impregnation methods, tested activity for AASR.
- Preparation methods plays crucial role in the Ni dispersion and the metal support interaction.
- Ni-complex/ALC catalyst showed more effective in terms of conversion and H₂ yield.
- The supports greatly influence the activity of Ni based catalysts in AASR.
- Ni-complex/ALC catalyst was more stable than Ni/ALC catalyst for AASR.

GRAPHICAL ABSTRACT



ARTICLE INFO

Article history:

Received 16 December 2019

Received in revised form

10 February 2020

Accepted 15 February 2020

Available online 11 March 2020

Keywords:

Hydrogen production

Acetic acid

Coke deposition

Nickel-complex

ABSTRACT

This study focuses on acetic acid steam reforming (AASR) for the production of hydrogen over synthesized a complex catalyst via metal-organic framework (MOF) process supported on Al₂O₃/La₂O₃/CeO₂ (ALC) named Ni-Complex/ALC. The catalytic activity and stability of the synthesized catalyst compared with a catalyst of the same composition prepared using nickel format precursor via wet impregnation wetness method. Catalytic reaction was tested for both catalysts under atmospheric pressure at different temperatures ranging from 300 to 650 °C, with S/C ratio = 6.5 and weight hour space velocity (WHSV) 1.05 h⁻¹. Acetic acid conversion and product distribution were observed for 36 h of reaction. The results showed that activity of the catalyst prepared using MOF process showed a better yield towards hydrogen production and stability against coke deposition due to regular pore structure and more amount of oxygen molecules available present on the surface. The yield of H₂ was found to be approx. 90%, i.e., close to the theoretical stoichiometric limit.

© 2020 Hydrogen Energy Publications LLC. Published by Elsevier Ltd. All rights reserved.

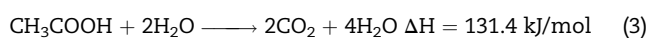
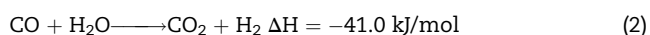
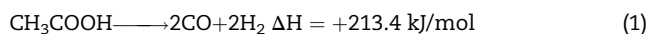
* Corresponding author.

E-mail address: asksinha.che@itbhu.ac.in (A. Kumar).<https://doi.org/10.1016/j.ijhydene.2020.02.097>

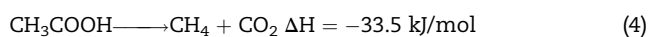
0360-3199/© 2020 Hydrogen Energy Publications LLC. Published by Elsevier Ltd. All rights reserved.

Introduction

In current times, because of the depletion of fossil fuel resources and growing concern related to increasing pollution, hydrogen is widely accepted as a promising alternative and sustainable for transportation fuel [1,2]. It offers several benefits and possesses high energy content ($\sim 122 \text{ MJ kg}^{-1}$), which is 2.8 times more than conventional fossil fuels and no generation of any pollutant on combustion as water is the only product formed during the combustion process [3]. Currently, H_2 is mainly generated via steam reforming of natural gas or petroleum-based sources and through coal gasification [4,5]. However, these techniques not only emit greenhouse gases and contribute to environmental pollution but also lead to the exhaustion of fossil reserves [6,7]. Alternative hydrogen can be produced using renewable energy sources such as biomass either through thermochemical process such as direct gasification combining with water gas shift reaction or production of bio-oil via fast pyrolysis steam reforming and via biological processes [8–11]. Hydrogen production from renewable biomass can mitigate environmental pollution as well as decrease dependency on fossil reserves. Bio-oils or pyrolysis oil obtained through fast pyrolysis of biomass and subsequent catalytic steam reforming has been considered as an economical and feasible way to generate hydrogen without harmful emission to greenhouse gases. Moreover, steam reforming of bio-oil is considered as a renewable and sustainable route for hydrogen production due to CO_2 neutral source of biomass growth [12]. Bio-oil, produced from fast pyrolysis of biomass is highly complex nature and contains various groups of oxygenated compounds like acids, esters, aldehyde, ketones, sugars, phenols, furfural as well as many others compounds [10,13]. Taking into account the complex nature of bio-oil, it is still a key challenge to develop and design an efficient and stable catalyst for hydrogen production from bio-oil steam reforming. Since, acetic acid (AcOH) one of the main component of raw bio-oil (up to 19 wt%) [14,15], has been chosen as a represented compound of bio-oil to explore and develop efficient catalyst for hydrogen production. AASR takes place via acetic acid decomposition (Eq. (1)), followed by the water gas shift reaction (WGSR) Eq. (2) simultaneously in the reactor. The overall steam reforming reactions are shown in Eq. (3).

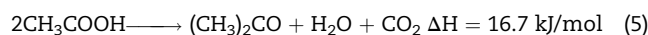


WGS reaction is favoured at low temperature and CO is combined with steam to produce H_2 and CO_2 , and resulting in the removal of produced CO. CH_4 may also form via thermal decomposition of acetic acid Eq. (4)



Acetone is also formed via ketonization at low reaction temperature and resulting in lower conversion. It is one of the

main intermediates for carbon formation in acetic acid reforming reaction.



AASR also involved complex reaction network pathways, which produces several undesired intermediates causing the generation of carbonaceous species over the catalyst surface. To enhance the production of H_2 and minimization of the intermediate gases during AASR, several researchers investigated various strategies, including modification of catalysts. In general noble metal catalysts such as; (Pt, Pd, Rh, Ru, Ir) have widely been reported for AASR [16,17]. These catalysts showed better activity towards H_2 production as well as less susceptibility for coke deposition in comparison to transition metals [18]. However, these catalysts are expensive, and therefore commercialization is difficult. So, at present great attention is focused on low-cost transition metals such as Ni, Co, and Fe during the AASR [19]. Among them, Ni-based catalysts have been extensively selected for steam reforming reaction because of having lower price compared to noble metals and excellent activity [20–25]. Ni showed high activity towards cleavage of C–C bond and O–H bond and contributed to form H_2 via adsorbed hydrogen atoms on catalyst surface [9,14,26,27]. However, the major disadvantage of Ni-based catalysts during steam reforming reaction is that, they are easily deactivated via coking and sintering of particles [13,28]. The coke formation is associated with various side reactions such as to the cracking, dehydration and polymerisation reaction on the acidic sites of the support. The reforming activity and selectivity of Ni-based catalysts depend on many factors viz. Catalysts preparation methods, type of supports, metal loading, use of the additive, and operating conditions [29]. Together with the active metal phase, proper support is also required to improve activity and stability, by the alleviation of coke deposition during AASR.

Carbon deposition is one of the most severe issues for Ni based catalyst than noble metal catalysts [19]. In addition, AASR suffers from severe hydrothermal environment, and catalysts get deactivated by sintering of active metal [30]. Carbon deposition may happen via. Decomposition of intermediates generated and through oligomerization of acetone during AASR [31]. Hence, various researchers have reported their works on measuring stable catalytic performance towards H_2 rich gas and suppressing coking during AASR [7,32–35]. Hu and Lu performed AASR over different transition metal catalysts (Ni, Co, Fe and Cu) supported on $\gamma\text{-Al}_2\text{O}_3$ and found that activities of Ni/ $\gamma\text{-Al}_2\text{O}_3$ and Co/ $\gamma\text{-Al}_2\text{O}_3$ catalysts were better. However, both catalysts deactivated due to coke deposition. Ni/ $\gamma\text{-Al}_2\text{O}_3$ catalyst showed much active and stable behaviour against coke deposition than Co/ $\gamma\text{-Al}_2\text{O}_3$ and other Fe and Cu based catalyst [34]. An et al. [32]. Reported that during AASR over the Ni/ $\gamma\text{-Al}_2\text{O}_3$, at 600 °C, increases in the Ni loading, supports cracking reaction of acetic acid while retards ketonization reaction. Deposited carbon species are also affected by loading from Ni e.g. carbidic type carbon decreased, and graphitic-type carbon increased with increase of Ni loading by 9–15 wt%. Maximum conversion and selectivity of H_2 was 90% and 50% respectively when supported on 12% Ni loading. The

total amount of deposited coke was same for all catalysts, while increase in Ni loading, crystalline coke increased. Li et al. [36] reported that crystalline carbon was formed from CH₄ decomposition and got transformed into inert graphitic carbon and was not quickly gasified because of Ni–C interaction. Basagiannis and Verykios performed AASR over Ni and Ru/ γ -Al₂O₃ at 700 °C (S/C = 5), and reported that modification of Ni or Ru/ γ -Al₂O₃ with Mg or La improves the conversion as well as H₂ selectivity. Coke formation also decreased from 4.65 to 0.1% over the other catalysts. However, La also promoted ketonization reactions and consequently produce acetone at lower temperatures [7].

Support also affects the dispersion of active metal and alter the electronic distribution by taking part in the reaction [37]. The γ -Al₂O₃ is widely accepted support in the steam reforming reaction because of its high surface area for metal dispersion and excellent thermal and chemical stability. However, Ni/ γ -Al₂O₃ gets easily deactivated by coke deposition during reforming reaction and substantial sintering due to presence of water vapor and high temperatures [38,39]. Due to strong acidic nature of Al₂O₃ and for the improvement of activity and stability of Ni-based catalyst, many researchers have suggested following strategies (1) modification in catalyst preparation (2) support modification (3) addition of promoters [24,40]. In order to neutralize the acid sites of γ -Al₂O₃ support, addition with basic promoters such as alkali and alkaline metals (Li, K, Mg, Ca, Ba, etc), are usually reported in literatures [24,29,41–43]. Another approach during steam reforming reaction to be mitigated by using various oxides support e.g. CeO₂, La₂O₃, CaO, BaO, or using as a modifier to alumina support. These oxide supports increase the catalyst activity as well as coke resistance capability [44]. Various researchers have investigated that basicity and redox properties of support material have strong effect to minimize the coke formation during AASR [31,45,46]. It is well known that CeO₂ has easy redox properties in terms of oxygen storage and release capacity because of easy transformation of Ce⁴⁺/Ce³⁺ which boosts the catalyst activity. Furthermore, it also enhances dispersion of Ni catalysts over the support surface because of its redox behaviour [47]. Incorporation of CeO₂ promotes oxidation reaction by providing oxygen atom from lattice of CeO₂ to the active metal which accelerate coke gasification resulting in low coke deposition [17,48]. Moreover, addition of CeO₂ also contributes to inhibition of sintering of active metal and also stabilize γ -Al₂O₃ support by preventing its phase transformation of [48]. On the other hand, addition of La₂O₃ showed a significant effect on thermal stability by preventing sintering of γ -Al₂O₃ particles through interactions between Al and La molecules, by creation of bonds La–O–Al after calcination. It also disperses the Ni metal particles and prevent the formation of NiAl₂O₄ which is susceptible to sintering [49]. In addition, La promote the WGS reaction which suppress the formation of coke on the catalyst surface by removal of adsorbed CO as well as reacts with CO₂ forming oxygen containing species which further helped to remove coke [6]. Lefferts et al. studied AASR over Ni/ZrO₂ catalyst and reported that catalytic activity gradually decreased due to extensive coke deposition. Whereas, addition of K and La in to the catalyst improved the activity as well as stability by suppressing coke accumulation [50]. Moreover, addition of

La₂O₃ also prevented metal sintering and stabilized the metal particles at high reaction temperatures [6]. Although both CeO₂ and La₂O₃ enhance the thermal stability property of γ -Al₂O₃, but La₂O₃ is more active due to insertion of lanthanum molecules into the crystal lattice of γ -Al₂O₃ forming spinel structures, while cerium remains on the surface in the form of CeO₂ [51]. Various catalyst preparation methods have been adopted to develop nano-porous structures particles with highly ordered structures and high surface area at a large scale for technology use. In this respect, metal-organic-frameworks (MOFs) exhibit excellent potential due to their controllable structure tunable functionality and pore size, special electrochemical properties, and high catalyst surface area [52,53]. Yang et al. investigated different and simple method for the synthesis of novel ZnO nanoparticles and hybrid ZnO@C nanostructured catalyst using MOF approach under different atmospheric conditions. The hierarchical 3D cubical structured nanoparticles of ZnO showed relatively high photocatalytic decomposition activity. Whereas, the hybrid ZnO@C composites showed high porosity with sufficient pore sizes which exhibited excellent adsorbing capacity for organic pollutants [54].

In the present study, Ni/ γ -Al₂O₃ catalysts impregnated with La₂O₃–CeO₂ have been prepared from two different methods (i) via MOF and (ii) wet impregnation method. Their catalytic activity and stability were evaluated for AASR for hydrogen production at different temperatures and time on stream. Various characterizations were applied to ascertain the chemical and textural properties of both the prepared catalysts, including H₂ temperature program reduction (TPR), X-ray diffraction (XRD), transmission electron microscopy (TEM), BET surface area by N₂ adsorption-desorption, and thermogravimetry analysis (TGA).

Experimental

Materials

Aluminum nitrate nanohydrate (Al(NO₃)₃·9H₂O, >98%, Merk Pvt Ltd.), Ammonium hydroxide (NH₄OH, >98% Fisher Scientific), Nickel chloride hexahydrate (NiCl₂·6H₂O, >98%, Fisher Scientific), Nickel (II) formate (Ni(HCO₂)₂·2H₂O, >98% Alfa Aesar), lanthanum nitrate (La(NO₃)₃·6H₂O, >98%, Central Drug House, Mumbai-India), Cerium(IV) sulfate tetrahydrate (Ce(SO₄)₂·4H₂O, >98%, Merk Pvt.Ltd.), 2,2' Bipyridine (C₁₀H₈N₂, >98%, Alfa Aesar), Propan -2OL ((CH₃)₂·CHOH, >98%, Fisher Scientific), Diethyl Ether ((C₂H₅)₂O, >98%, Fisher Scientific), and Ethanol (C₂H₆O, >98% Fisher Scientific) were used directly for the synthesis of support and catalysts.

Synthesis of Al₂O₃/La₂O₃/CeO₂(ALC) support material

Aluminum hydroxide gel of high surface area was prepared at 30 °C from concentrated solution of aluminum nitrate by adjusting pH 9 with the help of ammonia solution. The prepared hydrogel was kept 24 h for aging and appropriately rinsed with double distilled water to remove nitrate ions completely. Eventually, the product was dried in an oven and calcined in furnace at 110 °C and 800 °C respectively, each for 8 h to get γ -Al₂O₃ support. To obtain 3 wt% La₂O₃ yield in the

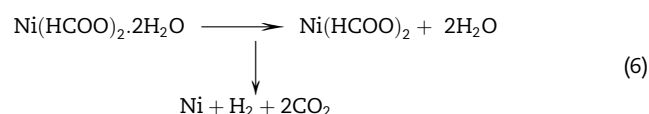
final support, γ - Al_2O_3 support was impregnated with the required amount of aqueous solution of $\text{La}(\text{NO}_3)_3 \cdot 6\text{H}_2\text{O}$. This concentration of La_2O_3 was chosen because it has been reported optimal for stabilizing the γ - Al_2O_3 support against sintering process [55,56].

The γ - Al_2O_3 - La_2O_3 support solution was then dried on a water bath (100 °C), and further dried in oven (110 °C) for overnight and finally calcined at 800 °C for 8 h. To obtain 9 wt% concentration of CeO_2 in the final support required amount of aqueous nitric acid solution of Cerium (IV) sulfate tetrahydrate was impregnated over prepared γ - Al_2O_3 - La_2O_3 support. The obtained mixture was dried in water bath with continuous stirring and subsequently in an oven at 110 °C for overnight and finally calcined at 550 °C for 8 h.

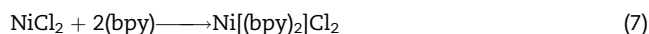
Synthesis of supported Ni catalyst

The above-synthesized γ - Al_2O_3 - La_2O_3 - CeO_2 (ALC) support was used to prepare Ni-based catalysts by two different methods. The nickel loading was 15% by weight in both cases.

Catalyst 1. The catalyst was synthesized by wet impregnation of support with a dilute ammoniacal solution of nickel formate ($\text{Ni}(\text{HCOO})_2 \cdot 2\text{H}_2\text{O}$). Requisite volume of the prepared solution was impregnated on the prepared alumina-lanthanum-cerium (ALC) support to obtain 15 wt% Ni in the final catalyst. The obtained mixture was dried in water bath with continuous stirring and subsequently in an oven at 110 °C for overnight and finally calcined at 550 °C for 4 h in a tubular reactor in the presence of N_2 flow. The advantage of using nickel formate precursor over other common precursors is that formate does not require external reducing agents like H_2 . On heating $\text{Ni}(\text{HCOO})_2 \cdot 2\text{H}_2\text{O}$ directly decomposes to nickel and a gaseous species [57].



Catalyst 2. This catalyst was prepared using $\text{Ni}[(\text{bpy})_2]\text{Cl}_2$ monometallic complex of nickel. Stoichiometric amount of nickel precursor ($\text{NiCl}_2 \cdot 6\text{H}_2\text{O}$) and organic ligand (2,2'-bipyridine) were taken for the preparation of the nano-metallic complexes via below given reaction.



1.47 g of NiCl_2 and 3.54 g of 2,2'-bipyridine organic ligand solutions were made in 20 mL of 2-propanol solvent separately. Both the solutions were mixed dropwise in a round bottom flask simultaneously with continuous stirring at 400 rpm for 4 h. The flow rate of each solution was maintained at 0.33 mL/min, and the temperature of flask was maintained at 40 °C. Fine mixture of Ni-complex ($\text{Ni}[(\text{bpy})_2]\text{Cl}_2$) was obtained, washed with ethanol, and ether until it is free from impurities. The final yield obtained after washing was 81% [58].

Finally, the prepared nickel complex and ALC support were further dissolved in methanol separately in the beaker. The solution of requisite amount of Ni-complex and ALC was taken and mixed dropwise in a round bottom flask at 400 rpm,

maintaining 40 °C for 3 h to obtain 15 wt% loading of Ni in the final catalyst. The prepared mixture was then filtered and dried for 12 h (110 °C) in an oven and calcined for 6 h in the tubular reactor at 650 °C to remove the ligand part in the presence of controlled flow of N_2 gas.

Characterization of catalysts

Surface area of catalysts and support, as well as pore size distribution of the catalyst, were measured by the N_2 adsorption/desorption cycles method using the (micrometric ASAP 2020) surface area analyzer. The sample catalysts were dried at 110 °C under argon flow before each measurement. Crystal phases and sizes in supports and catalysts were investigated via X-ray powder diffraction (XRD) techniques from a (Rigaku Ultima IV) using $\text{Cu-K}\alpha$ radiation source. Hydrogen temperature-programmed reduction (H_2 -TPR) results were obtained using micromeritics pulse chemisorption unit with TPD model no. 2920. 50 mg of the catalyst was pre-treated at 300 °C with constant flow of argon gas to remove moisture in a quartz made microreactor. Subsequently, to obtain the TPR profile, the sample was heated from 50 to 800 °C linearly at a heating rate of 5 °C/min with a constant flow of 5% H_2/Ar (40 mL/min). The catalysts were also peroxidised in the same instrument with the constant flow of oxygen (60 mL/h) from room temperature to 500 °C for 2 h before performing reduction analysis. The thermal conductivity detector measured any change in the composition of the exhaust gas. To observe the fine structure of prepared catalyst, transmission electron microscopy (TEM) was conducted by TechnaiG² at 200 kV accelerating voltage instrument. A scanning electron microscope (SEM, EDAX Novo Nano SEM 450) was performed for surface morphology of the catalyst. Photoelectron spectroscopy (XPS) of the catalysts was performed using the X-ray photoelectron spectroscopy (AMICUS, Kratos Analytical) using monochromated $\text{Mg-K}\alpha$ line (1253.6 eV) as an X-ray source. For the analysis of coke deposited on the surface of catalysts, thermal analysis (DT-TGA) was carried out using thermal analyzer (NETZSCH-Jupiter-STA-449F3) under a flow of O_2 (50 mL/min) with constant heating rate of 10 °C/min up-to 1000 °C. Decomposition of precursors, i.e., nickel formate and Ni-complex, were also studied by thermal analysis in an inert atmosphere of N_2 gas. N_2 gas was allowed to flow at 50 mL/min.

Experimental set-up

AASR was studied in a vertical quartz tubular reactor under steady-state conditions. The experimental schematic diagram was presented in Fig. 1. It consisted of three sections, viz, the feed preparation, the reaction, and the analysis section. The mixture was fed into a preheater to vaporize the feed before entering to the reactor section. Preheating section contained a tubular quartz tube surrounded with heating coil and insulated with ceramic wools. The temperatures of the preheating section were controlled from two variac connected in series. Activity test was carried out using the synthesized catalyst diluted with SiC particles (1:2w/w) (Particle size were of the range of 0.2–0.5 mm) to avoid channelling of flow and local

heating of the catalyst. No catalytic activity were found solely on SiC particles even at high reaction temperatures. The catalyst particles were placed in the centre of the reactor sandwiched between quartz wool. The length of tubular reactor was 50 cm, and internal diameter was 10 mm. The reactor was surrounded with electric furnace coupled with PID controller (Thermolyne, USA 79300). A K-type thermocouple was placed inside a vertical thermowell at the centre of reactor to measure the catalyst temperature. The thermocouple could move from the top to bottom of the reactor. 500 mg of catalyst diluted with SiC, as discussed above was placed in the central part of the reactor where the temperature variation along the length from the top to bottom of the catalyst bed was not more than 2 °C. The feed was a mixture of acetic acid and water. The two were premixed in a ratio to give steam to carbon ratio of 6.5:1(mole/mole) in the feed to the reactor. The premixed liquid mixture was fed at the rate of 2.5 mL/min through calibrated pump (Fluid Metering Inc, USA, Model RHSY). Nitrogen as a carrier gas was also introduced into the reactor at a flow rate of 30 mL/min. Accordingly, the inlet concentration of acetic acid was 4.85×10^{-6} mol/mL of N₂ and WHSV 1.05 h⁻¹. Products gases from the reactor were passed through a condenser set at 4 °C to gas-liquid separator for condensing water and any condensable vapors. The gaseous products and condensate liquid were analysed by Nucon (5700) make gas chromatograph (GC) separately. H₂, N₂, CO, CH₄, and CO₂ in the gaseous mixture were analysed by a GC equipped TCD (GC-TCD) with the Carbosieve SII column, and the condensate liquid was analysed by (GC-FID) equipped with Porapak Q column. To determine the calibration factors for TCD were achieved with the standard gas mixtures of known compositions (Chemtron Science Laboratory, Navi Mumbai) and for liquid self-prepared with iso-octane as the internal standard was used. All the experiments related to conversion, yield and stability tests of catalyst were performed at least twice for the same operating conditions, the

experimental data produced are approximately same with marginal difference.

Catalytic activities were measured in terms of conversion of acetic acid and yields of species (CO, CH₄, CO₂, and H₂). Conversion of acetic acid was defined in terms of C–C bond cleavage conversion, as given below.

Conversion of acetic acid, X_{AcOH} (%)

C – C bond cleavage conversion, X_{C-C}(%)

$$= \frac{\text{Moles of carbon in the product gases}}{\text{moles of acetic acid reacted}} \times 100 \quad (8)$$

Yield of a species in the products given in Eq. (9) is the ratio of moles of the species in the product to the number of moles of the same species formed on complete conversion of acetic acid to the species. Therefore, yield of CO, CH₄, CO₂ (%)

$$Y_{\text{CO, CH}_4, \text{CO}_2} = \frac{\text{moles of CO/ CH}_4/ \text{CO}_2 \text{ out}}{2 \times \text{moles of acetic acid reacted}} \times 100 \quad (9)$$

The yield of H₂ produced was calculated using in Eq. (10). It is the fraction of H₂ produced to the moles of H₂ on complete conversion of 1-mol acetic acid to H₂.

$$Y_{\text{H}_2} = \frac{\text{moles of H}_2 \text{ production}}{4 \times \text{moles of acetic acid reacted}} \times 100 \quad (10)$$

Results and discussion

Characterization of support and catalyst

Fig. 2. Presents the TG-DTA analysis of Ni(HCOO)₂·2H₂O performed from 23 to 1000 °C at a rate of 10 °C/min. It shows that the decomposition was a two-step process. In the first step, water molecules were removed at 200 °C and next to the anhydrous formate decomposed to Ni at 285 °C. The final weight was 32.6% of the initial, which matched nickel content

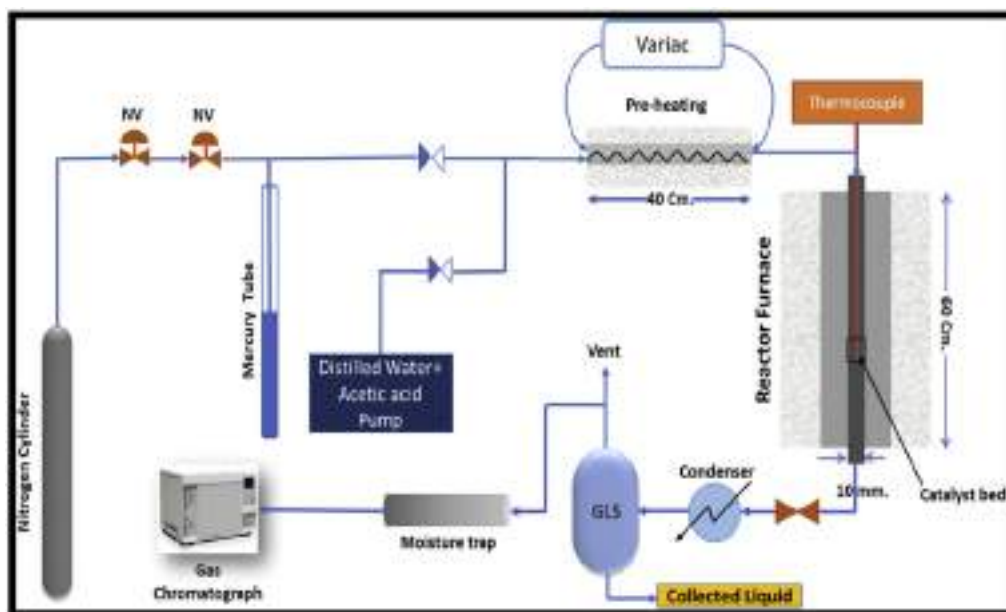


Fig. 1 – Schematic diagram of catalytic steam reforming.

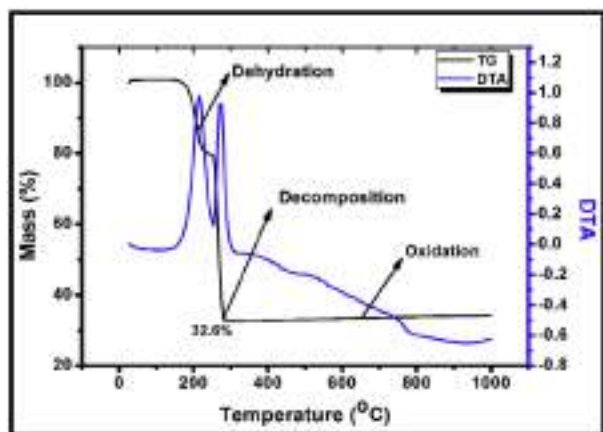


Fig. 2 – TGA profiles of nickel formate ($\text{Ni}(\text{HCOO})_2 \cdot 2\text{H}_2\text{O}$).

(32.9%) in $\text{Ni}(\text{HCOO})_2 \cdot 2\text{H}_2\text{O}$. It confirms that the nickel formate decomposed directly to metallic nickel in an inert atmosphere.

DT-TGA analyses of prepared $[\text{Ni}(2'2'\text{-bipy})_2\text{Cl}_2]$ (Fig. 3) showed that the precursor of nickel complex finally decomposed to Ni(0) with the removal of different volatiles compounds. The first decomposition peak at $\sim 200^\circ\text{C}$ is attributed to removal of H_2O coordinated with complex molecules along with 29.38% mass loss. However, it is not well defined and showed that formation of moieties occurred in the degradation process. The remaining three successive decomposition peaks attributed to the removal of bipyridine, hydrogen chloride and chlorine molecules, finally with a residue of 18.32% assigned to nickel-metal Ni(0). A similar report has been reported by Mazhar et al. [59].

Fig. 4. Illustrates the powder diffraction pattern (XRD) of nickel $[\text{Ni}(\text{bipy})_2]\text{Cl}_2$ complex prepared via MOF process. No peak corresponding to metal Ni salt or 2'2' bipyridine was observed. It shows that metal salt and ligand entirely reacted, resulting in the formation of monometallic complex of Ni [60]. Thus the complex of nickel prepared by MOF process gives Ni(0) finally after its decomposition in inert atmosphere.

XRD analyses of prepared Catalyst

All the XRD patterns of Al_2O_3 , ALC ($\text{Al}_2\text{O}_3\text{-La}_2\text{O}_3\text{-CeO}_2$), catalyst-1, and catalyst-2 are presented in Fig. 5. Several peaks of the support and prepared catalysts were identified with their d-value (calculated using Bragg's law) and matched with the standard values. It is observed that peaks correspond to $\gamma\text{-Al}_2\text{O}_3$, CeO_2 , and Ni, metal. The modified supports and reduced catalysts showed diffraction peaks at around $2\theta = 37.2^\circ$, 45.8° , and 66.7° , which were assigned to $\gamma\text{-Al}_2\text{O}_3$ (JCPDS 86–1410). The three high-intensity peaks of Ni⁰ observed at 44.5° ; at 51.8° and 76.5° correspond to (111), (200) and (220) planes. There is no characteristic peak of NiO at $2\theta = 37.3^\circ$ and 43.3° (JCPDS 78–0643) present. Catalysts showed the characteristics peaks of cubic fluorite crystal structure of CeO_2 were observed at $2\theta = 28.30^\circ$ (111), 33.13° (200), and 56.33° (311) in catalyst-1, catalyst-2 and support ALC respectively, which shows the segregation of the CeO_2 over the $\gamma\text{-Al}_2\text{O}_3$ [12]. Peaks of La_2O_3 corresponding to crystalline species La_2O_3 were not observed

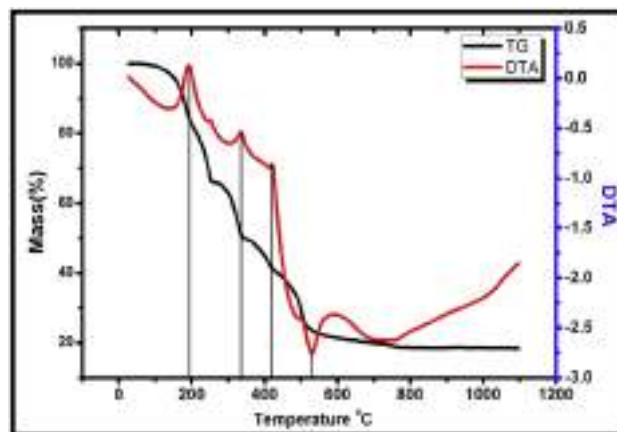


Fig. 3 – TGA and DTA profiles of Ni-complex.

in either of catalysts or the support ALC probably due to well dispersion and low amount of La_2O_3 in the samples or low crystallite size of La [61]. Crystallite size of Ni catalysts was calculated by Scherrer equation for the (200) peak and results are shown in Table 1. It is observed that the crystallite size of Ni in the catalyst 2 (prepared via MOF) had average crystallite of 37 nm, which is nearly 2.5 times than that of catalyst 1 (prepared from nickel formate). The MOF derived Ni particles showed ordered aggregates of Ni nanoparticles with 3 dimensions cubic structures, which consisted of faceted Ni crystals embedded with ALC support. Consequently, showed good catalytic activity compared to catalyst 1.

H_2 -TPR analysis

H_2 -TPR analysis was carried out in order to investigate the reduction behaviour and metal support interaction of the fresh samples of catalysts. Fig. 6 illustrates the H_2 -TPR patterns and reduction degree of both catalysts calcined in 550°C . The results showed that typically nickel species in both catalysts fully reduced in the temperature range $400\text{--}600^\circ\text{C}$. Fig. 6 also presents the reduction temperature (at the maximum) of pure nickel oxide prepared from calcination of $(\text{Ni}(\text{HCO}_2)_2 \cdot 2\text{H}_2\text{O})$ in the presence of air at 600°C was found at 329°C which. Referred to as “free” nickel oxide [62]. TPR explains the reduction behaviour of Ni depending on

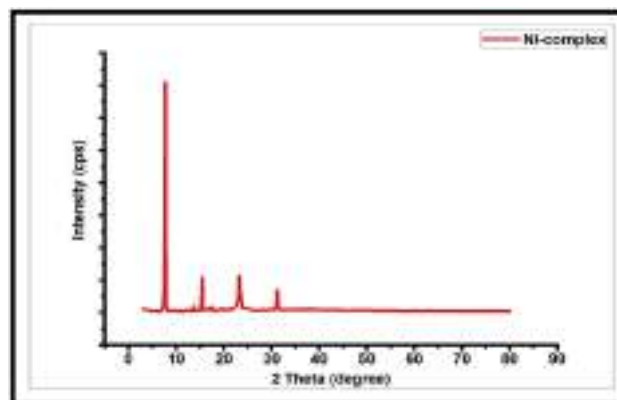


Fig. 4 – XRD pattern of monometallic complex of Ni.

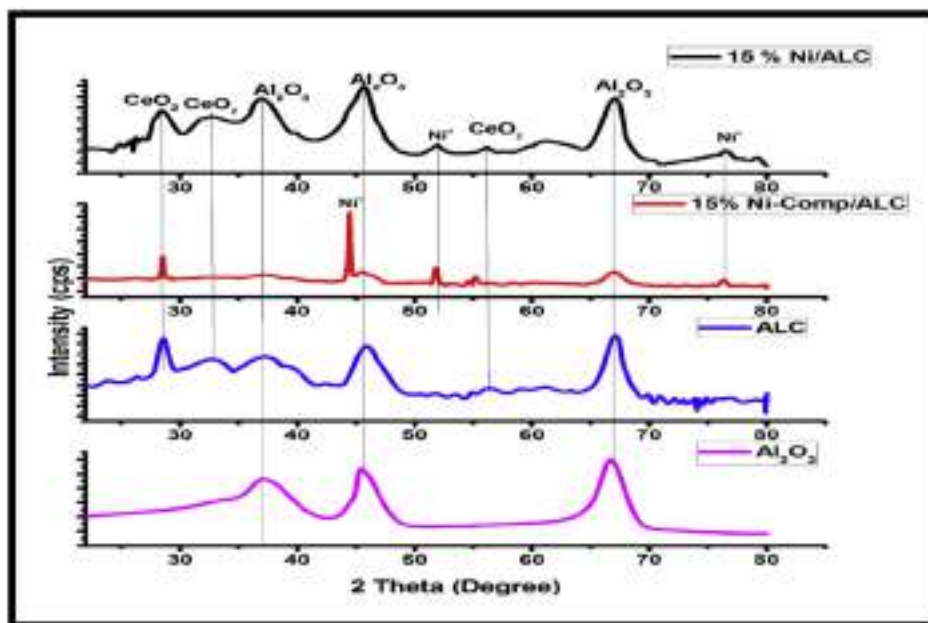


Fig. 5 – XRD Patterns of Alumina, ALC, catalyst 1 and catalyst 2.

Table 1 – Textural properties of synthesized catalysts.

Support/Catalyst	Surface area (m ² /g)	Pore volume (cm ³ /g)	Average pore size (nm)	Crystallite size of Ni ^a (nm)
γ-Al ₂ O ₃	169	0.61	9	–
Al ₂ O ₃ –La ₂ O ₃ –CeO ₂ (ALC)	133	0.43	8	–
15%Ni/ALC	110	0.27	9	14
15%Ni-comp/ALC	120	0.29	8	37

interactions with support. The reduction temperature (the maximum peak) for NiO in the catalyst-1 increased to 461 °C while reduction of catalyst 2 observed in two stages, two peaks appeared for catalyst-2, which also assigned to the reduction of NiO phase. The results are showing weak to medium interaction with the prepared support [40,61,63]. There are no reduction peaks related to the spinel (NiAl₂O₄) phase was appeared higher than 600 °C because the catalyst 1 was calcined at lower temperature of 550 °C and [64] it was also well reported that Ni and alumina particles could only react to form spinal phase at above 800 °C [65,66]. Moreover, addition of La with support was also hindered the prevention of NiAl₂O₄ and maintained the Ni active sites [67]. The observed TPR reduction peaks are also consistent and validated with the XRD results of catalysts. Incorporation of CeO₂ and La₂O₃ promoters weakened the NiO–Al₂O₃ interaction and facilitated the Ni species reduction earlier [61,68,69]. Catalyst-1 showed only one reduction peak near 461 °C, showing that weaker interaction with support. The reduction of nickel oxide species with strong interaction with the synthesized supports was significantly inhibited. However, in case of catalyst-2, it showed two earlier reduction peaks at temperatures 406 and 437 °C, due to a large number of “free” nickel oxide particles available on the support surface, resulting in high activity compared to Catalyst-1.

Surface area and pore size analysis

Table 1. Represents the textural properties of the synthesized support and catalysts. As can be observed that incorporation with La₂O₃ and CeO₂ resulted in a lower surface area, pore-volume, and average pore size. It is noticed that γ-Al₂O₃ has a high surface area of 169 m²/g, whereas, on the incorporation

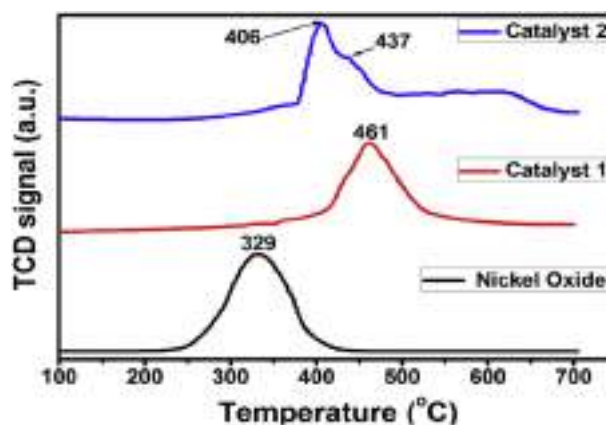


Fig. 6 – TPR profiles of 15%Ni-Comp/ALC catalyst, 15Ni/ALC, and pure Ni.

of La_2O_3 and CeO_2 , its surface area reduced to $133 \text{ m}^2/\text{g}$. Further, loading of 15% Ni, the surface area decreased to 110 and $120 \text{ m}^2/\text{g}$ for catalyst 1 and catalyst-2 respectively. The slightly higher surface area of MOFs derived 15%Ni-Complex/ALC might be due to the regular, three-dimensional framework and tunable pore size, and porosity and coordinating bonding of catalyst [70]. It is further observed that the $\gamma\text{-Al}_2\text{O}_3$ has a total pore volume of $0.61 \text{ cm}^3/\text{g}$ whereas, it is significantly lower at $0.43 \text{ cm}^3/\text{g}$ for synthesized ALC support. It has further decreased total pore volume of both catalysts and is also significant viz 0.27 and $0.29 \text{ cm}^3/\text{g}$ on incorporation of Ni for catalyst-1 and catalyst-2, respectively. The pore size distribution of alumina reveals its microporosity with having majority of pores of sizes less than 10 nm. While incorporation of lanthanum oxide and cerium oxide the microporosity reduced from 0.61 to $0.43 \text{ cm}^3/\text{g}$. Subsequently, when Ni was loaded on the support, the microporosity is further reduced. Since the surface area is also reduced with the incorporation of above components, it is concluded that such incorporations have also resulted in blockage of pores. It is obvious that Catalyst 2 has large surface area and smaller pore size distribution suggesting that catalyst 2 possess more active sites than catalyst 1.

TEM studies

Results of transmission electron microscopy and corresponding electron diffraction patterns of catalyst 1 and catalyst 2 are shown in Fig. 7. And Fig. 8, respectively. The images of TEM clearly shows that agglomerated small spherical type morphology, corresponding to CeO_2 . Moreover, dark road type fringes observed indicating alumina molecules, whereas small black areas could be marked as metal Ni particles. It is also observed from the TEM micrographs that Ni particles in catalyst 2 are better dispersed compared to catalyst 1. Based on the analysis, the size of the particles is approximately in between 12 and 20 nm range. However, despite having large crystallite sizes of Ni in catalyst 2, it showed better catalytic activity due to it consisted hierarchical nanoparticles of faceted Ni crystals supported on porous ALC support. The selected area electron diffraction (SAED) patterns for both the catalysts indicated clean and strong ring pattern which indicates characteristics of polycrystalline nature and rings analysis represent the planes of $\gamma\text{-Al}_2\text{O}_3$ (220, 311) and CeO_2 (111, 200) with crystalline structure matched with the corresponding hkl planes from XRD analysis. Diffraction rings of Ni could not be detected. It may be because of high dispersion of Ni in the size range of nanoparticles.

Scanning electron micrograph

SEM–EDAX analysis was performed on the catalysts to find out an idea on the textural morphology of the catalyst samples and shown in Fig. 9. In catalyst 1, the observed particles with rod-like particles while in case of catalyst 2 showed small dispersed particles and observed in a group of high cluster density and get agglomerated. During calcination, all ligands and associated coordinated ions were removed in presence of

inert atmosphere from the synthesized nickel complex supported catalyst as well as from $\text{Ni}(\text{HCOO})_2 \cdot 2\text{H}_2\text{O}$ supported catalyst. EDAX analysis has been given in separate S1 supplementary information.

X-ray photoelectron spectroscopy (XPS) studies of the catalysts

X-ray photoelectron spectroscopy analysis was carried out to investigate the oxidation state of chemical species and surface composition of the elements present on the surface of the catalysts. The subtraction of peak applied by Shirley type background across all the spectrum and the intensities were evaluated by integral calculation of each peak. The fitting and deconvolution of peaks were performed by using Lorentzian - Gaussian method [71]. Binding energies were calibrated with taking reference to carbon (C1s) binding energy at 284.6 eV. In both the catalysts, binding energies spectra of nickel and its characteristic peaks observed between 845 and 880 eV. The Ni 2p spectra of both the catalysts overlapped with the La3d, Ce3d peaks, and become uncertain about deconvoluting and quantified due to complex characteristics of peaks spectrum. Mostly, the main uncertainty encountered as a result of the overlapping of Ni $2p_{3/2}$ and La $3d_{3/2}$. Incorporation of Ni/ $\gamma\text{-Al}_2\text{O}_3$ with the La_2O_3 and CeO_2 significantly shifted the oxide peaks of nickel to the higher binding energies. The shifting towards higher binding energy indicated the increase of more oxygen vacancy as a result of the oxygen-deficient state. The H_2 -TPR analysis and XRD spectra of the catalysts supported over the ALC ternary oxide system also validated the above findings, showed weak to medium interaction of NiO with oxide supports. The presence of oxide peak of Ni in various forms on catalysts surface. It is tough to differentiate the binding energies of Ni $2p_{3/2}$ and La $3d_{5/2}$ because of the proximity of these peaks. However, the XPS spectrum peaks of La were observed in La (III) species at binding energy 855.3 and 835.5 eV, respectively. The surface concentration of La over both catalysts is very less due to well dispersion over $\gamma\text{-Al}_2\text{O}_3$ support and strong interaction with oxide support and nickel. However, in reduced catalysts, the XPS peak shifts to higher binding energy (855.3 eV), and this peak of La $3d_{5/2}$ (855.3) was not observed, probably due to overlapping with the strongest peak of Ni^{+2} peak in NiO, which is not reported here [55]. To understand the effect of cerium on the support surface as oxygen storage and releasing agent, a detailed study of cerium spectra as shown in Fig. 10 was carried out. XPS spectra of Ce3d is complex because of the formation of different compositions are present in the form of Ce^{3+} and Ce^{4+} species after deconvolution. The Ce3d core level showed multiple spin-orbital splitting corresponding to the Ce $3d_{5/2}$ and Ce $3d_{3/2}$ core species in the form of (u and v) are summarized in Tables 1 and 2, respectively. It is reported that XPS spectra of Ce3d core levels were formed of 10 different states of various spin-orbit doublets corresponding to different states of Ce^{3+} and Ce^{4+} on the surface of catalysts [55,72,73]. As a result, these 10 various peaks doublets proposed the presence of CeO_2 on the catalyst. The spectra of Ce3d peaks

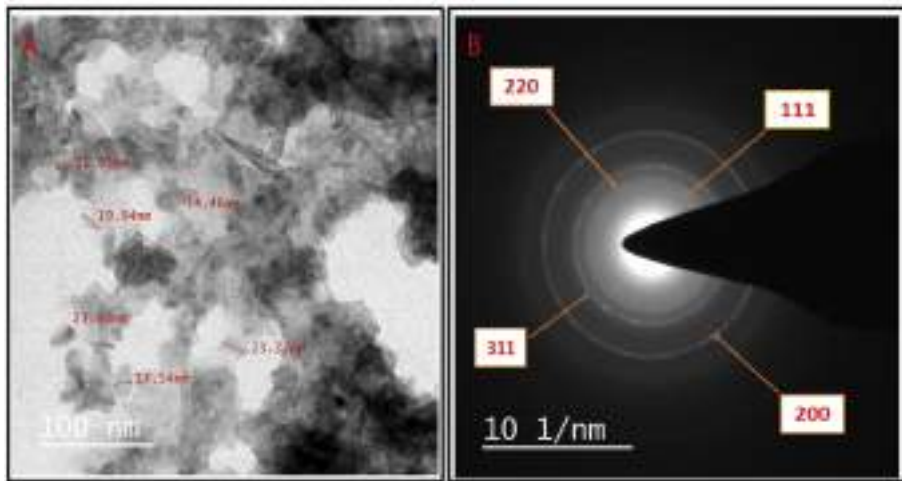


Fig. 7 – TEM image and SAED diffraction of catalyst 2.

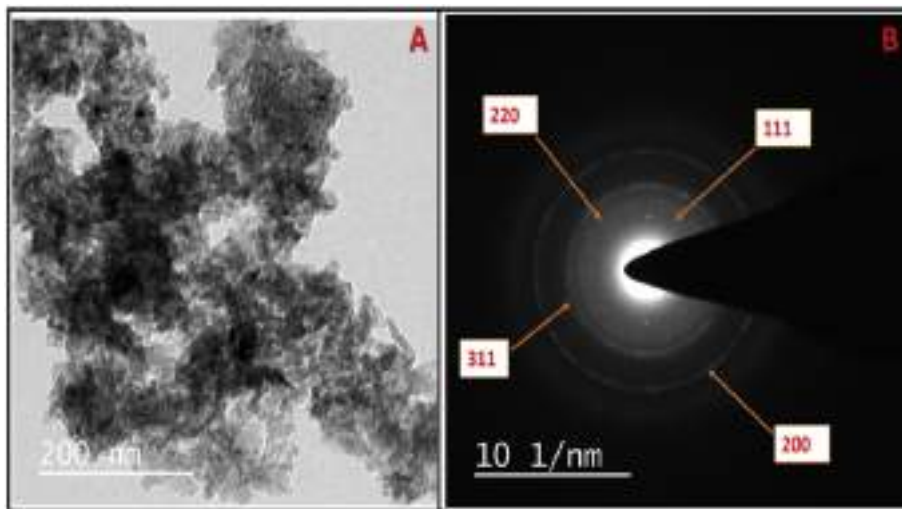


Fig. 8 – TEM images and SAED diffraction of catalyst 1.

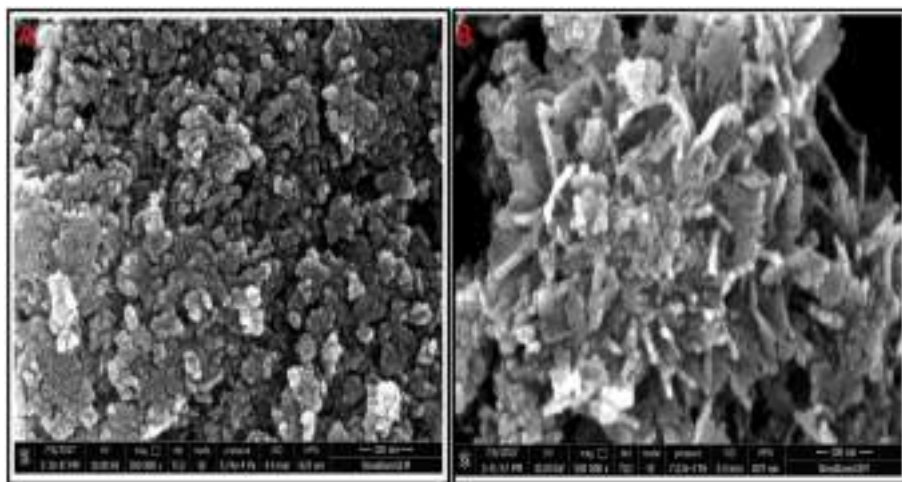


Fig. 9 – FE-SEM analysis of (A) Catalyst 1 and (B) Catalyst 2.

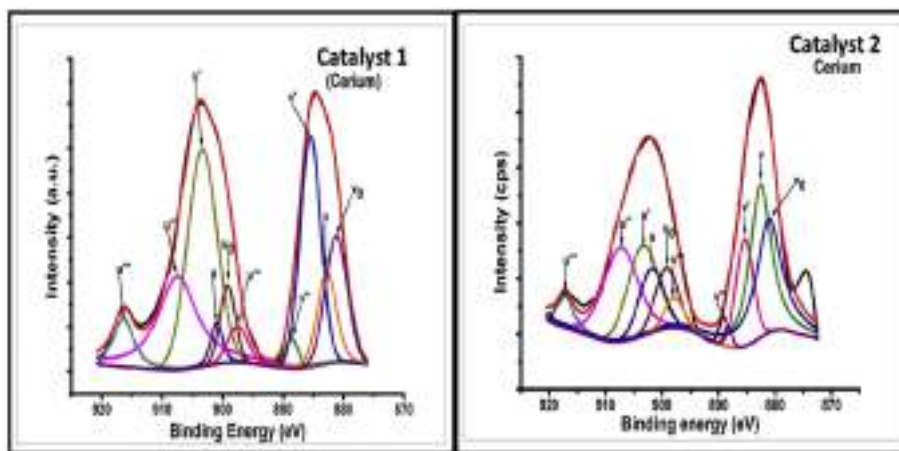


Fig. 10 – Ce 3 d XPS spectra of (A) catalyst 1 & (B) catalyst 2.

Table 2 – Pore size distribution of catalyst.

Species	Pore size range (nm) and corresponding pore volume (cm ³ /g)					Total pore volume (cm ³ /g)
	0 ≤ dp ≤ 10	10 ≤ dp ≤ 20	20 ≤ dp ≤ 40	40 ≤ dp ≤ 60	60 ≤ dp ≤ 80	
γ-Al ₂ O ₃	0.29	0.22	0.05	0.03	0.02	0.61
15% Ni/ALC	0.06	0.07	0.06	0.02	0.06	0.27
15% Ni-Comp/ALC	0.09	0.16	0.02	0.008	0.01	0.29

deconvoluted in split doublets (u'-v', u₀-v₀) are assigned to the Ce³⁺ species are given in Tables 3 and 4.

It is observed from Tables 3 and 4. The binding energy of Ce 3 d spectrum splits into co-existence of Ce³⁺ and Ce⁴⁺ oxidation states and is much more complicated. Both Ce₃₊ and Ce₄₊ are composed of five doublets (u₀, v₀), (u', v'), (u'', v''), (u''', v''') and (u, v) or in 10 peaks leveled as U and V corresponding to the spin-orbit splitting of Ce3d_{5/2} and Ce3d_{3/2} components (see Fig. 10 A. and 10 B) The results are also validated with the published results [74,75]. The deconvoluted spectra ascertain that the peak of Ce³⁺ state (v₀, v', u₀ and u') are stronger in comparison to the Ce⁴⁺ states (v, v'', v''', u, and u''). After reduction of the catalyst, the stronger content of Ce³⁺ species clearly attributed the more significant amount of oxygen vacancies available in the CeO₂ lattice. It was observed that before introduction of samples into XPS chamber, reduced catalysts get easily partially oxidized while it comes only a short period of time into the contact of ambient air. The CeO₂

provides mobilizable oxygen vacancies, which is useful for the prevention of coke formation over the catalyst surface. To accelerate the oxidation of carbon precursor over the catalyst surface, mobilizable oxygen was transferred from oxygen vacancies present in CeO₂ lattice. Hence, it is assumed that the catalysts having large amount Ce³⁺ species considered to be formed more oxygen vacancies. To evaluate the total fraction or relative amount of Ce³⁺ species present on catalyst surface sample (also allude as degree of reduction) was calculated in reference with total area of cerium species. To obtain a precise analysis of the total amount of the CeO₂ and the contribution of the spectrum from the Ce³⁺ and Ce⁴⁺ can be determined from the following equations (Eq. (11). & Eq. (12).) [76].

$$\text{Ce}^{3+} = u' + u_0 + v' + v_0 \quad (11)$$

$$\text{Ce}^{4+} = u''' + u'' + u + v''' + v'' + v \quad (12)$$

Table 3 – Binding energy (eV) (catalyst 1).

Binding Energies (eV)	Ce species	Peak assignment	Relative area (%)	Area
881.1	Ce ³⁺	v ₀	22.46	28116.59
882.6	Ce ⁴⁺	v	14.13	17688.2
885.4	Ce ³⁺	v'	9.93	12427.8
888.3	Ce ⁴⁺	v''	0.95	1186.80
897.8	Ce ⁴⁺	v'''	1.86	2330.97
899.2	Ce ³⁺	u ₀	4.45	5573.99
901.8	Ce ⁴⁺	u	8.50	10644.67
903.4	Ce ³⁺	u'	14.64	18323.38
907.3	Ce ⁴⁺	u''	19.05	23845.65
917.0	Ce ⁴⁺	u'''	4.01	5020.11

Table 4 – Binding energy (eV) (Catalyst 2).

Binding Energies (eV)	Ce species	Peak assignment	Relative area (%)	Area
881.2	Ce ³⁺	v ₀	10.18	6497.85
882.8	Ce ⁴⁺	v	7.06	4501.49
885.5	Ce ³⁺	v'	17.42	11112.51
888.6	Ce ⁴⁺	v''	1.50	956.84
897.5	Ce ⁴⁺	v'''	2.72	1737.75
899.2	Ce ³⁺	u ₀	7.24	4620.35
901.0	Ce ⁴⁺	u	3.63	2319.54
903.4	Ce ³⁺	u'	23.52	15001.92
907.5	Ce ⁴⁺	u''	18.37	11720.42
916.5	Ce ⁴⁺	u'''	8.34	5318.40

$$\text{Ce}^{3+} (\%) = \frac{\text{Ce}^{3+}}{\text{Ce}^{4+} + \text{Ce}^{3+}} \quad (13)$$

The concentration of Ce^{3+} and Ce^{4+} in CeO_2 can be estimated through Eq. (11) & Eq. (12). The concentration of Ce^{3+} in CeO_2 over both the catalyst was found to be around 51.34% and 58.37% for catalyst 1 and catalyst 2, respectively calculated from Eq. (13). It is noticed from Ce^{3+} calculation catalyst synthesized from MOF derived nickel complex showed more amount of Ce^{3+} species due to that more vacancies of oxygen are present in the catalyst. Consequently, catalyst 2 showed better catalytic activity and stable behaviour towards coke deposition.

Catalytic activity and yield of catalysts

Acetic acid conversions at different temperatures are displayed in Figs. 11 and 12 A for both the prepared catalysts as well as solely support. Due to the endothermicity of the reaction, conversion of acetic acid over both the catalysts as well as over the prepared support increases with increasing temperature. Thermodynamically, in all aspects, distribution of evolved hydrogen increases with increasing temperature whereas, the methane content decreases, to arrive a maximum. This is due to the promotion of steam reforming reaction (Eq. (1)), as temperature increases because it is an endothermic reaction since water-gas shift (Eq. (3)) is an exothermic reaction, the CO mol % increases at the expense of CO_2 as the temperature increases, also consuming H_2 (reverse reaction). Whereas methanation reaction (Eq. (6) and (7)) are prevented, as both are highly exothermic reactions. This leads to decrease of the H_2 content at high temperatures, at which methanation is almost completely unfavoured (CH_4 content below 0.2 mol %).

In the case of ALC support (Fig. 11.) AcOH does not completely convert even at high temperatures. It showed remarkable activity for the conversion of AcOH; however, it gives lower activity in terms of steam reforming and produces much less yield towards H_2 and CO_2 . The main products which are obtained in the gaseous phase at higher temperatures are H_2 , CO, CH_4 , CO_2 resulted from the thermal decomposition of the acetic acid and acetone is the main product at lower

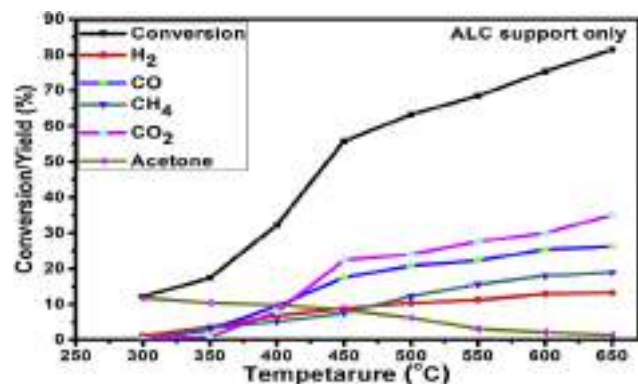


Fig. 11 – Conversion of AcOH and product distribution as a function of temperature over ALC support.

temperature produced via ketonization reaction. The yield of acetone was found to decrease with increase in reaction temperature and C1 products developments due to C–C bond cleavage. This result inferred that the only ALC support favours the ketonization reaction at lower temperature whereas at elevated temperature, C–C bond cleavage favours (Eq. (2)). The reforming activity becomes appreciably higher in case of when Ni was loaded over the support. Almost complete conversion of acetic acid and high H_2 yield obtained at temperature 600 °C. Without active metal catalysts on the support, only decomposition reaction is prominent for acetic acid conversion, and only marginal steam reforming activity might have occurred over the support surface.

The main out products during AASR in studied temperature range were H_2 and CO_2 with small amounts of CO and CH_4 were the major outcomes in both 15% Ni/ALC and 15% Ni-complex/ALC. Whereas, CH_4 , CO_2 , and acetone were the major outcomes over prepared support only. The small amount of CH_4 was generated over both nickels supported catalysts, but the yield of CO is high over the 15% Ni/ALC catalyst at higher temperatures. Whereas the yield of CO_2 and H_2 are more in case of 15% Ni-Comp/ALC compared to 15% Ni/ALC. The results also described that no ethylene formation was observed due to rapid decomposition as it produced. Evidently, catalytic activity due to homogeneous reaction and quartz wool was considered negligible during the reforming reaction. As displayed in Fig. 12 A, both catalysts produce approximately 100% conversion of acetic acid at 650 °C and S/C molar ratio 6.5. The high yield of CO_2 suggests the contribution of water gas shift reaction to a great extent. The dominance of H_2 and CO_2 at high temperature during reaction indicated that the main reactions are steam reforming and water-gas shift (WGS). Other intermediates like CO generated via decomposition and reverse water gas shift reaction at higher temperatures.

Stability test

The stability of both the catalysts was evaluated with more than 36 h time on stream (TOS). The catalyst 2 showed stable behaviour in terms of conversion as well as H_2 yield in comparison to catalyst 1. The better activity as well yield for H_2 are due to MOF derived nano-nickel particles form a regular, porous three-dimensional framework, tunable pore size, and available high surface area of the catalyst that enhances the activity of catalyst. Stability testing for both catalysts was performed at temperature 600 °C keeping with the same operating conditions for 36 h; results are shown in Fig. 13. The conversion and H_2 yield retain approximately the same during 10 h, but after that, 15% Ni/ALC catalysts showed a decreasing trend in the conversion as well as in H_2 yield. Catalyst 2 exhibited better stable behaviour for coke deposition of more than 36 h. The long stable behaviour of catalysts could be related with the addition of Ce and La promotion, which hinders coke formation. The decline in conversion and H_2 yield with time on steam for both the catalysts related to the coke deposition over the catalyst surface. The carbon deposition mainly occurred via thermal decomposition and the reaction intermediates generated during the AASR [29].

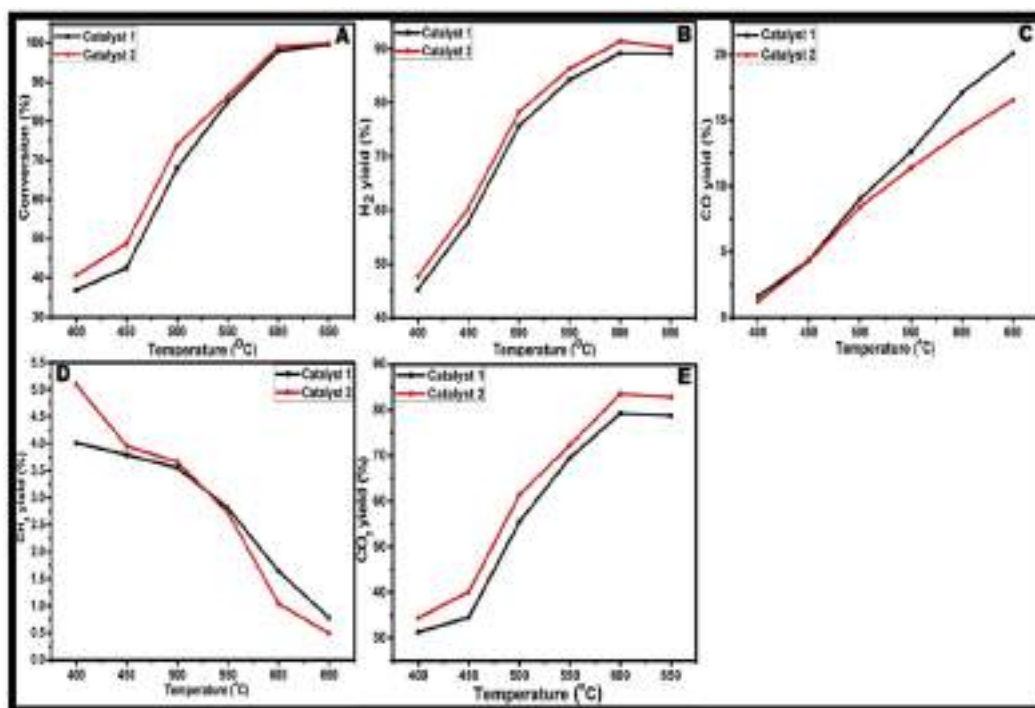


Fig. 12 – (A)–(E). Conversion of acetic acid and yield of the gaseous products over different Ni precursor and support (ALC) in the different temperature range of 400–650 °C. Experimental conditions: S/C mol ratio 6.5:1, mixture flow rate 2.5 mL/h.

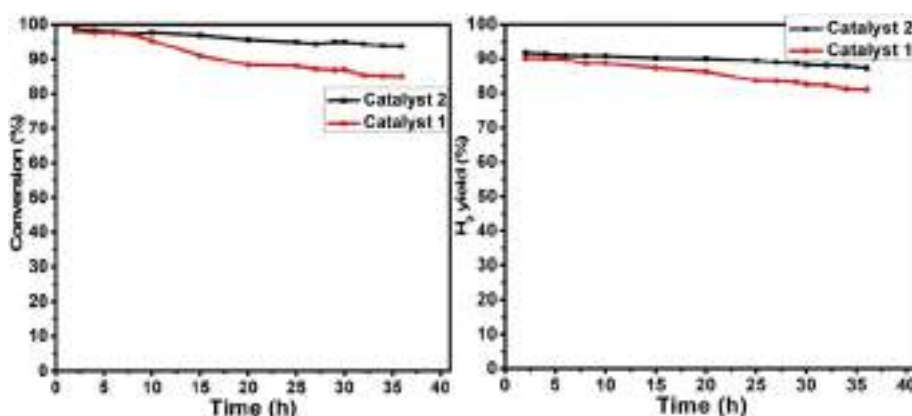


Fig. 13 – Conversion and yield of H₂(%) of catalyst 1 and catalyst 2, Reaction condition: temperature - 600 °C; N₂ flow rate- 30 mL/min; mixture flow rate - 2.5 mL/h; and S/C - 6.5 mol/mol.

DT-TGA analysis

DT-TGA analyses were carried out in oxygen after the stability test to determine the presence and type of carbonaceous species formed on the catalysts surface. Fig. 14 a. Shows the weight losses due to the combustion of coke deposited corresponding to catalyst 1 and catalyst 2, which were 29.0 and 24.1% respectively. The amount of coke deposited on catalysts 1 was slightly higher than catalyst 2 due to less catalytic activity. The results indicated that coke formed over the catalyst depends on Ni quality present at the surface of catalysts and its distribution. Moreover, low surface area suffers more coke

deposition. As displayed in Fig. 14b. Two distinct peaks one at temperature in the region of 350–400 °C and the second in the 550–600 °C range. It indicates the presence of two different carbonaceous species (amorphous and filamentous). The first peak was attributed to coke containing species like CH_x and C* (surface carbon) due to catalytic cracking reactions termed as amorphous coke [32], and second peaks assigned due to polymerisation of organics on catalyst surface termed as polymeric/filamentous coke especially on the surface of support [77]. Wang et al. also investigated the AASR over the Ni based catalyst and reported that adsorbed coke precursor CH_x* (x = 1–3) formed due to catalytic reaction are responsible

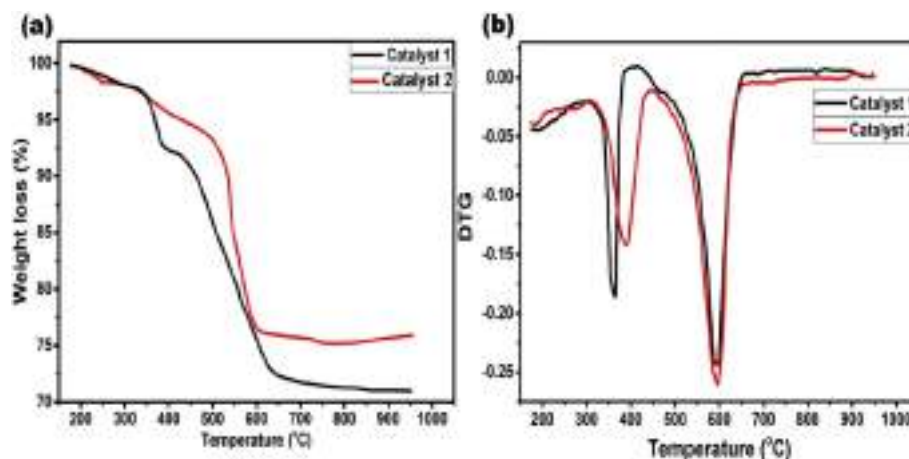


Fig. 14 – TGA-DTG profile of spent catalysts after stability test (a) TG (b) DTG.

for coke deposition [78]. Furthermore, it was also reported that at lower temperature coke deposition favoured significantly via the “Boudouard reaction”. However, at elevated temperature CH_4 cracking and intermediates formed via AcOH decomposition forming carbonaceous species (CH_x^*) which further responsible for coke deposition [79].

Conclusions

The $\gamma\text{-Al}_2\text{O}_3$ support incorporated with $\text{La}_2\text{O}_3\text{-CeO}_2$ prepared via two different methods were investigated in acetic acid steam reforming for hydrogen production. Incorporation of $\text{La}_2\text{O}_3\text{-CeO}_2$ in $\gamma\text{-Al}_2\text{O}_3$ enhances catalysts stability by preventing the rate of carbon deposition as well as sintering process. From the results, we could infer that both catalysts over modified ALC support exhibited approximately 100% conversion and high H_2 yield without much deactivation because of the incorporation of modified support over 36 h TOS. AASR and reverse water gas shift (RWGS) were the major reactions which govern the outlet gas distributions at high temperatures. However, catalyst 2 showed better results in terms of H_2 yield in comparison to catalyst 1 catalyst. Moreover, it's also found much stable nature up to 36 h towards coke deposition. Catalyst 2 exhibited slightly higher surface area and larger pore sizes due to the regular arranged ordered pore size and porosity and coordinating bonding of catalyst which improved the movement of reactants and catalytic activity. Moreover, it observed large number of free nickel particles and more Ce^{3+} vacancies on the support surface resulting in high catalytic activity and stability. Amorphous like carbon and filamentous-like carbon were observed over spent catalysts after stability test. Therefore, catalyst 2 showed better catalytic activity since it showed less coke deposition and high H_2 yield.

Appendix A. Supplementary data

Supplementary data to this article can be found online at <https://doi.org/10.1016/j.ijhydene.2020.02.097>.

REFERENCES

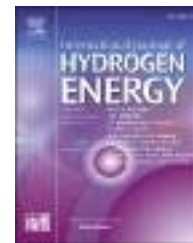
- [1] Mohanty P, Patel M, Pant KK. Hydrogen production from steam reforming of acetic acid over Cu–Zn supported calcium aluminate. *Bioresour Technol* 2012;123:558–65.
- [2] Goicoechea S, Ehrich H, Arias PL, Kockmann N. Thermodynamic analysis of acetic acid steam reforming for hydrogen production. *J Power Sources* 2015;279:312–22.
- [3] Takanae K, Aika K-i, Seshan K, Lefferts L. Sustainable hydrogen from bio-oil—steam reforming of acetic acid as a model oxygenate. *J Catal* 2004;227:101–8.
- [4] Peña MA, Gómez JP, Fierro JLG. New catalytic routes for syngas and hydrogen production. *Appl Catal Gen* 1996;144:7–57.
- [5] Xue Y-p, Yan C-f, Zhao X-y, Huang S-l, Guo C-q. Ni/La₂O₃-ZrO₂ catalyst for hydrogen production from steam reforming of acetic acid as a model compound of bio-oil. *Kor J Chem Eng* 2017;34:305–13.
- [6] Wang M, Zhang F, Wang S. Effect of La₂O₃ replacement on $\gamma\text{-Al}_2\text{O}_3$ supported nickel catalysts for acetic acid steam reforming. *Int J Hydrogen Energy* 2017;42:20540–8.
- [7] Basagiannis AC, Verykios XE. Catalytic steam reforming of acetic acid for hydrogen production. *Int J Hydrogen Energy* 2007;32:3343–55.
- [8] Mohanty P, Pant KK, Mittal R. Hydrogen generation from biomass materials: challenges and opportunities. *Wiley Interdisciplinary Reviews: Energy Environ* 2015;4:139–55.
- [9] Wang S, Cai Q, Zhang F, Li X, Zhang L, Luo Z. Hydrogen production via catalytic reforming of the bio-oil model compounds: acetic acid, phenol and hydroxyacetone. *Int J Hydrogen Energy* 2014;39:18675–87.
- [10] Kumar A, Chakraborty JP, Singh R. Bio-oil: the future of hydrogen generation. *Biofuels* 2017;8:663–74.
- [11] Fu P, Zhang A, Luo S, Yi W, Hu S, Zhang Y. Catalytic steam reforming of biomass-derived acetic acid over two supported Ni catalysts for hydrogen-rich syngas production. *ACS Omega* 2019;4:13585–93.
- [12] Italiano C, Bizkarra K, Barrio V, Cambra J, Pino L, Vita A. Renewable hydrogen production via steam reforming of simulated bio-oil over Ni-based catalysts. *Int J Hydrogen Energy* 2019;44:14671–82.
- [13] Hu X, Dong D, Shao X, Zhang L, Lu G. Steam reforming of acetic acid over cobalt catalysts: effects of Zr, Mg and K addition. *Int J Hydrogen Energy* 2017;42:4793–803.
- [14] Wang S, Li X, Zhang F, Cai Q, Wang Y, Luo Z. Bio-oil catalytic reforming without steam addition: application to hydrogen

- production and studies on its mechanism. *Int J Hydrogen Energy* 2013;38:16038–47.
- [15] Bertero M, de la Puente G, Sedran U. Fuels from bio-oils: bio-oil production from different residual sources, characterization and thermal conditioning. *Fuel* 2012;95:263–71.
- [16] Vagia EC, Lemonidou AA. Investigations on the properties of ceria–zirconia-supported Ni and Rh catalysts and their performance in acetic acid steam reforming. *J Catal* 2010;269:388–96.
- [17] Basagiannis AC, Verykios XE. Influence of the carrier on steam reforming of acetic acid over Ru-based catalysts. *Appl Catal B Environ* 2008;82:77–88.
- [18] Garcia La, French R, Czernik S, Chornet E. Catalytic steam reforming of bio-oils for the production of hydrogen: effects of catalyst composition. *Appl Catal Gen* 2000;201:225–39.
- [19] Zhang Z, Hu X, Li J, Gao G, Dong D, Westerhof R, et al. Steam reforming of acetic acid over Ni/Al₂O₃ catalysts: correlation of nickel loading with properties and catalytic behaviors of the catalysts. *Fuel* 2018;217:389–403.
- [20] Wang S, Zhang F, Cai Q, Li X, Zhu L, Wang Q, et al. Catalytic steam reforming of bio-oil model compounds for hydrogen production over coal ash supported Ni catalyst. *Int J Hydrogen Energy* 2014;39:2018–25.
- [21] Assaf PGM, Nogueira FGE, Assaf EM. Ni and Co catalysts supported on alumina applied to steam reforming of acetic acid: representative compound for the aqueous phase of bio-oil derived from biomass. *Catal Today* 2013;213:2–8.
- [22] Cheng F, Dupont V. Nickel catalyst auto-reduction during steam reforming of bio-oil model compound acetic acid. *Int J Hydrogen Energy* 2013;38:15160–72.
- [23] Hu X, Zhang L, Lu G. Pruning of the surface species on Ni/Al₂O₃ catalyst to selective production of hydrogen via acetone and acetic acid steam reforming. *Appl Catal Gen* 2012;427–428:49–57.
- [24] Choi I-H, Hwang K-R, Lee K-Y, Lee I-G. Catalytic steam reforming of biomass-derived acetic acid over modified Ni/γ-Al₂O₃ for sustainable hydrogen production. *Int J Hydrogen Energy* 2019;44:180–90.
- [25] Li Z, Hu X, Zhang L, Liu S, Lu G. Steam reforming of acetic acid over Ni/ZrO₂ catalysts: effects of nickel loading and particle size on product distribution and coke formation. *Appl Catal Gen* 2012;417–418:281–9.
- [26] Williams A, Jones JM, Ma L, Pourkashanian M. Pollutants from the combustion of solid biomass fuels. *Prog Energy Combust Sci* 2012;38:113.
- [27] Ni M, Leung DYC, Leung MKH. A review on reforming bio-ethanol for hydrogen production. *Int J Hydrogen Energy* 2007;32:3238–47.
- [28] Sugisawa M, Takanabe K, Harada M, Kubota J, Domen K. Effects of La addition to Ni/Al₂O₃ catalysts on rates and carbon deposition during steam reforming of n-dodecane. *Fuel Process Technol* 2011;92:21–5.
- [29] Kumar A, Singh R, Sinha ASK. Catalyst modification strategies to enhance the catalyst activity and stability during steam reforming of acetic acid for hydrogen production. *Int J Hydrogen Energy* 2019;44:12983–3010.
- [30] Sehested J, Gelten JAP, Helveg S. Sintering of nickel catalysts: effects of time, atmosphere, temperature, nickel-carrier interactions, and dopants. *Appl Catal Gen* 2006;309:237–46.
- [31] Hu R-r, Yan C-f, Zheng X-x, Liu H, Zhou Z-y. Carbon deposition on Ni/ZrO₂–CeO₂ catalyst during steam reforming of acetic acid. *Int J Hydrogen Energy* 2013;38:6033–8.
- [32] An L, Dong C, Yang Y, Zhang J, He L. The influence of Ni loading on coke formation in steam reforming of acetic acid. *Renew Energy* 2011;36:930–5.
- [33] Lemonidou AA, Vagia EC, Lercher JA. Acetic acid reforming over Rh supported on La₂O₃/CeO₂–ZrO₂: catalytic performance and reaction pathway analysis. *ACS Catal* 2013;3:1919–28.
- [34] Hu X, Lu G. Comparative study of alumina-supported transition metal catalysts for hydrogen generation by steam reforming of acetic acid. *Appl Catal B Environ* 2010;99:289–97.
- [35] Medrano JA, Oliva M, Ruiz J, García L, Arauzo J. Catalytic steam reforming of model compounds of biomass pyrolysis liquids in fluidized bed reactor with modified Ni/Al catalysts. *J Anal Appl Pyroly* 2009;85:214–25.
- [36] Li CY, Yu CC, Shen SK. Studies on the transformation of carbon species from CH₄ decomposition over a Ni/Al₂O₃ catalyst. *Hua Hsueh Hsueh Pao* 2000;58:1188–90.
- [37] Li Z, Hu X, Zhang L, Lu G. Renewable hydrogen production by a mild-temperature steam reforming of the model compound acetic acid derived from bio-oil. *J Mol Catal Chem* 2012;355:123–33.
- [38] Bizkarra K, Bermudez JM, Arcelus-Arillaga P, Barrio VL, Cambra JF, Millan M. Nickel based monometallic and bimetallic catalysts for synthetic and real bio-oil steam reforming. *Int J Hydrogen Energy* 2018;43:11706–18.
- [39] Basagiannis AC, Verykios XE. Reforming reactions of acetic acid on nickel catalysts over a wide temperature range. *Appl Catal Gen* 2006;308:182–93.
- [40] Abou Rached J, El Hayek C, Dahdah E, Gennequin C, Aouad S, Tidahy HL, et al. Ni based catalysts promoted with cerium used in the steam reforming of toluene for hydrogen production. *Int J Hydrogen Energy* 2017;42:12829–40.
- [41] Wang S, Zhang F, Cai Q, Zhu L, Luo Z. Steam reforming of acetic acid over coal ash supported Fe and Ni catalysts. *Int J Hydrogen Energy* 2015;40:11406–13.
- [42] Li X, Wang S, Cai Q, Zhu L, Yin Q, Luo Z. Effects of preparation method on the performance of Ni/Al₂O₃ catalysts for hydrogen production by bio-oil steam reforming. *Appl Biochem Biotechnol* 2012;168:10–20.
- [43] Chen SQ, Wang H, Liu Y. Perovskite La–Sr–Fe–O (Sr=Ca, Sr) supported nickel catalysts for steam reforming of ethanol: the effect of the A site substitution. *Int J Hydrogen Energy* 2009;34:7995–8005.
- [44] Iriundo A, Barrio VL, Cambra JF, Arias PL, Guemez MB, Sanchez-Sanchez MC, et al. Glycerol steam reforming over Ni catalysts supported on ceria and ceria-promoted alumina. *Int J Hydrogen Energy* 2010;35:11622–33.
- [45] Zhang F, Wang N, Yang L, Li M, Huang L. Ni–Co bimetallic MgO-based catalysts for hydrogen production via steam reforming of acetic acid from bio-oil. *Int J Hydrogen Energy* 2014;39:18688–94.
- [46] Mondal T, Kaul N, Mittal R, Pant KK. Catalytic steam reforming of model oxygenates of bio-oil for hydrogen production over La modified Ni/CeO₂–ZrO₂ catalyst. *Top Catal* 2016;59:1343–53.
- [47] Koo KY, Lee S-h, Jung UH, Roh H-S, Yoon WL. Syngas production via combined steam and carbon dioxide reforming of methane over Ni–Ce/MgAl₂O₄ catalysts with enhanced coke resistance. *Fuel Process Technol* 2014;119:151–7.
- [48] Kim TY, Kim SM, Lee WS, Woo SI. Effect and behavior of cerium oxide in Ni/γ-Al₂O₃ catalysts on autothermal reforming of methane: CeAlO₃ formation and its role on activity. *Int J Hydrogen Energy* 2013;38:6027–32.
- [49] Kim DH, Woo SI, Lee JM, Yang OB. The role of lanthanum oxide on Pd-only three-way catalysts prepared by co-impregnation and sequential impregnation methods. *Catal Lett* 2000;70:35–41.
- [50] Matas Güell B, Silva IMTd, Seshan K, Lefferts L. Sustainable route to hydrogen – design of stable catalysts for the steam

- gasification of biomass related oxygenates. *Appl Catal B Environ* 2009;88:59–65.
- [51] Alvarez-Galvan MC, Navarro RM, Rosa F, Briceño Y, Ridao MA, Fierro JLG. Hydrogen production for fuel cell by oxidative reforming of diesel surrogate: influence of ceria and/or lanthana over the activity of Pt/Al₂O₃ catalysts. *Fuel* 2008;87:2502–11.
- [52] Remya VR, Kurian M. Synthesis and catalytic applications of metal–organic frameworks: a review on recent literature. *Int Nano Lett* 2019;9:17–29.
- [53] Feng Y, Jiang H, Chen M, Wang Y. Construction of an interpenetrated MOF-5 with high mesoporosity for hydrogen storage at low pressure. *Powder Technol* 2013;249:38–42.
- [54] Yang SJ, Im JH, Kim T, Lee K, Park CR. MOF-derived ZnO and ZnO@C composites with high photocatalytic activity and adsorption capacity. *J Hazard Mater* 2011;186:376–82.
- [55] Navarro RM, Álvarez-Galván MC, Rosa F, Fierro JLG. Hydrogen production by oxidative reforming of hexadecane over Ni and Pt catalysts supported on Ce/La-doped Al₂O₃. *Appl Catal Gen* 2006;297:60–72.
- [56] Church JS, Cant NW, Trimm DL. Stabilisation of aluminas by rare earth and alkaline earth ions. *Appl Catal Gen* 1993;101:105–16.
- [57] Xia B, Lenggoro IW, Okuyama K. Preparation of nickel powders by spray pyrolysis of nickel formate. *J Am Ceram Soc* 2001;84:1425–32.
- [58] Ahmad M, Asghar A, Abdul Raman AA, Wan Daud WMA. Enhancement of treatment efficiency of recalcitrant wastewater containing textile dyes using a newly developed iron zeolite socony mobil-5 heterogeneous catalyst. *PLoS One* 2015;10:e0141348.
- [59] Parveen N, Nazir R, Mazhar M. Thermal degradation pathways of nickel (II) bipyridine complexes to size-controlled nickel nanoparticles. *J Therm Anal Calorim* 2013;111:93–9.
- [60] Abdul Raman AA, Ahmad M, Ahmed S. A two-step process for industrial scale production of nano heterometallic Catalysts. 2015.
- [61] de Freitas Silva T, Reis CGM, Lucrédio AF, Assaf EM, Assaf JM. Hydrogen production from oxidative reforming of methane on Ni/γ-Al₂O₃ catalysts: effect of support promotion with La, La–Ce and La–Zr. *Fuel Process Technol* 2014;127:97–104.
- [62] Zieliński J. Morphology of nickel/alumina catalysts. *J Catal* 1982;76:157–63.
- [63] Yang R, Wu J, Li X, Zhang X, Zhang Z, Guo J. Hydrotreating of crude 2-ethylhexanol over Ni/Al₂O₃ catalysts: influence of the Ni oxide dispersion on the active sites. *Appl Catal Gen* 2010;383:112–8.
- [64] Rynkowski JM, Paryjczak T, Lenik M. On the nature of oxidic nickel phases in NiO/γ-Al₂O₃ catalysts. *Appl Catal Gen* 1993;106:73–82.
- [65] Osorio-Vargas P, Flores-González NA, Navarro RM, Fierro JL, Campos CH, Reyes P. Improved stability of Ni/Al₂O₃ catalysts by effect of promoters (La₂O₃, CeO₂) for ethanol steam-reforming reaction. *Catal Today* 2016;259:27–38.
- [66] Lónyi F, Valyon J, Someus E, Hancsók J. Steam reforming of bio-oil from pyrolysis of MBM over particulate and monolith supported Ni/γ-Al₂O₃ catalysts. *Fuel* 2013;112:23–30.
- [67] Profeti LP, Dias JA, Assaf JM, Assaf EM. Hydrogen production by steam reforming of ethanol over Ni-based catalysts promoted with noble metals. *J Power Sources* 2009;190:525–33.
- [68] Melchor-Hernández C, Gómez-Cortés A, Díaz G. Hydrogen production by steam reforming of ethanol over nickel supported on La-modified alumina catalysts prepared by sol–gel. *Fuel* 2013;107:828–35.
- [69] Ismagilov IZ, Matus EV, Kuznetsov VV, Kerzhentsev MA, Yashnik SA, Prosvirin IP, et al. Hydrogen production by autothermal reforming of methane over NiPd catalysts: effect of support composition and preparation mode. *Int J Hydrogen Energy* 2014;39:20992–1006.
- [70] Furukawa H, Cordova KE, O’Keeffe M, Yaghi OM. The chemistry and applications of metal-organic frameworks. *Science* 2013;341:1230444.
- [71] Ranjan R, Sinha ASK. Optimizations of r GO supported CdS photo-electrocatalyst for dissociation of water. *Int J Hydrogen Energy* 2019;44:5955–69.
- [72] Masek K, Václavů M, Bábör P, Matolín V. Sn–CeO₂ thin films prepared by rf magnetron sputtering: XPS and SIMS study. *Appl Surf Sci* 2009;255:6656–60.
- [73] Óvári L, Krick Calderon S, Lykhach Y, Libuda J, Erdöhelyi A, Papp C, et al. Near ambient pressure XPS investigation of the interaction of ethanol with Co/CeO₂(111). *J Catal* 2013;307:132–9.
- [74] Pu J, Ikegami F, Nishikado K, Qian EW. Effect of ceria addition on NiRu/CeO₂Al₂O₃ catalysts in steam reforming of acetic acid. *Int J Hydrogen Energy* 2017;42:19733–43.
- [75] Zhang J, Wong H, Yu D, Kakushima K, Iwai H. X-ray photoelectron spectroscopy study of high-k CeO₂/La₂O₃ stacked dielectrics. *AIP Adv* 2014;4:117117.
- [76] Anandan C, Bera P. XPS studies on the interaction of CeO₂ with silicon in magnetron sputtered CeO₂ thin films on Si and Si₃N₄ substrates. *Appl Surf Sci* 2013;283:297–303.
- [77] Zhang C, Hu X, Yu Z, Zhang Z, Chen G, Li C, et al. Steam reforming of acetic acid for hydrogen production over attapulgite and alumina supported Ni catalysts: impacts of properties of supports on catalytic behaviors. *Int J Hydrogen Energy* 2019;44:5230–44.
- [78] Wang D, Montané D, Chornet E. Catalytic steam reforming of biomass-derived oxygenates: acetic acid and hydroxybenzaldehyde. *Appl Catal Gen* 1996;143:245–70.
- [79] Trane-Restrup R, Jensen AD. Steam reforming of cyclic model compounds of bio-oil over Ni-based catalysts: product distribution and carbon formation. *Appl Catal B Environ* 2015;165:117–27.

Available online at www.sciencedirect.com

ScienceDirect

journal homepage: www.elsevier.com/locate/he

Hydrogen production from acetic acid steam reforming over nickel-based catalyst synthesized via MOF process

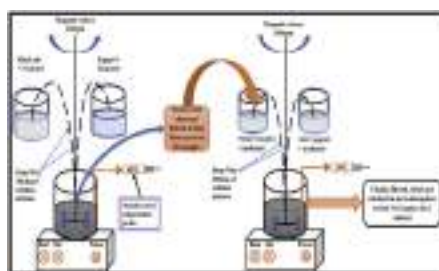
Ankit Kumar, A.S.K. Sinha*

Department of Chemical Engineering & Technology, Indian Institute of Technology (BHU), Varanasi, 221005, India

HIGHLIGHTS

- MOF derived Ni catalyst had excellent stability for steam reforming of acetic acid.
- Detailed activation, deactivation and regeneration studies were carried out.
- Nature of deposited coke was analysed.
- Microstructure changes in catalyst on use are also reported.

GRAPHICAL ABSTRACT



ARTICLE INFO

Article history:

Received 7 February 2020

Received in revised form

30 May 2020

Accepted 5 June 2020

Available online xxx

Keywords:

Hydrogen

Acetic acid

Steam reforming

Ni-complex catalyst

Coke deposition

ABSTRACT

In our earlier work, we have reported that Ni supported on γ -Al₂O₃-La₂O₃-CeO₂ (ALC) catalyst prepared via metal organic framework (MOF) was more active for acetic acid steam reforming (AASR) [1]. Here we report detailed study on the performance of this catalyst for AASR. Effects of operating conditions such as temperatures (400–650 °C), steam to carbon molar ratio (S/C) and feed flow rate (1.5–5.5 mL/h) were evaluated and optimized. Results showed an excellent activity for AASR at the molar ratio S/C = 6.5, feed flow rate = 2.5 mL/h and, at 600 °C with almost total conversion and more than 90% of H₂ yield. The ordered porous structure of embedded nickel supported catalyst promotes excellent steam reforming activity and water gas shift reaction even at low temperatures, which leads to the good stable behaviour up to 36 h of TOS. The coke formation was also significantly suppressed by ALC support. Catalyst regenerated by passing oxygen at 500 °C and followed by reduction in hydrogen also show a good activity. Catalysts were characterized by DT-TGA, XRD, TEM, H₂-TPR and N₂-adsorption-desorption to understand the micro structure and coke deposition behaviour.

© 2020 Hydrogen Energy Publications LLC. Published by Elsevier Ltd. All rights reserved.

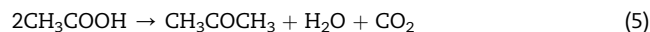
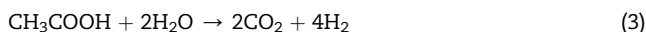
* Corresponding author.

E-mail address: asksinha.che@itbhu.ac.in (A.S.K. Sinha).<https://doi.org/10.1016/j.ijhydene.2020.06.040>

0360-3199/© 2020 Hydrogen Energy Publications LLC. Published by Elsevier Ltd. All rights reserved.

Introduction

Nowadays, increasing concern about severe environmental issues of climate change due to the greenhouse gases (e.g. CO, CO₂, CH₄) emission during consumption of fossil fuels, increasing energy demands and rapidly decreasing fossil reserves raises alarm towards renewable energy sources [2,3]. Hydrogen is widely considered a versatile clean source of energy and important feedstock for many industrial processes, transportation, electricity generation and household needs which can overcome the present demand. Currently, hydrogen is being produced in large quantities through non-renewable petroleum-based products which are one of the major causes of environmental pollution and climate changes [4]. As a result, more attention is drawn towards renewable hydrogen production via biomass and biomass derived bio-oils. Hydrogen production using biomass as a renewable energy source has gained significant attention because biomass being abundant around the globe and being CO₂ neutral [5–9]. There are two main established thermal processes to produce hydrogen from biomass. (I) direct gasification of biomass and (II) steam reforming of bio-oil obtained through fast pyrolysis process [10]. The later process of hydrogen production through biomass derived bio-oil has been gaining attention as a the most economical way to achieve hydrogen [11]. However, bio-oil is a complex mixture of carboxylic acids, aldehyde, esters, alcohols, ketones and lignin derived heavier hydrocarbons as well as are very unstable [12,13]. Acetic acid (AcOH) is one of the major components (12–19 wt %) [14,15] present in bio-oil and frequently chosen as a model compound to design efficient and stable catalysts for steam reforming of bio-oil [7,9,10,16–20]. Furthermore, unlike methanol and ethanol, acetic acid is non-flammable behaviour making it a safe source for hydrogen production [21]. However, Coking is a major challenge in steam reforming of acetic acid [22,23]. The most serious problem of coking is clogging the reactor and causing catalyst deactivation [24], which increases the operation cost in the process. Development of efficient and stable catalysts with the high resistivity towards coking has always been the focus of by several studies about steam reforming of acetic acid in recent years [25–32]. Therefore, AASR can provide a detailed understanding to design and develop efficient catalyst formulation for the various organic components of bio-oil steam reforming [33–35]. During acetic acid steam reforming (AASR), 4 mol of H₂ produced per mole of acetic acid reacted (Eq (3)). AASR proceeds according to the followings reactions, as shown in the Eqs (1)–(5) [36].



CO, CH₄, CH₃COCH₃ are the main undesired by-products formed during the reforming reactions leading towards decrease in the H₂ yield. Therefore, the development of highly active and efficient catalyst formulations have ever been since a research topic from past many years and remained a key challenge [37]. Nickel-based catalysts have been mainly developed or explored for steam reforming of oxygenated compounds due to the excellent ability of Ni catalysts to break C–C, O–H bond and lower cost and catalyst activity for WGS reaction [20,27,38–46]. However, major drawbacks with nickel-based catalysts are that, they deactivate easily due to coke deposition and via sintering during the steam reforming process [23,47]. The coke formation results due to the cracking, dehydration, ketonization of acetic acid and polymerization of organics on the acidic sites of the support [48]. Both active metal and supports suffers deactivation by coke deposition which also depends on operating conditions such as S/C ratio, space velocity and especially on reaction temperature. Furthermore, it has been also reported that at lower temperature coke deposition is favoured significantly via the “Boudouard reaction”. However, at elevated temperature CH₄ cracking and organic substrate absorb on the metallic sites via AcOH decomposition forming carbonaceous species (CH_x*) which are further responsible for coke deposition [49]. The reforming activity and selectivity of Ni-based catalysts depend on many factors viz. Catalysts preparation methods, type of supports, metal loading, use of the additive, and operating conditions [6]. Hence, various researches have been reported to increase stable catalytic performance for production of H₂ rich gas and suppressing coking during AASR [50–54]. Hu and Lu performed AASR over different transition metal catalysts (Ni, Co, Fe and Cu) supported on γ-Al₂O₃ and found that activity of Ni/γ-Al₂O₃ and Co/γ-Al₂O₃ catalysts were better. However, both catalysts encountered strong deactivation due to coke deposition, but Ni/γ-Al₂O₃ catalyst showed more activity and stable behaviour against coke deposition than Co/γ-Al₂O₃ and other Fe and Cu based catalyst [53]. An et al. [51] reported that during AASR over the Ni/γ-Al₂O₃, at 600 °C, an increases in the Ni loading, supports cracking reaction of acetic acid while retards ketonization reaction. Deposited carbon species are also affected by loading of Ni. It is reported that carbidic type carbon decreased, and graphitic-type carbon increased when Ni loading is increased from 9 to 15 wt%. It has been further reported that the maximum conversion and selectivity of H₂ was obtained 90% and 50% respectively with 12 wt% Ni loading. The total amount of deposited coke was same for all catalysts, while with the increase in Ni loading, crystalline coke increased. Li et al. [55] reported that crystalline carbon was formed from CH₄ decomposition and got transformed into inert graphitic carbon and was not quickly gasified because of Ni–C interaction. Basagiannis and Verekios [50] performed AASR over Ni and Ru/γ-Al₂O₃ at 700 °C (S/C = 5), and reported that modification of Ni or Ru/γ-

Al_2O_3 with Mg or La increased the conversion as well as H_2 selectivity. Whereas, Coke formation were also decreased from 4.65% to 0.1% over the other catalysts. However, La also promotes towards ketonization reactions and consequently produce acetone at lower temperatures. Various literatures have reported that supports are also responsible for catalytic conversion, H_2 yield and stability of catalysts during AASR [9,27,56]. The support also plays a crucial role for the dispersion of active metal as well as participate in catalytic reaction [57,58]. For example, Taknabe et al. [59] reported that during AASR over Pt/ZrO₂, not only Pt as active metal actively participate in reforming reaction but ZrO₂ also involved via dissociation of adsorbed steam which improved catalytic activity significantly. Generally, $\gamma\text{-Al}_2\text{O}_3$ is widely accepted support in the steam reforming reaction because of its high surface area for metal dispersion and excellent thermal and chemical stability. However, Ni/ $\gamma\text{-Al}_2\text{O}_3$ gets easily deactivated by coke deposition during reforming reaction and substantial sintering due to presence of water vapour and high temperatures [28,60]. $\gamma\text{-Al}_2\text{O}_3$ promote dehydration reactions that lead to deactivation of the catalysts. The basic supports also suffered deactivation due to coke deposition via other reactions include ketonization and oligomerization. Acetone is readily produced during decomposition of acetic acid which further act as a precursor for coke deposition [59]. Moreover, the support also influenced the metal support interaction as well as the reaction mechanism [61]. In order to neutralize the acid sites of $\gamma\text{-Al}_2\text{O}_3$ support, addition with basic promoters such as alkali and alkaline metals (Li, K, Mg, Ca, Ba, etc), usually reported in literatures [2,6,38,62,63]. Taking in to account the problem of deactivation of catalysts due to coke deposition and sintering at high reaction temperature, addition of small amount of oxides of rare earth metals such as cerium and lanthanum to the alumina support is reported beneficial to enhance the catalytic performance [64,65]. Various researches have reported neutralization of the acidic sites of $\gamma\text{-Al}_2\text{O}_3$ with rare earth metal oxides like CeO₂ and La₂O₃ during reforming reaction, which also improves the metal dispersion and metal support interactions. These alter the electronic distribution and metal dispersion of active metal [66,67]. The addition of La₂O₃ improves the thermal resistance of Al₂O₃, it strongly interacts with Ni active phase and increase dispersion of the fine nickel particles over the alumina and prevents sintering of Ni^o particles [68,69]. In addition, La promotes the WGS reaction which suppresses the formation of coke on the catalyst surface by removal of adsorbed CO as well as reacts with CO₂ forming oxygen containing species which further help to remove coke [64]. Leferts et al. studied AASR over Ni/ZrO₂ catalyst and reported that catalytic activity gradually decreased due to extensive coke deposition. Whereas, addition of K and La in to the catalyst improved the activity as well as stability by suppressing coke accumulation [70]. Moreover, addition of La₂O₃ also prevented metal sintering to stabilize the metal particles at high reaction temperatures [64]. Valle et al. [71] also reported that during steam reforming of aqueous phase of bio-oil, addition of La₂O₃ in Ni/ $\alpha\text{-Al}_2\text{O}_3$ catalyst not only increased the catalytic activity and H_2 yield but reduce the catalyst

deactivation also significantly. Likewise, the CeO₂ also presents excellent oxygen storage and release capacity owing to its facile redox property. Consequently, it favours coke gasification from the metallic surface and WGS reaction resulting in enhance catalyst stability and performance by alleviating the coke deposition on the catalyst surface during the steam reforming reaction [72–74]. The positive effect of CeO₂ over Rh/ZrO₂ supported catalysts have been reported in the oxidative steam reforming of bio-oil by Arandia et al. [75]. The results showed that addition of CeO₂ not only enhances the catalytic activity remarkably (conversion 100% and 92% H_2 yield) but also exhibited high stability by improving gasification and thermal combustion of coke. Moreover, CeO₂ also helps to improve WGS reaction during steam reforming reaction and also suppress metal sintering [67,76].

In addition to the structural and chemical properties of the support, the synthesis methods also play an important role in obtaining highly active and stable catalysts. Wang et al. [77] investigated that Ni/ATC (attapulgitic clay) catalyst prepared via impregnation, precipitation, and mechanical blending methods and reported that catalyst synthesized via precipitation method showed excellent activity in terms of conversion and H_2 yield as well as stability because of the strong interaction between Ni particles and ATC support. Yang et al. [78] investigated different and simple method for the synthesis of novel ZnO nanoparticles and hybride ZnO@C nanostructured catalyst via MOF approach under different atmospheric conditions. The hierarchical 3D cubical structured nanoparticles of ZnO showed relatively high photocatalytic decomposition activity. Whereas, the hybrid ZnO@C composites showed high porosity with sufficient pore sizes which exhibited excellent adsorbing capacity for organic pollutants.

In the present study, Ni-complex supported over $\gamma\text{-Al}_2\text{O}_3$ promoted by La₂O₃–CeO₂ (ALC) catalyst prepared via MOF process have been studied for the catalytic performance and reactivity for continuous acetic acid steam reforming. It is in order to mention that, in our earlier communication we had reported that the Ni catalyst which was prepared by decomposition of MOF was superior in performance compared to a catalyst of same composition prepared by decomposition of formate precursor via impregnation method [1]. The catalytic activity in terms of H_2 and CO₂ yield was interlinked with the structural and chemical properties of the catalyst, which are related to the interaction between nickel and ALC support. Moreover, effect of operating parameters such as temperatures, S/C ratio, mixture flow rate, catalyst stability, and coke deposition behaviour on catalyst before and after regeneration during the reaction were also evaluated.

Experimental

Material

Aluminium nitrate nonahydrate ($\text{Al}(\text{NO}_3)_3 \cdot 9\text{H}_2\text{O}$, >98%, Merk Pvt Ltd.), Ammonium hydroxide (NH_4OH , >98% Fisher Scientific), Nickel chloride hexahydrate ($\text{NiCl}_2 \cdot 6\text{H}_2\text{O}$, > 98%, Fisher Scientific), lanthanum nitrate ($\text{La}(\text{NO}_3)_3 \cdot 6\text{H}_2\text{O}$, >98%, Central

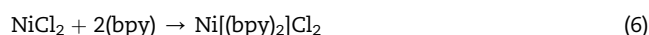
Drug House, Mumbai-India), Cerium (IV) sulfate tetrahydrate ($\text{Ce}(\text{SO}_4)_2 \cdot 4\text{H}_2\text{O}$, >98%, Merk Pvt. Ltd.), 2'2' Bipyridine ($\text{C}_{10}\text{H}_8\text{N}_2$, >98%, Alfa Aesar), Propan-2OL ($(\text{CH}_3)_2 \cdot \text{CHOH}$, >98%, Fisher Scientific), Diethyl Ether ($(\text{C}_2\text{H}_5)_2\text{O}$, >98%, Fisher Scientific), and Ethanol ($\text{C}_2\text{H}_6\text{O}$, >98% Fisher Scientific) were used directly for the synthesis of support and catalysts.

Synthesis of support material

Aluminium hydroxide gel of high surface area was prepared at 30 °C from concentrated solution of aluminium nitrate by adjusting pH 9 with the help of ammonia solution. The prepared hydrogel was kept for 24 h for aging and rinsed properly with double distilled water to remove nitrate ions completely. Eventually, the product was dried in an oven at 110 °C (8 h) and calcined in furnace at 800 °C (8 h) to get $\gamma\text{-Al}_2\text{O}_3$ support. $\gamma\text{-Al}_2\text{O}_3$ support was impregnated with the required amount of aqueous solution of La (NO_3)₃·6H₂O to obtain 3 wt% La₂O₃ in the final support. The $\gamma\text{-Al}_2\text{O}_3$ –La₂O₃ support solution was then dried on a water bath (100 °C), and further dried in oven (110 °C) for overnight and finally calcined at 800 °C for 8 h. The 3 wt% concentration of La₂O₃ was chosen because it has been reported optimal for stabilizing the $\gamma\text{-Al}_2\text{O}_3$ support against sintering process [79,80]. To obtain 9 wt% concentration of CeO₂ in the final support, required amount of aqueous nitric acid solution of Cerium (IV) sulfate tetrahydrate was impregnated over prepared $\gamma\text{-Al}_2\text{O}_3$ –La₂O₃ support. The mixture was dried in water bath with continuous stirring and subsequently in an oven at 110 °C for overnight and finally calcined at 550 °C for 8 h.

Synthesis of catalyst

This catalyst was prepared using Ni [(bpy)₂]Cl₂ monometallic complex of nickel. Stoichiometric amount of nickel precursor (NiCl₂·6H₂O) and organic ligand (2'2' bipyridine) were taken for the preparation of the nano-metallic complexes via below given reaction.



1.47 g of NiCl₂ and 3.54 g of 2'2'-bipyridine organic ligand solutions were dissolved in 20 mL of 2-propanol solvent separately. Both the solutions were mixed dropwise in a round bottom flask simultaneously with continuous stirring at 400 rpm for 4 h. The flow rate of each solution was maintained at 0.33 mL/min, and the flask was maintained at 40 °C temperature. Fine particles of Ni-complex (Ni [bpy]₂ Cl₂) were obtained these were washed repeatedly with ether until it is free from impurities [81]. The solution of requisite amount of Ni-complex and ALC prepared in methanol was taken and mixed dropwise in a round bottom flask at 400 rpm maintaining 40 °C for 3 h to obtain 15 wt% loading of Ni in the final catalyst. The prepared mixture was then filtered with ether, dried for 12 h (110 °C) in an oven and calcined for 6 h in the tubular reactor at 650 °C, with a controlled flow N₂ gas. Fig. 1, shows the schematic process flow representation of prepared catalyst. The advantage of Ni-complex precursor is that it directly decomposes to metallic Ni⁰ with the removal of different volatiles compounds after calcination in inert atmosphere. Therefore, it does not require external reducing agent like H₂ before catalytic reaction [82]. The detailed XRD

diffraction pattern and DT-TGA analysis of prepared Ni-complex (Ni [bpy]₂ Cl₂) was given in the previous manuscript [1].

Regeneration of catalyst

The stability of catalysts were performed at fixed operating conditions (Temp- 600 °C, Feed flow rate –2.5 mL/h and S/C –6 mol/mol). Regeneration of deactivated catalyst at 600 °C was performed in-situ in a fixed bed reactor by passing oxygen with a 60 mL/min flow rate at 500 °C for 3 h. The objective was to burn off deposited coke on the surface of catalyst. Subsequently, it was cooled down to room temperature and H₂ at 600 °C was blown over the catalyst for 3 h. It ensured that any oxidized nickel was reduced in the regenerated catalyst.

Characterization of catalyst

Surface area of catalysts and support as well as pore size distribution of the catalyst were measured by N₂ adsorption/desorption cycles method using the (micrometric ASAP 2020) surface area analyzer. Samples were heated at 350 °C for 6 h in vacuum for removing pre-adsorbed gases under argon flow before each measurement. Crystal phases distribution of support, fresh, deactivated and regenerated catalysts were investigated via X-ray powder diffraction (XRD) techniques from a (Rigaku Ultima IV) using Cu-K α radiation source. To ascertain the reduction behaviour of catalyst and interaction between supports and the metal, hydrogen temperature programmed reduction (H₂-TPR) analysis were carried out using micromeritics pulse chemisorption unit with TPD model no. 2920.50 mg of the catalyst was pre-treated at 300 °C with constant flow of argon gas to remove moisture in a quartz made microreactor. Subsequently, to obtain the TPR profile, the sample was heated from 50 to 800 °C linearly with rise in temperature at a heating rate of 5 °C/min with a constant flow of 5% H₂/Ar (40 mL/min). The catalysts were also peroxidised in the same instrument with the constant flow of oxygen from room temperature to 500 °C for 2 h before performing reduction analysis. Any change in the composition of the exhaust gas was measured by the thermal conductivity detector. To observe the fine structure of prepared catalyst, transmission electron microscopy (TEM) was conducted (Model TechnaiG² with 200 kV accelerating voltage). For the analysis of coke deposited on the surface of catalysts, thermal analysis (DT-TGA) was carried out using thermal analyzer (NETZSCH-Jupiter-STA-449F3) under a flow of air (50 mL/min) with constant heating rate of 10 °C/min up-to 1000 °C.

Experimental set-up

AASR was studied in a vertical quartz tubular reactor under steady state conditions. The experimental schematic diagram is shown in Fig. 2. It consisted of three sections, viz, the feed preparation, the test, and the analysis section. A mixture of known composition of acetic acid and water was fed into preheater to vaporize the feed before entering to the reactor section. Preheating section contained a tubular quartz pipe surrounded with heating coil and insulated with ceramic wools. The temperatures of the preheating section were controlled from two variac connected in series. Activity test

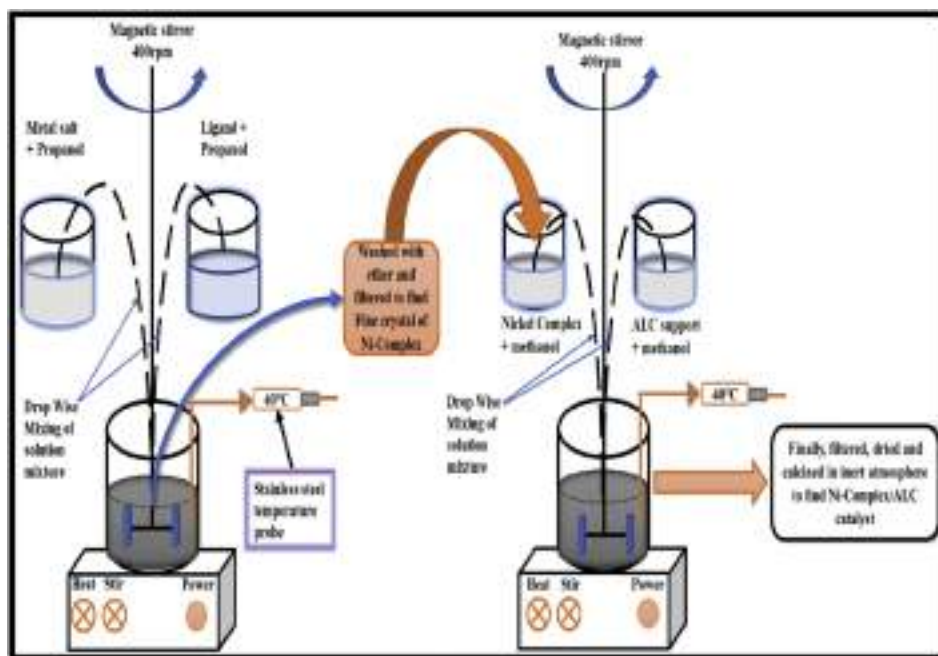


Fig. 1 – Process flow diagram for the Synthesis of Ni-Complex/ALC.

was carried out using the synthesized catalyst diluted with SiC particles (1:2w/w) (Particle size were of the range of 0.2–0.5 mm) to avoid channelling of flow and local heating of the catalyst. The catalyst particles were placed in the centre of the reactor sandwiched between quartz wool. The length of tubular reactor was 50 cm, and internal diameter was 10 mm. The reactor was surrounded with an electric furnace coupled with PID controller (Thermolyne, USA 79300). A K-type thermocouple was placed inside a vertical thermowell at the centre of reactor to measure the catalyst temperature. The thermocouple could move from the top to bottom of the reactor. 500 mg of catalyst diluted with SiC as discussed above

was placed in the central part of the reactor where the temperature variation along the length from the top to bottom of the catalyst bed was not more than 2 °C. The feed was a mixture of acetic acid and water. The two were premixed in a ratio to give steam to carbon ratio of 6.5:1 (mol/mol) in the feed to the reactor. The premixed liquid mixture was fed at the rate of 2.5 mL/min through calibrated pump (Fluid Metering Inc, USA, Model RHSY). Nitrogen as a carrier gas was also introduced into the reactor at a flow rate of 30 mL/min accordingly, the inlet concentration of acetic acid was 4.85×10^{-6} mol/mL of N_2 and WHSV 1.05 h^{-1} . Products gases from the reactor were passed through a condenser set at 4 °C to gas-liquid

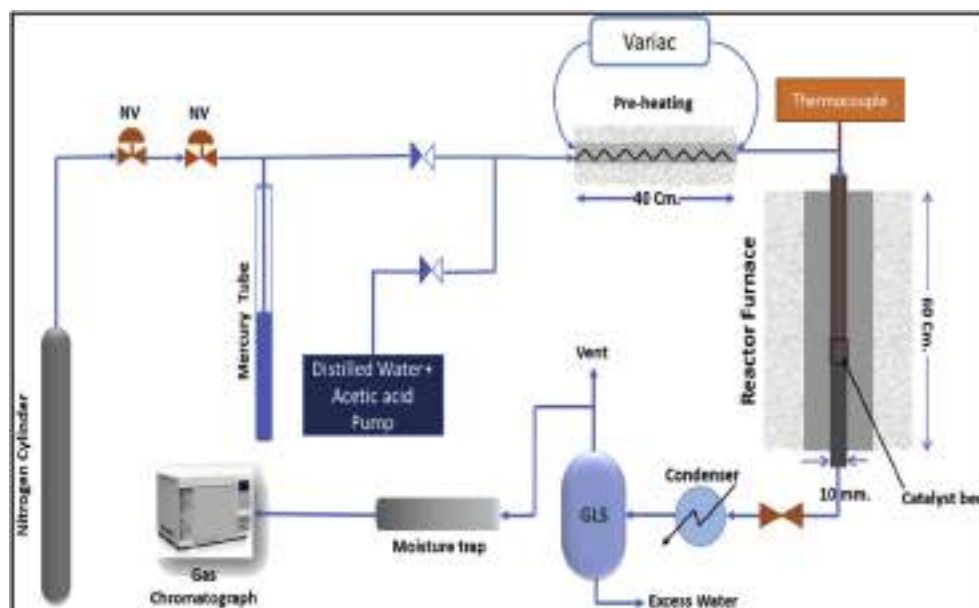


Fig. 2 – Schematic diagram of catalytic steam reforming.

separator for condensing liquids. The exit gas flow was measured intermittently by a soap bubble meter. The gaseous products and condensate liquid were analysed by gas Nucon make gas chromatograph (GC) separately. Concentrations of H_2 , N_2 , CO , CH_4 , and CO_2 in the gaseous fraction of the product were estimated by a GC equipped TCD with the Carbosieve SII column. Since the gas flow rate was known, the number of moles of individual gases in the output mixture could be calculated. The condensate liquid was analysed by (GC-FID) equipped with Porapak Q column. Calibration plots were prepared for quantitative analysis of gaseous products using standard gas mixtures of known compositions supplied by m/s Chemtron Science Laboratory, Navi Mumbai and for liquid self-prepared with iso-octane as the internal standard were used. All the experiments related to conversion, yield and stability tests of catalyst were performed at least twice for the same operating conditions, sometime it was repeated more than twice. All the times, the experimental data produced are approximately same with marginal difference.

Activity of catalysts was measured in terms of conversion of acetic acid and yields of species (CO , CH_4 , CO_2 , and H_2). Conversion of acetic acid was defined in terms of C–C bond cleavage conversion, as given below.

Yield of a species in the products given in Eq. (8) is the ratio of moles of the species in the product to the number of moles of the same species formed on complete conversion of acetic acid to the species. Therefore, yield of CO , CH_4 , and CO_2 (%)

$$Y_{CO, CH_4, CO_2} = \frac{\text{moles of } CO/CH_4/CO_2 \text{ produced}}{2 \times \text{moles of acetic acid fed}} \times 100 \quad (8)$$

$$\text{Conversion of acetic acid, } X_{AcOH} (\%) = \frac{\text{Moles of carbon in the product gases}}{2 \times \text{moles of acetic acid fed}} \times 100 \quad (7)$$

The yield of H_2 produced was calculated using in Eq. (9). It is the fraction of H_2 produced to the moles of H_2 on the complete conversion of 1-mole acetic acid to H_2 .

$$Y_{H_2} = \frac{\text{moles of } H_2 \text{ produced}}{4 \times \text{moles of acetic acid fed}} \times 100 \quad (9)$$

Result and discussion

Catalyst characterizations

Surface area and pore size analysis

N_2 adsorption – desorption isotherms of the support and fresh catalyst are shown in Fig. 3. These isotherms are of type IV typically exhibited by mesoporous materials Textural properties of support and the fresh & the used catalysts as determined by N_2 adsorption isotherms are shown in Table 1 and Table 2. The results show that, the impregnation of basic oxide promoters (La_2O_3 and CeO_2) on $\gamma-Al_2O_3$ leads to loss of surface area as well as the total pore volume of $\gamma-Al_2O_3$ support, probably due to covering of alumina pores walls by these

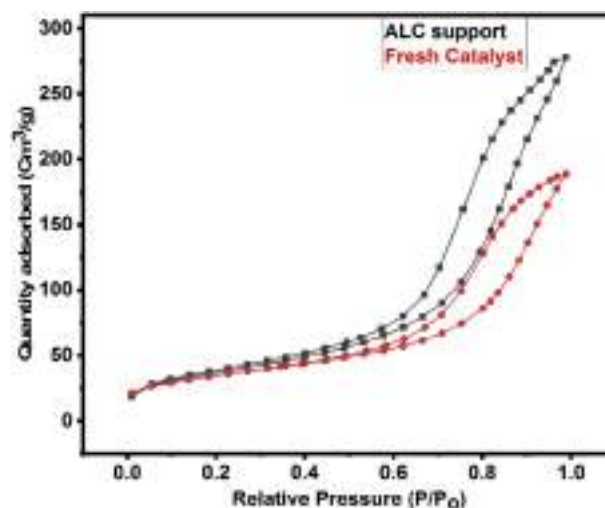


Fig. 3 – N_2 adsorption - desorption isotherms of the support and fresh catalyst.

metal mixed oxides or because of the lower surface area of these metal oxides which have low surface areas. Further, incorporation of nickel on ALC support leads to decrease in the surface area as well as the total pore volume. Pore size distribution (Table 2) shows that pores are mostly of size less than 20 Å. It is also observed that the fresh catalyst has a surface area of 120 m^2/g which is only marginal less than the surface area of ALC support. It is, therefore, concluded that Ni did not lead to any pore mouth blocking of support. On the

other hand, nickel was dispersed throughout the porous structure of the support. On deactivation, the surface area has decreased. The deactivated catalyst has 30% lower surface area in comparison to fresh catalyst. On regeneration, catalyst partially regain surface area to a large extent. It is indicative of that the deactivation was due to coke deposition. It is further observed from Table 1 that the total pore volumes do not change significantly. Therefore it is concluded that coke is deposited throughout the pore rather than being deposited on pore mouth and blocking the pores. It is also observed that on regeneration a fraction of larger pores has appeared (Table 2). It is indicative of collapse of pore structures of the support. Large size pores have appeared at the expense of smaller size pores.

XRD analyses of prepared catalyst

All the XRD patterns of support and the fresh catalyst, deactivated (after 36 h of run at 600 °C, ref. sec. Catalyst stability and regeneration studies) and regenerated catalyst (the deactivated catalyst regenerated as mentioned above in sec. Regeneration of catalyst) are presented in Fig. 4. Several peaks of the

Table 1 – Textural properties of synthesized catalysts.

Support/Catalyst	Surface area (m ² /g)	Total pore volume (cm ³ /g)	Crystallite size of Ni ^a (nm)
Al ₂ O ₃	169	0.61	–
Al ₂ O ₃ –La ₂ O ₃ –CeO ₂ (ALC)	133	0.43	–
Catalyst (Fresh)	120	0.29	37
Catalyst (Deactivated)	84	0.25	–
Catalyst (Regenerated)	110	0.27	40

^a (111) plane.

Table 2 – Pore size distribution of catalysts.

Species	Pore size range (Å) and corresponding pore volume (cm ³ /g)			
	0 ≤ d _p ≤ 20	20 ≤ d _p ≤ 40	40 ≤ d _p ≤ 60	60 ≤ d _p ≤ 80
Al ₂ O ₃ –La ₂ O ₃ –CeO ₂ (ALC)	0.38	0.05	–	–
Fresh Catalyst	0.25	0.02	0.01	.01
Deactivated catalyst	0.17	0.04	0.03	0.01
Regenerated Catalyst	0.06	0.13	0.06	0.02

D_p = pore diameter.

support and catalysts were identified with their d-value (calculated using Bragg's law) and matched with the standard values. Peaks correspond to γ -Al₂O₃, CeO₂, and Ni, metal. The MOF derived Ni particles in the catalyst showed ordered aggregates of Ni nanoparticles with 3 dimensions cubic structures, which consisted of faceted Ni crystals embedded with ALC support. Consequently, showed good catalytic activity. The support and catalysts showed diffraction peaks at around $2\theta = 37.2^\circ$, 45.8° , and 66.7° , which were assigned to γ -Al₂O₃ (JCPDS 86–1410). The three high-intensity peaks of Ni metal observed at 44.5° ; at 51.8° and 76.5° correspond to (111), (200) and (220) planes. No characteristic peak of NiO at $2\theta = 37.3^\circ$ and 43.3° (JCPDS 78–0643) present or corresponding to NiAl₂O₄

could be identified. Catalysts also showed the characteristic peaks of cubic fluorite crystal structure of CeO₂ at $2\theta = 28.30^\circ$ (111), 33.13° (200) and 56.33° (311) in catalysts and the support ALC respectively which shows the segregation of the CeO₂ over the γ -Al₂O₃ [83]. Cubic fluorite structures also helps to diffuse more oxygen and formation of oxygen vacancy [67]. No peak of La₂O₃ was observed in either of catalysts or the support ALC probably due to well dispersion and low amount of La₂O₃ in the catalysts [69]. The XRD diffraction patterns of prepared catalysts indicated that nickel observed was in the mainly metallic phase only on the synthesized support. It is also noteworthy that all the peaks corresponding to the nickel particles are in the highly ordered regular cubic structured over the surface of

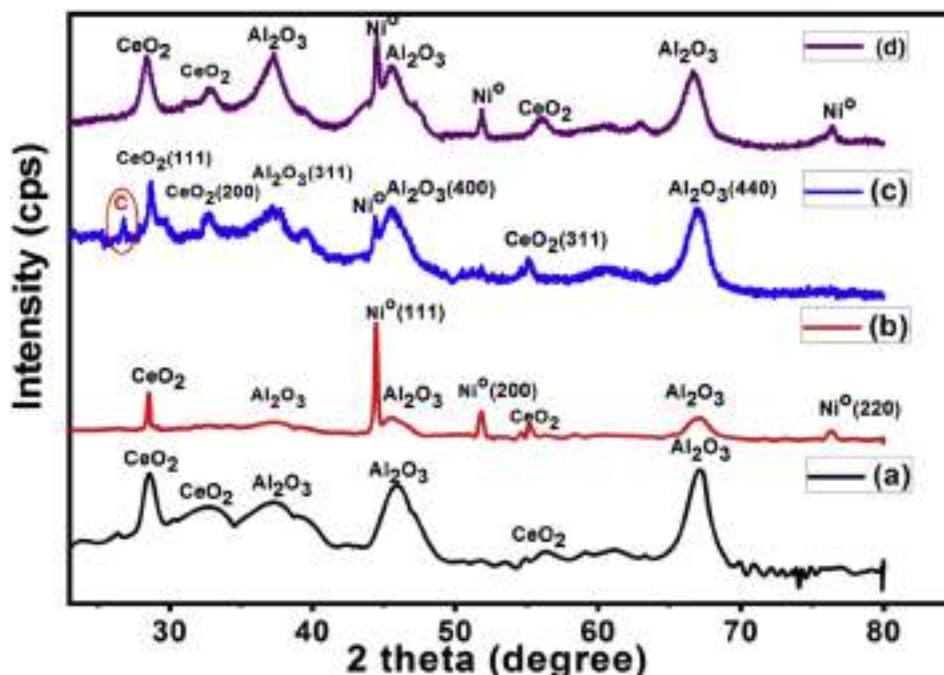


Fig. 4 – XRD patterns of (a) ALC support, (b) Fresh catalyst, (c) Deactivated, and (d) Regenerated catalyst.

ALC support. Average crystallite size of the catalysts (fresh, the deactivated and regenerated) was calculated by Scherrer equation for the (200) peak and results are shown in Table 1. It is observed that the crystallite size of Ni in fresh catalyst had 37 nm, while in case of deactivated catalyst Ni^o peak for the same plane (200) disappeared due to covering of coke formation. Crystallite size in the regenerated catalyst was 40 nm which was nearly equal to that of the fresh catalyst. Which represents coke has been gasified from the catalyst surface after the regeneration process. The XRD patterns of deactivated catalyst after 36 h reaction showed a peak $2\theta = 26.5^\circ$, attributed to graphitic carbon deposition on catalyst during reforming reaction. Above results lead to the conclusion that the deactivation of catalyst was due to deposition of coke on the surface. The DTA results, as discussed later, have shown that the deposited coke was of two types; i. e, amorphous and graphitic. Further, any significant sintering of nickel particles was not observed. Hence, it is not considered to be a cause of deactivation of the catalyst.

TPR analysis

TPR profiles of oxidized nickel supported catalyst and unsupported nickel oxide are shown in Fig. 5. Reduction of pure (unsupported), which is referred at free nickel oxide, NiO to Ni is observed at 329 °C [84]. However a shift in the reduction peak(s) is observed in catalyst compared to the reduction temperature of unsupported NiO. The catalyst showed a reduction peak at a higher temperature of 406 °C with a hump at 437 °C. In general, the metal support interaction hinders sintering of metal particles. In the present study, the crystallite size of Ni was almost stable after 36 h of run. This observation is attributed to the metal-support interaction observed in the catalyst. The use of metal organic framework precursor might have resulted into formation of a metal-support interaction in the catalyst.

TEM studies

TEM analysis was performed to obtain structural detail of prepared catalyst. Results of transmission electron microscopy and corresponding electron diffraction patterns of the

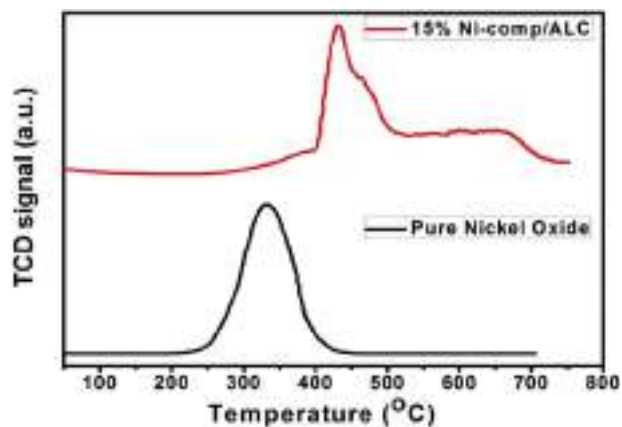


Fig. 5 – TPR profiles of 15%Ni-Comp/ALC catalyst and pure NiO.

catalyst is shown in Fig. 6(A-B). The TEM micrograms clearly shows homogeneously distributed particles, the small agglomerated spherical type morphology, corresponds to CeO₂. Moreover, dark road like particles morphology observed are alumina particles, whereas small black areas could be marked as metal Ni particles. It is also observed from the figure that Ni particles in catalyst are well dispersed. Size of the particles approximately ranged between 12 and 20 nm. The selected area electron diffraction (SAED) patterns of the catalyst indicated clean and strong ring pattern which indicates characteristics of polycrystalline nature. Rings analysis yields *d* – values 2.02, 2.42, 2.71 and 3.15 Å. The *d* values of 2.42, 2.71 and 3.15 Å correspond to planes of γ -Al₂O₃ (311) and CeO₂ (111) and CeO₂ (200) with crystalline structure matched with the corresponding *hkl* planes from XRD analysis. However the ring (corresponding to the *d* value 2.02 Å) could not be ubiquitously assigned to either γ -Al₂O₃ (400) with *d* value 2.0361 Å or Ni (111) with *d* value 1.981 Å. However both the peaks corresponding to γ -Al₂O₃ (400) and Ni (111) were observed in XRD analysis.

DTA/TG analysis

In order to determine and characterize the deposited coke over spent catalyst during steam reforming reactions, DT-TGA analysis of used catalysts was carried out. TGA of the used catalyst was carried out in the presence of oxygen from room temperature to 1000 °C with a heating rate of 10 °C/min shown in Fig. 7. The weight loss of the spent catalyst (catalyst after 36 h TOS) was observed 24.1%. Two types of coke species were found on the catalysts surface. The first peak observed at lower temperature between 350 and 400 °C has been attributed to coke combustion/oxidation of amorphous carbon. While second peak which appeared between 500 and 550 °C is attributed to oxidation of graphite or filamentous carbon associated to nickel particles [6,85]. It has been reported that the amorphous type coke generally unstable and easily oxidizable. It has been observed that for regenerated catalyst after 36 h TOS reaction, the coke formed over the catalyst surface via both type of carbon (amorphous and filamentous/graphitic) contributed in higher proportion (Fig. 7b). It is in order to mention that, the filamentous/graphitic coke formed over metallic sites showed comparatively less effect than amorphous coke on catalytic performance [6].

Activation, deactivation and regeneration studies

Effect of temperatures

Conversion of acetic acid and yield of products as a function of temperature are shown in Fig. 8. Experiments were performed in the temperature range of 400 and 650 °C with 2.5 mL/h (acetic acid/water mixture as feed) feed flow rate, S/C (steam to carbon in the feed) ratio of 6.5, and 0.5 g of catalyst. All the product samples during experiments were collected after achieving steady state. It was approximately 4 h after starting the run. All the experiments related to conversion, yield and stability tests of catalyst were performed at least twice for the same operating conditions (e.g. temperature, feed flow rate and S/C ratio) and all the data were collected when the temperature became constant at the desired value for at least

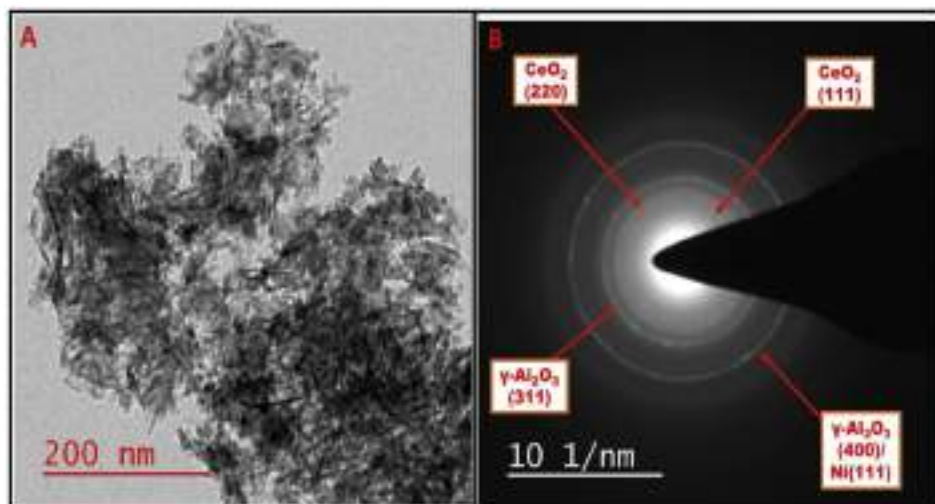


Fig. 6 – (A) TEM image (B) SAED diffraction of 15% Ni-Comp/ALC.

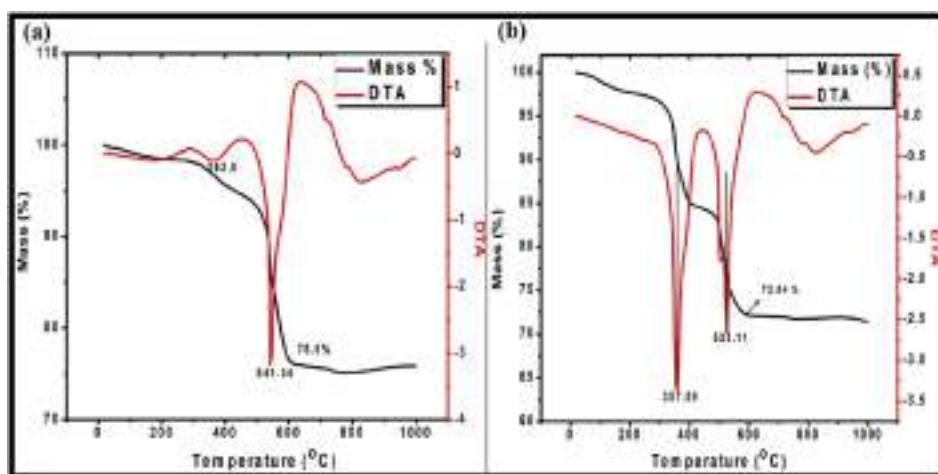


Fig. 7 – TG-DTA analysis of (a) deactivated and (b) regenerated deactivated catalyst after 36 h of TOS.

30 min with a deviation of less than 5 °C in. The experimental data produced were approximately same with marginal difference. The average value have been reported in the data. It

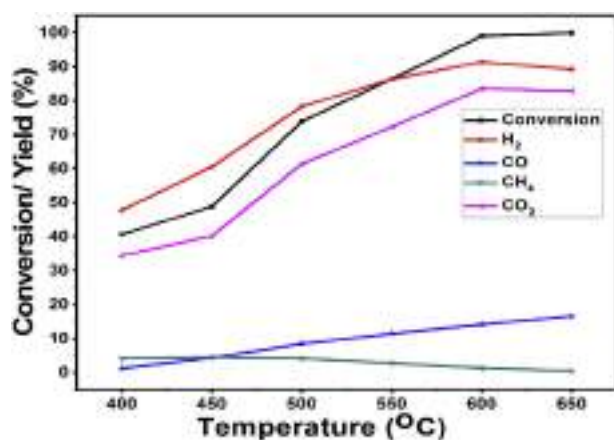


Fig. 8 – Conversion and yields of products over 15%Ni-Comp/ALC: S/C = 6.5, Feed flow rate = 2.5 mL/h, P = 1 atm.

could be seen from the Fig. 8, that catalyst showed activity for the reforming reactions even at initial lower temperature of 400 °C, where conversion of acetic acid reached about 40.44%. There were four major products; H₂, CO, CH₄, and CO₂. The conversion of acetic acid increased upon increasing reaction temperature up to 600 °C. Our results matched with the results obtained by previous research [9]. The production of methane decreased as temperature increased. During AASR, CH₄ is produced via thermal decomposition of acetic acid as well as from the methanation of CO and CO₂ [86]. However, according to thermodynamic study CH₄ formation occurred mainly via thermal decomposition at higher temperatures. The formation of CH₄ at high temperatures was almost negligible because at high-temperature CH₄ steam reforming reaction become favourable [22]. The production of CO increased monotonously with the increase in reaction temperatures. At high reaction temperature CO was produced possibly via the reverse water gas reaction (RWGS) whereas at lower temperature CO production might come from the thermal decomposition of acetic acid as catalyst showed poor activity towards RWGS [87]. H₂ yield increased with increasing

temperature, in the line of the thermodynamics prediction [9]. In previous research, similar trends were observed when Ni and Co based catalyst were studied during AASR. The C–C bond cleavage conversion and gaseous yields (H_2 , CO, CO_2) were increased with increasing temperatures [88]. From the results, it was observed that H_2 yield increased until 600 °C, and then decreased. Yield of CO_2 also increases up to 600 °C and decreased slightly after 600 °C. The decrease in H_2 and CO_2 yield at high temperatures has been attributed to RWGS reaction. Which is favoured at high reaction temperatures consequently dropped the concentration of H_2 and CO_2 . In the temperature range of 400–650 °C, almost complete conversion of acetic acid was obtained, and H_2 yield was 91.36% was achieved at 600 °C.

Effect of feed rate

The effect of acetic acid mixture flow rate was studied at a constant carrier gas flow rate and steam to carbon molar ratio ($S/C = 6.5$) at 600 °C shown in Fig. 9. The mixture flow rate was varied between 1.5 and 5.5 mL/h. Although feed flow rate of AcOH mixture did not have much effect on the conversion of acetic acid, however, H_2 and CO_2 yield declined significantly at higher flow rate due to the reduction in C–C bond cleavage and due to decrease in contact time between reactants and catalyst that prevents steam reforming process and dominate decomposition reaction. Takanabe et al. explained reaction pathways of AASR and reported that H_2 , CO, CH_4 and CO_2 were the main products formed via decomposition of CH_x species. Apparently, C–C bond cleavage played a significant role in acetic acid steam reforming [89]. With the increase in the flow rate of feed, the yield of other by-products such as CO and CH_4 increased remarkably. At 600 °C, CO was produced as a secondary by-product, probably due to RWGS reaction. It was observed from the results that at high feed flow rate, low conversion and high CO and CH_4 production probably, interaction between reactants and catalysts decreased which suppress the steam reforming reaction [4]. From Fig. 9, it is also observed that increasing the feed flow rate, H_2 and CO_2

yield percentage decreased, whereas CH_4 % increased. It is attributed to the fact that at a low feed flow rate, interaction of the reactants with the catalysts was excellent which improves steam reforming reaction dominated over thermal decomposition, leading to higher yield of H_2 and CO_2 . Whereas at higher flow rates, owing to lesser contact time with catalyst, thermal decomposition dominated over steam reforming.

Effect of steam to carbon molar ratio

Steam/carbon molar ratio (S/C) is one of the important parameters in the steam reforming process. A high S/C ratio prevents coke formation on the catalyst surface, and results in a better yield towards H_2 . Therefore, the effect of S/C was examined at 600 °C (reaction temperature at which yield of hydrogen was the highest) and constant feed flow rate of mixture. Fig. 10, showed the results where acetic acid conversion and product distribution were plotted as a function of the S/C molar ratio. It is observed from figure that both conversion and yield of acetic acid increased for H_2 and CO_2 monotonously with an increase in S/C ratio from 0 to 6.5 and further increase these levels off. On the contrary, the formation of by-products (CO, CH_4) decreased in high S/C ratio. At low S/C ratio decomposition reactions of acetic acid are favoured according to Eqs (1) and (2), leading to a large amount of CO and CH_4 . During AASR, adsorption of steam on catalyst surface plays a crucial role not only to suppress the formation of by-products (CO, CH_4 , C_2H_4 , CH_3COCH_3) via promotion of water gas shift (WGS) reaction but also enhances the removal of carbonaceous desorption over the catalyst surface. High S/C ratio promotes the adsorption of steam over the catalyst surface because of increased partial pressure [37]. It is observed from the results that additional steam can favor steam reforming reactions and suppress the generation of by-products. The similar results have been reported by Marquovich et al. [90] that lower S/C ratio would favor the lower rate of steam reforming reaction and consequently generation of a large amount of by-products, due to the low partial pressure of steam. Phongprueksathat et al. also reported that

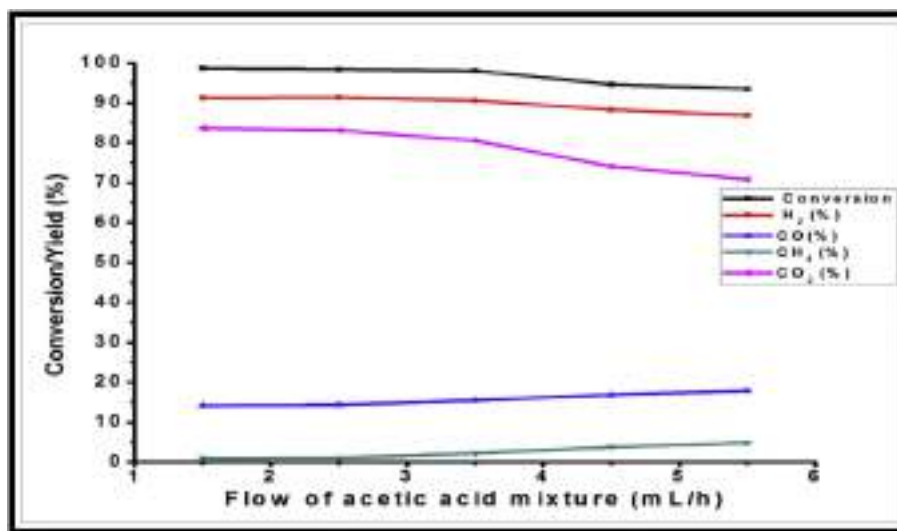


Fig. 9 – Effect of the feed flow rate of AcOH mixture on conversion and yield of products over 15%Ni-Comp/ALC; Temp 600 °C, S/C ratio - 6.5: 1, $P = 1$ atm

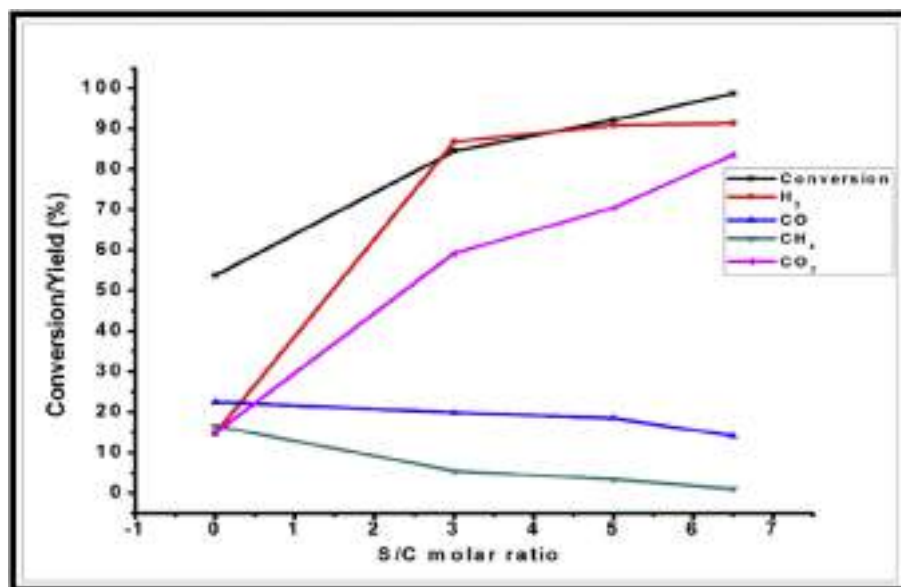


Fig. 10 – Effect of S/C ratio on conversion of AcOH and product distribution over 15%Ni-Comp/ALC at 600 °C, Feed flow rate– 2.5 mL/h, and P-1 atm

Ni/Ce_{0.75}Zr_{0.25}O₂ (CZO) supported catalyst promote C–C bond cleavage activity as well as increased H₂ yield at a higher S/C ratio [88]. Moreover, it could be seen from the results that at S/C = 0, the yield of H₂ is very low due to the absence of acetic acid steam reforming reaction, and the governing reactions are decomposition and ketonization. While, in the presence of steam, reforming reactions are dominated, and these reactions depressed significantly. As S/C ratio increases from 0 to 3, the steam reforming reaction dominated. The conversion and yield of H₂ increased remarkably.

However, due to the significant amount of CO generation, the yield of H₂ was still relatively low. The reason for this is that it was more difficult to remove CO from shift reaction in low steam ratios. The later runs made in the high S/C ratio demonstrated that CO yield decreased with increasing the S/C ratios. It is concluded that at higher S/C ratios, not only the response of the WGS reaction was promoted, but the RWGS reaction was also interrupted comparatively. As shown in Fig. 10, S/C = 6.5 and temp 600 °C were required for the maximum H₂ yield during AcOH steam reforming for hydrogen production.

Catalyst stability and regeneration studies

It has been reported by several researchers that catalyst deactivation is mainly because of the formation of severe coke deposition on catalytically active sites [6,90,91]. Keeping in mind that the catalyst exhibited the best conversion and selectivity of H₂ at T = 600 °C, S/C = 6.5 and mixture flow rate 2.5 mL/h. Stability of the catalyst was performed at these conditions. The stability test was performed for 36 h, and the result showed the dependence of the acetic acid conversion and H₂ yield on the reaction time on stream (TOS). As displayed in Fig. 11, initially, with the reaction time 20 h, both conversion of acetic acid and the yield of H₂ over the 15%Ni-Comp/ALC reduced. After 20 h TOS, AcOH conversion and the yield of H₂ did not change much after more than 36 h of

reaction. The conversion on the fresh catalyst declined from 98.69 to 93.73% in 36 h, and the yield of H₂ decreased from 91.36 to 87.26% after 36 h of reaction. The deactivation of catalyst was mainly due to the coke deposition over the active sites. Coke deposition takes place mainly due to polymerization or thermal decomposition of acetic acid or reaction intermediates at high temperatures [4]. The spent 15% Ni-Comp/ALC catalyst after 36 h were characterized by CHNS analysis; the total carbon % deposited was 23.46%. The type of coke deposited on catalyst was further characterized with DT-TGA in the air as discussed earlier. Lu et al. [92] have studied the coking and regeneration of Ni/γ-Al₂O₃ catalyst as well as effect of coke nature. They reported that catalyst deactivated due to toluene cracking at 700 °C within 0.5 h. The deactivated catalyst was repeatedly regenerated by calcining in air at 600 °C for 3 h. Results showed excellent conversion even after third regeneration and filamentous type of coke was formed over the catalyst surface. Wang et al. [93] also reported that supported Ni/Al/Mo spent catalysts after hydrogenation reaction of hydrocarbon were regenerated by passing oxygen at 550 °C for 3 h and suggested that at lower temperature coke could not be oxidized completely, whereas, at high-temperature, sintering of catalyst might occur. Therefore, regeneration of deactivated catalyst was performed in-situ in the reactor by passing oxygen with a 60 mL/min flow rate at 500 °C for 3 h and subsequently cooled to room temperature and reduced in the presence of H₂ at 600 °C for 3 h. The conversion and product distribution of regenerated catalyst is also displayed in Fig. 12. It was observed that catalyst activity approximately regained after regeneration. A slightly lower performance of regenerated catalyst slightly lowered compared to fresh catalyst may be due to the increase of Ni crystallite size (from 37 to 40 nm) as well as due to structural change in the support as observed in pore size analysis.

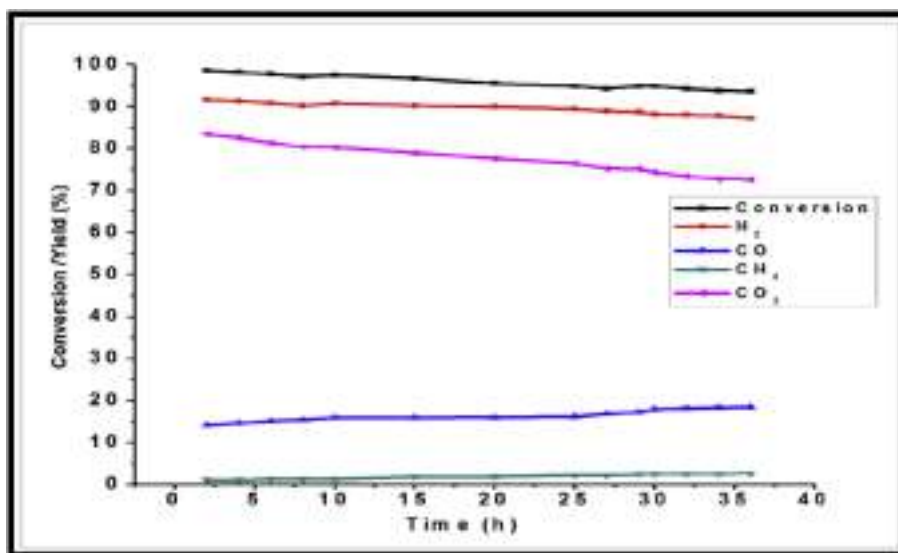


Fig. 11 – AcOH conversion and yield of gaseous product versus reaction time over 15%Ni-Comp/ALC catalyst. Reaction condition: temperature-600 °C; N₂; Feed flow rate-2.5 mL/h; and S/C- 6.5.

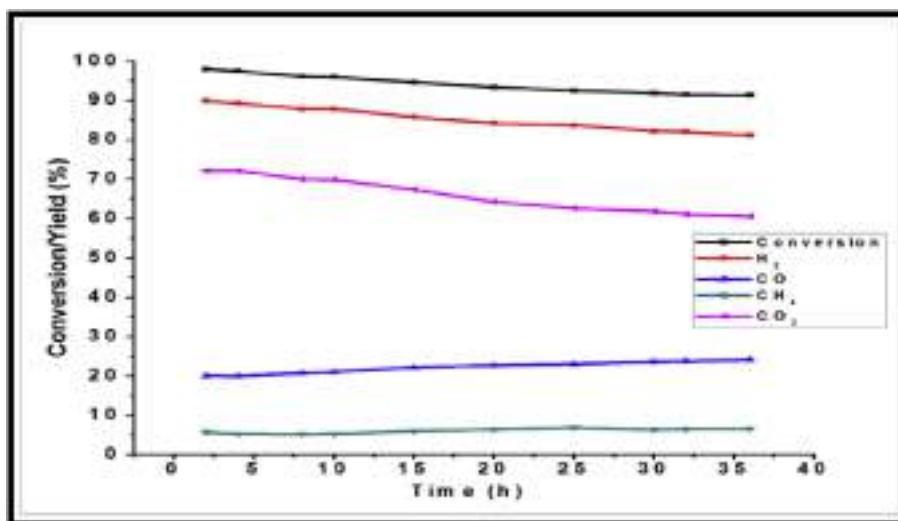


Fig. 12 – AcOH conversion and Yield of gaseous products versus reaction time over regenerated 15% Ni-Comp/ALC catalyst. Reaction condition: temperature-600 °C; N₂ flow rate- 30 mL/min; feed flow rate-2.5 mL/h; and S/C- 6.5 mol/mol.

Conclusions

A new porous ordered Ni-Complex/ALC catalyst was synthesized via MOF process was investigated. At constant operating conditions (S/C = 6.5, feed flow rate = 2.5 mL/h) the increase in the temperature range from 400 to 650 °C conversion increases while in case of H₂ yield it increases up to 600 °C and then slightly decreases after 600 °C due to RWGS reaction dominating at high temperature. The results showed that during the AASR, H₂, CO, CH₄, and CO₂ were main product gases whereas maximum hydrogen yield of 91.3% was obtained at temperature 600 °C. The temperatures and S/C ratio were observed to be the key parameters, while feed flow rate of AcOH/H₂O mixture

showed only marginal effect during AASR. The catalyst was deactivated by coke deposition. Amorphous as well as graphitic type of coke were found to get deposited on the surface of deactivated catalyst. Deactivated catalyst had lower surface area and pores of larger diameter compared to those of fresh catalyst. The deactivation studies of Ni-Complex/ALC catalyst showed excellent stability up to 36 h TOS. Catalyst regeneration of spent catalyst was achieved by flowing oxygen over the catalyst at 500 °C followed by reduction by H₂ gas. Regenerated catalyst regained the surface area, pore volume and nearly same activity as that of a fresh catalyst. Sintering of Ni particles was not significant. It has been attributed to the existence of nickel-support interaction.

REFERENCES

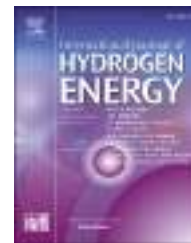
- [1] Kumar A, Sinha ASK. Comparative study of hydrogen production from steam reforming of acetic acid over synthesized catalysts via MOF and wet impregnation methods. *Int J Hydrogen Energy* 2020;45(20):11512–26.
- [2] Choi I-H, Hwang K-R, Lee K-Y, Lee I-G. Catalytic steam reforming of biomass-derived acetic acid over modified Ni/ γ -Al₂O₃ for sustainable hydrogen production. *Int J Hydrogen Energy* 2019;44:180–90.
- [3] Nabgan W, Tuan Abdullah TA, Mat R, Nabgan B, Gambo Y, Ibrahim M, et al. Renewable hydrogen production from bio-oil derivative via catalytic steam reforming: an overview. *Renew Sustain Energy Rev* 2017;79:347–57.
- [4] Zhang Z, Hu X, Li J, Gao G, Dong D, Westerhof R, et al. Steam reforming of acetic acid over Ni/Al₂O₃ catalysts: correlation of nickel loading with properties and catalytic behaviors of the catalysts. *Fuel* 2018;217:389–403.
- [5] Kumar A, Chakraborty JP, Singh R. Bio-oil: the future of hydrogen generation. *Biofuels* 2017;8:663–74.
- [6] Kumar A, Singh R, Sinha ASK. Catalyst modification strategies to enhance the catalyst activity and stability during steam reforming of acetic acid for hydrogen production. *Int J Hydrogen Energy* 2019;44:12983–3010.
- [7] Hu X, Zhang L, Lu G. Steam reforming of acetic acid over CuZnCo catalyst for hydrogen generation: synergistic effects of the metal species. *Int J Hydrogen Energy* 2016;41:13960–9.
- [8] Li Z, Wu Y, Lu G. Highly efficient hydrogen evolution over Co(OH)₂ nanoparticles modified g-C₃N₄ co-sensitized by Eosin Y and Rose Bengal under Visible Light Irradiation. *Appl Catal B Environ* 2016;188:56–64.
- [9] Nabgan W, Abdullah TAT, Mat R, Nabgan B, Jalil AA, Firmansyah L, et al. Production of hydrogen via steam reforming of acetic acid over Ni and Co supported on La₂O₃ catalyst. *Int J Hydrogen Energy* 2017;42:8975–85.
- [10] Xue Y-p, Yan C-f, Zhao X-y, Huang S-l, Guo C-q. Ni/La₂O₃-ZrO₂ catalyst for hydrogen production from steam reforming of acetic acid as a model compound of bio-oil. *Kor J Chem Eng* 2017;34:305–13.
- [11] Ma Z, Xiao R, Zhang H. Catalytic steam reforming of bio-oil model compounds for hydrogen-rich gas production using bio-char as catalyst. *Int J Hydrogen Energy* 2017;42:3579–85.
- [12] Staš M, Kubička D, Chudoba J, Pospíšil M. Overview of analytical methods used for chemical characterization of pyrolysis bio-oil. *Energy and Fuels* 2014;28:385–402.
- [13] Quitete CPB, Tavares RPA, Bittencourt RCP, Souza MMVM. Coking study of nickel catalysts using model compounds. *Catal Lett* 2016;146:1435–44.
- [14] Hoang TMC, Geerdink B, Sturm JM, Lefferts L, Seshan K. Steam reforming of acetic acid - a major component in the volatiles formed during gasification of humin. *Appl Catal B Environ* 2015;163:74–82.
- [15] Vagia EC, Lemonidou AA. Investigations on the properties of ceria-zirconia-supported Ni and Rh catalysts and their performance in acetic acid steam reforming. *J Catal* 2010;269:388–96.
- [16] Vagia EC, Lemonidou AA. Thermodynamic analysis of hydrogen production via autothermal steam reforming of selected components of aqueous bio-oil fraction. *Int J Hydrogen Energy* 2008;33:2489–500.
- [17] Vagia EC, Lemonidou AA. Thermodynamic analysis of hydrogen production via steam reforming of selected components of aqueous bio-oil fraction. *Int J Hydrogen Energy* 2007;32:212–23.
- [18] Garcia L, French R, Czernik S, Chornet E. Catalytic steam reforming of bio-oils for the production of hydrogen: effects of catalyst composition. *Appl Catal Gen* 2000;201:225–39.
- [19] Assaf PGM, Nogueira FGE, Assaf EM. Ni and Co catalysts supported on alumina applied to steam reforming of acetic acid: representative compound for the aqueous phase of bio-oil derived from biomass. *Catal Today* 2013;213:2–8.
- [20] Cheng F, Dupont V. Nickel catalyst auto-reduction during steam reforming of bio-oil model compound acetic acid. *Int J Hydrogen Energy* 2013;38:15160–72.
- [21] Hu X, Lu G. Steam reforming of acetic acid to hydrogen over Fe-Co catalyst. *Chem Lett* 2006;35:452–3.
- [22] Pu J, Luo Y, Wang N, Bao H, Wang X, Qian EW. Ceria-promoted Ni@Al₂O₃ core-shell catalyst for steam reforming of acetic acid with enhanced activity and coke resistance. *Int J Hydrogen Energy* 2018;43:3142–53.
- [23] Hu X, Dong D, Shao X, Zhang L, Lu G. Steam reforming of acetic acid over cobalt catalysts: effects of Zr, Mg and K addition. *Int J Hydrogen Energy* 2017;42:4793–803.
- [24] Vicente J, Montero C, Ereña J, Azkoiti MJ, Bilbao J, Gayubo AG. Coke deactivation of Ni and Co catalysts in ethanol steam reforming at mild temperatures in a fluidized bed reactor. *Int J Hydrogen Energy* 2014;39:12586–96.
- [25] Resende KA, Ávila-Neto CN, Rabelo-Neto RC, Noronha FB, Hori CE. Hydrogen production by reforming of acetic acid using La-Ni type perovskites partially substituted with Sm and Pr. *Catal Today* 2015;242:71–9.
- [26] Zhang F, Wang M, Zhu L, Wang S, Zhou J, Luo Z. A comparative research on the catalytic activity of La₂O₃ and Γ -Al₂O₃ supported catalysts for acetic acid steam reforming. *Int J Hydrogen Energy* 2017;42:3667–75.
- [27] Goicoechea S, Krалева E, Sokolov S, Schneider M, Pohl M-M, Kockmann N, et al. Support effect on structure and performance of Co and Ni catalysts for steam reforming of acetic acid. *Appl Catal Gen* 2016;514:182–91.
- [28] Basagiannis AC, Verykios XE. Reforming reactions of acetic acid on nickel catalysts over a wide temperature range. *Appl Catal Gen* 2006;308:182–93.
- [29] Basagiannis AC, Verykios XE. Influence of the carrier on steam reforming of acetic acid over Ru-based catalysts. *Appl Catal B Environ* 2008;82:77–88.
- [30] Chen G, Tao J, Liu C, Yan B, Li W, Li X. Hydrogen production via acetic acid steam reforming: a critical review on catalysts. *Renew Sustain Energy Rev* 2017;79:1091–8.
- [31] Goicoechea S, Krалева E, Ehrich H. Effect of Al₂O₃/ZnO ratio on Ni(Co)-AlZnOx catalysts for syngas production by steam reforming of acetic acid. *Catal Lett* 2017;147:1403–10.
- [32] Zhang C, Hu X, Yu Z, Zhang Z, Chen G, Li C, et al. Steam reforming of acetic acid for hydrogen production over attapulgite and alumina supported Ni catalysts: impacts of properties of supports on catalytic behaviors. *Int J Hydrogen Energy* 2019;44:5230–44.
- [33] Shejale AD, Yadav GD. Cu promoted Ni-Co/hydrotalcite catalyst for improved hydrogen production in comparison with several modified Ni-based catalysts via steam reforming of ethanol. *Int J Hydrogen Energy* 2017;42:11321–32.
- [34] Sahebdelfar S. Steam reforming of propionic acid: thermodynamic analysis of a model compound for hydrogen production from bio-oil. *Int J Hydrogen Energy* 2017;42:16386–95.
- [35] Mizuno T, Matsumura Y, Nakajima T, Mishima S. Effect of support on catalytic properties of Rh catalysts for steam reforming of 2-propanol. *Int J Hydrogen Energy* 2003;28:1393–9.
- [36] Basagiannis AC, Verykios XE. Catalytic steam reforming of acetic acid for hydrogen production. *Int J Hydrogen Energy* 2007;32:3343–55.
- [37] Wang D, Czernik S, Montané D, Mann M, Chornet E. Biomass to hydrogen via fast pyrolysis and catalytic steam reforming of the pyrolysis oil or its fractions. *Ind Eng Chem Res* 1997;36:1507–18.

- [38] Wang S, Zhang F, Cai Q, Zhu L, Luo Z. Steam reforming of acetic acid over coal ash supported Fe and Ni catalysts. *Int J Hydrogen Energy* 2015;40:11406–13.
- [39] Galdámez JR, García L, Bilbao R. Hydrogen production by steam reforming of bio-oil using coprecipitated Ni–Al catalysts. Acetic acid as a model compound. *Energy & Fuels* 2005;19:1133–42.
- [40] Iwasa N, Yamane T, Arai M. Influence of alkali metal modification and reaction conditions on the catalytic activity and stability of Ni containing smectite-type material for steam reforming of acetic acid. *Int J Hydrogen Energy* 2011;36:5904–11.
- [41] Thairachoencharittham S, Meeyoo V, Kitiyanan B, Rangsunvigit P, Rirksomboon T. Hydrogen production by steam reforming of acetic acid over Ni-based catalysts. *Catal Today* 2011;164:257–61.
- [42] Iwasa N, Yamane T, Takei M, Ozaki J-i, Arai M. Hydrogen production by steam reforming of acetic acid: comparison of conventional supported metal catalysts and metal-incorporated mesoporous smectite-like catalysts. *Int J Hydrogen Energy* 2010;35:110–7.
- [43] Hu X, Lu G. Inhibition of methane formation in steam reforming reactions through modification of Ni catalyst and the reactants. *Green Chem* 2009;11:724–32.
- [44] Hu X, Lu G. Acetic acid steam reforming to hydrogen over Co–Ce/Al₂O₃ and Co–La/Al₂O₃ catalysts—the promotion effect of Ce and La addition. *Catal Commun* 2010;12:50–3.
- [45] Zhao X, Xue Y, Yan C, Huang Y, Lu Z, Wang Z, et al. Promoted activity of porous silica coated Ni/CeO₂ZrO₂ catalyst for steam reforming of acetic acid. *Int J Hydrogen Energy* 2017;42:21677–85.
- [46] Kugai J, Velu S, Song C. Low-temperature reforming of ethanol over CeO₂-supported Ni–Rh bimetallic catalysts for hydrogen production. *Catal Lett* 2005;101:255–64.
- [47] Sugisawa M, Takanabe K, Harada M, Kubota J, Domen K. Effects of La addition to Ni/Al₂O₃ catalysts on rates and carbon deposition during steam reforming of n-dodecane. *Fuel Process Technol* 2011;92:21–5.
- [48] Li L, Jiang B, Tang D, Zhang Q, Zheng Z. Hydrogen generation by acetic acid steam reforming over Ni-based catalysts derived from La_{1–x}Ce_xNiO₃ perovskite. *Int J Hydrogen Energy* 2018;43:6795–803.
- [49] Trane-Restrup R, Jensen AD. Steam reforming of cyclic model compounds of bio-oil over Ni-based catalysts: product distribution and carbon formation. *Appl Catal B Environ* 2015;165:117–27.
- [50] Basagiannis AC, Verykios XE. Catalytic steam reforming of acetic acid for hydrogen production. *Int J Hydrogen Energy* 2007;32:3343–55.
- [51] An L, Dong C, Yang Y, Zhang J, He L. The influence of Ni loading on coke formation in steam reforming of acetic acid. *Renew Energy* 2011;36:930–5.
- [52] Lemonidou AA, Vagia EC, Lercher JA. Acetic acid reforming over Rh supported on La₂O₃/CeO₂–ZrO₂: catalytic performance and reaction pathway analysis. *ACS Catal* 2013;3:1919–28.
- [53] Hu X, Lu G. Comparative study of alumina-supported transition metal catalysts for hydrogen generation by steam reforming of acetic acid. *Appl Catal B Environ* 2010;99:289–97.
- [54] Medrano JA, Oliva M, Ruiz J, García L, Arauzo J. Catalytic steam reforming of model compounds of biomass pyrolysis liquids in fluidized bed reactor with modified Ni/Al catalysts. *J Anal Appl Pyrol* 2009;85:214–25.
- [55] Li CY, Yu CC, Shen SK. Studies on the transformation of carbon species from CH₄ decomposition over a Ni/Al₂O₃ catalyst. *Hua Hsueh Hsueh Pao* 2000;58:1188–90.
- [56] Wang S, Li X, Guo L, Luo Z. Experimental research on acetic acid steam reforming over Co–Fe catalysts and subsequent density functional theory studies. *Int J Hydrogen Energy* 2012;37:11122–31.
- [57] Wang S, Zhang F, Cai Q, Li X, Zhu L, Wang Q, et al. Catalytic steam reforming of bio-oil model compounds for hydrogen production over coal ash supported Ni catalyst. *Int J Hydrogen Energy* 2014;39:2018–25.
- [58] Borges R, Ferreira R, Rabelo-Neto RC, Noronha FB, Hori C. Hydrogen production by steam reforming of acetic acid using hydrotalcite type precursors. *Int J Hydrogen Energy* 2018;43:7881–92.
- [59] Takanabe K, Aika K-i, Seshan K, Lefferts L. Catalyst deactivation during steam reforming of acetic acid over Pt/ZrO₂. *Chem Eng J* 2006;120:133–7.
- [60] Bizkarra K, Bermudez JM, Arcelus-Arillaga P, Barrio VL, Cambra JF, Millan M. Nickel based monometallic and bimetallic catalysts for synthetic and real bio-oil steam reforming. *Int J Hydrogen Energy* 2018;43:11706–18.
- [61] Zanchet D, Santos JBO, Damyanova S, Gallo JMR, Bueno JMC. Toward understanding metal-catalyzed ethanol reforming. *ACS Catal* 2015;5:3841–63.
- [62] Li X, Wang S, Cai Q, Zhu L, Yin Q, Luo Z. Effects of preparation method on the performance of Ni/Al₂O₃ catalysts for hydrogen production by bio-oil steam reforming. *Appl Biochem Biotechnol* 2012;168:10–20.
- [63] Chen SQ, Wang H, Liu Y. Perovskite La–St–Fe–O (St=Ca, Sr) supported nickel catalysts for steam reforming of ethanol: the effect of the A site substitution. *Int J Hydrogen Energy* 2009;34:7995–8005.
- [64] Wang M, Zhang F, Wang S. Effect of La₂O₃ replacement on γ -Al₂O₃ supported nickel catalysts for acetic acid steam reforming. *Int J Hydrogen Energy* 2017;42:20540–8.
- [65] Pu J, Ikegami F, Nishikado K, Qian EW. Effect of ceria addition on Ni[sbnd]Ru/CeO₂[sbnd]Al₂O₃ catalysts in steam reforming of acetic acid. *Int J Hydrogen Energy* 2017;42:19733–43.
- [66] Bizkarra K, Bermudez J, Arcelus-Arillaga P, Barrio V, Cambra J, Millan M. Nickel based monometallic and bimetallic catalysts for synthetic and real bio-oil steam reforming. *Int J Hydrogen Energy* 2018;43:11706–18.
- [67] Isarapakdeetham S, Kim-Lohsoontorn P, Wongsakulphasatch S, Kiatkittipong W, Laosiripojana N, Gong J, et al. Hydrogen production via chemical looping steam reforming of ethanol by Ni-based oxygen carriers supported on CeO₂ and La₂O₃ promoted Al₂O₃. *Int J Hydrogen Energy* 2020;45:1477–91.
- [68] Feng H, Lan P, Wu S. A study on the stability of a NiO–CaO/Al₂O₃ complex catalyst by La₂O₃ modification for hydrogen production. *Int J Hydrogen Energy* 2012;37:14161–6.
- [69] de Freitas Silva T, Reis CGM, Lucrédio AF, Assaf EM, Assaf JM. Hydrogen production from oxidative reforming of methane on Ni/ γ -Al₂O₃ catalysts: effect of support promotion with La, La–Ce and La–Zr. *Fuel Process Technol* 2014;127:97–104.
- [70] Matas Güell B, Silva IMTD, Seshan K, Lefferts L. Sustainable route to hydrogen – design of stable catalysts for the steam gasification of biomass related oxygenates. *Appl Catal B Environ* 2009;88:59–65.
- [71] Valle B, Remiro A, Aguayo A, Bilbao J, Gayubo A. Catalysts of Ni/a-Al₂O₃ and Ni/La₂O₃-aAl₂O₃ for hydrogen production by steam reforming of bio-oil aqueous fraction with pyrolytic lignin retention. *Int J Hydrogen Energy* 2013;38:130.
- [72] Phongprueksathat N, Meeyoo V, Rirksomboon T. Steam reforming of acetic acid for hydrogen production: catalytic performances of Ni and Co supported on Ce_{0.75}Zr_{0.25}O₂ catalysts. *Int J Hydrogen Energy* 2019;44:9359–67.

- [73] Pu J, Luo Y, Wang N, Bao H, Wang X, Qian EW. Ceria-promoted Ni@ Al₂O₃ core-shell catalyst for steam reforming of acetic acid with enhanced activity and coke resistance. *Int J Hydrogen Energy* 2018;43:3142–53.
- [74] Pu J, Ikegami F, Nishikado K, Qian EW. Effect of ceria addition on NiRu/CeO₂Al₂O₃ catalysts in steam reforming of acetic acid. *Int J Hydrogen Energy* 2017;42:19733–43.
- [75] Arandia A, Remiro A, Oar-Arteta L, Bilbao J, Gayubo AG. Reaction conditions effect and pathways in the oxidative steam reforming of raw bio-oil on a Rh/CeO₂-ZrO₂ catalyst in a fluidized bed reactor. *Int J Hydrogen Energy* 2017;42:29175–85.
- [76] Han X, Yu Y, He H, Shan W. Hydrogen production from oxidative steam reforming of ethanol over rhodium catalysts supported on Ce–La solid solution. *Int J Hydrogen Energy* 2013;38:10293–304.
- [77] Wang Y, Chen M, Liang T, Yang Z, Yang J, Liu S. Hydrogen generation from catalytic steam reforming of acetic acid by Ni/attapulgit catalysts. *Catalysts* 2016;6:172.
- [78] Yang SJ, Im JH, Kim T, Lee K, Park CR. MOF-derived ZnO and ZnO@C composites with high photocatalytic activity and adsorption capacity. *J Hazard Mater* 2011;186:376–82.
- [79] Navarro RM, Álvarez-Galván MC, Rosa F, Fierro JLG. Hydrogen production by oxidative reforming of hexadecane over Ni and Pt catalysts supported on Ce/La-doped Al₂O₃. *Appl Catal Gen* 2006;297:60–72.
- [80] Church JS, Cant NW, Trimm DL. Stabilisation of aluminas by rare earth and alkaline earth ions. *Appl Catal Gen* 1993;101:105–16.
- [81] Ahmad M, Asghar A, Abdul Raman AA, Wan Daud WMA. Enhancement of treatment efficiency of recalcitrant wastewater containing textile dyes using a newly developed iron zeolite socony mobil-5 heterogeneous catalyst. *PloS One* 2015;10:e0141348.
- [82] Parveen N, Nazir R, Mazhar M. Thermal degradation pathways of nickel (II) bipyridine complexes to size-controlled nickel nanoparticles. *J Therm Anal Calorim* 2013;111:93–9.
- [83] Italiano C, Bizkarra K, Barrio VL, Cambra JF, Pino L, Vita A. Renewable hydrogen production via steam reforming of simulated bio-oil over Ni-based catalysts. *Int J Hydrogen Energy* 2019;44:14671–82.
- [84] Leary KJ. In: Jones Alan, McNicol Brian D, editors. Temperature programmed reduction for solid materials characterization (Chemical Industries Series, 24. Marcel Dekker, Inc.; 1986. p. 208. \$59.75. *AIChE Journal*. 1987;33:1407–8.
- [85] Nogueira FGE, Assaf PGM, Carvalho HWP, Assaf EM. Catalytic steam reforming of acetic acid as a model compound of bio-oil. *Appl Catal B Environ* 2014;160–161:188–99.
- [86] Goicoechea S, Ehrich H, Arias PL, Kockmann N. Thermodynamic analysis of acetic acid steam reforming for hydrogen production. *J Power Sources* 2015;279:312–22.
- [87] Robinson AM, Hensley JE, Medlin JW. Bifunctional catalysts for upgrading of biomass-derived oxygenates: a review. *ACS Catal* 2016;6:5026–43.
- [88] Phongprueksathat N, Meeyoo V, Rirksomboon T. Steam reforming of acetic acid for hydrogen production: catalytic performances of Ni and Co supported on CeO₂-75ZrO₂-25O₂ catalysts. *Int J Hydrogen Energy* 2019;44:9359–67.
- [89] Takanabe K, Aika K-i, Inazu K, Baba T, Seshan K, Lefferts L. Steam reforming of acetic acid as a biomass derived oxygenate: bifunctional pathway for hydrogen formation over Pt/ZrO₂ catalysts. *J Catal* 2006;243:263–9.
- [90] Markevich M, Czernik S, Chornet E, Montané D. Hydrogen from Biomass: steam reforming of model compounds of fast-pyrolysis oil. *Energy & Fuels* 1999;13:1160–6.
- [91] Sánchez-Sánchez MC, Navarro RM, Fierro JLG. Ethanol steam reforming over Ni/La–Al₂O₃ catalysts: influence of lanthanum loading. *Catal Today* 2007;129:336–45.
- [92] Lu P, Huang Q, Chi Y, Yan J. Coking and regeneration of nickel catalyst for the cracking of toluene as a tar model compound. *Energy & Fuels* 2017;31:8283–90.
- [93] Wang Y, Luo G, Xu X, Xia J. Deactivation of supported skeletal Ni catalyst and effect of regeneration temperature on its catalytic performance. *Catal Commun* 2014;57:83–8.

Available online at www.sciencedirect.com

ScienceDirect

journal homepage: www.elsevier.com/locate/ijhydene

Effect of catalyst layer with zeolite on the performance of a proton exchange membrane fuel cell operated under low-humidity conditions

Ankit Kumar ^a, Hsiao-Chun Su ^b, Yong-Song Chen ^{b,*},
Amornchai Arpornwichanop ^{c,**}

^a Department of Chemical Engineering & Technology, Indian Institute of Technology, (BHU), Varanasi-221005, India

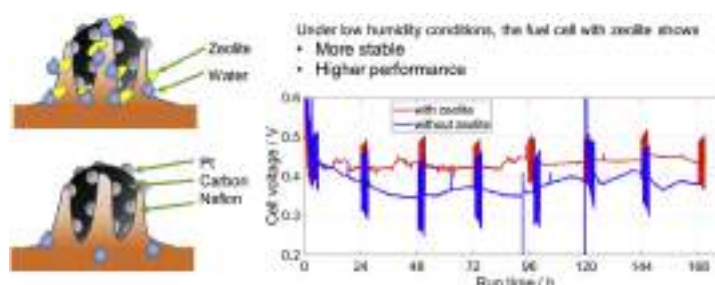
^b Department of Mechanical Engineering and Advanced Institute of Manufacturing with High-tech Innovations, National Chung Cheng University, 168, University Rd., Minhsiung Township, Chiayi county, 62102, Taiwan

^c Center of Excellence in Process and Energy Systems Engineering, Department of Chemical Engineering, Faculty of Engineering, Chulalongkorn University, Bangkok, 10330, Thailand

HIGHLIGHTS

- Optimum catalyst composition for dry hydrogen operation is obtained.
- Pt loadings are 0.1 and 0.7 mg cm⁻² for the anode and cathode, respectively.
- Nation-to-carbon ratio of 0.5 presents best cell performance.
- Zeolite-to-carbon ratio of 0.3 in the anode presents stable cell performance.
- Mass transport Impedance of the cell with zeolite is reduced.

GRAPHICAL ABSTRACT



ARTICLE INFO

Article history:

Received 10 July 2020

Received in revised form

3 February 2021

Accepted 4 February 2021

Available online 1 March 2021

Keywords:

Proton exchange membrane fuel cell

Low humidity

ABSTRACT

Proton exchange membrane fuel cells (PEMFCs) employ a proton conductive membrane as the separator to transport a hydrogen proton from the anode to the cathode. The membrane's proton conductivity depends on the water content in the membrane, which is affected by the operating conditions. A membrane electrode assembly (MEA) that can self-sustain water is the key component for developing a light-weight and compact PEMFC system without humidifiers. Hence, zeolite is employed to the anode catalyst layer in this study. The effect of the gas diffusion layer (GDL) materials, catalyst loading, binder loading, and zeolite loading on the MEA performance is investigated. The MEA durability is also investigated through the electrochemical impedance spectroscopy (EIS) method. The results suggest that the MEA with the SGL28BCE carbon paper, Pt loadings of 0.1 and

* Corresponding author.

** Corresponding author.

E-mail addresses: imeysc@ccu.edu.tw (Y.-S. Chen), amornchai.a@chula.ac.th (A. Arpornwichanop).

<https://doi.org/10.1016/j.ijhydene.2021.02.033>

0360-3199/© 2021 Hydrogen Energy Publications LLC. Published by Elsevier Ltd. All rights reserved.

Membrane electrode assembly
Durability
Zeolite

0.7 mg cm⁻² in the anode and cathode, respectively, Nafion-to-carbon weight ratio of 0.5, and zeolite-to-carbon weight ratio of 0.3 showed the best performance when the cell temperature is 60 °C and supplies with dry hydrogen and air from the environment. According to the impedance variation measured by EIS, the MEA with zeolite in the anode catalyst layer shows higher and more stable performance than those without zeolite.

© 2021 Hydrogen Energy Publications LLC. Published by Elsevier Ltd. All rights reserved.

Introduction

Among all types of fuel cells, the proton exchange membrane fuel cell (PEMFC) is considered as a promising power source for unmanned aerial vehicles due to high energy density, higher efficiency, and low emission [1,2]. Despite these advantages, cost and degradation of the membrane electrode assemblies (MEAs) remain as the main issue for PEMFC commercialization [3,4]. Moreover, the requirement of the cathode humidifier increases the weight and system complexity of PEMFCs and limits their applications. Since the 1960s [5], continuous attempts have been made to commercialize PEMFCs by achieving high-power density for an allocated cost. The PEMFC performance depends on various factors, such as the electrocatalytic activity in the catalyst layer (CL), physical property of gas diffusion layers (GDLs), MEA fabrication process, and operating conditions.

Researchers have been focusing on the catalyst loading reduction to reduce the cost of PEMFCs and to lower the ohmic resistance of CLs [6,7]. The CL consisting of a metal catalyst (Pt) and an ionic conductor (Nafion) is considered to be the key component of the MEA because of the hydrogen oxidation and oxygen reduction sites [8]. Carbon is a vital support material acting as a high-surface-area substrate for the structuring and proper dispersion of Pt or Pt-alloy nanoparticles [9–12]. However, carbon may suffer from low corrosion endurance because of the electrochemical oxidation of the carbon surface [13–16]. This shortcoming results in a Pt dissolution or aggregation, which causes the decay of performance and durability.

Appropriate Nafion content in the CL is also a factor to achieve high MEA performance. Several studies have been previously published on the effect of Nafion content in the CL on MEA performance. Passalacqua et al. [17] and Gamburzev et al. [18] reported the optimum Nafion content to be 33 wt%, while Qi and Kaufman [19] reported an optimum Nafion content of 30 wt%, irrespective of the Pt loading in the electrodes. Sasikumar et al. [20] have indicated the dependence of optimum Nafion content on Pt loading and independent of membrane thickness. Nafion loadings of 20, 40 and 50 wt% resulted in better performance at Pt loadings of 0.5, 0.25 and 0.1 mg Pt cm⁻², respectively.

Furthermore, Jeon et al. [21] and Kim et al. [22] studied the optimum ionomer content and found that it increased with decreasing humidity. The MEA with 20 wt% ionomer content at 87% humidity and the MEA with an ionomer content of 25 wt% at a relative humidity of 59% have shown the best performance. Cho et al. [23] showed the similar result,

presenting MEA drying became prominent over cathode flooding. Experimental data revealed that compared to that using a conventional single CL, the power density increased by 135.7% under a low-humidity operation of the PEMFC with a double-CL MEA. Kim et al. [24] studied the effect of the Nafion gradient on the CL of PEMFCs and revealed the achievement of a higher cell performance at higher-density regions.

PEMFC durability is also significantly dependent on the GDL composition. Various GDL parameters like thickness, carbon fiber arrangement, and hydrophobicity contribute to water management in fuel cells. Accordingly, studies on the influence of different GDLs on fuel cell performances have been conducted [25,26]. A few studies have shown that ionomer incorporation into a gas diffusion electrode (GDE) significantly increases the performance because of ink viscosity and dielectric constant [27]. The GDL hydrophobicity loss caused by the PTFE degradation, which results in the mass transport loss after a long-term operation, is a major issue [28,29].

The fabrication procedure of the MEA also significantly affects performance. Benítez et al. [30] experimentally showed that the MEA preparation by the electrospray method exhibited three times higher power density compared to that of the conventional impregnation method for the Pt loading of 0.5 mg cm⁻². Likewise, Millington et al. [31] performed a comparative study on the use of the ultrasonic spraying technology for preparing CL with that of hand-painted GDEs. Consequently, they confirmed that ultrasonic-sprayed GDEs at a low Pt loading exhibited a better performance compared to the latter. However, a limited number of reports on the use of ionomer concentration and additives in the catalyst ink along with humidification to be maintained during the cell operation exists. Chen et al. [32] reported about the gradient design of the Pt/C ratio and the Nafion content through a double-layer construction in the CL. The optimal gradient design exhibited a better performance at low-humidity operating conditions.

To enhance the performance of MEAs under low humidity environment, water-absorbent has been introduced to the MEA to keep generated water for membrane humidification. Nanocomposite membranes with inorganic or inorganic–organic particles dispersed in perfluorosulfonic acid (PFSA) had also recently been extensively studied [33–35]. Nowadays, zeolites are considered potential candidates for water absorbent materials in the membrane because of their thermostability and water retention capacity [36], which are attributed to their cationic mobility [37]. Some studies have shown the dispersion of the fine particles of zeolites for preparing the composite

membranes of PEMFCs (i.e., zeolite-PFSA [38], zeolite-sulfonated polyether ketone [39–41], and zeolite-polyfluoro ethylene [42,43]), but the particle aggregation and increase in transport resistance are still major issues [44,45]. To our best knowledge, the effects of zeolite in the CL on the MEA performance and durability have not been widely investigated.

This research presents the development of self-humidified MEAs for application under low-humidity environments. The CL is optimized after being sprayed through the ultrasonic method. Essential parameters, such as catalyst loading, ionomer concentration, zeolite addition, and GDL, are investigated. Furthermore, the I–V characteristic curves of the optimized values of the variables in a single cell with different operating conditions are measured and compared. Finally, the long-term operation under low-humidity conditions and the PEMFC impedance variation are studied via electrochemical impedance spectroscopy (EIS).

Experimental

Catalyst ink preparation

The catalyst inks used in the experiments were prepared using a 46.4% Pt/C (TEC10E50E, Tanaka K.K., Japan), ethanol, zeolite, and Nafion ionomer in isopropanol alcohol (IPA). The mixtures were uniformly stirred in a planetary mixer (ARE-310, Thinky, Japan) at 2000 rpm for 30 min. The catalyst inks were then sprayed by an ultrasonic spraying system (Prism 400BT, USI, USA). The spraying parameters were with a liquid flow rate of 0.4 mL min⁻¹, head speed of 60 mm s⁻¹, spray pitch of 5 mm, and head-to-substrate distance of 4 mm, as suggested by the manufacturer of the spraying system. The sonication power is normally less than 5 W depending on the spraying loading. The catalyst ink supplied from a syringe was continuously stirred by a rotating magnet to avoid deposition during the spraying process. The hot plate temperature was 95 °C to remove IPA during spraying. The catalyst was sprayed on three substrates individually and the catalyst weight on each substrate was compared. The weight difference was ensured to be less than 10% before catalyst was sprayed on both sides of the 25- μ m-thick membrane (Nafion HP, Dupont, USA) with an active area of 25 cm². The ink preparation and spraying procedures have not been optimized but kept consistent for all tests in this study.

The Pt loading on the anode side was fixed as 0.1 mg cm⁻², whereas that on the cathode side was selected as 0.3, 0.5, 0.7, and 1.0 Pt mg cm⁻². The Nafion solution (D2020, Dupont, USA) was mixed with Pt/C at various Nafion-to-carbon weight ratios (NC ratio) of 0.5:1, 0.6:1, 0.7:1, and 0.8:1.

Performance evaluation

The fuel cell was prepared by sandwiching the catalyst-coated membrane and different types of GDLs, flow field plates, current collectors, and end plates. In this experiment, the performances of GDLs from two different companies, namely Sigracet (SGL28BCE, SGL29BCE, and SGL38BCE) and CeTech (N1S1007 and GDL240), were tested. The cell performances of different samples of the NC ratio at different humidification

temperatures and cathode Pt loadings were recorded by a fuel cell testing system (HS330S, Hephase Energy, Taiwan). Pure hydrogen (99.99%) and air were fed into the anode and cathode with stoichiometric ratios of 1.2 and 2.2, respectively, for activation and performance evaluation. The MEAs were activated at a cell temperature of 70 °C for 12 h followed by performance evaluation, during which the fuel cell was operated at selected current density for 5 min to get stable voltage before moving to the next current density.

Different testing processes were performed at different cell and humidification temperatures, called C70H70, C70H60, C60H60, C60H50, C60H40, and C60H30, where CXHY stands for the cell temperature at X °C and the humidifier temperature at Y °C. Table 1 lists the operating conditions of the various cell and humidifier temperatures.

Results and discussion

Effect of GDL on the cell performance

For the investigation of the effect of GDL types on the cell performance, the anode and cathode Pt loadings were 0.1 and 0.3 mg cm⁻², respectively. The NC ratio was maintained as 0.7 for all the MEAs. Fig. 1 shows the current density of the MEAs measured at 0.6 V of the I–V characteristic curves for each of the five GDLs at six different testing cases. SGL28BCE provided a better performance when operated at C60H40, and C60H30, whereas GDL240 proved to be the right candidate under the operating conditions of C60H50, C60H60, C70H60 and C70H70, which can be attributed to its high air permeability. However, the cell performance using N1S1007 was inferior among all the GDLs because of its higher electrical resistivity.

Table 2 presents the typical properties of the GDLs, such as thickness, air permeability, and electrical resistivity. The presence of carbon-based microporous layers (MPLs) attached by sintering to the GDLs enhanced mechanical properties like shear stress, compression, and bending, which determined the electrical and thermal conductivities. The hydrophobic nature of SGL28BCE, SGL29BCE, and SGL38BCE GDLs is attributed to substrate loading with 5% PTFE of the GDLs. Among SGL28BCE, SGL29BCE, and SGL38BCE GDLs, SGL29BCE was not up to the mark in performance for the operating conditions C60H30 and C60H40, which may be attributed to less electrical conductivity through the plane compared to the other GDLs. However, SGL28BCE and SGL38BCE had similar performances at the low humidity conditions (C60H30 and C60H40). Furthermore, under low-humidity conditions, SGL28BCE and

Table 1 – Operating conditions.

Case	Cell temperature (C)	Humidifier temperature (C)	Relative humidity (%)
C70H70	70	70	100
C70H60	70	60	63.9
C60H60	60	60	100
C60H50	60	50	61.9
C60H40	60	40	37.0
C60H30	60	30	21.3

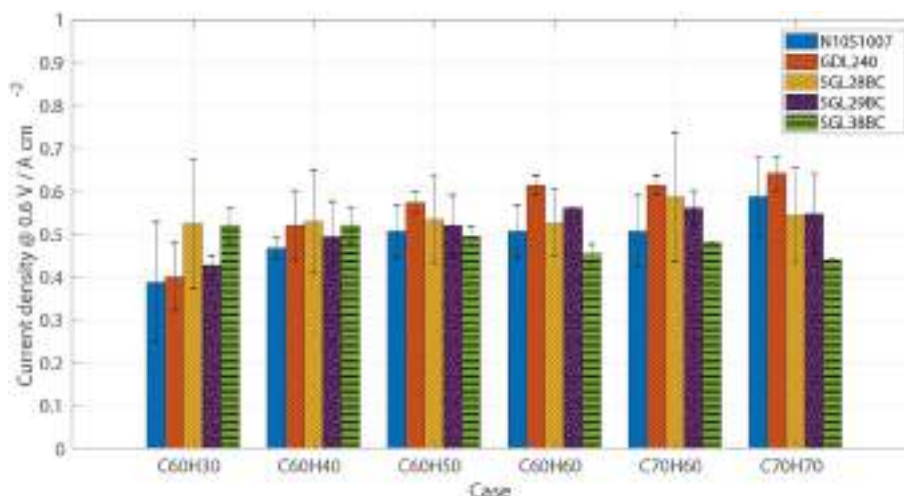


Fig. 1 – Current density measured at 0.6 V for different GDLs at different operating conditions.

Table 2 – Typical materials data of GDLs. (Ref: SGL Group and CeTech).

properties	Unit	N1S1007	GDL240	SGL28BCE	SGL29BCE	SGL38BCE
Thickness	μm	210	240	235	235	325
Air Permeability	Gurley sec	<225	<85			
	$\text{cm}^3 \text{cm}^{-2} \text{s}^{-1}$			0.5–0.7	0.4–1.6	0.2–0.4
Electrical Resistivity (through plane)	$\text{m}\Omega \text{cm}^2$	<15	<15	<11	<12	<11

SGL38BCE showed the best performances for C60H30 compared to all mentioned operating conditions. The larger error bars could be due to unsteady water transport at low humidity conditions. The current density was up to 0.52 A cm^{-2} at low humidification, with the possible reason being the lower air permeability that reduced the water vapor loss from the CL. For the SGL38BCE, the current density decreased at the maintained cell temperature of 60°C as the humidification temperature increased. This behavior may be attributed to the high water content at the high humidification. The generated water blocked the gas path in the GDL, resulting in flooding and increase of the concentration overpotential.

Effect of cathode CL composition on the cell performance

The effect of the cathode Pt loading on the PEMFC performances at various NC ratios with fully humidified reactants was studied using different testing processes. Fig. 2(a)–(d) show the current densities of the MEAs measured at 0.6 V for NC ratios of 0.5, 0.6, 0.7, and 0.8, respectively. The current densities at the NC ratios of 0.5 and 0.6 nearly increased with the increasing cathode Pt loading for all the testing processes, but decreased at the cathode loading of 1 mg Pt cm^{-2} , which could be caused by the thick CL. For the operating condition of C70H60, the cathode loadings of 0.5 and $0.7 \text{ mg Pt cm}^{-2}$ showed better MEA performances for the NC ratios of 0.5 and 0.6, respectively. Interestingly, the effect of the cathode loading on the performance decreased as the NC ratio increased from 0.7 onwards. Fig. 2(c) and (d) depict that the current density at 0.6 V decreased all throughout as the cathode Pt loading increased. The current density started to

decrease when the cathode Pt loading was higher than $0.5 \text{ mg Pt cm}^{-2}$ at the NC ratio of 0.8. Nafion is not electrically conductive; hence, the CL resistance increased with the increasing CL thickness at the higher NC ratio (Fig. 2(d)). This study aimed to develop an MEA for low-humidity operations; thus, the MEA performance at the operating condition of C60H30 has drawn attention. The optimal CL composition comprised an NC ratio of 0.5 and a cathode Pt loading of 0.7 mg cm^{-2} .

Fig. 3 depicts the variation in the current density at 0.6 V with respect to the NC ratio at the Pt loadings of $0.1 \text{ mg Pt cm}^{-2}$ in the anode and $0.7 \text{ mg Pt cm}^{-2}$ in the cathode. The performance significantly dropped with the increasing NC ratio at the saturated operating conditions, such as C70H70 and C60H60. At the high NC ratio, the saturated gases caused Nafion swelling in the CL, thereby blocking the activation sites on the catalyst surface. The swelling phenomenon can be relieved when the supplied gases were less saturated. The effect of the NC ratio on the MEA performance was less significant for the operating condition of C60H30. The optimal NC ratio for the low-humidity conditions was 0.5, whereas that for the high-humidity condition was 0.6.

Effect of zeolite on performance

Fig. 4 shows the effect of zeolite on the MEA performance. The anode and cathode Pt loadings were fixed at 0.1 and $0.7 \text{ mg Pt cm}^{-2}$, respectively. The NC ratio was determined as 0.5 in the previous section. The current density decreased with the increasing zeolite amount. The performance significantly dropped when the zeolite-to-carbon weight (ZC) ratio was higher than 0.3. Thus, the effect of increasing

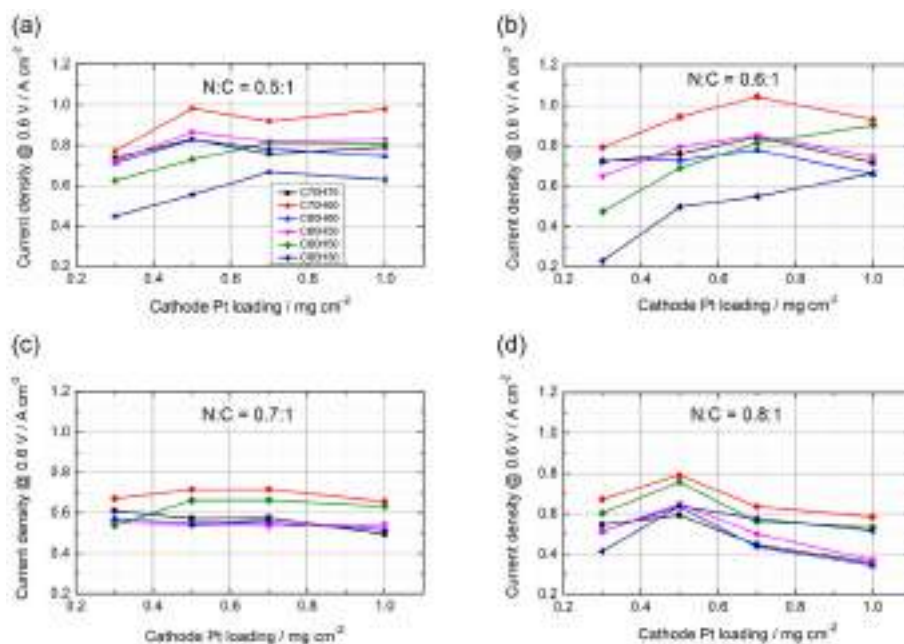


Fig. 2 – Effect of the cathode loading on the constant anode loading of $0.1 \text{ mg Pt cm}^{-2}$ anode for different operating conditions at NC ratios of (a) 0.5:1, (b) 0.6:1, (c) 0.7:1, and (d) 0.8:1 in the CL of the MEAs.

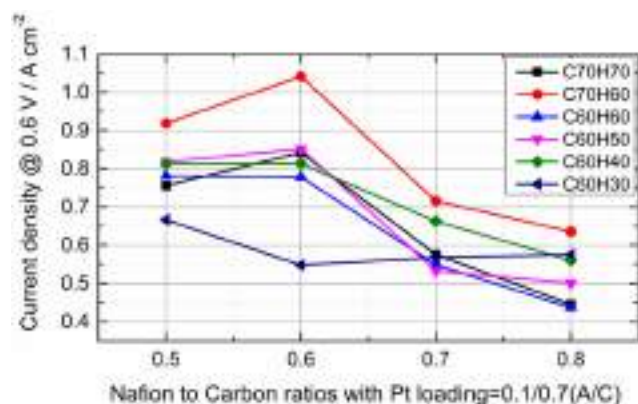


Fig. 3 – Effect of the NC ratio on the current density at 0.6 V for MEAs with Pt loadings of 0.1 and 0.7 mg Pt cm^{-2} in the anode and cathode, respectively.

the zeolite content on the performance under the operating condition of C60H30 was negligible. Such phenomenon is believed to be attributed to the non-electrically conductive nature of zeolite, which caused the increase of the internal resistance. Fig. 3 illustrates the measured current density of more than 0.65 A cm^{-2} without zeolite for C60H30. Fig. 4 depicts a current density near approximately 0.5 A cm^{-2} in the presence of zeolite. Consequently, we found that adding zeolite in the low-humidity operation negatively affects the performance. The result is opposite to the investigation carried out by Mercheri et al. [46], Yun et al. [47], and Devrim et al. [48]. However, the graph shows that the current density was nearly constant in the operating condition of C60H30. The ZC ratio of 0.3 was determined for the durability test considering the absorption of more water in the anode.

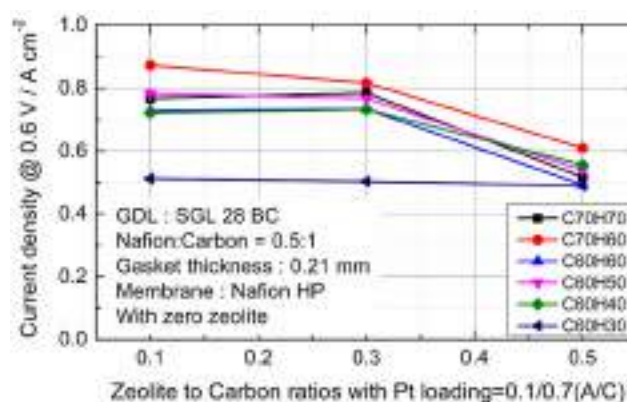


Fig. 4 – Plot of the current density at 0.6 V and ZC ratios for different operating conditions at Pt loadings of 0.1 and 0.7 mg Pt cm^{-2} in the anode and cathode, respectively.

Durability test

Fig. 5(a) and (b) illustrate the voltage variation during the long-term operation for the MEAs without and with zeolite in the anode, respectively. The MEAs used for the durability tests consisted of $0.1 \text{ mg Pt cm}^{-2}$ with a ZC ratio of 0.3 (or 0) in the anode and $0.7 \text{ mg Pt cm}^{-2}$ in the cathode. The NC ratios on both sides were 0.5. To meet practical operating conditions, hydrogen was not humidified, while air was passed through the humidifier maintained at a room temperature ranging between 21 (during the night) and 25 °C (during the day). The cell was operated at a constant current density of 0.6 A cm^{-2} with a cell temperature of 60 °C. The voltage was recorded continuously for 6 days. The EIS measurement was performed approximately every 24 h. The voltage of the MEA without zeolite showed a fluctuation between 0.35 and 0.4 V, as shown

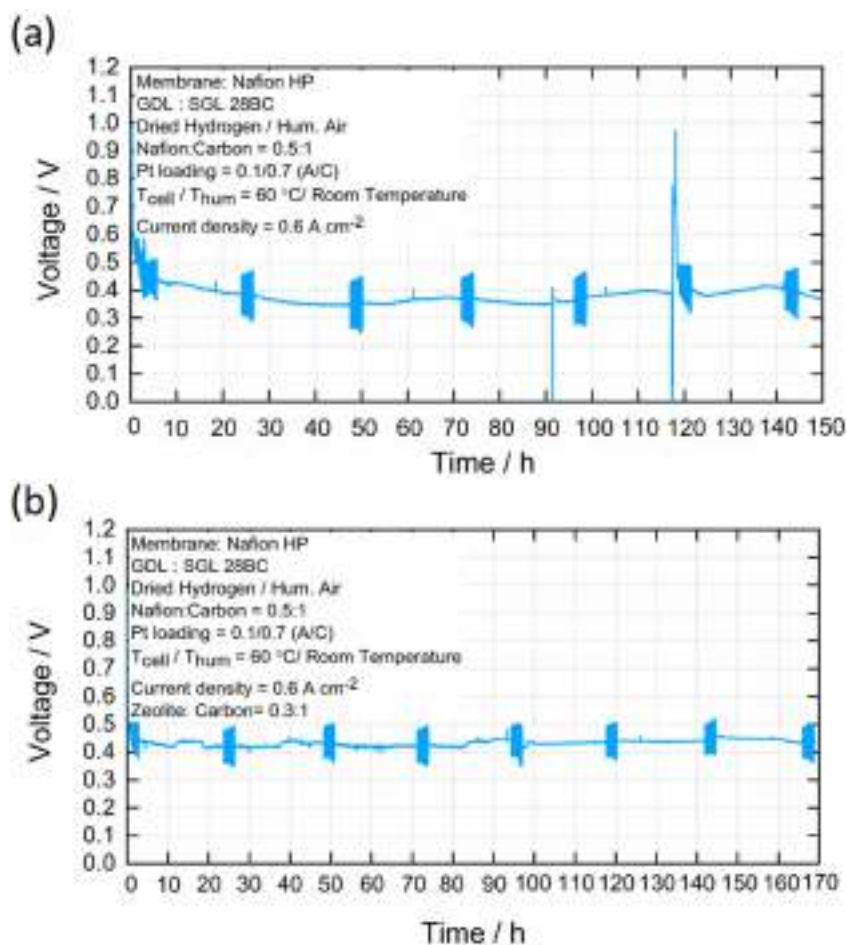


Fig. 5 – Durability test for the MEAs (a) without zeolite in the anode and (b) with zeolite in the anode. The MEA was operated at 0.6 A cm^{-2} and supplied with dry hydrogen and air passing a humidifier at room temperature.

in Fig. 5(a). On the contrary, the voltage of the MEA with zeolite was always above 0.42 V and comparatively more stable during the operation, as shown in Fig. 5(b). The anode was supplied with dry hydrogen; thus, the hydrophilic properties of the zeolite helped absorb the water diffused from the cathode to prevent the water from being carried by dry hydrogen, alleviating the water shortage in the anode.

Fig. 6(a) shows the Nyquist plot for the MEA without zeolite for long term operation. The interception of the first semi-circle at the high frequency represents the ohmic resistance of the cell, which showed a nearly stable value of approximately $0.22 \text{ } \Omega\text{-cm}^2$ during long term operation. The Bode plot shown in Fig. 6(b) also presents that change in impedance magnitudes at high frequency region was independent of operation time. However, at the low frequency region, the impedance magnitudes showed fluctuation with operating time. The slope of asymptotes at the low frequency region (below 10 Hz) gradually increased with operating time due to an increase in mass transfer resistance. The phase angle in both high and low frequency regions presented less variation with operating time but decreased in the intermediate region. The same results can be found in Le Canut's study [49]. For the MEA with zeolite in the anode, the impedance at high frequency showed the similar value of $0.22 \text{ } \Omega\text{-cm}^2$ during long

term operation, as shown in Fig. 6(c). This implied that the membrane hydration was maintained at a steady-state condition during the test period, regardless of the zeolite in the anode CL. The impedance magnitudes for MEAs with zeolite at low frequency showed smaller values and less fluctuations than those without zeolite did, as shown in Fig. 6(d). The less variation of phase angle in Fig. 6(d) after long term operation also indicated more stable performance of MEAs with zeolite than MEAs without zeolite.

An equivalent electric circuit as shown in Fig. 7(a), was employed to fit the experimental data, in which R_{Ω} , R_{an} , R_{ca} , and R_m represent ohmic resistance, anode charge transfer resistance, cathode charge transfer resistance, and mass transfer resistance, respectively. The constant phase element (CPE), CPE_{an} and CPE_{ca} are used to replace capacitors to improve the fit, whereas the capacitor C_m accounts for the mass transfer effect [50]. Fig. 7(b) presents the fitted impedance variation of the MEAs with and without zeolite. The anode impedances were approximately $0.1 \text{ } \Omega\text{-cm}^2$, regardless of the zeolite in the anode CL, because of the fast reaction kinetics of hydrogen oxidation. On the contrary, the cathode impedance showed a noticeable fluctuation at the range between 0.6 and 0.7 $\Omega\text{-cm}^2$ for the MEA with zeolite and between 0.5 and 0.7 $\Omega\text{-cm}^2$ for the MEA without

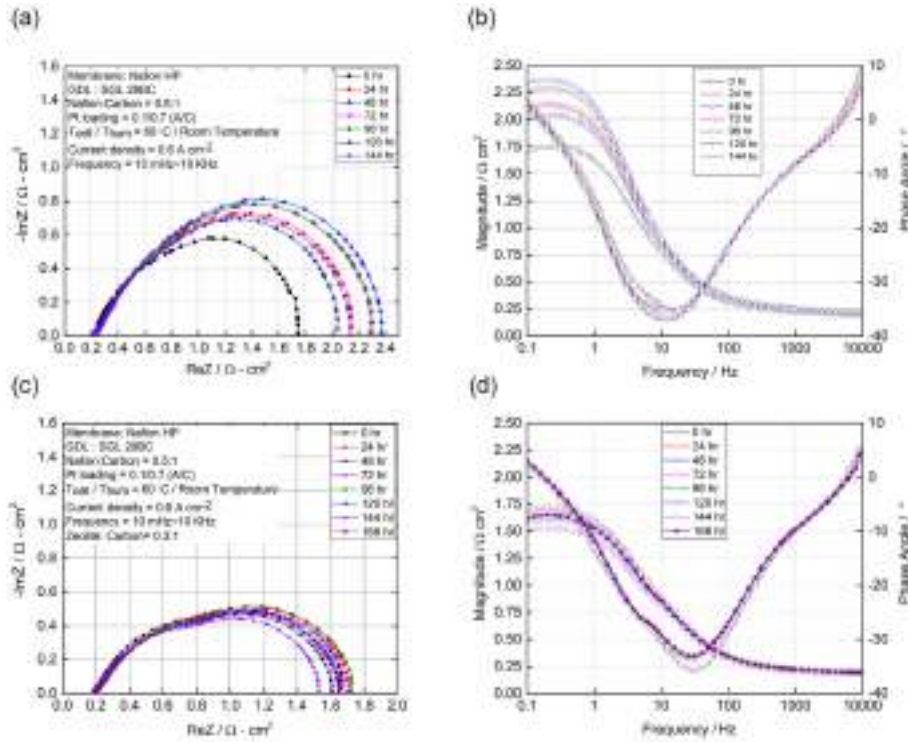


Fig. 6 – (a) Nyquist plots and (b) Bode plots for the MEA without zeolite; (c) Nyquist plots and (d) Bode plots for the MEA with zeolite. Both MEAs were operated at 0.6 A cm^{-2} under dry hydrogen and air passing the humidifier at room temperature.

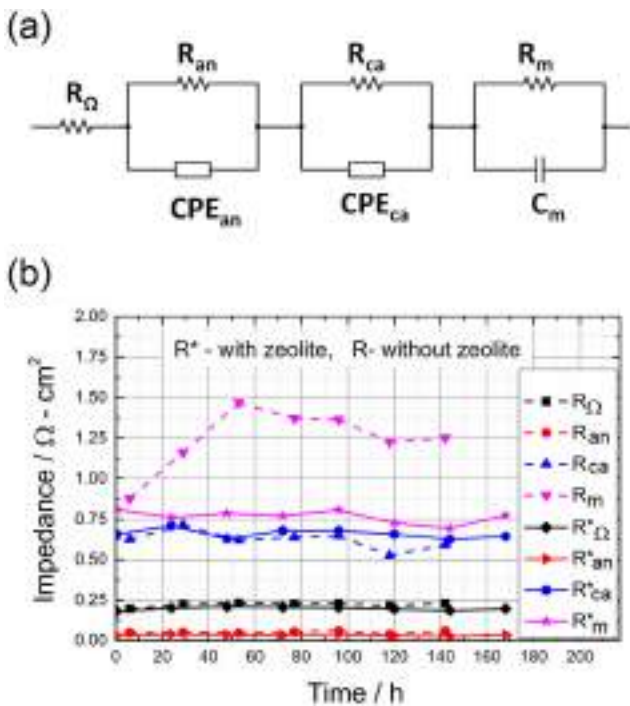


Fig. 7 – (a) Equivalent circuits of the obtained Nyquist plots of the MEAs. (b) Impedance variation with respect to operating time.

zeolite. The MEA without zeolite showed a concentration overpotential that was more significant than that of the MEA with zeolite. This results suggested that zeolite helped reduce concentration overpotential.

Conclusions

The MEA is one of key components influencing the performance of an open-cathode PEMFC, in which air is supplied from the environment with a low humidity. In this study, the effect of the manufacturing parameters on the MEA performance was investigated to develop MEAs under a low-humidity operation. The following conclusions can be drawn herein:

- (1) GDLs with lower air permeability and electrical resistivity provide a better cell performance because of the less water removing rate from the CL and the lower ohmic overpotential. The MEAs with the SGL28BCE carbon paper showed the best performance among all the tested carbon papers at low humidity conditions.
- (2) The optimal cathode Pt loading depended on the NC ratio and operating conditions. At the high NC ratio, the saturated gases caused Nafion swelling in the CL, which blocked the activation sites on the catalyst surface. The effect of the NC ratio on the MEA performance was less significant for the low-humidity operating conditions. The optimal cathode CL was composed of $0.7 \text{ mg Pt cm}^{-2}$ with an NC ratio of 0.5 for low-humidity conditions.
- (3) Although the presence of zeolite in the anode CL negatively affected the cell performance, the influence of zeolite on the performance was limited at low-humidity operations. The voltage of the MEA with zeolite was comparatively stable under the low-humidity conditions during the long-term operation. According to the

impedance variation measured by EIS, the zeolite in the anode reduced the concentration overpotential.

Declaration of competing interest

The authors declare that they have no known competing financial interests or personal relationships that could have appeared to influence the work reported in this paper.

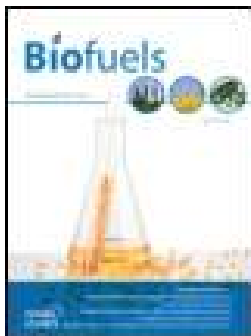
Acknowledgments

This work is financially supported by Ministry of Science and Technology under Grants 106-2221-E-194-033-MY3, 109-2622-E-008-029, and the Advanced Institute of Manufacturing with High-tech Innovations (AIM-HI) from The Featured Areas Research Center Program within the framework of the Higher Education Sprout Project by the Ministry of Education in Taiwan. A.A. would also like to thank the support by the Program Management Unit for Human Resources & Institutional Development, Research and Innovation – Chulalongkorn University, Thailand [Grant number B05F630077].

REFERENCES

- [1] Steele BCH, Heinzel A. Materials for fuel-cell technologies. *Nature* 2001;414:345–52. <https://doi.org/10.1038/35104620>.
- [2] Carrette L, Friedrich KA, Stimming U. Fuel cells: principles, types, fuels, and applications. *ChemPhysChem* 2000;1:162–93. [https://doi.org/10.1002/1439-7641\(20001215\)1:4<162::aid-cphc162>3.0.co;2-z](https://doi.org/10.1002/1439-7641(20001215)1:4<162::aid-cphc162>3.0.co;2-z).
- [3] Tawfik H, Hung Y, Mahajan D. Metal bipolar plates for PEM fuel cell—a review. *J Power Sources* 2007;163:755–67. <https://doi.org/10.1016/j.jpowsour.2006.09.088>.
- [4] Pei P, Chen H. Main factors affecting the lifetime of proton exchange membrane fuel cells in vehicle applications: a review. *Appl Energy* 2014;125:60–75. <https://doi.org/10.1016/j.apenergy.2014.03.048>.
- [5] Ren H, Chae J. Fuel cells technologies for wireless MEMS. *Wireless MEMS Networks and Applications*; 2016. p. 35–51. <https://doi.org/10.1016/B978-0-08-100449-4.00002-6>.
- [6] Hwang JJ. Sustainability study of hydrogen pathways for fuel cell vehicle applications. *Renew Sustain Energy Rev* 2013;19:220–9. <https://doi.org/10.1016/j.rser.2012.11.033>.
- [7] Cho KY, Jung HY, Sung KA, Kim WK, Sung SJ, Park JK, Choi JH, Sung YE. Preparation and characteristics of Nafion membrane coated with a PVDF copolymer/recast Nafion blend for direct methanol fuel cell. *J Power Sources* 2006;159:524–8. <https://doi.org/10.1016/j.jpowsour.2005.10.106>.
- [8] Yu X, Ye S. Recent advances in activity and durability enhancement of Pt/C catalytic cathode in PEMFC: Part II: degradation mechanism and durability enhancement of carbon supported platinum catalyst. *J Power Sources* 2007;172:145–54. <https://doi.org/10.1016/j.jpowsour.2007.07.048>.
- [9] Shahgaldi S, Hamelin J. Improved carbon nanostructures as a novel catalyst support in the cathode side of PEMFC: a critical review. *Carbon* 2015;94:705–28. <https://doi.org/10.1016/j.carbon.2015.07.055>.
- [10] Auer E, Freund A, Pietsch J, Tacke T. Carbons as supports for industrial precious metal catalysts. *Appl Catal* 1998;173:259–71. [https://doi.org/10.1016/S0926-860X\(98\)00184-7](https://doi.org/10.1016/S0926-860X(98)00184-7).
- [11] Litster S, McLean G. PEM fuel cell electrodes. *J Power Sources* 2004;130:61–76. <https://doi.org/10.1016/j.jpowsour.2003.12.055>.
- [12] Rodríguez-reinoso F. The role of carbon materials in heterogeneous catalysis. *Carbon* 1998;36:159–75. [https://doi.org/10.1016/S0008-6223\(97\)00173-5](https://doi.org/10.1016/S0008-6223(97)00173-5).
- [13] Willsau J, Heitbaum J. The influence of Pt-activation on the corrosion of carbon in gas diffusion electrodes—a dems study. *J Electroanal Chem Interfacial Electrochem* 1984;161:93–101. [https://doi.org/10.1016/S0022-0728\(84\)80252-1](https://doi.org/10.1016/S0022-0728(84)80252-1).
- [14] Kangasniemi KH, Condit DA, Jarvic TD. Characterization of vulcan electrochemically oxidized under simulated PEM fuel cell conditions. *J Electrochem Soc* 2004;151:E125–32. <https://doi.org/10.1149/1.1649756>.
- [15] Kinoshita K. Carbon: electrochemical and physicochemical properties. 1st ed. New York: Wiley; 1988. <https://doi.org/10.1002/bbpc.198800269>.
- [16] Joo JB, Kim P, Kim W, Kim Y, Yi J. Effect of the preparation conditions of carbon-supported Pt catalyst on PEMFC performance. *J Appl Electrochem* 2009;39:135–40. <https://doi.org/10.1007/s10800-008-9645-9>.
- [17] Passalacqua E, Lufano F, Squadrito G, Patti A, Giorgi L. Nafion content in the catalyst layer of polymer electrolyte fuel cells: effects on structure and performances. *Electrochim Acta* 2001;46:799–805. [https://doi.org/10.1016/S0013-4686\(00\)00679-4](https://doi.org/10.1016/S0013-4686(00)00679-4).
- [18] Gamburgzev S, Appleby A. Recent progress in performance improvement of the proton exchange membrane fuel cell (PEMFC). *J Power Sources* 2002;107:5–12. [https://doi.org/10.1016/S0378-7753\(01\)00970-3](https://doi.org/10.1016/S0378-7753(01)00970-3).
- [19] Qi Z, Kaufman A. Low Pt loading high performances cathodes for PEM fuel cells. *J Power Sources* 2003;113:37–43. [https://doi.org/10.1016/S0378-7753\(02\)00477-9](https://doi.org/10.1016/S0378-7753(02)00477-9).
- [20] Sasikumar S, Ihm JW, Ryu H. Dependence of optimum Nafion content in catalyst layer on platinum loading. *J Power Sources* 2004;132:11–7. <https://doi.org/10.1016/j.jpowsour.2003.12.060>.
- [21] Jeon S, Lee J, Rios GM, Kim HJ, Lee SY, Cho E, Lim TH, Jang JH. Effect of ionomer content and relative humidity on polymer electrolyte membrane fuel cell (PEMFC) performance of membrane-electrode assemblies (MEAs) prepared by decal transfer method. *Int J Hydrogen Energy* 2010;35:9678–86. <https://doi.org/10.1016/j.ijhydene.2010.06.044>.
- [22] Kim KH, Lee KY, Lee SY, Cho E, Lim TH, Kim HJ, Yoon SP, Kim SH, Lim TW, Jang JH. The effects of relative humidity on the performances of PEMFC MEAs with various Nafion® ionomer contents. *Int J Hydrogen Energy* 2010;35:13104–10. <https://doi.org/10.1016/j.ijhydene.2010.04.082>.
- [23] Cho MK, Park HY, Lee SY, Lee BS, Kim HJ, Henkensmeier D, Yoo SJ, Kim JY, Han J, Park HS, Jang JH. Effect of catalyst layer ionomer content on performance of intermediate temperature proton exchange membrane fuel cells (IT-PEMFCs) under reduced humidity conditions. *Electrochim Acta* 2017;224:228–34. <https://doi.org/10.1016/j.electacta.2016.12.009>.
- [24] Kim KH, Kim HJ, Lee KY, Jang JH, Lee SY, Cho E, Oh IH, Lim TH. Effect of Nafion® gradient in dual catalyst layer on proton exchange membrane fuel cell performance. *Int J Hydrogen Energy* 2008;33:2783–9. <https://doi.org/10.1016/j.ijhydene.2008.03.015>.
- [25] Prasanna M, Ha HY, Cho EA, Hong SA, Oh IH. Influence of cathode gas diffusion media on the performance of the

- PEMFCs. *J Power Sources* 2004;131:147–54. <https://doi.org/10.1016/j.jpowsour.2004.01.030>.
- [26] Williams MV, Begg E, Bonville L, Kunz HR, Fenton JM. Characterization of gas diffusion layer. *J Electrochem Soc* 2004;151:A1173–80. <https://doi.org/10.1149/1.1764779>.
- [27] Lee D, Hwang S. Effect of loading and distributions of Nafion ionomer in the catalyst layer for PEMFCs. *Int J Hydrogen Energy* 2008;33:2790–4. <https://doi.org/10.1016/j.ijhydene.2008.03.046>.
- [28] Thoben B, Siebke A. Influence of different gas diffusion layers on the water management of the PEFC cathode. *J New Mat Electrochem Sys* 2004;7:13–20.
- [29] Vielstich W, Lamm A, Gasteiger HA. *Handbook of fuel cells: fundamentals, technology and applications, fuel cell technology and applications*. Wiley; 2003. p. 609–16.
- [30] Benitez R, Soler J, Daza L. Novel method for preparation of PEMFC electrodes by the electrospray technique. *J Power Sources* 2005;151:108–13. <https://doi.org/10.1016/j.jpowsour.2005.02.047>.
- [31] Millington B, Whipple V, Pollet BG. A novel method for preparing proton exchange membrane fuel cell electrodes by the ultrasonic-spray technique. *J Power Sources* 2011;196:8500–8. <https://doi.org/10.1016/j.jpowsour.2011.06.024>.
- [32] Chen GY, Wang C, Lei YJ, Zhang J, Mao Z, Mao ZQ, Guo JW, Li J, Ouyang M. Gradient design of Pt/C ratio and Nafion content in cathode catalyst layer of PEMFCs. *Int J Hydrogen Energy* 2017;42:29960–5. <https://doi.org/10.1016/j.ijhydene.2017.06.229>.
- [33] Franke ME, Simon U. Proton mobility in H-ZSM5 studied by impedance spectroscopy. *Solid State Ionics* 1999;118:311–6. [https://doi.org/10.1016/S0167-2738\(98\)00436-6](https://doi.org/10.1016/S0167-2738(98)00436-6).
- [34] Franke ME, Simon U. Solvate-supported proton transport in zeolites. *ChemPhysChem* 2004;5:465–72. <https://doi.org/10.1002/cphc.200301011>.
- [35] Kreuer KD, Rabenau A, Weppner W. Vehicle mechanism, A new model for the interpretation of the conductivity of fast proton conductors. *Angew Chem Int Ed* 1982;21:208–9. <https://doi.org/10.1002/anie.198202082>.
- [36] Hibino T, Akimoto T, Iwahara H. Protonic conduction of mordenite-type zeolite. *Solid State Ionics* 1993;67:71–6. [https://doi.org/10.1016/0167-2738\(93\)90311-P](https://doi.org/10.1016/0167-2738(93)90311-P).
- [37] Yamamoto N, Okubo T. Ionic conductivity of single-crystal ferrierite. *Microporous Mesoporous Mater* 2000;40:283–8. [https://doi.org/10.1016/S1387-1811\(00\)00265-1](https://doi.org/10.1016/S1387-1811(00)00265-1).
- [38] Son DH, Sharma RK, Shul YG, Kim H. Preparation of Pt/Zeolite-Nafion composite membranes for self-humidifying polymer electrolyte fuel cells. *J Power Sources* 2007;165:733–8. <https://doi.org/10.1016/j.jpowsour.2006.11.090>.
- [39] Carbone A, Sacca A, Gatto I, Pedicini R, Passalacqua E. Investigation on composite S-PEEK/H-BETA MEAs for medium temperature PEFC. *Int J Hydrogen Energy* 2008;33:3153–8. <https://doi.org/10.1016/j.ijhydene.2008.01.029>.
- [40] Sengul E, Erdener H, Akay RG, Yucel H, Bac N, Eroglu I. Effects of sulfonated polyether-etherketone (SPEEK) and composite membranes on the proton exchange membrane fuel cell (PEMFC) performance. *Int J Hydrogen Energy* 2009;34:4645–52. <https://doi.org/10.1016/j.ijhydene.2008.08.066>.
- [41] Intaraprasit N, Kongkachuichay P. Preparation and properties of sulfonated poly (ether ether ketone)/Analcime composite membrane for a proton exchange membrane fuel cell (PEMFC). *J. Taiwan Inst. Chem. Eng.* 2011;42:190–5. <https://doi.org/10.1016/j.jtice.2010.05.002>.
- [42] Sancho T, Soler J, Pina MP. Conductivity in zeolite–polymer composite membranes for PEMFCs. *J Power Sources* 2007;169:92–7. <https://doi.org/10.1016/j.jpowsour.2007.01.079>.
- [43] Yahiro H, Konda Y, Okada G. Conductivity of zeolite/poly(tetrafluoroethylene) composite membrane in the presence of water vapor. *Phys Chem Chem Phys* 2003;5:620–3. <https://doi.org/10.1039/B207807D>.
- [44] Chen ZW, Holmberg B, Li WZ, Wang X, Deng WQ, Munoz R, Yan YS. Nafion/zeolite nanocomposite membrane by in situ crystallization for a direct methanol fuel cell. *Chem Mater* 2006;18:5669–75. <https://doi.org/10.1021/cm060841q>.
- [45] Lu JL, Lu SF, Jiang SP. Highly ordered mesoporous Nafion membranes for fuel cells. *Chem Commun* 2011;47:3216–8. <https://doi.org/10.1039/C0CC05560C>.
- [46] Mecheri B, Felice V, Zhang Z, D'Epifanio A, Licoccia S, Tavares AC. DSC and DVS investigation of water mobility in nafion/zeolite composite membranes for fuel cell applications. *J Phys Chem C* 2012;116:20820–9. <https://doi.org/10.1021/jp301762h>.
- [47] Yun YH, Kim SD, Park SW, Lee JY, Yi SC, Kim WJ. Cell performance of MEA fabricated with Pt-ZSM-5-carbon electrode for PEMFC. *Microporous Mesoporous Mater* 2010;131:122–7. <https://doi.org/10.1016/j.micromeso.2009.12.011>.
- [48] Devrim Y, Albostan A. Enhancement of PEM fuel cell performance at higher temperatures and lower humidities by high performance membrane electrode assembly based on Nafion/zeolite membrane. *Int J Hydrogen Energy* 2015;40:15328–35. <https://doi.org/10.1016/j.ijhydene.2015.02.078>.
- [49] Le Canut JM, Abouatallah RM, Harrington DA. Detection of membrane drying, fuel cell flooding, and anode catalyst poisoning on PEMFC stacks by electrochemical impedance spectroscopy. *J Electrochem Soc* 2006;153:A857–64. <https://doi.org/10.1149/1.2179200>.
- [50] Kang RJ, Chen YS. Experimental study on the effect of hydrogen sulfide on high-temperature proton exchange membrane fuel cells by using electrochemical impedance spectroscopy. *Catalysts* 2018;8:441. <https://doi.org/10.3390/catal8100441>.



Bio-oil: the future of hydrogen generation

Ankit Kumar, J.P. Chakraborty & Rupesh Singh

To cite this article: Ankit Kumar, J.P. Chakraborty & Rupesh Singh (2016): Bio-oil: the future of hydrogen generation, Biofuels

To link to this article: <http://dx.doi.org/10.1080/17597269.2016.1141276>



Published online: 01 Apr 2016.



Submit your article to this journal



View related articles



View Crossmark data

Bio-oil: the future of hydrogen generation

Ankit Kumar^a, J.P. Chakraborty ^a and Rupesh Singh^b

^aDepartment of Chemical Engineering, Indian Institute of Technology (B.H.U.), Varanasi, Varanasi- 221005 (UP), India; ^bDepartment of Chemical Engineering, Indian Institute of Technology Kanpur, Kanpur- 208016 (UP), India

ABSTRACT

Depleting non-renewable energy sources combined with stringent environmental norms necessitate researchers to search for alternative energy sources. Hydrogen (H₂) is one of the most promising alternatives if produced, stored and harnessed properly. Biomass derived bio-oil extracted through fast pyrolysis is an alternative source for sustainable H₂ generation via the reforming process. This review summarizes recent work done in the field of H₂ generation using steam reforming of bio-oil and the influence of operating parameters such as temperature, S/C ratio and type of catalyst used. Other than steam reforming, several other reforming techniques, such as oxidative steam reforming, aqueous phase reforming and partial oxidation, have also been discussed. Various catalytic systems with Ni, Pt and Ru on different supports have been investigated. Coke deposition on the catalyst surface over a long period of operation is the major shortcoming for reforming reaction which lowers the catalytic activity and requires frequent regeneration. Use of additives like MgO, K, Ca and addition of a small amount of O₂ reduces coke formation as well as increases the catalytic activity.

ARTICLE HISTORY

Received 15 November 2015
Accepted 7 January 2016

KEYWORDS

bio-oil; hydrogen generation; biomass

Introduction

Dependence on oil and electricity has made energy a vital component of our everyday needs.[1] At present continuously growing worldwide energy demand is largely met by fossil fuel reserves. These reserves are diminishing and are likely to become expensive in the near future. In order to meet the increasing energy demand, we will be forced to seek environmentally clean alternative energy resources.[2,3] The search for clean renewable energy sources has been intense over the last few years. Hydrogen, when produced from renewable energy resources like bio-oils, can be considered as a clean, inexpensive and efficient energy source having a very high energy content of 120.7 MJ/kg.[4]

Hydrogen is not only an energy carrier but also serves as an important raw material for fertilizers, oil refineries, methanol production and metallurgical industries.[2] Currently hydrogen is mainly obtained by steam reforming of fossil fuels (~ 48% from natural gas, ~30% from naphtha and ~18% from coal).[5] Out of the total H₂ produced, 49% is consumed during ammonia synthesis, 37% for petroleum refining, and 8% for methanol production.[6]

The main processes for production of commercial hydrogen are catalytic steam reforming of natural gas, light hydrocarbons and naphtha, partial oxidation of heavy residue as well as coal gasification.[7–9] All these processes utilize fossil resources and one of the

limitations of the current processes is the depletion of fossil fuels and CO₂ generation during the H₂ production. Renewable biomass can be an alternative source for H₂ production, as this renewable energy source does not contribute towards greenhouse emissions. [10,11] Biomass alludes to plants or plant-based materials which are explicitly known as lignocellulosic biomass. The major components that have been investigated in biomass are lignin (18–35%), cellulose (40–50%), hemicelluloses (20–40%), ash and water content.[12–14]

In recent years, the technologies that have been investigated currently for the production of hydrogen is steam gasification of biomass [15,16] and subsequent conversion of biomass to bio-oil via fast pyrolysis followed by steam reforming of bio-oil.[17–24] The latter process is one of the well proven and promising techniques for the production of H₂ rich gas.[25]

Bio-oil as a feedstock for H₂ generation

Bio-oil also known as pyrolysis oil/pyrolytic liquid is obtained from thermal decomposition of biomass, and is usually dark brown in color which is due to the degradation products of three main components namely cellulose, hemicelluloses and lignin.[26] Bio-oil can be readily stored and transported more easily in comparison to biomass; it is also used as a raw material for chemical production.[27,28] Bio-oil possesses nearly

Table 1. Physical properties of bio-oil (pine wood) produced at different temperatures.[111]

Bio-oil properties	Pyrolysis temperature (°C)			
	425	450	475	500
Density (kg/m ³)	1174 ± 40	1156 ± 17	1142 ± 26	1138 ± 31
pH	2.1 ± 0.09	2.2 ± 0.08	2.3 ± 0.07	2.4 ± 0.07
Water (wt%)	20.8 ± 3.9	21.0 ± 4.6	20.3 ± 2.8	20.6 ± 3.9
HHV (MJ/kg)	18.6 ± 0.8	19.1 ± 1.3	18.4 ± 0.5	19.7 ± 1.2
Ash (wt%)	0.12 ± 0.09	0.10 ± 0.06	0.12 ± 0.05	0.11 ± 0.03
Solid (wt%)	0.3 ± 0.17	0.4 ± 0.13	0.5 ± 0.21	0.7 ± 0.36

zero sulfur in comparison to crude oil, which makes it advantageous over the existing transportation fuels. It is a highly complex mixture of water and more than 300 oxygenated compounds like acids, alcohols, aldehydes, ketones, substituted phenolics and other complex oxygenates are obtained from biomass carbohydrate and lignin.[29,30] The different oxygenated compounds present in the bio-oil depend on the types of biomass used and also on the process conditions like temperature, residence time and heating rate. Table 1 shows the variation in physical properties, such as density, pH, calorific value, water content, solid content and ash content of the bio-oil derived from pine wood with variation in temperature

Water is the most abundant component in the bio-oil, and results from the original moisture present in the feedstock and as products of the dehydration reaction occurring during pyrolysis. The water content in bio-oil (15–30%) depends upon the feedstock and process conditions. There are different reports available which provides physical and chemical properties of bio-oil.[31,32] Table 2 shows the variation in elemental composition of bio-oil derived from different biomass as a feed stock. Bio-mass rich in protein (e.g. alfalfa, bark and grass hay) is expected to have higher organic nitrogen content when compared to materials having low protein content (e.g. debarked wood). The presence of bio-oil will not only affect the nitrogen oxide (NO_x) content of the combustion product but also the aging property of bio-oil.[33]

The chemical properties of bio-oils are different from petroleum derived fuels because of difference in the oxygen content, sulfur content and pH. The main elemental constituents of bio-oil are carbon (C), hydrogen (H), and oxygen (O), and hence its empirical chemical formula is given as C_nH_mO_k·xH₂O.[34] Crude bio-oil carries substantial amounts of water insoluble

materials (~50%), which includes lignin derived oligomeric phenolic compounds, which are difficult to be reformed.[2,35] These water insoluble materials are prone to form carbon over the catalyst surface leading to the rapid deactivation of the reformer catalysts. In the light of these limitations most of the work is focused upon the water soluble and volatile fractions of bio-oil for H₂ generation.[36] Different oxygenated compounds (acetic acid, ketones, different alcohols and their mixtures) were used as models of oxygenated organic compounds found in bio-oil to investigate the reforming behavior of bio-oil.[2,20,28,37–44]

Bio-oil issues

Bio-oil is combustible but is not miscible with conventional liquid fuels like gasoline or diesel due to its high water content. Because of high water (15–25 wt%) and oxygen content (35–45 wt% on dry basis) the lower heating values (LHV) of bio-oil is in the range 14–15 MJkg⁻¹. This LHV value is similar to that of biomass and is 40–45% of that for hydrocarbon fuels.[32] There are a series of identified challenges regarding the bio-oil's stability, viscosity and solids content. The high oxygen content in the bio-oil increases its acidity, and also reduces the stability of the bio-oil as oxygenates present in bio-oil can polymerize under storage.

Polymerization increases viscosity and average molar weight with time.[45–47] This polymerization might make upgrading of the bio-oil more difficult as complex molecules, which are more difficult to convert, could be formed. Aging of the bio-oil reduces the volatility, and results in phase separation and gum formation.[45] The bio-oil aging process could be accelerated by temperature, oxygen exposure, and UV light exposure.[48] The acidic nature of bio-oil is another problem which could corrode piping and process equipment hence corrosive resistant materials are needed, which makes the overall process more expensive. Therefore, long-term storage of the bio-oil brings severe changes in its physical and chemical properties. Some efforts have been carried out to enhance the storage stability of the bio-oils by adding additives like methanol.[49] For the above mentioned reasons, bio-oil is not suited for direct use as a fuel in engines or boilers.

Table 2. Comparison of elemental composition of bio-oils derived from different feed stocks.

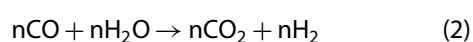
Feed stocks	Elements in bio-oil (wt%)					Moisture contents (wt%)	Ref.
	C	H	O*	N	S		
Beech wood	38.70	7.50	53.4	0.38	0.08	28.80	[29,107]
Pine wood	36.07	8.45	55.37	0.11	-	36.00	[36,84]
Corn stalk	47.34	7.29	42.70	2.63	0.05	71.57	[112]
Rice hull	31.70	8.40	59.80	0.13	0.05	-	[71]
Poplar	48.10	7.20	44.70	-	-	17.00	[85]
Hardwood	45.00	6.90	48.10	-	-	29.00	[85]
Cotton stalk	42.30	7.90	49.40	-	-	24.40	[4]

*Determined by difference

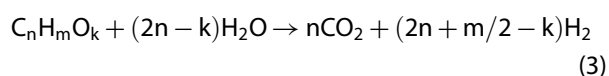
There are different methods for production of H₂ from bio-oil. This paper reviews the state of the art methods for H₂ production from bio-oil using different reforming techniques. Bio-oil contains large amounts of oxygenated organic compounds with a wide range of molecular weights. During storage, the chemical composition of the bio-oil changes towards thermodynamic equilibrium under storage condition, which results in a change in viscosity, molecular weight and solubility of its many compounds.[33] Bio-oil carries two main fractions. One is the hydrophilic carbohydrate or aqueous phase which contains a certain amount of water from dehydration reactions and moisture. The other is the hydrophobic phase composed of furan and aromatic based species, generally called pyrolytic lignin. The term pyrolytic lignin refers to the water insoluble phase oligomers that precipitate when water is added.

Steam reforming of bio-oil

Catalytic steam reforming of bio-oil is a technically viable process for production of H₂ as bio-oil has much higher energy density in comparison to biomass. It is an endothermic process in which hydrocarbons react with steam in the presence of a catalyst resulting in the formation of a mixture of CO and H₂ followed by a water gas shift reaction.[50] Standard Oil Co., USA, commissioned the first steam reforming plant of bio-oils in 1930.[51] The general chemical reaction scheme for the steam reforming of bio-oil is:

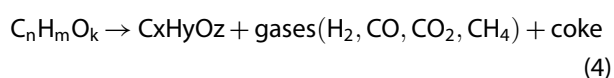


The overall reaction can be represented as:

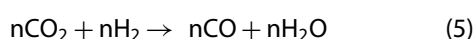


Because of formation of undesired product, due to side reactions (i.e. thermal decomposition of oxygenates, methanation, reverse water gas shift reaction), H₂ yield is lower than the stoichiometric yield.

Thermal decomposition of oxygenates



Reverse water gas shift reaction



Catalyst selection for steam reforming (SR)

The ideal bio-oil reforming catalyst must have high activity for reforming. In addition, it should also be highly selective towards hydrogen generation. The catalyst formulation should show resilience towards deactivation by coke formation which is one of the major challenges in bio-oil reforming reaction. Coke blocks the metal atoms and hence reduces activity. The steam reforming reaction for bio-oil has been widely explored via various catalysts, e.g., Ni-based catalysts,[19,23,42] Mg-doped catalysts [19,52] and noble metal-loaded catalysts.[20,53,54] Nickel based catalysts, being cost effective and also having high C-C bond breaking activity, are widely used for steam reforming of bio-oil in comparison to other reported metals.[55,56] The conversion of the oxygenates increases with the increasing Ni content in the catalytic system but a 10–15% Ni loading is generally preferred as higher loading results in significant catalyst deactivation due to sintering.[57] Noble metals (Pt, Ru, and Rh) are generally more effective than Ni-based catalysts and show less carbon deposition. They are not used in practical applications because of their high cost.[56] Specific activities of metals are reported to decrease in the order Rh, Ru > Ni, Pd, Pt > Re > Co.[58] As reported in literature, organic molecules dissociatively adsorb on metal sites whereby water molecules are adsorbed on the support (metal oxide i.e. Al₂O₃, MgO, etc.) surface. Hydrogen is produced via dehydrogenation of adsorbed organic molecules and reaction of adsorbed organic fragments with hydroxyl groups, which migrate from the alumina support to the metal/support interfaces.[58] In comparison to hydrocarbons, bio-oils are more reactive as they carry some C-O bonds. At elevated temperatures, the chance of carbon deposition increases because of the large size and thermal instability of constitutive molecules (cresol, furans, and phenols). Crude pyrolysis bio-oil as a feedstock was also used for H₂ generation. A major drawback of crude bio-oil reforming is coke deposition on the catalyst surface, which is mainly due to the presence of heavier molecules of olefins and aromatics. It was observed that incorporation of small amounts of K and La as additives prevents sintering and coke formation.[29,59–61] The use of ceria as support modifier in a Ni based catalyst improves hydrogen yield because of increased dispersion of metal over support. The presence of ceria promotes coke gasification which reduces the catalyst deactivation through coking.[57] Incorporation of MgO to Al₂O₃ support improves the adsorption and H₂O dissociation capacity, helping to keep the nickel metal surface free from carbon.[62] Basagiannis AC et al. [63] investigated catalytic steam reforming of the aqueous fraction of bio-oil over a series of Ru/MgO/Al₂O₃ catalysts supported on cordierite monoliths, ceramic foams and γ-Al₂O₃ pellets. Among all the investigated structured

materials, catalyst supported on Al_2O_3 pellets showed best performance because of efficient contact between gas phase and solid phase. Rioche C et al. [20] investigated the steam reforming of bio-oil (beech wood) over Pt and Rh catalysts over alumina and ceria-zirconia support. Use of ceria-zirconia leads to higher H_2 yield in comparison to alumina supported catalysts. As mentioned in previous literatures,[21] redox oxide plays a major role in steam activation. CeO_2 and $\text{Ce}_x\text{Zr}_{1-x}\text{O}_2$ facilitates water dissociation and supplies O for the oxidation of carbon on the surface because of their redox properties.[64–68] Magnesium and calcium aluminates as a catalyst support have less number of acidic sites in comparison to Al_2O_3 , which reduces the chances of carbon formation due to decomposition of oxygenated compounds present in bio-oil.[68] Selective poisoning of Ni-CeO₂/MgAl₂O₄ with sulfur in the form of SO₄ decreases the carbon deposition as well as the overall activity of the catalyst due to blockage of step sites on the Ni particles.[68] Incorporation of basic oxides like MgO and La₂O₃ to a Ni/Al₂O₃ catalyst increases the activity of the catalyst due to synergetic effect. Synthesized catalyst showed a maximum hydrogen yield of 71.42% at 800°C, with very slow deactivation in comparison to Ni/Al₂O₃ catalyst.[69]

Addition of Ru or MgO to Ni/Al₂O₃ catalyst increases the yield of H_2 production. The promotional effect to increase the H_2 yield was found considerably less for MgO in comparison to Ru. Maximum H_2 yield (80%) was achieved at 950 °C over Ru-Ni/Al₂O₃ catalyst (Ru = 0.5%) when Ni content was equal or greater than 10.7%.[70] A series of composite Ni/CeO₂-ZrO₂ catalyst performance for H_2 generation by steam reforming of bio-oil aqueous fraction was examined in a laboratory scale fixed bed reactor; the results were compared with commercial nickel based catalyst (Z417). Ni and Ce loading of 12 wt% and 7.5 wt% show the best performance for Ni/CeO₂-ZrO₂ catalyst. Maximum H_2 yield of 69.7% was obtained at W/B = 4.9 and T = 800°C. Under the same operating conditions, composite catalyst (Ni/CeO₂-ZrO₂) provides higher H_2 yield in comparison to commercial nickel-based catalysts (Z417).[71] Comparison of Pt/Ce_{0.5} Zr_{0.5}O₂ and Rh/Ce_{0.5} Zr_{0.5}O₂ monolithic catalysts for H_2 production in steam reforming of bio-oil shows that under similar reaction conditions Pt catalyst achieves higher H_2 yield in comparison to Rh.[72]

Due to the chemical complexity of the bio-oil with the additional issue of polymerization and aging makes it challenging to develop an effective catalyst. It is also difficult to establish kinetic modeling and reaction mechanism of the overall reforming process of bio-oil.[26,73] Since bio-oil is a complex mixture of many organic and lignin-derived oligomeric materials its steam reforming is studied either using its aqueous fraction of bio-oil or by using model compounds such

as methanol, ethanol, acetic acid, phenol, glycerol and cresol.[21,74–79]

Hu and Lu [80] investigated the steam reforming of acetic acid for H_2 generation using Ni, Co, Fe and Cu/Al₂O₃ catalysts. The catalytic activity decreases in the following order: Ni > Co > Fe > Cu. The difference in catalytic activity can be explained on the basis of difference in activities of metallic phases for cracking the bonds present in acetic acid molecules. Ni and Co metal species are active for cracking both C-C and C-H bonds. Fe is active to crack only the C-C bond while Cu can crack only the C-H bond. In comparison to Ni/Al₂O₃, Co/Al₂O₃ suffers the major drawback of coke formation which restricts its long term usage.

Reactor for steam reforming

Choice of reactor plays an important role in steam reforming of bio-oil. A fixed bed reactor is the commonly used reactor for steam reforming with both liquid and gas feeds.[21,37,81–83] Even though it is required to carry out the bio-oil steam reforming reaction at high S/C ratio, the reforming catalyst lasts no more than 3–4 h, after which the catalyst needs to be regenerated. Formation of carbonaceous deposition over the catalyst surface limits the operating time and hence fixed bed reactors are more susceptible to coke formation during steam reforming of bio-oil. Coking lowers the hydrogen yield and causes severe catalytic deactivation and reactor blockage. In contrast fluidized beds can be operated continuously by gasification of carbonaceous deposits on the catalyst surface.[18,35,75,84] In comparison to oxygenated model compounds such as ethanol and acetic acid, bio-oil (carrying larger compounds) does not vaporize completely when fed into the reactor and leaves behind a considerable amount of residual solid resulting in blockage of the feeding line along with the reactor.[22] The rapid heating rate of bio-oil causes thermal decomposition and coke formation resulting in deactivation of the catalyst. Researchers attempted different feeding techniques to overcome these problems. Using a spray nozzle to spray the bio-oil onto the catalyst bed helps in lowering the thermal decomposition and coke formation of bio-oil.[63,85] Adding the bio-oil drop wise has also been investigated to minimize the thermal decomposition of the bio-oil before the catalyst bed.[86] A triple-nozzle spraying system was employed for the aqueous bio-oil fraction in a laboratory reforming model which reduced the char formation in the reactor inlet.[22] Figure 1 shows the schematic diagram of a nozzle fed reactor.

Kechagiopoulos et al. [41,87] investigated the steam reforming of ethylene glycol, acetic acid and aqueous phase bio-oil over Ni/olivine catalysts in a pilot scale spouted bed reactor. In a spouted bed, rapid and sufficient mixing of hot particles and cold injected

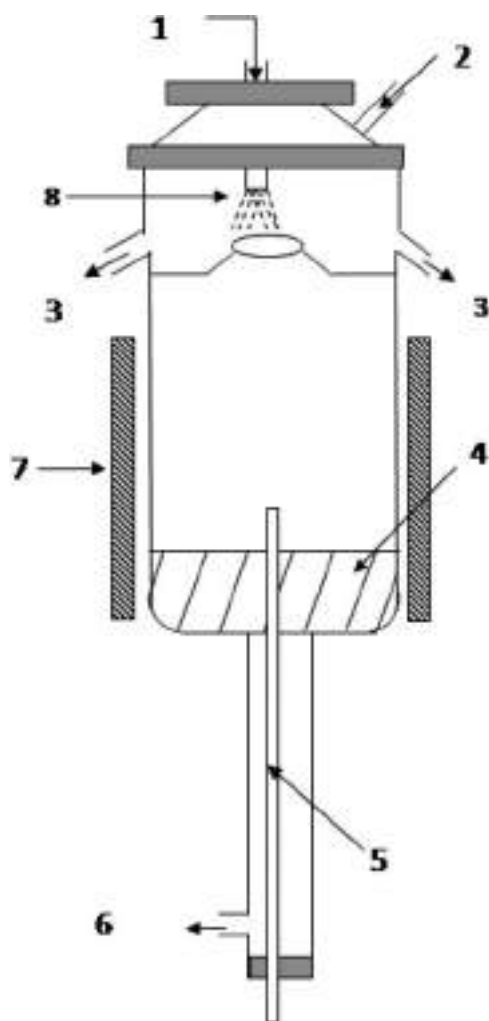


Figure 1. Schematic diagram of the nozzle fed reactor (Basiagiannis AC et al., [63]): (1) liquid inlet (bio-oil), (2) gas inlet, (3) excess liquid outlet, (4) catalyst bed or ceramic monolith/foam, (5) thermowell, (6) products, (7) furnace, (8) nozzle.

reactants along with continuous cyclic movement of solid particles lowers the coke buildup over the catalyst surface. Figure 2 shows the schematic representation of a spouted bed reactor.

Effect of operating parameters on steam reforming of bio-oil

Different operating parameters (temperature, space velocity and S/C) play a very important role in catalytic steam reforming of bio-oil. Steam reforming of bio-oil is an endothermic process and requires high reaction temperatures. Higher bio-oil conversion is favored at high reforming temperature, low pressure and high steam to hydrocarbon ratio.[20,88,89] As reported in literature, carbon conversion and hydrogen yield increases with increase in reaction temperature. The water gas shift reaction is exothermic in nature, carrying out the reaction at higher temperature (i.e. $\sim 950^{\circ}\text{C}$) increases CO yield because of reverse water gas shift reaction.[4,90,91] Thermodynamic studies show that high steam to carbon ratio (S/C) favors the

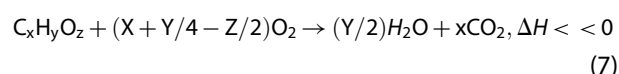
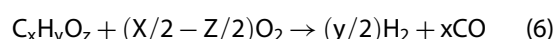
hydrogen formation.[72,78] Increase of steam favors both reforming as well as water-gas shift reaction. Higher S/C also improves carbon gasification (eliminates carbon deposition) on the catalyst surface.[4,92] The decrease in $W_b\text{HSV}$ (from 5.0 h^{-1} to 0.5 h^{-1}) at 700°C results in an increase in H_2 yield from 35% to 60.6%.[86] In a similar experiment, decrease in $W_b\text{HSV}$ from 0.8 h^{-1} to 0.2 h^{-1} resulted in an increase in H_2 yield from 33% to 57%.[93]

Other reforming techniques for H_2 production

To reduce the coke formation during steam reforming of bio-oil a higher S/C is required which makes the process less economically feasible for large scale generation of hydrogen. The few other reforming methods that are practiced for H_2 generation from bio-oil are briefly discussed below.

Partial oxidation (POX)

Partial oxidation is a highly exothermic catalytic/non-catalytic process and widely used method for production of hydrogen rich gas from organic molecules.[94] POX does not require any external heat supply. Compared with that in SR, bio-oil can be converted at relatively lower temperatures in POX.[94,95] Catalytic POX is advantageous over the non-catalytic process due to the heterogeneous reaction requiring lower temperatures and resulting in low soot formation.[96] The general reaction formula for partial oxidation (POX) is [85]:



Poplar wood oil mixed with methanol was used for non-catalytic POX to synthesis gas with a hydrogen yield as low as $\sim 25\%$.[97] Hu and Lu [60] investigated POX of bio-oil alone and further coupled it with dry reforming (DR) at atmospheric pressure. POX of bio-oil gives almost 100% conversion and $\sim 50\%$ H_2 yield at a temperature of 700°C . While coupled with dry reforming it also gives the same result at the same operating parameters. Rennard et al. [98] performed catalytic POX of bio-oil using ester and acids as a model compound over platinum and rhodium based catalysts for the production of synthesis gas.

Oxidative steam reforming (OSR)

The oxidative reforming process is a combination of endothermic steam reforming (SR) and exothermic catalytic partial oxidation (CPO) reactions.[99] In this process hydrocarbon fuel is reacted with both air and steam simultaneously to produce hydrogen.[100,101]

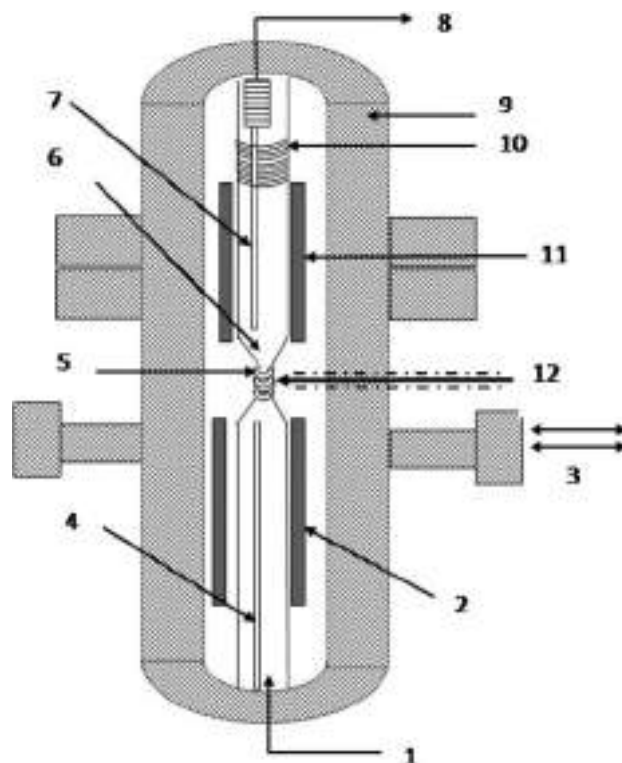
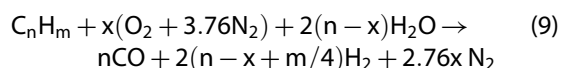
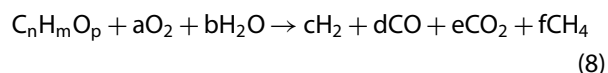


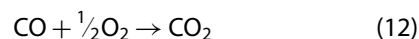
Figure 2. Schematic diagram of the spouted bed reactor [87]: (1) gas and steam inlet, (2) preheating zone, (3) inlet/outlet of electrical connections and thermocouples, (4) preheating zone thermocouples, (5) externally cooled injection nozzle, (6) reactor, (7) thermocouples, (8) products exit, (9) reactor shell, (10) cooling coil, (11) heating zones, (12) externally cooled organics inlet.

The general reaction formula for OSR, using air as the oxygen source and assuming that the products are only CO_2 and H_2 , can be expressed as follows:



The heat generated by this reaction can be controlled directly by adjusting the proportions of fuel, air/oxygen, and steam in the feed.[102] Oxidative steam reformers are simpler, smaller and lighter than steam reformers. The concentration of hydrogen produced by OSR reaction is higher than that of POX.[103] In oxidative steam reforming, the POX and SR take place in one reactor and oxygen facilitates a fast OSR reaction. The presence of oxygen suppresses cracking of hydrocarbons; consequently long chain hydrocarbons can also be reformed which otherwise yield coke.[98] Combination of oxidation reaction along with SR improves the reactor temperature control and in the process reduces the chances of hot spot formation. It also helps in protecting the catalyst from deactivation by carbon deposition.[104] However, the presence of any amount of O_2 lowers both the experimental and theoretical H_2 yield.[20,87,104,105] This is because in the presence of

molecular O_2 the following reactions take place.[106]



Vagia and Lemonidou [104] studied the effect of temperature and pressure on H_2 production. They found out that with an increase in pressure from 0 to 20 atm, H_2 fraction decreases from 0.6 to 0.47. The maximum H_2 yield was obtained at 900 K combining with low CO and CH_4 production. They also observed that at optimum reaction conditions ($T = 900\text{ K}$, $P = 1\text{ atm}$ and $S/C = 3$), 1 kmol of H_2 is produced from 0.245 kmol of simulated bio-oil (acetic acid/ethylene glycol/acetone) which is 20% lower than the H_2 yield achieved by SR method because part of the fuel is consumed during oxidation.

Sequential cracking/two stage reforming

It appears that carbon deposition on the catalyst surface is a key issue in bio-oil steam reforming. Therefore, a different concept has been applied. In this process, two steps were investigated for the conversion of crude pyrolysis bio-oil for H_2 production. In the first step, bio-oil is converted into synthesis gas without addition of water followed by catalytic steam reforming of generated gases.[29,107] A two stage reactor

Table 3. Comparative study of bio-oil reforming.

Catalyst	Experimental conditions	Outcome	Type of feed	Ref.
Pt, Pd, Rh (supported on CeO ₂ , ZrO ₂ and Al ₂ O ₃)	Fixed bed reactor. O/C: 0.54, S/C: 5–11 GHSV: 3090 h ⁻¹ liquid feed rate: 14 μl/min, Temp: 650–950°C	H ₂ yield >50% maintained over 9 h for 1% Pt-CeZrO ₂ Catalytic activity: 1% Rh-CeZrO ₂ > 1% Pt-CeZrO ₂ 1%Rh-Al ₂ O ₃ > 1% Pd-CeZrO ₂ > 1% Pt-Al ₂ O ₃ > 1% Pd-Al ₂ O ₃ . The ceria–zirconia supports were globally much more efficient than the alumina.	Beech wood oil	[20]
Commercial Ni based catalyst, ICI 46-4, UCI G-91	Fixed dual bed reactor, S/C: 5–10, GHSV: 1680 h ⁻¹ Temp: 500–900°C	Increase in S/C ratio increases H ₂ yield; based on ASPEN plus modeling established the thermodynamic model for typical bio-oil.	Poplar wood oil	[23]
Ni based catalyst (C11 NK)	Fixed bed reactor, S/C:2–7, Temp: 500–800°C, GHSV: 600 h ⁻¹ (for bio-oil), GHSV: 1500 h ⁻¹ (for model compounds).	Maximum H ₂ yield at 850°C (~ 60%) and at S/C: 6 (bio-oil), H ₂ yield up to 90% at temp 600°C and at S/C: >3 (acetone) among three analyzed model compounds acetone showed higher tendency towards coke formation.	Aqueous bio-oil (beech wood), acetone, ethylene glycol and acetic acid	[35]
Ni/CNT	Fixed bed reactor, S/C: 2–6, Temp: 350–550°C, GHSV: 1200 h ⁻¹	Higher Ni dispersion leads towards good low temperature reforming.	Bio-oil (saw dust, rice husk, cotton stalk)	[4]
Ni/Al ₂ O ₃ modified with Ca, Ce, Mg, Mn and Zn	Two stage fixed bed reactor, S/C: 3.5–9.0, Zone I Temp: 400°C, Zone II Temp: 600–900°C.	Modified Ni-Al catalysts showed excellent carbon deposition resistance. Ni-Mg-Al catalyst exhibited the highest stability of hydrogen production (56.46%) among the studied catalysts.	Aqueous bio-oil (corn stock)	[112]
Ni/modified dolomite	Fluidized bed, S/C: 2–5, Temp: 600–800°C	The increase in S/C from 2 to 5 results in increase in H ₂ yield with further increase in S/C does not show any pronounced effect on H ₂ yield. Increase in S/C decreases coke yield.	Aqueous bio-oil (saw dust)	[90]
Ni based catalyst (C11 NK)	Fluidized bed, S/C: 7–14, Temp: 800–850°C, GHSV: 700–1000 h ⁻¹	Maximum hydrogen yield from the aqueous bio-oil was about 80% of theoretical yield. Maximum hydrogen yield from the hemicellulose solution of a lignocellulosic biomass was about 70% of that for stoichiometric conversion.	Aqueous bio-oil (pine saw dust), aqueous bio-oil (hemi cellulose rich solution of poplar wood)	[18]
Cl ₂ A7-O ⁻ /M, (M = Mg, K, Ce) 0 wt% < Mg ≤ 36 wt%	Fixed bed reactor, S/C: 1.5–9, Temp: 200–800°C, GHSV = 4000–20000 h ⁻¹	C12A7-O ⁻ /18% Mg catalyst, shows H ₂ yield as high as 80%, and the maximum carbon conversion was 96% under the steam reforming condition (S/C >4.0, GHSV = 10,000 h ⁻¹ , T = 750°C).	Bio-oil	[92]
Ni/CeO ₂ -ZrO ₂ & Z417 (commercial), 5 wt% ≤ Ce ≤ 10 wt% 5 wt% ≤ Ni ≤ 12 wt%	Fixed bed reactor, Temp: 400–850°C, W/B: 3.2–5.8.	Ni/CeO ₂ -ZrO ₂ catalyst with Ni and Ce loading of 12 wt% and 7.5 wt% shows best result at W/B: 4.9, T = 800°C with maximum H ₂ yield of 69.7%, surpassing the H ₂ yield of commercial (Z417) catalyst at same reaction conditions.	Bio-oil (rice-hull)	[71]
Dolomite (primary) Ni/MgO (secondary)	Two stage fixed bed reactor, T: 700–900°C, S/C: 1–16, W _b H ₂ SV: 0.5–5.0 h ⁻¹ , GHSV: 3600 h ⁻¹ , S/CH ₄ : 1–4	Maximum H ₂ yield of 81.1% was obtained at 800°C with GHSV ≤ 3600h ⁻¹ .	Bio-oil	[86]
Pt and Rh/Ce _{0.5} Zr _{0.5} O ₂ (powder and deposited on cordierite monolith)	H ₂ yield of ~ 18 mmolgm ⁻¹ of bio-oil, double envelope stainless steel tubular reactor, T:700°C, liq. feed rate: 1–15 ml/h.	Monolithic supported catalyst gives stable and constant H ₂ production because of better soot gasification in comparison to packed bed.	Crude bio-oil (beech wood)	[107]
5% Ru dispersed over 15%MgO/Al ₂ O ₃	Nozzle fed reactor, Temp: 700–800°C, S/C: 7.2, W/ m _{organic} :0.05–0.2 g _{catalyst} .min/g _{organic} GHSV: 4880–16570 h ⁻¹	High activity was obtained for catalyst in pallet form; MgO in the catalyst enhances the O and/or-OH anion spill-over from the carrier onto the metal particles. High (GHSV) results in decrease in H ₂ selectivity because of formation of by products like CH ₄ and C ₂ H ₄	Aqueous bio-oil (beech wood)	[63]
Commercial C11-NK and NREL#20	Fluidized bed, S/C: 5.8, Temp: 850°C, GHSV: 920 h ⁻¹	Maximum H ₂ yield of 70–80%	Bio-oil (hard wood)	[59]
Ni/MgO, NiO: 7.2 wt%	Fluidized bed, S/C: 8–20, Temp: 500–800°C, W _b H ₂ SV: 0.2–0.8 h ⁻¹ .	H ₂ yield increases with increase in S/C. Maximum H ₂ yield of ~ 55% was obtained at S/C:20 and Temp = 800°C and WHSV 0.5 h ⁻¹ .	Bio-oil (rice husk)	[93]
Ni based commercial catalyst	Fixed bed reactor, S/C: 8–20, Temp: 650–850°C, liq. feed rate: 30 ml/h	Mole fraction of H ₂ and CO ₂ increases with increase in temperature from 650–850°C. Maximum H ₂ yield of 45% was obtained by incorporation of water at 850°C.	Bio-oil (rice husk)	[113]
Ni/Al ₂ O ₃ modified by Ca, Mg.	Bench scale fluidized bed reactor (U/U _{mf} = 10), Temp: 650°C, W/m _{organic} : 4–9 g _{catalyst} .min/g _{organic}	Mg modified catalyst shows the best performance because of less coke deposition.	Aqueous bio-oil (pine wood)	[84]
Ru-Ni/Al ₂ O ₃ , Ni-MgO/Al ₂ O ₃ .	Fixed bed reactor, liquid feed rate: 2.13 ml/h, Temp: 750–950°C, W _b H ₂ SV: 131 h ⁻¹ .	Addition of Ru and MgO to Ni/Al ₂ O ₃ increases H ₂ yield. H ₂ yield of 85% was obtained at 850°C over Ru-Ni/Al ₂ O ₃ .	Commercial bio-oil supplied by BTG group	[70]
Ni/Al ₂ O ₃ , Ni/ZrO ₂	Fixed bed tubular reactor, S/C: 5, liquid feed rate: 2.13 ml h ⁻¹ , Temp: 750–950°C, W _b H ₂ SV: 131 h ⁻¹	H ₂ yield of 60% was obtained for Ni/ZrO ₂ catalyst. Ni/ZrO ₂ based catalyst shows higher carbon formation tendency in comparison to Ni/Al ₂ O ₃ catalyst	Commercial bio-oil supplied by BTG group	[114]
Ni/Al ₂ O ₃ , Ni: 23, 28, 33 (relative atomic %)		28% is the optimum Ni content for maximum H ₂ generation.	Aqueous bio-oil (pine wood)	[36]

(continued)

Table 3. (Continued)

Catalyst	Experimental conditions	Outcome	Type of feed	Ref.
Ni/La ₂ O ₃ - α -Al ₂ O ₃	Fixed bed tubular reactor, S/C: 5.6, Temp: 600–800°C, W/m _{organic} : 0–5.0 g _{catalyst} ·min/g _{organic} Fluidized bed, S/C: 12, Temp: 600–800°C, space time: 0.10 -0.45 g _{catalyst} ·h (g _{bio-oil}) ⁻¹	Maximum H ₂ generation was obtained at 700°C further increase in temperature to 800°C results in decrease in H ₂ yield. Ni/La ₂ O ₃ - α -Al ₂ O ₃ catalyst was found highly stable, with high capacity for reforming coke precursor and high resistance to sintering with both properties being attributed to the presence of La ₂ O ₃ .	Aqueous bio-oil (pine wood)	[5]
Ni based commercial catalyst	Fixed bed tubular reactor, S/C: 8.2, Temp: 600–900°C, GHSV: 300–600 h ⁻¹	In comparison to investigated model compounds, aqueous phase of bio-oil gives 60% H ₂ yield because of high extent of coke formation.	Aqueous bio-oil (pine wood)	[35]
Ni/MgO-La ₂ O ₃ -Al ₂ O ₃	Fixed bed, S/C: 5–10, Temp: 700–900°C, LHSV: 0.8–2.5 h ⁻¹	Incorporation of basic oxide like MgO and La ₂ O ₃ to a Ni/Al ₂ O ₃ catalyst increases the activity of the catalyst due to synergetic effect. Maximum H ₂ yield of 71.42% at 800°C was obtained for Ni/MgO-La ₂ O ₃ -Al ₂ O ₃ catalyst	Bio-oil	[69]

system was chosen to reform bio-oil. Ni based catalyst Ni/MgO was used in the second stage to increase the yield of H₂ and also decrease the deactivation of the catalyst.[86] Bio mass derived crude oil is used for the production of H₂ via sequential cracking and steam reforming process using Pt/Ce_{0.5}Zr_{0.5}O₂ and Rh/Ce_{0.5}Zr_{0.5}O₂ catalyst deposited on cordierite monoliths. The best H₂ yield (70%, corresponding to ~49 mmol of H₂/g of bio-oil) was obtained with Pt catalyst at S/C ratio 10 at 780°C.[72] An efficient and promising approach for the production of H₂ from crude bio-oil was carried out via gasification-reforming dual fixed beds system using NiCuZnAl catalyst. The best H₂ yield of 81.4% with carbon conversion of 87.6% was obtained through the integrative process. The hydrogen productivity in sequential cracking is lower in comparison to continuous steam reforming. On the other hand catalyst regeneration due to coke deposition is comparatively easier.[29]

Aqueous phase reforming

Aqueous phase reforming (APR) is another process to generate H₂ using oxygenated hydrocarbons at low temperatures (~ 270°C) and high pressures (~ 60 bars). Similar to steam reforming, APR involves the breaking of C-C, C-H and O-H bonds.[2] Hydrogen production using this process produces low levels of CO in the effluent gases. Furthermore, steam generation and preheating of feed is not required which lowers the energy consumption during the process.[37] The main products in this reforming are H₂, CO₂, CO and small amounts of light alkanes.[42] Davada and co-workers [108] studied silica supported Ni, Pd, Pt, Ru, Rh, and Ir catalysts at temperature 483–498 K and high pressure of 22 bar using ethylene glycol for the production of hydrogen. Ni/olivine catalyst was tested for reforming of pine derived bio-oil in a fluidized bed reactor. Low surface area of support restricts higher Ni loading over olivine.[87] Shabaker et al. [109] studied the APR of methanol and ethylene glycol over Pt/Al₂O₃ catalysts.

They observed that at constant C/H₂O feed ratios, methanol and ethylene glycol shows similar reactivity over Pt/Al₂O₃ catalysts, which shows that for ethylene glycol the C-C bond cleave is not the rate determining step. However, H₂ generation was found to be higher for methanol in comparison to ethylene glycol. Huber et al. [11] investigated a series of Pt and Ni base catalysts including Sn-modified Raney Ni catalyst for the production of hydrogen from ethylene glycol, sorbitol and glycerol at a temperature of 225–265°C and pressures of 5–26 bar. The results obtained from the experiments depict that the Sn-modified Raney Ni catalyst achieved high activity equivalent to those found for the Pt/Al₂O₃ catalyst. Lehnert and Claus [110] studied the APR of glycerol with different particle sizes (1.6–3.2 nm) of Pt/Al₂O₃ catalyst; with no change in glycerol conversion (20%) enhanced hydrogen selectivity was observed for bigger catalyst particles size (3.2 nm) in comparison to smaller ones (1.6 nm), suggesting the structure dependency of the APR reaction. An increase in particle size results in an increase in the number of face atoms of metal crystallites whereas the number of edge and corner atoms decreases. The low degree of conversion and low production rate for APR requires large reactor volume and large recycle loops. Deactivation is also a major challenge with APR during the processing of heavier compounds.[73] A detailed comparative study of bio-oil reforming from the literature is discussed in Table 3.

Summary and conclusions

Hydrogen generation from renewable energy sources is needed to meet future energy demands. Steam reforming of bio-oil in the presence of an active catalyst is a promising route for sustainable hydrogen production. The catalyst formulation should show resilience towards deactivation by coke formation which is one of the major challenges in the bio-oil steam reforming reaction. The use of ceria as support modifier in a Ni based catalyst promotes coke

gasification which reduces the catalyst deactivation through coking. Incorporation of MgO to Al₂O₃ support improves the adsorption and H₂O dissociation capacity helping to keep the nickel metal surface free of carbon. Addition of a small amount of lanthanum also improves catalyst stability and decreases coke formation. Introduction of small amounts of O₂ also helps in bringing down coke formation, gasifying the carbonaceous material over the catalyst surface. Reactor choice plays an important role in steam reforming of bio-oil. The fixed bed reactor is the most commonly used reactor for steam reforming for both liquid and gas feeds. In comparison to different model compounds, reforming of aqueous phase of bio-oil yields less H₂ due to the high extent of coking. The use of fluidized bed and spouted bed reactors showed less coke formation in comparison to fixed bed reactors. Use of nozzle spray helps in uniform distribution of bio-oil over the catalyst bed. Other reforming techniques are also in the early stages of the study. Further investigation and research is required for industrial production of H₂ from bio-oil.

Nomenclature

GHSV	Ratio of volumetric flow rate to gas to volume of catalyst
W _b HSV	Ratio of mass of mass flow rate of bio-oil to mass of catalyst
Organics	Organic compounds contained in the aqueous fraction of pyrolysis liquids
S/C	moles of steam/moles of carbon
U/U _{mf}	Superficial gas velocity/velocity for minimum fluidization
wt%	Weigh percentage
W/m _{organic}	Catalyst weight/organic mass flow rate
W/B	Water/Bio-oil
O/C	moles of O ₂ /moles of carbon in the feed
HHV (MJ/kg)	High heating value

Disclosure statement

No potential conflict of interest was reported by the authors.

ORCID

J.P. Chakraborty  <http://orcid.org/0000-0001-7914-9358>

References

- [1] Kamat PV. Meeting the clean energy demand: nanostructure architectures for solar energy conversion. *J. Phys. Chem.* **2007**;C 111:2834–2860.
- [2] Kan T, Xiong J, Li X, et al. High efficient production of hydrogen from crude bio-oil via an integrative process between gasification and current-enhanced catalytic steam reforming. *Int. J. Hydrogen Energy* **2010**;35:518–532.
- [3] Mota N, Navarro RM, Alvarez-Galvan MC, et al. Hydrogen production by reforming of diesel fuel over

catalysts derived from LaCo_{1-x}Ru_xO₃ perovskites: Effect of the partial substitution of Co by Ru (x = 0.01–0.1). *J. Power Sources* **2011**;196:9087–9095.

- [4] Hou T, Yuan L, Ye T, et al. Hydrogen production by low-temperature reforming of organic compounds in bio-oil over a CNT-promoting Ni catalyst. *Int. J. Hydrogen Energy* **2009**;34:9095–9107.
- [5] Remiro A, Valle B, Aguayo AT, et al. Operating conditions for attenuating Ni/La₂O₃–αAl₂O₃ catalyst deactivation in the steam reforming of bio-oil aqueous fraction. *Fuel Process. Technol.* **2013**;115:222–232.
- [6] Kirtay E. Recent advances in production of hydrogen from biomass. *Energy Convers. Manage* **2011**;52:1778–1789.
- [7] Haryanto A, Fernando S, Murali N, et al. Current status of hydrogen production techniques by steam reforming of ethanol: A review. *Energy Fuels* **2005**;19:2098–2106.
- [8] Peña MA, Gómez JP, Fierro JLG. New catalytic routes for syngas and hydrogen production. *Appl. Catal.* **1996**;A 144:7–57.
- [9] Vaidya PD, Rodrigues AE. Insight into steam reforming of ethanol to produce hydrogen for fuel cells. *Chem. Eng. J.* **2006**;117:39–49.
- [10] Das D, Veziroglu TN. Hydrogen production by biological processes: A survey of literature. *Int. J. Hydrogen Energy* **2001**;26:13–28.
- [11] Huber GW, Shabaker JW, Dumesic JA. Raney Ni–Sn Catalyst for H₂ Production from Biomass-Derived Hydrocarbons. *Science* **2003**;300:2075–2077.
- [12] Hanaoka T, Inoue S, Uno S, et al. Effect of woody biomass components on air-steam gasification. *Biomass Bioenergy* **2005**;28:69–76.
- [13] McKendry P. Energy production from biomass (part 1): overview of biomass. *Bioresour. Technol.* **2002**;83:37–46
- [14] Yang H, Yan R, Chen H, et al. Characteristics of hemicellulose, cellulose and lignin pyrolysis. *Fuel* **2007**;86(12–13):1781–1788.
- [15] García L, Salvador ML, Arauzo J, et al. Catalytic steam gasification of pine sawdust. Effect of catalyst weight/biomass flow rate and steam/biomass ratios on gas production and composition. *Energy Fuels* **1999**;13:851–859.
- [16] Matsumura Y, Minowa T, Potic B, et al. Biomass gasification in near- and super-critical water: Status and prospects. *Biomass Bioenergy* **2005**;29:269–292.
- [17] Basagiannis AC, Veykios XE. Reforming reactions of acetic acid on nickel catalysts over a wide temperature range. *Appl. Catal.* **2006**;A 308:182–193.
- [18] Czernik S, French R, Feik C, et al. Hydrogen by catalytic steam reforming of liquid byproducts from biomass thermoconversion processes. *Ind. Eng. Chem. Res.* **2002**;41:4209–4215.
- [19] Garcia La, French R, Czernik S, et al. Catalytic steam reforming of bio-oils for the production of hydrogen: effects of catalyst composition. *Appl. Catal.* **2000**;A 201:225–239.
- [20] Rioche C, Kulkarni S, Meunier FC, et al. Steam reforming of model compounds and fast pyrolysis bio-oil on supported noble metal catalysts. *Appl. Catal.* **2005**;B 61:130–139.
- [21] Takanabe K, Aika K-i, Seshan K, et al. Sustainable hydrogen from bio-oil–Steam reforming of acetic acid as a model oxygenate. *J. Catal.* **2004**;227:101–108.
- [22] Wang D, Czernik S, Chornet E. Production of hydrogen from biomass by catalytic steam reforming of fast pyrolysis oils. *Energy Fuels* **1998**;12:19–24.

- [23] Wang D, Czernik S, Montané D, et al. Biomass to hydrogen via fast pyrolysis and catalytic steam reforming of the pyrolysis oil or its fractions. *Ind. Eng. Chem. Res.* **1997**;36:1507–1518.
- [24] Wang D, Montané D, Chornet E. Catalytic steam reforming of biomass-derived oxygenates: acetic acid and hydroxyacetaldehyde. *Appl. Catal.* **1996**;A 143:245–270.
- [25] Navarro R, Sanchez-Sanchez M, Alvarez-Galvan M, et al. Hydrogen production from renewable sources: biomass and photocatalytic opportunities. *Energy & Environmental Science* **2009**;2:35–54.
- [26] Ayalur Chattanathan S, Adhikari S, Abdoulmoumine N. A review on current status of hydrogen production from bio-oil. *Renewable Sustainable Energy Rev.* **2012**;16:2366–2372.
- [27] Raffelt K, Henrich E, Koegel A, et al. The BTL2 process of biomass utilization entrained-flow gasification of pyrolyzed biomass slurries. *Appl. Biochem. Biotechnol.* **2006**;129:153–164.
- [28] Vagia EC, Lemonidou AA. Thermodynamic analysis of hydrogen production via steam reforming of selected components of aqueous bio-oil fraction. *Int. J. Hydrogen Energy* **2007**;32:212–223.
- [29] Davidian T, Guilhaume N, lojoiu E, et al. Hydrogen production from crude pyrolysis oil by a sequential catalytic process. *Appl. Catal.* **2007**;B 73:116–127.
- [30] Zhang J, Toghiani H, Mohan D, et al. Product analysis and thermodynamic simulations from the pyrolysis of several biomass feedstocks. *Energy Fuels* **2007**;21:2373–2385.
- [31] Mohan D, Pittman CU, Steele PH. Pyrolysis of wood/biomass for bio-oil: A critical review. *Energy Fuels* **2006**;20:848–889.
- [32] Oasmaa A, Czernik S. Fuel oil quality of biomass pyrolysis oils. State of the art for the end users. *Energy Fuels* **1999**;13:914–921.
- [33] Diebold JP. A review of the chemical and physical mechanisms of the storage stability of fast pyrolysis bio-oils: National Renewable Energy Laboratory Golden, CO; **2000**.
- [34] Wang ZX, Dong T, Yuan LX, et al. Characteristics of bio-oil-syngas and its utilization in Fischer–Tropsch synthesis. *Energy Fuels* **2007**;21:2421–2432.
- [35] Kechagiopoulos PN, Voutetakis SS, Lemonidou AA, et al. Hydrogen production via steam reforming of the aqueous phase of bio-oil in a fixed bed reactor. *Energy Fuels* **2006**;20:2155–2163.
- [36] Bimbela F, Oliva M, Ruiz J, et al. Hydrogen production via catalytic steam reforming of the aqueous fraction of bio-oil using nickel-based coprecipitated catalysts. *Int. J. Hydrogen Energy* **2013**;38:14476–14487.
- [37] Basagiannis A, Vergykios X. Catalytic steam reforming of acetic acid for hydrogen production. *Int. J. Hydrogen Energy* **2007**;32:3343–3355.
- [38] Fatsikostas AN, Kondarides DI, Vergykios XE. Production of hydrogen for fuel cells by reformation of biomass-derived ethanol. *Catal. Today* **2002**;75:145–155.
- [39] Iordanidis AA, Kechagiopoulos PN, Voutetakis SS, et al. Autothermal sorption-enhanced steam reforming of bio-oil/biogas mixture and energy generation by fuel cells: Concept analysis and process simulation. *Int. J. Hydrogen Energy* **2006**;31:1058–1065.
- [40] Iulianelli A, Longo T, Basile A. CO-free hydrogen production by steam reforming of acetic acid carried out in a Pd–Ag membrane reactor: The effect of co-current and counter-current mode. *Int. J. Hydrogen Energy* **2008**;33:4091–4096.
- [41] Kechagiopoulos PN, Voutetakis SS, Lemonidou AA, et al. Sustainable hydrogen production via reforming of ethylene glycol using a novel spouted bed reactor. *Catal. Today* **2007**;127:246–255.
- [42] Markevich M, Czernik S, Chornet E, et al. Hydrogen from biomass: steam reforming of model compounds of fast-pyrolysis oil. *Energy Fuels* **1999**;13:1160–1166.
- [43] Ni M, Leung DY, Leung MK. A review on reforming bio-ethanol for hydrogen production. *Int. J. Hydrogen Energy* **2007**;32:3238–3247.
- [44] Resini C, Arrighi L, Concepción Herrera Delgado M, et al. Production of hydrogen by steam reforming of C3 organics over Pd–Cu/–Al₂O₃ catalyst. *Int. J. Hydrogen Energy* **2006**;31:13–19.
- [45] Demirbas A. Competitive liquid biofuels from biomass. *Appl. Energy* **2011**;88:17–28.
- [46] Oasmaa A, Meier D. Norms and standards for fast pyrolysis liquids: 1. Round robin test. *J. Anal. Appl. Pyrolysis* **2005**;73:323–334.
- [47] Zhang Q, Chang J, Wang T, et al. Review of biomass pyrolysis oil properties and upgrading research. *Energy Convers. Manage.* **2007**;48:87–92.
- [48] García-Pérez M, Chaala A, Roy C. Vacuum pyrolysis of sugarcane bagasse. *J. Anal. Appl. Pyrolysis* **2002**;65:111–136.
- [49] Diebold JP, Czernik S. Additives to lower and stabilize the viscosity of pyrolysis oils during storage. *Energy Fuels* **1997**;11:1081–1091.
- [50] Adhikari S, Fernando SD, Haryanto A. Hydrogen production from glycerol: An update. *Energy Convers. Manage.* **2009**;50:2600–2604.
- [51] Navarro R, Pena M, Fierro J. Hydrogen production reactions from carbon feedstocks: fossil fuels and biomass. *Chem. Rev.* **2007**;107:3952–3991.
- [52] Goula MA, Kontou SK, Tsiakaras PE. Hydrogen production by ethanol steam reforming over a commercial Pd/γ-Al₂O₃ catalyst. *Appl. Catal.* **2004**;B 49:135–144.
- [53] Satterfield CN. *Heterogeneous catalysis in industrial practice*. 2nd ed. New York, NY: McGraw Hill Book Co.; **1991**.
- [54] Trimm DL. Coke formation and minimisation during steam reforming reactions. *Catal. Today* **1997**;37:233–238.
- [55] Cheng F, Dupont V. Nickel catalyst auto-reduction during steam reforming of bio-oil model compound acetic acid. *Int. J. Hydrogen Energy* **2013**;38:15160–15172.
- [56] Sehested J. Four challenges for nickel steam-reforming catalysts. *Catal. Today* **2006**;111:103–110.
- [57] Garcia-Garcia I, Acha E, Bizkarra K, et al. Hydrogen production by steam reforming of m-cresol, a bio-oil model compound, using catalysts supported on conventional and unconventional supports. *Int. J. Hydrogen Energy* **2015**;40:14445–14455.
- [58] Rostrup-Nielsen J. *Catalytic steam reforming in Catalysis science and technology*. In: Anderson JR, Boudart M., editors. Berlin: Springer-Verlag.
- [59] Czernik S, Evans R, French R. Hydrogen from biomass-production by steam reforming of biomass pyrolysis oil. *Catal. Today* **2007**;129:265–268.
- [60] Hu X, Lu G. Bio-oil steam reforming, partial oxidation or oxidative steam reforming coupled with bio-oil dry reforming to eliminate CO₂ emission. *Int. J. Hydrogen Energy* **2010a**;35:7169–7176.
- [61] Lan P, Xu Q, Zhou M, et al. Catalytic steam reforming of fast pyrolysis bio-oil in fixed bed and fluidized bed reactors. *Chem. Eng. Technol.* **2010**;33: 2021–2028.

- [62] Llorca J, Corberan VC, Divins NJ, Fraile RO, Taboada E. Hydrogen from bioethanol. In: Gandia LM, Arzamendi G, Dieguez PM, editors. *Renewable hydrogen technologies: production, purification, storage, applications and safety*. 1st ed. Philadelphia: Elsevier Science; 2013.
- [63] Basagiannis AC, Verykios XE. Steam reforming of the aqueous fraction of bio-oil over structured Ru/MgO/Al₂O₃ catalysts. *Catal. Today* 2007;127:256–264.
- [64] Diagne C, Idriss H, Pearson K, et al. Efficient hydrogen production by ethanol reforming over Rh catalysts. Effect of addition of Zr on CeO₂ for the oxidation of CO to CO₂. *C.R. Chim.* 2004;7:617–622.
- [65] Gorte RJ. Ceria in catalysis: from automotive applications to the water–gas shift reaction. *AIChE journal* 2010;56(5):1126–1135.
- [66] Matas Güell B, Babich I, Nichols KP, et al. Design of a stable steam reforming catalyst—A promising route to sustainable hydrogen from biomass oxygenates. *Appl. Catal.* 2009;B 90:38–44.
- [67] Matas Güell B, Babich IV, Lefferts L, et al. Steam reforming of phenol over Ni-based catalysts – A comparative study. *Appl. Catal.* 2011;B 106:280–286.
- [68] Trane-Restrup R, Dahl S, Jensen AD. Steam reforming of ethanol: Effects of support and additives on Ni-based catalysts. *Int. J. Hydrogen Energy* 2013;38:15105–15118.
- [69] Lan P, Xu Q-L, Lan L-H, et al. Steam reforming of model compounds and fast pyrolysis bio-oil on supported nickel metal catalysts for hydrogen production. *Energy Sources, Part A: Recovery, Utilization, and Environmental Effects* 2012;34:2004–2015.
- [70] Salehi E, Azad FS, Harding T, et al. Production of hydrogen by steam reforming of bio-oil over Ni/Al₂O₃ catalysts: effect of addition of promoter and preparation procedure. *Fuel Process. Technol.* 2011;92:2203–2210.
- [71] Yan C-F, Cheng F-F, Hu R-R. Hydrogen production from catalytic steam reforming of bio-oil aqueous fraction over Ni/CeO₂–ZrO₂ catalysts. *Int. J. Hydrogen Energy* 2010;35:11693–11699.
- [72] Domine ME, Jojoi EE, Davidian T, et al. Hydrogen production from biomass-derived oil over monolithic Pt- and Rh-based catalysts using steam reforming and sequential cracking processes. *Catal. Today* 2008;133-135:565–573.
- [73] Trane R, Dahl S, Skjøth-Rasmussen MS, et al. Catalytic steam reforming of bio-oil. *Int. J. Hydrogen Energy* 2012;37:6447–6472.
- [74] Czernik S, French RJ, Magrini-Bair KA, et al. The production of hydrogen by steam reforming of trap grease progress in catalyst performance. *Energy Fuels* 2004;18:1738–1743.
- [75] Galdámez JR, García L, Bilbao R. Hydrogen production by steam reforming of bio-oil using coprecipitated Ni–Al catalysts. Acetic acid as a model compound. *Energy Fuels* 2005;19:1133–1142.
- [76] Goyal N, Pant KK, Gupta R. Hydrogen production by steam reforming of model bio-oil using structured Ni/Al₂O₃ catalysts. *Int. J. Hydrogen Energy* 2013;38:921–933.
- [77] Liguras DK, Kondarides DI, Verykios XE. Production of hydrogen for fuel cells by steam reforming of ethanol over supported noble metal catalysts. *Appl. Catal.* 2003;B 43:345–354.
- [78] Pant K, Jain R, Jain S. Renewable hydrogen production by steam reforming of glycerol over Ni/CeO₂ catalyst prepared by precipitation deposition method. *Korean J. Chem. Eng.* 2011;28:1859–1866
- [79] Polychronopoulou K, Costa CN, Efstathiou AM. The steam reforming of phenol reaction over supported-Rh catalysts. *Appl. Catal.* 2004;A 272:37–52.
- [80] Hu X, Lu G. Comparative study of alumina-supported transition metal catalysts for hydrogen generation by steam reforming of acetic acid. *Appl. Catal.* 2010;B 99:289–297
- [81] Kinoshita CM, Turn SQ. Production of hydrogen from bio-oil using CaO as a CO₂ sorbent. *Int. J. Hydrogen Energy* 2003;28:1065–1071
- [82] Wu C, Sui M, Yan YJ. A comparison of steam reforming of two model bio-oil fractions. *Chem. Eng. Technol.* 2008;31:1748–1753.
- [83] Zhang R, Wang Y, Brown RC. Steam reforming of tar compounds over Ni/olivine catalysts doped with CeO₂. *Energy Convers. Manage.* 2007;48:68–77.
- [84] Medrano J, Oliva M, Ruiz J, et al. Hydrogen from aqueous fraction of biomass pyrolysis liquids by catalytic steam reforming in fluidized bed. *Energy* 2011;36:2215–2224
- [85] Rennard D, French R, Czernik S, et al. Production of synthesis gas by partial oxidation and steam reforming of biomass pyrolysis oils. *Int. J. Hydrogen Energy* 2010;35:4048–4059.
- [86] Wu C, Huang Q, Sui M, et al. Hydrogen production via catalytic steam reforming of fast pyrolysis bio-oil in a two-stage fixed bed reactor system. *Fuel Process. Technol.* 2008;89:1306–1316.
- [87] Kechagiopoulos PN, Voutetakis SS, Lemonidou AA, et al. Hydrogen production via reforming of the aqueous phase of bio-oil over Ni/olivine catalysts in a spouted bed reactor. *Ind. Eng. Chem. Res.* 2009;48:1400–1408.
- [88] Lutz AE, Bradshaw RW, Keller JO, et al. Thermodynamic analysis of hydrogen production by steam reforming. *Int. J. Hydrogen Energy* 2003;28:159–167.
- [89] Navarro RM, Álvarez-Galván MC, Rosa F, et al. Hydrogen production by oxidative reforming of hexadecane over Ni and Pt catalysts supported on Ce/La-doped Al₂O₃. *Appl. Catal.* 2006;A 297:60–72.
- [90] Li H, Xu Q, Xue H, et al. Catalytic reforming of the aqueous phase derived from fast-pyrolysis of biomass. *Renewable Energy* 2009;34:2872–2877.
- [91] Seyedeyn-Azad F, Salehi E, Abedi J, et al. Biomass to hydrogen via catalytic steam reforming of bio-oil over Ni-supported alumina catalysts. *Fuel Process. Technol.* 2011;92:563–569.
- [92] Wang Z, Pan Y, Dong T, et al. Production of hydrogen from catalytic steam reforming of bio-oil using C12A7-O–based catalysts. *Appl. Catal.* 2007;A 320:24–34.
- [93] Xu Q, Lan P, Zhang B, et al. Hydrogen production via catalytic steam reforming of fast pyrolysis bio-oil in a fluidized-bed reactor. *Energy Fuels* 2010;24:6456–6462.
- [94] Salge JR, Deluga GA, Schmidt LD. Catalytic partial oxidation of ethanol over noble metal catalysts. *J. Catal.* 2005;235:69–78.
- [95] Pastore A, Mastorakos E. Syngas production from liquid fuels in a non-catalytic porous burner. *Fuel* 2011;90:64–76.
- [96] Bharadwaj SS, Schmidt LD. Catalytic partial oxidation of natural gas to syngas. *Fuel Process. Technol.* 1995;42:109–127.
- [97] Marda JR, DiBenedetto J, McKibben S, Evans RJ, et al. Non-catalytic partial oxidation of bio-oil to synthesis gas for distributed hydrogen production. *Int. J. Hydrogen Energy* 2009;34:8519–8534.

- [98] Rennard DC, Dauenhauer PJ, Tupy SA, et al. Autothermal catalytic partial oxidation of bio-oil functional groups: esters and acids. *Energy Fuels* **2008**;22:1318–1327.
- [99] Gutierrez A, Karinen R, Airaksinen S, et al. Autothermal reforming of ethanol on noble metal catalysts. *Int. J. Hydrogen Energy* **2011**;36:8967–8977.
- [100] Hoang DL, Chan SH. Experimental investigation on the effect of natural gas composition on performance of autothermal reforming. *Int. J. Hydrogen Energy* **2007**;32:548–556.
- [101] Peela NR, Kunzru D. Oxidative steam reforming of ethanol over Rh based catalysts in a micro-channel reactor. *Int. J. Hydrogen Energy* **2011**;36:3384–3396.
- [102] Harada M, Takanabe K, Kubota J, et al. Hydrogen production by autothermal reforming of kerosene over MgAlO_x-supported Rh catalysts. *Appl. Catal.* **2009**;A 371:173–178
- [103] Karatzas X, Dawody J, Grant A, et al. Zone-coated Rh-based monolithic catalyst for autothermal reforming of diesel. *Appl. Catal.* **2011**;B 101(3-4):226–238.
- [104] Vagia EC, Lemonidou AA. Thermodynamic analysis of hydrogen production via autothermal steam reforming of selected components of aqueous bio-oil fraction. *Int. J. Hydrogen Energy* **2008**;33:2489–2500
- [105] van Rossum G, Kersten SRA, van Swaaij WPM. Catalytic and noncatalytic gasification of pyrolysis oil. *Ind. Eng. Chem. Res.* **2007**;46:3959–3967.
- [106] Klouz V, Fierro V, Denton P, et al. Ethanol reforming for hydrogen production in a hybrid electric vehicle: process optimisation. *J. Power Sources* **2002**;105: 26–34.
- [107] Iojoiu EE, Domine ME, Davidian T, et al. Hydrogen production by sequential cracking of biomass-derived pyrolysis oil over noble metal catalysts supported on ceria-zirconia. *Appl. Catal.* **2007**;A 323:147–161
- [108] Davada RR, Shabaker JW, Huber, GW, et al. Aqueous-phase reforming of ethylene glycol on silica-supported metal catalysts. *Appl. Catal., B* **2003**; 43:13–26.
- [109] Shabaker JW, Davda RR, Huber GW, et al. Aqueous-phase reforming of methanol and ethylene glycol over alumina-supported platinum catalysts. *J. Catal.* **2003**;215:344–352.
- [110] Lehnert K, Claus P. Influence of Pt particle size and support type on the aqueous-phase reforming of glycerol. *Catal. Commun.* **2008**;9:2543–2546.
- [111] Thangalazhy-Gopakumar S, Adhikari S, Ravindran H, et al. Physicochemical properties of bio-oil produced at various temperatures from pine wood using an auger reactor. *Bioresour. Technol.* **2010**;101: 8389–8395.
- [112] Yao D, Wu C, Yang H, et al. Hydrogen production from catalytic reforming of the aqueous fraction of pyrolysis bio-oil with modified Ni–Al catalysts. *Int. J. Hydrogen Energy* **2014**;39:14642–14652.
- [113] Chen T, Wu C, Liu R. Steam reforming of bio-oil from rice husks fast pyrolysis for hydrogen production. *Bioresour. Technol.* **2011**;102:9236–9240.
- [114] Seyedejn Azad F, Abedi J, Salehi E, et al. Production of hydrogen via steam reforming of bio-oil over Ni-based catalysts: Effect of support. *Chem. Eng. J.* **2012**;180:145–150.



A comparative study on valuable products: bio-oil, biochar, non-condensable gases from pyrolysis of agricultural residues

Kedar Sahoo¹ · Ankit Kumar¹ · Jyoti Prasad Chakraborty¹

Received: 30 January 2020 / Accepted: 11 September 2020
© Springer Japan KK, part of Springer Nature 2020

Abstract

In this study, pyrolysis of agricultural residues, such as rice straw (RS), wheat straw (WS), and sugarcane bagasse (SB), was performed in a fixed-bed reactor. The experiments were carried out at varying operating conditions, such as temperature, heating rate, biomass particle size and sweeping gas flow rate, such that the bio-oil yield could be maximized. Small particle size and high heating rate contributed to more bio-oil yield as compared to large particle size and low heating rate. Physico-chemical properties of bio-oil samples, evaluated in a comparative manner with maximum focus devoted on analyzing the chemical constituents through GC–MS and FTIR analysis. Biochar was also examined through different physicochemical techniques (e.g., HHV, pH, SEM–EDX, FTIR, CHNS, ICP–AES) for understanding pyrolysis mechanism and its practical usability. Analysis of non-condensable gas through GC–TCD, revealed co-existence of H₂, CO, CO₂ and CH₄ molecules, with greater percentage of H₂ and CH₄ at high temperature resulted enhancement in calorific value.

Keywords Pyrolysis · RS · WS · SB · Fixed-bed

Introduction

Maximum of the world's energy resources are non-renewable and fulfilling through fossil fuel sector, those are depleting day by day due to their extensive uses, and also there is a rising concern for greenhouse gas emissions [1, 2]. These fundamental problems have created a tremendous amount of interest in the field of alternative and renewable fuels, which are environmentally benign as well as economically viable [3]. Biomass is a major source of energy; it provides approx. 10–14% energy demand of world [4]. Biomass, such as materials produced from microbial, animal, algae, agricultural waste, and forestry residues, is the renewable energy source, which converted into liquid fuels and value-added chemicals and used as high-potential feedstock for conventional petroleum-based energy sector around the world

[5–9]. Biomass has gained more attention because of its wide availability and low cost in comparison to other renewable energy sources [10–12]. Agricultural biomasses mainly comprise cellulose (30–60%), hemicellulose (20–35%) and lignin (15–30%) along with some resins and inorganic constituents and possess high-energy content [13]. They can be used for getting heat, power, synthesis gas, and chemicals through different thermo-chemical routes, such as combustion, gasification, pyrolysis, liquefaction, and enzymatic route, such as fermentation [14–19]. Among the various methods available for agricultural biomass conversion to the biofuels, pyrolysis is a promising technique which incurs lesser amount of cost and leads to the generation of high-energy-density bio fuel, performed in an inert atmosphere [20]. It is a thermo-chemical process that can efficiently produce bio-oil, gases and biochar. The yield and properties of products obtained from pyrolysis strongly depend on various factors viz. reactor design, operating conditions (temperature, heating rate, particle size, and sweeping gas flow rate etc.) as well as on type of biomass used [21–23]. Due to the diversity and heterogeneity in biomass composition and its typical thermal decomposition nature makes, resulting pyrolysis mechanism is very much complex [24]. Studies explained that there are three stages of pyrolysis reactions: (1) removal of free moisture (2) initial decomposition of

Electronic supplementary material The online version of this article (<https://doi.org/10.1007/s10163-020-01114-2>) contains supplementary material, which is available to authorized users.

✉ Jyoti Prasad Chakraborty
jpc.che@iitbhu.ac.in

¹ Department of Chemical Engineering and Technology,
Indian Institute of Technology (BHU), Varanasi, UP 221005,
India

long-chain molecules (3) followed by bio-oil decomposition and re-polymerization [25]. Since cellulose present in abundance amount in agricultural biomass, a simple decomposition mechanism explained by Waterloo helps to understand the reaction pathways for pyrolysis process [26]. Accordingly, at low temperature, cellulose gets depolymerized (300–450 °C) and subsequently defragmented at a higher temperature (~600 °C), and finally turns into carboxylic acid, alcohol, aldehyde, ketone, and anhydrosugars, etc. which are the major compounds found in bio-oil [24].

Indian economy is mostly agricultural-based because 60.6% of the cultivable land is being used by 53% of people, those belonging to rural India and who earn their livelihood through farming. So, a lot of agricultural wastes are generated every year, which are utilized directly for animal consumption or used as raw material for pulp and paper industry. However, storage, collection and transportation of residual biomass are very difficult and expensive. Therefore, it remained unutilized as a waste or directly burned in household stove or farms, causing serious environmental pollution and health hazards. A simple solution of this acute environmental problem arising from burning crop residues and unused biomass waste can be to solve through production of bio-oil and other value-added products locally through pyrolysis [11]. Bio-oil produced by pyrolysis of biomass is a free-flowing complex organic liquid dark brown in color, contains highly oxygenated organic compounds and having smoky odor [21, 27]. Bio-oil has an advantage over fossil fuel because it contains a very low amount of bonded nitrogen and sulfur resulting in lesser amount of greenhouse gas emission during combustion [19, 28]. However, it contains variety of value-added chemicals that can be used in different applications. The non-condensable gases produced during pyrolysis mainly comprise H₂, CO, CH₄, and CO₂ up to 95% [29, 30], which has high calorific value and further can be utilized for energy generation.

Apart from bio-oil and non-condensable gases, biochar (also called charcoal) is also the valuable solid product containing unconverted organic, inorganic and carbonaceous residues obtained from pyrolysis. According to the previous literatures [31, 32], biochar is mainly a carbon-rich compound with composition ranging from 53 to 96%, heating values ranging from 20 to 36 MJ/kg, and yields of biochar obtained from pyrolysis of different feedstock varied between 30 and 90%. The high HHV of biochar makes it a valuable combustible product, which can be substituted for coal also [33]. The highly porous surface structure of biochar confers it as a low-cost adsorbent material for removal of various organic and inorganics pollutants [25, 32] as well as in catalysis application also [34]. Biochar can also act as a fertilizer for soil amendment application [35] and can also contribute in carbon sequestration process [36].

Agricultural residues, such as wheat straw (WS), rice straw (RS), sugarcane bagasse (SB), are the largest and abundant by-products produced in the developing countries like India, Brazil, China, etc. [37, 38]. A lot of research has been carried out on pyrolysis of RS, WS and SB previously. Wang et al. [39] pyrolysed RS in a simple closed reactor at 523–773 K with 10 K/min heating rate. The maximum yield of liquid products was obtained at 693 K with H/C molar ratio of 1.65 and O/C molar ratio of 0.058 just in the range of petroleum. Park et al. [40] carried out slow pyrolysis of RS at different temperature range from 300 to 700 °C with a 10 °C/min heating rate. The yield of bio-oil and biochar obtained was same above 500 °C temperature. At 700 °C temperature, yield of bio-oil declined while gas yield increased. Balagurumurthy et al. [41] also performed pyrolysis of RS in the presence of hydrogen and nitrogen atmosphere. They observed that, higher yield of bio-oil was obtained under nitrogen atmosphere as compared to hydrogen environment. Pottmair et al. [42] performed pyrolysis of rice husk and WS in the wide temperature range from 290 to 900 °C at constant flow of nitrogen 100 mL/min with 50 °C/min heating rate. They reported that the bio-oil yield increases with rise in temperature from 290 to 900 °C for both the biomass. Varma et al. [43] conducted pyrolysis of SB in a semi-batch reactor at different temperature range of 350–650 °C with two heating rates (10 and 50 °C/min) and biomass particle sizes (<0.25 to 1.7 mm). They concluded that maximum bio-oil yield of 45.23% was obtained at temperature 500 °C with heating rate 50 °C/min, particle size of 0.5–0.6 mm and nitrogen flow rate of 100 cm³/min. Gonclaves et al. [44] evaluated the pyrolysis of SB in a fixed-bed reactor to investigate the product distributions at various operating conditions, such as temperature heating rate, particle size of biomass samples and sweeping gas flow rate of nitrogen. They reported highest bio-oil yield (0.5 g/g of biomass) at 600 °C, 15 °C/min heating rate and N₂ flow rate of 200 mL/min, with particle size ranging from 0.5 to 1.0 mm. Temperature and particles' sizes were the most significant factors for the maximum bio-oil yield. Also, Biswas et al. [11] performed a comparative study on fixed-bed pyrolysis of various agricultural residues, such as RS, husk, corn stover, WS at different temperatures range 300–450 °C with a fixed heating rate of 20 °C/min and nitrogen flow rate 50 mL/min and analyzed bio-oil produced during experimentation. Maximum bio-oil yields were varied for corn cob, WS, RS and rice husk were 47.3, 36.7, 28.4 and 38.1%, respectively [11]. Apart from this, Duong et al. [45] carried out thermal degradation of four types of Vietnamese biomasses, e.g. bagasse, corncob, rice husk and rice straw, through pyrolysis reaction for bio-oil production. This study has revealed that the bio-oil yield greatly depended on temperatures and sweeping gas flow rate, not the biomass particles size. Moreover rice husk and straw shown greater

production of bio-oil than bagasse and corn cob. Similarly, pyrolysis of agricultural residue has been extensively studied for bio-char production and those have specific uses. Adinaveen et al. [46] prepared porous biochar from rice straw by two-stage pyrolysis process and prepared porous carbons have been employed for fabrication of super-capacitor electrode. The physicochemical and nutrient properties of biochar have been investigated by several researchers for their plausible application in bioremediation, improvement of soil fertility, etc. Bera et al. [47] prepared biochar by pyrolysis of rice straw, wheat straw, maize stover and pearl millet stover by only variation of pyrolysis temperature. Temperature and biomass residue modified biochar properties significantly, those in turn improved soil nutrient on their application. Similar to above findings, Tan et al. [48] and Do et al. [49] reported in their investigation that the agronomic properties of biochar prepared by pyrolysis of agricultural residue, greatly influenced by reaction temperature and pyrolysis reaction atmosphere. Tan et al. in their research found that the limited oxygen cracking conditions improvised the biochar morphology and nutrient content as compared to inert nitrogen atmosphere. Also, Do et al. reported that at higher reaction temperature ($> 500\text{ }^{\circ}\text{C}$) improved biochar porosity but their calorific value was reduced. Derakhshan-Nejad et al. [50] prepared biochar from the pyrolysis of rice husk and maple leaves. The prepared biochar sample was used in soil amendment application for heavy metal immobilization. They found that phytoavailability of heavy metals Cd, Cu, Pb, Zn present in soil extensively declined in biochar-amended soil due to their immobilization process. The overall conclusion showed that all the biomasses are suitable to be used as a feedstock for bio-oil production in Indian sub-continent, due to abundant availability and very low sulfur and nitrogen contents.

Though a number of these types of studies have been performed till date, however, none of the work focused on the slow pyrolysis of different types of agricultural residues (crop residues) in addition to detailed and comparative analysis of all three pyrolysis products (bio-oil biochar, gases) through operating parameter variation. Moreover, there were only a few reports available regarding physicochemical properties of all three pyrolysis products in comparative manner with application oriented approach. This work also wanted to address issues with waste management as stubble burning poses serious threat to the environment. Hence, pyrolysis of surplus biomass available locally offers a sustainable solution.

The focus of this research is to study pyrolysis of three different kinds of biomass (SB, WS, RS) abundantly available in the campus of Banaras Hindu University, in a fixed-bed reactor. A comparative study regarding the yield of three primary pyrolysis products (bio-oil, biochar and non-condensable gases), along with variation in the yield

at various operating parameters viz. temperature, heating rate, sweeping gas flow rate, particles sizes were also studied extensively. Various physical properties of bio-oil and biochar were evaluated and significant focus was devoted on the chemical characterization through FTIR, GC-MS, ICP-AES, SEM and CHNS analysis for application oriented approach. Similarly, effect of inorganic constituents present in biochar on pyrolysis mechanism and product distribution were also thoroughly explained. Detailed composition of non-condensable gases (mainly producer gases) analyzed through gas chromatography (GC-TCD) techniques and variation of their energy values with temperature were studied carefully.

Materials and methods

Feedstock preparation

Feedstock chosen for this experiment was SB, RS, and WS, collected from agriculture farm of Banaras Hindu University. Each biomass was subjected to initial size reduction in a cutting mill (SM 300 Retsch Germany), washed thoroughly and sun-dried for 4–5 days followed by drying in an oven at $105\text{ }^{\circ}\text{C}$ for 4 h. The dried biomass was ground into small sizes in a disintegrator and sieved into three different sizes of 0.2–0.4 mm, 0.4–0.6 mm, and 0.6–0.8 mm.

Characterization methods

Characterization of biomass

The proximate analysis of biomass includes moisture content, volatile matter, ash content, and fixed carbon content and these were determined according to standards ASTM D1037 (1991), ASTM D3172, ASTM D2017 (1998), ASTM E1755, respectively. The ultimate analysis of three biomass samples was carried out in Euro-vector Elemental Analyzer. The functional groups present in biomass were also investigated at room temperature in the frequency range of $4500\text{--}500\text{ cm}^{-1}$ using a Fourier-transform infrared (FTIR) spectrometer (Thermo Electron Corporation, USA, FTIR procedure: S1, ESI). TGA of three biomass samples was carried out in the NETZSCH STA 449 F3 instrument. During each run, 7 mg of the sample was heated up to $900\text{ }^{\circ}\text{C}$ at a heating rate of $10\text{ }^{\circ}\text{C}/\text{min}$ starting from room temperature. The carrier gas used was argon with flow rate maintained at $100\text{ mL}/\text{min}$.

Characterization of liquid and gaseous products

Bio-oil samples were characterized by measuring their physical properties, such as density, pH, viscosity, ash content,

and calorific value. The pH of the bio-oil samples was measured with the digital pH meter (Eutech Instrument) and viscosity was measured with the help of Redwood Viscometer (I.P. 70/46, Gallenkamp, British Made) present in the laboratory. Ash content of bio-oil was determined by burning 10 g of bio-oil at around 600 °C in a muffle furnace overnight [51, 52]. The higher heating value of bio-oil was measured by a digital bomb calorimeter (model no. RSB-7, Rajdhani Scientific Instruments Corporation, New Delhi, India). The chemical characterization of bio-oil was performed by determining the organic functional groups present in it by a Thermo electron FTIR analyzer. GC–MS analysis of three bio-oil samples was performed in a GC–MS–QP 2010 plus ultra (Shimadzu company) equipped with a capillary column (HP-INNOWAX, 60 m × 0.25 mm id × with 0.250 µm film thickness) for determination of organic compounds present in them. Operating conditions and library specification for GC–MS analysis are provided in supporting information (S2, ESI). Non-condensable gases were collected in gas holders at different temperatures and analysis was carried out in a Centurion Scientific Gas chromatography thermal conductivity detector (GC-TCD). The GC was equipped with a Carbosieve SII column (40–60 mesh range) with a thermal conductivity detector. Column, detector, and injector temperatures were maintained at 60 °C, 80 °C, and 100 °C, respectively.

Characterization of biochar produced

Produced biochar samples were characterized through determination of their higher heating value (HHV) and pH. For measurement of pH 0.5 g of biochar, the sample was dissolved in 50 mL of distilled water and stirred for 30 h in a magnetic stirrer [30]. HHV was measured with the help of digital bomb calorimeter (model no. RSB-7, Rajdhani Scientific Instruments Corporation, New Delhi, India). Chemical characteristics of biochar samples were observed with the help of FTIR analysis, SEM/EDX (Evo 18 Research, Carl Zeiss, Oxford Instruments, Germany), CHNS (EuroEA elemental analyzer) and ICP-AES analysis (Thermo scientific model no. ICAP 6200 Duo). Prior to ICP analysis, biochar samples were dissolved in aquaregia solution and subjected to repeated filtration by diluting with deionized water followed by passing through Whatman #1 filter paper. Details regarding ICP-AES analysis procedure are provided in supplementary information (S3, ESI).

Experimental procedure

The experiment was performed in a tubular fixed-bed reactor made of quartz with the help of a split-tube single-zone furnace (NSW-104, New Delhi) programmed with a linear ramping rate. The reactor was made of quartz having length

65 cm and 2.5 cm in diameter. The height of the biomass bed was approx. 10 cm; id of the quartz reactor was 22 mm. The amount of biomass loaded was fed manually from the upper side of reactor by gently tapping the wall such that a packed bed shape could be obtained. The bed temperature was measured by inserting a thermocouple which touched the top portion of the biomass bed. The bed temperature was measured by inserting a thermocouple (temperature sensor) which touched the top portion of the biomass bed. Since the bed height is small and biomass particle has powder texture, the temperature variation due to thermal gradient can be overcome easily and biomass bed has nearly uniform temperature, sensed by thermocouple. The reactor had a provision of feeding line for carrier gas and thermowell (with K type thermocouple) for measurement of bed temperature. The sweeping gas (nitrogen) flow rate was controlled by a mass flow controller. A real-time picture of reactor set-up has been provided in the supplementary information file (Fig. S1, ESI). For every run 5 g of the biomass, the sample was taken, and produced vapors were condensed in a condenser placed at the bottom of reactor maintained at 4 °C with the help of re-circulation bath (Eyela, Japan). For the reproducibility of the result, every result was performed twice, and the average value was reported in the results. The condensable vapors were collected in the form of bio-oil in the separator. Condenser and its accessories were washed with acetone at the end of every run so as to collect the residual if any present in it. Acetone was evaporated in an oven at 70 °C and the calculated weight of residual bio-oil was added to the weight of bio-oil produced to obtain the final yield of bio-oil weight percentage. It was found that the residual bio-oil was present in condenser and its accessories within 5% of total product yield. The schematic of the experimental set-up is shown in Fig. 1. Pyrolysis of biomass samples of given sizes (mentioned earlier) was carried out at a temperature range of 350–650 °C in an interval of 50 °C

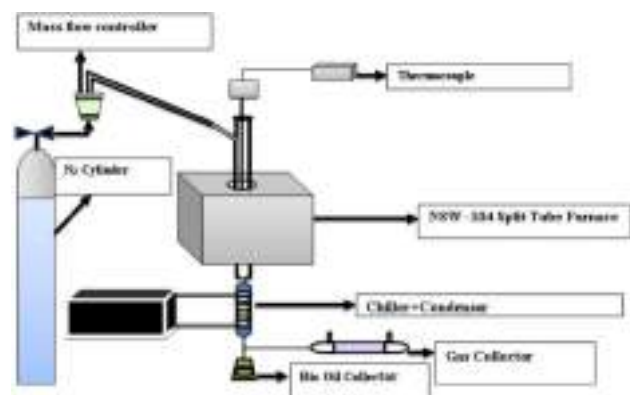
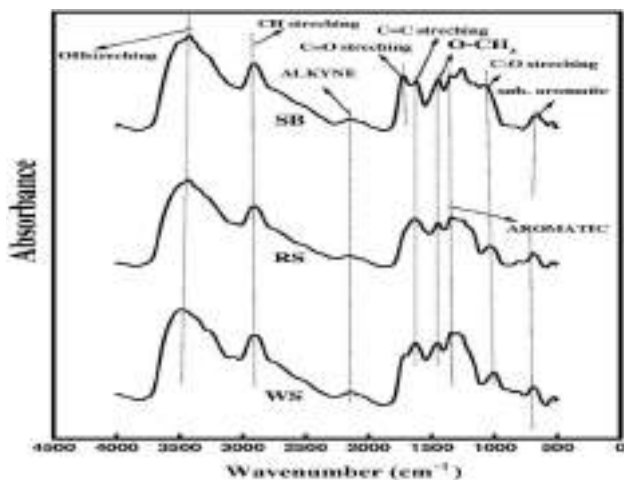


Fig. 1 Schematic diagram of experimental set-up

Table 1 Proximate and ultimate analyses of selected biomass samples (wt%)

Biomass	Moisture	Volatile matter	Ash	Fixed carbon	N	C	H	S	O	H/C	O/C
SB	6.0	89.50	1.90	8.60	0.88	44.04	6.18	Nd ^a	48.90	1.68	0.83
WS	7.0	81.00	7.53	11.47	1.15	42.16	5.57	Nd	51.12	1.58	0.90
RS	8.0	77.50	11.6	10.9	1.07	40.30	5.53	Nd	53.10	1.64	0.98

^aNot detected**Fig. 2** FTIR spectra of three biomass samples

with heating rates maintained at 20 °C/min and 100 °C/min and sweeping gas flow rate ranging from 30 to 100 mL/min.

Product yield was calculated using the following equations:

Yield of the products (on weight basis) was calculated as follows:

$$\text{Yield of bio-oil (wt\%)} = \left[\frac{\text{(bio-oil formed)}}{\text{(biomass-fed into the reactor)}} \right] \times 100, \quad (1)$$

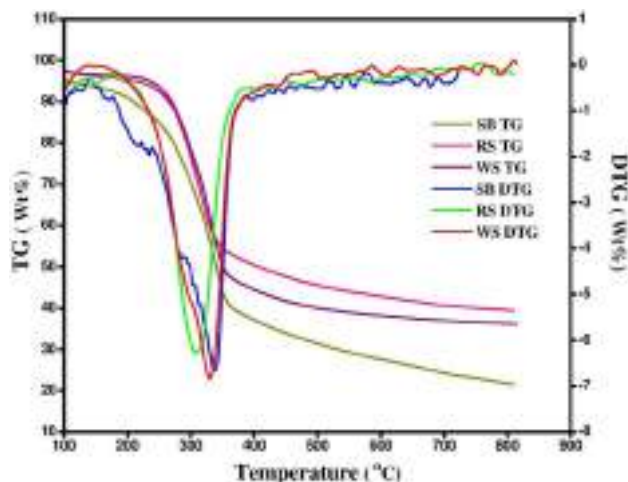
$$\text{Yield of biochar (wt \%)} = \left(\frac{\text{biochar formed}}{\text{biomass-fed into the reactor}} \right) \times 100, \quad (2)$$

$$\text{Yield of non-condensable gas (wt \%)} = 100 - (\text{yield of bio-oil} + \text{yield of biochar}). \quad (3)$$

Results and discussion

Characterization of biomass samples

The data for proximate and ultimate analyses of selected biomass samples are shown in Table 1. FTIR results of three biomass samples are provided in Fig. 2. Thermogravimetric analysis was carried out (Fig. 3) to identify the thermal

**Fig. 3** TG and DTG analysis of three biomass samples as a function of temperature

decomposition behavior of three biomass samples which in turn specify the suitable temperature range within which experiment has to be performed [53].

Proximate and ultimate analyses

As shown in Table 1, SB has the lowest ash content, moisture content and O/C ratio compared to other biomass samples. RS found to contain high amount of ash as compared to other biomass samples. All results are compared with the other works listed in Table 2 [1, 54, 55].

FTIR analysis

From Fig. 2, it is observed that the absorbance peak at 3490 cm^{-1} in the case of three biomass samples corresponds to OH stretching vibration which in turn confirms the presence of alcoholic and phenolic functional groups associated with cellulose as well as hemicellulose and lignin components, respectively, present in them. Cellulose is a homo-polymer of cellobiose monomers and hemicellulose is branched heterogeneous polymer of various sugar monomers like hexose, pentose, etc., all are associated with OH groups in their basic structures. Similarly, lignin is a highly branched 3D heteropolymer of hydroxyl- and methoxyl-substituted phenyl propane units mainly contribute to phenolic

Table 2 Proximate and ultimate analyses of selected biomass samples (from literature) (wt%)

Biomass	Moisture	Ash	N	C	H	O	S	Ref
SB	6.21	2.98	0.15	45.39	7.92	46.67	–	[1]
RS	5.68	14.11	1.07	47.50	6.55	44.88	–	[54]
WS	6.60	8.19	1.4	41.19	5.34	51.97	0.096	[55]

functional groups in all three biomass samples. C–H stretching vibration at wave no. 2910 cm^{-1} indicates the presence of alkanes, resulted from various carbohydrate monomers in three biomass samples [51, 56, 57]. The absorbance peak at 2140 cm^{-1} indicates the presence of alkyne functional group in 3 biomass samples [58]. Apart from this, the average intense absorption band at 1720 cm^{-1} indicates C=O stretching vibration, which confirms the presence of Quinone, aldehyde, and ketonic functional groups [51, 56, 57]. Its presence also validated from the fact that hemicellulose associated with various acetylated sugars. The medium-intense absorption band at 1620 cm^{-1} indicates C=C stretching vibration, which confirms the presence of alkenes and aromatic functional groups in above three biomass samples associated with lignin [56]. The absorbance peak at wave no. 1440 cm^{-1} in three biomass samples indicates O–CH₃ (methoxyl) functional groups contributing to the basic structure of phenyl propane units of lignin [58]. Infrared vibration at 1030 cm^{-1} which corresponds to C–O stretching or OH deformation, indicates the presence of ethers, esters in all three biomass samples those act as a connecting link between various monomers of lignocellulosic components as well as components of phenyl propane units associated with lignin. The more intense absorption band at wave no. 694 cm^{-1} in all three biomass samples indicates the presence of mono-, polycyclic, and substituted aromatic compounds contributing to the basic structure of lignocellulosic components of biomass [51].

Thermogravimetric analysis

The entire TGA profile (Fig. 3) can be distinguished into three stages. During the first stage between 50 and 220 °C, there is a slight change in the slope of TG curves for all three biomasses. This is an indication of slight decay in biomass weight (within 10%) due to the drying procedure and release of lighter volatiles in addition to bound moisture [59]. The second stage demarcated within a temperature range of 220–500 °C in TG curves contributed significantly to a drop in weight of biomass (~50%). This rapid weight loss is mainly because of the thermal decomposition of cellulose, hemicellulose, and lignin [58, 60]. During the third stage (500–900 °C), there is no significant loss in biomass weight due to thermal decomposition as indicated by the flat profile of the TG curve. Maximum weight loss rate occurs

at a temperature of 340 °C for SB and WS, while in case of RS, it is 320 °C. Maximum weight loss rates are 7%/min, 7.8%/min and 6.5%/min for SB, WS, and RS, respectively.

In lignocellulosic biomass, thermally degradable polymers are hemicellulose, cellulose, and lignin. Hemicellulose decomposed readily at a temperature range of 210–315 °C. Cellulose is more robust due to a long polymer of glucose without branches, thermally stable, and its pyrolysis temperature revolves around high temperature (315–400 °C). Lignin is full of aromatic rings with various branches hence, its degradation occurs at a wide temperature range (100–900 °C) [58]. Figure 3 consists of one major derivative weight loss peak in between 310 and 400 °C for all biomasses, and it is mainly due to the decomposition of cellulose. DTG curves consist of shoulder observed at a temperature < 300 °C, mainly due to hemicellulose decomposition. Small degradation peaks in DTG curve of three biomass samples at wide temperature range mainly due to decomposition of lignin.

Effect of pyrolysis reaction conditions on products distribution

Effect of temperature

The pyrolysis yield of products at different temperatures having a particle size of 0.2–0.4 mm, using a sweeping gas flow rate of 30 mL/min and a heating rate of 100 °C/min is shown in Fig. 4. The temperature had a significant effect on pyrolysis product distribution. The bio-oil yield was lowest at a temperature of 350 °C, and the yield increased up to 550 °C, and after that, there was a decreasing pattern. The maximum yield was obtained at a temperature of 550 °C in the case of SB and WS, but in the case of RS, maximum yield of bio-oil was obtained at 450 °C. SB produced highest bio-oil yield nearly 52.5%, and in the case of WS and RS maximum, bio-oil yield percentage is 37.2% and 33.3%, respectively. These results are similar to results obtained by several other researchers [51, 52, 57, 61, 62]. The evolution of minimum bio-oil yield and maximum char yield at 350 °C are due to the rigidity and lower thermal conductivity of biomass that inhibits its decomposition at low temperature [63]. At low-temperature pyrolysis, high char yield and low liquid yield are also reasonable because of the polymerization of volatilized organics [51]. But among three

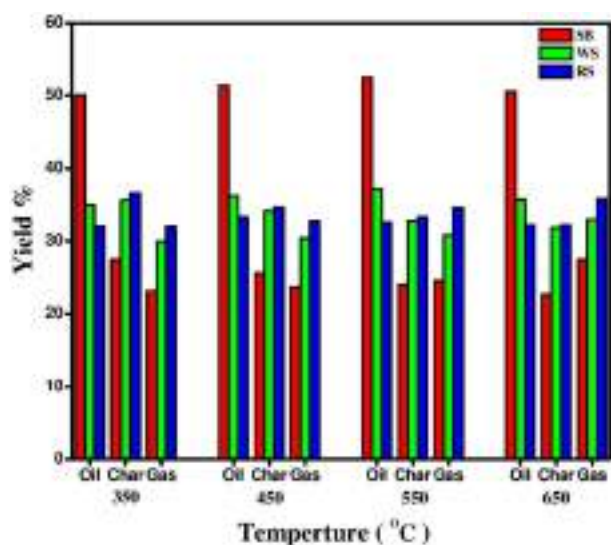


Fig. 4 Yield of pyrolysis products at different temperatures (heating rate of 100 °C/min, sweep gas flow rate of 30 mL/min and particle size of 0.2–0.4 mm)

biomasses, char yield was highest in the case of RS, since it contains a high amount of lignin [56, 64]. As the temperature increased, bio-oil yield also increased due to the rapid de-volatilization of biomass by primary decomposition with rising temperature. But at high temperature, i.e. after 550 °C in the case of SB and WS and 450 °C in the case of RS, the bio-oil yield started to decrease due to thermal and catalytic cracking of bio-oil or in other words, secondary reactions of the liquid fraction of volatiles [53, 62]. As temperature increased, the biochar yield decreased due to the decomposition of char at high temperature [62, 65]. Figure 4 also shows the increasing pattern of non-condensable gases with the rise in temperature, just because of the primary decomposition of biomass and secondary decomposition of biochar [62]. At a temperature above 550 °C, the rate of increase in gas yield was higher with the highest rate obtained at 650 °C because of secondary cracking of pyrolysis vapors or secondary reactions of bio-oil in vapor phase [53, 62, 66].

Effect of particle size

Effects of biomass particle size in the range of 0.2–0.8 mm at a heating rate of 100 °C/min, sweep gas flow rate of 30 mL/min and temperature of 550 °C for SB and WS and 450 °C for RS were studied on the pyrolysis product distribution, and results are shown in Fig. 5. It was observed that bigger particle size maximized the formation of char and non-condensable gases. But in the case of small-sized biomass particles, there was maximum amount of bio-oil produced instead of char and non-condensable gases. For small-size

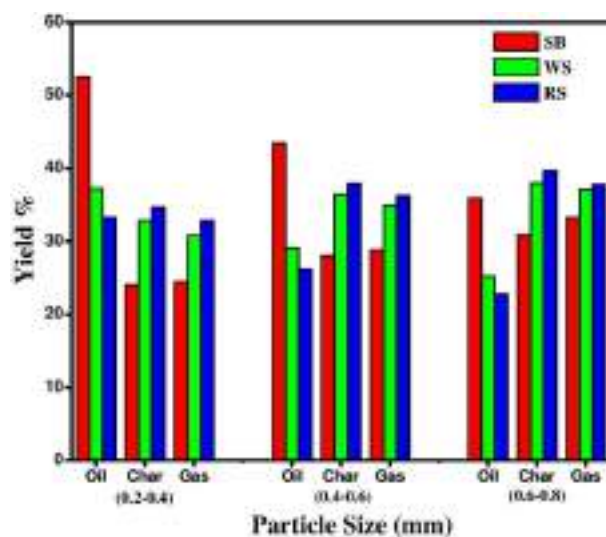


Fig. 5 Yield of pyrolysis products at different particle size (heating rate of 100 °C/min, sweep gas flow rate of 30 mL/min and temperature of 550 °C for SB and WS and 450 °C for RS)

particles, solid to solid heat transfer is faster and pyrolysis governs the reaction mechanism. Therefore, faster volatilization leads to higher liquid yield which was observed in case of all three biomass samples having small particle size (0.2–0.4 mm).

Similarly, as particle size increases, there is interaction among char produced and volatiles generated that lead to simultaneous cracking of bigger volatiles and polymerization of smaller volatiles [51]. This phenomenon was also observed in our experiment, as particle size increased char and non-condensable gas yield increased and reached maximum in case of biggest size biomass particles (i.e., 0.6–0.8 mm). Char and gas yields were highest in pyrolysis of all three kinds of biomass samples having particle size (0.6–0.8 mm). Moreover, as particle size increased from 0.2–0.4 to 0.6–0.8 mm, bio-oil yield decreased because large particle does not enhance the mass transfer and heat transfer associated with the cracking mechanism and non-uniform heating of particle as shown in the Fig. 5 [65–67]. Another reason for high char yield and low liquid yield with the increase in particle size is the rise in heat transfer resistance with distance from particle surface to center that impedes the quick heat transfer from a hot material to cold biomass, and thus reaction is not completed [68].

Effect of heating rate on product distribution

Pyrolysis experiment was conducted at two different heating rates of 20 °C/min and 100 °C/min at a sweep gas flow rate of 30 mL/min. It was found that bio-oil and gas yield increased with heating rate while char yield decreased. Figure 6 indicates that as the heating rate increased, bio-oil

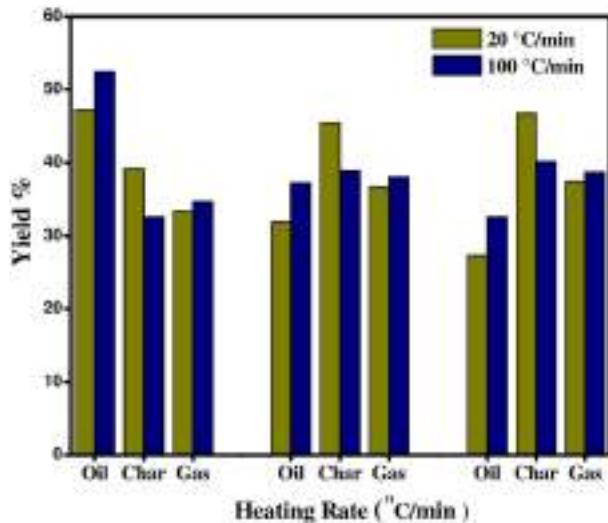


Fig. 6 Yield of pyrolysis products at a different heating rate (sweep gas flow rate of 100 mL/min)

yield increased. With the increase in heating rate from 20 to 100 °C/min, bio-oil yield increased from 47.2 to 52.5% in case of SB, 31.9 to 37.2% in WS and 27.3 to 32.6% in case of RS. Similarly, biochar yield decreased from 39.2 to 32.6%, 45.5 to 38.9%, and 46.7 to 40.1% in the case of SB, WS, and RS, respectively. Figure 6 also shows that non-condensable gas yield increased from 33.35 to 34.65% in case of SB, 36.7 to 38% in case of WS and 37.45 to 38.75% in case of RS. Rapid heating rate leads to rapid de-polymerization of solid biomass into primary volatiles those upon condensation produce more bio-oil hence, its yield was increased [66, 67]. While at low heating rate, dehydration to more stable anhydrous cellulose is limited and very slow that leads to more char formation. Moreover, the actual heating rate measured was 38 °C/min, for a theoretical heating rate of 45 °C/min in the furnace. Hence, we may expect that the actual heating rate was maintained within the bed around 85–90 °C/min, when the set value in the furnace was 100 °C/min. The thermal gradient within the bed was 4.35 °C/min in the radial direction. Hence, the predicted heating rate difference between two set values of experimentation mentioned in this manuscript was definitely responsible for the observed difference in product yield as contrary to some researchers [69], who those claimed that variation of heating rate does not have significant influence on product yield within the selected testing range.

Effect of the flow rate of sweeping gas on product distribution

For slow-to-moderate pyrolysis conditions as per this experiment, the carrier gas flow rate has significant influence on product distribution [51]. Hence, to ascertain the effect

of this reaction parameter on pyrolysis product yields, an additional experiment was designed for a certain biomass sample. Influence of the sweeping gas flow rate on product distribution of SB was carried out at 550 °C temperature, the particle size of 0.2–0.4 mm and fixed heating rate of 100 °C/min by varying the sweeping gas flow rate from 20 to 100 mL/min. The same effect can be observed for WS and RS not represented here.

It is observed from Fig. 7 that bio-oil yield was highest at a flow rate of 30 mL/min, and then it decreased. For bio-char and non-condensable gas, there is an initial decrease and then increase pattern, respectively, with an increase in flow rate. At low flow rate, the residence time of released volatiles in the reactor is high which influences more vapor-phase secondary cracking and re-polymerization reactions that lead to more char, gas and low liquid yield [70, 71]. To increase the bio-oil yield, the produced vapors should be quenched immediately to inhibit the onset of secondary reactions. As flow rate increased, bio-oil oil yield increased due to inhibition of cracking and re-polymerization reaction of vapors by rapid quenching [36, 51]. But at high sweeping gas flow rate, the yield of bio-oil decreased, whereas non-condensable gas and char yield increased as the effective time required for condensation of vapors was not sufficient enough. The increased amount of biochar at high sweeping gas flow rate may be correlated with the fact that, low availability of vapor-phase residence time slowed down the cracking of long polymeric chains of lignocellulosic biomass and smaller hydrocarbons [62, 65].

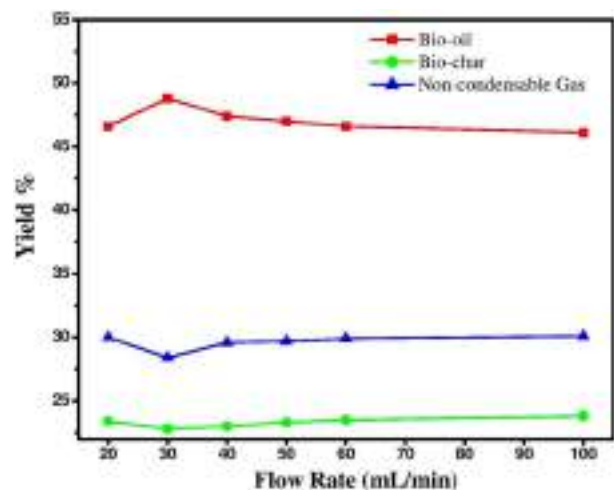


Fig. 7 Effect of sweep gas flow rate on pyrolysis product distribution of SB

Bio-oil characterization

Physical characterization

Table 3 demonstrates that bio-oil produced from three biomass samples is acidic in nature. The acidity of bio-oil is mainly due to the presence of carboxylic acids, phenolic compounds, and its derivatives [22]. The density of bio-oil found to be comparable or slightly heavier than diesel and fuel oil [62, 72]. This is mainly because of the presence of oxygenated heavy organic compounds, such as phenol [51]. The viscosity of produced bio-oil samples is lower as compared to the viscosity of diesel (1.58–4.99 cSt), biodiesel (1.66–5.24 cSt) [62]. The higher heating values (HHV) of bio-oil produced from all three biomass samples were investigated and found that in case of SB, it is maximum that may be correlated with its low moisture content and O/C ratio.

Chemical characterization

FTIR analysis From Fig. 8, it is illustrated that absorbance peak at 3370 cm^{-1} and 3390 cm^{-1} present in all bio-oil samples conforms to OH group which is an indication of the presence of phenol, alcohol, polymeric OH and to some extent water impurity [57, 73]. The strong absorbance peak at 1710 cm^{-1} in 3 bio-oil samples confirms the C=O stretching vibration, which in turn designates the presence of ketones, quinones, aldehyde, and carboxylic acid compounds. The slight absorbance peak at wave numbers 1660 cm^{-1} and 1510 cm^{-1} indicates C=C stretching so that there is a confirmation of alkene bond present in three bio-oil samples [74]. The medium-intense absorption band in 3 bio-oil samples at 1380 cm^{-1} is a simultaneous indication of C–H bending (alkane) and substituted aromatic compounds in bio-oils [51, 73, 75]. The broad peaks at 1260 cm^{-1} and 1050 cm^{-1} confirm the presence of alcohols, phenols, ether, and ester with CO stretching and OH deformation in 3 samples. The sharp absorbance peaks at wave numbers 775 and 727 cm^{-1} in case of SB bio-oil, at 739 cm^{-1} in case of WS oil, at 710 cm^{-1} in case of RS bio-oil specify the presence of mono-, polycyclic and substituted aromatic compounds in them [51, 75]. The high-intensity absorption peak at wave number 633 cm^{-1} in case of bio-oil produced from WS and

RS indicates the presence of aromatic compounds in them [76].

As mentioned previously, bio-oil contains various amounts of oxygenated organic compounds, such as acids, phenols, sugars, hydroxy aldehyde, hydroxy ketones, and alcohols, which are also substantiated from FTIR analysis. This leads to heterogeneity in bio-oil, which in turn affects the energy density, storage stability of bio-oil, miscibility with hydrocarbon fuels [77].

GC–MS analysis Table 4 presents a comparison of important compounds present in bio-oils (identified by GC–MS) obtained from pyrolysis of SB, WS, and RS. All three bio-oil samples mainly composed of benzene derivatives, nitrogenated, oxygenated, and aliphatic organic compounds in abundant quantities as inferred from their area % data in mass spectra. Tables S1–S3 (presented in ESI) give a list of all compounds identified by GC–MS for bio-oils obtained from pyrolysis of these three biomass samples. It was observed from Table 4 that ketones and ester compounds were found to be maximum in bio-oil obtained from WS, whereas furans and guaiacols were maximum in case of SB. Anhydro-sugars were available in significant quantity from SB, and it was also observed by David et al. [78]. Besides, alcohol was very high in bio-oil obtained from WS as well

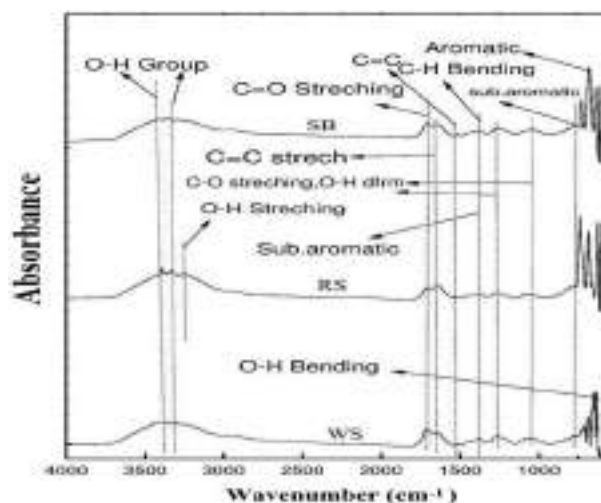


Fig. 8 FTIR spectra of bio-oil produced from three biomass samples

Table 3 Physical characteristics of bio-oil produced from selected biomass samples

Bio-oil from biomass	pH (25 °C)	Density (g/mL) (40 °C)	Viscosity (cSt) (40 °C)	Ash content (wt%)	HHV (MJ/kg) pyrolysis at 550 °C
SB	2.71	1.09	2.80	0.2	22.31
WS	2.87	1.05	1.89	0.2	18.12
RS	3.58	1.04	2.40	0.1	16.35

Table 4 GC–MS analysis of bio-oil obtained from pyrolysis of SB, WS (pyrolysis temperature 550 °C); and RS (pyrolysis temperature 450 °C); heating rate 100 °C/min; 0.2–0.4 mm particle size

Compound	SB ^a	WS ^a	RS ^a
Ketone	15.51	30.04	25.13
Furans	22.75	6.58	16.68
Ester	3.46	12.38	4.39
Guaiacol	11.66	8.26	7.04
Phenolics	10.91	10.99	1.38
Anhydro-sugar	23.99	0.33	4.58
Alcohols	–	26.96	27.54

as RS. It was also found that phenolic compounds and their derivatives comprised a greater portion of all three bio-oil samples. These mainly consist of phenol, 2-methoxyphenol, 3-methyl-phenol, 3-ethyl-phenol, 4-ethyl-guaiacol, 2-methoxy-4 vinyl phenol, 2,6 dimethoxy phenol, 2-methoxy-4-phenol, 2,6-dimethoxy-4(-2propenyl)-phenol, 2,6-dimethoxy-4(prop-1-en-1-yl) resulted from decomposition of lignin in all biomass samples. Decomposition of lignin and cellulose simultaneously gives rise to the production of aldehyde, ketone, and ester-related compounds, including also some oxygenated organic compounds. Acidic compounds found in all three bio-oil samples, such as 2,4-hexadienedioic acid, 2,4-benzene dicarboxylic acid, acetic acid, and butanoic acid, mainly evolved from the decomposition of hemicellulose in raw biomass. Cellulose decomposition also produces levoglucosan compound, such as 1,6-anhydro-beta-D-glucopyranose, which is found in produced bio-oil samples along with furan and its derivatives. Aliphatic, aldehyde, ketone, ester, alcohol (cyclopropyl methanol) and some of the carboxylic acid compounds present in all three bio-oil samples also formed from the decomposition of cellulose and hemicellulose as investigated by some researchers [78]. Presence of nitrogenous compound in bio-oil samples, such as 4-methyl pyridine, 3,5-dimethyl-1*H*-pyrazole, dinitro-glycoluril, guanosine, 6*H*-dipyrrole [1,2-A:1,2-D] pyrazine, 2,4-pyrimidinediamine, 5-[(3,4,5)-(trimethoxy phenyl) methyl], etc. is due to the presence of protein-based compounds in biomass. Presence of straight-chain hydrocarbon compound, such as 2-isocyanatopropane, is due to cracking of acidic compounds present in raw biomass samples [65, 78].

Non-condensable gas product distribution during pyrolysis

The non-condensable gases produced during pyrolysis of three types of biomass samples mainly comprised CO, CO₂, H₂ and CH₄ as analyzed by GC-TCD (Fig. S2, ESI). Since these gases contributed majority of producer gases used in

fuel applications, hence, non-condensable gases produced as a by-product could have better fuel application. The CO and CO₂ content was found to be high in non-condensable gases produced below 450 °C unlike high temperature. Maximum evolution of CO and CO₂ obtained at a very low temperature (~300 °C) and then there was a decreasing trend continued up to 650 °C. High yield of CO and CO₂ at low temperature mainly resulted due to cleavage of the C=O bond present in biomass samples. In addition to major CO and CO₂ contribution to gases, resulted from cracking of carbonyl (C=O) and carboxyl (–COOH) groups, respectively, some researchers also claimed that high yield of CO and CO₂ at low temperature is mainly due to decomposition of cellulose and hemicellulose [79], which was previously verified through TGA. Evolution of CH₄ gas started near 300 °C and continued rising up to 600 °C, then was a decreasing trend at high temperature. Major contribution towards CH₄ release was from O–CH₃ (methoxy) group associated with basic structure of phenyl propane units of lignin [80] unlike cellulose and hemicellulose. Amount of CH₄ in non-condensable gases was less compared to quantity of CO and CO₂. Hydrogen (H₂) gas was produced at much higher temperature ~500 °C, and then it followed an increasing trend with rise in temperature and was expected to rise above 650 °C (Fig. S2). The increasing evolution trend of H₂ at higher temperature was mainly due to cracking and reforming reaction of aromatic rings present in biomass. One noticeable observation from entire analysis of non-condensable gases, that temperature below 600 °C was responsible for the production of more amounts of CO, CO₂, CH₄ as a result of primary pyrolysis process, whereas at high temperature (650 °C and above), secondary pyrolysis and thermal cracking reactions dominated, resulting more amount of H₂ [76].

Non-condensable gas higher heating value (HHV) was evaluated with the help of mathematical formula provided by [81] by taking into consideration volume percentage of gases and represented as:

$$\text{HHV (MJ/Nm}^3\text{)} = (\text{H}_2\% \times 30.52 + \text{CO}\% \times 30.18 + \text{CH}_4\% \times 95) \times 0.0042 \quad (4)$$

According to Eq. (4), the higher heating value was calculated and found that with rise in temperature, the higher heating value of gases produced increased (Table 5) and at temperature above 600 °C, there was a decreasing trend. Increase in higher heating value with rise in temperature may have resulted due to increase in H₂ and CH₄ content in non-condensable gases, but at high temperature, CH₄ yield decreased ultimately reducing higher heating value. SB produced non-condensable gases with higher heating value less compared with RS and WS. This type of result may be ascertained from the fact that SB contained more amount of

Table 5 HHV of non-condensable gases and carbon conversion efficiency of biochar prepared from different biomass samples

Temperature	Biomass					
	SB		WS		RS	
	HHV (MJ/Nm ³)	η_c (%)	HHV (MJ/Nm ³)	η_c (%)	HHV (MJ/Nm ³)	η_c (%)
300	4.24	–	4.55	–	4.90	–
350	4.35	99.875	5.08	99.823	5.12	99.826
400	4.55	–	5.36	–	5.67	–
450	5.04	99.883	7.83	99.83	7.10	99.835
500	7.25	–	12.18	–	11	–
550	10.86	99.891	13.93	99.837	15.78	99.842
600	13.87	–	16.61	–	17.96	–
650	12.70	99.897	16.00	99.842	17.55	99.847

^a η_c : carbon conversion efficiency

Table 6 Physical characteristics of produced biochar samples from selected biomass

Biochar	Heating value (HHV) (MJ/kg)	pH (25 °C)	HHV(MJ/kg) raw biomass
SB	27.77	8.03	16.80
WS	17.72	10.07	13.93
RS	14.08	9.53	13.37

cellulose/hemicellulose and less amount of lignin, ultimately resulting gases devoid of high quantity of H₂ and CH₄, those that contribute more to HHV. Moreover, SB produced gases enriched with CO₂ as a result of cellulose decomposition.

Carbon conversion efficiency (CCE) related to production of non-condensable gases can be calculated according to formula provided by [82] and represented in Eq. (5):

$$\eta_C = \left[1 - \frac{m_{\text{biochar}}}{m_{\text{biomass}} \times \% C} \right] \times 100, \quad (5)$$

η_C = carbon conversion efficiency, m_{biochar} = amount of biochar produced, m_{biomass} = amount of biomass fed to reactor, %C = elemental carbon percentage in biomass.

Carbon conversion efficiency in case of SB biochar was found to be slightly higher than CCE of two other biomass samples (Table 5).

Biochar characterization

Physical characterization

Calorific values of biochar samples were measured with the help of laboratory bomb calorimeter and represented in Table 6. Interestingly, biochar calorific value is higher as compared to corresponding raw biomass. Hence, biochar can

be used in combustion, co-firing, and briquette application for providing heat energy. HHV of biochar is comparable to coal [83, 84], so it can be used as a substitute for fossil fuel in energy generation applications like running a boiler or stationary power generation. As three biochar samples are alkaline in nature (Table 6), their use as bio-fertilizer will help in controlling soil acidity for availing important plant nutrients and maintaining healthy environment for smooth functioning of beneficial soil bacteria [52]. Less pH value of biochar prepared from SB as compared to WS and RS may have resulted due to ample presence of acidic functional groups (–COOH, –OH) on its surface [85]. High acidity SB biochar among WS and RS may act as possible cation exchange site, from where cationic macro- and micronutrients may be readily available for plant intake purpose, hence, ultimately improving soil fertility and nutrient holding capability.

Chemical characterization

CHNS/ultimate analysis CHNS analysis of three biochar samples is described in Tables 7 and S4–S5. High percentage of carbon (as a major element) has been reported in produced biochar samples. Data regarding C and H weight percentage presented here have similar trends with that of represented earlier by Mullen et al. [83]. Within the pyrolytic temperature range of 350–50 °C, the concentration of carbon increases due to increase in degree of carbonization [86] and O, H decrease with rise in temperature due to decarboxylation and dehydration reactions [56]. Increased degree of carbonization with reduced oxygen content could have harnessed biochar in several fuel applications. Apart from this, high amounts of C, N contents in biochar make them good fertilizer application, which can replenish these elements in soil [83]. Moreover, probability of inducing soil nitrogen deficiency through biochar fertilizer application caused by microbial breakdown of carbon-rich substrates

Table 7 CHNS/ultimate analysis of biochar produced from SB

Char at temperature (°C)	C	H	N	S	O	H/C	O/C	(N+O)/C	HHV (MJ/kg)	Energy density	Energy yield %
350	68.42	3.81	0.98	Nd ^a	26.79	0.66	0.29	0.30	24.22	1.44	39.45
450	70.01	3.02	1.97	Nd	25.00	0.51	0.26	0.29	23.89	1.42	36.35
550	78.20	2.62	2.43	Nd	16.75	0.40	0.16	0.18	27.34	1.62	38.88
650	80.12	1.81	2.22	Nd	15.85	0.27	0.14	0.17	26.97	1.60	36.32

^aNot detected

can be countered by the fact that the carbon present in biochar is in condensed aromatic form, which is hardly easy to degrade. Since char contains little amount of nitrate as well as not balanced elementally, it is always advisable to use along with any nitrogenous fertilizer for soil amendment application. Another noticeable observation is that N content of biochar is high as compared to raw biomass, may be contributed due to adsorption N₂- or N-bearing organic compounds on the surface of solid char [76]. With increase in pyrolysis temperature, there is decrease in O/C and H/C ratio of biochar samples collected (Table 7). Generally, with rise in temperature, there is enhancement in carbonization as well as aromatization process, ultimately making the biochar more hydrophobic and non-polar in nature. This is also verified from the fact that there is a decremental nature of O/C and (N+O)/C ratio with rise in temperature in case of biochar. Biochar produced at high temperature with low H/C and O/C ratio is very much desirable during combustion process since it leads to reduction in energy losses and smoke generation. Similar type results have been reflected in case biochar generated at high temperatures, having high HHV with reduced polarity, thus making it as good-quality solid fuel as explained earlier. Van Krevelen diagram (Fig. 9) shows that biochar samples produced at high temperature (> 600 °C) have coordinates shifted towards region of fossil fuel [84]. Hence, their potential usability in energy generation by combusting individually or with synergistic manner in combination with lignite type fossil fuel in coal fired plant is highly desirable as confirmed through Van Krevelen diagram [87]. Carbon in biochar is highly stable and may be sequestered for thousands of years [88, 89]. Infact biochar produced from three biomass samples with H/C < 0.6 and O/C < 0.4 can be used in soil amendment applications [90]. Energy density and energy yield of biochar produced at different temperatures are evaluated according to formula developed by [91]. These are defined as:

Energy density : energy of biochar/energy of raw biomass, (6)

Energy yield (%) : yield of biochar × energy density. (7)

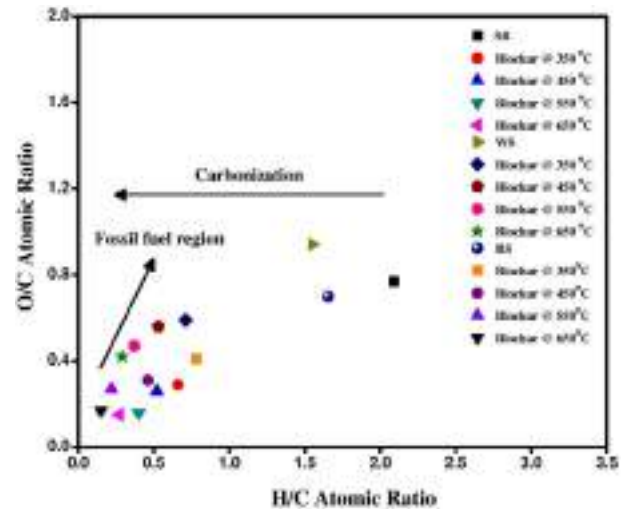


Fig. 9 Van Krevelen plot for different biomass samples with its biochar produced at different temperatures

From Tables 7 and S4–S5, it has been found that the energy yield of biochar decreases with increase, whereas energy density increases with rise in temperature. Energy density of biochar samples is highest at high-temperature conditions with maximum energy density going up to 1.60, 1.23 and 1.86, respectively, for SB, WS and RS at high temperature. The increasing trend of energy density with rise in temperature may be attributed to the minimization of low energy bonds, such as C–H, C–O and increment in high-energy C–C bond, during pyrolysis process due to carbonization process. Similarly, energy yield varies in between 39.45–36.32, 40.22–39.11, and 56.73–54.94% for SB, WS, and RS biochars. Variation of energy yield from biomass to biochar can be correlated with the biomass structure as well as amount of char resulted during pyrolysis process. Since RS produced maximum amount of biochar during pyrolysis process, hence, its energy yield found to be maximum. Biochar due to greater amount of fixed carbon, low H/C and O/C ratio as well as high-energy density can have better fuel property as compared to raw biomass.

FTIR analysis of biochar samples Pyrolysis is nothing but thermal decomposition of biomass at a specific temperature, ultimately resulting in breaking/cleavage of chemical bonds present in them and release of volatile gases corresponding to that temperature. So, a relationship established between the chemical structure of biochar produced (identified by FTIR) and composition of released gases at different final temperatures. Herein FTIR results of biochar produced at different temperatures are represented in comparison with raw biomass, to study the chemical changes occurring in biomass during pyrolysis process and its effect on released gases. As the chemical structures (functional groups) presented in three biomass samples shown similar representation in FTIR analysis (Fig. 2), thus the comparison is provided for only one biomass type, and same analysis can be followed for others.

Figure 10 shows that the sharp absorbance peak at wave number 3500 cm^{-1} (OH functional group) of raw biomass eventually diminishes to zero in case of biochar produced at $350\text{ }^{\circ}\text{C}$. This is an indication of dehydration reaction occurred during the pyrolysis process, which started near $300\text{ }^{\circ}\text{C}$ and produced a large amount of water that goes directly to the bio-oil. Medium intense absorption band between 2860 and 2970 cm^{-1} (C–H stretching) in the IR spectra of raw biomass diminishes to a very minimal value near $550\text{ }^{\circ}\text{C}$ as shown in spectra of biochar produced at that temperature. This mainly results due to the breaking of weak C–H (alkyl) bond and the formation of more CH_4 gases during pyrolysis within that temperature range. Slightly broad absorption band in raw biomass between 1700 and 1730 cm^{-1} is an indication of C=O functional group (carboxylic acid). The FTIR spectra of biochar (Fig. 10) collected within temperature $450\text{ }^{\circ}\text{C}$ show that this absorption band becomes narrow and its intensity also diminishes. This

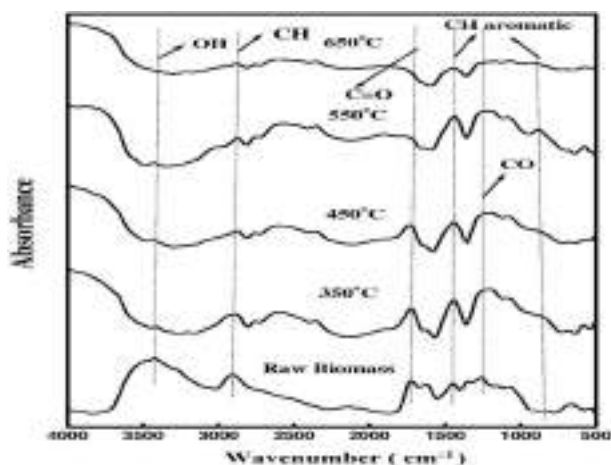


Fig. 10 FTIR spectra of SB biochar at different temperatures and its comparison with raw biomass

type of pattern appeared due to the formation of more CO and CO_2 gases within $450\text{ }^{\circ}\text{C}$ by breaking of C=O bond. Another interesting fact observed from the figure is that absorption band of functional groups, such as C–O (1450 and 1080 cm^{-1}) and CH aromatic ring (1440 and 890 cm^{-1}), increases with a rise in temperature. This increasing trend originated due to decreasing peaks of OH and CH alkyl groups. But after the final temperature reaching near about $650\text{ }^{\circ}\text{C}$, this increasing trend discontinued, and peak intensity decreased. These functional groups broke in a stepwise manner to produce more volatiles. Cracking and re-polymerization of aromatic rings gave rise to more H_2 gas evolution at high temperature ($600\text{ }^{\circ}\text{C}$) [53, 56, 76].

SEM analysis SEM analysis of biochar samples was carried out to study the textural property, surface morphology, and porous structure. The SEM images of biochar produced from SB, WS and RS, at low and high temperatures are shown in Fig. 11 along with SEM images of raw biomass for comparison purpose. From the SEM images, it is concluded that there was no porosity present on biomass surface, but with temperature rise, porosity and pore sizes increased. At $350\text{ }^{\circ}\text{C}$, small numbers of pores appeared on the surface of char. This is mainly due to low decomposition of volatile matter at that temperature when temperature increased and reached near $550\text{ }^{\circ}\text{C}$, a large number of fine pores developed on the surface of solid char as shown in Fig. 10 also pore size increased. In fact, at high temperature ($\sim 550\text{ }^{\circ}\text{C}$), there was the opening of more numbers of micro-sized pores which lead to the high surface area of produced biochar samples. These results were mainly due to the rapid release of volatile compounds during pyrolysis at this temperature [56]. Results obtained in this experiment were in accordance with the detailed study on biochar produced at different temperatures as previously reported by Yang et al. [76]. They explained the effect of pyrolysis temperature on the porosity and pore size of prepared biochar samples through SEM and BET analysis simultaneously. The trend regarding biochar porosity obtained in this pyrolysis reaction matches closely well with that of results obtained by Yang et al. But at a higher temperature, not studied here, these pores might block and combined, thus, shrunk in sizes due to plastic nature of char. Also, there will be large numbers of pore blockages due to melting and combination of minerals which were the main constituents of char produced at high temperature. Maximum de-volatilization occurred below $550\text{ }^{\circ}\text{C}$, therefore, maximum porosity developed within that temperature. The presence of large pores at the surface of biochar has many applications. It can be used as activated carbon for decolorization in the sugar industry, increase metal adsorption capacity by chemisorption method, etc. If this highly porous char is applied to the soil, it will contrib-

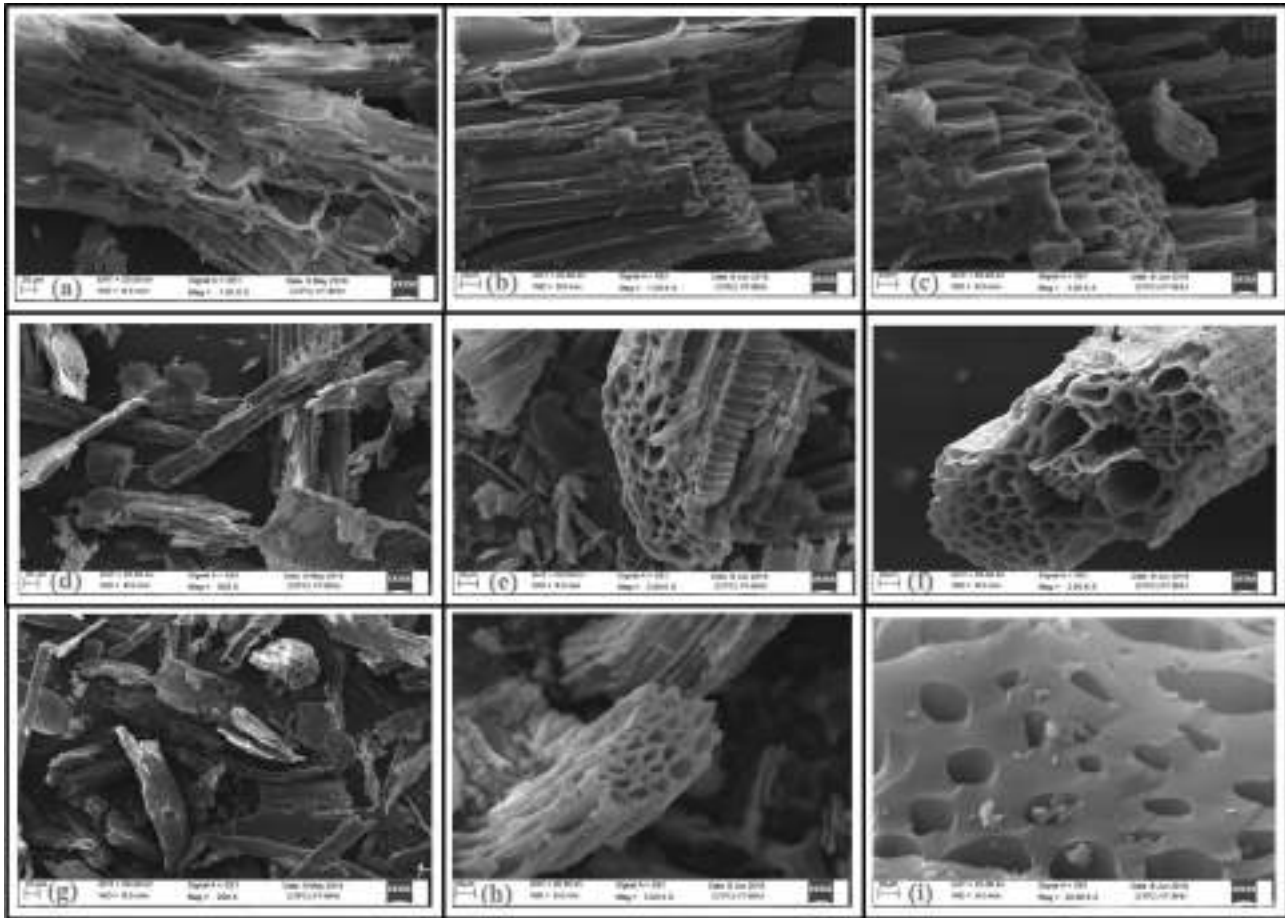


Fig. 11 SEM analysis of raw biomass and biochar produced at 350 °C and 550 °C (a) SB (d) WS (g) RS (b) SB biochar @ 350 °C (c) SB biochar @ 550 °C (e) WS biochar @ 350 °C (f) WS biochar @ 550 °C (h) RS biochar @ 350 °C (i) RS biochar @ 550 °C

ute more to the enhancement of soil quality and act as to subsequent sites for nutrient exchange [83].

EDX analysis The EDX analysis (Fig. S3, ESI) confirmed that biochar contains several inorganic elements, such as Ca, Si, K, P, Mg, Na. Biochar enriched with these elements, when applied to soil (especially acidic soil) as a fertilizer, provides important plant nutrients to soil [30, 56]. N P K present in biochar samples are the essential plant macro-nutrients that help in plant growth and fertility. Oxide and carbonate form of K and Na, whereas phosphate and sulfate form of Ca and Mg present in biochar are readily water-soluble, thus providing important macro- as well micronutrient contribution towards soil while being used as fertilizer, thus

promoting plant growth without any additional induction of toxicity [85]. Similarly, silica present in all the biochar samples in ample amount helps prevent drying up plant leaves and improves pollen fertility [92]. In addition, inorganic elements act as surface-charged species in the biochar, which help in removal of several pollutants from wastewater, such as Cd, Ni, Cu, and Zn, through chemisorption method [83]. Alkaline nature of biochar as previously described may be attributed to presence of these inorganic elements especially Ca, Mg carbonate along with organic hydroxyl and carboxyl functional groups [93].

ICP-AES analysis The inorganic elements present in studied biochar samples have been provided in Table 8. Most

Table 8 ICP-AES analysis of different biochar samples

Biochar	K	Ca	P	Zn	Na	Cu	Mn	Mg	Si
SB	4.023	0.9014	0.3461	0.1511	4.8664	0.0365	0.0321	3.82	7.65
WS	2.492	1.1650	0.0586	0.2115	3.3493	0.0243	0.4210	1.49	8.81
RS	3.050	1.4010	0.3062	0.1498	4.2295	0.0031	0.0351	1.65	9.16

abundant constituents of biomass minerals are Si, Ca, K, Na, and Mg with a lesser amount of S, P, Cu, Zn, Mn, and Al. These constituents remain as oxides, silicates, carbonates, sulfates, chlorides, and phosphates from [94]. Minerals/inorganic salts majorly present in biomass ash, decrease organic liquid yield with minimization of de-volatilization and initial decomposition temperature. They also catalytically promote char-forming secondary reactions [95]. Potassium and calcium catalyze biomass decomposition and char formation. The heterogeneous reaction between the mineral (Na+K) and pyrolysis vapor affects oil production. ICP analysis of biomass ash reveals that potassium concentration of SB is higher as compared to the other two biomass samples. Potassium is a strong catalyst for char gasification promoted in the presence of CO₂ and H₂O, thereby minimizing char yield as observed in case of SB. Similarly, combined effect K and Zn in SB also resulted in the production of more volatiles as compared to char. Similar trends were also observed in case of WS which resulted in more volatiles in terms of non-condensable gases unlike RS which ended up producing more char due to high lignin content. Due to the presence of Zn in biomass, there is a rise in initial decomposition temperature during pyrolysis whereas potassium has its reverse effect on biomass. TGA profile for three types of biomass samples indicated that the initial decomposition temperature of WS (~240 °C) is more as compared to other two biomasses due to presence of high amount of zinc in it. The initial pyrolysis decomposition temperatures were ~220 °C and ~230 °C for SB and RS, respectively, due to the high concentration of potassium in them as compared to zinc. Also, the combination of zinc and potassium played significant role in enhancing the number of volatile products produced during pyrolysis. SB has a moderately high amount of Na+K as compared to WS and RS; hence, there was larger decomposition and production of greater amount of volatiles clearly visible from SB weight loss profile in TGA. The weight loss was nearly (~50%) higher than WS (~47%) and RS (~42%). Another important finding is that the presence of Zn in biomass leads to generation of more gases while minimizing liquid yield. WS, on pyrolysis reaction produced higher gas yield as compared to the other two biomasses due to the high percentage of Zn in it. Ca and Mg present in biochar samples have concentration lower than Na and K since they have less solubility in water, hence not properly detected. Presence of nitrogen in prepared biochar samples along with all these inorganic elements mentioned above is important in plant nutrients, and those on subsequent application towards soil enhances soil fertility and promotes plant growth owing to their high solubility nature in water.

Generally, silica present in biomass has the property of arresting the carbon present in it, and thus reducing its conversion efficiency during formation of producer gas. Slight

increase in carbon conversion efficiency in case of biochar prepared from SB may have resulted due to presence of lesser amount of silica in its biomass as compared to WS and RS.

Pyrolysis product distribution and corresponding utilization

Though we have already discussed regarding wide usability of pyrolysis products obtained for different biomass samples, in this paragraph, we have briefly discussed each product quality based on their physiochemical properties. Based on yield % and heating value, sugarcane bagasse produced best-quality bio-oil which makes it suitable for best alternative liquid fuel in boiler and combustion engines after moderate upgrading. Bio-oil produced has comparable density and viscosity with diesel/fuel oil. Hence, greater volume of fuel injection, better atomization of fuel in burner, and uniform cylinder temperature ultimately lead to less NO_x emission while using in combustion engine. Though low viscosity enhances the shelf life of bio-oil; however, acidity and slightly higher ash content (~0.1%) can have issues with corrosion or kicking problem in engine, hence requiring moderate upgrading before use [96]. GC-MS analysis of bio-oil also revealed that it contains alcohol, anhydrosugar, furan and ketone compounds, those that can be directly consumed as fuel [97]. Also, phenolic compounds identified in bio-oil samples have attracted special attention due to their use in applications like fuel additives and chemical precursors [98, 99]. Detailed applications of identified chemical compounds present in bio-oils have been discussed in supplementary file (section S4, ESI). Biochar is produced in larger amounts for WS and RS and specifically maximized at bigger biomass particle size and low-temperature heating conditions. The yield of biochar was maximum for reaction carried out at low temperature; however, char produced at high temperature (> 600 °C) with low H/C and O/C ratio and high-energy density has calorific value comparable to fossil fuel (e.g. coal), hence it can be used in several energy generation applications like running a boiler furnace, co-firing, and briquetting etc. Apart from this, high porosity of biochar generated at moderate pyrolysis conditions and alkaline nature of biochar can be useful in applications like bio-fertilizer for providing important soil nutrients and carbon sequestration process. Apart from these, inorganic elements like (Si, Ca, K, Na, and Mg) are rich in biochar produced, hence can also be utilized in soil amendment application and use of it as an excellent adsorbent for waste water purification. Non-condensable gases generated at high-temperature pyrolysis conditions with less amount of CO₂ can be used as a fuel (synthesis gas) in combustion process and can be recycled and combusted to run the pyrolysis system [100].

In fact, non-condensable gases with relatively higher yield and enhanced HHV, generated from pyrolysis of WS and RS, can be used for energy generation applications.

Conclusion

Pyrolysis of three biomass samples was accomplished at different operating conditions to maximize bio-oil yield. The maximum bio-oil yield was obtained at a temperature of 550 °C for SB and WS, whereas for RS, it was 450 °C. Variation of the heating rate from 20 °C/min from 100 °C/min had no significant influence on optimizing the product yield in the chosen range. Biomass particle size had a great influence on the optimization of pyrolysis product yield. Bio-oil, which is the principal product in this experiment, was obtained at higher percentage within the particle size of 0.2–0.4 mm. The bigger particle size (0.6–0.8 mm) maximized the formation of char and gas during pyrolysis reaction. The flow rate of 30 mL/min was found to be best for maximizing bio-oil yield. TGA analysis of 3 biomass samples showed the similarity between decomposition behavior of SB and WS. RS showed slightly different thermal decomposition property, and maximum decomposition occurred within a temperature range of 220–500 °C. SB produced more CO, CO₂ as compared to other biomass, while RS exhibited the maximum yield of H₂ and CH₄. The bio-oil produced from three biomasses found to be acidic in nature and measured calorific value goes up to 10 MJ/kg. The comparable density with commercial fuel, low ash content, the low viscosity of produced bio-oil makes it suitable for use in an application like boiler combustion and IC engine. FTIR and GC–MS analysis of bio-oil showed that it contains chemical compounds, such as phenol, acids, alcohols, ester, ether, aromatic compounds, ketones, those can be exploited for commercial extraction purpose. CHNS, SEM/EDX, pH analysis of produced biochar indicated that it could be used as a commercial fertilizer in soil by replenishing soil nutrients. FTIR, CHNS, ICP-AES analyses data of biochar correlate biochar composition well with the pyrolysis product distribution. High calorific value of produced biochar samples compared to their precursor makes them suitable in combustion application with low NO_x and SO_x emission.

Acknowledgements This work was supported by the DST, New Delhi, vide sanction number, SR/FTP/ETA-56/2012, and Seed Money received from IIT (BHU), Varanasi.

References

- Sohaib Q, Muhammad A, Younas M (2017) Fast pyrolysis of sugarcane bagasse: effect of pyrolysis conditions on final product distribution and properties. *Energy Sourc Part A Recov Utilization Environ Eff* 39(2):184–190
- Kumar A, Sinha ASK (2020) Hydrogen production from acetic acid steam reforming over nickel-based catalyst synthesized via MOF process. *Int J Hydrog Energy*. <https://doi.org/10.1016/j.ijhydene.2020.06.040>
- Ren S, Ye XP, Borole AP, Kim P, Labbé N (2016) Analysis of switchgrass-derived bio-oil and associated aqueous phase generated in a semi-pilot scale auger pyrolyzer. *J Anal Appl Pyrol* 119:97–103
- Hernández C, Escamilla-Alvarado C, Sánchez A, Alarcón E, Ziarelli F, Musule R, Valdez-Vazquez I (2019) Wheat straw, corn stover, sugarcane, and Agave biomasses: chemical properties, availability, and cellulosic-bioethanol production potential in Mexico. *Biofuels Bioprod Biorefin* 13(5):1143–1159
- Wyman CE (1999) BIOMASS ETHANOL: technical progress, opportunities, and commercial challenges. *Annu Rev Energy Environ* 24(1):189–226. <https://doi.org/10.1146/annurev.energy.24.1.189>
- Mosier N, Wyman C, Dale B, Elander R, Lee YY, Holtzapple M, Ladisch M (2005) Features of promising technologies for pretreatment of lignocellulosic biomass. *Biores Technol* 96(6):673–686. <https://doi.org/10.1016/j.biortech.2004.06.025>
- Bridgwater AV (2003) Renewable fuels and chemicals by thermal processing of biomass. *Chem Eng J* 91(2):87–102. [https://doi.org/10.1016/S1385-8947\(02\)00142-0](https://doi.org/10.1016/S1385-8947(02)00142-0)
- Jestin-Fleury N (1994) International energy agency. World energy outlook. *Politique étrangère* 59(59):564–565
- Kumar A, Singh R, Sinha ASK (2019) Catalyst modification strategies to enhance the catalyst activity and stability during steam reforming of acetic acid for hydrogen production. *Int J Hydrog Energy* 44(26):12983–13010. <https://doi.org/10.1016/j.ijhydene.2019.03.136>
- Guo M, Song W, Buhain J (2015) Bioenergy and biofuels: history, status, and perspective. *Renew Sustain Energy Rev* 42:712–725
- Biswas B, Pandey N, Bisht Y, Singh R, Kumar J, Bhaskar T (2017) Pyrolysis of agricultural biomass residues: comparative study of corn cob, wheat straw, rice straw and rice husk. *Biores Technol* 237:57–63
- Kumar A, Sinha ASK (2020) Comparative study of hydrogen production from steam reforming of acetic acid over synthesized catalysts via MOF and wet impregnation methods. *Int J Hydrog Energy* 45(20):11512–11526. <https://doi.org/10.1016/j.ijhydene.2020.02.097>
- Worasuwannarak N, Sonobe T, Tanthapanichakoon W (2007) Pyrolysis behaviors of rice straw, rice husk, and corncob by TG-MS technique. *J Anal Appl Pyrol* 78(2):265–271
- Bridgwater AV, Peacocke GVC (2000) Fast pyrolysis processes for biomass. *Renew Sustain Energy Rev* 4(1):1–73. [https://doi.org/10.1016/S1364-0321\(99\)00007-6](https://doi.org/10.1016/S1364-0321(99)00007-6)
- Demirbas A (2009) Biorefineries: current activities and future developments. *Energy Convers Manag* 50(11):2782–2801
- Demirbas A (2004) Combustion characteristics of different biomass fuels. *Prog Energy Combust Sci* 30(2):219–230
- Demirbas A (2007) Progress and recent trends in biofuels. *Prog Energy Combust Sci* 33(1):1–18
- Chakraborty JP, Kunzru D (2009) High pressure pyrolysis of n-heptane. *J Anal Appl Pyrol* 86(1):44–52
- Kumar A, Chakraborty JP, Singh R (2017) Bio-oil: the future of hydrogen generation. *Biofuels* 8(6):663–674. <https://doi.org/10.1080/17597269.2016.1141276>
- Bilgen S (2016) Correlation for estimation of the chemical availability (energy) from ultimate analysis of pyrolytic oils obtained from fast pyrolysis of biomass. *Energy Sourc Part A Recove Utilization Environ Eff* 38(9):1286–1292

21. Demirbas A (2005) Pyrolysis of ground beech wood in irregular heating rate conditions. *J Anal Appl Pyrol* 73(1):39–43
22. Asadullah M, Rahman MA, Ali MM, Rahman M, Motin M, Sultan M, Alam M (2007) Production of bio-oil from fixed bed pyrolysis of bagasse. *Fuel* 86(16):2514–2520
23. Demiral İ, Şensöz S (2008) The effects of different catalysts on the pyrolysis of industrial wastes (olive and hazelnut bagasse). *Biores Technol* 99(17):8002–8007
24. Van de Velden M, Baeyens J, Brems A, Janssens B, Dewil R (2010) Fundamentals, kinetics and endothermicity of the biomass pyrolysis reaction. *Renew Energy* 35(1):232–242
25. Kan T, Strezov V, Evans TJ (2016) Lignocellulosic biomass pyrolysis: a review of product properties and effects of pyrolysis parameters. *Renew Sustain Energy Rev* 57:1126–1140. <https://doi.org/10.1016/j.rser.2015.12.185>
26. Boukis IP (1999) Fast pyrolysis of biomass in a circulating fluidised bed reactor. PhD Thesis, Chemical Engineering and Applied Chemistry, Aston University, Birmingham, UK
27. Karaosmanoğlu F, Tetik E (1999) Fuel properties of pyrolytic oil of the straw and stalk of rape plant. *Renew Energy* 16(1–4):1090–1093
28. Tsai W, Lee M, Chang Y (2007) Fast pyrolysis of rice husk: Product yields and compositions. *Biores Technol* 98(1):22–28
29. Aho A, Kumar N, Eränen K, Salmi T, Hupa M, Murzin DY (2008) Catalytic pyrolysis of woody biomass in a fluidized bed reactor: Influence of the zeolite structure. *Fuel* 87(12):2493–2501
30. Jensen PA, Sander B, Dam-Johansen K (2001) Pretreatment of straw for power production by pyrolysis and char wash. *Biomass Bioenergy* 20(6):431–446
31. Demirbas A (2004) Determination of calorific values of bio-chars and pyro-oils from pyrolysis of beech trunkbarks. *J Anal Appl Pyrol* 72(2):215–219
32. Ahmad M, Rajapaksha AU, Lim JE, Zhang M, Bolan N, Mohan D, Vithanage M, Lee SS, Ok YS (2014) Biochar as a sorbent for contaminant management in soil and water: a review. *Chemosphere* 99:19–33
33. Zhai M, Liu J, Wang Z, Guo L, Wang X, Zhang Y, Dong P, Sun J (2017) Gasification characteristics of sawdust char at a high-temperature steam atmosphere. *Energy* 128:509–518
34. Lee J, Kim K-H, Kwon EE (2017) Biochar as a catalyst. *Renew Sustain Energy Rev* 77:70–79
35. Hossain MK, Strezov V, Chan KY, Ziolkowski A, Nelson PF (2011) Influence of pyrolysis temperature on production and nutrient properties of wastewater sludge biochar. *J Environ Manag* 92(1):223–228
36. Pütün E, Uzun BB, Pütün AE (2006) Fixed-bed catalytic pyrolysis of cotton-seed cake: effects of pyrolysis temperature, natural zeolite content and sweeping gas flow rate. *Biores Technol* 97(5):701–710
37. Giddel M, Jivan A (2007) Waste to wealth, potential of rice husk in India a literature review. In: International conference on cleaner technologies and environmental management PEC, Pondicherry, India, pp 4–6
38. Chouhan S, Singh S, Pande A, Gautam U (2016) Adoption dynamics of improved sugarcane cultivation in Madhya Pradesh. *Indian Res J Extens Educ* 13(2):26–30
39. Wang C, Du Z, Pan J, Li J, Yang Z (2007) Direct conversion of biomass to bio-petroleum at low temperature. *J Anal Appl Pyrol* 78(2):438–444. <https://doi.org/10.1016/j.jaap.2006.10.016>
40. Park J, Lee Y, Ryu C, Park Y-K (2014) Slow pyrolysis of rice straw: analysis of products properties, carbon and energy yields. *Biores Technol* 155:63–70
41. Balagurumurthy B, Srivastava V, Kumar J, Biswas B, Singh R, Gupta P, Kumar KS, Singh R, Bhaskar T (2015) Value addition to rice straw through pyrolysis in hydrogen and nitrogen environments. *Biores Technol* 188:273–279
42. Pottmaier D, Costa MR, Farrow T, Oliveira AA, Alarcon O, Snape C (2013) Comparison of rice husk and wheat straw: from slow and fast pyrolysis to char combustion. *Energy Fuels* 27(11):7115–7125
43. Varma AK, Mondal P (2017) Pyrolysis of sugarcane bagasse in semi batch reactor: effects of process parameters on product yields and characterization of products. *Ind Crops Prod* 95:704–717
44. Gonçalves EV, Teodoro C, Seixas FL, Canesin EA, Olsen Scaliante MHN, Gimenes ML, De Souza M (2017) Pyrolysis of sugarcane bagasse in a fixed bed reactor: influence of operational conditions in the distribution of products. *Can J Chem Eng* 95(12):2249–2257
45. Duong TL, Nguyen DT, Nguyen HHM, Phan BMQ, Nguyen HL, Huynh TM (2019) Fast pyrolysis of Vietnamese waste biomass: relationship between biomass composition, reaction conditions, and pyrolysis products, and a strategy to use a biomass mixture as feedstock for bio-oil production. *J Mater Cycles Waste Manag* 21(3):624–632
46. Adinave T, Kennedy LJ, Vijaya JJ, Sekaran G (2015) Surface and porous characterization of activated carbon prepared from pyrolysis of biomass (rice straw) by two-stage procedure and its applications in supercapacitor electrodes. *J Mater Cycles Waste Manag* 17(4):736–747
47. Bera T, Purakayastha T, Patra A, Datta S (2018) Comparative analysis of physicochemical, nutrient, and spectral properties of agricultural residue biochars as influenced by pyrolysis temperatures. *J Mater Cycles Waste Manag* 20(2):1115–1127
48. Tan Z, Zou J, Zhang L, Huang Q (2018) Morphology, pore size distribution, and nutrient characteristics in biochars under different pyrolysis temperatures and atmospheres. *J Mater Cycles Waste Manag* 20(2):1036–1049
49. Do PT, Ueda T, Kose R, Nguyen LX, Okayama T, Miyanishi T (2019) Properties and potential use of biochars from residues of two rice varieties, Japanese Koshihikari and Vietnamese IR50404. *J Mater Cycles Waste Manag* 21(1):98–106
50. Derakhshan-Nejad Z, Jung MC (2019) Remediation of multi-metal contaminated soil using biochars from rice husk and maple leaves. *J Mater Cycles Waste Manag* 21(3):457–468
51. Asadullah M, Ab-Rasid NS, Kadir SASA, Azdarpour A (2013) Production and detailed characterization of bio-oil from fast pyrolysis of palm kernel shell. *Biomass Bioenergy* 59:316–324
52. Ogunjobi JK, Lajide L (2013) Characterisation of bio-oil and bio-char from slow-pyrolysed Nigerian yellow and white corn cobs. *J Sustain Energy Environ* 4(2):77–84
53. Yuan T, Tahmasebi A, Yu J (2015) Comparative study on pyrolysis of lignocellulosic and algal biomass using a thermogravimetric and a fixed-bed reactor. *Biores Technol* 175:333–341
54. Fu P, Hu S, Xiang J, Sun L, Su S, Wang J (2012) Evaluation of the porous structure development of chars from pyrolysis of rice straw: effects of pyrolysis temperature and heating rate. *J Anal Appl Pyrol* 98:177–183. <https://doi.org/10.1016/j.jaap.2012.08.005>
55. Trubetskaya A, Jensen PA, Jensen AD, Steibel M, Spliethoff H, Glarborg P, Larsen FH (2016) Comparison of high temperature chars of wheat straw and rice husk with respect to chemistry, morphology and reactivity. *Biomass Bioenergy* 86:76–87. <https://doi.org/10.1016/j.biombioe.2016.01.017>
56. Pütün AE, Özbay N, Önal EP, Pütün E (2005) Fixed-bed pyrolysis of cotton stalk for liquid and solid products. *Fuel Process Technol* 86(11):1207–1219
57. Apaydin-Varol E, Pütün E, Pütün AE (2007) Slow pyrolysis of pistachio shell. *Fuel* 86(12–13):1892–1899
58. Yang H, Yan R, Chen H, Lee DH, Zheng C (2007) Characteristics of hemicellulose, cellulose and lignin pyrolysis. *Fuel* 86(12–13):1781–1788

59. Chen W-H, Kuo P-C (2010) A study on torrefaction of various biomass materials and its impact on lignocellulosic structure simulated by a thermogravimetry. *Energy* 35(6):2580–2586
60. Stefanidis SD, Kalogiannis KG, Iliopoulou EF, Michailof CM, Pilavachi PA, Lappas AA (2014) A study of lignocellulosic biomass pyrolysis via the pyrolysis of cellulose, hemicellulose and lignin. *J Anal Appl Pyrol* 105:143–150
61. Şen N, Kar Y (2011) Pyrolysis of black cumin seed cake in a fixed-bed reactor. *Biomass Bioenergy* 35(10):4297–4304
62. Morali U, Şensöz S (2015) Pyrolysis of hornbeam shell (*Carpinus betulus* L.) in a fixed bed reactor: characterization of bio-oil and bio-char. *Fuel* 150:672–678
63. Lu Q, Li W-Z, Zhu X-F (2009) Overview of fuel properties of biomass fast pyrolysis oils. *Energy Convers Manag* 50(5):1376–1383
64. Carrier M, Joubert J-E, Danje S, Hugo T, Görgens J, Knoetze JH (2013) Impact of the lignocellulosic material on fast pyrolysis yields and product quality. *Biores Technol* 150:129–138
65. Garg R, Anand N, Kumar D (2016) Pyrolysis of babool seeds (*Acacia nilotica*) in a fixed bed reactor and bio-oil characterization. *Renew energy* 96:167–171
66. Demiral İ, Kul ŞÇ (2014) Pyrolysis of apricot kernel shell in a fixed-bed reactor: characterization of bio-oil and char. *J Anal Appl Pyrol* 107:17–24
67. Sensoez S, Angin D (2008) Pyrolysis of safflower (*Charthamus tinctorius* L.) seed press cake: part 1. The effects of pyrolysis parameters on the product yields. *Bioresour Technol* 99(13):5492–5497
68. Choi HS, Choi YS, Park HC (2012) Fast pyrolysis characteristics of lignocellulosic biomass with varying reaction conditions. *Renew Energy* 42:131–135
69. Şensöz S, Angin D (2008) Pyrolysis of safflower (*Charthamus tinctorius* L.) seed press cake: Part 1. The effects of pyrolysis parameters on the product yields. *Bioresour Technol* 99(13):5492–5497
70. Kim SW, Koo BS, Ryu JW, Lee JS, Kim CJ, Lee DH, Kim GR, Choi S (2013) Bio-oil from the pyrolysis of palm and Jatropha wastes in a fluidized bed. *Fuel Process Technol* 108:118–124
71. Park HJ, Park Y-K, Kim JS (2008) Influence of reaction conditions and the char separation system on the production of bio-oil from radiata pine sawdust by fast pyrolysis. *Fuel Process Technol* 89(8):797–802
72. Mohan D, Pittman CU Jr, Steele PH (2006) Pyrolysis of wood/biomass for bio-oil: a critical review. *Energy Fuels* 20(3):848–889
73. Kim S, Kim CH (2013) Bioethanol production using the sequential acid/alkali-pretreated empty palm fruit bunch fiber. *Renew Energy* 54:150–155
74. Părpăriță E, Brebu M, Uddin MA, Yanik J, Vășile C (2014) Pyrolysis behaviors of various biomasses. *Polym Degrad Stab* 100:1–9
75. Uzun BB, Pütün AE, Pütün E (2006) Fast pyrolysis of soybean cake: product yields and compositions. *Biores Technol* 97(4):569–576
76. Yang H, Yan R, Chen H, Lee DH, Liang DT, Zheng C (2006) Mechanism of palm oil waste pyrolysis in a packed bed. *Energy Fuels* 20(3):1321–1328
77. Vitasari CR, Meindersma GW, De Haan AB (2011) Water extraction of pyrolysis oil: the first step for the recovery of renewable chemicals. *Biores Technol* 102(14):7204–7210
78. David GF, Justo OR, Perez VH, Garcia-Perez M (2018) Thermochemical conversion of sugarcane bagasse by fast pyrolysis: high yield of levoglucosan production. *J Anal Appl Pyrol* 133:246–253
79. Dhyani V, Bhaskar T (2018) A comprehensive review on the pyrolysis of lignocellulosic biomass. *Renew Energy* 129:695–716. <https://doi.org/10.1016/j.renene.2017.04.035>
80. Yang H, Yan R, Chen H, Lee DH, Zheng C (2007) Characteristics of hemicellulose, cellulose and lignin pyrolysis. *Fuel* 86(12):1781–1788. <https://doi.org/10.1016/j.fuel.2006.12.013>
81. Guangul FM, Sulaiman SA, Ramli A (2014) Study of the effects of operating factors on the resulting producer gas of oil palm fronds gasification with a single throat downdraft gasifier. *Renew Energy* 72:271–283. <https://doi.org/10.1016/j.renene.2014.07.022>
82. Ahmad MI, Alauddin ZAZ, Soid SNM, Mohamed M, Rizman ZI, Rasat MSM, Razab M, Amini MHM (2015) Performance and carbon efficiency analysis of biomass via stratified gasifier. *ARPN J Eng Appl Sci* 10(20):9533–9537
83. Mullen CA, Boateng AA, Goldberg NM, Lima IM, Laird DA, Hicks KB (2010) Bio-oil and bio-char production from corn cobs and stover by fast pyrolysis. *Biomass Bioenergy* 34(1):67–74
84. Pütün AE, Özbay N, Apaydın Varol E, Uzun BB, Ateş F (2007) Rapid and slow pyrolysis of pistachio shell: effect of pyrolysis conditions on the product yields and characterization of the liquid product. *Int J Energy Res* 31(5):506–514
85. Carrier M, Hardie AG, Uras Ü, Görgens J, Knoetze J (2012) Production of char from vacuum pyrolysis of South-African sugar cane bagasse and its characterization as activated carbon and biochar. *J Anal Appl Pyrol* 96:24–32. <https://doi.org/10.1016/j.jaap.2012.02.016>
86. Al-Wabel MI, Al-Omran A, El-Naggar AH, Nadeem M, Usman ARA (2013) Pyrolysis temperature induced changes in characteristics and chemical composition of biochar produced from conocarpus wastes. *Biores Technol* 131:374–379. <https://doi.org/10.1016/j.biortech.2012.12.165>
87. Liu Z, Quek A, Kent Hoekman S, Balasubramanian R (2013) Production of solid biochar fuel from waste biomass by hydrothermal carbonization. *Fuel* 103:943–949. <https://doi.org/10.1016/j.fuel.2012.07.069>
88. Hansen J, Sato M, Kharecha P, Beerling D, Berner R, Masson-Delmotte V, Pagani M, Raymo M, Royer DL, Zachos JC (2008) Target atmospheric CO₂: where should humanity aim? arXiv:0804.1126.
89. Kim KH, Kim T-S, Lee S-M, Choi D, Yeo H, Choi I-G, Choi JW (2013) Comparison of physicochemical features of biooils and biochars produced from various woody biomasses by fast pyrolysis. *Renew Energy* 50:188–195
90. Anupam K, Swaroop V, Deepika Lal PS, Bist V (2015) Turning *Leucaena leucocephala* bark to biochar for soil application via statistical modelling and optimization technique. *Ecol Eng* 82:26–39. <https://doi.org/10.1016/j.ecoleng.2015.04.078>
91. Yan W, Acharjee TC, Coronella CJ, Vasquez VR (2009) Thermal pretreatment of lignocellulosic biomass. *Environ Progr Sustain Energy* 28(3):435–440
92. Tinwala F, Mohanty P, Parmar S, Patel A, Pant KK (2015) Intermediate pyrolysis of agro-industrial biomasses in bench-scale pyrolyser: product yields and its characterization. *Biores Technol* 188:258–264. <https://doi.org/10.1016/j.biortech.2015.02.006>
93. Apaydın-Varol E, Pütün AE (2012) Preparation and characterization of pyrolytic chars from different biomass samples. *J Anal Appl Pyrol* 98:29–36. <https://doi.org/10.1016/j.jaap.2012.07.001>
94. Raveendran K, Ganesh A, Khilar KC (1995) Influence of mineral matter on biomass pyrolysis characteristics. *Fuel* 74(12):1812–1822. [https://doi.org/10.1016/0016-2361\(95\)80013-8](https://doi.org/10.1016/0016-2361(95)80013-8)
95. Shafizadeh F (1968) Pyrolysis and combustion of cellulosic materials. In: Wolfrom ML, Tipson RS (eds) *Advances in carbohydrate chemistry*, vol 23. Elsevier, New York, pp 419–474

96. Zhang L, Shen C, Liu R (2014) GC–MS and FT-IR analysis of the bio-oil with addition of ethyl acetate during storage. *Front Energy Res* 2:3
97. Shah Z, Cataluña Veses R, Silva RD (2016) A comparative study and analysis of two types of bio-oil samples obtained from freshwater algae and microbial treated algae. *Mod Chem Appl* 4(3):1000185
98. Negahdar L, Gonzalez-Quiroga A, Otyuskaya D, Toraman HE, Liu L, Jastrzebski JT, Van Geem KM, Marin GB, Thybaut JW, Weckhuysen BM (2016) Characterization and comparison of fast pyrolysis bio-oils from pinewood, rapeseed cake, and wheat straw using ^{13}C NMR and comprehensive GC \times GC. *ACS Sustain Chem Eng* 4(9):4974–4985
99. Toraman HE, Vanholme R, Borén E, Vanwongerghem Y, Djokic MR, Yildiz G, Ronsse F, Prins W, Boerjan W, Van Geem KM (2016) Potential of genetically engineered hybrid poplar for pyrolytic production of bio-based phenolic compounds. *Biores Technol* 207:229–236
100. Mullen CA, Boateng AA, Hicks KB, Goldberg NM, Moreau RA (2010) Analysis and comparison of bio-oil produced by fast pyrolysis from three barley biomass/byproduct streams. *Energy Fuels* 24(1):699–706

Publisher's Note Springer Nature remains neutral with regard to jurisdictional claims in published maps and institutional affiliations.

An investigation of wireless S-DF hybrid satellite terrestrial relaying network over time selective fading channel

Indrajeet Kumar, Vikash Sachan*, Ravi Shankar, Ritesh Kumar Mishra

*Department of Electronics and Communication Engineering,
National Institute of Technology Patna, Patna 800005, India*

vikash.ece15@nitp.ac.in

ABSTRACT. This work investigates the performance of hybrid satellite terrestrial cooperative relaying communications network (HSTCN) over time-selective fading links arising due to the node mobility. Both satellite-to-destination (SD) and Satellite-to-relay (SR) links undergo the independent and identically distributed (i.i.d.) time-selective shadowed Rician fading, the terrestrial relay-to-destination links are assumed to be i.i.d. time-selective Nakagami-m faded. It evaluates the performance of such a network using multiple-input multiple-output (MIMO) space-time block-code (STBC) based selective decode-forward (S-DF) cooperation with imperfect CSI. An analytical approach is derived to evaluate the performance of the system in terms of per-frame average pairwise error probability (PEP) and asymptotic PEP floor. Further, a framework is developed for deriving the diversity order (DO). It demonstrates that full DO for cooperation protocol can be achieved when there is a knowledge of perfect CSI. A convex optimization (CO) framework is formulated for obtaining the optimal source-relay power allocation factors which significantly improve the end-to-end reliability of the system under power constraint scenarios. The results show the time selective nature of the links and imperfect CSI significantly degrades the system performance. Further, the impact of the satellite elevation angles at the terrestrial nodes is explicitly demonstrated through simulations. The error rate of the system is seen to reduce significantly with increasing satellite elevation angle at the relay when the SD link experiences frequent heavy shadowing and the RD links are relatively strong. However, for other scenarios when the RD links are relatively weak and SR links experience frequent heavy shadowing, significant performance improvement can be seen by increasing the satellite elevation angle at the destination user equipment. The analytical expressions show excellent agreement with the simulation results.

RÉSUMÉ. Cet article étudie la performance du réseau de communication de relais coopératif terrestre par satellite hybride (HSTCN, le sigle d'« hybrid satellite terrestrial cooperative relaying communications network » en anglais) sur les liaisons à évanouissement temporel sélectif en raison de la mobilité des nœuds. Les liaisons de satellite à destination (SD) et de satellite à relais (SR) sont soumises à un évanouissement temporel sélectif de Rician ombré indépendant et identique, les liaisons terrestres de relais à destination (RD) sont considérées indépendantes et identiques dans Nakagami -m à évanouissement temporel sélectif. Il évalue les

performances d'un tel réseau en utilisant une coopération de décodage -transfert sélectif basé sur un codage de bloc espace-temps ayant des entrées multiples et sorties multiples (MIMO, le sigle de «Multiple-Input Multiple-Output» en anglais) avec un CSI imparfait. Une approche analytique est dérivée pour évaluer les performances du système en termes de probabilité d'erreur par paire (PEP, le sigle de «Pairwise Error Probability» en anglais) moyenne par image et de plancher PEP asymptotique. En outre, un cadre est développé pour dériver l'ordre de diversité (OD). Cela démontre que l'OD complet pour la coopération de protocole peut être atteint lorsqu'il existe une connaissance du CSI parfait. Un cadre d'optimisation convexe (OC) est formulé pour obtenir les facteurs d'allocation de puissance source-relais optimaux qui améliorent de manière significative la fiabilité bout en bout du système dans des scénarios de contrainte de puissance. Les résultats montrent la nature sélective et temporelle des liaisons et du CSI imparfait dégrade considérablement la performance du système. De plus, l'impact des angles d'élévation des satellites terrestres aux nœuds est explicitement démontré par des simulations. Il semble que le taux d'erreur du système diminue considérablement avec l'augmentation de l'angle d'élévation du satellite au niveau du relais lorsque la liaison SD subit de fortes ombres fréquents et que les liaisons RD sont relativement fortes. Cependant, pour d'autres scénarios où les liaisons RD sont relativement faibles et que les liaisons SR subissent souvent une forte ombre, une amélioration significative des performances peut être constatée en augmentant l'angle d'élévation du satellite au niveau de l'équipement utilisateur de destination. Les résultats analytiques montrent un excellent accord avec les résultats de la simulation.

KEYWORDS: node mobility, selective decode-forward, space-time block code, hybrid satellite network, pairwise error probability.

MOTS-CLÉS: mobilité de nœud, décodage sélectif, codage de bloc espace-temps, réseau de satellites hybrides, probabilité d'erreur par paire.

DOI:10.3166/TS.35.103-120 © 2018 Lavoisier

1. Introduction

HSTCN are used in the context of mass broadcasting and navigation due to their ability to provide satellite coverage inside buildings and other shadowed areas. However, due to the rain, fog, poor angle of inclination, non-availability of line-of-sight (LOS), and low transmit power, the satellite coverage area is limited by the masking effect between the satellite and a terrestrial user. The masking effect becomes more severe in the case of low satellite elevation angles or when the user is indoors. The masking aberration also affects outdoor communication scenarios and its effect becomes more pronounced at lower satellite elevation angles. Further, mobility of the destination user-equipment (UE) and other cooperative UEs serving as relay nodes induces Doppler, which results in time-selective fading and the ensuing degradation of the end-to-end system performance (Varshney and Puri, 2017). Relay technology has thus become one of the core techniques in next-generation wireless communication systems. Therefore, HSTCN has been developed more recently to improve the performance as well as the coverage of the satellite networks (Ruan *et al.*, 2017).

In (Yang and Hasna, 2015), HSTCN is proposed, to avoid the masking effect. However, the work therein considers the amplify-and-forward (AF) protocol, which introduces noise amplification at the relay nodes. In (Sreng *et al.*, 2013), the authors investigated the symbol error rate (SER) performance of HSTCN. The closed form (CF) formulations for SER of quadrature phase shift keying (QPSK) and Quadrature amplitude modulation (QAM) signaling with maximum likelihood (ML) decoding over independent but not necessarily identically distributed shadowed rician fading channel are derived. These CF expressions are represented in terms of a finite sum of Lauricella hypergeometric functions. However, this work does not consider the impact of node mobility, elevation angles and imperfect CSI and on the PEP performance. In (Iqbal and Ahmed, 2011), the authors investigated the SER for a variable gain AF relaying network. Later, in (Bhatnagar and Arti, 2013), the authors investigated the performance of a fixed gain AF relaying system. Compared with variable-gain relaying, fixed-gain relaying appeals in practical applications for its ability to lower the implementation complexity since only statistic CSI is required. Further, several works such as (An *et al.*, 2014; Sharma *et al.*, 2016; Iqbal and Ahmed, 2015) have analyzed dual-hop HSTCN considering either AF or conventional decode-forward cooperative communication protocols at the relay node. However, in these works do not consider node mobility and imperfect CSI. In the authors investigated the node mobility and its impact on the per frame average PEP performance, especially employing the SDF cooperative protocol. However, in this work the authors do not consider MIMO and STBC and authors have not analyzed the diversity order and optimal power allocation. In (Halber and Chakravarty, 2018; Srikanth *et al.*, 2018) the author has described about the relay optimization.

This work investigates the performance of HSTCN over time-selective fading links with MIMO and STBC. Based multiple relays SDF cooperative communication system. It is observed that the node mobility and imperfect CSI lead to degradation of the system performance. Further, in case of static nodes and perfect CSI system gets full DO.

The rest of this paper is organized as follows. The system and channel models are discussed in Section II. In Section III, the moment generating function (MGF) and the average SEP are derived for different types of modulation schemes. The simulation and numerical results are presented in Section IV. The conclusion is finally drawn in Section V.

2. System model

We consider a HSTCN employing MIMO STBC S-DF relaying protocol, where K earth stations (terrestrial relay nodes) with N_R antennas selectively forwards the data received from the satellite to the destination. The schematic representation of HSTCN system is shown in Figure 1.

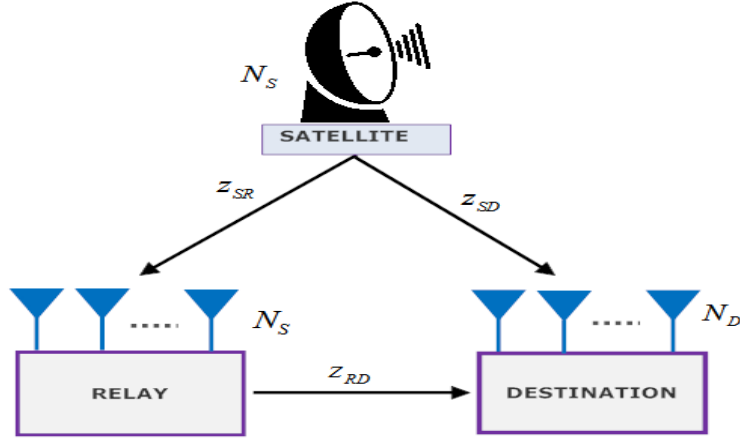


Figure 1. Schematic representation of HSTCN

In this work, we consider time-selective fading channel due to node mobility and imperfect CSI conditions. We assume all the fading channel links are time-selective in nature. Also, we assume links will not vary for one STBC to another STBC codeword matrix. It differs in a time-selective way from one STBC codeword to another STBC codeword within a block. Moreover, in contrast to previous papers (Varshney and Puri, 2017), the presence of a direct SD fading link with an elevation angle θ_{SD} is also assumed. The elevation angle for the fading link between SR is denoted by θ_{SR_r} , where $r = 1, 2, 3, \dots, K$. The time selective MIMO fading links can be modeled using first order autoregressive channel model (AR1) as (Varshnet and Hagannatham, 2017),

$$\mathbb{Z}_i(p) = v_i \mathbb{Z}_i(p-1) + \sqrt{1-v_i^2} E_i(p); \quad i \in \{SD, SR_r, R_rD\}. \quad (1)$$

Where the terms v_{SD} , v_{SR_r} and v_{R_rD} denote the correlation coefficients for the SD, SR and RD fading links respectively. These correlation coefficients can be evaluated using Jakes model as, $v = J_0(2\pi f_c v_p / R_S c)$, where v_p , R_S , $T_S = 1/R_S$, c , f_c and $J_0(\cdot)$ denote the relative velocity, symbol transmission rate, number of time slots, speed of light, carrier frequency and zeroth-order Bessel function of the 1st kind respectively. The random process $E_i(p)$ denotes the time-selective component of the associated link, distributed as zero mean circular shift complex Gaussian noise (ZMCSG) $\{i.e., \sim \mathbb{CN}(0, \sigma_{e_i}^2)\}$. In this system model, we consider that the DN employs low complexity maximal ratio combiner (MRC) receiver. However, it is difficult to get instantaneous CSI corresponding to the transmission of every STBC codeword due to the time-selective nature of the fading links. Hence, like works we assume imperfect CSI at the r^{th} relay node (RN) and DN.

The estimated channel matrices for RD, SR and SD links can be written as $\hat{\mathbb{Z}}_{RD}^{(r)}(1) = \mathbb{Z}_{RD}^{(r)}(1) + \mathbb{Z}_{\epsilon_{RD}}^{(r)}(1)$, $\hat{\mathbb{Z}}_{SR}^{(r)}(1) = \mathbb{Z}_{SR}^{(r)}(1) + \mathbb{Z}_{\epsilon_{SR}}^{(r)}(1)$ and $\hat{\mathbb{Z}}_{SD}(1) = \mathbb{Z}_{SD}(1) + \mathbb{Z}_{\epsilon_{SD}}(1)$ respectively, estimated at the beginning of each block and in this way used to detect each STBC codeword $X_S(p)$, $1 \leq p \leq M_b$ in the consequent block. The MIMO channel matrices $\mathbb{Z}_{SR_r}^{(r)}(1) \in \mathbb{C}^{N \times N}$, $\mathbb{Z}_{R_rD}^{(r)}(1) \in \mathbb{C}^{N_D \times N}$ and $\mathbb{Z}_{SD}(1) \in \mathbb{C}^{N_D \times N}$ are comprised of entries $h_{l,m}^{(SR_r)}(p)$, $h_{n,l}^{(R_rD)}(p)$ and $h_{n,m}^{(SD)}(p)$ which are ZMCSCG with variance $(\delta_{SR}^{(r)})^2$, $(\delta_{RD}^{(r)})^2$, $(\delta_{SR}^{(r)})^2$, $(\delta_{RD}^{(r)})^2$ and δ_{SD}^2 respectively. The channel error matrices $\mathbb{Z}_{\epsilon_{SR}}^{(r)}(1)$, $\mathbb{Z}_{\epsilon_{SD}}(1)$ and $\mathbb{Z}_{\epsilon_{RD}}^{(r)}(1)$ comprise of entries, which are ZMCSCG with variance $(\sigma_{\epsilon_{SR}}^{(r)})^2$, $\sigma_{\epsilon_{SD}}^2$ and $(\sigma_{\epsilon_{RD}}^{(r)})^2$ respectively. By using (1), $\mathbb{Z}_{SD}(p)$ can be modeled as,

$$\mathbb{Z}_{SD}(p) = \nu_{SD}^{p-1} \hat{\mathbb{Z}}_{SD}(1) - \nu_{SD}^{p-1} \mathbb{Z}_{\epsilon_{SD}}(1) + \sqrt{1 - \nu_{SD}^2} \sum_{i=1}^{p-1} \nu_{SD}^{p-i-1} E_{SD}(i). \quad (2)$$

Let N_D and N_S are the number of antennas employed at the DN and satellite node (SN) respectively. In order to keep the data rate of the SR link same as that of the RD link, we employ the same STBC at the RN and SN. This also means that $N_R = N_S = N$. The MIMO STBC S-DF based HSTCN relaying system can be described as follows. Let $\mathcal{C} = \{X_j[p]\}$ denotes the STBC codeword set, where each codeword of the set \mathcal{C} is expressed as, $X_j(p) \in \mathbb{C}^{N \times T_S}$ and $1 \leq j \leq |\mathcal{C}|$, where $|\mathcal{C}|$ denotes the cardinality of the codeword set \mathcal{C} . The received symbol block at the DN in case of direct SD transmission mode is modeled as,

$$Y_{SD}[p] = \sqrt{P_S / NR_C} \nu_{SD}^{p-1} \hat{\mathbb{Z}}_{SD}[1] X_S[p] + \tilde{W}_{SD}[p]. \quad (3)$$

Where P_S , N and R_C denote the total available power budget at the SN, number of antennas at the SN and STBC code rate respectively. For cooperation mode, the received symbol blocks at the RN and DN can be modeled as,

$$Y_{SR}^{(r)}[p] = \sqrt{P_S / NR_C} \nu_{SR_r}^{p-1} (\mathbb{Z}_{SR}^{(r)}[1] + \mathbb{Z}_{\epsilon_{SR}}^{(r)}[1]) X_S[p] + \tilde{W}_{SR}^{(r)}[p], \quad (4)$$

$$Y_{RD}^{(r)}[p] = \sqrt{\tilde{P}_r / NR_C} \nu_{R_rD}^{p-1} (\mathbb{Z}_{RD}^{(r)}[1] + \mathbb{Z}_{\epsilon_{RD}}^{(r)}[1]) X_S[p] + \tilde{W}_{RD}^{(r)}[p]. \quad (5)$$

Where, $\begin{cases} \tilde{P}_r = P_r; & \text{if relay decodes the symbol correctly} \\ \tilde{P}_r = 0; & \text{if relay decodes the symbol incorrectly.} \end{cases}$

In (4), P_r denotes the power available at the r^{th} relay.

The channel noise matrices $\tilde{W}_{SD}[p]$, $\tilde{W}_{SR}^{(r)}[p]$ and $\tilde{W}_{RD}^{(r)}[p]$ comprise of noise terms emerging because of the mobile nodes and imperfect CSI respectively. The effective noise variances N_{SD} , $N_{SR}^{(r)}$ and $N_{RD}^{(r)}$ for SD, SR and RD links can be modeled as,

$$\begin{aligned} N_{SD} &= N_0 + P_S (NR_C)^{-1} \nu_{SD}^{2(p-1)} N_a \sigma_{\epsilon_{SD}}^2 + P_S (NR_C)^{-1} (1 - \nu_{SD}^{2(p-1)}) N_a \sigma_{\epsilon_{SD}}^2, \\ N_{SR}^{(r)} &= N_0 + P_S (NR_C)^{-1} \nu_{SR_r}^{2(p-1)} N_a (\sigma_{\epsilon_{SR}}^{(r)})^2 + P_S (NR_C)^{-1} (1 - \nu_{SR_r}^{2(p-1)}) N_a (\sigma_{\epsilon_{SR}}^{(r)})^2, \quad (6) \\ N_{RD}^{(r)} &= N_0 + \tilde{P}_r (NR_C)^{-1} \nu_{R,D}^{2(p-1)} N_a (\sigma_{\epsilon_{RD}}^{(r)})^2 + \tilde{P}_r (NR_C)^{-1} (1 - \nu_{R,D}^{2(p-1)}) N_a (\sigma_{\epsilon_{RD}}^{(r)})^2, \end{aligned}$$

respectively. Where N_a denotes the number of non-zero M-PSK symbols transmitted per codeword. The advantage of using STBC code-word is that, it orthogonalizes the vector channel into a constant scalar channel by creating virtual parallel paths. The effective instantaneous signal to noise ratio (SNR) $\gamma_{SD}(p)$, $\gamma_{SR}^{(r)}(p)$ and $\gamma_{RD}^{(r)}(p)$ for the SD, SR and RD fading links respectively can be modeled as,

$$\begin{aligned} \gamma_{SD}(p) &= \frac{P_S \nu_{SD}^{2(p-1)} \left\| \hat{\mathcal{Z}}_{SD}(1)(X_S(p) - X_j(p)) \right\|_F^2}{2NR_C N_{SD}} = C_{SD}(p) \left\| \hat{\mathcal{Z}}_{SD}(1) \right\|_F^2, \\ \gamma_{SR}^{(r)}(p) &= \frac{P_S \nu_{SR_r}^{2(p-1)} \left\| \hat{\mathcal{Z}}_{SR}^{(r)}(1)(X_S(p) - X_j(p)) \right\|_F^2}{2NR_C N_{SR}^{(r)}} = C_{SR}^{(r)}(p) \left\| \hat{\mathcal{Z}}_{SR}^{(r)}(1) \right\|_F^2, \quad (7) \\ \gamma_{RD}^{(r)}(p) &= \frac{\tilde{P}_r \nu_{R,D}^{2(p-1)} \left\| \hat{\mathcal{Z}}_{RD}^{(r)}(1)(X_S(p) - X_j(p)) \right\|_F^2}{2NR_C N_{RD}^{(r)}} = C_{RD}^{(r)}(p) \left\| \hat{\mathcal{Z}}_{RD}^{(r)}(1) \right\|_F^2. \end{aligned}$$

The effective SNRs $\gamma_{SD}(p)$, $\gamma_{SR}^{(r)}(p)$ and $\gamma_{RD}^{(r)}(p)$ are Gamma distributed in nature, having a cumulative distribution function (CDF) and probability distribution function (PDF) are modeled as,

$$F_\gamma(t) = \gamma(\Theta, \Lambda t) \{ \Gamma(\Theta) \}^{-1}, \quad f_\gamma(t) = \Lambda^\Theta t^{\Theta-1} \{ \Gamma(\Theta) \}^{-1} e^{-\Lambda t}. \quad (8)$$

Where $\gamma(\dots)$ denotes the lower incomplete Gamma function and the quantities (Θ, Λ) will be equal to $\left[NN_D, \{ C_{SD}(p) \delta_{SD}^2 \}^{-1} \right]$, $\left[N^2, \{ C_{SR}^{(r)}(p) (\delta_{SR}^{(r)})^2 \}^{-1} \right]$ and $\left[NN_D, \{ C_{RD}^{(r)}(p) (\delta_{RD}^{(r)})^2 \}^{-1} \right]$ for the SR, SD, and RD SNR's respectively. Where $C_{SD}(p)$, $C_{SR}^{(r)}(p)$ and $C_{RD}^{(r)}(p)$ are given as,

$$\begin{aligned}
 C_{SD}(p) &= \left\{ \bar{\gamma}_{SD} \nu_{SD}^{2(p-1)} (NR_C)^{-1} \right\} \left\{ 1 + \bar{\gamma}_{SD} (NR_C)^{-1} \nu_{SD}^{2(p-1)} \tilde{\sigma}_{\epsilon_{SD}}^2 + \bar{\gamma}_{SD} (NR_C)^{-1} (1 - \nu_{SD}^{2(p-1)}) \tilde{\sigma}_{e_{SD}}^2 \right\}^{-1}, \\
 C_{SR}^{(r)}(p) &= \left\{ \bar{\gamma}_{SR} \nu_{SR}^{2(p-1)} (NR_C)^{-1} \right\} \left\{ 1 + \bar{\gamma}_{SR} (NR_C)^{-1} \nu_{SR}^{2(p-1)} (\tilde{\sigma}_{\epsilon_{SR}}^{(r)})^2 + \bar{\gamma}_{SR} (NR_C)^{-1} (1 - \nu_{SR}^{2(p-1)}) (\tilde{\sigma}_{e_{SR}}^{(r)})^2 \right\}^{-1}, \\
 C_{RD}^{(r)}(p) &= \left\{ \bar{\gamma}_{RD} \nu_{RD}^{p-1} (NR_C)^{-1} \right\} \left\{ 1 + \bar{\gamma}_{RD} (NR_C)^{-1} \nu_{RD}^{p-1} \tilde{\sigma}_{\epsilon_{RD}}^2 + \bar{\gamma}_{RD} (NR_C)^{-1} (1 - \nu_{RD}^{p-1}) \tilde{\sigma}_{e_{RD}}^2 \right\}^{-1}, \quad (9)
 \end{aligned}$$

respectively.

The quantities $(\tilde{\sigma}_{\epsilon_{SR}}^{(r)})^2$, $(\tilde{\sigma}_{e_{SR}}^{(r)})^2$, $(\tilde{\sigma}_{\epsilon_{RD}}^{(r)})^2$ and $(\tilde{\sigma}_{e_{RD}}^{(r)})^2$ are equivalent to $N_a(\sigma_{\epsilon_{SR}}^{(r)})^2$, $N_a(\sigma_{e_{SR}}^{(r)})^2$, $N_a(\sigma_{\epsilon_{RD}}^{(r)})^2$ and $N_a(\sigma_{e_{RD}}^{(r)})^2$ respectively.

The parameters $\bar{\gamma}_{SR}$, $\bar{\gamma}_{RD}$, $\bar{\gamma}_{SR}$, $\bar{\gamma}_{RD}$ and $\bar{\gamma}_{SD}$ are given as $\bar{\gamma}_{SR} = P_S/N_0$, $\bar{\gamma}_{RD} = P_r/N_0$ and $\bar{\gamma}_{SD} = P_S/N_0$ respectively. The quantities $(\tilde{\delta}_{SR}^{(r)})^2$, $\tilde{\delta}_{SD}^2$ and $(\tilde{\delta}_{RD}^{(r)})^2$ are defined as, $(\tilde{\delta}_{SR}^{(r)})^2 = (\delta_{SR}^{(r)})^2 + (\sigma_{\epsilon_{SR}}^{(r)})^2$, $\tilde{\delta}_{SD}^2 = \delta_{SD}^2 + \sigma_{\epsilon_{SD}}^2$ and $(\tilde{\delta}_{RD}^{(r)})^2 = (\delta_{RD}^{(r)})^2 + (\sigma_{\epsilon_{RD}}^{(r)})^2$ respectively. The terms $\tilde{\sigma}_{\epsilon_{SD}}^2$ and $\tilde{\sigma}_{e_{SD}}^2$ are equivalent to $N_a\sigma_{\epsilon_{SD}}^2$ and $N_a\sigma_{e_{SD}}^2$, respectively, $\lambda_{l_1}, \lambda_{l_2}, \dots, \lambda_{l_N}$ represents the singular values (SVs) obtained after performing the singular value decomposition (SVD) of the STBC codeword difference $X_S(p) - X_j(p)$, $\tilde{h}_{l,n}^{SD}$ represents the (\tilde{l}, n) coefficient of the matrix $\tilde{Z}_{SD}(1) = \tilde{Z}_{SD}(1)U_j$ for $1 \leq \tilde{l}, n \leq N$ and $U_j \in \mathbb{C}^{N \times N}$ is a unitary matrix, i.e., $U_j U = U U_j = I_{N \times N}$ and for Alamouti-STBC, $\lambda_{l_1} = \lambda_{l_2} = \dots = \lambda_{l_N} = \lambda$.

In this work we consider that SR and SD fading links are distributed as Shadowed-Rician and RD fading links are modeled as Nakagami-m fading channels. The SR channel matrix $H_{SR}[p] \in \mathbb{C}^{N_S \times N_R}$ contains independent and identically distributed (i.i.d.) Shadowed-Rician random variables (RVs), can be expressed as,

$$\underline{Z}_{SR}^{(r)}(p) = \underbrace{\bar{\underline{Z}}_{SR}^{(r)}(p)}_{\text{LOS COMPONENT}} + \underbrace{\tilde{\underline{Z}}_{SR}^{(r)}(p)}_{\text{SCATTERED COMPONENT}}. \quad (10)$$

The minimum antenna spacing for uncorrelated multipath scattered waves is $\lambda/2$, where λ denotes the wavelength. Very dense surrounding environment plays an important role in the correlation of the scatter component. Following the system model given in, the channel coefficients of LOS component $\bar{\underline{Z}}_{SR}^{(r)}(p)$ are i.i.d. Nakagami- m_i as RVs with variance Ω_i , where m_i denotes the shape parameter and its values ranges from 0.50 to ∞ . The scatter component channel matrix $\tilde{\underline{Z}}_{SR}^{(r)}(p)$ is comprised of entries which are distributed as i.i.d. complex Gaussian RVs with zero average value and variance $2b_i$.

3. Performance analysis of MIMO STBC S-SF based HSTCN relaying system

The instantaneous received SNR for SR link is modeled as,

$$(\gamma_{SR}^{(r)}(p))^i = (C_{SR}^{(r)}(p))^i \left\| \langle \hat{Z}_{SR}^{(r)}[1] \rangle^i \right\|^2; \quad i = 1, 2, \dots, N_S N_R. \quad (11)$$

By employing M-PSK modulation, the average PEP for the SR link is modeled as

$$P_E^{S \rightarrow R} \left((C_{SR}^{(r)}(p))^i, m_i, \Omega_i \right) \cong \xi_M \sum_{k=1}^{\eta M} \left(\sum_{i=1}^{N_S N_R} P_E^{S \rightarrow R} \left((C_{SR}^{(r)}(p))^i, m_i, \Omega_i, k \right) \right). \quad (12)$$

Where

$$P_E^{S \rightarrow R} \left((C_{SR}^{(r)}(p))^i, m_i, \Omega_i, k \right) = \int_0^\infty Q(\sqrt{g_k x}) f_{(\gamma_{SR}^{(r)}(p))^i}(x) dx. \quad (13)$$

$Q(\cdot)$ denotes the Q – function which is the tail probability of the Gaussian PDF; modulation specific parameters are defined as: $\xi_M = 2/\max(\log_2 M, 2)$, $\eta M = \max(M/4, 1)$, M is equal to 4 for QPSK and 2 for BPSK, and $g_k = 2 \sin^2((2k - 1)\pi/M)$. Also, $\max\{\cdot, \cdot\}$ selects greatest of the two positive integers; $(\gamma_{SR}^{(r)}(p))^i$ and $C_{SR}^i(p)$ denote the instantaneous and average SNR, respectively, for the SR link, and $f_{(\gamma_{SR}^{(r)}(p))^i}(x)$ denotes PDF of $(\gamma_{SR}^{(r)}(p))^i$.

In Appendix A, it is presented that the PDF of $(\gamma_{SR}^{(r)}(p))^i$ is modeled as,

$$f_{(\gamma_{SR}^{(r)}(p))^i}(x) \cong \alpha_i^{N_i} \sum_{l_i}^{c_i} \binom{c_i}{l_i} \beta_i^{c_i - l_i} \left(\begin{array}{l} J(x, l_i, d_i, (C_{SR}^{(r)}(p))^i) \\ + \epsilon_i \delta_i J(x, l_i, d_i + 1, (C_{SR}^{(r)}(p))^i) \end{array} \right). \quad (14)$$

Where

$$J(x, l_i, d_i, (C_{SR}^{(r)}(p))^i) = \frac{x^{d_i - l_i - 1}}{\{(C_{SR}^{(r)}(p))^i\}^{d_i - l_i} \Gamma(d_i - l_i)} \times {}_1F_1 \left(d_i; d_i - l_i; -\frac{(\beta_i - \delta_i)x}{(C_{SR}^{(r)}(p))^i} \right) \quad (15)$$

$\alpha_i = 0.5(2b_i m_i / (2b_i m_i + \Omega_i))^{m_i} / b_i$, $\beta_i = (0.5/b_i)$, $\delta_i = 0.5\Omega_i / (2b_i^2 m_i + b_i \Omega_i)$, $2b_i$ denotes the multipath component's average power, $c_i = (d_i - N_i)^+$, $\epsilon_i = m_i N_i - d_i$, $d_i = \max\{N_i, [m_i N_i]\}$ and $[z]$ denotes the largest integer not greater than

z ; $(z)^+$ indicates that if $z \leq 0$, then use $z = 0$; $z = 0$; $\Gamma(\cdot)$ denotes the Gamma function, and ${}_1F_1(\cdot; \cdot; \cdot)$ denotes the confluent hypergeometric function.

Substituting (14) in (13), we obtain,

$$p_E^{S \rightarrow R} \left((C_{SR}^{(r)}(p))^i, m_i, \Omega_i, k \right) \cong \alpha_i^{N_i} \sum_{l_i=0}^{c_i} \binom{c_i}{l_i} \beta_i^{c_i-l_i} \times \left(\kappa(l_i, d_i, (C_{SR}^{(r)}(p))^i, k) + \epsilon_i \delta_i \kappa(l_i d_i + 1, (C_{SR}^{(r)}(p))^i, k) \right) \quad (16)$$

Where,

$$\kappa(l_i, d_i, (\gamma_{SR}^{(r)}(p))^i, k) = \frac{1}{\{(\gamma_{SR}^{(r)}(p))^i\}^{-d_i-l_i} \Gamma(d_i-l_i)} \int_0^\infty x^{d_i-l_i-1} Q(\sqrt{g_k x}) \times {}_1F_1\left(d_i; d_i-l_i; -\frac{(\beta_i-\delta_i)x}{(C_{SR}^{(r)}(p))^i}\right) dx. \quad (17)$$

Using the relation given in $Q(\sqrt{g_k x})$ can be written as,

$$Q(\sqrt{g_k x}) = \frac{1}{2} \operatorname{erfc}\left(\sqrt{\frac{g_k x}{2}}\right) = \frac{1}{2\sqrt{\pi}} G_{12}^{20}\left(\frac{g_k x}{2} \middle| \frac{1}{0, 1/2}\right) \quad (18)$$

$${}_1F_1\left(d_i; d_i-l_i; -\frac{(\beta_i-\delta_i)x}{(C_{SR}^{(r)}(p))^i}\right) = \frac{\Gamma(d_i-l_i)}{\Gamma(d_i)} G_{12}^{11}\left(\frac{(\beta_i-\delta_i)x}{(C_{SR}^{(r)}(p))^i} \middle| \frac{1-d_i}{0, 1-d_i+l_i}\right) \quad (19)$$

Where $\operatorname{erfc}(\cdot)$ and $G_{p,q}^{m,n}(\cdot | \dots)$ denote the complementary error function and Meijer-G function respectively.

Substituting (18) and (19) into (17), $\kappa(l_i, d_i, (C_{SR}^{(r)}(p))^i, k)$ is given as,

$$\kappa(l_i, d_i, (C_{SR}^{(r)}(p))^i, k) = \frac{2^{d_i-l_i-1}}{2\sqrt{\pi}\Gamma(d_i)(C_{SR}^{(r)}(p))^i} \int_0^\infty x^{d_i-l_i-1} G_{12}^{22}\left(\frac{g_k x}{2} \middle| \frac{1}{0, 1/2}\right) G_{12}^{11}\left(\frac{(\beta_i-\delta_i)x}{(C_{SR}^{(r)}(p))^i} \middle| \frac{1}{0, 1/2}\right) dx. \quad (20)$$

The PEP for SR link can be obtained by substituting (16) into (12), as given below,

$$P_E^{S \rightarrow R} = \xi_M \sum_{k=1}^{\eta M} \left(\sum_{i=1}^{N_S N_R} \alpha_i^{N_i} \sum_{l_i=0}^{c_i} \binom{c_i}{l_i} \beta_i^{c_i - l_i} \times \right. \\ \left. \left(\frac{2^{d_i - l_i - 1}}{2\sqrt{\pi}\Gamma(d_i)(C_{SR}^{(r)}(p))^i} \int_0^\infty x^{d_i - l_i - 1} G_{12}^{22} \left(\frac{g_k x}{2} \middle| \frac{1}{0, 1/2} \right) G_{12}^{11} \left(\frac{(\beta_i - \delta_i)x}{(C_{SR}^{(r)}(p))^i} \middle| \frac{1}{0, 1/2} \right) dx + \right. \right. \\ \left. \left. \in_i \delta_i \frac{2^{d_i - l_i - 1}}{2\sqrt{\pi}\Gamma(d_i)(C_{SR}^{(r)}(p))^i} \int_0^\infty x^{d_i - l_i - 1} G_{12}^{22} \left(\frac{g_k x}{2} \middle| \frac{1}{0, 1/2} \right) G_{12}^{11} \left(\frac{(\beta_i - \delta_i)x}{(C_{SR}^{(r)}(p))^i} \middle| \frac{1}{0, 1/2} \right) dx \right) \right). \quad (21)$$

Following the similar approach, the PEP for the SD link can be written as,

$$P_E^{S \rightarrow D} \\ = \xi_M \sum_{k=1}^{\eta M} \left(\sum_{i=1}^{N_S N} \alpha_i^{N_i} \sum_{l_i=0}^{c_i} \binom{c_i}{l_i} \beta_i^{c_i - l_i} \right. \\ \left. \times \left(\frac{2^{d_i - l_i - 1}}{2\sqrt{\pi}\Gamma(d_i)(C_{SD}^i(p))^{d_i - l_i}} \int_0^\infty x^{d_i - l_i - 1} G_{12}^{22} \left(\frac{g_k x}{2} \middle| \frac{1}{0, 1/2} \right) G_{12}^{11} \left(\frac{(\beta_i - \delta_i)x}{C_{SD}^i(p)} \middle| \frac{1}{0, 1/2} \right) dx + \right. \right. \\ \left. \left. \in_i \delta_i \frac{2^{d_i - l_i - 1}}{2\sqrt{\pi}\Gamma(d_i)(C_{SD}^i(p))^{d_i - l_i}} \int_0^\infty x^{d_i - l_i - 1} G_{12}^{22} \left(\frac{g_k x}{2} \middle| \frac{1}{0, 1/2} \right) G_{12}^{11} \left(\frac{(\beta_i - \delta_i)x}{C_{SD}^i(p)} \middle| \frac{1}{0, 1/2} \right) dx \right) \right). \quad (22)$$

Instantaneous PEP for the event when $X_S[p] \in \mathbb{C}^{N \times T_S}$ is transmitted and $X_j[p] \in \mathbb{C}^{N \times T_S}$ is detected conditioned on the RD fading link instantaneous SNR $\gamma_{RD}^{(r)}(p)$ is modeled as,

$$P_{R \rightarrow D}(X_S[p] \rightarrow X_j[p] / \gamma_{RD}^{(r)}(p)) = Q\left(\sqrt{2\gamma_{RD}^{(r)}(p)}\right). \quad (23)$$

Where $Q(\cdot)$ denotes the Gaussian Q function, it is the area under the tail of a Gaussian curve, defined as, $Q(h) = \frac{1}{\sqrt{2\pi}} \int_h^\infty \exp(-u^2/2) du$. Average PEP $P_{R \rightarrow D}(X_S[p] \rightarrow X_j[p])$ be derived by averaging (23) over the PDF of $\gamma_{RD}^{(r)}(p)$, we use the MGF based approach. It can be modeled as,

$$P_{R \rightarrow D}(X_S[k] \rightarrow X_j[k]) = \frac{1}{\pi i} \int_0^{\pi i/2} M_{\gamma_{RD}^{(r)}(p)} \left[1 / \sin^2(\theta) \right] d\theta. \quad (24)$$

Where $M_{\gamma_{RD}^{(r)}(p)}(\cdot)$ denotes the MGF and is modeled as,

$$M_{\gamma_{RD}^{(r)}(p)} \left[1 / \sin^2(\theta) \right] = \left(\frac{1}{1 + \frac{\lambda_j^2 C_{RD}^{(r)}(p) (\tilde{\delta}_{RD}^{(r)})^2}{m_{RD} N_D N \sin^2(\theta)}} \right)^{m_{RD} N_D N}. \quad (25)$$

Following the detailed solution of (25) given in Appendix B, the average PEP for RD link is modeled as,

$$P_{R \rightarrow D}(X_S[p] \rightarrow X_j[p]) = \frac{1}{2\pi i} \left(\frac{1}{1 + \frac{\lambda_j^2 C_{RD}^{(r)}(p) (\tilde{\delta}_{RD}^{(r)})^2}{m_{RD} N_D N \sin^2(\theta)}} \right)^{m_{RD} N_D N} \frac{(m_{RD} N_D N - 1)! \sqrt{\pi}}{(m_{RD} N_D N)!} \times {}_2F_1 \left[m_{RD} N_D N, 0.50; m_{RD} N_D N + 1; 1 - \frac{1}{1 + \frac{\lambda_j^2 C_{RD}^{(r)}(p) (\tilde{\delta}_{RD}^{(r)})^2}{m_{RD} N_D N}} \right]. \quad (26)$$

The average PEP union bound can write as the summation of all PEP terms over the STBC codes $X_j[p] \in C$ as,

$$P_{R \rightarrow D}[p] \leq \sum_{X_j[p] \in C, X_j[p] \neq X_S[p]} P_{R \rightarrow D}(X_S[p] \rightarrow X_j[p]). \quad (27)$$

In relaying phase when relay correctly decodes the signal received from the source node then at the destination, we get the signal path from the source node as well as from the relay node. Using (22) and (27), the average PEP for cooperation modes, $P_{S \rightarrow D, R \rightarrow D}[k]$ can be written as,

$$P_{S \rightarrow D, R \rightarrow D}[k] = \xi_M \sum_{k=1}^{\eta M} \left(\sum_{i=1}^{N_S N} \alpha_i^{N_i} \sum_{l_i=0}^{c_i} \binom{c_i}{l_i} \beta_i^{c_i - l_i} \times \left(\frac{2^{d_i - l_i - 1}}{2\sqrt{\pi} \Gamma(d_i) (c_{SD}^i(p))^{d_i - l_i}} \int_0^\infty x^{d_i - l_i - 1} G_{12}^{22} \left(\frac{g_k x}{2} \middle| \frac{1}{0, 1/2} \right) G_{12}^{11} \left(\frac{(\beta_i - \delta_i)x}{c_{SD}^i(p)} \middle| \frac{1}{0, 1/2} \right) dx + \right. \right. \\ \left. \left. \in_i \delta_i \frac{2^{d_i - l_i - 1}}{2\sqrt{\pi} \Gamma(d_i) (c_{SD}^i(p))^{d_i - l_i}} \int_0^\infty x^{d_i - l_i - 1} G_{12}^{22} \left(\frac{g_k x}{2} \middle| \frac{1}{0, 1/2} \right) G_{12}^{11} \left(\frac{(\beta_i - \delta_i)x}{c_{SD}^i(p)} \middle| \frac{1}{0, 1/2} \right) dx \right) \right) \times$$

$$\sum_{X_j|p] \in C, X_j|p] \neq X_S[p]} \left\{ \frac{1}{2pi} \left(\frac{1}{1 + \frac{\lambda_j^2 C_{RD}^{(r)}(p)(\tilde{\delta}_{RD}^{(r)})^2}{m_{RD} N_D N \sin^2(\theta)}} \right)^{m_{RD} N_D N} \frac{(m_{RD} N_D N - 1)! \sqrt{pi}}{(m_{RD} N_D N)!} \times \right. \\ \left. {}_2F_1 \left[m_{RD} N_D N, 0.50; m_{RD} N_D N + 1; 1 - \frac{1}{1 + \frac{\lambda_j^2 C_{RD}^{(r)}(p)(\tilde{\delta}_{RD}^{(r)})^2}{m_{RD} N_D N}} \right] \right\}. \quad (28)$$

Therefore, the end-to-end PEP for HSTCN system can be written as,

$$P_E = P_E^{S \rightarrow R} \times P_E^{S \rightarrow D} + P_{S \rightarrow D, R \rightarrow D}[k] \times (1 - P_E^{S \rightarrow R}). \quad (29)$$

Substituting (28), (22) and (21) into (29), we will get the end-to-end PEP for HSTCN system.

4. Diversity order

The HSTCN system performance can be easily understood by assuming high SNR regimes. Coding gain (CG) and diversity gain (DG) are the two important parameters which help in analyzing the PEP performance of the system. CG is the measure in the difference between the SNR levels between the uncoded system and coded system required to reach the same PEP levels when used with the error correcting code (ECC). DG is the increase in signal-to-interference (SINR) ratio due to some diversity scheme, or how much the transmission power can be reduced when a diversity scheme is introduced, without a performance loss. DG is usually expressed in decibels, and sometimes as a power ratio. In general, the asymptotic value of the PEP can be written as,

$$\lim_{x \rightarrow \infty} P_E \approx \frac{(CG)^{-DG}}{\bar{\gamma}^{DG}}. \quad (30)$$

Where $\bar{\gamma}$ denotes the average SNR. The average PEP expression is expressed in terms of Meijer-G function. To find the system's asymptotic PEP, we need to find the asymptotic value of the Major-G function. For $(C_{SR}^{(r)}(p))^i \rightarrow \infty$ and $C_{SD}^i(p)$, asymptotically tight expression for Meijer-G function is given as,

$$G_{33}^{13} \left(\frac{2(\beta_i - \delta_i)}{C_{SD}^i(p) g_k} \middle| \begin{matrix} 1 - d_i, 1 - d_i + l_i, 1/2 - d_i + l_i \\ 0, -d_i + l_i, -d_i + l_i \end{matrix} \right) \rightarrow \frac{\Gamma(d_i) \Gamma(d_i - l_i + 1/2)}{\Gamma(d_i - l_i + 1)}, \quad (31)$$

At very high SNR, the term containing the product of probabilities can be ignored in (29). In addition, by using (31), assuming that $C_{SD}(p) = C_{SD}^i(p)$, and after some algebra, we can write the asymptotic average PEP of the system as,

$$p_e(C_{SD}(p), m_i, \Omega_i) \cong \xi_M \sum_{i=1}^2 p_{e_i}(C_{SD}(p), m_i, \Omega_i), \quad (32)$$

Where,

$$\begin{aligned} & p_{e_i}(C_{SD}(p), m_i, \Omega_i) \\ &= \frac{\alpha_i^{N_i}}{\sqrt{\pi}} \sum_{i=0}^{c_i} \binom{c_i}{l_i} \beta_i^{c_i-l_i} \frac{g_1^{l_i-d_i} 2^{d_i-l_i-1} \Gamma(d_i-l_i+1/2)}{C_{SD}(p)^{d_i-l_i} \Gamma(d_i-l_i+1)} \underbrace{\left(1 + \frac{2\epsilon_i \delta_i (d_i-l_i+1/2)}{(d_i-l_i+1) C_{SD}(p) g_1}\right)}_{A_i} \end{aligned} \quad (33)$$

For very large $C_{SD}(p)$, in (33), the term $A_i \rightarrow 1$; therefore, we obtain [],

$$\begin{aligned} & \lim_{C_{SD}(p) \rightarrow \infty} p_{e_i}(C_{SD}(p), m_i, \Omega_i) \\ &= \frac{\alpha_i^{N_i}}{\sqrt{\pi}} \sum_{i=0}^{c_i} \binom{c_i}{l_i} \beta_i^{c_i-l_i} g_1^{l_i-d_i} 2^{d_i-l_i-1} \frac{\Gamma(d_i-l_i+1/2)}{\Gamma(d_i-l_i+1)} \frac{1}{C_{SD}(p)^{d_i-l_i}}, \end{aligned} \quad (34)$$

At very high SNR, the decay of the term $p_{e_i}(C_{SD}(p), m_i, \Omega_i)$ is dominated by the lowest power of $C_{SD}(p)$; therefore, after some algebra, we obtain the asymptotic PEP of the considered scheme from (33) and (34), i.e.

$$\begin{aligned} \lim_{C_{SD}(p) \rightarrow \infty} p_e(C_{SD}(p), m_i, \Omega_i) &\cong \frac{\xi_M \alpha_1^{N_s} \Gamma(N_s+1/2) g_1^{-N_D} 2^{N_s-1}}{\sqrt{\pi} \Gamma(N_s+1)} \frac{1}{C_{SD}(p)^{N_s}} \\ &+ \frac{\xi_M \alpha_2^{N_D} \Gamma(N_D+1/2) g_1^{-N_D} 2^{N_D-1}}{\sqrt{\pi} \Gamma(N_D+1)} \frac{1}{C_{SD}(p)^{N_D}}. \end{aligned} \quad (35)$$

It can be seen from (35) that the DO of the satellite relay system is $\min\{N_s, N_D\} + NN_D$. This result indicates that if the relay has N_R transmit antenna, then no diversity gain can be achieved in the HSTCN by installing multiple antennas at the destination Earth station. Similarly, if the destination has N_D receive antenna, then it will experience no diversity gain due the MIMO based source Earth station. Hence, to experience the diversity advantage, the source and the destination must use multiple antennas, i.e., $N_i > 1$.

5. Simulation results

Simulations have been conducted in various conditions of node mobility over time varying channel. Simulation parameters are given as, $M = 4, K = 2$, noise variance

$N_0 = 1$. This section presents simulation results to demonstrate the performance of the HSTCN relaying network in various mobility scenarios. Figure 2 demonstrates the impact of the satellite elevation angles on the end-to-end PEP performance of the system for a scenario when all the links are quasi-static i.e., $\rho = 1$ and all elevation angles equal i.e., $\theta_{SR_1} = \theta_{SR_2} = \theta_{SR}$. It can be seen in Figure 2 that increasing the elevation angles results in a significant improvement in the end-to-end performance. This is because high elevation angles lead to favorable channel with infrequent light shadowing (ILS) in satellite-terrestrial links.

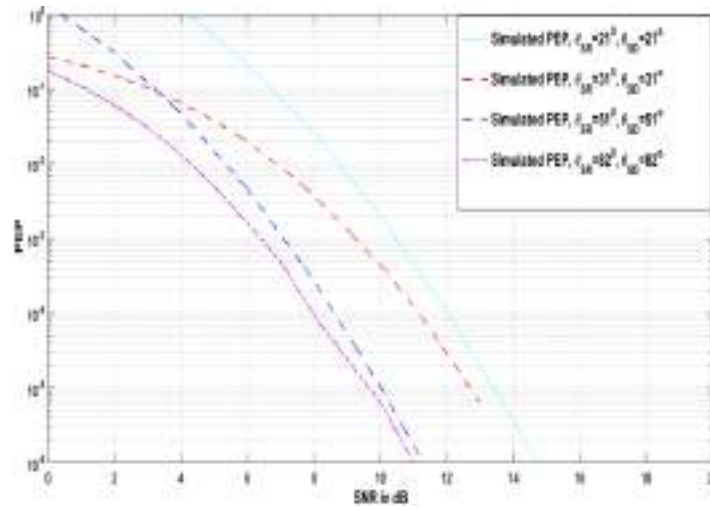


Figure 2. PEP versus SNR in dB performance of the MIMO STBC S-DF based HSTCN relaying network for various values of satellite elevation angle with $\theta_{SD}, \theta_{SR_1} = \theta_{SR_2} = \theta_{SR} \in \{21^\circ, 31^\circ, 51^\circ, 82^\circ\}, P_S = P_1 = P_2 = 1/3, m_{R_1D} = m_{R_2D} = m_{RD} = 0.60$ and $f_C = 5.9\text{GHz}, R_C = 9.6\text{Kbps}, P_S = P_1 = P_2 = 1/3, \rho_{SD} = \rho_{SR_1} = \rho_{SR_2} = \rho_{R_1D} = \rho_{R_2D} = \rho \in \{0.9856, 0.9889, 0.9989\}, \sigma_{eSD}^2 = \sigma_{eSR_r}^2 = \sigma_{eR_rD}^2 = \sigma_e^2 = \{0.09, 0.02\} \forall r$

6. Conclusion

This paper presents the performance analysis for a selective DF cooperative hybrid satellite-terrestrial system with multiple relays where the satellite-to-relay links experience non-identical time-selective shadowed Rician fading and the relay-destination terrestrial links are assumed to be nonidentical time-selective generalized Nakagami faded. Closed form expressions have been derived for the per-frame average SER and the asymptotic SER floor. Simulation results show the impact of terrestrial node mobility as well as the satellite elevation angles on the end-to-end performance.

Table 1. Lms channel parameters

Shadowing	b_i	m_i	Ω_i
Frequency heavy shadowing	0.063	0.739	8.97×10^{-4}
Average shadowing	0.126	10.10	0.835
Infrequent Light Shadowing	0.158	19.40	1.29

APPENDIX A

The j^{th} , $j = 1, 2, \dots, N_i$ entry of h_i is distributed as,

$$f_{|h_j^{(i)}|^2}(x) = \alpha_i e^{-\beta_i x} {}_1F_1(m_i; 1; \delta_i x), \quad x > 0. \quad (36)$$

The MGF of $|h_j^{(i)}|^2$ can be expressed as,

$$M_{|h_j^{(i)}|^2}(s) = E_{|h_j^{(i)}|^2} \left\{ e^{-s|h_j^{(i)}|^2} \right\} = \int_0^\infty e^{-sx} f_{|h_j^{(i)}|^2}(x) dx, \quad (37)$$

Where $E\{\cdot\}$ represents the expectation. By using in (37), it can be shown that,

$$M_{|h_j^{(i)}|^2}(s) = \frac{\alpha_i}{(s + \beta_i)} F\left(m_i, 1; 1; \frac{\delta_i}{(s + \beta_i)}\right), \quad (38)$$

where $F(\alpha, \beta; \gamma; z)$ is the Hypergeometric function. Next, by using in (38), we get,

$$M_{|h_j^{(i)}|^2}(s) = \alpha_i \frac{(s + \beta_i)^{m_i - 1}}{(s + \beta_i - \delta_i)^{m_i}}. \quad (39)$$

Under the assumption of i.i.d. entries in h_i , the moment generating function of $\|h_i\|^2$ can be written as,

$$M_{\|h_i\|^2}(s) = \prod_{j=1}^{N_i} M_{|h_j^{(i)}|^2}(s) = \alpha_i^{N_i} \frac{(s + \beta_i)^{c_i}}{(s + \beta_i - \delta_i)^{d_i}} \left(1 + \frac{\delta_i}{s + \beta_i - \delta_i}\right)^{\epsilon_i}. \quad (40)$$

It can be easily verified from TABLE I that $\beta_i \gg \delta_i$ for all kinds of shadowing. As $|s| \geq 0$, therefore $|\delta_i/(s + \beta_i - \delta_i)| \ll 1$. Since $\varepsilon_i < 1$, an extremely tight (very close to accurate) approximation, $(1 + z)^n \cong 1 + nz, |z| < 1$, can be used in (40), to find that,

$$M_{\|h_i\|^2}(s) = \alpha_i^{N_i} \sum_l^{c_i} \binom{c_i}{l_i} \beta^{c_i - l_i} \left(\frac{s^{l_i}}{(s + \beta_i - \delta_i)^{d_i}} + \frac{\varepsilon_i \delta_i s^{l_i}}{(s + \beta_i - \delta_i)^{d_i + 1}} \right). \tag{41}$$

Taking the inverse Laplace transform of (41) and after some algebra, we obtain (16).

APPENDIX B

To solve I_1 , let us change the variable by substitution $\cos^2 \theta = t$. This leads to,

$$\sin^2 \theta = 1 - \cos^2 \theta = 1 - t \quad -2 \cos \theta \sin \theta d\theta = dt \tag{42}$$

Thus, the limits of integral would change from 0 to 1 and the integrating variable $d\theta$ changes to

$$d\theta = \frac{dt}{-2\sqrt{t}\sqrt{1-t}} \tag{43}$$

Therefore, I_1 can now be given as

$$I_1 = \frac{a}{\pi} \int_0^1 \left(\frac{mN_t N_r}{mN_t N_r + \frac{b\bar{\gamma}}{(1-t)}} \right)^{mN_t N_r} \frac{dt}{2\sqrt{t}\sqrt{1-t}} \tag{44}$$

After rearrangements and mathematical manipulations, this integral can be represented in the standard form as,

$$I_1 = \frac{a}{2\pi} \left(\frac{2mN_t N_r}{mN_t N_r + b\bar{\gamma}} \right)^{mN_t N_r} \int_0^1 \frac{(1-t)^{mN_t N_r - \frac{1}{2}}}{\sqrt{t}} \left(1 - \frac{t}{1 + \frac{b\bar{\gamma}}{2mN_t N_r}} \right)^{-mN_t N_r} dt. \tag{45}$$

The above expression represents the integral in the standard form of the Gauss hypergeometric function defined as

$${}_2F_1(a, b; c; x) = \frac{\Gamma(c)}{\Gamma(c-a)\Gamma(a)} \int_0^1 t^{b-1} (1-t)^{c-b-1} (1-tx)^{-a} dt. \tag{46}$$

Comparing the above definition of the Gauss hypergeometric function with the expression of I_1 , the parameters can be obtained as $a = mN_tN_r$, $b = \frac{1}{2}$, $c = mN_tN_r + 1$ and $x = 1 - \frac{1}{1 + \frac{b\bar{\gamma}}{2mN_tN_r}}$ can be given as,

$$I_1 = \frac{a}{2\pi} \left(\frac{2mN_tN_r}{mN_tN_r + b\bar{\gamma}} \right)^{mN_tN_r} \frac{\Gamma(mN_tN_r)\Gamma\left(\frac{1}{2}\right)}{\Gamma(mN_tN_r + 1)} \times {}_2F_1\left(mN_tN_r, \frac{1}{2}; mN_tN_r + 1; 1 - \frac{1}{1 + \frac{b\bar{\gamma}}{2mN_tN_r}}\right) \tag{47}$$

References

Abdi A., Lau W. C., Alouini M. S., Kaveh M. (2003). A new simple model for land mobile satellite channels: First- and second-order statistics. *IEEE Transactions on Wireless Communications*, Vol. 2, No. 3, pp. 519-528. <https://doi.org/10.1109/TWC.2003.811182>

An K., Lin M., Ouyang J., Huang Y., Zheng G. (2014). Symbol error analysis of hybrid satellite-terrestrial cooperative networks with cochannel interference. *IEEE Communications Letters*, Vol. 18, No. 11, pp. 1947-1950. <https://doi.org/10.1109/LCOMM.2014.2361517>

Bhatnagar M. R. (2015). Performance evaluation of decode-and-forward satellite relaying. *IEEE Transactions on Vehicular Technology*, Vol. 64, No. 10, pp. 4827-4833. <https://doi.org/10.1109/TVT.2014.2373389>

Bhatnagar M. R., Arti M. K. (2013). Performance analysis of af based hybrid satellite-terrestrial cooperative network over generalized fading channels. *IEEE Communications Letters*, Vol. 17, No. 10, pp. 1912-1915. <https://doi.org/10.1109/LCOMM.2013.090313.131079>

Gradshteyn I. S., Ryzhik I. M. (2007). *Table of Integrals, Series, and Products*. <https://doi.org/10.2307/2007757>

Halber A., Chakravarty D. (2018). Wireless relay placement optimization in underground room and pillar mines. *Mathematical Modelling of Engineering Problems*, Vol. 5, No. 2, pp. 67-75. <https://doi.org/10.18280/mmep.050203>

- Iqbal A., Ahmed K. M. (2011). A hybrid satellite-terrestrial cooperative network over non identically distributed fading channels. *Journal of Communications*, Vol. 6, No. 7, pp. 581–589. <https://doi.org/10.4304/jcm.6.7.581-589>
- Iqbal A., Ahmed K. M. (2015). Impact of MIMO enabled relay on the performance of a hybrid satellite-terrestrial system. *Telecommunication Systems*, Vol. 58, No. 1, pp. 17-31. <https://doi.org/10.1007/s11235-014-9864-9>
- Ruan Y., Li Y., Wang C., Zhang R., Zhang H. (2017). Outage performance of integrated satellite-terrestrial networks with hybrid CCI. *IEEE Communications Letters*, Vol. 21, No. 7, pp. 1545-1548. <https://doi.org/10.1109/LCOMM.2017.2694005>
- Sharma N., Bansal A., Garg P. (2016). Performance of DF based dual-hop dual-path hybrid RF/FSO cooperative system. *Wireless Personal Communications*, Vol. 91, No. 2, pp. 1003-1021. <https://doi.org/10.1007/s11277-016-3510-7>
- Sreng S., Escrig B., Boucheret M. (2013). Exact outage probability of a hybrid satellite terrestrial cooperative system with best relay selection. *2013 IEEE International Conference on Communications (ICC)*, pp. 4520-4524. <https://doi.org/10.1109/ICC.2013.6655280>
- Srikanth B., Kumar H., Rao K. U. M. (2018). A robust approach for WSN localization for underground coal mine monitoring using improved RSSI technique. *Mathematical Modelling of Engineering Problems*, Vol. 5, No. 3, pp. 225-231. <https://doi.org/10.18280/mmep.050314>
- Varshney N., Jagannatham A. K. (2017). MIMO-STBC based multiple relay cooperative communication over time-selective Rayleigh fading links with imperfect channel estimates. *IEEE Transactions on Vehicular Technology*, Vol. 66, No. 7, pp. 6009-6025. <https://doi.org/10.1109/TVT.2016.2634924>
- Varshney N., Puri P. (2017). Performance analysis of decode-and-forward-based mixed MIMO-RF/FSO cooperative systems with source mobility and imperfect CSI. *Journal of Lightwave Technology*, Vol. 35, No. 11, pp. 2070-2077. <https://doi.org/10.1109/JLT.2017.2675447>
- Yang L., Hasna M. O. (2015). Performance analysis of amplify-and-forward hybrid satellite-terrestrial networks with cochannel interference. *IEEE Transactions on Communications*, Vol. 63, No. 12, pp. 5052-5061. <https://doi.org/10.1109/TCOMM.2015.2495278>

PAPER

Effect of hydrophilic bentonite nano particle on the performance of polyvinylchloride membrane

To cite this article: Pawan Kumar *et al* 2019 *Mater. Res. Express* **6** 126415

View the [article online](#) for updates and enhancements.



IOP ebooks™

Bringing you innovative digital publishing with leading voices to create your essential collection of books in STEM research.

Start exploring the collection - download the first chapter of every title for free.

Materials Research Express



PAPER

Effect of hydrophilic bentonite nano particle on the performance of polyvinylchloride membrane

RECEIVED
5 September 2019

REVISED
3 November 2019

ACCEPTED FOR PUBLICATION
18 November 2019

PUBLISHED
27 November 2019

Pawan Kumar, Shobhit Dixit and Vijay Laxmi Yadav

Department of Chemical Engineering and Technology, IIT-BHU, Varanasi-221005, Uttar Pradesh, India

E-mail: vlyadaviitbhu2014@gmail.com

Keywords: antifouling membrane, fouling ratio, hydrophilic bentonite, polyvinyl chloride

Abstract

In this research work, experiments were done to study the fouling behavior and performance of lab-made membranes using humic acid solution as feed. These membranes were prepared in lab using polyvinyl chloride membranes and Hydrophilic Bentonite nano particles via a non-solvent induced phase separation method. Membranes were further used in a dead-end filtration setup to filter a synthetic solution of humic acid and water to perform separation and fouling studies. Feed with different concentrations of humic acid was subjected to membrane system and performance was studied in terms of various parameters like flux, fouling ratio, flux recovery, relative flux, and rejection rate. Pure water flux, permeate flux, flux recovery, fouling ratio and rejection of humic acid of membranes increased in the presence of more hydrophilic Bentonite particles because of improved hydrophilicity. Total fouling was also affected, and irreversible fouling decreased in the presence of nano particle. However, agglomeration was observed between inorganic nano particles for 1.5 wt%. So membrane performance started decreasing by adding hydrophilic Bentonite nano particles more than 1%.

Introduction

Membrane separation processes are one of the most widely used technologies for water treatment because of their advantages of continuous and low-cost operation, easy to scale up, requiring less time and energy for the separation of undesired substances from raw water. Membrane separation processes do not involve heating and therefore use less energy than conventional thermal separation processes such as distillation, sublimation or crystallization [1, 2]. The efficiency of membrane separation processes depends on the selected membrane material, preparation method, and operating conditions. Usually polymeric and ceramic materials made membranes are used for application. Presently, a lot of commercial membranes are available, made of various polymers, such as, polytetrafluoroethylene [3], polysulfone [4], polyacrylonitrile [5], polyethylene [6], polyvinyl chloride [7], poly-ether-sulfone [8] and polyvinylidene fluoride (PVDF) [9].

Besides various advantages, membrane fouling is a major concern for a membrane manufacturer, which can critically reduce membrane performance [10]. In general, the strong hydrophilicity of membrane surface is desirable to minimize the membrane fouling caused by the adsorption of soluble natural organic matters and microorganisms, but hydrophilic polymers lack the required mechanical properties which are urgently required to increase the lifespan of membrane during backwashing or air flushing for membrane regeneration once the fouling occurs. Therefore, increase in the hydrophilicity and mechanical property for the membrane is of major concern for its potential practical application in the desired industrial or municipal areas [11, 12]. Polymer composites have shown an attractive solution to mitigate this problem. Many research studies have been done on polymer based composites for variety of applications [13–24]. Various researchers have prepared porous polymeric mix matrix membranes using many different nanomaterials to investigate their effect on antifouling properties and performance of membrane. Incorporation of these nanomaterials increases pore structure, higher hydrophilicity, surface morphology, strength which in turn results in better performance and antifouling nature of membrane [25–31].

Table 1. Composition of dope solution for membrane preparation.

Membrane	PVC (wt%)	PVP (wt%)	HB (wt%)	DMAc (wt%)
M1	19	1	0.0	80.0
M2	19	1	0.5	79.5
M3	19	1	1.0	79.0
M4	19	1	1.5	78.5
M5	19	1	2.0	78.0

In our previous published study [32], a polyvinyl chloride (PVC, MW = 80 000) based membrane was prepared and changes in its physical, chemical and mechanical properties were studied by blending different concentrations of Hydrophilic Bentonite (HB) containing majorly aluminium and silica. Then prepared membranes were characterized using different characterization instruments and techniques. Scanning electron microscope (SEM) was used for study of surface morphology and porous structure of membrane, x-ray diffraction (XRD) and Energy-dispersive x-ray spectroscopy EDX was used to verify the presence of bentonite content in polymer matrix, Drop shape analyzer (DSA) was used to determine contact angle for estimating change in hydrophobicity of composite membranes keeping size of water drop 0.3 mm and ultimate tensile machine (UTM) for mechanical properties of composite membranes as reported in previous study.

In this research work, the performance of different membranes prepared in lab was studied. Three feed samples of different concentrations of model organic foulant i.e. humic acid were prepared in lab. Humic acid (HA) is one of the major constituents of natural organic matter present in surface water. These elements are hazardous to human health and can cause dizziness, headache. It can also hamper central nervous system for a short period. Since it is so harmful to human health, it becomes essential to remove HA from water to mitigate its effect on human health [33, 34]. Performance of membranes was studied in terms of Flux, filtration capacity in terms of rejection and anti-fouling behavior was checked by calculating flux recovery and fouling ratios.

Materials and methods

Materials

Humic acid powder was purchased from Sigma-Aldrich and diluted with distilled water to prepare synthetic wastewater for experiments. It was used as received without any further treatment.

Filtration experiments

A lab-scale filtration setup was fabricated to perform the filtration experiments using prepared membranes for study. Membranes of different compositions (table 1) were prepared in lab, and then these were cut in spherical shape with effective diameter of 5 cm and fitted to the membrane cell. A new membrane can be compacted by applied pressure during the separation process, which in turn decreases the flux without membrane fouling. To eliminate the effect of compaction on flux, membranes were subjected to pure water first until a steady-state flux was attained. For this, membranes were first wetted for a half-hour at a transmembrane pressure of 1 atm and then at steady state pure water flux was calculated.

Humic acid was used as foulant to study the performance of membranes. Three different feeds of wastewater containing humic acid in concentration 10, 20 and 40 mg l⁻¹ were prepared and filtered through the membranes. Initially, the system was run over pure water only then Humic acid solution was filtered. Pure water flux, permeate flux containing HA in feed was calculated using following equation [35]:

$$J = \frac{V}{At} \quad (1)$$

Where J : water flux (PWF), V : the volume of water permeated, A : membrane area, and t : the time.

Fluxes obtained for pure water, and HA solution were denoted as J_0 and J_p . After completion of experiment membrane was again subjected to pure water to check the change in the performance of the membrane after fouling and pure water flux was measured. After this foulant layer deposited at membrane surface was scrapped and membrane was back washed. Later pure water was again run on membrane system and the flux was measured. Fluxes, calculated in those situations were denoted as J_1 and J_2 respectively.

With the help of the three flux information, fouling parameters of the membrane such as total fouling ratio (TFR), reversible fouling ratio (RFR), irreversible fouling ratio (IFR) and flux recovery (FR) were calculated.

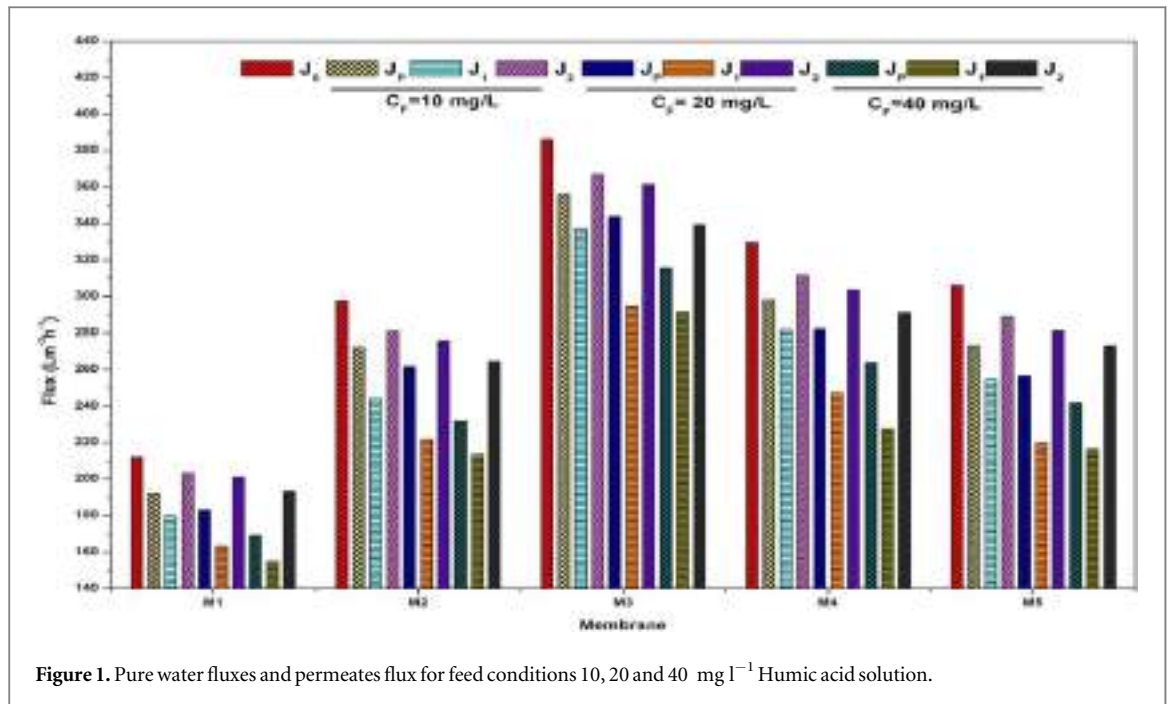


Figure 1. Pure water fluxes and permeates flux for feed conditions 10, 20 and 40 mg l⁻¹ Humic acid solution.

Following equations were used to measure the above parameters [36]:

$$\text{TFR} = \frac{J_0 - J_1}{J_0} \quad (2)$$

$$\text{RFR} = \frac{J_2 - J_1}{J_0} \quad (3)$$

$$\text{IFR} = \frac{J_0 - J_2}{J_0} \quad (4)$$

$$\text{FR} = \frac{J_2}{J_0} * 100\% \quad (5)$$

The concentration of humic acid at feed and permeates were calculated using spectrophotometric analysis and noted as C_F and C_P. These concentration values were used to measure percentage rejection through the membrane as follows [36]:

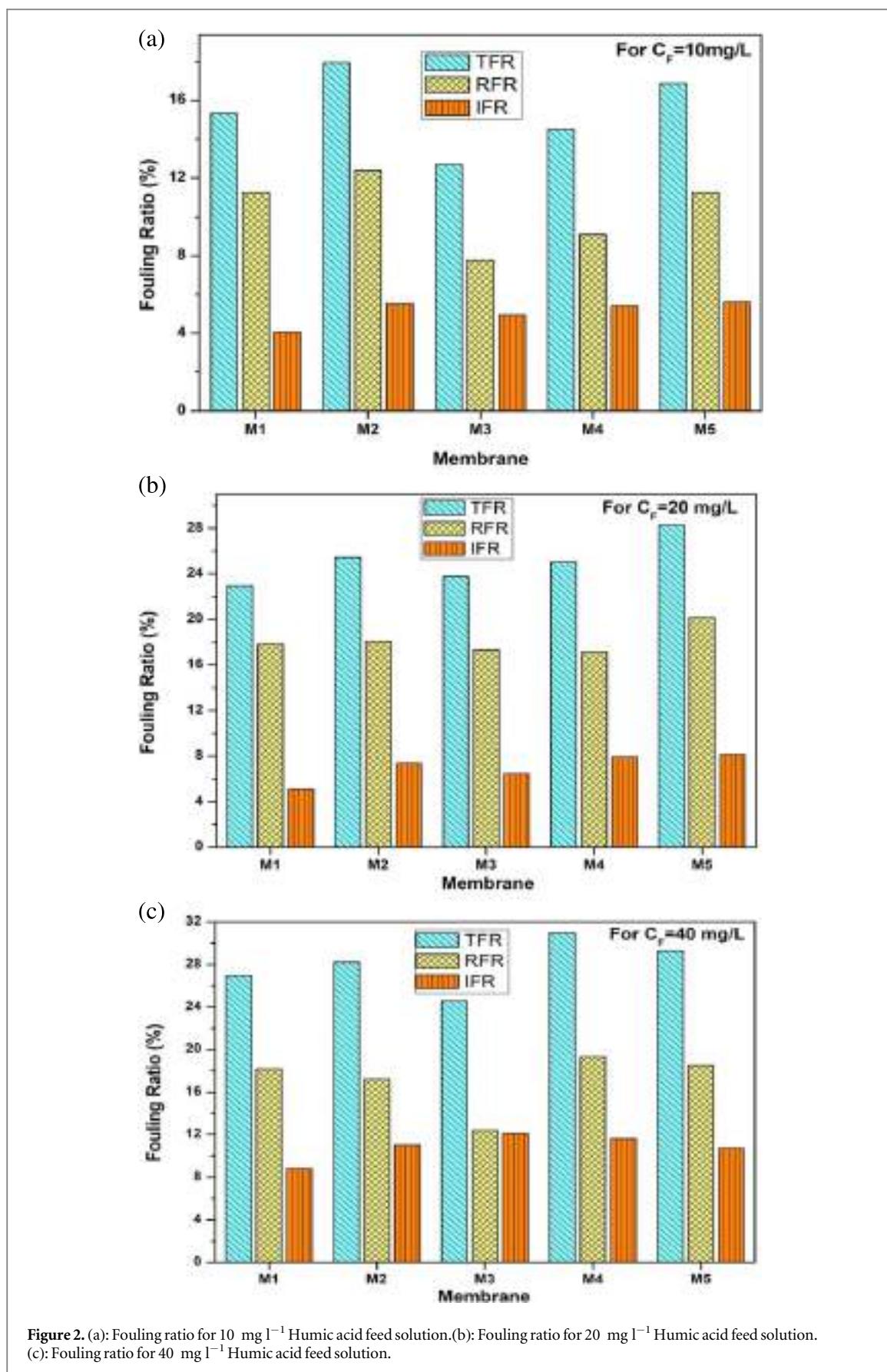
$$\text{Rejection} = \left[1 - \frac{C_P}{C_F} \right] * 100\% \quad (6)$$

$$\text{Relative flux} = \frac{J_P}{J_0} \quad (7)$$

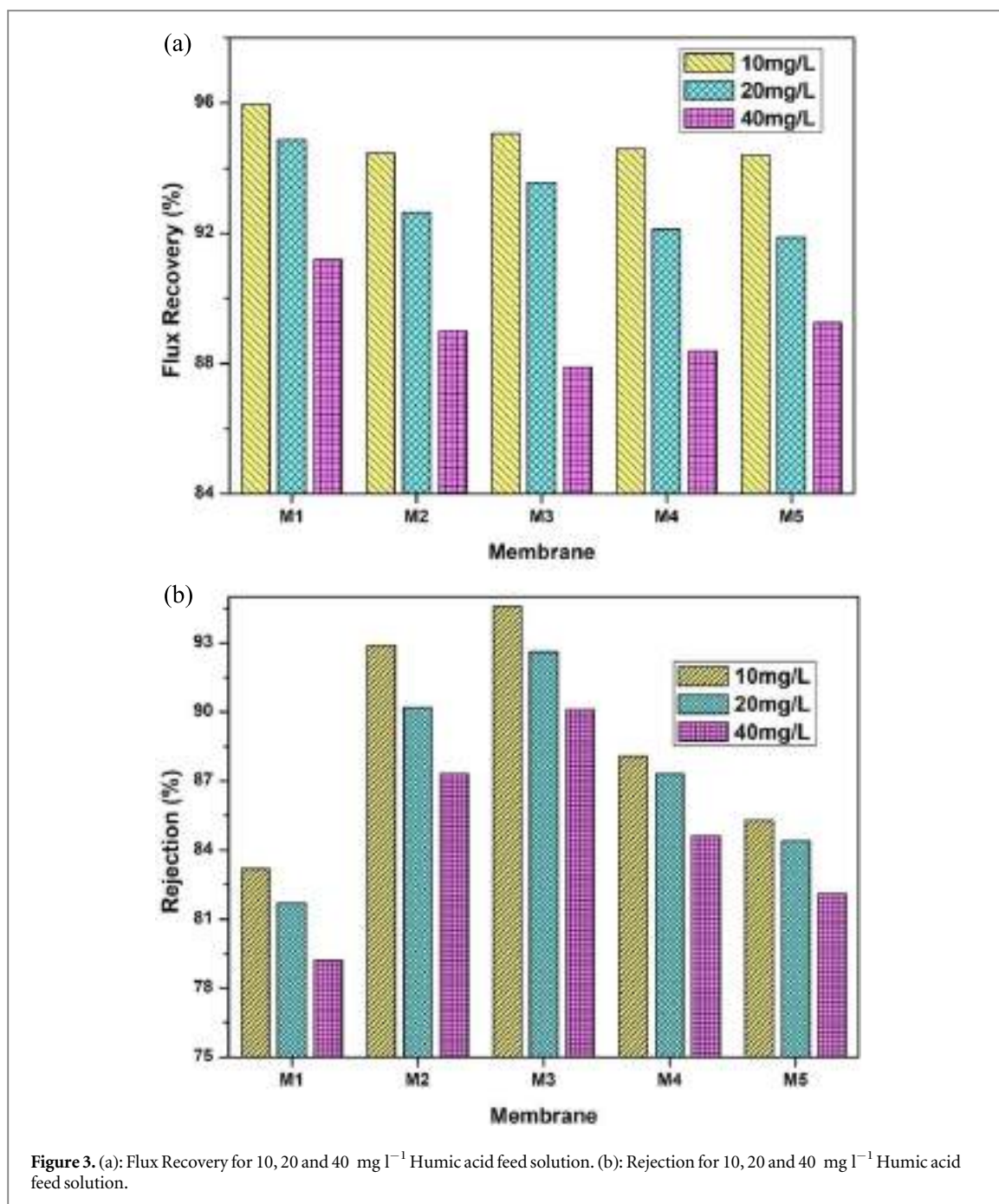
Result and discussions

Flux studies

After the initial pure water flux measurement J₀, the membrane system was subjected to the humic acid solution and flux for each membrane was calculated. Values of J₀, J_p, J₁, and J₂ were calculated for all three types of feeds containing 10, 20 and 40 mg l⁻¹ HA solution and shown in figure 1. For each feed fresh membrane was used for filtration so that the comparison of fluxes could be done properly. It was observed that flux for humic acid was lower than the pure water flux due to presence of humic acid particle in the feed stream, which creates extra resistance to membrane and decreases the flux. However, flux for humic acid solution of M₂ is much higher than the neat PVC membrane M₁. As found in our previous study [32], the mean pore size, as well as pore count, increased in M₂ which in-turn improved total pore area much higher than M₁. The higher flux values of M₂ were because of this reason. Such change in flux relative to pore size and improved hydrophilicity was also observed by Ghazanfari *et al* in their study [37]. It also increased with increasing content of HB in M₃ and started decreasing in M₄ and M₅. This improved flux of M₂, M₃ was the result of improved hydrophilicity and total pore area of membrane but because of particle agglomeration took place with higher concentration of HB, which in turn results in pore blockage which decreases the total pore area through which water passes through the membrane from feed side to permeate side. In a separate study similar



pattern was found by Rabiee *et al* [38] by using TiO_2 nano particle as filler to prepare composite membrane and found at high TiO_2 content, nanoparticles may cause pore blockage of the membranes, which leads to lower water flux. Flux through the membrane directly depends on this area, so as the pore area decreased flux start declining in M_4 and M_5 . A similar pattern was also observed for calculating J_1 and J_2 . Flux values were highest for M_3 but lower values found



for M₄ and M₅. Still these were much higher than neat PVC membrane M₁. So it was found that adding HB improve the flux of membrane relative to neat membrane M₁ and optimum performance was found at HB concentration 1% which was also supported by morphological studies.

As the total HA content is increased in feed solution to 20 and 40 mg l⁻¹, it was observed that flux declined to lower values for every situation. As the concentration is increased, more foulant was restricted by the membrane at feed side. This may increase resistance of membrane filtration due to pore blockage as well as concentration polarization due to formation of cake layer. After cake layer removal and backwashing when membranes were subjected to pure water. Again, it was shown that pure water flux J₂ at this condition is slightly lower to J₀. This reduction of flux was occurred because of irreversible fouling caused by foulant to the membrane. However, this flux was still much higher than the flux J₁ for all three feed conditions.

Antifouling properties

Membrane fouling is expressed as either reversible or irreversible fouling but TFR, RFR and IFR were the parameters to express the fouling behavior of membrane. Values of TFR, RFR and IFR were measured in all three feed conditions and shown in figures 2(a)–(c) respectively. For feed concentration 10 mg l⁻¹ membrane

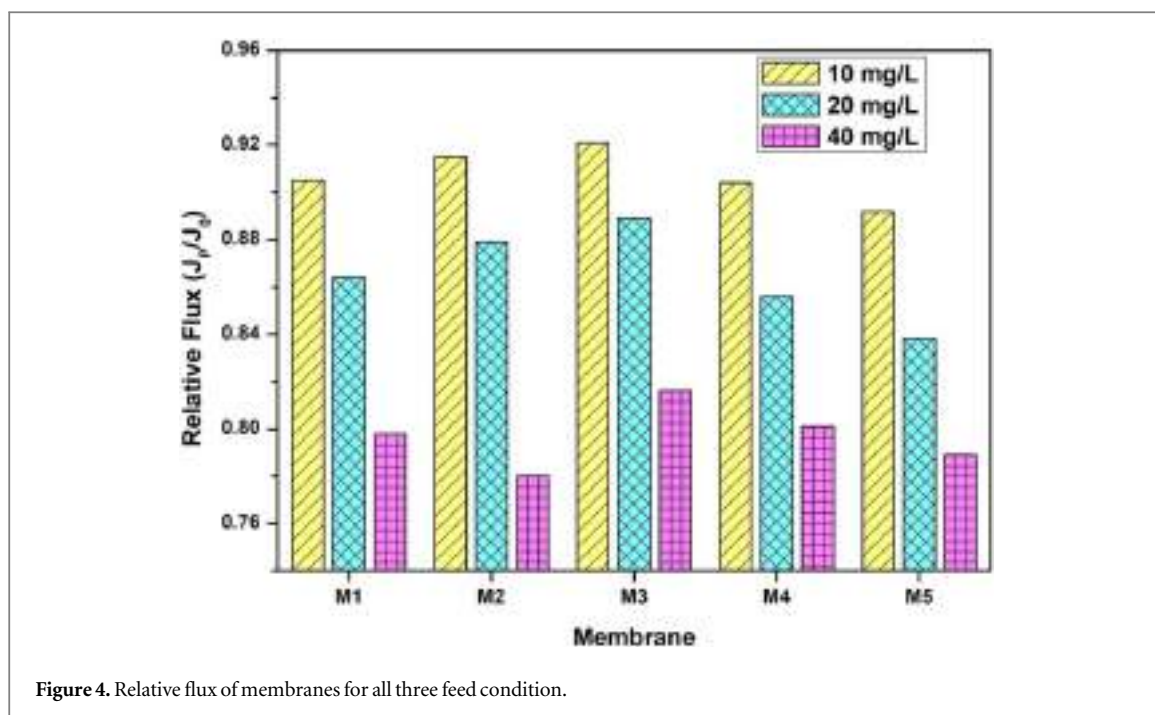


Figure 4. Relative flux of membranes for all three feed condition.

M₃ has shown lowest fouling as it was expected for this sample. Major fraction of fouling was because of reversible fouling which was 73.53%, 69.10%, 61.01%, 66.76% and 66.73% of total fouling of membranes M₁-M₅ respectively. Irreversible fouling, however, was highest for the membrane M₃. Few researchers have also reported such change in total fouling while studying performance of composite membranes [36, 39].

For 20 mg l⁻¹ feed sample, total fouling was higher than 10 mg l⁻¹ feed for all membrane samples. It was expected because of higher amount of foulant would make a thick layer of cake on the feed side membrane surface and increase the resistance created because of concentration polarization. However, here most of the fouling was reversible as the cake was removed and membrane was back washed. Reversible fouling for this condition was ranged between 68%–77% of total fouling for all five samples. Absolute values of irreversible fouling were also observed higher for 20 mg l⁻¹ as compared to 10 mg l⁻¹, which showed that some small pores were blocked more easily in the presence of higher amount of foulant available in feed [35].

Similarly, for feed 40 mg l⁻¹, we found the same pattern that total fouling, as well as irreversible fouling, increased. All membranes showed the major role of reversible fouling in creating total fouling except members M₃. This membrane showed almost equal ratio of both fouling types in total fouling. This membrane showed higher reversible fouling because of smaller range of pores which were easily fouled by foulant. However, M₃ still had lowest total fouling among all samples.

Rejection rate and flux recovery

The primary aim of any filtration operation is to filter out maximum possible targeted particle from the feed solution. For study the membrane performance, rejection rate was calculated using equation (6). Data obtained by calculations is shown in figures 3(a)–(c) for all three feed conditions respectively. The highest rejection was observed for M₃ membrane in 10 mg l⁻¹ feed condition. Since mean pore size of M₃ is smallest, so it was obvious for this membrane to show the maximum rejection rate. A similar pattern was found in next two feed condition but this time rejection rate declined. Increased total fouling could be the main reason for this decrease in rejection rate.

Another parameter to study fouling, i.e., flux recovery was also calculated using equation (5) and shown in figures 3(a)–(c). Flux recovery is reversely proportional to irreversible fouling. Higher irreversible fouling result in low recovery and lower irreversible fouling reflects the higher flux recovery [29, 37]. Ghazanfari *et al* reported that the flux recovery increased from 69% to 86% when the filler content was increased in base composite membrane. As the reversible fouling is increased with high amount of humic acid in feed, flux recovery also declined. For condition 10 mg l⁻¹, it was highest for membrane M₁ and valued for 95.93% and reduced to 94.86% and 91.18% for feed 20 mg l⁻¹ and 40 mg l⁻¹ respectively.

Relative flux

Relative flux is a parameter to observe how flux varies through a membrane when it is subjected to real operation as compared to pure water flow. This is a fractional value and ratio of flux of humic acid solution to pure water flux [28]. As it is shown in figure 4, for 10 mg l⁻¹ solution relative flux varies between 0.89–0.92. 0.92 was highest

relative flux for membrane M3. But as the amount of humic acid was increased in feed, flux through the membrane decreased because of various resistances provided by membrane and cake layer to the flow. For 40 mg l⁻¹ feed solution, relative flux dropped to a very low value 0.79 for membrane M5.

Conclusion

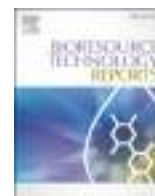
After understanding the variation in physical and chemical properties of PVC/HB membranes in our study, now we examined the effect of varying inorganic nano-filler on the performance of PVC membrane. Humic acid a common natural organic matter present in surface water was used as foulant to study the membrane performance. Three different feed samples of 10, 20 and 40 mg l⁻¹ was used to check membrane performance. Membrane M₃ containing 1% hydrophilic Bentonite showed the highest flux among all five samples. Total fouling ratio was least for this membrane sample rejection rate was higher even in high concentration feed samples. Highest flux observed in membrane M₃ for feed containing 10, 20 and 40 mg l⁻¹ humic acid was 356.1 LMH, 343.8 LMH and 315.7 LMH respectively.

ORCID iDs

Vijay Laxmi Yadav  <https://orcid.org/0000-0003-2926-7406>

References

- [1] Wee S-L, Tye C-T and Bhatia S 2008 *Sep. Purif. Technol.* **63** 500–16
- [2] Dharupaneedi S P, Nataraj S K, Nadagouda M, Reddy K R, Shukla S S and Aminabhavi T M 2019 *Sep. Purif. Technol.* **210** 850–66
- [3] Qin W, Xie Z, Ng D, Ye Y, Ji X, Gray S and Zhang J 2018 *Water Res.* **130** 343–52
- [4] Hwang T, Oh J-S, Yim W, Nam J-D, Bae C, Kim H-I and Kim K J 2016 *Sep. Purif. Technol.* **166** 41–7
- [5] Peng Y, Guo F, Wen Q, Yang F and Guo Z 2017 *Sep. Purif. Technol.* **184** 72–8
- [6] Akbari A, Yegani R, Pourabbas B and Behboudi A 2016 *Chem. Eng. Res. Des.* **109** 282–96
- [7] Marbelia L, Bilad M R, Bertels N, Laine C and Vankelecom I F J 2016 *J. Membr. Sci.* **498** 315–23
- [8] Khorshidi B, Hajinasiri J, Ma G, Bhattacharjee S and Sadrzadeh M 2016 *J. Membr. Sci.* **500** 151–60
- [9] Lai C Y, Groth A, Gray S and Duke M 2014 *Water Res.* **57** 56–66
- [10] Rana D and Matsuura T 2010 *Chem. Rev.* **110** 2448–71
- [11] Le-Clech P, Chen V and Fane T A G 2006 *J. Membr. Sci.* **284** 17–53
- [12] Fane A G and Fell C J D 1987 *Desalination* **62** 117–36
- [13] Jyothi M S, Reddy K R, Soontarapa K, Naveen S, Raghu A V, Kulkarni R V, Suhas D P, Shetti N P, Nadagouda M N and Aminabhavi T M 2019 *J. Environ. Manage.* **242** 415–29
- [14] Son D R, Raghu A V, Reddy K R and Jeong H M 2016 *Journal of Macromolecular Science, Part B* **55** 1099–110
- [15] Reddy K R, Karthik K, Prasad S B, Soni S K, Jeong H M and Raghu A V 2016 *Polyhedron* **120** 169–74
- [16] Han S J, Lee H-I, Jeong H M, Kim B K, Raghu A V and Reddy K R 2014 *Journal of Macromolecular Science, Part B* **53** 1193–204
- [17] Hassan M, Reddy K R, Haque E, Faisal S N, Ghasemi S, Minnett A I and Gomes V G 2014 *Compos. Sci. Technol.* **98** 1–8
- [18] Choi S H, Kim D H, Raghu A V, Reddy K R, Lee H-I, Yoon K S, Jeong H M and Kim B K 2012 *Journal of Macromolecular Science, Part B* **51** 197–207
- [19] Lee Y R, Kim S C, Lee H-I, Jeong H M, Raghu A V, Reddy K R and Kim B K 2011 *Macromol. Res.* **19** 66–71
- [20] Reddy K R, Jeong H M, Lee Y and Raghu A V 2010 *J. Polym. Sci., Part A: Polym. Chem.* **48** 1477–84
- [21] Reddy K R, Sin B C, Ryu K S, Kim J-C, Chung H and Lee Y 2009 *Synth. Met.* **159** 595–603
- [22] Reddy K R, Lee K-P, Lee Y and Gopalan A I 2008 *Mater. Lett.* **62** 1815–8
- [23] Reddy K R, Reddy C H V, Nadagouda M N, Shetti N P, Jaesool S and Aminabhavi T M 2019 *J. Environ. Manage.* **238** 25–40
- [24] Reddy K R, Gomes V G and Hassan M 2014 *Mater. Res. Express* **1** 015012
- [25] Saleh T A and Gupta V K 2012 *Sep. Purif. Technol.* **89** 245–51
- [26] Jafarzadeh Y, Yegani R and Sedaghat M 2015 *Chem. Eng. Res. Des.* **94** 417–27
- [27] Shokri E, Yegani R, Pourabbas B and Kazemian N 2016 *Appl. Clay Sci.* **132–133** 611–20
- [28] Maximous N, Nakhla G, Wan W and Wong K 2009 *J. Membr. Sci.* **341** 67–75
- [29] Wu T, Zhou B, Zhu T, Shi J, Xu Z, Hu C and Wang J 2015 *RSC Adv.* **5** 7880–9
- [30] Zhang Y, Shan X, Jin Z and Wang Y 2011 *J. Hazard. Mater.* **192** 559–67
- [31] Huang J, Arthanareeswaran G and Zhang K 2012 *Desalination* **285** 100–7
- [32] Kumar P, Dixit S and Yadav V L 2019 *Rasayan Journal of Chemistry* **12** 707–18
- [33] Waller K, Swan S H, DeLorenze G and Hopkins B 1998 *Epidemiology* **9** 134–40
- [34] Huang T-S, Lu F-J, Tsai C-W and Chopra I J 1994 *Journal of Endocrinological Investigation* **17** 787–91
- [35] Kusworo T D, Aryanti N, Quadratum and Utomo D P 2018 *Chem. Eng. J.* **347** 462–71
- [36] Behboudi A, Jafarzadeh Y and Yegani R 2016 *Chem. Eng. Res. Des.* **114** 96–107
- [37] Ghazanfari D, Bastani D and Mousavi S A 2017 *Journal of Water Process Engineering* **16** 98–107
- [38] Rabiee H, Farahani M H D A and Vatanpour V 2014 *J. Membr. Sci.* **472** 185–93
- [39] Taghaddosi S, Akbari A and Yegani R 2017 *Chem. Eng. Res. Des.* **125** 35–45



Optimization of process inputs for the synthesis of waste rice bran oil isolated *Pseudomonas aeruginosa* MTCC 424 biosurfactant using response surface methodology for oil recovery applications

Ashutosh Mishra^b, Ghazi Mohd Sawood^{a,*}, Shashi Bala Gautam^b, Rakesh Kumar Trivedi^c

^a Department of Chemical Engineering, Harcourt Butler Technical University, Kanpur 208002, India

^b Department of Chemical Engineering, Dr. AITH, Awadhपुरi, Kanpur 208024, India

^c Department of Oil Technology, School of Chemical Technology, Harcourt Butler Technical University, Kanpur 208002, India

ARTICLE INFO

Keywords:

Rice bran oil
Pseudomonas aeruginosa
Response surface methodology
Oil recovery

ABSTRACT

In this current study, the process variables i.e., the concentration of RBO (2–4%), pH (4–10), and incubation time (4–11 days) for the preparation of rhamnolipid biosurfactant based on *Pseudomonas aeruginosa* MTCC 424 and rice bran oil (RBO) were analyzed using response surface methodology-central composite design (RSM-CCD). At 5.02% of RBO, 7.3 pH, and 9.5 days of incubation time, maximum biosurfactant production was achieved. The process parameter was strongly affected by RBO, followed by the marginal effect of time and pH of incubation. The optimized biosurfactant was further analyzed using various techniques viz. surface tension measurement, Fourier transform infrared spectroscopy (FTIR), emulsifying ability test and oil displacement technique. As compared to synthetic chemical surfactant, the lower critical micelle concentration (CMC) (28.5 mN/m), impressive oil-free zone displacement ($17.26 \pm 0.18 \text{ cm}^2$) and benchmark emulsifying ability demonstrated the perfect use of the biosurfactant for oil recovery applications.

1. Introduction

At modern junction, massive uses of non-biodegradable toxic synthetic surfactants have drawn the attention of the scientists to fabricate a new biodegradable surfactant material for petroleum, detergent, food and soap industries applications (Singh et al., 2019). Generally, *Pseudomonas*, *Bacillus*, *Rhodococcus* and *Candida* genera are the most reliable biosurfactant used for various applications (Singh et al., 2019). The inherent virtues of biosurfactant materials made them suitable options for numerous applications such as food industry (Nitschke and Silva, 2018), agriculture (Sachdev and Cameotra, 2013), microbial oil recovery (Geetha et al., 2018), nanotechnology (Singh et al., 2017), and water remediation (Sharma et al., 2018), respectively. Hence, microbial biosurfactant materials are the perfect replacement of synthetic surfactant materials for environmental consideration. Although, the commercial success of biosurfactants is limited by the higher production cost of the synthesized materials.

The extensive use of vegetable oils for the domestic purposes in India creates environment imbalance conditions on disposal. The annual production of vegetable oils in India is 23 million metric tons. In

particular, a set of many vegetable oils such as mustard oil, sunflower oil, olive oil, rice bran oil, flaxseed oil, groundnut oil, palm oil, and sesame oil have been used for household purposes (Singh et al., 2019). However, the frequent use of vegetable oils encourages food safety and standards authority of India to fix the percentage limit i.e., 25% of polar compounds in the vegetable oils for preventing the health issues (Pathania and Jana, 2020). In addition, the problem associated with waste cooking oil is forming clogs in the pipe of the sewage system and damage the functioning of the reliable system. Hence, surging the use of cooking oils is breaching many environmental aspects. The strong needs to minimize the waste cooking oil and providing low cost biosurfactant materials trigger many scientists to provide the significant use of waste oil materials for regulating the environment aspects. In addition, many researchers have used waste vegetable oils for the production of biosurfactants (Cruz et al., 2018; Jimoh and Lin, 2020; Mitsui et al., 2019). Some researchers have also suggested the production of fatty acids from waste cooking oil.

Many authors have used waste vegetable oils such as rice bran oil, and soya bean oil, to attain the promising lower surface tension value and enormous emulsifying ability for various applications. The authors

* Corresponding author.

E-mail address: mohdsaud22@gmail.com (G.M. Sawood).

<https://doi.org/10.1016/j.biteb.2021.100653>

Received 9 January 2021; Received in revised form 6 February 2021; Accepted 6 February 2021

Available online 19 February 2021

2589-014X/© 2021 Elsevier Ltd. All rights reserved.

of this paper proved the perfect use of waste frying oil for the production of rhamnolipid using *Pseudomonas aeruginosa* as a microbial material (Pathania and Jana, 2020). Authors synthesized the rhamnolipid from *Pseudomonas aeruginosa* for enhanced oil recovery applications (Sharma et al., 2018). Ozdal et al. (2017) optimized the production of rhamnolipid prepared from *Pseudomonas aeruginosa* OG. In this study, the authors have used waste frying oil and chicken feather peptone materials as carbon sources. Deepika et al. (2016) optimized the production of biosurfactant prepared from *Pseudomonas aeruginosa* KVD-HR42. Kumar et al. (2015) applied Plackett–Burman design for the production of biosurfactant from *Pseudomonas aeruginosa* 2297 using sawdust and glycerol as a carbon source. Costa et al. (2010) studied the structural properties of the rhamnolipid produced from *Pseudomonas aeruginosa* L2-1. Kiran et al. (2010) prepared a novel lipopeptide biosurfactant material from marine *Brevibacterium aureum* for oil recovery applications. Till today, no experimental work has been conducted for optimizing the characteristics simultaneously (pH, incubation time and concentration of rice bran oil) of a biosurfactant based on *Pseudomonas aeruginosa* and rice bran oil using CCD coupled RSM technique for oil recovery applications.

By using mathematical and statistical tools, RSM is the best strategy to optimize the characteristics of the desired product simultaneously. Furthermore, RSM is the best alternative over time-consuming traditional approaches by offering the combined effects of all process variables to obtain remarkable responses. In this system, the RSM program provides a set of experiments. In addition, after successfully performed the desirable set of experiments, response data sheets are filled accordingly. CCD-RSM is used the response data for analyzing the behavior of the system. So, the key function of CCD-RSM is to optimize the independent variables for maximizing the dependent variables (Mohamed et al., 2018).

In this current study, a biosurfactant is synthesized using *Pseudomonas aeruginosa* and rice bran oil with a various set of experiments generated by CCD-RSM. The independent variables are pH, incubation time and concentration of rice bran oil, respectively. Moreover, the response is biosurfactant yield. In order to visualize the combined effects of all process variables, a quadratic model has been applied to observing the relationship between process variables and process output. The accuracy of the model was confirmed using analysis of variance (ANOVA) analysis. The optimized biosurfactant was analyzed using surface tension measurement, emulsifying ability, FTIR analysis, and oil displacement analysis.

2. Materials and method

2.1. Materials

Biosurfactant *Pseudomonas aeruginosa* MTCC 424 was purchased from the Institute of microbial Technology, Chandigarh, India. The culture was kept at a temperature of 4 °C for a period of 24 h for synthesis process. Agro-industrial residual oil i.e., rice bran oil was collected from the M/s Kanpur Edibles Private Limited, Kanpur, India. The residual was extracted using Soxhlet extraction method at a temperature of 68 °C for a period of 2 h. Rice bran agro-industrial residual oil was a key source of carbon in this paper. All required chemicals KH_2PO_4 , K_2HPO_4 , NaNO_3 , $\text{MgSO}_4 \cdot 7\text{H}_2\text{O}$, KCl , CaCl_2 , $\text{FeSO}_4 \cdot 7\text{H}_2\text{O}$, H_3BO_3 , $\text{CoCl}_2 \cdot 6\text{H}_2\text{O}$, $\text{CuSO}_4 \cdot 5\text{H}_2\text{O}$, $\text{MnSO}_4 \cdot \text{H}_2\text{O}$, $[\text{NH}_4]_6\text{Mo}_7\text{O}_{24}$, and ZnSO_4 were procured from Qualikems Fine Chem Private Limited, Gujarat.

2.2. Experimental design matrix for green biosurfactant using CCD-RSM

In this study, CCD-RSM was selected to attend the maximum yield of biosurfactant for oil recovery applications. RBO, pH, and incubation time were chosen as independent variables and the range of RBO (2–6%), pH (4–10) and incubation time (4–11 days), respectively (Razali et al., 2013; Tan et al., 2008).

The experimentally calculated actual values were very closely the predicted values provided by the CCD-RSM design are representing the accuracy of this model (Stat-Ease design software version-11) (Table 1). The maximum biosurfactant yield (g/L) is exhibiting the optimum combinations of process variables.

2.3. Cultivation of seed

The nutrient enriched agar slant was transferred to sterilized Erlenmeyer flask for the preparation of seed culture using 250 ml of nutritive broth. The required composition of nutritive broth is 1.07 g/L of beef extract, 2.05 g/L of yeast extract, 5.04 g/L of peptone, 5.02 g/L of NaCl, 15.10 g/L of agar and 1.0 L of distilled water, respectively, at pH 7. The cultures were developed under orbital agitation in the nutrient rich broth at a temperature of 32 °C with 100 rpm for the period of 16 to 18 h. Further, 3% (v/v) cell concentration has used a inoculum for the synthesis of biomass (Chaprão et al., 2018; Nawawi et al., 2010).

2.4. Isolation of *Pseudomonas aeruginosa* MTCC 424

The isolation process for microbes was occurred by employed the enrichment method. In this method, bacterial broth (3%) was inoculated in the agro-industrial residual oil i.e., rice bran oil carbon source (4%) supplemented with a minimal salt medium. The desired salt composition of minimal salt medium is 3 g/L of KH_2PO_4 , 2.5 g/L of K_2HPO_4 , 2.5 g/L of NaNO_3 , 1 g/L of $\text{MgSO}_4 \cdot 7\text{H}_2\text{O}$, 1 g/L of KCl , 0.02 g/L of CaCl_2 , and 1 ml/L of trace elements, respectively. In addition, the required composition of trace element solution is 0.12 g/L of $\text{FeSO}_4 \cdot 7\text{H}_2\text{O}$, 0.227 g/L of H_3BO_3 , 0.39 g/L of $\text{CoCl}_2 \cdot 6\text{H}_2\text{O}$, 0.018 g/L of $\text{CuSO}_4 \cdot 5\text{H}_2\text{O}$, 0.015 g/L of $\text{MnSO}_4 \cdot \text{H}_2\text{O}$, 0.027 g/L of $[\text{NH}_4]_6\text{Mo}_7\text{O}_{24}$, and 0.177 g/L of ZnSO_4 (0.177 g/L), respectively. The incubation process for the synthesis of biosurfactant cell was carried out at a temperature of 32 °C with 100 rpm for a period of 7 days (El-Sheshtawy et al., 2015; Moshtagh et al., 2019; Silva et al., 2010). The molecular weight of the synthesized biosurfactant is in the range of 1023–1071 (Suthar and Nerurkar, 2016).

2.5. Analysis techniques for synthesized biosurfactant

2.5.1. FTIR analysis

To study the functional group present in the green biosurfactant prepared from rice bran oil, FTIR analysis for biosurfactant was recorded. In this test, the sample material is prepared in pellet form and scanned over the wavelength range of 4000–500 cm^{-1} in the

Table 1
Actual value of biosurfactant response using CCD-RSM.

Run	Range of process variables			Actual value of response
	RBO (%)	pH	Incubation time (days)	Biosurfactant yield (g/L)
1	6.00	10.00	11.00	4.85
2	4.00	7.00	7.50	5.99
3	6.00	7.00	7.50	5.8
4	2.00	4.00	4.00	2.96
5	4.00	7.00	4.00	5
6	2.00	4.00	11.00	3.2
7	4.00	7.00	7.50	6.2
8	6.00	10.00	4.00	3.8
9	4.00	4.00	7.50	3.9
10	4.00	10.00	7.50	4.45
11	4.00	7.00	7.50	6.24
12	6.00	4.00	11.00	4.1
13	2.00	7.00	7.50	4.5
14	2.00	10.00	11.00	3.3
15	4.00	7.00	11.00	5.7
16	4.00	7.00	7.50	5.9
17	2.00	10.00	4.00	3.1
18	4.00	7.00	7.50	6.2
19	4.00	7.00	7.50	6.4
20	6.00	4.00	4.00	3.01

transmittance mode. The specification of FTIR machine is Thermo-Nicolet 5700, USA (Lan et al., 2015).

2.5.2. Emulsifying index

In order to elucidate the emulsifying ability of the prepared biosurfactant, the emulsifying capacity was examined using the emulsifying index. The emulsifying ability is calculated by adding 2 ml of oil with 2 ml of cell free broth in a test tube. In addition, the test tube containing solution is vortexed at high speed for 5 min and left for 24 h. The emulsifying ability is determined by using following equation (Ferhat et al., 2017).

$$\text{Emulsifying Index} = \frac{\text{Height of emulsion formed} \times 1000}{\text{Total height of the solution}} \quad (1)$$

2.5.3. Surface tension measurement

Surface tension of the synthesized biosurfactant was measured using the *du Nouy ring tensiometer*. Initially, the synthesized biosurfactant is collected from the fermentation media and placed in a sonicator for half an hour. Further, the resultant solution is kept in a centrifuge tube and centrifuged for half an hour. In this method, the platinum ring was carefully washed using acetone and red-hot heated in an ethyl alcohol flame for every concentration. critical micelle concentration (CMC) was investigated by plotting the graph between surface tension with different concentrations of biosurfactants. The procedure for measuring surface tension is repeated five times and using the averaged value for further investigation (Nawawi et al., 2010).

2.6. Oil displacement analysis

The oil displacement technique is an imperative technique the

$$Y_{BY} = -7.0429 + 0.96319 A + 2.39183 B + 0.44148 C + 0.027083 AB + 0.030357 AC - 9.52381E - 004BC - 0.14443A^2 - 0.17253B^2 - 0.0308355C^2 \quad (3)$$

analyzing the behavior of biosurfactants for crude oil separation applications. In this technique, a real crude oil (10 μ L) collected from IOCL, Mathura, India and poured in a glass plate and mixed with 40 ml of double deionized water. For analyzing the separation behavior of prepared biosurfactant, 1% of biosurfactant (5 μ L) is added in a glass plate. In addition, the real surfactants i.e., SDS and Triton X-100 were also added in separately in the same crude oil solution. After 24 h of incubation period, the diameters of the oil free zones were determined. This test is repeated three times and using the averaged value of the oil free zone. The following equation has been used for determining the diameter of the oil free zone (Deepika et al., 2016).

$$\text{Diameter of oil free zone (DOFZ)} = \pi \times (\text{radius})^2 \text{ cm}^2 \quad (2)$$

2.7. Foaming characteristics analysis

Foaming behavior analysis of optimized biosurfactant has been measured using of the Ross mile method (ASTMD 1173). The stability of foam height with time was demonstrated by observing the change in height in every 100 min (Wahyuningsih et al., 2019).

3. Results and discussion

3.1. ANOVA and RSM analyses for the yield of prepared biosurfactant

3.1.1. Reliability check for CCD-RSM model

The actual and predicted value graph for response depicts in Fig. 1. Actual value signifies the result obtained from experimental run and the

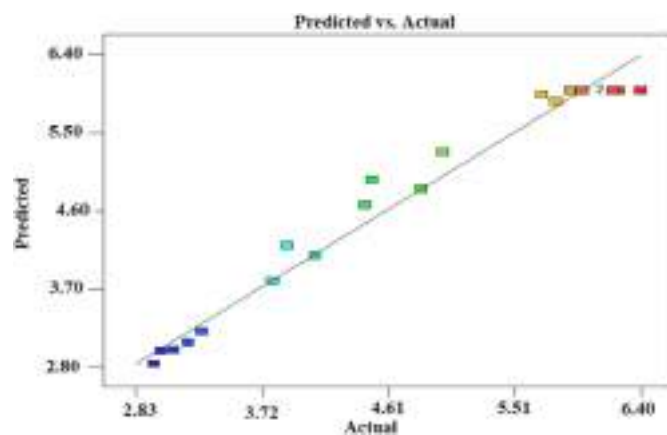


Fig. 1. Relationship between actual value and predicted value of biosurfactant yield.

predicted value illustrates the data originated from CCD-RSM tool. The actual value and the predicted value of response are very closer to each other. However, this is showing the correctness of the suggested model. Lu et al. (2009) also observed the similar outcomes in their published article. The reasonable R^2 values 0.9707 for biosurfactant yield illustrates the outcomes fit appropriately with the generated value of response.

3.2. Influence of process variables on biosurfactant yield

The second order polynomial equation for biosurfactant yield provided by CCD-RSM software depicts in Eq. (3).

Table 2 shows effective p and f values i.e., p value is less than 0.0001 and f value is 36.80, prove the perfectness of the ANOVA analyzed suggested model. In the table, linear terms are A, B, C, interaction terms are AB, BC, AC, and quadratic terms are A^2 , B^2 , C^2 , respectively. The reliable p-values for A, C, B^2 are <0.0001, <0.0001, 0.005, <0.0001, respectively. In addition, 0.30 standard deviation, and the difference between R^2 predicted biosurfactant yield and R^2 adjusted biosurfactant yield is less than 0.2 proven the correctness of RSM coupled CCD model (Xiangli et al., 2008).

3D plots explore the maximum production of biosurfactant with different process variables like RBO (%), pH and Incubation time (day) (Fig. 2). At pH 7, biosurfactant production increases with surging the concentration of RBO from 2 to 4% (Fig. 2(a)). This illustrates the remarkable effect of RBO concentration on biosurfactant production. At incubation time 7.5 days, the yield of biosurfactant raises up to 4% of RBO concentration (Fig. 2(c)). Similar trend is observed in the interactive pattern of pH and incubation time process variables for optimum production of biosurfactant (Fig. 2(e)).

3.3. Validation of the model

The optimized values provided by CCD-RSM i.e., 5.02% of RBO, 7.30 pH, and 9.52 days incubation period were performed. The Predicted value of biosurfactant yield (g/L) is 6.2043, respectively. CCD-RSM provided the collective effects of all independent variables on the response and confirmed the desirable characteristics of the prepared

Table 2
ANOVA analysis for biosurfactant yield from CCD-RSM model.

Source	Sum of squares	df	Mean square	F-value	p-Value		
Model	28.86	9	3.21	36.80	< 0.0001	Significant	
A-RBO	2.02	1	2.02	23.23	< 0.0007		
B-pH	0.54	1	0.54	6.23	0.0317		
C-Incubation time (days)	1.08	1	1.08	12.34	0.0056		
AB	0.21	1	0.21	2.42	0.1506		
AC	0.36	1	0.36	4.14	0.0691		
BC	8.000E-004	1	8.000E-004	9.178E-003	0.9256		
A ²	0.92	1	0.92	10.53	0.0088		
B ²	6.63	1	6.63	76.07	< 0.0001		
C ²	0.39	1	0.39	4.50	0.0599		
Residual	0.87	10	0.087				
Lack of fit	0.71	5	0.14	4.33	0.0668		Not significant
Cor total	29.74	19					
Std. dev.	0.30						
Mean	4.73						
C.V. %	6.24						
R ²	0.9707						
Adjusted R ²	0.9443						
Predicted R ²	0.8808						
Adeq precision	15.109						

biosurfactant can be achieved at optimum condition. The experimental result at predicted independent variables is 6.216 g/L, respectively for biosurfactant yield. The negligible error in results explored the validation of the CCD-RSM model.

3.4. FTIR analysis

FTIR analysis is a very precise analytical technique that provides the collective information of all functional groups present in the biosurfactant. The structural information of the synthesized biosurfactant was analyzed using FTIR analytical technique by scanning the sample over 4000–500 cm⁻¹ wavelength range.

In this FTIR analysis, the biosynthesized surfactant absorbed the infrared rays and generated various kinds of signals. In addition, that signal was examined by FTIR instrument and provides significant information about the functional groups present in the sample. Strong peak present at 3598 cm⁻¹ corresponds to stretching behavior of –OH group, respectively. The peak at 2987 cm⁻¹ represents the stretching vibration of methylene group, respectively. The peak at 1435 cm⁻¹ reveals the carboxylic group present in the sample, respectively. The peak at 1118 cm⁻¹ indicates rhamnose linkage exists in the sample, respectively. The peak at 714 cm⁻¹ corresponds to alkyl group, respectively. The collective information shows the sample is made from rhamnolipids. Sharma et al. (2018) prepared the rhamnolipids produced from *Pseudomonas aeruginosa* for oil recovery applications and observed similar results in their published article.

3.5. Emulsifying index

In order to investigate the emulsifying ability of the synthesized biosurfactant on crude oil, petrol, kerosene, hexane, heptane and hexadecane, the emulsifying capability of biosurfactant was examined (Fig. 3). In addition, the market suitability of the biosurfactant was determined by comparing the emulsifying index with renowned SDS and Tween-80 surfactants. The emulsifying ability of biosurfactant is 69 for crude oil, 55 for petrol, 66 for kerosene, 57 for hexane, 68 for heptane, and 74 for hexadecane, respectively. The emulsifying ability of SDS is 50 for crude oil, 51 for petrol, 62 for kerosene, 55 for hexane, 65 for heptane, and 80 for hexadecane, respectively. The emulsifying ability of Tween-80 is 60 for crude oil, 58 for petrol, 59 for kerosene, 30 for hexane, 61 for heptane, and 57 for hexadecane, respectively. It can be concluded from outcomes that the emulsifying ability of biosurfactant is higher for hexadecane. Moreover, the emulsifying ability of the prepared biosurfactant is showing comparable with other real chemical

surfactants. Sharma et al. (2018) prepared the biosurfactant and observed similar results for enhanced oil recovery applications. The emulsion stability of the prepared biosurfactant is also checked and found 55 days that is remarkable as compared to 20 days of chemical surfactants. The reported results are assuring the perfect use of biosurfactants for oil recovery applications.

3.6. Surface tension measurement

The surface tension characteristic of the optimized green biosurfactants at different concentrations has been examined using Du-Nouy international tensiometer. The surface tension is 77 mN/m for 20 mg/L, 69 mN/m for 40 mg/L, 59 mN/m for 60 mg/L, 45 mN/m for 80 mg/L, 31 mN/m for 100 mg/L, 28.5 mN/m for 120 mg/L, 28.43 mN/m for 140 mg/L, and 28.42 mN/m for 160 mg/L, respectively. These results reveal surface tension decreases significantly as surges the concentrations of optimized biosurfactant. In addition, this behavior reveals the absorption behavior of the material on the air-liquid interface. The critical micelle concentration (CMC) signifies the concentration of biosurfactant at which no further noticeable reduction in surface tension. The CMC value of synthesized and optimized biosurfactant is 28.5 mN/m observed at 120 mg/L of biosurfactant. Moraes et al. (2002) explained the similar results in their published article. The CMC value of biosurfactant prepared from *Pseudomonas* species is normally ranged from 50 to 200 mg/L, respectively (Kaya et al., 2014). Low value of CMC is correlated with remarkable ability of biosurfactant i.e., minimum biosurfactant is required to reduce surface tension. So as an outcome, the surface tension is 28.5 mN/m found at 120 mg/L of biosurfactant, respectively for enhanced oil recovery applications.

3.7. Oil displacement analysis

The oil displacement technique is an imperative technique the analyzing the behavior of biosurfactant for crude oil separation applications (Fig. 4). To visualize the ability of the prepared green biosurfactant, oil displacement technique was applied and the compared the quality with the market exist surfactant like SDS and Triton X-100. The DOFZ is 5.52 ± 0.2 cm² for SDS, 10.12 ± 0.15 cm² for Triton X-100 and 17.26 ± 0.18 cm² for prepared biosurfactant, respectively. Deepika et al. (2016) found 3.37 ± 0.12 cm² in *Pseudomonas* strain prepared from mangrove sediments and observed similar result in their published article. The reported result assures the remarkability of the prepared biosurfactant for oil cleaning vessel applications.

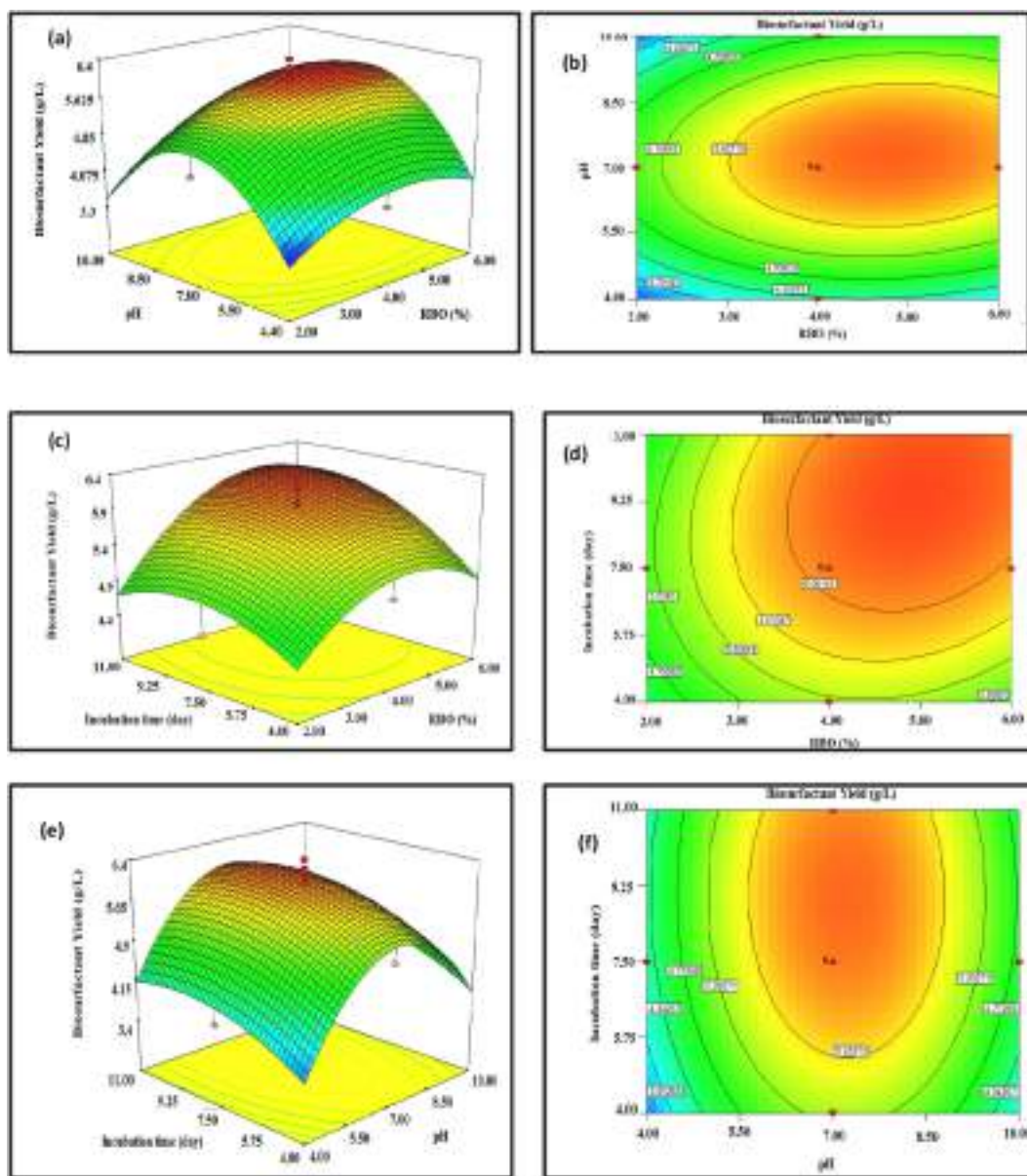


Fig. 2. Three dimensional response surface and contour plots of biosurfactant yield showing the effect of (a) and (b) pH and RBO (%); (c) and (d) incubation time (day) and RBO (%); (e) and (f) incubation time (day) and RBO (%).

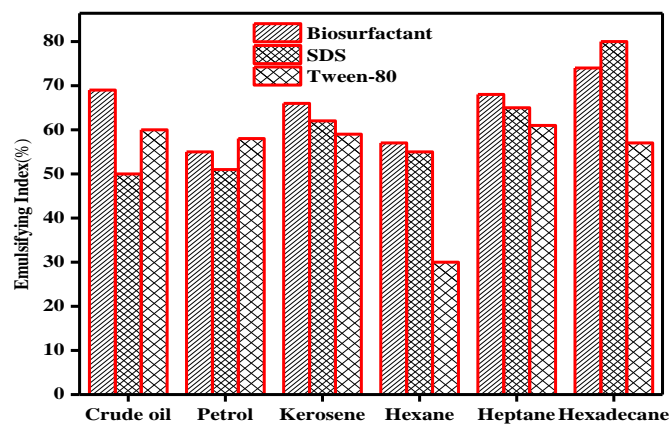


Fig. 3. Emulsifying abilities of biosurfactant, SDS, and Tween-80 for various oils.

3.8. Foaming characteristics of optimized biosurfactant

The foaming property of the optimized biosurfactant at different concentrations was analyzed using foam analyzing instrument. The foaming characteristics is usually illustrates the unsteady state behavior of the materials. The foam height is 65 mm for 20 mg/L, 69 mm for 40 mg/L, 76 mm for 60 mg/L, 79 mm for 80 mg/L, 85 mm for 100 mg/L, 88 mm for 120 mg/L and 88 mm for 140 mg/L, respectively at 25 °C (Fig. 5). The foam height is normally depends on the hydrophilic functional groups in the sample that minimizes the cohesive force present in the sample material. Wahyuningsih et al. (2019) reported similar results in their published article for enhanced oil recovery applications. The obtained results of optimized bio surfactant are showing reliable for oil recovery applications.

4. Conclusion

In this summary, the central composite design coupled with response surface methodology, is successfully applied for the preparation of

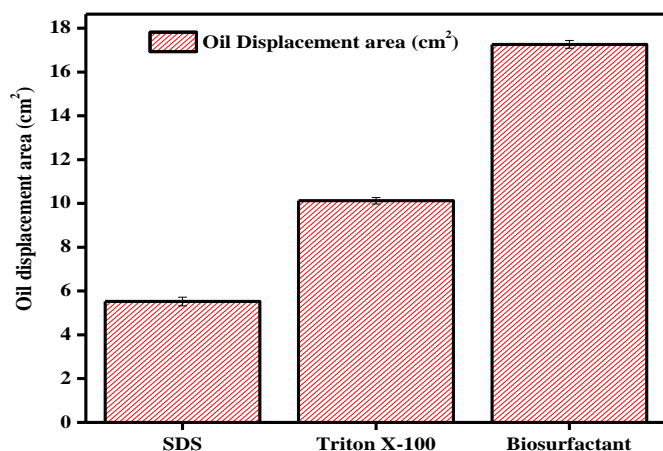


Fig. 4. Oil displacement analyses for optimized biosurfactant, Triton X-100 and SDS.

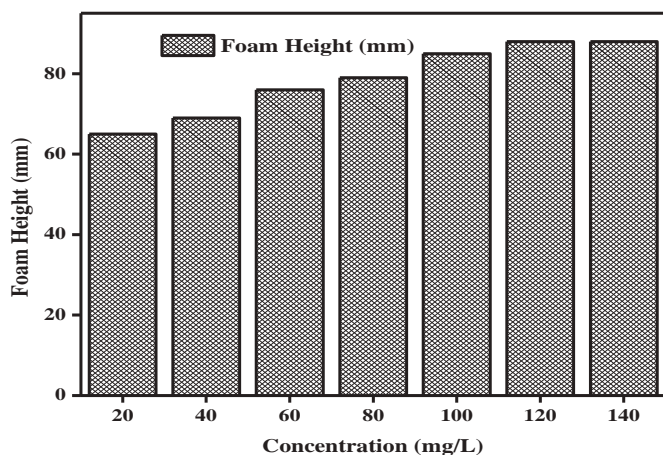


Fig. 5. Foaming characteristics analysis for optimized biosurfactant.

Pseudomonas aeruginosa MTCC 424 biosurfactant isolated from rice bran oil. The optimum values for concentration of rice bran oil, pH, and incubation time were 5.02%, 7.30, and 9.52 days, respectively. The optimum value of the response using process inputs was 6.2043 g/L, respectively. However, the equitable outcome with experimentally calculated value revealed the reliability of the CCD-RSM techniques. The benchmark emulsifying ability, lower CMC value, and remarkable oil displacement characteristics have confirmed the suitability for enhanced oil recovery applications.

CRedit authorship contribution statement

Conception and design of study: Ashutosh Mishra, Ghazi Mohd Sawood

Acquisition of data: Shashi Bala Gautam

Analysis and/or interpretation of data: Ashutosh Mishra, Ghazi Mohd Sawood, Rakesh Kumar Trivedi

Drafting the manuscript: Ashutosh Mishra, Ghazi Mohd Sawood

Revising the manuscript critically for important intellectual content: Ashutosh Mishra, Ghazi Mohd Sawood

Approval of the version of the manuscript to be published: Ashutosh Mishra, Ghazi Mohd Sawood, Shashi Bala Gautam, Rakesh Kumar Trivedi.

Declaration of competing interest

We wish to confirm that there are no known conflicts of interest associated with this publication and there has been no significant financial support for this work that could have influenced its outcome.

Appendix A. Supplementary data

Supplementary data to this article can be found online at <https://doi.org/10.1016/j.biteb.2021.100653>.

References

- Chaprão, M.J., Rufino, R.D., Luna, J.M., Santos, V.A., Sarubbo, L.A., 2018. Formulation and application of a biosurfactant from *Bacillus methylotrophicus* as collector in the flotation of oily water in industrial environment. *J. Biotechnol.* 285, 15–22. <https://doi.org/10.1016/j.jbiotec.2018.08.016>.
- Costa, S.G., Nitschke, M., Lépine, F., Déziel, E., Contiero, J., 2010. Structure, properties and applications of rhamnolipids produced by *Pseudomonas aeruginosa* L2-1 from cassava wastewater. *Process Biochem.* 45 (9), 1511–1516. <https://doi.org/10.1007/s12010-009-8707-8>.
- Cruz, J., Hughes, C., Quilty, B., Montagnoli, R., Bidoia, E., 2018. Agricultural feedstock supplemented with manganese for biosurfactant production by *Bacillus subtilis*. *Waste Biomass Valor.* 9, 613–618. <https://doi.org/10.1007/s12649-017-0019-6>.
- Deepika, K., Kalam, S., Sridhar, P.R., Podile, A.R., Bramhachari, P., 2016. Optimization of rhamnolipid biosurfactant production by mangrove sediment bacterium *Pseudomonas aeruginosa* KVD-HR42 using response surface methodology. *Biocatal. Agric. Biotechnol.* 5, 38–47. <https://doi.org/10.1016/j.bcab.2015.11.006>.
- El-Sheshtawy, H., Aiad, I., Osman, M., Abo-ELnasr, A., Kobisy, A., 2015. Production of biosurfactant from *Bacillus licheniformis* for microbial enhanced oil recovery and inhibition the growth of sulfate reducing bacteria. *Egypt. J. Pet.* 24 (2), 155–162. <https://doi.org/10.1016/j.ejpe.2015.07.018>.
- Ferhat, S., Alouaoui, R., Badis, A., Moulai-Mostefa, N., 2017. Production and characterization of biosurfactant by free and immobilized cells from *Ochrobactrum intermedium* isolated from the soil of southern Algeria with a view to environmental application. *Biotechnol. Biotechnol. Equip.* 31 (4), 733–742. <https://doi.org/10.1080/13102818.2017.1309992>.
- Geetha, S., Banat, I.M., Joshi, S.J., 2018. Biosurfactants: production and potential applications in microbial enhanced oil recovery (MEOR). *Biocatal. Agric. Biotechnol.* 14, 23–32. <https://doi.org/10.1016/j.biori.2018.09.001>.
- Jimoh, A.A., Lin, J., 2020. Biotechnological applications of *Paenibacillus* sp. D9 lipopeptide biosurfactant produced in low-cost substrates. *Appl. Biochem. Biotechnol.* 1–21. <https://doi.org/10.1007/s12010-020-03246-5>.
- Kaya, T., Aslim, B., Kariptaş, E., 2014. Production of biosurfactant by *Pseudomonas* spp. isolated from industrial waste in Turkey. *Turk. J. Biol.* 38 (3), 307–317. <https://doi.org/10.3906/biy-1303-18>.
- Kiran, G.S., Thomas, T.A., Selvin, J., Sabarathnam, B., Lipton, A., 2010. Optimization and characterization of a new lipopeptide biosurfactant produced by marine *Brevibacterium aureum* MSA13 in solid state culture. *Bioresour. Technol.* 101 (7), 2389–2396. <https://doi.org/10.1016/j.biortech.2009.11.023>.
- Kumar, A.P., Janardhan, A., Radha, S., Viswanath, B., Narasimha, G., 2015. Statistical approach to optimize production of biosurfactant by *Pseudomonas aeruginosa* 2297. *3 Biotech* 5 (1), 71–79. <https://doi.org/10.1007/s13205-014-0203-3>.
- Lan, G., Fan, Q., Liu, Y., Chen, C., Li, G., Liu, Y., Yin, X., 2015. Rhamnolipid production from waste cooking oil using *Pseudomonas* SWP-4. *Biochem. Eng. J.* 101, 44–54. <https://doi.org/10.1101/2020.03.09.983478>.
- Lu, S.Y., Qian, J.Q., Wu, Z.G., Ye, W.D., Wu, G.F., Pan, Y.B., Zhang, K.Y., 2009. Application of statistical method to evaluate immobilization variables of trypsin entrapped with sol-gel method. *J. Biochem. Technol.* 1 (3), 79–84. <https://doi.org/10.1155/2013/874050>.
- Mitsui, R., Yamada, R., Ogino, H., 2019. CRISPR system in the yeast *Saccharomyces cerevisiae* and its application in the bioproduction of useful chemicals. *World J. Microbiol. Biotechnol.* 35 (7), 111. <https://doi.org/10.1007/s11274-019-2688-8>.
- Mohamed, R., Al-Gheethi, A., Abdulrahman, A., Bin Sainudin, M.S., Bakar, S.A., Kassim, A.H.M., 2018. Optimization of ceramic waste filter for bathroom greywater treatment using central composite design (CCD). *J. Environ. Chem. Eng.* 6 (2), 1578–1588. <https://doi.org/10.1016/j.jece.2018.02.006>.
- Moraes, I., Benincasa, M., Monte Alegre, R., 2002. Production and characterization of rhamnolipids produced by a newly isolated strain of *Pseudomonas aeruginosa*. *Braz. J. Food Technol.* 5, 145–149. <https://doi.org/10.1590/0104-6632.20140314s00002473>.
- Moshagh, B., Hawboldt, K., Zhang, B., 2019. Optimization of biosurfactant production by *Bacillus subtilis* N3-1P using the brewery waste as the carbon source. *Environ. Technol.* 40 (25), 3371–3380. <https://doi.org/10.1080/09593330.2018.1473502>.
- Nawawi, W.M.F.W., Jamal, P., Alam, M.Z., 2010. Utilization of sludge palm oil as a novel substrate for biosurfactant production. *Bioresour. Technol.* 101 (23), 9241–9247. <https://doi.org/10.1016/j.biortech.2010.07.024>.
- Nitschke, M., Silva, S.S.e., 2018. Recent food applications of microbial surfactants. *Crit. Rev. Food Sci. Nutr.* 58 (4), 631–638. <https://doi.org/10.1080/10408398.2016.1208635>.

- Ozidal, M., Gurkok, S., Ozdal, O.G., 2017. Optimization of rhamnolipid production by *Pseudomonas aeruginosa* OG1 using waste frying oil and chicken feather peptone. *3 Biotech* 7 (2), 117. <https://doi.org/10.1007/2Fs13205-017-0774-x>.
- Pathania, A.S., Jana, A.K., 2020. Utilization of waste frying oil for rhamnolipid production by indigenous *Pseudomonas aeruginosa*: improvement through co-substrate optimization. *J. Environ. Chem. Eng.* 8 (5), 104304. <https://www.x-mol.com/paperRedirect/1288183012633788416>.
- Razali, N.F., Mohammad, A.W., Hilal, N., Leo, C.P., Alam, J., 2013. Optimisation of polyethersulfone/polyaniline blended membranes using response surface methodology approach. *Desalination* 311, 182–191. <https://doi.org/10.1016/j.desal.2012.11.033>.
- Sachdev, D.P., Cameotra, S.S., 2013. Biosurfactants in agriculture. *Appl. Microbiol. Biotechnol.* 97 (3), 1005–1016. <https://doi.org/10.1007/s00253-012-4641-8>.
- Sharma, R., Singh, J., Verma, N., 2018. Optimization of rhamnolipid production from *Pseudomonas aeruginosa* PBS towards application for microbial enhanced oil recovery. *3 Biotech* 8 (1), 20. <https://doi.org/10.1007/s13205-017-1022-0>.
- Silva, S., Farias, C., Rufino, R., Luna, J., Sarubbo, L., 2010. Glycerol as substrate for the production of biosurfactant by *Pseudomonas aeruginosa* UCP0992. *Colloids Surf. B* 79 (1), 174–183. <https://doi.org/10.1016/j.colsurfb.2010.03.050>.
- Singh, P., Ravindran, S., Suthar, J.K., Deshpande, P., Rokade, R., Rale, V., 2017. Production of biosurfactant stabilized nanoparticles. *Int J Pharma Bio Sci* 8, 701–707. <https://doi.org/10.22376/ijpbs.2017.8.2.b701-707>.
- Singh, P., Patil, Y., Rale, V., 2019. Biosurfactant production: emerging trends and promising strategies. *J. Appl. Microbiol.* 126 (1), 2–13. <https://doi.org/10.1111/jam.14057>.
- Suthar, H., Nerurkar, A., 2016. Characterization of biosurfactant produced by *Bacillus licheniformis* TT42 having potential for enhanced oil recovery. *Appl. Biochem. Biotechnol.* 180 (2), 248–260. <https://doi.org/10.1007/s12010-016-2096-6>.
- Tan, I., Ahmad, A., Hameed, B., 2008. Optimization of preparation conditions for activated carbons from coconut husk using response surface methodology. *Chem. Eng. J.* 137 (3), 462–470. <https://doi.org/10.1016/j.cej.2007.04.031>.
- Wahyuningsih, T.D., Kurniawan, Y.S., Amalia, S., Wardhani, T.A., Muriningsih, C., 2019. Diethanolamide derivatives as a potential enhanced oil recovery agent from Indonesian castor oil and used frying oil: isolation, synthesis, and evaluation as nonionic biosurfactants. *Rasayan J. Chem.* 12 (2), 741–748. <https://doi.org/10.31788/RJC.2019.1225140>.
- Xiangli, F., Wei, W., Chen, Y., Jin, W., Xu, N., 2008. Optimization of preparation conditions for polydimethylsiloxane (PDMS)/ceramic composite pervaporation membranes using response surface methodology. *J. Membr. Sci.* 311 (1–2), 23–33. <https://doi.org/10.1080/01496395.2011.594476>.



A comparative study of biosurfactant preparation by *Pseudomonas aeruginosa* MTCC 424 using rice bran oil and soybean oil substrates

Ashutosh Mishra^a and Rakesh Kumar Trivedi^{*b}

^aDepartment of Chemical Engineering, Dr. Ambedkar Institute of Technology for Handicapped, Awadhपुरi, Kanpur-208 024, Uttar Pradesh, India

^bDepartment of Oil Technology, Harcourt Butler Technical University, Kanpur-208 002, Uttar Pradesh, India

E-mail: rakeshtrivedi@hotmail.com

Manuscript received online 20 October 2020, revised and accepted 30 November 2020

Researchers world over are trying to find the low cost feed stocks for cost-effective production of biosurfactants in order to compete with the chemically synthesized traditional surfactants. In this study rhamnolipid biosurfactant was prepared by *Pseudomonas aeruginosa* MTCC 424 culture. The rice bran oil and soybean oil were the two substrates taken in the study, which were extracted from spent bleaching earth for use as low cost carbon source. Spent bleaching earth is a waste of vegetable oil processing industries and is usually disposed of in the landfills or waste dumps. *Pseudomonas aeruginosa* culture was preferred over other microorganisms due to its nutritional and biochemical versatility along with simple culture conditions. The two biosurfactants were screened using oil displacement, drop-collapse, cetyltrimethyl ammonium bromide agar plate, emulsification index and surface tension measurement tests. The chemical structure and composition were analyzed by Fourier transform infrared, nuclear magnetic resonance and thin layer chromatography spectroscopic test methods. The study proved residual rice bran oil based rhamnolipid biosurfactant as the better one compared to residual soybean oil based biosurfactant. Since the residual rice bran oil extracted from spent bleaching earth is a very cheap raw material, the present study is hoped to contribute to some extent in solving the issue of high production cost of biosurfactants.

Keywords: *Pseudomonas aeruginosa*, rhamnolipid biosurfactant, spent bleaching earth, rice bran oil, soybean oil.

Introduction

Surface active agents abbreviated as surfactants for ease of communication and expression are amphiphilic compounds of high relevance. Being amphiphilic compounds surfactants possess both hydrophilic and hydrophobic (lipophilic) characteristics with strong surface activity¹. The polar hydrophilic part has strong affinity towards polar solvents like water, acetic acid, methanol, etc., whereas non-polar hydrophobic part has affinity towards non-polar substances such as oils, fats, and greases². Surfactants are extensively used in the agricultural sector, foodstuff, cosmetics, medicine as well textile industries and for enhanced oil recovery from the rocks because of their ability to reduce overhead or interfacial tensions^{3,4}.

Nearly all commercial surfactants available today are chemically synthesized from hydrocarbon feedstock⁵. These surfactants are inherently toxic and non-degradable and of-

ten result in an additional source of pollution to already depleting natural habitat¹. Since the beginning of 21st century, increasing environmental awareness among consumers, more stringent environmental regulations across the globe, and advances in biotechnology have motivated the researchers and drawn the attention of industries as well to develop environmentally friendly surfactants as potential alternative to existing chemical surfactants^{6,7}.

Biological surfactants often called as biosurfactants are actually the biomolecules produced by a variety of microorganisms on various carbon sources. Biosurfactants do have both hydrophilic and hydrophobic affiliations just like conventional chemical surfactants. The hydrophilic component contains the carboxyl group of fatty acids or amino acids, the hydroxyl group of saccharides, the phosphoryl group of phospholipids, and peptides or proteins, whereas the hydrophobic part is comprised of hydrocarbon chain of saturated or

unsaturated fatty acids or sterol ring^{3,8,9}.

The active research on biosurfactants started in the 1960s that gained momentum over successive decades⁶. There is no satisfactory reason known to researchers till today for the microbial production of biosurfactants. Though conditions favoring biosurfactant production by microorganisms have been extensively studied and identified as carbon substrate, pH, temperature, incubation time, air flow, salt, and the concentration of minerals such as nitrogen and phosphorus¹⁰.

Biosurfactants are highly versatile compounds with multifunctional properties such as dispersion, foaming and detergency, emulsification and de-emulsification, moisturization, penetration, thickening, wetting and coating, coagulation, metal sequestration and corrosion inhibition^{1,9}. Due to these peculiar properties biosurfactants find potential applications in agriculture, cosmetics, fertilizers, foods, beverages, pharmaceuticals, textile processing, enhanced oil recovery, bioremediation of organics and metals^{11,12}. The growing interest in biosurfactants is mainly due to their ability to offer an alternative to chemically synthesized surfactants in terms of properties and performance. A partial list of advantages extended by biosurfactants include improved biodegradability¹³, environmentally friendly¹⁴, low toxicity, non-hazardous⁹, higher selectivity, mild production conditions using renewable materials and industrial waste/by-products as substrates^{6,15}, ability to function at extreme temperatures, pH and salt concentrations¹¹, and modification by biotechnology and genetic engineering⁵.

There is lack of consistency in available data on value of global biosurfactant market. Reis *et al.*⁷ reported the actual worth of inclusive biosurfactant market place at USD 1.7 billion in year 2011. Now one market research group reported the actual worth of global biosurfactant market in 2018 as USD 1.6 billion¹⁶, whereas another research group reported it as USD 4.7 billion for the same year¹⁷. The difference between the two values is quite big. One possible reason for this anomaly might be involuntary ignorance of the terms 'actual' and 'estimated'. Most market research groups have predicted a composite twelve-monthly enlargement rate of 3.5–5.6% for global biosurfactant market for the period 2018–2026. It would be worthwhile at this point to mention the size of global surfactant market for the sake of comparison, which was at USD 43.655 billion in 2017¹⁸. It is evident from these data that biosurfactants, despite their numerous advantages,

have not been yet able to seize an appreciable chunk of surfactant market. The major factors affecting the commercialization of biosurfactants are their high production cost (three to ten times over that for chemical surfactant)⁴ and low product yield⁵. All research efforts are now focused on reducing the cost for raw material and downstream processing in addition to increasing the product yield.

Mukherjee *et al.* (2006) suggested a three prong strategy to perk up the economy of biosurfactant manufacture. This includes exploiting high yielding strains, using cheap agro industrial wastes with the right nutrient balance, development of more efficient biochemical processes under optimum process conditions, and cost-effective downstream processing for maximum product recovery³. The intend of current exertion was to make a comparative swot of biosurfactant preparation by *Pseudomonas aeruginosa* MTCC 424 by means of rice bran oil and soybean oil extracted from spent bleaching earth discarded in a vegetable oil refinery. Different nutritional and environmental parameters including concentration of carbon, pH of media, incubation time and temperature were also studied for high biosurfactant yield. The biosurfactants thus produced were first screened using oil displacement method (ODM), the drop collapse method (DCM), the cetyltrimethyl ammonium bromide (CTAB) agar plate method, emulsification index (EI₂₄) and the surface tension (SFT) measurement and then characterized by various techniques such as Electro spray ionization-mass spectrometry (ESI-MS), Fourier transform infrared (FTIR) spectroscopy, Nuclear magnetic resonance (NMR) and Thin-layer chromatography (TLC).

Materials and methods

Chemicals:

All chemicals were of analytical or highest available grade purchased from Qualikems Fine Chem Private Limited, Gujarat and were used without further purification. Standard rhamnolipid biosurfactant (95% purity) was procured from Sigma Aldrich.

Agro-industrial feedstocks:

Two spent bleaching earth samples, one containing rice bran oil and the other containing soybean oil in range of 14–25%, were received as a generous gift from M/s Kanpur Edibles Private Limited, Kanpur, India. Residual oil in the spent bleaching earth was extracted by soxhlet extraction

Mishra *et al.*: A comparative study of biosurfactant preparation by *Pseudomonas aeruginosa* MTCC 424 using rice *etc.*

method using hexane as solvent. The optimum extraction temperature was 68°C and the optimum time was 2 h. The residual oil was used as sole carbon resource or substrate in this study.

Organism:

Pseudomonas aeruginosa MTCC 424 culture was acquired from Microbial Type Culture Collection and Gene Bank (MTCC), Institute of Microbial Technology (IMTECH), Chandigarh, India. The culture was preserved on nutrient agar tilt at 4°C for 24 h prior to further investigation.

Cultivation of seed culture:

The strain from 24 h culture on nutrient agar tilt was relocated to untainted Erlenmeyer flask containing 250 mL nutritive broth to get ready the seed ethnicity for biomass preparation. The nutritive broth was prepared as per following composition: beef extract (1.07 g/L), yeast extort (2.05 g/L), peptone (5.04 g/L), NaCl (5.02 g/L), agar (15.10 g/L) and distilled water (1.0 L) at pH 7.0. The microbial cultures were grown-up in this broth under orbital agitation at 100 rpm and 32°C for 16 to 18 h. The optical-density of the broth was measured at regular intervals by a spectrophotometer at wavelength of 600 nm (OD_{600}) until it reached a value of 0.7 equivalent to the inoculum of 10^7 colony form units (CFU)/mL. The cell concentration of 3% (v/v) was used as inoculum for biomass preparation^{15,19–21}.

Biosurfactant preparation, recovery and purification

Production medium:

Biosurfactant preparation was accomplished in two identical 3 L Erlenmeyer flasks each containing 1 L mineral salt medium of following composition²²: KH_2PO_4 (3.0 g/L), K_2HPO_4 (2.5 g/L), $NaNO_3$ (2.5 g/L), $MgSO_4 \cdot 7H_2O$ (1.0 g/L), KCl (1.0 g/L), $CaCl_2$ (0.02 g/L), and trace elements (1 ml/L). The trace element solution concentration was $FeSO_4 \cdot 7H_2O$ (0.120 g/L), H_3BO_3 (0.227 g/L), $CoCl_2 \cdot 6H_2O$ (0.39 g/L), $CuSO_4 \cdot 5H_2O$ (0.018 g/L), $MnSO_4 \cdot H_2O$ (0.015 g/L), $[NH_4]_6Mo_7O_{24}$ (0.027 g/L) and $ZnSO_4$ (0.177 g/L). The bacterial broth (3% v/v) was inoculated into the mineral salt medium supplemented with 4% residual rice bran oil (RRBO) and 6% residual soybean oil (RSBO) in respective flasks as sole carbon source for a comparative study. The medium had pH synchronized at 7.2 by addition of HCl or NaOH²³ and an air supply of 3 Lpm was maintained²⁴. Incubation for

biosurfactant preparation was carried out in incu-shaker at 32°C and 100 rpm for a seven days.

Biosurfactant recovery and purification:

Most researchers have followed the acid precipitation-cum-solvent extraction method to recover biosurfactant from broth culture^{4,5,15,20,22,25–28}. After seven days of incubation, the broth customs containing RRBO as sole carbon source was centrifuged at six thousand rpm for 30 min to attain the cell free supernatant. The cell free supernatant was then acidified with 6 N HCl to pH 2.0 and held at 4°C overnight with effervescent stirring in magnetic stirrer until rudimentary biosurfactant pellets appeared. The pellets were recovered from acidified broth by centrifugation at 8000 rpm for 20 min. The pellets were then dissolved in distilled water and modified to pH 7.0 with 1 N NaOH. Now the organic layer of the solution containing biosurfactant was separated by solvent extraction method. To do this, an equal volume of chloroform and methanol solvent mixture in 2:1 (v/v) proportion was mixed together. The resulting solution was vigorously stirred for 20 min and allowed to settle until phase separation. The organic layer was separated and the process was further repeated twice. Any remaining solvent from biosurfactant was removed by rotary evaporator. The biosurfactant thus obtained was dried in an oven at 105°C for 24 h and a brownish biomass product was obtained. The biosurfactant concentration was dictated by separating the weight of the dried biosurfactant with the absolute volume of unrefined biosurfactant solution and expressed in terms of rhamnase mg/mL (dry weight)¹⁴. Same procedure was followed to recover biosurfactant from the broth culture containing residual soybean oil as sole carbon source.

Test methods for biosurfactant screening and characterization:

The cell free supernatants from two broth cultures were initially screened for successful preparation of biosurfactant using ODM, DCM, CTAB agar plate method, EI24 and SFT measurement. ESI-MS was used to analyze the RRBO and RSBO used in the study as sole carbon sources. The substance design and biosurfactant product composition was measured with the help of FTIR, NMR and TLC methods.

Screening for biosurfactant production

Oil displacement method (ODM):

Oil displacement activities of two cell free supernatants

were determined by using the now widely recognized classic method described by Morikawa *et al.*⁸. The tests were performed in 150 mm diameter Petri dish filled with 40 ml of distilled water. Further 20 microliter of diesel oil was put onto the surface of the distilled water to form a thin film. 10 μ L of supernatant sample was softly put in the centre of the oil film. The formation of a clear zone by displacement of oil indicated the successful preparation of biosurfactant and the diameter of this circle gave a measure of biosurfactant activity. Tests were run in triplicate and the average clear zone diameters were reported¹.

Drop-collapse method (DCM):

The qualitative drop-collapse tests were performed in standard 96-well (8 mm i.d.) microtiter plate (12.7 \times 8.5 cm) polystyrene lids. The lids were carefully cleaned using hot water and ethanol, and was further dried before use. Each well was layered with 2 μ L of HP Milcy Turbo 15W-40 engine oil and left for 24 h at ambient conditions to confirm a consistent covering. 5 μ L cell free supernatant was carefully transferred into the center of each well using a glass syringe held at an angle of 45°. The drops were observed after 1 min with the help of a magnifying glass²³. If the drop collapsed and spread out completely over the surface of oil, the result was considered as positive (+) for biosurfactant preparation. If the drop remained beaded, the result was considered as negative (-) indicating lack of biosurfactant preparation²⁹.

Cetyltrimethyl ammonium bromide (CTAB) agar plate method:

Mineral salt medium (MSM) supplemented with 4% RRBO and 6% RSBO as carbon source and 0.5 mg.ml⁻¹ CTAB and 0.2 mg.ml⁻¹ methylene blue were used for determination of rhamnolipid biosurfactant. Different wells each of 4 mm dia and equally distant apart were made in blue agar plate using a cork borer. 30 μ L of culture extract were charged into specified wells and incubated at 32°C for 48–72 h. Development of dark blue halos around the bacterial strains is an indication of presence of rhamnolipid biosurfactant^{1,30}. CTAB agar plate method is basically a colorimetric technique in which colour reactions are carried out by binding a dye to the rhamnolipid biosurfactant. Here the cationic surfactant CTAB and the basic dye methylene blue form an insoluble ion pair with anionic rhamnolipid biosurfactant¹².

Emulsification index (EI₂₄):

Emulsification activities of the two cell free supernatants

were analyzed by using the time honored Cooper and Goldenberg method¹⁵. According to which, 2 mL of HP Milcy Turbo 15W-40 engine oil as a liquid hydrophobic compound was added to approach volume of cell free culture stock in a graduated screwcap test tube. The blend was twirled at high velocity for 2 min and afterward permitted to make due with 24 h at room temperature. EI₂₄ was then dictated by isolating the tallness of the emulsified layer by the absolute blend stature and duplicating this outcome by 100^{5,19,20,31,32}.

Emulsification index (%EI₂₄) = [Height of the emulsified layer/Total height of the mixture] \times 100 EI₂₄ is used to determine the ability of biosurfactant to emulsify the non-polar hydrophobic phase in polar hydrophilic phase. A good emulsifier should be able to retain at least 50% of initial emulsion volume after 24 h of its formation. The good emulsification activity of a biosurfactant is of paramount importance for its successful environmental and industrial application³¹.

Surface tension (SFT) measurement:

SFT measurements for two cell free supernatants with different carbon sources were made at the intervals of 24 h using a surface tensiometer (Usha Instruments, Kolkata) at room temperature following du Nuoy methodology as discussed by Bodour and Miller-Maier²³. 20 mL volume of each decontaminated surfactant arrangement was moved into a spotless 50 mL measuring utencil and set onto the tensiometer stage.

A 6-cm du Nuoy platinum wire ring was drenched into the solution and the power needed to get it through the fluid air interface was recorded from the graduated dial as surface pressure (dyn/cm). Between every estimation, the platinum wire ring was flushed multiple times with water, multiple times with CH₃COCH₃ and was permitted to dry. The alignment was done before every estimation with ultrapure refined water (ST = 71.5 mN/m \pm 0.5) and all estimations were made in three-fold^{5,21}.

Tensiometers utilize an ideally wettable ring swinging from an exactness equilibrium to gauge the surface strain. The test liquid placed on the tensiometer platform is elevated by a platform adjusting screw until the ring reaches below the surface of the liquid. The stage is currently brought down again so the fluid film created underneath the surface is extended. The power needed by the ring to break the surface

is estimated and used to figure the surface tension^{15,27}. Tensiometric measurements are widely applied in rhamnolipid research due to their simplicity¹².

Characterization of biosurfactant

Electro spray ionization-mass spectrometry (ESI-MS):

ESI-MS has been effectively applied in analysis of triglycerides, fatty acids, and rhamnolipids³³. This technique is based on the ionization of primary molecules, which are then picked by a mass analyzer as per their mass-to-charge ratio (m/z) and identified accordingly¹². The mass spectrometry of residual rice bran and soybean oils and of purified rhamnolipid biosurfactants were recorded on Waters Q-TOF Micromass Mass Spectrometer.

ESI-MS of vegetable oils were completed as followed. 250 μL of RRBO was taken in a flagon and dissolved in water-methanol (1:1 v/v) making the last volume to 1 mL. The entire arrangement was permitted to get comfortable two unmistakable layers. The top hydroalcoholic layer was disposed of and 10 μL formic corrosive was added to answer for positive particle mode examination. The arrangement was then infused with a needle siphon at a stream pace of 10 $\mu\text{L min}^{-1}$ and filtering was done preposterous 1200 m/z range. Regular ESI-MS conditions were: disintegration temperature 100°C, warmed slim temperature 100°C, hairlike voltage 3000 V, and cone voltage ± 40 V. ESI-MS of chose particles was accomplished by low-energy (15–30 V) collision instigated separation^{4,34}. Same method was applied for analysis of RSBO.

ESI-MS of purged rhamnolipid biosurfactants were proceeded as examined further. 2 mg of rhamnolipid combination was dissolved in 1 mL methanol:water (9:1, v/v) and blended altogether. The blend was sifted and aliquots of 0.1 mL were diluted to 1.9 mL of acetonitrile-water (7:3, v/v). The sample was then brought into the source with a syringe pump at a flow rate of 10 $\mu\text{L min}^{-1}$ keeping up the stock of nitrogen and auxiliary gas at 50 and 5 ml min^{-1} , individually. The checking was done more than 100–750 m/z range in negative ion mode. Typical ESI-MS conditions were: heated capillary temperature 250°C, mass analyzer temperature 100°C, capillary voltage 3000 V, and cone voltage 40 V. ESI-MS of selected ions was attained with low-energy (15–30 V) collision-induced dissociation^{4,14,28,35}.

Fourier transform infrared spectroscopy (FTIR):

FTIR has a proven capacity to identify chemical bonds in a molecule by producing a spectrum of characteristic infrared absorption bands that can be used as fingerprint to identify and characterize the sample¹⁴. FTIR absorption spectrums of purified biosurfactants were obtained with Perkin-Elmer spectrophotometer in a dry atmosphere over region of wave numbers 400–4000 cm^{-1} with 20 scan speed by the KBr pellet method. 10 mg freeze-dried pure biosurfactant was milled with 100 mg spectral grade KBr and compressed by a bench-top hydraulic press applying 7500 kg load for 20 min to obtain thin translucent pellets^{4,5,36}. KBr was used as a background reference³¹.

Nuclear magnetic resonance (NMR) spectroscopy:

NMR is a leading spectroscopy technique available to chemists to determine the precise structure and purity analysis of newly synthesized chemicals. The technique is based on transitions in atoms along with magnetic moment under effect of an external magnetic field¹². ¹H and ¹³C NMR spectrum of biosurfactants were obtained with JEOL JNM-ECS400 NMR spectrometer operating at 400 MHz. The purified biosurfactant was re-dissolved in chloroform-deuterated methanol (2:1 v/v) and spectra were determined at 30°C using tetramethylsilane (TMS) as internal standard³⁵.

Thin layer chromatography (TLC):

TLC of biosurfactants was conducted out following work of George and Jayachandran³⁷. The biosurfactants were dissolved in 1 ml chloroform. 100 μL of each biosurfactant was applied to a 10 cm \times 10 cm pre-covered silica gel TLC plate utilizing glass slim. The versatile stage utilized for the partition and investigation of biosurfactants included chloroform/methanol/acidic corrosive (65:15:2 v/v/v) solvents. The plate improvement chambers were soaked with the versatile stage for thirty minutes before advancement. The plates were put vertically in these improvement chambers. After advancement the biosurfactant spots were deliberately rejected off from the plates and suspended in a chloroform/methanol (1:2 v/v) blend in a glass tube. The dissolvable scratching combination was then vortexed at fast for 1 min and saved for extraction. After extraction, the silica was eliminated by centrifugation and the dissolvable was taken out by evaporation. The weight of the biosurfactant extricates were recorded^{11,37}.

Results and discussion

Biosurfactant activity analysis:

Purified biosurfactants based on RRBO and RSBO substrates were analyzed for their biosurfactant activity and found positive for oil displacement test, CTAB agar plate test, drop-collapse test, EI_{24} and SFT measurement (Table 1). RRBO based biosurfactant was found quite effective in oil displacement test with average clear zone diameter of 2.1 cm than RSBO based biosurfactant having average clear zone diameter of 1.2 cm. The test result indicated the presence of strong surface active properties in RRBO based biosurfactant. Rath *et al.* (2016) recommended that the lipase movement of *Pseudomonas aeruginosa* culture is fundamentally liable for corruption of triacylglycerol of two vegetable oils to free unsaturated fats, di and mono acyl glycerol which thus go about as forerunner for biosurfactant synthesis³⁸.

DCM registered complete spreading for RRBO based biosurfactant and partial spreading for RSBO based biosurfactant over the hydrophobic oil film. Both results were considered positive for biosurfactant production though with difference in their concentrations. Most researchers like the current one have applied the DCM for qualitative screening of biosurfactant production on account of its being a sensitive and easy method^{1,21,25,29–31,39}. However, according to Bodour *et al.* (1998), the procedure can be applied to quantitative screening of biosurfactant preparation as well. They also gave a reasonable account of the principle underlying in the method. A plain water drop bearing no surfactant will form a bead on a hydrophobic surface because such a surface repels the polar water molecules. On the contrary, when the water drop containing surfactant is placed on the hydrophobic surface, the interfacial tension among the drop and the surface is decreased and the water drop is spread over

the hydrophobic surface. The drop spread area depends on concentration of surfactant in drop and its ability to reduce surface and interfacial tension²³. Youssef *et al.* (2004) found that the DCM is not as sensitive as the ODM in detecting small amounts of biosurfactant production; though its ability to be performed in a microtiter plate makes it possible to carry out multiple analyses simultaneously²⁹.

CTAB methylene blue agar plate test was found positive for both rhamnolipid biosurfactants as confirmed by creation of dark blue halos around the bacterial colonies. Heyd *et al.* (2008) reported that spot diameter is a function of several key parameters such as rhamnolipid concentration, cell growth of bacteria culture, cultivation time, migration of rhamnolipids and loading level of agar plates¹².

The RRBO and RSBO substrate based two biosurfactants possessed good emulsion stabilizing capacity for HP Milcy Turbo 15W-40 engine oil as can be seen with their % EI_{24} values of 74.30 and 62.60, respectively. The RRBO based biosurfactant was found having better surface tension reducing ability than RSBO based biosurfactant in 96 h test. The results are satisfactory based on comparison with value of 28 to 27 mN/m reported for *Pseudomonas aeruginosa* in available literature^{15,40}. The lowering of surface tension of biosurfactant over a period of time is now a standard test method for selection of biosurfactant producing bacteria and to analyze the ability of biosurfactant produced in lowering of surface tension to an acceptable value²⁷.

Youssef *et al.*²⁹ reported to find an inverse linear relationship between the diameter of the clear zone in oil displacement test and the surface tension value of test biosurfactant. As evident from the Table 1, the RRBO based biosurfactant with large clear zone diameter has low surface tension. Similarly, Soltanighias *et al.*¹ found inverse linear

Table 1. Qualitative analysis of biosurfactant produced by *Pseudomonas aeruginosa*

Sr. No.	Name of test	Biosurfactant based on two oil substrates	
		RRBO	RSBO
1.	Oil displacement method	+++ (2.1 cm) ++ (1.2 cm)	
2.	Drop-collapse method	+++ (complete spreading)	+ (partial spreading)
3.	CTAB agar plate method	+ (dark blue)	+ (dark blue)
4.	Emulsification index (% EI_{24})	74.30%	62.60%
5.	Surface tension after 96 h	30.25 mN/m	46.46 mN/m

+ efficient / ++ very efficient

relationship between the drop size in drop-collapse test and surface tension of test biosurfactant. The drop-collapse test performed in present study was qualitative only and diameters were not measured, still the results obtained were in general agreement with the observations made in available literature.

Characterization of biosurfactant

Fourier transform infrared spectroscopy:

Figs. 1(A) and 1(B) show FTIR spectrums of dried biosurfactants synthesized using *Pseudomonas aeruginosa* grown on 4% RRBO and 6% RSBO substrates, respectively. FTIR spectrum of the RRBO based biosurfactant disclosed a peak at 3417.22 cm^{-1} which is characteristic of N-H bond stretching vibrations of amine groups^{14,22,41}. The adsorption peak $\sim 2926.91\text{ cm}^{-1}$ is supposed to be the asymmetric vibration of CH_2 and CH_3 groups of aliphatic chains. The accompanying symmetric stretch can be noticed at 2856.08 cm^{-1} ^{5,14,31,35,41,42}. The two characteristic peaks at 1722.59 cm^{-1} and 1651.38 cm^{-1} of C=O in COOH specified the presence of ester carbonyl group in the biosurfactant^{4,5,22,30,35,36,41,42}. The strong absorption band at 1572.77 cm^{-1} indicated the vibrations of C-O and C=O bonds in carboxyl esters³⁰. The absorption peak at 1402.03 cm^{-1} appeared due to the in plane bending of C-O-H corresponding

to carboxylic group⁴². The deformation vibration at 1377.86 cm^{-1} confirmed the presence of unsaturated alkyl group in aliphatic chain³⁰, whereas the C-O-C stretching vibrations at 1124.47 cm^{-1} marked the ether linkages in the chemical structures of the rhamnose rings^{4,30,36}. The vibration at wave number 1068.14 cm^{-1} can be assigned to C-O bonds^{5,14}. The absorption peak at 1050 cm^{-1} is indicative of the presence of polysaccharide or polysaccharide-identical substances in the biosurfactant⁴³. The prominent peak at 982.65 cm^{-1} was attributed to C-H bonding³¹. Further the absorption at 722.05 cm^{-1} indicated the presence of alkyl groups⁴.

FTIR spectrum of the RSBO biosurfactant can be described on similar lines. The absorption peaks at 3392.86 cm^{-1} and 1457.16 cm^{-1} indicated O-H bond stretching vibrations of -OH groups^{4,30,35,42}. The peaks at 2956.25 cm^{-1} , 2926.01 cm^{-1} , and 2855.90 cm^{-1} are attributed to C-H bond stretching of CH, CH_2 , and CH_3 groups in aliphatic chains^{4,5,14,31,35,41,42}. The two peaks at 1723.84 cm^{-1} and 1651.71 cm^{-1} implied the stretching vibrations of C=O in COOH suggesting the presence of ester compound in the biosurfactant^{4,5,22,30,35,36,41,42}. The strong absorption band at 1572.45 cm^{-1} expressed the stretching vibrations of C-O and C=O bonds in carboxyl esters³⁰. The absorption peaks at 1403.06 cm^{-1} and 1317.14 cm^{-1} were assigned to the C-O bending of ester carbonyl group^{35,42}. The C-O-C stretch-

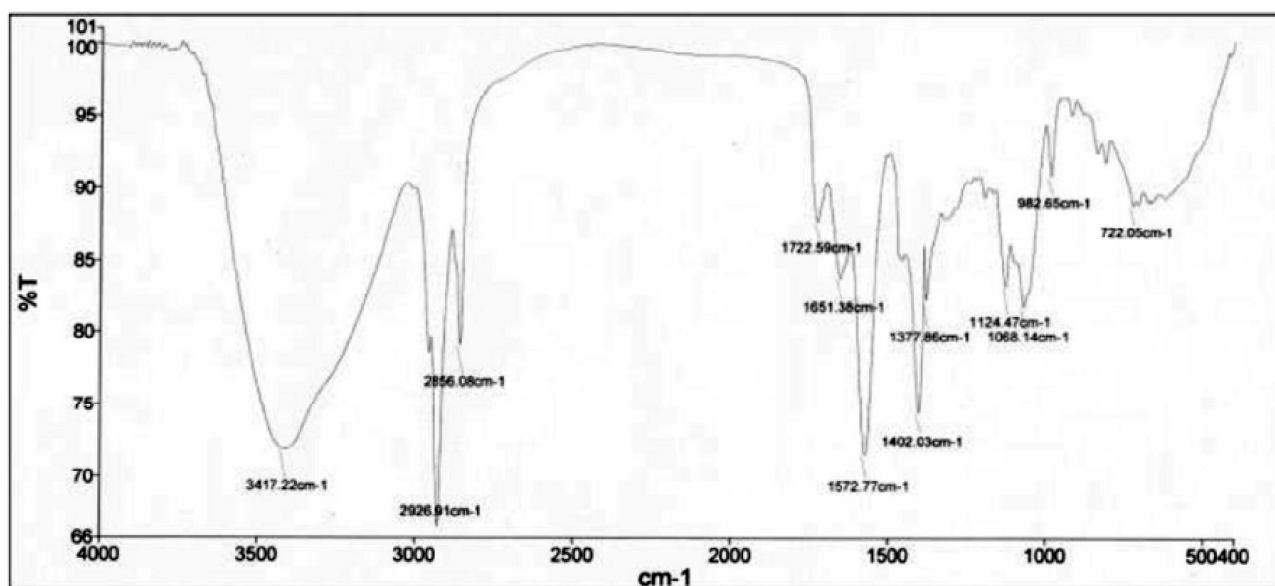


Fig. 1(A). FTIR spectrum of RRBO substrate based biosurfactant produced by *Pseudomonas aeruginosa*.

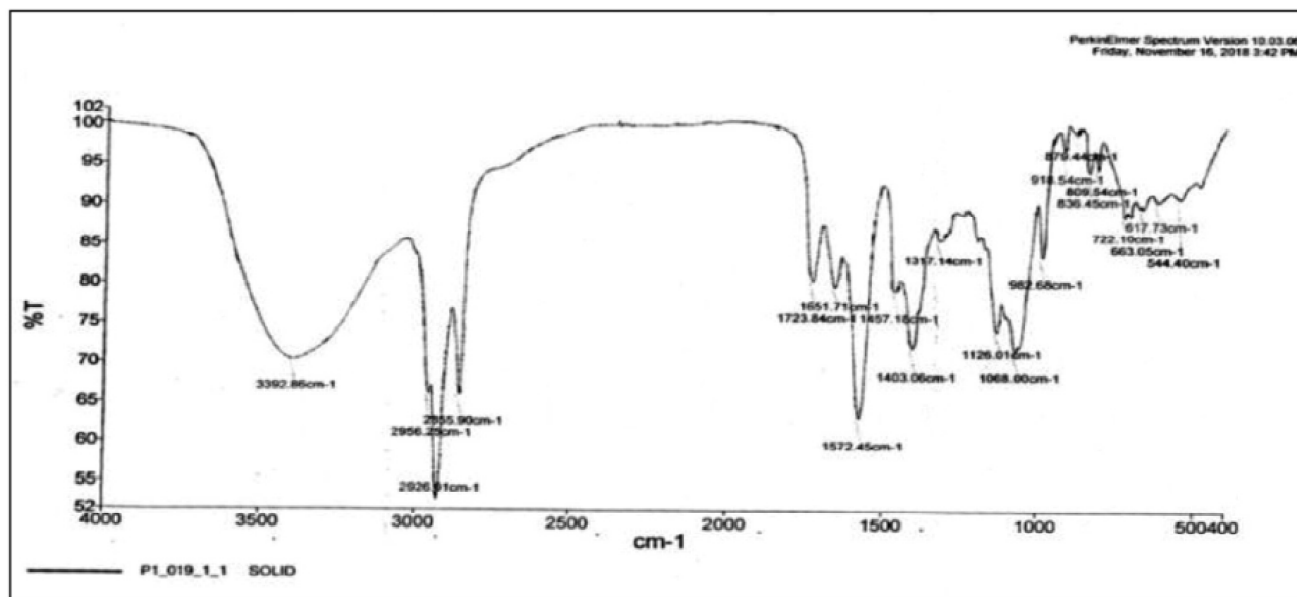


Fig. 1(B). FTIR spectrum of RSBO substrate based biosurfactant produced by *Pseudomonas aeruginosa*.

ing vibrations at 1126.01 cm^{-1} marked the ether linkages in the chemical structures of the rhamnose rings^{4,30,36}. The wave number 1068.00 cm^{-1} was assigned to C-O bonds^{5,14}, while the wavenumber 982.68 cm^{-1} was attributed to C-H bond stretching³¹. The α -pyranil II sorption band at 836.45 cm^{-1} demonstrated the presence of di-rhamnolipid in the biosurfactant³⁵. The band at 809.54 cm^{-1} represented C-H-OOP stretch of aromatic anhydride²⁵. Further the absorption at 722.10 cm^{-1} indicated the presence of alkyl groups⁴.

Hisatsuka *et al.*⁴⁴, da Rosa *et al.*⁴⁵, Mahalingam and Sampath³⁰, and Shekhar *et al.*²⁵ have reported that the *Pseudomonas aeruginosa* mostly produce lipid-carbohydrate compounds classified as rhamnolipid biosurfactants. FTIR analyses of the two biosurfactants in present study confirmed the findings of earlier studies.

Thin layer chromatography (TLC):

The purified rhamnolipid biosurfactants obtained with RRBO and RSBO carbon substrates were examined using TLC on silica gel plates. The first plate synthesized for RRBO substrate based biosurfactant exhibits the existence of two major spots having R_f values of 0.62 and 0.26 (Fig. 2(A)) indicating the presence of two major homologues in the biosurfactant sample. Similarly, the second plate prepared with RSBO carbon source based biosurfactant confirmed the

presence of two spots at R_f values of 0.55 and 0.19 (Fig. 2(B)). These results were then compared with the R_f values of mono- and di-rhamnolipid as mentioned in the available literature. According to Schenk *et al.*⁴⁶, Arino *et al.*⁴⁷, and Jadhav *et al.*⁴⁸, the R_f values of 0.74.0.55 and 0.40.0.19 relate to mono- and di-rhamnolipids, respectively. TLC analysis was thus successful in confirming further that *Pseudomonas aeruginosa* MTCC 424 strain has actually generated and developed rhamnolipid biosurfactant in present study.

Nuclear magnetic resonance (NMR) spectroscopy:

The ^1H and ^{13}C NMR spectroscopic analyses of the two biosurfactants were performed to confirm their rhamnose ring and long hydrocarbon chain structure¹². The ^1H and ^{13}C NMR spectra of RRBO substrate based rhamnolipid biosurfactants are shown in Figs. 3(A) and 3(B). The characteristic chemical shifts obtained in ^1H NMR spectra were 0.857 ppm for $-\text{CH}_3$, 1.232 ppm for $-(\text{CH}_2)_5$, 2.742 ppm for $-\text{CH}(\text{O})-\text{CH}_2-\text{COO}-$, 3.536 ppm for $-\text{O}-\text{CH}-$ lipid moiety, 4.101 ppm for $-\text{OH}$, and 5.308 ppm for $-\text{CH}-\text{O}-\text{C}-$ on rhamnose moiety. The ^{13}C NMR displayed chemical shifts of 76.773 ppm (characteristic of RL1) and 77.412 ppm (characteristic of RL2). All these results indicated the molecular structure of L-rhamnosyl- β -hydroxydecanoyl- β -hydroxydecanoate (RL1) and L-rhamnosyl-L-rhamnosyl- β -hydroxydecanoyl- β -hydroxy-

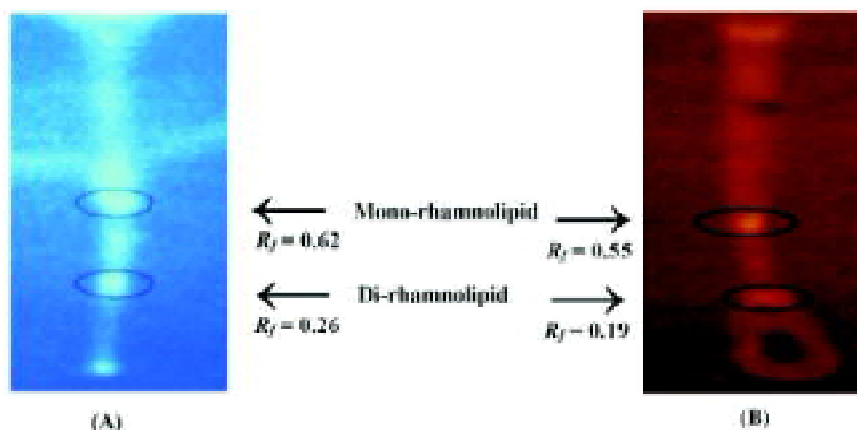


Fig. 2. TLC analysis of RRBO (A) and RSBO (B) substrate based rhamnolipid mixture synthesized by *Pseudomonas aeruginosa* MTCC 424 with chloroform/methanol/acetic acid (65:15:2, v/v/v) developing solvent system.

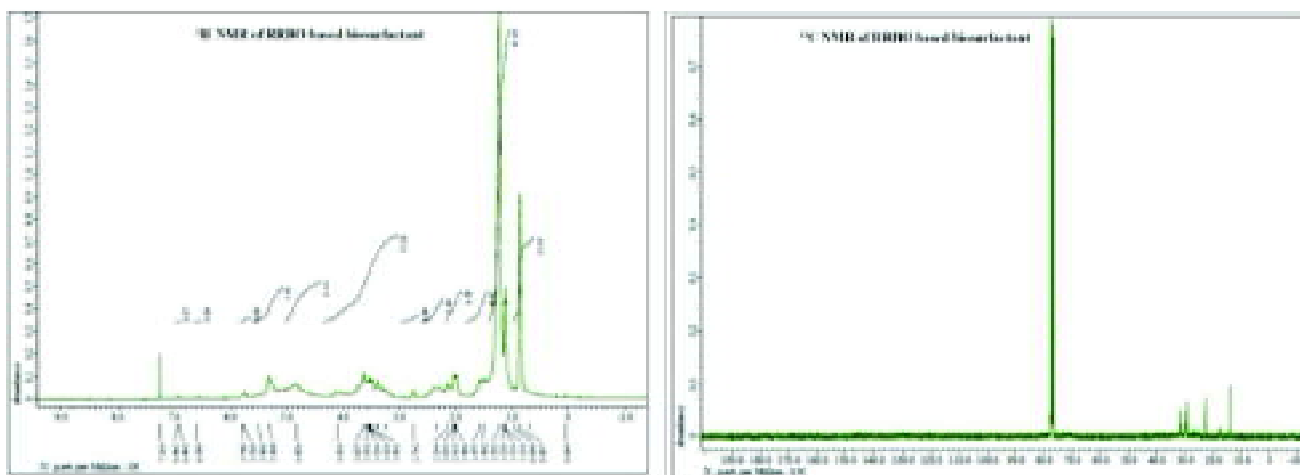


Fig. 3. ^1H NMR (A) and ^{13}C NMR (B) spectra of RRBO based biosurfactant.

decanoate (RL2), which are the principal glycolipids synthesized using *Pseudomonas aeruginosa*^{12,27}. The ^1H and ^{13}C NMR spectra of RSBO substrate based rhamnolipid biosurfactants are shown in Figs. 4(A) and 4(B). The distinguished chemical shifts appeared in two spectra were almost similar to that obtained with RRBO substrate based biosurfactant.

Results of NMR study for both surfactants are summarized in Table 2 and were found comparable with earlier studies of Ramana *et al.*⁴⁹, Wei *et al.*⁵⁰, Moussa *et al.*³⁵ and Sharma *et al.*⁴.

Electro spray ionization–mass spectrometry (ESI–MS):

Scanning of the two biosurfactants over 100 to 750 m/z in the negative ion mode allows for the selection of the different rhamnolipids. The two mass spectrums of targeted rhamnolipid mixtures are shown in Fig. 5. RRBO substrate based rhamnolipid biosurfactant (Fig. 5A) typically produced by *Pseudomonas aeruginosa* was consist of mono-rhamnolipid fragment ions at m/z 141.01 (RhaC8) and m/z 195.02 (RhaC10C12:1). The spectrum at m/z 333.57, 447.23, 475.36, and 503.23 represented mono-rhamnolipid pseudomolecular ions RhaC10, RhaC8C8, RhaC8C10/

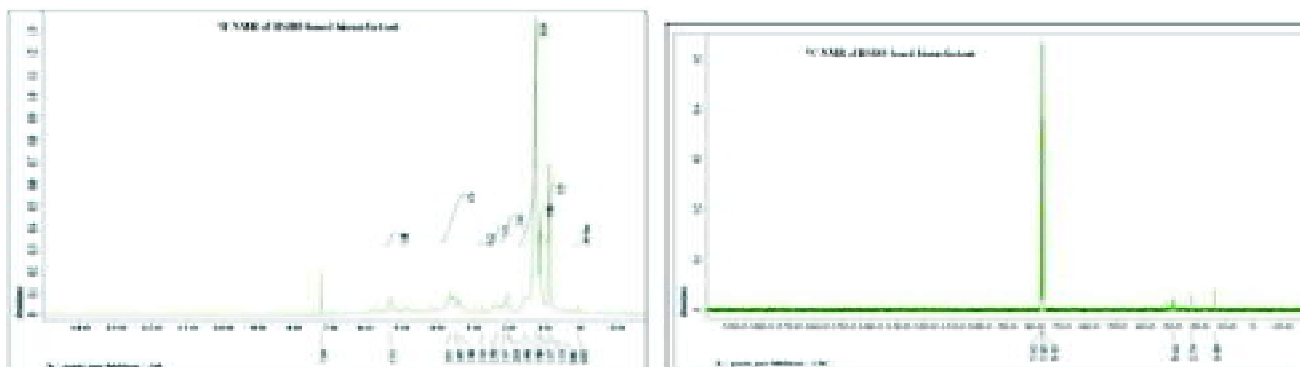


Fig. 4. ^1H NMR (A) and ^{13}C NMR (B) spectra of RSBO based biosurfactant.

Table 2. NMR analysis of the two biosurfactants

RRBO substrate based biosurfactant	RSBO substrate based biosurfactant	Analysis
^1H chemical shift (ppm)		
0.857	0.861	$-\text{CH}_3$ (on β -hydroxy fatty acids) ^{49,35}
1.232	1.237	$-(\text{CH}_2)_5-$ (on β -hydroxy fatty acids) ³⁵
2.742	2.745	$-\text{CH}(\text{O})-\text{CH}_2-\text{COO}-$ (on β -hydroxy fatty acids) ³⁵
3.536		$-\text{O}-\text{CH}-$ lipid moiety/C-2' and C-5' sugar moiety ⁵
4.101	4.100	$-\text{OH}$ (D_2O exchange) ⁴⁹
4.826		$-\text{CH}-\text{OH}$ (on rhamnose moiety) ³⁵
5.308	5.313	$-\text{CH}-\text{O}-\text{C}$ (on rhamnose moiety) ³⁵
^{13}C chemical shift (ppm)		
76.773	76.783	L-Rhamnosyl- β -hydroxydecanoyl- β -hydroxydecanoate (RL1) ¹²
77.412	77.422	L-Rhamnosyl-L-rhamnosyl- β -hydroxydecanoyl- β -hydroxydecanoate (RL2) ²⁷

RhaC10C8, and RhaC10C10, respectively. Spectrum at m/z 393.19 was detected to be di-rhamnolipid fragment ion (RhaRhaC12:1C12). The two peaks at m/z 621.78 and 649.27 were identified as di-rhamnolipid pseudomolecular ions RhaRhaC8C10/RhaRhaC10C8 and RhaRhaC10C10, respectively^{4,12,28}.

RSBO substrate based biosurfactant showed somewhat complex structure (Fig. 5B). The peak at m/z 141.03 was identified that of mono-rhamnolipid fragment ion (RhaC8)¹². The two adjacent peaks at m/z 353.99 and 354.07 represented rhamnolipid homologues with weak molecular ions⁴². The peak at m/z 621.86 was attributed to di-rhamnolipid pseudomolecular ion (RhaRhaC8C10/RhaRhaC10C8)¹², whereas the peak at m/z 680.66 designated dirhamnolipid

homologue (RhaRhaC10C12)³⁵. Spectrum at m/z 663.45 indicated the presence of carbohydrate moiety in biosurfactant structure⁴².

Mass spectrometric examination of two biosurfactants substantiated the existence of mono- and di-rhamnolipid structures in agreement with numerous previous studies. The opinion among researchers is divided on whether the mono-rhamnolipids are predominant components or the di-rhamnolipids are predominant components in rhamnolipid surfactant mixtures³⁵. In our study, the RRBO substrate based biosurfactant was found rich in di-rhamnolipid species as opposed to RSBO substrate based biosurfactant enriched in mono-rhamnolipid species. However, many peaks in RSBO substrate based biosurfactant were left unidentified poten-

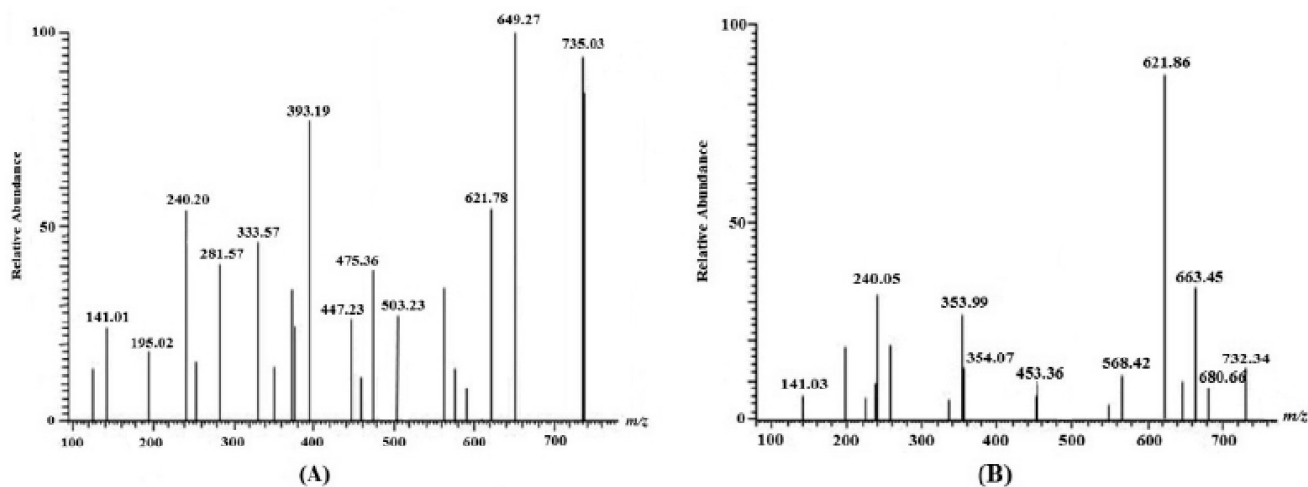


Fig. 5. ESI-MS spectrum of purified rhamnolipid mixtures produced by *Pseudomonas aeruginosa* cultures using RRBO (A) and RSBO (B) carbon substrates.

tially indicating towards poor surfactant structure, a fact already proved by previous tests in present study.

Electrospray ionization-mass spectrometry (ESI-MS) of RRBO and RSBO substrates:

Several well defined groups were identified in ESI-MS fingerprints of RRBO and RSBO through comparison with data reported by other researchers. In ESI-MS spectra of RRBO (Fig. 6A), the m/z 149.0249 and m/z 319.1689 were attributed to cinnamic acid and 4-norlempin aglicone, respectively³⁴. The ions at m/z 575.5056, 599.5067, and 601.5195 conformed to diacylglycerol fragments of PL^+ , LL^+ or OLn^+ , and LO^+ , respectively⁵¹. The spectra at m/z 853 reciprocated to PPL (C50:2), m/z 855 to PPO (C50:1), m/z 877 to PLL (C52:4), m/z 879 to PLO (C52:3), m/z 899 to LLLn or OLnLn (C54:7), m/z 901 to LLL or OLLn (C54:6), and m/z 915 to LLLn or OLnLn. Here O stands for oleic acid, L for linoleic acid, Ln for linolenic acid, and the P stands for palmitic acid⁵². In ESI-MS spectra of RSBO (Fig. 6B), the m/z 149.0259 was attributed to cinnamic acid³⁴. The m/z 263.2376 was considered to be RCO^+ ion reflecting linoleic fatty acid⁵¹. The ions at m/z 279.2329 and 377.2672 were regarded to be deprotonated linoleic acid (C18:2)³³ and hydroxytyrosillenoate³⁴, respectively.

One important deduction can be made from this interpretation of ESI-MS data of the two substrate oils. For RRBO, it

became possible to identify multiple groups with the help of reports of previous studies by other researchers, but for RSBO, hardly a few chemical groups were identified possibly indicating towards non-lipid character of soybean oil extracted from spent bleaching earth in this study. This might also be the principal reason for smaller production of biosurfactant even with higher percentage of soybean oil (6%) in comparison to ricebran oil (4%).

Factors affecting biosurfactant production

Various physicochemical factors like carbon and nitrogen source, variations in pH and temperature of the growth medium, oxygen flow rate, agitation speed, etc. affect biosurfactant production. Santos *et al.* (2016) have reported 30°C, in general, as the most favorable temperature for biosurfactant production by different bacterial strains⁶. The temperature range of 32.36°C is found to be most favorable particularly for *Pseudomonas aeruginosa* culture. The agitation speed of the growth medium has a decisive effect on biosurfactant production possibly by application of strain that provides an effective phase mixture and oxygen transfer¹⁵. In this study, the temperature in incu-shaker was maintained at 32°C, the agitation at 100 rpm, and the air flow at 3 Lpm. Other parameters like carbon source concentration, pH of the medium, and incubation time were varied in order to study their effect on rhamnolipid biosurfactant production.

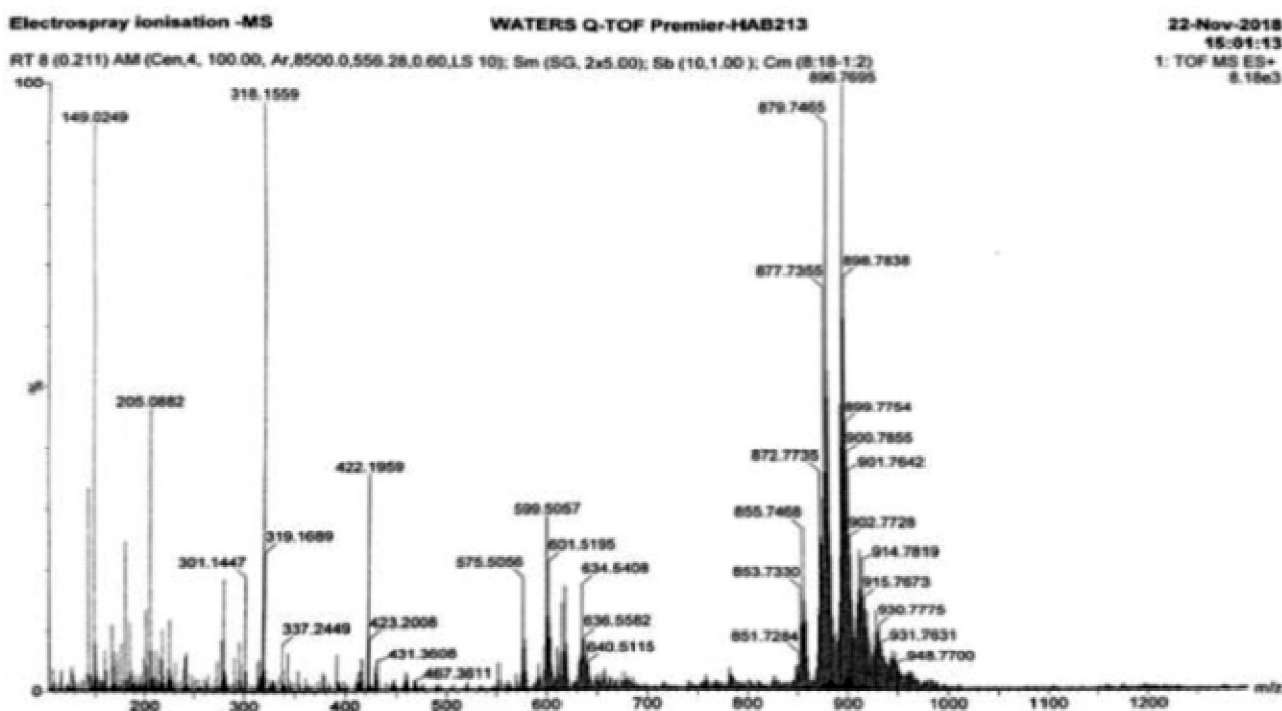


Fig. 6(A). ESI-MS spectra of RRBO substrate.

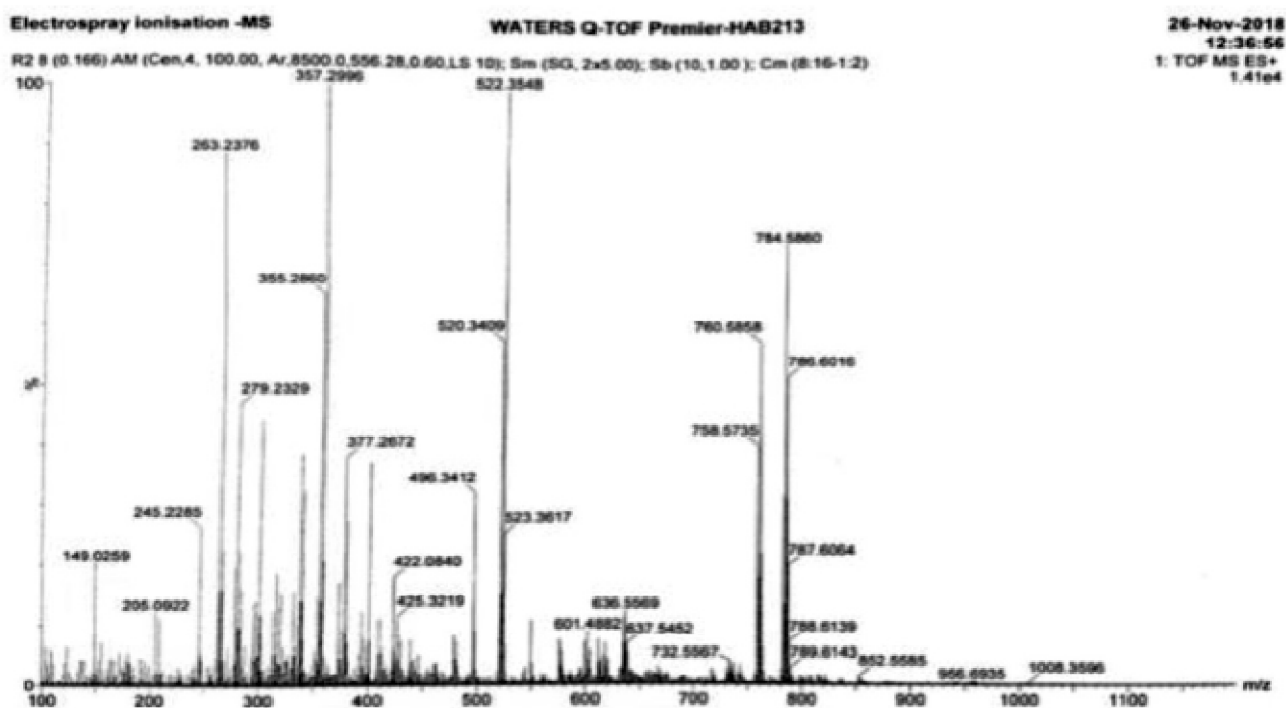


Fig. 6(B). ESI-MS spectra of RSBO substrate.

Effect of carbon source on biosurfactant production:

The need of a carbon source for successful growth and production of biosurfactants by microorganisms is beyond question⁶. Previous studies have found that biomass does not grow in absence of carbon source⁵³. In present study, RRBO and RSBO were used as cheap carbon sources in order to economize the large scale biosurfactant production⁵. The RRBO concentration of 4% obtained maximum rhamnolipid yield of 8.5 g/L by *Pseudomonas aeruginosa*. When RSBO was used as carbon source, the maximum rhamnolipid yield of 3.6 g/L was obtained at 6% carbon source concentration (Table 3). Though RRBO proved to be a better carbon source than RSBO in this study, the results validated the possibility of industrial scale biosurfactant synthesis using both RRBO and RSBO as low cost carbon sources.

Effect of pH on biosurfactant preparation:

The ideal pH of the growth medium for highest biosurfactant yield by *Pseudomonas aeruginosa* MTCC 424 using RRBO was reported to be 6.8. The biosurfactant production at this pH was 8.5 g/L. There was a sharp decrease in rhamnolipid concentration beyond this pH. The ideal pH for maximum biosurfactant generation with RSBO was re-

Table 3. Amount of rhamnolipid produced at different concentration of RRBO and RSBO substrates

RRBO concentration (%)	Rhamnolipid concentration (g/L)	RSBO concentration (%)	Rhamnolipid concentration (g/L)
1	1.0	1	2.0
2	3.9	2	2.4
3	6.0	3	2.8
4	8.5	4	3.0
5	5.2	5	3.2
-	-	6	3.6
-	-	7	3.5

ported to be 7.0 and the biosurfactant concentration was 5.0 g/L (Fig. 7).

Effect of incubation time on biosurfactant production:

The ideal incubation time for maximum rhamnolipid production using *Pseudomonas aeruginosa* MTCC 424 was found to be 7 days for both RRBO and RSBO carbon source based growth mediums. The maximum biosurfactant yield with RRBO was 8.0 g/L and 7.6 g/L with RSBO at optimum incubation time. Thereafter there was a reduction in biosurfactant concentration in both samples (Fig. 8).

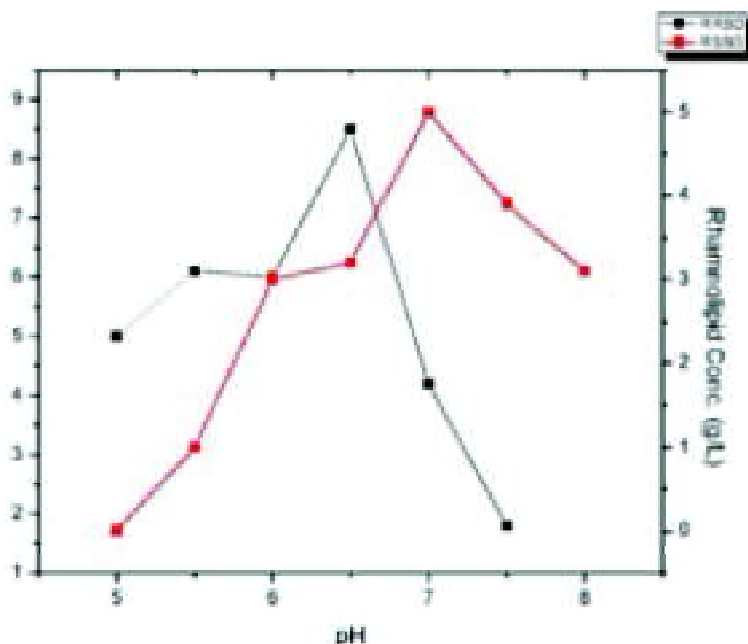


Fig. 7. Effect of pH on biosurfactant preparation using RRBO (4%) and RSBO (5%) as carbon source for incubation period of 7 days.

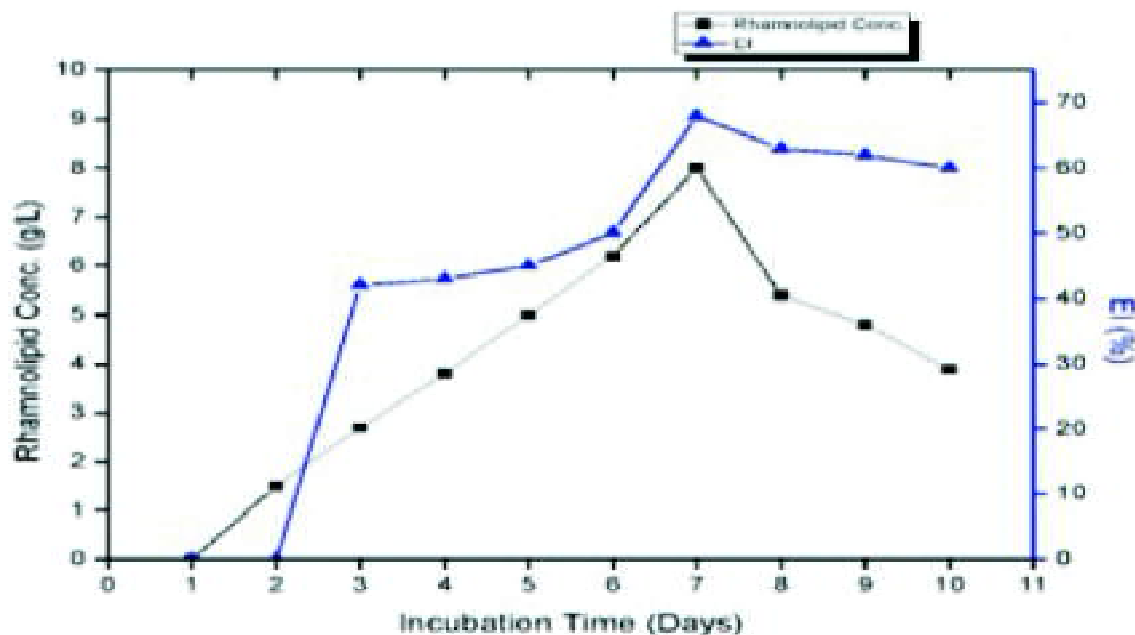


Fig. 8. Effect of incubation time on rhamnolipid production and emulsification index (%) with RRBO (4%) and RSBO (6%) as carbon source.

Conclusion

The two rhamnolipid biosurfactants were synthesized using *Pseudomonas aeruginosa* strain using RRBO and RSBO as low-cost substrates. Following conclusions were made out of this study:

(i) RRBO based biosurfactant was more effective than RSBO based biosurfactant in oil displacement test with larger clear zone diameter.

(ii) RRBO based biosurfactant displayed complete spreading over the hydrophobic film in drop-collapse test, whereas the RSBO based surfactant displayed partial spreading under the same conditions.

(iii) CTAB methylene blue agar plate test was positive for both biosurfactants.

(iv) RRBO based biosurfactant posted better emulsion stabilizing capacity than RSBO derived biosurfactant with same mineral engine oil.

(v) RRBO based biosurfactant registered larger reduction in surface tension than RSBO based biosurfactant in standard 96 h test.

The RRBO was found to be a better source of nutrition than RSBO for biosurfactant production. The oil used in this

study is very low-priced as it was extracted from the spent bleaching earth discarded in the edible oil processing industries.

References

1. T. Soltanighias, A. E. A. Singh, S. K. Satpute, A. G. Banpurkar, A. Koolivand and P. Rahi, *Environmental Sustainability*, 2019, **2**, 285.
2. N. Dave and T. Joshi, *Int. J. Appl. Chem.*, 2017, **13**, 663.
3. C. Syldatk and R. Hausmann, *Eur. J. Lipid Sci. Technol.*, 2010, **112**, 615.
4. R. Sharma, J. Singh and N. Verma, *Biotech*, 2018, **8**, 20.
5. M. Jadhav, A. Kagalkar, S. Jadhav and S. Govindwar, *Eur. J. Lipid Sci. Technol.*, 2011, **113**, 1347.
6. D. K. F. Santos, R. D. Rufino, J. M. Luna, V. A. Santos and L. A. Sarubbo, *Int. J. Mol. Sci.*, 2016, **17**, 401.
7. R. S. Reis, G. J. Pacheco, A. G. Pereira and D. M. G. Freire, *Biodegradation – Life of Science*, 2013, 31.
8. M. Morikawa, Y. Hirata and T. Imanaka, *Biochimica et Biophysica Acta (BBA) – Molecular and Cell Biology of Lipids*, 2000, **1488**, 211.
9. M. Pacwa-Płociniczak, G. A. Płaza, Z. Piotrowska-Seget and S. S. Cameotra, *Int. J. Mol. Sci.*, 2011, **12**, 633.
10. A. Yateem, M. T. Balba, Y. Al-Shayji and N. Al-Awadhi, *Soil and Sediment Contamination*, 2002, **11**, 41.
11. P. Das, X. P. Yang and L. Z. Ma, *Frontiers in Microbiology*, 2014, **5**, 1.

Mishra *et al.*: A comparative study of biosurfactant preparation by *Pseudomonas aeruginosa* MTCC 424 using rice etc.

12. M. Heyd, A. Kohnert, T. H. Tan, M. Nusser, F. Kirschhofer, G. Brenner-Weiss, M. Franzreb and S. Berensmeier, *Anal Bioanal. Chem.*, 2008, **391**, 1579.
13. K. V. Ramana, N. C. L. N. Charyulu and N. G. Karanth, *J. Chem. Tech. Biotechnol.*, 1991, **51**, 525.
14. R. Thavasi, V. R. M. S. Nambaru, S. Jayalakshmi, T. Balasubramanian and I. M. Banat, *Indian J. Microbiol.*, 2011, **51**, 30.
15. S. N. R. L. Silva, C. B. B. Farias, R. D. Rufino, J. M. Luna and L. A. Sarubbo, *Colloids and Surfaces B: Biointerfaces*, 2010, **79**, 174.
16. K. Ahuja and S. Singh, *Global Market Insights*, 2019.
17. L. Shastri and O. Sumant, *Allied Market Research*, 2018.
18. M. J. Chaprao, R. C. F. S. da Silva, R. D. Rufino, J. M. Luna, V. A. Santos and L. A. Sarubbo, *Journal of Biotechnology*, 2018, **285**, 15.
19. B. Moshtagh, K. Hawboldt and B. Zhang, *Environmental Technology*, 2018, 1.
20. W. M. F. W. Nawawi, P. Jamal and M. Z. Alam, *Bioresource Technology*, 2010, **101**, 9241.
21. H. S. El-Sheshtawy, I. Aiad, M. E. Osman, A. A. Abo-ELnasr and A. S. Kobisy, *Egyptian Journal of Petroleum*, 2015, **24**, 155.
22. A. A. Bodour and R. M. Miller-Maier, *Journal of Microbiological Methods*, 1998, **32**, 273.
23. M. Benincasa, A. Abalos, I. Oliveira and A. Manresa, *Antonie Van Leeuwenhoek*, 2004, **85**, 1.
24. S. Shekhar, A. Sundaramanickam, M. Panda and K. Saranya, *Inventi Rapid: Pharm Biotech & Microbio*, 2015, **4**, 1.
25. Y. Pecci, F. Rivardo, M. G. Martinotti and G. Allegrone, *J. Mass. Spectrom.*, 2010, **45**, 772.
26. N. M. P. R. e Silva, R. D. Rufino, J. M. Luna, V. A. Santos and L. A. Sarubbo, *Biocatalysis and Agricultural Biotechnology*, 2014, **3**, 132.
27. T. B. Lotfabad, N. Ebadipour, R. Roostaazad, M. Partovi and M. Bahmaei, *Colloids and Surfaces B: Biointerfaces*, 2017, **152**, 159.
28. N. H. Youssef, K. E. Duncan, D. P. Nagle, K. N. Savage, R. M. Knapp and M. J. McInerney, *Journal of Microbiological Methods*, 2004, **56**, 339.
29. P. U. Mahalingam and N. Sampath, *Euro. J. Exp. Bio.*, 2014, **4**, 59.
30. P. Talukdar, C. Sharma, A. Doley, K. Baruah, A. Borah, P. Agarwal and P. Deori, *Petroleum Science and Technology*, 2017, **35**, 2102.
31. A. S. Abu-Ruwaida, I. M. Banat, S. Haditirto, A. Salem and M. Kadri, *Acta Biotechnol.*, 1991, **11**, 315.
32. Y. Li, B. Jiang, Y. Lou, Q. Shi, R. Zhuang and Z. W. Zhan, *International Journal of Food Science & Technology*, 2019, 1.
33. R. R. Catharino, R. Haddad, L. G. Cabrini, I. B. S. Cunha, A. C. H. F. Sawaya and M. N. Eberlin, *Anal. Chem.*, 2005, **77**, 7429.
34. T. A. A. Moussa, M. S. Mohamed and N. Samak, *Braz. J. Chem. Eng.*, 2014, **31**, 867.
35. V. Saravanan and S. Vijayakumar, *J. Acad. Indus. Res.*, 2012, **1**, 264.
36. S. George and K. Jayachandran, *J. Appl. Microbiol.*, 2013, **114**, 373.
37. K. Rath, A. B. Singh, S. Chandan and R. S. Vatsala, *Journal of Scientific and Industrial Research*, 2016, **75**, 681.
38. D. K. Jain, D. L. Collins-Thompson, H. Lee and J. T. Trevors, *Journal of Microbiological Methods*, 1991, **13**, 271.
39. K. K. Gautam and V. K. Tyagi, *J. Oleo Sci.*, 2006, **55**, 155.
40. O. S. Amodu, S. K. O. Ntwampe and T. V. Ojumu, *BioResources*, 2014, **9**, 5045.
41. C. Hazra, D. Kundu, P. Ghosh, S. Joshi, N. Dandi and A. Chaudhari, *J. Chem. Technol. Biotechnol.*, 2011, **86**, 185.
42. Z. Li, C. Zhao, Y. Zhang and D. Zhao, 'The 5th International Conference on Bioinformatics and Biomedical Engineering', 2011, 1.
43. K. I. Hisatsuka, T. Nakahara, N. Sano and K. Yamada, *Agr. Biol. Chem.*, 1971, **35**, 686.
44. C. F. C. da Rosa, M. Michelon, J. F. D. M. Burkert, S. J. Kalil and C. A. V. Burkert, *African Journal of Biotechnology*, 2010, **9**, 9012.
45. T. Schenk, I. Schuphan and B. Schmidt, *Journal of Chromatography A*, 1995, **693**, 7.
46. S. Arino, R. Marchal and J. P. Vandecasteele, *Appl. Microbiol. Biotechnol.*, 1996, **45**, 162.
47. J. Jadhav, S. Dutta, S. Kale and A. Pratap, *Prep. Biochem. Biotechnol.*, 2018, **48**, 234.
48. K. V. Ramana and N. G. Karanth, *J. Chem. Tech. Biotechnol.*, 1989, **45**, 249.
49. Y. H. Wei, C. L. Chou and J. S. Chang, *Biochemical Engineering Journal*, 2005, **27**, 146.
50. A. Zeb and M. Murkovic, *Eur. J. Lipid Sci. Technol.*, 2010, **112**, 844.
51. R. C. Simas, R. R. Catharino, I. B. S. Cunha, E. C. Cabral, D. Barrera-Arellano, M. N. Eberlin and R. M. Alberici, *Analyst*, 2010, **135**, 738.
52. M. O. Ilori, C. J. Amobi and A. C. Odocha, *Chemosphere*, 2005, **61**, 985.

See discussions, stats, and author profiles for this publication at: <https://www.researchgate.net/publication/340114397>

Crack detection in a beam using wavelet transform and photographic measurements

Article in Structures - March 2020

DOI: 10.1016/j.istruc.2020.03.010

CITATIONS

21

READS

218

2 authors, including:



[Ravi Nigam](#)

Indian Institute of Technology (ISM) Dhanbad

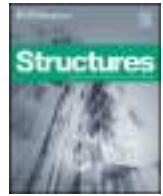
3 PUBLICATIONS 23 CITATIONS

SEE PROFILE

Some of the authors of this publication are also working on these related projects:



Early detection of fatigue crack on a rotor system. [View project](#)



Crack detection in a beam using wavelet transform and photographic measurements

Ravi Nigam, Sachin K. Singh*

Department of Mechanical Engineering, Indian Institute of Technology (ISM) Dhanbad, Dhanbad, Jharkhand, India

ARTICLE INFO

Keywords:

Discrete wavelet transform
Image edge detection
Slope discontinuity
Crack detection

ABSTRACT

An optimistic attempt for the detection of a crack in a beam using discrete wavelet transform is proposed. Finite element model of the simply supported beam with a transverse open crack is considered. Crack in a beam causes a slope discontinuity in the elastic line. The deflection of the beam is used to locate the slope discontinuity using wavelet transform. The effect of measurement noise on the wavelet decomposition level is studied. An inexpensive digital image based technique is employed to obtain the deflection of the cracked beam for experimental investigations. White pixels due to dust particles are removed using connected component algorithm. A suitable edge detection technique is selected for finding the edged image on the basis of peak signal to noise ratio values. The deflection of the non-cracked edge of the beam is used as an input signal for wavelet transform to detect the crack location. Detection of a crack in the beam with different crack depths is investigated experimentally. The proposed method works well with numerically simulated as well as experimentally measured cracked beam deflections.

1. Introduction

Beams are one of the most commonly used elements in several engineering structures, which play a vital role in the structural performance. Fatigue cracks arise in beams due to mechanical vibrations and cyclical loading. A growing crack in structures may lead to its catastrophic failure. Detection of cracks at an early stage increases safety and helps in scheduling corrective maintenance activity. Dimarogonas [1] and Wauer [2] presented the state-of-the-art reviews on detecting cracks using vibration techniques. The Crack detection using modal data based techniques has been used widely [3–6]. These techniques mainly track the changes in natural frequencies and mode shapes.

Formation of a crack in a beam reduces the local stiffness at the crack location and causes slope discontinuity in the beam elastic line [7]. The slope discontinuity is localized, and hence, detection of slope discontinuity reveals the presence of a crack in a beam. Singh and Tiwari [8,9] developed a crack detection and localization algorithm by using shaft deflections at different excitation frequencies. The algorithm was based upon detecting the slope discontinuity due to cracks in a shaft. The algorithm was verified experimentally for simply supported non-rotating shafts with two open cracks [10].

Wavelet transform (WT) is very effective signal processing tool for detecting discontinuity in a noisy signal [11,12]. In literature, wavelet based signal processing techniques are broadly used for the detection of

slope discontinuity in a beam elastic line [13–17]. One of the first applications of WT to detect crack in a beam was presented by Surace and Ruotolo [18]. These wavelet based methods are popular due to their ability to detect meticulous changes in the signal. Chasalevris and Papadopoulos [19] discussed the dynamic behavior of a beam with two transverse surface cracks. Wavelet analysis along with the changes in natural frequencies was used to obtain the positions and size of the cracks. Most of the studies based on WT have been verified on simulated beam responses without their experimental validation. Some of them have been verified experimentally [20,21].

Patsias and Staszewski [22] used a digital camera based optical measurement to identify the damage location in the cracked beam. The mode shape was obtained by analyzing the image sequence of a vibrated cantilever beam (CB). This mode shape was further analyzed using orthogonal WT for damage identification. Crack localization in the CB using continuous wavelet transform was discussed by Rucka and Wilde [23]. Efficiency of both Coiflet and Gaussian wavelets were verified analytically and experimentally. The deflection line of the cracked beam was computed by using commercial finite element software. The wavelet analysis was conducted on the static deflection of the beam. In the experimental part, they have put several illuminating points along the beam length to get the beam deflection using photographic method. The precision of the method depends on the photographic resolution. Coiflet wavelet of order two and Gaussian wavelets

* Corresponding author.

E-mail addresses: ravinigam.16dr000281@mech.ism.ac.in (R. Nigam), sachinks@iitism.ac.in (S.K. Singh).

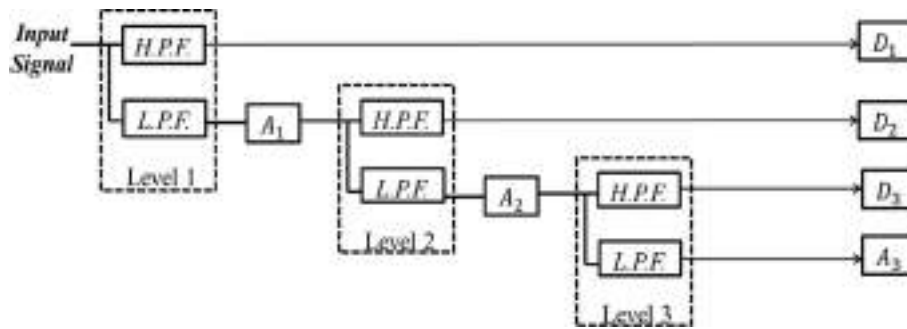


Fig. 1. DWT decomposition tree.



Fig. 2. Discretized model of a beam with an open crack.

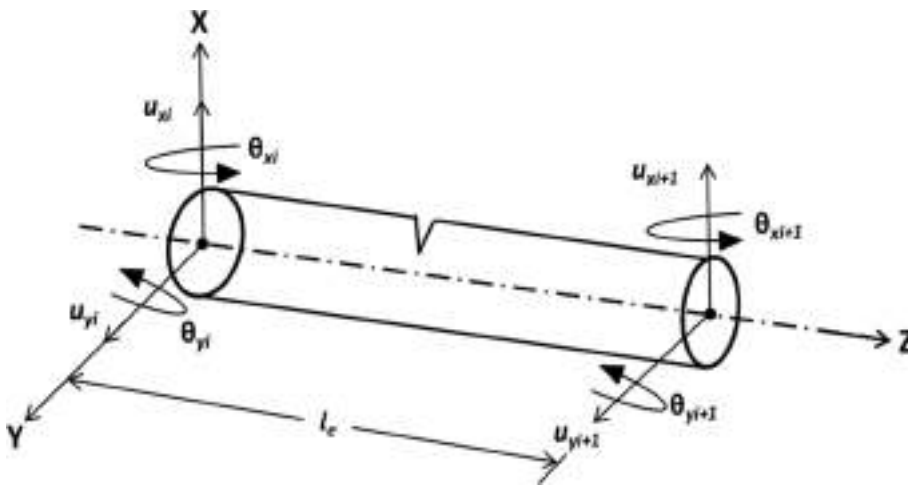


Fig. 3. Cracked beam element with generalized displacement at nodes i and $i + 1$.

Table 1
Material properties and dimensions for numerical simulation.

Parameter	Value
Beam length, L (m)	1
Diameter of the circular beam, h (m)	0.01
Poisson's ratio, ν	0.3
Density, ρ (Kg/m^3)	7800
Young's modulus, E (N/m^2)	2.06×10^{11}
Number of finite elements	4000
Location of cracked element from the left support	2500
Crack depth ratio (α/h)	0.33

of order four were used and found to be effective in determining the crack location.

Pakrashi et al. [24] performed a wavelet and kurtosis based technique on the mode shape of simply supported beam (SSB). In the presence of high measurement noise, this technique detected the crack location for different crack depth ratios. A digital camera based experiment was accomplished on a single cracked SSB to validate the simulation work. A notch was made by sawing into the lower section of the beam to mimic a cracked beam. The image of the deflected cracked

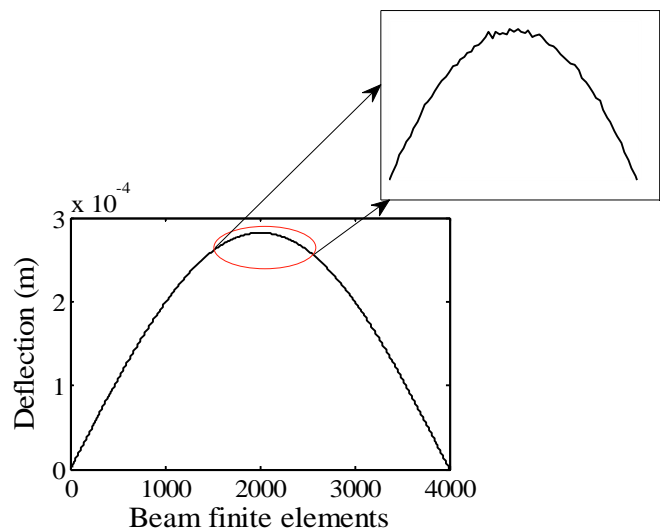


Fig. 4. Response of the cracked beam with noise.

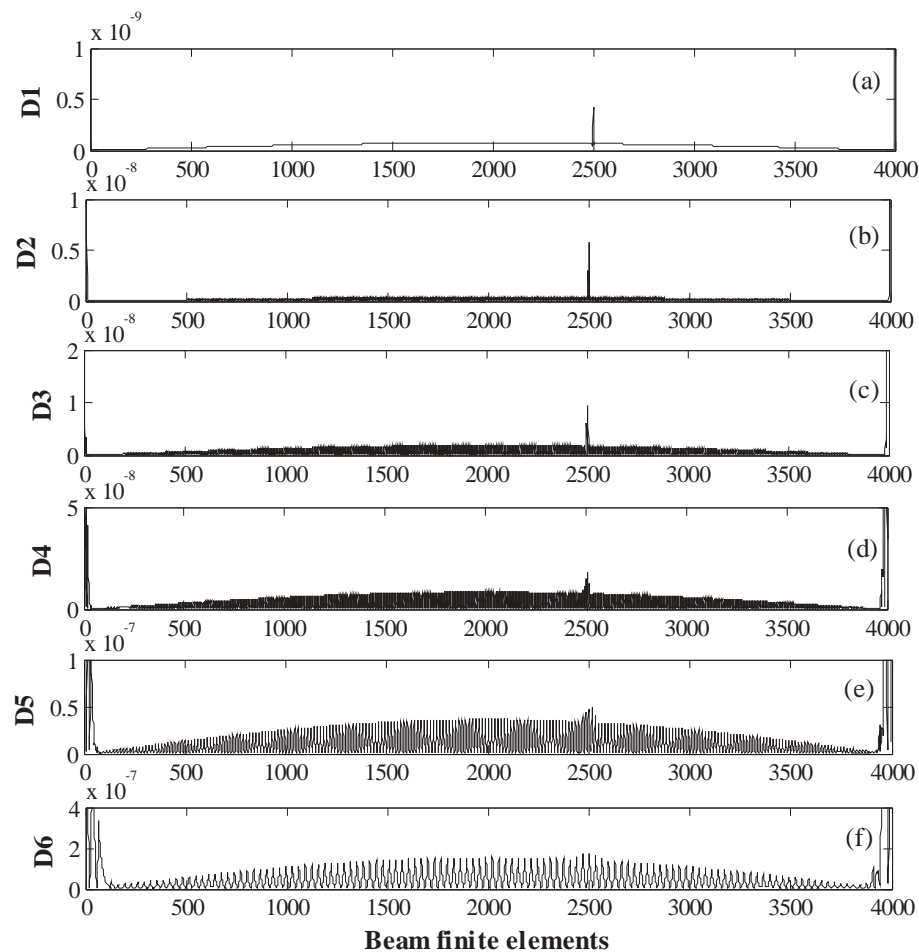


Fig. 5. Wavelet detail coefficients without noise (a) I level; (b) II level; (c) III level; (d) IV level; (e) V level; (f) VI level.

beam was captured using a digital camera and further processed for finding the cracked edge. To locate the crack, the deflection of the cracked edge was used as an input signal for the WT. This obtains the discontinuity in the image. However in a real scenario, the cracks are very fine and may not be visible to camera and hence, detection of discontinuity in the image will not be possible. Hence the crack detection algorithm should be able to identify the discontinuity in beam elastic line. The beam elastic line can be obtained by measuring the deflection of non-cracked edge of the beam.

In the present study, an inexpensive digital camera based experiment is performed. In this experimental work, image processing based edge detection technique (EDT) is used to detect the edges of the deflected cracked CB image. The non-cracked edge is identified from the edge contours of the beam image. This deflected edge is taken as an input signal for further wavelet analysis for identifying the crack location in the beam. This method may also be employed in case of hidden cracks that exist inside the beam. The method would be useful for the damage detection in wind turbine blades, shafts, aircraft wings, and steel bridges. For the simulation part, the finite element model of a SSB and a CB with a single crack is considered. The vertical response of the cracked beam is considered as an input signal for wavelet analysis. To imitate actual experimentation, white Gaussian noise is added in the simulated response.

The present paper is organized as follows: A brief description of the image-edge detection concept and wavelet transformation is given in Section 2. The finite element model of the cracked beam is presented in Section 3. Stiffness of a cracked beam element is also discussed in this section. Simulated response of the cracked beam with noise is presented in Section 4. Also, WT based crack detection results with the effect of

measurement noise on the wavelet decomposition level are presented in this section. Next, experimental verification of the simulation work is presented in Section 5. Moreover, experimentation procedure, removal of white pixels due to dust particles using connected component algorithm, selection of suitable EDT and detailed discussion of experimental results are discussed in this section. Finally, a brief conclusion is presented in Section 6.

2. Theoretical background

A crack in a beam introduces a slope discontinuity in its elastic line during vibration. Detection of a slope discontinuity reveals the presence of a crack in the beam. In the present work, a photographic method is used to get the deflection of a cracked beam. Canny EDT is used for getting the edge of the beam from the beam images. Discrete wavelet transformation (DWT) is used for finding the slope discontinuity from the cracked beam deflection. The concept of Canny edge detection is introduced in Section 2.1. A brief discussion of DWT is presented in Section 2.2.

2.1. Image edge detection

Edge is a location in the image where a sudden change in the intensity of pixels occurs. For the present work, beam deflection is obtained by detecting edge of the image. Mostly, the EDT's are based on the threshold value of intensity gradient as edges have higher pixel intensity values than its surrounding. Different EDT's, such as: Roberts, Canny, Sobel, and Prewitt are used for the edge detection in a digital image [25]. In the present work, the Canny EDT is used for getting the

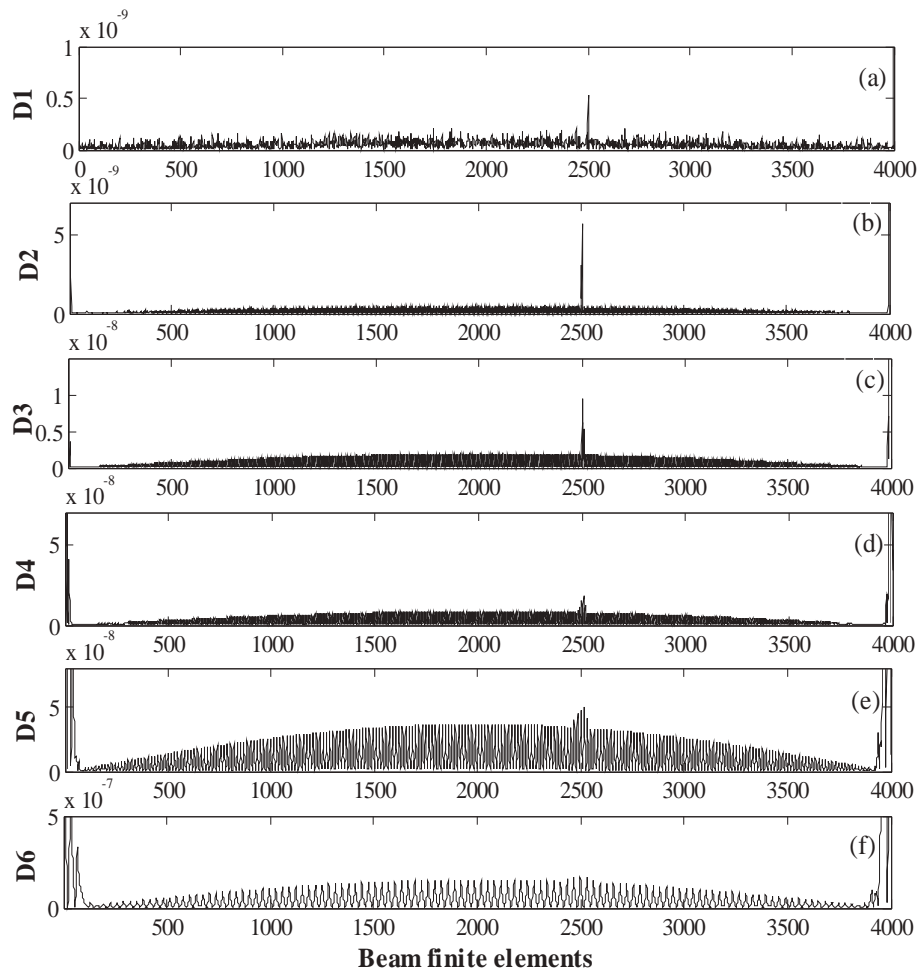


Fig. 6. Wavelet detail coefficients at SNR 120 dB: (a) I level; (b) II level; (c) III level; (d) IV level; (e) V level; (f) VI level.

edge of the beam from the digital image.

2.1.1.1. Canny edge detector

This detector uses a multi-step algorithm for the detection of edges in an image. It consists of the following steps [25]:

2.1.1.1.1. Smoothing of the input image with a Gaussian filter $G(u, v)$. The edge detection results are generally affected by image noise [25]. It is important to filter out the noise to prevent false detection, affected by noise. The effect of noise is reduced by convolving 2D Gaussian kernel $G(u, v)$ with the source image $f(x, y)$, where the Gaussian kernel is denoted by [25]:

$$G(u, v) = \frac{1}{2\pi\sigma^2} e^{-\frac{u^2+v^2}{2\sigma^2}} \tag{1}$$

where u and v are the horizontal and vertical dimensions of the Gaussian kernel. The term σ is the standard deviation (also called space constant) of the Gaussian distribution. The smoothed image $f_s(x, y)$ is obtained by:

$$f_s(x, y) = f(x, y) * G(u, v) \tag{2}$$

Here the asterisk denotes a convolution operation.

2.1.1.1.2. Computing the intensity gradient of the smoothed image. The intensity gradient estimates the strength and direction at every point of the image. It is obtained by filtering with Sobel kernel in both horizontal and vertical directions. It uses a pair of 3×3 kernels. These kernels are basically two dimensional convolution matrices containing

positive and negative coefficients. The size of each kernel is usually much smaller than the source image and values of the kernel coefficients determine the nature of the process [25]. The kernels are given by,

$$M_x = \begin{bmatrix} -1 & -2 & -1 \\ 0 & 0 & 0 \\ +1 & +2 & +1 \end{bmatrix} \quad M_y = \begin{bmatrix} -1 & 0 & +1 \\ -2 & 0 & +2 \\ -1 & 0 & +1 \end{bmatrix}$$

Here M_x and M_y are kernels in the horizontal (x) and vertical (y) directions. Convoluting M_x and M_y with the smoothed image estimates the gradient in (x) and (y) directions, respectively.

$$g_x = M_x * f_s(x, y) \tag{3}$$

$$g_y = M_y * f_s(x, y) \tag{4}$$

Hence, gradient magnitude $|g|$ is defined as:

$$|g| = \sqrt{g_x^2 + g_y^2} \tag{5}$$

The gradient's direction is calculated by using:

$$\alpha(x, y) = \tan^{-1} \frac{g_y}{g_x} \tag{6}$$

2.1.1.1.3. Non maximum suppression and hysteresis. After getting the gradient of the image, non-maximum suppression is used for selecting the best pixel for the edges when there are multiple possibilities in a local neighborhood. It works by finding the pixel with the maximum value in an edge. Hence, only the thin lines remain in the resultant

image. Also, a double thresholding criterion is used for the selection of an edge.

2.2. Discrete wavelet transform (DWT)

The WT of a signal is expressed as: [11]

$$W_{\tau,s}(x) = \frac{1}{\sqrt{s}} \int_{-\infty}^{+\infty} p(x)\psi\left(\frac{x-\tau}{s}\right)dx \tag{7}$$

here, $p(x)$ is the input signal and $\psi\left(\frac{x-\tau}{s}\right)$ is translated and scaled version of the mother wavelet $\psi(x)$. Here $\tau \in \mathbb{R}$ is the translation parameter, $s \in \mathbb{R}^+$ is the scale parameter and the variable x is the location along the spatial domain. The WT is called dyadic WT when the scaling is selected as a power of two. The dyadic WT is interpreted as multilevel decomposition of the signal [11]. This gives a way to the DWT. The DWT of a signal $p(x)$ can be expressed as:

$$\psi_{i,k}(x) = 2^{i/2}\psi(2^i x - k) \tag{8}$$

where $\psi(x)$ is the mother wavelet, k is the translation index and i is the scale index. Scaling is done in the form of 2^i ; $i = 1, 2, 3, \dots, m$; where m is the decomposition level. Translation occurs at integer multiples of $2^i k$; $k = 1, 2, 3, \dots, n$; where n is the number of data points. DWT is equivalent to passing a signal with discrete multi-stage filter banks.

The coefficients obtained after the high pass filter (H.P.F.) and low pass filter (L.P.F.) are called detail coefficients and approximate coefficients, respectively. Fig. 1 shows the flow diagram of DWT up to 3 levels, where A_i and D_i are the approximation and detail coefficients respectively.

3. Mathematical modeling of a cracked beam

The Timoshenko beam theory is used in the modeling of the beam for transverse vibration. In the present study, the finite element method is used to develop the discretized model of a SSB. The beam contains an open transverse surface crack. Discretized model of a SSB is presented in Fig. 2.

Each node of the beam element has two degrees of freedom (DOF) for translation and two DOF for rotation. A cracked beam element and its generalized displacements at the nodes are shown in Fig. 3.

The length of a beam element is l_e . The generalized displacement vector at the i^{th} node is given by,

$$X_i = \begin{bmatrix} u_{xi} \\ u_{yi} \\ \theta_{xi} \\ \theta_{yi} \end{bmatrix} \tag{9}$$

where u_{xi}, u_{yi} are translational DOF along x and y directions and θ_{xi}, θ_{yi} are rotational DOF along x and y directions, respectively. The governing equation of motion, after assembly, is written as:

$$[M]\{\ddot{X}\} + [D]\{\dot{X}\} + [K]\{X\} = \{F\} \tag{10}$$

here, $[M], [D], [K]$ are the assembled mass, damping and stiffness matrices of the beam system, respectively. The term $\{X\}$ is the assembled nodal displacement vector of the beam system. The term $\{F\}$ is the harmonic excitation force, given by,

$$\{F\} = \{F_0\}\sin\omega t \tag{11}$$

Here $\{F_0\}$ is the magnitude of applied force, ‘ ω ’ is the frequency of

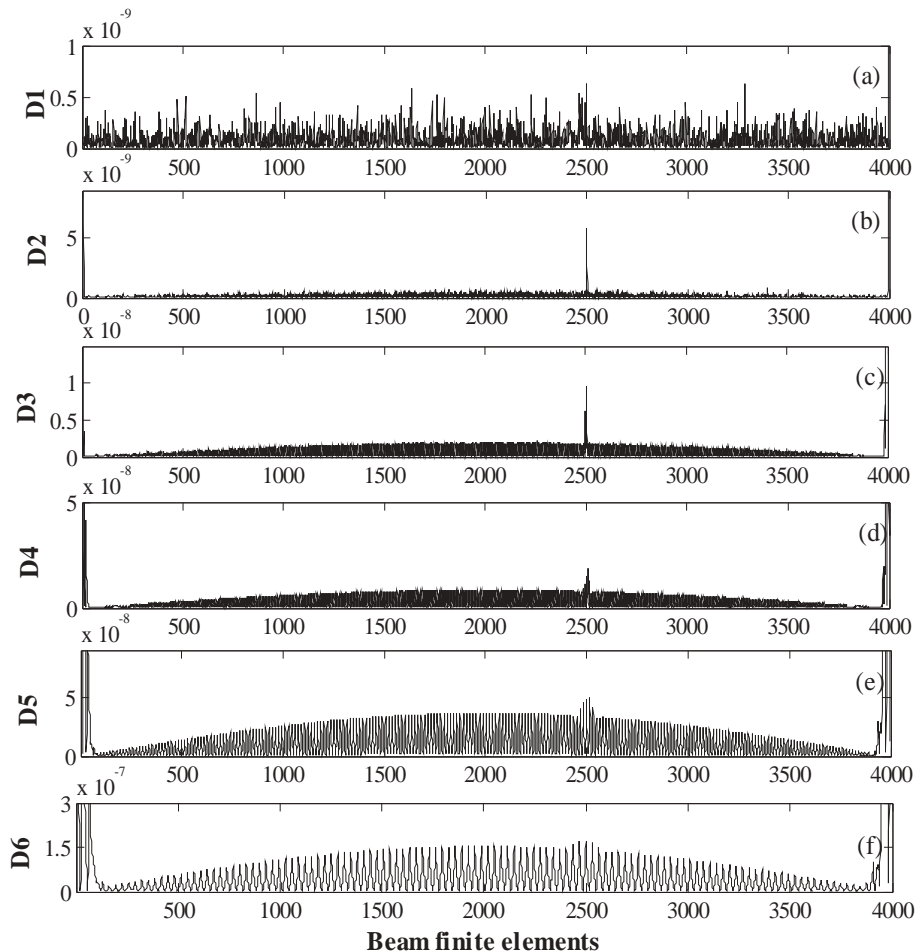


Fig. 7. Wavelet detail coefficients at SNR 110 dB: (a) I level; (b) II level; (c) III level; (d) IV level; (e) V level; (f) VI level.

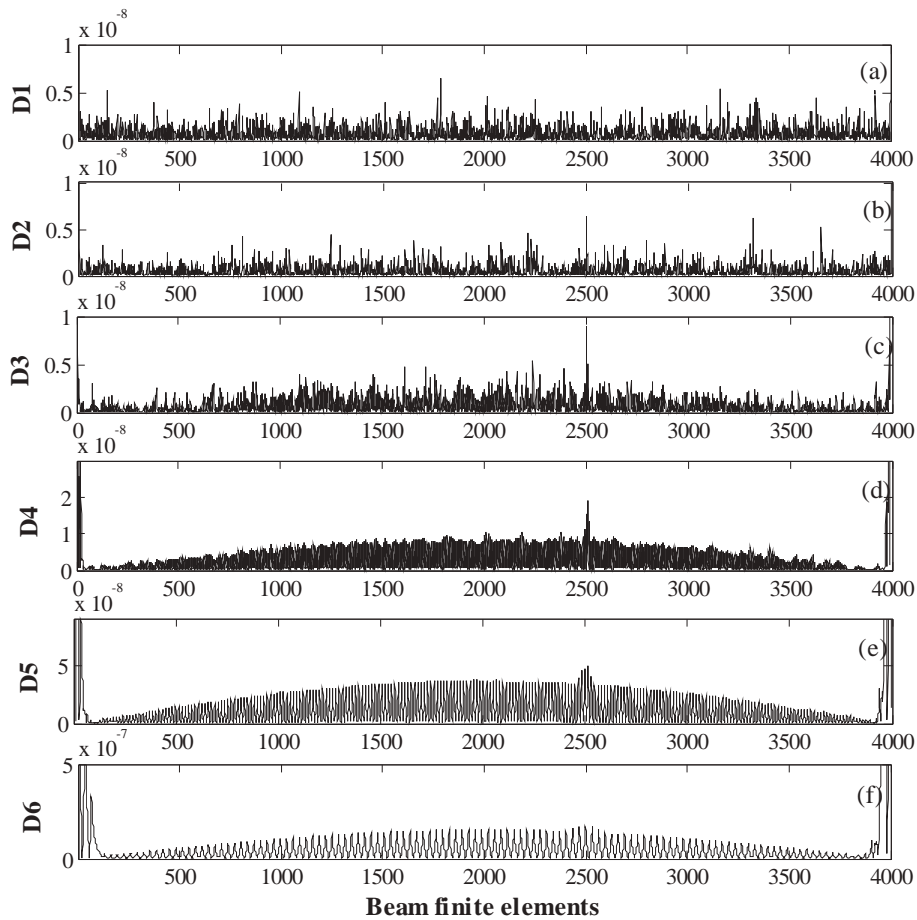


Fig. 8. Wavelet detail coefficients at SNR 90 dB: (a) I level; (b) II level; (c) III level; (d) IV level; (e) V level; (f) VI level.

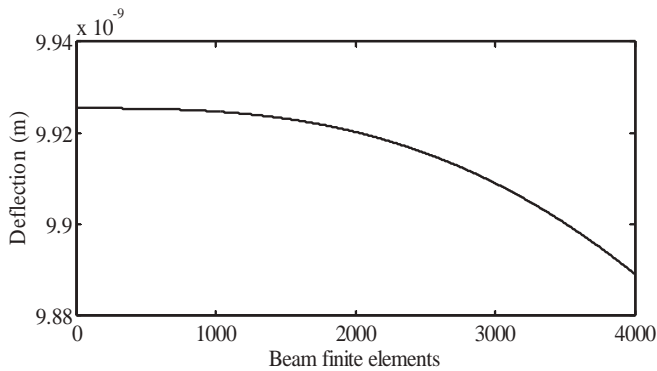


Fig. 9. Response of the cracked CB with noise.

excitation, and 't' is the time.

The damping is considered to be proportional damping [26]. The term [D] can be written as:

$$[D] = a_0[M] + a_1[K] \tag{12}$$

Here the terms a_0 and a_1 are Rayleigh damping factors.

The presence of a crack in a beam element introduces additional flexibility. The total flexibility matrix of the cracked element is given as,

$$[C] = [C_0] + [C_c] \tag{13}$$

The term $[C_0]$ is the flexibility matrix of the beam element without a crack. The term $[C_c]$ is the additional flexibility in the beam element due to a crack, can be expressed as,

$$[C_c] = \begin{bmatrix} C_{22} & 0 & 0 & 0 \\ 0 & C_{33} & 0 & 0 \\ 0 & 0 & C_{44} & C_{45} \\ 0 & 0 & C_{54} & C_{55} \end{bmatrix}$$

where $[C_{22}]$, $[C_{33}]$, $[C_{44}]$, $[C_{55}]$, are the direct and $[C_{45}]$, $[C_{54}]$ are the cross-coupled flexibility coefficients. The stiffness of the cracked element of the beam is given as [27]

$$[K_c]^e = [T][C]^{-1}[T]^T \tag{14}$$

where [T] is a transformation matrix, expressed as:

$$[T] = \begin{bmatrix} -1 & 0 & 0 & 0 \\ 0 & -1 & 0 & 0 \\ 0 & l_e & -1 & 0 \\ -l_e & 0 & 0 & -1 \\ 1 & 0 & 0 & 0 \\ 0 & 1 & 0 & 0 \\ 0 & 0 & 1 & 0 \\ 0 & 0 & 0 & 1 \end{bmatrix}$$

Now, the governing equation of motion of the beam system can be written as:

$$[M]\{\ddot{X}\} + [D_c]\{\dot{X}\} + [K_c]\{X\} = \{F\} \tag{15}$$

The term $[D_c]$ is the assembled damping matrix and $[K_c]$ is the assembled damping matrix of the cracked beam system.

4. Numerical simulation results

A SSB with a transverse open crack is considered. External forcing in vertical direction is considered to excite the beam. Responses of the

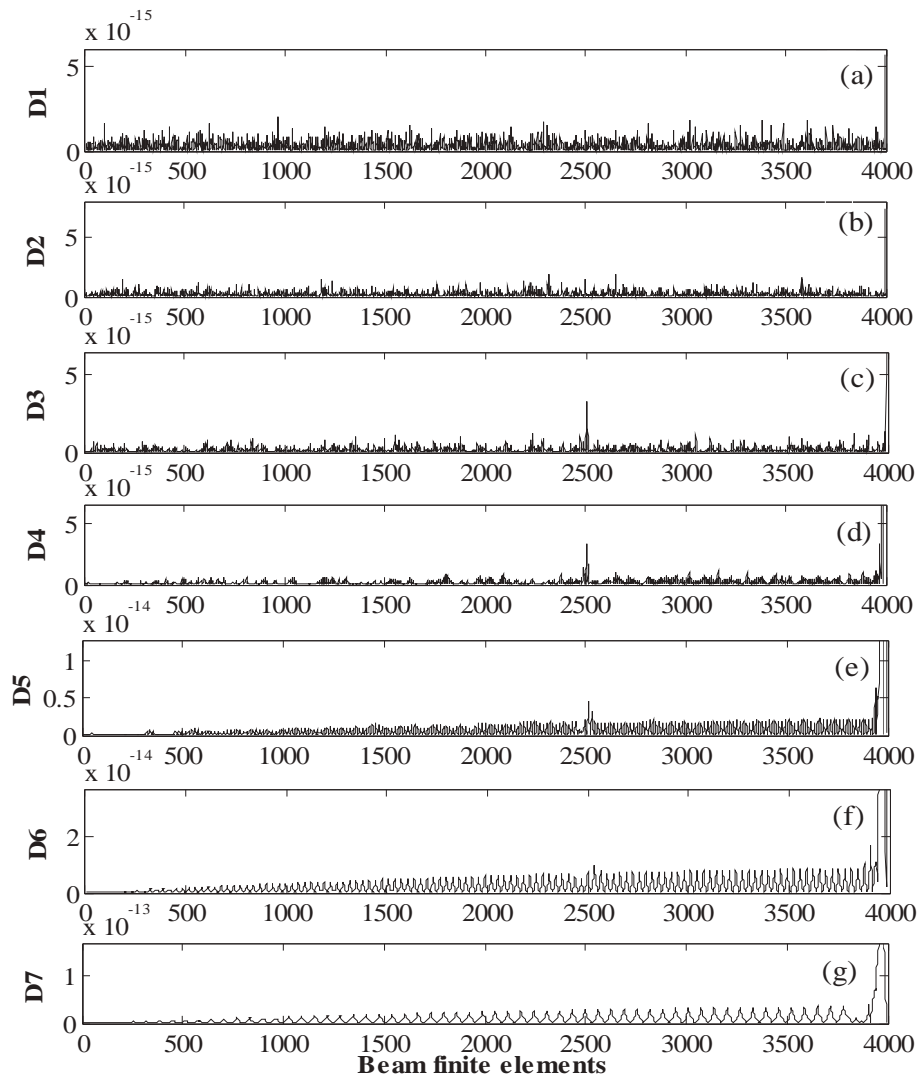


Fig. 10. Wavelet detail coefficients (for CB) at 80 SNR (a) I level; (b) II level; (c) III level; (d) IV level; (e) V level; (f) VI level; (g) VII level.

Table 2
Physical parameters of the cracked beam for the experiment.

Parameter	Case-1	Case-2	Case-3
Length of beam, L (m)	1	1	1
Width of beam, w (m)	0.05	0.05	0.05
Thickness of beam, t (m)	0.006	0.006	0.006
Depth of crack, α (m)	0.004	0.003	0.002
Location of crack from the left end (m)	0.58	0.58	0.58
Pixel location of a crack from the left end of the beam image (pixel number)	2499	2691	2371

intact and cracked beams are generated using Eq. (10) and Eq. (15), respectively. Vertical deflection response is used for the wavelet analysis. White Gaussian noise is added to the simulated response to represent the measurement noise. The noise level (SNR) is kept at 90 dB. The material properties and the dimensions for the simulation are given in Table 1. For simplicity, the simulation study is based on the first mode of the cracked beam. Therefore, the cracked beam is excited near the first natural frequency. Response of the cracked beam is plotted in Fig. 4. This cracked beam response is taken as an input signal for further wavelet analysis.

4.1. Wavelet based crack detection

DWT with Coiflet wavelet of order one is applied on the simulated responses of the cracked beam to reveal the existence of the crack in the beam. The wavelet detail coefficients for the simulated response, without measurement noise, are shown in Fig. 5. Next, the algorithm is tested at different SNR to observe the effect of measurement noise. The wavelet detail coefficients at SNR 120 dB, 110 dB and 90 dB are shown in the Figs. 6–8, respectively.

Fig. 6 shows the first six levels of wavelet detail coefficients at SNR 120 dB. A clear and dominant spike at the crack position is seen in the first three levels of decomposition. The effect of slope discontinuity diminishes in the subsequent decomposition levels. The first six levels of wavelet detail coefficients at SNR 110 dB are shown in Fig. 7. The first clear dominant peak at the crack location is observed at II decomposition level. With increase in noise, at SNR of 90 dB, the first clear dominant peak at crack location shifts to III level of decomposition as shown in Fig. 8. The larger values of detailed coefficients at the two ends are due to the boundary effect of WT.

The input signal for DWT, i.e., the beam deflection, has the information of slope discontinuity at the crack location. However, the signal is contaminated with measurement noise. The slope discontinuity due to the crack is composed of a wide range of frequency components. Without measurement noise in the signal, the slope discontinuity is

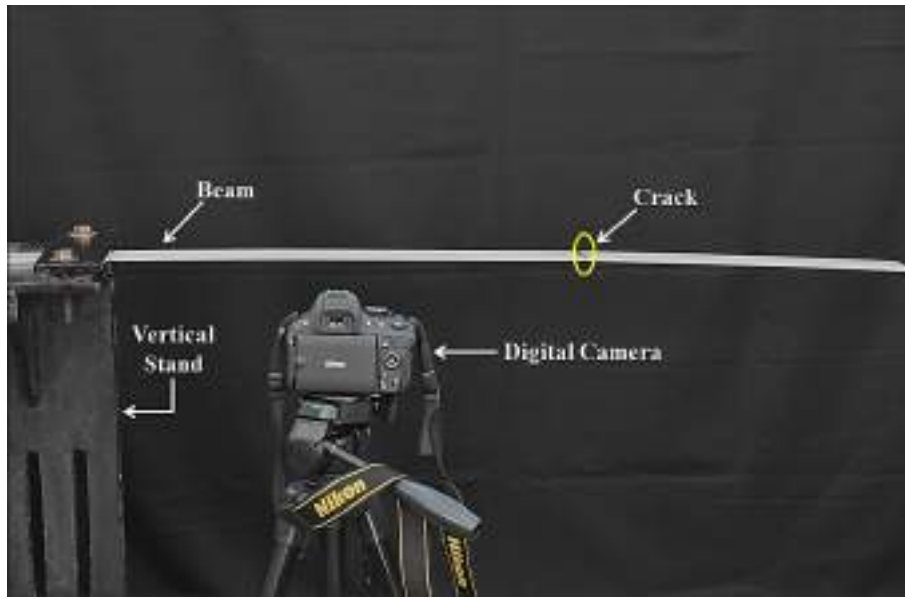


Fig. 11. Experimental set-up of cracked beam.

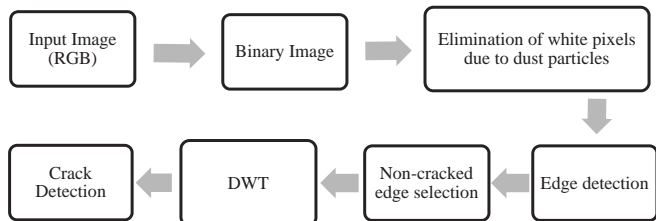


Fig. 12. Steps of the experimental procedure.

observable in first few decomposition levels, as shown in Fig. 5. When the input signal is contaminated with measurement noise, the initial levels of decomposition will be affected more by the measurement noise. Considering the measurement noise to be mainly consisting of high frequency components, the effect of noise will reduce with an increase in the decomposition level. Hence, with the higher noise of SNR 90 dB, the slope discontinuity is not observable at initial decomposition levels, shown in Fig. 8. As the effect of noise reduces with

increase in decomposition level, a clear peak is observed at D3 level, as shown in Fig. 8(c). However, localisation deteriorates at higher decomposition levels due to low frequency content at higher decomposition levels.

The algorithm is verified with CB also. The input signal of wavelet analysis is shown in Fig. 9. The material properties and the dimensions for the simulation are given in Table 1.

The first seven levels of wavelet detail coefficients at SNR 80 dB are shown in Fig. 10. A clear and dominant spike at the crack location is seen from III to V decomposition level. The effect of slope discontinuity diminishes in the subsequent decomposition levels.

5. Experimental validation

In order to validate the simulation work, a digital camera based experiment is performed. The experiment is carried out on three CB's with different crack depths, as shown in Table 2.

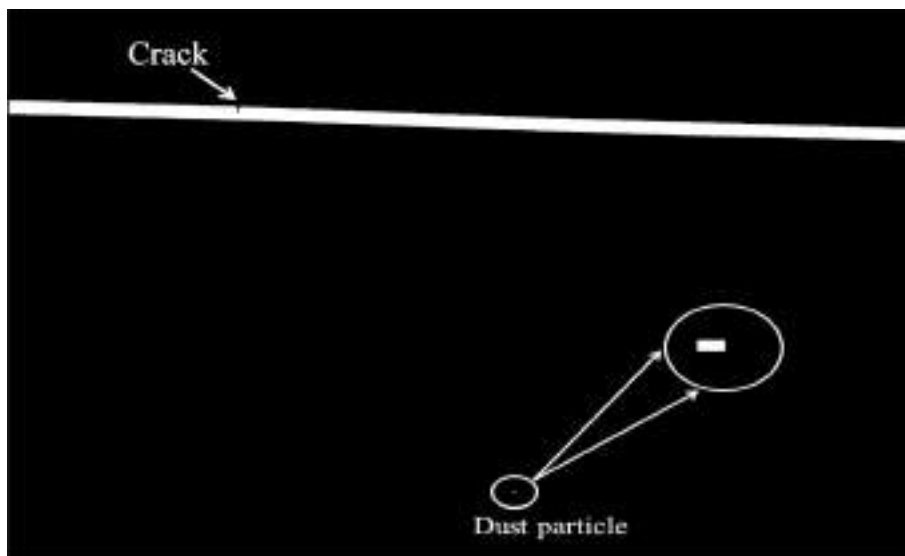


Fig. 13. Binary image of a portion of the beam with dust particle.

Table 3
PSNR values computed for EDT's.

EDT	PSNR value (dB)		
	(Case-1)	(Case-2)	(Case-3)
Roberts	23.14	23.06	23.04
Sobel	18.08	17.97	17.88
Canny	5.96	6.02	5.95
Prewitt	18.33	18.20	18.04

5.1. Experimental set-up

The arrangement of the set-up consists of a CB, vertical stand and a black fabric background, is shown in the Fig. 11. The material properties of the beam are taken as: Poisson's ratio $\nu = 0.3$, Young's modulus $E = 206$ GPa and Density $\rho = 7800$ Kg/m³. An open crack is created by machining a notch into the upper section of the beam. The width of the notch is 2 mm. The surface representing beam's thickness is polished by sand paper to reduce noises in the image.

5.2. Experimental procedure

Free end of the CB is given initial displacement to obtain free vibration of the beam. Deflected shape of the cracked beam is captured by Nikon D-5100 digital camera. Size of the captured image is

4928 × 3264 pixels. Out of all the captured images, only the clear and sharp images with beam deflection closer to the maximum beam deflection position are considered for further analysis. Steps of the experimental procedure are shown in Fig. 12.

The digital picture is saved as JPEG image in RGB color space and subsequently converted into binary image. Any binary image contains only two values 0 and 1, where 0 and 1 refers to black and white color pixel, respectively. The binary image is shown in Fig. 13. The image contains dust particle also. One such dust particle is shown in zoomed view in Fig. 13.

Dust particles in the source image are present as white pixels in the binary image. Presence of these white pixels will distort the beam deflection. Hence, connected component algorithm is used to remove the white pixels due to dust particles. The connected component algorithm is discussed in Section 5.2.1.

5.2.1. Removal of white pixels due to dust particles using connected component

Effect of dust particles in the captured image is eliminated by using connected component analysis [28]. In the present work, 8-neighbourhood component analysis is performed to identify the number of connected components, present as noise (white pixels) in the image. Next, it estimates the number of pixels in each connected component. The identified connected components are replaced with black pixels if number of pixels in each connected component is less than a predefined

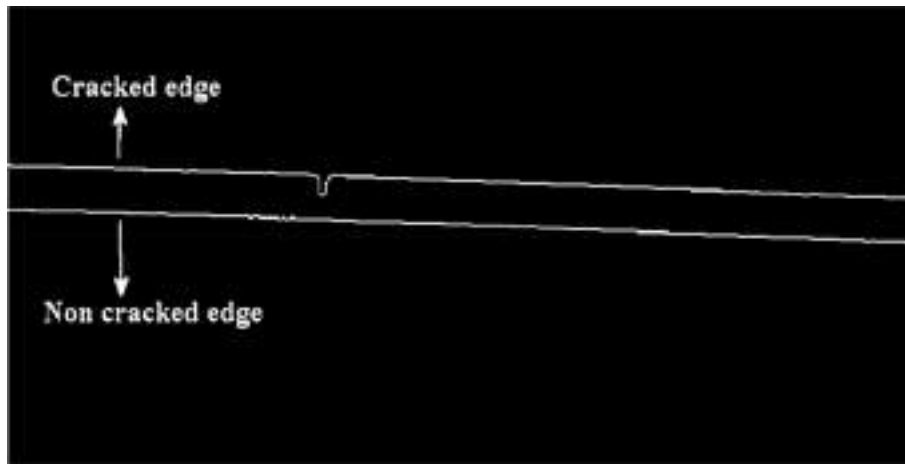


Fig. 14. Edge contours of a cracked beam image.

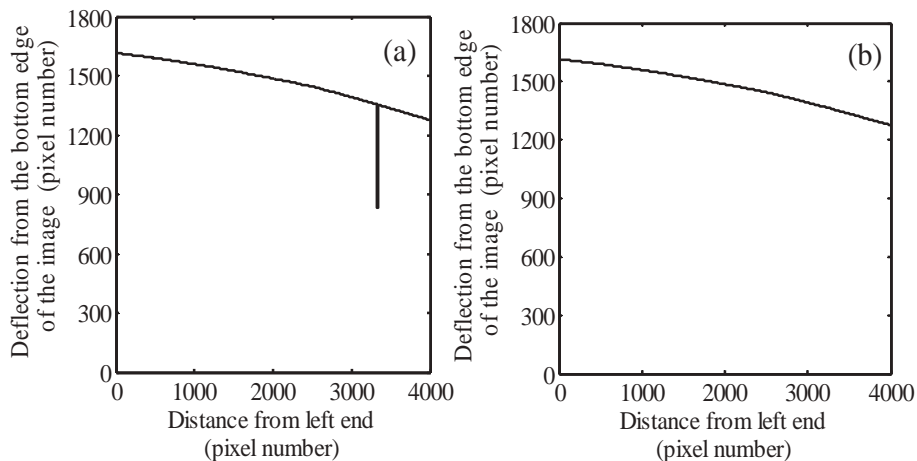


Fig. 15. Experimentally measured beam deflection (non-cracked edge): (a) without using connected component algorithm; (b) with using connected component algorithm.

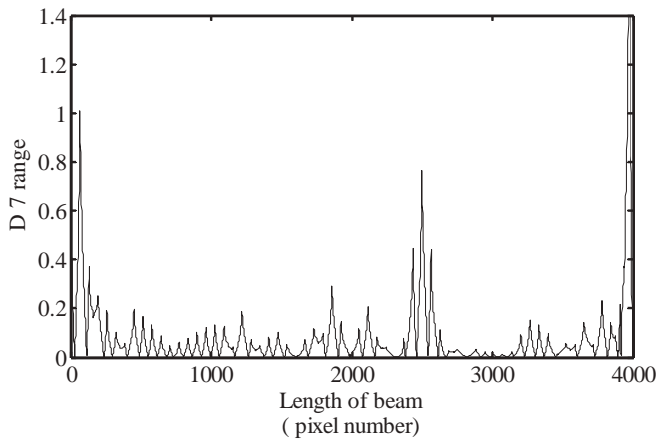


Fig. 16. Wavelet detail coefficients for a crack of 4 mm depth.

threshold value. Sizes of dust particles are small and hence the number of connected white pixels due to the dust particles is less. For the present work, the threshold value of the connected component is taken to be 500 pixels.

5.2.2. Selection of suitable EDT

Several EDT’s, such as: Roberts, Sobel, Canny, and Prewitt are used for the edge detection in a digital image [23]. It is important to select suitable EDT for finding edges of the deflected beam image. For the present experimental analysis, the selection of suitable EDT is based on the peak signal to noise ratio (PSNR) values. PSNR is described as [29],

$$PSNR = 10 \log_{10} \left(\frac{R^2}{MSE} \right) \tag{16}$$

where R represents the maximum possible pixel value of the input image. MSE is the cumulative squared error between the noisy and noise-free edged image. The higher difference between the noisy and noise-free edge detected image gives the higher value of MSE . So a better EDT should have lower PSNR value. MSE can be calculated as,

$$MSE = \frac{1}{A \times B} \sum_{a=1}^A \sum_{b=1}^B \{f_1(b, a) - f_2(b, a)\}^2 \tag{17}$$

where $f_1(b, a)$ and $f_2(b, a)$ are the noise-free edge detected image and noisy edge detected image, respectively. A and B are the numbers of rows and columns of the input image, respectively.

For a noisy image, the zero mean Gaussian white noise with

Table 4
Physical parameters of the crack near fixed end.

Parameter	(Case-4)	(Case-5)
Depth of crack, α (m)	0.002	0.004
Location of crack from the left end (m)	0.15	0.15
Pixel location of crack from the left end of the beam image (pixel number)	451	387

variance of 0.01 is added to the original image. The PSNR values for the edge detected images corresponding to the three images (case 1, 2 and 3 of Table 2) are given in Table 3. PSNR values from the four EDT, Roberts, Sobel, Canny, and Prewitt are presented.

It can be observed from Table 3 that the Canny EDT has the least PSNR value among the four tested EDT’s. It should be noted that PSNR value should be low for effective edge detection in an image [30]. Hence, in the present work, Canny EDT is used for finding edged image from the cracked beam images. The edged image corresponding to the image in Fig. 13 is shown in Fig. 14. Here, a notch is machined in the upper edge of the cantilever beam and that edge is referred to as the cracked edge. There is no crack in the lower edge, and hence the lower edge is referred to as the non-cracked edge.

The lower side of the edged image represents the non-cracked edge. Beam deflection is obtained by detecting the lower edge of the beam from the edged image. The white pixel index from the bottom of the edged image gives the beam deflection.

The beam deflection, with and without using the connected component algorithm, is shown in Fig. 15.

The beam deflection without using the connected component algorithm is distorted. This distortion is due to the presence of dust particles which are present as white pixels in the binary image. Use of connected component algorithm removes the white pixels due to the dust particles and gives a distortion-less beam deflection.

The images of the CB with different crack depths are captured in different lighting conditions in the room. For all the cases of different crack depths in the beam, the crack is located at the same location from the fixed end. However, the location of a crack in the CB image for different cases is different due to change in position and angle of the camera.

5.3. Experimental results and analysis

The non-cracked edge of the beam is used to get the beam deflection using image edge detection. The first 4000 pixels from left end of the detected edge are considered for wavelet analysis. The beam deflection

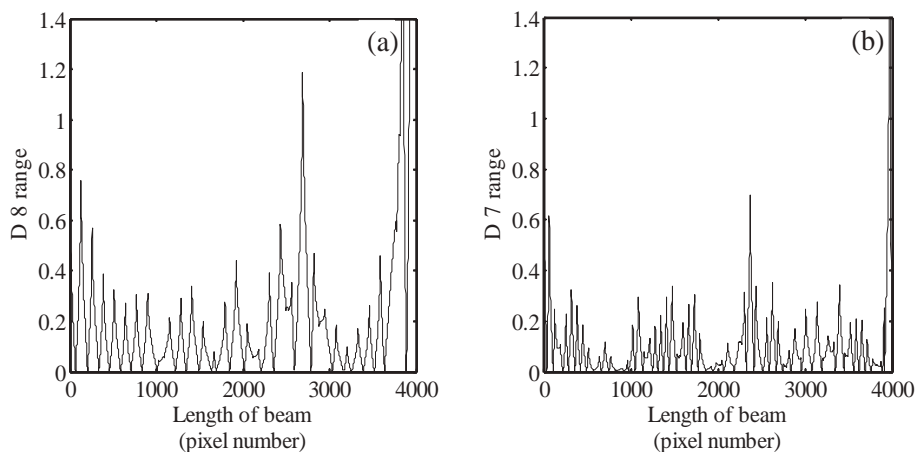


Fig. 17. Wavelet detail coefficients for a crack of depth: (a) 3 mm; (b) 2 mm.

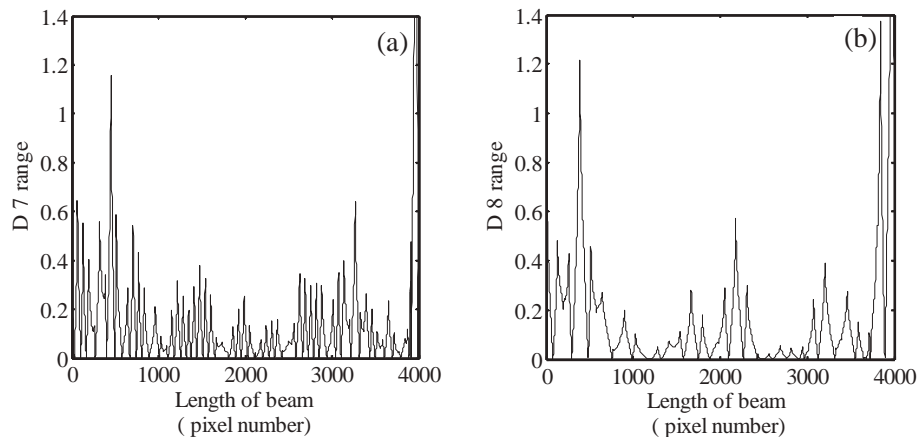


Fig. 18. Wavelet detail coefficients for a crack near fixed end of depth: (a) 2 mm; (b) 4 mm.

shown in Fig. 15(b), with a 4 mm crack depth (case 2 of Table 2), is analyzed up to twelve levels of wavelet decomposition, and the seventh level decomposed signal (D7) is identifying the crack location, as shown in Fig. 16. For experiment with 3 mm crack depth (case 2 of Table 2), the eighth level of decomposition (Fig. 17(a)) shows a dominant spike at the crack location. In case of 2 mm depth of crack (case 3 of Table 2), the seventh level (D7) of decomposition clearly shows the crack location in Fig. 17(b). In contrast to the simulation results (Figs. 6–8), in all the three experimental cases, a dominant peak at the crack is observed only at a single decomposition level. This could be due to the presence of a different kind of noise in the real experiments as compared to the noise model used in simulations. In simulations, Gaussian noise was considered to model the measurement noise. A dominant peak in the detail coefficients is observed in the close vicinity of crack location along the beam length. Also, dominance of the peak near the crack location increases with crack depth. It is found that Coiflet wavelet of order 1 (coif1) works better in detecting the crack location compared to the other studied wavelets, such as Coiflet of order 2 (coif2) and 4 (coif4), Symlet of order 4 (sym4) and 5 (sym5), and Daubechies of order 2 (db2) and 4 (db4) etc. The compact support of coif1 leads to higher peaks at the crack location [31].

Additionally to extend the experimental results, the algorithm is applied when the crack is located near the fixed end of CB. Physical parameters of the crack are given in Table 4. The detail coefficients for both the cases are shown in Fig. 18. Hence, the present algorithm works well for crack near the fixed ends also. It is observed that the border distortion zone covers approximately 380 pixels at the free end (right side) for case 2 of Table 2, which is maximum among the different cases studied. It is approximately 10% of the full signal. Since the length of the beam is 1 m, therefore the crack can be located between 0.10 m and 0.9 m from the fixed end without being affected by the boundary effects. The border distortion will also depend on the measurement resolution. More data points per unit length will be available at higher measurement resolution. Hence, it is expected that the border distortion zone will shrink at higher measurement resolution.

There would be some challenges while applying the algorithm in real world environment. Some of the probable challenges are unfavourable background colour, non-uniform background, dusty environment, non-smooth surface, and poor lighting conditions. The colour intensity of the foreground object should be different from the colour intensity of the background for proper edge detection. An unfavourable background colour along with non-uniform background is expected to degrade the edge detection step of the algorithm. The efficiency of the proposed algorithm is expected to reduce in case of more dust particles in the image. The tunable parameter, i.e., the threshold value, in the connected component analysis can be adjusted to minimise the effect of dust particles. Case specific modifications in edge detection

techniques are recommended for situations, such as unfavourable background colour and poor lighting conditions.

6. Conclusions

A wavelet based crack detection method is presented to find the crack location in the beam. Effect of measurement noise on the crack detection is studied with simulated cracked beam responses. With high measurement noise, the slope discontinuity is detected at higher wavelet decomposition levels as the initial levels are corrupted by measurement noise.

A low-cost digital image based experiment is accomplished to validate the proposed methodology. The effect of dust particles in the captured image is eliminated by using connected component algorithm, which helps in getting a distortion-less input signal for the WT. The beam deflections from the beam image are obtained by using EDT. A suitable EDT is selected on the basis of PSNR values, and the Canny operator is found to be the most suitable among the tested techniques. The present algorithm is suitable of finding the crack location from the deflection of non-cracked edge of the beam.

Numerical simulation and experimental results show that the proposed method is suitable and effective for detecting the crack location correctly. Poor edge detection due to adverse conditions, such as unfavorable background colour, and poor lighting conditions may reduce the efficiency of the proposed algorithm. Future work can be done by modifying the edge detection technique to improve the working of the algorithm under such adverse conditions. Further, this algorithm may be tested for minimum crack depth that it can identify.

Funding

The authors are grateful for the financial support provided by the Department of Science and Technology (DST), India under sanction order number “YSS/2015/001555”.

Declaration of Competing Interest

The authors declare that they have no known competing financial interests or personal relationships that could have appeared to influence the work reported in this paper.

Appendix A. Supplementary data

Supplementary data to this article can be found online at <https://doi.org/10.1016/j.istruc.2020.03.010>.

References

- [1] Dimarogonas AD. Vibration of cracked structures: a state of the art review. *Eng Fract Mech* 1996;55:831–57.
- [2] Wauer J. On the dynamics of cracked rotors: a literature survey. *Appl Mech* 1990;43:13–7.
- [3] Kam TY, Lee TY. Detection of crack in structures using modal test data. *Eng Fract Mech* 1997;42:381–7.
- [4] Armon D, Ben-Hain Y, Barun S. Crack detection in beams by rank-ordering of eigen-frequency shifts. *Mech Syst Signal Process* 1991;24:153–8.
- [5] Ismail F, Ibrahim A, Martin HR. Identification of fatigue cracks from vibration testing. *J Sound Vib* 1990;140:305–17.
- [6] Cawley P, Adams RD. The location of defects in structures from measurements of natural frequencies. *J Strain Anal Eng Des* 1979;14:49–57.
- [7] Aboudi J. Stiffness reduction of cracked solids. *Eng Fract Mech* 1987;5:637–50.
- [8] Singh SK, Tiwari R. Identification of multiple cracks in a shaft system using transverse frequency response function. *Mech Mach Theory* 2010;45:1813–27.
- [9] Singh SK, Tiwari R. Detection and localization of multiple cracks in a stepped shaft. *Fatigue Fract Eng Mater Struct* 2012;36:85–91.
- [10] Singh SK, Tiwari R. Detection and localisation of multiple cracks in a shaft system: an experimental investigation. *Meas J Int Meas Confed* 2014;53:182–93.
- [11] Mallat SG. A wavelet tour on signal processing. New York: Academic Press; 2009.
- [12] Ten Daubechies I. Lectures on wavelets. Pennsylvania: Society Ind Appl Math; 1992.
- [13] Quek ST, Wang Q, Zhang L, Ang KK. Sensitivity analysis of crack detection in beams by wavelet technique. *Int J Mech Sci* 2001;43:2899–910.
- [14] Zhu XQ, Law SS. Wavelet-based crack identification of bridge beam from operational deflection time history. *Int J Solids Struct* 2006;43:2299–317.
- [15] Wang Q, Deng X. Damage detection with spatial wavelets. *Int J Solids Struct* 1999;36:3443–68.
- [16] Rucka M. Damage detection in beams using wavelet transform on higher vibration modes. *J Theor Appl Mech* 2011;49:399–417.
- [17] Gentile A, Messina A. On the continuous wavelet transforms applied to discrete vibrational data for detecting open cracks in damaged beams. *Int J Solids Struct* 2003;40:295–315.
- [18] Surace C, Ruotolo R. Crack detection of a beam using the wavelet transforms. *Proc 12th Int Modal Anal Conf* 1994:1141–7.
- [19] Chasalevris AC, Papadopoulos CA. Identification of multiple cracks in beams under bending. *Mech Syst Signal Process* 2006;20:1631–73.
- [20] Zhong S, Oyardiji SO. Detection of cracks in simply-supported beams by continuous wavelet transform of reconstructed modal data. *Comput Struct* 2011;89:127–48.
- [21] Wu N, Wang Q. Experimental studies on damage detection of beam structures with wavelet transform. *Int J Eng Sci* 2011;49:253–61.
- [22] Patsias S, Staszewskiy WJ. Damage detection using optical measurements and wavelets. *Struct Heal Monit* 2002;1:5–22.
- [23] Rucka M, Wilde K. Crack identification using wavelets on experimental static deflection profiles. *Eng Struct* 2006;28:279–88.
- [24] Pakrashi V, Basu B, Connor AO. Structural damage detection and calibration using a wavelet kurtosis technique. *Eng Struct* 2007;29:2097–108.
- [25] Gonzalez RC, Woods RE. *Digital Image Processing*. Pearson Education; 2018.
- [26] Andres S, L. Notes 08 Modal analysis of MDOF systems with proportional damping; 2008:1–10.
- [27] Sekhar AS, Prabhu BS. Transient analysis of a cracked rotor passing through the critical speed. *J Sound Vib* 1994;173:415–21.
- [28] Pramanik R, Bag S. Shape decomposition-based handwritten compound character recognition for Bangla OCR. *J Vis Commun Image Represent* 2018;50:123–34.
- [29] Najafipour A, Babae A, Shahrtash SM. Comparing the trustworthiness of signal-to-noise ratio and peak signal-to-noise ratio in processing noisy partial discharge signals. *IET Sci Meas Technol* 2013;7:112–8.
- [30] Poobathy D, Chezian RM. Edge detection operators: peak signal to noise ratio based comparison. *Int J Image, Graph Signal Process* 2014;10:55–61.
- [31] Wei D, Bovik AC. Generalized Coifflets with nonzero-centered vanishing moments. *IEEE Trans Circuits Syst II* 1998(45):988–1001.

BIOLOGICAL METHODS OF WATER PURIFICATION

Dairy Effluent Biodegradation by Endogenous Fungal Isolates in the Integrated Wastewater Treatment System

Ravish Singh Rajput^{a, *, **}, Manish Singh^b, and Sanjay Kumar Singh^c

^a Government Engineering College, Kannauj, 209732 India

^b Department of Biotechnology, Dr. Ambedkar Institute of Technology for Handicapped, Kanpur, 208024 India

^c Institute of Engineering and Technology, Lucknow, 226021 India

*e-mail: ravishrajput@reck.ac.in

**e-mail: ravishrajput@gmail.com

Received October 27, 2020; revised December 26, 2020; accepted March 24, 2021

Abstract—The dairy industry is the fastest growing industry in the world. Discharged water is more easily contaminated with high levels of organic substances, pollutants and microbes. Consuming raw milk effluents can cause disease transmission to living beings and can be harmful to the environment. The present investigation was carried out for the characterization and its biodegradation process of dairy effluents using locally selected isolated fungi. For the biodegradation process, three species of fungi such as ASP, ALT, FUS were isolated and identified from dairy wastewater using the CFU method. During the monsoon, the dairy farm (CMP) collected the seasonal milk effluent. Aeration followed by filtration for degradation was performed. During the research some physicochemical parameters such as pH, BOD, COD, TDS, TSS, TKN, etc., were analyzed. Effluents from milk processing and ASP fungal isolate have been found to have a high capacity to break down organic matter. The BOD₅ and COD value of the crude effluent improved by 87.75 and 81.02%, respectively, after 5 days. Biodegradation with fungal isolates can be a perfect method for treating dairy wastewater. This treatment technique can be used for industrial purposes, starting from selected fungal isolates, *Aspergillus* was more vital than *Alternaria* and *Fusarium* species for the biodegradation of organic content in dairy effluents. After studying all the aspects considered, aeration followed by filtration was extremely effective in reaching the most notable level of contamination present in wastewater. The possible reason could be related to the high adsorption capacity of activated carbon and assimilation by sawdust. Activated coal and sawdust can remove an assortment of organic matter from contaminated water. At long last, biodegradation of dairy wastewater by chosen fungal isolates is viable treatment technology, particularly on account of using locally isolated fungal strains.

Keywords: dairy effluent, biodegradation, fungal isolates, physiochemical parameters

DOI: 10.3103/S1063455X22010076

INTRODUCTION

In the dairy industry with the help of various processes such as cooling, pasteurization and homogenization, raw milk is transformed into different products such as market milk, butter, cheese, yogurt, condensed milk, powdered milk (milk powder) and ice cream. The dairy industry is sensitive to water and requires a large volume of water for various operations such as heating, cooling, cleaning, etc. [1]. In milk processing, a large effluent discharge volume of 3 L per liter of milk has been reported [2–4]. This effluent was highly polluted with organic and inorganic content with the unacceptable value of BOD [5], COD, high concentration of dissolved and suspended solids such as FOG (fat, oil, fat) and fungal nutrients such as ammonia, minerals, phosphates and nitrates [6]. These nutrients produce unwanted toxic chemicals in high concentrations. Many isolates of heterotrophic bacteria and fungi have been reported to have been influential discharges. Fungi isolates are capable of degrading compounds that include fats, oils, and proteins. Maximum decomposition occurs when nitrogen, phosphorous, and other essential inorganic nutrients are present in the wastewater [7]. Fungi isolates also provide food for many organisms [8]. Microbes combine with the oxygen in the water to generate multiple energy, this oxygen is also essential for flora and fauna in the aquatic environment. In the 2010 Gaddet study, steroidal estrogens were also found in high concentrations in effluent from untreated dairy farms [9]. The consumption of contaminated dairy effluents can cause the transmission of diseases to living beings and the death of aquatic life [10]. Increased

industrialization without proper control of effluents containing toxic chemicals has led to serious environmental pollution [11]. Taking into account the importance of fungi in the removal of organic pollutants, the three most abundant fungal isolates were selected, such as *Aspergillus* sp. (ASP), *Alternaria* sp. (ALT), and *Fusarium* sp. (FUS). During the last decade, numerous researchers have also defined the process and applications of biodegradation of dairy effluents using microbes, where fungi seem to reveal a better degradation rate of organic matter [12]. The fungal cell and its enzymes play an important role in the biodegradation of organic compounds [13]. In the present work, our objective is to examine the efficiency of selected fungal isolates in the monsoon season (July 2020) to treat wastewater from the dairy industry under aerobic and anaerobic conditions. After the study, it was found that the degradation of dairy effluents by fungal isolates can be a very economical and efficient technique for the removal of the organic pollutant from wastewater CMP.

EXPERIMENTAL

Sample Collection

Samples were collected from Cow milk plant (CMP) Kannauj, U.P. (India), along with two other plants of District Kannauj. After sample collection, the discharge rate of wastewater was also measured from the dairy plant's outlet. The flow rate of wastewater from the plant was measured by a differential pressure flow meter. The sample was collected in a sterile 5-liter container from the identified site. The container was washed with alcohol and distilled water and dried in a hot air oven for 15 min at 30°C and was allowed to cool at room temperature. After sample collection, the cap of the container was tightly locked and placed at below 4°C temperature to avoid any physiochemical change in effluent [14]. An antibiotic (Chloramphenicol 500 mg/L) was added to the influent to inhibit bacterial growth and incubated for 5 days at room temperature (27°C) [15].

Isolation and Identification of Fungal Cells

Dairy effluent samples were serially diluted (10^{-1} – 10^{-5}) and total dilution up to 10^{-5} was made. For the culture of fungi potato dextrose agar (PDA) medium was used. One mL of the diluted sample was inoculated into a 250 mL Erlenmeyer flask containing 100 mL of enrichment cultural media potato dextrose broth (2.5 mg in 100 mL DW) at 27°C for 2 days. The cultures were repeatedly streaked on PDA medium and incubated at 27°C for five days to obtain a pure culture [16]. A high-resolution LCD microscope (Wuzhou DMS 653) was used to determine the morphological characteristics of the isolated fungi. The isolated fungi were identified by colony morphology and microscopic observation by using Lactophenol cotton blue staining method. Potato Dextrose Agar (PDA) and Potato Dextrose Broth (PDB) medium were used for the maintenance of isolated fungal cultures [17]. All the culture of fungi was developed in the biotechnology laboratory of AITH Kanpur.

Characterization of Isolated Fungal

The three fungal strains were isolated from influent based on colony morphology and microscopic examination. These fungal strains were isolated during monsoon season at room temperature and identified as *Alternaria* sp. (ALT), *Aspergillus* sp. (ASP), and *Fusarium* sp. (FUS). The colonies were found to be the blackcolor with granular surface shows the presence of *Aspergillus* sps. while the greyish green colony shows *Alternaria*, and the pink color colony shows *Fusarium* [18].

Experimental Set Up for Analysis of Physiochemical Parameter

To experimental set up for study was developed according to Porwal et al. [16]. According to this model, an assembly was prepared by using two plastic bottles with a capacity of 2 L. Each bottle was reused to form two columns namely the primary tank and the secondary tank. These bottles were cut from the bottom side and turned upside down to form columns. Both inverted bottles (column) were mounted on a frame. Holes were drilled at the required locations in the bottles and clear silica tubes were attached. An aerator was used for two days to provide a continuous supply of air to maintain the desired level of dissolved oxygen. For filtration, the sawdust was collected from the sawmill. It was washed thoroughly with clean water to remove the organic and inorganic matter and it was dried by direct sunlight for 1 day. This purified sawdust was used for filtration; the dimension of sawdust was 1.0 mm sieve size. The activated carbon dust and purified sawdust were used for filtration, and both columns were washed with alcohol and distilled water, respectively.

Now 1 L of autoclaved affected milk water was poured into the main tank at room temperature, then 10 mL inoculum was added to the milk water. To affect a sufficient air supply, an aerator was inserted from the top side of the main tank for 2 days continuously, and the tank was covered with aluminum foil. Aeration was provided to the influent for degradation by fungal isolates. After 2 days the aeration was stopped and the influent was allowed to stand for 1 h to precipitate. The treated water from the primary tank was allowed to enter the secondary tank through a transparent silicone tube. In the secondary tank, water filtration was performed using a 2 cm layer of activated carbon powder and a layer of 2 cm sawdust layer (1.0 mm sieve size). Once the filtration process was completed, the treated effluent was analyzed with parameters such as pH, TDS (total dissolved solids), TSS (total suspended solids), BOD (biological oxygen demand), COD (chemical oxygen demand), hardness total and TKN (total nitrogen Kjeldahl).

Parameter Analysis Method

The analysis of the required physicochemical parameters was carried out with the standard method according to the Maiti water analysis manual [19]. The pH value was determined with the digital pH meter, the TDS was measured with the TDS meter while the TSS was determined by the standard method. The BOD was analyzed using (BOD Incubator manufactures KHERA KI-216) standard procedure with nutrient mix and 5 days incubation at 20°C and COD was analyzed with (COD Digestion Unit manufactures KHERA KI-162) method of oxidation with dichromate. Colors and odor are physical parameters, both physically evaluated.

RESULTS AND DISCUSSION

Characterization of Influent

First of all control experiment was performed with untreated water of dairy effluent and obtained results of physiochemical parameters were summarized in Table 1. The influent water was light grey as in appearance with an unpleasant odor, after treatment water was clear without odor. Some variation in color and odor of the effluent might be due to the presence of microorganism and fungal isolates, which play an important role in the decomposition of organic matter.

Characterization of Treated Effluent

The experiment was carried out using three selected fungal isolates for the treatment process. Obtained values of the physiochemical parameter of treated dairy effluent after aeration in the primary tank and filtration in the secondary tank are summarized in Table 1. Here sawdust and activated carbon were used as a filter media which led to the removal of total suspended solids and consequently in the color improvement [20]. After all processes, the effluent was used for the characterization of the physiochemical parameter. Results show that the color and value of other physiochemical parameters of dairy effluent were changed. This change may be attributed to the degradation of organic materials by fungal isolates.

pH

The pH of effluent depends on the nature of the end product of the dairy plant, and it varies from 4.7 to 11 pH at 190–330°C. It was observed that the pH value range in aeration and filtration was varying from 6.12 to 7.61. Untreated wastewater under control experiment was slightly acidic (pH 6.37) due to the microbial action on organic compounds and it decomposes into similar acid and this acidic water could harm the soil and aquatic flora and fauna [21]. Overall after filtration, the pH of treated water by ALT was 6.19 acidic in nature while ASP treated water shows alkaline in nature (pH 7.61) and the pH of FUS treated water was also observed in acidic near to neutral 6.65. Hence ASP and FUS sp. play an important role in control the pH of dairy effluent (Table 1).

Turbidity

Decrease in turbidity was observed on the fifth day of filtration, the decrement in turbidity may be due to fungal isolates. The total turbidity removal efficiency was observed as 82.47, 97.17, and 89.77% for ALT, ASP, and FUS respectively (Table 1). Turbidity was reduced due to the consumption of organic materials under anaerobic conditions by the fungi through growth. *Aspergillus* (ASP) shows that the highest reducing power (97.17%) during filtration in anaerobic conditions among the three fungal isolates.

Table 1. Analysis of physiochemical parameters of dairy effluent control and after degradation using fungal isolates

Parameters	pH	Turbidity, NTU	TDS, mg/L	TSS, mg/L	Total alkalinity (CaCO ₃), mg/L	Total hardness (CaCO ₃), mg/L	TKN, mg/L
Control	6.37 ± 0.08	1147.37 ± 1.12	1706.08 ± 0.80	736.24 ± 0.41	616.66 ± 8.809	518.346 ± 6.014	104.043 ± 6.154
Fungal isolates + effluent		<i>Alternaria</i> sp.					
2nd day (AR)	6.32 ± 0.14	385.97 ± 09.81	1531.85 ± 4.44	680.66 ± 0.57	604.12 ± 1.64	518.30 ± 6.014	102.18 ± 0.08
3rd day	6.12 ± 0.04	267.37 ± 02.01	682.54 ± 9.87	477.01 ± 1.73	738.42 ± 3.41	513.21 ± 0.52	87.82 ± 2.25
5th day (AF)	6.19 ± 0.10	201.56 ± 8.76	600.85 ± 0.55	8.16 ± 0.42	729.35 ± 0.64	511.10 ± 4.55	91.70 ± 5.36
	Acidic	82.47↓	35.17↓	97.53↓	18.27↑	1.39↓	11.82↓
Fungal isolates + effluent		<i>Aspergillus</i> sp.					
2nd day (AR)	6.69 ± 0.14	72.36 ± 1.16	1090.25 ± 1.25	602.29 ± 0.92	610.69 ± 7.89	514.58 ± 2.19	93.65 ± 2.01
3rd day	7.17 ± 0.07	48.10 ± 1.64	473.12 ± 4.53	214.34 ± 0.47	589.96 ± 0.35	509.33 ± 0.84	64.82 ± 0.83
5th day (AF)	7.61 ± 0.02	32.35 ± 1.15	381.95 ± 6.62	8.65 ± 0.37	578.84 ± 0.19	491.11 ± 4.03	50.33 ± 1.57
Overall % change	Basic	97.17↓	77.60↓	98.82↓	6.02↓	5.25↓	51.60↓
Fungal isolates + effluent		<i>Fusarium</i> sp.					
2nd day (AR)	6.38 ± 0.28	198.56 ± 2.83	990.45 ± 5.29	632.30 ± 0.92	720.23 ± 1.10	514.97 ± 3.18	98.55 ± 2.91
3rd day	6.65 ± 0.13	147.56 ± 1.85	677.33 ± 2.29	518.92 ± 1.14	714.92 ± 1.10	513.00 ± 0.17	63.13 ± 1.31
5th day (AF)	6.65 ± 0.08	117.30 ± 1.25	616.61 ± 13.88	38.68 ± 0.42	713.48 ± 2.97	510.67 ± 1.01	68.99 ± 1.07
Overall % change	Acidic	89.77↓	35.53↓	95.02↓	15.70↑	1.48↓	33.66↓

AR—After aeration (48 h); AF—after filtration; TDS—total dissolved solids; TSS—total suspended solids; NTU—nephelometric turbidity unit.

Biological Oxygen Demand (BOD)

The value of BOD in dairy effluent was observed as 1093.24 mg/L that was higher than standard norms as per environmental protection law. This high value of BOD shows the presence of organic matter, lactose, detergents, proteins, and inorganic salts in the wastewater. After treatment (filtration) it was noticed that the maximum removal of organic matters was done by *Aspergillus* species (89.20%). In the same order the removal rate was observed for other fungal isolates as 30.85, 34.63%, for FUS, ALT, respectively (Table 2). During the treatment process, it was observed that the removal value was a decline with the number of days as Table 2 and Fig. 1. After analysis noticed that during aeration first and the second day the BOD value was declined sharply because of the continuous supply of air to maintain the desired level of dissolved oxygen (Table 2). During aeration, it was also noticed that BOD value was diminishing with the decrease of microbial colonies simultaneously. Yathavamoorthi et al. have been reported a good correlation between microbes and BOD and TSS [22]. Although the high growth of fungal isolates had consumed the oxygen present in the treatment column. The continuous and additional aeration in the column was decreasing the BOD value. Different types of microorganisms require different levels of oxygen to digest organic matter, which is very useful for multiplication and growth.

Chemical Oxygen Demand (COD)

The COD content was significantly reduced with ASP, ALT, FUS during aerobic treatment. The maximum efficient deformation in ASP, during filtration on the fifth day of removal, was 81.02% (Table 2). This is confirmed by the COD flow of the result after ASP, ALT, and FUS significantly reduce aeration. Like 81.02, 55.93, and 41.22%, respectively (Fig. 2). ASP has effective removal power of the effluent during aeration, whereas FUS showed the least removal power in COD. The decrement in COD values might be due to more quantity of nutrients of fungi present in the form of dissolved and organic substances which may be helpful for the growth of fungal isolates [23].

Table 2. Variation in colony counting, BOD, and COD in dairy effluent control and treated with fungal isolates

Sample	Fungal growth <i>h</i> in CFU/mL $\times 10^6 \downarrow$	BOD, mg/L					COD, mg/L				
		control \downarrow	2nd day (AR)*	3rd day	5th day (AR)*	overall % change	control	2nd day (AR)*	3rd day	5th day (AF)*	overall % change
Control	68	1093.24 \pm 0.68	NA	NA	NA	NA	2318.59 \pm 0.05	NA	NA	NA	NA
<i>Alternaria</i> sp.	126	1093.24 \pm 0.68	864.32 \pm 0.14	712.08 \pm 0.47	714.43 \pm 7.91	34.63 \downarrow	2318.59 \pm 0.05	1715.90 \pm 9.28	990.52 \pm 7.0	1021.2 \pm 8.86	55.93 \downarrow
<i>Aspergillus</i> sp.	232	1093.24 \pm 0.68	889.32 \pm 1.68	130.15 \pm 5.14	123.82 \pm 3.93	89.20 \downarrow	2318.59 \pm 0.05	1785.59 \pm 1.05	415.17 \pm 3.31	440.44 \pm 1.67	81.02 \downarrow
<i>Fusarium</i> sp.	142	1093.24 \pm 0.68	918.52 \pm 1.26	773.53 \pm 0.31	755.75 \pm 2.25	30.85 \downarrow	2318.59 \pm 0.05	2129.59 \pm 1.09	1363.32 \pm 6.07	1362.77 \pm 5.72	41.22 \downarrow

BOD₅—Biological oxygen demand (5 days at 20°C), COD—chemical oxygen demand, NA—not available.

Total Dissolved Solid (TDS)

Among the three fungal isolates, only ASP showed greater removal power for total dissolved solids (77.60%) in the filtration treatment, while FUS has (35.53%), while the minimum reduction power has been observed in ALT as (35.17%), Table 1. The presence of a high level of total dissolved solids is due to the organic and inorganic matter present in the effluent. We know that a lot of solids dissolve in plain water. The high content of TDS reduces the usefulness of the water for potable irrigation and industrial purposes [24].

Total Suspended Solid (TSS)

Suspended solids in wastewater generates from gelatinous milk and other dairy products. The decreasing value of the total suspended solid in the treated milk effluent after aeration and filtration was summarized in Table 1. After aeration and filtration, the percentage of suspended solid was observed as 98.82, 97.53, and 95.02% in ASP, FUS, and ALT, respectively. From the data obtained it is clear that ALT has a low decomposition power, while ASP shows a remarkable ability to remove suspended solids. However, after the suspended solid decomposition aeration rate was low, after the filtration decomposition rate it increased very rapidly from 602.29 ± 0.92 to 8.65 ± 0.37 for ASP 98.82%. The efficiency of decomposition is attributed to the use of organic substances with the help of the fungus that further insulates from the adsorption capacity of the used filter substances, sawdust and Charcoal powder.

Total Hardness

In hard water, the amount of calcium, magnesium, carbonate, bicarbonate, sulfate, and other ions are present in excess. During the period of study, after five days of the treatment with fungal isolates, the hardness was obtained as 1.39, 1.48, and 5.25% for ALT, FUS, and ASP, respectively (Table 1). The result shows that the higher value of hardness in dairy effluent was due to discharge of carbonate, bicarbonate, caustic soda, etc.

Total Kjeldahl Nitrogen (TKN)

TKN is the approved parameter used to determine the organic nitrogen and ammonia from wastewater. The TKN amount of effluent for discharge should not be greater than 100 mg/L as per guidelines of environmental protection rule 1986 [3]. Nitrogen generally arises from milk protein in different forms like urea [25], nucleic acid, and ammonium ions. NH_4^+ is the first inorganic ion produced during the aeration treatment of dairy wastewater. Aeration treatment depends on microorganism growth in an oxygen-rich environment. In this study removal of TKN was measured as 11.82, 33.66, and 51.60% for ALT, FUS, and ASP respectively after 48 h aeration against untreated water Average TKN removal efficiency is summarized in Table 1. Based on the obtained result it is proved that *Aspergillus* sp. has a great ability to decompose organic nitrogen while *Alternaria* sp. showed less competence for degradation of organic nitrogen.

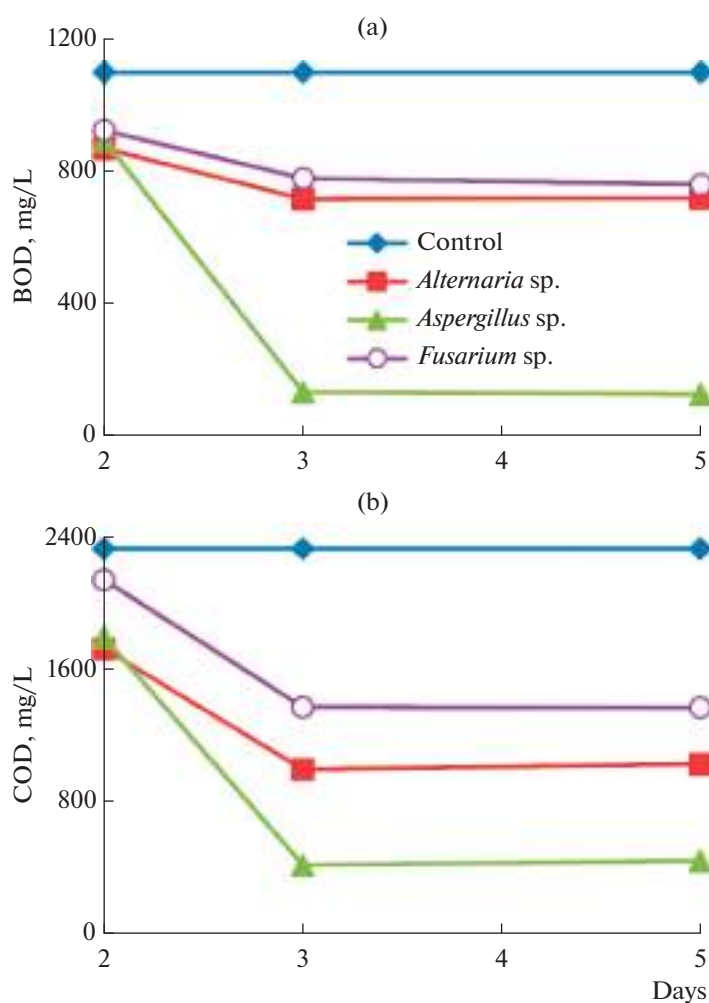


Fig. 1. Variation in BOD (a) and COD (b) removal of dairy effluent by *Alternaria* sp., *Aspergillus* sp., *Fusarium* sp. fungal isolates.

CONCLUSIONS

In this study, some points were detected by the results obtained after the degradation of the milk effluent treated with fungal isolates. The degradation efficiency of dairy effluent was examined by the consortium of *Alternaria*, *Aspergillus* and *Fusarium* species because the availability of the fungal isolates chosen above is very abundant in nature, which is why they were selected for the study. Two processes were involved in the treatment, aeration and filtration process. This treatment process can be a very economical and efficient technique for CMP wastewater treatment. The research results also show that it is the best treatment after filtration as there has been a significant reduction in all selected water parameters. Aerobic treatment to be reliable and economical to generate a high quality effluent after analysis found that *Aspergillus* has a great ability to remove BOD (87.75%) and COD (81.02%) under aerobic conditions because the high growth of fungal isolates had consumed the oxygen present in the treatment column. Continuous and additional aeration was responsible for the decrease in BOD and COD value. During the study, it was also observed that turbidity was also reduced when mixing *Aspergillus*, for the CMP milk effluent a higher removal rate of turbidity (97.17%) and total suspended solids (98.82%). The three mushroom isolates chosen above can be used as an inexpensive, potent and environmentally friendly way to withstand a wide range of toxins from wastewater. Biodegradation with fungal isolates is an appropriate method for treating dairy effluents. In this treatment method, the fungal isolates can be used on a commercial scale. The fungal isolates chosen as *Aspergillus* were more effective than *Alternaria* and *Fusarium* sp. for the biodegradation process of organic matter in dairy effluents. After all, the results show that aeration followed by filtration was very effective in achieving the highest rate of removal of organic substances (pollutants) present

in the wastewater. The possible reason could be associated with the high adsorption capacity of activated carbon and absorption by sawdust. Activated carbon and sawdust have the ability to remove a variety of organic compounds from contaminated water. Finally, the biodegradation of dairy effluents by selected fungal isolates is an effective treatment technology, especially when using locally isolated fungal strains.

ACKNOWLEDGMENTS

Authors are thankful to Director CMP Kannauj, India for providing a sample of the dairy plant and the necessary facilities to complete it.

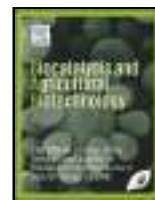
CONFLICT OF INTEREST

The authors declare that they have no conflicts of interest.

REFERENCES

1. Kumar A.V., Sarkar B., Chakrabarti P.P., and Kale V., Wastewater treatment in dairy industries possibility of reuse, *Desalination*, 2006, vol. 195, pp. 141–152.
2. Vourch M., Balannec B., Chaufer B., and Dorange, G., Treatment of dairy industry wastewater by reverse osmosis for water reuse, *Desalination*, 2008, vol. 219, nos. 1–3, pp. 190–202.
3. General standards for discharge of environmental pollutants, Part A: Effluents, *Environ. Prot. Rules*, 1986, vol. 6, pp. 545–546.
4. Janczukowicz, W., Zieliński, M., and Dębowski, M., Biodegradability evaluation of dairy effluents originated in selected sections of dairy production, *Bioresour. Technol.*, 2008, vol. 99, pp. 4199–4205.
5. Das, S. and Santra, S.C., Simultaneous biomass production and mixed origin wastewater treatment by five environmental isolates of Cyanobacteria, *Biologija*, 2010, vol. 56, nos. 1–4, pp. 9–13.
6. Sabah, G., Jatau, E., and Whang, C., Assessment of biodegradation ability of *Aspergillus niger* isolated from mechanic workshops soil on refinery effluent and petroleum hydrocarbons, *Int. J. Sci. Res.*, 2016, vol. 6, no. 3, pp. 381–389.
7. Rhodes, C.J., Applications of bioremediation and phytoremediation, *Sci. Prog.*, 2013, vol. 96, no. 4, pp. 417–427.
8. Machida, M. and Gomi, K., *Aspergillus*: Molecular biology and genomics, *Biotechnol. J.*, 2010, vol. 5, pp. 336–337.
9. Gadd, B.J., Northcott, G.L., and Tremblay, L.A., Passive secondary biological treatment systems reduce estrogens in dairy shed effluent, *Environ. Sci. Technol.*, 2010, vol. 44, no. 19, pp. 7601–7606.
10. Maghsoodi, V., Samadi, A., and Ghobadi, Z., Biodegradation of effluents from dairy plant by bacterial isolates, *Iran. J. Chem. Chem. Eng.*, 2007, vol. 26, no. 1, pp. 55–59.
11. Rajput, M.S., Dwivedi, V., and Awasthi, S.K., Enzymatic degradation of pyridine raffinate using response surface and artificial neural network simulation, *Indian J. Exp. Biol.*, 2020, vol. 58, pp. 584–592.
12. *Plant-Microbe Interactions in Agro-Ecological Perspectives*, vol. 2: *Microbial Interactions and Agro-Ecological Impacts*, Singh, D.P., Singh, H.B., and Prabha, R., Eds., Singapore: Springer, 2017, p. 593.
13. Kshirsagar, A.D., Application of bioremediation process for wastewater treatment using aquatic fungi, *Int. J. Curr. Res.*, 2013, vol. 5, no. 7, pp. 1737–1739.
14. Demirel, B., Yenigun, O., and Onay, T., Anaerobic treatment of dairy wastewaters: A review, *Process. Biochem.*, 2005, vol. 40, no. 8, pp. 2583–2595.
15. Hageskal, G., Knutsen, A.K., Gaustad, P., Hoog, G.S., and Skaar, I., Diversity, and significance of mold species in Norwegian drinking water, *Appl. Environ. Microbiol.*, 2006, vol. 72, no. 12, pp. 7586–7593.
16. Porwal, H.J., Mane, A.V., and Velhal, S.G., Biodegradation of dairy effluent by using microbial isolates obtained from activated sludge, *Water Resour. Ind.*, 2015, vol. 9, pp. 1–15.
17. Tatah, S., Ogodo, A.C., Kaa, L.C., and Agwaranze, D.I., The potential use of *Alternaria alternata* in bioremediation of wastewater contaminated by hexavalent chromium ion, *FUW Trends Sci. Technol. J.*, 2016, vol. 1, no. 1, pp. 115–118.
18. Kaur, A. and Chaman, S., International bioaugmentation for dairy wastewater, *J. Sci. Res.*, 2014, vol. 3, no. 9, pp. 316–320.
19. Maiti, S.K., *Handbook of Methods in Environmental Studies*, vol. 1: *Water and Waste Water Analysis*, Jaipur: ABD, 2004, p. 21.
20. Passeggi, M., Lopez, I., and Borzacconi, L., Integrated anaerobic treatment of dairy industrial wastewater and sludge, *Water Sci. Technol.*, 2009, vol. 59, pp. 501–506.

21. Slavov, A.K., General characteristics, and treatment possibilities of dairy wastewater, *Food Technol. Biotechnol.*, 2017, vol. 55, no. 1, pp. 14–28.
22. Yathavamoorthi, R., Surendraraj, A., and Farvin, K.H.S., Enteric bacteria and water quality of freshwater prawn *Macrobrachium rosenbergii* in culture environment from Kerala, *J. Fish. Aquat. Sci.*, 2010, vol. 5, no. 4, pp. 282–292.
23. Kowsalya, R., Noorjahan, C.M., Karunakaran, C.M., Deecaraman, M., and Vijayalakshmi, M., Physico-chemical characterization of brewery effluent and its degradation using native fungus *Aspergillus niger*, *J. Ind. Pollut. Control*, 2010, vol. 26, no. 2, pp. 171–176.
24. Al-Wasify, R.S., Ali, M.N., and Hamed, S.R., Biodegradation of dairy wastewater using bacterial and fungal local isolates, *Water Sci. Technol.*, 2017, vol. 76, no. 11, pp. 3094–3100.
25. Jimenez, G., Mateos, P.A., Guzman, F.R., and Martin, J.P., Biomineralization of organic matter as affected by pH, *Water Res.*, 2000, vol. 34, pp. 1215–1224.



Biodegradation of pyridine raffinate by microbial laccase isolated from *Pseudomonas monteilii* & *Gamma proteobacterium* present in woody soil

Manish Singh Rajput^a, Vinay Dwivedi^{b,*}, S.K. Awasthi^c

^a Department of Biotechnology, Dr. Ambedkar Institute of Technology for Handicapped, Kanpur, 208024, U P, India

^b Department of Biotechnology, Naraina Vidyapeeth Engineering & Management Institute, Kanpur, 208020, U P, India

^c Harcourt Butler Technical University, Kanpur, 208002, U P, India

ARTICLE INFO

Keywords:

Microbial laccase
Pyridine raffinate
Pseudomonas monteilii
Gamma proteobacterium
Biodegradation

ABSTRACT

Two novel laccase enzyme-producing strains *Pseudomonas monteilii* and *Gamma proteobacterium* were isolated from woody soil sample and their productions were optimized. Maximum production of laccase was achieved at temperature (37 °C), pH (7), carbon source (glucose) and nitrogen source (yeast extract) for both the isolates. The produced extracellular laccases were extracted by centrifugation at 14000 rpm and 4 °C for 15 min. The extracted laccases were also optimized for the specific substrate to enzyme concentration ratio, pH, temperature and the results were 1:9, 6.0, 25 °C for strain *Pseudomonas monteilii* and 2:8, 8.0, 40 °C for strain *Gamma proteobacterium* respectively.

The novelty of this work is here we use extracted bacterial laccase enzyme was subjected to pyridine raffinate according to optimized process parameters, a reduction in absorbance was observed up to 51% for strain *Pseudomonas monteilii* and 59.5% for strain *Gamma proteobacterium* in 140 min. The study signifies the biotransformation of pyridine raffinate into some other simpler products as it provides a novel way to bioremediate pyridine raffinate. This innovative remediation process displays a route towards reasonable treatment techniques where physical and chemical procedures appear to fall flat.

1. Introduction

Pyridine raffinate is an organic discharge of the pyridine manufacturing industry containing mainly pyridine; a heterocyclic aromatic compound along with formaldehyde, picolines, and phenolics. It is a water-soluble (Li et al., 2009), a highly alkaline mixture (pH 10–12), slightly pale in color with penetrating nauseating odor (“Pyridine [C5H5N - PubChem,” n.d.). Apart from a lab reagent, pyridine has found its applications in adhesives, aerosols, bleaching agents, electroplating industry, fuel additives, industrial solvents and as a raw material in paint, dyes, pharmaceutical and several other industrial processes. Pyridine is also an important agent in the manufacturing of several different key products such as vitamins, food flavorings, rubber products, insecticides and herbicides (“Pyridine [C5H5N - PubChem,” n.d.).

Despite its industrial usefulness pyridine has several health hazards. Researchers have reported pyridine carcinogenicity in rats (Hasegawa et al., 1993), in human-derived liver cell lines (Majer et

al., 2005), in the mammary gland of rat (Huber et al., 1997) and many more. Due to its hazardous behavior, pyridine is of foremost concern among all the organic heterocyclic compounds (Saroja, 2018).

Pyridine is listed as a priority organic pollutant by the United States Environmental Protection Agency (USEPA). According to the latest report published by NBC, Global Pyridine Market size is expected to grow at USD 747.89 million by 2023 (“Pyridine Market Research Report- Forecast to 2023 | MRF, n.d.). Being a priority organic pollutant, such growth would also affect the environment at a high cost.

Several physical, chemical and biological methodologies for biodegradation of pyridine raffinate have been reported. Physical and chemical methods have the disadvantages of being costly and less effective, however, biological treatment methods are preferred as they are cost-effective and environment-friendly (Sims, O'Loughlin and Crawford, 1989). From the perspective of the heterocyclic nature of pyridine, it is recalcitrant to microbial activity. However, with time,

* Corresponding author.

E-mail addresses: msrbitech@gmail.com (M.S. Rajput), drvinay@yahoo.com (V. Dwivedi), skahbti@yahoo.co.in (S.K. Awasthi).

<https://doi.org/10.1016/j.bcab.2020.101650>

Received 29 November 2019; Received in revised form 14 April 2020; Accepted 8 May 2020

Available online 16 May 2020

1878-8181/© 2020 Elsevier Ltd. All rights reserved.

because of the ability of the microbes to deliver increasingly phenotypic species and their differential ways to utilize various substrates for their metabolism, they are able to degrade pyridines and their derivatives (Sun et al., 2011).

Laccases are copper-containing polyphenol oxidoreductases first reported in exudates of Japanese lacquer tree *Rhus vernicifera* (Yoshida, 1883) and degrades pyridine ring as reported by several researchers (Rajput and Mishra, 2019). The mechanism of laccase activity involves utilizing oxygen as an electron donor and helping in the oxidation of different compounds such as phenols, polyphenols, aromatic amines by four-electron transfer resulting in the reduction of O₂ to H₂O and formation of reactive substrate radicals (Claus, 2004; Riva, 2006). Some substrates are two-electron donors resulting in one step oxidation-reduction reaction, copper-I accepts electron and reactive substrate radicals take part in further non-enzymatic reactions (Kersten et al., 1990). The occurrence of laccase had been found in fungus such as *Aspergillus sp.*, *Coriopsis gallica*, *Funaliatrogii*, *Streptomyces cyaneus*, *Penicillium oryzae* etc (Baldrian, 2006; Thurston, 2019), plants such as *Camelia sinensis*, *Schinus molle*, *Musa paradisiaca*, *Forsinthususpensa*, *Pinus sp.* etc (Dean and Eriksson, 1994; Dwivedi et al., 2011) and bacteria (Bugg et al., 2011; Sharma et al., 2007). Laccases are the center of attraction for effluent treatment discharged from industries because of their wide range of oxidoreductase activity (Claus, 2004). Laccases have also been reported thermally (D'Souza-Ticlo et al., 2009) and pH stable (Singh et al., 2007) which makes them more diversified in the bioremediation process. The first bacterial laccase was isolated in 1999 from *Azospirillum lipoferum* (Diamantidis et al., 2000). Martins et al. (2002) isolated and characterized bacterial laccase from *Bacillus subtilis* endospore coat (Martins et al., 2002). Many researchers used microbial species as whole to bioremediate the complex heterocyclic compounds. Chandra et al. (2009) reported *Bacillus sp. co-culture* can degrade formaldehyde free pyridine raffinate (Chandra et al., 2009). Little work has been reported on pyridine raffinate degradation with bacterial laccase. In the present study, we have succeeded to bioremediate the pyridine raffinate with the help of enzyme laccase.

2. Material and methods

2.1. Chemicals and growth medium

Solvents viz Tris-Base, Phosphate buffer, EDTA and Propyl alcohol were obtained from Thomas Baker Chemicals Private Limited, New Delhi, India. Salts viz. Na₂HPO₄, CaSO₄, NaCl, ZnSO₄, C₆H₅FeO₇, MnSO₄·H₂O, K₂Cr₂O₇, NaHCO₃, NaH₂PO₄, and CH₃COONa were obtained from Central Drug House, New Delhi, India and media components viz. agar, yeast extract, sucrose, glucose, tryptone, peptone were obtained from Sisco Research Laboratories Pvt. Ltd. (SRL), New Delhi, India. Guaiacol was procured from Thermo Fisher Scientific India Pvt. Ltd., Mumbai, India. All reagents were of analytical grade and extra pure quality.

2.2. Collection of soil sample

Collection of soil sample was done aseptically from Gupta Timbers (26°30'06.6"N 80°15'15.9"E), Kalyanpur, Kanpur, Uttar Pradesh, India. The first layer of soil up to 10 cm was removed using a sterile spatula. After that, using another sterile spatula soil sample was transferred into pre autoclaved beaker and covered with aluminum foil instantly. The sample was then transferred to a Petri dish and kept at room temperature for 6 h in a glove box by maintaining aseptic conditions to normalize the temperature of the soil sample and to remove moisture. Dried soil was filtered using 34 μ sieve and 1 g was weighed out for serial dilution protocol.

2.3. Selection and screening of Laccase producing colonies

The filtered sample weighed out was serially diluted to get more prominent isolates from microbe-rich dense soil culture. A total dilution up to 10⁻⁶ was made and inoculated on sterile pre-prepared nutrient agar Petri plates (Hi-Media Laboratories, Mumbai, India) using spread plate culture technique in a laminar cabinet (Microflow Sterile Concepts India Pvt Ltd., Chennai, India). After sterilizing it against possible contamination, 20 μ L of well-mixed sample from 10⁻⁴, 10⁻⁵, 10⁻⁶ dilutions were transferred into three different Petri plates in triplicate and spread it with the help of a sterile spreader. These Petri plates were then incubated at 37 °C temperature, humidity and light-controlled incubator for 24 h to allow the growth of microbes. After that different colonies were marked and streaked out in quadrant form onto sterilized pre-prepared nutrient agar Petri plates for further isolation of pure colony.

Specified M162 medium (Degryse et al., 1978) was used to isolate laccase producing bacterial species. Modified M162 medium composition (g/l): CaSO₄·2H₂O (0.4), MgCl₂·6H₂O (2.0), glucose (1.0), yeast extract (3.0), C₆H₅FeO₇ solution (0.01 M) (5.0), K₂HPO₄ (0.5), NH₄NO₃ (0.5), NaH₂PO₄ (0.5), Na₂HPO₄ (0.5) and 10 ml of micronutrients containing g/l of MnSO₄·H₂O (2.28), Na₂MO₄·2H₂O (0.05), CoCl₂·6H₂O (0.09), CuSO₄ (0.025), H₃BO₄ (0.5), ZnSO₄·7H₂O (0.5) & 0.5 ml H₂SO₄. Agar (1%) used as a solidifying agent in SSF (Rajput and Mishra, 2019) and 2 mM Guaiacol was used as a standard substrate. Laccase producing bacteria produce brown colonies when grown on this medium after 72 h at 37 °C temperature (Kaur et al., 2017) and the identification of laccase producing bacterial strains by probing into its morphological and biochemical characteristics by referring Bergey's Manual of Determinative Bacteriology (Bergey et al., 1984) and then after strains were further cross-verified by Chromous Biotech Pvt. Ltd. Bengaluru, India. Service Number: BI-525, India.

2.4. Isolation of crude Laccase

Colonies were allowed to grow on differential broth media for 5 days at 37 °C and 150 rpm in an orbital shaker (Scigenics Biotech Private Limited, Chennai, India). After 5 days the flasks were drawn from the shaker and culture mixture was centrifuged (Elektrocraft Pvt. Ltd., MP400R, Mumbai, India) at 14000 rpm for 15 min and 0–4 °C in a high-speed research centrifuge. The supernatant was collected and stored at 4 °C for further use as a crude enzyme source and the pellet was discarded.

2.5. Laccase production & optimization

In the process of laccase production parameters like time, temperature, pH, carbon, and nitrogen sources were optimized. Experimental cultures were incubated for 5 days and their laccase activity was measured at a regular interval of 12 h for optimization of time. The effect of temperature and pH on enzyme production was determined by incubating the inoculated flask under different conditions (temperature 27–42 °C), pH (5–9) in a controlled environment (Niladevi et al., 2009; Singh et al., 2007). Glucose, fructose, and sucrose were separately investigated to determine the effect of the carbon source while yeast extract, tryptone and peptone as nitrogen sources to examine its effect on laccase production.

2.6. Total protein content determination

Total protein estimation was done according to the Lowry method (Walker et al., 2003). The method relies on a biuret reaction in which peptide bonds from protein react with copper under alkaline conditions to produce copper ions. The reactions result in a strong blue color, which depends partly on tyrosine and tryptophan content. The

method is sensitive down to about 0.01 mg of protein/ml and is best used on solutions with concentrations in the range 0.01–1.0 mg/ml of protein.

2.7. Characterization of enzyme

2.7.1. Standard substrate concentration

To standardize the procedure for bioremediation of pyridine raffinane, guaiacol as a standard substrate was used for determining optimum substrate to enzyme concentration. A total reaction mixture of 4 ml was taken as constant having varying concentrations of enzyme to substrate ratio. The enzyme to substrate ratio was varied as 1:9, 2:8, 3:7 and 4:6 respectively.

2.7.2. pH

The reaction mixture containing enzyme & guaiacol was incubated at an optimum concentration determined in the previous step with varying pH from 5 to 9 measured using pH meter (Cole-Parmer India, Mumbai, India). After initial incubation, samples were drawn at a regular interval of 20 min and optical density was measured at 450 nm for guaiacol and 501 nm for pyridine raffinane using a UV spectrophotometer (G Biosciences Pvt. Ltd., Noida, India).

2.7.3. Temperature

Estimated optimum pH and enzyme-substrate concentration ratio obtained from previous studies were kept constant and the temperature was varied between 27 and 42 °C under a controlled environment (Niladevi et al., 2009).

2.7.4. Laccase activity

Laccase activity was determined using Guaiacol assay (Sheikhi et al., 2012). 2 mM dilution of guaiacol was prepared in absolute ethanol. The total reaction mixture of 4 ml containing 3.5 ml of pre-prepared phosphate buffer of pH 8.0, 400 µL of 2 mM guaiacol and 100 µL of crude enzyme extract was used. A total of 6 test tubes containing the same reaction mixture were prepared. Guaiacol has been reported as an efficient substrate for laccase assay. The intense brown color development due to oxidation of guaiacol by laccase can be correlated to its activity often read at 450 nm. The mixture was incubated at 35 °C for 15 min and absorbance was read at 450 nm using a UV spectrophotometer. Enzyme activity was expressed as International Units (IU), where 1 IU is defined as the amount of enzyme required to oxidize 1 µmol of guaiacol per min. The laccase activity in IU/ml is calculated by the formula (Abd El Monsef, Hassan and Ramadan, 2016).

$$\text{Laccase activity (IU/ml)} = \frac{\Delta A_{450} \times V}{v \times \Delta t \times e}$$

Where,

ΔA_{450} = Change in absorbance at 450 nm

V = Total volume mixture (ml)

v = Enzyme volume (ml)

Δt = Change in time

e = Extinction coefficient for guaiacol (12.1 mM/cm)

3. Results and discussion

3.1. Isolation and screening of laccase producing bacterial strains

Eight different colonies were obtained after serially diluting 1 mg of soil into 6 different test tubes and were spread onto pre-prepared nutrient agar plates. They were further marked out and were permitted to grow on modified M162 selection media where 2 mM of guaiacol as a substrate was added to the medium. Laccase producing bac-

terium produces reddish-brown colonies on this medium. Colonies corresponding to 1st and 5th of Petri plates produced reddish-brown colonies and hence marked as TS₁ and TS₅. Guaiacol allows enhanced melanization by laccase producing strains and hence helps in identification.

3.2. Laccase production & optimization

The concentration and nature of the carbon source used in the medium showed a significant effect on enzyme production. The addition of fructose, glucose, and sucrose as different carbon sources increases the production of laccase (measured in terms of maximum laccase activity). Optimization studies for carbon sources in the presence of guaiacol were performed. Glucose (0.265 & 0.238 IU/ml) showed higher activity in comparison to sucrose (0.255 & 0.169 IU/ml) and fructose (0.219 & 0.198 IU/ml) respectively for strain TS₁ and TS₅ (Fig. 1). Similar results were reported by many researchers in the case of the utilization of specified carbon sources (Mikiashvili et al., 2006). Yeast extract, urea, ammonium sulphate, ammonium nitrate, peptone and tryptone are most commonly used nitrogen sources for the bacterial and fungal laccase production. We optimized preferred nitrogen sources tryptone, peptone and yeast extract against laccase activity and found that yeast extract demonstrated higher activity (0.250 & 0.255 IU/ml) compared to peptone (0.231 & 0.238 IU/ml) and tryptone (0.223 & 0.232 IU/ml) respectively for strain TS₁ and TS₅ (Fig. 2). Experiments have suggested that laccase production increases as ni-

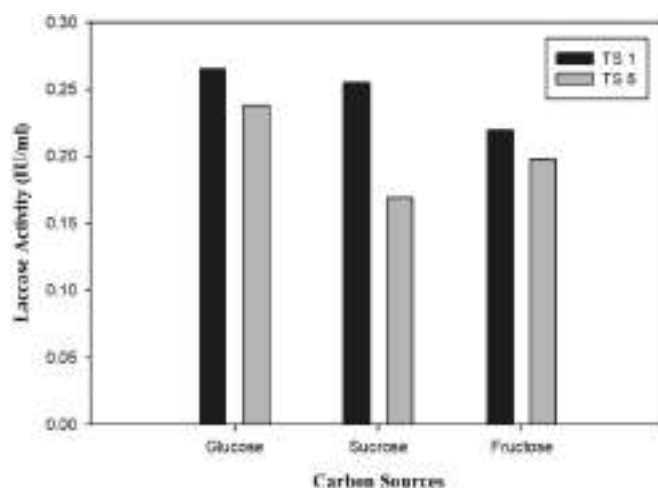


Fig. 1. Laccase activity against carbon sources for laccase production.

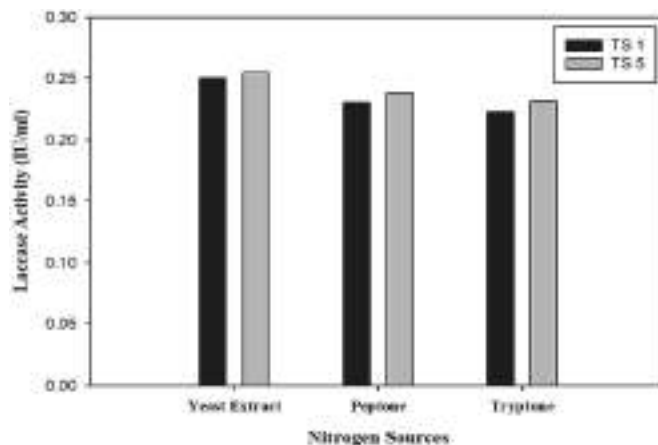


Fig. 2. Laccase activity against nitrogen sources for laccase production.

trogen depleted, attained a maximum and then started falling off (Keyser et al., 1978).

Laccase being thermostable, temperature does not have a very significant effect on laccase activity whereas the optimal temperature varies with strain (Thurston, 2019). In this study, we optimized laccase activity against varied temperature range (27–42 °C) and discovered that both the strains showed higher activity at 37 °C (Fig. 3).

The ideal pH worth changes relying upon the substrate since the instrument of the response with compound laccase fluctuates. Many reports suggest that the bell profile occurs in the case of laccase activity. The potential difference between the phenolic substrate and the T1 copper (First copper inactive moiety of laccase) can increase the oxidation of the substrate while the hydroxide (OH⁻) is bonded to the T2/T3 copper center which help to determine the optimal pH value for the laccase activity (Kunamneni et al., 2007). Laccase production was higher at pH 7.0 for both the strains (Fig. 4). Substantial laccase production was displayed by many researchers in the pH range from 3.0 to 8.0 (Cordi et al., 2007).

3.3. Morphological and molecular identification of laccase producing strains

3.3.1. Gram staining

A high-resolution LCD microscope (Wuzhou New Found Instrument Company Ltd., DMS653, China) was used to determine the morphological characteristics of the bacterium. Gram-stained slides were analyzed under the microscope at 100X resolution and the colonies were found to be pink colored, rod-shaped, motile, multi-flagella, the center raised and margins slightly tapered smooth bacterium (Fig. 5).

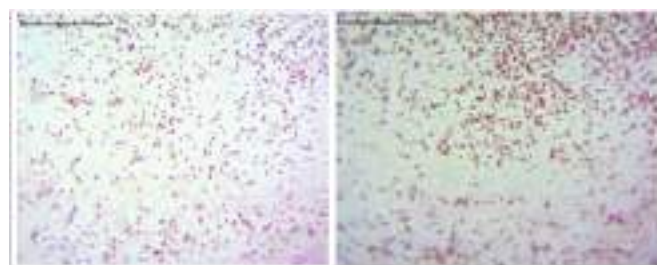


Fig. 5. Gram-stained isolate strain TS1 (left) and TS5 (right).

3.3.2. Molecular identification of bacterial strains using 16S rRNA sequencing

3.3.2.1. PCR amplification conditions. In this study DNA amplification was done under the mentioned protocol for the identification of the samples TS1 and TS5 in which DNA was taken 1 µl, 16S forward primer (400 ng) 1 µl, 16S Reverse Primer (400 ng) 1 µl, dNTPs (2.5 mM each) 4 µl, 10X Taq DNA polymerase Assay Buffer 10 µl, Taq DNA polymerase enzyme (3U/µl) 1 µl, nuclease free water X 7 µl, Total reaction volume 250 µl, all PCR work done by Chromous Biotech Pvt. Ltd. PCR thermal cycles and conditions are mentioned in Table 1.

Forward and reverse primers were used for amplification of 16S rDNA sequence: Prokaryotic 16S rRNA specific primer were used in this study: (The PCR product size was expected ~1.5 kb) and the used primers sequences were-

16S Forward Primer: 5' – AGAGTTTGTATCMTGGCTCAG – 3'
16S Reverse Primer: 5' – TACGGYTACCTTGTTACGACTT – 3'

The bacterial cultures were isolated and identified to their nearest species using the 16S rDNA sequence. In Fig. 6 sample TS1(1), TS5 (2) and 500bp DNA ladder (L) was loaded in 1% agarose gel to determine

Table 1
PCR cycle condition.

Temperature °C	95 °C	94 °C	50 °C	72 °C	72 °C
Time	5min	30sec	30sec	1.30min	7min
Cycle	35				

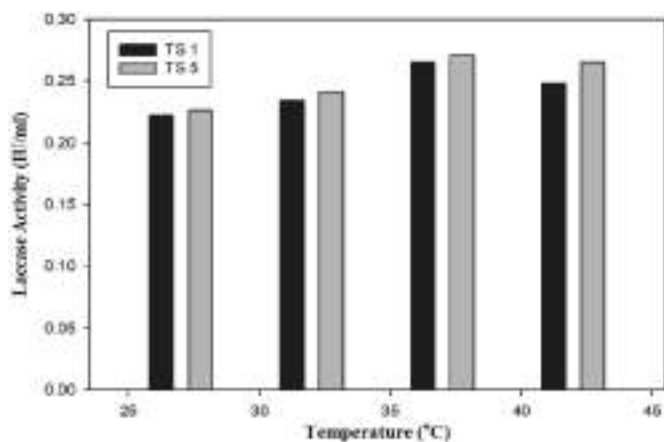


Fig. 3. Laccase activity at different temperatures for laccase production.

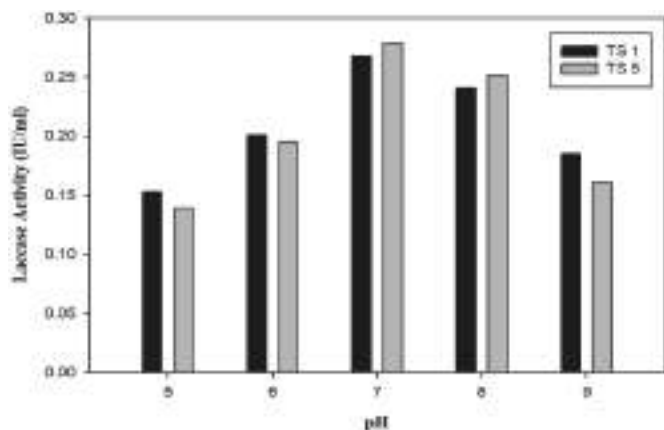


Fig. 4. Laccase activity at different pH for laccase production.

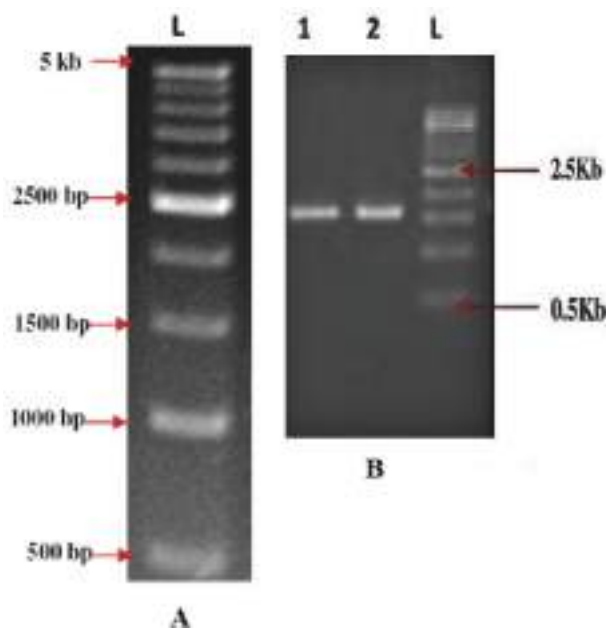


Fig. 6. PCR products loaded on 1% Agarose gel, A: 500bp DNA Ladder, 1: Sample-TS1, 2: Sample-TS5, L: Ladder.

the size of the samples after PCR for 16S rDNA analysis. The 16S rDNA sequence of the isolates was compared with the 16S rDNA GenBank database using BLASTn. Genomic DNA from the isolated strains was isolated and 1.5 kb 16S-rDNA fragment was amplified bi-directionally using high-fidelity PCR. The obtained PCR product was sequenced bi-directionally. Phylogenetic tree builder was used for sequences aligned with system software aligner. A distance matrix was generated using the Jukes-Cantor with corrected distance model. While generating the distance matrix, only alignment model positions were used, alignment inserts were ignored and the minimum comparable position was considered 200. The tree was created using weight or with alphabet size 4 and length size 1000. The entire analysis gave matched with *Pseudomonas sp.* FBF57 partial 16S rRNA gene, isolate FBF57 and next nearest locus was found as *Pseudomonas monteilii* strain PS38 (Fig. 7). The sample was found to be *Gamma proteobacterium symbiont of Calliphora excellent IROM* gene for 16S ribosomal RNA (Fig. 8).

From the above analysis it has very clear that our organisms of interest was belong to the prokaryotes (Bacteria) system. With the use of advanced molecular biology approaches and bio-informatics tool *Pseudomonas monteilii* & *Gamma proteobacterium* was found confirmed organisms.

3.3.3. Laccase activity determination with reference to guaiacol as a standard substrate

Laccase activity was determined by performing the enzyme-substrate reaction between guaiacol as substrate and crude enzyme extract as a laccase source. A UV-Visible spectrophotometer was used to display absorbance at a specific interval of 20 min for 120 min. Laccase activity results are shown below (Fig. 9). The enzyme to substrate ratio was taken as 1:4 as reported from the literature (Rajput and Mishra, 2019). Initially, guaiacol was present in good quantity so the reaction was fast but as the substrate started depleting, the reaction rate became slower.

3.4. Laccase characterization

3.4.1. Effect of substrate concentration, pH and temperature on laccase activity

Laccase obtained from the crude extracts was subjected to standard substrate guaiacol for determining the optimum concentration for its maximum activity. Laccase being substrate-specific enzyme, an excessive amount of substrate concentration would have caused substrate inhibition. Moreover, low concentration would not have allowed attaining the proper rate of reaction. Entities already present in crude extract may also participate in the reaction and affect it adversely. In the case of only one substrate, it has been well known that by increasing substrate concentration, the rate of reaction increases then achieves a maximum, beyond which, rate of reaction will not be affected by substrate concentration. Fig. 10 shows maximum laccase activity at the enzyme to substrate ratio 1:9 for *Pseudomonas monteilii* and 2:8 for *Gamma proteobacterium*.

To signify that enzyme is active (different subunits of enzymes behave differently at diverse pH) and stable it becomes necessary to validate enzyme activity and stability at varied pH. The activity of *Pseudomonas monteilii* was found best at pH 8.0 and that of *Gamma proteobacterium* at pH 6.0 (Fig. 11). The results of this study infer that laccase from *Gamma proteobacterium* strain is much more pH stable than its counterpart (*Pseudomonas monteilii*) and was in accordance with other researches (Cordi et al., 2007; Kunamneni et al., 2007).

Optimum temperature for laccase activity was found at 25 °C for *Gamma proteobacterium*, while that of *Pseudomonas monteilii* at 40 °C (Fig. 12). Enzymatic reactions are temperature specific and their stability depends on the temperature of the reaction mixture and environment. Mostly laccases are thermally stable and research has shown that laccase activity can vary from moderate to higher temperature highly depending on strain type (Nyanhongo et al., 2002; Palmeiri et al., 1993).



Fig. 7. Phylogenetic tree generated by the concatenation of the 16SrRNA sequences Data retrieved from NCBI database (Sequence ID: HG805731.1).

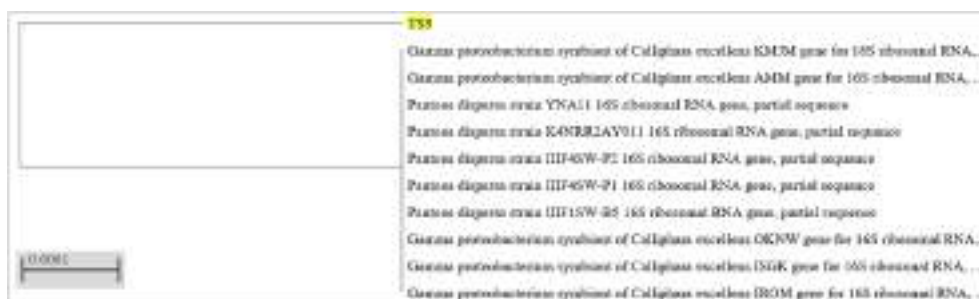


Fig. 8. Phylogenetic tree generated by the concatenation of the 16SrRNA sequences Data retrieved from the NCBI database (Sequence ID: LC473101.1).

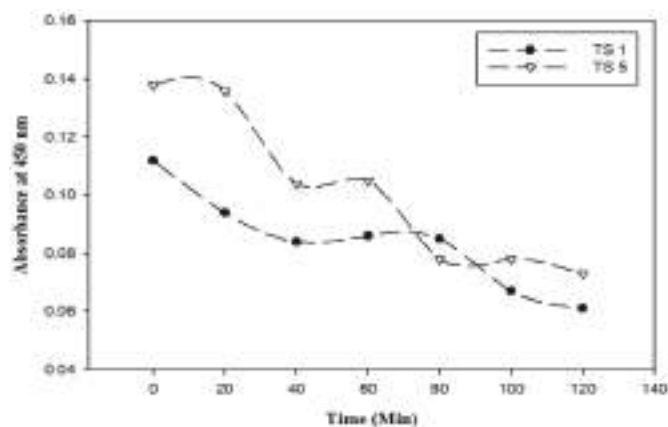


Fig. 9. Laccase activity determination using Guaiacol as standard substrate.

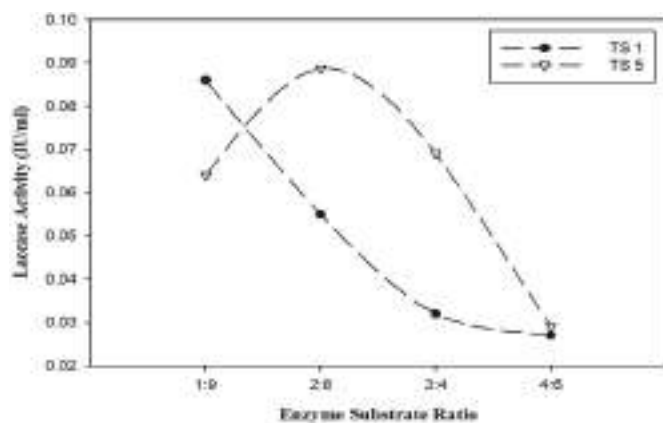


Fig. 10. Optimum substrate concentration determination for pyridine raffininate degradation.

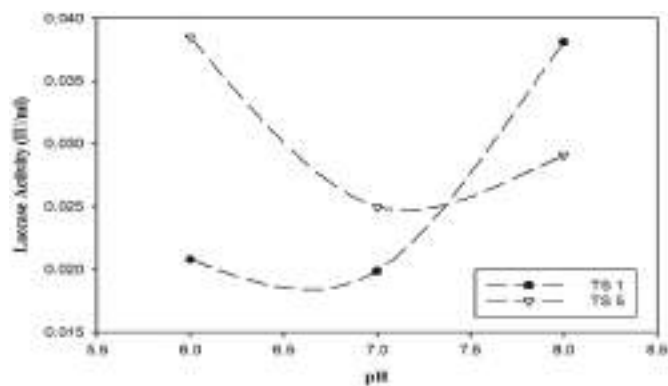


Fig. 11. Optimum pH determination for pyridine raffininate degradation.

3.5. Specific activity measurement

Specific activity is the measure of enzyme purity. It is the ratio of enzyme activity to total protein concentration. Specific activity for crude enzyme extract from *Pseudomonas monteilii* was found to be 0.089 IU/ml, while that of *Gamma proteobacterium* was 0.1217 IU/ml.

3.6. Pyridine raffininate degradation

After the characterization of laccase with standard substrate guaiacol, the best conditions were chosen to perform assay with pyridine raffininate. Extracted enzymes were tested for bioremediation in terms

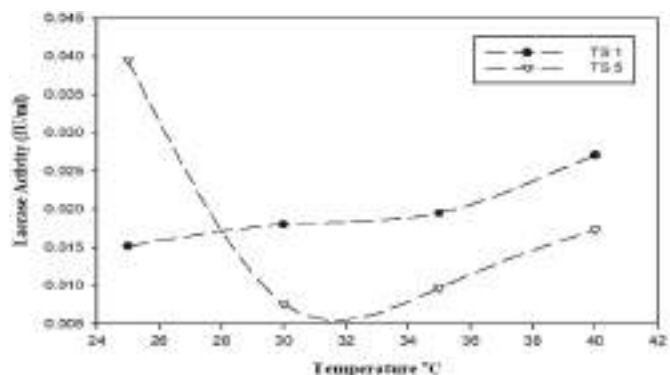


Fig. 12. Optimum temperature determination for pyridine raffininate degradation.

of reduction in optical density (Shi et al., 2015; Singh et al., 2007; Wang et al., 2012).

We determined the optimized conditions viz; enzyme-substrate concentration (1:9), pH(6), temperature(25 °C) for strain *Pseudomonas monteilii*, and enzyme-substrate concentration(2:8), pH(8), temperature(40 °C) for strain *Gamma proteobacterium* and applied the same for the degradation of pyridine raffininate. After initial incubation of 20 min the absorbance of pyridine raffininate increases slightly then it starts decreasing till 120 min and further seems to become a plateau (Fig. 13). Absorbance decreased up to 51% in 140 min for strain *Pseudomonas monteilii* while 59.5% reduction was observed in case of strain *Gamma proteobacterium*. This experiment signifies that pyridine raffininate can be degraded using bacterial laccase.

4. External validation of process parameters

High-Performance Liquid Chromatography (HPLC) was used to accurately determine the degradation percentage of pyridine compound by initially using 50 ppm pure pyridine from BDH instead of pyridine raffininate sample. According to the time course degradation study (Fig. 14a and 14b), the maximum pyridine degradation ($46.323 \pm 5\%$) was observed at 140 min of incubation. HPLC (LC-20AD, Shimadzu, and Tokyo, Japan) was used for the analysis with injection volume 20 μ L at 25 °C and acetonitrile (ACN) as a mobile phase. The reaction mixture without laccase was used as a control for this experiment. All the analysis were carried out in triplicates. The results have been compared with their controls. Both the chromatogram (control and laccase-mediated degradation of pyridine) showed single dominant peaks at a retention time of 2.005, 2.077 min, respectively. The control chromatograms did not show any absolute peaks. However, the laccase treated chromatograms showed their solute peaks at retention time at 1.376 & 1.276 min. The results implied laccase mediated degradation of pyridine. The degradation of toxic pyridine by

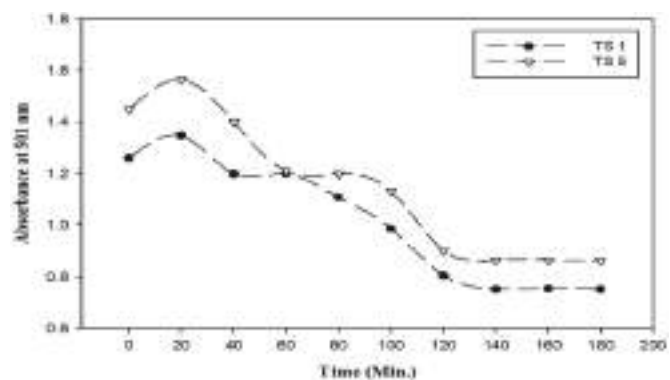


Fig. 13. Pyridine raffininate degradation, absorption read at 501 nm.

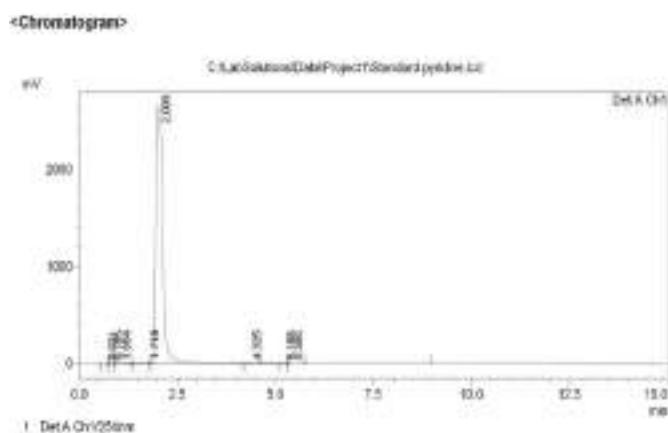


Fig. 14a. Chromatogram of standard 50 ppm pyridine.

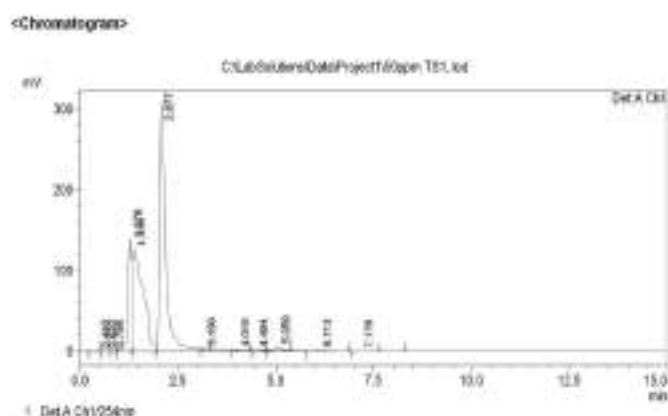


Fig. 14b. Chromatogram of treated 50 ppm pyridine.

Pseudomonas monteilii and *Gamma proteobacterium* suggest a potential alternative for the degradation of pollutants in the ecosystem.

5. Conclusion

Many studies have already reported the potential of laccases in bioremediation of complex phenolic and aromatic substances. However, the persistent and complicated structure and nature of pyridine raffinate has led to little studies regarding its biodegradation. In this study, laccases have been selected to evaluate biodegradation of pyridine raffinate (highly alkaline) as these enzymes have better tolerance towards high pH and show thermal stability. Laccase obtained from isolates of *Pseudomonas monteilii* (enzyme-substrate concentration (1:9), pH (6), temperature (25 °C)) and *Gamma proteobacterium* (enzyme-substrate concentration (2:8), pH (8), temperature (40 °C)) showed around 51 and 59.5% degradation of toxic and carcinogenic pyridine raffinate in 140 min respectively and further by HPLC method 46.323 ± 5% reduction was observed. The outcomes of this investigation suggested a potential route for combating pyridine raffinate pollution in an ecologically compatible and economical manner.

Authors statement

We are submitting revised manuscript entitled “Biodegradation of Pyridine Raffinate by microbial laccase isolated from *Pseudomonas monteilii* & *Gamma proteobacterium* present in Woody Soil” for possible evaluation. We mutually agree with all necessary changes which have been made in this revised manuscript. We affirm that this manuscript is original, has not been published before

and is not currently being considered for publication elsewhere. We affirm that the novelty in results/findings, or significance of results.

Declaration of competing interest

None.

Acknowledgment:

The authors gratefully acknowledge the support of Director, Dr. Ambedkar Institute of Technology for Handicapped, Kanpur for providing the space and resources for successful completion of this comprehensive research and Chromous Biotech Pvt Ltd, Bangaluru, India for 16s RNA based bacterial identification.

This research did not receive any specific grant from funding agencies in the public, commercial, or not-for-profit sectors.

Appendix A. Supplementary data

Supplementary data to this article can be found online at <https://doi.org/10.1016/j.bcab.2020.101650>.

References

- Abd El Monssef, R.A., Hassan, E.A., Ramadan, E.M., 2016. Production of laccase enzyme for their potential application to decolorize fungal pigments on aging paper and parchment. *Ann. Agric. Sci. (Cairo)*. <https://doi.org/10.1016/j.aosas.2015.11.007>.
- Baldrian, P., 2006. Fungal laccases—occurrence and properties. *FEMS (Fed. Eur. Microbiol. Soc.) Microbiol. Rev.* 30 (2), 215–242.
- Bergey, D.H., Hendricks, D., Holt, J.G., Sneath, P.H.A., 1984. *Bergey's Manual of Systematic Bacteriology*, vol. 2. Williams & Wilkins.
- Bugg, T.D.H., Ahmad, M., Hardiman, E.M., Singh, R., 2011. The emerging role for bacteria in lignin degradation and bio-product formation. *Curr. Opin. Biotechnol.* 22 (3), 394–400.
- Chandra, R., Bharagava, R.N., Kapley, A., Purohit, H.J., 2009. Isolation and characterization of potential aerobic bacteria capable for pyridine degradation in presence of picoline, phenol and formaldehyde as co-pollutants. *World J. Microbiol. Biotechnol.* 25 (12), 2113–2119.
- Claus, H., 2004. Laccases: structure, reactions, distribution. *Micron* 35 (1–2), 93–96.
- Cordi, L., Minussi, R.C., Freire, R.S., Durán, 2007. Fungal laccase: copper induction, semi-purification, immobilization, phenolic effluent treatment and electrochemical measurement. *Afr. J. Biotechnol.* 6 (10), 1255–1259.
- D'Souza-Ticlo, D., Sharma, D., Raghukumar, C., 2009. A thermostable metal-tolerant laccase with bioremediation potential from a marine-derived fungus. *Mar. Biotechnol.* 11 (6), 725–737.
- Dean, J.F.D., Eriksson, K.-E.L., 1994. Laccase and the deposition of lignin in vascular plants. *Holzforchung-International Journal of the Biology, Chemistry, Physics and Technology of Wood* 48 (s1), 21–33.
- Degryse, E., Glandsdorff, N., Piérard, A., 1978. A comparative analysis of extreme thermophilic bacteria belonging to the genus *Thermus*. *Arch. Microbiol.* 117 (2), 189–196.
- Diamantidis, G., Effosse, A., Potier, P., Bally, R., 2000. Purification and characterization of the first bacterial laccase in the rhizospheric bacterium *Azospirillum lipoferum*. *Soil Biol. Biochem.* 32 (7), 919–927.
- Dwivedi, U., Singh, P., Pandey, V., Kumar, A., 2011. Laccases from new fungal sources and its promising application. *J. Mol. Catal. B Enzym.* 68, 117–128.
- Hasegawa, R., Sano, M., Tamano, S., 1993. Pyridine (PhIP) carcinogenicity in rats. *Mutat. Res. Fund. Mol. Mech. Mutagen* 376 (1–2), 115–122.
- Huber, W.W., McDaniel, L.P., Kaderlik, K.R., Teitel, C.H., Lang, N.P., Kadlubar, F.F., 1997. Chemoprotection against the formation of colon DNA adducts from the food-borne carcinogen 2-amino-1-methyl-6-phenylimidazo [4, 5-b] pyridine (PhIP) in the rat. *Mutat. Res. Fund. Mol. Mech. Mutagen* 376 (1–2), 115–122.
- Kaur, K., Singh, G., Gupta, V., Capalash, N., Sharma, P., 2017. Impact of phosphate and other medium components on physiological regulation of bacterial laccase production. *Biotechnol. Prog.* 33 (2), 541–548.
- Kersten, P.J., Kalyanaraman, B., Hammel, K.E., Reinhammar, B., Kirk, T.K., 1990. Comparison of lignin peroxidase, horseradish peroxidase and laccase in the oxidation of methoxybenzenes. *Biochem. J.* 268 (2), 475–480.
- Keyser, P., Kirk, T.K., Zeikus, J.G., 1978. Ligninolytic enzyme system of *Phanerochaete chrysosporium*: synthesized in the absence of lignin in response to nitrogen starvation. *J. Bacteriol.* 135 (3), 790–797.
- Kunamneni, A., Ballesteros, A., Plou, F.J., Alcalde, M., 2007. A Review Article. pp. 233–245.
- Li, B., Lei, Z., Huang, Z., 2009. Surface-treated activated carbon for removal of aromatic compounds from water. *Chem. Eng. Technol.* 32 (5), 763–770.
- Majer, B.J., Hofer, E., Cavin, C., Lhoste, E., Uhl, M., Glatt, H.R., et al., 2005. Coffee diterpenes prevent the genotoxic effects of 2-amino-1-methyl-6-phenylimidazo [4, 5-b] pyridine (PhIP) and N-nitrosodimethylamine in a human derived liver cell line (HepG2). *Food Chem. Toxicol.* 43 (3), 433–441.

- Martins, L.O., Soares, C.M., Pereira, M.M., Teixeira, M., Costa, T., Jones, G.H., Henriques, A.O., 2002. Molecular and biochemical characterization of a highly stable bacterial laccase that occurs as a structural component of the *Bacillus subtilis* endospore coat. *J. Biol. Chem.* 277 (21), 18849–18859.
- Mikiashvili, N., Wasser, S.P., Nevo, E., Elisashvili, V., 2006. Effects of carbon and nitrogen sources on *Pleurotus ostreatus* ligninolytic enzyme activity. *World J. Microbiol. Biotechnol.* 22 (9), 999–1002.
- Niladevi, K.N., Sukumaran, R.K., Jacob, N., Anisha, G.S., Prema, P., 2009. Optimization of laccase production from a novel strain—*Streptomyces psammoticus* using response surface methodology. *Microbiol. Res.* 164 (1), 105–113.
- Nyanhongo, G.S., Gomes, J., Gübitz, G., Zvauya, R., Read, J.S., Steiner, W., 2002. Production of laccase by a newly isolated strain of *Trametes modesta*. *Bioresour. Technol.* 84 (3), 259–263.
- Palmeiri, G., Giardina, P., Marzullo, L., Desiderio, B., Nittii, G., Cannio, R., Sannia, G., 1993. Stability and activity of a phenol oxidase from the ligninolytic fungus *Pleurotus ostreatus*. *Appl. Microbiol. Biotechnol.* 39 (4–5), 632–636.
- Pyridine | C5H5N - PubChem. n.d., Retrieved April 5, 2020, from: <https://pubchem.ncbi.nlm.nih.gov/compound/pyridine>.
- Pyridine Market Research Report- Forecast to 2023 | MRFR. n.d., Retrieved April 5, 2020, from: <https://www.marketresearchfuture.com/reports/pyridine-market-3198>.
- Rajput, M.S., Mishra, B.N., 2019. Biodegradation of pyridine raffinate using bacterial laccase isolated from garden soil. *Biocatalysis and Agricultural Biotechnology*. <https://doi.org/10.1016/j.bcab.2018.10.020>.
- Riva, S., 2006. Laccases: blue enzymes for green chemistry. *Trends Biotechnol.* 24 (5), 219–226. <https://doi.org/10.1016/j.tibtech.2006.03.006>.
- Saroja, A.K., 2018. Biodegradability enhancement of industrial organic raffinate containing pyridine and its derivatives by CWAO using ceria promoted MnOx/Al2O3 catalyst at atmospheric pressure. *Chem. Eng. J.* 334, 985–994.
- Sharma, P., Goel, R., Capalash, N., 2007. Bacterial laccases. *World J. Microbiol. Biotechnol.* 23 (6), 823–832.
- Sheikhi, F., Ardakani, M.R., Enayatizamir, N., Rodriguez-Couto, S., 2012. The determination of assay for laccase of *Bacillus subtilis* WPI with two classes of chemical compounds as substrates. *Indian J. Microbiol.* 52 (4), 701–707.
- Shi, X., Liu, Q., Ma, J., Liao, H., Xiong, X., Zhang, K., et al., 2015. An acid-stable bacterial laccase identified from the endophyte *Pantoea ananatis* Sd-1 genome exhibiting lignin degradation and dye decolorization abilities. *Biotechnol. Lett.* 37 (11), 2279–2288.
- Sims, G.K., O'Loughlin, E.J., Crawford, R.L., 1989. Degradation of pyridines in the environment. *Crit. Rev. Environ. Sci. Technol.* 19 (4), 309–340.
- Singh, G., Capalash, N., Goel, R., Sharma, P., 2007. A pH-stable laccase from alkali-tolerant γ -proteobacterium JB: purification, characterization and indigo carmine degradation. *Enzym. Microb. Technol.* 41 (6–7), 794–799.
- Sun, J.-Q., Xu, L., Tang, Y.-Q., Chen, F.-M., Liu, W.-Q., Wu, X.-L., 2011. Degradation of pyridine by one *Rhodococcus* strain in the presence of chromium (VI) or phenol. *J. Hazard Mater.* 191 (1–3), 62–68.
- Thurston, C. F. (2019). Article 1, 1(1 994), 19–26.
- Walker, J.M., Waterborg, J.H., Matthews, H.R., 2003. The Lowry Method for Protein Quantitation. *Basic Protein and Peptide Protocols*, pp. 1–4 (January). <https://doi.org/10.1385/0-89603-268-x:1>.
- Wang, W., Zhang, Z., Ni, H., Yang, X., Li, Q., Li, L., 2012. Decolorization of industrial synthetic dyes using engineered *Pseudomonas putida* cells with surface-immobilized bacterial laccase. *Microb. Cell Factories* 11 (1), 75.
- Yoshida, H., 1883. Chemistry of lacquer (urushi). *J. Chem. Soc. Trans.* 43 (47), 472. <https://doi.org/10.1039/ct8834300472>.



Enzymatic degradation of pyridine raffinate using response surface and artificial neural network simulation

Manish Singh Rajput^{1*}, Vinay Dwivedi^{2*} & SK Awasthi³

¹Department of Biotechnology, Dr. Ambedkar Institute of Technology for Handicapped, Kanpur, Uttar Pradesh, India

²Department of Biotechnology, Naraina Vidyapeeth Engineering & Management Institute Kanpur, Uttar Pradesh, India

³Harcourt Butler Technical University, Kanpur, Uttar Pradesh, India

Received 31 January 2020; revised 17 March 2020

Pyridine is a heterocyclic aromatic compound present in pyridine raffinate, an organic discharge of the pyridine manufacturing industry. Besides pyridine, raffinate also contains formaldehyde, picolines and phenolics. Earlier, we isolated *Gamma proteobacterium* from timber soil for laccase production and optimized the involved process parameters. Here, we studied the optimization of process parameters for biodegradation of pyridine raffinate with the help of mathematical modeling [central composite design with response surface methodology (CCD-RSM) and artificial neural network (ANN)]. The results predicted ANN to be a better tool for optimization of pyridine raffinate degradation. CCD was used to develop the best fit second-order polynomial quadratic regression equation. Prediction of degradation percentage for pyridine raffinate was done using the equation which was found to be 71.60% at temperature 36.76°C, pH 7.45 and inoculum concentration 1.96 mL/10mL. The predicted response was experimentally validated in the wet lab to verify the degradation efficiency. The outcome was 65.76±2%, further confirmed by Gas Chromatography-Flame Ionization Detector (GC-FID). The result of GC-FID () data showed no trace of pyridine (Area 0%) which was reduced from initial area of 1.38% pyridine in raffinate sample.

Keywords: Backpropagation, Biodegradation, Central composite design (CCD), Industrial pollution, Laccase production, Organic pollutant, RSM

The increased industrialization without proper monitoring of effluents comprising toxic chemicals has led to serious environmental pollution. One such chemical is pyridine and its derivatives which are frequently found in the industrial and agricultural effluents. Due to its recalcitrant nature, the United States Environment Protection Agency (USEPA) has listed pyridine as a priority organic pollutant¹. Utilization as a raw material in paint, dyes and pharmaceuticals along with its use in the alcohol denaturation process and to formulate products, such as medicine, vitamins, adhesives and in waterproofing of fabrics are some of the applications of pyridine^{2,3}. Pyridine has carcinogenic properties, and hence an exposure limit of 5 ppm averaged over a 10 h work-shift has been recommended by Occupational Safety and Health Administration (OSHA), American Conference of Governmental Industrial Hygienists (ACGIH).

Pyridine raffinate is a pale, toxic, obnoxious odour organic effluent released from different manufacturing industries, such as pharmaceuticals agrochemicals, food, latexes and others⁴. The raffinate consists of various heterocyclic aromatic hydrocarbon compounds, such as formaldehyde, phenolics and picolines along with pyridine and is highly alkaline (pH 12.0) and water soluble⁵. Among the various treatment methods investigated *viz.* sorption, zeolites and biodegradation⁶, the biological treatment approach has been found to be most cost-effective. In this work, we opted for ex-situ bioremediation approach for degrading pyridine raffinate using bacterial extracellular enzyme laccase. The extensive applications of laccase have enhanced its industrial importance in areas like delignification of lignocellulosic material, waste detoxification and textile dye decolourization. The large amount of wastewater requiring treatment creates hindrance in the industrial application of enzyme assisted treatment technologies. High costs, limited operating stability, intolerance to unfavourable environmental conditions, and challenging recovery and recyclability are among the many other

*Correspondence:

Phone: +91 98684 21746 (Mob.)

E-Mail: drvinay@yahoo.com (VD); msrbiotech@gmail.com (MSR)

drawbacks encountered while using soluble native enzymes for treatment⁷. Although laccase can be obtained from both bacteria and fungi, bacterial laccases are comparatively better for industrial use which could be attributed to their ability to perform in a broader range of temperature and pH and greater stability against different physical and chemical inhibitions.

In this study, we explored degradation of pyridine raffinate using laccase and to enhance the degradation process by optimizing the involved process parameters. Pyridine raffinate degradation was used as a model in this study for optimization of industrial degradation of pyridine and validation of the hypothesis was performed with central composite design (CCD). CCD is beneficial and efficient in providing information on the effects of variables involved in the experiment and overall experimental error in a minimum number of required runs (CCD-RSM). Box & Wilson developed response surface methodology (RSM) with the objective of improving yield from various industries⁸. The optimization of multiple parameters is performed in a stepwise manner by conducting a statistically designed experiment followed by determination of coefficient estimate, analysis of the response and finally checking the adequacy of the model.

In this study, we focused on optimizing the process parameter for degradation of pyridine raffinate using the diversity of isolated bacterial laccase to enhance the removal of pyridine on which only limited information is available. Furthermore, in order to screen the optimum process parameters, we used simulation tools like CCD-RSM⁹⁻¹¹ and ANN which is well known for optimization in biotechnology, life science, process industries¹². We intend to select and screen the degradation parameters and further validate the parameters to apply in the industrial trial.

Materials and Methods

All chemicals used in this study were of analytical grade procured from Sigma Aldrich, Hi-media, BDH (British Drug House). The media and their ingredients were purchased from Hi-Media. Pure pyridine was used as a control sample and was procured from Thomas Baker.

Microorganism

Laccase producing bacteria was isolated from a soil sample in our previous study¹³. The bacteria were morphologically and biochemically characterized and identified as *Pseudomonas fluorescens* (Gamma proteobacterium).

Collection of pyridine raffinate sample

Plastic containers (Capacity 250 mL) were used to aseptically collect pyridine raffinate from M/S Jubilant Organosys Ltd, Gajraula (UP), India. The freshly collected pyridine raffinate samples were transparent, pale with pungent smell of formaldehyde, phenol, picoline, and pyridine.

Growth media

Solvents *viz.* Tris-Base, Phosphate buffer, EDTA and Propyl alcohol were obtained from Thomas Baker Chemicals Private Limited, New Delhi, India. Salts *viz.* Na₂HPO₄, CaSO₄, NaCl, ZnSO₄, C₆H₅FeO₇, MnSO₄.H₂O, K₂Cr₂O₇, NaHCO₃, NaH₂PO₄ and CH₃COONa were obtained from Central Drug House, New Delhi, India and media components *viz.* agar, yeast extract, sucrose, glucose, tryptone, peptone were obtained from Sisco Research Laboratories Pvt. Ltd. (SRL), New Delhi, India. Guaiacol was procured from Thermo Fisher Scientific India Pvt. Ltd., Mumbai, India. All reagents were of analytical grade and extra pure quality.

Laccase production media

The production of laccase was done in 250 mL Erlenmeyer flask, containing 50 mL of modified production media (g/l): 0.4 CaSO₄.2H₂O, 2.0 MgCl₂.6H₂O, 1.0 glucose, 5.0 Ferric citrate solution 0.01M, 0.5 Na₂HPO₄, 0.5 NaH₂PO₄, 0.5 NH₄NO₃, 0.5 K₂HPO₄, 3.0 yeast extract, 3.0 tryptone. pH was adjusted to 8.0 using 5N NaOH prior to sterilization (121°C, 15 lbs, 15 min). About 1% v/v inoculum (1×10⁴ cells/mL)¹⁴ was used for media inoculation and incubation was done at 30°C at 120 rpm for 5 days. After incubation was over, the culture broth was centrifuged at 10000 ×g for 10 min at 4°C and the supernatant was used as crude enzyme to measure laccase activity.

Process optimization

Experimental design and modeling

In this study, our aim was to obtain the optimum values of process parameters (temperature, pH and inoculum concentration) for efficient and optimized degradation of pyridine raffinate using CCD-RSM and ANN as statistical tools. RSM had been used as a prediction tool for process optimization¹⁵. As much as 20 experiments were conducted employing a three-level-three factor CCD taking into consideration the temperature (°C), pH and inoculum concentration (g/L) (Table. 1).

The influence of independent experimental factors and their interaction on pyridine raffinate degradation was predicted using a 2³ rotatable CCD followed by RSM. Many researchers have successfully used CCD-

Table 1 — Range of parameters (independent variables) chosen for CCD

Factor	Name	Units	Type	Minimum	Maximum	Coded Low	Coded High	Mean	Std. Dev.
A	Temp.	°C	Numeric	19.89	45.11	-1 ↔ 25.00	+1 ↔ 40.00	32.50	6.36
B	pH		Numeric	4.64	11.36	-1 ↔ 6.00	+1 ↔ 10.00	8.00	1.70
C	Inoculum conc.	g/l	Numeric	0.4887	3.01	-1 ↔ 1.00	+1 ↔ 2.50	1.75	0.6359

RSM for optimization and improved the degradation of PAHs¹⁶.

The best fit second-order polynomial quadratic regression equation (Eq.1) was generated with the help of the response obtained through a CCD,

$$Y = \beta_0 + \beta_1A + \beta_2B + \beta_3C + \beta_{11}A^2 + \beta_{22}B^2 + \beta_{33}C^2 + \beta_{12}AB + \beta_{13}AC + \beta_{23}BC \quad (\text{Eq. 1})$$

where, Y is the dependent variable (percentage of pyridine raffinate degradation); β_0 represents the offset value whereas $\beta_1, \beta_2, \beta_3$ are coefficients of linear terms; $\beta_{11}, \beta_{22}, \beta_{33}$ are quadratic coefficients and $\beta_{12}, \beta_{13}, \beta_{23}$ denote interaction coefficients. A, B, C represent the independent variables, viz., Temperature (°C), pH and inoculum concentration (g/L), respectively. Significance tests and analysis of variance (ANOVA) on each response were conducted to analyze the effect of the parameters and their interaction on the response in order to check the adequacy of the model. Design Expert 9.0 (State-Ease Inc., USA) was employed for the plotting three-dimensional surface plots. The value of α was calculated as 1.5 where $\alpha = 2k/4$ ($k=3$, the number of variables). Table 2 represents the coded values of all independent variables and the experimental value of the only response variable Y (percentage of pyridine raffinate degradation) along with predicted values. The coefficients were calculated by Design-Expert 9.0.6.2.

Artificial neural network (ANN) modeling

A multilayered feed-forward ANN with error backpropagation (BP) was employed using MATLAB R2016a (MathWorks Inc., USA). Constant improvement of the network with proper mapping between input and output layers and error reduction is desired which is achieved by a strict learning scheme for proper training of the network^{17,18}. The network was trained with Levenberg-Marquardt back-propagation algorithm (trainlm) in order to obtain the weights and biases. This algorithm typically requires more memory but less time. Minimization of error at each iteration during process optimization is most commonly done by a feed forward network with backpropagation¹⁹. The developed ANN architecture was used to optimize pyridine raffinate degradation using input neurons network topology. The number of hidden layer neurons was recognized by the

Table 2 — Experimental plan, range and levels of independent variables (A), (B) and (C)

Run	Temp. (°C)	pH	Inoculum (mL/10 mL)	Exp. removal (%)	RSM	ANN
1	25	6	1	25.63	20.99	25.74597
2	40	6	1	46.97	48.5	47.54515
3	25	10	1	42.97	43.72	40.81833
4	40	10	1	74.93	70.98	74.68941
5	25	6	2.5	30.92	35.13	31.58764
6	40	6	2.5	93.23	92.73	90.35077
7	25	10	2.5	36.36	35.08	38.33328
8	40	10	2.5	87.54	92.43	88.00668
9	20	8	1.75	16.36	17.06	14.15993
10	45	8	1.75	89.47	88.42	89.45637
11	32.5	4.5	1.75	47.05	46.81	47.22412
12	32.5	11.5	1.75	65.79	65.67	67.66411
13	32.5	8	0.5	37.46	41.34	37.69763
14	32.5	8	3.0	75.5	71.27	75.84445
15	32.5	8	1.75	61.55	57.55	58.06888
16	32.5	8	1.75	63.36	57.55	58.06888
17	32.5	8	1.75	48.11	57.55	58.06888
18	32.5	8	1.75	56.06	57.55	58.06888
19	32.5	8	1.75	58.73	57.55	58.06888
20	32.5	8	1.75	57.41	57.55	58.06888

training of several ANN topologies. The optimal one was selected on the basis of minimization of mean square error (MSE) and overall correlation coefficient (R) to improve the generalization ability of ANN topology. Overall, 20 experimental data points were used to construct and train the neural network model. About 70% of the overall data set was used for training the network model while 30% (15% + 15%) for testing and validation of the model. Training automatically stops as soon as improvement in generalization stops. This was indicated by an increase in the mean square error of the validation samples. The training of the neural network was performed until the MSE reaches a constant low value with accompanying overall correlation coefficient (R value) close to 1.

Results and Discussion

Pyridine raffinate degradation:

Laccase was initially characterized by standard substrate guaiacol after which the best conditions were chosen to perform assay with pyridine raffinate. The bioremediation capability of the extracted enzyme was tested by analyzing the reduction in

optical density. Conical flasks (250 mL) each with 100 mL pyridine raffinate were inoculated with crude laccase enzyme and incubated according to CCD for evaluating degradation performance. Then, 5 mL of sample was taken aseptically at optimized time; 140 min and centrifuged (Elektrocraft Pvt. Ltd., MP400R, Mumbai, India) at 5000 rpm for 10 min¹³. The analysis of pyridine bioremediation was performed in terms of optical density reduction in the supernatant, observed at 501nm by a UV spectrophotometer (G Biosciences Pvt. Ltd., Noida, India) (Table 2).

The response expressed as percentage of pyridine raffinate degradation was calculated from Eq.2,

$$\% \text{ Degradation} = \frac{(C_0 - C_t)}{C_0} \times 100 \quad (\text{Eq. 2})$$

where C₀ is the initial optical density (OD) and C_t is the OD after time t (min).

Optimization of pyridine raffinate degradation

Central composite design (CCD) was employed for the experimental optimization of pyridine raffinate degradation. CCD model was used for experimental run, using temperature (A), pH (B), and inoculum concentration (C) as a variable parameter. The experimental run and the respective responses (i.e. degradation of pyridine raffinate in g/L) have been shown in Table 2. Error produced during the experiment was estimated before applying the RSM, ANN model for optimization.

Optimization by RSM modeling

The degradation of pyridine raffinate ranged between 16.36 and 93.23% removal. The experimental data was simulated using RSM for interaction analysis and response plot. The ANOVA model for pyridine raffinate degradation is shown in Table 3.

The model F-value of 35.86 implied model to be significant with only a 0.01% chance that an F-value this large could occur due to noise. P-values less than 0.0500 indicated the significant model terms which was A, B, C, AC, BC in this case. Model terms with values greater than 0.10 indicated insignificance and if insignificant model terms are many (not counting those required to support hierarchy), model reduction may improve the model. The Lack of Fit F-value of 0.8295 implied an insignificant lack of fit relative to the pure error. There was 57.88% chance that a Lack of Fit F-value this large could occur due to noise. Non-significant lack of fit is good as it implies the model to fit. The predicted R² of 0.8621 was in reasonable agreement with the adjusted R² of 0.9429; the difference was less than 0.2. Adeq precision

measures the signal to noise ratio. A ratio greater than 4 is desirable and in this case a ratio of 20.961 indicated an adequate signal. Hence, the model was suitable to be used to navigate the design space.

Final equation regarding code factors

$$\text{Pyridine raffinate degradation (\%)} = -97.46393 + 2.48722\text{Temperature} + 11.42961 \text{pH} + 1.49961\text{Inoculum} - 0.004250\text{Temperature} * \text{pH} + 1.33756\text{Temperature} * \text{Inoculum} - 3.79583\text{pH} * \text{Inoculum} - 0.030233\text{Temperature}^2 - 0.115346\text{pH}^2 - 0.782526\text{Inoculum}^2 \dots\dots\dots(\text{Eq. 3})$$

Predictions regarding the response for given levels of each factor can be made by using Eq. 3 in terms of actual factors where the levels should be specified in the original units for each factor. Fig. 1 depicts the interaction between the actual and predicted response. Further, the interaction graph and contour plot showing the relationship between two parameters keeping the remaining as constant is also presented. The interaction between inoculum concentration and pH is shown in

Table 3 — Analysis of variance (ANOVA) for pyridine raffinate degradation

Source	Sum of Squares	df	Mean Square	F-value	p-value
Model	8413.99	9	934.89	35.86	<0.0001*
A-temperature	6147.29	1	6147.29	235.80	<0.0001
B-pH	429.27	1	429.27	16.47	0.0023
C-inoculum	1081.39	1	1081.39	41.48	<0.0001
AB	0.0325	1	0.0325	0.0012	0.9725
AC	452.85	1	452.85	17.37	0.0019
BC	259.35	1	259.35	9.95	0.0103
A ²	41.68	1	41.68	1.60	0.2348
B ²	3.07	1	3.07	0.1177	0.7387
C ²	2.79	1	2.79	0.1071	0.7502
Residual	260.70	10	26.07		
Lack of fit	118.20	5	23.64	0.8295	0.5788**
Pure error	142.50	5	28.50		
Cor total	8674.69	19			

[*significant; **not significant]

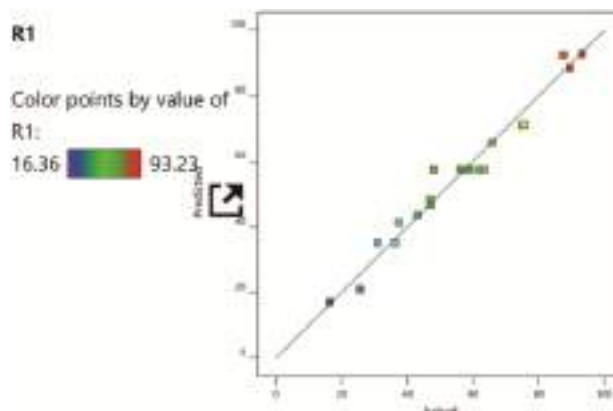


Fig. 1 — Relation between actual response and predicted response

Fig. 2A at a constant temperature 32.5 °C. Similarly, the interaction between pH and temperature at a constant inoculum concentration of 1.75% is represented in Fig. 2B and interaction between inoculum concentration and temperature at constant pH 8 is represented in Fig. 2C. The optimum degradation of pyridine raffinate through RSM was evaluated at pH 7.45, temp 36.76°C

and inoculum 1.96%. Fig. 3 depicts the optimum levels of the different parameters with the corresponding outcome for pyridine raffinate degradation.

Optimization by Artificial Neural Network (ANN)

Initially, for the ANN model, the input data was divided as training (70%), validation (15%) and testing (15%) and the performance of training is

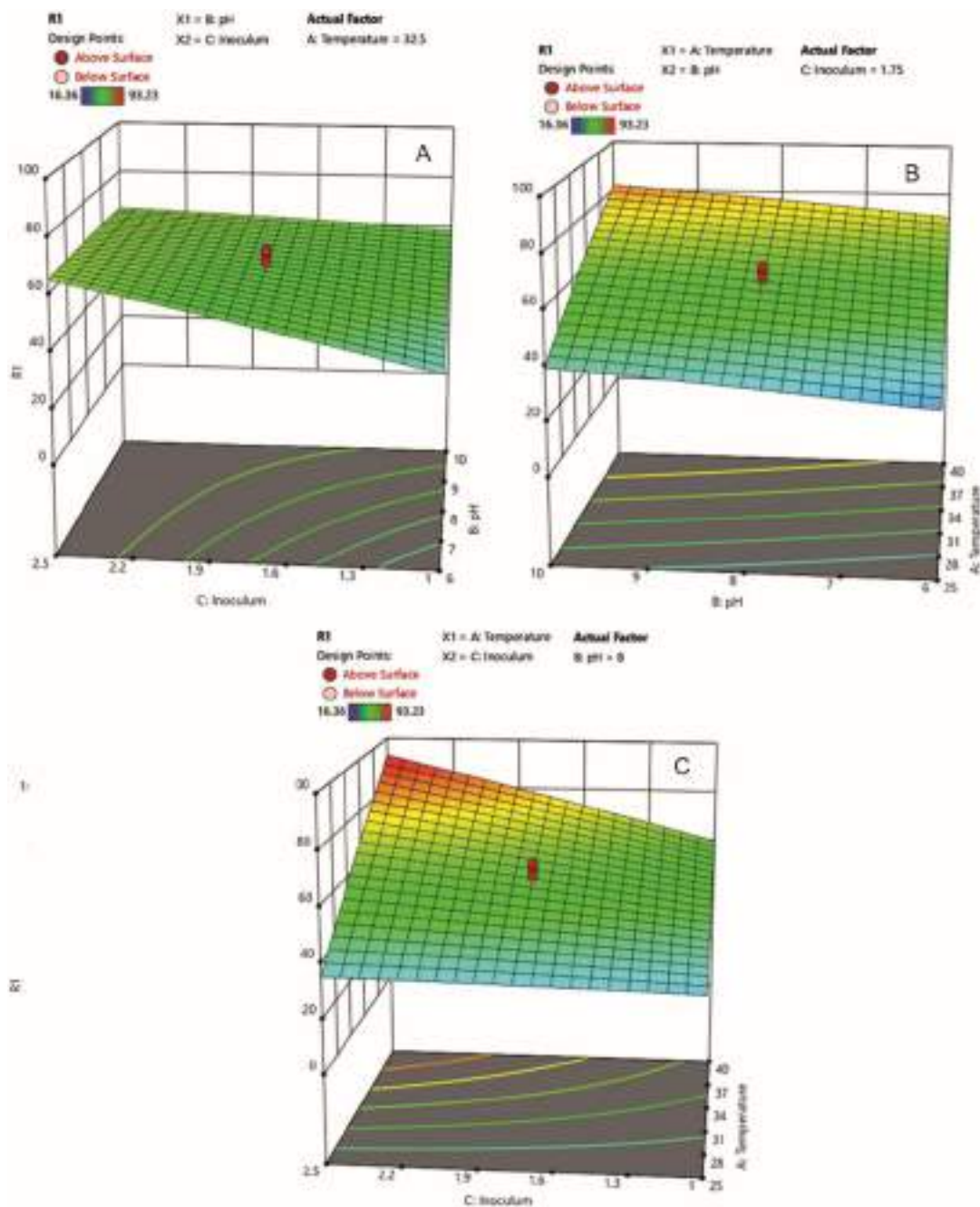


Fig. 2 — Contour graph interaction between (A) inoculum concentration and pH; (B) pH and temperature; and (C) inoculum concentration and temperature

depicted in Fig. 4A. The ANN model with suitable R^2 values of training (0.9848), validation (0.9981) and testing (0.9977) is represented in Fig. 4B. The overall model was best fit to a linear equation with R^2 value 0.99013 which was not close to R^2 value of RSM data set which was 0.9699. This indicates that accurate

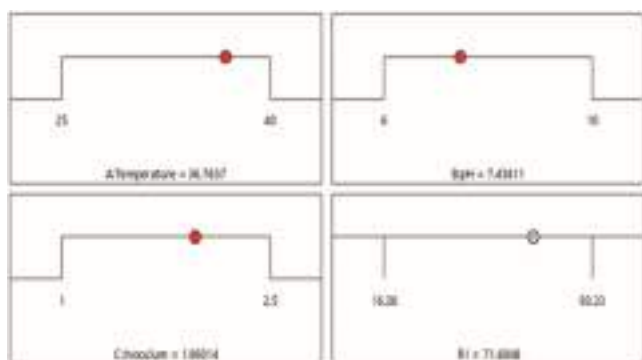


Fig. 3 — Optimum outcome of parameters

simulation for pyridine raffinate degradation (target) was provided by the developed ANN model and the experimental results were reproduced with greater precision. The quality of the data used to develop the ANN model was further estimated by error histogram plot which indicated most of the errors to range between -0.4276 to 0.3349 (Fig. 4C). The collection of more data points was necessitated in order to improve the model due to the presence of a large number of outliers in this model.

External validation by GC analysis

The GC-Flame ionization detector (GC-FID) was used to analyze the presence of pyridine along with other volatile and semi-volatile compounds in the raffinate and to validate the data regarding pyridine removal after microbial laccase treatment. Analysis of sample was performed by Agilent GC7890B with headspace 7697B (Agilent Technologies) to detect the compounds present using a GsBP-624 capillary

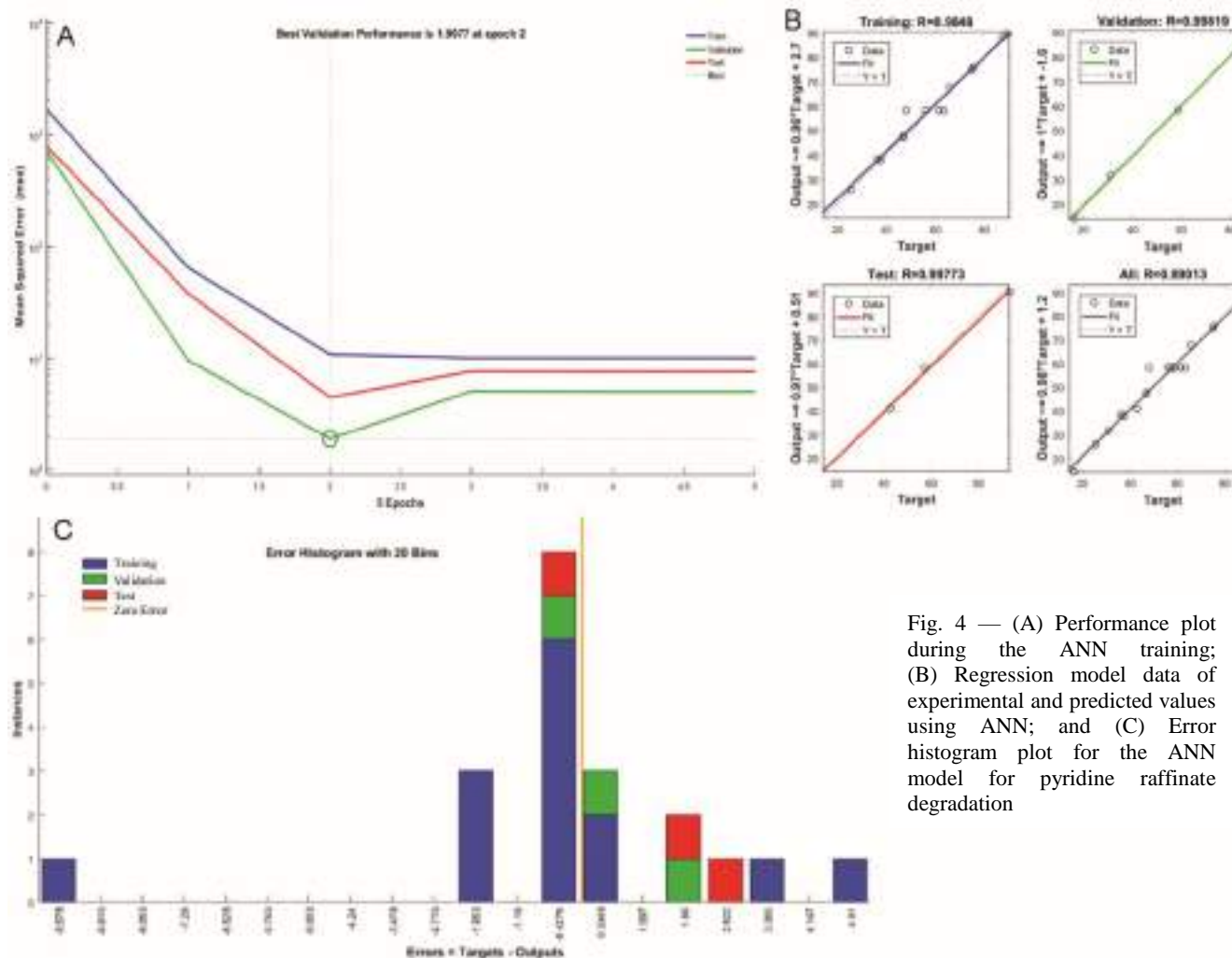


Fig. 4 — (A) Performance plot during the ANN training; (B) Regression model data of experimental and predicted values using ANN; and (C) Error histogram plot for the ANN model for pyridine raffinate degradation

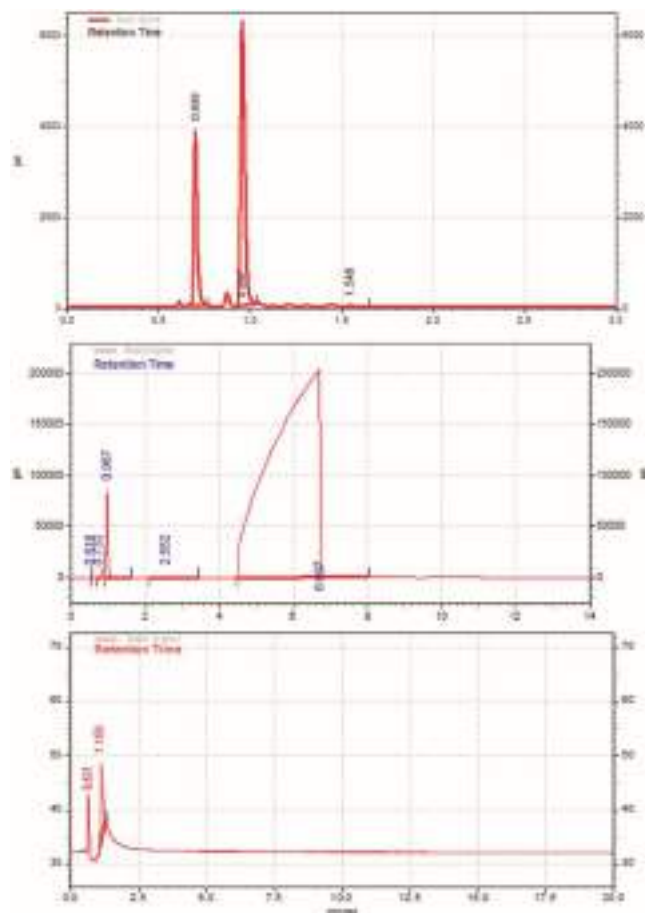


Fig. 5 — GC chromatogram of (A) pure pyridine analysis; (B) pyridine raffinate analysis; and (C) Analysis of pyridine raffinate after treatment by microbial laccase

column (30 m X 0.32 mm X 1.80 μ m film thickness) (Agilent Technologies). Hydrogen was used as a carrier gas at a flow rate of 36 mL/min and the sample volume loaded was 1.0 μ L. The column temperature was set at 100°C for 15 min. The volatile compounds present were detected by comparing their retention times depicted in the gas chromatogram to that of pure standard compound. The detection of the elements was done using a flame ionization detector. The chromatograms are shown in Fig. 5A-C. Fig. 5A indicates chromatogram for pure pyridine to be used as control with base material which depicts the peak with retention time and percentage (%) area for pyridine as 0.957 min and 65.10%, respectively; the retention time for base material was 0.699 min. (34.42%). The chromatogram in Fig. 5B depicts the different compounds present in the pyridine raffinate sample. The peak with retention time at 0.967 min. was confirmed as pyridine (1.38%) since the retention time

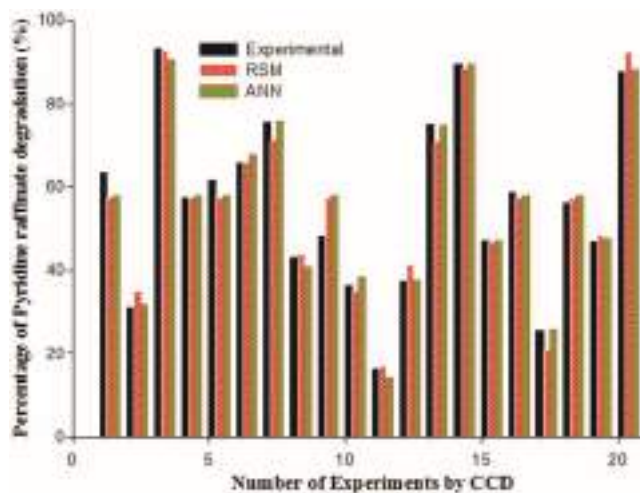


Fig 6 — Comparative analysis of experimental vs. CCD-RSM vs. ANN data

corresponded to that of pure pyridine peak in control. Another prominent peak was obtained at 6.697 min. (98.5%). The identification of the compounds associated with the other peaks is to be done in our future studies. The analysis of the pyridine raffinate sample after treatment with microbial laccase validated the removal of pyridine by the enzyme. The chromatogram in Fig. 5C showed two peaks at 0.631 min. (21.00%) and 1.10 min. (77.93%), respectively, none of which corresponded to the peak for pyridine in the chromatogram mentioned in Fig. 5B. This indicates the potential degradation of the pyridine in the raffinate sample after treatment by microbial laccase since 0% area was observed.

Comparing CCD-RSM and ANN data

The comparison of RSM and ANN data for validation has also been done in previous studies^{15,20}. Fig. 6 depicts the comparison between CCD-RSM and ANN response where the data points of ANN response showed no overfitting. Also, the model was found to be statistically more suitable when compared to the RSM response. The experimental and predicted values of pyridine raffinate degradation by RSM and ANN are illustrated in Table 2. R^2 and mean square error (MSE) was employed as the basis for comparison of predictive capabilities of RSM and ANN models. R^2 values for the predicted model of RSM were found to be 0.9699 and that for the ANN model was 0.9901 whereas the MSE values for RSM and ANN models were 28.50 and 1.9077, respectively. One of the limitations with the RSM model is its ability to generalize data by only quadratic equations while ANN models demonstrate

higher predictive capability attributed to the non-linear polynomials of the system. The comparative predictive supremacy of ANN over experimental response has also been reported²¹. The selection of model type (RSM or ANN) mainly depends upon the type of data set to be used. RSM models are more appropriate in case of the limited number of components for obtaining the relation between input and output components and for sensitivity analysis²². However, on the other hand, ANN possesses the ability to learn and generalize the behaviour of any complex process and represents non-linearities in a much-rectified way²³.

Conclusion

In this study, we demonstrated degradation of the environmental pollutant pyridine raffinate by microbial laccase. We estimated the optimum process parameters required for adequate degradation of pyridine raffinate using central composite design with further analysis of the experimental outcome by coupling RSM and ANN model. ANN was found to be a better and improved tool for optimization of pyridine raffinate degradation. The predicted degradation of pyridine raffinate through the model was found to be 71.60% at temperature 36.76°C, pH 7.45 and inoculum concentration 1.96 mL/10 mL. The actual run had limitation of incubation temperature, therefore instead of 36.76°C, temperature was approximated at 37°C. At this condition, the actual degradation was determined by UV spectroscopy in terms of OD reduction and further validated by GC-FID. The optimum result was 65.76% which was further validated by GC-FID analysis to confirm the depicted area percentage (1.38%) of pyridine in the pyridine raffinate sample. After treatment by microbial laccase, the chromatogram showed no trace of pyridine (0% area) in the treated sample. Hence, microbial laccase could show potential in remediation of pyridine raffinate discharged into terrestrial and aquatic environment. Also, mathematically designed experiments (CCD-RSM/ANN) have great potential in the field of process optimization.

Acknowledgement

The authors acknowledge CSIR-CIMAP, Lucknow for GC analysis.

Conflict of Interest

Authors declare no conflict of interests.

References

- 1 Sushma & Saroha AK, Treatment of industrial organic raffinate containing pyridine and its derivatives by coupling of catalytic wet air oxidation and biological processes. *J Clean Prod*, 162 (2017) 973.
- 2 Mohan D, Singh KP, Sinha S & Gosh D, Removal of pyridine derivatives from aqueous solution by activated carbons developed from agricultural waste materials. *Carbon*, 43 (2005) 1680.
- 3 Lataye DH, Mishra IM & Mall ID, Removal of pyridine from liquid and gas phase by copper forms of natural and synthetic zeolites. *Ind Eng Chem Res*, 45 (2006) 3934.
- 4 Sharma VK, Singh J & Yadav OP, Physicochemical studies of some surfactants in water and in water+ pyridine mixture. *Indian J Chem*, 35A (1996) 337.
- 5 Singh BB & Chandra R, Comparative Chronic Toxicity of Pyridine, α -Picoline, and β -Picoline to *Lemma minor* L. and *Chlorella vulgaris* B. *Bull Environ Contam Toxicol*, 75 (2005) 482.
- 6 Li J, Cai W & Cai J, The characteristics and mechanisms of pyridine biodegradation by *Streptomyces* sp. *J Hazard Mater*, 165 (2009) 950.
- 7 Bilal M, Rasheed T, Nabeel F, Iqbal HM & Zhao Y, Hazardous contaminants in the environment and their laccase-assisted degradation—a review. *J Environ Manage*, 234 (2019) 253.
- 8 Box GE, The exploration and exploitation of response surfaces: some general considerations and examples. *Biometrics*, 10 (1954) 16.
- 9 Udeh KO & Achremowicz B, Optimization of cultivation medium composition of an L-lysine producing mutant: the use of response surface methodology. *Acta Microbiol Pol*, 42 (1993) 171.
- 10 Saval S, Pablos L & Sanchez S, Optimization of a culture medium for streptomycin production using response-surface methodology. *Bioresour Technol*, 43 (1993) 19.
- 11 Ergun M & Mutlu SF, Application of a statistical technique to the production of ethanol from sugar beet molasses by *Saccharomyces cerevisiae*. *Bioresour Technol*, 73 (2000) 251.
- 12 Myers RH, Montgomery DC, Vining GG, Borror CM & Kowalski SM, Response surface methodology: a retrospective and literature survey, *J Qual Technol*, 36 (2004) 53.
- 13 Rajput MS, Dwivedi V & Awasthi SK, Biodegradation of pyridine raffinate by microbial laccase isolated from *Pseudomonas monteilii* & Gamma proteobacterium present in woody soil. *Biocatal Agric Biotechnol*, 26 (2020). doi.org/10.1016/j.bcab.2020.101650.
- 14 Barathi S & Vasudevan N, Utilization of petroleum hydrocarbons by *Pseudomonas fluorescens* isolated from a petroleum-contaminated soil. *Environ Int*, 26 (2001) 413.
- 15 Pandey AK, Pandey K, Pandey A, Morya VK & Singh LK, Response surface and artificial neural network simulation for process design to produce L-lysine by *Corynebacterium glutamicum* NCIM 2168. *Indian J Biotechnol*, 18 (2019) 269.
- 16 Sachaniya BK, Gosai HB, Panseriya HZ & Dave BP, Bioengineering for multiple PAHs degradation for contaminated sediments: Response surface methodology (RSM) and artificial neural network (ANN). *Chemometr*

- Intell Lab Syst*, 202 (2020). doi.org/10.1016/j.chemolab.2020.104033.
- 17 Little JN & Shure L, *Signal Processing Toolbox User's Guide*, (The MathWorks, Inc., Massachusetts, U.S). 1993.
 - 18 Witek-Krowiak A, Chojnacka K, Podstawczyk D, Dawiec A & Pokomeda K, Application of response surface methodology and artificial neural network methods in modelling and optimization of biosorption process. *Bioresour Technol*, 160 (2014) 150.
 - 19 Turan NG, Mesci B & Ozgonenel O, The use of artificial neural networks (ANN) for modeling of adsorption of Cu (II) from industrial leachate by pumice. *Chem Eng J*, 171 (2011) 1091.
 - 20 Das S, Bhattacharya A, Haldar S, Ganguly A, Gu S, Ting YP & Chatterjee PK, Optimization of enzymatic saccharification of water hyacinth biomass for bio-ethanol: Comparison between artificial neural network and response surface methodology. *Sustain Mater Technol*, 3 (2015) 17.
 - 21 Desai KM, Survase SA, Saudagar PS, Lele SS & Singhal RS, Comparison of artificial neural network (ANN) and response surface methodology (RSM) in fermentation media optimization: case study of fermentative production of scleroglucan. *Biochem Eng J*, 41 (2008) 266.
 - 22 Bezerra MA, Santelli RE, Oliveira EP, Villar LS & Escaleira LA, Response surface methodology (RSM) as a tool for optimization in analytical chemistry. *Talanta*, 76 (2008) 965.
 - 23 Hajmeer MN, Basheer IA & Najjar YM, Computational neural networks for predictive microbiology II. Application to microbial growth. *Int J Food Microbiol*, 34 (1997) 51.

Analysis of transmit antenna selection based selective decode forward cooperative communication protocol

Vikash Sachan*, Indrajeet Kumar, Ravi Shankar, Ritesh Kumar Mishra

Department of Electronics and Communication Engineering,
National Institute of Technology Patna, Patna-800005, India

vikash.ece15@nitp.ac.in

ABSTRACT. In this work, we consider a single relay multiple input multiple output (MIMO) space-time block-code (STBC) based relaying system for two strategies using transmit antenna selection (TAS) technique. We consider the Rayleigh distribution between source to destination (SD), relay to destination (RD) and source to relay (SR) fading channel links. In first selection strategy, we consider selective decode and forward (SDF) protocol between the relay and destination and in second selection strategy, we consider STBC SDF protocol between RD fading channel links. We derive the closed form expressions for SER, SER upper bound and diversity order (DO). The optimal power allocation factors (OPFs) are derived for the both strategies, which minimize the SER of the relaying system. Simulation results show that the second strategy performs better than the first one for the same DO.

RÉSUMÉ. Dans ce travail, nous considérons un système de relais à base de code de blocs spatio-temporels (STBC) à entrées multiples et sorties multiples (MIMO) à relais unique pour deux stratégies utilisant la technique de sélection d'antenne d'émission (TAS). Nous considérons les liaisons de canaux à évanouissements de la distribution de Rayleigh entre source vers destination (SD), relais vers destination (RD) et source vers relais (SR). Dans la première stratégie de sélection, nous considérons le protocole de décodage et de transmission sélectifs (SDF) entre le relais et la destination. Et dans la deuxième stratégie de sélection, nous considérons le protocole STBC SDF entre les liaisons de canaux à évanouissements RD. Nous dérivons les expressions de forme fermée pour SER, limite supérieure et ordre de diversité (DO). Les facteurs optimaux d'allocation de puissance (OPFs) sont dérivés pour les deux stratégies, ce qui minimise le SER du système de relais. Les résultats de la simulation montrent que la deuxième stratégie est plus performante que la première pour le même OD.

KEYWORDS: multiple input multiple output, space-time-block-code, selective decode and forward, pairwise error probability.

MOTS-CLÉS: entrée multiple et sortie multiple, code spatio-temporel, décodage et transmission sélectifs, probabilité d'erreur paire.

DOI:10.3166/TS.35.47-60 © 2018 Lavoisier

1. Introduction

MIMO is proven, cost-effective technology, high spectral efficiency, provides antenna diversity and reduces channel fading. Cooperative communication attains ominously high data rates in 4G/5G communication systems due to their ability to create a virtual array of antennas (Ibrahim *et al.*, 2008). With increasing emphasis on Femto, small and Pico cell networks, cooperative systems are a promising solution for 5G systems. The most famous relaying protocols are amplify-and-forward (AF), decode-and-forward (DF) and SDF protocols (Khattabi and Matalgah, 2015; Ryu *et al.*, 2018; Shankar *et al.*, 2017; Shankar *et al.*, 2017). Also by using MIMO and STBC together, better end-to-end error performance has been achieved and it will enhance the data transmission rate.

In references (Varshney and Puri, 2017; Varshney *et al.*, 2015), the author analyzed the pairwise error probability (PEP) of MIMO STBC S-DF cooperative communication protocol. The authors derived the closed-form PEP expressions for dual phase and multiple phase cooperation protocol, derive the DO and OPFs.

In the works (Amarasuriya *et al.*, 2011; Yang *et al.*, 2014), the authors investigated TAS based cooperation network. In study (Amarasuriya *et al.*, 2011), AF based relaying is investigated and it is shown that two sub-optimal TAS technique achieves DOs $M_D + M_R \min(M_S, M_D)$ and $M_R + M_S M_D$. In study (Yang *et al.*, 2014), TAS for full duplex AF relaying protocol is extensively investigated.

In study (Krishna and Bhatnagar, 2014), the author investigated the symbol error rate (SER) performance of two sub-optimal TAS strategies having only one relay SDF cooperation network. Closed form and upper bound expressions of SER for SDF systems have been taken for both TAS strategies.

In study (Krishna and Bhatnagar, 2016), the authors investigated the single-relay MIMO DF relaying network with M_S, M_R and M_D number of antennas are employed in source, relay and destination. In study (Jin and Shin, 2013), the authors offered the selection of a new source transmit antenna based on the channel state information. It is shown that source transmit antenna selection achieves the full DO of $M_S M_D + M M_R \min(M_S, M_D)$. In study (Halber and Chakravarty, 2018), the author has investigated the relay for the optimization purpose.

In this paper, investigation of the single relay MIMO STBC based SDF system employing M-ary PSK by deriving the closed form PEP expressions and PEP upper bounds has been done. The closed form SER expression for two sub-optimal selection strategies has been derived. There are consideration two criteria for antenna selection 1) Maximization of SNR of SD and RD fading channel links and 2) Maximization of SNR of RD and SR fading channel links. Also, we investigated the DO and optimal power allocation.

In this paper, section 2 gives the System Model. Section 3, describes SER analysis. Section 4, shows the Simulation results and discussions. Section 5 provides the conclusion for our proposed method.

2. System model

Consider a MIMO SDF cooperative communication system employing single relay, as given in Figure 1. The relay, source, and destination nodes are employed with M_R , M_S and M_D number of antennas, respectively. Only in the case of successful decoding relay node, the signal will be forwarded to the destination node, otherwise it will be inactive state. Let $H_{SR} \in \mathbb{C}^{M_R M_S}$, $H_{SD} \in \mathbb{C}^{M_D M_S}$ and $H_{RD} \in \mathbb{C}^{M_D M_R}$ denote the channel matrix from SR, SD and RD respectively. Let $h_{d_i s_j} \in H_{SD}$, $h_{r_i s_j} \in H_{SR}$ and $h_{d_i r_j} \in H_{RD}$ denote the channel coefficients for SD, SR and RD fading links. The channel coefficient is modeled as the zero mean complex Gaussian circular shift (ZMCGCS) random variable (RV) with unit variance. Let $Q_{d_i r_j} = |h_{d_i r_j}|^2$, $Q_{r_i s_j} = |h_{r_i s_j}|^2$ and $Q_{d_i s_j} = |h_{d_i s_j}|^2$ denote the exponentially distributed instantaneous channel gains from the j^{th} transmitter (Tx) to i^{th} receiver (Rx) antenna in the RD, SR and SD fading channel. δ_{SD}^2 , δ_{SR}^2 and δ_{RD}^2 denote the average channel gain for SD, SR and RD fading link respectively. The transmission of signals can be divided into two steps, one transmission phase and one relaying phase. In broadcast phase using Time Division Multiple Access (TDMA), the signal from the source is being transmitted to both destination and relay in T_1 time slots. In relaying phase, the relay node forwards the signal correctly decoding to the destination node using STBC technique.

2.1. The Broadcast phase

Let $X_1 \in \mathbb{C}^{T_1 \times 1}$ denotes the symbol vector, each symbol has unit energy, i.e., $E\{X_1^H X_1\} = 1$. Let $y_{SD} \in \mathbb{C}^{T_1 \times 1}$ and $y_{SR} \in \mathbb{C}^{T_1 \times 1}$ denote received symbol vector at the destination and relay node, modeled as,

$$y_{SD} = \sqrt{P_S} h_{D_i S_j} x + w_{SD} \quad (1)$$

$$y_{SR} = \sqrt{P_S} h_{R_i S_j} x + w_{SR} \quad (2)$$

Where $w_{SD} \in \mathbb{C}^{T_1 \times 1}$, $w_{SR} \in \mathbb{C}^{T_1 \times 1}$, denote the noise vector, modeled as ZMCGCS RV with noise variance N_0 . Let y_{SD}^k denote the received symbol at k^{th} time slot, modeled as,

$$y_{SD}^k = \sqrt{P_S} h_{D_i S_j} x^k + w_{SD}^k \quad (3)$$

Let us define α_{SD} , the weight factor for SD fading link, the SNR is maximized when $\alpha_{SD} = h_{D_i S_j}^H$. Also the maximized SNR is given as, $\lambda_{SD} = \frac{P_S}{N_0} |h_{D_i S_j}|^2$. Following similar procedure, weight factor and maximized SNR for SR fading link is given as, $\alpha_{SR} = h_{R_i S_j}^H$ and $\lambda_{SR} = \frac{P_S}{N_0} |h_{R_i S_j}|^2$ respectively.

2.2. The relaying phase

2.2.1. Strategy I-single Tx and Rx antenna between the relay and destination nodes

In relaying phase, the relay node selects one aerial in a random manner to transmitter and receiver selects one aerial randomly to receive, as given in Figure 2. Let $y_{RD}^{k+T_1}$ denote the received symbol block at the destination at the $k + T_1$ time corresponding to transmission of x^k data, modeled as,

$$y_{RD}^{k+T_1} = \sqrt{P_R} h_{D_i S_j} x^k + w_{RD}^k \quad (4)$$

The weight vector α_{RD} of the RD link and maximum SNR is given as $\alpha_{RD} = h_{D_i R_j}^H$ and $\lambda_{RD} = \frac{P_R}{N_0} |h_{D_i R_j}|^2$ respectively. Cooperation mode SNR is modeled as,

$$\lambda = \frac{P_S |h_{D_i S_j}|^2 + P_R |h_{D_i R_j}|^2}{N_0} \quad (5)$$

2.2.2. Strategy II-STBC between relay and destination

In strategy II broadcast phase is similar to strategy I. Relay generated the STBC code-word block $X \in \mathbb{C}^{M_R \times T_2}$ after receiving the transmitted vector $X_1 \in \mathbb{C}^{T_1 \times 1}$ at T_2 time slot. According to the STBC transmission from the relay node, the symbol block received on the destination node has been modeled as,

$$Y_{RD} = \sqrt{P_R / M_R} H_{RD} X + W_{RD} \quad (6)$$

Where $H_{RD} \in \mathbb{C}^{M_D M_R}$ denote channel matrix for RD fading link and W_{RD} denote the noise vector for RD fading link respectively, modeled as ZMCGCS RV with noise variance N_0 . Assuming perfect CSI availability at receiver terminal and uncorrelated noise component, the maximum likelihood (ML) decoding of X is given as [1],

$$\hat{X} = \arg \max_{X \in C} \|Y_{RD} - \sqrt{P_R / M_R} H_{RD} X\|_F^2 \quad (7)$$

Where C denotes the STBC code-word set and $|C|$ denote the cardinality of the code-word set C

3. SER analysis

3.1. SER analysis for strategy I

In Figure 2, it has given the various steps involve in the broadcast phase and in the other phase of selecting the antennas in strategy I. Broadcast phase is comprised of

two steps. Broadcast phase involves the selection of i^{th}, j^{th} and k^{th} aerials respectively, shown in Figure 2.

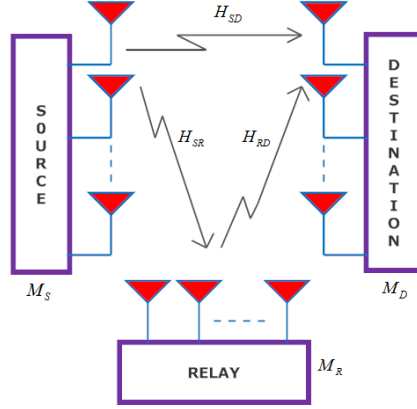


Figure 1. Selection strategy I

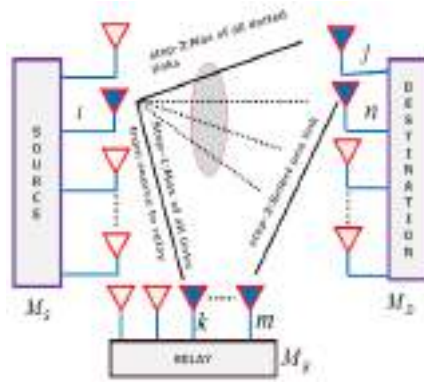


Figure 2. Selection strategy II

In step 1, i^{th} antenna at the source and k^{th} antenna at the relay is selected depending on the maximum instantaneous gain Q_{SR} of all fading links. In step 2, j^{th} antenna at the destination node has been selected depending on the maximum instantaneous gain Q_{SD} of the fading channels displayed as dotted lines. Lastly, in step 3, one antenna is selecting between m^{th} antenna at the relay node and n^{th} antenna at the destination node. Q_{SR} , Q_{SD} and Q_{RD} are given as,

$$Q_{SR} = \max(Q_{S_1,R_1}, Q_{S_2,R_2}, \dots, Q_{S_{M_S},R_{M_R}}), 1 \leq i \leq M_S, 1 \leq k \leq M_R$$

$$Q_{SD} = \max(Q_{S_i D_1}, Q_{S_i D_2}, \dots, Q_{S_i D_{M_D}}), 1 \leq j \leq M_D, Q_{RD} = Q_{R_i D_i}, 1 \leq m \leq M_R, 1 \leq n \leq M_D \quad (8)$$

The cumulative distribution function (CDF) and probability distribution function (PDF) of the Q_{SD} , Q_{SR} and Q_{RD} is modeled as [8],

$$\begin{aligned} F_{Q_{SD}}(Q) &= \left(1 - \exp\left(\frac{-Q}{\delta_{SD}^2}\right)\right)^{M_D}, \\ f_{Q_{SD}}(Q) &= \frac{M_D}{\delta_{SD}^2} \exp\left(\frac{-Q}{\delta_{SD}^2}\right) \left(1 - \exp\left(\frac{-Q}{\delta_{SD}^2}\right)\right)^{M_D-1}, \\ F_{Q_{SR}}(Q) &= \left(1 - \exp\left(\frac{-Q}{\delta_{SR}^2}\right)\right)^{M_S M_R}, \\ F_{Q_{RD}}(Q) &= \left(1 - \exp\left(\frac{-Q}{\delta_{RD}^2}\right)\right), \\ f_{Q_{RD}}(Q) &= \frac{1}{\delta_{RD}^2} \exp\left(\frac{-Q}{\delta_{RD}^2}\right), \end{aligned} \quad (9)$$

In study (Shankar *et al.*, 2017), the end-to-end error Probability is given as,

$$P_E^I = P_{S \rightarrow D, R \rightarrow D} \times (1 - P_{S \rightarrow R}) + P_{S \rightarrow D} \times P_{S \rightarrow R}. \quad (10)$$

Let $\psi(\lambda_{SD})$ represents the instantaneous symbol error rate of M-PSK modulation, given as (Varshney *et al.*, 2015),

$$\psi(\lambda_{SD}) = \frac{1}{\pi} \int_0^{(\frac{M-1}{M})\pi} \exp\left(\frac{-b}{\sin^2 \theta} \lambda_{SD}\right) d\theta, \quad (11)$$

Where $b = \sin^2(\pi/M)$, $\theta(\alpha)$ denotes the Gaussian Q function, defined as (Varshney *et al.*, 2008), $\theta(\alpha) = \frac{1}{\pi} \int_0^{\frac{\pi}{2}} \exp\left(\frac{-x^2}{\sin^2 \theta}\right) d\theta$ and $b = \sin^2\left(\frac{\pi}{M}\right)$.

The SER for SD link can be derived as (Varshney *et al.*, 2017),

$$\begin{aligned} P_{S \rightarrow D} &= E_{Q_{SD}}\{\psi(\lambda_{SD})\} = \int_0^\infty \psi(Q_{SD}) f_{Q_{SD}}(Q) dQ \\ &= \frac{M_D}{\pi \delta_{SD}^2} \int_0^\infty \int_0^{(\frac{M-1}{M})\pi} \exp\left(-\left(\frac{b P_S}{N_0 \sin^2 \theta} + \frac{1}{\delta_{SD}^2}\right) Q\right) \left(1 - \exp\left(\frac{-Q}{\delta_{SD}^2}\right)\right)^{M_D-1} d\theta dQ \end{aligned} \quad (12)$$

By using the expression, $(1-x)^M = \sum_{m=0}^{M-1} \binom{M}{m} (-1)^m x^m$, we further simplify $P_{S \rightarrow D}$ as,

$$P_{S \rightarrow D} = M_D \sum_{j=0}^{M_D-1} \binom{M_D-1}{j} (-1)^j F\left(\frac{b P_S \delta_{SD}^2}{N_0 \sin^2 \theta} + j + 1\right), \quad (13)$$

Following the similar procedure, SER for the SER link can be derived as,

$$\begin{aligned}
 P_{S \rightarrow R} &= E_{\beta_{SR}} \{\psi(\lambda_{SR})\} \\
 &= M_S M_R \sum_{i=0}^{M_S M_R - 1} \binom{M_S M_R - 1}{i} (-1)^i F \left(\frac{b P_S \delta_{SR}^2}{N_0 \sin^2 \theta} + i + 1 \right), \quad (14)
 \end{aligned}$$

The SER for the cooperation mode can be written as,

$$\begin{aligned}
 P_{S \rightarrow D, R \rightarrow D} &= E_{f_{Q_{SD}} f_{Q_{RD}}} \{\psi(\lambda)\} \\
 &= \frac{1}{\prod_0} \int_0^{\frac{(M-1)\pi}{M}} \int_0^\infty \psi(Q_{SD}) f_{Q_{SD}}(Q_{SD}) dQ_{SD} \int_0^\infty \psi(\lambda_{RD}) f_{\beta_{RD}}(Q_{RD}) dQ_{RD} \\
 &= M_D \sum_{j=0}^{M_D - 1} \binom{M_D - 1}{j} (-1)^j F \left(\left(\frac{b P_S \delta_{SD}^2}{N_0 \sin^2 \theta} + j + 1 \right) \left(\frac{b P_R \delta_{RD}^2}{N_0 \sin^2 \theta} + 1 \right) \right), \quad (15)
 \end{aligned}$$

Substituting (13), (14) and (15) into (10), end to end SER for selection strategy I is expressed in (16).

$$\begin{aligned}
 P_E^I &= M_D \sum_{j=0}^{M_D - 1} \binom{M_D - 1}{j} (-1)^j F \left(\frac{b P_S \delta_{SD}^2}{N_0 \sin^2 \theta} + j + 1 \right) \\
 &\quad \times M_S M_R \sum_{i=0}^{M_S M_R - 1} \binom{M_S M_R - 1}{i} (-1)^i F \left(\frac{b P_S \delta_{SR}^2}{N_0 \sin^2 \theta} + i + 1 \right) \\
 &\quad + M_D \sum_{j=0}^{M_D - 1} \binom{M_D - 1}{j} (-1)^j F \left(\left(\frac{b P_S \delta_{SD}^2}{N_0 \sin^2 \theta} + j + 1 \right) \left(\frac{b P_R \delta_{RD}^2}{N_0 \sin^2 \theta} + 1 \right) \right) \\
 &\quad \times \left(1 - M_S M_R \sum_{n=0}^{M_S M_R - 1} \binom{M_S M_R - 1}{n} (-1)^n F \left(\frac{b P_S \delta_{SR}^2}{N_0 \sin^2 \theta} + n + 1 \right) \right), \quad (16)
 \end{aligned}$$

3.1.1. SER upper bound

For deriving the SER upper bound, we assume $1 - P_{S \rightarrow R} \approx 1$ at high SNR regimes. Tight SER upper bound of P_E^I can be given in (17),

$$\begin{aligned}
 P_E^I &= \frac{M_S M_R M_D}{\pi^2} \int_0^{\frac{(M-1)\pi}{M}} \int_0^{\frac{(M-1)\pi}{M}} \left(\sum_{n=0}^{M_S M_R - 1} \binom{M_S M_R - 1}{n} \times \frac{(-1)^n}{\left(\frac{b P_S \delta_{SR}^2}{N_0 \sin^2 \theta} + n + 1 \right)} \right) \times \\
 &\quad \left(\sum_{m=0}^{M_D - 1} \binom{M_D - 1}{m} \times \frac{(-1)^m}{\left(\frac{b P_S \delta_{SD}^2}{N_0 \sin^2 \theta} + m + 1 \right)} \right) \\
 &\quad \times d\theta_1 d\theta_2 + \\
 &M_D \sum_{j=0}^{M_D - 1} \binom{M_D - 1}{j} \times (-1)^j \times \left[\frac{1}{\pi} \int_0^{\frac{(M-1)\pi}{M}} \frac{1}{\left(\frac{b P_R \delta_{RD}^2}{N_0 \sin^2 \theta} + j + 1 \right)} \times \frac{1}{\left(\frac{b P_R \delta_{RD}^2}{N_0 \sin^2 \theta} + 1 \right)} d\theta \right] \quad (17)
 \end{aligned}$$

Applying the approximation,

$$\sum_{n=0}^N \binom{N}{n} (-1)^n \frac{1}{x+ny} = \frac{N!y^N}{\prod_{n=0}^N (x+ny)} \quad (18)$$

We can write tight SER upper bound for the selection strategy I as,

$$P_E^I \leq \frac{M_S M_R M_D (M_S M_R - 1)! (M_D - 1)! B_0 B_1}{\pi^2 \left(\frac{b P_S \delta_{SR}^2}{N_0}\right)^{M_S M_R} \left(\frac{b P_S \delta_{SD}^2}{N_0}\right)^{M_D}} + \frac{M_D (M_D - 1)! B_1}{\pi \left(\frac{b P_S \delta_{SD}^2}{N_0}\right)^{M_D} \left(\frac{b P_R \delta_{RD}^2}{N_0}\right)} \quad (19)$$

Where $B_0 = \int_0^{\left(\frac{M-1}{M}\right)\pi} (\sin \theta_1)^{2M_S M_R} d\theta_1$, $B_1 = \int_0^{\left(\frac{M-1}{M}\right)\pi} (\sin \theta_2)^{2M_D} d\theta_2$.

3.1.2. Optimal power allocation

Substituting $P_R = P_0 - P_S$ in (19) and differentiating the resultant expression w.r.t. P_S and after equating it to zero, we can get,

$$K_1 (M_S M_R + M_D) P_S^{-(M_S M_R + M_D + 1)} + K_2 (P - P_S)^{-1} M_D P_0^{-(M_D + 1)} - K_2 P_S^{-(M_D)} (P - P_S)^{-2} = 0, \quad (20)$$

Where K_1 and K_2 are appropriately defined constant terms, given below,

$$K_1 = \frac{M_S M_R M_D (M_S M_R - 1)! (M_D - 1)! B_0 B_1}{\pi^2 \left(\frac{b \delta_{SR}^2}{N_0}\right)^{M_S M_R} \left(\frac{b \delta_{SD}^2}{N_0}\right)^{M_D}}, K_2 = \frac{M_D (M_D - 1)! B_1}{\pi \left(\frac{b \delta_{SD}^2}{N_0}\right)^{M_D} \left(\frac{b \delta_{RD}^2}{N_0}\right)}$$

Solution of (20) will give optimal powers for source and relay nodes.

3.1.3. DO calculation

Substituting $Q_0 = \frac{P_S}{P}$, $Q_1 = \frac{P_R}{P}$, (19) can be written as, (21),

$$P_e \leq \frac{M_S M_R M_D (M_S M_R - 1)! (M_D - 1)! B_0 B_1}{\pi^2 (b \delta_{SR}^2)^{M_S M_R} (b \delta_{SD}^2)^{M_D} Q_0^{-(M_S M_R + M_D)} (P/N_0)^{-(M_S M_R + M_D)}} + \frac{M_D (M_D - 1)! B_2}{\pi Q_0^{-M_D} (b \delta_{SD}^2)^{M_D} (b \beta_1 \delta_{RD}^2) (P/N_0)^{-(M_D + 1)}}, \quad (21)$$

DO expression is given as,

$$DO = - \lim_{SNR \rightarrow \infty} \frac{\log(P_E^I)}{\log(SNR)_D} \min(S_R)$$

3.2. SER strategy II

In this selection strategy, the SD and SR link is having a similar error probability to the previous strategy. In this strategy between the relay and destination fading link

we apply STBC. Let us define the PEP as the error probability when STBC codeword X_n is of confused with STBC codeword X_l . The PEP can be modeled as,

$$P(X_n \rightarrow X_l | H_{RD}) = Q \left(\sqrt{\frac{P_R}{2M_R N_0} H_{RD} \|X_n - X_l\|_F^2} \right).$$

Averaging the PEP over the probability distribution of the fading channel, the average pairwise error probability can be derived as,

$$P(X_n \rightarrow X_l) = G \left(\prod_{k=1}^{M_R} \left(1 + \frac{P_R \lambda_{k,l} \sigma_{RD}^2}{4N_0 M_R \sin^2 \theta} \right)^{M_D} \right) = E_{H_{RD}} \{P(X_n \rightarrow X_l | H_{RD})\},$$

Where $\lambda_{1,l}, \lambda_{1,l}, \dots, \lambda_{M_R,l}$, are the non-zero singular values of $(X_n - X_l)(X_n - X_l)^H$ and $G(x(\theta)) = \int_0^{\frac{\pi}{2}} \frac{1}{x(\theta)} d\theta$. For RD link the PEP can be upper bounded using union bound, which is very tight on high SNR,

$$\begin{aligned} P_{R \rightarrow D} &\leq \sum_{X_l \in C, l \neq n}^{|\mathcal{C}|} P_{R \rightarrow D}(X_n \rightarrow X_l) = \\ &\sum_{X_l \in C, l \neq n}^{|\mathcal{C}|} G \left(\prod_{k=1}^{M_R} \left(1 + \frac{P_R \lambda_{k,l} \delta_{RD}^2}{4N_0 M_R \sin^2 \theta} \right)^{M_D} \right) \quad (22) \\ P_{S \rightarrow D, R \rightarrow D} &= E_{f_{Q_{SD} f_{Q_{RD}}}} \{ \psi(\lambda) \} \\ &= \frac{1}{\Pi} \int_0^{\frac{(M-1)\Pi}{M}} \int_0^\infty \psi(\lambda_{SD}) f_{Q_{SD}}(Q_{SD}) dQ_{SD} \times \int_0^\infty \psi(\lambda_{RD}) f_{Q_{RD}}(Q_{RD}) dQ_{RD} d\theta \\ &\simeq \frac{1}{\Pi} \int_0^{\frac{(M-1)\Pi}{M}} \int_0^{\frac{(M-1)\Pi}{M}} \int_0^\infty \psi(\lambda_{SD}) f_{Q_{SD}}(Q_{SD}) dQ_{SD} \times \\ &\quad \int_0^\infty \psi(\lambda_{RD}) f_{Q_{RD}}(Q_{RD}) dQ_{RD} d\theta_1 d\theta_2 \\ &= M_D \sum_{m=0}^{M_D-1} \binom{M_D-1}{m} (-1)^m F \left(\frac{b P_S \delta_{SD}^2}{N_0 \sin^2 \theta} + m + 1 \right) \times \\ &\quad \sum_{X_l \in C, l \neq n}^{|\mathcal{C}|} G \left(\prod_{k=1}^{M_R} \left(1 + \frac{P_R \lambda_{k,l} \sigma_{RD}^2}{4N_0 M_R \sin^2 \theta} \right)^{M_D} \right), \quad (23) \end{aligned}$$

The end-to-end error probability for selection strategy II is given as,

$$P_E^{II} = P_{S \rightarrow D} \times P_{S \rightarrow R} + P_{S \rightarrow D, R \rightarrow D} \times (1 - P_{S \rightarrow R}) \quad (24)$$

Substituting (13), (14) and (23) into (24), we are getting (25),

$$\begin{aligned} P_E^{II} &= M_D \sum_{j=0}^{M_D-1} \binom{M_D-1}{j} (-1)^j F \left(\frac{b P_S \delta_{SD}^2}{N_0 \sin^2 \theta} + j + 1 \right) \\ &\times M_S M_R \sum_{i=0}^{M_S M_R - 1} \binom{M_S M_R - 1}{i} (-1)^i F \left(\frac{b P_S \delta_{SR}^2}{N_0 \sin^2 \theta} + i + 1 \right) \end{aligned}$$

$$\begin{aligned}
& +M_D \sum_{m=0}^{M_D-1} \binom{M_D-1}{m} (-1)^m F \left(\frac{bP_S \delta_{SD}^2}{N_0 \sin^2 \theta} + m + 1 \right) \\
& \times \sum_{X_l \in C, l \neq n}^{|C|} G \left(\prod_{k=1}^{M_R} \left(1 + \frac{P_R \lambda_{k,l} \sigma_{RD}^2}{4N_0 M_R \sin^2 \theta} \right)^{M_D} \right)
\end{aligned} \quad (25)$$

Table 1. Optimal power allocation for SR link for selection strategy I

Number of Antennas	Q_0	Q_1
$M_S = 1, M_R = 1, M_D = 1,$	0.60	0.40
$M_S = 2, M_R = 2, M_D = 2$	0.70	0.30
$M_S = 2, M_R = 3, M_D = 3$	0.73	0.27

3.2.1. SER upper bound

Replacing $1 - P_{S \rightarrow R} \approx 1$ at high SNR, we can write $P_{S \rightarrow D, R \rightarrow D}$ as (26),

$$\begin{aligned}
P_{S \rightarrow D, R \rightarrow D} & \leq \frac{M_D}{\pi^2} \int_0^{\frac{(M-1)\pi}{M}} \sum_{m=0}^{M_D-1} \binom{M_D-1}{m} (-1)^m \frac{1}{\left(\frac{bP_S \delta_{SD}^2}{N_0 \sin^2 \theta} + m + 1 \right)} d\theta \\
& \times \sum_{X_l \in C, l \neq n}^{|C|} \int_0^{\frac{(M-1)\pi}{M}} \frac{1}{\prod_{k=1}^{M_R} \left(1 + \frac{P_R \lambda_{k,l} \sigma_{RD}^2}{4N_0 M_R \sin^2 \theta} \right)^{M_D}} d\theta,
\end{aligned} \quad (26)$$

Using an expression given in (18), $P_{S \rightarrow D, R \rightarrow D}$ is approximated as,

$$P_{S \rightarrow D, R \rightarrow D} \leq \frac{M_D (M_D - 1)! I_2^2}{\pi^2 \left(\frac{bP_S \delta_{SD}^2}{N_0} \right)^{M_D} \left(\frac{P_R \sigma_{RD}^2}{4N_0 M_R} \right)^{M_D}} \quad (27)$$

Table 2. Optimal power allocation for SR link for selection strategy II

Number of Antennas	Q_0	Q_1
$M_S = 1, M_R = 1, M_D = 1$	0.60	0.40
$M_S = 2, M_R = 2, M_D = 2$	0.53	0.47
$M_S = 3, M_R = 3, M_D = 3$	0.48	0.52

Finally, the SER upper bound for strategy II can be written as,

$$P_E^{II} \leq \frac{M_S M_D M_R (M_S M_R - 1)! (M_D - 1)! B_0 B_1}{\pi^2 \left(\frac{bP_S \delta_{SR}^2}{N_0} \right)^{M_S M_R} \left(\frac{bP_S \delta_{SD}^2}{N_0} \right)^{M_D}} + \frac{M_D (M_D - 1)! I_2^2}{\pi^2 \left(\frac{bP_S \delta_{SD}^2}{N_0} \right)^{M_D} \left(\frac{P_R \sigma_{RD}^2}{4N_0 M_R} \right)^{M_D}} \quad (28)$$

Where, $z = \sum_{X_l \in C, l \neq n} |C_l| \lambda_l$, $\lambda_l = \prod_{k=1}^{M_R} \lambda_{k,l}$, $I_2 = \frac{1}{\pi} \int_0^{\frac{(M-1)\pi}{2}} (\sin \theta)^{2M_D} d\theta$.

3.2.2. DO analysis

Substituting $P_S = Q_0 P$, $P_R = Q_1 P$, we can express SER upper bound as,

$$P_E^u \leq \frac{M_S M_D M_R (M_S M_R - 1)! (M_D - 1)! B_0 B_1}{\pi^2 (b Q_0 \delta_{SR}^2)^{M_S M_R} (b Q_0 \delta_{SD}^2)^{M_D} \left(\frac{P}{N_0}\right)^{M_S M_R + M_D}} + \frac{M_D (M_D - 1)! I_2 I_4}{\pi^2 (b Q_0 \sigma_{SD}^2)^{M_D} \left(\frac{Q_1 \sigma_{RD}^2 z}{4 M_R}\right)^{M_D} \left(\frac{P}{N_0}\right)^{2 M_D}}, \quad (29)$$

DO expression is given as,

$$DO = -\lim_{SNR \rightarrow \infty} \frac{\log(P_E^u)}{\log(SNR)} = M_D \min(M_S M_R, M_D). \quad (30)$$

3.2.3. Optimal power allocation

Substituting $P_R = P_S - P$ in (28) and differentiating it with respect to P_S , after equating it to zero, the resultant expression we get,

$$K_1 \times (M_S M_R + M_D) (P_S)^{-M_S M_R - M_D - 1} + K_2 \begin{bmatrix} M_D (P_S)^{M_D} \times (P - P_S)^{-(M_D + 1)} \\ -M_D (P_S)^{-(M_D + 1)} (P - P_S)^{M_D} \end{bmatrix} = 0 \quad (31)$$

Where K_1 and K_2 are appropriately defined constant terms. Solution of equation (31) will provide the optimal power for source and relay nodes.

4. Simulation results and discussions

We analyzed the SER performance of the single relay relaying network for the identical and best possible power factors Q_0 and Q_1 . In Figure 3, the plots show that analytical results are in close agreement with simulated results. Also, SER simulated matches the SER upper bounds at high SNR regimes. It can be seen from the given graph that S2 performance is better than that of S1 and SER for optimal power outperforms SER for equal power allocation.

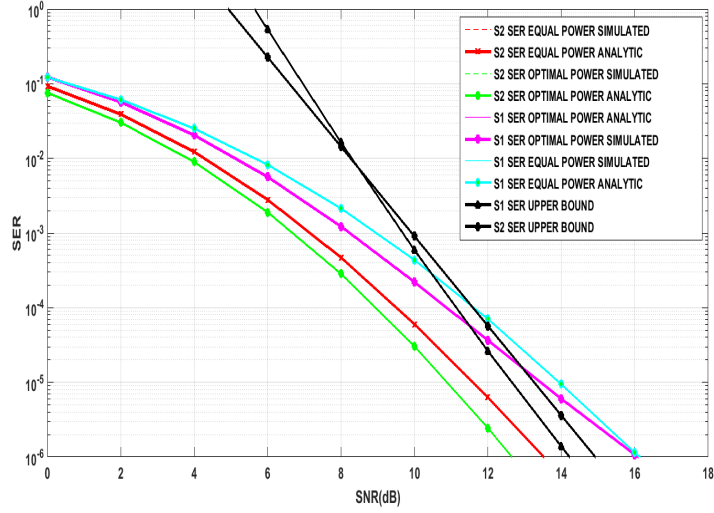


Figure 3. SER Simulated, SER Analytic, SER Upper bound for single relay relaying network with $M = 4, N_0 = 1, M_S = M_R = M_D = 2, \delta_{SD}^2 = \delta_{SR}^2 = \delta_{RD}^2 = 2, Q_0 = 0.70, Q_1 = 0.30$ for selection strategy S1 and $Q_0 = 0.53, Q_1 = 0.47$ for selection strategy S2

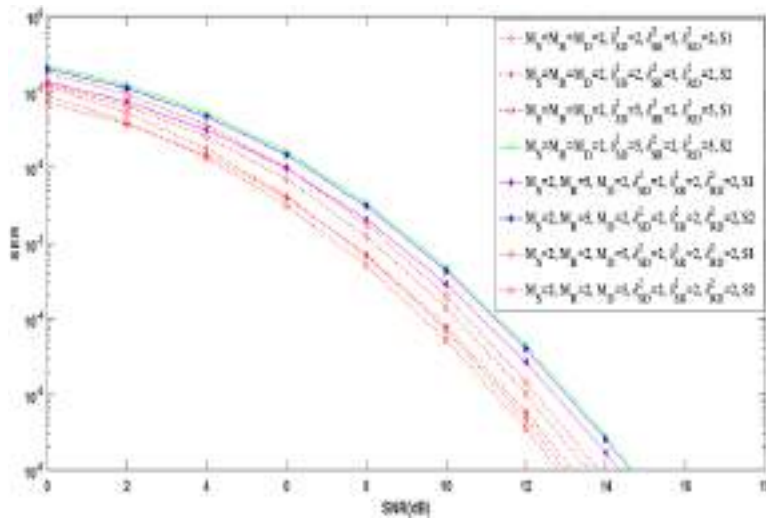


Figure 4. Comparison between selection strategy S1 and selection strategy S2 for various antenna configurations and various values of channel variables

In Figure 4, we show a comparison between selection strategy S1 and S2 in different channel conditions and different antenna configurations with $M = 4, N_0 = 1$. Figure 4, shows that when $M_S = 2, M_R = 5, M_D = 2, \delta_{SD}^2 = \delta_{SR}^2$ and $\delta_{RD}^2 = 2$, SER performance of strategy S2(DO=10) is better than strategy S1 (DO=8); and when $M_S = 2, M_R = 2, M_D = 5, \delta_{SD}^2 = \delta_{SR}^2$ and $\delta_{RD}^2 = 2$, SER performance of strategy S1(DO=10) are better than strategy S2 (DO=8). Lastly, when $M_S = 2, M_R = 2, M_D = 2, \delta_{SD}^2 = 2, \delta_{SR}^2 = 5, \delta_{RD}^2 = 2$ i.e., strategy S1 and S2 have same DO, SER performance of S1 is better than S2 by 3dB because it is based on the maximization of the SNR of source-to-destination fading link which is strong in this scenario; when $M_S = 2, M_R = 2, M_D = 2, \delta_{SD}^2 = 5, \delta_{SR}^2 = 2, \delta_{RD}^2 = 5$, the strategy S2 performs better (1dB gain) because it is based on maximization of SNR of the relay to the destination and source-to-relay fading link which are strong in this scenario.

5. Conclusion

We investigated the SER performance of two antenna selection strategy S1 and S2 for S-DF relaying network over time invariant Rayleigh fading links. We presented the closed form expression for SER analytic and SER upper bound for both antenna selection strategies. Analytical outcomes have been validated with simulated outcomes. We have conducted simulations for various antenna configurations and various channel gains. We can select the antenna selection strategy which has maximum DO for that particular antenna configuration. In case both the strategies give the same DO then one can choose strategy I, when source-to-destination link is strong and strategy II, when source-to-destination link is weak as compared to source-to-relay and relay-to-destination fading links.

References

- Amarasuriya G., Tellambura C., Ardakani M. (2011). Performance analysis framework for transmit antenna selection strategies of cooperative MIMO AF relay networks. *IEEE Transactions on Vehicular Technology*, Vol. 60, No. 7, pp. 3030-3044. <https://doi.org/10.1109/TVT.2011.2157371>
- Halber A., Chakravarty D. (2018). Wireless relay placement optimization in underground room and pillar mines. *Mathematical Modelling of Engineering Problems*, Vol. 5, No. 2, pp. 67-75. <https://doi.org/10.18280/mmep.050203>
- Ibrahim A. S., Sadek A. K., Su W., Liu K. J. R. (2008). Cooperative communications with relay-selection: When to cooperate and whom to cooperate with? *IEEE Transactions on Wireless Communications*, Vol. 7, No. 7, pp. 2814-2827. <https://doi.org/10.1109/TWC.2008.070176>
- Jin X., No J., Shin D. (2013). Source transmit antenna selection for MIMO decode-and-forward relay networks. *IEEE Transactions on Signal Processing*, Vol. 61, No. 7, pp. 1657-1662. <https://doi.org/10.1109/TSP.2013.2241053>
- Khattabi Y., Matalgah M. M. (2015). Conventional AF cooperative protocol under nodes-mobility and imperfect-CSI impacts: Outage probability and Shannon capacity. *2015 IEEE*

Wireless Communications and Networking Conference (WCNC), pp. 13-18.
<https://doi.org/10.1109/WCNC.2015.7127437>

Krishna V. S., Bhatnagar M. R. (2014). Performance analysis of sub-optimal transmit and receive antenna selection strategies in single relay based DF cooperative MIMO networks. *2014 Twentieth National Conference on Communications (NCC)*, pp. 1-6.
<https://doi.org/10.1109/NCC.2014.6811367>

Krishna V. S., Bhatnagar M. R. (2016). A joint antenna and path selection technique in single-relay-based DF cooperative MIMO networks. *IEEE Transactions on Vehicular Technology*, Vol. 65, No. 3, pp. 1340-1353. <https://doi.org/10.1109/TVT.2015.2414511>

Ryu G., Jang D., Jeong U., Ko K. (2018). BER performance analysis of orthogonal space-time block codes in cooperative MIMO DF relaying networks. *2018 IEEE International Conference on Communications (ICC)*, pp. 1-6. <https://doi.org/10.1109/ICC.2018.8423038>

Shankar R., Kumar I., Kumari A., Pandey K. N., Mishra R. K. (2017). Pairwise error probability analysis and optimal power allocation for selective decode-forward protocol over Nakagami-m fading channels. *2017 International Conference on Algorithms, Methodology, Models and Applications in Emerging Technologies (ICAMMAET)*, pp. 1-6.
<https://doi.org/10.1109/ICAMMAET.2017.8186700>

Shankar R., Pandey K. N., Kumari A., Sachan V., Mishra R. K. (2017). C(0) protocol based cooperative wireless communication over Nakagami-m fading channels: PEP and SER analysis at optimal power. *2017 IEEE 7th Annual Computing and Communication Workshop and Conference (CCWC)*, pp. 1-7.
<https://doi.org/10.1109/CCWC.2017.7868399>

Varshney N., Krishna A. V., Jagannatham A. K. (2015). Selective DF protocol for MIMO STBC based single/multiple relay cooperative communication: End-to-end performance and optimal power allocation. *IEEE Transactions on Communications*, Vol. 63, No. 7, pp. 2458-2474. <https://doi.org/10.1109/TCOMM.2015.2436912>

Varshney N., Puri P. (2017). Performance analysis of decode-and-forward-based mixed MIMO-RF/FSO cooperative systems with source mobility and imperfect CSI. *Journal of Lightwave Technology*, Vol. 35, No. 11, pp. 2070-2077.
<https://doi.org/10.1109/JLT.2017.2675447>

Yang K., Cui H., Song L., Li Y. (2014). Joint relay and antenna selection for full-duplex AF relay networks. *2014 IEEE International Conference on Communications (ICC)*, pp. 4454-4459. <https://doi.org/10.1109/ICC.2014.6884022>

Uplink Sum Rate and Capacity of Hybrid Precoding mmWave Massive MIMO System

Vikash Sachan*, Ritesh Kumar Mishra

Department of Electronics and Communication Engineering, National Institute of Technology Patna, India

Corresponding Author Email: vikash.ece15@nitp.ac.in

<https://doi.org/10.18280/ts.360205>

Received: 15 January 2019

Accepted: 3 April 2019

Keywords:

MIMO, massive MIMO, millimeter wave, hybrid precoding and combining

ABSTRACT

Massive multiple input multiple output (MIMO) systems offer an improvement in the uplink sum rate with increasing the number of base station antennas. Massive MIMO system needs the perfect channel state information (perfect CSI) and imperfect channel state information (imperfect CSI) for deriving the achievable sum rate. The Uplink sum rate is derived for the ZF receiver and the MRC receiver with perfect CSI and imperfect CSI. The zero forcing (ZF) receiver outperforms maximal ratio combining (MRC) receiver. With imperfect CSI as the number of users increases the uplink sum rate also increases. The channel capacity is derived for the Millimeter wave (mmWave) MIMO system employing MMSE receiver. The mmWave massive MIMO system requires a large number of radio frequency (RF) chains where as the number of the RF chains increases the capacity of the system also improves.

1. INTRODUCTION

Current wireless networks operate at the carrier frequency below 6 GHz. The mmWave massive MIMO system works beyond 6 GHz. The massive MIMO system at mmWave range gives the benefits of a large bandwidth without compromising on device size and therefore it is facilitating the 5G technology. The mmWave massive MIMO works beyond 6 GHz [1-2]. Due to the large available bandwidth of the mmWave frequencies, high transmission rates can be achieved. IEEE 802.11 ad-WLAN standard based on the mmWave provides data rates of 6 Gbps at frequencies around 60 GHz. But there are several problems to implement these types of systems due to rain attenuation, atmospheric absorption and severe path loss [3]. However, small chips are having huge number of antenna arrays at frequencies beyond 6 GHz and can provide high received signal power [4]. Analysis of systems with and without channel state information has been done [5-8]. There is a great deal of interest in the multiuser multiple input multiple output (MU-MIMO) containing a high number of antennas in a base station (BS). High number of MU-MIMO systems are serving hundreds of users by providing hundreds of antenna arrays. The design and analysis of MU-MIMO systems is appealing substantial interest in the latest research areas [9-11]. Small scale fading can be averaged out due to high antenna array. The cost of each antenna is low because the real size of the antenna is small. As the number of BS antenna increases, the random channel vectors become orthogonal between BS and the users. One important advantage of the large MIMO system is that there is a reduction in the transmitting power. In the uplink, decreasing the transmit power of the node will result in improving the battery life. In the downlink, the large amount of power consumed by the base stations is exhausted by the power amplifiers, associated circuits and cooling circuits [12-14]. Wireless backhaul is challenging in closely dispersed small cells in urban environments. Although the length is too small, operating expenditures can be high for optical fiber

deployment due to dense deployment of small cell BS. So ideally, high data rate is provided by low cost mmWave technology. The mmWave can enable high data rate and low latency connectivity between vehicles and also provides high speed communication between vehicles and cloud for data processing and storage. This can support the mmWave-based vehicle to infrastructure communication. The mmWave can be employed in high speed systems such as mobile phones and virtual reality headsets. There are many challenges for the mmWave MIMO systems and several differences exist between different mmWave MIMO networks. Sub 6 GHz places new constraints on hardware. The hardware challenge at the mmWave are high frequency carrier and bandwidth of the communication channel. One more hardware challenge at mmWave is a large array at both the source and destination due to small wavelength. So large number of analog to digital converters (ADCs) are required by the high number of antennas. By increasing the resolution of the ADCs, the design complexity of the system increases. There are many solutions that have been proposed for mmWave networks such as hybrid beam forming architectures, beam space signal processing and low rate ADC methods [15-17]. The mmWave systems and low frequency systems are having some common properties like multipath delay spread, Doppler shift and angle spread. Also the mmWave has many differences with respect to a low frequency system such as high sensitivity to blockages and strong differences between line of sight (LOS) and non line of sight propagation conditions. High number of antenna arrays at the source and destination makes MIMO signal processing a reality, but this is more challenging at mmWave frequencies due to hardware constraint and different channel characteristics. Thus the novel solutions are needed to overcome hardware constraints, channel modeling and signal processing with large arrays. These will have a significant impact on the design and implementation of the mmWave communication network to maintain active connections with multiple BS's to achieve diversity and overcome blockages.

Relays and cooperative diversity can enhance coverage and improve signal strength in the mmWave mobile network.

This paper is organized as follows. In section 2, we analyzed the system model for MU-MIMO System. The achievable sum rate is derived for MU-MIMO Systems employing the ZF and MRC receivers with Perfect CSI and imperfect CSI. In section

3, we derived the capacity of optimal precoder/combiner for the mmWave massive MIMO system. Simulation results are shown in section 4. Section 5 shows the conclusion.

2. SYSTEM MODEL OF MU-MIMO SYSTEM

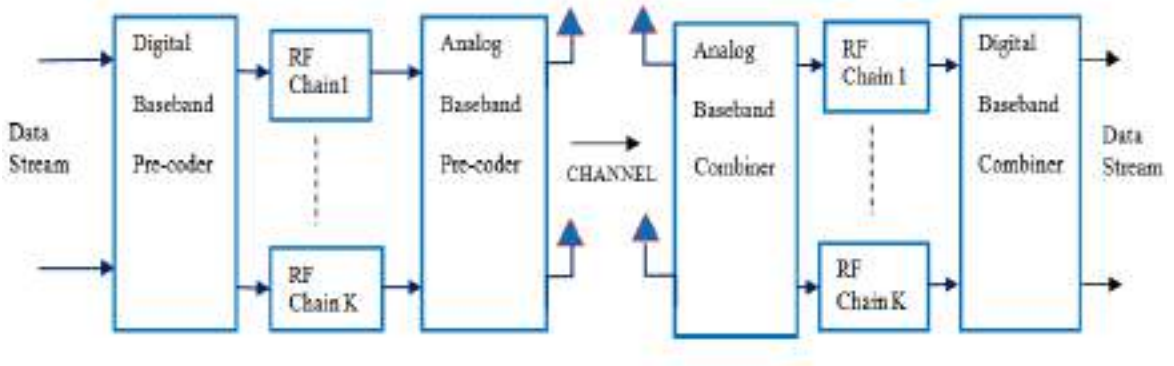


Figure 1. System model of the hybrid mmWave precoder/combiner

2.1 Perfect CSI for MU-MIMO systems

The system model of MU-MIMO system can be shown as,

$$y = \sqrt{P_U} \begin{bmatrix} b_{11} & b_{12} & \dots & b_{1K} \\ b_{21} & b_{22} & \dots & b_{2K} \\ \vdots & \vdots & \ddots & \vdots \\ b_{M1} & b_{M2} & \dots & b_{MK} \end{bmatrix} \begin{bmatrix} x_1 \\ x_2 \\ \vdots \\ x_K \end{bmatrix} + \begin{bmatrix} n_1 \\ n_2 \\ \vdots \\ n_M \end{bmatrix} \quad (1)$$

$$y = \sqrt{P_U} Bx + n \quad (2)$$

where P_U denotes the average transmitted power of each user. B represents the $M \times K$ channel matrix between the BS and K users and models fast fading, geometric attenuation and log-normal shadow fading. $1^{st}, 2^{nd}, \dots, M^{th}$ row of the B matrix is shown as b_1, b_2, \dots, b_M . b_{mk} is the channel coefficient between mk^{th} user and m^{th} antenna from the BS. x is the transmitted data and n is a vector of additive white Gaussian noise with mean zero and variance unity.

The coefficient b_{mk} can be shown as [13],

$$b_{mk} = h_{mk} \sqrt{\lambda_k} \quad (3)$$

where h_{mk} is the fast fading coefficient between k^{th} user and m^{th} antenna of BS. λ_k is modeled as geometric attenuation and shadow fading.

$$B = HC^{1/2} \quad (4)$$

where H is $M \times K$ matrix having fast fading coefficient between K user and BS, i.e. $[H]_{mk} = h_{mk}$ and C is $K \times K$ diagonal matrix, i.e. $[C]_{kk} = \lambda_k$.

For perfect channel state information

$$r = A^H y \quad (5)$$

$$A = \begin{cases} B & \text{for MRC} \\ B(B^H B)^{-1} & \text{for ZF} \end{cases} \quad (6)$$

After linear detection, the received vector is given by

$$r = \sqrt{P_U} A^H Bx + A^H n \quad (7)$$

Considering the MU-MIMO system, the received vector r at the BS can be written as,

$$r = \sqrt{P_U} \sum_{i=1}^K a_k^H b_i x_i + a_k^H n \quad (8)$$

By taking user 1 without loss as the desired user,

$$r = \sqrt{P_U} a_k^H b_1 x_1 + \sqrt{P_U} \sum_{i=2}^K a_k^H b_i x_i + a_k^H n \quad (9)$$

The signal to interference noise ratio (SINR) can be given as,

$$SINR = \frac{P_U |a_k^H b_1|^2}{P_U \sum_{i=2}^K |a_k^H b_i|^2 + \|a_k\|^2} \quad (10)$$

The achievable rate for single cell MU-MIMO can be written as,

$$R_{p,k} = E \left[\log_2 \left(1 + \frac{\frac{e_U}{\sqrt{M}} |b_k^H b_1|^2}{\frac{e_U}{\sqrt{M}} \sum_{i=2}^K |b_k^H b_i|^2 + \frac{e_U}{\sqrt{M}} \|b_k\|^2 \sum_{i=1}^K \frac{\lambda_i}{\tau P_U \lambda_{i+1}} + \|b_k\|^2} \right) \right] \quad (11)$$

$$R_{p,k} = E \left[\log_2 \left(1 + \frac{\frac{P_U |a_k^H b_1|^2}{M}}{\frac{P_U \sum_{i=2}^K |a_k^H b_i|^2 + \|a_k\|^2}{\rightarrow 0}} \right) \right] \quad (12)$$

The rate scaling is given as,

$$\log_2(1 + SINR) = \log_2(1 + e_U \lambda_k) \quad (13)$$

where e_U denote the total transmit power.

The achievable rate for very large value of M can be written as,

$$R_{p,k} = E[\log_2(1 + e_U \lambda_k)] \quad (14)$$

In case of MRC, A=G so $a_k = b_k$.

$$R_{p,k}^{MRC} = E \left[\log_2 \left(1 + \frac{P_U |b_k^H b_1|^2}{P_U \sum_{i=2}^K |b_k^H b_i|^2 + \|b_k\|^2} \right) \right] \quad (15)$$

The power of each user is inversely related to the number of antennas, $P_U = \frac{e_U}{M}$.

$$R_{p,k}^{MRC} = E \left[\log_2 \left(1 + \frac{\frac{e_U}{M} |b_k^H b_1|^2}{\|b_k\|^2} \right) \right] \quad (16)$$

When M is very large,

$$R_{p,k}^{MRC} = E \left[\log_2 \left(1 + \frac{\frac{e_U}{M} |b_k^H b_1|^2}{\|b_k\|^2} \right) \right] \quad (17)$$

By using inequality, $R_{p,k}^{MRC} \geq \hat{R}_{p,k}^{MRC}$. The lower bound on the achievable rate can be given as,

$$\hat{R}_{p,k}^{MRC} = \log_2 \left(1 + \frac{P_U (M-1) \lambda_k}{P_U \sum_{i=1}^K \lambda_i + 1} \right) \quad (18)$$

When, $P_U = \frac{e_U}{M}$, then

$$\hat{R}_{p,k}^{MRC} = \log_2 \left(1 + \frac{P_U (M-1) \lambda_k}{P_U \sum_{i=1}^K \lambda_i + 1} \right) \quad (19)$$

$$R_{ip,k} = E \left[\log_2 \left(1 + \frac{P_U \left| \left((b_k^H b_k)^{-1} \right)^H b_k \right|^2}{P_U \sum_{i=1, i \neq k}^K \left| \left((b_k^H b_k)^{-1} \right)^H b_i \right|^2 + P_U \left\| \left((b_k^H b_k)^{-1} \right)^H b_k \right\|^2 + \sum_{i=1, i \neq k}^K \frac{\lambda_i}{\tau P_U \lambda_i + 1} + \left\| (b_k^H b_k)^{-1} \right\|^2} \right) \right] \quad (28)$$

In case of MRC, A=G so $\hat{a}_k = \hat{b}_k$.

When M is very large, $M \rightarrow \infty$

$$\hat{R}_{p,k}^{MRC} = \log_2(1 + \lambda_k e_U) \quad (20)$$

In case of ZF, $A = B(B^H B)^{-1}$ so $a_k = (b_k^H b_k)^{-1}$.

The Achievable sum rate for the ZF receiver can be given as,

$$R_{p,k}^{ZF} = E \left[\log_2 \left(1 + \frac{P_U \left| \left((b_k^H b_k)^{-1} \right)^H b_1 \right|^2}{P_U \sum_{i=2}^K \left| \left((b_k^H b_k)^{-1} \right)^H b_i \right|^2 + \left\| \left((b_k^H b_k)^{-1} \right)^H b_k \right\|^2} \right) \right] \quad (21)$$

$$R_{p,k}^{ZF} = E \left[\log_2 \left(1 + \frac{\frac{e_U}{M} \left| \left((b_k^H b_k)^{-1} \right)^H b_1 \right|^2}{\frac{e_U \sum_{i=2}^K \left| \left((b_k^H b_k)^{-1} \right)^H b_i \right|^2 + \left\| \left((b_k^H b_k)^{-1} \right)^H b_k \right\|^2}{\rightarrow 0}} \right) \right] \quad (22)$$

$$R_{p,k}^{ZF} = E \left[\log_2 \left(1 + \frac{\frac{e_U}{M} \left| \left((b_k^H b_k)^{-1} \right)^H b_1 \right|^2}{\left\| \left((b_k^H b_k)^{-1} \right)^H b_k \right\|^2} \right) \right] \quad (23)$$

By using inequality, $R_{p,k}^{ZF} \geq \hat{R}_{p,k}^{ZF}$. The lower bound on the achievable rate can be given as,

$$\hat{R}_{p,k}^{ZF} = \log_2(1 + P_U (M-K) \lambda_k) \quad (24)$$

when $P_U = \frac{e_U}{M}$, then

$$\hat{R}_{p,k}^{ZF} = \log_2 \left(1 + \frac{e_U}{M} (M-K) \lambda_k \right) \quad (25)$$

When M is very large, $M \rightarrow \infty$

$$\hat{R}_{p,k}^{ZF} = \log_2(1 + e_U \lambda_k) \quad (26)$$

2.2 Imperfect CSI for MU-MIMO systems

In case of imperfect CSI, the signal to interference noise ratio can be given as [13],

$$SINR = \frac{P_U |\hat{a}_k^H \hat{b}_k|^2}{P_U \sum_{i=1, i \neq k}^K |\hat{a}_k^H \hat{b}_i|^2 + P_U \|\hat{a}_k\|^2 \sum_{i=1, i \neq k}^K \frac{\lambda_i}{\tau P_U \lambda_i + 1} + \|\hat{a}_k\|^2} \quad (27)$$

The Achievable sum rate can be given as,

$$R_{ip,k}^{MRC} = E \left[\log_2 \left(1 + \frac{P_U |\hat{b}_k^H \hat{b}_k|^2}{P_U \sum_{i=1, i \neq k}^K |\hat{b}_k^H \hat{b}_i|^2 + P_U \|\hat{b}_k\|^2 \sum_{i=1}^K \frac{\lambda_i}{\tau P_U \lambda_i + 1} + \|\hat{b}_k\|^2} \right) \right] \quad (29)$$

$$R_{ip,k}^{MRC} = E \left[\log_2 \left(1 + \frac{P_U |\hat{b}_k|^4}{P_U \sum_{i=1, i \neq k}^K |\hat{b}_k^H \hat{b}_i|^2 + P_U \|\hat{b}_k\|^2 \sum_{i=1}^K \frac{\lambda_i}{\tau P_U \lambda_i + 1} + \|\hat{b}_k\|^2} \right) \right] \quad (30)$$

Put, $P_U = \frac{e_U}{\sqrt{M}}$

$$R_{ip,k}^{MRC} = E \left[\log_2 \left(1 + \frac{\frac{e_U}{\sqrt{M}} |\hat{b}_k^H \hat{b}_k|^2}{\frac{e_U}{\sqrt{M}} \sum_{i=1, i \neq k}^K |\hat{b}_k^H \hat{b}_i|^2 + \frac{e_U}{\sqrt{M}} \|\hat{b}_k\|^2 \sum_{i=1}^K \frac{\lambda_i}{\tau P_U \lambda_i + 1} + \|\hat{b}_k\|^2} \right) \right] \quad (31)$$

The achievable uplink rate of the k^{th} user for the MRC receiver using imperfect CSI, Rayleigh fading and $M > K + 1$ is bounded as,

$$\hat{R}_{ip,k}^{ZF} = \log_2 (1 + \tau \lambda_k^2 e_U^2) \quad (37)$$

Let $P_U = \frac{e_U}{\sqrt{M}}$, then

$$\hat{R}_{ip,k}^{MRC} = \log_2 \left(1 + \frac{\tau \frac{e_U}{\sqrt{M}} (M-1) \lambda_k^2}{\left(\tau \frac{e_U}{\sqrt{M}} \lambda_k + 1 \right) \sum_{i=1, i \neq k}^K \lambda_i + (\tau+1) \lambda_k + \frac{1}{\frac{e_U}{\sqrt{M}}}} \right) \quad (32)$$

When M is very large, $M \rightarrow \infty$

$$\hat{R}_{ip,k}^{MRC} = \log_2 (1 + \tau \lambda_k^2 e_U^2) \quad (33)$$

In case of ZF, $\hat{A} = \hat{B}(\hat{B}^H \hat{B})^{-1}$ so $\hat{a}_k = (\hat{b}_k^H \hat{b}_k)^{-1}$.

$$R_{ip,k}^{ZF} = E \left[\log_2 \left(1 + \frac{P_U |((\hat{b}_k^H \hat{b}_k)^{-1})^H \hat{b}_k|^2}{P_U \sum_{i=1, i \neq k}^K |((\hat{b}_k^H \hat{b}_k)^{-1})^H \hat{b}_i|^2 + P_U \left\| (\hat{b}_k^H \hat{b}_k)^{-1} \right\|^2 \sum_{i=1}^K \frac{\lambda_i}{\tau P_U \lambda_i + 1} + \left\| (\hat{b}_k^H \hat{b}_k)^{-1} \right\|^2} \right) \right] \quad (34)$$

The achievable uplink rate of the k^{th} user for the ZF receiver using imperfect CSI, Rayleigh fading and $M > K + 1$ is bounded as,

$$\hat{R}_{ip,k}^{ZF} = \log_2 \left(1 + \frac{\tau P_U^2 \lambda_k^2}{(\tau P_U \lambda_k + 1) \sum_{i=1}^K \frac{P_U \lambda_i}{\tau P_U \lambda_i + 1} + \tau P_U \lambda_i + 1} \right) \quad (35)$$

As $P_U = \frac{e_U}{\sqrt{M}}$

$$\hat{R}_{ip,k}^{ZF} = \log_2 \left(1 + \frac{\tau \frac{e_U^2}{M} \lambda_k^2}{\left(\tau \frac{e_U}{\sqrt{M}} \lambda_k + 1 \right) \sum_{i=1}^K \frac{\frac{e_U}{\sqrt{M}} \lambda_i}{\tau \frac{e_U}{\sqrt{M}} \lambda_i + 1} + \tau \frac{e_U}{\sqrt{M}} \lambda_i + 1} \right) \quad (36)$$

When M is very large, $M \rightarrow \infty$.

3. OPTIMAL PRECODER/COMBINER FOR mmWAVE MIMO SYSTEM

Received matrix Y can be given as [16-17],

$$Y = \sqrt{P} W_{BB}^H W_{RF}^H H_n F_{RF} F_{BB} + \tilde{N} \quad (38)$$

where $F_{RF} = N_T \times N_T$, $W_{RF} = N_R \times N_R$, $F_{BB} = N_T \times N_T^{Beam}$ and $W_{BB} = N_R \times N_R^{Beam}$.

Number of RF chains = N_{RF} .

The channel model can be written as,

$$H_n = \underbrace{A_B}_{N_R \times G} \times \underbrace{H}_{G \times G} \times \underbrace{A_T^H}_{G \times N_T} \quad (39)$$

where G is the number of directional cosine vectors and H_n is the sparse combination of directional vector at the transmitter/receiver.

The equivalent sensing matrix is given as,

$$\begin{aligned} \text{vec}(Y) &= \sqrt{P} Q_S \text{vec}(H) + \text{vec}(\tilde{N}) \\ y &= \sqrt{P} Q_S h + \tilde{n} \end{aligned} \quad (40)$$

Equivalent sensing matrix $Q_S = \text{size } N_T^{Beam} N_R^{Beam} \times G^2$.

$$Q_S = (F_{BB}^T F_{RF}^T A_T^*) \otimes (W_{BB}^H W_{RF}^H A_R) \quad (41)$$

The channel estimation problem can be formulated as,

$$\begin{aligned} \arg \min_{h} & \|y - \sqrt{P} Q_S h\|_2 \|y - A h\|_2 \\ y &= H x + n = H F_{RF} F_{BB} s + n \end{aligned} \quad (42)$$

$$(W_{RF}^{opt}, W_{BB}^{opt}) = \arg \min_{W_{RF}, W_{BB}} E \|s - W_{BB}^H W_{RF}^H y\|^2 \quad (43)$$

where $W_{BB}^H = N_S \times N_{RF}$ and $W_{RF}^H = N_{RF} \times N_R$.

The MMSE estimate is shown as,

$$\hat{s} = W_{MMSE}^H Y \quad (44)$$

$$W_{MMSE}^H = E (s y^H) E (y y^H)^{-1} = R_{sy} R_{yy}^{-1}$$

Finally MMSE estimate can be written as,

$$\hat{s} = \left\| R_{yy}^{1/2} (W_{MMSE} - W_{RF} W_{BB}) \right\|_F^2 \quad (45)$$

MMSE minimization can be given as,

$$(W_{RF}^{opt}, W_{BB}^{opt}) = \arg \min_{W_{RF}, W_{BB}} E \left\| R_{yy}^{1/2} (W_{MMSE} - W_{RF} W_{BB}) \right\|_F^2 \quad (46)$$

The capacity can be given as,

$$C = B \log_2 (1 + SINR) \quad (47)$$

4. SIMULATION RESULTS

Figure 2 shows that there is a much improvement in the uplink sum rate for the ZF receiver than MRC receiver with perfect channel state information in the massive MIMO system. The uplink sum rate also increases as the number of base station antenna increases. In figure 3, comparison of uplink sum rate for varying number of users is done. The uplink sum rate is higher as the number of users increases with imperfect channel state information in the massive MIMO system. In figure 4, it is shown that as the number of transmit and receive antenna increases, the capacity of the mmWave massive MIMO system increases. Capacity of hybrid MIMO outperforms conventional MIMO system. Figure 5 shows an improvement in the capacity of the system as the number of radio frequency chain increases.

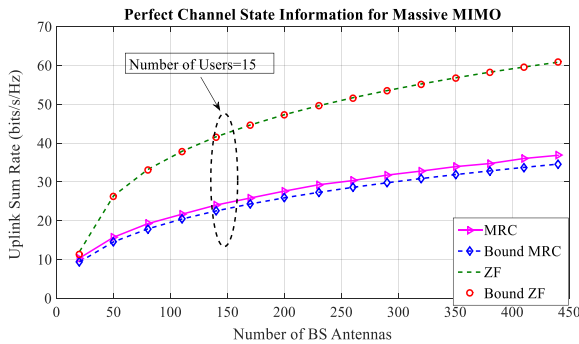


Figure 2. Numerically evaluated values and lower bounds of uplink sum rate for different number of base station antenna for MRC and ZF receiver with with perfect channel state information for K=15 (Number of Users)

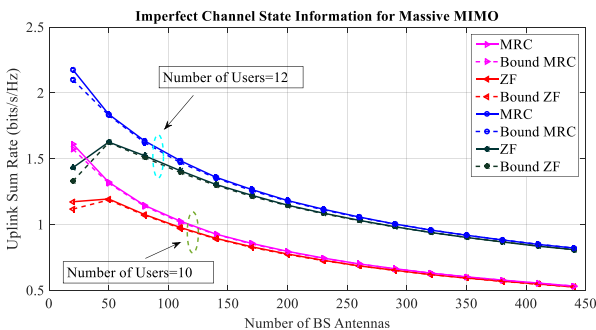


Figure 3. Comparison of numerically evaluated values and lower bounds of uplink sum rate for different number of base station antenna for MRC and ZF receiver with imperfect channel state information for K=10 (Number of Users) and K=12 (Number of Users)

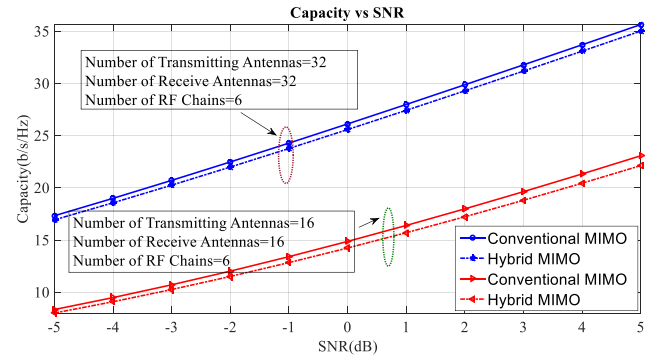


Figure 4. Comparison of Capacity versus signal to noise ratio for Conventional MIMO and Hybrid MIMO with $T_x = 32, R_x = 32, n_{RF} = 6$ and $T_x = 16, R_x = 16, n_{RF} = 6$

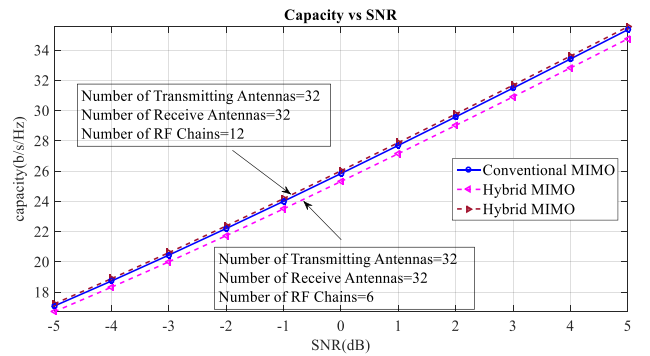


Figure 5. Comparison of Capacity versus signal to noise ratio for Conventional MIMO and Hybrid MIMO with $T_x = 32, R_x = 32, n_{RF} = 12$ and $T_x = 32, R_x = 32, n_{RF} = 6$

5. CONCLUSION

Massive MIMO systems offer an improvement in the uplink sum rate with increasing the number of base station antennas. ZF forcing receiver outperforms the MRC with perfect CSI and Imperfect CSI. With imperfect CSI, as the number of users increases the uplink sum rate also increases. In the mmWave massive MIMO system, there is an improvement in channel capacity as the number of transmit and receive antenna increases. Further, as the number of the RF chains decreases, the capacity of the mmWave massive MIMO system with MMSE receiver also degrades.

REFERENCES

- [1] Magrini, A., Lazzari, S., Marengo, L., Guazzi, G. (2017). A procedure to evaluate the most suitable integrated solutions for increasing energy performance of the building's envelope, avoiding moisture problems. International Journal of Heat and Technology, 35(4): 689-699. <https://doi.org/10.18280/ijht.350401>
- [2] Rappaport, T.S., Sun, S., Mayzus, R., Zhao, H., Azar, Y., Wang, K., Wong, G.N., Schulz, J.K., Samimi, M., Gutierrez, F. (2013). Millimeter wave mobile communications for 5G cellular: It will work! In IEEE Access, 1: 335-349. <http://dx.doi.org/10.1109/ACCESS.2013.2260813>
- [3] Andrews, J.G., Bai, T., Kulkarni, M.N., Alkhatieb, A., Gupta, A.K., Heath, R.W. (2017). Modeling and

- analyzing millimeter wave cellular systems. In IEEE Transactions on Communications, 65(1): 403-430. <http://dx.doi.org/10.1109/TCOMM.2016.2618794>
- [4] MacCartney, G.R., Samimi, M.K., Rappaport, T.S. (2015). Exploiting directionality for millimeter-wave wireless system improvement. 2015 IEEE International Conference on Communications (ICC), 2416-2422. <http://dx.doi.org/10.1109/ICC.2015.7248687>
- [5] Sachan, V., Shankar, R., Mishra, R.K. (2017). Selective Decode-forward cooperative communication over Nakagami-m fading channel with channel estimation error. Journal of Telecommunication, Electronic and Computer Engineering (JTEC), 9(2-6): 85-90.
- [6] Sachan, V., Kumar, I., Shankar, R., Mishra, R.K. (2018). Analysis of transmit antenna selection based selective decode forward cooperative communication protocol. Traitement du Signal, 35(1): 47-60. <http://dx.doi.org/10.3166/TS.35>
- [7] Sachan, V., Shankar, R., Kumar, I., Mishra, R.K. (2019). Performance analysis of SM-MIMO system employing binary PSK and M-ary PSK techniques over different fading channels. Procedia Computer Science, 152: 323-332. <http://dx.doi.org/10.1016/j.procs.2019.05.010>
- [8] Shankar, R., Kumar, G., Sachan, V., Mishra, R.K. (2018). An investigation of two phase multi-relay S-DF cooperative wireless network over time-variant fading channels with incorrect CSI. Procedia Computer Science, 125: 871-879. <http://dx.doi.org/10.1016/j.procs.2017.12.111>
- [9] Ngo, H.Q., Larsson, E.G., Marzetta, T.L. (2013). Energy and spectral efficiency of very large multiuser MIMO systems. In IEEE Transactions on Communications, 61(4): 1436-1449. <http://dx.doi.org/10.1109/TCOMM.2013.020413.110848>
- [10] Hoydis, J., ten Brink, S., Debbah, M. (2013). Massive MIMO in the UL/DL of cellular networks: How many antennas do we need? IEEE Journal on Selected Areas in Communications, 31(2): 160-171. <http://dx.doi.org/10.1109/JSAC.2013.130205>
- [11] Yang, H., Marzetta, T.L. (2013). Performance of conjugate and zeroforcing beamforming in large-scale antenna systems. IEEE Journal on Selected Areas in Communications, 31(2): 172-179. <http://dx.doi.org/10.1109/JSAC.2013.130206>
- [12] Rusek, F., Persson, D., Lau, B.K., Larsson, E.G., Marzetta, T.L., Edfors, O., Tufvesson, F. (2013). Scaling up MIMO: Opportunities and challenges with very large arrays. IEEE Signal Processing Magazine, 30(1): 40-60. <http://dx.doi.org/10.1109/MSP.2011.2178495>
- [13] Ngo, H.Q., Larsson, E.G., Marzetta, T.L. (2013). The multicell multiuser MIMO uplink with very large antenna arrays and a finite-dimensional channel. In IEEE Transactions on Communications, 61(6): 2350-2361. <http://dx.doi.org/10.1109/TCOMM.2013.032713.120408>
- [14] Kumar, I., Sachan, V., Shankar, R., Mishra, R.K. (2018). An investigation of wireless S-DF hybrid satellite terrestrial relaying network over time selective fading channel. Traitement du Signal, 35(2): 103-120. <http://dx.doi.org/10.3166/ts.35.103-120>
- [15] Jose, J., Ashikhmin, A., Marzetta, T.L., Vishwanath, S. (2011). Pilot contamination and precoding in Multi-Cell TDD systems. In IEEE Transactions on Wireless Communications, 10(8): 2640-2651. <http://dx.doi.org/10.1109/TWC.2011.060711.101155>
- [16] Ayach, O.E., Rajagopal, S., Abu-Surra, S., Pi, Z., Heath, R.W. (2014). Spatially sparse precoding in millimeter wave MIMO systems. In IEEE Transactions on Wireless Communications, 13(3): 1499-1513. <http://dx.doi.org/10.1109/TWC.2014.011714.130846>
- [17] Alkhateeb, A., El Ayach, O., Leus, G., Heath, R.W. (2014). Channel estimation and hybrid precoding for millimeter wave cellular systems. In IEEE Journal of Selected Topics in Signal Processing, 8(5): 831-846. <http://dx.doi.org/10.1109/JSTSP.2014.2334278>

NOMENCLATURE

B	band width
C	channel capacity
e	total transmitted power
k	single antenna user
M	Base station antenna
n	additive white Gaussian noise
N	number of radio frequency chain
P	average transmitted power
x	transmitted data
r	received vector
R	achieved sum rate

Greek symbols

λ	geometric distribution
τ	length of pilot sequence

Subscripts

u	number of user
---	----------------



A comparative study on valuable products: bio-oil, biochar, non-condensable gases from pyrolysis of agricultural residues

Kedar Sahoo¹ · Ankit Kumar¹ · Jyoti Prasad Chakraborty¹

Received: 30 January 2020 / Accepted: 11 September 2020
© Springer Japan KK, part of Springer Nature 2020

Abstract

In this study, pyrolysis of agricultural residues, such as rice straw (RS), wheat straw (WS), and sugarcane bagasse (SB), was performed in a fixed-bed reactor. The experiments were carried out at varying operating conditions, such as temperature, heating rate, biomass particle size and sweeping gas flow rate, such that the bio-oil yield could be maximized. Small particle size and high heating rate contributed to more bio-oil yield as compared to large particle size and low heating rate. Physico-chemical properties of bio-oil samples, evaluated in a comparative manner with maximum focus devoted on analyzing the chemical constituents through GC–MS and FTIR analysis. Biochar was also examined through different physicochemical techniques (e.g., HHV, pH, SEM–EDX, FTIR, CHNS, ICP–AES) for understanding pyrolysis mechanism and its practical usability. Analysis of non-condensable gas through GC–TCD, revealed co-existence of H₂, CO, CO₂ and CH₄ molecules, with greater percentage of H₂ and CH₄ at high temperature resulted enhancement in calorific value.

Keywords Pyrolysis · RS · WS · SB · Fixed-bed

Introduction

Maximum of the world's energy resources are non-renewable and fulfilling through fossil fuel sector, those are depleting day by day due to their extensive uses, and also there is a rising concern for greenhouse gas emissions [1, 2]. These fundamental problems have created a tremendous amount of interest in the field of alternative and renewable fuels, which are environmentally benign as well as economically viable [3]. Biomass is a major source of energy; it provides approx. 10–14% energy demand of world [4]. Biomass, such as materials produced from microbial, animal, algae, agricultural waste, and forestry residues, is the renewable energy source, which converted into liquid fuels and value-added chemicals and used as high-potential feedstock for conventional petroleum-based energy sector around the world

[5–9]. Biomass has gained more attention because of its wide availability and low cost in comparison to other renewable energy sources [10–12]. Agricultural biomasses mainly comprise cellulose (30–60%), hemicellulose (20–35%) and lignin (15–30%) along with some resins and inorganic constituents and possess high-energy content [13]. They can be used for getting heat, power, synthesis gas, and chemicals through different thermo-chemical routes, such as combustion, gasification, pyrolysis, liquefaction, and enzymatic route, such as fermentation [14–19]. Among the various methods available for agricultural biomass conversion to the biofuels, pyrolysis is a promising technique which incurs lesser amount of cost and leads to the generation of high-energy-density bio fuel, performed in an inert atmosphere [20]. It is a thermo-chemical process that can efficiently produce bio-oil, gases and biochar. The yield and properties of products obtained from pyrolysis strongly depend on various factors viz. reactor design, operating conditions (temperature, heating rate, particle size, and sweeping gas flow rate etc.) as well as on type of biomass used [21–23]. Due to the diversity and heterogeneity in biomass composition and its typical thermal decomposition nature makes, resulting pyrolysis mechanism is very much complex [24]. Studies explained that there are three stages of pyrolysis reactions: (1) removal of free moisture (2) initial decomposition of

Electronic supplementary material The online version of this article (<https://doi.org/10.1007/s10163-020-01114-2>) contains supplementary material, which is available to authorized users.

✉ Jyoti Prasad Chakraborty
jpc.che@iitbhu.ac.in

¹ Department of Chemical Engineering and Technology, Indian Institute of Technology (BHU), Varanasi, UP 221005, India

long-chain molecules (3) followed by bio-oil decomposition and re-polymerization [25]. Since cellulose present in abundance amount in agricultural biomass, a simple decomposition mechanism explained by Waterloo helps to understand the reaction pathways for pyrolysis process [26]. Accordingly, at low temperature, cellulose gets depolymerized (300–450 °C) and subsequently defragmented at a higher temperature (~600 °C), and finally turns into carboxylic acid, alcohol, aldehyde, ketone, and anhydrosugars, etc. which are the major compounds found in bio-oil [24].

Indian economy is mostly agricultural-based because 60.6% of the cultivable land is being used by 53% of people, those belonging to rural India and who earn their livelihood through farming. So, a lot of agricultural wastes are generated every year, which are utilized directly for animal consumption or used as raw material for pulp and paper industry. However, storage, collection and transportation of residual biomass are very difficult and expensive. Therefore, it remained unutilized as a waste or directly burned in household stove or farms, causing serious environmental pollution and health hazards. A simple solution of this acute environmental problem arising from burning crop residues and unused biomass waste can be to solve through production of bio-oil and other value-added products locally through pyrolysis [11]. Bio-oil produced by pyrolysis of biomass is a free-flowing complex organic liquid dark brown in color, contains highly oxygenated organic compounds and having smoky odor [21, 27]. Bio-oil has an advantage over fossil fuel because it contains a very low amount of bonded nitrogen and sulfur resulting in lesser amount of greenhouse gas emission during combustion [19, 28]. However, it contains variety of value-added chemicals that can be used in different applications. The non-condensable gases produced during pyrolysis mainly comprise H₂, CO, CH₄, and CO₂ up to 95% [29, 30], which has high calorific value and further can be utilized for energy generation.

Apart from bio-oil and non-condensable gases, biochar (also called charcoal) is also the valuable solid product containing unconverted organic, inorganic and carbonaceous residues obtained from pyrolysis. According to the previous literatures [31, 32], biochar is mainly a carbon-rich compound with composition ranging from 53 to 96%, heating values ranging from 20 to 36 MJ/kg, and yields of biochar obtained from pyrolysis of different feedstock varied between 30 and 90%. The high HHV of biochar makes it a valuable combustible product, which can be substituted for coal also [33]. The highly porous surface structure of biochar confers it as a low-cost adsorbent material for removal of various organic and inorganics pollutants [25, 32] as well as in catalysis application also [34]. Biochar can also act as a fertilizer for soil amendment application [35] and can also contribute in carbon sequestration process [36].

Agricultural residues, such as wheat straw (WS), rice straw (RS), sugarcane bagasse (SB), are the largest and abundant by-products produced in the developing countries like India, Brazil, China, etc. [37, 38]. A lot of research has been carried out on pyrolysis of RS, WS and SB previously. Wang et al. [39] pyrolysed RS in a simple closed reactor at 523–773 K with 10 K/min heating rate. The maximum yield of liquid products was obtained at 693 K with H/C molar ratio of 1.65 and O/C molar ratio of 0.058 just in the range of petroleum. Park et al. [40] carried out slow pyrolysis of RS at different temperature range from 300 to 700 °C with a 10 °C/min heating rate. The yield of bio-oil and biochar obtained was same above 500 °C temperature. At 700 °C temperature, yield of bio-oil declined while gas yield increased. Balagurumurthy et al. [41] also performed pyrolysis of RS in the presence of hydrogen and nitrogen atmosphere. They observed that, higher yield of bio-oil was obtained under nitrogen atmosphere as compared to hydrogen environment. Pottmair et al. [42] performed pyrolysis of rice husk and WS in the wide temperature range from 290 to 900 °C at constant flow of nitrogen 100 mL/min with 50 °C/min heating rate. They reported that the bio-oil yield increases with rise in temperature from 290 to 900 °C for both the biomass. Varma et al. [43] conducted pyrolysis of SB in a semi-batch reactor at different temperature range of 350–650 °C with two heating rates (10 and 50 °C/min) and biomass particle sizes (<0.25 to 1.7 mm). They concluded that maximum bio-oil yield of 45.23% was obtained at temperature 500 °C with heating rate 50 °C/min, particle size of 0.5–0.6 mm and nitrogen flow rate of 100 cm³/min. Gonclaves et al. [44] evaluated the pyrolysis of SB in a fixed-bed reactor to investigate the product distributions at various operating conditions, such as temperature heating rate, particle size of biomass samples and sweeping gas flow rate of nitrogen. They reported highest bio-oil yield (0.5 g/g of biomass) at 600 °C, 15 °C/min heating rate and N₂ flow rate of 200 mL/min, with particle size ranging from 0.5 to 1.0 mm. Temperature and particles' sizes were the most significant factors for the maximum bio-oil yield. Also, Biswas et al. [11] performed a comparative study on fixed-bed pyrolysis of various agricultural residues, such as RS, husk, corn stover, WS at different temperatures range 300–450 °C with a fixed heating rate of 20 °C/min and nitrogen flow rate 50 mL/min and analyzed bio-oil produced during experimentation. Maximum bio-oil yields were varied for corn cob, WS, RS and rice husk were 47.3, 36.7, 28.4 and 38.1%, respectively [11]. Apart from this, Duong et al. [45] carried out thermal degradation of four types of Vietnamese biomasses, e.g. bagasse, corncob, rice husk and rice straw, through pyrolysis reaction for bio-oil production. This study has revealed that the bio-oil yield greatly depended on temperatures and sweeping gas flow rate, not the biomass particles size. Moreover rice husk and straw shown greater

production of bio-oil than bagasse and corn cob. Similarly, pyrolysis of agricultural residue has been extensively studied for bio-char production and those have specific uses. Adinaveen et al. [46] prepared porous biochar from rice straw by two-stage pyrolysis process and prepared porous carbons have been employed for fabrication of super-capacitor electrode. The physicochemical and nutrient properties of biochar have been investigated by several researchers for their plausible application in bioremediation, improvement of soil fertility, etc. Bera et al. [47] prepared biochar by pyrolysis of rice straw, wheat straw, maize stover and pearl millet stover by only variation of pyrolysis temperature. Temperature and biomass residue modified biochar properties significantly, those in turn improved soil nutrient on their application. Similar to above findings, Tan et al. [48] and Do et al. [49] reported in their investigation that the agronomic properties of biochar prepared by pyrolysis of agricultural residue, greatly influenced by reaction temperature and pyrolysis reaction atmosphere. Tan et al. in their research found that the limited oxygen cracking conditions improvised the biochar morphology and nutrient content as compared to inert nitrogen atmosphere. Also, Do et al. reported that at higher reaction temperature ($> 500\text{ }^{\circ}\text{C}$) improved biochar porosity but their calorific value was reduced. Derakhshan-Nejad et al. [50] prepared biochar from the pyrolysis of rice husk and maple leaves. The prepared biochar sample was used in soil amendment application for heavy metal immobilization. They found that phytoavailability of heavy metals Cd, Cu, Pb, Zn present in soil extensively declined in biochar-amended soil due to their immobilization process. The overall conclusion showed that all the biomasses are suitable to be used as a feedstock for bio-oil production in Indian sub-continent, due to abundant availability and very low sulfur and nitrogen contents.

Though a number of these types of studies have been performed till date, however, none of the work focused on the slow pyrolysis of different types of agricultural residues (crop residues) in addition to detailed and comparative analysis of all three pyrolysis products (bio-oil biochar, gases) through operating parameter variation. Moreover, there were only a few reports available regarding physicochemical properties of all three pyrolysis products in comparative manner with application oriented approach. This work also wanted to address issues with waste management as stubble burning poses serious threat to the environment. Hence, pyrolysis of surplus biomass available locally offers a sustainable solution.

The focus of this research is to study pyrolysis of three different kinds of biomass (SB, WS, RS) abundantly available in the campus of Banaras Hindu University, in a fixed-bed reactor. A comparative study regarding the yield of three primary pyrolysis products (bio-oil, biochar and non-condensable gases), along with variation in the yield

at various operating parameters viz. temperature, heating rate, sweeping gas flow rate, particles sizes were also studied extensively. Various physical properties of bio-oil and biochar were evaluated and significant focus was devoted on the chemical characterization through FTIR, GC-MS, ICP-AES, SEM and CHNS analysis for application oriented approach. Similarly, effect of inorganic constituents present in biochar on pyrolysis mechanism and product distribution were also thoroughly explained. Detailed composition of non-condensable gases (mainly producer gases) analyzed through gas chromatography (GC-TCD) techniques and variation of their energy values with temperature were studied carefully.

Materials and methods

Feedstock preparation

Feedstock chosen for this experiment was SB, RS, and WS, collected from agriculture farm of Banaras Hindu University. Each biomass was subjected to initial size reduction in a cutting mill (SM 300 Retsch Germany), washed thoroughly and sun-dried for 4–5 days followed by drying in an oven at $105\text{ }^{\circ}\text{C}$ for 4 h. The dried biomass was ground into small sizes in a disintegrator and sieved into three different sizes of 0.2–0.4 mm, 0.4–0.6 mm, and 0.6–0.8 mm.

Characterization methods

Characterization of biomass

The proximate analysis of biomass includes moisture content, volatile matter, ash content, and fixed carbon content and these were determined according to standards ASTM D1037 (1991), ASTM D3172, ASTM D2017 (1998), ASTM E1755, respectively. The ultimate analysis of three biomass samples was carried out in Euro-vector Elemental Analyzer. The functional groups present in biomass were also investigated at room temperature in the frequency range of $4500\text{--}500\text{ cm}^{-1}$ using a Fourier-transform infrared (FTIR) spectrometer (Thermo Electron Corporation, USA, FTIR procedure: S1, ESI). TGA of three biomass samples was carried out in the NETZSCH STA 449 F3 instrument. During each run, 7 mg of the sample was heated up to $900\text{ }^{\circ}\text{C}$ at a heating rate of $10\text{ }^{\circ}\text{C}/\text{min}$ starting from room temperature. The carrier gas used was argon with flow rate maintained at $100\text{ mL}/\text{min}$.

Characterization of liquid and gaseous products

Bio-oil samples were characterized by measuring their physical properties, such as density, pH, viscosity, ash content,

and calorific value. The pH of the bio-oil samples was measured with the digital pH meter (Eutech Instrument) and viscosity was measured with the help of Redwood Viscometer (I.P. 70/46, Gallenkamp, British Made) present in the laboratory. Ash content of bio-oil was determined by burning 10 g of bio-oil at around 600 °C in a muffle furnace overnight [51, 52]. The higher heating value of bio-oil was measured by a digital bomb calorimeter (model no. RSB-7, Rajdhani Scientific Instruments Corporation, New Delhi, India). The chemical characterization of bio-oil was performed by determining the organic functional groups present in it by a Thermo electron FTIR analyzer. GC–MS analysis of three bio-oil samples was performed in a GC–MS-QP 2010 plus ultra (Shimadzu company) equipped with a capillary column (HP-INNOWAX, 60 m × 0.25 mm id × with 0.250 µm film thickness) for determination of organic compounds present in them. Operating conditions and library specification for GC–MS analysis are provided in supporting information (S2, ESI). Non-condensable gases were collected in gas holders at different temperatures and analysis was carried out in a Centurion Scientific Gas chromatography thermal conductivity detector (GC-TCD). The GC was equipped with a Carbosieve SII column (40–60 mesh range) with a thermal conductivity detector. Column, detector, and injector temperatures were maintained at 60 °C, 80 °C, and 100 °C, respectively.

Characterization of biochar produced

Produced biochar samples were characterized through determination of their higher heating value (HHV) and pH. For measurement of pH 0.5 g of biochar, the sample was dissolved in 50 mL of distilled water and stirred for 30 h in a magnetic stirrer [30]. HHV was measured with the help of digital bomb calorimeter (model no. RSB-7, Rajdhani Scientific Instruments Corporation, New Delhi, India). Chemical characteristics of biochar samples were observed with the help of FTIR analysis, SEM/EDX (Evo 18 Research, Carl Zeiss, Oxford Instruments, Germany), CHNS (EuroEA elemental analyzer) and ICP-AES analysis (Thermo scientific model no. ICAP 6200 Duo). Prior to ICP analysis, biochar samples were dissolved in aquaregia solution and subjected to repeated filtration by diluting with deionized water followed by passing through Whatman #1 filter paper. Details regarding ICP-AES analysis procedure are provided in supplementary information (S3, ESI).

Experimental procedure

The experiment was performed in a tubular fixed-bed reactor made of quartz with the help of a split-tube single-zone furnace (NSW-104, New Delhi) programmed with a linear ramping rate. The reactor was made of quartz having length

65 cm and 2.5 cm in diameter. The height of the biomass bed was approx. 10 cm; id of the quartz reactor was 22 mm. The amount of biomass loaded was fed manually from the upper side of reactor by gently tapping the wall such that a packed bed shape could be obtained. The bed temperature was measured by inserting a thermocouple which touched the top portion of the biomass bed. The bed temperature was measured by inserting a thermocouple (temperature sensor) which touched the top portion of the biomass bed. Since the bed height is small and biomass particle has powder texture, the temperature variation due to thermal gradient can be overcome easily and biomass bed has nearly uniform temperature, sensed by thermocouple. The reactor had a provision of feeding line for carrier gas and thermowell (with K type thermocouple) for measurement of bed temperature. The sweeping gas (nitrogen) flow rate was controlled by a mass flow controller. A real-time picture of reactor set-up has been provided in the supplementary information file (Fig. S1, ESI). For every run 5 g of the biomass, the sample was taken, and produced vapors were condensed in a condenser placed at the bottom of reactor maintained at 4 °C with the help of re-circulation bath (Eyela, Japan). For the reproducibility of the result, every result was performed twice, and the average value was reported in the results. The condensable vapors were collected in the form of bio-oil in the separator. Condenser and its accessories were washed with acetone at the end of every run so as to collect the residual if any present in it. Acetone was evaporated in an oven at 70 °C and the calculated weight of residual bio-oil was added to the weight of bio-oil produced to obtain the final yield of bio-oil weight percentage. It was found that the residual bio-oil was present in condenser and its accessories within 5% of total product yield. The schematic of the experimental set-up is shown in Fig. 1. Pyrolysis of biomass samples of given sizes (mentioned earlier) was carried out at a temperature range of 350–650 °C in an interval of 50 °C

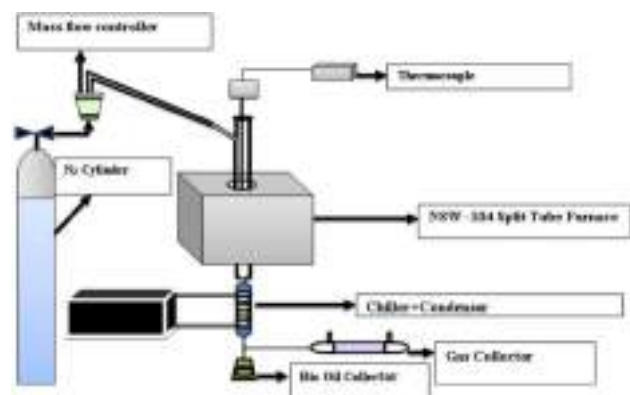
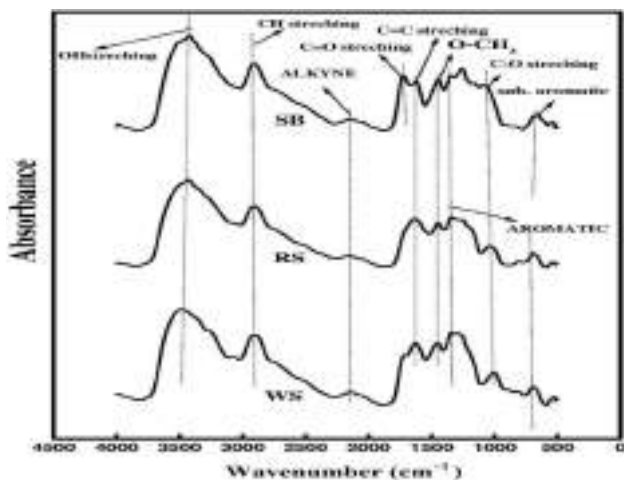


Fig. 1 Schematic diagram of experimental set-up

Table 1 Proximate and ultimate analyses of selected biomass samples (wt%)

Biomass	Moisture	Volatile matter	Ash	Fixed carbon	N	C	H	S	O	H/C	O/C
SB	6.0	89.50	1.90	8.60	0.88	44.04	6.18	Nd ^a	48.90	1.68	0.83
WS	7.0	81.00	7.53	11.47	1.15	42.16	5.57	Nd	51.12	1.58	0.90
RS	8.0	77.50	11.6	10.9	1.07	40.30	5.53	Nd	53.10	1.64	0.98

^aNot detected**Fig. 2** FTIR spectra of three biomass samples

with heating rates maintained at 20 °C/min and 100 °C/min and sweeping gas flow rate ranging from 30 to 100 mL/min.

Product yield was calculated using the following equations:

Yield of the products (on weight basis) was calculated as follows:

$$\text{Yield of bio-oil (wt\%)} = \left[\frac{\text{(bio-oil formed)}}{\text{(biomass-fed into the reactor)}} \right] \times 100, \quad (1)$$

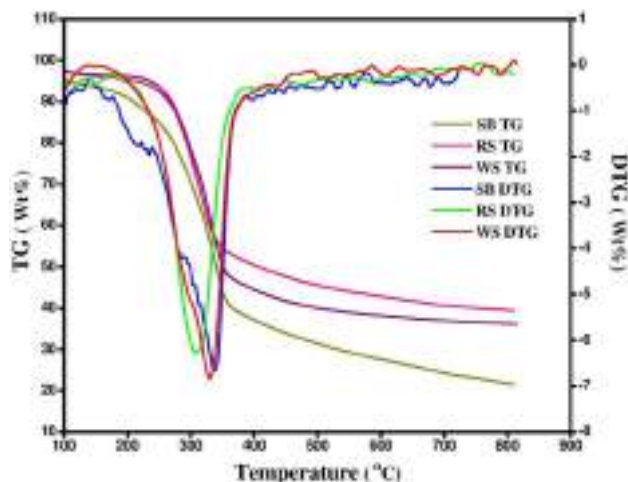
$$\text{Yield of biochar (wt \%)} = \left(\frac{\text{biochar formed}}{\text{biomass-fed into the reactor}} \right) \times 100, \quad (2)$$

$$\text{Yield of non-condensable gas (wt \%)} = 100 - (\text{yield of bio-oil} + \text{yield of biochar}). \quad (3)$$

Results and discussion

Characterization of biomass samples

The data for proximate and ultimate analyses of selected biomass samples are shown in Table 1. FTIR results of three biomass samples are provided in Fig. 2. Thermogravimetric analysis was carried out (Fig. 3) to identify the thermal

**Fig. 3** TG and DTG analysis of three biomass samples as a function of temperature

decomposition behavior of three biomass samples which in turn specify the suitable temperature range within which experiment has to be performed [53].

Proximate and ultimate analyses

As shown in Table 1, SB has the lowest ash content, moisture content and O/C ratio compared to other biomass samples. RS found to contain high amount of ash as compared to other biomass samples. All results are compared with the other works listed in Table 2 [1, 54, 55].

FTIR analysis

From Fig. 2, it is observed that the absorbance peak at 3490 cm^{-1} in the case of three biomass samples corresponds to OH stretching vibration which in turn confirms the presence of alcoholic and phenolic functional groups associated with cellulose as well as hemicellulose and lignin components, respectively, present in them. Cellulose is a homo-polymer of cellobiose monomers and hemicellulose is branched heterogeneous polymer of various sugar monomers like hexose, pentose, etc., all are associated with OH groups in their basic structures. Similarly, lignin is a highly branched 3D heteropolymer of hydroxyl- and methoxyl-substituted phenyl propane units mainly contribute to phenolic

Table 2 Proximate and ultimate analyses of selected biomass samples (from literature) (wt%)

Biomass	Moisture	Ash	N	C	H	O	S	Ref
SB	6.21	2.98	0.15	45.39	7.92	46.67	–	[1]
RS	5.68	14.11	1.07	47.50	6.55	44.88	–	[54]
WS	6.60	8.19	1.4	41.19	5.34	51.97	0.096	[55]

functional groups in all three biomass samples. C–H stretching vibration at wave no. 2910 cm^{-1} indicates the presence of alkanes, resulted from various carbohydrate monomers in three biomass samples [51, 56, 57]. The absorbance peak at 2140 cm^{-1} indicates the presence of alkyne functional group in 3 biomass samples [58]. Apart from this, the average intense absorption band at 1720 cm^{-1} indicates C=O stretching vibration, which confirms the presence of Quinone, aldehyde, and ketonic functional groups [51, 56, 57]. Its presence also validated from the fact that hemicellulose associated with various acetylated sugars. The medium-intense absorption band at 1620 cm^{-1} indicates C=C stretching vibration, which confirms the presence of alkenes and aromatic functional groups in above three biomass samples associated with lignin [56]. The absorbance peak at wave no. 1440 cm^{-1} in three biomass samples indicates O–CH₃ (methoxyl) functional groups contributing to the basic structure of phenyl propane units of lignin [58]. Infrared vibration at 1030 cm^{-1} which corresponds to C–O stretching or OH deformation, indicates the presence of ethers, esters in all three biomass samples those act as a connecting link between various monomers of lignocellulosic components as well as components of phenyl propane units associated with lignin. The more intense absorption band at wave no. 694 cm^{-1} in all three biomass samples indicates the presence of mono-, polycyclic, and substituted aromatic compounds contributing to the basic structure of lignocellulosic components of biomass [51].

Thermogravimetric analysis

The entire TGA profile (Fig. 3) can be distinguished into three stages. During the first stage between 50 and 220 °C, there is a slight change in the slope of TG curves for all three biomasses. This is an indication of slight decay in biomass weight (within 10%) due to the drying procedure and release of lighter volatiles in addition to bound moisture [59]. The second stage demarcated within a temperature range of 220–500 °C in TG curves contributed significantly to a drop in weight of biomass (~50%). This rapid weight loss is mainly because of the thermal decomposition of cellulose, hemicellulose, and lignin [58, 60]. During the third stage (500–900 °C), there is no significant loss in biomass weight due to thermal decomposition as indicated by the flat profile of the TG curve. Maximum weight loss rate occurs

at a temperature of 340 °C for SB and WS, while in case of RS, it is 320 °C. Maximum weight loss rates are 7%/min, 7.8%/min and 6.5%/min for SB, WS, and RS, respectively.

In lignocellulosic biomass, thermally degradable polymers are hemicellulose, cellulose, and lignin. Hemicellulose decomposed readily at a temperature range of 210–315 °C. Cellulose is more robust due to a long polymer of glucose without branches, thermally stable, and its pyrolysis temperature revolves around high temperature (315–400 °C). Lignin is full of aromatic rings with various branches hence, its degradation occurs at a wide temperature range (100–900 °C) [58]. Figure 3 consists of one major derivative weight loss peak in between 310 and 400 °C for all biomasses, and it is mainly due to the decomposition of cellulose. DTG curves consist of shoulder observed at a temperature < 300 °C, mainly due to hemicellulose decomposition. Small degradation peaks in DTG curve of three biomass samples at wide temperature range mainly due to decomposition of lignin.

Effect of pyrolysis reaction conditions on products distribution

Effect of temperature

The pyrolysis yield of products at different temperatures having a particle size of 0.2–0.4 mm, using a sweeping gas flow rate of 30 mL/min and a heating rate of 100 °C/min is shown in Fig. 4. The temperature had a significant effect on pyrolysis product distribution. The bio-oil yield was lowest at a temperature of 350 °C, and the yield increased up to 550 °C, and after that, there was a decreasing pattern. The maximum yield was obtained at a temperature of 550 °C in the case of SB and WS, but in the case of RS, maximum yield of bio-oil was obtained at 450 °C. SB produced highest bio-oil yield nearly 52.5%, and in the case of WS and RS maximum, bio-oil yield percentage is 37.2% and 33.3%, respectively. These results are similar to results obtained by several other researchers [51, 52, 57, 61, 62]. The evolution of minimum bio-oil yield and maximum char yield at 350 °C are due to the rigidity and lower thermal conductivity of biomass that inhibits its decomposition at low temperature [63]. At low-temperature pyrolysis, high char yield and low liquid yield are also reasonable because of the polymerization of volatilized organics [51]. But among three

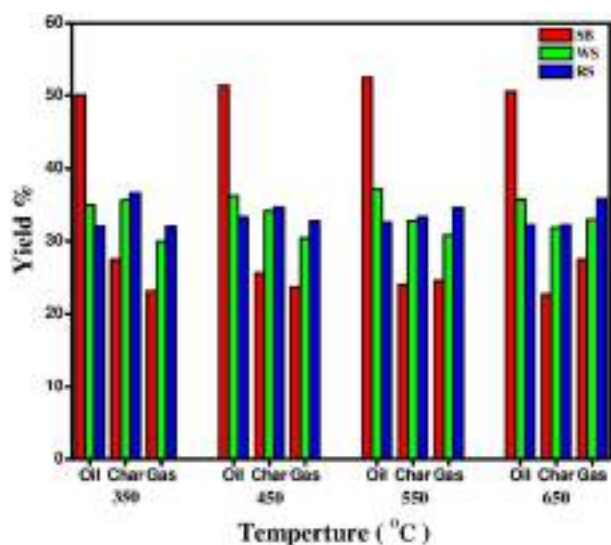


Fig. 4 Yield of pyrolysis products at different temperatures (heating rate of 100 °C/min, sweep gas flow rate of 30 mL/min and particle size of 0.2–0.4 mm)

biomasses, char yield was highest in the case of RS, since it contains a high amount of lignin [56, 64]. As the temperature increased, bio-oil yield also increased due to the rapid de-volatilization of biomass by primary decomposition with rising temperature. But at high temperature, i.e. after 550 °C in the case of SB and WS and 450 °C in the case of RS, the bio-oil yield started to decrease due to thermal and catalytic cracking of bio-oil or in other words, secondary reactions of the liquid fraction of volatiles [53, 62]. As temperature increased, the biochar yield decreased due to the decomposition of char at high temperature [62, 65]. Figure 4 also shows the increasing pattern of non-condensable gases with the rise in temperature, just because of the primary decomposition of biomass and secondary decomposition of biochar [62]. At a temperature above 550 °C, the rate of increase in gas yield was higher with the highest rate obtained at 650 °C because of secondary cracking of pyrolysis vapors or secondary reactions of bio-oil in vapor phase [53, 62, 66].

Effect of particle size

Effects of biomass particle size in the range of 0.2–0.8 mm at a heating rate of 100 °C/min, sweep gas flow rate of 30 mL/min and temperature of 550 °C for SB and WS and 450 °C for RS were studied on the pyrolysis product distribution, and results are shown in Fig. 5. It was observed that bigger particle size maximized the formation of char and non-condensable gases. But in the case of small-sized biomass particles, there was maximum amount of bio-oil produced instead of char and non-condensable gases. For small-size

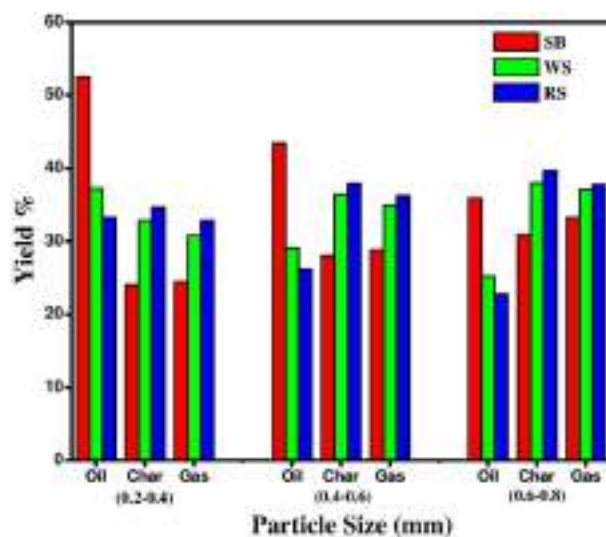


Fig. 5 Yield of pyrolysis products at different particle size (heating rate of 100 °C/min, sweep gas flow rate of 30 mL/min and temperature of 550 °C for SB and WS and 450 °C for RS)

particles, solid to solid heat transfer is faster and pyrolysis governs the reaction mechanism. Therefore, faster volatilization leads to higher liquid yield which was observed in case of all three biomass samples having small particle size (0.2–0.4 mm).

Similarly, as particle size increases, there is interaction among char produced and volatiles generated that lead to simultaneous cracking of bigger volatiles and polymerization of smaller volatiles [51]. This phenomenon was also observed in our experiment, as particle size increased char and non-condensable gas yield increased and reached maximum in case of biggest size biomass particles (i.e., 0.6–0.8 mm). Char and gas yields were highest in pyrolysis of all three kinds of biomass samples having particle size (0.6–0.8 mm). Moreover, as particle size increased from 0.2–0.4 to 0.6–0.8 mm, bio-oil yield decreased because large particle does not enhance the mass transfer and heat transfer associated with the cracking mechanism and non-uniform heating of particle as shown in the Fig. 5 [65–67]. Another reason for high char yield and low liquid yield with the increase in particle size is the rise in heat transfer resistance with distance from particle surface to center that impedes the quick heat transfer from a hot material to cold biomass, and thus reaction is not completed [68].

Effect of heating rate on product distribution

Pyrolysis experiment was conducted at two different heating rates of 20 °C/min and 100 °C/min at a sweep gas flow rate of 30 mL/min. It was found that bio-oil and gas yield increased with heating rate while char yield decreased. Figure 6 indicates that as the heating rate increased, bio-oil

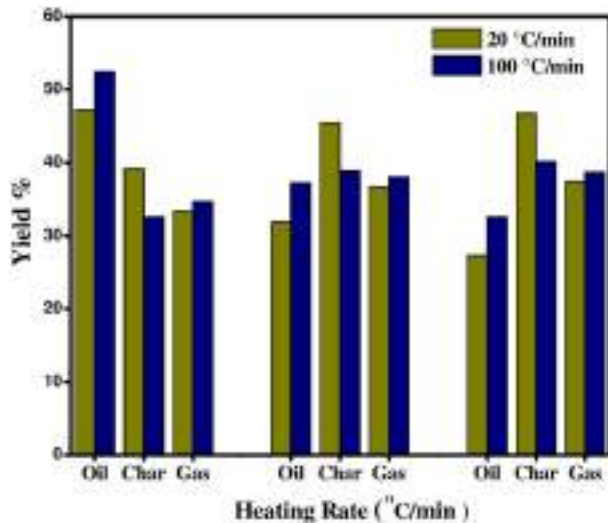


Fig. 6 Yield of pyrolysis products at a different heating rate (sweep gas flow rate of 100 mL/min)

yield increased. With the increase in heating rate from 20 to 100 °C/min, bio-oil yield increased from 47.2 to 52.5% in case of SB, 31.9 to 37.2% in WS and 27.3 to 32.6% in case of RS. Similarly, biochar yield decreased from 39.2 to 32.6%, 45.5 to 38.9%, and 46.7 to 40.1% in the case of SB, WS, and RS, respectively. Figure 6 also shows that non-condensable gas yield increased from 33.35 to 34.65% in case of SB, 36.7 to 38% in case of WS and 37.45 to 38.75% in case of RS. Rapid heating rate leads to rapid de-polymerization of solid biomass into primary volatiles those upon condensation produce more bio-oil hence, its yield was increased [66, 67]. While at low heating rate, dehydration to more stable anhydrous cellulose is limited and very slow that leads to more char formation. Moreover, the actual heating rate measured was 38 °C/min, for a theoretical heating rate of 45 °C/min in the furnace. Hence, we may expect that the actual heating rate was maintained within the bed around 85–90 °C/min, when the set value in the furnace was 100 °C/min. The thermal gradient within the bed was 4.35 °C/min in the radial direction. Hence, the predicted heating rate difference between two set values of experimentation mentioned in this manuscript was definitely responsible for the observed difference in product yield as contrary to some researchers [69], who those claimed that variation of heating rate does not have significant influence on product yield within the selected testing range.

Effect of the flow rate of sweeping gas on product distribution

For slow-to-moderate pyrolysis conditions as per this experiment, the carrier gas flow rate has significant influence on product distribution [51]. Hence, to ascertain the effect

of this reaction parameter on pyrolysis product yields, an additional experiment was designed for a certain biomass sample. Influence of the sweeping gas flow rate on product distribution of SB was carried out at 550 °C temperature, the particle size of 0.2–0.4 mm and fixed heating rate of 100 °C/min by varying the sweeping gas flow rate from 20 to 100 mL/min. The same effect can be observed for WS and RS not represented here.

It is observed from Fig. 7 that bio-oil yield was highest at a flow rate of 30 mL/min, and then it decreased. For bio-char and non-condensable gas, there is an initial decrease and then increase pattern, respectively, with an increase in flow rate. At low flow rate, the residence time of released volatiles in the reactor is high which influences more vapor-phase secondary cracking and re-polymerization reactions that lead to more char, gas and low liquid yield [70, 71]. To increase the bio-oil yield, the produced vapors should be quenched immediately to inhibit the onset of secondary reactions. As flow rate increased, bio-oil oil yield increased due to inhibition of cracking and re-polymerization reaction of vapors by rapid quenching [36, 51]. But at high sweeping gas flow rate, the yield of bio-oil decreased, whereas non-condensable gas and char yield increased as the effective time required for condensation of vapors was not sufficient enough. The increased amount of biochar at high sweeping gas flow rate may be correlated with the fact that, low availability of vapor-phase residence time slowed down the cracking of long polymeric chains of lignocellulosic biomass and smaller hydrocarbons [62, 65].

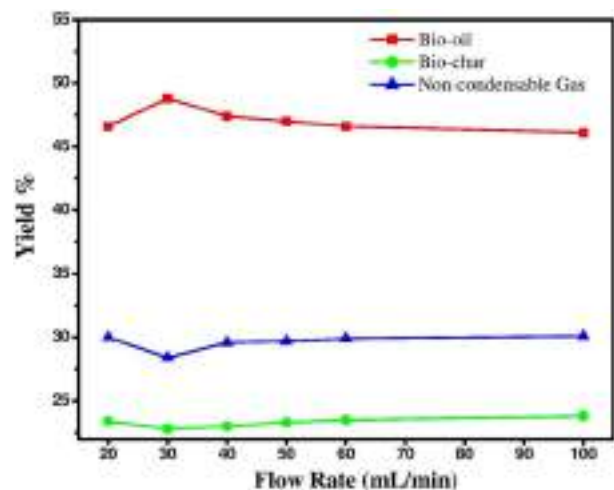


Fig. 7 Effect of sweep gas flow rate on pyrolysis product distribution of SB

Bio-oil characterization

Physical characterization

Table 3 demonstrates that bio-oil produced from three biomass samples is acidic in nature. The acidity of bio-oil is mainly due to the presence of carboxylic acids, phenolic compounds, and its derivatives [22]. The density of bio-oil found to be comparable or slightly heavier than diesel and fuel oil [62, 72]. This is mainly because of the presence of oxygenated heavy organic compounds, such as phenol [51]. The viscosity of produced bio-oil samples is lower as compared to the viscosity of diesel (1.58–4.99 cSt), biodiesel (1.66–5.24 cSt) [62]. The higher heating values (HHV) of bio-oil produced from all three biomass samples were investigated and found that in case of SB, it is maximum that may be correlated with its low moisture content and O/C ratio.

Chemical characterization

FTIR analysis From Fig. 8, it is illustrated that absorbance peak at 3370 cm^{-1} and 3390 cm^{-1} present in all bio-oil samples conforms to OH group which is an indication of the presence of phenol, alcohol, polymeric OH and to some extent water impurity [57, 73]. The strong absorbance peak at 1710 cm^{-1} in 3 bio-oil samples confirms the C=O stretching vibration, which in turn designates the presence of ketones, quinones, aldehyde, and carboxylic acid compounds. The slight absorbance peak at wave numbers 1660 cm^{-1} and 1510 cm^{-1} indicates C=C stretching so that there is a confirmation of alkene bond present in three bio-oil samples [74]. The medium-intense absorption band in 3 bio-oil samples at 1380 cm^{-1} is a simultaneous indication of C–H bending (alkane) and substituted aromatic compounds in bio-oils [51, 73, 75]. The broad peaks at 1260 cm^{-1} and 1050 cm^{-1} confirm the presence of alcohols, phenols, ether, and ester with CO stretching and OH deformation in 3 samples. The sharp absorbance peaks at wave numbers 775 and 727 cm^{-1} in case of SB bio-oil, at 739 cm^{-1} in case of WS oil, at 710 cm^{-1} in case of RS bio-oil specify the presence of mono-, polycyclic and substituted aromatic compounds in them [51, 75]. The high-intensity absorption peak at wave number 633 cm^{-1} in case of bio-oil produced from WS and

RS indicates the presence of aromatic compounds in them [76].

As mentioned previously, bio-oil contains various amounts of oxygenated organic compounds, such as acids, phenols, sugars, hydroxy aldehyde, hydroxy ketones, and alcohols, which are also substantiated from FTIR analysis. This leads to heterogeneity in bio-oil, which in turn affects the energy density, storage stability of bio-oil, miscibility with hydrocarbon fuels [77].

GC–MS analysis Table 4 presents a comparison of important compounds present in bio-oils (identified by GC–MS) obtained from pyrolysis of SB, WS, and RS. All three bio-oil samples mainly composed of benzene derivatives, nitrogenated, oxygenated, and aliphatic organic compounds in abundant quantities as inferred from their area % data in mass spectra. Tables S1–S3 (presented in ESI) give a list of all compounds identified by GC–MS for bio-oils obtained from pyrolysis of these three biomass samples. It was observed from Table 4 that ketones and ester compounds were found to be maximum in bio-oil obtained from WS, whereas furans and guaiacols were maximum in case of SB. Anhydro-sugars were available in significant quantity from SB, and it was also observed by David et al. [78]. Besides, alcohol was very high in bio-oil obtained from WS as well

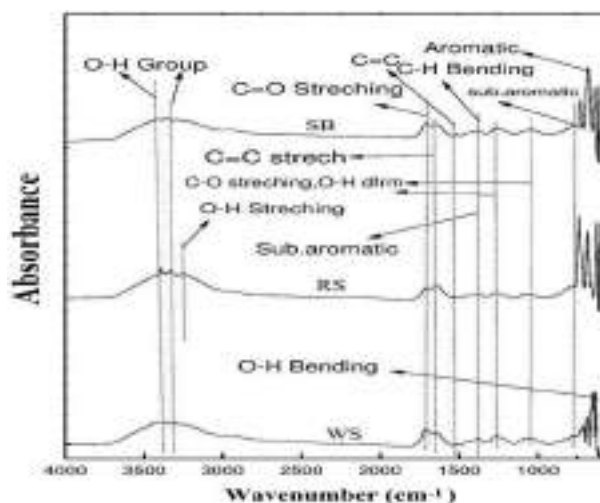


Fig. 8 FTIR spectra of bio-oil produced from three biomass samples

Table 3 Physical characteristics of bio-oil produced from selected biomass samples

Bio-oil from biomass	pH (25 °C)	Density (g/mL) (40 °C)	Viscosity (cSt) (40 °C)	Ash content (wt%)	HHV (MJ/kg) pyrolysis at 550 °C
SB	2.71	1.09	2.80	0.2	22.31
WS	2.87	1.05	1.89	0.2	18.12
RS	3.58	1.04	2.40	0.1	16.35

Table 4 GC–MS analysis of bio-oil obtained from pyrolysis of SB, WS (pyrolysis temperature 550 °C); and RS (pyrolysis temperature 450 °C); heating rate 100 °C/min; 0.2–0.4 mm particle size

Compound	SB ^a	WS ^a	RS ^a
Ketone	15.51	30.04	25.13
Furans	22.75	6.58	16.68
Ester	3.46	12.38	4.39
Guaiacol	11.66	8.26	7.04
Phenolics	10.91	10.99	1.38
Anhydro-sugar	23.99	0.33	4.58
Alcohols	–	26.96	27.54

as RS. It was also found that phenolic compounds and their derivatives comprised a greater portion of all three bio-oil samples. These mainly consist of phenol, 2-methoxyphenol, 3-methyl-phenol, 3-ethyl-phenol, 4-ethyl-guaiacol, 2-methoxy-4 vinyl phenol, 2,6 dimethoxy phenol, 2-methoxy-4-phenol, 2,6-dimethoxy-4(-2propenyl)-phenol, 2,6-dimethoxy-4(prop-1-en-1-yl) resulted from decomposition of lignin in all biomass samples. Decomposition of lignin and cellulose simultaneously gives rise to the production of aldehyde, ketone, and ester-related compounds, including also some oxygenated organic compounds. Acidic compounds found in all three bio-oil samples, such as 2,4-hexadienedioic acid, 2,4-benzene dicarboxylic acid, acetic acid, and butanoic acid, mainly evolved from the decomposition of hemicellulose in raw biomass. Cellulose decomposition also produces levoglucosan compound, such as 1,6-anhydro-beta-D-glucopyranose, which is found in produced bio-oil samples along with furan and its derivatives. Aliphatic, aldehyde, ketone, ester, alcohol (cyclopropyl methanol) and some of the carboxylic acid compounds present in all three bio-oil samples also formed from the decomposition of cellulose and hemicellulose as investigated by some researchers [78]. Presence of nitrogenous compound in bio-oil samples, such as 4-methyl pyridine, 3,5-dimethyl-1*H*-pyrazole, dinitro-glycoluril, guanosine, 6*H*-dipyrrole [1,2-A:1,2-D] pyrazine, 2,4-pyrimidinediamine, 5-[(3,4,5)-(trimethoxy phenyl) methyl], etc. is due to the presence of protein-based compounds in biomass. Presence of straight-chain hydrocarbon compound, such as 2-isocyanatopropane, is due to cracking of acidic compounds present in raw biomass samples [65, 78].

Non-condensable gas product distribution during pyrolysis

The non-condensable gases produced during pyrolysis of three types of biomass samples mainly comprised CO, CO₂, H₂ and CH₄ as analyzed by GC-TCD (Fig. S2, ESI). Since these gases contributed majority of producer gases used in

fuel applications, hence, non-condensable gases produced as a by-product could have better fuel application. The CO and CO₂ content was found to be high in non-condensable gases produced below 450 °C unlike high temperature. Maximum evolution of CO and CO₂ obtained at a very low temperature (~300 °C) and then there was a decreasing trend continued up to 650 °C. High yield of CO and CO₂ at low temperature mainly resulted due to cleavage of the C=O bond present in biomass samples. In addition to major CO and CO₂ contribution to gases, resulted from cracking of carbonyl (C=O) and carboxyl (–COOH) groups, respectively, some researchers also claimed that high yield of CO and CO₂ at low temperature is mainly due to decomposition of cellulose and hemicellulose [79], which was previously verified through TGA. Evolution of CH₄ gas started near 300 °C and continued rising up to 600 °C, then was a decreasing trend at high temperature. Major contribution towards CH₄ release was from O–CH₃ (methoxyl) group associated with basic structure of phenyl propane units of lignin [80] unlike cellulose and hemicellulose. Amount of CH₄ in non-condensable gases was less compared to quantity of CO and CO₂. Hydrogen (H₂) gas was produced at much higher temperature ~500 °C, and then it followed an increasing trend with rise in temperature and was expected to rise above 650 °C (Fig. S2). The increasing evolution trend of H₂ at higher temperature was mainly due to cracking and reforming reaction of aromatic rings present in biomass. One noticeable observation from entire analysis of non-condensable gases, that temperature below 600 °C was responsible for the production of more amounts of CO, CO₂, CH₄ as a result of primary pyrolysis process, whereas at high temperature (650 °C and above), secondary pyrolysis and thermal cracking reactions dominated, resulting more amount of H₂ [76].

Non-condensable gas higher heating value (HHV) was evaluated with the help of mathematical formula provided by [81] by taking into consideration volume percentage of gases and represented as:

$$\text{HHV (MJ/Nm}^3\text{)} = (\text{H}_2\% \times 30.52 + \text{CO}\% \times 30.18 + \text{CH}_4\% \times 95) \times 0.0042 \quad (4)$$

According to Eq. (4), the higher heating value was calculated and found that with rise in temperature, the higher heating value of gases produced increased (Table 5) and at temperature above 600 °C, there was a decreasing trend. Increase in higher heating value with rise in temperature may have resulted due to increase in H₂ and CH₄ content in non-condensable gases, but at high temperature, CH₄ yield decreased ultimately reducing higher heating value. SB produced non-condensable gases with higher heating value less compared with RS and WS. This type of result may be ascertained from the fact that SB contained more amount of

Table 5 HHV of non-condensable gases and carbon conversion efficiency of biochar prepared from different biomass samples

Temperature	Biomass					
	SB		WS		RS	
	HHV (MJ/Nm ³)	η_c (%)	HHV (MJ/Nm ³)	η_c (%)	HHV (MJ/Nm ³)	η_c (%)
300	4.24	–	4.55	–	4.90	–
350	4.35	99.875	5.08	99.823	5.12	99.826
400	4.55	–	5.36	–	5.67	–
450	5.04	99.883	7.83	99.83	7.10	99.835
500	7.25	–	12.18	–	11	–
550	10.86	99.891	13.93	99.837	15.78	99.842
600	13.87	–	16.61	–	17.96	–
650	12.70	99.897	16.00	99.842	17.55	99.847

^a η_c : carbon conversion efficiency

Table 6 Physical characteristics of produced biochar samples from selected biomass

Biochar	Heating value (HHV) (MJ/kg)	pH (25 °C)	HHV(MJ/kg) raw biomass
SB	27.77	8.03	16.80
WS	17.72	10.07	13.93
RS	14.08	9.53	13.37

cellulose/hemicellulose and less amount of lignin, ultimately resulting gases devoid of high quantity of H₂ and CH₄, those that contribute more to HHV. Moreover, SB produced gases enriched with CO₂ as a result of cellulose decomposition.

Carbon conversion efficiency (CCE) related to production of non-condensable gases can be calculated according to formula provided by [82] and represented in Eq. (5):

$$\eta_c = \left[1 - \frac{m_{\text{biochar}}}{m_{\text{biomass}} \times \%C} \right] \times 100, \quad (5)$$

η_c = carbon conversion efficiency, m_{biochar} = amount of biochar produced, m_{biomass} = amount of biomass fed to reactor, %C = elemental carbon percentage in biomass.

Carbon conversion efficiency in case of SB biochar was found to be slightly higher than CCE of two other biomass samples (Table 5).

Biochar characterization

Physical characterization

Calorific values of biochar samples were measured with the help of laboratory bomb calorimeter and represented in Table 6. Interestingly, biochar calorific value is higher as compared to corresponding raw biomass. Hence, biochar can

be used in combustion, co-firing, and briquette application for providing heat energy. HHV of biochar is comparable to coal [83, 84], so it can be used as a substitute for fossil fuel in energy generation applications like running a boiler or stationary power generation. As three biochar samples are alkaline in nature (Table 6), their use as bio-fertilizer will help in controlling soil acidity for availing important plant nutrients and maintaining healthy environment for smooth functioning of beneficial soil bacteria [52]. Less pH value of biochar prepared from SB as compared to WS and RS may have resulted due to ample presence of acidic functional groups (–COOH, –OH) on its surface [85]. High acidity SB biochar among WS and RS may act as possible cation exchange site, from where cationic macro- and micronutrients may be readily available for plant intake purpose, hence, ultimately improving soil fertility and nutrient holding capability.

Chemical characterization

CHNS/ultimate analysis CHNS analysis of three biochar samples is described in Tables 7 and S4–S5. High percentage of carbon (as a major element) has been reported in produced biochar samples. Data regarding C and H weight percentage presented here have similar trends with that of represented earlier by Mullen et al. [83]. Within the pyrolytic temperature range of 350–50 °C, the concentration of carbon increases due to increase in degree of carbonization [86] and O, H decrease with rise in temperature due to decarboxylation and dehydration reactions [56]. Increased degree of carbonization with reduced oxygen content could have harnessed biochar in several fuel applications. Apart from this, high amounts of C, N contents in biochar make them good fertilizer application, which can replenish these elements in soil [83]. Moreover, probability of inducing soil nitrogen deficiency through biochar fertilizer application caused by microbial breakdown of carbon-rich substrates

Table 7 CHNS/ultimate analysis of biochar produced from SB

Char at temperature (°C)	C	H	N	S	O	H/C	O/C	(N+O)/C	HHV (MJ/kg)	Energy density	Energy yield %
350	68.42	3.81	0.98	Nd ^a	26.79	0.66	0.29	0.30	24.22	1.44	39.45
450	70.01	3.02	1.97	Nd	25.00	0.51	0.26	0.29	23.89	1.42	36.35
550	78.20	2.62	2.43	Nd	16.75	0.40	0.16	0.18	27.34	1.62	38.88
650	80.12	1.81	2.22	Nd	15.85	0.27	0.14	0.17	26.97	1.60	36.32

^aNot detected

can be countered by the fact that the carbon present in biochar is in condensed aromatic form, which is hardly easy to degrade. Since char contains little amount of nitrate as well as not balanced elementally, it is always advisable to use along with any nitrogenous fertilizer for soil amendment application. Another noticeable observation is that N content of biochar is high as compared to raw biomass, may be contributed due to adsorption N₂- or N-bearing organic compounds on the surface of solid char [76]. With increase in pyrolysis temperature, there is decrease in O/C and H/C ratio of biochar samples collected (Table 7). Generally, with rise in temperature, there is enhancement in carbonization as well as aromatization process, ultimately making the biochar more hydrophobic and non-polar in nature. This is also verified from the fact that there is a decremental nature of O/C and (N+O)/C ratio with rise in temperature in case of biochar. Biochar produced at high temperature with low H/C and O/C ratio is very much desirable during combustion process since it leads to reduction in energy losses and smoke generation. Similar type results have been reflected in case biochar generated at high temperatures, having high HHV with reduced polarity, thus making it as good-quality solid fuel as explained earlier. Van Krevelen diagram (Fig. 9) shows that biochar samples produced at high temperature (> 600 °C) have coordinates shifted towards region of fossil fuel [84]. Hence, their potential usability in energy generation by combusting individually or with synergistic manner in combination with lignite type fossil fuel in coal fired plant is highly desirable as confirmed through Van Krevelen diagram [87]. Carbon in biochar is highly stable and may be sequestered for thousands of years [88, 89]. Infact biochar produced from three biomass samples with H/C < 0.6 and O/C < 0.4 can be used in soil amendment applications [90]. Energy density and energy yield of biochar produced at different temperatures are evaluated according to formula developed by [91]. These are defined as:

Energy density : energy of biochar/energy of raw biomass, (6)

Energy yield (%) : yield of biochar × energy density. (7)

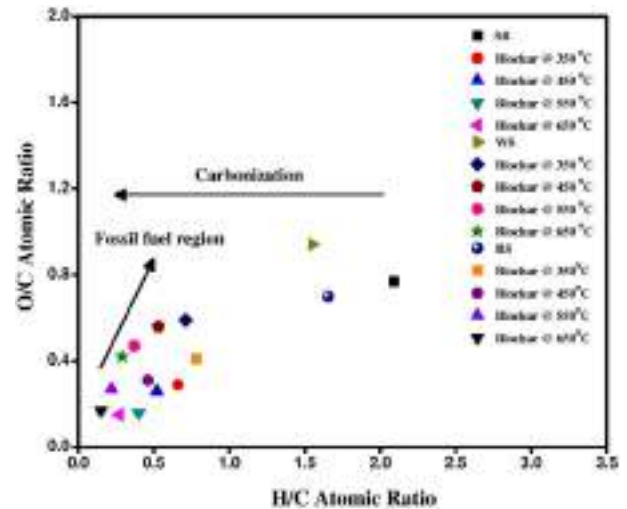


Fig. 9 Van Krevelen plot for different biomass samples with its biochar produced at different temperatures

From Tables 7 and S4–S5, it has been found that the energy yield of biochar decreases with increase, whereas energy density increases with rise in temperature. Energy density of biochar samples is highest at high-temperature conditions with maximum energy density going up to 1.60, 1.23 and 1.86, respectively, for SB, WS and RS at high temperature. The increasing trend of energy density with rise in temperature may be attributed to the minimization of low energy bonds, such as C–H, C–O and increment in high-energy C–C bond, during pyrolysis process due to carbonization process. Similarly, energy yield varies in between 39.45–36.32, 40.22–39.11, and 56.73–54.94% for SB, WS, and RS biochars. Variation of energy yield from biomass to biochar can be correlated with the biomass structure as well as amount of char resulted during pyrolysis process. Since RS produced maximum amount of biochar during pyrolysis process, hence, its energy yield found to be maximum. Biochar due to greater amount of fixed carbon, low H/C and O/C ratio as well as high-energy density can have better fuel property as compared to raw biomass.

FTIR analysis of biochar samples Pyrolysis is nothing but thermal decomposition of biomass at a specific temperature, ultimately resulting in breaking/cleavage of chemical bonds present in them and release of volatile gases corresponding to that temperature. So, a relationship established between the chemical structure of biochar produced (identified by FTIR) and composition of released gases at different final temperatures. Herein FTIR results of biochar produced at different temperatures are represented in comparison with raw biomass, to study the chemical changes occurring in biomass during pyrolysis process and its effect on released gases. As the chemical structures (functional groups) presented in three biomass samples shown similar representation in FTIR analysis (Fig. 2), thus the comparison is provided for only one biomass type, and same analysis can be followed for others.

Figure 10 shows that the sharp absorbance peak at wave number 3500 cm^{-1} (OH functional group) of raw biomass eventually diminishes to zero in case of biochar produced at $350\text{ }^{\circ}\text{C}$. This is an indication of dehydration reaction occurred during the pyrolysis process, which started near $300\text{ }^{\circ}\text{C}$ and produced a large amount of water that goes directly to the bio-oil. Medium intense absorption band between 2860 and 2970 cm^{-1} (C–H stretching) in the IR spectra of raw biomass diminishes to a very minimal value near $550\text{ }^{\circ}\text{C}$ as shown in spectra of biochar produced at that temperature. This mainly results due to the breaking of weak C–H (alkyl) bond and the formation of more CH_4 gases during pyrolysis within that temperature range. Slightly broad absorption band in raw biomass between 1700 and 1730 cm^{-1} is an indication of C=O functional group (carboxylic acid). The FTIR spectra of biochar (Fig. 10) collected within temperature $450\text{ }^{\circ}\text{C}$ show that this absorption band becomes narrow and its intensity also diminishes. This

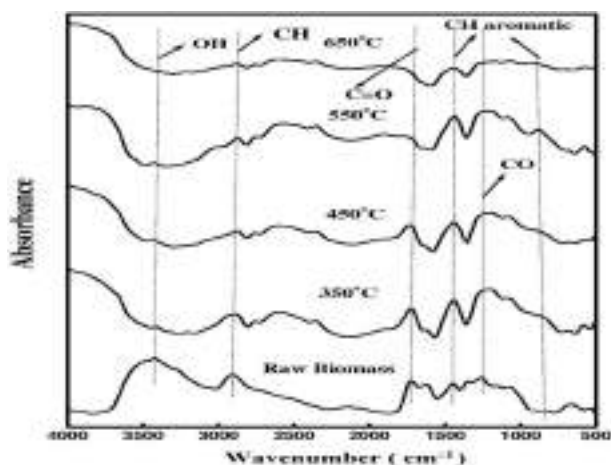


Fig. 10 FTIR spectra of SB biochar at different temperatures and its comparison with raw biomass

type of pattern appeared due to the formation of more CO and CO_2 gases within $450\text{ }^{\circ}\text{C}$ by breaking of C=O bond. Another interesting fact observed from the figure is that absorption band of functional groups, such as C–O (1450 and 1080 cm^{-1}) and CH aromatic ring (1440 and 890 cm^{-1}), increases with a rise in temperature. This increasing trend originated due to decreasing peaks of OH and CH alkyl groups. But after the final temperature reaching near about $650\text{ }^{\circ}\text{C}$, this increasing trend discontinued, and peak intensity decreased. These functional groups broke in a stepwise manner to produce more volatiles. Cracking and re-polymerization of aromatic rings gave rise to more H_2 gas evolution at high temperature ($600\text{ }^{\circ}\text{C}$) [53, 56, 76].

SEM analysis SEM analysis of biochar samples was carried out to study the textural property, surface morphology, and porous structure. The SEM images of biochar produced from SB, WS and RS, at low and high temperatures are shown in Fig. 11 along with SEM images of raw biomass for comparison purpose. From the SEM images, it is concluded that there was no porosity present on biomass surface, but with temperature rise, porosity and pore sizes increased. At $350\text{ }^{\circ}\text{C}$, small numbers of pores appeared on the surface of char. This is mainly due to low decomposition of volatile matter at that temperature when temperature increased and reached near $550\text{ }^{\circ}\text{C}$, a large number of fine pores developed on the surface of solid char as shown in Fig. 10 also pore size increased. In fact, at high temperature ($\sim 550\text{ }^{\circ}\text{C}$), there was the opening of more numbers of micro-sized pores which lead to the high surface area of produced biochar samples. These results were mainly due to the rapid release of volatile compounds during pyrolysis at this temperature [56]. Results obtained in this experiment were in accordance with the detailed study on biochar produced at different temperatures as previously reported by Yang et al. [76]. They explained the effect of pyrolysis temperature on the porosity and pore size of prepared biochar samples through SEM and BET analysis simultaneously. The trend regarding biochar porosity obtained in this pyrolysis reaction matches closely well with that of results obtained by Yang et al. But at a higher temperature, not studied here, these pores might block and combined, thus, shrunk in sizes due to plastic nature of char. Also, there will be large numbers of pore blockages due to melting and combination of minerals which were the main constituents of char produced at high temperature. Maximum de-volatilization occurred below $550\text{ }^{\circ}\text{C}$, therefore, maximum porosity developed within that temperature. The presence of large pores at the surface of biochar has many applications. It can be used as activated carbon for decolorization in the sugar industry, increase metal adsorption capacity by chemisorption method, etc. If this highly porous char is applied to the soil, it will contrib-

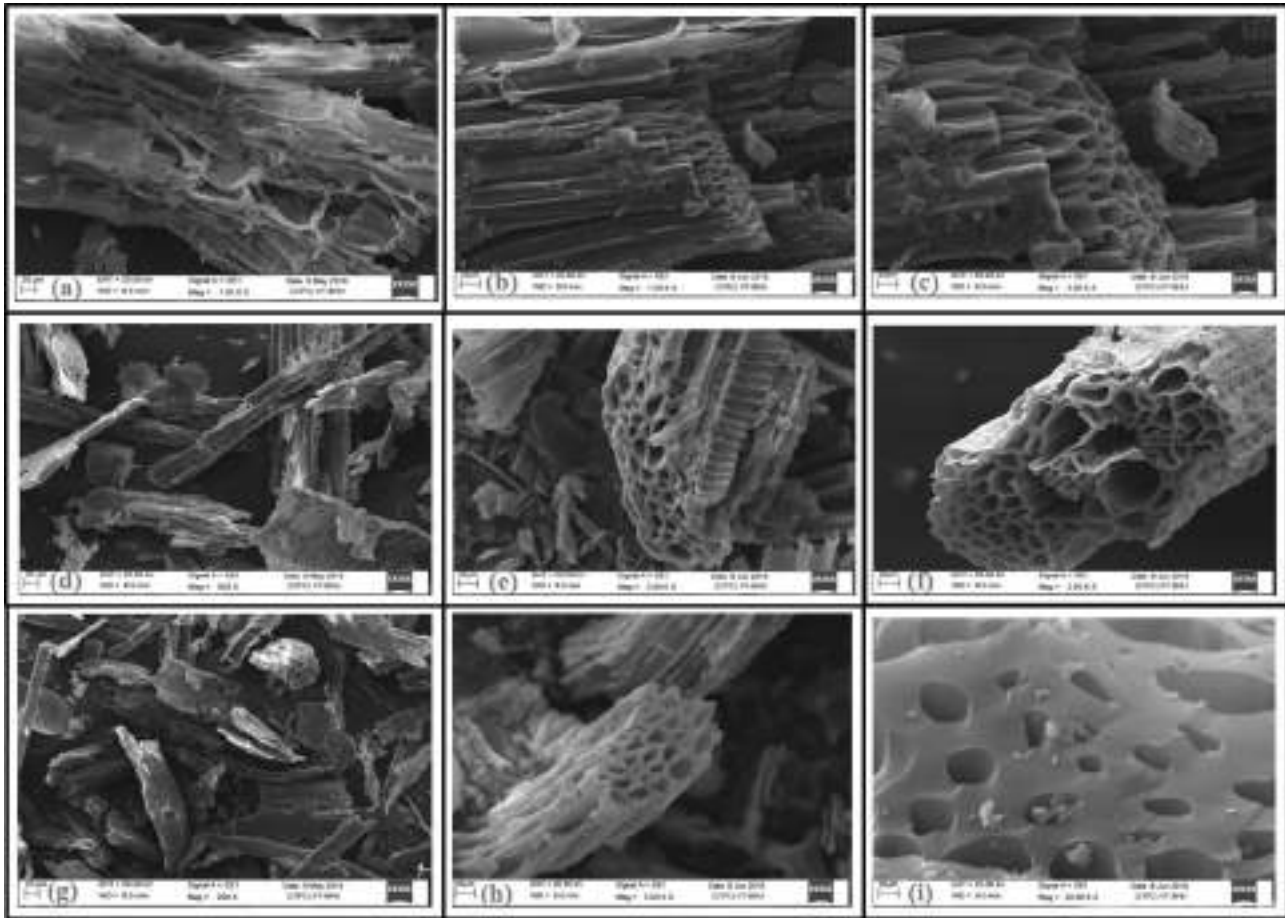


Fig. 11 SEM analysis of raw biomass and biochar produced at 350 °C and 550 °C (a) SB (d) WS (g) RS (b) SB biochar @ 350 °C (c) SB biochar @ 550 °C (e) WS biochar @ 350 °C (f) WS biochar @ 550 °C (h) RS biochar @ 350 °C (i) RS biochar @ 550 °C

ute more to the enhancement of soil quality and act as to subsequent sites for nutrient exchange [83].

EDX analysis The EDX analysis (Fig. S3, ESI) confirmed that biochar contains several inorganic elements, such as Ca, Si, K, P, Mg, Na. Biochar enriched with these elements, when applied to soil (especially acidic soil) as a fertilizer, provides important plant nutrients to soil [30, 56]. N P K present in biochar samples are the essential plant macro-nutrients that help in plant growth and fertility. Oxide and carbonate form of K and Na, whereas phosphate and sulfate form of Ca and Mg present in biochar are readily water-soluble, thus providing important macro- as well micronutrient contribution towards soil while being used as fertilizer, thus

promoting plant growth without any additional induction of toxicity [85]. Similarly, silica present in all the biochar samples in ample amount helps prevent drying up plant leaves and improves pollen fertility [92]. In addition, inorganic elements act as surface-charged species in the biochar, which help in removal of several pollutants from wastewater, such as Cd, Ni, Cu, and Zn, through chemisorption method [83]. Alkaline nature of biochar as previously described may be attributed to presence of these inorganic elements especially Ca, Mg carbonate along with organic hydroxyl and carboxyl functional groups [93].

ICP-AES analysis The inorganic elements present in studied biochar samples have been provided in Table 8. Most

Table 8 ICP-AES analysis of different biochar samples

Biochar	K	Ca	P	Zn	Na	Cu	Mn	Mg	Si
SB	4.023	0.9014	0.3461	0.1511	4.8664	0.0365	0.0321	3.82	7.65
WS	2.492	1.1650	0.0586	0.2115	3.3493	0.0243	0.4210	1.49	8.81
RS	3.050	1.4010	0.3062	0.1498	4.2295	0.0031	0.0351	1.65	9.16

abundant constituents of biomass minerals are Si, Ca, K, Na, and Mg with a lesser amount of S, P, Cu, Zn, Mn, and Al. These constituents remain as oxides, silicates, carbonates, sulfates, chlorides, and phosphates from [94]. Minerals/inorganic salts majorly present in biomass ash, decrease organic liquid yield with minimization of de-volatilization and initial decomposition temperature. They also catalytically promote char-forming secondary reactions [95]. Potassium and calcium catalyze biomass decomposition and char formation. The heterogeneous reaction between the mineral (Na+K) and pyrolysis vapor affects oil production. ICP analysis of biomass ash reveals that potassium concentration of SB is higher as compared to the other two biomass samples. Potassium is a strong catalyst for char gasification promoted in the presence of CO₂ and H₂O, thereby minimizing char yield as observed in case of SB. Similarly, combined effect K and Zn in SB also resulted in the production of more volatiles as compared to char. Similar trends were also observed in case of WS which resulted in more volatiles in terms of non-condensable gases unlike RS which ended up producing more char due to high lignin content. Due to the presence of Zn in biomass, there is a rise in initial decomposition temperature during pyrolysis whereas potassium has its reverse effect on biomass. TGA profile for three types of biomass samples indicated that the initial decomposition temperature of WS (~240 °C) is more as compared to other two biomasses due to presence of high amount of zinc in it. The initial pyrolysis decomposition temperatures were ~220 °C and ~230 °C for SB and RS, respectively, due to the high concentration of potassium in them as compared to zinc. Also, the combination of zinc and potassium played significant role in enhancing the number of volatile products produced during pyrolysis. SB has a moderately high amount of Na+K as compared to WS and RS; hence, there was larger decomposition and production of greater amount of volatiles clearly visible from SB weight loss profile in TGA. The weight loss was nearly (~50%) higher than WS (~47%) and RS (~42%). Another important finding is that the presence of Zn in biomass leads to generation of more gases while minimizing liquid yield. WS, on pyrolysis reaction produced higher gas yield as compared to the other two biomasses due to the high percentage of Zn in it. Ca and Mg present in biochar samples have concentration lower than Na and K since they have less solubility in water, hence not properly detected. Presence of nitrogen in prepared biochar samples along with all these inorganic elements mentioned above is important in plant nutrients, and those on subsequent application towards soil enhances soil fertility and promotes plant growth owing to their high solubility nature in water.

Generally, silica present in biomass has the property of arresting the carbon present in it, and thus reducing its conversion efficiency during formation of producer gas. Slight

increase in carbon conversion efficiency in case of biochar prepared from SB may have resulted due to presence of lesser amount of silica in its biomass as compared to WS and RS.

Pyrolysis product distribution and corresponding utilization

Though we have already discussed regarding wide usability of pyrolysis products obtained for different biomass samples, in this paragraph, we have briefly discussed each product quality based on their physiochemical properties. Based on yield % and heating value, sugarcane bagasse produced best-quality bio-oil which makes it suitable for best alternative liquid fuel in boiler and combustion engines after moderate upgrading. Bio-oil produced has comparable density and viscosity with diesel/fuel oil. Hence, greater volume of fuel injection, better atomization of fuel in burner, and uniform cylinder temperature ultimately lead to less NO_x emission while using in combustion engine. Though low viscosity enhances the shelf life of bio-oil; however, acidity and slightly higher ash content (~0.1%) can have issues with corrosion or kicking problem in engine, hence requiring moderate upgrading before use [96]. GC-MS analysis of bio-oil also revealed that it contains alcohol, anhydrosugar, furan and ketone compounds, those that can be directly consumed as fuel [97]. Also, phenolic compounds identified in bio-oil samples have attracted special attention due to their use in applications like fuel additives and chemical precursors [98, 99]. Detailed applications of identified chemical compounds present in bio-oils have been discussed in supplementary file (section S4, ESI). Biochar is produced in larger amounts for WS and RS and specifically maximized at bigger biomass particle size and low-temperature heating conditions. The yield of biochar was maximum for reaction carried out at low temperature; however, char produced at high temperature (> 600 °C) with low H/C and O/C ratio and high-energy density has calorific value comparable to fossil fuel (e.g. coal), hence it can be used in several energy generation applications like running a boiler furnace, co-firing, and briquetting etc. Apart from this, high porosity of biochar generated at moderate pyrolysis conditions and alkaline nature of biochar can be useful in applications like bio-fertilizer for providing important soil nutrients and carbon sequestration process. Apart from these, inorganic elements like (Si, Ca, K, Na, and Mg) are rich in biochar produced, hence can also be utilized in soil amendment application and use of it as an excellent adsorbent for waste water purification. Non-condensable gases generated at high-temperature pyrolysis conditions with less amount of CO₂ can be used as a fuel (synthesis gas) in combustion process and can be recycled and combusted to run the pyrolysis system [100].

In fact, non-condensable gases with relatively higher yield and enhanced HHV, generated from pyrolysis of WS and RS, can be used for energy generation applications.

Conclusion

Pyrolysis of three biomass samples was accomplished at different operating conditions to maximize bio-oil yield. The maximum bio-oil yield was obtained at a temperature of 550 °C for SB and WS, whereas for RS, it was 450 °C. Variation of the heating rate from 20 °C/min from 100 °C/min had no significant influence on optimizing the product yield in the chosen range. Biomass particle size had a great influence on the optimization of pyrolysis product yield. Bio-oil, which is the principal product in this experiment, was obtained at higher percentage within the particle size of 0.2–0.4 mm. The bigger particle size (0.6–0.8 mm) maximized the formation of char and gas during pyrolysis reaction. The flow rate of 30 mL/min was found to be best for maximizing bio-oil yield. TGA analysis of 3 biomass samples showed the similarity between decomposition behavior of SB and WS. RS showed slightly different thermal decomposition property, and maximum decomposition occurred within a temperature range of 220–500 °C. SB produced more CO, CO₂ as compared to other biomass, while RS exhibited the maximum yield of H₂ and CH₄. The bio-oil produced from three biomasses found to be acidic in nature and measured calorific value goes up to 10 MJ/kg. The comparable density with commercial fuel, low ash content, the low viscosity of produced bio-oil makes it suitable for use in an application like boiler combustion and IC engine. FTIR and GC–MS analysis of bio-oil showed that it contains chemical compounds, such as phenol, acids, alcohols, ester, ether, aromatic compounds, ketones, those can be exploited for commercial extraction purpose. CHNS, SEM/EDX, pH analysis of produced biochar indicated that it could be used as a commercial fertilizer in soil by replenishing soil nutrients. FTIR, CHNS, ICP-AES analyses data of biochar correlate biochar composition well with the pyrolysis product distribution. High calorific value of produced biochar samples compared to their precursor makes them suitable in combustion application with low NO_x and SO_x emission.

Acknowledgements This work was supported by the DST, New Delhi, vide sanction number, SR/FTP/ETA-56/2012, and Seed Money received from IIT (BHU), Varanasi.

References

- Sohaib Q, Muhammad A, Younas M (2017) Fast pyrolysis of sugarcane bagasse: effect of pyrolysis conditions on final product distribution and properties. *Energy Sour Part A Recov Utilization Environ Eff* 39(2):184–190
- Kumar A, Sinha ASK (2020) Hydrogen production from acetic acid steam reforming over nickel-based catalyst synthesized via MOF process. *Int J Hydrog Energy*. <https://doi.org/10.1016/j.ijhydene.2020.06.040>
- Ren S, Ye XP, Borole AP, Kim P, Labbé N (2016) Analysis of switchgrass-derived bio-oil and associated aqueous phase generated in a semi-pilot scale auger pyrolyzer. *J Anal Appl Pyrol* 119:97–103
- Hernández C, Escamilla-Alvarado C, Sánchez A, Alarcón E, Ziarelli F, Musule R, Valdez-Vazquez I (2019) Wheat straw, corn stover, sugarcane, and Agave biomasses: chemical properties, availability, and cellulosic-bioethanol production potential in Mexico. *Biofuels Bioprod Biorefin* 13(5):1143–1159
- Wyman CE (1999) BIOMASS ETHANOL: technical progress, opportunities, and commercial challenges. *Annu Rev Energy Environ* 24(1):189–226. <https://doi.org/10.1146/annurev.energy.24.1.189>
- Mosier N, Wyman C, Dale B, Elander R, Lee YY, Holtzapple M, Ladisch M (2005) Features of promising technologies for pretreatment of lignocellulosic biomass. *Biores Technol* 96(6):673–686. <https://doi.org/10.1016/j.biortech.2004.06.025>
- Bridgwater AV (2003) Renewable fuels and chemicals by thermal processing of biomass. *Chem Eng J* 91(2):87–102. [https://doi.org/10.1016/S1385-8947\(02\)00142-0](https://doi.org/10.1016/S1385-8947(02)00142-0)
- Jestin-Fleury N (1994) International energy agency. World energy outlook. *Politique étrangère* 59(59):564–565
- Kumar A, Singh R, Sinha ASK (2019) Catalyst modification strategies to enhance the catalyst activity and stability during steam reforming of acetic acid for hydrogen production. *Int J Hydrog Energy* 44(26):12983–13010. <https://doi.org/10.1016/j.ijhydene.2019.03.136>
- Guo M, Song W, Buhain J (2015) Bioenergy and biofuels: history, status, and perspective. *Renew Sustain Energy Rev* 42:712–725
- Biswas B, Pandey N, Bisht Y, Singh R, Kumar J, Bhaskar T (2017) Pyrolysis of agricultural biomass residues: comparative study of corn cob, wheat straw, rice straw and rice husk. *Biores Technol* 237:57–63
- Kumar A, Sinha ASK (2020) Comparative study of hydrogen production from steam reforming of acetic acid over synthesized catalysts via MOF and wet impregnation methods. *Int J Hydrog Energy* 45(20):11512–11526. <https://doi.org/10.1016/j.ijhydene.2020.02.097>
- Worasuwannarak N, Sonobe T, Tanthapanichakoon W (2007) Pyrolysis behaviors of rice straw, rice husk, and corncob by TG-MS technique. *J Anal Appl Pyrol* 78(2):265–271
- Bridgwater AV, Peacocke GVC (2000) Fast pyrolysis processes for biomass. *Renew Sustain Energy Rev* 4(1):1–73. [https://doi.org/10.1016/S1364-0321\(99\)00007-6](https://doi.org/10.1016/S1364-0321(99)00007-6)
- Demirbas A (2009) Biorefineries: current activities and future developments. *Energy Convers Manag* 50(11):2782–2801
- Demirbas A (2004) Combustion characteristics of different biomass fuels. *Prog Energy Combust Sci* 30(2):219–230
- Demirbas A (2007) Progress and recent trends in biofuels. *Prog Energy Combust Sci* 33(1):1–18
- Chakraborty JP, Kunzru D (2009) High pressure pyrolysis of n-heptane. *J Anal Appl Pyrol* 86(1):44–52
- Kumar A, Chakraborty JP, Singh R (2017) Bio-oil: the future of hydrogen generation. *Biofuels* 8(6):663–674. <https://doi.org/10.1080/17597269.2016.1141276>
- Bilgen S (2016) Correlation for estimation of the chemical availability (energy) from ultimate analysis of pyrolytic oils obtained from fast pyrolysis of biomass. *Energy Sour Part A Recov Utilization Environ Eff* 38(9):1286–1292

21. Demirbas A (2005) Pyrolysis of ground beech wood in irregular heating rate conditions. *J Anal Appl Pyrol* 73(1):39–43
22. Asadullah M, Rahman MA, Ali MM, Rahman M, Motin M, Sultan M, Alam M (2007) Production of bio-oil from fixed bed pyrolysis of bagasse. *Fuel* 86(16):2514–2520
23. Demiral İ, Şensöz S (2008) The effects of different catalysts on the pyrolysis of industrial wastes (olive and hazelnut bagasse). *Biores Technol* 99(17):8002–8007
24. Van de Velden M, Baeyens J, Brems A, Janssens B, Dewil R (2010) Fundamentals, kinetics and endothermicity of the biomass pyrolysis reaction. *Renew Energy* 35(1):232–242
25. Kan T, Strezov V, Evans TJ (2016) Lignocellulosic biomass pyrolysis: a review of product properties and effects of pyrolysis parameters. *Renew Sustain Energy Rev* 57:1126–1140. <https://doi.org/10.1016/j.rser.2015.12.185>
26. Boukis IP (1999) Fast pyrolysis of biomass in a circulating fluidised bed reactor. PhD Thesis, Chemical Engineering and Applied Chemistry, Aston University, Birmingham, UK
27. Karaosmanoğlu F, Tetik E (1999) Fuel properties of pyrolytic oil of the straw and stalk of rape plant. *Renew Energy* 16(1–4):1090–1093
28. Tsai W, Lee M, Chang Y (2007) Fast pyrolysis of rice husk: Product yields and compositions. *Biores Technol* 98(1):22–28
29. Aho A, Kumar N, Eränen K, Salmi T, Hupa M, Murzin DY (2008) Catalytic pyrolysis of woody biomass in a fluidized bed reactor: Influence of the zeolite structure. *Fuel* 87(12):2493–2501
30. Jensen PA, Sander B, Dam-Johansen K (2001) Pretreatment of straw for power production by pyrolysis and char wash. *Biomass Bioenergy* 20(6):431–446
31. Demirbas A (2004) Determination of calorific values of bio-chars and pyro-oils from pyrolysis of beech trunkbarks. *J Anal Appl Pyrol* 72(2):215–219
32. Ahmad M, Rajapaksha AU, Lim JE, Zhang M, Bolan N, Mohan D, Vithanage M, Lee SS, Ok YS (2014) Biochar as a sorbent for contaminant management in soil and water: a review. *Chemosphere* 99:19–33
33. Zhai M, Liu J, Wang Z, Guo L, Wang X, Zhang Y, Dong P, Sun J (2017) Gasification characteristics of sawdust char at a high-temperature steam atmosphere. *Energy* 128:509–518
34. Lee J, Kim K-H, Kwon EE (2017) Biochar as a catalyst. *Renew Sustain Energy Rev* 77:70–79
35. Hossain MK, Strezov V, Chan KY, Ziolkowski A, Nelson PF (2011) Influence of pyrolysis temperature on production and nutrient properties of wastewater sludge biochar. *J Environ Manag* 92(1):223–228
36. Pütün E, Uzun BB, Pütün AE (2006) Fixed-bed catalytic pyrolysis of cotton-seed cake: effects of pyrolysis temperature, natural zeolite content and sweeping gas flow rate. *Biores Technol* 97(5):701–710
37. Giddel M, Jivan A (2007) Waste to wealth, potential of rice husk in India a literature review. In: International conference on cleaner technologies and environmental management PEC, Pondicherry, India, pp 4–6
38. Chouhan S, Singh S, Pande A, Gautam U (2016) Adoption dynamics of improved sugarcane cultivation in Madhya Pradesh. *Indian Res J Extens Educ* 13(2):26–30
39. Wang C, Du Z, Pan J, Li J, Yang Z (2007) Direct conversion of biomass to bio-petroleum at low temperature. *J Anal Appl Pyrol* 78(2):438–444. <https://doi.org/10.1016/j.jaap.2006.10.016>
40. Park J, Lee Y, Ryu C, Park Y-K (2014) Slow pyrolysis of rice straw: analysis of products properties, carbon and energy yields. *Biores Technol* 155:63–70
41. Balagurumurthy B, Srivastava V, Kumar J, Biswas B, Singh R, Gupta P, Kumar KS, Singh R, Bhaskar T (2015) Value addition to rice straw through pyrolysis in hydrogen and nitrogen environments. *Biores Technol* 188:273–279
42. Pottmaier D, Costa MR, Farrow T, Oliveira AA, Alarcon O, Snape C (2013) Comparison of rice husk and wheat straw: from slow and fast pyrolysis to char combustion. *Energy Fuels* 27(11):7115–7125
43. Varma AK, Mondal P (2017) Pyrolysis of sugarcane bagasse in semi batch reactor: effects of process parameters on product yields and characterization of products. *Ind Crops Prod* 95:704–717
44. Gonçalves EV, Teodoro C, Seixas FL, Canesin EA, Olsen Scaliante MHN, Gimenes ML, De Souza M (2017) Pyrolysis of sugarcane bagasse in a fixed bed reactor: influence of operational conditions in the distribution of products. *Can J Chem Eng* 95(12):2249–2257
45. Duong TL, Nguyen DT, Nguyen HHM, Phan BMQ, Nguyen HL, Huynh TM (2019) Fast pyrolysis of Vietnamese waste biomass: relationship between biomass composition, reaction conditions, and pyrolysis products, and a strategy to use a biomass mixture as feedstock for bio-oil production. *J Mater Cycles Waste Manag* 21(3):624–632
46. Adinavee T, Kennedy LJ, Vijaya JJ, Sekaran G (2015) Surface and porous characterization of activated carbon prepared from pyrolysis of biomass (rice straw) by two-stage procedure and its applications in supercapacitor electrodes. *J Mater Cycles Waste Manag* 17(4):736–747
47. Bera T, Purakayastha T, Patra A, Datta S (2018) Comparative analysis of physicochemical, nutrient, and spectral properties of agricultural residue biochars as influenced by pyrolysis temperatures. *J Mater Cycles Waste Manag* 20(2):1115–1127
48. Tan Z, Zou J, Zhang L, Huang Q (2018) Morphology, pore size distribution, and nutrient characteristics in biochars under different pyrolysis temperatures and atmospheres. *J Mater Cycles Waste Manag* 20(2):1036–1049
49. Do PT, Ueda T, Kose R, Nguyen LX, Okayama T, Miyanishi T (2019) Properties and potential use of biochars from residues of two rice varieties, Japanese Koshihikari and Vietnamese IR50404. *J Mater Cycles Waste Manag* 21(1):98–106
50. Derakhshan-Nejad Z, Jung MC (2019) Remediation of multi-metal contaminated soil using biochars from rice husk and maple leaves. *J Mater Cycles Waste Manag* 21(3):457–468
51. Asadullah M, Ab-Rasid NS, Kadir SASA, Azdarpour A (2013) Production and detailed characterization of bio-oil from fast pyrolysis of palm kernel shell. *Biomass Bioenergy* 59:316–324
52. Ogunjobi JK, Lajide L (2013) Characterisation of bio-oil and bio-char from slow-pyrolysed Nigerian yellow and white corn cobs. *J Sustain Energy Environ* 4(2):77–84
53. Yuan T, Tahmasebi A, Yu J (2015) Comparative study on pyrolysis of lignocellulosic and algal biomass using a thermogravimetric and a fixed-bed reactor. *Biores Technol* 175:333–341
54. Fu P, Hu S, Xiang J, Sun L, Su S, Wang J (2012) Evaluation of the porous structure development of chars from pyrolysis of rice straw: effects of pyrolysis temperature and heating rate. *J Anal Appl Pyrol* 98:177–183. <https://doi.org/10.1016/j.jaap.2012.08.005>
55. Trubetskaya A, Jensen PA, Jensen AD, Steibel M, Spliethoff H, Glarborg P, Larsen FH (2016) Comparison of high temperature chars of wheat straw and rice husk with respect to chemistry, morphology and reactivity. *Biomass Bioenergy* 86:76–87. <https://doi.org/10.1016/j.biombioe.2016.01.017>
56. Pütün AE, Özbay N, Önal EP, Pütün E (2005) Fixed-bed pyrolysis of cotton stalk for liquid and solid products. *Fuel Process Technol* 86(11):1207–1219
57. Apaydin-Varol E, Pütün E, Pütün AE (2007) Slow pyrolysis of pistachio shell. *Fuel* 86(12–13):1892–1899
58. Yang H, Yan R, Chen H, Lee DH, Zheng C (2007) Characteristics of hemicellulose, cellulose and lignin pyrolysis. *Fuel* 86(12–13):1781–1788

59. Chen W-H, Kuo P-C (2010) A study on torrefaction of various biomass materials and its impact on lignocellulosic structure simulated by a thermogravimetry. *Energy* 35(6):2580–2586
60. Stefanidis SD, Kalogiannis KG, Iliopoulou EF, Michailof CM, Pilavachi PA, Lappas AA (2014) A study of lignocellulosic biomass pyrolysis via the pyrolysis of cellulose, hemicellulose and lignin. *J Anal Appl Pyrol* 105:143–150
61. Şen N, Kar Y (2011) Pyrolysis of black cumin seed cake in a fixed-bed reactor. *Biomass Bioenergy* 35(10):4297–4304
62. Morali U, Şensöz S (2015) Pyrolysis of hornbeam shell (*Carpinus betulus* L.) in a fixed bed reactor: characterization of bio-oil and bio-char. *Fuel* 150:672–678
63. Lu Q, Li W-Z, Zhu X-F (2009) Overview of fuel properties of biomass fast pyrolysis oils. *Energy Convers Manag* 50(5):1376–1383
64. Carrier M, Joubert J-E, Danje S, Hugo T, Görgens J, Knoetze JH (2013) Impact of the lignocellulosic material on fast pyrolysis yields and product quality. *Biores Technol* 150:129–138
65. Garg R, Anand N, Kumar D (2016) Pyrolysis of babool seeds (*Acacia nilotica*) in a fixed bed reactor and bio-oil characterization. *Renew energy* 96:167–171
66. Demiral İ, Kul ŞÇ (2014) Pyrolysis of apricot kernel shell in a fixed-bed reactor: characterization of bio-oil and char. *J Anal Appl Pyrol* 107:17–24
67. Sensoez S, Angin D (2008) Pyrolysis of safflower (*Charthamus tinctorius* L.) seed press cake: part 1. The effects of pyrolysis parameters on the product yields. *Bioresour Technol* 99(13):5492–5497
68. Choi HS, Choi YS, Park HC (2012) Fast pyrolysis characteristics of lignocellulosic biomass with varying reaction conditions. *Renew Energy* 42:131–135
69. Şensöz S, Angin D (2008) Pyrolysis of safflower (*Charthamus tinctorius* L.) seed press cake: Part 1. The effects of pyrolysis parameters on the product yields. *Bioresour Technol* 99(13):5492–5497
70. Kim SW, Koo BS, Ryu JW, Lee JS, Kim CJ, Lee DH, Kim GR, Choi S (2013) Bio-oil from the pyrolysis of palm and Jatropha wastes in a fluidized bed. *Fuel Process Technol* 108:118–124
71. Park HJ, Park Y-K, Kim JS (2008) Influence of reaction conditions and the char separation system on the production of bio-oil from radiata pine sawdust by fast pyrolysis. *Fuel Process Technol* 89(8):797–802
72. Mohan D, Pittman CU Jr, Steele PH (2006) Pyrolysis of wood/biomass for bio-oil: a critical review. *Energy Fuels* 20(3):848–889
73. Kim S, Kim CH (2013) Bioethanol production using the sequential acid/alkali-pretreated empty palm fruit bunch fiber. *Renew Energy* 54:150–155
74. Părpăriță E, Brebu M, Uddin MA, Yanik J, Vășile C (2014) Pyrolysis behaviors of various biomasses. *Polym Degrad Stab* 100:1–9
75. Uzun BB, Pütün AE, Pütün E (2006) Fast pyrolysis of soybean cake: product yields and compositions. *Biores Technol* 97(4):569–576
76. Yang H, Yan R, Chen H, Lee DH, Liang DT, Zheng C (2006) Mechanism of palm oil waste pyrolysis in a packed bed. *Energy Fuels* 20(3):1321–1328
77. Vitasari CR, Meindersma GW, De Haan AB (2011) Water extraction of pyrolysis oil: the first step for the recovery of renewable chemicals. *Biores Technol* 102(14):7204–7210
78. David GF, Justo OR, Perez VH, Garcia-Perez M (2018) Thermochemical conversion of sugarcane bagasse by fast pyrolysis: high yield of levoglucosan production. *J Anal Appl Pyrol* 133:246–253
79. Dhyani V, Bhaskar T (2018) A comprehensive review on the pyrolysis of lignocellulosic biomass. *Renew Energy* 129:695–716. <https://doi.org/10.1016/j.renene.2017.04.035>
80. Yang H, Yan R, Chen H, Lee DH, Zheng C (2007) Characteristics of hemicellulose, cellulose and lignin pyrolysis. *Fuel* 86(12):1781–1788. <https://doi.org/10.1016/j.fuel.2006.12.013>
81. Guangul FM, Sulaiman SA, Ramli A (2014) Study of the effects of operating factors on the resulting producer gas of oil palm fronds gasification with a single throat downdraft gasifier. *Renew Energy* 72:271–283. <https://doi.org/10.1016/j.renene.2014.07.022>
82. Ahmad MI, Alauddin ZAZ, Soid SNM, Mohamed M, Rizman ZI, Rasat MSM, Razab M, Amini MHM (2015) Performance and carbon efficiency analysis of biomass via stratified gasifier. *ARPN J Eng Appl Sci* 10(20):9533–9537
83. Mullen CA, Boateng AA, Goldberg NM, Lima IM, Laird DA, Hicks KB (2010) Bio-oil and bio-char production from corn cobs and stover by fast pyrolysis. *Biomass Bioenergy* 34(1):67–74
84. Pütün AE, Özbay N, Apaydın Varol E, Uzun BB, Ateş F (2007) Rapid and slow pyrolysis of pistachio shell: effect of pyrolysis conditions on the product yields and characterization of the liquid product. *Int J Energy Res* 31(5):506–514
85. Carrier M, Hardie AG, Uras Ü, Görgens J, Knoetze J (2012) Production of char from vacuum pyrolysis of South-African sugar cane bagasse and its characterization as activated carbon and biochar. *J Anal Appl Pyrol* 96:24–32. <https://doi.org/10.1016/j.jaap.2012.02.016>
86. Al-Wabel MI, Al-Omran A, El-Naggar AH, Nadeem M, Usman ARA (2013) Pyrolysis temperature induced changes in characteristics and chemical composition of biochar produced from conocarpus wastes. *Biores Technol* 131:374–379. <https://doi.org/10.1016/j.biortech.2012.12.165>
87. Liu Z, Quek A, Kent Hoekman S, Balasubramanian R (2013) Production of solid biochar fuel from waste biomass by hydrothermal carbonization. *Fuel* 103:943–949. <https://doi.org/10.1016/j.fuel.2012.07.069>
88. Hansen J, Sato M, Kharecha P, Beerling D, Berner R, Masson-Delmotte V, Pagani M, Raymo M, Royer DL, Zachos JC (2008) Target atmospheric CO₂: where should humanity aim? arXiv:0804.1126.
89. Kim KH, Kim T-S, Lee S-M, Choi D, Yeo H, Choi I-G, Choi JW (2013) Comparison of physicochemical features of biooils and biochars produced from various woody biomasses by fast pyrolysis. *Renew Energy* 50:188–195
90. Anupam K, Swaroop V, Deepika Lal PS, Bist V (2015) Turning *Leucaena leucocephala* bark to biochar for soil application via statistical modelling and optimization technique. *Ecol Eng* 82:26–39. <https://doi.org/10.1016/j.ecoleng.2015.04.078>
91. Yan W, Acharjee TC, Coronella CJ, Vasquez VR (2009) Thermal pretreatment of lignocellulosic biomass. *Environ Progr Sustain Energy* 28(3):435–440
92. Tinwala F, Mohanty P, Parmar S, Patel A, Pant KK (2015) Intermediate pyrolysis of agro-industrial biomasses in bench-scale pyrolyser: product yields and its characterization. *Biores Technol* 188:258–264. <https://doi.org/10.1016/j.biortech.2015.02.006>
93. Apaydın-Varol E, Pütün AE (2012) Preparation and characterization of pyrolytic chars from different biomass samples. *J Anal Appl Pyrol* 98:29–36. <https://doi.org/10.1016/j.jaap.2012.07.001>
94. Raveendran K, Ganesh A, Khilar KC (1995) Influence of mineral matter on biomass pyrolysis characteristics. *Fuel* 74(12):1812–1822. [https://doi.org/10.1016/0016-2361\(95\)80013-8](https://doi.org/10.1016/0016-2361(95)80013-8)
95. Shafizadeh F (1968) Pyrolysis and combustion of cellulosic materials. In: Wolfrom ML, Tipson RS (eds) *Advances in carbohydrate chemistry*, vol 23. Elsevier, New York, pp 419–474

96. Zhang L, Shen C, Liu R (2014) GC–MS and FT-IR analysis of the bio-oil with addition of ethyl acetate during storage. *Front Energy Res* 2:3
97. Shah Z, Cataluña Veses R, Silva RD (2016) A comparative study and analysis of two types of bio-oil samples obtained from freshwater algae and microbial treated algae. *Mod Chem Appl* 4(3):1000185
98. Negahdar L, Gonzalez-Quiroga A, Otyuskaya D, Toraman HE, Liu L, Jastrzebski JT, Van Geem KM, Marin GB, Thybaut JW, Weckhuysen BM (2016) Characterization and comparison of fast pyrolysis bio-oils from pinewood, rapeseed cake, and wheat straw using ^{13}C NMR and comprehensive GC \times GC. *ACS Sustain Chem Eng* 4(9):4974–4985
99. Toraman HE, Vanholme R, Borén E, Vanwongerghem Y, Djokic MR, Yildiz G, Ronsse F, Prins W, Boerjan W, Van Geem KM (2016) Potential of genetically engineered hybrid poplar for pyrolytic production of bio-based phenolic compounds. *Biores Technol* 207:229–236
100. Mullen CA, Boateng AA, Hicks KB, Goldberg NM, Moreau RA (2010) Analysis and comparison of bio-oil produced by fast pyrolysis from three barley biomass/byproduct streams. *Energy Fuels* 24(1):699–706

Publisher's Note Springer Nature remains neutral with regard to jurisdictional claims in published maps and institutional affiliations.



Arsenate adsorption from aqueous solution using iron-loaded *Azadirachta indica* roots: batch and fixed-bed column study

Ghazi Mohd Sawood*, S.K. Gupta

Department of Chemical Engineering, Harcourt Butler Technical University, Kanpur, India, Tel. +91 9918040404; emails: mohdsaud22@gmail.com (G.M. Sawood), skgupta@hbtu.ac.in (S.K. Gupta)

Received 21 October 2019; Accepted 9 June 2020

ABSTRACT

Batch and fixed-bed column studies were carried out to investigate the potential of an economic and eco-friendly adsorbent (iron impregnated *Azadirachta indica* roots (AIR)), for the remediation of arsenate. Maximum adsorption of 96.811% ($q_{e,exp} = 10.586 \mu\text{g/g}$) was obtained at an initial arsenate concentration of 100 $\mu\text{g/L}$, pH of 6.0, adsorbent dose of 1 g/L and contact time of 30 min. The presence of co-existing anions like PO_4^{3-} , SiO_3^{2-} decreases the adsorption capacity whereas cation does not have any effect on the same. Kinetics, isotherms, and thermodynamic studies were also conducted for understating the adsorption process in a better way. The adsorption data fitted best in the Langmuir model ($R^2 = 0.9918$ and $q_{max} = 29.82 \mu\text{g/g}$), which reveals the removal takes place as monolayer adsorption with homogenous energy levels. Adsorption kinetics study reveals that the pseudo-second-order kinetics ($R^2 = 0.9966$, $q_e = 10.2832$) controls the adsorption process. Thermodynamics studies show exothermic and spontaneous adsorption of arsenate on Fe-AIR. In fixed-bed column operations, effects of various operating parameters like bed height, the influent concentration of As(V), flow rate, column diameter were investigated to evaluate the removal efficiency. At optimum experimental conditions ($C_i = 1,000 \mu\text{g/L}$, bed height = 9 cm, flow rate = 3 mL/min, column diameter = 3 cm and pH 7.0), maximum uptake ($q_e = 93.3 \mu\text{g/g}$) with maximum breakthrough (450 min) was achieved. Breakthrough curves were used to analyze the effect of operating parameters on adsorption. Thomas model was used to determine the saturated concentration and the Yoon–Nelson model was applied to determine the required time for 50% adsorbate breakthrough. The present system developed for arsenate remediation is rapid, economic, and reproducible and can be applied to any resource of arsenic-contaminated water. The Fe-AIR fixed column can be regenerated and reused many times. The adsorption capacity decreases to 31.5% after 5 cycles.

Keywords: Arsenate; Fe-AIR; Breakthrough curve; Column operation; Regeneration

1. Introduction

Arsenic in drinking water is considered as a potential threat to human health. It is ranked as the number one carcinogenic substance and listed as number five among potentially toxic elements according to the Comprehensive Environmental Response, Compensation, and Liability act [1]. More than 70 countries, including the United States,

Southeast Asian countries, China, Hungary, Chile, etc. were affected by arsenic contamination [2]. Due to highly toxic nature towards human health, the maximum allowable Arsenic concentration in drinking water has been reduced to 10 from 50 $\mu\text{g/L}$ by the World Health Organization (WHO) [3]. Under different redox situations and pH, arsenic is present in various oxidation states (-3, 0, 3, and 5) in the aquatic system and its chemistry is complicated. Under

* Corresponding author.

oxidizing conditions and in the pH range of 5–7, As(V) is dominating species in the form of HAsO_4^{2-} , HAsO_4^{-1} , and HAsO_4 while under mild reducing conditions, As(III) predominates and exists as $\text{H}_3\text{AsO}_3^{-2}$, $\text{H}_3\text{AsO}_3^{-1}$, or H_3AsO_3 [4]. In human bodies, Arsenate readily reduces to arsenite at low dosages. It is important to treat the total arsenic rather than the distribution of arsenate and arsenite from the contaminated water [5]. Only the conversion of arsenite to arsenate does not reduce arsenic toxicity. Thus it is necessary to develop efficient As(V) removal technologies after pre-oxidation of contaminated water. There are various methods including coagulation and flocculation, membrane filtration, ion exchange, electrochemical precipitation, and adsorption were proposed for the Arsenic remediation from drinking water [6]. It has been reported that along with technical barriers, economic hurdles are also very prominent in arsenic remediation as arsenic-containing groundwater mostly found in developing countries. Therefore, cheaper and technically good methods are required for the treatment of arsenic-contaminated water. Out of the mentioned methods, electrochemical precipitation has the problem of disposal of waste, membrane filtration, and ion exchange technique are less cost-efficient methods [7]. The wide use of the adsorption process is in comparison to other arsenic remediation techniques is due to its simplicity in operation, low cost of operation, and availability [8].

In the recent past, the demand for biosorption and agro-based adsorption processes increased. This hike in the demand can be attributed to the fact that they are relatively very cheap, their bulk abundance, easy regeneration, and generation of minimum sludge. Moreover, this class of adsorbent also tends to form the metal complex of their functional group with metal ions which in turn result in high affinity [9]. Lignin, hydrocarbons of water, hemicellulose, proteins, functional groups of starch are the essential components derived from agro-waste that are responsible for forming a metal complex, which results in sequestering [10].

The powdered form of roots of the *Azadirachta indica* tree is a very good example of non-conventional bio-adsorbent. In the recent past, adsorbents synthesized from bark and leaves of *Azadirachta indica* tree draw the attention of researchers, due to its easy availability across the globe. 90% of As(III) removal at pH 5 was reported using zinc oxide nanoparticle entrenched on leaf extract of *Azadirachta indica* [11]. At 6 pH and 100 $\mu\text{g/L}$ arsenic concentration, 79% of arsenic removal from the groundwater reported using modified bark powder of *Azadirachta indica* [12]. Under optimized experimental conditions (0–500 $\mu\text{g/L}$, pH of 6.5), 89% of As(III) removal achieved using powdered bark of *Azadirachta indica* [13]. Remediation of other pollutants including Zn(II) [14], Cd(II) [15], Cr(VI) [16] and dyes [17] from aqueous solution also investigated using *Azadirachta indica* powder. Earlier the roots of water hyacinth plant (81% arsenic removal at 6.0 pH and 10 mg/L concentration [18], eucalyptus (94% removal at pH = 6.0, $t = 47.5$ min, $C_0 = 2.75$ mg/L and $m = 1.5$ mg/L)), ribwort plantain, lichens, mosses, Chinese brake fern, crowberry, *Tamarix* and many more plants were used for arsenic removal still, not a single research has reported removal of As(V) using roots of *Azadirachta indica* tree.

These findings attributed to great interest in analyzing the possibility for application of [19] powdered roots

of *Azadirachta indica* tree in the remediation of As(V) from aqueous solution. Since the unmodified barks or leaves of *Azadirachta indica* tree has proven to be reasonably significant adsorbents for the removal of As(III) and other pollutants, it is essential to modify the properties of adsorbents to achieve better efficiencies for As(V) removal. Various researches show that iron and its compounds are very effective adsorbents for the remediation of arsenic from water, but due to their fragile nature and the high cost, they cannot be used alone. Many Fe based adsorbents are used for As(III) removal [19–23] but very few such adsorbents were used for As(V) remediation [24,25]. In the present study, surface modification of *Azadirachta indica* root (AIR) carbon is carried out using the impregnation of Fe.

The present study aimed at (i) evaluation of equilibrium adsorption and kinetics using iron impregnated *Azadirachta indica* carbon (new adsorbent) in batch and fixed-bed column operations, (ii) to find the optimum flow velocity, bed height, maximum uptake capacity through the fixed bed column operations to bring the Arsenic concentration in the prescribed domain as per WHO limits. Vast studies carried out where removal of Arsenic is done through different activated carbons using the static batch runs [26]. Very few experiments were conducted in the past using column-based dynamic operations. The novelty of the work is the performance evaluation of *Azadirachta indica* roots derived activated carbon, followed by its impregnation using iron metal. The column experiment which was performed has direct relevance with the large scale industrial operations.

2. Materials and methods

2.1. Apparatus and reagents

Chemicals of analytical grade procured from Merck India limited and used without further purification. Acid washing of glassware followed by rinsing with double distilled water and subjected to oven drying at every stage. Double distilled water was used to prepare reagents. NaOH and HCL having molarity 0.1 were used to maintain the pH.

2.2. Instruments used

Agilent (Laos) inductively coupled mass spectrophotometer (ICPMS)-7900 used to find the concentration of arsenate. The pH of the sample was measured by Hanna (Rhode Island, United States) edge multi parameter pH meter-HI2020. For the study of morphology and Fe-distribution of impregnated iron, Fe-ACs was fractured for exposing internal structure using energy-dispersive X-ray spectroscopy (EDX) coupled with a scanning electron microscope (Carl Zeiss EVO 50, Germany). On the exposed region, no further polishing was done to avoid the spooliation of the surface characteristics of Fe-AIR. Determination of Fe-species was done through X-ray diffraction (XRD) analysis by using Bruker D8 focus (United States) X-ray diffractometer having $\text{Cu-K}\alpha$ X-radiation source and $\lambda = 1.5418$ Å. Brunauer–Emmett–Teller (BET) multipoint technique (Autosorb iQ) was used to evaluate the surface area of impregnated and non-impregnated AIR at 77 K.

2.3. Preparation of arsenic(V) solution

Sodium arsenate ($\text{NaHAsO}_4 \cdot 7\text{H}_2\text{O}$) used to prepare the stock solution of arsenate. Then after, by the dilution of stock solution, required concentrations were obtained. NaOH or H_2SO_4 solution used to control the pH.

2.4. Collection and preparation of adsorbent

The adsorbents which are used in the present work is activated carbon derived from roots of *Azadirachta indica* (Neem) tree, which are further modified by the impregnation procedure with iron salt. The alteration in the structure of pore of activated carbon and enhancement in its surface area is achieved by the impregnation process [27]. More quantity of iron was preferred in the Iron impregnation as the active phase is recognized by the impregnated Iron which is responsible for enhancing adsorption capacity [28].

AIR was purchased from a local timber house. Repeated washing of roots with distilled water was done to remove dust and other impurities, followed by oven drying at 65°C for 30–36 h. After the removal of moisture, the roots were grounded to obtain powder form. The product thus obtained was sieved. The dried mixture was placed in a muffle furnace at 750°C for 6 h. Washing of the product (activated carbon) thus produced was done with distilled water [29]. The washed activated carbon was dried in a hot air oven at 90°C for 6 h. Desiccators are used to store produced activated carbon.

2.4.1. Iron impregnation on the adsorbent

The iron salt solution which is used in the current study for the impregnation, of the activated carbon was obtained by dissolving the ferrous chloride salt in the distilled water. The impregnation method involving thermochemical reactions by ferrous chloride solution was used to coat the activated carbon. The pH of the slurry was maintained at 8 by use of NaOH that enhances the negative charge abundance of activated carbon which in turn enhances the impregnation process [30]. Fifty grams of AC was added to a 500 mL glass beaker filled with a 0.5 M FeCl_2 solution. To prevent precipitation and ferrous oxidation, no headspace was provided. A magnetic stirrer was used for through stirring of AC in the ferrous salt solution. The suspension temperature was controlled and maintained at 70°C . After stirring 24 h, the suspension was collected and filtered by using filter paper. Oven drying at 100°C for 6 h was done to obtain the required solid phase. After complete drying of the solid phase, the product was cooled and washed thoroughly until a clear supernatant was obtained. Post-treatment of the thus obtained product with 1 N NaOH provides the stabilization step in the development of the iron impregnated activated carbon [31].

2.5. Experimental setup

2.5.1. Batch experiments

In the batch experiments, different parameters like time of contact (15–75 min), a dose of adsorbent (0.25–1.25 g), pH (2–10), initial As(V) concentration (50–250 $\mu\text{g/L}$) and

operating temperature (313–328 K) were studied to analyze their effects on As(V) adsorption. In the experimental procedure, a known quantity of Fe-AIR was added to a 250 mL Erlenmeyer flask filled with a 100 mL solution of sodium arsenate ($\text{NaHAsO}_4 \cdot 7\text{H}_2\text{O}$), after pH adjustment. The magnetic stirring of the suspension, thus formed was done till the equilibrium conditions were achieved. After stirring, the suspension was allowed to settle down and filtered using a $0.22 \mu\text{m}$ syringe filter. The obtained filtrate was collected, and the arsenic concentrations were recorded using ICPMS. The following equation [32] was used to calculate adsorption (removal) efficiency:

$$\text{Adsorption (removal) efficiency} = \frac{(C_i - C_e)}{C_i} \times 100 \quad (1)$$

where C_i and C_e are the arsenate concentration before and after treatment in the sample solution.

At equilibrium, the As(V) uptake capacity of Fe-AIR was estimated by the following equation [33]:

$$q_e (\text{uptake capacity}) = \frac{(C_i - C_e)}{M} \times V \quad (2)$$

where M is the mass of the adsorbent and V is the volume of the solution.

The effect of co-existing ions on the adsorption of As(V) was observed at room temperature. The As(V) solution was further spiked with the salts of competing ion, including phosphate (PO_4^{3-}), sulfate (SO_4^{2-}), silicate (SiO_3^{2-}), and nitrate (NO_3^-). At optimum pH and adsorbent dose, the co-existing ion salt solutions were added to 100 ml Erlenmeyer flask, which was already filled with As(V) solution. The suspension thus obtained was subjected to stirring for 10 h. The suspension was filtered through a syringe filter and the resulting concentration was observed as before.

2.5.2. Column experiments

Two experimental setups were constructed for analyzing the adsorptive behavior of As(V) in packed bed reactors. The D.I water spiked with 100 $\mu\text{g/L}$ As(V) at pH of 6 was circulated through the empty column to test the As(V) adsorption in constituents of setup (tubing and column). A little adsorption in the column at the very initial stage was observed, which was vanished off after 3 h, and no adsorption was observed in tubes. Each experimental setup comprise of heat resistant borosilicate glass column (*Reactor 1*: I.D = 2 cm; H = 30 cm and *Reactor 2*: I.D = 3 cm; H = 30 cm). Both columns were rinsed using 15% nitric acid followed by washing with deionized water at 6 pH for 8 h. Then after, Fe-AIR adsorbent was loaded into the columns. To obtain different bed heights (3, 6, and 9 cm), varying amounts of Fe-AIR (4.17, 10.98, and 17.81 g) were used to pack the column. Layers of glass wool (1 cm) at the ends were used to avoid floating. After loading is done, As(V) spiked water was circulated into the columns by peristaltic pumps with different flow rates (3, 6, and 9 mL/min). The effluents from the column were collected through the weir. Adjustment of optimum pH was done to ensure

the maximum Arsenic uptake for desired concentration and pumped in down-flow mode was used to maintain the desired flow rate. When the concentration of effluent exceeds the value of 99% initial arsenic concentration, the operation was stopped. The hydraulic head of 6 inches was maintained. All samples were collected and refrigerated until their analysis.

Under identical conditions, the blank control test was performed. The amount of As(V) lost during the test was subtracted from the experimental results. All the experiments were performed in triplicate at room 25°C (room temperature). The average experimental values were reported, and the standard deviation was represented using error bars. The relative experimental error was within ±5%.

3. Result and discussion

3.1. Characterization

The scanning electron microscopy (SEM) images (25 kV; 20 μm) of uncarbonized AIR and Fe-AIR at 5000 magnification are shown in Figs. 1 and 2, respectively. SEM images of virgin AIR show smooth and non-porous morphology whereas, SEM image of Fe-AIR reveals the presence of rough, porous, heterogenous, and non-uniform surface. The cavities and heterogeneity of adsorbent support the high adsorption capacity[34]. EDX determined the presence of Fe and Cl, which are known to be good binding agents [35].

The BET surface areas, pore-volume, and pore width of Fe-AIR and virgin AIR are given in Table 2. A reduction in

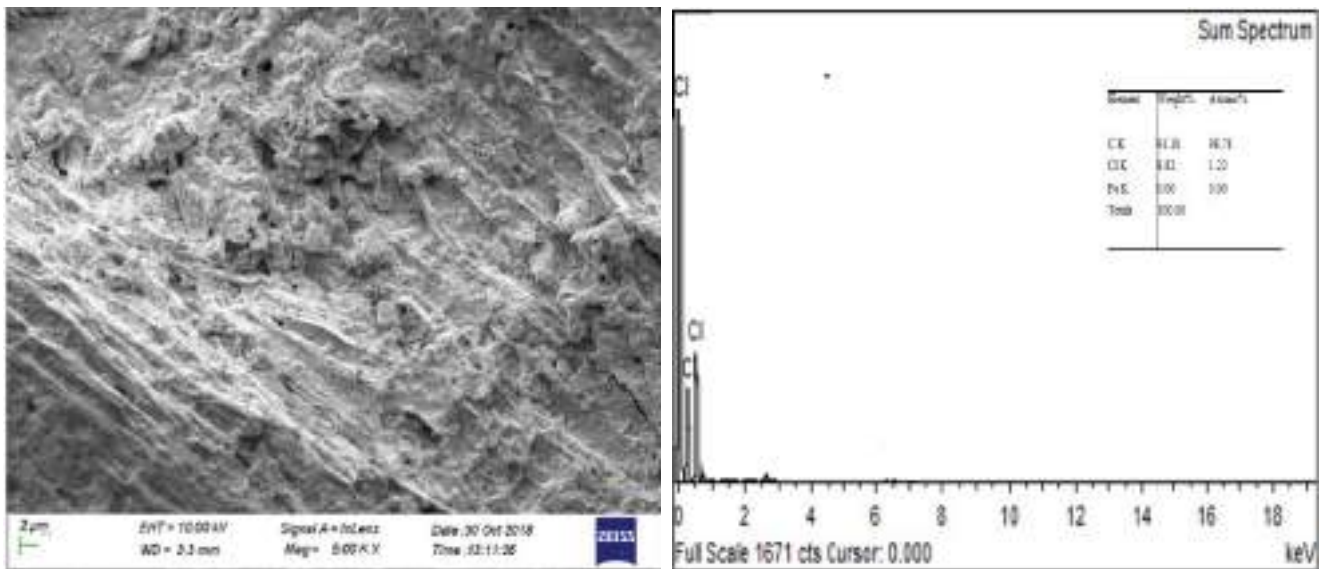


Fig. 1. SEM micrograph and EDX image of AIR.

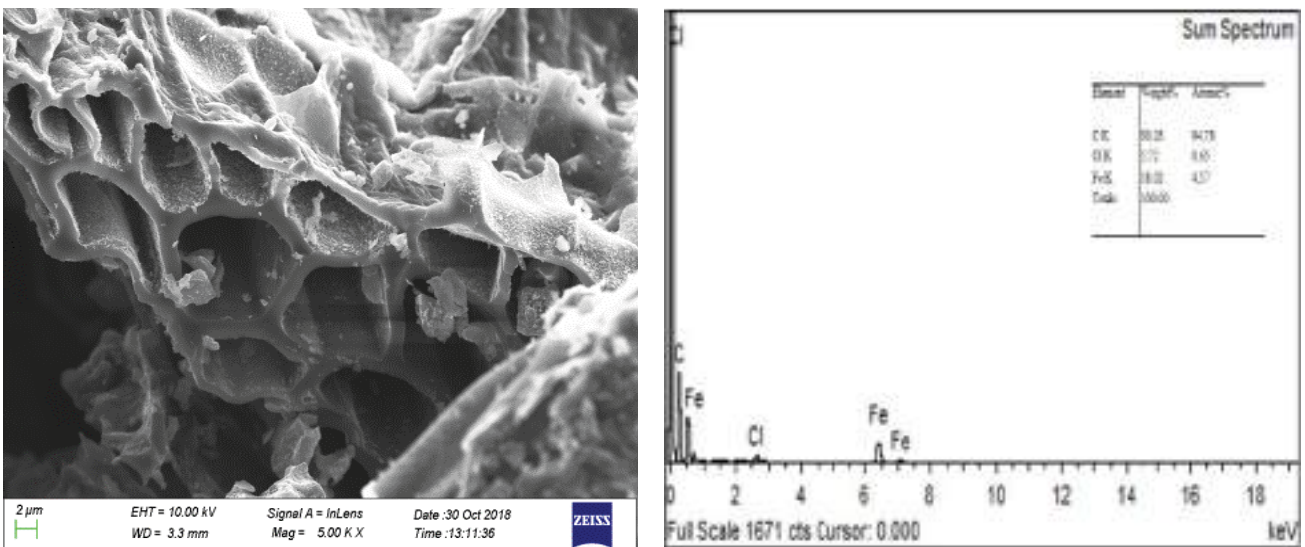


Fig. 2. SEM micrograph and EDX image of Fe-AIR.

Table 1
Physiochemical properties of Fe-AIR

Analysis	Value
Moisture content	11.18%
pH _{zpc}	6.91
pH _{slurry}	6.17
Specific gravity	0.216
Porosity	78%
Particle size	238 μm

Table 2
BET results of virgin AIR and Fe-AIR

	Fe-AC	Virgin AC
Surface area (m^2/g)	358.916	631.355
Pore volume (cc/g)	0.159	0.198
Pore width (\AA)	5.996	23.878

the surface area of Fe-AIR was observed when compared to the surface area of virgin AC. This reduction in surface area can be attributed to the awning of the AIR surface during the impregnation process by iron oxide particles [36]. The pore volume and pore width also decrease in the same fashion as that of BET surface areas from virgin AC to Fe-AC [37]. The pore width of the Fe-AIR lies in the range of 5–15 \AA , which suggests the microporous nature of the adsorbent used in the present study.

Fig. 3 shows the XRD pattern of virgin AIR and Fe-AIR. The XRD plot analysis revealed that the basic structure of AIR carbon is amorphous. Broader peaks were obtained in a 2θ range of 10° – 35° . The peaks of Fe-AIR can be attributed to oxides of iron [38]. The marked peaks of the Fe-AIR plot show the face-centered cubic structure of Fe(II) oxide.

Comparing d values and plot pattern of Fe-AIR with magnetite, it was observed that the peaks of the plots correspond to magnetite which was adsorbed on to the surface of Fe-AIR. No peak corresponds to any other form of Fe was observed. Crystalline nature of adsorbent results from the loading of iron. The absence of a sharp peak in the remaining part of the plot shows porosity and amorphous nature. The appreciable adsorption capacity of Fe-AIR towards arsenic is due to the crystalline, amorphous structure [39].

The electronic state and elemental composition of Fe-AIR in the present study were determined by X-ray photoelectron spectroscopy (XPS) scan. The distribution of the elements on the Fe-AIR was analyzed using the survey scan. Then the concentration of C, O, N, and Fe in the Fe-AIR were measured using utility scans. Fig. 4 shows various positions of peaks of Fe, C, O, and N determined by XPS scan of Fe-AIR. From Fig. 4, it can be seen that the carbon-1s peak was detected at 224.0 eV. The N-1s peak of Fe-AIR was observed at 342.0 eV, which may be due to R-NH₂ (amino) groups in AIR carbon [40]. Strong Fe peaks were observed which can be attributed to effective impregnation of Fe on to AIR. A primary band of Fe at 681.0 eV was observed along with its secondary band at 723.0 eV. The Satellite band of Fe at 698.0 eV can be due to the oxidation state of Fe³⁺ [41]. The presence of Fe³⁺ in Fe-AIR the sample reveals that iron(III) oxide, iron(III) oxide, or residual iron(III) chloride was present on the surface of the sample [42]. No zero-valent Fe was observed on to the Fe-AIR surface in the Fe-2p spectra.

3.2. Batch operations results

3.2.1. Effect of initial arsenate concentration

The influence of initial As(V) concentration on the adsorption of arsenate onto Fe-AIR and AIR, in the concentration range of 50–250 $\mu\text{g}/\text{L}$ is shown in Fig. 5. It can be seen that with increasing concentration of Arsenate, the percentage of removal decreases for both adsorbents. In the

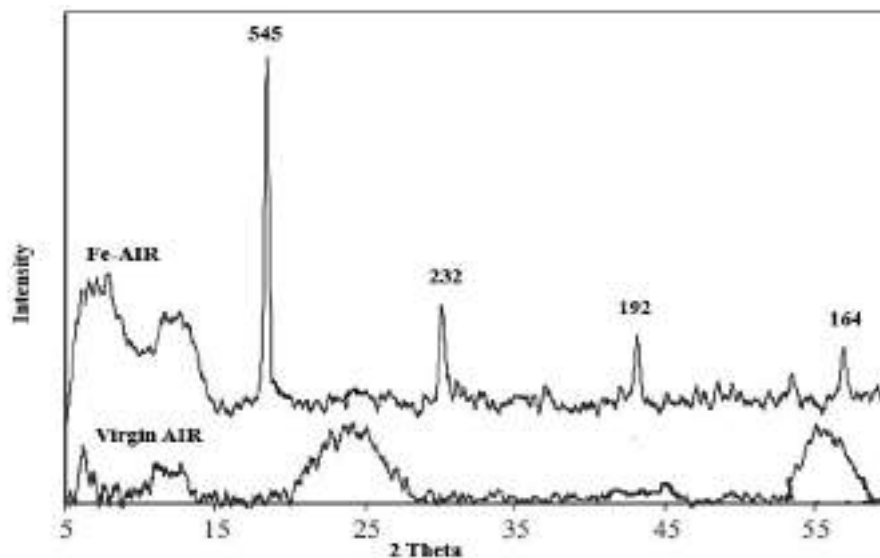


Fig. 3. XRD pattern of Fe-AIR.

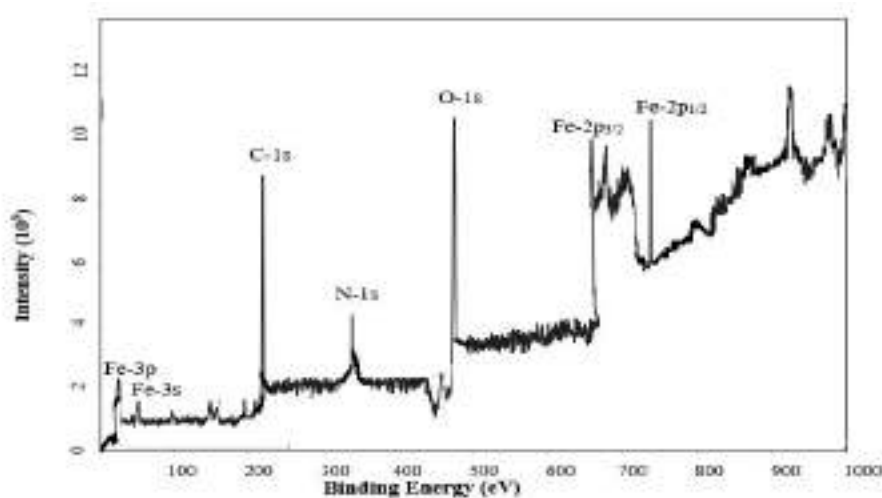


Fig. 4. XPS scans for Fe-AIR.

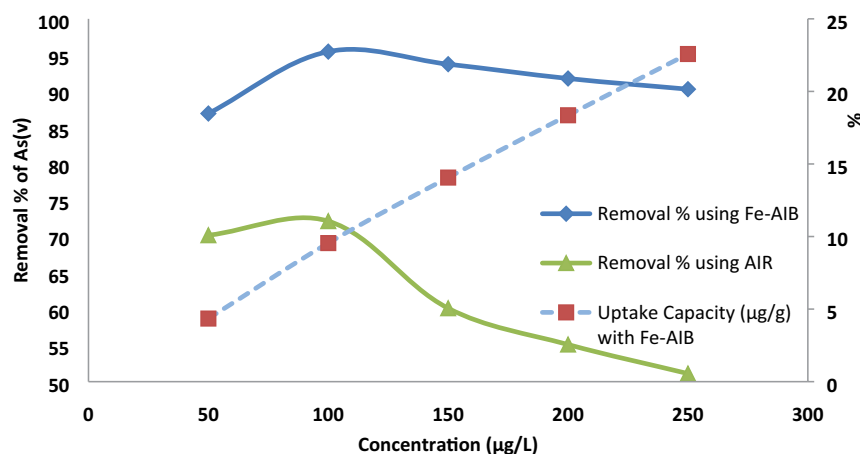


Fig. 5. Effect of initial arsenic concentration on adsorption of arsenate by Fe-AIR.

case of Fe-AIR, removal percentage increases from 90.30% at 250 µg/L to 95.48% at 100 µg/L. Though the adsorption capacity of AIR is comparatively low, the removal percentage increases from 51.11% at 250 µg/L to 72.11% at 100 µg/L, in the same pattern as that in the case of Fe-AIR. The same trend was observed earlier for the adsorption of As(V) with varying initial concentrations [43]. At low As(V) concentration, the adsorption capacity increases due to significant interaction of As(V) ions with the active binding sites and, decrement at high concentration can be attributed to less availability of highly energized binding sites onto the surface of adsorbents [44]. But the amount of Arsenate adsorbed per unit mass of Fe-AIR increases with increasing arsenate concentration in the test solution. This increment can be attributed to reduced solute uptake from solution with an increase in arsenate concentration [45].

3.2.2. Effect of pH on zeta potential and As(V) adsorption

The influence of pH on the As(V) adsorption at AIR and Fe-AIR surface was investigated with an initial As(V)

concentration of 100 µg/L. To each test solution, 1 g of AIR and Fe-AIR was added and equilibrated for 75 min, then after pH and As(V) uptake was recorded. Although adsorption capacity of AIR is very low, maximum As(V) adsorption (73%) onto AIR obtained at pH 4. The adsorption of arsenate is more prominent at acidic conditions. In the pH range of 2–10, anionic behavior is exhibited by As(V) and is replaced by AsO_4^{3-} , HAsO_4^{2-} and H_2AsO_4^- . Under acidic conditions, the surface is positively charged and the accompanying ions balance the positive charge. In this way, ion exchange can take place with anionic species that are already there in a test solution. [46]. It can be seen from Fig. 6 that maximum removal is achieved at pH 5.0–6.0. The isoelectric point (IEP) of Fe-AIR was observed at 6.3, below which Fe-AIR particles are positively charged. The optimum removal of 96.811% (17.7 µg/g) by the Fe-AIR was achieved at a pH of 6.0, which is very close to the IEP point. The following equation will give the surface reaction:



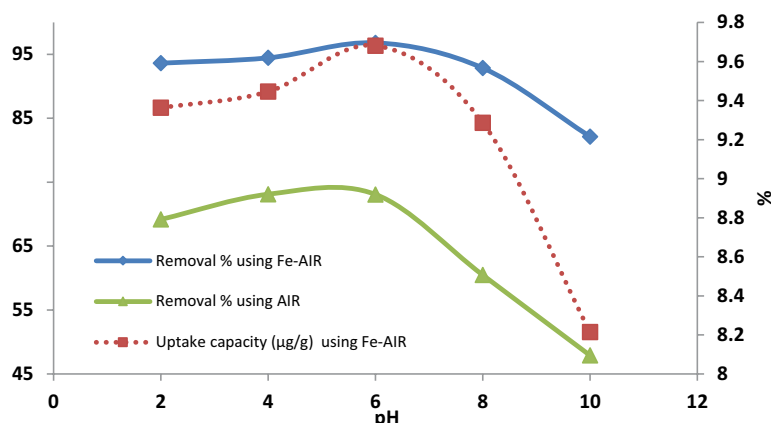


Fig. 6. pH effect on adsorption of As(V) by Fe-AIR.



It can be seen from Fig. 7 that the zeta potential values decrease with increasing pH. This can be attributed to decrement in negative charge on to the surface with increasing pH values. The decrease in negative charge species of As ($\text{H}_2\text{AsO}_4^{2-}$ and HAsO_4^-) is due to the dominance over the adsorption mechanism by electrostatic repulsive forces [47]. After adsorption of As(V) on Fe-AIR, the value of zeta potential decreases. The reason behind this decrement may be the adsorption process resulting from chemisorption and electrostatic attraction (due to inner and outer surface complexation). The final pH of the suspension was lower than the initial pH when the pHs values are greater than 6. This trend can be attributed to the liberation of H^+ ions by Fe-AIR and adsorption of OH^- ions on to the surface at high pHs [48].

There exists one more factor which depends on pH and influences the arsenate adsorption efficiency: pH_{pzc} (point of zero charge) of the adsorbent. The surface charges are more active in acidic conditions which result in a more positive surface charge of Fe-AIR, and hence the attraction towards arsenate is more. The charge on to the surface gets negative when the value of pH exceeds the point of zero charge value due to electrostatic effect (repulsive) and hence the

adsorption capacity of Fe-AIR towards arsenate reduces under basic conditions. The influence of pH on adsorption capacity reported at 5–6 pH values shows the maximum adsorption as these values are less than the point of zero charge (6.9).

3.2.3. Effect of adsorbent dose

The effect of the dose of AIR and Fe-AIR on adsorption of As(V) is illustrated in Fig. 8. The adsorption experiment carried out at an optimum pH of 6 and 100 µg/L initial As(V) concentration. The percentage removal of As(V) was increased from 19.725% to 95.88% as the dose of Fe-AIR increases from 0.25 to 1 g. likewise for AIR removal percentage increases from 23.42% to 67.6% for the same dosages. The increase in adsorption capacities of AIR and Fe-AIR may be due to an increase in surface area, which in turn provides a higher number of active adsorption sites [49]. But above a dose of 1.0 g, the removal of As(V) was negligible for both the adsorbents. This can be attributed to achieving maximum adsorption at a dose of 1.0 g, and hence even with further addition in adsorbent dose, the number of ions will remain unchanged. Similarly, 10 g/L of Fe loaded zeolites shows 98% As(V) removal for 100 µg/L of arsenate concentration [50]. Besides, percent removal

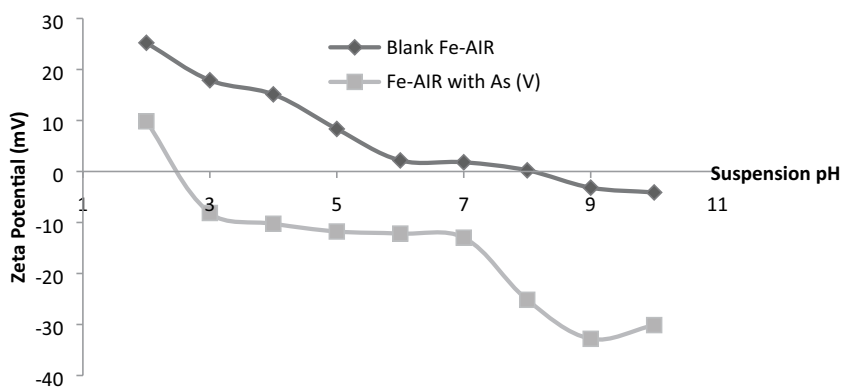


Fig. 7. Zeta-potential of Fe-AIR with and without As(V).

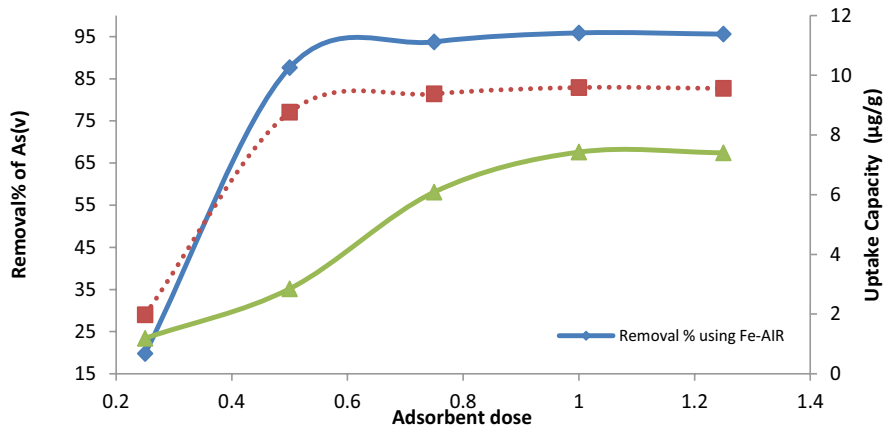


Fig. 8. Effect of dose on arsenate adsorption by Fe-AIR.

of As(V) increases from 20% to 92% using 25–500 mg/L Fe-zeolite [51]. Also, 1 g/L of Fe impregnated bamboo charcoal yields 89% arsenate removal under controlled experimental conditions [52]. More than 97% removal capacity using Fe-biomass carbon (1.5 g/L) was achieved for a test solution containing 10 mg/L of As(V) [53]. Therefore current study shows that a lesser amount of Fe-AIR brings down the As(V) concentration to the prescribed limits. The residual Fe concentrations were also measured after adsorption, and it was observed that at the optimum adsorbent dose the amount of Fe in spent Fe-AIR was 0.152 mg/L. The spent amount was under the maximum permissible limit of Fe (0.2 mg/L) in drinking water by WHO and Fe-AIR can be used as a safe and efficient adsorbent for arsenate removal.

3.2.4. Effect of contact time

The rate of adsorption of As(V) on AIR and Fe-AIR was studied in the time range of 15–75 min Fig. 9 adsorption of As(V) on Fe-AIR is quite rapid, with 94.747% removal of the initial amount within 30 min of operation, and attained equilibrium after approximately 60 min. This behavior is common for As(V) adsorption and has been reported earlier in the literature [40,54]. Larger concentration gradient and

availability of higher adsorption sites attribute to the quick adsorption in the initial stage [54]. After 30 min, no remarkable changes in adsorption capacity were found. Though, the time of contact of 75 min was chosen for maximum removal to take place for the sake of optimization of other process parameters. The adsorption capacity of Fe-AIR was 95.887% at equilibrium ($t = 60$ min).

3.2.5. Influence of the coexisting ions

The results of batch experiments were analyzed by taking As(V) alone as the adsorbate in the test solution. However, in actual practice, several other ions may also be present in contaminated water which can affect the adsorption of As(V) ions. The influence of the presence of other ions including PO_4^{3-} , SO_4^{2-} , SiO_3^{2-} and NO_3^- on the adsorption capacity of Fe-AIR was investigated in a representative test. The percentage removal of As(V) in the absence and presence of competing ions is given in Fig. 10. It was observed that the adsorption capacity of As(V) on Fe-AIR reduced by in the presence of phosphate (PO_4^{3-}) anions. Remarkable reduction in removal percentage was also observed in the presence of SO_4^{2-} anions. The high interference in As(V) adsorption in the presence of phosphates and silicates ions

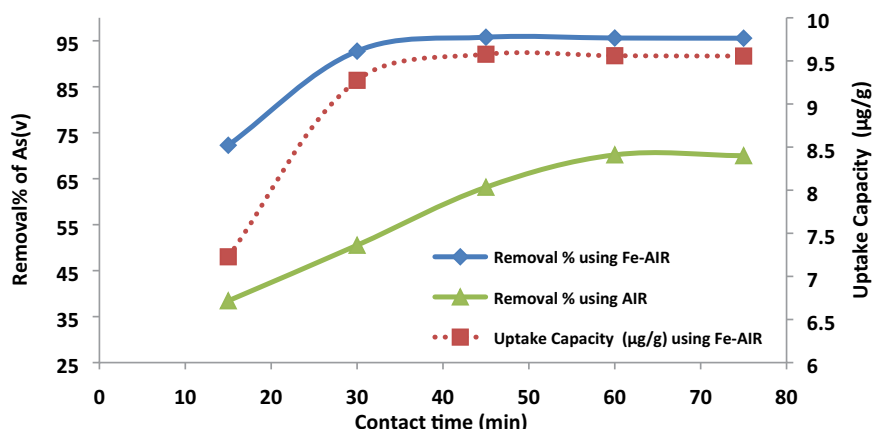


Fig. 9. Effect of contact time on adsorption of arsenate by Fe-AIR.

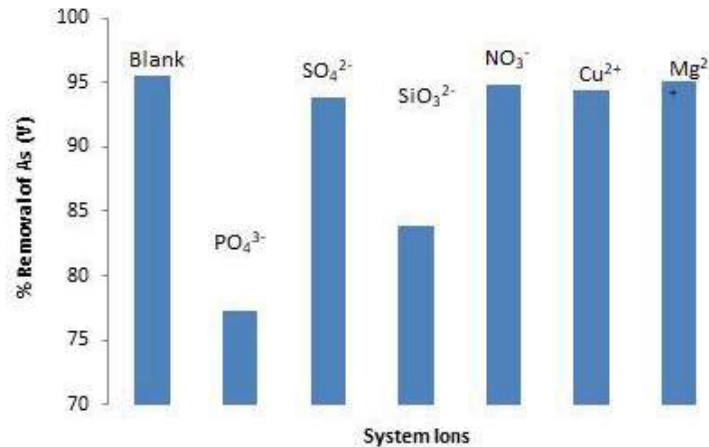


Fig. 10. Effect of co-existing ions on the adsorption of As(V). (Experiment conditions: initial As(V) concentration 100 µg/L; adsorbent dosage 1.0 g/L; solution pH 6.0; agitation speed 60 rpm).

may be attributed to the strong adsorption of these anions onto the Fe oxide surface due to inner core complexation. PO₄³⁻ and SiO₃²⁻ get adsorb by Iron oxide when Complex on the surface is formed with a surface R–OH group [55]. Also, it can be concluded that phosphates and silicates ions possess the same chemical properties as that of arsenate in aqueous solution. Similar results were reported earlier for the removal of As(V) in test solution using the same nature of adsorbents [56,57].

The presence SO₄²⁻ and NO₃⁻ anion does not possess a remarkable impact on the adsorption of As(V) ions. The adsorption of these anions can be due to outer and inner surface complexation. Moreover, their binding ability with oxides of metals is very less when compared to arsenate [58]. The presence of cations does not interfere with the adsorption of As(V).

3.3. Equilibrium adsorption isotherm study for batch process

Isotherm study gives the relationship between the adsorbent and adsorbate. In the current study Langmuir,

Freundlich, Dubinin–Radushkevich (D-R) and, Temkin isotherms equations were used to quantify the removal capacity of Fe-AIR for the adsorption of Arsenate. Langmuir, Freundlich, Temkin models are very significant for chemisorption although the Langmuir and Freundlich isotherm models are equally important for physisorption. Analysis of the physical adsorption of gases and vapors on porous adsorbent is done by D-R isotherm. The assumption of the Langmuir model is based on the fact that adsorbate molecules are bound as a monolayer on to specific sites of the adsorbent surface [59]. Multilayer and heterogeneous adsorption on the adsorbent surface is given by the empirical equation of the Freundlich model. This model takes the assumption that there is an uneven allocation of adsorption sites on the heterogeneous surface [43]. Temkin model gives a corrected adsorption theory involving adsorbate–adsorbent and adsorbate–adsorbate interactions. In the adsorption layer, with an increase in coverage, there is a decrement in the heat of adsorption of all molecules. By taking into account, all the reactions in adsorbate–adsorbent and adsorbate–adsorbate interactions, the adsorption theory was corrected [60]. D-R

Table 3
Isotherm data for sorption of arsenate by Fe-AIR

Adsorption isotherm	Equation	Parameters	Values	R ²
Langmuir isotherm	$\frac{1}{q_e} = \frac{1}{q_{\max} K_L C_e} + \frac{1}{q_{\max}}$	(5) q_{\max} (µg/g) K_L (L/µg)	29.82393 0.102678	0.9918
Freundlich isotherm	$\log q_e = \log K_F + \frac{1}{n} \log C_e$	(6) K_F (µg/g) $1/n$	2.5661 0.5086	0.9899
Temkin isotherm	$q_e = \frac{RT}{b_T} (\ln A_T + \ln C_e)$	(7) A_T (L/µg) b_T (J/mol)	0.720396 324.2599	0.9829
D-R isotherm	$\ln q_e = \ln q_{\max} - \frac{1}{2E^2} \left\{ RT \ln \left(1 + \frac{1}{C_e} \right) \right\}^2$	(8) q_{\max} (µg/g) E (J/mol)	20.05692 7.8991	0.8728

isotherm uses Gaussian energy distribution over a heterogeneous surface to express the mechanism of adsorption. D-R isotherm model is temperature dependent, which is a unique feature on its own [61].

Various correlation coefficients and constants of four adsorption isotherms are evaluated and shown in Table 3. It can be seen from the table, the correlation coefficient for the Langmuir ($R^2 = 0.9918$) model is highest among all four models which shows that the Langmuir model is most relevant to express the equilibrium adsorption of As(V) on Fe-AIR. The removal takes place as monolayer adsorption with homogenous energy levels. Since the separation factor (R_L) value is between 0 and 1, we can say that the adsorption process is favorable. The degree of heterogeneity is given by Freundlich constant (K_F) and another constant n . A graph between $\log(q_e)$ vs. $\log(C_e)$ yields the K_F and $1/n$ values. The value of $1/n$ is coming out to be 0.5086 ($1/n$ value lying between 0 and 1) which shows that adsorption is favorable [62]. Temkin isotherm analysis reveals that the value of heat of adsorption related Temkin constant (B) is 7.6232 which is less than the typical bonding energy range of ion exchange process. The low R^2 value for Temkin isotherm suggests that removal of As(V) by Fe-AIR does not closely follow the isotherm [63]. The E value calculated from the D-R isotherm model equation comes out to be smaller than the typical bonding energy range (8–16 kJ/g) for the process of ion exchange. Thus E value suggests that the adsorption process onto the surface of Fe-AIR may not be only ion exchange mechanism or chemisorption. Thus for adsorption of As(V) by Fe-AIR, pore filling can also be a feasible process [64].

3.4. Kinetic study

The adsorption mechanism, the description of ways of adsorbate molecule transfer and dependency of reaction rate on different variables were studied using kinetics of adsorption. In the present study, to investigate the adsorption mechanism on Fe-AIR at pH 7, 1 g adsorbent at a concentration of 100 $\mu\text{g/L}$ at 298 K temperature, the pseudo-first-order, pseudo-second-order and, intraparticle diffusion models were used. The assumption in the first-order model states that the solute withdrawal rate is proportional to the quantity of adsorbent withdrawal and contrast of concentration at saturation. The rate equation of pseudo-first-order is given by equation [65]:

$$\log\{(q_e) - (q_t)\} = \log\{q_e\} - \frac{k_1}{2.303}t \quad (9)$$

where the quantity of As(V) adsorbed after time t and at equilibrium ($\mu\text{g/g}$) is denoted by q_t and q_e respectively. k_1 is the rate constant for first-order model.

Pseudo-second-order kinetic model assumes that the adsorption process is controlled by chemical adsorption. The rate equation of the second-order model is given by equation [66]:

$$\frac{t}{(q_t)} = \frac{1}{(k_2)(q_e)^2} + \frac{t}{(q_e)} \quad (10)$$

where k_2 is the rate constant for the second-order model. q_t is the arsenate adsorbed after time t and q_e is the arsenate adsorbed on Fe-AIR at equilibrium.

The interphase diffusion plot gives the mechanism of the adsorption process. The Weber–Morris intraparticle model is given by equation [67]:

$$q_t = k_{pi}t^{0.5} + C \quad (11)$$

where q_t is arsenic adsorbed on Fe-AIR after time t , k_{pi} is the intraparticle diffusion rate constant, and constant C gives the thickness of the boundary layer.

Different kinetic model parameters are given in Table 4. The determination coefficient (R^2) will provide the goodness of fit in different models. Higher the value of R^2 , the better will be a description of the kinetics of As(V) adsorption by Fe-AIR. For the entire As(V) concentration range, the first-order model does not give a great fit to experimental data due to the lower determination coefficient. Moreover, adsorption capacity at equilibrium predicted by the first-order model was not in good agreement with the experimental values of q_e . Hence the pseudo-first-order kinetic model was not found suitable for the prediction of the sorption kinetics of As(V) on to Fe-AIR. According to the intraparticle diffusion model, the uptake plot ought to be linear if in the adsorption process, diffusion is twisted and the intraparticle diffusion model is rate-controlling step if the lines originate through the origin. Due to lower R^2 values, the intraparticle diffusion model failed to get fitted

Table 4
Kinetic parameters for adsorption of arsenate by Fe-AIR

Kinetic model	Equation	Parameters	Values	R^2
Pseudo-first-order	$\log\{(q_e) - (q_t)\} = \log\{q_e\} - \frac{k_1}{2.303}t$	q_e k_1	1.7155 0.001317	0.9017
Pseudo-second-order	$\frac{t}{(q_t)} = \frac{1}{(k_2)(q_e)^2} + \frac{t}{(q_e)}$	q_e k_2	10.2832 0.020992	0.9966
Intraparticle diffusion	$q_t = k_{pi}t^{0.5} + C$	k_{pi} C	1.214 5.081	0.8815

with kinetic data and suggests that the rate-controlling step was not intraparticle diffusion for the sorption of Arsenate on to Fe-AIR. Furthermore, the value of the determination coefficient of the pseudo-second-order model was reported as 0.996, which was much higher in comparison to the other models. Also, it was observed that the gap between the experimentally obtained adsorption capacity and the equilibrium adsorption capacity is very narrow for the various concentrations of arsenate which suggest that arsenate on to Fe-AIR follows pseudo-second-order kinetics.

3.5. Thermodynamic studies

Thermodynamics studies provide insight into the nature of the reaction (endothermic or exothermic), entropy, and enthalpy changes resulting from adsorption and change in Gibb's energy. Thermodynamic parameters including change in Gibbs free energy (ΔG°), change in enthalpy (ΔH°), and change in entropy (ΔS°) can be evaluated using equations provided in Table 5 [68]. The negative value of ΔG° reveals that the adsorption is feasible and spontaneous, maybe resulting from columbic attraction. Also, decrement in ΔG° values with increment in temperature propound that adsorption of As(V) on Fe-AIR is even more favorable at elevated temperatures. The positive value of ΔH° (5.33092×10^{-3}) reveals that the adsorption of As(V) on Fe-AIR is an endothermic process [69]. The degree of randomness of the system has been defined as entropy. A positive value of entropy change confers the structural changes that occurred on the surface of adsorbent during the adsorption process and randomness increases in the adsorption system at solid-liquid interphase [70].

3.6. Column operations results

3.6.1. Effect of bed height

The bed depth of the adsorbent in the column is a key parameter for adsorption as segregation of metal ions is dependent on the amount of adsorbent inside the column. The influence of bed depth on breakthrough was analyzed by carrying out adsorption experiments in bed height ranging from 3–9 cm, at optimum pH, constant influent Arsenate concentration (1,000 $\mu\text{g/L}$) and, flow rate (3.0 mL/min). Breakthrough curves for adsorption of As(V) on Fe-AIR are shown in Fig. 11. The effect of bed height can be evaluated from the shape of the breakthrough and time needed

to attain a breakthrough point. Larger bed heights result in the availability of more time for interaction of Fe-AIR with As(V), which in turn enhances the diffusion of As(V) ions into the Fe-AIR and adsorption capacity of Fe-AIR increases with increasing bed height [71]. Similar results showing the increment in exhaustion time with increasing bed height were reported earlier in literature [72,73].

3.6.2. Effect of flow rate

The flow rate is an important parameter that affects the adsorption process in a continuous flow column to a great extent. In the current study, the influence of flow rate on Arsenate adsorption by Fe-AIR was investigated by varying the flow rate from 3.0 to 9.0 mL/min and keeping the influent arsenate concentration (1,000 $\mu\text{g/L}$), bed height (9.0 cm) and pH constant. The breakthrough curve is shown in Fig. 12. It was observed that for higher flow rates, a quicker breakthrough was achieved. With decreasing flow rates, a significant increase in breakthrough time was noted. At a low inlet flow rate of As(V), time available for interaction with Fe-AIR was more which in turn results in increased removal of As(V) ions in the column. Fundamental of mass transfer demonstrates the variation in adsorption capacity and slope of the breakthrough curve. The explanation is that increased flow rate results in enhanced mass transfer rate and the amount of As(V) adsorbed onto mass transfer zone (unit bed height) increases, due to which faster saturation was achieved [74]. Less residence time of As(V) ions in column resulted in reduced adsorption capacities at an increased flow rate and solutes leave the column before the occurrence of equilibrium. These findings were in good agreement with results referred to the previous literature [75,76].

3.6.3. Effect of influent As(V) concentration

The influence of varying As(V) concentration ranging from 1,000–1,500 $\mu\text{g/L}$ with 9 cm of Fe-AIR bed height and influent As(V) flow rate of 3 mL/min is shown by the breakthrough curve in Fig. 13. As can be seen from fig, in the time interval of 400 min, the C_t/C_i values reach 0.50, 0.67 and 0.89 when influent concentration was 1,000; 1,250; and 1,500 $\mu\text{g/L}$ respectively. It is observed that with increasing influent As(V) concentration, the breakthrough time decreases. A slower and dispersed breakthrough

Table 5
Thermodynamic parameters for adsorption of arsenate by Fe-AIR

Thermodynamics parameters	Equation	Values	
		Temp. (K)	ΔG° (KJ/mol)
Standard Gibbs free energy	$\Delta G^\circ = -RT \ln K_c$	313	-1.79076
		(12) 318	-1.82576
		323	-1.85492
		328	-1.88409
Standard enthalpy change	$\log K_c = \frac{\Delta S^\circ}{2.303R} - \frac{\Delta H^\circ}{2.303RT}$	$\Delta H^\circ = 1.58007$	
Standard entropy change		(13) $\Delta S^\circ = 5.33092 \times 10^{-3}$	

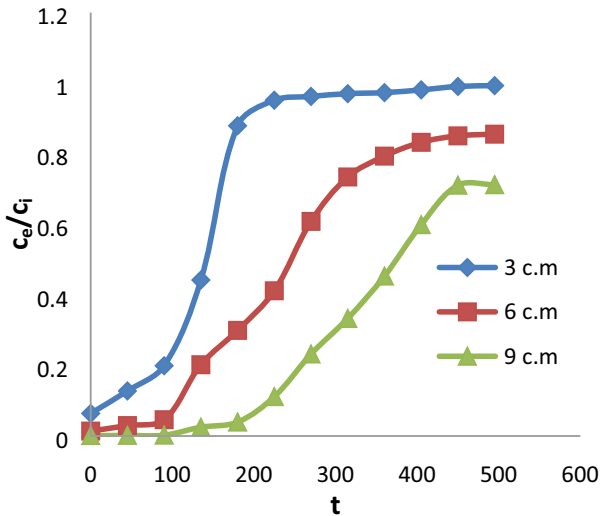


Fig. 11. The breakthrough curve for arsenate adsorption by Fe-AIR at different bed height.

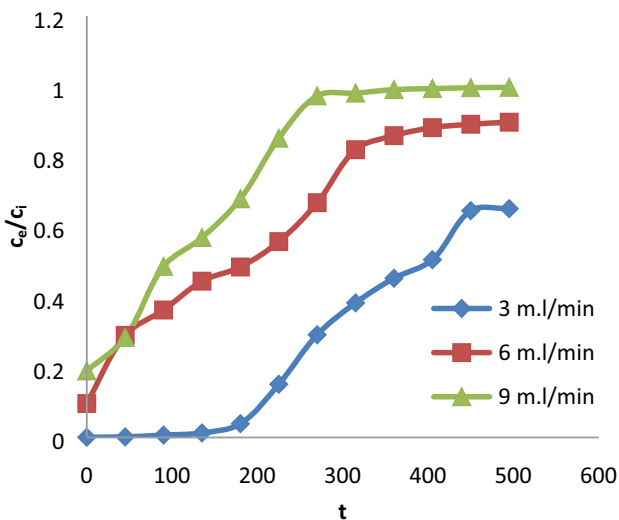


Fig. 12. The breakthrough curve for arsenate adsorption by Fe-AIR at different flow rates.

was analysed at lower concentration and sharper breakthrough curves were obtained at higher concentration. This can be attributed to slow transport of As(V) ions resulted from a decreased diffusion coefficient. The slope of the curve became steeper with increasing influent concentration. These findings show that the rate of saturation and breakthrough time was influenced by the variation of concentration gradient which means the process of diffusion is dependent on concentration. The loading rate of As(V) ions increases with increasing influent concentration along with the increase in driving force and the length of the adsorption zone decreases [77]. Similar behaviour was observed for As(V) removal by Fe-oxide based adsorbent [78], Arsenate adsorption on untreated dolomite powder [79]. With increasing influent concentration, the increase in adsorption capacity was expected due to enhanced driving

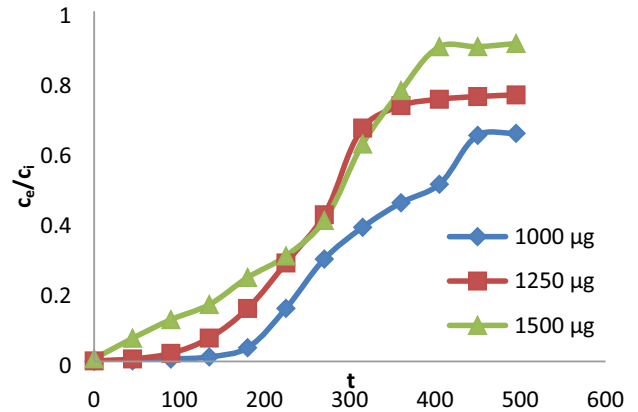


Fig. 13. The breakthrough curve for arsenate adsorption by Fe-AIR at different influent concentration.

force facilitated by a higher concentration difference for the adsorption process. The largest bed capacity of 90.02 µg/g was achieved using 1,000 µg/L influent As(V) concentration, 9 cm bed height, and 3 mL/min flow rate. The present result is in agreement with fixed bed adsorption operations which were reported earlier [80,81].

3.6.4. Effect of the column diameter

The effect of the column diameter (2 and 3 cm) at a fixed bed height of 9 cm, a flow rate of 3.0 mL/min, and normal pH is shown in Fig. 14. It was observed that maximum removal of 92.785% was achieved using a 3 cm diameter column having the same height and influent metal concentration like that of a 2 cm diameter column. This can be attributed to the fact that larger depth is achieved in the column having a larger diameter which in turn increases the interaction between the As(V) solution and the adsorbent permitting better adsorption of As(V) ion at available binding sites of Fe-AIR [82].

3.6.5. Thomas model application

One of the most extensively used and general models for packed column studies is the Thomas model. The assumptions used in the Thomas model are that axial dispersion is not there and it follows Langmuir adsorption kinetics, provided that the second-order kinetics is obeyed by rate deriving force. A constant separation factor is also assumed but applies to unfavorable or favorable isotherm. Thomas model also possesses some disadvantages like its derivation is based on second-order kinetics. Interphase mass transfer often controls adsorption and is not limited by chemical kinetics. Some errors may result from all these discrepancies while the adsorption process is being modeled using the Thomas model [83]. The model has the following linearized form:

$$\frac{C_t}{C_0} = \frac{1}{1 + \exp\left(K_{TH}q_0 \frac{m}{Q} - K_{TH}C_0t\right)} \quad (14)$$

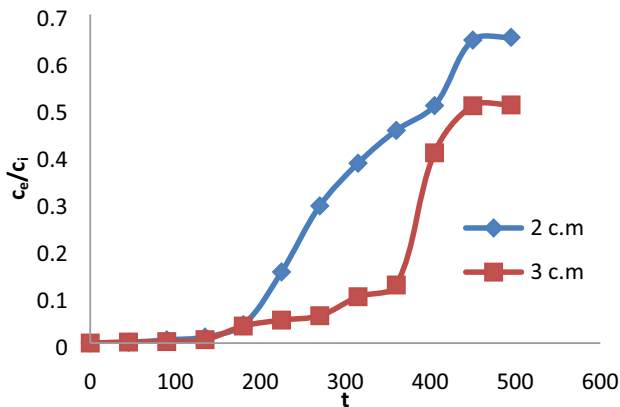


Fig. 14. The breakthrough curve for arsenic adsorption by Fe-AIR at different column diameters.

where C_0 and C_t are As(V) concentrations initially and after time t respectively, q_0 is As(V) uptake per gram ($\mu\text{g/g}$) of Fe-AIR at equilibrium, m is the mass of As(V) in grams, the flow rate is given by Q (mL/min) and K_{TH} is Thomas constant (L/ $\mu\text{g min}$). Table 6 shows the values of Thomas constants and As(V) uptake capacity at different bed heights, flow rates, influent arsenic concentration, and column diameters. It can be seen from the table that all the mentioned parameters affect Thomas constant and As(V) uptake capacity. The values of As(V) uptake capacity increase and Thomas constant (K_{TH}) reduces with increasing bed height. With increasing flow rates, the values of As(V) uptake capacity decreases and Thomas constant (K_{TH}) increases. Also, with increasing influent arsenic concentration, K_{TH} decreases and As(V) uptake capacity increases. Also with an increase in column diameter, both K_{TH} and q_0 values increases. The same trend has been reported earlier [84].

Table 6
Column operation modeling results onto Fe-AIR column

Process parameters		Thomas model results			Yoon–Nelson model results	
Bed height (cm)	q_{exp} ($\mu\text{g/g}$)	K_{TH} (mL/min μg)	q_0 ($\mu\text{g/g}$)	R^2	K_{YN}	τ
3	70.75	0.017	64.21	0.83	0.010	135.30
6	85.33	0.012	76.52	0.95	0.015	287.17
9	89.15	0.010	90.89	0.93	0.016	388.03
Flow rate (mL/min)						
3	89.1541	0.0067	90.8981	0.9339	0.0168	388.0347
6	84.0307	0.0084	81.2042	0.9468	0.0084	187.3247
9	76.2183	0.0104	63.2949	0.9521	0.0157	97.3405
Conc. in ($\mu\text{g/L}$)						
1,000	89.1541	0.0104	90.0222	0.9339	0.0133	388.0347
1,250	90.2231	0.0095	90.8981	0.9245	0.0153	332.2661
1,500	92.6643	0.0088	91.0536	0.9548	0.0168	280.0608
Column dia. (cm)						
2	89.1541	0.01045	90.8981	0.9339	0.0168	388.0347
3	93.3372	0.01605	97.4687	0.7455	0.0160	449.6885

3.6.6. Yoon–Nelson model application

Yoon–Nelson model does not concentrate on the nature of adsorbent, adsorbate properties, and any physical aspects of adsorption bed and it's a straightforward physical assumption. Yoon–Nelson model states that adsorption rate decrement is proportional to adsorption of adsorbate and adsorbent breakthrough [85]. The following expression is used:

$$\ln \frac{C_t}{C_0} = K_{\text{YN}} t - K_{\text{YN}} \tau \quad (15)$$

where K_{YN} is velocity constant and τ is the time needed for fifty percent adsorbate breakthrough. The values of τ and K_{YN} can be obtained from the intercept and slope of the linear graph of $\ln C_t/C_0$ and t . The table shows values of T and K_{YN} at various bed heights, flow rates, influent arsenic concentration, and column diameters. It can be concluded from Table 6 that with increasing influent arsenic concentration, the K_{YN} values increase. This may be attributed to the fact that with increment in initial concentration, vying for the binding sites among adsorbate molecules increases which results in enhanced uptake capacity of Fe-AIR. The values of K_{YN} increases with an increase in bed height and decrease with an increase in column diameter.

3.6.7. Regeneration and reuse of Fe-AIR

For a feasible adsorption process, it is important to have efficient regeneration and reuse of adsorption medium. To test the same, the 9 cm exhausted Fe-AIR media was regenerated using NaOH (10%). The recovery profile of arsenate through desorption is shown in Fig. 15. It can be concluded from the calculations that for 99% arsenate recovery, 12-bed volumes are sufficient. Almost 83.5% of adsorbed arsenate was eluted during the first two bed volumes and

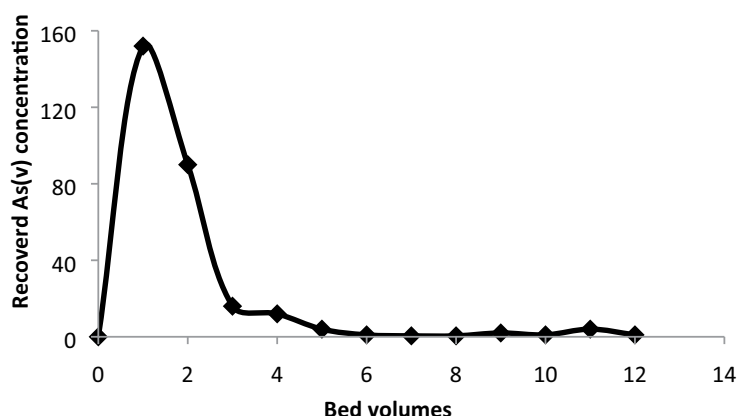


Fig. 15. Concentration profile of arsenate during regeneration.

the rest get removed in the next 10 bed volumes. From these findings, it can be concluded that the active sites of Fe-AIR particles are accessible through the pore network among the particles, which suggests that there occurs no clogging in pores.

After regeneration, excess NaOH was removed through the conditioning process where media was subjected to hot water, due to which the pH was decreased. The concentration of dissolved iron in the regenerant spent was reported as 0.02 mg/L, which is very low in comparison to the amount of iron present in the medium. So it was assumed that the total amount of Fe in the medium remains unaltered. Fig. 16 shows six adsorption cycles. It can be seen from the figure that appreciable decrement of 31.4% in the removal percentage was observed after 5 cycles. Hence it can be concluded from regeneration and reuse analysis that Fe-AIR proffers an inexpensive approach to the removal of arsenate from water.

3.6.8. Adsorption capacity comparison of different adsorbents from the literature for removal of As(V)

The adsorption potential of Fe-AIR needs to be compared with other adsorbents used for the purpose to justify

its validity. The value of q_{\max} at different operating conditions is listed in Table 7. It is not possible to compare the adsorption capacity of Fe-AIB and Fe-AIL directly with other adsorbents due to different operating conditions. However, the adsorbent used in the present study shows good adsorption capacity when compared with other adsorbents. The variation in adsorption capacity for different adsorbents are due to difference in individual properties (functional group, surface structure, available surface area) of adsorbents

4. Conclusion

A methodology of Fe impregnation was applied to synthesize a porous cost-effective arsenate adsorbent (Fe-AIR) from the *Azadirachta indica* roots carbon. The adsorption capacity and efficiency of Fe-AIR for remediation of arsenate from contaminated waters were investigated. Batch operations were conducted under various operating conditions to analyze the adsorption capacity of Fe-AIR. The maximum removal of arsenate species on Fe-AIR from arsenate spiked deionized water is reported to be 96.811%. Analysis of the effect of competing ions reveals that the presence of phosphate and sulfate anions reduces the adsorption capacity whereas the presence of cations does not affect the

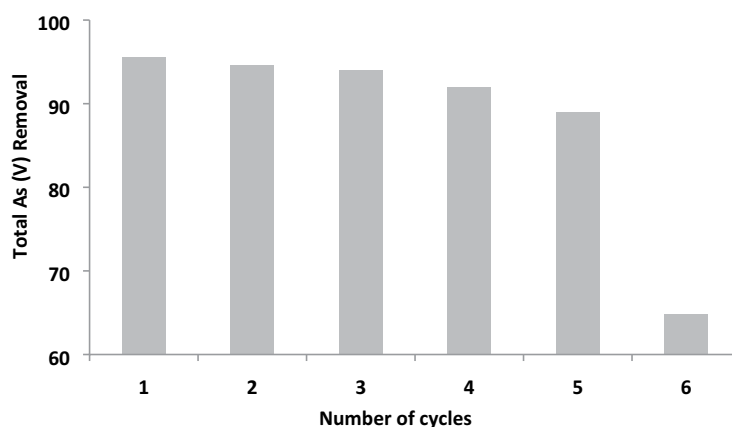


Fig. 16. Variation in percentage removal of As(V) by repetitive use of Fe-AIR.

Table 7
Comparison of adsorption capacity of various adsorbent adsorbents used for As(V) remediation

Adsorbent	Conditions	q_{\max} (mg/g)	Reference
Green marine algal-based biochar	pH 4.0; flow rate 5 mL/min; dose 12.66 g	7.67	[86]
Lamdong laterite soil	pH 3.0; flow rate 11.2 mL/min; bed depth 2.7 cm	0.47	[87]
Activated alumina impregnated by Fe oxide	pH 12.0; flow rate 16 mL/min; bed depth 6 cm	0.46	[88]
Biopolymer chitosan sorbent	pH 7.0; flow rate 8 mL/min; bed depth 8 cm	1.90	[89]
Fe-oxide coated cement	pH 6.0; flow rate 1.35 mL/min; bed depth 10 cm; influent concentration 2.7 mg/L	2.3	[90]
Waste of rice husk	pH 5.0–6.0; flow rate 6.7 mL/min; bed depth 5 cm; influent concentration 0.1 mg/L	0.007	[32]
Iron-zein beads	pH 6.0; flow rate 4 mL/min; bed depth 3 cm; influent concentration 0.5–100 mg/L	1.95	[91]
Composite of Fe oxides and carbon with eucalyptus wood	pH 3.0; flow rate 5.136 mL/min; dose 2 g; influent concentration 20 mg/L	10.49	[92]
Poly LDHs	pH 8.0; flow rate 7 mL/min; initial concentration 50 mg/L	1.73	[93]
Iron impregnated <i>Azadirachta indica</i> roots carbon (Fe-AIR)	pH 6.0; flow rate 3.0 mL/min; bed depth 3 cm; influent concentration 1 mg/L	0.093	Present study

adsorption process. The batch process was evaluated by various isotherms and kinetic models. Langmuir isotherm best fits the batch operation data. From the results of adsorption kinetics, it can be seen that the second-order kinetics controls the adsorption. The exothermic nature of adsorption was observed. Spontaneous adsorption on Fe-AIR was indicated from negative values of ΔG° . To analyze the practical applicability of Fe-AIR in the removal of Arsenate species, column operations were employed. The experimental data of column operations fits well with Thomas model and Yoon–Nelson model for arsenic influent concentration ranging from 1,000–1,500 ppb at a flow rate of 3 mL/min. Following adsorption, about 99% of Fe-AIR fixed bed was regenerated effectively with 10% sodium hydroxide within 12-bed volumes. Not much depression in efficiency is reported in the first five cycles, which makes Fe-AIR responsive to reuse and regeneration and thus cost-effective in use. Through arsenic incorporation in Portland cement, arsenic solidification is possible so there will not be an issue of secondary pollution. Moreover, the developed fixed column treatment process is easy to handle, reproducible, rapid, and economic so it is a suitable and appropriate approach for arsenic remediation in local areas.

Acknowledgment

The authors would like to thank Post Graduation Research Lab, IIT Kanpur for providing assistance with SEM, XRD, BET, and FTIR analysis.

References

- [1] M. Kobya, R.D.C. Soltani, P.I. Omwene, A. Khataee, A review on decontamination of arsenic-contaminated water by electrocoagulation: reactor configurations and operating cost along with removal mechanisms, *Environ. Technol. Innovation*, 17 (2020) 100519.
- [2] S. Alka, S. Shahir, N. Ibrahim, T.-T. Chai, Z. Mohd Bahari, F. Abd Manan, The role of plant growth promoting bacteria on arsenic removal: a review of existing perspectives, *Environ. Technol. Innovation*, 17 (2020) 100602.
- [3] P. Kumarathilaka, S. Seneweera, Y.S. Ok, A.A. Meharg, J. Bundschuh, Mitigation of arsenic accumulation in rice: an agronomical, physico-chemical, and biological approach – a critical review, *Crit. Rev. Environ. Sci.*, 50 (2020) 31–71.
- [4] S.K. Gupta, K.Y. Chen, Arsenic removal by adsorption, *Water Pollut. Control Fed.*, 50 (1978) 493–506.
- [5] A. Maiti, S. DasGupta, J.K. Basu, S. De, Batch and column study: adsorption of arsenate using untreated laterite as adsorbent, *Ind. Eng. Chem. Res.*, 47 (2008) 1620–1629.
- [6] F. Fu, Q. Wang, Removal of heavy metal ions from wastewaters: a review, *J. Environ. Manage.*, 92 (2011) 407–418.
- [7] M.E. Argun, S. Dursun, C. Ozdemir, M. Karatas, Heavy metal adsorption by modified oak sawdust: thermodynamics and kinetics, *J. Hazard. Mater.*, 141 (2007) 77–85.
- [8] A. Demirbas, Heavy metal adsorption onto agro-based waste materials: a review, *J. Hazard. Mater.*, 157 (2008) 220–229.
- [9] D. Sud, G. Mahajan, M.P. Kaur, Agricultural waste material as potential adsorbent for sequestering heavy metal ions from aqueous solutions—a review, *Bioresour. Technol.*, 99 (2008) 6017–6027.
- [10] S.E. Bailey, T.J. Olin, R.M. Bricka, D.D. Adrian, A review of potentially low-cost sorbents for heavy metals, *Water Res.*, 33 (1999) 2469–2479.
- [11] D. Gnanasangeetha, D. SaralaThambavani, Modelling of As³⁺ adsorption from aqueous solution using *Azadirachta indica* by artificial neural network, *Desal. Water Treat.*, 56 (2015) 1839–1854.
- [12] T.R. Choudhury, M. Amin, S. Quraishi, A. Mustafa, Arsenic(III) removal from real-life groundwater by adsorption on Neem Bark (*Azadirachta indica*), *Int. Res. J. Pure Appl. Chem.*, (2014) 594–604.
- [13] P. Roy, U. Dey, S. Chattoraj, D. Mukhopadhyay, N.K. Mondal, Modeling of the adsorptive removal of arsenic(III) using plant biomass: a bioremedial approach, *Appl. Water Sci.*, 7 (2017) 1307–1321.
- [14] A. Bhattacharya, S. Mandal, S. Das, Adsorption of Zn(II) from aqueous solution by using different adsorbents, *Chem. Eng. J.*, 123 (2006) 43–51.
- [15] D. Tiwari, S.P. Mishra, M. Mishra, R. Dubey, Biosorptive behavior of Mango (*Mangifera indica*) and Neem (*Azadirachta*

- indica*) bark for Hg²⁺, Cr³⁺, and Cd²⁺ toxic ions from aqueous solutions: a radiotracer study, *Appl. Radiat. Isot.*, 50 (1999) 631–642.
- [16] A. Bhattacharya, T. Naiya, S. Mandal, S. Das, Adsorption, kinetics and equilibrium studies on removal of Cr(VI) from aqueous solutions using different low-cost adsorbents, *Chem. Eng. J.*, 137 (2008) 529–541.
- [17] R. Srivastava, D.C. Rupainwar, A comparative evaluation for adsorption of dye on Neem bark and Mango bark powder, *Indian J. Chem. Technol.*, 18 (2011) 67–75.
- [18] S.W. Al Rmalli, C.F. Harrington, M. Ayub, P.I. Haris, A biomaterial based approach for arsenic removal from water, *J. Environ. Monit.*, 7 (2005) 279–282.
- [19] S. Zhu, J. Zhao, N. Zhao, X. Yang, C. Chen, J. Shang, Goethite modified biochar as a multifunctional amendment for cationic Cd(II), anionic As(III), roxarsone, and phosphorus in soil and water, *J. Cleaner Prod.*, 247 (2020) 119579.
- [20] H. Lyu, J. Tang, M. Cui, B. Gao, B. Shen, Biochar/iron (BC/Fe) composites for soil and groundwater remediation: synthesis, applications, and mechanisms, *Chemosphere*, 246 (2020) 125609.
- [21] S. Ali, M. Rizwan, M.B. Shakoor, A. Jilani, R. Anjum, High sorption efficiency for As(III) and As(V) from aqueous solutions using novel almond shell biochar, *Chemosphere*, 243 (2020) 125330.
- [22] T. Chen, X. Quan, Z. Ji, X. Li, Y. Pei, Synthesis and characterization of a novel magnetic calcium-rich nanocomposite and its remediation behavior for As(III) and Pb(II) co-contamination in aqueous systems, *Sci. Total Environ.*, 706 (2020) 135122.
- [23] J. Cui, Q. Jin, Y. Li, F. Li, Oxidation and removal of As(III) from soil using novel magnetic nanocomposite derived from biomass waste, *Environ. Sci. Nano*, 6 (2019) 478–488.
- [24] L. Verma, M.A. Siddique, J. Singh, R.N. Bharagava, As(III) and As(V) removal by using iron impregnated biosorbents derived from waste biomass of *Citrus limmeta* (peel and pulp) from the aqueous solution and ground water, *J. Environ. Manage.*, 250 (2019) 109452.
- [25] H. Zeng, Y. Yu, F. Wang, J. Zhang, D. Li, Arsenic(V) removal by granular adsorbents made from water treatment residuals materials and chitosan, *Colloids Surf., A*, 585 (2020) 124036.
- [26] M.K. Mondal, R. Garg, A comprehensive review on removal of arsenic using activated carbon prepared from easily available waste materials, *Environ. Sci. Pollut. Res.*, 24 (2017) 13295–13306.
- [27] I. Shah, R. Adnan, W.S. Wan Ngah, N. Mohamed, Iron impregnated activated carbon as an efficient adsorbent for the removal of Methylene blue: regeneration and kinetics studies, *PLoS One*, 10 (2015) e0122603.
- [28] Y. Sudaryanto, T. Deitiana, W. Irawaty, H. Hindarso, S. Ismadji, High surface area activated carbon prepared from cassava peel by chemical activation, *Bioresour. Technol.*, 97 (2006) 734–739.
- [29] S. Rahdar, M. Taghavi, R. Khaksefidi, S. Ahmadi, Adsorption of arsenic(V) from aqueous solution using modified saxaul ash: isotherm and thermodynamic study, *Appl. Water Sci.*, 9 (2019) 87.
- [30] Gh. Ghanizadeh, M.H. Ehrampoush, M.T. Ghaneian, Application of iron impregnated activated carbon for removal of arsenic from water, Iran. *J. Environ. Health Sci. Eng.*, (ISSN: p-ISSN: 1735–1979), 7 (2010) 145–156.
- [31] Q. Chang, W. Lin, W.-c. Ying, Preparation of iron-impregnated granular activated carbon for arsenic removal from drinking water, *J. Hazard. Mater.*, 184 (2010) 515–522.
- [32] M.N. Amin, S. Kaneco, T. Kitagawa, A. Begum, H. Katsumata, T. Suzuki, K. Ohta, Removal of arsenic in aqueous solutions by adsorption onto waste rice husk, *Ind. Eng. Chem. Res.*, 45 (2006) 8105–8110.
- [33] B.M. Lekić, D.D. Marković, V.N. Rajaković-Ognjanović, A.R. Dukić, L.V. Rajaković, Arsenic removal from water using industrial by-products, *J. Chem.*, 2013 (2013) 9.
- [34] M.A. Alam, W.A. Shaikh, M.O. Alam, T. Bhattacharya, S. Chakraborty, B. Show, I. Saha, Adsorption of As(III) and As(V) from aqueous solution by modified *Cassia fistula* (golden shower) biochar, *Appl. Water Sci.*, 8 (2018) 198.
- [35] M.L. Paul, J. Samuel, N. Chandrasekaran, A. Mukherjee, Comparative kinetics, equilibrium, thermodynamic and mechanistic studies on biosorption of hexavalent chromium by live and heat killed biomass of *Acinetobacter junii* VITSUKMW2, an indigenous chromite mine isolate, *Chem. Eng. J.*, 187 (2012) 104–113.
- [36] S. Nethaji, A. Sivasamy, A.B. Mandal, Preparation and characterization of corn cob activated carbon coated with nano-sized magnetite particles for the removal of Cr(VI), *Bioresour. Technol.*, 134 (2013) 94–100.
- [37] M. Dinesh, S. Ankur, V.K. Singh, M. Alexandre-Franco, C.U. Pittman Jr., Development of magnetic activated carbon from almond shells for trinitrophenol removal from water, *Chem. Eng. J.*, 172 (2011) 1111–1125.
- [38] T. Depci, Comparison of activated carbon and iron impregnated activated carbon derived from Gölbaşı lignite to remove cyanide from water, *Chem. Eng. J.*, 181 (2012) 467–478.
- [39] L.G. Sorokhaibam, V.M. Bhandari, M.S. Salvi, S. Jain, S.D. Hadawale, V.V. Ranade, Development of newer adsorbents: activated carbons derived from carbonized *Cassia fistula*, *Ind. Eng. Chem. Res.*, 54 (2015) 11844–11857.
- [40] D.D. Gang, B. Deng, L. Lin, As(III) removal using an iron-impregnated chitosan sorbent, *J. Hazard. Mater.*, 182 (2010) 156–161.
- [41] B. Sunkara, J. Zhan, I. Kolesnichenko, Y. Wang, J. He, J.E. Holland, G.L. McPherson, V.T. John, Modifying metal nanoparticle placement on carbon supports using an aerosol-based process, with application to the environmental remediation of chlorinated hydrocarbons, *Langmuir*, 27 (2011) 7854–7859.
- [42] M. Descostes, F. Mercier, N. Thromat, C. Beaucaire, M. Gautier-Soyer, Use of XPS in the determination of chemical environment and oxidation state of iron and sulfur samples: constitution of a data basis in binding energies for Fe and S reference compounds and applications to the evidence of surface species of an oxidized pyrite in a carbonate medium, *Appl. Water Sci.*, 165 (2000) 288–302.
- [43] M.B. Baskan, A. Pala, Batch and fixed-bed column studies of arsenic adsorption on the natural and modified clinoptilolite, *Water Air Soil Pollut.*, 225 (2014) 1798.
- [44] P. Chutia, S. Kato, T. Kojima, S. Satokawa, Arsenic adsorption from aqueous solution on synthetic zeolites, *J. Hazard. Mater.*, 162 (2009) 440–447.
- [45] H. Nollet, M. Roels, P. Lutgen, P. Van der Meer, W. Verstraete, Removal of PCBs from wastewater using fly ash, *Chemosphere*, 53 (2003) 655–665.
- [46] R. Ansari, M. Sadegh, Application of activated carbon for removal of arsenic ions from aqueous solutions, *E-J. Chem.*, 4 (2007) 103–108.
- [47] L.H. Velazquez-Jimenez, J.A. Arcibar-Orozco, J.R. Rangel-Mendez, Overview of As(V) adsorption on Zr-functionalized activated carbon for aqueous streams remediation, *J. Environ. Manage.*, 212 (2018) 121–130.
- [48] N.D.G. Chau, Z. Sebesvari, W. Amelung, F.G. Renaud, Pesticide pollution of multiple drinking water sources in the Mekong Delta, Vietnam: evidence from two provinces, *Environ. Sci. Pollut. Res.*, 22 (2015) 9042–9058.
- [49] Y. Li, F.S. Zhang, F.R. Xiu, Arsenic(V) removal from aqueous system using adsorbent developed from a high iron-containing fly ash, *Sci. Total Environ.*, 407 (2009) 5780–5786.
- [50] M. Macedo-Miranda, M. Olguin, Arsenic sorption by modified clinoptilolite-heulandite rich tuffs, *J. Inclusion Phenom. Macroscopic Chem.*, 59 (2007) 131–142.
- [51] C.-S. Jeon, K. Baek, J.-K. Park, Y.-K. Oh, S.-D. Lee, Adsorption characteristics of As(V) on iron-coated zeolite, *J. Hazard. Mater.*, 163 (2009) 804–808.
- [52] X. Liu, H. Ao, X. Xiong, J. Xiao, J. Liu, Arsenic removal from water by iron-modified bamboo charcoal, *Water Air Soil Pollut.*, 223 (2012) 1033–1044.
- [53] H.L. Rahman, H. Erdem, M. Sahin, M. Erdem, Iron-incorporated activated carbon synthesis from biomass mixture for enhanced arsenic adsorption, *Water Air Soil Pollut.*, 231 (2020) 6.

- [54] T.G. Asere, S. Mincke, J. De Clercq, K. Verbeke, D.A. Tessema, F. Fufa, C.V. Stevens, G. Du Laing, Removal of arsenic(V) from aqueous solutions using chitosan–red scoria and chitosan–pumice blends, *Int. J. Environ. Res. Public Health*, 14 (2017) 895.
- [55] S. Goldberg, Chemical modeling of anion competition on goethite using the constant capacitance model, *Soil Sci. Soc. Am. J.*, 49 (1985) 851–856.
- [56] M. Mkandawire, Y.V. Lyubun, P.V. Kosterin, E.G. Dudel, Toxicity of arsenic species to *Lemma gibba* L. and the influence of phosphate on arsenic bioavailability, *Environ. Toxicol.*, 19 (2004) 26–34.
- [57] M.A. Rahman, H. Hasegawa, K. Ueda, T. Maki, M.M. Rahman, Arsenic uptake by aquatic macrophyte *Spirodela polyrhiza* L.: interactions with phosphate and iron, *J. Hazard. Mater.*, 160 (2008) 356–361.
- [58] X. Meng, S. Bang, G.P. Korfiatis, Effects of silicate, sulfate, and carbonate on arsenic removal by ferric chloride, *Water Res.*, 34 (2000) 1255–1261.
- [59] S. Ahmadi, C.A. Igwegbe, Adsorptive removal of phenol and aniline by modified bentonite: adsorption isotherm and kinetics study, *Appl. Water Sci.*, 8 (2018) 170.
- [60] S. Ahmadi, A. Banach, F.K. Mostafapour, D. Balarak, Study survey of cupric oxide nanoparticles in removal efficiency of ciprofloxacin antibiotic from aqueous solution: adsorption isotherm study, *Desal. Water Treat.*, 89 (2017) 297–303.
- [61] A.O. Dada, A.P. Olalekan, A.M. Olatunya, O. Dada, Langmuir, Freundlich, Temkin and Dubinin–Radushkevich isotherms studies of equilibrium sorption of Zn²⁺ unto phosphoric acid modified rice husk, *IOSR J. Appl. Chem.*, 3 (2012) 38–45.
- [62] N.K. Mondal, R. Bhaumik, T. Baur, B. Das, P. Roy, J.K. Datta, Studies on defluoridation of water by tea ash: an unconventional biosorbent, *Chem. Sci. Trans.*, 1 (2012) 239–256.
- [63] M. Chiban, G. Carja, G. Lehutu, F. Sinan, Equilibrium and thermodynamic studies for the removal of As(V) ions from aqueous solution using dried plants as adsorbents, *Arabian J. Chem.*, 9 (2016) S988–S999.
- [64] P.S. Blanes, M.E. Bordoni, J.C. González, S.I. García, A.M. Atria, L.F. Sala, S.E. Bellú, Application of soy hull biomass in removal of Cr(VI) from contaminated waters: kinetic, thermodynamic and continuous sorption studies, *J. Environ. Chem. Eng.*, 4 (2016) 516–526.
- [65] S.S. Bagali, B.S. Gowrishankar, A.S. Roy, Optimization, kinetics, and equilibrium studies on the removal of lead(II) from an aqueous solution using banana pseudostem as an adsorbent, *Engineering*, 3 (2017) 409–415.
- [66] S. Ghorai, K. Pant, Equilibrium, kinetics and breakthrough studies for adsorption of fluoride on activated alumina, *Sep. Purif. Technol.*, 42 (2005) 265–271.
- [67] L. Liu, S. Fan, Y. Li, Removal Behavior of Methylene blue from aqueous solution by tea waste: kinetics, isotherms and mechanism, *Int. J. Environ. Res. Public Health*, 15 (2018) 1321.
- [68] T. Sumathi, G. Alagumuthu, Adsorption studies for arsenic removal using activated *Moringa oleifera*, *Int. J. Chem. Eng.*, 2014 (2014) 6.
- [69] E. Bazrafshan, F. Kord Mostafapour, S. Rahdar, A.H. Mahvi, Equilibrium and thermodynamics studies for decolorization of Reactive black 5 (RB5) by adsorption onto MWCNTs, *Desal. Water Treat.*, 54 (2015) 2241–2251.
- [70] V.K. Gupta, Equilibrium uptake, sorption dynamics, process development, and column operations for the removal of copper and nickel from aqueous solution and wastewater using activated slag, a low-cost adsorbent, *Ind. Eng. Chem. Res.*, 37 (1998) 192–202.
- [71] N. Teutscherova, J. Houška, M. Navas, A. Masaguer, M. Benito, E. Vazquez, Leaching of ammonium and nitrate from acrisol and calcsol amended with holm oak biochar: a column study, *Geoderma*, 323 (2018) 136–145.
- [72] P. Singh, S.K. Singh, J. Bajpai, A.K. Bajpai, R.B. Shrivastava, Iron crosslinked alginate as novel nanosorbents for removal of arsenic ions and bacteriological contamination from water, *J. Mater. Res. Technol.*, 3 (2014) 195–202.
- [73] K. Vijayaraghavan, J. Jegan, K. Palanivelu, M. Velan, Batch and column removal of copper from aqueous solution using a brown marine alga *Turbinaria ornata*, *Chem. Eng. J.*, 106 (2005) 177–184.
- [74] P.V. Nidheesh, R. Gandhimathi, S.T. Ramesh, T.S.A. Singh, Adsorption and desorption characteristics of crystal violet in bottom ash column, *J. Urban Environ. Eng.*, 6 (2012) 18–29.
- [75] A. Ahmad, B. Hameed, Fixed-bed adsorption of reactive azo dye onto granular activated carbon prepared from waste, *J. Hazard. Mater.*, 175 (2010) 298–303.
- [76] S. Ghorai, K. Pant, Investigations on the column performance of fluoride adsorption by activated alumina in a fixed-bed, *Chem. Eng. J.*, 98 (2004) 165–173.
- [77] J. Goel, K. Kadirvelu, C. Rajagopal, V.K. Garg, Removal of lead(II) by adsorption using treated granular activated carbon: batch and column studies, *J. Hazard. Mater.*, 125 (2005) 211–220.
- [78] H. Zeng, M. Arashiro, D.E. Giammar, Effects of water chemistry and flow rate on arsenate removal by adsorption to an iron oxide-based sorbent, *Water Res.*, 42 (2008) 4629–4636.
- [79] G. Ayoub, M. Mehawej, Adsorption of arsenate on untreated dolomite powder, *J. Hazard. Mater.*, 148 (2007) 259–266.
- [80] T. Padmesh, K. Vijayaraghavan, G. Sekaran, M. Velan, Biosorption of Acid blue 15 using fresh water macroalga *Azolla filiculoides*: batch and column studies, *Dyes Pigm.*, 71 (2006) 77–82.
- [81] I. Tan, A. Ahmad, B. Hameed, Adsorption of basic dye using activated carbon prepared from oil palm shell: batch and fixed bed studies, *Desalination*, 225 (2008) 13–28.
- [82] Z. Asif, Z. Chen, Removal of arsenic from drinking water using rice husk, *Appl. Water Sci.*, 7 (2017) 1449–1458.
- [83] Z. Aksu, F. Gönen, Biosorption of phenol by immobilized activated sludge in a continuous packed bed: prediction of breakthrough curves, *Process Biochem.*, 39 (2004) 599–613.
- [84] T. Padmesh, K. Vijayaraghavan, G. Sekaran, M. Velan, Batch and column studies on biosorption of acid dyes on fresh water macro alga *Azolla filiculoides*, *J. Hazard. Mater.*, 125 (2005) 121–129.
- [85] H. Patel, Fixed-bed column adsorption study: a comprehensive review, *Appl. Water Sci.*, 9 (2019) 45.
- [86] R. Senthilkumar, D. Reddy Prasad, L. Govindarajan, K. Saravanakumar, B. Naveen Prasad, Synthesis of green marine algal-based biochar for remediation of arsenic(V) from contaminated waters in batch and column mode of operation, *Int. J. Phytorem.*, 22 (2020) 279–286.
- [87] P.T.T. Nguyen, Y. Sanou, S. Pare, H.M. Bui, Removal of arsenic from groundwater using Lamdong laterite as a natural adsorbent, *Pol. J. Environ. Stud.*, 29 (2020) 1305–1314.
- [88] M.N. Haque, G. Morrison, G. Ferrusquia, M. Gutierrez, A. Aguilera, I. Cano-Aguilera, J. Gardea-Torresdey, Characteristics of arsenic adsorption to sorghum biomass, *J. Hazard. Mater.*, 145 (2007) 30–35.
- [89] C.-C. Chen, Y.-C. Chung, Arsenic removal using a biopolymer chitosan sorbent, *J. Environ. Sci. Health, Part A*, 41 (2006) 645–658.
- [90] S. Kundu, A. Gupta, As(III) removal from aqueous medium in fixed bed using iron oxide-coated cement (IOCC): experimental and modeling studies, *Chem. Eng. J.*, 129 (2007) 123–131.
- [91] S. Thanawatpooantawee, A. Imyim, N. Praphairaksit, Iron-loaded zein beads as a biocompatible adsorbent for arsenic(V) removal, *J. Ind. Eng. Chem.*, 43 (2016) 127–132.
- [92] Y. Li, Y. Zhu, Z. Zhu, X. Zhang, D. Wang, L. Xie, Fixed-bed column adsorption of arsenic(V) by porous composite of magnetite/hematite/carbon with eucalyptus wood microstructure, *J. Environ. Eng. Landscape Manage.*, 26 (2018) 38–56.
- [93] H.N. Nhat Ha, N.T. Kim Phuong, T. Boi An, N.T. Mai Tho, T. Ngoc Thang, B. Quang Minh, C. Van Du, Arsenate removal by layered double hydroxides embedded into spherical polymer beads: batch and column studies, *J. Environ. Sci. Health, Part A Toxic/Hazard. Subst. Environ. Eng.*, 51 (2016) 403–413.



Kinetic equilibrium and thermodynamic analyses of As (V) removal from aqueous solution using iron-impregnated *Azadirachta indica* carbon

Ghazi Mohd Sawood¹ · S. K. Gupta¹

Received: 28 January 2020 / Accepted: 28 April 2020
© The Author(s) 2020

Abstract

Arsenic emerges out as a potential threat to human health and vegetation in recent past. Therefore, the present study aimed at adsorption of As (V) from the aqueous solution using Fe-AIB and Fe-AIL (iron-impregnated activated carbon synthesized from the powder of bark and leaves of *Azadirachta indica* tree). The removal of As (V) by Fe-AIB and Fe-AIL was examined under different experimental conditions. The Fe-AIB showed up to 96% As (V) removal at pH of 6.0, and up to 90% removal was observed with Fe-AIL at pH 4.0. Although the kinetic data fit best in the pseudo-second-order model, there are various other processes like intraparticle diffusion, pore diffusion and film diffusion that controls the overall rate. Mechanistic frameworks related to the adsorption process were analysed using various isotherm models. Langmuir and Freundlich models clearly explain As (V) adsorption by Fe-AIB and Fe-AIL. Thermodynamic analysis reveals the spontaneous adsorption on Fe-AIB. Moreover, it also confers the endothermic nature of the adsorption process for both the adsorbents. The presence of co-existing ions like PO_4^{3-} and SiO_3^{2-} negatively interfered the removal or arsenate uptake, whereas ions like SO_4^{2-} and NO_3^- do not significantly affect the adsorption process. Consistently greater than 90% As (V) removal up to few cycles for both the adsorbents was observed in regeneration studies. Significant reusability characteristics was possessed by both the spent adsorbents, which makes them potentially efficient for large-scale practical application with enhanced performance.

Keywords Adsorption · Arsenate · Adsorption isotherms · Fe-AIB · Fe-AIL

Introduction

Arsenic is a heavy metal and presents in abundance, primarily in environment and earth's crust. For living beings, arsenic is an essential element as it has wide use in pharmaceutical, agriculture and electronic industries, but toxicity caused by arsenic is an emerging issue (Hare et al. 2019). More than two hundred million people are affected by arsenic-contaminated groundwater worldwide, especially in Ganga–Brahmaputra and Indo-Gangetic plains. Recent research shows some new areas like Amazon basin also getting effected by As contamination (Upadhyay et al. 2019). Arsenic contamination of groundwater can be caused by natural sources, including weathering of minerals and rocks.

Anthropogenic activities like processing of ore, extraction of metals, smelting, excessive use of fertilizer and pesticides cause transport and mobilization of As and highly induces its concentration in groundwater (Ranjan 2019). Arsenic exists in inorganic and organic form in an aqueous system. The organic form is of not much relevance as it easily gets detoxify through methylation. Inorganic As exists in rarely found oxidation states of -3 and 0 and very commonly found oxidation states of $+3$ and $+5$ in water system depending upon the redox conditions (Shankar et al. 2014). Pentavalent arsenic co-exists in the anionic form such as AsO_4^{3-} , H_2AsO_4^- and is predominant species under oxidizing conditions (surface water). Trivalent arsenic exists in the non-anionic form such as $\text{As}(\text{OH})_3$, $\text{AsO}_2\text{OH}^{2-}$, $\text{As}(\text{OH})_4^-$, AsO_3^{3-} and $\text{AsO}_2\text{OH}^{2-}$ and dominates under mild reducing conditions (groundwater) (Cullen and Reimer 1989; Singh and Pant 2004). Most of the As compounds do not possess any colour or smell; their presence in edible food or water cannot be detected easily and presents a serious threat to human health and environment (Mandal and Suzuki 2002).

✉ Ghazi Mohd Sawood
mohdsaud22@gmail.com

¹ Department of Chemical Engineering, Harcourt Butler Technical University, Kanpur, India

USEPA declared arsenic as Group A carcinogenic compound and considered as a severe potential threat to living being across the globe. Because of the notorious behaviour of As towards human health, the prescribed limit for As consumption by WHO is decreased to 10 ppb, which earlier was 50 ppb. There are various pathways through which As enters the human body, but ingestion of water and food is widespread (Smeester and Fry 2018). Mostly all organs of humans can be adversely affected by As toxicant. Basically, the effect on human health can be chronic or acute, which greatly depends on the amount of consumption and type of As (Ferrecio et al. 2013). Wide range of biochemical mechanism including mitosis activation, genotoxic damage induction, depletion of DNA fixing mechanism, signal cascades perturbation, etc., was proposed for arsenic as carcinogen (Tchounwou et al. 2019). Long-term consumption of

As-contaminated water may result in As poisoning, also known as arsenicosis. Its pathological and clinical manifestations have been largely reported, and it comprises of pathologies related to skin, fibrosis of lungs and liver, atherosclerosis, loss of hearing and neurologic impairment in children (Tchounwou et al. 2015). In present work, the arsenic effect on human health has been distinguished as non-carcinogenic effects and carcinogenic effects (Table 1).

Due to easy oxidation of arsenite to arsenate, As (V) is in much more abundance in comparison with arsenite (Rango et al. 2013). Therefore, the present study aimed to remove As (V) from water. Due to the severity of arsenic threat, numerous arsenic removal technologies have been developed in recent past. A compact summary of them is given below (Tripathy and Raichur 2008; Nicomel et al. 2016; Asere et al. 2017).

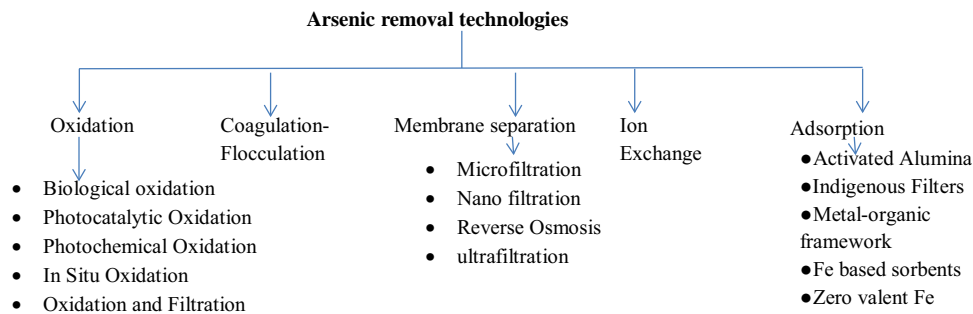


Table 1 Ways in which As effects human health

Non-carcinogenic effects

Cardiovascular effect	Elevated blood pressure, hypertension and CVD were linked with chronic As consumption. Research shows areas exposed to prolonged As consumption are much prone to ischaemic heart diseases (IHD) (Tseng 2009)
Respiratory effects	Apart from lung cancer, there are many other effects on the respiratory system related to As poisoning. Research suggests the link of arsenicosis with chronic bronchitis. Moreover, vital capacity in children decreased by As (Smith et al. 2006)
Reproductive effect	The deleterious impact is shown by inorganic As on the reproductive system. Women affected by chronic As consumption shows positive trends towards premature delivery, complications in pregnancy and elevated fetal loss (Kwok et al. 2006)
Haematological effects	Haematological imbalance can be induced at higher rates with As exposure. Arsenic can be diabetogenic and can be a cause of type II diabetes (Tseng et al. 2000)
Neuropathic effects	Studies suggest that consumption of As in early age may affect the neurobehavioral system in the later phase of life. One of the most common issues related to the nervous system is peripheral neuropathy (Tsai et al. 2003)
Dermatologic effects	Keratoses, hypopigmentation and other types of skin lesions are common indicators of arsenicosis (Ahsan et al. 2000)
Effects on intellectual function and memory	A research on children in Mexico shows that with an increase in the concentration of As in urine, there is a decrement in verbal IQ, intellectual function and memory (Wasserman et al. 2004)

Carcinogenic effects

Skin cancer	As the skin is one of the target organs in human by As, skin cancer induced by UV and intra-epidermal carcinomas can be greatly enhanced by inorganic As (Rossman et al. 2004)
Bladder cancer	Epidemiological studies show that the rate of bladder cancer and urinary system is positively linked to high As consumption, although there is an infrequent risk of bladder cancer in areas in which As exposure is less than 100 ppb (Baris et al. 2016)
Lung cancer	With increased As ingestion rates, mortality from this type of cancer increased. The risk of lung cancer increases with cigarette smoke as As and cigarette smoke are synergistic (Chen et al. 2004)
Liver cancer	There is huge risk of hepatocellular carcinoma and angiosarcoma, when arsenic exposure is combined with other genetic and environmental risk factors (Albores et al. 1996)

All techniques listed above, other than adsorption, require high fixed and running cost along with skilled human resources. Adsorption technique due to its low operational and fixed cost, easy operability, regeneration and less toxic sludge formation have the upper hand than other technologies, especially in developing regions (Boddu et al. 2008). Commercially available activated carbon is quite expensive, so in developing countries processes involving natural and locally available adsorbents were considered to be more promising due to their low investment and less impact on the environment (Asere et al. 2019). Being environment friendly, abundance and high efficiency, great interest is shown towards Fe-based adsorbents (Fe-based nanoparticles, Fe-based LDHs, zero-valent Fe, Fe-impregnated activated carbon, Fe-impregnated biomass and Fe-impregnated inorganic minerals) by the researchers in recent past for remediation of As (Hao et al. 2018).

The carbon obtained from the powdered bark and leaves of *Azadirachta indica* tree has proven to be excellent sorption materials for As (V) remediation. Because of abundance of these base materials, *Azadirachta indica* bark and leaves have drawn the attention of researchers in recent past for arsenate adsorption. At an optimum pH 5, maximum removal of arsenite, i.e. 90 per cent, was reported using ZnO nanoparticles doped into the *Azadirachta indica* leaves extract (Gnanasangeetha and SaralaThambavani 2015). By using the bark powder of *Azadirachta indica* at an optimum influent concentration 100 µg/L and 6pH, 79 per cent of arsenate was removed from the ground water (Choudhury et al. 2014). Also, at an initial concentration of 0–500 µg/L and Ph 6.5, maximum arsenite removal of 89 per cent was reported using the bark powder of *Azadirachta indica* (Roy et al. 2017) Moreover, *Azadirachta indica* powder in carbonized or uncarbonized form was frequently used earlier for the remediation of other contaminants including dyes (Srivastava and Rupainwar 2011), Cd(II) (Tiwari et al. 1999) Zn(II) (Bhattacharya et al. 2006) and Cr(VI) (Bhattacharya et al. 2008). Other plants bio-sorbents including Tamarix were also used for arsenate removal from the aqueous solution (Zhu et al. 2020).

These findings laid interest in exploring the probability for application of carbon obtained from the bark and leaves of *Azadirachta indica* for remediation of arsenate from aqueous solution. Also, there are numerous researches that have shown the compatibility of Fe oxides for arsenic removal, but due to high cost and fragile nature it cannot be used alone. Large number of iron-doped adsorbents were used earlier for arsenite remediation (Zhu et al. 2020; Lyu et al. 2020; Ali et al. 2020; Chen et al. 2020; Cui et al. 2019), but very less iron-impregnated adsorbents were used for arsenate removal (Verma et al. 2019; Zeng et al. 2020). In the present study, surface-modified bark and leaves of *Azadirachta indica* derived carbon were used for arsenate removal from the aqueous solution.

The present study aimed to develop low cost adsorbent derived from the impregnation of Fe on to the carbon derived from leaves (Fe-AIL) and bark (Fe-AIB) of *Azadirachta indica* tree and evaluation of kinetics, equilibrium and thermodynamics adsorption and kinetics studies of arsenate removal from aqueous solution, The novelty of the work is the performance evaluation of *Azadirachta indica* derived activated carbon, followed by its impregnation using iron metal, which was never been studied. The characterization of synthesized adsorbent was done through various analytical methods including scanning electron microscopy (SEM), energy-dispersive X-ray analysis (EDX), X-ray powder diffraction (XRD) and Brunauer–Emmett–Teller (BET) multipoint technique. The Fe-impregnated adsorbents have been used for the removal of As (V) at different operating conditions such as concentration, dose, time and pH after the treatment process; the testing of residual As (V) was done through ICP-MS.

Materials and method

Materials

Reagent-grade sodium arsenate ($\text{NaHAsO}_4 \cdot 7\text{H}_2\text{O}$), iron (II) chloride, hydrochloric acid, sodium hydroxide and sulphuric acid were procured from Merc India Ltd. Arsenate stock solution was prepared by dissolving 0.416 grams of sodium arsenate in deionized water and slowly rising the volume to 1 litre. 0.1 N NaOH or 0.1 N H_2SO_4 solution was used to control the pH. Deionized water was used to prepare the solutions for adsorption, synthesis and dilution.

Synthesis of Fe-AIB and Fe-AIL adsorbents

Activated carbon synthesized from the bark and leaves of *Azadirachta indica* tree was used in the present study. After pre-treatment, powdered bark and leaves are subject to sieving followed by carbonization in muffle furnace at 750 °C for 6 h and 3 h, respectively, with the circulation of N_2 gas. The activated carbon thus produced was subject to Fe impregnation using FeCl_2 salt solution. Series of thermochemical reaction takes place during the impregnation process. In the impregnation process, 50 g of activated carbon was added to a 0.5 M FeCl_2 solution and stirred at 70 °C for 24 h. NaOH was used to maintain the pH of suspension at 8 to increase the negative charge abundance. The filtrate was washed multiple times to remove the colloidal precipitates and iron salt attached to the surface of Fe-AIB or Fe-AIL (Kalaruban et al. 2019). The impregnation process using iron results in rearrangement of the pore structure of activated carbon and better affinity towards adsorbate (Shah et al. 2015).

Techniques used for characterization

Before the porosity and surface area measurement, degassing of AC and Fe-AC, at 300 °C for 18 h under vacuum, was done. The surface area was measured using Nitrogen adsorption isotherm at 77 °C by Brunauer–Emmett–Teller (BET) method. Average pore diameter and total pore volume were evaluated by Barrett–Joyner–Halenda method using Autosorb iQ. The surface morphology of samples and Fe distribution on activated carbon was studied using Carl Zeiss EVO 50 EDX coupled with scanning electron microscope operating at 20kv. XRD analysis for determining Fe species was done using Bruker D8 focus X-ray diffractometer having $\lambda = 1.5418 \text{ \AA}$ and 2θ ranging between 5° and 80°.

Batch adsorption experiments

A series of Erlenmeyer flask (250 ml) containing 100 µg/L of 100 ml As (V) solution stirred in magnetic stirrer at a rate of 60 rpm was used to determine equilibrium time and optimum dose in the batch experiment. Volumetric flasks were used to prepare a standard solution. For investigating the effect of time of contact on overall removal, time of contact was varied from 15 to 75 min. By diluting the stock solution, concentrations ranging from 50 to 250 µg/L of As (V) were prepared. 0.1 M hydrochloric acid and 0.1 M sodium hydroxide were used to maintain the pH, and adsorbent dose was varied from 0.25 to 1.25 g while investigating the adsorption isotherm. To study the effect of temperature in a range 25–65 °C on uptake of As (V) by Fe-AIB or Fe-AIL, 1 g adsorbent was added to 100 ml of As(III) with initial concentration of 100 µg/L stirred at a rate of 60 rpm for various temperatures. Inductively coupled mass spectrophotometer (ICP-MS) was used to analyse the filtrate of solution to determine residue As (V). The quantity of adsorbed As (V) or the uptake capacity and percentage removal of arsenate was determined using Eqs. (1) and (2) (Yadav et al. 2014).

$$q_e (\mu\text{g/g}) = \frac{(c_i - c_e)V}{W} \quad (1)$$

and,

$$\text{Percentage As (V) removal} = \frac{c_i - c_e}{c_i} \times 100 \quad (2)$$

where c_i and c_e correspond to initial and equilibrium concentration of arsenate (µg/L), V is the volume of arsenate solution (L), and W represents the mass of adsorbent (gm).

Desorption and regeneration analysis

In desorption analysis, series of Erlenmeyer flask filled with 50 ml arsenate solution (100 µg/L) was used to treat

1 gm of the adsorbent. The adsorbent loaded with arsenate was filtered. To remove unadsorbed arsenate, the adsorbent subjected to multiple washing with deionized water. Then, the adsorbent was subject to hydroxide treatment at various concentrations, followed by filtration. The volume used for adsorption (V_a) was 50 ml, and that for desorption (V_d) was 25 ml, maintaining the V_d/V_a equals 0.5 (Chiban et al. 2016). The analysis of filtrate was done to evaluate the desorbed arsenate. Following equation was used to find out the amount of desorbed arsenate:

$$\text{Percent desorption} = \frac{\text{released arsenate } (\mu\text{g/L})}{\text{initially arsenate adsorbed } (\mu\text{g/L})} \times 100 \quad (3)$$

In regeneration studies, 50 ml arsenate solution (100 µg/L) was used to treat 1 gm of the adsorbent and allowed to filter after attaining the equilibrium. For time equal to adsorption period, the hydroxide treatment (20 ml NaOH) of adsorbent was done. Then, the filtration was done and filtrate was analysed for arsenate desorbed. Excess NaOH was removed by multiple washing of adsorbent. Again, the adsorbent was treated with 50 ml arsenate solution (100 µg/L).

Under identical conditions, the blank control test was performed. The amount of As (V) lost during the test was subtracted from the experimental results. All the experiments were performed in triplicate at room 25 °C (room temperature). The average experimental values were reported, and the standard deviation was represented using error bars. The relative experimental error was within $\pm 5\%$ (Table 2).

Results and discussion

Characterization of Fe-AIB and Fe-AIL adsorbents

The BET surface area, pore width and pore volume of Fe-AIB and Fe-AIL are presented in Tables 3 and 4. The analysis shows decrement in surface area, pore width and pore volume after the Fe impregnation in both the samples. This decrease may be attributed to the blocking of some pores

Table 2 Physio-chemical properties of Fe-AIR

Analysis	Value	
	Fe-AIB	Fe-AIL
Moisture content (%)	10.95	13.81
pH _{zpc}	6.76	5.41
pH _{slurry}	6.23	5.19
Specific gravity (%)	0.227	0.208
Porosity	81	74
Particle size (µm)	227	251

Table 3 BET results of virgin AIB and Fe-AIB

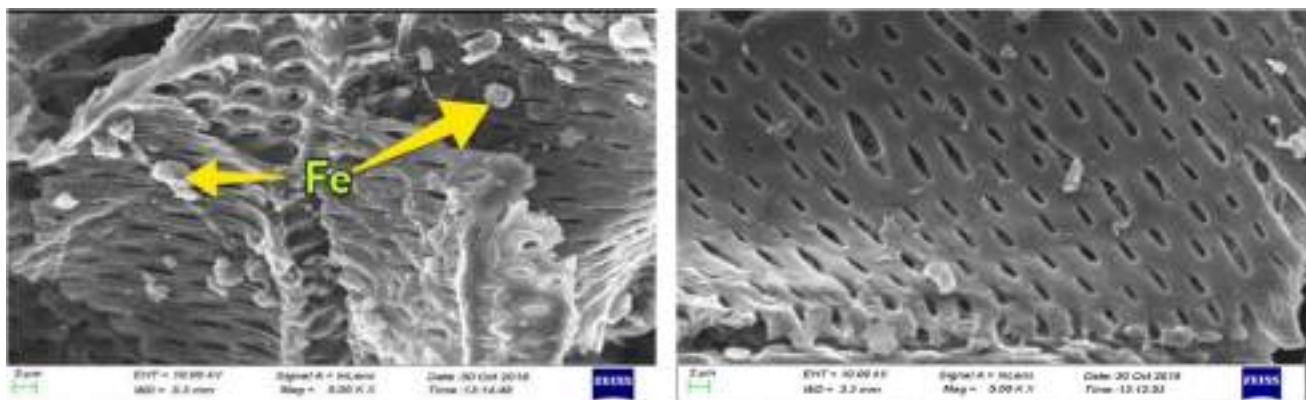
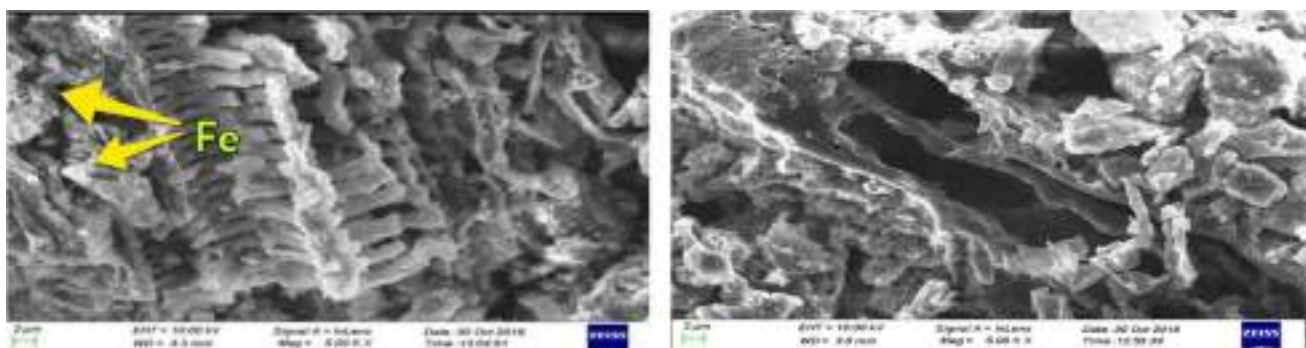
	BET surface area (m ² /g)	Pore volume (cm ³ /g)	Pore width (Å)
Virgin AIB	878.139	0.247	14.358
Fe-AIB	352.442	0.193	6.956

Table 4 BET results of virgin AIL and Fe-AIL

	BET surface area (m ² /g)	Pore volume (cm ³ /g)	Pore width (Å)
Virgin AIL	359.732	0.169	6.135
Fe-AIL	192.116	0.092	2.974

The SEM micrographs of Fe-AIB and Fe-AIL reveal the surface morphology. It shows a very porous structure of Fe-AIB, as a large number of pores and grooves can be clearly seen (Fig. 1), which may have resulted in a large surface area of the material. The micrographs of Fe-AIL (Fig. 2) show fewer pores and heterogeneity as in comparison with the Fe-AIB. In some of the pores, the aggregates of Fe can be seen in the micrographs of both adsorbents.

The distribution of surface elements of Fe-AIB and Fe-AIL examined by EDAX is presented in Figs. 3 and 4, respectively. The EDAX analysis reveals that both the adsorbents mostly comprise of C, Cl and Fe, indicating mixed metal oxide composition. Cl and Fe are known to be good binding agents. Fe oxide is the dominant species of adsorbents as per the analysis of chemical composition.

**Fig. 1** SEM micrograph of Fe-AIB**Fig. 2** SEM micrograph of Fe-AIL

in samples due to Fe coating. Same trends of decrement in surface area, pore width and pore volume due to Fe incorporation have also been reported earlier (Ryu et al. 2017). The average pore width of Fe-AIB was reported lying in the range of 5–15 Å, which reveals its microporous nature; on the other hand, Fe-AIL falls in the mesoporous category as the pore width of Fe-AIL is less than 5 Å.

The XRD pattern of prepared Fe-AIB and Fe-AIL is illustrated in Figs. 5 and 6. Fe-AIB and Fe-AIL show a peak at 2θ equal to 18° and 25° , respectively, which depicts the amorphous pattern of both the adsorbents. However, the peak in case of Fe-AIB is border and sharper as compared to the peak of Fe-AIL. This pattern of the peak is common in

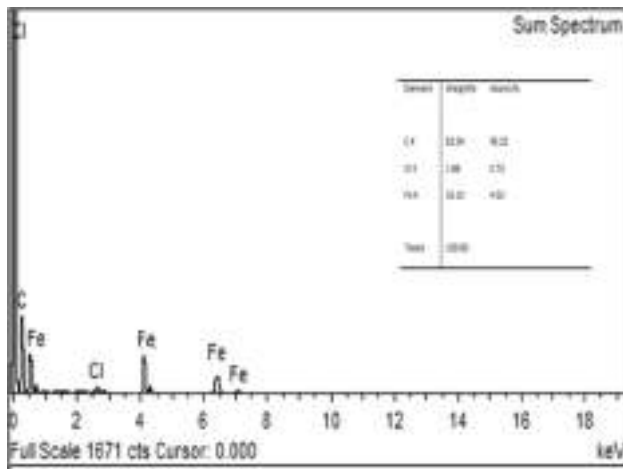


Fig. 3 EDX image and elemental composition of Fe-AIB

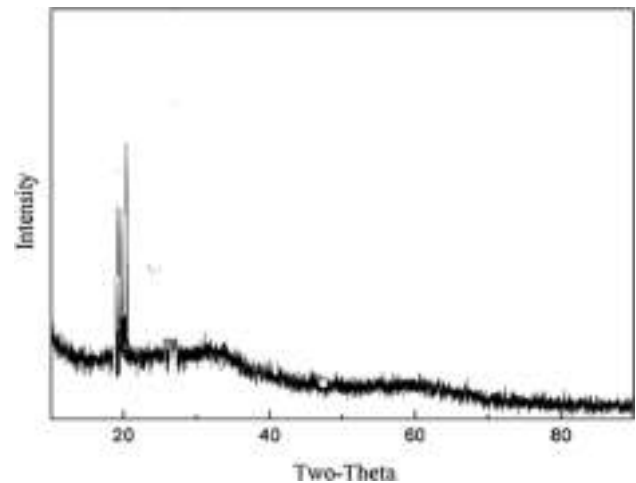


Fig. 5 XRD curve for Fe-AIB

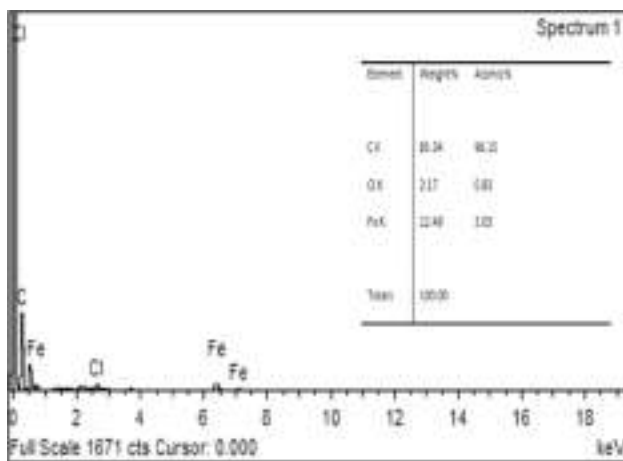


Fig. 4 EDX image and elemental composition Fe-AI

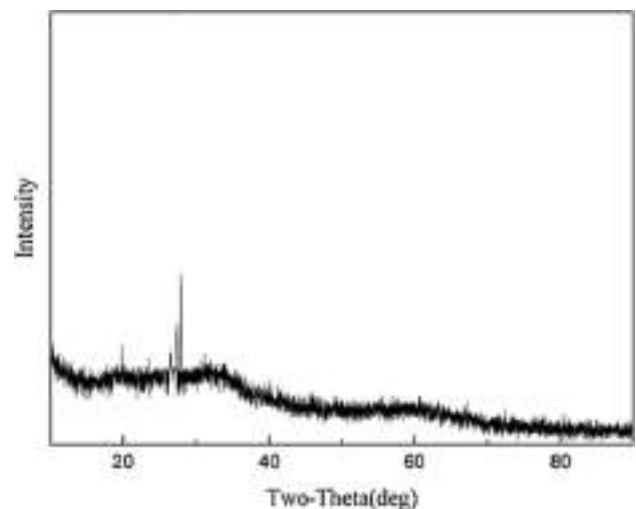


Fig. 6 XRD curve for Fe-AIL

amorphous material containing pyrolytic carbon with amorphous iron oxide and micro-graphitic structure (Naeem et al. 2016). XRD spectrum near to baseline subjects to amorphous nature of both adsorbents. From the literature, it can be concluded that amorphous nature of adsorbents is good for adsorption (Yakun et al. 2011).

The FTIR spectra of Fe-AIB and Fe-AIL recorded in the scale of 5000–450 cm^{-1} , before and after adsorption, are shown in Fig. 7. At 3206.5 cm^{-1} and 3504.2 cm^{-1} in Fe-AIB and Fe-AIL spectra (before adsorption), a characteristic peak appears which may correspond to O–H stretching or chemisorbed water content (Liu et al. 2014). In the As(V) adsorbed Fe-AIB and Fe-AIL, the peak shifted to 3241.7 cm^{-1} and 3432.1 cm^{-1} , respectively. A weak adsorption band appears at 1520.7 cm^{-1} after adsorption of arsenate on Fe-AIB, which can be assigned to C=C stretching of the aromatic ring (Ravikovich and Neimark 2006). A sharp peak before adsorption

in Fe-AIB 1000.2 cm^{-1} at and small peak 1028.6 cm^{-1} at in Fe-AIL may result from C–OH stretching of COOH (Jadhav et al. 2015). After As (V) adsorption, the peak shifted to 1096.4 cm^{-1} in Fe-AIB and to 1152.3 cm^{-1} in Fe-AIL. A sharp peak at 892.4 cm^{-1} appears in Fe-AIB after adsorption may attribute to the interaction of metal and oxygen (Shah et al. 2015). No such peak is found in case of Fe-AIL.

Effect of initial arsenic concentration

The adsorptive behaviour of arsenate was analysed in the concentration range of 100–300 $\mu\text{g/L}$ at pH 6.0, adsorbent dose of 1 g, stirring rate of 60 rpm and 25 $^{\circ}\text{C}$ temperature for the time of contact of 1 h, as shown in Fig. 8. The trend shows decrement in percentage removal of As (V) on

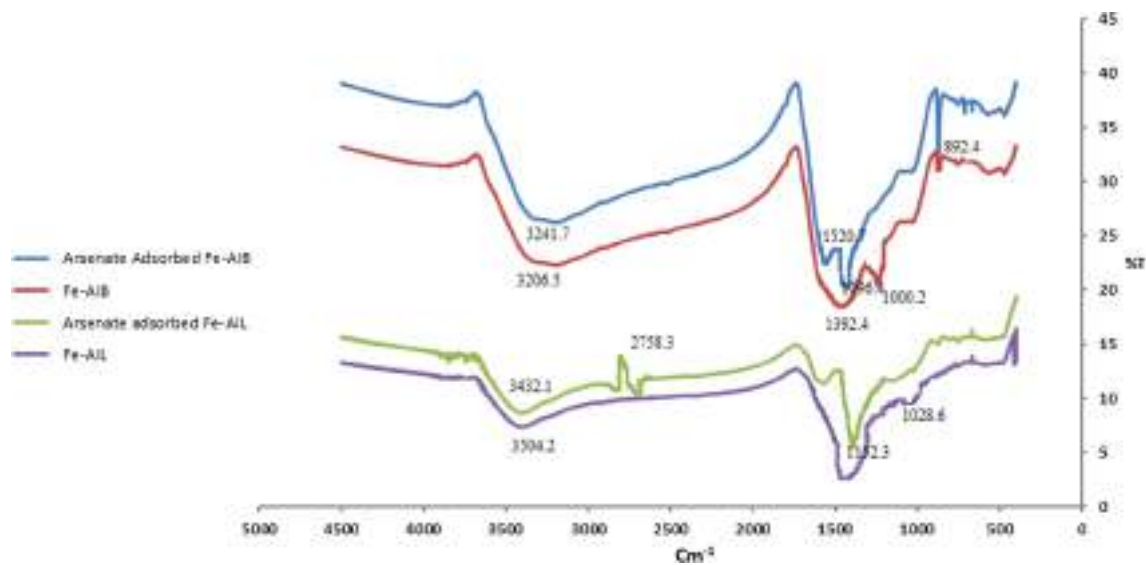
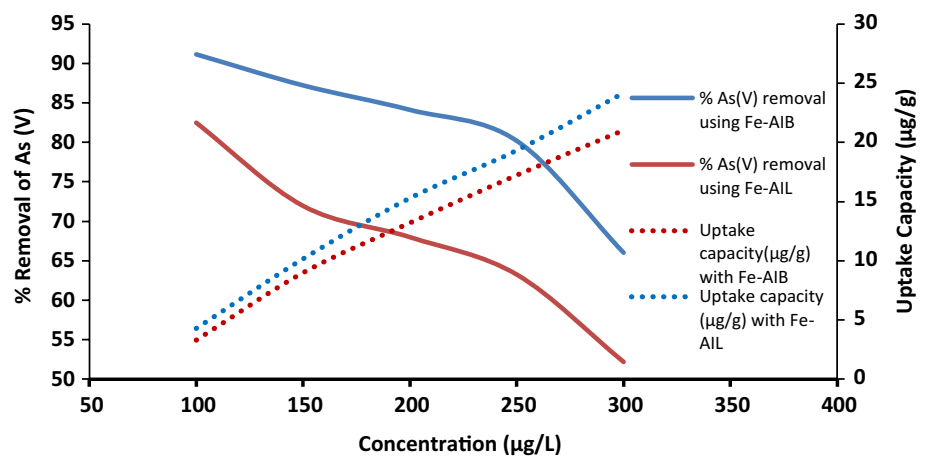


Fig. 7 FTIR spectra of Fe-AIB and Fe-AIL before and after adsorption

Fig. 8 Effect of initial arsenic concentration on adsorption of As (V) by Fe-AIB and Fe-AIL



Fe-AIB and Fe-AIL with increase in initial As (V) concentration. This decrement may result from the saturation of active adsorption sites.

The ratio of ion and adsorbent increases which saturates the higher energy sites, and efficiency of adsorption gets decreased (Mondal et al. 2012). But with increase in As (V) concentration, the quantity of As (V) adsorbed per unit mass of Fe-AIB and Fe-AIL increases. This increase may be attributed to lowering in resistance to the uptake of As (V) with increase in concentration (Bhaumik et al. 2011).

Effect of adsorbent dose

To attain the maximum capacity of adsorption of Fe-AIB and Fe-AIL and hence the maximum percentage of As (V) removal from the water phase, the adsorbent dose varied

from 0.25 to 1.25 g/L. Further addition from 1 g/L in case of Fe-AIB and 0.75 g/L in case of Fe-AIL does not reduce the As (V) residual concentration. These findings are shown in Fig. 9. This increase in As (V) removal percentage with increase in dose may be due to enhanced surface area and availability of more adsorption sites (Božić et al. 2009). The saturation in removal efficiency of Fe-AIB after 1.00 g/L and of Fe-AIR after 0.75 g/L may be due to attainment of maximum adsorption. Hence, the number of ions remains constant even with further increase in adsorbent dose (Thapa and Pokhrel 2012).

Effect of time of contact

The impact of contact time on adsorption of As (V) using Fe-AIB and Fe-AIL was studied in the time span of 15–75 min

Fig. 9 Effect of adsorbent dose on adsorption of As (V) by Fe-AIB and Fe-AIL

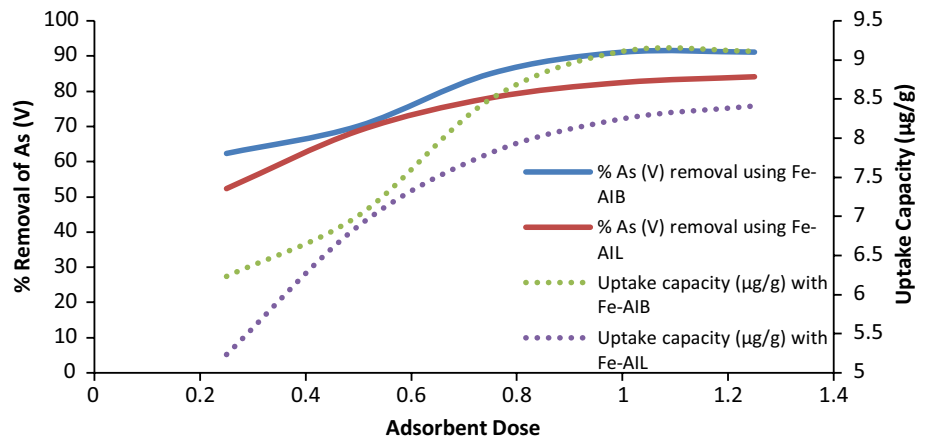
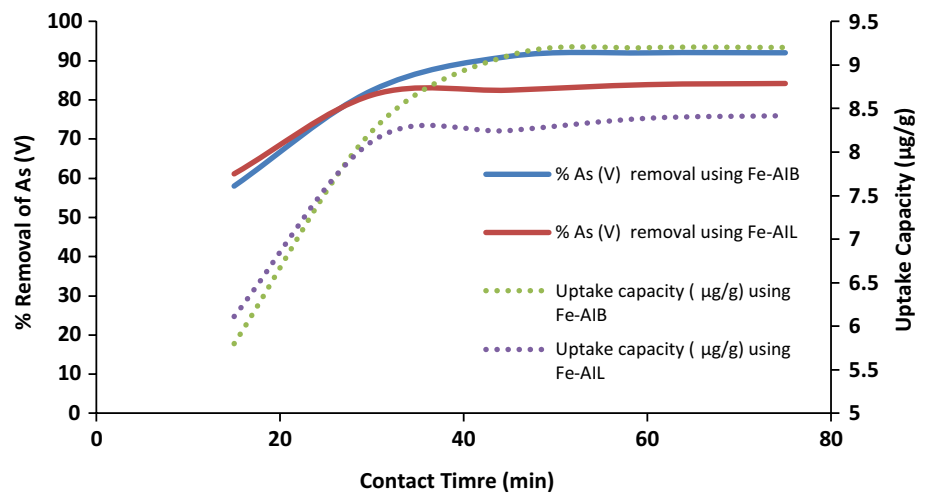


Fig. 10 Effect of contact time on adsorption of As (V) by Fe-AIB and Fe-AIL



at pH 6.0, and 1.0 g dose is shown in Fig. 10. The per cent As (V) ion removal as a function of contact time depicts biphasic nature on the surface of both the adsorbents with a quick uptake up to 45 min for Fe-AIB and 30 min for Fe-AIL and gradually attains equilibrium after that. After that, no significant change in per cent As (V) removal was observed. The availability of a large number of binding sites on the surface of adsorbent at an initial phase may result in quick adsorption. Due to repulsive forces between As (V) molecules on the surface of adsorbent and bulk phase in the later phase, the occupancy of left out vacant sites became difficult (Rajesh 2010).

Effect of pH

At an optimum concentration of 100 µg/L, the uptake capacity and per cent removal of As (V) as a function of pH by Fe-AIB and Fe-AIL are shown in Fig. 11. For Fe-AIB, the optimum per cent removal obtained as 93.997 (9.337 µg/g) was attained at 6.0 pH. HAsO_4^{2-} and H_2AsO_4^- were the predominant species in the pH range

of 2–10. In the pH spectrum of 4–6, the arsenate species exist mainly as H_2AsO_4^- and HAsO_4^{2-} in pH range of 8–10. Both the species co-exist in the 6–8 pH range. At optimum pH, the probable mechanism is adsorption of HAsO_4^{2-} (anionic species) on to positively charged adsorption sites through the bonding with R-OH group present on the Fe-AIB surface (Kumari et al. 2005). The decrement in removal efficiency at high pH can be attributed to dominance of density of OH^- ions, which results in their competition with anionic arsenate species. Moreover, at alkaline pH, R-OH, R-COOH and R-CO-NR groups of Fe-AIB are negatively charged and result in repulsive force between the anionic arsenate species and the adsorbent (Sarı and Tuzen 2010). For Fe-AIL, the optimum removal of 88.698% was obtained at 4.0 pH. This can be attributed to the fact that arsenate species are efficiently adsorbed at acidic conditions. Adsorption of As (V) by Fe-AIL is supposed to be performed by anion exchange along with physiochemical adsorption. Under acidic conditions, the surface of adsorbent is positively charged, which get balanced by their escort anions (Ansari and Sadegh 2007).

Fig. 11 Effect of pH on adsorption of As (V) by Fe-AIB and Fe-AIL

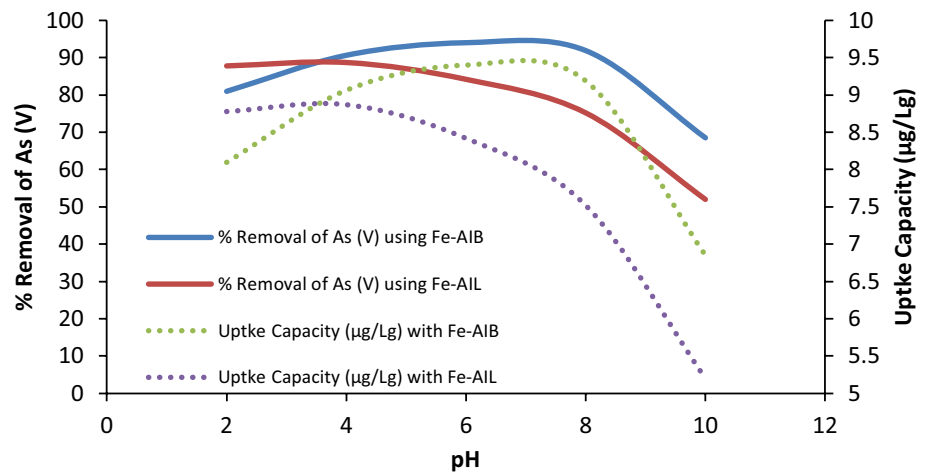
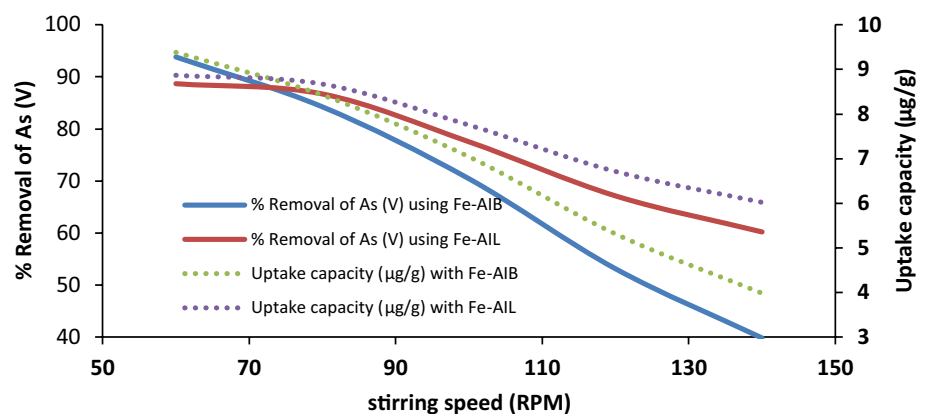


Fig. 12 Effect of stirring rate on adsorption of As (V) by Fe-AIB and Fe-AIL



Effect of stirring rate

The effect of different rates of stirring varying from 60 and 120 rpm at optimum conditions was analysed for Fe-AIB and Fe-AIL and is presented in Fig. 12. For both the adsorbents, it was observed that the removal efficiency decreases with increase in stirring rate. This decreasing trend of removal efficiency can be due to the fact that less time is available for the interaction of arsenate ions and surface of the adsorbent for interaction at high agitation speeds which also can separate the ions that are loosely bounded (Roy et al. 2014). Removal percentage of As (V) drastically decreases with increase in stirring rate. This decrease in removal percentage can be attributed to the fact that less time of contact available for adsorbent and adsorbate and hence results in reduced adsorption when the rate of stirring increases.

Effect of temperature

The impact of temperature on the removal of As (V) by Fe-AIB and Fe-AIL at various temperatures ranges from 303 to 325 K. Figure 13 presents that removal percentage using Fe-AIB increases from 91.525 to 94.614% when temperature

changes from 301 to 313 K and then decreased. The same trend was observed using Fe-AIL, where removal percentage changes from 88.175 to 90.432% when temperature changes from 303 to 308 K and declines after that. This may be attributed to the fact that both the adsorbents are losing their adsorption capacity at elevated temperatures by means of denaturation. Also arsenate ions (solute) move with high rates at elevated temperature and time available for their interaction with active sites of adsorbent decreases (Kanwal et al. 2012).

Adsorption kinetics analysis

The physicochemical study of adsorption kinetics is significant as it provides valuable information about reaction mechanism involved and pathways of reaction. Moreover, it also provides the uptake rate of solute, which describes the residence time of solute on the surface of the adsorbent. In the current study, the As (V) adsorption kinetics and mechanism of adsorption on the prepared adsorbents were evaluated at various temperatures. Pseudo-first-order, Pseudo-second-order, Elovich equation, Bangham model and intraparticle diffusion models were used to evaluate

Fig. 13 Effect of temperature on adsorption of As (V) by Fe-AIB and Fe-AIL

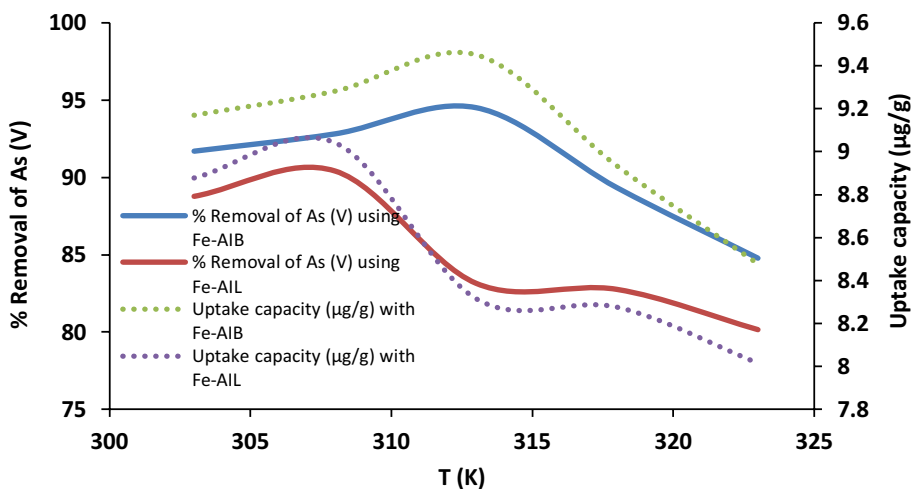


Table 5 Kinetic parameters for adsorption of arsenic by Fe-AIB and Fe-AIL

Kinetic model	Parameters	Fe-AIB		Fe-AIL	
		Values	R ²	Values	R ²
Pseudo first order	<i>q_{e,exp}</i> (μg/g)	10.9917	0.915	9.4702	0.821
	<i>q_e</i> (μg/g)	5.8159		1.3452	
	<i>K₁</i> (g/μg-min)	0.0017		0.0004	
Pseudo second order	<i>q_{e,exp}</i> (μg/g)	10.9917	0.997	9.4702	0.991
	<i>q_e</i> (μg/g)	11.7708		9.1313	
	<i>K₂</i> (g/μg-min)	0.0074		0.0031	
Intraparticle diffusion	<i>k_{pi}</i> (μg/g min ^{0.5})	0.7642	0.844	0.6049	0.865
	<i>C</i>	3.4874		4.0144	
Elovich model	<i>α</i> (μg g ⁻¹ min ⁻¹)	12.1553	0.959	1.87552	0.920
	<i>β</i>	0.4288		0.5406	
Bangham kinetic model	<i>k_r</i> (μg/g-min)	9.6421	0.92	3.1479	0.891
	<i>m</i>	3.1968		4.0069	

the obtained data. Parameters of the five models are listed in Table 5. The R² (coefficients of determination) values determine the goodness-to-fit model. Relatively higher values of coefficients of determination show that the model well describes the kinetics of As (V) adsorption by the adsorbents.

The Lagergren first-order equation assumes that the overall rate of adsorption is proportional to the difference in concentrations at saturation and the cumulative quantity of solute uptake. The pseudo-first-order rate equation is expressed as Eq. (4) (Depci et al. 2012)

$$\text{Log}\{(q_e) - (q_t)\} = \text{Log}\{q_e\} - \frac{k_1}{2.303}t \tag{4}$$

where the quantity of As (V) adsorbed after time *t* and at equilibrium (μg/g) is denoted by *q_t* and *q_e*, respectively. *k₁* is the rate constant for the first-order model. Lower values of R² and vast gap between the calculated and experimental

values of maximum solute adsorbed (Table 6) show that Pseudo-first-order model is unsuitable for explaining the mechanism for the As (V) uptake by and Fe-AIL.

Ho and Mckay second-order model assumes that sharing of electrons through chemisorption controls the rate of adsorption. It deals more with mechanism of chemical reaction. The pseudo-second-order kinetic equation is as Eq. (5) (Bayramoglu et al. 2009)

$$\frac{t}{(q_t)} = \frac{1}{(k_2)(q_e)^2} + \frac{t}{(q_e)} \tag{5}$$

where *k₂* is the rate constant for the second-order model, *q_t* is the arsenate adsorbed after time *t*, and *q_e* is the arsenate adsorbed on Fe-AIB and Fe-AIL at equilibrium. The slope of plot *t/q_t* versus *t* would yield *q_e* (adsorption capacity at equilibrium). From Table 6, it can be seen that the difference between *q_e* and *q_{e,exp}* values is very less along with good R²

Table 6 Isotherm data for adsorption of arsenate by Fe-AIB and Fe-AIL

Adsorption isotherm	Parameters	Fe-AIB		Fe-AIL	
		Values	R ²	Values	R ²
Langmuir isotherm	q _{max} (μg/g)	36.9636	0.9937	29.1812	0.9989
	K _L (L/μg)	0.0516		0.1145	
	R _L	0.1623		0.0803	
Freundlich isotherm	K _F (μg/g)	2.1712	0.9899	1.0362	0.9912
	n	1.6130		1.2786	
Temkin isotherm	A _T (L/μg)	0.7203	0.983	0.0453	0.970
	b _T (J/mol)	324.2599		79.4315	
	B	8.7199		5.7896	
D–R isotherm	q _{max} (μg/g)	21.9289	0.9037	19.1885	0.9169
	E (J/mol)	45.342		6.3845	

value, so it can be concluded that second-order model can very well approximate adsorption reaction mechanism.

Weber–Morris intraparticle diffusion graph is used to evaluate the mechanism involved in the adsorption process. The Weber–Morris intraparticle model is given by eq. (6) (Bazarafshan 2017)

$$q_t = k_{pi}t^{0.5} + C \tag{6}$$

where q_t is arsenic adsorbed on Fe-AIB and Fe-AIL after time t, k_{pi} is the intraparticle diffusion rate constant, and constant C gives the thickness of the boundary layer. A low value of C implies less effect of the boundary layer on the process of adsorption. q_t versus t^{0.5} correspond to multi-linearity plot having two adsorption stages. First linear portion represents mass transfer at faster rates through film diffusion, and the second portion corresponds to uptake of As (V) through intraparticle diffusion. It is conferred that intraparticle diffusion and film diffusion takes place simultaneously as the straight line is not passing through origin (Nandi et al. 2009). The values of k_{pi}, C and R² values from the table infer that during adsorption of As (V) on Fe-AIB and Fe-AIL, one of the rate controlling steps is intraparticle diffusion.

Elovich model explains the phenomenon of chemisorption with negligible desorption. This model assumes that adsorption rate decreases as the surface coverage increases with time. Elovich model is given by Eq. (7) (Juang and Chen 1997)

$$\frac{dq_t}{dt} = \alpha \exp(-\beta q_t) \tag{7}$$

where α (mg g⁻¹ min⁻¹) a is the rate constant for initial adsorption, and β is the rate constant for desorption. The simplified form of Eq. (7) can be written as:

$$q_t = \frac{\ln(\alpha\beta)}{\beta} + \frac{\ln(t)}{\beta} \tag{8}$$

q_t versus t yield a plot in the present study for both the adsorbents indicate switching from one active site to another site having different kinetics of the reaction. For the case of Fe-AIB, Elovich plot can be subdivided into two stages. In the first stage, the adsorption takes place at a faster rate on to the adsorbent surface, and in a later stage, the adsorption takes place in the inner surface may be in micropore (Chien and Clayton 1980). No such trend was observed in the Elovich plot of Fe-AIB, suggesting that a major portion of the adsorption process takes place on the outer surface of Fe-AIL.

Bangham kinetic model was used to investigate the role of pore diffusivity in the present study. The linear form of Bangham kinetic equation will be given by Eq. (9) (El Saliby et al. 2013)

$$q_t = (k_r)t^{1/m} \tag{9}$$

where q_t is the quantity (μg/g) of As (V) adsorbed at time t (min), k_r is the rate constant for As (V) adsorption, and factor 1/m represents the intensity of adsorption. From the Bangham plot for Fe-AIB, the value of K_r comes out to be very close to the obtained value of adsorbed amount (q_{e,exp}) and linear nature of obtained curve suggests pore diffusion plays an important role in the adsorption of As (V) (Taştan et al. 2012). For Fe-AIL, the straight line obtained is not very linear, suggesting its deviation from Bangham model. It can be observed that the overall reaction rate cannot be controlled by pore diffusion alone, but also by film diffusion and intraparticle diffusion.

Adsorption isotherms models

Adsorption isotherms are mathematical models used to predict adsorbate distribution among the solid–liquid phase, and obtained data are helpful in evaluating the mechanism of adsorption. There are numerous models used in the literature to enumerate experimental findings of adsorption isotherm. The Langmuir (LM), Freundlich (FM), Temkin (TM) and Dubinin–Radushkevich models (D–RM) are the most frequently used models. In the current study, these four models were used to explain the relationship among the adsorbed quantity of As (V) on Fe-AIB and Fe-AIL with its concentration at equilibrium.

LM Isotherm

The obtained data were fitted to LM adsorption isotherm at equilibrium by assuming adsorbent having identical finite number of active sites upon which monolayer adsorption

taking place. Following equation in linear is used to express isotherm (Langmuir 1918):

$$\frac{1}{q_e} = \frac{1}{q_{\max} K_{LC_e}} + \frac{1}{q_{\max}} \quad (10)$$

where q_e is the As (V) concentration at equilibrium on the Fe-AIB and Fe-AIL ($\mu\text{g/g}$), C_e is the equilibrium arsenate concentration in the solution ($\mu\text{g/l}$), q_{\max} ($\mu\text{g/g}$) is the adsorption capacity (maximum) of the adsorbent, and K_L ($l/\mu\text{g}$) is the Langmuir constant and is associated with the free energy of adsorption. The value of all these parameters obtained from the plot of $1/q_e$ versus $1/c_e$ is presented in Table 6. Higher values of R^2 (above 0.99) for both the adsorbents represent a good fit of LM to adsorption of As (V) on the adsorbents. Separation factor (R_L) is one of the important parameters of LM isotherm which tells whether the adsorption is favourable or not and mathematically can be expressed as given in Eq. (11)

$$R_L = \frac{1}{1 + K_L C_i} \quad (11)$$

R_L values lying in between 0 and 1 correspond to favourable adsorption (Bulut et al. 2007). In the present study, the values of R_L obtained from both the adsorbents are presented in Table 6. It can be seen that the R_L value for Fe-AIB is 0.1623 and for Fe-AIL is 0.0803, indicating the favourable adsorption.

FM Isotherm

Then, the obtained data were fitted to FM adsorption isotherm, which assumes that free energy of adsorption is heterogeneous in nature and varies with the surface coverage (Freundlich 1906). Mathematical expression of FM isotherm can be give by Eq. (12)

$$\log q_e = \log K_F + \frac{1}{n} \log C_e \quad (12)$$

where K_F and n are FM isotherm constant and can be evaluated from the linear plot of $\log q_e$ versus $\log c_e$. n indicates how favourable adsorption process is. $1/n$ values in the range 0–1 are measure of intensity of adsorption and heterogeneity of surface; heterogeneity increases as the value approaches 0. $1/n$ value below 1 corresponds to normal LM isotherm. The values of FM isotherm constants and R^2 for Fe-AIB and Fe-AIL are also presented in Table 6. The numerical value of n for Fe-AIB is 1.6130 and for Fe-AIL is 1.2786, indicating that As (V) ions are adsorbed favourably. FM model does have good agreement with experimental data as the values of R^2 are high for both the adsorbent. The capacity of the microparticle to remove As (V) confers by these findings.

TM Isotherm

The TM isotherm is derived from LM isotherm, assuming that energy of adsorption decreases with surface coverage, resulting from repulsive forces acting on the surface (Temkin 1940). The linear form of isotherm equation can be represented as:

$$q_e = (B) \ln A_T + (B) \ln C_e \quad \text{where } B = \frac{RT}{b_T} \quad (13)$$

b (J/mol) where corresponds to TM isotherm constant, T (K) is absolute temperature, and R (J/mol-K) is the universal gas constant. B is a dimensionless constant associated with the heat of adsorption. A_T ($L/\mu\text{g}$) is adsorption constant related to the binding energy. The TM isotherm plot for Fe-AIB and Fe-AIL is presented in Fig. 14, and the parameters of isotherm are listed in Table 6. The value B for Fe-AIB is 8.7199 and for Fe-AIL is 5.7896. The range of binding energy for the mechanism of ion exchange is 8–16 kJ/mol. The low value of binding energy in case of Fe-AIL suggests weak interaction between the solute and adsorbent, and the probable mechanism could be ion exchange. The comparative low value of R^2 for both the adsorbents infers that As (V) adsorption does not closely follow TM isotherm.

D–RM Isotherm

The D–RM isotherm is more general in nature than LM as there is no assumption of homogenous surface or constant potential of adsorption. The linear form of D–RM Isotherm is expressed as:

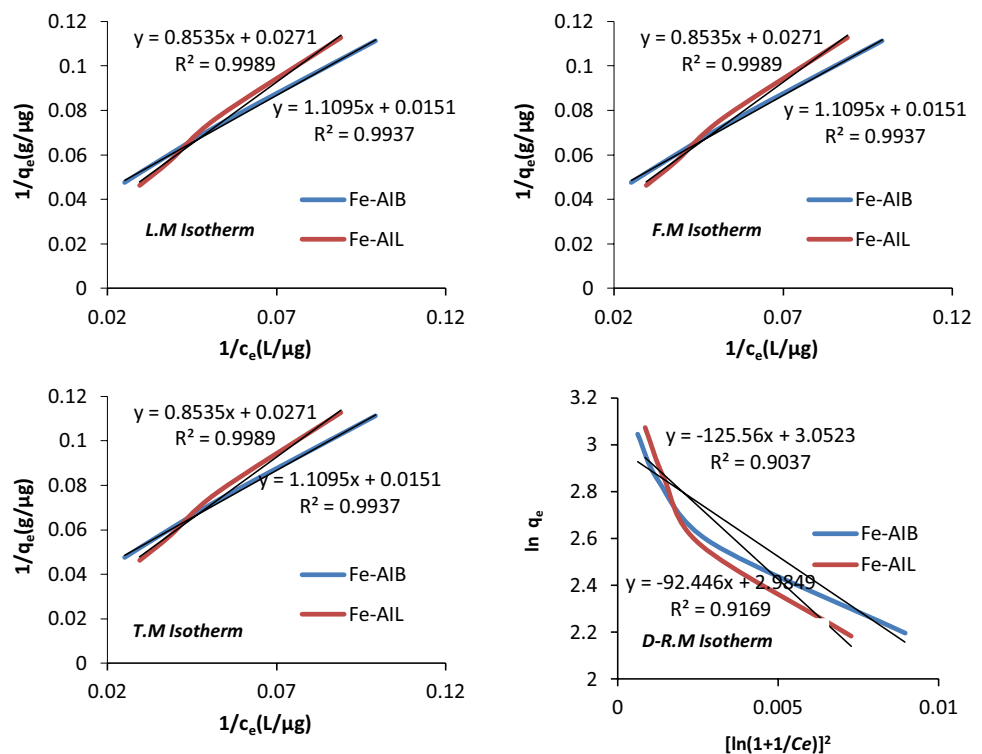
$$\ln q_e = \ln q_{\max} - \frac{1}{2E^2} \left\{ RT \ln \left(1 + \frac{1}{c_e} \right) \right\}^2 \quad (14)$$

where E (kJ/mol) represents mean adsorption energy. Other parameters of Eq. (14) are the same as discussed in earlier equations. If the E value for adsorption lies in the range 8–16, chemisorption is dominating phenomenon. For E values less than 8, physio-sorption dominates (Wu et al. 2012). The E value for Fe-AIB is greater than 8, and it corresponds to chemisorption. For Fe-AIL, E value is less than 8 which indicates physical adsorption and suggests that sorption process onto the surface of Fe-AIL may not be only ion exchange mechanism or chemisorption. Thus for adsorption of As (V) by Fe-AIL, pore filling can also be a feasible process.

Thermodynamic assessments

The thermodynamic analysis is used to determine the spontaneity of the process. Also, the analysis reveals endothermic or exothermic nature of the reaction, change in entropy or

Fig. 14 Four adsorption equilibrium plots: LM isotherm, FM isotherm, TM isotherm, D–RM isotherm. (Experimental conditions: dose, 1 g; contact time, 60 min; pH, 6.0; temperature, 25 °C; agitation speed, 80 rpm)



change in ΔG° (Gibbs free energy) and basis of excitation. Various thermodynamic parameters like ΔH° (enthalpy change), ΔS° (entropy change) and ΔG° can be calculated from the following equations (Balarak et al. 2016):

$$\Delta G^\circ = -RT \ln K_c \tag{15}$$

where K_c is equilibrium thermodynamic constant. Other parameters of Eq. (15) are the same as discussed in earlier equations. The slope and intercept of a linear plot between $\log K_c$ and $-1/T$ from Eq. (16) would yield ΔH° and ΔS° , respectively.

$$\text{Log } K_c = \frac{\Delta S^\circ}{2.303R} - \frac{\Delta H^\circ}{2.303RT} \tag{16}$$

The findings of thermodynamic assessments for adsorption of As (V) on Fe-AIB and Fe-AIL are presented in

Table 7. For Fe-AIB, it can be seen from the table that all the values of ΔG° at different temperatures are negative which infers about spontaneous nature of adsorption of As (V) on to Fe-AIB, while the decrement in values of ΔG° with increase in temperature shows that spontaneity increases with increase in temperature (Bulut and Tez 2007). The values of ΔH° and ΔS° are $34.6891 \text{ kJ mol}^{-1}$ and $13.4454 \text{ kJ mol}^{-1}$ for Fe-AIB. The typical standard value of ΔH° falls in the range $20.9\text{--}418.4 \text{ kJ/mol}$ for the heat of chemical reactions, so it can be concluded that adsorption with Fe-AIB takes place through chemisorption and nature of the process was endothermic. The positive value of ΔS° confirms the increment of free active sites at the interface of solid–liquid during adsorption. For Fe-AIL, the positive value of ΔG° implies increment in randomness of the process of adsorption. The positive value of ΔH° and ΔS° infers that the nature of adsorbent is endothermic and randomness

Table 7 Thermodynamic parameters for adsorption of As (V) by Fe-AIB and Fe-AIL

Thermodynamics parameters	Temp (K)	Fe-AIB	Fe-AIL
		ΔG° (KJ/mol)	ΔG° (KJ/mol)
Standard Gibb’s free energy	298	−2.6326	6.9815
	308	−2.7318	6.3114
	318	−2.7511	5.9887
	328	−2.7888	5.7719
	338	−2.7891	5.7413
Standard enthalpy change	ΔH° (kJ mol ^{−1})	34.6891	1.1918
Standard entropy change	ΔS° (kJ mol K ^{−1})	13.4454	7.0912

of the process increases with temperature (Bazrafshan et al. 2015).

Effect of co-existing ions

Arsenic-contaminated groundwater might also contain various anions that can hamper the process of adsorption and can be competitor for As (V) ions for adsorption. Phosphate (PO_4^{3-}), sulphate (SO_4^{2-}), silicate (SiO_3^{2-}) and nitrate (NO_3^-) are the major co-existing ions with arsenic, which has the potential to inhibit its adsorption. For understanding the influence of co-existing ions on the removal of arsenate, solution of As (V) was spiked with PO_4^{3-} , SO_4^{2-} and NO_3^- and As (V) removal was determined. At a constant pH 6, phosphate and silicate ions cause the most significant depression in removal percentage of As (V), for both the adsorbents as shown in Fig. 15. The most massive reduction in percentage removal is observed due to the presence of phosphate ions and then by silicate ions under experimental conditions. It is majorly these two anions which compete with As (V) species to be adsorbed by Fe-AIB and Fe-AIL. Due to inner core complexation, PO_4^{3-} and SiO_3^{2-} get strongly adsorbed by surface of Fe oxide. PO_4^{3-} adsorbs Fe oxide when complex on the surface is formed with surface R-OH group (Goldberg 1985).

On the other hand, nitrate and sulphate ions have minimal impact on per cent removal of As (V). SO_4^{2-} and NO_3^- can get adsorb on to the surface by complexation of the outer and inner surface. Also their binding ability with metal oxides is poor as in comparison with As (V) (Meng et al. 2000). Hence, the adsorption of As (V) was significantly influenced by phosphate and silicate ions.

Desorption and regeneration capacity

Reusability of adsorbent with good adsorption capacity, without losing its inherent characteristics, is essential from

economic perspective. For a big-scale application or industrial use, it is crucial to make repetitive use of the active sites of the worn adsorbent. This will not only cut down the cost of operation but also will deteriorate the risk of the secondary pollutant. Significant performance for adsorption as well as for desorption is the essential characteristics of an efficient adsorbent. Different types of eluents were used in the past for the evaluation of adsorption–desorption characteristics. In the present study, NaOH solutions of different strengths were used to analyse desorption performance, and their influence on desorption of is presented in Fig. 16. The use of NaOH solution for desorption of As(V) was based on anticipation that the probability of OH⁻ ions to compete with already adsorbed As (V) on Fe-AIB and Fe-AIL. Strong alkalis much supports the desorption of As (V) ions. It can be seen from Fig. 16 that with increase in strength of sodium hydroxide solution, the percentage desorption keeps on increasing for both the adsorbents. 49.1% of adsorbed arsenate ion from Fe-AIB desorbs when 0.02 M sodium hydroxide solution was used. The value goes up to 71.3% when the concentration of sodium hydroxide solution was 0.1 M. Concerning Fe-AIL, high removal percentage (up to 88.78) was achieved at higher concentration (0.1 M). Both Fe-AIB and Fe-AIL are subjected to analysis for reusability as shown in Fig. 17. For Fe-AIB, appreciable decrement is observed after 5 cycles, while in Fe-AIL, the trend of decrements starts after third cycle only.

Adsorption capacity comparison of different adsorbents from the literature for removal of As (V)

The adsorption potential of Fe-AIB and Fe-AIL needs to be compared with other adsorbents used for the same purpose to justify their validity. The value of q_{max} at different operating conditions is listed in Table 8. It is not possible to compare the adsorption capacity of Fe-AIB and Fe-AIL directly with other adsorbents due to different operating conditions.

Fig. 15 Effect of co-existing ions on the adsorption of As(V). (Experiment conditions: initial As(V) concentration 100 $\mu\text{g/L}$, adsorbent dosage 1.0 g/L, solution pH 6.0, agitation speed 60 rpm)

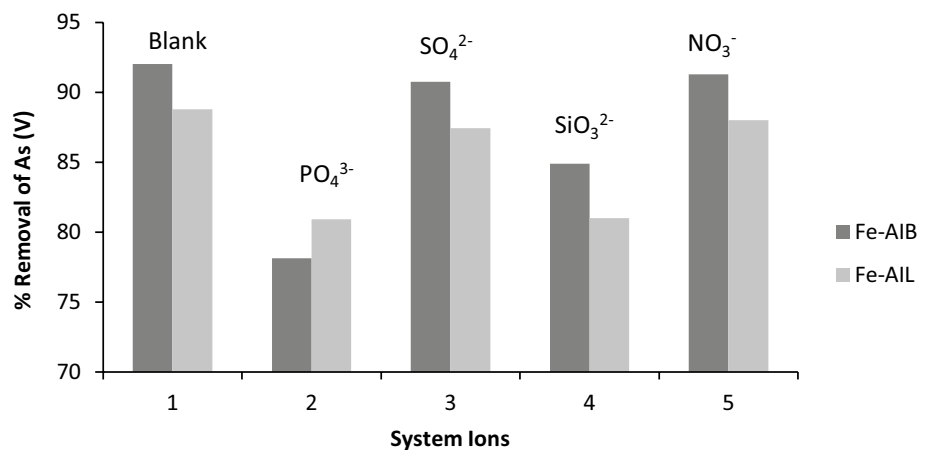


Fig. 16 desorption study on Fe-AIB and Fe-AIL by NaOH as desorbing agent

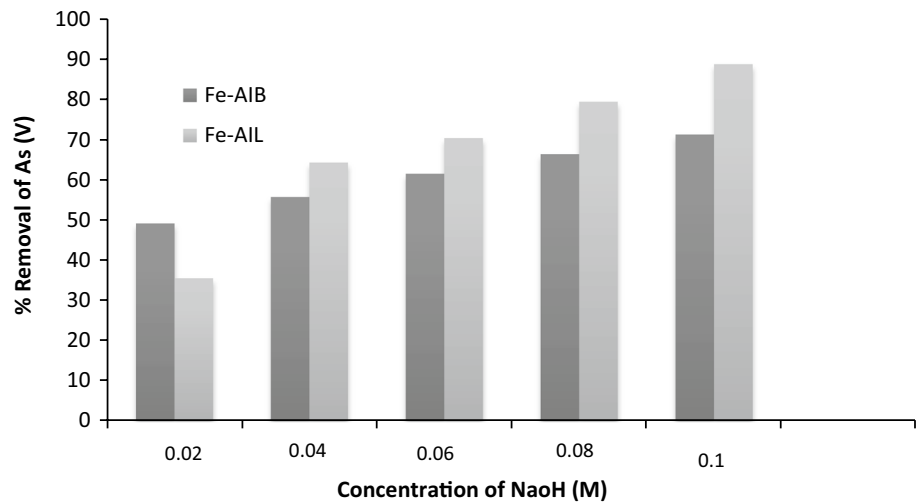


Fig. 17 Variation in percentage removal of As(VI) by repetitive use of Fe-AIB and Fe-AIL

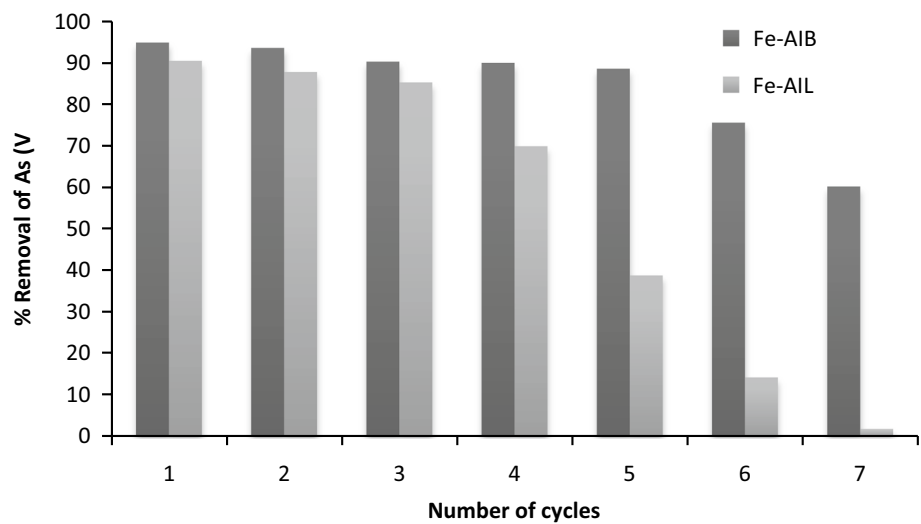


Table 8 Comparison of adsorption capacity of various adsorbent adsorbents used for As (V) remediation

Adsorbent	Initial pH	T (K)	Dose (g/L)	Conc. (mg/L)	q _{max} (mg/g)	References
Manganese oxide loaded sand	4.5	298	2.00	1–100	0.09	Chang et al. (2009)
Laterite (Raw)	5.5	302	20.0	0.2–20	0.51	Maiti et al. (2008)
Coal mine drainage sludge coated polyurethane	6.0	298	1.0	1–100	7.3	Kumar et al. (2020)
Fe-Hickory biochar	5.8	298	1.0	0.1–55	16.0	Hu et al. (2015)
FeCl ₃ treated lemon residues	6.5	298	0.1	1–100	0.474	Marín-Rangel et al. (2012)
Waste Fe–Mn oxides embedded in chitosan	6.0–6.5	298	1.0	100	26.80	Ociński and Mazur (2020)
Amino-functionalized γFe ₂ O ₃ -β-Zeolite	5.0	353	10	5–50	30	Faalzadeh and Faghihian (2015)
Thioglycolated sugarcane carbon	6.0	303	1.0	15	0.085	Roy et al. (2013)
Fe-AIB	6.0	298	1.0	0.1–0.3	0.365	Present study
Fe-AIL	4.9	298	1.0	0.1–0.3	0.298	Present study

However, both the adsorbents used in the present study show good adsorption capacity when compared with other adsorbents. The variation in adsorption capacity for different adsorbents is due to difference in individual properties (functional group, surface structure and available surface area) of adsorbents (Ozsoy and Kumbur 2006).

Conclusion

The present study shows that macro- and microparticles synthesized from the *Azadirachta indica* tree, like Fe-AIL and Fe-AIB, can be used as efficient adsorbent for the remediation of As (V)-contaminated wastewater. It has been observed that various process parameters like pH, adsorbent dose, contact time, initial arsenate concentration, operating temperature and stirring rate affect the process of adsorption. Adsorption studies under different experimental conditions indicate rapid adsorption of As (V) in the first 45 min for Fe-AIB and 30 min for Fe-AIL, thereafter it slowly increases to attain equilibrium in about one hour. The maximum removal of As (V) was noted at 6.0 pH using Fe-AIB and at 4.0 with Fe-AIL. The removal percentage of As (V) from aqueous solution by Fe-AIB was 96.5% (36.5 $\mu\text{g/g}$) and 90.3% for Fe-AIL. In the analysed range of concentration, the equilibrium data were very well fitted to Langmuir (LM), Freundlich (FM), Temkin isotherm (TM) and reasonably will be fitted to Dubinin–Radushkevich (D–RM) isotherm. The arsenate adsorption kinetics onto Fe-AIB and Fe-AIL follows second-order equation. Different thermodynamic parameters including ΔG° , ΔS° and ΔH° were calculated by using adsorption isotherm data at various temperatures. For Fe-AIB, negative values of ΔG° imply spontaneous adsorption and positive value of ΔG° for Fe-AIL indicates the endothermic nature of its interaction with As (V) ions for adsorption. The efficacy is evaluated in terms of reusability. By analysing adsorption/desorption trends of Fe-AIB and Fe-AIL, we can conclude that Fe-AIB is more suitable than Fe-AIL for continuous flow operation. A consistent high efficiency of approximately 90 per cent after the repeated operation even after five cycles reflects high regeneration capacity of Fe-AIB.

Acknowledgments The authors would like to thank Post-Graduation Research Laboratory, IIT Kanpur, for providing assistance with SEM, XRD, BET and FTIR analysis.

Funding The author(s) received no specific funding for this work.

Compliance with ethical standards

Conflict of interest The authors declare that they have no conflict of interest.

Open Access This article is licensed under a Creative Commons Attribution 4.0 International License, which permits use, sharing, adaptation, distribution and reproduction in any medium or format, as long as you give appropriate credit to the original author(s) and the source, provide a link to the Creative Commons licence, and indicate if changes were made. The images or other third party material in this article are included in the article's Creative Commons licence, unless indicated otherwise in a credit line to the material. If material is not included in the article's Creative Commons licence and your intended use is not permitted by statutory regulation or exceeds the permitted use, you will need to obtain permission directly from the copyright holder. To view a copy of this licence, visit <http://creativecommons.org/licenses/by/4.0/>.

References

- Ahsan H et al (2000) Associations between drinking water and urinary arsenic levels and skin lesions in Bangladesh. *J Occup Environ Med* 42(12):1195–1201
- Albores A et al (1996) Enhanced arsenite-induced hepatic morphological and biochemical changes in phenobarbital-pretreated rats. *Toxicol Pathol* 24(2):172–180
- Ali S et al (2020) High sorption efficiency for As (III) and As (V) from aqueous solutions using novel almond shell biochar. *Chemosphere* 243:125330
- Ansari R, Sadegh M (2007) Application of activated carbon for removal of arsenic ions from aqueous solutions. *J Chem* 4(1):103–108
- Asere T et al (2017) Removal of arsenic (V) from aqueous solutions using chitosan–red scoria and chitosan–pumice blends. *Int J Environ Res Public Health* 14(8):895
- Asere TG, Stevens CV, Du Laing G (2019) Use of (modified) natural adsorbents for arsenic remediation: a review. *Sci Total Environ* 676:706–720
- Balarak D et al (2016) Kinetic, isotherms and thermodynamic modeling for adsorption of acid blue 92 (ab92) from aqueous solution by modified azolla filicoides. *Fresenius Environ Bull* 25(5):1322–1331
- Baris D et al (2016) Elevated bladder cancer in Northern New England: the role of drinking water and arsenic. *JNCI: J Natl Cancer Inst* 108(9):1–9
- Bayramoglu G et al (2009) Biosorption of phenol and 2-chlorophenol by *Funalia trogii* pellets. *Biores Technol* 100(10):2685–2691
- Bazarafshan E (2017) Efficiency of combined processes of coagulation and modified activated bentonite with sodium hydroxide as a biosorbent in the final treatment of leachate: kinetics and thermodynamics. *J Health Res Commun* 3(3):58–69
- Bazrafshan E et al (2015) Equilibrium and thermodynamics studies for decolorization of reactive black 5 (RB5) by adsorption onto MWCNTs. *Desal Water Treat* 54(8):2241–2251
- Bhattacharya A, Mandal S, Das S (2006) Adsorption of Zn (II) from aqueous solution by using different adsorbents. *Chem Eng J* 123(1–2):43–51
- Bhattacharya A et al (2008) Adsorption, kinetics and equilibrium studies on removal of Cr(VI) from aqueous solutions using different low-cost adsorbents. *Chem Eng J* 137(3):529–541
- Bhaumik R et al (2011) Predicting iron adsorption capacity and thermodynamics onto calcareous soil from aqueous solution by linear regression and neural network modeling. *Univ J Environ Res Technol* 1(4):486–499
- Boddu VM et al (2008) Removal of arsenic (III) and arsenic (V) from aqueous medium using chitosan-coated biosorbent. *Water Res* 42(3):633–642
- Božić D et al (2009) Adsorption of heavy metal ions by sawdust of deciduous trees. *J Hazard Mater* 171(1–3):684–692

- Bulut Y, Tez Z (2007) Adsorption studies on ground shells of hazelnut and almond. *J Hazard Mater* 149(1):35–41
- Bulut Y, Gözübenli N, Aydın H (2007) Equilibrium and kinetics studies for adsorption of direct blue 71 from aqueous solution by wheat shells. *J Hazard Mater* 144(1–2):300–306
- Chang Y-Y, Lee S-M, Yang J-K (2009) Removal of As (III) and As (V) by natural and synthetic metal oxides. *Colloids Surf A* 346(1–3):202–207
- Chen C-L et al (2004) Ingested arsenic, cigarette smoking, and lung cancer risk: a follow-up study in arseniasis-endemic areas in Taiwan. *JAMA* 292(24):2984–2990
- Chen T et al (2020) Synthesis and characterization of a novel magnetic calcium-rich nanocomposite and its remediation behaviour for As (III) and Pb(II) co-contamination in aqueous systems. *Sci Total Environ* 706:135122
- Chiban M et al (2016) Equilibrium and thermodynamic studies for the removal of As (V) ions from aqueous solution using dried plants as adsorbents. *Arab J Chem* 9:S988–S999
- Chien S, Clayton W (1980) Application of Elovich equation to the kinetics of phosphate release and sorption in soils 1. *Soil Sci Soc Am J* 44(2):265–268
- Choudhury TR et al (2014) Arsenic (III) removal from real-life groundwater by adsorption on neem bark (*Azadirachta indica*). *Int Res J Pure Appl Chem* 4:594–604
- Cui J et al (2019) Oxidation and removal of As (III) from soil using novel magnetic nanocomposite derived from biomass waste. *Environ Sci: Nano* 6(2):478–488
- Cullen W, Reimer K (1989) Arsenic speciation in the environment. *Chem Rev* 89:713–764
- Depci T, Kul AR, Önal Y (2012) Competitive adsorption of lead and zinc from aqueous solution on activated carbon prepared from Van apple pulp: study in single- and multi-solute systems. *Chem Eng J* 200–202:224–236
- El Saliby I et al (2013) Adsorption and photocatalytic degradation of methylene blue over hydrogen–titanate nanofibres produced by a peroxide method. *Water Res* 47(12):4115–4125
- Faalzadeh M, Faghihian H (2015) Separation of arsenic from aqueous solutions by amino-functionalized γ -Fe₂O₃- β -zeolite. *Sep Sci Technol* 50(7):958–964
- Ferreccio C et al (2013) Case-control study of arsenic in drinking water and kidney cancer in uniquely exposed Northern Chile. *Am J Epidemiol* 178(5):813–818
- Freundlich H (1906) *Stoichiometrie und Verwandtschaftslehre. Zeitschrift fuer Physikalische Chemie* 57:385–470
- Gnanasangeetha D, SaralaThambavani D (2015) Modelling of As³⁺ adsorption from aqueous solution using *Azadirachta indica* by artificial neural network. *Desalin Water Treat* 56(7):1839–1854
- Goldberg S (1985) Chemical modeling of anion competition on goethite using the constant capacitance model. *Soil Sci Soc Am J* 49(4):851–856
- Hao L et al (2018) A critical review on arsenic removal from water using iron-based adsorbents. *RSC Adv* 8(69):39545–39560
- Hare V et al (2019) Arsenic toxicity and its remediation strategies for fighting the environmental threat. In: Bharagava RN, Chowdhary P (eds) *Emerging and eco-friendly approaches for waste management*. Springer, Berlin, pp 143–170
- Hu X et al (2015) Batch and column sorption of arsenic onto iron-impregnated biochar synthesized through hydrolysis. *Water Res* 68:206–216
- Jadhav AH et al (2015) Preparation, characterization, and kinetic study of end opened carbon nanotubes incorporated polyacrylonitrile electrospun nanofibers for the adsorption of pyrene from aqueous solution. *Chem Eng J* 259:348–356
- Juang R-S, Chen M-L (1997) Application of the Elovich equation to the kinetics of metal sorption with solvent-impregnated resins. *Ind Eng Chem Res* 36(3):813–820
- Kalaruban M et al (2019) Iron-impregnated granular activated carbon for arsenic removal: application to practical column filters. *J Environ Manag* 239:235–243
- Kanwal F et al (2012) Isothermal and thermodynamical modeling of chromium (III) adsorption by composites of polyaniline with rice husk and saw dust. *J Chil Chem Soc* 57(1):1058–1063
- Kumar R et al (2020) Waste sludge derived adsorbents for arsenate removal from water. *Chemosphere* 239:124832
- Kumari P et al (2005) Arsenic removal from the aqueous system using plant biomass: a bioremediation approach. *J Ind Microbiol Biotechnol* 32(11–12):521–526
- Kwok RK, Kaufmann RB, Jakariya M (2006) Arsenic in drinking-water and reproductive health outcomes: a study of participants in the Bangladesh integrated nutrition programme. *J Health Popul Nutr* 24:190–205
- Langmuir I (1918) The adsorption of gases on plane surfaces of glass, mica and platinum. *J Am Chem Soc* 40(9):1361–1403
- Liu J et al (2014) ZnCl₂ activated electrospun carbon nanofiber for capacitive desalination. *Desalination* 344:446–453
- Lyu H et al (2020) Biochar/iron (BC/Fe) composites for soil and groundwater remediation: synthesis, applications, and mechanisms. *Chemosphere* 246:125609
- Maiti A et al (2008) Batch and column study: adsorption of arsenate using untreated laterite as adsorbent. *Ind Eng Chem Res* 47(5):1620–1629
- Mandal BK, Suzuki KT (2002) Arsenic round the world: a review. *Talanta* 58(1):201–235
- Marín-Rangel VM et al (2012) As (V) biosorption in an aqueous solution using chemically treated lemon (*Citrus aurantifolia* swingle) residues. *J Food Sci* 77(1):T10–T14
- Meng X, Bang S, Korfiatis GP (2000) Effects of silicate, sulfate, and carbonate on arsenic removal by ferric chloride. *Water Res* 34(4):1255–1261
- Mondal NK et al (2012) Studies on defluoridation of water by tea ash: an unconventional biosorbent. *Chem Sci Trans* 1(2):239–256
- Naeem S et al (2016) Sorption properties of iron impregnated activated carbon web for removal of methylene blue from aqueous media. *Fibers Polym* 17:1245–1255
- Nandi BK, Goswami A, Purkait MK (2009) Adsorption characteristics of brilliant green dye on kaolin. *J Hazard Mater* 161(1):387–395
- Nicomel N et al (2016) Technologies for arsenic removal from water: current status and future perspectives. *Int J Environ Res Public Health* 13(1):62
- Ociński D, Mazur P (2020) Highly efficient arsenic sorbent based on residual from water deironing—Sorption mechanisms and column studies. *J Hazard Mater* 382:121062
- Ozsoy HD, Kumbur H (2006) Adsorption of Cu (II) ions on cotton boll. *J Hazard Mater* 136(3):911–916
- Rajesh KR et al (2010) Equilibrium and kinetic studies on sorption of malachite green using *Hydrilla verticillata* biomass
- Rango T et al (2013) Mobilization of arsenic and other naturally occurring contaminants in groundwater of the Main Ethiopian Rift aquifers. *Water Res* 47(15):5801–5818
- Ranjan A (2019) Spatial analysis of arsenic contamination of groundwater around the world and India
- Ravikovitch PI, Neimark AV (2006) Density functional theory model of adsorption on amorphous and microporous silica materials. *Langmuir* 22(26):11171–11179
- Rossman TG, Uddin AN, Burns FJ (2004) Evidence that arsenite acts as a cocarcinogen in skin cancer. *Toxicol Appl Pharmacol* 198(3):394–404
- Roy P et al (2013) Removal of arsenic (III) and arsenic (V) on chemically modified low-cost adsorbent: batch and column operations. *Appl Water Sci* 3(1):293–309

- Roy P, Mondal N, Das K (2014) Modeling of the adsorptive removal of arsenic: a statistical approach. *J Environ Chem Eng* 2(1):585–597
- Roy P et al (2017) Modeling of the adsorptive removal of arsenic (III) using plant biomass: a bioremedial approach. *Appl Water Sci* 7(3):1307–1321
- Ryu S-R et al (2017) Adsorption of As (III) and As (V) in groundwater by Fe–Mn binary oxide-impregnated granular activated carbon (IMIGAC). *J Taiwan Inst Chem Eng* 72:62–69
- Sari A, Tuzen M (2010) Biosorption of As (III) and As (V) from aqueous solution by lichen (*Xanthoria parietina*) biomass. *Sep Sci Technol* 45(4):463–471
- Shah I et al (2015) Iron impregnated activated carbon as an efficient adsorbent for the removal of methylene blue: regeneration and kinetics studies. *PLoS ONE* 10(4):e0122603
- Shankar S, Shanker U, Shikha (2014) Arsenic contamination of groundwater: a review of sources, prevalence, health risks, and strategies for mitigation. *Sci World J* 2014:304524
- Singh TS, Pant K (2004) Equilibrium, kinetics and thermodynamic studies for adsorption of As (III) on activated alumina. *Sep Purif Technol* 36(2):139–147
- Smeester L, Fry RC (2018) Long-term health effects and underlying biological mechanisms of developmental exposure to arsenic. *Curr Environ Health Rep* 5(1):134–144
- Smith AH et al (2006) Increased mortality from lung cancer and bronchiectasis in young adults after exposure to arsenic in utero and in early childhood. *Environ Health Perspect* 114(8):1293–1296
- Srivastava R, Rupainwar DC (2011) A comparative evaluation for adsorption of dye on Neem bark and mango bark powder. *Indian J Chem Technol* 18:67–75
- Taştan BE, Duygu E, Dönmez G (2012) Boron bioremoval by a newly isolated *Chlorella* sp. and its stimulation by growth stimulators. *Water Res* 46(1):167–175
- Tchounwou P et al (2015) Arsenic and cancer, handbook of arsenic toxicology. Elsevier Inc., Amsterdam
- Tchounwou PB et al (2019) State of the science review of the health effects of inorganic arsenic: perspectives for future research. *Environ Toxicol* 34(2):188–202
- Temkin M (1940) Kinetics of ammonia synthesis on promoted iron catalysts. *Acta physiochim. URSS* 12:327–356
- Thapa S, Pokhrel MR (2012) Removal of as (III) from aqueous solution using Fe(III) loaded pomegranate waste. *J Nepal Chem Soc* 30:29–36
- Tiwari D et al (1999) Biosorptive behaviour of Mango (*Mangifera indica*) and Neem (*Azadirachta indica*) bark for Hg^{2+} , Cr^{3+} and Cd^{2+} toxic ions from aqueous solutions: a radiotracer study. *Appl Radiat Isot* 50(4):631–642
- Tripathy SS, Raichur AM (2008) Enhanced adsorption capacity of activated alumina by impregnation with alum for removal of As (V) from water. *Chem Eng J* 138(1–3):179–186
- Tsai S-Y et al (2003) The effects of chronic arsenic exposure from drinking water on the neurobehavioral development in adolescence. *Neurotoxicology* 24(4–5):747–753
- Tseng C-H (2009) A review on environmental factors regulating arsenic methylation in humans. *Toxicol Appl Pharmacol* 235(3):338–350
- Tseng C-H et al (2000) Long-term arsenic exposure and incidence of non-insulin-dependent diabetes mellitus: a cohort study in arseniasis-hyperendemic villages in Taiwan. *Environ Health Perspect* 108(9):847–851
- Upadhyay MK et al (2019) An assessment of arsenic hazard in groundwater–soil–rice system in two villages of Nadia district, West Bengal, India. *Environ Geochem Health* 41:1–15
- Verma L et al (2019) As (III) and As (V) removal by using iron impregnated biosorbents derived from waste biomass of *Citrus limmeta* (peel and pulp) from the aqueous solution and ground water. *J Environ Manag* 250:109452
- Wasserman GA et al (2004) Water arsenic exposure and children's intellectual function in Arahazar, Bangladesh. *Environ Health Perspect* 112(13):1329–1333
- Wu Y et al (2012) The characteristics of waste *Saccharomyces cerevisiae* biosorption of arsenic (III). *Environ Sci Pollut Res* 19(8):3371–3379
- Yadav SK, Singh DK, Sinha S (2014) Chemical carbonization of papaya seed originated charcoals for sorption of Pb(II) from aqueous solution. *J Environ Chem Eng* 2(1):9–19
- Yakun H et al (2011) Fluoride removal by lanthanum alginate bead: adsorbent characterization and adsorption mechanism. *Chin J Chem Eng* 19(3):365–370
- Zeng H et al (2020) Arsenic (V) removal by granular adsorbents made from water treatment residuals materials and chitosan. *Colloids Surf A* 585:124036
- Zhu S et al (2020) Goethite modified biochar as a multifunctional amendment for cationic Cd (II), anionic As (III), roxarsone, and phosphorus in soil and water. *J Clean Prod* 247:119579

Publisher's Note Springer Nature remains neutral with regard to jurisdictional claims in published maps and institutional affiliations.



Optimization of Arsenate Adsorption over Aluminum-Impregnated Tea Waste Biochar Using RSM–Central Composite Design and Adsorption Mechanism

Ghazi Mohd. Sawood¹; Ashutosh Mishra²; and S. K. Gupta³

Abstract: Aluminum-impregnated tea waste activated carbon (Al-TC) synthesized for adsorption of arsenate at optimum conditions. The Al-TC produced through slow pyrolysis of tea waste followed by the impregnation of anhydrous aluminum. The operating conditions (initial metal concentration, pH, contact time, and adsorbent dose) were optimized using response surface methodology–central composite design statistical technique, with percentage arsenate removal as a targeted response. The response surface analyses and analysis of variance reveals an excellent fit of experimental data into the quadratic model, and the interactive effect of pH and initial concentration was highly significant on arsenate removal capacity. The obtained optimal conditions corresponding for good percentage arsenate removal were at 100 µg/L, pH 6.0, adsorbent dose 1.0 g, and contact time 1 h. The synthesized mesoporous adsorbent possesses a high surface area of 396 m²/g and an excellent uptake capacity of 99.6 µg/g. The probable mechanism for adsorption proposes that electrostatic forces and hydrogen bonding are responsible for adsorption of arsenic species (H₂AsO₄⁻ and H₃AsO₄) at pH 2.0, the arsenic species, including HAsO₄²⁻ and H₂AsO₄⁻ are removed through adsorption and ion exchange at pH 6.0, and weak adsorption of AsO₄³⁻ through ion exchange at pH 10.0. Coexisting PO₄³⁻ and SiO₃²⁻ ions negatively affect the arsenate adsorption whereas CO₃²⁻, SO₄²⁻, Ca²⁺, and Mg²⁺ ions do not have a significant impact on the adsorption process. The arsenate's using Al-TC obeyed the Langmuir isotherm model and the kinetic data best fits into the pseudo-second order model. The adsorption process has proven to be spontaneous and endothermic. The produced Al-TC can be used very effectively for the treatment of arsenate containing aqueous media. DOI: 10.1061/(ASCE)HZ.2153-5515.0000581. © 2020 American Society of Civil Engineers.

Author keywords: Tea waste; Aluminum impregnation; Arsenate; Response surface methodology (RSM); Adsorption mechanism.

Introduction

For human societies, groundwater serves as the chief water resource and accounts for approximately 65% annual water supply. Several heavy metals contaminate the groundwater. These heavy metals are one of the main hazards associated with water resources; contamination by arsenic is one of them. Millions of people from countries including India, Bangladesh, Taiwan, China, Japan, Canada, New Zealand, and the United States are dependent on groundwater containing the elevated arsenic level for drinking purposes (Mohan and Pittman 2007). Arsenic is a chemical element present in group-15 of the periodic table and is a p-block element with atomic number 15 and atomic mass 33 (Golami et al. 2009). Arsenic is nonbiodegradable and a natural component of earth present in the environment in both organic and inorganic form. The organic form includes mono-methyl arsenate (MMA, dimethyl, and arsenate-DMA) whereas the inorganic form includes arsine, which is highly toxic and flammable. It is one of the most dangerous contaminants for underground water and is a highly toxic in the organic form (Kumaresan and Riyazuddin 2001). Arsenic contamination

of groundwater results from both natural and anthropogenic activities that cause harmful effects on the environment and human health. The chief anthropogenic sources include burning fossil fuels, mining, smelting, and combustion of wood (Ranjan 2019). The main natural source includes weathering of minerals and rocks, volcanic eruptions, and all biological activities (Kanel et al. 2005). There are many ways arsenic enters the human body, but encystation through the food chain is predominant. Several diseases are caused by arsenic such as dysfunction in the digestive system, shock leading to death, dysfunction of the respiratory system, and hypertension (Sawood and Gupta 2020). The International Agency for Research of Cancer (IARC) declared inorganic arsenic as a group A carcinogenic compound that poses the greatest threat to human health (Adlnasab et al. 2019; Fakhri et al. 2018). Some carcinogenic effects are skin cancer, bladder cancer, lung cancer, and liver cancer. Arsenic exposure is linked to cardiovascular effect, such as elevated blood pressure, hypertension, coronary heart disease (CHD), stroke, and peripheral arterial disease (Tseng 2009). Owing to arsenic's toxic nature, the World Health Organization (WHO) has set a 10 µg/L allowable limit of arsenic in drinking water. Arsenic chemistry in water is prominently affected by aquatic system viz precipitation, oxidation-reduction, and ligand exchange (Baskan and Pala 2011). The compounds of arsenic such as arsenious acid, arsenic acid, methyl arsenic acid, dimethyl arsenic, arsenate, and arsenite are perceived in the environment. The aquatic system majorly comprises arsenic with +3 (arsenite) and +5 (arsenate) oxidation states (Eljamal et al. 2011). Out of arsenic's two forms observed in naturally contaminated water, arsenite has proven to be more toxic than the arsenate. The arsenate species predominates under oxidizing and aerobic conditions, and under moderately reducing and anaerobic conditions, the arsenite species predominates (Patel et al. 2020). For remediation of hazards caused by arsenate in the aquatic system, many techniques are available that ensure the supply of arsenic-free water or reduce the

¹Ph.D. Scholar, Dept. of Chemical Engineering, Harcourt Butler Technical Univ., Kanpur, UP 208002, India (corresponding author). Email: mohdsaud22@gmail.com

²Assistant Professor, Dept. of Chemical Engineering, Dr.AITH, Awadhपुरi, Kanpur, UP 208024, India. Email: ashutosh@aith.ac.in

³Associate Professor, Dept. of Chemical Engineering, Harcourt Butler Technical Univ., Kanpur, UP 208002, India. Email: skgupta@hbtu.ac.in

Note. This manuscript was submitted on July 30, 2020; approved on September 22, 2020; published online on November 25, 2020. Discussion period open until April 25, 2021; separate discussions must be submitted for individual papers. This paper is part of the *Journal of Hazardous, Toxic, and Radioactive Waste*, © ASCE, ISSN 2153-5493.

quantity of arsenic in groundwater. Mainly these technologies are coagulation-flocculation, membrane separation (microfiltration, reverse osmosis, ultrafiltration), oxidation (e.g., biological-oxidation, photocatalytic oxidation, oxidation and filtration), ion exchange, and adsorption (activated alumina metal-organic framework, Fe-based sorbents) (Asere et al. 2017; Nicomel et al. 2016; Tripathy and Raichur 2008; Uthappa et al. 2020). Adsorption has been established as one of the best arsenic removal technologies in recent decades. Compared with the other arsenic removal techniques, adsorption is effective due to its low processing cost, easy regeneration, and sludge-free or minimal sludge operation (Boddu et al. 2008).

Activated carbon is considered organic adsorbent and has been widely used to remediate different contaminants from the aquatic system. How activation takes place can alter the functional group. The activated carbon possesses high adsorption capacity due to various forms of active groups (e.g., carbonic, hydroxyl, carboxylic acid) and a large surface area (Kanel et al. 2005). Low-cost adsorbents attracted the researchers to remediate heavy metals as they are less expensive than synthetic activated carbons and membrane separation. The process of biosorption by agro-wastes and other natural bio sorbents is considered an ecofriendly approach and has proved to be nonhazardous and cost-effective for remediation of heavy metals from the aquatic system. Biochar, which is finely powdered charcoal and possesses high surface area, is prepared by pyrolysis of biomass at a high temperature in the absence or limited supply of oxygen. Although biochar reportedly has limited adsorption capabilities for the remediation of arsenate from contaminated water. Biochars derived from rice husk are reported to have 25% arsenate removal (21.4 $\mu\text{g/g}$ arsenate uptake) with 90 $\mu\text{g/L}$ aqueous solution. The sewage sludge and municipal waste biochar adsorb 53% (46.8 $\mu\text{g/g}$ arsenate uptake) and 55% (49.2 $\mu\text{g/g}$ arsenate uptake), respectively, at the same initial arsenate concentration, which is less in comparison with removal by sandy loam soil (60% or 53.9 $\mu\text{g/g}$ arsenate uptake) (Agrafioti et al. 2014). Biochar derived from perilla leaf results in 76% arsenate removal (3.85 mg/g arsenic uptake) at the pyrolysis temperature of 300°C and 7 pH (Niazi et al. 2018a). Arsenate mitigation using Japanese oak wood biochar was investigated, and the batch experiments show a maximum arsenic removal capacity of 3.89 mg/g (92%) (Niazi et al. 2018b). Empty fruit bunch biochar at 8.0 pH reported having maximum arsenic removal of 5.1 mg/g (Samsuri et al. 2013). Solid waste-based biochar under optimum conditions shows 3.548 $\mu\text{g/g}$ arsenate uptake (Agrafioti et al. 2014). Moreover, MSW was also investigated for its suitability

in arsenate removal and proven to be a good biosorbent having 24.4 mg/g uptake capacity (Jin et al. 2014). Banana pith biochar shows a maximum adsorption capacity of 120 $\mu\text{g/g}$ at room temperature (Lata et al. 2019). Significant quantities of tea waste result from tea leaves extraction, carried out to produce bottled and instant teas. Tea wastes are porous, and their network structure mainly consists of hemicelluloses and cellulose, condensed tannins, structural proteins, and lignin (Cai et al. 2015). Proper recycling of tea wastes can result in a cheap source of biomass, and resolves the environmental issues related to the tea waste's simple disposal. The biomass synthesized from tea waste contains amine, carboxyl, and phenolic hydroxyl groups that synergize in physicochemical with metal ions through ion exchange or inner-sphere complex formation (Cai et al. 2015). The capability of tea waste and its biochars to effectively remediate the water containing heavy metals has already been reported (Ng et al. 2013; Pal and Maiti 2019; Panneerselvam et al. 2011).

The surface modification of biochars has been attempted by many researchers in the recent past to enhance biochar's adsorption capacity for arsenate removal (Table 1). The surface modifications include metal oxide/hydroxide addition (Alchouron et al. 2020; Huo et al. 2020; Maghsodi et al. 2018; Nguyen et al. 2020; Singh et al. 2020) and alkaline activation (Jin et al. 2014; Senthilkumar et al. 2020). Iron has been reported as the most common metal impregnated into biochar for arsenate remediation, although manganese and nickel were also used as impregnating materials (Khojasteh et al. 2016). Iron oxides/hydroxides have already proven to be efficient adsorbents for arsenic removal, due to which their decoration on biochars has been found very effective for arsenic remediation (Goldberg and Johnston 2001). However, the high temperature (500°C–600°C) requirement for pyrolysis, and high Fe to biochar mass ratio results in increased cost of manufacturing (Hognon et al. 2014; Zhang et al. 2016). In addition, as a consequence of an anoxic state that supports the reducing dissolution of Fe oxides/hydroxides to liberate ferrous ions, the iron-impregnated biochar may be unsuitable for seizing arsenate (Liu et al. 2019; Maher et al. 2018). Under anoxic conditions, the aluminum oxides/hydroxides are chemically more stable, so they are better alternatives for surface modification of biochars. A comparative performance evaluation study of Fe and Al in the pH range 3–9 reported decreased arsenate adsorption at 7–9 pH due to Fe dissolution, whereas Al maintained approximately 100% adsorption irrespective of the change in pH (Nagar et al. 2010).

To the best of our understanding and knowledge, the use of aluminum loaded tea waste biochar (Al-TC) for the remediation

Table 1. Comparison of adsorption capacities of arsenate using metal/oxide/hydroxides modified adsorbents

Adsorbent	Optimum conditions	q_{max} (mg/g)	References
MnO ₂ loaded sand	pH 4.5, Temperature 298 K, Concentration 1–100 mg/L, Dose 2.0 g	0.09	(Chang and Lin 2009)
Fe loaded Hickory biochar	pH 5.8, Temperature 298, Concentration 0.1–55 mg/L, Dose 0.1 g	16	(Hu et al. 2015)
Fe (III) chloride treated lemon waste	pH 6.5, Temperature 298, Concentration 1–100 mg/L, Dose 1.0 g	0.48	(Marin-Rangel et al. 2012)
Fe/Mn loaded chitosan	pH 6.0, Temperature 298, Concentration 1–100 mg/L, Dose 1.0 g	26.8	(Ociński and Mazur 2020)
Fe–Al hydroxides	pH 5.5, Temperature 298, Concentration 50–250 mg/L, Dose 2.2 g	78.62	(Masue et al. 2007)
MnFe ₂ O ₄ magnetic nanomaterial	pH 3.0, Temperature 298, Concentration 10 mg/L, Dose 0.3 g	90.4	(Zhang et al. 2010)
Iron oxide	pH 7.0, Concentration 275 mg/L, Dose 1.0 g	93.94	(Wei et al. 2019)
Nano needle array-decorated biochar fibres			
$\gamma\text{Fe}_2\text{O}_3$ - β -Zeolite	pH 5.0, Temperature 353 K, Concentration 35 mg/L, Dose 10.0 g	30	(Faalzadeh and Faghiehian 2015)
Fe-AIL	pH 4.9, Temperature 298 K, Concentration 0.3 mg/L, Dose 1.0 g	0.298	(Sawood and Gupta 2020)
Al impregnated waste tea biochar	pH 6.0, Temperature 298 K, Concentration 0.3 mg/L, Dose 1.0 g	0.099	This study
waste tea biochar	pH 6.0, Temperature 298 K, Concentration 0.3 mg/L, Dose 1.0 g	0.078	This study

of arsenate has not been reported yet. Owing to better chemical properties and favorable surface structure, tea waste biochar is expected to be a superior support of Al oxide instead of chars from other biomass and zeolites. The present study's objective was to evaluate and test Al-TC as an efficient and cost-effective alternative arsenate adsorbent. Batch adsorption arsenate operations were carried out to evaluate the influence of process parameters, including initial concentration, adsorbent dose, contact time, coexisting ions, and pH on arsenate removal capacity. The experimental design was used to optimize the arsenate removal test by applying central composite design (CCD) under response surface methodology (RSM) using Design-Expert software (Version 12.0.0, Stat. Ease. Inc., USA). Outcomes from chemical, structural, and morphological characterization analysis were clubbed to propose the mechanism of arsenate removal. The acquired result facilitates a scientific basis for enhanced removal application of Al-impregnated biochar to remediate of arsenate pollution.

Materials and Methods

All chemicals used in the present work were procured from M/S, Merck India Ltd., and were of analytical grade. All sample bottles and glassware were washed with a solution of detergent and rinsed with water. Afterward, these items were subjected to soaking in 15% HNO₃ solution for 12 h. Deionized (DI) water was used to prepare the aqueous solutions. Standard arsenate solutions (1,000 µg/L) were prepared by dissolving Na₂HAsO₄·7H₂O in DI water and slowly raising the volume up to 1 L.

In the present study, tea refuse was selected as the base material for biochar synthesis due to its abundant availability as waste by-products in India. The infused tea waste was collected from local tea vendors of Kanpur City, India. Tea residue was washed multiple times with DI water followed by oven drying at 70°C for 36 h. The dried product was pyrolyzed at 650°C for 4 h under an inert environment (in the absence of oxygen by circulating N₂) in a muffle furnace. The biochar thus produced was allowed to cool down and was washed multiple times with the double distilled water to remove any residual impurities or ash content. The washed char was oven dried at 90°C for 12 h and then placed in a desiccator and stored.

Instrumentation

For the analysis of arsenate concentration, Agilent inductively coupled mass plasma spectrophotometer (ICP-MS)-7900 was used. A number of pHs of different samples and solutions were investigated using a Hanna edge pH meter-HI2020. Morphological investigations of Al-TC and aluminum distribution on to char were carried out by fracturing the adsorbent to expose its internal structure using a Carl Zeiss EVO 50 scanning electron microscope (SEM). X-ray diffractometer (Bruker D8 focus) with $\lambda = 1.5418 \text{ \AA}$ and two theta angle range between 5° and 80° was used for determining Al-species. The surface area, pore size, and pore width of virgin tea waste char and Al-TC were determined using Autosorb iQ BET multipoint equipment.

Preparation of Al-Impregnated Biochar

The tea residue biochar was rinsed multiple times with DI water and dried in an oven at 70°C until the constant weight was achieved. Next, 10 g of tea residue biochar was added to a 0.5 M

aluminum sulphate solution (100 mL) in a 250 mL beaker and subjected to vigorous magnetic stirring for 12 h. After that, a dropwise infusion of 4 M ammonium hydroxide to the solution was performed until the pH attained a value of 8.0, at which almost all Al precipitated as follows:



The suspension thus formed was allowed to settle for 12 h and then dried in the oven at 110°C. The resultant solid product was washed multiple times and then oven dried at 70°C for 12 h. The dried solid was grounded and screened by allowing it to pass through a 60-mesh sieve. The obtained Al-impregnated tea residue biochar was labeled as Al-TC and stored before use.

Adsorption Process

RSM was applied for experimental design and optimization. A CCD suggested model was used for designing the number of experiments required. Initial concentration, time of contact, adsorbent dose, and pH were the significant parameters analyzed for the adsorption process. Batch operations designed by RSM were carried out by adding a definite quantity of Al-TC in an arsenate-spiked solution (100 mL) in a conical flask (250 mL) at room temperature. The mixture was subjected to magnetic stirring at 120 rpm for 45 min. The suspension was allowed to settle for 1 h and then filtered through a 0.22-µm syringe filter. The filtrate thus obtained was analyzed to determine the remaining arsenate concentration, using an ICP-MS. The percentage arsenate removal from aqueous solution was evaluated as follows:

$$\% \text{ arsenate removal} = \frac{(c_i - c_e)}{c_i} \times 100 \quad (2)$$

where c_i = initial arsenate concentration (µg/L); and c_e = arsenate concentration (µg/L) after treatment in the sample solution.

At equilibrium, the arsenate uptake capacity of Al-TC was evaluated by

$$\text{Uptake capacity } (q_e) = \frac{(c_i - c_e)}{M} \times V \quad (3)$$

where M = mass (g) of the adsorbent; and V (L) = volume of the solution.

Design of Experiment and Optimization by RSM

Optimization of the process parameters was performed using the design of experiment, which results in enhanced performance characteristics. Moreover, designing the experiments minimizes the error and number of runs (Asfaram et al. 2015). In the present work, the experiment for arsenate adsorption uses CCD with four factors [initial arsenate concentration (A), dose of adsorbent (B), contact time (C), and pH (D)] at five levels with 30 runs. The experimental design points along with values (coded) used in the experimental matrix are listed in Table 2. The numbers of factorial points are 2^n , axial points are $2n$ and central points are N_c . The central points in CCD determined data reproducibility and experimental errors. The variables (independent) with maximum and minimum levels were coded as +1 and -1, respectively. To maintain the rotation of design, the axial point's location was kept at a distance from the center. In the present study, the value was set at two (rotatable). The CCD-generated data was evaluated by multiple regression for fitting the second-order model given in the

following (Bagheri et al. 2019):

$$Y = \beta_0 + \sum_{i=1}^4 \beta_i X_i + \sum_{i=1}^4 \sum_{j=1}^4 \beta_{ij} X_i X_j + \sum_{i=1}^4 \beta_{ii} X_i^2 \quad (4)$$

where Y = percentage of adsorption (predicted response); β_0 = model const.; β_i = linear coeff.; β_{ii} = quadratic coeff.; β_{ij} = interaction coeff.; and X_i, X_j = independent variables (Torrades and García-Montaño 2014).

The modeling was conducted by adjusting first or second order equation to the outcome of the response. An analysis of variance (ANOVA) was conducted to affirm the suitability of the predicted model by evaluating R^2 (regression coefficient) value, lack of fit, and the F -value (Fisher test value). After validation, the model can be presented in 3D graphs to create a surface response to find the best possible operating conditions.

Kinetics and Adsorption Isotherm Run

To investigate the process kinetics, 1 g Al-TC was added to five flasks containing arsenate-spiked water (100 mL). The initial arsenate concentration was fixed to 100 $\mu\text{g/L}$. After that, stirring was done in magnetic stirrers at 120 rpm. The samples were collected in 15, 30, 45, 60, and 75 min. The suspension thus obtained was filtered using a syringe filter, and the filtrate was analyzed for residual arsenate ions. Since variation in pH of the solution can alter the isotherm, the adsorption isotherm test was carried out at fixed a pH (7.0). Next, 0.25–1.25 g of Al-TC was added to different flasks,

Table 2. 2^4 experimental CCD matrix

Std	Run	Factor 1 A: concentration ($\mu\text{g/L}$)	Factor 2 B: adsorbent dose (g)	Factor 3 C: time of contact (min)	Factor 4 D: pH	Response 1 as (V) removal percent
16	1	300	1.25	75	10	79.81
24	2	200	0.75	45	6	93.34
15	3	100	1.25	75	10	80.55
20	4	100	1.25	75	6	99.62
23	5	100	1.25	75	6	99.62
30	6	100	1.25	75	6	99.62
29	7	100	1.25	45	6	97.62
28	8	200	0.75	45	6	93.34
4	9	300	1.25	15	2	82.57
8	10	300	1.25	75	2	87.14
17	11	100	0.75	45	6	93.19
27	12	200	0.75	45	6	93.34
22	13	200	0.75	75	6	94.58
10	14	300	0.25	15	10	63.86
1	15	100	0.25	15	2	74.19
25	16	200	0.75	45	6	93.34
21	17	200	0.75	15	6	86.50
5	18	100	0.25	75	2	77.88
11	19	100	1.25	15	10	77.71
19	20	200	0.25	45	6	79.15
2	21	300	0.25	15	2	72.13
13	22	100	0.25	75	10	74.37
9	23	100	0.25	15	10	66.33
18	24	100	0.75	45	6	95.19
26	25	200	0.75	45	6	93.34
14	26	300	0.25	75	10	75.47
6	27	300	0.25	75	2	74.37
12	28	300	1.25	15	10	73.45
7	29	100	1.25	75	2	89.43
3	30	100	1.25	15	2	84.71

which were already filled with 100 mL of arsenate solution. Magnetic stirring followed by filtration was completed before analyzing the arsenate.

Desorption and Regeneration Analysis

Here, 1 g of Al-TC was treated using a 50 mL As (V) solution (100 $\mu\text{g/L}$) kept in a different Erlenmeyer flask during desorption studies. The Al-TC was washed multiple times with DI water to remove the unadsorbed As (V). The hydroxide treatment was given to the washed Al-TC at different concentrations before filtration. To maintain the ratio of the volume of desorption (V_d) to the volume of adsorption (V_a) equal to 0.5, V_d was taken as 25 mL and V_a was taken as 50 mL. The obtained filtrate was analyzed to discover the residual arsenate concentration. The percentage of arsenate desorb was estimated using

$$\text{Desorption \%} = \frac{\text{Arsenate Released } (\mu\text{g/L})}{\text{Initially adsorbed Arsenate } (\mu\text{g/L})} \times 100 \quad (5)$$

Here, 1 g of adsorbent was added to 50 mL As (V) solution (100 $\mu\text{g/L}$) during regeneration studies, and once the equilibrium was reached the suspension was filtered. The adsorbent was treated with 20 mL sodium hydroxide (0.1 M) for the time interval equals to equilibrium time. After hydroxide treatment, the filtration was carried out again, and thus obtained filtrate was analyzed for the desorbed arsenate quantity. Repeated washing was completed for rinsing off excess sodium hydroxide.

The blank control test was carried out under similar conditions. The quantity of arsenate wasted during the test was excluded from the results of the experiment. All the experiments were performed in triplicate at room temperature (25°C). The average experimental values were reported, and the standard deviation was represented using error bars. The experimental error (relative) was within $\pm 3\%$.

Results and Discussion

Characterization of Al-TC

The Al-TC was reported as stable under basic, dilute acidic, and aqueous conditions. At zero charge pH, the behavior of Al-TC was neutral. The physiochemical properties of Al-TC are summarized in Table 3. The yield of Al-TC and the precursor was 54.3% and 46.1%, respectively. The difference of 8.2% in the obtained value can be attributed to the hindrance caused by an Al oxide

Table 3. Physiochemical properties of Al-TC

Analysis	Value
Moisture content (%)	09.2
C (%)	51.2
N (%)	0.0
O (%)	7.1
H (%)	1.9
Ash (%)	39.6
Yield (%)	54.3
O/C	0.1
H/C	0.0
pH _{zpc}	6.6
pH _{slurry}	6.0
Specific gravity	0.3
Porosity (%)	81
Particle size (μm)	207

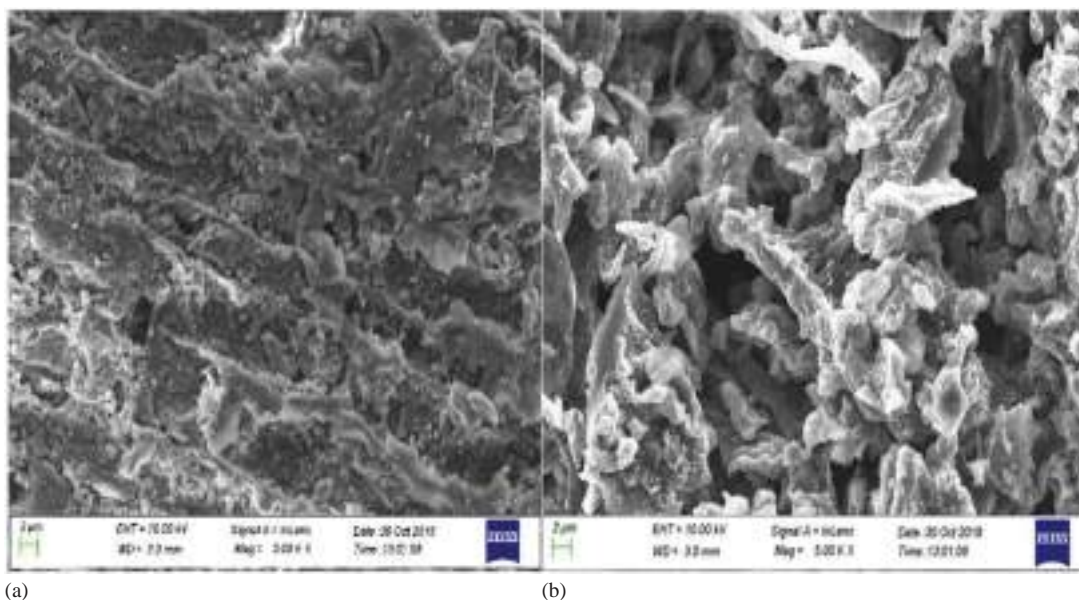


Fig. 1. SEM micrographs of (a) precursor; and (b) Al-TC.

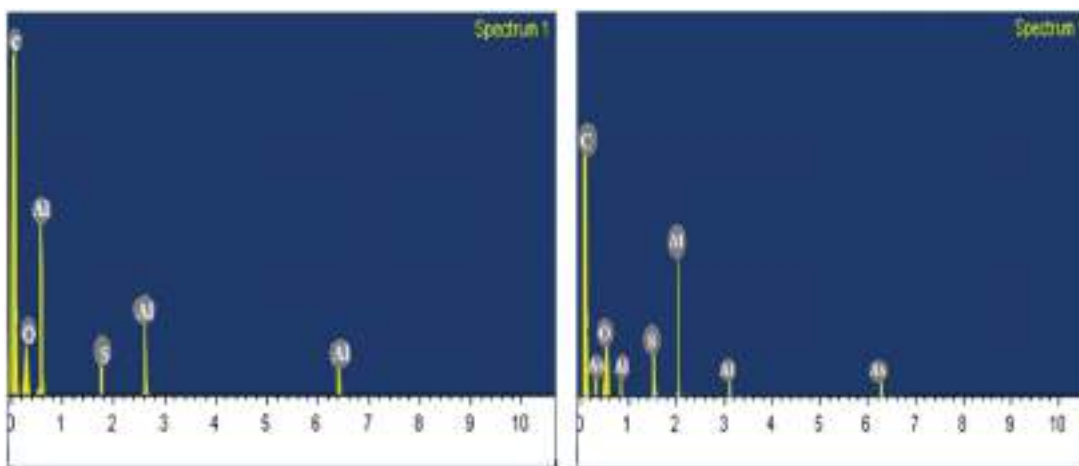


Fig. 2. EDS spectra of Al-TC and arsenate-laden Al-TC.

covering of the biochar surface during pyrolysis. The finding suggests that the yield can be increased by pretreatment of biochar with Al oxide/hydroxide (He et al. 2020). The pH_{pzc} (point of zero charge) is a prime indicator of ionic species preference and surface charge of adsorbent (Chen et al. 2011). The corresponding pH_{pzc} of Al-TC reported equal to $pH_{initial}$ when $\Delta pH = 0$. The pH_{pzc} value was 6.62 for Al-TC. Under acidic conditions, the higher activity of surface charges leads to positive charge abundance on the surface of Al-TC, which results in strong attraction toward arsenate ions (Tan et al. 2020). The adsorption of arsenate reduces under basic conditions. When the pH value exceeds pH_{pzc} value, the negative charge prevails on the adsorbent's surface due to electrostatic repulsive forces (Alkurdi et al. 2020). In the present study, the maximum removal was reported under 5.5–6.5 pH.

The precursor might contain volatile components and other unknown impurities that become texturized by analysis of SEM micrographs (Fig. 1). It was observed that large numbers of pores with great protuberances were developed by activating the precursor (IR = 1.4) at a high temperature (650°C). The formation of pores can be due to deprivation of volatile components, C in the form of CO_2 and CO, and reversible inclusion of the aluminum

element during the process (Auta and Hameed 2011). The increased pore volume and surface area of Al-TC could surge the active sites and area of contact, which results in enhanced arsenate removal capacity (Wu et al. 2013; Yu et al. 2015). Energy dispersive spectroscopy (EDS) spectra of the Al-TC prior and after adsorption are shown in Fig. 2. Signal peaks were observed on the surface of Al-TC sample. The major elemental constituents of the biosorbent were C, O, Al, and S. O and Al are the chief elements of $Al_2(SO_4)_3$. The presence of S can be ascribed due to SO_4^{2-} , resulting from residual aluminum hydroxide during synthesis of material (Liu et al. 2019).

The S_{BET} (BET surface area) was reported as 465 and 396 m^2/g for the tea waste char and Al-TC, respectively. The small decrease in BET surface area after Al impregnation can be attributed to the precursor and Al-TC having almost the same specific surface area and the aluminum coating did not significantly block the opening of the pore of biochar. The specific surface area of the precursor can be compared with some of the commercially available activated carbon (Auta and Hameed 2011; Low et al. 2008). Pore volume and pore diameter also decrease after Al impregnation (Mohan et al. 2011). The analysis also reveals the microporous nature of

Al-TC, as the pore width is in the range 5–15 Å. A detailed result of BET analysis is listed in Table 4.

The FTIR spectra of Al-TC recorded in the range of 5,000–500 cm^{-1} , pre- and post-adsorption are shown in Fig. 3. The FTIR analysis is used for the verification of functional groups associated with the surface. The abundance of C and O was observed in Al-TC, which comprise C–O group (at 1,059 cm^{-1}) (Ding et al. 2016), carboxyl groups (C=O at 1,592 cm^{-1}) (Ding et al. 2018), methylene groups ($-\text{CH}_2$ at 2,922 cm^{-1}), and hydroxyl group ($-\text{OH}$ at 3,384 cm^{-1}) (Darby et al. 2016). The FTIR spectra analysis was also used to depict the evident shifts of peaks or emergence of new peaks after the adsorption process. It shows the development of new chemical bonds, indicating chemisorption (due to surface complexation). A new peak was observed at 881 cm^{-1} in As (V) laden Al-TC, which can be attributed to As–O presence (Thanh et al. 2016). As–O peak in arsenate-laden biochar implies surface complexation of functional groups with As species during arsenate adsorption onto Al-TC. The C–O peak shifts to 1,029 cm^{-1} after adsorption due to C–O stretching. The sharp peak at 1,702 cm^{-1} can be attributed to aromatic C–C stretching (Ravikovitch and Neimark 2006). New peaks or peak shifts cannot be observed if the adsorption of arsenate is under the limit of detection, particularly for the sorption of black char.

The XRD spectra of Al-TC before and after adsorption are shown in Fig. 4. The result of XRD analysis confers the amorphous nature of produced biochar. It can be observed from Fig. 4 that three distinct peaks (at 14.9°, 22.7°, and 34.3°) are present in the XRD spectra of Al-TC after adsorption while there exist no such obvious peaks before the adsorption. The peaks obtained in the spectra of the post-treatment sample can be due to the presence of crystalline minerals or AlOOH (diaspore). The hydrolysis of

aluminum chloride hexahydrate results in the formation of AlOOH during the adsorption process (Liu et al. 2019).

When the colloidal particles surface slides, there exists a potential known as zeta potential. The sign and values of zeta potential are associated with charges on the surface of colloidal particles (Yin et al. 2020). The analysis presented in Fig. 5 shows the negative value of the zeta potential of the precursor in the pH range of 4–10. The mentioned analysis reveals that precursor carries the negative charge in the given pH range, which is in agreement with previous studies (Yuan et al. 2011). The de-protonation of functional groups of oxygen on the biochar led to the origination of negative charge abundance. Zeta potential of precursor became more negative with an increase in the pH value of suspension, due to an enhanced functional group ($-\text{OH}$ and $-\text{COOH}$) dissociation (Shaheen et al. 2019). The value of the zeta potential of Al-TC changes from negative to positive. These findings suggest that the positive charge increases and negative charge decreases on the surface of biochar after Al impregnation. This could be due to complex formation between Al and the functional groups' atoms on the surface of biochar. In addition, negative charge decreases up to an extent due to the surface coverage of biochar by Al oxide/hydroxide (Peng et al. 2019). The coverage of the surface of biochar by Al favored the arsenate adsorption on biochar.

Adsorption Mechanism of Arsenate on Al-TC

Usually, the electrostatic sorption does not affect the zeta potential or surface charge of the particles. The location of adsorbed (electrostatically) ions is the diffusion layer situated on the surface of the particle (Xu et al. 2016). Although the zeta potential or surface charge can be changed by specific adsorption by the formation of chemical bonds due to the penetration of adsorbed ions into the stern layer on the surface of particles. Both the diffusion layer and the stern layer are part of electric dual layers.

From Fig. 5, it can be seen that the zeta potential values of the arsenate-laden precursor and the arsenate-laden Al-TC changes from positive to negative, revealing that specific adsorption of arsenate took place (Yan et al. 2018). The specific adsorption mechanism for the present work is also supported by the shift of FTIR spectra after adsorption of arsenate onto Al-TC. The $-\text{OH}$ peak on the surface of Al-TC shifted from 3,384 to 3,391 cm^{-1} , after

Table 4. BET results of Virgin TC and Al-TC

BET parameters	Al-TC	TC (Virgin)
S_{BET} (m^2/g)	396.1	465.7
S_{ext} (m^2/g)	97.1	123.5
$S_{\text{ext}}/S_{\text{BET}}$ (%)	24.4	26.4
S_{mic} (m^2/g)	231.4	301.7
$S_{\text{mic}}/S_{\text{BET}}$ (%)	58.3	66.0
Pore volume (cc/g)	0.181	0.213
Pore width (Å)	7.108	25.563

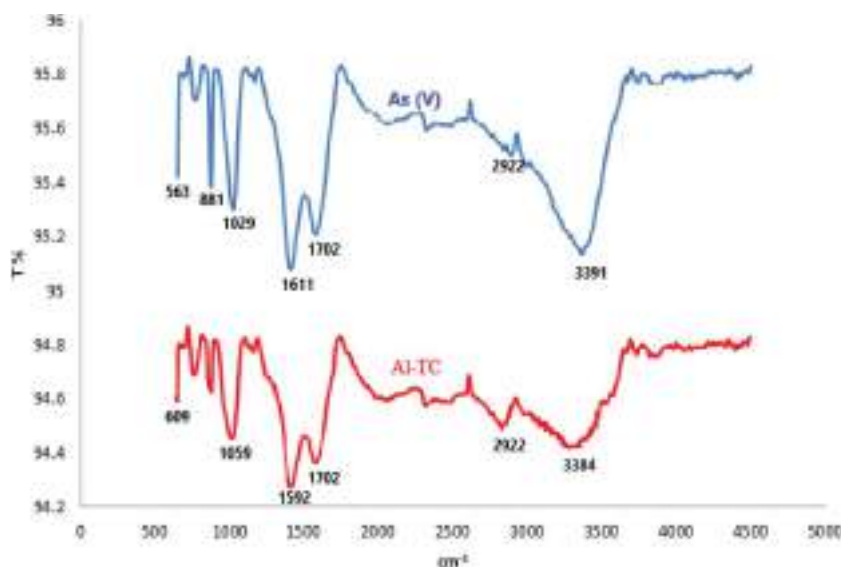


Fig. 3.1. FTIR spectra of pre- and post-adsorption of Al-TC.

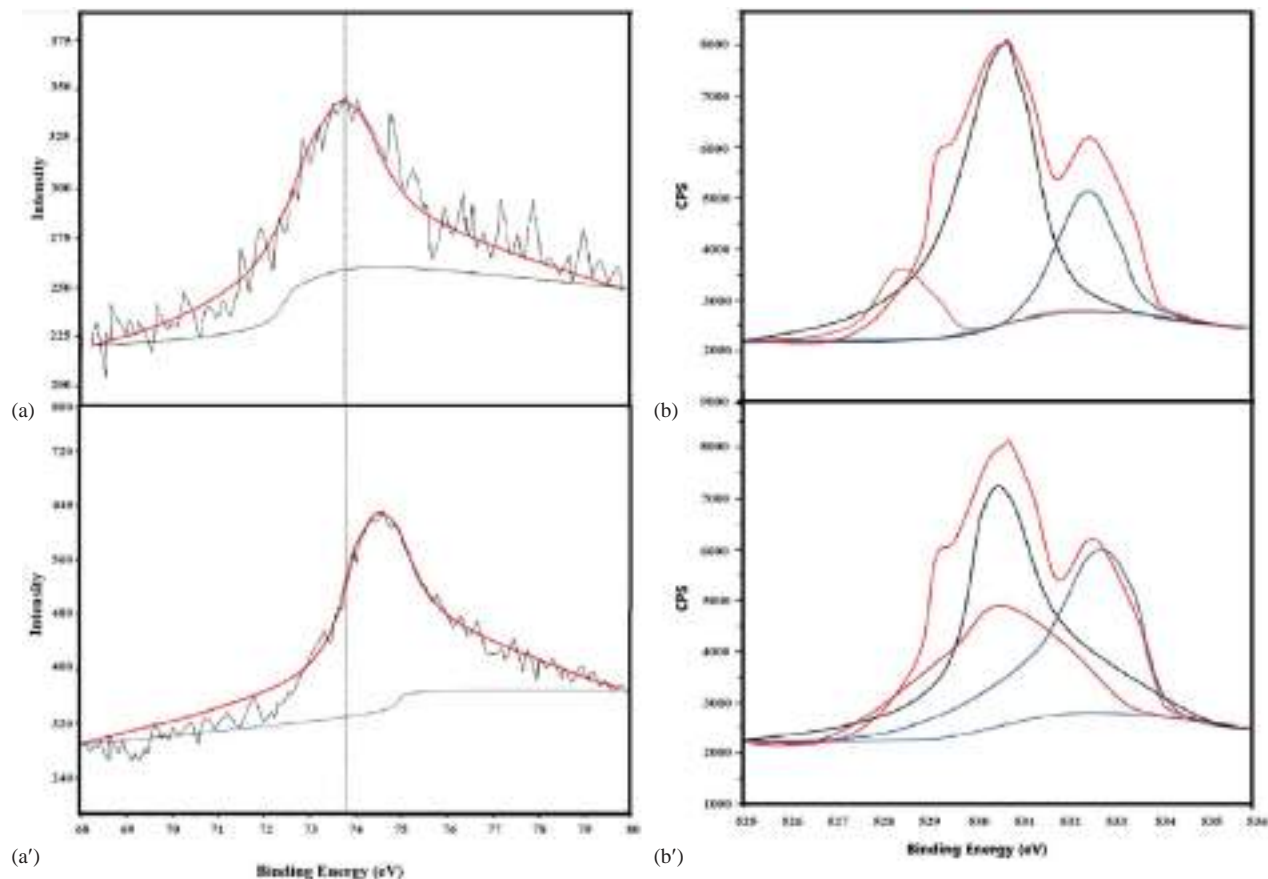


Fig. 3.2. Al₂p XPS spectra of Al-TC before (a) and after (a') adsorption. The O1s XPS spectra of Al-TC before (b) and after (b') adsorption.

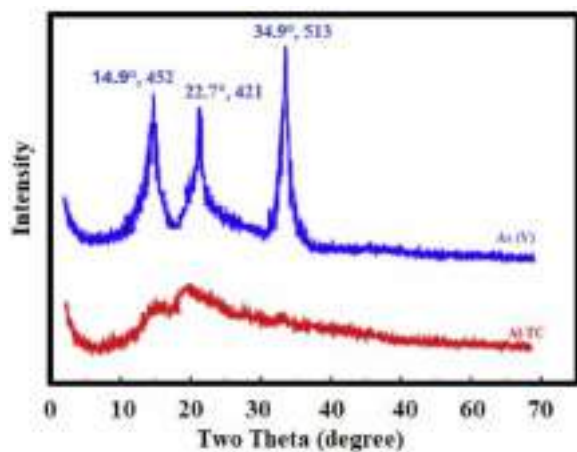


Fig. 4. XRD spectra of Al-TC before and after adsorption.

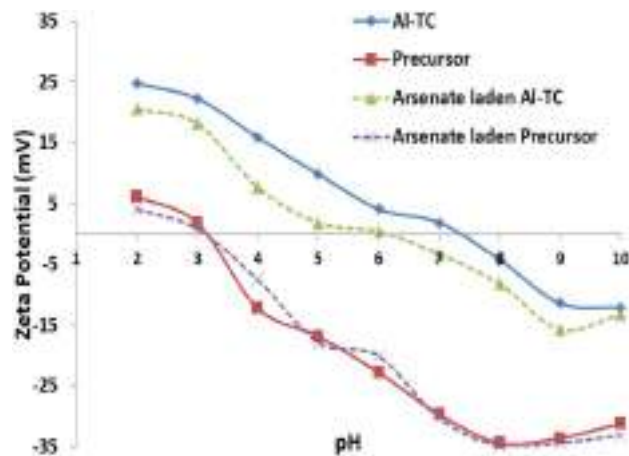


Fig. 5. Zeta potential of precursor and Al-TC before and after As (V) adsorption.

arsenate adsorption. Moreover, the appearance of new peak at 881 cm^{-1} is also noteworthy and suggests a new chemical bond formation after arsenate adsorption.

The chief mechanism of the specific adsorption of arsenate on Al-TC is the formation of chemical bonds (Al-O-As), due to the exchange of ligand between arsenate and R-OH groups, on the surface of Al oxides. The formation of identical chemical bonds (Fe-O-As) was observed earlier while studying arsenate removal using Fe modified biochar (Pan et al. 2015). Thus the zeta potential analysis in combination with FTIR spectra confers that arsenate was adsorbed mainly by Al-impregnated tea waste biochar (Al-TC).

The XPS analysis of Al modified tea waste char before and after adsorption is shown in Fig. 3.2 the appearance of a new As peak on Al-TC suggests the successful adsorption on its surface. The increase in the oxygen atom ratio could be ascribed to efficient arsenate adsorption. The surface morphology, ash content, and arsenate loading are the factors that influence the arsenate removal capacity by carbon-based adsorbents. The Al₂p peaks (Figs. 3.2(a and a')) corresponding to binding energies of 73.53 eV were shifted to 74.49 eV after adsorption of arsenate in the Al-TC. The shifts in Al₂p peaks can be attributed to the interactions between Al oxides/hydroxides and arsenate, involving

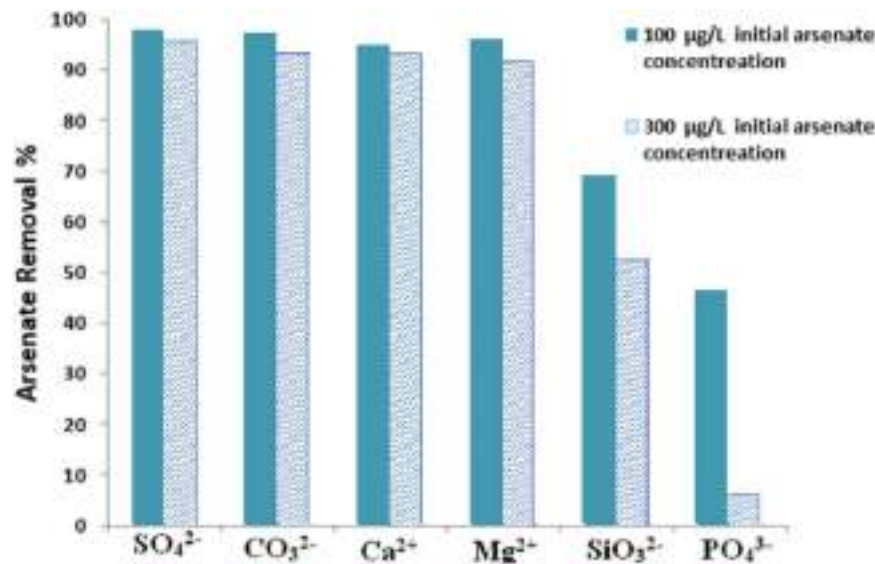


Fig. 6. Effect of coexisting ions on adsorption of arsenate using Al-TC.

development of As-O-Al and Al-As bonds (Peng et al. 2019). The O1s spectra [Figs. 3.2(b and b')] shows a relatively stronger peak at 530.5 eV after arsenate adsorption (Barboux et al. 1992), which could result from the overlapping of the oxygen element in arsenate. Moreover, in O1s spectra, two distinct stronger peaks of oxygen appeared corresponding to C-O (533.1 eV) and C=O=C (533.4 eV) bonds (Matienzo 1991).

Effect of Coexisting Ions on Arsenate Adsorption

The effect of coexisting ions on arsenate adsorption using Al-TC is shown in Fig. 6. It is a well-known fact that arsenic is present in natural water along with other ions, including PO₄³⁻ (phosphate), CO₃²⁻ (carbonate), SO₄²⁻ (sulphate), Ca²⁺ (calcium), and Mg²⁺ (magnesium). Instead of the formation of inner surface complexation with α -AlOOH, CO₃²⁻, SO₄²⁻, Ca²⁺, and Mg²⁺ have a very minimal adverse impact on arsenate adsorption in the given range of concentration. This can be attributed to these ions' relatively lower binding ability with the metal ions (Wei et al. 2019). Even a very high concentration of CO₃²⁻ does not have a significant impact on arsenate adsorption (Radu et al. 2005). Presence of SO₄²⁻ decreases the arsenate removal to a very little extent, due to formation of outer surface complexation with metal oxides rather than the adsorption favorable inner surface complexation at pH < 6 (Lefèvre 2004). In contrast, PO₄³⁻ and SiO₃²⁻ ions hinder the adsorption of arsenate and kept increasing inhibition with increasing concentration, especially PO₄³⁻ ions. This can be due to their ability to form inner surface complexation with Al oxides/hydroxides, similar to arsenate ions (Liu et al. 2019; Youngran et al. 2007). In particular, PO₄³⁻ ions are chemically very similar to arsenate. Thus, PO₄³⁻ and SiO₃²⁻ ions will compete with arsenate ions for active adsorption sites, especially PO₄³⁻ ions, resulting in suppressed uptake of arsenate. The removal efficiency can be improved by increasing the dose of Al-TC appropriately.

RSM-CCD

The CCD was employed to investigate the effect of independent parameters, including initial arsenate concentration (A), the dose of adsorbent (B), contact time (C), and pH (D) in 3 levels, low

(coded as -1), basal (coded as 0), and high (coded as 1). For all sets of experiments, the star points were selected as +2 for + α and -2 for - α . A random performance of complete design was conducted to minimize the effect of uncontrolled variables and to evaluate the quadratic, main, and interaction effects. In addition, the development of RSM was done by considering all the relevant interaction in the CCD for expressing the nature of surface response in the process, and critical factors optimization. Justification of adequacy and significance of the model was provided using ANOVA. The significance of various terms in the model was evaluated using Prob > F value. After discarding all nonsignificant terms (based on the selected level of confidence), the eventual coded factor RSM model was predicted to evaluate the given equation's adsorption efficiency as

$$\begin{aligned} \text{Adsorption Efficiency (\%)} = & 92.17 - 1.03A + 5.22B + 3.02C \\ & - 3.18D - 0.36AB + 0.2AC \\ & + 0.22AD - 0.28BC - 0.86BD \\ & + 0.85CD + 2.54A^2 - 4.58B^2 \\ & - 0.46C^2 - 12.58D^2 \end{aligned} \quad (6)$$

A correlation between predicted and actual adsorption (%) of arsenate on Al-TC is shown in Fig. 7. It is clear from the figure that there is good agreement between the experimental values and the predicted model, which is validated by the high value of the correlation coefficient ($R^2 = 0.991$). However, the observed deviation in the predicted values may be due to the nonlinear effect of the examined parameters, influence of nonrelevant terms, and confined number of experiments (Roy et al. 2014).

The ANOVA is given in Table 5 and is used to predict the cubic, individual, and interaction effect of the independent variables on the adsorption of arsenate on Al-TC. The results suggest that the quadratic model (P -value < 0.05) has a significant contribution. The determination coefficient described the standard of the polynomial model as a basis of the extent of deviation through the mean elucidated by the model, and the values of Adj- $R^2 =$ and $R^2 =$ show a good correlation between the predicted and exponential data (Dil et al. 2019). The value of the signal to noise ratio (adequate precision) greater than four indicates the RSM model's worth. The adequate S/N value (25.062) shows a significant

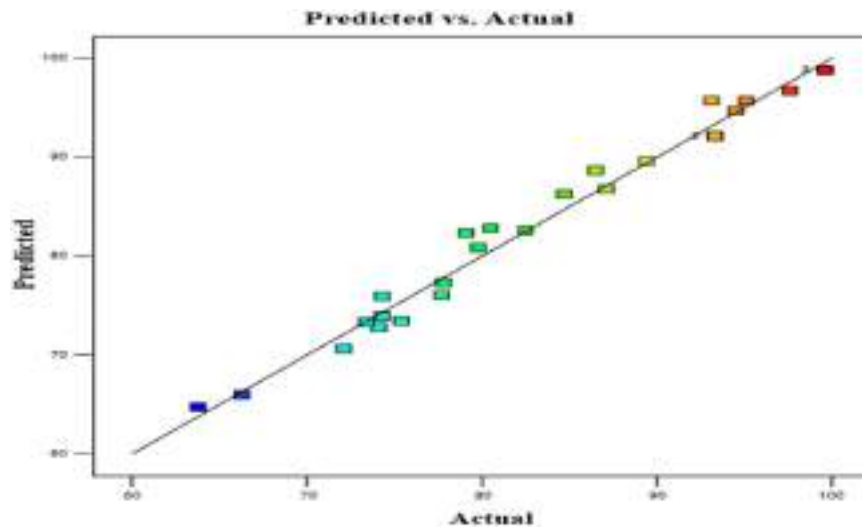


Fig. 7. Plot between the predicted and experimental data for arsenate adsorption.

Table 5. ANOVA and model fit summary for CCD

Parameter/Source	Value	Sum of squares	df	Mean square	F-value	p-value	Remarks	Std. dev.	R ²	Adjusted R ²	Predicted R ²	PRESS	Remarks
Model	—	3,103.77	14	221.70	60.05	<0.0001	Significant	—	—	—	—	—	—
A—Concentration	—	16.81	1	16.81	4.55	0.0498	—	—	—	—	—	—	—
B—Adsorbent dose	—	480.12	1	480.12	130.04	<0.0001	—	—	—	—	—	—	—
C—Time of contact	—	169.09	1	169.09	45.80	<0.0001	—	—	—	—	—	—	—
D—pH	—	161.29	1	161.29	43.69	<0.0001	—	—	—	—	—	—	—
AB	—	2.20	1	2.20	0.5957	0.4522	—	—	—	—	—	—	—
AC	—	0.6614	1	0.6614	0.1791	0.6781	—	—	—	—	—	—	—
AD	—	0.8100	1	0.8100	0.2194	0.6462	—	—	—	—	—	—	—
BC	—	1.37	1	1.37	0.3700	0.5521	—	—	—	—	—	—	—
BD	—	11.90	1	11.90	3.22	0.0927	—	—	—	—	—	—	—
CD	—	11.56	1	11.56	3.13	0.0971	—	—	—	—	—	—	—
A ²	—	12.27	1	12.27	3.32	0.0883	—	—	—	—	—	—	—
B ²	—	39.83	1	39.83	10.79	0.0050	—	—	—	—	—	—	—
C ²	—	0.5444	1	0.5444	0.1474	0.7064	—	—	—	—	—	—	—
D ²	—	266.64	1	266.64	72.22	<0.0001	—	—	—	—	—	—	—
Residual	—	55.38	15	3.69	—	—	—	—	—	—	—	—	—
Lack of fit	—	53.38	8	6.67	23.35	0.0002	Not significant	—	—	—	—	—	—
Pure error	—	2.00	7	0.2857	—	—	—	—	—	—	—	—	—
Cor total	—	3159.15	29	—	—	—	—	—	—	—	—	—	—
Std. dev.	1.92	—	—	—	—	—	—	—	—	—	—	—	—
Mean	84.81	—	—	—	—	—	—	—	—	—	—	—	—
C.V. %	2.27	—	—	—	—	—	—	—	—	—	—	—	—
R ²	0.991	—	—	—	—	—	—	—	—	—	—	—	—
Adj. R ²	0.972	—	—	—	—	—	—	—	—	—	—	—	—
Predicted R ²	0.912	—	—	—	—	—	—	—	—	—	—	—	—
Linear	—	—	—	—	—	—	—	7.91	0.5051	0.4259	0.3059	2192.62	—
2FI	—	—	—	—	—	—	—	8.93	0.5200	0.2674	-0.5581	4922.32	—
Quadratic	—	—	—	—	—	—	—	1.92	0.991	0.972	0.912	340.24	Suggested
Cubic	—	—	—	—	—	—	—	0.5151	0.9993	0.9976	—	—	Aliased

RSM model signal that can be utilized for navigating the design (Bagheri et al. 2019).

Simultaneous Effects of Interactive Adsorption Variables

For the analysis of effects of process variables (initial arsenate concentration, dose of adsorbent, contact time, and pH) on arsenate adsorption, 3D response surface plots were generated. The response surface plots representing the influence of significant

process variables on the arsenate adsorption efficiency are shown in Figs. 8(a–f).

Effect of pH on Arsenate Adsorption

The speciation of the solution (adsorbate) and surface chemistry of biosorbent become strongly influenced by the system pH in environmental studies. Arsenate can coexist in polluted water as H₃AsO₄, HAsO₄²⁻, H₂AsO₄⁻, and AsO₄³⁻ ions with the pK_a value

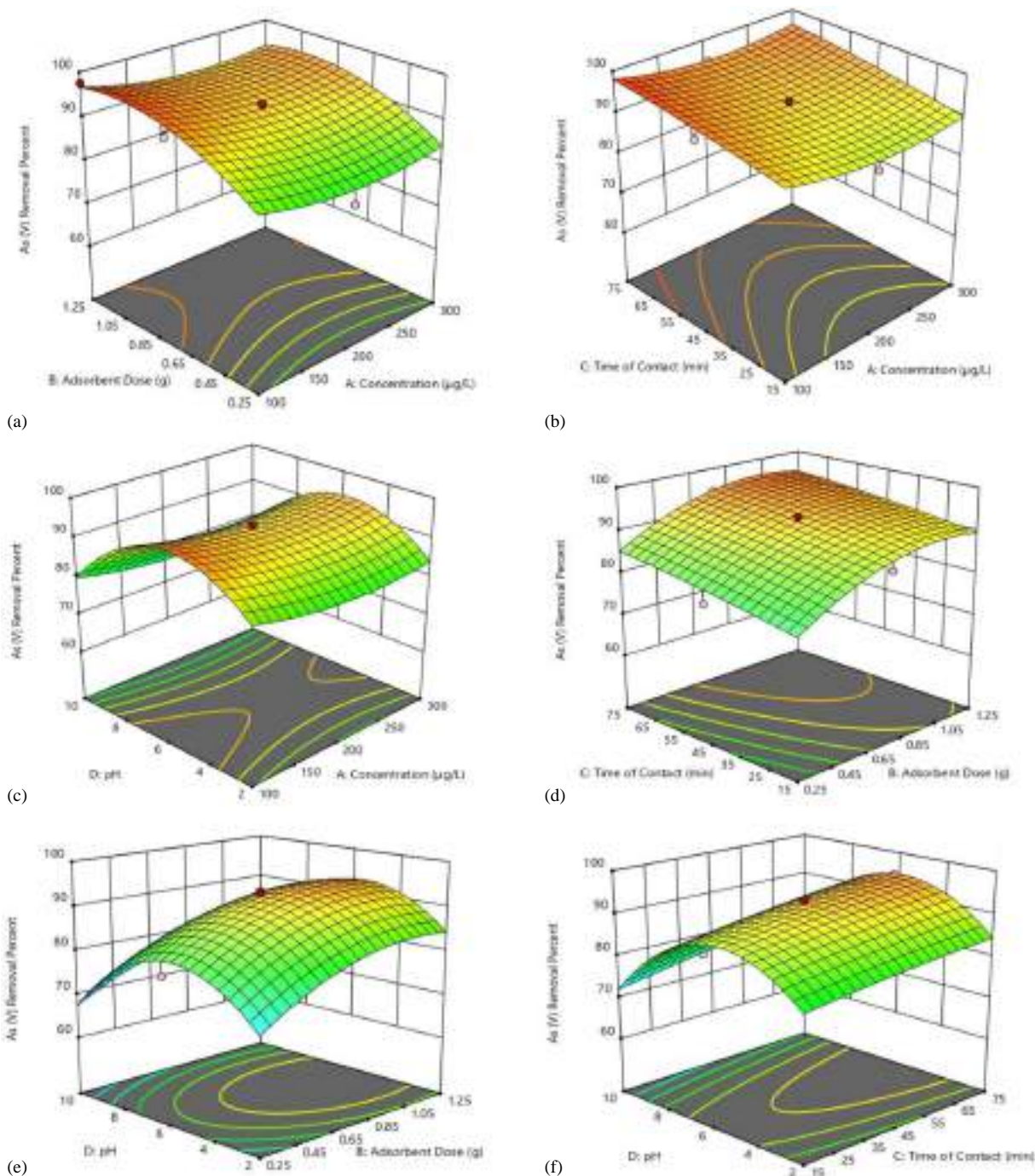


Fig. 8. Three-dimensional response surface plots for simultaneous interactive effects of (a) adsorbent dose and initial concentration at pH 6.0, contact time 45 min; (b) contact time and initial concentration at pH 6.0, adsorbent dose 1.0 g; (c) pH and initial concentration at adsorbent dose 1.0 g, contact time 45 min; (d) contact time and adsorbent dose at pH 6.0, initial concentration 100 µg/L; (e) pH and adsorbent dose at contact time 45 min, initial concentration 100 µg/L; and (f) pH and contact time at adsorbent dose 1.0 g, initial concentration 100 µg/L.

in the range of 2.3–11.6. Therefore, the arsenate adsorption of Al-TC was quantitatively analyzed in the 2–10 pH range.

Figs. 8(c–f) show the influence of pH on adsorption efficiency of arsenate in the test solution. From the given figures it can be observed that the acidic conditions are more favorable for arsenate adsorption. The removal efficiency of arsenate steeply increased in the pH range 2–6.5 and decreased thereafter at any adsorbent dose, initial arsenate concentration, or contact time. The explanation for this could be based on anionic behavior of arsenate at pH < 6.5, and replacement by $\text{H}_2\text{AsO}_4^{2-}$, HAsO_4^{2-} , and AsO_4^{3-} ions.

The protonation of metal oxides ions ($=\text{Al}-\text{OH}_2^+$) is highly favored under acidic conditions, due to which the electrostatic interaction increase between negatively charged arsenate ions (e.g., HAsO_4^{2-}), and the metal oxides. The attractive electrostatic forces result in enhanced adsorption of arsenate. In other words, the accompanying ions balance the positive charge of the surface under acidic conditions, the R-OH group on the Al-TC surface forms a chemical bond with active sites. The subsequent bond formation led to the ion exchange with anionic species that are already present in solution (Ansari and Sadegh 2007). This trend

of enhanced removal efficiency of arsenate under acidic conditions has been observed previously in the literature (Sierra-Trejo et al. 2020; Wan et al. 2020).

The optimum removal was achieved in the pH range 5.5–6.6, which is close to the isoelectric point (i.e., $p=6.6$) of Al-TC. Below the isoelectric point, the particles of the adsorbent are positively charged. As the pH increases above 6.5, the removal capacity decreases and attains a minimum value at pH 10. The decreased removal capacity at higher pHs can be due to the increase in negative charge abundance ($=Al-O$) and arsenate ions, which led to the repulsive electrostatic forces between the metal oxides and adsorbate ions in the solution (Xue et al. 2019). The R-COOH, R-OH, and R-CO-NR functional groups on the adsorbent's surface are negatively charged at $pH > 6.5$. The ligand exchange and electrostatic interaction in mechanisms reported for arsenate removal on metal oxide surface are strongly dependent on system pH. Specifically, the ligand exchange of arsenate with surface $=Al-O$ and $=Al-OH_2^+$ is reported frequently in the literature (Kumar et al. 2020; Maiti et al. 2010), and can be shown as



Effect of Initial Arsenate Concentration

The dependence of arsenate adsorption on initial concentration is presented in Figs. 8(a–c). The data reveals that initial concentration of adsorbate determines the concentration at equilibrium along with the kinetic character and uptake rate of arsenate. It can be observed from the results that percentage removal decreases with initial arsenate concentration. This decrease in the percentage removal can be attributed to the scarcity of the active sites on the adsorbent's surface. Moreover, increased initial concentration of arsenate offers a decreased driving force to overcome the resistance offered by mass transfer from the adsorbate ions in the solution to the adsorbent. This phenomenon results in a greater collision between the arsenate and surface of Al-TC, due to which uptake of arsenate increases (Da'na and Sayari 2011). A similar trend of decreasing removal of arsenate with increasing initial concentration has been reported very often in literature (Shahid et al. 2019; Su et al. 2020). However, with increasing initial arsenate concentration, the actual quantity of arsenate adsorbed per unit mass of Al-TC increased at the interface of adsorbate and adsorbent. The increased amount of arsenate adsorbed can be due to decrement in solute uptake resistance from the solution with increment in arsenate concentration (Nollet et al. 2003).

Effect of Adsorbent Dose

The effect of Al-TC dose on removal of arsenate from the aqueous solution is illustrated in Figs. 8(a, d, and e). The results show that the removal percentage of arsenate increases gradually with the increasing adsorbent dose attaining a maximum value and negligible effect thereafter. This increase in removal percentage may be due to an enhanced surface area with an increasing mass of adsorbent. The enhanced surface area results in a larger number of active sites available for adsorption (Zeng et al. 2020). Moreover, the increased removal might result from the presence of appropriate functional groups on the surface of the Al-TC, which helps in the adsorption of arsenate (Bhattacharya et al. 2006). After a specific dose, unaffected adsorption may be due to the attainment of saturation or maximum adsorption (Foroutan et al. 2019). The same trend of variation in arsenate removal percentage with the

adsorbent dose has been reported earlier (Salih et al. 2019; Sheralala et al. 2019).

Optimization

Design-Expert 12.0 software was used to optimize the experimental results. By using the maximum removal percentage as the target of optimization, the obtained optimum conditions were as follows: initial arsenate concentration of 100 $\mu\text{g/L}$, initial pH of 6.0, and adsorbent dosage of 1.0 g and contact time of 1 h. The result reveals that 100% removal was achieved under optimum conditions.

For the validation of optimization, under optimal conditions a distinct batch experiment was conducted. A thorough investigation was made to compare the predicted and observed response values under optimum conditions. The observed response value is the actual experimental value and the predicted value is the obtained value from Eq. (6). The obtained result of the observed value was 99.6%, whereas that of the predicted value was 100%. As both the predicted and the observed values are in good agreement with each other, the model's performance was validated.

Adsorption Isotherm Study

The adsorption isotherm analysis gives details about the distribution of adsorbate between solid and mobile phases at equilibrium. The information thus produced can be utilized by the researcher to optimize process variables for adsorption and set up the most suitable correlation. Freundlich, Langmuir, Temkin, and Dubinin-Radushkevich (D-R) isotherm models were used in the present study to express equilibrium characteristics (Fig. 9).

The Freundlich isotherm model is based on multilayer adsorption on the heterogeneous surface of the adsorbent. This model assumes that the active sites for adsorption are unevenly allocated on the surface. The linear form of the Freundlich isotherm model can be expressed as following (Murcia-Salvador et al. 2020):

$$\ln q_e = \ln K_f + \frac{1}{n} \ln C_e \quad (9)$$

where C_e = arsenate concentration at equilibrium; q_e = quantity of adsorbed arsenate; n and K_f = Freundlich coefficients. The n value gives the feasibility of the adsorption process whereas K_f denotes the adsorption capacity. The slope and intercept of $\ln q_e$ versus $\ln C_e$ plot yields values of n and K_f . The value of factor $1/n$ falling in the range 0–1 gives the degree of heterogeneity of the surface. The present study results show that the adsorption surface of Al-TC is highly heterogeneous from the value of $1/n$ (0.114), and the adsorption process is feasible. Analogous results of heterogeneity of adsorbents have been reported (Abukhadra et al. 2020). The obtained isotherm parameter for arsenate adsorption is given in Table 6.

Langmuir isotherm model assumes that monolayer adsorption take place on the active sites of the adsorbent's surface. The linear form of the Langmuir isotherm model can be expressed as the following (Singh and Pant 2004):

$$\frac{1}{q_e} = \frac{1}{q_{\max} K_L C_e} + \frac{1}{q_{\max}} \quad (10)$$

The Langmuir parameters (q_{\max} and K_L) can be evaluated from the slope and intercept of linear $1/q_e$ versus $1/C_e$ plot. Here, R_L is dimensionless, which can be used to describe the essential features of the Langmuir model. This dimensionless constant can be expressed as $R_L = 1/(1 + K_L C_i)$. The R_L value gives the measure of favorability of the adsorption process. The nature of adsorption is considered as unfavorable for $R_L > 1$, favorable for $0 < R_L < 1$, and

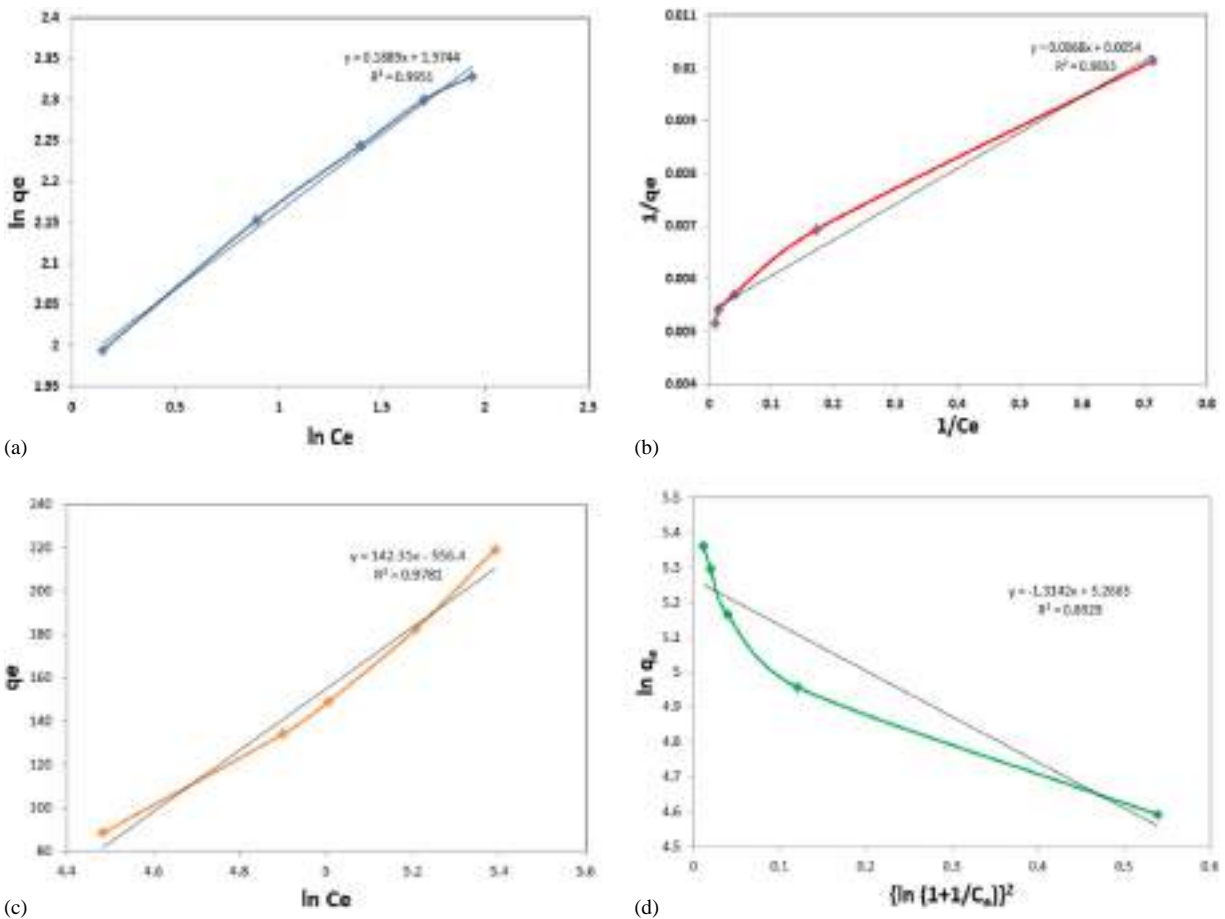


Fig. 9. (a) Freundlich isotherm; (b) Langmuir isotherm; (c) Temkin isotherm; (d) D-R isotherm model at pH 6.0, 1 g adsorbent dose, initial concentration 100–300 $\mu\text{g/L}$.

Table 6. Freundlich, Langmuir, Temkin, D-R models for arsenate adsorption on AL-TC at 298 K

Isotherm	Parameters	Value	R^2
Freundlich	N	8.741	0.995
	K_F ($\mu\text{g/g}$)	108.45	
Langmuir	q_{\max} ($\mu\text{g/g}$)	217.91	0.985
	R_L	0.005	
Temkin	A_T ($\text{L}/\mu\text{g}$)	1.118	0.978
	B (J/mol)	6.94	
D-R	E (kJ/mol)	7.11	0.892
	x_M ($\mu\text{g/g}$)	32.44	

irreversible for $R_L = 0$. The obtained data of the Langmuir parameters is given in Table 6. It can be seen from the table that the obtained R_L value is 0.005, which means the adsorption process is favorable. The correlation coefficient ($R^2 = 0.995$) for the Langmuir model is highest among the studied isotherm models, which validate that the Langmuir model is most suitable to express the equilibrium arsenate adsorption on AL-TC.

The Temkin isotherm model is used to investigate the effect of arsenate (adsorbate) interaction with AL-TC (adsorbent). The Temkin isotherm model assumes (i) the decrease in surface energy (heat of adsorption) of all molecules due to increased interaction between adsorbate and adsorbent with increasing coverage, and (ii) the binding energy is uniformly distributed and used to

characterize the adsorption. The linear form of the Temkin isotherm can be expressed as (Said et al. 2018)

$$q_e = \frac{RT}{b_T} (\ln A_T + \ln C_e) \quad (11)$$

where A_T = binding constant at equilibrium; constant B ($B = RT/b_T$) is associated with the heat of adsorption; and $1/b_T$ = a measure of adsorption capacity of the adsorbent. The result of the Temkin isotherm analysis is given in Table 6. Here, B 's obtained value is 6.94, which is lower than the classical ion-exchange bonding energy range and shows the interaction between the arsenate ions and AL-TC is weak. A similar trend has been reported in the literature (Jain and Agarwal 2017).

The D-R adsorption isotherm models are usually implied for studying the physisorption of vapors and gases over porous adsorbent. The linear form of D-R isotherm can be represented as (Bordoloi et al. 2017)

$$\ln q_e = \ln X_M - \frac{1}{2E^2} \left\{ RT \ln \left(1 + \frac{1}{C_e} \right) \right\}^2 \quad (12)$$

The slope and intercept of $\ln q_e$ versus $\ln (1 + 1/C_e)^2$ can be used to calculate the D-R isotherm constants E and X_M . The D-R isotherm model analysis result is listed in Table 6. The obtained E value is 7.11, less the typical ion exchange associated binding energy range (8–16 kJ/mol). The value of E indicates that the process of adsorption on AL-TC is not only governed by chemisorption or ion exchange mechanism, but also the filling of pores phenomenon could be a feasible process (Bagali et al. 2017).

Adsorption Kinetics

To investigate the order of reaction and the rate limiting step in the process of adsorption of arsenate on Al-TC, three kinetic models (pseudo-first order, pseudo-second order, and intraparticle diffusion models) were used to fit the kinetics. The adsorption rate was studied by the application of kinetics of pseudo-first order and pseudo-second order. The linear form of pseudo-first order model can be expressed as (Tariq et al. 2018)

$$\ln[q_e - q_t] = \ln q_e - K_1 t \quad (13)$$

where q_e and q_t = amount of adsorbed arsenate on Al-TC at equilibrium; and K_1 is the rate constant of pseudo-first order. The slope of $\ln(q_e - q_t)$ versus t can be used to determine the value of K_1 . The pseudo-first order kinetic model is based on the uptake capacity of the adsorbate. This model assumes that the overall rate of adsorption is proportional to the difference in uptake of solute and equilibrium concentration. The general form of the pseudo-second order model can be given as (Yu et al. 2016)

$$\frac{t}{q_t} = \frac{1}{(k_2)(q_e)^2} + \frac{t}{q_e} \quad (14)$$

where K_2 is the adsorption rate constant of the pseudo-second order. The intercept on linear t/q_t versus t plot would yield the value of K_2 . The pseudo-second order kinetic model assumes that chemical adsorption controls the rate of adsorption by sharing electrons between adsorbate and adsorbent. The general equation for intraparticle diffusion model (McKay and Poots) can be given as (Kim and Kim 2019)

$$q_t = k_p t^{0.5} + C \quad (15)$$

where k_p = rate constant associated with intraparticle diffusion; and constant C = boundary layer thickness. The slope and intercept of q_t versus $t^{0.5}$ plot can be used to find the values of k_p and C . The values of rate constant associated with intraparticle diffusion are calculated to determine its contribution in arsenate adsorption. A linear plot passing through the origin ($C=0$) is the prerequisite for intraparticle diffusion to be a rate limiting step. In the current study, surface diffusion is shown by the initial section of the curve. Furthermore, the value $C \neq 0$ can be attributed to the fact that the rate of adsorption is not solely controlled by intraparticle diffusion but also to some extent by boundary layer mechanism (Okoli et al. 2017).

From Table 7, the data of kinetic studies was well fitted in pseudo-first order, pseudo-second order, and intraparticle diffusion models. However, the R^2 (correlation coefficient) value of pseudo-second order is higher than the pseudo-first order and q_e (calculated) values of pseudo-second order are close to q_e (experimental) in comparison with q_e (calculated) values of pseudo-first order, which confers that pseudo-second order equation is preferable than the pseudo-first order equation. It can be concluded that pseudo-second order equation and intraparticle diffusion model controls the adsorption process. Fig. 10(c) shows that the “zero” point was not crossed by experimental data, which suggests that the chief rate controlling step is intraparticle diffusion (Mohan et al. 2002).

From Table 7, the correlation coefficient of pseudo-second order equation is higher than the intraparticle diffusion equation. It could be attributed to the fact that arsenate removal from the aqueous solution cannot be abandoned relative to quantity of arsenate in the solution. Moreover, the dependency of the intraparticle diffusion is mainly on the concentration of the solid phase (Yang and Al-Duri 2001; Yang et al. 2003). Owing to the previously mentioned reasons, the R^2 value of intraparticle diffusion equation is low.

Table 7. Kinetics model parameters for arsenate adsorption on AL-TC at 298 K

Kinetic Model	Parameters	Value	R^2
Pseudo-first order	q_e	90.21	0.960
	K_1	0.1701	
Pseudo-second	q_e	99.74	0.998
	K_2	0.0238	
Intraparticle diffusion	K_{pi}	0.8148	0.899
	C	2.118	

Thermodynamic Analysis

In the present study, the thermodynamic analysis was performed to evaluate Gibb's free energy (ΔG^0), enthalpy change (ΔH^0), and entropy change (ΔS^0), which suggests the feasibility, behavior of adsorption process, and spontaneity of the reactions (Fig. 11). For determination of thermodynamic parameters, the Vant Hoff equation was used as follows (Dashamiri et al. 2016):

$$\Delta G^0 = -RT \ln K_C \quad (16)$$

$$\ln K_C = \frac{\Delta S^0}{R} - \frac{\Delta H^0}{RT} \quad (17)$$

where K_C = equilibrium. Here, K_C is equal to ratio of the arsenate concentration on the surface to the concentration at equilibrium. The slope and intercept of $\ln K_C$ versus $1/T$ were used to calculate ΔH^0 and ΔS^0 . The obtained thermodynamic parameters are listed in Table 8. The negative value of ΔG^0 over the entire range of temperature implies the feasibility and spontaneity of the process may be due to columbic attraction. Furthermore, it is noteworthy that the ΔG^0 values decrease with an increase in temperature. This trend suggests that the adsorption process is favorable at high temperatures. A similar trend was reported earlier (Alam et al. 2018). The positive value of enthalpy change (ΔH^0) reveals that the adsorption process is endothermic in nature. The positive value of entropy change (ΔS^0) can be attributed to increased randomness at the interface (solid-liquid). Moreover, the positive ΔS^0 also advocates the physisorption phenomenon for arsenate removal using Al-TC.

Desorption and Regeneration

The desorption analysis and adsorption-desorption cycles were carried out to discover the regeneration capacity of Al-TC. Sodium hydroxide solution was selected for desorption and regeneration, as arsenate shows poor adsorption performance at a pH greater than 9. A NaOH solution with different dilutions (0.1%, 0.5%, 1%, 5%, 10%) was added to the arsenate-laden Al-TC. It can be seen from the Fig. 12 the optimum NaOH concentration for desorption of arsenate from loaded Al-TC was reported as 1%. As shown in Fig. 13, adsorption-desorption cycles of Al-TC were repeated up to five cycles. Cycle 1 represents the percent removal of fresh Al-TC. After one complete cycle, the arsenate removal percentage dropped by 6% only. The decrease in the percent removal of Al-TC was observed after the successive adsorption-desorption cycle. However, the reduction in removal efficiency was not high and it maintained over 65% after five successive adsorption-desorption cycles. The significant decrease in removal percentage initially can be attributed to occupancy of adsorption sites by arsenate ions resulting from the previous runs and inefficiency of the desorption process to detach ions from the laden adsorbent. Moreover,

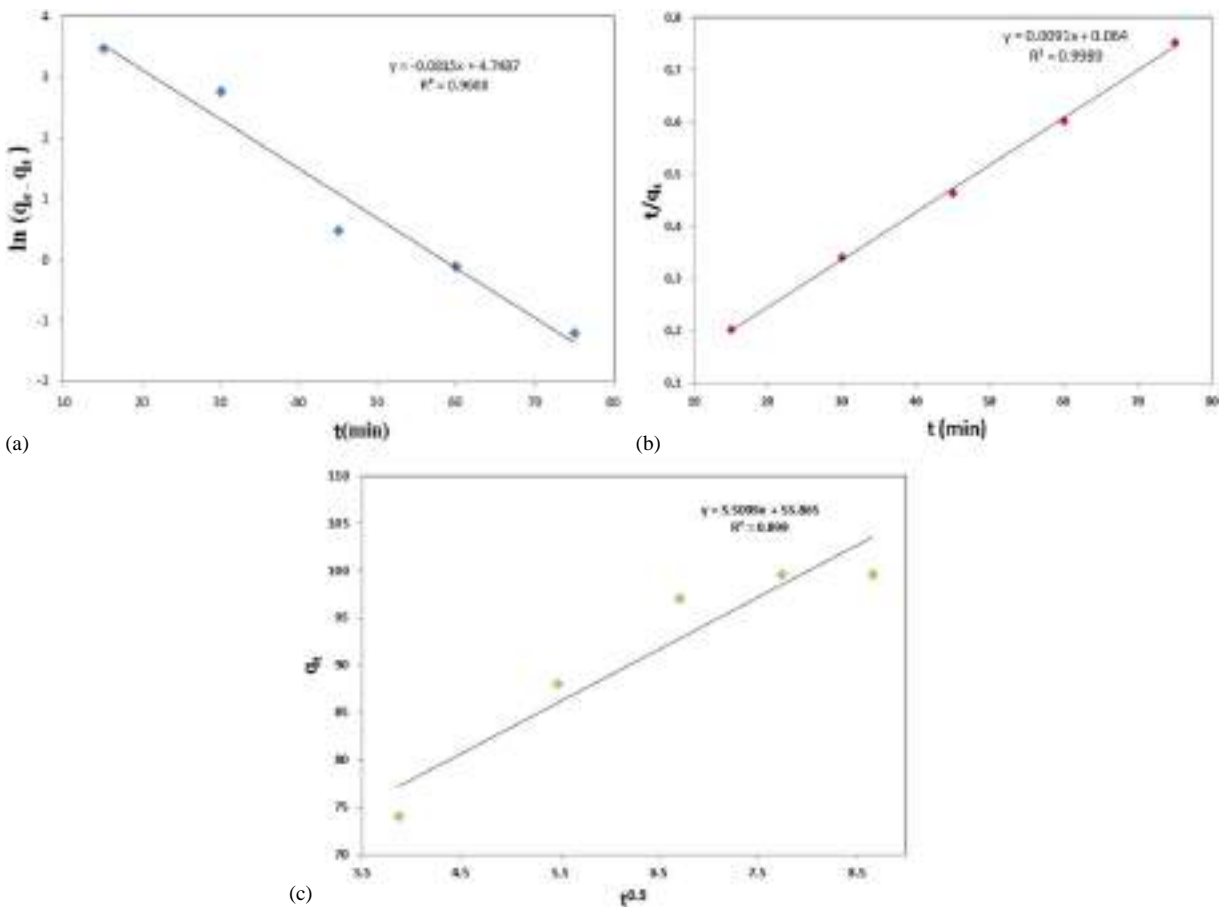


Fig. 10. (a) pseudo-first order kinetics; (b) pseudo-second order kinetics; and (c) intra particle diffusion at contact time 15–75 min, pH 6.0, 1 g adsorbent dose, initial concentration 100 $\mu\text{g/L}$.

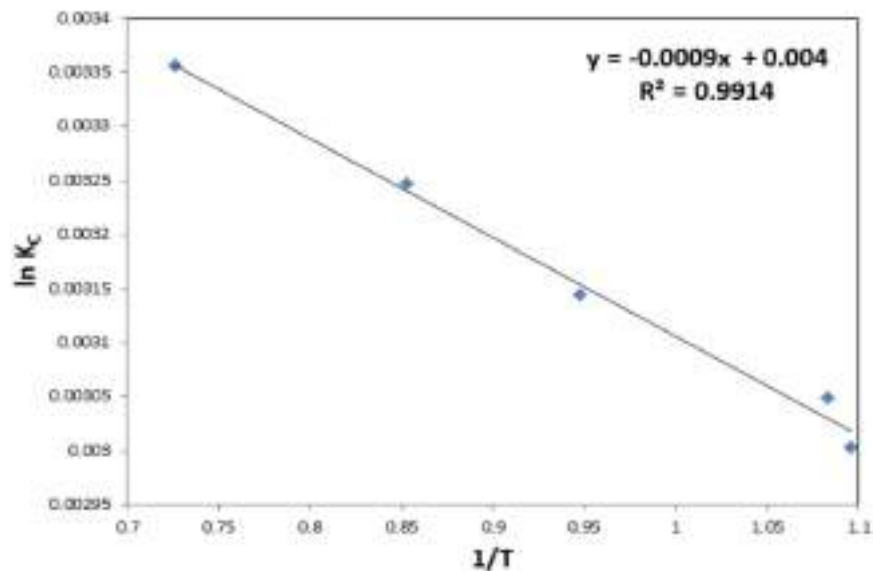


Fig. 11. Thermodynamic curve of $\ln k_c$ as $1/T$ at 1 g adsorbent dose, initial concentration 100 $\mu\text{g/L}$ and 6.0 pH.

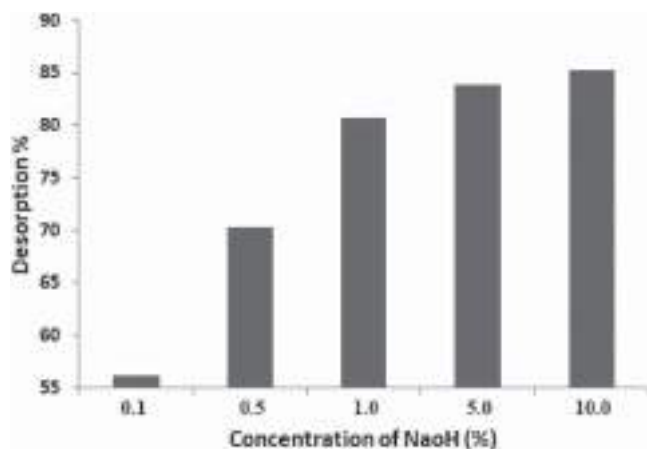
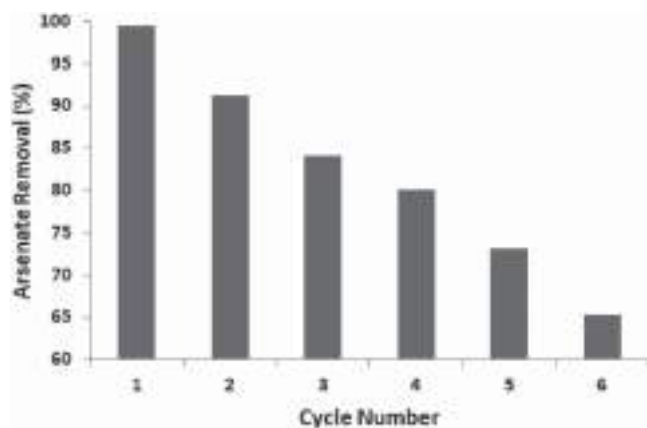
loss of materials would also occur during the regeneration process. These defects obstruct the practical applicability of any adsorbent. However, there was no prominent crush or weight loss shown by Al-TC, which reveals the commendable mechanical strength of Al-TC.

Batch Operation Performance Using Real Contaminated Ground Water

The proposed biosorbent Al-TC was adequately tested for arsenate remediation from samples of real contaminated ground water.

Table 8. Thermodynamic parameters for arsenate removal using Al-TC

Thermodynamic parameters	Values	
	Temp (K)	ΔG^0 (kJ/mol)
Standard Gibb's free energy	298	-1.6514
	308	-3.2204
	318	-7.1809
	328	-9.9835
	338	-14.7315
Standard change in enthalpy (ΔH^0)	53.4711 kJ/mol	
Standard change in entropy (ΔS^0)	0.0915 kJ/mol k	

**Fig. 12.** Percentage desorption of arsenate from Al-TC with increasing concentration of NaOH.**Fig. 13.** Adsorptive nature of Al-TC for five cycles of regeneration.

Natural samples of arsenic-contaminated ground water were taken from arsenic-affected areas of the Burdwan district, W.B., India. Maximum total inorganic arsenic concentration was reported as 258 $\mu\text{g/L}$ out of all the collected samples. Arsenic removal from contaminated ground water [$\text{As(V)} = 153 \mu\text{g/L}$ and $\text{As(III)} = 105 \mu\text{g/L}$] using batch experiments at optimal was performed. After treating real contaminated ground water by proposed batch operations, the water quality results pre- and post-adsorption under analysis are listed in Table 9. The analysis of batch operations using contaminated ground water samples, comprising both arsenate and arsenite ions, reveals that Al-TC is efficient in removal of both As (V) and As(III) from natural contaminated ground water. However, the arsenic concentration in samples after adsorption was not reported lower than the prescribed limit set by WHO. Dual step

Table 9. Removal of arsenate by Al-TC and physiochemical properties of water

Parameter	Pre-adsorption	Post-adsorption
As(V) ($\mu\text{g/L}$)	153	23.6
As(III) ($\mu\text{g/L}$)	105	14.8
As (Total) ($\mu\text{g/L}$)	258	38.4
Phosphate (mg/L)	1.3	0.4
Sulphate (mg/L)	4.1	2.8
Fluoride (mg/L)	0.8	0.0
Ca (mg/L)	133.8	93.4
Mg (mg/L)	53.6	32.4
Na (mg/L)	42.3	41.8
K (mg/L)	3.1	2.8
Carbonates (mg/L)	47.8	32.7
Bicarbonates (mg/L)	231.1	183.5
TDS (mg/L)	578.3	490.3
pH	7.1	7.0

of adsorption can be incorporated when the contaminant concentration cannot be remediated below the allowable limits through one stage adsorption. Thus, the current study proposes a two-step adsorption using Al-TC to decrease the arsenic contamination below safe limits.

Conclusion

Typically arsenate does not strongly adhere to the surface of biochar, which restricts its application in the arsenate's commercial treatment. In this research, aluminum hydroxide (anhydrous) has been impregnated for the surface modification of tea waste biochar, and provided ample active sites for adsorption of arsenate on the surface of biochar. Mechanistic analysis reveals the obtained product possesses inner surface complexes, showing the importance of ligand exchange in the adsorption of arsenate on the Al oxide/hydroxide of the synthesized adsorbent. Strong bonding resulting from the irreversible nature of inner surface complexation ensures reliable and efficient arsenate adsorption during the treatment of aqueous media using new adsorbent. The effect of operating parameters on the removal of arsenate was analyzed and optimized by using CCD combined with RSM. The Langmuir isotherm model explained the equilibrium data well, and the experimental data best fits into the pseudo-second order kinetic model. The thermodynamic study reveals the spontaneous and endothermic nature of the adsorption process. The adsorbent has shown excellent removal capacity with maximum uptake of 99.6 $\mu\text{g/g}$ in contrast with similar adsorbents from the literature. The developed adsorbent is good at regeneration with 1.0 M NaOH and it was observed that even after six complete cycles, the removal percentage does not fall below 65%.

The study calls attention to extend the application of biochar for remediation of severe pollutants through surface modification. This study also shows that anhydrous aluminum oxide-impregnated tea waste biochar is an effective novel adsorbent for preventing groundwater pollution. Future study would aim at the column analysis for the performance of Al-TC for arsenate remediation under continuous conditions.

Data Availability Statement

All data, models, and code generated or used during the study appear in the published article.

Acknowledgments

The authors would like to thank Post Graduation Research Lab, IIT Kanpur for providing assistance with SEM, XRD, BET, FTIR, XPS analysis.

References

- Abukhadra, M. R., M. A. El-Meligy, and A. M. El-Sherbeeney. 2020. "Evaluation and characterization of Egyptian ferruginous kaolinite as adsorbent and heterogeneous catalyst for effective removal of safranin-O cationic dye from water." *Arabian J. Geosci.* 13 (4): 169. <https://doi.org/10.1007/s12517-020-5182-6>.
- Adniasab, L., N. Shekari, and A. Maghsodi. 2019. "Optimization of arsenic removal with $\text{Fe}_3\text{O}_4@/\text{Al}_2\text{O}_3@/\text{Zn-Fe}$ LDH as a new magnetic nano adsorbent using Box-Behnken design." *J. Environ. Chem. Eng.* 7 (2): 102974. <https://doi.org/10.1016/j.jece.2019.102974>.
- Agrafioti, E., D. Kalderis, and E. Diamadopoulos. 2014. "Arsenic and chromium removal from water using biochars derived from rice husk, organic solid wastes and sewage sludge." *J. Environ. Manage.* 133: 309–314. <https://doi.org/10.1016/j.jenvman.2013.12.007>.
- Alam, M. A., W. A. Shaikh, M. O. Alam, T. Bhattacharya, S. Chakraborty, B. Show, and I. Saha. 2018. "Adsorption of As(III) and As(V) from aqueous solution by modified *Cassia fistula* (golden shower) biochar." *Appl. Water Sci.* 8 (7): 198. <https://doi.org/10.1007/s13201-018-0839-y>.
- Alchouron, J., C. Navarathna, H. D. Chludil, N. B. Dewage, F. Perez, C. U. Pittman Jr, A. S. Vega, and T. E. Mlsna. 2020. "Assessing South American *Guadua chacoensis* bamboo biochar and Fe_3O_4 nanoparticle dispersed analogues for aqueous arsenic(V) remediation." *Sci. Total Environ.* 706: 135943. <https://doi.org/10.1016/j.scitotenv.2019.135943>.
- Alkurdi, S. S., R. A. Al-Juboori, J. Bundschuh, L. Bowtell, and S. McKnight. 2020. "Effect of pyrolysis conditions on bone char characterization and its ability for arsenic and fluoride removal." *Environ. Pollut.* 262: 114221. <https://doi.org/10.1016/j.envpol.2020.114221>.
- Ansari, R., and M. Sadegh. 2007. "Application of activated carbon for removal of arsenic ions from aqueous solutions." *E-J. Chem.* 4: 103–108. <https://doi.org/10.1155/2007/829187>.
- Asere, T. G., S. Mincke, J. De Clercq, K. Verbeken, D. A. Tessema, F. Fufa, C. V. Stevens, and G. Du Laing. 2017. "Removal of arsenic(V) from aqueous solutions using chitosan–red scoria and chitosan–pumice blends." *Int. J. Environ. Res. Public Health* 14 (8): 895. <https://doi.org/10.3390/ijerph14080895>.
- Asfaram, A., M. Ghaedi, S. Agarwal, I. Tyagi, and V. K. Gupta. 2015. "Removal of basic dye Auramine-O by ZnS:Cu nanoparticles loaded on activated carbon: Optimization of parameters using response surface methodology with central composite design." *RSC Adv.* 5 (24): 18438–18450. <https://doi.org/10.1039/C4RA15637D>.
- Auta, M., and B. Hameed. 2011. "Optimized waste tea activated carbon for adsorption of Methylene Blue and Acid Blue 29 dyes using response surface methodology." *Chem. Eng. J.* 175: 233–243. <https://doi.org/10.1016/j.cej.2011.09.100>.
- Bagali, S. S., B. S. Gowrishankar, and A. S. Roy. 2017. "Optimization, kinetics, and equilibrium studies on the removal of lead(II) from an aqueous solution using banana pseudostem as an adsorbent." *Engineering* 3 (3): 409–415. <https://doi.org/10.1016/J.ENG.2017.03.024>.
- Bagheri, R., M. Ghaedi, A. Asfaram, E. A. Dil, and H. Javadian. 2019. "RSM-CCD design of malachite green adsorption onto activated carbon with multimodal pore size distribution prepared from *Amygdalus scoparia*: Kinetic and isotherm studies." *Polyhedron* 171: 464–472. <https://doi.org/10.1016/j.poly.2019.07.037>.
- Barboux, Y., M. Dekiok, D. Le Maguer, L. Gengembre, D. Huchette, and J. Grimblot. 1992. "Bulk and surface analysis of a Fe-PO oxydehydrogenation catalyst." *Appl. Catal., A* 90 (1): 51–60. [https://doi.org/10.1016/0926-860X\(92\)80247-A](https://doi.org/10.1016/0926-860X(92)80247-A).
- Askani, M. B., and A. Pala. 2011. "Removal of arsenic from drinking water using modified natural zeolite." *Desalination* 281: 396–403. <https://doi.org/10.1016/j.desal.2011.08.015>.
- Bhattacharya, A. K., S. N. Mandal, and S. K. Das. 2006. "Adsorption of Zn(II) from aqueous solution by using different adsorbents." *Chem. Eng. J.* 123 (1–2): 43–51. <https://doi.org/10.1016/j.cej.2006.06.012>.
- Boddu, V. M., K. Abburi, J. L. Talbott, E. D. Smith, and R. Haasch. 2008. "Removal of arsenic (III) and arsenic (V) from aqueous medium using chitosan-coated biosorbent." *Water Res.* 42 (3): 633–642. <https://doi.org/10.1016/j.watres.2007.08.014>.
- Bordoloi, N., R. Goswami, M. Kumar, and R. Kataki. 2017. "Biosorption of Co (II) from aqueous solution using algal biochar: Kinetics and isotherm studies." *Bioresour. Technol.* 244: 1465–1469. <https://doi.org/10.1016/j.biortech.2017.05.139>.
- Cai, H., G. Chen, C. Peng, L. Xu, X. Zhu, Z. Zhang, Y. Dong, G. Shang, F. Ke, and H. Gao. 2015. "Enhanced removal of fluoride by tea waste supported hydrous aluminium oxide nanoparticles: Anionic polyacrylamide mediated aluminium assembly and adsorption mechanism." *RSC Adv.* 5 (37): 29266–29275. <https://doi.org/10.1039/C5RA01560J>.
- Chang, Q., and W. Lin. 2009. "Development of GAC-Iron adsorbent for arsenic removal." *Proc. Water Environ. Fed. 2009* (16): 1552–1571.
- Chen, S., Q. Yue, B. Gao, Q. Li, and X. Xu. 2011. "Removal of Cr(VI) from aqueous solution using modified corn stalks: Characteristic, equilibrium, kinetic and thermodynamic study." *Chem. Eng. J.* 168 (2): 909–917. <https://doi.org/10.1016/j.cej.2011.01.063>.
- Da'na, E., and A. Sayari. 2011. "Adsorption of copper on amine-functionalized SBA-15 prepared by co-condensation: Equilibrium properties." *Chem. Eng. J.* 166 (1): 445–453. <https://doi.org/10.1016/j.cej.2010.11.016>.
- Darby, I., C.-Y. Xu, H. M. Wallace, S. Joseph, B. Pace, and S. H. Bai. 2016. "Short-term dynamics of carbon and nitrogen using compost, compost-biochar mixture and organo-mineral biochar." *Environ. Sci. Pollut. Res.* 23 (11): 11267–11278. <https://doi.org/10.1007/s11356-016-6336-7>.
- Dashmiri, S., M. Ghaedi, K. Dashtian, M. R. Rahimi, A. Goudarzi, and R. Jannesar. 2016. "Ultrasonic enhancement of the simultaneous removal of quaternary toxic organic dyes by CuO nanoparticles loaded on activated carbon: Central composite design, kinetic and isotherm study." *Ultrason. Sonochem.* 31: 546–557. <https://doi.org/10.1016/j.ultsonch.2016.02.008>.
- Dil, E. A., M. Ghaedi, and A. Asfaram. 2019. "Application of hydrophobic deep eutectic solvent as the carrier for ferrofluid: A novel strategy for pre-concentration and determination of mefenamic acid in human urine samples by high performance liquid chromatography under experimental design optimization." *Talanta* 202: 526–530. <https://doi.org/10.1016/j.talanta.2019.05.027>.
- Ding, Z., Y. Wan, X. Hu, S. Wang, A. R. Zimmerman, and B. Gao. 2016. "Sorption of lead and methylene blue onto hickory biochars from different pyrolysis temperatures: Importance of physicochemical properties." *J. Ind. Eng. Chem.* 37: 261–267. <https://doi.org/10.1016/j.jiec.2016.03.035>.
- Ding, Z., X. Xu, T. Phan, X. Hu, and G. Nie. 2018. "High adsorption performance for As(III) and As(V) onto novel aluminum-enriched biochar derived from abandoned Tetra Paks." *Chemosphere* 208: 800–807. <https://doi.org/10.1016/j.chemosphere.2018.06.050>.
- Eljamal, O., K. Sasaki, and T. Hirajima. 2011. "Numerical simulation for reactive solute transport of arsenic in permeable reactive barrier column including zero-valent iron." *Appl. Math. Modell.* 35 (10): 5198–5207. <https://doi.org/10.1016/j.apm.2011.04.040>.
- Fakhri, Y., A. Mohseni-Bandpei, G. O. Conti, M. Ferrante, A. Cristaldi, A. K. Jeihooni, M. K. Dehkordi, A. Alinejad, H. Rasoulzadeh, and S. M. Mohseni. 2018. "Systematic review and health risk assessment of arsenic and lead in the fished shrimps from the Persian gulf." *Food Chem. Toxicol.* 113: 278–286. <https://doi.org/10.1016/j.fct.2018.01.046>.
- Faalzadeh, M., and H. Faghilian. 2015. "Separation of arsenic from aqueous solutions by amino-functionalized $\gamma\text{-Fe}_2\text{O}_3\text{-}\beta\text{-zeolite}$." *Sep. Sci. Technol.* 50 (7): 958–964.
- Foroutan, R., R. Mohammadi, A. S. Adeleye, S. Farjadfar, Z. Esvandi, H. Arfaeinia, G. A. Sorial, B. Ramavandi, and S. Sahebi. 2019. "Efficient arsenic(V) removal from contaminated water using natural clay and clay composite adsorbents." *Environ. Sci. Pollut. Res.* 26 (29): 29748–29762. <https://doi.org/10.1007/s11356-019-06070-5>.

- Golami, M., H. Mohammadi, and S. Mokhtari. 2009. "Application of reverse osmosis technology for arsenic removal from drinking water." *J. Adv. Med. Biomed. Res.* 17 (68): 9–20.
- Goldberg, S., and C. T. Johnston. 2001. "Mechanisms of arsenic adsorption on amorphous oxides evaluated using macroscopic measurements, vibrational spectroscopy, and surface complexation modeling." *J. Colloid Interface Sci.* 234: 204–216. <https://doi.org/10.1006/jcis.2000.7295>.
- He, X., J. Jiang, Z. Hong, X. Pan, Y. Dong, and R. Xu. 2020. "Effect of aluminum modification of rice straw-based biochar on arsenate adsorption." *J. Soils Sediments* 20: 3073–3082. <https://doi.org/10.1007/s11368-020-02595-2>.
- Hognon, C., C. Dupont, M. Gâteau, and F. Delrue. 2014. "Comparison of steam gasification reactivity of algal and lignocellulosic biomass: Influence of inorganic elements." *Bioresour. Technol.* 164: 347–353. <https://doi.org/10.1016/j.biortech.2014.04.111>.
- Huo, J.-B., K. Gupta, C. Lu, H. C. B. Hansen, and M.-L. Fu. 2020. "Recyclable high-affinity arsenate sorbents based on porous Fe₂O₃/La₂O₃CO₃ composites derived from Fe-La-C frameworks." *Colloids Surf., A* 585: 124018. <https://doi.org/10.1016/j.colsurfa.2019.124018>.
- Hu, X., Z. Ding, A. R. Zimmerman, S. Wang, and B. Gao. 2015. "Batch and column sorption of arsenic onto iron-impregnated biochar synthesized through hydrolysis." *Water Res.* 68: 206–216.
- Jain, A., and M. Agarwal. 2017. "Kinetic equilibrium and thermodynamic study of arsenic removal from water using alumina supported iron nano particles." *J. Water Process Eng.* 19: 51–59. <https://doi.org/10.1016/j.jwpe.2017.07.001>.
- Jin, H., S. Capareda, Z. Chang, J. Gao, Y. Xu, and J. Zhang. 2014. "Biochar pyrolytically produced from municipal solid wastes for aqueous As(V) removal: Adsorption property and its improvement with KOH activation." *Bioresour. Technol.* 169: 622–629. <https://doi.org/10.1016/j.biortech.2014.06.103>.
- Kanel, S. R., B. Manning, L. Charlet, and H. Choi. 2005. "Removal of arsenic(III) from groundwater by nanoscale zero-valent iron." *Environ. Sci. Technol.* 39 (5): 1291–1298. <https://doi.org/10.1021/es048991u>.
- Khojasteh, D., M. Kazerooni, S. Salarian, and R. Kamali. 2016. "Droplet impact on superhydrophobic surfaces: A review of recent developments." *J. Ind. Eng. Chem.* 42: 1–14. <https://doi.org/10.1016/j.jiec.2016.07.027>.
- Kim, Y.-S., and J.-H. Kim. 2019. "Isotherm, kinetic and thermodynamic studies on the adsorption of paclitaxel onto Sylopute." *J. Chem. Thermodyn.* 130: 104–113. <https://doi.org/10.1016/j.jct.2018.10.005>.
- Kumar, R., C.-U. Kang, D. Mohan, M. A. Khan, J.-H. Lee, S. S. Lee, and B.-H. Jeon. 2020. "Waste sludge derived adsorbents for arsenate removal from water." *Chemosphere* 239: 124832. <https://doi.org/10.1016/j.chemosphere.2019.124832>.
- Kumaresan, M., and P. Riyazuddin. 2001. "Overview of speciation chemistry of arsenic." *Curr. Sci.* 80: 837–846.
- Lata, S., R. Prabhakar, A. Adak, and S. R. Samadder. 2019. "As(V) removal using biochar produced from an agricultural waste and prediction of removal efficiency using multiple regression analysis." *Environ. Sci. Pollut. Res.* 26 (31): 32175–32188. <https://doi.org/10.1007/s11356-019-06300-w>.
- Lefèvre, G. 2004. "In situ Fourier-transform infrared spectroscopy studies of inorganic ions adsorption on metal oxides and hydroxides." *Adv. Colloid Interface Sci.* 107 (2–3): 109–123. <https://doi.org/10.1016/j.cis.2003.11.002>.
- Liu, Q., L. Wu, M. Goring, and Y. Deng. 2019. "Aluminum-impregnated biochar for adsorption of arsenic(V) in urban stormwater runoff." *J. Environ. Eng.* 145 (4): 04019008. [https://doi.org/10.1061/\(ASCE\)EE.1943-7870.0001503](https://doi.org/10.1061/(ASCE)EE.1943-7870.0001503).
- Low, B.-T., Y.-P. Ting, and S. Deng. 2008. "Surface modification of Penicillium chrysogenum mycelium for enhanced anionic dye removal." *Chem. Eng. J.* 141 (1–3): 9–17. <https://doi.org/10.1016/j.cej.2007.10.004>.
- Maghsodi, A., L. Adlnasab, M. Shabaniyan, and M. Javanbakht. 2018. "Optimization of effective parameters in the synthesis of nanopore anodic aluminum oxide membrane and arsenic removal by prepared magnetic iron oxide nanoparticles in anodic aluminum oxide membrane via ultrasonic-hydrothermal method." *Ultrason. Sonochem.* 48: 441–452. <https://doi.org/10.1016/j.ultsonch.2018.07.003>.
- Maher, A., M. Kitazume, M. Janbaz, R. Miskewitz, S. Douglas, and D. Yang. 2018. "Utilization of pneumatic flow tube mixing technique (PFTM) for processing and stabilization of contaminated soft sediments in the NY/NJ Harbor." *Mar. Georesour. Geotechnol.* 36 (3): 271–279. <https://doi.org/10.1080/1064119X.2016.1257668>.
- Maiti, A., J. K. Basu, and S. De. 2010. "Development of a treated laterite for arsenic adsorption: Effects of treatment parameters." *Ind. Eng. Chem. Res.* 49 (10): 4873–4886. <https://doi.org/10.1021/ie100612u>.
- Marín-Rangel, V. M., R. Cortés-Martínez, R. A. C. Villanueva, M. G. Garnica-Romo, and H. E. Martínez-Flores. 2012. "As (V) biosorption in an aqueous solution using chemically treated lemon (*Citrus aurantifolia* swingle) residues." *J. Food Sci.* 77 (1): T10–T14.
- Masue, Y., R. H. Loeppert, and T. A. Kramer. 2007. "Arsenate and arsenite adsorption and desorption behavior on coprecipitated aluminum: Iron hydroxides." *Environ. Sci. Technol.* 41 (3): 837–842.
- Matienzo, L. 1991. "Surface reactions of poly(ether ether ketone) with He²⁺ ions." *Polymer* 32 (16): 3057–3061. [https://doi.org/10.1016/0032-3861\(91\)90209-2](https://doi.org/10.1016/0032-3861(91)90209-2).
- Mohan, D., and C. U. Pittman Jr. 2007. "Arsenic removal from water/wastewater using adsorbents—a critical review." *J. Hazard. Mater.* 142 (1–2): 1–53. <https://doi.org/10.1016/j.jhazmat.2007.01.006>.
- Mohan, D., A. Sarswat, V. K. Singh, M. Alexandre-Franco, and C. U. Pittman Jr. 2011. "Development of magnetic activated carbon from almond shells for trinitrophenol removal from water." *Chem. Eng. J.* 172 (2–3): 1111–1125. <https://doi.org/10.1016/j.cej.2011.06.054>.
- Mohan, S. V., N. C. Rao, and J. Karthikeyan. 2002. "Adsorptive removal of direct azo dye from aqueous phase onto coal based sorbents: A kinetic and mechanistic study." *J. Hazard. Mater.* 90 (2): 189–204. [https://doi.org/10.1016/S0304-3894\(01\)00348-X](https://doi.org/10.1016/S0304-3894(01)00348-X).
- Murcia-Salvador, A., J. A. Pellicer, M. I. Rodríguez-López, V. M. Gómez-López, E. Núñez-Delgado, and J. A. Gabaldón. 2020. "Egg by-products as a tool to remove direct Blue 78 dye from wastewater: Kinetic, equilibrium modeling, thermodynamics and desorption properties." *Materials* 13 (6): 1262. <https://doi.org/10.3390/ma13061262>.
- Nagar, R., D. Sarkar, K. C. Makris, and R. Datta. 2010. "Effect of solution chemistry on arsenic sorption by Fe- and Al-based drinking-water treatment residuals." *Chemosphere* 78 (8): 1028–1035. <https://doi.org/10.1016/j.chemosphere.2009.11.034>.
- Ng, I.-S., X. Wu, X. Yang, Y. Xie, Y. Lu, and C. Chen. 2013. "Synergistic effect of trichoderma reesei cellulases on agricultural tea waste for adsorption of heavy metal Cr(VI)." *Bioresour. Technol.* 145: 297–301. <https://doi.org/10.1016/j.biortech.2013.01.105>.
- Nguyen, T. T. Q., P. Loganathan, T. V. Nguyen, and S. Vigneswaran. 2020. "Removing arsenic from water with an original and modified natural manganese oxide ore: Batch kinetic and equilibrium adsorption studies." *Environ. Sci. Pollut. Res.* 27 (5): 5490–5502. <https://doi.org/10.1007/s11356-019-07284-3>.
- Niazi, N. K., I. Bibi, M. Shahid, Y. S. Ok, E. D. Burton, H. Wang, S. M. Shaheen, J. Rinklebe, and A. Lüttge. 2018a. "Arsenic removal by perilla leaf biochar in aqueous solutions and groundwater: An integrated spectroscopic and microscopic examination." *Environ. Pollut.* 232: 31–41. <https://doi.org/10.1016/j.envpol.2017.09.051>.
- Niazi, N. K., I. Bibi, M. Shahid, Y. S. Ok, S. M. Shaheen, J. Rinklebe, H. Wang, B. Murtaza, E. Islam, and M. F. Nawaz. 2018b. "Arsenic removal by Japanese oak wood biochar in aqueous solutions and well water: Investigating arsenic fate using integrated spectroscopic and microscopic techniques." *Sci. Total Environ.* 621: 1642–1651. <https://doi.org/10.1016/j.scitotenv.2017.10.063>.
- Nicomel, N. R., K. Leus, K. Folens, P. Van Der Voort, and G. Du Laing. 2016. "Technologies for arsenic removal from water: Current status and future perspectives." *Int. J. Environ. Res. Public Health* 13 (1): 62. <https://doi.org/10.3390/ijerph13010062>.
- Nollet, H., M. Roels, P. Lutgen, P. Van der Meer, and W. Verstraete. 2003. "Removal of PCBs from wastewater using fly ash." *Chemosphere* 53 (6): 655–665. [https://doi.org/10.1016/S0045-6535\(03\)00517-4](https://doi.org/10.1016/S0045-6535(03)00517-4).

- Ociński, D., and P. Mazur. 2020. "Highly efficient arsenic sorbent based on residual from water deironing—Sorption mechanisms and column studies." *J. Hazard. Mater.* 382: 121062.
- Okoli, C. P., P. N. Diagbaya, I. O. Anigbogu, B. I. Olu-Owolabi, and K. O. Adebowale. 2017. "Competitive biosorption of Pb(II) and Cd(II) ions from aqueous solutions using chemically modified moss biomass (*Barbula lambarenensis*)." *Environ. Earth Sci.* 76 (1): 33. <https://doi.org/10.1007/s12665-016-6368-9>.
- Pal, D., and S. K. Maiti. 2019. "Abatement of cadmium (Cd) contamination in sediment using tea waste biochar through meso-microcosm study." *J. Cleaner Prod.* 212: 986–996. <https://doi.org/10.1016/j.jclepro.2018.12.087>.
- Pan, J.-J., J. Jiang, W. Qian, and R.-k. Xu. 2015. "Arsenate adsorption from aqueous solution onto Fe(III)-modified crop straw biochars." *Environ. Eng. Sci.* 32 (11): 922–929. <https://doi.org/10.1089/ees.2014.0540>.
- Panneerselvam, P., N. Morad, and K. A. Tan. 2011. "Magnetic nanoparticle (Fe₃O₄) impregnated onto tea waste for the removal of nickel(II) from aqueous solution." *J. Hazard. Mater.* 186 (1): 160–168. <https://doi.org/10.1016/j.jhazmat.2010.10.102>.
- Patel, M., A. Kumari, and A. K. Parida. 2020. "Arsenic tolerance mechanisms in plants and potential role of arsenic hyperaccumulating plants for phytoremediation of arsenic-contaminated soil." In *Plant ecophysiology and adaptation under climate change: Mechanisms and perspectives II*, edited by M. Hasanuzzaman, 137–162. Berlin: Springer.
- Peng, Y., Y. Sun, R. Sun, Y. Zhou, D. C. Tsang, and Q. Chen. 2019. "Optimizing the synthesis of Fe/Al (Hydr)oxides-Biochars to maximize phosphate removal via response surface model." *J. Cleaner Prod.* 237: 117770. <https://doi.org/10.1016/j.jclepro.2019.117770>.
- Radu, T., J. L. Subacz, J. M. Phillippi, and M. O. Barnett. 2005. "Effects of dissolved carbonate on arsenic adsorption and mobility." *Environ. Sci. Technol.* 39 (20): 7875–7882. <https://doi.org/10.1021/es050481s>.
- Ranjan, A. 2019. "Spatial analysis of arsenic contamination of groundwater around the world and India." *Int. J. Innov. Stud. Soc. Human.* 4 (10): 6–15.
- Ravikovich, P. I., and A. V. Neimark. 2006. "Density functional theory model of adsorption on amorphous and microporous silica materials." *Langmuir* 22 (26): 11171–11179. <https://doi.org/10.1021/la0616146>.
- Roy, P., N. Mondal, and K. Das. 2014. "Modeling of the adsorptive removal of arsenic: A statistical approach." *J. Environ. Chem. Eng.* 2 (1): 585–597.
- Said, K. A. M., N. Z. Ismail, R. L. Jama'in, N. A. M. Alipah, N. M. Sutan, G. G. Gadung, R. Bainsi, and N. S. A. Zauzi. 2018. "Application of Freundlich and Temkin isotherm to study the removal of Pb(II) via adsorption on activated carbon equipped polysulfone membrane." *Int. J. Eng. Technol.* 7 (3.18): 91–93. <https://doi.org/10.14419/ijet.v7i3.18.16683>.
- Salih, S. S., A. Mahdi, M. Kadhom, and T. K. Ghosh. 2019. "Competitive adsorption of As(III) and As(V) onto chitosan/diatomaceous earth adsorbent." *J. Environ. Chem. Eng.* 7 (5): 103407. <https://doi.org/10.1016/j.jece.2019.103407>.
- Samsuri, A. W., F. Sadegh-Zadeh, and B. J. Seh-Bardan. 2013. "Adsorption of As(III) and As(V) by Fe coated biochars and biochars produced from empty fruit bunch and rice husk." *J. Environ. Chem. Eng.* 1 (4): 981–988. <https://doi.org/10.1016/j.jece.2013.08.009>.
- Sawood, G. M., and S. K. Gupta. 2020. "Kinetic equilibrium and thermodynamic analyses of As (V) removal from aqueous solution using iron-impregnated *Azadirachta indica* carbon." *Appl. Water Sci.* 10: 1–18. <https://doi.org/10.1007/s13201-020-01217-z>.
- Senthilkumar, R., D. M. Reddy Prasad, L. Govindarajan, K. Saravanakumar, and B. S. Naveen Prasad. 2020. "Synthesis of green marine algal-based biochar for remediation of arsenic(V) from contaminated waters in batch and column mode of operation." *Int. J. Phytorem.* 22 (3): 279–286. <https://doi.org/10.1080/15226514.2019.1658710>.
- Shaheen, S. M., N. K. Niazi, N. E. Hassan, I. Bibi, H. Wang, D. C. Tsang, Y. S. Ok, N. Bolan, and J. Rinklebe. 2019. "Wood-based biochar for the removal of potentially toxic elements in water and wastewater: A critical review." *Int. Mater. Rev.* 64 (4): 216–247. <https://doi.org/10.1080/09506608.2018.1473096>.
- Shahid, M. K., S. Phearom, and Y.-G. Choi. 2019. "Adsorption of arsenic (V) on magnetite-enriched particles separated from the mill scale." *Environ. Earth Sci.* 78 (3): 65. <https://doi.org/10.1007/s12665-019-8066-x>.
- Sherlala, A., A. Raman, M. M. Bello, and A. Buthiyappan. 2019. "Adsorption of arsenic using chitosan magnetic graphene oxide nanocomposite." *J. Environ. Manage.* 246: 547–556. <https://doi.org/10.1016/j.jenvman.2019.05.117>.
- Sierra-Trejo, P. V., E. Guibal, and J. F. Louvier-Hernández. 2020. "Arsenic sorption on chitosan-based sorbents: Comparison of the effect of molybdate and tungstate loading on As(V) sorption properties." *J. Polym. Environ.* 28 (3): 934–947. <https://doi.org/10.1007/s10924-020-01654-6>.
- Singh, P., A. Sarswat, C. U. Pittman JR, T. Mlsna, and D. Mohan. 2020. "Sustainable Low-Concentration Arsenite [As(III)] Removal in Single and Multicomponent Systems Using Hybrid Iron Oxide-Biochar Nanocomposite Adsorbents-A Mechanistic Study." *ACS Omega* 5 (6): 2575–2593. <https://doi.org/10.1021/acsomega.9b02842>.
- Singh, T. S., and K. K. Pant. 2004. "Equilibrium, kinetics and thermodynamic studies for adsorption of As(III) on activated alumina." *Sep. Purif. Technol.* 36 (2): 139–147. [https://doi.org/10.1016/S1383-5866\(03\)00209-0](https://doi.org/10.1016/S1383-5866(03)00209-0).
- Su, J., T. Lyu, H. Yi, L. Bi, and G. Pan. 2020. "Superior arsenate adsorption and comprehensive investigation of adsorption mechanism on novel Mn-doped La₂O₃CO₃ composites." *Chem. Eng. J.* 391: 123623. <https://doi.org/10.1016/j.cej.2019.123623>.
- Tan, P., Y. Zheng, and Y. Hu. 2020. "Efficient removal of arsenate from water by lanthanum immobilized electrospun chitosan nanofiber." *Colloids Surf., A* 589: 124417. <https://doi.org/10.1016/j.colsurfa.2020.124417>.
- Tariq, M. A., A. I. Durrani, U. Farooq, and M. Tariq. 2018. "Efficacy of spent black tea for the removal of nitrobenzene from aqueous media." *J. Environ. Manage.* 223: 771–778. <https://doi.org/10.1016/j.jenvman.2018.06.080>.
- Thanh, D. N., Z. Bastl, K. Černá, P. Ulbrich, and J. Lederer. 2016. "Amorphous nanosized Al–Ti–Mn trimetal hydrous oxides: Synthesis, characterization and enhanced performance in arsenic removal." *RSC Adv.* 6 (103): 100732–100742. <https://doi.org/10.1039/C6RA11347H>.
- Torrades, F., and J. García-Montaña. 2014. "Using central composite experimental design to optimize the degradation of real dye wastewater by Fenton and photo-Fenton reactions." *Dyes Pigm.* 100: 184–189. <https://doi.org/10.1016/j.dyepig.2013.09.004>.
- Tripathy, S. S., and A. M. Raichur. 2008. "Enhanced adsorption capacity of activated alumina by impregnation with alum for removal of As(V) from water." *Chem. Eng. J.* 138 (1–3): 179–186. <https://doi.org/10.1016/j.cej.2007.06.028>.
- Tseng, C.-H. 2009. "A review on environmental factors regulating arsenic methylation in humans." *Toxicol. Appl. Pharmacol.* 235 (3): 338–350. <https://doi.org/10.1016/j.taap.2008.12.016>.
- Uthappa, U., G. Sriram, O. Arvind, S. Kumar, G. M. Neelgund, D. Losic, and M. D. Kurkuri. 2020. "Engineering MIL-100(Fe) on 3D porous natural diatoms as a versatile high performing platform for controlled isoniazid drug release, Fenton's catalysis for malachite green dye degradation and environmental adsorbents for Pb²⁺ removal and dyes." *Appl. Surf. Sci.* 528: 146974. <https://doi.org/10.1016/j.apsusc.2020.146974>.
- Wan, P., M. Yuan, X. Yu, Z. Zhang, and B. Deng. 2020. "Arsenate removal by reactive mixed matrix PVDF hollow fiber membranes with UIO-66 metal organic frameworks." *Chem. Eng. J.* 382: 122921. <https://doi.org/10.1016/j.cej.2019.122921>.
- Wei, Y., S. Wei, C. Liu, T. Chen, Y. Tang, J. Ma, K. Yin, and S. Luo. 2019. "Efficient removal of arsenic from groundwater using iron oxide nanonetwork array-decorated biochar fibers with high Fe utilization and fast adsorption kinetics." *Water Res.* 167: 115107. <https://doi.org/10.1016/j.watres.2019.115107>.
- Wu, X., Y. Zhang, X. Dou, B. Zhao, and M. Yang. 2013. "Fluoride adsorption on an Fe–Al–Ce trimetal hydrous oxide: Characterization of adsorption sites and adsorbed fluorine complex species." *Chem. Eng. J.* 223: 364–370. <https://doi.org/10.1016/j.cej.2013.03.027>.
- Xu, R.-k., N. P. Qafoku, E. Van Ranst, J.-y. Li, and J. Jiang. 2016. "Adsorption properties of subtropical and tropical variable

- charge soils: Implications from climate change and biochar amendment." *Adv. Agron.* 135 (4): 1–58. <https://doi.org/10.1016/bs.agron.2015.09.001>.
- Xue, Q., Y. Ran, Y. Tan, C. L. Peacock, and H. Du. 2019. "Arsenite and arsenate binding to ferrihydrite organo-mineral coprecipitate: Implications for arsenic mobility and fate in natural environments." *Chemosphere* 224: 103–110. <https://doi.org/10.1016/j.chemosphere.2019.02.118>.
- Yan, J., Y. Xue, L. Long, Y. Zeng, and X. Hu. 2018. "Adsorptive removal of As(V) by crawfish shell biochar: Batch and column tests." *Environ. Sci. Pollut. Res.* 25 (34): 34674–34683. <https://doi.org/10.1007/s11356-018-3384-1>.
- Yang, X.-Y., and B. Al-Duri. 2001. "Application of branched pore diffusion model in the adsorption of reactive dyes on activated carbon." *Chem. Eng. J.* 83 (1): 15–23. [https://doi.org/10.1016/S1385-8947\(00\)00233-3](https://doi.org/10.1016/S1385-8947(00)00233-3).
- Yang, X., S. R. Otto, and B. Al-Duri. 2003. "Concentration-dependent surface diffusivity model (CDSDM): Numerical development and application." *Chem. Eng. J.* 94 (3): 199–209. [https://doi.org/10.1016/S1385-8947\(03\)00051-2](https://doi.org/10.1016/S1385-8947(03)00051-2).
- Yin, Z., Y. Ma, B. Tanis-Kanbur, and J. W. Chew. 2020. "Fouling behavior of colloidal particles in organic solvent ultrafiltration." *J. Membr. Sci.* 599: 117836. <https://doi.org/10.1016/j.memsci.2020.117836>.
- Youngran, J., F. Maohong, J. Van Leeuwen, and J. F. Belczyk. 2007. "Effect of competing solutes on arsenic(V) adsorption using iron and aluminum oxides." *J. Environ. Sci.* 19 (8): 910–919. [https://doi.org/10.1016/S1001-0742\(07\)60151-X](https://doi.org/10.1016/S1001-0742(07)60151-X).
- Yu, C., F. Wang, C. Zhang, S. Fu, and L. A. Lucia. 2016. "The synthesis and adsorption dynamics of a lignin-based hydrogel for remediation of cationic dye-contaminated effluent." *React. Funct. Polym.* 106: 137–142. <https://doi.org/10.1016/j.reactfunctpolym.2016.07.016>.
- Yu, Y., L. Yu, and J. P. Chen. 2015. "Adsorption of fluoride by Fe–Mg–La triple-metal composite: Adsorbent preparation, illustration of performance and study of mechanisms." *Chem. Eng. J.* 262: 839–846. <https://doi.org/10.1016/j.cej.2014.09.006>.
- Yuan, J.-H., R.-K. Xu, and H. Zhang. 2011. "The forms of alkalis in the biochar produced from crop residues at different temperatures." *Bioresour. Technol.* 102 (3): 3488–3497. <https://doi.org/10.1016/j.biortech.2010.11.018>.
- Zeng, H., Y. Yu, F. Wang, J. Zhang, and D. Li. 2020. "Arsenic(V) removal by granular adsorbents made from water treatment residuals materials and chitosan." *Colloids Surf., A* 585: 124036. <https://doi.org/10.1016/j.colsurfa.2019.124036>.
- Zhang, S., H. Niu, Y. Cai, X. Zhao, and Y. Shi. 2010. "Arsenite and arsenate adsorption on coprecipitated bimetal oxide magnetic nanomaterials: MnFe₂O₄ and CoFe₂O₄." *Chem. Eng. J.* 158 (3): 599–607.
- Zhang, F., X. Wang, J. Xionghui, and L. Ma. 2016. "Efficient arsenate removal by magnetite-modified water hyacinth biochar." *Environ. Pollut.* 216: 575–583. <https://doi.org/10.1016/j.envpol.2016.06.013>.



Cite this: DOI: 10.1039/d1ew00385b

Selective As(v) capture by a novel magnetic green Fe-biochar composite in a packed column: an application of central composite design†

Ghazi Mohd Sawood,^a Shobhit Dixit,^b Gaurav Mishra^b and S. K. Gupta^a

Arsenic contamination in groundwater is a prominent global issue due to its substantial toxicological impacts on the environment and human health. Herein, a fixed-bed column experiment was carried out for feasibility analysis of using a novel Fe-impregnated *Azadirachta indica* biochar matrix for arsenate removal. The adsorbent was characterized by SEM, EDAX, BET, XRD, TGA, VSM, and XPS analysis. Statistical RSM with central composite design is applied to examine the synergistic effects of process parameters on the adsorption of arsenate. A high R^2 value of 0.994 predicted by ANOVA established the adequate regression of the proposed model. At a bed height of 18.0 cm, flow rate of 3.0 mL min⁻¹, pH 7 and initial arsenate concentration of 500 µg L⁻¹, the arsenate uptake capacity of Fe-AIB was found to be 149 µg g⁻¹. Various mathematical models including the Thomas, Yoon Nelson, Adams–Bohart and BDST models were used to analyse the column experiment data. The Thomas model best defines the nature of the breakthrough curves at various conditions. The BDST model manifested good agreement with experimental results and obtained high R^2 values, showing the significant applicability of this model for the current fixed-bed column system. The regeneration of columns was conducted using 10% NaOH.

Received 6th June 2021,
Accepted 13th September 2021

DOI: 10.1039/d1ew00385b

rsc.li/es-water

Water impact

A substantial lab-scale investigation was conducted to estimate the performance of a fixed-bed column by a novel adsorbent Fe-AIB having an adsorption capacity of 1.49 mg L⁻¹, using different influent concentrations, bed heights, pH and flow rates. The experimental data obtained in the present work were competently simulated in the central composite design model. The simultaneous effect shows that the breakthrough time increases but with a slight decrease in uptake capacity as the bed height and influent concentration increase. The breakthrough time, along with the uptake capacity, increases at low flow rates. The Thomas model can determine the nature of the breakthrough curves; this may imply that the controlling step of the adsorption process is neither internal nor external diffusion in the column. The BDST model demonstrated excellent agreement with the experimental results and obtained high R^2 values, confirming the applicability of the BDST model for the fixed-bed column system of the present study. The regeneration and successive reuse of the adsorbent offered an inexpensive approach for the remediation of arsenate from aqueous systems. The effluent water quality treated by Fe-AIB was proven to be completely safe for human consumption. The foremost performance of the Fe-AIB packed column was its capacity, *i.e.*, approximately 90 litres of arsenate contaminated water per day (of 500 µg L⁻¹ brought down to below 10 µg L⁻¹), suggesting the suitability of the Fe-AIB adsorbent for water filters in households in rural regions without power requirements. Overall, it can be deduced that the statistical model application is an efficient approach for modelling, optimization and design of the arsenate adsorption system. The experimental results shown in the present investigation can surely be hypothesized for the establishment and design of an effective arsenate remediation plan while treating contaminated groundwater.

Introduction

Arsenic is a major contaminant in both wastewater and potable water resulting from anthropogenic and natural

activities including application of arsenical insecticides, ore mining, rock weathering *etc.* Arsenic can cause a potential threat to human health and aquatic life.^{1,2} The chronic effects of arsenic consumption may include disorders associated with the digestive and respiratory tracts, renal and liver diseases, reproductive system disorders, carcinogenic effects, neurasthenia, arsenicosis, and dystrophia.^{3,4} Therefore, efforts are required to mitigate the arsenic load in aquatic systems. Developing low-cost, efficient and sustainable techniques for the remediation of arsenic from contaminated water resources has attracted remarkable attention.

^a Department of Chemical Engineering, Harcourt Butler Technical University, Kanpur, India. E-mail: mohdsaud22@gmail.com

^b Department of Chemical Engineering and Technology, IIT BHU, Varanasi, Uttar Pradesh, 221005, India

† Electronic supplementary information (ESI) available. See DOI: 10.1039/d1ew00385b

Catalytic degradation, membrane filtration, ion exchange, solvent extraction, steam stripping, oxidation and microbial degradation are the primary technologies which have been utilized for remediation of arsenic from aquatic systems. These methods have been shown to be less successful owing to increased energy consumption, increased resource requirements, and the generation of toxic metabolites.^{5,6} Adsorption technique is generally recognized for the treatment of arsenic due to its economic efficiency, simplicity of operation, and eco-friendliness. Various materials, including clay minerals, activated carbon, metal oxides, sludge, gels, and resins, have been intensively utilised as adsorbents by researchers for arsenic mitigation from contaminated water.⁷

Due to the presence of high surface area, surface charges, active sites, and functional groups, the potential of commercial biochar as an adsorbent for arsenic species has piqued researchers' interest considerably.^{8,9} To meet these requirements, carbonized *Azadirachta indica* bark is used as a substitute adsorbent. Various studies have been conducted which report efficient removal of homogenous and cationic adsorbates using carbon derived from the bark and leaves of *Azadirachta indica* tree.^{10–12} However, due to its lower interference capacity and heterogeneous nature, biochar application is inconsistent to some degree.¹³ Furthermore, the majority of biochars is ineffective in remediating anionic pollutants such as arsenate. Thus, modifying the surface area, surface charges, functional groups, ash content, and hydrophilicity/hydrophobicity of biochar through physical, chemical, mechanical, or thermal treatments may enhance the removal capacity and selectivity of biochar.^{5,14}

In the recent past, various technologies have been developed for the synthesis of engineered biochar with increased adsorption capacity to inorganic and organic contaminants. For example neutral Fe oxide minerals (hematite, goethite, and magnetite) and low-cost, naturally abundant Fe affluent lateritic soil have proven to be effective in remediation of arsenic from aquatic reservoirs.¹⁵ The composite of Fe–Mn biochar was reported to have approximately 20 times greater arsenate adsorption capacity in comparison to pristine biochar.¹⁶ The enhanced uptake capacity of the composite can be attributed to the presence of MnFe_2O_4 (bimetal oxides) and Fe_2O_3 and MnO (metal oxides). Moreover, hydrolysis of Fe salt on hickory biochar was carried out for the sorption of arsenate.¹⁷ Fe-impregnated biochar, prepared by mixing Fe salt solution with the biochar on a magnetic stirrer, manifested enhanced arsenate adsorption capacity (maximum uptake of $2160 \mu\text{g g}^{-1}$).¹⁸ However, the synthesized composite adsorbent showed negligible magnetism, making it inappropriate for practical applications in terms of recollection of iron traces from the spent adsorbent. Thorough exploration into the effectiveness of arsenate adsorption by a low-cost, magnetically effective and re-generable adsorbent is needed urgently.

Thus, the overarching objective of this study is to synthesise modified *Azadirachta indica* carbon through iron

impregnation (Fe-AIB) and to investigate the use of Fe-AIB for arsenate remediation in aqueous solution. Statistical modelling of the column adsorption experiments were carried out to evaluate the optimization potential and sensitivity analysis, using response surface methodology (RSM)–central composite design (CCD). Various models have been employed to investigate the combined as well as the individual effects of the process variable that influences the process of adsorption. Moreover, adsorption–desorption analyses were conducted to reuse and regenerate the spent adsorbent. In unison, a thorough study for the eco-friendly, easy, and economical exposition of catastrophic $\text{As}(\text{v})$ contamination has been carried out that can be easily applied in underdeveloped countries. The obtained result from the present research is presented as well as discussed.

Materials and methods

Reagents and apparatus

The chemicals used were AR grade and procured from M/S, Merck India Ltd. Double distilled water was used to prepare all standards and reagents. The arsenate solution was prepared by using sodium arsenate hydrate ($\text{NaHAsO}_4 \cdot 7\text{H}_2\text{O}$). Iron(II) chloride was used for impregnation purposes. A stock solution of arsenate was prepared by dissolving 0.416 g of $\text{NaHAsO}_4 \cdot 7\text{H}_2\text{O}$ in DI water. 0.1 M NaOH and HCl solutions were added to adjust the pH of arsenate whenever necessary. The glassware were soaked in 15% HNO_3 for thorough cleaning and rinsed with double distilled water before using.

Instruments and software

The pH of various solutions during the experiment was measured using a digital pH meter (Hanna multi parameter pH meter-HI2020) with ± 0.01 unit accuracy. For providing a continuous supply of arsenate solution to the fixed-bed column, a peristaltic pump (Stenner-85mhp17) was used. For the synthesis of *Azadirachta indica* char, a muffle furnace (METZER METZ-2011) was used. For the morphological and iron distribution analysis of Fe-AIB and Fe-AIL, energy dispersive X-ray coupled with SEM (Carl Zeiss model-EVO-50) was used. Arsenate was determined using ICP-MS. Each sample was examined thrice, and reproducibility was found to be within $\pm 5\%$ of experimental results. Before analysis, calibration was conducted on a daily basis using a freshly prepared standard of arsenate. Blank runs were conducted to ensure that no adsorption transpires on the walls of the column.

Preparation and characterization of adsorbent

Azadirachta indica carbon was synthesised by carbonization (at 750°C under a controlled environment) of powdered bark of *Azadirachta indica* tree which was collected from local timber houses of Kanpur, UP, India. AIB having size in the range $200\text{--}250 \mu\text{m}$ was rinsed with DI water for the removal of dirt, and the resultant product was oven-dried at 80°C for

24 h for the volatilization of organic impurities. To prepare iron impregnated *Azadirachta indica* carbon (Fe-AIB), a mixture of 0.5 M iron(II) chloride and 50 g *Azadirachta indica* carbon was subjected to a gentle stirring of 50 rpm for 24 hours. The impregnation process results in a series of thermochemical reactions. To maintain the slurry pH for greater charge abundance, NaOH was added to the mixture. The obtained filtrate was subjected to multiple washing to remove the colloidal precipitates and iron salt traces which stick to the surface of activated carbon. The washed filtrate was oven-dried at 100 °C for 4 h.

Experimental setup

The Fe-AIB adsorbent was packed within glass (borosilicate) columns with a length of 55 cm and an internal diameter of 2 cm; to obstruct the flotation of particles of adsorbent at the top and to provide uniform flow distribution, a layer of glass wool over glass beads was provided.

All the experiments were carried out in a downflow manner at pH 7.0 in the column study. A peristaltic pump was used to pump the arsenate-spiked water through the packed bed of Fe-AIB. The impact of various process parameters like influent arsenate concentration, bed height, inlet flow rate and pH at different throughput volumes was investigated and studied. Samples of effluent at fixed time intervals were collected and examined for arsenate concentration. The arsenate-spiked water was allowed to pass through the Fe-AIB bed in a downflow manner at a volumetric flow rate of 3 ml min⁻¹, bed depths of 3, 6, and 9 cm and initial arsenate concentration of 1000 µg L⁻¹. The influence of flow rate on the removal of arsenate was analysed at 3, 6 and 9 mL min⁻¹ for an influent arsenate concentration of 1000 µg L⁻¹ and bed depth of 9 cm. The column operations were stopped as the effluent arsenate concentration surpassed 99% influent concentration. Conventional mathematical models, including the Thomas model, Yoon Nelson model, and BDST model, were used to study the column performance and breakthrough curve analysis. All experiments were conducted at room temperature (25 ± 2 °C).

Experimental design

The optimum conditions related to the mitigation of arsenate using Fe-AIB were investigated, and the variable interactions were estimated by using central composite design in response surface methodology (RSM). Four independent variables (influent arsenate concentration, bed depth, influent flow rate, and pH) were selected. All-inclusive 30 sets of remediation combinations were examined by using Design-Expert software (version 12.0.0, Stat-Ease Inc., USA). 2nd-order polynomials were used in order to fit the obtained experimental data. The model adequacy was examined by using the lack-of-fit test, sequential F-test, and other requisite measurements. The data generated by CCD were estimated by multiple regressions to fit the second-order model given by eqn (1) (Fig. 1).¹⁹

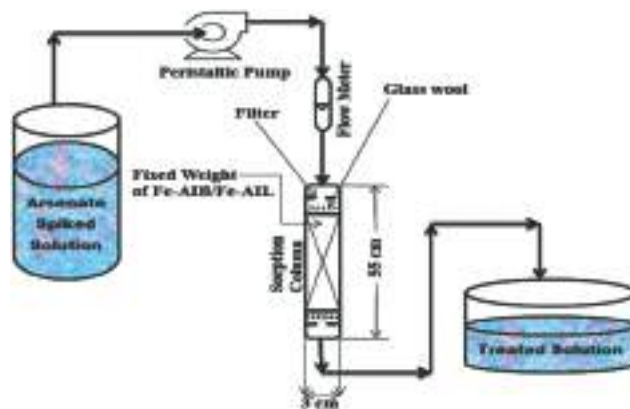


Fig. 1 Experimental setup for continuous adsorption.

$$Y = \beta_0 + \sum_{i=1}^4 \beta_i X_i + \sum_{i=1}^4 \sum_{j=1}^4 \beta_{ij} X_i X_j + \sum_{i=1}^4 \beta_{ii} X_i^2 \quad (1)$$

where Y is the breakthrough time (predicted response), β_0 is a model constant, β_i is a linear coefficient, and X_i and X_j are independent variables.

Results and discussion

Characterization of Fe-AIB

The iron content of Fe-AIB and pristine biochar were 16.10% and 0.05%, respectively, revealing the adequate Fe impregnation into the biochar. The reported specific surface areas of Fe-AIB and pristine biochar were 352 m² g⁻¹ and 877 m² g⁻¹, respectively, suggesting that Fe impregnation may have filled or blocked pores on the biochar surfaces. Hence, specific surface areas cannot be regarded as the deciding factor in sorption of arsenate onto Fe-AIB. Surface morphology is revealed by the SEM micrographs of Fe-AIB. A large number of pores and grooves can be clearly seen (Fig. 2b); it shows a very porous structure of Fe-AIB, which may have resulted in a large surface area of the material. Aggregates of Fe can be seen in the micrographs of the adsorbent. The distribution of Fe-AIB surface elements analysed by EDAX is shown in Table 1. The EDAX analysis shows that the adsorbent contains mainly C, Cl and Fe, suggesting the composition of mixed metal oxide. Chlorine and iron are well-known binding agents. As per the study of chemical composition, Fe oxide is the dominant adsorbent species.

Table 1 presents the BET surface area, pore width and pore volume of Fe-AIB. The study indicates a decrease in the surface area, pore width and pore volume in the samples after Fe impregnation. This decrease can be due to the blockage of the pores resulting from Fe coating in samples. Previously, a similar trend was seen in surface area, pore width and pore volume due to iron doping.²⁰ Fe-AIB's average pore width was found to be in the range of 5–15 Å, which shows its microporous nature.²¹



Fig. 2 SEM images (25 kV; 20 μm) of (a) uncarbonized AIB, (b) Fe-AIB, and (c) arsenate-laden Fe-AIB.

XRD analysis was carried out to investigate the crystalline structure of the modified biochars derived from the bark of *Azadirachta indica* (Fig. 3). The diffraction peaks corresponding to 2 theta values of 18° for Fe-AIB show the amorphous nature of the carbonised adsorbent.²² In the spectrum of Fe-AIB, the peaks at two theta values of 30.6° and 34.4° correspond to the presence of γ -Fe₂O₃ and Fe₃O₄ spinel structure, respectively.²³ The absence of any noticeable peaks in the two theta range of 35–90° in the spectrum reveals the replacement by the amorphous form of Fe in Fe-AIB, which is more favourable than the crystalline form of Fe oxide in adsorption of arsenic.²⁴ XRD analysis confirms that the crystalline nature of the material may be influenced by the process of impregnation.

To study the mechanism of arsenate adsorption on Fe-AIB, shifts of binding energy were analysed for C, O, Fe and As using XPS analysis (Fig. 4). As carbon and oxygen can alter the reactivity of surfaces in XPS data, their spectrum is very significant. A similar pattern has also been recorded previously in surface area. The C 1s XPS spectra (Fig. 5) for the precursor could be de-convoluted into 4 peaks corresponding to binding energies at 284.9 (C–C and C–H), 285.2 (C–O), 287.5 (C=O), and 290.3 eV (O–C=O). After impregnation, the peaks at 287.5 and 290.3 eV appeared at 287.1 and 289.4 eV, respectively, and the peak at 287.5 was shown with the enhanced area, revealing carbon surface oxidation resulting from the deposition of Fe.²⁵

Table 1 Physicochemical properties of Fe-AIB and pristine biochar

Analysis	Fe-AIB	Pristine biochar
Element (weight %)		
C	82.04	98.16
Cl	1.86	1.79
Fe	16.10	0.05
Moisture content (%)	10.95	11.14
pH _{zpc}	6.76	—
Particle density (g cm ⁻³)	1.33	—
Average particle size (μm)	226	—
Specific surface area (m ² g ⁻¹)	352	877
Pore width (Å)	6.9	14.38

The O 1s spectra (Fig. 6) for the unmodified *Azadirachta indica* carbon could be de-convoluted into 2 peaks corresponding to a binding energy of 484.9 eV representing the O–C functional group and the other at a binding energy of 486.0 eV representing the O–C=O group. After Fe impregnation, a new peak of oxygen at 488.7 is shown owing to the oxygen of Fe oxide. The peaks of Fe were located at BE = 704.2 eV for these impregnated carbons. These data correspond to Fe³⁺ characteristics.²⁶ The peaks of unmodified AIB carbon at 484.9 eV reduced to lower values with increased area, indicating the unmodified carbon's oxidation during the impregnation process.

The As 3d spectra of Fe-AIB are presented in Fig. 7. The binding energies of HASO₄²⁻ = 45.0 eV and H₂AsO₄ = 46.1 eV are shown. The arsenate distribution was evaluated by deconvolution of As 3d spectra. For the impregnated product, a peak corresponding to 45.0 eV was observed, which reveals HASO₄²⁻ as the dominant species. On the surface of Fe-impregnated activated carbon, the HASO₄²⁻ dominance shows the dominant nature of protonated complexes.²⁷ Moreover, the analysis of As 3d spectra shows no conversion of arsenate to poisonous arsenite during the adsorption process.

Complexes of arsenate are disassociated as HASO₄²⁻ and H₂AsO₄ species.²⁸ The probable mechanism of adsorption in

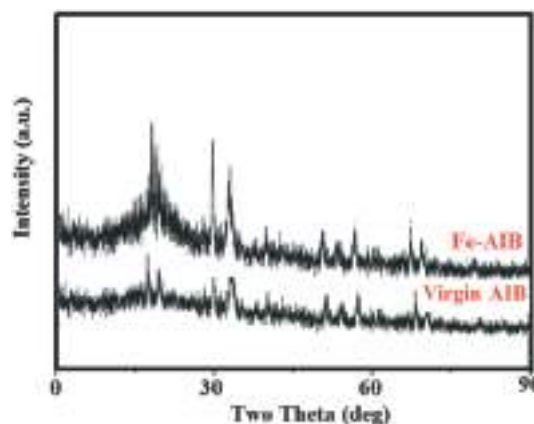


Fig. 3 XRD pattern of Fe-AIB.

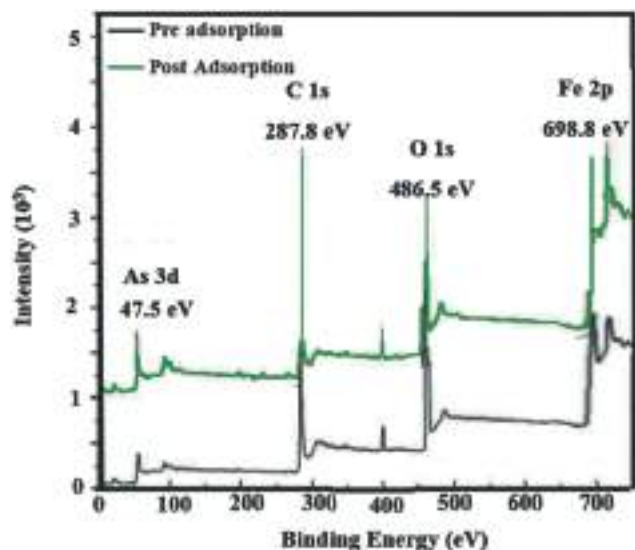


Fig. 4 XPS scans for Fe-AIB.

Fe-impregnated biochars is the substitution of the O ligand of As(v) molecules by the microparticles of Fe on the surface of carbon through the formation of bi- and mono-dentate complexes on the surface (Fig. 10).²⁹ The peak intensity for Fe₃O₄ and OH was relatively unaltered for Fe-AIB, which shows better results, whereas it increased for C=O, confirming the predominance of bidentate complexes on the Fe-impregnated char. The characteristic bands for Fe 2p (Fig. 8) were shifted after arsenate adsorption. The significant peak shift of Fe after As(v) adsorption at B.E. = 698.3 eV is observed in the figure. The corresponding energy can be attributed to Fe³⁺ ions.

The adsorption of arsenate on Fe-AIB shows a negative direction shift in zeta potential (Fig. 9). The shift can be attributed to increased negativity of the surface charge on Fe-AIB resulting from arsenate adsorption. The zeta potential

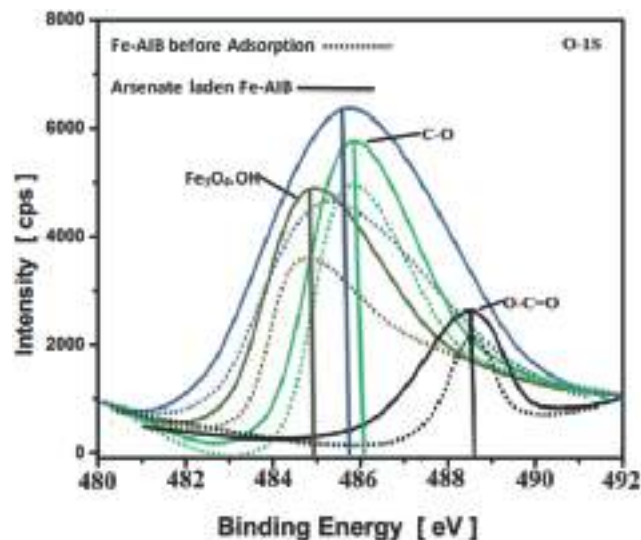


Fig. 6 O 1s spectra of Fe-AIB before and after arsenate adsorption.

shift induced by the adsorption of arsenate became more conspicuous with a decrement in pH, consistent with the trend of adsorption of arsenate with pH. Arsenate is firmly bound to the adsorbent surface during adsorption, and several negative charges transferred to the biochar's surface, although if arsenate was electrostatically adsorbed, the electrostatic double layer would have carried negative charges on Fe-AIB and, consequently, would not alter the zeta potential and surface charge of the adsorbent. The same trend of alterations in surface charge and zeta potential on metal oxides induced by arsenate adsorption was previously reported.^{30–32}

TGA curves comprise an expeditious weight loss phase and a stable phase. Thermal decomposition led to a significant weight loss for the precursor at temperatures between 400 and 600 °C, which was significantly different

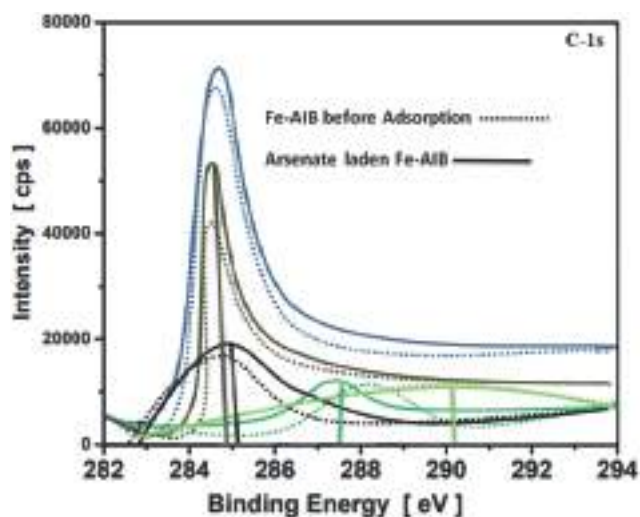


Fig. 5 C 1s spectra of Fe-AIB before and after arsenate adsorption.

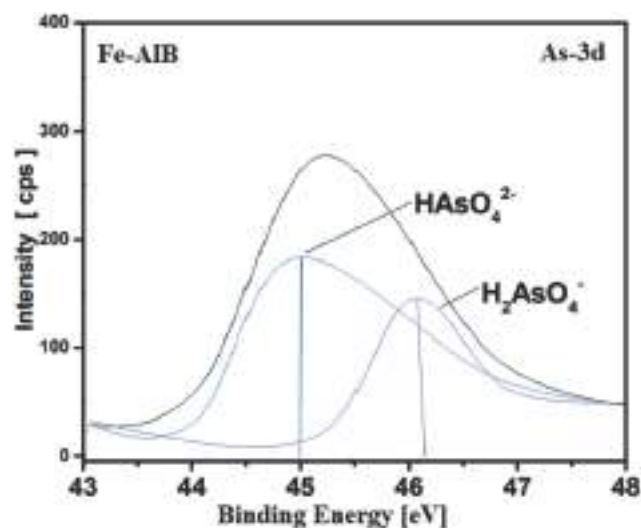


Fig. 7 As 3d spectra of Fe-AIB after arsenate adsorption.

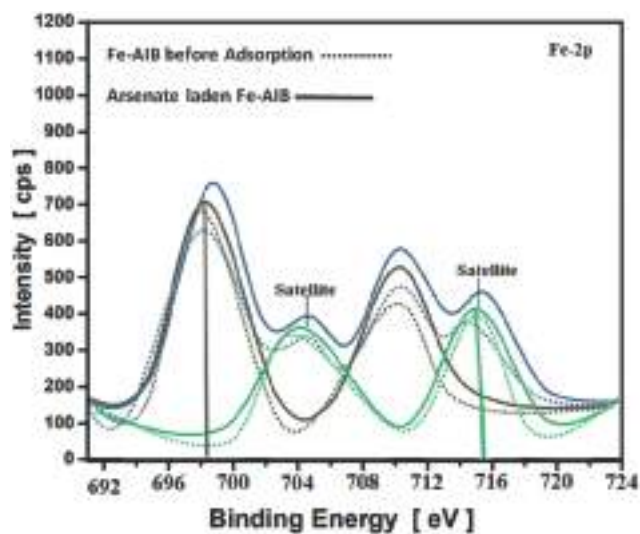


Fig. 8 Fe-2p spectra of Fe-AIB before and after arsenate adsorption.

from that of Fe-AIB and arsenate-laden Fe-AIB. The residual weights in comparison to the original weight were 3.75% for the precursor, 8.55% for Fe-AIB, and 10.45% for arsenate-laden Fe-AIB. The obtained result is in good agreement with previous studies where the metal oxide modified biochar possesses greater thermal stability in comparison to pristine char.^{33–36} This can be attributed to the transition of metal oxides in the course of the heating process.

The thermal modification and thermogravimetric characteristics of various metal oxides in the presence of oxygen and under inert atmosphere have been investigated in the literature.³⁷ Initially, the mass of Fe-AIB shows unstable behaviour; it kept decreasing with a smaller slope during the initial period and a quicker slope in the later period (Fig. 11). The temperature–weight relationship manifested a negative slope with $R^2 = 0.94$ at temperatures up to 450 °C. This slow loss in mass during the initial period can be attributed to loss of water captured in the inner layers of Fe. The higher thermal stability of Fe-AIB can be due to the strong mechanical properties of bark biochar which is stable at a higher temperature in the presence of air.³⁸

Vibrating sample magnetometry (VSM) was used for the analysis of magnetization of Fe-AIB and the magnetic

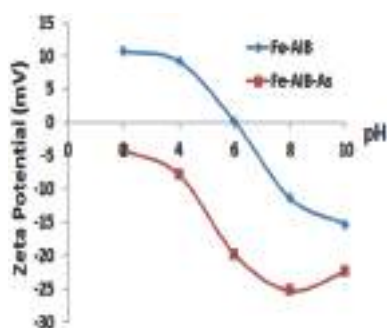


Fig. 9 Zeta potentials of Fe-AIB before and after arsenate adsorption.

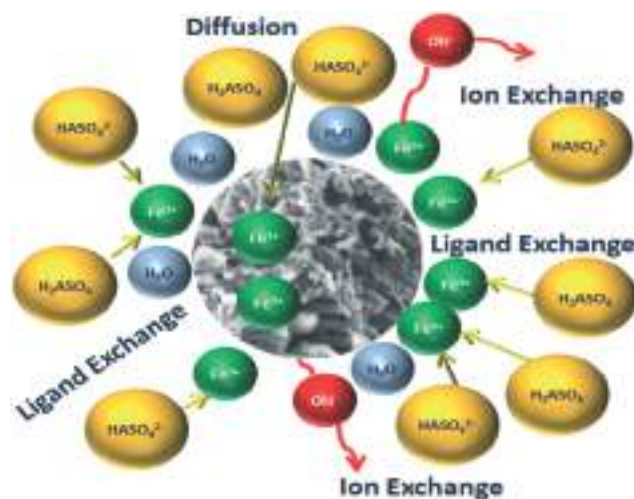


Fig. 10 Schematic demonstration of arsenate adsorption on Fe-AIB.

characteristics are presented in Fig. 12. The study reveals that Fe-AIB can be easily separated by using a magnet. The saturation magnetization (SM) of Fe-AIB was reported to be 39 emu g^{-1} .³⁹ This shows that a sufficient amount of Fe was successfully impregnated into the adsorbent.

Model evaluation and analysis of variance (ANOVA)

To define a valid model, the existing linear, quadratic, cubic and 2 FI were tested to fit the actual response. The evaluations of these models was done on the grounds of obtained scores from the sum of squares sequential model and revealed that the highest score is possessed by the quadratic model. High model significance was supported by higher F values and lower p values; consequently, the quadratic model was estimated to be adequate and was chosen to continue the process.

Analysis of variance (ANOVA) was used to evaluate further the significance and adequacy of the selected quadratic

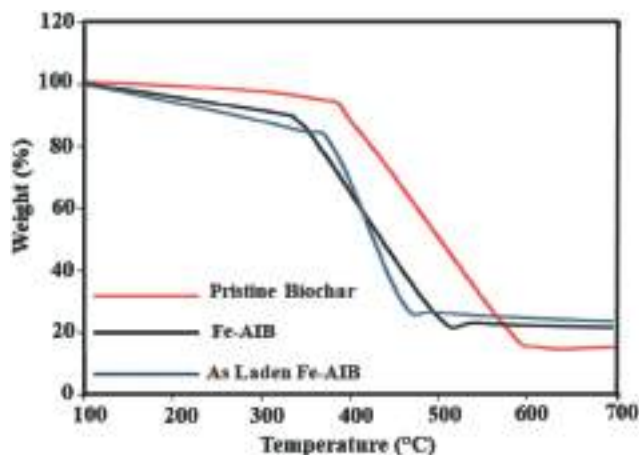


Fig. 11 Thermogravimetric (TG) curves of AIB.

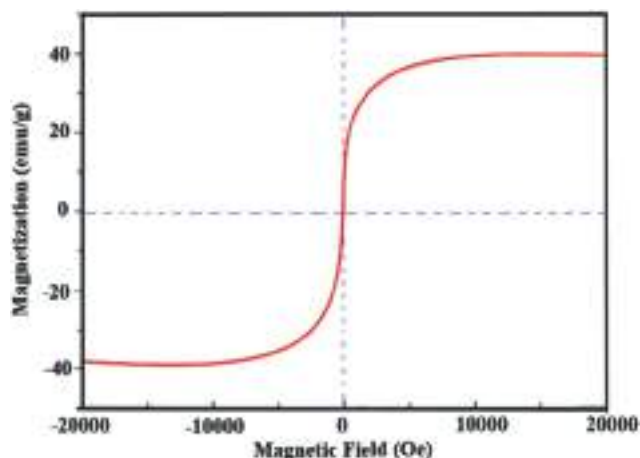


Fig. 12 Magnetization curves of Fe-AIB.

model (Table 2). This was confirmed by the p value (probability value), F value (Fisher variation ratio), coefficient of determination, predicted R^2 , adjusted R^2 , lack of fit and adequate precision. The comparison of design point predicted value ranges with prediction error was given by signal-to-noise ratio (adequate precision). A significant discrimination model prevails if the ratio > 4 . The measure of the proportion of variation around newly generated data and the mean are given by predicted R^2 and adjusted R^2 , respectively. The p value represents the measurement of significance of different variables, and the F value is a measure of the data variation about its mean.^{40–42} ANOVA was used for the validation of the adopted quadratic model which gives evidence including low p values (< 0.0001), high F values (197.10), lack of fit being non-significant (6.38), high values of coefficient of determination (0.994), predicted R^2 (0.968), adjusted R^2 (0.989) and adequate precision (50).

The empirical relation between the independent variables and the breakthrough time given in terms of regression

coefficient by the adopted model can be expressed as the following equation:

$$Y = 817.489 + -33.9228 \times A + -89.6274 \times B + 285.289 \times C + -11.0367 \times D + 11.7083 \times AB + -21.2976 \times AC + -18.0837 \times AD + -16.2018 \times BC + -6.83366 \times BD + 12.5736 \times CD + -1.70343 \times A^2 + 15.1038 \times B^2 + 28.8215 \times C^2 + -42.9537 \times D^2$$

where A (influent As(v) concentration), B (inlet flow rate), C (bed height) and D (pH) are in coded factors. The model equation generated by regression analysis reveals that the interacting as well as the main effect of bed depth, influent arsenate concentration, influent flow rate and pH are of high significance ($p < 0.0001$). The validation of the selected quadratic model was done by ANOVA, which gives evidence including low p values (< 0.0005) and high F value.

Variable interaction

The 3D response surface plots and contour plots were generated to analyse the interaction among various independent variables and their respective effects on breakthrough time (response). 3D response surface plots are the response surface's projection in the 3D plane, whereas contour plots are in the 2D plane. The combined analysis yields better understanding of variable effects along with their interaction on the breakthrough time as a function of three and two variables at a time.

Fig. 13a shows the combined effect of influent arsenate concentration and influent flow rate on the breakthrough time through the response surface and contour plot for column operation. Within the experimental range, with the increase in the influent flow rate and influent arsenate concentration, the breakthrough time decreases. The decrease in breakthrough time can be attributed to the availability of limited active sites on the adsorbent which

Table 2 Analysis of variance (ANOVA) of the Fe-AIB adsorbent using CCD

Source	Sum of squares	df	Mean square	F value	p value
Model	1.774×10^6	14	1.267×10^5	197.10	< 0.0001
A - influent As(v) concentration	19025.64	1	19025.64	29.59	< 0.0001
B - inlet flow rate	1.349×10^5	1	1.349×10^5	209.76	< 0.0001
C - bed height	1.244×10^6	1	1.244×10^6	1935.02	< 0.0001
D - pH	1689.43	1	1689.43	2.63	0.1258
AB	2023.74	1	2023.74	3.15	0.0963
AC	6665.30	1	6665.30	10.37	0.0057
AD	3919.17	1	3919.17	6.10	0.0260
BC	4012.22	1	4012.22	6.24	0.0246
BD	559.66	1	559.66	0.8705	0.3656
CD	2026.82	1	2026.82	3.15	0.0961
A^2	6.72	1	6.72	0.0105	0.9199
B^2	484.65	1	484.65	0.7539	0.3989
C^2	1728.55	1	1728.55	2.69	0.1219
D^2	6157.53	1	6157.53	9.58	0.0074
Residual	9643.53	15	642.90		
Lack of fit	8942.70	10	894.27	6.38	0.0270
Pure error	700.83	5	140.17		
Cor total	1.784×10^6	29			

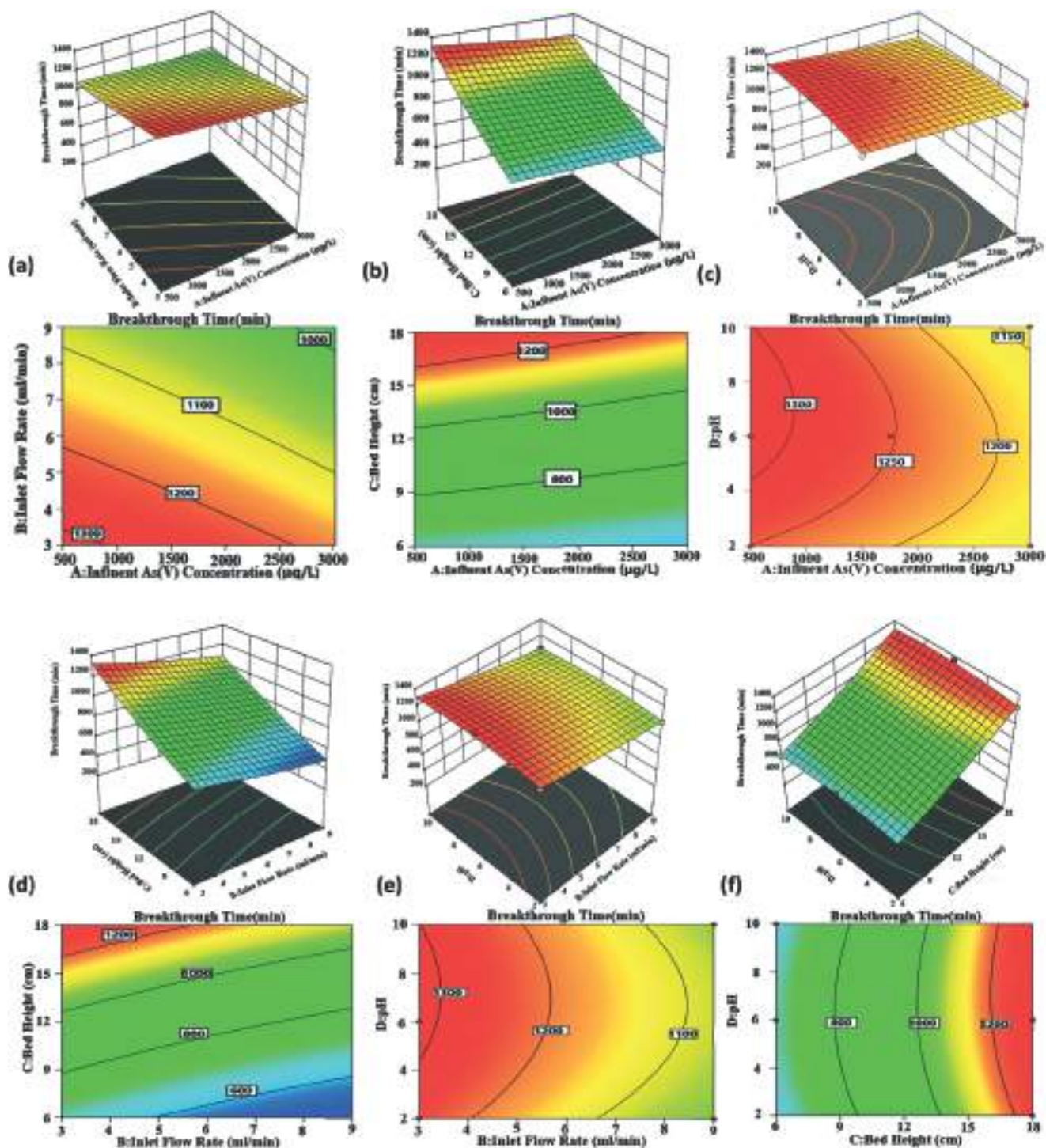


Fig. 13 3D response surface plots and 2D contour plot of Fe-AIB for simultaneous interactive effects of (a) influent flow rate and inlet concentration at pH 7.0, bed height 18.0 cm, (b) bed height and inlet concentration at pH 7.0, influent flow rate 3 ml min^{-1} , (c) pH and inlet concentration at bed height 18.0 cm, influent flow rate 3 ml min^{-1} , (d) bed height and influent flow rate at pH 7.0, inlet concentration $600 \mu\text{g L}^{-1}$, (e) pH and influent flow rate at bed height 18.0 cm, inlet concentration $600 \mu\text{g L}^{-1}$ and (f) pH and bed height at influent flow rate 3 ml min^{-1} , inlet concentration $600 \mu\text{g L}^{-1}$.

becomes saturated after the uptake of a particular concentration.^{40,43} At elevated influent flow rates, the resultant poor efficiency can be due to decreased time of residence of arsenate in the column, and its diffusion within

the pores of the adsorbent is less frequent which in turn enables the solute to exit the column before the attainment of equilibrium. Due to the mentioned event, a quick breakthrough was achieved.^{44,45}

Fig. 13b shows the combined effect of influent arsenate concentration and bed height on the breakthrough time through the response surface and contour plot for column operation using Fe-AIB. The breakthrough time (response function) increases with an increase in bed height, whereas it decreases with increased influent concentration. This could be because an increased dose of adsorbent with an increase in bed height yields an increased number of active sites for arsenate interaction with the enhanced surface area. As a result, the solute has ample chance to be adsorbed onto the active sites, and late breakthrough is achieved.^{40,46}

Fig. 13c shows the combined effect of pH and influent arsenate concentration on the response through the response surface and contour plot for column operation. Fe-AIB worked exceptionally well within the tested range of pH. Arsenic acid (H_3AsO_4) is triprotic, and the corresponding dissociation constants are $\text{p}K_{\text{a}11/4}$ 2.21, $\text{p}K_{\text{a}21/4}$ 6.94 and $\text{p}K_{\text{a}31/4}$ 11.49. With the increase in pH, a gradual decrease in breakthrough time was reported. This can be ascribed to the integrated effect of the enhancement in divalent As(v) species fraction and the decrease in the quantity of protonated species of R-CH (NH_2)-COOH in PAA with enhancement in the influent pH. In the pH range 4.6–7.0, monovalent and divalent As(v) species dominates; ion exchange phenomenon resulted in the mentioned pH range. In the pH range 2.2–4.6, the arsenate species remains non-dissociated, and monovalent anion and H_3AsO_4 dominate.^{47–49}

The combined effect of bed height and flow rate on the response factor (breakthrough time) for column operations of adsorption of arsenate on Fe-AIB is shown in Fig. 13d. The combined effect of bed height and the flow rate has a significant influence on the breakthrough time. With an increase in bed height, the breakthrough time increases, whereas it decrease with increasing flow rate. The pattern of such a breakthrough can be described in terms of inadequate residence time for arsenate and adsorbent interaction in the column as well as the availability of sufficient active sites for adsorption, as mentioned earlier.^{47,48}

Breakthrough time prediction by the combined effect of solution pH and bed height is shown in Fig. 13f. The breakthrough time increases with an increase in pH, whereas it decreases with an increase in influent arsenate concentration. This can be attributed to enhanced surface area availability with increased bed height, resulting in an increased number of active sites for adsorption. Moreover, as the pH of the solution

increases, the uptake of arsenate for the adsorbent decreases. This can be attributed to the fact that when the pH_{pzc} is more than the pH of the solution, the surface of the adsorbent becomes positive charge dominant. In contrast, the arsenate surface resulted in a more negative in the mentioned pH. Hence, the anion which was negatively charged is strongly attracted toward the surface of the adsorbent and results in increased adsorption at lower pH.^{47,50}

Thus, analysis of 3D response surface plots and contour plots reveals that breakthrough time, *i.e.* column service time decrease with the influent flow rate, influent concentration, pH, and increases with the bed depth.

A review of the literature reveals that very few studies have been reported for column operations. Most of the research has been conducted in batch operations for arsenate remediation. In contrast to the column operations, the obtained data from batch operations are often not applicable in household/industrial remediation systems, as the time of contact is less to reach equilibrium. The increased equilibrium removal capacity of arsenate in column (fixed bed) reactors ensures the suitability of the adsorbent to be used in filter units for arsenate mitigation. Hence, a comparison of the arsenate uptake capacity of Fe-AIB with that of other adsorbents of the same nature reported in the literature has been made (Table 7). Although, due to varying experimental conditions, a direct comparison of Fe-AIB/with other adsorbents is difficult, still it is observed that the arsenate removal capacity on Fe-AIB is worthy of comparison with and better than that of other adsorbents for arsenate mitigation in column operations. The outcomes reveal the suitability of Fe-AIB and Fe-AL for the remediation of arsenate from aqueous solution using a downflow continuous fixed-bed column.

The potential objective of using the Design-Expert software is to minimize, maximize, in range, target and fix to factors only (precise value). The required objective was selected for each response and variable from the menu in numerical optimization.^{51,52} By seeking from 100 initial points in the changes of the response surface, the finest response was found to be 1321.828 min when the variables were kept at $500 \mu\text{g L}^{-1}$ of influent arsenate, 3.0 ml min^{-1} influent flow rate, pH of 7.246, and bed height of 18.0 cm.

Confirmation column runs were performed in duplicate at optimal conditions for the sake of validation. The experimental data which coexist in good agreement with

Table 3 Adams–Bohart model parameters for As(v) adsorption on Fe-AIB

C_i ($\mu\text{g L}^{-1}$)	h (cm)	Q (ml min^{-1})	d (cm)	K	N_0	R^2
1000	3	3	2	0.034	148.14	0.59
1000	6	3	2	0.028	67.87	0.72
1000	9	3	2	0.014	47.15	0.79
1000	9	6	2	0.015	48.88	0.63
1000	9	9	2	0.015	48.19	0.61
1000	9	3	3	0.016	48.92	0.74
1250	9	3	3	0.01	32.69	0.75
1500	9	3	3	0.0068	37.33	0.78

Table 4 Modeling outcomes of arsenate adsorption on Fe-AIB packed-bed column

Process parameters	q_{exp} ($\mu\text{g g}^{-1}$)	Thomas model results			Yoon–Nelson model results	
		k_{th} ($\text{ml min}^{-1} \mu\text{g}$)	q_0 ($\mu\text{g g}^{-1}$)	R^2	K_{YN}	T
Bed height (cm)						
3	111.4711	0.0158	106.6347	0.7571	0.0128	128.9249
6	127.0649	0.0128	138.6136	0.9491	0.0158	282.6839
9	136.7064	0.0111	143.182	0.9087	0.0171	383.4361
Flow rate (mL min^{-1})						
3	136.7064	0.0111	143.182	0.9087	0.0171	383.4361
6	99.41522	0.0127	95.7494	0.8687	0.0127	128.2085
9	85.0841	0.0189	82.9062	0.76	0.0164	85.1237
Conc ($\mu\text{g L}^{-1}$)						
1000	136.7064	0.0111	134.182	0.9087	0.0171	383.4361
1250	138.1012	0.0089	143.624	0.9738	0.0112	288.4184
1500	141.0321	0.0065	147.3377	0.9898	0.0098	263.0469
Column diam (cm)						
2	136.7064	0.011181	143.182	0.9087	0.017181	383.4361
3	142.7872	0.018989	149.0885	0.912	0.018989	399.259

optimum results obtained from central composite design confirm that the adsorbent may be economically viable and effective for arsenate mitigation in aquatic systems.

Fixed-bed column breakthrough models

Adams–Bohart model. This model assumes that the rate of adsorption is proportional to both the concentration of the adsorbate and the adsorbent's residual capacity. The Adams–Bohart model is used for the explanation of the early part of the breakthrough curve.⁵³

$$\ln\left(\frac{C_e}{C_i}\right) = KC_i t - KN_0 \frac{Z}{U}$$

where U is the linear velocity (cm min^{-1}), K is a kinetic constant ($\text{l mg}^{-1} \text{min}^{-1}$), Z is the bed height of the packed bed (cm), and N_0 is the maximum removal capacity (mg l^{-1}). The plot of $\ln\left(\frac{C_e}{C_i}\right)$ vs. t would yield the values of N_0 and K . The experimental data have been incorporated in the model,

and using regression analysis (linear), the values obtained corresponding to N_0 and K are presented in Table 3. The values of N_0 and K do not show a significant variation with change in flow rates. Moreover, the values of N_0 and K decrease as the bed height increases. Additionally, the value of N_0 increases and K decreases with an increase in influent arsenate concentration. This model relies on the theory of surface reaction and presumes the non-instantaneous behaviour of equilibrium. Therefore, the rate of adsorption is proportional to the arsenate concentration and residual capacity of the adsorbent. In addition, the Adams–Bohart model is applicable to the mass transfer restricted rate of adsorption and low concentration regions.⁵⁴ The vast difference between the experimental and predicted values of the breakthrough and the low values of determination coefficient (R^2) implies that the Adams–Bohart model is not efficient to speculate the data of experiments with both the adsorbents.

The Thomas model. The Thomas model assumes that the Langmuir kinetics has been followed by the adsorption process in the fixed-bed column operation without any axial dispersion because the driving force of rate follows the second-order kinetics.^{55,56} The linear form of the Thomas model can be represented as follows:

$$\ln\left(\frac{c_0}{c_t} - 1\right) = k_{\text{th}} q_0 \frac{m}{Q} - (k_{\text{th}} C_0 t)$$

where k_{th} represents the constant of the Thomas model ($\text{ml min}^{-1} \text{mg}^{-1}$), q_0 is the uptake capacity of arsenate on Fe-AIB

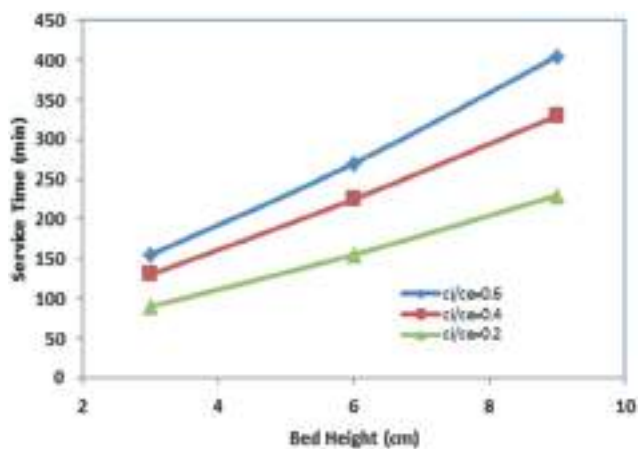


Fig. 14 Bed height vs. service time curve at various values of c_i/c_e in the column for arsenate adsorption on Fe-AIB.

Table 5 BDST model parameters for As(v) adsorption onto Fe-AIB

c_i/c_e	K ($\text{L mg}^{-1} \text{min}^{-1}$)	N_0 (mg L^{-1})	R^2	t_e	t_p
0.2	0.075	9.907	0.998	120	116.20
0.4	0.063	14.156	0.999	360	349.42
0.6	0.032	17.691	0.997	280	261.76

Table 6 Process parameters of sorption for four desorption cycles of arsenate onto Fe-AIB

Cycle no.	Breakthrough volume (ml)	Breakthrough time (min)	Exhaustion time (min)	Uptake capacity ($\mu\text{g g}^{-1}$)	Elution time (min)
I	2317	600	861	149.9	352
II	2108	585	894	145.4	301
III	1952	570	917	144.3	275
IV	1721	480	952	141.7	243

($\mu\text{g g}^{-1}$), m is the adsorbent mass (g), and Q is the flow rate (ml min^{-1}).

The linear form of this model, $(\ln C_0/C_t - 1)$ vs. t , was used to find out the values of q_0 and k_{th} from the Thomas equation. The evaluated values of the model parameters and R^2 (regression coefficients) are given in Table 4. A comparative analysis of the predicted breakthrough attained at different process parameters has been performed. It can be seen from the table that with an increase in influent concentration and bed height, the value of q_0 increases but that of k_{th} decreases. In contrast, with the increase in influent flow rate the value of q_0 is decreased and k_{th} increased. While this model certainly shows excellent adaptation for the experimental conditions related to adsorption, it does not give a good co-relation for the rupture curve prediction. This is noticed when a gap is obtained between the experimental adsorption capacity and the adsorption capacity evaluated using the model. Therefore, while this model is most extensively used for expressing the behaviour of the bio-sorption process in column experiments, its chief limitation is second-order kinetics based derivation and presumes that bio-sorption is not only restricted by the chemical reaction but also governed by interfacial mass transfer. This mentioned inconsistency can produce errors while using the method for modelling of biosorption processes.^{57,58}

The Yoon–Nelson model. This model assumes that the probability decrement rate of adsorption corresponding to each molecule of adsorbate is proportional to adsorption of adsorbate probability and breakthrough of adsorbate

probability. The linearized Yoon–Nelson model can be expressed as

$$\ln\left(\frac{c_0}{c_0 - c_t}\right) = K_{YN}t - \tau K_{YN}$$

where K_{YN} is the Yoon–Nelson rate constant (min^{-1}), and τ is the required time for 50% breakthrough of the adsorbate. The linearized plot between $\ln(c_0/c_0 - c_t)$ vs. t would yield the values of parameters K_{YN} and τ with respect to influent arsenate concentration, bed height, flow rate, and column diameter and are presented in Table 4. The experimental data for both Fe-AIB adsorbents reveal a great fit to the model with R^2 (regression coefficient) equal to 0.995. It can be observed that the calculated and obtained τ values are very near, showing the goodness of the Yoon–Nelson model to be fitted by experimental data.

BDST model. The BDST model is a semi-empirical model in column analysis, which allows the quickest prediction of the performance of an adsorbent. This model assumes that the adsorption rate is governed by the surface reaction between the unconsumed adsorbent's capacity and the adsorbate.^{59,60} The BDST model can estimate the interaction between the bed height of the column and service time. A linearized form of the BDST model is given by equation

$$t = \frac{N_0 Z}{UC_i} - \frac{1}{KC_i} \ln\left(\frac{C_i}{C_e} - 1\right)$$

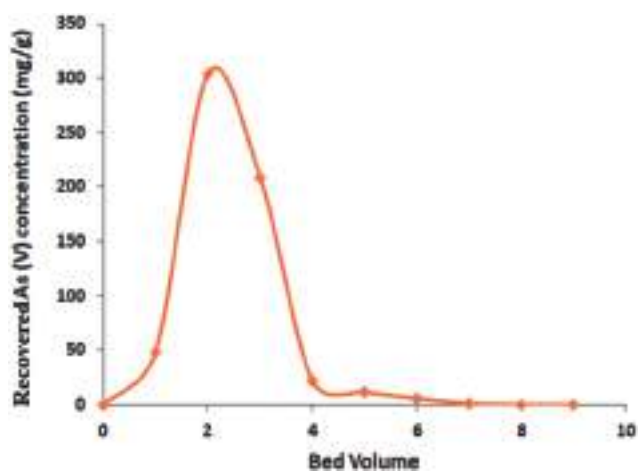


Fig. 15 Concentration profile of arsenate in the regenerant for Fe-AIB during regeneration with 10% sodium hydroxide.

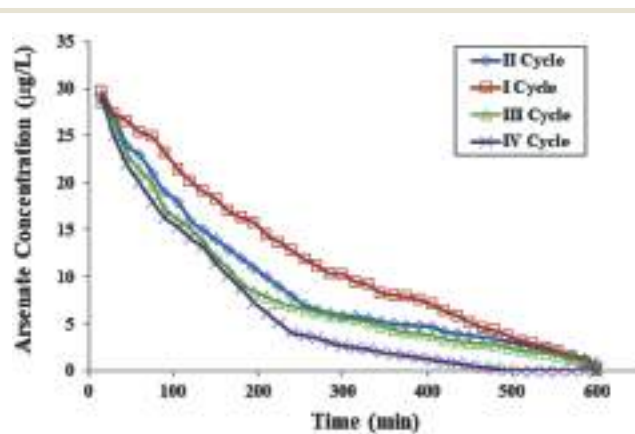


Fig. 16 Elution curves for desorption of arsenate during four cycles (10% NaOH; flow rate = 3 mL min^{-1}).

Table 7 Uptake capacity comparison of different adsorbents in a packed-bed column for arsenate removal

Adsorbents	Operating conditions	Uptake capacity ($\mu\text{g g}^{-1}$)	Ref.
Activated alumina	pH 7.2; bed depth 6 cm; $16 \text{ mm}^3 \text{ cm}^{-1}$; 0.2 mm particle size	0.007	61
Sand coated with siderite	Flow rate 148 mL min^{-1} , bed depth 15 cm, influent concentration 500 mg L^{-1}	1.09	62
Hydrous Fe_2O_3 impregnated with $\text{C}_8\text{H}_6\text{O}_2$ resin coated activated carbon	Influent concentration 1470 mg L^{-1} , flow rate 1.57 mL min^{-1} , pH 6.8	1.52	63
Laterite (natural) (NA)	Temperature $27 \text{ }^\circ\text{C}$, pH 5.5, bed depth 30 cm, inlet concentration $1000 \mu\text{g L}^{-1}$, average particle size 0.273 mm , flow rate 5 mL min^{-1}	0.147	64
Fe-impregnated sugarcane-based carbon (Fe-SCC)	Temperature $30 \text{ }^\circ\text{C}$, concentration 600 mg L^{-1} , adsorbent dose 9.0 g , pH 7, particle size 250 mm , flow rate 1.2 mL min^{-1}	0.084	48
Rice polish	Temperature $30 \text{ }^\circ\text{C}$, concentration 1000 mg L^{-1} , dose 30.5 g , pH 7.0, particle size less than 178 mm , flow rate 1.6 mL min^{-1}	0.067	45
Hybrid of goethite structure Fe_2O_3 and anion exchange resin (polymeric)	Dose 45 g , pH 7.5, concentration $500 \mu\text{g L}^{-1}$, particle size 0.35 mm flow rate 8 mL min^{-1}	3.22	65
Zein-Fe beds	Bed height 3 cm, conc $0.5\text{--}100 \text{ mg L}^{-1}$, pH 6.0, influent flow rate 4 mL min^{-1}	1.95	66
Laterite soil	Temperature $30 \text{ }^\circ\text{C}$, bed height 2.7 cm , flow rate 11 mL min^{-1} , pH 3.0	0.47	67
Fe_2O_3 doped alumina	Temperature $30 \text{ }^\circ\text{C}$, bed height 6 cm , flow rate 16 mL min^{-1} , pH 12.0	0.46	68
Chitosan base biopolymer adsorbent	Bed height 8 cm , flow rate 8 mL min^{-1} , pH 7.0, particle size 300 mm	1.90	49
LDH (poly)	Inlet conc 50 mg L^{-1} , inlet flow rate 7 mL min^{-1} , pH 8.0	1.73	69
Fe-impregnated <i>A. indica</i> root (Fe-AIR) carbon	Bed height 9 cm , influent conc 1 mg L^{-1} , flow rate 3.0 mL min^{-1} , pH 6.0	0.92	70
Fe-impregnated <i>A. indica</i> bark (Fe-AIB) carbon	Influent arsenate conc $500 \mu\text{g L}^{-1}$, influent flow rate 3.0 mL min^{-1} , pH 7.0, bed height 18.0 cm	1.49	Present study

where k is the rate constant corresponding to the BDST model ($\text{L mg}^{-1} \text{ min}^{-1}$), N_0 represents the capacity of adsorption in the BDST model ($\mu\text{g L}^{-1}$), and Z is the height of the packed bed (cm). The values of the BDST model parameters, k and N_0 were obtained by the linear plot between bed height and service time c_i/c_e equal to 0.2, 0.4 and 0.6, as shown in Fig. 14. The predicted service time and experimental service time at the bed height of 9 cm , flow rate of 3 mL min^{-1} and influent concentration of $1000 \mu\text{g L}^{-1}$ were calculated and are shown in Table 5. It can be observed from the table that there is a good agreement between the predicted and the experimental service time. Therefore it can be concluded that the BDST model is acceptable for the Fe-AIB system. Also, the high R^2 values verify the applicability of the BDST model for the current system.

Regeneration and reuse of Fe-AIB

A good adsorption operation needs numerous reuses of the adsorbent, which significantly lowers the process cost and reliance on a constant supply of adsorbents. The current study used 10% sodium hydroxide to regenerate the exhausted Fe-AIB medium after the run. The profiles for arsenate recovery during desorption of Fe-AIB are presented

in Fig. 15. The analysis shows that 12-bed volumes of Fe-AIB were required for about 99% recovery of arsenate. The first 4-bed volumes elute approximately 93.4% of the adsorbed quantity, and the desorption of the remaining takes place in the remaining 8-bed volumes. These findings suggest that the active sites of the adsorbent's particles are easily approachable through the pore networking among various

Table 8 Water physicochemical parameters and remediation of arsenate using Fe-AIB

Process parameters (unit)	Before adsorption	After adsorption
As(v) ($\mu\text{g L}^{-1}$)	155	7.14
As(III) ($\mu\text{g L}^{-1}$)	131	11.40
TDS (mg L^{-1})	611.4	478.12
Conductivity ($\mu\text{S cm}^{-1}$)	3.7	3.3
Ca^{2+} (mg L^{-1})	133.4	91.7
Mg^{2+} (mg L^{-1})	45.9	19.1
Carbonates (mg L^{-1})	39.7	30.1
Bicarbonates (mg L^{-1})	234.4	161.9
Na^+ (mg L^{-1})	40.3	39.3
K^+ (mg L^{-1})	2.9	2.1
Cl^- (mg L^{-1})	35.4	12.3
Fe (mg L^{-1})	16.1	3.1
SO_4^{2-} (mg L^{-1})	4.1	3.3
PO_4^{3-}	1.7	0.1
F^- (mg L^{-1})	0.7	Below detection limit

particles. That is to say, pore clogging does not take place, which is strongly supported by the fact that is a very constant flow rate during adsorption–desorption runs, and the process comes out to be reversible.

To discard the excess NaOH found in the medium and thus to maintain the pH, the Fe-AIB beds were reconditioned with hot water after regeneration. The dissolved Fe content in the exhaust regenerant is negligible (0.03 to 0.05 mg L⁻¹) in comparison to the Fe present in the medium during regeneration, which led to the assumption that the total Fe concentration in Fe-AIB is unchanged after the regeneration. After rinsing the Fe-AIB media, they were basically prepared for the succeeding adsorption cycles. Up to the fourth sorption cycle, the iron content was practically non-detectable. Fig. 16 shows consecutive sorption–desorption cycles for Fe-AIB; as the regeneration cycle continued, the breakthrough time decreased and the exhaustion time increased, resulting in a widened mass-transfer zone. However, all four cycles demonstrated a high capacity for arsenate adsorption. It is always preferable to choose an eluent that has no effect on the sorbent's physical properties or uptake capacity. For the present system, 10% sodium hydroxide works well, with desorption efficiencies above 99% for all four cycles. The eco-friendly and economic benefits of reusing Fe-AIB, along with its high sorption capability, make it an appealing treatment option for arsenic-containing solutions (Table 6).

Performance evaluation of fixed-bed column using real groundwater

The proposed biosorbent Fe-AIB was convincingly examined for the mitigation of arsenate from contaminated groundwater samples. Eighty natural contaminated groundwater samples were garnered from an arsenate-contaminated region of Burdwan district (Purbasthali Block-II), West Bengal, India. Our initial analysis confirms the presence of 286 µg L⁻¹ of inorganic arsenic out of eighty water samples of tube wells. Mitigation of inorganic arsenic from the sample (total arsenic = 286 µg L⁻¹, arsenite = 131 µg L⁻¹, and arsenate = 155 µg L⁻¹) through a column experiment conducted under optimal conditions of 18 cm bed height of both adsorbents and flow rate 3 mL min⁻¹. After processing 20 L of contaminated water by the proposed column experiments, the water quality results on pre and post adsorption under analysis are given in Table 8. The column run results using real contaminated water samples, containing both arsenite and arsenate ions, reveals that Fe-AIB is efficient to remediate both inorganic arsenic species from contaminated groundwater.

Conclusion

A substantial lab-scale investigation was conducted to estimate the performance of a fixed-bed column using a novel adsorbent Fe-AIB having an adsorption capacity of 1.49

mg L⁻¹, with different influent concentrations, bed heights, pH and flow rates. The experimental data obtained in the present work were competently simulated in the central composite design model. The simultaneous effect shows that the breakthrough time increases but with a slight decrease in uptake capacity as the bed height and influent concentration increase. The breakthrough time, along with the uptake capacity, increases at low flow rates. The Thomas model can determine the nature of the breakthrough curves; this may imply that the controlling step of the adsorption process is neither internal nor external diffusion in the column. The BDST model demonstrated excellent agreement with the experimental results and obtained high R² values, confirming the applicability of the BDST model for the fixed-bed column system of the present study. The regeneration and successive reuse of the adsorbent offered an inexpensive approach for the remediation of arsenate from aqueous systems. The effluent water quality treated by Fe-AIB was proven to be completely safe for human consumption. The foremost performance of the Fe-AIB packed column was its capacity, *i.e.*, approximately 90 litres of arsenate-contaminated water per day (of 500 µg L⁻¹ brought down to below 10 µg L⁻¹), suggesting the suitability of the Fe-AIB adsorbent for water filters in households in rural regions without power requirements. Overall, it can be deduced that the statistical model application is an efficient approach for modelling, optimization and design of the arsenate adsorption system. The experimental results shown in the present investigation can surely be hypothesized for the establishment and design of an effective arsenate remediation plan while treating contaminated groundwater.

Conflicts of interest

We wish to confirm that there are no known conflicts of interest associated with this publication and there has been no significant financial support for this work that could have influenced its outcome.

References

- 1 M. U. Rehman, R. Khan, A. Khan, W. Qamar, A. Arafah, A. Ahmad, A. Ahmad, R. Akhter, J. Rinklebe and P. Ahmad, Fate of arsenic in living systems: implications for sustainable and safe food chains, *J. Hazard. Mater.*, 2021, 126050.
- 2 Q. Y. Chen and M. Costa, Arsenic: a global environmental challenge, *Annu. Rev. Pharmacol. Toxicol.*, 2021, **61**, 47–63.
- 3 M. Bissen and F. H. Frimmel, Arsenic—a review. Part I: occurrence, toxicity, speciation, mobility, *Acta Hydrochim. Hydrobiol.*, 2003, **31**, 9–18.
- 4 P. Ziarati, B. Hochwimmer, L. Cruz-Rodriguez, N. Tanideh, A. Iraj and B. Kamyab-Moghadam, Lung Cancer Disease and Arsenic: The Medical Geology as Key, *J. Med. Discovery*, 2021, **6**, 1–16.
- 5 M. Ahmad, M. Ahmad, A. R. Usman, A. S. Al-Faraj, A. S. Abduljabbar and M. I. Al-Wabel, Biochar composites with

- nano zerovalent iron and eggshell powder for nitrate removal from aqueous solution with coexisting chloride ions, *Environ. Sci. Pollut. Res.*, 2018, **25**, 25757–25771.
- 6 S. Foteinis, A. G. Borthwick, Z. Frontistis, D. Mantzavinos and E. Chatzisymeon, Environmental sustainability of light-driven processes for wastewater treatment applications, *J. Cleaner Prod.*, 2018, **182**, 8–15.
 - 7 G. Sawood and S. Gupta, Arsenic remediation of the waste water using adsorbent: a review, *Int. J. Eng. Technol. Sci. Res.*, 2018, **5**, 1054–1070.
 - 8 G. M. Sawood, A. Mishra and S. Gupta, Optimization of Arsenate Adsorption over Aluminum-Impregnated Tea Waste Biochar Using RSM–Central Composite Design and Adsorption Mechanism, *J. Hazard. Toxic Radioact. Waste*, 2021, **25**, 04020075.
 - 9 G. M. Sawood and S. Gupta, Kinetic equilibrium and thermodynamic analyses of As (V) removal from aqueous solution using iron-impregnated *Azadirachta indica* carbon, *Appl. Water Sci.*, 2020, **10**, 1–18.
 - 10 S. Kumar, A. Gupta and J. Yadav, *Fluoride removal by mixtures of activated carbon prepared from Neem (Azadirachta indica) and Kikar (Acacia arabica) leaves*, 2007.
 - 11 K. G. Bhattacharyya and A. Sharma, Kinetics and thermodynamics of methylene blue adsorption on neem (*Azadirachta indica*) leaf powder, *Dyes Pigm.*, 2005, **65**, 51–59.
 - 12 W. D. Costa, A. M. da Silva Bento, J. A. S. de Araújo, J. M. C. Menezes, J. G. M. da Costa, F. A. B. da Cunha, H. D. M. Coutinho, F. J. de Paula Filho and R. N. P. Teixeira, Removal of copper (II) ions and lead (II) from aqueous solutions using seeds of *Azadirachta indica* A. Juss as bioadsorbent, *Environ. Res.*, 2020, **183**, 109213.
 - 13 J. Ahmad, S. Naeem, M. Ahmad, A. R. Usman and M. I. Al-Wabel, A critical review on organic micropollutants contamination in wastewater and removal through carbon nanotubes, *J. Environ. Manage.*, 2019, **246**, 214–228.
 - 14 L. Trakal, Z. Michálková, L. Beesley, M. Vítková, P. Ouředníček, A. P. Barceló, V. Ettler, S. Číhalová and M. Komárek, AMOchar: Amorphous manganese oxide coating of biochar improves its efficiency at removing metal (loid) s from aqueous solutions, *Sci. Total Environ.*, 2018, **625**, 71–78.
 - 15 S. Aredes, B. Klein and M. Pawlik, The removal of arsenic from water using natural iron oxide minerals, *J. Cleaner Prod.*, 2013, **60**, 71–76.
 - 16 S. Wang, B. Gao, Y. Li, Y. Wan and A. E. Creamer, Sorption of arsenate onto magnetic iron–manganese (Fe–Mn) biochar composites, *RSC Adv.*, 2015, **5**, 67971–67978.
 - 17 X. Hu, Z. Ding, A. R. Zimmerman, S. Wang and B. Gao, Batch and column sorption of arsenic onto iron-impregnated biochar synthesized through hydrolysis, *Water Res.*, 2015, **68**, 206–216.
 - 18 R. He, Z. Peng, H. Lyu, H. Huang, Q. Nan and J. Tang, Synthesis and characterization of an iron-impregnated biochar for aqueous arsenic removal, *Sci. Total Environ.*, 2018, **612**, 1177–1186.
 - 19 A. Mishra, G. M. Sawood, S. B. Gautam and R. K. Trivedi, Optimization of process inputs for the synthesis of waste rice bran oil isolated *Pseudomonas aeruginosa* MTCC 424 biosurfactant using response surface methodology for oil recovery applications, *Bioresour. Technol. Rep.*, 2021, **14**, 100653.
 - 20 S.-R. Ryu, E.-K. Jeon, J.-S. Yang and K. Baek, Adsorption of As (III) and As (V) in groundwater by Fe–Mn binary oxide-impregnated granular activated carbon (IMIGAC), *J. Taiwan Inst. Chem. Eng.*, 2017, **72**, 62–69.
 - 21 G. M. Sawood and S. Gupta, Kinetic equilibrium and thermodynamic analyses of As (V) removal from aqueous solution using iron-impregnated *Azadirachta indica* carbon, *Appl. Water Sci.*, 2020, **10**, 1–18.
 - 22 Q. Yang, X. Wang, W. Luo, J. Sun, Q. Xu, F. Chen, J. Zhao, S. Wang, F. Yao and D. Wang, Effectiveness and mechanisms of phosphate adsorption on iron-modified biochars derived from waste activated sludge, *Bioresour. Technol.*, 2018, **247**, 537–544.
 - 23 Y. Han, X. Cao, X. Ouyang, S. P. Sohi and J. Chen, Adsorption kinetics of magnetic biochar derived from peanut hull on removal of Cr (VI) from aqueous solution: effects of production conditions and particle size, *Chemosphere*, 2016, **145**, 336–341.
 - 24 D. Mohan, A. Sarswat, V. K. Singh, M. Alexandre-Franco and C. U. Pittman Jr, Development of magnetic activated carbon from almond shells for trinitrophenol removal from water, *Chem. Eng. J.*, 2011, **172**, 1111–1125.
 - 25 S. R. Chowdhury, E. K. Yanful and A. R. Pratt, Arsenic removal from aqueous solutions by mixed magnetite–maghemite nanoparticles, *Environ. Earth Sci.*, 2011, **64**, 411–423.
 - 26 S. Zhang, X.-y. Li and J. P. Chen, An XPS study for mechanisms of arsenate adsorption onto a magnetite-doped activated carbon fiber, *J. Colloid Interface Sci.*, 2010, **343**, 232–238.
 - 27 A. M. Pintor, B. R. Vieira, C. C. Brandão, R. A. Boaventura and C. M. Botelho, Complexation mechanisms in arsenic and phosphorus adsorption onto iron-coated cork granulates, *J. Environ. Chem. Eng.*, 2020, **8**, 104184.
 - 28 J. G. Hering, I. A. Katsoyiannis, G. A. Theoduloz, M. Berg and S. J. Hug, *Arsenic Removal from Drinking Water: Experiences with Technologies and Constraints in Practice*, American Society of Civil Engineers, 2017.
 - 29 J. A. Arcibar-Orozco, D.-B. Josue, J. C. Rios-Hurtado and J. R. Rangel-Mendez, Influence of iron content, surface area and charge distribution in the arsenic removal by activated carbons, *Chem. Eng. J.*, 2014, **249**, 201–209.
 - 30 J.-J. Pan, J. Jiang, W. Qian and R.-k. Xu, Arsenate adsorption from aqueous solution onto Fe (III)-modified crop straw biochars, *Environ. Eng. Sci.*, 2015, **32**, 922–929.
 - 31 Y. Arai, E. J. Elzinga and D. L. Sparks, X-ray absorption spectroscopic investigation of arsenite and arsenate adsorption at the aluminum oxide–water interface, *J. Colloid Interface Sci.*, 2001, **235**, 80–88.
 - 32 A. Jain, K. P. Raven and R. H. Loeppert, Arsenite and arsenate adsorption on ferrihydrite: Surface charge reduction and net OH-release stoichiometry, *Environ. Sci. Technol.*, 1999, **33**, 1179–1184.
 - 33 M. Ahmad, A. R. Usman, Q. Hussain, A. S. Al-Farraj, Y. F. Tsang, J. Bundschuh and M. I. Al-Wabel, Fabrication and evaluation of silica embedded and zerovalent iron

- composited biochars for arsenate removal from water, *Environ. Pollut.*, 2020, **266**, 115256.
- 34 X. Xu, Z. Xu, B. Gao, L. Zhao, Y. Zheng, J. Huang, D. C. Tsang, Y. S. Ok and X. Cao, New insights into CO₂ sorption on biochar/Fe oxyhydroxide composites: Kinetics, mechanisms, and in situ characterization, *Chem. Eng. J.*, 2020, **384**, 123289.
- 35 Y. Wang, Q. Yang, J. Chen, J. Yang, Y. Zhang, Y. Chen, X. Li, W. Du, A. Liang and S.-H. Ho, Adsorption behavior of Cr (VI) by magnetically modified *Enteromorpha prolifera* based biochar and the toxicity analysis, *J. Hazard. Mater.*, 2020, 122658.
- 36 Y. Zhou, B. Gao, A. R. Zimmerman, H. Chen, M. Zhang and X. Cao, Biochar-supported zerovalent iron for removal of various contaminants from aqueous solutions, *Bioresour. Technol.*, 2014, **152**, 538–542.
- 37 S. Wang, B. Gao, Y. Li, A. Mosa, A. R. Zimmerman, L. Q. Ma, W. G. Harris and K. W. Migliaccio, Manganese oxide-modified biochars: preparation, characterization, and sorption of arsenate and lead, *Bioresour. Technol.*, 2015, **181**, 13–17.
- 38 C. Gonzalez, J. Gutierrez, J. González-Velasco, A. Cid, A. Arranz and J. Arranz, Transformations of manganese oxides under different thermal conditions, *J. Therm. Anal. Calorim.*, 1996, **47**, 93–102.
- 39 Z. Zhou, Y.-g. Liu, S.-b. Liu, H.-y. Liu, G.-m. Zeng, X.-f. Tan, C.-p. Yang, Y. Ding, Z.-l. Yan and X.-x. Cai, Sorption performance and mechanisms of arsenic (V) removal by magnetic gelatin-modified biochar, *Chem. Eng. J.*, 2017, **314**, 223–231.
- 40 S. Chowdhury, S. Chakraborty and P. D. Saha, Response surface optimization of a dynamic dye adsorption process: a case study of crystal violet adsorption onto NaOH-modified rice husk, *Environ. Sci. Pollut. Res.*, 2013, **20**, 1698–1705.
- 41 D. C. Montgomery, *Montgomery Design and Analysis of Experiments*, 1997.
- 42 Y. Abdollahi, A. Zakaria, K. A. Matori, K. Shameli, H. Jahangirian, M. Rezayi and T. Abdollahi, Interactions between photodegradation components, *Chem. Cent. J.*, 2012, **6**, 1–5.
- 43 E. Kumar, A. Bhatnagar, M. Ji, W. Jung, S.-H. Lee, S.-J. Kim, G. Lee, H. Song, J.-Y. Choi, J.-S. Yang and B.-H. Jeon, Defluoridation from aqueous solutions by granular ferric hydroxide (GFH), *Water Res.*, 2009, **43**(2), 490–498.
- 44 P. Roy, N. K. Mondal, S. Bhattacharya, B. Das and K. Das, Removal of arsenic (III) and arsenic (V) on chemically modified low-cost adsorbent: batch and column operations, *Appl. Water Sci.*, 2013, **3**, 293–309.
- 45 D. Ranjan, M. Talat and S. Hasan, Rice polish: an alternative to conventional adsorbents for treating arsenic bearing water by up-flow column method, *Ind. Eng. Chem. Res.*, 2009, **48**, 10180–10185.
- 46 A. Gupta and N. Sankaramakrishnan, Column studies on the evaluation of novel spacer granules for the removal of arsenite and arsenate from contaminated water, *Bioresour. Technol.*, 2010, **101**, 2173–2179.
- 47 H. Genç-Fuhrman, H. Bregnhøj and D. McConchie, Arsenate removal from water using sand–red mud columns, *Water Res.*, 2005, **39**, 2944–2954.
- 48 P. Roy, N. Mondal and K. Das, Modeling of the adsorptive removal of arsenic: a statistical approach, *J. Environ. Chem. Eng.*, 2014, **2**, 585–597.
- 49 C.-C. Chen and Y.-C. Chung, Arsenic removal using a biopolymer chitosan sorbent, *J. Environ. Sci. Health, Part A: Toxic/Hazard. Subst. Environ. Eng.*, 2006, **41**, 645–658.
- 50 M. Kanematsu, T. M. Young, K. Fukushi, P. G. Green and J. L. Darby, Individual and combined effects of water quality and empty bed contact time on As (V) removal by a fixed-bed iron oxide adsorber: Implication for silicate pre-coating, *Water Res.*, 2012, **46**, 5061–5070.
- 51 J. P. Maran and S. Manikandan, Response surface modeling and optimization of process parameters for aqueous extraction of pigments from prickly pear (*Opuntia ficus-indica*) fruit, *Dyes Pigm.*, 2012, **95**, 465–472.
- 52 N. H. Zabaruddin, L. C. Abdullah, N. H. Mohamed and T. S. Y. Choong, Optimization Using Response Surface Methodology (RSM) for Biodiesel Synthesis Catalyzed by Radiation-Induced Kenaf Catalyst in Packed-Bed Reactor, *Processes*, 2020, **8**, 1289.
- 53 S. Lawrance, J. Bajpai and A. Bajpai, Designing fixed bed column and batch studies of Chitosan nanoparticles for defluoridation of drinking water, *J. Dispersion Sci. Technol.*, 2011, **32**, 1256–1265.
- 54 K. U. Ahamad and M. Jawed, Kinetics, equilibrium and breakthrough studies for Fe (II) removal by wooden charcoal: A low-cost adsorbent, *Desalination*, 2010, **251**, 137–145.
- 55 A. C. da Costa Rocha, G. Scaratti, C. D. Moura-Nickel, T. L. da Silva, M. G. A. Vieira, R. M. Peralta, R. A. Peralta, A. de Noni and R. d. F. P. M. Moreira, Economical and technological aspects of copper removal from water using a geopolymer and natural zeolite, *Water, Air, Soil Pollut.*, 2020, **231**, 1–15.
- 56 M. A. E. de Franco, C. B. de Carvalho, M. M. Bonetto, R. de Pelegrini Soares and L. A. Féris, Removal of amoxicillin from water by adsorption onto activated carbon in batch process and fixed bed column: kinetics, isotherms, experimental design and breakthrough curves modelling, *J. Cleaner Prod.*, 2017, **161**, 947–956.
- 57 K. Tan and B. Hameed, Insight into the adsorption kinetics models for the removal of contaminants from aqueous solutions, *J. Taiwan Inst. Chem. Eng.*, 2017, **74**, 25–48.
- 58 J. López-Cervantes, D. I. Sánchez-Machado, R. G. Sánchez-Duarte and M. A. Correa-Murrieta, Study of a fixed-bed column in the adsorption of an azo dye from an aqueous medium using a chitosan–glutaraldehyde biosorbent, *Adsorpt. Sci. Technol.*, 2018, **36**, 215–232.
- 59 S. Baral, N. Das, T. Ramulu, S. Sahoo, S. Das and G. R. Chaudhury, Removal of Cr (VI) by thermally activated weed *Salvinia cucullata* in a fixed-bed column, *J. Hazard. Mater.*, 2009, **161**, 1427–1435.
- 60 K. Nithya, A. Sathish and P. S. Kumar, Packed bed column optimization and modeling studies for removal of chromium ions using chemically modified *Lantana camara* adsorbent, *J. Water Process. Eng.*, 2020, **33**, 101069.

- 61 M. N. Amin, S. Kaneco, T. Kitagawa, A. Begum, H. Katsumata, T. Suzuki and K. Ohta, Removal of arsenic in aqueous solutions by adsorption onto waste rice husk, *Ind. Eng. Chem. Res.*, 2006, **45**, 8105–8110.
- 62 H. Guo, D. Stüben and Z. Berner, Adsorption of arsenic (III) and arsenic (V) from groundwater using natural siderite as the adsorbent, *J. Colloid Interface Sci.*, 2007, **315**, 47–53.
- 63 J. Ming Zhuang, E. Hobenshield and T. Walsh, Arsenate sorption by hydrous ferric oxide incorporated onto granular activated carbon with phenol formaldehyde resins coating, *Environ. Technol.*, 2008, **29**, 401–411.
- 64 A. Maiti, S. DasGupta, J. K. Basu and S. De, Batch and column study: adsorption of arsenate using untreated laterite as adsorbent, *Ind. Eng. Chem. Res.*, 2008, **47**, 1620–1629.
- 65 M. R. Boldaji, R. Nabizadeh, M. H. Dehghani, K. Nadafi and A. H. Mahvi, Evaluating the performance of iron nanoparticle resin in removing arsenate from water, *J. Environ. Sci. Health, Part A: Toxic/Hazard. Subst. Environ. Eng.*, 2010, **45**, 946–950.
- 66 S. Thanawatpootawee, A. Imyim and N. Praphairaksit, Iron-loaded zein beads as a biocompatible adsorbent for arsenic (V) removal, *J. Ind. Eng. Chem.*, 2016, **43**, 127–132.
- 67 P. T. Thanh Nguyen, S. Yacouba, S. Pare and H. M. Bui, Removal of Arsenic from Groundwater Using Lamdong Laterite as a Natural Adsorbent, *Pol. J. Environ. Stud.*, 2020, **29**, 1–10.
- 68 M. N. Haque, G. Morrison, G. Perrusquia, M. Gutierrez, A. Aguilera, I. Cano-Aguilera and J. Gardea-Torresdey, Characteristics of arsenic adsorption to sorghum biomass, *J. Hazard. Mater.*, 2007, **145**, 30–35.
- 69 H. N. Nhat Ha, N. T. Kim Phuong, T. Boi An, N. T. Mai Tho, T. Ngoc Thang, B. Quang Minh and C. Van Du, Arsenate removal by layered double hydroxides embedded into spherical polymer beads: Batch and column studies, *J. Environ. Sci. Health, Part A: Toxic/Hazard. Subst. Environ. Eng.*, 2016, **51**, 403–413.
- 70 G. M. Sawood and S. Gupta, Arsenate adsorption from aqueous solution using iron-loaded *Azadirachta indica* roots: batch and fixed-bed column study, *Desalin. Water Treat.*, 2020, **203**, 292–308.

RESEARCH

Open Access

Global host metabolic response to *Plasmodium vivax* infection: a ^1H NMR based urinary metabonomic study

Arjun Sengupta¹, Soumita Ghosh¹, Angika Basant^{2,3}, Suhas Malusare¹, Parul Johri¹, Sulabha Pathak², Shobhona Sharma^{2*} and Haripalsingh M Sonawat^{1*}

Abstract

Background: *Plasmodium vivax* is responsible for the majority of malarial infection in the Indian subcontinent. This species of the parasite is generally believed to cause a relatively benign form of the disease. However, recent reports from different parts of the world indicate that vivax malaria can also have severe manifestation. Host response to the parasite invasion is thought to be an important factor in determining the severity of manifestation. In this paper, attempt was made to determine the host metabolic response associated with *P. vivax* infection by means of NMR spectroscopy-based metabonomic techniques in an attempt to better understand the disease pathology.

Methods: NMR spectroscopy of urine samples from *P. vivax*-infected patients, healthy individuals and non-malarial fever patients were carried out followed by multivariate statistical analysis. Two data analysis techniques were employed, namely, Principal Component Analysis [PCA] and Orthogonal Projection to Latent Structure Discriminant Analysis [OPLS-DA]. Several NMR signals from the urinary metabolites were further selected for univariate comparison among the classes.

Results: The urine metabolic profiles of *P. vivax*-infected patients were distinct from those of healthy individuals as well as of non-malarial fever patients. A highly predictive model was constructed from urine profile of malarial and non-malarial fever patients. Several metabolites were found to be varying significantly across these cohorts. Urinary ornithine seems to have the potential to be used as biomarkers of vivax malaria. An increasing trend in pipercolic acid was also observed. The results suggest impairment in the functioning of liver as well as impairment in urea cycle.

Conclusions: The results open up a possibility of non-invasive analysis and diagnosis of *P. vivax* using urine metabolic profile. Distinct variations in certain metabolites were recorded, and amongst these, ornithine may have the potential of being used as biomarker of malaria. Pipercolic acid also showed increasing trend in the malaria patient compared to the other groups.

Keywords: *Plasmodium vivax*, NMR, metabonomics, metabolites, biomarker

Background

Malaria is caused by parasites of the genus *Plasmodium*. The five *Plasmodium* species that are responsible for human malaria are *Plasmodium vivax*, *Plasmodium falciparum*, *Plasmodium malariae*, *Plasmodium ovale* and

Plasmodium knowlesi [1]. Every year, 200-300 million people are affected with malaria with an annual mortality rate of nearly one million [2]. Sub-Saharan Africa and Southeast Asia are some of the most affected regions. In India, *P. vivax* is the predominant cause of clinical malaria [3].

Metabonomics is a comparatively recently developed technology defined as the global, dynamic response of living organism towards genetic and environmental perturbations [4]. The technique involves the NMR or mass

* Correspondence: sharma@tifr.res.in; hms@tifr.res.in

¹Department of Chemical Sciences, Tata Institute of Fundamental Research, Homi Bhabha Road, Mumbai 400 005, India

²Department of Biological Sciences, Tata Institute of Fundamental Research, Homi Bhabha Road, Mumbai 400 005, India

Full list of author information is available at the end of the article

spectra analysis of biofluids such as urine and serum, etc. followed by multivariate analyses using Principal Component Analysis [PCA] or Orthogonal Partial Least Square - Discriminant Analysis [OPLSDA]. Essentially this provides the clustering of the samples into classes. This also provides the identity of specific NMR/mass spectral signature[s] that are responsible for the clustering/classification. This, in turn, leads to identification of the metabolite[s] that are specifically perturbed in response to the stress factor [genetic or environmental] under investigation [5]. Metabonomics, although a relatively new technology, is being used extensively in pharmacological industry [6,7]. Metabonomic analysis is also being utilized in identification of novel biomarkers and/or metabolic characterization during different diseases, such as diabetes [8] and congenital heart disease [9].

Malaria is an ancient infectious disease that has afflicted humans since pre-historic times. Severity in the clinical malarial disease occurs frequently, and has been well documented for *P. falciparum* infections [10,11]. The severity or pathogenicity is likely to be due to metabolic complications arising as a result of host parasite interactions in which the pathogen may divert the host nutrients, and/or release toxic metabolites. Metabolomic analysis will allow a direct read out for such complications. Using axenic cultures, the changes in metabolomic profiles have been documented for the intraerythrocytic stages of *P. falciparum* [12-14]. However, there have been very few studies on the effects on the metabolic profile of the host during malarial infection. Although body fluids such as urine and plasma are amenable to such metabolomic analysis, very few reports exist of such studies. Urine, as an easily available fluid, is also a very good reporter of the overall metabolic status of the whole organism. Systemic level analysis of host metabolic response towards malaria is delineated only in two rodent model studies. In one of the studies, existence of sexual dimorphism was shown in the alterations of sera, urine and brain metabolic profile in the rodent model of malaria [15]. In another study Nicholson and co-workers delineated the global metabolic response to *Plasmodium berghei* infection [16]. No metabolomic information exists so far for human patient samples. In particular, very little is known for *P. vivax* patients, although it has been observed recently that *P. vivax* can cause high levels of pathological complications [17,18].

In this report, a NMR based metabonomic approach is delineated to study the urine samples of *P. vivax* malaria patients and try to correlate the changes observed in them to the known and reported biochemical processes. The paper describes a study of global host metabolic responses towards *P. vivax* infection. The results ascertain differences in metabolic response in the urinary

metabolic profile of the *P. vivax* infected persons with respect to that of healthy individuals and also with the patients of non-malarial fever. The differential metabolites are delineated, raising the possibility of a non-invasive diagnosis of malaria.

Methods

Ethical aspects

This study was approved by and carried out according to the guidelines of the Local Institutional Ethics Committee. Informed consent was obtained prior to sample collection.

Sample collection

Midstream urine samples (~10 ml) of malaria-infected individuals were collected from local pathological laboratories in sterile tubes containing a final concentration of 0.02% sodium azide. The inclusion criteria followed to recruit the subjects in the study were as follows- (1) Adult males (age ranging from 30 to 50 years), (2) Malaria cohort of those patients that tested positive for *P. vivax* by blood smear microscopy and (3) Subjects able to consent through informed consent document. Certain exclusion criteria were also followed viz. (1) All females and males < 30 and > 50 years of age, (2) Patients with *P. falciparum* and mixed *P. falciparum/P. vivax* infections and (3) Patients with other chronic diseases and/or previous history of any type of malarial infection. In total 53 individuals (all males) were recruited for the study: 21 *P. vivax*-infected patients, 21 healthy controls and 12 patients with non-malarial fever. Their age ranges were: malaria patients: 35 ± 3.95 years: healthy individuals: 44 ± 3.18 years: and non-malarial fever patients: 40.5 ± 5.33 years (median \pm standard error). The samples were transported from the site of collection to the laboratory at 0°C and were immediately processed [19].

Sample preparation for NMR experiments

An aliquot (800 μ L) of collected urine sample was mixed with 400 μ L phosphate buffer (an 81:19 (v/v) mixture of 0.2 M Na_2HPO_4 and 0.2 M NaH_2PO_4 ; pH 7.4, made in deionized and 0.22 mm filtered water). This mixture was homogenized and left to stand for 5 min at ambient temperature following which it was centrifuged for 6 min at 6000 g to remove any suspended matter. The clear supernatant (600 μ L) was transferred to 5 mm NMR tube (Wilmad, USA) and 50 μ L D_2O , containing 2, 2-dimethyl-2-silapentane-5-sulfonic acid (DSS) at 0.01% final concentration, was added to it. D_2O served as a field-frequency lock and DSS was the internal chemical shift reference. The samples were stored frozen at -20°C until required for NMR experiments.

NMR experiments

The NMR spectra were acquired on AVANCE 500 MHz Bruker NMR spectrometer equipped with a 5 mm broad-band inverse probe. The operating frequency on this machine was 500.13 MHz for ^1H . For the 1D experiments the spectral width was 12.01 ppm, an excitation pulse of 9 μs ($\sim 70^\circ$), and a relaxation delay of 1 s between consecutive pulses. This resulted in an acquisition time of 0.68 s and a cycle time of 1.68 s. A total of 64 transients were acquired into 8,192 data points. The water suppression routine involved excitation sculpting using gradients. For processing the FIDs were subjected to exponential multiplication leading to an additional line broadening of 0.20 Hz. A sine bell apodization was also used prior to Fourier transformation. The ^1H NMR spectra were manually phase and baseline corrected. For identification of metabolites two dimensional (2D) experiments were performed on selected samples. 2D COSY spectra were acquired with 32 transients in the direct dimension for each of the 256 increments in the indirect dimension. The spectral width was 12.01 in both the dimensions. The pulse width used was 11.80 μs with a delay of 1.5 s. The processing parameters of the data included a QSINE window function, exponential multiplication of 0.20 and 0.30 Hz in the direct and indirect dimension respectively, followed by Fourier transformation in both the dimensions. The 2D TOCSY experiments were performed using similar acquisition parameters. The processing parameters were also identical with an extra Gaussian multiplication of 0.10 Hz prior to Fourier transformation in both the dimensions. The 2D spectra aided in assignment of the NMR resonances to the specific metabolites. In addition, comparison with reported experimental and calculated spectra was done using Human Metabolome Data Base (<http://www.hmdb.ca/search/spectra>).

Data reduction and analyses

The frequency domain ^1H NMR spectra were manually phased and baseline corrected. For data reduction the individual spectrum (0.50 to 9.50 ppm) were divided into frequency bins of width 0.04 ppm each resulting in a total of 191 bins per spectrum. Each bin was integrated using MestReC 4.7.0. In order to avoid the artefacts of water suppression and the variable concentration of urea, the region 4.3 to 6.6 ppm was excluded from the binning procedure. The integrals were normalized to the total intensity of the spectrum to compensate for the inter-sample dilution effects. This was achieved by an algorithm developed in-house. The data was mean-centered (the average value of each bin for all samples was subtracted from individual integrals) and Pareto scaled. The preceding operation resulted in similar weight being given to all the bins and the

resultant multivariate models were not dominated by bins representing metabolites high in concentration. Next, the data so generated served as input for PCA and OPLS-DA, which were performed on the SIMCA-P + 12.0 platform (Umetrics, Umea, Sweden).

PCA is an unsupervised pattern recognition technique where no class identity is assigned to the samples *a priori*. This helps in visualizing any pattern that is present in the data and also identifies the outliers. The class specific segregation can be refined using OPLS-DA. This is a supervised technique where class specificity is assigned towards the sample set *a priori*. This aided in the visualization of the data as scores plot. In such a plot each point represents a spectrum and the pattern and the segregation in the data can be visualized. This pattern is due to one or more spectral bin(s) which can be visualized using a loadings plot where each point represents a spectral bin. The OPLS-DA model is judged using two parameters. R^2X signifies the total explained variation in the data whereas the Q^2 (cum) explains the extent of separation between the classes as well as the predictability of the model.

Integration of NMR peaks

The spectral bins contributing to the variation seen in the OPLS-DA models (visualized in terms of scores plot) were assigned to specific metabolites as described in the previous section. For further quantification of these metabolites, univariate analysis of the NMR spectral peaks was performed in the following way: the peak of the metabolite contributing to the variation in the OPLS-DA model was assigned in the one-dimensional NMR spectral profiles of the individuals. These peaks were integrated, normalized to the whole region of the spectral profile and compared between the classes concerned using student's *t*-test to judge the significance in their difference across the classes.

Results

Multivariate statistical analysis

^1H NMR spectra of urine samples from patients and healthy individuals were recorded followed by multivariate statistical analyses. Representative ^1H NMR spectra from individual belonging to the three groups are shown in Figure 1 [I-III]. These samples were from individuals infected with *P. vivax*, patients with non-malarial fever or healthy volunteers. For this analysis, only adult male samples were used. The individuals with infection had been referred to the pathology laboratories with malaria-like clinical symptoms (chills, fever, splenomegaly, etc.) and their infection status was confirmed by standard peripheral blood smears.

The multivariate analysis was performed on two data sets obtained from the ^1H NMR spectra of urine samples.

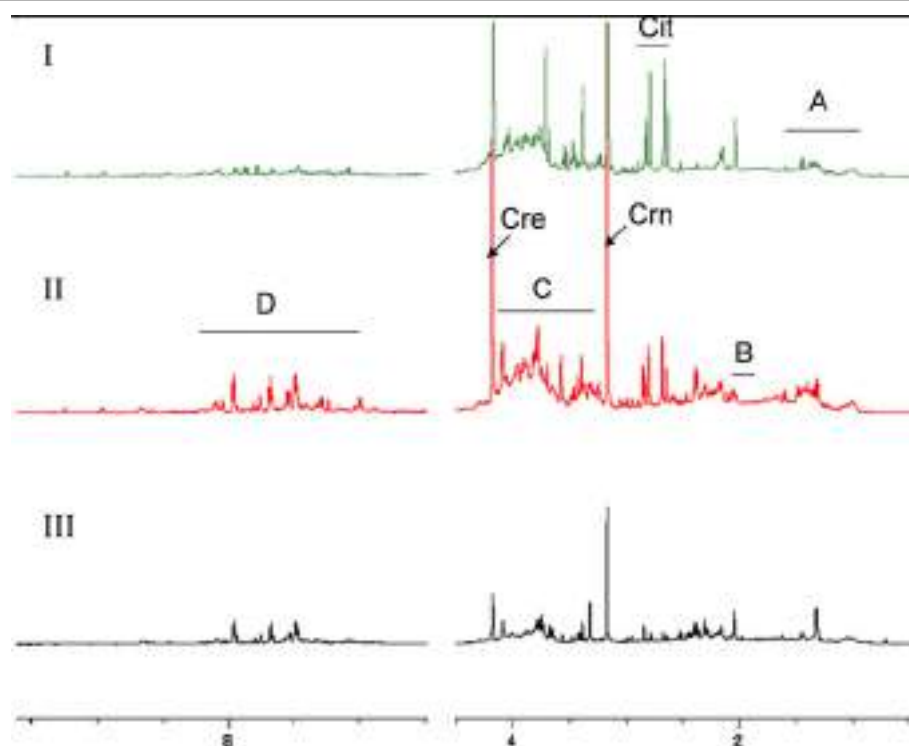


Figure 1 Representative urine ^1H NMR spectral profile of I. Adult male patient with non-malarial fever, II. Adult male healthy individual and III. Adult male infected with *Plasmodium vivax*. However, due to high variability in the urine profiles of across individuals, a direct comparison of the spectral profile is not possible. Keys: A: Branched chain amino acid and small chain fatty acids, B: acetate and N-acetyl groups of acetylated amino acids, C: glucose, carbohydrates and amino acid alpha protons, D: Aromatic amino acids and metabolites, Cit: citrate, Crn: creatine/ phosphocreatine/creatinine and Cre: creatine. The Urea and water regions were excluded from the figure.

The first data set consisted of urine from *P. vivax*-infected individuals and healthy controls. The second data set consisted of patients with malaria and non-malarial fever. Earlier data analysis by PCA of the ^1H NMR spectra of urine from the healthy individuals and *P. vivax*-infected persons showed an inherent segregation between the two classes [20]. The R^2X value was found to be 0.72 [20]. In the current study the OPLS-DA model was built to visualize the class specific segregation and to obtain the significant bins contributing to the variation across the classes, i.e. *P. vivax*-infected patients and healthy controls or non-malarial fever patients. The OPLS-DA scores plot from the urinary NMR metabolic profile of *P. vivax*-infected individuals and healthy controls is shown in Figure 2. This model also showed segregation of classes with $R^2X = 0.41$ and $Q^2(\text{cum}) = 0.67$. However, the spread is typical of human samples since there is enormous variation in genetic backgrounds as well as food habits. This is to say, the samples under consideration have factors other than malaria, which led to a larger scatter among them. To ensure that the effect of sex does not confound the analysis it was restricted to male patients only. In spite of all these factors, the $Q^2(\text{cum})$ was found to be significantly high, therefore it

implicated a considerable difference in the urinary metabolic profile of malarial patients and healthy individuals. OPLS-DA models made from NMR profile of urine samples of malaria patients and non malarial fever patients showed $Q^2(\text{cum}) = 0.89$ and $R^2X = 0.67$. This indicates a very good separation between the urinary profile of malaria patients and non-malarial fever patients, which is also evident from the PCA and OPLS-DA scores plot shown in Figures 3 and 4 respectively. In order to identify the spectral bins varying significantly between the classes, the loadings S-plot from the two models were analysed along with the Variable importance on Projection (VIP) values (Tables 1 and 2). The loadings S-plots are shown in Figure 5 (malarial patients and healthy individuals) and Figure 6 (malarial patients and non malarial fever patients). The bins accepted for further analysis are shown in Table 1 (malarial patients and healthy individuals) and Table 2 (malarial patients and non-malarial fever patients) along with their loadings and VIP values.

In order to identify the metabolites corresponding to the spectral bins found significant two-dimensional NMR techniques such as COSY and TOCSY were employed, matching of the chemical shifts with values reported in metabolite databases such as Human

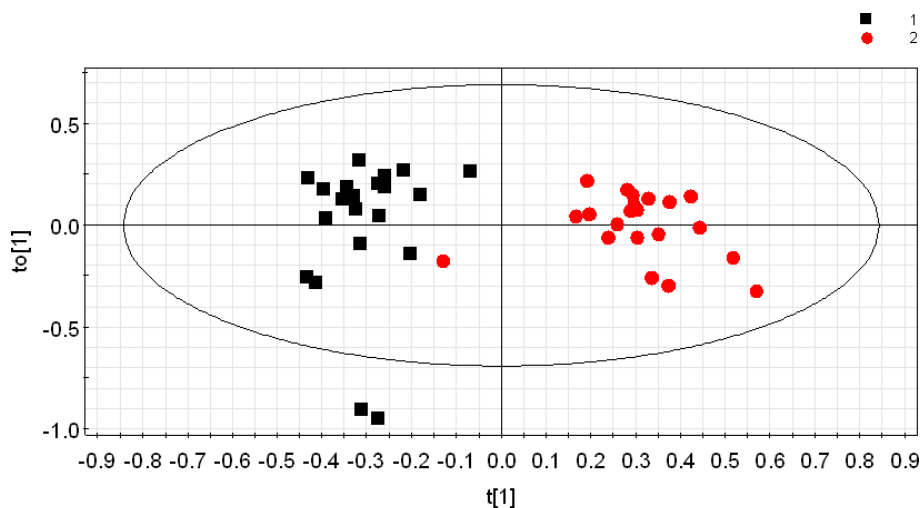


Figure 2 OPLS-DA scores plot showing the variation between urinary metabolic profiles of the *Plasmodium vivax*-infected patients and healthy individuals. This model was constructed from ^1H NMR data of urine from 21 *P. vivax*-infected individuals and 21 healthy individuals. The subjects were all male. Each point in the plot represents one sample ^1H NMR spectra. Black square = *P. vivax*-infected individual and red circle = healthy individual. The $t[1]$ axis represents the predictive variation among the classes and the $to[t1]$ axis represents the variation orthogonal to the class specific variation. The statistical parameters of the model were as follows- $R^2X = 0.41$ and $Q^2(\text{cum}) = 0.67$. The ellipse is a 95% Hotelling's T^2 ellipse.

Metabolome Database (HMDB). The compounds so identified are listed in Tables 3 and 4, for the malaria vs healthy and malaria vs non-malaria fever patients, respectively.

Integration of spectral peaks and univariate analysis

In order to compare the relative concentrations of the metabolites identified from OPLS-DA models, the

corresponding ^1H NMR spectral peak(s) were integrated. The results are presented in Figures 7 and 8 for the malaria patients compared with healthy individuals and patients with non-malaria fever respectively. Most of the metabolites showed significant variation across the classes. For example, the levels of valerylglycine, pipecolic acid, phenylpyruvic acid increased in the urine of malaria patients (Figure 7A, D, E) while the relative

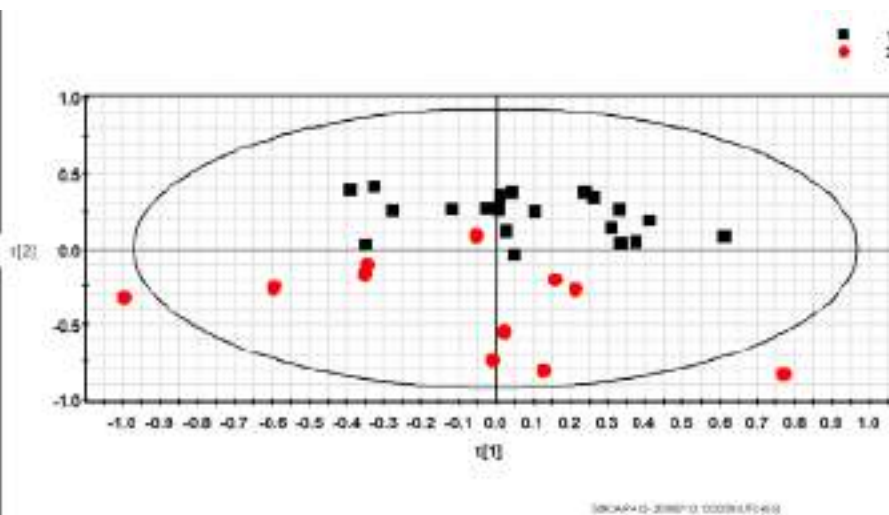


Figure 3 PCA scores plot showing the variation between urinary metabolic profiles of *Plasmodium vivax*-infected individuals and non-malarial fever patients. The PCA scores plot demonstrates that the infection by the parasite brings in considerable variation in the urine profile of the individuals. Here the variation is seen along PC2. This PCA model was constructed from ^1H NMR of 21 patients with *P. vivax* infection and 12 patients with non-malarial fever. All of the patients were male. Each point represents one sample ^1H NMR urine profile. Black square = *P. vivax*-infected individuals and red circles = non-malarial fever patients. R^2X for the model = 0.67.

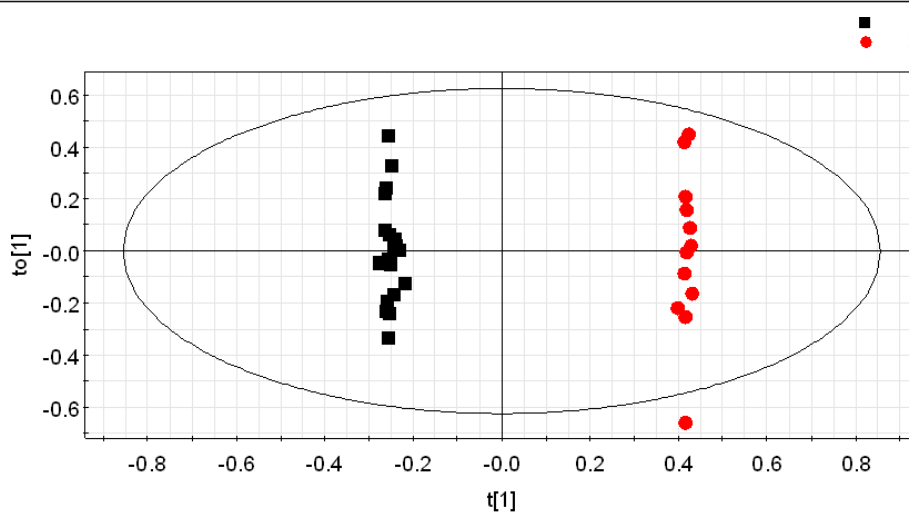


Figure 4 OPLS-DA scores plot showing the variation between urinary metabolic profiles of *Plasmodium vivax*-infected individuals and non-malarial fever patients. This model was constructed from ^1H NMR data of urine from 21 *P. vivax*-infected individuals and 12 patients with non-malarial fever. All of the subjects were male. Each point in the plot represents one sample ^1H NMR spectra. Black square = *P. vivax*-infected individual and red circle = non-malarial fever patients. The $t[1]$ axis represents the predictive variation among the classes and the $to[1]$ axis represents the variation orthogonal to the class specific variation. The statistical parameters of the model were as follows- $R^2X = 0.67$ and Q^2 (cum) = 0.89. The ellipse is a 95% Hotelling's T^2 ellipse.

levels of tyrosine, glucose and N-acetylglutamate decreased in the malaria patients in comparison to that of healthy individuals (Figure 7G, H, K). Some spectral resonances had overlap from more than one metabolite (Figure 7F, I). These signals showed significant variation across the three groups. Since the contribution of individual metabolites towards such signals could not be ascertained, they are mentioned here collectively.

Several metabolites also showed significant variation across malaria and non-malarial fever patients. Among them, glucose and ornithine were increased in the urine profile of the malaria patients significantly (Figure 8B,

D), while a significant decrease in N-butyrate and acetate levels was observed (Figure 8E, F).

From Figures 7, 8 and Tables 3 and 4, it is evident that there is little overlap between the sets of metabolites found to be varying across the classes. Therefore metabolites showing differences between malaria patients and healthy individuals (Figure 7, Table 3) were integrated in the spectral profile of non-malarial fever patients and were compared with the malaria patients using univariate statistics (Figure 9A-I). Significant enhancement was observed in the concentration of N-acetyloronithine and tyrosine (Figure 9A, C; $p < 0.05$ for

Table 1 OPLS-DA model bins selected for assignment of metabolites based on differences between patients of *vivax* malarial and healthy individuals

Increased/Decreased	Bin (Chemical shift)	Loading values	Variable importance on projection (VIP) values
Increased in urine metabolic profile of <i>P.vivax</i> infected patients	2.16	-0.20	3.09
	1.40	-0.12	2.11
	7.48	-0.11	2.04
	3.48	-0.15	2.10
	7.44	-0.12	1.79
	1.20	-0.09	1.58
Decreased in urine metabolic profile of <i>P.vivax</i> infected patients	3.04	0.37	5.61
	3.68	0.20	2.36
	3.80	0.17	2.29
	3.00	0.11	1.93
	2.04	0.10	1.51

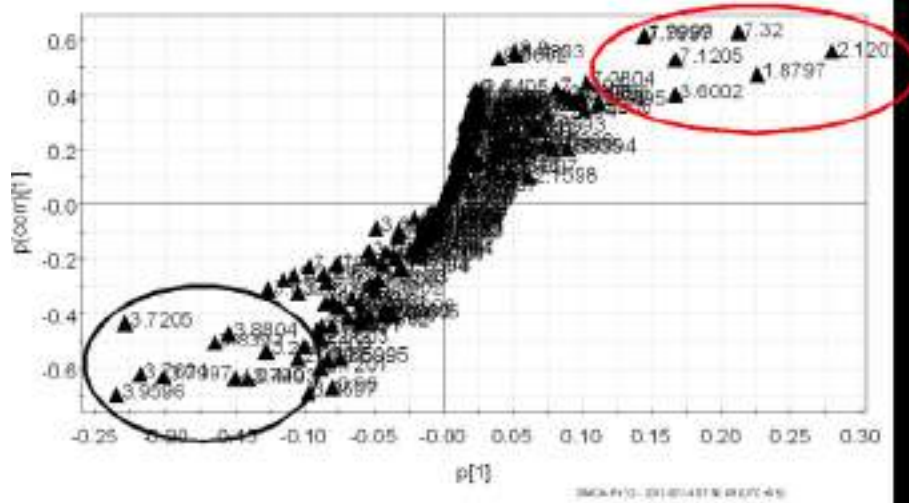


Figure 6 A Representative OPLS-DA loadings S- plot showing relative contribution of bins/spectral variables to clustering of *Plasmodium vivax*-infected patients and non-malarial fever patients. This plot corresponds to Figure 4. Each point in the figure represents a bin. The p[corr][1] axis represents the correlation of the bin towards the predictive variation shown in Figure 1. The p[1] axis represents the magnitude of the spectral bins. Bins from region circled in red represents the bins that decreased in the *P. vivax*-infected individuals. Bins from region circled in black represents the bins that increased in the *P. vivax*-infected individuals. Among them, bins with high p[corr][1] [< -0.4 for decreased and > 0.4 for increased], high p[1] (listed in Table 2) and VIP above cut-off are selected for further analysis.

minor metabolite in fatty acid break down. The elevation of the urinary acylglycines is an indication of impaired β -oxidation of fatty acid [25]. Therefore, it may be concluded that the impairment in fatty acid β -oxidation is associated with febrile condition.

Data presented here also indicates a disturbance in the phenylalanine metabolism. Phenylalanine is known to be metabolized by phenylalaninehydroxylase and tetrahydrobiopterin (THBP) to tyrosine. Alteration of this pathway leads to the formation of phenylpyruvate. Usually phenylpyruvate is a minor metabolite of phenylalanine. However, in patients with phenylketonuria, the phenylalanine-tyrosine pathway is blocked leading to excess formation of phenylpyruvate [26]. A significantly enhanced excretion of phenylpyruvic acid in the malarial patients compared to healthy individuals was observed in our experiments (Figure 7E). This ‘phenylketonuric condition’ is probably arising out of an impaired phenylalanine

metabolism. The data also suggests a possible increase in the biopterin concentration in the urine of malaria patients (Figure 7F). Some atypical form of phenylketonuria has been characterized by an increase in the urinary biopterin, which is caused by malfunction of dihydropteridinereductase (DHPR) [26]. Hyperphenylalaninemia is associated with severe *P. falciparum* malaria in African children [27]. However, this does not seem to be the case in the present study as the phenylpyruvic acid excretion is not significantly different between the malaria and non-malarial fever patients (Figure 9E). Although, the overlapped peaks of phenylalanine and hippurate showed a significant increase in the urine of malaria patients compared to that of non-malarial fever patients (Figure 8A), this cannot be taken to an indication of hyperphenylalaninemia. The hyperphenylalaninemic condition may be an associated complication of fever. However, there seems to be no study that deals with the metabolite

Table 3 Urinary metabolites perturbed in the *Plasmodium vivax*-infected patients compared to healthy individuals.

Classes compared	Metabolites increased in <i>P. vivax</i> -infected individuals	Metabolites decreased in <i>P. vivax</i> -infected individuals
<i>P. vivax</i> -infected individuals and healthy controls	Valerylglycine	Creatine/Phosphocreatine
	N - acetylornithine	Tyrosine
	Salicylurate	Glucose
	pipecolic acid	Guanidoacetate
	Phenylpyruvate	Alanine
	biopterin, 3- hydroxybutyrate	N - acetylglutamate

Figure 7 indicates the bin corresponding to each metabolite

Table 4 Urinary metabolites perturbed in the *Plasmodium vivax*-infected patients compared to non-malarial fever patients.

Classes compared	Metabolites increased in <i>P. vivax</i> -infected individuals	Metabolites decreased in <i>P. vivax</i> -infected individuals
<i>P. vivax</i> -infected individuals and patients with non-malarial fever	L-phenylalanine	N-butyrate
	Hippurate	Acetate
	Glucose	
	Glutamine	
	Alanine	
	Ornithine	

Figure 8 indicates the bin corresponding to each metabolite

profiling during fever in humans, therefore it remains an interesting aspect to be investigated.

Ornithine is a part of the urea cycle. In the first step of the cycle, ornithinecarbamoyltransferase (OCT) acts on ornithine and carbamoylphosphate to begin the natural detoxification of ammonia. Earlier reports suggested that elevation of serum value of OCT can be a potential marker of malaria and this was associated with the damage of the liver cells in the liver stage of the parasite [27,28].

Perturbation of OCT levels are likely to result in an impaired urea cycle. Urea cycle is the major pathway for ammonia detoxification in mammals. Earlier reports indicated ammonia toxicity during malaria in mice model [29]. Observation of significant increase in the urinary level of both ornithine (Figure 8D) and N-acetylornithine (Figure 9A) in malaria patients (compared to non-malarial fever patients) and an increased level of N-acetylornithine (compared to healthy individuals) (Figure 7B) also points to possible hepatic injury and impaired urea cycle resulting in ammonia toxicity during *P. vivax* infection. In the light of results presented here, earlier reports of statistically significant decrease of ornithine in the plasma of patients with clinical malaria [27] may be interpreted as an enhanced excretion of ornithine in malaria patients.

Pipecolic acid is a minor metabolite of lysine catabolism. In humans, pipecolic acid is found to be associated with chronic liver disease, pyridoxine dependent epilepsy and Zellweger syndrome [30-32]. Recent studies in the murine malaria model show elevated pipecolic acid level in the urine of NMRI mice [16]. Liver dysfunction is associated with malaria. However, the cause for the elevated pipecolic acid during malaria remains unclear. Although statistically not very significant, this metabolite was present in larger quantities in the urine of malarial patients compared with non-malarial fever patients (Figure 9D). Earlier studies showed hyperlysinaemia in the sera of *P. berghei* ANKA infected mice [15]. Hyperlysinaemia is often related to activation of minor metabolic pathway hence an enhanced pipecolic acid excretion

[33]. From the data reported here and earlier data from murine malaria model it seems likely that lysine metabolism is perturbed during the course of malarial infection. However, the underlying biochemical reason remains to be addressed.

The non-malarial fever category serves as a control for general fever related changes that are not specific to *P. vivax* infection. Febrile illnesses are often likely to be misdiagnosed as malaria. Lundqvist and co-workers showed that borreliosis can be misdiagnosed as malaria due to the similarity in the symptoms [34]. Poorly executed microscopy also sometimes adds on to this, leading to malaria overdiagnosis and overuse of anti-malarial in malaria endemic regions [35,36]. In this report, it is shown that the non-malarial fevers can be separated from vivax patients on the basis of the urinary metabolite profile of the patients. The urine metabolomic profile seems to be significantly different in these two categories (Figures 3 and 4). This is due to the difference in the levels of Phenylalanine, hippurate, glucose, glutamine, alanine, and ornithine which are increased in the urine of the *P. vivax*-infected individuals and n-butyrate and acetate which are decreased in these patients (Figure 8, Table 4). Pipecolic acid also showed a higher trend in the urine of malaria patients compared to non-malarial fever patients (Figure 9D). As is evident from a very high $Q^2(\text{cum})$ which is equal to 0.89 from the OPLS-DA model made from the urinary metabolite profile of the non-malarial fever patients and *P. vivax*-infected individuals, urinary metabolic profiles have a potential to be of diagnostic use for detecting malaria and to differentiate malaria from other non-malarial fevers.

Conclusions

This study reports on the understanding of the host metabolic changes in terms of the urinary metabolite profile of the *P. vivax*-infected patients. Urinary metabolite profile of malaria patients were found to be distinct from both healthy individuals and those of non-malarial fever patients. Among several changes in metabolism, a

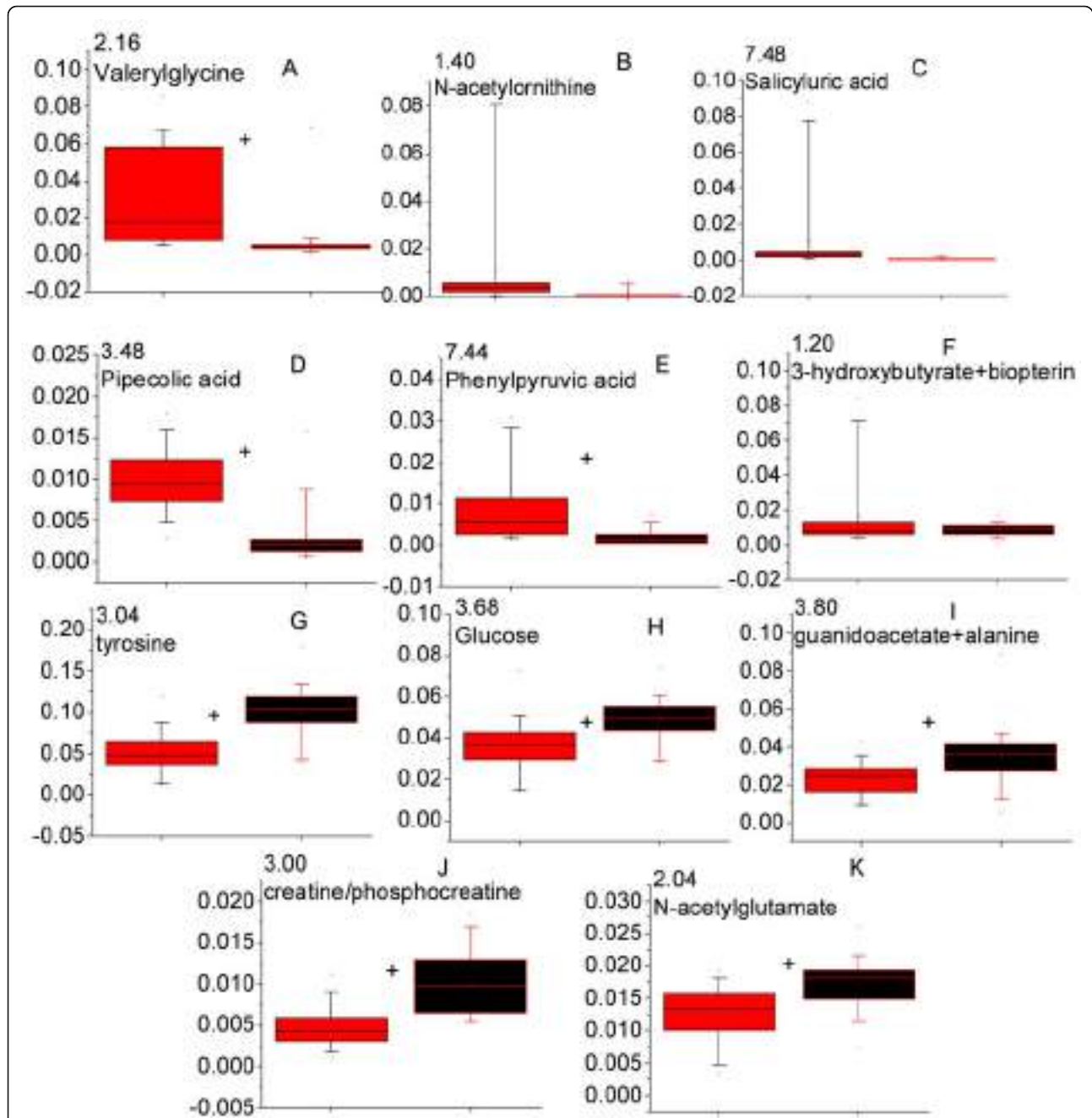


Figure 7 The level of perturbed metabolites in the urine of *Plasmodium vivax*-infected and healthy individuals. All peak intensities were calculated in terms of actual integrated value of individual NMR spectral peak normalized to the total spectral intensity. Panels with more than one metabolite represent an overlap in the peak of metabolites in the spectrum. Red = *P. vivax*-infected individuals and black = healthy individuals. + indicates $p < 0.05$.

disruption in the urea cycle in terms of ornithine excretion was noted, along with an elevated level of pipecolic acid indicating possible hepatic injury. Ornithine, therefore, promises to be candidate biomarker for malarial infection. Moreover, an extremely predictive model was constructed from urinary metabolite profile of the

clinical malaria patients and individuals with non-malarial fever. This might help in the non-invasive diagnosis of malarial infection. Malaria-specific signatures were observed in the urine and showed that the urine profile of malaria patients cluster separately from different groups of control populations in spite of the high

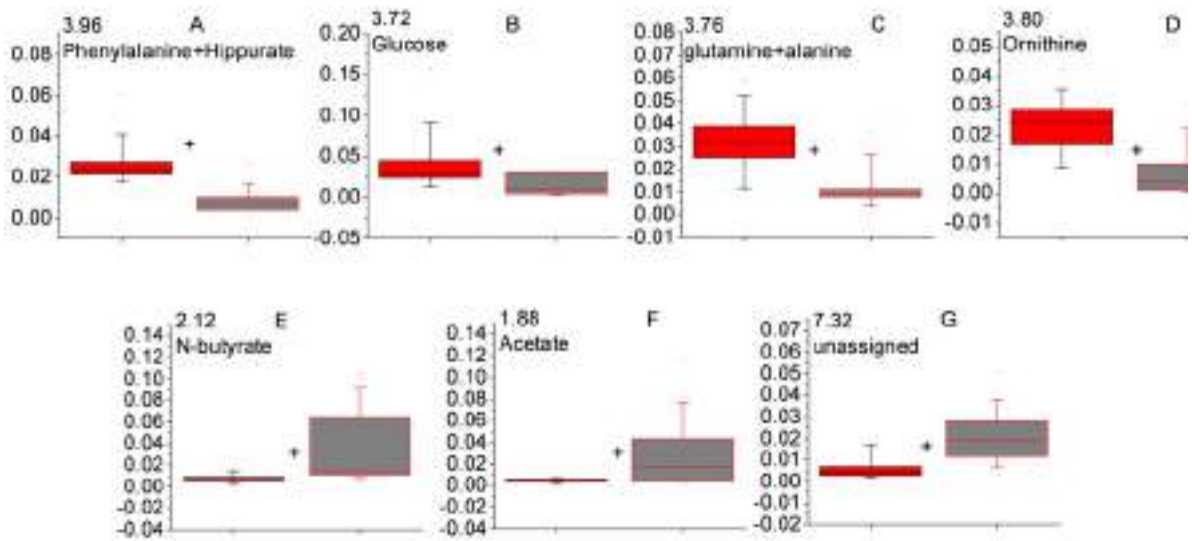


Figure 8 The level of perturbed metabolites in the urine of *Plasmodium vivax*-infected and non-malarial fever patients. All peak intensities were calculated in terms of actual integrated value of individual NMR spectral peak normalized to the total spectral intensity. Panels with more than one metabolite represent an overlap in the peak of metabolites in the spectrum. Red = *P. vivax*-infected individuals and grey = non-malarial fever patient. + indicates $p < 0.05$.

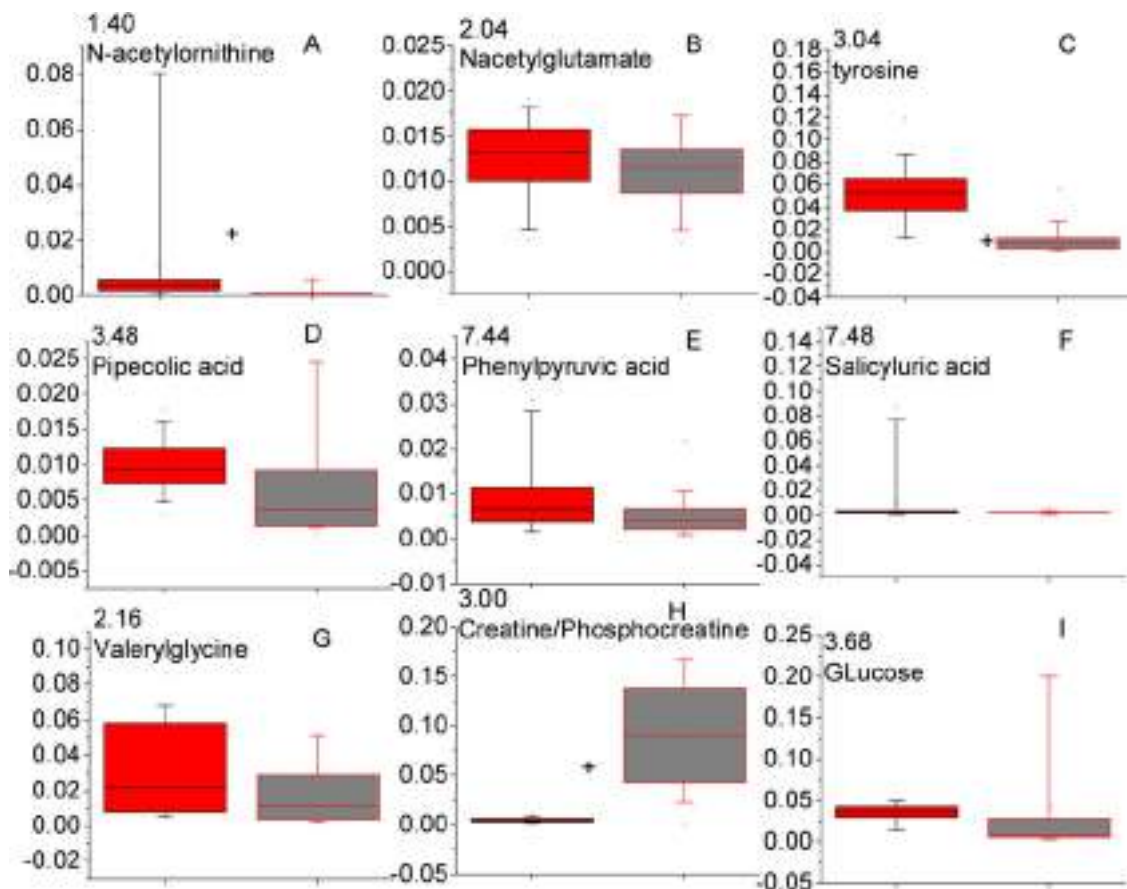


Figure 9 The level of perturbed metabolites in the urine of *Plasmodium vivax*-infected and non-malarial fever patients. Only those peaks are integrated which showed no overlap in the spectra and showed significant variation across the *P. vivax*-infected patients and healthy individuals. All peak intensities were calculated in terms of actual integrated value of individual NMR spectral peak normalized to the total spectral intensity. Red = *P. vivax*-infected individuals and grey = non-malarial fever patient. + indicates $p < 0.05$.

variability of urine metabolites across individuals. This study, therefore opens up the possibility of finding out malaria specific biomarkers in the urine, which might help in non invasive diagnosis of the infection in the long run. Many parameters, such as genetic make up, food habits and lifestyle, may influence urine metabolite patterns. In order to circumvent such confounding parameters, a longitudinal follow up and comparison of urine from cohorts of malaria patients and other control subjects will provide further specific information regarding disease related changes in patients of *P. vivax* malaria.

Competing interests

The authors declare that they have no competing interests.

Authors' contributions

AS, SG, SM, PJ were involved in collection and processing of the samples, NMR experiments, statistical analyses and model building and interpretation of the data. AS and SG, in addition, drafted the manuscript. SP, SS and HMS conceived the study, interpreted the data and were involved in writing the manuscript. All authors read and approved the final manuscript.

Acknowledgements

The authors are grateful to the National Facility for High-field NMR, TIFR and Dr R.Y. Agarkar of TIFR Medical section for all their help. We thank Dr S. Bhayani and Dr A. Mehta for help in sample collection. AS thanks the Council of Scientific and Industrial Research, Govt. of India for the Shyama Prasad Mukherjee Fellowship.

Author details

¹Department of Chemical Sciences, Tata Institute of Fundamental Research, Homi Bhabha Road, Mumbai 400 005, India. ²Department of Biological Sciences, Tata Institute of Fundamental Research, Homi Bhabha Road, Mumbai 400 005, India. ³The Division of Biological Sciences, University of Chicago, 5812, S. Ellis Avenue, Chicago, IL 60637, USA.

Received: 24 October 2011 Accepted: 23 December 2011

Published: 23 December 2011

References

1. Trampuz A, Jereb M, Muzlovic I, Prabhu R: **Clinical review: Severe malaria.** *Crit Care* 2003, **7**:315-323.
2. Wim Van Lerberghe TE, Kumanan R, Abdelhay M: **World Malaria Report.** *World Malaria Report (Editor eds.)* World Health Organization; 2008.
3. Joshi H, Prajapati KS, Verma A, Kang'a S, Carlton JM: **Plasmodium vivax in India.** *Trends Parasitol* 2008, **24**:228-235.
4. Nicholson JK, Lindon JC: **Systems biology: metabonomics.** *Nature* 2008, **455**:1054-1056.
5. Lindon JC, Holmes E, Nicholson JK: **Pattern recognition methods and applications in biomedical magnetic resonance.** *Prog NMR Spec* 2001, **39**:1-40.
6. Lindon J, Holmes E, Nicholson J: **Metabonomics techniques and applications to pharmaceutical research & development.** *Pharma Res* 2006, **23**:1075-88.
7. Robertson DG, Reilly MD, Cantor GH, John CL, Jeremy KN, Elaine H: **Metabonomics in preclinical pharmaceutical discovery and development.** *The Handbook of Metabonomics and Metabolomics* Amsterdam: Elsevier Science B.V; 2007, 241-277.
8. Yuan K, Kong H, Guan Y, Yang J, Xu G: **A GC-based metabonomics investigation of type 2 diabetes by organic acids metabolic profile.** *Journal Chroma B* 2007, **850**:236-240.
9. Brindle JT, Antti H, Holmes E, Tranter G, Nicholson JK, Bethell HWL, Clarke S, Schofield PM, McKilglin E, Mosedale DE, Grainger DJ: **Rapid and noninvasive diagnosis of the presence and severity of coronary heart disease using 1H-NMR-based metabonomics.** *Nat Med* 2002, **8**:1439-1445.
10. Planche T, Dzeing A, Nqou-Milama E, Kombila M, Stackpole PW: **Metabolic complications of severe malaria.** *Curr Top Microbiol Immunol* 2005, **295**:105-136.
11. Mackintosh CL, Beeson JG, Marsh K: **Clinical Features and pathogenesis of severe malaria.** *Trends Parasitol* 2004, **20**:597-603.
12. Olszewski KL, Morrissey JM, Wilinski D, Burns JM, Vaidya AB, Rabinowitz JD, Llinas M: **Host parasite interaction revealed by Plasmodium falciparum Metabolomics.** *Cel Host Microb* 2009, **5**:191-199.
13. Plata G, Hsiao TL, Olszewski KL, Llinas M, Vitkup D: **Reconstruction and Flux- balance analysis of the Plasmodium falciparum metabolic network.** *Mol Syst Biol* 2010, **6**:408-422.
14. Teng R, Junankar PR, Bubb WA, Rae C, Kirk K: **Metabolite profiling of the intraerythrocytic malaria parasite Plasmodium falciparum.** *NMR Biomed* 2009, **22**:292-302.
15. Basant A, Rege M, Sharma S, Sonawat HM: **Alterations in urine, serum and brain metabolomic profiles exhibit sexual dimorphism during malaria disease progression.** *Malar J* 2010, **9**:110.
16. Li JV, Wang Y, Saric J, Nicholson JK, Dirnhofer S, Singer BH, Tanner M, Wittlin S, Holmes E, Utzinger JR: **Global metabolic responses of NMRI mice to an experimental Plasmodium berghei infection.** *J Prot Res* 2008, **7**:3948-3956.
17. Rogerson SJ, Carter R: **Severe vivax malaria: newly recognised or rediscovered?** *PLoS Med* 2008, **5**:875-877.
18. Kochar DK, Das A, Kochar SK, Saxena V, Sirohi P, Garg S, Kochar A, Khatri MP, Gupta V: **Severe Plasmodium vivax malaria: a report on serial cases from Bikaner in Northwestern India.** *Am J Trop Med Hyg* 2009, **80**:194-198.
19. Lauridsen M, Hansen SH, Jaroszewski JW, Cornett C: **Human urine as test material in 1H NMR-based metabonomics: recommendations for sample preparation and storage.** *Anal Chem* 2007, **79**:1181-1186.
20. Sengupta A, Ghosh S, Sonawat HM, Basant A, Sharma S, Kshirsagar NA, Gogtay N: **A urine 1H NMR based metabonomic approach to understand the host metabolic response towards plasmodium vivax infection.** In *Proceedings of International Conference on Systems in Medicine and Biology: 16-18 December 2010.* Edited by: Manjunatha M. Kharagpur; 2010:172-176, IEEE.
21. Anvikar A, Singh D, Singh R, Dash A, Valecha N: **Vivax malaria presenting with cerebral malaria and convulsions.** *Acta Parasitol* 2010, **55**:96-98.
22. Koibuchi T, Nakamura T, Miura T, Endo T, Nakamura H, Takashi T, Kim HS, Watawa Y, Washizaki K, Yoshikawa K: **Acute disseminated encephalomyelitis following Plasmodium vivax malaria.** *J Infect Chemo* 2003, **9**:254-256.
23. Beg MA, Khan R, Baig SM, Gulzar Z, Hussain R, Smego Ra Jr: **Cerebral involvement in benign tertian malaria.** *Am J Trop Med Hyg* 2002, **67**:230-232.
24. Mehta M, Sonawat HM, Sharma S: **Malaria parasite-infected erythrocytes inhibit glucose utilization in uninfected red cells.** *FEBS Letters* 2005, **579**:6151-6158.
25. Kimura M, Yamaguchi S: **Screening for fatty acid beta oxidation disorders: Acylglycine analysis by electron impact ionization gas chromatography-mass spectrometry.** *J Chrom B: Biomed Sci Appl* 1999, **731**:105-110.
26. Jon CN, Ching-Lun L, Sheldon M, Seymour K, Klaus B: **Neopterin and biopterin levels in patients with atypical forms of phenylketonuria.** *J Neurochem* 1980, **35**:898-904.
27. Lopansri BK, Anstey NM, Stoddard GJ, Mwaikambo ED, Boutlis CS, Tjitra E, Maniboye H, Hobbs MR, Levesque MC, Weinberg JB, Granger DL: **Elevated plasma phenylalanine in severe malaria and implications for pathophysiology of neurological complications.** *Infect Immun* 2006, **74**:3355-3359.
28. Sampath SLS, Somani BL, Sharma YV, Arora MM, Ambade VN: **Serum Ornithine carbamoyl transferase as a surrogate marker in malaria.** *Med J AFI* 2002, **58**:315-8.
29. Pernet MF, Kober F, Confort-Gouny S, Fur YL, Dalmaso C, Coltel N, Liprandi A, Gulian JM, Grau GE, Cozzone PJ, Viola A: **Magnetic resonance spectroscopy reveals an impaired brain metabolic profile in mice resistant to cerebral malaria infected with Plasmodium berghei ANKA.** *J Biol Chem* 2007, **282**:14505-14514.
30. David MD, Patricia T, Caroline A, Peter C: **Cerebro-hepato-renal syndrome of Zellweger: a report of eight cases with comments upon the incidence, the liver lesion, and a fault in pipecolic acid metabolism.** *J Pediatrics* 1975, **86**:382-387.
31. Hironaka K, Tatsuaki H, Masako N, Kenzo T: **Plasma levels of pipecolic acid in patients with chronic liver disease.** *Hepatology* 1988, **8**:286-289.

32. Barbara P, Sylvia S-I, Eduard P, Wolfgang E, Eduard AS, Cornelis J: **Pipecolic acid elevation in plasma and cerebrospinal fluid of two patients with pyridoxine-dependent epilepsy.** *Ann Neurol* 2000, **48**:121-125.
33. Dancis J, Hutzler J, Cox RP: **Familial hyperlysinemia with lysine ketoglutarate- reductase insufficiency.** *J Clin Invest* 1969, **48**:1447-52.
34. Lundqvist J, Larsson C, Nelson M, Andersson M, Bergstrom S, Persson C: **Concomitant infection decreases the malaria burden but escalates relapsing fever borreliosis.** *Infect Immun* 2010, **78**:1924-30.
35. Shillcutt SD, Morel CM, Coleman PG, Mills AJ, Goodman CA: **Cost-effectiveness of malaria diagnosis in sub-Saharan Africa: the role of rapid diagnostic tests in rural settings with high *Plasmodium falciparum* transmission.** *A report for WHO-UNICEF-UNDP-World Bank Special Programme for Research and Training in Tropical Diseases (TDR)* 2006.
36. Elhassan EM, Haggaz AED, Magzoub MM, Adam I: **Non-malarial fever among pregnant women in Medani Hospital, Sudan: diagnostic uncertainty and overtreatment with quinine.** *Asian Pacific J Trop Med* 2010, **3**:392-394.

doi:10.1186/1475-2875-10-384

Cite this article as: Sengupta *et al.*: Global host metabolic response to *Plasmodium vivax* infection: a ¹H NMR based urinary metabolomic study. *Malaria Journal* 2011 **10**:384.

**Submit your next manuscript to BioMed Central
and take full advantage of:**

- Convenient online submission
- Thorough peer review
- No space constraints or color figure charges
- Immediate publication on acceptance
- Inclusion in PubMed, CAS, Scopus and Google Scholar
- Research which is freely available for redistribution

Submit your manuscript at
www.biomedcentral.com/submit





A Highly Reliable and Cost-effective Service Model for Finite Population Clouds: Analysis and Implementation

Rohit Sharma¹ · Raghuraj Singh²

Received: 31 March 2020 / Accepted: 2 June 2021
© King Fahd University of Petroleum & Minerals 2021

Abstract

Cloud computing is the delivery of on-demand, network accessed and easily configurable computing resources on a pay-as-you-go basis. These resources are dynamically assigned and can be scaled up and down in response to users' needs. An increasing number of businesses are switching to cloud based computing systems for internal uses. Hence, there is a need to explore queuing theory to model systems bound by the constraint of a finite user population. In this work, a model for the analysis of request stage of finite population cloud computing systems has been presented. The losses in the system due to impatient users owing to balking and reneging in the system have also been taken into account in the model. A scheduling method to improve the load balancing of the request stage of the system has been introduced. A cost and reliability measurement scheme has been used to analyse the performance/cost trade-off associated with request stage of the system. The results obtained have been presented and compared with existing model working in the same domain. Experimental results show that improved cost saving (as high as $\approx 91\%$) and high throughput rate can be achieved by applying the proposed CCRM scheme.

Keywords Request stage cloud reliability · Queuing theory

1 Introduction

Cloud computing is the delivery of different services through the internet. These resources include tools and applications like data storage, servers, databases, networking, and software. This service archetype evolved as a utility to offer groups of computing and data resources on a rental basis in contrast to the traditional purchase and use patterns [1,2]. Cloud services and resources are supplied based on several fundamental models, including Infrastructure as a Service (IaaS), Platform as aService (PaaS), and Software as a Service (SaaS). For example, clouds like HPE, VMware and

Salesforce utilise computing and data resource, programming interfaces and software as services, respectively.

A number of works have been published to study the cost of establishing and operating a cloud computing setup [3–6]. This cost often portrayed as a function of the resources provisioned for any computation system. There is a trade-off between the profitability of maintaining the system and redundancies in the system to tolerate faults that may be caused due to a variety of reasons. An over-provisioned system can greatly improve the Quality of Service (QoS) but drastically increase the cost of maintenance. On the other hand, an under-provisioned system may reduce the economic cost of the system but also cause increased losses and errors in the system apart from the increased latency in the queue. These errors include timeout errors as well as overflow errors [7].

Traditionally, a Service Level Agreement (SLA) is drawn between the cloud service providers and customers in terms of the guaranteed performance levels. The SLA is negotiated in accordance to users expectations and system abilities [5,6]. It covers performance and quality guideline for services to be offered by cloud service provider. Cloud computing systems are designed to minimise the number of SLA violations

✉ Rohit Sharma
rohit6615@rediffmail.com

¹ R. Sharma ✉
Department of Computer Science & Engineering, Dr.
Ambedkar Institute of Technology for Handicapped, Kanpur
208024, India
e-mail: rohit6615@rediffmail.com

² R. Singh
Department of Computer Science & Engineering, Harcourt
Butler Technical University, Kanpur 208002, India

as they reduce the profits to the provider. An optimal control policy (OCP) was suggested by Chiang et al. that helps in making decisions in terms of computing resources used, cost and system capacity in order to maximise profit [3]. Performance analysis is therefore necessary for achieving performance guarantee in a service-oriented system. Atmaca et al. proposed an easy to implement approximate solution which can take care of QoS parameters, while customers and cloud service providers meet their SLA requests [5].

The degree of cloud reliability on a cloud computing system is described as the probability of successful completion of cloud service in a specific period of time. It can be viewed mainly in terms of request stage reliability, i.e. minimisation of overflow and timeout errors [7]. As described in Figs. 1 and 2, overflow errors or balking is mainly due to impatient users who withdraws from the system as request queue run out of space. Similarly, timeout errors or renegeing is due to impatient users who withdraws after joining the request queue due to long waiting [7].

The relationship between input queue length and computing resource cost with performance indicators like average number of tasks in the system, balking probability and response time in terms of immediate service was analysed for $M/G/m/m+r$ queuing systems [14]. Optimal resource provisioning problem [15] is extended by inducing impatient user behaviour (balking and renegeing) with reliability measure scheme, and it was applied to finite population private clouds.

In this work, we analyse the effect of system control on operational costs and performance of finite population cloud under varying request arrival rates. The effect of impatient user behaviour (balking and renegeing) and variable size request queue on server utilisation and throughput rates was then studied. The question of how to increase the request stage reliability of any cloud service system has also been discussed. Additionally, a load aware request scheduling approach was shown. Finally, the presented model has been compared with an existing model by means of the cost calculation and reliability measure algorithm proposed [8]. The main contributions of this work is as follows:

1. The variations of request arrival rates due to impatient users along with issues of wastage resources for a population bounded finite request queue cloud service system are studied by considering some established performance factors and losses in the service system.
2. A cost calculation and reliability measure scheme (CCRM Scheme) is proposed, which gives us operational cost and a measure of request stage reliability for our proposed model.
3. Simulations are designed for the above-mentioned model by taking into consideration the balking and renegeing threat imposed by impatient users. Experimental results

show that improved cost saving and high throughput rate can be achieved by applying our policy.

Section 2 summarises the existing related work on queuing systems with finite request buffers, impatient user behaviour and cost and reliability modelling of cloud computing systems. In Sect. 3, we describe the proposed population controlled multi-server queuing system with finite but variable size request queue along with behavioural considerations of rejected and impatient users. The mathematical equations that have been used to model the system and calculate various performance parameters have been listed in Subsection 4. In Sect. 5, the cost calculation and reliability measure (CCRM) algorithm has been described. The algorithm gives us an insight to the overall cost and request stage reliability measure of the constraint optimisation problems. A load aware request scheduling algorithm was also given that efficiently schedules the requests to the computing resources. Comparison of results over carefully designed test cases is shown in Sect. 6. The conclusion of entire work, along with the future scope, is given in Sect. 7.

2 Related Work

This section discusses relevant works in the field of cloud computing that form the basis of this work. Our work extensively uses queuing theory for its theoretical foundation. The equations used are taken from various sources including the work by Goswami et al. [9,10] and [3,8] Similar works that have used queuing theory to model cloud computing systems have been discussed in Subsection 2.1. Studies that utilise performance parameters to improve the QoS of cloud computing systems are discussed in Subsection 2.2 The works dealing with cost and reliability analysis for cloud computing systems have been discussed in Subsection 2.3.

2.1 Queuing Models for Cloud Computing

A number of works have been published regarding the performance analysis of miscellaneous systems considered under impatient user behaviour. A comprehensive review of related work has been studied. Probabilistic representation of patient and restless users in a telephone system was presented by Zhao et al. [11]. Critical parameters needed for performance analysis of a telephone system like the average waiting time spent by a client in the queue and probability of a customer to be treated as a patient one were also determined. However, the study proceeded with an assumption of infinite user population. Additionally, an assumption of a single provider was used, and hence, the question of load balancing in the system was left unexplored.

Fig. 1 Balking in request queue

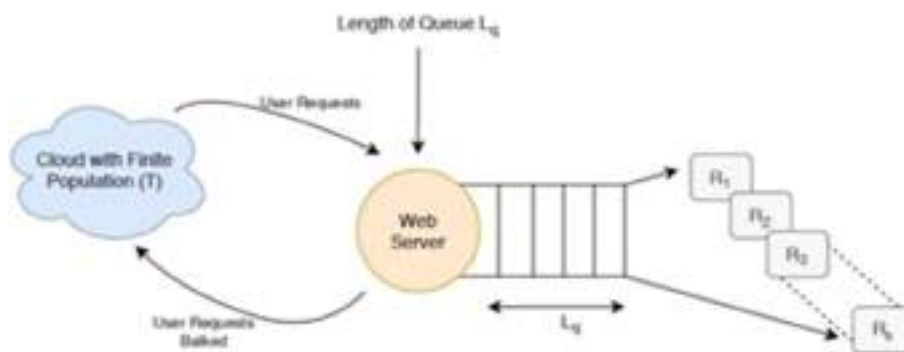
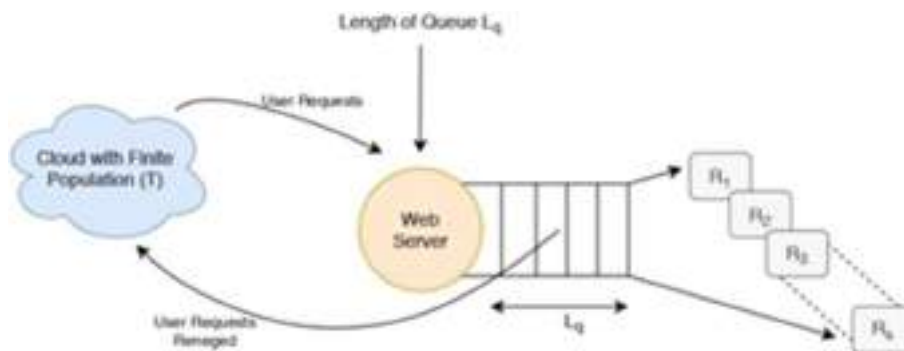


Fig. 2 Reneging in request queue



In the work presented by Mandelbaum et al., a linear relationship between the probability of a user reneging from the request queue and the response time in the queue was established for $M/M/n+G$ queuing systems [12]. The asymptotic ratio between probabilities of leaving was computed for the system under the assumption that the rate of arrival may sometime tends to zero. The work focused solely on the impatient customers who exhibited a reneging behaviour and does not explore the phenomenon of balking.

An analytical cost model for $M/G/1/N$ queuing system was proposed in by Doran et al. [13]. Doran, Lipsky and Thompson explored the inter-relation between size of queue, customer loss, and mean service time and the distribution of diverse service time. It focuses on the cost of customer losses versus cost of customer delays by varying size of buffer and speed of processor; however, the user population in their work has been assumed to be finite as well which is not representative of systems utilised by small and medium businesses (SMEs) and many private networks. In [14], Ghosh et al. described a rate control problem associated with a single server system. A problem of infinite horizon cost-minimisation was considered, while obtaining a definite optimal strategy for limiting diffusion control problem (also known as the Brownian control problem or BCP) includes a threshold-type optimal rejection process and a feedback-type optimal drift control. This solution was further used to develop an asymptotically optimal control policy. Service systems with finite user population are an important field of research in cloud resources foundation especially in privately

owned clouds used by small enterprises; however, it has only a little mention in previous works.

A notable work in the modelling of finite population in cloud computing models has been by Goswami et al [9,10]. They modelled the system as a $M/M/R/K/K$ model and presented an analytical formulation for the same. A number of parameters were used in this study to study the presented model. The work, however, did not incorporate the complexities of the system caused by presence of impatient users which often results in large costs to the cloud provider [11]. Additionally, the user population was constrained to be equal to the size of the buffer in the system.

Mehdi et al. assessed the impact of the proposed model on impatient jobs [15,16]. The algorithm proposed maps the jobs to inspiration by using minimum completion time (MCT) scheduling algorithm. However, this only proposed an algorithm to value the impact of the proposed model on impatient jobs. Detailed study in performance factors of the model was ignored.

2.2 Delay Information-Based Cloud Management System with Fixed Population (Finite) and Request Queues

Modelling of cloud computing systems has been a well-explored research area. In [6,17], cloud centres were modelled using $M/M/m/m$ queuing system, and its service performance was examined under the well-defined fault recovery environment. In their work, the submitted request

first arrived in the request queue of the Cloud Management System, if the request queue is partially empty otherwise the request queue was blocked which resulted in a failed service. Performance of cloud service was analysed by its service response time, and its probability density function for different states of the system was derived. The cost optimisation of the complete system was, however, not addressed in the system

Because of improving the QoS of Cloud Management System, in [18] delay information in terms of lengths of request queues etc. was floated to legitimate users of Cloud Systems. State information is communicated by instances so that all participants find the “World” consistent in appearance. VCM can share the inter cloud application placement information [19]. An efficient and exact predictive service latency mechanism was given by Lim et al. [20], which was used for cloud resource estimation.

2.3 Cost and Reliability Awareness in Cloud Management Systems

In cloud computing, cost optimisation is an essential research area which is less explored and needs to be addressed [21,22]. Few works like Selvarani et al. [23] proposed a cost-effective job grouping algorithm through which group of tasks work dynamically assigned to the resources provided. This scheduling algorithm simultaneously gives both, the cost of resources and the computing performance obtained. Sorting of user tasks was done on the basis of individual cloud resource processing capability, which significantly improved the computation/communication ratio. The work done by Selvarani et al. focussed on cost reduction in cloud networks but ignored the phenomenon of impatient users and hence reneging and balking behaviour of users was ignored.

A cost-aware market theory-based resource scheduling paradigm was proposed by [24,25] for computing scheduled resources in accordance with current user requirements. The work focussed on presenting a dynamic load balancing algorithm and the cost modelling of the system and the phenomenon of impatient users and their effect on the cloud computing system were not explored. In the work presented by hadji et al. [26], an algorithm was proposed for resource allocation in clouds which is based on maximum flow and minimum cost module. Hadgi et al. worked towards the optimal dynamic positioning of the effective resources. Hwang et al. proposed a two-stage policy for service handlers to optimise their overall cost of service provisioning [27]. Firstly, the minimum amount of reserved resources for long-term use were computed through an analytical formula, and secondly, Kalman filters were used to obtain resources demanded. In light of the literature review conducted by the authors, the cost optimisation for a cloud computing system operating on a finite buffer size and user population coupled with the

reliability analysis of the system has not been conducted till date and needs to be explored further.

3 Structure of the Proposed Model

In this section, the proposed model has been discussed in parts. The model is a stochastic model with the state transition probabilities given in Subsection 3.1 which describes the Markovian birth-death process employed. The behaviour of impatient users has been discussed in Subsection 3.2. The various losses in the system have been described in the following subsections. The balking probability has been described in Subsection 3.3, system blocking probability in Subsection 3.4, and the reneging probability has been described in the Subsection 3.5. The model description is shown in Fig. 3. As depicted in Fig 3, requests from users enter the request queue through a web service which gives information of the expected response time to the end users. Some impatient users may leave the system at this point. These request drops are counted as balking losses. The request scheduler, then categorises and transfers the waiting requests to the corresponding data and computing resources. The dynamic system controls vary the size and count of the request queue along with data/computing resources in accordance to the varying load conditions. The various variables and symbols used in the model have been described in Table 1 as well as the required places of use.

3.1 A Finite Population Multi-Server Queuing System with Variable Size Request Queue

The proposed model, is a $M/M/S/K/T$ Markov queue intended to study the behaviour of the request phase of cloud computing systems which have a finite source of users. User requests are assumed to arrive at a mean rate of λ following a Poisson distribution, while inter-service times follow an exponential distribution with a mean service rate of μ [28]. The queuing system follows the First-Come-First-Serve (FCFS) queue discipline.

The expressions for request arrival rate and service rate are given as in Equation 1 and equation 2 [9,10]. Where n is the number of users in the queue, K is the maximum length of the request queue, and S is the maximum number of servers provisioned to the system. The probability P_n is the steady-state probability of having n users in the queue and is modelled as a Markov birth and death process. This steady-state probability can be calculated as Equation 3 which can be further simplified as Equation 4. In the particular case when $K = S$, that is a case where the requests are rejected right away without any waiting time, then we obtain the relation in Equation 5. P_n represents the steady-state probability of having exactly n users in the system. The sum of probabilities has to be unity

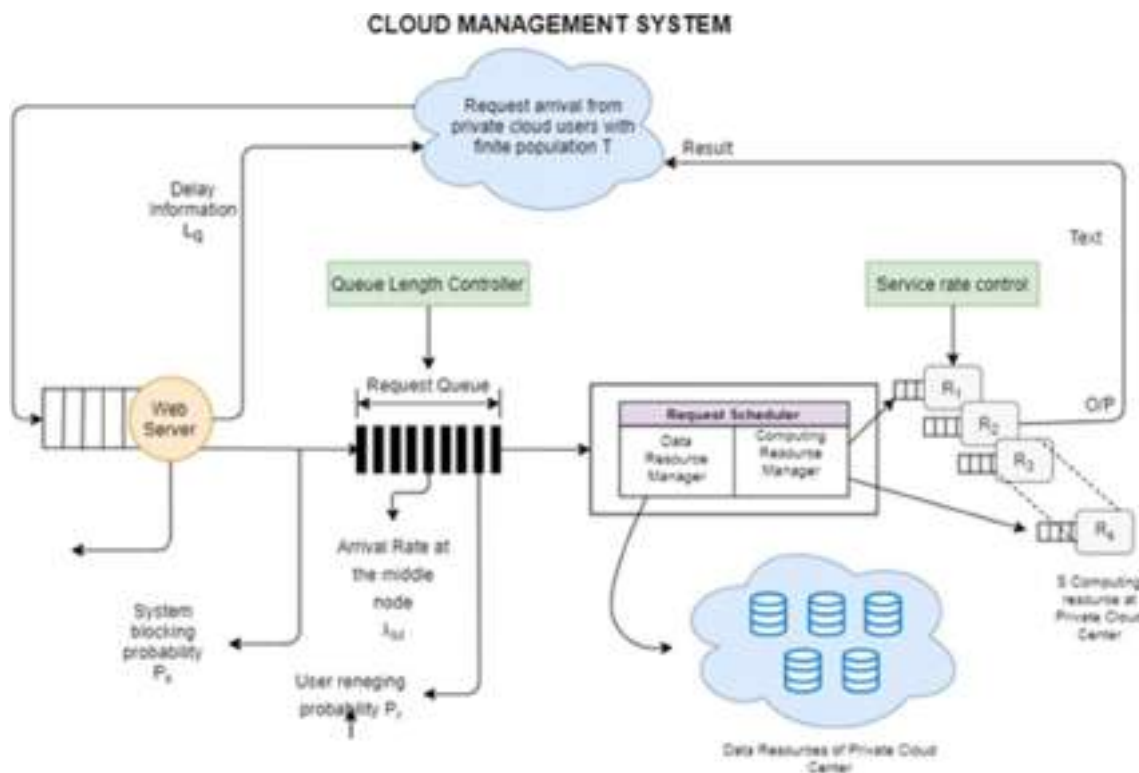


Fig. 3 Cloud service model with finite population and buffer with provisions for impatient user environment

(axiomatically). Hence, P_n in the request queue satisfies the general probability equation $\sum_{n=0}^K P_n = 1$. The equations can be solved to arrive at an expression of P_0 which represents the steady-state probability of having no users in the queue and hence having no waiting time involved. The above-mentioned equations upon substitution can be transformed as 6 and the expression of P_0 can be hence derived as 7. In steady state, system utilisation is equal to $\rho = \lambda / (s\mu)$, when $\lambda \leq S\mu$, but when $\lambda > S\mu$ the request queue is eventually filled and leads to system blocking, reducing the request stage reliability of the system. However, when then the queue is filled the system demonstrates forced balking (or blocking) and all the requests beyond K are dropped.

3.2 A Finite and Variable Size Request Queue with Impatient Users

Impatient user is defined by their behaviour of balking and reneging. Balking occurs when the user notices the length of the queue (number of users already in the queue) and chooses not to enter the queue. Reneging on the other hand occurs when the user after entering the queue experiences latency in response and ends up dropping the request before being services. The length of request queue, L_q and the response time of the queue, W_q , are the main factors responsible for the user balking and reneging behaviours. As described in Figs. 4

and 5, system blocking loss λ_K can be reduced by increasing the request queue size, K ; however, it results in an increased balking and reneging rates which consequently degrades the user experience. Similarly, decreasing the request queue size increases the system blocking loss, but it reduces the balking and reneging cost.

It is the responsibility of the cloud provider to manage the provisioning of resources and keep a check over the losses in the system. The primary function of any Cloud Management System (CMS) includes controlling the length of the request queue (choosing K) with managing computing servers (choosing S). Figure 3 shows the proposed cloud service model for a finite population, which has a variable size request queue with S computing servers.

3.3 Overall Balking Probability of the System

The expected queuing length of the request queue is to be predicted and propagated to each and every users of the cloud [29–31]. The length of the request queue L_q can be obtained as in Equation 8 which can be simplified into Equation 9. There can be few user requests that leave the system due to excessive queue length after waiting for some time in the queue. These are accounted for as reneging losses. The CMS keeps a record of balking and reneging rates. These rates are the potential customers that could have been served and

Fig. 4 Effect of increasing the size of request queue

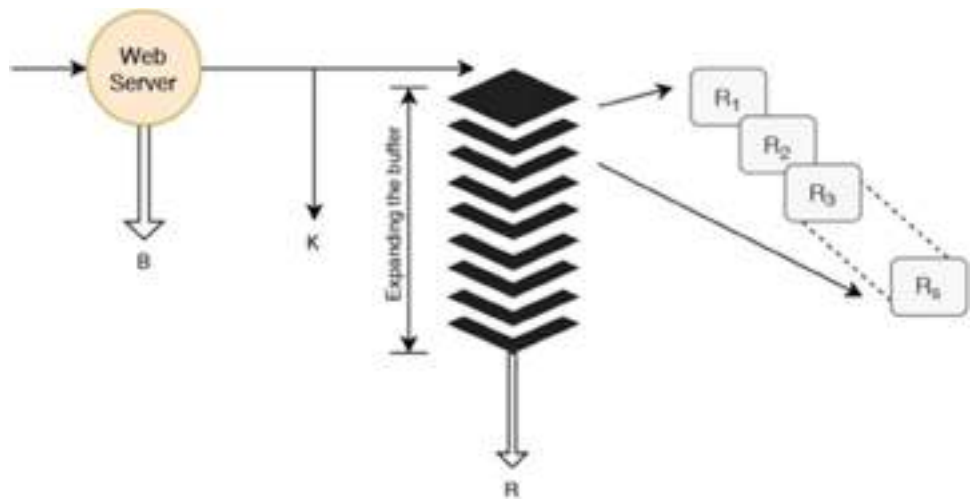
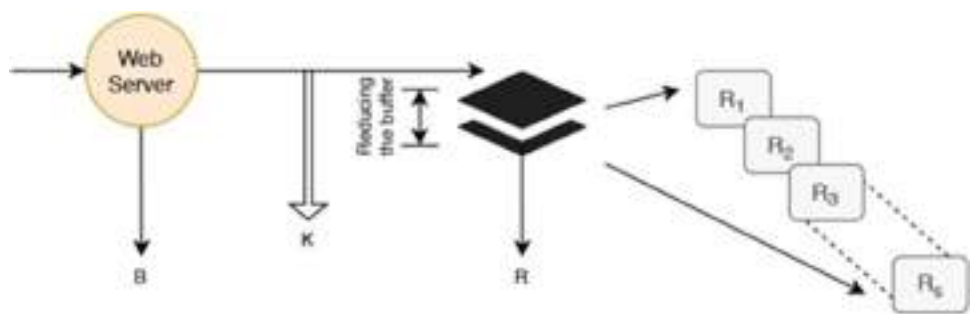


Fig. 5 Effect of decreasing the size of the request queue



hence would have added to the revenue of the firm. Hence, these losses reduce the profit of the system and contribute to the economic cost of the cloud providing firm. The notations that are used in this paper pertaining to the losses are also mentioned in Table 1.

We use the balking and the reneging factor to define impatient users as discussed in later subsections. We define balking factor Ω_b as per Equation 10. The Dividing average balking rate λ_b by Length of the request queue L_q and initial arrival rate, possible balking factor can be identified. The balking factor is a measure of the behavioural balking of the users and is obtained from the records of the CMS regarding the data of the requests retracted in the system. Setting $\Omega_b = 0$ would give us the behaviour of the queuing system when the users do not show any balking behaviour. The balking probability is obtained by multiplying the length of the queue with the potential balking factor as in Equation 11. With arrival rate λ , the average balking rate may be obtained in Equation 12.

3.4 Overall System Blocking Probability

The system blocking probability measures the proportion of request that are forced to leave the system due to lack of space in the request queue. In this work, we distinguish these dropped requests from the balking losses owing to the fact that these requests would have been dropped in the absence of

impatient users as well. At this point in the system, the arrival rate of the request is $\lambda - \lambda_b$. The size of the request queue is K , the blocking probability is obtained in Equation 13. The average system blocking rate λ_K can hence be obtained as Equation 14. In accordance with the request balking rate and the system blocking rate, the arrival of the request, at the middle node of the request queue λ_M , can be calculated, referring to Equation 15.

3.5 Overall Reneging Probability of the System

Based of λ_M , the overall system performances at the MN queue is denoted by P_n^* and the mean length of the queue L_q^* is obtained by substituting λ by λ_M in Equations 1-9. The final expression of L_q^* can be referred to in Equation 16. W_q^* (Predicted waiting time) for the request queue is calculated by using Little's law [32]. According to the law, the average arrival rate multiplied by mean response time equals the number of requests waiting to serviced, it has been written as Equation 17. Little's law can be used to calculate the waiting times in the request queue as per Equations 18, 19 and 20. The average reneging rate λ_r when divided by the average waiting time and the arrival the at the middle of the request queue gives the reneging factor. Similar to the balking factor Ω_b , the reneging factor Ω_r is also obtained from the logs of the CMS regarding the retraction of requests in the system.

The renegeing factor Ω_r is defined as per Equation 21. The average renegeing probability of the system P_r is obtained by multiplying the average time and the potential renegeing factor as shown in Equation 22. The expected rate of renegeing is calculated by multiplying the arrival rate of requests in the queue with the probability of renegeing as in Equation 23. For a system having a finite waiting buffer and impatient users, the final throughput rate λ_r can be calculated by subtracting the balking, renegeing and system blocking rates from the request arrival rate as in Equation 24. The final system utilisation is obtained as per Equation 25.

4 Mathematical Modelling

The mathematical modelling of the system and the equations involved in the study have been discussed in this section. The various symbols and their respective descriptions can be referred to in Table 1. The meaning of the symbols has also been described at the first instance that they have been used in the preceding section. The equations pertaining to the modelling of the request queue with S servers and a finite buffer of size K with a user population size T have been listed in Subsection 4.1. The equations related to the modelling of impatient users along with the equations used to calculate the renegeing, balking and system blocking probability are listed in Subsection 4.2.

4.1 Modelling of the Finite Population Queue

The arrival rate and the service rate of the system queue can be derived as per the following Equations [9]

$$\lambda_n = \begin{cases} (T - n)\lambda, & 0 \leq n \leq K - 1 \\ 0, & K \leq n \end{cases} \tag{1}$$

$$\mu_n = \begin{cases} n\mu, & 1 \leq n \leq S - 1 \\ S\mu, & S \leq n \leq K \end{cases} \tag{2}$$

$$P_n = \begin{cases} P_0 \prod_{i=0}^n \frac{\lambda(T-i)}{(i+1)\mu}, & 0 \leq n \leq S - 1 \\ P_0 \prod_{i=0}^{S-1} \frac{\lambda(T-i)}{(i+1)\mu} \prod_{i=S}^{n-1} \frac{\lambda(T-i)}{S\mu}, & S \leq n \leq K \end{cases} \tag{3}$$

The above expression for steady-state probability can be mathematically represented as:

$$P_n = \begin{cases} \frac{\lambda^n}{\mu^n} \binom{T}{n} P_0, & 1 \leq n \leq S - 1 \\ \frac{n!}{S!S^{n-S}} \frac{\lambda^n}{\mu^n} \binom{T}{n} P_0, & S \leq n \leq K \end{cases} \tag{4}$$

$$P_n = \frac{\binom{T}{n} \left(\frac{\lambda^n}{\mu^n}\right)}{\sum_{i=1}^K \binom{T}{i} P \frac{\lambda^i}{\mu^i}} \tag{5}$$

$$\sum_{n=0}^K P_n = P_0 + \sum_{n=0}^{S-1} P_n + \sum_{n=S}^K P_n \tag{6}$$

$$P_0 = \left[\sum_{n=0}^{S-1} \frac{\lambda^n}{\mu^n} \binom{T}{n} + \sum_{n=S}^K \frac{n!}{S!S^{n-S}} \frac{\lambda^n}{\mu^n} \binom{T}{n} \right]^{-1} \tag{7}$$

4.2 Modelling the Phenomenon of Impatient Users in Terms of Balking and Renegeing

The mean length of the queue in steady state is given by the following equations:

$$L_q = \sum_{n=S+1}^K (n - S)P_n = \sum_{n=S+1}^K \frac{(n - S)n!}{S!S^{n-S}} \frac{\lambda^n}{\mu^n} \binom{T}{n} \tag{8}$$

$$L_q = \frac{P_0 \times \lambda^S}{S!} \times \sum_{n=S+1}^K (n - S) \times \binom{T}{n} \times \left(\frac{\rho}{S}\right)^{n-S} \times n! \tag{9}$$

The balking factor has been defined as:

$$\Omega_b = \frac{\lambda_b}{L_q \lambda} \tag{10}$$

This factor is utilised to calculate the balking probability of the system. The balking probability is calculated as:

$$P_b = L_q \times \Omega_b \tag{11}$$

$$\lambda P_b = \lambda_b \tag{12}$$

The steady-state probability of encountering an overflow in the request queue is given as:

$$P_k = P_0 \times \frac{K!}{S! \times S^{K-S}} \times \left(\frac{\lambda - \lambda_b}{\mu}\right)^K \times \binom{T}{n} \tag{13}$$

The steady-state rate of buffer overflow (overflow in the request queue) is given as:

$$\lambda_K = (\lambda - \lambda_b) P_K \tag{14}$$

The final rate of request arrival that enter the queue is given as:

$$\lambda_M = \lambda - \lambda_b - \lambda_K \tag{15}$$

The steady-state length of the queue after accounting for the losses is given as:

$$L_q^* = \sum_{n=S+1}^K \frac{(n - S) \times n!}{S!S^{n-S}} \times \left(\frac{\lambda_M^n}{\mu^n}\right) \times \binom{T}{n} \times P_0^* \tag{16}$$

Table 1 Key terms and notations

Description	Symbol	Description	Symbol
Population of users which are allowed to access the system	T	Number of servers provisioned in the system	S
Maximum length of request queue	K	Mean arrival rate of requests	λ
Mean service rate	μ	Length of request queue in service rate	L_q
Balking factor	Ω_b	Reneging factor	Ω_r
Steady-state probability of having n users in queue	P_n	Balking probability	P_b
Reneging probability	P_r	Request allocation probability	P_i
Uniform load allocation probability	P_{ul}	K size system blocking probability	$P_n n=K$
Average balking rate	λ_b	Average reneging rate	λ_r
K size system blocking rate	λ_k	Arrival rate at Middle Node (MN)	λ_M
System throughput rate	λ_f	Steady state of having N users in M N queue	P_n^*
Length of MN queue in steady state	L_q^*	Predicted waiting time	W_q^*

Using little’s law [32] the waiting time in the queue can be calculated as:

$$L = \lambda W \tag{17}$$

$$W_q^* = \frac{L_q^*}{\lambda_M} \tag{18}$$

The length of queue

$$L_s^* = L_q^* + \rho^* \tag{19}$$

$$W_s = \frac{L_s^*}{\lambda_M} \tag{20}$$

The reneging factor similar to the balking factor is defined as follows:

$$\Omega_r = \frac{\lambda_r}{W_q^* \lambda_M} \tag{21}$$

The reneging probability and the reneging rate are calculated on the same lines as the balking probability and balking rate, respectively:

$$P_r = W_q^* \times \Omega_r \tag{22}$$

$$\lambda_M \times P_r = \lambda_r \tag{23}$$

The final throughput rate is hence calculated as:

$$\lambda_F = \lambda - \lambda_b - \lambda_k - \lambda_r \tag{24}$$

$$\rho_F = \frac{\lambda_M - \lambda_r}{S\mu} \tag{25}$$

5 Outline of the Cost Calculation and Reliability Measurement Scheme (CCRM Scheme)

The CCRM scheme has been proposed to minimise the cost of maintaining the cloud computing system and to monitor the reliability of the system which ensures an adequate QoS to avoid SLA violations. The cost model employed in the scheme has been discussed in Subsection 5.1. The algorithm for cost calculation and reliability measurement has been discussed in 5.2. Additionally, a request allocation policy to maintain uniform load for the server resources has been discussed in 5.3. Since the CEA policy proposed by Chiang et al. has been used to compare the performance of the model, a brief introduction to the work done by Chiang et al. has been given in Subsection 5.4 and further details for the same can be accessed in [3,8]

5.1 The Cost Study

The behaviour of the presented model can be compared with other models in the same domain by employing a cost model. The cost model employed includes the effect of losses incurred due to system blocking, reneging and balking as well as the cost of the infrastructure employed to establish the cloud system. The cost under consideration in this work is the economic cost of the system which includes both implicit and explicit costs involved [33]. The various components of costs considered in the system are listed in Table 2, and the equation of the cost model employed in this work is given in Equation 26.

The virtual machines (VMs) are active when service requests are accepted and submitted into the variable size request queue. However, due to balking and reneging, some requests will untimely leave the system making some extra

Table 2 Coefficients of cost term

Infrastructure usage cost	
Cost incurred due to varying capacity request queue per unit of placeholder for request	C_1
Cost incurred by power consumption of resources per unit of service rate per unit of time	C_2
Cost incurred in maintaining appropriate Server Count in the system per unit of time	C_3
Losses in the system	
Costs incurred by intolerant users depicted balking	C_4
Costs incurred by intolerant users depicted renegeing	C_5
System overflow cost due to exhausted waiting queue	C_6
Costs due to unnecessary engaging of VMs due to timeout errors	C_7
Overall system performance cost	
Penalty of system overflow	C_8
Cost of holding jobs in the system	C_9
Cost incurred by jobs waiting in the system	C_{10}

VMs active. Therefore, the cost of unnecessarily activating VMs without releasing them is also to be considered. Operational costs (infrastructure cost, system losses and system performance cost) with balking and renegeing probabilities are all dependent on service rate, variable size request queue length, request arrival rate and the number of servers provisioned to the system. Therefore, a cost function is designed with variable size request queue and service rates as its decision parameters. It should be noted that the cost function varies greatly from firm to firm. In this work however, we use a fixed cost function. The units of the coefficients need to be chosen in such a way that the equation is always dimensionally correct. The cost function in this work has also been chosen in such a way that the cost is dimensionless and unit less.

$$\begin{aligned}
 cost &= f(\mu, \delta, \lambda, S) \\
 cost &= \delta C_1 + \left(\frac{\mu}{\rho_F}\right) C_2 + \left(\frac{S}{\rho_F}\right) C_3 + \lambda_r C_4 \\
 &\quad + \lambda_b C_5 + \lambda_K C_6 + \lambda_r C_7 + \rho_K C_8 + L_s C_9 + W_s C_{10}
 \end{aligned}
 \tag{26}$$

Request stage reliability of the proposed queuing system is dependent upon overflow and timeout errors. These errors are directly proportional to system blocking probability (P_k) and system renegeing probability (P_r). Therefore, we have devised a reliability index which will give a measure of overall request stage reliability.

$$R = -[\log_{10}(P_K) + \log_{10}(P_r)] \tag{27}$$

Since $0 \leq P_K \leq 1$ and $0 \leq P_r \leq 1$, a negative sign has been appended to the equation to keep the reliability index positive. According to this construction, the greater the value

of the index the more reliable and error free the system can be considered.

5.2 Cost Calculation and Reliability Measure Scheme

We propose the following cost calculation and reliability measure algorithm (CCRM scheme). The scheme is proposed for comparing the performance of the proposed algorithm with other models

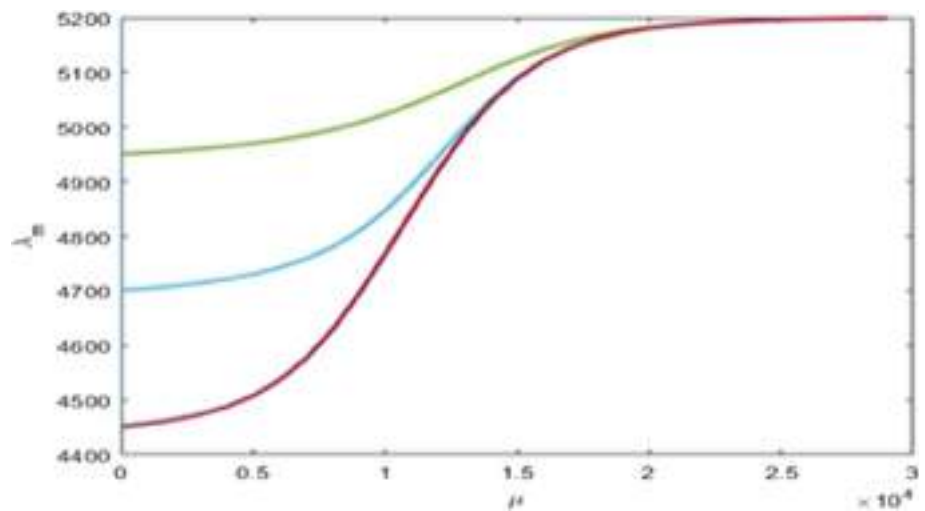
CCRM algorithm
Input
-The mean request arrival rate λ
-The potential balking and renegeing factors [Ω_b, Ω_r]
-The cost matrix [$C_1, C_2, C_3, C_4, C_5, C_6, C_7, C_8, C_9, C_{10}$]
-The total number of computing resources S
-The upper limit of the service rate and the buffer size in the server farm μ and δ
Output
- $f(\mu, \delta, \lambda, S)$

5.3 Request Allocation Strategy

Below is the algorithm for request allocation for population bounded cloud. This algorithm allocates K requests to the S number of servers. It is assumed that all servers are homogeneous with each one having its own local queue and service is delivered in a steady state

$$P_{UL} = P_0 + P_{1S} + P_{2S} + P_{3S} + \dots + P_{wS} \tag{28}$$

Fig. 6 Request arrival rate at the MN queue for values of μ and the given δ values. (Green - $\delta = T/2$, Blue - $\delta = T/4$, Red - $\delta = T/8$)



Algorithm

start

1. For $i = 1; i = q; i = i + 1$
- (a) Assign $\mu_i =$ The current service rate.
2. For $j = 1; j = t; j = j + 1$
- (a) Assign $\delta_j =$ The current buffer size.
3. Calculate L_q and λ_b using equations (7)-(11)
4. Calculate P_q and λ_q using equation (3) and (12)-(14)
5. Assign $\lambda_M = \lambda - \lambda_b - \lambda_q$
6. Assign The arrival rate at the middle of the request queue as λ_M
7. Compute $L_q^*, W_q^*, L_s^*, W_s^*$ and λ_r using equation (15)-(23)
8. $\lambda_F = \lambda_M - \lambda_r$
9. Assign The expected final throughput rate as λ_F
10. Compute ρ_F using equations (24)-(25)
11. Compute the cost function by bringing out all the cost parameters into the developed cost

End

Load aware request allocation algorithm

Start

For $i=0; i \leq K; i++$

For $j = 0; j \leq S - 1; j++$

 If $i == j \% S$

 Allocate request[i] to server[j]

 Break

End

Where w is a whole number and $wS \leq K$ When buffer size K is an integral multiple no. of servers S , users would be equally distributed in the local queue of each server. Thus, the uniform load allocation probability P_{UL} is given as

$$P_{UL} = P_0 + \sum_{n=1}^w P_0 \frac{(vS)!}{S!S^{vS-S}} \frac{\lambda^{vS}}{\mu^{vS}} \binom{T}{vS}$$

$$P_{UL} = P_0 \left(1 + \frac{T!S^S}{S!} \sum_{u=1}^v \frac{\rho^{uS}}{(T-uS)!} \right) \tag{29}$$

5.4 Cost-Effective Policy in an Abandoned System (CEA) Policy-Based Queuing System

The CEA policy is a queuing theory-based policy which deals with impatient users in a system with a finite buffer size. We have used the CEA policy proposed by Chiang et al. [3,8] to

compare the performance of the CCRM policy as discussed in this paper. In the work by Chiang et al., the presence of impatient users in the system has been modelled using balking and reneging and are modelled using the parameters Ω_b and Ω_r which is similar to the work done in this paper. The CEA policy, however, makes an assumption of a infinite user population contrary to this work which is modelled for a finite user population. In addition, the work by Chiang et al. does not attempt to quantify the reliability of the system using their proposed model. The detailed mathematical modelling of the CEA policy has been discussed in detail in the papers [3,8].

6 Result and Discussion

The model proposed in this work been analysed in this section. The performance of the model with respect to the change in various input variables has been observed in terms of cost, throughput rate and system losses and reported in Subsection 6.1. The performance of the load balancing strategy has also been discussed in the same subsection. Various parameters for the calculations have been supplied. In Subsection 6.2, the model has been compared to the CEA policy presented by Chiang et al. [3,8]. The specific work has been selected since the authors found the work appropriate for

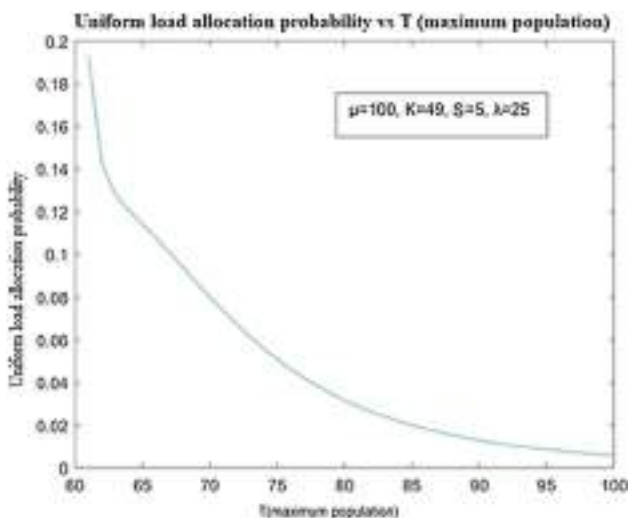


Fig. 7 Variation in the Uniform load allocation probability on changing the maximum population

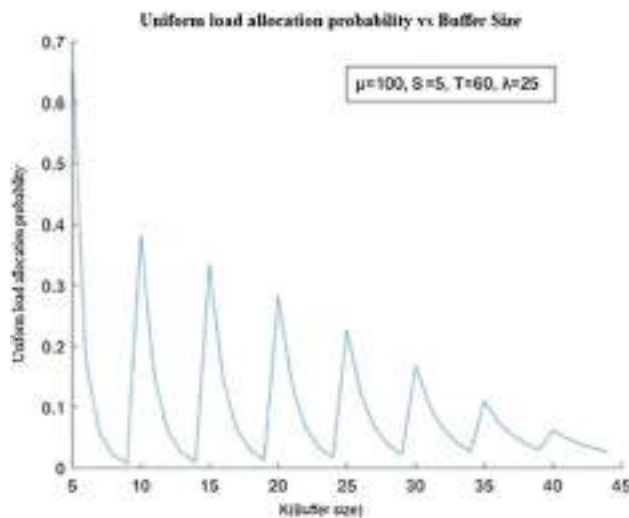


Fig. 9 Variation in the Uniform load allocation probability on changing the buffer size

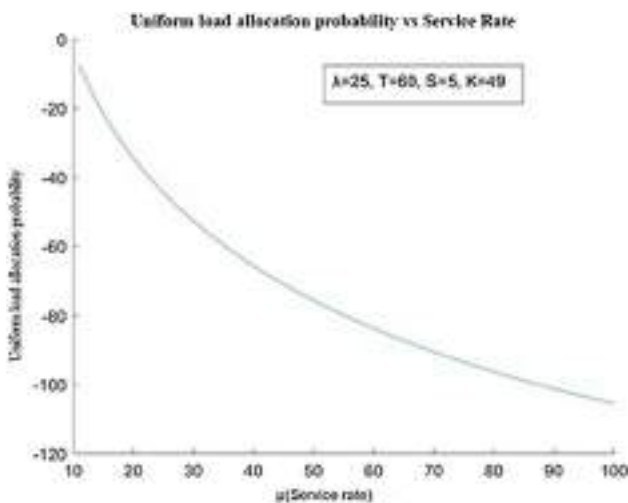


Fig. 8 Variation in the Uniform load allocation probability on changing the service rate

comparison. The CEA policy also deals with impatient users and employs a cost model for comparing their own work.

6.1 System Behaviour

The behaviour of the developed model was observed by varying the input parameters involved. All computations were performed on MATLAB. In Fig. 6, the effect of the service rate of the servers, μ and the maximum length of the queue, δ have been varied for $\lambda = 5200$ request/min, $\Omega_r = \Omega_b = 0.006$, $S = 5$ and total population $T = 150$. Even though the value of the total population of the system used here is meagre compared to the real-world applications of cloud computing systems, the authors lacked the computational infrastructure to calculate the results for higher values

of T ; however, the authors are convinced that the results are scalable and should offer an insight into the modelling of cloud computing systems serving a finite population of users. The value of δ was kept as $T/2, T/4, T/8$. The graph shows that the difference in δ results in a different initial point for the graph, i.e. there is difference in the throughput rate of at lower values of μ ; however, the difference diminishes as the service rate increases. It is within expectations that all the requests pass through when the service rate is extremely high. However, the effect of increasing δ is also within expectations as this allows the system to hold a larger number of requests.

The behaviour of the Uniform load allocation policy was also studied under various values of the user population T in Fig. 7. The parameters for this calculation have been given as $\mu = 100$ requests per minute per server, Number of servers $S = 5$, $K = 9$ and the arrival rate of the requests $\lambda = 25$. Here, we see that the increase in the population results in a steady decrease in the probability of having a balanced load. This is reasonable as the load on the system becomes less manageable as the population of the system increases.

In Fig. 8, we see the variation in the Resource allocation probability on varying the service rate while $T = 60$, $S = 5$, $K = 49$ and $\lambda = 25$. Here, we see that on increasing the service rate the uniform resource allocation probability decreases gradually and becomes constant after increasing the population which is for the same reason as the behaviour of Fig. 7. On the other hand, the effect of the service rate on the system is demonstrated in Fig. 9 where it was noticed that the behaviour resembles a saw tooth pattern. We observed that on increasing the buffer size the resource allocation probability falls from the peak value to lowest value and then after again increasing the buffer size it increases to next high-

Fig. 10 Reneging probability under various μ and δ values

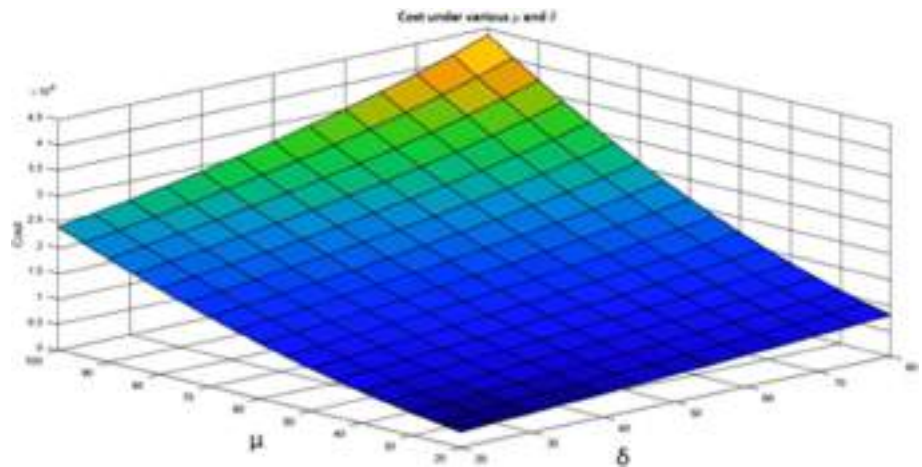
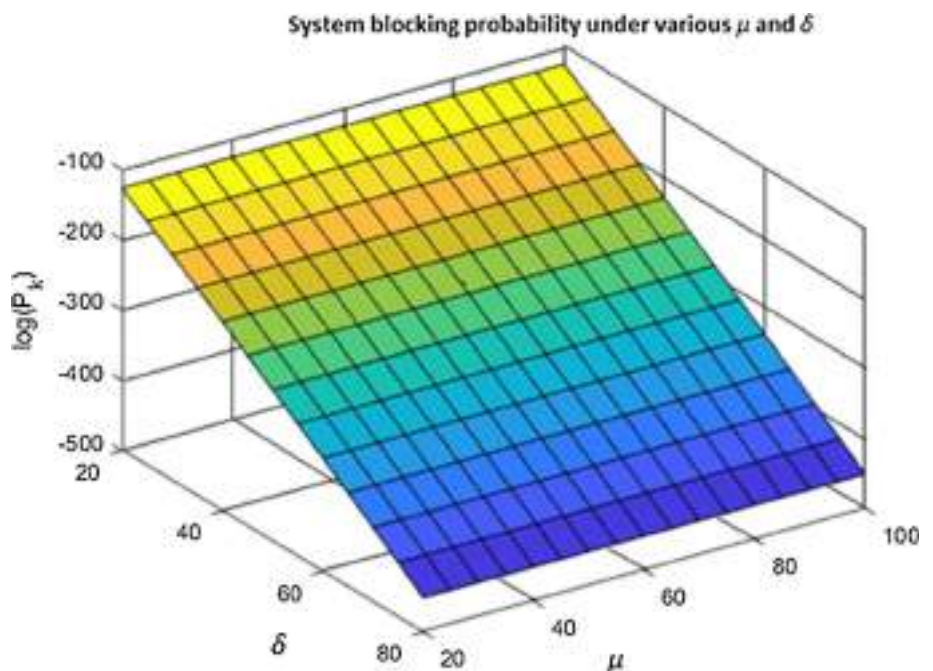


Fig. 11 Cost distribution under various μ and δ values



est level and so on and the distance between the high and low peaks reduces as K is increased. This is mathematically explained by the term w being an integer in equation (29). Hence, the peaks are observed when K can be written as an integer multiple of S . The values for Figs. 7 and 9 are taken at $T = 60, S = 5, \mu = 100$ and $\lambda = 25$.

The cost and losses of the system were also studied as per the models discussed in the previous sections. The calculations have been done at $\lambda = 100, \Omega_b = \Omega_r = 0.006$ and the number of servers provisioned for the system $S = 5$. The cost matrix assumed for this work is $[C_1, C_2, C_3, C_4, C_5, C_6, C_7, C_8, C_9, C_{10}] = [20, 30, 200, 60, 60, 60, 50, 10, 5, 5]$ in experiments. $S = 5$. The cost increases more with increased service rate, while variation in buffer size will not have much effect on our cost function. For the same parameters, the system blocking probability P_K and reneging probability P_r are

plotted in Figs. 10 and 12, respectively. It must be noted that since system blocking probability $0 \leq P_k \leq 1$. The value of $\log_{10}(P_K)$ is negative which is reflected in the plots. It is observable that the reneging probability increases as δ increases. This has been observed by Dai et al. as well [7]. On the other hand, the system blocking probability decreases as the value of δ increases.

The server utilisation in a system is reflected by the value of P_0 . This is due the physical significance of P_0 that in steady state it is the probability at any given time of having the request queue empty, and hence, the servers are un-utilised. The value of P_0 is plotted in Fig. 13. It is clear that the server utilisation increases upon increasing request queue length and increasing service rate. It is clear from the results that higher service rates result in lower server utilisation but smaller queue length.

Fig. 12 System blocking probability under various μ and δ values

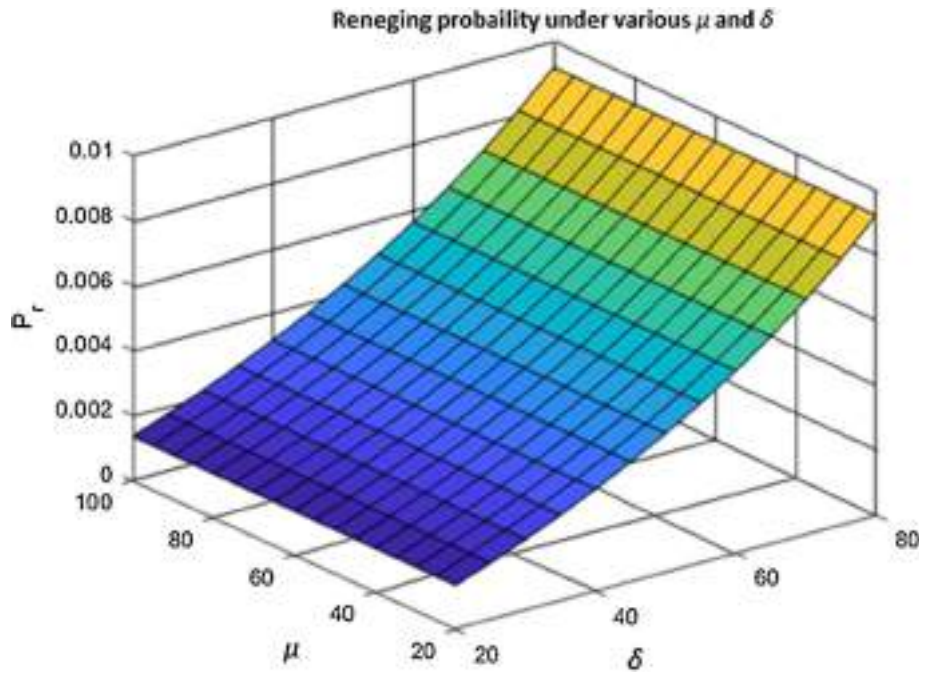


Fig. 13 P_0 under various μ and δ values

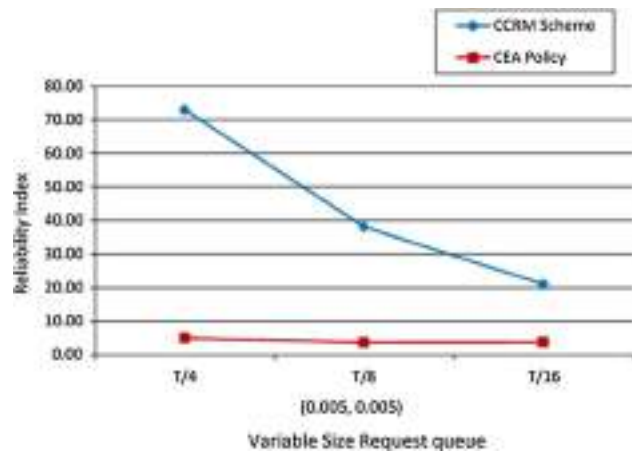
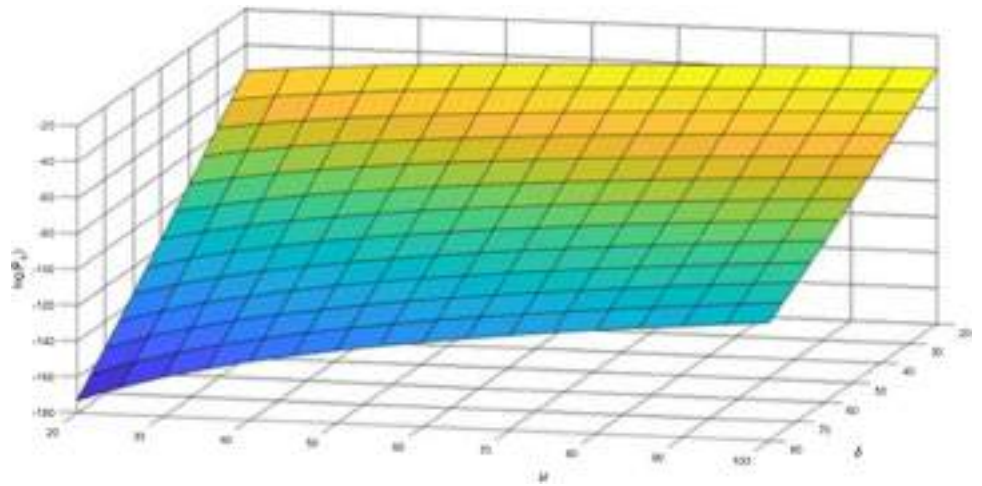


Fig. 14 Comparison of the reliability index in CEA Scheme vs CCRM Scheme

6.2 Comparison of Results

Although to the best of our knowledge this finite population queuing model is unique its kind, some similar approaches have been presented in [34,35]. The work presented by Chiang et al. serves as a great platform for comparison of results. That is because they adopt a $M/M/R/K$ queuing model and include impatient users in their analysis [3,8]. Hence, their work presents a suitable basis for comparison.

Almost every user reacts differently to degrees of latency, as an individual feeling, tolerance and satisfaction, etc., are the potential factors which may directly or indirectly influence user decision. The comparison has been done for cases which are different sets of values for Ω_b and Ω_r . These

Fig. 15 Comparison of the economic cost in CEA Scheme vs CCRM Scheme

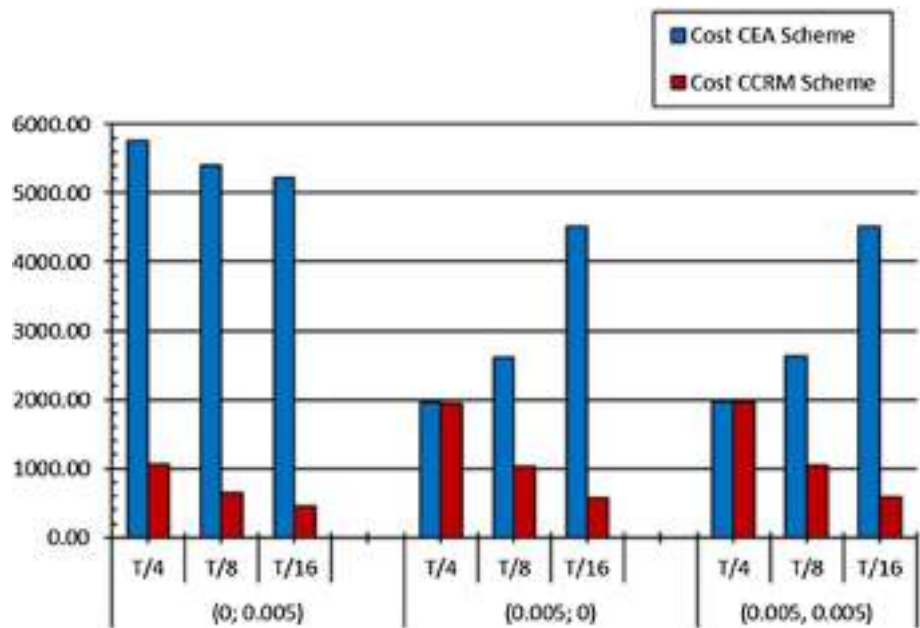
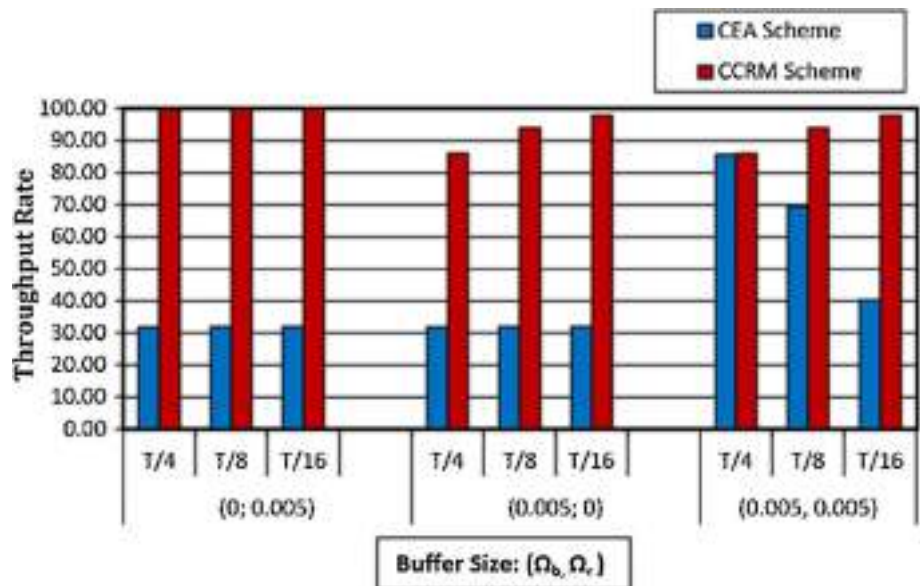


Fig. 16 Comparison of the throughput rate in CEA Scheme vs CCRM Scheme



comparisons have been done at $\lambda = 100, \mu = 8, S = 4$ and $T = 128$

- $(\Omega_b, \Omega_r) = (0; 0.005)$, system is without balking but users are reneging.
- $(\Omega_b, \Omega_r) = (0.005; 0)$, system is without reneging but balking exists.
- $(\Omega_b, \Omega_r) = (0.005; 0.005)$, system possesses both threats of users doing balking and reneging.

Reliability index of both considered policies is calculated for variable sizes of request queue δ on the X-axis, and results are shown in Fig. 14. The proposed CCRM Policy clearly

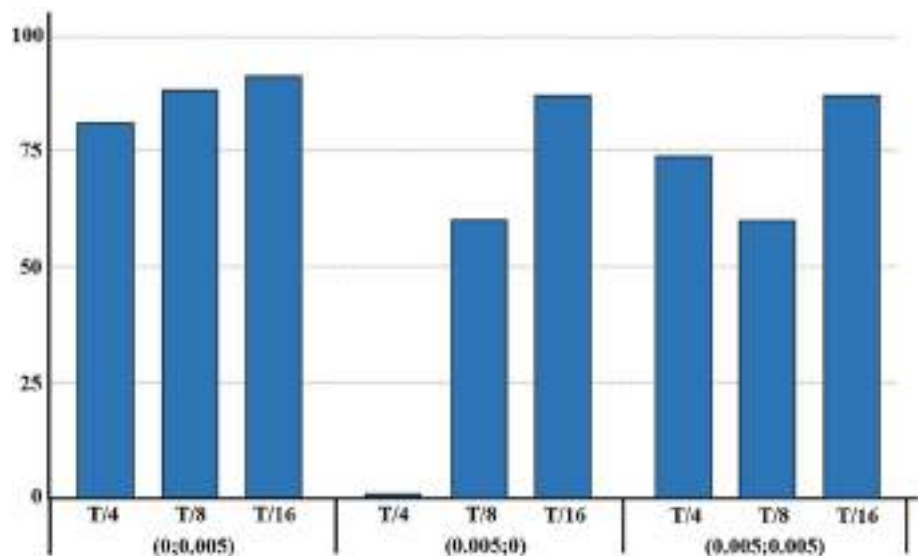
Table 3 Throughput rate and cost for CCRM and CEA scheme for $T = 150, R = 4, K = T/16, \lambda = 100, \mu = 0.8$

(U_b, U_r)	CCRM scheme		CEA scheme	
	λ_r	Cost	λ_r	Cost
(0, 0.005)	99.980	$4.51E + 02$	31.963	$5.22E + 03$
(0.005, 0)	98.001	$5.75E + 02$	40.292	$4.51E + 03$
(0.005, 0.005)	93.941	$5.77E + 02$	40.282	$4.51E + 03$

shows a higher value of reliability index which decreases in both the schemes as the value of δ decreases.

While comparing costs of both models under variable size request queue length for a total population $T = 150$,

Fig. 17 Cost improvement



the results consistently show that the CCRM scheme has a lower economic cost as compared to the CEA model. The cost comparison is presented in Fig. 15. The costs show a decreasing trend with decrease in the request queue length for CCRM scheme, while the trend varies for the CEA scheme. The comparisons of throughput rates are shown in Fig. 16; demonstrate high levels of throughput rate for our system. The exact values for the throughput for the two schemes can be referred to in Table 3.

The cost improvement for the various cases is plotted in Fig. 17. The relative improvement rate varies highly in terms of cost reduction. The cost improvement is due to a number of reasons. The first and foremost reason is the fact the model presented is designed to serve a finite population of users, where the CEA scheme is designed with an infinite user population. The second reason is the higher throughput rate of the model as observed in Fig. 16. The cost function also presents major consequences since in economics and the management of any firm the determination of cost function is a complicated ordeal as discussed by a number of works [36,37].

7 Conclusion and Scope for Future Work

A large number of organisations across the world are using private and community clouds. These clouds often have strict population constraints and security policy. These clouds serve a heterogeneous user base and face the challenges of having impatient users as well. In this study, a model for analysing such clouds has been presented. The comparison of the presented work with another work in the same domain was also presented along with the improvement obtained in terms of the economic cost of the system. As for future work,

we plan to develop a highly controlled policy for private clouds which can take traffic load control mechanism and larger population sample for its purpose.

Funding Not applicable

Availability of Data and Material All the data have been obtained by using the codes which can be obtained from the link mentioned in the next section.

Declarations

Conflicts of Interest/competing interests The authors have no conflicting interests.

Code Availability The codes used in this work are available in an open-source GitHub directory [here](#). All the codes were written by the authors on MATLAB 2016.

References

1. Sivathanu, Sankaran; Liu, Ling; Yiduo, Mei; Pu, Xing: Storage management in virtualized cloud environment. In 2010 IEEE 3rd international conference on cloud computing, pages 204–211. IEEE, (2010)
2. Zhang, Rui; Liu, Ling: Security models and requirements for healthcare application clouds. In 2010 IEEE 3rd international conference on cloud computing, pages 268–275. IEEE, (2010)
3. Chiang, Yi.-Ju.; Ouyang, Yen-Chieh.: Profit optimization in SLA-aware cloud services with a finite capacity queuing model. *Math. Prob. Eng.* **1–11**, 2014 (2014)
4. Keskin, Tayfun; Taskin, Nazim: A pricing model for cloud computing service. In 2014 47th Hawaii international conference on system sciences, pages 699–707. IEEE, (2014)
5. Atmaca, Tulin, Begin, Thomas, Brandwajn, Alexandre, Castel-Taleb, Hind: Performance evaluation of cloud computing centers with general arrivals and service. *IEEE Trans. Parallel Distrib. Syst.* **27(8)**, 2341–2348 (2016)

6. Khazaei, H., Mistic, J., Mistic, V.B.: Performance analysis of cloud computing centers using M/G/m/m+r queuing systems. *IEEE Trans. Parallel Distrib. Syst.* **23**(5), 936–943 (2012)
7. Dai, Yuan-shun.; Yang, Bo; Dongarra, Jack; Zhang, Gewei: Cloud Service Reliability : Modeling and Analysis. In 15th IEEE Pacific Rim international symposium on dependable computing, pages 1–17. Citeseer, (2009)
8. Chiang, Yi.-Ju., Ouyang, Yen-Chieh., Hsu, Ching-Hsien. : Performance and cost-effectiveness analyses for cloud services based on rejected and impatient users. *IEEE Trans. Serv. Comput.* **9**(3), 446–455 (2016)
9. Goswami, V.; Patra, S.S.; Mund, G.B.: Performance analysis and optimal resource usage in finite population cloud environment. *Proceedings of 2012 2nd IEEE international conference on parallel, distributed and grid computing, PDGC 2012*, pages 679–684, (2012)
10. Goswami, V.; Patra, S.S.; Mund, G.B.: Performance analysis of cloud with queue-dependent virtual machines. 2012 1st international conference on recent advances in information technology, RAIT-2012, pages 357–362, (2012)
11. Quennel, Zhao; Yiqiang; Alfa Sule, Attahiru. : Performance analysis of a telephone system with both patient and impatient customers. *Telecommun. Syst.* **4**(1), 201–215 (1995)
12. Mandelbaum, Avi, Zeltyn, Sergey: The impact of customers' patience on delay and abandonment: some empirically-driven experiments with the M/M/ n + G queue. *OR Spectrum* **26**(3), 377–411 (2004)
13. Doran, Derek; Lipsky, Lester; Thompson, Steve: Cost-based optimization of buffer size in M/G/1/N systems under different service-time distributions. *Proceedings - 2010 9th IEEE international symposium on network computing and applications, NCA 2010*, pages 28–35, (2010)
14. Ghosh, Arka P., Weerasinghe, Ananda P.: Optimal buffer size and dynamic rate control for a queueing system with impatient customers in heavy traffic. *Stoch. Process. Their Appl.* **120**(11), 2103–2141 (2010)
15. Mehdi: Impatient Task Mapping in Elastic Cloud using Genetic Algorithm. *J. Comput. Sci.* **7**(6), 877–883 (2011)
16. Mehdi, Nawfal A.; Mamat, Ali; Ibrahim, Hamidah; Syrmabn, Shamala K.: Virtual machines cooperation for impatient jobs under cloud paradigm. *World Academy of science, engineering and technology* **51**(Section III), 1119–1125 (2011)
17. Khazaei, Hamzeh, Mistic, J., Mistic, Vojislav B.: Performance analysis of cloud computing centers using M/G/m/m+r queuing systems. *IEEE Trans. Parallel Distrib. Syst.* **23**(5), 936–943 (2012)
18. Cappos, Justin; Beschastnikh, Ivan; Krishnamurthy, Arvind; Anderson, Tom: Seattle: A Platform for Educational Cloud Computing. In *Proceedings of the 40th ACM technical symposium on Computer science education - SIGCSE '09*, page 111, New York, New York, USA, (2009). ACM Press.
19. Shouraboura, Caroline, Bleher, Pavel: Placement of applications in computing clouds using Voronoi diagrams. *J. Intern. Serv. Appl.* **2**(3), 229–241 (2011)
20. Ping Lim, Boon; Kit Chong, Poh; Kandasamy Karuppiah, Ettikan; Mohamad Yassin, Yaszrina; Nazir, Amril; Noor Batcha, Mohamed Farid: FARCREST: Euclidean Steiner Tree based cloud service latency prediction system. 2013 IEEE 10th Consumer Communications and Networking Conference, CCNC 2013, pages 859–860, (2013)
21. Quarati, Alfonso; Agostino, Daniele; Galizia, Antonella; Mangini, Matteo; Clematis, Andrea: Delivering Cloud Services with QoS Requirements: An Opportunity for ICT SMEs. In Kurt Vanmecheelen, Jörn Altmann, and Omer F Rana, editors, *Economics of Grids, Clouds, Systems, and Services*, pages 197–211, Berlin, Heidelberg, (2012). Springer Berlin Heidelberg.
22. Mishra, Suchintan; Narayan Sahoo, Manmath; Kumar Sangaiah, Arun; Bakshi, Sambit; D: Nature-inspired cost optimisation for enterprise cloud systems using joint allocation of resources. *Enterprise Information Systems* **15**(2), 174–196 (2021)
23. Selvarani S.; Sudha Sadhasivam, G.: Improved cost-based algorithm for task scheduling in cloud computing. 2010 IEEE international conference on computational intelligence and computing research, ICCIC 2010, pages 620–624, (2010)
24. Yang, Zhi; Yin, Changqin; Liu, Yan: A Cost-Based Resource Scheduling Paradigm in Cloud Computing. In 2011 12th international conference on parallel and distributed computing, applications and technologies, pages 417–422. IEEE, (2011)
25. Yang, Bo., Tan, Feng, Dai, Shun, Yuan, : Performance evaluation of cloud service considering fault recovery. *J. Supercomput.* **65**(1), 426–444 (2013)
26. Hadji, Makhlof; Zeghlache, Djamel: Minimum cost maximum flow algorithm for dynamic resource allocation in clouds. *Proceedings - 2012 IEEE 5th international conference on cloud computing, CLOUD 2012*, pages 876–882, (2012)
27. Hwang, Ren-Hung., Lee, Chung-Nan., Chen, Yi.-Ru., Zhang-Jian, Da-Jing. : Cost optimization of elasticity cloud resource subscription policy. *IEEE Trans. Serv. Comput.* **7**(4), 561–574 (2014)
28. Shortle, John F., Thompson, James M., Gross, Donald, Harris, Carl M.: *Fundamentals of Queueing Theory*. Wiley Series in Probability and Statistics. Wiley, Hoboken, NJ, USA (2018)
29. Cao, Jiuxin; Yang, Liu; Zheng, Xiao; Liu, Bo; Zhao, Lei; Ni, Xudong; Dong, Fang; Mao, Bo: Social attribute based web service information publication mechanism in delay tolerant network. In 2011 14th IEEE international conference on computational science and engineering, pages 435–442. IEEE, (2011)
30. Armony, Mor, Maglaras, Constantinos: Contact centers with a callback option and real-time delay information. *Op. Res.* **52**(4), 527–545 (2004)
31. Guo, Pengfei, Zipkin, Paul: Analysis and comparison of queues with different levels of delay information. *Manag. Sci.* **53**(6), 962–970 (2007)
32. John, D.C.: Little. A Proof for the Queuing Formula: $L = \lambda W$. *Operations Research* **9**(3), 383–387 (1961)
33. Ullah, Amjad, Li, Jingpeng, Shen, Yindong, Hussain, Amir: A control theoretical view of cloud elasticity: taxonomy, survey and challenges. *Clust. Comput.* **21**(4), 1735–1764 (2018)
34. Nathuji, Ripal; Kansal, Aman; Ghaffarkhah, Alireza: Q-Clouds: Managing Performance Interference Effects for QoS-Aware Clouds. In *Proceedings of the 5th European conference on Computer systems - EuroSys '10*, volume 298, page 237, New York, New York, USA, (2010). ACM Press.
35. Calheiros, Rodrigo N.; Ranjan, Rajiv; Buyya, Rajkumar: Virtual machine provisioning based on analytical performance and QoS in cloud computing environments. In 2011 international conference on parallel processing, pages 295–304. IEEE, (2011)
36. Bradley, John, Gerald, Fitz, John; Kearney, Ide. : Modelling supply in an open economy using a restricted cost function. *Econ. Modell.* **10**(1), 11–21 (1993)
37. Brown, Randall S., Caves, Douglas W., Christensen, Laurits R.: Modelling the structure of cost and production for multiproduct firms. *South. Econ. J.* **46**(1), 256 (1979)



Performance evaluation and reliability analysis of predictive hardware failure models in cloud platform using ReliaCloud-NS

Rohit Sharma*

Department of Computer Science and Engineering,
Dr. Ambedkar Institute of Technology for Handicapped U.P.,
208024, Kanpur, India

Email: rohit6615@rediffmail.com

*Corresponding author

Raghuraj Singh

Department of Computer Science and Engineering,
Harcourt Butler Technical University,
208002, Kanpur, India

Email: raghurajsingh@rediffmail.com

Abstract: Cloud computing systems at the present time established as a promising trend in providing the platform for coordinating large number of heterogeneous tasks and aims at delivering highly reliable cloud computing services. It is most necessary to consider the reliability of cloud services and timely prediction of failing hardware in cloud data centres so that it ensures correct identification of the overall time required before resuming the service after the failure. In this paper reliability of two recently introduced predictive hardware failure models has been analysed. The first model is on the basis of two open data sources, i.e., self-monitoring, analysis and reporting technology (SMART), windows performance counters and the second model is based on FailureSim which is a neural networks-based system for predicting hardware failures in data centres is done over our carefully designed two test cloud simulations of 144 VMs and 236 VMs. The results are thoroughly compared and analysed with the help of ReliaCloud-NS that allow researchers to design a CCS and compute its reliability.

Keywords: cloud computing system; CCS; virtual machines; VM; Monte Carlo simulation; MCS; neural networks; annual failure rate; AFR; self-monitoring, analysis and reporting technology; SMART.

Reference to this paper should be made as follows: Sharma, R. and Singh, R. (2021) 'Performance evaluation and reliability analysis of predictive hardware failure models in cloud platform using ReliaCloud-NS', *Int. J. Cloud Computing*, Vol. 10, No. 3, pp.207–224.

Biographical notes: Rohit Sharma is a Research Scholar at the Dr. APJ Abdul Kalam Technical University, Lucknow, India and currently working as an Assistant Professor in the Department of Computer Science and Engineering, Dr. Ambedkar Institute of Technology for Handicapped, Kanpur, India. He received his BTech and MTech in Computer Science and Engineering from the U.P. Technical University, Lucknow. His research interests include cloud computing and computational intelligence.

Raghuraj Singh is working as a Professor and Head in the Department of Computer Science and Engineering at Harcourt Butler Technical University, Kanpur, India. His research interests are in the field of software engineering, computer networks, soft computing and cloud computing. He has guided several MTech and PhD candidates. He has published a number of papers in reputed international journals and conferences. He is a senior member of CSI, ACM, IETE and ISTE and an editor and reviewer of peer-reviewed journals.

1 Introduction

In past two decades, the cloud computing technology is found to be a widespread emerging trend in various service domains. It is the most cost effective, transparent and scalable way of providing wide categories of computing resources and in accordance with the needs of both individual and corporate customers. End users always need a highly available and highly reliable cloud, and cloud providers want to build highly utilised systems which can optimise their profit. It is recognised that the reliability requirements of a cloud differ while considering its individual components. The general reliability of the cloud management system is a function of the reliability of its components and their interfaces (Singh et al., 2014).

Cloud computing can be illustrated as the operation of heavy computing resources that includes hardware and software package that are delivered to clients as a service over an outsized scale network. The name 'cloud' has been originated from the employment of a cloud-shaped representation as associate abstraction for the advanced infrastructure that is contained in a very system diagrams. The origination of the term 'cloud computing' is very vague; however it appears to be derived from the practice of using schematic diagrams of computing and communications systems. The word cloud is employed as an allegory for the big scale network that is supported by the standardised use of a cloud-like form to denote a network on telephone schematics associated later to depict the web in network diagrams as an abstraction of the underlying infrastructure it represents. The cloud image (Gibbs, 2012) was used to represent the web as early as 1994. The elemental thought of cloud computing essentially dates back to the 1950s once there was associate availableness of huge scale mainframe in establishments and companies.

Owing to the pricey nature of mainframe, there arise a necessity to search out another answer for allowing the multiple users for accessing and sharing equivalent central processor time thereby truncating the chance of periods of inactivity (also termed as time-sharing) (Liu, 2007). As computers became additionally prevailing, scientists and technologists explored ways to create large-scale computing power on the market to cater additional users through sharing, experimenting with algorithms to produce the best use of the infrastructure, platform and applications with prioritised access to the computer hardware and potency for the tip users.

The high value of those powerful computing systems has forced several prime organisations to require associate in nursing initiative to explore higher value effective answer exploitation sharing. The prime organisation can embody IBM, GE, National CSS, etc., who took the initiative to launch and marketed time sharing. With the ascension of net technology and standards, varied merchandise and demands of distributed computing were on high increase. The presence of pervasive high computing

network, value effective computing devices, storage devices together with massive scale use of virtualisation of hardware, service headed design has paved the trail for top demands in new technology, therefore known as ‘cloud computing’ (Cepeda et al., 2010).

The reliability of the system is found to be affected with the changes within the active phase of the system. In a recent study (Alexandrov and Dimov, 2013), the passive and active redundancy in cloud is explained considering the study related with prototype service deployed in the Amazon web services cloud. However, very few researches have been conducted based on the study of software engineering in the development of software systems intended for execution in cloud technology.

Another study was done to provide detailed characteristics on CCS component failure and detailed analysis based on the predictors involved in the failure.

A case study on diverse existing architectural approaches developed for estimating reliability and availability for the execution of software in the cloud is conducted (Villalpando and Edouardo, 2014).

There are diverse existing machine learning approaches for estimating reliability by predicting hardware failures and results obtained from them indicate that high levels of reliability can be obtained by using these approaches. The first considered predictive hardware failure model (Ganguly et al., 2016) based on SMART technology takes into account the node data of reported high sector counts and predict future disk failures on that basis. In the worst case it will predict at least 50% of disk failures and thus replacing this predicted to be malfunctioning hard disk timely will eventually increases the overall reliability of the CCS.

Another model (Davis et al., 2017) predicting the overall hardware malfunctioning in cloud data centres includes not only hard disk but CPU and memory failures as well. This neural network-based simulator model FailureSim is designed for predicting the hardware faults in cloud-based data centres. This model can effectively predict host failure in cloud with 89% efficiency. These results of hardware prediction when combined with efficient hardware replacement policy may lead to overall improvement in reliability of a particular cloud computing system (CCS). A designed test case simulation of 144 VMs and 236 VMs over ReliaCloud-NS [non-sequential Monte Carlo simulation (MCS) based reliability assessment tool] is considered for result analysis upon both models.

The rest of this paper is ordered as:

- Section 2 ‘previous work on cloud reliability’ a comprehensive review on previous literature work is done that is relevant to the proposed methodology.
- Section 3 ‘outline of ReliaCloud-NS’ is an introduction to simulation environment used for analysing our proposed methodology.
- Section 4 ‘our approach’ presents how two predictive hardware failure models could affect the overall reliability of a CCS.
- Section 5 ‘test system design for CCS’ details the characteristics of our two especially designed test cases of 144 VMs and 256 VMs.
- In Sections 6, 7 and 8 ‘reliability estimation of primary cloud model’ predictive future disk failure model based on S.M.A.R.T. data and the one based on FailureSim presents the results of reliability obtained over our proposed test cases.

- Section 9 ‘simulation result analysis and key findings’ insights gathered during CCS reliability assessments and CCS design finally.
- Section 10 ‘conclusion and future work’ concludes the paper with a summary as well as directions for future work.

2 Previous work on cloud reliability

With globalisation, organisations are spread across the globe and their operations will involve data transfers between their global offices. This will lead to the need for the services, which can use anywhere with an economical way. Developers introduce a new idea based on the internet, which no need to use large outlay of hardware and can have the most of the services that required. These widely popular services supported by 1,000 servers without cost and implementation time consideration (Armburst et al., 2010).

This solution can be solved the huge problems for those companies which has the wide office or wide users (Vaquero et al., 2008).

However, at the same time there are few questions rising up which asking about performance, reliability and security in CCSs. The most of the industrial company wants to know can be trusted to these systems or how can be sure the services always available to the client (Mell and Grance, 2009).

Cloud computing is one of the major technologies predicted to revolutionise the future of computing. The model of delivering IT as a service has several advantages. It enables current businesses to dynamically adapt their computing infrastructure to meet the rapidly changing requirements of the environment (Marston et al., 2011).

A cloud is a form of parallel and distributed system possessing a group of inter-connected and virtualised computers that are dynamically scheduled and highlighted as one or more unified computing resources based on service-level agreements established through conciliation between the service provider and consumers (Buyya et al., 2008).

Various studies and works references reliability, availability and related issues in cloud services. The cloud service customer requires efficient quality services which are secured and reliable from the providers. Significance of customer satisfaction reflects as assurance of service provider through feedback in terms of QoS metrics like customer support, reliability, availability and user feedback (Govindaraj and Jaisankar, 2017).

Feedback of customers in terms of QoS, employment models, reviews, security and portability parameters ascertained that it is necessary to secure resources involved in the virtualised data centres to maintain the integrity and privacy of the data. Data colouring and software watermarking methods was found to protect shared data objects and extremely scattered software modules. These research factors were answered using multiple data sources which were commonly collected by network operators (Hwang and Li, 2010).

Subsequently, the research was seen to provide the solutions for devices or links that are not reliable, creating failures, which impact the network traffic and are having network redundancy. These research factors were answered using multiple data sources which were commonly collected by network operators (Gill et al., 2011b).

Recent studies has considered the terms such as ‘reliability’ and ‘availability’ and focused on CCS while in general cases the term refers to growing stability of the system through active management or redundancy (Bauer and Adams, 2012).

These researches were found to provide the base for exposing certain gaps in knowledge based on the need for standardised CCS system models for testing and the definition of utility grade metrics for evaluating availability [though a single, non-utility grade metric expected resource availability has been developed (Ferrari et al., 2012)].

Cloud computing paradigm is seen to be an emerging trend in providing resources to users in transparent manner like other utilities. This was found to develop techniques for evaluation that provide reliability as a quantitative metric for a CCS and used for efficient expansion and planning. Much close information about nature of CCS reliability and its design are revealed (Zhang et al., 2014).

A fresh work was proposed to analyse the reliability of cloud services considering the factors such as overflow, timeout and missing data resource. Further the reliability model was postulated on the basis of request stage and execution stage reliability (Dai et al., 2009).

Another related work utilised fault tree for different tasks and further diverse sub graphs were identified in the execution stage reliability modelling. These parameters were known as MSST and different MSSTs were intersected for the development of MEST. This research was limited in proposing the development while the execution of the approach was yet to be performed (Meçe and Driza, 2013).

Consequently, mathematical solutions were developed considering the mathematical uncertainty principle as the historical data were untraceable and the manual components were found to contribute to 20%–90% of the failures (Guo et al., 2014).

Furthermore, a recent research developed additional features considering the conventional challenges in the employment of cloud computing without investments for developing infrastructures as well as training of employees as per the need of the provider (Jain and Singh, 2014).

Fault tolerance is found to be a significant part of improving the service reliability in cloud computing services. Further, it was noticed that less reliable device such as HDD, would compensate the negative effect on system (Zhang et al., 2014).

Research on reliability also focuses at conceptual issues (Page, 2012), hierarchical graphs, priority graphs and application of grid computing for dynamic scalability in the cloud. Cloud computing paradigm removes the need to procure, arrange and uphold the resources. This was found to reduce the overall incentives incurred in operational costs in hardware, software and human effort, taking into account the use of cloud services in various industries (Ahuja and Mani, 2012).

The research in Wang et al. (2012) presents a hierarchical system for computing availability of a CCS which focuses on the response time of user requirements for resources. This research was found to postulate an availability aware model to explore the computing resources for both vertical and horizontal scaling.

A reliable cloud system was proposed that would contemplate and evade applications that are commonly dependent with complex internal structures (Chen et al., 2017). Consequently, numerous virtual machine (VM) parameters such as RAM and number of processors were varied to analyse the performance of cloud for different VM systems. From this research it was seen that VM characteristics affects the time taken for cloudlet execution (Kumar and Aramudhan, 2013).

Also, a recent research in Lin and Chang (2010) described the employment of computer network (CN) as a multistate network with different states due to partial failure, or edges maintenance (physical lines) and nodes (switches or routers). This approach can also be used in hardware failure prediction models for CCSs. It is necessary to consider suitable technique for distributing appropriate amount of data on the receiving nodes (Schmidt et al., 2010).

Therefore, the aforementioned researches provide a comprehensive review on various literatures based on the reliability of cloud computing services and it has been revealed that the major cause of decreased reliability in CCS is due to component level failures. In order to improve the reliability of CCS two predictive hardware failure models on SMART technology (Ganguly et al., 2016) and neural network-based FailureSim (Davis et al., 2017) were thoroughly examined in the upcoming sections.

Some technical issues in cloud computing will include load balancing, security, reliability, ownership. Here is a rundown on most of the current issues concerning cloud computing:

- *Load balancing*: load levelling is usually mechanised to implement failover – the continuance of a service when the failure of 1 or additional of its parts. The components are monitored frequently and once one becomes non-responsive, the load balancer is up on and now not sends traffic to it. This can be an inherent feature from grid-based computing for cloud-based platforms. Energy conservation and resource consumption do not seem to be continuously attentiveness once discussing cloud computing; but with correct load levelling in place of resource consumption are often unbroken to a minimum. This is not only serves to keep cost low and enterprise ‘greener’, it also puts less stress on the circuits of each individual design making them more potentially last longer (Kaur, 2012).
- *Security*: while a leading edge cloud services provider will employ data storage and transmission encryption, user authentication, and authorisation (data access) practices, many people worry about the vulnerability of remote data to such criminals as hackers, thieves, and disgruntled employees. Cloud providers are enormously sensitive to this issue and apply substantial resources to mitigating concern (Kuyoro et al., 2011).
- *Reliability*: some people worry also about whether a cloud service provider is financially stable and whether their data storage system is trustworthy. Most cloud providers attempt to mollify this concern by using redundant storage techniques, but it is still possible that a service could crash or go out of business, leaving users with limited or no access to their data. A diversification of providers can help alleviate this concern, albeit at a higher cost (Deng et al., 2010).
- *Ownership*: once data has been relegated to the cloud, some people worry that they could lose some or all of their rights or are unable to protect the rights of their customers. Many cloud providers are addressing this issue with well-crafted user-sided agreements. That said, users would be wise to seek advice from their favourite legal representative. Never use a provider who, in their terms of service, lays any kind of ownership claim over your data (Agrawal, 2011).

3 Outline of ReliaCloud-NS

ReliaCloud-NS is a GUI-based web application build over MVC architecture and used for executing non sequential version of MCSs for evaluating the CCS reliability. The basic activities of ReliaCloud-NS includes designing individual components (like VMs, VM groups, clusters etc.) and eventually CCS itself, simulating CCSs for reliability estimation, and analysing results from previous simulations. ReliaCloud-NS also evaluates CCS reliability convergence curve. ReliaCloud-NS holds both request able and available resources that a user can use easily; it has a feature that let users to create their own CCS.

Snyder et al. (2015) studies have demonstrated, offered and scrutinise an original approach in re-considering the reliability of CCSs with the help of non-sequential MCS. It was demonstrated that non-sequential MCS gives us a flexible and efficient way to determine CCS reliability upon a set of four distinct resources, i.e., CPU, memory, bandwidth and HDD. We have used an allocation algorithm which allocates VMs in a static manner. In this scheme, the same quantity of each VM units is used for each parallel trial. This static VM allocation algorithm allows for much replicated simulations with a non-monotonic variance on the resulting reliability indicator across corresponding trials. In our proposed work, we consider the case where static allotment algorithm assign VMs in a static manner. Here all checks of a sole simulation have similar VM distributions. This allocation strategy results in firm bound on the reliability variance of recurring simulations as only stochastic behaviour is coming from within the MCS algorithm. The annual failure rates (AFR) of various hardware components were determined in Nightingale et al. (2011) and was given in Table 1. Each of the above distinct entities considered for simulation are bounded to a predefined AFR. The AFRs used were congregated and projected from the review of the research work in the current literature that evaluates hardware failures of CCSs (Nightingale et al., 2011; Kim et al., 2009; Vishwanath and Nagappan, 2010; Gill et al., 2011b; Birke et al., 2012).

Table 1 AFR used in the simulations

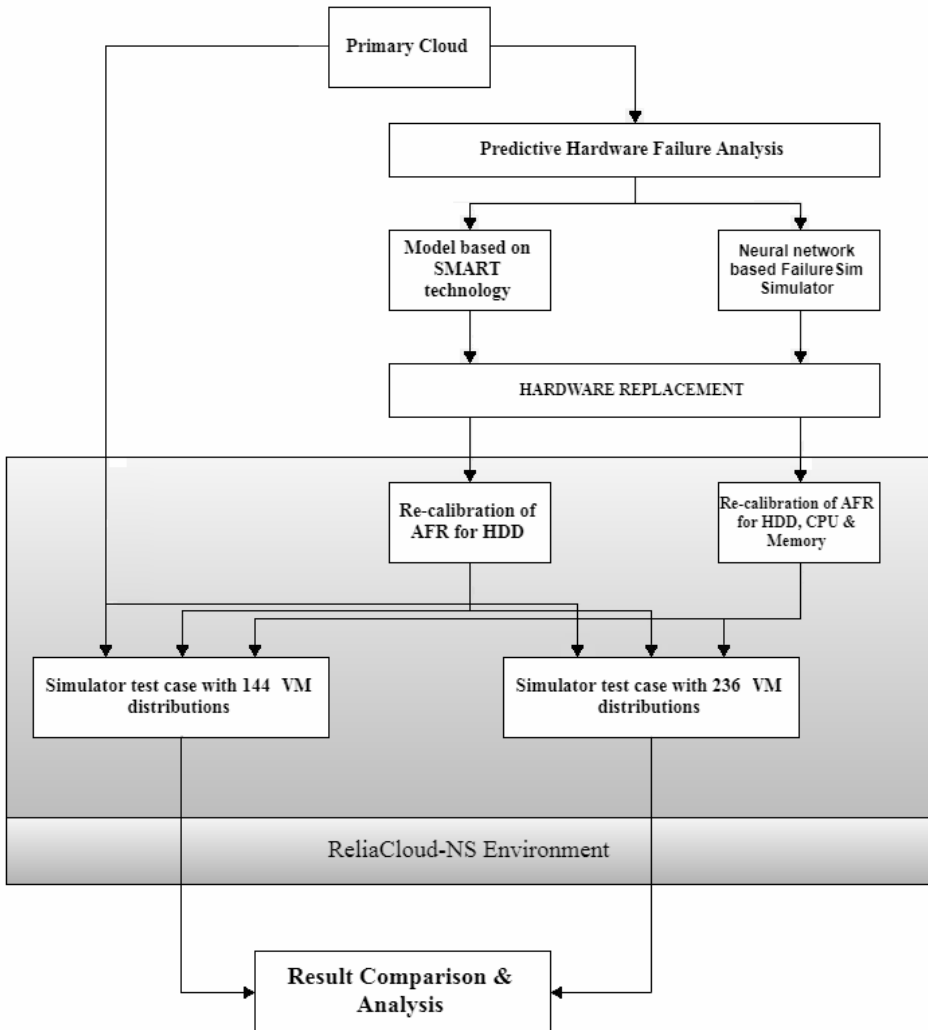
<i>Component</i>	<i>AFR</i>
CPU	2%
Memory	1%
Hard disk drives	8%
Bandwidth	1%

4 Our approach

There are different reliability tools of cloud computing focusing on fault tolerance, redundancy, check pointing and the most important hardware reliability, while the work in assessment of reliability in a CCS is broadly classified into calculating request stage reliability which deals with timeout and overflow errors and execution stage reliability in which failure of hardware and particularly hard disk is considered. Disk failures are the root cause to outages in running services over CCS. These faults are mostly due to mechanical hardware shortcomings that are always reflected in the analysed data used to observe HDDs. The process involved in the measurement of the overall quality of service

provided was described by the performance indicator evaluation for cloud computing (Bardsiri and Hashemi, 2014). Considering a practical CCS it was observed that during a fault or failure the edges and nodes of the system have various capacities or states. Recently, a mixture of two free data sources self-monitoring, analysis and reporting technology (S.M.A.R.T. or SMART) data and windows performance counters were used to develop an appropriate model where it was seen that the behaviour of these data sources are dissimilar and *complicated* (Ganguly et al., 2016). Also, study indicates the employment of FailureSim, a simulator based on CloudSim for the prediction of failures in a CCS. This system was found to provide the relevant information's from the cloud and act as classifier for classifying the status of the hardware using neural network.

Figure 1 Framework used for reliability analysis of NN-based FailureSim simulation model and predictive hardware failure-based SMART technology model



4.1 Proposed probabilistic algorithm for static VM distributions

As we are using static allocation policy for performance evaluation and reliability analysis of predictive failure models in this entire work with a single VM group, this very algorithm will give us the no. of VMs allocated to a single *VMinstance* of the used VM group. This algorithm is traced to design for our made test cases as discussed in Section 5. In this algorithm below *VMs available* refers to the total number of VMs to be allocated on to a CCS. *N* refers to the total number of *VMinstances* in a considered *VM group*. VM instance *i* is a single instance of considered VM group, *Probi* is the probability of a single VM and *VMtotalcount* is the total number of VMs allocated to the cloud. A single *VMinstance* is using the resources as per Table 2 of the test-case CCS. The algorithm is given as follows:

```

Select from SET_OF (VMs available)
  A VM group with set of N VMinstances
  For i = 1 to N
  For each VM instance i do
    Assign probability as Probi = 1/N to each VM instance i
  end For
end For
Need:  $\sum Probi = 1$  and  $0 \leq Probi \leq 1$ 
Pick VMtotalcount = |VMs available|
For i = 1 to N
  No. of allotted VMs to each VM instances i of VM group is
     $VMtotalcount * Probi$ 
end for

```

5 Test system design for CCS

We have carefully designed, couple of our homogeneous test CCSs (test-case CCS – 144 VMs and 236 VMs) for our ReliaCloud-NS. The first test suite is designed for high utilisation of HDD resource. The summary of an initially designed test-case simulation showing configuration of each VM is given in Table 2. This data is further used to design the first CCS test suite having a provision of 144 VMs for allocation and it is depicted in Table 3.

Table 2 Initial test-case CCS for individual VMs

	<i># of cores</i>	<i>Memory (GB)</i>	<i>HDD (GB)</i>	<i>Bandwidth (Mbps)</i>
Available	500	500	25,000	75,000
Each VM	2	2	160	160

Table 3 Test-Case CCS – 144 VMs

	# of cores	Memory (GB)	HDD (GB)	Bandwidth (Mbps)
Available	500	500	25,000	75,000
Requested	288	288	23,040	23,040
Difference	212	212	3,400	51,960
Utilisation	0.576	0.576	0.9216	0.3072

The other test-case is re-designed taking two facts in view firstly to enable cloud provider to serve many more VMs to the CCS and secondly providing those resources individually to the CCS who exhibit maximum failures, i.e., HDD who has a maximum value of AFR bound to it. While designing these test cases, we have taken into account the static distribution algorithm of previous section. The VM group considered is having four VM instances with an assigned probability of 0.25 and each VM instance is having 36 VMs assigned in first test-case and 59 VMs in the second test-case.

Table 4 Test-case CCS – 236 VMs (extra 15,000 HDD’s)

	# of cores	Memory (GB)	HDD (GB)	Bandwidth (Mbps)
Available	500	500	40,000	75,000
Requested	472	472	37,760	37,760
Difference	28	28	240	37,240
Utilisation	0.944	0.944	0.993	0.503

6 Reliability estimation of primary cloud model

The first reliability estimation upon ReliaCloud-NS averaged over 20 trials is act upon the 144 VM test-case suites. The results from this trial are shown in Figures 2 and 3. It is clear that the HDD resource is the root cause of all failures as 139 out of total 156 failures are due to HDD breakdown. This is probably due to the high exploitation of the HDD resource (92.16%) and low usage of all other resources (57.6% for CPU and memory and 30.72% utilisation for bandwidth).

Figure 2 Reliability convergence curve for the first test-case CCS (144 VMs) as shown in Table 3 and simulated over ReliaCloud-NS (see online version for colours)

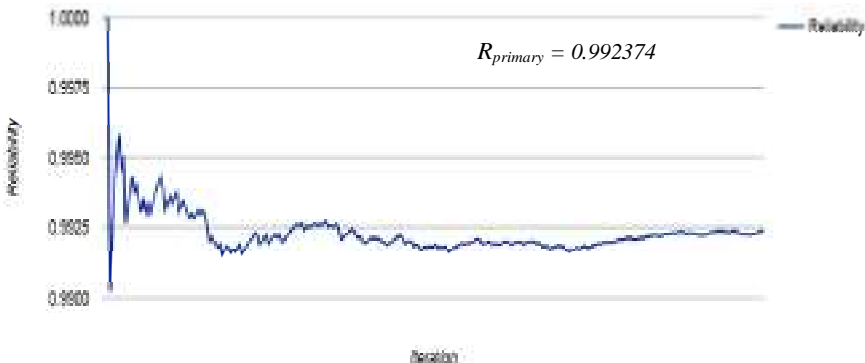


Figure 3 Component failures by resource type for the first test-case CCS (144 VMs) as shown in Table 3 and simulated over ReliaCloud-NS (see online version for colours)



The above results are carried upon a total sample size of 20,456 out of which 156 failures were detected and thus reliability $R_{primary}$ of 0.992374 was shown. The extra HDD resource and more VMs for allocation on the cloud in effect allow for a much higher employment percentage of the other resources. These parameters were already considered while developing the second test case of 236 VMs (Table 4). The second reliability estimation upon ReliaCloud-NS averaged over 20 trials is acted upon 236 VM test-case suite with 15,000 extra HDD's. The results were also found upon of this typical trial and are shown in Figures 4 and 5.

Figure 4 Reliability convergence curve for the second test-case CCS (236 VMs) as shown in Table 4 and simulated over ReliaCloud-NS (see online version for colours)

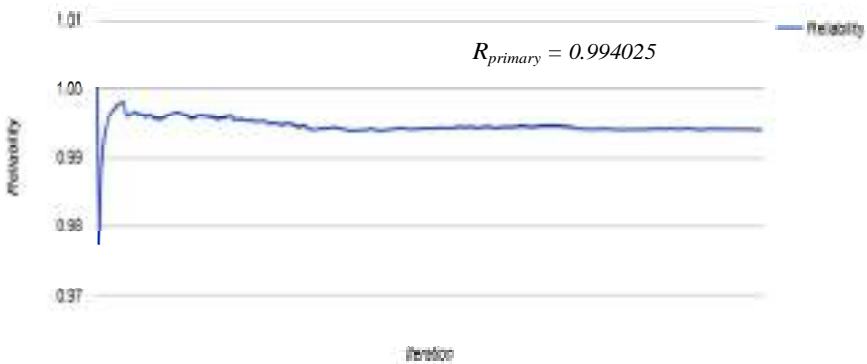
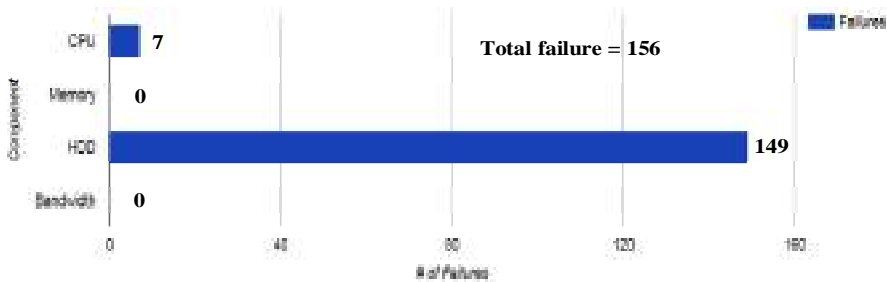


Figure 5 Component failures by resource type for the second test-case CCS (236 VMs) as shown in Table 4 and simulated over ReliaCloud-NS (see online version for colours)



7 Reliability estimation of predictive future hardware failure model based on S.M.A.R.T data

A comprehensive study of having a highly fault tolerant structure of Azure Fabric software by Ganguly et al. (2016) suggests that maximum failures resulting in a VM breakdown is due to disk issues. To build a predictive model identifying future HDD failures, they use a combination of two open data sources – S.M.A.R.T or SMART data and windows performance counters. Nature of both these complex data sources varies a lot but review studies shows that in the worse case it will predict at most 50% of disk failures and thereby decreasing the AFR of the hard disk drives to 4%. We have performed the whole reliability simulation of earlier mentioned test cases of 144 VMs and 256 VMs after recalibrating AFR for the worst case of 50% efficiency.

Figure 6 Pattern of reliability convergence for the initial test-case CCS (144 VMs) simulation as shown in Table 3 (see online version for colours)

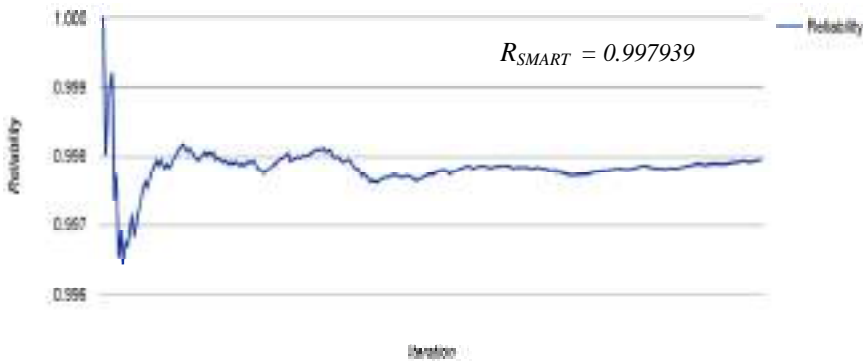
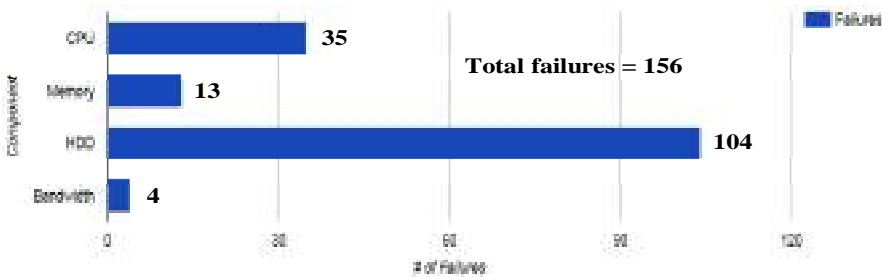


Figure 7 Component failures by resource type for the initial test-case CCS (144 VMs) with extra HDD’s simulation as shown in Table 3 (see online version for colours)



The primary drawback of this model is that it only predicts the future failure possibilities of hard disk drives and remaining hardware parameters like CPU, memory and bandwidth remains untouched. Significant losses in cloud data centres are due to hardware failures. Therefore, the ability to accurately predict the information about

failing hardware is of great importance and therefore we in the next section considers a NN-based hardware failure prediction model which can predict failing hardware in terms of HDD, CPU and memory.

Figure 8 Pattern of reliability convergence for the initial test-case CCS (236 VMs) simulation as shown in Table 4 (see online version for colours)

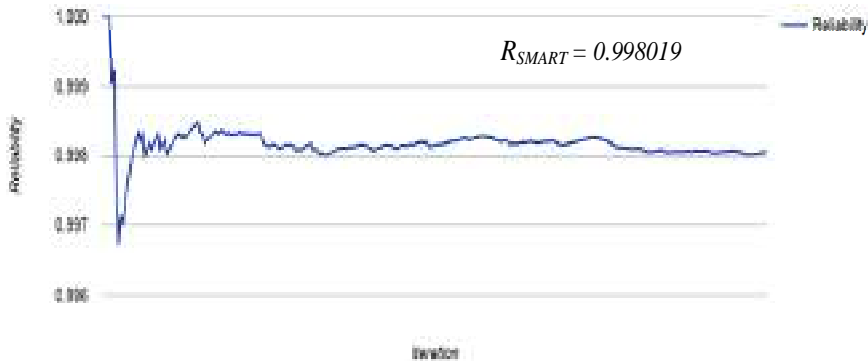


Figure 9 Component failures by resource type for the initial test-case CCS (236 VMs) as shown in Table 4 (see online version for colours)



8 Reliability estimation of predictive future disk failure model based on FailureSim

Davis et al. (2017) proposed a simulator, namely FailureSim which is an extension module of CloudSim and supports prediction of failing hardware. FailureSim collects performance related data from the cloud itself and categorise the status of the hardware using a neural network. Performance information is read from hosting hardware and stored in a variable length windowing vector. Using conventional host failure performance models, FailureSim was able to effectively predict host failure in the cloud with around 89% accuracy. This categorised data and algorithm can determine about the failing hardware with 89% accuracy. Assuming that there is no amending cost in any predictable CPU, memory or hard disks failures we can again alter the AFR values of

CPU, memory and hard disk to 0.22%, 0.11% and 0.88%. These AFR values were updated in ReliaCloud NS. The test cases of Tables 3 and 4 were executed over it and results are as under.

Figure 10 Pattern of reliability convergence for the initial test-case CCS (144 VMs) simulation as shown in Table 3 (see online version for colours)

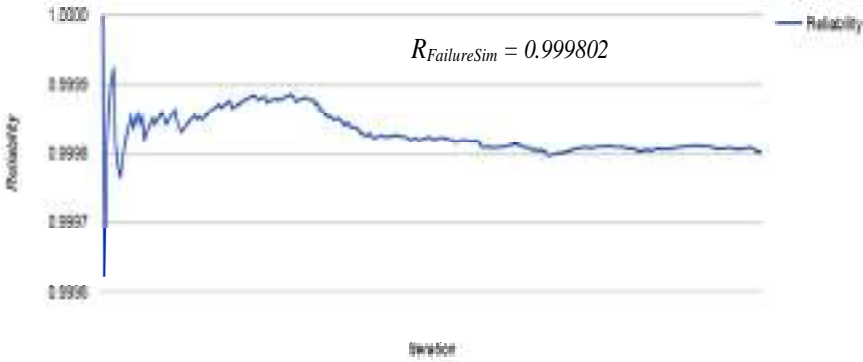


Figure 11 Component failures by resource type for the initial test-case CCS (144 VMs) simulation as shown in Table 3 (see online version for colours)

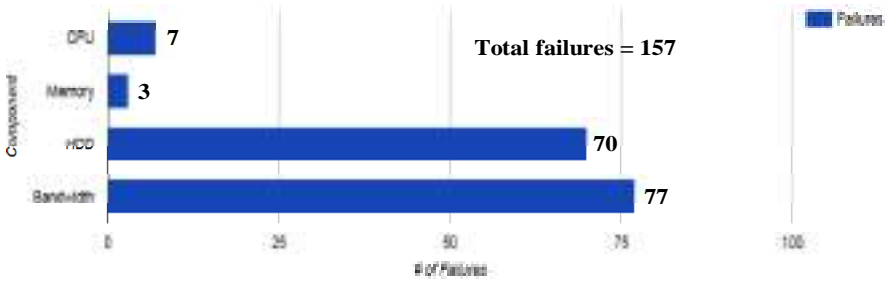


Figure 12 Pattern of reliability convergence for the initial test-case CCS (236 VMs) simulation as shown in Table 4 (see online version for colours)

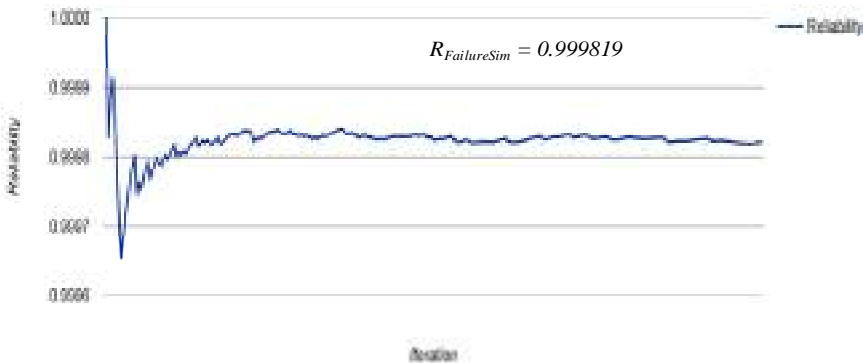
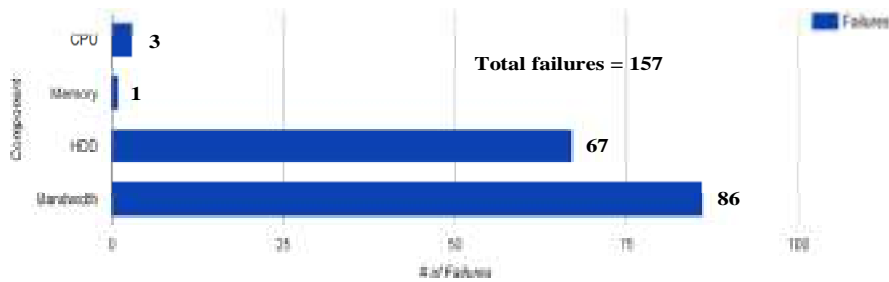


Figure 13 Component failures by resource type for the initial test-case CCS (236 VMs) with extra HDD's simulation as shown in Table 4 (see online version for colours)



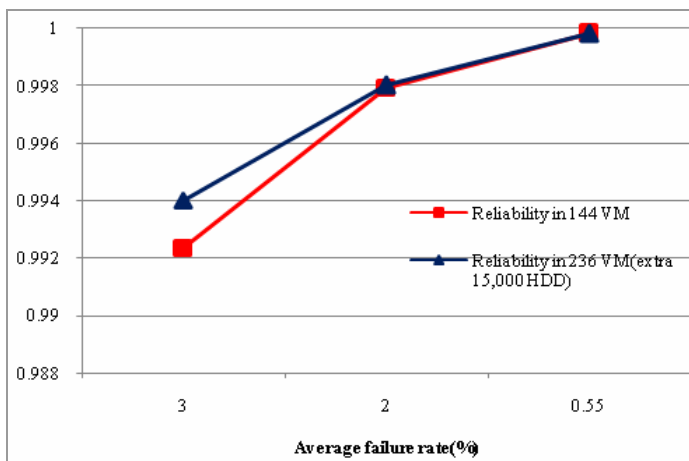
9 Simulation result analysis and key findings

A simulation software application namely ReliaCloud-NS has been assessed, which performs reliability estimation of CCSs using non-sequential MCS with a new static VM distributions policy. This assessment tool is recalibrated for AFR values and reliability of two predictive hardware failure models based on SMART technology and NN-based FailureSim simulator was tested on two simulation beds of 144 VMs and 236 VMs. Results were written in Table 5.

Table 5 Reliability and failure rate assessment in all three models

	Average failure rate (%)	Reliability in 144 VM	Reliability in 236 VM (extra 15,000 HDD)
$R_{primary}$	3	0.992374	0.994025
R_{SMART}	2	0.997939	0.998019
$R_{FailureSim}$	0.55	0.999802	0.999819

Figure 14 Graph representing convergence of reliability of considered models with decreasing average failure rate (see online version for colours)



Following findings can be drawn from the above curve between average failure rate and reliability:

- 1 For a given CCS if we predict hardware failures with the help of both these models and timely replace the identified failing hardware components the reliability improves significantly.
- 2 CCS having large no of VMs and extra hardware components has little significance in improving cloud reliability as compared to any decrement of AFR in this case due to prediction of failing hardware.

10 Conclusions and future work

The recent advances in the CCS have led to the replacement of the need for the storage devices. This makes the cloud computing infrastructure vulnerable to hardware failures and the corresponding service outages. This paper has surveyed various techniques implemented in CCS to review their ability in providing accurate, rapid, reliable and efficient services. The analysis of reliability as a metric was done on two predictive hardware failure models and it was concluded that reliability of a static VM allocation-based CCS increase with the efficient hardware failure prediction and it is always better if CCS is in the low utilisation of hardware resources. Although cost of replacement of predicted hardware components is not considered and ReliaCloud-NS only considers CPU, hard disk, memory and bandwidth this work can be extended to GPU's, databases and software packages. It is an important fact that individual component failing cannot be traced the MCS algorithm and therefore this property can also be added.

References

- Agrawal, R. (2011) 'Legal issues in cloud computing', *IndicThreads.com Conference on Cloud Computing*, June.
- Ahuja, S.P. and Mani, S. (2012) 'Availability of services in the era of cloud computing', *Network and Communication Technologies*, 6 June, Vol. 1, No. 1, p.2.
- Alexandrov, T. and Dimov, A. (2013) 'Software availability in the cloud', in *Proceedings of the 14th International Conference on Computer Systems and Technologies 2013*, ACM, June 28, pp.193–200.
- Armbrust, M., Fox, A., Griffith, R., Joseph, A.D., Katz, R., Konwinski, A. and Zaharia, M. (2010) 'A view of cloud computing', *Communications of the ACM*, Vol. 53, No. 4, pp.50–58.
- Bardsiri, A.K. and Hashemi, S.M. (2014) 'QoS metrics for cloud computing services evaluation', November, *I.J. Intelligent Systems and Applications*, Vol. 12, pp.27–33, DOI: 10.5815/ijisa.2014.12.04.
- Bauer, E. and Adams, R. (2012) *Reliability and Availability of Cloud Computing*, 1st ed., Wiley-IEEE Press, Piscataway, New Jersey.
- Birke, R., Chen, L.Y. and Smirni, E. (2012) *Data Centers in the Wild: a Large Performance Study*, Technical Report, April, IBM [online] [https://domino.research.ibm.com/library/cyberdig.nsf/papers/OC306B31CF0D3861852579E40045F17F/\\$File/rz3820.pdf](https://domino.research.ibm.com/library/cyberdig.nsf/papers/OC306B31CF0D3861852579E40045F17F/$File/rz3820.pdf).
- Buyya, R., Yeo, C.S. and Venugopal, S. (2008) 'Market-oriented cloud computing: vision, hype, and reality for delivering IT services as computing utilities', *HPCC*, pp.5–1.

- Cepeda, D., Ding, R., Ahmed, M. and Diaz, R. (2010) *Clustered Environments*, Report.
- Chen, R., Akkus, I.E., Viswanath, B., Rimal, I. and Hilt, V. (2017) 'Towards reliable application deployment in the cloud', in *Proceedings of the 13th International Conference on Emerging Networking Experiments and Technologies*, ACM, pp.464–477.
- Dai, Y-S., Yang, B., Dongarra, J. and Zhang, G. (2009) 'Cloud service reliability: modeling and analysis', in *15th IEEE Pacific Rim International Symposium on Dependable Computing*, pp.1–17.
- Davis, N.A., Rezgui, A., Soliman, H., Manzanares, S. and Coates, M. (2017) 'FailureSim: a system for predicting hardware failures in cloud data centers using neural networks', *2017 IEEE 10th International Conference on Cloud Computing (CLOUD)*, pp.544–551, ISSN: 2159-6190.
- Deng, J., Huang, S.C-H., Han, Y.S. and Deng, J.H. (2010) 'Fault-tolerant and reliable computation in cloud computing', *GLOBECOM Workshops (GC Wkshps)*, IEEE.
- Ferrari, A., Puccinelli, D. and Giordano, S. (2012) 'Characterization of the impact of resource availability on opportunistic computing', in *MCC Workshop on Mobile Cloud Computing*, ACM, Helsinki, Finland, pp.35–40.
- Ganguly, S., Consul, A., Khan, A., Bussone, B., Richards, J. and Miguel, A. (2016) 'A practical approach to hard disk failure prediction in cloud platforms: big data model for failure management in datacenters', *IEEE Second International Conference on Big Data Computing Service and Applications (BigDataService)*, pp.105–116.
- Gibbs, S. (2012) 'Cloud computing', *International Journal of Innovative Research in Engineering & Science*, July, Vol. 1, No. 1, ISSN 2319-5665.
- Gill, P., Jain, N. and Nagappan, N. (2011a) 'Understanding network failures in data centers: measurement, analysis, and implications', in *ACM SIGCOMM Computer Communication Review*, ACM, Vol. 41, No. 4, pp.350–361.
- Gill, P., Jain, N. and Nagappan, N. (2011b) 'Understanding network failures in data centers: measurement, analysis, and implications', in *Proceedings of the ACM SIGCOMM 2011 Conference, SIGCOMM'11*, ACM, New York, NY, USA, pp.350–361.
- Govindaraj, P. and Jaisankar, N. (2017) 'A review on various trust models in cloud environment', *Journal of Engineering Science & Technology Review*, 1 March, Vol. 10, No. 2, pp.213–219.
- Guo, C., Zheng, X. and Liu, J. (2014) *Uncertain Random Fault Tree Analysis based on Cloud Security Protection Framework*, Vol. 18, No. 10, pp.288–295.
- Hwang, K. and Li, D. (2010) 'Trusted cloud computing with secure resources and data coloring', *IEEE Internet Computing*, September, Vol. 14, No. 5, pp.14–22.
- Jain, J. and Singh, R. (2014) *Improving Service Reliability in Cloud Computing Environment*, 22 March [online] <https://www.ijser.org/researchpaper/Improving-Service-Reliability-in-Cloud-Computing-Environment.pdf> (accessed October 2014).
- Kaur, J. (2012) 'Comparison of load balancing algorithms in a cloud', *International Journal of Engineering Research and Applications*, May–June, Vol. 2, No. 3, pp.1169–1173.
- Kim, D.S., Machida, F. and Trivedi, K.S. (2009) 'Availability modeling and analysis of a virtualized system', in *15th IEEE Pacific Rim International Symposium on Dependable Computing*, Shanghai, China, pp.365–371.
- Kumar, V.S. and Aramudhan, M. (2013) 'Performance analysis of cloud under different virtual machine capacity', *International Journal of Computer Applications*, 1 January, Vol. 68, No. 8 [online] <http://citeseerx.ist.psu.edu/viewdoc/download?doi=10.1.1.404.1248&rep=rep1&type=pdf>.
- Kuyoro, S.O., Ibikunle, F. and Awodele, O. (2011) 'Cloud computing security issues and challenges', *International Journal of Computer Networks (IJCN)*, Vol. 3, No. 5, pp.245–255.
- Lin, Y-K. and Chang, P-C. (2010) 'Estimation of maintenance reliability for a cloud computing network', *International Journal of Operations Research*, May, Vol. 7, No. 1, pp.53–60.
- Liu, C.L. (2007) 'Computing and communication: there's so much that we share', *ICESA*.

- Marston, S., Li, Z., Bandyopadhyay, S., Zhang, J. and Ghalsasi, A. (2011) 'Cloud computing – the business perspective', *Decision Support Systems*, Vol. 51, No. 1, pp.176–189.
- Meçe, E.K. and Driza, E. (2013) 'An approach to evaluate the reliability of web applications in cloud computing using dynamic fault trees', in *BCI (Local)*, p.150.
- Mell, P. and Grance, T. (2009) *Draft Nist Working Definition of Cloud Computing*, 3rd June [online] <https://nvlpubs.nist.gov/nistpubs/Legacy/SP/nistspecialpublication800-145.pdf>.
- Nightingale, E.B., Douceur, J.R. and Orgovan, V. (2011) 'Cycles, cells and platters: an empirical analysis of hardware failures on a million consumer PCs', in *Proceedings of the Sixth Conference on Computer Systems, Ser. EuroSys'11*, ACM, New York, NY, USA, pp.343–356.
- Page, S. (2012) *Cloud Computing-Availability*, ISA/BIT Learning Centre, Tech. Rep.
- Schmidt, M., Fallenbeck, N., Smith, M. and Freisleben, B. (2010) 'Efficient distribution of virtual machines for cloud computing', in *2010 18th Euromicro International Conference on Parallel, Distributed and Network-Based Processing (PDP)*, IEEE, pp.567–574.
- Singh, L.K., Vinod, G. and Tripathi, A.K. (2014) 'Impact of change in component reliabilities on system reliability estimation', *ACM SIGSOFT Software Engineering Notes*, Vol. 39, No. 3, pp.1–6.
- Snyder, B., Ringenberg, J., Green, R.C., Devabhaktuni, V. and Alam, M. (2015) 'Evaluation and design of highly reliable and highly utilized cloud computing systems', *Journal of Cloud Computing*, Vol. 4, DOI: 10.1186/s13677-015-0036-6.
- Vaquero, L.M., Roderer-Merino, L., Caceres, J. and Lindner, M. (2008) 'A break in the clouds: towards a cloud definition', *ACM SIGCOMM Computer Communication Review*, Vol. 39, No. 1, pp.50–55.
- Villalpando, B. and Edouardo, L. (2014) *A Performance Measurement Model for Cloud Computing Applications*, Doctoral dissertation, École de technologie supérieure.
- Vishwanath, K.V. and Nagappan, N. (2010) 'Characterizing cloud computing hardware reliability', in *Proceedings of the 1st ACM Symposium on Cloud Computing, SoCC'10*, ACM, New York, NY, USA, June, pp.193–204.
- Wang, W., Chen, H. and Chen, X. (2012) 'An availability-aware approach to resource placement of dynamic scaling in cloud', in *IEEE Fifth International Conference on Cloud Computing*, Honolulu, Hawaii, June, pp.930–931.
- Zhang, C., Green, R. and Alam, M. (2014) 'Reliability and utilization evaluation of a cloud computing system allowing partial failures', in *2014 IEEE 7th International Conference on Cloud Computing (CLOUD)*, IEEE, June, pp.936–937.

Resource provisioning optimisation for cloud computing systems serving multi-class requests

Rohit Sharma*

Department of Computer Science and Engineering,
Dr. Ambedkar Institute of Technology for Handicapped,
Kanpur – 208024, Uttar Pradesh, India
Email: rohit6615@rediffmail.com

*Corresponding author

Prateek Gupta

Department of Mechanical Engineering,
Indian Institute of Technology,
Kanpur – 208016, Uttar Pradesh, India
Email: ptkgupta@iitk.ac.in

Raghuraj Singh

Department of Computer Science and Engineering,
Harcourt Butler Technical University,
Kanpur – 208002, Uttar Pradesh, India
Email: raghurajsingh@rediffmail.com

Abstract: With many organisations switching to cloud-based systems, the variety of domains using cloud services is increasing steadily. Often, companies own private cloud computing systems to cater to their own needs and reduce dependency on third-party services. These systems serve a multitude of requests of different classes that often require different types of resources. A queuing network-based cost model has been employed to quantify the economics of the system, and an optimisation problem has been set up. In the cost function, higher-order terms have been used which accounts for diminishing marginal productivity. This law is used in microeconomics to study the behaviour of cost for individual service-producing entities, i.e., firms. In this study, the cost of the system has been optimised by calculating the optimal quantity of resources provisioned to the cloud system and the behaviour of the cost of maintaining a profitable cloud-computing system has been discussed.

Keywords: cloud computing; request phase; queuing theory; multi-class.

Reference to this paper should be made as follows: Sharma, R., Gupta, P. and Singh, R. (2022) 'Resource provisioning optimisation for cloud computing systems serving multi-class requests, *Int. J. Ad Hoc and Ubiquitous Computing*, Vol. 40, No. 4, pp.239–249.

Biographical notes: Rohit Sharma is a research scholar at the Dr. APJ Abdul Kalam Technical University, Lucknow, India and currently working as an Assistant Professor in the Department of Computer Science and Engineering, Dr. Ambedkar Institute of Technology for Handicapped, Kanpur, India. He received his BTech and MTech in Computer Science and Engineering from the U.P. Technical University, Lucknow. His research interests include cloud computing, cloud reliability and computational intelligence.

Prateek Gupta is a Bachelors-Masters dual degree in Technology from the Department of Mechanical Engineering at Indian Institute of Technology Kanpur, India. His area of interest is molecular dynamics, conventional manufacturing and cloud computing systems.

Raghuraj Singh received his PhD from the U.P. Technical University, Lucknow, India in 2006, MS from the BITS, Pilani, India in 1997 and BTech in Computer Science and Engineering from the Harcourt Butler Technological Institute, Kanpur, India in 1990. Currently, he is working as Professor and the Head at the Computer Science and Engineering Department of Harcourt Butler Technical University, Kanpur, India.

1 Introduction

Cloud computing is defined by National Institute of Standards and Technology (NIST) as a model for enabling ubiquitous, convenient, on-demand network access to a shared pool of configurable computing resources (e.g., networks, servers, storage, applications, and services) that can be rapidly provisioned and released with minimal management effort or service provider interaction as provided by Mell et al. (2011). With a growing number of enterprises switching over to cloud-based services to meet their internal demands, the analysis of these systems has become imperative to run an enterprise profitably (Etro, 2014; Ellman et al., 2018; Mach and Schikuta, 2011; Greenberg et al., 2008). The formulation of a cost model is a complicated problem in the field of economics due to the increasingly complex nature of the service provider systems (Chun and Choi, 2014; Ellman et al., 2018; Mach and Schikuta, 2011). The types of requests served in the system and the scheduling algorithms employed in the systems are just a few of the many factors of complexity faced by engineers that the cloud providers can tweak to increase the quality of service (QoS) (Ansari et al., 2019; Ferrand et al., 2018; Ayesta et al., 2017). Since most firms grow gradually over time, the technology stack of the firm changes over time, and the resources utilised in the production of the service are often heterogeneous. Such systems are often studied as multi-class systems to model the differences between the different types of resources employed (Anselmi and Casale, 2013). The technological infrastructure of firms also changes over time. These hardware components include data centres (Sampatrao et al., 2017), storage devices, networking components along with data and computational physical resources (Gill and Buyya, 2020). Cloud physical resources like computing servers, storage H/W, and single-tenant bare metal servers are also allocated to users by cloud service providers either elastically or dynamically according to user demand and the services provided by the firms (Guo et al., 2014; Xiong and Perros, 2009). The allocation of these resources to different users depends highly on the structure of the queuing network implemented in the system and the scheduling algorithm employed.

There are three significant service models implemented on cloud systems – infrastructure as a service (IaaS), platform as a service (PaaS) and software as a service (SaaS). The IaaS model provides the fundamental computational, network, and storage resources for customers on-demand. PaaS models offer the customers hardware, software, and infrastructure to develop, deploy, manage, and run applications created by them or acquired from a third-party pay-as-you-go basis. SaaS, on the other hand, provides access to users to a service provider's cloud-based software. Users access the applications on a cloud while the infrastructure, platform, data, application code, security, availability, and performance of the application cloud are managed and owned by the cloud provider (Armbrust et al., 2010).

There are various measurements of the quality of service used in the industry for quantifying the performance of cloud systems. Response time, throughput rate, and server availability are the major ones studied in literature (Mansouri et al., 2019; Xiong and Perros, 2009). The most well-known method of improving the QoS of a given system is to increase the number of relevant resources allocated to the system. However, the increase in the resources provisioned for the system also increases the cost the firm has to pay to keep the system operational. This trade-off is the driving force of the research on optimising the high-performance computing systems used for commercial purposes. In order to guarantee a minimum level of QoS to the customer, a service level agreement (SLA) is drawn between the service provider and the user. There have been several studies published discussing the different SLA policies used by cloud providers (Hussain et al., 2017; Maarouf et al., 2015). A low rate of SLA violations is necessary to establish the system's reliability from a consumer perspective. SLA violations in this work have been measured in terms of overflow errors in the system. The relevant formulations have been discussed in the subsequent sections. In literature, several schemes have been used to quantify the reliability of a system. However, for this work, the throughput rate of the system and the average queue length has been used as a measure of the reliability of the system.

There is abundant literature on the use of queuing theory to model cloud computing systems (Anselmi and Casale, 2013; de Assunção et al., 2010; Guo et al., 2014). These publications consider several scenarios that are observed in these queues, including reneging, abandonment, balking, etc. (Bai et al., 2015; Chiang et al., 2016; Chiang and Ouyang, 2014). Similarly, several works have proposed different cost models to characterise the efficiency and performance of the systems in question (Chiang et al., 2016; Chiang and Ouyang, 2014; Ellman et al., 2018; Saha et al., 2016). However, very few studies have discussed the cost functions and viability of their cost models using the micro-economic law of proportions and economic costs into account while differentiating between the fixed cost and the variable cost of the system (Mach and Schikuta, 2011). Even from the studies that have considered these factors, the work is focused mainly on the consumer side of the transaction, and the producer side of the transaction is seldom discussed. In this work, our focus is on the system's producer-side economics. The main contributions of this work are summarised as follows:

- A stochastic model to analyse the performance of the request phase of a cloud computing system has been proposed. The model is based on queuing theory, and hence the results can be studied analytically in the form of closed-loop equations.
- The model proposed takes multiple classes of requests entering the system into consideration and hence models them as a queuing network.

- The cost analysis of the system has been done on the producer side, i.e., to reduce the cost of production of the cloud services. The cost function has been modelled based on principles of microeconomics.
- To account for the diminishing marginal productivity of variable resources, the second-order term for the resources has also been included in the cost model however the formulation can be easily extended to higher-order terms.
- The problem of making decisions for resource allocation has been formulated as an optimisation problem to reduce costs taking SLA considerations and the costs of violating them into account.

The rest of the paper has been organised as follows. The relevant literature for this work has been summarised in Section 2. An overview of the system under consideration has been given in Section 3 while the detailed structure of the system has been discussed in Subsection 3.1. The analytical modelling of the system has been extensively explained in Subsection 3.2. The cost model, along with all the relevant microeconomics theory, has been discussed in detail in Subsection 3.3. The methodology of the study has been discussed in Section 4. The GitHub directory for accessing the codes used for this work, as well as the software tools for the work, have also been mentioned in the opening paragraph of this section. The results have been discussed in Section 5. The behaviour of the system has been discussed in Subsections 5.1 to 5.3 and the cost analysis of the system has been presented in Subsection 5.4. The concluding remarks for the work, as well as the improvements in the work that can be implemented in the future, have been discussed in Section 6.

2 Related work

As mentioned in the previous sections, a number of works have been conducted on the use of queuing theory to model cloud computing systems (Anselmi and Casale, 2013; de Assunção et al., 2010; Guo et al., 2014). A few of these works concentrated exclusively on multi-class systems (Vetha and Devi, 2017). A number of these works have also looked at the SLA contracts and their effect on the cloud providers. The problem of cost optimisation in cloud computing systems has also been studied in literature, however most of the work in literature in this domain has been on the consumer side, and the number of works that combine multi-class queues and a cost optimisation model is not explored in enough depth.

An extensive review of the various SLAs was presented by Slimani et al. (2021). The work was a review paper which presented various key results on the basis of which SLAs are drafted. They also identified the major SLA violations that take place in the cloud computing industry and the economic cost associated with them. A number of works studying SLAs and their effects on the cloud providers have been presented.

Anselmi and Casale (2013) studied the revenue maximisation of multi-class queues. They used a revenue maximisation approach which aimed at calculating the optimal size of user population for a cloud computing system. They also used queuing theory to model their cloud computing system. However in a realistic setting the cloud computing market is more of an oligopoly instead of monopoly and hence the model they used applies only for large cloud service providers whereas our model is aimed at MSME level-firms.

Liu et al. (2020) presented a model to optimise the resource provisioning and allocation for a cloud-based system according to micro-economic theory in mobile edge computing. They presented a market-based model and focused on the consumer-side economics of the system contrary to the producer side economic approach presented in this paper. They formulated a utility maximisation problem for optimising the allocation of resources to optimise the utility of the consumer constrained to the budget of the consumer. In this work we have formulated a cost minimisation problem for the cloud provider, hence focusing on maximising utilisation of the resources needed to produce the cloud computing service and maintaining it. The study of the cloud computing system using queuing theory is however outside the scope of the work by Liu et al.

In the work reported by Xiong and Perros (2009) a relationship was obtained between the number of customers for a given system, the resources employed, and the best possible quality of service that can be delivered. In the study, the consumers were assumed to give utmost priority to the system's response time, which was hence used as the measure of QoS or as a key performance indicator (KPI), and the throughput rate of the system was ignored. More importantly the economic costs of the system were not discussed in the work.

In Wardat et al. (2018), a revenue model for cloud systems was proposed. According to their work electricity consumption cost is a considerable share of the costs in a cloud computing system. In our work we have included the electricity consumption cost as variable costs which is in agreement with their theory. They proposed server consolidation as an effective technique to reduce these costs. They further present an expansion strategy for cloud service providers to increase revenue by server consolidation while maintain service quality in agreement with the SLAs signed.

Mach and Schikuta (2011) provided a comprehensive economic study on the costs of cloud computing systems. They classified costs of a cloud computing system into variable costs and fixed costs and used micro-economic theory to model the marginal costs of the systems similar to the approach followed in this work. Their work focussed on the depreciation cost of the infrastructure as well but neglected the inner workings of the cloud computing system and the losses due to SLA violations which have been accounted for in this paper.

In Saha et al. (2016), a revenue model is proposed for cloud data centres that use the Cobb-Douglas production

function to model productivity. In this work, the authors used the Lagrangian multiplier for optimising the revenue of the firm contrary to the numerical methods utilised in this work. Similarly, in work by Sampatrao et al. (2017) a Cobb-Douglas function was used as the production function of a cloud computing system. The Cobb-Douglas function was employed to satisfy the law of proportions in the cost function employed. In Mansouri et al. (2019), the cost optimisations were performed on a dynamic system. Chen and Meyn (1999) conducted an optimisation on queuing network using a value iteration method. The work was directed towards multi-class scheduling problems. Several scheduling strategies involving the use of resources from the clouds are examined, and it was shown that these strategies achieve a balance between performance and usage cost and improve service response time.

de Assunção et al. (2010) proposed a costing model that systematically evaluates cloud services combining compute, disk storage, and memory requirements. They provided an insight into the various strategies upon technology tools and processes used in cloud management optimisation.

3 System description

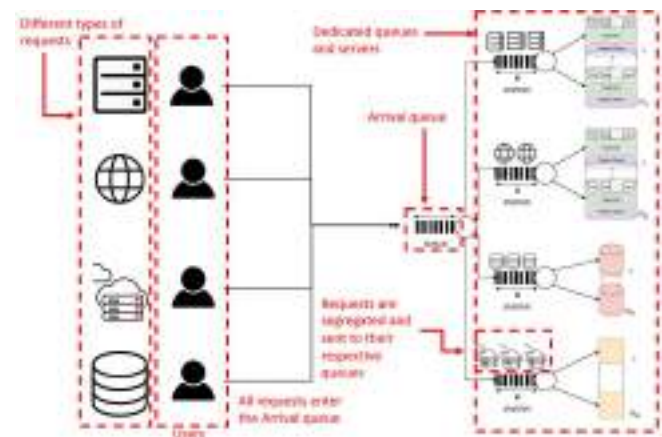
A cloud computing system can be divided into two parts, i.e., the request phase and the execution phase (Dai et al., 2009). In this work, the request phase of a multi-class multi-server cloud computing system has been modelled. We aim to optimise the operational cost of the system by calculating the optimal number of servers to be employed for each class of requests that are served. A description of the structure of the cloud computing system studied has been discussed in Subsection 3.1 modelling of the request phase has been accomplished using queuing theory in Subsection 3.2. The modelling of the cost function and the constrained cost optimisation function has been discussed in Subsection 3.3.

3.1 System structure

A schematic of the structure of the system being studied is given in Figure 1. The structure used is quite simple, and similar structures for cloud computing systems have been used in literature for studying multi-class systems (Bai et al., 2015; Vetha and Devi, 2017). Any request that comes from the user population is pushed into the scheduler queue (also referred to as the arrival queue as in Figure 1), all the requests received by the cloud first enter this queue. This scheduler queue is serviced by a scheduler. The scheduler might be a dedicated physical unit, or simply a software cloud monitoring system (CMS) (Li et al., 2017). The purpose of the scheduler is to segregate the incoming requests into various classes and forward them to the dedicated server queues where they are serviced by the respective dedicated servers. Cloud computing systems consist of various different types of requests each of which requires different set of hardware parameters.

These different types include computing requests, storage requests, bare metal server requests, web requests etc. or may even represent requests with different priority groups (Ellens et al., 2012). In this work we assume that different classes of requests require different hardware requirements and hence dedicated servers for each class are used. Furthermore the scheduler has been assumed to be a single entity for this work. Hence a $M/M/1/K$ queuing model has been used to model the scheduler queue. This queue is henceforth referred to as the scheduler queue. The scheduler node is assumed to be well equipped to handle the segregation of the requests. Hence for this queue, the service time has been assumed to be much lower than the request inter-arrival time. Different methods in which classes can be formed along with the segregation of requests into various classes have been studied extensively in literature and hence it is not a subject of study in this work (Ansari et al., 2019; Çil et al., 2011; Mayekar et al., 2015; Vetha and Devi, 2017). As shown in Figure 1, each class of requests has been allotted to their dedicated servers (Narman et al., 2014). These dedicated servers have their separate queues that have been called as service queues in this work. Hence, the requests are pushed into the service queue for their respective class, where they wait to be serviced by the dedicated servers. During the entire run-time, the system's state is monitored and logged by the CMS for gathering data regarding consumer behaviour and to gather data to characterise the utilisation of the system as well as fault monitoring.

Figure 1 Schematic of the system being modelled (see online version for colours)



3.2 Analytical modelling

The whole system can be modelled as a stochastic process that has been modelled using a queuing theory. Queuing theory has been used extensively in the literature to study cloud computing systems (Chiang et al., 2016; Dai et al., 2009; Cui et al., 2017; El Kafhali and Salah, 2018; Liu et al., 2020; Wang and Xia, 2019). The scheduler queue has been modelled as a $M/M/1/K$ queue. K is the buffer size of the queue. The arrival rate of the requests has been assumed to be in a Poisson distribution. The inter-service

rates for the various servers have been assumed to be exponentially distributed. The various symbols and notations used in the analytical part of the work have been listed in Table 1. The mean arrival rate of the requests in the scheduler queue is λ_S and the average service time for the scheduler is μ_S . This assumption of an exponentially distributed inter-arrival and inter-service time has been used extensively to study stochastic processes in different studies (Cui et al., 2017; Liu et al., 2020; Zhao et al., 2019). (As described in the Subsection 3.1, $\rho_S < 1$ where $\rho_S = \lambda_S/\mu_S$) In this work, the service time of the scheduler for different requests has been taken to be independent of the request class. The buffer size (or the maximum size) of the scheduler queue is K_S . The throughput rate of the queue is hence given as λ_S^f in equation (1).

$$\lambda_S^f = \lambda \left(1 - \rho^{K_S} \left(\frac{1 - \rho}{1 - \rho^{K_S+1}} \right) \right) \quad (1)$$

The number of requests passing through the scheduler belonging to each class can be predicted by the class fraction matrix $\Omega_{N \times 1}$ which is given as follows in equation (2):

$$\Omega_{N \times 1} = \begin{bmatrix} f_1 \\ f_2 \\ f_3 \\ \vdots \\ f_N \end{bmatrix} \quad (2)$$

This matrix is a theoretical construction and can be obtained by the CMS. The i^{th} row in the matrix represents the fraction of requests for the i^{th} class from all the requests received. Where N is the number of classes of requests served by the system. It must be noted that $f_i \geq 0 \forall 0 < i \leq N$ and $i \in N$. f_i is defined as in equation (3):

$$\Lambda_{N \times 1} = \lambda_S^f \Omega_{N \times 1} = \lambda_S^f \begin{bmatrix} f_1 \\ f_2 \\ f_3 \\ \vdots \\ f_N \end{bmatrix} = \begin{bmatrix} \lambda_1 \\ \lambda_2 \\ \lambda_3 \\ \vdots \\ \lambda_N \end{bmatrix} \quad (3)$$

where λ_i is the mean arrival rate of requests of class i and $\Lambda_{N \times 1}$ represents the class distribution matrix representing the arrival rate for different classes in the system. Let the i^{th} queue serve the i^{th} class of requests. The individual class specific queues can be modelled as independent $M/M/R/K$ queues. The mean arrival and service time of the i^{th} queue is given by λ_i and μ_i respectively. Similarly the number of servers dedicated to the i^{th} queue is R_i and the buffer size is K_i . The value of ρ_i is defined as $\rho_i = \lambda_i/\mu_i$. In this study we aim to find the optimal value of R_i for the system. The steady state probability of having n requests in the i^{th} queue is given as π_i^n . It is calculated as per equation (4):

$$\pi_i^n = \begin{cases} \pi_i^0 \frac{(\rho_i)^n}{n!}, & \text{if } 0 \leq n \leq R_i - 1 \\ \pi_i^0 \frac{n!}{R_i! R_i^{n-R_i}} \rho_i^n, & \text{if } R_i \leq n \leq K_i \end{cases} \quad (4)$$

The value of π_i^0 is derived from the axiom that $\sum_{m=0}^{K_i} \pi_i^m = 1$. Equation (4) substituted in this equation

can be used to derive the value of π_i^0 and hence the value of π_i^n can be obtained from equation (5):

$$\pi_i^0 = \left[\sum_{n=0}^{R_i} \frac{\rho_i^n}{n!} + \frac{\rho_i^{R_i}}{R_i!} \sum_{n=R_i}^{K_i} \left(\frac{\rho_i}{R_i} \right)^{n-R_i} \right]^{-1} \quad (5)$$

Table 1 List of variables and notations used throughout the paper along with their meanings

Symbol	Description
λ_S	Mean arrival rate in scheduler queue
ρ_S	λ_S/μ_S ρ_S for scheduler
λ_S^f	Throughput rate of scheduler queue
λ_i	Throughput rate of i^{th} service queue
R_i	Number of server units in i^{th} service queue
π_i^n	Steady state probability of having n requests in i^{th} service queue
P_i^{loss}	Probability of a request being dropped due to overflow error in i^{th} service queue
λ_i^f	Throughput rate of i^{th} service queue
L	Variable factors of production
C_{var}	Expenditure on variable factors of production
Q_L	Marginal product of variable factors of production
C	cost of production of goods and services
μ_S	Mean service rate of scheduler
K_S	Buffer size of scheduler queue
$\Omega_{N \times 1}$	Class fraction matrix representing fraction of requests for N different classes
$\Lambda_{N \times 1}$	Class distribution matrix representing rate of requests for N different classes
ρ_i	λ_i/μ_i
μ_i	Service rate of i^{th} service queue
K_i	Buffer size of i^{th} service queue
L_i	Average number of requests in i^{th} service queue at steady state
λ_i^{loss}	Average drop rate of i^{th} service queue
K	Fixed factors of production
C_{fixed}	Expenditure on fixed factors of production
Q	Output of production
$\phi_{N \times 3}$	Cost matrix of a system containing N classes and three terms in the cost function (cost function for individual queue)
L_i	Average number of requests in the buffer of the i^{th} queue in steady state

The average number of requests in the queue is given as per equation (6) and the steady state probability of a given request to be dropped due to overflow errors (Dai et al., 2009) is given in the equation (7):

$$L_i = \sum_{n=0}^{K_i} n \pi_i^n \quad (6)$$

$$P_i^{\text{loss}} = \pi_i^{K_i} = \pi_i^0 \left(\frac{\rho_i^{K_i}}{R_i! R_i^{K_i-R_i}} \right) \quad (7)$$

Hence the throughput rate for the i^{th} queue and the average drop rate is given in equation (8) and 9:

$$\lambda_i^f = \lambda_i (1 - P_i^{\text{loss}}) \quad (8)$$

$$\lambda_i^{\text{loss}} = \lambda_i P_i^{\text{loss}} \quad (9)$$

3.3 Cost model and optimisation problem formulation

Micro-economics is the branch of economics that deals with the modelling of individual firms and consumers. In order to produce goods and services any firm (the cloud service provider in this case) requires a number of resources (Pindyck et al., 1995). These resources are termed as the factors of production and are considered as inputs for production (Gans et al., 2011). The factors of production can usually be classified into two groups as shown in Figure 2 in the short run, i.e., fixed and variable. The fixed factors of production are the inputs whose amount can not be changed in the short run. For a cloud computing system, an example of these factors would be the infrastructure allocated for the system, the upper administration and management of the firm, the heavy equipment employed in the cloud system, cooling etc and is usually represented using the variable K . On the other hand, variable factors of production are the resources whose quantity can be changed in the short term example number of low level staff and maintenance personnel, electricity consumption, the number of servers employed in the system has been assumed to be the variable factors of production and are represented as L . The various variables and symbols used in this subsection have also been listed in Table 1 for reference.

A similar classification is also performed in terms of the cost of the system. The system's fixed cost is defined as the cost independent of the firm's output, while its variable cost is defined as the part of the costs that vary with the quantity of the goods/services produced. This classification has been studied extensively in the domain of cloud computing by Mach and Schikuta (2011). The construction of a realistic cost model is a pervasive topic in research in economics for any given firm, and the domain of cloud computing is no exception (Etro, 2014; Greenberg et al., 2008; Mach and Schikuta, 2011). The cost of production of goods and services is hence given in equation (10):

$$C = C(K, L) = C_{fixed} + C_{var} \quad (10)$$

where K is the amount of the fixed factor of production, L is the variable factor of production and C stands for the cost of production. Assuming Q as the output (number of units of goods produced) we define the marginal product of variable factors of production in equation (11):

$$Q_L = \frac{Q(K, L + \Delta L) - Q(K, L)}{\Delta L} = \frac{\partial}{\partial L} Q(K, L) \quad (11)$$

The law of diminishing marginal productivity states that keeping the level of fixed factors of production constant, the marginal product of an input declines as the quantity of the input increases Which is mathematically states as in equation (12). This is also called the law of diminishing returns and follows from the law of proportions. In other words, for each additional unit of the variable resource employed, the firm has to pay an enormous economic cost.

$$\frac{\partial}{\partial L} Q_L(K, L) = \frac{\partial^2}{\partial L^2} Q(K, L) <= 0 \quad (12)$$

In this work, we are considering the system in the short run, and hence it becomes imperative for the validity of the

analysis to use a cost function that complies with the law of diminishing marginal productivity. Since we are working in the context of cloud computing the cost of requests dropped by the servers also need to be taken into account since they result in violations of SLAs (Slimani et al., 2021). Hence for a given queue, the cost function used is as equation (13):

$$C = C_0 \lambda^{loss} + C_1 R + C_2 R^2. \quad (13)$$

The marginal cost of R is hence given as equation (14):

$$C_R = C_0 \frac{\Delta \lambda^{loss}}{\Delta R} + C_1 + 2C_2 R \quad (14)$$

Since the $2C_2 R$ term is increasing in R and C_1 is a constant, the proposed cost model follows the law of diminishing marginal productivity. The cost model takes into account the variable costs in the system. The variable costs include the number of servers employed in the system, i.e., R_i and the rate at which requests are dropped λ_i^{loss} . Literature is abundant on the dynamics of SLAs that are used by different companies when serving clients in the cloud computing industry (de Carvalho et al., 2017; Chiang et al., 2016; El Kafhali and Salah, 2018; Hussain et al., 2017; Li et al., 2017; Slimani et al., 2021). The SLA dictates the QoS that the cloud provider needs to provide. In order to extend the cost model to cover the whole queuing system, the cost of the system is represented in a generalised for N request classes using the cost matrix Φ . It should be noted that $\phi_{i,j} = C_{i,j-1}$

$$\Phi = \begin{bmatrix} C_{1,0} & C_{1,1} & C_{1,2} \\ C_{2,0} & C_{2,1} & C_{2,2} \\ \vdots & \vdots & \vdots \\ C_{N,0} & C_{N,1} & C_{N,2} \end{bmatrix} \quad (15)$$

$$cost = \sum_{i=1}^{i=N} \Phi_{i1} \lambda_i^{loss} + \Phi_{i2} R_i + \Phi_{i3} (R_i)^2 \quad (16)$$

The optimal resource provisioning is hence formulated as an optimisation problem:

$$\text{Minimise: } cost(\lambda_i, \mu_i, R_i, K_i) \quad \forall, 0 < i \leq N, i \in \mathbb{N} \quad (17)$$

$$\text{Such that: } 0 < R_i \leq K_i \quad \forall, 0 < i \leq N, i \in \mathbb{N} \quad (18)$$

$$0 < N \quad (19)$$

Φ for the case varies as per the infrastructure available to the service provider. The value C_1 is the linear coefficient of R and C_2 represents the phenomenon that increasing the fixed capital without increasing the infrastructure and other resources proportionally result in increasing costs per unit employed of the machine.

4 Methodology

All numerical calculations were performed using MATLAB using live scripts. All the relevant codes for the work have been uploaded to a GitHub directory (<https://github.com/prateekkggupta/Resource-provisioning-optimisation.git>) and

are available in the public domain. The graphs have been plotted using R language on RStudio, which is available as an open-source software (R Core Team, 2013; RStudio Team, 2020). A system as described in the previous sections has been simulated on MATLAB. The various values used in the results have been obtained after sufficient pilot experiments and literature review. The various parameters of the system were varied to observe the behaviour of the KPIs of the systems. The KPIs used in the study have been extensively used in literature to characterise the performance of (El Kafhali and Salah, 2018) cloud computing systems. The cost system was then added to the system to simulate the economics of the firm. The data for different resource allocations for each of the service queue was extracted and used to calculate the optimal resource provisioning for each of the service queues.

5 Results and discussion

In this section, the behaviour of the system as described in Section 3 has been discussed. Subsections 5.1 to 5.3 discuss the behaviour of the $M/M/R/K$ queuing model used primarily in the second stage of the queuing network under consideration. The $M/M/1/K$ queuing model can be simply studied as a particular case of the $M/M/R/K$ model for which $R = 1$. This implies that the results of the $M/M/R/K$ can be used directly to analyse that queue as well. The behaviour of the system in terms of the steady state probability of having n requests in the queue for a single queue for different values of the service rate (processing rate) of the server has been discussed in Subsection 5.1. The behaviour of the system in terms of the average length of the queue in the system with respect to

the buffer size of the system for a given value of arrival rate and service rate for different values of R has been discussed in Subsection 5.2. The losses in the system along with the probability distribution, P_n have also been noted in Subsection 5.3. In Subsection 5.4, the results of the cost model proposed were studied. The cost model was applied to a system as described in the previous section. Different costs for different classes of requests were used to get a comprehensive picture of the effects of the cost function.

5.1 System behaviour with respect to service rate μ

The steady-state probability of the queue having n requests in the servers has been shown in Figure 3. The figure has been plotted for a $M/M/R/K$ system which is representative of any individual class of requests in the system as described in Subsection 3.2. The data has been plotted for $\lambda = 100$ requests/min, $R = 5$ and $K = 25$. It has been noticed that after $n = 5$ the curves can be classified as increasing ($\mu = 17, 18, 19$), constant ($\mu = 20$) or decreasing ($\mu = 21, 22$).

For all the values of μ (service rate) simulated the plot shows a kink at $n=R$. The kink can be explained by the piece-wise definition of the probability function in equation (4). The nature of the slope of the plot varies for different values of μ . for the value of $\lambda > R\mu$ The slope of the plot is negative, the slope is positive for $\lambda < R\mu$ and the slope ≈ 0 for $\lambda = R\mu$. This can be explained physically as the when the rate of request arrival (λ) is greater than the rate of processing $R\mu$ the system tends to be under-provisioned and hence the requests overflow and vice versa for the case when the arrival rate is lower than the processing capacity.

Figure 2 Classification of factors of production (see online version for colours)

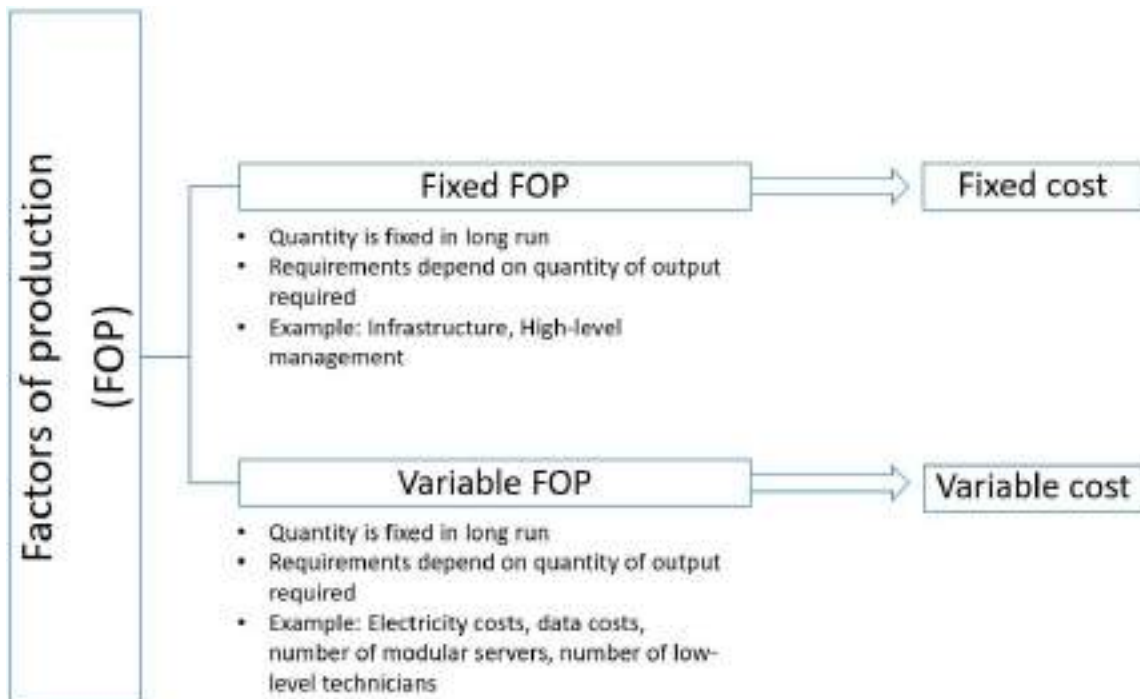
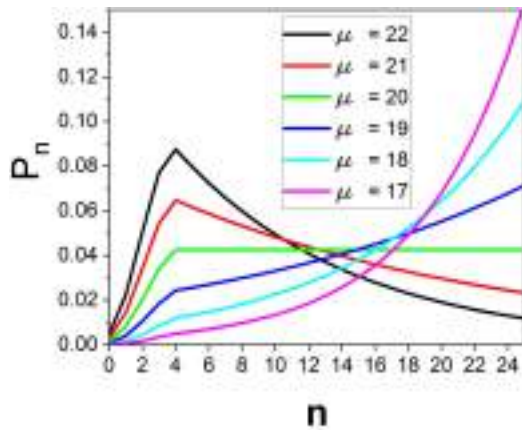


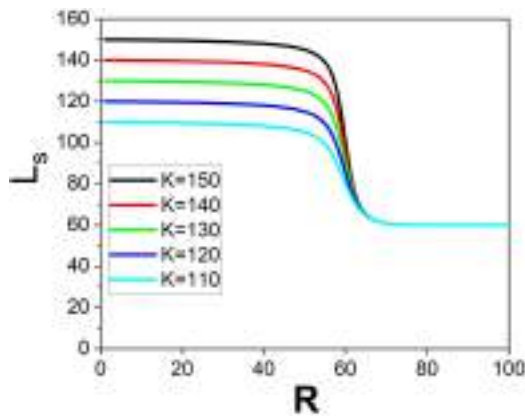
Figure 3 P_n v/s n for various values of μ (see online version for colours)



5.2 System behaviour with respect to buffer size (K)

The average number of requests in the system has been plotted in Figure 4. The curves have been plotted for different values of buffer size K . The mean arrival rate for this graph is taken as $\lambda = 1200$ requests/minute, and the service rate has been taken as $\mu = 20$ requests per minute. A sudden change in slope for the curves is observed in the neighbourhood of $R = 60$ which occurs to be the value for which $\rho = 1$ or $\lambda = R\mu$ after which the system tends to reduce the queue length to a constant value, i.e., $L_s \approx \lambda/\mu$. However, it is essential to emphasise the behaviour of the average queue length, L_s for $\rho < 1$. In this range, the system tends to use up all the buffer available. This is because the system is not fast enough to serve the requests as they come, and the requests end up piling in the buffer, eventually overflowing. This implies that any increment of the value of K for the system will not be helpful as the requests will take up any available space in the buffer irrespective of the size of the buffer.

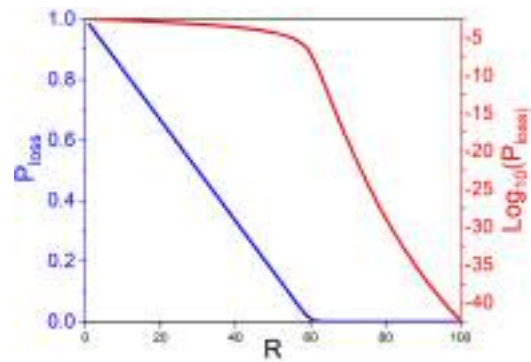
Figure 4 Length of queue L_s v/s R for different values of K (see online version for colours)



5.3 Overflow rate with respect to number of servers deployed R

The curve for this loss probability has been given in Figure 5. It was observed that the value of K does not result in any significant difference in the curves as long as $K > 100$. The decrease in the probability of dropping a request decreases approximately linearly and then becomes negligible. Similar behaviour has also been noted for the $M/M/R/K$ queuing system in the literature (Ghosh et al., 2013, 2014; El Kafhali and Salah, 2018).

Figure 5 Overflow probability v/s R (see online version for colours)



5.4 Cost and performance analysis

In this subsection the cost model suggested in Subsection 3.3 has been applied on a cloud computing system as described in Subsection 3.1. The system studied serves four different types of requests. Each the class of requests requires different type of infrastructure to be processed and is serviced by its dedicated queue. The cost for servicing each type of requests is also different since the infrastructure to process them is different. The four classes of requests in this case are web requests (abbreviated as wr), computing requests (abbreviated as cr), storage request (abbreviated as sr) and bare metal server request (abbreviated asbm). The data used in this study is given in Table 2. The behaviour of the cost of the system has been discussed in Subsection 5.4.1. The behaviour of the length of queue and the performance of the system at optimised resource provisioning R_i has been described in Subsection 5.4.2.

5.4.1 Behaviour of cost of the system with respect to resource provisioning

In Figure 6 of different classes of the system have been studied. The shape of the curves for all classes in the curve is quite similar as all the classes share the same $M/M/R/K$ queuing model. The pattern can be summarised as follows. A similar analysis of the revenue of cloud computing systems has been observed in work by Mach and Schikuta (2011):

- A positive Y-intercept, which results from the $\approx 100\%$ drop rate of the queue.
- A decreasing cost of the system. The decrease is due to the increase in the throughput rate of the system, which results in a lower number of SLA violations since the value of λ_i^{loss} decreases.
- The decrease in the costs due to fewer SLA violations supersedes the cost of adding additional servers to the queues.
- As the rate of decrease of the drop rate of the queue decreases, the cost of increasing R_i becomes more prominent compared to the former. The cost of the queue hence begins increasing. This results in the positive sloped region of the curve.

The position and existence of an optimisation point are very much subjected to the cost function used and the constraint of the computing system. Depending on the values, the optimum may lie on the boundaries of the cost curve, i.e., $R_i = 0$ in which case it might not be profitable to serve the particular class of requests or at $R_i = K_i$ in which case the value of K_i can be increased to get the optimisation point. Subsection 3.3. The optimum points for the given data have been tabulated in Table 3. The system losses in the respective queues decrease monotonically with an increasing R_i as seen in Figure 7. On the other hand, every unit of R_i added to the queue also adds a particular cost to the system. Hence a point of minima is obtained as per the optimisation problem set up in subsection. An important point to be noted is that the optimisation might not necessarily be obtained at the point where a majority of requests are being served (Chun and Choi, 2014; Laverty et al., 2014).

Table 2 Parameters for calculations involved in obtaining Figures 6 and 7

Parameter	Value	Unit
λ_{tb}	12,800	Requests per minute
μ_{tb}	64,000	Requests per minute
N	4	-
$\Omega_{N \times 1}$	$[0.4 \ 0.3 \ 0.2 \ 0.1]^T$	-
μ	$[50, 45, 40, 35]^T$	Requests per minute
Φ	$\begin{bmatrix} 0.75 & 10 & 0.15 \\ 0.65 & 10 & 0.3 \\ 1 & 9 & 0.15 \\ 2 & 10 & 0.3 \end{bmatrix}$	As per equation (16)

Table 3 Results for optimisation of system based on parameters given in Table 2, total cost = 6,770.6

i	Class name	P_i^{loss}	Cost	R_i^*
1	Web request	11.14%	2,579.8	91
2	Computing request	0.06%	2,187.2	32
3	Storage request	0	1,213.3	63
4	Bare metal server request	0	790.3	37

Figure 6 Cost of the system v/s R_i for different classes (see online version for colours)

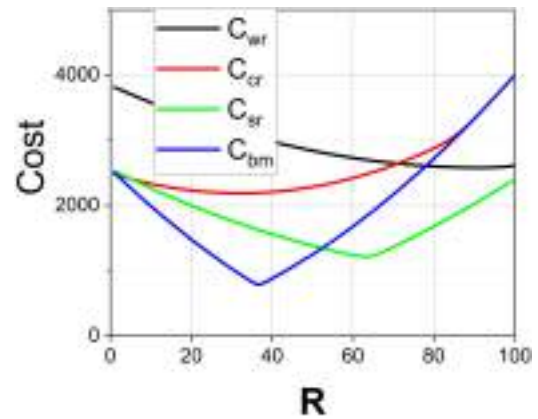
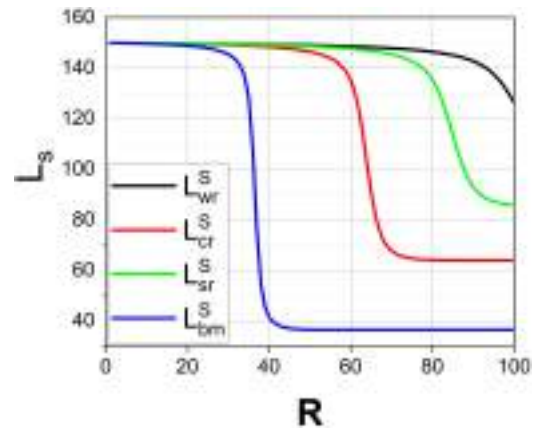


Figure 7 Loss probability v/s R_i for different classes (see online version for colours)



5.4.2 Performance of the system at the obtained optimisation point

As shown in the data about $i = 1$ the optimisation does not imply a 100% (approximately) throughput rate. For example in the case of $i = 1$ the throughput rate is $\approx 88.86\%$. However, the position of the optimisation point depends highly on the parameters of the cost function and the equation of the cost function employed. The allowed drop rate of the system is often dictated by the SLA between the cloud provider and the customers using the services. In that case, additional constraints may be added in the system, which has been done as in work by Chiang et al. (2016).

6 Conclusions and future scope

6.1 Conclusions

In this work, we model a cloud computing system based on queuing network that serves multiple classes of requests. A micro-economically viable cost model was set-up and applied to a cloud computing system. The cost model was utilised to observe the behaviour of the cost of the system and detect over-provisioning and under-provisioning of the

systems. A optimisation problem was set up in terms of the cost model discussed and optimal resource provisioning was calculated for each of the classes of requests taking the SLA violations into considerations. It was also concluded that it is possible to run a profitable cloud computing system while tolerating a certain amount of SLA violations.

6.2 Scope for future research

The queuing network studied was a simple one and consisted of a single scheduler node. However the multitude of queueing systems with different architectures are in use in the industry and hence there is a need to study and model these architectures. Queueing theory was used to model the arrival and service of the system as a stochastic process and hence the results discussed pertain to a steady state. Additionally the work only analyses the queuing system in steady state and phenomenon like burst arrivals have not been taken into account and can be a subject of study in the future. Also, the study focused only on the request phase of the system. The model studied was static, and further work can be done on dynamic provisioning of resources that depict a more realistic situation, especially to the adaptiveness of the systems in the future. The effects of the QoS agreements can also be taken into account in the cost model and performance analysis to develop cost functions that are a more realistic depiction of the industry.

References

- Ansari, S., Debo, L. and Iravani, S. (2019) 'Optimal policy in single-server multi-class queueing systems with abandonment', *SSRN Electronic Journal*, pp.1–19 [online] <https://ssrn.com/abstract=3453227> or <http://dx.doi.org/10.2139/ssrn.3453227>.
- Anselmi, J. and Casale, G. (2013) 'Heavy-traffic revenue maximization in parallel multiclass queues', *Performance Evaluation*, Vol. 70, No. 10, pp.806–821.
- Armbrust, M., Fox, A., Griffith, R., Joseph, A.D., Katz, R., Konwinski, A., Lee, G., Patterson, D., Rabkin, A., Stoica, I. et al. (2010) 'A view of cloud computing', *Communications of the ACM*, Vol. 53, No. 4, pp.50–58.
- Ayesta, U., Jacko, P. and Novak, V. (2017) 'Scheduling of multi-class multi-server queueing systems with abandonments', *Journal of Scheduling*, Vol. 20, No. 2, pp.129–145.
- Bai, W-H., Xi, J-Q., Zhu, J-X. and Huang, S-W. (2015) 'Performance analysis of heterogeneous data centers in cloud computing using a complex queueing model', *Mathematical Problems in Engineering*, Vol. 2015, No. 4, pp.1–15.
- Chen, R.R. and Meyn, S. (1999) 'Value iteration and optimization of multiclass queueing networks', *Queueing Systems*, Vol. 32, Nos. 1–3, pp.65–97.
- Chiang, Y.J. and Ouyang, Y.C. (2014) 'Profit optimization in sla-aware cloud services with a finite capacity queueing model', *Mathematical Problems in Engineering*, Vol. 2014, Article ID 534510, 11pp [online] <https://doi.org/10.1155/2014/534510>.
- Chiang, Y.J., Ouyang, Y.C. and Hsu, C.H.R. (2016) 'Performance and cost-effectiveness analyses for cloud services based on rejected and impatient users', *IEEE Transactions on Services Computing*, Vol. 9, No. 3, pp.446–455.
- Chun, S.H. and Choi, B.S. (2014) 'Service models and pricing schemes for cloud computing', *Cluster Computing*, Vol. 17, No. 2, pp.529–535.
- Çil, E.B., Karaesmen, F. and Örmeci, E.L. (2011) 'Dynamic pricing and scheduling in a multi-class single-server queueing system', *Queueing Systems*, Vol. 67, No. 4, pp.305–331.
- Cui, H., Li, Y., Liu, X., Ansari, N. and Liu, Y. (2017) 'Cloud service reliability modelling and optimal task scheduling', *IET Communications*, Vol. 11, No. 2, pp.161–167.
- Dai, Y-S., Yang, B., Dongarra, J. and Zhang, G. (2009) 'Cloud service reliability: modeling and analysis', *15th IEEE Pacific Rim International Symposium on Dependable Computing*, pp.1–17, Citeseer.
- de Assunção, M.D., di Costanzo, A. and Buyya, R. (2010) 'A cost-benefit analysis of using cloud computing to extend the capacity of clusters', *Cluster Computing*, Vol. 13, No. 3, pp.335–347.
- de Carvalho, C.A.B., Andrade, R.M.C., de Castro, M.F., Coutinho, E.F. and Agoulmine, N. (2017) 'State of the art and challenges of security SLA for cloud computing', *Computers and Electrical Engineering*, Vol. 59, Special Issue, pp.141–152.
- El Kafhali, S. and Salah, K. (2018) 'Modeling and analysis of performance and energy consumption in cloud data centers', *Arabian Journal for Science and Engineering*, Vol. 43, No. 12, pp.7789–7802.
- Ellens, W., Ivkovic, M., Akkerboom, J., Litjens, R. and van den Berg, H. (2012) 'Performance of cloud computing centers with multiple priority classes', *2012 IEEE Fifth International Conference on Cloud Computing*, pp.245–252, IEEE.
- Ellman, J., Lee, N. and Jin, N. (2018) 'Cloud computing deployment: a cost-modelling case-study', *Wireless Networks*, Vol. 2.
- Etro, F. (2014) 'The economics of cloud computing', *Cloud Technology: Concepts, Methodologies, Tools, and Applications*, Vol. 4, No. 2, pp.2135–2148.
- Ferrand, Y.B., Magazine, M.J., Rao, U.S. and Glass, T.F. (2018) 'Managing responsiveness in the emergency department: comparing dynamic priority queue with fast track', *Journal of Operations Management*, July, Vols. 58–59, Part of Special Issue: SI: EURO 2018, pp.15–26.
- Gans, J., King, S. and Mankiw, N.G. (2011) *Principles of Microeconomics*, Cengage Learning, Monash University, Australia.
- Ghosh, R., Longo, F., Naik, V.K. and Trivedi, K.S. (2013) 'Modeling and performance analysis of large scale IaaS Clouds', *Future Generation Computer Systems*, Vol. 29, No. 5, pp.1216–1234.
- Ghosh, R., Longo, F., Xia, R., Naik, V.K. and Trivedi, K.S. (2014) 'Stochastic model driven capacity planning for an infrastructure-as-a-service cloud', *IEEE Transactions on Services Computing*, Vol. 7, No. 4, pp.667–680.
- Gill, S.S. and Buyya, R. (2020) 'Failure management for reliable cloud computing: a taxonomy, model, and future directions', *Computing in Science & Engineering*, Vol. 22, No. 3, pp.52–63.
- Greenberg, A., Hamilton, J., Maltz, D.A. and Patel, P. (2008) 'The cost of a cloud', *ACM SIGCOMM Computer Communication Review*, Vol. 39, No. 1, pp.68–73.

- Guo, L., Yan, T., Zhao, S. and Jiang, C. (2014) 'Dynamic performance optimization for cloud computing using M/M/m queueing system', *Journal of Applied Mathematics*, Vol. 2014, pp.1–8.
- Hussain, W., Hussain, F.K., Hussain, O.K., Damiani, E. and Chang, E. (2017) 'Formulating and managing viable SLAs in cloud computing from a small to medium service provider's viewpoint: a state-of-the-art review', *Information Systems*, Vol. 71, pp.240–259.
- Laverty, J.P., Wood, D.F. and Turcek, J. (2014) 'Micro and macro economic analysis of cloud computing', *Issues in Information Systems*, Vol. 15, No. 2, pp.293–302.
- Li, X., Liu, Y., Kang, R. and Xiao, L. (2017) 'Service reliability modeling and evaluation of active-active cloud data center based on the IT infrastructure', *Microelectronics Reliability*, Vol. 75, pp.271–282.
- Liu, G., Xiao, Z., Tan, G.H., Li, K. and Chronopoulos, A.T. (2020) 'Game theory-based optimization of distributed idle computing resources in cloud environments', *Theoretical Computer Science*, Vol. 806, pp.468–488.
- Maarouf, A., Marzouk, A. and Haqiq, A. (2015) 'A review of SLA specification languages in the cloud computing', *2015 10th International Conference on Intelligent Systems: Theories and Applications, SITA 2015*, pp.0–5.
- Mach, W. and Schikuta, E. (2011) 'A consumer-provider cloud cost model considering variable cost', *Proceedings – IEEE 9th International Conference on Dependable, Autonomic and Secure Computing, DASC 2011*, pp.628–635.
- Mansouri, Y., Toosi, A.N. and Buyya, R. (2019) 'Cost optimization for dynamic replication and migration of data in cloud data centers', *IEEE Transactions on Cloud Computing*, Vol. 7, No. 3, pp.705–718.
- Mayekar, P., Venkateswaran, J., Gupta, M.K. and Hemachandra, N. (2015) 'Performance analysis and decomposition results for some dynamic priority schemes in 2-class queues', *2015 13th International Symposium on Modeling and Optimization in Mobile, Ad Hoc, and Wireless Networks, WiOpt 2015*, pp.115–122.
- Mell, P., Grance, T. et al. (2011) *The NIST Definition of Cloud Computing*, Special Publications 800-145, Computer Security Division Information Technology Laboratory National Institute of Standards and Technology Gaithersburg, MD 20899-8930, September.
- Narman, H.S., Hossain, M.S. and Atiquzzaman, M. (2014) 'DDSS: dynamic dedicated servers scheduling for multi priority level classes in cloud computing', *2014 IEEE International Conference on Communications, ICC 2014*, pp.3082–3087.
- Pindyck, R.S., Rubinfeld, D.L. and Mehta, P.L. (1995) *Microeconomics*, Vol. 4, Prentice Hall, Englewood Cliffs, NJ.
- R Core Team (2013) *R: A Language and Environment for Statistical Computing*, R Foundation for Statistical Computing, Vienna, Austria.
- RStudio Team (2020) *RStudio: Integrated Development Environment for R*, RStudio, PBC, Boston, MA.
- Saha, S., Sarkar, J., Dwivedi, A., Dwivedi, N., Narasimhamurthy, A.M. and Roy, R. (2016) 'A novel revenue optimization model to address the operation and maintenance cost of a data center', *Journal of Cloud Computing*, Vol. 5, No. 1, p.1.
- Sampatrao, G.S., Dey, S.R., Goswami, B., Prasanna, S.M.S. and Saha, S. (2017) 'A study of revenue cost dynamics in large data centers', *Proceedings of the Second International Conference on Internet of things, Data and Cloud Computing – ICC '17*, pp.1–14, ACM Press, New York, New York, USA.
- Slimani, S., Hamrouni, T. and Ben Charrada, F. (2021) 'Service-oriented replication strategies for improving quality-of-service in cloud computing: a survey', *Cluster Computing*, Vol. 24, No. 1, pp.361–392.
- Vetha, S. and Devi, V.K. (2017) 'Dynamic resource allocation in cloud using queuing model', *Journal of Industrial Pollution Control*, Vol. 33, No. 2, pp.1547–1554.
- Wang, X. and Xia, Y. (2019) 'Performance evaluation and cost optimal service quality prediction of cloud computing systems in unreliable environments', *2019 IEEE International Conference on Power, Intelligent Computing and Systems, ICPICS 2019*, pp.241–249.
- Wardat, M., Al-Ayyoub, M., Jararweh, Y. and Khreishah, A.A. (2018) 'Cloud data centers revenue maximization using server consolidation: modeling and evaluation', *IEEE INFOCOM 2018 – IEEE Conference on Computer Communications Workshops (INFOCOM WKSHPS)*, April, pp.172–177, IEEE.
- Xiong, K. and Perros, H. (2009) 'Service performance and analysis in cloud computing', *2009 Congress on Services – I, Part 1*, pp.693–700, IEEE.
- Zhao, W., Wang, X., Jin, S., Yue, W. and Takahashi, Y. (2019) 'An energy efficient task scheduling strategy in a cloud computing system and its performance evaluation using a two-dimensional continuous time Markov chain model', *Electronics (Switzerland)*, Vol. 8, No. 7, pp.775–790.



Hypergeometrically Represented Responsive and Reliable Cloud Service Model for Personal and Private Clouds

Rohit Sharma¹ · Prateek Gupta² · Raghuraj Singh³

Accepted: 7 February 2022

© The Author(s), under exclusive licence to Springer Science+Business Media, LLC, part of Springer Nature 2022

Abstract

Last two decades have witnessed a tremendous evolution and growth of cloud computing paradigm and reliability estimation techniques. In spite of recent advancements in this field, very little work has been reported over population bounded personal and private clouds. In this work, a highly responsive and reliable queuing model for finite population clouds has been proposed. The model has an explicit feature of varying length of the waiting queue in accordance with the incoming requests and suggesting the number of virtual machines needed per physical machine. This model has been represented in a generalized hypergeometric representation which is a simple way to represent queuing based cloud service model. The performance parameters like server utilization, response time and request stage reliability of the proposed model were thoroughly analyzed and compared with the popular existing cloud queuing model and improvement in server utilisation has been observed.

Keywords Finite population cloud systems · Request stage reliability · Hypergeometric series · Queuing systems · Markovian queues

1 Introduction

Cloud computing design refers to enabling ubiquitous, easy and on demand network access for a shared repository of computer configurable resources like networks, storage, servers, applications and services. These resources are easily provisioned, amended and used by having minimum administrative attempt and service provider communication [1].

Cloud adoption rate is growing faster than predicted. According to Gartner, it is expected that the overall cloud market will grow from \$182.4 billion in 2018 to \$331.2 billion in 2022 with a growth rate of $\approx 12.6\%$ [2]. The adoption of cloud technologies is enabling enterprises, big and small, to be agile, innovative, competitive and capable of

✉ Rohit Sharma
rohit6615@rediffmail.com

¹ Department of Computer Science & Engineering, Dr. Ambedkar Institute of Technology for Handicapped, Kanpur 208024, India

² Department of Mechanical Engineering, Indian Institute of Technology, Kanpur 208016, India

³ Department of Computer Science & Engineering, Harcourt Butler Technical University, Kanpur 208002, India

creating differentiated customer experiences. 74% have adopted cloud to improve customer experience, and 71% use cloud to create enhanced products and services while downsizing legacy systems and reducing costs. More and more organizations are considering cloud adoption strategy in accordance to escalating market expectations that might be better served by born-on-the-cloud competitors or leading-edge cloud adopters, their risk capacity, business needs and investment viability [3].

The highest growing cloud adoption model is that of private clouds which are largely suitable for small enterprises and companies working under strict population constraints. This category of cloud computing environment which is designed to serve a limited number of users is growing, largely amongst organizations across the world [2, 4]. Private clouds may be sub-categorized as on-premise clouds and externally hosted clouds. The major difference between the two is the positioning, deployment, maintenance and control of their data centers and Enterprise Resource Planning (ERP) software. In an on-premise cloud it is the responsibility of the organization itself to take care of its data centers which are situated inside the organization while in externally hosted private clouds data centers are hosted and maintained outside the organization. On-premise private clouds are less affected by price increase, data leakage and external security threats but have higher maintenance costs and lower flexibility as compared to the externally hosted private clouds [5]. Similarly, reliability of private clouds is difficult to spot because of their broad range of service availability, heterogeneously distributed network and connected but diverse and largely varied software/hardware components.

Queuing theory has been observed to be an efficient way of studying cloud computing models [6–13]. Although a variety of queuing models for improving the performance of cloud service management system by reducing the waiting time, improving performance and availability of resources to maintain QoS are available but very little work has been done on queuing systems with dynamic virtual machine provisioning dedicated to finite population private clouds. Therefore, there is a requirement for these private clouds to be modeled by an efficient reliable and dedicated finite population queuing system. The greatest challenge while modeling such specific cloud service systems is to have a check on its request stage reliability which can be optimized by modeling the system with a queuing model intended to minimize the overflow and timeout errors.

After their introduction by Euler as power series expansions, hypergeometric functions were found extremely useful in theory of partitions, number theory [14], finite vector spaces, different combinatorial identities [15] and different applications to applied physics [16]. But, they have never been used for representational and characterization purposes to any cloud queuing model. In this work, all important parameters of the proposed model have been represented using hypergeometric representations. Finite population models are an important part in the study of the availability of limited resources in a realistic environment. Hypergeometric series allow us to model the discrete event model into differential equations that can be applied to systems dealing with continuous flow of resources. This work focuses on the application of hypergeometric series in modelling the reliability of cloud computing systems, however the same principles can be applied in most of the applications that are modelled as a markovian queue in a finite population setting. This also opens opportunities for using different methods to solve differential equations in applications involving discrete event simulations. For example in an assembly line where the maintenance of breaking down machines are modelled as a markovian queue, the limited size of the assembly line implies that a finite population model functions well for theorizing the efficiency and reliability of the maintenance system [17].

The main contributions of this work can be summarized as:-

- This work proposes a service model dedicated for population bounded On-premise and externally hosted private clouds which are becoming extremely popular for both large and small business organizations where high responsiveness for the service requests generated by their workforce is extremely vital. The proposed model is designed in such a way that it will incorporate all the user requests and accordingly set the upper bound for the VMs allowed per Physical Server.
- All standard model parameters are represented using hypergeometric representation which gives it a logical insight and opens up the idea of analyzing a Queuing System in terms of properties of hypergeometric functions.
- Simulation results show that the model fully utilizes the available resources and request stage reliability can be optimized by varying due time for incoming requests .

In Sect. 2 the literature review on applications of hypergeometric functions to various areas of science and engineering covering cloud reliability and service models having finite buffer size and population has been presented. Section 3 describes the proposed cloud service model having a variable size request queue incorporating all the incoming requests for private and community clouds. Probabilistic terms of all the performance parameters are represented in terms of special terminating generalized hypergeometric series. In Sect. 4 the request stage reliability of the system is analyzed in terms of timeout errors. Numerical results depicting enhanced system performance and comparison of results has been presented in Sect. 5. Significant conclusions of the proposed work along with the future scope is given in Sect. 6.

2 Related Work

Modeling of cloud service systems is a perplexing research areas in recent times. A large number of queuing models are available for cloud data centers which aim to provide improved performance efficiency, decreased energy usage and dynamicity. A cloud computing system can be dissected into two stages for the purpose of analysis i.e. the request stage and the execution stage [18–20]. A number of tools have been developed for the analysis and assessment of the execution stage of the system [21–23] including ReliaCloud-NS [24] and network CloudSim [25]. However, in this work we focus on the performance of request stage part of the systems in which the user population is highly restricted. The earliest work in finite source queues was done by Kameda [7] in which he investigated finite-source queuing model and obtained the utilization factor of the processor in an analytical form and also demonstrated that it is independent of the queue discipline. Goswami et al. proposed an analytical finite population queuing model and carried out performance evaluation of private cloud computing systems. [13, 26] Another notable work in the study of finite population queuing systems was done by Louchard [9] where the author studied several stochastic variables for various arrival and service distributions including non markovian queues. The work focused on single server queuing systems and showed that the stochastic variables have weak convergence in some time regions as compared to Gaussian processes and Brownian motions.

Chiang et al. proposed a CEA policy for M/M/R/K cloud service model to solve a constraint optimization problem with decreased system losses. In this work authors

modeled the system losses using the concept of balking and reneging [8, 27]. Their studies were then formulated into a cost function over the parameters of the system and an optimized system was achieved. A model to minimize energy cost for cloud computing systems was discussed in Kumar et al. [28]. In Liu et al, authors used game theory to give an economic model for resource provisioning and utilisation in IT infrastructure of organisations [4]. Ellens et al. proposed resource provisioning in cloud data centers using M/M/C/C queuing system [29]. Their work also depicted the importance of priority scheduler in any cloud service system. Ahuja et al. modelled a retrial queueing system with optional service and finite population subjected to balking [30]. In Kalyanaraman et al. A M/G/1 queueing system was studied with bernoulli vacations to account for server breakdowns [12]. Among all the mathematical tools used to study the reliability of queueing systems hypergeometric functions have been observed to be useful [31, 32].

A comprehensive survey work is done by George E Andrews in order to study applications of hypergeometric functions to physics, combinatorial identities, finite vector spaces and partitions number theory [31]. The properties of basic q-hypergeometric series were used by Economou et. al. to model synchronized abandonments of impatient users in single server queues [33]. The work focused on 2-dimensional continuous time markovian chains and the effect of failure times on impatient users. A similar study on M/M/1 queueing systems was conducted by Ammar [34] in order to conduct a transient analysis of the behaviors of impatient users. Yuen-Shun Dai et. al had systematically modeled the reliability of cloud services [18]. Kafhali et al. presented a performance oriented model for cloud computing systems and validated it using their model using discrete event simulations [10, 35].

It is a model with quality dimensions and metrics that targets general cloud services. CLOUDQUAL contains six quality dimensions, i.e., usability, availability, reliability, responsiveness, security, and elasticity, of which usability is subjective, whereas others are objective. If hardware failures or software faults occur, they may decrease reliability. Through CLOUDQUAL one can check the reliability [36].

From the literature review it is evident that a lot of work has been done to improve the performance efficiency, decreased energy usage and dynamicity of cloud computing systems by analyzing and proposing modifications in the queueing theory. However the literature is quite thin in application of queueing models on systems involving a finite population of users where the quantity of the user population is not many magnitude higher than the resource pool. Moreover the literature review also highlights the lack of metrics available for measuring the reliability of systems that function with such low user populations. In this paper, we aim to fill this research gap by proposing such a model which has intuitive metrics for quantifying the reliability of the system. Moreover, we propose to apply the concept of hypergeometric functions to investigate the application of finite population and finite capacity queueing system in the cloud computing. The use of hypergeometric series and the respective notations associated with it has been described in Sect. 1. We have calculated the results for such systems analytically and the results have been compared with the work presented by Kafhali et al [35]. After the literature review the authors were unable to find any work that discusses the reliability of finite population models that utilise hyper-geometric systems. The distinction between peak load and low load and its mathematical implications has also been omitted in any work that deals with a finite population cloud computing system modelled as markovian queues. Moreover the use of hypergeometric series to

calculate metrics useful for quantification of the reliability of the system also add to the novelty of this work to the best of the authors' knowledge.

3 Model Description

The proposed model is based on $M/M/C/m/K$ (m varies from 0 to K) queuing system having Poisson's distribution with mean arrival rate of λ and an exponential inter-service time with a mean rate of $1/\mu$. The poisson distribution and exponential inter-service time has been observed to be a widely used assumption in this field [8, 10, 34, 37]. The model is primarily suited for both on-premise and externally hosted private clouds which work under strict population constraints. All incoming requests arrive to the request scheduler and eventually to the request queue from a pool of finite population K , permitted to access the resources of private cloud. There are C identical servers and a request queue of length m . High responsiveness is a key feature needed in finite population private clouds and therefore it is desirable that each and every incoming request must be attended by its cloud management system [38, 39]. It will eliminate the possibility of overflow errors and result in improving the request stage reliability of the system. Queue length controller takes data of request count from the scheduler and varies the request queue with respect to the request count. The system is designed such that, at steady state it always maintains the request queue length to the total number of arriving incoming requests i.e. $m = K$. Apart from that, the dynamic VM provisioning mechanism of the system will give the maximum number of VMs, U allowed over the hypervisor layer of the physical machine on the basis of simple equation of $U = K/C$, where K varies in variably as shown in Fig. 1. This allows the private cloud data center to maintain the request drop rate to minimum.. To the best of our knowledge hypergeometric representation of queuing systems is not been studied earlier. Our proposed model is represented in ${}_2F_0$, which is defined as special terminating generalized hypergeometric series two parameters in numerator and zero parameters in denominator. This novel representation is a unique and efficient language to represent all performance parameters of this queuing model.

The conditional and probabilistic mathematical expressions representing our queuing model are expressed in terms of hypergeometric functions. We have assumed First Come First Serve queuing discipline and the usual system parameters are obtained in i) low load & ii) Peak load conditions. The request arrival and service rates can be obtained from,

$$\lambda_n = \begin{cases} (K - n)\lambda, & \text{if } 0 \leq n \leq m - 1 \\ 0, & \text{otherwise} \end{cases} \tag{1}$$

$$\mu_n = \begin{cases} n\mu, & \text{if } 0 \leq n \leq C \\ C\mu, & \text{if } n > C \end{cases} \tag{2}$$

The probability that n users may enter the system is obtained by P_n which is separately defined for two ranges. $0 \leq n \leq C - 1$ and $C \leq n \leq m - 1$. The probability function P_n can be obtained by,

$$P_n = \begin{cases} P_0 \binom{K}{n} \rho^n, & \text{if } 0 \leq n \leq C-1 \\ P_0 \binom{K}{n} \frac{n!}{C!C^{n-C}} \rho^n, & \text{if } C \leq n \leq m \end{cases} \quad (3)$$

Working of the model is such that the dynamic system controls will automatically adjust the service queue length in accordance with the incoming requests from the scheduler since the system is modelled for population bounded private clouds, it is very much feasible to stretch the request queue length in accordance to the considered finite population K .

3.1 Low Load Case

When incoming requests are almost equal to the computing resources, all requests are automatically assigned to computing resources. It is the case where request queue length $m = K$ & $K \leq C - 1$. Therefore the normalising equation would be,

$$\sum_{n=0}^K \binom{K}{n} \rho^n P_0 = 1 \quad (4)$$

or,

$$\left[\frac{K!}{K! \times 0!} \rho^0 + \frac{K!}{(K-1)! \times 1!} \rho^1 + \frac{K!}{(K-2)! \times 2!} \rho^2 + \dots + \frac{K!}{0! \times K!} \rho^K \right]^{-1} = P_0$$

or,

$$P_0 = \left[\sum_{r=0}^K \left(\frac{(K-r+1)_r}{r!} \right) \rho^r \right]^{-1}$$

or,

$$P_0 = [{}_1F_0(K-r+1; \rho)]^{-1} \quad (5)$$

Where, ${}_1F_0(K-r+1; \rho)$ is a finite terminating hypergeometric series. Since $\frac{\lambda}{\mu} < 1$, higher order terms of the series may be neglected, and therefore it is a solution for the differential equation,

$$(1-\rho) \frac{dy}{dz} - (K-r+1)y = 0 \quad (6)$$

with its solution as

$$y = C_1 \times {}_1F_0(K-r+1, -; \rho) \quad (7)$$

where C_1 is a constant.

3.2 Peak Load Case

When the total population of any finite population cloud is made to access and use the computing resources and $K \gg C$, dynamic system controls will automatically expand the request queue length to accommodate all the incoming requests. This will eventually increase the length of the request queue and hence the normalising equations would be written as,

$$\sum_{n=C}^m P_0 \binom{K}{n} \frac{n!}{C! C^{n-C}} \rho^n \approx 1 \tag{8}$$

or,

$$\frac{P_0 \rho^C K!}{C!} \sum_{n=C}^m \frac{1}{(K-C)!} \left(\frac{\rho}{C}\right)^{n-C} \approx 1$$

or,

$$\frac{P_0 \rho^C K!}{C!} \left[\frac{1}{(K-C)!} + \frac{1}{(K-C-1)!} \left(\frac{\rho}{C}\right) + \dots + \frac{1}{(K-m)!} \left(\frac{\rho}{C}\right)^{m-C} \right] = 1$$

The equation can be rewritten as

$$\frac{P_0 \rho^C K!}{C!(K-C)!} \sum_{r=0}^{m-C} \frac{\left(\frac{\rho}{C}\right)^r}{(K-C-r)!} (K-C)! = 1$$

or,

$$P_0 \times \binom{K}{C} \times \rho^C \sum_{r=0}^{m-C} \frac{(-1)^r \left(\frac{\rho}{C}\right)^r (K-C)!}{(K-C-r)!} = 1$$

or,

$$P_0 \times \binom{K}{C} \times \rho^C \sum_{r=0}^{m-C} \frac{(-K-C)_r \left(\frac{-\rho}{C}\right)^r \times (1)_r}{r!} = 1 \tag{9}$$

Dynamic system controls, of our proposed model will eventually allow all the incoming requests into the system's request queue i.e. $m = K$ and the equations becomes as follows,

$$P_0 = \left[\binom{K}{C} \times \rho^C {}_2F_0 \left(-K-C, 1; \left(\frac{-\rho}{C}\right) \right) \right]^{-1} \tag{10}$$

Where, ${}_2F_0(-K-C, 1; (-\rho/C))$ is a special finite terminating hypergeometric series with its differential equation expressed as,

$$\frac{\rho^2}{C^2} \times \frac{d^2y}{dz^2} + \left((2 + C - K) \left(\frac{-\rho}{C} \right) - 1 \right) \frac{dy}{dz} + (C - K)y = 0 \tag{11}$$

It is interesting, to note that the function ${}_2F_0$ is a solution of a second order linear ordinary differential equation, which defines the relationship between the hypergeometric function ${}_2F_0$, defined over a wider domain of argument by analytic continuation, and its rate of change. The recursion formula for the hypergeometric series ${}_2F_0$ is given as,

$$\frac{d}{dz} \left({}_2F_0(-K - C, 1; (-\rho/C)) \right) = (C - K) {}_2F_0((C - K + 1), 2; (-\rho/C)) \tag{12}$$

Similarly, in the present peak load condition, Probability of having n elements present in the system can hypergeometrically be represented as,

$$P_n = P_0 \binom{K}{C} \rho^C \times \left\{ (n - C)^{\text{th}} \text{ term of the hypergeometric series } {}_2F_0(-K - C, 1; (-\rho/C)) \right\}$$

or

$$P_n = P_0 \binom{K}{C} \rho^C \times \left(\frac{(-K - C)_{n-C} \times (1)_{n-C} \times \left(\frac{-\rho}{C} \right)^{n-C}}{(n - C)!} \right) \tag{13}$$

The expected length of Queue L_q of the system is given by-

$$L_q = \rho^C \binom{K}{C} P_0 \times \sum_{n=c+1}^K \left((n - C) (-K - C)_{n-C} \left(\frac{-\rho}{C} \right)^{n-C} \right) \tag{14}$$

$$L_s = L_q + \frac{\lambda}{C\mu} \tag{15}$$

Similarly, the well known Little’s equations are written as,

$$W_s = \frac{L_s}{\lambda} \tag{16}$$

$$W_q = \frac{L_q}{\lambda} \tag{17}$$

In order to measure the performance of the system in terms of the resource provisioning we also define the server utilisation \underline{U}_s , mean number of busy servers \underline{C} .

$$\underline{C} = \sum_{k=1}^C P_k + \sum_{k=C+1}^N CP_k \tag{18}$$

$$U_s = \underline{C}/C \tag{19}$$

4 Reliability Modelling and Analysis

The main function of any cloud management system is to manage the request queue in which all the incoming user requests are collected before reaching for different cloud services [20]. These incoming requests are prone to queue overflow and request timeout errors. In the request stage, if the buffer length is too large then the timeout error loss increases and if the buffer is too small, it increases the risk of overflow errors. Therefore a queuing system intended for minimizing these errors would significantly increase the request stage reliability of the system. [18]. As dynamic controls of the proposed system are designed in a way that allows all the incoming requests to enter the request queue, the probability of overflow errors is minimum. However, due to long request queue, timeout errors are likely to be high. Hence it becomes imperative to study the timeout errors in the system for the sake of establishing the reliability of the system. Since the timeout errors are of major importance, in this study we have defined the reliability index in terms of the probability of getting timeout errors as per equation 20. According to this definition the lower the reliability index for a given configuration, the more unreliable the system is and vice versa.

$$\text{Reliability Index} = -\log_{10}(P_T(t_r)) \tag{20}$$

Since service time of our system is finite, probability of timeout errors is high. These timeout errors pose a serious threat to the reliability and availability of resources of the cloud. According to [18] the probability of timeout errors in infinite population models are obtained by a probability density function integrated over due time. The due time t_r is defined as the time for which an incoming request is allowed to wait in the request queue before being dropped. Since queue length of the request stage of is quantified to an integer, for the proposed model it can be calculated in discrete terms.

A heuristic algorithm formulated to model the reliability of the system is as follows.

Inputs :

1. m - number of empty spaces for holding incoming requests (buffer size) (varies from C to K)
2. K - Total population allowed to access the cloud system
3. C - Number of servers available to the system
4. λ - Arrival rate
5. μ - Service rate
6. t_r - Due time, iterated from t_{r1} to t_{r2}

Algorithm For each value of t_r follow the following steps from 1-5

Step 1 Calculate L_n^q using the following equation for $n \in [C + 1, K]$ where n is an integer.

$$L_n^q = \sum_{i=c+1}^n (k - c)P_i \quad (21)$$

Step 2 Calculate W_n^q using little's rule from equation (16) for $n \in [C + 1, K]$ where n is an integer

Step 3 Obtain N as a function of T_r as per the following relation.

$$N(t_r) = \{max(n) | W_n^q < t_r\} \quad (22)$$

Step 4 The probability of encountering timeout error as a function of t_r is defined as $P_t(t_r)$

$$P_t(t_r) = \sum_{i=0}^{i=N} W_i^q \quad (23)$$

Step 5 We calculate the reliability index as defined in equation (20)

Outputs :

1. $P_t(t_r)$
 2. Reliability index
-

Table 1 Table of variables

Symbol	Description
n	Number of users entering the queuing system
λ	Mean arrival of requests
μ	Mean service rate of requests
m	Size of requested queue (varies from 0 to K)
C	Number of computing resources
P_0	probability of zero users in the system
P_n	Probability of n users in the system
W_s	Waiting time of system
W_q	Waiting time of queue
${}_x F_y$	Finite terminating generalized hypergeometric series with x parameters in the numerator and y parameters in the denominator.

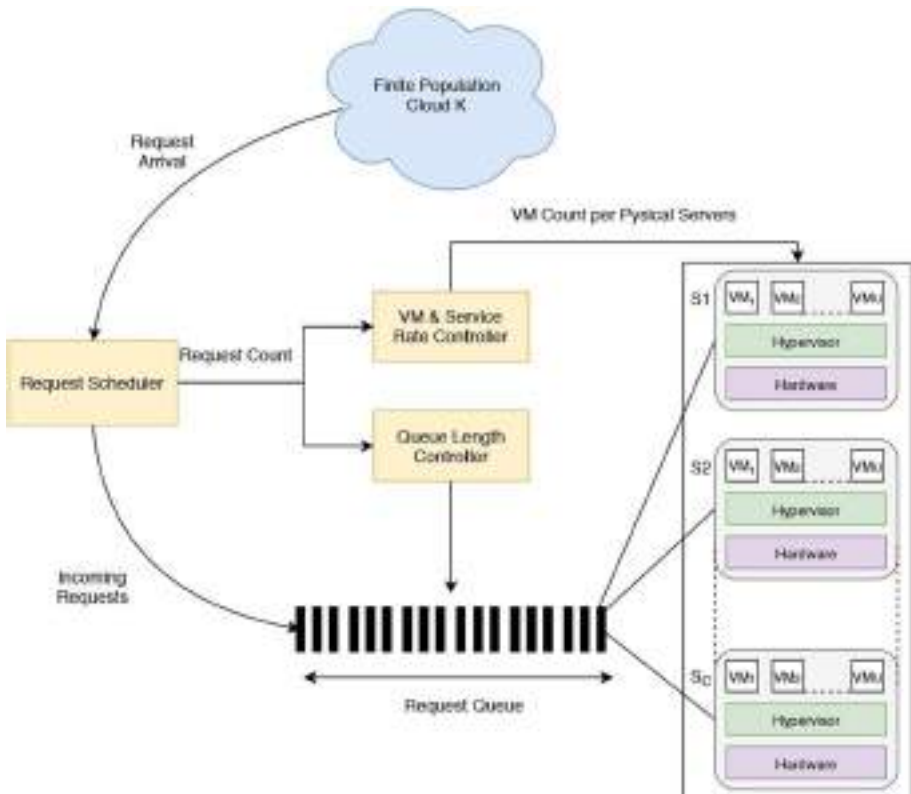
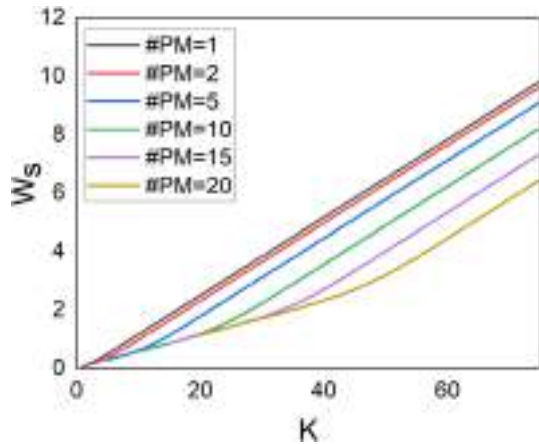


Fig. 1 Schematic of the model employed

Table 2 Parameters for calculations involved in obtaining Figs. 2, 3 and 4

Parameter	Value
λ	7.5
μ	10
C	1–20
K	1–80

Fig. 2 W_s (Waiting time) v/s K (Buffer size) with different number of physical machines provisioned to the system

5 Results and Discussion

In this section we discuss the performance of the proposed system using various indicators mentioned in the previous sections. All the numerical calculations in this work were performed using MATLAB. In order to get a clear picture of the model performance with respect to the inputs provided, mean arrival rate λ , population or system capacity K and the number of servers C (also abbreviated as #PM in all figures) available to the system have been varied in Sect. 5.1. The parameters of performance of the system are then compared with the well established $M/M/C/K/\infty$ queuing system [40–42] and the system presented by Kafhali et al. [10, 35] in Sect. 5.2. Some quantities have been used in a non-dimensional form in order to facilitate the comparison. The results reported in this section have been calculated analytically using MATLAB as per the mathematical modelling mentioned in the preceding sections and all the graphs have been plotted using OriginLab. The parameters of the simulations/calculations have been mentioned in Tables 2, 3, and 5 and the notations for the variables are the same as used in Table 1. The values used for reporting the findings in this work were decided based on preliminary experiments and findings by the authors.

5.1 Model Performance

In Figs. 2, 3 and 4 the system waiting time W_s , Server utilization U_s , and the system length L_s had been calculated for different populations of the user source. Parameters given in table 2 have been used for these calculations.

Fig. 3 L_s (Queue length) v/s K (Buffer size) with different number of physical machines provisioned to the system

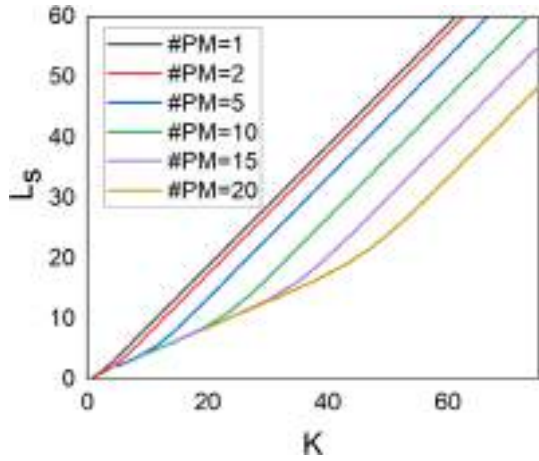


Fig. 4 U_s (Utilisation ratio) v/s K (Buffer size) of the system for different number of physical machines provided to the system

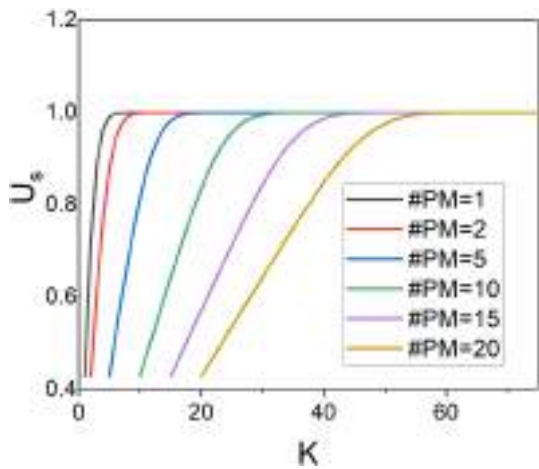


Table 3 Parameters for calculations involved in obtaining Figs. 5, 6 and 7

Parameter	Value
λ	0.1 – 9.9
μ	10
C	1–20
K	40

Figure 2 shows that W_s tends to increase uniformly as the population on the system is increased. The curves tend to increase linearly as the population of the system is increased. This increase is in direct correlation with Fig. 3 which can be derived from the former using Little’s law in equation 16 [43]. This is because the system being highly responsive is utilising all the available servers as observed in Fig. 4 and hence as the population of the system increases, the load on the system increases due to a larger number of users.

Fig. 5 U_s (Utilisation ratio) v/s λ (Request arrival rate) for the system for different quantities of physical machines provisioned

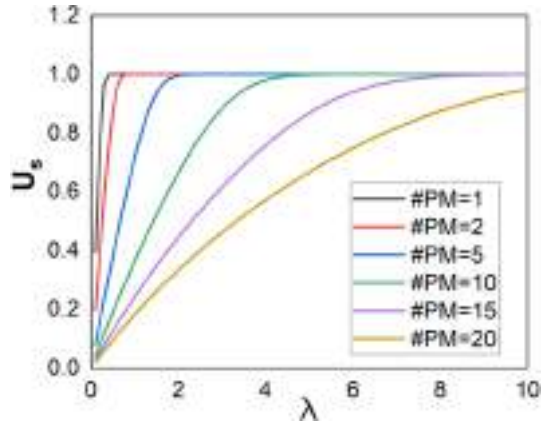


Fig. 6 W_q (Waiting time) v/s λ (Request arrival rate) of the system for different number of physical machines provisioned

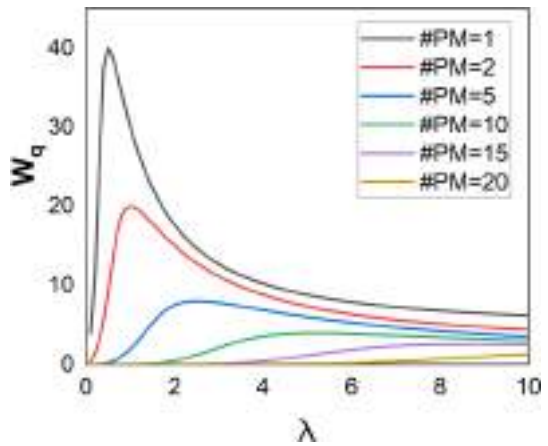


Fig. 7 L_s (Length of queue) v/s λ (Request arrival rate) of the system for different number of physical machines provisioned for the system

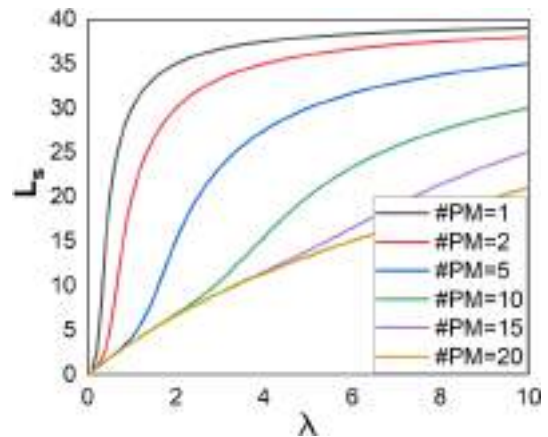


Fig. 8 Reliability index of the system v/s $\rho (= \lambda/\mu)$ for different values of buffer size of the system

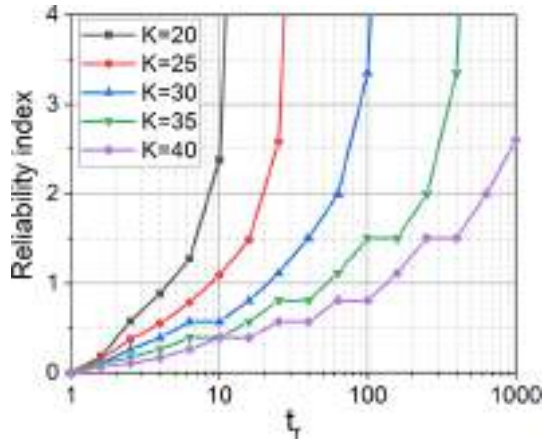


Table 4 Reliability index for different values of mean arrival rate, ($C = 10, \mu = 10$)

$\log(t_r)$	$\lambda = 1$	$\lambda = 2$	$\lambda = 3$	$\lambda = 4$	$\lambda = 5$	$\lambda = 6$	$\lambda = 7$	$\lambda = 8$	$\lambda = 9$
0.5	0.332	0.195	0.232	0.223	0.168	0.189	0.144	0.14	0.167
1	0.332	0.381	0.38	0.416	0.325	0.378	0.314	0.322	0.391
1.5	0.695	0.655	0.78	0.701	0.579	0.517	0.616	0.656	0.569
2	1.214	1.02	1.019	0.885	0.752	0.693	0.834	0.902	0.806
2.5	1.214	1.473	1.586	1.1	0.961	1.177	1.106	1.214	1.504
3	1.886	2.548	2.282	1.638	1.507	1.497	1.848	2.08	2.602
3.5	3.662	6.35	5.992	2.759	2.252	2.33	2.921	2.54	3.76

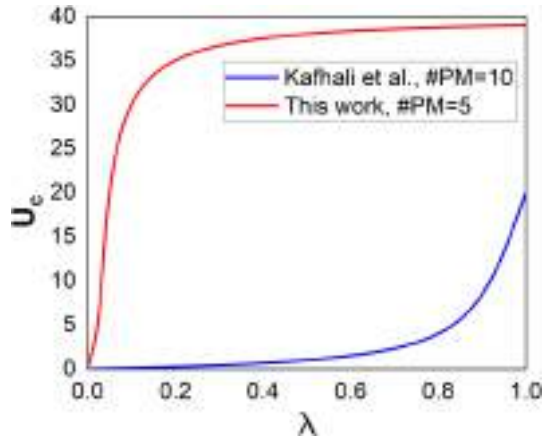
The performance of the system with respect to the mean arrival rate λ can be observed in Figs. 5, 6 and 7 for parameters given in table 3.

It was observed that Figs. 4 and 5 show a similar nature i.e. the system shows a tendency to employ all the available servers for a given task. The waiting time of the system W_s and length of the system L_s on the other hand show a different behaviour as compared to Figs. 2 and 3. This shows that while the increase in population results in a linear increase in the mean response time, an increase in the request arrival rate may necessarily not have the same result. This can be explained in terms of the server utilization U_s and the system capacity K . Initially when the server utilization is low the requests are not being completed fast enough since the number of servers employed is low, hence the steady increase in W_s and L_s . However, as the server utilization saturates, all the available servers are being used at full capacity, decreasing the waiting time. Thus the waiting time of the queue and the length of the queue stabilizes. This becomes more evident when Figs. 5 and 6 are observed in conjunction. The value of λ corresponding to peaks in the value of W_q are very close to the values of λ at which the U_s curve starts saturating. In the case when number of physical machines $\#PM = 20$ since the lambda corresponding to saturation of U_s is not achieved in the range of the X-axis there is no peak observed in this range of the X-axis.

The reliability of the system has also been studied using the reliability index defined as per equation 20 in Fig. 8. The reliability of the system has been calculated at $C = 5$,

Table 5 Parameters for calculations involved in obtaining Figs. 9 and 10

Parameter	Value
ρ	0.1 – 9.9
μ	10
C	5,10
K	40
μ_1	25

Fig. 9 U_c (Utilisation ratio) v/s ρ ($= \lambda/\mu$) for the system for different modelling schemes

$\lambda = 9$, $\mu = 10$ and N varying from 10 to 40 for different due time. The Table 4 shows the values of reliability index for different values of arrival rate at $C = 10$, $\mu = 10$. The graph clearly shows that the reliability of the system decreases as the population of the system is increased. As per the definition of reliability index the greater the index, the more reliable the system is deemed. The graph for $K = 35$ shows some erratic discontinuities in the slope of the curve which increases as the value of K increases. This erratic nature in the curves is because of the discrete placeholders in the queue and the assumption that n in equation 13 is always a whole number. However it must be noted that the values in table 4 for column $\lambda = 2$ and $\lambda = 3$ are greater than that of other columns. This attributed to the same property of the system which causes the peak in the Fig. 6.

5.2 Model Comparison

The proposed model has been compared with the model presented by Kafhali et al. [10, 35] in Figs. 9 and 10 as well as with the well established $M/M/C/K/\infty$ model [40–42] in Figs. 9 and 11. The parameters used for obtaining Figs. 9 and 10 are presented in table 5.

The parameter ρ has been used in the comparison to keep the comparisons dimensionless. The parameter μ has been taken in accordance with [35]. It also needs to be noted that the value of ρ needs to be between 0 and 1 to confirm the convergence of the hypergeometric series for case where $K \rightarrow \infty$. The nature of figure shows that the presented work attempts to utilise the available resources to their full capacity. The difference in the waiting time for the system has been showed in Fig. 10. A higher queue length at lower loads

Fig. 10 W_s (Waiting time) $v/s \rho$ ($= \lambda/\mu$) for different modelling schemes and number of physical machines provisioned for the system

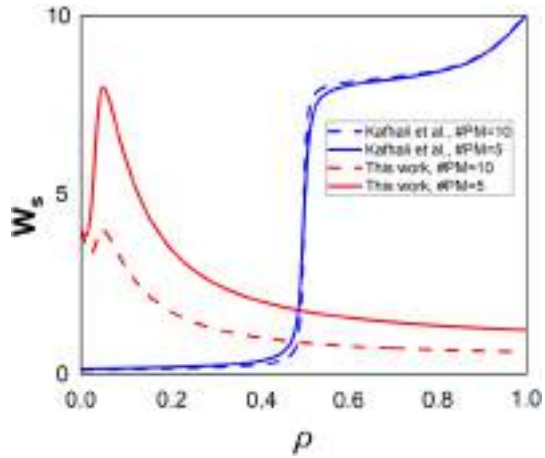
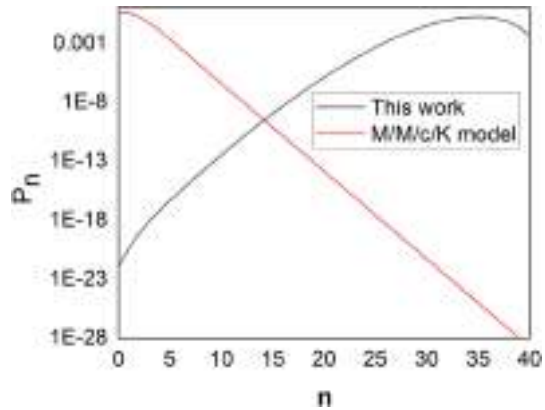


Fig. 11 P_n (Probability distribution for having n users in the queue) $v/s n$ for the system



for finite population models has been discussed in Louchard et al. [9] which when used in conjunction with equation 16 predicts the results accurately. This reduces the possibility of over-provisioning of resources [8, 44, 45]. In most organisations with their own IT infrastructure, there is an oversupply of resources which causes an increased implicit economic cost and maintenance cost [4] which can be avoided by higher utilisation of resources. The lower response time in is also beneficial for maintaining the quality of service as per the SLA agreements in times of high loads which is a highly sought after trait in a system. A lower waiting time in the queue is beneficial in reducing renegeing errors in the system [8, 27, 46].

Figure 11 shows the major difference between the presented model and the $M/M/c/K$ model. A similar probability distribution is expected in Kafhali et al. since it is also based of stochastic processes using the $M/M/1/K$ model. The reason for this contrast in the probability distribution in the presented work is the combination term in equation 3 which increases monotonically as the value of n increases while the ρ^n term decrease monotonically. The presented system has a greater probability of having more users in the queue at any given time which explains the higher system utilisation.

6 Conclusion and Future Work

Developing a request stage reliable queuing system dedicated to private clouds having finite population concerns is very little touched in most existing studies. In order to explore this research area we have analyzed and designed a new queuing system for private and community clouds. The mathematical expression of this model is developed using a unique and novel hypergeometric notation. All probabilistic terms of the model are represented in terms of a special terminating hypergeometric series. The model is compared with a similar recent work on cloud data centers and a significant improvement in the system parameters like server utilization and system response time is observed. The analysis and simulation results compliment each other to conclude the correctness of our analytical model.

The model parameters are represented in terms of hypergeometric representations and it can work exclusively for finite population private clouds which is an important and perplexing research area. The system is also designed such that it has negligible overflow errors. A discrete probabilistic mathematical analysis has been done to obtain and minimize the timeout errors by varying due time. This helps in improving system request stage reliability.

In future, it may be planned to study the overall characteristics of any queuing system in light of various properties of hypergeometric functions.

Declarations

Conflict of interest The authors declare that they have no conflict of interest.

References

1. Mell, P., & Grance, T. et al. (2011). The NIST definition of cloud computing
2. Costello, K., & Hippold, S. (2019). Gartner forecasts worldwide public cloud revenue to grow 17.5 percent in 2019. Connecticut: Stamford. Dostupno na: <https://www.gartner.com/en/newsroom/press-releases/2019-04-02-gartner-forecasts-worldwide-public-cloud-revenue-to-g> [10. rujna 2019]
3. Karpovich, B., Kesterson-Townes, L., & Rishi, S. (2017). *Beyond agility-How cloud is driving enterprise innovation*. New York, USA: IBM Institute for Business Value.
4. Liu, G., Xiao, Z., Tan, G. H., Li, K., & Chronopoulos, A. T. (2020). Game theory-based optimization of distributed idle computing resources in cloud environments. *Theoretical Computer Science*, 806, 468. <https://doi.org/10.1016/j.tcs.2019.08.019>
5. Fisher, C., et al. (2018). Cloud versus on-premise computing. *American Journal of Industrial and Business Management*, 8(09), 1991.
6. Santhi, K., & Saravanan, R. (2017). Performance analysis of cloud computing using batch queueing models in healthcare systems. *Research Journal of Pharmacy and Technology*, 10(10), 3331. <https://doi.org/10.5958/0974-360X.2017.00591.1>
7. Kameda, H. (1982). A Finite-source queue with different customers. *Journal of ACM*, 29(2), 478. <https://doi.org/10.1145/322307.322320>.
8. Chiang, Y. J., Ouyang, Y. C., & Hsu, C. H. R. (2016). Performance and cost-effectiveness analyses for cloud services based on rejected and impatient users. *IEEE Transactions on Services Computing*, 9(3), 446. <https://doi.org/10.1109/TSC.2014.2365783>.
9. Louchard, G. (1994). Large finite population queueing systems. The single-server model. *Stochastic Processes and their Applications*, 53(1), 117. [https://doi.org/10.1016/0304-4149\(94\)90060-4](https://doi.org/10.1016/0304-4149(94)90060-4).
10. El Kafhali, S., & Salah, K. (2017). Stochastic modelling and analysis of cloud computing data center. In *2017 20th Conference on Innovations in Clouds, Internet and Networks (ICIN)* (IEEE, 2017). <https://doi.org/10.1109/ICIN.2017.7899401>

11. Chen, H.P., & Li, S.C. (2010). A queueing-based model for performance management on cloud. Proc. - 6th Intl. Conference on Advanced Information Management and Service, IMS2010, with ICMA2010 - 2nd International Conference on Data Mining and Intelligent Information Technology Applications pp. 83–88
12. Kalyanaraman, R., & Nagarajan, P. (2019). Bulk arrival, fixed batch service queue with unreliable server, Bernoulli vacation and with delay time. In *AIP Conference Proceedings*, vol. 2177, p. 020034. <https://doi.org/10.1063/1.5135209>
13. Sahoo, C. N., & Goswami, V. (2016). Performance evaluation of cloud centers with high degree of virtualization to provide mapreduce as service. *International Journal of Advances in Soft Computing and its Applications*, 8(3), 193.
14. Andrews, G.E., & Garvan, F. (2018). *Analytic Number Theory, Modular Forms and Q-Hypergeometric Series: In Honor of Krishna Alladi's 60th Birthday*, University of Florida, Gainesville, March 2016, vol. 221 (Springer)
15. Bringmann, K., Lovejoy, J., & Rolen, L. (2018). On Some Special Families of q-hypergeometric Maass Forms. *International Mathematics Research Notices*, 2018(18), 5537. <https://doi.org/10.1093/imrn/rnx057>
16. Andrews, G. E. (1974). Applications of basic hypergeometric functions. *SIAM review*, 16(4), 441.
17. Pradhan, S., Damodaran, P., & Srihari, K. (2008). Predicting performance measures for Markovian type of manufacturing systems with product failures. *European Journal of Operational Research*, 184(2), 725. <https://doi.org/10.1016/j.ejor.2006.11.016>. <https://www.sciencedirect.com/science/article/pii/S0377221706011520>
18. Dai, Y. S., Yang, B., Dongarra, J., & Zhang, G. (2009). in *15th IEEE Pacific Rim International Symposium on Dependable Computing* (Citeseer, 2009). Cloud service reliability: Modeling and analysis. (pp. 1–17)
19. Kaur, G., & Kumar, R. (2015). A review on reliability issues in cloud service. *International Journal of Computer Applications*, 975, 8887.
20. Gill, S. S., & Buyya, R. (2020). Failure management for reliable cloud computing: A taxonomy, model, and future directions. *Computing in Science & Engineering*, 22(3), 52. <https://doi.org/10.1109/MCSE.2018.2873866>.
21. Zio, E., & Podofillini, L. (2003). Monte Carlo simulation analysis of the effects of different system performance levels on the importance of multi-state components. *Reliability Engineering & System Safety*, 82(1), 63. [https://doi.org/10.1016/S0951-8320\(03\)00124-8](https://doi.org/10.1016/S0951-8320(03)00124-8).
22. Bahwairath, K., Tawalbeh, L., Benkhelifa, E., Jararweh, Y., & Tawalbeh, M. A. (2016). Experimental comparison of simulation tools for efficient cloud and mobile cloud computing applications. *EURASIP Journal on Information Security*, 2016(1), 15. <https://doi.org/10.1186/s13635-016-0039-y>
23. Fakhfakh, F., Kacem, H. H., & Kacem, A. H. (2017). Simulation tools for cloud computing: A survey and comparative study. In *2017 IEEE/ACIS 16th International conference on Computer and Information Science (ICIS)* (IEEE, 2017) (pp. 221–226). <https://doi.org/10.1109/ICIS.2017.7959997>
24. Snyder, B., Green, R. C., Devabhaktuni, V., & Alam, M. (2018). ReliaCloud-NS: A scalable web-based simulation platform for evaluating the reliability of cloud computing systems. *Software: Practice and Experience*, 48(3), 665. <https://doi.org/10.1002/spe.2541>.
25. Garg, S.K., & Buyya, R. (2011). NetworkCloudSim: Modelling Parallel Applications in Cloud Simulations. In *2011 Fourth IEEE Int. Conf. Util. Cloud Comput.* (IEEE), Vm, pp. 105–113. <https://doi.org/10.1109/UCC.2011.24>
26. Goswami, V., Patra, S. S., & Mund, G. B. (2012). Performance analysis and optimal resource usage in finite population cloud environment. In *2012 2nd IEEE International conference on parallel, distributed and grid computing* (IEEE, 2012). pp. 679–684. <https://doi.org/10.1109/PDGC.2012.6449902>
27. Chiang, Y. J., & Ouyang, Y. C. (2014). Profit optimization in sla-aware cloud services with a finite capacity queueing model. *Mathematical Problems in Engineering*. <https://doi.org/10.1155/2014/534510>.
28. Kumar, R., Sahoo, G., Yadav, V., & Malik, P. (2017). Minimizing the energy consumption of cloud computing data centers using queueing theory. In *Advances in Computational Intelligence* (Springer, 201–210).
29. Ellens, W., Ivkovic, M., Akkerboom, J., Litjens, R., & van den Berg, H. (2012). Performance of Cloud Computing Centers with Multiple Priority Classes. In *2012 IEEE Fifth International conference on cloud computing* (IEEE, 2012). pp. 245–252. <https://doi.org/10.1109/CLOUD.2012.96>
30. Ahuja, A., Jain, A., & Jain, M. (2019). Finite population multi-server retrial queueing system with an optional service and balking. *International Journal of Computers and Applications*, 41(1), 53. <https://doi.org/10.1080/1206212X.2018.1505023>

31. Andrews, G. E. (1974). Applications of basic hypergeometric functions. *SIAM Review*, 16(4), 441. <https://doi.org/10.1137/1016081>
32. Beukers, F. (2014). Hypergeometric Functions, How Special Are They? *Notices of the American Mathematical Society*, 61(01), 48. <https://doi.org/10.1090/noti1065>
33. Economou, A., & Kapodistria, S. (2010). Synchronized abandonments in a single server unreliable queue. *European Journal of Operational Research*, 203(1), 143. <https://doi.org/10.1016/j.ejor.2009.07.014>.
34. Ammar, S. I. (2015). Transient analysis of an M/M/1 queue with impatient behavior and multiple vacations. *Applied Mathematics and Computation*, 260, 97. <https://doi.org/10.1016/j.amc.2015.03.066>.
35. El Kafhali, S., & Salah, K. (2018). Modeling and analysis of performance and energy consumption in cloud data centers. *Arabian Journal for Science and Engineering*, 43(12), 7789. <https://doi.org/10.1007/s13369-018-3196-0>.
36. Xianrong Zheng, P., & Martin, K. Brohman. (2014). Li Da Xu, CLOUDQUAL: A Quality Model for Cloud Services. *IEEE Transactions on Industrial Informatics*, 10(2), 1527. <https://doi.org/10.1109/TII.2014.2306329>. <http://ieeexplore.ieee.org/document/6740846/>.
37. Badian-Pessot, P., Lewis, M. E., & Down, D. G. (2019). Optimal control policies for an M/M/1 queue with a removable server and dynamic service rates. *Probability in the Engineering and Informational Sciences*. <https://doi.org/10.1017/S0269964819000299>
38. Toka, L., Haja, D., Korosi, A., & Sonkoly, B. (2019). Resource provisioning for highly reliable and ultra-responsive edge applications. In *2019 IEEE 8th International conference on cloud networking (CloudNet)* (IEEE, 2019), pp. 1–6. <https://doi.org/10.1109/CloudNet47604.2019.9064131>
39. Satyanarayanan, M. (2017). The emergence of edge computing. *Computer*, 50(1), 30.
40. Robertazzi, T. G. (2012). *Computer networks and systems: queueing theory and performance evaluation*. Springer.
41. Borovkov, A. (2012). *Stochastic processes in queueing theory* (Vol. 4). Springer.
42. Medhi, J. (2002). *Stochastic models in queueing theory*. Elsevier.
43. Little, J. D. C. (1961). A proof for the queuing formula: $L = \lambda W$. *Operations Research*, 9(3), 383. <https://doi.org/10.1287/opre.9.3.383>.
44. Ghobaei-Arani, M., Jabbehdari, S., & Pourmina, M. A. (2016). An autonomic approach for resource provisioning of cloud services. *Cluster Computing*, 19(3), 1017. <https://doi.org/10.1007/s10586-016-0574-9>.
45. Singh, S., & Chana, I. (2016). A survey on resource scheduling in cloud computing: Issues and challenges. *Journal of grid computing*, 14(2), 217. <https://doi.org/10.1007/s10723-015-9359-2>.
46. Madhu, J., & Amita, B. (2012). Retrial queue with threshold recovery, geometric arrivals and finite capacity. *Journal of Operations Management*, 3(1), 1039. https://doi.org/10.1007/978-81-322-0491-6_96.

Publisher's Note Springer Nature remains neutral with regard to jurisdictional claims in published maps and institutional affiliations.



Rohit Sharma is a research scholar at Dr. APJ Abdul Kalam Technical University, Lucknow, India and currently working as Assistant Professor in Department of Computer Science and Engineering, Dr. Ambedkar Institute of Technology for Handicapped, Kanpur, India. He received his B.Tech and M.Tech degree in Computer Science & Engineering from U.P. Technical University, Lucknow. His Research interest include Cloud Computing & Computational Intelligence.



Prateek Gupta is a Bachelors-Masters dual degree in technology at the department of mechanical engineering at Indian Institute of Technology Kanpur, India., His area of interest is molecular dynamics, conventional manufacturing and cloud computing systems. He has also done extensive work on the additive manufacturing and use of CT-scans to study topology of porous media.



Raghuraj Singh received his Ph.D. degree from U. P. Technical University, Lucknow, India in 2006 and M. S. degree from BITS, Pilani, India in 1997 and B. Tech. in Computer Science and Engineering degree from Harcourt, Butler Technological Institute, Kanpur, India in 1990. He is currently working, as Professor and Head at Computer Science and Engineering Department, of Harcourt Butler Technical University, Kanpur, India. His research interest, includes Software Engineering, Human Computer Interaction and Mobile Ad hoc Networks and Cloud reliability. Dr. Singh has published about 140 research papers in National and International Journals and Conferences. Prof. Singh has supervised 26 M. Tech. and 12 Ph.D. theses and supervising 9 Ph.D. scholars.

Biodegradation of ciprofloxacin by white rot fungus *Pleurotus ostreatus*

Sushil Kumar Singh¹ · Robinka Khajuria¹ · Loveleen Kaur¹

Received: 23 January 2017 / Accepted: 28 February 2017 / Published online: 27 April 2017
© Springer-Verlag Berlin Heidelberg 2017

Abstract Unrestricted and reckless use of antibiotics has resulted in their accumulation in environment. This, in turn, has led to the emergence of multiple drug-resistant microbes. The present study focuses on degradation of ciprofloxacin (CIP) by an edible white rot fungus *Pleurotus ostreatus*. Effect of CIP was determined on radial growth and biomass of *P. ostreatus*. Titrimetric and spectrophotometric assays were carried out to assess the degrading potential of *P. ostreatus* towards CIP. It was found that CIP has a stimulatory effect on growth and enzyme activity of *P. ostreatus*. Maximum enzyme (glucanase, ligninases, laccase) production was observed at the highest concentration of CIP (500 ppm). Antibiotic degradation of about 68.8, 94.25 and 91.34% was estimated after 14 days of incubation at 500 ppm CIP using Titrimetric, Indigo carmine and Methyl orange assay, respectively. Degradation of CIP was further validated by high performance liquid chromatography (HPLC) and microbiological analysis. HPLC analysis revealed 95.07% degradation while microbiological test also exhibited a decreased antimicrobial activity of degraded products against *Escherichia coli*, *Staphylococcus aureus* and *Streptococcus pyogenes*. To the best of our knowledge, this is the first study wherein *P. ostreatus* was used for the degradation of ciprofloxacin.

Keywords Antibiotic resistance · Bioremediation · CIP · *Pleurotus ostreatus* · HPLC

Introduction

Antibiotics are among the most frequently prescribed medicaments in modern day medicine (Hernandez et al. 2012). Between 2005 and 2009, the units of antibiotics sold in India specifically increased by about 40%. Increased sales of cephalosporins were particularly striking, with sales increasing by 60% though some increase was seen in most antibiotic classes, making India world's largest consumer of antibiotics (Shah et al. 2015). Being non-degradable in nature, most of these antibiotics persist in the environment for long periods. Antibiotics like ciprofloxacin (CIP) degrade very slowly and may persist in soil in its original form for up to 1–4 months, thus creating a microenvironment for the development of antibiotic resistant strains (Laxminarayan et al. 2013). CIP is one of the most widely used second-generation broad spectrum quinolone which has been detected in domestic wastewaters in concentrations of up to 1000–6000 ng/l, that causes the possible occurrence of selective pressures and the consequent selection of resistant bacteria (Batt et al. 2007). This problem of extensive and unrestricted use of antibiotics has aggravated to such magnanimous proportions that it is becoming increasingly difficult to treat diseases caused by such resistant strains. It has now, therefore, become necessary to search for new methods for effective degradation of antibiotics persisting in the environment.

A number of methods including physical and chemical have been adopted for treatment of water contaminated with antibiotics (Hernandez et al. 2012; Hubicka et al. 2013). However, these methods are largely ineffective and end up adding more pollutants into the environment. An alternative lies in the use of living organisms for remediation of these antibiotics. Bioremediation involves the use of microbes to remove or breakdown complex hazardous

✉ Loveleen Kaur
loveleensays@gmail.com

¹ School of Bioengineering and Biosciences, Lovely Professional University, Phagwara, Punjab 1440111, India

substances into simpler, less toxic or nontoxic substances. The process is generally 60–70% less costly than other technologies (Laxminarayan et al. 2013). Fungi such as *Gloeophyllum striatum* (Wetzstein et al. 1999), *Phanerochaete chrysosporium* (Guo et al. 2014; Martens et al. 1996) and *Trametes versicolor* (Rodríguez-Rodríguez et al. 2012) have been reported for their use in bioremediation of antibiotics. The aim of this study was to evaluate the potential use of mycelium of a basidiomycetous fungus *Pleurotus ostreatus* for degradation of CIP.

Pleurotus ostreatus (*P. ostreatus*), is a temperate edible mushroom which forms oyster shaped fruiting bodies that can be grown on different agricultural wastes in a temperature range of 25–28 °C (Ahmed et al. 2009). The ability of *P. ostreatus* as bioremediation agent has been attributed to the production of various enzymes such as laccase, manganese peroxidase, lignin peroxidases, xylanases, etc. which are important for various metabolic reactions such as substrate utilization as well as degradation of pollutants (Martens et al. 1996; Espindola et al. 2007; Rana and Rana 2011; Jegatheesan et al. 2012; Singh et al. 2012).

Materials and methods

Growth studies

Mycelium of *P. ostreatus* was maintained on Potato dextrose agar (PDA) medium at 25 ± 2 °C. The effect of different concentrations of CIP (100, 200, 300, 400 and 500 ppm) on growth of *P. ostreatus* mycelium and biomass production was studied by inoculating mycelium bits (5 mm) in PDA and Potato dextrose broth (PDB), respectively. One-way ANOVA was used to determine whether there was any significant effect of concentration of CIP used on the radial growth of *P. ostreatus* with increase in incubation time by calculating Critical Difference (CD) at 5%.

Enzymatic studies

Effect of different concentrations (100–500 ppm) of CIP on Endo-β-D-1,4-glucanase (Miller 1959), Laccase (Jegatheesan et al. 2012), Hemicellulase (Bucht and Erikson 1968), Lignin peroxidase (Tien and Kirk 1984) and Manganese peroxidase (Kuwahara et al. 1983) produced by *P. ostreatus* was determined after 7 and 14 days of incubation. Culture broth devoid of CIP was used as control.

Degradation of CIP

Two different approaches, viz., titrimetric and spectrophotometric were used to estimate the amount of CIP degraded by *P. ostreatus*.

Titrimetric analysis

The amount of CIP degraded by *P. ostreatus* was determined according to Basavaiah et al. (2006). A 10 ml aliquot of standard solution containing 100–500 ppm of CIP was placed in a 100 ml volumetric flask. The solution was acidified by adding 5 ml of 5 M sulfuric acid. 10 ml of 0.025 M cerium sulfate was added to content in the flask, mixed well and kept aside for 15 min. Finally, the unreacted oxidant was back titrated with 0.025 M Ferrous Ammonium Sulfate (FAS) solution using one drop of ferroin indicator. Simultaneously, a blank titration was performed and the amount of drug left in the aliquot was calculated from the amount of cerium sulfate reacted. Standard curve of FAS was used to calculate the amount of CIP degraded.

Spectrophotometric analysis

Spectrophotometric determination of degraded CIP was carried out by methyl orange method and Indigo carmine method (Basavaiah et al. 2006; Nijhu et al. 2011).

Indigo carmine method

20 µg of spent broth was added to 4 ml distilled water. 1 ml of 5 M sulfuric acid was added to each tube followed by addition of 500 µg/ml of cerium sulfate solution (0.025 M). The contents were mixed well and kept aside for 10 min with occasional swirling at room temperature. 1 ml of indigo carmine was added to each tube and absorbance was measured at 610 nm after 5 min. Standard curve was prepared for determination of degraded amount of CIP.

Methyl orange method

10 µg of spent broth was added to 4 ml of distilled water. 1 ml of 5 M sulfuric acid and 250 µg/ml of cerium sulfate (0.025 M) were added to above mixture and kept at room temperature for 10 min with occasional swirling. Finally, 1 ml of methyl orange was added and absorbance was measured at 520 nm. Standard curve was prepared for determination of degraded amount of CIP.

Validation of CIP bioremediation

High performance liquid chromatography (HPLC)

HPLC was carried out to validate the degradation results obtained in the above mentioned assays. AC18 column with acetonitrile as mobile phase was used for chromatography (Singh et al. 2013). A standard run of pure CIP was performed to comparatively assess the samples taken, i.e., 100 and 500 ppm concentrations of CIP.

Antimicrobial activity of degraded products

Antibacterial activity of degraded products formed post incubation with *P. ostreatus* was evaluated against *Escherichia coli*, *Staphylococcus aureus* and *Streptococcus pyogenes* on Mueller–Hinton agar plates by disc diffusion method and compared with antibacterial activity of different CIP concentrations (Thillaimaharani et al. 2013; Hernandez et al. 2012).

Results and discussion

Radial growth studies

Radial growth studies of *P. ostreatus* on PDA at different concentrations of CIP revealed that there was no inhibitory effect of CIP on the growth of the fungus. On the contrary, as the concentration of the antibiotic was increased, a subsequent increase was observed in the radial growth. It was also seen that with the increase in incubation period, there was an increase in the radial growth of the fungus, with maximum growth being observed on the 6th day at all concentrations. However, 4th day onwards, there was no substantial change in the growth rate even when the concentration of CIP was increased (Table 1). Maximum

growth was observed at an antibiotic concentration of 500 ppm, exhibiting a 27% increase as compared to the control. CD at 5% showed a significant effect of concentrations of CIP used on the radial growth of *P. ostreatus*. Such significant increase in the growth of the fungi in presence of antibiotics has not been reported before. Use of antibiotics as growth promoters in animal feeds has been well documented (Dibner and Richards 2005; Butaye et al. 2003; Miles et al. 2006; Wegener et al. 1999) but the stimulatory effect of antibiotics specifically ciprofloxacin on the growth of *P. ostreatus* has not been reported before. The stimulatory effect of CIP on the fungus can be supported by the fact that increased fungal microbiota growth is a common side effect of antibiotic therapy (Noverr et al. 2004). This can be probably due to decrease in competition with bacterial species for food and space and reduction in microbial metabolites that depress growth (Dibner and Richards, 2005), there by stimulating fungal growth. Further, work needs to be carried out to understand the mechanism behind the growth stimulatory effect of ciprofloxacin on *P. ostreatus*.

Biomass studies

Biomass studies showed that after 7 days of incubation, maximum growth (3.703 gm wet weight/1.436 gm dry weight) was observed in medium having concentration of 500 ppm of CIP while lowest biomass production (2.448 g wet weight/1.194 g dry weight) was seen at 100 ppm. The trend continued up to 14 days of incubation where maximum growth was observed at 500 ppm (3.965 g wet weight/3.965 g dry weight) and lowest at 100 ppm (3.128 g wet weight/1.398 g dry weight). CD (5%) revealed a significant increase in mycelial growth at increasing concentrations of CIP (Table 2). Biomass studies also exhibited a pattern similar to the one observed in radial mycelium growth studies.

Table 1 Effect of different concentrations of CIP on radial growth of *P. ostreatus*

Concentration of CIP used (ppm)	Radial Growth of <i>P. ostreatus</i> (mm) ^a					
	Day 1	Day 2	Day 3	Day 4	Day 5	Day 6
0 (control)	7.5 ± 0.228	9.0 ± 0.000	19.0 ± 0.577	34.0 ± 0.000	46.0 ± 1.154	55.0 ± 1.154
100	8.0 ± 1.154	11.0 ± 0.000	22.5 ± 1.443	34.0 ± 3.464	50.0 ± 4.612	74.0 ± 0.000
200	8.5 ± 0.866	11.5 ± 0.866	23.0 ± 1.410	36.0 ± 1.732	50.0 ± 1.154	74.0 ± 0.577
300	9.5 ± 0.288	12.0 ± 1.154	26.0 ± 1.154	39.0 ± 0.577	53.0 ± 0.577	75.0 ± 0.000
400	11.0 ± 0.000	13.0 ± 0.000	26.5 ± 1.443	40.0 ± 0.000	55.0 ± 5.196	75.5 ± 0.288
500	11.5 ± 0.288	14.0 ± 0.000	26.5 ± 1.154	40.5 ± 4.33	55.5 ± 0.288	75.5 ± 0.288
CD 5%	1.967	1.816	3.559	NS	NS	1.703

NS not significant

^a Average of three replicates with standard error; Medium used-PDA; Temperature: 25 ± 2 °C

Table 2 Effect of different concentrations of CIP on wet and dry weight of *P. ostreatus* after 7 and 14 days of incubation

Concentration of CIP used (ppm)	Wet weight(gm) ^a		Dry weight (gm) ^a	
	7 Days	14 Days	7 Days	14 Days
0 (control)	2.448 ± 0.002	2.686 ± 0.000	1.194 ± 0.000	1.389 ± 0.002
100	2.503 ± 0.000	3.128 ± 0.000	1.254 ± 0.000	1.596 ± 0.000
200	2.521 ± 0.000	3.143 ± 0.000	1.291 ± 0.000	1.604 ± 0.000
300	2.901 ± 0.000	3.457 ± 0.000	1.400 ± 0.001	1.609 ± 0.000
400	3.094 ± 0.000	3.816 ± 0.000	1.415 ± 0.001	1.614 ± 0.000
500	3.703 ± 0.000	3.965 ± 0.000	1.436 ± 0.001	1.647 ± 0.001
CD 5%	0.008	0.003	0.003	0.002

Medium used-PDB; Incubation temperature-25 ± 2 °C

^a Average of three replicates with standard error

Endo-β-D-1,4-glucanase, hemicellulase, lignin peroxidase, manganese peroxidase and laccase activity of *Pleurotus ostreatus*

P. ostreatus produces different extracellular enzymes to utilize the substrate. The effect of various concentrations of CIP on production of endo-β-D-1,4-glucanase, hemicellulase, laccase, lignin peroxidase and manganese peroxidase was determined. It was observed that with the increase in antibiotic concentration, the enzymatic activity of the fungus also increases. In case of endo-β-D-1,4-glucanase, hemicellulase, laccase, lignin peroxidase and manganese peroxidase, maximum activity was observed at 500 ppm CIP after 14 days of incubation. *P. ostreatus* exhibited a maximum endo-β-D-1,4-glucanase specific activity 392.94 μmol/min/mg as compared to 58 μmol/min/mg of specific activity observed in the absence of antibiotic in the control. Similarly, maximum specific activity of 331.40, 0.0256 and 23.864 μmol/min/mg, was observed for hemicellulase, lignin peroxidase and manganese peroxidase, respectively, after 14 days of incubation at 500 ppm antibiotic concentration (Table 3). Enzymatic activities were determined after 7 and 14 days only so as to evaluate the profile of enzymes being produced by the fungus. The work was not designed to optimize the conditions for enzyme production. A similar pattern was observed in the enzyme activities of laccase with maximum enzyme activity at 500 ppm CIP after 14 days of incubation (Data Not Provided). CD at 5% revealed significant increase in the activities of all the enzymes at different concentrations of CIP.

Sandhu and Arora (1985) reported the induction of laccase production in *Polyporus sanguineus* in the presence of different phenolic compounds and protein synthesis inhibitors. They further proposed that laccase thus represents a mechanism to eliminate these toxic compounds by enzymatic transformation. Hence the possibility that the white rot fungi might sense the antibiotic as phenolic

substrates and detoxify them, cannot be ruled out. Similarly, *Phlebia radiata* has been shown to produce lignin-modifying enzymes for detoxification purposes when toxic compounds are present in its environment (Rogalski et al. 1991) Froehner and Eriksson (1974) have reported that inhibition of extracellular protein synthesis in *Neurospora crassa*, stimulated laccase production in the presence of cycloheximide, owing to normal protein turnover. Dhawan et al. (2005) also reported the stimulatory effect of Apramycin sulfate (200 mg/l) on laccase production (18.2 U/ml) in *Pycnoporus cinnabarinus*. Similarly, Praveen et al. (2012) reported an increase in Lac, LiP and MnP production by *Stereum ostrea* and *Phanerochaete chrysosporium* in media supplemented with Tetracycline at a concentration of 200 ppm. The stimulation of ligninolytic enzyme production by certain antibiotics could be attributed to the fact that the fungi might be treating antibiotics as phenolic compounds and adopting the mechanism used for their detoxification for degradation antibiotics.

Degradation of CIP

Titrimetric analysis

Titrimetric analysis was used as one of the methods for the determination of degradation of CIP by *P. ostreatus*. On determining the concentration of FAS remaining after oxidation by cerium sulfate and calculating the % degradation thereof, it was found that the maximum degradation (68.8%) was obtained after 14 days of incubation at 500 ppm CIP (Table 4). This can be attributed to the fact that with the increase in CIP concentration, an increase in radial growth and enzyme production was observed, which in turn may have led to the increased biodegradation of the antibiotic. These results also suggest that the concentration of CIP in environment may significantly affect the biodegradation of antibiotic by the fungus.

Table 3 Effect of different concentrations of CIP on Enzyme activity of *P. ostreatus* after 7 and 14 days of incubation

Concentration of CIP used (ppm)	Enzyme activity (in $\mu\text{mol}/\text{min}/\text{mg}$) ^a							
	Endo- β -D-1,4-glucanase		Hemicellulase		Lignin peroxidase		Manganese peroxidase	
	7 Days	14 Days	7 Days	14 Days	7 Days	14 Days	7 Days	14 Days
0 (control)	35.53	58.00	43.40	62.84	0.0117	0.0129	4.295	13.779
100	51.93	99.73	58.68	105.99	0.0134	0.0159	4.704	13.863
200	53.81	164.86	65.02	144.10	0.0161	0.0184	4.805	15.454
300	94.20	185.52	71.78	164.82	0.0184	0.0212	5.426	15.909
400	94.30	269.95	82.73	235.97	0.0208	0.0222	6.231	21.786
500	112.87	392.94	93.69	331.40	0.0244	0.0256	7.441	23.864
CD 5%	0.101	0.162	0.121	0.181	0.001	0.001	0.029	NS

Medium used-PDB; Incubation temperature- 25 ± 2 °C

NS non significant

^a Average of three replicates with standard error

Table 4 Percent degradation of CIP by *P. ostreatus* after 7 and 14 days of incubation by Titrimetric and Spectrophotometric Analysis

Concentration of CIP used (ppm)	Percent degradation of CIP					
	Titrimetric analysis		Spectrophotometric analysis			
	7 Days	14 Days	Indigo carmine method		Methyl orange method	
			7 Days	14 Days	7 Days	14 Days
0 (control)	ND	ND	ND	ND	ND	ND
100	12.0	46.0	81.60	86.50	79.20	85.80
200	41.0	52.0	83.40	90.90	81.05	88.00
300	57.3	61.3	87.13	91.00	85.37	90.26
400	60.5	63.0	90.87	93.00	88.97	90.30
500	65.4	68.8	93.50	94.25	88.92	91.34
CD 5%	4.847	4.691	0.55	0.75	0.168	0.161

ND not detected

Spectrophotometric analysis

Indigo carmine assay

Spectrophotometric determination of CIP using Indigo carmine method also exhibited a pattern similar to that obtained in titrimetric analysis. Percent degradation increased with the increasing concentration of CIP. 81.50% degradation of CIP was carried out by *P. ostreatus* after 7 days of incubation when 100 ppm CIP was initially taken. This increased to 86.50% after 14 days of incubation. A maximum degradation of 94.25% was achieved at CIP concentration of 500 ppm, after 14 days of incubation (Table 4).

Methyl orange assay

Showed that after 14 days of incubation, about 86.50% of CIP was degraded when 100 ppm of CIP was originally

supplemented in the broth. As observed above, degradation increased with the increase in antibiotic concentration with highest degradation (91.34%) obtained at 500 ppm of CIP, after 14 days of incubation (Table 4).

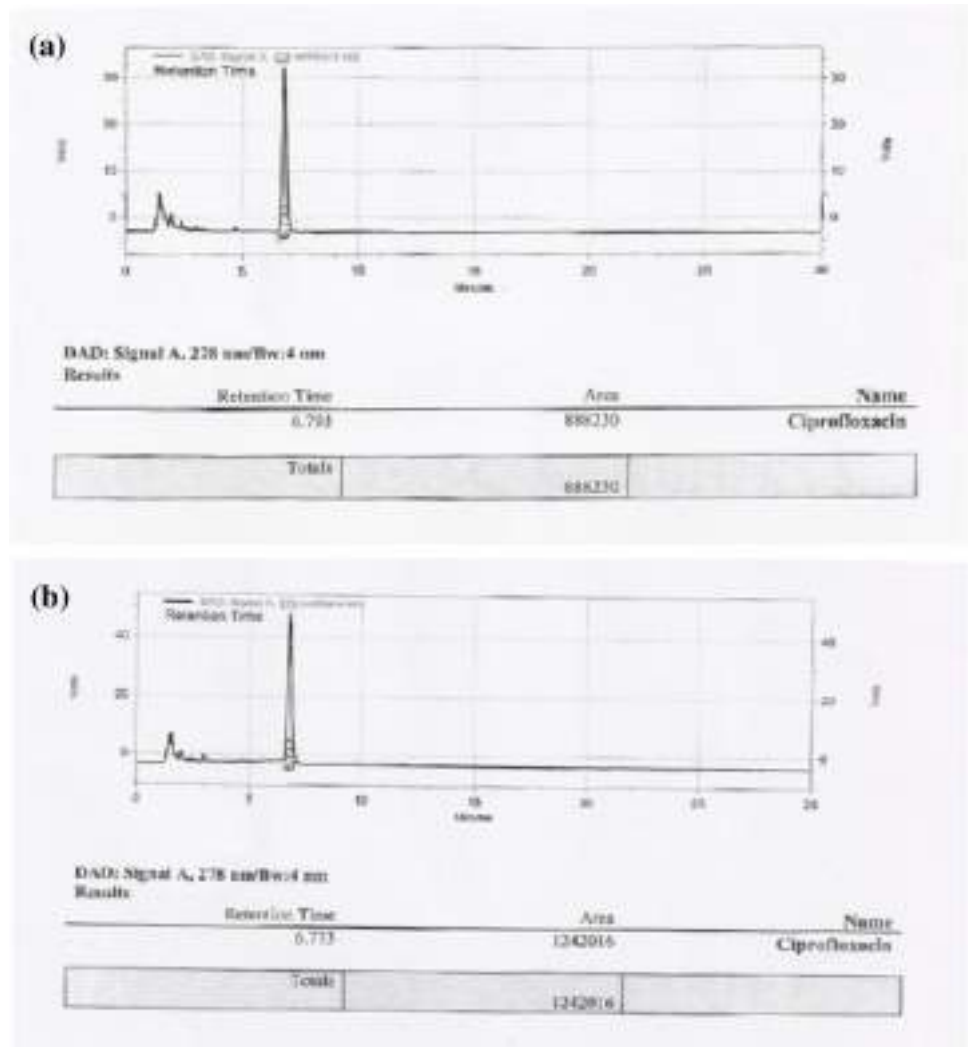
These results suggest that spectrophotometric methods are more sensitive in determination of CIP as compared to titrimetric method and Indigo carmine assay was a more sensitive method than methyl orange assay.

Validation of CIP bioremediation

High performance liquid chromatography (HPLC)

Validation of the results obtained by titrimetric and spectrophotometric methods was carried out by HPLC. On comparison with CIP standard, a degradation of 82.3% of 100 ppm CIP and 95.07% for 500 ppm CIP was observed after 14 days of incubation with *P. ostreatus* (Fig. 1).

Fig. 1 Chromatogram for CIP
a 100 ppm **b** 500 ppm after
 treatment with *P. ostreatus* for
 14 days



These results are in agreement with the results obtained by titrimetric and spectrophotometric analysis.

Antimicrobial activity of degraded products

Antimicrobial activity of degraded CIP was determined against *Escherichia coli*, *Staphylococcus aureus* and *Streptococcus pyogenes*. It was observed that the inhibitory action of CIP degradation products produced after incubation with *P. ostreatus* for 14 days was less as compared to standard CIP (100 and 500 ppm CIP solution). When 100 ppm CIP was used, a zone of inhibition of 2.5, 2.0 and 2.8 cm for *E. coli*, *S. aureus* and *S. pyogenes*, respectively, was observed whereas when degradation product obtained after incubation of 100 ppm CIP with *P. ostreatus* for 14 days was used, an inhibition zone of about 1.9, 1.7 and 2.3 cm for *E. coli*, *S. aureus* and *S. pyogenes* was observed. This corresponds to a 24, 15 and 17% decrease in the antimicrobial activity against *E. coli*, *S. aureus* and *S. pyogenes*, respectively. Similarly, for 500 ppm CIP used, a

zone of 4.0, 3.6 and 3.4 cm for *E. coli*, *S. aureus* and *S. pyogenes* was obtained while with degradation product obtained after incubation of 500 ppm CIP with *P. ostreatus* for 14 days, a zone of inhibition of 2.9, 2.6 and 2.6 cm for *E. coli*, *S. aureus* and *S. pyogenes* was observed, exhibiting an average decrease of 26.3% in the antimicrobial activity of CIP (Table 5).

When these results were compared by calculating CD5% using one-way ANOVA, they suggested a significant decrease in the antimicrobial activity of degraded products produced when CIP was incubated with *P. ostreatus*. These results are supported by Wetzstein et al. (1999) who found that another fungus *Gloeophyllum striatum* reduced the activity of CIP in liquid culture to 0–33% after 13 weeks.

These results are also in agreement with the growth and enzymatic studies of *P. ostreatus* in presence of CIP. The stimulatory effect of CIP concentration on the growth of *P. ostreatus* can be attributed to an increase in amount of enzyme production in the presence of CIP. Extracellular

Table 5 Antimicrobial activity of degradation products of ciprofloxacin against *Escherichia coli*, *Staphylococcus aureus* and *Streptococcus pyogenes*

Concentration of CIP used (in ppm)	Zone of inhibition (in cm) ^a								
	<i>E. coli</i>			<i>S. aureus</i>			<i>S. pyogenes</i>		
	CIP degradation products	CIP	CD 5%	CIP degradation products	CIP	CD 5%	CIP degradation products	CIP	CD 5%
D/w	ND	ND	–	ND	ND	–	ND	ND	–
0(Control)	1.5	3.0	0.226	1.6	3.8	0.358	2.0	3.6	0.358
100	1.9	2.5	0.226	1.7	2.0	0.226	2.3	2.8	0.240
200	1.9	3.0	0.226	2.5	2.8	0.226	2.5	3.0	0.226
300	2.3	3.4	0.358	2.5	3.0	0.321	2.5	3.2	0.330
400	2.6	3.6	0.321	2.6	3.4	0.330	2.1	3.2	0.160
500	2.9	4.0	0.179	2.6	3.6	0.330	2.6	3.4	0.320

Medium used—Mueller Hinton Agar; Temperature conditions 37 ± 2 °C

D/w distilled water, CIP ciprofloxacin, ND not detected

^a Average of triplicates

enzymes of *P. ostreatus* have been found to have a degradative effect on various environmental pollutants in past studies (Tellez et al. 2013; Collins et al. 1997) and can possibly be involved in the degradation of CIP using similar metabolic pathways. These results are of much significance since they indicate that treatment of CIP containing effluent with *P. ostreatus* might effectively decrease antimicrobial activity of the antibiotic, thereby leading to a negative effect on the development of antibiotic resistant bacteria in nature.

Conclusion

1. *Pleurotus ostreatus*, a basidiomycetous fungus has shown a considerable biodegradation potential towards antibiotic ciprofloxacin. Not only was *P. ostreatus* found to have a high tolerance to CIP, but it was also observed that CIP has a stimulatory effect on the fungus as observed by increased mycelial growth and enzyme activity.
2. Spectrophotometric methods were better at detection of CIP than titrimetric methods with Indigo carmine assay being the most sensitive assay in detection of CIP.
3. The products produced after degradation of CIP were found to have a reduced antimicrobial activity against test microorganisms as detected from their zones of inhibition.
4. To the best of our knowledge, the effect of ciprofloxacin on growth of *P. ostreatus* and its subsequent degradation by the fungus has not been reported before.

Funding This research did not receive any specific grant from funding agencies in the public, commercial, or not-for-profit sectors.

Compliance with ethical standards

Conflict of interest The authors declare that there is no conflict of interest.

References

- Ahmed SA, Kadam JA, Mane VP, Patil SS, Baig MMV (2009) Biological efficiency and nutritional contents of *Pleurotus florida* (Mont.) Singer cultivated on different agro-wastes. *Nat Sci* 7(1):44–48
- Basavaiah K, Nagegowda P, Somashekar BC, Ramakrishna V (2006) Spectrophotometric and titrimetric determination of CIP based on reaction with cerium (IV) Sulfate. *Sci Asia* 32:403–409
- Batt AL, Kim S, Aga DS (2007) Comparison of the occurrence of antibiotics in four fullscale wastewater treatment plants with varying designs and operations. *Chemosphere* 68(3):428–435
- Bucht B, Eriksson KE (1968) Extracellular enzyme system utilized by the rot fungus *Stereum sanguinolentum* for the breakdown of cellulose. I. Studies on the enzyme production. *Arch Biochem Biophys* 124(1):135–141
- Butaye P, Devriese LA, Haesebrouck F (2003) Antimicrobial growth promoters used in animal feed: effects of less well known antibiotics on gram-positive bacteria. *Clin Microbiol* 16(2):175–188
- Collins PJ, Field JA, Teunissen P, Dobson ADW (1997) Stabilization of lignin peroxidases in white rot fungi by tryptophan. *Appl Environ Microbiol* 63(7):2543–2548
- Dhawan S, Lal R, Hanspal M, Kuhad RC (2005) Effect of antibiotics on growth and laccase production from *Cyathus bulleri* and *Pycnoporus cinnabarinus*. *Biores Technol* 96:1415–1418
- Dibner JJ, Richards JD (2005) Antibiotic growth promoters in agriculture: history and mode of action. *Poult Sci* 84(4):634–643
- Espindola LHS, Espindola FS, Freitas GRD, Brandeburgo MAM (2007) Biodegradation of red 40 dye by the mushroom *Pleurotus florida*. *Biosci J* 23(3):90–93

- Froehner SC, Eriksson KEL (1974) Induction of *Neurospora crassa* laccase with protein synthesis inhibitors. *J Bacteriol* 120(1):450–457
- Guo X, Zhu Z, Li H (2014) Biodegradation of sulfamethoxazole by *Phanerochaete chrysosporium*. *J Mol Liq* 198:169–172
- Hernandez F, Rivera A, Ojeda A, Zayas T, Cedillo L (2012) Photochemical degradation of the CIP antibiotic and its microbiological validation. *J Environ Sci Eng A1*:448–453
- Hubicka U, Zmudzki P, Talik P, Witek BZ, Krzek J (2013) Photodegradation assessment of CIP, moxifloxacin, norfloxacin and ofloxacin in the presence of excipients from tablets by UPLC-MS/MS and DSC. *Chem Cent J* 7:133
- Jegatheesan M, Kumaran MS, Eyini M (2012) Enhanced production of laccase enzyme by the white-rot mushroom fungus *Pleurotus florida* using response surface methodology. *Int J Curr Res* 4(10):025–031
- Kuwahara M, Glenn JK, Morgan MA, Gold MH (1984) Separation and characterization of two extracellular H₂O₂-dependent oxidases from ligninolytic cultures of *Phanerochaete chrysosporium*. *KEBS Lett* 69(2):247–250
- Laxminarayan R, Duse A, Wattal C, Zaidi AKM, Wertheim HFL, Sumpradit N, Vlieghe E, Hara GL, Gould IM, Goossens H, Greko C, So AD, Bigdeli M, Tomson G, Woodhouse W, Ombaka E, Peralta AQ, Qamar FN, Mir F, Kariuki S, Bhutta ZA, Coates A, Bergstrom R, Wright GD, Brown ED, Cars O (2013) Antibiotic resistance—the need for global solutions. *Lancet Infect Dis* 13(12):1057–1098
- Martens R, Wetzstein HG, Zadrzil F, Capelari M, Hoffmann P, Schmeer N (1996) Degradation of the fluoroquinolone enrofloxacin by wood-rotting fungi. *Appl Environ Microbiol* 62(11):4206–4209
- Miles RD, Butcher GD, Henry PR, Littell RC (2006) Effect of antibiotic growth promoters on broiler performance, intestinal growth parameters, and quantitative morphology. *Poult Sci* 85(3):476–485
- Miller GL (1959) Use of dinitrosalicylic acid reagent for determination of reducing sugar. *Anal Chem* 31(3):426–428
- Nijhu RS, Jhankar YM, Sutradhar KB (2011) Development of an assay method for simultaneous determination of CIP and naproxen by UV spectrophotometric method. *Stamford J Pharma Sci* 4(1):84–90
- Noverr MC, Noggle RM, Toews GB, Huffnagle GB (2004) Role of antibiotics and fungal microbiota in driving pulmonary allergic responses. *Infect Immun* 72(9):4996–5003
- Praveen K, Usha KY, Rajasekhar Reddy B (2012) Effect of antibiotics on ligninolytic enzymes production from *Stereum ostrea* and *Phanerochaete chrysosporium* under submerged fermentation. *Int J Pharm Pharm Sci* 4(3):135–138
- Rana IS, Rana AS (2011) Lignocellulolytic enzyme profile of *Agaricus* and *Pleurotus* species cultured on used tea leaves substrate. *Adv Bio Tech* 11(6):10–14
- Rodríguez-Rodríguez CE, García-Galán MA, Blázquez P, Díaz-Cruz MS, Barceló D, Caminal G, Vicent T (2012) Continuous degradation of a mixture of sulfonamides by *Trametes versicolor* and identification of metabolites from sulfapyridine and sulfathiazole. *J Hazard Mater* 213–214:347–354
- Rogalski J, Lundell TK, Leonowicz A, Hatakka AI (1991) Influence of aromatic compounds and lignin on production of ligninolytic enzymes by *Phlebia radiata*. *Phytochem* 30(9):2869–2872
- Sandhu DK, Arora DS (1985) Laccase production by *Polyporus sanguineus* under different nutritional and environmental conditions. *Experientia* 41:355–356
- Shah Z, Dighe A, Londhe V (2015) Pharmacoeconomic study of various brands of antibiotic medications in India. *World J Parma Res* 4(3):1600–1606
- Singh MP, Pandey AK, Vishwakarma SK, Srivastava AK, Pandey VK (2012) Extracellular xylanase production by *Pleurotus* species on lignocellulosic wastes under in vivo condition using novel pretreatment. *Cell Mol Biol (Noisy-le-grand)* 58(1):170–173
- Singh RN, Sahoo S, Mishra U, Garnaik B, Sahoo SK, Hati D (2013) Stability indicating RP-HPLC method development and validation of norfloxacin. *Am J Adv Drug Deliv* 1(5):743–758
- Tellez MT, Diaz R, Sanchez C, Godinez GD (2013) Hydrolytic enzymes produced by *Pleurotus* species. *Afr J Microbiol Res* 7(4):276–281
- Thillaimaharani KA, Sharmila K, Thangaraju P, Karthick M, Kalaiselvam M (2013) Studies on antimicrobial and antioxidant properties of oyster mushroom *Pleurotus florida*. *Int J Pharm Sci Res* 4(4):1540–1545
- Tien M, Kirk TK (1984) Lignin-degrading enzyme from *Phanerochaete chrysosporium*: purification, characterization, and catalytic properties of a unique H₂O₂-requiring oxygenase. *Proc Natl Acad Sci* 81(8):2280–2284
- Wegener HC, Aarestrup FM, Jensen LB, Hammerum AM, Bager F (1999) Use of antimicrobial growth promoters in food animals and *Enterococcus faecium* resistance to therapeutic antimicrobial drugs in Europe. *Emerg Infect Dis* 5(3):329–335
- Wetzstein HG, Stadler M, Tichy HV, Dalhoff A, Karl W (1999) Degradation of CIP by basidiomycetes and identification of metabolites generated by the brown rot fungus *Gloeophyllum striatum*. *Appl Environ Microbiol* 65(5):1556–1563

MOLECULAR DOCKING STUDIES OF *CURCUMA LONGA* AND *ALOE VERA* FOR THEIR POTENTIAL ANTICANCER EFFECTS

PARUL TRIPATHI, SAAD SABIR SIDDIQUI, ANJU SHARMA, PARUL JOHRI, ADITI SINGH*

Amity Institute of Biotechnology, Amity University Uttar Pradesh, Lucknow Campus, Malhaur, Gomti Nagar Extension, Lucknow – 226 028, Uttar Pradesh, India. Email: asingh3@lko.amity.edu

Received: 28 November 2017, Revised and Accepted: 12 January 2018

ABSTRACT

Objective: In this paper, docking study is presented to use these phytochemicals for their prospective role in various types of cancers.

Methods: A group of the different set of phytochemicals (aloesin, barbaloin, curcumin, and emodin) were taken and docked into the active sites of Topoisomerase I, a 91-kDa monomer (having 765 amino acids), is encoded by a single copy gene (Top 1) located on chromosome 20q12–13.2 using Autodock4 Software. The docking studies of the selected proteins were also docked to study the anticancerous property of the selected phytochemicals.

Result: These studies were based on binding energy, docking energy and other relevant scores that revealed emodin could be the potential lead molecule for the inhibition of signal potent for different types of cancer. Furthermore, the important residues for potential drug target were identified.

Conclusion: This paper is an initial step toward a rational design of novel selective and potent phytochemicals inhibitors for the treatment of deadly disease cancer.

Keywords: Anticancer, Docking, Phytochemicals.

© 2018 The Authors. Published by Innovare Academic Sciences Pvt Ltd. This is an open access article under the CC BY license (<http://creativecommons.org/licenses/by/4.0/>) DOI: <http://dx.doi.org/10.22159/ajpcr.2018.v11i4.23995>

INTRODUCTION

Plants and their extracts have been used to treat human diseases since ancient time. Among the many medicinal and therapeutic properties, plants such as *Andrographis paniculata*, *Arachis hypogaea*, *Datura innoxia*, *Aloe vera*, and *Curcuma longa* have also been explored for their cancer chemotherapeutic potential [1-5]. In *C. longa* (Indian spice turmeric) the most active component is curcumin, the yellow substance belonging to polyphenols superfamily. It has been extensively used in Ayurvedic medicine for centuries, as it is nontoxic and has a variety of therapeutic properties including antioxidant, analgesic, anti-inflammatory, and antiseptic activity [6,7]. Recently, curcumin has also been found to possess anticancer activities because of its effect on a variety of biological pathways involved in mutagenesis, oncogene expression, cell cycle regulation, apoptosis, tumorigenesis, and metastasis [7-9].

The herb *A. vera* is widely used in Ayurveda, homoeopathy as well as allopathy for its wide medicinal properties. The most active plant part extract is leaf gel which has more than 200 different biologically active substances having antimicrobial, anti-inflammatory, anthelmintic, wound healing, and also anticancer activities [10-12]. The most significant anthraquinones in aloe gel are aloesin, aloe-emodin (AE), and barbaloin. Aloesin is a potent and selective inhibitor of tyrosinase and exhibits direct inhibitory effects on melanogenesis [13]. However, little is known about the role of aloesin in anticancer activity. Barbaloin is C-glucoside of AE anthrone, and has strong inhibitory effect on histamine release, cathartic, and anticancer activity. AE, the hydroxyanthraquinone has been studied to possess *in vitro* and *in vivo* anti-neuroectodermal tumor activity [14].

Many cell cycle molecules and genes have been studied to be involved in cancer pathogenesis. Targeting such proteins and

molecules may be a good strategy for anticancer therapy. In the current study, molecular docking was performed to find out the target protein for these four potential anticancer compounds (aloesin, barbaloin, curcumin, and emodin), their respective binding energies along with the number of hydrogen bonds and other hydrophobic interactions.

METHODS

Structure retrieval

Selection of the target proteins has been done through literature search [15-18]. Proteins who have anticancer properties been selected for the study. The three-dimensional crystal structures of all 14 target proteins were retrieved from the protein data bank (PDB) (<https://www.rcsb.org/pdb/home/home.do>) (Table 1).

C. longa and *A. vera* are very well known for their therapeutic properties, so it was decided to check their anticancerous effect *in silico*. The two-dimensional structures of ligand molecules (aloesin, barbaloin, curcumin, and emodin) were downloaded from PubChem database (<https://pubchem.ncbi.nlm.nih.gov>) (Table 2).

Docking studies

The docking studies were performed by AutoDock 4 Software. AutoDock 4 Software serves as a valid and acceptable docking application to study the interactions of small compounds with proteins. All protein structures and ligands were prepared for docking studies using various parameters such as addition of polar hydrogen atoms, merging of non-polar hydrogen atoms and defining the rotatable bonds for each ligand. Finally, Kollman united atom charge, and atom type parameter was added. The grid parameters (60* 60* 60) for all proteins were set in such a way that it includes the active site. The

Lamarckian genetic search algorithm was employed, and docking was set to 20 runs. All other parameters were set to the default values such as maximum number of energy evaluation was set as 25,00,000 per run and maximum number of generations in the genetic algorithm was increased to 2,70,000 (Fig. 1).

RESULTS

The results obtained after docking aloesin, barbaloin, curcumin, and emodin (Table 2) with 14 different proteins (Table 1) were evaluated on the basis of energy. The binding energy obtained from docking interactions, ligand efficiency and inhibition constant values calculated by AutoDock 4 were considered as the primary parameters for studying the

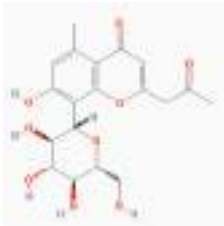
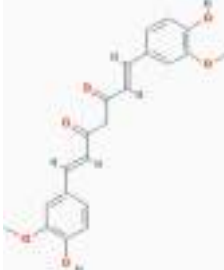
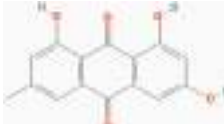
docking behavior of ligands with our proteins (Table 3). Binding energy is a measure of the affinity of ligand-protein complex or is the difference between the energy of complex and the sum of energies of each molecule separately. Inhibition constant is an indication of how potent an inhibitor is, it is concentration required to produce half maximum inhibition. The ligand efficiency is binding energy per atom of ligand to protein and is defined as the calculated pKi divided by the number of heavy atoms in the ligand; the smaller is the ligand efficiency, the more promising is the docking. Optimal parameters were used as criteria to interpret the best pose among the 10 conformations generated by the software AutoDock 4. The molecular docking studies provide valuable information about the residues involved in the enzyme-substrate interaction.

Table 1: Proteins used as target for docking studies

S. No	Name	PDB ID	Length	Experimental info	Resolution
1	Topo I	1k4t	592	X-ray diffraction	2.1 Å
2	NF-KB	1nfk	312	X-ray diffraction	2.3 Å
3	Caspase 3	1pau	504	X-ray diffraction	2.5 Å
4	Caspase 8	1qtn	479	X-ray diffraction	1.2 Å
5	PKC	1yrk	13	X-ray diffraction	1.7 Å
6	CDK2	2bhh	298	X-ray diffraction	2.6 Å
7	EGFR	2itx	324	X-ray diffraction	2.98 Å
8	MMP-9	2ovx	159	X-ray diffraction	2.0 Å
9	CFLIP	3h13	271	X-ray diffraction	2.2 Å
10	COX-2	3ln1	552	X-ray diffraction	2.4 Å
11	mTOR	3oaw	951	X-ray diffraction	2.75 Å
12	HER2 Protein	3pp0	308	X-ray diffraction	2.25 Å
13	Topo II β	3qx3	12	X-ray diffraction	2.16 Å
14	MPO	4c1m	467	X-ray diffraction	2.0 Å

PDB: Protein data bank, EGFR: Epidermal growth factor receptor

Table 2: Ligand molecules used for docking studies

S. No	Name	PubChem CID	Chemical formula	Molecular weight (g/mol)	2D structure
1	Aloesin	160190	C ₁₉ H ₂₂ O ₉	394.376 g/mol	
2	Barbaloin	12305761	C ₂₁ H ₂₂ O ₉	418.398 g/mol	
3	Curcumin	969516	IC ₂₁ H ₂₀ O ₆ /C ₂₁ H ₂₀ O ₆	368.385 g/mol	
4	Emodin	3220	C ₁₅ H ₁₀ O ₅	270.24 g/mol	

2D: Two-dimensional

Aloesin showed the lowest binding energy of -3.16 kcal/mol, ligand efficiency of -0.11, and inhibition constant of 4.79 μM, with Protein kinase C (1yrk) out of the 14 proteins. The best-docked conformation of aloesin showed hydrogen-binding interactions with the active residues Lys96, Leu3, and Leu122 of 1yrk with a binding free energy -3.16 kcal/mol (Fig. 2).

Barbaloin showed the lowest binding energy of -2.9 kcal/mol and -2.93 kcal/mol with protein 1qtn and 3oaw, respectively, out of 14 proteins selected as a receptor for docking. Both proteins were found to have same ligand efficiency (-0.1) and inhibition constant (7.16 μM) with barbaloin inferring equal affinity of binding. The best-docked conformation of barbaloin showed hydrogen-binding interactions with the active residues Asn452, Ser451, Tyr412, Thr503, Gly368, and Arg413 of 1qtn (Fig. 3).

When barbaloin was docked with protein 3oaw, hydrogen bonds are formed with Asn452, Ser451, Tyr412, Thr503, Gly368, and Arg413 residues (Fig. 4).

Curcumin binds best with epidermal growth factor receptor (2itx) getting the binding energy of -4.0 kcal/mol. The ligand efficiency

and inhibition constant of curcumin with 2itx are 1.18 and -0.15 μM respectively. The best-docked conformation of curcumin showed hydrogen-binding interactions with the active residues Asn700, Pro999, Gln701, Glu697, and Pro1019 of 2itx (Fig. 5).

Emodin binds best with topo I (1k4t) getting the binding energy of -5.71 kcal/mol. The measured ligand efficiency and inhibition constant with 1k4t observed are 65.38 and -0.29 μM, respectively. The best-docked conformation of emodin showed hydrogen-binding interactions with active residues Trp416, Glu356, and Ile377 active residues of 1k4t (Fig. 6).

The H-bonding stabilizes the ligand and the target site and helps alter binding affinity and drug efficacy. The result presented in this paper provides a novel *in silico* based approach to design drug lead at the hydrophobic core of ligand and protein interphase. The weak hydrogen bonds can be broken and exchanged for another kind of bond depending on the chemical environment at the target, ligand, and target-ligand interphase. The summarized details of the hydrogen bonds studied are listed in Table 4.

Table 3: Describes the data obtained from docking log file for every ligand-receptor docking

Ligand molecules	Docking parameters	Proteins													
		1k4t	1nfk	1pau	1qtn	1yrk	2bhh	2itx	2ovx	3h13	3ln1	3oaw	3pp0	3q×3	4c1m
Aloesin	Binding energy (kcal/mol)	-1.14	-0.88	-1.15	-2.02	-3.16	-2.2	-2.79	-2.59	-1.28	-1.35	-0.88	-1.46	-0.9	-1.17
	Inhibition constant*(μM)	146.5	224.8	142.9	32.8	4.79	24.51	9.04	12.62	115.7	101.9	224.6	84.37	218.2	139.4
	Ligand efficiency	-0.04	-0.03	-0.03	-0.07	-0.11	-0.08	-0.1	-0.09	-0.05	-0.05	-0.07	-0.05	-0.03	-0.04
Barbaloin	Binding energy (kcal/mol)	-2.06	-1.01	-0.26	-2.9	-1.15	-2.15	-1.39	-2.04	-0.96	-1.06	-2.93	-0.6	-1.33	-1.14
	Inhibition constant*(μM)	30.73	180.7	640.6	7.47	144.1	26.48	95.74	32.22	197.5	165.9	7.16	363.9	105.2	146.9
	Ligand efficiency	-0.07	-0.03	-0.01	-0.1	-0.04	-0.07	-0.05	-0.07	-0.03	-0.04	-0.1	-0.02	-0.04	-0.04
Curcumin	Binding energy (kcal/mol)	-3.21	-2.39	-2.01	-2.93	-1.98	-3.38	-4	-2.58	-1.49	-2.51	-1.6	-1.59	-1.77	-2.53
	Inhibition constant*(μM)	4.47	17.61	33.49	7.06	35.13	3.36	1.18	12.94	80.98	14.42	66.7	68.54	50.31	13.96
	Ligand efficiency	-0.12	-0.09	-0.07	-0.11	-0.07	-0.13	-0.15	-0.1	-0.06	-0.09	-0.06	-0.06	-0.07	-0.09
Emodin	Binding energy (kcal/mol)	-5.71	-4.68	-3.36	-3.8	-3.33	-3.68	-3.71	-5	-3.6	-4.39	-3.93	-4.11	-3.89	-3.83
	Inhibition constant*(μM)	65.38	370.5	3.42	1.65	3.61	2.01	1.91	217	2.31	609.9	1.1	996	1.4	1.55
	Ligand efficiency	-0.29	-0.23	-0.17	-0.19	-0.17	-0.18	-0.19	-0.25	-0.18	-0.22	-0.2	-0.21	-0.19	-0.19

*The change in binding free energy is related to the inhibition constant using the equation: $\Delta G = RT \ln K_i$, where R is the gas constant 1.987 cal K⁻¹ mol⁻¹, and T is the absolute temperature assumed to be 298.15 K

Table 4: Summarized hydrogen bonding interactions for all the proteins and their ligands

S. No	Protein name	Compound	Interaction	Amino acid involved in interaction
1	Aloesin	Protein kinase C (1yrk)	Hydrogen bond	Lys96, Leu3, Leu122
2	Barbaloin	Caspase 8 (1qtn)	Hydrogen bond	Asn452, Ser451, Tyr412, Thr503, Gly368, Arg413
3	Barbaloin	mTOR (3oaw)	Hydrogen bond	Asn452, Ser451, Tyr412, Thr503, Gly368, Arg413
4	Curcumin	EGFR (2itx)	Hydrogen bond	Asn700, Pro999, Gln701, Glu697, Pro1019
5	Emodin	Topo I (1k4t)	Hydrogen bond	Trp416, Glu356, Ile377

EGFR: Epidermal growth factor receptor

Table 5: Energy in KJ/mol for ligand complex with top scoring proteins

S. No	Ligand (zinc IDs/name)	Protein (PDB ID)	VDW (kcal/mol)	Electrostatic energy (KJ/mol)
1	Aloesin	1yrk	6.82	-0.1
2	Barbaloin	a) 1qtn	-8.53	-0.64
		b) 3oaw	-8.99	-0.22
3	Curcumin	2itx	-9.32	-0.19
4	Emodin	1k4t	-8.44	-0.09

PDB: Protein data bank, VDW: Van der Waals

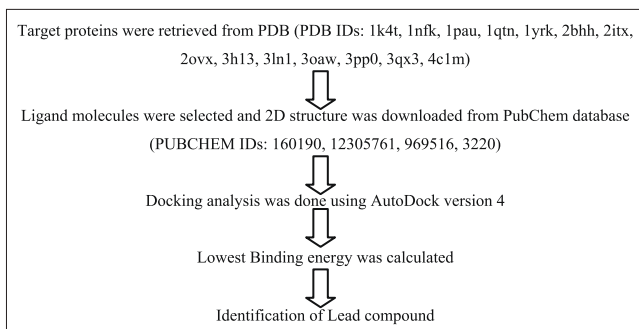


Fig. 1: Flowchart for methodology

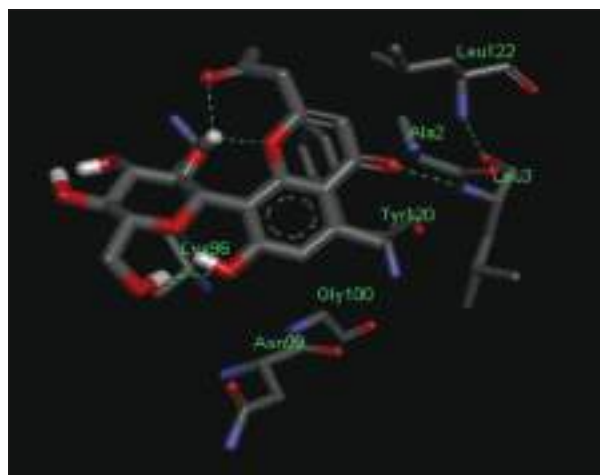


Fig. 2: Docked complex of aloesin (160190) with protein kinase C (1yrk) in ribbon representation and their interacting residues; dotted lines showing the hydrogen bond interaction

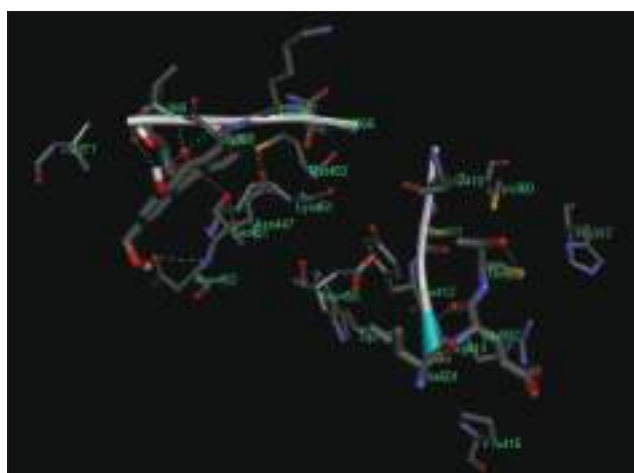


Fig. 3: Docked complex of barbaloin (12305761) with caspase 8 (1qtn) in ribbon representation and their interacting residues; dotted lines showing the hydrogen bond interaction

Ligands and best-docked proteins along with their van der Waals value and electrostatic energy (KJ/mol) are shown in Table 5.

CONCLUSION

The protein-ligand interaction plays a significant role in structure-based drug designing. The data suggest that emodin and curcumin have potential therapeutic value in cancer. Since the compounds do not exhibit side effects, it has been designated for several clinical trials as a treatment of human cancer, yet its mechanism of action remains

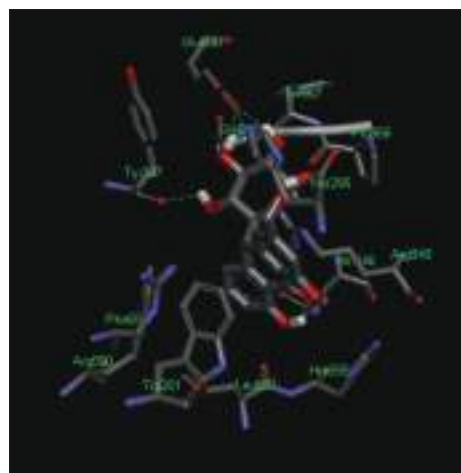


Fig. 4: Docked complex of barbaloin (12305761) with mTOR (3oaw) in ribbon representation and their interacting residues; dotted lines showing the hydrogen bond interaction

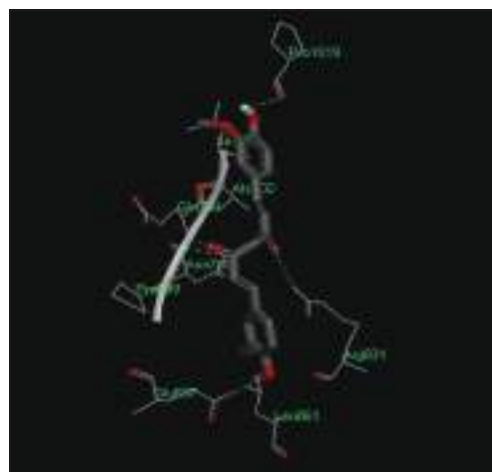


Fig. 5: Docked complex of curcumin (969516) with epidermal growth factor receptor (2itx) in ribbon representation and their interacting residues; dotted lines showing the hydrogen bond interaction



deoxyribonucleic acid (DNA) Topoisomerase I catalyze single-strand breaking and rejoining in a DNA double helix in an ATP-independent manner [19].

Therefore, this study states the importance of compounds from *C. longa* and *A. vera* and their use to enhance protein-ligand studies, *in silico*. From the docking results, it is possible to conclude that emodin could be a potential Topo I inhibitor. In this study, the molecular docking was applied to explore the binding mechanism and to correlate its docking score with the activity of plant-derived compounds. The results of our present study can be useful for the design and development of novel compounds having better inhibitory activity against several types of cancers. This potential agent will be a promising candidate and can further be validated in wet lab studies for its proper function and can proceed for clinical trials [20].

AUTHOR'S CONTRIBUTION

Authors Sharma A, Tripathi P and Siddiqui SS make substantial contributions to conception and design, acquisition of data, lab work and analysis and interpretation of data. Authors Singh A and Johri P participate in drafting the article or revising it critically for important intellectual content. All the authors gave final approval of the version to be submitted and any revised version.

CONFLICTS OF INTEREST

The authors have declared that no conflict of interest exists.

REFERENCES

- Huidrom S, Deka M. Determination of antioxidant property of *Andrographis paniculata*. Indian J Drugs Dis 2012;1:12-7.
- Tripathi P, Singh A. Indigenous Asian plants against cancer: A comprehensive review. Int J Plant Res 2015;5:80-6.
- Tripathi P, Singh A. Natural resources from plants in the treatment of cancer: An update. Asian J Pharm Clin Res 2017;10:13-22.
- Vermillion K, Holguin FO, Berhow MA, Richins RD, Redhouse T, O'Connell MA, et al. Dinoxin B, a withanolide from *Datura innoxia* leaves with specific cytotoxic activities. J Nat Prod 2011;74:267-71.
- Yadav DN, Yogesh K, Aswani A. Antioxidant activity of peanut (*Arachis hypogaea* L.) skin extract: Application in soybean and mustard oil. Int J Food Process Technol 2014;1:26-31.
- Akram M, Shahab-uddin, Ahmed A, Usmanghani K, Hannan A, Mohiuddin E, et al. *Curcuma longa* and curcumin: A review article. Rom J Biol Plant Biol 2010;55:65-70.
- Wilken R, Veena MS, Wang MB, Srivatsan ES. Curcumin: A review of anti-cancer properties and therapeutic activity in head and neck squamous cell carcinoma. Mol Cancer 2011;10:12.
- Vallianou NG, Evangelopoulos A, Schizas N, Kazazis C. Potential anticancer properties and mechanisms of action of curcumin. Anticancer Res 2015;35:645-51.
- Jerah A, Hobani Y, Kumar BV, Bidwai A. Curcumin binds *in silico* to anti-cancer drug target enzyme MMP-3 (human stromelysin-1) with affinity comparable to two known inhibitors of the enzyme. Bioinformation 2015;11:387-92.
- Sahu PK, Giri DD, Singh R, Pandey P, Gupta S, Shrivastava AK, et al. Therapeutic and medicinal uses of *Aloe vera*: A review. Pharmacol Pharm 2013;4:599-610.
- Hashemi SA, Madani SA, Abediankenari S. The review on properties of *Aloe vera* in healing of cutaneous wounds. Biomed Res Int 2015;2015:714216.
- Tripathi P, Singh A. *Aloe vera*: Plant with diverse therapeutic properties. Everyman's Sci 2016;1:6-9.
- Zhang LQ, Lv RW, Qu XD, Chen XJ, Lu HS, Wang Y, et al. Aloesin suppresses cell growth and metastasis in ovarian cancer SKOV3 cells through the inhibition of the MAPK signaling pathway. Anal Cell Pathol (Amst) 2017;2017:8158254.
- Ahirwar K, Jain SK. Aloe-emodin novel anticancer herbal drug. Int J Phytomed 2011;3:27-31.
- Kumar NA, Sharmila R, Akila K, Jaikumar B. *In-silico* approach for the assessment of oral cancer property on *Limonia acidissima*. Int J Pharm Sci Res 2016;7:1271-75.
- Sanghani HV, Ganatra SH, Pande R. Molecular-docking studies of potent anticancer agent. J Comput Sci Syst Biol 2012;5:12-5.
- Norleena PG, Amin AR, Bayraktar S, Pezzuto JM, Shin DM, Khuri FR, et al. Cancer prevention with natural compounds. Semin Oncol 2010;37:258-81.
- Huang Q, Lu G, Shen HM, Chung MC, Ong CN. Anti-cancer properties of anthraquinones from rhubarb. Med Res Rev 2007;27:609-30.
- Adhikari A, Mahar KS. DNA targeted anthraquinone derivatives: An important anticancer agent. Int J Pharm Pharm Sci 2016;8:17-25.
- Bairam R, Muppavarapu SM, Sreekanth S. Synthesis, characterization, biological evaluation and docking of some novel substituted 1, 3-thiazine derivatives. Int J Pharm Pharm Sci 2017;9:233-42.



Spectrophotometric and conductometric study of the interaction of saponin with chromium(VI) and lead(II)

S. K. Upadhyay¹ · O. Hari¹

Received: 19 September 2018 / Revised: 7 December 2018 / Accepted: 2 January 2019
© Islamic Azad University (IAU) 2019

Abstract

The removal of heavy metals from contaminated soil/water by biosurfactants depends on the ability of biosurfactant to form complexes with metals. The interaction of quillaja saponin, a nonionic natural biosurfactant, with heavy metal ions, viz. chromium(VI) and lead(II), has been studied spectrophotometrically and conductometrically in order to obtain detailed information for the saponin–metal complexes. Both the methods indicate complex formation between saponin and metal ions. Critical micelle concentration of saponin in the absence and presence of metal ions obtained by both the methods was in good agreement. The thermodynamic parameters, viz. free energy, enthalpy and entropy change, for micellization have been determined.

Keywords Saponin · Chromium(VI) · Lead(II) · Biosurfactant complexes

Introduction

Biosurfactants which are surface-active compounds of natural origin and obtained by either microbiological synthesis (Deleu and Paquot 2004) or extraction from plants are effective at wide range of pH, extreme temperature and environment salinity (Cameotra and Makkar 1998; Cameotra and Singh 2004; Desai and Banat 1997; Rodrigues et al. 2006). Moreover, the biosurfactants have higher biodegradability, ecological safety and low toxicity (Tang et al. 2017a; Kiran et al. 2010; Kanga et al. 1997). The effect of biosurfactant, viz. rhamnolipids, on removal of 2,4,2,4-tetrabrominated biphenyl ether by *Phanerochaete chrysosporium* has recently been analyzed with a combined approach of experiments and molecular docking (Liu et al. 2018).

Biosurfactants have been found to have higher selectivity and affinity for heavy metals (Hong et al. 2002; Chen et al. 2008) and therefore, have been used for remediation of heavy metals from the liquid waste streams, soils and

water (Abyanesh and Fazaelipour 2016). Metal–biosurfactant binding may include ion exchange, precipitation dissociation, counterion dissociation or electrostatic attraction (Miller 1995). The removal of heavy metals from contaminated soil/water depends on the ability of biosurfactant to form complexes with metal (Lai et al. 2009; Mulligan 2005).

Saponins, a class of nonionic biosurfactants, are naturally occurring glycosides of steroids, alkaloids and triterpenoids. Saponin is a natural product with high biodegradability, surface activity, environmental compatibility and low toxicity (Tang et al. 2017a). It has some carbonyl and hydroxyl with stronger capability of complexing with heavy metals (Chen et al. 2008) and, therefore, has been found to be ideally suited for bioremediation of metals at very low concentration. During the removal of heavy metals (viz. Cu, Zn, Cr, Pb, Ni, etc.) with sequential sludge washing techniques, Gao et al. (2012) and Huang and Liu (2013) observed that saponin has a strong ability to form complexes with these metals.

Green preparation of saponin complexes with divalent heavy metal ions has been optimized by direct combination between crude extract of *Olea Europaea* and *Citrus Auvantiaue* (Ashwini and Shantaram 2016). Saponin–metal complexes exhibited major absorption peaks in wavelength range of 320–400 nm (Aziz et al. 2017), while most of the saponin itself has a normal absorption peak in range of 250–350 nm (Bano 1985). The optimum concentration of

Editorial responsibility: Agnieszka Galuszka.

✉ S. K. Upadhyay
upadhyay_s_k@rediffmail.com

¹ Department of Applied Science, Dr. Ambedkar Institute of Technology for Handicapped UP, Awadhपुरi, Kanpur 208024, India



heavy metals and crude extract was equal to 120 ppm and 600–1000 ppm, respectively. However, information about stability constant and other thermodynamic parameters of these complexes is not available.

Our objective was to investigate the detailed information for the complex formations between saponin and metals. In the present investigation, the complex formation between saponin and two heavy metal ions, viz. chromium(VI) and lead(II), has been studied electrochemically and conductometrically and the results are reported in present communication.

Saponin used was a triterpene glycoside extracted from quillaja bark containing β -D-glucuronic acid with carboxyl group of sugar moiety (Hong et al. 2002; Hostettmann and Marston 1995). Saponin molecule contains one hydrophobic fused ring of triterpenes. It is different from conventional surfactants in hydrophobic tail, as conventional surfactants have long and straight chain of hydrocarbons. Two hydrophilic sugar chains having various functional groups are connected at the two ends C-3 and C-28 of the hydrophobic triperpene backbone, in which one end carries β -D-glucuronic acid group and other end carries non-ionic glycoside groups (Chen et al. 2008; Higuchi 1987).

Materials and methods

Materials

Saponin (Product Number 84510) was obtained from Sigma-Aldrich Chemical Pvt. Ltd. (Bangalore, India). It was brown powder and used without further purification. The aqueous solutions of saponin were prepared using distilled water. The critical micelle concentration (CMC) of saponin was determined by surface tension measurement and was found to be 0.10% (wt%). According to element analysis of saponin percentage composition of carbon, oxygen and hydrogen were 43, 51 and 6, respectively.

Analytical-grade chemicals $K_2Cr_2O_7$ (99.9% purity, Thomas Baker, Mumbai, India), lead nitrate $Pb(NO_3)_2$ (99.5% purity, Rankem, New Delhi, India) and sodium hydroxide (98.0% purity, Qualigens fine chemicals, Mumbai, India) were used. Double distilled water was used throughout experiments for the preparation of the solutions.

UV–visible spectroscopy

Spectrophotometric studies were performed in a UV–visible spectrophotometer model BT-UVS-DB8-E made by

BenchTop Lab System, India. A square quartz cell having 10 mm thickness and 1 nm silt width was used.

Electrical conductivity

Specific conductivity of solutions was measured on a digital conductivity meter model EI-641 made by ESICO, India. The instrument can be used to measure specific conductivity in the range of 0.01 μ S to 199.9 mS. Solution of $KCl_{(aq)}$ was used for the calibration of the instrument. The data were recorded up to ± 0.05 accuracy.

Results and discussion

The solutions were kept for 20 min at 308 K to establish the equilibrium. The chemical destruction of natural products like saponin may be predominant in acidic and alkaline medium. It has also been observed (Aziz et al. 2017) that the volume of saponin–metal complexes prepared in strong acidic or alkaline medium was less than that prepared in slightly alkaline conditions. Therefore, the interaction of saponin with metal ions has been studied in slightly alkaline conditions.

UV–visible spectroscopy

The spectra of saponin in pure water in the absence and in the presence of metal ions lead(II) and chromium(VI) were taken. Double distilled water was used for the preparation of all samples and for reference of simple UV–visible spectra. The maximum absorption was observed at 310 and 312 nm in case of aqueous solution of saponin. In the presence of chromium(VI) and lead(II), the additional absorption peaks were also observed at 338 nm and 318 nm, respectively. The results are reported in Fig. 1. The interaction between saponin and metal ions is confirmed by additional absorption peaks in the presence of metal ions. It has been observed that most of the saponin has a normal absorption peak in range of 250–350 nm (Bano 1985). The peak of saponin has been found to be shifted toward longer wave length (red shift) due to complexation with metal ions.

The gradual increase in the absorption with the concentration of saponin at λ_{max} (Fig. 2) in the absence as well as in the presence of metal ions indicates the incorporation of metal ions within the micelles. CMC of saponin with and without metal ions has been determined through the intersection of two straight lines (at lower and higher concentrations of saponin) plotted between (Absorbance) versus saponin (wt%) (Fig. 2). CMC of saponin was found to increase in the presence of metal ions (Table 2).

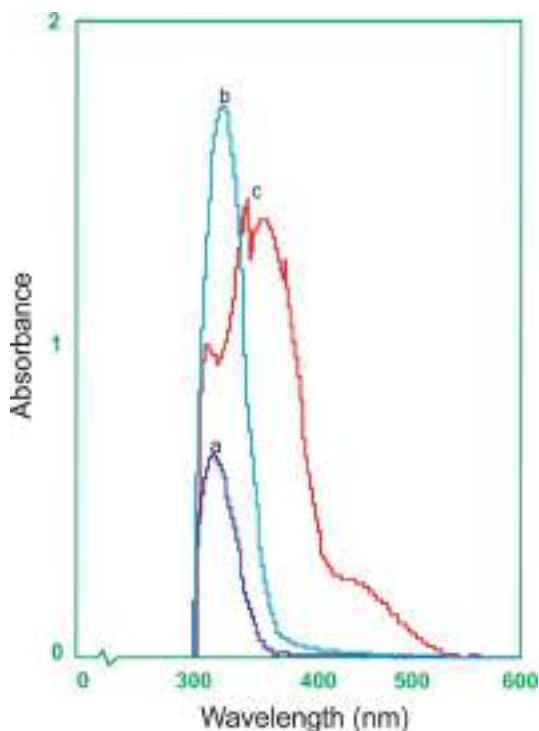


Fig. 1 Spectra of saponin in the absence and presence of metal ion at 308 K. a, saponin (wt .05%); b, saponin (wt .05%) + Cr^{VI} (wt. 06%); c, saponin (wt .05%) + Pb^{II} (wt .032%)

CMC of saponin in the presence of metal ions has also been obtained by considering difference in absorbance (ΔA), i.e., (absorbance of solution consisting saponin and metal ions) – (absorbance of metal ions). The results are represented graphically in the form of ΔA versus (saponin) in Fig. 3, and CMC of saponin in the presence of metal ions obtained from Fig. 3 is given in Table 1. It can be observed from Table 1 that CMC of saponin in the presence of metal ions obtained from Figs. 2 and 3 is in a good agreement.

The differential spectroscopy can be used for the qualitative and quantitative measurement of metal–surfactant interaction (Younas et al. 2017a, b; Noor et al. 2018). The following equation, reported by Kawamura et al. (1989), has been used for calculation of partition coefficient (K_x) for metal–surfactants interaction;

$$\frac{1}{\Delta A} = \frac{1}{K_c \Delta A_\infty (C_a + C_s^m)} + \frac{1}{\Delta A_\infty} \quad (1)$$

where ΔA is difference in absorbance, i.e., (absorbance of solution consisting saponin + metal ion) – (absorbance of solution consisting only metal ion); K_c is the partition constant and related to partition coefficient (K_x) as $K_x = K_c n_w$, where n_w is number of moles of water present per dm^{-3}

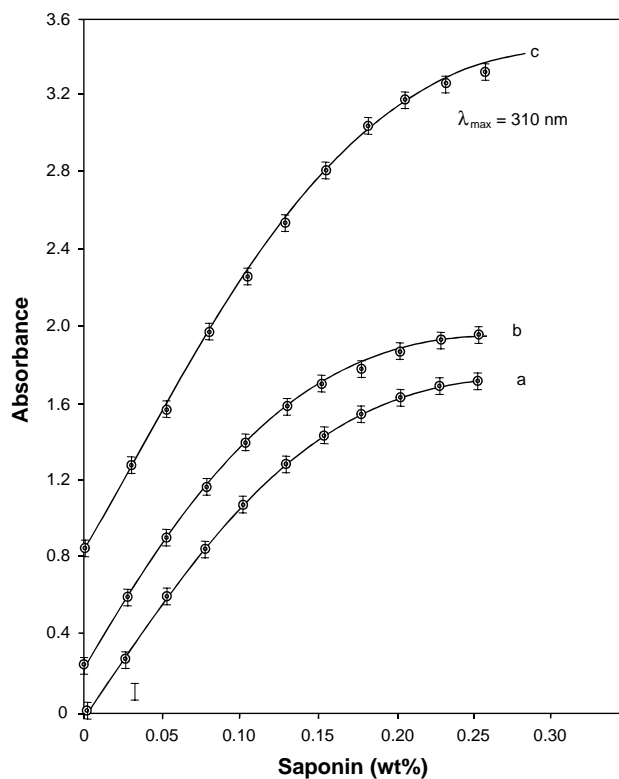


Fig. 2 Plots of absorbance (A) versus saponin concentration (wt%) at 308 K in the absence and presence of metal ions. a, saponin; b, saponin + Cr^{VI} (wt .06%); c, saponin (wt .05%) + Pb^{II} (wt .032%)

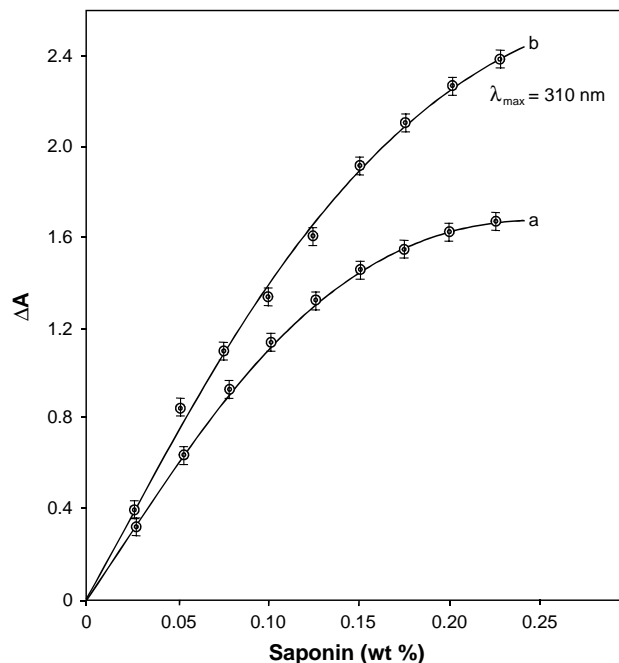


Fig. 3 Plots of (ΔA) versus saponin concentration (wt%) at 308 K in the absence and presence of Cr^{VI} and Pb^{II}. where, ΔA is (absorbance of solution consisting saponin and metal ions) - (absorbance of metal ions). a, saponin + Cr^{VI} (wt .06%); b, saponin + Pb^{II} (wt .032%)

Table 1 CMC and partition parameters by spectroscopic data

System (aqueous medium)	CMC (wt%) obtained		$10^4 K_c$	$10^5 K_x$	ΔG_p kJmol ⁻¹
	From Fig. 2	From Fig. 3			
Saponin (wt .05%)	0.110	–	–	–	–
Saponin (wt .05%) + Cr ^{VI} (wt .028%)	0.125	0.120	1.5	8.33	– 24.65
Saponin (wt .05%) + Pb ^{II} (wt .024%)	0.175	0.175	1.3	7.30	– 24.18

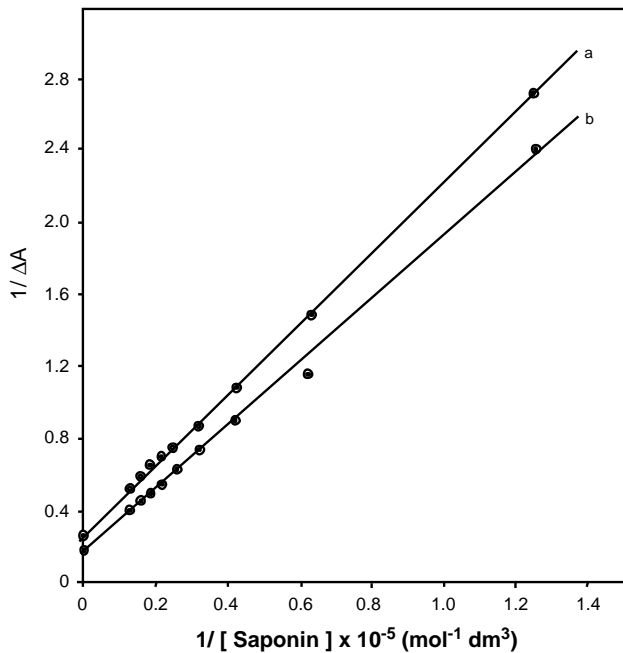


Fig. 4 Plots of $(1/\Delta A)$ versus $1/\text{saponin}$ concentration (wt%) at 308 K in the absence and presence of Cr^{VI} and Pb^{II}. where, ΔA is (absorbance of solution consisting saponin and metal ions) – (absorbance of metal ions). a, saponin + Cr^{VI} (wt .06%); b, saponin + Pb^{II} (wt .032%) concentration of saponin has been taken in mol dm^{-3}

(Kawamura et al. 1989; Shah et al. 2009; Usman and Siddiq 2013).

ΔA_∞ is the difference in absorbance (i.e., ΔA) at infinite dilution; C_a is concentration of additive (metal ions) and

$C_s^m = C_s - \text{CMC}_0$, where C_s is concentration of saponin and CMC_0 represents CMC of surfactant in water.

The plots of $1/\Delta A$ versus $1/[\text{Saponin}]$ in the presence of lead(II) and chromium(VI) are shown in Fig. 4. With the help of slopes and intercepts of these plots, the values of partition constant (K_c) and partition coefficients (K_x) have been calculated and are given in Table 1.

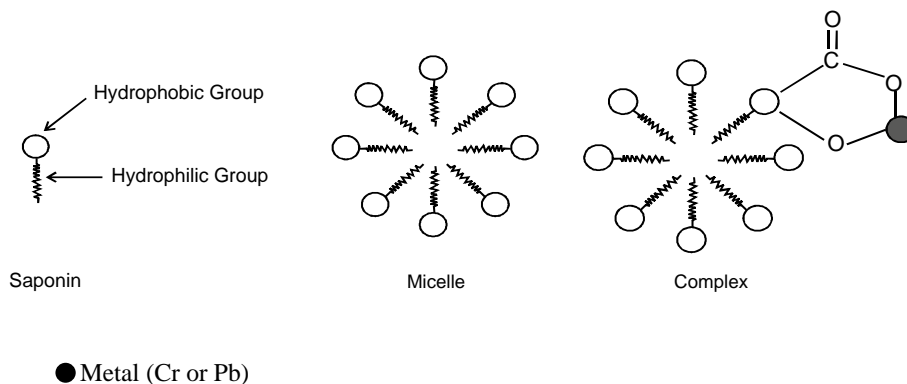
The standard free energy change of partitions was calculated using the following equation;

$$\Delta G_p = -RT \ln K_c \quad (2)$$

The spontaneity in partitioning phenomenon and system stability is indicated by negative value of ΔG_p (Table 1). The higher value of K_x (8.33×10^5) in case of chromium(VI) than that in case of lead(II) ($K_x = 7.30 \times 10^5$) indicates that chromium(VI) partitioned more in saponin micelles than lead(II).

It has been observed that saponin removes heavy metals from soils effectively in comparison with conventional surfactants. The desorption mechanism by saponin was not because of ion exchange or micelle formation but was mainly due to complexation between metal and saponin by formation of stronger bond between metal and carbonyl group in saponin (Mulligan et al. 1999; Hong et al. 2000). The reaction between metal ions with carbonyl and hydroxyl groups of saponin is also reported by Jian Tang et al. (2017a) during the removal of heavy metals with sequential sludge washing techniques using saponin.

On the basis of above facts and observed experimental results during present investigations, the complex formation between metal ion and saponin may be considered as follows



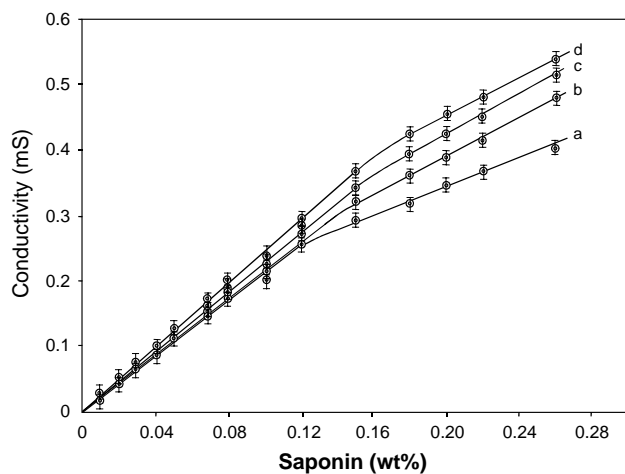


Fig. 5 Plots of conductivity versus saponin concentration (wt%) at 308 K. a, b, c and d represent the plots in the presence of nil, .015, .030 and .045% of Cr^{VI} , respectively

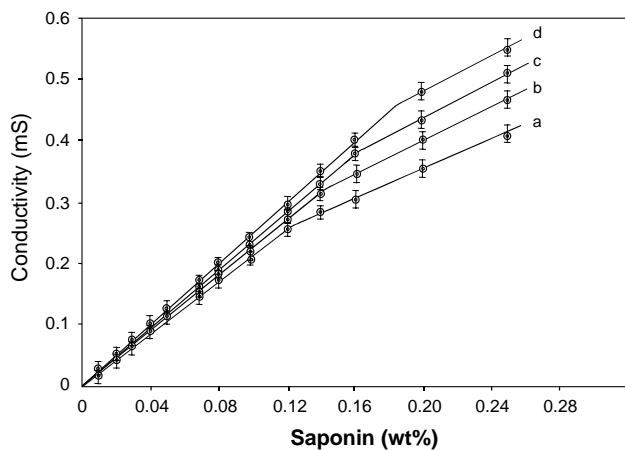


Fig. 6 Plots of conductivity versus saponin concentration (wt%) at 308 K. a, b, c and d represent the plots in the presence of nil, .008, .016 and .024% of Pb^{II} , respectively

Specific conductivity

The specific conductivity of solutions of saponin and saponin–metal ion complexes by taking three different concentrations of chromium(VI)/lead(II) was measured at 308 K. The temperature of thermostat was maintained constant within ± 0.5 °C. Each solution was kept for 15–20 min to establish the equilibrium. The establishment of equilibrium was checked by taking a series of readings after 20 min until no significant change was observed.

The plot of specific conductivity versus concentration of aqueous solution of saponin (wt%) in the presence of chromium(VI) and lead(II) is given in Figs. 5 and 6, respectively. It is observed that specific conductivity increases on increasing saponin concentration in solution. Further, an increase in conductivity was observed on increasing metal ion concentration in the solution. The CMC values were obtained from these plots of (conductivity) versus saponin concentration. The concentration at which micellization starts is evident from the change in the slope of the plot, and that particular concentration has been taken as the CMC in present investigations. The values of CMC in the absence of metal ion and in the presence of different concentrations of chromium(VI) and lead(II) are given in Table 2. The values of CMC observed by conductivity measurement (Table 2) were also in agreement with values of CMC determined spectrophotometrically (Table 1). A slight variation in CMC obtained by spectrophotometric and conductometric methods may be explained as CMC gives the range of the concentration where micellization starts.

Generally, the CMC of saponin depends upon its source. Due to difference in chemical and molecular structures of the sources and thus due to change in hydrophobicity of the molecules, temperature and pH, the CMC of saponin varies from 0.045 to 0.15% (wt).

The thermodynamic parameters, viz. (ΔG_m) change in free energy, (ΔH_m) change in enthalpy and (ΔS_m) change

Table 2 CMC and thermodynamic parameters for micellization obtained by conductivity data

Saponin–metal complex	CMC (wt%)	10^5 CMC (mol dm ⁻³)	β	$-\Delta G_m$ (kJmol ⁻¹)	$-\Delta H_m$ (kJmol ⁻¹)	ΔS_m (JK ⁻¹)
Saponin	0.120	1.90	0.63	33.40	23.35	32.60
Saponin + Cr^{VI} (wt .014%)	0.140	2.20	0.66	32.15	22.70	30.66
Saponin + Cr^{VI} (wt .028%)	0.165	2.62	0.77	31.10	22.15	29.02
Saponin + Cr^{VI} (wt .042%)	0.180	2.85	0.80	30.13	21.79	27.05
Saponin + Pb^{II} (wt .008%)	0.135	2.14	0.67	29.08	20.70	27.18
Saponin + Pb^{II} (wt .016%)	0.160	2.54	0.80	28.14	20.34	25.34
Saponin + Pb^{II} (wt .024%)	0.170	2.70	0.84	27.25	19.98	23.60

$[\text{OH}^-] = 1 \times 10^{-3}$ moldm⁻³ except in case of saponin



in entropy of micellization in the absence as well as in the presence of metal ions, have been computed using following equations (Usman and Siddiq 2013; Usman et al. 2010, 2013).

$$\Delta G_m = (2 - \beta)RT \ln X_{cmc} \quad (3)$$

$$\Delta H_m = -2.303(2 - \beta)RT^2 \left[\frac{\partial \log X_{cmc}}{\partial T} \right] \quad (4)$$

$$\Delta G_m = \Delta H_m - T\Delta S_m \quad (5)$$

where universal gas constant ($8.314 \text{ J mol}^{-1} \text{ K}^{-1}$) is denoted by R , at CMC X_{cmc} is the mole fraction of surfactant and β is the degree of dissociation. Degree of dissociation before and after mobilization has been calculated by the ratio of slopes in conductivity–concentration plots. $\beta = \frac{S_2}{S_1}$ where S_1 and S_2 represent slopes of straight lines before and after micellization.

The outcome of CMC, β , ΔG_m , ΔH_m and ΔS_m of micellization for aqueous media of saponin in the absence and presence of metal ions is reported in Table 2. It is clear from data obtained (Table 2) that CMC of saponin increases on increasing metal ion content in the solution. An increase in CMC is caused by metal ions primarily because of structure breaking effect. As the metal ion content in saponin increases, the work of micellization increases due to adsorption of metal ion making micellization less convenient and hence resulting an increase in CMC. This is also supported by less rise in entropy, ΔS_m (Table 2) on increasing metal ion content in solution. The negative magnitude of ΔG_m indicates the spontaneity of micellization. On increasing metal ion content in solution, ΔG_m becomes less negative (Table 2). This observation again suggests that micellization becomes less favorable at risen metal ion content in solution.

The negative value of ΔG_m suggests the exothermic nature of process. On increasing metal ions content in saponin, the value of ΔG_m becomes less negative suggesting that micelle formation is favored by entropy as well as enthalpy driven for saponin–metal complexes.

The effect of temperature on the CMC of saponin was also studied. The CMC of saponin was found to be 0.12, 0.14 and 0.16 (wt%) at 308, 313 and 318 K, respectively. The value of $\left[\frac{\partial \log X_{cmc}}{\partial T} \right]$ was nearly .005.

Conclusion

Although the complexation between heavy metals and saponin by formation of a bond between metal and carbonyl and hydroxyl groups of saponin (Mulligan et al. 1999; Hong et al. 2000; Tang et al. 2017b) is reported, the partition parameters for the complex formation between saponin and metal ions, viz. chromium(VI) and lead(II), and thermodynamic parameters for the micellization of saponin in the presence of these ions are reported first time in the present investigation. The partitioning of chromium(VI) in saponin micelle was found to be more in comparison with the partition of lead(II). Further studies on the role of these complexes in removal of chromium/lead in contaminated water are in progress.

Acknowledgement The authors are thankful to Prof. Rachna Asthana, Director, AITH, Kanpur, for her keen interest and providing necessary facilities for the work.

References

- Abyanesh S, Fazaalipoor MH (2016) Evaluation of Rhamnolipid (RL) as a biosurfactant for the removal of chromium from aqueous solutions by the precipitation flotation. *J Environ Manage* 165:184–187
- Ashwini S, Shantaram M (2016) Preliminary phytochemical and biochemical composition of different solvent extracts of red seaweed *Gracilaria corticata* from surathkal beach, Karnataka in India. *Int J Life Sci Technol* 13:106–110
- Aziz MA, Ashour A, Madbouly H, Melad S, Kerikshi KE (2017) Investigations on green preparation of heavy metal saponin complexes. *J Water Environ Nanotechnol* 2(2):103–111
- Bano N (1985) Phytochemical studies on saponins and sapogenins of *guatacum officinale*. HEJ Research Institute of chemistry,



- International Center for Chemical and Biological Sciences, University of Karachi (Karachi)
- Cameotra SS, Makkar RS (1998) Synthesis of biosurfactants in extreme conditions. *Appl Microbiol Biotechnol* 50:520–529
- Cameotra SS, Singh P (2004) Enhancement of metal bioremediation by use of microbial surfactants. *Biochem Biophys Res Commun* 319(2):291–297
- Chen W-J, Hasiao L-C, Chen KK-Y (2008) Metal desorption from copper (II)/nickel (II)-spiked kaolin as a soil component using plant derived saponin biosurfactant. *Process Biochem* 43:488–498
- Deleu E, Paquot M (2004) Renewable vegetables resources to microorganisms: new trends in surfactants. *C R Chim* 7:641–646
- Desai JD, Banat IM (1997) Microbial production of surfactants and their commercial potential. *Microbiol Mol Rev* 61:47–64
- Gao L, Kano N, Sato Y, Li C, Zhang S, Imaizumi H (2012) Behavior and distribution of heavy metals including rare earth elements, thorium, and uranium in sludge from industry waste treatment plant and recovery method of elements by biosurfactants application. *Bioinorg Chem Appl*. <https://doi.org/10.1155/2012/173819>
- Higuchi R (1987) Structure of desacylsaponins obtained from the bark of the *Quillaja saponaria*. *Phytochemistry* 26:229–235
- Hong KJ, Tokunaga S, Ishigami Y (2000) Extraction of Heavy metals from MSW incinerator fly ash using saponin. *Chemosphere* 41:345–352
- Hong KJ, Tokunaga S, Kajiuchi T (2002) Evaluation of remediation process with plant-derived biosurfactant for recovery of heavy metals from contaminated soil. *Chemosphere* 49:379–387
- Hostettmann K, Marston A (1995) Saponin. Cambridge University Press, Cambridge, pp 1–4
- Huang W, Liu ZM (2013) Biosorption of Cd(II)/Pb(II) from aqueous solution by biosurfactant-producing bacteria: isotherm kinetic characteristics and mechanism studies. *Colloids Surf B Biointerfaces* 105:113–119
- Kanga SH, Bonner JS, Page CA, Mills MA, Autenrieth RL (1997) Solubilization of naphthalene from crude oil using biosurfactants. *Environ Sci Tech* 31:556–561
- Kawamura H, Manabe M, Miyamoto Y, Fuzita Y, Tokunaga S (1989) Partition coefficients of homologous. Omega-phenylalkanols between water and sodium dodecyl sulfate micelles. *J Phys Chem* 93:5536–5540
- Kiran GS, Thomas TA, Selvin J (2010) Production of a new glycolipid biosurfactant from marine *Nocardiosis lucentensis* MSA04 in solid state cultivation. *Colloids Surf B* 78:8–16
- Lai CC, Huang YC, Wei YH, Chang JS (2009) Bio-surfactant enhanced removal of total petroleum hydrocarbons from contaminated soil. *J Hazard Mater* 167:609–614
- Liu Z, Shao B, Zeng G, Chen M, Li Z, Liu Y, Jiang Y, Zhong H, Liu Y, Yan M (2018) Effect of rhamnolipid on the removal of 2,4,2,4-tetrabrominated biphenyl ether (BDE-47) by *Phanerochaete chrysosporium* analyzed with a combined approach of experiments and molecular docking. *Chemosphere* 210:922–930
- Miller RM (1995) Biosurfactant facilitated remediation of contaminated soil. *Environ Health Perspect* 103:59–62
- Mulligan CN (2005) Environmental applications for biosurfactants. *Environ Pollut* 133:183–198
- Mulligan CN, Yong RN, Gibbs BF (1999) Heavy metal removal from sediments by Bio-surfactants. *J Hazard Mater* 85:111–125
- Noor S, Younas N, Rashid MA, Nazir S, Usman M, Naz T (2018) Spectroscopic, conductometric and biological investigation of [Ni(phen)₃]F₂·EtOH·MeOH·8H₂O complex in anionic micellar media. *Colloidal Interface Sci Commun* 27:26–34
- Rodrigues L, Banat IM, Teixeira J, Oliveria R (2006) Biosurfactants: potential applications in medicine. *J Antimicrob Chemother* 57:609–618
- Shah A, Khan AM, Usman M, Qureshi RUMANA, Siddiq M, Shah SS (2009) Thermodynamic characterization of dexamethanose sodium phosphate and its complex with DNA as studied by conductometric and spectroscopic techniques. *J Chil Chem Soc* 54:134–137
- Tang J, He J, Liu T, Xin X (2017a) Removal of heavy metals with sequential sludge washing techniques using saponin: optimization conditions, kinetics, removal effectiveness, binding intensity, mobility and mechanism. *RSC Adv*. 7:33385–33401



- Tang J, He J, Liu T, Xin X, Hu H (2017b) Removal of heavy metal from sludge by the combined application of a biodegradable biosurfactant and complexing agent in enhanced electrokinetic treatment. *Chemosphere* 189:599–608
- Usman M, Siddiq M (2013) Surface and micellar properties of chloroquine diphosphate and its interactions with surfactants and human serum albumin. *J Chem Therodyn* 58:182–190
- Usman M, Khan A, Siddiq M (2010) Thermodynamic properties of amphiphilic antidepressant drug citalopram HBr. *J Chem Soc Pak* 32:1–6
- Usman M, Cheema MA, Khan A, Farooki ZH, Mosquera V, Siddiq M (2013) A comparative study of thermodynamic properties of structurally related phenothiazine drugs in aqueous solution. *J Chil Chem Soc* 58:1842–1845
- Younas N, Rashid MA, Nazir S, Usman M, Sarfraz RA, Jamil A, Whitwood AC (2017a) Spectroscopic and conductometric study of interaction of anionic surfactants with [Co(phen)₃]F₂·2H₂O complex. *J Mol Liq* 240:351–360
- Younas N, Rashid MA, Nazir S, Usman M, Nazir S, Noor S, Basit A, Jamil M (2017b) solubilization of Ni Imidazole complex in micellar media of anionic surfactants, sodium dodecyl sulfate and sodium stearate. *J Surfactants Deterg* 20:1311–1320





IJRASET

International Journal For Research in
Applied Science and Engineering Technology



INTERNATIONAL JOURNAL FOR RESEARCH

IN APPLIED SCIENCE & ENGINEERING TECHNOLOGY

Volume: 10 **Issue:** V **Month of publication:** May 2022

DOI: <https://doi.org/10.22214/ijraset.2022.42118>

www.ijraset.com

Call:  08813907089

E-mail ID: ijraset@gmail.com

A Review Paper on Rice Quality Analysis Using Image Processing Technique

Mohd. Kaif Khan¹, Mukund Mohan², Pradyumn Jaiswal³, Prashant Kumar⁴, Prerna Srivastava⁵

^{1, 2, 3, 4} Electronics Engineering, Dr. Ambedkar Institute Of Technology for Handicapped, Kanpur, UP

⁵ Assistant Professor, Electronics Engineering, Dr. Ambedkar Institute of Technology for Handicapped, Kanpur

Abstract: In rice production industry as per the market demand, good quality rice evolution is very important in the present time. The factors for rice quality such as its whiteness, shape, milling degree, chalkiness, cracks and polish are the important factors for to evaluate the rice quality. Quality of rice becomes necessity nowadays for to defend the consumers from using sub standard products, the quality of rice is an important necessity. In the world population more than half people are the primary consumer of rice. It is one of the most important foods to provide energy, protein, essential vitamin and minerals, fiber grain, beneficial antioxidants, and carbohydrates. It is complicated by using the rice kernel manually for rice quality analysis because due to time consuming and having a chance for error with the bias of human perception. To overcome such issues and achieve the rice quality, the image processing technique has a wide scope. The main motive of this paper is to review different techniques that calculate the quality of rice using the image processing technique.

Keywords: Rice quality, Chalkiness, Crackiness, Whiteness, Image Processing

I. INTRODUCTION

Rice grain plays out a very vital role to fulfill human needs. They are real source products of Asian populace and numerous different nations. The quality of rice is characterized in its surrounding of its extent components, for example, Protein, Carbohydrates, etc. In figure 1 represents the cross sectional of rice seed. The rice kernel is contained bran coat and a hull, both of them which are withdrawn by shining is known as white rice.

1) *Rice shell, hull:* Hull bounded the bran coat, and the endosperm

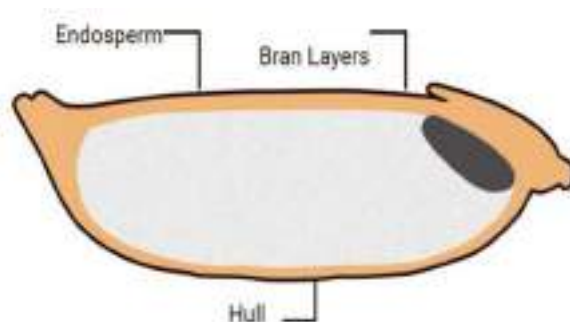


Figure 1 Cross section of Rice Seed.

2) *Bran Layers:* Bran consists of the pericarp, the seed coat and the aleurone layer

3) *Endosperm:* The endosperm is the most commonly consumed portion of the rice grain and mediates the transfer of nutrients from the vegetative tissues to metal rich environment

II. LITERATURE SURVEY

In the research methodologies, the main research area is the Systematic Literature Review (SLR). To review the existing information about rice quality evaluation is the main cause for undertaking the SLR methodology. Additionally, it provides detail information about our domain existing techniques, research questions and future challenges for the rice quality based on the image processing technique. The main aim is to examine or detect the relevant literature based on image processing technique. In Systematic Literature Review, we followed different steps. The SLR process phases illustrated as follows:



A. *Research Papers*

- 1) B.S. Anami. et al., (2015), proposed a method for recognition of paddy varieties from bulk paddy grain image samples based on color texture features extracted from color co-occurrence matrices. The color texture features are extracted from H, S and I color planes and their combinations. The color texture features are used for recognition of 15 paddy varieties. The reduced feature set of the HS plane includes Energy, Entropy and Correlation features from Hue plane and Energy, Entropy, Contrast, and Correlation features from Saturation plane. The paddy grain images are recognized using a multilayer feedforward artificial neural network. The considered fifteen paddy varieties have given the recognition accuracy of 92.33%.
- 2) Guzman. J.D et al., (2011) proposed the use of a machine vision system and multilayer neural networks for automatic identification of the sizes, shapes, and variety of samples of 52 rice grains belonging to five varietal groups of rice in the Philippines. Thirteen grain features extracted from each sample image using multilayer neural networks. The Artificial Neural Networks classifiers developed were able to identify the grain sample sizes and shapes at overall average accuracies of 98.76 per cent and 96.67 percent, respectively.
- 3) Verma, B., (2010) proposed relatively faster computer vision system to analyse and sort rice kernels. A series of measurements were done using image processing techniques namely smoothing, binarization, etc. on three varieties of Indian rice namely Marked Supreme, Marked Golden (export quality), Half Basmati. The extracted parameters area, perimeter, maximum length, maximum width, compactness and elongation from processed images were measured.
- 4) Rad. S.J.M, et al., (2011), proposed an algorithm for classifying five different Iranian varieties of rice, using the color and texture features. The proposed algorithm consists of several steps: image acquisition, segmentation, feature extraction, feature selection, and classification. Sixty color and texture features were extracted from rice kernels. The set of features contains redundant, noisy or even irrelevant information, so features were examined by four different algorithms. Finally twenty-two features were selected as the superior ones.
- 5) Mousavi Rad. S.J. et al., (2012), proposed an algorithm for identifying five different varieties of rice, using the morphological features. The proposed algorithm consists of several steps: image acquisition, segmentation, feature extraction, feature selection, and classification. Eighteen morphological features were extracted from rice kernels. The set of features contains redundant, noisy or even irrelevant information, so features were examined by four different algorithms. Finally six features were selected as the superior ones. A back propagation neural network-based classifier was developed to classify rice varieties.
- 6) Aulakh. J.S. et al., (2012), have proposed image processing techniques for grading of rice samples based on their sizes. The images were captured using a Flat Bed Scanner (FBS) and then converted to binary image to which they apply morphological operations and by the objects features were extracted by finding the properties of the connected components and get the information regarding connectivity, image size, numobjects, pixelidylist.
- 7) Silva.C.S et al., (2013), proposed a classification of rice seeds obtained through a machine vision combined with neural network architecture. A total of 9 different rice varieties were considered for the study. Algorithms were developed to extract thirteen morphological features, six color features and fifteen texture features from color images of individual seed samples. A different neural network models were developed for individual and combined feature set. High classification accuracy was given by textural features than morphological and colour features. Out of these feature sets, texture features produced high classification accuracy. Especially texture features obtained from red colour band produced better predictions.

III. METHOD FOR QUALITY ANALYSIS OF RICE

In this section, we review some existing method of quality analysis of rice.

A. *Based on Whiteness*

Chalkiness is one of the most important appearance quality indicators. Therefore, clarification of the heredity of chalkiness and its molecular mechanisms will contribute to reduction of rice chalkiness. Although a number of QTLs related to chalkiness were mapped, few of them have been cloned so far.

B. *Based on Size & Shape*

Simply speaking, long grain rice will have a longer cylindrical shape, whereas short grain rice will be shorter and wider. This rice has milled grains that are at least three to four times as long as they are wide. Due to its starch composition, it is separate, light and fluffy when cooked.



IV. FUTURE SCOPE

- 1) Different types of grain and its varieties are used for the detail analysis of quality products related to the accuracy and efficiency performance.
- 2) For the experiment purpose instead scanner we can use conveyor belt with vibration mechanism for using the appropriate hardware.
- 3) The collection, assessment, protection and trade of rice germplasm and circulation of enhanced plant material to various national and local research focus.
- 4) Development of innovation for incorporated nuisance, illness and supplement the board for different cultivating circumstances.

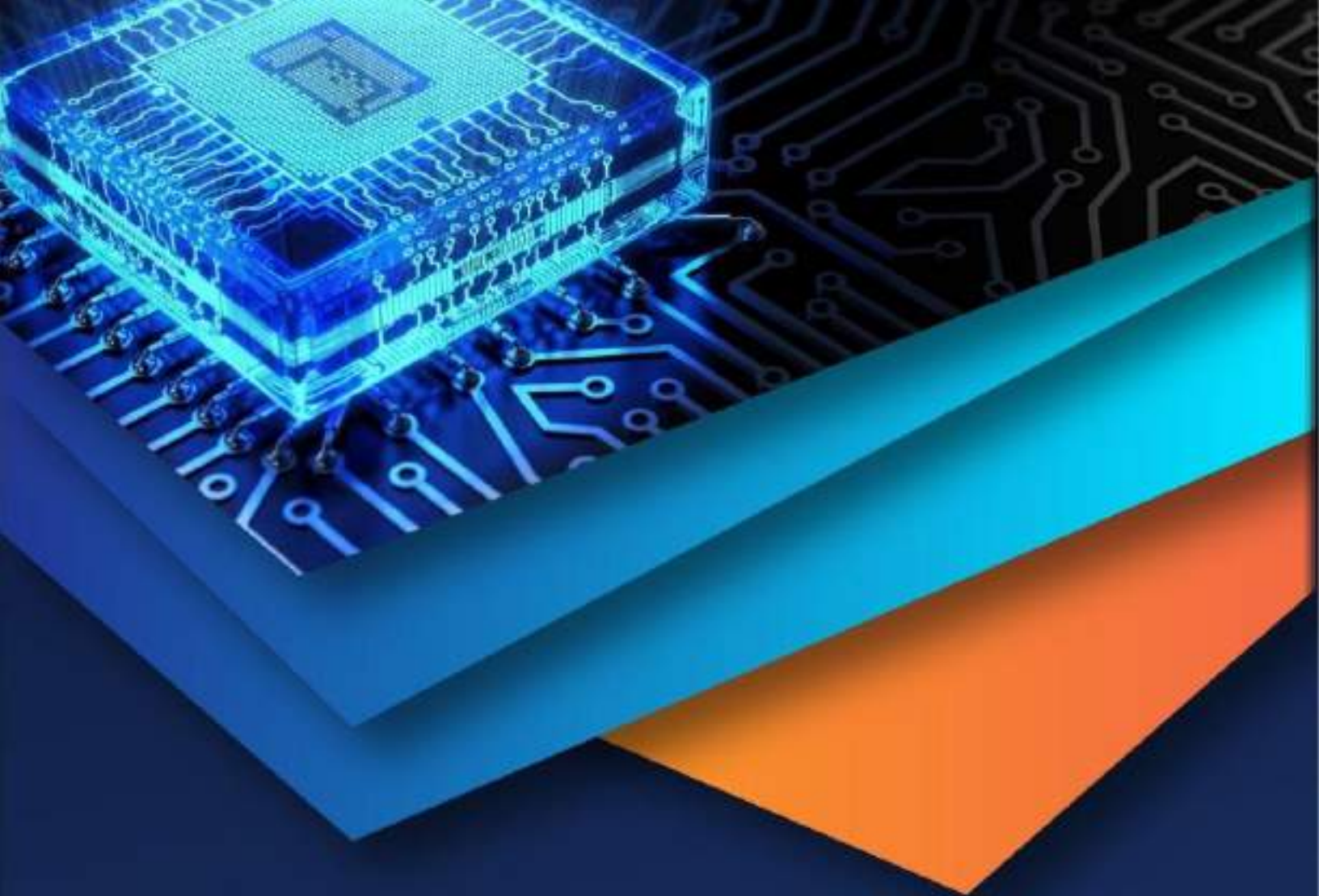
V. CONCLUSION

This paper presented a survey on using image processing techniques used in an automated rice grading system in agricultural context. Most of the work in this field use image processing method like background subtraction feature extraction and training and classification.

There is number of applications and method to select for implementation to real time need. While the existing rice classification method sustaining the need of today, there are more and more new method are evolving to assist and ease the rice classification.

REFERENCES

- [1] S.Durai, M.Thanjai Vadivel, T.Sujithra, Grading of Rice Quality by Chalky area analysis Using simple Digital Image Processing Techniques, International Journal of Pure and Applied Mathematics, 114(12): 657665, 2017.
- [2] B.S. Anami, Naveen N.M. and Hanamaratti N.G. 2015. Behavior of HSI Color Co-Occurrence Features in Variety Recognition from Bulk Paddy Grain Image Samples. International Journal of Signal Processing, Image Processing and Pattern Recognition. 8(4).
- [3] Neelam Jyoti Gupta. 2015. Identification and Classification of Rice Varieties Using Neural Network By Computer Vision. International Journal of Advanced Research in Computer Science and Software Engineering. 5(4): 992-997.
- [4] Vidya Patil, V. S. Malemath. 2015. Quality Analysis and Grading Of Rice Grain Images. International Journal of Innovative Research in Computer and Communication Engineering. 3(6): 5672-5678.
- [5] Tahir W.P.N., Hussin N., Htike Z.Z. and Naing W.Y.N. 2015. Rice grading using image processing.
- [6] A. Chauguleand S.N. Mali. Evaluation of Texture and Shape Features for Classification of Four Paddy Varieties, Journal of Engineering, 2014.
- [7] Pazoki A.R., Farokhi F. and Pazoki, Z., 2014. Classification of Rice Grain Varieties Using Two Artificial Neural Networks (MLP and Neuro-Fuzzy). Journal of Animal and Plant Sciences. 24: 336-343.
- [8] Kaur G. And Verma B. 2013. Measurement Standards based Grading of Rice Kernels by Separating Touching Kernels for Embedded Imaging Applications. International Journal of Electronics, Communication & Instrumentation Engineering Research and Development. 3: 127-134.
- [9] Silva C.S. and U. Sonnadara, Classification of Rice Grains Using Neural Networks, Proceedings of Technical Sessions, 29: 9-14, 2013.
- [10] Aulakh, J. S. and V.K. Banga, Grading of rice grains by image processing. International journal of engineering research & technology (IJERT) 1(4), 2012.
- [11] Guzman J.D. 2011. Classification of Philippine Rice Grains Using Machine Vision and Artificial Neural Networks. World Conference on Agricultural Information and IT, Tokyo, Japan. pp. 24-27
- [12] Guangrong L. 2011, August. Detection of Chalk Degree of Rice Based On Image Processing. In Intelligence Science and Information Engineering (ISIE), 2011 IEEE International Conference on. pp. 515-518.
- [13] Verma B. 2010. Image Processing Techniques For Grading and Classification Of Rice. International Conference on Computer and Communication Technology. pp. 220-223.



10.22214/IJRASET



45.98



IMPACT FACTOR:
7.129



IMPACT FACTOR:
7.429



INTERNATIONAL JOURNAL FOR RESEARCH

IN APPLIED SCIENCE & ENGINEERING TECHNOLOGY

Call : 08813907089  (24*7 Support on Whatsapp)

Framework for Assessing Efficient Water Consumption Attributes and Their Relative Importance in Office Complexes

Gaurav Chandra*, Manjari Chakraborty¹ and A.K. Sinha²

Department of Architecture, Dr. Ambedkar Institute of Technology for Handicapped, Kanpur, 208024, India

¹Department of Architecture, Birla Institute of Technology, Mesra Ranchi, 835215, India

²Department of Civil Engineering, Birla Institute of Technology, Mesra Ranchi, 835215, India

✉ gauravchandra1@gmail.com

Received September 26, 2016; revised and accepted May 3, 2017

Abstract: Globally, the water availability is getting difficult due to over extraction of ground water and rapid population growth. The Indian national water supply is expected to fall down by 50% below the demand by 2030. In the last decade, in spite of alluvial aquifers of the Indo-Gangetic plains, the over extraction of the ground water is making the scene catastrophic in the state of Uttar Pradesh (U.P.), India. Therefore, to overcome this water stress condition in the urban areas of U.P., it is needed to achieve water sustainability in office complexes (major consumers of the drinking water supply of a city) based on the analysis of water resource management of the area. In this study, to develop water management attribute framework for office complexes, expert opinion based Delphi technique followed by Analytic Hierarchy Process (AHP) is adopted.

The determination and pairwise comparison of the components are computed using Delphi technique, while AHP is used to calculate the weights representing their relative importance. Finally, the water supply, consumption and financial aspects are found as crucial components with 0.378, 0.422 and 0.20 relative weights respectively. Thus, the developed framework rates the attributes (components, indicators and sub-indicators) with their relative importance (based on weights) which would intelligently assist decision makers to design priority issues and programmes for efficient water management system in the geographical area under consideration.

Key words: Water sustainability, office complexes, AHP, Delphi, India.

Introduction

Nowadays, the urban scenario clearly reflects the fact that water resources management is an intricate issue, which contains dependence upon environment to help in the prediction of indefinite climatic events, i.e., rainfall events. These fluctuations in urban hydrological cycles are mainly due to intensified anthropogenic pursuits. As a result, this is causing prevalent flooding and dry events to be ordinary for countries like India. The foremost reasons for urban water conflicts include anthropogenic

activities, such as an excessive runoff from concrete surfaces, restricted infiltration, and fragile management decisions and policies. The requirement of freshwater resources intake is intensifying worldwide (Morrison et al., 2000); equally, the ecological deterioration and inconsistent use of limited natural resources are creating pressure on urban water systems. Worldwide, as the complexity of urban water issues has intensified, a wide-ranging research has been done to use the sustainability measures with water resource problems (Loucks et al., 2000; Ashley et al., 2004; Starkl and Brunner, 2004; Mays, 2006; Giupponi et al., 2006).

*Corresponding Author

and implementation of the concepts of urban water sustainability.

The concept of 'multi-criteria decision method based water sustainability' works as a prototype for the assessment of urban water issues (Lai et al., 2008). However, several objectives and stakeholders demonstrate the judgements in urban water resource utilities. The complexity of urban system imposes decision makers to come up with practical judgements; several researchers use Multi-Criteria Decision Making (MCDM) approach to deal with urban water issues, for implementing sustainable development principles. MCDM is widely used in water related decision support systems (Harmancioglu and Alpaslan, 1992; Eder et al., 1997; Tkach and Simonovich, 1997; Tiwari et al., 1999; Gupta et al., 2000; Raju et al., 2000; De Marchi et al., 2000; Mahmoud and Garcia, 2000; Flug et al., 2000; Kholgi, 2001; Hamalainen et al., 2001; Joubert et al., 2003; Srdjevic et al., 2004; Janssen et al., 2005; Fassio et al., 2005; Khalil et al., 2005; Pietersen, 2006; Maia and Schumann, 2007; Zarghami et al., 2008; Qin et al., 2008; Makropoulos et al., 2008).

Several researches have been reviewed, which shows that sustainable urban water management can be achieved with indicator-based approach (Jakeman et al., 2005). Recent studies regarding development of Water Sustainability indices, i.e., development of Water Poverty Index (WPI) Canadian Water Sustainability Index (CWSI), Watershed Sustainability Index (WSI), and West Java Water Sustainability Index (WJWSI), used the MCDM. These water indices are site-specific, which limits their universal aptness. Possibly, the development of a similar type of index will be a solution for the urban water issues in U.P. In this connection, this study provides a preliminary framework to develop water sustainability index for office complexes in the state of U.P.

Methodology

Due to the acuteness of water scarcity and drought challenges in various regions of the country, as discussed above there is a need to conserve this finite natural resource and to achieve water sustainability in buildings, i.e. commercial, industrial, institutional etc. Since, after the residential sector, the commercial (office) complexes are the second largest consumers of water, consuming at an average of approx. 20-25% water of the total consumption of a city (Chanan et al., 2003; EPA Water Sense, 2009; Morton, 2011; Pieterse-Quirijns et al., 2013), assessing the efficient water

consumption attributes in office complexes would be a significant step towards water sustainability. Notably, the aforesaid attributes would be much suitable for a mid level office complex where approximately 100 persons work, as these types of offices are large in numbers in this segment, and the application of the outcome of this research would be significant to produce major effects regarding communal water sustainability. In assessing the attributes there is a need to form consensus among the water experts opinions; therefore widely accepted Delphi technique has been used.

In past years, Delphi technique has been used for selection of indicators or parameters in various fields, i.e., education fields, different information systems, transportation, surface engineering, various strategic planning, water quality, etc. This technique has the advantages of using several judgements of diverse respondents from different backgrounds. Delphi is based on the information derived from consensus of respondents and stakeholders, thus it underpins the initial settings for mass decision-making. Significantly, in Delphi technique, minority views (e.g., a small group of respondents) are not always overlooked and consequently used in decision-making process.

Jolson & Rossow (1971) and Rowe & Wright (1999) mentioned that application of Delphi technique produces more accurate, less uncertain and bias-free results as compared to other alternative group decision-making methods. The Delphi technique has a better accuracy rate as it eliminates variance up to an admissible limit. Notably, the variance can be reduced as some of the respondents change their opinions (e.g., not their judgements) as they get aware of the facts presented in previous rounds by the other respondents. In general, the primarily designed framework can be included in the first questionnaire, which can refine or update the existing acquaintance of respondents.

It has been observed that Delphi technique has been extensively used in decision-making process, and it is supposed that this technique can be a useful method for attaining consensus in the selection of components, indicators and thresholds for the development of a water sustainability index.

To develop the primary framework for water sustainability assessment, a set of parameters is to be conceptualized. Therefore, similar types of water sustainability indices developed earlier in different regions of the world were rigorously reviewed and studied. Some of the relevant and available indices are Water Poverty Index (WPI), Canadian Water

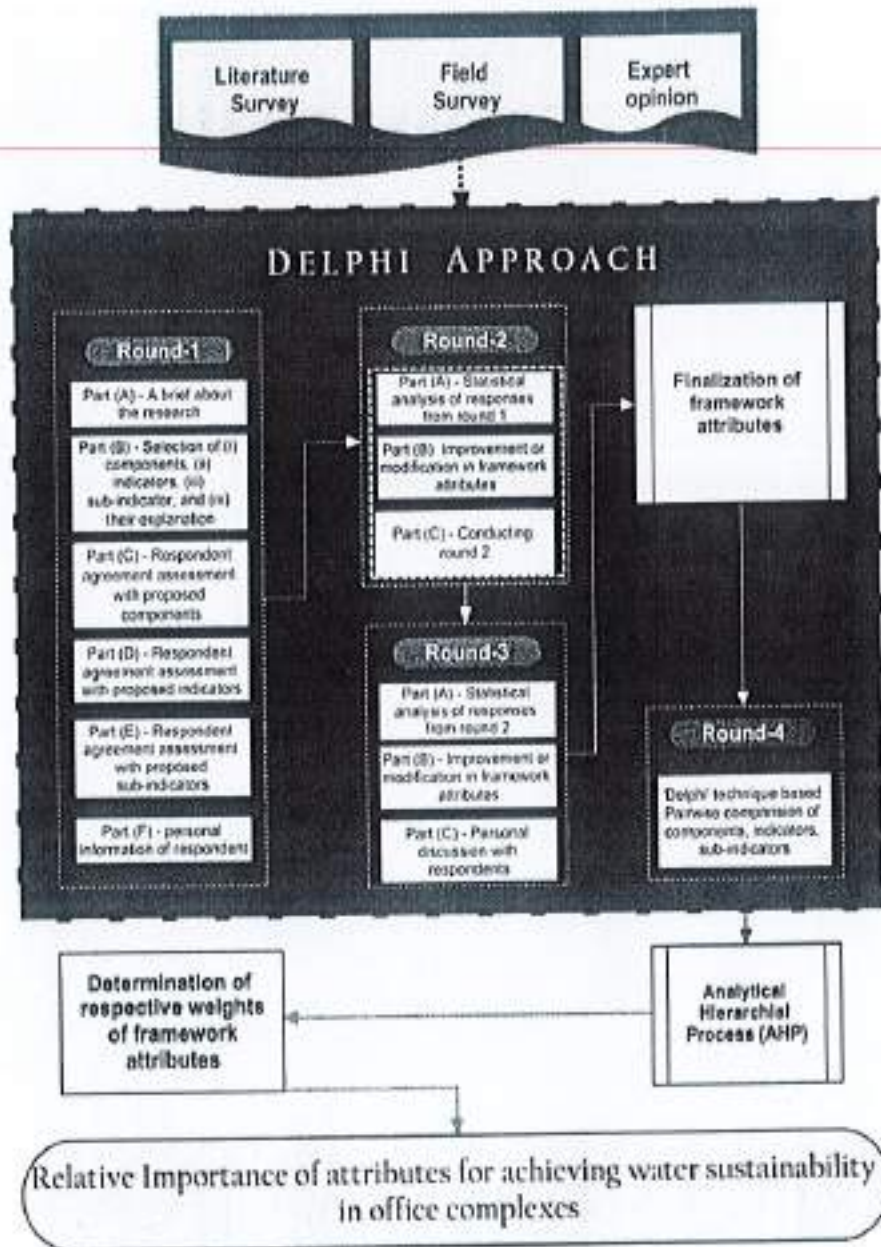


Figure 1: The methodology for preliminary framework for selection of attributes.

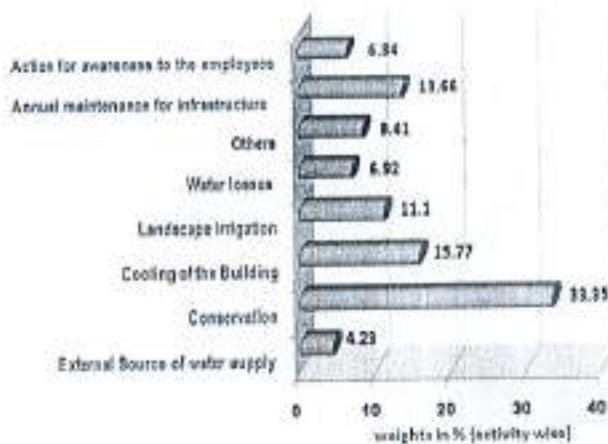


Figure 2: Weights (%) of different activities for efficient water management in office complexes.

Result and Discussion

The Delphi technique is quite helpful in developing "Group response" or "Expert consensus" by analyzing the opinions/feedbacks/suggestions of the group experts through a series of intelligently designed questionnaires incorporating relevant information/details/contents. Delphi technique consists of the introduction of weighted opinions of a group of individuals as a whole for achieving a group response through a structured group communication process; thus, initial solution frameworks can be designed for complex decision problems. Based on the literature study, expert opinions, adoption of Delphi technique to form a consensus among the opinions of the respondents to

Participant inclination is decisive, particularly for the development of an effective and feasible building water-efficiency strategy.

4. System is desired to explain the importance of water and to reckon the development of cost/benefit paradigms of 'Aqua^U' buildings water-competence, interventions and designs.
5. Urban buildings water-efficiency movements should be rationally planned to be less interfering, they should be uninterrupted and focused at refining civic awareness of water processes related to office complexes.
6. To promote an improved verification system, especially in office complexes water consumption pattern, policy makers must provide flawless management strategies and criterions for water-saving fixtures, end-uses and water recycling stuffs. This may be through accreditation, ratings, i.e., Water Efficiency Rating Tool (WERT), survey-level audits, benchmark modelling, performance metrics, cost-recovery methods and ISO certification schemes.
7. Water efficiency programmes must be expanded to city's old domestic buildings with flexible promotional activities with some appropriate incentives.

Urban planners and hydrologists are trying to define new concepts to lessen the energy consumption substantially in office complexes. The attributes' weights obtained from the present study may have some ambiguity factors so far, as it is based on the personal opinion of the regional experts. A possibility of occurring some experimental inaccuracies may also be there, while conducting the field survey. In this study, the uncertainty analysis has not been carried out; if done, it may yield some more superior outcomes. To use the developed framework the regional settings should be re-scrutinized to attain the required outcome. The outcomes of this study would play a key role in attaining urban water sustainability, and underpinning a prototype for the development of water sustainability indices for the 'Aqua^U' buildings. The lowering down of water consumption and achieving the zero water discharge conditions in buildings by adopting the water efficient tools and practices would be a step towards the solution of the problem. Office complexes being the major consumers of the urban drinking water supply should be given acceleration to achieve water consumption efficiency. As a result, it would regulate the limited water supply with maintaining its quality, reduce energy consumptions and would improve the

financial condition of the institute. The cumulative efforts would improve the water resource conditions along with the safeguard of ecosystems of the peripheral urban societies.

References

- Asian Water Development Outlook (2013). Measuring Water Security in Asia and the Pacific. Asia-Pacific Water Forum. ISBN: 978-92-9092-988-8 (Print).
- Ashley, R., Blackwood, D., Butler, D. and P. Jowitt (2004). Sustainable Water Services. London: IWA Publishing.
- Bin, L. (2009). Benchmarking Water Use in Office Building, 1-2
- Chanan, V., White, S., Howe, C. and M. Jha (2003). Sustainable water management in commercial office buildings. Innovations in Water: Ozwater Convention & Exhibition, Perth, 6-10 April 2003.
- De Marchi, B., Funtowicz, S.O., Cascio, S. and G. Munda (2000). Combining participative and institutional approaches with multi criteria evaluation: An empirical study for water issues in Troina, Sicily. *Ecological Economics*, 34: 267-282.
- Eder, G., Duckstein, L. and H.P. Nachtnebel (1997). Ranking water resource projects and evaluating criteria by multi criterion Q-analysis: An Austrian case study. *Journal of Multi-Criteria Decision Analysis*, 6: 259-271.
- EPA Water Sense (2009). Efficiency in the Commercial and Institutional Sector. Consideration for a Water Sense Program.
- Fassio, A., Giupponi, C., Hiederer, R. and C. Simota (2005). A decision support tool for simulating the effects of alternative policies affecting water resources: An application at the European scale. *Journal of Hydrology*, 304: 462-476.
- Flug, M., Seitz, L.H. and J.F. Scott (2000). Multi criteria decision analysis applied to Glen Canyon Dam. *Journal of Water Resource Planning and Management*, 126(5): 270-276.
- Giupponi, C., Jakeman, A.J., Karrssenberg, D. and M.P. Hare (2006). Sustainable Management of Water Resources. Massachusetts: Edward Elgar Publishing Limited.
- Gupta, A.P., Harboe, R. and M.T. Tabucanon (2000). Fuzzy multiple-criteria decision making for crop area planning in Narmada River Basin. *Agricultural Systems*, 63: 1-18.
- Hamalainen, R.P., Kettunen, E., Marttunen, M. and H. Ehtamo (2001). Evaluating a framework for multi-stakeholder decision support in water resources management. *Group Decision and Negotiation*, 10(4): 331-353.
- Harmancioglu, N.B. and N. Alpaslan (1992). Water quality monitoring network design: A problem of multi-objective decision making. *Water Resources Bulletin*, 28(1): 179-192.

WSI_{OC}: The Water Sustainability Index for Office Complexes

Gaurav Chandra*, Manjari Chakraborty¹ and A.K. Sinha²

Department of Architecture, Dr. Ambedkar Institute of Technology for Handicapped, Kanpur 208024, India

¹Department of Architecture, Birla Institute of Technology, Mesra, Ranchi 835215, Jharkhand, India

²Department of Civil Engineering, Birla Institute of Technology, Mesra, Ranchi 835215, Jharkhand, India

✉ gauravchandra1@gmail.com

Received May 31, 2017; revised and accepted March 28, 2018

Abstract: Water as a natural resource although covering almost two-third part of the universe, a fifth of the global population is facing acute water scarcity and unavailability of fresh drinking water due to the increasing anthropogenic pressure worldwide. In the Indian sub-continent ~23% of the total population is classified as under the class of absolute water scarcity, and ~54% people are facing high water stress condition. In spite of alluvial aquifers of the Indo-Gangetic plains water table has declined in the northern region of the country, which may lead to a disaster. Water sustainability so should be our priority. This study aims to assess the building water management systems with a relative importance of certain associated attributes. Thus, a water sustainability index (WSI_{OC}) is developed for office complexes (e.g., 26 sampled buildings) of major cities of Uttar Pradesh (U.P.) India, based on the framework of water sustainability attributes comprising water supply, consumption and financial aspects.

The framework attributes were determined using Delphi technique followed by AHP and linear regression method. The (WSI_{OC})_{absolute} value ranges from 31 to 74, which represents the building water management performance as moderate and high, respectively. In order to revive the menacing scenario related to the water efficiency in buildings, a need for priority action is evaluated accordingly. Certainly, the developed WSI_{OC} will act as a guiding tool for the water policy makers, consultants and architects to formulate their ideas for sustainable urban environment.

Key words: Water scarcity, water sustainability index (WSI), office buildings, WSI_{OC}

Introduction

Nowadays, the water availability to every human on the earth is getting difficult. In spite of the global availability of water and having renewable characteristics, a fifth of the world's population is facing water scarcity (Hering and Ingold, 2012). The United Nations reports reflect that 85% of the world population lives in the driest part of the earth, while ~6 to 8 million people die every year due to water related diseases (KPMG, 2012; UN-DESA, 2013). The international water management institute

(IWMI) estimated that ~1.4 billion people of the world population will experience severe water scarcity in the first quarter of the 21st century (Seckler et al., 1999). Several studies show that due to the rapid population growth and climate change ~37 countries of the world are facing high water stress with a score > 80% stress index. The burgeoning industrial development and urbanization are the foremost reasons for the water crisis (Singh et al., 2002; Dixit and Tiwari, 2008). In the changing world, the water management practices should gradually be improved accordingly.

*Corresponding Author

Water sustainability may be an effective approach to overcome the water scarcity problem for urban areas, and it depends on the water resources and services catering the need of the present, as well as for future, without significant deterioration in the system. Several studies related to the effective water management have been conducted to ensure the availability of fresh drinking water for the future generations (Madungwe and Sakuringwa, 2007; Hoque et al., 2006; Mossalanejad, 2011).

In case of the Indian sub-continent the national water supply is expected to fall down 50% below the demand by 2030, if the fact is not taken and act upon seriously (Shiao et al., 2015). As of April 2015, the usable water resources are estimated as 1123 billion cubic metre (BCM)/yr, against the total availability of 1869 BCM/yr (Suhag, 2016). In last decade, the over extraction of ground water is making the scene catastrophic in the state of Uttar Pradesh (U.P.), India. Therefore, this study advocates the development and implementation of the concepts of urban water sustainability. In spite of alluvial aquifers of the Indo-Gangetic plains water table has declined in the northern region of the country; consequently the state of Uttar Pradesh (U.P.) is facing critical geo-environmental problems, e.g., sanitization of the surface water. The disproportionate extraction of ground water, traditional agricultural mechanisms, absence of institutional monitoring for rainfall, industrial and domestic water demands, with an inadequate water resources management are the causal factors for water stress in this region.

In last decade, the average decline of water table in Allahabad, Gautambudh Nagar (Noida), Ghaziabad, Kanpur, Lucknow, Meerut and Varanasi being 0.62, 0.76, 0.79, 0.65, 0.70, 0.91 and 0.68 m/year respectively (UP-GWD, 2016) shows that these cities are prone to severe water scarcity. In the state of U.P. the annual replenishable ground water resource, net annual ground water availability, and annual ground water draft are as 76.35, 70.18, and 48.78 BCM, respectively. The stage of ground water development was 69% (2004), 72% (2009) and at present is 70%. The number of stressed blocks in the year 2011 were 261, of which the over exploited, critical and semi-critical blocks are listed as 111, 68 and 82 respectively. The area identified for artificial recharge of ground water is ~45,180 km², with a quantity of surface water to be recharged is ~14,022 MCM (UP-GWD, 2016).

In urban environment, to achieve the water sustainability in a particular building (Note: in this study, buildings considered are office complex [OC],

in which ~100 persons are working), an inclusive knowledge of the current conditions of water resources is necessary along with the demand, type of use, conservation and consumption pattern. Notably, in California and Canada the institutional (office) and commercial buildings consume ~27% (Seneviratne, 2007) and ~19% (REALPAC, 2011) respectively of the total water supply of the city, which is a major part of the supplied drinking water. Whereas, in U.S.A. the office buildings consume almost 9% of the total water consumption of the city (EPA, 2009).

Remarkably, office buildings are not only one of the major contributors to resource exhaustion, they are also the most evident and enduring components of an organization's assurance to implement the sustainability. The indicators are competent to conclude, focus and integrate the complexity of the environment to convenient and significant information (Godfrey and Todd, 2001; Warhurst, 2002). The 'sustainable water management improves tomorrow's cities health' (SWITCH) is an approach to develop scientific, technological and socioeconomic solutions for the effective management of water in the city of the future 2050, begins by defining sustainability indicators (SI) for the urban water system (Feyen et al., 2009).

The development of different WSI's (i.e., water poverty index [WPI], Canadian water sustainability index [CWSI], watershed sustainability index [WSI] and West Java water sustainability index [WJWSI]) have been developed using sustainability dimensions. These indices act as a holistic tool to assess the current status of water related issues, as well as communicating the evaluated information in the community, which in turn will assist to improve the regional water management policy. Particularly, these indices are site-specific that limits their worldwide implementation. Therefore, this study attempts to develop an indicator based WSI_{OC} for city's office complexes that can resolve the issues related to the water scarcity in the state of U.P. The WSI_{OC} would be able to assist decision makers with an evaluation of availability of urban water resources in short and long term perspectives in the U.P. region, and to determine which actions should or should not be taken in an attempt to make society sustainable.

Materials and Methods

Step 1: Development of framework attributes

The consensus among the water experts' opinions has been evaluated to determine the framework attributes using Delphi technique. Based on the

experts' consultation, an initial evaluation about water consumption in the office complexes has been performed, and a survey questionnaire was used to determine the components, indicators and sub-indicators. The questionnaire was circulated to the respondents in three rounds including their detailed interviews. The feedback received from the respondents after each round has been analyzed. Therefore, the 67% (2/3 opinions to form a consensus) of the respondents agreed and suggested significant corrections in order to determine the implementation of the parameters, and afterward these modifications were incorporated in the framework (Table 1).

The components, indicators and sub-indicators were finalized with a requirement to list their respective threshold values e.g., minimum and maximum values (Table 1). To determine these respective threshold values a survey questionnaire was prepared to collect the primary data from the office complexes (26 sample buildings, i.e., public and private, from 13 'A' cities of the UP state). These threshold values were used for the next round questionnaire, e.g., round 4, with their respective components, indicators and sub-indicators.

In round 4, the relative importance of the attributes was assessed using a consensus among the opinions of the respondents regarding the pair-wise comparison between the attributes. Afterward, the AHP was used for the analysis of feedback received from the preceding round. The results obtained, are therefore, the relative weights of the components, indicators and sub-indicators.

Step 2: Normalization of the attributes and calculation of modified sub-sub index values for respective indicators.

Clearly, some of the attributes are having different measurement units (Table 1); therefore, here, it is necessary either to convert these units into the similar units for all or make them unitless, which is known as the normalization of the data. The normalization method should take into account the data properties and the objectives of the indicator (JRC-EC, 2005a). Thus, to normalize the primary data and neutralizing the further ambiguities related to the scale effects in Table 1 data, it is necessary to obtain sub-index values for sub-indicators. The sub-sub index values (S_i) of sub-indicators have been calculated as follows.

Case I: When X_{max} is the most preferred value and X_{min} is the least preferred value of the i^{th} sub-indicator.

$$S_i = 1 - [(X_i - X_{min}) / (X_{max} - X_{min})] \quad (1)$$

Case II: When X_{max} is the most preferred value and X_{min} is the least preferred value of the i^{th} sub-indicator.

$$S_i = [(X_i - X_{min}) / (X_{max} - X_{min})] \quad (2)$$

where X_i is observed value of an i^{th} sub-indicator, in a sample office complex, S_i = sub-sub index value of the i^{th} sub-indicator, X_{min} = observed minimum value of i^{th} sub-indicator, among all the sample office complex, i.e., 26 and X_{max} = observed maximum value of i^{th} sub-indicator, among all the sample office complex, i.e., 26.

Finally, the attribute data have been normalized using Eqs (1) and (2).

Significantly, for index calculation, the inclusion of two major factors (i.e., rainfall and groundwater depletion) is necessary to assess the impact of different climatic and hydrological conditions on the final index values. It has been hypothesized that the effect of these two factors can potentially modify the sub-sub index values. Therefore, the yearly average rainfall for the study area has been calculated using last five years (2009-2013) rainfall data. A coefficient of modification (C_{MR}) representing the rainfall impact on the scale of one, has been derived from the average rainfall data (Table S1). Similarly, the influence of groundwater depletion on the scale of one has been assessed by deriving a coefficient of modification (C_{MGD}) from historically measured groundwater data (Table S2). Thereafter, the integrated coefficient of modification (C_M) has been developed by the multiplication of the coefficients i.e., C_{MR} and C_{MGD} , representing the combined effect of rainfall and groundwater depletion. The C_M has been calculated using Eq. (3).

$$C_M = C_{MR} \times C_{MGD} \quad (3)$$

The S_i values have been multiplied to the C_M to get the modified sub-sub index values (S_{Si}). The respective weight of i^{th} sub-indicator (SIW_i), where, $\sum_{i=1}^n SIW_i = 1$, and $0 \leq SIW_i \leq 1$, calculated from AHP, have been multiplied with S_{Si} to calculate the modified sub-index (S_{sw}) value at sub-indicator level using equations (4) to (9), as presented below:

$$S_{Si} = 1 - [(X_i - X_{min}) / (X_{max} - X_{min})] \times C_M \quad (4)$$

$$S_{sw} = SIW_i \times [1 - \{(X_i - X_{min}) / (X_{max} - X_{min})\} \times C_M] \quad (5)$$

$$S_{sw} = SIW_i \times [(X_i - X_{min}) / (X_{max} - X_{min})] \quad (6)$$

$$S_{Si} = [(X_i - X_{min}) / (X_{max} - X_{min})] \times C_M \quad (7)$$

$$S_{sw} = SIW_i \times [\{(X_i - X_{min}) / (X_{max} - X_{min})\} \times C_M] \quad (8)$$

$$S_{sw} = SIW_i \times [1 - \{(X_i - X_{min}) / (X_{max} - X_{min})\}] \quad (9)$$

Table 1: Developed conceptual framework of attributes with respective weights

Sl.	Components	Component weight through AHP CW_i	Indicators (Sub components)	Sub-indicators	Sub-indicator weight through AHP SIW_{ij}	Threshold			Data availability
						Unit	Max	Min	
1.	Water supply	0.378	External source of water supply (Ground water)	---	0.112	%	100 ^b	40 ^a	Water supply standards and data collected by field surveys.
				Adopting water savings techniques	0.164	%	100 ^a	0.0 ^b	
			Conservation	Reuse of waste water	0.469	%	100 ^a	0.0 ^b	Institutional standards and data collected from field surveys.
				Rainwater harvesting	0.255	%	100 ^a	0.0 ^b	
				Toilets	0.061	Lt./cap/day	16.0 ^b	10.0 ^a	
				Pantry	0.040	Lt./cap/day	6.0 ^b	4.0 ^a	
				Air cooling (Desert coolers)	0.131	Lt./cap/day	25.0 ^b	10.0 ^a	
				A.C. (Cooling towers)	0.243	Lt./min./Ton	6.5	0.0	
			Water demand	Maintenance of complex (Floor Cleansing etc.)	0.098	Lt./sq.mt./day	0.40 ^b	0.20 ^a	
				Landscape Irrigation	0.263	Lt./sq. mt. area/day	10.0 ^b	2.4 ^a	
Water losses (leakage & misuse)	0.164	%		13.0 ^b	8.0 ^a				

3. Financial aspect	0.20	Price to pay to municipality for supply water (metered usage)	Not to be considered for Sub-Index value	Rs.	Yearly fixed charges from local body.*	No appropriate records are found in office.
Annual budget for water consumption		Electricity charges for pumping etc..	Not to be considered for Sub-Index value	Rs.	No separate record is found.	
Annual maintenance of infrastructure		Motors, supply pipelines and plumbing items etc.	0.430	Rs./sq. mt./year	250.0 ^b	Yearly running expenditure data is collected from office records.
Action for awareness to the employees		STP/WWTP	0.253	Rs./year	1.0 lac	0.0
		Activities for promotion of awareness for water savings	0.317	Rs./year	1.0 ^a lac	0.0 ^b lac

Note: a: Preferable, b: not preferable, c: > 0 preferable, < 0 not preferable

*Since most of the sample buildings are using municipal water supply facility partially/fully, the management of the office pays a fixed amount to the municipal body every year. Presently, in U.P., there is no arrangement of having water meters in the premises, to record the water consumption per month/year. Thus, the municipal body has fixed the per year water charges rate for the buildings as per their rules.

Table 2: Method of calculating modified sub-index (S_{im}) values at sub-indicator level

SI	Component	CW_i	Sub-indicator	SIW_i	S_i	$S_{im} = SIW_i \times S_i$
1.	Water supply	0.378	External source of water supply (Ground water)	0.112	eq. (4)*	eq. (5)*
			Adopting water savings techniques	0.164	eq. (2)	eq. (6)
			Reuse of waste water	0.469	eq. (7)*	eq. (8)*
			Rainwater harvesting	0.255	eq. (2)	eq. (6)
2.	Water use (Consumption)	0.422	Toilets	0.061	eq. (1)	eq. (9)
			Pantry	0.040	eq. (1)	eq. ((9)
			Air cooling (Desert coolers)	0.131	eq. (1)	eq. ((9)
			A.C. (Cooling towers)	0.243	eq. (1)	eq. ((9)
			Maintenance of complex (Floor cleaning etc.)	0.098	eq. (1)	eq. ((9)
			Landscape irrigation	0.026	eq. (1)	eq. ((9)
			Water losses (Leakage & misuse)	0.164	eq. (1)	eq. ((9)
			3.	Financial aspect	0.141	Motors, supply pipelines & plumbing items etc.
STP/WWTP	0.253	eq. (1)	eq. ((9)			
Activities for promotion of awareness for water savings	0.317	eq. (1)	eq. ((9)			

*The S_i values have been designated as S_{ij} because of the inclusion of the integrated coefficient of modification (C_{ij}) in the calculation, therefore the S_{ij} values have been calculated using Equations (4) and (7). Similarly, the S_{im} values have been obtained using equations (5) and (8) for respective sub-indicators.

Finally, the S_{im} values were calculated using equations [4-9] (Table 2). Consequently, the S_{im} values were calculated for different types of office complexes under consideration (Table S3 to S6).

Step 3: The linear aggregation method (JRC-EC, 2005b) was used to develop the composite or aggregated water sustainability index (WSI_{OC}) for the sample office complexes under consideration using equation (10), as follows.

$$WSI_{OC} = \sum_{i=1}^n SI_i \quad (10)$$

$$SI_1 = [\sum_{i=1}^4 S_{im}] \times CW_{1,1}; \text{ where, in case of } S_{im} \text{ } i^{th} \text{ sub indicator} = 1, 2 \dots n \text{ (} n = 4 \text{) (Table S7)}$$

$$SI_2 = [\sum_{i=5}^{11} S_{im}] \times CW_{1,2}; \text{ where, in case of } S_{im} \text{ } i^{th} \text{ sub indicator} = 5, 6 \dots n \text{ (} n = 11 \text{) (Table S7)}$$

$$SI_3 = [\sum_{i=12}^{14} S_{im}] \times CW_{1,3}; \text{ where, in case of } S_{im} \text{ } i^{th} \text{ sub indicator} = 12, 13 \dots n \text{ (} n = 14 \text{) (Table S7)}$$

where WSI_{OC} represents the aggregated index; $SI = \sum SI_1 + SI_2 + SI_3$; S_{im} is the modified sub-index value of i^{th} sub-indicator, from 1, 2 ... n ($n = 14$); and CW_i is the weight of the i^{th} component, where $\sum_{i=1}^n CW_i = 1$, where $i = 1, 2, \dots n$ ($n = 3$), and $0 \leq CW_i \leq 1$.

Step 4: To make the use of WSI_{OC} easier and implementable, it was required to present it in a simpler or absolute form. Therefore, it was necessary to know about the maximum index value (WSI_{OC}^{max}) which a sample office complex might achieve, based on taking all the S_i values of all the sub-indicators taken into consideration. The S_i for all the sub-indicators except external source of water supply (ground water) and reuse of waste water was calculated as 1 [maximum value among all the sample office complexes] (Table S3). The S_i for indicators [external source of water supply (ground water) and reuse of waste water] was calculated 0.8 for each of them (Table S3), showing the associated impacts of combined influences of climate and hydrological conditions, which has been discussed under step 2. Hence, the (WSI_{OC}^{max}) was computed as 0.96, which is based on the average of maximum values attained by all the three components (Table 3).

Step 5: At last, to determine the 'priority of action' in terms of efforts to make the office complexes more sustainable for water resource development in this region, a classification scheme was developed (Table 5), which is based on the absolute index values ($WSI_{OC}^{absolute}$) (Table 4). Thereafter, the performance of water management system and relative 'priority of action' for sample office complexes were determined (Table 6).

Table 3: Calculation of maximum index value (WSI_{OC})_{max} based on maximum S_j values incurred from Tables S3 to S6

SI - Component	CW _i	Sub-indicator	SIW _i	S _j	S _{in} = SIW _i × S _j
1. Water supply	0.378	External source of water supply (Ground water)	0.112	0.8*	0.0896
		Adopting water savings techniques	0.164	1	0.164
		Reuse of waste water	0.469	0.8*	0.375
		Rainwater harvesting	0.255	1	0.255
		Total	1	-	0.884
		Max. value attained by Component 1	-	-	-
2. Water use (Consumption)	0.422	Toilets	0.061	1	0.061
		Pantry	0.040	1	0.040
		Air cooling (Desert coolers)	0.131	1	0.131
		A.C. (Cooling towers)	0.243	1	0.243
		Maintenance of complex (Floor cleansing etc.)	0.098	1	0.098
		Landscape irrigation	0.263	1	0.263
		Water losses (leakage and misuse)	0.164	1	0.164
		Total	1.00	-	1.00
Max. value attained by Component 2	-	-	-	-	
3. Financial aspect	0.200	Motors, supply pipelines and plumbing items etc.	0.430	1	0.430
		STP/WWTP	0.253	1	0.253
		Activities for promotion of awareness for water saving	0.317	1	0.317
		Total	1.00	-	1.00
		Max. value attained by Component 3	-	-	0.2 × 1 = 0.2
Grand Total of max. values of C1, C2, C3	-	-	0.334 + 0.422 + 0.2 = 0.956 ≈ 0.96		

Table 4: The classification scheme developed to determine the performance of water management system

Absolute index value interval	Performance of water management system	Priority of Action	No. of sample buildings
0-25	Poor	Very high	Nil
25-50	Moderate	High	18
50-75	High	Moderate	08
75-100	Very high	Low	Nil

Results and Discussion

1. External source of water supply (through bore well)
It is observed that all the sample office complex authorities are extracting ground water from 40%-100% to meet out their daily water demands, as either the municipal water supply facility is not available at some of the office complexes or the quality/quantity of municipal water is not as per the required standards (Table S3, column no. 4). Clearly, the majority of sample office complexes are extracting high amount of ground water to meet their daily water requirements;

similarly many other different types of complexes are practicing the same. This community action acts as the foremost factor for decreased water table, which results in severe water scarcity in this area.

2. Reuse of waste water

In this study, it has been found that thirteen (13) out of twenty six (26) samples are not reusing the waste water (Table S3, column no. 12), and draining it into public sewer. Moreover, only six and seven sample office complexes are reusing ~25-50% and 50-100% of the waste water in their secondary uses, respectively. The office management authorities are aware about

Table 5: Performance and recommendations based on absolute index value of all the sample office complexes (U.P., India)

Sl.	City/ District	Type of building	Aggregated index value (out of value 1) (WSI_{OC})	(WSI_{OC}) _{absolute} with respect to (WSI_{OC}) _{max}	Absolute index value	Performance of water management system	Priority of action
1	2	3	4	5	6	7	8
1	Agra	Public	0.3187	33.19	33	Moderate	High
		Private	0.4614	48.06	48	Moderate	High
2	Aligarh	Public	0.3637	37.88	38	Moderate	High
		Private	0.3100	32.29	32	Moderate	High
3	Allahabad	Public	0.4029	41.96	42	Moderate	High
		Private	0.4903	51.07	51	High	Moderate
4	Bareilly	Public	0.3156	32.88	33	Moderate	High
		Private	0.3397	35.39	35	Moderate	High
5	G.B.Nagar (Noida)	Public	0.5341	55.64	56	High	Moderate
		Private	0.6981	72.72	73	High	Moderate
6	Ghaziabad	Public	0.5438	56.65	57	High	Moderate
		Private	0.5403	56.28	56	High	Moderate
7	Gorakhpur	Public	0.3513	36.59	37	Moderate	High
		Private	0.3497	36.42	36	Moderate	High
8	Jhansi	Public	0.3858	40.19	40	Moderate	High
		Private	0.4315	44.95	45	Moderate	High
9	Kanpur	Public	0.3436	35.79	36	Moderate	High
		Private	0.7056	73.50	74	High	Moderate
10	Lucknow	Public	0.5103	53.16	53	High	Moderate
		Private	0.5722	59.60	60	High	Moderate
11	Meerut	Public	0.3684	38.38	39	Moderate	High
		Private	0.3980	41.46	41	Moderate	High
12	Moradabad	Public	0.3411	35.53	36	Moderate	High
		Private	0.3474	36.19	36	Moderate	High
13	Varanasi	Public	0.2924	31.19	31	Moderate	High
		Private	0.4409	45.93	46	Moderate	High

Note: Max. Index Value (WSI_{OC})_{max} = 0.96, Refer Table 3

the importance of water consumption and its reuses; therefore these six office complexes have been retrofitted with limitations to reuse the waste water. The later seven office complexes are situated in national capital region (NCR), Kanpur and Lucknow. These have fully/partially adopted the mandates guided by the sustainable building rating systems i.e., LEED, GRIHA etc. Furthermore, it has been found in the selected samples that the institutions with having significant budgetary provisions and awareness for environmental security are coming forward to follow the water sustainability guidelines. Eight sample office complexes have not adopted any

water saving techniques i.e., water saving fixtures, fittings etc. whereas, only eleven and seven sample office complexes have adopted ~20-50% and 50-100% for water savings techniques, respectively.

3. Rain water harvesting (RWH)

Out of twenty six sample office complexes, seven (five public and two private) are not conserving rain water and not adopting RWH systems (Table S4, column no. 8), which shows the ignorance of the government water resource management policy mandates. While, ten and nine sample office complexes (situated in NCR, Kanpur and Lucknow) are practicing the RWH from 35-50%

and 50-100%, respectively, for their secondary uses. The implementation of RWH is strongly recommended.

4. Toilet, Pantry, Air cooling (Desert cooler), and Maintenance of complex (Floor Cleansing etc.)

It has been found that the private office complexes situated in NCR, Kanpur and Lucknow regions are consuming less water as compared to other cities under consideration.

5. A.C. (Cooling towers)

The office complexes are having air cooling and / or window unit cooling facilities except eight office complexes of NCR, Kanpur and Lucknow, which are having central air conditioning facilities in their campuses.

6. Landscape irrigation

The water consumption in landscape irrigation (watering green areas) activities in public office complexes is quite less, which is almost half of the consumption of water used for the same activity in private office complexes. Notably, in public office complexes proper maintenance has not been done for landscapes and green areas, as compared to the private office complexes of NCR, Kanpur and Lucknow. Even the water consumption per unit green area is comparatively low as compared to the existing literatures.

7. Water Losses (Leakage and misuse)

The water losses are found almost within considerable limits in the sample office complexes as compared to the value ranging from 7.5-25% with 15% being the most common value for commercial buildings (Beecher, 2002). Private sector buildings of NCR, Kanpur and Lucknow are having minimum water losses due to their better maintenance and measures as compared to other sample office complexes of different cities.

8. Annual maintenance (Motors, supply pipelines, plumbing items etc.)

The annual maintenance cost including water supply motors, lines, drainage disposal system etc. in all the twenty six sample office complexes ranges from 110-250 Rs./m²/year of the built up area. The public sector office complexes are spending less; therefore no proper maintenance is found in these buildings in comparison to private complexes.

9. Annual maintenance for sewage treatment plant (STP) / waste water treatment plant (WWTP)

Only seven sample office complexes of NCR, Kanpur and Lucknow are having sewage/waste water treatment facilities among the office complexes under consideration. Therefore, all the discharge (water/sewage) is drained out in the cities' common sewer lines. The amount incurred in the operation and

maintenance in this activity, as informed by the person concerned (supervisor) is an approximate value, since no separate accounting has been found in records for this purpose.

10. Promotional activities for awareness generation for water saving

Significantly, all the sample office complexes, except Aligarh (private building), Bareilly (public building), Meerut (private and public) (Table S6, column no. 16), management has an annual budget to hold programmes/seminars to make aware to the users for water savings in the premises. Though, the amount allocated by them is too less for the promotional activities, it is satisfactory that the system is quite aware of the alarming condition of water scarcity/stress issues, and thus initiated a step toward water savings by make the users aware of the fact.

It is obvious that if any of the sample office complex adopts and follows all the norms and guidelines of efficient water management than the (WSI_{OC})_{max} value of 0.96 possibly can be achieved (Table 3). It is because the S₀ for sub-indicators i.e., external source of water supply and reuse of waste water is 0.8, as it is derived by multiplying S₁ value 1 (a building consuming only 40% of the ground water through bore well and reusing 100% waste water) by the C_M (Table 3) value 0.8. The value 0.96 can be assessed as the best or ideal condition among the sample building considered in this study. Conversely, if any sample office complex does not adopt the sustainability criteria and fails to follow the normal water saving practices, then the minimum index value would be achieved as 0.0, which can be assessed as the worst condition regarding the water sustainability in that very building.

To assess the overall status of water management system of the samples among themselves, it would be easier to use the [(WSI_{OC})_{absolute}] values derived from equation (11), as mentioned below.

$$\begin{aligned} [(WSI_{OC})_{absolute}]^{avg} &= \frac{(WSI_{OC})_{absolute}}{\text{number of total sample complexes}} \\ &= \frac{1162.89}{26} = 44.73 \end{aligned} \quad (11)$$

Sample buildings having (WSI_{OC})_{absolute} below [(WSI_{OC})_{absolute}]^{avg} = 15

~58% of the total samples

Sample buildings having (WSI_{OC})_{absolute} above [(WSI_{OC})_{absolute}]^{avg} = 11

~42% of the total samples

It is therefore concluded that ~58% buildings of the total sampled office complexes are not showing efficient water management practices that is not satisfactory, while remaining ~42% buildings of the total samples showing comparatively better water management practices.

There is no office complex found in the category of poor performance, eighteen office complexes are found in the category of moderate performance and need high priority of action, while only eight office complexes are found in the category of high performance and need moderate priority of action. Notably, office complexes with having possibility of low priority action are absent. Remarkably, the signs of the perfect water sustainability practices are scarce in the area under consideration. This study suggests that the incorporation of the water sustainability measures can improve the performance of the sub-indicators leading to the reduced water stress in the area.

Conclusion

Interestingly, in spite of the limited number of sample office complexes, this study provides a synoptic and explicit measure of the urban water consumption pattern in the state of U.P. India. The $(WSI_{OC})_{absolute}$ values show that the office complexes taken into consideration are not adopting appropriate water management practices. To achieve urban sustainability, the office complexes of each sector, e.g., residential, industrial, commercial etc. should be designed and constructed according to the 'Green Building Rating Systems', which lead to increased water use efficiency at a larger scale. Additionally, the water sustainability mandates should not be limited up to the urban environment, but also implementable for the agriculture sector as it demands plenty of water. The proposed WSI_{OC} lays the scientific and technical foundation for the research related to the urban water management systems in arid and semi arid urban zones. Nonetheless, a few limitations still exist in the proposed WSI_{OC} , but inclusion of diverse parameters with thorough baseline survey at a time is arduous.

The developed WSI_{OC} works as a composite index, and would facilitate better results for other geographical location provided if the selection of the attribute is re-scrutinized. Significantly, the consensus based selection of the framework attributes and application of AHP, signify the robustness of the proposed WSI_{OC} . It is suggested that a mechanism for the consistent

monitoring of actual water consumption in the office complexes should be implemented, and the threshold values of water consumption in these complexes should be maintained accurately, to further establish the more simplified and explanatory index. It is suggested that the WSI_{OC} should be developed for large scale office complexes of different types in different geographical settings to establish its universal aptness.

In this study, the weights of the attributes are calculated through AHP, followed by arithmetic (linear) aggregation method to develop the index. Since in the linear aggregation method, perfect substitutability and compensability occurs, among all sub-indices. In future, the weighting methods other than AHP, i.e., MAUT, ELECTRE, PROMETHEE, and DRSA can be used in combination with geometric aggregation method having limited substitutability and compensability. A comparative study can be performed to assess the performance of different combinations of the aggregation methods with MCDMs for better acceptability of the WSI_{OC} results.

This study suggests that it should be mandatory to design and construct the large scale office complexes as per the guidelines of the sustainable building rating systems i.e., LEED, GRIHA, etc., to make office complexes more water efficient. Some incentives should be given to the managements and the staff persons, for adopting sustainable building rating systems and contributing actively for water savings in the complex respectively, so that the activities for water savings in the community can be promoted at a large scale. It is recommended that the proper allocation of the funds either from government or private organizations should be made available for conducting water saving programmes, seminars, workshops and placing relevant information i.e., slogans, hoarding etc. at different places in their campus for making the public aware and conscious to conserve water.

Acknowledgements

The authors are thankful to Professor Dr. N.R. Mandal, Department of Architecture, School of Planning and Architecture (SPA), Bhopal, and Mr. Kartar Singh, Assistant Professor, Department of Remote Sensing, School of Earth Sciences, Banasthali University, for their scientific and technical support in design as well as dissemination of this research work. Their expertise and guidance are highly appreciated.

Supplementary Tables

Table S1: Calculation of coefficient of modification for rainfall impact (C_{MR})

Range of rainfall (mm)	Points scored	Coefficient of modification for rainfall impact (C_{MR})
450-600	5	.33
601-750	4	.27
751-900	3	.20
901-1050	2	.13
1051-1200	1	.07
Total	15	1.00

Table S2: Calculation of coefficient of modification for ground water depletion (C_{MGD})

Range of yearly ground water depletion (mt.)	Points scored	Coefficient of modification for ground water depletion (C_{MGD})
.50-.60	5	.33
.61-.70	4	.27
.71-.80	3	.20
-.81-.90	2	.13
.91-1.0	1	.07
Total	15	1.00

Table S3: Sub index value for indicators (External source of water supply (ground water) and reuse of waste water)

Sl.	City/ District	Type of office complex	External source of water supply (ground water)							Reuse of waste water				
			X_i (%)	(S_i)	Ground water depletion (mt./yr)	Average rainfall (Last 5 years) (mm)	(C_{MR})	(S_{MR})	SIW_1	S_{im}	X_j (%)	(S_j)	SIW_2	S_{jm}
1	2	3	4	5	6	7	8	9	10	11	12	13	14	15
1	Agra	Public	100	0	0.5	502	1	0	0.112	0	0	0	0.469	0
		Private	100	0	0.5	502	1	0	0.112	0	0	0	0.469	0
2	Aligarh	Public	100	0	0.5	590	1	0	0.112	0	0	0	0.469	0
		Private	100	0	0.5	590	1	0	0.112	0	0	0	0.469	0
3	Allahabad	Public	100	0	0.62	878	0.7	0	0.112	0	0	0	0.469	0
		Private	75	0.42	0.62	878	0.7	0.294	0.112	0.032	25	0.25	0.469	0.082
4	Barcilly	Public	100	0	0.6	1085	0.6	0	0.112	0	0	0	0.469	0
		Private	100	0	0.6	1085	0.6	0	0.112	0	0	0	0.469	0
5	G.B.Nagar (Noida)	Public	50	0.833	0.76	581	0.8	0.666	0.112	0.074	60	0.6	0.469	0.225
		Private	50	0.833	0.76	581	0.8	0.666	0.112	0.08	100	1	0.469	0.375
6	Ghaziabad	Public	50	0.833	0.79	456	0.8	0.666	0.112	0.074	60	0.6	0.469	0.225
		Private	50	0.833	0.79	456	0.8	0.666	0.112	0.074	60	0.6	0.469	0.225
7	Gorakhpur	Public	70	0.5	0.7	1166	0.5	0.25	0.112	0.028	0	0	0.469	0
		Private	60	0.67	0.7	1166	0.5	0.335	0.112	0.037	0	0	0.469	0
8	Jhansi	Public	70	0.5	0.85	779	0.5	0.25	0.112	0.028	30	0.3	0.469	0.07
		Private	50	0.833	0.85	779	0.5	0.417	0.112	0.046	30	0.5	0.469	0.117
9	Kanpur	Public	100	0	0.65	654	0.8	0	0.112	0	0	0	0.469	0
		Private	40	1	0.65	654	0.8	0.8	0.112	0.089	100	1	0.469	0.375
10	Lucknow	Public	50	0.833	0.7	810	0.7	0.583	0.112	0.065	80	0.8	0.469	0.263
		Private	50	0.833	0.7	810	0.7	0.583	0.112	0.065	60	0.6	0.469	0.197
11	Meerut	Public	100	0	0.91	560	0.6	0	0.112	0	20	0.2	0.469	0.056
		Private	100	0	0.91	560	0.6	0	0.112	0	30	0.3	0.469	0.084
12	Moradabad	Public	100	0	0.7	1051	0.5	0	0.112	0	0	0	0.469	0
		Private	100	0	0.7	1051	0.5	0	0.112	0	0	0	0.469	0
13	Varanasi	Public	100	0	0.68	804	0.7	0	0.112	0	0	0	0.469	0
		Private	100	0	0.68	804	0.7	0	0.112	0	50	0.5	0.469	0.164

Table S4: Sub index values for indicators (Water saving technique, rain wt. harvested, toilet and pantry)

SI	City/ District	Type of office complex	Water saving technique			Qty. of rain wt. harvested			Consumption for toilet			Consumption for pantry						
			X_i (%)	(S_j)	SIW_i	S_m	X_i (%)	(S_j)	SIW_i	X_i (%)	(S_j)	SIW_i	X_i (%)	(S_j)	SIW_i	S_m		
1	2	3	4	5	6	7	8	9	10	11	12	13	14	15	16	17	18	19
1	Agra	Public	0	0	0.164	0	0	0	0.255	0	13	0.5	0.061	0.031	4	1	0.04	0.04
		Private	20	0.2	0.164	0.032	100	1	0.255	0.255	11	0.83	0.061	0.051	6	0	0.04	0
2	Aligarh	Public	0	0	0.164	0	50	0.5	0.255	0.127	12	0.67	0.061	0.041	4	1	0.04	0.04
		Private	0	0	0.164	0	0	0	0.255	0	14	0.33	0.061	0.02	5	0.5	0.04	0.02
3	Allahabad	Public	25	0.25	0.164	0.041	40	0.4	0.255	0.102	12	0.67	0.061	0.041	4	1	0.04	0.04
		Private	50	0.5	0.164	0.082	100	1	0.255	0.255	13	0.5	0.061	0.031	6	0	0.04	0
4	Bareilly	Public	0	0	0.164	0	0	0	0.255	0	11	0.83	0.061	0.051	5	0.5	0.04	0.02
		Private	0	0	0.164	0	25	0.25	0.255	0.064	12	0.67	0.061	0.041	5	0.5	0.04	0.02
5	G.B.Nagar (Noida)	Public	100	1	0.164	0.164	100	1	0.255	0.255	11	0.83	0.061	0.051	4	1	0.04	0.04
		Private	100	1	0.164	0.164	100	1	0.255	0.255	10	1	0.061	0.061	6	0	0.04	0
6	Ghaziabad	Public	60	0.6	0.164	0.098	100	1	0.255	0.255	12	0.67	0.061	0.041	5	0.5	0.04	0.02
		Private	100	1	0.164	0.164	100	1	0.255	0.255	14	0.33	0.061	0.02	6	0	0.04	0
7	Gorakhpur	Public	0	0	0.164	0	40	0.4	0.255	0.102	12	0.67	0.061	0.041	4	1	0.04	0.04
		Private	0	0	0.164	0	50	0.5	0.255	0.128	14	0.33	0.061	0.02	5	0.5	0.04	0.02
8	Jhansi	Public	50	0.5	0.164	0.082	50	0.5	0.255	0.128	12	0.67	0.061	0.041	4	1	0.04	0.04
		Private	30	0.3	0.164	0.049	80	0.8	0.255	0.204	13	0.5	0.061	0.031	6	0	0.04	0
9	Kanpur	Public	25	0.25	0.164	0.041	35	0.35	0.255	0.089	11	0.83	0.061	0.051	5	0.5	0.04	0.02
		Private	100	1	0.164	0.164	100	1	0.255	0.255	10	1	0.061	0.061	5	0.5	0.04	0.02
10	Lucknow	Public	100	1	0.164	0.164	100	1	0.255	0.255	13	0.5	0.061	0.031	5	0.5	0.04	0.02
		Private	100	1	0.164	0.164	100	1	0.255	0.255	16	1	0.061	0.061	5	0.5	0.04	0.02
11	Meerut	Public	40	0.4	0.164	0.065	0	0	0.255	0	12	0.67	0.061	0.041	5	0.5	0.04	0.02
		Private	50	0.5	0.164	0.082	0	0	0.255	0	14	0.33	0.061	0.02	4	1	0.04	0.04
12	Moradabad	Public	40	0.4	0.164	0.065	0	0	0.255	0	11	0.83	0.061	0.051	4	1	0.04	0.04
		Private	50	0.5	0.164	0.082	40	0.4	0.255	0.102	15	0.17	0.061	0.01	6	0	0.04	0
13	Varanasi	Public	0	0	0.164	0	0	0	0.255	0	10	1	0.061	0.061	4	1	0.04	0.04
		Private	50	0.5	0.164	0.082	50	0.5	0.255	0.128	12	0.67	0.061	0.041	5	0.5	0.04	0.02

Table S5: Sub index value for indicators (Desert cooling, air conditioning, and maintenance of complex and landscape irrigation)

Sl	City/ District	Type of off. Com.	Desert cooling				Air conditioning				Maintenance of complex				Landscape irrigation				
			X _i (%)	(S _i)	SIW _i	S _{im}	X _i (%)	(S _i)	SIW _i	S _{im}	X _i (%)	(S _i)	SIW _i	S _{im}	X _i (%)	(S _i)	SIW _i	S _{im}	
1		3	4	5	6	7	8	9	10	11	12	13	14	15	16	17	18	19	
1	Agra	Public	25	0	0.131	0	0	1	0.243	0.243	0.243	1	0.098	0.098	3.5	0.86	0.263	0.226	
		Private	22	0.5	0.131	0.065	0	1	0.243	0.243	0.243	0.5	0.098	0.049	6	0.53	0.263	0.139	
2	Aligarh	Public	25	0	0.131	0	0	1	0.243	0.243	0.243	1	0.098	0.098	2.4	1	0.263	0.263	
		Private	20	0.83	0.131	0.108	0	1	0.243	0.243	0.243	0.5	0.098	0.049	5	0.66	0.263	0.174	
3	Allahabad	Public	24	0.17	0.131	0.022	0	1	0.243	0.243	0.243	1	0.098	0.098	2.5	0.99	0.263	0.260	
		Private	21	0.67	0.131	0.087	0	1	0.243	0.243	0.243	0.35	0.098	0.025	6	0.53	0.263	0.139	
4	Bareilly	Public	23	0.33	0.131	0.043	0	1	0.243	0.243	0.243	0.75	0.098	0.074	3	0.92	0.263	0.242	
		Private	21	0.67	0.131	0.087	0	1	0.243	0.243	0.243	0.3	0.5	0.098	0.049	7	0.4	0.263	0.105
5	G.B.Nagar (Noida)	Public	25	0	0.131	0	6.25	0.04	0.243	0.01	0.35	0.25	0.098	0.025	4	0.79	0.263	0.208	
		Private	22	0.5	0.131	0.065	4.5	0.31	0.243	0.075	0.4	0	0.098	0	8	0.26	0.263	0.068	
6	Ghaziabad	Public	25	0	0.131	0	6.5	0	0.243	0	0.3	0.5	0.098	0.049	4	0.79	0.263	0.208	
		Private	23	0.33	0.131	0.043	5.5	0.154	0.243	0.037	0.35	0.25	0.098	0.025	8	0.26	0.263	0.068	
7	Gorakhpur	Public	22	0.5	0.131	0.065	0	1	0.243	0.243	0.243	0.3	0.5	0.098	0.049	5	0.66	0.263	0.174
		Private	20	0.83	0.131	0.108	0	1	0.243	0.243	0.243	0.4	0	0.098	0	7	0.4	0.263	0.105
8	Jhansi	Public	25	0	0.131	0	0	1	0.243	0.243	0.243	0.25	0.75	0.098	0.074	7	0.4	0.263	0.105
		Private	22	0.5	0.131	0.065	0	1	0.243	0.243	0.243	0.3	0.5	0.098	0.049	10	0	0.263	0.000
9	Kanpur	Public	24	0.17	0.131	0.022	6	0.077	0.243	0.019	0.28	0.6	0.098	0.059	3	0.92	0.263	0.242	
		Private	21	0.67	0.131	0.087	5.5	0.015	0.243	0.004	0.31	0.45	0.098	0.044	8	0.26	0.263	0.068	
10	Lucknow	Public	24	0.17	0.131	0.022	6.25	0.04	0.243	0.01	0.35	0.25	0.098	0.025	6	0.53	0.263	0.139	
		Private	21	0.67	0.131	0.087	5.88	0.095	0.243	0.023	0.31	0.45	0.098	0.044	10	0	0.263	0.000	
11	Meerut	Public	22	0.5	0.131	0.065	0	1	0.243	0.243	0.243	1	0.098	0.098	3.6	0.84	0.263	0.221	
		Private	19	1	0.131	0.131	0	1	0.243	0.243	0.243	0.3	0.5	0.098	0.049	6	0.53	0.263	0.139
12	Moradabad	Public	24	0.17	0.131	0.022	0	1	0.243	0.243	0.243	0.25	0.75	0.098	0.074	5	0.66	0.263	0.174
		Private	21	0.67	0.131	0.087	0	1	0.243	0.243	0.243	0.35	0.25	0.098	0.025	7	0.4	0.263	0.105
13	Varanasi	Public	25	0	0.131	0	0	1	0.243	0.243	0.243	0.3	0.5	0.098	0.049	4	0.79	0.263	0.208
		Private	21	0.67	0.131	0.087	0	1	0.243	0.243	0.243	0.35	0.25	0.098	0.025	6	0.53	0.263	0.139

Table S6: Sub index value for indicators [Water losses, annual maintenance (motor, supp.), annual maintenance (STP/WWTP) and activities for promotion of awareness for water savings]

Sl	City/ District	Type of office complex	Water Losses						Annual Maintenance (Motor, Supp.)						Annual Maintenance (STP/WWTP)						Activities for promotion of awareness for water savings					
			X _i (%)	(S _i)	SIW _i	S _{om}	X _i (Rs/ sqm/yr)	(S _i)	SIW _i	S _{om}	X _i (Rs/ sqm/yr)	(S _i)	SIW _i	S _{om}	X _i (Rs/ sqm/yr)	(S _i)	SIW _i	S _{om}	X _i (Rs/ sqm/yr)	(S _i)	SIW _i	S _{om}				
1			4	5	6	7	8	9	10	11	12	13	14	15	16	17	18	19								
1	Agra	Public	11	0.4	0.164	0.065	120	0.07	0.43	0.030	0	0	0.253	0	25,000	0.25	0.317	0.079								
		Private	9	0.8	0.164	0.131	150	0.29	0.43	0.124	0	0	0.253	0	65,000	0.65	0.317	0.206								
2	Aligarh	Public	12	0.2	0.164	0.032	110	0	0.43	0	0	0	0.253	0	20,000	0.2	0.317	0.063								
		Private	10	0.6	0.164	0.098	125	0.107	0.43	0.046	0	0	0.253	0	0	0	0.317	0								
3	Allahabad	Public	12	0.2	0.164	0.032	130	0.143	0.43	0.061	0	0	0.253	0	40,000	0.4	0.317	0.126								
		Private	10	0.6	0.164	0.098	160	0.36	0.43	0.154	0	0	0.253	0	40,000	0.4	0.317	0.126								
4	Bareilly	Public	12	0.2	0.164	0.032	140	0.21	0.43	0.090	0	0	0.253	0	0	0	0.317	0								
		Private	10	0.6	0.164	0.098	160	0.36	0.43	0.154	0	0	0.253	0	20,000	0.2	0.317	0.063								
5	G.B.Nagar (NoIDA)	Public	13	0	0.164	0	175	0.46	0.43	0.197	1,00,000	1	0.253	0.253	50,000	0.5	0.317	0.158								
		Private	8	1	0.164	0.164	225	0.82	0.43	0.352	1,00,000	1	0.253	0.253	1,00,000	1	0.317	0.317								
6	Ghaziabad	Public	11	0.4	0.164	0.065	170	0.43	0.43	0.184	1,00,000	1	0.253	0.253	75,000	0.75	0.317	0.237								
		Private	9	0.8	0.164	0.131	180	0.5	0.43	0.215	1,00,000	1	0.253	0.253	60,000	0.6	0.317	0.190								
7	Gorakhpur	Public	13	0	0.164	0	150	0.29	0.43	0.124	0	0	0.253	0	30,000	0.3	0.317	0.095								
		Private	11	0.4	0.164	0.065	170	0.43	0.43	0.184	0	0	0.253	0	20,000	0.2	0.317	0.063								
8	Jhansi	Public	12	0.2	0.164	0.032	155	0.32	0.43	0.137	0	0	0.253	0	25,000	0.25	0.317	0.079								
		Private	10	0.6	0.164	0.098	170	0.43	0.43	0.184	0	0	0.253	0	50,000	0.5	0.317	0.158								
9	Kanpur	Public	9	0.8	0.164	0.131	175	0.46	0.43	0.197	0	0	0.253	0	40,000	0.4	0.317	0.126								
		Private	8	1	0.164	0.164	220	0.79	0.43	0.339	1,00,000	1	0.253	0.253	1,00,000	1	0.317	0.317								
10	Lucknow	Public	12	0.2	0.164	0.032	185	0.54	0.43	0.232	75,000	0.75	0.253	0.19	40,000	0.4	0.317	0.126								
		Private	11	0.4	0.164	0.065	250	1	0.43	0.43	1,00,000	1	0.253	0.253	80,000	0.8	0.317	0.253								
11	Meerut	Public	12	0.2	0.164	0.032	140	0.21	0.43	0.090	0	0	0.253	0	0	0	0.317	0								
		Private	10	0.6	0.164	0.098	160	0.36	0.43	0.154	0	0	0.253	0	0	0	0.317	0								
12	Moradabad	Public	11	0.4	0.164	0.065	135	0.176	0.43	0.075	0	0	0.253	0	30,000	0.3	0.317	0.095								
		Private	10	0.6	0.164	0.098	150	0.29	0.43	0.124	0	0	0.253	0	20,000	0.2	0.317	0.063								
13	Varanasi	Public	12	0.2	0.164	0.032	125	0.107	0.43	0.046	0	0	0.253	0	25,000	0.25	0.317	0.079								
		Private	11	0.4	0.164	0.065	135	0.176	0.43	0.075	0	0	0.253	0	35,000	0.35	0.317	0.111								

Table S7: Calculation of final water sustainability index (WSI_{OC}) of sample office complexes of U.P. India

Representation of the columns is given below

Sl.	City/District	Type of office complex	4	5	6	7	8	9	10	11	12	13	14	15	16	17	18	19	20	21	22	23	24	25	26	27	
1	Agra	Public	0.000	0.000	0.000	0.000	0.000	0.378	0.000	0.031	0.040	0.000	0.243	0.098	0.226	0.066	0.704	0.422	0.297	0.030	0.000	0.079	0.109	0.200	0.022	0.3189	
		Private	0.000	0.033	0.000	0.255	0.258	0.378	0.109	0.051	0.000	0.046	0.243	0.049	0.139	0.131	0.679	0.422	0.395	0.125	0.000	0.000	0.206	0.331	0.200	0.066	0.5702
2	Aligarh	Public	0.000	0.000	0.000	0.128	0.128	0.378	0.000	0.041	0.040	0.000	0.243	0.098	0.263	0.033	0.718	0.422	0.351	0.000	0.000	0.000	0.063	0.063	0.200	0.013	0.4119
		Private	0.000	0.000	0.000	0.000	0.000	0.378	0.000	0.020	0.020	0.109	0.243	0.049	0.174	0.098	0.713	0.422	0.301	0.046	0.000	0.000	0.000	0.046	0.200	0.049	0.3100
3	Allahabad	Public	0.000	0.041	0.000	0.102	0.143	0.378	0.054	0.041	0.040	0.022	0.243	0.098	0.260	0.033	0.737	0.422	0.365	0.001	0.000	0.127	0.188	0.200	0.038	0.4570	
		Private	0.073	0.082	0.082	0.255	0.452	0.378	0.171	0.031	0.000	0.088	0.243	0.025	0.139	0.068	0.624	0.422	0.434	0.155	0.000	0.127	0.282	0.200	0.056	0.6812	
4	Bareilly	Public	0.000	0.000	0.000	0.064	0.064	0.378	0.024	0.041	0.020	0.088	0.243	0.049	0.105	0.098	0.644	0.422	0.296	0.155	0.000	0.000	0.063	0.218	0.200	0.044	0.3639
		Private	0.000	0.000	0.640	0.225	0.719	0.378	0.272	0.051	0.040	0.000	0.010	0.025	0.208	0.000	0.333	0.422	0.412	0.198	0.253	0.159	0.609	0.200	0.122	0.8059	
5	G. B. Nagar (NoIDA)	Public	0.075	0.164	0.225	0.255	0.874	0.378	0.330	0.061	0.000	0.066	0.075	0.000	0.068	0.164	0.434	0.422	0.514	0.353	0.253	0.317	0.923	0.200	0.185	1.0286	
		Private	0.080	0.164	0.375	0.255	0.655	0.378	0.247	0.041	0.020	0.000	0.043	0.037	0.025	0.068	0.131	0.324	0.409	0.185	0.253	0.238	0.076	0.200	0.135	0.7907	
6	Ghaziabad	Public	0.075	0.164	0.225	0.255	0.719	0.378	0.272	0.020	0.000	0.040	0.066	0.243	0.049	0.174	0.000	0.632	0.422	0.307	0.125	0.000	0.095	0.220	0.209	0.044	0.4003
		Private	0.028	0.000	0.000	0.128	0.166	0.378	0.063	0.020	0.020	0.000	0.109	0.243	0.000	0.105	0.066	0.563	0.422	0.300	0.185	0.000	0.063	0.248	0.200	0.050	0.4122
7	Gorakhpur	Public	0.038	0.000	0.000	0.128	0.166	0.378	0.116	0.041	0.040	0.000	0.243	0.074	0.105	0.033	0.535	0.422	0.242	0.138	0.000	0.079	0.217	0.200	0.063	0.5023	
		Private	0.028	0.000	0.070	0.128	0.168	0.378	0.116	0.041	0.040	0.000	0.066	0.243	0.049	0.000	0.098	0.486	0.422	0.263	0.185	0.000	0.159	0.343	0.200	0.069	0.5891
8	Jhansi	Public	0.047	0.049	0.117	0.204	0.417	0.378	0.158	0.031	0.000	0.066	0.243	0.049	0.000	0.098	0.486	0.422	0.279	0.198	0.000	0.127	0.325	0.200	0.005	0.3028	
		Private	0.000	0.041	0.000	0.089	0.120	0.378	0.049	0.051	0.020	0.022	0.004	0.044	0.068	0.164	0.449	0.422	0.524	0.340	0.232	0.190	0.127	0.449	0.200	0.182	1.0598
9	Kanpur	Public	0.090	0.164	0.375	0.255	0.884	0.378	0.334	0.061	0.020	0.088	0.004	0.044	0.068	0.164	0.449	0.422	0.401	0.232	0.138	0.000	0.079	0.217	0.200	0.063	0.5023
		Private	0.065	0.164	0.263	0.255	0.748	0.378	0.283	0.031	0.020	0.022	0.010	0.025	0.139	0.033	0.279	0.422	0.385	0.430	0.253	0.254	0.937	0.200	0.187	0.8298	
10	Lucknow	Public	0.065	0.164	0.197	0.255	0.682	0.378	0.258	0.061	0.020	0.088	0.023	0.044	0.000	0.066	0.301	0.422	0.350	0.090	0.000	0.000	0.000	0.000	0.200	0.018	0.4144
		Private	0.065	0.164	0.197	0.255	0.682	0.378	0.258	0.061	0.020	0.088	0.023	0.044	0.000	0.066	0.301	0.422	0.350	0.090	0.000	0.000	0.000	0.000	0.200	0.018	0.4144
11	Meerut	Public	0.000	0.066	0.056	0.000	0.122	0.378	0.046	0.041	0.020	0.066	0.243	0.049	0.139	0.098	0.721	0.422	0.367	0.155	0.000	0.000	0.000	0.155	0.200	0.031	0.4608
		Private	0.000	0.082	0.084	0.000	0.166	0.378	0.063	0.020	0.040	0.131	0.243	0.049	0.139	0.098	0.721	0.422	0.367	0.155	0.000	0.000	0.000	0.155	0.200	0.031	0.4608
12	Mirzapur	Public	0.000	0.066	0.000	0.102	0.143	0.378	0.054	0.041	0.040	0.022	0.243	0.098	0.260	0.033	0.737	0.422	0.365	0.001	0.000	0.127	0.188	0.200	0.038	0.4570	
		Private	0.000	0.082	0.000	0.102	0.184	0.378	0.070	0.010	0.000	0.088	0.243	0.025	0.105	0.068	0.569	0.422	0.310	0.125	0.000	0.000	0.063	0.168	0.200	0.038	0.4171
13	Varanasi	Public	0.000	0.000	0.000	0.000	0.000	0.378	0.000	0.061	0.040	0.000	0.243	0.049	0.208	0.033	0.654	0.422	0.267	0.046	0.000	0.000	0.079	0.125	0.200	0.025	0.2924
		Private	0.000	0.082	0.164	0.128	0.374	0.378	0.141	0.041	0.020	0.088	0.243	0.025	0.139	0.066	0.621	0.422	0.404	0.076	0.000	0.000	0.111	0.187	0.200	0.037	0.5823

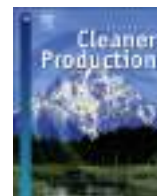
Interpretation

Column no. 4 - S_{m-1} ; Column no. 5 - S_{m-2} ; Column no. 6 - S_{m-3} ; Column no. 7 - S_{m-4} ; Column no. 8 represents, $S_{i=1}^{n-1} S_{m-i}$; where $i = 1, 2, \dots, n$ ($n = 4$); Column no. 9 - $CW_{i=1}$; Column no. 10 - SI_1 ; Column no. 11 - S_{m-5} ; Column no. 12 - S_{m-6} ; Column no. 13 - S_{m-7} ; Column no. 14 - S_{m-8} ; Column no. 15 - S_{m-9} ; Column no. 16 - S_{m-10} ; Column no. 17 - S_{m-11} ; Column no. 18 represents, $\sum_{i=5}^n S_{m-i}$; where $i = 5, 6, \dots, n$ ($n = 11$); Column no. 19 - $CW_{i=2}$; Column no. 20 - SI_2 ; Column no. 21 - S_{m-12} ; Column no. 22 - S_{m-13} ; Column no. 23 - S_{m-14} ; Column no. 24 represents, $\sum_{i=12}^n S_{m-i}$; where $i = 12, 13, \dots, n$ ($n = 14$); Column no. 25 - $CW_{i=3}$; Column no. 26 - SI_3 ; Column no. 27 represents, $\sum_{i=1}^n SI_i$; where $i = 1, 2, \dots, n$ ($n = 3$).

Note: CW_j is the weight of the j^{th} component, where $\sum_{j=1}^n CW_j = 1$, where $i = 1, 2, \dots, n$ ($n = 3$), and $0 \leq CW_j \leq 1$.

References

- Beecher, J. (2002). Survey of state water agency water loss reporting practices. AWWA – American Water Works Association, Denver.
- Dixit, S. and S. Tiwari (2008). Impact assessment of heavy metal pollution of Shahpura Lake, Bhopal, India. *Int. J. Environ. Res.*, **2(1)**: 37-42.
- Environmental Protection Agency, Water Sense (2009). Efficiency in the commercial and institutional sector. Consideration for a water sense program.
- Feyen, J., Shannon, K. and M. Neville (Eds.) (2009). Water and urban development paradigms towards an integration of engineering, design and management approaches. London: CRC Press.
- Godfrey, L. and C. Todd (2001). Defining thresholds for freshwater sustainability indicators within the context of South African water resource management. Paper presented at the 2nd WARFA/Water net symposium: Integrated water resource management: Theory, Practice, Cases. Cape Town.
- Hering, J.G. and K.M. Ingold (2012). Water resources management: What should be integrated? *Science*, **336(6086)**: 1234-1235.
- Hoque, B.A., Hallman, K., Levy, J., Bouis, H., Ali, N., Khan, F., Khanam, S., Kabir, M., Hossain, S. and M.S. Alam (2006). Rural drinking water at supply and household levels: Quality and management. *Int. J. Hyg. Environ. Health*, **209(5)**: 451-460.
- Joint Research Centre-European Commission (2005a). Tools for composite indicators buildings. Italy, EUR 21682 EN.
- Joint Research Centre-European Commission (2005b). Constructing consistent composite indicators: The issue of weights, Luxembourg, EUR 21834 EN.
- Klynveld Peat Marwick Goerdeler (2012). Sustainable insight, Water scarcity: A dive into global reporting trends, United Kingdom (U.K.), 121050.
- Madungwe, E. and S. Sakuringwa (2007). Grey water reuse: A strategy for water demand management in Harare? *Phys. Chem. Earth*, **32(15)**: 1231-1236.
- Mossalanejad, A. (2011). The role of economic policy and environment in sustainable development. *Int. J. Environ. Res.*, **5(2)**: 395-402.
- Real Property Association of Canada (2011). Water Management: A Benchmark for Canadian office buildings. Version 1.01.
- Seckler, D., Barker, R. and U. Amarasinghe (1999). Water scarcity in the twenty-first century. *Int. J. Water Resour. D.*, **15(1-2)**: 29-42.
- Seneviratne, M. (2007). A practical approach to water conservation for commercial and industrial facilities. Oxford: Elsevier Ltd.
- Shiao, T., Maddocks, A., Carson, C. and E. Loizeaux (2015). 3 Maps explain India's growing water risks. WRI – World Resource Institute.
- Singh, S.P., Deepa, P. and S. Rashmi (2002). Hydrobiological studies of two ponds of Satna (M.P.), India. *Eco. Environ. Cons.*, **8(3)**: 289-292.
- Suhag, R. (2016). Overview of ground water in India. PRS 'Legislative Research'.
- The United Nations Department of Economic and Social Affairs (2013). International decade for action "water for life" 2005-2015.
- U.P. Ground Water Department (2016). Status of groundwater level and figures.
- Warhurst, A. (2002). Sustainability indicators and sustainability performance management. International Institute for Environment and Development (IIED), Warwick, England.



Optimization of polyethylene/polypropylene/alkali modified wheat straw composites for packaging application using RSM

Shobhit Dixit, Vijay Laxmi Yadav*

Department of Chemical Engineering and Technology, IIT BHU, Varanasi, 221005, Uttar Pradesh, India

ARTICLE INFO

Article history:

Received 10 June 2019

Received in revised form

26 August 2019

Accepted 28 August 2019

Available online 29 August 2019

Handling Editor: Zuotai Zhang

Keywords:

Polyethylene

Polypropylene

Wheat straw

Packaging

ABSTRACT

The objective of this research was to synthesize the optimized packaging film based on polyethylene (PE), polypropylene (PP) and alkali treated-wheat straw (WS) using central composite design (CCD). In this paper, effects of three independent factors viz. polyethylene (1.8–1.08 g), polypropylene (1.2–0.72 g), and alkali treated-wheat straw (0–1.2 g) on three dependent variables viz. tensile strength, elongation at break (%) and water vapor transmission rate (WVTR) of packaging film were investigated. Response surface methodology (RSM) provided the combination for an optimum film, which was 1.8 g of polyethylene, 1.2 g of polypropylene and 1.192 g of alkali treated-wheat straw giving 45.018 MPa tensile strength, 120% elongation limit and $51.740 \text{ g/m}^{-2}\text{day}^{-1}$ water vapor transmission rate, respectively for packaging application. The film prepared using the optimized results further characterized using several characterization techniques such as scanning electron microscopy (SEM), X-ray diffraction (XRD), mechanical testing, contact angle, water vapor transmission rate and optical characteristics test. This result demonstrated the perfect use of treated-agro-waste in a polymer matrix for green packaging application.

© 2019 Elsevier Ltd. All rights reserved.

1. Introduction

A set of different combination of synthetic polymers such as polyethylene, polystyrene, polyamide, polypropylene, polyethylene terephthalate and polyvinyl chloride are frequently used for packaging application. However, frequent use of non-biodegradable polymers is correlated with the surging plastics wastes. The worldwide production of polymers has grown from 1.5 million ton in 1950 to about 322 million ton in 2015 (Bajracharya et al., 2016; Díaz et al., 2018; Dixit and Yadav, 2019; Fazeli et al., 2018). Hence, increasing plastic wastes have affected several environmental aspects. In particular, many environment reports have also proved that polymeric wastes imbalanced the surrounding chains (Law and Thompson, 2014). Therefore, the imbalanced environment triggers towards disturbance in the lifecycle of many organisms. Dire need of minimizing polymeric wastes provoked many researchers to develop new biodegradable materials as a replacement of synthetic polymers. In addition, many authors have also used abundantly available wheat straw in the polymer matrix for minimization of polymer wastes and also synthesizing a high mechanically stable

biodegradable polymer (Bourmaud and Baley, 2007, 2009). Some authors have also reported the polymer blended with pre-treated biomass exhibiting a remarkable high mechanical strength and benchmark thermal stability as compared to native biomass-based composite film (Hou et al., 2014; Laadila et al., 2017).

Many authors used a combination of polyethylene and polypropylene to attain promising melting point, water resistance and higher resistance to fatigue (Gamage et al., 2009; Jo et al., 2018). However, non-biodegradability of synthesized composites encouraged authors to prepare biodegradable composites using green fiber in a polymer matrix (Mansor et al., 2018; Xie and Hung, 2018). These green fibers are low in density, economical, easily available and provide benchmark mechanical stability to composites. The synthesis of biodegradable packaging film has been encouraged widely, such as the development of a composite involving polymer and abundantly available wheat straw as a packaging matrix. Several authors have reported the suitability of agro-waste blended polymer composites for packaging applications (Ayrilmis et al., 2013; Babaei et al., 2014; Bledzki et al., 2010; Colín-Chávez et al., 2014; Panthapulakkal and Sain, 2015; Pereira et al., 2015; Thakur et al., 2014). Some authors focused on alkali treatment of biomass for increasing the suitability with polymer matrix and enhancing the mechanical stability of composites (da Silva et al., 2013; Hou et al., 2014; Pigatto et al., 2012; Zegaoui

* Corresponding author.

E-mail address: vlyadaviitbhu2014@gmail.com (V.L. Yadav).

et al., 2018). Sometimes Nano-clay and Nano-silver have also been incorporated with polyethylene as a packaging matrix for food preserving application (Ayrilmis et al., 2013; Jiang et al., 2018; Jo et al., 2018; Naskar et al., 2018; Sabetzadeh et al., 2016; Saha et al., 2018; Wu et al., 2017). Authors optimized the mechanical properties of natural rubber incorporated poly (3-hydroxybutyrate-co-3-hydroxyvalerate) matrix for food packaging applications using RSM (Zhao et al., 2019). In this study, gluten/carboxymethyl cellulose/cellulose nanofiber composite is synthesized and optimized water vapor permeability, color and mechanical properties of the composite using RSM analysis (Bagheri et al., 2019). Several studies have also provoked to synthesize oxygen scavenging packaging film using low-density polyethylene matrix (Kim and Holtzaple, 2005; Semanová et al., 2016). This study examined the tensile property of biocomposite synthesized from polylactic acid and treated cellulosic waste (Laadila et al., 2017).

In order to replace the time consuming conventional methods, RSM is the best choice to optimize the parameters according to our application. RSM is a combination of mathematical and statistical techniques which provide the optimize condition by analysing the relative importance of all affecting factors (Bezerra et al., 2008; Oyekanmi et al., 2019a). RSM is used to observe the simultaneously effects of different independent variables for getting the benchmark output response. Many authors claimed the suitability of using the central composite design of RSM to optimize the independent variables in their research article (Mohamed et al., 2018; Oyekanmi et al., 2019b). RSM is generally a technique to move from analysis under fixed conditions to optimized conditions. It is an empirical model that provides a desirable set of experiments. However, a desirable set of experiments provide response data that is used by RSM to predict the nature of the system (Leardi, 2009). So probably, the primary function of RSM is to optimize the process parameters that maximize the response (Abdulrahman Oyekanmi et al., 2019).

In the current research, polyethylene/polypropylene has been blended with alkali treated-wheat straw with the different set of compositions provided by RSM in terms of mass of polyethylene, polypropylene and alkali treated-wheat straw and to analyse the effect on outcomes. Moreover, outcomes are tensile strength, elongation at break (%) and water vapor transmission rate. A quadratic model was applied to depict a relationship between mechanical properties and the mass ratio of polymer/biomass. Moreover, various statistical techniques were used to obtain the optimum mass of polymer and biomass with remarkable tensile strength, moderate elongation at break (%) and lowest water vapor transmission rate. The resultant biocomposite film was characterized using XRD, SEM, Mechanical testing, WVTR, contact angle and optical characteristics test.

2. Materials and methods

2.1. Materials

Wheat straw, an agricultural waste was collected from a local farm near BHU, Varanasi after harvesting the main product. Initially, wheat straw was washed with distilled water and dried in the presence of sunlight. The average particle size of wheat straw was from 0.177 to 0.125 mm. Polymers such as polyethylene and polypropylene were procured from Sigma Aldrich, USA. Moreover, chemicals such as xylene and sodium hydroxide for alkali treatment were purchased from Fisher Scientific, USA.

2.2. Alkali pre-treatment of wheat straw

Pre-treatment of lignocellulosic material is a favourable way for

making biomass suitable for polymer blending. The main motive of using pre-treatment is to reduce the obstacle hemicellulose and lignin content. According to Kim et al., pre-treatment can precisely be used for refining biomass or surging the cellulose content of the biomass for polymer blending (Islam et al., 2011; Kim and Holtzaple, 2005; Yang et al., 2013). Mostly it can be frequently done by using some chemicals like alkali, acid, solvent and salts. In this pre-treatment, 5 g wheat straw was chemically treated with 5 W/V % of sodium hydroxide at 60 °C for 1 h. The desirable residue was filtered and used for reinforcing polymer composites (Nargotra et al., 2018).

2.3. Experimental design and optimization for polyethylene/polypropylene/alkali treated-wheat straw based biocomposite film

In this study, RSM was chosen to determine the favourable condition for the synthesis of PE/PP/alkali treated-wheat straw. RSM has many advantages over conventional methods such as it requires less number of experiments and experiment data provides optimized parameters, less time consumption and cost minimization. All experiments are lined-up on the basis of CCD. CCD provided the two sets of factors such as center points and axial points. In the set of experiments, center points of experiments are generally repeated for maintaining the accuracy of the experiments. Moreover, axial point values are fitting above and below the center points of the two factorial levels (Razali et al., 2013).

A film having high mechanical strength, elongation at break (%) in range and low WVTR were optimized using CCD model. In this experiment, three independent variables existed viz: polyethylene (1.8–1.08 g), polypropylene (1.2–0.72 g), and alkali treated-wheat straw (0–1.2 g). The number of experiments was 20 derived from the following equation (1) (Tan et al., 2008).

$$N = 2^n + 2n + n_c \quad (1)$$

where number of independent variables (n) was 3, number of replicates at central points (n_c) was 6 and thus total number of experiments was 20.

Table 1 depicts a CCD for PE/PP/Alkali treated-WS biocomposite film prepared by using Stat-Ease Design-Expert design expert software (version-11). The experimentally calculated actual value was closer to the predicted value given by design software proving the reliability of RSM. Tensile strength represents the mechanical stability of a biocomposite film, elongation at break (%) exhibits the flexibility of a biocomposite film and WVTR signifies the water vapor migration rate through the film for packaging application. Responses (tensile strength, elongation limit and WVTR) obtained from experiments were used for the optimization of the independent variables. In order to optimize the parameters, the second order polynomial equation was applied from CCD model. The general mathematical form of the second order equation is shown in the following equation (2).

$$Y = b_0 + \sum_{i=1}^k b_i X_i + \sum_{i=1}^k b_{ij} X_i^2 + \sum_{i < j}^k \sum_j^k b_{ij} X_i X_j + \epsilon \quad (2)$$

where b_0 represents the regression coefficient, k represents the number of parameters used in CCD model, i represent the linear coefficient, j represents the quadratic coefficients and ϵ represents the random error.

In order to check the reliability of the mathematical equation provided by RSM, analysis of variance (ANOVA) was used. This ANOVA analysis inspected the suitability of the polynomial second

Table 1
Mechanical and water vapor migration responses based on actual and predicted value using RSM.

Range of actual variable				Actual and predicted value of response					
Run	PE (g)	PP(g)	Alkali treated-WS (g)	Tensile strength (MPa)		Elongation at break (%)		WVTR (g.m ⁻² .day ⁻¹)	
				Actual value	Predicted value	Actual value	Predicted value	Actual value	Predicted value
1	1.08	0.72	1.2	41.00	41.04	123.00	123.03	70.00	69.40
2	1.08	0.96	0.6	39.00	38.43	125.00	124.65	63.00	62.71
3	1.44	0.96	0.6	39.50	39.35	124.00	124.37	57.50	58.42
4	1.08	1.2	1.2	39.50	39.99	123.50	123.68	63.00	63.27
5	1.8	0.72	1.2	43.00	43.09	120.00	120.03	59.00	58.84
6	1.44	0.96	0	36.00	36.33	126.00	125.95	56.25	55.11
7	1.44	0.96	0.6	39.12	39.35	124.30	124.37	59.00	58.42
8	1.8	1.2	1.2	45.00	45.04	120.00	119.93	52.00	51.73
9	1.44	0.96	0.6	39.10	39.35	125.00	124.37	58.50	58.42
10	1.8	0.96	0.6	42.00	42.23	125.00	125.15	55.00	54.92
11	1.8	1.2	0	41.00	41.04	128.00	128.03	51.25	51.94
12	1.44	0.96	1.2	43.00	42.33	121.00	120.85	60.00	60.77
13	1.8	0.72	0	36.00	35.59	130.00	129.88	54.00	53.83
14	1.44	1.2	0.6	40.00	39.43	124.50	124.35	57.00	56.06
15	1.44	0.96	0.6	38.50	39.35	124.20	124.37	59.00	58.42
16	1.08	0.72	0	33.00	33.04	125.00	125.13	57.50	57.87
17	1.08	1.2	0	35.50	35.49	124.00	124.03	56.70	56.96
18	1.44	0.96	0.6	39.40	39.35	123.70	124.37	57.25	58.42
19	1.44	0.72	0.6	37.00	37.23	125.00	124.95	59.50	60.07
20	1.44	0.96	0.6	39.80	39.35	124.60	124.37	58.50	58.42

order equation using several factors like determination coefficient (R^2), adjusted determination of coefficient (R^2_{adj}), F value, p-value, degree of freedom (DF) to examine the statistical fitness of the CCD model. The value of p less than 0.05 is indicating a well-suited model for the experiments. The 3-D graphical plots also illustrated the individual and mutual effects of the independent variables on tensile strength, elongation at break (%) and WVTR of PE/PP/Alkali treated-WS biocomposite film.

2.4. Synthesis of polyethylene/polypropylene/alkali treated-wheat straw

Films with different composition recommended by RSM software were synthesized using solution casting method. A film with different composition exhibited the total weight of the film. Polyethylene and polypropylene both are non-polar, saturated and high molecular weight hydrocarbons and xylene is aliphatic hydrocarbon. Both simultaneously dissolve in xylene solvent at high temperature. The film was synthesized by dispersing a known amount of polyethylene and polypropylene in xylene at a temperature of 130 °C. The polymeric solution was mechanically stirred at 400 rpm for an hour. Subsequently, native-wheat straw was added in a solution. Then, the solution was mechanically stirred at 600 rpm for half an hour. The bio-composite solution was cast in a petri dish. Moreover, the cast solution was kept in an oven at 50 °C for 24 h and the film was detached safely. In a similar manner, the film using alkali treated-wheat straw based polymeric composite was also prepared. In addition, bio-composite films were also preserved using aluminium foil and placed in a desiccator for preventing film to attain moisture.

2.5. Characterization of polyethylene/polypropylene/alkali treated-wheat straw bio-composite film

2.5.1. SEM analysis

The surface morphology of PE/PP, PE/PP/Native-wheat straw and PE/PP/Alkali treated- WS composite films was analysed using SEM analysis (EVO - Scanning Electron Microscope MA15/18, CARL ZEISS MICROSCOPY LTD., USA) at a 20 kV voltage with 500 X

magnification. In the sample preparation process, initially, gold coating was done on film to make it conductive for SEM analysis.

2.5.2. XRD analysis

The XRD analysis of PE/PP, PE/PP/Native-wheat straw and PE/PP/Alkali treated- WS composite films was performed using an X-ray diffractometer (XRD, model mini flux II, Rigaku, Japan) with a Cu K α radiation ($\lambda = 0.154$ nm). The XRD was conducted at 2 theta values of 5°- 70° with a scanning rate of 5°/min at 40 kV operating voltage (Perumal et al., 2018).

2.5.3. Mechanical testing

The mechanical strength such as tensile strength, elongation at break (%) and tensile modulus of PE/PP, PE/PP/Native-wheat straw and PE/PP/Alkali treated- WS composite films were determined using the universal testing machine (INSTRON 5982 Floor Model System, US). The mechanical testing was performed using ASTM D0882 having gauge length 5 mm with testing speed 30 mm/min (Haddar et al., 2018). The thickness of the films was 0.25 ± 0.2 mm.

2.5.4. Contact angle measurement

In order to signify the water-resistant property of the film, the water contact angles of PE/PP, PE/PP/Native-wheat straw and PE/PP/Alkali treated- WS composite films were examined by using the sessile drop method (KRUSS DSA25 Series, Germany) at room temperature. In this measurement, a droplet of water was placed on the film surface and the droplet was allowed to expand on the film surface for 1 s. Subsequently, water contact angle of the film was recorded. This procedure was repeated 5 times and the average value of the contact angle was calculated (Simmons et al., 2016; Tsuchiya et al., 2019).

2.5.5. WVTR test

In this test, WVTR of PE/PP, PE/PP/Native-wheat straw and PE/PP/Alkali treated- WS composite films were determined. Initially, a wet chamber was prepared by a glass beaker tightly covered with bio-composite film. Subsequently, the weight of the wet chamber was measured and it was placed in an incubator at 23 °C. The relative humidity of incubator was maintained at 53–55%.

Moreover, the change in weight of bio-composite film was observed regularly at an interval of 24 h. Based on the weight loss through the film, WVTR was calculated using the following equation (3) (Răpă et al., 2016; Sirviö et al., 2014).

$$WVTR = \frac{WC1 - WC2}{WC1 * A * day} \quad (3)$$

where WC1 and WC2 represent the initial and final weight of the wet chamber and A represents the exposed area of the wet chamber.

2.5.6. Optical characteristics test

Transparency test for PE/PP, PE/PP/Native-wheat straw and PE/PP/Alkali treated- WS composite films were analysed using Elico SL 210 UV VIS spectrophotometer. In this test, the film was directly exposed in the spectrophotometer at a visible wavelength of 400–800 nm. Moreover, a blank compartment was also used as a reference in the spectrophotometer (Saha et al., 2018).

3. Results and discussion

3.1. RSM and ANOVA analysis

3.1.1. ANOVA and RSM analysis for tensile strength, Elongation at break and WVTR of PE/PP/Alkali treated-WS biocomposite film

3.1.1.1. *Data adequacy check of the model.* After conducting the set of experiments provided by RSM, the resultant data were analysed using ANOVA analysis. Fig. 1 exhibits the actual and predicted responses (tensile strength, elongation at break (%) and WVTR) in which actual values are dependent variable data of specific experiment and the predicted values were provided by the RSM model. Figure reveals that all points lie around the diagonal line in the graph of predicted value vs. actual value. According to Lu et al. (2009), variable data points lying on the straight line suggest the adequacy of the model. This behaviour of the graph represents that the results fit well with the predicted value. The higher R^2 value 0.9820 for tensile strength, 0.9870 for elongation at break (%) and

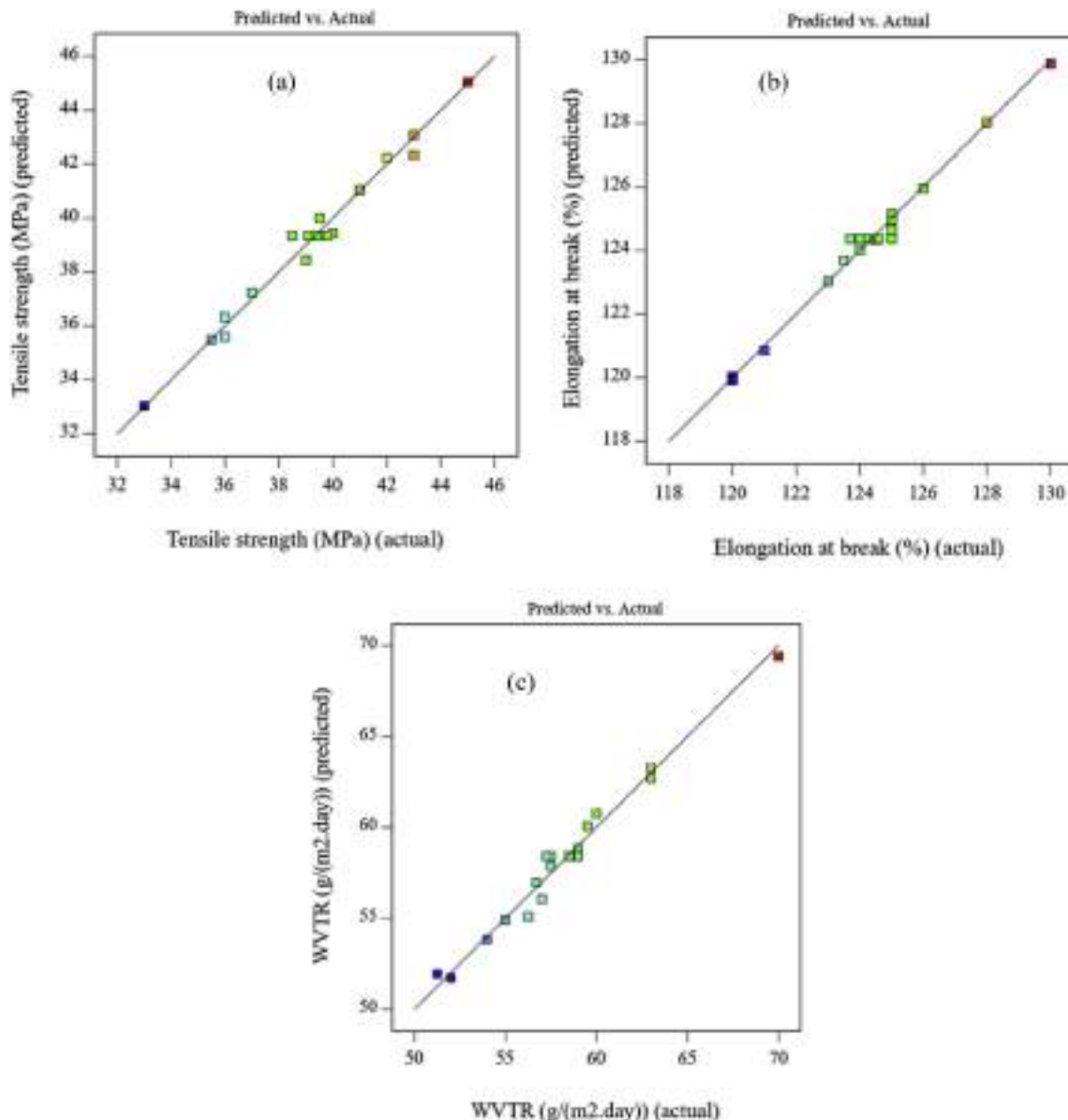


Fig. 1. Relationship between actual and predicted values of model (a) Tensile strength and (b) Elongation at break (%) (c) Water vapor transmission rate.

0.9768 for WVTR assure the reliability of the model. These outcomes are similar to the results reported by Satapathy et al. (Satapathy and Das, 2014).

3.1.1.2. Effect of process variables on tensile strength. The RSM model for the tensile strength of the biocomposite film is shown in following equation (4).

$$Y_{TS} = + 31.71964 - 24.50631 A + 29.69886 B + 11.73030 C + 8.68056 AB - 0.578704 AC - 6.07639 BC + 7.56874 A^2 - 17.69255 B^2 - 0.053030 C^2 \quad (4)$$

Where linear terms (A, B, C), interaction terms (AB, BC, AC) and quadratic terms (A^2 , B^2 , C^2), are there in the mathematical equation. According to ANOVA analysis, all the factors followed the second-order quadratic model for tensile strength. The p value < 0.05 and higher F value signify the suitability of the model. Value of $p < 0.0001$ and the F-value of 60.67 indicate that the model is well suited to the experiments (Table 2). A p-value is generally expressing the probability of error that is correlated with the validation of the observed result (Xiangli et al., 2008). The p-value for linear terms, interaction term, and quadratic terms are less than 0.05 showing the benchmark impact of process parameters on tensile strength. The standard deviation of the model is found to be 0.5293. Hence it can be concluded that the results show the reliability of the RSM model.

3-D graphical response plots illustrate the interactions between the independent variables and dependent variables for tensile strength (Fig. 2). Fig. 2(a) reveals the low and high concentration of polypropylene, tensile strength continuously increases with the polyethylene concentration (1.08 g–1.8 g). This signifies the remarkable effect of polyethylene on tensile strength. Similar behaviour is illustrated from interaction pattern of polyethylene and alkali treated-WS (Fig. 2(c)), and polypropylene and alkali treated-WS (Fig. 2(e)) for tensile strength of biocomposite film. These results assure the considerable interaction of independent parameters for optimization of the tensile strength of biocomposite film and also encourage the use of alkali treated-WS in the synthesis of composite film for packaging application.

3.1.1.3. Effect of process variables on elongation at break (%). The statistical equation for elongation at break (%) of bio-composite film is shown in the following equation.

$$Y_{EAB} = +130.16727 - 3.65846 A - 9.34186 B + 8.97727 C - 2.17014 AB - 8.96991 AC + 3.03819 BC + 4.10354 A^2 + 4.89268 B^2 - 2.68939 C^2 \quad (5)$$

ANOVA analysis provides a significant model of p-value < 0.0001 and F value 84.22 for elongation at break (%) of the bio-composite film. In this analysis, p-value < 0.05 for linear term (A, B, C), interaction term (AC, BC) and quadratic term (A^2 , C^2) assures the remarkable impact of these independent variables on elongation at break (%) of PE/PP/Alkali treated-WS biocomposite film and proving the suitability of CCD model (Table 3).

Fig. 3 represents the 3-D plots of the independent and dependent variables for elongation at break (%) of biocomposite. At low and high concentration of polypropylene, there is a decrease in elongation at break (%) with increasing the concentration of polyethylene from 1.08 g to 1.8 g (Fig. 3(a)). The same pattern was found in the case of polyethylene and alkali treated-WS in RSM plot for elongation at break (%) of biocomposite film (Fig. 3(c)). But on the other hand, interaction pattern of polypropylene and alkali treated-WS exhibits that at high and low concentration of alkali treated-WS, there is no significant influence on elongation at break (%) at certain concentration of polypropylene (Fig. 3(e)). Thus it can be concluded that the value of elongation at break (%) is found to be in a range (120–125%) with the addition of alkali treated-WS in the composite film for packaging application.

3.1.1.4. Effect of process variables on WVTR. RSM model suggests the following equation which optimizes the process parameters for WVTR of PE/PP/Alkali treated-WS biocomposite film.

$$Y_{WVTR} = + 63.71182 - 12.36774 A + 12.96922 B + 25.89845 C - 2.82118 AB - 7.55208 AC - 9.07118 BC + 3.05135 A^2 - 6.15530 B^2 - 1.33207 C^2 \quad (6)$$

The statistical equation provided by ANOVA analysis shows p value < 0.05 and higher F value (46.82) assuring the suitability of the model for WVTR. The p value < 0.05 of individual process variables (A, B, C) and interaction process variables (AC, BC) signify the role of independent variables on WVTR of PE/PP/Alkali treated-WS biocomposite film for optimization of the process model (Table 4).

Response surface plots for water vapor transmission rate are shown in Fig. 4. A desirable decrement in WVTR is observed in the interaction pattern of polyethylene and polypropylene as shown in Fig. 4(a). This result indicates that a higher concentration of

Table 2
ANOVA analysis for the tensile strength of PE/PP/alkali treated-WS from CCD model.

Source	Sum of Squares	df	Mean Square	F-value	p-value	
Model	152.96	9	17.00	60.67	<0.0001	significant
A-Polyethylene	36.10	1	36.10	128.86	<0.0001	
B-Polypropylene	12.10	1	12.10	43.19	<0.0001	
C-Alkali Treated biomass	90.00	1	90.00	321.25	<0.0001	
AB	4.50	1	4.50	16.06	0.0025	
AC	0.1250	1	0.1250	0.4462	0.5193	
BC	6.13	1	6.13	21.86	0.0009	
A^2	2.65	1	2.65	9.44	0.0118	
B^2	2.86	1	2.86	10.19	0.0096	
C^2	0.0010	1	0.0010	0.0036	0.9535	
Residual	2.80	10	0.2802			
Lack of Fit	1.81	5	0.3626	1.83	0.2608	not significant
Pure Error	0.9883	5	0.1977			
Cor Total	155.76	19				
Std. Dev.	0.5293		R²	0.9820		
Mean	39.32		Adjusted R²	0.9658		
C.V. %	1.35		Predicted R²	0.8950		
			Adeq Precision	32.0625		

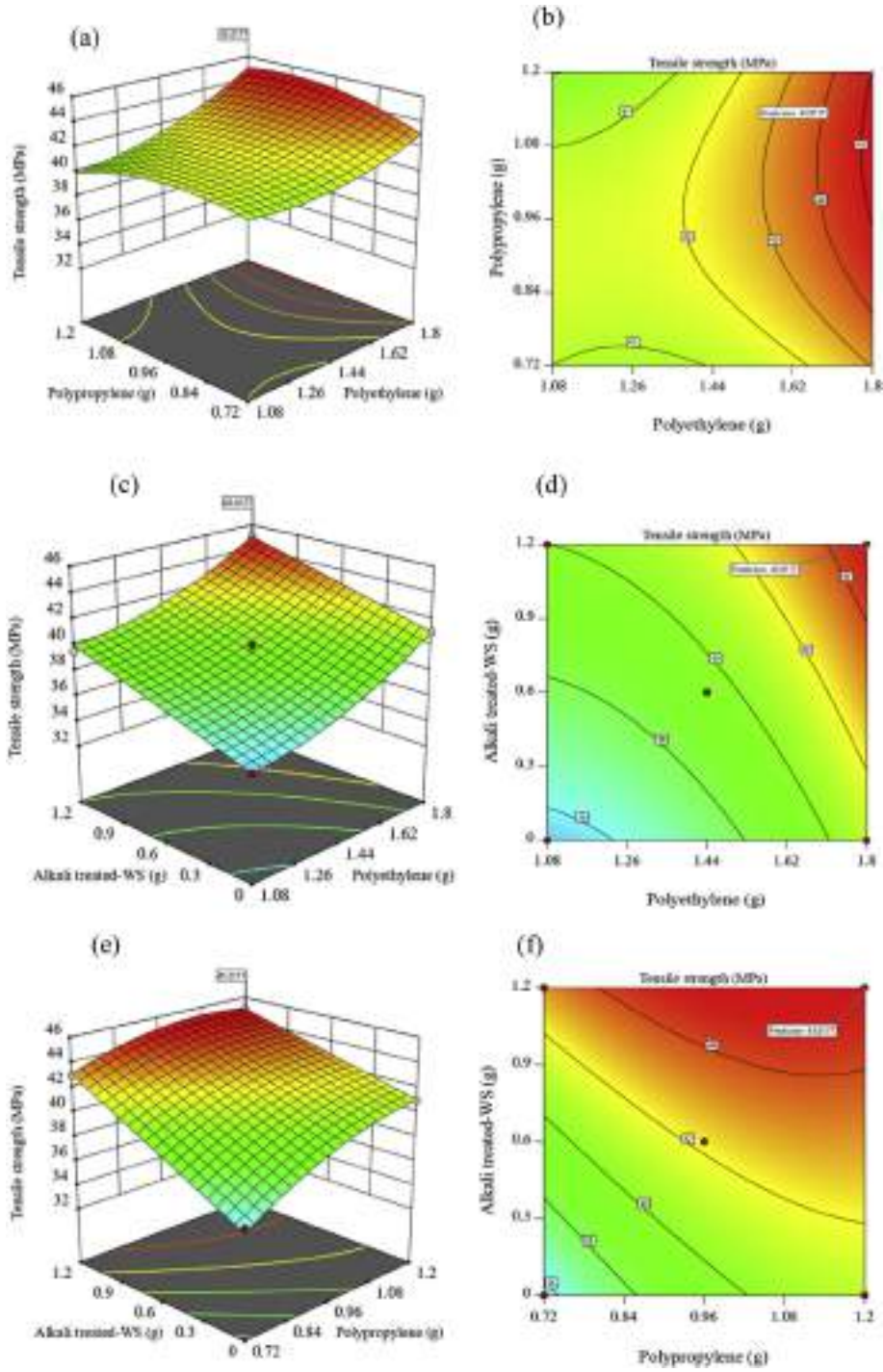


Fig. 2. Three dimensional response surface and contour plots of tensile strength showing the effect of (a) and (b) polypropylene and polyethylene; (c) and (d) alkali treated-WS and polyethylene; (e) and (f) alkali treated-WS and polypropylene.

Table 3
ANOVA analysis for elongation at break (%) of PE/PP/alkali treated-WS from CCD model.

Source	Sum of Squares	df	Mean Square	F-value	p-value	
Model	101.06	9	11.23	84.22	<0.0001	significant
A-Polyethylene	0.6250	1	0.6250	4.69	0.0556	
B-Polypropylene	0.9000	1	0.9000	6.75	0.0266	
C-Alkali Treated biomass	65.02	1	65.02	487.68	<0.0001	
AB	0.2812	1	0.2812	2.11	0.1770	
AC	30.03	1	30.03	225.23	<0.0001	
BC	1.53	1	1.53	11.48	0.0069	
A ²	0.7778	1	0.7778	5.83	0.0364	
B ²	0.2184	1	0.2184	1.64	0.2295	
C ²	2.58	1	2.58	19.33	0.0013	
Residual	1.33	10	0.1333			
Lack of Fit	0.2933	5	0.0587	0.2821	0.9045	not significant
Pure Error	1.04	5	0.2080			
Cor Total	102.40	19				
Std. Dev.	0.3651		R²	0.9870		
Mean	124.29		Adjusted R²	0.9753		
C.V. %	0.2938		Predicted R²	0.9632		
			Adeq Precision	38.5361		

polypropylene and polyethylene is correlated with the lower water vapor transmission rate of the composite film. Similar patterns of interaction pattern are observed for polyethylene and alkali treated-WS, and polypropylene and alkali treated-WS for WVTR (Fig. 4(c) and (e)). At lower and higher concentration of polyethylene and polypropylene, WVTR continuously decreases with surging the contribution of alkali treated-WS in the composite film. So probably, this outcome assures the successful substitution of Polymer with alkali treated-WS for packaging application.

3.2. Optimization of the statistical model

The optimization run was performed with 1.8 g of polyethylene, 1.2 g of polypropylene and 1.192 g of alkali treated-WS. Predicted responses at optimum parameters provided by RSM are 45.018 MPa for tensile strength, 120% for elongation at break and 51.740 g m⁻² day⁻¹ for water vapor transmission rate. The RSM study shows that desirable properties could be obtained with optimized conditions. The experimental results with the optimized parameters yield 45.010 MPa for tensile strength, 119.98 for elongation at break (%) and 51.890 g m⁻² day⁻¹ for water vapor transmission rate. The error in all results is found to be very less. This small error in results exhibits the reliable response is obtained using CCD process optimization technique.

3.3. Characterization of the optimized polyethylene/polypropylene/alkali treated-wheat straw bio-composite film

The synthesized PE/PP, PE/PP/Native-wheat straw and PE/PP/Alkali treated-wheat straw composite films were characterized using SEM, XRD, mechanical testing, contact angle, WVTR and Optical characteristics test.

3.3.1. SEM analysis

In order to elucidate the surface morphology of PE/PP, PE/PP/Native-wheat straw and PE/PP/Alkali treated-wheat straw composite films, SEM analysis was performed. 10x magnification SEM images have been depicted to examine the adhesion of polymer and treated-biomass. Fig. 5(a) exhibits the plain surface of PE/PP based composite. Fractured SEM image of PE/PP/Native-wheat straw composite film is observed in Fig. 5(b). Uniform distribution of alkali treated-WS in the matrix is observed in Fig. 5(c).

This surface behaviour of treated-WS based polymer composites was revealing the strong biomass-polymer matrix adhesion

existence. In addition, treated-WS is strongly encapsulated in PE/PP matrix which restricts the penetration by problematic ingredients. Sabetzadeh et al. (2016) used nano clay for reinforcement of polyethylene/starch based film and observed the same results as discussed earlier. The strong adhesion was correlated with the higher mechanical strength which is confirmed in mechanical testing of the film as reported in Table 5.

3.3.2. XRD analysis

The crystalline changes in PE/PP, PE/PP/Native-wheat straw and PE/PP/Alkali treated-wheat straw composite films were analysed by using XRD analysis and are shown in Fig. 6. There are five principle peaks observed for PE/PP, PE/PP/Native-wheat straw and PE/PP/Alkali treated-wheat straw composite films which are around 13°, 16°, 18°, 21° and 23° respectively. The peak at 21.5° for PE/PP, 21.35° for PE/PP/Native-wheat straw and 21.48° for Alkali treated-WS are showed higher intensity in XRD spectrum.

Comparable peak height at around 21° for both composite films is showed the increase of cellulose crystallinity in the polymer matrix. Pickering et al. described that the increase in cellulose crystallinity was correlated with the decrement in the amorphous region after pre-treatment (Islam et al., 2011). So probably, the use of alkali treated-WS for blending with polymer matrix was maintaining the hydrophobicity of polymer matrix film which is confirmed in the contact angle measurement test of the film. Same results were reported by Kalia et al. (Kalia and Vashistha, 2012) in previous studies.

3.3.3. Mechanical testing

In this test, the mechanical stability of PE/PP, PE/PP/Native-wheat straw and PE/PP/Alkali treated-wheat straw composite films has been investigated. Tensile strength and flexibility tests for PE/PP, PE/PP/Native-wheat straw and PE/PP/Alkali treated-wheat straw composite films have been summarized in Table 5. The tensile strength of PE/PP, PE/PP/Native-wheat straw and PE/PP/Alkali treated-wheat straw composite films are 46.5 MPa, 34 MPa, and 45.010 MPa respectively. On the other hand, the elongation limit of PE/PP, PE/PP/Native-wheat straw and PE/PP/Alkali treated-wheat straw composite films are 122.05%, 116.20% and 119.98% respectively.

A notable decrement in tensile strength is observed for polymer incorporated with native-wheat straw. Moreover, this signified a poor adhesion found between polymer and native-wheat straw. A positive increase in tensile strength from 34 MPa to 45.010 MPa was

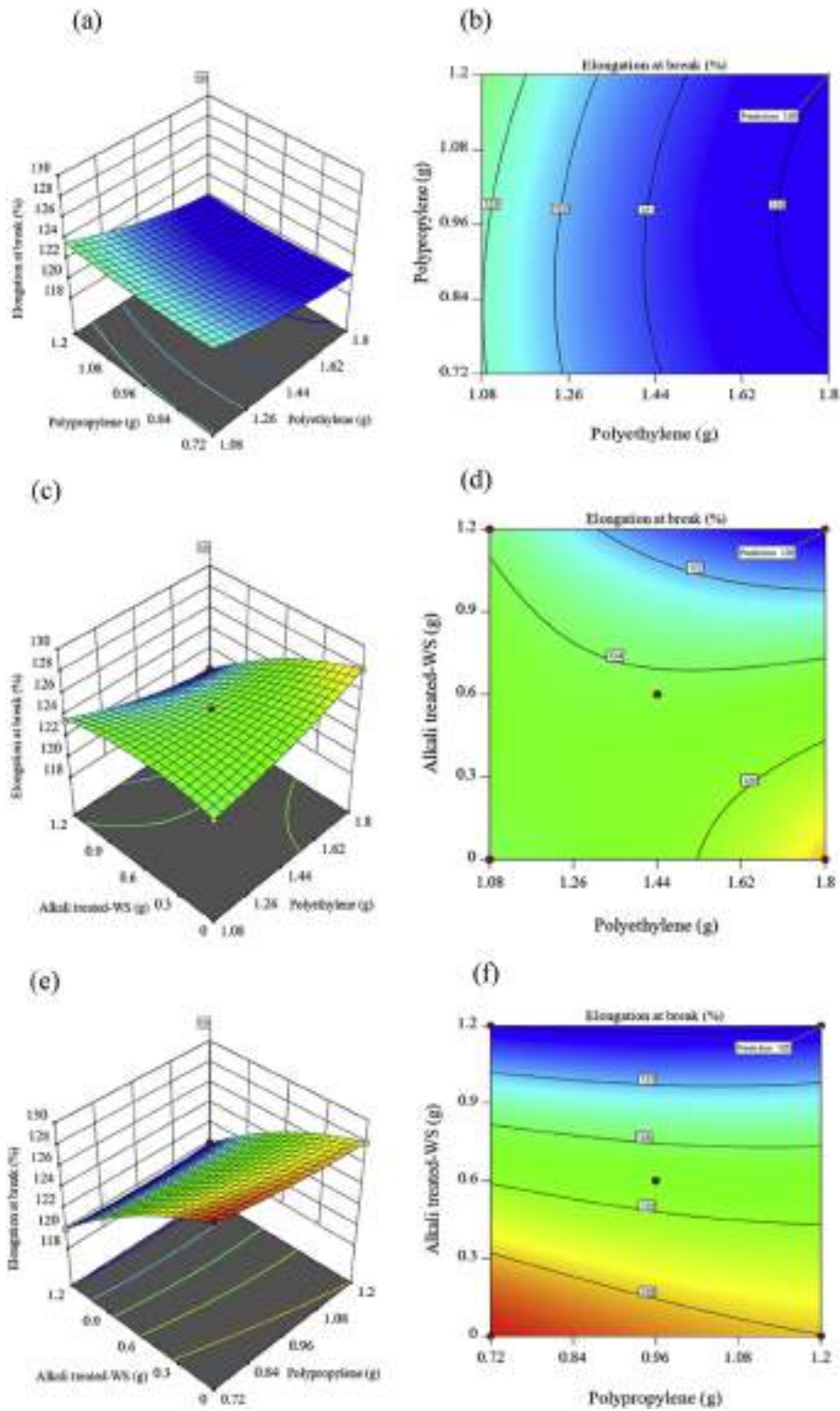


Fig. 3. Three dimensional response surface and contour plots of elongation at break showing the effect of (a) and (b) polypropylene and polyethylene; (c) and (d) alkali treated-WS and polyethylene; (e) and (f) alkali treated-WS and polypropylene.

Table 4
ANOVA analysis for water vapor transmission rate of PE/PP/alkali treated-WS from CCD model.

Source	Sum of Squares	df	Mean Square	F-value	p-value	
Model	309.01	9	34.33	46.82	<0.0001	significant
A-Polyethylene	151.71	1	151.71	206.88	<0.0001	
B-Polypropylene	40.20	1	40.20	54.82	<0.0001	
C-Alkali Treated biomass	80.09	1	80.09	109.22	<0.0001	
AB	0.4753	1	0.4753	0.6482	0.4395	
AC	21.29	1	21.29	29.03	0.0003	
BC	13.65	1	13.65	18.61	0.0015	
A ²	0.4301	1	0.4301	0.5865	0.4615	
B ²	0.3457	1	0.3457	0.4714	0.5080	
C ²	0.6324	1	0.6324	0.8624	0.3749	
Residual	7.33	10	0.7333			
Lack of Fit	4.53	5	0.9062	1.62	0.3054	not significant
Pure Error	2.80	5	0.5604			
Cor Total	316.35	19				
Std. Dev.	0.8563		R²	0.9768		
Mean	58.20		Adjusted R²	0.9560		
C.V. %	1.47		Predicted R²	0.8576		
			Adeq Precision	29.1897		

observed in polymer blended with alkali treated-wheat straw which is similar to the results published by Nyambo et al. (2011) in their research article.

A clear decrease in flexible limit was observed in polymer incorporated with untreated-wheat straw biomass. Sanchez et al. (Sánchez-Safont et al., 2018) prepared different lignocellulosic waste based packaging film and reported similar results in their article. Moreover, the elongation limit is increased from 116.20% to 119.98% after blending of treated-wheat straw with the polymer matrix. The flexible limit is improved by enhancing the suitability of fiber in the polymer matrix using alkali treatment.

There is a remarkable improvement in mechanical stability after incorporated treated-wheat straw with the polymer matrix. Hence, it can be stated that polymer incorporated with treated-wheat straw is exhibiting the suitability of polymeric composite films in packaging application.

3.3.4. Contact angle

Water-repelling behaviour of polymeric composite films was investigated using contact angle test. Contact angle values for PE/PP, PE/PP/Native-wheat straw and PE/PP/Alkali treated-wheat straw composite films are depicted in Table 5.

The contact angle values for both polymeric composite films are comparable and higher than 90°. It can be attributed to the existence of weak surface energy between film and liquid as compared to surface tension of the water. This test outcome suggested the use of alkali treated-WS in a polymer matrix for green reinforcement packaging application (Baek et al., 2012; Tang et al., 2009).

3.3.5. WVTR test

In this test, water vapor barrier properties for composite films were estimated and the values are depicted in Table 5. WVTR for PE/PP, PE/PP/Native-wheat straw and PE/PP/Alkali treated-wheat straw composite films are 47.50, 132.10 and 51.890 g m⁻².day⁻¹ respectively.

WVTR for PE/PP/Native-WS composite film is high due to the unsuitable blending of biomass in a polymer matrix which was confirmed in SEM analysis. It has better water affinity as compared to other polymeric composite films. Sánchez -Safont et al. (Sánchez-Safont et al., 2018) and Tănase et al. (2015) have reported similar results in their research articles. After the dispersion of alkali treated-wheat straw in the polymer matrix in place of native-wheat straw, WVTR is decreased due to the roughness of

composite film, which is showing better compatibility of treated biomass in polymer matrix. As an outcome, PE/PP/Alkali treated-wheat straw has become a better substitute for polymer composite film for packaging application.

3.3.6. Optical characteristics test

In order to elucidate the transparency of the film, visible light transmission rate for PE/PP and PE/PP/Alkali treated-WS composite films were examined. Light transmission rates over 400–800 nm wavelength range for composite films are shown in Table 5.

The light transmission rate for alkali treated-WS based composite film is estimated to be less as compared to the polymer composite film. This could be due to the blending of treated-biomass in the polymer matrix. In addition, film still has hazing transparency due to the uniform distribution of wheat straw in the polymer matrix. Similar results were reported by Paul et al. (Zeng et al., 2005) and Liu et al. (2014) in previous studies. Thus, PE/PP/Alkali treated-WS green composite with haze transparency could be used for packaging application.

4. Conclusions

The response surface methodology for PE/PP/Alkali treated-WS biocomposite film was successfully applied with 0.996 selectivity. The optimum concentrations for polyethylene, polypropylene and wheat straw were 1.8 g, 1.2 g and 1.192 g respectively. The optimized results for tensile strength, elongation at break (%) and water vapor migration rate using independent variables for biocomposite film were 45.018 MPa, 120% and 51.740 g m⁻².day⁻¹ respectively. The optimum results predicted by RSM were equable with the experimental results. However, the equable results were showing the accuracy of CCD-RSM model. In addition, the optimized film was also characterized using SEM, XRD, mechanical testing, contact angle and optical characteristics test. SEM and XRD analysis showed roughened surface of treated-WS in the polymer matrix. Contact angle test explored the higher melting point of film with benchmark water repelling property. Optical characteristics explained the hazing transparency of film. So it can be concluded that these outcomes were associated with the use of treated-WS for better mechanical strength, lower water migration rate with moderate elongation for promising green packaging application.

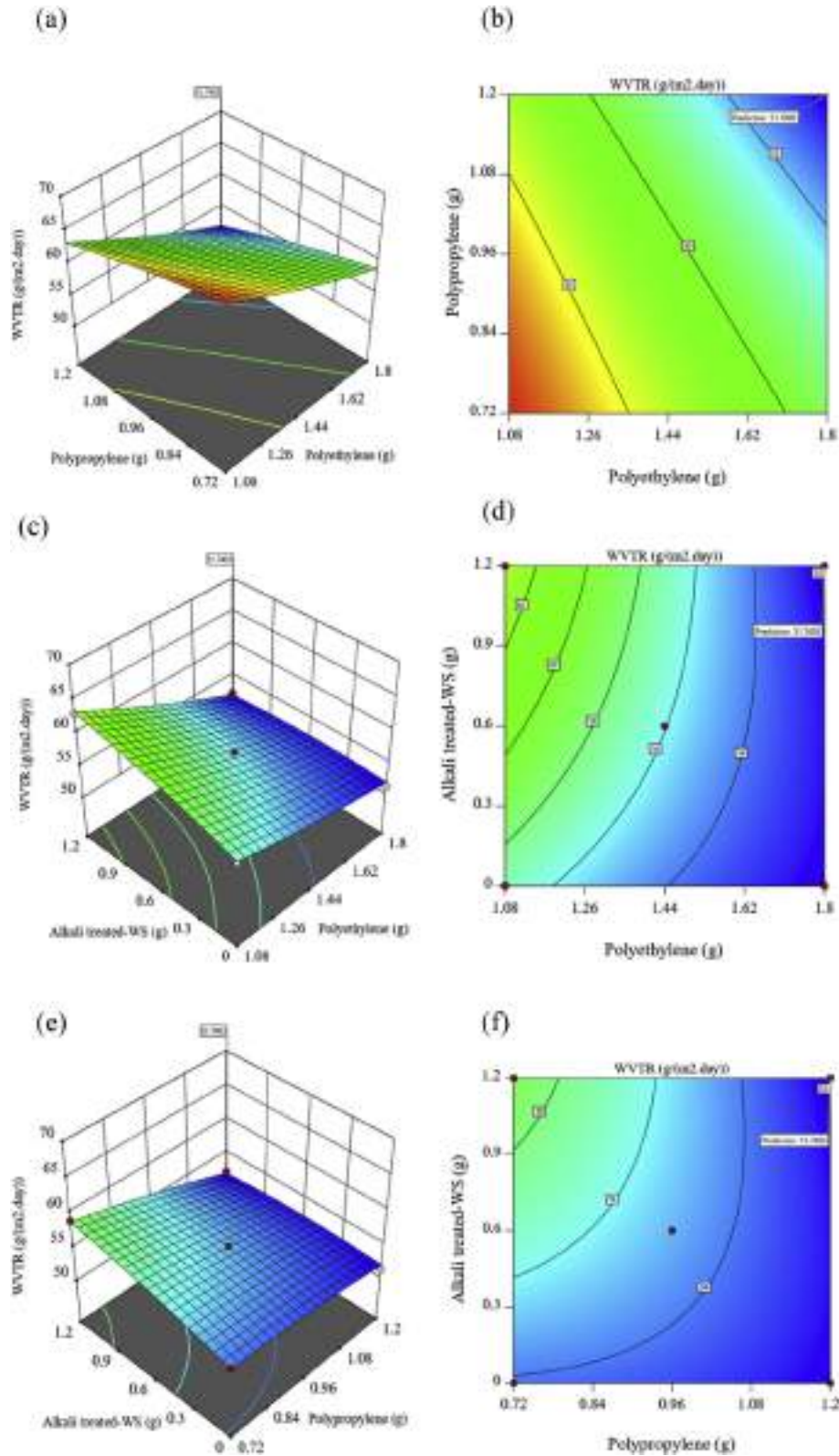


Fig. 4. Three dimensional response surface and contour plots of water vapor transmission rate showing the effect of (a) and (b) polypropylene and polyethylene; (c) and (d) alkali treated-WS and polyethylene; (e) and (f) alkali treated-WS and polypropylene.

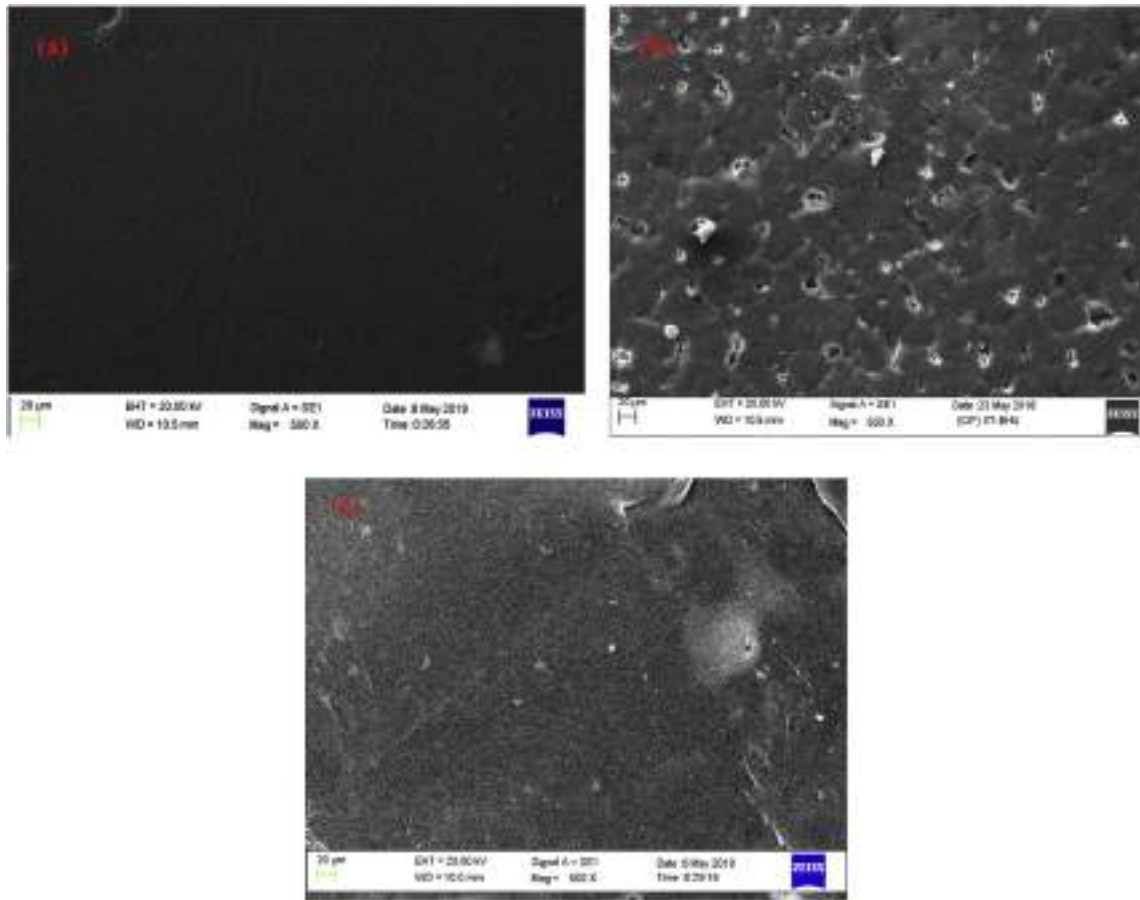


Fig. 5. SEM analysis of all polymeric composite films (a) PE/PP film (b) PE/PP/native-WS (c) PE/PP/alkali treated-WS composite films.

Table 5

Tensile strength, elongation at break, contact angle, water vapor transmission rate and optical characteristics property of polymeric composite films.

Composite film	Tensile strength (MPa)	Elongation at break (%)	Contact angle (deg)	WVTR ($\text{g m}^{-2} \text{ day}^{-1}$)	Light transmission rate through a different visible wavelength range(nm)		
					400	600	800
PE/PP	46.5	122.05	$121^\circ \pm 4$	47.50	30.5 ± 0.02	34.30 ± 0.01	41.20 ± 0.02
PE/PP/Native-WS	34 ± 1	116.20	$92^\circ \pm 2$	132.10	5.5 ± 0.02	7.70 ± 0.04	8.2 ± 0.03
PE/PP/NaOH treated-WS	45.010	119.98	$117^\circ \pm 5$	51.890	10.25 ± 0.05	15.4 ± 0.04	18.65 ± 0.07

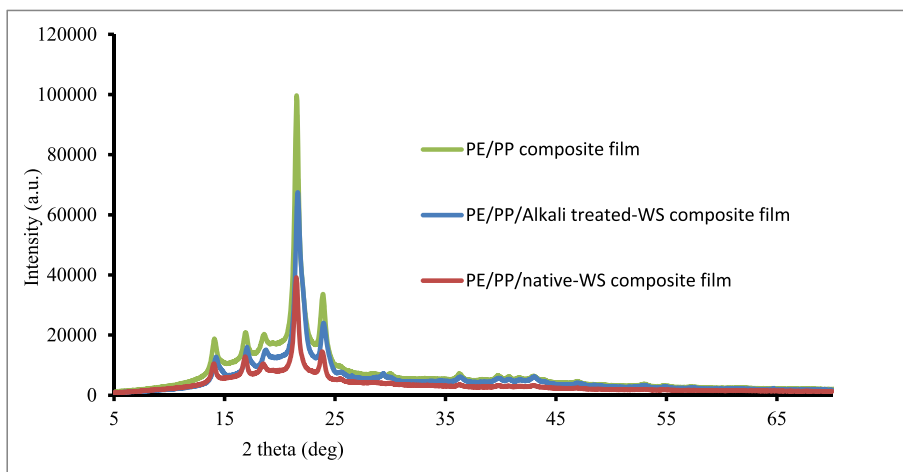


Fig. 6. XRD analysis of all polymeric composite films (a) PE/PP film (b) PE/PP/native-WS (c) PE/PP/alkali treated-WS composite films.

Acknowledgement

The authors are very thankful to Head, Department of Chemical Engineering and Technology, IIT (BHU) for providing essential facilities for different types of analysis such as XRD and SEM.

Appendix A. Supplementary data

Supplementary data to this article can be found online at <https://doi.org/10.1016/j.jclepro.2019.118228>.

References

- Abdulrahman Oyekanmi, A., Abd Latiff, A.A., Daud, Z., Saphira Radin Mohamed, R.M., Ismail, N., Ab Aziz, A., Rafatullah, M., Hossain, K., Ahmad, A., Kamoldeen Abiodun, A., 2019. Adsorption of cadmium and lead from palm oil mill effluent using bone-composite: optimisation and isotherm studies. *Int. J. Environ. Anal. Chem.* 99 (8), 707–725.
- Ayrimlis, N., Kaymakci, A., Akbulut, T., Elmas, G.M., 2013. Mechanical performance of composites based on wastes of polyethylene aluminum and lignocellulosics. *Compos. B Eng.* 47, 150–154.
- Babaei, L., Madanipour, M., Farsi, M., Farajpoor, A., 2014. Physical and mechanical properties of foamed HDPE/wheat straw flour/nanoclay hybrid composite. *Compos. B Eng.* 56, 163–170.
- Baek, Y., Kang, J., Theato, P., Yoon, J., 2012. Measuring hydrophilicity of RO membranes by contact angles via sessile drop and captive bubble method: a comparative study. *Desalination* 303, 23–28.
- Bagheri, V., Ghanbarzadeh, B., Ayaseh, A., Ostadrahimi, A., Ehsani, A., Alizadeh-Sani, M., Adun, P.A., 2019. The optimization of physico-mechanical properties of bionanocomposite films based on gluten/carboxymethyl cellulose/cellulose nanofiber using response surface methodology. *Polym. Test.* 78, 105989.
- Bajracharya, R.M., Manalo, A.C., Karunasena, W., Lau, K.-t., 2016. Characterisation of recycled mixed plastic solid wastes: coupon and full-scale investigation. *Waste Manag.* 48, 72–80.
- Bezerra, M.A., Santelli, R.E., Oliveira, E.P., Villar, L.S., Escalera, L.A., 2008. Response surface methodology (RSM) as a tool for optimization in analytical chemistry. *Talanta* 76 (5), 965–977.
- Bledzki, A.K., Mamun, A.A., Volk, J., 2010. Physical, chemical and surface properties of wheat husk, rye husk and soft wood and their polypropylene composites. *Compos. Appl. Sci. Manuf.* 41 (4), 480–488.
- Bourmaud, A., Baley, C., 2007. Investigations on the recycling of hemp and sisal fibre reinforced polypropylene composites. *Polym. Degrad. Stab.* 92 (6), 1034–1045.
- Bourmaud, A., Baley, C., 2009. Rigidity analysis of polypropylene/vegetal fibre composites after recycling. *Polym. Degrad. Stab.* 94 (3), 297–305.
- Colín-Chávez, C., Soto-Valdez, H., Peralta, E., 2014. Diffusion of carotenoids from mono and bilayer polyethylene active packaging into soybean oil. *Food Packag. Shelf Life* 1 (2), 170–178.
- da Silva, L.V., Júnior, J.H.S.A., Angrizani, C.C., Amico, S.C., 2013. Short beam strength of curaua, sisal, glass and hybrid composites. *J. Reinf. Plast. Compos.* 32 (3), 197–206.
- Díaz, S., Ortega, Z., McCourt, M., Kearns, M.P., Benítez, A.N., 2018. Recycling of polymeric fraction of cable waste by rotational moulding. *Waste Manag.* 76, 199–206.
- Dixit, S., Yadav, V.L., 2019. Comparative study of polystyrene/chemically modified wheat straw composite for green packaging application. *Polym. Bull.* 1–20. <https://doi.org/10.1007/s00289-019-02804-0>.
- Fazeli, M., Keley, M., Biazar, E., 2018. Preparation and characterization of starch-based composite films reinforced by cellulose nanofibers. *Int. J. Biol. Macromol.* 116, 272–280.
- Gamage, G.R., Park, H.-J., Kim, K.M., 2009. Effectiveness of antimicrobial coated oriented polypropylene/polyethylene films in sprout packaging. *Food Res. Int.* 42 (7), 832–839.
- Haddar, M., Elloumi, A., Koubaa, A., Bradai, C., Migneault, S., Elhalouani, F., 2018. Synergetic effect of *Posidonia oceanica* fibres and deinking paper sludge on the thermo-mechanical properties of high density polyethylene composites. *Ind. Crops Prod.* 121, 26–35.
- Hou, X., Sun, F., Yan, D., Xu, H., Dong, Z., Li, Q., Yang, Y., 2014. Preparation of lightweight polypropylene composites reinforced by cotton stalk fibers from combined steam flash-explosion and alkaline treatment. *J. Clean. Prod.* 83, 454–462.
- Islam, M.S., Pickering, K.L., Foreman, N.J., 2011. Influence of alkali fiber treatment and fiber processing on the mechanical properties of hemp/epoxy composites. *J. Appl. Polym. Sci.* 119 (6), 3696–3707.
- Jiang, H., Wei, Y., Cheng, Q., Zhu, Z., 2018. Scratch behavior of low density polyethylene film: effects of pre-stretch and aging. *Mater. Des.* 157, 235–243.
- Jo, Y., Garcia, C.V., Ko, S., Lee, W., Shin, G.H., Choi, J.C., Park, S.-J., Kim, J.T., 2018. Characterization and antibacterial properties of nanosilver-applied polyethylene and polypropylene composite films for food packaging applications. *Food Biosci.* 23, 83–90.
- Kalia, S., Vashistha, S., 2012. Surface modification of sisal fibers (Agave sisalana) using bacterial cellulase and methyl methacrylate. *J. Polym. Environ.* 20 (1), 142–151.
- Kim, S., Holtzapfel, M.T., 2005. Lime pretreatment and enzymatic hydrolysis of corn stover. *Bioresour. Technol.* 96 (18), 1994–2006.
- Laadila, M.A., Hegde, K., Rouissi, T., Brar, S.K., Galvez, R., Sorelli, L., Cheikh, R.B., Paiva, M., Abokitse, K., 2017. Green synthesis of novel biocomposites from treated cellulose fibers and recycled bio-plastic polylactic acid. *J. Clean. Prod.* 164, 575–586.
- Law, K.L., Thompson, R.C., 2014. Microplastics in the seas. *Sci* 345 (6193), 144–145.
- Leardi, R., 2009. Experimental design in chemistry: a tutorial. *Anal. Chim. Acta* 652 (1–2), 161–172.
- Liu, G., Song, Y., Wang, J., Zhuang, H., Ma, L., Li, C., Liu, Y., Zhang, J., 2014. Effects of nanoclay type on the physical and antimicrobial properties of PVOH-based nanocomposite films. *LWT - Food Sci. Technol. (Lebensmittel-Wissenschaft -Technol.)* 57 (2), 562–568.
- Lu, S.-Y., Qian, J.-Q., Wu, Z.-G., Ye, W.-D., Wu, G.-F., Pan, Y.-B., Zhang, K.-Y., 2009. Application of statistical method to evaluate immobilization variables of trypsin entrapped with sol-gel method. *J. Biochem. Technol.* 1 (3), 79–84.
- Mansor, M.R., Mustafa, Z., Fadzullah, S.H.S.M., Omar, G., Salim, M.A., Akop, M.Z., 2018. Recent Advances in Polyethylene-Based Biocomposites, Natural Fibre Reinforced Vinyl Ester and Vinyl Polymer Composites. Elsevier, pp. 71–96. <https://doi.org/10.1016/B978-0-08-102160-6.00003-2>.
- Mohamed, R., Al-Gheethi, A., Abdulrahman, A., Sainudin, M.S.b., Bakar, S.A., Kassim, A.H.M., 2018. Optimization of ceramic waste filter for bathroom grey-water treatment using central composite design (CCD). *J. Environ. Chem. Eng.* 6, 1578–1588.
- Nargotra, P., Sharma, V., Gupta, M., Kour, S., Bajaj, B.K., 2018. Application of ionic liquid and alkali pretreatment for enhancing saccharification of sunflower stalk biomass for potential biofuel-ethanol production. *Bioresour. Technol.* 267, 560–568.
- Naskar, A., Khan, H., Sarkar, R., Kumar, S., Halder, D., Jana, S., 2018. Anti-biofilm activity and food packaging application of room temperature solution process based polyethylene glycol capped Ag-ZnO-graphene nanocomposite. *Mater. Sci. Eng. C* 91, 743–753.
- Nyambo, C., Mohanty, A.K., Misra, M., 2011. Effect of maleated compatibilizer on performance of PLA/wheat Straw-Based green composites. *Macromol. Mater. Eng.* 296, 710–718.
- Oyekanmi, A.A., Ahmad, A., Hossain, K., Rafatullah, M., 2019a. Adsorption of Rhodamine B dye from aqueous solution onto acid treated banana peel: response surface methodology, kinetics and isotherm studies. *PLoS One* 14, 1–20. <https://doi.org/10.1371/journal.pone.0216878>.
- Oyekanmi, A.A., Ahmad, A., Hossain, K., Rafatullah, M., 2019b. Statistical optimization for adsorption of Rhodamine B dye from aqueous solutions. *J. Mol. Liq.* 281, 48–58.
- Panthapulakkal, S., Sain, M., 2015. The Use of Wheat Straw Fibres as Reinforcements in Composites, Biofiber Reinforcements in Composite Materials. Elsevier, pp. 423–453. <https://doi.org/10.1533/9781782421276.4.423>.
- Pereira, P.H.F., Rosa, M.d.F., Cioffi, M.O.H., Benini, K.C.C.d.C., Milanese, A.C., Voorwald, H.J.C., Mulinari, D.R., 2015. Vegetal fibers in polymeric composites: a review. *Polímeros* 25 (1), 9–22.
- Perumal, A.B., Sellamuthu, P.S., Nambiar, R.B., Sadiku, E.R., 2018. Development of polyvinyl alcohol/chitosan bio-nanocomposite films reinforced with cellulose nanocrystals isolated from rice straw. *Appl. Surf. Sci.* 449, 591–602.
- Pigatto, C., Santos Almeida Júnior, J.H., Luiz Ornaghi Júnior, H., Rodrigues, A.L., Mählmann, C.M., Amico, S.C., 2012. Study of polypropylene/ethylene-propylene-diene monomer blends reinforced with sisal fibers. *Polym. Compos.* 33 (12), 2262–2270.
- Răpă, M., Miteluş, A.C., Tănase, E.E., Grosu, E., Popescu, P., Popa, M.E., Rosnes, J.T., Sivertsvik, M., Darie-Niță, R.N., Vasile, C., 2016. Influence of chitosan on mechanical, thermal, barrier and antimicrobial properties of PLA-biocomposites for food packaging. *Compos. B Eng.* 102, 112–121.
- Razali, N.F., Mohammad, A.W., Hilal, N., Leo, C.P., Alam, J., 2013. Optimisation of polyethersulfone/polyaniline blended membranes using response surface methodology approach. *Desalination* 311, 182–191.
- Sabetzadeh, M., Bagheri, R., Masoomi, M., 2016. Effect of nanoclay on the properties of low density polyethylene/linear low density polyethylene/thermoplastic starch blend films. *Carbohydr. Polym.* 141, 75–81.
- Saha, N.R., Roy, I., Sarkar, G., Bhattacharyya, A., Das, R., Rana, D., Banerjee, R., Paul, A.K., Mishra, R., Chattopadhyay, D., 2018. Development of active packaging material based on cellulose acetate butyrate/polyethylene glycol/aryl ammonium cation modified clay. *Carbohydr. Polym.* 187, 8–18.
- Sánchez-Safont, E.L., Aldureid, A., Lagarón, J.M., Gámez-Pérez, J., Cabedo, L., 2018. Biocomposites of different lignocellulosic wastes for sustainable food packaging applications. *Compos. B Eng.* 145, 215–225.
- Satopathy, M.K., Das, P., 2014. Optimization of crystal violet dye removal using novel soil-silver nanocomposite as nanoadsorbent using response surface methodology. *J. Environ. Chem. Eng.* 2 (1), 708–714.
- Semanová, J., Sklářsová, B., Šimon, P., Šimko, P., 2016. Elimination of polycyclic aromatic hydrocarbons from smoked sausages by migration into polyethylene packaging. *Food Chem.* 201, 1–6.
- Simmons, L., Tsuchiya, K., Numata, K., 2016. Chemoenzymatic modification of silk fibroin with poly (2, 6-dimethyl-1, 5-phenylene ether) using horseradish peroxidase. *RSC Adv.* 6 (34), 28737–28744.
- Sirviö, J.A., Kolehmainen, A., Liimatainen, H., Niinimäki, J., Hormi, O.E., 2014. Biocomposite cellulose-alginate films: promising packaging materials. *Food Chem.* 151, 343–351.

- Tan, I., Ahmad, A., Hameed, B., 2008. Optimization of preparation conditions for activated carbons from coconut husk using response surface methodology. *Chem. Eng. J.* 137 (3), 462–470.
- Tănase, E.E., Popa, M.E., Răpă, M., Popa, O., 2015. PHB/Cellulose fibers based materials: physical, mechanical and barrier properties. *Agric. Agric. Sci. Procedia* 6, 608–615.
- Tang, C.Y., Kwon, Y.-N., Leckie, J.O., 2009. Effect of membrane chemistry and coating layer on physiochemical properties of thin film composite polyamide RO and NF membranes: I. FTIR and XPS characterization of polyamide and coating layer chemistry. *Desalination* 242 (1–3), 149–167.
- Thakur, V.K., Thakur, M.K., Gupta, R.K., 2014. Raw natural fiber-based polymer composites. *Int. J. Polym. Anal. Charact.* 19 (3), 256–271.
- Tsuchiya, K., Ifuku, N., Koyama, Y., Numata, K., 2019. Development of regenerated silk films coated with fluorinated polypeptides to achieve high water repellency and biodegradability in seawater. *Polym. Degrad. Stab.* 160, 96–101.
- Wu, L.-B., Su, Q.-Z., Lin, Q.-B., Peng, W.-D., Chen, C.-F., Wang, Z.-W., Hu, C.-Y., 2017. Impact of migration test method on the release of silver from nanosilver-polyethylene composite films into an acidic food simulant. *Food Packag. Shelf Life* 14, 83–87.
- Xiangli, F., Wei, W., Chen, Y., Jin, W., Xu, N., 2008. Optimization of preparation conditions for polydimethylsiloxane (PDMS)/ceramic composite pervaporation membranes using response surface methodology. *J. Membr. Sci.* 311 (1–2), 23–33.
- Xie, J., Hung, Y.-C., 2018. UV-A activated TiO₂ embedded biodegradable polymer film for antimicrobial food packaging application. *LWT* 96, 307–314.
- Yang, S.-T., El-Ensashy, H., Thongchul, N., 2013. *Bioprocessing Technologies in Biorefinery for Sustainable Production of Fuels, Chemicals, and Polymers*. John Wiley & Sons.
- Zegaoui, A., Derradji, M., Ma, R.-k., Cai, W.-a., Medjahed, A., Liu, W.-b., Dayo, A.Q., Wang, J., Wang, G.-x., 2018. Influence of fiber volume fractions on the performances of alkali modified hemp fibers reinforced cyanate ester/benzoxazine blend composites. *Mater. Chem. Phys.* 213, 146–156.
- Zeng, Q., Yu, A., Lu, G., Paul, D., 2005. Clay-based polymer nanocomposites: research and commercial development. *J. Nanosci. Nanotechnol.* 5 (10), 1574–1592.
- Zhao, X., Ji, K., Kurt, K., Cornish, K., Vodovotz, Y., 2019. Optimal mechanical properties of biodegradable natural rubber-toughened PHBV bioplastics intended for food packaging applications. *Food Packag. Shelf Life* 21, 100348.

Relation Classification: How well do Neural Network Approaches Work?

Sri Nath Dwivedi¹[0000-1111-2222-3333], Harish Karnick^{2,3}[1111-2222-3333-4444], and Renu Jain³[2222--3333-4444-5555]

¹ AITH, Kanpur

² IIT, Kanpur srinath.vedi@gmail.com

³ UIET, Kanpur

hk@iitk.ac.in, jainrenu@gmail.com

Abstract. Relation classification is a well known task in NLP. It classifies relations that occur between two entities in sentences by assigning a label from a pre-defined set of abstract relation labels. A benchmark data set for this task is the SemEval-2010 Task 8 data set. Neural network approaches are currently the methods that give state-of-art results on a wide range of NLP problems. There is also the claim that the models trained on one task carry over to other tasks with only a small amount of fine tuning. Our experience suggests that for the relation classification problem while a wide variety of neural network methods work reasonably well it is very hard to improve performance significantly by including different kinds of syntactic and semantic information that intuitively should be important in signalling the relation label. We think that improved performance will be hard to achieve without injecting controlled class specific semantic information into the classification process.

In our experimentation we have given many different kinds of syntactic and semantic information by tagging suitable words with relevant semantic/syntactic tags. We have also tried various embedding methods like Google embeddings, FastText, Word-to-vec and BERT. None of these make a substantial difference in the performance which hovers between 82% to 85%.

Surprisingly, when we looked at the top three classification performance it was above 96% that is 11 to 14 percent above the top one performance. This implies that it should be possible to boost the correct label from the second or third position to the first position by suitable semantic inputs and architectural innovations. We have experimented with an architecture that gives supplementary information about words in the sentence as well as the sentence itself in parallel with the main stream of information, namely the sentence itself. In one such case we are able to boost performance to state-of-art levels. A systematic investigation is ongoing.

1 Introduction

Relation classification identifies the type of relationship that exists between two given entities in a sentence - we consider only binary relationships. The type of this relationship depends on other words present in the sentence and more generally on the meaning that the sentence is trying to convey. Sentences usually have multiple entities and a single entity can be related to multiple other entities in the sentence. The type of this relation

can be different in each case. So, in relation classification data sets it is necessary to mark the two entities whose relation is to be classified. The reason relation classification can be an interesting and challenging problem is the types of relation labels that are specified. The relation labels can be abstract, directed and there can be subtle differences between two or more labels that often depend on the meaning of the entire sentence. One such well known data set is the SEMEVAL-2010 Task 8 data set (henceforth Semeval data set). The Semeval data set has 9 bi-directional relations (giving 18 actual labels) and a nineteenth catch all label OTHER where none of the other eighteen labels are appropriate. The data set was labelled by human volunteers who were given detailed instructions for each label type.

From inspection of the Semeval data set it is clear that the relation type can often depend on linguistic markers like *is-x*, *x-of*, *in-x*, *from-x to-y*, *caused* (prepositions, verbs and nouns) that are proximate to the entities and/or the relation word(s). But in several cases the relation type is sensitive to the overall meaning of the sentence which implies that words distant from the entities and/or relation word influence the label type. We consider some examples below:

1. *The <e1> singer </e1>, who performed three of the nominated songs, also caused a <e2> commotion </e2> on the red carpet.* Relation label: Cause-Effect(e1, e2).
2. *The <e1> radiation </e1> from the atomic <e2> bomb explosion </e2> is a typical acute radiation.* Relation label: Cause-Effect(e2, e1). Clashes with Entity-Origin(e1, e2).
3. *A person infected with a <e1>flu</e1> <e2>virus</e2> strain develops antibodies against the virus.* Relation label: Cause-Effect(e2, e1).
4. *A person infected with a <e1>Corona</e1> <e2>virus</e2> strain develops antibodies against it.* Relation label: OTHER (Given by the authors based on labelling guidelines).
5. *A volunteer injected, during the phase-2 trials in India started by Oxford and AstraZeneca, with a <e1>flu</e1> <e2>vaccine</e2> developed antibodies against it.* Relation label: OTHER (Given by authors based on labelling guidelines).

The first three sentences are from the data set or guideline documents. The last two were created and labelled by the authors using the guidelines. It is clear that words like *caused* in example 1 and *from* in example 2 signal the type of the relation. However, note that due to the labelling guidelines example 2 has been labelled Cause-Effect(e2, e1) because specifically radiation, light or heat is in the negative list for Entity-Origin. Otherwise the word *from* often signals an Entity-Origin relation. There are many such exceptions or subtleties in the labelling guidelines. Examples 3, 4 and 5 show why it can be hard to label correctly. One can argue that *flu* qualifies/ describes/ elaborates the word *virus* and *vaccine* in examples 3 and 5 respectively much as the word *Corona* does in example 4. While *flu* is caused by a *virus* in the context of the sentence the relation between *flu* and *virus* is better interpreted as one where *flu* is a qualifier or descriptor of the *virus* instead of *virus* being a cause of the *flu*. But the guidelines mean that example 3 is classified as Cause-Effect while in an almost identical looking sentence, example 4, the relation will be OTHER. The label set does not contain a label such as Entity-Descriptor or Entity-Qualifier. Example 5 shows how a very similar sentence (the relative clause is a garden path merely to increase the distance between *injected* and the entities) can never

be classified as Cause-Effect in spite of being structurally similar and having significant overlap with example 3. The point is that both the relation types and the guidelines that specify certain subtle semantic differences and exceptions that give a contra or pro indication for a label are at least slightly arbitrary.

The interesting question is whether task agnostic neural network approaches work well in such settings and if yes how well do they work and what do the results indicate.

For example, *New Delhi is the capital of India*. In this sentence *New Delhi* and *India* are the two entities that are related by *is-capital-of* giving the relation *is-capital-of(Delhi, India)*. There are many relational linguistic markers like *is-x*, *x-of*, *in-x*, *from-x to-y*, *caused* etc. that often signal the presence of a relation and also indicate the type of the relation.

We have seen that relation types are influenced by specific words that are proximate to the entities and relation words as well as by the overall meaning of the sentence that is sensitive to words that are distant. So, it is plausible that a neural network architecture with some kind of combination of a convolutional neural network and a recurrent neural network should be able to learn such relational dependencies between the two entities. Consequently, there is a reasonably large body of work that has used a wide variety of neural networks to do relation classification. A benchmark data set used for this is SemEval-2010 Task 8. Table 1 shows the top results from various such attempts since mid 2016 and we see that the F1 values have ranged between approximately 87% and 90%. The current best performance is 90.2%. The top performers include rather specialized networks and performance enhancing tweaks. We are more interested in seeing whether simple class specific semantic information can be encoded in these networks to enhance performance.

2 Related Work

In this section we briefly review the work on relation classification.

[31] proposed an RNN (Recurrent Neural Network) model and averaged model parameters to stabilize learning and improve generalization. They achieved an F1 score of 79.40%. This work was based on earlier work in [18], [27]. [4] used an LSTM network and shortest dependency paths to get an F1 of 83.7%. [5] used a combination of RNN, CNN and attention and got an F1 of 83.7%. [26] used attention in LSTMs to get an F1 of 84.0%. [25] classified relations via ranking and achieved an F1 of 84.10%. [2] used a CNN (Convolutional Neural Network), incorporated shortest dependency paths and used negative sampling for subjects and objects and achieved an F1 of 85.4%. [3] compared RNNs and CNNs and claimed RNNs work better than CNNs. What is evident from the above is that a wide variety of neural network architectures and addition of basic linguistic information like part-of-speech, dependencies, etc. do not substantially change performance.

We now review more recent work that tries to inject more specific ‘semantic’ information into the model learning process.

[6] used a GCN (Graphical CNN) along with extra information from a knowledge base. [24] claimed that entities participating in a relation influence its type more than the high-level linguistic information obtained through NLP tools. It used an end-to-end

RNN incorporating an entity aware attention mechanism with a latent entity typing method. [23] [TRE] combined unsupervised and supervised learning to improve relation classification. A Transformer for relation extraction (TRE) makes use of pre-trained deep language representations instead of using explicit linguistic features of the language. It is combined with a self-attentive Transformer architecture to model long range dependencies between entities. [14] [Att-Pooling-CNN] uses a CNN with entity-specific and relation-specific attention helping the model to learn what is more relevant for a given classification. [22] [Entity-Aware BERT] was built on top of pre-trained self-attentive models to identify the positions of the entities and used Bidirectional Encoder Representations from Transformers (BERT) as the transformer-based encoder. [21] [KnowBert-W+W] incorporated contextual word knowledge from knowledge bases (KBs) consisting of high quality, human-curated knowledge rather than using unstructured, unlabeled text. They have presented a general method to insert multiple KBs into a large pre-trained model with a Knowledge Attention and Re contextualization (KAR) mechanism that is inserted between two layers of a pre-trained model like BERT. [20] [R-BERT] incorporated entity-level information like location of entities, marking the entities as first and second into a pre-trained BERT language model to improve relation classification. [19] [BERTEM+MTB] developed models that produced task agnostic relation representations using entity-linked text and learnt mappings from relation statements to relation representations. [29] [EP GNN] used an entity pair graph to represent the correlations between entity pairs and implemented an entity pair based CNN model. In the above methods, semantic guidance is being provided by emphasizing entities and/or relations in some way and also by incorporating extra knowledge via KBs or from unsupervised corpora processed in specific ways. The results obtained are summarized in table 1.

3 Baseline

For our work we used the models described in [1] as the baseline. The basic model has two layers consisting of a CNN layer and a Bidirectional Gated Recurrent Unit (Bi-GRU) layer. GoogleNews-vectors-negative300 were used and three different models of the two layer architecture were constructed for the models that used fusion. These models were:

1. CBGRU-ME: contains a CNN layer, a Bi-GRU layer, max pooling and entity pooling.
2. CBGRU-A: is the same as the previous model except that instead of max pooling and entity pooling attention pooling is used.
3. CBGRU-MEA: is a combination of the previous two models that is CNN, Bi-GRU layers, max pooling, entity pooling and attention pooling. This is the model that has been used.

The architecture is shown in figure 1. Two methods were used for fusing the results from the three models: a) a voting scheme where the winning label had the highest number of votes and b) summing softmax probabilities of each classifier where the winning label had the highest summed probability. The performance details of the different individual models and the two models that use model fusion can be found in [1]. We use the voting model with a performance of 83.70%(F1) as our baseline. So, we have a strong baseline.

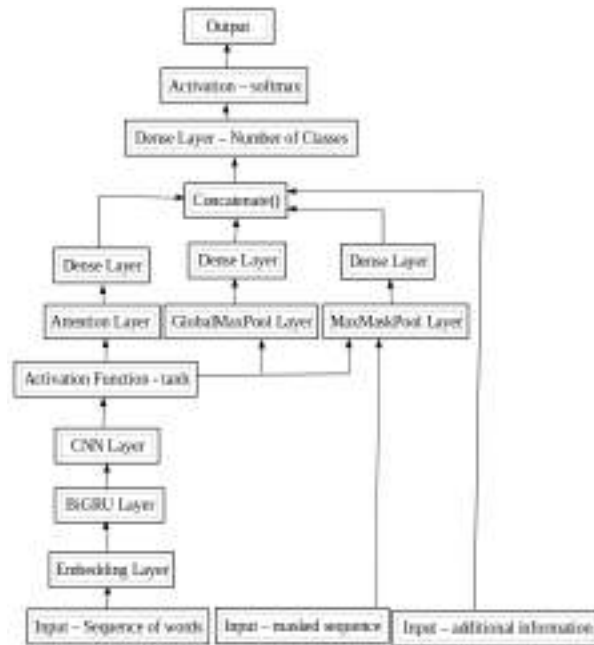


Fig. 1. Architecture Diagram

4 Experiments

Our objective was to improve the accuracy of the baseline system used for relation classification by introducing simple class specific ‘semantic’ guidance in the form of extra information that can be easily computed from the learning set itself. A series of experiments were performed to examine the effects on the accuracy of a standard model of a CNN and Bi-GRU neural network by inserting different types of syntactic and semantic information. The process of experimentation involved 4 steps: 1. Identifying the types of linguistic information that plays an important role in relation classification 2. Extracting that information from the given dataset either by using available NLP tools or implementing statistical approaches. 3. Exploring different methods to insert the extracted linguistic information in the training and testing data 4. Running the model and compare the accuracy of models. To compare the performances of various experiments, a base experiment where only the entities were marked was taken and the accuracy of this was 83.70%.

4.1 Experiments after the inclusion of English specific linguistic knowledge:

First Experiment:

Experience with the English language suggests that verbs, prepositions and nouns representing entities are strong indicators of the type of relation that exists between

Rank	Method	F1	Reference	Year
1	RESIDE	84.0	[6]	2018
2	Entity Attention Bi-LSTM	85.2	[24]	2019
3	TRE	87.1	[23]	2019
4	Att-Pooling-CNN	88.0	[14]	2016
5	Entity-Aware BERT	89.0	[22]	2019
6	KnowBert-W+W	89.1	[21]	2019
7	R-BERT	89.25	[20]	2019
8	BERTEM + MTB	89.5	[19]	2019
9	EP GNN	90.2	[29]	2019

Table 1. Performance of recent models

the entities in a sentence. To reconfirm this, a few sentences of each relation were examined manually and it appeared that prepositions and a few specific kind of main verbs play an important role in many relations and can be treated as a strong clue to the type of the relation. However, it was observed that prepositions either attached to the main verb of the sentence or attached to the second entity play a significant role in relation classification though many times this clue is ambiguous and indicate two or three relations instead of a single relation. We calculated different class specific statistics for words and created a list of the top N prepositions arranged in descending order of highest occurrence statistics for each relation class. Then for each sentence, in that relation class, the top ranked preposition word in the sentence was tagged with the semantic begin-end tags. These newly tagged sentences formed the learning set for training a standard CBGRU-MEA model. Relation based tagging was done in the training data set through an algorithm and in the test data, all prepositions were tagged. The accuracy achieved was only around 80%. A detailed analysis of miss-classified sentences showed that around 50% sentences of type OTHER were misclassified due to the occurrence of prepositions in these sentences making the system classify them into one of the more specific relation types.

4.2 Second Experiment:

It is known that most of the time, the type and the action denoted by the main verb of any sentence defines the relationship of its subject and object entities present in the sentence. Hence, we experimented by putting emphasis on the verb relation in the sentence. To extract the relation verb, knowledge graph and NLTK tools were used and then the training as well as testing data were tagged by introducing special markers. The accuracy achieved was 84.37% which was a slight improvement over the base level but not significant.

Another similar experiment was done by finding the shortest dependency path (SDP) between the marked entities. We thought SDP contained enough information between the two entities to identify their relationship. We used SpaCy to find the SDP of a sentence. The SDP information was added in training and as well as during testing and the accuracy achieved was 82.84% which was again very close to base level.

4.3 Third Experiment: Adding Syntactical Category of each word:

Each sentence of training data and testing data was parsed using NLTK tools to get the syntactic category of each word and then the part of speech of each word was attached with the word to check the effect of adding word level syntactical information. The accuracy achieved was 84.51% which was again slightly higher than the base model.

Fourth Experiment: After adding syntactic information, we also added some semantic information for entities and the main verb of the sentence. This was done with the help of Wordnet semantic tags representing a class of nouns and verbs. But, again there was no improvement.

In addition to this, many other experiments were performed like marking higher frequency verbs and nouns, increasing the training data set by adding more sentences by using the hyponyms of each entity word and the main verb, etc. but the accuracy did not improve as expected.

4.4 Using different word embeddings:

For the base line models, Google embeddings of size 300 were used. However, it was observed that there are many words for which Google embeddings are not available and so the Google average embedding had to be used for all such words. To avoid the average embedding, we generated embeddings using FastText and WordtoVec but found that the accuracy of the model went down slightly instead of improving. We also used the BERT word vector representation (of 768 size) and the results obtained were comparable to those from the Google embeddings. Hence, we concluded that Google embeddings could be used in future experiments.

4.5 Experiments by taking Top 3 choices:

We tried tagging some sentences manually using the Semeval Task 8 guidelines and found that in many instances, it was very difficult even for us to distinguish between two similar types of relations. For example, Content-Container or Component-Whole and several other pairs like Entity-Origin, Cause-Effect. This has been elaborated in the introduction. Therefore, we set the system to output top 3 choices identified by the system and then checked whether the top 3 choices contained the correct label or not. To our surprise the accuracy was 96.55% which was very encouraging. This meant that the system had to learn to distinguish the right type from a very limited set of possible types.

5 Data Set, Experiments and Results

The SemEval-2010 Task 8 data set has 9 categories and an *OTHER* category for relations that do not belong to any of the nine (giving a total of 10 categories). Since each relation is a binary relation the entity order matters, so if R is the relation and e_1, e_2 are

Expt. No.	Semantic input	Tagging Status	F1 score
a)	None	Entities	83.70%
b)	Class based prepositions	Entities and prepositions	80.38%
c)	Relation Verb	Entities and Relation Verb	84.37%
d)	Shortest Dependency Path	Entities and Relation word	82.84%
e)	Part Of Speech	Entities and POS of every word	84.89%
f)	Hyponyms	Entities	82.21%
g)	Semantic Information of entities and verb	Entities and semantic tags	82.78%
h)	Top 3 tags	Entities	90.64%

Table 2. Table: Experiment Results

entities $R(e_1, e_2)$ and $R(e_2, e_1)$ are different relations unless R is symmetric. None of the SemEval-2010 Task 8 relations, not including *OTHER*, is symmetric. So, there are $9 \times 2 + 1 = 19$ class labels.

Only 9 classes (order agnostic) were used to calculate the statistic for words that were semantically tagged.

There are 8000 sentences for training and 2717 sentences for testing. Each sentence has two entities marked by entity start and end tags. It also has a relation label indicating the type of relation between the tagged entities.

Experimentation is still in its early stages. We report results on eight experiments in the form of table below. Our best result which matches the state-of-art is obtained using a two stage network by giving the top 3 labels obtained from the standard CNN-BiGRU classifier as additional input while training a second stage classifier. This has given us an F1 score of 90.64%. These are early results and need to be confirmed with more extensive experimentation on the Semeval and other data sets.

6 Discussion and Conclusions

We saw that vanilla neural network methods work reasonably well reaching an F1 score close to the mid eighties. However, adding various kinds of specific syntactic and/or semantic information to the neural network does not significantly change performance. At the same time the top-3 performance is significantly better - almost 12% better - reaching 96.55% using just the baseline architecture. We hypothesized that it should be possible to teach the network to distinguish the top label when it is present in the top-3. Our initial attempt did this by training a two stage network where in the second stage the network is trained with the top 3 labels as input and we got a state-of-art performance of 90.64%. We think a systematic and controlled way to add very specific semantic information in parallel should be able to help improve classification performance. We saw that a two stage model that first learns to predict the top three labels and then separately learns to choose the correct label from the top 3 performs surprisingly well.

7 Acknowledgement

I would like to express my gratitude to Sahitya Patel, M.Tech, IIT Kanpur and Pawan Kumar, Ph.D student of IIT Kanpur. They were very helpful and provided me technical support required for the experiments.

Bibliography

- [1] Sahitya Patel: Multi-Way Classification of Relations Between Pairs of Entities, IIT Kanpur MTech thesis (2018)
- [2] Xu, Kun and Feng, Yansong and Huang, Songfang and Zhao, Dongyan: Semantic relation classification via convolutional neural networks with simple negative sampling. arXiv preprint(2015). arXiv:1506.07650
- [3] Zhang, Dongxu and Wang, Dong: Relation classification via recurrent neural network arXiv preprint(2015). arXiv:1508.01006
- [4] Yan, Xu and Mou, Lili and Li, Ge and Chen, Yunchuan and Peng, Hao and Jin, Zhi: Classifying relations via long short term memory networks along shortest dependency path. arXiv preprint (2015). arXiv:1508.03720
- [5] Zhang, Xiaobin and Chen, Fucui and Huang, Ruiyang: A combination of RNN and CNN for attention-based relation classification. journal: Procedia computer science, volume: 131, pages: 911–917, year: 2018, publisher: Elsevier
- [6] Vashishth, Shikhar and Joshi, Rishabh and Prayaga, Sai Suman and Bhattacharyya, Chiranjib and Talukdar, Partha: Reside: Improving distantly-supervised neural relation extraction using side information. journal: arXiv preprint arXiv:1812.04361, year: 2018
- [7] Cho, Kyunghyun and Van Merriënboer, Bart and Gulcehre, Caglar and Bahdanau, Dzmitry and Bougares, Fethi and Schwenk, Holger and Bengio, Yoshua: Learning phrase representations using RNN encoder-decoder for statistical machine translation. journal: arXiv preprint arXiv:1406.1078, year: 2014.
- [8] Kim, Jonggu and Lee, Jong-Hyeok: Multiple range-restricted bidirectional gated recurrent units with attention for relation classification. journal: arXiv preprint arXiv:1707.01265, year: 2017
- [9] Liu, Yang and Wei, Furu and Li, Sujian and Ji, Heng and Zhou, Ming and Wang, Houfeng: A dependency-based neural network for relation classification. journal: arXiv preprint arXiv:1507.04646, year=2015.
- [10] Miwa, Makoto and Bansal, Mohit: End-to-end relation extraction using lstms on sequences and tree structures. journal: arXiv preprint arXiv:1601.00770, year: 2016
- [11] Nguyen, Thien Huu and Grishman, Ralph: Combining neural networks and log-linear models to improve relation extraction. journal: arXiv preprint arXiv:1511.05926, year: 2015
- [12] Qin, Pengda and Xu, Weiran and Guo, Jun: An empirical convolutional neural network approach for semantic relation classification. journal: Neurocomputing, volume: 190, pages: 1–9, year: 2016, publisher: Elsevier
- [13] Vu, Ngoc Thang and Adel, Heike and Gupta, Pankaj and Schütze, Hinrich: Combining recurrent and convolutional neural networks for relation classification. journal: arXiv preprint arXiv:1605.07333, year: 2016.
- [14] Wang, Linlin and Cao, Zhu and De Melo, Gerard and Liu, Zhiyuan: Relation classification via multi-level attention cnns. publisher: Tsinghua University, Beijing, year=2016.

- [15] Xu, Kun and Feng, Yansong and Huang, Songfang and Zhao, Dongyan: Semantic relation classification via convolutional neural networks with simple negative sampling. journal: arXiv preprint arXiv:1506.07650, year=2015
- [16] Xu, Yan and Jia, Ran and Mou, Lili and Li, Ge and Chen, Yunchuan and Lu, Yangyang and Jin, Zhi: Improved relation classification by deep recurrent neural networks with data augmentation. journal: arXiv preprint arXiv:1601.03651, year: 2016.
- [17] Yan, Xu and Mou, Lili and Li, Ge and Chen, Yunchuan and Peng, Hao and Jin, Zhi: Classifying relations via long short term memory networks along shortest dependency path. journal: arXiv preprint arXiv:1508.03720, year: 2015.
- [18] Blunsom, Phil and Hermann, Karl Moritz: The Role of Syntax in Vector Space Models of Compositional Semantics. year: 2013.
- [19] Soares, Livio Baldini and FitzGerald, Nicholas and Ling, Jeffrey and Kwiatkowski, Tom: Matching the Blanks: Distributional Similarity for Relation Learning. journal: arXiv preprint arXiv:1906.03158, year: 2019.
- [20] Wu, Shanchan and He, Yifan: Enriching Pre-trained Language Model with Entity Information for Relation Classification. journal: arXiv preprint arXiv:1905.08284, year: 2019.
- [21] Peters, Matthew E and Neumann, Mark and Logan, IV and Robert, L and Schwartz, Roy and Joshi, Vidur and Singh, Sameer and Smith, Noah A: Knowledge Enhanced Contextual Word Representations. journal: arXiv preprint arXiv:1909.04164, year: 2019.
- [22] Wang, Haoyu and Tan, Ming and Yu, Mo and Chang, Shiyu and Wang, Dakuo and Xu, Kun and Guo, Xiaoxiao and Potdar, Saloni: Extracting Multiple-Relations in One-Pass with Pre-Trained Transformers. journal: arXiv preprint arXiv:1902.01030, year: 2019.
- [23] Alt, Christoph and Hübner, Marc and Hennig, Leonhard: Improving relation extraction by pre-trained language representations. journal: arXiv preprint arXiv:1906.03088, year: 2019.
- [24] Lee, Joohong and Seo, Sangwoo and Choi, Yong Suk: Semantic Relation Classification via Bidirectional LSTM Networks with Entity-Aware Attention Using Latent Entity Typing. journal: Symmetry, volume: 11, number: 6, pages: 785, year: 2019, publisher: Multidisciplinary Digital Publishing Institute
- [25] Santos, Cicero Nogueira dos and Xiang, Bing and Zhou, Bowen: Classifying relations by ranking with convolutional neural networks. arXiv preprint (2015). arXiv:1504.06580
- [26] Zhou, Peng and Shi, Wei and Tian, Jun and Qi, Zhenyu and Li, Bingchen and Hao, Hongwei and Xu, Bo: Attention-based bidirectional long short-term memory networks for relation classification. In: 54th Annual Meeting. on Proceedings, (Volume 2: Short Papers), pages207–212,. Association for Computational Linguistics, (2016).
- [27] Socher, Richard and Huval, Brody and Manning, Christopher D and Ng, Andrew Y: Semantic compositionality through recursive matrix-vector spaces. In: Proceedings of the 2012 joint conference on empirical methods in natural language processing and computational natural language learning. on Proceedings, organization: Association for Computational Linguistics, year: 2012.

- [28] Socher, Richard and Bauer, John and Manning, Christopher D and Ng, Andrew Y: Parsing with compositional vector grammars. In: 51st Annual Meeting. on Proceedings, Association for Computational Linguistics (Volume 1: Long Papers), pages=455–465, year=2013.
- [29] Zhao, Yi and Wan, Huaiyu and Gao, Jianwei and Lin, Youfang: Improving Relation Classification by Entity Pair Graph. In: Asian Conference on Machine Learning, pages: 1156–1171, year: 2019.
- [30] Wang, Linlin and Cao, Zhu and De Melo, Gerard and Liu, Zhiyuan: Relation classification via multi-level attention cnns. In: 54th annual meeting. on Proceedings, Association for Computational Linguistics (volume 1: long papers), pages: 1298–1307, year: 2016
- [31] Hashimoto, Kazuma and Miwa, Makoto and Tsuruoka, Yoshimasa and Chikayama, Takashi: Simple customization of recursive neural networks for semantic relation classification. In: Conference on Preceedings, Empirical Methods in Natural Language Processing, pages=1372–1376, year=2013
- [32] Cai, Rui and Zhang, Xiaodong and Wang, Houfeng: Bidirectional recurrent convolutional neural network for relation classification. In: the 54th Annual Meeting on Preceedings, the Association for Computational Linguistics (Volume 1: Long Papers) pages: 756–765, year: 2016.
- [33] Qin, Pengda and Xu, Weiran and Guo, Jun: Designing an adaptive attention mechanism for relation classification. In: 2017 International Joint Conference on Neural Networks (IJCNN), pages: 4356–4362, year: 2017, organization: IEEE.
- [34] Manning, Christopher and Surdeanu, Mihai and Bauer, John and Finkel, Jenny and Bethard, Steven and McClosky, David: The Stanford CoreNLP natural language processing toolkit. In: 52nd annual meeting on Proceedings, the association for computational linguistics: system demonstrations. pages: 55–60, year: 2014
- [35] Yu, Mo and Gormley, Matthew and Dredze, Mark: Factor-based compositional embedding models. In: NIPS Workshop on Learning Semantics, on Proceedings, pages: 95–101, year: 2014.
- [36] Sahitya Patel, <http://172.28.64.70:8080/jspui/handle/123456789/17624>

Protein Characterization at atomic level: A Novel approach for sequence analysis

Parul Johri^{1*}, Mala Trivedi¹, Drishti Srivastava¹, Aman Kumar¹ Singh and Mohammed Haris Siddiqui²

¹Amity Institute of Biotechnology, Amity University Uttar Pradesh, Lucknow Campus, Malhaur, Gomti Nagar Extension, Lucknow, Uttar Pradesh, India

²Department of Bioengineering, Integral University Lucknow Uttar Pradesh, India

* Corresponding Author: pjohri@lko.amity.edu; +91 9838144680

Abstract

Carbon being the most omnipresent element in all the organic compounds is of great importance with regards to its structure and function. The fundamental structure of protein is composed of amino acids arranged in linear chain and folded to a globular form. All twenty amino acids consist of combination of only five different atoms that are Carbon, Nitrogen, Oxygen, Hydrogen and Sulphur. Depending on the property of their side chain the amino acids are classified as hydrophobic and hydrophilic. The allocation of the hydrophobic residue in a protein contributes majorly towards protein folding, protein interaction, active site formation and other biological functions. As carbon is the most important element which contributes to hydrophobic interaction in proteins, the hydrophobic amino acids characteristically have greater number of carbon atoms. In the present study, we have analyzed 4,306 protein sequences of *Escherichia coli*, a gram negative, facultative anaerobic, rod shaped bacterium. All the protein sequences of *Escherichia coli* were scanned to get a profound view on carbon content and its distribution. The sequences were retrieved from proteome section of UniprotKB (<http://www.uniprot.org/uniprot/>) database and atomic percentages were calculated with the aid of a dynamic programming algorithm and Microsoft Excel. The analysis of the atomic percentages calculated for the proteins revealed that there is a precise range of carbon percentage for all the *Escherichia coli* proteins

(30%-33% carbon). Also the different categories of protein like transport protein, repressor protein, catalytic protein, inhibitory protein etc have discrete range of carbon percentages which could be further linked to their exact activity

Keyword : Carbon, *E. Coli*, dynamic programming, proteins.

Introduction:

Proteins make almost 50% of the dry weight of the cells and are present in profound amount, than any other biomolecules. Proteins are basically organic compounds composed of amino acids arranged in linear chain and folded to a globular form (1). All 20 amino acids consist of combinations of only five different atoms Carbon, Nitrogen, Hydrogen, Sulphur, Oxygen. Depending on the properties of their side chains, the amino acids are classified as hydrophobic and hydrophilic (2; 3; 4). The distribution of hydrophobic residues in a protein contributes majorly towards protein folding, protein interactions, formation of core, active site formation and other biological functions (5).

Materials and Methods:

A hydropathy plot maps the hydrophobic regions against the hydropathy indices of the amino acids in the protein. It gives a clear idea of level of hydrophobicity in a protein. The hydrophobicity and carbon distribution profile of a protein is studied with help of a hydropathy plot (Fig. 1 and Fig. 2). In the carbon distribution profile

obtained, it was possible to locate the hydrophobic, hydrophilic and also the active sites in the protein. The hydropathy plot does not give information on the active sites of a protein (6; 7; 8; 9). So it was postulated that the carbon distribution profile is a better alternative to hydropathy plot.

Escherichia coli, a gram negative, facultative anaerobic, rod shaped bacterium was the model

organism used by us in our study. The entire project commenced by the retrieval of protein sequences of *Escherichia coli* from the public repository of protein sequences i.e UniprotKB database(<http://www.uniprot.org/uniprot/>). There were 4,306 protein sequences of *Escherichia coli*(strain K12) present in the proteome section of the database. Each and every sequence was scanned by us using the script written in perl

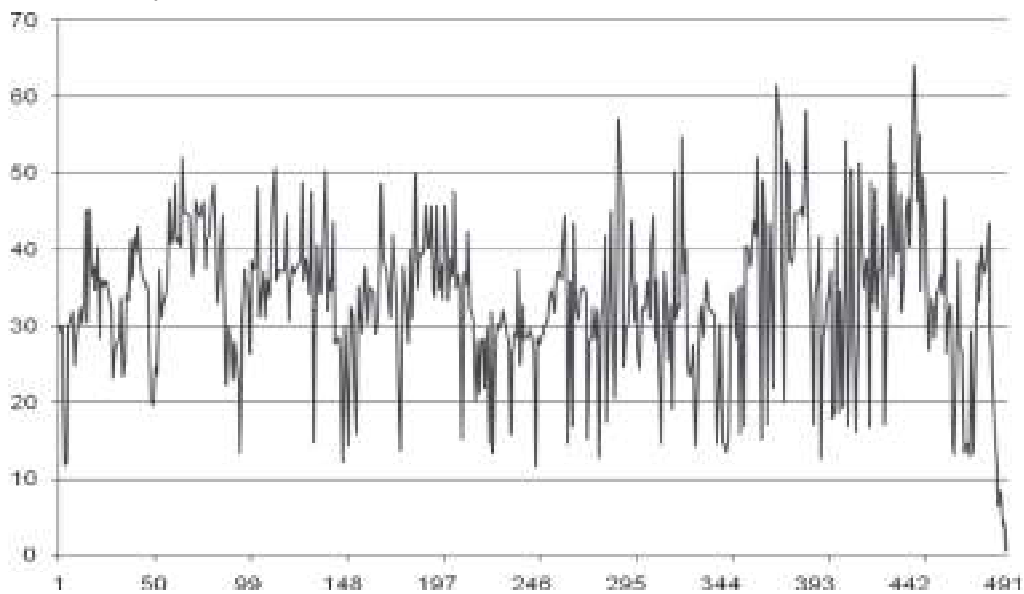


Fig. 1: Carbon distribution plot for GLUT1

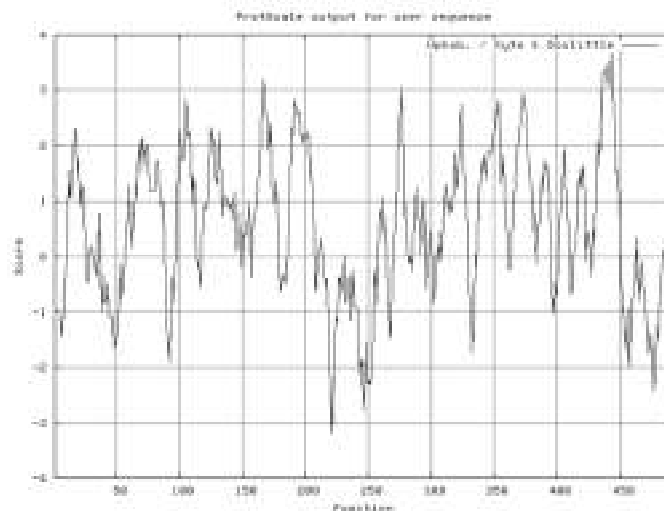


Fig. 2: Hydropathy plot from ProtScale for GLUT1

programming based on the dynamic algorithm designed (Fig. 3) (10; 11; 12; 13). So the atomic composition of each and every protein sequence was extracted and were formulated into the excel sheet. After that the respective percentage of carbon was calculated on basis of number of carbon atoms and number of total atoms present in every protein sequences.

Proteins were also classified into broad categories on basis of their function like transport protein, catalytic protein, regulatory protein etc.

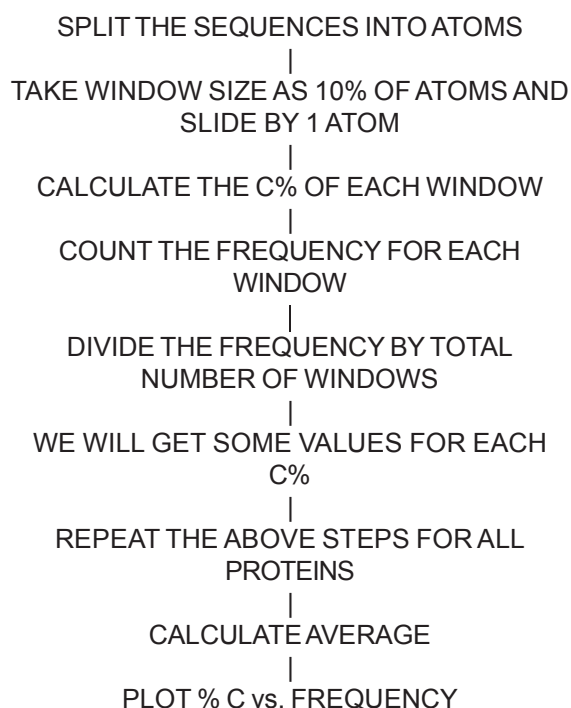


Fig. 3: Flow chart for the dynamic programming algorithm

The scrutiny of the atomic percentages calculated for the proteins revealed that there is a specific range of carbon percentage for all the *Escherichia coli* proteins that is 30%-33%. Broad classification of proteins also showed that all proteins strictly followed the range.

Results and Discussion:

We got amazing results from our research work. Carbon percentages in all the protein

sequences lied between 30%-33% no matter which types of amino acids where present in protein sequences (Table 1). So we can conclude that on the basis of carbon atoms, demarcation can be done. And after analyzing the carbon content in every proteins, percentages of other components can be taken out and studied for further uses. The atomic level analysis of the protein sequence does lead to a new venture of scrutiny of many long stranded questions.

The arenas of molecular biology, pharmacy, drug designing, enzymology, proteomics and many other fields including genomics and phylogenetic are wedged on certain facets which can possibly be answered by the carbon content analysis of protein sequences. The carbon level analysis of protein sites for post translational modification would lead towards new and profound ways of understanding them (14).

Carbon percentage in protein sequence would be the next parameter for prediction of secondary protein structure. Developments in microarray technologies, which would be based on the carbon content of protein, are required. Chromatography techniques which imply carbon as a parameter may also evolve. Drug development and designing must be implied for detection of active site and potential drugs based on carbon content. The development of tool for prediction of ligand binding site in globular proteins, based on average carbon percentage and distribution, was developed for mouse mitochondrial aspartate aminotransferase. This technique has huge potential to further develop for a large spectrum of proteins (15).

Table 1: Carbon percentages in various types of proteins in *E. coli*

S.No	Types of Protein	Range of Carbon (%)
1	Regulatory proteins	29.95%-32.32%
2	Catalytic Proteins	30.82%-32.97%
3	Transport protein	30.37%-32.15%
4	Enzymatic proteins	29.91%-33.65%
5	Transfer proteins	31.13%-32.58%

A new and fascinating concept is of '**Carbon bar coding**'. The concept is to make carbon as the structure for width of bars. The protein sequence may be converted into its carbon bar code which would be universal. This presentation would be path breaking and very convenient size wise.

Acknowledgement:

Authors are grateful to Dr. A. K. Chauhan, Founder President & Mr. Aseem Chauhan, Chancellor Amity University Haryana & Chairperson Amity Lucknow for providing necessary facilities and support. We also extend our gratitude to Maj. Gen. K.K Ohri, AVSM (Retd.), Pro Vice Chancellor, Amity University, Uttar Pradesh Lucknow Campus for constant support and encouragements.

References

1. Johri, P. and Gokhale, M. (2013). A New Perspective for Sequence Analysis – Carbon content. *Research and Review: Journal of Computational Biology*, 2:1-6.
2. Rajasekaran, E., Akila, K. and Vennila, J.J. (2011). Carbon Contents of H1N1 Proteins. *International Conference on Biosciences, Biochemistry and Bioinformatics*, 5:27-29.
3. Akila, K. and Rajasekaran, E. (2009). What Might be the Difference in Viral Proteins? *International Journal of Bioinformatics Research*, 1:1-3.
4. Rajasekaran, E., Asha, J. and Klaus, H. (2012). Magnitude of Thymine In Different Frames of Messenger RNAs. *International Journal of Bioinformatics Research*, 4:273-275.
5. Senthil, R., Sathish, S., Vennila, J.J. and Rajasekaran, E. (2011). Prediction of Ligand Binding Site in Globular Proteins. *Journal of Advance Bioinformatics Application and Research*, 2:98-99.
6. Akila, K., Kaliaperumal, R. and Rajasekaran, E. (2012). Carbon Distribution to Toxic Effect in Toxin Proteins. *Bioinformation Discussion at the Interface of Physical and Biological Science*, 8:720-721.
7. Rajasekaran, E. and Vijayasarathy, M. (2011). CARBANA: Carbon Analysis Program for Protein Sequences. *Bioinformatics*, 5:455-457.
8. Rajasekaran, E. (2012) CARd: Carbon Distribution Analysis Program for Protein Sequences. *Bioinformatics*, 8:508-512.
9. Chase, M.W. and Fay, M.F. (2009). Barcoding of Plants and Fungi. *Science*, 325:682-683.
10. Nsimama, P.D., Mamboya, A.F., Amri, E. and Rajasekaran, E. (2012). Correlation Between The Mutated Colour Tunings and Carbon Distributions in Luciferase Bioluminescence. *Journal of Computational Intelligence In Bioinformatics*, 5:105-112.
11. Rajasekaran, E., Rajadurai, M., Vinobha, C.S. and Senthil, R. (2008). Are The Proteins Being Hydrated During Evolution ? *Journal of Computational Intelligence In Bioinformatics*, 1:115-118.
12. Akila, K., Sneha, N. and Rajasekaran, E. (2012). Study of Carbon Distribution at Protein Regions of Disorder. *Journal of Bioscience, Biochemistry and Bioinformatics*, 2:58-60.
13. Johri, P., Trivedi, M. and Siddiqui, M.H, and Gokhale, M. (2016). A Study On The Presence and Distribution of Carbon Percentage in and Around the Sites of Glycosylation for Eukaryotic Proteins. *Journal of Chemical and Pharmaceutical Research*, 8:52-63.
14. Johri, P., Trivedi, M., Singh, A. and Siddiqui, M.H. (2016). Towards The Atomic Level Protein Sequence Analysis. *Journal of Chemical and Pharmaceutical Research*, 8:204-207.
15. Johri, P. (2013). Atomic Level Sequence Analysis- a Review. *International Journal of Computational Bioinformatics and Insilco*

Comparative Genomics Analysis of *Cryptosporidium Parvum* and Repurposing of Triazole Derivative as Anti-Cryptosporidial Agents

Kalpna¹, R.K Srivastava² and Ravindra Nath³

¹Department of Biotechnology, Dr. Ambedkar Institute of Technology for Handicapped, Kanpur, India.

²Rural Division Extension, Central Institute for Medicinal and Aromatic Plant, Lucknow, India.

³University Institute of Engineering and Technology, CSJM University, Kanpur, India.

*Corresponding Author E-mail : kalpna@aith.ac.in

<http://dx.doi.org/10.13005/bpj/1869>

(Received: 07 October 2019; accepted: 17 January 2020)

Cryptosporidium, a member of phylum apicomplexa is considered as an opportunistic pathogen for humans as well as other important livestock. It is a causative agent for water-borne infectious diarrheal like disease cryptosporidiosis with a comparatively high mortality rate among children and immunocompromised patients worldwide. The statistics shows that cryptosporidiosis is among the top three threats for the survival of infants, especially in developing countries. To date, no fully effective drug therapy is available to treat cryptosporidiosis. Therefore, the discovery and development of an effective anti-cryptosporidial drug with a novel mechanism of action have become an insistent task for controlling cryptosporidiosis. The literature revealed that various heterocyclic aromatic compounds have various invincible biological properties such as anti-fungal, anti-bacterial and anti-parasitic. Among these, Triazole is one of the most promising candidates that grab attention by researchers, chemists, microbiologists, and pharmacologists through various success stories. Triazole nucleus is present in various natural anti-infective and medicinal compounds. In this research, we have collected triazole compounds from various published works and create a database of these novel compounds for further exploration as anti-cryptosporidial compounds. It is hoped that this research provides new insights for rational anti-cryptosporidial chemotherapeutic agents who will be more active and less toxic.

Keywords: Cryptosporidiosis; IMPDH; Molecular Docking; Triazole; Virtual Screening.

Cryptosporidiosis is an infectious disease caused by protozoan parasite *Cryptosporidium*. To date, 27 species and 60 genotypes of the parasite have been identified worldwide. Among them, *C. parvum* and *C. hominis* are mainly responsible for human cryptosporidiosis.¹ Human cryptosporidiosis is marked off by greenish watery, profuse fetid diarrhea, dehydration, abdominal

pain, fever, and vomiting while failing to gain weight and malnutrition are few symptoms in chronic cases. Immunocompetent host recovers within two weeks in absence of any treatment, but the situation becomes worst in children and host having impaired immune system. In immunocompromised individuals such as those affected by Human Immunodeficiency Virus (HIV)

experience unmanageable lethal diarrhea². This acute diarrheal disease remains the largest threat to the health of young children and agriculturally important livestock worldwide³. The field reports of GEMS (The Global Enteric Multicenter Study) procured by three-year case-control study over 22000 children of aged five years at seven divergent sites covering Africa and Asia continent manifested parasite second diarrhoea causing agent after rotavirus⁴.

Cryptosporidium infection accounts for 20 % and 9 % diarrheal cases in the young population of developing nations and developed nations respectively. In parallel, the findings of Global Network for the study of Malnutrition and Enteric Diseases (MAL-ED) obtained through a five-year-long birth cohort study in 2145 children of age group 0-24 months at eight public sites in South America, Asia and Africa proclaimed *Cryptosporidium* species among top five agents that are liable for diarrhoeal mortality in first year of life⁴. In India, the highest occurrence of cryptosporidiosis is noted in southern and northern regions in infants and young children⁵.

The cryptosporidium life cycle consisted of both sexual and asexual stages that complete in a single host. Infected hosts shed oocysts in defecation that are infective as well as environmentally resistant phase⁶. Oocysts outlive in extreme environmental conditions and remain unpretentious to chemicals, environmental stresses and even most ultra-water purification drinking and sewage water treatment methods. Pathogenesis begins when oocysts are ingested by the host. Four spindle-like *Sporozoites* released into the gastrointestinal tract followed by differentiation to trophozoites inside parasitophorous vacuoles that are extracytoplasmic to intestinal epithelial cells. Trophozoites initiate an asexual cycle and undergo two consecutive merogony producing type I and type II meronts. Subsequently, type I merozoites and type II merozoites differentiate from type I and type II meronts respectively. Type I merozoites infect neighbor cells whereas type II merozoites develop into microgamonts (male gametes) and macrogamonts (female gametes) marks the initiation of the sexual phase of reproduction. Than fertilization in between microgametes and macrogametes results in oocysts development. As a result of sporogony, thick-walled oocysts which

released in feces and thin-walled oocysts that remain in the host⁷.

Now it is established that for such widespread and prevalence of cryptosporidiosis there are mainly two reasons the first one is that infected person sheds large number oocysts that are immediate infective stages to a healthy person. Transmission takes place through a fecal-oral route either directly or indirectly. Another reason is the lack of a fully effective chemotherapeutic agent to treat cryptosporidiosis in all patients⁸.

The identification of drug-target enzymes that differ in human counterparts led to the foundation of comparative genomics. Previous studies revealed that *Cryptosporidium* has many unique metabolic pathways in comparison to other apicomplexan species⁹.

However, there is no potential drug/antibiotic against this protozoan disease. The currently available drugs such as decuquinat, sulphaquinoxaline, halofuginone, paromomycin have shown less efficiency. FDA approved nitazoxanide has shown potential effect however in immunodeficiency case it is not effective¹⁰. Controlling this disease is very difficult because the oocytes of *C. parvum* are. Thus, it is important to identify the possible drugs to control this life-threatening disease.

MATERIALS AND METHODS

Retrieval of Proteome and Identification of Non-Homologous Crucial Proteins

Complete genome of *C. parvum* was retrieved by using the National Center for Biotechnology Information (NCBI) database (<http://www.ncbi.nlm.nih.gov/genomes/apicomplexa/>) in fasta format¹¹. All the sequences manually inspected and short sequences (less than 100 amino acids) were stricken out because short proteins have the least chance to be as essential genes. The CryptoDB (<http://CryptpoDB.org>) database was chosen to access essential genes of the parasite¹².

Selection of Non-Homologous Proteins

The CD-HIT is a suite of a program that is very useful in comparing and clustering of proteins and nucleotides. The whole proteome of *C. parvum* was submitted to the CD-HIT server (weizhong-lab.ucsd.edu/cdhit-web-server/cgi-bin/index.cgi?cmd=cd-hit) for filtration of analogous,

paralogous and homologous proteins¹³. All the default parameter was chosen except sequence identity cut-off reset to 0.7. The non-homologous proteins of the parasite were obtained through BLAST P analysis as opposed to the human genome with expectation value cut-off reset at 10⁻⁴ and other parameters were chosen as default¹¹. The non-homologous proteins of the parasite were submitted to the CryptoDB database (<http://CryptoDB.org>) for the extraction of essential parasite genes. At this step expectation value (E-value) cut-off and bit score cut-off were chosen 10⁻¹⁰ and 100 respectively and the rest of the parameters were chosen as a default¹⁴.

Metabolic Pathway Analysis

KASS-KEGG Automatic Annotation server (<http://www.genome.jp/kegg/kass/>) was selected for metabolic pathway analysis. KASS program is helpful in the functional annotation of the genome. This analysis results in an assignment of functional role to each gene. This is also helpful in the retrieval of unique proteins for the drug targets¹⁵.

Target Protein Model Generation

Template selection is a process of identifying a suitable protein that shares nearly the same structure of the query protein which doesn't possess the 3D structure. Template selection is very important in comparative protein modeling. Templates can be chosen by various tools such as BLAST, FASTA, Swiss-model, etc¹⁶. In the case of BLAST and FASTA, the sequence of the protein in FASTA format can be uploaded and the templates can be manually selected by considering the score value and the E value¹⁷. In the case of the Swiss-Model server, it automatically chooses the template and models the protein structure. In this study, we choose the BLAST tool for generating a respective template. In this tool, a high level of sequence identity should guarantee a more accurate alignment between the target sequence and template structure¹⁸. The sequence of CpIMPDH was retrieved from Uniprot and submitted for BLAST against PDB protein for obtaining perspective 3D structure¹⁹. Hits which fulfilled criteria of query coverage > 95 %, sequence identity >80 % and PDB structure resolution < 3.0 Å were selected as a template for homology modeling of IMPDH

Inosine 5'-monophosphate dehydrogenase (IMPDH) is the most important molecular agent

when looking for target-specific drug designing because this protozoan parasite cannot reclaim guanosine and therefore relies on IMPDH for guanine nucleotides synthesis to survive. Interestingly, *C. parvum* seems to have acquired the IMPDH gene from proteobacteria through lateral gene transfer and IMPDH of *C. parvum* is functionally and structurally distinct from eukaryotic IMPDH enzymes²⁰. Therefore, mutational or inhibitory action against the IMPDH gene is considered to be effective and target specific. In silico identification and optimization of therapeutic inhibitors are cost and time effective. Here most effective additional inhibitors derivatives have been identified and optimized to inactivate the functional domain of IMPDH for treating cryptosporidiosis. Previously we also reported a new chemical scaffold using a structure-based pharmacophore approach against IMPDH of *C. parvum*.²¹

Active Site Prediction of Target Protein

CASTp 3.0, Computed Atlas of Surface Topography of Proteins (<http://www.sts.bioe.uic.edu/castp>) is a free online tool which scans structural geometry of macromolecule and shows cavities on physio-chemical properties of residues of surrounding residues²². Modeled structure of IMPDH protein submitted to this tool for the spotting of binding pockets. The most prominent binding sites would be selected for further in-silico analysis.

Ligand Data Set Preparation for Virtual Screening

Virtual screening is the foundation pillar for computer-aided drug design paradigm. In this computer-assisted process, virtual evaluation of large chemical libraries is accomplished by docking molecules into target protein and also prioritization of chemical compounds on the basis of binding affinities²³.

In this study, we have chosen the PubChem (<https://pubchem.ncbi.nlm.nih.gov>) database for finding new molecular scaffolds that selectively interact with the target protein. NCBI operated PubChem database store biochemical information of small molecules under Pccompounds, Pcbioassay, and Pcsubstances subsets²⁴.

Triazole is five-membered heterocyclic ring compounds with molecular formula C₂H₃N₃. The relative positioning of the nitrogen atom in

the ring, triazole exists in two isomeric forms and each isomer presents two tautomers. Triazole derivatives interact with biomolecule by forming various noncovalent interactions and thus exploited as medicinal drugs²⁵. These compounds were considered for the study.

To date, Pccomounds contain 461,626 triazole compounds, 261, 784 triazole substances and 1507 triazole bioassays. Among 1507 bioassay compounds, a dataset of 30 triazole compounds is prepared by filtering undesirable small fragments, covalent salts, and conformers, etc.

The 2D structures of chemical compounds were drawn in Marvin Sketch²⁶. The PDB coordinates of 30 triazole derivatives were obtained after converting their respective mol files in Open

Babel²⁷. Ligand dataset comprises 30 triazole derivatives²⁵ and detailed information regarding ligands is provided in Table 1.

The PDB coordinates of ligand were converted into pdbqt format after the addition of Gasteiger charges, merging non-polar hydrogens, detecting aromatic carbons and setting up a torsion tree.

Molecular Docking Studies

Molecular docking studies provide significant insights into binding interactions of the ligand with the target protein. AutoDock 4.2 tools were employed for this study²⁸. This tool performs rigid docking where ligands and targets are allowed to interact in a rigid state without bond angle, bond length as well as torsional angle alteration.

Table 1. Triazole Derivate ligands (from PubChem database) for Molecular Docking

S. No	Compound Name	Compound ID
1	N-(4-chlorophenyl)-2-(1-naphthalenyloxy)propanamide	S8000001
2	N-(4-chlorophenyl)- \acute{a} -(1-naphthalenyloxy) benzene acetamide	S8000002
3	N-(4-chlorophenyl)-3-methyl-2-(1-naphthalenyloxy)butanamide	S8000003
4	2-bromo-N-(4-chlorophenyl)propanamide	S8000004
5	N-(4-chlorophenyl)-2-[[4-quinolinyl]oxy]propanamide	S8000005
6	1-[(1-methyl-2-propyn-1-yl)oxy]naphthalene	S8000006
7	1-(1-methylethyl)-2-propyn-1-yl]oxy]naphthalene	S8000007
8	1-(4-chlorophenyl)-4-(2-methyl-1-(1-naphthalenyloxy)propyl)-1H-1,2,3-triazole	S8000008
9	1-(4-chlorophenyl)-4-(1-(naphthalene-1-yloxy)ethyl)-1H-1,2,3-triazole	S8000009
10	1-(2,6-dichlorophenyl)-4-(1-(naphthalen-1-yloxy)ethyl)-1H-1,2,3-triazole	S8000010
11	4-(1-(4-chloronaphthalen-1-yloxy)ethyl)-1-(4-chlorophenyl)-1H-1,2,3-triazole	S8000011
12	4-(1-(1-(4-chlorophenyl)-1H-1,2,3-triazol-4-yl)ethoxy)quinoline	S8000012
13	4-((1-(4-chlorophenyl)-1H-1,2,3-triazol-4-yl)methoxy)quinoline	S8000013
14	4-(1-(1-(3,4-dichlorophenyl)-1H-1,2,3-triazol-4-yl)ethoxy)quinolone	S8000014
15	4-(4-(1-(quinolin-4-yloxy)ethyl)-1H-1,2,3-triazol-1-yl)benzotrile	S8000015
16	2-chloro-4-(4-(1-(quinolin-4-yloxy)ethyl)-1H-1,2,3-triazol-1-yl)benzotrile	S8000016
17	(R)-4-(1-(1-(3,4-dichlorophenyl)-1H-1,2,3-triazol-4-yl)ethoxy)quinolone	S8000017
18	(S)-4-(1-(1-(3,4-dichlorophenyl)-1H-1,2,3-triazol-4-yl)ethoxy)quinolone	S8000018
19	(R)-2-chloro-4-(4-(1-(quinolin-4-yloxy)ethyl)-1H-1,2,3-triazol-1-yl)benzotrile	S8000019
20	(S)-2-chloro-4-(4-(1-(quinolin-4-yloxy)ethyl)-1H-1,2,3-triazol-1-yl)benzotrile	S8000020
21	(R)-5-(1-(1-(4-chlorophenyl)-1H-1,2,3-triazol-4-yl)ethoxy)quinolone	S8000021
22	4-(1-(1-(4-chlorophenyl)-1H-1,2,3-triazol-4-yl)ethoxy)quinoline 1-oxide	S8000022
23	4-(1-(1-(3,4-dichlorophenyl)-1H-1,2,3-triazol-4-yl)ethoxy)quinoline 1-oxide	S8000023
24	5-(1-(1-(4-chlorophenyl)-1H-1,2,3-triazol-4-yl)ethoxy)quinoline 1-oxide	S8000024
25	(R)-4-(1-(1-(4-chlorophenyl)-1H-1,2,3-triazol-4-yl)ethoxy)quinoline 1-oxide	S8000025
26	(R)-5-(1-(1-(4-chlorophenyl)-1H-1,2,3-triazol-4-yl)ethoxy)quinoline 1-oxide	S8000026
27	(R)-5-(but-3-yn-2-yloxy)quinoline 1-oxide	S8000027
28	ethyl \acute{a} -bromocyclopropaneacetate	S8000028
29	2-cyclopropyl-2-(1-naphthalenyloxy)acetic acid	S8000029
30	N-(4-chlorophenyl)-2-cyclopropyl-2-(1-naphthalenyloxy)acetamide	S8000030

RESULTS

Metabolic pathway analysis and selection of essential protein in *C. parvum*

C. parvum has eight chromosomes with 10.4 Mb genome (Mbp) size that codes for total 18538 proteins sequences²⁹. Parasite lacks several key enzymes in comparisons with the host for example it scavenges or transport building block biomolecule from the host in spite of de novo biosynthesis. The whole-genome sequence is manually curated for any observable anomaly CD-HIT (<http://weizhong-lab.ucsd.edu>) suite of the programme is used for redundancy removal and non -paralogs proteins identification. the whole genome in FASTA format is submitted to cd-hit (http://weizhong-lab.ucsd.edu/cdhit_suite/cgi-bin/index.cgi?cmd=cd-hit) non-homologous proteins were again subjected to BLAST P analysis against the Crypto DB database with 10-10 E-value threshold. This resulted in 323 essential proteins that are described as an essential protein for the propagation of parasite inside the host.

Metabolic Pathway Analysis in *Cryptosporidium Parvum*

Metabolic pathway analysis shows that parasite has intensely diminished metabolic machinery. Further analysis also suggests that parasite has a scarcity of apicoplast and mitochondrial proteins. Carbohydrates, amino

acids, and nucleic acid anabolic functions are also reduced. Parasite depends preponderatingly on glycolysis for energy production. Parasite metabolic machinery perfectly matches with its unique life cycle.

Target Protein Model Generation

In the results of the BLAST search against PDB, only one-reference protein 3FFS has a high level of sequence identity and the identity of the reference protein with the domain is 99%¹⁶.

After this, we have chosen 3FFS (PDB ID) as a reference structure for modeling the Inosine Monophosphate dehydrogenase domain. Coordinates from the reference protein (3FFS) to the structurally variable regions (SVRs), structurally constant regions (SCRs), C-termini and C-termini were assigned to the target sequence based on the satisfaction of spatial restraints³⁰.

The sequence of the reference structures was extracted from the respective structure files and aligned with the target sequence using the default parameters in ClustalW.

The Cladogram tree between the Inosine Monophosphate dehydrogenase and template are at a close distance 0.33 indicates both are closely related in origin³¹.

The 3FFS structure was used as the templates for building the 3D model of the Inosine Monophosphate dehydrogenase using MODELLER9V7³².

Table 2. List of essential protein of *Cryptosporidium parvum* which could be a promising target for drug development

Target Enzyme	Function / Pathway in which the target enzyme is involved
Mucin- like proteins	Parasite-host cell interaction and immune invasion
Glycosylphosphatidyl-inositol anchored proteins	Pathogenesis
N-acetylglucosaminyl transferases	Fatty acid biosynthesis
P-type ATPase (CpATpase)	Transporting cations
Thrombospondin-related adhesive proteins (TRAPs)	Parasite gliding motility and host-parasite interaction
Lactate Dehydrogenase (LDH)	Energy production
Malate Dehydrogenase (MDH)	Energy production
Inosine Monophosphate Dehydrogenase (CpIMPDH)	Purine and pyrimidine biosynthesis
Thymidine Kinase (TK)	DNA Biosynthesis
Polyamine enzymes	Polyamine Biosynthesis
Dihydrofolate reductase-thymidylate synthetase	Folate Biosynthesis Pathway
Cryptosporidium Calcium-dependent protein kinase (CpCDPK1)	Host Cell invasion
Clan CA cysteine protease	Host cell invasion

The peptide bond of a polypeptide chain N-Ca (phi angle) and Ca-C (psi angle) bond remain free to rotate whereas bond between Cβ-N (omega angle) remain rigid due to p-p interaction. Although the value of phi and psi angle ranges from -180°C to +180°C but because of steric hindrances, only a few limited values are allowed. These dihedral angles describe specific secondary conformation of the protein. Ramachandran Plot helps in

determining secondary structure and assists in structure prediction simulations³³.

The final structure was further checked by the verify3D graph and the results have been shown in Figure 6. The overall scores indicate an acceptable protein environment.

After the refinement process, validation of the model was carried out using Ramachandran plot calculations computed with the PROCHECK

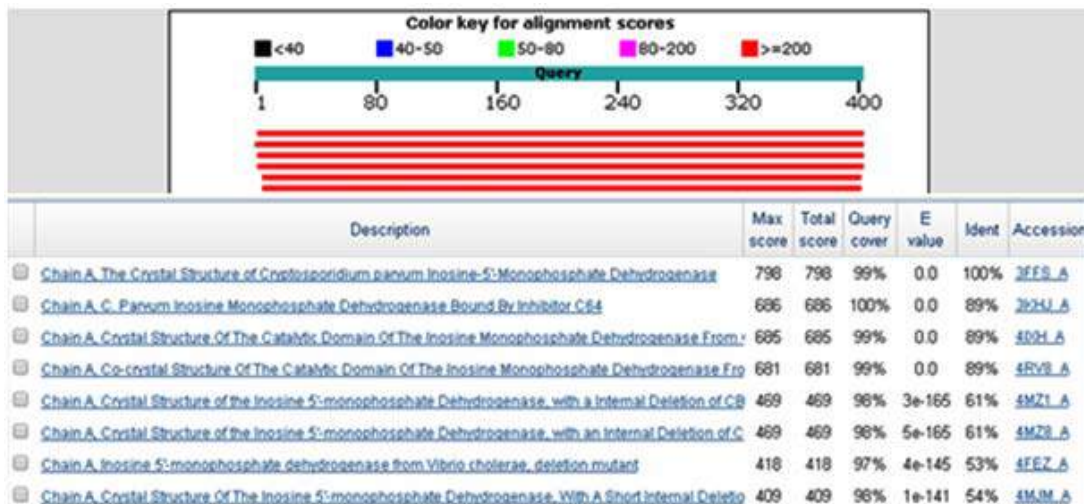


Fig. 1. BLAST result with a similar template having 99% identity with Inosine Monophosphate dehydrogenase

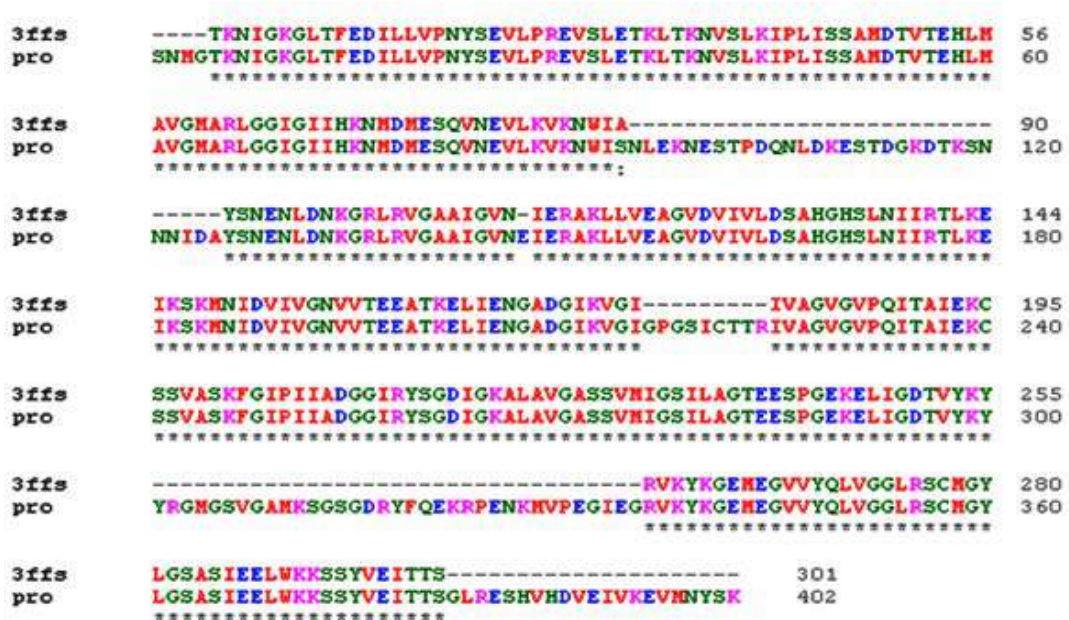


Fig. 2. Alignment of Inosine Monophosphate dehydrogenase with template 3FFS

program³⁴. The α and β dihedral angle distributions of the Ramachandran plots of non-glycine, non-proline residues are in the permissible range. The RMSD (Root Mean Square deviation) deviation for covalent bonds and covalent angles relative to the standard dictionary of Inosine Monophosphate dehydrogenase was -0.4 and -0.8 Å. Altogether 95% of the residues of Inosine Monophosphate dehydrogenase was in favored and allowed regions. The overall PROCHECK G-factor of Inosine Monophosphate dehydrogenase was -2.15 and the verify3D environment profile was good.

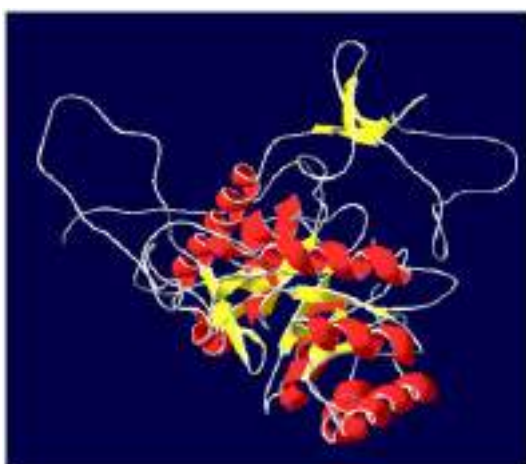


Fig. 3. Three-dimensional structure of Inosine Monophosphate dehydrogenase with 10 helices and 8 sheets

The structural superimposition of the 3FFS template and Inosine Monophosphate dehydrogenase is shown in Figure 8. The weighted root mean square deviation of trace between the template and final refined models is 0.41Å . This final refined model was used for the identification of the active site with the domain Inosine Monophosphate dehydrogenase.

Since Inosine Monophosphate dehydrogenase and the 3FFS are well conserved in both sequence and structure; their biological

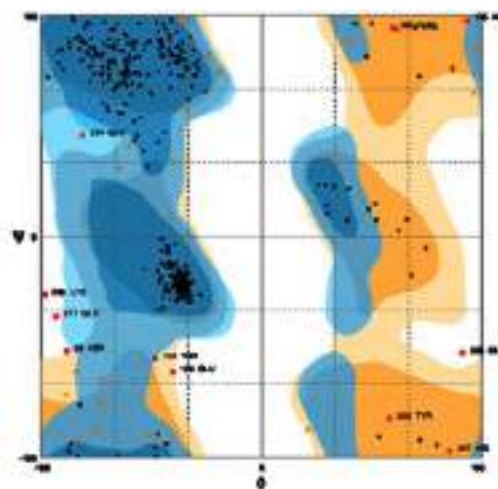


Fig. 4. Ramachandran plot analysis for Inosine Monophosphate dehydrogenase indicating the suitable positions of amino acids

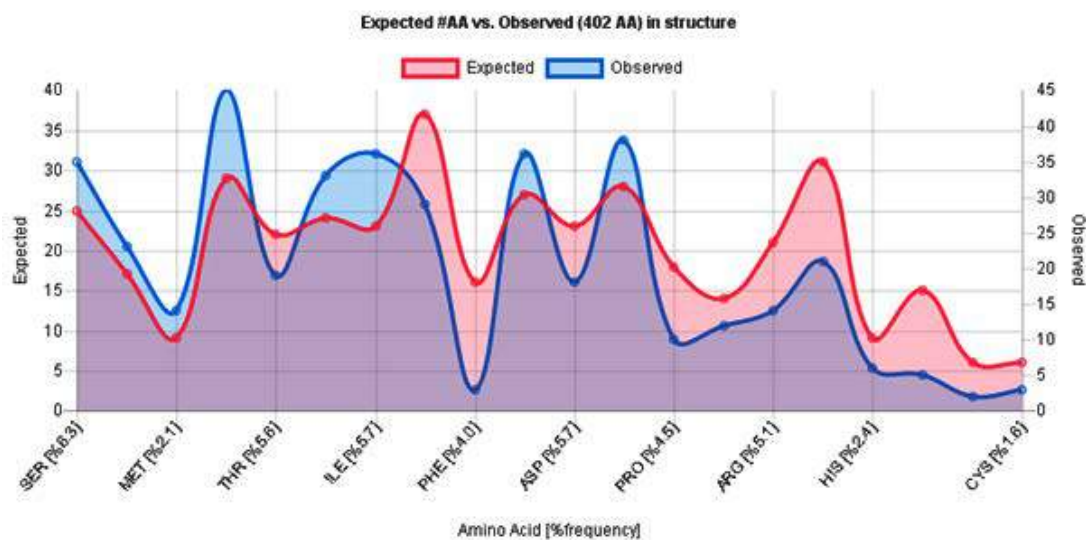


Fig. 5. The 3D profiles verified results of the Inosine Monophosphate dehydrogenase model; overall quality score indicates residues are reasonably folded

function should be identical. In fact from the structure comparison of template, a final refined model of Inosine Monophosphate dehydrogenase domain using SPDBV program and was shown in Figure 8.

Active Site Identification

The predicted model was submitted to the CASTp tool for the exploration of major binding pockets. Top three binding pockets in terms of surface area and volume selected. The details of these potential binding sites are given in supplementary table number 1 shown in figure 9. We observed that THR 11, PHE12, GLU13, SER22, LEU25, SER 48, ALA 49, MET 50, ASP 163, SER 164,

ALA 165, HIS 166, SER 169, ASN 191, VAL 193, LYS 210, GLY 212, ILE 213, VAL 214, VAL 229, GLN 231, ALA 234, ASP 252, ARG 256, TYR 257 and ASP 260 are binding cavity residues.

AutoDock 4.2 a freely accessible computational tool for docking of small molecules to target receptor macromolecule. Bound water molecules and heteroatoms were removed from the target protein. Further, Polar hydrogens and rotatable bonds were selected. This step was followed by the computation of the Gasteiger charge. Target protein preparation was accomplished by choosing amino-acid residues in the active site based on the

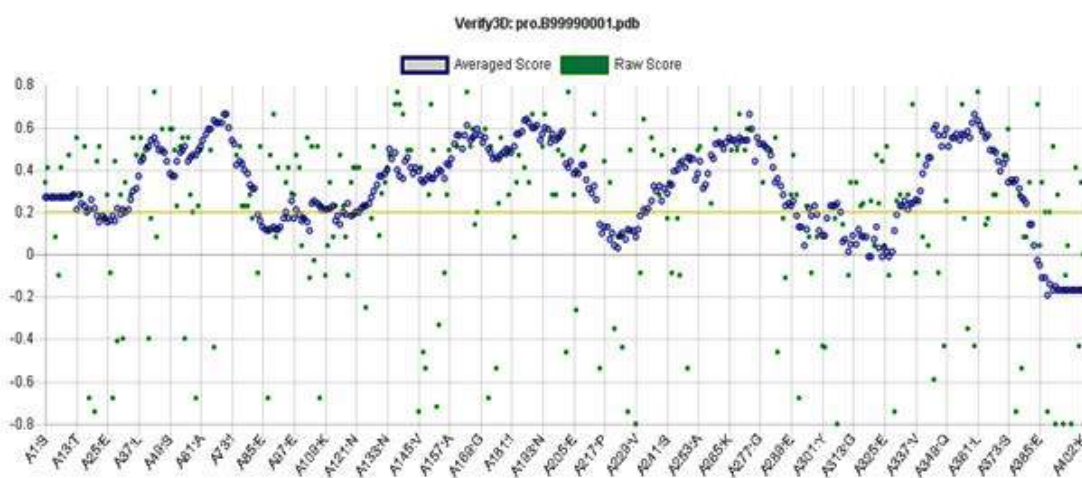


Fig. 6. Verify 3D analysis of Inosine Monophosphate dehydrogenase

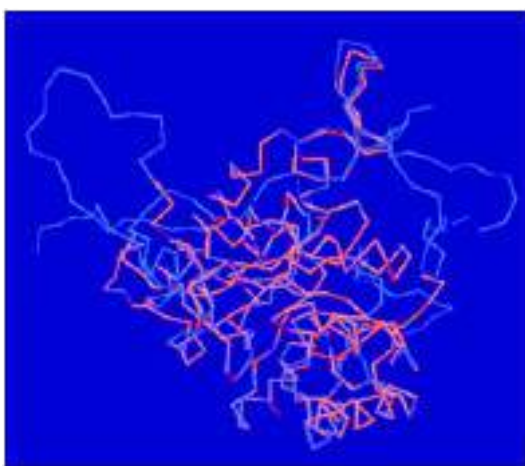


Fig. 7. Superimposition Inosine Monophosphate dehydrogenase (represented in blue color) and 3FFS (represented in red color)

AutoGrid method. Amino acid residues present in the binding sites include Ser164, Ala165, Ser169, His166, Ser22, Val24, Leu25, Pro26, Asn171, Asn191, and Asp252. Binding site residues were selected and three-dimensional grid boxes were created.

AutoDock exploits the Lamarckian-Genetic algorithm for the accurate placement of ligand into the active site. Docking was executed by considering all stereochemical configurations of chemical compounds. Top 100 poses of ligands were considered for docking in order to enhance the accuracy and efficacy. Information regarding docking scores is given in Table 2 in ascending order of free binding energy.

DISCUSSION

IMPDH is an attractive target for the treatment of *C. parvum* infections. In the present study, we have analyzed the efficacy of 30 triazole derivatives in combating *C. parvum* infections by executing in-silico methodologies. Molecular docking studies were carried out to identify the efficacy of 30 triazole compounds with CpIMPDH protein. Amino acid residues present in the binding sites include Ser164, Ala165, Ser169, His166, Ser22, Val24, Leu25, Pro26, Asn171, Asn191, and Asp252. The results of the docking study revealed significant interactions of triazole derivatives with IMPDH. Among 30 compounds,

4-(1-(4-chloronaphthalen-1-yloxy) ethyl)-1-(4-chlorophenyl)-1H-1,2,3-triazole (compound ID: S8000011) showed highest free binding energy of -12.19 kcal/mol. This result is coherent with the interactions made by previously reported inhibitors with CpIMPDH. From the docking results, it is evident that chemical compounds possessing both electron releasing and electron-withdrawing groups exhibited good free binding energy values. The presence of electron-withdrawing groups enhances H-bonding potential. When the number of electrons withdrawing groups are dominant in the chemical structure, electrons from these groups will be utilized for stabilizing chemical compounds by resonance stabilization interactions. Hence,



Fig. 8. Amino acid residues in the active site domain of *C. parvum* IMPDH shown in red color

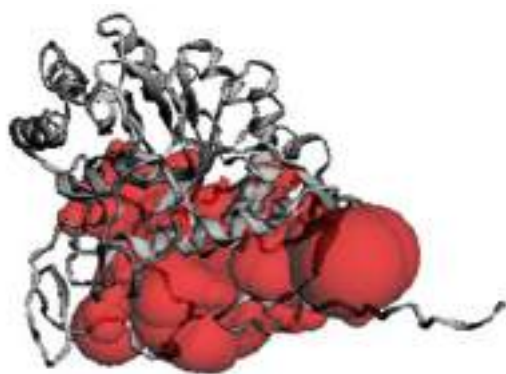


Fig. 9. Active site identification in *Cryptosporidium parvum* IMPDH. Molecular Docking

these electrons can't be used in making significant interactions with the target protein. This is evident in ethyl α -bromocyclopropaneacetate (Compound ID: S8000011), which exhibited the lowest free binding energy.

CONCLUSION

The binding efficacies of 30 triazole derivatives, with IMPDH, were analyzed by executing docking studies. Among 30 compounds 4-(1-(4-chloronaphthalen-1-yloxy)ethyl)-1-(4-chlorophenyl)-1H-1,2,3-triazole (Compound ID: S8000011) showed higher free binding energy score with significant interactions with the target

Table 3. Molecular Docking result (in term of free binding energy) of Triazole derivative with IMPDH protein of *C.parvum*

S. No	Compound ID	Free Binding Energy (Kcal/mol)
1	S8000011	-12.19
2	S8000022	-12.06
3	S8000012	-11.7
4	S8000024	-11.95
5	S8000021	-11.66
6	S8000020	-11.6
7	S8000013	-11.42
8	S8000009	-11.4
9	S8000025	-11.29
10	S8000015	-11.29
11	S8000023	-11.17
12	S8000016	-11.12
13	S8000010	-10.94
14	S8000017	-10.09
15	S8000014	-10.83
16	S8000018	-10.83
17	S8000019	-10.54
18	S8000026	-10.34
19	S8000005	-10.2
20	S8000008	-9.9
21	S8000001	-9.17
22	S8000029	-7.18
23	S8000030	-7.08
24	S8000004	-6.79
25	S8000003	-6.66
26	S8000002	-6.24
27	S8000027	-5.72
28	S8000006	-5.2
29	S8000007	-2.4
30	S8000028	0.1

protein. Hence, this could be a promising antagonist for IMPDH. But the efficacy of this compound as IMPDH inhibitor has to be proven by conducting in -vitro and in-vivo studies.

REFERENCES

1. L. Xiao, R. Fayer, U. Ryan, and S. J. Upton, "Cryptosporidium taxonomy: recent advances and implications for public health.," *Clin. Microbiol. Rev.*, (2004).
2. L. Xiao, "Molecular epidemiology of cryptosporidiosis: An update," *Exp. Parasitol.*, (2010).
3. S. Bhalchandra, D. Cardenas, and H. D. Ward, "Recent Breakthroughs and Ongoing Limitations in Cryptosporidium Research," *F1000 Research*, (2018).
4. D. A. Shoultz, E. L. de Hostos, and R. K. M. Choy, "Addressing Cryptosporidium Infection among Young Children in Low-Income Settings: The Crucial Role of New and Existing Drugs for Reducing Morbidity and Mortality," *PLoS Negl. Trop. Dis.*, (2016).
5. J. A. Platts-Mills *et al.*, "Pathogen-specific burdens of community diarrhoea in developing countries: A multisite birth cohort study (MAL-ED)," *Lancet Glob. Heal.*, (2015).
6. D. P. Clark, "New insights into human Cryptosporidiosis," *Clinical Microbiology Reviews.* (1999).
7. G. J. Leitch and Q. He, "Cryptosporidiosis-an overview," *Journal of Biomedical Research.* (2011).
8. N. F. Rossle and B. Latif, "Cryptosporidiosis as threatening health problem: A review," *Asian Pacific Journal of Tropical Biomedicine.* (2013).
9. H. Sparks, G. Nair, A. Castellanos-Gonzalez, and A. C. White, "Treatment of Cryptosporidium: What We Know, Gaps, and the Way Forward," *Current Tropical Medicine Reports.* (2015).
10. M. M. Cabada and A. C. White, "Treatment of cryptosporidiosis: Do we know what we think we know?," *Current Opinion in Infectious Diseases.* (2010).
11. D. L. Wheeler *et al.*, "Database resources of the National Center for Biotechnology Information," *Nucleic Acids Res.*, (2008).
12. M. Heiges, "CryptoDB: a Cryptosporidium bioinformatics resource update," *Nucleic Acids*

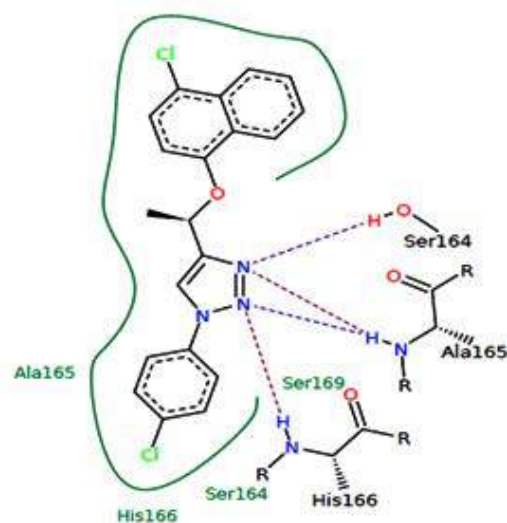


Fig. 10. Post –docking interactions between the active site of CpIMPDH with ligand S8000011

- Res.*, (2006).
13. Y. Huang, B. Niu, Y. Gao, L. Fu, and W. Li, "CD-HIT Suite: A web server for clustering and comparing biological sequences," *Bioinformatics*, (2010).
 14. A. Morris, J. Pachebat, G. Robinson, R. Chalmers, and M. Swain, "Identifying and resolving genome misassembly issues important for biomarker discovery in the protozoan parasite, cryptosporidium," in *BIOINFORMATICS 2019–10th International Conference on Bioinformatics Models, Methods and Algorithms, Proceedings; Part of 12th International Joint Conference on Biomedical Engineering Systems and Technologies, BIOSTEC 2019*, (2019).
 15. H. Ogata, S. Goto, K. Sato, W. Fujibuchi, H. Bono, and M. Kanehisa, "KEGG: Kyoto encyclopedia of genes and genomes," *Nucleic Acids Research*. (1999).
 16. S. F. Altschul, W. Gish, W. Miller, E. W. Myers, and D. J. Lipman, "Basic local alignment search tool," *J. Mol. Biol.*, (1990).
 17. W. R. Pearson, "Finding protein and nucleotide similarities with FASTA," *Curr. Protoc. Bioinforma.*, (2016).
 18. N. Guex and M. C. Peitsch, "SWISS-MODEL and the Swiss-PdbViewer: An environment for comparative protein modeling," *Electrophoresis*, (1997).
 19. A. Bateman *et al.*, "UniProt: The universal protein knowledgebase," *Nucleic Acids Res.*, (2017).
 20. L. Hedstrom, G. Liechti, J. B. Goldberg, and D. R. Gollapalli, "The Antibiotic Potential of Prokaryotic IMP Dehydrogenase Inhibitors," *Curr. Med. Chem.*, (2011).
 21. R. K. Srivastava and R. Nath, "Structure based drug designing against Inosine Monophosphate Dehydrogenase Receptor of Cryptosporidium parvum," in *2018 International Conference on Bioinformatics and Systems Biology (BSB)*, 2018, pp. 128–130.
 22. W. Tian, C. Chen, X. Lei, J. Zhao, and J. Liang, "CASTp 3.0: computed atlas of surface topography of proteins.," *Nucleic Acids Res.*, (2018).
 23. L. G. Ferreira, R. N. Dos Santos, G. Oliva, and A. D. Andricopulo, "Molecular docking and structure-based drug design strategies," *Molecules*. (2015).
 24. S. Kim *et al.*, "PubChem substance and compound databases," *Nucleic Acids Res.*, (2016).
 25. S. K. Maurya *et al.*, "Triazole inhibitors of Cryptosporidium parvum inosine 52 - monophosphate dehydrogenase," *J. Med. Chem.*, (2009).
 26. ChemAxon, "Marvin Sketch," <https://www.chemaxon.com/products/marvin/>, (2013).
 27. P. W. Rose *et al.*, "The RCSB protein data bank: Integrative view of protein, gene and 3D structural information," *Nucleic Acids Res.*, (2017).
 28. W. Forli, S. Halliday, R. Belew, and A. Olson, "AutoDock Version 4.2," *Citeseer*, (2012).
 29. M. S. Abrahamsen *et al.*, "Complete Genome Sequence of the Apicomplexan, Cryptosporidium parvum," *Science (80-.)*, (2004).
 30. N. N. Umejiego, C. Li, T. Riera, L. Hedstrom, and B. Striepen, "Cryptosporidium parvum IMP dehydrogenase: Identification of functional, structural, and dynamic properties that can be exploited for drug design," *J. Biol. Chem.*, (2004).
 31. J. D. Thompson, D. G. Higgins, and T. J. Gibson, "CLUSTAL W: Improving the sensitivity of progressive multiple sequence alignment through sequence weighting, position-specific gap penalties and weight matrix choice," *Nucleic Acids Res.*, (1994).
 32. J. A. R. Dalton and R. M. Jackson, "Homology-modelling protein-ligand interactions: Allowing for ligand-induced conformational change," *J. Mol. Biol.*, (2010).
 33. L. L. Porter and G. D. Rose, "Redrawing the Ramachandran plot after inclusion of hydrogen-bonding constraints," *Proc. Natl. Acad. Sci. U. S. A.*, (2011).
 34. R. A. Laskowski, M. W. MacArthur, D. S. Moss, and J. M. Thornton, "PROCHECK: a program to check the stereochemical quality of protein structures," *J. Appl. Crystallogr.*, (1993).



Identification of novel anti-cryptosporidial inhibitors through a combined approach of pharmacophore modeling, virtual screening, and molecular docking

Kalpana Katiyar^{a,*}, Ramesh Kumar Srivastava^b, Ravindra Nath^c

^a Dr. Ambedkar Institute of Technology for Handicapped, Kanpur, Uttar Pradesh, India

^b Central Institute of Medicinal and Aromatic Plants, India

^c Chatrapati Sahu Ji Maharaj University, Kanpur, India

ARTICLE INFO

Keywords:

Cryptosporidiosis
 COVID-19 pandemic
 Inosine 5'-Monophosphate dehydrogenase
 Pharmacophore
 Virtual screening
 Molecular docking
 Molecular simulation

ABSTRACT

Background and objective: Cryptosporidiosis is a diarrheal disease that affects millions of people worldwide and can cause dire effects in immunocompromised, HIV/AIDS patients and younger children. *Cryptosporidium* species are causative agents for cryptosporidiosis. The presently available chemotherapeutic options are not fully effective in curbing the menace of disease in all patients. The deprived experimental traceability of the pathogen, lack of a suitable in-vivo model are few factors that hindered the development of reliable chemotherapeutic options despite continuous efforts. The underway COVID-19 pandemic widens this gap as most of the scientific resources and researches shifted priority. The genome sequencing of the *Cryptosporidium parvum* (*C. parvum*) has discovered many new targets, such as Inosine 5'-Monophosphate Dehydrogenase (IMPDH), Lactate Dehydrogenase and many more. The parasite uses the host adenosine pool to synthesize guanine nucleotide in a streamlined pathway, where IMPDH catalyzes the first rate-limiting step. The present study aims to discover new anti-cryptosporidial agents that work against the IMPDH of the parasite.

Methodology and results: In this study, The PharmaGist (<https://bioinfo3d.cs.tau.ac.il/PharmaGist/>) tool was deployed for the pharmacophore model generation employing previously reported *Cryptosporidium parvum* IMPDH (CpIMPDH) inhibitors having IC₅₀ values ranging from 0.009 μM to 0.028 μM. The model having the highest scores was used as a 3D query for high throughput screening of the Zinc database via ZINC pharmer (<http://zincpharmer.csb.pitt.edu/>) tool. The screened 'hits' were further subjected to molecular docking in the active site of CpIMPDH (PDB ID: 4IXH), Lipinski's rule of 5, and SwissADME (<http://www.swissadme.ch/>) filter. Finally, the best three 'hits' or proposed leads (ZINC09672610, ZINC16511373, and ZINC39780256) docked CpIMPDH were further subjected to 50 ns molecular dynamic simulation (MDL) analysis for stability analysis.

Conclusion and significance: The ZINC09672610 and ZINC39780256 compounds show excellent in-silico inhibitory efficacy against CpIMPDH. These compounds were used as a starting point for the discovery and development of new anti-cryptosporidial compounds. Future anti-cryptosporidial agents could be designed by utilizing these three molecules.

1. Introduction

The current underway pandemic of COVID-19 is the most prolonged, destructive, and deadly outbreak of the infectious disease since the flu pandemic of the year 1918. The COVID-19 pandemic changed the health care system's focus to resolve the problems of the COVID-19 pandemic, which placed severe limits on access to public health facilities available to minimize the burden of parasitic infectious diseases. The drug

discovery and development project is currently facing an obstacle in fund investment and shifting the priority of scientific resources on other parasitic disease programs due to the burden imposed by the COVID-19 pandemic [1].

Amid the current pandemic, this article tried to provide a detailed overview of cryptosporidiosis, lack of treatment and proposes new lead molecules for drug production to curb cryptosporidiosis and fill the research gap.

* Corresponding author.

E-mail addresses: kalpna@aith.ac.in (K. Katiyar), rksrivastava@cimap.res.in (R.K. Srivastava), rnkatiyar@gmail.com (R. Nath).

<https://doi.org/10.1016/j.imu.2021.100583>

Received 4 April 2021; Accepted 19 April 2021

Available online 8 May 2021

2352-9148/© 2021 The Authors.

Published by Elsevier Ltd.

This is an open access article under the CC BY-NC-ND license

(<http://creativecommons.org/licenses/by-nc-nd/4.0/>).

Cryptosporidium is a protozoan coccidian parasite responsible for the occurrence of the chronic disease cryptosporidiosis. E. Tyzzer first detected the *Cryptosporidium species(spp.)* in 1936 during the in-vivo analysis of the infected mice model. Later on, the first case of human cryptosporidiosis was discovered in 1976, and the parasite emerged quickly with many diarrhoeal illnesses worldwide [2].

Phylogenetically, the parasite belongs to phylum Apicomplexa, family Cryptosporidiidae and genus *Cryptosporidium*. About 30–35 species are incorporated in the genus *Cryptosporidium*, among which *C. parvum* and *C. hominis* are accountable for more than 90% of cryptosporidiosis cases in humans [3,4]. The parasite primarily infects gastrointestinal microvillus epithelial cells, which results in epithelial cell death leading to villous atrophy, malabsorption, and altered intestinal permeability accompanied by fever, abdominal pain, vomiting, and diarrhea [5].

The Global Multicentre Study classified the *Cryptosporidium spp.* as the second most prevalent factor responsible for moderate to severe diarrhea in young children within Asia and Africa [6]. The European Network for foodborne in 2016 graded *Cryptosporidium spp.* as the second and eighth highest priority foodborne pathogenic parasite in northern, western, eastern, and southwestern Europe [7]. However, the estimation of cryptosporidiosis disease magnitude remains a more challenging factor to quantify because long-term consequences are associated with parasite infection [8]. Fortunately, most infections are self-limited in immunocompetent hosts, but it might be life-threatening in immunosuppressed and HIV-infected hosts. It is projected that 80% of mortality of AIDS patients are due to opportunistic infections of *Toxoplasma gondii*, *Cryptosporidium spp.*, *Microsporidia spp.*, and *Cyclospora cayatanensis*, and *Isoospora belli* instead of the virus itself. Even usually, each third of the casualties of AIDS patients are linked to intestinal opportunistic parasitic infections [9]. A recent systematic review investigated that 30.7% and 77% of pre-school children were found infected with parasites in the pre-urban area of Zambia and slum-dwelling areas in Bangladesh [10].

The parasite completes its lifecycle in a single host and consists of both sexual and asexual stages. The sporulated oocysts, the only environmental stage, are the ultimate infection source and infect humans through multiple routes. The oocysts are also responsible for carrying on infection to a fresh host [11]. Cryptosporidiosis is spread through the ingestion of animal or human origin oocysts released with feces that contaminate water and food resource. Fecal-oral route transmission either directly or indirectly is considered the most common mode of transmission. The typical direct process for fecal-oral transmission is person-to-person contact, ingestion of infected eatables, and zoonosis [12]. Oocysts survive adverse environmental conditions and are resistant to commonly used drinking water and wastewater treatment method, hence *Cryptosporidium spp.* Oocysts are considered type B bioterrorism agents [13].

The parasite possesses peculiar physiological adaptation features compared with their sibling's apicomplexan. The habitat of the parasite is intracellular but extra-cytoplasmic. The parasite scavenges most of the host's biomolecules, so de-novo biosynthesis of amino acids, nucleotides, and fatty acids is missing. The parasite is also accompanied by rudimentary mitochondria lacking cytochrome-based respiratory chain proteins, thus relying on glycolysis for energy production [14]. The IMPDH (EC 1.1.1.205) is a rate-limiting enzyme for catalysis of Inosine 5'-Monophosphate (I.M.P.) to Xanthosine 5'-Monophosphate (XMP) with concurrent reduction of NAD⁺. The XMP is further catalyzed by G.M.P. synthase into Guanosine 5'-monophosphate (G.M.P.). Subsequently, a series of enzymatic reactions catalyzes G.M.P. into building blocks of nucleic acids (G.T.P., dGTP) [15]. The Adenine and guanine nucleotides are essential for cell growth and proliferation, and thus suppressing CpIMPDPH leads to a decline in proliferation and growth of the parasite [16].

In a study, Nwakaso N.Umejiego et al. emphasizes that when substrate IMP(Inosine-5'-monophosphate) and NAD⁺ bind within the active site of IMPDH, a unique conformational change takes place. The flap-like active site cysteine residue attack IMP and simultaneously transfer hydride ion to NAD⁺, and a conjugate of Enzyme -XMP (E-XMP) formed. Following conformational change facilitates NADH release and hydrolysis of E-XMP. The hydrolysis of E-XMP is a partially rate-limiting step. The authors have found that the kinetic properties of CpIMPDPH and human IMPDH are different, and ribavirin and mycophenolic acid (MPA) blocks CpIMPDPH catalysis in vivo models [17]. Another research study discovered a new CpIMPDPH inhibitor class through high throughput screening and in-vitro assay development for inhibition analysis [18]. The CpIMPDPH gene is passed from an ϵ -proteobacterium via the lateral gene transfer process, so it differs from that of the human counterpart in terms of kinetics [19]. A systematic review of studies has shown that CpIMPDPH is an outstanding drug target not only for cryptosporidiosis cure but also for other parasitic diseases. This review also presented a narrative overview of different inhibitors developed against CpIMPDPH [20,21]. There is ample evidence supporting the druggability aspect of CpIMPDPH. The comparative genomics analysis revealed that the IMPDH, Lactate dehydrogenase, Fatty acyl-coenzyme A Synthetase (LC-ACS) of *Cryptosporidium parvum* are some non-homologous proteins that have a different evolutionary origin and kinetic properties compared with the host [22]. The parasite is unable to synthesize purines de novo and scavenges nucleotides from the host cell. The parasite, like obligate intracellular bacteria *Chlamydia* and *Rickettsia*, possess a minimal set of genes [23]. In this way, the parasite is master in utilizing host metabolic resources for their growth and development. Parasite complex life cycle and high metabolic demand for nucleotides also make CpIMPDPH a critical drug target for developing next-generation antibiotics.

Paromomycin, an aminoglycoside, shows a modest activity against *C. parvum*, but it is less effective in AIDS patients [24]. Azithromycin, an azalide antibiotic, when given in combination with paromomycin, shows promising results in a small open-label trial in HIV patients (n = 11) with cryptosporidiosis [25]. Nitazoxanide (NTZ) and its two metabolites, tizoxanide and tizoxanide -glucuronide, show promising results in-vivo in mice, rats, and piglets against *C. parvum* infection [26]. Despite the general wellbeing and economic effects of *Cryptosporidium*, there are no preventive antibiotics treatment alternatives for humans that have been constrained to date. The primary affirmed treatment, nitazoxanide, decreases the span of diarrhea in immunocompetent grown-ups, yet is just reasonably effective in infants or children [27]. In-vivo and in-vitro models for the study of *C. parvum* pathogenesis are gnotobiotic piglets, neonatal calves, immunodeficient and immunocompetent mice, HCT -8 cell lines, cell-free culture, Hollow fiber technology, silk-protein scaffold model, colon-explants, lung, and small intestine organoids, and stem-cell-derived cultures. These models are highly technology expensive and associated with limitations [28].

The Computer-aided Drug Design (CADD) technologies override these hindrances along with other plummy aspects. The CADD technologies are broadly classified into ligand-based drug design (Pharmacophore-based approach), structure-based drug design (molecular docking-based approach), and quantitative structure-property and quantitative structure-activity relationships [29]. When one or more molecule possesses the same biological activity, than pharmacophore derived from them represent their essential features obligatory for biological activity. The pharmacophore can be used as 3D queries for high-throughput and in-silico screening, lead discovery, optimization of the lead for designing new molecules with desired features, and also helpful in assessing similarity and diversity among molecules [30,31]. On the other hand, pharmacophore could be exploited for the alignment of molecular chemical features or to develop predictive 3D QSAR models [32]. Current feature alignment and activity-based 3D QSAR modeling

are the two methods that can be used to form optimal ligand-based pharmacophore models. The D.S., Catalyst Hypothesis, Phase, and M. O.E. are tools commonly used for this purpose. A structure-based perspective can be used to generate the pharmacophore when three-dimensional (3D) structural information of the chosen target is known [33].

This work aims to discover a novel molecular entity that acts as a CpIMPDPH inhibitor with improved efficacy. To address the aim outlined above, we performed pharmacophore modeling, high throughput virtual screening, molecular docking, free energy calculation, and molecular dynamics simulation analysis to ascertain the critical interactions between ligands and catalytic pockets responsible for CpIMPDPH inhibitory activity. The highest active three compounds selected from the ZINC database are subjected to 50 ns molecular dynamic simulations to validate the proposed binding mode and binding affinity. A schematic representation of the methodology followed in this research is shown in Fig. 1.

2. Material and methods

2.1. Pharmacophore generation

The pharmacophore reflects three-dimensional(3D) 3D molecular interacting ecosystem of ligand and receptor (protein or nucleic acid). A 3D pharmacophore represents a summary of chemical features such as hydrogen bond (H-bond), ionic charges, lipophilic and aromatic contacts accountable for the functional and biological response initiation when ligands and receptor associate. Thus, a 3D pharmacophore model is used for extracting particular molecules laden with desired chemical features from the chemical space of millions of compounds stored in the form of databases. Methods of 3D pharmacophore derivation can be categorized as molecular field-based, substructure pattern-based, and feature-based, relying on how the pharmacophore attributes are deduced [34].

The PharmaGist tool (<https://bioinfo3d.cs.tau.ac.il/PharmaGist/>) was used to generate the 3D pharmacophore model on substructure-pattern based approach. When ligands interact with the receptor, ligand might have many potentially feasible conformations. PharmaGist deploys multiple flexible alignment processes for each input ligands separately. Candidate pharmacophores are generated in which one of the ligands serves as a pivot (the algorithm picks each input ligand to

serve as a pivot) on which the other target ligands are aligned. Based on the physicochemical features and pharmacophore score, the best pharmacophore is selected and downloaded in mol2 format for further analysis [35].

2.2. Virtual screening

The ZINCPharmer (<http://zincpharmer.csb.pitt.edu/>), an online tool, was used for the high throughput screening of small molecules against a submitted pharmacophore query [36]. The ZINC Purchasable (<https://zinc.docking.org/>) subset of the ZINC database, containing 22,724,825 molecules, was chosen for virtual screening that could provide a new chemical moiety to act as an inhibitory ligand for CpIMPDPH [37]. The molecules which showed maximum homology to the query pharmacophore were strained out. Subsequently, these strained or 'hit molecules' further subjected to Lipinski's rule of five filters, which states that drugs must consist of molecules with molecular weight <500D, HBD<5, HBA <10, and an octanol/water partition coefficient (LogP) value < 5. Filtered molecules are now supposed as 'potential lead molecules' and passed to the next filter of docking and ADME filter [38].

2.3. Molecular docking

CpIMPDPH (PDB ID: 4IXH) (<https://www.rcsb.org/>), protein in complex with a ligand Q21 or (2s)-2-(Naphthalen-1-Yloxy)-N-[2-(Pyridin-4-Yl)-1,3- Benzoxazol-5-Yl] Propanamide was selected for the binding mode confirmation of potential lead molecules [39].

The purpose of this exercise is to validate whether the filtered hit molecules bind in the target protein active site amino acid residues with precise orientation. The strained 'hits' ligand were subjected to docking by the AutoDock Vina tool (<http://vina.scripps.edu/>) [40].

Before docking, the target protein is prepared by removing water molecules and polar hydrogen atoms to neutralize ionization of both basic and acidic amino acid residues. The MMFF force field was used for the energy minimization of the target protein. The information about the active site was retrieved through literature search, PDBsum(<http://www.ebi.ac.uk/thornton-srv/databases/cgi-bin/pdbsum/>), and binding interactions were generated through the LIGPLOT⁺ tool [41]. The active site was marked off as a sphere of 10 Å around the native ligand (Q21) in the target protein(PDB ID:4IXH). The grid box was laid down to 50x50x50 X.Y.Z. Points. The best-docked pose of hits with higher

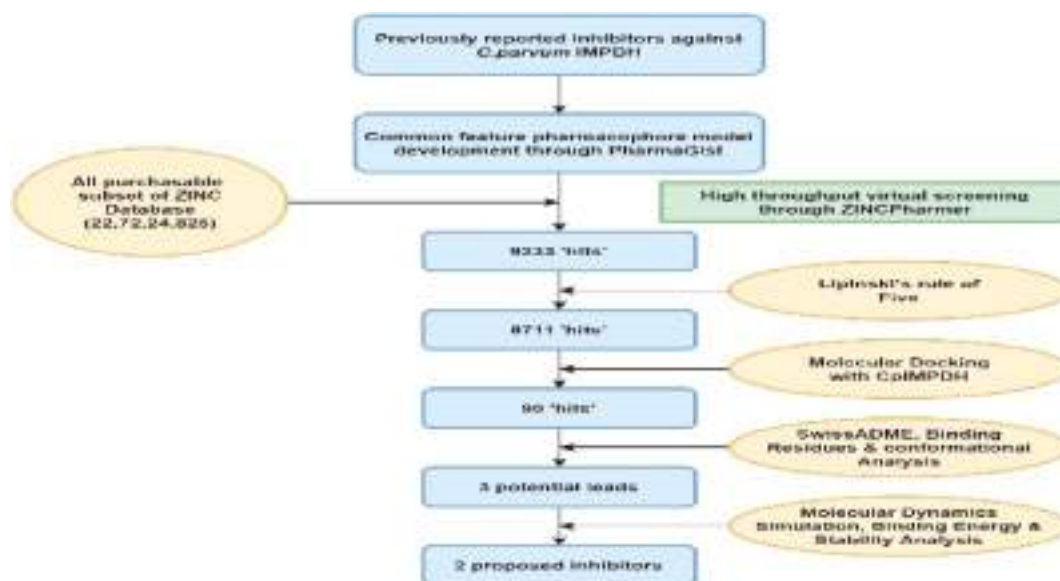


Fig. 1. Schematic representation of methodology followed in this research.

binding-free energy compared to reference ligand and that demonstrate interaction with the important active site residues with requisite geometry was selected as more desirable potential lead molecules.

2.4. Molecular dynamic simulations

Molecular dynamic (MD) simulations were performed to evaluate the stability, binding interactions of the selected lead compound in the active site of CpIMPDPH (PDB ID:4IXH). The MD simulation is a valuable analysis for determining the static and dynamic behavior of protein-ligand complex over a span of time. The MD simulation also shed light on the conformational, topology facet and 3D coordinate of biomolecule complex.

LiGRO, a GUI-based tool, was used to prepare the setup files of the protein-ligand system for the MD simulations using Gromacs 5.1.5, and the ACPYPE tool was used to generate the topology and parameter files for the ligands [42–44]. The system was solvated with Tip3P water molecules in a cubic box such that the distance of every atom of the protein-ligand system with the water box edge was 2 nm. The system charge was neutralized with a 0.15 M concentration of NaCl. The solvated system was equilibrated under N.V.T. and N.P.T. ensemble using modified Berendsen thermostat and Parinello-Rahman barostat at 310.15K and 1.0 atm respectively for one ns each, followed by the production run of 50ns at 310.15K and 1.0 atmosphere (atm) pressure. SHAKE algorithm was employed on the covalent bonds with hydrogen atoms. Time step integration of 2 femtoseconds (fs) was applied, and the frames were stored every 10 picoseconds (ps). After the production run, trajectories were analyzed for the RMSD(Root Mean Square Deviation), RMSF, and hydrogen bonding profile data obtained from the MD simulations.

The binding energy of the lead molecules with the protein 4IXH was calculated with the MMPBSA(Molecular Mechanics Poisson-Boltzmann Surface Area) tool of Gromacs using the last 100 frames from the metastable region of 45–50 nanoseconds (ns) of the MD trajectories with the values of solute and solvent dielectric constants set to 1 and 80, respectively [45].

A comprehensive analysis of interaction energy was performed on the best stable simulated complex of each protein and ligand complex. The average values of protein-ligand interaction energy were recorded in the term of the Gibbs free energy [46].

$$\Delta G = (\text{EE})_{\text{vander waal energy}} + (\text{EE})_{\text{electrostatic energy}} + (\text{EE})_{\text{polar solvation energy}} + (\text{EE})_{\text{SASA}} + (\text{EE})_{\text{SAV energy}} + (\text{EE})_{\text{WCA energy}}$$

Where: ΔG -binding free energy

SASA – Solvent accessible surface area or non-polar solvation energy

The free energy of each molecular entity was calculated as follows-

$$G = E_{\text{vdw}} + E_{\text{ele}} + E_{\text{int}} + G_{\text{PB}} + G_{\text{SA-TS}}$$

Where- E_{vdw} = Van Der Waal free energy

E_{ele} = Electrostatic free energy
 E_{int} = internal free energy
 G_{PB} = Polar free energy
 G_{SA} = Non-Polar free energy
 TS = Solute entropic proportion

The binding free energy of protein-ligand complex(ΔG_{bind}) was calculated as follows-

$$\Delta G_{\text{bind}} = G_{\text{complex}} - G_{\text{protein}} - G_{\text{ligand}}$$

The G_{complex} , G_{protein} , and G_{ligand} are free energy of protein-ligand complex, protein, and ligand, respectively [47].

3. Results and discussion

3.1. Pharmacophore model generation

The pharmacophore models were derived from three known active (Q21 or (2s)-2-(Naphthalene-1-Yloxy)-N-[2-(Pyridin-4-Yl)-1,3-Benzoxazol-5-Yl]propanamide; N09 or N-(4-Chloro-3-Methoxyphenyl)-2-(4-Oxochromeno[4,3-C]pyrazol-1(4h)-Yl)acetamide; C64 or N-(4-Bromophenyl)-2-[2-(1,3-Thiazol-2-Yl)-1h-Benzimidazol-1-Yl]co-crystallized with protein structure (PDB ID:4IXH,4QJ1,3KHJ) and shown in supplementary figure 1 [48].

The Multiple flexible alignments of input ligands generated the pharmacophore model, and all shared features of the input ligands are also considered during model generation. The Hydrogen bond donor (HBD), Hydrogen bond acceptor (HBA), Aromatic ring (AR), hydrophobic (HYD), positive ionizable (PI), negative ionizable (N.I.) features are chosen as essential features of the model. All the generated pharmacophores are then compared based on scores, and total highlights were mapped with active, and decoys compounds, and details are shown in Table 1 and Fig. 2A.

The pharmacophore, having the highest score (around 33.068) and covering maximum features of input ligands, was selected as a query pharmacophore for virtual screening. It is a six-feature pharmacophore having three AR, one HBD, and two HBA and shown in Fig. 2B. One of the aromatic features is disabled during virtual screening as the previous research validated that only two AR features are essential in this case [49].

A target-based and ligand-based pharmacophore feature was developed recently for *C. parvum* inosine 5'-monophosphate dehydrogenase (CpIMPDPH) [50]. Their pharmacophore model has two- AR, one of the hydrophobic-aliphatic and hydrogen bond donors in CpIMPDPH. Further, this allowed a conformational structure for the NAD⁺ binding site for IMPDPH [51].

3.2. Virtual screening

The obtained pharmacophore was then submitted to the ZINC-Pharmer server for virtual screening to capture potential 'hit ligands.' The pharmacophore uploaded in mol2 format, and it was run with features-2AR, 1HBD, and 2HBA. Here we have disabled one of the AR features as it creates a steric hindrance to the other AR features. Out of 22,724,825 ligands molecules, virtual screening analysis returned 9233 potential 'hit ligands' that correctly matched with features present in the query pharmacophore model. These potential hits were additionally segregated based on Lipinski's rule of 5. This filter reduces the number of the molecule to 8711 hits ligands or a drug like a molecule. Further, these molecules were virtually screened by molecular docking with the target protein(PDB ID:4IXH).

3.3. Molecular docking

The AutoDock Vina is used for molecular docking simulations. The filtered hit ligands (8711) docked into the active site of the *C. parvum* IMPDPH (PDB ID: 4IXH) receptor protein. The literature analysis have shown that Glu329, Met 302,Gly303,Met308,Ala165,Tyr358,Thr221, Val327,Met326,Ser354,Ser169,Ser22,Gly357,Pro26, Leu25 and Val24 are amino acid residues making contacts with ligand during catalysis process. Docking protocol was validated by re-docking Q21, C64, and N09 ligand, which are in a complex in 4IXH,3KHJ, and 4QJ1 protein, respectively. The docking result showed that C64, Q21, N09 ligands interact within the same binding pocket. All three ligands gave comparable binding-free energy. The docking results of selected ligands are shown in Table 2. In this docking simulation, receptor protein (CpIMPDPH) side chains allowed for limited conformational flexibility, and flexible-ligand docking mode was selected.

Eventually, 8711 hit ligand molecules docked onto receptor protein,

Table 1
Detailed information on generated pharmacophore models from PharmaGist Tool.

Pharmacophore model	The score of the pharmacophore model	Total features of the pharmacophore model	A.R.	HY	HBD	HBA
1	33.068	6	3	0	1	2
2	18.371	3	2	0	1	0
3	18.371	3	2	0	0	1
4	18.371	3	2	0	0	1
5	18.371	3	2	0	0	1
6	18.371	3	2	0	0	1
7	14.697	3	1	0	1	1
8	14.697	3	1	0	0	2
9	14.697	3	1	0	0	2

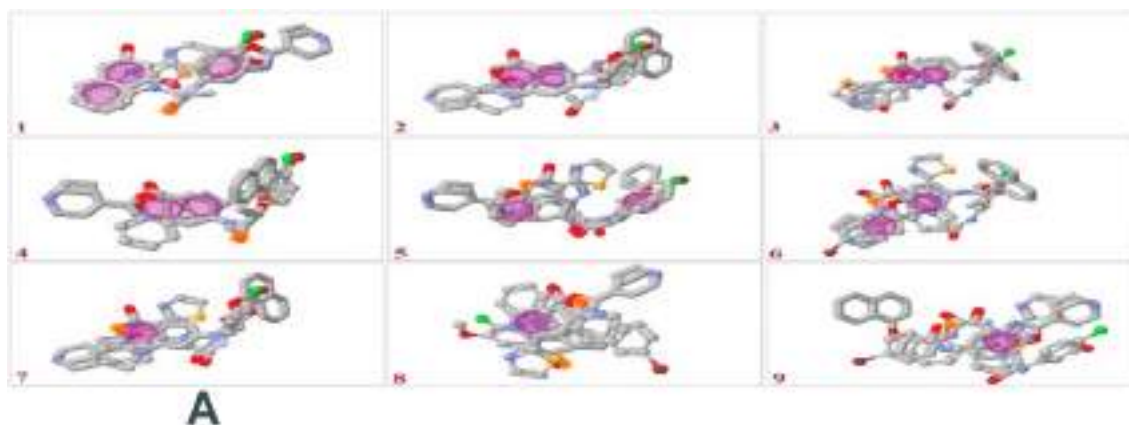


Fig. 2A. The top 9 pharmacophore model of *C. parvum* IMPDH inhibitors generated by PharmaGist and mapping of training set compound onto the pharmacophore (numbers on the bottom represent their sequence as per Table 1)(Here: round meshes, feature; orange, hydrogen bond acceptor; purple, aromatic; white, hydrogen bond donor.). (For interpretation of the references to colour in this figure legend, the reader is referred to the Web version of this article.)

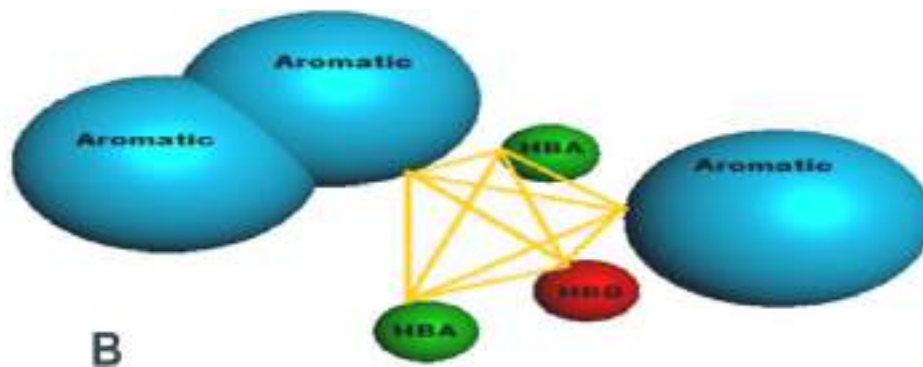


Fig. 2B. Geometric parameter of best-selected pharmacophore model which used as a 3D query in the virtual screening process. (Here: H.B.A., hydrogen bond acceptor; HBD, hydrogen bond donor).

Table 2
Docking results were obtained from AutoDock Vina by re-docking Q21, C64, and N09 ligand in 4IXH (PDB id) chain B receptor protein.

Receptor Protein	Docked Ligand	Interacting amino acid residues	Binding energy (kcal/mol)
4IXH	Q21	GLY 214:HN→O3	-9.5
	C64	SER 48: H.G. →N4 GLY212: O→HZ	-8.9
N09		GLY 214:HN→O2	-9.0
		THR 221: HG1→ O1	
		THR 221: HG1→ O3	

and ligand conformations were ranked in descending order of their binding free energy. The docking energy calculated by AutoDock is a combination of Vander Waal energy, electrostatic energy, hydrogen bonding energy, and desolvation energy. The docking results were analyzed cautiously, and the binding-free energy of all of them was analyzed. At this stage, the top 10% of the hit ligands, which satisfy the chosen criteria for docking, were chosen. These top 10% hit ligands were again re-docked to the same active site in triplicate times for validating docking calculations. This exercise strained out three lead molecules (ZINC9672610, ZINC16511373, and ZINC39780256). The selected lead molecules were found to possess high free binding energy than the reference ligands and have shown interaction with essential active-site amino acid residues. The details of selected leads, along with their binding orientation and binding residues, are shown in Fig. 3. Fig. 3 is divided into three (A, B, C) subparts which are further divided into

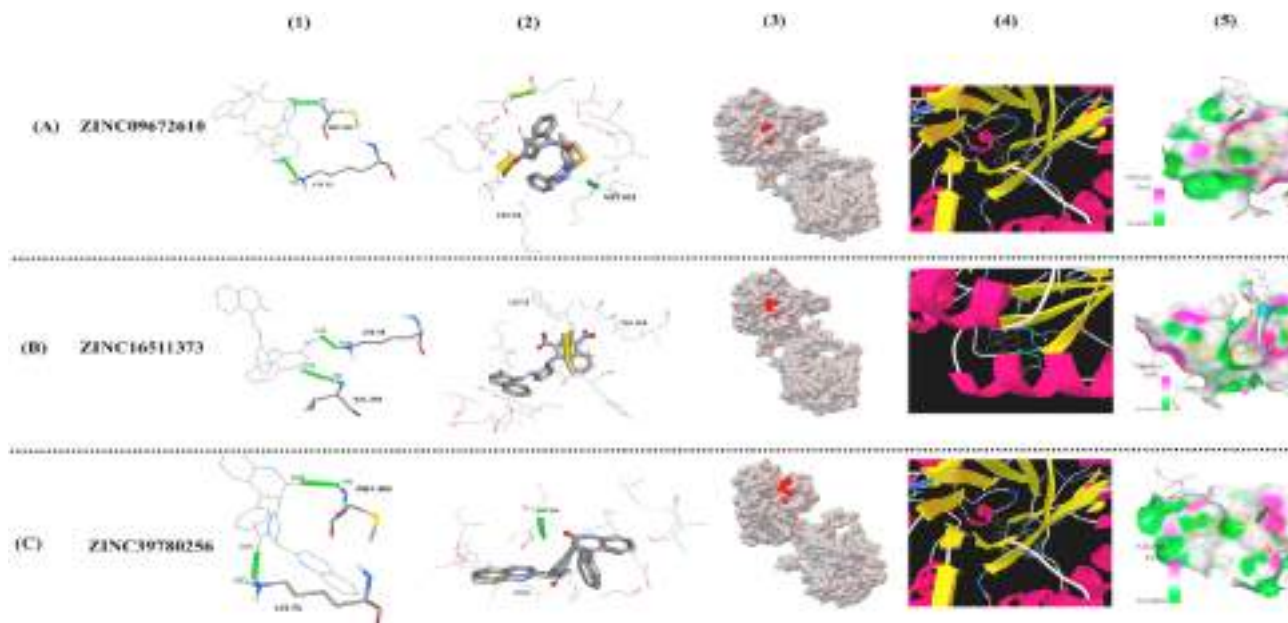


Fig. 3. Binding orientation of ZINC9672610 (A), ZINC16511373 (B) and ZINC39780256 (C) hit within the pocket of 4IXH (PDB ID) receptor protein (different poses). Images were generated with the help of AutoDock Tool.

(1,2,3,4,5) sub-subparts to show a different aspect of interaction.

- (1). The thick stick represents target protein where a thin stick represents ligand and green solid sphere represent interacting residues along with interacting atom between ligand and target.
- (2). A thick stick represents ligand, whereas a thin stick represents a target, and dotted green lines indicate hydrogen bond.
- (3). Ligand (red) in the binding cavity of target protein (grey).
- (4). Ligand (stick) and target protein (ribbon) secondary structure model complex.
- (5) Molecular surface model of the target protein and ligand displaying features of the binding cavity (image generated with Discovery Studio Tool)

The details of the binding free energy and the amino acid residues of the selected lead molecules involved in this interaction are enlisted in

Table 3
Statistical docking result of three best ligands with 4IXH (PDB ID) protein showing interacting residue, bond length, and binding energy.

ZINC ID	2D structure	Interacting residue(s)	Bond length (Å)	Binding Energy (Kcal/mol)
ZINC16511373 7th conformer		LYS 73B: HZ1→O35 VAL 143B: HN→O34	2.083 2.18	-11.2
ZINC39780256 6th conformer		L.Y.S. 73B: HZ→O35 MET 302B: HN→O34	1.840 2.113	-10.4
ZINC9672610 12th conformer		LYS73B: HZ1→N28 MET 302B: HN→N30	2.245 2.242	-10.2

Table 3. These ligands also possess good pharmacokinetics and drug-likeness properties as determined through the SwissADME tool (<http://www.swissadme.ch/>), and results are shown in Table 4 [52].

These molecules attained a better molecular geometry in the target protein's chosen active site and simultaneously formed hydrogen bonding with essential amino acid residue. ZINC16511373 ZINC39780256 and ZINC09672610, displayed binding affinity of -11.2, -10.4 and -10.2 kcal/mol, respectively. The seventh conformer, ZINC16511373, builds hydrogen bonds with LYS73 and Val143. The sixth conformer of ZINC39780256 exhibited one hydrogen bond with LYS73 along with hydrophobic interactions. The twelfth conformer of ZINC9672610 builds two hydrogen bonds with MET302 and Lys 73. The bond lengths of all hydrogen bonds are also in the permissible range. The binding pose of ZINC09672610, ZINC16511373, and ZINC39780256 also displayed geometrical symmetry with the query Pharmacophore. In chemical word, the ZINC39780256, is known as [3R]-3-[C3S]-2-acetyl-3-[(2-quinonyl)-3,4-dihydropyrazol-5-yl]-4-phenyl-3H-quinolin-2-one. It is a derivative of quinoline. The ZINC09672610 (2-[-[4-(3,4-dimethylphenyl)-5-(4-pyridyl)-1,2,4-triazole-3-yl]sulfonyl]acetyl]-3-methyl [(3)-[2-[(2,4-dinitro-1-naphthyl)amino]phenyl]iminomethyl]naphthalen-2-ol.

3.4. Molecular dynamic simulation

The structural conduct and pliability of receptor CpIMPDH (PDB:4IXH) docked with reference ligand, and selected ligands were examined in terms of binding free energy and hydrogen bond profile analysis. The free energy of binding scores and plot is shown in Fig. 4 and Fig. 5, respectively. The ZINC16511373 ligand showed the highest free energy of binding (-120.002 kJ/mol) with the target protein 4IXH, followed by ZINC3980256 (-118.651 kJ/mol) and ZINC9672610 (-103.920 kJ/mol). The hydrophobic (van der waal) interactions were more dominant than the electrostatic interactions in all three cases. The ZINC16511373 ligand formed up to 5 hydrogen bonds with receptor (4IXH) protein while ZINC3980256 and ZINC9672610 formed up to 2 and 9 hydrogen bonds, respectively, with the receptor(4IXH) throughout the trajectory (Fig. 3).

The overall stability of the free target protein (4IXH) and ligand-

Table 4
Pharmacokinetics and drug-likeness properties of three best ligands generated from SwissADME tool. .

LIGAND ID	LIGAND FORMULA	MW(g/mol)	Number of Heavy atoms	Number of Aromatic Heavy atoms	Number of rotatable bonds	Number of Hydrogen bond acceptor	Number of Hydrogen bond donor	GI absorption	BBB permeant	log Kp(cm/s)	Lipinski Violation	Leadlike	Synthetic accessibility
ZINC16511373	C27H18N4O5	478.5	36	26	6	6	2	low	no	-4.16	0	0	3.99
ZINC39780256	C29H22N4O2	458.5	35	22	4	5	0	high	yes	-6.5	0	0	4.83
ZINC9672610	C27H26N6O2S	498.6	36	23	6	5	1	high	no	-6.75	0	2	4.23

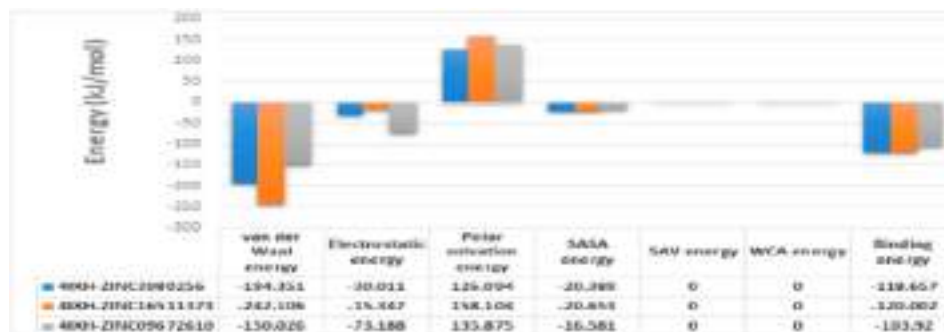


Fig. 4. The binding energy graph of the ligand-protein complex.

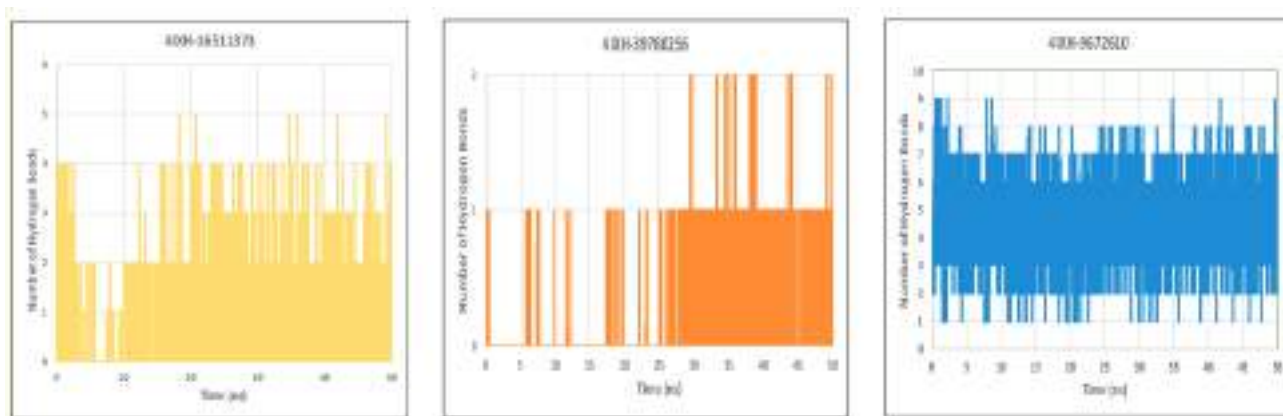


Fig. 5. The plot of hydrogen bond formed by the lead molecules (ZINC16511373, ZINC39780256, ZINC9672610) with target protein (PDB ID:4IXH) throughout 50 ns time scale.

complexed target protein was monitored based on the RMSD values, as shown in Fig. 6. Compared with the free target protein (4IXH), all the ligand-4IXH complexes followed different conformational changes in the beginning and middle of the trajectories. Finally, they attained the metastable state after 35ns interval, pertaining to the fact that the docked ligands stabilized themselves in the active site pocket in the later part of the trajectory, which is also demonstrated by the RMSF values in Fig. 7, where the RMSF values of the lead molecules complexed protein residues were significantly lower than the free target (4IXH) protein. Hence the binding of the lead molecules stabilized the target protein (4IXH).

The stability of ligands is further accessed by calculating the inhibition constant (ki) value using the binding free energy. The Ki value is calculated as follows-

$$\Delta G = -RT \ln K_i$$

ΔG -Gibbs free energy, R-universal gas constant, T-temperature

The Ki values of complex1 (4IXH-ZINC09672610), Complex 2 (4IXH-16511373) and complex 3 (4IXH-39780256) are 3.082×10^{-9} nM, 6.17×10^{-12} nM and 1.19×10^{-2} nM respectively. All these values are in an acceptable range when compared with reference ligands.

4. Conclusion

Even after the enormous public health consequences laid by cryptosporidiosis, there is a gap among disease and effective medications. The gap became more widens due to the COVID-19 pandemic.

There is almost no part of the globe that will remain unaffected by the COVID-19 pandemic in terms of health care crisis or a resulting financial recession. Awareness is increasing the short-term and long-term impacts of COVID-19 on drug development, clinical research, and other related areas. To address this problem, we developed a comprehensive screening workflow for the selection of CpIMPDPH inhibitors. In this study, a 3D pharmacophore model was generated from the known structurally diverse inhibitor using the PharmaGist tool. The pharmacophore model having the highest score along with the maximum number of features was chosen. The pharmacophore model consists of three AR, one HBD, and two HBA features and is used as a 3D query for the virtual scanning of the ZINC purchasable drug database. By placing distinct filters, the database suppressed to a total of 8711 molecules or 'hits.' These hits were subjected to docking to the active site of *C. parvum* IMPDPH (PDB ID: 4IXH) receptor protein by AutoDock Vina to explore the binding stability and conformation. The 'hits' were sorted



Fig. 6. The RMSD graph depicting the behavior of free target (4IXH) protein and ligand-complexed protein over a 50 ns timescale.

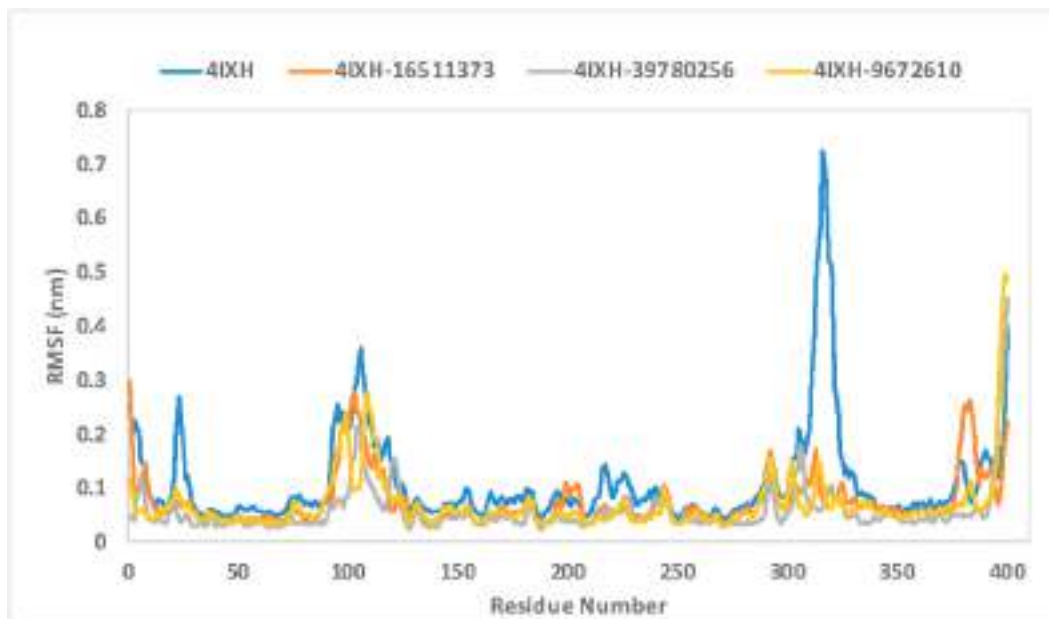


Fig. 7. The RMSF plot of the free target protein (4IXH) and ligand-complexed protein.

out on the basis of their interaction with active-site residues as well as on the basis of binding energy affinity. The ZINC09672610, ZINC16511373 and ZINC39780256 ligand has satisfied all criteria and fetched out from the ZINC database as a lead molecule. These three lead molecules were also passed the pharmacokinetics and drug-likeness filter. The MD simulation analysis of these three lead molecules was performed to validate the binding stability in the target protein. The hydrogen bond interaction profile, RMSD, and RMSF analysis of free and lead-protein complex are reinforcing the docking analysis. The

inhibition constant (K_i) values of these lead molecules were also analyzed and found satisfactory. It was observed that ZINC39780256, a quinolin derivative is having a basic structure similar to a recently discovered inhibitor of CpIMPDH [18]. The ZINC09672610 is a member of triazole family. The triazole derivative is extensively studied for its antibacterial, antifungal, anticancer, antiviral, and anti-inflammatory behavior [53]. The ZINC16511373 is a new heterocyclic compound that has hitherto not been analyzed in the scientific text as a CpIMPDH inhibitor. These lead molecules might provide guidelines in designing

novel *anti*-cryptosporidial drugs for treating *Cryptosporidium* infections in children and adults. In the Future, *in vivo* studies will be performed to further validate the inhibitory potential of these novel molecules against CpIMPDPH.

The main potential limitation of the present study is that the *in-silico* model of research.

Declaration of competing interest

The authors declare that they have no known competing financial interests or personal relationships that could have appeared to influence the work reported in this paper.

Acknowledgment

The authors acknowledge the Director, Dr. Ambedkar Institute of Technology for Handicapped, for providing a research facility.

Appendix A. Supplementary data

Supplementary data to this article can be found online at <https://doi.org/10.1016/j.imu.2021.100583>.

References

- Nicola M, et al. The socio-economic implications of the coronavirus pandemic (COVID-19): a review. *Int J Surg* 2020. <https://doi.org/10.1016/j.ijsu.2020.04.018>.
- Tyzzar EE. A sporozoan found in the peptic glands of the common mouse. *Exp Biol Med* 2013. <https://doi.org/10.3181/00379727-5-5>.
- Gerace E, Lo Presti VDM, Biondo C. Cryptosporidium infection: epidemiology, pathogenesis, and differential diagnosis. *Eur. J. Microbiol. Immunol.* 2019;9(4): 119–23.
- Clark DP. New insights into human Cryptosporidiosis. *Clin Microbiol Rev* 1999;12(4):554–63.
- Shirley DAT, Moonah SN, Kotloff KL. Burden of disease from cryptosporidiosis. *Curr Opin Infect Dis* 2012;25(5):555. <https://doi.org/10.1097/QCO.0b013e328357e569>.
- Kotloff KL, et al. Burden and aetiology of diarrhoeal disease in infants and young children in developing countries (the Global Enteric Multicenter Study, GEMS): a prospective, case-control study. *Lancet* 2013;382(9888):209–22. [https://doi.org/10.1016/S0140-6736\(13\)60844-2](https://doi.org/10.1016/S0140-6736(13)60844-2).
- Carter BL, Chalmers RM, Davies AP. Health sequelae of human cryptosporidiosis in industrialised countries: a systematic review. *Parasites Vectors* 2020;13(1):1–14.
- Bhalchandra S, Cardenas D, Ward HD. Recent breakthroughs and ongoing limitations in cryptosporidium research. *F1000Research* 2018. <https://doi.org/10.12688/f1000research.15333.1>.
- Mohebbi M, Yimam Y, Woreta A. Cryptosporidium infection among people living with HIV/AIDS in Ethiopia: a systematic review and meta-analysis. *Pathog Glob Health* 2020;114(4):183–93.
- Dong S, et al. Prevalence of Cryptosporidium infection in the global population: a systematic review and meta-analysis. *Acta Parasitol* 2020;65:882–9.
- Tandel J, et al. Life cycle progression and sexual development of the apicomplexan parasite *Cryptosporidium parvum*. *Nat. Microbiol.* 2019;4(12):2226–36.
- Shrivastava AK, Kumar S, Smith WA, Sahu PS. Revisiting the global problem of cryptosporidiosis and recommendations. *Tropenmed Parasitol* 2017;7(1):8.
- Tzipori S, Ward H. Cryptosporidiosis: biology, pathogenesis and disease. *Microb Infect* 2002. [https://doi.org/10.1016/S1286-4579\(02\)01629-5](https://doi.org/10.1016/S1286-4579(02)01629-5).
- Swarna LS, Parkinson J. Genomics of apicomplexan parasites. *Crit Rev Biochem Mol Biol* 2017. <https://doi.org/10.1080/10409238.2017.1290043>.
- Juvala K, Shaik A, Kirubakaran S. Inhibitors of inosine 5'-monophosphate dehydrogenase as emerging new generation antimicrobial agents. *Medchemcomm* 2019;10(8):1290–301.
- Pawlowic MC, et al. Genetic ablation of purine salvage in *Cryptosporidium parvum* reveals nucleotide uptake from the host cell. *Proc Natl Acad Sci Unit States Am* 2019;116(42):21160–5.
- Umejiego NN, Li C, Riera T, Hedstrom L, Striepen B. *Cryptosporidium parvum* I.M.P. Dehydrogenase. *J Biol Chem* 2004;279(39):40320–7. <https://doi.org/10.1074/jbc.m407121200>.
- Shigetomi K, Sarwono AEY, Ichikawa S, Ubukata M. Novel adenosine-derived inhibitors of *Cryptosporidium parvum* inosine 5'-monophosphate dehydrogenase. *J Antibiot (Tokyo)* 2019;72(12):934–42.
- Gollapalli DR, MacPherson IS, Liechti G, Gorla SK, Goldberg JB, Hedstrom L. Structural determinants of inhibitor selectivity in prokaryotic I.M.P. dehydrogenases. *Chem Biol* 2010. <https://doi.org/10.1016/j.chembiol.2010.07.014>.
- Aey S, et al. Repurposing existing drugs: identification of irreversible IMPDH inhibitors by high-throughput screening. *J Enzym Inhib Med Chem* 2019. <https://doi.org/10.1080/14756366.2018.1540474>.
- Fotie J. Inosine 5'-monophosphate dehydrogenase (IMPDH) as a potential target for the development of a new generation of antiprotozoan agents. *Mini Rev Med Chem* 2016. <https://doi.org/10.2174/1389557516666160620065558>.
- Sk G, et al. Validation of I.M.P. dehydrogenase inhibitors in a mouse model of cryptosporidiosis. *Antimicrob Agents Chemother* 2014. <https://doi.org/10.1128/A.A.C.02075-13.L.K>. <http://sfx.library.uu.nl/utrecht?sid=EMBASE&issn=00664804&id=doi:10.1128%2FAAC.02075-13&atitle=Validation+of+IMP+dehydrogenase+inhibitors+in+a+mouse+model+of+cryptosporidiosis&title=Antimicrob.+Agents+Chemother.&title=Antimicrobial+Agents+and+Chemotherapy&volum e=58&issue=3&spage=1603&epage=1614&aulast=Gorla&aufirst=Suresh+Kumar&aunit=S.K.&aufull=Gorla+S.K.&coden=AMACC&isbn=&pages=1603-1614&date=2014&aunit1=S&aunitm=K>.
- Hedstrom L, Liechti G, Goldberg JB, Gollapalli DR. The antibiotic potential of prokaryotic I.M.P. Dehydrogenase inhibitors. *Curr Med Chem* 2011. <https://doi.org/10.2174/092986711795590129>.
- Gargala G. Drug treatment and novel drug target against *Cryptosporidium*. *Parasite* 2013. <https://doi.org/10.1051/parasite/2008153275>.
- Kadappu KK, V Nagaraja M, V Rao P, Shastry BA. Azithromycin as treatment for cryptosporidiosis in human immunodeficiency virus disease. *J Postgrad Med* 2002; 48(3):179.
- Rossignol JF, Kabil SM, El-gohary Y, Younis AM. Effect of nitazoxanide in diarrhea and enteritis caused by *Cryptosporidium* species. *Clin Gastroenterol Hepatol* 2006. <https://doi.org/10.1016/j.cgh.2005.12.020>.
- Lunde CS, et al. Identification of a potent benzoxaborole drug candidate for treating cryptosporidiosis. *Nat Commun* 2019. <https://doi.org/10.1038/s41467-019-10687-y>.
- Love MS, McNamara CW. Phenotypic screening techniques for *Cryptosporidium* drug discovery. *Expet Opin Drug Discov* 2021;16(1):59–74.
- Leelananda SP, Lindert S. Computational methods in drug discovery. *Beilstein J Org Chem* 2016. <https://doi.org/10.3762/bjoc.12.267>.
- Gao Q, Yang L, Zhu Y. Pharmacophore based drug design approach as a practical process in drug discovery. *Curr Comput Aided-Drug Des* 2010. <https://doi.org/10.2174/157340910790980151>.
- Kumar A, Zhang KYJ. Advances in the development of shape similarity methods and their application in drug discovery. *Front. Chem.* 2018;6:315.
- Krusemark CJ. Drug design: structure- and ligand-based approaches. 2012.
- Kapetanovic IM. Computer-aided drug discovery and development (CADD): in silico-chemico-biological approach. *Chem Biol Interact* 2008. <https://doi.org/10.1016/j.cbi.2006.12.006>.
- Yadav DK, Kumar S, Teli MK, Kim M. Ligand-based pharmacophore modeling and docking studies on vitamin D receptor inhibitors. *J Cell Biochem* 2020;121(7): 3570–83.
- Schneidman-Duhovny D, Dror O, Inbar Y, Nussinov R, Wolfson HJ. PharmaGist: a webserver for ligand-based pharmacophore detection. *Nucleic Acids Res* 2008. <https://doi.org/10.1093/nar/gkn187>.
- Koes DR, Camacho CJ. ZINCPharmer: pharmacophore search of the ZINC database. *Nucleic Acids Res* 2012. <https://doi.org/10.1093/nar/gks378>.
- Irwin JJ, Shoichet BK. ZINC - a free database of commercially available compounds for virtual screening. *J Chem Inf Model* 2005. <https://doi.org/10.1021/ci049714>.
- Pollastri MP. Overview on the rule of five. *Current Protocols in Pharmacology* 2010. <https://doi.org/10.1002/0471141755.ph0912s49>.
- Kim Y, Maltseva N, Mulligan R, Makowska-Grzyska M, Gu M, Gollapalli D. Crystal structure of the catalytic domain of the inosine monophosphate dehydrogenase from *Bacillus anthracis* in the complex with I.M.P. And the inhibitor P200. *RCSB Protein Data Bank* 2017.
- Forli W, Halliday S, Belew R, Olson A. AutoDock version 4.2. CiteSeer; 2012.
- Laskowski RA, Swindells MB. LigPlot+: multiple ligand-protein interaction diagrams for drug discovery. *J Chem Inf Model* 2011. <https://doi.org/10.1021/ci200227u>.
- Abraham MJ, et al. GROMACS: high performance molecular simulations through multi-level parallelism from laptops to supercomputers. *Software* 2015;1:19–25.
- Bernardi A, Faller R, Reith D, Kirschner KN. ACPYPE update for nonuniform 1–4 scale factors: conversion of the GLYCAM06 force field from AMBER to GROMACS. *Software* 2019;10:100241.
- Kagami LP, das Neves GM, da Silva AWS, Caceres RA, Kawano DF, Eifler-Lima VL. LIGRO: a graphical user interface for protein–ligand molecular dynamics. *J Mol Model* 2017;23(11):1–6.
- Kumari R, Kumar R, Consortium OSDD, Lynn A. g_mmpbsa A GROMACS tool for high-throughput MM-PBSA calculations. *J Chem Inf Model* 2014;54(7):1951–62.
- Genheden S, Ryde U. The MM/PBSA and MM/GBSA methods to estimate ligand-binding affinities. *Expet Opin Drug Discov* 2015;10(5):449–61.
- Low C-F, Shamsir MS, Mohamed-Hussein Z-A, Baharum SN. Evaluation of potential molecular interaction between quorum sensing receptor, LuxP and grouper fatty acids: *in-silico* screening and simulation. *PeerJ* 2019;7:e6568.
- Sun Z, et al. Synthesis, *in vitro* evaluation and cocrystal structure of 4-oxo-[1] benzopyrano [4, 3-c] pyrazole cryptosporidium parvum inosine 5'-monophosphate dehydrogenase (cp IMPDH) inhibitors. *J Med Chem* 2014;57(24):10544–50.
- Gollapalli DR, MacPherson IS, Liechti G, Gorla SK, Goldberg JB, Hedstrom L. Structural determinants of inhibitor selectivity in prokaryotic I.M.P. dehydrogenases. *Chem Biol* 2010;17(10):1084–91.

- [50] Gorla SK, et al. Selective and potent urea inhibitors of cryptosporidium parvum inosine 5'-monophosphate dehydrogenase. *J Med Chem* 2012. <https://doi.org/10.1021/jm3007917>.
- [51] Li RJ, Wang YL, Wang QH, Huang WX, Wang J, Cheng MS. Binding mode of inhibitors and *Cryptosporidium parvum* I.M.P. dehydrogenase: a combined ligand- and receptor-based study. *SAR QSAR Environ Res* 2015. <https://doi.org/10.1080/1062936X.2015.1043341>.
- [52] Daina A, Michielin O, Zoete V. SwissADME: a free web tool to evaluate pharmacokinetics, drug-likeness and medicinal chemistry friendliness of small molecules. *Sci Rep* 2017. <https://doi.org/10.1038/srep42717>.
- [53] Dong H-R, Wu J-G. Design, synthesis and anticancer activity evaluation of aziridine-1, 2, 3-triazole hybrid derivatives. *Heterocycl Commun* 2018;24(2): 109–12.

Simulation of language competition by bilingual agents

Rakesh Kumar

Department of Computer Science and Engineering,
National Institute of Technical Teachers Training and Research,
Sector-26, Chandigarh 160019, India
Email: raakeshdhiman@gmail.com

ShivKishan Dubey*

Department of Computer Science and Engineering,
Dr. Ambedkar Institute of Technology for Handicapped,
Awadhपुरi, Kanpur 208024, India
Email: shiv.aith06@gmail.com

*Corresponding author

Abstract: In the language transmission, a person shares different ways of own lexicons to others and each one is able to reproduce new lexicons through the old ones. Our objective is to explore how lexicons can be modified in synchronic or diachronic scenarios during the interaction of two different languages (L1 or L2) community agents. In this research, a new model has been proposed within language competition game strategy using bilingual agents. The outcome of shared lexicons in the synchronic scenario is that massive codes of second-language are affected and propagated into future generation successfully. Initially, we take matured agents who are stimulated by iterated learning model (ILM) and equipped with own grammar rules. Using Levenshtein Distance, these agents modify own old lexicons and generate new ones for the next generation. This game strategy is restricted to synchronic only and found that second language always wins this game.

Keywords: NLP; natural language processing; iterated learning model; language acquisition; bilingualism; exposure ratio.

Reference to this paper should be made as follows: Kumar, R. and Dubey, S. (2018) 'Simulation of language competition by bilingual agents', *Int. J. Knowledge and Learning*, Vol. 12, No. 4, pp.362–378.

Biographical notes: Rakesh Kumar is an Assistant Professor of Computer Science and Engg department in the N.I.T.T.R Chandigarh. He earned his PhD in Computer Engineering from NIT Kurukshetra. His current research interest is in NLP, mobile ad-hoc networks and wireless sensor networks.

ShivKishan Dubey received his Post graduate in Computer Science from Punjab University. He is currently an Assistant Professor in Dr. Ambedkar Institute of Technology for Handicapped, Kanpur. His research interests include Linguist analysis and Natural language processing.

1 Introduction

Humans communicate through speech or writing; they always use entities like phrases, sentences and structured collection of words. How human languages are emerged and evolved, is a fundamental question in the social and cognitive sciences. Human language shows many unique features such as semantic structure, open mindedness, and compositionality that are unmatched elsewhere in other forms of communication. The languages of other species have a limited lexicon, linguistic pattern-learning (Saffran et al., 2008), and basic syntactic structure (Karl and Frisch, 1967) and no other species has linguistic behaviour as complex and diverse as that of human language behaviour (Boysen et al., 1980; Chomsky, 1965). Everyone believes that the internal and external representation of language is inseparably connected with and part of the human language development process. However, there is a lack of historical data for the analysis of natural language evolution. The development of human language is a largely unobserved temporal event. It means, we can say that these are not various phases of language development. With the help of experiments, researchers have studied and concluded how children acquire languages, explore how languages could have originated and exactly what the process acquire by child for language development. We can observe three following stages of language development as below.

Origin: In this phase, we study how organisms came under communication and the tools for creation and acquisition of existing language.

Emergence: An individual already possesses the general or specific mechanisms to acquire any language. It also includes the development of a shared lexicon among a population. A lexicon represents a systematic mapping between signals and meanings. The signals must be distinguishable from one another. We assume meanings are mental entities of an individual that they want to convey to another individual with the help of some representational medium that we call language. Signals are strings of symbols and its mapping with meanings is completely arbitrary.

Evolution: Here we study how language evolves over time. This is the study of emergence with properties of language such as grammar composition, syntax based structure, word order and their subsequent evolution.

In this paper, a new model has been proposed by using bilingual agents within a game strategy to explore the concept of language modernisation. The work is based upon a strategy of language-competition game, which has been played among bilingual agents during communication phase. The outcome of this work will suggest that if lexicons are being used in the synchronic environment, massive second-language's codes are affected and propagated into next generation for successful communication.

The rest of the paper is organised as follows: – In the following section, we have introduced a short overview of Language development. Then bilingualism with acquisition and role of this terminology over population is explained. Section 3 gives a careful literature review of previous related works on the basis of monolingual and bilingual developmental. Section 4 presents the problem in existing works and proposes a new model by using bilingual agents within a game strategy. Section 5 provides the implementation details of the proposed work with algorithms over bilingual acquisition in

synchronic environment that uses the concept of global dictionary. Section 6 discusses the results of our proposed work with all simulations of exposure at word and sentence level. Section 7 concludes the paper and gives the direction for future research.

2 Bilingual overview

Universally all agents (humans) express own thoughts in one language, but when we talk about different agents belongs from different society and cultures, they express differently. In particular context, peoples use particular language for particular essence to generate an idea of bilingualism. Simply we say bilingualism is ability to use two languages. There is two class of bilingualism. First classification is known as simultaneous and another is sequential. A process of Simultaneous is to learn two languages at one time and sequential process is to learn one later on other language (Ipurange, 2015).

2.1 Acquisition of bilingual language

Language acquisition is a process by which human learn, how to use language in communication. Chomsky's linguistic theory states that we are born with inherent ability to learn language with little guidance. Infants learn their first language, while bilingual learners learn how to use second language with native language. Exposure of both languages may be varying (Nakamura et al., 2009). True-balanced bilingualism occurs when individual agents are equally fluent to produce utterance which is rare (Quinonez, 2015).

2.2 Role of population and topology

It has been observed that major elements like social groups, their different behaviours and various geographical regions are affecting language development (Dunbar, 1996). It is not an ideal model and every one does not concur with it. Various researchers assumed that no any such type of homogeneous interaction among agents at all population level. Nettle (1999) shows that with the help of population structure it is difficult to determine, whether linguistic changes will propagate in a population. Wang et al. (2002) extended Nettle's work and found that there are some agents that can affect the spread of a linguistic variation. Magu (2007) worked on a model of "lexicon learning to multiple population structures" and showed that the acquisition (learning) is directly influenced by population structure.

3 Previous studies over language development

Problem of language emergence and evolution is not containing sufficient amount of documented data. Either languages emerged long time ago or new language did not emerge frequently. As previous theories stated that language-development is mostly found scenario in the society either monolingual or second language acquisition (Tria et al., 2015). Authors have given different types of recipes about language – acquisition by using hypothesis, robotics game, iterated schemes and its evolution.

3.1 Monolingual development

Steels (2000) published a paper 'Language as a complex system', a simulation scheme used with robotics agents. In this model, robotic agents mounted over cameras, negotiate a virtual world where objects had different features. Initially agents had no semantic knowledge. However, they were gifted with memory to store lexicons. Agents were also gifted with sensors that can transmit value of different attributes for any object perceived. A game of discrimination is played between two agents. Agent participated in interaction to identify an object with guess. Speaker agent selects one object and tries to differentiate it from given scene. Aizenberg (2003) discussed over dynamics of language death. They found that scopes of various languages depend on one fixed alarming rate and this rate is directly proportionate to as adopted by current generation. They developed a model of language competition which explained the survival nature of historical languages like Scottish, Welsh and Roman etc. Results are collected from highly connected population with no spatial or social structure. Their practical implementation had been performed over 42 regions of different land regions like Peru, Scotland and Ireland etc.

Minett and Wang (2008) proposed an extension model of monolingual speakers as discussed by Aizenberg et al. (2003). They presented a mathematical model about language competition and estimated theory of monolingual and bilingual speakers. Their theory was focused on two strategies; one is language maintenance and second is availability of educational resources for bilingual speakers. They also presented fully connected social structures that were jointly interconnection of neighbourhood (as speakers). Due to this phenomenon, they achieved success of probability of language maintenance.

Kirby et al. (2003) published a paper "Iterated learning: A framework for emergence of language". In this model, two computation models were described to emergence of language. In mathematical model, language compositional stability changes with cultural frames. Mostly, the stability of compositional language is equal to holistic languages, emergence rate with equal frequency over cultural frames. While in other cases, languages emergence may vary. Neural network model investigates the evolution of holistic communication over different environmental structures.

3.2 Bilingual development

Castello et al. (2008) proposed a socially equivalent language model which is agent based and addressed the role of bilingualism. According to agent based model, random selection of each agent computed the local density of language for each community in particular iteration. Agent changed the state of language according to probabilistic model whereas results in the form of probabilities reflect the shift from mono-lingualism to bilingualism.

Nakamura et al. (2009) presented a framework that multi-language evolution is a self organising process. These creoles made a new language community. They introduced degree of exposure from society language to Creole community. BA Model reflected exposure ratio α to determine exposure of learners to speakers and their neighbours or parents.

Tria et al. (2015) proposed a model to find out emergence of languages contact, which was easily modified to different language contact in the domain of spatial and time resolution. Experimental setup exposes that how language spoken by two communities

developed with the passage of time and results in the form of language adaptation by two communities.

Uriarte and San (2012) gone towards language competition in the complex social structures based community. It might be the variation in fractions of speakers languages evolved in a definite time. They reviewed over some advancement and focused on few aspects. First, they have studied with shifting of two-state models to three-state models for bilingual speakers. Second, they have found effect of interaction in social networks using some real barriers. Finally, they have shown how to analyse the issue of bilingualism.

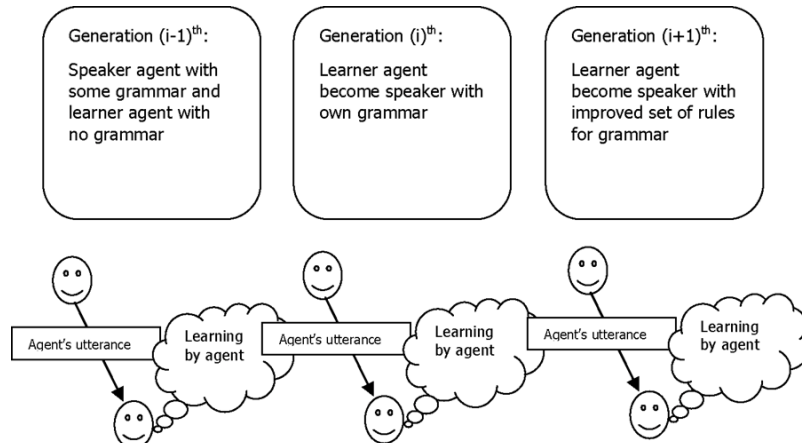
Milroy and Pieter (1983) have done detailed analysis over one speaker two languages, which was supporting concept of bilingualism. In a large scale, they introduced modernisation of languages and discussed bilingualism as a second language development by people in society. Their complete research about bilingual speakers heavily focused upon basic concept of code switching and code mixing which was very important event occurred during acquisition of second language learning.

Nakamura et al. (2015) presented an agent based simulation model to describe how language groups emerge using ILM on social networks. They focus on language group's emergence with the help of exposure ratio α which is acquired by group of agents as G_i and infant speaks as G_p (linguistic input from his/her parents) with the proportion of $1-\alpha$. In order to establish a comparison between languages, Nakamura defines distance in languages by Levenshtein distance and established a formula between E and I-languages.

4 Problem formulation and proposed work

Previous study of language acquisition maximally based upon monolingual development and bilingualism has been implemented by using only language dynamics equation. We have implemented bilingualism in the form of language competition game which is highly abstract.

Figure 1 Agent based iterated learning model



Source: Kirby et al. (2003)

4.1 Existing framework

Using an agent based iterated learning model (Kirby et al., 2003), where agents equipped with identical set of meanings, an internal language and induction algorithm that can move towards more compositional grammars. Individuals start as ‘listeners’ and become matured agents as ‘speakers’. According to Figure 1, in which an agent of i th generation receive its linguistic input from its parent of $(i - 1)$ th generation then apply an induction algorithm on the learner, now learner become a speaker to provide linguistic inputs to $(i + 1)$ th generation.

4.2 Assumptions

- All agents must be matured i.e., they must be efficient to produce utterance in own language.
- Agents have only produced utterances in the form of level-1 grammar during game of language competition which is shown in Figure 2.
- Agents are having sample of words from different categories as Table 1. For L1 community noun and predicate phrases are as [eat, take, give, like, go] and [ram, pen, apple] and for L2 community noun and predicate phrases are as [Khana, Dena, Lena, Pasand, Jana] and [Ram, Kalam, Seb].

Figure 2 Level-1 grammar for language L1 and L2

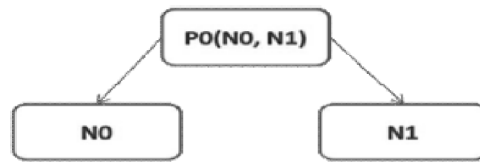
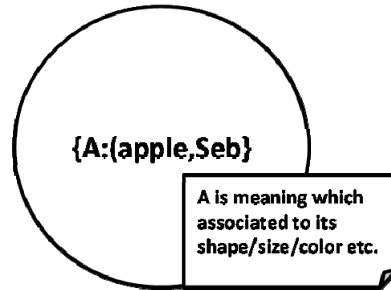


Table 1 Word used in simulation for two different languages L_1 and L_2

Predicate	Language L_1	Language L_2
Verb	$ev_1, ev_2, ev_3, ev_4, ev_5$	$hv_1, hv_2, hv_3, hv_4, hv_5$
Noun	$en_1, en_2, en_3, en_4, en_5$	$hn_1, hn_2, hn_3, hn_4, hn_5$

4.3 Concept of universal dictionary

Any real world object can be defined in terms of its colour, shape, length, height and size etc. In our model, dictionary is collection of such type of definition which has been used for conveying meaning (or code) among agents of different language communities during communication. for example: ‘apple’ is a real world object and in most of cases it can be defined using its shape or colour as Figure 3. In our model, dictionary has been used as following: {‘A’: <apple, seb>, ‘M’: <mango, aam>, ‘E’: <eat, khana>, ‘G’: <go, jana>, ‘Rm’: <ram, Ram>}.

Figure 3 Meaning of 'apple' used in dictionary

4.4 Proposed framework

- a All speaker and learner agents will select a random meaning from predefined set.
- b After that, agents of different language's groups will generate own utterance/meaning space during learning. (In previous model, only meanings of one language could be generated from predefined set).
- c On the basis of diachronic scenario, agents will learn grammar from own previous generation. In our model as Figure 4, due to synchronicity agents will take utterances and learn grammar from same generation also.

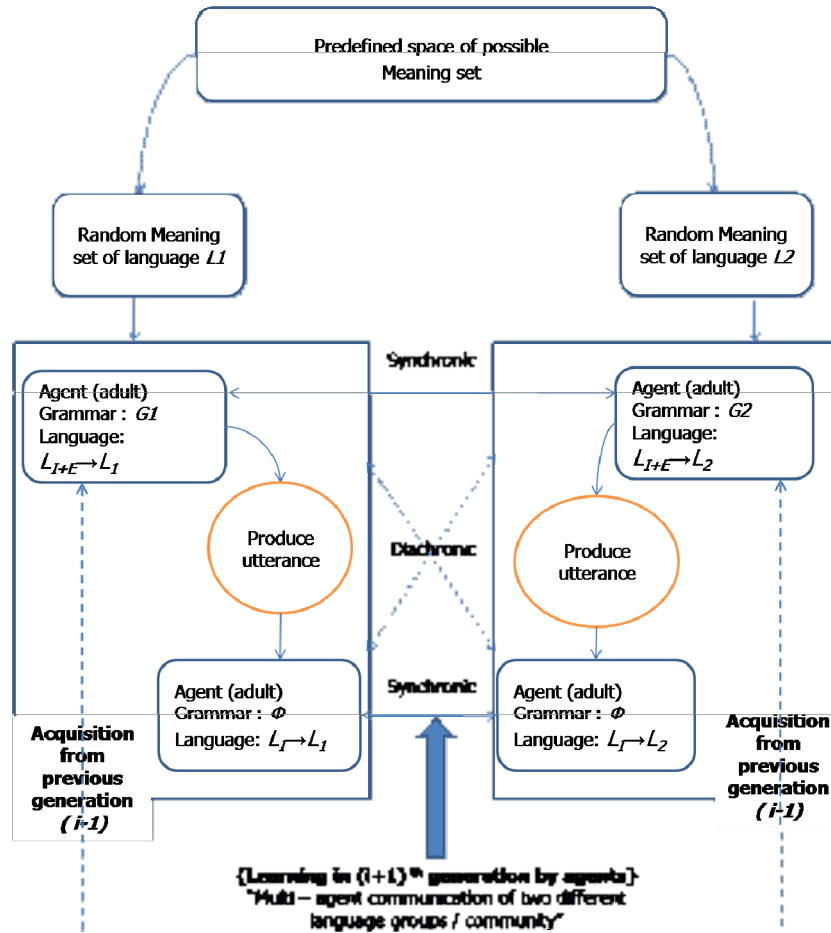
Loop for (g) and (h) upto -k iterations: where k represents no of generation for acquisition

- d Agents of language L_1 and L_2 , will expose own utterance by the procedure *Language_exposure()* and update own random meaning space.
- e Using *Grammar_exposure()*, agents of language L_1 and L_2 will update their rules during acquisition of language L_1 and L_2 respectively.
- f After k iterations, results will gain in terms of updating utterance/meaning space and grammar rules, which will be performed by *induction_method()*. If so, count the exposure ratio which will reflect bilingual acquisition.
- g In extended induction method, code-switching and code-mixing will update the level-1 acquisition (Figure 2) only.
- h Finally, matured agents have an ability to express language L_1 and L_2 after stabilisation of grammar G_1 and G_2 .

5 Implementation of proposed framework

We describe the experimental setup and the learning model for bilingualism we used in this paper. We seek to extend the major role of induction used in iterated learning model proposed by Kirby to realistic model of bilingual community. We have perform experiments with multiple agents who randomly communicate within synchronic environment.

Figure 4 Proposed framework of bilingual acquisition using linguistic transmission (see online version for colours)



5.1 Process with concept of dictionary

Our model assume that mature agents are participating in communication who are fully equipped with own meaning space and grammar rules. When these agents try to communicate to each other, their intentions towards understand about meaning (or code) of produced utterances during communication as following procedure of *produce_utterance_speaker()* and *listener_B()*.

According to Algorithm 1, speaker agent takes part in communication first with produces any random utterance from own sample and transfer to listener. Now listener agent process this utterance and use concept of dictionary as an Algorithm 2 for *listener_B()*.

Algorithm 1: produce random utterance by speaker agent

```

1 Produce_utterance_Speaker ();
   Input  : Speaker_sample={apple, ram, eat}      Output : utterance
2 utterance_A=random.choice(Speaker_sample);
3 return (uttarance_A);

```

Algorithm 2: Processing by listener against produced utterance by speaker agent using dictionary

```

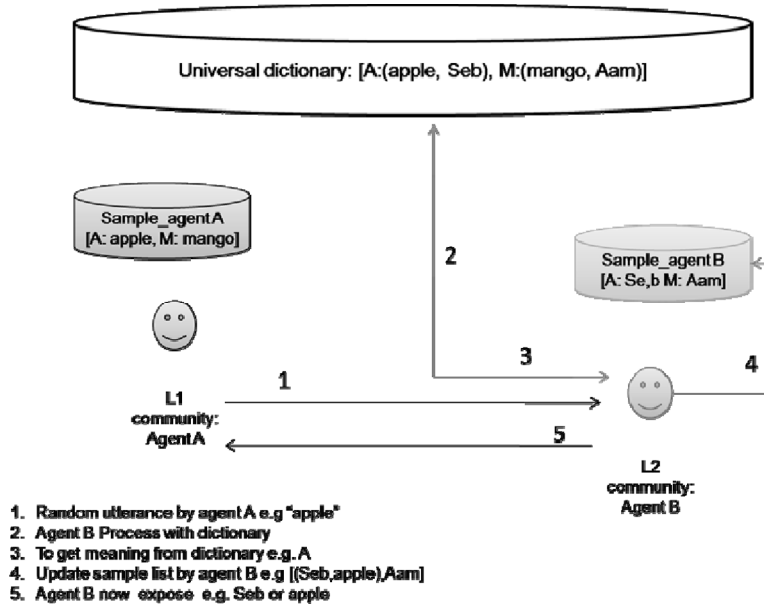
1.Listener_B (utterance_A):
   Input  : listener_sample={Seb,Ran,Khana}  Output : utterance
2. If utterance_A is in listener_sample then
   return random.sample(utterance_A; randrange(1;len(utterance_A)));
3. else
   find_meaning(utterance_A);    /* return code to listener
   if code is in listener_sample then
   valueget_value(code);        /* meaning from dictionary
   append utterance_A to listener_sample ; /* updation of listener
                                   sample e.g. (Seb,apple),Ran,Khan
   else
   insert utterance_A to listener_sample ; /*updating of sample
                                   by acceptance e.g (apple),Ran,Khana*/
4. return ( random.choice(utterance_A,value));

```

According to procedure of listener_B(), listener agent gets utterance by speaker agent and processes over dictionary. Finally listener agent updates own sample against produced utterance by speaker agent and able to produce utterances to agent of other language-community.

5.2 Exposure of word switching

In the word level exposure, there are two methods involve for acquisition. As studies found, concept of code mixing and code switching which are to be help for bilingual acquisition. In our model, we have used this concept as word mixing and word switching. According to monolingual scenario, agents are equipped with one language-meaning space but these agents when come into another language community. They suddenly acquire new words and map them in own meaning spaces. Process of mapping in various agents may be differing. Agents who mapped words and store them into own meaning space can produce utterance in form of borrowing (word-switching) as Figure 5.

Figure 5 Exposure of utterance at word level by switching

For example: an Agent A of L1 community has meaning space [apple, mango] and communicate to agent B of L2 community who has meaning space [seb, aam]. Now both agents come into conversation and agent B produce seb. Agent A does process of mapping and after completion of mapping process, B updates own meaning space by using process of word-switching as Figure 5.

5.3 Exposure of word mixing

Very often the language utterance code/expression is used in the form of code mixing. According to Ayeomoni (2006), "code mixing is assembly of various linguistic units such as affixes, words, phrases and clauses from a cooperative activity where the participants, in order to infer what is intended, must reconcile what they hear with what they understand". Our model describes code (word) mixing by Figure 6 where initially global words are represented as expression or object definition. [A, B, C, D,...Z], which will same for both language community.

5.4 Sentence generation using proposed model by agents of two different language communities

As our model, in which agents of different language communities are act like a matured agents that means they are fully equipped with own grammar rules (affected by Kirby's induction algorithm model) and own updated word spaces with global world (dictionary) coding syntax. For bilingualism, agents of two different communities may be contact to each other and learning will be achieved according the rules of fix meaning from different utterances by using word mixing or switching. Learning will be reflected by updating their old meaning space to new one. This rule will make extension of previous induction mechanism for learning two languages.

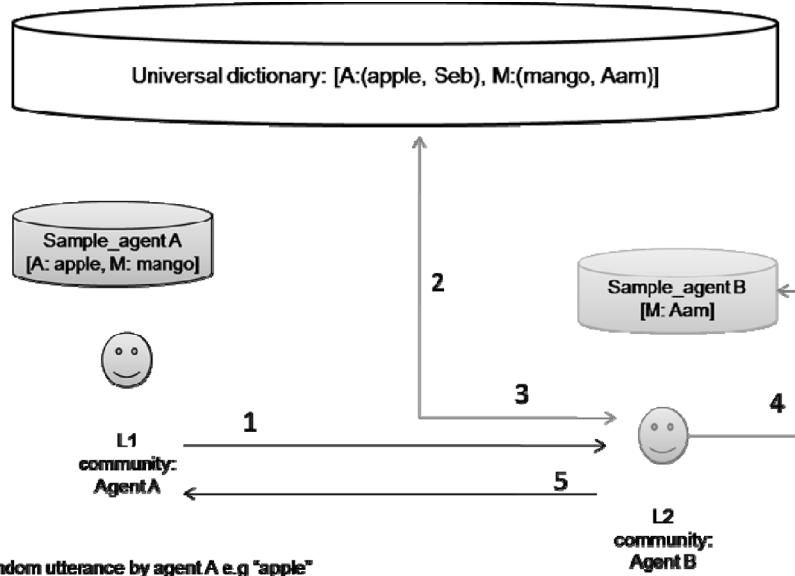
Algorithm 3: produce random sentence (utterances) by speaker agent for one language community

```

1  Speaker_A_utterance ():
    Input: Noun_sample={apple,ram} , Verb_sample={eat} Output: utterance
2  Utterance= random.choice(Noun_sample) +
              random.choice(Verb_sample) +
              random.choice(Noun_sample);
3  Return (utterance)

```

Figure 6 Exposure of utterance at word level by mixing



1. Random utterance by agent A e.g "apple"
2. Agent B Process with dictionary
3. To get meaning from dictionary e.g. A
4. Insert rule in sample list by agent B e.g [apple,Aam]
5. Agent B now expose only by apple or acquire substring(apple)

For example: Initial grammar for both agents of different language communities is as.

For language L1: Grammar of level- 1 is eat (ram, apple) → R eat A

For language L2: Grammar of level- 1 is Khana (Ram, Seb) → R S Khana.

Now Speaker agent of L1 community started to expose own grammar in terms of utterances via some random sentences to listener agent of L2 community. After some repetitions of above utterances grammar rules can be updated and set by following rule where updated grammar is as.

For Agent L1: S/V (N0, N1) → (N0/R → N0) eat (N1/A → Seb)

For Agent L2: S/V (N0, N1) → (N0/R → N0) (N1/A → apple) Khana

Algorithm 4: Exposure by listener Agent against produced utterance by speaker agent

```

1  listener_B_exposure (utterance_A; global_dictionary) :
   Input  : Noun_sample={Seb, Ran} Verb_sample={Khana}
   Output : utterance
2  temp_list=split_sentence() / split sentence by agent for mapping with
   dictionary ./
3  text = nltk.word_tokenize(utterance_A)
4  foreach k < no_of_generation do
   utterance_B = [ ], i = 0
5     foreach l <= length (temp_list) do
       temp = find_key(text,temp_list [l] )
6     if temp is NP then
       utterance_B.insert (0, temp_list[l] )
7     else if temp is NP and as Object participate then
       y = list_A [l]
8     foreach item in Noun_sample of Agent B do
9         if y found in item then
           utterance_B.insert(l, random.choice(item))
10    else if temp is VP then
       x = list_A [l]
11    foreach item in Verb_sample of Agent B do
12        if x found in item then
           utterance_B.insert(2,random.choice(item))

```

According to above sample examples, agents are able to generate sentences (exposure of utterances) using word mixing and switching using own grammar (set of rules exposed by Kirby et al. (2003) ILM model). In an Algorithm 3, we have first used speaker-agent's utterance (of level-1 grammar) of L1 community, after that agent of L2 community will be try to produce utterances for stabilising communication using Algorithm 4. We have used some additional module for sentence generation like *nltk.word_tokenize()* which will help to identify words category like noun(subject), verb and noun(object) participate. Next procedure used by listener agent of another language community which has first argument is *Speaker_A_utterance* and second argument is *global_dictionary*.

In this procedure (Algorithm 4), any listener agent has called two important arguments speaker utterance and global dictionary. Listener agent are also equipped with own noun and verb sample. As agent get utterance from speaker, first split the sentence and then categorise it according to own noun and verb predicates.

Process of sentence generation is repeatedly applied until fixed numbers of generations are available. During this scenario, agent checks that appearing word is noun predicate or verb predicate. If found word is Noun predicate then insert it at initial position (if agent belongs to L2 community, otherwise insert it at last position (for object predicates).

If found word is verb predicate then insert it at last position (if agent belongs to L2 community, otherwise insert at middle position (at first position). Procedure takes some random amount of time taken by listener agent which is depending on the length of sentences. As length of speaker utterances is increased, production of agent's utterance is slow.

The whole procedure has been implemented for bilingual acquisition in synchronic scenario between speaker of L2 community and listener of L1 community.

6 Results and discussion

In order to estimate the strength and effectiveness of the proposed bilingual acquisition in synchronic environment a careful performance evaluation has been carried out on a self-designed dataset. Results of this implementation has been categorised into sub sections.

6.1 Language competition at word level

The above bilingual acquisition simulated at word level language Competition shows how agent of L2 community affects the bilingualism when agent of L1 community give an utterance of its own language to L2 community agents. The knowledge samples of Agent A are [eat, apple, mango, ram] and agent A will produce random utterance eat to agent B.

```
>>speaker produce uttrance is "eat" and learner will be try to produce
utterance for eat
```

```
>>Now learner learner present sample is ['seb', 'aam', 'khana', 'jana',
'Ram']
```

```
-----
>>learner find meaning from universal dictionry is ( E ) and now try to
produce utterance for [ eat ] where ( ['e', 'a', 't'], 3) → (target word,
length)
```

```
-----
>>'new updated meaning space of Learner is:
```

```
['seb', 'aam', ('tea', 'khana'), ('at', 'khana'), ('tae', 'khana'), ('t',
'khana'), ('ae', 'khana'), ('ae', 'khana'), ('ae', 'khana'), ('eta',
'khana'), ('ta', 'khana'), ('eat', 'khana'), ('e', 'khana'), 'khana',
'jana', 'Ram']
```

Learner agents are trying to acquire knowledge during acquisition for stabilising its own samples (or knowledge-base) using synchronic communication.

According to the graph in Figure 7, L2 community agent has produced most suitable utterance after acquisition of string 'eat' against "Khana". It was clearly seen that in the graph no other utterances (like tea, at, e, ae, ta, eta and t) touched Levenstine Distance 0 (as mentioned in vertical axis) except string "eat".

Agents are facing situation of random picking of utterance among two different utterances of same meaning. Following Figure 8 are showing this interesting situation at word levels and results are being found in experiment that probability of unsuccessful exposure of string (eat) is 0.46 (12/26) and probability of successful exposure is 0.50 (13/26) It has been also found that lesser the length of the produced string more accurate the results on Bilingualism.

Figure 7 Exposure by Learner agent of L2 community from sample (*eat, Khana*)

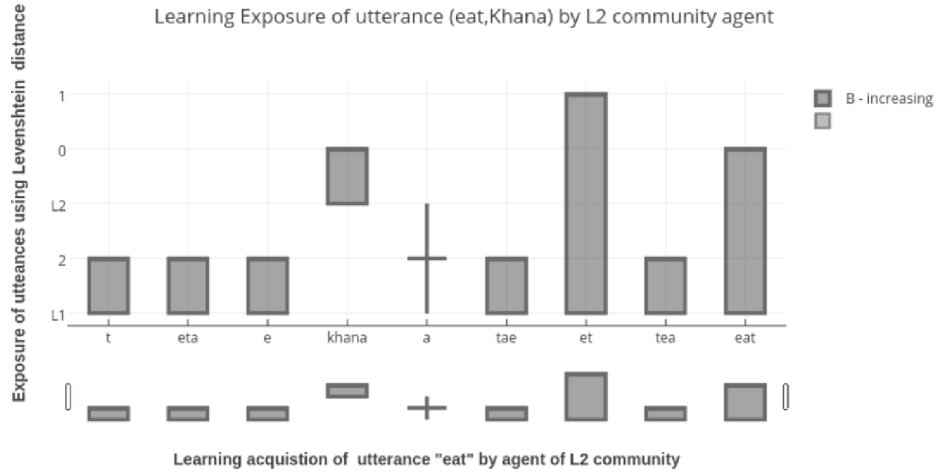
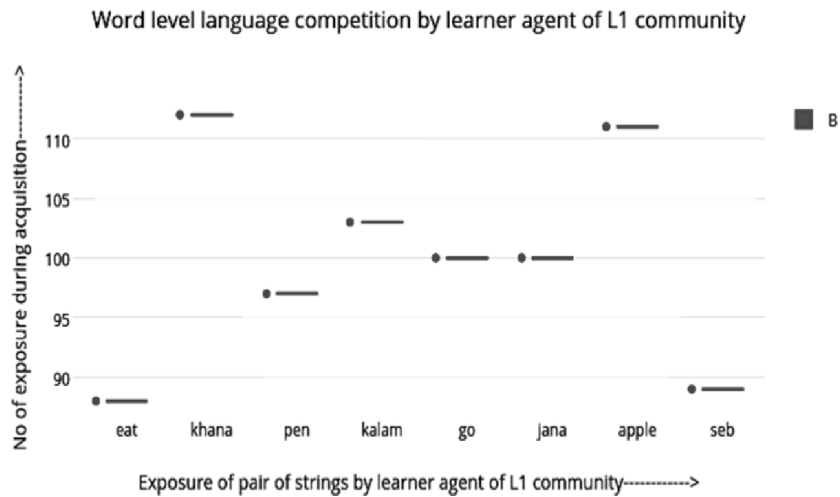


Figure 8 Language competition at word level by learner agent of L1 community



6.2 Language competition at sentence level

Sentences are learned by our own grammar rules as specified in our result set i.e., for L1 (subject, verb, object) or for L2 (subject, object, verb). These rules are implemented in our simulation that includes conditional clauses and had executed within loop of certain generation. In our scenario, Agent A (of L1 community) who is equipped with own grammar rule < S, V, O > produces some random utterances in terms of random choice of word from own samples and agent B (of L2 community and equipped with grammar of < S, O, V > produces following results as below.

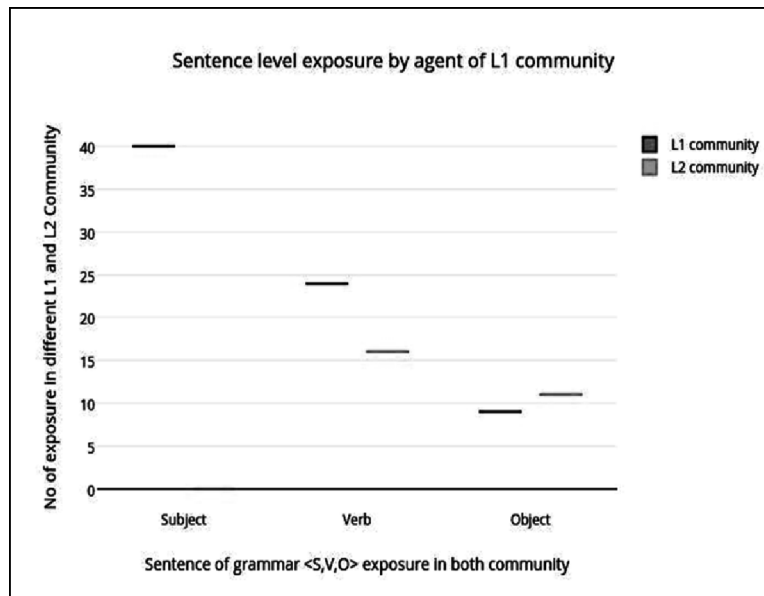
('Ram' → 'NNP')

('eats' → 'VBZ')

('apple' → 'NN')

(0, ['Ram', 'khana'])	(0, ['Ram', 'seb', 'khana'])
(1, ['Ram', 'eats'])	(1, ['Ram', 'apple', 'eats'])
(2, ['Ram', 'khana'])	(2, ['Ram', 'apple', 'khana'])
(3, ['Ram', 'eats'])	(3, ['Ram', 'seb', 'eats'])
(4, ['Ram', 'khana'])	(4, ['Ram', 'seb', 'khana'])
(5, ['Ram', 'eats'])	(5, ['Ram', 'apple', 'eats'])
(6, ['Ram', 'eats'])	(6, ['Ram', 'seb', 'eats'])
(7, ['Ram', 'eats'])	(7, ['Ram', 'seb', 'eats'])
(8, ['Ram', 'eats'])	(8, ['Ram', 'apple', 'eats'])
(9, ['Ram', 'khana'])	(9, ['Ram', 'apple', 'khana'])
(10, ['Ram', 'khana'])	(10, ['Ram', 'seb', 'khana'])
(11, ['Ram', 'eats'])	(11, ['Ram', 'seb', 'eats'])
(12, ['Ram', 'khana'])	(12, ['Ram', 'seb', 'khana'])
(13, ['Ram', 'eats'])	(13, ['Ram', 'apple', 'eats'])
(14, ['Ram', 'eats'])	(14, ['Ram', 'seb', 'eats'])
(15, ['Ram', 'eats'])	(15, ['Ram', 'seb', 'eats'])
(16, ['Ram', 'khana'])	(16, ['Ram', 'apple', 'khana'])
(17, ['Ram', 'khana'])	(17, ['Ram', 'seb', 'khana'])
(18, ['Ram', 'khana'])	(18, ['Ram', 'apple', 'khana'])
(19, ['Ram', 'eats'])	(19, ['Ram', 'seb', 'eats'])

Figure 9 Sentence level language competition by learner agent of L₁ community



Learner agent tried to acquire stabilisation at exposure of sentence level. Agent keeps own grammar rule and updated samples so that agent create successful setup of communication. As following Figure 9, sample sentence produce by agent of L1 community is < Ram eat apple >, but it can produce different samples for stabilising communication with agent of L2 community using word switching procedure.

7 Conclusions and future work

In this paper, a model has been proposed for bilingual acquisition in synchronic environment and the proposed algorithm is applied to the environment that shows that second language (L2) always wins the race of assumed language competition game. Matured-agents of two different language communities join in synchronic scenario and interact with each other to learn and acquire utterances of each other. The resulting cross utterances may lead to modified language as well as new utterances. Our research work predicts the possibility of second language acquisition in synchronic environment.

In future, we plan to extend this work for generating multi-level and nested sentence resulting it to become a more realistic model of bilingual (second language) acquisition. This particular area of research in perplexing field of Natural language processing may be used for development of cross compilers. The compilers based on this work may even support more than one language at a time.

References

- Aizenberg, J., Tkachenko, A., Weiner, S. and Addadi, L. (2003) 'Modeling the dynamics of language death', *Nature*, Vol. 424, p.900.
- Ayeomoni, M.O. (2006) 'Code-switching and code-mixing: style of language use in childhood in Yoruba speech community', *Nordic Journal of African Studies*, Vol. 15, pp.90–99.
- Brighton, H. (2005) *Linguistic Evolution and Induction by Minimum Description Length*, Applications to Linguistics, Psychology and Neuroscience, Ontos Verlag, Frankfurt, pp.13–40.
- Brighton, H. (2006) 'Compositional syntax from cultural transmission', *Artificial Life*, Vol. 8, pp.25–54.
- Briscoe, T. (1998) 'Language as a complex adaptive system: co-evolution of language and of the language acquisition device', *Proceedings of the 8th Computational Linguistics in the Netherlands Meeting*, Nijmegen, Rodopi, pp.3–40.
- Castello, X., Eguiluz, V.M. and Miguel, M.S. (2008) 'Modelling language competition: bilingualism and complex social networks', *Proceedings of the 7th International Conference (EVOLANG7)*, Barcelona, IFISC, pp.59–66.
- Chomsky, N. (1967) *Aspects of the Theory of Syntax*, MIT Press, Cambridge.
- Donald, W. (2007) 'Some issues in the study of language contact', *Journal of Language Contact*, Vol. 1, pp.22–40.
- Dunbar, R. (1996) *Grooming, Gossip and the Evolution of Language*, Harvard University Press, Cambridge.
- Frisch, V. and Karl, D. (1967) *The Dance Language and Orientation of Bees*, Harvard University Press, Cambridge.
- Ipurange, K. (2015) *What is Bilingualism?*, 2015, <http://leap.tki.org.nz/> (Accessed 5 June, 2016).

- Ke, J., Minett, J.W., Au, C.P. and Wang, W. (1999) 'Self-organization and selection in the emergence of vocabulary', *Complexity*, Vol. 7, pp.41–54.
- Kirby, S., Smith, K. and Brighton, H. (2003) 'Iterated learning: a framework for the emergence of language', *Artificial Life*, Vol. 9, No. 4, pp.371–386.
- Komarova, N.L. and Nowak, M.A. (2003) 'Language dynamics in finite populations', *Journal of Theoretical Biology*, Vol. 221, pp.445–457.
- Magu, J.P. (2007) 'On the importance of population structure in computational models of language evolution', *Proceedings of the 31st Pennsylvania Linguistic Colloquium on Language Evolution; Social Network*, Philadelphia, USA, pp.0041–0043.
- Milroy, L. and Muysken, P. (1995) *Code-Switching and Grammatical Theory of One Speaker Two Languages: Cross-Disciplinary Perspectives on Code-Switching*, Cambridge University Press, Cambridge.
- Milroy, L. and Pieter, M. (1983) *One Speaker, Two Languages Cross-Disciplinary Perspectives on Code-Switching*, Cambridge University Press, Cambridge.
- Minett, W. and Wang, S.Y. (2008) 'Modelling endangered languages: the effects of bilingualism and social structure', *Lingua*, Vol. 118, pp.19–45.
- Nakamura, M., Hashimoto, T. and Tojo, S. (2009) 'Self-organization of creole community in a scale-free network', *Third IEEE International Conference on Self-Adaptive and Self-Organizing Systems (SASO09)*, San Francisco, IEEE. pp.293–294.
- Nakamura, M., Hashimoto, T. and Tojo, S. (2015) 'Simulation of emergence of local common languages using iterated learning model on social networks', *Advanced in Intelligent System*, Vol. 8, pp.374–388.
- Nakamura, M., Matoba, R. and Tojo, S. (2015) 'Simulation of emergence of language groups using iterated learning model on social networks', *Cognitive*, Vol. 21, pp.175–180.
- Nettle, D. (1999) 'Using social impact theory to simulate language change', *Lingua*, Vol. 108, Nos. 2–3, pp.95–117.
- Quinonez, L. (2015) *A Resource Guide for Early Hearing Detection and Intervention: Language Acquisition for Bilingual Child, 2015*, http://infanthearing.org/ehdi-ebook/2016_ebook (Accessed 12 September, 2016).
- Saffran, J., Hauser, M.D., Siebel, R., Kapfhamer, J., Tsao, F. and Cushman, F. (2008) 'Grammatical pattern learning by human infants and cotton-top tamarin monkeys', *Cognition*, Vol. 107, No. 2, pp.479–500.
- Savage, E.S., Duane, M., Rumbaugh, P. and Boysen, S. (1980) 'Do apes use language?', *American Scientist*, Vol. 68, No. 1, pp.49–61.
- Smith, A.D.M. (2001) 'Establishing communication systems without explicit meaning transmission', *Springer*, Vol. 2159, pp.381–390.
- Steels, L. (2000) 'Language as a complex adaptive system', *Parallel Problem Solving from Nature (PPSN)*, Vol. 1917, pp.17–26.
- Stob, M., Osherton, D. and Weinstein, S. (1986) *Systems That Learn An Introduction to Learning Theory for Cognitive and Computer Scientist*, MIT Press, Cambridge.
- Tria, F., Servedio, V.D., Mufwene, S.S. and Loreto, V. (2015) 'Modeling the emergence of contact languages', *PLoS ONE*, Vol. 10, pp.375–384.
- Uriarte, J. and San, M. (2012) 'Modeling two-language competition dynamics', *Advances in Complex Systems*, Vol. 15, No. 3, pp.1250048–1.

DEINKING OF OLD USED PAPERS USING CRUDE RHAMNOLIPID BIOSURFACTANT

ASHUTOSH MISHRA¹ AND RAKESH KUMAR TRIVEDI^{2*}

¹Department of Chemical Engineering, Dr. Ambedkar Institute of Technology for Handicapped,
Kanpur 208 024, (U.P.) India

²Department of Oil Technology, Harcourt Butler Technical University, Kanpur 208 002, (U.P.) India

(Received 20 October, 2020; accepted 23 December, 2020)

ABSTRACT

Surfactants are having a great role in world chemical industries majorly used in laundry detergents, household, and personal care products along with pharmaceuticals. Apart from this surfactants have special use in the pulp and paper industry for the deinking process that makes new paper from the old paper. Generally, anionic synthetic surfactants are using for this purpose. As the synthetic surfactants are non-biodegradable and non-eco-friendly, this study was conducted by replacing these surfactants with the rhamnolipid biosurfactant, which was manufactured in the laboratory with the help of *Pseudomonas aeruginosa* MTCC 424 using residual oil from vegetable oil processing industry. After manufacturing the new hand sheet, the brightness % and the ash content were checked. The brightness efficiency and ash content were found 58 percent and 8.97 percent, respectively. The optimum concentration of the crude rhamnolipid biosurfactant of concentration 0.9 g/L was used 0.12 percent at pH 9.

KEY WORDS : Rhamnolipid biosurfactant, *Pseudomonas aeruginosa*, Brightness efficiency, Ash content, Pulp consistency

INTRODUCTION

Surfactants have a vital role in the field of chemical technology. These have major applications in the field of agriculture such as pesticides, herbicides, insecticides, sanitizers, spermicides (nonoxynol-9), and fungicides. Surfactants also have versatile applications in food processing, pharmaceutical, oil, and paint and as well as for industrial and home cleaning solutions (Borchardt, 2003; Bruhn, 2009). These also include applications as emulsifiers, foaming agents or wetting agents for lowering surface tension and interfacial tension. Surfactants are widely used for cleaning, dispersing agents, soaps, adhesives, various detergents, wax related products, paints, softeners, emulsifiers, inks, anti-fogging agents, fabric washing, anti-foaming agent, etc. These also have major applications for personal care and household products like shampoos, shower gel, hair conditioner, and toothpaste, etc (Miranda *et al.*, 2010). For industrial

or household safety, surfactants play a vital role such as fire fighting agents and in pipelines as liquid drag-reducing agents. In oil exploration wells, alkali surfactant polymers are used to mobilize oil. Surfactants are also used in plastic industries as plasticizer for making nanocellulose, ferrofluids, and leak detectors. In the current research, surfactants are used with quantum dots for identifying the electrical properties and reactions on their surface which is required for the growth and assembly of dots. Therefore, the mechanism of surfactant arrangement on the quantum dots surface and deinking of recycled papers is required to understand the process. Previously synthetic surfactants are in a wide range application due to their low cost and they can be easy to synthesize the synthetic surfactants in the industries. If the biodegradability of synthetic surfactants is considered, it harms the environment and human health as well. Therefore, with the help of biosurfactants we overcome this problem of

environmental issues as well as toxicity towards living organism. In this study we conclude the wide application of biosurfactant for the deinking of old used papers for recycling as well as for environmental issues related to the paper industry (Allix *et al.*, 2010; Wasserman *et al.*, 1965). Generally inkjets and flexographic water-based inks are difficult to deink. A column flotation cell is designed for the deinking of used paper without the addition of an agitator (Chaiarrekij *et al.*, 2001). The formulated design method is capable of significant savings of electrical energy, capital costs, and maintenance costs which ultimately benefits the environment.

Cellulose is used in place of conventional chemicals for deinking of old used papers (Pelach *et al.*, 2003). In enzymatic treatments the enzyme efficacy is improved with particular consistency and repulping time which is analyzed with shear factor. The office recovered papers were recycled for removing the ink using biological deinking technology with cellulase and resinase enzymes (Viesturs *et al.*, 1999). The enzyme treatment with acidic pH reduces the ink particle size and enhances ink removal effectiveness as compared to alkaline pH. The addition of hydrocarbon oil surfactant eliminates the darkness of pulp and improves the cleanliness of paper. The mechanism of cellulase enzyme for removing the ink particles using biodeinking technology is explicitly explained (Vyasa *et al.*, 2003; Lee *et al.* 2007). The Anionic surfactants are generally used for removing the black toner ink from laser-printed paper nowadays. The foam is generated due to the addition of surfactants which tend to decrease surface tension. The efficacy of deinking affects with flotation time, pH and, quantity of fatty acid soap. The problem continues with association of pigments, inks and other paper grade quality. As per the literature of recycling, the surfactants are broadly classified into three stages (Abraha *et al.*, 2019; Allix *et al.* 2008; Zhao *et al.*, 2004). In the first stage, the ink particles are detached from fiber which is dispersed in the system and restricts them to re-deposit on the further deinking process. For the second stage, the ink particles are agglomerated with the case of the surfactant. In this stage, hydrophobicity plays an important role which later absorbs on paper fiber. The surface of fiber is changed from hydrophilic to more hydrophobic. In the third stage the hydrophobic end is attached to the surface during the processing of the flotation stage for achieving

the higher yield. Current research emphasizes simple, cheap, biodegradable, and effective recycling of used paper.

MATERIALS AND METHODS

Materials

The following conventional chemicals were used in this study.

- i. Lemon Juice
- ii. Baking Soda(1N)
- iii. Sodium silicate
- iv. Crude rhamnolipid Surfactant
- v. C.B.S.X.
- vi. Polyethylene Glycol

Methods

The pulping is the first stage of deinking process in which the printed used papers were dispersed in water to release ink and fiber particles. In this research, the conventional process was replaced by the natural process for releasing the ink. The natural lemon juice and baking soda were used in place of toxic chemicals like hydrogen peroxide and crude rhamnolipid biosurfactant was used in place of synthetic surfactant.

Making the oven-dried pulp:

For making the pulp following materials were used
 25 % old magazine papers (Cricket Samrat)
 25% used newspapers (Times of India)
 25% used handwritten copies by students (Classmate brand)
 25 % recovered computer printout

For the process of this research, all the materials were well crushed and then soaked overnight in the bucket of distilled water for proper disintegration. Samsung mixer (501 - 750 watts) was used for disintegrating the particles. Then these particles were passed through the centrifuge for dewatering and dewatered material again well mixed into very fine pulp which was dried at room temperature. For the determination of air-dried pulp, consistency of the pulp was calculated using 250g oven-dried pulp. Pulp consistency is expressed as percentage which is defined as follows:

$$\frac{\text{Dry weight of pulp fibers}}{\text{Weight of the suspension}}$$

As the pulping consistency increases, the deinking efficiency decreases. For 1-2% of the pulp

consistency, the maximum efficacy of deinking was observed.

To find the consistency, a small amount of air-dried pulp is taken, weighed (X) and mixed with water in a small beaker, and suction filtered through a previously weighed filter paper (F). The weighed filter paper with the filtrate was dried in a rapid drier and again weighed (Y).

$$\text{Consistency (C)} = \frac{X-Y}{X} 100$$

Weight of air-dried pulp needed to get 250

$$\text{g oven dried pulp} = \frac{250 \times 100}{C}$$

PULPING

For calculating 250g oven dried pulp, the weight of air dried pulp was required. Water was added in 90 percent of the total weight of the pulp. In every set of experiments, the amount of water and the weight of pulp were varied according to the batch of raw material or recovered paper used. The oven-dried pulp was assorted properly with sufficient amount of water and kept in a water bath at 60 °C for 30 minutes. After this time, the chemicals were added to the pulp and the pH was measured. Then the mixture was kept in a water bath for another 30 minutes and the resultant pH was measured after one hour at 60 °C.

Flotation: After pulping, the pulp was diluted to 1% consistency to achieve higher microfilament yield and pulp was further transferred to a flotation machine, which could be a mechanical flotation cell or a flotation column. Laboratory flotation cell (as per developed in the lab Fig.1.) was used for the current study to achieve higher consistency.

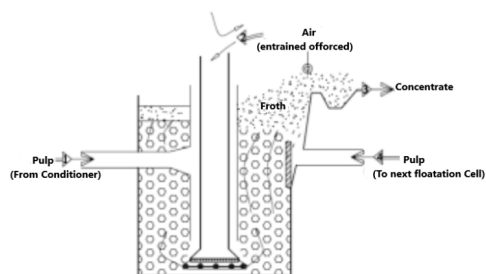


Fig. 1. Flotation cell

After flotation the froth was scraped off and the distilled water was used for washing of deinked pulp. The deinked pulp was dried and for testing it was converted to hand sheets from the pulp. The brightness was measured using brightness tester (Model PCE-WNM 100) made by PCE instruments and ash content was calculated through Muffle

furnace.

Making the brightness sheet

The brightness of the initial pulp, the pulp after pulping, and deinked pulp could be found out by making the brightness sheet/ hand sheets of the respective pulp. The Technical Association of the Pulp and Paper Industry (TAPPI), TAPPI Test Method T218om91 (Buchner Funnel Procedure) provided the technique by which the hardness sheets were prepared.

RESULTS AND DISCUSSION

The current study was performed to achieve better deinking of used paper as well as to achieve higher consistency in the floatation phase. The effect of water based ink for different values of pH is given in Table 1.

Table 1: Effect of pH on removal of ink

The alkaline medium generates dark colored froth (Fig. 2a), whereas the acidic medium generates lighter color froth (Fig. 2b). The study establishes the fact that alkaline medium has the ability to agglomerate the ink particles while medium forces ink particles to disperse. The color difference is monitored for the pH values of 6 and 10 which are acidic and alkaline regions respectively.

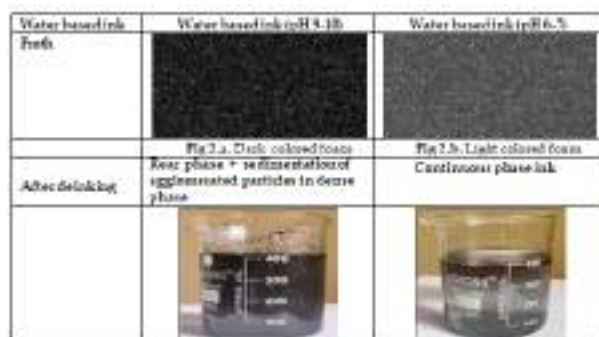


Fig. 2(a) and Fig. 2(b) show the agglomerated ink particles after flotation by application of alkaline and acidic medium, respectively. The difference in the colors of two froths is visible.

Various important surface characteristics has been shown by the FTIR spectra of rhamnolipid biosurfactant treated pulp. The rhamnolipid treated pulp is in good agreement with the previous studied literature. The -OH stretching corresponding to hydrogen bonding is depicted by the band at 3477.92 cm⁻¹. The stretching can be attributed to increase cellulase content of the pulp. The band at 3041.24 cm⁻¹ corresponds to asymmetric

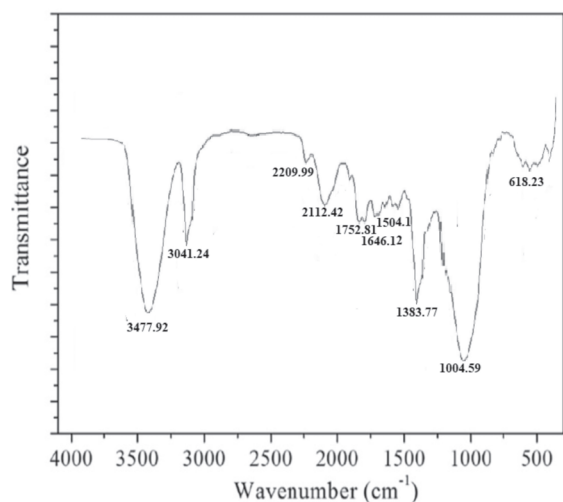


Fig 3. FTIR spectra of Rhamnolipid Biosurfactant treated pulp

–CH vibrations of CH, CH₂, CH₃. The band at 1752.81 cm⁻¹ was assigned to vibrations of C = O stretching in ester, COOH, β-C= O indicating the enrichment of spent lignin in functional groups after rhamnolipid treatment . This variation can be due to the aliphatic chain degradation. The band at 1646.12 cm⁻¹ can be attributed to C=O stretching of carbonyl groups, due to bio surfactant action on aromatic ring of lignin. The sharp band at 1504.01 cm⁻¹ can be attributed to –CH₃ stretching combined with skeletal aromatic vibrations with deformation in the plane, which shows that some O–CH₃ has been removed during rhamnolipid treatment. The band at 1383.77 cm⁻¹ has been assigned to C–H aliphatic stretching in phen–OH and CH₃. Appearance of band at 1004.59 can be attributed to syringyl groups degradation.

Distribution of detached ink before floatation is presented in Fig 4.a the diameter of the ink was measured by using dot analyzer (Beta Breye Braille Dot Print Analyzer by Beta Screen Corporation). Majority of the detached ink has been reported less than 10 μm. With the decrement in the ink diameter,

there observed a rapid increase in number of ink. Furthermore, the Fig. 4.b suggests that number of inks lesser than 3 μm might be larger than the reported value. If the growth of bubble goes along with surfacing, the ink removal might get effected. So, the distribution of bubbles starting from the lower position to upper position was measure. It was observed that in pulp slurry, same even distribution at upper and lower position and less growth of bubbles was occurred. The result might be attributed to the retardation of bubble growth in presence of pulp.

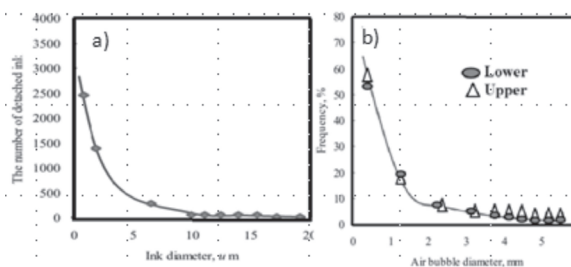


Fig. 4(a). Size distribution of detached ink before floatation; (b) distribution of bubbles at different positions in pulp slurry

Fig. 5 shows the effect of rhamnolipid concentration and brightness percent on the floatation process. Deinking efficiency increases with increasing concentration up to 0.9 g/l. The brightness was 58 using 0.9 g/l of crude rhamnolipid. Since the anionic species of surfactants and the ink particles form a micelle which has the same polarity. The negatively charged particles are strongly favored as compared to alkaline pH range particles by the floatation process. The two adjacent surfaces are interconnected through the bridging mechanism in which the calcium is predominant. As a result, there is a strong bonding between surface functional groups and carboxyl groups which exist on ink particles and collector, respectively. Higher surfactant concentration reduces the floatability but increase the collision frequency. This effect can also

Table 2. Ink removal results using various Deinking solution at different times

Deinking solution	Ink removal					
	20 min	40 min	60 min	80 min	100 min	>120 min
Biosurfactant* (0.12%)	90%	100%	100%	100%	100%	100%
Lemon juice (0.5%)	14%	25%	35%	40%	60%	100%
Baking soda (1N)	100%	100%	100%	100%	100%	100%
Sodium silicate (0.1%)	15%	24%	36%	48%	52%	63%
C.B.S.X. (1%)	10%	12%	14%	14%	14%	14%
PEG (0.08%)	5%	7%	7%	7%	7%	7%

results above CMC for the biosurfactant. Rhamnolipid supported the formation of admicelles on carbon black as well as paper which indicates the carboxylate group and carbon surface strongly interacted. With the help of this phenomenon we resulted in the wider application of soaps in flotation deinking operations.

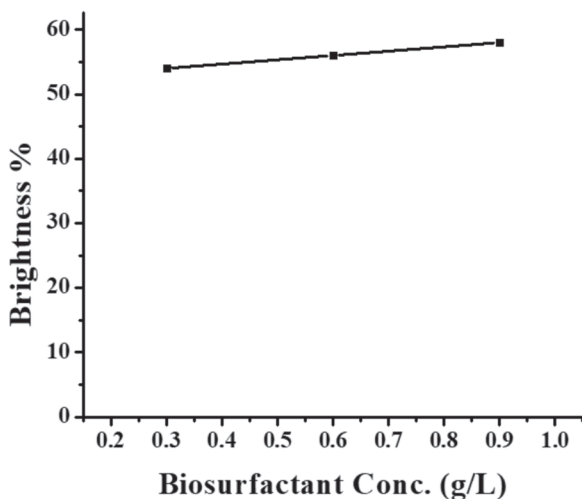


Fig. 5. Effect of Biosurfactant conc. on brightness of the floating product.

Table 2 shows the percentage removal of ink with different time duration for different deinking solutions. The area covered with alkaline agents is immediately cleaned in alkaline medium by adding the drop of surfactant. Crude Rhamnolipid biosurfactant produced by *Pseudomonas aeruginosa* is used for this purpose. Acidic agents had lower removal of water-based ink. This research studied the sustainable application of biosurfactant on the recycling of paper during the deinking process.

In the current study we observed the effect of biosurfactant on the removal of ink from pulp. Biosurfactant having a pH of 6.3 is used which is found to be best. It is observed that Acidic solutions showed poor deinkability as well as behaves as poor dispersants. However, biosurfactants showed better ability to deink from the pulp surface, but the negative effect shows by scattering the ink particles

in the environment. Table 3 shows the effect of deinking for different pH values in the solutions.

Measurement of brightness (%) ISO

As brightness is the prime indicator of the Deinking efficiency. The brightness pads (Fig. 6 and 7) made both from the deinked pulp treated with synthetic surfactant and from the deinked pulp samples treated with crude rhamnolipid biosurfactant were compared for optical property, in order to evaluate the influence of biosurfactants on the deinking of old used papers. The pulp brightness (%) is measured on an ISO brightness color tester according to the TAPPI (Technical Association of Pulp and Paper Industry) standard T452 om 87. Pulp brightness (ISO) is defined as follows:

$$\frac{\text{Radiance of wavelength 457 nm of a paper specimen}}{\text{Perfect reflecting diffuser}}$$

Magnesium oxide is taken as a perfect reflecting diffuser. Before taking the brightness, one filter paper is peeled off from one side of the brightness sheet. The percentage of brightness is also referred to as brightness index (BI). The brightness is measured with Elrepho' Photo-electric reflectance photometer. At different places of the sheet prepared, the brightness is measured and the values are calculated as the mean of all (TAPPIT 452 om 92). The digital value presented the percentage value of the brightness of the sheet prepared. Table 4 shows the brightness and dirt count for different deinking agents.



Fig. 6. Handsheets made from synthetic surfactant



Fig. 7. Handsheets made from Rhamnolipid Biosurfactant

Table 3. Effect of deinking for different pH values in the solutions

Deinking solutions	pH	Observations
Surfactant*	6.3	Good for deinking but No. agglomeration
Lemon Juice	3	Good for deinking but No. agglomeration
Baking Soda (IN)	11	Good for deinking but No. agglomeration
Sodium silicate	9	Good for deinking but No. agglomeration
C.B.S.X. & Polyethylene Glycol	2-4	No ink detachment/Good ink agglomeration

Table 4. Brightness (%) and dirt count (ppm) for different deinking agents

Deinking Agent	Handsheet	
	Brightness %	Dirt Count (ppm)
Biosurfactant*	67	50
Baking Soda (1N)	38	98
Sodium silicate	34	107
C.B.S.X.	25	227
Polyethylene Glycol	16	243

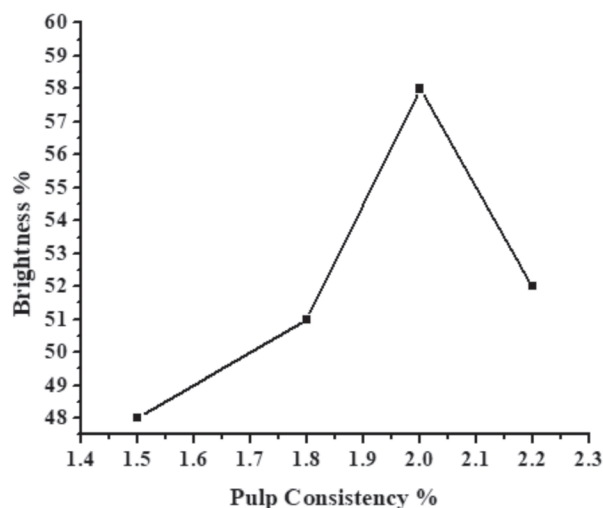


Fig. 8. Effect of Pulp Consistency on brightness.

Fig. 8. shows the effect of the consistency of paper pulp with biosurfactants in the stage of pulping. A brightness of 58% was obtained with 0.9 g/L of rhamnolipid biosurfactants. The brightness is almost constant with pulping consistency up to 2% and then decreased.

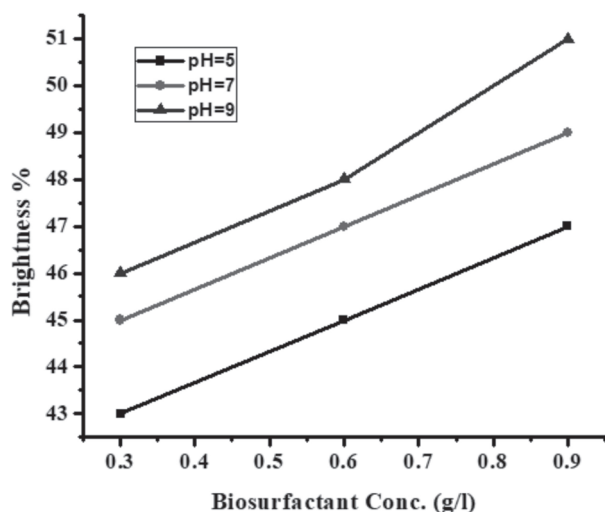


Fig. 9. Effect of Biosurfactant conc. and pH on brightness of 13% pulp.

Fig. 9. shows the effect of biosurfactant concentration and pH on the brightness of paper pulp. The higher brightness is achieved by with increasing the concentration of biosurfactant. The maximum brightness is obtained at 0.9 g/L for crude rhamnolipid biosurfactant. The brightness increases with increasing pH up to 9, which means a higher alkaline medium is to be maintained. Alkalinity enables the swelling of the fibers which results in easy removal of printing ink by the effect of breaking the bond between fibers and print. It also supported increasing final brightness and hydrolysed ester groups in print particle networks.

Ash content Measurement (%)

Ash content calculation is another very important parameter to know deinking efficiency. Ash content is obtained by burning the pulps in a Muffle furnace(Make : Nabertherm, Model : L3/12) according to TAPPI standards. Both initial and deinked pulps in a quantity of 100 ml are taken for this measurement. The brightness pads and consistency sheets are prepared similarly to the previous method. Empty and pulp containing the weight of crucibles are measured and then put in a desiccators. The ready consistency pads are positioned in every crucible and kept in the furnace for 45minutes (the set temperature for ashing was around 600 °C). After ashing, weights of the

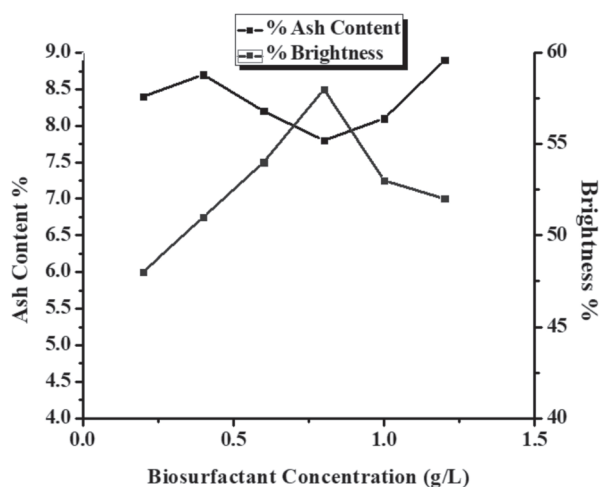


Fig. 10. Effect of Biosurfactant conc. on brightness and ash content of pulp.

crucibles are measured and the ash present is calculated in percentage by the formula, weight of ash/ weight of oven dried pulp×100. Fig.10. describes the effect of biosurfactant concentration on brightness and ash content of pulp.

CONCLUSION

Optimization of the most efficient biosurfactant concentration

The optimum concentration of rhamnolipid biosurfactant produced by *Pseudomonas aeruginosa* MTCC 424 preparing using residual rice bran oil as a sole substrate for the deinking of old used papers is found to be 0.9g/l. A decrease in the percentage of brightness is observed with an increase in biosurfactant concentration. The percentage of ash is also found to be lowest when 0.9 g/l of biosurfactant is added to the pulp before deinking.

ACKNOWLEDGEMENTS

We are thankful for M/S- Bajaj Kagaj Limited Unnao for providing us guidance and laboratory facilities for this research. We are also grateful to Indian Institute of Technology Kanpur and for facilitating laboratories.

REFERENCES

- Abraha, M. and Kifle, Z. 2019. Deinking of Black Toner Ink from Laser Printed Paper by Using Anionic Surfactant. *Biomol. Eng.* 4 (1) : 23-30.
- Allix, J., Beneventi, D., Carré, B., Nortier, P., Zeno, E. and Angelier, M.C. 2008. Understanding the role of surface active substances in flotation deinking mills by coupling surfactant and ink balance with process simulation *TAPPI J.* 9 : 31.
- Allix, J., Beneventi, D., Zeno, E. and Nortier, P. 2010. Flotation de-inking of 50% ONP/50% OMG recovered papers mixtures using nonionic surfactant, soap, and surfactant/soap blends. *Bioresour.* 5 (4) : 2702-27019.
- Borchardt, J.K. 2003. Recent developments in paper deinking technology. *Pulp Paper Can* 104 (5) : 32.
- Bruhn, C.M. 2009. Understanding 'green' consumers. *Food Technol- Chicago.* 63 (7) : 28-35.
- Chaiarrekij, S., Gupta, H., Amato, W. and Ramarao, B. 2000. Experimental results in deinking of recycled fibers by column flotation. Faculty of science and engineering, University of New York. 4.
- Lee, C., Darah, I. and Ibrahim, C. 2007. Enzymatic deinking of laser printed office waste papers: some governing parameters on deinking efficiency. *Bioresour. Technol.* 98 (8) : 1684-1689.
- Miranda, C. R., Bobu, E., Grossmann, H., Stawicki, B. and Blanco, S.Á. 2010. Factors influencing a higher use of recovered paper in the European paper industry. *Cellul. Chem. Technol.* 44 (10) : 419-430.
- Pelach, M., Pastor, F., Puig, J., Vilaseca, F. and Mutje, P. 2003. Enzymic deinking of old newspapers with cellulase. *Process Biochem.* 38 (7) : 1063-1067.
- Viesturs, U., Leite, M., Eisimonte, M., Eremeeva, T. and Treimanis, A. 1999. Biological deinking technology for the recycling of office waste papers. *Bioresour. Technol.* 67 (3) : 255-265.
- Vyas, S. and Lachke, A. 2003. Biodeinking of mixed office waste paper by alkaline active cellulases from alkalotolerant *Fusarium* sp. *Enzyme Microb. Technol.* 32 (2) : 236-245.
- Wasserman, A.E. 1965. Absorption and fluorescence of water-soluble pigments produced by four species of *Pseudomonas*. *Appl. Microbiol.* 13 (2) : 175-180.
- Zhao, Y., Deng, Y. and Zhu, J. 2004. Roles of surfactants in flotation deinking. *Prog. Pap. Recycl.* 1 : 41-45.

SYNTHESIS AND CHARACTERIZATION OF BIOSURFACTANT USING WASTE FROM OIL PROCESSING INDUSTRY AS SUBSTRATE BY *Pseudomonas aeruginosa* (MTCC 424)

Ashutosh Mishra¹ and Rakesh Kumar Trivedi^{2,*}

¹Department of Chemical Engineering, Dr. Ambedkar Institute of Technology for Handicapped, Kanpur-208024, (U.P.) India

² Department of Oil Technology, Harcourt Butler Technical University, Kanpur-208002, (U.P.) India

*E-mail: rakeshtrivedi@hotmail.com

ABSTRACT

The purpose of this study was to produce biosurfactant by the waste of vegetable oil (soya bean and rice bran) processing industries like spent bleaching earth which contains approximately 14 to 25% residual oil respectively. More oil % was found in the spent on rice bran so here the same was used. The spent bleaching earth is a type of waste solid substance which is generated as an ingredient of the cleansing and decolorization process in the edible oil industry. It is usually deposited in the landfills or waste dumps. *Pseudomonas* was selected for its nutritional and biochemical versatility as well as for the simplicity of the culture conditions. The process opted for the growth of bacteria was steam sterilization and dry heat sterilization followed by microbial culture in basal salt medium with residual oil. Further biosurfactant was screened by various examination methods such as surface tension measurement, emulsification assay E24, CTAB methylene blue assay, oil dislocation (displacement), drop collapse and effect of environmental factors on biosurfactant activity was studied. Rhamnolipid biosurfactant produced by *Pseudomonasaeruginosa* is determined by the formation of insoluble ion pairs with various cationic substances. Emulsification index (%) shows the positive result for drop collapse, oil displacement, and CTAB methylene blue assay. The NMR and FTIR analysis show that the concentration and purely screened Rhamnolipid product contained L-rhamnosyl-b-hydroxydecanoyl-b-hydroxydecanoate (RL1) and L-rhamnosyl L-rhamnosyl-bhydroxydecanoyl-b-hydroxydecanoate (RL2). Effect of environmental factors like salt, temperature and pH on surface tension was studied to analyze the solubility of biosurfactant. The optimum pH was found 6.8 and the optimum concentration of rhamnolipids produced was 8.5 g/l.

Keywords: Biosurfactant, Spent Bleach Earth, Rice Bran, *Pseudomonas aeruginosa*, CTAB-MB, NMR, FTIR

© RASĀYAN. All rights reserved

INTRODUCTION

Biosurfactant, which is basically surface-active agents, are synthesized by microorganisms. Biosurfactant is to be used than chemical surfactants because of some very valuable characteristics such as lower toxicity, the very low value of critical micelle concentration, better biodegradability, good environmental compatibility, etc. Biosurfactant has major applications to degradation the pollutants. The production which includes isolation, identification and characterization of biosurfactant by an assortment of microorganisms have already been reviewed deeply¹. Glycolipids and lipopeptides are some commonly isolated biosurfactant which also includes Rhamnolipids, which is produced by *Pseudomonasaeruginosa*², sophorolipids from *Candida* sp.³, as well as surfactin and iturin produced by *Bacillus subtilis* strains⁴. Biosurfactants are classified according to their surface activity and molecular weight. Lower molecular weight surface active agents are called Biosurfactant whereas higher molecular weight substances are called Bio-emulsifier. Some common biosurfactant is glycolipids, phospholipids, polymeric

biosurfactants and lipopeptides (surfactin). Among these, rhamnolipids, sophorolipids and trehalolipids are some best popular glycolipids.⁵

To cultivate the bacteria for biosurfactant production, the dairy waste, sugar industry byproducts, fruit and vegetable (edible and non-edible oil) processing industries, breweries, distillery, etc. are the major sources. Million ton of hazardous pollutants are treated with biosurfactant to reduce, reuse and recycle the waste. For the laboratory use, some microorganisms and biosurfactants are cultivated from the cheap alternative substrate like waste olive oil crush runoff, dissipate blistering oil, vegetable processing plant squander like spent bleaching earth, soapstock, molasses, whey and distillery waste etc.⁷⁻¹²

For increasing the yield of biosurfactant the bacteria cultivation should have the optimal environment and culture conditions to enhance productivity. Some factors affecting biosurfactant production are:

- a. C-Source
- b. N- Source
- c. Salts and minerals
- d. Environmental conditions
- e. Aeration and Agitation

Biosurfactant has an advantage over chemical surfactant like inferior venomous, superior biodegradability, reduced CMC concentration values, etc. It has an ample variety of relevance in oil, foodstuff and cosmetic industries as well as in therapeutic agent and pollutant removal.

EXPERIMENTAL

Substrate Used

RO (Residual Oil) from spent bleaching earth from Kanpur Edible Oil, vegetable oil processing industry situated in Rania, Kanpur.

Microorganisms and Culture Conditions

Strain *Pseudomonas aeruginosa* (424) was used which was produced in Microbial Type Culture Collection and Gene Bank (MTCC), Chandigarh.

Apparatus Required

- i. Autoclave: vertical model: PSM-550-B2-11CD was used for steam sterilization of media.
- ii. Oven: Make Samsung used for dry heat sterilization.
- iii. Laminar air flow: Horizontal make Science Tech Mahindra was used to provide sterilize condition for culture maintenance.
- iv. Incubator shaker: Model JEQ-4(0) was used for maintaining growth condition.
- v. Separating funnel and water bath are used to separate the phases of different densities and to maintain temperature.

Fermentation Media

All chemicals of make qualikems CDH were used. The nutrient issue was cast-off for grounding to inoculums. Main Symphony of the nutrient bisque was warned as beef extort 1.0 g, yeast extorts 2.0 g, peptone 5.0 g, NaCl 5.0 g in one liter of distilling water. In the nutrient bisque, 15.0 g of agar is to be added for preparing nutrient agar. The cultures were developed in this bisque for 16-18 hr at room temperature. The composition is utilized for the synthesis of biosurfactant as per given in Table-2 and 3 and 4% (w/w) residual rice bran oil (RO). The RO in the samples were anticipated by spent through soxhlet extraction method using hexane as solvent. The optimum temp was found out at 68⁰C and the optimum time was found 2 hours. It was used as the sole carbon source.

Then microbial culture was incubated for 48 hrs in an incubator shaker at 100 rpm, 25⁰C. The culture was inoculated to basal salt medium (BSM) with each substrate and yeast extract to enhance the growth. They were incubated for 48-72 hrs in an incubator shaker at 100 rpm, 25⁰C. Froth was detected and then centrifuged for 15 min at 6000 rpm to attain cell gratis supernatant.

Drop Collapse Test

The method used was developed by Bodour and Maier (1998).¹⁴

Emulsification Test

The method to determine the EI used was developed by Saravanan, V. et al. 2012. The EI (E 24) is the height (cm) divided by total height (cm), multiplied by 100.¹⁵

$$\text{Emulsification Index (E24)} = \frac{\text{The height of the emulsion layer achieved}}{\text{total height procured}} \times 100$$

Table-1: Mineral Salt Medium Compositions

Components	Quantity (g/l)
NaNO ₃	1.0
KH ₂ PO ₄	1.0
K ₂ HPO ₄	2.0
MgSO ₄	1.0
CaCl ₂	0.02
FeSO ₄	0.002
KCl	1.0
Trace elements	1 ml/l

Table-2: Media Components

KH ₂ PO ₄	0.7 g/l
Na ₂ HPO ₄	0.9 g/l
NaNO ₃	2 g/l
MgSO ₄ .7H ₂ O	0.4 g/l
CaCl ₂ . 2H ₂ O	0.1 g/l
Trace Elements	2 ml/l
CTAB	0.2 g/l
Methylene Blue	0.005 g/l
Agar	15 g/l

Oil Spreading Technique

This technique was used to correlate surfactant activity, which is commonly known as the displacement of oil activity. The method used was developed by Masaaki Morikawa et al., 2000.¹⁶

CTAB-MB

The test is specifically used for the detection of anionic biosurfactant. A gloomy blue aperture region around the culture should be considered positive for anionic biosurfactant production.¹⁷

MBAS Assay

Rhamnolipid production was qualitatively analyzed by methylene blue Active Substance assay (MBAS) proposed by Hayashi in 1975.¹⁶

Surface Tension Measurement

The surface tension of cell-free culture broth was measured by DuNouy ring method and the instrument used was a Surface Tensionmeter (USHA INST., Kolkata-73). The surface tension of cell-free culture broth was measured by DuNouy ring method.¹⁸

Rhamnolipid Biosurfactant Recovery

The culture was centrifuged at 6000 rpm for 15 minutes. The supernatant obtained was used for the extraction method. Then to reduce the pH to approximately 2, 6N conc. HCl was added in supernatant so that it may precipitate. Thus obtained the acidified suspension was kept for overnight in the refrigerator. Chloroform: methanol (2:1 v: v) solvent mixture was used to extract the biosurfactant by using separating funnel. This step was repeated twice. Ethyl acetate was used for the washing of the Organic phase obtained at the bottom. The aqueous phase was discarded. The organic phase was kept open for overnight. It was filtered to obtain crude biosurfactant for further column chromatography, TLC, FTIR, and NMR analysis.

Purification and Characterization of Rhamnolipid Biosurfactant column chromatography

Liquid column chromatography was used for these variances of rhamnolipids. 50g of activated silica gel 60-CHCl₃ slurry was used for the separation of the polar lipids in a 26×3.3cm column. 5g sample of rudimentary rhamnolipid primed was loaded in the column in 10ml Chloroform and then to evade the neutral lipids the column was cleaned away with chloroform. Then at a flow rate of 1 ml/min and 20 ml fractions were collected by applying the mobile phases of chloroform: methanol in sequence; 50:3

v/v(1000ml), 50:5v/v(200ml) and 50:50v/v(100ml)²⁰. A concluding cleanse washing with half-half CHCl₃:

CH₃OH detached any remaining rhamnolipid from the column. Fractions were pooled and solvent of vigorous fractions enclosing biosurfactant was fade away to dryness beneath vacuum with a rotor evaporator(make - BUCHI™ Rotavapor™ R-300) at 40⁰ C under a bridged pressure.

Thin Layer Chromatography

The fractions from the liquid column chromatography thus obtained. Further 1 ml CHCl₃ and 100µl of each sample was taken and the samples were dissolving followed by applying to a 20×20 silica gel TLC plate and developed in a solvent system of chloroform : methanol : acetic acid (65:15:2v/v/v). The separated spots on these preparative TLC plates were carefully scraped and collected separately. From these silica gel scrapings, the rhamnolipids were extracted thrice with 8ml of CHCl₃: CH₃OH(1:2v/v). The solvent scraping mixture was vortexed for 1 minute followed by centrifugation and settled down the silica gel for 10 minutes and pipetted off the solvent.²⁹

Effect of Environmental Factors on Biosurfactant Activity

The outcomes of the accumulation of dissimilar concentrations of salt (sodium chloride) on the bustle of the biosurfactant were investigated in the cell-free broth. Specific concentrations of salt (sodium chloride)(2–10%, weight/vol) were additionally provided and the surface tension was determined as described above. The cell-free broth was also maintained at a constant temperature (5,70, 100 and 120⁰C) for 60 min and used for surface tension and emulsification measurements. The consequence of the pH on the surface tension was investigated after fine-tuning of the bisque pH to 2, 4,6,8,10,12 and 14 with 6.0 Molar NaOH or HCl.¹⁹

Application of Biosurfactant in Hydrophobic Contaminant Cleaning Test

To determine the cleaning ability of the biosurfactant, the inner walls of a beaker were coated with motor oil. Fifty ml of the cell-free culture broth were added to the beaker, which was vortexed for 1.0 min and allowed to stand for 6 h.²⁰

NMR and FTIR Analysis

Purified rhamnolipid samples are analyzed with the magnetic nuclear response (NMR) and FTIR. JEOL JNM-ECS400 spectrometer manufactured by Tokyo, Japan was used for ¹H and ¹³C spectrum. FTIR studies were done on PerkinElmer Spectrum Version 10.03.06 manufactured by the USA.²¹

RESULTS AND DISCUSSION

Rhamnolipids, produced by *Pseudomonas* species are a kind of glycolipids. The strain was developed on basal salt medium (BSM) and was further screened for biosurfactant production by different assays. Rhamnolipids biosurfactants produced by *Pseudomonas aeruginosa* was determined by the formation of insoluble ion pairs with various cationic substances.

Oil Displacement Assay

10 µl of oil was added to the surface of 10 ml distilled water in a plate. A thin layer of oil was formed on the surface of the water. 10 µl of cell-free supernatant was placed on the center of oil layer where the clear zone was formed by displacing oil showed the presence of biosurfactant.

Drop Collapse Assay

2 µl of oil was applied on Petri plate and 2-3 µl of cell-free supernatant was placed on oil drop. It was observed after 1 min. The result was considered positive for biosurfactant production when the drop was flat and the rounded drops were scored as negative. The diameter (mm) of the drop was observed and shown in Table-4.

CTAB Methylene Blue Assay

This test is specific for the identification of anionic biosurfactant producers. Instead of CTAB other cationic detergents can also be used. Cell-free supernatant was loaded into each well prepared in

methylene blue agar plate. The plate was then incubated at 37°C for 48-72 h. A dark blue hole zone around the culture was considered positive for anionic biosurfactant production.

MBAS Assay

Rhamnolipid production by the strains *Pseudomonas aeruginosa* MTCC 424 was qualitatively analyzed by Methylene Blue Active Substance assay (MBAS). The method was based on the formation of a complex between an anionic surfactant and the cationic dye methylene blue, followed by the extraction of the complex into chloroform and measurement of the absorbance (Table- 6) of the blue chloroform layer at 655nm. The blue tint of the anionic surfactant-methylene blue complex was observed at the bottom layer of chloroform which confirmed the production of an anionic biosurfactant thus obtained by *Pseudomonas aeruginosa* MTCC424.

Emulsification Assay (E24)

2 ml of oil was added to each test tube where cell-free supernatant was suspended and the mixture was vortexed for 1 min and allowed to stand for 24 hrs. Emulsion layer was formed which was calculated by the known (given above) formula.

Table-3: Emulsification Index for Different Substrate

Substrate	DCA (Dia in mm)	ODA	CTAB	EI (%)
RO	+ 5.0	+	+	72.20
Control	-	-	-	25.92

+ = positive result

- = negative result

Table-4: Surface Tension Measurement

Substrate	Surface Tension Reduction on increasing Concentration of Sample			
RO	64.77	61.10	59.44	56.46
Control	71.49	71.48	71.44	71.44

Surface Tension Measurement

The surface Tension was decreased throughout the growth of the strain data as given in Table-5.

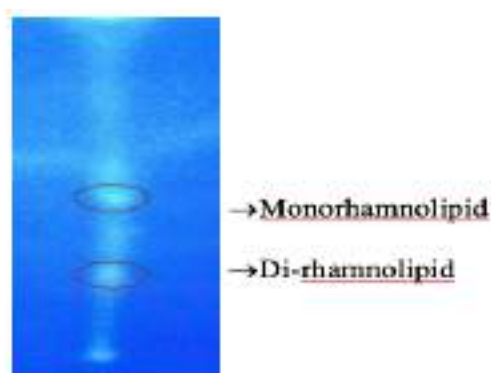


Fig.-1: Thin Layer Chromatography Strip Analysis

Column Chromatography

The rhamnolipid components produced by the strain *P. aeruginosa* MTCC 424 using residual rice bran as the substrates were recovered from the batch cultures by centrifugation followed by acid precipitation and solvent extraction. Ethyl Acetate was used as an organic solvent used for the extraction. silica gel column chromatography was used for the further purification of the resulting partially purified rhamnolipid components and collected fractions were analyzed by TLC in order to monitor the separation of the components.

Thin Layer Chromatography

As shown in Fig.-1, the Blue acne investigative of carbohydrate units were noticed on spraying with anisaldehyde reagent (Sigma Aldrich) in silica plates encumbered with crude extract of the biosurfactant produced by *Pseudomonas aeruginosa* MTCC424. When the similar plates were bared with iodine vapor, yellow acne investigative of lipids benevolent equivalent Retention factor as that of glycosyl units was acquired on the identical section. The occurrence of both glycosyl units and lipid moieties on the same acne indicated that the sample was a glycolipid and the Retention factor acquired was 0.62, analogous to that of rhamnolipids.²⁸ In the previous study, the presence of both glycosyl units and lipid moieties on the spot with Rf value 0.65 indicated the presence of a rhamnolipid biosurfactant. Another spot with a lower Rf value 0.26 was seen with this sample which also showed the presence of glycosyl and carbohydrate moiety. These results showed that the strain *Pseudomonas aeruginosa* MTCC424 was able to grow and produce rhamnolipid biosurfactant.

Optimization of Incubation Time on Biosurfactant Production

The optimum incubation time for rhamnolipid production by *Pseudomonas aeruginosa* MTCC424 using residual rice bran was found to be 7 days (Fig.-2).

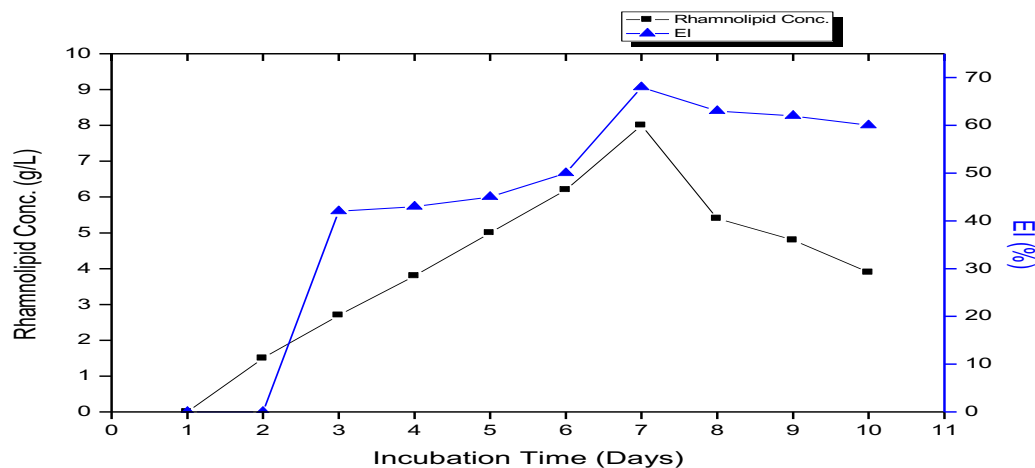


Fig.- 2 : Effect of Incubation Time on Rhamnolipid Production and Emulsification Index(%) with Mineral Oil by *Pseudomonas aeruginosa* MTCC424 using Residual Rice Bran (4%) Oil as the Solitary Carbon Source.

Optimization of Substrate Concentration on Biosurfactant Production

The rhamnolipid production by both bacterial strains was studied with varying concentrations of selected substrates in the growth medium. The rhamnolipid production by *Pseudomonas aeruginosa* MTCC 424 showed a significant increase with the increase in the rice bran concentration and attained the maximum yield when 4% rice bran oil was used as the carbon source(Fig.-3).

Optimization of pH on Biosurfactant Production

The optimum pH of the medium for maximum biosurfactant yield by *Pseudomonas aeruginosa* MTCC424 using residual rice bran was found to be 6.8(Fig.-5). The production decreased with the increase in pH beyond 6.8.

Effect of Environmental Factors on Biosurfactant Activity

Salinity, temperature and pH are various parameters on which the production of biosurfactant depends.²⁰ Therefore the effect on the variation of these parameters on the production of biosurfactant was tested and described as per given in Table-6. At pH 2,4 and 6, a very slight increase in surface tension was found. At pH in the range from 3-5(acidic) the rhamnolipid produced by *P.aeruginosa* as analyzed and found complete inactivation of the emulsifying capacity, but at higher values ie 6-9 no significant changes. With

the different concentration of salt, it was observed that the surface tension of the cell-free broth containing the biosurfactant proved stable. It was observed that at NaCl concentration above 10%, there was approximately no reduction in surface tension caused by a biosurfactant produced from the bacterial strain.²² The surface tension of the cell-free broth underwent small changes at different temperatures tested, with an as light increase at 5°C, but the results were unaltered at (26–27mN/m) at high temperatures (70, 100 and 120 °C).

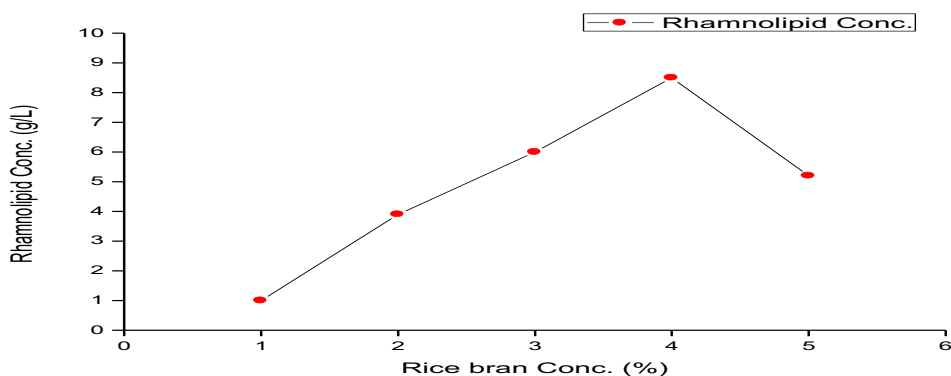


Fig.-3: Effect of Concentration of Rice Bran as the Carbon Source on Biosurfactant Production using *Pseudomonas aeruginosa* MTCC424 (pH 6.8, Incubation Time 7 days).

Chemical Characterization of Purified Biosurfactant

As revealed in Fig.-6 the FTIR analysis, an extensive elongate at 3417 cm^{-1} that was an attributed elongation mode of -OH group can be experiential undoubtedly. The symmetric elongate (-C-H) of $-\text{CH}_2-$ and $-\text{CH}_3$ groups of aliphatic manacles were represented by the absorption bands around 2927 cm^{-1} , 2856 cm^{-1} and 1402 cm^{-1} represented, and an absorption band at 722 cm^{-1} was assigned to $-(\text{CH}_2)_n-$ ($n = 6$) group. Also, a concerted assimilation band at 1572 cm^{-1} and 1068 cm^{-1} indicated the company of $-\text{C}=\text{O}$ group and $-\text{C}-\text{O}-\text{C}-$ group, respectively. Additionally, a weak absorption band at 1722 cm^{-1} , 1651 cm^{-1} , 1377 cm^{-1} , 1124 cm^{-1} and 982 cm^{-1} was the unsaturated alkyl double bond ($-\text{C}=\text{C}-$) of aliphatic chains. Compared with the previous literature²³, these main chemical structure groups were in agreement with the characteristic of rhamnolipid.

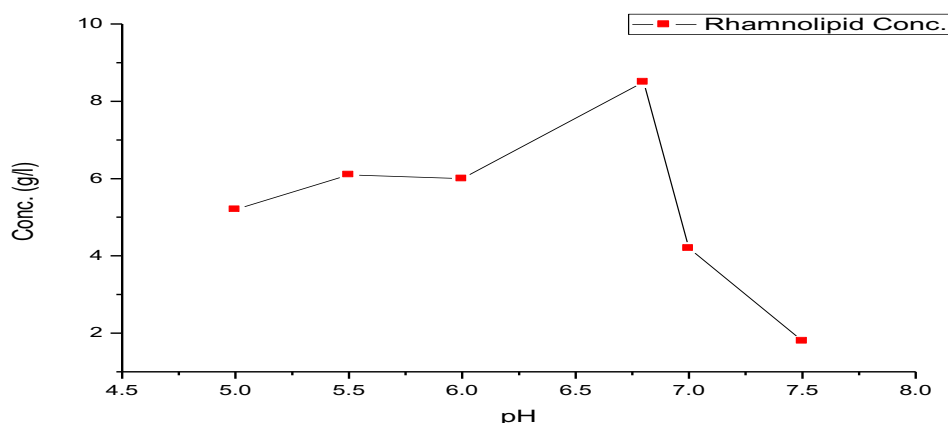
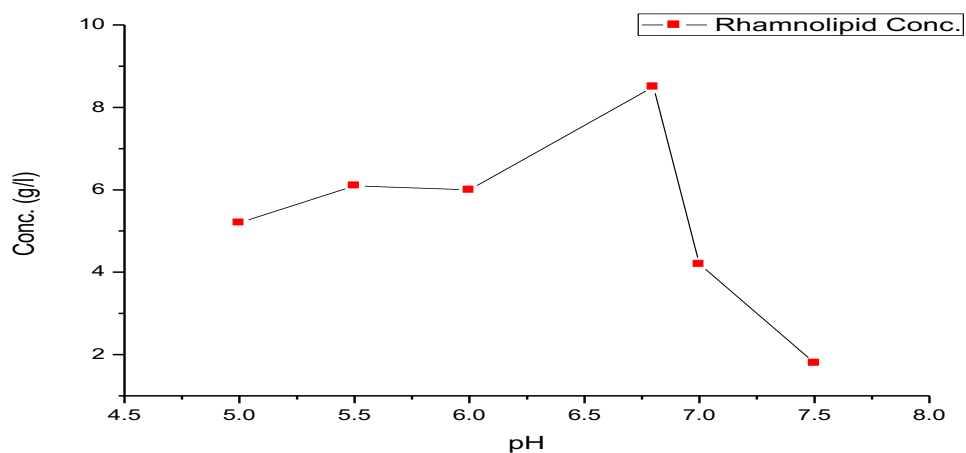
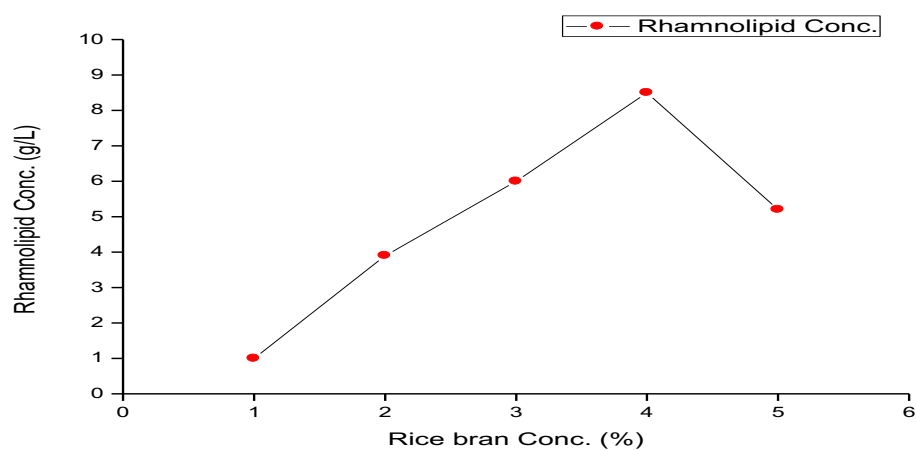


Fig.-4: Effect of pH on Biosurfactant Production by *Pseudomonas aeruginosa* MTCC424 using Rice Bran Oil as the Carbon Source at 4% Level (Incubation Time 7 days).

The detail chemical structure groups of the biosurfactant were identified by NMR. Structure information is obtained from three parameters: chemical shifts of the absorption frequency, coupling (mutual influence of adjacent nuclei), and integral height.²⁴



(a)



(b)

Fig.-5: (a)pH Versus Rhamnolipids Concentration produced from *P. aeruginosa* MTCC424, (b) Residual Rice Bran Oil(%) Concentration Vs Rhamnolipid produced (g/l) Concentration

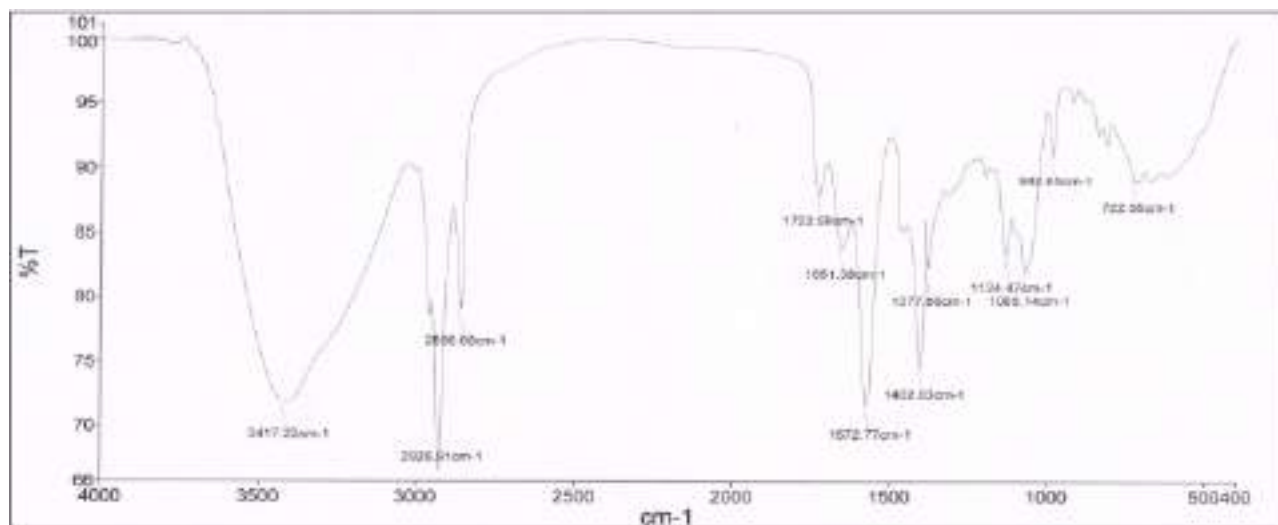
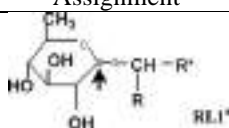
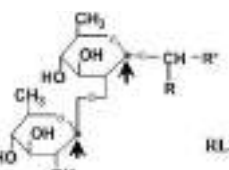


Fig.-6: FT-IR Spectra of the purified Biosurfactant produced by *Pseudomonas ae.* 424.

Table-5: Effect of Salt Concentration, Temperature and pH on Surface Tension (ST) of Cell-Free Broth Containing Biosurfactant from *P.aeruginosa* MTCC424 with 4% RO for 48 h at 100 rpm and 25 °C.

	ST (mN/m)
NaCl (%)	
0.0	25.9 ± 0.03
3.0	26.2 ± 0.05
6.0	27.1 ± 0.06
9.0	27.2 ± 0.04
10.0	27.5 ± 0.08
12.0	27.7 ± 0.01
15.0	27.7 ± 0.02
Temperature (°C)	
5	29.1 ± 0.04
70	26.2 ± 0.07
100	27.9 ± 0.03
120	27.1 ± 0.02
pH	
2	32.9 ± 0.06
3	33.2 ± 0.04
4	33.5 ± 0.06
5	33.8 ± 0.05
6	33.7 ± 0.01
7	33.8 ± 0.01
8	33.7 ± 0.09
9	33.7 ± 0.07

Table: 6 Chemical Shift of cleansed Rhamnolipid in ¹H NMR and ¹³C NMR Spectra

¹ H Chemical Shift (ppm)	Multiplicity	Assignment
0.856	Triplet	--CH ₃
1.232	Multiplet	---(CH ₂) ₆ --
2.742	Doublet	--CH ₂ --COO--
4.100	Multiplet	--O--CH--
5.308	Multiplet	--COO--CH--
¹³ C Chemical shift (ppm)		Assignment
76.773		
77.412		

^aRL1 (rhamnolipid 1): L-rhamnosyl-b-hydroxydecanoyl-b-hydroxydecanoate

^bRL2 (rhamnolipid 2): L-rhamnosyl L-rhamnosyl-b-hydroxydecanoyl-b-hydroxydecanoate

The purified rhamnolipid was analyzed by NMR as shown in Fig.-7 and Table-6. In the ¹H NMR study The distinguishing chemical shifts pragmatics were 0.855 ppm (for --CH₃), 1.232 ppm (for --(CH₂)₆--), 2.742 ppm (for --CH₂--COO--), 4.100 ppm (for --O--CH--), and 5.308 ppm (for --COO--CH--). The ¹³C NMR also displayed chemical shifts of 76.773 ppm (characteristic of RL1) and 77.412 ppm (characteristic of RL2). All those results indicate the molecular structure of L-rhamnosyl-b-

hydroxydecanoyl-b-hydroxydecanoate (RL1) and L-rhamnosyl-Lrhamnosyl-b-hydroxydecanoyl-b-hydroxydecanoate (RL2), which are common rhamnolipids types produced by *P. aeruginosa* strains.^{21,22}

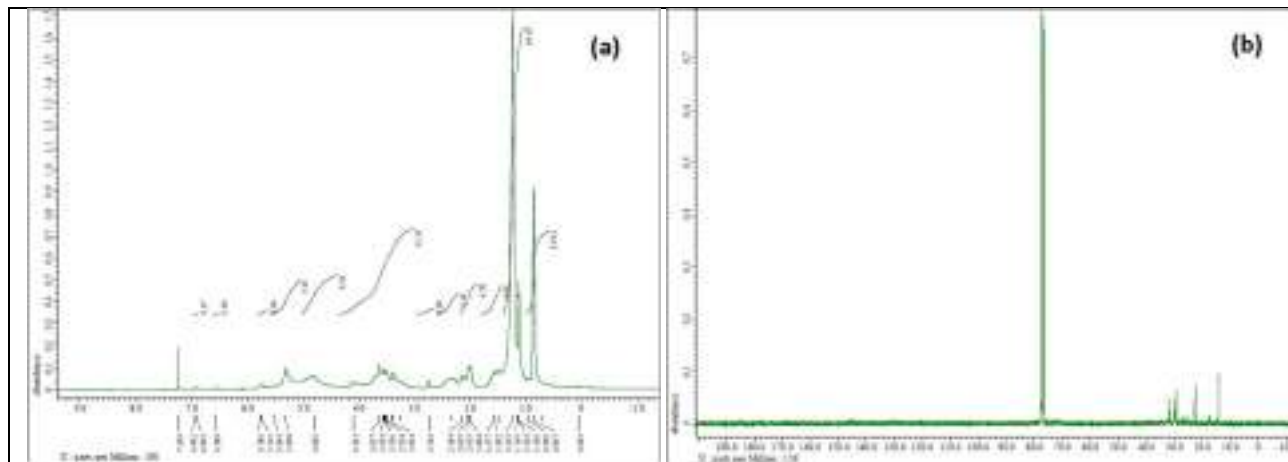


Fig.-7: (a) ^1H NMR Spectra, (b) ^{13}C NMR Spectra of the purified Biosurfactant produced by *Pseudomonas ae.* 424

CONCLUSION

The present study emphasis on strategies such as the use of cheaper substrates like spent earth which is a waste product of the vegetable oil processing industry so as to reduce the cost of the production of biosurfactant as compare to the conventional substrates like glucose and glycerol etc. and to the optimization of their production parameters. The main obstacle in the production of biosurfactant on a large scale is the costly substrates. In this study using the cheaper substrate like spent earth can make biosurfactant production economically feasible. Some other cheaper substrates like plant-derived oils, oil waste, distillery waste, etc are best supportive for biosurfactant production. Here optimization and production strategy have to be studied for the culture medium to increase the productivity of biosurfactant. The yield of rhamnolipids produced was 8.5 g/l. The optimum pH at which the maximum yield of rhamnolipids found was 6.8. In the whole study, the best results were obtained when pure biosurfactant was used, it reduced insufficient production cost and thus improved the adequate industrial application.

ACKNOWLEDGMENT

I am thankful to MTCC Chandigarh for providing the bacteria culture and Kanpur edible oil (Mayur Group) for providing spent earth. I am also thankful to the Department of Biotechnology, AITH Kanpur, Deptt of Oil Technology, HBTU Kanpur and IIT Kanpur for providing laborites facilities and Director AITH Kanpur for her kind support. I am also thankful to our colleagues who provided impending and proficiency that significantly assisted to follow a line of investigation and research.

REFERENCES

1. J. D. Desai, *J. Sci. Ind. Res.*, **46**, 440(1987).
2. A. Daverey and K. Pakshirajan, *App. Biochem. Biotech.*, **158**, 663(2008), DOI:10.1007/s12010-008-8449-z
3. F. Ahimou, P. Jacques, M. and Dele, *Enz. Mtcrob. Techno.*, **27**, 749(2000), DOI:10.1016/S0141-0229(00)00295-7
4. M. Nitschke, S. G. V. A. Coasta and J. Contiero, *Biotech. Prog.*, **1**, 593(2005).
5. S. Mukherjee, P. Das and R. Sen, *TRENDS in Biotechnology*, **24(11)**, 509(2006), DOI: 10.1016/j.tibtech.2006.09.005
6. A. Fiechter, *Tibtech.*, **10**, 208(1992), DOI:10.1016/0167-7799(92)90215-H
7. K. Dubey and A. Juwarkar, *World Journal of Microbiology and Biotechnology*, **17(1)**, 61(2001), DOI:10.1023/A:1016606509385
8. Y. Zhang, and R. M. Miller, *Appl. Environ. Microbiol.*, **58**, 3276 (1992).

9. M. E. Mercade, M. A. Manresa, *J. American Oil Chem. Soc.*, **71(1)**, 61(1994), DOI:10.1007/BF02541473
10. Z. A. Raza, A. Rehman, M. S. Khan and Z. M. Khalid, *Biodegradation*, **18(1)**, 115(2007), DOI:10.1007/s10532-006-9047-9
11. R. Makkar and S. Cameotra, *Applied Microbiology and Biotechnology*, **58(4)**, 428(2002), DOI:10.1007/s00253-001-0924-1
12. S. Maneerat, *Songklanakar J. Sci. Technol.*, **27(3)**, 675(2005).
13. G. Dashiny, *Oil Recovery from Palm Oil Solid Wastes* (Doctoral Dissertation, Dissertation University, Malaya Pahang) (2009).
14. A. A. Bodour and R. M. Miller-Maier, *Journal of Microbiological Methods*, **32(3)**, 273 (1998), DOI:10.1016/S0167-7012(98)00031-1
15. V. Saravanan and S. Vijayakumar, *J. Acad. Indus. Res.*, **1(5)**, 264(2012).
16. Noha H. Youssef et al., *Journal of Microbiological Methods*, **56(3)**, 339(2004), DOI:10.1016/j.mimet.2003.11.001
17. N. M. Pinzon and L. K. Ju, *Biotechnology Letters*, **31(10)**, 1583(2009), DOI: 10.1007/s10529-009-0049-7
18. A. A. Bodour and R. M. Miller-Maier, *Journal of Microbiological Methods*, **32(3)**, 273(1998), DOI:10.1016/S0167-7012(98)00031-1
19. M. O. Ilori, C. J. Amobi and A. C. Odocha, *Chemosphere*, **61(7)**, 985(2005), DOI: 10.1016/j.chemosphere.2005.03.066
20. I. M. Banat, *Bioresource Technology*, **51(1)**, 1(1995), DOI: 10.1016/0960-8524(94)00101-6
21. M. Heyd, A. Kohnert, T.H. Tan, M. Nusser, F. Kirschhöfer, G. Brenner-Weiss, M. Franzreb and S. Berensmeier, *Analytical and Bioanalytical Chemistry*, **391(5)**, 1579(2008), DOI:10.1007/s00216-007-1828-4
22. N. M. P. R. e Silva, R. D. Rufino, J. M. Luna, V. A Santos and L. A. Sarubbo, *Biocatalysis and Agricultural Biotechnology*, **3(2)**, 132(2014), DOI: 10.1016/j.bcab.2013.09.005
23. S. Lang, D. Wullbrandt, *Appl. Microbiol. Biotechnol.*, **51**, 22(1999), DOI:10.1007/s002530051358
24. O. Pornsunthorntawe, P. Wongpanit, S. Chavadej, M. Abe and R. Rujiravanit, *Bioresource Technology*, **99(6)**, 1589(2008), DOI:10.1016/j.biortech.2007.04.020

[RJC-5073/2018]

Research Article

Toxicity Mitigation of Textile Dye Reactive Blue 4 by Hairy Roots of *Helianthus annuus* and Testing Its Effect in *In Vivo* Model Systems

Kanchanlata Tungare ¹, Rinkey Shahu ², Vyankatesh Zambare ³, Payal Agarwal ², Renitta Jobby ^{2,4}, Nazima Nisar,⁵ Nadiyah M. Alabdallah ⁶, Fatimah A. Al-Saeed ⁷, Parul Johri,⁸ Sachidanand Singh,⁹ Mohd Saeed ¹⁰ and Pamela Jha ¹¹

¹School of Biotechnology and Bioinformatics, D. Y. Patil Deemed to be University, Plot No. 50, Sector 15, CBD Belapur, 400614 Navi Mumbai, Maharashtra, India

²Amity Institute of Biotechnology, Amity University Maharashtra, Mumbai Pune Expressway, Bhatan, Post Somatane, Panvel, Mumbai, Maharashtra 410206, India

³Huck Institutes of the Life Sciences, The Pennsylvania State University, University Park PA 16802, USA

⁴Amity Centre of Excellence in Astrobiology, Amity University, Maharashtra-Pune Expressway, Bhatan, Panvel, Mumbai, Maharashtra 410206, India

⁵Department of Clinical Laboratory Sciences, College of Applied Medical Sciences, King Khalid University, Abha, Saudi Arabia

⁶Department of Biology, College of Science, Imam Abdulrahman Bin Faisal University, P.O. Box 1982, 31441 Dammam, Saudi Arabia

⁷Department of Biology, College of Science, King Khalid University, Abha, Saudi Arabia

⁸Department of Biotechnology, Dr. Ambedkar Institute of Technology for Handicapped, Kanpur 208001, India

⁹Department of Biotechnology, Smt. S. S. Patel Nootan Science & Commerce College, Sankalchand Patel University, Visnagar, 384315 Gujarat, India

¹⁰Department of Biology, College of Sciences, University of Hail, Hail, Saudi Arabia

¹¹Department of Biological Sciences, Sunandan Divatia School of Science, NMIMS Deemed to be University, Vile Parle (West), Mumbai 400056, India

Correspondence should be addressed to Mohd Saeed; mo.saeed@uoh.edu.sa and Pamela Jha; pamelajha@gmail.com

Received 16 May 2022; Revised 24 June 2022; Accepted 25 June 2022; Published 25 July 2022

Academic Editor: Abdelaaty Shahat

Copyright © 2022 Kanchanlata Tungare et al. This is an open access article distributed under the Creative Commons Attribution License, which permits unrestricted use, distribution, and reproduction in any medium, provided the original work is properly cited.

An anthraquinone textile dye, Reactive Blue 4 (RB4), poses environmental health hazards. In this study, remediation of RB4 (30–110 ppm) was carried out by hairy roots (HRs). UV-visible spectroscopy and FTIR analysis showed that the dye undergoes decolourization followed by degradation. In addition, toxicity and safety analyses of the bioremediated dye were performed on *Allium cepa* and zebrafish embryos, which revealed lesser toxicity of the bioremediated dye as compared to untreated dye. For *Allium cepa*, the highest concentration, i.e., 110 ppm of the treated dye, showed less chromosomal aberrations with a mitotic index of 8.5 ± 0.5 , closer to control. Two-fold decrease in mortality of zebrafish embryos was observed at the highest treated dye concentration indicating toxicity mitigation. A higher level of lipid peroxidation (LPO) was recorded in the zebrafish embryo when exposed to untreated dye, suggesting a possible role of oxidative stress-inducing mortality of embryos. Further, the level of LPO was significantly normalized along with the other antioxidant enzymes in embryos after dye bioremediation. At lower concentrations, mitigated samples displayed similar antioxidant activity comparable to control underlining the fact that the dye at lesser concentration can be more easily degraded than the dye at higher concentration.

1. Introduction

The textile industry is one of the major industries using dyes of various kinds. Nearly 80,000 tonnes of dyestuff are produced in India, and approximately 10,000 textile dyes are manufactured commercially on a global scale. Globally, the production of textile dye is 7×10^5 metric tons, of which 30% of dyes are used superfluously [1]. 2% of these dyes fail to adhere to fibre and consequently discharge into effluents, implying that the textile dyeing process generates harmful wastewater [2]. The most frequently used dyeing compounds are azo dyes followed by anthraquinone dyes owing to their stability against microbial degradation and photolysis [3, 4]. Azo groups and aromatic groups of anthraquinone dyes are resistant to chemical degradation and are liable to accumulate in the environment with a very high degree of persistence [1]. Anthraquinone dyes are the second most abundantly produced dyes on a global scale. While numerous groups have investigated the remediation of azo dyes, less attention has been dedicated to the degradation of anthraquinone dyes [5]. Industrial effluents containing these substances have a detrimental influence on natural water bodies and aquatic life, while also offering an implicit hazardous and even carcinogenic risk to humans [6]. Therefore, amelioration of these effluents is imperative and research on it is a pressing priority.

Existing methods for textile wastewater treatment include physical and chemical, in addition to certain engineered techniques such as adsorption, electrolysis, oxidation, and photoionization. The majority of the procedures discussed above have significant disadvantages, including high costs, low efficiency, and the generation of hazardous intermediates [7]. Adsorption, on the other hand, requires less land space, offers more flexibility in the design and operation, generates fewer toxic elements, and extends increased removal of contaminants. However, it leads to concentration of pollutants from textile effluents to the adsorbent and does not ensure complete removal of the pollutant. Therefore, it is of importance to determine if the plant species are capable of transforming or degrading the dye into simpler, nontoxic products. Hairy roots (HRs) from various plant species are extensively used to assess tolerance, accumulation, and/or elimination of environmental pollutants [8, 9]. Additionally, HR crops also serve as *in vivo* model systems to investigate phytoremediation processes and mechanisms [10]. Amidst all the pollutants that endanger biodiversity, industrial dye-based effluents present the most serious threat [11]. Textile colours in extremely low quantities in effluent and their byproducts are likewise hazardous to the ecology [12]. Hence, only the adsorption process is not enough, and degradation of the dyes also becomes critical. Numerous researchers have described the use of HRs to degrade dyes; however, there is limited data investigating the safe nature of the bioremediated dyes using *in vitro* models. Among the plants used for remediation of pollutants, sunflower (*Helianthus annuus*) is well known for remediation of pollutants like phenol and heavy metals [13]. Hence, the present study is aimed at evaluating the bioremediation potential of HRs towards an anthraquinone textile dye RB4, and toxicity

analysis of the degraded dye products was performed using *in vivo* model systems. The outcomes from this study are expected to further standardize the use of HRs as an effective bioremediation agent for a broad range of textile dyes.

2. Materials and Methods

2.1. Raw Materials and Chemicals. Hairy roots were obtained from explants of *Helianthus annuus*. The textile dyes RB4, Direct Black B (DBB), Reactive Green 19 (RG19), Reactive Orange 84 (RO84), Reactive Yellow 17 (RY17), Reactive Red 35 (RR35), Reactive Red M8B (RRM8B), Reactive Red M5B (RRM5B), Reactive Violet 5R (RV5R), and Reactive Violet 13 (RV13) were obtained from Apex Industries, Ahmedabad, India. All other chemicals used were of high analytical grade.

2.2. Preparation of Hairy Roots. *Agrobacterium rhizogenes* MTCC532 was used for HR induction in leaf explants of *Helianthus annuus*, and molecular confirmation was done by PCR [14].

2.3. Decolourization of Textile Dyes. The capacity of HRs to decolourize 10 textile dyes for 120 h was performed, and percent decolourization was calculated by the method of Jha et al. [14] using the following formula:

$$\% \text{Decolourization} = \frac{\text{Initial absorbance} - \text{final absorbance}}{\text{Initial absorbance}} \times 100. \quad (1)$$

2.4. Effect of Different Parameters on Decolourization of Dyes. The study was carried out by incubating HRs and selected dye (RB4) solution of varying pH (1.8, 2.8, 3.8, 4.8, 5.8, 6.8, and 7.8), temperatures ($27 \pm 2^\circ\text{C}$, $35 \pm 2^\circ\text{C}$, and $45 \pm 2^\circ\text{C}$), initial dye concentrations (30, 50, 70, 90, and 110 ppm), and biomass dosages (10-50 g/L). The decolourization (%) was calculated (see Section 2.3) for each sample with varying parameters.

2.5. Phytodegradation Analysis of Dyes by HRs

2.5.1. UV-Visible Spectroscopy. The absorbance of the supernatant obtained at 0 h and during decolourization of RB4 by HRs was taken in a UV-Vis spectrophotometer (Shimadzu UV-Vis Spectrophotometer 2800) at 595 nm wavelength.

2.5.2. Fourier Transform Infrared Spectroscopy (FTIR). The metabolites extracted, after decolourization of RB4, were mixed with spectroscopically pure KBr in the ratio of 5:95. The analysis was performed in the mid-IR region of $400\text{-}4000\text{ cm}^{-1}$ with 16 scan speeds using the PerkinElmer 783 Spectrophotometer and compared with control [14].

2.6. Toxicity Analysis

2.6.1. Allium cepa Test. The first set of bulbs was exposed to water (control), the second set to untreated dye (110 ppm), and the third set to treated dye (110 ppm) for 120 h. The cells were checked for different types of chromosomal aberrations [15].

2.6.2. Zebrafish Maintenance and Fish Embryo Toxicity (FET) Test. The embryos of wild-type zebrafish were used and maintained as per Westerfield 2000. Fertilized eggs in the cleavage period until the blastula stage were selected under an inverted microscope (Nikon ECLIPSE TS100) for subsequent experiments. An *in vivo* toxicity test was performed as per the Organization for Economic Cooperation and Development (OECD) test guideline no. 236. For this study, healthy zebrafish embryos were placed in 6-well culture plates (15 embryos per well). 30 mL per well samples of each untreated and treated dye was used in the range of 30, 50, 70, 90, and 110 ppm, respectively. Embryos in sterile distilled water were used as a control. The plates were then kept in the dark at $26 \pm 2^\circ\text{C}$. The embryos exposed from 24 to 96 h (every 24 h) were used for toxicity and biochemical analyses. The embryos exposed to the untreated and treated dye were evaluated for hatching, mortality, tail malformations, heartbeat, coagulation, malformation of somites, development of eyes, pigmentation, and edemas [16, 17]. All the experiments were conducted in triplicate.

2.7. Biochemical Assays. The embryos were homogenized in an ice-cold buffer (0.1 M Tris-HCl, 0.1 mM EDTA, and 0.1% Triton X-100 (*v/v*), pH 7.8). The homogenates were centrifuged, and the supernatants were used for the measurement of total protein and malondialdehyde (MDA) content as per Rajneesh et al. [18], superoxide dismutase (SOD) activity as per Bewley et al. [19], succinate dehydrogenase (SDH) as per Singh et al. [20], catalase (CAT) assay as per Bhoori et al. [21], and peroxidase (POX) assay as per Bhunia et al. [22].

2.8. Statistical Analysis. Each analysis was performed using GraphPad Prism 8.4.2 in triplicate, and the results were represented as mean \pm SD. The significance of the difference among the groups was assessed using a two-way analysis of variance (ANOVA) test followed by Tukey's post hoc test of the difference between all group means. Symbols used for significance are * $p < 0.05$, ** $p < 0.01$, and *** $p < 0.001$.

3. Results and Discussion

3.1. Screening of Textile Dyes. As the dyes used in the textile processing industry are of varying chemical structures, the effluents from the industry significantly vary to a large extent in composition. Therefore, it was important to evaluate the decolourization efficiency of HRs for different dyes. All the dyes were screened, and decolourization was observed in the range of 10% to 90% (Figure 1) after 24 h, 48 h, and 120 h of incubation. The dye, which showed maximum decolourization, was RB4, i.e., 90% after 120 h (Figure S1). The absorbance of supernatants at 120 h of decolourized RB4 was taken in a UV-visible spectrophotometer and compared with that of an untreated sample (Figure 2(b)). The decolourization percentage varied with different dyes, which might be attributed to their structural differences [23], increased structural complexities due to high molecular weight, and occurrence of inhibitory groups such as NO_2 and SO_3Na [24].

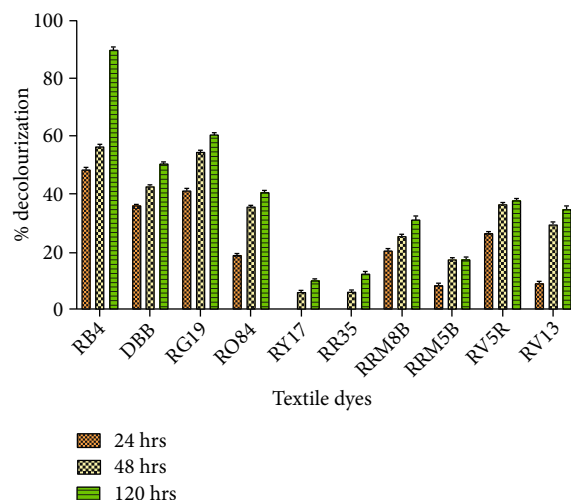


FIGURE 1: Decolourization of different dyes by hairy roots: untreated dye (U) and treated dye (T).

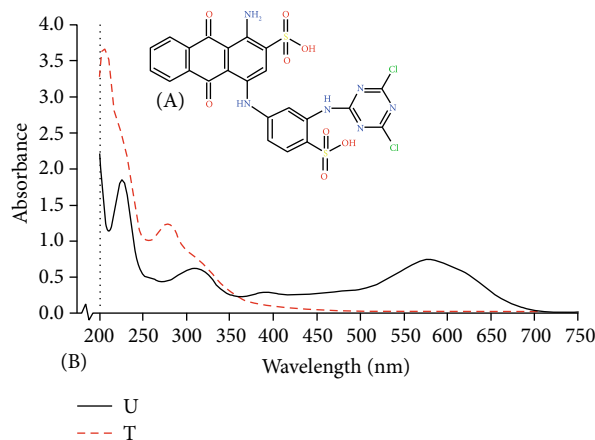


FIGURE 2: (a) Structure of RB4 and (b) UV-visible spectrum of RB4 untreated dye (U) and treated dye (T).

3.2. Effect of Different Parameters on Dye Decolourization by HRs. Maximum decolourization was observed at pH 4.8-5.8 (Figure S2), while temperature from 25 to 45°C (Figure S3) did not substantially affect decolourization. Therefore, all further experiments were conducted at 25°C and medium pH 5.8. Maximum decolourization (>90%) was observed at a biomass dosage of 40 g/L and 50 g/L (Figure S4). Decolourization was observed to be inversely proportional to the dye concentration ranging 30-110 ppm. The lowest concentration decolourized to 99%, and the highest was 51% (Figure S5).

3.3. FTIR. The FTIR spectrum of untreated and treated samples showed a variation in the molecular structure which is due to biodegradation of dye (Figure 3). In untreated dye, band at 3430.10, 2132.05, 1020-1220, and 691.45-548.19 cm^{-1} represents O-H stretching vibration of hydrogen-bonded hydroxyl groups in polymeric association, C=C stretching bond of alkynes molecule, alkyl amine, and halogen compound (chloro compound) (C-Cl), respectively. Similar broad bands at 3420.87 and 3442.87 cm^{-1} ,

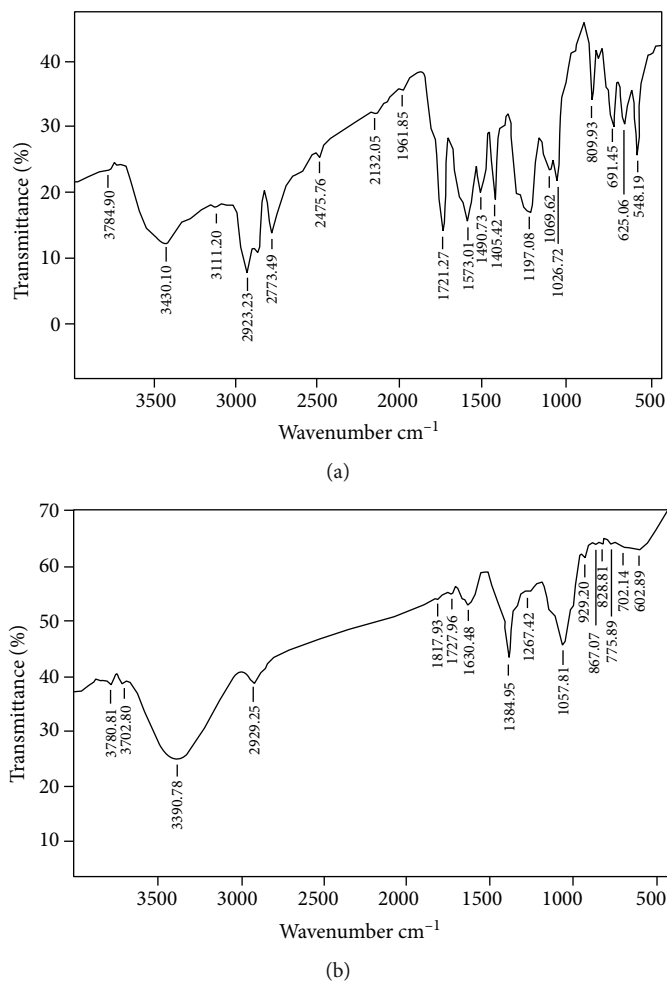


FIGURE 3: FTIR spectrum of RB4: (a) untreated dye and (b) treated dye.

respectively, representing $-NH-$ and hydroxyl ($-OH$) extensions in the RB4 spectrum were also reported by Afreen et al. [25] and Atteke et al. [26]. In our study, FTIR spectrum of treated dye showed bands at 3390.78, 1727.96, 1630.48, and 702.14-602.89 cm^{-1} which are attributed to the presence of bonded $N-H/C-H/O-H$ stretching of amines and amides, ketones, aromatic ring ($C=C$ in plane) stretching symmetric, and halogen compound ($C-Cl$), respectively. In another study, the difference in bands obtained in FTIR spectra of Reactive Red 198 and after its decolorization by HRs of *Tagetes patula* also indicated the degradation of the dye [27]. In a previous study, the FTIR spectra of another azo dye, Reactive Green 19A, also indicated similar functional groups like sulfonic groups and azo groups at the same wavenumbers as shown in our results [11]. Also, our previous study had reported the presence of azo groups in parent dye Acid Red 114 and the absence of these groups along with the emergence of new bands in treated dye by HRs of *Ipomoea carnea*, thereby suggesting the degradation of dye [28].

3.4. Toxicity Analysis

3.4.1. *Allium cepa* Test. Higher plants are recognized as excellent genetic models to detect environmental mutagens

and are frequently used in monitoring studies. Among the plant species, *Allium cepa* has been used to evaluate DNA damage, such as chromosome aberrations and disturbances in the mitotic cycle. Meristematic mitotic cells of *A. cepa* are established as capable constituents for cytotoxicity analysis [29]. In the present study, cytotoxic implications of treated and untreated dye were analyzed based on the mitotic index (MI) and chromosomal aberrations (Table 1). The MI of bulbs grown in 110 ppm untreated dye was found to be 6.5 ± 0.15 , which is statistically lower than cells in distilled water, whereas the MI of bulbs grown in 110 ppm treated dye was found to be improved and significantly closer to distilled water samples. Likewise, the percentage of aberrant cells at 110 ppm untreated dye was statistically higher ($p < 0.001$) than that of distilled water cells and significantly decreased to 10% in the case of cells exposed to the treated dye. In another study, toxicity analysis of the treated textile dye, RR35, using *A. cepa* root cells demonstrated improvement in cell viability, root length, mitotic index, and chromosomal aberrations when compared to untreated dye [30]. Different types of chromosomal abnormalities in treated and untreated dye samples like sticky metaphase, disturbed metaphase, anaphasic bridge, disturbed anaphase, and laggards have been previously

TABLE 1: Phytodegradation analysis of RB4 and its degradation products.

	Number of cells examined	Average number of roots	Mitotic index (MI)	% aberrant
Distilled water	510	14 ± 1.16	9.8 ± 0.52	4.0 ± 1.15
Untreated (110 ppm)	470	8 ± 1.15 ^{ns}	6.5 ± 1.10 ^{ns}	38 ± 0.55 ^{a***}
Treated (110 ppm)	480	12 ± 1.15 ^{ns}	8.5 ± 0.55 ^{ns}	10 ± 1.15 ^{aNS,b**}

The data represent mean ± SD. Symbols in the figure represent that comparisons are made between ^asample dye vs. control ($p < 0.001$) and ^btreated dye vs. untreated ($p < 0.01$). Statistical significance: *** $p < 0.001$ and ** $p < 0.01$. NS: nonsignificant.

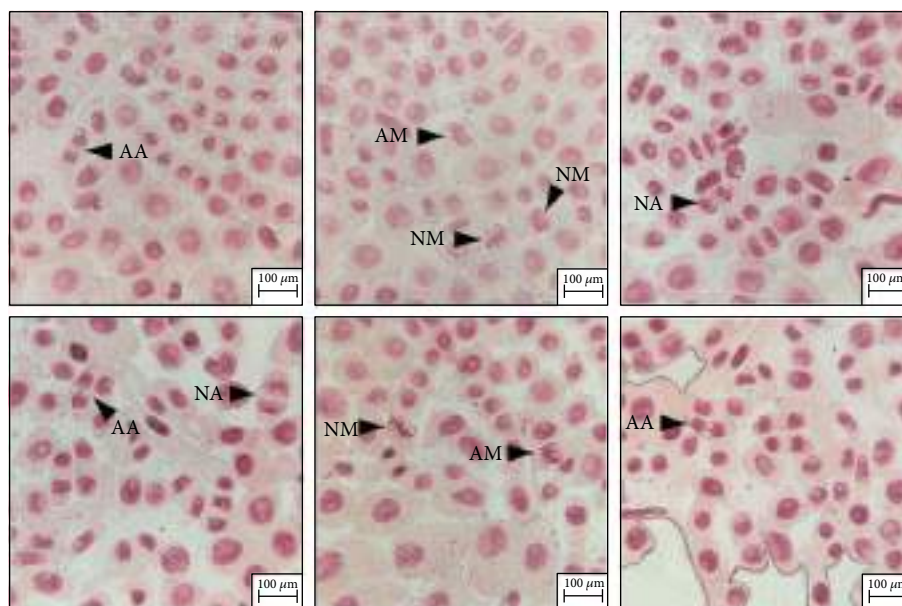


FIGURE 4: Stages of mitosis in root tips of *Allium cepa*: NM: normal metaphase; AM: abnormal metaphase; NA: normal anaphase; AA: abnormal anaphase.

reported [31]. Our microscopic results showed a significantly higher number of cell alterations in untreated than in control, with the most common being binucleate cells (Figure 4). In addition, untreated dye cells are shown to have more laggards than the cells exposed to treated dye, which is indicative of the genotoxic nature of the nonremediated dye.

3.4.2. FET. The zebrafish (*Danio rerio*) has immense advantages like small size, short life cycle, ease of breeding and maintenance, genetic similarities with humans, and high fecundity as a model system. It has been widely used as an effective biomarker in environmental toxicology. Zebrafish embryo serves as an alternative to the higher vertebrate model for which ethical consideration has become more contentious [32], thus gaining immense popularity in revealing the repercussion of natural or man-made chemicals [17]. In the FET test, control embryos showed a normal growth pattern, while a constant abnormal hatching pattern was observed in the case of test samples from 30 ppm to 110 ppm. Embryos reared in treated dye showed equivalent hatching rate as control whereas the ones in untreated dye exhibited a slightly delayed hatching at all concentrations under consideration (Figures 5(a) and 5(b)). At 96 hpf, embryos in untreated dye showed around 58% hatching (30, 50, 70, and 90 ppm) and 53% hatching for 110 ppm dye,

whereas embryos at all the concentrations of treated dye showed 78% hatching, which accounts for nearly 26% amelioration in toxicity posttreatment of dye using HRs. This delayed hatching of the eggs can be attributed to abridged expression of hatching-specific enzymes and embryonic movements that reduce the ability of the embryo to break the egg envelope as reported for other RB dyes [7]. Heart rate was also measured after 24 hpf till 96 hpf, but no significant difference was observed between control and both types (untreated and treated) of test samples (data not shown).

Zebrafish mortality is another important parameter to account for the dye toxicity. The untreated dye sample was observed to affect embryo survival percentage, even at the lowest concentration, but a sharp decline was observed at 70 and 90 ppm, i.e., 71.1% and 5%, respectively. Least survival percentage was noted in 110 ppm of untreated dye which seems to be quite close to the survival percentage of 90 ppm dye-exposed embryos. This major drop of the survival curve in 70 and 90 ppm of untreated dye seems to get flattened at 110 ppm. Upon bioremediation, improvement in the embryo survival was observed as shown in Figures 5(c) and 5(d). The survival percentage in 70 and 90 ppm of treated dye was recorded to be 88.9 and 82.2%, whereas the highest concentration of 110 ppm treated dye showed 77.8% survival. Therefore, the toxicity induced by untreated dye seems to be significantly

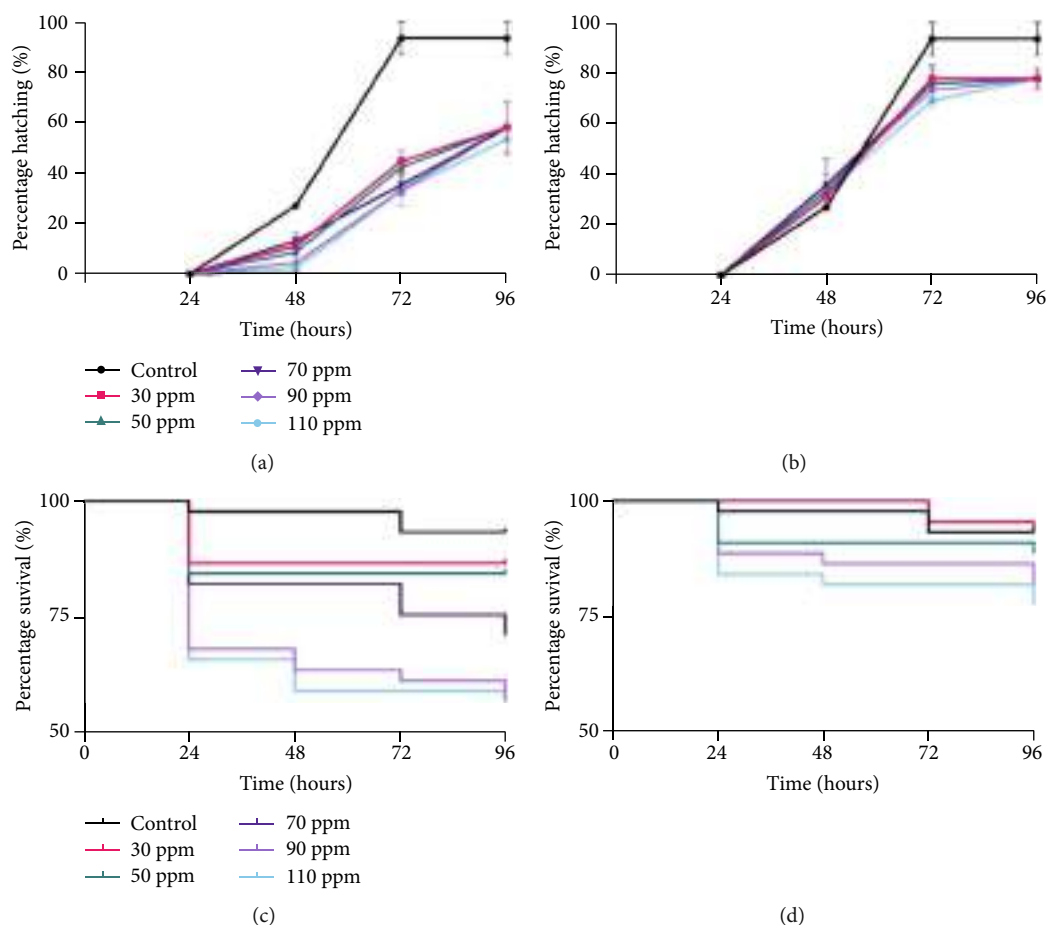


FIGURE 5: Ramification of RB4 dye and bioremediated dye on embryo hatching and survival rates. (a, b) Percentage hatching of embryos reared at different concentrations of untreated dye and treated dye, respectively. (c, d) Kaplan-Meier survival curves for zebrafish embryos reared at different concentrations of untreated dye and treated dye, respectively.

mitigated indicating the promising nature of HRs in the bioremediation of textile dyes.

Zebrafish embryos were monitored at every 24 h intervals till 96 hpf. A striking difference between the growth patterns was observed between the embryos reared at all the concentrations of untreated dye and treated dye (Figures 6(a) and 6(b)). Embryos raised at 50 ppm dye and above showed delayed hatching and other morphological deformities both before and after the bioremediation of RB4. 90% of the embryos displayed hyperpigmentation at 72 hpf and 96 hpf, respectively, for untreated dye samples (90 ppm and 110 ppm), while the extent of hyperpigmentation was reduced to around 50% of embryos after dye treatment. Though yolk sac edema (YSE) was prevalent in the embryos in untreated dye samples (except for 70 ppm), pericardial edema was absent. Bioremediation of RB4 ameliorated YSE, as YSE was absent in the embryos in treated dye samples. No deformity germane to somite formation was observed. A prominent spinal curvature (SC) was visible in embryos at 72 hpf and 96 hpf of 50 ppm and 70 ppm (96 hpf) untreated samples. This SC was reversed upon dye bioremediation. But SC observed at 96 hpf of 90 ppm and 110 ppm was irreversible. Lastly, tail malformation (TM) was observed in 50% embryos reared at 70 ppm at 96 hpf

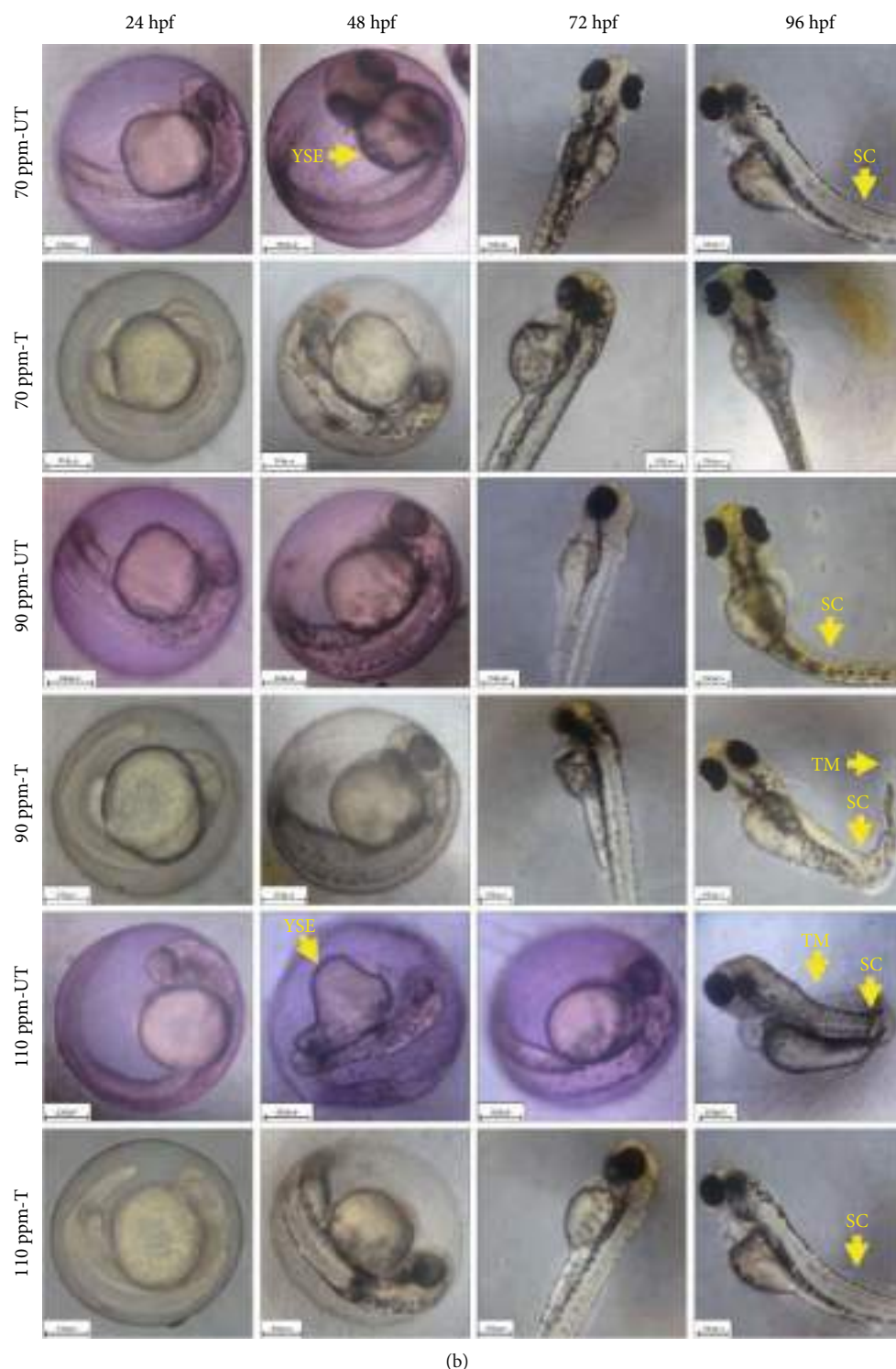
and in 90% embryos reared at 90 ppm and 110 ppm of untreated dye samples. At 110 ppm and 96 hpf, the embryo displayed entangling of the tail around the embryo axis. This may happen due to the defects at the molecular level which involve malformation of the tail and motor proteins required for the tail movement. Bioremediated dye samples displayed better results while nullifying TM for 70 ppm at the same time interval and reducing the deformity to 10% in the case of 90 ppm and 110 ppm samples. To the best of our knowledge, the toxicity of RB4 on the molecular cell signaling of zebrafish is not available. It is previously known that zebrafish T-box genes namely *spadetail* (*spt*) and *no tail* (*ntl*) are involved in the formation of the medial floor plate that in turn gives rise to the tail where *pipetail* (*ppt*) and *kugelig* (*kgg*) play an important role [33, 34]. Other textile azo dyes, namely, DB38, RO16, and DR28, induce toxicity in the early developmental stages of zebrafish that includes the curved tail, delayed hatching, and YSE, respectively [16]. Therefore, in the same context, RB4 could be attributed to interfering with the tail formation pathway in zebrafish embryos by influencing the expression of these proteins.

3.5. Biochemical Assays. If the rate of reactive oxygen species (ROS) formation is greater than the rate of their elimination,



(a)

FIGURE 6: Continued.



(b)

FIGURE 6: (a) Photomicrograph representing morphological abnormalities in zebrafish caused by RB4 dye and bioremediated dye exposure at various concentrations (0-50 ppm). The dashed yellow line represents the normal spinal axis. YSE: yolk sac edema; SC: spinal curvature. (b) Photomicrograph representing morphological abnormalities in zebrafish caused by RB4 dye and bioremediated dye exposure at various concentrations (70-110 ppm). The dashed yellow line represents the normal spinal axis. YSE: yolk sac edema; SC: spinal curvature; TM: tail malformation.

then the inactivation of enzymes, damage of the DNA, and peroxidation of unsaturated fats can further destroy the integrity of the cell [35]. The activities of enzymes like

SOD, CAT, and glutathione peroxidase (GPx) are used as redox biomarkers under oxidative stress to measure the status of scavenging capacities that can nullify ROS generated

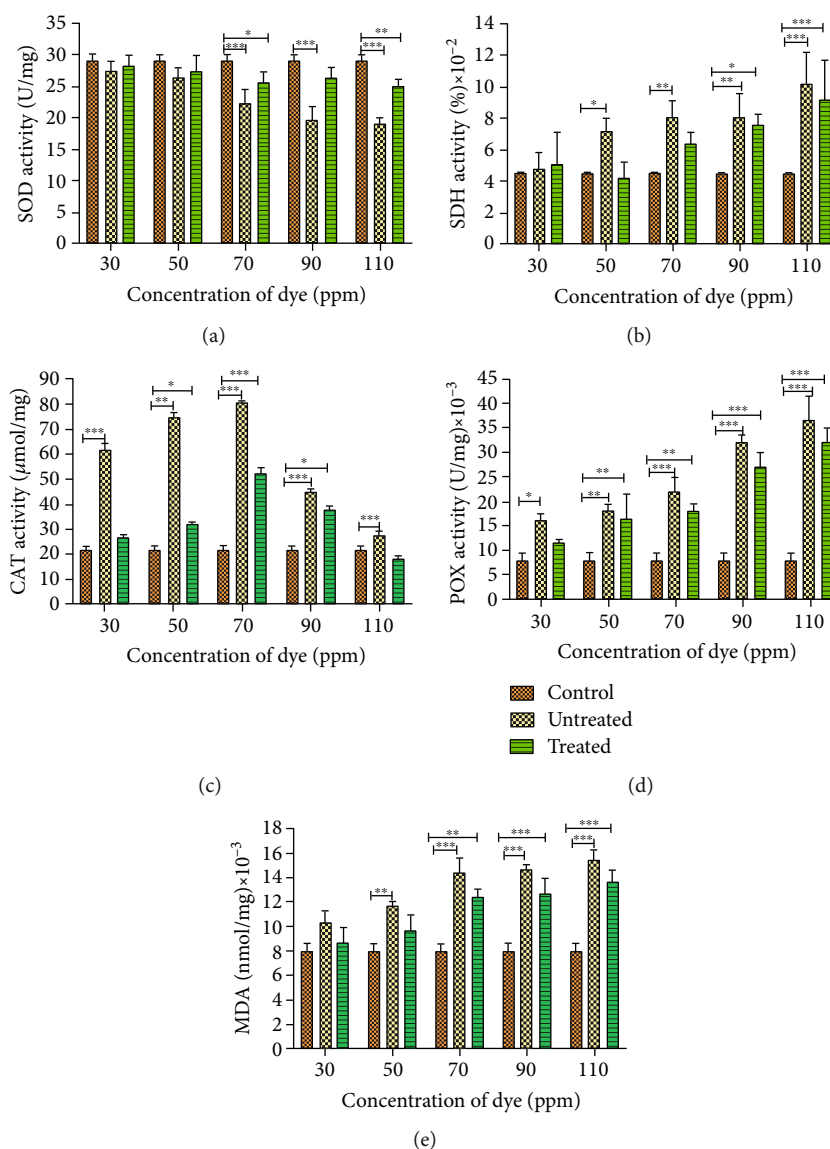


FIGURE 7: Oxidative stress profile of zebrafish larva exposed to untreated and treated dye: (a) SOD; (b) SDH; (c) CAT; (d) POX; (e) LPO.

by environmental contaminants [36]. In this study, activities of SOD, SDH, CAT, POX, and MDA levels in zebrafish larvae were investigated in treated and untreated dye samples (Figure 7). The SOD activity in untreated samples showed a declining trend with a significant decrease of ~1.2-fold at 70 ppm ($p < 0.001$) which continued to decline by ~1.5-fold at 110 ppm, which may be attributed to a high level of oxidative stress generated beyond the preventive potential of the existing SOD level [37]. Similar decreasing trends in SOD activities are reported wherein zebrafish larvae were exposed to increasing dimethyl phthalate concentration [38] or pesticide endosulfan [39]. In treated samples, SOD activity was found to be relatively closer to the control for initial concentrations and marginal decline at the maximum concentration, i.e., 110 ppm ($p < 0.01$). The higher levels of SOD in treated samples (i.e., 70-110 ppm), compared to untreated samples, suggest that to protect cells from free radicals, more proteins are required that bolster the enzymatic activity

against oxidants [40]. SDH activity was found to increase in both untreated and treated dyes with respect to the control (Figure 7(b)). However, samples treated with 110 ppm of untreated and treated dye showed an increased SDH activity by 2.38-fold and 2.26-fold, respectively, as compared to control. In untreated samples, the relative concentration of H₂O₂ was slightly higher as compared to the treated samples ($p < 0.01$). Due to low levels of SDH in the untreated dye, there was an escalated production of H₂O₂. Excess H₂O₂ buildup due to SOD and SDH activity becomes toxic to cells. As CAT and POX enzymes catalyze the conversion of H₂O₂ to molecular oxygen and water, the activity of these enzymes was evaluated. A change in CAT activity after exposure to dye is shown (Figure 7(c)). At lower concentrations of untreated dye (30-70 ppm), there was a significant increase ($p < 0.001$) in CAT activity by 3-, 3.75-, and 4-fold, respectively, in comparison to control, in order to reduce or counterbalance the excessive ROS production. But at 90 and

110 ppm of dye exposure, there was a significant reduction in CAT activity ($p < 0.05$). After a threshold concentration of dye exposure, the CAT could no longer eliminate the increased oxidative stress generated, and thus, CAT activity reduces [38]. In another study, Meireles et al. reported a decline in the CAT activity to 1.55-, 1.44-, and 1.25-fold when Red Disperse dyes, i.e., DR60, DR73, and DR78, were used, respectively [41]. According to Cong et al., exposure to a higher concentration of dye can cause oxidative damage leading to reduced CAT activity, consequentially depleting CAT and SOD enzymes [38]. In our study, at the lowest concentration of treated dye exposure (30 ppm), there was a negligible increase in CAT, and at a higher concentration, i.e., 70 ppm, activity was found to have increased significantly ($p < 0.001$) by ~2.5-fold as compared to control. With a further increase in dye concentration (>70 ppm) of treated samples, a significant decline ($p < 0.001$) was observed. This investigation showed remarkably low levels of CAT activity in treated samples when compared to untreated samples from 30 to 110 ppm. This can occur in view of SOD enzyme dysfunction caused by stress-induced inactivation of its active site [42] in untreated dye. In Figure 7(a), SOD levels in untreated samples were reduced as compared to treated samples, leading to curtailed H_2O_2 production, and may thus result in deficiency of CAT synthesis in untreated dye. POX catalyses the removal of H_2O_2 by oxidising a substrate pyrogallol to purpurogallin [43]. POX activity in both treated and untreated samples produced a rising trend as compared to control (Figure 7(d)). For any given concentration, the POX activity of untreated dye was distinctly higher than that of treated dye. A higher POX activity is a consequence of high H_2O_2 levels. Increased POX is associated with tissue damage and can lead to disruption in larval development [44]. The lower POX activity in treated samples may occur due to minimized oxidative stress in treated samples. It is therefore noted that these antioxidant enzymes are adept at capturing H_2O_2 and superoxide anions which lead to the protection of organisms from oxidative stress conditions [45].

Free radicals induce lipid peroxidation, wherein degradation of lipid peroxides leads to the production of many subproducts including MDA, the levels of which can be used to determine the severity of oxidative damage evoked in larvae [46]. The untreated dye exhibits a rising trend in MDA levels with a significant increase of ~1.7-fold ($p < 0.001$) at 70 ppm with respect to control (Figure 7(e)). At lower concentrations (i.e., 30-50 ppm), the level of MDA was relatively closer to control, but at a slightly higher concentration, i.e., 70 ppm, ~1.5-fold rise in MDA levels was observed. In the presence of high dye toxicity (i.e., 90 ppm onwards), the ability of antioxidant enzymes to eliminate ROS reduces, and therefore, the residual free radicals attack unsaturated fatty acids inciting an increase in MDA content of larvae [46]. Analogous results were observed using naphthalene sulfonic acid (NSA), metanilic acid (MA), and acid blue 113 (AB113) textile dye [47] and fungicide azoxystrobin [48], where an apparent rise in MDA content of zebrafish was paralleled with an increase in concentration. A similar observation was reported by Mao et al. using pesticides [49]. In our study

as well, the content of MDA in treated samples is fairly reduced as compared to that in untreated RB4 samples. This suggests the occurrence of minimized MDA formation or the ability to scavenge them as an important measure for preventing cell damage in hairy root bioremediated samples. Similar results were proclaimed in a study by Cong et al., where oxidative damage in fish, treated with a low concentration of DMP for 24h, was effectively exterminated by the cause of its antioxidant mechanisms [38].

In the untreated samples, the concentration of dye, i.e., 50 ppm onwards, causes severe damage in embryos. But in the treated samples of 50 and 70 ppm, the activity of antioxidant enzymes such as SOD, SDH, CAT, POX, and LPO content (Figure 7) indicates toxicity amelioration after treatment with HRs as there was delayed hatching, morphological deformities, and the absence of YSE in zebrafish embryos. These enzymes have been known to play an important role in early stress even at relatively low concentrations of dye, helping to reduce ROS [50]. However, at a further increase in the concentration of dye, i.e., 90 and 110 ppm, the ROS produced is also high, which cannot be remediated by HRs, in the severity of stress like embryo hyperpigmentation. These may be due to stress-induced inhibition or changes in the subunit of the antioxidant enzymes [51]. Several reports have shown the toxic nature of different anthraquinone dyes, but to the best of our knowledge, this is the first report on comprehending the repercussion of untreated and bioremediated RB4 dye on zebrafish embryos thereby contributing to the rudimentary understanding of the impact of remediated RB4 on ecosystems.

4. Conclusion

In summary, we emphasize the need to develop nontoxic dyes or efficient methods to treat industrial effluents having synthetic dyes. The HRs used in this study were found to be effective in the degradation of potentially toxic textile dyes, and treated dye was found to be less toxic in comparison to untreated, after *in vivo* toxicity assessment. We also hypothesize that RB4 might be hindering the normal cellular pathway for tail formation further contributing to the increased mortality in embryos. The expression of different antioxidant enzymes during dye exposure corroborates the synchronous activity of antioxidant machinery to protect developmental toxicity in zebrafish embryos. This study thus suggests that HRs can be accounted as viable candidates for the treatment of RB4-contaminated effluents. This study has added novel approaches of remediation-based investigation to understand the activity of enzymes under dye stress in a process to develop a system for degradation of high dye concentration with minimal or no residual toxicity.

Data Availability

The data used to support the findings of this study are included within the article.

Conflicts of Interest

The authors declare that there is no conflict of interest regarding the publication of this article.

Authors' Contributions

KT performed zebrafish experiments and wrote the manuscript. RS performed experiments of hairy root induction and antioxidant experiments. VZ wrote the original draft, prepared figures, and reviewed and edited the manuscript. PA and RJ wrote the original draft, did editing, and prepared a graphical abstract. NN, NA, and FS prepared the manuscript, edited the paper, and funded the work. PJ and SS helped in analysis of results and draft preparation. MS helped in data analysis and draft editing. PJ conceptualized the study, did standardization of methods, wrote original drafts, and reviewed raw data.

Acknowledgments

The authors are grateful to the Scientific Research Deanship at King Khalid University, Abha, Saudi Arabia, for their financial support through a general research project under grant number GRP-280-43.

Supplementary Materials

Figure S1: (A) untreated dye, (B) treated dye (with HRs) at 0 h, and (C) treated dye (with HRs) at 120 h. Figure S2: effect of different pH on % decolourization by HRs. Figure S3: effect of different temperatures on % decolourization by HRs. Figure S4: effect of different biomass dosages on % decolourization by HRs. Figure S5: effect of different concentrations of dye on % decolourization by HRs. (*Supplementary Materials*)

References

- [1] S. Lalnunhlmi and V. Krishnaswamy, "Decolorization of azo dyes (Direct Blue 151 and Direct Red 31) by moderately alkaliphilic bacterial consortium," *Brazilian Journal of Microbiology*, vol. 47, no. 1, pp. 39–46, 2016.
- [2] C. Zaharia and D. Suteu, "Coal fly ash as adsorptive material for treatment of a real textile effluent: operating parameters and treatment efficiency," *Environmental Science and Pollution Research International*, vol. 20, no. 4, pp. 2226–2235, 2013.
- [3] J. Forss and U. Welander, "Biodegradation of azo and anthraquinone dyes in continuous systems," *International Biodeterioration & Biodegradation- INT BIODETERIOR BIODEGRAD*, vol. 65, no. 1, pp. 227–237, 2011.
- [4] A. U. Chaudhari, D. Paul, D. Dhotre, and K. M. Kodam, "Effective biotransformation and detoxification of anthraquinone dye Reactive Blue 4 by using aerobic bacterial granules," *Water Research*, vol. 122, pp. 603–613, 2017.
- [5] E. Routoula and S. V. Patwardhan, "Degradation of anthraquinone dyes from effluents: a review focusing on enzymatic dye degradation with industrial potential," *Environmental Science & Technology*, vol. 54, no. 2, pp. 647–664, 2020.
- [6] H. B. Mansour, R. Mosrati, K. Ghedira, and L. Chekir-Ghedira, "Decolorization of textile wastewater by *Pseudomonas putida*: toxicity assessment," *Environmental Engineering Science*, vol. 28, no. 7, pp. 489–495, 2011.
- [7] S. Barathi, C. Karthik, S. Nadanasabapathi, and I. A. Padikasan, "Biodegradation of textile dye Reactive Blue 160 by *Bacillus firmus* (Bacillaceae: Bacillales) and non-target toxicity screening of their degraded products," *Toxicology Reports*, vol. 7, pp. 16–22, 2020.
- [8] A. N. Kagalkar, U. B. Jagtap, J. P. Jadhav, V. A. Bapat, and S. P. Govindwar, "Biotechnological strategies for phytoremediation of the sulfonated azo dye Direct Red 5B using *Blumea malcolmii* Hook," *Bioresource Technology*, vol. 100, no. 18, pp. 4104–4110, 2009.
- [9] E. Agostini, M. A. Talano, P. S. González, A. L. W. Oller, and M. I. Medina, "Application of hairy roots for phytoremediation: what makes them an interesting tool for this purpose?," *Applied Microbiology and Biotechnology*, vol. 97, no. 3, pp. 1017–1030, 2013.
- [10] P. M. Doran, "Application of plant tissue cultures in phytoremediation research: incentives and limitations," *Biotechnology and Bioengineering*, vol. 103, no. 1, pp. 60–76, 2009.
- [11] V. H. Lokhande, S. Kudale, G. Nikalje, N. Desai, and P. Suprasanna, "Hairy root induction and phytoremediation of textile dye, Reactive green 19A-HE4BD, in a halophyte, *Sesuvium portulacastrum* (L.) L.," *Biotechnology Reports*, vol. 8, pp. 56–63, 2015.
- [12] V. H. Lokhande, B. K. Gor, N. S. Desai, T. D. Nikam, and P. Suprasanna, "Sesuvium portulacastrum, a plant for drought, salt stress, sand fixation, food and phytoremediation. A review," *Agronomy for Sustainable Development*, vol. 33, no. 2, pp. 329–348, 2013.
- [13] O. B. Ojuederie and O. O. Babalola, "Microbial and plant-assisted bioremediation of heavy metal polluted environments: a review," *International Journal of Environmental Research and Public Health*, vol. 14, no. 12, p. 1504, 2017.
- [14] P. Jha, R. Jobby, K. Subhash, N. Modi, A. Dhaneshwar, and N. Desai, "Biodegradation of phenol using hairy roots of *Helianthus annuus* L.," *International Biodeterioration & Biodegradation*, vol. 77, pp. 106–113, 2013.
- [15] L. Wu, H. Yi, and M. Yi, "Assessment of arsenic toxicity using *Allium/Vicia* root tip micronucleus assays," *Journal of Hazardous Materials*, vol. 176, no. 1–3, pp. 952–956, 2010.
- [16] G. A. R. de Oliveira, J. de Lapuente, E. Teixidó, C. Porredón, M. Borràs, and D. P. de Oliveira, "Textile dyes induce toxicity on zebrafish early life stages," *Environmental Toxicology and Chemistry*, vol. 35, no. 2, pp. 429–434, 2016.
- [17] K. Tungare, M. Bhorl, K. S. Racherla, and S. Sawant, "Synthesis, characterization and biocompatibility studies of carbon quantum dots from *Phoenix dactylifera*," *Biotech*, vol. 10, no. 12, p. 540, 2020.
- [18] C. P. Rajneesh, A. Manimaran, K. R. Sasikala, and P. Adaikappan, "Lipid peroxidation and antioxidant status in patients with breast cancer," *Singapore Medical Journal*, vol. 49, no. 8, pp. 640–643, 2008.
- [19] M. C. Bewley, V. Graziano, K. Griffin, and J. M. Flanagan, "The asymmetry in the mature amino-terminus of ClpP facilitates a local symmetry match in ClpAP and ClpXP complexes," *Journal of Structural Biology*, vol. 153, no. 2, pp. 113–128, 2006.
- [20] K. Singh, V. Mhatre, M. Bhorl, and T. Marar, "Vitamins E and C reduce oxidative stress and mitochondrial permeability

- transition caused by camptothecin – an *in vitro* study,” *Toxicological Environmental Chemistry*, vol. 95, no. 4, pp. 646–657, 2013.
- [21] M. Bhorl, K. Singh, T. Marar, and M. K. Chilakapati, “Exploring the effect of vitamin E in cancer chemotherapy—a biochemical and biophysical insight,” *Journal of Biophotonics*, vol. 11, no. 9, article e201800104, 2018.
- [22] A. Bhunia, S. Durani, and P. P. Wangikar, “Horseradish peroxidase catalyzed degradation of industrially important dyes,” *Biotechnology and Bioengineering*, vol. 72, no. 5, pp. 562–567, 2001.
- [23] E. Zabłocka-Godlewska, W. Przystaś, and E. Grabińska-Sota, “Decolourisation of different dyes by two pseudomonas strains under various growth conditions,” *Water, Air, and Soil Pollution*, vol. 225, no. 2, p. 1846, 2014.
- [24] M. Ramya, B. Anusha, S. Kalavathy, and S. Devilaksmi, “Biodecolorization and biodegradation of Reactive Blue by *Aspergillus* sp.,” *African Journal of Biotechnology*, vol. 6, 12, 2007.
- [25] S. Afreen, T. N. Shamsi, M. A. Baig et al., “A novel multicopper oxidase (laccase) from cyanobacteria: purification, characterization with potential in the decolorization of anthraquinonic dye,” *PLoS One*, vol. 12, no. 4, article e0175144, 2017.
- [26] C. Attéké, S. Mounguengui, J.-B. S. Tchinda, M. K. Ndikontar, É. Gelhaye, and P. Gérardin, “Biodegradation of Reactive Blue 4 and Orange G by *Pycnoporus sanguineus* strain isolated in Gabon,” *Journal of Bioremediation & Biodegradation*, vol. 4, no. 7, 2013.
- [27] P. Patil, N. Desai, S. Govindwar, J. P. Jadhav, and V. Bapat, “Degradation analysis of Reactive Red 198 by hairy roots of *Tagetes patula* L. (Marigold),” *Planta*, vol. 230, no. 4, pp. 725–735, 2009.
- [28] P. Jha, R. Jobby, and N. S. Desai, “Remediation of textile azo dye acid Red 114 by hairy roots of *Ipomoea carnea* Jacq. and assessment of degraded dye toxicity with human keratinocyte cell line,” *Journal of Hazardous Materials*, vol. 311, pp. 158–167, 2016.
- [29] R. Chakraborty, A. K. Mukherjee, and A. Mukherjee, “Evaluation of genotoxicity of coal fly ash in *Allium cepa* root cells by combining comet assay with the *Allium* test,” *Environmental Monitoring and Assessment*, vol. 153, no. 1–4, pp. 351–357, 2009.
- [30] R. K. Soni, N. S. Bhatt, H. A. Modi, and P. B. Acharya, “Decolorization, degradation and subsequent toxicity assessment of reactive Red 35 by *Enterococcus gallinarum*,” *Current Biotechnology*, vol. 5, no. 4, pp. 325–336, 2016.
- [31] A. H. Kuchy, A. A. Wani, and A. N. Kamili, “Cytogenetic effects of three commercially formulated pesticides on somatic and germ cells of *Allium cepa*,” *Environmental Science and Pollution Research International*, vol. 23, no. 7, pp. 6895–6906, 2016.
- [32] C. D. Jayasinghe and U. A. Jayawardena, “Toxicity assessment of herbal medicine using zebrafish embryos: a systematic review,” *Evidence-Based Complementary and Alternative Medicine*, vol. 2019, Article ID 7272808, 17 pages, 2019.
- [33] S. L. Amacher, B. W. Draper, B. R. Summers, and C. B. Kimmel, “The zebrafish T-box genes *no tail* and *spadetail* are required for development of trunk and tail mesoderm and medial floor plate,” *Development*, vol. 129, no. 14, pp. 3311–3323, 2002.
- [34] M. Hammerschmidt, F. Pelegri, M. C. Mullins et al., “Mutations affecting morphogenesis during gastrulation and tail formation in the zebrafish, *Danio rerio*,” *Development*, vol. 123, no. 1, pp. 143–151, 1996.
- [35] A. Ayala, M. F. Muñoz, and S. Argüelles, “Lipid peroxidation: production, metabolism, and signaling mechanisms of malondialdehyde and 4-hydroxy-2-nonenal,” *Oxidative Medicine and Cellular Longevity*, vol. 2014, Article ID 360438, 31 pages, 2014.
- [36] E. B. Kurutas, “The importance of antioxidants which play the role in cellular response against oxidative/nitrosative stress: current state,” *Nutrition Journal*, vol. 15, no. 1, p. 71, 2016.
- [37] M. Puerto, S. Pichardo, A. Jos et al., “Differential oxidative stress responses to pure microcystin-LR and microcystin-containing and non-containing cyanobacterial crude extracts on Caco-2 cells,” *Toxicol*, vol. 55, no. 2–3, pp. 514–522, 2010.
- [38] B. Cong, C. Liu, L. Wang, and Y. Chai, “The impact on antioxidant enzyme activity and related gene expression following adult zebrafish (*Danio rerio*) exposure to dimethyl phthalate,” *Animals (Basel)*, vol. 10, no. 4, p. 717, 2020.
- [39] B. Muazzam, K. Munawar, I. A. Khan et al., “Stress response and toxicity studies on zebrafish exposed to endosulfan and imidacloprid present in water,” *Journal of Water Supply: Research and Technology-Aqua*, vol. 68, no. 8, pp. 718–730, 2019.
- [40] R. S. Kuder and G. H. Philip, “Antioxidant enzymatic activities and lipid peroxidation in liver and ovary of zebrafish (*Danio rerio*) exposed to deltamethrin,” *Chemistry and Ecology*, vol. 33, no. 8, pp. 739–749, 2017.
- [41] G. Meireles, M. A. Daam, A. L. M. Sanches et al., “Red disperse dyes (DR 60, DR 73 and DR 78) at environmentally realistic concentrations impact biochemical profile of early life stages of zebrafish (*Danio rerio*),” *Chemico-Biological Interactions*, vol. 292, pp. 94–100, 2018.
- [42] T. Fukai and M. Ushio-Fukai, “Superoxide dismutases: role in redox signaling, vascular function, and diseases,” *Antioxidants & Redox Signaling*, vol. 15, no. 6, pp. 1583–1606, 2011.
- [43] K. Hernandez, A. Berenguer-Murcia, R. C. Rodrigues, and R. Fernandez-Lafuente, “Hydrogen peroxide in biocatalysis. A dangerous liaison,” *Current Organic Chemistry*, vol. 16, no. 22, pp. 2652–2672, 2012.
- [44] J. Vicente, U. Höfle, J. M. Garrido et al., “Wild boar and red deer display high prevalences of tuberculosis-like lesions in Spain,” *Veterinary Research*, vol. 37, no. 1, pp. 107–119, 2006.
- [45] Y. Han, T. Liu, J. Wang, J. Wang, C. Zhang, and L. Zhu, “Genotoxicity and oxidative stress induced by the fungicide azoxystrobin in zebrafish (*Danio rerio*) livers,” *Pesticide Biochemistry and Physiology*, vol. 133, pp. 13–19, 2016.
- [46] X. Huang, Y. Li, T. Wang, H. Liu, J. Shi, and X. Zhang, “Evaluation of the oxidative stress status in zebrafish (*Danio rerio*) liver induced by three typical organic UV filters (BP-4, PABA and PBSA),” *International Journal of Environmental Research and Public Health*, vol. 17, no. 2, p. 651, 2020.
- [47] J. Tippabathani, J. Nellore, P. Kathirkannan, and V. Nachiyar, “Developmental effects of three textile chemicals on locomotor activity, antioxidant markers and acetylcholine esterase activity in zebrafish,” *Indian Journal of Experimental Biology*, vol. 58, pp. 212–218, 2020.
- [48] S. Han, B. Kang, J. Lee et al., “A trifloxystrobin fungicide induces systemic tolerance to abiotic stresses,” *The Plant Pathology Journal*, vol. 28, no. 1, pp. 101–106, 2012.
- [49] L. Mao, W. Jia, L. Zhang et al., “Embryonic development and oxidative stress effects in the larvae and adult fish livers of

zebrafish (*Danio rerio*) exposed to the strobilurin fungicides, kresoxim-methyl and pyraclostrobin,” *Science of The Total Environment*, vol. 729, article 139031, 2020.

- [50] S. Kusvuran, S. Kiran, and S. S. Ellialtioglu, *Antioxidant enzyme activities and abiotic stress tolerance relationship in vegetable crops*, IntechOpen, 2016.
- [51] T. Abedi and H. Pakniyat, “Antioxidant enzymes changes in response to drought stress in ten cultivars of oilseed rape (*Brassica napus* L.),” *Czech Journal of Genetics and Plant Breeding*, vol. 46, no. 1, pp. 27–34, 2010.

Hello Messaging based Aodv Routing Protocol and Its Simulation

Abhishek Prabhakar

*Assistant Professor, Department of Computer Science and Engineering,
Dr. Ambedkar Institute of Technology for Handicapped, Awadhपुरi, Kanpur, Uttar Pradesh, India.*

Orcid Id: 0000-0002-8475-0137

Dr. Amod Tiwari

Director, Naraina Colloge of Engineering and Technology, Panki, Kanpur, Uttar Pradesh, India.

Prof Vinay Kumar Pathak

VC, APJ Abdul Kalam Technical university, Lucknow, Uttar Pradesh, India.

Abstract

Routing is the method, which is used to maintain, the wireless communication of ad-hoc network. It has various discoveries and different paths between every node within a network. The process of preparing Routing table itself is called Routing. Routing uses the concept of switching. In switching an incoming packet is transferred to destination using MAC address. It is done within the network. The efficiency of a dynamic ad-hoc routing protocols is mainly based on the changes in network topology. The transmission via wireless medium increase the security of message transmission. It prevents the unauthorized access and provides security and offers authentication and access-control to the transmission of Messages. The, increasing day-by-day use of wireless media has reduced the works of humans and their access to the wireless devices. As, everything has its Merits and Demerits the, wireless media also have both Merits and Demerits, the disadvantage as included minimizing size and cost security and loss, mobility signal fading etc.

In this paper, we adaptively optimize the performance of AODV protocol using simulation results. The proposed fuzzy algorithm used to model the uncertainty measurements for updating local connectivity successfully in time and provide an overview of the Research Issues and Challenges in wireless networks and wireless network performance.

Keywords: Hello messages, AODV, wireless communication, Ad-hoc Network

INTRODUCTION

Every node is working as router in mobile, ad-hoc network, which is having no infrastructure. In this network, each node has its own local neighbors and it will communicate to these neighbors, that are out of its transmission range and it called

as Multihop. These networks suffer from nodes mobility causes continual link breaks. Local Connectivity Management is one of the techniques to update, the routing protocol knowledge about these neighbors. One of those techniques is periodically broadcasting short beacon messages (called hello messages)[1].

We adaptively optimize the maximum time period that taken before the node transfer the next hello message to its neighbors in this paper. During a fixed period of time the number of sent hello messages has been directly affected. The co-relation between the periodical interval for the transmission of hello message and reconstruction of topology deals with optimization. The decision of increasing or decreasing the frequency of hello messages is made during a fixed period of time through a fuzzy logic system. Fuzzy set theory provides high flexibility and it is used to model complex systems.

Ad-hoc On Demand Distance Vector (AODV) [9] routing protocol is used in this method. Routers are used as per needed by per node and they determined the route, as it is a reactive routing protocol. The, two parameter used are: Hello-Interval (HI) and allowed-hello-loss. The link between the neighbors and the node is broken, only when the neighbor does not get any packet (hello message) for allowed hello-loss.

The growth in wireless networks [2] over the last few years resembles the rapid growth of the internet over the last decade. Wireless communication is done with each other not via visible medium in spite of this wireless networks are used. The immense growth of internet-wireless, wireless home networking & cellular telephony enjoys wireless communication [4]. WLAN technology [3] allow high speed of wireless network access and mobile network access.



Figure 1: Infrastructure wireless network

The stored data, can be accessed by all people, even when are outside in travelling journeys etc. Wireless communication is hacked by hacker for exploiting the networks. Security Measurements are used to prevent the unauthorized access.

RELATED WORK

The utilization of hello message in Local Connectivity Management (LCM) in various comparisons are used as metric, for those ad-hoc routing protocols. Research has also focused on the usage of mathematical methods to estimate the stability of the links in ad-hoc networks. The lifetime expectations of these methods mainly depend on the choice of links we use. The, main creator of AODV protocol Perkins *et al.*[9] gives detailed description why hello messages has been used and the disadvantages of using these message. They mentioned that they will investigate other ways to eliminate drawbacks of these messages. The frequency optimizations of hello messages remove all of its disadvantages and give its advantages, which are mentioned in this page.

Lundgren *et al.* [10] evidence says that sometimes mismatch occur between the actual connectivity status and the router due to unreliable implement action of hello message. This mismatch is known as "*communication gray zones*". In these zones in spite of neighbor's reach ability are sensed by hello message but the actual data message cannot be exchanged between router and its neighbors. To, remove this drawback one such routing protocol [5] called position-based routing protocols, are introduced. The presence and the current position are indicated by these protocols.

In this each node broadcast a sort hello message to have the presence. GPS tracking is used on topology-based routing protocols. The proposed method of wireless network communication [4] can be extended for these types of protocols and the main focus, in these references is mainly on topology-based routing protocol only.

TYPES OF WIRELESS NETWORK

Taxonomy Of Wireless Networks

The wireless communication is one of important adapting feature for the latest technologies. In the wireless communication the packets are arranged in small segments and transmitted, this is the distinguishing features which are not present in other networks.

IEEE 802.11

A computer is also called a host, workstation, node and Wireless Local Area Network (WLAN) communication is the main feature of IEEE 802.11. It was developed and the standard was first introduced in 1997. It was envisioned for home and office environments for wireless local area connectivity and supports three types of transmission technologies. The IEEE 802.11 mainly works for 3 types as technologies which is in generally used for transmission namely:

- Direct Sequence Spread Spectrum (DSSS)
- Frequency Hopping Spread Spectrum (FHSS)
- Infrared (IR)

IEEE 802.11 has two types of wireless networks, namely, the infrastructure networks and the ad hoc networks.

Infrastructure Networks

The infrastructure type of wireless network (Fig 1) is a network with an Access Point (AP), in which all stations (STAs) must be associated with an AP to access the network. Stations communicate with each other through the AP. In infrastructure wireless network device installations can be set up with a fixed topology to which a wireless host can connect via a fixed point known as a base station or an access point. The latter is connected to the backbone network often via a wired link. Cellular network and most of the wireless local area networks (WLANs) operate as static infrastructure networks. All wireless hosts within the transmission coverage of the base station can connect to it and use it to communicate with the backbone network. The communications initiated

from or destined to a wireless host have to pass through the base station to which the host connects directly.

Ad Hoc Networks

Ad-hoc networks are the second access Methods for, the wireless communication. Ad-hoc network, is used where there is not all user can reach. It is also, called independent mode of access of network. The topology and wireless communication is use in ad-hoc network, an example of ad-hoc network is packet radio network. The users in one region can directly communicate within the transmission range of the receiver. If the sender wants to communicate with the receiver, which is out of transmission range, then it should have to firstly convey the message to the user, which is inside range, Then this receiver acts as new sender & send to the user which is out of the converge transmission. This provides a relay to the sender that Message transmitted to transmission. The main purpose of this transmission is that it offers flexibility and easiness to the transfer of the message. No fixed infrastructure network is needed. Ad-hoc network does not have any device to connect the links. In spite of advantages, there are still various drawbacks of ad-hoc network. It is complex system routing because of various topology changes due to the host mobility. Secondly it is quite difficult. Normal Users cannot predict the actual message transmission.

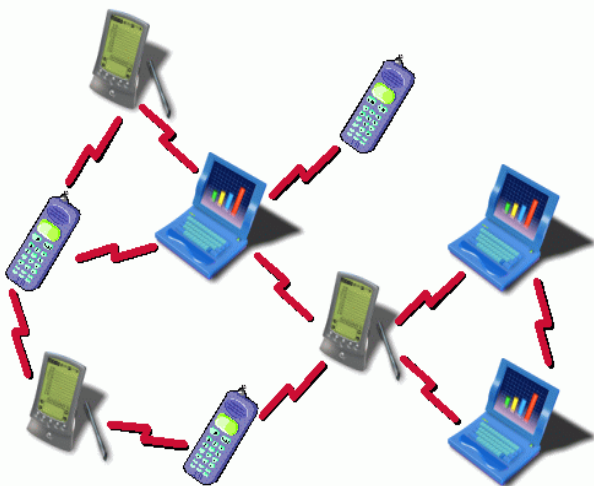


Figure 2: Ad Hoc wireless network

AODV WITH FUZZY HELLO INTERVAL

This part of the paper deals with the, the proposed concept using fuzzy Hello Intervals values that is used with AODV protocol for the transmission of hello messages. In this part we have further classifications, as two subsections; in this section we study the effect of some node parameters on Hello Intervals.

Algorithm: Effect of Node Transmission Power and Node Speed on HI

The transmission of Hello messages is done between the nodes and its neighbors on the basis of main parameters. Transmission power is one of the proposed main parameter for determining the present nodes neighbors in the ad-hoc network. Transmission power abbreviated as, (T_r Power) is the power strength through which the signal transmission takes place between the nodes. The free space propagation model [12], determines the signal power degraded in the transmission of hello messages of the proposed system.

The received signal strength is given by:

$$P_r(d) = \frac{P_t G_t G_r \lambda^2}{(4\pi)^2 d^2 L}$$

Where,

P_r stands for receive powers (in watts),

P_t stands for transmit powers(in watts),

G_t and G_r are the transmit and receive antenna gains,

d is the separated distance between the transmitter-receiver,

L is a system loss factor ($L = 1$ in our simulations which indicates no loss in the system hardware), and λ is the carrier wavelength (in meters) which is related to the carrier frequency (f_c) as:

$$\lambda = \frac{c}{f_c} \quad \text{Where } c \text{ is the speed of light } (3 \times 10^8 \text{ m/s}).$$

```
#include <stdio.h>
```

```
int main()
```

```
{
```

```
    Long Gt, Gr, Pt, Pr ;
```

```
    Printf("%1%1%1,&Gt&Gr&Pt)
```

```
    for (Gt=1;Gt<Pt; Gt++)
```

```
    {
```

```
        for(Gr=1;Gr<Pr; Gr++)
```

```
        {
```

```
            for(Pt=1;Pt<Pt; Pt++)
```

```
                Value (Pt*Gt*Gr);
```

```
                Printf("%1 ",Pr);
```

```
            }
```

```
        }
```

```
    }
```

For Node Speed on HI

Network Topology concept is mainly used in dynamic routing changes of ad-hoc networks. As the mobility of nodes is not restricted, due to which it causes the routing protocols of dynamic changes.

If the transmission between the neighboring nodes is faster, due to this sometimes causes links break down between these two nodes and increases probability of breaking links and loss of information. The movements of transmission of message between the nodes are measured by the speed. High-speed transmission between the nodes has huge probability of losing links between the current neighbors and acquired the default nodes.

Galluccio et.al. [11] Calculated the neighborhood time, T_n , between two node $n1$ and $n2$ as:

$$T_n = \frac{2 \times \sqrt{R^2 - P_{n1}^2}}{v_{n1}}$$

Where R is the transmission range, P_{n1} is the position of $n1$ according to $n2$, and v_{n1} is the relative velocity and can be calculated as:

$$v'_{n1} = \sqrt{v_{n1}^2 + v_{n2}^2 - 2v_{n1}v_{n2} \cos(\phi)}$$

Where v_{n1} is the magnitude of the vector v_{n1} , v_{n2} is the magnitude of the vector v_{n2} , and Φ is the angle between them. This assumption of T_n is accurate only with constant relative velocity.

```
{
int n1, n2, Tn, R, Pn1, Vn1, Vn2, Vn*;
float phi;
for (n1=0; n1<Tn; n1++)
for (n2=0; n2<Tn; n2++)
}
Value (Vn1*)
CalculateTime(Tn) / for transmission data
}
```

Fuzzification, Inference and Defuzzification :

Fuzzification is a mathematical process where the crisp input values are transformed into the membership values of the fuzzy logic. There is a continuous sequencing of fuzzification, inference and defuzzification is used. Firstly, the process of fuzzification is done, and then the inference engine calculates the fuzzy output using the fuzzy rules.

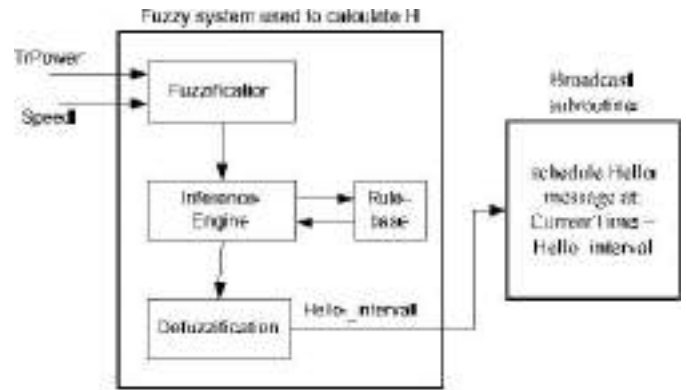


Figure 4: Block-diagram for the basic elements of the fuzzy system.

Defuzzification is a process used to convert the fuzzy output to a crisp value; Hello interval (HI) value in this case. The basic block diagram of the basic elements of the fuzzy system is shown in the figure of fuzzification, inference and defuzzification.

RESEARCH CHALLENGES OF WIRELESS NETWORKS

Since wireless networks are bandwidth limited, some of the key challenges in wireless networks are increase data rate, minimizing size, cost, low power networking, security of user and Quality of Service (QoS).

Signal Fading:

As in wireless communication, the message is propagated on an open changing route; unprotected mediums and signals can be distorted and weakened. As the same signal can disperse and travel on some other routes due to reflection, diffraction, congestion and scattering caused by different uncertain hurdles used by different hackers before it is received by receiver. Due to these different routes the dispersed signals on various paths may take different times to reach the destination.

Mobility

The wireless communication is not wired, so there is not at all any constraint like that of wired networks among devices. Ongoing mobility is maintained to roam the transmitted message here and there.

Power and Energy

To maintain the energy levels in any system it is necessary to have power conservation mechanism, all the devices should perform effectively and efficiently to work in different

surroundings. The transmission between the receiver and the sender must be done in intelligent manner so that time and task both are maintained for communication purpose.

Data Rate

The data compression algorithm and interference mitigation through error-resilient coding, power control, and the data transfer protocol is done by the various functions and techniques used by different routing methods. Thus it is important to have a well understanding of topic and knowledge that results a thought design in order to achieve high data transfer rates during transmission.

Security:

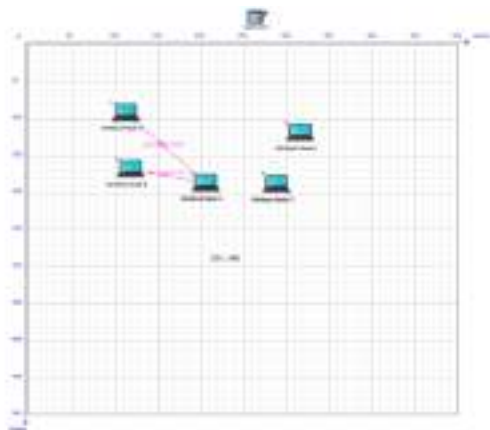
Security [6] is a big concern in wireless networking, especially in m-commerce and e-commerce applications Virtual private network (VPN) is an option to make access to fixed access networks reliable. Since hackers are getting smarter, it is imperative that wireless security features must be updated constantly.

Quality of Service (QoS):

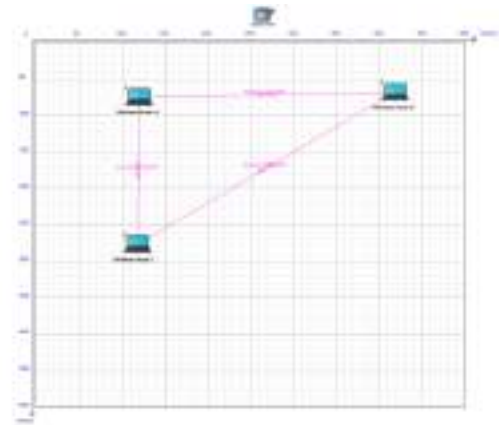
Quality of Service [8] is a measure of network performance that reflects the network's transmission quality and service availability. For each flow of network traffic, QoS can be characterized by four parameters:

- Reliability
- Jitter
- Bandwidth
- Delay

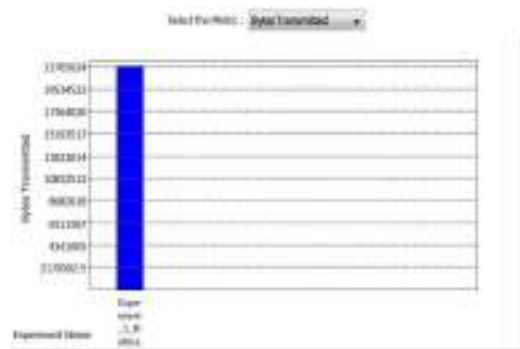
Simulation



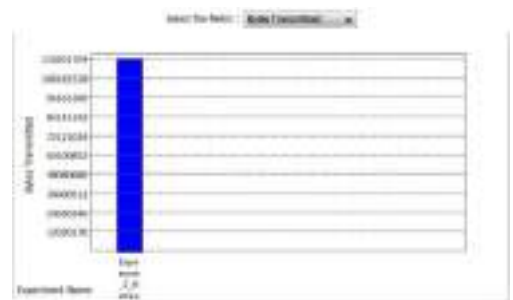
Environment1



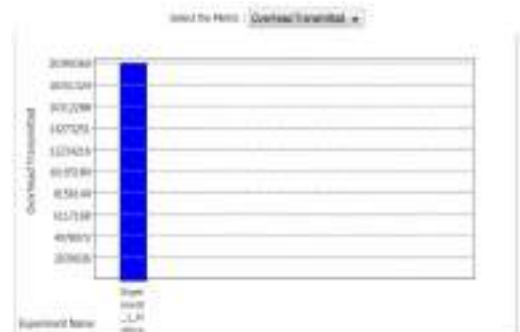
Environment 2



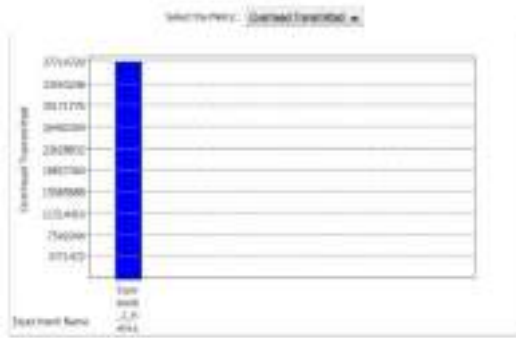
Environment1



Environment2



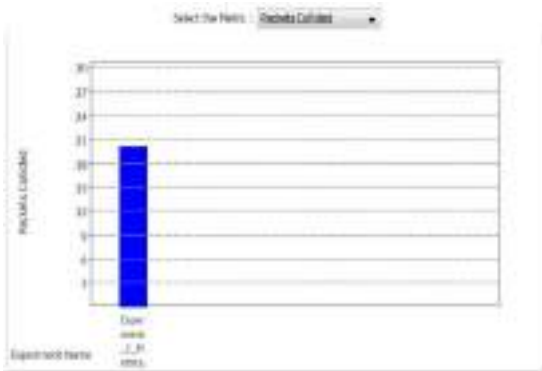
Environment1



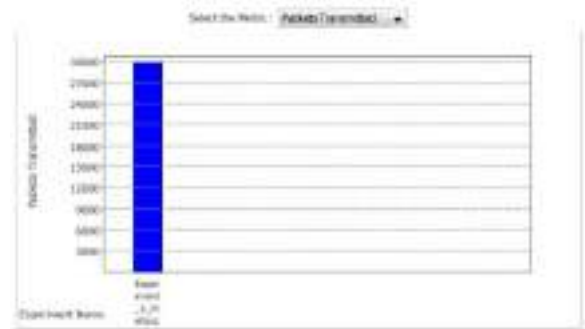
Environment2



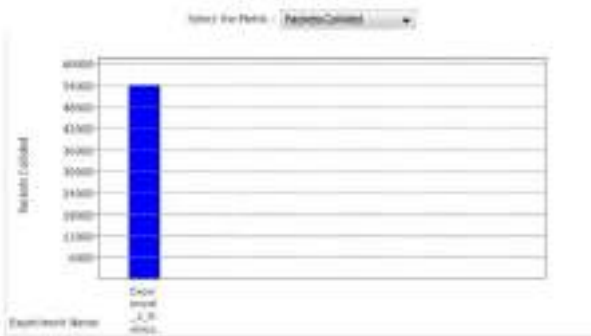
Environment2



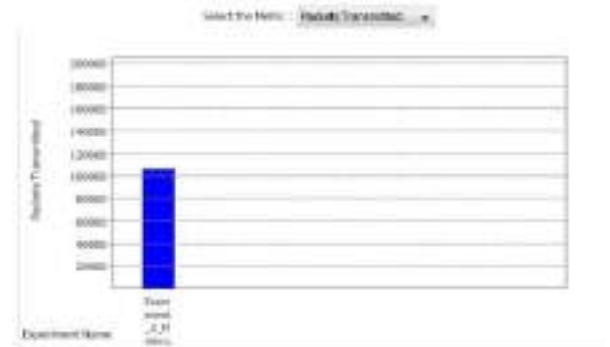
Environment1



Environment1



Environment2



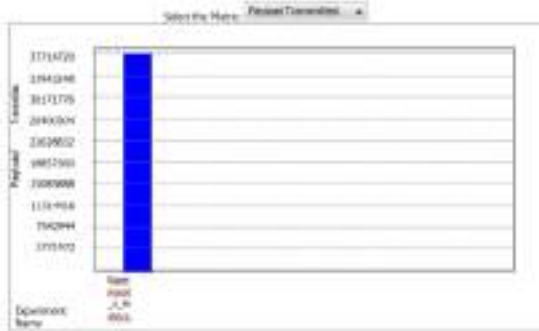
Environment2



Environment1



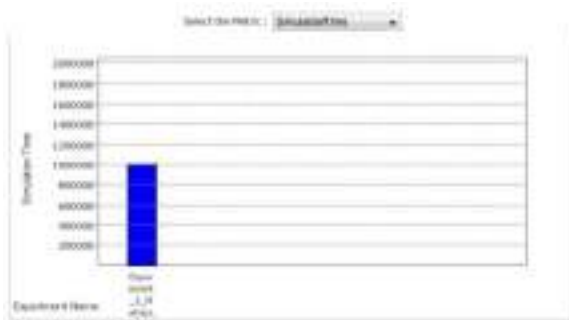
Environment1



Environment2



Environment1



Environment2

SIMULATION AND RESULTS

We have simulated AODV using Netsim simulator developed by tetcos .This is suited for various routing algorithm having dynamic topologies. Our aim is to show that working of AODV is quick and accurate. AODV also works in large networks and calculating optimum values in every parameter. The network layer, application layer and transport layer has been properly configured for each node.

Simulation environment:-

We have created two different environments. In environment 1 we have taken 5 nodes(1,2,3,4,5) in which (1,3) and (2,3) are connected wirelessly as ad-hoc network. In environment 2, nodes (1,3) (2,3)(1,2) are connected in ad-hoc way where any node can transfer packet to any node .Nodes are placed randomly within a fixed size LxL grid . During the simulation nodes are free to move anywhere in grid area .If the nodes are

larger in number then there is continuous change in topology of network. For both the simulation environment 1 and environment 2 we have calculated byte transmitted, overhead transmitted, packets collided , packets errata ,packet transmitted ,payload transmitted and simulation time as shown in graph and values in table1 shown below in results.

RESULTS

Our results show that AODV can find routes quickly and with accuracy. AODV is good choice for ad-hoc network. It is useful in battlefield communication, emergency, conferencing etc.

Table 1

Parameter	Environment 1	Environment 2
Bytes Transmitted	21705024	120201704
Overhead Transmitted	20390360	37714720
Packets collided	20	54000
Packets Errata	32	24
Packets Transmitted	30000	100000(approx)
Payload Transmitted	20390360	37714720
Simulation Time(sec)	100000	1000000

We have seen the final results in environment 1 and environment 2. The byte transferred is of major difference and has been increased in environment 2. Similarly for the overhead transmission the transmitted data has increased in environment 2. But the packets errata has decreased in environment 2 in spite of large volume of data being transferred in environment 2 .This shows the accuracy of the protocol as shown in table 1. The main focus of result is that the AODV protocol will be helpful for Ad-hoc network.

CONCLUSION

In this research paper, a novel approach for local connectivity management in ad-hoc routing protocols has been presented for the transmission of hello messages between the nodes and its neighbors. This wireless communication provides an efficient way, to the transmission of messages, as it is unprotected still the transmission is faster between the nodes. A logical idea is probably mainly used to optimize the nodes transmission range and speed and used to decide the hello messages interval. As the wireless communication the message is propagated is an open, Changing, unprotected medium, and the signals can be distorted and weakened. The routing procedure that has been developed has been used in

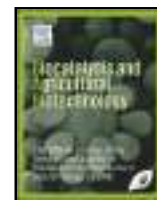
the context of the AODV routing protocol. There are various types of routing methods is used like- Distance vector routing and link state routing. The main advantages of using routing protocols that it provides no duplicate packets and no traffic problems. In spite of this entire if we use routing shortest path is not guaranteed but ad-hoc networks can work properly. The routing is mainly used for the internet purpose, where each node works as a host or hop. Military networks are used routing algorithms to determine the routers; they do not care of flooding at all. Various results produced by each methods provides that, the efficiency of the proposed AODV protocol method in terms of routing overhead, bytes transmitted ,packets errata ,packets collided and payload transmitted using simulation results. Overall, the work presented here has given us an insight that the ad-hoc routing protocols configuration parameters might be determined more accurately and dynamically.

FUTURE SCOPE

There is large need to increase the capabilities of protocol. AODV should support large population with optimum efficiency. We look for development of protocol for quality of service(qos) with fixed network and internet .In future we can develop error free environment as we have shown that the packets errata is decreased from 32 to 24 in spite of large volume of data in environment 2.

REFERENCES

- [1] Chakeres I. D. and Royer E. M., "The Utility of Hello Messages for Determining Link Connectivity," in *Proceedings of the 5th International Symposium on Wireless Personal Multimedia Communications (WPMC)*, Honolulu, Hawaii, pp. 504-508, October 2002.
- [2] http://en.wikipedia.org/wiki/Wireless_network.
- [3] D. Tang and M. Baker. Analysis of a Local-Area Wireless Network. In *Proceedings of ACM MobiCom'00*, pages 1–10, August 2000.
- [4] Rappaport T. S., *Wireless Communications: Principles & Practice*, Prentice Hall, pp. 70-74, 1996.
- [5] Royer E. M. and Toh C. K., "A Review of Current Routing Protocols for Ad-Hoc Mobile Wireless Networks," *IEEE Personal Communications Magazine*, vol. 6, no. 2, pp. 46-55, April 1999.
- [6] Chip Craig J. Mathias Principal, Farpoint Group COMNET 2003 —Wireless Security: Critical Issues and Solutions| 29, January 2003.
- [7] IEEE 802.11-1999, IEEE Standard for Local and Metropolitan Area Networks Specific Requirements – Part 11: Wireless LAN Medium Access Control (MAC) and Physical Layer (PHY) Specifications, June 12, 1999.
- [8] Jim Kurose- Open issues and challenges in providing quality of service in high-speed networks| Computer.
- [9] Perkins C. E. and Royer E. M., "Ad-Hoc On-Demand Distance Vector Routing," in *Proceedings of the 2nd IEEE Workshop on Mobile Computing Systems and Applications*, New Orleans, USA, pp. 90-100, February 1999.
- [10] Lundgren H., Nordstrom E., and Tschudin C., "Coping with Communication Gray Zones in IEEE 802.11b Based Ad Hoc Networks," in *Proceedings of the 5th ACM International Workshop on Wireless Mobile Multimedia (WoWMoM'2002)*, Atlanta, Georgia, USA, pp. 49-55, 2002.
- [11] Galluccio L., Leonardi A, Morabito G and Pallazo S., "Tradeoff between energy efficiency and timeliness of neighbour discovery in self organizing Ad-hoc and sensor networks in proceedings of 38th Annual Hawaii International conference on system sciences (HICSS'05),USA ,vol 9 ,no 9,pp. 286.1-286.10 ,2005.
- [12] Tapan K. Sarkar, Zhong Ji, Kyungjunj Kim, Abdellatif Medour "A survey of various propagation models for mobile communications", *IEEE Antennas and propagation magazine* vol 45 , no 3,June 2003



Biodegradation of pyridine raffinate by microbial laccase isolated from *Pseudomonas monteilii* & *Gamma proteobacterium* present in woody soil

Manish Singh Rajput^a, Vinay Dwivedi^{b,*}, S.K. Awasthi^c

^a Department of Biotechnology, Dr. Ambedkar Institute of Technology for Handicapped, Kanpur, 208024, U P, India

^b Department of Biotechnology, Naraina Vidyapeeth Engineering & Management Institute, Kanpur, 208020, U P, India

^c Harcourt Butler Technical University, Kanpur, 208002, U P, India

ARTICLE INFO

Keywords:

Microbial laccase
Pyridine raffinate
Pseudomonas monteilii
Gamma proteobacterium
Biodegradation

ABSTRACT

Two novel laccase enzyme-producing strains *Pseudomonas monteilii* and *Gamma proteobacterium* were isolated from woody soil sample and their productions were optimized. Maximum production of laccase was achieved at temperature (37 °C), pH (7), carbon source (glucose) and nitrogen source (yeast extract) for both the isolates. The produced extracellular laccases were extracted by centrifugation at 14000 rpm and 4 °C for 15 min. The extracted laccases were also optimized for the specific substrate to enzyme concentration ratio, pH, temperature and the results were 1:9, 6.0, 25 °C for strain *Pseudomonas monteilii* and 2:8, 8.0, 40 °C for strain *Gamma proteobacterium* respectively.

The novelty of this work is here we use extracted bacterial laccase enzyme was subjected to pyridine raffinate according to optimized process parameters, a reduction in absorbance was observed up to 51% for strain *Pseudomonas monteilii* and 59.5% for strain *Gamma proteobacterium* in 140 min. The study signifies the biotransformation of pyridine raffinate into some other simpler products as it provides a novel way to bioremediate pyridine raffinate. This innovative remediation process displays a route towards reasonable treatment techniques where physical and chemical procedures appear to fall flat.

1. Introduction

Pyridine raffinate is an organic discharge of the pyridine manufacturing industry containing mainly pyridine; a heterocyclic aromatic compound along with formaldehyde, picolines, and phenolics. It is a water-soluble (Li et al., 2009), a highly alkaline mixture (pH 10–12), slightly pale in color with penetrating nauseating odor (“Pyridine [C5H5N - PubChem,” n.d.). Apart from a lab reagent, pyridine has found its applications in adhesives, aerosols, bleaching agents, electroplating industry, fuel additives, industrial solvents and as a raw material in paint, dyes, pharmaceutical and several other industrial processes. Pyridine is also an important agent in the manufacturing of several different key products such as vitamins, food flavorings, rubber products, insecticides and herbicides (“Pyridine [C5H5N - PubChem,” n.d.).

Despite its industrial usefulness pyridine has several health hazards. Researchers have reported pyridine carcinogenicity in rats (Hasegawa et al., 1993), in human-derived liver cell lines (Majer et

al., 2005), in the mammary gland of rat (Huber et al., 1997) and many more. Due to its hazardous behavior, pyridine is of foremost concern among all the organic heterocyclic compounds (Saroja, 2018).

Pyridine is listed as a priority organic pollutant by the United States Environmental Protection Agency (USEPA). According to the latest report published by NBC, Global Pyridine Market size is expected to grow at USD 747.89 million by 2023 (“Pyridine Market Research Report- Forecast to 2023 | MRF, n.d.). Being a priority organic pollutant, such growth would also affect the environment at a high cost.

Several physical, chemical and biological methodologies for biodegradation of pyridine raffinate have been reported. Physical and chemical methods have the disadvantages of being costly and less effective, however, biological treatment methods are preferred as they are cost-effective and environment-friendly (Sims, O'Loughlin and Crawford, 1989). From the perspective of the heterocyclic nature of pyridine, it is recalcitrant to microbial activity. However, with time,

* Corresponding author.

E-mail addresses: msrbitech@gmail.com (M.S. Rajput), drvinay@yahoo.com (V. Dwivedi), skahbti@yahoo.co.in (S.K. Awasthi).

because of the ability of the microbes to deliver increasingly phenotypic species and their differential ways to utilize various substrates for their metabolism, they are able to degrade pyridines and their derivatives (Sun et al., 2011).

Laccases are copper-containing polyphenol oxidoreductases first reported in exudates of Japanese lacquer tree *Rhus vernicifera* (Yoshida, 1883) and degrades pyridine ring as reported by several researchers (Rajput and Mishra, 2019). The mechanism of laccase activity involves utilizing oxygen as an electron donor and helping in the oxidation of different compounds such as phenols, polyphenols, aromatic amines by four-electron transfer resulting in the reduction of O₂ to H₂O and formation of reactive substrate radicals (Claus, 2004; Riva, 2006). Some substrates are two-electron donors resulting in one step oxidation-reduction reaction, copper-I accepts electron and reactive substrate radicals take part in further non-enzymatic reactions (Kersten et al., 1990). The occurrence of laccase had been found in fungus such as *Aspergillus sp.*, *Corioliopsis gallica*, *Funaliatrogii*, *Streptomyces cyaneus*, *Penicillium oryzae* etc (Baldrian, 2006; Thurston, 2019), plants such as *Camelia sinensis*, *Schinus molle*, *Musa paradisiaca*, *Forsinthususpensa*, *Pinus sp.* etc (Dean and Eriksson, 1994; Dwivedi et al., 2011) and bacteria (Bugg et al., 2011; Sharma et al., 2007). Laccases are the center of attraction for effluent treatment discharged from industries because of their wide range of oxidoreductase activity (Claus, 2004). Laccases have also been reported thermally (D'Souza-Ticlo et al., 2009) and pH stable (Singh et al., 2007) which makes them more diversified in the bioremediation process. The first bacterial laccase was isolated in 1999 from *Azospirillum lipoferum* (Diamantidis et al., 2000). Martins et al. (2002) isolated and characterized bacterial laccase from *Bacillus subtilis* endospore coat (Martins et al., 2002). Many researchers used microbial species as whole to bioremediate the complex heterocyclic compounds. Chandra et al. (2009) reported *Bacillus sp. co-culture* can degrade formaldehyde free pyridine raffinate (Chandra et al., 2009). Little work has been reported on pyridine raffinate degradation with bacterial laccase. In the present study, we have succeeded to bioremediate the pyridine raffinate with the help of enzyme laccase.

2. Material and methods

2.1. Chemicals and growth medium

Solvents viz Tris-Base, Phosphate buffer, EDTA and Propyl alcohol were obtained from Thomas Baker Chemicals Private Limited, New Delhi, India. Salts viz. Na₂HPO₄, CaSO₄, NaCl, ZnSO₄, C₆H₅FeO₇, MnSO₄·H₂O, K₂Cr₂O₇, NaHCO₃, NaH₂PO₄, and CH₃COONa were obtained from Central Drug House, New Delhi, India and media components viz. agar, yeast extract, sucrose, glucose, tryptone, peptone were obtained from Sisco Research Laboratories Pvt. Ltd. (SRL), New Delhi, India. Guaiacol was procured from Thermo Fisher Scientific India Pvt. Ltd., Mumbai, India. All reagents were of analytical grade and extra pure quality.

2.2. Collection of soil sample

Collection of soil sample was done aseptically from Gupta Timbers (26°30'06.6"N 80°15'15.9"E), Kalyanpur, Kanpur, Uttar Pradesh, India. The first layer of soil up to 10 cm was removed using a sterile spatula. After that, using another sterile spatula soil sample was transferred into pre autoclaved beaker and covered with aluminum foil instantly. The sample was then transferred to a Petri dish and kept at room temperature for 6 h in a glove box by maintaining aseptic conditions to normalize the temperature of the soil sample and to remove moisture. Dried soil was filtered using 34 μ sieve and 1 g was weighed out for serial dilution protocol.

2.3. Selection and screening of Laccase producing colonies

The filtered sample weighed out was serially diluted to get more prominent isolates from microbe-rich dense soil culture. A total dilution up to 10⁻⁶ was made and inoculated on sterile pre-prepared nutrient agar Petri plates (Hi-Media Laboratories, Mumbai, India) using spread plate culture technique in a laminar cabinet (Microflow Sterile Concepts India Pvt Ltd., Chennai, India). After sterilizing it against possible contamination, 20 μ L of well-mixed sample from 10⁻⁴, 10⁻⁵, 10⁻⁶ dilutions were transferred into three different Petri plates in triplicate and spread it with the help of a sterile spreader. These Petri plates were then incubated at 37 °C temperature, humidity and light-controlled incubator for 24 h to allow the growth of microbes. After that different colonies were marked and streaked out in quadrant form onto sterilized pre-prepared nutrient agar Petri plates for further isolation of pure colony.

Specified M162 medium (Degryse et al., 1978) was used to isolate laccase producing bacterial species. Modified M162 medium composition (g/l): CaSO₄·2H₂O (0.4), MgCl₂·6H₂O (2.0), glucose (1.0), yeast extract (3.0), C₆H₅FeO₇ solution (0.01 M) (5.0), K₂HPO₄ (0.5), NH₄NO₃ (0.5), NaH₂PO₄ (0.5), Na₂HPO₄ (0.5) and 10 ml of micronutrients containing g/l of MnSO₄·H₂O (2.28), Na₂MO₄·2H₂O (0.05), CoCl₂·6H₂O (0.09), CuSO₄ (0.025), H₃BO₄ (0.5), ZnSO₄·7H₂O (0.5) & 0.5 ml H₂SO₄. Agar (1%) used as a solidifying agent in SSF (Rajput and Mishra, 2019) and 2 mM Guaiacol was used as a standard substrate. Laccase producing bacteria produce brown colonies when grown on this medium after 72 h at 37 °C temperature (Kaur et al., 2017) and the identification of laccase producing bacterial strains by probing into its morphological and biochemical characteristics by referring Bergey's Manual of Determinative Bacteriology (Bergey et al., 1984) and then after strains were further cross-verified by Chromous Biotech Pvt. Ltd. Bengaluru, India. Service Number: BI-525, India.

2.4. Isolation of crude Laccase

Colonies were allowed to grow on differential broth media for 5 days at 37 °C and 150 rpm in an orbital shaker (Scigenics Biotech Private Limited, Chennai, India). After 5 days the flasks were drawn from the shaker and culture mixture was centrifuged (Elektrocraft Pvt. Ltd., MP400R, Mumbai, India) at 14000 rpm for 15 min and 0–4 °C in a high-speed research centrifuge. The supernatant was collected and stored at 4 °C for further use as a crude enzyme source and the pellet was discarded.

2.5. Laccase production & optimization

In the process of laccase production parameters like time, temperature, pH, carbon, and nitrogen sources were optimized. Experimental cultures were incubated for 5 days and their laccase activity was measured at a regular interval of 12 h for optimization of time. The effect of temperature and pH on enzyme production was determined by incubating the inoculated flask under different conditions (temperature 27–42 °C), pH (5–9) in a controlled environment (Niladevi et al., 2009; Singh et al., 2007). Glucose, fructose, and sucrose were separately investigated to determine the effect of the carbon source while yeast extract, tryptone and peptone as nitrogen sources to examine its effect on laccase production.

2.6. Total protein content determination

Total protein estimation was done according to the Lowry method (Walker et al., 2003). The method relies on a biuret reaction in which peptide bonds from protein react with copper under alkaline conditions to produce copper ions. The reactions result in a strong blue color, which depends partly on tyrosine and tryptophan content. The

method is sensitive down to about 0.01 mg of protein/ml and is best used on solutions with concentrations in the range 0.01–1.0 mg/ml of protein.

2.7. Characterization of enzyme

2.7.1. Standard substrate concentration

To standardize the procedure for bioremediation of pyridine raffinane, guaiacol as a standard substrate was used for determining optimum substrate to enzyme concentration. A total reaction mixture of 4 ml was taken as constant having varying concentrations of enzyme to substrate ratio. The enzyme to substrate ratio was varied as 1:9, 2:8, 3:7 and 4:6 respectively.

2.7.2. pH

The reaction mixture containing enzyme & guaiacol was incubated at an optimum concentration determined in the previous step with varying pH from 5 to 9 measured using pH meter (Cole-Parmer India, Mumbai, India). After initial incubation, samples were drawn at a regular interval of 20 min and optical density was measured at 450 nm for guaiacol and 501 nm for pyridine raffinane using a UV spectrophotometer (G Biosciences Pvt. Ltd., Noida, India).

2.7.3. Temperature

Estimated optimum pH and enzyme-substrate concentration ratio obtained from previous studies were kept constant and the temperature was varied between 27 and 42 °C under a controlled environment (Niladevi et al., 2009).

2.7.4. Laccase activity

Laccase activity was determined using Guaiacol assay (Sheikhi et al., 2012). 2 mM dilution of guaiacol was prepared in absolute ethanol. The total reaction mixture of 4 ml containing 3.5 ml of pre-prepared phosphate buffer of pH 8.0, 400 µL of 2 mM guaiacol and 100 µL of crude enzyme extract was used. A total of 6 test tubes containing the same reaction mixture were prepared. Guaiacol has been reported as an efficient substrate for laccase assay. The intense brown color development due to oxidation of guaiacol by laccase can be correlated to its activity often read at 450 nm. The mixture was incubated at 35 °C for 15 min and absorbance was read at 450 nm using a UV spectrophotometer. Enzyme activity was expressed as International Units (IU), where 1 IU is defined as the amount of enzyme required to oxidize 1 µmol of guaiacol per min. The laccase activity in IU/ml is calculated by the formula (Abd El Monsef, Hassan and Ramadan, 2016).

$$\text{Laccase activity (IU/ml)} = \frac{\Delta A_{450} \times V}{v \times \Delta t \times e}$$

Where,

ΔA_{450} = Change in absorbance at 450 nm

V = Total volume mixture (ml)

v = Enzyme volume (ml)

Δt = Change in time

e = Extinction coefficient for guaiacol (12.1 mM/cm)

3. Results and discussion

3.1. Isolation and screening of laccase producing bacterial strains

Eight different colonies were obtained after serially diluting 1 mg of soil into 6 different test tubes and were spread onto pre-prepared nutrient agar plates. They were further marked out and were permitted to grow on modified M162 selection media where 2 mM of guaiacol as a substrate was added to the medium. Laccase producing bac-

terium produces reddish-brown colonies on this medium. Colonies corresponding to 1st and 5th of Petri plates produced reddish-brown colonies and hence marked as TS₁ and TS₅. Guaiacol allows enhanced melanization by laccase producing strains and hence helps in identification.

3.2. Laccase production & optimization

The concentration and nature of the carbon source used in the medium showed a significant effect on enzyme production. The addition of fructose, glucose, and sucrose as different carbon sources increases the production of laccase (measured in terms of maximum laccase activity). Optimization studies for carbon sources in the presence of guaiacol were performed. Glucose (0.265 & 0.238 IU/ml) showed higher activity in comparison to sucrose (0.255 & 0.169 IU/ml) and fructose (0.219 & 0.198 IU/ml) respectively for strain TS₁ and TS₅ (Fig. 1). Similar results were reported by many researchers in the case of the utilization of specified carbon sources (Mikiashvili et al., 2006). Yeast extract, urea, ammonium sulphate, ammonium nitrate, peptone and tryptone are most commonly used nitrogen sources for the bacterial and fungal laccase production. We optimized preferred nitrogen sources tryptone, peptone and yeast extract against laccase activity and found that yeast extract demonstrated higher activity (0.250 & 0.255 IU/ml) compared to peptone (0.231 & 0.238 IU/ml) and tryptone (0.223 & 0.232 IU/ml) respectively for strain TS₁ and TS₅ (Fig. 2). Experiments have suggested that laccase production increases as ni-

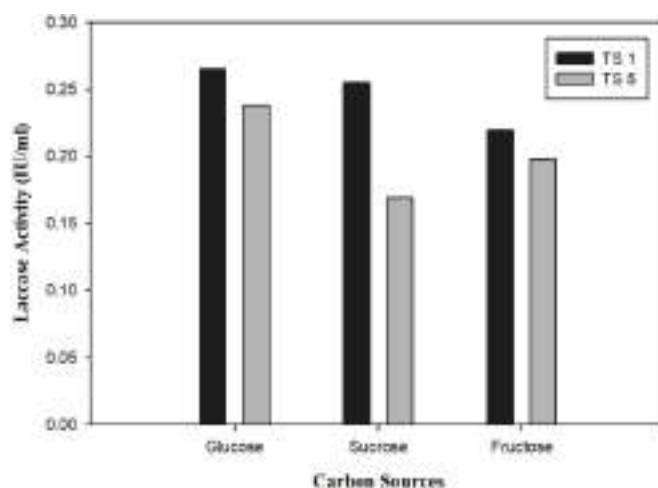


Fig. 1. Laccase activity against carbon sources for laccase production.

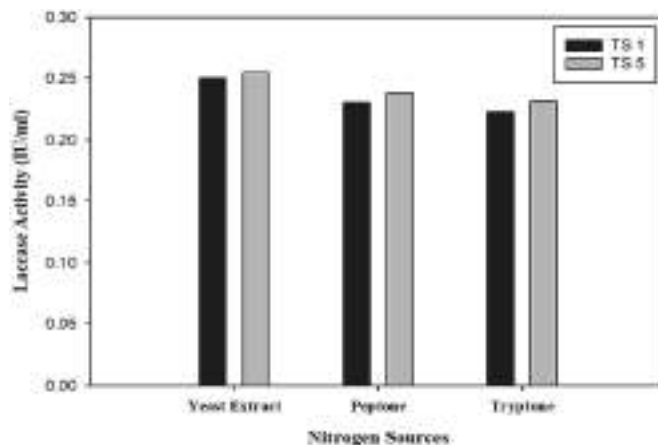


Fig. 2. Laccase activity against nitrogen sources for laccase production.

trogen depleted, attained a maximum and then started falling off (Keyser et al., 1978).

Laccase being thermostable, temperature does not have a very significant effect on laccase activity whereas the optimal temperature varies with strain (Thurston, 2019). In this study, we optimized laccase activity against varied temperature range (27–42 °C) and discovered that both the strains showed higher activity at 37 °C (Fig. 3).

The ideal pH worth changes relying upon the substrate since the instrument of the response with compound laccase fluctuates. Many reports suggest that the bell profile occurs in the case of laccase activity. The potential difference between the phenolic substrate and the T1 copper (First copper inactive moiety of laccase) can increase the oxidation of the substrate while the hydroxide (OH⁻) is bonded to the T2/T3 copper center which help to determine the optimal pH value for the laccase activity (Kunamneni et al., 2007). Laccase production was higher at pH 7.0 for both the strains (Fig. 4). Substantial laccase production was displayed by many researchers in the pH range from 3.0 to 8.0 (Cordi et al., 2007).

3.3. Morphological and molecular identification of laccase producing strains

3.3.1. Gram staining

A high-resolution LCD microscope (Wuzhou New Found Instrument Company Ltd., DMS653, China) was used to determine the morphological characteristics of the bacterium. Gram-stained slides were analyzed under the microscope at 100X resolution and the colonies were found to be pink colored, rod-shaped, motile, multi-flagella, the center raised and margins slightly tapered smooth bacterium (Fig. 5).

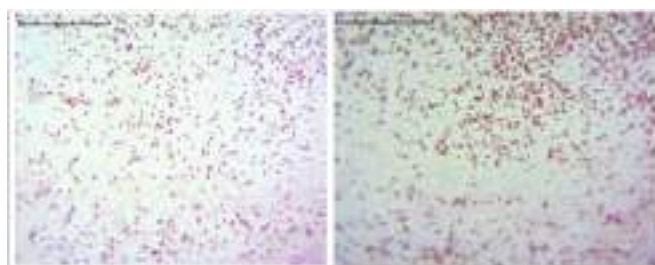


Fig. 5. Gram-stained isolate strain TS1 (left) and TS5 (right).

3.3.2. Molecular identification of bacterial strains using 16S rRNA sequencing

3.3.2.1. PCR amplification conditions. In this study DNA amplification was done under the mentioned protocol for the identification of the samples TS1 and TS5 in which DNA was taken 1 µl, 16S forward primer (400 ng) 1 µl, 16S Reverse Primer (400 ng) 1 µl, dNTPs (2.5 mM each) 4 µl, 10X Taq DNA polymerase Assay Buffer 10 µl, Taq DNA polymerase enzyme (3U/µl) 1 µl, nuclease free water X 7 µl, Total reaction volume 250 µl, all PCR work done by Chromous Biotech Pvt. Ltd. PCR thermal cycles and conditions are mentioned in Table 1.

Forward and reverse primers were used for amplification of 16S rDNA sequence: Prokaryotic 16S rRNA specific primer were used in this study: (The PCR product size was expected ~1.5 kb) and the used primers sequences were-

16S Forward Primer: 5' – AGAGTTTGTATCMTGGCTCAG – 3'
16S Reverse Primer: 5' – TACGGYTACCTTGTTACGACTT – 3'

The bacterial cultures were isolated and identified to their nearest species using the 16S rDNA sequence. In Fig. 6 sample TS1(1), TS5 (2) and 500bp DNA ladder (L) was loaded in 1% agarose gel to determine

Table 1
PCR cycle condition.

Temperature °C	95 °C	94 °C	50 °C	72 °C	72 °C
Time	5min	30sec	30sec	1.30min	7min
Cycle	35				

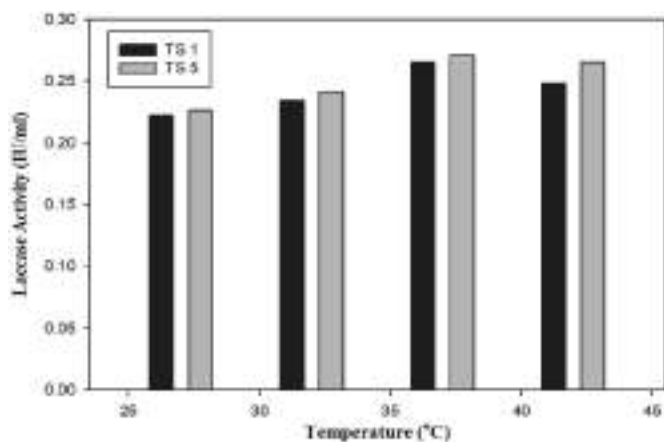


Fig. 3. Laccase activity at different temperatures for laccase production.

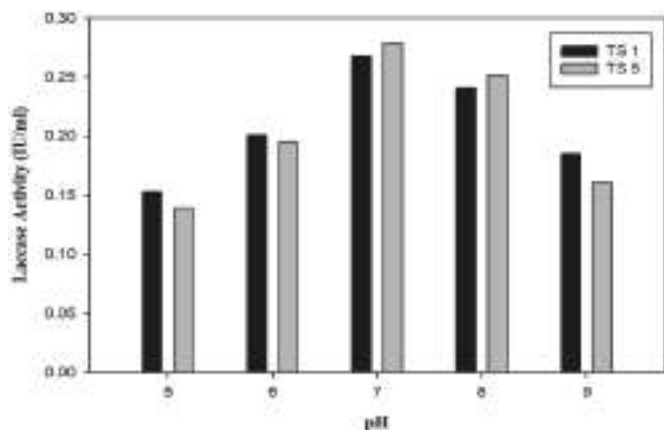


Fig. 4. Laccase activity at different pH for laccase production.

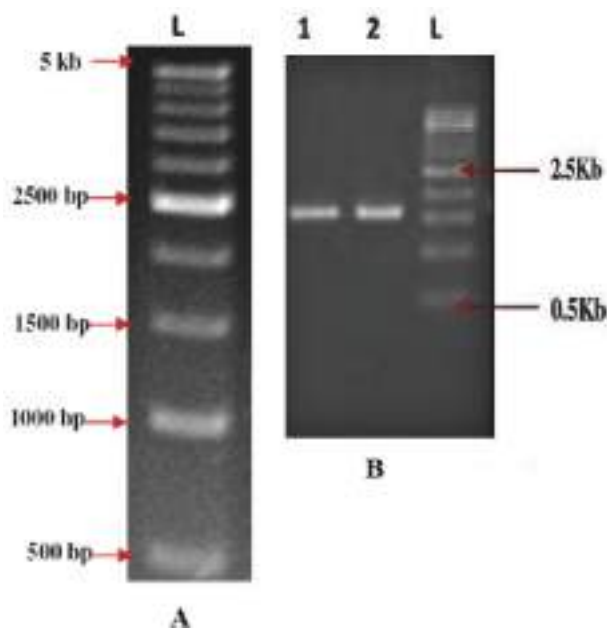


Fig. 6. PCR products loaded on 1% Agarose gel, A: 500bp DNA Ladder, 1: Sample-TS1, 2: Sample-TS5, L: Ladder.

the size of the samples after PCR for 16S rDNA analysis. The 16S rDNA sequence of the isolates was compared with the 16S rDNA GenBank database using BLASTn. Genomic DNA from the isolated strains was isolated and 1.5 kb 16S-rDNA fragment was amplified bi-directionally using high-fidelity PCR. The obtained PCR product was sequenced bi-directionally. Phylogenetic tree builder was used for sequences aligned with system software aligner. A distance matrix was generated using the Jukes-Cantor with corrected distance model. While generating the distance matrix, only alignment model positions were used, alignment inserts were ignored and the minimum comparable position was considered 200. The tree was created using weight or with alphabet size 4 and length size 1000. The entire analysis gave matched with *Pseudomonas sp.* FBF57 partial 16S rRNA gene, isolate FBF57 and next nearest locus was found as *Pseudomonas monteilii* strain PS38 (Fig. 7). The sample was found to be *Gamma proteobacterium symbiont of Calliphora excellent IROM* gene for 16S ribosomal RNA (Fig. 8).

From the above analysis it has very clear that our organisms of interest was belong to the prokaryotes (Bacteria) system. With the use of advanced molecular biology approaches and bio-informatics tool *Pseudomonas monteilii* & *Gamma proteobacterium* was found confirmed organisms.

3.3.3. Laccase activity determination with reference to guaiacol as a standard substrate

Laccase activity was determined by performing the enzyme-substrate reaction between guaiacol as substrate and crude enzyme extract as a laccase source. A UV-Visible spectrophotometer was used to display absorbance at a specific interval of 20 min for 120 min. Laccase activity results are shown below (Fig. 9). The enzyme to substrate ratio was taken as 1:4 as reported from the literature (Rajput and Mishra, 2019). Initially, guaiacol was present in good quantity so the reaction was fast but as the substrate started depleting, the reaction rate became slower.

3.4. Laccase characterization

3.4.1. Effect of substrate concentration, pH and temperature on laccase activity

Laccase obtained from the crude extracts was subjected to standard substrate guaiacol for determining the optimum concentration for its maximum activity. Laccase being substrate-specific enzyme, an excessive amount of substrate concentration would have caused substrate inhibition. Moreover, low concentration would not have allowed attaining the proper rate of reaction. Entities already present in crude extract may also participate in the reaction and affect it adversely. In the case of only one substrate, it has been well known that by increasing substrate concentration, the rate of reaction increases then achieves a maximum, beyond which, rate of reaction will not be affected by substrate concentration. Fig. 10 shows maximum laccase activity at the enzyme to substrate ratio 1:9 for *Pseudomonas monteilii* and 2:8 for *Gamma proteobacterium*.

To signify that enzyme is active (different subunits of enzymes behave differently at diverse pH) and stable it becomes necessary to validate enzyme activity and stability at varied pH. The activity of *Pseudomonas monteilii* was found best at pH 8.0 and that of *Gamma proteobacterium* at pH 6.0 (Fig. 11). The results of this study infer that laccase from *Gamma proteobacterium* strain is much more pH stable than its counterpart (*Pseudomonas monteilii*) and was in accordance with other researches (Cordi et al., 2007; Kunamneni et al., 2007).

Optimum temperature for laccase activity was found at 25 °C for *Gamma proteobacterium*, while that of *Pseudomonas monteilii* at 40 °C (Fig. 12). Enzymatic reactions are temperature specific and their stability depends on the temperature of the reaction mixture and environment. Mostly laccases are thermally stable and research has shown that laccase activity can vary from moderate to higher temperature highly depending on strain type (Nyanhongo et al., 2002; Palmeiri et al., 1993).

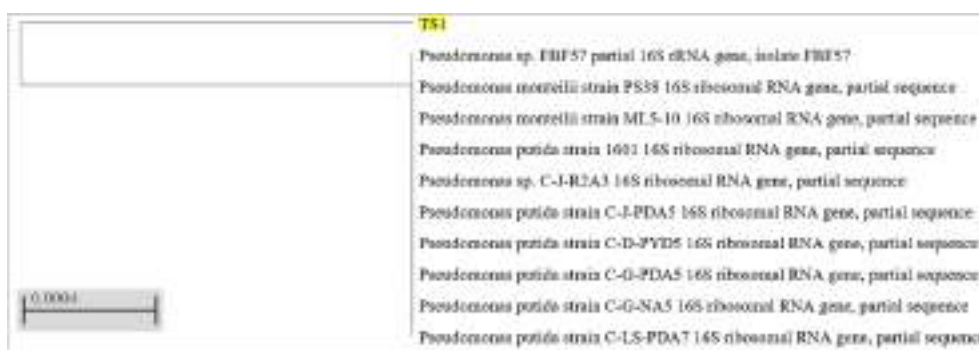


Fig. 7. Phylogenetic tree generated by the concatenation of the 16SrRNA sequences Data retrieved from NCBI database (Sequence ID: HG805731.1).

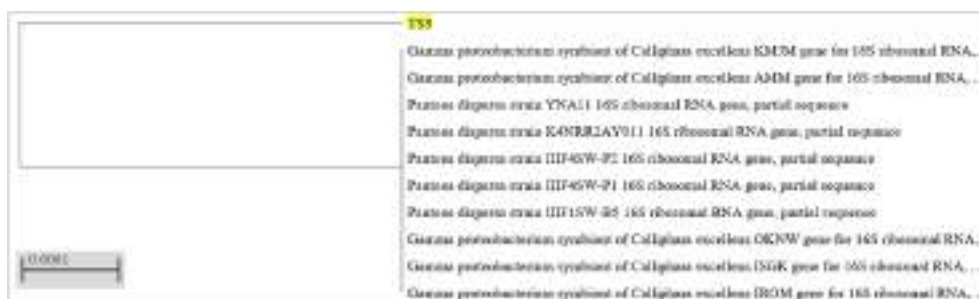


Fig. 8. Phylogenetic tree generated by the concatenation of the 16SrRNA sequences Data retrieved from the NCBI database (Sequence ID: LC473101.1).

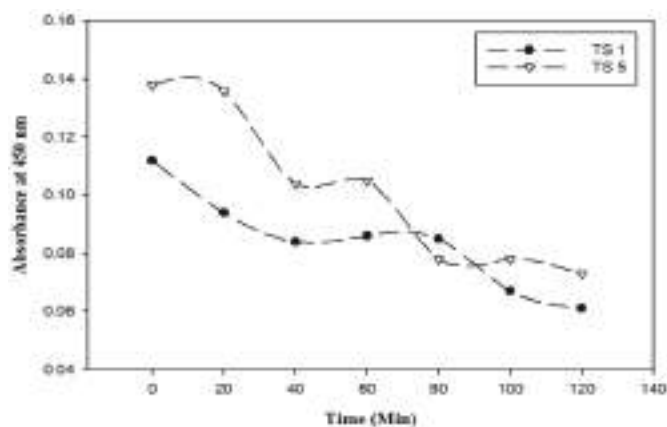


Fig. 9. Laccase activity determination using Guaiacol as standard substrate.

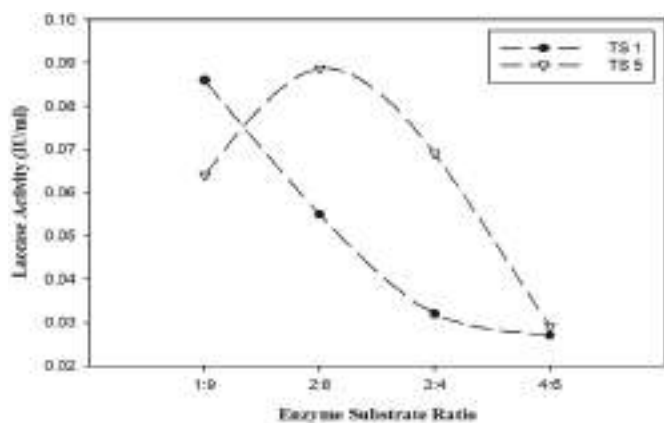


Fig. 10. Optimum substrate concentration determination for pyridine raffinate degradation.

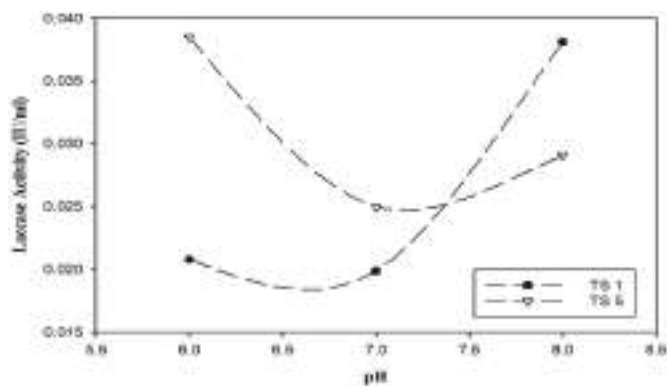


Fig. 11. Optimum pH determination for pyridine raffinate degradation.

3.5. Specific activity measurement

Specific activity is the measure of enzyme purity. It is the ratio of enzyme activity to total protein concentration. Specific activity for crude enzyme extract from *Pseudomonas monteilii* was found to be 0.089 IU/ml, while that of *Gamma proteobacterium* was 0.1217 IU/ml.

3.6. Pyridine raffinate degradation

After the characterization of laccase with standard substrate guaiacol, the best conditions were chosen to perform assay with pyridine raffinate. Extracted enzymes were tested for bioremediation in terms

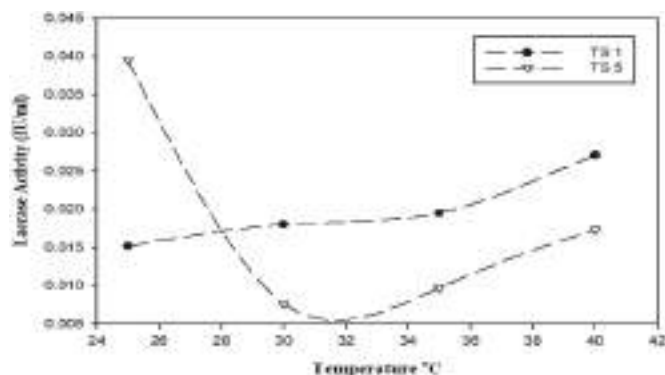


Fig. 12. Optimum temperature determination for pyridine raffinate degradation.

of reduction in optical density (Shi et al., 2015; Singh et al., 2007; Wang et al., 2012).

We determined the optimized conditions viz; enzyme-substrate concentration (1:9), pH(6), temperature(25 °C) for strain *Pseudomonas monteilii*, and enzyme-substrate concentration(2:8), pH(8), temperature(40 °C) for strain *Gamma proteobacterium* and applied the same for the degradation of pyridine raffinate. After initial incubation of 20 min the absorbance of pyridine raffinate increases slightly then it starts decreasing till 120 min and further seems to become a plateau (Fig. 13). Absorbance decreased up to 51% in 140 min for strain *Pseudomonas monteilii* while 59.5% reduction was observed in case of strain *Gamma proteobacterium*. This experiment signifies that pyridine raffinate can be degraded using bacterial laccase.

4. External validation of process parameters

High-Performance Liquid Chromatography (HPLC) was used to accurately determine the degradation percentage of pyridine compound by initially using 50 ppm pure pyridine from BDH instead of pyridine raffinate sample. According to the time course degradation study (Fig. 14a and 14b), the maximum pyridine degradation ($46.323 \pm 5\%$) was observed at 140 min of incubation. HPLC (LC-20AD, Shimadzu, and Tokyo, Japan) was used for the analysis with injection volume 20 μ L at 25 °C and acetonitrile (ACN) as a mobile phase. The reaction mixture without laccase was used as a control for this experiment. All the analysis were carried out in triplicates. The results have been compared with their controls. Both the chromatogram (control and laccase-mediated degradation of pyridine) showed single dominant peaks at a retention time of 2.005, 2.077 min, respectively. The control chromatograms did not show any absolute peaks. However, the laccase treated chromatograms showed their solute peaks at retention time at 1.376 & 1.276 min. The results implied laccase mediated degradation of pyridine. The degradation of toxic pyridine by

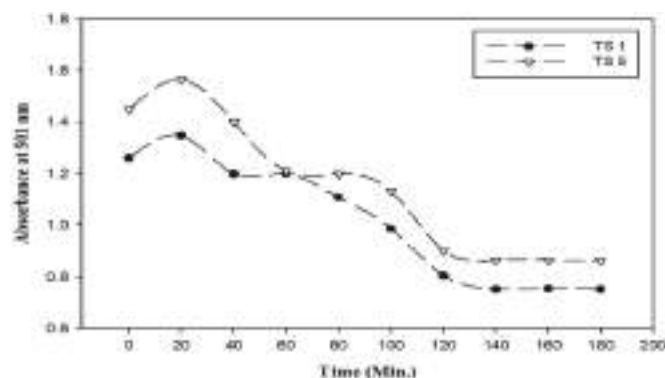


Fig. 13. Pyridine raffinate degradation, absorption read at 501 nm.

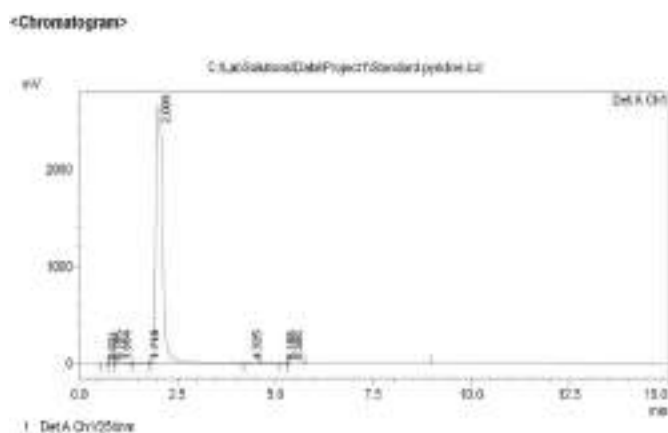


Fig. 14a. Chromatogram of standard 50 ppm pyridine.

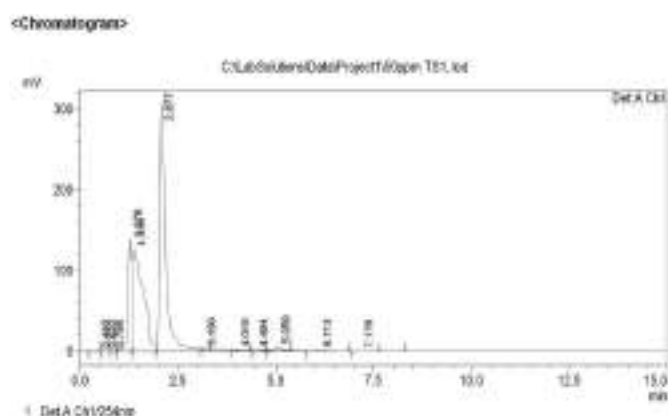


Fig. 14b. Chromatogram of treated 50 ppm pyridine.

Pseudomonas monteilii and *Gamma proteobacterium* suggest a potential alternative for the degradation of pollutants in the ecosystem.

5. Conclusion

Many studies have already reported the potential of laccases in bioremediation of complex phenolic and aromatic substances. However, the persistent and complicated structure and nature of pyridine raffinate has led to little studies regarding its biodegradation. In this study, laccases have been selected to evaluate biodegradation of pyridine raffinate (highly alkaline) as these enzymes have better tolerance towards high pH and show thermal stability. Laccase obtained from isolates of *Pseudomonas monteilii* (enzyme-substrate concentration (1:9), pH (6), temperature (25 °C)) and *Gamma proteobacterium* (enzyme-substrate concentration (2:8), pH (8), temperature (40 °C)) showed around 51 and 59.5% degradation of toxic and carcinogenic pyridine raffinate in 140 min respectively and further by HPLC method 46.323 ± 5% reduction was observed. The outcomes of this investigation suggested a potential route for combating pyridine raffinate pollution in an ecologically compatible and economical manner.

Authors statement

We are submitting revised manuscript entitled “Biodegradation of Pyridine Raffinate by microbial laccase isolated from *Pseudomonas monteilii* & *Gamma proteobacterium* present in Woody Soil” for possible evaluation. We mutually agree with all necessary changes which have been made in this revised manuscript. We affirm that this manuscript is original, has not been published before

and is not currently being considered for publication elsewhere. We affirm that the novelty in results/findings, or significance of results.

Declaration of competing interest

None.

Acknowledgment:

The authors gratefully acknowledge the support of Director, Dr. Ambedkar Institute of Technology for Handicapped, Kanpur for providing the space and resources for successful completion of this comprehensive research and Chromous Biotech Pvt Ltd, Bangaluru, India for 16s RNA based bacterial identification.

This research did not receive any specific grant from funding agencies in the public, commercial, or not-for-profit sectors.

Appendix A. Supplementary data

Supplementary data to this article can be found online at <https://doi.org/10.1016/j.bcab.2020.101650>.

References

- Abd El Monssef, R.A., Hassan, E.A., Ramadan, E.M., 2016. Production of laccase enzyme for their potential application to decolorize fungal pigments on aging paper and parchment. *Ann. Agric. Sci. (Cairo)*. <https://doi.org/10.1016/j.aos.2015.11.007>.
- Baldrian, P., 2006. Fungal laccases—occurrence and properties. *FEMS (Fed. Eur. Microbiol. Soc.) Microbiol. Rev.* 30 (2), 215–242.
- Bergey, D.H., Hendricks, D., Holt, J.G., Sneath, P.H.A., 1984. *Bergey's Manual of Systematic Bacteriology*, vol. 2. Williams & Wilkins.
- Bugg, T.D.H., Ahmad, M., Hardiman, E.M., Singh, R., 2011. The emerging role for bacteria in lignin degradation and bio-product formation. *Curr. Opin. Biotechnol.* 22 (3), 394–400.
- Chandra, R., Bharagava, R.N., Kapley, A., Purohit, H.J., 2009. Isolation and characterization of potential aerobic bacteria capable for pyridine degradation in presence of picoline, phenol and formaldehyde as co-pollutants. *World J. Microbiol. Biotechnol.* 25 (12), 2113–2119.
- Claus, H., 2004. Laccases: structure, reactions, distribution. *Micron* 35 (1–2), 93–96.
- Cordi, L., Minussi, R.C., Freire, R.S., Durán, 2007. Fungal laccase: copper induction, semi-purification, immobilization, phenolic effluent treatment and electrochemical measurement. *Afr. J. Biotechnol.* 6 (10), 1255–1259.
- D'Souza-Ticlo, D., Sharma, D., Raghukumar, C., 2009. A thermostable metal-tolerant laccase with bioremediation potential from a marine-derived fungus. *Mar. Biotechnol.* 11 (6), 725–737.
- Dean, J.F.D., Eriksson, K.-E.L., 1994. Laccase and the deposition of lignin in vascular plants. *Holzforchung-International Journal of the Biology, Chemistry, Physics and Technology of Wood* 48 (s1), 21–33.
- Degryse, E., Glandsdorff, N., Piérard, A., 1978. A comparative analysis of extreme thermophilic bacteria belonging to the genus *Thermus*. *Arch. Microbiol.* 117 (2), 189–196.
- Diamantidis, G., Effosse, A., Potier, P., Bally, R., 2000. Purification and characterization of the first bacterial laccase in the rhizospheric bacterium *Azospirillum lipoferum*. *Soil Biol. Biochem.* 32 (7), 919–927.
- Dwivedi, U., Singh, P., Pandey, V., Kumar, A., 2011. Laccases from new fungal sources and its promising application. *J. Mol. Catal. B Enzym.* 68, 117–128.
- Hasegawa, R., Sano, M., Tamano, S., 1993. Pyridine (PhIP) carcinogenicity in rats. *Mutat. Res. Fund. Mol. Mech. Mutagen* 376 (1–2), 115–122.
- Huber, W.W., McDaniel, L.P., Kaderlik, K.R., Teitel, C.H., Lang, N.P., Kadlubar, F.F., 1997. Chemoprotection against the formation of colon DNA adducts from the food-borne carcinogen 2-amino-1-methyl-6-phenylimidazo [4, 5-b] pyridine (PhIP) in the rat. *Mutat. Res. Fund. Mol. Mech. Mutagen* 376 (1–2), 115–122.
- Kaur, K., Singh, G., Gupta, V., Capalash, N., Sharma, P., 2017. Impact of phosphate and other medium components on physiological regulation of bacterial laccase production. *Biotechnol. Prog.* 33 (2), 541–548.
- Kersten, P.J., Kalyanaraman, B., Hammel, K.E., Reinhammar, B., Kirk, T.K., 1990. Comparison of lignin peroxidase, horseradish peroxidase and laccase in the oxidation of methoxybenzenes. *Biochem. J.* 268 (2), 475–480.
- Keyser, P., Kirk, T.K., Zeikus, J.G., 1978. Ligninolytic enzyme system of *Phanerochaete chrysosporium*: synthesized in the absence of lignin in response to nitrogen starvation. *J. Bacteriol.* 135 (3), 790–797.
- Kunamneni, A., Ballesteros, A., Plou, F.J., Alcalde, M., 2007. A Review Article. pp. 233–245.
- Li, B., Lei, Z., Huang, Z., 2009. Surface-treated activated carbon for removal of aromatic compounds from water. *Chem. Eng. Technol.* 32 (5), 763–770.
- Majer, B.J., Hofer, E., Cavin, C., Lhoste, E., Uhl, M., Glatt, H.R., et al., 2005. Coffee diterpenes prevent the genotoxic effects of 2-amino-1-methyl-6-phenylimidazo [4, 5-b] pyridine (PhIP) and N-nitrosodimethylamine in a human derived liver cell line (HepG2). *Food Chem. Toxicol.* 43 (3), 433–441.

- Martins, L.O., Soares, C.M., Pereira, M.M., Teixeira, M., Costa, T., Jones, G.H., Henriques, A.O., 2002. Molecular and biochemical characterization of a highly stable bacterial laccase that occurs as a structural component of the *Bacillus subtilis* endospore coat. *J. Biol. Chem.* 277 (21), 18849–18859.
- Mikiashvili, N., Wasser, S.P., Nevo, E., Elisashvili, V., 2006. Effects of carbon and nitrogen sources on *Pleurotus ostreatus* ligninolytic enzyme activity. *World J. Microbiol. Biotechnol.* 22 (9), 999–1002.
- Niladevi, K.N., Sukumaran, R.K., Jacob, N., Anisha, G.S., Prema, P., 2009. Optimization of laccase production from a novel strain—*Streptomyces psammoticus* using response surface methodology. *Microbiol. Res.* 164 (1), 105–113.
- Nyanhongo, G.S., Gomes, J., Gübitz, G., Zvauya, R., Read, J.S., Steiner, W., 2002. Production of laccase by a newly isolated strain of *Trametes modesta*. *Bioresour. Technol.* 84 (3), 259–263.
- Palmeiri, G., Giardina, P., Marzullo, L., Desiderio, B., Nittii, G., Cannio, R., Sannia, G., 1993. Stability and activity of a phenol oxidase from the ligninolytic fungus *Pleurotus ostreatus*. *Appl. Microbiol. Biotechnol.* 39 (4–5), 632–636.
- Pyridine | C5H5N - PubChem. n.d., Retrieved April 5, 2020, from: <https://pubchem.ncbi.nlm.nih.gov/compound/pyridine>.
- Pyridine Market Research Report- Forecast to 2023 | MRFR. n.d., Retrieved April 5, 2020, from: <https://www.marketresearchfuture.com/reports/pyridine-market-3198>.
- Rajput, M.S., Mishra, B.N., 2019. Biodegradation of pyridine raffinate using bacterial laccase isolated from garden soil. *Biocatalysis and Agricultural Biotechnology*. <https://doi.org/10.1016/j.bcab.2018.10.020>.
- Riva, S., 2006. Laccases: blue enzymes for green chemistry. *Trends Biotechnol.* 24 (5), 219–226. <https://doi.org/10.1016/j.tibtech.2006.03.006>.
- Saroja, A.K., 2018. Biodegradability enhancement of industrial organic raffinate containing pyridine and its derivatives by CWAO using ceria promoted MnOx/Al2O3 catalyst at atmospheric pressure. *Chem. Eng. J.* 334, 985–994.
- Sharma, P., Goel, R., Capalash, N., 2007. Bacterial laccases. *World J. Microbiol. Biotechnol.* 23 (6), 823–832.
- Sheikhi, F., Ardakani, M.R., Enayatizamir, N., Rodriguez-Couto, S., 2012. The determination of assay for laccase of *Bacillus subtilis* WPI with two classes of chemical compounds as substrates. *Indian J. Microbiol.* 52 (4), 701–707.
- Shi, X., Liu, Q., Ma, J., Liao, H., Xiong, X., Zhang, K., et al., 2015. An acid-stable bacterial laccase identified from the endophyte *Pantoea ananatis* Sd-1 genome exhibiting lignin degradation and dye decolorization abilities. *Biotechnol. Lett.* 37 (11), 2279–2288.
- Sims, G.K., O'Loughlin, E.J., Crawford, R.L., 1989. Degradation of pyridines in the environment. *Crit. Rev. Environ. Sci. Technol.* 19 (4), 309–340.
- Singh, G., Capalash, N., Goel, R., Sharma, P., 2007. A pH-stable laccase from alkali-tolerant γ -proteobacterium JB: purification, characterization and indigo carmine degradation. *Enzym. Microb. Technol.* 41 (6–7), 794–799.
- Sun, J.-Q., Xu, L., Tang, Y.-Q., Chen, F.-M., Liu, W.-Q., Wu, X.-L., 2011. Degradation of pyridine by one *Rhodococcus* strain in the presence of chromium (VI) or phenol. *J. Hazard Mater.* 191 (1–3), 62–68.
- Thurston, C. F. (2019). Article 1, 1(1 994), 19–26.
- Walker, J.M., Waterborg, J.H., Matthews, H.R., 2003. The Lowry Method for Protein Quantitation. *Basic Protein and Peptide Protocols*, pp. 1–4 (January). <https://doi.org/10.1385/0-89603-268-x:1>.
- Wang, W., Zhang, Z., Ni, H., Yang, X., Li, Q., Li, L., 2012. Decolorization of industrial synthetic dyes using engineered *Pseudomonas putida* cells with surface-immobilized bacterial laccase. *Microb. Cell Factories* 11 (1), 75.
- Yoshida, H., 1883. Chemistry of lacquer (urushi). *J. Chem. Soc. Trans.* 43 (47), 472. <https://doi.org/10.1039/ct8834300472>.

SEQUENCING AND *IN SILICO* ANNOTATIONS OF A NOVEL *PSEUDOMONAS* STRAIN

SHWETA SACHAN, PARUL JOHRI*, MALA TRIVEDI AND ADITI SINGH

Amity Institute of Biotechnology, Amity University Uttar Pradesh,
Lucknow Campus, Malhaur, Gomti Nagar Extension, Lucknow- 226028 (UP)

(Received 9 March, 2017; accepted 25 April, 2017)

Key words : BLAST, GenBank, *Pseudomonas aeruginosa*, Phylogenetic analysis, Restriction sites.

Abstract—Symbioses of soil micro-organisms have proved to be of fundamental importance for plant or crop adaptation. In order to discover a microbial species for lipase enzyme production, we isolated the organisms found in the soil of sugarcane field. The strains were isolated, identified and a total of six different bacterial strains were obtained. All were assessed for their lipolytic potential, in which only one gram negative strain was found to be most active. The bacteria was identified as *Pseudomonas* and further confirmed by 16s rRNA sequencing technique. The sequence came out to be a novel sequence and was deposited in the global nucleotide sequence repository Genbank database of NCBI (accession ID: KX946966.1). The sequence was additionally annotated using bioinformatics tools. The sequence statistic was calculated, AT%-GC%, number of codons, translational frames, phylogenetic analysis, homology search and restriction site identification was done for the curation of meta data of the sequence. The number of codons in the sequence was 479. The Blast result showed that our sequence was homologous with the *Pseudomonas aeruginosa* species, giving 0 e value and 2630 as bit score. This sequence can further be analyzed for its biochemical and physiological characteristics and could be commercially used in various industries for enzymatic production.

INTRODUCTION

Microorganisms constitute an important source of biodiversity in soils and are an integral part of terrestrial ecosystems (Lecomte *et al.*, 2011). They contribute to major biological functions such as nutrient and gas cycling, biogeochemical processes and the decomposition and transformation of organic matter. Moreover, the discovery that soil microbes may translate into benefits for biotechnology, management of agricultural, forest, and natural ecosystems, biodegradation of pollutants, and waste treatment systems maximized the need of scientists for the isolation and their characterization (Bhardwaj *et al.*, 2012). Operations such as the production of antibiotics and enzymatic activities from microorganisms of soil constitute objectives of industry in their effort to cope with the increase of population on earth and disturbance of environment and may also ameliorate the effects of global climate change (Stefanis *et al.*, 2013).

In our previous studies, we have identified a lipolytic strain of *Pseudomonas* isolated from the soil of sugarcane crop field. The soil samples were

grown on the tributyrin agar medium and the colonies which showed a clear wide zone had been isolated and stored for further use. For the production of lipase, bacterial colonies were cultured in nutrient medium in shake flask cultures for 24 hr at 37°C. Enzyme is extracted by centrifugation at 10,000 rpm at 4°C for 10 min and activity of lipase was checked as described previously (Sachan *et al.*, 2017).

The isolated bacterium was also subjected to the next generation sequencing technique: 16S rRNA technique and the sequence obtained was deposited in the primary database for nucleotides, GenBank database of NCBI (<http://www.ncbi.nlm.nih.gov/genbank/>). The sequence was further analyzed and annotated using different online tools of bioinformatics.

MATERIALS AND METHODS

Sequencing and submission

The bacterial colony identified was further sequenced using the 16S rRNA technique by automated Sanger sequencing method (ABI 3130xl

*Corresponding author's email : pjohri@lko.amity.edu; asingh3@lko.amity.edu

analyzer, a 16-capillary machine). The sequence came out to be 1,432bp long rRNA segment. This was then submitted to the Genbank (<http://www.ncbi.nlm.nih.gov/genbank/>) database of NCBI (<http://www.ncbi.nlm.nih.gov/>) using the BankIT (<http://www.ncbi.nlm.nih.gov/WebSub/?tool=genbank>) online tool (Benson *et al.*, 1996). The sequence was provided with a unique identification number (Accession Number) KX946966.1. Further the sequence was annotated using bioinformatics tools for analysis.

Sequence annotations

The sequence identified was subject to homology search using BLAST (Basic Local Alignment Search Tool) (<http://blast.ncbi.nlm.nih.gov/Blast.cgi>) tool of NCBI. 16S ribosomal RNA sequences (Bacteria and Archaea) were taken as the target database for the identification of most similar sequences using BLAST 2.5.0 (Wheeler *et al.*, 2007).

The numbers of codons were recorded using the Codon Usage Database (<http://www.kazusa.or.jp/codon/countcodon.html>) tool. The rRNA sequence was further translated into its corresponding six reading frames using the TRANSLATE (<http://web.expasy.org/translate/>) tool of ExPASy server taking into consideration the standard genetic codes (Bairoch *et al.*, 2003; Gasteiger *et al.*, 2003).

The sequence statistics was studied using the online tool Genomatix software suite (<http://www.genomatix.de/cgi-bin/tools/tools.pl>). The base content (AT %, GC%, mono nucleotides, Dinucleotides, tri nucleotides etc) was studied for the sequence (Sachan *et al.*, 2016; Johri *et al.*, 2016).

For multiple sequence alignment and phylogenetic tree construction, CLUSTAL Omega tool of EMBL-EBI (<http://www.ebi.ac.uk/Tools/msa/clustalo/>) was used. Clustal Omega is a new multiple sequence alignment program that uses seeded guide trees and HMM profile-profile techniques to generate alignments between three or

more sequences. Total of 14 sequences of *Pseudomonas aeruginosa* were selected for building the phylogenetic tree. The tree made was further analyzed for clustering.

The virtual digestion of the sequence was done using the online tool Restriction Mapper (<http://www.restrictionmapper.org/>). All the enzymes were selection for digestion and analysis (Fig. 1).

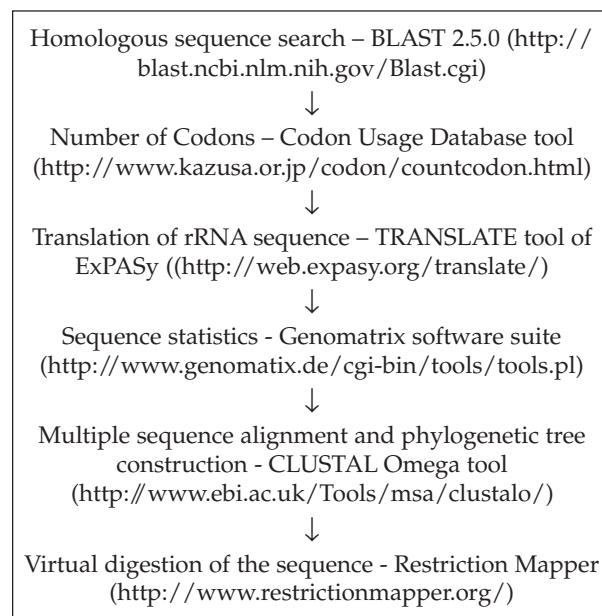


Fig. 1. Flow Chart of Sequence Annotation

RESULTS AND DISCUSSION

The Blastn result showed that the sequence showing maximum score and 0 e value was from *Pseudomonas aeruginosa* stain ATCC 10145 16S rRNA gene (NR_114471.1). This proves that the sequence belongs to *Pseudomonas aeruginosa* family only and it will possess all the characteristics of this species (Table 1).

The codon usage database counted total of 479 codons in our sequence using the standard codon

Table 1. Blastn result of the sequences showing maximum score

S. No.	Organism Name	Max Score/Total Score	Query Cover	E Value	% Identity	Accession Number
1	<i>Pseudomonas aeruginosa</i> ATCC 10145	2630/2630	99%	0.0	99%	NR 114471.1
2	<i>Pseudomonas aeruginosa</i> DSM50071	2628/2628	99%	0.0	99%	NR 117678.1
3	<i>Pseudomonas aeruginosa</i> NBRC 12689	2603/2603	98%	0.0	99%	NR 113599.1
4	<i>Pseudomonas otitidis</i> MCC10330	2527/2527	100%	0.0	98%	NR 043289.1
5	<i>Pseudomonas aeruginosa</i> DSM50071	2484/2484	100%	0.0	98%	NR 026078.1

table. The nucleotide sequence was further subjected to in silico translation using online tool of ExPASy server. All the six translational reading frames of our sequence were obtained showing the ORFs (Supplementary material 1).

The sequence statistics were calculated using the Genomatix online suite. The AT-content of the sequence was obtained as 45.79%, the GC-content was recorded as 54.21%. Further the mono, di and tri nucleotides were also calculated and the results are as under (Table 2-4).

The phylogenetic tree was constructed using CLUSATAL OMEGA tool of EBI. The tree showed that our sequence does not group with any of the

existing sequences and lay as an outlier. The sequence still need to be classified and characterize using various biochemical tests (Fig. 2).

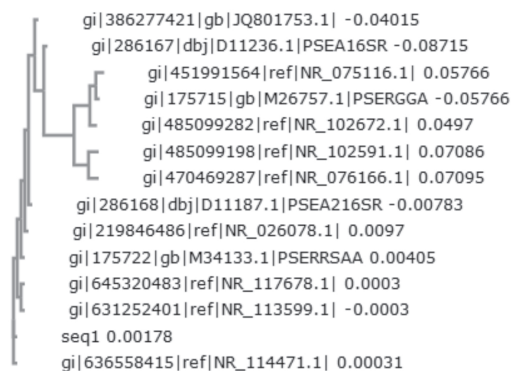


Fig. 2. Phylogenetic tree of all strains of *Pseudomonas aeruginosa*

Table 2. The AT & GC percent of mono nucleotides

Bases	In bp	In %
A	362	25.19%
C	328	22.83%
G	451	31.38%
T	296	20.60%

Table 3. The AT & GC percent of di- nucleotides

	First nucleotide	Second nucleotide			
		A	C	G	T
	A	102	86	109	65
	C	78	78	94	77
	G	111	98	142	100
	T	70	66	106	54

Table 4. The AT & GC percent of tri- nucleotides

	First nucleotide	Second/third nucleotide															
		AA	AC	AG	AT	CA	CC	CG	CT	GA	GC	GG	GT	TA	TC	TG	TT
	A	20	26	33	23	18	23	24	21	23	30	28	28	14	19	21	11
	C	20	21	26	11	19	11	22	26	18	21	31	24	18	12	30	17
	G	35	19	29	28	24	24	27	22	41	26	42	33	22	25	35	18
	T	27	20	20	3	17	20	21	8	29	21	41	15	16	10	20	8

Table 5. Virtual restriction digestion using restriction mapper

Name	Sequence	Site length	Overhang	frequency	Cut position
BamHI	GGATCC	6	Five_prime	1	822
EcoRII	CCWGG	5	Five_prime	8	77, 120, 608, 723, 781, 867, 969, 1202
MaeIII	GTNAC	4	Five_prime	8	271, 295, 469, 1084, 1109, 1149, 1350, 1390
HindII	GTYRAC	6	Blunt	2	809, 862
BglII	AGATCT	6	Five_prime	1	831
SmaI	CCCGGG	6	Blunt	2	600, 1370
FauI	CCCGC	5	Five_prime	1	924
HincII	GTYRAC	6	Blunt	2	809, 862

The sequence was subjected to virtual restriction digestion using the online tool restriction mapper. Many enzymes and chemicals were used for finding out their potential restriction sites in our sequence. The detailed results of all the restriction sites obtained are given in the table below (table 5). Many of the enzymes were found as non cutters namely HindIII, EcoRI, EcoRV, Acl1, Mva1269I etc.

CONCLUSION

In silico biology is a thorough, expanding and complex science. Once a gene is sequenced, the

hypothesizing of gene function, repeats, basic statistic, homologous sequence search and many more add on details are mostly computed computationally. The online tools of bioinformatics plays a crucial role in the annotation of sequences. In the present work, we have tried to add some more meta data to the isolated and sequenced stretch of a novel 16s rRNA sequence. The most similar homologue was identified, the AT and GC content was calculated, the restriction sites of most important restriction enzymes and chemicals were identified, along with the phylogenetic studies of the similar sequences. The computational or in silico approaches that has been highlighted in this paper for annotating 16s rRNA sequence apprehends the efficacy of various tools of bioinformatics. These tools are pre-requisite in predicting genes, homologues and ancestors thereby facilitating experimental analysis of nucleic acid sequences and can be explored and utilized further so that it can be beneficial for therapeutic purposes.

REFERENCES

- Bairoch, A., Gasteiger, E., Gattiker, A., Hoogland, C. and Lachaize, C. et al., 2003. The ExPASy proteome WWW server.
- Benson, D.A., Boguski, M., Lipman, D.J. and Ostell, J. 1996. GenBank. *Nucleic Acids Res.* 24 : 1-5.
- Bhardwaj, V. and Garg, N. 2012. Importance of Exploration of Microbial Biodiversity. *ISCA J. Biol. Sci.* 1 (3): 78 - 83.
- Gasteiger, E., Gattiker, A., Hoogland, C., Ivanyi, I., Appel, R.D. and Bairoch, V., 2003. ExPASy: the proteomics server for in-depth protein knowledge and analysis. *Nucleic Acids Res.* 31 (13): 3784-3788.
- Lecomte, J., St-Arnaud, M. and Hijri, M. 2011. Isolation and identification of soil bacteria growing at the expense of arbuscular mycorrhizal fungi. *FEMS Microbiol. Lett.* 317 (1): 43 -51.
- P Johri, P., Trivedi, M., Singh, A. and Siddiqui, M.H., 2016. Towards the atomic level protein sequence analysis. *J. Chem. Pharm. Res.* 8 (5): 204-207.
- Sachan, S., Chandra, V.Y., Yadu, A. and Singh, A., 2017. Cobalt has Enhancing Effect on Extracellular Lipases Isolated from *Pseudomonas aeruginosa* JCM5962(T). *Int. J. PharmTech Res.* 10 (1): 45 -49.
- Sachan, S., Johri, P., Trivedi, M., Singh, A. and Siddiqui, M.H., 2016. Study of carbon distribution at glycosylation sites in *Arabidopsis thaliana*. *J. Chem. Pharm. Res.* 8 (6): 77-83.
- Stefanis, C., Alexopoulos, A., Voidarou, C., Vavias S. and Bezirtzoglou, E. 2013. Principal methods for isolation and identification of soil microbial communities. *Folia Microbiologica.* 58 (1): 6 -68.
- Wheeler, D.L., Barrett, T., Benson, D.A., Stephen, H. and Canese, K. et al., 2007. Database resources of the National Center for Biotechnology Information. *Nucleic Acids Res.* 36: 13-21.



Selection of suitable mother wavelet along with vanishing moment for the effective detection of crack in a beam

Ramnivas Kumar, Ravi Nigam, Sachin K Singh^{*}

Department of Mechanical Engineering, Indian Institute of Technology (ISM) Dhanbad, Dhanbad, Jharkhand 826004, India

ARTICLE INFO

Communicated by Jerome Antoni

Keywords:

Crack detection
Measurement resolution
Wavelet selection
Vanishing moments

ABSTRACT

Presence of crack in a beam causes a slope discontinuity at the crack location in the operational deflection shape (ODS). Detecting the slope discontinuity in ODS can reveal the presence of crack in a beam. Wavelet transform is a powerful technique to detect discontinuity in a signal. Efficient detection of the crack using wavelet transform depends primarily upon the wavelet family and the number of vanishing moments. In the present work, suitable mother wavelet along with optimum number of vanishing moment is obtained for the effective detection of crack in a beam. *Crack detectability* is defined to quantify the effectiveness of different mother wavelet and vanishing moments. Finite element analysis is used for getting the simulated ODS. Higher resolution measurement of ODS is the requisite for effective wavelet based crack detection. Photographic method is used for obtaining the high resolution measurement of ODS for the experimental verification. The present methodology works well with the experimentally obtained ODS of the cracked beam. It is capable of detecting crack near the end support also.

1. Introduction

A beam is a critical part of rotating machinery. Fluctuating load, along with stress concentration, causes crack in a beam. Presence of a crack in a beam increases the flexibility of the beam near the crack. This ultimately changes the dynamic response of the beam. This change in dynamic response is widely used for crack detection. A detailed review of vibration based crack detection technique was presented by Dimarogonas [1], Sekhar [2], and Sabnavis et al [3].

A great number of research works have been done towards the development of crack models. Adams et al. [4] modeled a cracked bar by a linear spring of infinitesimally small length and obtained a relation between the crack depth and the change in natural frequency. Dimarogonas and Massouros [5] modeled a continuous rotor with a circumferential crack. They used the strain energy release rate function to calculate the flexibility at the vicinity of a crack. Chasalevris and Papadopoulos [6] computed the flexibility matrix of a shaft due to crack. The flexibility matrix was expressed as a function of depth and the rotation angle of the crack. *B-spline* curve fitting was used to interpolate the flexibility coefficients at all the rotational angles from the known values of flexibility coefficients.

The appearance of a crack in a beam lowers the natural frequency of the system. Several researchers have utilized this concept to identify the crack in a beam [7–9]. Although the change in natural frequencies are easy to determine with high degree of accuracy, the

^{*} Corresponding author.

E-mail addresses: ramnivas.18dr0111@mech.iitism.ac.in (R. Kumar), ravinigam.16dr000281@mech.ism.ac.in (R. Nigam), sachinks@iitism.ac.in (S.K. Singh).

natural frequency of a system may change due to several other reasons, such as, environmental degradation and wear. Several researchers have used the mode shape for the detection of crack in beams [10–14]. Mode shapes are spatial domain signals. Existence of a crack in the beam causes slope discontinuity in the mode shape. Detection of the slope discontinuity reveals the presence of crack in the beam. Pandey et al. [15] used the curvature mode shape concept to detect the crack in a cantilever beam. Operating deflection shape (ODS) is the deflection of a structure at a particular excitation frequency [16]. ODSs depend on the forces or loads applied to a structure. Singh and Tiwari [17] used ODSs at several excitation frequencies for the detection of crack in a shaft system. They proposed *crack probability functions* as an indicator of the crack in a shaft system.

Some recent methods proposed in the literature use wavelet transform for the detection of crack in a beam [18–21]. The wavelet transform is a powerful tool to detect the subtle changes in a signal. A detailed review of wavelet-based crack detection technique was presented by Peng and Chu [22]. An important property of a wavelet, which affects its ability to detect the subtle changes present in a signal is the number of vanishing moments [23]. Wavelet transform of a signal with n vanishing moment is equivalent to n^{th} order derivative of the signal with a smoothing function [24]. Loutridis et al. [25] used continuous wavelet transform (CWT) with Symlet mother wavelet of fourth order to detect the crack position. They also used an intensity factor by using Hoelder exponent to relate the size of the crack to the coefficients of the wavelet transform. Rucka and Wilde [13] used CWT with Gaussian and Coiflet wavelets with four vanishing moments to detect the crack position in cantilever beams. Hong et al. [26] used CWT with Mexican hat wavelet and found that the minimum number of vanishing moments to extract the crack position in a beam should be two. Douka et al. [27] suggest that the wavelet with higher vanishing moments gives a more stable performance. However, wavelets with a large number of vanishing moments have higher support length that may result in poor crack localization [28]. So an optimum value of vanishing moment must be determined in order to develop the robust wavelet based crack detection algorithm. In the present work, a suitable mother wavelet along with the number of vanishing moments is found out by defining *crack detectability*. Different wavelet families along with their vanishing moments are studied and a suitable wavelet is selected to detect the location of crack along a beam.

Although many works have been reported on the use of wavelet transform for the detection of crack in a beam, crack detection near the end support is still a challenge [29]. In wavelet based techniques, the abrupt change in wavelet coefficients near the end of the signal, termed as end effect, restricts the detection of crack near the end supports. Although some simulation works have been reported to reduce the end effect [30,31], Mardasi et al. [29] made an experimental study to detect a crack in a beam using wavelet analysis. They used the triangular and Hanning windows on the raw data to reduce the end effects of CWT. The algorithm applies CWT repetitively to detect the crack. A scanning laser vibrometer with 25 mm scanning range was used for a beam of length 750 mm. Hence, the entire length of a beam cannot be covered in a single measurement. Also, the crack near the end supports of the beam was not considered. The scanning laser vibrometer was positioned in such a way that the crack was located near the end of the vibrometer's scanning range. In the present work, a photographic method is used to get the experimental ODS and the proposed algorithm is able to detect crack near the end support also.

Considering experimental measurement of ODS of a beam, the measurement resolution is the number of data points per unit length of the beam. Detection and accurate localization of a crack using wavelet transform depend upon the measurement resolution of the ODS. The measurement resolution of mode shape is a crucial aspect in vibration based damage detection methods [32]. Some researchers have made an extensive study based on simulated ODSs. Zhong and Oyadiji [33] studied the effect of sampling interval to detect the location of crack by using wavelet transform. Lorenzo et al. [34] made an extensive study to assess the optimum number of sampling interval to identify the location of crack by using CWT. Traditional sensors such as accelerometer and impedance head are used to obtain the deflection shape [35,36]. Getting high measurement resolution with traditional sensors is a tedious task. High measurement resolution can be obtained by using a scanning laser vibrometer [37], however it is costly. In the present work photographic method is used to get the high resolution measurement of ODS for the experimental verification. Initially, simulated ODSs are obtained by the finite element method (FEM) to study the effect of noise on *crack detectability* for different wavelet families. The mathematical model for getting the simulated responses is presented in the next section.

2. Mathematical model of the cracked beam element

The Timoshenko beam theory is used to generate the cracked beam response. The finite element method is used to discretize the beam, as shown in Fig. 1. The elemental mass and stiffness matrices for the Timoshenko beam model are taken from the reference [38]. A local flexibility matrix is used to model the transverse crack in the beam. A cracked element with 4 degrees of freedom at each node

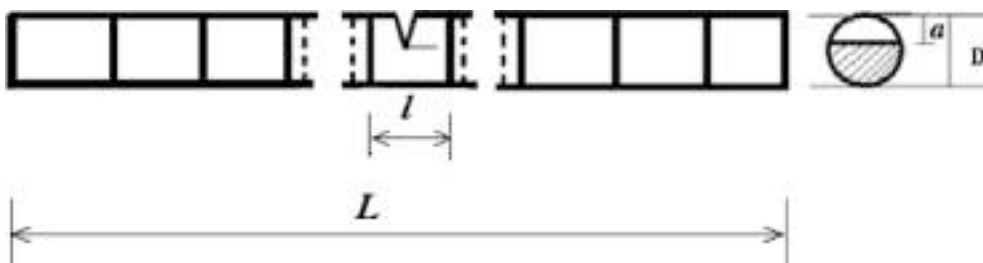


Fig. 1. Finite element discretization of a cracked beam of crack depth a .

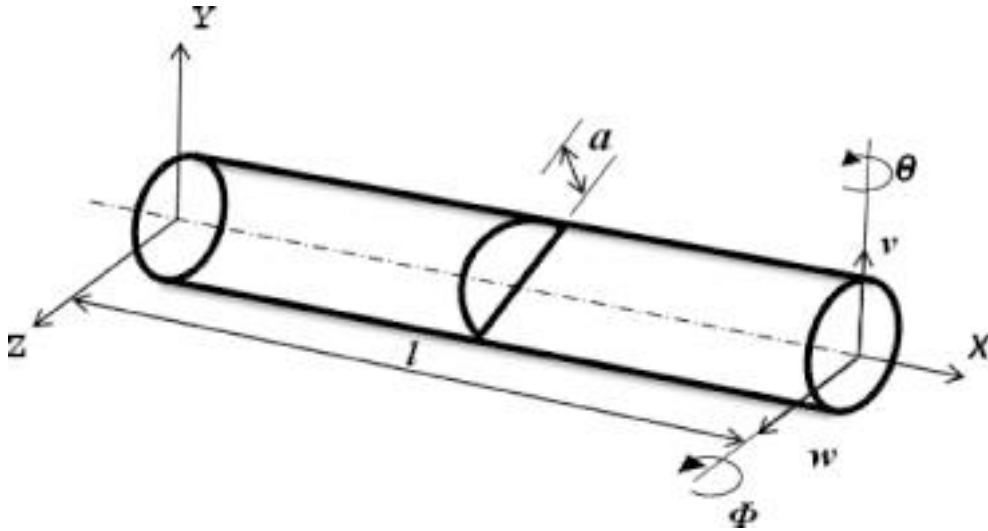


Fig. 2. A finite element with a crack.

and element length of l is shown in Fig. 2.

The elemental equations of motion for the intact and cracked elements are:

$$[M]^e \{\ddot{q}\}^e + [D_{wc}]^e \{\dot{q}\}^e + [K_{wc}]^e \{q\}^e = \{F\}^e \tag{1}$$

and

$$[M]^e \{\ddot{q}\}^e + [D_c]^e \{\dot{q}\}^e + [K_c]^e \{q\}^e = \{F\}^e \tag{2}$$

where, $[M]^e$, $[D]^e$, and $[K]^e$ are the elemental mass, damping, and stiffness matrices, respectively; and vectors $\{F\}^e$ and $\{q\}^e$ are the elemental force and response vectors, respectively. The subscripts 'c' and 'wc' are used for cracked and intact elements, respectively. The displacement vector at each node is given as

$$\{q\}^e = [v \ w \ \theta \ \phi]^T \tag{3}$$

Here, v and w are the translational degrees of freedom along the y and z-axis, respectively. θ and ϕ are the rotational degrees of freedom about the y and z-axis, respectively. Axial and torsional motions are not considered. Proportional damping is considered. The damping matrix of a beam element without crack can be written as [39]

$$[D]_{wc} = a_0[M]^e + a_1[K_{wc}]^e \tag{4}$$

and the damping matrix for a cracked element is given by,

$$[D]_c = a_0[M]^e + a_1[K_c]^e \tag{5}$$

Here, a_0 and a_1 are the Rayleigh damping constants. These constants depend upon the first two natural frequencies of the system [39]. The additional flexibility due to a crack is given by [40],

$$[C_C]^e = \begin{bmatrix} C_{22} & 0 & 0 & 0 \\ 0 & C_{33} & 0 & 0 \\ 0 & 0 & C_{44} & C_{45} \\ 0 & 0 & C_{54} & C_{55} \end{bmatrix} \tag{6}$$

Here the coefficients C_{ij} quantify the additional flexibility due to a crack, and its value depends upon the size of the crack. Total flexibility for a cracked element is given by [40]

Table 1
Parameters for cracked beam simulation.

Parameters	Values for simulation
Radius of the beam (R)	0.005 m
Crack depth ratio (a/R)	0.7
Length of the beam (L)	1 m
Modulus of elasticity (E)	$2.06 \times 10^{11} \text{ N/m}^2$
Number of finite element (N)	500
Location of cracked element	162 from the left end
Excitation frequency (ω)	10 rad/s.
Location of excitation	20 cm from the left end
Amplitude of excitation	$0.0024\omega^2$

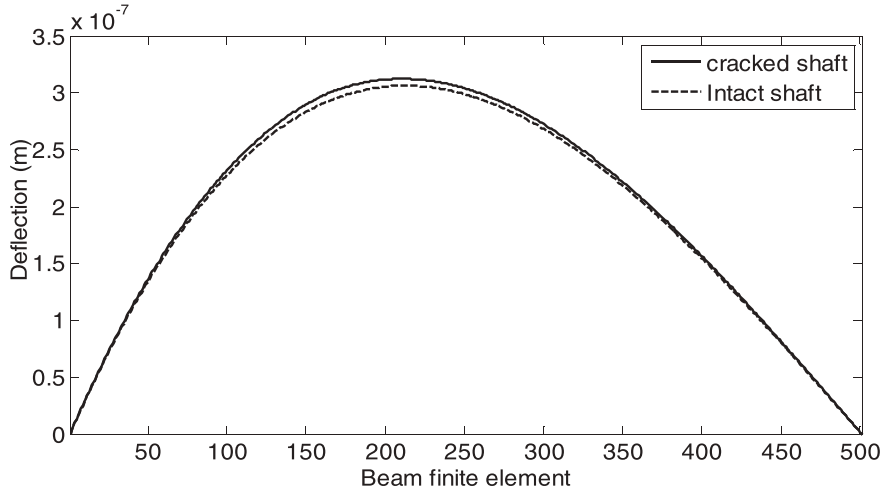


Fig. 3. ODS at excitation frequency of 10 rad/s.

$$[C] = [C_0] + [C_c] \quad (7)$$

Here, $[C_0]$ is the flexibility matrix of an element without crack and $[C_c]$ is the additional flexibility due to the crack. Stiffness of the cracked element is obtained as [41]

$$[K]^e = [T][C]^{-1}[T]^T \quad (8)$$

where $[T]$ is the transformation matrix, given by [41]

$$[T]^T = \begin{bmatrix} -1 & 0 & 0 & -l & 1 & 0 & 0 & 0 \\ 0 & -1 & l & 0 & 0 & 1 & 0 & 0 \\ 0 & 0 & -1 & 0 & 0 & 0 & 1 & 0 \\ 0 & 0 & 0 & -1 & 0 & 0 & 0 & 1 \end{bmatrix} \quad (9)$$

The elemental matrices are combined to get the global matrix. The finite element codes are written in Matlab. The ODS is generated for simply supported conditions and for a harmonic excitation in the vertical direction. The beam parameters used for generating the simulated cracked beam ODS are given in Table 1.

The cracked and uncracked beam ODSs are shown in Fig. 3. The presence of a crack in a beam changes the dynamics of the beam as a whole, but locally it causes a discontinuity in the ODS at the crack location. However, the slope discontinuity is not observed directly from the ODS (Fig. 3). In the present work, a wavelet based algorithm is presented to detect the slope discontinuity in the ODS.

In a real situation, the ODS of the system will be affected by some measurement noise. Hence, measurement noise is added to the simulated ODS for the development of a noise-robust crack detection algorithm.

3. Detection of crack using wavelet transform

3.1. Addition of noise

The presence of measurement noise suppresses the crack information present in the ODS of the beam. This makes the crack detection intricate, as dummy singularities are introduced due to noise. Hence, white Gaussian noise is added to the simulated ODS to see the effect of measurement noise. Signal to noise ratio (SNR) is considered to quantify the measurement noise as, $SNR = 20 \log_{10} \left(\frac{\sigma_s}{\sigma_n} \right)$. Here σ_s is the standard deviation of the signal and σ_n is the standard deviation of the noise. Noise is added by using the Gaussian random number generator. The noisy ODS, $f(\omega)$, at an excitation frequency, ω , is given by

$$f(\omega) = q(\omega) + n \tag{10}$$

Here, $q(\omega)$ is the ODS at excitation frequency ω , and n is the measurement noise.

Wavelets are good at detecting slope discontinuity in a noisy signal. In the present work, the discrete wavelet transform (DWT) is used to detect the crack location along the beam length. Wavelet transform is discussed briefly in the subsequent section.

3.2. Wavelet transform

A function $\psi(x)$ is said to be a wavelet if its Fourier transform $\Psi(\omega)$ fulfills the wavelet acceptability condition [23]

$$\int_{-\infty}^{+\infty} \frac{|\Psi(\omega)|^2}{\omega} d\omega < +\infty \tag{11}$$

This condition suggests that the average value of the wavelet must be zero, i.e., area underneath the curve must be zero

$$\int_{-\infty}^{+\infty} \psi(x) dx = 0 \tag{12}$$

and that the Fourier transform of wavelet function at $\omega = 0$ must be zero, i.e.,

$$\Psi(0) = 0 \tag{13}$$

The CWT of a signal can be expressed as:

$$W_{u,s}(x) = \frac{1}{\sqrt{s}} \int_{-\infty}^{+\infty} f(x) \psi\left(\frac{x-u}{s}\right) dx \tag{14}$$

where, $f(x)$ is the input signal and $\frac{1}{\sqrt{s}} \Psi\left(\frac{x-u}{s}\right)$ is translated and scaled version of the mother wavelet $\Psi(x)$. Here, u is the translation parameter, s is the scale parameter and the variable x is the location along the spatial domain. The translation is the shifting of the wavelet along the span, and scaling is the stretching of the wavelet. If scaling is selected as a power of two, the wavelet transform is called the dyadic orthonormal wavelet transform. The dyadic orthonormal wavelets offer the formation of DWT [23]. The DWT gives a

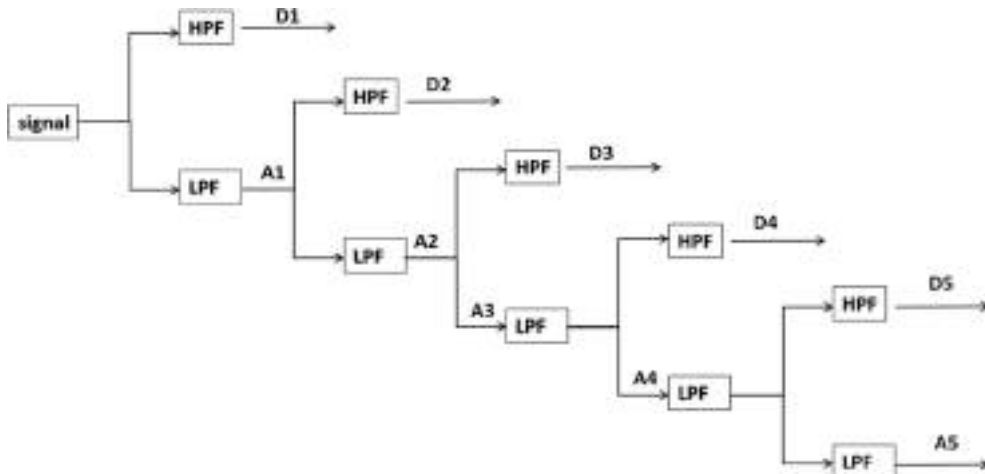


Fig. 4. The discrete wavelet transform as a multilevel filter bank.

Table 2
Characteristics of selected wavelet having multilevel decomposition properties.

Wavelet family name	Order	No of vanishing moments	Support width
Daubechies N (dbN)	$N = 1, 2, 3, \dots$	N	$2N - 1$
Symlet N (symN)	$N = 1, 2, 3, \dots$	N	$2N - 1$
Coiflet N (coifN)	$N = 1, 2, 3, 4, 5$	$2N$	$6N - 1$
Biorthogonal N_r, N_d (bior N_r, N_d)	$N_r = 1, N_d = 1, 3, 5$		
	$N_r = 2, N_d = 2, 4, 6, 8$		
	$N_r = 3, N_d = 1, 3, 5, 7, 9$	$N_r - 1$	$2N_d + 1$
	$N_r = 4, N_d = 4$		
	$N_r = 5, N_d = 5$		
	$N_r = 6, N_d = 8$		
Reverse Biorthogonal N_d, N_r (rbio N_d, N_r)	$N_d = 1, N_r = 1, 3, 5$		
	$N_d = 2, N_r = 2, 4, 6, 8$		
	$N_d = 3, N_r = 1, 3, 5, 7, 9$		
	$N_d = 4, N_r = 4$	$N_d - 1$	$2N_r + 1$
	$N_d = 5, N_r = 5$		
	$N_d = 6, N_r = 8$		

multilevel decomposition of the signal. The first level of decomposition is equivalent to scaling at scale 2, the second level of decomposition means scaling at scale 4, and so on. The *Approximate* coefficients $A1, A2, A3, \dots$ and the *detailed* coefficients $D1, D2, D3, \dots$ are obtained at each level of decomposition. This decomposition is equivalent to low-pass and high-pass filtering of the signal [23]. A low-pass filter (LPF) allows the passes of signals with a frequency lower than the cutoff frequency and attenuates signals with frequencies higher than the cutoff frequency. On the other hand, a high-pass filter (HPF) allows the passes of signals with a frequency higher than the cutoff frequency and attenuates signals with frequencies lower than the cutoff frequencies. Fig. 4 shows the multilevel decomposition of a signal using DWT.

Crack in a beam causes a local slope discontinuity in the operational deflection shape (ODS) of the beam. The local slope discontinuity can't be observed directly due to measurement noise in the signal. Discrete wavelet transform has an excellent property to detect a discontinuity in a noisy signal. There are various mother wavelets designed for different purposes. The most common mother wavelets providing the multilevel decomposition properties are Daubechies, Symlets, Coiflets, biorthogonal, reverse biorthogonal and discrete Meyer. Out of all the aforesaid mother wavelets, a suitable mother wavelet needs to be selected for efficient detection of the crack from the ODS. Apart from the suitable mother wavelet, the number of vanishing moments plays an important role in efficient crack detection. A wavelet has n vanishing moments if it possesses the following [23]:

$$\int_{-\infty}^{+\infty} x^n \Psi(x) dx = 0, \quad n = 0, 1, 2, \dots, n - 1 \tag{15}$$

Hence, a wavelet with n vanishing moments is orthogonal to polynomials up to degree $n-1$. The relation among the number of vanishing moments, order and support width for different wavelet families are presented in Table 2. In the case of biorthogonal wavelets, N_r is the order of reconstruction filter, and N_d is the order of the decomposition filter. The support width of the mother wavelet is inversely proportional to the localization of discontinuity. Wavelet with higher vanishing moments gives a more stable performance. However, larger support width leads to poor localization. The effect of vanishing moments on *crack detectability* is discussed in the following section.

4. Results and discussion

The capability of wavelet transform to detect a local discontinuity in a signal depends on certain parameters like measurement resolution, wavelet decomposition level, type of mother wavelets, and the number of vanishing moments. For ODS, measurement resolution is the number of data points per unit length of the beam. Selection of these parameters is discussed in the subsequent sections.

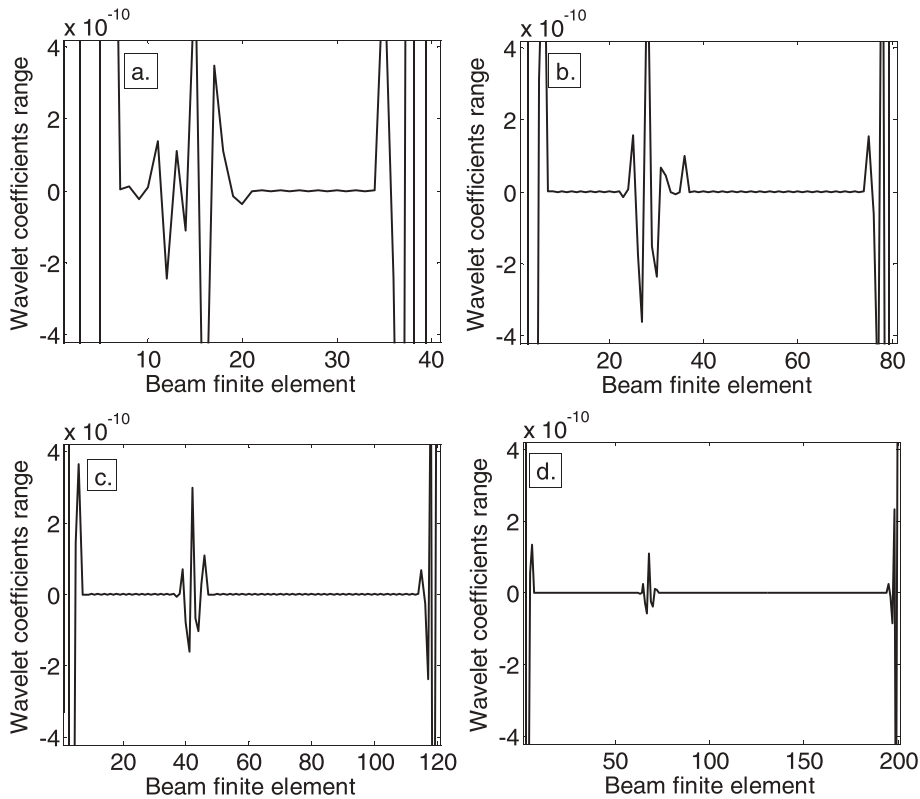


Fig. 5. D1 coefficients at different levels of measurement resolution.

4.1. Measurement resolution for the ODS

A one meter long simply supported beam is considered for simulated response using FEM. The crack depth ratio is the ratio of crack depth to the radius of the beam. A single crack of crack depth ratio 0.7 is considered at 1/3rd distance from the left support. ODS is obtained at 10 rad/s. The number of datapoints along the beam length is varied to study the effect of measurement resolution on the crack detectability. Hence, ODS is obtained using 40, 80, 120, and 200 finite elements. Responses at finite element nodes are considered to be the measurement data for the ODS. The ODS with different data points is taken as the input signal for the wavelet transform. The D1 coefficients are plotted in Fig. 5. A spike is obtained at the location of the crack in the beam. However, the spike gets localized with an increase in measurement resolution. Hence for all the subsequent numerical simulations, the beam is discretized into 500 finite elements to get good localisation.

Localization of discontinuity in the detailed coefficients depends upon the level of decomposition also. Wavelet coefficients up to the sixth level of decomposition are shown in Fig. 6. A very clear and localized spike due to crack is observed in the first level of decomposition and the localization degrades with the increase in the level of decompositions. Basically, the high frequency components modeling the discontinuity are filtered out at the initial level of decomposition. The selection of suitable mother wavelet with the number of vanishing moments is discussed in the subsequent section.

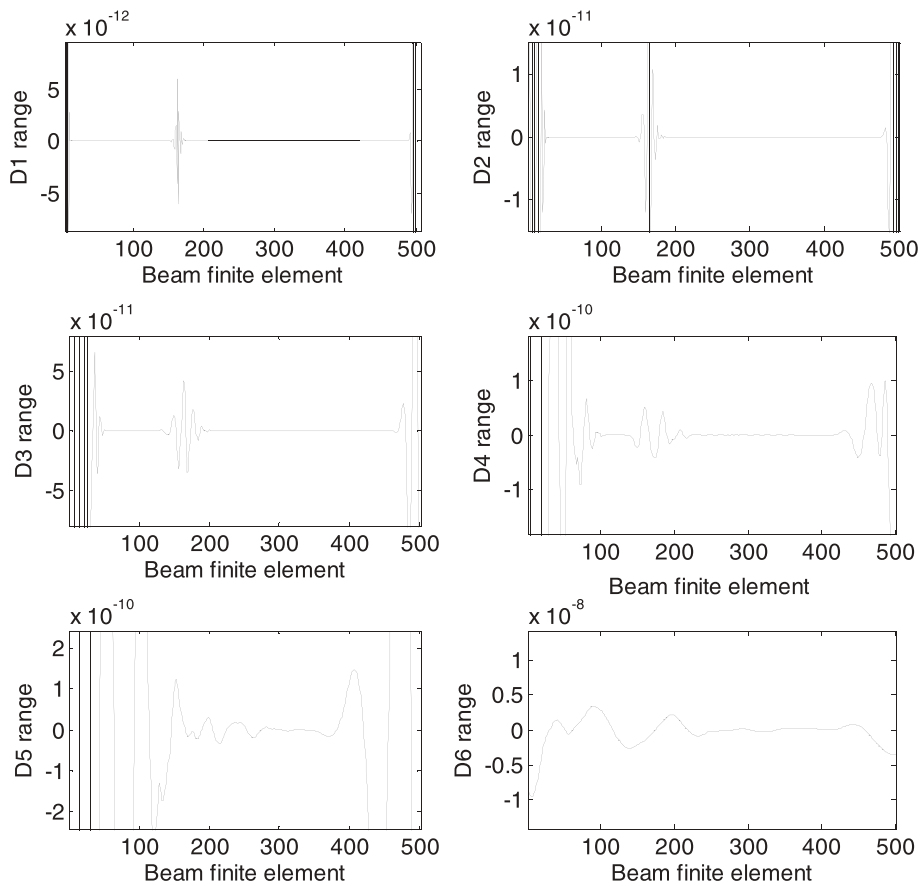


Fig. 6. Wavelet coefficients of ODS at 10 rad/s.

4.2. Selection of suitable mother wavelet

Efficient detection of a crack from the measured ODS depends upon the selected mother wavelet. For selecting the suitable mother wavelet, “crack detectability” is introduced as,

$$Crack\ detectability = Amplitude\ of\ spikes\ due\ to\ crack - Maximum\ amplitude\ of\ spikes\ due\ to\ noise \tag{16}$$

The *amplitude of spikes due to crack* is the maximum value of detailed coefficients near the known crack location. The *maximum amplitude of spikes due to noise* is the maximum value of detailed coefficients in the non-crack region. This definition is used for the purpose of selecting the suitable mother wavelet along with vanishing moments for efficient crack detection. Hence, the crack position

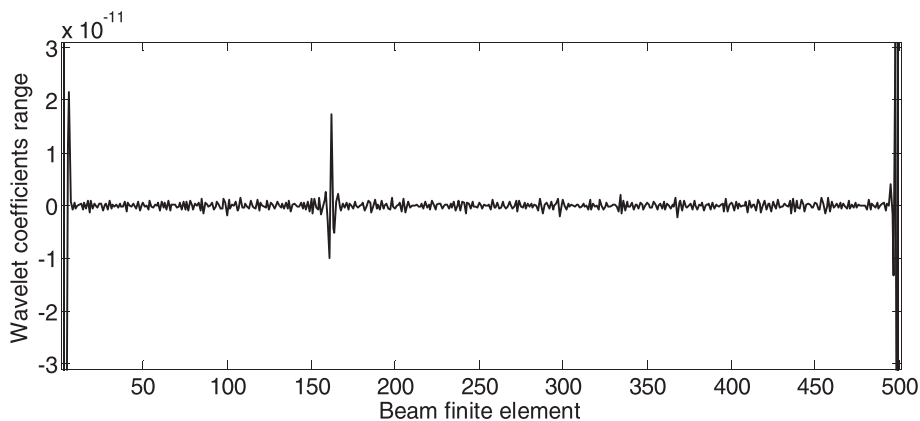


Fig. 7. D1 wavelet coefficients of an ODS of a cracked beam.

is assumed to be known. The wavelet transform is the convolution between the signal and the dilated and translated wavelets. The beam deflection is a spatially distributed signal with finite length. For a finite-length signal, the convolution between the signal and wavelets gives an end effect at the two ends of the signal, as shown in Fig. 7. Hence the decomposed signal near the two ends is neglected while calculating 'crack detectability'.

Change in crack detectability with the order of different mother wavelets is studied. Crack detectability for different mother wavelets are plotted in Fig. 8. Three noise conditions are taken to observe the trend. As expected, crack detectability reduces with an increase in noise level. For a particular mother wavelet, the crack detectability depends on the number of vanishing moments. The slope discontinuity in an ODS is composed of higher order polynomial, whereas, remaining parts of ODS are composed of a lower order polynomial. A wavelet of n^{th} order vanishing moment annihilates n^{th} order signal [23]. Hence wavelet with low number of vanishing moment annihilates polynomial of low order. For detecting the slope discontinuity, the wavelet should annihilate the parts of ODS without crack. This will give importance to the higher order polynomial induced by the crack. Hence, initially increasing the number of vanishing moment increases the crack detectability by gradually giving more importance to the higher order polynomials at the crack location. However, wavelets with higher vanishing moments have longer support width and less spatial resolution [29]. This leads to decrease in crack detectability with an increase in the number of vanishing moments. The two opposing trends give the first maxima in the plots of Fig. 8. From Fig. 8, it is observed that the crack detectability increases with the number of vanishing moments up to a certain value (optimum value), then it starts decreasing. In the case of Coiflet wavelet the crack detectability decreases monotonically because of its wider span.

By tracing the maxima in each of the plots, it can be observed that db3, sym4, coif1, bior2.4, and rbio2.2 are giving good results in their respective families. However, among these wavelets, the highest crack detectability is observed for the case of reverse biorthogonal wavelet of order 2.2, i.e., rbio2.2, as shown in Fig. 8(f). Hence, the rbio2.2 mother wavelet is chosen for further study.

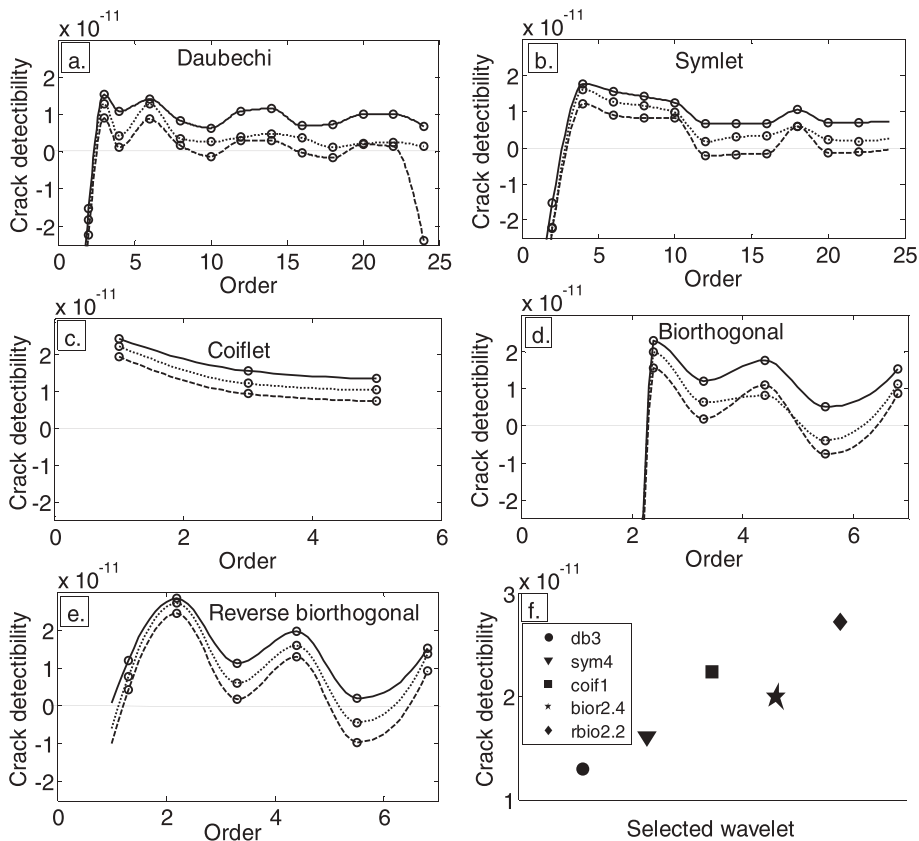


Fig. 8. Variation of crack detectability with vanishing moment, No noise; ... 90 SNR; — 85 SNR.

4.3. Detection of crack location

Crack detection using rbio2.2 wavelet is tested with three numerical simulations. Parameters for numerical simulations are given in Table 3. From simulations, the first and second natural frequencies of the beam are 125 rad/s and 500 rad/s, respectively. For Simulation I and II, the excitation at 10 rad/s is considered. In these cases the ODS is dominated by the first mode. Whereas for simulations III and IV, the excitation frequency of 480 rad/s is considered. In these cases, the ODSs are dominated by the second mode.

Table 3
Parameters for numerical simulations.

Parameters	Simulation I	Simulation II	Simulation III	Simulation IV	Simulation V
Number of finite element	500	500	500	500	500
Crack depth ratio (a/r)	0.7	0.7	0.7	0.7	0.7
Excitation (rad/s)	10	10	480	480	10
Crack location	0.32	0.066	0.32	0.5	0.066 & 0.58

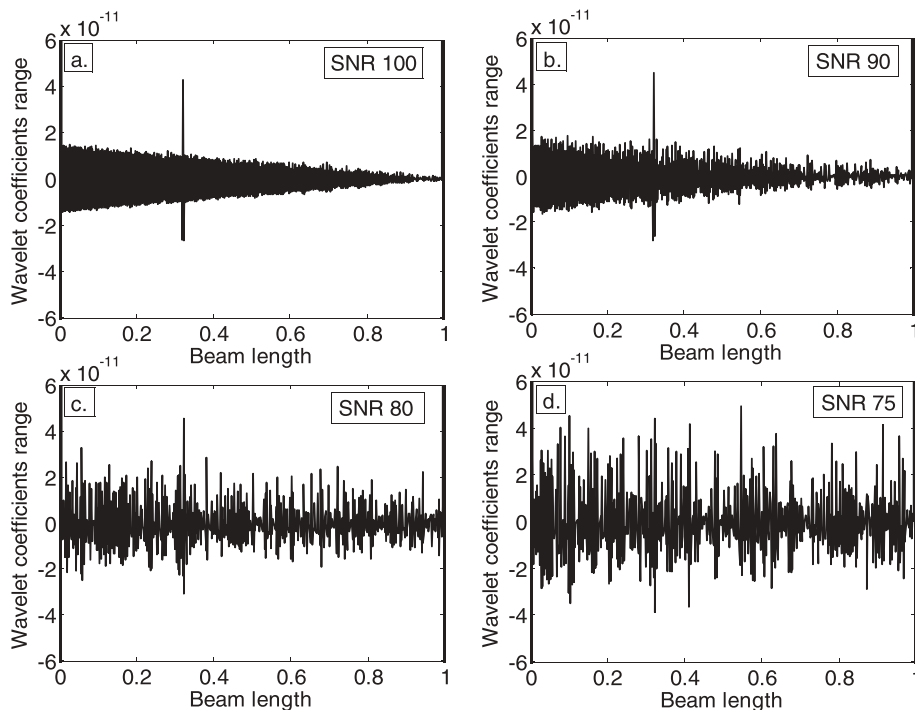


Fig. 9. DWT of ODS at excitation frequency of 10 rad/s and a crack at 0.32 m from left end support.

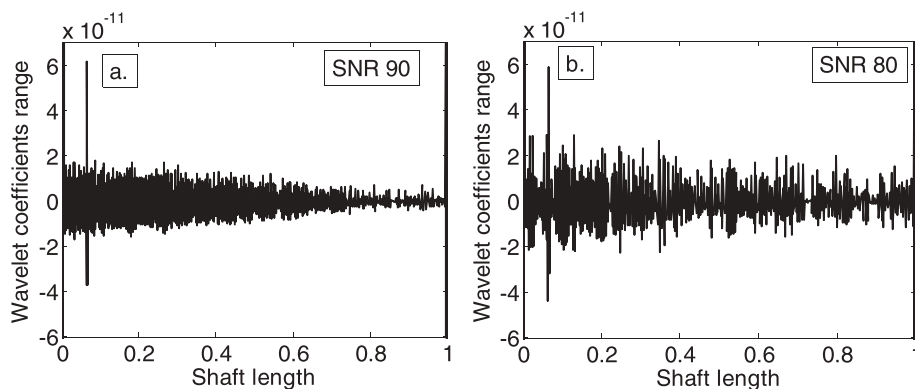


Fig. 10. DWT of ODS at excitation frequency of 10 rad/s and a crack at 0.066 m from left end support.

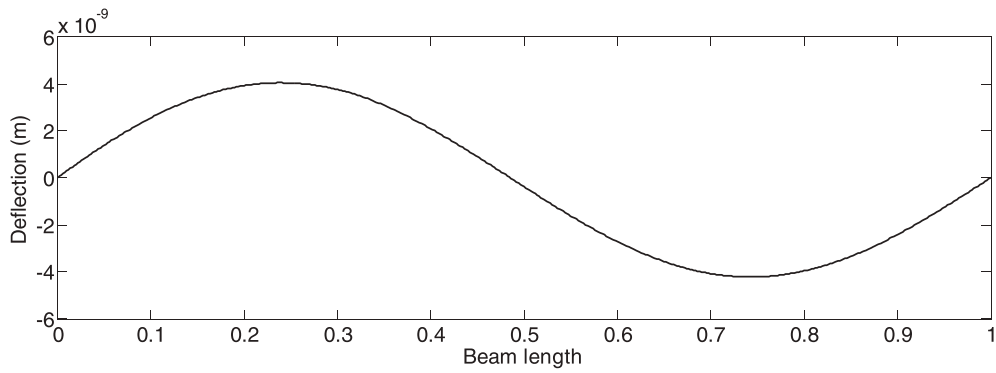


Fig. 11. ODS of the cracked beam at the excitation frequency of 480 rad/s.

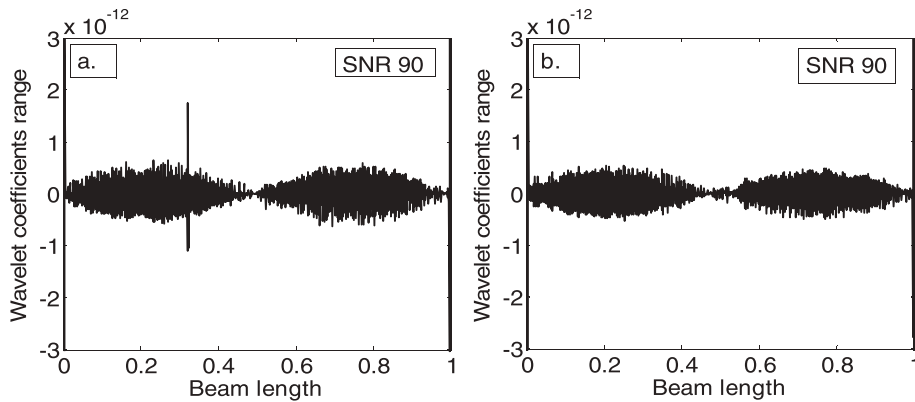


Fig. 12. DWT of ODS at 480 rad/s with different crack location from left end: (a) Crack at 0.32 m and (b) crack at 0.5 m.

500 datapoints are taken over a beam of length 1 m. For Simulation I, four different noise levels are considered to see the effect of measurement noise. The D1 coefficients at four different noise levels are shown in Fig. 9. Clear spikes at the crack locations are observed for the low noise cases. In simulation II the crack is taken very close to the edge of the beam. The D1 coefficients at SNR 90 and SNR 80 are plotted in Fig. 10(a) and (b), respectively. The ODS for simulation III is plotted in Fig. 11, and the D1 coefficient is plotted in Fig. 12(a). In simulation IV, the crack position is taken close to the node of the vibrating beam and no clear spike is seen in the D1 coefficient, as plotted in Fig. 12(b). The cracks nearby the nodes remain undetected due to negligible bending moment.

The algorithm is tested for multi-crack detection also. In simulation V, two cracks are located at 0.066 m and 0.58 m from the left end of the beam. The DWT coefficients are plotted in Fig. 13. Two spikes at the crack locations are seen at the 90 dB of noise level.

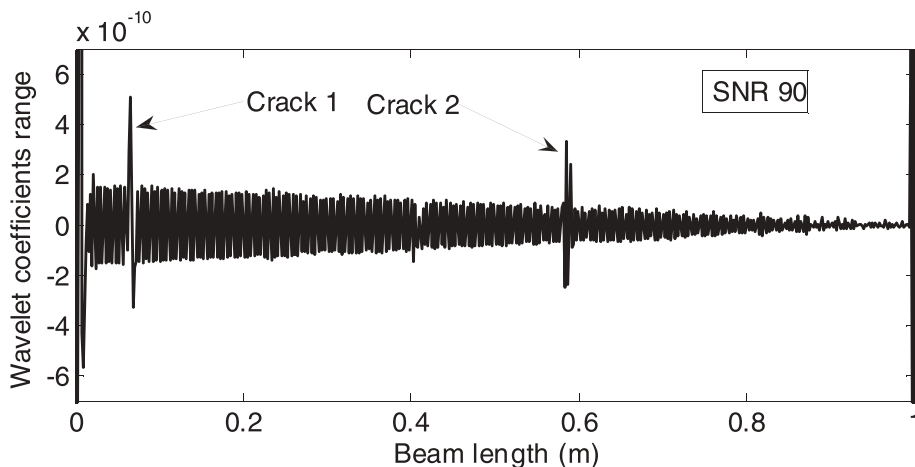


Fig. 13. DWT of ODS at 10 rad/s with two cracks, located at 0.066 m and 0.58 m from the left end.

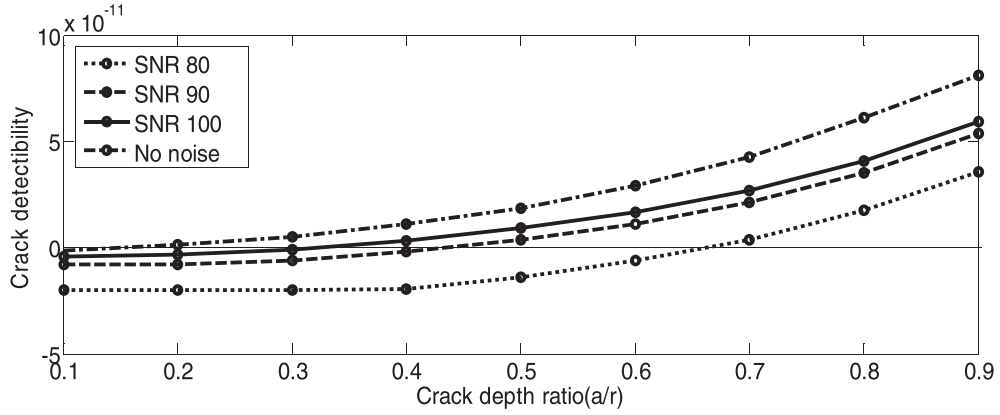


Fig. 14. Variation of crack detectability with crack depth (at 10 rad/s, crack position 0.32 m from left end).

For all the numerical simulations, the crack depth ratio is taken to be 0.7. The algorithm can be tested for lower crack depth ratio also. The variation of crack detectability with the crack depth ratio is shown in Fig. 14. From Fig. 14, it can be observed that the algorithm can detect smaller cracks with less measurement noise. However, in real applications, the SNR in a particular measurement is not known. Still, experiments can be performed in a particular set of conditions, and a similar plot from experimental data can be obtained.

5. Experimental validation

A cantilever beam of 1 m length with a rectangular cross-section (50 mm × 6 mm) is taken to see the variation of crack detectability with the number of vanishing moments. Four experimental cases are taken. The parameters for experimental setups are given in Table 4. The cracks are created by using a hacksaw blade. In experiment I, an open crack of depth 4 mm is created at a distance of 0.58 m from the fixed end. The experimental setup is shown in Fig. 15. The beam is excited freely by giving initial displacement at the free end. The images are captured by using a Digital camera (Make: NIKON, Model: D5100). The camera is positioned at a lateral distance of 2.5 m from the beam, and axially at the center of the beam. A black color screen is used in the background for getting a good contrast between the beam and the background. A tripod is used to adjust the camera height and to prevent the camera shaking. A proper setting of the camera is established to capture the deflected shape of the vibrating beam. The shutter speed, aperture, and ISO of the camera are set at 1/160, F 3.7, and 3200, respectively. The captured frames are saved as a JPG image and subsequently transformed into a binary image using the Matlab image processing toolbox. The transformed binary image is shown in Fig. 16(a). The Sobel operator is used to extract the edges from the binary image [42]. In the Sobel operator, the first order central finite difference scheme is used to calculate the intensity gradients in the x and y directions. This results in masks, M_x and M_y , for calculating the intensity gradients in the x and y directions, respectively. These masks are two dimensional convolution matrices containing positive and negative coefficients. The Sobel operator masks are given by [42]:

$$M_x = \begin{bmatrix} -1 & -2 & -1 \\ 0 & 0 & 0 \\ +1 & +2 & +1 \end{bmatrix}; M_y = \begin{bmatrix} -1 & 0 & +1 \\ -2 & 0 & +2 \\ -1 & 0 & +1 \end{bmatrix}$$

Convolving M_x and M_y with the binary image, $f(x,y)$, estimates the gradient in the x and y directions, respectively.

$$G_x = M_x * f(x, y) \tag{17}$$

$$G_y = M_y * f(x, y) \tag{18}$$

Here the asterisk denotes a convolution operation. The intensity gradient estimates the strength and direction of the edge. The gradient magnitude $|G|$ is defined as:

$$|G| = \sqrt{G_x^2 + G_y^2} \tag{19}$$

Table 4
Parameters for free vibration experiments.

	Experiment I	Experiment II	Experiment III	Experiment IV	Experiment V
Crack location	0.58 m	0.58 m	0.58 m	0.066 m	0.066 m & 0.58 m
Crack depth	4 mm	3 mm	2 mm	4 mm	3 mm

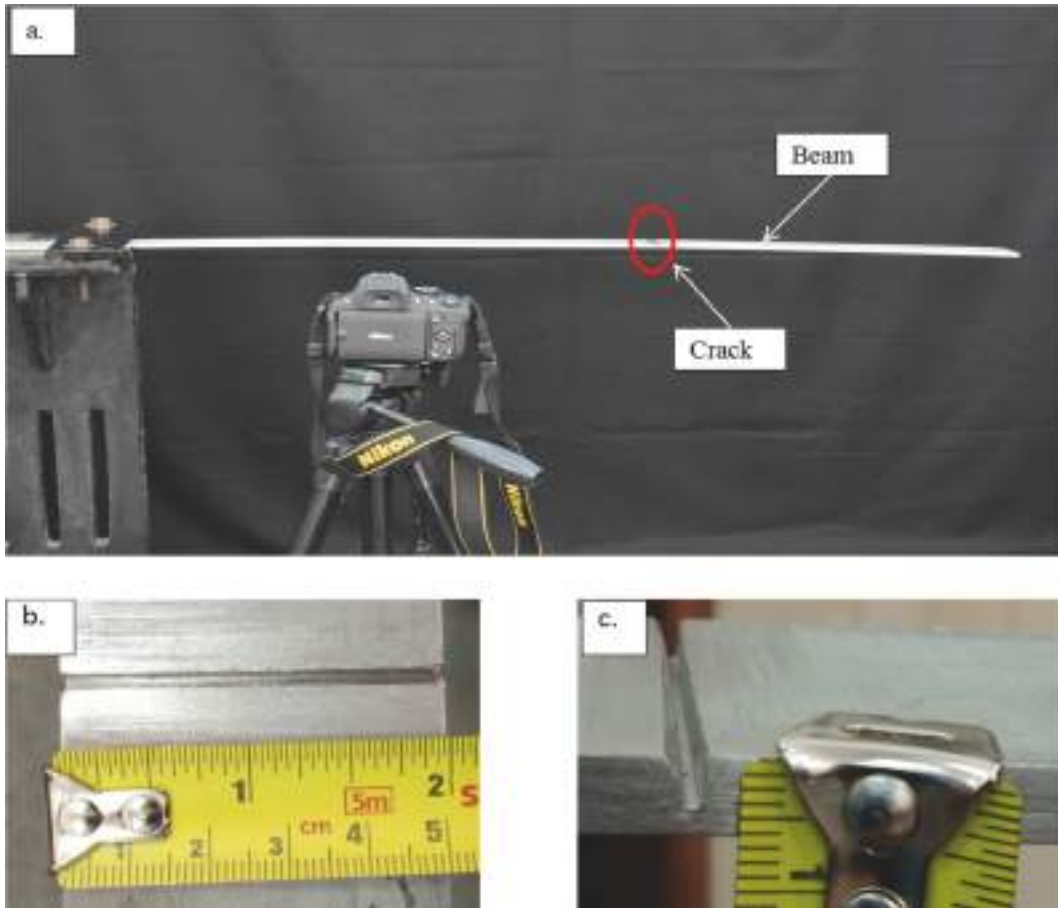


Fig. 15. Experimental setup for crack detection: (a) The beam with digital camera, (b) Length of crack, and (c) Depth of open crack.

The gradient direction is calculated as:

$$\alpha(x, y) = \tan^{-1} \left(\frac{G_y}{G_x} \right) \quad (20)$$

The magnitude and direction of the gradient is calculated at all the points of the image. The edge detection is made by thresholding the gradient of the image. The returned image after the application of the Sobel operator is called the edged image. The extracted edges from the binary image are shown in Fig. 16 (b). The deflected shape of the beam is obtained by detecting the un-cracked edge from the edged image. In the present work, the lower edge of the beam is the un-cracked edge. The first white pixel index from the bottom of the edged image gives the beam deflection shape, as shown in Fig. 17(a). A weighted regression is used to smooth the signal. The kernel used for giving weight at each data point is given as,

$$W_i = \left(1 - \left(\frac{x_i - x_{i-h}}{h} \right)^3 \right)^3, i = 1, 2, 3, \dots \quad (21)$$

Here, x_i is the i^{th} data point, W_i is the corresponding weight and h is the window size in the considered span. The DWT with rbio2.2 mother wavelet is applied on the smoothed signal of experiment I. The wavelet detailed coefficients are shown in Fig. 17(b). A clear spike is observed at the crack location.

For comparison purposes, the crack detection using the beam static deflection is presented. The static deformation of the beam with a crack at 0.58 m from the left support of the beam is obtained. The wavelet coefficients are plotted in Fig. 18. The wavelet coefficients from the static deflection do not give clear crack information.

For experiment 1, the variation of *crack detectability* with the order of wavelet is plotted in Fig. 19. The *crack detectability* increases up to an optimum order for the Daubechi, Symlet, biorthogonal and reverse biorthogonal wavelet. Overall trends in the plots are similar to those obtained with simulated ODSs (Fig. 8). Although oscillations have increased in some of the plots, the choice of a suitable mother wavelet along with vanishing moment depends only upon the maxima. The highest *crack detectability* for the studied mother wavelets is plotted in Fig. 19(f). Hence, the reverse biorthogonal wavelet of order 2.2 is the most suitable mother wavelet among the studied wavelets.

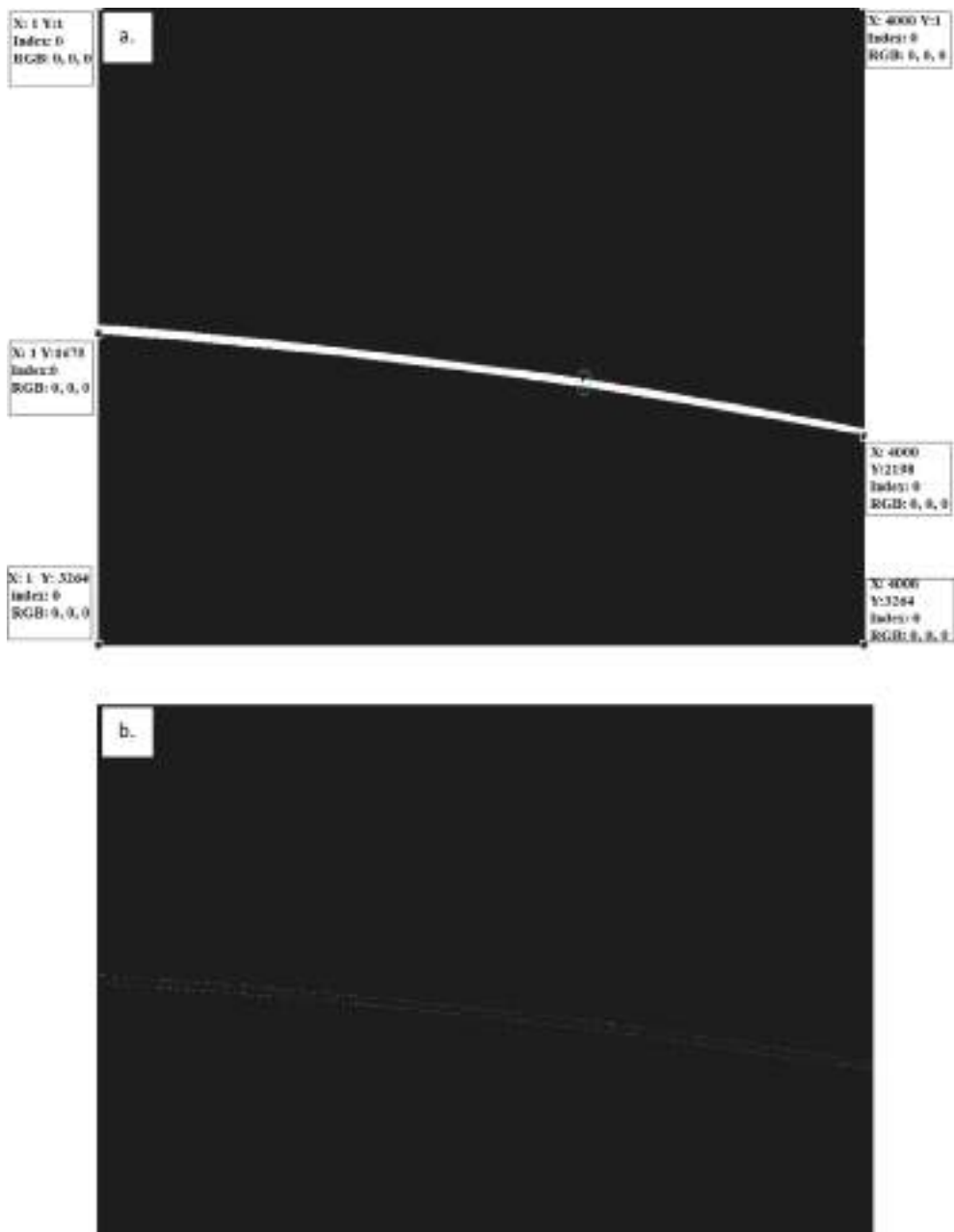


Fig. 16. Edge extraction from JPEG image: (a) Binary image, and (b) Extracted edges from the binary image.

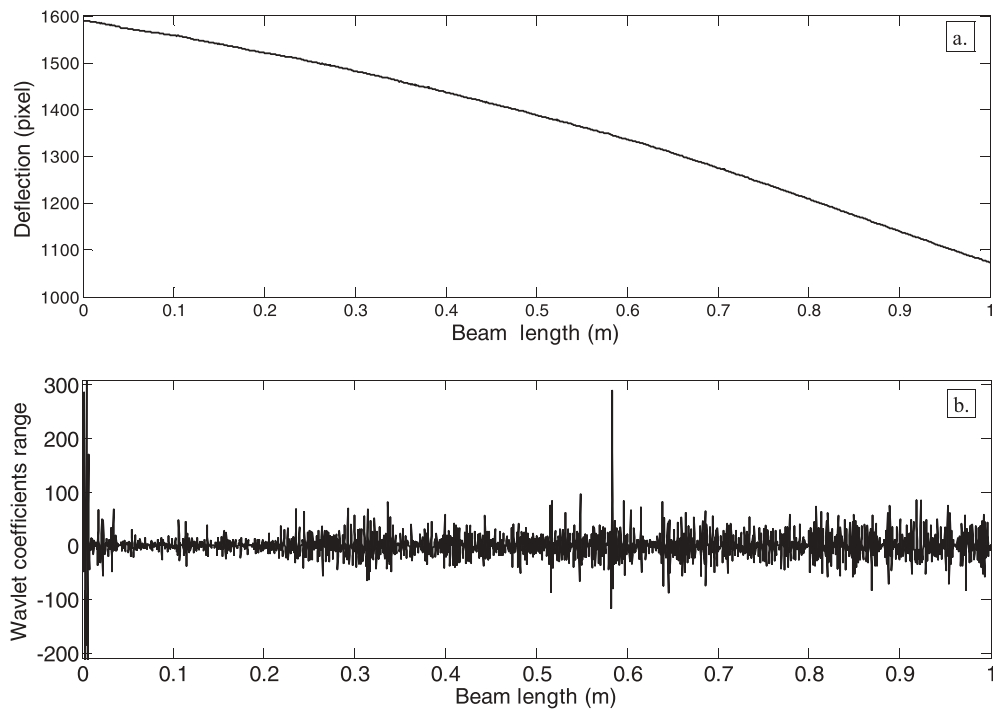


Fig. 17. Crack detection in a beam; (a) Deflection shape of beam, and (b) Wavelet detailed coefficients.

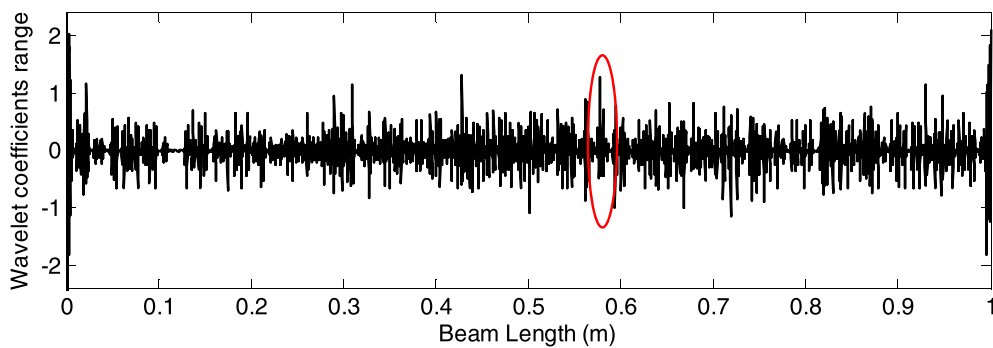


Fig. 18. DWT coefficients of the static deflection of a beam with a crack at 0.58 m from the fixed support.

The algorithm is tested for cracks of smaller depths also. A crack of crack depth 3 mm is taken for experiment II, and a crack of crack depth 2 mm is taken for experiment III. The wavelet detailed coefficients for experiments II and III are plotted in Figs. 20 and 21, respectively. A clear spike is shown at the crack locations in both cases. In experiment IV, a crack is introduced near the clamped end (0.066 m from the clamped end). The DWT coefficients with `rbio2.2` are shown in Fig. 22. Since the ODS has a higher measurement resolution, more data points are available per unit length of the beam. Hence, the end effect shrinks near the end supports. This makes the proposed method capable of detecting crack near the end support also. The present method is suitable for detecting multi-crack also as it is based on detecting the slope discontinuity due to the cracks and the slope discontinuity is localised. In experiment V, two cracks of crack depth 3 mm each are created at locations 0.066 m and 0.058 m from the left end. The DWT coefficients are plotted in Fig. 23. Clear spikes are observed at the crack locations.

Fig. 24 shows the variation of *crack detectability* with the crack depth. *Crack detectability* for experimental cases I, II, and III are taken. Since the order of y-limit is not similar in all three cases (i.e., Fig. 17(b), Figs. 20, 21), the *crack detectability* is normalized with their *rms* values. *Crack detectability* is increasing with the crack depth. Similar observations were obtained for the simulated ODS also (Fig. 14.). Figs. 14 and 24 show the variation of *crack detectability* with crack size. The intersection of *crack detectability* curves with the horizontal axis gives the minimum crack sizes that the algorithm can detect. From Fig. 14, it can be observed that the minimum crack size depends on the SNR values of the measurements. The noise level in a measurement depends primarily upon the lighting conditions, camera quality, and proper edge detection techniques. A low noise measurement will lead to the detection of smaller cracks in the beam.

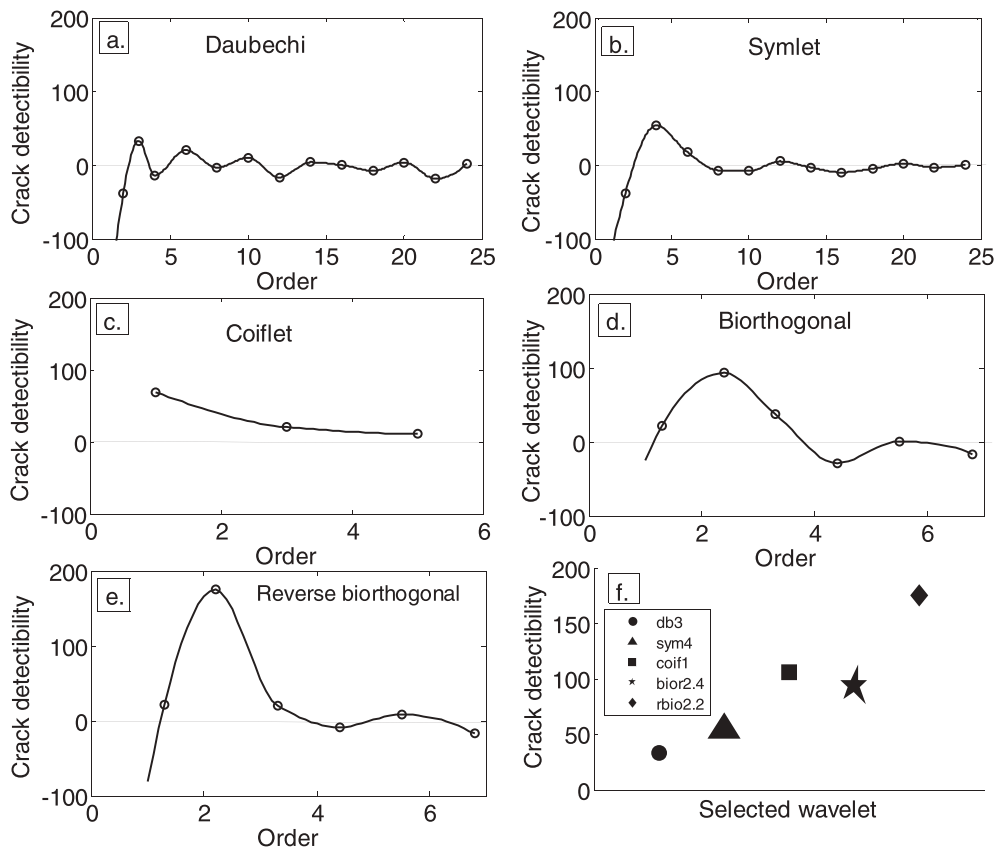


Fig. 19. Experimental verification of variation of crack detectability with vanishing moment.

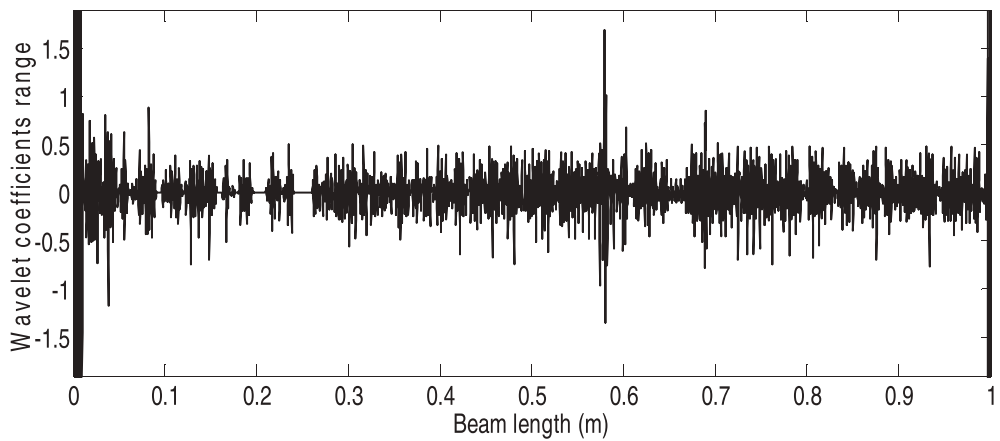


Fig. 20. DWT coefficients for experiment II.

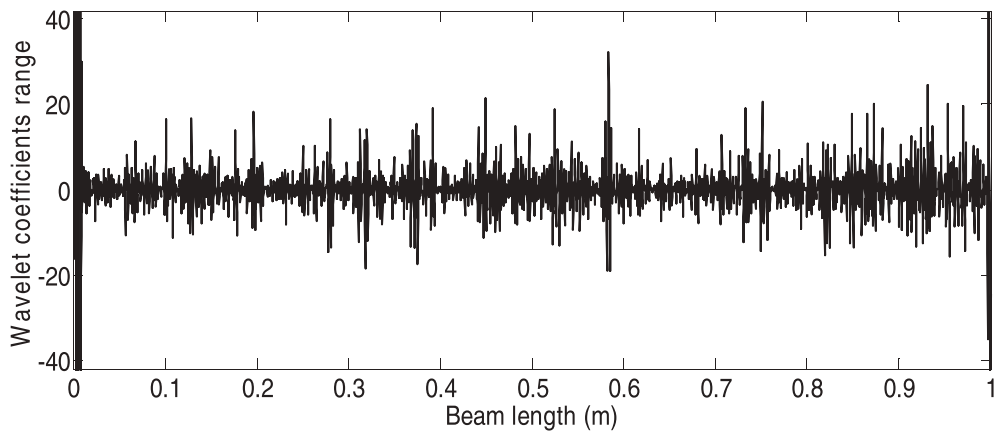


Fig. 21. DWT coefficients for experiment III.

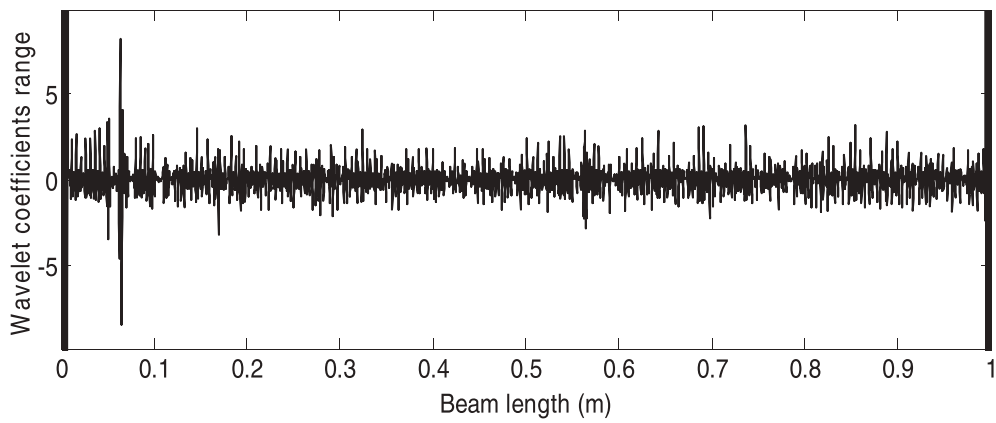


Fig. 22. DWT coefficients for experiment IV.

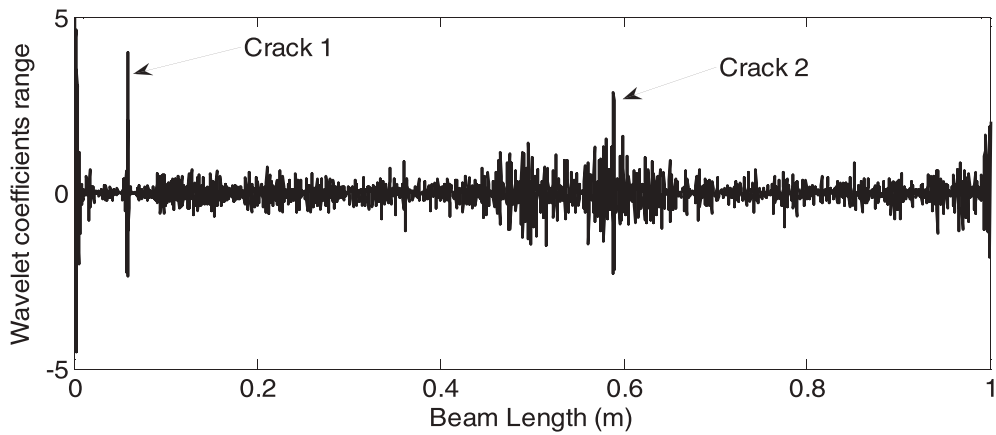


Fig. 23. DWT coefficients for experiment V.

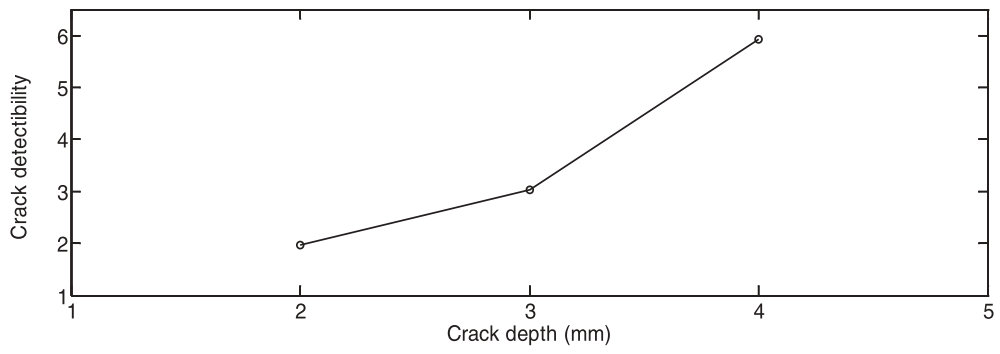


Fig. 24. Variation of crack detectability with crack depth.

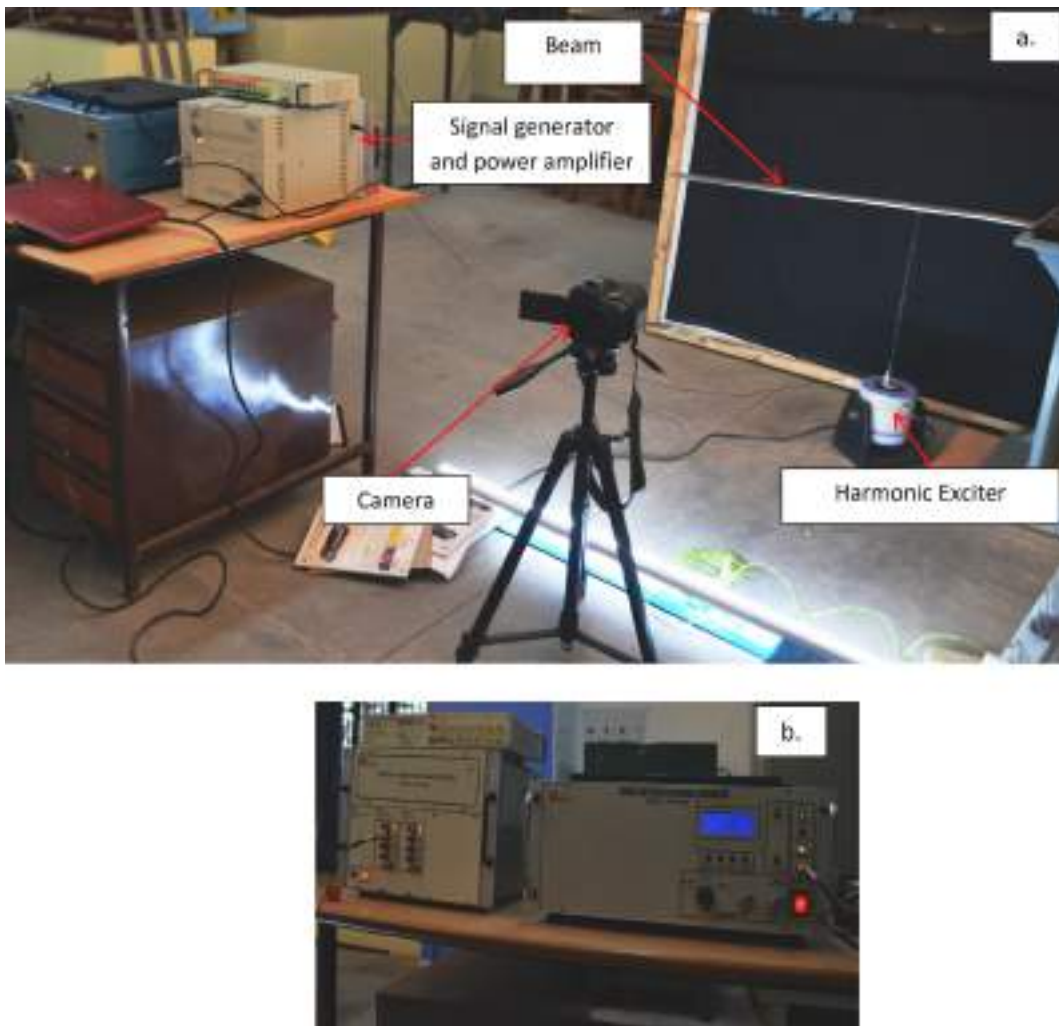


Fig. 25. Forced vibration experimental setup for crack detection: (a) The beam with a digital camera and harmonic exciter, (b) Signal generator and power amplifier.

Table 5
Parameters for forced vibration experiments.

	Experiment VI	Experiment VII
Crack location	0.58 m	0.066 m
Crack depth	4 mm	2 mm
Excitation frequency	3 Hz	3 Hz

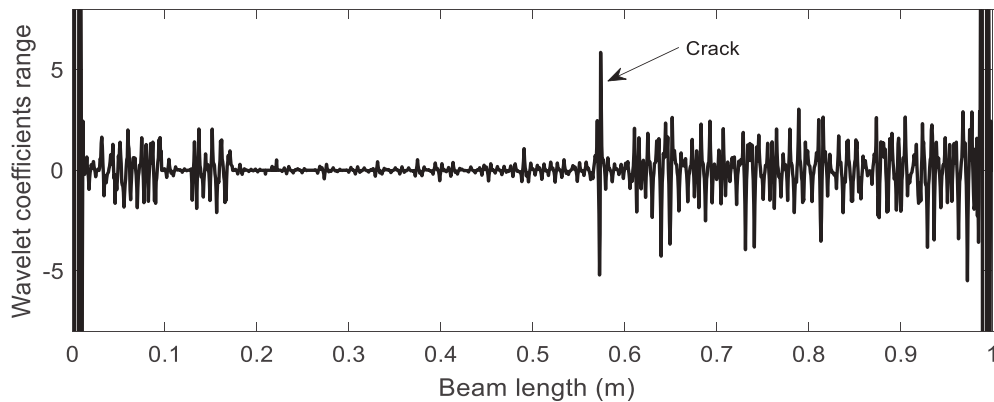


Fig. 26. DWT coefficients for experiment VI.

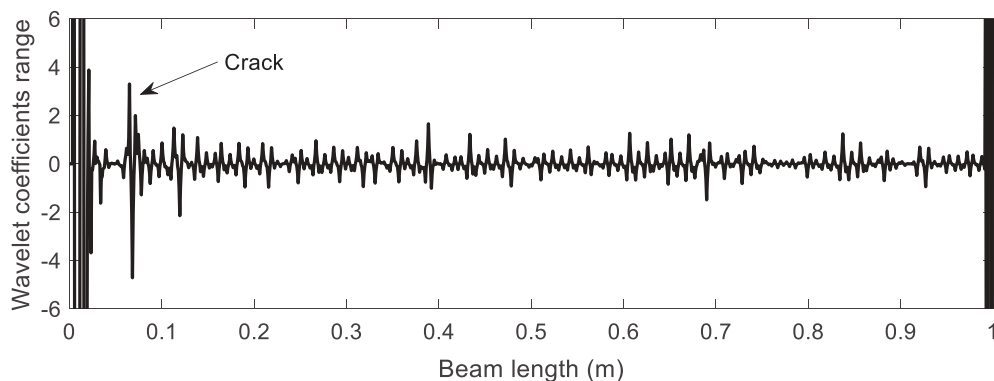


Fig. 27. DWT coefficients for experiment VII.

Slope discontinuity in the beam elastic line arises due to the local change in the stiffness value. The algorithm requires a deflected shape of the beam for the application of the algorithm. The slope discontinuity due to a crack will arise in both cases, the free vibration case and the forced vibration case. To observe this, now the algorithm is experimentally tested with the forced vibration responses of the beam. In the forced vibration, the exciter unit is present in the captured images. Hence the pixel measurement is taken from the top, and the cracked edge is kept as the lower edge. The first white pixel index from the top of the edged image gives the beam deflection. The experimental setup for the measurement of deflection shape under forced vibration is shown in Fig. 25. A cantilever beam of 1 m length with a rectangular cross-section (50 mm \times 6 mm) is taken for testing. An electromagnetic exciter (make: Micron- Roorkee, India; Type MEV 0010) is used for the excitation. Two experimental cases are taken. The parameters for experimental setups are given in Table 5.

The wavelet detailed coefficients for experiments VI and VII are plotted in Figs. 26 and 27, respectively. Clear spikes are seen at the crack locations in both cases.

6. Conclusion

Crack in a beam is detected using discrete wavelet transform of the operational deflection shape of the beam. *Crack detectability* is defined in order to study the effectiveness of different wavelet families and the number of vanishing moments in detecting the crack. Initially, the crack detectability increases with the number of vanishing moments; however, a further increase in the number of vanishing moments reduces the crack detectability due to an increase in support width. An optimum number of vanishing moments is obtained for effective crack detection. The reverse biorthogonal wavelet of order 2.2 is found to have better crack detection capability among the studied wavelets. The proposed methodology for selecting the suitable mother wavelet and the optimum vanishing moment

is verified experimentally. Wavelet transformation based algorithm needs high resolution measurement of the operational deflection shape of the beam. Photographic method is used to get high resolution measurement of operational deflection shape. The proposed methodology is able to detect cracks near the end support also.

CRedit authorship contribution statement

Ramnivas Kumar: Conceptualization, Methodology, Software, Writing - Original draft preparation, Data acquisition. **Ravi Nigam:** Software, Data acquisition. **Sachin K Singh:** Supervision, Writing - Reviewing and Editing, Visualization, Investigation.

Declaration of Competing Interest

The authors declare that they have no known competing financial interests or personal relationships that could have appeared to influence the work reported in this paper.

Acknowledgement

This work is supported by research grant from Science & Engineering Research Board India, through project File No. YSS/ 2015/ 001555.

References

- [1] A.D. Dimarogonas, Vibration of cracked structures: A state of the art review, *Eng Fract Mech* 55 (5) (1996) 831–857, [https://doi.org/10.1016/0013-7944\(94\)00175-8](https://doi.org/10.1016/0013-7944(94)00175-8).
- [2] A.S. Sekhar, Multiple crack effects and identification, *Mech Syst Signal Process* 22 (2008) 845–878, <https://doi.org/10.1016/j.ymssp.2007.11.008>.
- [3] G. Sabnavis, R.G. Kirk, M. Kasarda, D. Quinn, Cracked shaft detection and diagnostics: A literature review, *Shock Vib Dig* 36 (4) (2004) 287–296, <https://doi.org/10.1177/0583102404045439>.
- [4] R.D. Adams, P. Cawley, C.J. Pye, B.J. Stone, A Vibration technique for non-destructively assessing the integrity of structures, *Journal of Mechanical Engineering Science* 20 (1978) 93–100, https://doi.org/10.1243/JMES_JOUR_1978_020_016_02.
- [5] A.D. Dimarogonas, G. Massouros, Torsional vibration of a shaft with a circumferential crack, *Engineering Fracture Mechanics* 15 (3–4) (1981) 439–444, [https://doi.org/10.1016/0013-7944\(81\)90069-2](https://doi.org/10.1016/0013-7944(81)90069-2).
- [6] A.C. Chasalevris, C.A. Papadopoulos, Identification of multiple cracks in beams under bending, *Mech Syst Signal Process* 20 (7) (2006) 1631–1673, <https://doi.org/10.1016/j.ymssp.2006.03.008>.
- [7] A. Morassi, M. Rollo, Identification of two cracks in a simply supported beam from minimal frequency measurements, *JVC/Journal Vib Control* 7 (5) (2001) 729–739, <https://doi.org/10.1177/107754630100700507>.
- [8] A.A. Masoud, S. Al-Said, A new algorithm for crack localization in a rotating Timoshenko beam, *JVC/Journal Vib Control* 15 (10) (2009) 1541–1561, <https://doi.org/10.1177/1077546308097272>.
- [9] A. Labib, D. Kennedy, C.A. Featherston, Crack localisation in frames using natural frequency degradations, *Comput Struct* 157 (2015) 51–59, <https://doi.org/10.1016/j.compstruc.2015.05.001>.
- [10] P.F. Rrzos, Identification of crack location and magnitude in a cantilever beam from the vibration mode, *J Sound Vib* 138 (1990) 381–388, [https://doi.org/10.1016/0022-460X\(90\)90593-O](https://doi.org/10.1016/0022-460X(90)90593-O).
- [11] K. Roy, S. Ray-Chaudhuri, Fundamental mode shape and its derivatives in structural damage localization, *J Sound Vib.* 332 (21) (2013) 5584–5593, <https://doi.org/10.1016/j.jsv.2013.05.003>.
- [12] E.-T. Lee, H.-C. Eun, Damage detection of damaged beam by constrained displacement curvature, *J mech sci technol.* 22 (6) (2008) 1111–1120, <https://doi.org/10.1007/s12206-008-0310-3>.
- [13] M. Rucka, K. Wilde, Crack identification using wavelets on experimental static deflection profiles, *Eng Struct.* 28 (2006) 279–288, <https://doi.org/10.1016/j.engstruct.2005.07.009>.
- [14] C.R. Farrar, G.H. James III, System identification from ambient vibration measurements on a bridge, *J. Sound Vib.* 205 (1) (1997) 1–18, <https://doi.org/10.1006/jsvi.1997.0977>.
- [15] A.K. Pandey, M. Biswas, M.M. Samman, Damage detection from changes in curvature mode shapes, *J Sound Vib.* 145 (2) (1991) 321–332, [https://doi.org/10.1016/0022-460X\(91\)90595-B](https://doi.org/10.1016/0022-460X(91)90595-B).
- [16] S.K. Singh, R. Tiwari, Identification of a multi-crack in a shaft system using transverse frequency response functions, *Mech Mach Theory* 45 (12) (2010) 1813–1827, <https://doi.org/10.1016/j.mechmachtheory.2010.08.007>.
- [17] S.K. Singh, R. Tiwari, Detection and localisation of multiple cracks in a shaftsystem: An experimental investigation, *Meas J Int Meas Confed* 53 (2014) 182–193, <https://doi.org/10.1016/j.measurement.2014.03.028>.
- [18] A.K. Darpe, A novel way to detect transverse surface crack in a rotating shaft, *J Sound Vib* 305 (1-2) (2007) 151–171, <https://doi.org/10.1016/j.jsv.2007.03.070>.
- [19] S. Zhong, S.O. Oyadiji, Crack detection in simply supported beams without baseline modal parameters by stationary wavelet transform, *Mech Syst Signal Process* 21 (4) (2007) 1853–1884, <https://doi.org/10.1016/j.ymssp.2006.07.007>.
- [20] Q. Wang, X. Deng, Damage detection with spatial wavelets, *Int J Solids Struct* 36 (23) (1999) 3443–3468, [https://doi.org/10.1016/S0020-7683\(98\)00152-8](https://doi.org/10.1016/S0020-7683(98)00152-8).
- [21] H. Kim, H. Melhem, Damage detection of structures by wavelet analysis, *Eng. Struct.* 26 (3) (2004) 347–362, <https://doi.org/10.1016/j.engstruct.2003.10.008>.
- [22] Z.K. Peng, F.L. Chu, Application of the wavelet transform in machine condition monitoring and fault diagnostics: A review with bibliography, *Mech Syst Signal Process* 18 (2) (2004) 199–221, [https://doi.org/10.1016/S0888-3270\(03\)00075-X](https://doi.org/10.1016/S0888-3270(03)00075-X).
- [23] S. Mallat, A Wavelet Tour of Signal Processing, *A Wavelet Tour Signal Process* (2009), <https://doi.org/10.1016/B978-0-12-374370-1.X0001-8>.
- [24] Wilde K. Modal diagnostics of civil engineering structures 2008. ISBN 978–83–7348–227–2.
- [25] S. Loutridis, E. Douka, A. Trochidis, Crack identification in double-cracked beams using wavelet analysis, *J Sound Vib* 277 (4-5) (2004) 1025–1039, <https://doi.org/10.1016/j.jsv.2003.09.035>.
- [26] J.-C. Hong, Y.Y. Kim, H.C. Lee, Y.W. Lee, Damage detection using the Lipschitz exponent estimated by the wavelet transform: applications to vibration modes of a beam, *Int J Solids Struct* 39 (7) (2002) 1803–1816, [https://doi.org/10.1016/S0020-7683\(01\)00279-7](https://doi.org/10.1016/S0020-7683(01)00279-7).
- [27] E. Douka, S. Loutridis, A. Trochidis, Crack identification in beams using wavelet analysis, *Int J Solids Struct* 40 (13-14) (2003) 3557–3569, [https://doi.org/10.1016/S0020-7683\(03\)00147-1](https://doi.org/10.1016/S0020-7683(03)00147-1).
- [28] Daubechies I. Ten lectures on wavelets. Society for industrial and applied mathematics, 1992. ISBN-13: 978-0-898712-74-2.
- [29] A.G. Mardasi, N. Wu, C. Wu, Experimental study on the crack detection with optimized spatial wavelet analysis and windowing, *Mech Syst Signal Process* 104 (2018) 619–630, <https://doi.org/10.1016/j.ymssp.2017.11.039>.

- [30] M. Rucka, K. Wilde, Application of continuous wavelet transform in vibration based damage detection method for beams and plates, *J Sound Vib* 297 (3-5) (2006) 536–550, <https://doi.org/10.1016/j.jsv.2006.04.015>.
- [31] A. Messina, Refinements of damage detection methods based on wavelet analysis of dynamical shapes, *Int J Solids Struct* 45 (14-15) (2008) 4068–4097, <https://doi.org/10.1016/j.ijsolstr.2008.02.015>.
- [32] E. Sazonov, P. Klinkhachorn, Optimal spatial sampling interval for damage detection by curvature or strain energy mode shapes, *J Sound Vib* 285 (4-5) (2005) 783–801, <https://doi.org/10.1016/j.jsv.2004.08.021>.
- [33] S. Zhong, S.O. Oyadiji, Sampling interval sensitivity analysis for crack detection by stationary wavelet transform, *Struct. Control Health Monit* (2011), <https://doi.org/10.1002/stc>.
- [34] L. Montanari, A. Spagnoli, B. Basu, B. Broderick, On the effect of spatial sampling in damage detection of cracked beams by continuous wavelet transform, *J Sound Vib* 345 (2015) 233–249, <https://doi.org/10.1016/j.jsv.2015.01.048>.
- [35] S. Zhong, S.O. Oyadiji, Detection of cracks in simply-supported beams by continuous wavelet transform of reconstructed modal data, *Comput. Struct* 89 (1-2) (2011) 127–148, <https://doi.org/10.1016/j.compstruc.2010.08.008>.
- [36] Y. BAMNIO, E. DOUKA, A. TROCHIDIS, Crack identification in beam structures using mechanical impedance, *J Sound Vib* 256 (2) (2002) 287–297, <https://doi.org/10.1006/jsvi.2001.4209>.
- [37] S.I. Ishak, G.R. Liu, H.M. Shang, S.P. Lim, Non-destructive evaluation of horizontal crack detection in beams using transverse, *J Sound Vib* 252 (2002) 343–360, <https://doi.org/10.1006/jsvi.2001.4043>.
- [38] Rao J S., *Rotor Dynamics*, New age international publishers, , 1996. ISBN:9780470217870.
- [39] Clough RW, and Penzien H., *Dynamics of structures*, McGraw-Hill Computers & Structures, Inc.1995.
- [40] C.A. Papadopoulos, A.D. Dimarogonas, Coupled longitudinal and bending vibration of rotating shaft with an open crack, *J Sound Vib* 117 (1987) 81–93, [https://doi.org/10.1016/0022-460x\(87\)90437-8](https://doi.org/10.1016/0022-460x(87)90437-8).
- [41] A.K. Darpe, K. Gupta, A. Chawla, Coupled bending, longitudinal and torsional vibrations of a cracked rotor, *J Sound Vib*. 269 (1–2) (2004) 33–60, [https://doi.org/10.1016/S0022-460X\(03\)00003-8](https://doi.org/10.1016/S0022-460X(03)00003-8).
- [42] R.C. Gonzalez, R.E. Woods, *Digital Image Processing*, Pearson Education, 2018. ISBN-13:9780133356779.



4th International Conference on Advances in Energy Research 2013, ICAER 2013

Biofuel from wastes an economic and environmentally feasible resource

Devendra Pratap Singh^{a*}, Rakesh Kumar Trivedi^b

^aDepartment of Applied Chemistry, Dr. A.P.J.S. Kanpur-208024, India

^bProfessor & Head, Department of Oil and Paint Technology H. B.T.I., Kanpur 208002

Abstract

Environmental arguments centre on the need to reduce greenhouse gas (GHG) emissions for the sake of both the global and local environments. In this respect, the replacement of fossil fuels by biofuels in the transportation sector is necessary to help the reduction of GHG. Climate change impacts have spurred researchers and industry to look at alternate clean energy options. The concentration of CO₂ in the earth's atmosphere was about 280 parts per million by volume (ppm) in 1750, before the Industrial Revolution began. By 1994 it was 358 ppm and rising by about 1.5 ppm per year. If emissions continue at the 1994 rate, the concentration will be around 500 ppm, nearly double the preindustrial level, by the end of the 21st century. Carbohydrate biomass is considered as the future feedstock for bio ethanol production because of its low cost and its huge availability.

The major carbohydrate materials found in great quantities to be considered, is wheat bran, sugarcane bagasse and rape straw, which can be easily converted in to ethanol by following pretreatment either by acid or enzyme, hydrolysis and distillation process under feasible conditions. The effects of different pH and temperature with enzymatic saccharification treatment on conversion of these biomasses were studied. The produced glucose was fermented to bioethanol, using *Saccharomyces cerevisiae* yeast in combination with pentose fermenting enzymes as *Pichia stipitidis* and the amount of produced bio ethanol was measured by gas chromatography. Enzyme treatment at 30°C and pH 5 is an effective treatment method for converting lignocelluloses to glucose. Up to 23.35% glucose v/v could be achieved after enzyme treatment from bagasse than others. Fermentation of treated lignocelluloses shown that glucose after 3 days fermentation the maximum bio ethanol of 19.25% (v/v) by *Saccharomyces cerevisiae* and 26.75% (v/v) was attained in case of sugarcane bagasse by using *Pichia stipitidis* in combination with *S. cerevisiae*. This process is expected to be useful for the bio ethanol production from wheat bran, sugarcane bagasse and rape straw as a source of carbohydrate renewable biomass from abundant agricultural by product.

© 2014 Devendra Pratap Singh. Published by Elsevier Ltd. This is an open access article under the CC BY-NC-ND license (<http://creativecommons.org/licenses/by-nc-nd/3.0/>).

Selection and peer-review under responsibility of Organizing Committee of ICAER 2013

Keywords: Biomass, Carbohydrates, Fermentation, Pre-treatment, Saccharification.

* Corresponding author. Tel.: +91-512-2583221, fax: +91-512-2583418.
E-mail address: dr.pratap2012@gmail.com

1. Introduction

In the past few years there have been important advances in the field of alternative transportation fuels, primarily bio ethanol and biodiesel. Only biodiesel and bio ethanol are considered in this report due to their similar inherent properties compared to fossil-based fuels, especially auto ignitibility. There is a longer-term potential for other bio fuels such as biobutanol and biogas but little research effort has been seen in either regular or small engines. Bio ethanol is an alcohol, made by fermenting any biomass with a high content of carbohydrates through a process similar to beer brewing. Today, bio ethanol is made from starches and sugars. In the future, cellulose and hemicellulose fibrous material will be used. For the production of ethanol as bio fuels, pre-treatment is the initial process to degrade the biomass into carbohydrates, so that it may be converted in to monomers and latter on fermentation of sugars is the valuable process by which ethanol is obtained. Chemical treatment is generally used to remove lignin content of agro residues. Chemical pre-treatment by alkali or acid hydrolysis are common in paper and pulp industries to recover cellulose for paper production. These treatments tend to be expensive hence are not used for bioconversion purposes. Pretreatment with acid or alkali is common chemical method that has the effect of increasing the surface area of the agro-industrial residue due to the swelling and disruption of lignin. Pretreatment is the pre step to release the components of lignocellulosic biomass. Agro-residues consist of lignocelluloses that is compact, partly crystalline structure consisting of linear and crystalline polysaccharides cellulose, branched non cellulosic and non-crystalline hetero polysaccharides (hemicelluloses), and branched (non crystalline) lignin [1]. During the process some of the compounds are formed which inhibits the direct fermentation, so it is necessary to remove them so that an efficient products form. Detoxification of dilute-acid lignocelluloses hydrolysates by treatment with $\text{Ca}(\text{OH})_2$ (over liming) efficiently improves the production of fuel ethanol, but is associated with drawbacks like sugar degradation and CaSO_4 precipitation. In factorial designed experiments, in which pH and temperature were varied, dilute-acid spruce hydrolysates were treated with $\text{Ca}(\text{OH})_2$, NH_4OH or NaOH . The concentrations of sugars and inhibitory compounds were measured before and after the treatments. The ferment ability was examined using the yeast *Saccharomyces cerevisiae* and compared with reference fermentations of synthetic medium without inhibitors [2].

Biodiesel is made by combining alcohol (usually bio ethanol) with vegetable oil, animal fat, or recycled cooking grease. These materials contain triglycerides and other components depending on type. Some of the feedstocks are palm oil, coconut oil, canola oil, corn oil, cottonseed oil, flax oil, soy oil, peanut oil, sunflower oil, rapeseed oil and algae. It can be used as an additive to reduce vehicle emissions or in its pure form as a renewable alternative fuel for diesel engines. In the near future, agricultural residues such as corn Stover (the stalks, leaves, and husks of the plant) and wheat straw will also be used. Biodiesel is one of the future fuels for the engines that help to reduce the global warming and other harmful pollutants. Converting vegetable oils into their esters of methyl and ethyl alcohols is known as Bio-diesel. Ester formation is a possible way to overcome almost all the problems associated with vegetable oils. By the process of esterifications the high viscosity of vegetable oils could be brought down to acceptable limits. Esters can be produced from oils and fats by 3 methods. i) Base catalyzed transesterifications of oil with alcohol. ii) Direct acid catalyzed esterifications of oil with methanol. iii) Conversion of oil to fatty acids and then to alkyl esters with acid catalysts. The first method is preferred because it is economical. The conversion of vegetable oil (Triglyceride Esters) to methyl esters through Tran's esterifications process, this reduces the molecular weight to one-third, reducing the viscosity by a factor of 8 and increasing the volatility. Vegetable oil is mixed with alcohol, NaOH as catalyst. The mixture is heated and maintained at 650C for one hour, while heating, the solution is stirred continuously with stirrer. Two distinct layers are formed, the lower layer is glycerine and the upper layer is ester. The upper layer is separated with moisture and the ester is removed by using calcium chloride. It is observed that 90% of ester is obtained from vegetable oil. Experimental research has been done on various blends of gasoline and ethanol, and results have shown that 7.5% addition of ethanol was the best suitable for SI engine with reduced CO emission [3]. Biodiesel reduces particulate, carbon monoxide, and sulphur dioxide emissions compared to diesel fuel.

Lignocellulose is an important structural component of woody plants and consists of cellulose, hemicelluloses, and lignin. The cellulose molecules, which are polymers with six carbon sugars linked in long chains, and five carbon sugar chains called hemicelluloses, are reinforced by cross linked organic molecules called lignin. This structure is very difficult for microbes to break down into simple sugars. In order to exploit the structural sugars from plant fibers for bio ethanol, the recalcitrance of biomass must be overcome in a way that is cost competitive in current markets. The kind of cost-reducing measures that bio-refineries are working towards are

efficient de-polymerization of cellulose and hemicelluloses, efficient fermentation (including pentose and hexose sugars) that can handle inhibitory compounds, optimizing process integration, and a cost efficient use of lignin [18,19]. Table 1 shows the composition of different biomass.

Table 1. Effect of pH on glucose content of sugarcane baggase

Lignocellulosic substrate	Cellulose (%)	Hemicellulose (%)	Lignin (%)
Sugarcane bagasse	45	35	15
Wheat straw	30	50	15
Rice straw	52.1	24	18
Rape straw	33.4	30	17
Rice bran	30.4	22	16
Wheat bran	31.3	23	17.5

In recent years, bio fuels producers have achieved significant improvements in crop production and processing efficiencies and today the volume of bio fuels produced in a specific planted area is several times higher than it used to be. Improved production methods and technologies are expected to increase efficiencies even further. In a simplified way, bio fuels can be sub-divided into two large categories: substitute for diesel (biodiesel) and substitute for petroleum (ethanol). This division is based on the key properties of the two products. On the one hand, biodiesel (which replaces diesel in cars) is produced from oil rich plants (e.g. rapeseed, sunflower, algae, etc.) by mixing the vegetable oil (90%) with methanol (10%) in the process called trans-esterifications. On the other hand, bio ethanol (which replaces petrol in cars) – also known as alcohol – is produced through the fermentation of sugar from cereals (wheat, maize, etc.) or sugary feedstock's (sugarcane, sugar beet). Since biodiesel is derived from vegetable oils or animal fats made up of esters, these vegetable oils are renewable biological sources. It has been reported that they emit substantially lower quantity of harmful pollutants compare to conventional diesel; Researchers also found that comparable engine performance with diesel was achieved at relatively lower emission [4, 5]. The merits of using biodiesel instead of conventional diesel are has comparable energy density, cetane number, heat of vaporization, and stoichiometric air /fuel ratio [6]. Biodiesel is also non-toxic and rate of biodegradation is much faster than conventional diesel. Green house gases effects were least in case of biodiesel [7, 8].

Use of Bio ethanol in motor engines is beneficial to the environment, because it produce CO_2 from combustion engines which is absorbed by plants these plants provide lignocelluloses, which turns in ethanol as shown in Fig. 1, it is a recycle process which helps to control global warming and air pollutants. Another environmental benefit of ethanol as a fuel is that the emission of carbon monoxide, nitrogen oxides and hydrocarbons in general is less compared to gasoline [9]. However, ethanol-containing fuels will contribute to an increased emission of formaldehyde and acetaldehyde [10]. Nevertheless, the environmental damage caused by reactive aldehydes is far less than that of poly-nuclear aromatic compounds, which are emitted when gasoline is combusted [9].

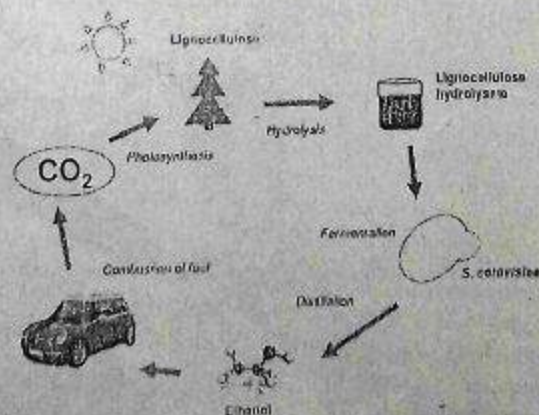


Figure 1. Production of Ethanol from lignocelluloses

The choice of microorganism and strain is very important not only for high sugar utilization, ethanol tolerance, and ethanol producing properties, but also for the robustness and the ability to withstand inhibitors. The selection of

microorganism may be influenced by its ability to ferment pentose sugars. The fraction of pentose sugars is generally low in softwood hydrolysates, but if hardwood or agricultural residues are considered, the ability to ferment Pentoses becomes more important. There are several naturally occurring microorganisms that can utilize pentoses. *E. coli* is a natural pentose fermenter, but it gives low ethanol yields. This problem has been addressed by genetic engineering to increase the ethanol production. *S. cerevisiae* and *Z. mobilis* are excellent ethanol producers, but they are unable to metabolize Pentoses. Recombinant strains that are able to utilize pentose sugars have been developed for both *Z. mobilis* and *S. cerevisiae* studied by [11, 12]. However, the genetically engineered pentose-fermenting *S. cerevisiae* strains have not yet been especially successful; this is due to problems like low pentose fermentation rates, low ethanol yields, and redox imbalances [13].

2. Material and Methods

2.1. Material

Wheat bran, sugarcane bagasse, Rice bran and rape straw were used for the treatment process. Before pretreatment these biomasses are reduced in to smaller particles after milling and crushing (particle size $<180 \mu\text{m}$). Glucose was obtained from hydrolysis of wheat bran, sugarcane bagasse, Rice bran and rape straw. After the hydrolysis hydrolyzed biomass were kept at 18°C until use [14].

2.2. Dilute acid pretreatment

For the comparative result equal amount of biomasses were pretreated in two ways one is acid treatment where 2-3% acid (H_2SO_4) was used for the pre-treatment method. In this content acid soaked biomass slurry was autoclaved at 121°C for 30 minutes. To separate the solid and liquid fraction centrifuge method was used. The dilution and pH was maintained at 5 by adding alkali of centrifuged biomass before fermentation process.

2.3. Enzyme Pretreatment

150 g of each biomass were suspended in 500 mL H_2O in ratio of 3:10 (w/v) sugarcane bagasse and added of 0.1 mL of α -amylase enzyme. The pH of sample was adjusted at pH 5, 5.5, and 6. The sample was incubated in water bath 100°C for 30 minutes, after that the mixture was applied for second enzymatic treatment (0.2 ml of glucoamylase). Finally, hydrolysate was pressed through cheese cloth. The amount of reducing sugar in juice was measured.

2.4. Fermentation

The pre-treated samples from 2.2 and 2.3 were carried out for fermentation experiments. The yeast *S. cerevisiae* was used for fermentation (1.5g, 3.0g, and 4.5g). After 3 fermentation days the ethanol content was measured by gas chromatography. All the measurements were duplicated and the data reported are average of two replications. Yeast *S. cerevisiae* was also used with *Pichia stipititis* for both the fermentation of pentose and hexose. Equal amount of both the yeast and *P. stipititis* were taken for the efficient hydrolysis and fermentation of both Pentoses and hexoses sugar present in the hydrolyzed.

3. Result and Discussion

3.1. Effect of enzyme pre-treatment methods on glucose content of sugarcane bagasse

For the maximum production of ethanol hydrolyzed biomass (both acid and enzyme pretreated) were fermented at different pH scale, after fermentation the maximum result was obtained at pH 5 for the sugarcane bagasse. From the Table: 2, it is clear that, increasing pH showed reverse effect on glucose concentration in sample. This is expected because of conversion of carbohydrate to glucose [15]. The highest glucose up to 23.35 % glucose on the sugarcane

bagasse basis could be obtained on pH 5. Hence pH 5 at 30°C was found optimum for fermentation; hence it was taken for all the hydrolyzed biomass for fermentation.

Table 2. Effect of pH on glucose content of sugarcane bagasse

pH	Temperature (°C)	Glucose (%)
5	30	23.35
5.5	30	22.80
6	30	22.00
5	40	21.05
5.5	40	19.43
6	40	18.95

3.2. Effect of acid pre-treatment methods on glucose content of sugarcane bagasse

150 g of each biomass were suspended in 500 mL dilute acid of different concentration in the ratio of 3:10 (w/v) sugarcane bagasse. The percentage of cellulose converted and the available form of substrate after enzymatic hydrolysis of various concentrations of acid pre-treated corncob samples were calculated based on the amount of sugar released. The results are presented in the Table 3. The results show that the percentage of cellulose conversion increased with the increased concentrations of acid used for pre-treatment and it was also noted that the available form of substrate reduced with increased concentrations of acid. Since maximum sugars were obtained at 3% acid pre-treatment (optimum), hence it was used for further pre-treatment of other biomasses.

Table 3. Effect of acid pre-treatment on carbohydrate content of sugarcane bagasse

Sample	Sample-Acid used for Pre-treatment (%)	Cellulose Conversion (%)	Available Substrate (%)
S1	0.5	11.8	88.2
S2	1.0	12.8	87.2
S3	1.5	13.6	86.4
S4	2.0	14.2	85.8
S5	2.5	15.2	84.8
S6	3.0	16.0	84

3.3. Fermentation of enzyme treated biomass

Bio ethanol was produced by using *S. cerevisiae* and *S. cerevisiae* in combination with *Pichia stipitidis* at pH 5 and 30°C. 3.0g of each enzyme were taken which yields maximum ethanol 19.25% by using *S. cerevisiae* while 26.75% was found by using *S. cerevisiae* and *p. stipitidis*, for sugarcane bagasse. It can be seen in Figure 2 that pH 5.0 tended to give higher ethanol concentration at 30°C. Therefore, pH 5.0 was chosen for ethanol fermentation. This was supported by [16].

Table 4. Production of Ethanol % (v/v) at 30°C and pH 5 of enzyme treated biomass.

Biomass (150g)	Sugar (%)	Ethanol (%) by	
		<i>S. cerevisiae</i>	<i>S. cerevisiae</i> & <i>P. stipitidis</i>
Sugarcane bagasse	23.35	19.25	26.75
Wheat Bran	20.74	17.47	21.17
Rape Straw	22.75	18.09	25.48
Rice bran	21.03	17.95	24.28

Production of bio ethanol in Table 2 shows that pH 5 at temperature 60°C had higher quantities of bio ethanol produced and bio ethanol content of 19.25%, 17.47%, 18.09%, 17.95% (v/v) was recorded maximum for bagasse, wheat bran rape straw and rice bran. This confirms that the higher sugar content in the juice, the more bio ethanol can be produce which was also found similar according to the [17]. It was observed that the sugar content was directly proportional to the quantities of the ethanol collected. Therefore, the higher the sugar content, the more the ethanol can be produced [17]. By using *Pichia stipitidis* in combination with *S. cerevisiae* maximum ethanol was found 26.75%, 21.17%, 25.48% and 24.28% for sugarcane bagasse, wheat bran rape straw and rice bran. The high

yield of ethanol production is due to the conversion of pentose sugar by *P. stipitidis*, because *S. cerevisiae* is only able to ferment hexose sugar as shown in fig. 2

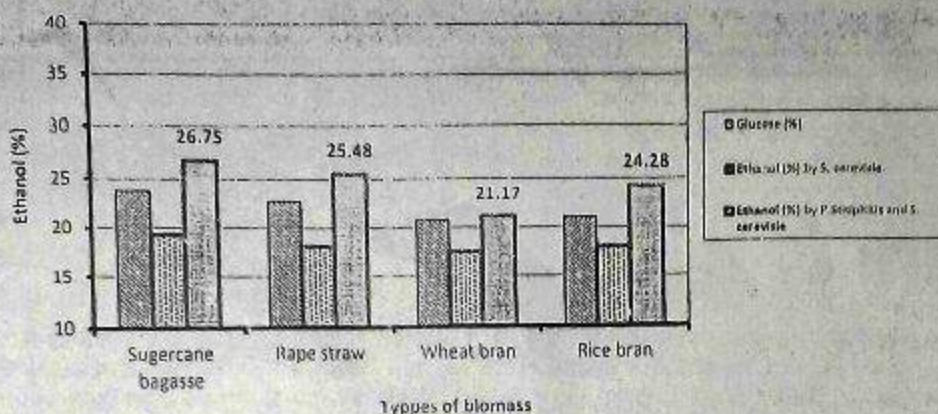


Fig. 2 Production of Ethanol % (v/v) at 30°C and pH 5 from enzyme treated biomass

3.4. Fermentation of acid treated biomass

The feasibility of bio-alcohol production of cellulosic wastes especially sugarcane bagasse was made in this study. From the previous studies it was noted that increased acid concentration used for the pretreatment purpose enhanced the sugar release during enzymatic hydrolysis. Fermentation studies also proved that increased acid concentration yielded more amount of alcohol.

Table 5. Production of Ethanol % (v/v) at 30°C and pH 5 of acid treated biomass.

SN	Types of biomass samples	Ethanol % (v/v) by	
		<i>S. cerevisiae</i>	<i>S. cerevisiae</i> & <i>P. stipitidis</i>
1	Sugarcane bagasse	24.25	35.38
2	Wheat Bran	21.47	31.25
3	Rape Straw	23.95	34.37
4	Rice bran	23.05	33.98

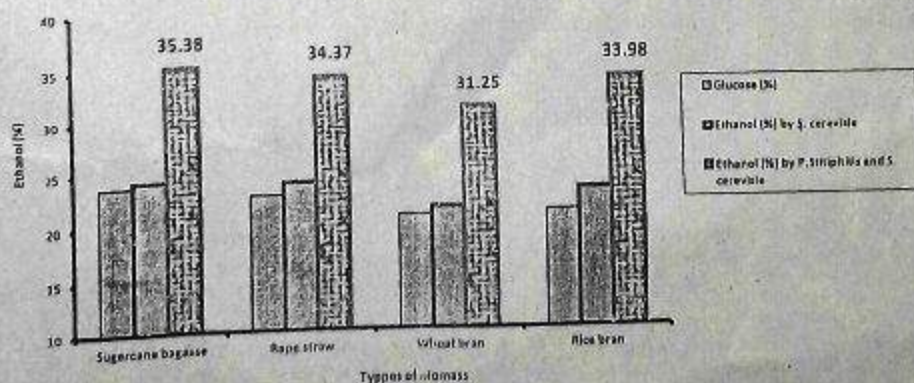


Fig. 3. Production of Ethanol % (v/v) at 30°C and pH 5 from Acid treated biomass

Alcohol content of about 25.38% (Table 5) was detected in the 72 hours of fermentation broth containing the hydrolysed sample pretreated with 3% sulphuric acid. This study proved that sugars released by means of enzymatic

hydrolysis of pretreated bagasse are of fermentable category and alcohol can be produced efficiently using a suitable fermenting strain *Saccharomyces cerevisiae*. Table-5 represents the total Ethanol Production from the kinds of agricultural wastes. The comparative study of production of ethanol from acid treated and enzyme treated biomasses are presented in Fig. 3. Maximum ethanol was found by acid treatment than enzymatic treatment because in acid treatment both Pentoses and hexoses sugar was present.

It is clear from the fig.2 and fig.3 that acid treated biomass yields maximum ethanol but there may be chance of formation of inhibitors so that experiments were done very carefully. The maximum ethanol was counted as 35.38% for sugarcane bagasse by fermentation with *S. cerevisiae* & *P. stipitius* of acid treated, while in case of enzyme treated biomass it was 26.75%.

4. Conclusion

If bio fuels continue their rapid growth around the globe, the impact on the agricultural sector can be significant. Increased jobs and economic development for rural areas in both industrialised and developing countries is one possibility, if governments put the appropriate policies in place and enforce them. The more involved farmers are in the production, processing, and use of bio fuels, the more likely they are to benefit from them. It can be concluded that it is possible to successively use sugarcane bagasse, wheat bran and rape straw for bio ethanol. Enzyme treatment at 30°C and pH 5 is an effective treatment method for converting biomass to glucose. Up to 23.35% glucose w/v could be achieved after enzyme treatment. Fermentation of enzyme treated biomasses shown that glucose after 3 days fermentation the maximum bio ethanol of 19.25% (v/v) was attained by *S. cerevisiae* and 26.75% by *S. cerevisiae* & *P. stipitius*, while Fermentation of acid treated biomasses shown that reducing sugar after 3 days fermentation the maximum bio ethanol of 24.25% (v/v) was attained by *S. cerevisiae* and 35.38% by *S. cerevisiae* & *P. stipitius*. Production of bio ethanol has been considered to be one of economical way for the utilization of rice bran. So the manufacture of glucose could easily be undertaken as an additional source of income.

Biofuels can play a significant role in the context of a broader transformation of the transportation sector but alone they will not solve all of the world's transportation-related energy problems. To achieve their full potential in providing security of supply, environmental and social benefits, bio fuels need to represent an increasing share of total transport fuel compared to oil. While it is recognised that bio fuels have the capacity to reduce greenhouse gas emissions compared to fossil fuels, their production and use are not entirely without environmental implications. Depending on the crop type and other factors, carbon emissions are not always lower than for traditional fuels. Production of biofuel from biomasses has recycle process to keep the environment green and safe from the reduction of harmful gases. On a small scale, biofuels are currently produced from Lignocellulosic waste and algae with relatively large greenhouse gas savings compared to fossil fuels, of around 70%. Hence biofuel production and its utilization technologies must be a one of the way and more efficient in terms of net lifecycle greenhouse gas (GHG) emission reductions while at the same time biofuels are socially and environmentally sustainable.

References

- [1] Glasser WG, Kaar WE, Jain RK, Sealey JE (2000) Isolation options for non-cellulosic hetero polysaccharides. *Cellulose* 7: 299-317.
- [2] Ariksson, B., Sjöde, A., Nilvebrant, N.-O., Jönsson, L.J. (2006), Optimal conditions for alkaline detoxification of dilute-acid lignocellulose hydrolysates. *Appl. Biochem. Biotechnol.*, 130, 599-611.
- [3] Hakan Bayraktar (2005) "Experimental and theoretical investigation of using gasoline-ethanol blends in spark-ignition engines", *Renewable Energy* Vol. 30 pp1733-1747.
- [4] Aliuso S., Aurientina M., Police G. and Prati M. V. (1993), "The effect of methyl-ester of rapeseed oil on combustion and emissions of DI diesel engines", *SAE Paper 93-2801*.
- [5] Peterson C. and Reece D., (1995), "Emissions characteristics of ethyl and methyl ester of rapeseed oil compared with low sulphur diesel control fuel in a chassis dynamometer test of a pickup truck", *Transactions of ASAB*, Vol. 39, No.(3), pp.805-816.
- [6] Agarwal A. K. (2007) "Biofuels (alcohols and biodiesel) applications as fuels for internal combustion engines." *Progress in Energy and Combustion Science* Vol.33, pp 233-271.
- [7] Murugesan A, Umerani C, Subramanian R, Nedunchezian N; (2009) "Bio-diesel as an alternate fuel for diesel engines – a review", *Renew Sustain Energy Rev*, Vol.13 No. (3), pp 653-662.
- [8] Alar M, Balat H, A. (2008) "Critical review of bio-diesel as a vehicular fuel", *Energy Convers Manage*, Vol.49 No. (10), pp 2727-41.
- [9] Hsieh, W.-D., Chen, R.-H., Wu, T.-L., Lin, T.-H. (2002), Engine performance and pollutant emission of an SI engine using ethanol-gasoline blended fuels. *Atmos Environ*, 36, 403-410.

- [10] Leong, S.H., Muttamara, S., Laortanakul, P. (2002), Applicability of gasoline containing ethanol as Thailand's alternative fuel to curb toxic VOC pollutants from automobile emission. *Atmos. Environ.*, 36, 3495-3503.
- [11] Aristidou, A., Penttilä, M. (2000), Metabolic engineering applications to renewable resource utilization. *Curr. Opin. Biotechnol.*, 11, 187-198.
- [12] Hahn-Hägerdal, B., Wahlborn, C.F., Gardonyi, M., Van Zyl, W.H., Cordero Otero, R.R., Jonsson, L.J. (2001), Metabolic engineering of *Saccharomyces cerevisiae* for xylose utilization. *Adv. Biochem. Eng. Biotechnol.*, 73, 53-84.
- [13] Sonderegger, M., Jeppsson, M., Hahn-Hägerdal, B., Sauer, U. (2004), The molecular basis for anaerobic growth of *Saccharomyces cerevisiae* on xylose investigated by global gene expression and metabolic flux analysis. *Appl. Environ. Microbiol.*, 70, 2307-2317.
- [14] Khongsay, N., Laopaiboon, L.; and Laopaiboon. 2010. Growth and Batch Fermentation of *Saccharomyces cerevisiae* on Sweet Sorghum Stem Juice Under Normal and Very High Gravity Conditions. *Biotechnology*, 2010, ISSN 1682- 296X © 2010 Asian Network for Scientific Information.
- [15] Yoswanta, N., Phuriphat, P., Treyawuthiwat, P. 2009. Bioethanol Production from Rice Straw. *International Conference on Science Technology and Innovation for Sustainable Well-Being (STISWB)*.
- [16] Thuesombat, P., Thanonkeo, P., Laopaiboon, L., Laopaiboon, P., Yunchalard, S., Kaewkannetra, P. and Thanonkeo, S., 2007, The Batch Ethanol Fermentation of Jerusalem Artichoke Using *Saccharomyces cerevisiae*, *KMITL Sci. Tech. J.* 7, S2, 93-96.
- [17] Yamba, F.D., Wamukwamba, C.K., Matsika, E., and Sangiso, M. 2007. Investigation into the Production and Use of Bioethanol from Sweet Sorghum as an Alternative Fuel. Department of Mechanical Engineering, School of Engineering, University of Zambia, Lusaka.
- [18] Galbe, M., Süssner, P., Wingren, A., Zacchi, G. I., s.l. *Applied Biochemistry and Biotechnology*, 2007, Vol. 124, 1101-1117, Process Engineering Economics of Bioethanol Production.
- [19] Hahn-Hägerdal, B., Galbe, M., Gorwa-Grauslund M.F., Liden, G., Zacchi, G. I2, and s.l.: *TRENDS in Biotechnology*, 2006, Vol. 24. Bioethanol – The fuel of tomorrow from the residues of today

EVALUATION OF DAIRY EFFLUENT DETOXIFICATION AND REMOVAL EFFICIENCY IN AN INTEGRATED WASTEWATER TREATMENT SYSTEM USING LOW-COST ADSORBENTS

R. S. Rajput^{1,✉}, M. Singh², P. Kumar³ and N. K. Srivastava⁴

¹Department of Chemistry Rajkiya Engineering College, Kannauj, 209732 (U.P.) India

²Dr. Ambedkar Institute of Technology for Handicapped, Kanpur, 208024 (U.P.) India

³Department of Chemical Engineering Institute of Engineering & Technology, 22602, Lucknow (U.P.) India

⁴Department of Chemical Engineering Dr. B. R. Ambedkar National Institute of Technology, 144011, Jalandhar (Punjab) India

✉Corresponding Author: ravishrajput@gmail.com

ABSTRACT

Dairy effluent typically contains lipids, lactose, and whey proteins, all of which contribute to a rise in biological oxygen demand, chemical oxygen demand, and other water parameters. Physicochemical characteristics of wastewater can be reduced by biological, chemical, and Physicochemical treatments. The adsorption technique is attractive for the removal of organic compounds in wastewater among the numerous Physicochemical treatment methods. Two low-cost adsorbents were chosen for this work, and a comparative analysis was performed. The goal of this study was to find a new application of rice husk ash and sugarcane bagasse ash. When rice husk ash and sugarcane bagasse ash were employed, the removal of organic pollutants, biological oxygen demand, chemical oxygen demand and other parameters from dairy effluent were evaluated and compared. The organic pollutants, color, biological oxygen demand, and chemical oxygen demand have all been removed from dairy effluent using rice husk ash and sugarcane bagasse ash as adsorbents. At room temperature, rice husk ash adsorbents were reported to remove up to 73.11 % of biological oxygen demand, with a maximum dose of 800mg/L, whereas sugarcane bagasse adsorbents were removed 78.17 % with the same dose. The Chemical oxygen demand removal efficiency was also evaluated and compared to rice husk ash and sugarcane bagasse ash which were 89.12% and 81.23%, respectively with a dosage of 800 mg/L at 7.4 pH.

Keywords: Dairy Effluent, Adsorbent, Rice Husk Ash, Sugarcane Bagasse, Physicochemical Parameters

RASAYAN J. Chem., Vol. 15, No.1, 2022

INTRODUCTION

The dairy industry is the fastest growing industry in the world. Dairy effluent is more easily contaminated with high levels of organic substances, pollutants, and microbes. The dairy industry is sensitive to water and requires a large volume of water for various operations such as heating, cooling, cleaning, etc.¹ In milk processing, a large effluent discharge volume of 03 liters per liter of milk has been reported.²⁻⁴ The present investigation was carried out for the detoxification of organic contaminants, color, Turbidity, BOD (Biological oxygen demand), COD (Chemical oxygen demand), and degree of efficiency of dairy effluents using low-cost adsorbents like rice husk ash (RHA) and sugarcane bagasse ash (SBA), which were obtained from rice and sugar mill individually. During monsoon, dairy effluent was collected from the dairy plant (CMP) Kannauj, U.P., India. In the present investigation, the adsorption technique is used for detoxification and removal of color, odor. During the investigation, various Physicochemical parameters i.e. pH, BOD, COD, TDS (Total dissolved solids), TSS (Total suspended solid), etc. were analyzed.

The biological, chemical and Physicochemical treatments are ways to reduce the Physicochemical properties of effluent^{5,6} to the desired values. The adsorption technique was shown to be the most effective at removing organic compounds and reducing COD in wastewater among the other

Physicochemical treatment methods.⁷ Commercial activated carbon is successful in removing organic contamination, but it comes at a high initial cost and its regeneration problem in system.⁸ Therefore, rice husk ash and sugarcane bagasse ash were chosen as low-cost adsorbents in this study. Rice husk ash has been widely used as an efficient adsorbent for filtration to filter solid-liquid systems such as colloids, highly compatible fine solid particles, or difficult-to-filter materials.⁹ Recent studies on RHA have shown excellent adsorption properties which help in reducing the color, odor, COD, BOD and organic contaminants.¹⁰ RHA is compared to sugarcane bagasse, which generally possesses biosorption of organic compounds due to high-quality fibers and surface, while rice husk ash material exhibits both physical adsorptions for removal of organic compounds and adsorption chemistry (ion exchange) to remove some ions and metals. The physical adsorption of RHA is due to its porous structure and high surface area.¹¹ SBA is a by-product sugarcane industry. In addition to this SBA are a low-cost absorbent and high availability. After crushing and extracting the sugarcane juice, a fibrous residue from the sugarcane stalks remains.¹² Which we call SBA. SBA is a form of industrial waste that contains 50% cellulose, 25% hemicellulose, and 25% lignin.¹³ These agricultural wastes pave the path to use as low-cost adsorbents which effectively reduce the cost of the process for reducing the wastewater contamination.¹⁴ Bagasse from sugarcane exhibits biosorption characteristics. Bio adsorption is a kind of adsorption that can be used to remove contaminants from biological materials that are not metabolically active.⁷ The biosorption process has several advantages over traditional treatment methods, including cheap cost, high efficiency, reduced chemical use, no need for extra nutrients, biosorbent regeneration capacity, and metal recovery.¹² Sugarcane bagasse ash has a porous character due to its specific gravity, structure, and vesicular consistency.¹⁵

EXPERIMENTAL

Sample Collection

Samples were collected from the Cow milk plant (CMP) Kannauj, U.P. (India). After sample collection, the discharge rate of wastewater was also measured from the dairy plant's outlet. The flow rate of wastewater from the plant was measured by a differential pressure flow meter. The sample was collected in a sterile 5L container from the identified site. The container was washed with alcohol and distilled water and dried in a hot air oven for 15 minutes at 30°C and was allowed to cool at room temperature. After sample collection, the cap of the container was tightly locked and placed below 4°C to avoid any physicochemical change in the effluent.¹⁶ An antibiotic (Chloramphenicol 500 mg/L) was added to the influent to inhibit bacterial growth and incubated for 3 days at room temperature (27°C).¹⁷

Preparation of Rice Husk Ash

Rice husk ash was obtained from a local rice mill of Kannauj, Uttar Pradesh, India. It was washed with distilled water, dried for 2 hours at 60°C, washed again with acetone and NaOH (0.3M) to remove dirt and other impurities, and then dried for 4 hours at 60°C.¹⁸ RHA was obtained by heating rice husk samples at 500°C for 6 hours in a muffle furnace. Obtain RHA was grey in color because it was completely burned. The average particle size of RHA is 0.20mm and has a specific gravity of 2.10.¹⁹

Preparation of Sugarcane Bagasse Ash

Sugarcane was obtained from a mill in Sitapur, Uttar Pradesh, India. It was cleaned with distilled water to remove dirt and suspended impurities, then dried for 2 hours at 80°C, cooled, then washed again with acetone and distilled water to remove any remaining contaminants, and dried for 4 hours at 100°C to remove moisture. After drying, 250g bagasse was burned in a muffle furnace at 1200°C for 5 hours to generate SBA.²⁰ The average particle size of SBA is 0.30mm, and the specific gravity is 1.95.²¹

Chemicals and Instrumentation

Analytical reagent grade (AR) chemicals were used in this study. Chemical oxygen demand (COD) was analyzed with COD Digestion Unit, KHERA KI-162, BOD by BOD Incubator KHERA KI-216, double beam UV-visible spectrophotometer (Systronics 2203), FTIR spectrophotometer (Perkin-Elmer RX1) as KBr pellets and pH by digital pH meter.

General Procedure

The adsorbent dosage for each batch of RHA and SBA was changed between 200mg/L to 1000mg/L at 27°C for each experiment. In 1000 mL of dairy wastewater, the desired amount of adsorbent was added. At 27°C, this mixture was shaken at a constant speed of 150 rpm in a temperature-controlled shaker for the necessary amount of time. At the end of the set time interval, the adsorbent was filtered from treated water and Physicochemical parameters were analyzed.¹⁸ For data consistency, all experiments were repeated twice. In all of the experiments, the standard deviations for duplicate experiments were less than 5%. The characteristics of the effluent and treated water are shown in Table-1. The percentage of removal was calculated using the following formula:

$$\% \text{ Removal Efficiency} = \frac{C_i - C_t}{C_i} \times 100 \quad (1)$$

Where C_i is the initial concentration of waste water, C_t is after 't' time concentration.

RESULTS AND DISCUSSION

Characterization of Dairy Wastewater

Initial sets of experiments were performed with untreated dairy wastewater and obtained results of physicochemical parameters and percentage of removal were summarized in Table-1. The untreated wastewater was light grey in appearance with an unpleasant odor, after adsorbent treatment water was clear without odor. Some variation in color and odor of the effluent is due to the biosorption property of rice husk ash or bagasse ash, which plays an important role in the removal of impurities.

Characterization of Treated Dairy Wastewater

The experiments were carried out using two selected adsorbents RHA and SBA for the treatment process. The contact time of wastewater and adsorbent was taken as 12 hrs. The obtained values of the Physicochemical parameter of treated dairy wastewater are summarized in Table-1. RHA and SBA as adsorbents leads to the removal of total suspended solids and consequently in the color reduction²². The treated water was used for the characterization of the Physicochemical parameters. Results show that the color and value of other Physicochemical parameters of dairy effluent were changed. This change may be attributed to the biosorption of organic materials by the adsorbents.

Characterization of Adsorbents

The absorption bands for such adsorbent materials are usually broad and diffuse, according to IR spectra studies of rice husk ash and Sugarcane bagasse. It was determined which chemical groups matched the wavenumber of bands cm^{-1} . The Sugarcane bagasse has an OH group in cellulose (1261 cm^{-1}) and a presence of β -glycosidic linkage (910 cm^{-1}) in addition to the normal bands ester carbonyl (1730 cm^{-1}) groups, while in rice husk had (3400 cm^{-1}) OH groups, 2926 cm^{-1} (C-H groups), and $1641\text{--}1738 \text{ cm}^{-1}$ (C = O) groups were observed.

Adsorbent Dosage

The experiments were done under Constant temperature (27°C), agitation speed (250 rpm), constant pH approximately 6.0, and varying adsorbent dosage (200, 400, 600, 800, and 1000 mg/L) were used. As seen in figure1, the percentage removal of parameters varies with adsorbent dosage. It was observed that as the dosage was increased the percentage of removal was also increased. The release of soluble organic molecules contained in plant products may be responsible for the growth in COD, BOD and other parameters value. In RHA, the percentage removal was fairly high, reaching 800 mg/L after 4 hours, whereas in SBA, it was only 600 mg/L. After that, up to 1000 mg/L, there was no more decline. It should be mentioned that trials were carried out for dosages of more than 1000 mg/L, yet adsorption and desorption did not change. Although these adsorbent materials are porous in nature, the porous volume is coupled with multiple minute pores, resulting in extra diffusion resistance and a reduction in removal.

pH

The pH of the effluent is an important parameter that determines the effectiveness of bioadsorption investigations. This affects not only the surface charge of the biosorbent, but also the type and concentration of organic molecules in effluent solution, as well as the degree of dissociation of functional groups in the active site of the adsorbent. The pH was changed between 6.6 and 7.81 in the range from acidic to strongly alkaline, while other parameters were maintained such as the dosage of the adsorbent from 200 mg/L to 1000 mg/L, temperature 27° C and rotation speed 250 revolutions per minute. Removals of organic components from the samples were increased with increasing pH. This shows that the removal of organic products is more effective at more than 7 pH. The adsorbent surface is negatively charged at higher pH values due to the dissociation of functional groups, while at lower pH values it has a net positive charge. The surface of the rice hulls and sugarcane bagasse ash protonate and become positive at low pH values, and the surface is linked by hydrogen ions, which represent the interactions between organic molecules and binding sites through attractive interactions.

Total Dissolve Solid

SBA has a higher total dissolved solid removal power (88.15%) than RHA (87.10%). The presence of organic and inorganic compounds in the effluent produces high amount of TDS. Water contains a large number of solids, as we all know. Both RHA and SBA have Oxygen atoms in various forms, each with a lone pair of electrons. Hardness is caused by the presence of cation in water. The interaction of these cations with the negative charge of adsorbents helps in the removal of TDS.

Turbidity

The removal efficiency of RHA and SBA were tested after 2hrs. and 4 hrs. of treatment by the filtration process. It was observed that after the addition of RHA and SBA, turbidity drastically changed with the increased amount of dosage as shown in Table-1. For the observation of turbidity, various amounts of adsorbents were used such as 200mg, 400mg, 600mg, 800mg, 1000mg in 250mL of effluent at 6.37 pH which was the original pH of the effluent. The turbidity of RHA and SBA treated water was observed with different dosages and time and it was found that SBA treated water has more % removal efficiency (87.28%) with a dose 600mg at 7.52 pH after 4 h, while in RHA treated water % removal efficiency (80.21%) with dose 600mg at 7.1 pH after 4 h which was less than SBA. The Turbidity Removal Efficiency of sugarcane bagasse is high due to the presence of high-grade fibres and surface area, while in RHA physical adsorption occurs due to porous structure and surface area.²³⁻²⁵

COD

The COD of dairy wastewater samples treated with two different adsorbents RHA and SBA is calculated. It indicates a continuous removal of organic pollutants by adsorption on the surface of rice husk ash and sugarcane bagasse ash. Table-1 showed that the COD concentration decreased with adsorbent dosage. Equation-1 was used to compute the percentage of COD removed. Table-1 shows that the % removal increases gradually as the time and the dosage increase. It can be attributed to the fact that greater time (4 h) becomes available for the organic substances to stick with the adsorbent surface, as well as surface adsorption increases with dosage. At the 27°C, the maximum percentage removal in COD using RHA and SBA were found to be 89.12%, 83.17%, respectively. RHA was found to be highly efficient for removing organic pollutants from dairy wastewater. The percentage removal of 89.12% within 4h using a dose of 800mg/L was obtained at 7.4 pH.

BOD

Figure-1 shows the effect of adsorbent dose on the reduction of BOD. It may be seen that the % of BOD removal efficiency increases with increase in the adsorbent dose up to some extent and thereafter for further increase in the adsorbent dose for 4 h contact time. The % removal of BOD was higher in the case of SBA(89.20%) followed by RHA(73.11%) due to their Physicochemical adsorption properties and high-grade fibers. The removal of BOD by SBA has sharply increased from 36.33% to 89.20% with an adsorbent dose from 200mg to 1000mg. However, with a further increase in the adsorbent dose, there was

no appreciable increase in the BOD removal. Maximum BOD removal by SBA, RHA was found to be 89.20%, 73.11%, respectively with an adsorbent dose of 800mg/L. Hence SBA has great ability to remove the BOD of dairy wastewater.

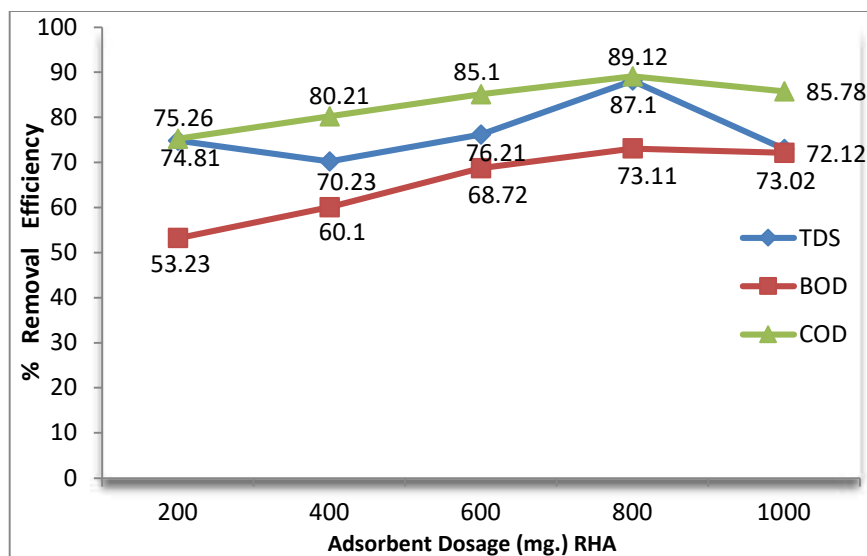


Fig.-1: % RHA's Removal Efficiency for BOD, COD, and TDS is measured in %

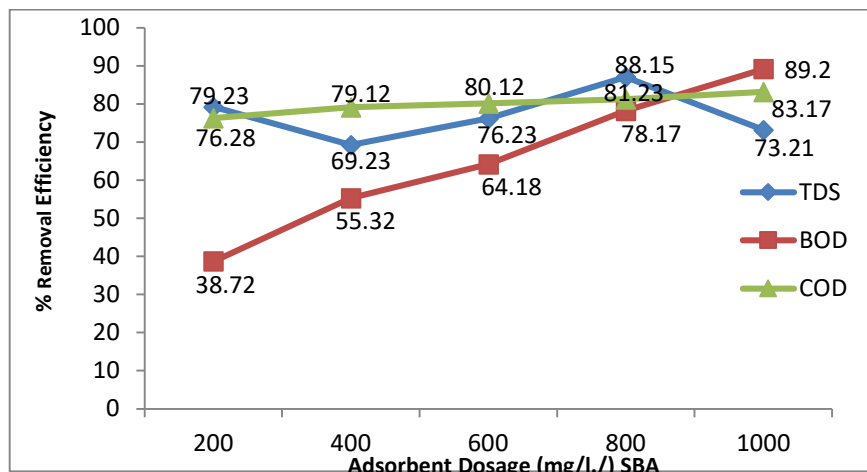


Fig.-2: SBA's Removal Efficiency for BOD, COD, and TDS is measured in %

Table-1: Analysis of Physicochemical Parameters of Dairy Effluent Control and after Treatment

Parameters		pH	Turbidity (NTU)	TDS (mg/L)	TSS (mg/L)	BOD3	COD
Control	Grey in Color	6.37 ± 0.08	1147.37 ± 1.12	1706.08 ± 0.80	736.24 ± 0.41	1093.24 ± 0.68	2318.59 ± 0.05
Doasage (mg.)	Time (Hrs.)	(RHA) Adsorbent + Effluent (Removal Efficiency in % Except pH)					
200mg.	2	6.6	68.84	71.23	72.1	48.66	70.19
	4	6.8	70.01	74.81	75.1	53.23	75.26
	6	6.8	70.1	74.81	76.12	53.2	75.21
400mg.	2	6.9	73.85	68.71	70.21	58.23	76.78
	4	7.1	77.25	70.23	74.23	60.1	80.21
	6	7.1	77.4	70.38	74.2	61.89	80.2
600mg.	2	6.9	79.32	73	76.18	63.28	82.32

	4	7.1	80.21	76.21	77.18	68.72	85.1
	6	7.1	80.21	76.78	77.2	69.21	86.21
800mg.	2	7.4	81.43	83	85.1	68.72	86.2
	4	7.4	81.56	87.15	90.2	73.11	89.12
	6	7.39	81.52	87.15	90.12	73.1	89.01
1000mg.	2	7.2	80.01	73.02	78.02	68.7	84.98
	4	7.3	79.56	73.02	79.18	72.12	85.78
	6	7.31	80.12	73.1	80.01	72.12	86.13
(SBA) Adsorbent + Effluent (Removal efficiency in % Except pH)							
200mg.	2	7.81	73.21	79.93	72.18	36.33	75.98
	4	7.9	75.26	79.23	73.28	38.72	76.28
	6	7.89	75.32	80.1	73.25	37.85	77.21
400mg.	2	7.56	77.24	70.12	70.2	51.78	78.72
	4	7.71	79.58	69.23	74.23	55.32	79.12
	6	7.66	79.5	69.2	74.21	55.32	79.1
600mg.	2	7.48	74.51	76.2	75.23	64.21	76.48
	4	7.52	87.28	76.23	77.18	64.18	80.12
	6	7.5	86.32	74.52	77.21	64.19	80.11
800mg.	2	7.3	66.11	86.5	80.1	76.01	77.23
	4	7.37	65.72	88.15	82.12	78.17	81.23
	6	7.35	65.85	88.14	81.89	78.1	81.19
1000mg.	2	6.9	62.71	71.78	72.28	80.38	72.01
	4	7.1	62.12	73.21	78.31	89.2	83.17
	6	7.11	62.12	73.21	78.31	89.2	83.17

CONCLUSION

The results obtained after using the RHA and SBA adsorbent for the treatment of dairy wastewater showed certain points in this investigation. The results reveal that SBA and rice husk may be utilized efficiently as adsorbents for the treatment of dairy effluents, as they can remove up to 89.2% and 73.11% of BOD₃ respectively, using an adsorbent dose of 800 mg/L, pH 7.37-7.4 at 27°C. This treatment method can be a very cost-effective and efficient way to handle CMP wastewater. The results also suggest that it is the best treatment after filtering, as all of the specified parameters have been significantly reduced. The pH regulates the electrostatic interactions between adsorptive-adsorbent, which have a significant impact on the adsorption process.

ACKNOWLEDGEMENT

The authors are thankful to Director CMP Kannauj, India for providing a sample of the dairy plant and the necessary facilities to complete it.

REFERENCES

1. B. Sarkar, P. P. Chakrabarti, A. Vijaykumar and V. Kale, *Desalination*, **195**, 141(2006), <https://doi.org/10.1016/j.desal.2005.11.015>
2. M. Vourch, B. Balanec, B. Chaufer, and G. Dorange, *Desalination*, **219**, 190(2008), <https://doi.org/10.1016/j.desal.2007.05.013>
3. N. Nouria, E. Benyagoub, A. Mellouk, and Y. Benmoussa, *Applied Water Science*, **229**,1(2020), <https://doi.org/10.1007/s13201-020-01309-w>
4. W. Janczukowicz, M. Zieliński, and M. Dębowski, *Bioresour. Technol.*, **99**, 4199(2008), <https://doi.org/10.1016/j.biortech.2007.08.077>
5. A. Vermaand, A. Singh, *International Journal of Current Microbiology and Applied Sciences*, **6**, 1769 (2017), <http://dx.doi.org/10.20546/ijemas.2017.602.213>
6. A. K. Slavov, *Food Technology and Biotechnology*, **55**, 14(2017), <http://dx.doi.org/10.17113/ftb.55.01.17.4520>
7. G. Crini, *Progress in Polymer Science*, **30**, 38(2005), <https://doi.org/10.1016/j.progpolymsci.2004.11.002>

8. M. T. Yagub, T. K. Sen, S. Afroze, and H. M. Ang, *Advances in Colloid and Interface Science*, **209**, 172(2014), <https://doi.org/10.1016/j.cis.2014.04.002>
9. G. M. Gadd, *Journal of Chemical Technology and Biotechnology*, **84**, 13(2009), <https://doi.org/10.1002/jctb.1999>
10. D. V. S. Bhagavanulu, *International Research Journal of Engineering and Technology*, **2**, 327(2015).
11. R. D. Khonde and S. L. Pandharipande, *International Journal of Computer Applications*, **41**,1(2012), <http://dx.doi.org/10.5120/5526-7567>
12. M. Fomina, G. M. Gadd, *Bioresource Technology*, **160**, 3(2014), <https://doi.org/10.1016/j.biortech.2013.12.102>
13. E.M. Soliman, S.A. Ahmed and A.A. Fadl, *Desalination*, **278**, 18(2011), <https://doi.org/10.1016/j.desal.2011.04.072>
14. A. Farhadi, A. Ameri and S. Tamjidi, *Physical Chemistry Research*, **9**, 211(2021), <http://dx.doi.org/10.22036/PCR.2021.256683.1852>
15. D. Gisi, G. Lofrano, M. Grassi and M. Notarnicola, *Sustainable Materials and Technologies*, **9**, 10(2016), <https://doi.org/10.1016/j.susmat.2016.06.002>
16. B. Demirel, O.Yenigun, and T. Onay, *Process Biochemistry*, **40**, 2583(2005), <https://doi.org/10.1016/j.procbio.2004.12.015>
17. G. Hageskal, A.K. Knutsen, P. Gaustad, G. S. Hoog, and I. Skaar, *Applied and Environmental Microbiology*, **72**, 7586 (2006), <https://doi.org/10.1128/AEM.01628-06>
18. J. Fito, N. Tefera, and S.W.H.V. Hulle *Chemical and Biological Technologies in Agriculture*, **6**, 6 (2019), <https://doi.org/10.1186/s40538-019-0144-5>
19. M. Ghorbani, and H. Eisazadeh, *Composites: Part B*, **45**, 1(2013), <https://doi.org/10.1016/j.compositesb.2012.09.035>
20. Y. Maung, T. Than Win, Aye Thidao, S. S. Htwe, and K. K. Soe, *International Journal of Technical Research and Applications*, **3**, 84(2015)
21. J. P. Kushwaha, V. C. Srivastava and I. D. Mall, *Critical Reviews in Food Science and Nutrition*, **51**, 442 (2011), <https://doi.org/10.1080/10408391003663879>
22. D.D. Bui, J. Hu, P. Stroeven, *Cement & Concrete Composites* **27**, 357(2005), <https://doi.org/10.1016/j.cemconcomp.2004.05.002>
23. E. Arif, M. W. Clark, N. Lake, *Construction and Building Materials*, **128**, 287(2016), <https://doi.org/10.1016/j.conbuildmat.2016.10.091>
24. Qing Xu, Tao Ji, San-Ji Gao , Zhengxian Yang, and Nengsen Wu, *Materials*, **12**, 39,1(2019), <https://doi.org/10.3390/ma12010039>
25. U. Pathak, P. Das, P. Banerjee, and S. Datta, *Journal of Thermodynamics*, **1**, Article ID 3746316(2016), <https://doi.org/10.1155/2016/3746316>

[RJC-6727/2021]

Analytical Study of A Two-Phase Model For Steady Flow of Blood in A Circular Tube

S.R. Verma and Anuj Srivastava

Department of Mathematics, D.A-V. College, Kanpur (U.P.), India

Abstract:

The present paper deals with a mathematical model of blood flow through narrow circular tube. The model consists of a core region of suspension of all the erythrocytes assumed to be a power law fluid and a peripheral cell-depleted layer of plasma as a Newtonian fluid. The system of differential equations has been solved analytically. The expressions for velocity profile, Bluntness parameter, flow rate, the ratio of core hematocrit to discharge hematocrit (H_c/H_D), apparent viscosity (μ_{app}), and the ratio of tube hematocrit to discharge hematocrit (H_T/H_D) and shear stress at the wall have obtained. Some of them have been discussed through graphs.

Key words: Two-phase blood flow, cell-depleted layer, Bluntness, Hematocrit, apparent viscosity.

I. Introduction:

Blood is composed of two major components; the cellular component and the plasma component. In an average adult, the blood volume is approximately 5 litre of which approximately 55% to 60% is plasma and the remaining portion is cellular. More than 99% of the cellular component is composed of red blood cells. The most common way to quantify the percent of blood that is cellular is by quantifying the packed red blood cell volume, which is termed the hematocrit. Hematocrit or red blood cell (RBC) concentration and the shear rate are the principal independent variables for describing the apparent viscosity of blood and other RBC suspension. The formation of RBC aggregates at low shear rates may affect blood flow in the microcirculation. The experimental evidence suggests that hematocrit distribution in the microvasculature is not uniform: RBCs tend to concentrate near the center of the vessel, thus forming and RBC-depleted plasma layer near the wall. RBCs are non-uniformly distributed not only within, but also among the micro vessels. The heterogeneous distribution of RBCs and other blood cells has important implications for microvascular hemodynamic and molecular transport.

The two important mechanisms that cause non-proportional distribution of RBCs and plasma in the microcirculation are "cell screening and "plasma skimming". The cell screening mechanism (Cokelet, 1976 [1]; Pries *et al.*, 1981 [2]), involves direct cell-cell and cell wall-fluid mechanical interactions near the orifice of a side branch.

These interactions cause the RBC trajectories to deviate from the fluid stream lines; which would exist in the absence of the cells. The plasma skimming mechanism is related to the non uniform

distribution of RBCs at the inlet cross- section of arteriolar bifurcations, in particular the formation of a cell-depleted layer near the vascular wall (Tateishi *et al.*, 1994 [3]; Yamaguchi *et al.*, 1992 [4]). For the "ideal" plasma skimming case, when the flow fraction in the branch is less than 0.5 the discharge hematocrit in the branch becomes lower than in the parent vessel.

When blood flows through tubes, the two-phase nature of blood as a suspension becomes important as the diameter of the red blood cell (RBC) becomes comparable to the tube diameter. The following are some of the effects observed in vitro and in vivo:

- (i) Fahraeus - Lindqvist effect: dependence of apparent viscosity on tube diameter;
- (ii) Fahraeus effect: dependence of tube or vessel hematocrit on tube diameter;
- (iii) Existence of a cell-free or cell-depleted layer near the wall;
- (iv) Blunt velocity profile;
- (v) Phase separation effect: disproportionate distribution of red blood cells and plasma at vessel bifurcation.

Fournier [5] have been developed several models to interpret these effects. Pries *et al.* [6] reviewed biophysical aspects of micro-vascular blood flow in vivo as well as in vitro.

Nair *et al.* [7] used a two-phase model for the blood in modeling transport of oxygen in arterioles. They considered a cell-rich cone surrounded by a cell-free plasma layer.

In the cell-rich core, the radial hematocrit distribution was expressed as a power law profile with maximum at the center of the tube. The thickness of the cell-free layer was chosen on the basis of geometrical consideration in terms of RBC size and radius of the tube. However, the

dependence of the thickness on the cell free layer on hematocrit was not taken into account. **Seshadri and Jaffrin [8]** modeled the outer layer as cell-depleted having a lower hematocrit than in the core. The apparent viscosity and the mean tube hematocrit were taken from the measurements obtained in glass tubes. The concentration of RBCs in the cell-depleted layer was assumed to be 50% of that in the core. **Gupta et al., [9]** divided the outer layer into a cell-free plasma layer and cell-depleted layer. In both these studies, the velocity profile in the core was assumed to follow a power law. **Pries et al. [10,11,12]** derived empirical relationship of the relative apparent viscosity and mean tube hematocrit as parametric functions of tube diameter and discharge hematocrit from in vitro **Pries et al. [10,12]** and in vivo **Pries et al. [11]** data.

Numerical modeling can provide information for various hematocrits. Hematocrit is known to affect the viscous properties of blood (**Merril, E.W. [13]** and **Chien, S. et. al. [14]**) and physiological abnormalities in hematocrit are associated with diseases which alter the blood composition (**Chien, S. et. al. [14]**; **Halvorsen, S.[15]**; **Skovborg, R. [16]** and **Leblond, P.F. et. al. [17]**). For example, over production of red blood cells (polycythemia) increases whole blood viscosity, while iron deficiency (anemia) decreases blood viscosity. Changes in blood composition may influence wall shear stress patterns in the arterial system, which may in turn play a role in the sequence of arterial diseases. Effect of hematocrit on wall shear rate in oscillatory flow has been studied by **Kathleen and John [18]** and found that increase in hematocrit produced a decrease in the peak wall shear rate in both the straight and curved artery models and a corresponding decrease in wall shear rate reversal on the inside wall of the curved artery model.

Das et al., [19] considered the effect of nonaxisymmetric hematocrit distribution on non-Newtonian blood flow in small tubes. Eccentric hematocrit distribution is considered such that the axis of the cylindrical core region of red cell suspension is parallel to the axis of the blood vessel but not coincident. Human blood is described by Quemada's rheological model and cat blood is

described by Casson's model. Velocity distribution, shear stress, apparent viscosity and Fahraeus effect have been calculated numerically. These are strongly influenced by the eccentricity factor, the core radius and the tube hematocrit. **Maithili Sharan and Popel [20]** proposed a two-phase model for flow of blood in narrow tubes with increased effective viscosity near the wall. The model consists of a central core of suspended erythrocytes and a cell-free layer surrounding the core. A system of nonlinear equation is solved numerically to estimate bluntness, core radius and core hematocrit. Variation of apparent viscosity and tube hematocrit with the tube diameter and the discharge hematocrit in vitro have been discussed. **Davod Alizadehard et al., [21]** investigated the deformation of RBCs in micro vessels for a variety of vessel diameter (8-50 μ m), Hematocrit (20-45%) and shear rates (20-150 S^{-1}) and comparing the apparent viscosity with experimental results.

The aim of the present investigation is to study the flow of blood as a two-phase model. The behavior of blood is considered as power law in core region and cell-depleted layer as Newtonian fluid. Analytical expressions for velocity profile, bluntness parameter, flow rate, ratio of core hematocrit to discharge hematocrit (H_c/H_D), apparent viscosity and ratio of tube hematocrit to discharge hematocrit (H_T/H_D), shear stress at the wall have obtained. The results are discussed graphically.

II. Mathematical Analysis:

The geometry of the model is shown in Fig.1. The steady laminar two layer model for the blood flow within a cylindrical tube of radius R consisting a central core of radius r_h and effective viscosity μ_c which contains an erythrocyte suspension of uniform hematocrit H_c and a cell-free layer outside the core containing plasma with an effective viscosity μ_0 . The blood is considered as non-Newtonian power law fluid in core region and plasma is Newtonian fluid in cell free layer.

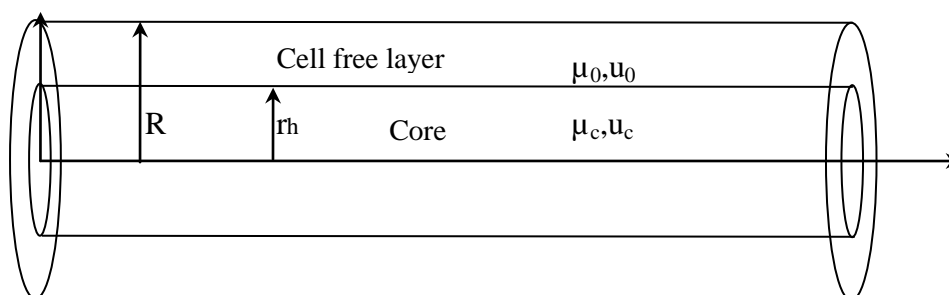


Fig.1. Geometry of the flow model

2.1 Governing equation and boundary conditions:-

The constitutive equation of motion for incompressible steady fully developed flow in a tube reduces to:

$$-\frac{\partial p}{\partial z} + \frac{\mu_c}{r} \frac{\partial}{\partial r} \left[r \left(\frac{\partial u_c}{\partial r} \right)^n \right] = 0, \quad 0 \leq r < r_h \quad (1)$$

for the central core with red blood cells and

$$-\frac{\partial p}{\partial z} + \frac{\mu_0}{r} \frac{\partial}{\partial r} \left[r \left(\frac{\partial u_0}{\partial r} \right) \right] = 0, \quad r_h < r < R \quad (2)$$

for the cell-free layer, where u_c and u_0 are the velocities in the cone and plasma layer respectively, p is the hydraulic pressure and r and z represent the radial and axial direction in the tube.

The boundary conditions are:

- (a) the velocity gradient vanishes along the axis of the tube:

$$\frac{\partial u_c}{\partial r} = 0 \quad \text{at } r = 0 \quad (3)$$

- (b) No slip condition is assumed at the wall;

$$u_0 = 0 \quad \text{at } r = R \quad (4)$$

- (c) The velocity and shear stress are continuous at the interface of plasma and the core:

$$(i) \quad u_c = u_0 \quad \text{at } r = r_h \quad (5)$$

$$(ii) \quad \mu_c \frac{\partial u_c}{\partial r} = \mu_0 \frac{\partial u_0}{\partial r} \quad \text{at } r = r_h \quad (6)$$

2.2 Solution of the problem

The solution of equation (1) and (2), subject to the boundary conditions (3) - (6) is given by

$$u_c(\xi) = -\frac{R^2}{4\mu_0} \frac{\partial p}{\partial z} \left[1 - \lambda^2 + \frac{\mu_0}{\mu_c} \alpha \lambda^{\frac{n+1}{n}} \right] \left[1 - \frac{\frac{\mu_0}{\mu_c} \alpha}{1 - \lambda^2 + \frac{\mu_0}{\mu_c} \alpha \lambda^{\frac{n+1}{n}}} \xi^{\frac{n+1}{n}} \right]; \quad 0 \leq \xi \leq \lambda, \quad (7)$$

$$u_0(\xi) = -\frac{R^2}{4\mu_0} \frac{\partial p}{\partial z} [1 - \xi^2]; \quad \lambda \leq \xi \leq 1 \quad (8)$$

where

$$\xi = \frac{r}{R}, \quad \lambda = \frac{r_h}{R}, \quad \alpha = 2^{\frac{2n-1}{n}} \left(\frac{n}{n+1} \right) \left(\frac{R}{\mu_c} \frac{\partial p}{\partial z} \right)^{\frac{1-n}{n}}$$

$\alpha=1$ for $n = 1$ (Newtonian fluid) and $\frac{\partial p}{\partial z}$ is pressure gradient along the length of the tube.

Velocity in the core $u_c(\xi)$ can be expressed as

$$u_c(\xi) = u_{\max} \left(1 - B \xi^{\frac{n+1}{n}} \right) \quad (9)$$

where,

$$u_{\max} = -\frac{R^2}{4\mu_0} \frac{\partial p}{\partial z} \left[1 - \lambda^2 + \frac{\mu_0}{\mu_c} \alpha \lambda^{\frac{n+1}{n}} \right] \quad (10)$$

$$B = \frac{\frac{\mu_0}{\mu_c} \alpha}{1 - \lambda^2 + \frac{\mu_0}{\mu_c} \alpha \lambda^{\frac{n+1}{n}}} \quad (11)$$

The parameter B is the bluntness of the velocity profile. When $n = 1$ and $\mu_c \rightarrow \mu_0$ then $B \rightarrow 1$ which give the velocity profile becomes parabolic throughout the entire cross-section of the tube and fluid in both layer in Newtonian.

The volumetric flow rate of the blood is given by

$$Q = 2\pi R^2 \int_0^\lambda u_c(\xi) \xi d\xi + 2\pi R^2 \int_\lambda^1 u_0(\xi) \xi d\xi \quad (12)$$

The expression for the flow rate Q is obtained as the evaluation of integrals in (12) with the velocity equations (7) and (8) as:

$$Q = -\frac{\pi R^4}{8\mu_0} \frac{\partial p}{\partial z} \left[1 - \lambda^4 + \frac{2(n+1)}{3n+1} \left(\frac{\mu_0}{\mu_c} \alpha \right) \lambda^{\frac{3n+1}{n}} \right] \quad (13)$$

Mass balance of the cells in the tube is defined as:

$$QH_D = 2\pi \int_0^1 \xi u(\xi) h(\xi) d\xi \quad (14)$$

Where H_D is the discharge hematocrit and $h(\xi)$ is hematocrit function related to core hematocrit H_C as:

$$h(\xi) = \begin{cases} H_c & 0 \leq \xi < \lambda \\ 0 & \lambda < \xi \leq 1 \end{cases} \quad (15)$$

Using (7) and (8) in (14) with (15) we obtain

$$QH_D = -\frac{\pi R^4 H_c}{8\mu_0} \frac{\partial p}{\partial z} \left[2\lambda^2 (1 - \lambda^2) + \frac{2(n+1)}{3n+1} \frac{\mu_0}{\mu_c} \alpha \lambda^{\frac{3n+1}{n}} \right] \quad (16)$$

The ratio H_C/H_D can be obtain from equations (13) and 16) as:

$$\frac{H_C}{H_D} = \frac{1 - \lambda^4 + \frac{2(n+1)}{3n+1} \frac{\mu_0}{\mu_c} \alpha \lambda^{\frac{3n+1}{n}}}{2\lambda^2 (1 - \lambda^2) + \frac{2(n+1)}{3n+1} \frac{\mu_0}{\mu_c} \alpha \lambda^{\frac{3n+1}{n}}} \quad (17)$$

Equation (13) can be written as:

$$Q = -\frac{\pi R^4}{8\mu_{app}} \frac{\partial p}{\partial z} \quad (18)$$

Where μ_{app} is the apparent viscosity of total tube flow given by

$$\mu_{app} = \frac{\mu_0}{\left[1 - \lambda^4 + \frac{2(n+1)}{3n+1} \frac{\mu_0}{\mu_c} \alpha \lambda^{\frac{3n+1}{n}} \right]} \quad (19)$$

The tube hematocrit H_T is defined as:

$$H_T = 2 \int_0^1 h(\xi) \xi d\xi \quad (20)$$

Using equation (15) in (20), we get

$$H_T = \lambda^2 H_C \quad (21)$$

The average velocity of the blood $\left(\bar{U}\right)$ is given as

$$\bar{U} = \frac{Q}{\pi R^2} \quad (22)$$

From equation (10) and (22) the maximum velocity U_{\max} can be expressed as:

$$\frac{u_{\max}}{\bar{U}} = \frac{2\mu_{app}}{\mu_0} \left[1 - \lambda^2 + \frac{\mu_0}{\mu_C} \alpha \lambda^{\frac{n+1}{n}} \right] \quad (23)$$

The shear stress at the wall is defined as

$$\tau_w = -\frac{1}{2} \frac{\partial p}{\partial z} R \quad (24)$$

Using equation (18), and (22) in (24), the expression for the shear stress at the wall is obtained as

$$\tau_w = \frac{4 \mu_{app} \bar{U}}{R} \quad (25)$$

Equation (17), (19) and (21) express H_C , μ_{app} and H_T in terms of λ , H_D , μ_0 and μ_C .

III. Results and Discussion:-

In order to discuss the results of the theoretical model proposed in the study, the analytical expression for velocity profile, Bluntness parameter, flow rate, the ratio of core hematocrit to discharge hematocrit $\left(H_C/H_D\right)$, apparent viscosity, the tube hematocrit to discharge hematocrit $\left(H_T/H_D\right)$ and shear stress at the wall have been obtained. It may be noted that if we put $n=1$ in present model the results are obtained for both layer is Newtonian.

To discuss the problem, the Bluntness, B; ratio H_C/H_D , apparent viscosity, μ_{app} and ratio H_T/H_D obtained analytically in equation (11), (17), (19) and (21) respectively have been plotted in Figures 2 to 8. For numerical calculations we take $R = 100 \mu m$, $\frac{\partial p}{\partial z} = -75 \times 10^3 \text{ dyne/cm}^3$, $\mu_C = 3.8 \text{ cP}$, $\mu_0 = 1.2 \text{ cP}$.

The parameters B in equation (11) is the bluntness of the velocity profile in core. The parameter depends on the thickness of the cell-free layer. Figure 2 show the variation of bluntness parameter with tub radius R for $n = 3/4$ and $n = 5/4$. It is observe that the numerical values of B for $n=5/4$ are less than that for $n = 3/4$. Bluntness parameter B is plotted in Figure 3 with λ for different values of non-Newtonian parameter. For $n = 3/4$ bluntness parameter B first decreases upto $\lambda=0.2$ and then increases upto $\lambda = 0.6$ and again decreases upto $\lambda = 1$.

Bluntness parameters profile is near about similar for $n = 1$, and $n = 5/4$ but the values for $n = 1$ in greater than that of $n = 5/4$.

Figures 4 and 5 show are variation of ratio H_C/H_D with λ and with R for different values of n. H_C/H_D decreases with λ fastly upto $\lambda=0.4$ and then decreases slowly for $n = 1$ and $n = 5/4$ but increase upto $\lambda=0.5$ then decrease fastly upto $\lambda = 0.6$ and again increase. From figure 4 it is observe that when $n < 1$ the character in very different. Figure 5 shown that H_C/H_D increases fastly upto $R=125 \mu m$ and then slow effect is obtained for $n = 3/4$ whereas H_C/H_D decreases very slowly for $n = 5/4$. Numerical values for $n = 5/4$ of H_C/H_D are greater than that for $n = 3/4$.

The variation of apparent viscosity (μ_{app}) with λ for different value of non-Newtonian parameter n is shown in figure 6. μ_{app} increase slowly with λ upto 0.6 and fastly for $n = 1$ and $n = 5/4$ but the character is very different for $n = 3/4$. The trend of figure are same for $n = 1$ and $n = 5/4$ but numerical values for $n = 5/4$ for different λ are greater than that of $n = 1$.

From figure 7, it is observed that the ratio H_T / H_D increase with λ for $n = 1$ and $n = 5/4$ in similar trend but increases fastly upto $\lambda = 0.4$ then decreases upto $\lambda = 0.7$ and again increases.

Effect of tube radius R on H_T / H_D is plotted in Figure 8 for $n = 3/4, 5/4$. H_T / H_D increase with R for $n = 3/4$ and decreases with R for $n = 5/4$. Numerical values for $n = 5/4$ of H_T / H_D are greater than that for $n = 5/4$.

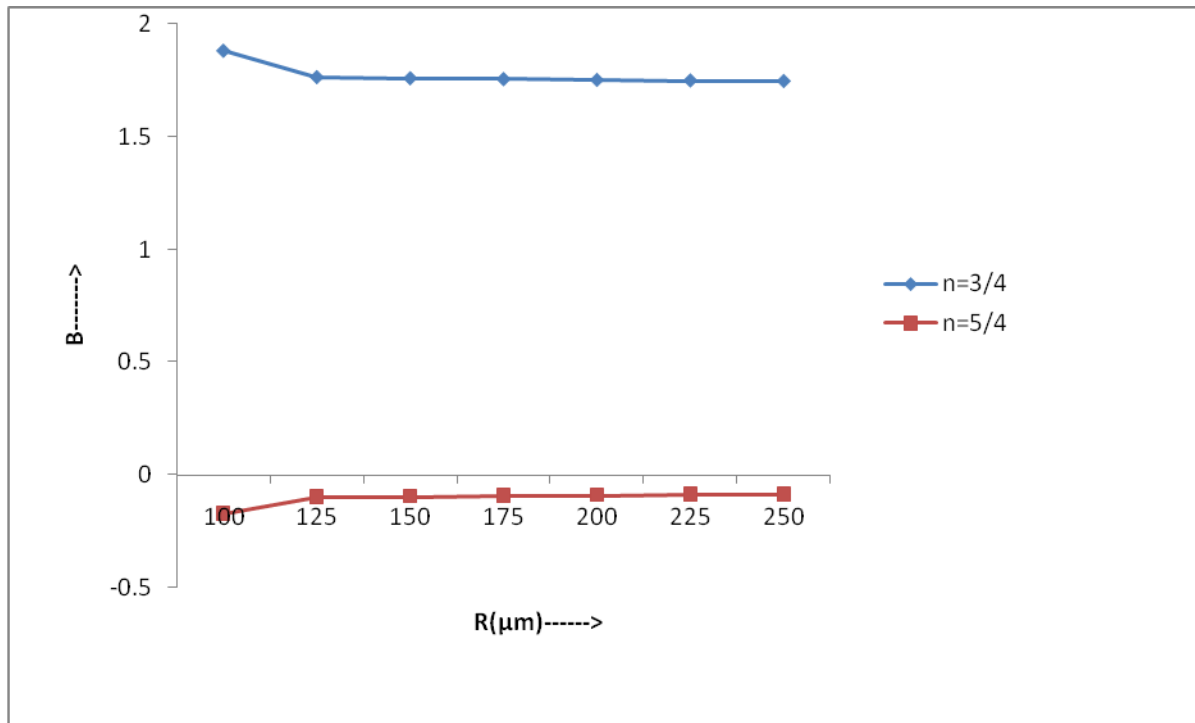


Fig. 2: Variation of Bluntness parameter (B) with R

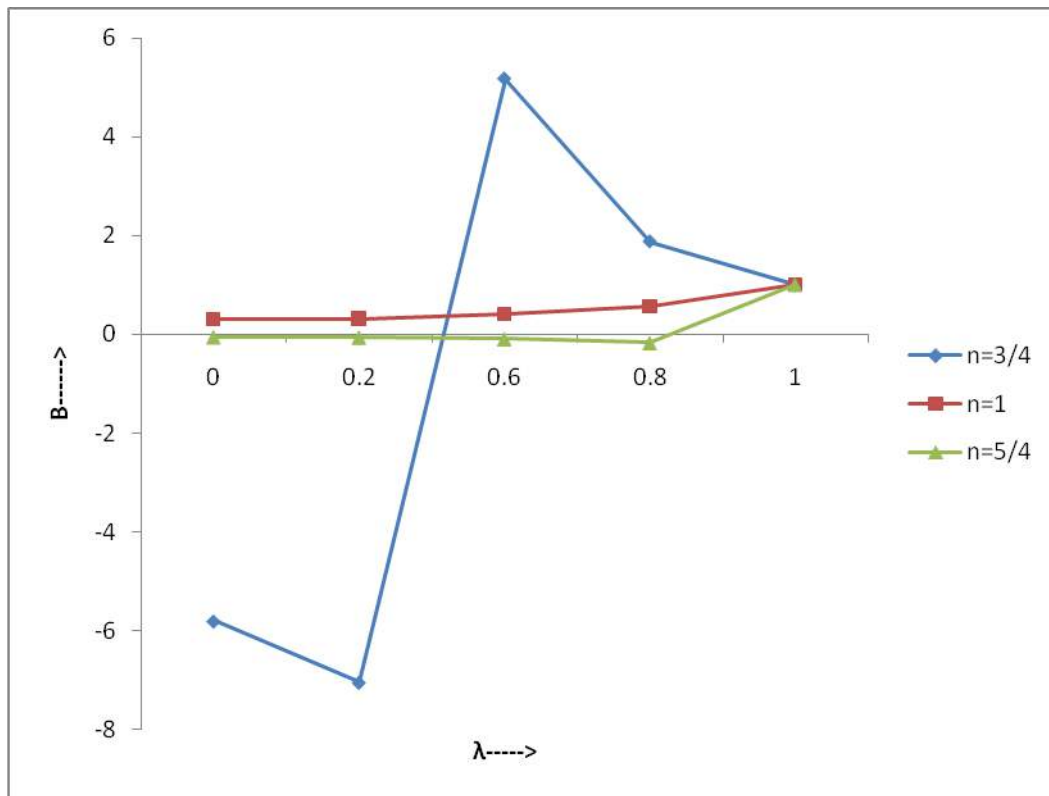


Fig.3: Variation of Bluntness parameter (B) with λ

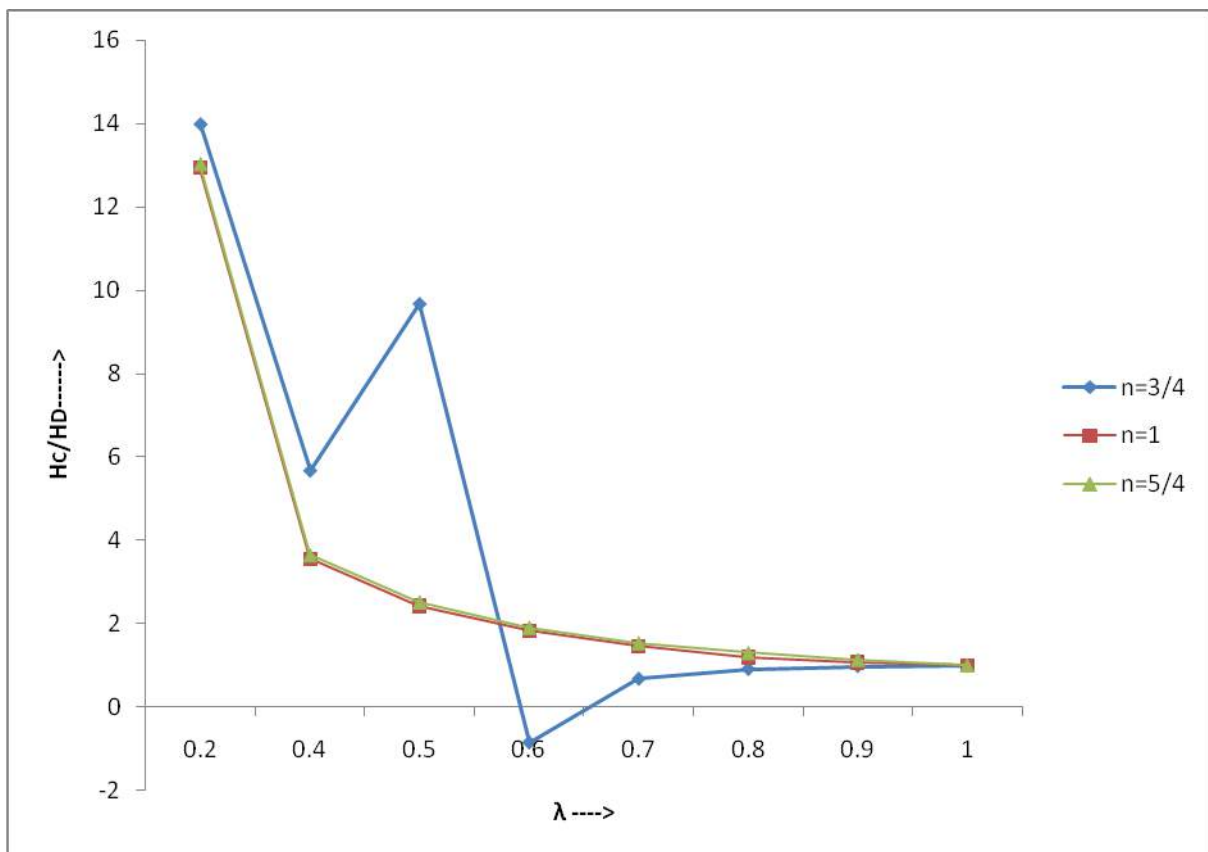


Fig.4: Variation of HC/HD with λ

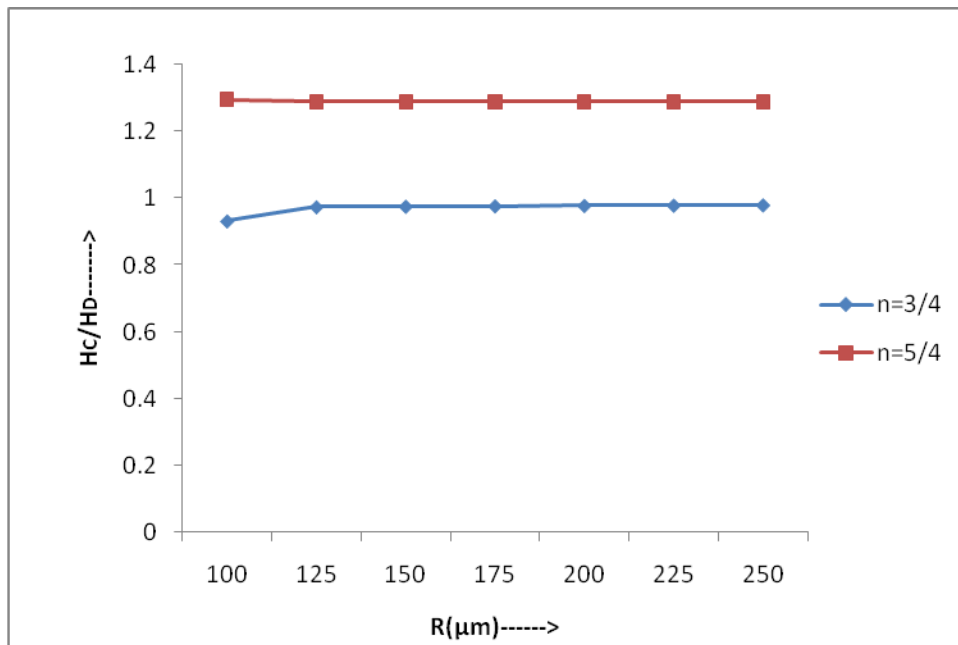


Fig. 5: Variation of HC/HD with R

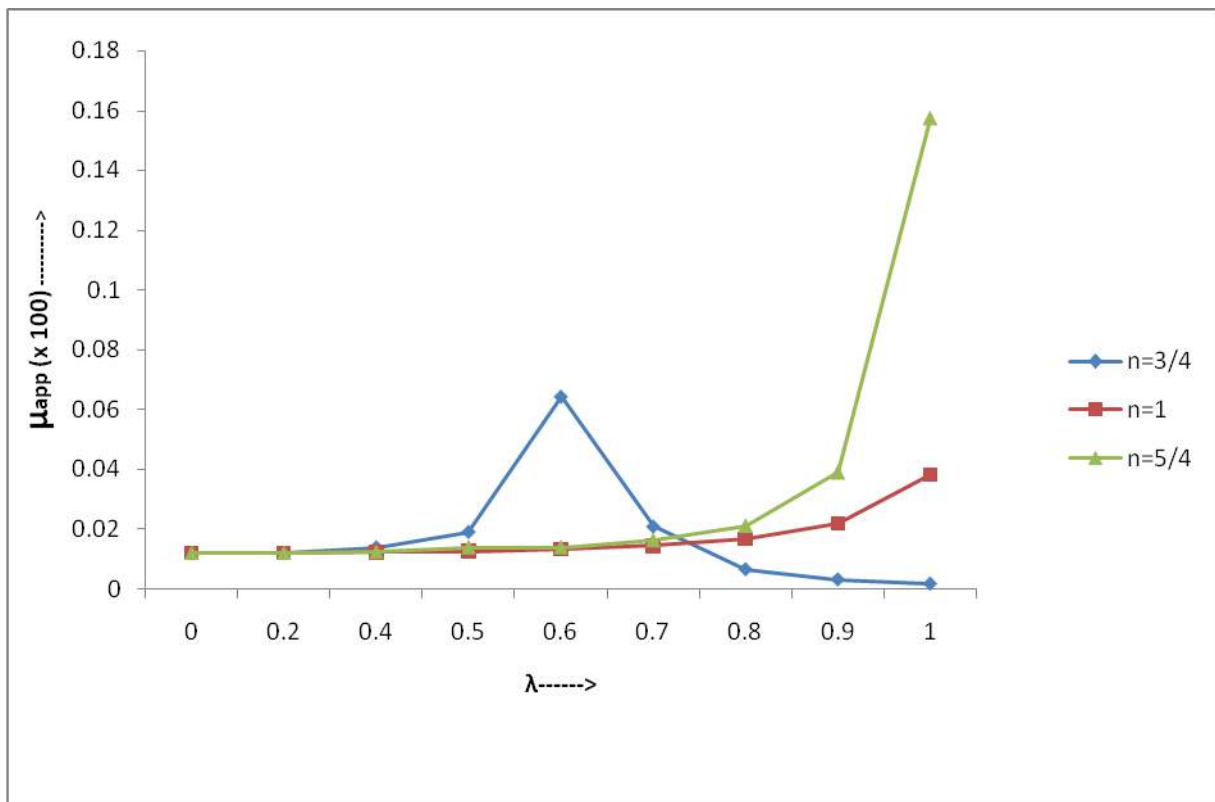


Fig. 6: Variation of apparent viscosity (μ_{app}) with λ

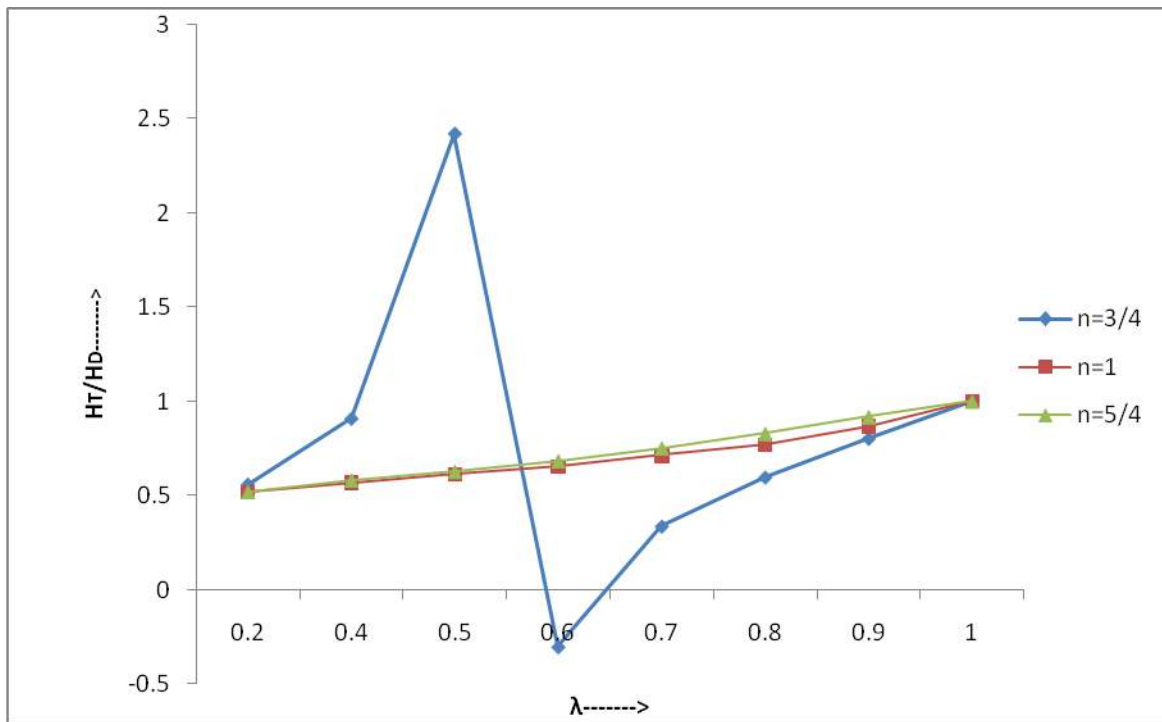


Fig.7: Variation of HT/HD with λ

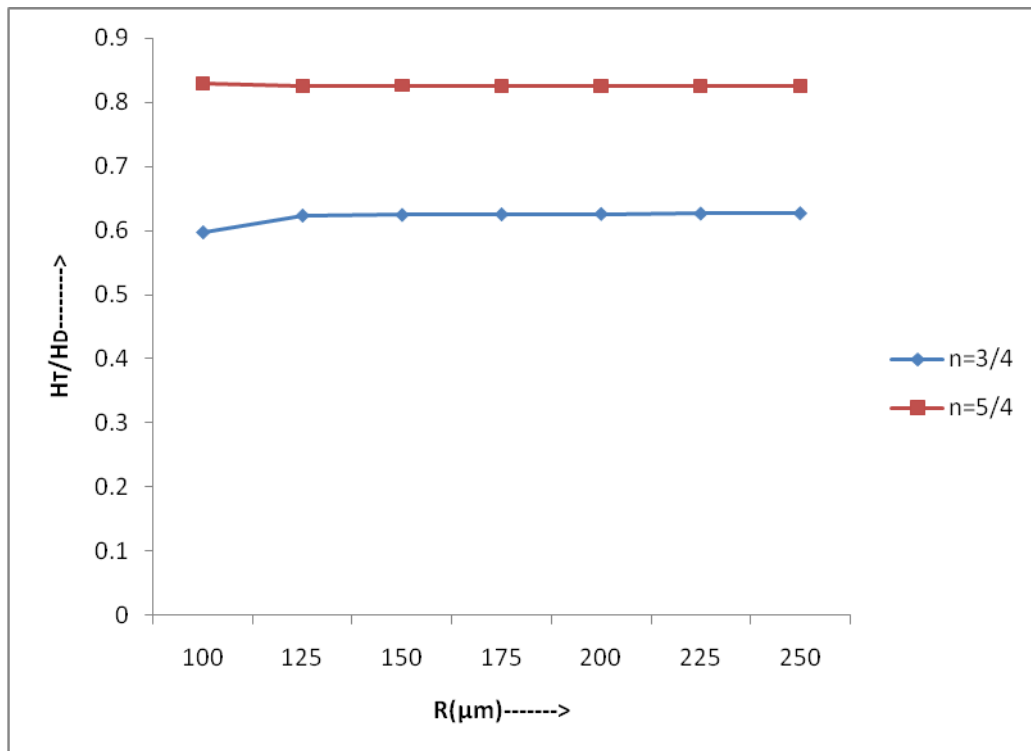


Fig. 8: Variation of HT/HD with R

References

- [1.] Cokelet, G.R. Macroscopic rheology and tube flow of human blood. In: *Microcirculation. Volume 1. Grayson J, Zingg W, Eds; New York: Plenum;* pp. 9-31, 1976.
- [2.] Pries, A.R., Albrecht, K.H. and Gachtgens, P. Model studies on phase separation at a capillary orifice. *Biorheology, 18;* pp. 355-367, 1981.
- [3.] Tateish, N., Suzuki, Y., Soutani, M. and Maeda, N. Flow dynamics of erythrocytes in microvessels of isolated rabbit mesentery: Cell free layer and flow resistance. *Journal of Biomechanics, 27,* pp. 1119-1125, 1994.
- [4.] Yamaguchi, S., Yamakura, T. and Niimi, H. Cell free layer in cerebral microvessels. *Biorheology, 29,* pp. 251-260, 1992.
- [5.] Fournier, R.L. Basic Transport Phenomena in Biomedical Engineering, Taylor and Francis, *Philadelphia,* pp. 312, 1999.
- [6.] Pries, A.R., Secomb, T.W. and Gaehtgens, P. Biophysical aspects of blood flow in the microvasculature, *Cardiovasc. Res. 32,* pp. 654-667, 1996.
- [7.] Nair, P.K., Hellums, J.D. and Olson, J.S. Prediction of oxygen transport rates in blood flowing in large capillaries. *Microvasc. Res. 38,* pp. 269-285, 1989.
- [8.] Seshadri, V. and Jaffrin, M.Y. Anomalous effects in blood flow through narrow tubes: a model. IN *SERM - Euromech. 92, 71,* pp. 265-282, 1977.
- [9.] Gupta B.B., Nigam, K.M. and Jaffrin, M.Y. A three- layer semi-empirical model for flow of blood and other particulate suspensions through narrow tubes. *J. Biomech. Eng. 104,* pp. 129-135; 1982.
- [10.] Pries, A.R., Neuhaus, D. and Gaehtgens, P. Blood viscosity in tube flow: dependence on diameter and hematocrit. *Am.J. Physiol. 263,* H1770-H1778, 1992.
- [11.] Pries, A.R., Secomb, T.W., Gaehtgens, P. and Gross J.F. Blood flow in microvascular networks: experiments and simulation. *Circ. Res. 67,* pp. 826-834, 1990.
- [12.] Pries, A.R., Secomb, T.W., Gesser, T., Sperandio, M.B., Gachtgens, P. and Gorss, J.F. Resistance to blood flow in microvessels in vivo. *Circ. Res. 75,* pp. 904-915, 1994.
- [13.] Merrill, E.W. Rheology of blood, *Physiol. Rews. 49,* pp. 863-888, 1969.
- [14.] Chien, S., Dormandy, J., Ernst, E., and Matrai A. eds., *Clinical Hemorheology, Martinus Nijhoff publishers, Dordrecht,* 1987.
- [15.] Halvorsen, S. Regulation of Erythropoiesis. In. *J. Microcir. Clin. Exp.,* pp. 109-114, 1984.
- [16.] Skovborg, R., Nielsen, A.V., Schlichtkrull, J., and Ditzel, J. Blood viscosity in Diabetic Patients *Lancet, 1.* pp. 129-131, 1966.
- [17.] Leblond, P.F., Lacelle, P.L. and Weed, R.I., Cellular Deformability: A possible determination of the normal release of maturing erythrocytes from the bone marrow. *Blood, 7,* pp. 40-46, 1971.
- [18.] Kathleen K. Brookshier and John M. Tarbell, Effect of hematocrit on well shear rate in oscillatory flow: Do the elastic properties of blood play a role? *Biorheology, 28,* pp.569-587, 1991
- [19.] Das, B., Johnson, P.C. and Popel, A.S., Effect of non axisymmetric hematocrit distribution on non-Newtonian blood flow in small tubes. *Biorheology 35: 1,* pp. 69-87, 1998
- [20.] Maithili Sharan and Aleksander S. Popel, A two-phase model for flow of blood in narrow tubes with increased effective viscosity near the wall. *Biorheology 38,* pp. 415-428, 2001.
- [21.] Davod Alizadehrad, Yohsuke Imai, Keita Nakaaki, Takuji Ishikwa and Takami Yamaguchi, Quantification of red blood cell deformation at high-hematocrit blood flow in microvessels. *J. of Bio mechanism 45,* pp. 2684-2689, 2012.

A Literature Review on Ultra-Wideband Circular Polarization Antenna

*ShwetaTripathi¹ Garima Saini²

1. Department of Electronics Engineering

Dr. Ambedkar Institute of Technology for Handicapped Awadhपुरi Kanpur

2. Department of Electronics & Communication Engineering

National Institute of Technical Teachers Training and Research Chandigarh

1.shweta@aith.ac.in

Abstract—This literature gives worldwide, technical overview of circularly polarized (CP) antennas for numerous packages in wireless communication, highlighting on the current trends within the outlet work. The object additionally affords a relative take a look at of diverse studies reported within the open composition, with a goal to emphasize the contribution of CP antenna systems in the progressive evolution of the wifi communication technology. The number one motive of this evaluate is to (i) highlight the modes used by extraordinary researchers to represent and examine the wonderful attributes within CP antennas locate their appeals in present scenario of wifi conversation, (ii) supply a sensible perspective of the succeeding range of the take a look at, based upon the sooner and current kingdom of art studies trends and (c) deliver a notional and realistic assist to present-day antenna creators to help the manner of promoting of revolution and numerous system combination. In conclusion, the article additionally casts a few light upon the succeeding scope of research in the grip of CP antenna contributions.

Key Words— Circular polarization (CP), End-fire, Helix Shaped Antenna, Low Profile, Antenna Array.

I. INTRODUCTION

Circular-separated horns (CP) received positive size comments in the wi-fi agreement considering they could turn off the multi-street screen, avoid friction and separation, and aid in ductile flexibility of receiving and moving horns. Many CP antennas tested over the following decagons include a helical antenna [1], [2], a winding antenna [3], a patch antenna [4], [5], disconnected -dipole antenna [6], etc. Among those CPs mounted horns, tail horns can emit CP stop-fire radiation, high gain, and wide bandwidth [7], which are in great command to display a space tracking package. However, conventional radio horns are not suitable for over-designed and space-intensive needs, as their profiles are generally high.

Numerous attempts have been made to map company and coffee-outlines helical antennas. In [8], a low pitch angle and small wide variety of turns had been operated in a helical antenna to note a low-profile ordering. In [9], a hemispherical helical antenna changed into provided to benefit a thick length, low profile in addition to CP radiation over a huge angular range. Further, twist line become hired in a executed helical antenna to perish the full duration of the antenna [10]. Although the profiles may be adeptly perished, these antennas are not planar systems, which may additionally outcome in aerodynamic pulls out if they may be leaded up. Way of considering something, a planar helix which is being considered for a role on the surfaces of the attachments, and place of pass phase may be either square or rectangular. Square helical antennas were informed circular polarization with stop-hearth radiation [11]–[13]. In [13], a square helical antenna was joined into a semiconductor silicon layer, reaching desirable CP production whilst supporting the layer big of 0.22 λ_0 at the center repetition. In general, the square cross section can destroy the profile of the helical antenna. The square planar helix has made many demands on the creation of lazy waves [14] - [16] and brightly colored horns [17], [18], but little research has been done on the antennas of existing fire stations. It is well known that in an effort to see the division around, two electric fields with the same proportions and phase difference are 90°. In rectangular square helicopters, two electric fields can be formed by currents running along the right sides of the helix, respectively. It has been predicted for miles that if one rectangle is too long for the other, the size of the two electric fields would be at odds with the original levels. As a result, a summons remains to be obtained for the CP radiation to stop the operation of the low-level rectangular helical antenna cables, which may be required to obtain a low-level condition.

In this presented article, a rectangular helical antenna is mounted with fast-featured connectors made through hole-hole holes, which are lower and can reach the CP of the fire-end radiation. Apart from the limiting currents in the clean holes and outside the helix that form a direct and indirect separation, respectively, the modern day on the inner edges of the plane of the plane plays a major role in reducing the amplitude of a well-constructed electric horizontal edge. Installation, small helix and side wall handling work inside the antenna to increase axial bandwidth (AR) bandwidth and radiation association. The proposed planar helical antenna has the subsequent advantages:

(1) The antenna can advantage vast impedance and AR bandwidths. Marvelous CP performance with give up fire place emission is

completed over a 34% frequency band.

(2) The antenna has a completely low profile, which is only $0.11\lambda_0$ at the center frequency. It is far convenient to be scaled on the wings of the modified towering organs and aircraft.

(3) The structure is very simple, spacious and low cost. It can be easily constructed using the recorded circuit board technology

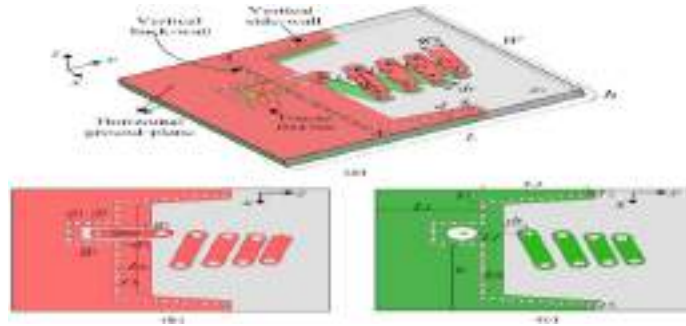


Fig. 1. Layout of the planar helical antenna. (a) Perspective view; (b) top; and (c) bottom layers of the substrate [14].

II. ANTENNA Layout

The layout of the presented planar helical horn is shown in Fig. 1. The helix has a rectangular flow section, which focuses on the use of engraved strips with straight connected parts made using composite holes. As shown in Fig. 1 (a), the length and width of the antenna are prominent L and W , respectively. ϵ_r and h form dielectric flexibility and substrate density, respectively. The thru-hole width of the helix is dv , and the pitch angle between the upper and lower points is α . The diameter of all the uniform strands is uniform, that passes through W_s . The time line in the bottom layer of the layer is indicated with the help of L_{si} ($i = 1, 2, 3, 4$) with the helix tip. To improve AR and radiation development, the helix is decreased in line with the subsequent ratio:

$$r = \frac{L_{S2}}{L_{S1}} = \frac{L_{S3}}{L_{S2}} = \frac{L_{S4}}{L_{S3}} \tag{1}$$

Commonly speak me, a wide handling aircraft which is vertical to the axis of the helix have to be united in the helical antenna to achieve a good CP radiation ultimately-fireplace radiation. In this two metal plates are duplicated on both top and bottom substrates of the layer to shape the horizontal floor planes.

III. ANTENNA AUDIT

A. Normal mode helix

A standard mode helix test is established on the separation date that currently provides the helix length. In addition, the helix can be installed as a series of small loops and fast dipole antennas. The width of the short dipole is the same as the order between the turns of the helix, as the width of the loop is the same as the width of the helix. Because the helix scales are much smaller than the wavelength, the sample path is freed from the rotation distance. It is possible to calculate the total value of the long helix method by using a combination of small loop fields and a short pole connected to a series. In doing so, the effect of electrical discipline is displayed as:

$$E_{\phi} = \eta * \frac{k^2 I D^2}{16r} * e^{-jkT} * \sin \theta \tilde{\theta}$$

$$E_{\theta} = jk_{\eta} * \frac{IS}{4\pi r} * e^{-jkT} \sin \theta \tilde{\theta}$$

The axial ratio becomes

$$AR = \left| \frac{E_a}{E_b} \right| = \frac{2S\lambda}{\pi^2 D^2}$$

Normal mode helix can be split in a circular manner once the condition $AR = 1$ is satisfied. This condition is satisfied when the helix width and the space between the points are associated with

$$C = \sqrt{2S\lambda}$$

It is miles expressed that the polarization of this mode is as in all guidelines debarring alongside the z-axis in which the field is zero. It is also visible from the equation that the maximum radiation takes place at $\theta=90^\circ$, that is, in a plane normal to the helix axis.

B. Axial-Mode Helix

Compare the helix case of normal mode, the simple logical functions of the axial synthetic helix no longer work. Thus, the effects of radiation and the spread of modern technology are being achieved by using new and limited, logical and numerical techniques. Modern release of standard axial-mode helix. As it is written, today's issue can be divided into two regions. Near the feed circuit, the cutting edge ended uniformly to a small, at the same time as the current size of the continuous helix is particularly smooth. Since the field adjacent to the feed is slightly limited until the helix period, the current can be like a moving wave of constant amplitude.

Using this measurement, the identification of the axial-mode helix remote field can be calculated automatically. There are two remote field research techniques. In the first method, the N-flip helix is considered to be a group of N elements with a spacing equal to S. The field design is obtained by repeating the formation of a single turn of the helix with an array factor. The result is

$$F(\theta) = C_0 \cos \theta \frac{\sin(N\frac{\Psi}{2})}{\sin(\frac{\Psi}{2})}$$

Where C_0 is a constant coefficient and $\Psi = kS \cos \theta + \alpha$, Here, α is the phase shift between successive elements and is given as

$$\alpha = -2\pi - \frac{\pi}{N}$$

In the above equation $\cos \theta$ is the element pattern and $\frac{\sin(N\frac{\Psi}{2})}{\sin(\frac{\Psi}{2})}$ is the array factor for a smooth arranging of N-equally-spaced elements.

The Hansen-Woodyard condition is satisfied. This situation is compulsory so that it will acquire harmony between the calculated and calculated sketches. In a second approach, the entire field is immediately planned by connecting the contributions of the current components from one end of the helix to another. The current is examined to be a travelling wave of fixed amplitude. The current distribution at an arbitrary point on the helix is written as

$$\vec{I}(l) = I_0 e^{-jg\varphi} \hat{l}$$

In the above equation, l = the length of wire from the starting of the helix to a random point.

$$g = \frac{\omega L_T}{pc\varphi_m}$$

L_T = the total length of the helix

p = phase velocity of wave propagation along the helix relative to the velocity of light c .

ϕ = azimuthal coordinate of an arbitrary point

\hat{l} = unit vector along the wire

$\hat{l} = -x \sin \varphi + \hat{y} \varphi + \hat{z} \sin \alpha$

According to Hansen-Woodyard condition,

$$p = \frac{1}{\sin \alpha + \left(\frac{2N+1}{N}\right) * \frac{\lambda \cos \alpha}{c}} = 2\pi N$$

C. Experimental Relations for Radiation Properties of Axial-Mode Helix

Approximate statements for radiation effects of an axial-mode helix have also been obtained experimental. A synopsis of the approximate formulas for radiation attributes is marked out below. These formulas are valid when $12^\circ < \alpha < 15^\circ$ and $\frac{3}{4} < C/\lambda < 3/4$ and $N > 3$.

The terminal impedance of a helix radiating in the axial mode is almost resistive with values between 100 and 200 ohms. Lesser values, even close to 50 ohms, may be completed by way of well properly drawing the feed. Approximate statements, primarily based on a huge wide variety of measurements, have been carried out, and they are used to manipulate some of parameters. The input impedance (purely resistive) is obtained by

$$R \cong 140 \left(\frac{C}{\lambda}\right)$$

Which is accurate to about $\pm 20\%$, the half-power beam width by

$$HPBW(\text{degrees}) \cong \frac{52\lambda^{\frac{3}{2}}}{C\sqrt{NS}}$$

The beam width between nulls by

$$FNBW(\text{degrees}) \cong \frac{115\lambda^{\frac{3}{2}}}{C\sqrt{NS}}$$

The Directivity is given by

$$D \cong \frac{15NC^2s}{\lambda^3}$$

The axial ratio (for the condition of enlarged directivity) by

$$AR = \frac{2N + 1}{2N}$$

IV LITERATURE REVIEW

The 3-detail introduction will want to break the strength into three qui-amplitude alerts with 0° , 120° , and 240° segment flow. The proposed established order is accumulated of three similar additives which are in addition assigned around a vital axis. A ground aircraft with a disk or binomen shape is with the aid of nature extra healthy for this solution. The disk shape is supplied as a way to come to be bigger the antenna frequency bandwidth. Then, the antennas are constructing on a pinnacle PCB, as shown in Figure 2. By using a vertical interchanged F antenna phenomenon, those radiating elements are seeded on the edges of the disc with the nourishing lines gusting out from the disk middle. The pinnacle layer is attached to the ground plane at the bottom membrane by means of 1mm diameter metal wires. The antenna is duplicated and upgraded with a three DEM. For readability and in view of the make up uniformity, most effective S11 and S21 are allotted. A maximum coupling between the upgrading ports of eight dB is duplicated. Considering that the three assisting ports are cater with a 120° segment shift, power will be dissipated, because of the riposting. Nevertheless, the loss will cling at the manner the two blended signals may be recombined at the third port.

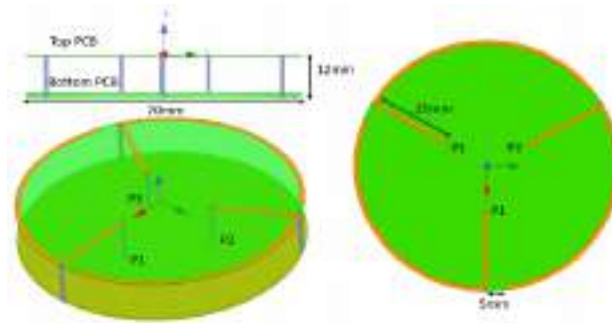


Figure 2 Top, side and 3D view of the radiating structure [23]

Frame Working and Calculations

Frame Work Creation

The presented notion has been forged on a low cost membrane that is 1.6 mm-thick FR4 Epoxy with the $\epsilon_r = 4.4$ and $\tan\delta = 0.02$. The exceptional factors of the antenna are provided in Figure 3. The keeping apart elements are positioned on the top beam that combine to the reproducing circuit and the floor plane at six points by means of the use of the 1mm diameter metallic wires. The three inner factors hyperlink to the three output ports of feeding circuit, whilst the three outer factors are incised to the floor plane.



Figure 3: Picture of Prototype [24]

Antenna Measurement

The reflection co-efficient of the prototype was estimated. Because of the design matter, the bandwidth of the computation results was much smaller than the replica. Nevertheless, considering a -10 dB, a 27 MHz frequency bandwidth from 860 to 887 MHz was accomplished this is exceptional for the utility. The 3D radiation layout became computed the use of close to field superstar Lab station from Satimo. The antenna had a total efficiency of -1.7 dB at 868 MHz. The computation suggests a peak RHCP gain of three dBic at 868 MHz and a 50 MHz (844–894 MHz) $-three$ dB RHCP Gain frequency bandwidth. Moreover, a 14MHz–3dB axial ratio bandwidth was performed in the censure direction.

Circularly polarized wearable antennas for ISM band applications

A plethora of circularly polarized wearable antenna designs has been reported in the literature recently aimed for (2.4–2.4835 GHz) industrial–scientific–medical(ISM) band applications. Hertleer *et al.* [23] introduced a truncated patch antenna to be exploited in protective garments of firefighters. The thickness of the antenna is 3.94 mm using foam as a substrate. Circularly polarized radiation is generated by cutting the corners of the patch radiator and deflecting the feed point slightly off the patch diagonal. The geometry is simple and hence easy to realize utilizing textile materials. To achieve an optimal performance, the authors recommend to use a

ground plane at least 1.5 times larger than the patch. It is also found that some bending directions cause more deterioration to the antenna performance than others, hence, such positioning must be avoided.

Another design of a wearable circularly polarized ISM band antenna is reported by Luet *et al.* [24]. The design is aimed for power transmission in a wirelessly powered, battery-less temperature sensor system to communicate over a distance of 1.7 m with 50 mW transmitted off a base station. The reported antenna is based on a two-layered patch with no ground plane. To achieve a reasonable performance in the vicinity of human body, the optimal height is selected as 10 mm. The handedness of circular polarization is found to be depending on the bending direction, which must be taken into account when aligning the antenna.

Tronquo *et al.* [25] have developed a nearly circularly polarized wearable patch antenna for ISM band applications. Instead of truncating the corners, a rectangular slot in the centre of the radiator is introduced to excite the two orthogonal current modes. Fleece is used as a substrate material and FlecTron fabric is chosen for the ground plane and the radiator. All layers are sewn together while the antenna is fed by a Sub Miniature version A (SMA) connector. The effect of bending over 3.75 and 6 mm radii is analysed in terms of return loss measurements.

Kuhjani and Neshati [26] have proposed a dual-band circularly polarized wearable antenna for 2.4 and 5.7 GHz bands. The antenna is fed by a microstrip via an aperture in the ground plane. The substrate under the patch radiator is based on a 2.56-mm thick fleece fabric with a permittivity close to 1. Altogether, the antenna consists of four textile layers and the total thickness is approximately 3.7 mm. The dimensions of the radiator are 43 mm × 43 mm. The two frequency bands with circular polarization are achieved by truncating the corners and cutting several symmetrical grooves on the rectangular radiator. The authors found that the higher band of the antenna is more sensitive to bending than the lower band and that bending increases back lobe radiation. However, SAR values remained below EU limit levels even when the antenna is bent. Locher *et al.* [27] have investigated the design of wearable Bluetooth antennas for the 2.4–2.4835 GHz ISM band. The authors presented an elaborate analysis on the properties of substrate and conductive materials in addition to attachment methods. The advantages and drawbacks of probe and microstrip feeding methods are also presented. Detailed measurement results and analysis are provided for a truncated corner circularly polarized antenna on a 3.5-mm thick felt substrate and a linearly polarized antenna on a 6-mm thick spacer fabric. Measurement results show that the circularly polarized antenna is more sensitive to bending over a radius of 37.5 mm than in a linear one. It is worth noting that bending changes the effective dimensions of the radiator and consequently affects the two orthogonal current modes of the circularly polarized antenna. The thickness might change slightly during operation which in turn affects the effective permittivity of the substrate. Consequently, the beam-width of the circularly polarized antenna is narrowed down, and the purity of the circular polarization is degraded. The degradation level depends on the bending direction extent. As Kellomaki *et al.* noted in [28], the main lobe direction may vary with frequency, and hence the angle information is needed.

Circularly polarized wearable Antennas for Personal Satellite Communication and Navigation

In addition to ISM-band antennas, other popular applications of circularly polarized wearable antennas are GPS and satellite communication. Some solutions include dual-band operation for both navigation and personal communication. Elliot *et al.* [29] used a hybrid with two fabric feed lines to generate circular polarization in their wearable dual-band antenna design. The design consists of a stacked patch antenna for GPS at 1,575 MHz and global navigation satellite systems (GNSS) at 1,227 MHz. The thickness of the antenna is 3.9 mm, length and width are 91 mm × 91 mm. The authors found that multilayer textile patch and especially the feed-line structure is challenging to realize. However, it allows placing a low noise amplifier (LNA) for the receiver end closer to the antenna and hence losses and noise due to long cabling can be minimized. Circular polarization is estimated by LHCP and RHCP gain radiation patterns.

A patch antenna with a central rectangular slot aimed for Iridium satellite phone communication is reported by Kaivanto *et al.* [30]. The substrate of the antenna is based on Cordura fabric sheets, while the radiator and the ground plane are based on woven conductive textiles with electric conductivity close to that of copper foil. Circular polarization is generated by adjusting the dimensions of the slot and the radiating element. Deflecting the feed point slightly from the diagonal of the radiator is another design parameter. The antenna is fed by an SMA connector. The

effect of bending is studied by measuring the antenna bent on a cylinder of 50-mm radius in four layouts. Results show that changing the bending directions affect the antenna performance differently. Hence in practice, the worst cases can be avoided by placing the antenna in a way where bending in the undesirable direction is improbable.

Another design reported by Kaivanto *et al.* [31] based on a circularly polarized dual-band antenna for personal satellite communication at iridium band (1621.35–1626.50 MHz), and for navigation at L1 band (1,575 MHz). To excite a wide band circular polarization, the slot at the centre of the rectangular patch is shaped as a polygon. The substrate layer consists of two different dielectric textile sheets: Cordura and a ballistic textile. The ground plane and patch radiator are twisted using silver and copper plated, low-loss nylon fabric. To retain the design as bend able as possible and to avoid losses caused by adhesives, the layers are sewn together. The effect of four defined bending directions on the antenna performance is investigated as described in the previous section. It is worth mentioning that no significant changes in total efficiency or RHCP gain were observed, whereas one bending direction remarkably degraded the circular polarization purity. An active wearable dual-band antenna for L1 GPS (1,575 MHz) and iridium (1616–1626.5 MHz) satellite phone is reported by Dierck *et al.* [32]. Enhanced signal reception with over 25 dBi gain is achieved by applying a LNA underneath the radiating element. The authors proposed a method of enlarging the bandwidth of circular polarization by using a discrete hybrid coupler, which fixes 90° phase difference between feed lines. As the circular polarization is generated by the coupler instead of radiator reshaping, the antenna is found to be less sensitive to bending effects and fabrication inaccuracies. The reported probe-free planar patch antenna is fed by two perpendicular feed lines, which are coupled to the radiator via an aperture. A

GPS antenna intended for rescue workers is reported by Vallozzi *et al.* [33]. As the antenna is required to tolerate harsh environmental conditions, fire-resistant and water-repellent materials are picked. The antenna is based on a truncated corners patch with a ground plane. In addition to free space, an evaluation of a real life scenario performance of the antenna integrated within a rescue worker jacket is conducted.

Kellomaki *et al.* [28] have conducted a comparative study by investigating bending effects on different GPS antenna topologies. In addition to circularly polarized truncated corner patch antenna fed by a microstrip line, a linearly polarized dipole, an elliptically polarized inverted-F antenna, and a wideband circular slot antenna are compared. According to return loss measurements, the last two types are found to be virtually immune to bending effects, whereas the dipole antenna is found to be the most sensitive.

In [42], a low-CPW-powered CPW antenna output a 2.45 GHz (ISM band) antenna was introduced with wireless biomedical applications. The small introduced antenna produced the maximum impedance bandwidth and axial ratio bandwidth compared to other reported structures. Price simulations are performed with parametric studies and it is found that the measured antenna results are consistent with the simulation. The antenna is powerful with a variety of tissue delivery. Antenna connecting margins are also calculated to show its wireless communication capability. In addition, SAR distributions are still being distributed at an acceptable level. Therefore, the proposed antenna is very durable, economical, easy to build, well-built and will occupy very little space in IMD.

In [43] a quadrilateral-shaped antenna shaped UWB CPW presented (CP) was introduced. An antenna model was developed, with its calculated results presented, which are applicable to modern communication systems. The results show that the antenna has wideband circular polarization (CP) with 56.64% fractional ARBW and ultra-wideband (UWB) IMBW (S_{11}) of 137.1%. In addition, the components of a single antenna are arranged in a detailed sequence with a systematic arrangement of 1*2 and 2*2 objects and their performance with comparison. The performance of the proposed antenna (one item) has been compared to the performance of recently released functions and is shown to be attractive. Compared to well-classified value antennas, the proposed antenna has a combined size, with better impedance comparisons with bandwidth of 3 dB axial ratio. The introduced antenna is useful for C-band, In band and X-band satellite communications.

In [44] reliable mathematical analysis and rigid design of circular horns were presented using limited follow-up. In [44], the method is easy to use and allows for a significant reduction in computer costs compared to standard analysis conducted by EM Monte Carlo. In the example of a compact microstrip CP antenna, the improvement in yield (considering the same distribution of production resistance) from 63.5% in small construction to 99% in improved production construction was achieved with about 300 full antenna EM antenna simulation.

In [45] the UWB CP antenna an unspecified novel in with a solid size based on tapered slot element material. The UWB tapered slot radiation object was first designed and discussed to improve bandwidth performance, respectively, with a tapered slot structure. Next, a compact dual-feed network is used to entertain the fallen harbors. Finally, a round metal wire was introduced to improve the low-level radiation feature. In order to ensure the composition, a certain type was made and measured. The measured results show that the corresponding bandwidth of 10-dB impedance bandwidth and 3-dB axial ratio (AR) bandwidth is 105.8% (1.85 GHz ~ 6 GHz), with a maximum gain of 8 dBic available. Compared to other recently reported CP antennas, the proposed one not only has the largest operating bandwidth, but also has stable and consistent radiation patterns with a combined volume of $0.33 \lambda \times 0.33 \lambda \times 0.3 \lambda$. All of that fits makes it ideal for modern wireless systems.

In [46] Three UWB CP slot antennas for UWB door mounting systems and other related applications are suggested in this paper, including a bidding antenna, a solid light antenna, and a meshed display antenna. By using a curved and slightly curved square structure, these antennas detect wave mode, and thus display the wideband feature. The "unlimited balun" offers the simplest and wideband features in the feed structure. The meshed reflector structure helps to achieve UWB-directed CP radiation with a low-level structure. And the shape of the space also leaves a completely complete plane of the plane that offers the opportunity to combine other elements, e.g. filter or amplifier, in the antenna to save space for the whole system. The results show that the horns presented show the desirable features of low cost, low cost, high bandwidth, and easy construction, making these antennas suitable for UWB wireless applications, such as in-door installation systems.

In [47] an ultra-wideband circular antenna is proposed and investigated in this paper. To improve the FBR, a composite hole is inserted. The proposed antenna has a CP bandwidth of 96.6% and a standard 30dB FBR within its range of operating frequency, making the antenna very promising for wireless systems.

In [48] a compact UWB circular separated by an Archimedean spiral antenna was introduced and its properties investigated. Extended arms and illuminated opponents are used to reduce the size of the antenna, and cross-spacing of the cross enhances the circular material. The results show that the proposed antenna has a wide bandwidth ranging from 2 GHz to 6 GHz (VSWR <2.5 and AR <3) with a combined size of $36 \times 36 \times 20 \text{ mm}^3$ ($0.24\lambda_{2G} * 0.24\lambda_{2G} * 0.24\lambda_{2G}$). The results indicate that the proposed antenna is suitable for wireless communication systems and low-visibility applications.

In [49] a circular UWB antenna is proposed and used. UWB performance is available in two patches. The two orthogonal modes of RHCP radiation are enhanced by using a double-Y-shape coupling slot. By reducing radiation exposure, AR bandwidth is also enhanced. The size of the proposed antenna is limited to $28 \times 28 \times 15 \text{ mm}^3$. Both the resulting and measured results show that the gain of the proposed UBW horn is better than 8.5 dB. 50% AR range and 71% IBW are available. Alternatively, the diameter of the antenna power beam is about 70° , cross-polarization 1.

In [50], a modified line of annular ring planar monopole antenna fed with a line of tapered microstrip was successfully applied and measured. A monopole antenna is constructed with a base slot and a stub that produces a rotating current of the CP wave radiation at a wide frequency range. The current surface around the clock side was confirmed by this design and LHCP was observed. Measurement results reveal that the proposed antenna receives a 10-dB loss bandwidth of 120.86% (2.96-12 GHz) and a 3-dB AR bandwidth of 81.42% (4.02-9.54 GHz) in the Z direction. In addition, high stable radiation efficiency (> 88%) is achieved with a

good broad spectrum of LHCP pattern. Percentage of the UWB frequency range covered by the ARBW of the proposed antenna is 72%, which is wider than other CP antennas presented in open literature. This antenna is a good member of the broadband CP application within the UWB frequency range.

In [51], a new bandwidth consolidation process, not available in any existing wideband method, is proposed according to mode analysis. By adjusting the position and size of the short loading structure, the high frequency mode ($TM_{20} - TM_{50}$) has been reduced and combined with the high frequency antenna duplicate mode (TM_{10}). These five methods form a broad band of performance. This network can be added to the proposed patch antenna to implement the UWB CP patch antenna. The patch size is only $0.5\lambda_0 \times 0.5\lambda_0$, and the height is only $0.1\lambda_0$ (λ_0 , the center frequency size in the free space). Compared to other reported patch antennas, the integrated feature of the patch antenna is maintained and the bandwidth is very wide. Compared to other types of UWB antennas, the size is significantly reduced and the radiation pattern is not as functional and uniform. This proposed new method, with various parameters to increase bandwidth in all other ways, makes the integration of more than 3 channels accessible to the clip antenna. Depending on the method proposed in this paper, an unlimited number of modes may also be included. These results provide a guide to designing UWB CP patch antennas and provide CP antenna design with a much wider bandwidth than existing antennas.

Wearable Circular Antenna for Personal Satellite Communication and Navigation

The first step after deciding on the type of antenna is to choose the right antenna item according to the design requirements. When choosing a dielectric substrate, one needs to show the electrical and mechanical properties of the object.

Table 1: Electrical Parameters of Dielectric substrate fabrics

Fabrics	ϵ_x	ϵ_y	ϵ_z	$\tan\delta_x$	$\tan\delta_y$	$\tan\delta_z$
Ballistic textile	1.46	1.46	1.38	0.003	0.003	0.002
Cordura	1.88	1.91	1.67	0.009	0.010	0.005

For some common electro-textiles, the electrical properties are documented and available. In many other cases, however, the permittivity and loss tangent of the textile are unknown and hence need to be characterized. When determining the electrical parameters, it must be taken into account that textiles are often an isotropic, and hence the parameters of interest need to be determined separately in three orthogonal directions.

The dielectric materials used for the antenna discussed here are Cordura and a ballistic textile. Their electrical parameters are listed in Table 1. The conductive material is a low-loss, woven nylon fabric, plated with copper. The surface resistance of this fabric is $0.03 \Omega/\sqrt{2}$.

The next step is to optimize the antenna dimensions. Now a days, numerical simulations are widely used, as most simulation packages provide a fast and reliable solution. However, in the case of a textile antenna, the designer needs to be more careful as the anisotropic textiles are often challenging to model. Moreover, inaccuracies are inevitable in the manufacturing process of textile antennas, and hence it is often common to end up with measurement results diverged from simulation ones. It is also worth noting that 100% realistic setups cannot be simulated such as wrinkles, air gaps, or stretching that might occur during bending. Hence, it is always advisable to confirm the simulated results by measurements. The proposed antenna is first simulated using CST Microwave Studio and followed by prototype fabrication once the optimized dimensions are obtained. The required operational bandwidth is 51 MHz to cover a 10 dB return loss between the start of L1 band and the upper end of iridium band. It is also recommended to achieve larger bandwidth than the required one to compensate for possible frequency shifts caused by operational and environmental variables. The geometry and layout of the proposed antenna is depicted in Fig. 4. The measurements of the radiator is approximately $65 \text{ mm} \times 65 \text{ mm}$, and the coordinates of the feed point in milli-meters are $x = 3, y = 11.5$, where the origin is at the center of the antenna.

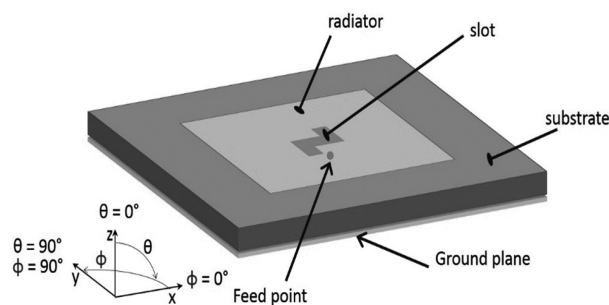


Figure 4: The structure of the circularly polarized antenna [26]

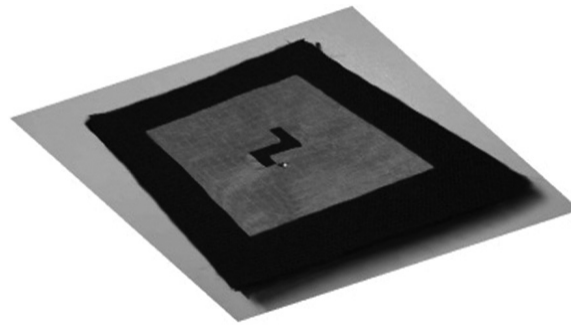


Figure 5: The manufactured antenna prototype [27]

To avoid any additional losses due to glue or other adhesives and to ensure durable attachment of the antenna structures, all fabric layers are sewn together. The fabricated prototype is shown in Fig. 5.

The next step is to determine the return loss and bandwidth for measurements (S11). The antenna is first measured with a space arrangement in the free space, then twisted to x and y above the Rohacell half cylinder with a radius of 50 mm. The directions for bending and setting are 6 and 7 figs, respectively.

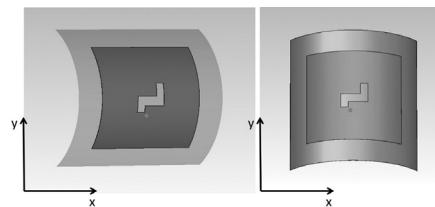


Figure 6: The antenna bent in y-direction (left) and in x-direction (right).[28]

Table of Parameters Considered For Helix Shaped Antenna

Ref. no.	Feed	Shape	Methodology	Size(mm ³)	Impedance B.W.	ARBW
42	CPW	Circular	Asymmetric square slots in ground	120*120*75	99.25% 2.4-2.5Ghz	63.56% 2.4-2.5Ghz
43.	CPW	Quadrilateral	Asymmetric ground plane	Linear array of 1*2 and 2*2	137.1% 3.1-17.5	56.64% 5.91-10.58
45	Dual feed network	2 crossed printed tapered slot	Dial shaped parasitic metallic strip	53*53*48	108% 1.8-6 Ghz	107% 1.8-6 Ghz
46	Microstrip	Circular	Elliptical shaped slots in ground	75*75*0.5	110% 2.94-10.06 Ghz	89% 3.19-8.26Ghz
47.	Single feed	T shaped	Composed cavity	-----	106.5% 0.9-2.95	96.6% 1-2.87
48.	Tapered wideband balun	Spiral	Planar Archimedean spiral antenna	36*36*20	1.9-8.5Ghz	2-6Ghz
49	microstrip	Rectangular	Four layers with different parasitic patches	28*28*15	71% 3.28-6.76Ghz	49.8% 3.61-6.05Ghz
50	Tapered microstrip	Rectangular	Annual ring patch and rectangular slot in ground	30*34*1.6	120.86% 2.96-12Ghz	81.42% 4.02-9.54Ghz
51.	Coaxial	Quarter printed ring	Open ends with curved delay line	55*55*1.6	50.2% 1.99-3.22Ghz	27% 2.3-2.9Ghz
52.	Sequential phase feeding	Square ring double layer	stacked patches	0.88λ*0.88λ*0.12 λ	43.2% 4.65-7.21Ghz	26.5% 4.9-6.4Ghz
53.	Coaxial	Conical	Tapered metal strip rolled in conical shape	40*40*40	81% 2.1-5Ghz	58% 2.4-4.36Ghz

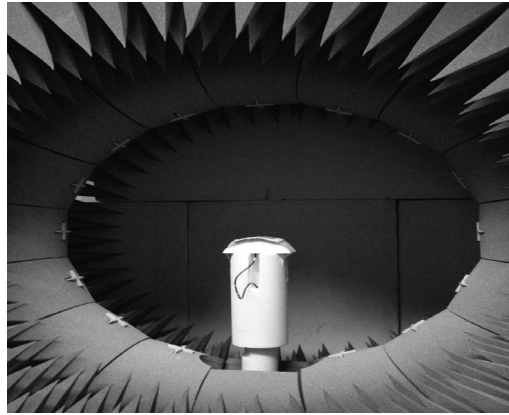


Figure 7: Antenna measurement set-up.[31]

A Dual Frequency Microstrip Patch Antenna for High-Precision GPS Applications

The antenna described is a quadruple feed stacked shorted annular circular patch antenna operating at L1 and E5a-E5b bands of Galileo. In this geometry, two shorted circular annular patches are side by side printed on two assembled membranes discriminated by an air gap. The main characteristic of this antenna is that the radiation pattern can be altered by differing the relation between the external and internal radii. Furthermore, the stacked shorted circular circular patch can be designed to avoid surface wave emissions diminishing back and lateral radiations and improving efficiency. In the following point the coaxial feeding is described in order to better understand the achieved results in the simulation.

Coaxial feeding Feed/Probe Coupling

One of the basic implements of conveying electricity to a micro-strip spot is by means of the use of a probe surpassed thru the membrane and fused to the spot. This probe can be the internal conductor of the coaxial line or a strip line through an aperture in the ground plane. The position of the notch needs to be at the factor where the great impedance match is completed. The coupling of the feed contemporary current J_z to the E_z field consequences in excitation in the patch. The coupling may be obtained by the following equation:

$$\text{Coupling} = \iiint_v E_z J_z dv \cong \cos\left(\frac{\pi x_0}{L}\right)$$

Where x_0 is the aperture balance from the edge of the spot. It can be seen that the coupling is maximum at the threshold of the patch.

II. CONCLUSIONS

The given work furnishes a better overall performance in RHCP gain and bandwidth for a smaller most dimension. It have to also be pointed that the use of a higher fee and lower-loss fabric ($\tan\delta = 0.001$) would boom the antenna benefit by 0.6dB. The PRMS antenna outlines the use of an opening antenna and MS is provided. Antenna segmentation can be automatically restored to LHCP, RHCP and LP by rotating the MS in the center relative to the opening. The polarization re-configurable belongings has been inspected and reported the use of the identical circuit. There produced and computed performances in terms of polarization re-configurability, performance, advantage and radiation sample, have been provided.

REFERENCES

- [1] H. A. Wheeler, "A helical antenna for circular polarization," Proc. IRE, vol. 35, no. 12, pp. 1484–1488, Dec. 1947.
- [2] J. M. Tranquilla and S. R. Best, "A study of the quadrifilar helix antenna for global positioning system (GPS) applications," IEEE Trans. Antennas Propag., vol. 38, no. 10, pp. 1545–1550, Oct. 1990.
- [3] H. Nakano, H. Oyanagi, and J. Yamauchi, "A wideband circularly polarized conical beam from a two-arm spiral antenna excited in phase," IEEE Trans. Antennas Propag., vol. 59, no. 10, pp. 3518–3525, Oct. 2011.
- [4] J. Huang, "Microstrip antenna developments at JPL," IEEE Antennas Propag. Mag., vol. 33, no. 3, pp. 33–41, Jun. 1991.
- [5] Y. M. Pan, S. Y. Zheng, and B. J. Hu, "Wideband and low-profile omnidirectional circularly polarized patch antenna," IEEE Trans. Antennas Propag., vol. 62, no. 8, pp. 4347–4351, Aug. 2014.
- [6] J. W. Baik, K. J. Lee, W. S. Yoon, T. H. Lee, and Y. S. Kim, "Circularly polarised printed crossed dipole antennas with broadband axial ratio," Electron. Lett., vol. 44, no. 13, pp. 785–786, Jun. 2008.
- [7] D. J. Kraus and R. J. Marhefka, Antennas: For All Applications, 3rd ed. New York, NY, USA: McGraw-Hill, 2002.
- [8] H. Nakano, H. Takeda, T. Honma, H. Mimaki, and J. Yamauchi, "Extremely low-profile helix radiating a circularly polarized wave," IEEE Trans. Antennas Propag., vol. 39, no. 6, pp. 754–757, Jun. 1991.
- [9] H. T. Hui, K. Y. Chan, and E. K. N. Yung, "The low-profile hemispherical helical antenna with circular polarization radiation over a wide angular range," IEEE Trans. Antennas Propag., vol. 51, no. 6, pp. 1415–1418, Jun. 2003.
- [10] M. G. Ibambe, Y. Letestu, and A. Sharaiha, "Compact printed quadrifilar helical antenna," Electron. Lett., vol. 43, no. 13, pp. 697–698, 2007.
- [11] H. L. Knudsen, "Radiation field of a square, helical beam antenna," J. Appl. Phys., vol. 23, no. 4, pp. 483–491, Apr. 1952.
- [12] J. P. Casey and R. Bansal, "Square helical antenna with a dielectric core," IEEE Trans. Antennas Propag., vol. 30, no. 4, pp. 429–436, Nov. 1988.
- [13] N. Benjati and J. Oberhammer, "Three-dimensional micromachined silicon substrate integrated millimeter-wave helical antennas," IET Microw. Antennas Propag., vol. 7, no. 4, pp. 291–298, Jan. 2013.

- [14] C. Chua, S. Aditya, and Z. Shen, "Planar helix with straight-edge connections in the presence of multilayer dielectric substrates," *IEEE Trans. Electron. Devices*, vol. 57, no. 12, pp. 3451–3459, Dec. 2010.
- [15] S. Aditya and R. K. Arora, "Guided waves on a planar helix," *IEEE Trans. Microw. Theory Tech.*, vol. 27, no. 10, pp. 860–863, Oct. 1979.
- [16] C. F. Fu, Y. Y. Wei, W. X. Wang, and Y. B. Gong, "Dispersion characteristics of a rectangular helix slow-wave structure," *IEEE Trans. Electron. Devices*, vol. 55, no. 12, pp. 3582–3589, Dec. 2008.
- [17] H. Ma and H. Y. D. Yang, "Miniaturized integrated folded helical antennas," in *Proc. IEEE Antennas Propag. Soc. Int. Symp.*, Jul. 2011, pp. 753–756.
- [18] D. Seo, Y. Yu, S. Jeon, and J. Choi, "An integrated two-wire helical antenna for Bluetooth application," in *Proc. IEEE Antennas Propag. Soc. Int. Symp.*, Jun. 2007, pp. 3552–3555.
- [19] D. Deslandes and K. Wu, "Accurate modeling, wavenumbers, and design considerations of a substrate integrated waveguide," *IEEE Trans. Microw. Theory Tech.*, vol. 54, no. 6, pp. 2516–2526, Jun. 2006.
- [20] L. C. Kuo and H. R. Chuang, "A study of printed dipole antennas for wireless communication applications," *J. Electromagn. Waves Appl.*, vol. 21, no. 5, pp. 637–652, Jan. 2007.
- [21] K. G. Thomas and G. Praveen, "A novel wideband circularly polarized printed antenna," *IEEE Trans. Antennas Propag.*, vol. 60, no. 12, pp. 5564–5570, Dec. 2012.
- [22] C. A. Balanis, *Antenna Theory Analysis and Design*, 3rd ed. Hoboken, NJ, USA: Wiley, 2005.
- [23] Hertleer, C., Rogier, H., Vallozzi, L. & Van Langenhove, L., A textile antenna for off-body communication integrated into protective clothing for firefighters *IEEE Transactions on Antennas and Propagation*, 57(4), pp. 919–925, April 2009.
- [24] Lui, K.W., Murphy, O.H. & Toumazou, C., A wearable wideband circularly polarized textile antenna for effective power transmission on a wirelessly powered sensor platform. *IEEE Transactions on Antennas and Propagation*, 61(7), pp. 3873–3876, July 2013.
- [25] Tronquo, A., Rogier, H., Hertleer, C. & Van Langenhove, L., Robust planar textile antenna for wireless body LANs operating in 2.45 GHz ISM band. *Electronics Letters*, 42(3), pp. 142–143, 2006.
- [26] Kuhjani, A. & Neshati, M.H., Design investigation of a dual-band circularly polarized wearable antenna. *Second Iranian Conference on Engineering Electromagnetics (IECCM)*, 8–9 January 2014.
- [27] Locher, I., Klemm, M., Kirstein, T. & Troster, G., Design and characterization of purely textile patch antennas. *IEEE Transactions on Advanced Packaging*, 29(4), pp. 777–788, November 2006.
- [28] Kellomaki, T., Heikkinen, J. & Kivikoski, M., Effects of bending GPS antennas. *Asia-Pacific Microwave Conference APMC*, pp. 1597–1600, 12–15 December 2006.
- [29] Elliot, P.G., Rosario, E.N., Rama Rao, B., Davis, R.J. & Marcus, N.M., E textile microstrip patch antennas for GPS. *IEEE/ION Position Location and Navigation Symposium (PLANS)*, pp. 66–73, 23–26 April 2012.
- [30] Kaivanto, E., Lilja, J., Berg, M., Salonen, E. & Salonen, P., Circularly polarized textile antenna for personal satellite communication. *Proceedings of the Fourth European Conference on Antennas and Propagation (EuCAP)*, pp. 1–4, 12–16 April 2010.
- [31] Kaivanto, E., Berg, M., Salonen, E. & de Maagt, P., Wearable circularly polarized antenna for personal satellite communication and navigation. *IEEE Transactions on Antennas and Propagation*, 59(12), pp. 4490–4496, December 2011.
- [32] Dierck, A., Rogier, H. & Declercq, F., A wearable active antenna for global positioning system and satellite phone. *IEEE Transactions on Antennas and Propagation*, 61(2), pp. 532–538, February 2013.
- [33] Vallozzi, L., Vandendriessche, W., Rogier, H., Hertleer, C. & Scarpello, M.L., Wearable textile GPS antenna for integration in protective garments. *Proceedings of the Fourth European Conference on Antennas and Propagation (EuCAP)*, pp. 1–4, 12–16 April 2010.
- [34] H. Oraizi and R. Pazoki, "Wideband circularly polarized aperture-fed rotated stacked patch antenna," *IEEE Trans. Antennas Propag.*, vol. 61, no. 3, pp. 1048–1054, Mar. 2013.
- [35] J. Wu, Y. Yin, Z. Wang, and R. Lian, "Broadband circularly polarized patch antenna with parasitic strips," *IEEE Antennas Wireless Propag. Lett.*, vol. 14, pp. 559–562 (2015)
- [36] S.-P. Pan, J.-Y. Sze, and P.-J. Tu, "Circularly polarized square slot antenna with a largely enhanced axial-ratio bandwidth," *IEEE Antennas Wireless Propag. Lett.*, vol. 11, pp. 969–972, 2012.
- [37] Y. He, W. He, and H. Wong, "A wideband circularly polarized cross-dipole antenna," *IEEE Antennas Wireless Propag. Lett.*, vol. 13, pp. 67–70, 2014.
- [38] Z. Chen and Z. Shen, "Planar helical antenna of circular polarization," *IEEE Trans. Antennas Propag.*, vol. 63, no. 10, pp. 4315–4323, Oct. 2015.
- [39] X. Tang, B. Feng, and Y. Long, "The analysis of a wideband strip-helical antenna with 1.1 turns," *Int. J. Antennas Propag.*, vol. 2016, Jan. 2016, Art. no. 5950472.
- [40] S. Fu, Q. Kong, S.-J. Fang, and Z. Wang, "Optimized design of helical antenna with parasitic patch for L-band satellite communications," *Prog. Electromagn. Res. Lett.*, vol. 44, pp. 9–13, 2014.
- [41] V. Kaim, B. K. Kanaujia, S. Kumar, H. C. Choi, K. W. Kin and K. Rambabu, "Ultra miniature circularly polarized CPW-fed implantable antenna design and its validation for biotelemetry applications" *springer nature in (2020)*[10:6795].
- [42] Prashant Chaudhary, Ashwani Kumar, "Compact ultra-wideband circularly polarized CPW-fed monopole antenna" *international journal Electronics communication (AEIJ)* 107 (2019) 137-145.
- [43] Slawomir Koziel, Adrian Bekasiewicz, "Statical analysis and robust design of circularly polarized antennas using sequential approximate optimization" *warsaw university of technology* 2018:978-83-949421-1-3.
- [44] X. Ding, Z. Zhao, "A compact unidirectional ultra wideband circularly polarized antenna based on cross tapered slot radiation element" Dec. 21, 2017, IEEE, NNSF China (Nos 61571086, 61721001 and 61727803).
- [45] Yong sheng pan and Yuan dan Dong, "Low profile low cost ultra wideband circularly polarized slot antennas" 30 oct 2019, "IEEE/Access 2019.2950521."
- [46] L. Zang, Steven Gao, Qi Leuo, "Single feed ultra wide band circularly polarized antenna with enhanced front to back ratio" IEEE DOI 10.1109/TAP.2015.2501844
- [47] Y.W.Zhong, G. M. Yang, J.Y. Mo and L. R. Zheng "Compact circularly polarized Archimedean spiral antenna for ultra wideband communication applications" DOI: 10.1109/LAWP.2016-2560258, IEEE.
- [48] Jia Wei, Xing Jiag and Lin Peng "ultra wideband and high gain circularly polarized antenna with double Y shape slot" DOI:10.1109/ LAWP. 2016.2647318, IEEE.
- [49] M. Midya, S. bhattacharjee, M. Mitra "Circularly Polarized planar monopole antenna for ultra wideband applications" *International journal of RF and microwave computer aided engineering*, 4 July 2019.
- [50] Chao Sun et al "A design of compact ultra wideband circularly polarized microstrip patch antenna" DOI: 10.1109 / TAP. 2019.2922759; IEEE.
- [51] Y.He, W.He, H.Wond, "A wideband circularly polarized cross dipole antenna" vol.13,2014 , IEEE 2014 pages-67-70.
- [52] Kang Ding, Yan jie wu et al, "A stacked patch antenna with broadband circular polarization and flat gains" IEEE 2017.
- [53] J. N. Mei, D. W. Ding, and G. Wang, "Design of compact wideband circularly polarized conical helix," in *Proc. Int. Conf. Comput. Inf. Syst. Ind. Appl.*, 2015, pp. 139–141.

Design and System Stability of Integrated Renewable Energy Source

Chandra Prakash Varma

Department of Electronics Engineering, Dr. Ambedkar Institute of Technology for Handicapped (U.P.), Awadhपुरi, Kanpur, India

Tel: 0-800-549-5175 E-mail: cpvermaith2007@gmail.com

Yaduvir Singh

Department of Electrical Engineering, Harcourt Butler Technical University, Nawabganj, Kanpur, India

Tel: 0-708-130-0508 E-mail: dryaduvirsingh@gmail.com

Abstract

The development of IES technology resolves issues of energy safety, improve social efficiency, and renewable energy sources. There are many potential benefits associated with IES technologies. It is being known now as an important strategic research direction in the field of international energy. Renewable energy sources play an important role in the modern energy system. Rapid adoption of distributed generation sources and micro grids powered by renewable sources like photovoltaic, wind, tidal, fuel cells is being reported as one of the major results of increasing global demand for energy all over the world. Two types of sizing methods viz. iterative method and artificial intelligence method are being used. Modern techniques, based on single artificial intelligence (AI) algorithms, are more popular than classical algorithms owing to their capabilities in solving complex optimization problems. Optimal sizing of a stand-alone integrated renewable energy system (IRES) which may be comprised of micro hydro power (MHP), biogas, biomass, solar, wind energy etc. is an important research problem. It is modelled as a demand response (DR) strategy based on energy consumption scheduling of appliances. Multi-objective optimization with stochastic modelling becomes necessary to correctly identify the trade-offs between cost and reliability. Other technical issues are system stability, voltage at point of common coupling (PCC) and system integrating distributed generation. Integrating hybrid distributed generation in a distribution network requires an advanced controller, which is critical for ensuring high quality and stability of voltage at PCC and frequency of the power system. For controlling voltage at PCC and for controlling system frequency and making system stable, controller is used for Proportional-Integral (PI) & Proportional-Integral Derivative (PID) controllers are being considered for investigation. Pareto-based approaches are more efficient way to obtain good solutions close to global optimum. Stand-alone Hybrid Renewable Energy Systems (SA-HRES) contains more than one objective function and many constraints. Reliability assessment helps in assessment by power system operators, planners, designers and engineers. Reliability assessment optimizes the power outage cost. A Non-linear robust control technique using improved particle swarm optimization (IPSO) control is reported to have been implemented as a master control technique for the control of interlinking converter (IC) between AC and DC micro grids.

Keywords

Demand Response, Distributed Generation, Firefly algorithm, Optimization, Point of Common Coupling.

1. Introduction

Electrical power is considered as one of the most commonly sought commodities of mankind. HRESs are being used in the standalone mode for individual houses or in microgrids (MGs) in remote areas [4,5]. The energy demand is increasing in islands and remote areas in recent years. Therefore, standalone HRES or MGs with RES is reported as a promising and sustainable solution to supply the growing population and industries in remote areas and islands with clean and cost effective electrical power [7,8]. The optimal design of HRESs is observed as a complicated task since the optimal configuration depends on the knowledge of environmental conditions, energy sources, technical specifications, and load profiles [9]. An overview of some of the sizing algorithms and has also been discussed the optimal sizing process of two HRESs. Few single artificial algorithms for standalone and grid-connected applications have been discussed. Optimal sizing of different hybrid system combinations for standalone and grid-connected applications have been discussed which covers some of the artificial and classical sizing methodologies. Hybrid energy systems based on solar, wind and fuel cell energy sources covering only multi-objective optimization algorithms have been discussed. The feasibility analysis, control, and modeling of HREs with some artificial optimization techniques have also discussed [10].

The main function of a power system is reported to supply electricity to its customers at optimal operating costs with the assurance of a reasonable quality and continuity at all times [11]. Reliability is being reported as the probability that a power system will perform its functions adequately without any failure within a stipulated period of time [12]. The reliability study can be utilized to assess the performance of the distribution system based on the availability of suitable input component data and the configuration of the system. The reliability assessment could also be used to identify the malfunctional components that need urgent replacement in the distribution system as well as recommending the numbers of new components that should be incorporated in order to improve the reliability of the networks. The reliability technique has been accepted as a benchmark for power system design and operation at all phases of the power system, i.e. conceptual, design, planning and operational phases owing to these technical and economic attributes. This review work explored renewable energy resources to ameliorate the reliability of the distribution system and to reduce the cost that is associated with the power outage. Renewable DG units can enhance reliability of the distribution system in order to optimize greenhouse gas emissions and also the fuel consumption cost of the conventional power systems [13–15]. The reliability assessment of the distribution system in the presence of wind turbine generation (WTG), energy storage system (ESS) and photovoltaic (PV) have been drawn the attention of many researchers. The impact of renewable DG and battery storage units on the reliability of a conventional distribution system have been studied in [16]. The power network is no more passive, as such, the power flow and voltage profile are being determined by both generation and load with the high penetration of renewable generations (RGs) in the distribution network (DN). Many approaches based on control strategies are being proposed. The review of proposed voltage control strategies is presented in order to accommodate the voltage variation due to RG penetration [17].

Energy resources are very important economically and politically for all countries. Optimization of hybrid renewable energy systems might be complicated due to difficulties like the use of many energy resources, the sizing and high investment costs required. A variety of optimization models have been developed or investigated by many researchers such as renewable energy models, emission reduction models, energy planning models, energy supply and demand models, estimation models and control models [18-20]. An integrated energy system (IES) is being reported as a custom-designed configuration of different renewable technologies. The term IES is being referred to the interactions and interdependencies of energy supply systems, e.g. combined electricity and district heating systems; combined electricity and gas systems; and combined electricity, gas, and district heating systems. The development of IES technology is help a resolve issues of energy safety, improve social efficiency, and promote the development of new energy resources and renewable energy sources. There are so many potential benefits associated with IES technologies, it is being known now an important strategic research direction in the field of international energy. Much of the recent energy research in IESs has been demonstrated the use of multi-energy complementary technology in the operational analysis of IESs. Combined heat and power (CHP) technology is being reported as one of the basic concepts of multi-energy complementarily, and could be provided electrical power and thermal energy for space heating, cooling, domestic hot water, industrial processes, and so on. Previous studies have shown that there are various types of IES uncertainty problems caused by the multitude of intermittent RESs and stochastic energy loads. As research into these uncertainties continues, the dependencies between multiple energies have been identified and modelled using a copula-based approach [21-22]. The uncertainty and limited storability of wind and photovoltaic power could be due to output fluctuations and power curtailment, which severely impedes the utilization of renewable energy [23]. The modelling constraints could be divided into three categories: resource type, station type, and grid type [24-26]. Renewable energy sources play important role in the modern energy system with rapid development. Rapid adoption of distributed generation sources and micro grids powered by renewable sources like photovoltaic, wind, tidal, fuel cells are being reported as one of the major results of increasing global demand for energy all over the world. The integration of these energy sources to form a hybrid system is being considered as an excellent option for distributed energy production. Grouping a few distributed energy resources, a storage system and loads together is being formed a small grids or micro grids. This concept has been proposed to well manage the local DG units and its loads with higher capacity and more control flexibility compared to a single DG system. There are being several

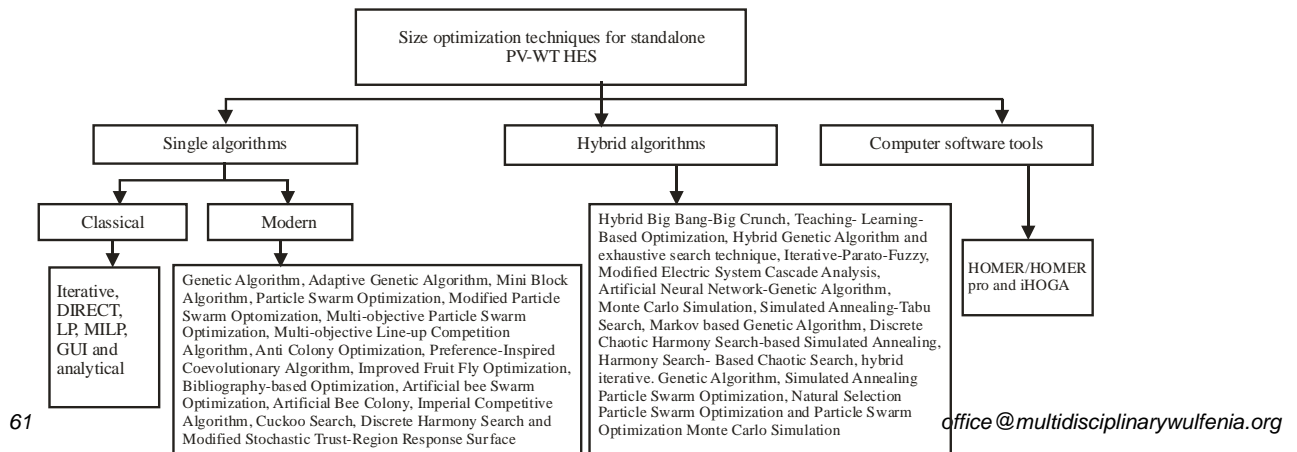
ways to integrate different alternative energy sources to form a hybrid system. These methods could be generally classified into two categories: AC coupling and DC coupling; the main two types of micro-grids namely AC micro grid and DC micro grid. A hybrid alternative energy system could be either be stand-alone or grid-connected if utility grid is available. Control of hybrid AC/DC micro grid under island operational conditions is being investigated [27]. A novel hybrid centralized and distributed control of a hybrid AC-DC micro grids is presented. A hybrid centralized master controller using IPSO based on the control of modified interlinking converter that utilizes Three Level Neutral Point Clamped Converter (3LNPC2) has been reported [28].

2. Sizing methods

Accurate dynamic performance of solar and wind energy system are not being represented by these methods. Hence, it is necessary to develop a unit sizing method which avoids complexity in designing the system and explains perfectly frequency response of the system in dynamic performance criteria. It is necessary to develop centralized and multilevel controlling technique which avoids the potential complexity of communication system and large computation as burden which is subjected to single point failure. Cournot, Stackelberg, Bertrandduopoly concepts are used to find out the exact system cost and salvage value of integrated system in view of increased day by day installation of HRES [1].

Due to the increasing cost and harmful emissions of fossil fuels, hybrid renewable energy systems (HRESs) is the growing trend to use standalone source. Intermittency and high net present cost are being the challenges associated with solar and wind energy systems. In this context, optimal sizing is being told as a key factor to attain a reliable supply at a low cost through these standalone systems. Therefore, a growing interest has been reported to develop algorithms for size optimization in standalone HRESs. The optimal sizing methodologies can be broadly categorized as classical algorithms, modern techniques and software tools. Modern techniques, based on single artificial intelligence (AI) algorithms, are more popular than classical algorithms owing to their capabilities in solving complex optimization problems [10].

Optimal sizing of a stand-alone integrated renewable energy system (IRES) which may be comprised the resources of micro hydro power (MHP), biogas, biomass, solar, wind energy etc. A demand response (DR) strategy is modelled based on energy consumption scheduling of appliances. Using integer linear programming (ILP), a DR strategy based on energy consumption scheduling of appliances can be modeled. The different combinations of system components without and with DR strategy are being considered and optimized for power reliability criteria of 0% and 5% unmet load. For 0% unmet load, the optimum size of IRES with the suggested DR strategy consists of 50 kW MHP system, 50 kW biogas system, 40 kW biomass gasifier system, 12 numbers of 4.2 kW rated small wind turbine, 17 numbers of 235Wp rated PV module, 89 numbers of 150 Ah rated battery and 50 kW converter. It has been found that significant amount of savings in system sizes and costs are obtained with DR strategy compared to system without DR. It has been found that reduction of 1.82 kW and 23 kW in peak hourly energy consumption during summer and winter seasons respectively are obtained with DR strategy in comparison of system without DR. Size optimization of the proposed IRES without and with DR strategy can be performed using discrete harmony search (DHS) algorithm [2]. In recent years, hybrid algorithms are being used for optimization over single algorithm. Hybrid algorithms provide better optimization results over single algorithm. Modern methods such as artificial algorithms and hybrid algorithms provide more accurate optimization results than software tools as they have the ability to solve multi-objective optimization problems [10].



3. System Security and Reliability

The ability of the system to respond to disturbances and maintain stable operating conditions is being termed as system security [20]. Reliability assessment is one of the key indicators to measure the impact of the renewable distributed generation (DG) units in the distribution networks and to minimize the cost associated with power outage [16].

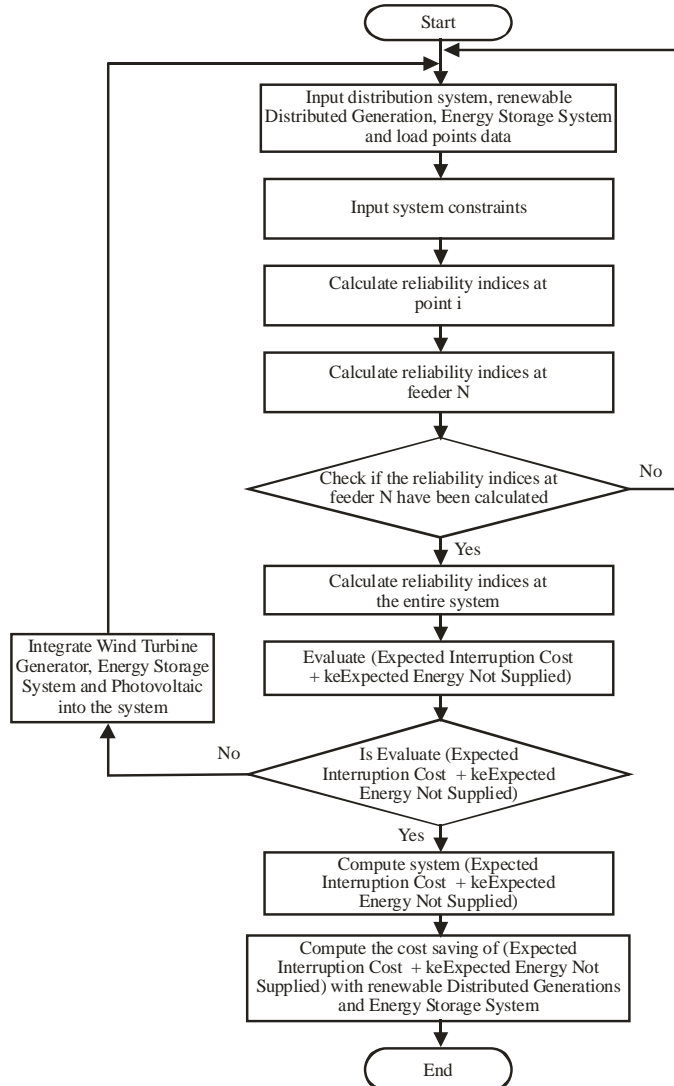


Fig. 2. Reliability estimation and improvement [16].

Two stage approach is used for off-grid mining operations for analysis of variability effects on the optimal design and reliability of an integrated energy system. Solutions of deterministic non-linear programming (NLP) optimization problem creates various possible energy system designs. Capital cost for a number of input scenarios is minimised. Two measures of reliability are loss of power supply probability (LPSP) and energy index of reliability (EIR). These two measures are being evaluated for each design. It is based on the minimization of the external energy that is required to satisfy load demands for variety of input conditions. Measures of reliability should consider the frequency and extent of demand satisfaction. It is being reported that range of system capacities and capital cost increase with increased variability, with demand satisfaction worsening. Multi-objective optimization with stochastic modeling becomes necessary to correctly identify the trade-offs between cost and reliability [3]. Markov model can be developed to access the stochastic characteristics of the major components of the renewable DG resources as well as their influence on the reliability of a conventional distribution system [16].

Some of the most common used indices in the power generation (hybrid renewable energy) system reliability assessment are termed as loss of load expectation (LOLE), loss of energy expectation (LOEE) and Loss of Power Supply Probability (LPSP).

a) Loss of load expected (LOLE)

$$LOLE = \sum_{h=1}^H \sum_{i \in S} P_i \times T_i \quad (1)$$

where S: all loss of load states of the system, Pi: probability the system encountering state i, Ti: time (hour) of load exceeds the production capacity, and H: annual time period considered 8760 h.

b) Loss of energy expected (LOEE)

The expected value of energy that hasn't been supplied is termed as LOEE. It occurs when the available electric generation capacity can not meet the hourly load demand. It is given as

$$LOEE = \sum_{h=1}^H \sum_{i \in S} P_i \times LOE_i \quad (2)$$

where S: all loss of energy states of the system, Pi: probability the system encountering state i, and LOEi: amount of loss of energy (kWh) when the system couldn't be supply expected energy at time step h.

c) Loss of power supply probability (LPSP)

LPSP is given as

$$LPSP = \frac{LOEE}{\sum_{h=1}^H LD} \quad (3)$$

where LD (kWh): load demand (kWh) at time step h.

d) Deficiency of power supply probability (DPSP)

DPSP is given as

$$DPS = \sum_{t=1}^T LD(t) - E_{sist}(h) \quad (4)$$

$$DPSP = \frac{\sum_{t=1}^T DPS(t)}{\sum_{t=1}^T LD(t)} \quad (5)$$

DPS (power supply fault) is a condition that occurs when the main power generation components and/or backup units of the hybrid renewable energy system can not meet the load demand. $E_{sist}(h)$ (kWh/year) means supplied energy by the hybrid renewable energy system at hour t.

e) Loss of Load probability (LLP)

It is given as

$$LLP = \frac{\sum_{t=1}^{8760} ES(t)}{\sum_{t=1}^{8760} LD(t)} \quad (6)$$

where $ES(t)$: power shortage (kWh) at the hour.

First order reliability method (FORM) can be estimated the failure probabilities. They are crucial for ensuring the reliability of the gas supply and surplus power absorption. FORM optimization model can be solved by Hasofer Lind and Rackwitz Fiessler (HLRF) algorithm. A mathematical case has been reported to demonstrate the use of the FORM in the estimation of failure probability, and the results are being validated using the Latin hypercube sampling theories, including the Iman and Stein methods. The results of a failure probability analysis for an ideal IES are also provided. The failure probability can be used to improve IES operation and planning to ensure better reliability. In contrast to Monte Carlo methods, the FORM method does not require many samples [22].

4. Controller Design

Several technical issues, especially system stability like voltage at point of common coupling (PCC) and system can be caused an integrating distributed generation to power systems. Current existing power systems should be upgraded to the advanced power grid in order to complete address the issue. There is need to make a controller for power grid become 'advanced', particularly in terms of stability and flexibility. The controller is capable to control the above issue after integration of hybrid

distributed generation system into the utility grid. Different energy sources in the system are being integrated through a DC bus into the utility grid. The firefly algorithm for optimization of controllers of several classical controllers such as Proportional-Integral (PI) and Proportional-Integral-Derivative (PID) in grid connected hybrid Wind/PV distributed generation system are being successfully applied and it has been concluded that the designed value of optimum gain of several controllers for control the voltages at PCC and system frequency by FA Technique are robust because they perform well in both condition i.e. nominal operating condition as well as in fault at work. Optimum values of K_P , K_I and K_D of PID controllers used for frequency control and voltage control are obtained at nominal operating conditions for various disturbances and fault occurrences. The overall control strategy of grid connected hybrid energy system should be robust and work well. Integrating hybrid distributed generation in a distribution network requires an advanced controller, which is critical to ensuring high quality and stability of voltage at PCC and frequency of the power system [29].

5. System stability and other technical issues

Investigations have been carried out on a grid connected hybrid Wind/PV distributed generation system as shown in Fig. 3 consisting of a permanent magnet synchronous generator (PMSG) based variable speed wind energy conversion of a 6 KW, PV array 1 KW & utility grid. Hybrid system is connected through utility grid & load through command dc link and DC-AC convertor. A single switch three-phase switch-mode rectifier is being used which is being controlled to extract maximum power from the fluctuating wind. Individual dc–dc boost converters have been used to control the power flow to the load through dc link in PV system. A simple and effective control with dc–dc converters is being used for maximum power point tracking and hence maximum power extracting from and the solar photo voltaic systems. For controlling voltage at PCC & for controlling system frequency and making system stable, controller has been designed. Proportional-Integral (PI) & Proportional-Integral Derivative (PID) controllers are being considered for investigation.

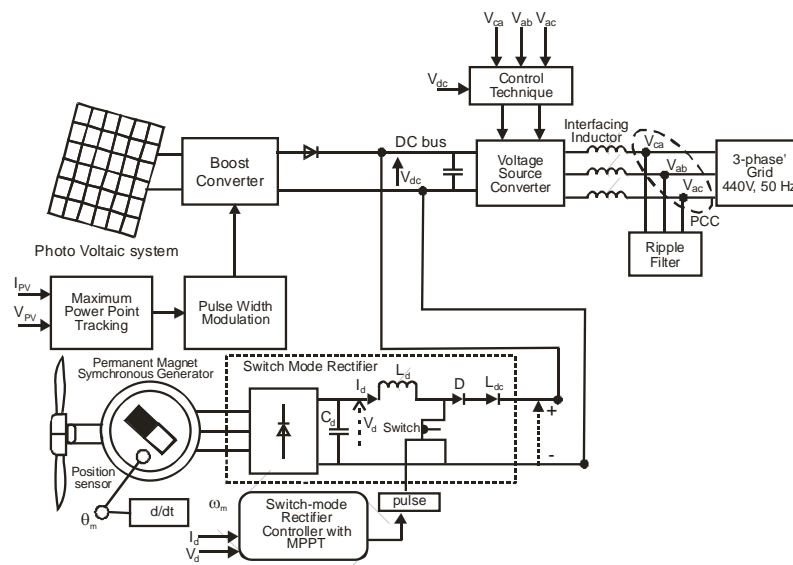


Fig. 3. Schematic diagram of proposed grid connected hybrid wind/PV distributed generation system [30].

Firefly algorithm is used for optimization of different controller’s parameter of the presented system. The cost function used in the hybrid distributed generation system is reported as the integral squared error (ISE) given by Eq. (7):

$$J = \int_0^T [(\Delta f)^2 + (\Delta V)^2] dt \tag{7}$$

Flow chart of Firefly Algorithm for voltage regulation and frequency control at PCC has been shown in Fig. 4. There are two issues in FA. As reported, there is variation of light intensity and formulation of the attractiveness. The attractiveness of a fire fly is determined by its brightness or light intensity which in turn is associated with the objective function. For maximization problems, the brightness I of a fire fly at a particular location x can be chosen as $I(x)/f(x)$. It should be seen in the eyes of the beholder or judged for relative attractiveness ρ by the other fire flies. Thus, it should vary with the distance r_{ij} between fire fly i and fire fly j . As light

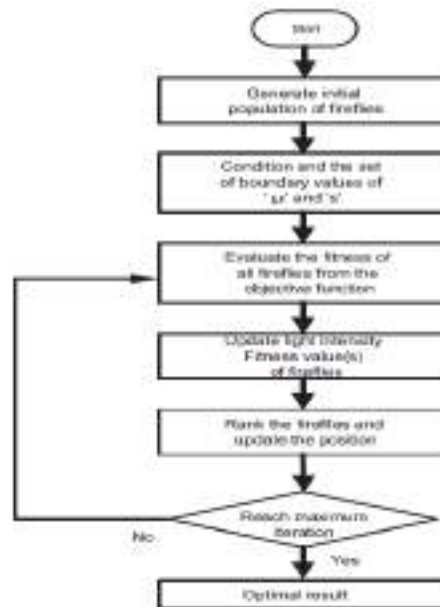


Fig. 4. Flowchart of firefly algorithm for voltage regulation and frequency control [30].

6. Result and discussions

As most standalone hybrid energy systems are being used for remote and rural areas, in many cases, the load profile data are unavailable. The accuracy of load profile immensely influenced the size optimization results. Therefore, more research is required in the field of load profile estimation and forecasting to establish and construct more accurate predictions for the load profile. The new technique not only focuses on the variables of technical and climate specifications in forecasting process but also being included social factors. The peaks of solar irradiation and wind speed influence the size optimization solutions. Therefore, usage of hourly annual solar and wind data rather than daily or monthly data is being recommended as hourly data contain the troughs and peaks of solar irradiation and wind speed. Based on the review studies, the manufacturing costs of hybrid system components are being reported as the main reason of the high initial costs of HES, which require a significant reduction to lessen initial system cost. This reduction will be decrease payback time and increase return on investment which will eventually increase social acceptance and human development index.

Optimization of hybrid renewable energy systems designed to be remote from the grid (SA-HRES) might be reported as single-objective optimization problems including optimization of system elements sizes to minimize total costs, but might be also comprised multi-objective optimization problems including targets such as system management, control or environmental optimization. As observed in the results of studies evaluating optimization problems as single or multiple objective problems, for single-objective optimization problems in addition to classic methods such as the least squares method, linear programming and iterative optimization techniques, meta-heuristic methods such as PSO and genetic algorithms might be applied. For multiobjective optimization techniques, in addition to classic methods, Pareto-based optimization approaches such as PSO and MOPSO, evolutionary algorithms, genetic algorithms and NSGA-II are being frequently used. Pareto-based approaches could be provided Pareto-front which contains a few solutions according to domination relations. Result of this, Pareto-based approaches are being more efficient way to obtain good solutions close to global optimum. SA-HRES is being contained more than one objective function and many constraints. This situation is being expanded solution space and computational

Alternatively, while using Pareto-approaches, SA-HRES multi objective optimization problem could be divided to sub problems as a solution way to overcome these difficulties. The main differences between the simulation results and real or other applications are being reported as the model parameters and probability distributions, which depend on the operating characteristics and geographical environment.

The most popular hybrid combination for islands and remote rural areas are the solar, wind, diesel generator, and battery storage based hybrid energy system as it provides more reliable and continuous power supply. Finding the optimum size of each element is to reduce the cost while maintaining the reliability and social acceptance. Hybrid algorithms have recently been extensively applied for the sizing optimization of standalone solar and wind hybrid system. Moreover, software computer tools are also used widely for sizing and designing of standalone solar and wind system. However, using modern methods such as artificial algorithms and hybrid algorithms are more accurate optimization results than software tools as they have the ability to solve multi-objective optimization problems. The reliability assessment technique applied in this paper is being told as one of the key performance indicators to assess the impact of using the WTG, PV and ESS in the conventional distribution system. Reliability technique is being reported one of the key performance indicators to measure the impact of renewable DG resources in the conventional power distribution system. It could be deduced from the results obtained from the simulation that the power utilities should encourage the integration of renewable energy into their distribution systems as an alternative way to increase the reliability of their networks. This work could be extended to evaluate the effect of renewable energy resources on a large distribution system. In addition, reliability assessment could be assisted the power system operators, planners, designers and engineers to optimize the power outage cost in a conventional distribution system with the application of renewable energy resources.

Voltage control derived from power flow as a result of high penetration of RG in the DS is being reported as one of the major concerns of the DNOs. Feeder voltage needs to be maintained within the permissible range against RG connection so that voltage variation is not being affected consumer voltage supply quality and reliability. The paper is being reviewed the impact of RG on DS with voltage control strategies and presents the aspect of smart grid technologies in voltage control as the most appropriate voltage control at varying wind speed and PV irradiance. Mitigation of voltage imbalances as a result of voltage fluctuation and intermittency could be provided if the voltage and reactive power control equipment are being operated based on smart grid technologies, especially at the demand side integration and energy storage. The combination of electrical energy storage and demand side measures one operating from the supply side (Energy Storage), the other from the demand side (DSI), would be potentially allowed generation plant, both traditional and renewable, to operate in a more cost effective manner. Co-ordination of voltage control devices and RG for voltage profile improvement could further be investigated.

7. Conclusions

Realistic solutions, the SA-HRES problem requires multi-objective solutions that each function could be grouped in different optimization classes. Each solution has been reported trade-off between total system cost, reliability, environmental aspects and so on. Furthermore, for each type component design and/or selection variables also could be grouped in positive continuous, integer, and combinatorial selection variables. A method is presented for estimating the failure probability of an IES based on a first order reliability method, and considers the issues of gas supply shortage and the limited capacity of the grid to absorb it. To calculate the failure probabilities in an IES, the stochastic behaviours, dependencies, and limits of multiple energy sources might be considered. The FORM method, solved by HLRF theory, is being used to calculate the failure probabilities of a gas supply shortage and the absorption limits of the grid.

The relationship between power generation and output fluctuations should be further discussed under various resource situations. The constraints of the power grid should be refined. The detailed coordinated operation of multi-energy should be explored. Compensating for wind power and photovoltaic power with hydropower is being reported to be an effective solution for output

fluctuations in power curtailment. Establishing a model for a hydro-wind photovoltaic system is necessary to investigate the mechanisms underlying the coordinated operation of diverse energies. A hybrid centralized and distributed control technique for a hybrid renewable energy system consisting of AC/DC micro grids is proposed. The models of the DER and coordination control schemes are being proposed for the all embedded converters to maintain stable system operation. The control schemes power flow between AC and DC micro grids. This is being achieved the proper power sharing and enhances operational reliability. Various salve control methods have been incorporated to harness the maximum power from DC and AC sources and to facilitate coordination of the power exchange between DC and AC grid. A Non-linear robust control technique using improved particle swarm optimization (IPSO) control is being implemented as a master control technique for the control of interlinking converter (IC) between AC and DC micro grids.

References:

1. Khare, Vikas, Nema, Savita and Baredar, Prashant, (2016). Solar-wind hybrid renewable energy system: A review. *Renewable and Sustainable Energy Reviews* 58 23–33.
2. Chauhan, Anurag and Saini, R.P. (2017). Size optimization and demand response of a stand-alone integrated renewable energy system. *Energy* 124 59-73.
3. Amusata, Oluwamayowa O., Shearing, Paul R. and Fraga, Eric S. (2016). Optimal integrated energy systems design incorporating variable renewable energy sources. *Computers and Chemical Engineering* 95 21–37.
4. Cheng M, Zhu Y. (2014). The state of the art of wind energy conversion systems and technologies: a review. *Energy Convers Manage*;88:332–47.
5. Koohi-Kamali S, Rahim NA. (2016). Coordinated control of smart microgrid during and after islanding operation to prevent under frequency load shedding using energy storage system. *Energy Convers Manage*;127:623–46.
6. Blechinger P, Cader C, Bertheau P, Huyskens H, Seguin R, Breyer C. (2016). Global analysis of the techno-economic potential of renewable energy hybrid systems on small islands. *Energy Policy*; 98:674–87.
7. Petrakopoulou F. (2016). On the economics of stand-alone renewable hybrid power plants in remote regions. *Energy Convers Manage*;118:63–74.
8. Singh S, Singh M, Kaushik SC. (2016). Feasibility study of an islanded microgrid in rural area consisting of PV, wind, biomass and battery energy storage system. *Energy Convers Manage*;128:178–90.
9. Zahraee SM, Khalaji Assadi M, Saidur R. (2016). Application of artificial intelligence methods for hybrid energy system optimization. *Renew Sustain Energy Rev*;66:617–30.
10. Monaaf D.A. Al-falahi, S.D.G. Jayasinghe and H. Enshaei, (2017). A review on recent size optimization methodologies for standalone solar and wind hybrid renewable energy system, *Energy Conversion and Management* 143 252–274.
11. Adegboye BA, Ekundayo KR. (2011). Reliability assessment of 4.2 MW single shaft typhoon gas fired turbine power generation station (2003–2008). *Adv Mater Res*;367:143–50.
12. Zhang P, Li W, Li S, Wang Y, Xiao W. (2013). Reliability assessment of photovoltaic power systems: review of current status and future perspectives. *Appl Energy*;104:822–33.
13. Zhao H, Guo S, Fu L. (2014). Review on the costs and benefits of renewable energy power subsidy in China. *Renew Sustain Energy Rev*;37:538–49.
14. Hossain MS, Madlool NA, Rahim NA, Selvaraj J, Pandey AK, Khan Abdul Faheem (2016). Role of smart grid in renewable energy: an overview. *Renew Sustain Energy Rev*;60:1168–84.
15. Sreedharan P, Farbes J, Cutter E, Woo CK, Wang J (2016). Micro grid and renewable generation integration: University of California, San Diego. *Appl Energy*;169:709–20.
16. Adefarati, T. and Bansal, R.C. (2017). Reliability assessment of distribution system with the integration of renewable distributed generation. *Applied Energy* 185 158–171.
17. Petinrin, J.O. and Shaaban, Mohamed, (2016). Impact of renewable generation on voltage control in distribution systems. *Renewable and Sustainable Energy Reviews* 65 770–783.

-
- algorithms and tools for renewable energy: a review. *Renew Sustain Energy Rev*;39:640–54.
19. Jebaraj S and Iniyar S. (2006). A review of energy models. *Renew Sustain Energy Rev*;10(4):281–311.
 20. Tezer, Tuba, Yaman, Ramazan and Yaman, Gülşen (2017). Evaluation of approaches used for optimization of stand-alone hybrid renewable energy systems. *Renewable and Sustainable Energy Reviews* 73 840–853.
 21. Fu X, Sun H, Guo Q, Pan Z, Zhang X, Zeng S. (2017). Probabilistic power flow analysis considering the dependence between power and heat. *Appl Energy*;191: 582-92.
 22. Xueqian Fu, Qinglai Guo, Hongbin Sun, Xiurong Zhang and Li Wang, (2017). Estimation of the failure probability of an integrated energy system based on the first order reliability method. *Energy* 134 1068-1078.
 23. Acker TL, Robitaille A, Holttinen H, Piekutowski M, Tande JOG (2012). Integration of wind and hydropower systems: results of IEA wind task 24. *Wind Eng*;36(1):1-18.
 24. Cheng CT, Wu XY, Shen JJ, Liao SL (2011). Short-term optimal operation methods of large-scale hydropower plantsI.general overview. *Shuili Xuebao*;9: 1017-24.
 25. Wu XY, Cheng CT, Shen JJ, Luo B, Liao SL, Li G (2015). A multi-objective short term hydropower scheduling model for peak shaving. *Int J Electr Power Energy Syst*;68:278-93.
 26. Xianxun Wang, Yadong Mei, Yanjun Kong, Yuru Lin and Hao Wang, (2017). Improved multi-objective model and analysis of the coordinated operation of a hydro-wind-photovoltaic system. *Energy* 134 813-839.
 27. Ding Guangqian, Gao Feng, Zhang Song, Loh Poh Chiang, Blaabjerg Frede (2014). Control of hybrid AC/DC microgrid under islanding operational conditions. *J Mod Power Syst Clean Energy*;2(3):223–32.
 28. Saad, Naggat H., El-Sattar, Ahmed A. and Mansour, El-Aziz M. (2018). A novel control strategy for grid connected hybrid renewable energy systems using improved particle swarm optimization. *Ain Shams Engineering Journal* 9 2195–2214.
 29. Chaurasia, Giraja Shankar, Singh, Amresh Kumar, Agrawal, Sanjay and Sharma, N.K. (2017). A meta-heuristic firefly algorithm based smart control strategy and analysis of a grid connected hybrid photovoltaic/wind distributed generation system. *Solar Energy* 150 265–274.
 30. Bacchetti, Elisa (2017). A design approach with method and tools to support SMEs in designing and implementing Distributed Renewable Energy (DRE) solutions based on Sustainable Product-Service System (S.PSS). *Procedia CIRP* 64 229 – 234.
 31. Bajpai, Prabodh and Dash, Vaishalee (2012). Hybrid renewable energy systems for power generation in stand-alone applications: A review", *Renewable and Sustainable Energy Reviews* 16 2926–39.
 32. Duong Minh Bui, Keng-Yu Lein, Shi-Lin Chen, Yin-Chen. Lu, Chen-Min Chan and Yung-Ruei Chang, (2015). Investigate dynamic and transient characteristics of microgrid operation and develop a fast-scalable-adaptable algorithm for fault protection system. *Electric Power Systems Research*, 120 214-233.

Optimum Scheduling Techniques for Integrated Renewable Energy Source

Chandra Prakash Varma

Department of Electronics Engineering, Dr. Ambedkar Institute of Technology for Handicapped (U.P.), Awadhपुरi, Kanpur, India

Tel: 0-800-549-5175 E-mail: cpvermaith2007@gmail.com

Yaduvir Singh

Department of Electrical Engineering, Harcourt Butler Technical University, Nawabganj, Kanpur, India

Tel: 0-708-130-0508 E-mail: dryaduvirsingh@gmail.com

Abstract

Optimal Power Flow (OPF) is being used to dispatch available generation in such a way that minimizes a particular objective function. The need for new transmission and/or generation capacity, improving load following, the potential benefits of grid-integrated storage technologies is being included decreasing, providing spinning reserve, correcting frequency, voltage, and power factors, as well as the indirect environmental advantages gained through facilitating an increased penetration of RERs. Differential search algorithm (DSA) is being stated as a recent literature described application of state-of-the-art evolutionary algorithm (EA). Success history based parameter adaptation technique of differential evolution (SHADE) is being employed for the optimization problem. Optimal scheduling contains Equality and inequality constraints and Real time optimal power flow (RT-OPF) model. Indirect soft linking approaches is being required the construction of new dedicated sectoral models and more challengingly handling the interface between the two models in order to arrive at consistent results. The direct integration methodologies for ESOMs that improve the technical representation directly increase the optimality of solution.

Keywords

Generator rate constraints, Integrated Renewable Energy Source, Optimal power flow, Solar Energy System, Variable renewable energy.

1. Introduction

By Optimal Power Flow (OPF) method, the operation of power systems has been informed for a long time. It is being used to dispatch available generation in such a way that minimizes a particular objective function. It could be represented the network and nodal power balance equations. It is also being maintained the limits on bus voltage, branch power flows, and generator's active and reactive power outputs [2,3]. The needs for new transmission and/or generation capacity, improving load following, the potential benefits of grid-integrated storage technologies are being included i.e. decreasing, providing spinning reserve, correcting frequency, voltage, and power factors, as well as the indirect environmental advantages gained through facilitating an increased penetration of renewable energy resources RERs [4]. For the wind-solar-storage generation system considering the correlation among wind power output, solar PV power output and load demand, an optimal scheduling approach is being proposed [5]. The various

aspects of hybrid renewable energy system including the pre-feasibility analysis, optimum sizing, modeling, control aspects and reliability issues, a comprehensive review are being presented [1,6].

Differential search algorithm (DSA) is being stated as a recent literature described application of state-of-the-art evolutionary algorithm (EA) where a few standard objectives in OPF are being optimized for IEEE bus systems with thermal generators [8]. Standard group search optimization algorithm is being reported as improved with adaptive group search optimization (AGSO) to perform similar study on OPF [9]. As reported by Chiab AE et al (2016), it is being performed OPF calculation with more complex objectives of multi-fuel options and considers valve-point effect in thermal generators in applying backtracking search optimization algorithm (BSA) [10]. As reported by Bouchekara HREH et al (2016), improved colliding bodies optimization (ICBO) algorithm is being used where number of colliding bodies are increased in each iteration to enhance performance of the algorithm when applied to the problem of OPF [11]. As reported by Mohammed AAA (2017), moth swarm algorithm (MSA) on numerous objectives of OPF for various bus systems is being applied effectiveness of the algorithm in terms of fast execution time and quick convergence [12]. Independent System Operator (ISO) is being reported as to bear the penalty cost as surplus power goes wasted if not utilized. On contrary, overestimation is the scenario when the generated power is being reported as less than the scheduled power. To mitigate power demand, ISO is being needed to keep spinning reserve which adds up to the operating cost of the system. Success history based parameter adaptation technique of differential evolution (SHADE) is being employed for the optimization problem. SHADE is being combined with an effective constraint handling technique called superiority of feasible solutions (SF) [8]. In economic and societal wellbeing, electricity has been reported a crucial role. In the form of electricity, the global energy consumption was 18% in 2013. In addition, electricity power generation and transmission has been contributed to climate change through greenhouse gas emissions. With generation of electricity, a quarter of global emissions are being associated. From electricity generation, there are being reported various national and international targets for reducing greenhouse gas (GHG) emissions. The power sector has been considered a crucial role, as it is responsible for 31.8% of the global GHG emissions. The considered objectives are being included economic as well as environmental measures. They have been reported the particle swarm optimization PSO algorithm to be very efficient in finding the Pareto optimal solutions, establishing the trade-off between the competing objectives [13-15]. It is being expected to require the transition to a low-carbon energy system the electricity sector to integrate large amounts of variable renewable energy sources (VRES) [17]. To bridge this gap, numerous methodologies have recently been developed [18-21]. A review of prominent methodologies is being developed in this paper to better capture the economic and technical challenges related to the integration of VRES in two families of long-term planning models, namely long-term energy system optimization models (ESOMs) and Integrated Assessment Models (IAMs), which focus on global long-term scenarios. The users of long-term planning models are being allowed this analysis to select a methodology (or combination of methodologies) to suit their needs. Additionally, the analysis is being exposed the needs for further research [16].

2. Optimal Scheduling

As reported in a comparison between the deterministic and stochastic scenarios, it

is being suggested that the economic performance of the stochastic (i.e., more realistic) model is superior to the average deterministic scenario [13]. The simulation results for various IEEE 30 and 300 bus test systems etc. with Genetic Algorithm (GA) and Two-Point Estimate Method (2PEM) are being reported which test the effectiveness of optimal scheduling strategy. Results for sample systems with GA and two-point estimate based optimal power flow, and GA and Monte Carlo Simulation (MCS) can be obtained to ascertain the effectiveness of method. The interior Point method is being compared also with some of the results [1].

The objective function is formulated as,

Minimize

(1)

$$\sum_{i=1}^{N_G} C_{Gi}(P_{Gi}) + \sum_{j=1}^{N_W} C_{Wj}(P_{Wj}) + \sum_{k=1}^{N_S} C_{Sk}(P_{Sk}) + \sum_{i=1}^{N_G} C_{RTi}(P_{Dev,i})$$

where N_G : number of thermal generators, N_W : number of wind generators, and N_S : number of solar PV generators

The first term is the fuel cost of conventional thermal generators, and it is expressed as,

$$C_{Gi}(P_{Gi}) = a_i + b_i P_{Gi} + c_i P_{Gi}^2 \quad (2)$$

P_{Gi} : scheduled power output from i^{th} conventional thermal generator in MWs, $C_{Gi}(P_{Gi})$: fuel cost function of conventional thermal generators, and a_i , b_i , and c_i fuel cost coefficients of i^{th} conventional thermal generating unit.

A linear cost function is used for the scheduled wind power and it is expressed as,

$$C_{Wj}(P_{Wj}) = d_j P_{Wj} \quad (3)$$

P_{Wj} : scheduled wind power generation from j^{th} wind farm in MWs, $C_{Wj}(P_{Wj})$: cost function of wind energy generator, and d_j : direct cost coefficient of j^{th} wind farm/generator.

A linear cost function is being expressed as the use for the scheduled solar PV power, and it is,

$$C_{Sk}(P_{Sk}) = t_k P_{Sk} \quad (4)$$

where P_{Sk} : power output from k^{th} solar PV plant (MW), and t_k : direct cost coefficient of k^{th} solar PV plant.

A quadratic real time adjustment cost function is used to calculate the mean adjustment cost (MAC), and is given by

$$C_{RTi}(P_{Dev,i}) = C_{RTi} \left(\left| PDA - PRT \right| \right) = x_i + y_i P_{Dev,i} + z_i P_{Dev,i}^2 \quad (5)$$

where $P_{Dev,i}$: deviation power from i^{th} conventional thermal generator, and x_i , y_i and z_i the cost coefficients of i^{th} conventional thermal generator in real-time.

2.1 Equality and inequality constraints

The equality and inequality constraints are presented here.

a) Nodal power balance constraints

The sum of power generated by conventional thermal generators, wind farms and solar PV modules is equal to the sum of the total demand and losses in the system.

$$P_i = V \sum_{j=1}^n [V_j [G_{ij} \cos(\delta_i - \delta_j) + B_{ij} \sin(\delta_i - \delta_j)]] - P_{Gi} - P_{Di} \quad (6)$$

$$Q_i = V \sum_{j=1}^n [V_j [G_{ij} \sin(\delta_i - \delta_j) + B_{ij} \cos(\delta_i - \delta_j)]] - Q_{Gi} - Q_{Di} \quad (7)$$

where

$$P_{Gi} = \sum_{j=1}^{N_G} P_{Gj} + \sum_{k=1}^{N_W} P_{Wk} + \sum_{i=1}^{N_S} P_{Si}$$

P_{Di} and Q_{Di} are the load active and reactive power, respectively. $Y_{ij} = G_{ij} + j B_{ij}$; i, j : i th and j th entry of the nodal admittance matrix. G_{ij} and B_{ij} : transfer conductance and susceptance between bus i and bus j , respectively.

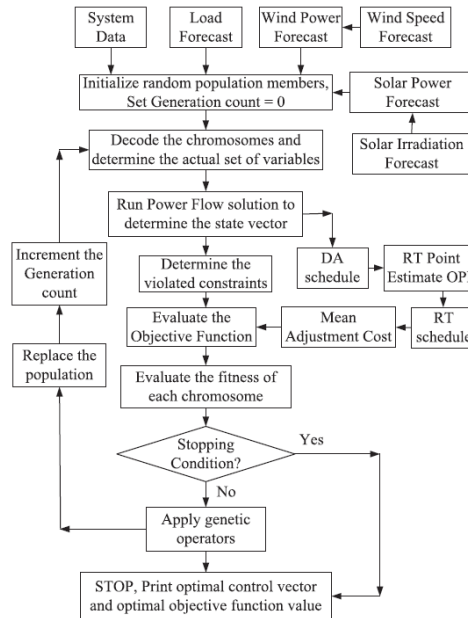


Fig. 1. Flowchart of solution procedure for optimal scheduling with RERs and storage [1].

b) Generator constraints

The minimum, maximum limits and generator rate constraints (GRC) of power is being restricted to the output power of each thermal generator, is restricted by their.

$$\max[P_{Gi}^{\min} \cdot P_{Gi}^0 - R_{Gi}^{down}] \leq P_{Gi} \leq \min[P_{Gi}^{\max} \cdot P_{Gi}^0 - R_{Gi}^{up}] \tag{8}$$

The power output of each wind generator is restricted by, $0 \leq P_{wj} \leq Prj$ $j = 1, 2, \dots, N_w$ (9)

where Prj is submitted as part of the wind producer energy offer. In DA scheduling, the wind power (P_{wj}) varies in the following range

$$0 \leq P_{wj} \leq P_{wf,j} \quad j = 1, 2, \dots, N_w \tag{10}$$

where $P_{wf,j}$ is the forecasted wind power from j th wind generator, which is obtained from the forecasted wind speed.

The maximum penetration of solar PV to system is given by,

$$| P_{Sk} | \leq P_{sk}^{\max} \quad k = 1, 2, \dots, N_s \tag{11}$$

where P_s (MW) is the solar PV active power generation (unknown), and $P_{max S}$ (MW) is the available maximum active power generation (known) subject to solar irradiation and temperature. (13)

Generator voltage magnitudes (V_G), generator reactive power (Q_G) are restricted by their lower and upper limits, and they are represented by

$$V_{Gi}^{\min} \leq V_{Gi} \leq V_{Gi}^{\max} \quad i, (N_G + N_w + N_s)$$

$$Q_{Gi}^{\min} \leq Q_{Gi} \leq Q_{Gi}^{\max} \quad i, (N_G + N_w + N_s)$$

c) Security constraints

These constraints include the limits on load bus voltage magnitudes (VDi), line flow limits (Sij) and transformer tap (TTt) constraints.

$$V_{Di}^{\min} \leq V_{Di} \leq V_{Di}^{\max} \quad i = 1, 2, \dots, N_i \quad (14)$$

$$|S_{ij}| \leq S_{ij}^{\max} \quad (15)$$

$$TT_t^{\min} \leq TT_t \leq TT_t^{\max} \quad (16)$$

$t = 1, 2, \dots, N_T$
 where N_I : number of load demands, S_{ij} : MVA (mega-volt ampere) flow, S_{max} ij : maximum thermal limit of line between bus i and bus j . TT_t : transformer tap settings, and N_T : number of transformer taps

2.2 Real time optimal power flow (RT-OPF) model

Probabilistic RT-OPF is being used to calculate the mean adjustment cost (MAC), and the two-point estimate OPF is used to solve this RTOPF problem. This two-point estimate method (2PEM) uses deterministic OPF. The deterministic and probabilistic RT-OPF models are formulated next:

2.2.1 Deterministic RT-OPF model

In this model, the objective is to minimize the deterministic mean adjustment cost (MAC), and is formulated as,

$$\min \text{imize} \sum_{i=1}^{N_G} C_{RTi}(P_{Dev,i}) = \sum_{i=1}^{N_G} C_{RTi}(|P_{Gi}^{DA} - P_{Gi}^{RT}|) \quad (17)$$

Subjected to equality and inequality constraints.

2.2.2 Probabilistic RT-OPF model

In this model, the objective is to minimize the MAC due to uncertainty in wind generation, solar PV power and load demand forecasts. For probabilistic RT-OPF, the uncertain random variable is due to uncertainties in wind generation, solar PV power and load demand at real time. Hence,

$$\min \text{imize} \sum_{i=1}^{N_G} C_{RTi}(P_{Dev,i}) = \sum_{i=1}^{N_G} C_{RTi}(|P_{Gi}^{DA} - P_{Gi}^{RT}|) \quad (18)$$

where P_{Gi}^{RT} is a random variable. Subjected to equality and inequality constraints. This problem is being solved using two-point estimate OPF. In real time (RT), if the scheduled wind power (P_{Wj}) varies in $\pm x$ %, then

$$P_{\max}^{\min} = P_{Wf,j} - \left(\frac{x}{100} \times P_{Wf,j}\right) \quad (19)$$

and

$$P_{\max}^{\max} = P_{Wf,j} + \left(\frac{x}{100} \times P_{Wf,j}\right) \quad (20)$$

Therefore, in real time optimal power flow (RT-OPF),

$$P_{\max}^{\min} \leq P_{\max} \leq P_{\max}^{\max} \quad (21)$$

and the similar expressions are valid for solar PV power generation also.

2.3 Wind energy system

Weibull Probability Density Function (PDF) is being used for the wind speed and then, transformed to the corresponding wind power distribution for use in proposed optimal scheduling model.

For a given wind speed input, the wind power output is expressed as,

$$p = \begin{cases} 0 & \text{for } v < v_1 \text{ and} \\ p_r \left(\frac{v - v_1}{v_r - v_1} \right)^{\frac{1}{\alpha}} & v > v_o \\ p_r & \text{for } v_1 \leq v \leq v_r \end{cases} \quad (22)$$

where p is power output of wind energy generator in MWs, v is the wind speed (in m/sec), and v_i , v_o , v_r are the cut-in, cut-out and rated wind speeds, respectively.

2.3.1 Uncertainty modeling of wind energy system

The wind speed is modeled by using Weibull Probability Density Function (PDF), and is expressed as,

$$f(v) = \left(\frac{k}{c}\right) \left(\frac{v}{c}\right)^{k-1} \exp\left[-\left(\frac{v}{c}\right)^k\right] \quad 0 < v < \infty \quad (23)$$

For the Weibull PDF, the corresponding Cumulative Distribution Function (CDF) is expressed as,

$$F_v(v) = 1 - \exp\left[-\left(\frac{v}{c}\right)^k\right] \quad (24)$$

If it is assumed that the wind speed has a given distribution, such as the Weibull, it is then necessary to convert that distribution to a wind power distribution. For a linear transformation, in general, such as that described as below

$$P = T(V) = aV + b \quad (25)$$

and

$$f_p(p) = \int_v [T^{-1}(p)] \left| \frac{dT^{-1}(p)}{dp} \right| = \int_v \left(\frac{p-b}{a} \right) \left| \frac{1}{a} \right| \quad (26)$$

The wind generation output in the continuous range ($v_i \leq v \leq v_r$) is given by,

$$p = p_r \left(\frac{v-v_i}{v_r-v_i} \right) = \left(\frac{p_r}{v_r-v_i} \right) v - \left(\frac{v_i}{v_r-v_i} \right) \quad (27)$$

where

$$a = \left(\frac{p_r}{v_r-v_i} \right) \quad \text{and} \quad b = - \left(\frac{v_i}{v_r-v_i} \right)$$

According to the theory for function of random variables, Eq. (26) will take the form,

$$f_p(p) = \frac{khv_i}{p_r c} \left(\frac{1 + \frac{hp}{p_r}}{c} \right)^{(k-1)} \times \exp\left[- \left(\frac{1 + \frac{hp}{p_r}}{c} \right)^k \right] \quad (28)$$

where $h = (v_r/v_i) - 1$ is an intermediary parameter. The wind power output in discrete range can also be considered. The sum of the probability of discrete and continuous function should be 1.

2.3.4 Solar energy system

In the presence of battery storage, the power output of solar PV cell (P_{PV}) and the power output of solar energy system (P_S) are being different. The power balance in solar energy system is represented as,

$$P_S = P_{PV} (G) + P_B - P_U \quad (29)$$

It is assumed that there is being no spillage power (P_U (MW)) from PV. The effect of spillage power of the aggregated battery is also governed. The solar PV power output can be controlled by the power tracking control scheme or to be charged into the batteries. Hence, the maximum penetration of solar PV to system is

$$|P_S| \leq P_S^{\max} \quad (30)$$

It is assumed that the battery voltage remains constant during the scheduling period. The maximum charge and discharge capacity of battery is being represented by Eq. (31). However, this limit depends on the rating of the battery. P_B is the power charge/discharge to/from battery (MW). P_B is positive for discharging and negative for charging.

$$P_B < P_B < \bar{P}_B \quad (31)$$

where P_B is the aggregated discharging power limit (positive) for all batteries (MW), and \bar{P}_B is the aggregated charging power limit (negative) of all batteries (MW). The effect of spillage power of the aggregated battery is

being ignored.

If C_{init} and C are aggregated battery state of charge of all batteries (kAh) at the beginning and the end of the scheduling period (say 1 h). The contribution of solar PV module to the grid during interval ' Δt ' (1h) is

$$P_S = P_{PV}(G) + \frac{(C_{init} - C)V_B}{\eta_B \Delta t} \quad (32)$$

where V_B : battery voltage, η_B : efficiency during the charging period (75%), and $P_{PV}(\cdot)$: solar irradiation to energy conversion function of the solar PV generator or power output from solar PV cell, and is given by

$$P_{PV}(G) = \begin{cases} P_{sr} \left(\frac{G^2}{G_{std} R_c} \right) & \text{for } 0 < G < R_c \\ P_{sr} \left(\frac{G}{G_{std}} \right) & \text{for } G > R_c \end{cases} \quad (33)$$

Solar PV cell temperature is ignored.

where, G : Solar irradiation forecast (W/m^2), G_{std} : In the standard environment, the solar irradiation is set as $1000 W/m^2$, R_c : A certain irradiation point set as $150 W/m^2$, P_{sr} : Rated equivalent power output of the solar PV generator, and P_B : Power charge/discharge to/from the battery

2.3.4.1 Uncertainty modeling of solar PV system

The power output of solar PV generator mainly depends on irradiance. The distribution of hourly irradiance at a particular location usually follows a bi-modal distribution, which can be considered as a linear combination of two uni-modal distributions. The uni-modal distribution functions can be modeled by Weibull, Beta and Log-normal PDFs. The Weibull probability distribution function is expressed as,

$$f_G(G) = \omega \left(\frac{k_1}{c_1} \right) \left(\frac{G}{c_1} \right)^{k_1-1} \exp\left[-\left(\frac{G}{c_1}\right)^{k_1}\right] + (1-\omega) \left(\frac{k_2}{c_2} \right) \left(\frac{G}{c_2} \right)^{k_2-1} \exp\left[-\left(\frac{G}{c_2}\right)^{k_2}\right] \quad 0 < G < \infty \quad (34)$$

where ω is weight parameter in the range between 0 and 1 ($0 < \omega < 1$). k_1 , k_2 and c_1 , c_2 are the shape and scale factors, respectively.

2.3.4.2 Normal distribution for load demand uncertainty

The future system load demand is uncertain at any given period of time. Normally used two probability density functions (PDFs) for modeling load demand uncertainty are Normal and Uniform PDFs. The PDF of normal distribution for uncertain load ' l ' is given by

$$f_l(l) = \frac{1}{\sigma_L \sqrt{2\pi}} \times \exp\left[-\frac{(l - \mu_L)^2}{2\sigma_L^2}\right] \quad (35)$$

where μ_L and σ_L are the mean and standard deviation of the uncertain load, respectively.

2.4 Optimal Power Flow

Optimal power flow problem is being formulated with all relevant system parameters including generator outputs and solved subsequently to obtain the optimal settings. Weibull and lognormal probability distribution functions are being used for forecasting wind and solar photovoltaic power output respectively. The objective function is being considered reserve cost for overestimation and penalty cost for underestimation of intermittent renewable sources. Emission factor is also included in objectives. Success history based adaptation technique of differential evolution algorithm can also be adopted for the optimization problem. The algorithm thus combined and constructed can give optimum results satisfying all network constraints.

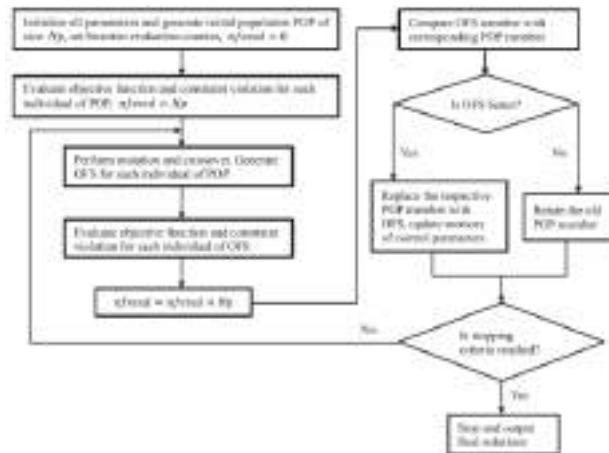


Fig. 2. Flowchart for implementation of SHADE-SF[7].

State-of-the-art evolutionary algorithm, SHADE, is being employed for the optimization. Flowchart is given in Fig. 2. The algorithm is combined with an effective constraint handling technique, SF. Therefore, the use of proper constraint handling method in constrained optimization problems is being must. Besides, due to fast convergence of SHADE-SF algorithm to global optima, it can be applied successfully to other multimodal, highly non-linear, constrained optimization problems [7].

2.5 Comparison of modeling methodologies

An overview of the different methodologies and their respective advantages and disadvantages is being presented in Table 1. Indirect soft linking approaches is being required the construction of new dedicated sectoral models and more challengingly handling the interface between the two models in order to arrive at consistent results. The direct integration methodologies for ESOMs that improve the technical representation directly increase the optimality of solution [16].

3. Result and discussions

It is being proposed solution approach to optimal power flow (OPF) problem with stochastic wind and solar power in the network. Uncertainties of intermittent renewable sources are being modelled with different probability density functions. Integration method of all the sources is being discussed in detail. Generation cost incorporating all sources is being optimized and variation of generation cost with change in cost coefficients of uncertain sources is being studied. State-of-the-art evolutionary algorithm, SHADE, is being employed for the optimization. The algorithm is being combined with an effective constraint handling technique, SF. Violating physical or security constraints of network components may be compromised system safety, lead to excessive losses, malfunction and often failure of the component. So,

operating the network within defined limits is being pre-requisitioned for secure and correct operation. In ESOMs and IAMs, the aim of this paper was to review the current state of play with regards to how integration challenges of VRES. In future, a key motivator in this was to aid future research by presenting and contrasting these methodologies so that, energy system modellers can select and apply methodologies best suited to their situation. Failure to sufficiently capture the integration challenges of VRES leads to unrealistic assessment of the difficulties associated with achieving a low carbon energy system and thus leading to sub-optimal energy system planning.

Table 1: Tabular comparison of modelling methodologies [16].

Methodology		Strengths	Limitations and challenges
Soft-link to an operational power system model	Uni-directional soft-link	<ul style="list-style-type: none"> Accurate assessment of operational costs, fuel consumption and greenhouse gas emissions High level of temporal and technical detail allows assessment of power system reliability. Good robustness check of energy system model Results 	<ul style="list-style-type: none"> Need for a UCED model in addition to the ESOM/IAM Does not increase the optimality of the solution: Can possibly overestimate integration costs of VRES, because the ESOM investments are not adjusted to account for the UCED challenges
	Bi-directional soft-link	<ul style="list-style-type: none"> Allows for increased optimality of the solution Iterative procedure has a lower computational cost than a single integrated ESOM/IAM with the same level of detail Accurate assessment of costs, fuel consumption and greenhouse gas emissions High level of temporal and technical detail allows assessment of power system reliability. Good robustness check of energy system model Results 	<ul style="list-style-type: none"> Need for a UCED model in addition to the ESOM/IAM Feedback to ESOM/IAM highly dependent on modeller skill and judgement Optimality and convergence of the solution cannot be guaranteed
Direct integration methodologies for ESOMs	Semi-dynamic balancing using typical days with increased resolution	<ul style="list-style-type: none"> Allows for increased optimality of the solution Ease of implementation Retains chronology which allows the capture of the benefits associated with within-day storage systems and other types of flexibility 	<ul style="list-style-type: none"> Averaging of VRES generation data of different days leads to smoothing of VRES output. Reliable operation of the modelled power system in the short term (hourly) is difficult to assess Endogenous determination of the value of flexibility requires to include additional constraints, which further increase computational cost Computational complexity increases with an increasing number of time-slices Chronology is lost making it impossible to assess the need for flexibility and the value of flexibility options Reliable operation of the modelled power system in the short term (hourly) is difficult to assess
	Integral balancing based on approximating the joint probability distribution of the load and VRES generation	<ul style="list-style-type: none"> Allows for increased optimality of the solution The variability of the load and VRES generation can be captured relatively well using a limited number of time-slices The correlation between different time series is accounted for. This way, the RLDC will be approximated well for varying shares of VRES. Ease of implementation 	
	Semi-dynamic balancing using representative historical periods	<ul style="list-style-type: none"> Allows the strong increase of the optimality of the solution The variability of the load and VRES generation can be captured well using a limited number of time-slices The correlation between different time series can be accounted for. This way, the RLDC will be approximated well for varying shares of VRES. Retains chronology which allows an endogenous determination of the value of flexibility options such as within-day storage. 	<ul style="list-style-type: none"> Reliable operation of the modelled power system in the short term (hourly) is difficult to assess Good selection of representative historical periods requires implementation of a specific selection algorithm/model Difficult to capture the impact of medium-term variations (e.g., periods of two weeks with almost no wind) Endogenous determination of the value of flexibility requires to include additional constraints, which further increase computational cost
	Using stochastic programming as a means to address modelling uncertainties	<ul style="list-style-type: none"> The requirement for back-up capacity is endogenous removing the need for a commonly used peak constraint. Hedges against not having enough flexibility generation capacity in the power system. Detailed quantification of uncertainty Can be combined with methodologies that increase intra-annual time resolution Can incorporate several historical RES profiles Measures the costs of disregarding uncertainty Measures the cost of eliminating uncertainty (and hence provides insights about the order of magnitude of supports required in investments in back-up capacity and storage options) 	<ul style="list-style-type: none"> Strongly increases computational complexity Stochastic modelling requires a representation of the uncertain parameters that are specific to the model used Requires advanced scenario tree generation techniques and reduction algorithms Requires a solid understanding of probability concepts and sampling techniques Can impose difficulties in interpreting the results Obtained

	Stylized integration of operational Constraints	<ul style="list-style-type: none"> • Allows for increased optimality of the solution • Ease of implementation • Allows to mimic the impact of different constraints with only a minor increase in computational complexity 	<ul style="list-style-type: none"> • Requires calibration using more detailed models • General validity cannot be guaranteed
	Modelling ancillary services markets in long-term energy system models	<ul style="list-style-type: none"> • Allows to increase the optimality of the solution • Captures the most influential technical constraint • Can be combined with a low level of temporal Detail 	<ul style="list-style-type: none"> • Uncertainties related to endogenous sizing the need for operating reserves over long time horizons • Requires using additional variables and constraints which increase computational complexity
Direct integration methodologies for IAMS	Parametrization of residual load duration curves	<ul style="list-style-type: none"> • Allows for increased optimality of the solution • The correlation between different time series is fully accounted for. This way, the RLDC will be approximated well for varying shares of VRES • Only a requires a limited increase in computational complexity compared to a timeslice Approach 	<ul style="list-style-type: none"> • Chronology is lost, making it impossible to directly assess the need for flexibility and the value of flexibility options • Parametrization of the impact of short-term storage requires pre-processing of the RLDC using a more detailed model • The spatial aspect of VRE integration (effect of transmission grid on pooling variability) cannot be endogenously calculated, but rather needs to be included in the RLDC data ex-ante. • Reliable operation of the modelled power system in short-term (hourly) is difficult to assess

4. Conclusions

Due to fast convergence of SHADE-SF algorithm to global optima, it can be applied successfully to other multimodal, highly non-linear, constrained optimization problems. For future work on OPF front, the authors are being proposed possible integration of small hydro-generators with variable river flow, storage in the form of batteries or pumped hydro in the network with large number of buses. Accurate model of doubly fed induction generators for wind turbines, FACTS devices can also be incorporated for detailed study. The comparison between the deterministic and stochastic scenarios have been suggested that the economic performance of the stochastic (i.e., more realistic) model is superior to the average deterministic scenario. Indirect soft linking approaches require the construction of new dedicated sectoral models and – more challengingly – handling the interface between the two models in order to arrive at consistent results.

References:

- [1] Reddy, S. Surender, (2017). Optimal scheduling of thermal-wind-solar power system with storage. *Renewable Energy* 101 1357-1368.
- [2] Carpentier, J., (1979). Optimal power flows. *Int. J. Elect. Power Energy Syst.* 1 (1) (Apr. 1979) 3-15.
- [3] Momoh, J.A. et al, (1997). Challenges to optimal power flow. *IEEE Trans. Power Syst.* 12 (1) (Feb. 1997) 444-447.
- [4] Gayme, D. and Topcu, U., (2013). Optimal power flow with large-scale storage integration. *IEEE Trans. Power Syst.* 28 (2) (May 2013) 709-717.
- [5] Yang, G., Zhou, M., Lin, B., Du, W., (2013). Optimal scheduling the wind-solar-storage hybrid generation system considering wind-solar correlation, *IEEE PES Asia-Pacific Power and Energy Engineering Conference (APPEEC)*, pp. 1-6.
- [6] Khare. V., Nema, S., Baredar, P., (2016). Solar wind hybrid renewable energy system: a review. *Renew. Sustain. Energy Rev.* 58 (May 2016) 23-33.

- [7] Biswas, Partha P., Suganthan, P.N. and Amaratunga, Gehan A.J. (2017). Optimal power flow solutions incorporating stochastic wind and solar power. *Energy Conversion and Management* 148 1194–1207.
- [8] Kadir, Abaci and Volkan, Yamacli, (2016). Differential search algorithm for solving multiobjective optimal power flow problem. *Int J Electr Power Energy Syst*;79:1–10.
- [9] Narges, Daryani, Tarafdar, Hagh Mehrdad, Saeed, Teimourzadeh, (2016). Adaptive group search optimization algorithm for multi-objective optimal power flow problem. *Applied Soft Comput*;38:1012–24.
- [10] Chaib AE, Bouchekara HREH, Mehasni R, Abido MA. (2016). Optimal power flow with emission and non-smooth cost functions using backtracking search optimization algorithm. *Int J Electr Power Energy Syst*;81:64–77.
- [11] Bouchekara HREH, Chaib AE, Abido MA, El-Sehiemy RA. (2016). Optimal power flow using an improved colliding bodies optimization algorithm. *Appl Soft Comput*;42:119–31.
- [12] Mohamed AAA, Mohamed YS, El-Gaafary AA, Hemeida AM. (2017). Optimal power flow using moth swarm algorithm. *Electric Power Sys Res*;142:190–206.
- [13] Mahdi Sharifzadeh, Helena Lubiano-Walochik and Nilay Shah, (2017). Integrated renewable electricity generation considering uncertainties: The UK roadmap to 50% power generation from wind and solar energies. *Renewable and Sustainable Energy Reviews* 72 385–398.
- [14] Kornelakis A, Koutroulis E. Methodol Des (2009). Optim Econ Anal grid-Connect Photovolt Syst IET. *Renew Power Gen*;3:476–92.
- [15] Kornelakis A., (2010). Multiobjective Particle Swarm Optimization for the optimal design of photovoltaic grid-connected systems. *Sol Energy*;84:2022–33.
- [16] Collins, Seán et al, (2017). Integrating short term variations of the power system into integrated energy system models: A methodological review. *Renewable and Sustainable Energy Reviews* 76 839–856.
- [17] Luderer G, Krey V, Calvin K, Merrick J, Mima S, Pietzcker R, et al. (2014), The role of renewable energy in climate stabilization: results from the EMF27 scenarios. *Clim Change*;123:427–41.
- [18] Poncelet K, Delarue E, Six D, Duerinck J, D’haeseleer W., (2016). Impact of the level of temporal and operational detail in energy-system planning models. *Appl Energy*;162:631–43.
- [19] Pietzcker RC, Ueckerdt F, Carrara S, de Boer HS, Després J, Fujimori S, Johnson N, Kitous A, Scholz Y, Sullivan P, Luderer G, (2016). System integration of wind and solar power in integrated assessment models: a cross-model evaluation of new approaches", *Energy Econ*, n.d., doi:<http://dx.doi.org/10.1016/j.eneco.2016.11.018>.
- [20] Pfenninger S, Hawkes A, Keirstead J. (2014). Energy systems modeling for twenty-first century energy challenges. *Renew Sustain Energy Rev*;33:74–86.
- [21] Hidalgo Gonzalez I, RUIZ CASTELLO P, SGOBBI A, NIJS W, Quoilin S, ZUCKER A, et al. (2015). Addressing flexibility in energy system models. European Commission Joint Research Centre Institute for Energy and Transport; 2015, retrieved from [HTTPS://SETIS.EC.EUROPA.EU/SITES/DEFAULT/FILES/REPORTS/ADDRESSING-FLEXIBILITY-IN-ENERGY-SYSTEM-MODELS.PDF](https://setis.ec.europa.eu/sites/default/files/reports/addressing-flexibility-in-energy-system-models.pdf).

Multi junction Cells and Their Utility for Power Generation

Prof. S. K. Misra

Head of the Department

Department of Electrical Engineering

Harcourt Butler Technological Institute, Kanpur 208002

skmisraee@gmail.com

Chandra Prakash Varma

Assistant Professor, Department of Electronics Engineering

Dr. Ambedkar Institute of Technology for Handicapped, Kanpur 208024

governa_2003@rediffmail.com

Amit Jaisal

Lecturer, Department of Electronics Engineering

Dr. Ambedkar Institute of Technology for Handicapped, Kanpur 208024

jaisalmit@gmail.com

Abstract – Currently, the best lab examples of traditional silicon solar cells have efficiencies around 25%, while lab examples of multi-junction cells have demonstrated performance over 43%. Commercial examples of tandem cells are widely available at 35% under one-sun illumination, and improve to around 40% under concentrated sunlight and this CPV can be utilized for power generation. However, this efficiency is gained at the cost of increased complexity and manufacturing price.

I. INTRODUCTION

Multi-junction solar cells or tandem cells are solar cells containing several p-n junctions. Each junction is tuned to a different wavelength of light, reducing one of the largest inherent sources of losses, and thereby increasing efficiency. Traditional single-junction cells have a maximum theoretical efficiency of 34%, a theoretical "infinite-junction" cell would improve this to 87% under highly concentrated sunlight. The ordering of the layers of a multi-junction solar device are decided by their individual band gaps - i.e. the wavelengths of light they will absorb. On the top - closest to the sun - goes the layer with the largest band gap. Subsequent layers are then positioned in descending order of their band gaps. The highest energy photons (e.g. ultra violet to blue light) are captured by the top layer, and the bottom layer captures the lower energy photons (red to infra red) which pass through the other layers.

II. MULTIJUNCTION SOLAR CELL DESIGN

Multijunction cells use a combination of semiconductor materials to more efficiently capture a larger range of photon energies. They do so without sacrificing photovoltage or creating losses of heat to the degree of single-junction cells.

A. BANDGAP SELECTION

Consider the spectrum of sunlight split and distributed over a variety of semiconductor materials by using a prism. In that case, a different semiconductor material

could be selected (Fig. 1a) that would best match each portion of the spectrum. Although such an arrangement is reasonable in theory, mechanically maintaining such a design would be problematic. A more viable solution is to stack, or grow, multiple layers of semiconductors with decreasing band gaps. The figure 1 shows both kind of band gap selection.

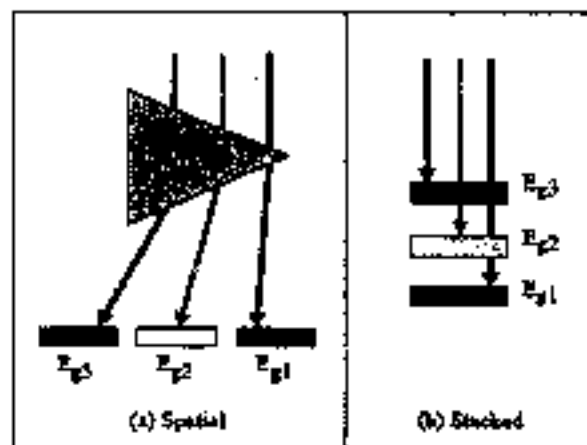


Fig 1: Alternate configurations for multi-junction spectral splitting.

Alloys of Group III and Group V elements, as well as other related compounds, lend themselves well to the design of multi-junction cells. Indium phosphide (InP), gallium antimony (GaSb), and the more commonly used GaAs are examples of such III-V materials. By carefully adjusting the compositions, a range of bandgap energies can be achieved. Such selections are usually made in conjunction with lattice-constant constraints.

B. LATTICE MATCHING

To produce optical transparency and maximum current conductivity between the top and bottom cells in monolithic multi-junction devices, all layers must have similar crystal, or lattice, structures. The lattice constant is a measure of the distance between atom locations in a crystal pattern and has a strong

descriptive correlation with the overall crystal structure. It is extremely desirable to match the lattice constants of the various layers.

Mismatch in the crystal lattice constants creates defects or dislocations in the lattice where recombination centers can occur. Recombination results in the loss of photogenerated minority carriers (e.g., electrons drop from the conduction band back into the valence band) and significantly degrades the photovoltaic quality of the device. Such effects will decrease the open-circuit voltage, short-circuit current density (J_{sc}), and fill factor, which represents the relationship, or balance, between current and voltage for effective power output.

C. CELL OPTIMIZATION

Bandgap and lattice matching are central to multijunction solar cell designs. But to maximize the efficiency of multijunction devices, other characteristics are also desirable. Foremost of these for a monolithic (grown all in one piece), series-connected, two-terminal multijunction device is that each of the subcells should have matched currents. That is, they should absorb photons at the same overall rate, thus producing the same current.

CI. CURRENT MATCHING

By the nature of its series connection, the output current of the multijunction solar cell is limited to the smallest of the currents produced by any of the individual junctions. For this reason, it is desirable to design each junction to produce the same amount of photocurrent.

The current produced by a semiconductor junction depends on a number of factors, but most notably, the number of incident photons exceeding the semiconductor's bandgap and the material's absorptivity. If the photons that exceed the bandgap of the material are in abundance, then cell layers need a minimal thickness to collect the desired current. Likewise, if the absorptivity of a material is relatively high, the photons must pass through less of the material before being absorbed.

In practice, for the GaInP/GaAs/Ge cell, this situation implies a relatively thick Ge layer because of its lower absorptivity. Further, there are design distinctions between terrestrial versions and space versions of the cell to account for the differing number of UV and near-IR photons for these two different environments.

C2. POWER PRODUCTION

One may note that as additional cell layers are added, the level of total current necessarily decreases. This phenomenon occurs because a fixed total number of photons are distributed over increasing numbers of cell layers, which decreases the amount available for electron promotion in any one cell layer. The tradeoff, however, is that the electrons promoted are, overall, more energetic and have a greater electric potential. As additional cell layers are added in series, the voltage each layer produces must be summed with the others. Therefore, the total voltage of a multi-junction solar cell is greater than that of a single-junction solar cell.

Multijunction designs, as compared to single-junction designs, have reduced currents. But this loss is more than compensated for by increases in voltages, so overall power (the product of current and voltage) is greater.

D. CONCENTRATION SYSTEMS

Concentrators are a vital component of terrestrial multijunction solar cell systems. By dramatically increasing the total power produced by a given solar cell 100- to 1200-fold, the increased cost of that cell is more readily justified. In addition, high solar concentrations actually work to improve the performance of multijunction solar cells. Concentrator systems are varied and generally scalable.

The next generation of multijunction solar cells may have four layers. The most direct path to such an achievement is to develop a 1.0-eV bandgap material that is lattice matched with the GaInP, GaAs, and Ge of the present triple-junction solar cell. The theoretical results of such efforts are summarized in the Fig 2.

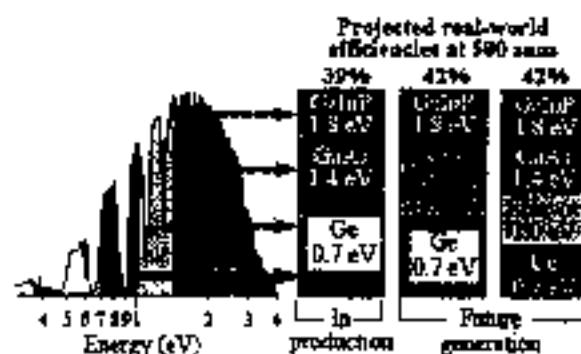


Fig 2: Projected Real World 500 Sun Concentrator efficiencies of multijunction cells

III. PROGRESS IN III-V SOLAR CELLS

Figure 3 shows progress in world record conversion efficiency of compound solar cells. In the 1980s, GaAs single-junction and AlGaAs/GaAs dual-junction cells were developed. InGaP material was proposed instead of AlGaAs which had quality problem due to oxygen. In the 1990s, InGaP(In)/GaAs/Ge triple-junction cells were developed by combining with GaAs/Ge hetero-epitaxial technique. Since 2000, the triple-junction cells have been practically used for space and developed for terrestrial concentrator. Efficiency of the cell reached to 32% (1sun) and 40% (1000sun). Recently, InGaP (~1.7eV)/InGaAs (~1.2eV)/Ge lattice mismatch cell which has lower band-gap for both top and middle cells has been developed to obtain current matching among three cells and the maximum efficiency has reached to 40.7% (340sun) at Spectrolab and 41.1% (434sun) at Fraunhofer-ISE. The invert epitaxial structure of InGaP/GaAs/InGaAs(1eV) cell attaining the same current matching has been developed by using 1eV InGaAs lattice mismatch bottom cell and the world record efficiency of 33.3% (1sun) and 40.8% (326sun) has been achieved.

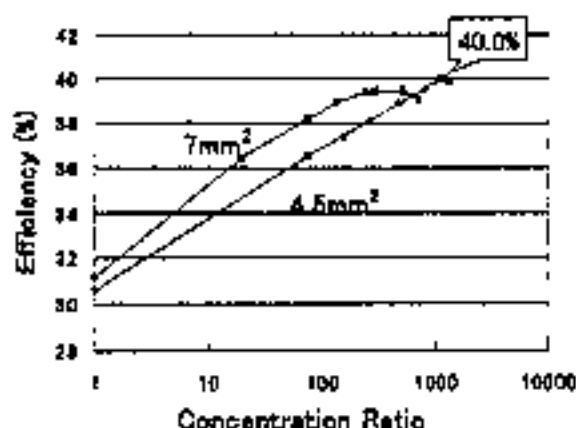


Fig 7: Efficiency as a function of concentration ratio for the cells with different size.

V. UTILITY IN POWER GENERATION

Comparing to the existing level of maturity of Si technology in the PV industry, it could be said that multijunction CPV from III-V semiconductors could be in its early stages of development. In contrast, multijunction CPV has gone through extensive device performance improvements and grueling qualifications tests which have catapulted prototype designs out from the laboratory into the field in just a few years. From these, there are several material systems that have been candidates for producing next-generation high efficiency solar cells. Metamorphic structures, for example, have been receiving considerable attention since the solar cell that set the new efficiency record of 40.8% was based on this material system but of equal importance is the lattice-matched system. In the last 11 years, solar cells built from these material systems have shared and enjoyed record-breaking efficiencies, and it is likely that this pace will continue in the coming years since there is, however, still more room for further refinements in the device structure, and their manufacturing methods.

A parameter that influences multijunction cell production, and therefore impacting the overall CPV system feasibility is cost. Throughout this review, some points were touched upon regarding costs. For the end-user to take advantage of CPV generated electricity, the overall installed systems costs must be minimized so that delivering power to the meter is affordable. In terms of cost breakdown, this means that the cell, module assembly, inverter and installations must all be reduced, each presently corresponding to about US \$3/W, \$2/W, \$1/W and \$3/W, respectively. The CPV roadmap rolled out by the solar initiative programs, which are federally-funded solar energy technologies program, is targeting installed systems to be \$3-5/W by 2015, equating to localized cost of electricity (LCOE) of 7-8 ¢/kWh. Then, a likely scenario for the above cost breakdown (in the same order presented above) based on this LCOE using multijunction CPV would be 50¢/W, \$1/W, \$1/W and \$1.5/W, with the last term

selected quite aggressively. This is assuming that cell cost per area of wafer processed is \$3-5/cm², and commercial device efficiencies are 36%-40%. There is a good chance these cost objectives can be achieved ahead of time considering the present rate of success from some system component manufacturers. As a matter of fact, volume production of multijunction solar cells at Spectrolab is now costing slightly less than \$1/W. Companies abroad are working toward this goal. As an example, a few companies are currently targeting CPV for commercial introduction in the utilities market and remote areas for off-grid power generation. Triple junction solar cells made from GaInP/GaInAs/Ge are being used in dense array systems in Australia by Solar Systems PTY which is developing 33 kW CPV systems using these cells which will possibly enhance or displace their Si technology. When operating under concentrated sunlight, a multijunction CPV system with much less solar cell area than cells in a Si or in a thin film panel generates almost twice as much power. Just like in the dense array business, there is a market for point-focus systems which is also hunting in on installations at the utility scale. Amonix, another manufacturer of CPV in the US is currently evaluating 3-junction solar cells for possible use in their Si-based, 25 kW, point-focus system for deployment to take place in the near future. Companies in other countries, primarily in Europe, such as Germany and Spain, are also making strides toward developing and expanding CPV. Concentrix Solar, for example, has recently deployed its CX5000 system using 3-junction cells capable of generating 5.75 kW. As of this writing, Concentrix has installed 300 kW of CPV. Further, demonstration projects are now underway at the Castilla La Mancha test site in Spain where a group of CPV companies have gathered to install their systems; an effort sponsored by ISFOC (Instituto de Sistemas Fotovoltaicos de Concentraci3n or Institute of Photovoltaic Systems under Concentration) to install up to 3 MW of CPV for pilot power plant programs. There is much momentum in the solar PV field, and it is moving in a positive direction. Right now there is an upsurge in the amount of PV produced in the world due to many incentive programs, capital investment and cost reduction. Cell volume production has increased as a result of this growth, and more companies have entered this market to reap the benefits that others are currently gathering. It is expected that the annual electricity delivered to the consumer in the globe will reach tens of GW (10⁹ Watts), with a substantial portion produced from perhaps 45% to over 50% high-efficiency multijunction CPV, in the years ahead. Hopefully, this will be the beginning to topple fossil fuel-burning which is responsible for climate change.

CONCLUSION

Theoretical efficiencies are still much higher than laboratory multijunction efficiencies. And researchers are designing approaches for solar cells with efficiencies greater than 50%, while solar cells with 41% efficiency are likely to be available imminently in

Effect Of Magnetic Field On Steady Blood Flow Through An Inclined Circular Tube

S.R. Verma And Anuj Srivastava

Department of Mathematics
D.A-V.(P.G.) College, Kanpur(U.P.),India

ABSTRACT

The present paper is devoted to study the flow of an incompressible viscous, electrically conducting fluid (blood) in a rigid inclined circular tube in the presence of transverse magnetic field. The blood is considered to be Newtonian fluid. The analytical expression for velocity profile and flow rate are obtained. The velocity profile and flow rate for various values of Hartmann number and inclination angle have been shown graphically. The bluntness appears in velocity profile and this bluntness decrease by increasing magnetic field.

Keywords : Incompressible fluid, transverse magnetic field, Hartmann number.

I. INTRODUCTION

The study of the rheological properties of blood can allow a better understanding of blood circulation. This depends on numerous factors such as the driving force of the heart, the shape, as well as mechanical and physiological behaviour of the vascular walls. The experimental and theoretical studies of blood flow phenomena are very useful for the diagnosis of a number of cardiovascular diseases and development of pathological patterns in human physiology and for other practical applications.

The study of magneto hydrodynamic flow problems through a tube has found an applications in many fields like MHD power generation, blood flow measurements, etc. The application of MHD principles in medicine and biology is of interest in the literature of bio-mathematics (Vardanyan [1], Sud et. al. [2], [3]). Blood can be regarded as a magnetic fluid appeared in which red blood cells, magnetic in nature due to iron oxide in it. The movement of blood in an externally applied magnetic field is governed by magneto hydrodynamic principles. By Lenz's law, the Lorentz's force will oppose the motion of conducting fluid. The MHD principles may be used to decelerate the flow of blood in a human arterial system and therefore it is useful in the treatment of certain cardiovascular disorders (Korchevskii and Marochunik [4]) and in the diseases with accelerated blood circulation like haemorrhages and hypertension etc.

Magnetic field interactions with blood flow have been studied by many workers. The idea of

electromagnetic fields in medical research was firstly given by Kolin [5] and later Korchevskii and Marochunik [4] discussed the possibility of regulating the movement of blood in human system by applying magnetic field. Vardanyan [6] studied the effect of magnetic field on blood flow theoretically and obtained steady solutions for velocity profile and flow rate by neglecting the induced fields.

A large number of theoretical and experimental attempts have been made in the literature to explain the blood flow behavior when it flows through the vessels of circulatory system of living beings. Many investigators have used single-phase homogeneous Newtonian viscous fluid (Womersley [7], McDonald [8], Whitmore [9], Copley and Stainsby [10], Attinger [11], Fung [12], Lew and Fung [13].)

Various mathematical models have been investigated by several workers to examine the behaviour of blood flow under the influence of magnetic fields (Chaturani and Bhartiya [14], Tiwari [15], Abdel Wahab M. and Salem S.I. [16], Sanyal et al [17], Verma, S.R. ([18],[19],[20]), Verma and Srivastava [21].) Chaturani and Bhartiya [14] studied two layered magneto hydrodynamic flow through parallel plates with applications to blood flow and noticed that magnetic field help in reducing the cell injury and the dialysis time. Sanyal et. al. [17] investigated the characteristics of blood flow in a rigid inclined circular tube with periodic body acceleration under the influence of a uniform magnetic field and point out that flow velocity deviates with various parameters and this deviation of flow velocity can be regulated by a proper use of magnetic field. Chaturani and Upadhyay [22] studied the gravity flow of fluid with couple stress along an inclined plane with application to blood flow. Many researchers (Rathod and Thippeswamy [23], Leonid et. al.[24], Chen and Tzuoo [25], Astarita et. al. [26], Verma, S.R. [27]) investigated the nature of blood flow in a inclined vessel or surface.

In the present paper, it is proposed to develop a mathematical model to study the characteristics of steady flow of blood through an inclined circular tube in the presence of transverse magnetic field. In the analysis we consider blood as a Newtonian fluid. The analytical expression of blood flow velocity and flow rate are obtained. The effect of magnetic field, inclination angle on blood

flow, flow rate of blood has been discussed.

II. MATHEMATICAL FORMULATION AND ANALYSIS

Let us consider a one-dimensional laminar steady blood flow through a uniform straight and inclined rigid circular tube in the presence of transverse magnetic field. The equations governing the flow in cylindrical polar coordinates as -

$$\frac{\partial u}{\partial z} = 0 \quad (1)$$

$$\frac{\partial p}{\partial r} = 0 \quad (2)$$

$$-\frac{\partial p}{\partial z} + \mu \nabla^2 u + \rho g \sin \theta - \sigma B_0^2 u = 0 \quad (3)$$

Where $\nabla^2 = \frac{1}{r} \left(\frac{\partial}{\partial r} \left(r \frac{\partial}{\partial r} \right) \right)$

Here u is the axial velocity, ρ is the density of blood, μ is the coefficient of viscosity of blood, g is the acceleration due to gravity, θ is inclination angle, $\frac{\partial p}{\partial z}$ is pressure gradient, B_0 is the transverse component of magnetic field and σ is the electrical conductivity of the medium.

The boundary conditions are

$$u = 0 \quad \text{at} \quad r = R_0 \quad (4)$$

$$\frac{\partial u}{\partial r} = 0 \quad \text{at} \quad r = 0 \quad (5)$$

where R_0 is the radius of tube.

Let us introduce the following transformation

$$y = \frac{r}{R_0} \quad (6)$$

Then the governing equation (3) becomes

$$\frac{\partial^2 u}{\partial y^2} + \frac{1}{y} \frac{\partial u}{\partial y} - M^2 u = \frac{R_0^2}{\mu} \left(\frac{\partial p}{\partial z} - \rho g \sin \theta \right) \quad (7)$$

Where $M = B_0 R_0 \sqrt{\frac{\sigma}{\mu}}$ is the Hartmann number.

The corresponding boundary conditions (4) and (5) takes the form

$$u = 0 \quad \text{at} \quad y = 1 \quad (8)$$

$$\frac{\partial u}{\partial y} = 0 \quad \text{at} \quad y = 0 \quad (9)$$

The expression for velocity u obtained as the solution of equation (7) under the boundary conditions (8) and (9) is given as

$$u = \frac{R_0^2}{\lambda^2 \mu} \left(\frac{\partial p}{\partial z} - \rho g \sin \theta \right) \left[1 - \frac{J_0(\lambda y)}{J_0(\lambda)} \right] \quad (10)$$

where $\lambda^2 = -M^2$ and J_0 is the Bessel's function of zero order.

Volume flow rate Q is given by

$$Q = \int_0^{R_0} 2 \pi u r dr \quad (11)$$

Using equation (10) in (11), the expression for flow rate is obtained as

$$Q = \frac{2\pi R_0^4}{\lambda^2 \mu} \left(\frac{\partial p}{\partial z} - \rho g \sin \theta \right) \left[\frac{1}{2} - \frac{1}{\lambda} \frac{J_1(\lambda)}{J_0(\lambda)} \right] \quad (12)$$

Where J_1 is the Bessel's function of first order.

III. RESULTS AND DISCUSSION

The theoretical results such as velocity profile, flow rate for the effect of magnetic field on steady laminar flow of blood through a rigid inclined circular tube are obtained in this analysis. Numerical solutions of velocity profile and flow rate are shown through tables and graphs for different value of y , Hartmann number M and inclination angle θ .

Velocity profile and flow rate equations (10) and (12) can be written as after neglecting higher order terms of small quantities as

$$u = \frac{R_0^2}{\mu} \left(\rho g \sin \theta - \frac{\partial p}{\partial z} \right) \left[\left(\frac{1}{4} - \frac{3}{64} M^2 - \frac{1}{2304} M^4 \right) - \left(\frac{1}{4} - \frac{1}{16} M^2 + \frac{3}{256} M^4 \right) y^2 - \left(\frac{1}{64} M^2 - \frac{1}{256} M^4 \right) y^4 - \left(\frac{1}{2304} M^4 \right) y^6 \right] \quad (13)$$

$$Q = \frac{\pi R_0^4}{\mu} \left(\rho g \sin \theta - \frac{\partial p}{\partial z} \right) \left[\frac{1}{8} - \frac{1}{48} M^2 - \frac{1}{4608} M^4 \right] \quad (14)$$

For the purpose of computation of numerical results, we have made use of the following values :

$$R_0 = 100 \times 10^{-4} \text{ cm}, \quad g = 980 \text{ cm/sec}^2, \\ \rho = 1.06 \text{ gm/cm}^3,$$

$$\frac{\partial p}{\partial z} = -67.5 \times 10^3 \text{ dyne/cm}^3$$

The variation of velocity profile with y for different value of M is shown in Fig.1. From the figure it is clear that the velocity for $\theta = 30^\circ$ maximum velocity occurs for $M = 0.0$ and then gradually decreases as Hartmann number M increases. It is also clear that the bluntness appears in velocity profile and this bluntness decreases by increasing magnetic field.

Fig.2 shows that variation of velocity profile with M for different value of y and $\theta = 30^\circ$, the velocity profile decreases as M increases and figure shows that velocity is maximum at the axis and decreases as y increases. The bluntness is same as Fig.1.

For fixed $y = 0.6$, the variation of velocity with M and θ are given through Table-1. From table it is clear that velocity increases as inclination angle θ increases but very slowly for fixed M . Velocity profile decreases as M increases for any fixed θ .

Table-2 shows the variation of velocity with θ and y for fixed Hartmann number $M = 1.0$. From numerical values, we can see that velocity increases as θ increases by decreases as y increases and back flow exist near the wall. There is no backflow when $M = 0$.

In the absence of Magnetic field $M = 0.0$, the variation of velocity with θ and y is computed and given through Table-3. From that we see that velocity decreases with y and become zero at the wall and increases as inclination angle θ increases. There is no back flow at the wall in this case.

The variation of flow rate with inclination angle θ and Hartmann number M is given through Table-4. Flow rate increases with θ for any fixed M but decreases with increasing M . Therefore by using an external magnetic field, a remarkable thing is that we can regulate the blood flow and treatment some of diseases such as bleeding and clotting.

From above discussion it may be noticed that the transverse magnetic field effects largely on the axial flow velocity of blood and by taking appropriate value of M , we may regulate the axial flow velocity. By applying proper magnetic field attached with those instruments we can regulate the blood flow and enhance patient's activities. Movement of hemoglobin in blood vessels is accelerated while calcium and cholesterol deposits in blood are decreased. Even the other unwanted materials adhered to the inner side of blood vessels, which provoke high blood pressure, are decreased and made to vanish. The blood is cleansed and circulation is increased. The activity of the heart increases and pains disappear.

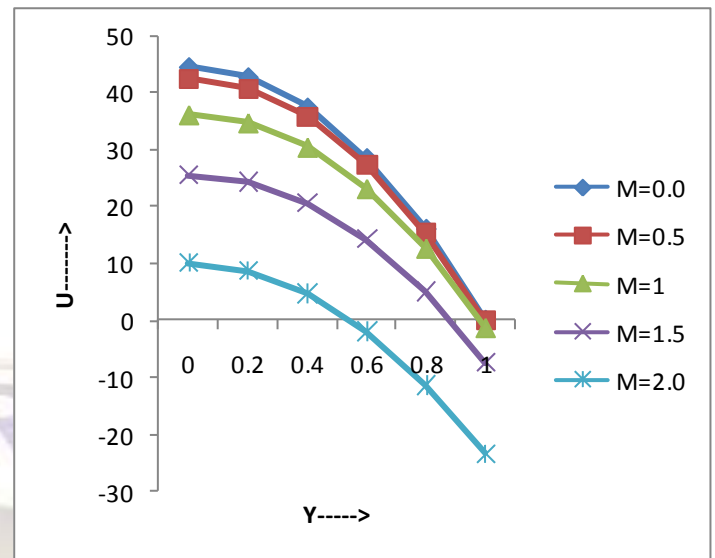


Figure 1: Variation of u with y for different M at $\theta = 30^\circ$

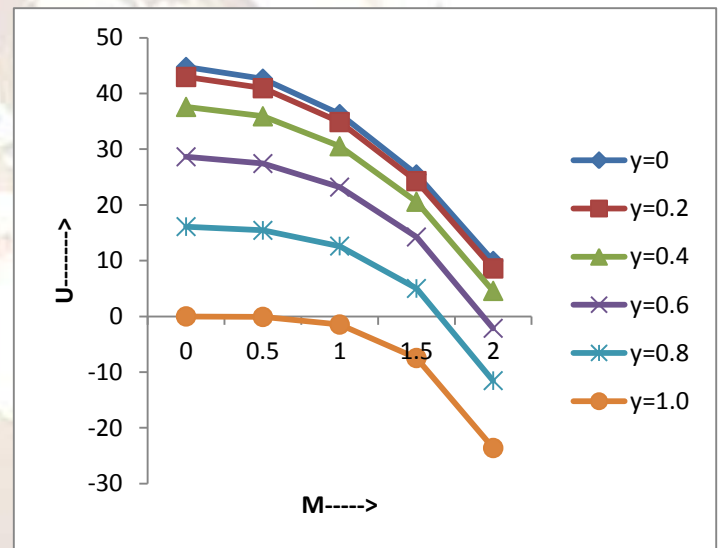


Figure 2: Variation of u with M for different y at $\theta = 30^\circ$

Table: 1
Variation of u (cm/sec) with M and θ for $y = 0.6$

$\theta \downarrow M \rightarrow$	0°	15°	30°	45°	60°
0.0	28.42	28.54	28.65	28.73	28.80
0.5	27.213	27.321	27.42	27.51	27.57
1.0	23.020	23.112	23.197	23.271	23.327
1.5	14.141	14.197	14.249	14.294	14.329
2.0	-	-	-	-	-
	2.1138	2.1222	2.1300	2.1368	2.1420

Table: 2

Variation of u (cm/sec) with θ and y for M = 1.0

θ → y↓	0°	15°	30°	45°	60°
0.0	36.023	36.167	36.300	36.415	36.503
0.2	34.6022	34.7400	34.8684	34.9787	35.0634
0.4	30.3036	30.4243	30.5367	30.6333	30.7074
0.6	23.0207	23.1124	23.1979	23.2713	23.3276
0.8	12.5228	12.5727	12.6192	12.6591	12.6898
1.0	-1.4459	-1.4516	-1.4570	-1.4616	-1.4652

Table: 3

Variation of u (cm/sec) with θ and y for M = 0.0

y → θ ↓	0.0	0.2	0.4	0.6	0.8	1.0
0°	44.40 73	42.63 10	37.30 21	28.42 07	15.98 66	0. 0
15°	44.58 42	42.80 08	37.45 07	28.53 39	16.05 03	0. 0
30°	44.74 90	42.95 90	37.58 92	28.63 94	16.10 96	0. 0
45°	44.89 05	43.09 49	37.70 81	28.72 99	16.16 06	0. 0
60°	44.99 12	43.19 92	37.79 93	28.79 95	16.19 97	0. 0

Table: 4

Variation of Q with θ and M

θ → M ↓	0°	15°	30°	45°	60°
0.0	0.006 96	0.006 99	0.0070 2	0.0070 44	0.0070 62
0.5	0.006 67	0.006 70	0.0067 3	0.0067 5	0.0067 7
1.0	0.005 79	0.005 82	0.0058 4	0.0058 6	0.0058 8
1.5	0.004 29	0.004 31	0.0043 3	0.0043 4	0.0043 5
2.0	0.002 13	0.002 14	0.0021 48	0.0021 54	0.0021 6

REFERENCES

[1] Vardanyan, V.A. (1973). Effect of magnetic field on blood flow. *Biophysics*, 18, p. 515.
 [2] Sud, V.K., Suri, P.K. and Mishra, R.K. (1974). Effect of magnetic field on oscillating blood flow in arteries. *Study Biophysics*, 46, p. 163.
 [3] Sud, V.K., Suri, P.K. and Mishra, R.K.

(1978). Laminar flow of blood in an elastic tube in the presence of magnetic field. *Studia Biophysica*, 69, p. 175.
 [4] Korchevskii, E.M. and Marochunik, L.S. (1965). Magneto hydrodynamic version of movement of blood. *Biophysics*, 10, P. 411.
 [5] Kolin, A. (1936). Electromagnetic flow meter : principle of method and its applications to blood flow measurement. *Proc. Soc. Exp. Biol. Med.*, 35, P. 53.
 [6] Vardanyan, V.A. (1973). Effect of magnetic field on blood flow. *Biophysics*, 18, p. 515.
 [7] Womersley, J.R. (1954). Method for the calculation of velocity, rate of flow and viscous drag in arteries when the pressure gradient is known, *J. Physiol.* 127, p. 38.
 [8] McDonald, D.A. (1960). Blood flow in arteries. *Arnold, London*.
 [9] Whitmore, R.L. (1963). Hemorheology and hemodynamics. *Biorheology* 1, p. 201.
 [10] Copley, A.L. and Stainsby, G. (1960). Flow properties of blood. *Pergamon press, Oxford*.
 [11] Attinger, E.O. (1964). Pulsatile blood flow. *McGraw - Hill, New York*.
 [12] Fung, Y.C. (1964). Biomechanics, its scope, history and some problems of continuum mechanics in physiology. *Applied Mechanics Review* 21, p. 1.
 [13] Lew, H.S. and Fung, Y.C. (1970). Entry flow into blood vessels at arbitrary Reynolds number. *Journal of Biomechanics* 3, P. 23.
 [14] Chaturani, P. and Bhartiya Saxena, S. (2001). Two-layered magneto hydrodynamic flow through parallel plates with applications. *Indian J. pure appl. Math.* 32(1), p. 55.
 [15] Tiwari Vandana (1998). Effect of magnetic field on a simple blood flow in a arterial region. *J.M.A.C.T.* 31, p. 183.
 [16] Abdel Wahab M. and Salem S.I. (2012). Magneto hydrodynamic blood flow in a narrow tube. *World Research Journal of Biomaterials* 1, No.-1, p. 1.
 [17] Sanyal, D.C., Das, K. and Debnath, S. (2007). Effect of magnetic field on pulsatile blood flow through an inclined circular tube with periodic body acceleration. *Journal of Physical Sciences*, 11, p. 43.
 [18] Verma, S.R. (2003). Effect of magnetic field on Couette flow of Newtonian fluid with application to blood flow. *J. PAS*, 9, p. 185.
 [19] Verma, S.R. (2005). Theoretical study of

- MHD flow of fluid through parallel plates with application to blood flow. *Proc. XV Ann. Conf. PAS.*, p. 72.
- [20] Verma, S.R. (2011). Two-layered two-phase magneto hydrodynamic fluid model of blood flow through narrow circular vessels. *J. Tensor society* 5, p. 27.
- [21] Verma, S.R. and Srivastava Anuj (2012). Effect of magnetic field on unsteady blood flow through a narrow tube. *International J.S.F.M.* 3, No.1, p. 85.
- [22] Chaturani, P. and Upadhya, V.S. (1977). Gravity flow of fluid with couple stress along an inclined plane with application to blood flow. *Biorhedogy*, 14, p. 237.
- [23] Rathod, V.P. and Thippeswamy, G. (1999). Gravity flow of pulsatile blood through closed rectangular inclined channel with micro-organisms. *The Mathematical Education*, 33, No.-1, p. 40.
- [24] Leonid, B., Laure, P., Dias, F. and Bridges, T.J. (1999). Linear pulse structure and signaling in a film flow on an inclined plane. *J. Fluid Mech.*, 396, p. 37.
- [25] Chen, T.S. and Tzuoo, K.L. (1982). Vortex instability of free convection flow over horizontal and inclined surface. *J. Heat Transfer*, 104, p. 637.
- [26] Astarita, G., Mariucxi, G. and Polumbo, G. (1964). Non-Newtonian gravity flow on inclined surface. *Ind. Engg. Chem. Fundam.*, 3, p. 333.
- [27] Verma, S.R.(2006).Theoretical analysis of steady blood flow along an inclined plane influenced by the gravity force. *Jnanabh.* 36, p. 183.

Role of data mining and machine learning techniques in medical imaging

Abhishek Agnihotri

Department of Computer Science and Engineering,
Harcourt Butler Technical University,
Kanpur, India
Email: abhiagni1991@gmail.com

Vikash Yadav*

Department of Computer Science and Engineering,
ABES Engineering College,
Ghaziabad, India
Email: vikas.yadav.cs@gmail.com
*Corresponding author

Vandana Dixit Kaushik

Department of Computer Science and Engineering,
Harcourt Butler Technical University,
Kanpur, India
Email: vandnadixitk@yahoo.com

Abstract: Medical images are ubiquitous images among all images around us. Due to the expansion in the use of medical images and growing resolution and size of medical images, medical image processing became the subclass of image processing and this field is continuously gaining the attention of researchers all around the world. There is a need to handle medical images for better diagnostic purposes and this gave rise to cope up with the techniques of image processing like data mining and machine learning together. Data mining and machine learning techniques gave rise to use the computer-based application in the diagnostic purpose for better, reliable and fast diagnosis of patient, detection of lesions, change detection and more important better therapy and diagnosis planning. In this paper various data mining and machine learning techniques are given which are used in the field of medical imaging.

Keywords: medical imaging; machine learning; neural network; Bayesian classification; support vector machine; decision tree.

Reference to this paper should be made as follows: Agnihotri, A., Yadav, V. and Kaushik, V.D. (2020) 'Role of data mining and machine learning techniques in medical imaging', *Int. J. Advanced Intelligence Paradigms*, Vol. 15, No. 3, pp.340–351.

Biographical notes: Abhishek Agnihotri received his BTech in Information Technology in 2012 from the Gautam Buddha Technical University (formerly UP Technical University), Lucknow, U.P., India and MTech in Computer Science and Engineering in 2017 from the Dr. A.P.J. Abdul Kamal Technical

University, Lucknow, U.P., India. He is currently working as a Lecturer in the Department of Computer Science and Engineering, Harcourt Butler Technical University, Kanpur, UP, India. He has more than three years of teaching experience and his areas of interest are data structures, algorithms, data mining, machine learning, medical imaging and image processing.

Vikash Yadav received his BTech in Computer Science and Engineering in 2009 from the Dr. Ambedkar Institute of Technology for Handicapped, Kanpur (UP India), MTech in Software Engineering in 2013 from the Motilal Nehru National Institute of Technology, Allahabad (UP India) and PhD in Computer Science and Engineering from the Dr. APJ Abdul Kalam University (Formerly UP Technical University) Lucknow, (UP India) in the field of image processing. He is currently working as an Assistant Professor in the Department of Computer Science and Engineering, ABES Engineering College, Ghaziabad, India and has more than seven years of teaching/research experience and published more than 25 research papers in various national/international conferences/journals. His area of interest includes data structure, data mining, image processing and big data analytics.

Vandana Dixit Kaushik received her BE in Computer Science in 2000 from the Pune University and PhD in Computer Science and Engineering in 2011 from the UP Technical University, Lucknow. She is currently working as an Assistant Professor in the Department of Computer Science and Engineering, Harcourt Butler Technical University, Kanpur and more than 16 years of teaching experience. She is a member of various technical committees and published more than 35 research papers in various national/international conferences/journals. Her area of interest includes database management system and image processing.

1 Introduction

Information density for imaging studies has been greatly increased due to advancements in medical technology. This may result increased contrast resolution allowing evaluation of more subtle structures from previously possible, increased temporal image acquisition rate, increased spatial resolution facilitating greater anatomical detail. It is estimated that, Medical images will consists of one fourth of total amount of data stored electronically and this large data store widen the scope for data mining techniques. Data mining is carrying out interesting and hidden patterns stored in large data warehouse using the power of machine learning, statistics, artificial intelligence and DBMS techniques. Computer aided diagnosis (CAD) algorithms have ability to quantify bodily structures and various lesions, extract features automatically and create features that can be used for mining to discover new knowledge. CAD algorithms are also used for change detection, i.e., to automatically measure lesions inside the body, tumours from images at different time and point to determine whether lesions and tumour size has changed. These methods are also used for therapy monitoring and diagnosis. The proper use of data mining techniques can heighten the quality of diagnosis, prediction and disease classification. Data mining is one of the basic foundations of machine learning but it does not have capability to learn and apply knowledge on its own without human interaction. Data Mining is used as an information or knowledge source for Machine Learning and helps Machine learning to look at patterns and learn from them to adapt behaviour of patterns

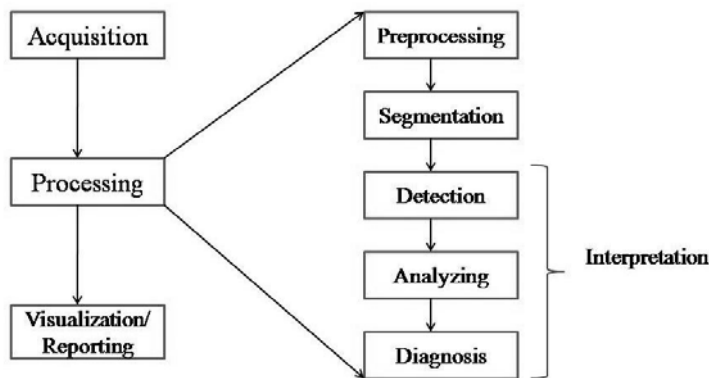
to achieve better results for future incidents. With technological advancements in medical imaging such as tomosynthesis, positron emission tomography (PET), cone beam/multislice CT, electrical impedance tomography, diffuse optical tomography, digital radiography, computed radiography using film digitisers or storage phosphor imaging plates, diffusion-weighted magnetic resonance imaging, 3D ultrasound imaging, the demands for advance machine learning algorithms and applications in the medical imaging has increased. Tasks in medical imaging demand knowledge from patient data for prior knowledge to come out with the detection and diagnosis of abnormality in medical data. In Section 3 and 4, we described the role of data mining and machine learning in medical imaging and furthermore described the promising and effective techniques that are gaining much more attention before and now in this field to make medical and clinical task easy.

2 Basic medical image processing system

By the development of computing technologies, the essence of basics of image processing techniques in the field of computer assisted diagnosis is much more important to determine the understanding of physical nature, to understand the functional process of different parts of the human body for medical intervention and clinical analysis. Medical diagnosis based on digital images of human body helps to understand the nature of biological systems of human body. These images may be of organs or body parts. These Images, like any other information source, need to be analysed to better understand the disordered system to the internal and external level using radiology devices or modern observatory. In Figure 1, the medical image processing system is shown. Images are acquired using different modalities for different medical and clinical analysis and for diagnosis purposes. Mainly, medical images are of two varieties: projection images and slice images. Projection images show 3D human body projection on a 2D image and slice images show the measured value distribution in 2D slice. The main imaging techniques for digital images in medical are X-ray imaging (fluoroscopy, mammography, computed tomography), magnetic resonance imaging [MR angiography, blood oxygen level dependency (BOLD) imaging, perfusion imaging, diffusion imaging], ultrasound imaging, nuclear imaging (Scintigraphy, SPECT, PET), photography, electro encephalogram (EEG) and magneto encephalogram (MEG). Each of these techniques produces images that are used for further analysis. Information produced by each of these techniques is related to functional and physiological attributes; so, the selection is always intended to maintain this relationship. After acquisition of medical images, different techniques, mentioned in the Sections 5 and 6 are used to process these images for clinical and medical purposes. The step of processing is further subdivided into processes as in the figure. Preprocessing is one of the important steps in medical imaging due to inconsistent, incomplete and noisy data. MRI and CT images comprise ring, volume effect, staircase, equipment-based and patient specific artefacts. All of these are removed by preprocessing steps for further analysis. Widely used denoising approaches are Gabor filter, Adaptive median filter, morphological operations, Mean or average filter, Image normalisation, weighted median filter, Weiner filter and histogram equalisation (Jeyavathana et al., 2016). Segmentation is used to give greater knowledge than a medical image has. Dividing an image into regions with a few properties such as contrast, colour,

brightness, texture and grey level is called segmentation process. The input is digital image (grey scale) and the abnormalities are outputs in this process. Different methods are used for the segmentation of medical image regions are Pixel-based methods [thresholding (adaptive thresholding, OTSU's thresholding)], edge-based detection methods (Gray histogram, gradient), region-based methods (region growing, region split and merge), model-based methods (deformable model, level set-based model), texture-based methods (statistical, structural), Artificial neural network-based methods, fuzzy theory-based methods and genetic algorithm-based methods (Song and Ying, 2015). After this, abnormalities or lesions are detected using different advanced techniques and images are analysed for the treatment and diagnosis purpose. Image compression is one of the most important features in Medical Imaging. A hybrid Image compression technique is used for this purpose (Yadav et al., 2015) which can compress the images so that it can be easily transfer via some communication channel.

Figure 1 Basic medical image processing system



3 Data mining

Data mining is a process of extracting patterns and useful information from large data set. It is also called knowledge discovery from databases (KDD process). Various techniques and algorithms like classification, clustering, association rules, regression, decision trees, genetic algorithm, nearest neighbour and neural network are used for different purposes in medical imaging. Pictures stored in picture-archiving and communication systems (PACS) or in other image databases give opportunities to learn about the temporal and specific features, such as lesions in images of the image objects and this gives the opportunity to use data mining that allow to discover the relevant knowledge from the database to analyse and diagnose images. Data mining helps to extract some additional knowledge of specific features of different classes and in the same way they are in the image. Data mining also used in the decision making and for other task that enables to create automatic image diagnose system that could be important in case of no knowledge for decision making (Perner, 2002). The high level features of an image can also be used to identify an infected medical image (Yadav and Kaushik, 2018).

4 Machine learning

Machine learning is a branch of artificial intelligence and it enables to extract the meaningful patterns from examples, which is a factor of human intelligence. In the recent years, Machines has proved itself that they can learn and master tasks that were considered too complex for machines, showing that ML algorithms are useful components for decision support system and CAD. In some cases, ML algorithms enable computers to see the patterns that are out of human perception. A Rapid rise to adapt machine learning techniques to gain information from medical Images and in various radiological imaging tasks (such as detection, diagnosis, risk assessment, prognosis and therapy response, and in multi-omics disease discovery) has grown up with the advancements in both computers and imaging. Machine learning provides techniques, tools and methods that can help to solve various prognostic and diagnostic problems in various medical domains. Diagnostic parameters and their combinations are important for prognosis in analysis (for, e.g., extracting medical knowledge for the purpose of outcome research, therapy support and planning, predicting disease progression, and for patient management system) and for this purpose, ML is being used. ML is also promising in efficient and effective monitoring by intelligent alarming, to interpret uninterrupted data, data analysis such as regularities detection in the data. Medical image interpretation system based on computing applications consist of major applications area provides significant assistance in the field of medical diagnosis. Mostly, these systems are developed in consideration to emulate the expertise of doctor to identify the malignant regions in various minimally invasive imaging procedures (for, e.g., endoscopy, computed tomography, confocal microscopy, ultrasonography, MRI or computed radiography) (Magoulas and Prentza, 1999). Machine learning is providing an opportunity for the improvement in decision support in medical image interpretation (Giger, 2018). Machine learning algorithms-based CAD reduces interpretation times by helping physicians to interpret medical imaging findings. These algorithms performed well in some challenging tasks such as segmentation of pulmonary embolism with computed tomographic angiography, detection and diagnosis of breast cancer with mammography, segmentation of brain tumour with magnetic resonance imaging, and detect brain's cognitive state with functional medical resonance imaging in diagnosis of neurological disease (Alzheimer disease) (Erickson et al., 2017).

5 Classification

Classification can play an important role in diagnosis purpose in medical image processing. Using both gray scale and colour medical images, there are many classifications created. Classification assigns an incident or physical objects into one of a set of predefined categories. Medical image databases containing images of different modalities used for image classification. Types of different classification techniques used in medical image processing are explained in this section.

5.1 *Decision tree induction*

Decision tree methodology has become popular in the area of medical research. Decision tree may use in the diagnosis of a medical condition from the symptoms pattern in which classes defined by the decision tree decide the type of diagnosis given to patient. Decision tree model are formed by selecting the most relevant input variables by decision tree methods and are used to formulate clinical hypothesis and inform subsequent research. After selecting the relevant variables, importance of variables is computed. Mostly, the importance of variable is calculated by the records it have. Decision tree analysis also plays an important role in handling missing values. Either missing values are classified as a separate category or variables are to be set for prediction and replace these missing values with the predicted values. It is usual to have many categories of one categorical variables or heavily skewed continuous data in medical research. In these conditions, decision tree models can help in deciding how ranges are formed by subdividing heavily skewed variables or how to form more manageable no. of categories by collapsing categorical variables. The decision tree, a powerful technique, is used for classification, interpretation, Prediction and data manipulation that involves various potential applications in the area of medical research.

5.2 *Bayesian classification*

Bayesian theorem is based on statistics and probability theory. The mathematical form of Bayesian theorem is

$$P(A | B) = P(B | A)P(A)/P(B) \quad (1)$$

where, $P(A)$, prior probability, is initial degree of belief in A and, $P(B)$, prior probability, is the initial degree of belief in B, $P(A|B)$, the posterior, degree of belief in A, having accounted for B.

Naïve Bayes Classifier appeals to physician because it requires little data for training in comparison to other classifiers. It is naturally robust to noisy and missing data. All the available information is used in the explanation of decision. This classifier is based on Bayes theorem. Attributes are independent, i.e., no dependency between all attributes. Karabatak (2015) proposed a simple weighted naïve Bayes classifier which detects the breast cancer. The accuracy of this proposed method is highest (98.54%) in comparison to C4.5 (94.74%), RIAC (94.99), LDA (96.80), SVM (97.20), NEFCLASS (95.60), neuro-rule, optimised LVQ (96.70), BIG-LVQ (96.80), SFC (95.57). Bayesian classifier is a very promising technique in medical image processing. Bayesian classifier takes 7 min on an average for the segmentation of all types of tumour in comparison to fuzzy clustering.

5.3 *Neural network*

Neural network is a very promising technique in medical image processing. There are many types of neural network used in the different fields of medical image processing.

- 1 In the feed forward neural network, there are no cycles and loops exist. Information moves only in forward direction from the input nodes to the output nodes through hidden nodes (if any). It is widely used in preprocessing, segmentation and recognition.
- 2 A cellular neural network features a multi-dimensional array of neuron and local interconnections among the cells. Cellular neural network is widely used only for preprocessing (construction and restoration).
- 3 Probabilistic neural network organises its operations into a multilayered feed forward network with four layers, i.e., input layer, hidden layer, pattern/summation layer output layer. It is often used in the segmentation and recognition.
- 4 Fuzzy neural network is a multilayer feed forward neural network that uses learning algorithm inspired by neural network theory to determine its parameters by processing data samples.

This neural network is used in preprocessing, segmentation and recognition. Other types of neural networks like Self organising feature neural network, convolution neural network, massive training neural network, neural ensemble and adaptive resonance theory neural network are used in one or more of the techniques (preprocessing, segmentation, registration, recognition) (Shi et al., 2009).

5.4 Support vector machine

The principle of structural risk minimisation is the basis of SVM learning. SVM performs well in case it applied to data outside the training set because it does not minimise an objective function based on training samples rather it attempts to minimise a bound on the generalisation error. It has been observed that in many applications, SVM-based approaches are able to outperform competing methods. Medical image processing plays an important role in the computer added diagnosis. In different diagnosis systems, SVM performed well in comparison to other classifiers and it has been using solely or with the combination of other techniques in the wellbeing of medical research. Zhou et al. (2006) proposed the one class SVM classifier technique based on query for image segmentation. This technique extracts the brain tumours from the clinical MR images. Selvaraj et al. (2007) proposed a classification technique which identifies the normal and abnormal brain slices from MRI data for identification of tumour. Chaplot et al. (2006) proposed a novel method by taking wavelets as input for neural network SOM and SVM for the classification of MR images of human brain as either normal or abnormal and it has shown that SVM performed well with the classification rate of 98% in comparison to neural network SOM with the classification rate of 94%. SVM also performs in the detection of objects from the medical images and it has been observed from different studies that SVM can perform well in object detection. Micro calcifications clusters are the early indicator of breast cancer in women and the early detection of MC clusters can prevent or help in diagnosis of breast cancer. El-Naqa et al. (2002) proposed a method which uses SVM in the detection of micro calcifications from mammograms. SVM is a promising technique in the different areas of medical image processing like classification, object detection, feature extraction.

5.5 Association rules

Association rule is a process of data mining which finds correlations, frequent patterns or casual structures from data sets found in different kinds of databases such as transactional database, relational database and other information repositories. Many effective algorithms have been proposed, the most popular are FP tree growth and Apriori. Let, $I = \{i_1, i_2, \dots, i_n\}$, called items, a set of n binary attributes and, $D = \{t_1, t_2, \dots, t_n\}$, called database, a set of transactions Such that any transaction t_i , where $1 \leq i \leq n$, in D is a set of items in I .

Association rules are widely used for feature selection, content-based image retrieval (CBIR) in medical domain, discover frequent patterns. Breast cancer is one of the main causes of deaths especially in the developing countries. Currently, there are no solutions to prevent breast cancer; the only solution is to detect it in the early phase. The most reliable method to detect cancer in the early phase is mammography. Digital mammograms are considered as the most difficult among medical images to be read due to differences in the tissues types and their low contrast. Antonie et al. (2002) proposed the classification system for digital mammograms with the accuracy of 80.33%. CAD systems and CBIR are widely used resources in medicine. CAD increases the accuracy of diagnosis and improves the consistency for interpretation of images with the use of second opinion (computer results). Ribeiro et al. (2009b) proposed the feature selection through association rules (FAR) method for continuous feature selection using the features of image and image categories to improve the CBIR system and also proposed the image diagnosis enhancement through association (IDEA) method to improve the CAD system to assist radiologist for diagnosis of medical images. Ribeiro et al. (2009a) proposed StARMiner algorithm that uses the statistical association rule to select the most relevant features of image in image dataset. In the discrimination of images, StARMiner performs well in comparison to relief-F and DTM algorithm.

6 Clustering

The process of identifying the objects of similar classes is called clustering. Clustering helps to identify sparse and dense regions in object space. It is an ‘unsupervised learning process’ that group together the samples of similar data, although, the classification criteria may differ from each other. It can discover correlations and overall distribution pattern among data attributes. Clustering techniques can be categorised because they are differing in various ways. These techniques are computationally complex and require dataset entries into the memory, that’s why these techniques do not find favour in the medical research field. Researchers have developed hundreds of clustering algorithms from a different scientific discipline. In this section, we’ll focus on the widely used clustering techniques in the medical imaging field.

6.1 K-means clustering algorithm

K-means algorithm, fall into the category of unsupervised methods, is a widely used technique because of its simplicity. It is suitable technique for the pixel-based medical image segmentation and the key issue in this algorithm is to select the feature

space. There are many improved versions of k-means clustering algorithms have been proposed for the better performance of the segmentation process for different purposes in computer-based medical diagnosis. Sulaiman and Isa (2010) proposed the adaptive-fuzzy-K-means clustering algorithm for image segmentation and conclude that this algorithm outperforms the moving k-means (MKM) and fuzzy c-means (FCM) algorithms in order to better segmented images. Numbers of modified k-means algorithms are proposed for the better segmentation purpose. Fuzzy k-means (FKM), fuzzy moving k-means (FMKM), adaptive moving k-means (AMKM) and fuzzy adaptive moving k-means (AFMKM) are the algorithms which are relatively accurate and fast in comparison to other segmentation methods.

6.2 Fuzzy c-means clustering algorithms

Fuzzy c-means algorithm is widely used in the application of medical image segmentation and it is more suitable for MR images because pixels are assigned to fuzzy clusters in this are without labels. The standard fuzzy c-means technique provides no filtering that's why quality of Images remains poor. Many researchers proposed different modified fuzzy c-means algorithm for better segmentation process. Zhang and Chen (2004) proposed a robust clustering approach [kernelised fuzzy c-means (KFCM)] that is simple and computationally inexpensive for medical image segmentation applications. Szilagyi et al. (2003) proposed another approach to improve the speed of segmentation process of MR brain images; it is a useful tool for virtual brain endoscopy.

6.3 Expectation maximisation (EM) algorithm

This algorithm is widely used in reconstruction of medical images, especially in the tomography context like PET and single photon emission computed tomography (SPECT) for both purposes, to determine the maximum likelihood (ML) solution and as a framework by which algorithms can be developed and spawned. EM algorithm consists of two repetitive steps, i.e., expected distribution (E-step) and maximisation (Mstep). Probability distribution is created by an initial guess for model's parameters and this probability distribution is pulled off to include the new data. These steps are repeated until stability is reached. EM algorithm borne the number of developments. space-alternating generalised expectation-maximisation (SAGE) algorithm, regularised EM algorithms (one-step-late algorithm, EMS algorithm, ICM-EM algorithm, and penalised SAGE algorithm) is the developments and advancements of EM algorithm (Kay, 1997). These algorithms are more commonly used for image reconstruction. De Pierro (1995) proposed a modified EM algorithm, which is a natural advancement of EM algorithm, to penalise likelihood estimation in tomography (emission tomography). Boudjelal et al. (2017) proposed a novel kernel-based regularisation technique, to reconstruct the image that is more robust and effective to remove background noise in comparison to standard MLEM. Approaches defined in Yan (2011), Teng et al. (2016) and Han and Xue (2015) are more efficient and robust algorithms for image reconstruction.

6.4 Hierarchical clustering

Hierarchical clustering is a technique of cluster analysis which builds clusters hierarchy. The bottom-up approach is known as agglomerative clustering and Top down approach is known as divisive clustering. Michel et al. (2012) proposed a approach which uses hierarchical approach to infer brain states based on fMRI resulting in reduced technical difficulty to optimise the parcellation with respect to information spatial organisation within image. Hierarchical clustering is used solely or with the combination of other techniques for different purposes in medical applications. Pooshfam and Abdullah (2009) proposed a more accurate and effective method for brain image processing based on hierarchical clustering. This approach of brain mapping consists of four stages equating, registration, wrapping and rendering steps that promises physicians, researchers, and surgeon to work with more accuracy in brain. Segmentation based on hierarchical clustering is a generic unsupervised segmentation technique in which dissimilar regions in digital images are segmented. Selvan et al. (2017) described that how hierarchical cluster analysis helps to visualise the imaging data of different medical image modalities to help diagnosis. Hierarchical clustering is also an important approach for medical image segmentation. Segmentation approaches are presented in Ohkura et al. (1998), Galbiati et al. (2009) and Reddy et al. (2013) for medical images which show that this technique is more effective and reliable technique for segmentation process.

7 Challenges in medical

Imaging-dealing with large amount of data, i.e., Giga to Terabyte data is a challenging task regarding medical image data mining, image management, medical image visualisation, bioimaging and neuro-imaging. Medical image acquisition, difficulty in image content-based queries and its acceptance by physician, virtual reality in medical visualisation, CBIR (Yadav et al., 2016) and image content-based queries is also a difficult task in medical image processing, A lot of approaches have been proposed in this particular area but still it is not widely accepted by the physicians because of less reliability and less accuracy. Realistic applications for better CAD ranging from detection to diagnosis is still a challenging task which require more work to apply it in the real time for better, reliable and fast diagnosis.

8 Conclusions

Now a day's medical imaging is a wide area of research and a lot of work has already been done in this area, still more is left. This paper presents the overview and functionalities of data mining and machine learning techniques for the clinical purposes from detection to diagnosis including prediction, data process description, therapy and treatment planning etc through medical imaging. Different approaches are performed better in different domains and their contribution in particular step for application development is discussed.

References

- Antonie, M.L., Zaiane, O.R. and Coman, A. (2002) 'Associative classifiers for medical images', in *Pacific-Asia Conference on Knowledge Discovery and Data Mining*, May, pp.68–83, Springer, Berlin, Heidelberg.
- Boudjelal, A., Messali, Z. and Elmoataz, A. (2017) 'A novel kernel-based regularization technique for PET image reconstruction', *Technologies*, Vol. 5, No. 2, p.37.
- Chaplot, S., Patnaik, L.M. and Jagannathan, N.R. (2006) 'Classification of magnetic resonance brain images using wavelets as input to support vector machine and neural network', *Biomedical Signal Processing and Control*, Vol. 1, No. 1, pp.86–92.
- De Pierro, A.R. (1995) 'A modified expectation maximization algorithm for penalized likelihood estimation in emission tomography', *IEEE Transactions on Medical Imaging*, Vol. 14, No. 1, pp.132–137.
- El-Naqa, I., Yang, Y., Wernick, M.N., Galatsanos, N.P. and Nishikawa, R.M. (2002) 'A support vector machine approach for detection of microcalcifications', *IEEE Transactions on Medical Imaging*, Vol. 21, No. 12, pp.1552–1563.
- Erickson, B.J., Korfiatis, P., Akkus, Z. and Kline, T.L. (2017) 'Machine learning for medical imaging', *Radiographics*, Vol. 37, No. 2, pp.505–515.
- Galbiati, J., Allende, H. and Becerra, C. (2009) 'Dynamic image segmentation method using hierarchical clustering', in *Iberoamerican Congress on Pattern Recognition*, November, pp.177–184, Springer, Berlin, Heidelberg.
- Giger, M.L. (2018) 'Machine learning in medical imaging', *Journal of the American College of Radiology*, Vol. 15, No. 3, pp.512–520.
- Han, M. and Xue, Y. (2015) 'Application of expectation maximization algorithm in magnetic induction tomography', *Biomedical Engineering Letters*, Vol. 5, No. 3, pp.221–228.
- Jeyavathana, R.B., Balasubramanian, R. and Pandian, A.A. (2016) 'Survey: analysis on preprocessing and segmentation techniques for medical images', *International Journal of Research and Scientific Innovation (IJRSI)*, June, Vol. III, No. VI, June, ISSN 2321-2705.
- Karabatak, M. (2015) 'A new classifier for breast cancer detection based on Naïve Bayesian', *Measurement*, Vol. 72, pp.32–36.
- Kay, J. (1997) 'The EM algorithm in medical imaging', *Statistical Methods in Medical Research*, Vol. 6, No. 1, pp.55–75.
- Magoulas, G.D. and Prentza, A. (1999) 'Machine learning in medical applications', in *Advanced Course on Artificial Intelligence*, July, pp.300–307, Springer, Berlin, Heidelberg.
- Michel, V., Gramfort, A., Varoquaux, G., Eger, E., Keribin, C. and Thirion, B. (2012) 'A supervised clustering approach for fMRI-based inference of brain states', *Pattern Recognition*, Vol. 45, No. 6, pp.2041–2049.
- Ohkura, K., Nishizawa, H., Obi, T., Yamaguchi, M. and Ohyama, N. (1998) 'Hierarchical clustering method for the segmentation of medical images', in *Medical Imaging 1998: Image Processing*, June, Vol. 3338, pp.1306–1314, International Society for Optics and Photonics.
- Perner, P. (2002) 'Image mining: issues, framework, a generic tool and its application to medical image diagnosis', *Engineering Applications of Artificial Intelligence*, Vol. 15, No. 2, pp.205–216.
- Pooshfam, H. and Abdullah, R. (2009) 'A proposed method for brain medical image registration by hierarchical clustering algorithm', in *Modelling & Simulation, 2009, AMS'09, Third Asia International Conference on*, IEEE, May, pp.315–319.
- Reddy, K.S., Basha, S., Prashanth, B. and Reddy, K.S. (2013) *A Hierarchical Clustering Algorithm Based Computer Aided Molecular Modeling with Haematoxylin & Eosin Images of Colon Cancer*.
- Ribeiro, M.X., Balan, A.G., Felipe, J.C., Traina, A.J. and Traina, C. (2009a) 'Mining statistical association rules to select the most relevant medical image features', in *Mining Complex Data*, pp.113–131, Springer, Berlin, Heidelberg.

- Ribeiro, M.X., Bugatti, P.H., Traina Jr., C., Marques, P.M., Rosa, N.A. and Traina, A.J. (2009b) 'Supporting content-based image retrieval and computer-aided diagnosis systems with association rule-based techniques', *Data & Knowledge Engineering*, Vol. 68, No. 12, pp.1370–1382.
- Selvan, A.N., Cole, L.M., Spackman, L., Naylor, S. and Wright, C. (2017) 'Hierarchical cluster analysis to aid diagnostic image data visualization of MS and other medical imaging modalities', *Imaging Mass Spectrometry: Methods and Protocols*, pp.95–123.
- Selvaraj, H., Selvi, S.T., Selvathi, D. and Gewali, L. (2007) 'Brain MRI slices classification using least squares support vector machine', *International Journal of Intelligent Computing in Medical Sciences and Image Processing*, Vol. 1, No. 1, pp.21–33.
- Shi, Z., He, L., Suzuki, K., Nakamura, T. and Itoh, H. (2009) 'Survey on neural networks used for medical image processing', *International Journal of Computational Science*, Vol. 3, No. 1, p.86.
- Song, Y.Y. and Ying, L.U. (2015) 'Decision tree methods: applications for classification and prediction', *Shanghai Archives of Psychiatry*, Vol. 27, No. 2, p.130.
- Sulaiman, S.N. and Isa, N.A.M. (2010) 'Adaptive fuzzy-K-means clustering algorithm for image segmentation', *IEEE Transactions on Consumer Electronics*, Vol. 56, No. 4.
- Szilágyi, L., Benyo, Z., Szilágyi, S.M. and Adam, H.S. (2003) 'MR brain image segmentation using an enhanced fuzzy c-means algorithm', in *Engineering in Medicine and Biology Society, 2003, Proceedings of the 25th Annual International Conference of the IEEE*, September, Vol. 1, pp.724–726.
- Teng, Y., Sun, H., Guo, C. and Kang, Y. (2016) 'ADMM-EM method for-norm regularized weighted least squares PET reconstruction', *Computational and Mathematical Methods in Medicine*.
- Yadav, V. and Kaushik, V.D. (2018) 'Detection of melanoma skin disease by extracting high level features for skin lesions', *International Journal of Advanced Intelligence Paradigms (IJAIP)*, DOI: 10.1504/IJAIP.2018.10012484.
- Yadav, V., Verma, M. and Kaushik, V.D. (2015) 'A hybrid image compression technique for medical image', *IEEE International Conference on Computational Intelligence and Communication Networks (CICN-15)*, December, pp.222–227.
- Yadav, V., Verma, M., Kaushik, V.D. (2016) 'Content based image retrieval in medical image database', *IEEE International Conference on Advanced Computing and Software Engineering (ICACSE-2016)*, October, pp.73–77, pp.14–15, ISBN: 978-93-86256-05-8.
- Yan, M. (2011) *General Convergent Expectation Maximization (EM)-Type Algorithms for Image Reconstruction with Background Emission and Poisson Noise*, CAM report, pp.11–56.
- Zhang, D.Q. and Chen, S.C. (2004) 'A novel kernelized fuzzy c-means algorithm with application in medical image segmentation', *Artificial Intelligence in Medicine*, Vol. 32, No. 1, pp.37–50.
- Zhou, J., Chan, K.L., Chong, V.F.H. and Krishnan, S.M. (2006) 'Extraction of brain tumor from MR images using one-class support vector machine', in *Engineering in Medicine and Biology Society, 2005, IEEE-EMBS 2005, 27th Annual International Conference of the*, January, pp.6411–6414, IEEE.

SUSTAINABLE USE OF RECYCLED CONSTRUCTION AND DEMOLISHED CONCRETE/MASONRY AGGREGATES IN INDIA

Er. S. K. Singh Gaur¹

¹Sr. lecturer, Civil Engineering, A.I.T.H., Awadhपुरi, Kanpur

Abstract - Many structures that were constructed during 1970 or before are now in need of either major repairs or possible replacement. This is because some of such structures are now reaching the end of their design life, or may not have been constructed according to the specifications or do not receive the required maintenance while in service. Demolition or maintenance work on such structures results in large amount of concrete and masonry rubbles. The advantages of recycling coarse aggregates from discarded old concrete and masonry include lower environmental pollution, reduction in valuable land fill space and savings in natural aggregate resource

Key Words: Natural coarse aggregate NCA, recycled coarse aggregate RCA, recycled concrete RC, recycled coarse masonry RCM, construction and demolished aggregate CDA

1. INTRODUCTION

The construction industry in India is growing very fast at an annual rate of 10 % over last 10 years as against the world average of 5.5 % per annum .The built -up area is expected to increase almost five times from 21 billion sqft in 2005 to approximately 104 billion sqft in 2030 as per C.S.E. report.

There was a tremendous increase in infrastructural development activities in last few decades due to overall development of country in all socio economic fields. As per up dates of Budget 2018-19, infrastructural proposed schemes & reforms are as under:

- Railways, roadways, airways along rail and road linkages and defence and connectivity infrastructure received major emphasis.
- Highest budget allocations for the rail, road and rural infrastructure including rural roads and rural housing.
- A new scheme for revitalising school architecture by the year 2022, 'Revitalising of Infrastructure and Systems in Education' scheme launched.
- Dedicated funding for affordable housing to make schemes like 'Pradhan Mantri Awas Yojana' more accessible.
- 1 crore houses to be built under PMAY out of which 50 lakh houses will be built in the urban area.
- To attain the motto of 'House for all' by the end of the year 2022. 50 lakh more houses will be constructed in the urban areas.
- Target to build 100 smart cities under the ambitious 'Smart City' project among which 99 cities have been selected. Emphasis will be on offering solar facilities, smart road and smart infrastructure.
- Upgradation and renovation work to be conducted for the improvement of 600 railway stations in India.
- New tunnel in Sera Pass will be built in order to promote tourism in India, especially in the north-eastern part of the country.
- Target of constructing 2 crore more toilets under 'Swachh Bharat Mission' in this financial year.
- Under road infrastructure, plans for completion of 9,000 km of National Highway and 3.7 lakh km rural road construction plan.
- Plan to build 2 new planning & architecture schools for IITs and 1 Rail University in Vadodara for boosting railway operation.
- Construction of 1 government medical college for every 3 parliamentary constituencies along with the improvement of 24 district-level colleges.
- Top 10 tourist sites in the country will be converted into exceptional tourist destinations through marketing, branding and private funding.

This immense surge in infrastructural development will need tremendous amount of energy, water & material, but they also create waste. This waste, generated in construction, maintenance and disposal phases of a building, is called construction and demolition (referred as construction and demolition aggregates CDA) waste. This includes wastes from demolished structures, renovation in the real estate sector and construction and repair of roads, flyovers, bridges etc. along with debris produced from natural activities such as landslides & volcanic eruption etc.

Globally, cities generate about 1.3 billion tonne of solid waste per year. This volume is expected to increase to 2.2 billion tonne by 2025, says a 2012 report by the World Bank. Building materials account for about half of all materials used and about half the solid waste generated worldwide.

But recycled construction and demolition aggregates (CDA) can be an invaluable source of construction material. In fact the recent controversy in India over sand mining has put the spotlight on the need to recycle and substitute naturally sourced construction material such as sand and stone aggregates.

2. CONSTRUCTION & DEMOLITION WASTE GENERATED IN INDIA

The Union ministry of forest and environment (MOEF) has agreed that there is no systematic database on C&D waste available in India. As per the estimates of Centre for Science and Environment (CSE), since 2005, India has newly constructed 5.75 billion Sq m, of additional floor space with almost one billion Sq m in 2013 itself. If

(according to the Technology Information, Forecasting and Assessment Council's, TIFAC, thumb rule) a new construction generates about 40 to 60 kg of CDA per sq m, then taking an average of 50 kg per sq m, India would have produced about 287 MT of this construction and demolition waste.

This estimate only account for new construction. Demolition and maintenance /repair related waste also generates additional waste. The waste produced per sq m of demolition is 10 times that generated during construction, as per TIFAC, about 288 MT of construction & demolition waste would have generated in year of study alone because of demolition work assuming 10% of building constructed till that time were demolished.

TIFAC also says building repair or renovations must have produced an average of 155 MT CDA waste, in the year of study.

Thus, the total CDA waste generated in India just by buildings, in one year amounts to an amount approximately 530 MT, which is 44 times higher than the official estimates collected by different agencies in India.

Not surprisingly, in India, if CDA waste is quantified, it will be more than all the other types of solid wastes put together.

Where this all CDA waste is going? A lot of it being used illegally as landfill for water bodies and water lands around urban areas. The rest is just being dumped in open areas, thus affecting the environment adversely.

Indian Construction Industry is highly employment intensive and accounts for approximately 50% of the capital outlay in successive 5-Year Plans of our country. The Projected investment in this industrial sector continues to show a growing trend.

Construction activity leads to generation of solid wastes, which include sand, gravel, concrete, stone, bricks, wood, metal, glass, plastic, paper etc. The management of construction and demolition waste is a major concern for town planners due to the increasing quantum of demolition's rubble, continuing shortage of dumping sites, increase in transportation and disposal cost and above all growing concern about pollution and environmental deterioration.

Construction waste is bulky and heavy and is mostly unsuitable for disposal by incineration or composting. The growing population in the country and requirement of land for other uses has reduced the availability of land for waste disposal. Re-utilization or recycling is an important strategy for management of such waste.

Apart from mounting problems of waste management, other reasons which support adoption of reuse/ recycling strategy are-reduced extraction of raw materials, reduced transportation cost, improved profits and reduced environmental impact. Above all, the fast depleting reserves of conventional natural aggregate has necessitated the use of recycling/ re-use technology, in order to be able to conserve the conventional natural aggregate for other important works.

3. VARIOUS CONSTITUENTS OF CONSTRUCTION & DEMOLITION WASTE IN INDIA

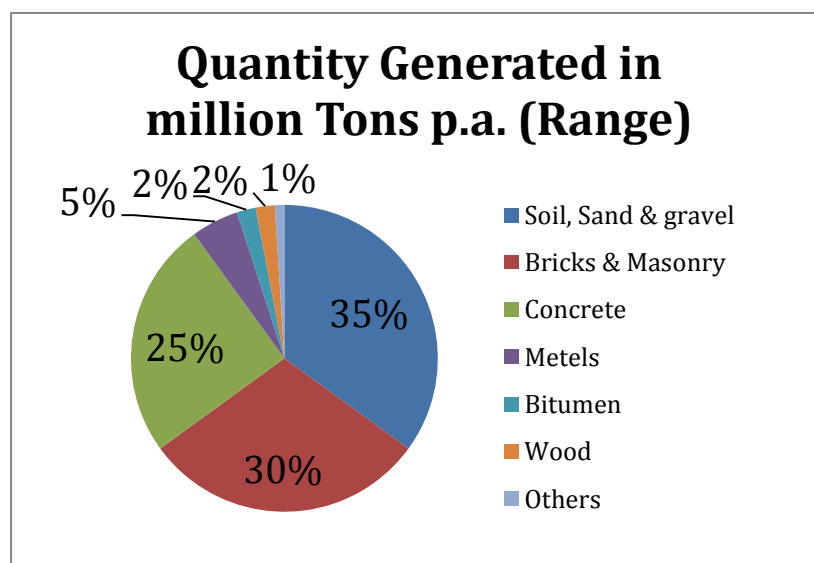
Waste is generated at different stages of construction process. Waste during construction activity relates to excessive cement mix or concrete left after work is over, rejection/ demolition caused due to change in design or wrong workmanship etc.

Concrete appears in two forms in the waste. Structural elements of building have reinforced concrete, while foundations have mass non-reinforced concrete. Excavations produce topsoil, clay, sand, and gravel. This may be either re-used as filler at the same site after completion of excavation work or moved to another site. Large quantum of bricks and masonry arise as waste during demolition. These are generally mixed with cement, mortar or lime. Stone arises during excavations or by demolition of old buildings.

Metal waste is generated during demolition in the form of pipes, conduits, and light sheet material used in ventilation system, wires, and sanitary fittings and as reinforcement in the concrete. Metals are recovered and recycled by re-melting. Timber recovered in good condition from beams, window frames, doors, partitions and other fittings is reused. However, wood used in construction is often treated with chemicals to prevent Termite infestation and warrants special care during disposal.

Bituminous material arises from Road planning, water proofing compounds, breaking and digging of Roads for services and utilities. Other miscellaneous materials that arise as waste include glass, plastic material, paper, etc. The total quantum of waste from construction industry is estimated to be 12 to 14.7 million tons per annum. Quantity of different constituents of waste that arise from Construction Industry in India is estimated as follows (As per TIFAC 2000 Report):

Constituent	Quantity Generated in million Tons p.a. (Range)	% of Different Constituents
Soil, Sand & gravel	4.20 to 5.14	35
Bricks & Masonry	3.60 to 4.40	30
Concrete	2.40 to 3.67	25
Metals	0.60 to 0.73	5
Bitumen	0.25 to 0.30	2
Wood	0.25 to 0.30	2
Others	0.10 to 0.15	1



Contractor executes construction project on a labour contract basis or on turnkey basis. Small housing projects, executed by owners, are predominantly executed on labour contract basis and strict supervision is required to control waste generation during construction process. Typically, waste generation ranges between 5 to 7%. In larger projects, where execution is on turnkey basis or through one's own team of professionals, material wastage is within 3%.

Services of demolition contractor are taken when old building is to be demolished due to deterioration of the building or to make way for construction of a new building. Demolition contractor specializes in planned deconstruction so that recovery of good material can be maximized for re-use. Recovery rate varies from 25% in old buildings to as high as 75% in new buildings.

4. RECYCLING OF CONSTRUCTION & DEMOLITION WASTE AS A REMEDY

Recycling of demolition waste was first carried out after the Second World War in Germany to tackle the problem of disposing large amounts of demolition waste caused by the war and simultaneously generate raw material for reconstruction.

Considerable research has been carried out in U.S.A, Japan, U.K, France, Germany, and Denmark etc. for recycling concrete, masonry & bricks, bituminous and other constituents of waste from Construction Industry. These studies have demonstrated possibility of using construction waste to substitute new materials of recycling.

In view of significant role of recycled construction material and technology in the development of urban infrastructure, Technology, Information, Forecasting and Assessment Council (TIFAC) have commissioned a techno-market survey on 'Utilization of waste from Construction Industry.

5. PRESENT STATUS OF PRODUCTION & REUSE OF CONSTRUCTION & DEMOLITION WASTE IN INDIA

Management of solid waste is the responsibility of Municipal Bodies or health officers. They notify landfill sites for disposal of solid waste. Whereas responsibility of removing the construction & demolition waste is primarily of the builder or the owner, it is usually assigned to the demolition contractor. Items, that cannot be re-used, are disposed off to landfill site.

Hard core material from demolition operation is required for land fill activities to provide daily cover over domestic waste, bulk fill capping, hard standings etc. Some Municipal Corporations require demolition waste for their landfill activities, while others want to minimize it to prolong useful life of landfill sites. However, all respondents are unanimous that in the long run, recycling of waste from construction industry is necessary in view of limited landfill space and increasing quantum of demolition waste.

Different constituents of waste are not segregated prior to disposal. Municipal Authorities incur cost of Rs 60 to 80 per ton of waste, but presently no charge is levied by them on the owner or builders.

Builders/ Owners bear the cost of transportation, which at present range between Rs. 250 to Rs 500 per truckload depending on the distance of demolition site from landfill area. Though directives exist for disposal of waste to landfill areas, presently penal action against violators is practically not taken.

Presently management of waste from construction industry in India, comprise of the following elements:

- Re-use of materials salvaged in good condition during demolition.
- All metal items are sent for re-melting through scrap dealers.
- Disposal of other items to low lying sites.

According to findings of survey, the most dominant reason for not adopting recycling of waste from Construction Industry is "Not aware of the recycling techniques". While 70% of the respondents have cited this as one of the reasons, 30% of the respondents have indicated that they are not even aware of recycling possibilities. The response of industries, which can use the recycled product, indicates that presently, the specifications do not provide for use of recycled product in the construction activity. Sixty Seven percent of the respondents from user industry have indicated non-availability of recycled product as one of the reasons for not using it. Concrete and masonry constitute more than 50% of waste generated by the Construction Industry. Recycling of this waste by converting it to aggregate offer dual benefit of saving landfill space and reduction in extraction of natural raw material for new construction activity.

6. CONVENTIONAL METHODS OF RECYCLING & REUSE OF CONSTRUCTION & DEMOLITION WASTE IN INDIA

Basic method of recycling of concrete and masonry waste is to crush the debris to produce a granular product of given particle size. Plants for processing of demolition waste are differentiated based on mobility, type of crusher and process of separation.

There are three types of recycling plants Viz. Mobile, Semi-Mobile and Stationary plant. In the Mobile plant, the material is crushed and screened and ferrous impurities are separated through magnetic separation. The plant is transported to the demolition site itself and is suited to process only non-contaminated concrete or masonry waste.

In the semi-mobile plant, removal of contaminants is carried out by hand and the end product is also screened. Magnetic separation for removal of ferrous material is carried out. End product quality is better than that of a Mobile unit.

Above plants are not capable to process a source of mixed demolition waste containing foreign matter like metal, wood, plastic, hardbound etc. Stationary plants are equipped for carrying out crushing, screening as well as purification to separate the contaminants. Issues necessary to be considered for erection of a Stationary plant are: plant location, road infrastructure, availability of land space, provision of weigh-bridge, provision for storage area etc.

Different types of sorting devices and screens are used for separating contaminants from end-product and grading the recycled product in various grain sizes. Vibrating screens, star screens or disc-separators are used for removal of impurities. Three main processes used for purification are:

- Dry Process
- Wet Process
- Thermal Process

Properties of recycled aggregate have to be compared to those of natural aggregate to evaluate its suitability for applications in construction industry. Density of recycled aggregate is lower and water absorption is higher than that of original aggregate. This is primarily due to mortar adhering to the concrete and higher porosity of bricks that are recycled.

7. PROBABLE USES OF CONSTRUCTION & DEMOLITION WASTE IN INDIA

Non awareness of recycling possibilities is one of the main barriers due to which waste is disposed to landfill. Absence of technology for recycling is another major hurdle for recycling of construction waste.

Once technology is known, availability of feedstock in sufficient quantities and of requisite quality is another bottleneck for its widespread use.

The acceptability of the recycled material is hampered due to poor image associated with recycling activity in India. Customer specifications do not permit use of materials recycled from Waste.

Cost of disposal of waste from construction industry to landfill has a direct bearing on recycling operations. High dumping costs induce diversion of waste for recycling.

The problem of dumping huge quantity of waste caused by a disaster and the difficulty in finding sufficient quantity of building material for reconstruction can be solved by recycling this waste. Usually, quick removal of debris is necessary to start the rehabilitation the waste can be reused for strengthening riverbanks or for producing aggregates for construction of road or building blocks. Experience of recycling operations at two disaster sites, have proven the feasibility of recycling demolition waste. In one of project, most of the debris had been transported and temporarily disposed off. Yet, recycling was carried out successfully. These experiences are relevant to India, in view of damage suffered in recent earthquake in Kumauni and Garhwali regions.

The raw material for construction is costly in hills due to high cost of transportation. Similarly, cost of waste disposal is also high thereby making recycling an attractive proposition. However, present volume of concrete, bricks and masonry waste are low to justify investment in recycling units.

Technology for producing recycled aggregate from concrete, bricks and masonry is quite simple. A mobile unit is best suited to process demolition waste of uniform quality. It can be procured at low investment. It can be useful for low quantum of waste and can be moved to the demolition site avoiding cost of Waste transportation. A fixed recycling plant requires higher volumes of demolition waste to justify high investment in complex, screening and separation systems, which are necessary to process mixed demolition waste. It has to be located in a place, where large volume of waste is available and the market for recycled product is close by. Unless the market for recycled aggregate is developed, economic viability of such a unit would be questionable. Indian manufactures are producing crushers, which can be used with suitable modification in a recycling unit to break concrete, bricks and masonry. A comparative study shows that a jaw crusher or impact crusher may be used.

Recycling of bituminous material by hot in-situ recycling technique is advantageous due to savings in consumption of asphalt and energy, avoidance of material transportation and possibility of using the technique for road maintenance and repairs. Cold in-situ technique is more suited to roads having lighter traffic, which appear less probable in Indian conditions. Hence, a thorough evaluation is warranted before its adoption.

Recycled aggregate can be used as general bulk fill, sub-base material in road construction, fills in drainage projects and for making new concrete.

While using recycled aggregate for filler application, care must be taken that it is free of contaminants to avoid risk of ground water pollution. Mixed debris with high gypsum, plaster, should not be used as fill.

Use of recycled aggregate as sub-base for road construction is widely accepted in most countries. It is possible to use crushed concrete as coarse fraction of gravel in sub-base for road, but crushed brick is not suitable owing to its high bitumen requirement and high void content.

For using recycled aggregate to make new concrete, water absorption of the recycled aggregate must be determined in the laboratory to decide the mix design. Use of fine recycled aggregate for concrete making is not recommended as it increases the water demand and lowers the strength and durability of concrete. Pre-soaking of recycled aggregate is suggested to take care of high water absorption so that concrete of uniform quality is produced.

Concrete made from recycled aggregate has lower compression strength caused by the bond characteristic of recycled aggregate and the fresh mortar. Fraction of less than 2mm of recycled aggregate brings about the largest reduction in strength of recycled aggregate concrete (RAC). Fine aggregates also reduce frost resistance of recycled aggregate concrete. Drying shrinkage of recycled concrete is higher than that of concrete with conventional aggregate. Workability of concrete decreases with increased portions of demolition waste. Upto 30% of natural coarse aggregate can be substituted, by coarse recycled aggregate, without any impact on the quality of concrete.

Feasibility analysis has been carried out for a 25000 tons/annum recycling plant to produce recycled aggregate from waste concrete and Masonry & bricks. The location of the recycling plant should be so chosen that there is (a) Availability of feed stock (b) Market for recycled product and (c) It is difficult to dispose of the waste by other means. Equipment like Crushers, conveyors, screens etc. can be sourced from Indian manufacturers, who supply similar machines to Natural aggregate producers. Necessary modifications for adapting the equipment for crushing concrete/ Masonry/ Bricks can be carried out. Due to marked preference of the customers to use natural aggregate, Recycled aggregates have to be marketed at a discount to achieve sale of 25000-tons/ year in 2/3 years time. The unit is viable but its operation is highly sensitive to fluctuations in sale price of recycled aggregate and capacity utilization of the plant.

8. PROBLEMS ASSOCIATED WITH USE OF CDA WASTE

Problem associated with use of recycled aggregate, for manufacture of new concrete, is the possibility of contaminants in original debris passing into new concrete. Such impurities reduce the strength of the concrete. Waste glass is a problem because it is alkali reactive with cement paste under wet conditions. Organic substances like wood, textile fabrics, paper and other polymeric materials are unstable in concrete. Paints may entrain air in concrete.

Test results of aggregate properties and concrete properties prove repeatedly recycled concrete to be both durable and of good quality in all respects. Therefore, existing concrete structures, in addition to providing an aggregate source for the immediate future, may continue to generate an adequate supply of aggregate for concrete construction in the more distant future after once being recycled.

Recycled aggregate of best quality for concrete production is obtained when it is graded. Although there are no standards drawn up in India for recycled aggregate and recycled aggregate concrete, specification drawn in other countries are useful as a guideline.

In Hot in-situ recycling, the upper layer of the road is pre-heated and the asphalt is loosened by milling devices. It is mixed together with recycling agent and the mixture is spread along the road and compacted. In India, recycling of bituminous material is not practiced. In developed countries, special purpose machine has been built, which carry out the total process of hot in-situ recycling. It is important that the project for recycling is properly evaluated to ensure that the potential benefits of hot in-place recycling are realized.

9. MEASURES NEEDED TO PROMOTE THE USE OF CONSTRUCTION & DEMOLITION AGGREGATES

Creating awareness & dissemination of information is essential to build public opinion and instill confidence in favor of recycling option. There is a need to create market for the recycled products by involving the Construction Industry to use recycled materials in their construction projects.

Development of standards for recycled materials would provide producers with targets and users an assurance of quality of material. Standards formulated in other countries can be a guideline for development of specification in our country.

Commissioning of a pilot plant as a demonstration unit can help in breaking barriers against recycling of construction & demolition waste. Imposition of charge on Sanitary landfill can induce builders and owners to divert the waste for recycling.

Government support and commitment is vital for development of recycling industry. Development of policy supported by proper regulatory framework can provide necessary impetus. It will also help in data compilation, documentation and control over disposal of waste material.

Low returns from investment in recycling units can be offset by providing suitable fiscal incentives by the Government for gestation period. These are warranted in the long-term interest of reducing pollution and conserving valuable resources.

Environmental impact of recycling has both advantages and disadvantages. Advantages are reduced disposal of waste to landfill sites and reduced mineral extraction. Disadvantages are problems of Noise and Dust emission and risk of ground water pollution. The problem of noise can be managed by using silencers and providing acoustic enclosures while water spray is useful to control dust emission.

Based on evaluation of the technology, review of Waste Management practices in India and other countries, and assessment of constraints to recycling option in the country, following recommendations along with implementation & action plan are proposed:

There is a need to create awareness about the problems of waste management and the necessity to adopt reuse and recycling options for waste from Construction Industry. It is recommended that Seminars, Conferences and Workshops be held in different parts of the Country. Simultaneously, other media should also be exploited to create an environment in favor of Recycling.

Interpretation on the above may result in bringing out publication/ brochures highlighting the short and long term benefits of recycling strategy and indicating case histories of utilisation of construction industry waste, especially in India. Circulation of these brochures especially in construction industry research departments, field/design organisations in Central/ State government may generate sufficient confidence for promotion/ adoption of recycling strategy for their works. Equally important is the need to generate sufficient Database regarding efficacy and field adoptability of the recycling strategy in the country.

A coordinated action should be taken up by NGO's, environmentalist, government offices and industry representatives. The recycling technology for construction waste has to be established on a pilot scale in India. It is recommended that pilot scale plant for producing recycled aggregates is established and application of recycled aggregates in different construction activities is demonstrated. Central Road Research Institute or Central Building Research Institute may be involved to put up a pilot plant and establish use of recycled aggregate in road and building construction. The most common application of recycled aggregate in other countries is its usage as sub-base material in construction of roads. At first, recycled aggregates should be tried for this application. Produce from Pilot plant should be evaluated by Central Road Research Institute for using it as sub-

base for Road. Accordingly, specifications for Road construction should be modified so that recycled aggregate is used in this application.

Manufacturers of Crushers, screens and separating equipment should be involved to provide necessary equipment for the recycling unit. Presently, manufacturers of such equipment in India are suppliers to Natural Aggregate Industry. Suitable modifications, as may be required, can be carried out by manufacturers to their product for processing Construction Waste. Manufacturers of Crushers, Screens and material Handling Equipment should take up this work. Quality standards/ codes of Practice regarding various aspects of product control and acceptance criteria for use of recycled aggregate in recycled aggregate concrete and other works should be formulated. This would help in setting a target product quality for producers and assure the user of a minimum quality requirement, thus encouraging him to use it. Specifications drawn in other countries like Japan, Netherlands, and Germany etc. can be a useful guideline.

BIS in coordination with Construction Industry, Research Laboratories involved in producing recycled aggregate should take up this work.

Government should formulate and implement policy for Management of waste from Construction and other Industries. It should clearly set out goals for recycling of Waste as a means of reducing pollution and conserving valuable resources. Government of India in consultation with State governments, Pollution Control Boards should formulate this plan.

Such an elaborate system can be developed and implemented in two steps. In the short term, requirement of applying for permission for demolition process with mandatory requirement to provide details of the projected quantities, types and disposal routes can be introduced. In the long term, along with permission for demolition, commitment of segregation of constituents of waste and recycling should be submitted. Government of India should undertake this work in coordination with Construction Industry, Municipal Corporations and Pollution Control Boards.

Based on success of demonstration unit, Municipal Authorities of Metropolitan cities should put up facility for recycling of construction and demolition waste adjacent to their landfill sites. The waste from Construction Industry can be used in this plant for making recycled aggregates. Charges should be imposed on disposal of construction waste to landfill site. This is to induce the builders/ owners to divert the waste to recycling.

Municipal Corporation Authorities of Metropolitan Cities should take up this work under guidance of agency, which has put up the pilot plant. If necessary, assistance from foreign consultants/ experts may also be taken.

Mobile recycling units should be used at sites where demolition waste of one type is being generated for example demolition of railway platform, airport runway, waste of prefabricated concrete structure etc. Once the concept of recycling is widely accepted, Mobile units can be owned by Organizations undertaking demolition work. Large scale construction companies who in their course of business have to frequently undertake demolition of structures can also have their own mobile recycling units.

The builder/ owner must segregate different constituents of waste before its disposal to landfill site. In this respect, Municipal Authorities can impose a differential charge so that disposal of mixed waste is charged at a higher price than segregated waste. The builders/ owners/ demolition contractors should maximize segregation of waste constituents. Municipal authorities to introduce differential Landfill levy.

To take care of the problem of noise and dust emission associated with recycling, suitable measure like erection of acoustic screening around the equipment, use of mufflers/silencers and water spraying equipment should be made mandatory in a recycling unit.

Equipment manufacturers should ensure incorporation of these features in their machines.

- In the initial phase, fiscal incentives should be provided by the Government to the recycling industry by way of:
 - Financing the purchase of equipment at lower interest rate
 - Tax exemptions/ holidays.
 - Subsidy during initial gestation period of the recycling plant.

- Government of India in coordination with State Governments should provide the Tax exemptions/ holidays. Municipal authority that will benefit should provide subsidy while Financial Institutes should provide assistance for purchase of equipment at lower interest rates.
- Hot Recycling technique for recycling of bituminous material should be taken up for R&D. A small pilot plant should be established. Based on this experience, Hot In-situ technique should be developed. Alternatively, equipment available from abroad for Hot In-situ process may be evaluated for financial viability. Central Road Research Institute should undertake this exercise.
- Estate developers and builders undertake demolition of old buildings in urban centers to develop new complexes for residential/ commercial use. They should be educated and involved in recycling activity so that the demolition waste generated is used at the same site, leading to substantial saving in cost as follows:
 - Reduction in cost of transportation of demolition waste for disposal.
 - Reduction in material cost by utilizing recycled aggregate produced from demolition waste.
 - Savings accruing in transportation cost of raw material.
 - Estate builders and property developers should take the initiative, since they are going to benefit by way of cost reduction in their new construction project.
- Lot of demolition waste is caused by natural calamities and disasters like earthquake witnessed recently and few years ago in Kumauni/ Garhwali region. Possibility of recycling such waste for reconstruction locally should be explored with the help of International agencies having expertise in this field. Government of India/ State Governments should take the initiative and encourage local administration to explore such possibility by taking help of agencies experienced in carrying out this type of rehabilitation work.
- Necessary R&D work should be taken up for developing technology for reconstruction of houses utilizing waste from construction Industry.

Central Building Research Institute/ National Building Organization should take up this assignment. Time has arrived to accord priority to environmental pollution and sustainable development. Recycling of waste from Construction Industry achieves this objective.

10. CONCLUDING REMARKS

Though there has been extensive research carried out on recycled/ demolished waste yet there is neither simple and cost effective method nor any approved design mix theory available for use of construction and demolished waste. Though RCA can be used up to 25% to 30% replacement level of NCA without significant adverse effects on hardened, fresh and durability properties of concrete. Yet further investigations are needed to confirm the beneficial effects of RCA for more effective use in construction industry. After thoroughly reviewing the literature on RCA/RCM, the following research needs have been identified.

- To study on the potential use of RCA in the production of high strength, high performance, light weight concrete.
- To study the potential use of RCA/RCM on performance of concrete specimens by replacing coarse aggregate partially or fully.
- To study the addition of super plasticizer in improvement of workability and strength of concrete specimens prepared with RCA/RCM as coarse aggregate.
- To study the effect of aggressive chemical environment on concrete blended with RCA/RCM.
- To investigate the effect of RCA/RCM on target concrete strength on durability and fire resistance of concrete
- To study on the effect of RCA/RCM on the plastic shrinkage, rheological properties and segregation resistance of concrete.

REFERENCES

1. Press Information Bureau GOI, Ministry of Environment, Forest and Climate change March 2016
2. TIFAC –Technology Information Assessment Council, “Utilization of waste from Construction Industry ”
3. Guidelines on Environment Management of Construction and Demolished waste,” A Report of Central Pollution Control Board of India”, March 2017
4. Oikonomou, N.. Recycled concrete aggregates,. Cement & Concrete Composites, (2005) 27, 315-318.

5. Exteberria M., Vasquez E.& Mari A.R., Influence of amount of recycled coarse aggregates and production process on properties of recycled aggregate concrete, *Cement and Concrete Research*, (2007). 37, 735-742.
6. Silva R.V., De Brito J., & Dhir R.K., Properties and composition of recycled aggregates from construction and demolition waste suitable for concrete production. *Construction and Building Materials*, (2014) 65, 201-217.

Performance of Concrete with Demolished Concrete as Coarse Aggregate on Strength, Durability and Fire Resistance

S. K. Singh Gaur¹ and Sunil Kumar²

Abstract : This study analyses the suitability of demolished concrete as coarse aggregate by comparing the strength, durability and fire resistance of three different mixes MC-1, MC-2, MC-3, with 20%, 40% and 100% replacement of natural coarse aggregate with recycled coarse aggregate, for a constant water cement ratio (W/C) of 0.45 and a slump of 100 ± 20 mm, with mix M-1 made with natural aggregates (NA) and having a design mix ratio of 1:1.76:2.28 as per IS 10262. It is observed that almost same strength and durability as that of mix M-1, is obtained by mix MC-1 with 20% replacement of natural coarse aggregate (NCA) by recycled coarse aggregate (RCA). Whereas mix MC-2(40% RCA) has achieved the target strength but strength and durability reduces as the percentage of RCA is increased beyond 40%. Recycled aggregate concrete up to 40% replacement of NCA with RCA has got almost same resistance to severe weathering environment of 10000 ppm MgSO₄ solution at an age of 120 days curing in this solution. Residual compressive strength of recycled aggregate concrete (RAC) at elevated temperatures was satisfactory and comparable with the control mix.

Keywords : *Natural Coarse Aggregate (NCA); Natural Aggregate (NA); Recycled Coarse Aggregate (RCA); Recycled Aggregate Concrete (RAC); Natural Aggregate Concrete (NAC); B.I.S. Bureau of Indian Standards; Water Ratio (W/C); Polycarboxylate Ether.*

INTRODUCTION

Conventionally, sand and coarse aggregate used as concrete ingredients, are of geological origin. River sand, which is used as a natural fine aggregate in concrete and mortar production is facing problem of availability in many areas of India and abroad. Moreover, natural coarse aggregate is produced by crushing the natural rocks in crushers and producing a large quantity of stone dust as a byproduct of coarse aggregate production. This stone dust needs a lot of land fill area for disposal; thus causing environmental pollution and ecological imbalance in nature.

Moreover, many structures constructed during 1970 or before are now in need of either major repairs or possible replacement. This is because some of such structures are now reaching the end of their design life. Many other structures, either have not been constructed according to the specifications or do not receive the required maintenance while in service. A

large amount of concrete and masonry rubble is produced in demolition and maintenance of these old structures. The advantages of reusing the recycled concrete, rubble and stone dust as alternative coarse aggregate & fine aggregate respectively include lower environmental pollution, reduction in valuable land fill space and savings in natural aggregate resources. There has been increasing concern worldwide on the long-term performance of concrete. The selection of construction material should be dependent not only on the strength, dimensional stability and mechanical properties of the material, but also on its durability. The chemical attack has a variety of forms, including chloride ion permeation and the resulting corrosion of reinforcing steel, Sulphate attack carbonation, alkali aggregate reaction, leaching and efflorescence. A structure or structural element required to have fire resistance for heat transmission and failure. Fire resistance of concrete elements depend upon details of

¹Senior Lecturer, Civil Engineering, A.I.T.H., Awadhपुरi, Kanpur - 208024, India.

²Professor, Civil Engineering Department, H.B.T.U., Kanpur - 208002, India.
Email: sushil@aith.ac.in

member size, cover to steel reinforcement detailing and type of aggregate used in concrete. The current state of knowledge on durability and fire resistance of concrete made with waste aggregates such as, recycled concrete is lacking. It is envisaged that the studies to be taken up in this research work, will provide useful experimental results which will be of value in improving the quality of construction, reduce environmental pollutions and save natural aggregate resources.

LITERATURE REVIEW

Nagraj and Banu (1996) reported that by adding super plasticizers in the concrete made with rock dust and pebbles increases the workability of the concrete without increasing cement content. Tavakoli and Soroushian (1996) in their research found out that the strength of recycled aggregate concrete is affected by the strength of the demolished concrete, percentage of the coarse aggregate in the demolished concrete, the ratio of top size of aggregate in the original demolished concrete to that of the recycled aggregate, and the Los Angeles abrasion loss as well as the water absorption of the demolished recycled aggregate. Shukla et al (1998) have used stone dust as replacement for natural sand in concrete and concluded that the presence of stone dust in concrete reduces the workability of the concrete. Limbachiya et.al (2000) studied use of recycled concrete aggregate in high strength concrete. Ajdukiewlcz and Kliszczewicz (2000) have observed the mechanical properties of high performance and high strength concretes prepared by using recycled aggregates. In their work, they used recycled aggregates obtained from concrete with compressive strength 40-70 MPa. Olorunsojo and Padayachee (2002) observed the durability of concrete by replacing natural coarse aggregate with different percentages of recycled concrete aggregates (0%, 50% 100%). Gomez-Sobern (2002) investigated the porosity of recycled concrete made with substitution of recycled concrete aggregate. Sahu et.al (2003) conducted an experimental investigation for use of crushed stone dust as fine aggregate in concrete and concluded that the concrete made with different proportions of stone dust can produce concrete of comparable compressive , tensile strength and modulus of rupture and having a lower

degree of shrinkage. C. S. Poon et al (2004) revealed by scanning electron microscope that normal aggregate cement inter facial zone had mainly loose and pervious hydrates whereas high performance concrete aggregate cement inter facial zone had mainly dense hydrates. Keun-Hyeok Yang et al (2008) investigated that the properties of fresh and hardened concrete containing recycled aggregate were dependent on the relative water absorption of aggregates. A.K. Padmini and K. Ramamurthy (2009) found that parent concrete required relatively higher water cement ratio than RAC to gain a particular compressive strength. Marta Sanchez de Juan, Pilar Alaejos Gutierrez found that the attached mortar present in recycled aggregate unfavorably affects properties of RAC because mortar is a pervious material with high water absorption and lesser coefficient of Los Angeles abrasion value. Tabesh and Abdelfatah (2009) studied influence of recycled concrete aggregates on strength properties of concrete. They found in their study that compressive and splitting tensile strength of concrete made with recycled coarse aggregate depends on the mix proportions of original concrete. In general, it was concluded that the strength of the recycled aggregate concrete can be 10-25% lesser than that of the natural coarse aggregate concrete. Kou & Poon (2012) used fly ash to overcome the lower quality of recycled aggregate. They inferred from their studies that one of the practical ways to utilize a higher percentage of recycled aggregate in concrete is by replacing 25-35 % of fine aggregate by fly ash. Yehia et al (2015) observed the suitability of producing concrete with 100% replacement of NCA with recycled aggregate to fulfill the durability and strength requirements for different applications. They concluded in their study that concrete with acceptable strength and durability could be produced if one could achieve high packing density. Bhashya V, Ramersg G et al studied the effect of replacing sand with recycled fine aggregate. They found in their study that reduction in compressive and tensile strength occurs while using fine recycled concrete aggregate as replacement of natural sand. Hammad Salahuddin et al carried out experimental work to see the effect of elevated temperature on mechanical properties of recycled aggregate concrete and they found that compressive strength of RAC

reduces with increase in temperature with a comparable residual strength in RAC at different temperatures.

AIMS AND OBJECTIVES OF THE RESEARCH

It is clear from the review of earlier research work that the current state of knowledge in durability and fire resistance of concrete produced with recycled demolished concrete, is lacking in some areas and further extensive research is needed in this field. The aim of this study was to conduct an extensive experimental investigation to see the performance of recycled aggregate concrete on durability and fire resistance. The specific objectives of this research was to study the potential use of RCA on performance of concrete specimens by replacing coarse aggregate partially or fully on compressive strength in normal curing conditions and curing in aggressive chemical environment of 10000 PPM solution of MgSO₄ along with exposing the concrete samples to varying temperature ranges to investigate the durability of RAC in higher temperatures. Although, extensive work has been done on the improvement of durability and fire resistance of concrete and many researchers worked on the utilization of recycled and demolished concrete in concrete production but limited study is available on durability and fire resistance of concrete produced with recycled demolished concrete. The recycled concrete comes from different sources and is used in production of different grades of concrete. Hence, to establish a firm conclusion on use of the waste construction materials for present and future use, an extensive experimental investigation is needed involving aggregates of different sources and different aggregate gradation in producing mix proportions of different grades having long term durability and enhanced fire resistance.

RESEARCH METHODOLOGY

Test Method

The experimental program consisted of testing of all ingredients of concrete and properties of fresh and hardened concrete specimens. Cement, river sand, natural coarse aggregate, recycled demolished concrete rubbles and water were tested as per B.I.S. tests. The mechanical properties of natural and recycled aggregate were found out as per IS 383:2016. The fresh concrete was tested for workability by using slump test. Concrete specimens were tested according

to B.I.S. procedure for compressive strength comparison by taking mix M-1 (having ratios as 1:1.76:2.28 designed as per IS 10262 with use of natural aggregate) as bench mark, with the mixes MC-1, MC-2, MC-3 after a curing period 7, 28, 90 and 120 days in water (total 48 samples) and after 120 days curing in 10000 ppm MgSO₄ 7H₂O solution respectively (total 12 samples), to see the performance of processed concrete in severe environment. Magnesium sulphate solution was periodically replaced after a period of 30 days to maintain proper concentration of MgSO₄ 7H₂O. The concrete specimens were also tested for fire resistance in a diesel fired muffle furnace by exposing the concrete samples to fire for a period of one hour duration to varying temperatures of 2000C, 4000C, 6000C and 800 0C respectively (total 48 samples) and then allowed to cool in air to attain normal room temperature before compressive strength testing.

Aggregate Gradation

The recycled concrete aggregate was obtained from the different demolition sites. For consistency, the recycled concrete aggregate was crushed to 20 mm down size with the help of jaw crushers in stages and the gradation of RCA, NCA and sand was assured by standard sieve analysis as per IS 383:2016.

Material Used in Research Work

- I. Cement : PPC conforming to IS 1489
- II. Sand : Obtained from Betwa river (Conforming to zone II)
- III. Coarse aggregate : Obtained from Kabrai crusher (As per gradation chart *figure 1*)
- IV. Demolished concrete (RCA) : Obtained from local demolished sites
- V. MgSO₄ 7H₂O: 10,000 ppm concentration
- VI. Admixture : Polycarboxylate ether (conforming to IS-9103)

Properties of Ingredients

Properties of different ingredients were calculated as per B.I.S. are and given in *Table 1*:

Mix Proportions

In order to compare results objectively, a control mix M-1 (prepared with NA) having a design mix ratio of 1:1.76:2.28 as per IS 10262, was needed as a benchmark to compare the results with mixes MC-1 (80%NCA, 20%RCA), MC-2 (60%NCA, 40%RCA), and MC-3 (0%NCA, 100%RCA).

All concrete mixes were proportioned for 100 ±20 mm slump suitable for pumping with a constant w/c of 0.45 for all four mixes as per Table 2. Admixture conforming to IS 9103 (polycarboxylate ether) was used in different concrete mixes to maintain the desired slump.

Experimental Design

Total 108 number of cubes with size 100mm x 100mm

x100mm were casted for testing durability and fire resistance of mixes M-1(100%NCA), MC-1 (80%NCA and 20%RCA), MC-2 (60%NCA and 40%RCA),MC-3 (0%NCA and 100%RCA).

RESULTS AND DISCUSSION

Dose of admixture was observed to obtain the desired slump of 100±20 mm for different mixes M-1, MC-1, MC-2, MC-3 and compressive strength of all samples

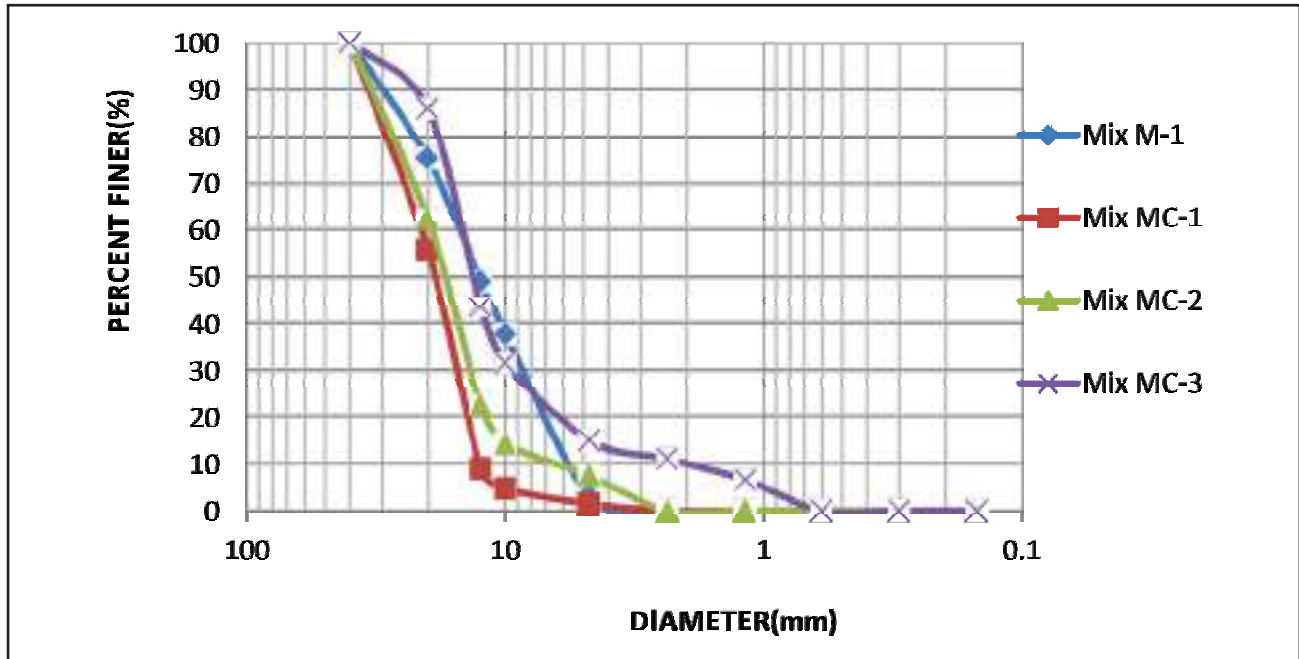


Figure 1 : Gradation Curves for Different Mixes Obtained After Sieve Analysis

Table 1: Properties of Sand, NCA, RCA Used in Present Research Work

Ingredients	Properties										Remark
	Normal Consistency (%)	Setting Time (min)		Compressive Strength (Mpa)		Specific Gravity	Bulk Density (kg/m ³)	Fineness Modulus	Water Absorption (%)	Sieving Zone	
		Initial	Final	7 days	28 days						
Cement (PPC)	31.5	185	315	32.7	41.4	3.15	-	-	-	-	Conforming to IS 1489
Fine Aggregate (Natural Sand)	-	-	-	-	-	2.68	1690	3.03	1.0	II	As per IS 383
Natural Coarse Aggregate	-	-	-	-	-	2.75	1490	7.35	0.5	-	-
Recycled Coarse Aggregate	-	-	-	-	-	2.72	1537	7.07	4.32	-	-

Table 2: Concrete Mix Ratios Adopted in Present Research Work

Mix ID	Cement (kg/m ³)(PPC)	Fine Aggregate (kg/m ³)	Coarse Aggregate (kg/m ³)		Water (kg/m ³)	W/C Ratio	Admix % weight of Cement
			NCA	RCA			
M-1(100% NCA)	437	772	1000	-	197	0.45	0.17
MC-1(80%NCA 20% RCA)	437	772	800	198	197	0.45	0.30
MC-2(60%NCA 40% RCA)	437	772	600	396	197	0.45	0.43
MC-3(100%RCA)	437	772	-	989	197	0.45	0.74

Table 3: Compressive Strength Test Results for Different Mixes in Water Curing

Mix ID	Compressive Strength at Different Curing Periods			
	7 Days	28 Days	90 Days	120 Days
M-1	30.33	41.67	43.50	44.83
MC-1	27.67	40.67	42.50	46.33
MC-2	16.00	30.33	33.50	37.59
MC- 3	16.00	28.16	32.16	34.00
Mean	23.90	35.20	37.90	40.7
Std. Deviation	6.00	6.54	5.56	5.45

Table 4: Compressive Strength for Different Mixes Exposed to 10000ppm MgSO₄.7H₂O Solution

Mix ID	Compressive Strength in water after 120 days of curing	Compressive Strength in 1000 ppm solution after 120 days of curing	% Reduction in Compressive Strength
M-1	44.83	41.50	7.43
MC-1	46.33	43.33	6.48
MC-2	37.59	34.66	7.80
MC-3	34.00	30.33	10.80

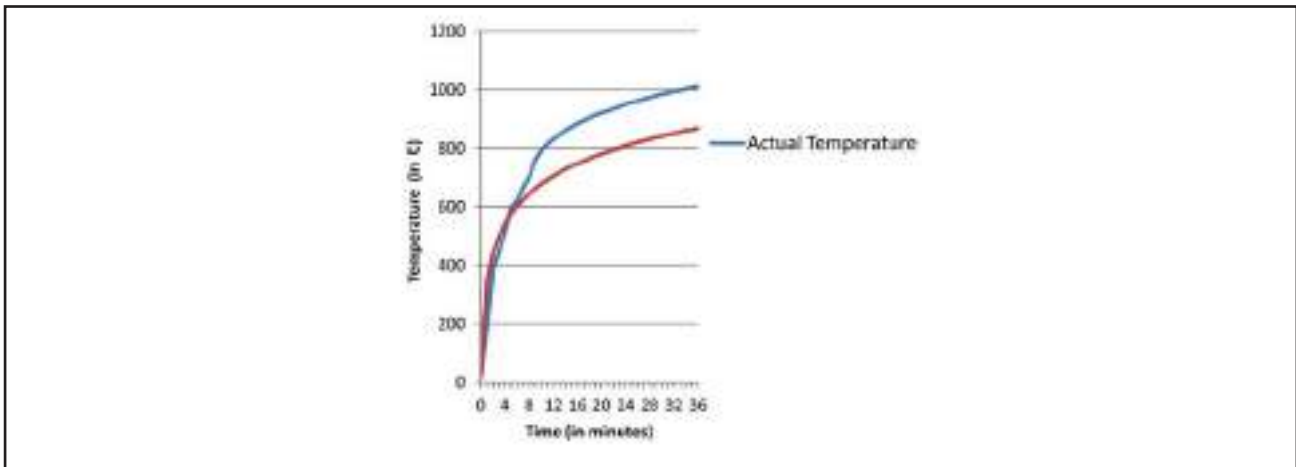


Figure. 2: Actual and Standard Fire Curves for Measuring Fire Resistance of Different Mixes

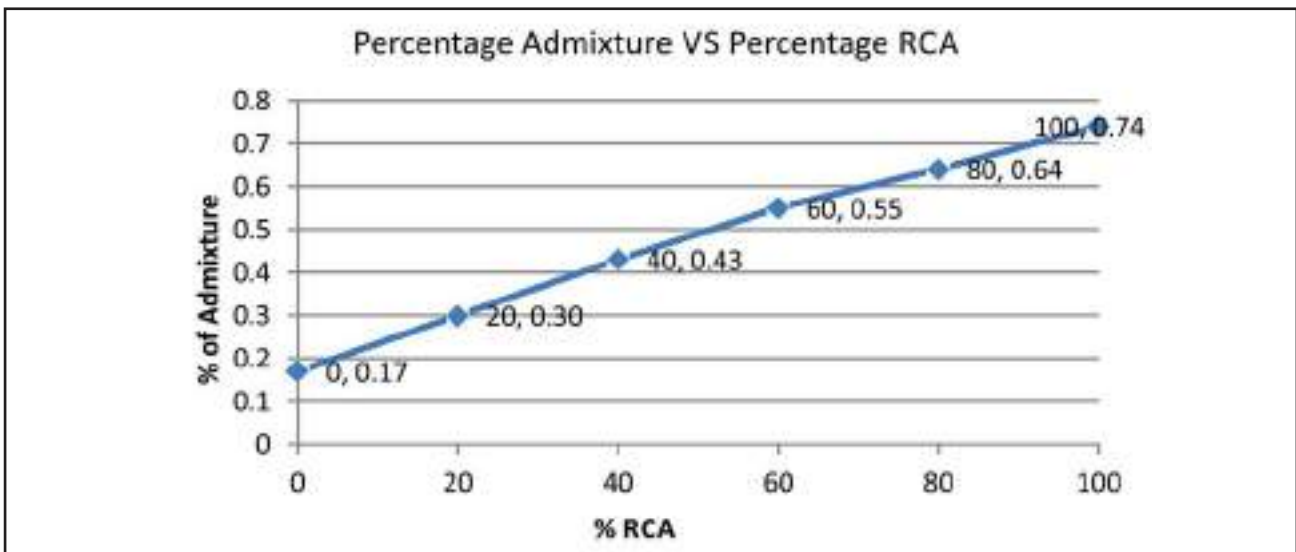


Figure 3: Dose of Admixture Required for a Slump of 100 ± 20 mm

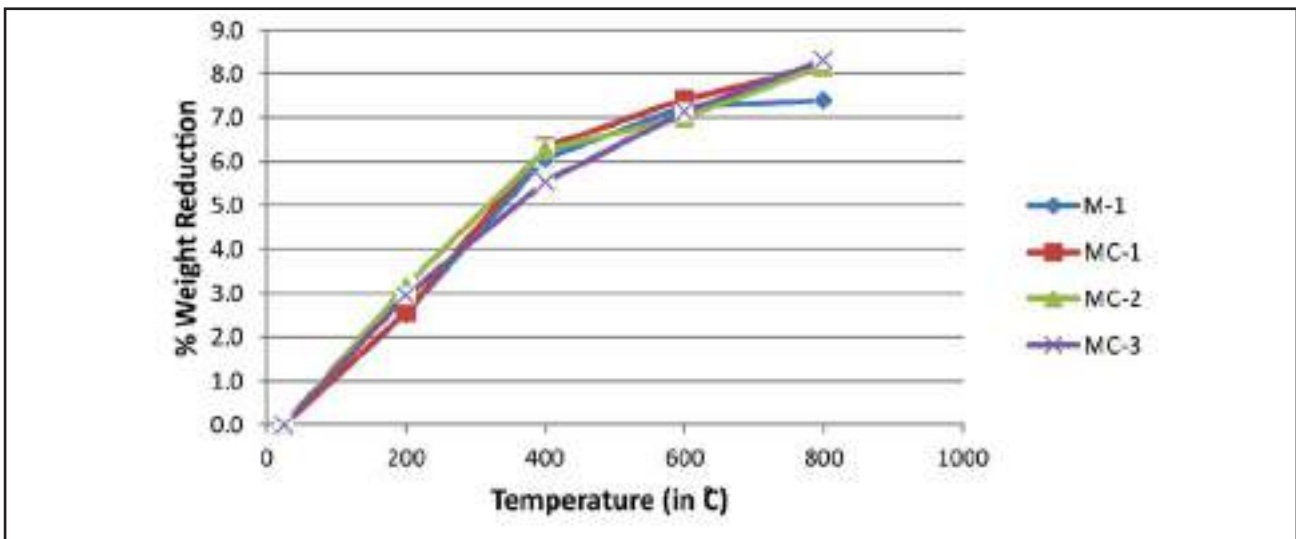
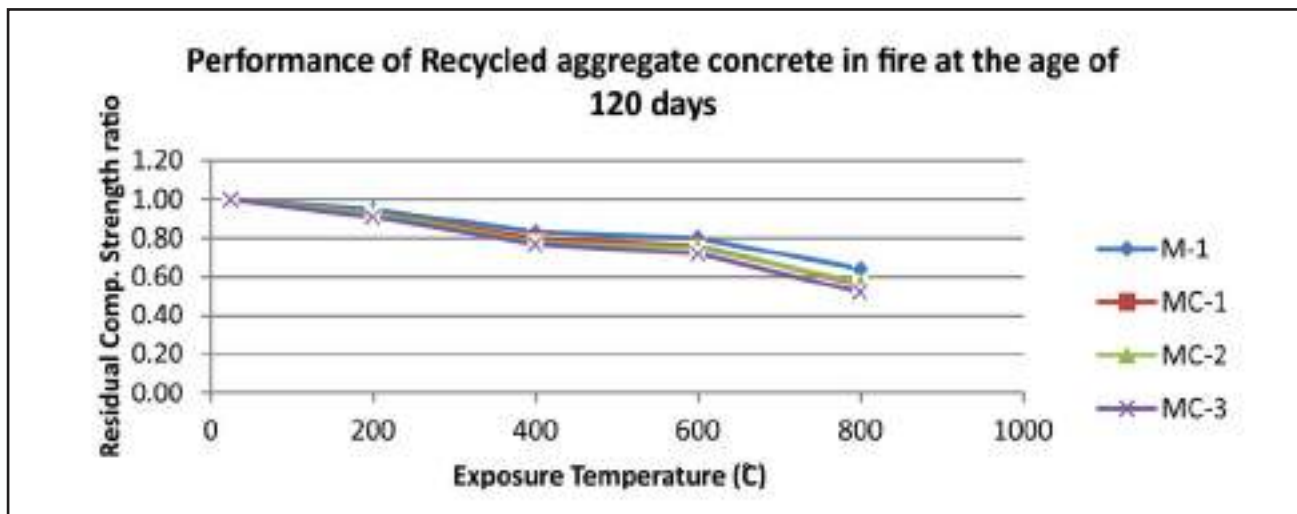


Figure 4: Reduction in Weight with Temperature for Different Mixes

Table 5: Compressive Strength for Different Mixes at Different Temperatures

Performance of Recycled Aggregate Concrete in Fire at the Age of 120 Days										
Mix	Comp. Strength room temp (N/mm ²)	At room Temp	At 200°C		At 400°C		At 600°C		At 800°C	
		Residual Comp. Strength Ratio	Comp. Strength (N/mm ²)	Residual Comp. Strength Ratio	Comp. Strength (N/mm ²)	Residual Comp. Strength Ratio	Comp. Strength (N/mm ²)	Residual Comp. Strength Ratio	Comp. Strength (N/mm ²)	Residual Comp. Strength Ratio
M-1	44.83	1.00	42.67	0.95	37.33	0.83	36.00	0.80	28.50	0.64
MC-1	46.33	1.00	43.16	0.93	37.00	0.80	35.00	0.76	26.00	0.56
MC-2	37.67	1.00	35.00	0.93	29.50	0.78	28.33	0.75	21.50	0.57
MC-3	34.00	1.00	31.00	0.91	26.33	0.77	24.50	0.72	17.67	0.52

**Figure 5: Residual Compressive Strength Ratio at Different Temperature for Different Mixes**

was found out in a compression testing machine of 100 tonne capacity after a curing period of 7, 28, 90 and 120 days in water and after 120 days curing in 10000 ppm MgSO₄.7H₂O Solution respectively, to see the performance of the processed concrete in severe environment. PPC was used in this research work, which has a slower rate of hydration in comparison to OPC and RCA was used as a substitute for NCA, which had adhered mortar and having high water absorption of 4.32%, thus further reducing the hydration process of concrete. At the same time, to visualize the weathering action of MgSO₄ solution, a considerable long period was needed. Therefore, a curing period of 120 days was adopted in this research work. The concrete specimens were also tested for fire resistance in a diesel fired muffle furnace exposed to

fire as per actual fire as shown in fire diagram, for a period of one hour duration to varying temperatures of 2000C, 4000C, 6000C and 800 0C respectively.

Dose of Admixture for Different Mixes

It was observed that the dose of admixture increases as percentage of replacement of RCA increases to achieve the same workability (pumpable concrete with 100 ±20 mm slump) with 0.45 as W/C ratio for all mixes. Increased dose of admixture is required as RCA has previously adhered mortar and having angular aggregates which reduce the workability of RAC in comparison to NAC. Thus, requiring an increased dose of admixture with increase in percentage of RCA to attain same level of workability.

Compressive Strength

The results of compressive strength for different mixes

after a curing period of 7, 28, 90 and 120 days are shown in table 3. It is observed from the table that the compressive strength for all mixes increases as curing period is increased. Rate of strength growth for all mixes is high, i.e., up to 28 days and a lesser growth rate is observed later on in all cases. Mix MC-1 shows almost same compressive strength as mix M-1 and it achieved 3.35% higher strength at 120 days curing. This increase in compressive strength probably occurred due to better interlocking of angular aggregate of recycled concrete with concrete paste. Whereas mixes MC-2, MC-3 have shown a reduction in compressive strength of 47.25% at 7 days curing, which subsequently reduces to 16.15% and 24.16% respectively, for 120 days curing period. Mix MC-2 has almost achieved the target strength at 120 days with initially a low compressive strength of 16 N/mm², which implies that desired compressive strength is achievable up to 40% replacement of NCA with RCA for a characteristic strength of 30 N/mm². It is seen from the data that as percentage of RCA is increased, there is a considerable loss in initial compressive strength but as the age of concrete increases, this loss reduces, thus showing a retarded growth of compressive strength due to presence of adhered mortar with recycled concrete aggregate needing more water for chemical reaction. Strength loss in RAC beyond 20% increase of RCA occurred due to adhered mortar having a lesser crushing strength as compared to virgin aggregate.

Magnesium Sulphate Attack

All four mixes were exposed to 10000 ppm MgSO₄.7H₂O solution for a period of 120 days. It was observed from test data that mix M-1, MC-1 and MC-2 show almost same resistance to severe Sulphate attack. Mix MC-3(100% RCA) shows a high percentage deterioration in comparison to Mix M-1(100% NCA). It is indicative of the fact that in this duration, concrete up to 40% replacement of NCA with RCA has got equally good resistance to severe Sulphate attack as NCA concrete.

Fire Resistance

Samples of all four mixes were exposed to fire in varying temperature ranges of 200°C, 400°C, 600°C and 800°C for a period one hour duration. The weight loss of all samples was observed after cooling

the samples to room temperature and results were plotted in figure 4. It was observed that all four mixes show a loss of weight varying between 2.55% to 3.17% for an exposure temperature of 200°C with no visible cracks on specimen surface. At a temperature of 400°C, there occurred a loss of weight varying between 5.53% to 6.32% due to loss of moisture, with no visible cracks on surface of the samples. At 600°C temperature, average percentage loss in weight of samples was around 7% with fine hair cracks on samples of all four mixes along with a change in colour of samples from greyish to whitish colour. At 800°C temperature, samples of all mixes showed a decrease of around 8% in weight and the colour of samples was almost white with visible cracks on surfaces. It was also observed from the test data of samples as shown in table 5 that there occurred no significant loss in compressive strength up to 200°C, with minimum 4.82% loss for reference mix and maximum 8.82% loss for mix MC-3 made up with 100% RCA. At a temperature of 400°C, maximum loss of 22.56% in compressive strength occurred in Mix MC-3 with decreasing loss in strength of 21.69%, 20.14% 16.73% for mix MC-2, MC-1 and M-1 respectively. At 600°C temperature, % loss in compressive strength was observed as 19.7%, 24.45%, 24.79% and 27.94% for mixes M-1, MC-1, MC-2 and MC-3 respectively. Indicating that as percentage of RCA increases, fire resistance is decreases. At 800°C temperature, percentage loss in compressive strength was observed as 36.43%, 43.88%, 42.93% and 48.03% for mixes M-1, MC-1, MC-2 and MC-3 respectively. In this temperature range spalling and visible cracks were seen in samples of all four mixes, thus showing that at about 800°C, concrete had lost almost 40% to 50% of its virgin compressive strength thus making it not usable for major structural works as upper surface of the sample was almost burnt irrespective of the percentage replacement of NCA with RCA.

CONCLUSIONS

In this research work, experimental work was carried out to see the performance of concrete made with varying percentages (0%, 20%, 40% and 100%) of RCA for a controlled w/c of 0.45 and 100 ±20 mm slump, on strength, durability and fire resistance after 120 days curing in water and 10000 ppm

MgSO₄.7H₂O solution respectively. Fire resistance was also observed at different temperature ranges after exposing the samples to fire for a period of one hour. The following conclusions are inferred from the experimental research work:

- Concrete made with RCA up to 40% replacement of NCA found to achieve the desired target strength in 120 days curing in water and for a higher percent replacement of NCA with RCA (up to 100 % replacement) showed to have a concrete of 75% target strength of design mix.
- At the same curing period of 120 days in 10000 ppm solution of Magnesium Sulphate with cyclic replacement of solution after 30 days, (to maintain consistent SO₄⁻ concentration) recycled aggregate concrete showed almost same resistance to this environment up to 40% replacement of NCA with RCA.
- As the percentage replacement of RCA increases, compressive strength of recycled aggregate concrete reduces at all exposure temperature ranges.
- NAC showed slightly less mass loss as compared to RAC, when exposed to fire. Mass loss was 2.55% for mix M-1(100 % NCA) and 2.95% for mix MC-3 (100% RCA) at a temperature of 200°C, whereas it was observed 7.39% for mix M-1 and 8.32% for mix MC-3 at an elevated temperature of 800°C.
- Residual compressive strength of recycled concrete at different elevated temperature ranges was comparable with the control mix.

Acknowledgment

The authors are thankful to Harcourt Butler Technical University for providing laboratory facilities for performing this research work.

References

- Padmini, A. K., Ramamurthy, K., & Mathews, M. S. (2009). Influence of parent concrete on the properties of recycled aggregate concrete. *Construction and Building Materials*, 23(2), 829-836.
- Sahu, A. K., Kumar, S., & Sachan, A. K. (2003). Crushed stone waste as fine aggregate for concrete. *Indian concrete journal*, 77(1), 845-848.
- Ajdkiewicz, A., & Kliszczewicz, A. (2002). Influence of recycled aggregates on mechanical properties of HS/HPC. *Cement and concrete composites*, 24(2), 269-279.
- Bhashya V, Ramersg G et al (2020). Performance evaluation of concrete by using recycled aggregate ICJ Vol.94, No. 1, pp. 51-57.
- Poon, C. S., Shui, Z. H., & Lam, L. (2004). Effect of microstructure of ITZ on compressive strength of concrete prepared with recycled aggregates. *Construction and Building Materials*, 18(6), 461-468.
- Olorunsogo, F. T., & Padayachee, N. (2002). Performance of recycled aggregate concrete monitored by durability indexes. *Cement and concrete research*, 32(2), 179-185.
- Gómez-Soberón, J. M. (2002). Porosity of recycled concrete with substitution of recycled concrete aggregate: An experimental study. *Cement and concrete research*, 32(8), 1301-1311.
- Salahuddin, H., Nawaz, A., Maqsoom, A., & Mehmood, T. (2019). Effects of elevated temperature on performance of recycled coarse aggregate concrete. *Construction and Building Materials*, 202, 415-425.
- Yehia, S., Helal, K., Abusharkh, A., Zaher, A., & Istaitiyeh, H. (2015). Strength and durability evaluation of recycled aggregate concrete. *International journal of concrete structures and materials*, 9(2), 219-239.
- Shyam Prakash, K., & Rao, C. H. (2016). Study on compressive strength of quarry dust as fine aggregate in concrete. *Advances in Civil Engineering*, 2016.
- Yang, K. H., Chung, H. S., & Ashour, A. F. (2008). Influence of Type and Replacement Level of Recycled Aggregates on Concrete Properties.
- Kou, S. C., & Poon, C. S. (2012). Enhancing the durability properties of concrete prepared with coarse recycled aggregate. *Construction and building materials*, 35, 69-76.
- Limbachiya, M. C., Leelawat, T., & Dhir, R. K. (2000). Use of recycled concrete aggregate in high-strength concrete. *Materials and structures*, 33(9), 574-580.
- Marta Sanchez de Juan, Pilar Alaejos Gutierrez, (2009). Study on the influence of attached mortar content on the properties of recycled concrete aggregate, *Construction and Building Material* 23, 872-877.
- Nagaraj, T. S., & Banu, Z. (1996). Efficient utilization of rock dust and pebbles as aggregates in Portland cement concrete.
- Tabsh, S. W., & Abdelfatah, A. S. (2009). Influence of recycled concrete aggregates on strength properties of concrete. *Construction and building materials*, 23(2), 1163-1167.
- Shukla, M., Sahu, A. K., & Sachan, A. K. (1998). Performance of Stone dust as fine aggregate replacing sand in concrete and mortar. In *National Seminar on Advances in Special concretes Indian Concrete Institute* (pp. 241-248).
- Tavakoli, M., & Soroushian, P. (1996). Strengths of recycled aggregate concrete made using field-demolished concrete as aggregate. *Materials Journal*, 93(2), 178-181.



Mathematical models for performance of concrete by replacing natural sand with stone dust

Er. S. K. Singh Gaur¹, Dr. Sunil Kumar²

¹Senior Lecturer, Civil Engineering,
A.I.T.H. Awadhपुरi, Kanpur,
sushil@aith.ac.in

²Professor, Civil Engineering
H.B.T.U., Kanpur,
suniljaddon@live.in

Abstract: This study is carried out to evaluate the performance of concrete by replacing natural sand with granite stone dust. Compressive strength of concrete was observed by replacing natural sand with granite stone dust in ratio of 20%, 40% and 100% for a constant W/C of 0.45 and a slump of 100 ±20 mm to have pump able properties in concrete. A total of four concrete mixes MS-1, MS-2, MS-3 (with 20%, 40% and 100% replacement of natural sand) including a reference mix M-1 (having 100% natural fine aggregate) with a design mix ratio of 1:1.76:2.28 as per IS 10262, were casted. Mechanical properties of NA and stone dust were studied and different concrete mixes were tested for compressive strength after 7, 28, 90 and 120 days of water curing. Samples of all four mixes were also subjected to different temperature ranges of 200°C, 400°C, 600°C and 800°C for duration of one hour after a curing period of 120 days. A mathematical model was developed to observe the compressive strength for different replacement ratios of sand with stone dust at different age and at different temperature exposures and it was observed that age of concrete has a positive correlation with strength whereas % replacement of sand and temperature has a negative effect on strength.

Keywords: Natural coarse aggregate NCA, natural aggregate NA, Green concrete, Construction and demolition waste (C & D waste), Stone dust, Recycled aggregate concrete RAC, Polycarboxylate ether.

(Article history: Received: 16th October 2021 and accepted 21st December 2021)

I. INTRODUCTION

Construction of new structures due to rapid advancement of cities require a huge amount of natural aggregates, which in turn produce several types of ecological imbalances due to blasting, quarrying, transportation etc. The construction industry in India is growing very fast at an annual rate of 10% over last 10 years, as against the world average of 5.5% per annum. The built up area is expected to increase almost five times from 21 billion sqft to approximately 104 billion sqft in 2030 as per C.S.E. report [1]. In order to fetch the demand of new construction a lot of natural resources are needed. On the other hand demolition of old structures due to over ageing, changes in architectural and functional requirements along with natural disasters produce a substantial amount of construction waste, which is generally stacked in form of landfills.

According to the Building Material Promotion Council (BMPTC), India generates an estimated 150 million MT of construction and demolition (C&D) waste every year as against the official recycling of 6500 MT per day, which is about 1.5% of total waste generated per day. The rest of the waste lies in form of landfills. With increasing demand of natural aggregates for new construction and huge amount of landfills required for construction wastes, generated by demolition activities creates an ecological imbalance thus creating the concept of green concrete by use of recycled construction waste. The advantages of reusing the recycled

concrete, rubble & stone dust as alternative coarse & fine aggregate respectively include lower environmental pollution, reduction in valuable land fill space and savings in natural aggregate resources. The use of old construction material in new projects is not a new concept. The recycling industry has become well established in Europe since the end of World War II. In Europe about 30% of demolished waste is recycled. Some other countries like Netherland and Belgium have achieved recycling rates of 90% [2]. In India 53 cities were expected to set up recycling facilities to recover materials from C&D wastes by 2017, but only 13 cities have done that by 2020 [1]. Keeping the global scenario in mind and to have a proper balance of demand of aggregates in construction works, Indian government has taken strong steps by forming guidelines on environment management of construction and demolition wastes under the guidance of Ministry of Environment, Forest and Climate change. In order to create confidence in different sectors of construction industry, it is essential to look after the viability of use of C & D waste in new construction works. Though stone dust is used as a replacement for sand in India for non structural members, but to use stone dust as a substitute of natural sand, in major works, there is a need for proper assessment of strength properties of hardened concrete in ordinary as well as under exposure to high temperature conditions.

II. REVIEW OF LITERATURE WORK

Keeping in view the significance of the research work and problems associated, efforts have been made to review

the literature available on various aspects of the research. Only a few researchers have worked on concrete made with inert and waste materials like stone dust, recycled demolished concrete/ masonry rubbles, glass etc. Frondistou-Yann's evaluated and compared the mechanical properties of conventional concrete and concrete made from recycled concrete. He found that recycled concrete best matches the mechanical behavior of conventional concrete^[3]. Nagraj and Banu 1996 reported that the addition of super plasticizers in concrete made with rock dust and pebbles enhance the workability of the mix without enhancing cement content^[4]. Test results by Tavakoli and Soroushian (1996) indicated that the strength of recycled aggregate concrete was affected by the strength of the original concrete, percentage of the coarse aggregate in the original concrete, the ratio of top size of aggregate in the original concrete to that of the recycled aggregate, and the Los Angeles abrasion loss as well as the water absorption of the recycled aggregate^[5]. Shukla et al (1998) have used stone dust as fine aggregate replacing sand in concrete and concluded that the presence of stone dust reduces the workability of concrete^[6]. Limbachiya et al (2000) studied use of recycled concrete aggregate in high strength concrete^[7]. Ajdukiewicz and Kliszczewicz (2000) examined the mechanical properties of high performance and high strength concretes made with recycled aggregates. In their work, they considered recycled aggregates produced from concrete with compressive strength 40-70 Mpa^[8]. Sunil kumar, Sahu a.k. and Sachan a.k., (2003) investigated the effect of partial replacement of river sand with crushed stone dust at a replacement level of 20%, 40% on compressive strength of concrete. They observed that there was a significant increase in compressive strength of concrete in both the replacement levels of natural sand with stone dust. They further observed that there was a significant increase in splitting tensile strength of concrete in both the replacement levels of natural sand with stone dust.^[9] Tabesh and Abdelfatah (2009) studied influence of recycled concrete aggregates on strength properties of concrete. The compressive and splitting tensile strength of concrete made with recycled coarse aggregate depend on the mix proportions. In general it was observed that the strength of recycled concrete can be 10-25% lower than that of conventional concrete made with natural coarse aggregate^[21]. Yehia et al (2015) discussed the suitability of producing concrete with 100% recycled aggregate to meet durability and strength requirements for different applications. Their results showed that concrete with acceptable strength and durability could be produced if high packing density is achieved^[12]. The durability aspect and fire resistance of concrete has been studied by many researchers in the past decades^[10,13]. Vijayalakshmi et.al. (2013) investigated the effect of replacement of river sand with granite powder on splitting tensile strength of concrete at a replacement level from 0% to 25% at 28 days of curing. They observed that inclusion of granite powder as a replacement of river sand did not much affect the splitting tensile strength at lower replacement levels of 5%, 10% and 15%. At these replacement levels, the splitting tensile strength was similar or slightly lower than that of control concrete. However, increase in substitution rate beyond 15%, there was a significant decrease in splitting tensile strength of concrete^[11].

On the basis of literature review, it was observed that no mathematical relationship was found to assess the compressive strength of concrete with variable % of stone dust along with age and different temperature ranges.

Therefore a regressive experimental analysis was carried out to establish a relationship for compressive strength of green concrete with varying age, different % of stone dust and varying temperature ranges.

III. METHODOLOGY OF RESEARCH WORK

A. Test method

The experimental program consisted of testing of all ingredients of concrete and properties of fresh and hardened concrete specimens. Cement, river sand, natural coarse aggregate, recycled concrete, water were tested as per B.I.S. procedures. The mechanical properties of aggregates were found out as per IS 383:2016. The fresh concrete was tested for workability by using slump test. The hardened concrete tests consisted of testing of concrete cubes specimens at the age of 7, 28, 90 and 120 days in accordance with the relevant method of testing recommended by B.I.S. by taking M-1 mix (1:1.76:2.28 designed as per IS 10262 with use of natural aggregates) as bench mark, with the mixes MS-1(20% stone dust), MS-2(40% stone dust), MS-3(100% stone dust), The concrete specimens were also tested for fire resistance in a diesel fired muffle furnace exposed to actual fire as per plotted fire exposure curve, for a period of one hour duration to varying temperatures of 200⁰C, 400⁰C, 600⁰C and 800⁰C respectively and then allowed to cool in air to attain normal room temperature before compressive strength testing.

B. Aggregate gradation

The gradation of natural aggregates and stone dust was assured by standard sieve analysis as per IS 383:2016. As per sieve analysis sand and stone dust both belongs to Zone II and were having fineness modulus as 3.03 and 2.28 respectively.

C. Material used in research work

- | | |
|---------------------|---|
| 1) Cement | : PPC conforming to IS 1489 |
| 2) Sand | : Obtained from Betwa river (Conforming to zone II) |
| 3) Coarse aggregate | : Obtained from Kabrai crusher |
| 4) Admixture | : polycarboxylate ether (conforming to IS-9103) |

D. Properties of ingredients

Properties of different ingredients were calculated as per B.I.S. and given in table-1.

TABLE 1. PROPERTIES OF SAND, NCA, STONE DUST USED IN PRESENT RESEARCH WORK

Ingredients	Properties										Remark
	Normal consistency (%)	Setting time (min)		Compressive strength (Mpa)		Specific gravity	Bulk density (kg/m ³)	Fineness modulus	Water absorption (%)	Sieving zone	
		Initial	Final	7 days	28 days						
Cement	31.5	185	315	32.7	41.4	-	-	-	-	-	Conforming to IS 1489
Fine aggregate (natural sand)	-	-	-	-	-	2.68	1690	3.03	1.0	II	As per IS 383
Stone dust	-	-	-	-	-	2.70	1595	2.28	8.03	II	As per IS 383
Natural coarse aggregate	-	-	-	-	-	2.75	1490	7.35	0.5	-	-

E. Mix proportions

In order to compare results objectively, a control mix M-1 (prepared with NA) having a characteristic strength $f_{ck}=30\text{MPa}$, and a mean target strength $f'_{ck} = 38.25 \text{ MPa}$ was needed as benchmark to compare the results with mixes MS-1(80% sand, 20% stonedust), MS-2(60% sand, 40% stonedust), and MS-3(0% sand, 100%

stonedust). All concrete mixes were proportioned for 100 ± 20 mm slump suitable for pumping with a constant W/C of 0.45 for all four mixes as per table-2. Admixture conforming to IS 9103 (Polycarboxylate ether) was used in different concrete mixes to maintain the desired slump.

TABLE 2. CONCRETE MIX RATIOS ADOPTED IN PRESENT RESEARCH WORK

Mix ID	Cement (kg/m ³)	Coarse Aggregate (kg/m ³)	Fine Aggregate (kg/m ³)		Water (kg/m ³)	W/C Ratio	Admix % weight of cement
			Sand	Stone dust			
M-1(100% NCA)	437	1000	772	-	197	0.45	0.17
MS-1(80% sand 20% stone dust)	437	1000	618	156	197	0.45	0.21
MS-2(60% sand 40% stone dust)	437	1000	464	312	197	0.45	0.33
MS-3(100% stone dust)	437	1000	-	780	197	0.45	0.63

F. Testing of specimens

Total 96 numbers of cubes with size 100mmX100mmX100mm were casted for finding out a mathematical model for compressive strength with variable % of stone dust and curing age along with exposure of hardened concrete to varying range of fire temperature as per exposure curve shown in figure 1. Twelve beams (including 3 number of beams of reference mix M-1) of size 100mmx100mmx500mm each casted and cured for 28 days for finding out flexural strength of green concrete.

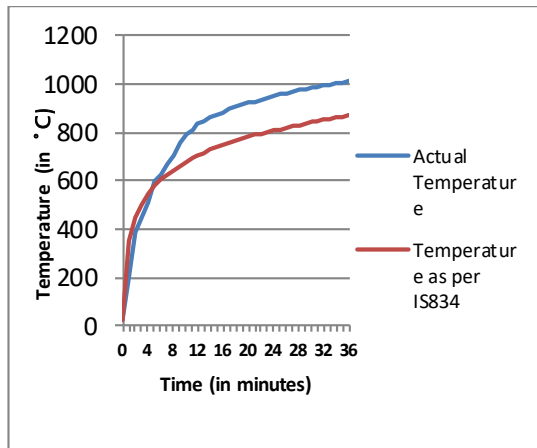


Fig. 1. Actual and standard fire curves for different mix analysis

IV. RESULTS AND DISCUSSION

Effect of admixture was seen to obtain desired slump of 100±20 mm for different mixes M-1, MS-1, MS-2, MS-3 and compressive strength of all samples was found out in a compression testing machine of 100 tonne capacity after a curing period of 7,28,90 and 120 days in water to see the performance of processed concrete. The concrete specimens were also tested for fire resistance in a diesel fired muffle furnace exposed to actual fire for a period of one hour duration to varying temperatures of 200°C,400°C, 600°C and 800 °C respectively and then cooling down to room temperature before compressive strength testing.

A. Dose of admixture for different mixes

It was observed that dose of admixture increases as % of replacement of stone dust increases to achieve same workability (pump able concrete with 100 ±20 mm slump) with 0.45 as W/C ratio for all mixes.

B. Compressive Strength

The results of compressive strength for different mixes after a curing period of 7, 28, 90 and 120 days are shown in table 3. It is observed from the table that compressive strength for all mixes increases as curing period is increased.

TABLE 3. COMPRESSIVE STRENGTH TEST RESULTS FOR DIFFERENT MIXES IN WATER CURING

Mix Designation	7 days		28 days		90 days		120days	
	Density	Comp. Str.	Density	Comp. Str.	Density	Comp. Str.	Density	Comp. Str.
M-1	2515	28.0	2565	41.0	2455	44.5	2505	46.0
	2520	32.0	2575	40.0	2405	42.0	2520	43.0
	2565	31.0	2605	44.0	2505	44.0	2565	45.5
MS-1	2451	30.0	2455	42.0	2435	48.0	2460	50.0
	2453	32.0	2451	44.0	2445	43.5	2453	47.0
	2455	28.0	2456	41.5	2450	45.0	2450	48.0
MS-2	2460	38.0	2465	46.0	2465	49.0	2455	54.0
	2458	36.0	2460	42.0	2455	48.0	2460	52.0
	2456	32.5	2452	43.0	2460	47.0	2465	49.0
MS-3	2459	23.0	2465	36.5	2463	43.5	2470	44.0

	2463	21.5	2463	40.0	2465	41.0	2456	42.0
	2467	20.0	2455	39.0	2467	40.0	2460	41.0

A total of 48 test samples were tested for compressive strength with varying % of stone dust along with varying curing period in days. A multiple variable regression analysis was performed by taking % of stone dust, curing period in days and density of different samples in Kg/m³ as independent variables. After regression analysis it was found that density of samples does not have a good correlation with compressive strength. Therefore it was left in further analysis and only two independent variables were considered and we found following mathematical model for compressive strength of green concrete:-

$f_{cc} = 34.78 + 0.127 A - 0.0495 S$, where A is age in days & S is % of stone dust as substitute for natural sand.

$R = 0.787, R^2 = 0.619$ (valid for 0% to 100% replacement level of stone dust and up to 120 days age)

A total of 60 compressive strength tests were performed for obtaining a correlation between compressive strength as dependent variable and replacement percentage of sand and temperature as independent variables for a curing age of 120 days and 0% to 100% replacement level of sand with stone dust and for a temperature range of room temperature to 800^oc.

$$f_{cc} = 50.47 - 0.0254T - 0.0646S$$

(valid for 0% to 100% replacement of sand & for room temp. to 800^oC)

$R = 0.922, R^2 = 0.851$ where T is temp. in ^oc and S is % of Stone dust as substitute for natural sand.

C. Mathematical model for flexural strength of concrete obtained by substituting sand with stone dust

Flexural strength of green concrete was calculated experimentally with help of 12 beams (including 3 number of beams of reference mix M-1) of size 100mmx100mmx500mm each casted and cured for 28 days by substituting natural fine aggregate (sand) with C&D waste granite stone dust in ratio of 20% (MS-1), 40% (MS-2) and 100% (MS-3).

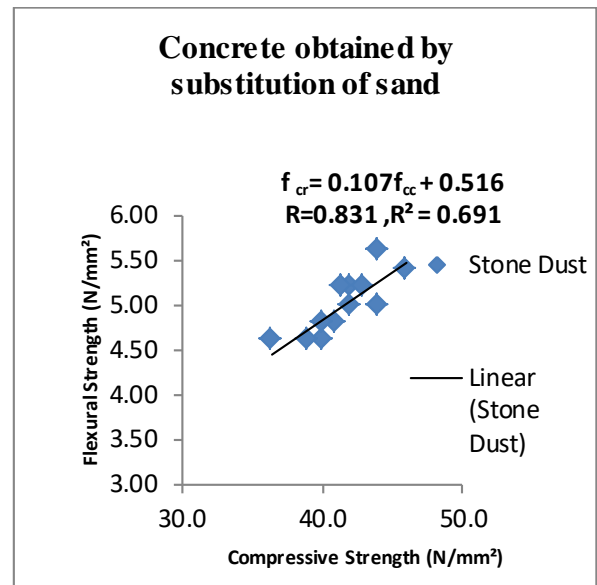


Fig. 2. Flexural. Strength VS Comp. strength for MS-1, MS-2 & MS-3 mix concrete

A better flexural strength in comparison to NAC is observed experimentally in case of substitution of sand with stone dust and justified with empirical formula. A larger % difference was observed between experimental values and values obtained by formula recommended by IS code, in case of concrete obtained by substituting sand with stone dust.

V. CONCLUSIONS

From the experimental results and by further multivariable mathematical regression analyses following conclusions have been drawn:

- For a particular W/C ratio, workability of green concrete reduces with increase in % of stone dust and desired workability is achievable by addition of admixture. The dose of admixture increases with increase in % of stone dust.
- Effect of age of green concrete has got a positive correlation with compressive strength and it is found that one day increase in age of green concrete increases compressive strength by 0.127 MPa. Whereas by 1% increase in stone dust quantity, compressive strength of green concrete decreases by 0.0495 MPa, which shows that 100% sand can be successfully replaced with stone dust with only 4.95% strength reduction in compressive strength.
- Better flexural strength was observed in case of green concrete, therefore it is concluded from present research work that sand can be economically substituted with stone dust up to 40 % replacement values and yielding

better strength properties as can be calculated from empirical formulae obtained in research work.

- Temperature as well as % of stone dust has a negative correlation with compressive strength. It is found that by 1⁰C increase in temperature, compressive strength of green concrete reduces by 0.0254 MPa and a unit % increase in stone dust quantity, reduces the compressive strength of green concrete by 0.0646 MPa at higher temperature which shows that when 100% sand was replaced with stone dust then only 6.46 % reduction in compressive strength was observed at different temperature ranges. Therefore strength properties of green concrete can be very well estimated with above derived mathematical formulae.

VI. REFERENCES

- [1] cseindia.org, press release August 25, 2020
- [2] Sami W. Tabsh, Akmal S. Abdelfatrah, Influence of recycled concrete aggregates on strength properties of concrete, Construction and Building Materials. 23 (2009) 1163-1167
- [3] Frondistou-Yannas S, Waste concrete as aggregate for new concrete. ACI J 1977; 74(8):373-6.
- [4] Nagaraj, T.S. and Zahida Banu, Efficient utilization of rock dust and pebbles as aggregate in Portland cement concrete, The Indian Concrete Journal, Vol 70, No 1, 1996, pp 1-4.
- [5] Tavakoli M, Soroushian P., Strengths of recycled aggregate concrete made using field-demolished concrete as aggregate. ACI Mater J 1996;93(2):182-90.
- [6] Shukla M., Sahu A.K. and Sachan A.K., Performance of stone dust as fine aggregate replacing sand in concrete and mortar, National Seminar on Advances in Special Concretes. Indian Concrete Institute, Bangalore, India, 1998, pp 241-248.
- [7] M. C. Limbachiya, T. Leelawat and R. K. Dhir, Use of recycled concrete aggregate in high strength concrete, materials and Structures/Mat&iaux et Constructions, Vol. 33, November 2000, pp 574-580
- [8] Ajdukiewicz A, Kliszczewicz A., Influence of recycled aggregates on mechanical properties of HS/HPC. Cement and Concrete Comp 2002;24:269-79.
- [9] A.K. Sahu, Sunil Kumar and A.K. Sachan, Crushed stone waste as fine aggregate for concrete, * The Indian Concrete Journal, January 2003, Page No. 845-848
- [10] Vieira J.P.B.et al (2011), Post fire residual mechanical properties of concrete made with recycled concrete coarse aggregate, Cement and concrete research journal, Volume 41, issue(5), pages 533-541.
- [11] Vijayalakshmi M., Sekar A.S.S., Prabhu G.G., Strength and durability properties of concrete made with granite industry waste, Construction and Building Materials 46 (2013) 1-7
- [12] Sherif Yehia*, Kareem Helal, Anaam Abusharkh, Amani Zaher, and Hiba Istaitiyeh, Strength and Durability Evaluation of Recycled Aggregate Concrete. International Journal of Concrete Structures and materials Vol.9, No. 2, pp. 219-239, June 2015
- [13] Bhashya V, Ramersg G et al, Performance evaluation of concrete by using recycled aggregate ICJ Vol.94, No. 1, pp. 51-57, Jan 2020.

AUTHOR PROFILE



Er. S. K. Singh Gaur
 B.E. (CIVIL) I.I.T. ROORKEE, M.E. (Civil)
 Sr. lecturer, Civil Engineering,
 A.I.T.H. Awadhपुरi, Kanpur
 Area of interest: Structural engineering
 and Recycled construction material,
 Concrete technology
 Email: sushil@aith.ac.in, Contact:
 9839026833



Dr. Sunil Kumar
 Professor, Civil Engineering
 Department, H.B.T.U., Kanpur
 B.Sc. (Civil engg.), M.Tech. Phd.
 Area of interest: Structural Analysis,
 Advanced RCC Design, Waste
 Utilization
 Email: suniljadon@live.in, Contact:
 98398168200

Palm Print Recognition Based on PCA and its Variants

Ravi Kumar Kanaujia
M.tech Scholar
NIT Hamirpur (H.P.)
India-177005
Mob. No.-7831939329
ravikanaujia9911@
gmail.com

Er. Amit Kaul
Assistant Professor
NIT Hamirpur (H.P.)
India-177005
Mob.No.-9418132834
amitkaul9@gmail.com

Ravinder Nath
Associate Professor
NIT Hamirpur (H.P.)
India-177005
Mob. No.-9418095509
r.nath1964@gmail.com

Abstract

In present era, automatic personal recognition is a serious problem that needs to be overcome properly. Palm print recognition is one of the most reliable and successful biometric solutions due to its numerous advantages such as stable line features, low resolution imaging, low cost capturing device, non-intrusive and user friendly. In this article, performance comparisons of palm print recognition techniques based on subspace approaches (PCA, 2DPCA, 2D²PCA) have presented. The experimental results are evaluated on three benchmark databases (CASIA, Cropped palm images and IIT Delhi) in terms of recognition rate and computation time.

1. Introduction

The development of accurate and reliable security systems is a matter of our convenience, and in this context biometrics system has seen as a highly effective automatic mechanism for personal authentication. Authentication by biometric verification is becoming increasingly common in corporate and public security systems, consumer products and point of sale applications. Biometrics is the science and technology of measuring and analyzing biological data. In information technology, biometrics refers to technologies that measure and analyze human body characteristics, such as fingerprints, eye retinas and irises, voice patterns, facial patterns and hand measurements, for authentication purposes.

Palmprint recognition refers to the process of determining whether two palmprints are from the same persons on line patterns of the palm. A Palm is having principal lines, wrinkles and ridges. There are three principal lines. In general, biometric systems identify a person using physical characteristics, such as fingerprint, iris, face, palmprint and ear, or behavioral characteristics, such as signature, gait and keystroke .

Among them, palmprint based biometric recognition methods have currently been attracting more attention. Palm print is the inner part of hand which consist lines and points such as heart line, head line and life line respectively. Wrinkles are more irregular than the principal lines. The lines which are not principal lines or wrinkles, are called as ridges and they exist all over the palm. These line and point patterns are always unique, even in the monozygotic twins. The interesting part is that the ridge structure is permanent. This ridge structure is unique and having the low dimensional features. The palmprint recognition system has advantages over the other physiological biometric systems. Some of the advantages are fixed line structure, low intrusiveness, low cost capturing device, low resolution imaging. Thus palmprint recognition is a very interesting research area. A lot of work has already been done in this area, but there is still a lot of scope to make the systems more efficient.

In this paper, the most popular PCA, 2D-PCA and 2D²-PCA approaches are used to extract the palm features from two standard palmprints datasets (CASIA [20] and PolyU cropped [22]). The extracted features are classified using Euclidean distance to evaluate the performance in terms of recognition rate and computation time.

The rest of the paper organised as follow. In section 2 Literature review has been introduced. In section 3 of paper, discussed about the proposed subspace approaches contains methodology of PCA, 2D-PCA, 2D²-PCA and Euclidean distance. Section 4 and section 5 contain the results, discussion and conclusion respectively. At last acknowledgement in section 6 has been introduced and in 7th section references has been given.

2. Literature Review

In order to provide an accurate and efficient authentication system, there has been research in the area of palmprint recognition system. For this, a number of relevant papers have been reviewed.

Generally, palmprint based recognition approaches can be categorized into three types: line-based, subspace-based and texture-based approaches. Line based approaches, which also called structural based approaches, employ a set of structural features of palmprints such as principle lines, wrinkles, datum points, ridges and crease points. These approaches either develop edge detectors or use the existing edge detection methods to extract palm lines [1]. Wu et al. used Sobel masks to compute the magnitude of palm lines [2]. In [3], datum points of the palmprints are used as features. Datum points are defined as end points of the principle lines. Han et al. proposed a palmprint based system which uses Sobel masks and morphologic operators to extract the structural features of palmprint [4]. In [5], Canny edge operator is used to extract the palm lines. In general, line-based approaches can successfully extract the majority of lines and ridges correctly. However, the high complexity of these methods is the main drawback in using line based approaches. Besides, a significant computational power is required to determine and match the line segments. Subspace-based approaches utilize numerous techniques such as principle component analysis (PCA) [6], Fisherpalm [7], and independent component analysis (ICA) [8] to extract the palmprint features. These approaches also called appearance-based approach in the literature of face recognition [1]. Subspace-based approaches do not make use of any prior knowledge of palmprints. Lu et al. proposed an approach based on the PCA to extract the palm features [6]. They used the Karhunen-loeve transform to project the original image into a small set of feature space called 'eigenpalms'. In [7], Fisher linear discriminant (FLD) is used to project the original palmprint images into the lower dimensional feature space called 'Fisherpalm space'. In another approach, ICA is employed to extract the palm features [8]. In general, these approaches are more computational effective but suffer from dependency to the training data sets. In texture based approaches, texture can be defined as the spatial relationship of pixel values in an image region [9]. Some interesting techniques to analyze the palmprint texture are Gabor filters [10,11], discrete cosines transform (DCT) [12,13], morphological techniques [14], Fourier Transform [17] and wavelet Transforms [16–20]. Zhang et al. used Gabor filters to extract the palm features [10]. They called these features as Palm codes. In [11], Palm codes in varying direction are fused to present the features which are called Fusion code. In [12], DCT is used to extract the palmprint and face features. Meraoumia et al. proposed a method to use two dimensional Block based Discrete Cosine Transform (2D-BDCT) [13]. They divided a palmprint into overlapping and equal-sized blocks and applied DCT over each block. Han et al. proposed a method based on the morphological operator to

extract the palmprint features [14]. In [16–20], palmprint features are extracted by using various families of Wavelet transform. In general, texture based methods have strong mathematical foundations and fast implementations which make them suitable for palmprint authentication applications. In [16], the wavelet energy features are defined for palm-print representation and the performance of the proposed system has been analyzed for different wavelets. Zhang et al. defined a set of statistical signatures for palmprint classification [17]. Accordingly, wavelet transform is applied to palmprint image and the directional context of each wavelet sub-band is computed. Then, a set of statistical signatures, which includes density, spatial dispersivity, gravity center and energy, is defined to characterize the palmprint. In [18], sequential modified haar transform is applied to palmprint image to compute the modified haar energy features. Zhang et al. proposed an image similarity metric called 'complex wavelet structural similarity index' for palmprint classification. In the information extracted from multiple wavelets is combined using the fusion at feature level. On the other hand, some other approaches utilized wavelet transform for extracting the palmprint and fingerprint features. Yang et al. introduced a biometric verification system based on fingerprint, palmprint and hand geometry. In this system, palmprint and fingerprint features are extracted by using the discrete wavelet transform and integrated by fusion at feature level. Then, the integrated textural features are combined with hand geometry features by means of the fusion at matching score level. In Lu et al. applied wavelet zero-crossing for representing the 1D fingerprint and palmprint features. Although, these approaches employed wavelet based techniques for efficient authentication systems, their performance are highly dependent on the type of wavelet transform. Therefore, how to choose the suitable wavelet transform is a critical issue in some wavelet based approaches [16].

3. Methodology Used

The feature extraction and classification are the two major steps in any recognition process. In this work the performance evaluation of feature extraction and classification algorithm are tested on two different sets of palm print images. PCA and 2D-PCA are used as a feature extractor separately in combination with Euclidean distance.

(i) Principal component analysis

PCA is a well-known feature extraction and data representation technique widely used in the areas of pattern recognition, computer vision and signal processing, etc. In this work, PCA transforms the 2D

palm image matrices into 1D image vectors column by column or row by row. It is described as follows.

Let us consider a set of M palmprint images, i_1, i_2, \dots, i_M the average palm of the set is defined as:

$$\bar{i} = \frac{1}{M} \sum_{j=1}^M i_j \quad (1)$$

Each palmprint image differs from the average palm \bar{i} , by the vector Φ_i . A covariance matrix is constructed where:

$$C = \sum_{j=1}^M \Phi_j \Phi_j^T \quad (2)$$

Then, eigenvectors, V_k and eigenvalues, λ_k with symmetric matrix C are calculated. V_k determine the linear combination of M difference images with Φ to form the eigenpalms:

$$b_i = \sum_{k=i}^M V_k \Phi_k \quad (3)$$

From these eigenpalms, $K (< M)$ eigenpalms are selected to correspond to the K highest eigenvalues. The set of palmprint images, $\{i\}$ is transformed into its eigenpalm components (projected into the palm space) by the operation:

$$\omega_{nk} = b_k(i_n - \bar{i}) \quad (4)$$

where $n = 1, \dots, M$ and $k = 1, \dots, K$.

$$\Omega_n = [\omega_{n1}, \omega_{n2}, \dots, \omega_{nK}]$$

The weights obtained form a vector that describes the contribution of each eigenpalm in representing the input palm image, treating eigenpalms as a basis set for palm images.

(ii) 2D-PCA-

2D-PCA is based on two dimensional matrices as opposed to the standard PCA, which is based on 1D vectors. In this paper, we first indicate that 2D-PCA is essentially working in the row or column direction of palm images.

Consider an m by n random image matrix A . Let $X \in \mathbb{R}^{n \times d}$ be a matrix with orthonormal columns, $n \geq d$. Projecting A onto X yields an m by d matrix. $Y = AX$. In 2DPCA, the total scatter of the projected samples was used to determine a good projection matrix X . The method used is :

$$\begin{aligned} J(X) &= \text{trace} \{E[(Y-EY)(Y-EY)^T]\} \\ &= \text{trace} \{E[(AX-E(AX))(AX-E(AX))^T]\} \\ &= \text{trace} \{X^T E[(A-EA)^T (A-EA)] X\} \end{aligned} \quad (5)$$

Eq.(5) results from $\text{trace}(RS) = \text{trace}(SR)$

Eq.[5]. Now defines the palm image covariance matrix $K = [(A - EA)^T (A - EA)]$, which is an $n \times n$ nonnegative definite matrix. Let us consider M training palm images, denoted by $m \times n$ matrices $A_r (r=1, 2, 3, \dots, M)$, and denote the average image as $\bar{A} = \frac{1}{M} \sum_r A_r$. Then K can be solved by

$$K = \frac{1}{M} \sum_{k=1}^M [(A_r - \bar{A})^T (A_r - \bar{A})] \quad (6)$$

It has been shown that the optimal value for the projection matrix X_{opt} is composed by the orthonormal eigenvectors X_1, \dots, X_d of K corresponding to the d largest eigenvalues, i.e. Because the size of K is only $n \times n$, computing its eigenvectors is very relevant. Also, as in PCA the value of d can be controlled by setting a threshold as follows:

$$\frac{\sum_{i=1}^d \lambda_i}{\sum_{i=1}^n \lambda_i} \geq \theta_i \quad (7)$$

Where $\lambda_1, \lambda_2, \lambda_3, \dots, \lambda_n$ is the biggest eigen values of K and θ is the preset threshold set.

(iii) 2D²-PCA

A simultaneously way of presenting 2DPCA and Alternate 2DPCA is (2D)²PCA which uses the projection matrices X and Z of 2DPCA and Alternate 2DPCA respectively. (2D)²PCA Preserves the accuracy of 2DPCA but eliminates the large number of coefficient requirement of 2DPCA [10]. Suppose we have obtained the projection matrices X and Z , projecting the m by n image A onto X and Z simultaneously, yielding a q by d matrix C_{trn}

$$C_{trn} = Z^T A X$$

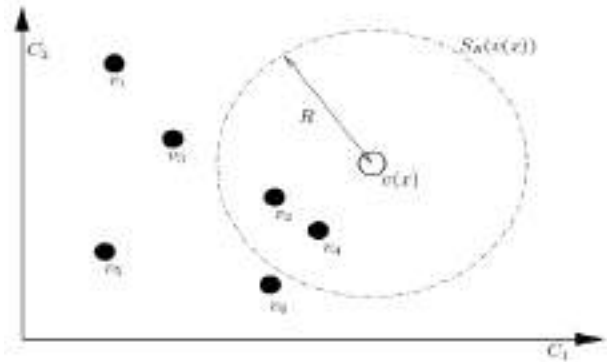
The matrix C_{trn} is also called the coefficient matrix in image representation, which can be used to reconstruct the original image A . When used for face recognition, the matrix C_{trn} is also called the feature matrix. After projecting each training image $A_{trn} (trn = 1, 2, \dots, M)$ onto X and Z , we obtain the training feature matrices $C_{trn} (trn = 1, 2, \dots, M)$. Repeating the same for test image A_{test} we get the test feature matrix C_{test} . Then the nearest neighbor classifier is used for classification. Here the distance between C_{trn} and C_{test} is defined by

$$d(C_{trn}, C_{test}) = \|C_{trn} - C_{test}\| = \sqrt{\sum_{i=1}^q \sum_{j=1}^d (C_{trn}^{(i,j)} - C_{test}^{(i,j)})^2} \quad (8)$$

(iv) Euclidean Distance

Euclidean distance is the distance between two points in Euclidean space. Now the procedure of calculation of Euclidean distance is as follows: The distance between two points in one dimension is simply the absolute value of the difference between their coordinates. Mathematically, this is shown as $|p_1 - q_1|$ where p_1 is the first coordinate of the first point and q_1 is the first coordinate of the second point.

Generalized, the distance between two points $P = (p_1, p_2, \dots, p_n)$ and $Q = (q_1, q_2, \dots, q_n)$ in n dimensions. This general solution can be given as $((p_1 - q_1)^2 + (p_2 - q_2)^2 + \dots + (p_n - q_n)^2)^{1/2}$.



Comparison of a pixel value with a set of sample in Euclidean colour

[4] Results and discussions

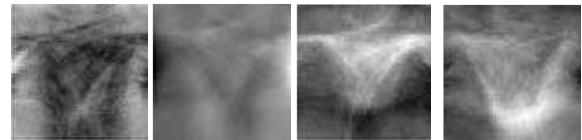
Although 2D-PCA and 2D²-PCA obtain higher recognition accuracy than PCA, a vital unresolved problem of 2D-PCA and 2D²-PCA are that it need many more coefficients for palm image representation than PCA. The percentage recognition rates of PCA and 2D-PCA, 2D²-PCA are shown in Table 1, Table 2 and Table 3 respectively. Classifier is tested, namely Euclidean distance. Euclidean distance is the simplest distance matching algorithm among all. Cosine measure can be used since 2D-PCA allows the columns vectors to be non-orthogonal, and the angles and distances between images differ from each other. Table 1 shows the performance recognition rates of PCA using :

Table 1: PRR by PCA

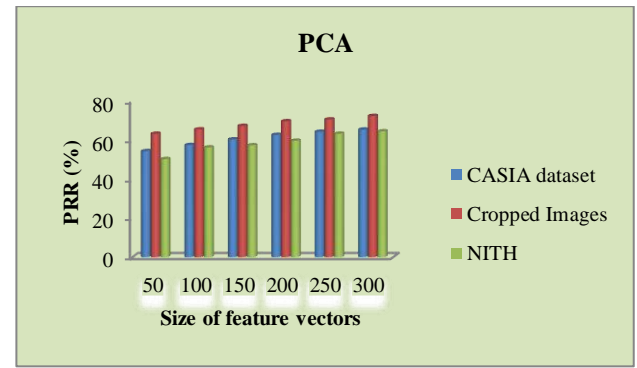
PRR (%)							
Feature vector size	50	100	150	200	250	300	350
NITH	50.1	56.1	57.2	59.5	63.1	64.3	67.1
CASIA	54.2	57.3	60.2	62.5	64.1	65.2	68.9
Cropped images	63.1	65.3	67.1	69.5	70.4	72.18	73.5

these distance metrics.

(i) PCA (after applying pca gives this type of images)



Graph Representation of PCA results:

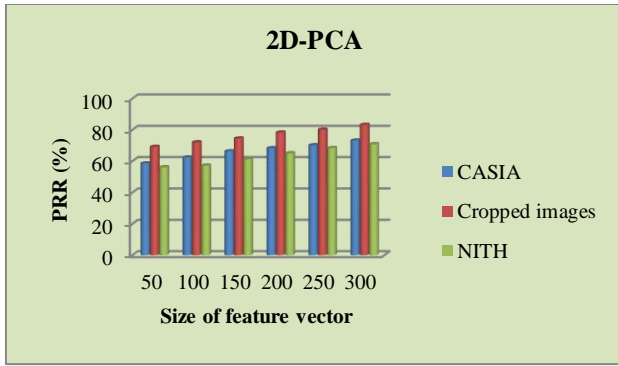


The percentage recognition rate by 2D-PCA is shown in Table 2 as follows:

Table 2: PRR by 2D-PCA

CRR (%)							
Feature vector size	50	100	150	200	250	300	350
NITH	56.2	57.2	61.2	65.1	68.4	70.9	73.4
CASIA	58.6	62.4	66.3	68.3	70.2	73.2	78.
Cropped images	69.2	72.1	74.5	78.3	80.1	83.2	85.2

Graph Representation of 2D-PCA



(ii) 2D-PCA (after applying the 2D-PCA)

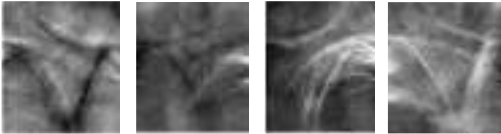
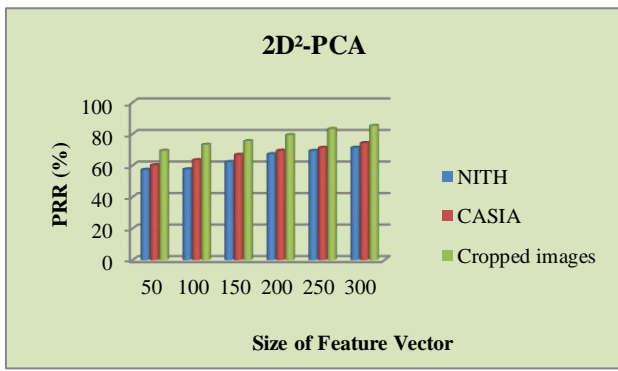


Table 3- PRR by 2D²-PCA

CRR (%)							
Feature vector size	50	100	150	200	250	300	350
NITH	57.3	57.6	62.2	67.2	69.3	71.3	74.4
CASIA	60.1	63.4	66.8	69.4	71.2	74.2	79.3
Cropped images	69.4	73.2	75.5	79.3	83.2	85.2	87.5

Graph Representation of 2D²-PCA



[5] Conclusion

Palm print identification systems measure and compare ridges, lines and Minutiae found on the palm. Palm print is a unique and reliable biometric characteristic with high usability. The 2D-PCA and 2D²-PCA give more better results than PCA because its computational time is less than computational time in PCA. So 2D-PCA and 2D²-PCA are more convenient than PCA. If we apply PCA in cropped palm images then it gives more better result than CASIA database. In 2D-PCA, 2D²-PCA CASIA database gives better results.

[6] Acknowledgements

This work was supported in part by a grant from the faculties of Electrical department from signal processing and control branch in National Institute of Technology Hamirpur.

[7] References

[1] A. Kong, D. Zhang, M. Kamel, A survey of palmprint recognition, *Pattern Recogn.* 42 (7) (2009) 1408–1418.

[2] X. Wu, K.Wang, D. Zhang, HMMsbased palmprint identification, *LCNS Springer* 3072 (2004) 775–781.

[3] D. Zhang, W. Shu, Two novel characteristics in palmprint verification: datum point invariance and line feature matching, *Pattern Recogn.* 32 (4) (1999) 691–702.

[4] C. Han, H. Cheng, C. Lin, K. Fan, Personal authentication using palm-print features, *Pattern Recogn.* 36 (2) (2003) 371–381.

[5] X. Wu, K. Wang, D. Zhang, Fuzzy direction element energy feature (FDEEF) based palmprint identification, in: *Proceedings of International Conference on Pattern Recognition*, vol. 1, 2002, pp. 95–98.

[6] G. Lu, D. Zhang, K. Wang, Palmprint recognition using Eigenpalms features, *Pattern Recogn. Lett.* 24 (9–10) (2003) 1473–1477.

[7] X. Wu, D. Zhang, K. Wang, Fisherpalms based palmprint recognition, *Pattern Recogn. Lett.* 24 (2003) 2829–2838.

[8] L. Shang, D.S. Huang, J.X. Du, Z.K. Huang, Palmprint recognition using ICA based on winner-take-all network and radial basis probabilistic neural network, *LCNS 3972* (2006) 216–221.

[9] S. Drabycz, R. Stockwell, J. Mitchell, Image texture characterization using the discrete orthonormal S-Transform, *J. Digit. Imaging* 22 (6) (2009) 696–708.

[10] D. Zhang, J. You, Online Palmprint identification, *IEEE Trans. Pattern Anal. Matching Intell.* 25 (9) (2003) 1041–1050.

[11] W.K. Kong, D. Zhang, Competitive coding scheme for palm print verification, in: *Proceedings of the 17th International Conference on Pattern Recognition*, 2004, pp. 520–523.

[12] X.Y. Jing, D. Zhang, A face and palmprint recognition approach based on discriminant DCT feature extraction, *IEEE Trans. Syst. Man Cybern. Part B* 34 (6) (2004) 2405–2415.

[13] A. Meraoumia, S. Chitroub, A. Bouridane, Gaussian modeling and discrete Cosine transform for efficient and automatic palmprint identification, in: *International Conference on Machine and Web Intelligence (ICMWI)*, 2010, pp. 121–125.

[14] C.C. Han, H.L. Cheng, K.C. Fan, C.L. Lin, Personal authentication using palmprint features, *Pattern Recogn.* 36 (2) (2003) 371–381.

[15] W. Li, D. Zhang, Z. Xu, Palmprint identification by Fourier transform, *Int. J. Pattern Recogn. Artif. Intell.* 16 (4) (2002) 417–432.

[16] X.Q. Wu, K.Q. Wang, D. Zhang, Wavelet based palmprint recognition, in: *Proceedings of the First International Conference on Machine Learning and Cybernetics 3*, 2002, pp. 1253–1257.

[17] L. Zhang, D. Zhang, Characterization of palmprints by wavelet signatures via directional context modeling, *IEEE Trans. Syst. Man Cybern. Part B* 34 (3) (2004) 1335–1347.

[18] E.W.K. Yih, G. Sainarayanan, A.N.G. Chekima, Palmprint identification using sequential modified Haar wavelet energy, in: *International Conference on Signal Processing, Communications and Networking*, 2008, pp. 411–416.

[19] Lu, G., David, Z., Wang, K., “Palmprint recognition using eigenpalms features”, *Pattern Recognition Letters*, 24(9-10), pp 1473-1477 (2003).

[20] J. Yang, D. Zhang, A.F. Frangi, and J.Y. Yang, “Two-dimensional PCA: a new approach to appearance-based face representation and recognition,” *IEEE Trans. on Pattern Analysis and Machine Intelligence*, vol. 26, no. 1, pp. 131-137, Jan. 2004.

[21] CASIA Palmprint Database, (<http://biometrics.idealtest.org/dbDetailForUser.do?id=5>)

[22] A. Jain, R. Bolle, S. Pankanti, *Biometrics: Personal Identification in Networked Society*, Kluwer Academic Publishers, Dordrecht, 1999.

[23] PolyU (<http://www.comp.polyu.edu.hk/biometrics>) Palmprint database.

Study of Various Generation and Bandwidth Sharing Issues in Mobile Network

Abhishek Prabhakar^a, Dr. Amod Tiwari^b, Prof Vinay Kumar Pathak^c

^aAsstt. Prof., Dr,AITH Kanpur, India.

^bDirector, NCET Kanpur, India.

^cVC, APJ Abdul Kalam Technical university, Lucknow, India.

Abstract

An important performance index of a mobile system among other indices is “number of users” that a system can support. For a system to be supported by a single base station catering to large number of users there is need of high power transmitter. The enhancement in the capacity can also be achieved by using an array of lower power transmitter in cellular array arrangement. Security however remains an important concern for all mobile networks. The kind of infrastructure in new generation networks has been observed to be packet and IP based. An important improvement seen in 4G systems over 3G systems is that it provides broadband internet access in addition to usual voice and other services. This can be made use of in Laptops using wireless modems, smart phones and in other mobile services. In transferring data using wireless communication at high speed in mobile phones and other data terminals, 4generation long term evaluation (4G LTE) is much in use. An effort has been made to analyze the next generation mobile networks in light of threats to security of access points in networks supported by cellular networks.

Keywords: Ad-hoc network; mobile generation; AODV; DSR; mobile network security

1. INTRODUCTION

Over the last decade, there has been lot of development in mobile technology. The systems that have been upgraded from first generation to second to third and now some companies have launched even 4G systems. The technology too has changed a great deal. The first generation (1G) wireless systems while use frequency division multiple access(FDMA)as multiple access technology, the second generation (2G) wireless system use digital transmission communication system that have been in use for some time are those in the first generation and second generation. Third generation system are also under use these days. .The first generation (1G) wireless communication system use frequency division multiple access (FDMA) as the multiple access technology. The second generation (2G) wireless system use digital transmission .The multiple access technology makes use of both time division multiple access (TDMA) and code division multiple access (CDMA).The third generation (3G) is based on CDMA as multiple access technology also support multimedia services. The Cellular system is changing very fast. In cellular communication technology the change in the nature of service, on compatible transmission technology, and new frequency bands have been observed to have been used frequently. With introduction of Wireless LAN (WLAN) technology, networks have been able to achieve connectivity with useable amount of bandwidth .The Mobile devices used while travelling, such as mobile smart phones, laptops allowed users to access data with more flexibility especially when people on the move. At present, the wireless networks though are quite in vague they are unsafe and are prone to attack by attackers .The main elements that a new generation of mobile network contain are given in figure 1. As is seen in figure they are mainly femtocell and wifi. While using wireless communication [1], data has to be protected by applying security checks and this is done at several levels. The present paper seeks to analyze the mobile networks and the potential threats that a system, specially, cellular network is faced with regarding bandwidth sharing issues..



Figure 1. Next Generation of Mobile Networks

2. RELATED WORK

A commercially available femtocell can be modified and used to track phones intercept communication and even modify traffic. A security analysis of femtocells [2] was conducted by Borgaoankar et. al. They pointed out several security drawbacks which allowed a hacker to attack femtocell's firmware. They also showed how location verification techniques can be surrounded and how an attacker can use a femtocell from an unregistered location to avoid roaming charges [3].

The use of honeypot system [4] to detect infected mobile devices proposed by Lance spitzner et al. Their system analyzed and monitored the communication aspect of the mobile devices. The honeypot however has not been designed to detect or analyze attacks against the mobile networks. A method to use nomadic honeypots[5] to collect threat intelligence directly on smart phones was proposed by Liebergeld et al. The solution they proposed allowed to contain attacks even in case of complete capture of smart phone operating system. It required modification of Smartphone firmware. Software to prevent against attacking and exploiting pocket pc's Smartphone [6] was proposed by mulliner et al. This includes vulnerability analysis of smart phones.

3. GENERATION OF MOBILE NETWORKS

The first to arrive were the first generation of wireless telephones known as 1G .They were introduced in 1980's,used analog telecommunications standard .They were replaced by second generation known as 2G during 1990's and used digital telecommunication signal .The main difference between 1G and 2G system has been while the radio signals that used 1G systems were analog ,those used by 2G have been digital. This generation included data access to mobile phones. 2G cellular telecom networks were commercially launched on the GSM(Global system for mobile communication) standard in Finland by Radiolinja. The technology used in second generation 2G systems provided the services like sending text messages ,picture messages and multimedia messages(MMS). All text messages sent over 2G were first digitally encrypted and then the data was transferred in such a way that only the authorised receiver could receive and read it.

The third generation, 3G mobile phones use the technology that allows them to access the internet. This enables the users to surf web page, make video calls and download music. In addition to this the access to the internet is even faster .3G telecommunications networks support services that provide higher data transfer rate .The applications of 3G technology used include wireless voice telephony ,mobile internet access video calls and mobileTV .General packet radio service (GPRS)is a packet oriented mobile data service on 2G and 3G cellular communications.GPRS provides data rates of 56-114 kbit/sec.2G cellular technology combined with GPRS is sometimes described as 2.5G i.e. a technology between 2G and 3G generation of

mobile telephony. 4G refers to fourth generation of mobile phone technology. A 4G system provide high speed internet access. 4G provide mobile web access, gaming and IP telephony mobile TV, cloud computing and video conferencing. 4G technology offers increased voice, video and higher data rates. 5G or fifth generation of mobile network provide next mobile standards beyond current 4G standards. 5G technology are theoretical and not real. 5G is also called as complete wireless communication and having no limitations. 5G transmission has high transmission speed .It offers worldwide connectivity and high data rate capabilities. The hand held phones have more –power, large memory and good quality of audio and video. The speed in 5G technology can extend up to 1Gbps having low cost than previous generations. The user can connect with various wireless devices. 5G provides high resolution for cell phone users with 25Mbps connectivity speed. Uploading and downloading can be up to 1Gbps and supports virtual private network. 5G is sixth sense technology with AI (Artificial intelligence) capabilities. 5G uses IPV6 technology and IP is assigned as per connected network and geographical location. 5G uses UWB (ultra wide band) networks having bandwidth of 4000Mbps which is much higher than today's wireless networks .

4. MOBILE AD-HOC NETWORKS (MANETS)

MANET is short term used spontaneously in wireless network of mobile nodes communicating with each other without the interaction of any fixed infrastructure or central control. Usually it is a system in which mobile nodes or mobile station serving as routers interconnected by wireless links. Network communication and management tasks are usually performed in a distributed manner .Since the nodes moves or adjust their transmission and reception parameters, MANET topology may vary from time to time. The use of ad-hoc networks in mobiles makes use of advanced networking mechanism. The ad-hoc wireless network does not need any infrastructure in other words it is a network without a base station .In mobile network since the nodes are mobile the likelihood of change in topology randomly over a period is fair .The technology used enables the system to be decentralized where the inclusive network activity including discovering the topology and the delivery of message need to be executed by the nodes themselves by incorporating the routing functionality over mobile nodes.

Chances of likelihood of mobile networks being corrupted:

The use of wireless links makes the network susceptible to attacks.. In Wired networks, attackers do not need physical access to the network to carry out these attacks. The Wireless networks have lower bandwidths than wired networks and hence attacker can exploit network bandwidth with ease.

Dynamic Topology:

In mobile ad-hoc network nodes are free to move, they can leave or join the network and can move independently. This leads to frequent changes in network topology. In dynamic environment it is difficult to differentiate between the malicious and normal behavior of network. A node sending disruptive routing information may be said to be in malicious mode. MANET nodes can leave and join the network, and move independently. As a result the network topology can change frequently. It is hard to differentiate normal behavior of the network from malicious behavior in this dynamic environment. For example, a node sending disruptive routing information can be a malicious node. Nodes with inadequate physical protection are prone to being hacked.

4.1 Cooperation:

Routing algorithms in MANETs usually assume that nodes behave according to expectation and are not malicious. If attacker can become important routing agent it can disrupt network by rejecting or disobeying protocol specification. In this way a node behaving as functioning to other nodes and participating in overall decision making mechanism can affect network significantly. So cooperation between nodes is of most importance. As a result, a malicious attacker can easily become an important routing agent and disrupt network operations by disobeying the protocol specifications. For example, a node can pose as a neighbor to other nodes and participate in collective decision-making mechanisms, possibly affecting networking significantly. So cooperation between nodes is of most importance and at the same time the differentiation between nodes that follow protocols and those don't should also be clear. This is serious shortcomings in such network. MANET don't have clear line of defense and hackers may attack from all directions. The line of demarcation between the internal network from the outside world is not very clear. Therefore the decision on the point where the traffic monitoring and access control mechanism should be deployed becomes difficult. The network information on MANET's is distributed across nodes that can only see the packet sent and receive in their transmission range whereas in wired network all traffic goes through switches, routers or gateways.

4.2 Limitations:

There are number of devices which use MANET's ranging from laptops to other handheld devices like PDA's and mobile phones. They generally employ different computing and storage capabilities and constitute the focus of new attacks. The mobile nodes generally run on battery, this has further paved way for new types of attacks targeting this aspect as well. In present day networks the introduction of

additional security features increasing the computation ,communication and management load poses serious challenge for network that are already resource constrained.

5. Ad-hoc ROUTING PROTOCOLS

Ad-hoc routing protocol deals with how mobile nodes decide which way to route packets between devices in a mobile Ad-hoc network. In MANETS initially nodes are not familiar with topology; rather they have to discover it. New mobile node announces its presence and should listen for announcements broadcast by its neighbors.

Ad-hoc Routing Protocol May be classified as under:-

5.1 Proactive (table driven) routing protocol:-

This type of protocol maintains fresh list of destinations and their routes by periodically distributing routing tables throughout the network. Examples are DSDV (Destination sequenced distance vector) routing protocol.

5.2 Reactive (on demand routing protocol):-

This type of protocol finds a route on demand by flooding the network with route requests packets. Examples are Dynamic source routing (DSR) and AODV (Ad-hoc on demand distance vector routing protocol)

5.3 Hybrid (both proactive and reactive):-

This type of protocol combines the advantage of both proactive and reactive routing protocols.

5.4 Hierarchical routing protocols:-

With this type of protocols the choice of proactive and reactive routing depends on hierarchical level where a mobile node resides

6. AODV ROUTING PROTOCOL

Ad-hoc on demand distance vector routing protocol (AODV) work best under dynamic link conditions as they offer quick adaptability. It is reactive routing protocol that discovers route only when they are required. They are also suited to low processing and memory overhead ,low network utilization and determine unicast routes to destination within Ad-hoc network[7] .It is believed that AODV can handle low ,moderate and high mobile rates along with variety of data traffic loadings. The

security provisions however are not taken care of that well. AODV functions mainly on three types of messages: (a) Route request RREQ messages.(b)route reply RREP messages(c)Route error(RERR) messages. When clear route for destination is not available to another node, the node start discovering the route by broadcasting a RREQ message .The routing table of the nodes within the neighborhood are organized to optimize the response time to local movements. The neighbor in turn broadcast the packet to neighbors till it reaches a node that has recent route information about destination.figure2 (a) the nodes receiving RREP messages and requesting route in the node, they update their routing table with new routes. Due to mobility of nodes in the network or due to transmission errors wireless network come across frequent link breakages .The Ad-hoc on demand distance vector routing enables the mobile nodes to respond to link breakages and changes appropriately at the same time. When AODV is functional the nodes can control their connectivity in two ways:-(a) Linking layer notification using control packets like link layer acknowledgement messages i.e. ACK or RTS-CTS (b) Passive acknowledgement i.e. notification by listning on channel to find out if the next node forwards the packet or not.AODV uses only symmetric links because the route reply packet follows the reverse path of route request packet figure.2 (b)

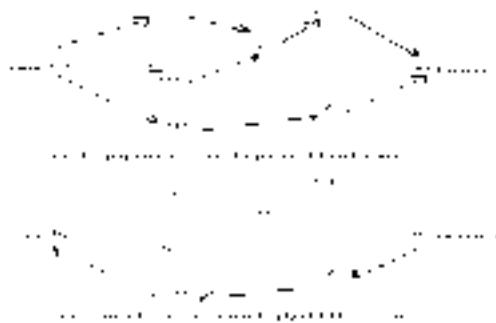


Figure 2

DSR (Dynamic source routing):-

This protocol is similar to AODV but the route is maintained in the packet header. In this routing the intermediate nodes do not route information and also there is no requirement of periodic route advertisement. Intermediate nodes propagating a route request; add their ID in the packet header figure 3. When a packet reaches destination, route reply is returned.



Figure 3. Route discoveries in DSR

7. PROACTIVE VS REACTIVE PROTOCOLS

Proactive: - It is more efficient when routes are used many times. It requires periodic route update .If the nodes are mobile it affects entire network.

Reactive:-It is more efficient when routes are used occasionally. In this approach node first find the route before transmission of data. There is no requirement of periodic route update.

8. CHALLENGING ISSUES IN MANETs

Some of the most challenging issues in MANETs are following-

- (a) Limited wireless range.
- (b) Broadcast nature of wireless
- (c) Routing problem.
- (d) Packet losses
- (e) Battery constraints
- (f) Security issues

9. ATTACKS AGAINST MOBILE NETWORKS

Among the ways to destroy the target devices most dangerous types are flooding and the denial of service(DoS) and distributed denial of service(DDoS).They could be accomplished individually or organised using botnet [8,9].Increasingly high number of requests could put most of the firewall security system out of service due to limitation in state tables. Therefore a denial of service (DoS) or distributed denials of service mode of protection service or product are employed against attacks coming from internet. Generally it is recommended that DDoS protection be placed in the ISP's side [10]. Various types of attacks which can be done on cellular communication networks are as follows:

9.1 Denial of Service attacks (DoS)

“Denial of Service (DoS) kind of attack is a attack that renders computer or a network incapable of providing normal services”.DoS attack are normally carried out against a service running on a specific IP address in order to deny access to legitimate users and cause damage to service owner. The most common types of DoS attacks targets the computer network bandwidth or connectivity.Bandwidth attacks flood network with such a high volume of traffic that all available network resources are consumed and legitimate user requests cannot be completed .Connectivity attacks flood a computer with such number of requests that all available operating system resources are consumed and computer cannot process the legitimate user requests. The focus is mostly on local attacks i.e. jamming, as well as threats against Radio access networks RAN that could be leveraged from a single attacker.

9.2 Distributed Denial of Service attacks (DDoS)

DDoS are IP packet-based attacks launched at the network infrastructure. “A DDoS attack uses many computers to launch a number of DoS attack against the targets. A DDoS attack happens when multiple system flood the bandwidth of resources of a targeted system. In DoS attack a hacker uses a single internet connection to flood a target with fake requests usually to exhaust server resources. DDoS are launched with multiple connected devices that are distributed across internet. Unlike single source Dos attack DDoS attempts to target network infrastructure with huge amount of traffic. If pass bandwidth is p, where p is prime than with the help of Euler function

$$\Phi(p)=p-1.....(1)$$

Where $\Phi(p)$ is totient function[11] which counts the positive integer upto given integer n that are relatively prime to p .

Since all numbers less than p are relatively prime to p. If $m = p^a$ (where a is a power of pass bandwidth p) is a power of a prime, then the numbers that have a common factor with m are the multiples of p: p , 2p, 3p, ..., $p^{a-1}(p)$. There are p^{a-1} of these multiples, so the number of factors relatively prime to p^a is

$$\phi(p^a) = p^a - p^{a-1}.....(2)$$

$$= p^{a-1} (p - 1).....(3)$$

$$= p^a \left(1 - \frac{1}{p}\right).....(4)$$

p^a is pass bandwidth of network.

9.3 Insider attacks

An insider attack is also known as insider threat. Insiders have advantage over external hackers because they have authorized system access and also know network architecture and system procedures. Usually organisation focus on external architecture, so there is less security against insider attacks. Now take a general m divisible by p . Let $\phi_p(m)$ be the number of positive integers $\leq m$ not divisible by p . As before, $p, 2p, \dots, (m/p)p$ have common factors, so

$$\phi_p(m) = m - \frac{m}{p} \dots\dots\dots(4)$$

$$\phi_p(m) = m \left(1 - \frac{1}{p}\right) \dots\dots\dots(5)$$

Where m is multiple factor of passed bandwidths

9.4 Overview of threats against mobility availability

Threats include all those potential factors or platforms that challenge the smooth running of the system from outside. These are based on attack platforms, the scope, the difficulty or cost incurred to launch such an attack and finally an estimate of the impact against the availability of an LTE network. The larger the impact the more is the chances of getting affected within the scope of attack. A smart jamming attack despite being of local nature has potential to block one or more multiple sections at very low cost. The cost of a signalling amplification attack or a threat against the HSS (home subscriber subsystem) is larger because it requires a large botnet of infected devices.

10. RESULT ANALYSIS

By comparing equation (5) and equation (4) at passing same band width. Yield

$$p^\alpha \left(1 - \frac{1}{p}\right) = m \left(1 - \frac{1}{p}\right) = \phi_p(m)$$

for higher degree calculation taking log both side

$$\log[p^\alpha (1 - 1/p)] = \log[m(1 - 1/p)] = \log[\Phi(p)]$$

From the above equation we can yield $\Phi(p) = m \ln \ln(p)$

Table 1.0 Relation between input data and pass bandwidth

P	1/2	1	3/2	2	5/2
$\Phi(p) = m \ln \ln(p)$	1000	2000	3000	4000	5000

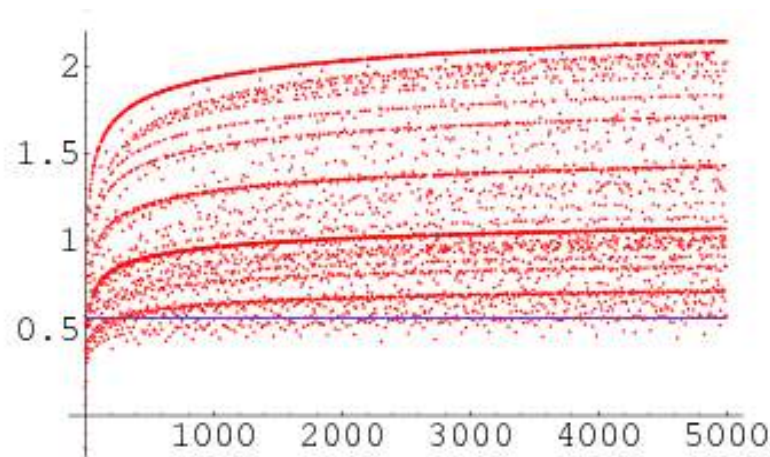


Figure 4: Passed p bandwidth with m multiple factor

11. CONCLUSION

Results after applying above equation on different values of P (passed bandwidth-Y-axis) and number of users (x-axis) are shown in table 1.0 and it is also represented graphically in figure 4 shown above. If we increase the bandwidth and number of users simultaneously then after some time the number of users will increase but at optimum level the bandwidth remains constant or unchanged. The conclusion of research paper is that passed bandwidth is directly affected with number of users but at a constant bandwidth (p) where $0 \leq p \leq 2$ means that number of users does not affect bandwidth in a given transmission area.

Wireless technologies enable devices to communicate without an actual wired connection and used in areas where it is difficult to build connection using wires. Long term evaluation (LTE) provides increased speeds and greater bandwidth and gives users what they want, which is faster access to applications. Cellular Networks are open to attacks such as DDoS, DoS, channel jamming, message forgery etc. Therefore, it is necessary that security features are also added that prevent such attacks.

REFERENCES

- [1] http://en.wikipedia.org/wiki/Wireless_network
- [2] en.wikipedia.org/wiki/Femtocell
- [3] en.wikipedia.org/wiki/Roaming
- [4] Lance (2002). Honeypots tracking hackers. Addison-Wesley. pp. 68–70. ISBN 0-321-10895-7
- [5] L4android: A generic operating system framework for secure smartphones - Lange, Liebergeld, et al. – 2011
- [6] <http://www.mulliner.org/pocketpc/>
- [7] Perkins C., Belding-Royer E., Das S., “RFC 3561: Ad hoc On-Demand Distance Vector (AODV) Routing”, <http://www.ietf.org/rfc/rfc3561.txt>, 2003
- [8] Tyagi, A.K.; Aghila G. A wide scale survey on botnet. Int. J. Comput. Appl. 2011, 34, 9–22.
- [9] Sharma, R.K.; Chandel, G.S. Botnet detection and resolution challenges: A survey paper. Int. J. Comput. Inf. Technol. Bioinforma. 2009, 1, 10–15.
- [10] Douligieris, C.; Mitrokotsa, A. DDoS attacks and defence mechanisms: Classification and state-of-the-art. Comput. Netw. 2004, 44, 643–666
- [11] J J Sylvester 1879, “on certain ternary cubic form equation”: American journal of mathematics 357-393: Sylvester coins the term totient on page 361.

Design of Floating Point Vedic Multiplier using VHDL**Garima Singh**Research Scholar M.Tech ECE
Bansal I.E.T ,Lko(India)
garima.sitm@rediffmail.com**Sushil Kumar Agrawal**Prof. (Director)
Bansal I.E.T ,Lko(India)
skagrawal10@rediffmail.com**B.R.Singh**H.O.D Dept. Of ECE
Bansal I.E.T ,Lko(India)
brs1973@rediffmail.com**Abstract:**

In this paper we proposed the configuration of fast Vedic Multiplier utilizing the strategies of Ancient Indian Vedic Mathematics that have been changed to enhance execution. Vedic Multiplication Technique is utilized to execute IEEE 754 Floating point multiplier. For mantissa increase we are utilizing Urdhvatriyakbhyam sutra for the sub-current and over stream cases are taken care of. The multiplier's inputs are given in IEEE 754, 32 bit group. The Vedic Mathematics is the old arrangement of science which has a one of a kind system of counts in view of 16 Sutras. Our work has demonstrated the effectiveness of Urdhvatriyakbhyam– Vedic technique for duplication which strikes a distinction in the real procedure of augmentation. It empowers parallel era of moderate items, dispenses with undesirable increase ventures with zeros and scaled to higher piece levels utilizing Karatsuba calculation with the similarity to various information sorts. The Urdhva tiryakbhyam Sutra is most effective Sutra (Algorithm), giving least defer for increase of a wide range of numbers, either small or large. We implement this multiplier using VHDL. We implement our work by Xilinx ISE tool i.e. responsible for synthesis also. For simulation we are using Modelsim 10.2a.

Keywords: IEEE 754, Vedic Multiplier, Modelsim, Xilinx, VHDL.

I. Introduction

Multipliers are key segments of numerous superior frameworks, for example, microchips, FIR channels, computerized signal processors, and so on. Execution of a framework is for the most part dictated by the execution of the multiplier on the grounds that the multiplier is by and large the slowest component in the framework. Since augmentation overwhelms the execution time of most DSP application so there is need of fast multiplier. Moreover, it is by and large the most zone devouring. Thus, enhancing the territory and pace of the multiplier is a noteworthy outline issue. Be that as it may, speed and range are typically clashing imperatives so that enhancing speed comes about for the most part in bigger territories. Thus, an entire range of multipliers with various region speed imperatives has been outlined with completely serial multipliers toward one side of the range and completely parallel Multipliers at the flip side. These multipliers have moderate execution in both pace and zone. Twofold drifting point numbers augmentation is one of the essential capacities utilized as a part of advanced sign handling (DSP) application. The IEEE 754 standard gives the organization to representation of Binary Floating point numbers in PCs. The Binary Floating

point numbers are spoken to in Single and Double configurations. The Single accuracy arrangement comprises of 32 bits and the Double exactness position comprises of 64 bits. The organizations are made out of 3 fields; Sign, Exponent and Mantissa. An average focal preparing unit dedicates a lot of handling time in executing math operations, especially augmentation operation. Most superior DSP frameworks depend on equipment duplication to accomplish high information throughput. Augmentation is a critical basic number juggling operation. Execution limitations can likewise be tended to by applying elective innovations. A change at the level of outline usage by the insertion of another innovation can regularly make practical a current minor calculation or design. This venture manages the "Configuration of rapid gliding point multiplier utilizing antiquated strategy". In this task Vedic Multiplication Technique is utilized to actualize IEEE 754 Floating point multiplier. For computation of mantissa unit The Vedic sutra is utilized. A change at the usage level of outline by the insertion of another innovation can regularly make reasonable a current negligible calculation or engineering. Execution limitations can likewise be tended to by applying elective innovations.

II. Related Work

Sushma S. Mahakalkar et al, they chipped away at the key and the center of all the Digital Signal Processors (DSPs) are its multipliers and the velocity of the DSPs is mostly dictated by the rate of its multiplier. IEEE coasting point arrangement was a standard organization utilized as a part of all preparing components since Binary drifting point numbers augmentation is one of the fundamental capacities utilized as a part of computerized sign handling (DSP) application. In that work VHDL execution of Floating Point Multiplier utilizing old Vedic science is introduced. The thought for planning the multiplier unit is received from old Indian science "Vedas". The Urdhva Tiryakbhyam sutra (strategy) was chosen for execution since it is material to all instances of increase. Augmentation of two no's utilizing Urdhva Tiryakbhyam sutra is performed by vertically and across, transversely implies askew increase and vertically implies straight above duplication and taking their whole. The component is any multi-bit duplication can be diminished down to single piece augmentation and expansion utilizing this strategy. Because of these recipes, the convey proliferation from LSB to MSB is decreases because of one stage era of halfway item [1].

Tariquzzaman et al, took a shot at the FPGA based 64 bit RISC processor with Vedic multiplier component actualized utilizing VHDL .The VHDL code is adaptable dialect and

backings FPGA. Framework On-Chip (SoC) and Spartan 3E unit. In today's innovation RISC processor assumes an essential part and RISC framework abbreviate execution time by decreasing the clock cycle per direction and it can address colossal measure of memory up to 16 Exabyte. Augmentation is Fundamental capacity number juggling operation in Digital sign preparing application, for example, FFT, Convolution. Average multiplier requires significant measure of calculation time to actualize result, along these lines productivity of Vedic strategy for augmentation enhances the execution this is the one of a kind system of calculation in view of 16 sutra (Methods). It likewise dispenses with the undesirable duplication step. This work depends on Nikhlam sutra [2].

Aritra Mitra et al, proposed a Vedic Multiplication Technique which used to actualize Floating point multiplier. The Urdhvatriyakbhyam sutra will be utilized for the increase of Mantissa. The undercurrent and over stream cases will be taken care of. The inputs to the multiplier in 32 bit design. The multiplier is outlined in VHDL or VERILOG and reenacted utilizing Modelsim [3].

Bhagyashree Hardiya et al, dealt with augmentation of the drifting point numbers portrayed in IEEE 754 single accuracy substantial. Coasting point multiplier is done utilizing VHDL .Implementation in VHDL(VHSIC Hardware Description Language) is utilized in light of the fact that it permit direct execution on the equipment while in other dialect they need to change over them into HDL then just can be actualized on the equipment. In drifting point duplication, including of the two numbers is finished with the assistance of different sorts of adders yet for increase some additional moving is required. This coasting point increase handles different conditions like flood, sub-current, standardization, adjusting. In this work they utilize IEEE adjusting strategy for perform the adjusting of the came about number. This work surveys the execution of an IEEE 754 single accuracy coasting point multiplier created by numerous scientists [4].

Remadevi R, proposed a calculation for duplicating drifting point numbers which was a basic necessity for DSP applications including substantial element range. This work concentrates just on single accuracy standardized twofold trade design focused for Xilinx Spartan-3 FPGA in light of VHDL. The multiplier was confirmed against Xilinx gliding point multiplier center. It handles the flood and sub-current cases. Adjusting is not executed to give more exactness when utilizing the multiplier as a part of a Multiply and Accumulate (MAC) unit [6].

III. Methodology

The performance of Mantissa calculation Unit dominates overall performance of the Floating Point Multiplier. This unit requires unsigned multiplier for multiplication of 24x24 BITS. The Vedic Multiplication technique is chosen for the implementation of this unit. This technique gives promising result in terms of speed and power [6].The Vedic multiplication system is based on 16 Vedic sutras or

aphorisms, which describes natural ways of solving a whole range of mathematical problems. Out of these 16 Vedic Sutras the Urdhva-triyakbhyam sutra is suitable for this purpose. In this method the partial products are generated simultaneously which itself reduces delay and makes this method fast. The method for multiplication of two, 3 BITS number is shown Figure 3.4. Consider the numbers A and B where $A = a_2a_1a_0$ and $B = b_2b_1b_0$. The LSB of A is multiplied with the LSB of B:

$$s_0 = a_0b_0;$$

Then a_0 is multiplied with b_1 , and b_0 is multiplied with a_1 and the result are added together as:

$$c_1s_1 = a_1b_0 + a_0b_1;$$

Here c_1 is carry and s_1 is sum. Next step is to add c_1 with the multiplication results of a_0 with b_2 , a_1 with b_1 and a_2 with b_0 .

$$c_2s_2 = c_1 + a_2b_0 + a_1b_1 + a_0b_2;$$

Next step is to add c_3 with the multiplication results of a_1 with b_2 and a_2 with b_1 .

$$c_3s_3 = c_2 + a_1b_2 + a_2b_1;$$

Similarly the last step

$$c_4s_4 = c_3 + a_2b_2;$$

Now the final result of multiplication of A and B is $c_4s_4s_3s_2s_1s_0$.

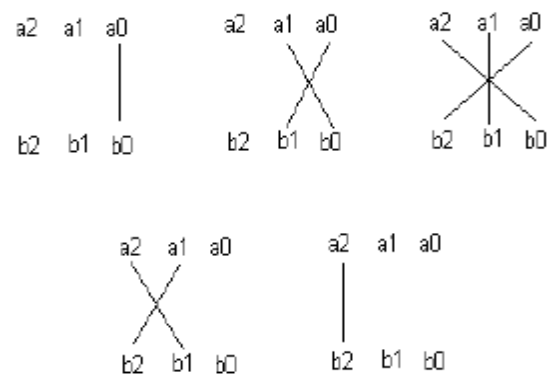


Fig 1. The Vedic Multiplication method

For Multiplier, first the basic blocks, that are the 2x2 bit multipliers have been made and then, using these blocks, 4x4 block has been made by adding the partial products using carry save adders and then using this 4x4 block, 8x8 bit block, 16x16 bit block and then finally 32 x 32 bit Multiplier as shown in figure 3.5 has been made [5].

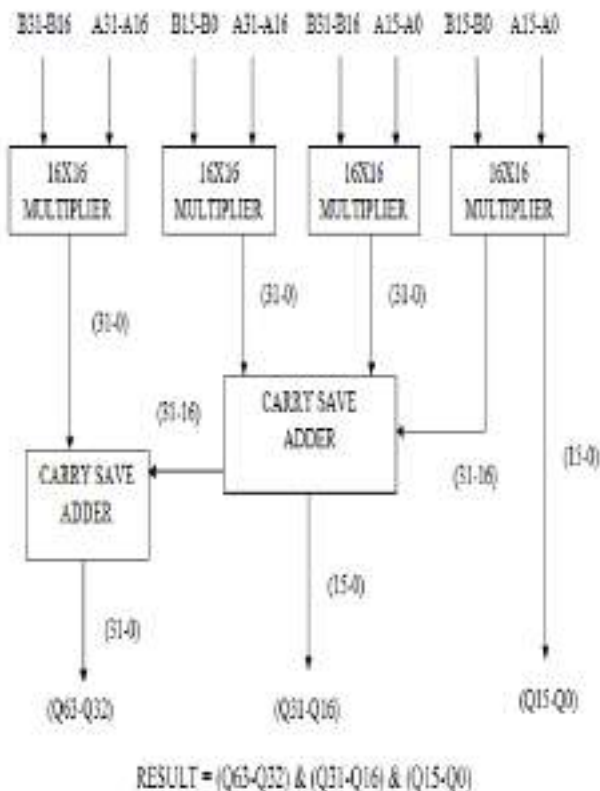


Fig. 2. 32X32 Bits proposed Vedic Multiplier

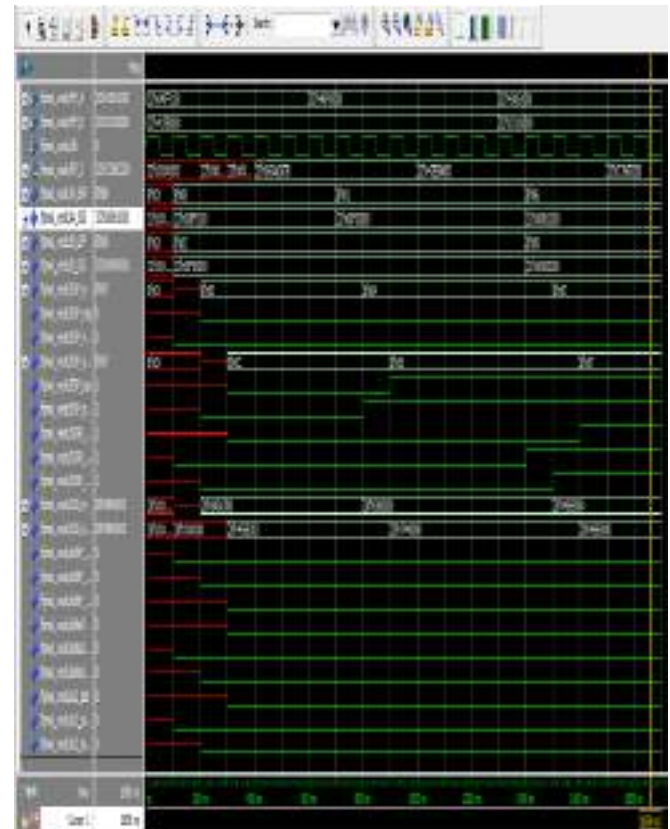


Fig. 3. Simulation Result of Case I

The design starts first with Multiplier design, that is 2x2 bit multiplier as shown in figure 3.6. Here, “Urdhva Tiryakbhyam Sutra” or “Vertically and Crosswise Algorithm”[3] for multiplication has been effectively used to develop digital multiplier architecture. This algorithm is quite different from the traditional method of multiplication, which is to add and shift the partial products.

IV. Result and Discussion

We have taken two inputs ‘A’ and ‘B’ as a multiplier and multiplicand these are floating point signed value we are perform multiplier using Vedic Algorithm between these inputs and will be stored in other output port which we have taken as ‘Z’ all operations are performing on positive edge of clock.

For case I we take value of ‘A’ is 134.0625 and value of ‘B’ is -2.25. Here ‘A’ is unsigned floating pint number and ‘B’ is Signed Floating Point Number. Now we have to convert value of ‘A’ to binary format after normalize we get 1.00001100001×2^7 then we have to convert it into IEEE-32 floating point format then we get 0 10000110 0000110000100000000000 then convert it into hexadecimal format we get 0x43061000. Now we have to convert value of ‘B’ to binary format after normalize we get -1.001×2^1 then we have to convert it into IEEE-32 floating point format then we get 1 10000000 0010000000000000000000 then convert it into hexadecimal format we get 0xC0100000. After multiplication using Vedic Multiplier we get 0xC396D200 the value of this hexadecimal no. is -301.640625 fig 4.1 shows the simulation result of this data.

For case II we take value of ‘A’ is -14.5 and value of ‘B’ is -0.375. Here ‘A’ is signed floating pint number and ‘B’ is also a signed Floating Point Number. Now we have to convert value of ‘A’ to binary format after normalize we get -1.1101×2^3 then we have to convert it into IEEE-32 floating point format then we get 1 10000010 1101000000000000000000 then convert it into hexadecimal format we get 0xC1680000. Now we have to convert value of ‘B’ to binary format after normalize we get -1.1×2^{-2} then we have to convert it into IEEE-32 floating point format then we get 1 01111101 1000000000000000000000 then convert it into hexadecimal format we get 0xBEC00000. After multiplication using Vedic Multiplier we get 0x40AE0000 the value of this hexadecimal no. is 5.4375 fig 4.2 shows the simulation result of this data.

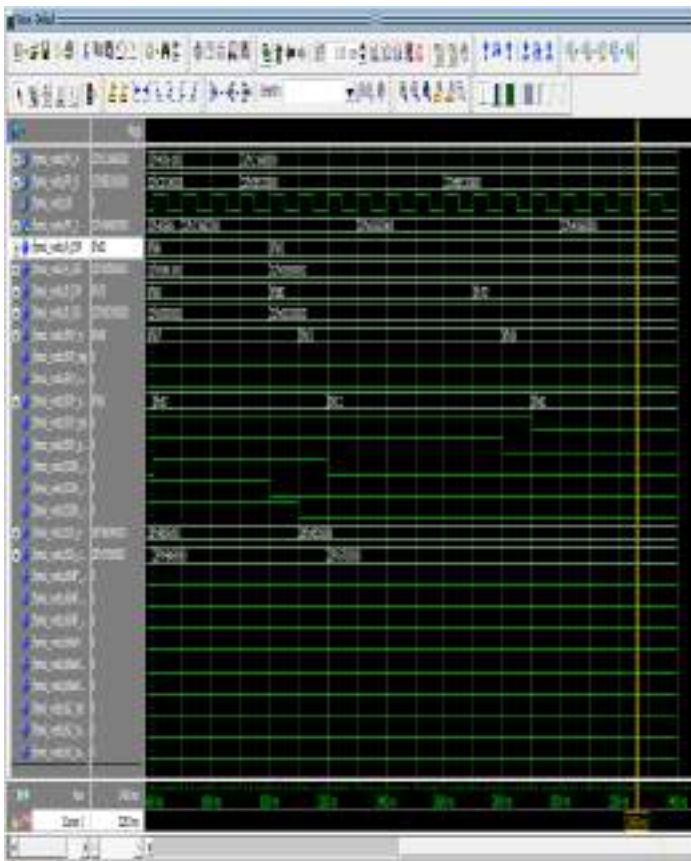


Fig. 4. Simulation Result of Case II

V. Conclusion

The Floating Point numbers are the basic necessity in the current scenario of digital design based systems. Hence we implemented, the design of Floating point number in IEEE32 bit format, on Spartan 3E- XC3S250-5-CP132. The design is based on Vedic method of multiplication. The worst case propagation delay in the Optimized Vedic floating point multiplier case is 4.788 ns. It is therefore seen that the Vedic floating point number multipliers are much faster than the conventional multipliers. This gives us method for hierarchical floating point multiplier design. So the design complexity gets reduced for inputs of large no of bits and modularity gets increased. Urdhva tiryakbhyam sutra algorithm is been used which can reduce the delay and hardware requirements for multiplication of Floating point numbers. FPGA based simulation and Synthesis of this floating point multiplier shows that hardware realization of the Vedic mathematics algorithms is easily possible. The high speed multiplier algorithm exhibits improved efficiency in terms of speed.

References:

- [1] Sushma S. Mahakalkar et al, "Review on floating point multiplier using ancient techniques" IOSR Journal of Electrical and Electronics Engineering (IOSR-JEEE) e-ISSN: 2278-1676, p-ISSN: 2320-3331 PP 01-04.
- [2] Tariquzzaman et al, "FPGA implementation of 64 bit RISC processor with Vedic multiplier using VHDL" IOSR Journal of Electrical and Electronics Engineering (IOSR-JEEE) e-ISSN: 2278-1676, p-ISSN: 2320-3331 PP 12-16.

[3] Aritra Mitra et al, "Design of Floating Point Multiplier based on Vedic Multiplication Technique" School of Electronics Engineering Electronics And Telecommunication Kalinga Institute of Industrial Technology BHUBANESWAR-751024.

[4] Bhagyashree Hardiya et al "Implementation Of Floating Point Multiplier Using VHDL" Technology and Engineering (BEST: IJMITE) Vol. 1, Issue 3, Dec 2013, 199-204 © BEST Journals.

[5] S Venkateswara Reddy et al, "Design And Implementation Of 32 Bit Multiplier Using Vedic Mathematics" International Journal of Advanced Research in Electrical, Electronics and Instrumentation Engineering (An ISO 3297: 2007 Certified Organization) Vol. 2, Issue 8, August 2013.

[6] Remadevi R, "Design and Simulation of Floating Point Multiplier Based on VHDL" Remadevi R / International Journal of Engineering Research and Applications (IJERA) ISSN: 2248-9622 www.ijera.com Vol. 3, Issue 2, March - April 2013, pp.283-286.

[7] Dinesh Kumar et al, "Simulation and Synthesis Of 32-Bit Multiplier Using Configurable Devices" International Journal of Advances in Engineering & Technology, Jan. 2013. ©IJAET ISSN: 2231-1963.

[8] Poornima M et al, "Implementation of Multiplier using Vedic Algorithm" International Journal of Innovative Technology and Exploring Engineering (IJITEE) ISSN: 2278-3075, Volume-2, Issue-6, May 2013.

Production of Biodiesel Using Immobilized *Pseudomonas* Fluorescence

Devendra Pratap Singh ¹, Hemant Kumar ²

¹Department of Applied Sciences, ² [Department](#) of Biotechnology
(Dr. Ambedkar Institute of Technology for Handicapped, Kanpur 208024, India)
(¹Dr.pratap2012@gmail.com, ² hemantkumarhbti@gmail.com)

ABSTRACT

Transesterification of vegetable oils is an important reaction that produces fatty acid alkyl esters, methyl and ethyl esters which are excellent substitutes for diesel fuel. Biodiesel prepared by catalyzed mild transesterification has become of much current interest for alternative fuel production. In the present study the ability of a commercial immobilized *Pseudomonas fluorescens* MTCC 103 to catalyze the transesterification of *Jatropha* oil and methanol was investigated. The cell of *P. fluorescens* was easily immobilized within the sodium alginate during batch process. The important parameters like reaction temperature, pH, oil/methanol molar ratio, amount of beads and reaction time was studied. From the study it was found that highest yield of biodiesel was obtained at the optimum conditions of at temperature 40°C, pH of 7.0, molar ratio of 1:4, amount of beads of 3 g and reaction time of 48 h. The physical properties of the products were analyzed and the results were compared with conventional petroleum based diesel and it was found that the product can be used as an effective alternate fuel in existing diesel engine without any hardware engine modifications.

Keywords – Biodiesel, conventional, environmental, economical, Transesterification.

1. INTRODUCTION

Increasing energy demand, climate change and carbon dioxide (CO₂) emission from fossil fuels make it a high priority to search for low-carbon energy resources. Bio fuels represent a key target for the future energy market that can play an important role in maintaining energy security. It is primarily considered as potentially cheap, low-carbon energy source. Most life-cycle studies of bio fuels have found that bio-ethanol made from corn or sugarcane generally reduces greenhouse gases, replacing gasoline (petrol) [1]. Biodiesel can be produced from any biological feedstock that contains oil or animal fat, through a chemical process (called “transesterification”), reacting feedstock oil or fat with methanol and a potassium hydroxide catalyst. Soybean, sunflower, rapeseed and palm fruit are oil-seed

crops used to produce biodiesel. Animal fat, or even used frying oil can be used to produce biodiesel too. Biodiesel also includes synthetic diesel fuel made through gasification or some other approach. The biodiesel process involves well-established technologies that are not likely to change significantly in the future, but efficiency can be improved by large scale production. Biodiesel, which is the name of a clean burning, renewable diesel fuel replacement made from vegetable oils or animal fats. The methyl ester of vegetable oil or what we now call Biodiesel is very similar to the petrochemical based diesel fuel that it replaces so does not require any vehicle or storage modifications.

Renewable source of energy undergo quick recycling, reproducing and replacement within a reasonable time maintain themselves (like biodiesel, LPG, biogas etc.) but nonrenewable energy source which do not undergo recycling and replacement for example fossil fuels (like coal, petroleum etc.) The main advantage of using this alternative fuel are its renewability, better quality exhaust gas emission, its biodegradability and, given that all the organic carbon present is photosynthetic in origin, it does not contribute to a net rise in the level of carbon dioxide in the atmosphere, and consequently to the greenhouse effect (if the carbon dioxide emitted from fertilizer production is not taken into account).

Biodiesel can be used as a pure fuel or blended with petroleum in any percentage, B5, a blend of 5% Biodiesel and 95% by volume of petroleum diesel has shown improvements in performance, enhanced lubricity and some reduction in emissions. A blend of 20 percent by volume Biodiesel with 80 percent by volume petroleum diesel called B20, has demonstrated significant environmental benefits with a minimum increase in cost. The other way to fuel a diesel engine with vegetable oil is to reduce the oil’s viscosity before it gets into the tank and in this way; neither the engine nor vehicles need modification.

1.1 BIODIESEL

Biodiesel is defined as: a fuel composed of mono-alkyl esters of long chain Fatty acids derived from vegetable oils or animal fats, designated B100. A “mono-alkyl ester” is the

product of the reaction of a straight chain alcohol, such as methanol or ethanol, with a fat or oil (triglyceride) to form glycerol (glycerin) and the esters of long chain fatty acids [2]. Biodiesel, defined as “a substitute for, or an additive to diesel fuel that is derived from the oils and fats of plants and animals”. The transesterification reaction of oil to give mixtures of fatty acids methyl esters. Biodiesel almost completely eliminates lifecycle carbon dioxide emissions. When compared to petro-diesel it reduces emission of particulate matter by 40%, unburned hydrocarbon by 68%, carbon monoxide by 44%, sulphates by 100%, poly cyclic hydrocarbon (PAH) by 80%, and the carcinogenic nitrate PAH by 90% on an average. The use of biodiesel complements the working of the catalyst and can help a current EURO-1 motor attain the EURO-111 standards [3].

1.2 PETRODIESEL

Diesel is produced from petroleum, and is sometimes called petro diesel when there is a need to distinguish it from diesel obtained from other sources. “As a hydrocarbon mixture, it is obtained in the fractional distillation of crude oil between 250°C and 350°C at atmospheric pressure”. Petro diesel is considered to be a fuel oil and is about 18% denser than gasoline. Diesel fuel, however, often contains higher quantities of sulfur; reduction in level of sulfur is essentially required in diesel fuels. High levels of sulfur in diesel are harmful for the environment. It prevents the use of catalytic diesel particulate filters to control diesel particulate emissions, as well as more advanced technologies, such as nitrogen oxide (NOx) adsorbers (still under development), to reduce emissions. However, lowering sulfur also reduces the lubricity of the fuel, meaning that additives must be put into the fuel to help lubricate engines. Biodiesel is an effective lubricity additive.

1.3 CHEMICAL COMPOSITION OF BIODIESEL

Most of biodiesel consists of alkyl usually methyl esters instead of the alkanes and aromatic hydrocarbons of petroleum diesel. However biodiesel has combustion properties very similar to regular diesel including combustion energy and cetane ratings paraffin biodiesel also exists. Due to the purity of the source, it has a higher quality than petro diesel. Petroleum derived diesel is composed of about 75% saturated hydrocarbons (primarily paraffin's including *n*, *iso*, and cycloparaffins), and 25% aromatic hydrocarbons (including naphthalene's and alkyl benzenes). The average chemical formula for common diesel fuel is $C_{12}H_{26}$, ranging from approx. $C_{10}H_{22}$ to $C_{15}H_{32}$.

Biodiesel is derived from vegetable oils. The major components of vegetable oils are triglycerides. Triglycerides are esters of glycerol (see above; an alcohol with a hydroxyl group on each of its three carbon atoms) with long-chain acids, commonly called fatty acids. The comparison of the rational names of the fatty acids with their structural formula

show the position of the double bonds is defined by numbers. The number of carbon atoms is counted by beginning with the first carbon having the functional group defining the fatty compound as acid or ester.

1.4 COMPARISON BETWEEN PETRO & BIODIESEL

Biodiesel can be obtained from vegetable oil and animal fats (bio-lipids, using transesterification). Biodiesel is a non-fossil fuel alternative to petro diesel. It can also be mixed with petro diesel in any account in modern engines, though when first using it, the solvent properties of the fuel tend to clear out all the garbage that has built up from the petro diesel and can clog fuel filters.

Properties	Petrodiesel	Biodiesel
Density 20°C	0.815	0.891
Viscosity 20°C	4.736	6.483
Flash point	>60	>105
Residue carbon w/w	<0.025	<0.005
Ash % w/w	<0.025	<0.005
Heat KJ/Kg	44950	39425

Table: 1 Comparison properties of Petro diesel and Biodiesel

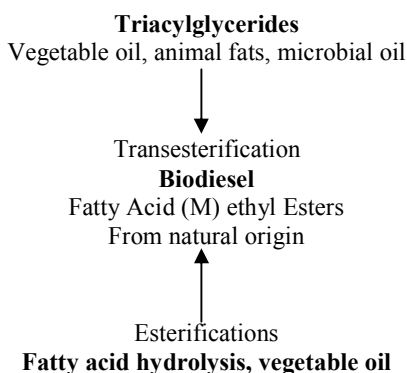
Biodiesel has a lower gel point than regular diesel, but is comparable to diesel. This can be overcome by using a biodiesel/petro diesel, blend, or by installing a small heater in your fuel system, but this is only necessary during the colder months. There have been reports that a diesel biodiesel mix results in lower emissions than either can achieve alone. A small percentage of biodiesel can be used as an additive in low-sulfur formulations of diesel to increase the lubricating ability that is lost when the sulfur is removed.

1.4 PRODUCTION PROCESS (TRANSESTERIFICATION)

Chemically, transesterification (also called alcoholysis) means taking a triglyceride molecules or a complex fatty acid, neutralizing the free fatty acids, removing the glycerin and creating an alcohol. A catalyst is usually used to improve the reaction rate and yield. The transesterification reaction is an equilibrium reaction. In this reaction, however a large amount of methanol was used to shift the reaction equilibrium to the right side and produce more methyl esters, the proposed product. Alcohols are primary or secondary monohydric aliphatic alcohols having 1-8 carbon atoms. Among the alcohols that can be used in the transesterification reaction are methanol, ethanol, propanol, butanol and amyl alcohol. Methanol and ethanol are used most frequently.

Ethanol is a preferred alcohol in the transesterification process compared to methanol because it is derived from agricultural products and is renewable and biologically less objectionable in the environment, however methanol is used

because of its low cost and its physical and chemical advantages (polar and shortest chain alcohol).



The transesterification reaction can be catalyzed by alkalis, acids or enzymes. Several alcoholysis catalysts, known to be effective for reactions between simple alcohols and oil, were evaluated and found to be ineffective toward alcoholysis of ethylene glycol with oil under traditional reaction conditions.

Commonly acids are used in this process; these include sulfuric acid. A high yield of alkyl esters is achieved however high temperature is required to speed up the process. Transesterification process under acid catalyses condition needs to be done in absence of water in order to avoid formation of carboxylic acid, which reduces the yield alkyl ester. The proper determination of the alcohol/vegetable oil ratio influences the final yield. With the use of this type of catalyst excess amount of alcohol is required to complete the transesterified process.

Base catalyzed transesterification process is more efficient and is less corrosive than acid catalyses process which makes it more applicable to industrial use. Base catalysts for transesterification process includes metal hydroxides like sodium or potassium hydroxide, carbonates and metal alkoxides. Metal hydroxides are readily available but are less reactive. Increasing the concentration of the catalyst in the mixture accelerates the reaction. The condition of activity of this catalyst is under anhydrous conditions. However, this cannot be avoided as water is formed during the reaction between hydroxides and alcohol. The yield of alkyl esters is reduced as water hydrolyses the ester, forming soap. Soap forms an emulsion with glycerol making recovery of glycerol difficult. The commonly catalyst used is sodium hydroxide due to its economical availability. However, potassium hydroxide has been reported to be a superior catalyst in the production of biodiesel. Fatty acid was covalently attached to lipase from *Phycomycetia*, yielding a modified lipase of higher specific activity in hydrolytic reaction in organic solvents [4]. The initial rate of transesterification by modified lipase was almost 40 times that of native lipase in organic solvent.

2. MATERIALS & METHODS

2.1 MICROORGANISM (CULTURE)

Pseudomonas fluorescens, MTCC -103 strains procured from Microbial Type Culture Collection, Chandigarh (India) was used in this work. The culture was maintained on agar slant & stored at 4°C in refrigerator. The non-edible crude *Jatropha* oil was purchased commercially and was stored at 4°C to avoid rancidity of the vegetable oil.

2.2 MEDIA & CULTIVATION

Medium for *Pseudomonas fluorescens* was used as MTCC 103 (Nutrient agar). Beef Extract 1g, Yeast Extract 2g, Peptone 5g, NaCl 5g, Distilled H₂O 1 lit, Agar 30g, pH=7. Nutrient agar medium was used for revive of culture. The culture was maintained on nutrient agar medium. After three days incubation at 25°C, the agar slants were stored at 4°C. Inocula were grown aerobically in 250 ml Erlenmeyer flask containing the liquid medium at 25°C in an Orbital Shaker at 200 rpm for 24 h. Active cells were centrifuged in a centrifuge (3000 rpm) for 5 min. after that washed with sterile water. This step repeated at least three times & then used as inoculums.

2.3 CELLS IMMOBILIZATION BY ENTRAPMENT

The sodium alginate entrapment of cells was performed according to the standard method. Alginate solution with a concentration range of 0.5 - 10% was used for the cell immobilization and was prepared by dissolving sodium alginate in boiling water and autoclaved at 121°C for 15 min. Both alginate slurry and cell suspension was mixed and stirred for 10 min to get a uniform mixture the alginate/ cell mixture which was extruded drop by drop into a cold sterile 0.2 M CaCl₂ solution through a sterile 5 ml pipette from 5 cm height and kept for curing at 4°C for 1 h. The beads were hardened by resuspending into a fresh CaCl₂ solution for 24 h at 4°C with gentle agitation. Finally these beads were washed with distilled water to remove excess calcium ions and untrapped cells. When the beads are not being used, they are preserved in 0.86% sodium chloride solutions in the refrigerator.

2.4 CALCULATIONS

2.4.1 Specific gravity:-The specific gravity was determined with a specific gravity bottle or pycnometer. The temperature at which the specific gravity was determined 30°C/30°C. The specific gravity was calculated by the formulae:

$$\text{Specific gravity at } 30^{\circ}\text{C} / 30^{\circ}\text{C} = \frac{A - B}{C - B}$$

Where *A* = weight in g of the specific gravity bottle with oil at 30°C,

B = weight in g of the specific gravity bottle, and

C = weight in g of the specific gravity bottle with water at 30°C

The specific gravity of the fuels at 15.6 °C was also employed to find the specific gravity at other temperatures by using the ASTM D1250 Petroleum Measurement Tables (1953)[13,14].

2.4.2 Viscosity of oil: Viscosity is measured by Oswald-viscometer from the following formula

$$\text{Viscosity } (\eta) = n_w \frac{t_s \times d_s}{T_w \times d_w}$$

Where

η_s = Viscosity of the sample in cp at room temperature

η_w = Viscosity of the water in cp at room temperature

t_s = time of flow of sample (vol=v) in sec.

t_w = time of flow of water (vol=v) in sec.

d_s = density of sample in g/l at room temperature

d_w = density of water in g/l at room temperature

2.4.3 Acid Value: Weigh accurately about 2 g of oil sample dissolve it in 25 ml of alcohol (ethanol) and add 2 to 3 drop of 1 % phenolphthalein titrated against by 0.1 N NaOH gives pink color (end point).

$$\text{Acid Value} = \frac{NEV}{W}$$

2.4.4 Iodine value: Iodine value was calculated by-

$$\text{Iodine Value} = \frac{V_b - V_s}{W} N 12.69$$

Where Wt. of oil = w g

Vol. of hypo used against sample solution = V_s ml

Vol. of hypo used against blank solution = V_b ml

Normality of hypo solution = N

2.4.5 Saponification value: It was also calculated by the formula

$$\text{Saponification value} = \frac{56.1(B - S) N}{W}$$

Where

B = volume in ml of standard hydrochloric acid required for the blank

S = volume in ml of standard hydrochloric acid required for the sample

N = normality of the standard hydrochloric acid, and

W = weight in g of the material taken for the test

X g of the sample requires X mg KOH

1 g of the sample requires x/w mg KOH

Specific gravity, Iodine value and others was measured using the standard method [15&16]. Capillary stopper relative specific gravity bottle (pycnometer bottle) of 50 ml capacity was used to determine specific gravity of biodiesel.

3. RESULT & DISCUSSION

In present work experiments were carried out to growth of culture, *Pseudomonas fluorescens* procured from MTCC, Chandigarh and maintained it on agar slant, cell immobilized by entrapment, characteristics of Jatropa oil, conversion of oil to biodiesel by transesterification and to determine the effects of various parameter (temperature, pH, reaction time, amounts of beads, oil alcohol molar ratio) on the production of biodiesel by transesterification reaction.

3.1 DETERMINATION OF CHARACTERISTICS OF JATROPHA OIL

Chemically oil and fats are triesters of glycerol. Depending upon the physical state of an ester it is called fat (if solid) or oil (if liquid) at room temperature. The following observations were calculated as shown in Table2.

S. N.	Characteristics of oil	Value
1.	Saponification value	13.89 mg KOH/g oil
2.	Specific gravity at 30°C / 30°C	0.92379
3.	Viscosity of oil	52.780 mm ² /s at 303 K
4.	Acid value (with ethanol)	9.8 mg KOH/g oil
	Acid value (with ethanol)	13.2 mg KOH/g oil

Table: 2 Characteristics of Jatropa Oil

3.2 OPTIMIZATION OF TRANSESTERIFICATION REACTION FOR BIODIESEL PRODUCTION

3.2.1 Effect of temperature on the transesterification reaction: Effect of temperature on the transesterification reaction was examined at the temperature range from 30°C to 45°C. Four conical flasks containing 50 ml of Jatropa oil, 3 ml hexane, methanol (1:4 molar ratio of oil/methanol) and 3g beads of immobilized cell concentration. These flasks incubated four different temperatures respectively 30°C, 35°C, 40°C and 45°C at 100 rpm for 48 h. Figure 4.5.1 Shows that the highest percentage conversion at 40°C is 76% and thereafter decreases due to denature of the enzyme.

3.2.2 Effect of pH on the transesterification reaction: Effect of pH on biodiesel production from Jatropa oil using immobilized cells of *Pseudomonas fluorescens* was studied by conducting experiments with different pH as 5.5, 6.0, 6.5, 7.0, and 7.5. The constant reaction mixtures such as 50 ml of Jatropa oil, 3 ml hexane, methanol (1:4 molar ratio of oil/methanol) and 3g immobilized cell concentration in a conical flasks. These flasks were incubated at a constant optimum temperature of 40°C for 48 h reaction period. Figure 2, Shows that the yield of biodiesel was found to be increasing with increasing pH and maximum 76% was

obtained at pH 7.0. Thereafter decreased when pH increased beyond 7.0.

3.2.3 Effect of Effect of reaction time on the transesterification reaction: Effect of time on conversion of fatty acid into their corresponding esters increases with

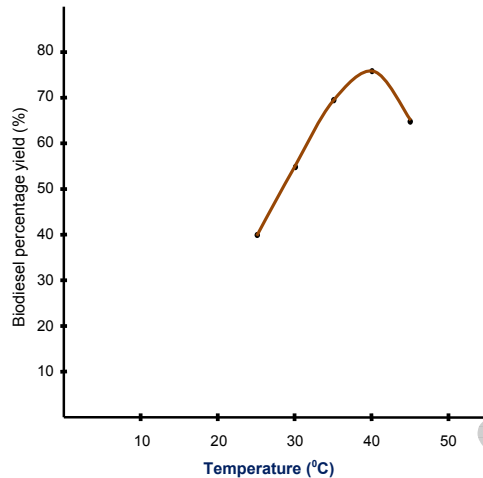


Fig. 1 Effect of temperature on biodiesel yield during transesterification of Jatropha oil using immobilized *Pseudomonas fluorescens*.

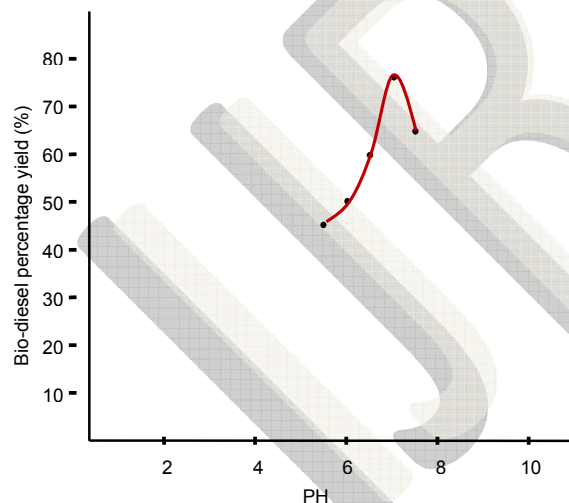


Fig 2. Effect of pH on biodiesel yield during transesterification of Jatropha oil using immobilized *Pseudomonas fluorescens*.

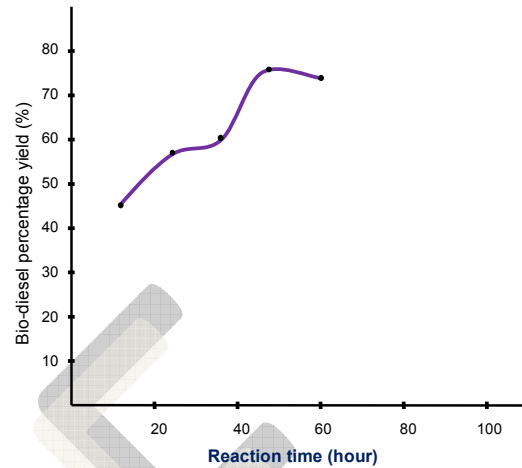


Figure 3. Effect of reaction time on biodiesel yield during transesterification of Jatropha oil using immobilized *Pseudomonas fluorescens*.

-time. The reaction mixture containing 50 ml of oil, 3 ml hexane, methanol (1:4 molar ratio of oil/methanol) and 3g beads of immobilized cells was taken in a conical flask. These flasks were incubated at optimum temperature 40°C in a different time interval as 12, 24, 36, 48 and 60 h. Figure 3, Shows that on increasing the reaction time, the percentage yield of biodiesel increases till 48 h. thereafter slightly decreases, further increases in the reaction time does not have effect on the production of biodiesel.

3.2.4 Effect of amount of beads on the transesterification reaction: The amount of immobilized beads also effect on production of biodiesel from Jatropha oil. Experiments were carried out at different amount of beads as 1, 2, 3, 4, and 5g at constant levels of 50 ml Jatropha oil, 3 ml hexane and methanol (1:4 molar ratio of oil/methanol) at optimum condition of temperature 40°C , pH 7.0 and reaction time 48 h.

Figure 4 Shows that on increasing the amount of beads the percentage yield of biodiesel increases till 4 g (74%) and thereafter slightly decreases. Further does not have effect on production yield. So 4g bead was chosen at the optimum amount of beads.

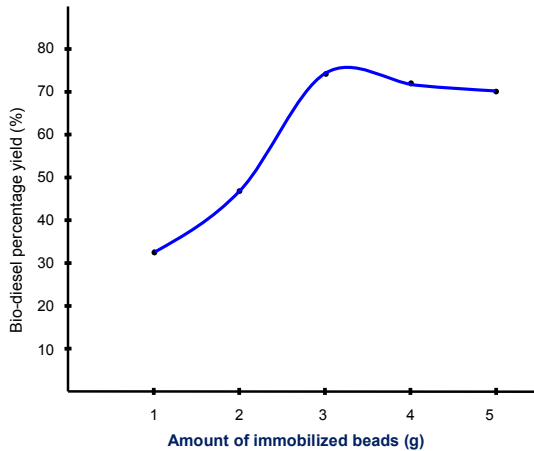


Figure 4. Effect of immobilized beads on biodiesel yield during transesterification of Jatropha oil using immobilized *Pseudomonas fluorescens*.

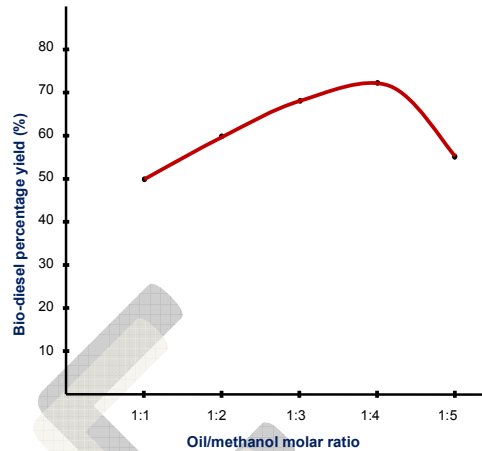


Figure 5. Effect of oil/methanol ratio on biodiesel yield during transesterification of Jatropha oil using immobilized *Pseudomonas fluorescens*.

3.2.5 Effect of oil / alcohol molar ratio on the transesterification reaction: Oil/ alcohol molar ratios also effect on the yield of biodiesel, because to shift the transesterification reaction in forward direction. It is necessary to use either an excess amount of alcohol or to remove one of the products from the reaction or mixture. Experiments were carried out with different molar ratios of 1:1, 1:2, 1:3, 1:4, and 1:5 (oil to methanol) at constant levels of 50 ml Jatropha oil, 3 ml hexane and 3g immobilized cell concentration in a conical flasks. This reaction mixture incubated at optimum conditions such as temperature 40°C, pH 7.0 and reaction time 48 h. Figure 5 Shows that the increasing the molar ratio, the yield of biodiesel was found to be increasing and a maximum yield of 72% were obtained at molar ratio of 1:4. Further yield of biodiesel was found to be decreasing with increasing molar ratio beyond 1:4. It is due to the inhibition of excess methanol reduces the enzyme activity.

3. CONCLUSION

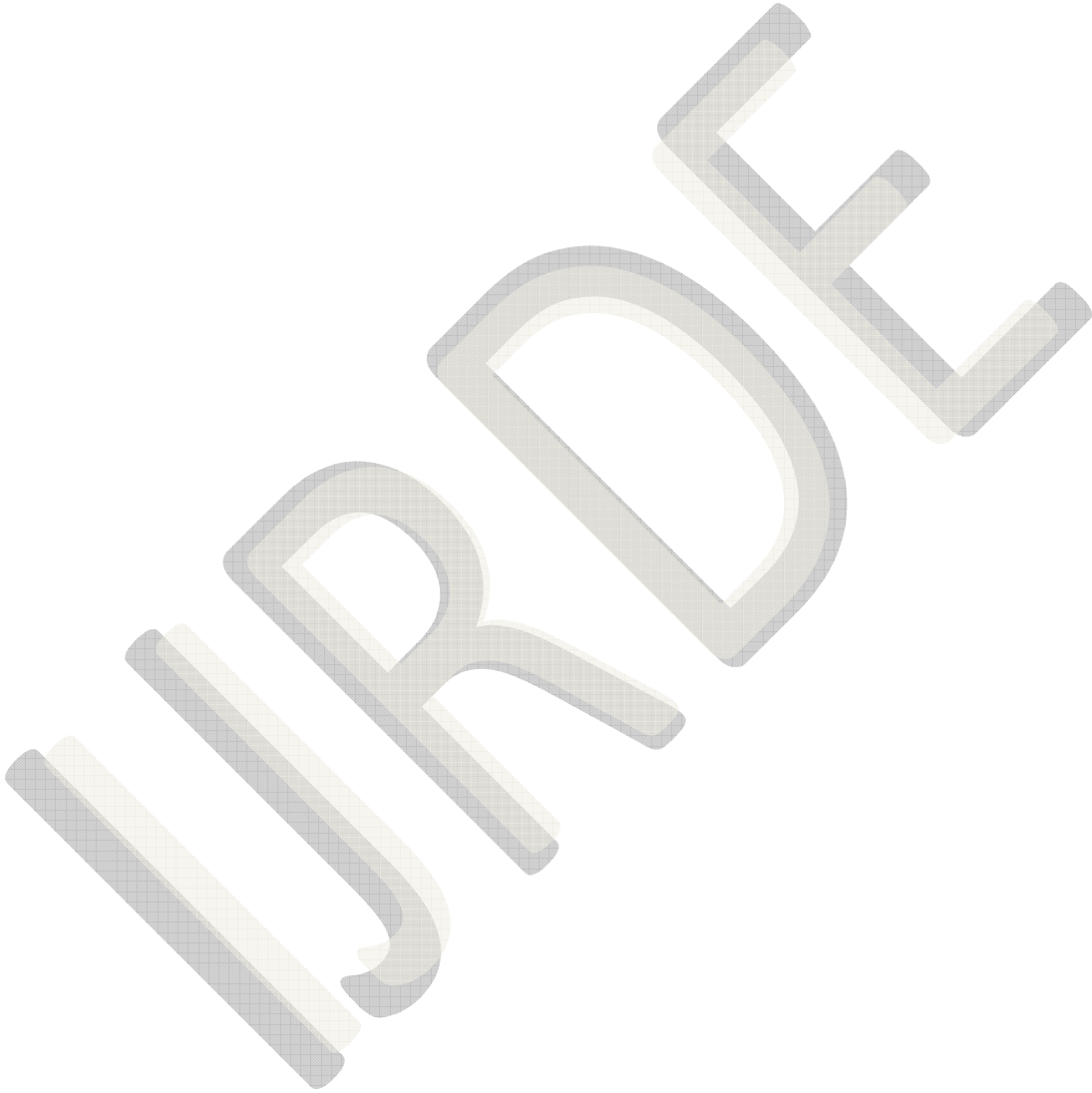
There are several methods are available for producing biodiesel but transesterification of natural oil is currently the method of choice. The purpose of the process is to lower the viscosity of oil. The transesterification was carried out using Jatropha oil and short chain alcohols such as methanol and ethanol by the immobilized cells of *Pseudomonas fluorescens* MTCC 103 under specific condition.

Optimization of various transesterification parameters such as temperature, pH, reaction time, amount of beads and oil/alcohol molar ratio; which affects the biodiesel yield. The maximum yield of 76% was obtained at optimum values of temperature 40°C, pH, reaction time 48 h, amount of beads 4g and molar ratio of oil to alcohol 1:4. The biodiesel produced was analyzed for its physical properties and compared with the petroleum based diesel. The specific gravity, viscosity slightly lower than that of diesel, whereas the diesel index is much higher and the smoke point is slightly lower.

Elevated NOx emissions have been considered as one of the major problems of biodiesel and biodiesel blends as compared to petroleum diesel in diesel engines [5-9]. Earlier combustion that causes more rapid cylinder pressure rise and higher combustion temperature was believed to be one of the main causes [10-12]. This suggests that NOx emissions could be reduced by retarding the combustion timing of the fuel in diesel engines, which can be achieved by adjusting injection timing according to the concentration of biodiesel in petroleum diesel. Therefore, a means to detect the concentration of biodiesel in its diesel blends will be necessary.

REFERENCES

- [1] Hall, D. O., Mynick, H. E. & Williams, R. H., (1991) Cooling the greenhouse with bioenergy. *Nature*, 353:11.
- [2] Jon Van Gerpen, (1999). *A Book "Biodiesel Production and Fuel Quality"* <http://www.uidaho.edu>
- [3] Damier Chrysier et al. (2004). Development, mobility and Environment a case for production and use of biodiesel from Jatropha plantation in India.
- [4] Motoake Murakami, Yoshihiro Kawasaki, Masami Kawanari and Hideo Okai (2003). *Transesterification of oil by fatty acid-modified lipase*, JAOCS, Vol. 70(6), 571-574.
- [5] Choi, C. Y., and R. D. Reitz. 1999. A numerical analysis of the emissions characteristics of biodiesel blended fuels. *Trans. ASME, J. Eng. for Gas Turbines and Power* 121(1): 31-37.
- [6] Sharp, C. A., S. A. Howell, and J. Jobe. 2000. The effect of biodiesel fuels on transient emissions from modern diesel engines: Part I. Regulated emissions and performance. *SAE Paper No. 2000-01-1967*. Warrendale, Pa.: SAE.
- [7] McCormick, R. L., M. S. Graboski, A. M. Herring, and T. L. Alleman. 2001. Impact of biodiesel source material and chemical structure on emissions of criteria pollutants from a heavy-duty engine. *Environ. Sci. & Tech.* 35(9): 1742-1747.
- [8] Grimaldi, C. N., L. Postriotti, M. Battistoni, and F. Millo. 2002. Common rail HSDI diesel engine combustion and emissions with fossil/bio-derived fuel blends. *SAE Tech. Paper 2002-01-6085*. Warrendale, Pa.: SAE.
- [9] Hansen, A. C., M. R. Gratton, and W. Yuan. 2006. Diesel engine performance and NOx emissions from oxygenated bio fuels and blends with diesel. *Trans. ASABE* 49(3): 589-595.
- [10] Tat, M., and J. H. Van Gerpen. 2003. Fuel property effects on biodiesel. *ASAE Paper No. 036034. St. Joseph, Mich.: ASAE*.
- [11] Yuan, W., A. C. Hansen, M. E. Tat, J. H. Van Gerpen, and Z. Tan. 2005. Spray, ignition and combustion modeling of biodiesel fuels in a DI diesel engine. *Trans. ASAE* 48(3): 933-940.
- [12] Yuan, W., A. C. Hansen, and Q. Zhang. 2007. Computational modeling of NOx emissions from biodiesel combustion. *Intl. J. Vehicle Design* 45(1/2): 12-32.
- [13] ASTM-IP Petroleum Measurement Tables. 1953. Prepared jointly by American Society for Testing Materials [and] the Institute of Petroleum. *ASTM Designation: D1250, IP Designation: 200*.
- [14] ASTM D1298-99e2. 2003. Standard Test Method for Density, Relative Density (Specific Gravity), or API Gravity of Crude Petroleum and Liquid Petroleum Products by Hydrometer Method.
- [15] ASTM data series publication. 1975. Viscosity index tables for Celsius temperatures. (Ds39B), (05-039020-12).
- [16] Indian Standard Methods of Sampling and Test for Butterfat's, Fifth edition, December, (1995).



Production of Biodiesel Using Immobilized *Pseudomonas* Fluorescence

Devendra Pratap Singh¹, Hemant Kumar²

¹Department of Applied Sciences, ² [Department](#) of Biotechnology
(Dr. Ambedkar Institute of Technology for Handicapped, Kanpur 208024, India)
(¹Dr.pratap2012@gmail.com, ²hemantkumarhbti@gmail.com)

ABSTRACT

Transesterification of vegetable oils is an important reaction that produces fatty acid alkyl esters, methyl and ethyl esters which are excellent substitutes for diesel fuel. Biodiesel prepared by catalyzed mild transesterification has become of much current interest for alternative fuel production. In the present study the ability of a commercial immobilized *Pseudomonas fluorescens* MTCC 103 to catalyze the transesterification of *Jatropha* oil and methanol was investigated. The cell of *P. fluorescens* was easily immobilized within the sodium alginate during batch process. The important parameters like reaction temperature, pH, oil/methanol molar ratio, amount of beads and reaction time was studied. From the study it was found that highest yield of biodiesel was obtained at the optimum conditions of at temperature 40°C, pH of 7.0, molar ratio of 1:4, amount of beads of 3 g and reaction time of 48 h. The physical properties of the products were analyzed and the results were compared with conventional petroleum based diesel and it was found that the product can be used as an effective alternate fuel in existing diesel engine without any hardware engine modifications.

Keywords – Biodiesel, conventional, environmental, economical, Transesterification.

1. INTRODUCTION

Increasing energy demand, climate change and carbon dioxide (CO₂) emission from fossil fuels make it a high priority to search for low-carbon energy resources. Bio fuels represent a key target for the future energy market that can play an important role in maintaining energy security. It is primarily considered as potentially cheap, low-carbon energy source. Most life-cycle studies of bio fuels have found that bio-ethanol made from corn or sugarcane generally reduces greenhouse gases, replacing gasoline (petrol) [1]. Biodiesel can be produced from any biological feedstock that contains oil or animal fat, through a chemical process (called “transesterification”), reacting feedstock oil or fat with methanol and a potassium hydroxide catalyst. Soybean, sunflower, rapeseed and palm fruit are oil-seed

crops used to produce biodiesel. Animal fat, or even used frying oil can be used to produce biodiesel too. Biodiesel also includes synthetic diesel fuel made through gasification or some other approach. The biodiesel process involves well-established technologies that are not likely to change significantly in the future, but efficiency can be improved by large scale production. Biodiesel, which is the name of a clean burning, renewable diesel fuel replacement made from vegetable oils or animal fats. The methyl ester of vegetable oil or what we now call Biodiesel is very similar to the petrochemical based diesel fuel that it replaces so does not require any vehicle or storage modifications.

Renewable source of energy undergo quick recycling, reproducing and replacement within a reasonable time maintain themselves (like biodiesel, LPG, biogas etc.) but nonrenewable energy source which do not undergo recycling and replacement for example fossil fuels (like coal, petroleum etc.) The main advantage of using this alternative fuel are its renewability, better quality exhaust gas emission, its biodegradability and, given that all the organic carbon present is photosynthetic in origin, it does not contribute to a net rise in the level of carbon dioxide in the atmosphere, and consequently to the greenhouse effect (if the carbon dioxide emitted from fertilizer production is not taken into account).

Biodiesel can be used as a pure fuel or blended with petroleum in any percentage, B5, a blend of 5% Biodiesel and 95% by volume of petroleum diesel has shown improvements in performance, enhanced lubricity and some reduction in emissions. A blend of 20 percent by volume Biodiesel with 80 percent by volume petroleum diesel called B20, has demonstrated significant environmental benefits with a minimum increase in cost. The other way to fuel a diesel engine with vegetable oil is to reduce the oil’s viscosity before it gets into the tank and in this way; neither the engine nor vehicles need modification.

1.1 BIODIESEL

Biodiesel is defined as: a fuel composed of mono-alkyl esters of long chain Fatty acids derived from vegetable oils or animal fats, designated B100. A “mono-alkyl ester” is the

product of the reaction of a straight chain alcohol, such as methanol or ethanol, with a fat or oil (triglyceride) to form glycerol (glycerin) and the esters of long chain fatty acids [2]. Biodiesel, defined as “a substitute for, or an additive to diesel fuel that is derived from the oils and fats of plants and animals”. The transesterification reaction of oil to give mixtures of fatty acids methyl esters. Biodiesel almost completely eliminates lifecycle carbon dioxide emissions. When compared to petro-diesel it reduces emission of particulate matter by 40%, unburned hydrocarbon by 68%, carbon monoxide by 44%, sulphates by 100%, poly cyclic hydrocarbon (PAH) by 80%, and the carcinogenic nitrate PAH by 90% on an average. The use of biodiesel complements the working of the catalyst and can help a current EURO-1 motor attain the EURO-111 standards [3].

1.2 PETRODIESEL

Diesel is produced from petroleum, and is sometimes called petro diesel when there is a need to distinguish it from diesel obtained from other sources. “As a hydrocarbon mixture, it is obtained in the fractional distillation of crude oil between 250°C and 350°C at atmospheric pressure”. Petro diesel is considered to be a fuel oil and is about 18% denser than gasoline. Diesel fuel, however, often contains higher quantities of sulfur; reduction in level of sulfur is essentially required in diesel fuels. High levels of sulfur in diesel are harmful for the environment. It prevents the use of catalytic diesel particulate filters to control diesel particulate emissions, as well as more advanced technologies, such as nitrogen oxide (NOx) adsorbers (still under development), to reduce emissions. However, lowering sulfur also reduces the lubricity of the fuel, meaning that additives must be put into the fuel to help lubricate engines. Biodiesel is an effective lubricity additive.

1.3 CHEMICAL COMPOSITION OF BIODIESEL

Most of biodiesel consists of alkyl usually methyl esters instead of the alkanes and aromatic hydrocarbons of petroleum diesel. However biodiesel has combustion properties very similar to regular diesel including combustion energy and cetane ratings paraffin biodiesel also exists. Due to the purity of the source, it has a higher quality than petro diesel. Petroleum derived diesel is composed of about 75% saturated hydrocarbons (primarily paraffin's including *n*, *iso*, and cycloparaffins), and 25% aromatic hydrocarbons (including naphthalene's and alkyl benzenes). The average chemical formula for common diesel fuel is $C_{12}H_{26}$, ranging from approx. $C_{10}H_{22}$ to $C_{15}H_{32}$.

Biodiesel is derived from vegetable oils. The major components of vegetable oils are triglycerides. Triglycerides are esters of glycerol (see above; an alcohol with a hydroxyl group on each of its three carbon atoms) with long-chain acids, commonly called fatty acids. The comparison of the rational names of the fatty acids with their structural formula

show the position of the double bonds is defined by numbers. The number of carbon atoms is counted by beginning with the first carbon having the functional group defining the fatty compound as acid or ester.

1.4 COMPARISON BETWEEN PETRO & BIODIESEL

Biodiesel can be obtained from vegetable oil and animal fats (bio-lipids, using transesterification). Biodiesel is a non-fossil fuel alternative to petro diesel. It can also be mixed with petro diesel in any account in modern engines, though when first using it, the solvent properties of the fuel tend to clear out all the garbage that has built up from the petro diesel and can clog fuel filters.

Properties	Petrodiesel	Biodiesel
Density 20°C	0.815	0.891
Viscosity 20°C	4.736	6.483
Flash point	>60	>105
Residue carbon w/w	<0.025	<0.005
Ash % w/w	<0.025	<0.005
Heat KJ/Kg	44950	39425

Table: 1 Comparison properties of Petro diesel and Biodiesel

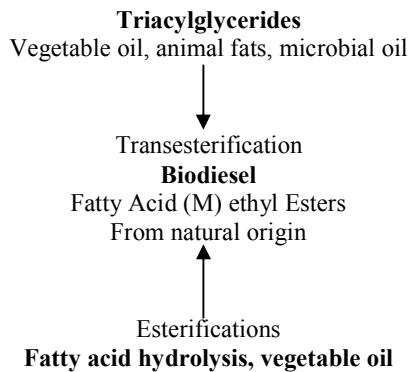
Biodiesel has a lower gel point than regular diesel, but is comparable to diesel. This can be overcome by using a biodiesel/petro diesel, blend, or by installing a small heater in your fuel system, but this is only necessary during the colder months. There have been reports that a diesel biodiesel mix results in lower emissions than either can achieve alone. A small percentage of biodiesel can be used as an additive in low-sulfur formulations of diesel to increase the lubricating ability that is lost when the sulfur is removed.

1.4 PRODUCTION PROCESS (TRANSESTERIFICATION)

Chemically, transesterification (also called alcoholysis) means taking a triglyceride molecules or a complex fatty acid, neutralizing the free fatty acids, removing the glycerin and creating an alcohol. A catalyst is usually used to improve the reaction rate and yield. The transesterification reaction is an equilibrium reaction. In this reaction, however a large amount of methanol was used to shift the reaction equilibrium to the right side and produce more methyl esters, the proposed product. Alcohols are primary or secondary monohydric aliphatic alcohols having 1-8 carbon atoms. Among the alcohols that can be used in the transesterification reaction are methanol, ethanol, propanol, butanol and amyl alcohol. Methanol and ethanol are used most frequently.

Ethanol is a preferred alcohol in the transesterification process compared to methanol because it is derived from agricultural products and is renewable and biologically less objectionable in the environment, however methanol is used

because of its low cost and its physical and chemical advantages (polar and shortest chain alcohol).



The transesterification reaction can be catalyzed by alkalis, acids or enzymes. Several alcoholysis catalysts, known to be effective for reactions between simple alcohols and oil, were evaluated and found to be ineffective toward alcoholysis of ethylene glycol with oil under traditional reaction conditions.

Commonly acids are used in this process; these include sulfuric acid. A high yield of alkyl esters is achieved however high temperature is required to speed up the process. Transesterification process under acid catalyses condition needs to be done in absence of water in order to avoid formation of carboxylic acid, which reduces the yield alkyl ester. The proper determination of the alcohol/vegetable oil ratio influences the final yield. With the use of this type of catalyst excess amount of alcohol is required to complete the transesterified process.

Base catalyzed transesterification process is more efficient and is less corrosive than acid catalyses process which makes it more applicable to industrial use. Base catalysts for transesterification process includes metal hydroxides like sodium or potassium hydroxide, carbonates and metal alkoxides. Metal hydroxides are readily available but are less reactive. Increasing the concentration of the catalyst in the mixture accelerates the reaction. The condition of activity of this catalyst is under anhydrous conditions. However, this cannot be avoided as water is formed during the reaction between hydroxides and alcohol. The yield of alkyl esters is reduced as water hydrolyses the ester, forming soap. Soap forms an emulsion with glycerol making recovery of glycerol difficult. The commonly catalyst used is sodium hydroxide due to its economical availability. However, potassium hydroxide has been reported to be a superior catalyst in the production of biodiesel. Fatty acid was covalently attached to lipase from *Phycomycetia*, yielding a modified lipase of higher specific activity in hydrolytic reaction in organic solvents [4]. The initial rate of transesterification by modified lipase was almost 40 times that of native lipase in organic solvent.

2. MATERIALS & METHODS

2.1 MICROORGANISM (CULTURE)

Pseudomonas fluorescens, MTCC -103 strains procured from Microbial Type Culture Collection, Chandigarh (India) was used in this work. The culture was maintained on agar slant & stored at 4°C in refrigerator. The non-edible crude *Jatropha* oil was purchased commercially and was stored at 4°C to avoid rancidity of the vegetable oil.

2.2 MEDIA & CULTIVATION

Medium for *Pseudomonas fluorescens* was used as MTCC 103 (Nutrient agar). Beef Extract 1g, Yeast Extract 2g, Peptone 5g, NaCl 5g, Distilled H₂O 1 lit, Agar 30g, pH=7. Nutrient agar medium was used for revive of culture. The culture was maintained on nutrient agar medium. After three days incubation at 25°C, the agar slants were stored at 4°C. Inocula were grown aerobically in 250 ml Erlenmeyer flask containing the liquid medium at 25°C in an Orbital Shaker at 200 rpm for 24 h. Active cells were centrifuged in a centrifuge (3000 rpm) for 5 min. after that washed with sterile water. This step repeated at least three times & then used as inoculums.

2.3 CELLS IMMOBILIZATION BY ENTRAPMENT

The sodium alginate entrapment of cells was performed according to the standard method. Alginate solution with a concentration range of 0.5 - 10% was used for the cell immobilization and was prepared by dissolving sodium alginate in boiling water and autoclaved at 121°C for 15 min. Both alginate slurry and cell suspension was mixed and stirred for 10 min to get a uniform mixture the alginate/ cell mixture which was extruded drop by drop into a cold sterile 0.2 M CaCl₂ solution through a sterile 5 ml pipette from 5 cm height and kept for curing at 4°C for 1 h. The beads were hardened by resuspending into a fresh CaCl₂ solution for 24 h at 4°C with gentle agitation. Finally these beads were washed with distilled water to remove excess calcium ions and untrapped cells. When the beads are not being used, they are preserved in 0.86% sodium chloride solutions in the refrigerator.

2.4 CALCULATIONS

2.4.1 Specific gravity:-The specific gravity was determined with a specific gravity bottle or pycnometer. The temperature at which the specific gravity was determined 30°C/30°C. The specific gravity was calculated by the formulae:

$$\text{Specific gravity at } 30^{\circ}\text{C} / 30^{\circ}\text{C} = \frac{A - B}{C - B}$$

Where *A* = weight in g of the specific gravity bottle with oil at 30°C,

B = weight in g of the specific gravity bottle, and

C = weight in g of the specific gravity bottle with water at 30°C

The specific gravity of the fuels at 15.6 °C was also employed to find the specific gravity at other temperatures by using the ASTM D1250 Petroleum Measurement Tables (1953)[13,14].

2.4.2 Viscosity of oil: Viscosity is measured by Oswald-viscometer from the following formula

$$\text{Viscosity } (\eta) = n_w \frac{t_s \times d_s}{T_w \times d_w}$$

Where

η_s = Viscosity of the sample in cp at room temperature

η_w = Viscosity of the water in cp at room temperature

t_s = time of flow of sample (vol=v) in sec.

t_w = time of flow of water (vol=v) in sec.

d_s = density of sample in g/l at room temperature

d_w = density of water in g/l at room temperature

2.4.3 Acid Value: Weigh accurately about 2 g of oil sample dissolve it in 25 ml of alcohol (ethanol) and add 2 to 3 drop of 1 % phenolphthalein titrated against by 0.1 N NaOH gives pink color (end point).

$$\text{Acid Value} = \frac{NEV}{W}$$

2.4.4 Iodine value: Iodine value was calculated by-

$$\text{Iodine Value} = \frac{V_b - V_s}{W} N 12.69$$

Where Wt. of oil = w g

Vol. of hypo used against sample solution = V_s ml

Vol. of hypo used against blank solution = V_b ml

Normality of hypo solution = N

2.4.5 Saponification value: It was also calculated by the formula

$$\text{Saponification value} = \frac{56.1(B - S) N}{W}$$

Where

B = volume in ml of standard hydrochloric acid required for the blank

S = volume in ml of standard hydrochloric acid required for the sample

N = normality of the standard hydrochloric acid, and

W = weight in g of the material taken for the test

X g of the sample requires X mg KOH

1 g of the sample requires x/w mg KOH

Specific gravity, Iodine value and others was measured using the standard method [15&16]. Capillary stopper relative specific gravity bottle (pycnometer bottle) of 50 ml capacity was used to determine specific gravity of biodiesel.

3. RESULT & DISCUSSION

In present work experiments were carried out to growth of culture, *Pseudomonas fluorescens* procured from MTCC, Chandigarh and maintained it on agar slant, cell immobilized by entrapment, characteristics of Jatropa oil, conversion of oil to biodiesel by transesterification and to determine the effects of various parameter (temperature, pH, reaction time, amounts of beads, oil alcohol molar ratio) on the production of biodiesel by transesterification reaction.

3.1 DETERMINATION OF CHARACTERISTICS OF JATROPHA OIL

Chemically oil and fats are triesters of glycerol. Depending upon the physical state of an ester it is called fat (if solid) or oil (if liquid) at room temperature. The following observations were calculated as shown in Table2.

S. N.	Characteristics of oil	Value
1.	Saponification value	13.89 mg KOH/g oil
2.	Specific gravity at 30°C / 30°C	0.92379
3.	Viscosity of oil	52.780 mm ² /s at 303 K
4.	Acid value (with ethanol)	9.8 mg KOH/g oil
	Acid value (with ethanol)	13.2 mg KOH/g oil

Table: 2 Characteristics of Jatropa Oil

3.2 OPTIMIZATION OF TRANSESTERIFICATION REACTION FOR BIODIESEL PRODUCTION

3.2.1 Effect of temperature on the transesterification reaction: Effect of temperature on the transesterification reaction was examined at the temperature range from 30°C to 45°C. Four conical flasks containing 50 ml of Jatropa oil, 3 ml hexane, methanol (1:4 molar ratio of oil/methanol) and 3g beads of immobilized cell concentration. These flasks incubated four different temperatures respectively 30°C, 35°C, 40°C and 45°C at 100 rpm for 48 h. Figure 4.5.1 Shows that the highest percentage conversion at 40°C is 76% and thereafter decreases due to denature of the enzyme.

3.2.2 Effect of pH on the transesterification reaction: Effect of pH on biodiesel production from Jatropa oil using immobilized cells of *Pseudomonas fluorescens* was studied by conducting experiments with different pH as 5.5, 6.0, 6.5, 7.0, and 7.5. The constant reaction mixtures such as 50 ml of Jatropa oil, 3 ml hexane, methanol (1:4 molar ratio of oil/methanol) and 3g immobilized cell concentration in a conical flasks. These flasks were incubated at a constant optimum temperature of 40°C for 48 h reaction period. Figure 2, Shows that the yield of biodiesel was found to be increasing with increasing pH and maximum 76% was

obtained at pH 7.0. Thereafter decreased when pH increased beyond 7.0.

3.2.3 Effect of Effect of reaction time on the transesterification reaction: Effect of time on conversion of fatty acid into their corresponding esters increases with

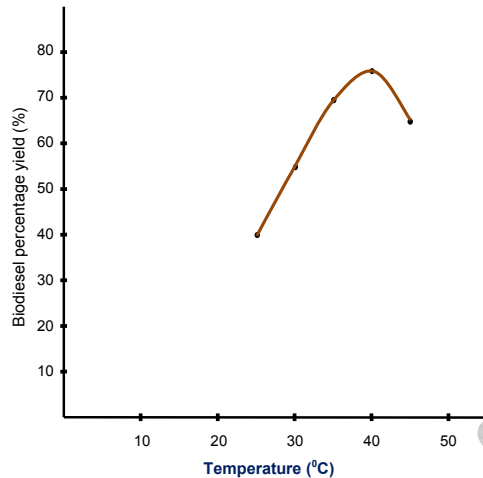


Fig. 1 Effect of temperature on biodiesel yield during transesterification of Jatropha oil using immobilized *Pseudomonas fluorescens*.

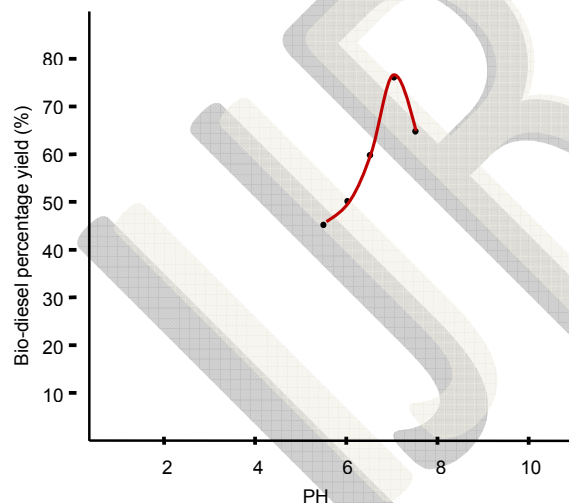


Fig 2. Effect of pH on biodiesel yield during transesterification of Jatropha oil using immobilized *Pseudomonas fluorescens*.

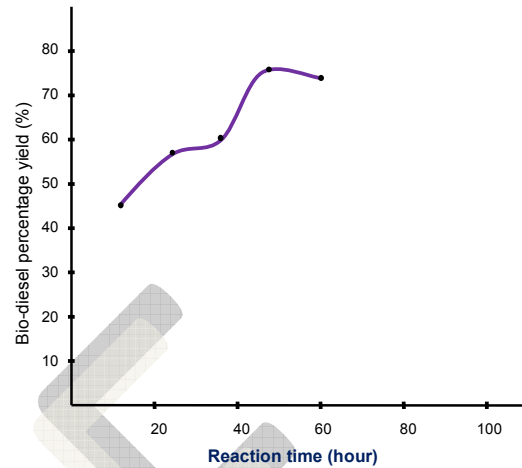


Figure 3. Effect of reaction time on biodiesel yield during transesterification of Jatropha oil using immobilized *Pseudomonas fluorescens*.

-time. The reaction mixture containing 50 ml of oil, 3 ml hexane, methanol (1:4 molar ratio of oil/methanol) and 3g beads of immobilized cells was taken in a conical flask. These flasks were incubated at optimum temperature 40°C in a different time interval as 12, 24, 36, 48 and 60 h. Figure 3, Shows that on increasing the reaction time, the percentage yield of biodiesel increases till 48 h. thereafter slightly decreases, further increases in the reaction time does not have effect on the production of biodiesel.

3.2.4 Effect of amount of beads on the transesterification reaction: The amount of immobilized beads also effect on production of biodiesel from Jatropha oil. Experiments were carried out at different amount of beads as 1, 2, 3, 4, and 5g at constant levels of 50 ml Jatropha oil, 3 ml hexane and methanol (1:4 molar ratio of oil/methanol) at optimum condition of temperature 40°C , pH 7.0 and reaction time 48 h.

Figure 4 Shows that on increasing the amount of beads the percentage yield of biodiesel increases till 4 g (74%) and thereafter slightly decreases. Further does not have effect on production yield. So 4g bead was chosen at the optimum amount of beads.

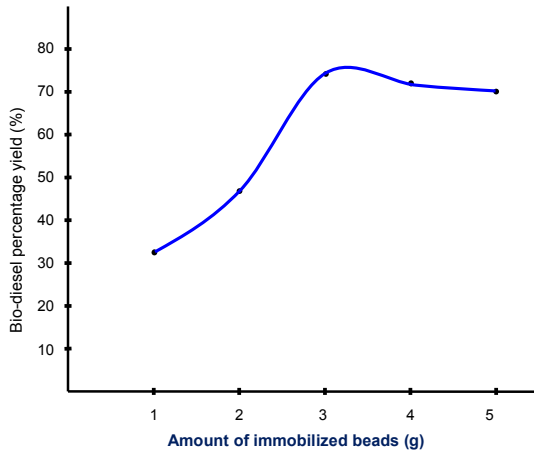


Figure 4. Effect of immobilized beads on biodiesel yield during transesterification of Jatropha oil using immobilized *Pseudomonas fluorescens*.

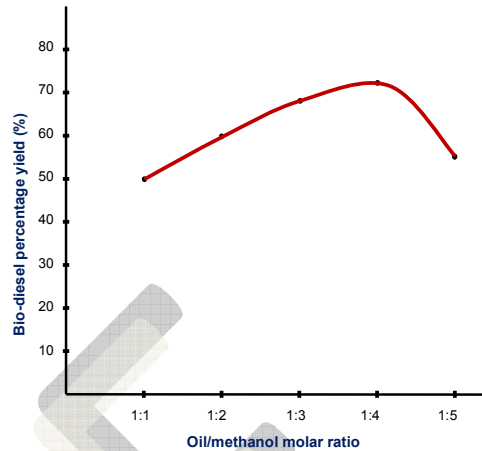


Figure 5. Effect of oil/methanol ratio on biodiesel yield during transesterification of Jatropha oil using immobilized *Pseudomonas fluorescens*.

3.2.5 Effect of oil / alcohol molar ratio on the transesterification reaction: Oil/ alcohol molar ratios also effect on the yield of biodiesel, because to shift the transesterification reaction in forward direction. It is necessary to use either an excess amount of alcohol or to remove one of the products from the reaction or mixture. Experiments were carried out with different molar ratios of 1:1, 1:2, 1:3, 1:4, and 1:5 (oil to methanol) at constant levels of 50 ml Jatropha oil, 3 ml hexane and 3g immobilized cell concentration in a conical flasks. This reaction mixture incubated at optimum conditions such as temperature 40°C, pH 7.0 and reaction time 48 h. Figure 5 Shows that the increasing the molar ratio, the yield of biodiesel was found to be increasing and a maximum yield of 72% were obtained at molar ratio of 1:4. Further yield of biodiesel was found to be decreasing with increasing molar ratio beyond 1:4. It is due to the inhibition of excess methanol reduces the enzyme activity.

3. CONCLUSION

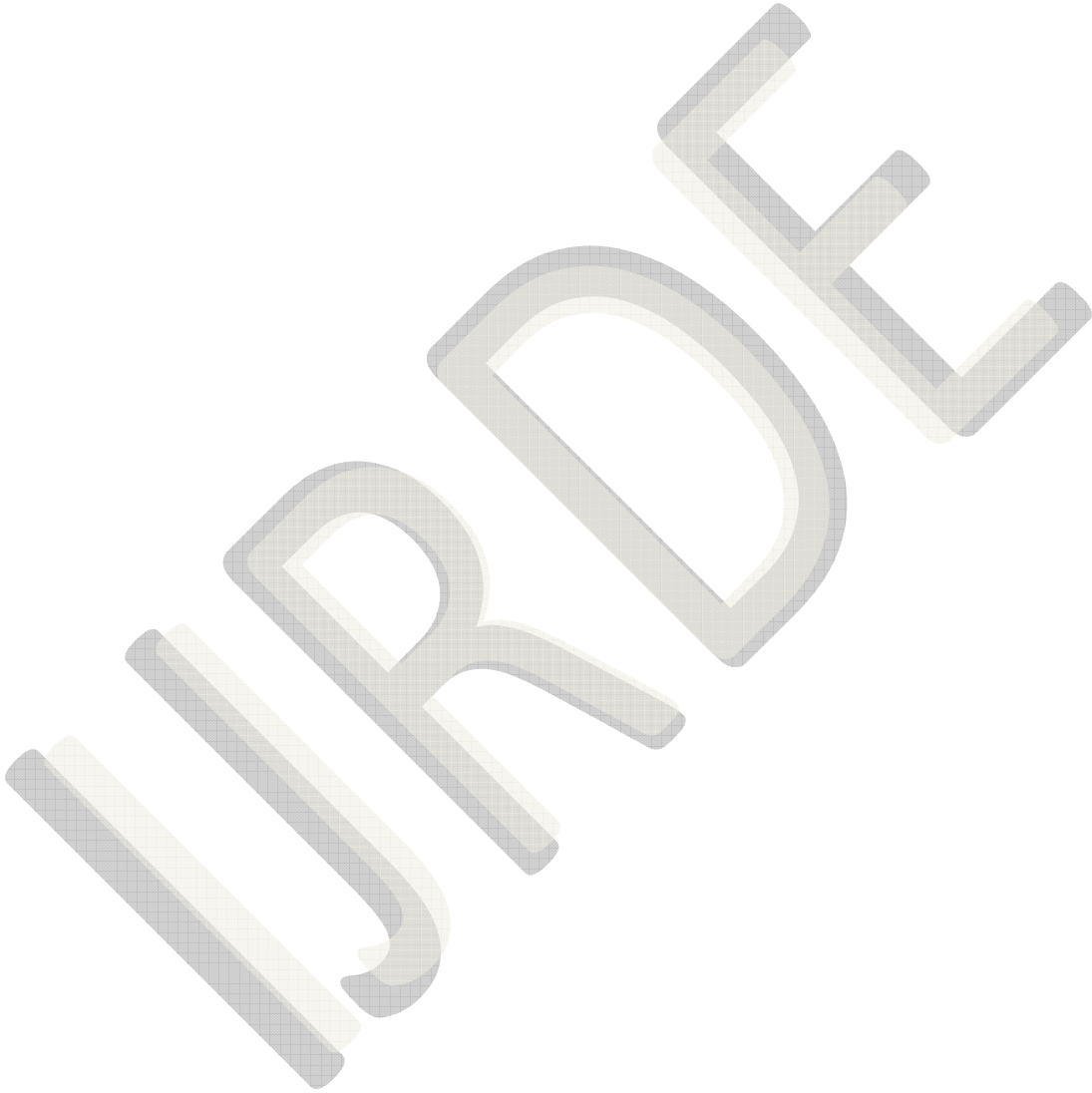
There are several methods are available for producing biodiesel but transesterification of natural oil is currently the method of choice. The purpose of the process is to lower the viscosity of oil. The transesterification was carried out using Jatropha oil and short chain alcohols such as methanol and ethanol by the immobilized cells of *Pseudomonas fluorescens* MTCC 103 under specific condition.

Optimization of various transesterification parameters such as temperature, pH, reaction time, amount of beads and oil/alcohol molar ratio; which affects the biodiesel yield. The maximum yield of 76% was obtained at optimum values of temperature 40°C, pH, reaction time 48 h, amount of beads 4g and molar ratio of oil to alcohol 1:4. The biodiesel produced was analyzed for its physical properties and compared with the petroleum based diesel. The specific gravity, viscosity slightly lower than that of diesel, whereas the diesel index is much higher and the smoke point is slightly lower.

Elevated NOx emissions have been considered as one of the major problems of biodiesel and biodiesel blends as compared to petroleum diesel in diesel engines [5-9]. Earlier combustion that causes more rapid cylinder pressure rise and higher combustion temperature was believed to be one of the main causes [10-12]. This suggests that NOx emissions could be reduced by retarding the combustion timing of the fuel in diesel engines, which can be achieved by adjusting injection timing according to the concentration of biodiesel in petroleum diesel. Therefore, a means to detect the concentration of biodiesel in its diesel blends will be necessary.

REFERENCES

- [1] Hall, D. O., Mynick, H. E. & Williams, R. H., (1991) Cooling the greenhouse with bioenergy. *Nature*, 353:11.
- [2] Jon Van Gerpen, (1999). *A Book "Biodiesel Production and Fuel Quality"* <http://www.uidaho.edu>
- [3] Damier Chrysier et al. (2004). Development, mobility and Environment a case for production and use of biodiesel from Jatropha plantation in India.
- [4] Motoake Murakami, Yoshihiro Kawasaki, Masami Kawanari and Hideo Okai (2003). *Transesterification of oil by fatty acid-modified lipase*, JAOCS, Vol. 70(6), 571-574.
- [5] Choi, C. Y., and R. D. Reitz. 1999. A numerical analysis of the emissions characteristics of biodiesel blended fuels. *Trans. ASME, J. Eng. for Gas Turbines and Power* 121(1): 31-37.
- [6] Sharp, C. A., S. A. Howell, and J. Jobe. 2000. The effect of biodiesel fuels on transient emissions from modern diesel engines: Part I. Regulated emissions and performance. *SAE Paper No. 2000-01-1967*. Warrendale, Pa.: SAE.
- [7] McCormick, R. L., M. S. Graboski, A. M. Herring, and T. L. Alleman. 2001. Impact of biodiesel source material and chemical structure on emissions of criteria pollutants from a heavy-duty engine. *Environ. Sci. & Tech.* 35(9): 1742-1747.
- [8] Grimaldi, C. N., L. Postriotti, M. Battistoni, and F. Millo. 2002. Common rail HSDI diesel engine combustion and emissions with fossil/bio-derived fuel blends. *SAE Tech. Paper 2002-01-6085*. Warrendale, Pa.: SAE.
- [9] Hansen, A. C., M. R. Gratton, and W. Yuan. 2006. Diesel engine performance and NOx emissions from oxygenated bio fuels and blends with diesel. *Trans. ASABE* 49(3): 589-595.
- [10] Tat, M., and J. H. Van Gerpen. 2003. Fuel property effects on biodiesel. *ASAE Paper No. 036034. St. Joseph, Mich.: ASAE*.
- [11] Yuan, W., A. C. Hansen, M. E. Tat, J. H. Van Gerpen, and Z. Tan. 2005. Spray, ignition and combustion modeling of biodiesel fuels in a DI diesel engine. *Trans. ASAE* 48(3): 933-940.
- [12] Yuan, W., A. C. Hansen, and Q. Zhang. 2007. Computational modeling of NOx emissions from biodiesel combustion. *Intl. J. Vehicle Design* 45(1/2): 12-32.
- [13] ASTM-IP Petroleum Measurement Tables. 1953. Prepared jointly by American Society for Testing Materials [and] the Institute of Petroleum. *ASTM Designation: D1250, IP Designation: 200*.
- [14] ASTM D1298-99e2. 2003. Standard Test Method for Density, Relative Density (Specific Gravity), or API Gravity of Crude Petroleum and Liquid Petroleum Products by Hydrometer Method.
- [15] ASTM data series publication. 1975. Viscosity index tables for Celsius temperatures. (Ds39B), (05-039020-12).
- [16] Indian Standard Methods of Sampling and Test for Butterfat's, Fifth edition, December, (1995).



ICGSEE-2013[14th – 16th March 2013]
International Conference on Global Scenario in Environment and Energy

Acid And Alkaline Pretreatment Of Lignocellulosic Biomass To Produce Ethanol As Biofuel

Devendra Pratap Singh¹, Rakesh Kumar Trivedi^{2*}

¹Department of Applied Chemistry, Dr. Ambedkar Institute of Technology for Handicapped, Kanpur 208024, India.

²Department of Oil and Paint Technology, Harcourt Butler Technological Institute, Kanpur 208002, India.

*Corres. Author: rakeshtrivedi@hotmail.com

Abstract: Ethanol obtained from biomass has potential to become an important sustainable transportation fuel in the near future. Renewable energy sources, such as lignocellulosic biomass, are environmentally friendly because they emit less pollution without contributing net carbon dioxide to the atmosphere. Among kinds of biomass, lignocellulosic biomass is a very useful feedstock to economically produce environmentally friendly biofuels. The main goal of the research described in this paper is to investigate the process of pretreated biomass, effect of inhibitors and ethanol fermentation as an efficient bio fuel source for the society, as well as to examine whether it is used and beneficial for the society, which helps to control the global warming. Processing of lignocellulosic biomass to ethanol consists of four major operations: (a) Pretreatment (b) Acid or enzymatic hydrolysis (c) Fermentation and (d) Ethanol separation/purification. In this paper alkali and acid method of pretreatment was used to examine their effect on ethanol production. Effective parameters such as pH, Nutrient media and sugar concentration also effected the enzymatic growth and production of ethanol from lignocellulosic biomasses.

Production of ethanol from agricultural and forestry residues, municipal solid waste, energy crops, and other forms of lignocellulosic biomass could improve energy security, reduce trade deficits, decrease urban air pollution, and contribute little, if any, net carbon dioxide accumulation to the atmosphere. The use of production of ethanol is more beneficial and economical because most of the lignocellulosic agricultural wastes are converted in to ethanol as biofuel in urban areas. Biofuels should ideally create the environmental, economic and social benefits to the communities in India, but modification in process and car engine should be needed. Bioethanol is also made from different Algal biomass in the terms of third generation of biofuel. In fact, not only are they environmentally friendly, but they have also been shown to get just as good of gas mileage as petroleum based fuels. It will eventually totally replace petroleum fuels, but that remains to be seen. Ethanol is made from agricultural wastes is less polluting than diesel and oil based fuels, and gets better gas mileage than many of the alternatives.

Keywords: Bio ethanol, Biomass, Pretreatment, Inhibitors, fermentation, hydrolysis, sugar.

Introduction:

Biomass is a renewable energy resource derived from the carbonaceous waste of various human and natural activities. It is derived from numerous sources, including the by-products from the timber industry, agricultural crops, raw material from the forest, major parts of household waste and wood. Biomass is available in different forms in the country, it cannot be defined easily because all things, which are dead and produces energy on combustion is a part of biomass either it may consist different thing. Liquid fuels are prepared by those types of biomass which consist starch, cellulose and another different forms of carbohydrates followed by fermentation in a feasible conditions. Biomass is an important source of energy and the most important fuel worldwide after coal, oil and natural gas. Biofuels are referred to liquid, gas and solid fuels predominantly produced from biomass. Lignocellulosic materials are the world's most widely available low-cost renewable resources to be considered for ethanol production.

Biofuel is a renewable energy source produced from natural (biobased) materials, which can be used as a substitute for petroleum fuels. The most common biofuels, such as ethanol from corn, wheat or sugar beet and biodiesel from oil seeds, are produced from classic food crops that require high-quality agricultural land for growth. However, bioethanol is a petrol additive/substitute that can be produced from plentiful, domestic, cellulosic biomass resources such as herbaceous and woody plants, agricultural and forestry residues, and a large portion of municipal and industrial solid waste streams. The best biofuels from biomasses are bioethanol and biodiesel. Production of bioethanol from biomass is one way to reduce both the consumption of crude oil and environmental pollution. There is also a growing interest in the use of vegetable oils for making biodiesel, which is less polluting than conventional petroleum diesel fuel^{16,17}. Bioethanol fuel is mainly produced by the sugar fermentation process, although it can also be manufactured by the chemical process of reacting ethylene with steam. Bioethanol is one of the cheapest biofuel which is produced by different types of lignocellulosic biomass. Bioethanol is produced from different resources of biomass by using different process, such as pretreatment, hydrolysis and fermentation. Production of ethanol from agricultural and biodegradable wastes provides a variable solution to multiple environmental problems simultaneously creating sink for waste and renewable energy production as well. Using ethanol-blended fuel for automobiles can significantly reduce petroleum use and greenhouse gas emissions²⁷.

Alkaline pretreatment is basically a delignification process, in which a significant amount of hemicellulose is solubilised as well. The action

mechanism is believed to be saponification of intermolecular ester bonds cross linking xylan hemicelluloses and other components, for example, lignin and other hemicellulose. Alkaline pretreatment also removes acetyl and various uronic acid substitutions on hemicellulose that reduce the accessibility of hemicellulose and cellulose to enzymes². Several types of acids, concentrated or diluted, can also be used, such as sulphurous, sulphuric, hydrochloric, hydrofluoric, phosphoric, nitric and formic acid for the pretreatment and acid hydrolysis of lignocellulosic biomass. Sulphuric and hydrochloric acids are the most commonly used catalysts for hydrolysis of lignocellulosic biomass¹⁴. Dilute acid process is the oldest technology for converting cellulose biomass to ethanol. The main step is essentially hemicellulose hydrolysis. In simple terms, acid catalyzes the breakdown of long hemicellulose chains to form shorter chain oligomers and then to sugar monomers that the acid can degrade. However, because hemicellulose is amorphous, less severe conditions are required to release hemicellulose sugars²⁸⁻³⁰. The goal of the pretreatment process is to break down the lignin structure and disrupt the crystalline structure of cellulose, so that the acids or enzymes can easily access and hydrolyze the cellulose^{15,16,20}. Pretreatment can be the most expensive process in biomass-to-fuels conversion but it has great potential for improvements in efficiency and lowering of costs through further research and development^{13,17}. Pretreatment is an important tool for biomass-to-biofuels conversion processes and is the subject of this review article. The digestibility of NaOH-treated hardwood was reported to increase from 14% to 55% with a decrease of lignin content from 24-55% to 20%. However, no effect of dilute NaOH pretreatment was observed for Lignocelluloses with lignin content greater than 26%¹⁹. Dilute NaOH pretreatment was also found to be effective for the hydrolysis of straws with relatively low lignin contents of 10-18%¹.

Material and Methods:

Lignocellulosic dry samples (Sugarcane baggase, wheat straw, rape straw etc.) were taken from agricultural rural areas. All the biomass samples were dried in to oven and cut in to small pieces by milling. The method of producing ethanol from lignocelluloses involves reducing the size of biomass to smaller particles prior and using acid or enzyme treatments to hydrolyze the biomass to sugars. Some of the reducing sugars are glucose, galactose, lactose and maltose. The Nelson-Somogyi method is one of the classical and widely used methods for the quantitative determination of reducing sugars²⁴.

For the fermentation of pretreated, wet biomass was mixed with distilled water to obtain a solution with 10% solid content and then divided in 250-ml flasks containing 100 ml of slurry with pH 5. Yeast enzymes were grown in PDA slant in incubator. The fermentation process started with the addition of 1.0 mL of the activated yeast culture, 0.30 g of yeast extract, and 0.1 g of KH_2PO_4 into the hydrolyzates in each flask. Fermentation was conducted at 30°C for 24-36 hours in an incubator shaker operating at 150 rpm under anaerobic conditions.

Alkaline Pretreatment:

Alkaline pretreatment of lignocellulosic materials causes swelling, leading to decreased crystallinity, increased internal surface area, disruption of the lignin structure, and separation of structural linkages between lignin and carbohydrates^{10,11}. Alkali pretreatment refers to the application of alkaline solutions such as NaOH, $\text{Ca}(\text{OH})_2$ (lime) or ammonia to remove lignin and a part of the hemicelluloses, and efficiently increase the accessibility of enzyme to the cellulose.

For the alkaline hydrolysis of the samples three alkaline solution NaOH, $\text{Ca}(\text{OH})_2$ of equal concentration were taken and each lignocellulosic biomasses were treated as in the following manner Ground biomass 3g of each crop was placed in a 1000ml Erlenmeyer flask and 300 ml of 3% (w/v) NaOH solution was added to it. The flask was cotton plugged and autoclaved at 121°C for 30 min. The material obtained after treatment was dark in colour which was then filtered through muslin cloth and washed under running distilled water until no colour was visible in the wash water. The neutralized residue was pressed manually to remove excess water and used for the enzymatic hydrolysis. Small portion of the treated biomass was dried in the oven at 70°C for 24 h and ground to fine particle size in a Laboratory Mill for the compositional analysis studies.

Acid Pretreatment: Acid pretreatment is the one of the pretreatment method which is used to degrade the biomass component in to fermentable sugars by further acid hydrolysis or using enzymatic hydrolysis. There are two types dilute and concentrated acid treatment is used for the biomass degradation. The advantage of the acid hydrolysis is that acids can penetrate lignin without any preliminary pre-treatment of biomass, thus breaking down the cellulose and hemicelluloses polymers to form individual sugar molecules. The main advantage of the dilute hydrolysis process is the low amount of acid required (2-3%). However this process is carried out at high temperatures to achieve acceptable rates of cellulose conversion. The high

temperature increases the rates of hemicellulose sugars decomposition thus causing the formation of toxic compounds such as furfural and 5-hydroxymethyl-furfural (HMF). Detoxification, activated charcoal, Calcium hydroxide over-liming etc are the process used to remove inhibitors^{3-5,32}. The acid concentration used in the concentrated acid hydrolysis process is in the range of 10-30%. The process occurs at low temperatures, producing high hydrolysis yields of cellulose (i.e. 90% of theoretical glucose yield). However, this process requires large amounts of acids causing corrosion problems to the equipments.

For the pretreatment with acid the following process has been used:- Prepare biomass samples as necessary (grinding, blending, etc.) Weigh out 3g of biomass into a pre weighed aluminium tray (do replicates of this). Be sure to record the weight of the biomass as well as the weight of the tray. Place the trays in a 105°C oven overnight. Prepare 3% (w/w) sulphuric acid. Once the moisture content is determined, weigh the amount of wet biomass correlating to 1.5g dry mass to a 125ml flask. (Record this weight and repeat for all samples). Apply 45ml of 0.8% sulphuric acid to each sample. Autoclave it at 121°C for 30 min. Centrifuge the obtained at 1500 rpm for 10 minutes. Separate the solid part, wash with distilled water and again make slurry by adding known concentration of acid, autoclaved again at 121°C for 30min. immediately after the cycle is finished, remove the samples and filter it. Wash the biomass with 200ml water using the filter. Maintain pH at 5.0, and dilute it for enzymatic hydrolysis.

Result and Discussion:

To determine the composition of biomass after Acid, Alkaline biomass samples of different kinds, Determination of Structural Carbohydrates and Lignin in Biomass” and “Determination of Ash in Biomass,” refined by NREL researchers²³. The Sugar concentrations of the biomasses were measured by HPLC also. Contents of three main components of cellulose, hemicelluloses and lignin in the initial biomasses was found, are shown in Table 1. The other components of the initial biomass samples were extractives, ash and protein. The biomasses taken were contained 55 to 62 % cellulose after acid treatment of biomasses. The low lignified corncob and rice straw contained 8 to 15% lignin and 60 to 62% cellulose. Besides the corncobs had the highest content of hemicelluloses, 12% after acid treatment of samples.

Study of the enzymatic hydrolysis of the initial biomass samples showed that initial biomass(untreated) sample cannot be considered as appropriate feedstock for enzymatic hydrolysis due to

insufficient yield of reducing sugars. Low utilization rate of the biomass moreover increasing lignin content worsened enzymatic digestibility of the samples. The biomass samples were pretreated with 3% sulphuric acid for acidic study, and the cellulose % was found in the range of 55-62%, while hemicelluloses % was found 6-12%. The biomasses taken were contained 15-31% of lignin after acidic treatment and enzymatic hydrolysis. The cellulose % was found maximum by using 3% sodium hydroxide for alkaline study at moderate temperatures. The biomasses taken were contained 62-78% Cellulose after alkaline treatment; it was found maximum 78% in rice straw and minimum 62% in wheat bran sample. The comparative results are shown in Fig: 1, 2 for kinds of biomasses.

Table: 1 Percentage of Cellulose, Hemicellulose and Lignin in the Biomass sample Pretreated with Acid (AC), Alkali (AL)

Overall Parameters	Rice Straw		Corncobs		Barley Straw		Wheat Bran	
	AC	AL	AC	AL	AC	AL	AC	AL
Cellulose (%)	62	78	60	73	55	65	58	62
Hemicelluloses (%)	7	15	12	17	7	16	6	14
Lignin (%)	15	5	20	8	26	12	31	16
Yield of Reducing Sugar (%)	49	82	45	78	40	65	34	46

The final result showed some improvement of the enzymatic digestibility of the acid pretreated biomass in comparison with untreated samples. However the digestibility characteristics were insufficient, the utilization rate of biomass was in the range 30-42% and yield of reducing sugars was in the range 34-49% for acid pretreated biomass and 46-82% for alkali treated biomass. It is clear that after acidic pretreatment of biomasses and in case of alkali pretreatment of the biomass caused decreases of both of hemicelluloses and lignin as in Table: 1 and Fig: 1,2. Simultaneously increasing cellulose content was observed which should promote the enzymatic digestibility of the pretreated biomass.

Hence the experiment showed that, pretreatment of the biomass samples with dilute alkali solution caused considerable rise of the utilization rate and yield of sugars after enzymatic hydrolysis of alkali pretreated biomass in comparison with acid pretreated samples. This result is in agreement with the findings of other researchers³¹.

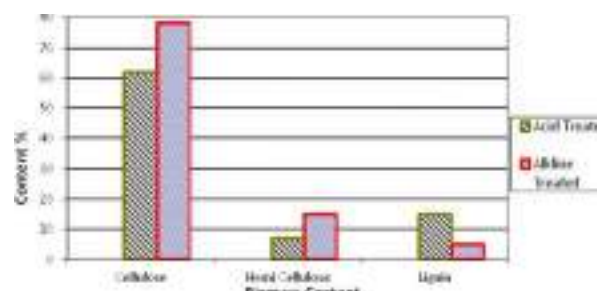


Fig. 1:Percentage of Cellulose, Hemicelluloses and Lignin in Rice Straw

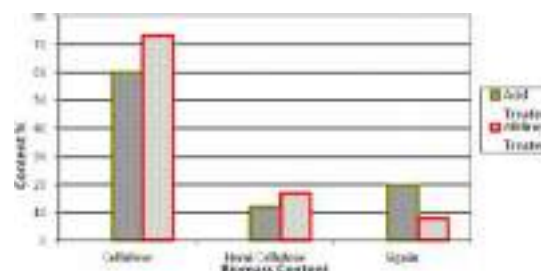


Fig. 2: Percentage of Cellulose, Hemicelluloses and Lignin in Corn Cobs

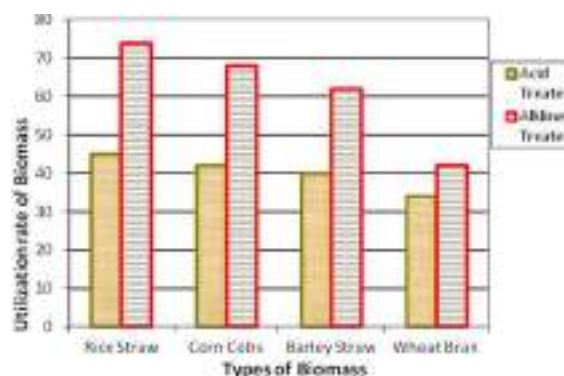


Fig. 3: Utilization rate of biomass (UR) after enzymatic hydrolysis of untreated, Acid and Alkali pretreated biomass sample

From the previous studies it was noted that increased acid concentration used for the pretreatment purpose enhanced the sugar release during enzymatic hydrolysis. But it was found optimum at 3%. Fermentation studies also proved that optimum acid concentration yielded more amount of alcohol. Alcohol content of about 8.9 g l⁻¹ (Table 2) was detected in the 48 hours of fermentation broth containing the hydrolyzed sample pretreated with 3% sulphuric acid. This study proved that sugars released by means of enzymatic hydrolysis of pretreated corncob are of fermentable category and alcohol can be produced efficiently using a suitable fermenting strain *Saccharomyces cerevisiae*.

Hence it is clear that at 3% of acid sample ethanol yield was found maximum at optimum temperature and pH value. Fig. 4 represents the data

of maximum alcohol yield and cellulose conversion. On the basis of above discussion we were also used different kinds of biomasses and their results of cellulose conversion from the following Table: 3 represents the ethanol yield at optimum acid concentration of 3% and optimum temperature and other conditions as discussed for corncob.

Table2: S1 to S7 – Biomaas samples of Alcohol Production on Acid Pretreated corncob through Fermentation with *Saccharomyces cerevisiae*.

S No	Sample-Acid used for Pretreatment w/w (%)	Ethanol gl^{-1}
S1	0.0	1.4
S2	0.5	3.8
S3	1.0	4.9
S4	1.5	5.6
S5	2.0	6.8
S6	2.5	7.7
S7	3.0	8.9

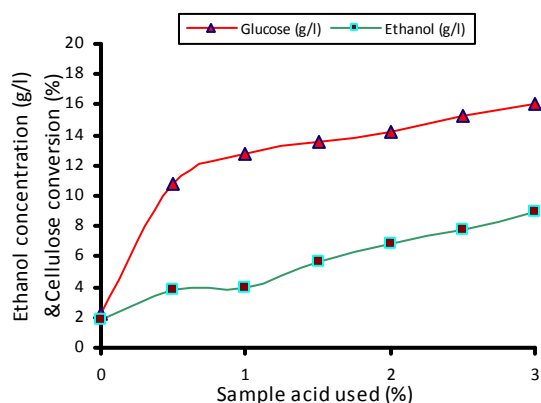


Figure: 4 Comparison of total Cellulose conversion (%) and Ethanol fermentation with *Saccharomyces cerevisiae* at different sample used of acid.

Table 3: Alcohol Production on (3.0%) acid pretreated kinds of biomass through Fermentation with *Saccharomyces cerevisiae*.

SNo	Types of biomass samples	Ethanol gl^{-1}
1	Corn cob	8.9
2	Cassava	7.4
3	Wheat Straw	6.2
4	Rape Straw	7.9

According to Table: 3, it is concluded that the maximum ethanol yield was found 8.9g/l in corncob and minimum ethanol yield was found in wheat straw (6.2 g/l). These data shows that degradation of biomass by acid pretreatment and enzymatic hydrolysis followed by fermentation gives sustentative yield of ethanol production.

To check the pretreatment process three sample of alkaline solution were also taken in the manner of same concentration. 3% alkaline using different basic solutions, results are shown by alkali pre-treatment with NaOH solution has the most impact on sugarcane bagasse structure (Table 4). Furthermore regarding lower molecular weight of NaOH in comparison with KOH and $Ca(OH)_2$, using this base is equal to less consumption of material while at the same time the resulted solid has the better composition for ethanol production. Compositional analysis of pretreated bagasse shows that residual solid is rich in glucose. Therefore pretreatment effect in this condition is dissolution of lignin and partially hemicelluloses. Hence it was found that Alkaline pretreatment with NaOH is more optimum than KOH and $Ca(OH)_2$. The percentage of glucose by alkali pretreatment with NaOH was found 58%, which was maximum than pretreatment by KOH (54%) and by $Ca(OH)_2$ (40%). Therefore, NaOH solution was chosen for pretreatment of other biomasses for ethanol production. After this pre-treatment, solid composition was found 58% (w/w) glucose. On behalf of the method the following results was obtained after pretreatment of kinds of biomasses as in (Table 4).

Table 4: Effect of different basic solutions on sugarcane bagasse composition

SN.	Base	g/g of Solids	% Glucose in solid after pretreatment
1	NaOH	0.4	58
2	KOH	0.56	54
3	$Ca(OH)_2$	0.74	40

From the data it is concluded that alkaline hydrolysis of different kinds of biomass is more effective parameter than others. Alkaline hydrolysis is so very effective in comparison to acid hydrolysis. Fig: 5 show the ethanol yield by fermentation with *Saccharomyces cerevisiae* at optimum temp 30°C and Optimum pH 5.

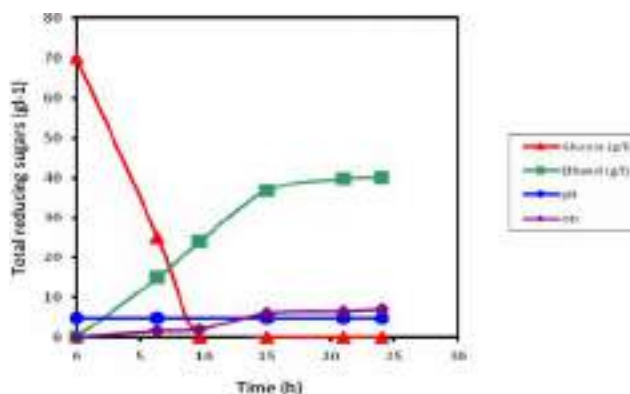


Fig 5: Fermentation of 70 g⁻¹ Glucose medium (Bagasse) by *Saccharomyces cerevisiae* (temp 30°C, pH5)

Conclusion:

The biomass pretreatment and the intrinsic structure of the biomass itself are primarily responsible for its subsequent hydrolysis. The conditions employed in the chosen pretreatment method will affect various substrate characteristics, which, in turn, govern the susceptibility of the substrate to hydrolysis and the subsequent fermentation of the released sugars. Therefore, pretreatment of biomass is an extremely important step in the synthesis of biofuels from lignocellulosic biomasses, and there is a critical need to understand the fundamentals of various processes, which can help in making a suitable choice depending on the structure of the biomass substrate and the hydrolysis agent. Pretreatment is the initial step to degrade the biomass content. Pre-treatment's are usually focused on lignin and hemicelluloses removal, cellulose crystallinity reduction and accessible surface area increase. Without pretreatment it is not possible to convert biomass content in to reducing sugars and further fermented in to ethanol as biofuel. Pretreatment of lignocellulosic and algal biomass can be held in three ways Acid, Alkali and enzymatic pretreatment. Pretreatment with acid autoclaving at 121°C for 30 min, is an effective and cheap parameter in comparison to enzymatic degradation and other methods. Acid pretreatment had a greater influence on the sugar release through enzymatic hydrolysis. An increase in acid severity in terms of concentration resulted in higher sugar releases. By the experimental analysis 3% by volume of acid was found optimum.

Acid pretreatment is effective but in the controlled concentration, because at higher concentration is the cause of formation of inhibitors which inhibits the fermentation process in to ethanol. In this study and work, optimum acid concentration

was found 2-3%. Alkaline hydrolysis is also effective for pretreatment of biomass but after alkaline hydrolysis further enzymatic hydrolysis is need for better result. Alkaline pretreatment with 3% NaOH solutions was found optimum than KOH and Lime Water Ca(OH)₂. Pretreatment. Alkaline hydrolysis reduces the lignin component during degradation which enhances the alcohol production in comparison to acidic pretreatment because at high concentration of acid sugar concentration decreases, due to formation of inhibitors. In presence of higher sugar concentration Furfural, a pentose degradation product and HMF as inhibitors 5-hydroxymethylfurfural, a hexose degradation product and lignin degradation products are formed which decreases the ethanol yield and production. Detoxification is the method to avoid the formation of inhibitors.

Compared with acid processes, alkaline processes cause less sugar degradation, and many of the caustic salts can be recovered and/or regenerated. Sodium, potassium, calcium, and ammonium hydroxides are suitable alkaline pretreatment agents. Of these four, sodium hydroxide has been studied the most^{9,18,25}. Alkali pretreatment can be carried out at ambient conditions, but pretreatment times are on the order of hours or days rather than minutes or seconds. Dilute NaOH treatment of lignocellulosic materials has been found to cause swelling, leading to an increase in internal surface area, a decrease in the degree of polymerization, a decrease in crystallinity, separation of structural linkages between lignin and carbohydrates, and disruption of the lignin structure^{11,12}. Hence it is cleared that dilute acid hydrolysis of biomass yields higher sugar concentration but at high concentration of acid decreases the sugar concentration decreases and in case of alkaline hydrolysis the lignin component is decreases, it was also satisfied by some of the researcher²⁶.

The choice of the pretreatment technology used for a particular biomass depends on its composition and the byproducts produced as a result of pretreatment. These factors significantly affect the costs associated with a pretreatment method. There have been some reports comparing various pretreatment methods for biomass^{28-30,21,22}. The pretreatments were compared after enzyme treatment using a cellulase enzyme system. The acid or water impregnation followed by steam explosion of agricultural waste/straw was the best pretreatment in terms of the resulting glucose concentration in the liquid hydrolysate after enzymatic hydrolysis.

References:

1. Bjerre, A. B.; Olesen, A. B.; Fernqvist, T. Pretreatment of wheat straw using combined wet oxidation and alkaline hydrolysis resulting in convertible cellulose and hemicellulose. *Biotechnol. Bioeng.* 1996, 49, 568–577.
2. Chang, V., Burm, B., Holtzapple, M. (1997), Lime pretreatment of switchgrass. *Applied Biochemistry and Biotechnology*, 63-65: 3-19.
3. Chandel, A.K., Singh, O.V., Narasu, M.L. & Rao, L.V. (2011b) Bioconversion of *Saccharum spontaneum* (wild sugarcane) hemicellulosic hydrolysate into ethanol by mono and co-cultures of *Pichia stipitis* NCIM3498 and thermotolerant *Saccharomyces cerevisiae*- VS3. *N. Biotechnol.*, DOI 10.1016/j.nbt.2010.12.002.
4. Chandel, A.K., Narasu, M.L., Rudravaram, R., Ravindra, P., Narasu, M.L. & Rao, L.V. (2009) Bioconversion of de-oiled rice bran (DORB) hemicellulosic hydrolysate into ethanol by *Pichia stipitis* NCIM3499 under optimized conditions. *Int. J. Food Eng.*, Vol. 2, pp. 1–12.
5. Chandel, A.K., Singh, O.V., Chandrasekhar, G., Rao, L.V. & Narasu, M.L. (2011a) Bioconversion of novel substrate, *Saccharum spontaneum*, a weedy material into ethanol by *Pichia stipitis* NCIM3498. *Bioresource Technol.*, Vol. 102, pp. 1709- 1714.
6. Demirbas A. Biofuels sources, biofuel policy, biofuel economy and global biofuel projections. *Energy Convers Manage* 2008; 49:2106–16.
7. Demirbas A. Present and future transportation fuels. *Energy Sources Part A* 2008; 30:1473–83.
8. Demirbas A. New liquid biofuels from vegetable oils via catalytic pyrolysis. *Energy Educ. Sci. Technol.* 2008; 21:1–59.
9. Elshafei, A. M.; Vega, J. L.; Klasson, K. T.; Clausen, E. C.; Gaddy, J. L. The saccharification of corn stover by cellulase from *Penicillium funiculosum*. *Bioresour. Technol.* 1991, 35, 73–80.
10. Fan L T, Gharpuray M M, Lee Y -H. *Cellulose Hydrolysis Biotechnology Monographs*. Berlin: Springer, 1987; 57 p.
11. Fan, L. T.; Gharpuray, M. M.; Lee, Y.-H. *Cellulose Hydrolysis; Biotechnology Monographs*; Springer: Berlin; Vol. 3, p 57.
12. Fox, D. J.; Gray, P. P.; Dunn, N. W.; Warwick, L. M. Comparison of alkali and steam (acid) pretreatments of lignocellulosic materials to increase enzymic susceptibility: Evaluation under optimized pretreatment conditions. *J. Chem. Tech. Biotech.* 1989, 44, 135–146.
13. Galbe, M.; Zacchi, G. Pretreatment of lignocellulosic materials for efficient bioethanol production. *Adv. Biochem. Eng./Biotechnol.* 2007, 108, 41–65.
14. Lenihan, P.; Orozco, A.; O’Neil, E.; Ahmad, M., N., M.; Rooney, D., W. & Walker G., M. (2010). Dilute acid hydrolysis of lignocellulosic biomass. *Chemical Engineering Journal*, Vol. 156, No.2,(January, 2010), pp. 395-403.
15. Lee, J. Biological conversion of lignocellulosic biomass to ethanol. *J. Biotechnol.* 1997, 56, 1–24.
16. Lee, D.; Yu, A. H. C.; Wong, K. K. Y.; Saddler, J. R. Evaluation of the enzymatic susceptibility of cellulosic substrates using specific hydrolysis rates and enzyme adsorption. *Appl. Biochem. Biotechnol.* 1994, 45 (45), 407–415.
17. Lynd, L. R.; Elander, R. T.; Wyman, C. E. Likely features and costs of mature biomass ethanol technology. *Appl. Biochem. Biotechnol.* 1996, 57 (58), 741–761.
18. MacDonald, D. G.; Bakhshi, N. N.; Mathews, J. F.; Roychowdhury, A.; Bajpai, P.; Moo-Young, M. Alkali treatment of corn stover to improve sugar production by enzymatic hydrolysis. *Biotechnol. Bioeng.* 1983, 25, 2067–2076.
19. Millet, M. A.; Baker, A. J.; Scatter, L. D. Physical and chemical pretreatment for enhancing cellulose saccharification. *Biotech. Bioeng. Symp.* 1976, 6, 125–153.
20. Mosier, N. S.; Wyman, C.; Dale, B.; Elander, R.; Lee, Y. Y.; Holtzapple, M.; Ladisch, M. R. Features of promising technologies for pretreatment of lignocellulosic biomass. *Bioresour. Technol.* 2005, 96, 673–686.
21. Rosgaard, L.; Pedersen, S.; Meyer, A. S. Comparison of different pretreatment strategies for enzymatic hydrolysis of wheat and barley straw. *Appl. Biochem. Biotechnol.* 2007, 143, 284–296.
22. Silverstein, R. A.; Chen, Y.; Sharma-Shivappa, R. R.; Boyette, M. D.; Osborne, J. A comparison of chemical pretreatment methods for improving saccharification of cotton stalks. *Bioresour. Technol.* 2007, 98, 3000–3011.
23. Sluiter A, Hames B, Ruiz R, Scarlata C, Sluiter J, Templeton D. 2005. Determination of ash in biomass. Golden, CO: National Renewable Energy Laboratory.
24. Somogyi, M. (1952). *J. Biol. Chem.*, 200, 245.
25. Soto, M. L.; Dominguez, H.; Nunez, M. J.; Lema, J. M. Enzymatic saccharification of alkali-treated sunflower hulls. *Bioresour. Technol.* 1994, 49, 53–59.
26. Sun, Y., Cheng, J. (2002), Hydrolysis of lignocellulosic materials for ethanol production: A review. *Bioresource Technology*, 83: 1-11.
27. Wang M, Saricks C, Santini D (1999) Effects of fuel ethanol use on fuel-cycle energy and greenhouse gas emissions. Argonne National

- Laboratory, Centre for Transportation Research, Energy System Division, ANL/ESD-38.
28. Wyman C E. Biomass ethanol: technical progress, opportunities, and commercial challenges. *Annu. Rev. Energy. Env.*, 1999; 24: 189–226.
 29. Wyman, C.E. *Handbook on bioethanol: production and utilization*; Taylor & Francis: Washington DC, USA, 1996.
 30. Wyman, C. E.; Dale, B. E.; Elander, R. T.; Holtzapple, M.; Ladisch, M. R.; Lee, Y. Y. Comparative sugar recovery data from laboratory scale application of leading pretreatment technologies to corn stover. *Bioresour. Technol.* 2005, 96, 2026–2032.
 31. Xu, J., Wang J., Sharma-Shivappa, R.R. and Cheng, J.J. (2011). “Enzymatic hydrolysis of switch grass and Bermuda grass pretreated with different chemical methods” *Bio Resource.* 6 (3), 2990-2003.
 32. Yang, B. & Wyman, C.E. (2008) Pretreatment: the key to unlocking low-cost cellulosic ethanol. *Biofuels Bioproduct Bioref.*, Vol. 2, pp. 26–40.



Reliability Analysis of Cloud Computing Systems Serving Multi-Class Requests

Divya Srivastava¹, Rohit Sharma² and Anuj Srivastava³

¹Department of Computer Science and Engineering, Indian Institute of Technology Jodhpur srivastavadivya.90@gmail.com

²Department of Computer Engineering and Engineering, Dr. Ambedkar Institute of Technology for Handicapped, Kanpur rohit6615@rediffmail.com

³Department of Mathematics, Dr. Ambedkar Institute of Technology for Handicapped, Kanpur anuj_srivas1984@rediffmail.com

Abstract: The current era of the internet has laid focus on Cloud Computing systems. We find the application of CCS in almost all the domains, such as the medical field, pharmacy sector, IT sector, etc. However, the reliability of CCS is of utmost importance for its smooth applicability. In this paper, we perform the reliability analysis of CCs using the ReliaCloud-NS simulation framework. We have carefully framed our test cases to cover the broad domain where CCS is used. Along with reliability analysis, the study on components of CCS, i.e., HDD, CPU, Bandwidth and memory, is performed, illustrating its failure in various VMs. We have tried our best to perform the analysis of CCs broadly to make this work valuable for almost all the domains where CCS is used.

Index Terms: Cloud Computing System, Reliability analysis, ReliaCloud-NS, Application of CCS, AWS. Introduction

I. INTRODUCTION

The adoption of cloud technologies enables enterprises, big and small, to be agile, innovative, and competitive, and create differentiated customer experiences. The cloud adoption rate is growing faster than predicted. A report from Gartner says that the expected growth in the cloud market will be from \$182.4 billion in 2018 to \$331.2 billion in 2022, a growth rate of approximately 12.6% [1]. The question organizations are asking is what strategy they should adopt to move to the cloud.

Cloud computing reliability has gained popularity owing to rapid growth in demand for cloud computing services. As mentioned in [2], the cloud forms the heart of almost all internet-based activities; for example, it is used in social networking sites such as Facebook, Twitter, Snapchat, etc. It has found its application in almost every research sector, life sciences [3], natural sciences [4] or applied science. This growth in demand for cloud computing and the high demand on cloud services necessitates the requirement for quantitative ways for cloud services

evaluation from a reliability standpoint efficiently.

Non-sequential Monte Carlo Simulation (MCS) is used to calculate the reliability of a CCS due to its high computational efficiency. The general steps followed by the non-sequential MCS algorithm are sampling, classification, calculation, and convergence. A non-sequential MCS-based simulation software ReliaCloud-NS has been used to perform reliability evaluations of carefully designed CCSs. The feature of ReliaCloud-NS to create and simulate complex CCS's is used to develop compute, memory, and storage-intensive clusters along with their suitable VM instances. We have also presented the simulation results, showing that ReliaCloud-NS can provide user-friendly charts and graphs that characterize CCS reliability.

In section 2 the literature review on CCS reliability with an outline of popular cloud simulation software and tools is given. Section 3 introduces and provides us with the idea of MCS-based Cloud reliability software ReliaCloud-NS and the description of VM types and clusters used for simulation. In section 4, the execution stage reliability of the system is obtained and analyzed. Numerical results depicting enhanced system reliability and comparison of results has been presented in section 5. Significant conclusions of the proposed work, along with the future scope is given in section 6.

II. RELATED WORK

CCS's plethora of works is done to model user requests and data transmission issues. However, one critical aspect of system failure in a CCS is hardware failure which is less addressed. The focus on failing hardware in CCS's begins in [5], where examination of hardware failures occurring in multiple data centers are thoroughly verified to identify the explicit rates of failure for various components, i.e., disks, CPUs, memory, and RAID controllers. The main conclusion of their work is that the largest source of failure in almost all data centers is disk

failure—the evaluation of intermittent hardware failures is countered in [6]. The review of failures occurring in DRAM, CPU, and disks in customer PC's continue in [7]. The most important outcome of this work is for recurring faults, as it suggests that an already failed PC component is likely to fail shortly soon. This paper also examines hidden failures such as DRAM's 1-bit failures[8]. A comprehensive failure evaluations at all levels of the CCS and systems overall reliability is obtained in [9]. To prevent failure of cloud computing system, authors in [10] proposed a service model for finite population clouds. It analyze the resource request stage of finite population cloud computing system. Then the losses incurred in the system due to impatient users are accounted from which the scheduling strategy is prepared to load balance the request stage of model.

The issue of network failures in Cloud Data Centers is addressed in [11,12]. These studies conclude to the fact that cloud data center networks and switches have high reliability, and faults in their load balancers are due to software failures. Network failure causes only minor faults, and redundancy in cloud resources is not always a positive thing. The study of resource utilization and general workloads in data centers and the study of various hardware components in it, including disks, CPU's and memory, was carried out in [13]. The facility of modeling and simulation of application schedulers for the multiple administrative domain distributed systems is provided by GridSim [14]. Their work is extended in [15] an which incorporates data grids in the simulations. Similarly, the simulation environment for evaluation of cluster, grid, and peer-to-peer heuristics and algorithms for distributed computing systems is SimGrid [16,17]. They also provide multiple user interfaces and APIs to assist researchers and developers in simulating scheduling heuristics and algorithms or even developing new applications for distributed computing systems. CloudSim presented in [18] forms an extensible toolkit for modelling cloud environments and performs evaluation of existing and new resource provisioning algorithms. Various other software packages are extensions of CloudSim, including CloudAnalyst, Cloudbus Toolkit, and NetworkCloudSim[19]. CloudAnalyst is a reliable tool for simulating hugely levelled cloud environments and presents insights on distributed applications and services among cloud infrastructure to optimize the application performance including providers using service brokers [20]. Cloudbus Toolkit is a group of softwares forming a system for enhancing the functionality of market-oriented resource management which involves support for federated clouds and energy-aware resource allocation to create green clouds [21]. NetworkCloudSim proposed in [22] is a tool for modeling the advanced application models, which includes highly parallel applications utilizing message passing or scalable network models. EMUSIM [23] is an open-source integrated environment for emulation and simulation to model, evaluate, and validate cloud computing applications' performance. iCanCloud is a GUI-based open-source simulator used for

modeling and simulating CCSs from a cost and performance perspective for a fixed set of applications running on specific hardware [24]. MAScloud is multiple agents and iCanCloud [25] based framework for optimizing the cost and performance of Cloud computing systems. GreenCloud is a simulation environment for energy-aware cloud computing data centers. It captures details for various components such as servers, switches, and links, realistic packet-level communications, and enables assessing power management techniques such as frequency and voltage scaling and the dynamic shutdown of network components [27]. [5] proposes a new, scalable algorithm based on non-sequential Monte Carlo Simulation (MCS) to evaluate the reliability of large-scale cloud computing systems (CCS) and develops appropriate performance measures. It also proposes a new iterative algorithm that leverages the MCS method to design highly reliable and utilized CCSs. The implementation, architecture, and use of ReliaCloud-NS allow users to evaluate a cloud computing system (CCS) and design a CCS to a pre-defined reliability level for both public and private clouds [28].

III. METHODOLOGY

In this work, we performed a detailed analysis for reliability of CCS using ReliaCloud-NS. We have categorized the user request for CCS into three categories of virtual machines. The virtual machines under these categories are then specified, and their reliability analysis is performed in the robust scenario.

A. *ReliaCloud-NS*

ReliaCloud-NS, proposed by Snyder et al. in [5] is a GUI-based web application for executing non-sequential Monte Carlo simulations (MCSs) to evaluate the CCS reliability. Along with assessing reliability, it enables the user to design a CCS for both public and private cloud to a specified reliability level. Their software comprises various types of CCS components, virtual machine allocation systems and simulation schemes. The basic functionality of ReliaCloud-NS includes designing individual components (like VM's, VM groups, clusters etc.), creating CCS, simulating CCSs for estimating reliability and result analysis obtained after simulation.

It is built over MVC architecture, enabling the non-sequential MCS algorithm to work in parallel mode using many cores. Each parallel trial can execute in its own thread and be simulated simultaneously. Non-sequential MCS in ReliaCloud-NS facilitates a flexible and efficient way to compute CCS reliability using a set of four different resources, i.e., CPU, memory, Bandwidth and Hard Disk Drive (HDD). These basic resources are combined to form Virtual Machines (VMs) and clusters. A VM is a fundamental reusable component of ReliaCloud-NS for requesting resources, while a cluster is a basic reusable component for allocating available resources.

ReliaCloud-NS components can be categorized in an hierarchical manner. The basic components are CPU, memory, Bandwidth and HDD. The components form VM or cluster. The

collection of individual VMs forms VM groups while the collection of clusters forms the cloud. VM groups can be considered as a simulation-facing resource-requesting component.

B. Proposed User-driven Simulation System

We proposed our simulation system to meet the demand of a real-life scenario, where the user wants access to the cloud for a specific type of resource. In real-scenario, among the four basic components, viz., CPU, memory, Bandwidth and HDD, user requirement focuses on one component as per its task. The task is either, computing or storage-intensive or memory-based. For example, cloud is used for saving user data, hence storage-intensive task.

Considering the above-mentioned real scenario, we frame our clusters and VMs accordingly to meet such requirements. Figure 1 shows our division of framework of clusters based on the incoming request.

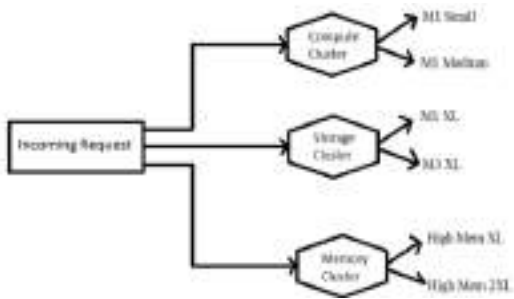


Fig. 1. Framework of clusters based on the incoming request.

We divide user requests into three clusters of resources: compute cluster, storage cluster, and memory cluster. Here, as their names suggest, compute cluster emphasizes computation capability, storage cluster ensures high storage capacity, and memory cluster focuses on large memory size needed during computation. Table 1 gives specifications for each of the cluster type.

Table 1: VM categories specifications used in our user-driven simulations

VM Category	VM Name	# of Cores	Memory (GB)	HDD Size (GB)	Bandwidth (Mbps)
Compute VM's	M1 Small	2	2	160	100
	M1 Medium	4	4	410	500
Storage VM's	M1 XL	16	16	1690	1000
	M3 XL	26	16	1690	1000
Memory VM's	High Mem XL	13	18	420	500
	High Mem 2XL	26	35	850	1000

IV. EXPERIMENT

Based on the above configuration of cluster and VM categories, we frame our experimental setup comprising test cases designed for each cluster. Three test cases of VMs categories are made for each of the clusters according to their type. Compute cluster is given 3 VM test cases, where test case 1, test case 2 and test case 3 comprises 20 VMs, 30 VMs, and 50 VMs, respectively, each belonging to compute VM category. Storage Cluster is given 3 VM test cases, where test case 1, test case 2 and test case 3 comprises 20 VMs, 30 VMs and 50 VMs, respectively, each belonging to the storage VM category. Memory Cluster is given 3 VM test cases, where test case 1, test case 2 and test case 3 comprises 20 VMs, 30 VMs and 50 VMs, respectively, each belonging to the memory VM category.

Each type of cluster has specific instances of each resource available with them depending upon its type. For example, Compute cluster has 250 cores, 300 GB Memory, 25000 GB HDD and 30000 Mbps Bandwidth available with them. Now, each of the test cases demands these resources. Test case 1 is for Compute VM category comprising 20 VM's request for 64 cores, 64 GB memory, 6200 GB HDD and 6800 Mbps Bandwidth. From these Available instances of resources and requested resources, the utilization is computed as mentioned in equation 1.

$$Utilization = \frac{RequestedResourceInstance}{AvailableResourceInstance} \tag{1}$$

Similarly, utilization is computed for the remaining 2 test cases of compute cluster. Table 3 gives insights for all the test cases, resource status and utilization corresponding to each test case for compute cluster.

Table 2: Details for test cases, resource status, and utilization for compute cluster

Compute_Cluster	Resources Status	# of Cores	Memory (GB)	HDD Size (GB)	Bandwidth (Mbps)
	Available Instances	250	300	25000	30000
20 VM's	Requested	64	64	62,00	68,00
	Difference	186	236	18,800	23,200
	Utilization	0.2560	0.2133	0.2480	0.2267
30 VM's	Requested	96	96	9300	10200
	Difference	154	204	15700	19800
	Utilization	0.3834	0.3200	0.3720	0.3400
50 VM's	Requested	160	160	15,500	17,000
	Difference	90	140	9,500	13,000
	Utilization	0.6400	0.5333	0.6200	0.5667

Similar procedure is applied for computing utilization for storage and memory cluster. Their details are given in table 4 and 5 respectively

Table 3: Details for test cases, resource status and utilization for storage cluster

Storage_Cluster	Resources Status	# of Cores	Memory (GB)	HDD Size (GB)	Bandwidth (Mbps)
	Available Instances	1500	1000	100,000	60,000
20 VM's	Requested	440	320	33,800	20,000
	Difference	1,060	680	66,200	40,000
	Utilization	0.2933	0.3200	0.3380	0.3333
30 VM's	Requested	660	480	50,700	30,000
	Difference	840	520	49,300	30,000
	Utilization	0.4400	0.4800	0.5070	0.5000
50 VM's	Requested	1,100	800	84,500	50,000
	Difference	400	200	15,500	10,000
	Utilization	0.7333	0.8000	0.8450	0.8333

Table 4: Details for test cases, resource status and utilization for memory cluster

Memory_Cluster	Resources Status	# of Cores	Memory (GB)	HDD Size (GB)	Bandwidth (Mbps)
	Available Instances	1500	2000	50,000	60,000
20 VM's	Requested	416	564	13,560	16,000
	Difference	1,084	1,436	36,440	44,000
	Utilization	0.2773	0.2820	0.2712	0.2667
30 VM's	Requested	624	846	20,340	24,000
	Difference	876	1,154	29,660	36,000
	Utilization	0.4160	0.4230	0.4068	0.4000
50 VM's	Requested	1,040	1,410	33,900	40,000
	Difference	460	590	16,100	20,000
	Utilization	0.6933	0.7050	0.6780	0.6667

V. RESULT

We compute reliability for the experimental setup described above. Three test cases are designed for VM's demand for resources from cluster as per their need according to their type.

We create the total samples for each test case and compute the reliability of the system. Table 6 reports the total number of samples created for each test case of the VM type for clusters and the average reliability calculated for the total number of samples.

We also report the pictorial representation of results based on failure reports and reliability values. Here we depict, the number of failures accounted for each component (CPU, Memory, HDD, Bandwidth), Ratio of M1Small and M1Medium VM used and the reliability graph over the number of iterations. Figure 2-10 shows these results for each VM test case over all three clusters.

It can be seen from figure 2-4, for compute cluster, maximum failure is reported for HDD followed by CPU, Bandwidth and memory. In the storage cluster, as shown in Figures 5-7, regular fashion is CPU and HDD failure compared to Bandwidth and memory failure. It is also interesting to note that when the percentage of M3XL VM is more than M1XL, we encounter more CPU failure than HDD failure. Similar to compute cluster shown in figure 8-10, maximum failure is reported for HDD followed by CPU, Bandwidth and memory in the memory cluster.

Table 5: Total samples and average reliability for every VM test case of each cluster

CLUSTER NAME	VM Test Cases	Total Samples	Reliability
Compute_Cluster	20 VM's	236,385	0.999336
	30 VM's	218,837	0.999283
	50 VM's	210,925	0.999256
Storage_Cluster	20 VM's	230,148	0.999318
	30 VM's	209,141	0.999249
	50 VM's	182,269	0.999139
Memory_Cluster	20 VM's	235,533	0.999333
	30 VM's	235,320	0.999333
	50 VM's	219,526	0.999285

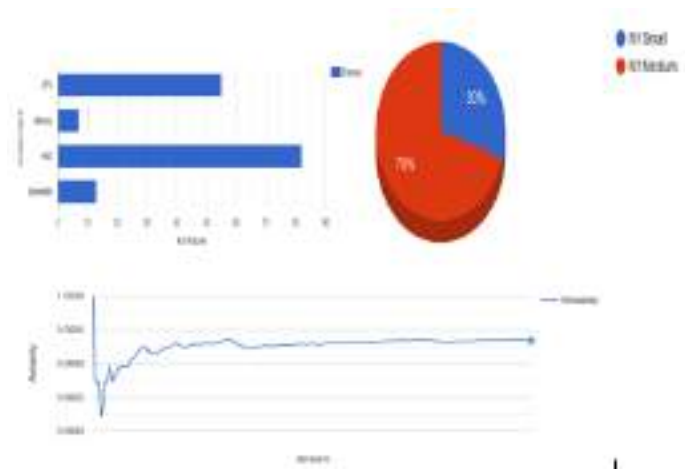


Figure 2 Pictorial representation of result for an instance of 20VM for Compute cluster

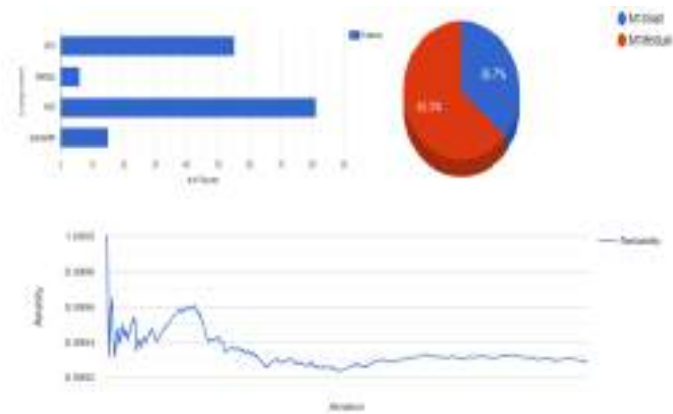


Figure 3 Pictorial representation of result for an instance of 30VM for Compute cluster

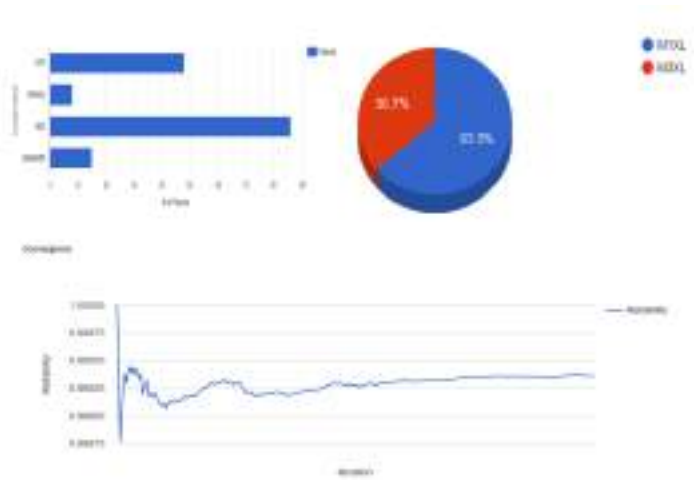


Figure 6 Pictorial representation of result for an instance of 30VM for the storage cluster

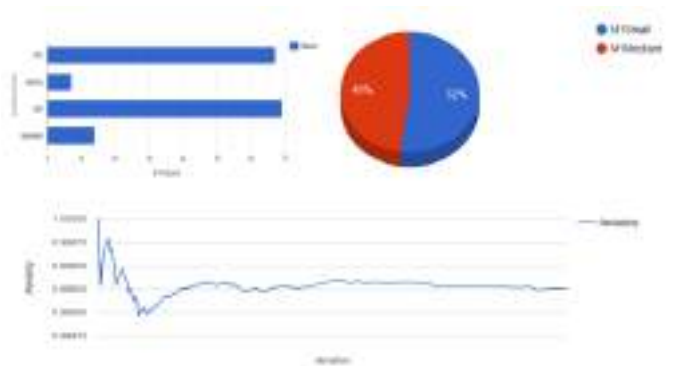


Figure 4 Pictorial representation of result for an instance of 50VM for Compute cluster

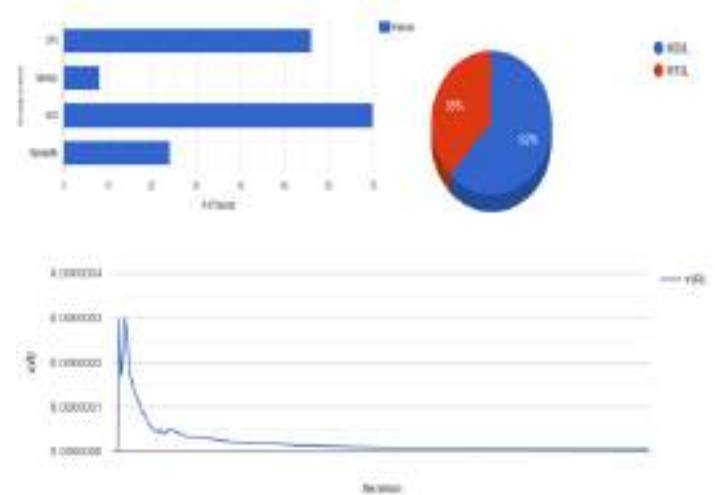


Figure 7 Pictorial representation of result for an instance of 50VM for the storage cluster

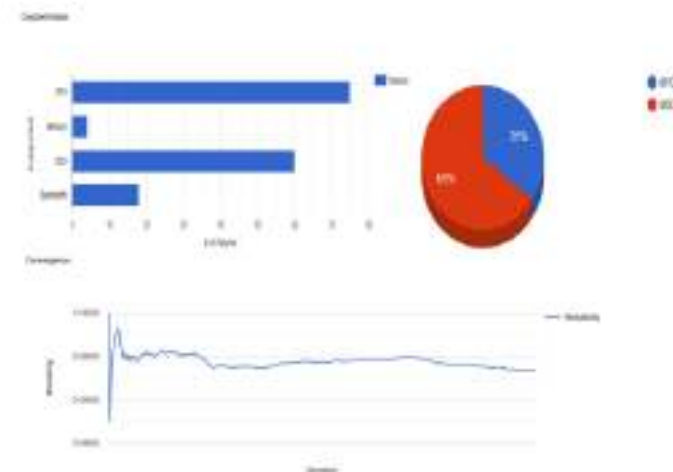


Figure 5 Pictorial representation of result for an instance of 20VM for the storage cluster



Figure 8 Pictorial representation of result for an instance of 20VM for memory cluster

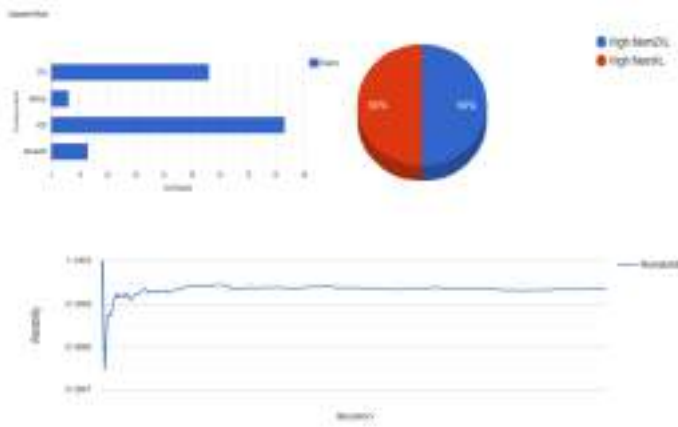


Figure 9 Pictorial representation of result for an instance of 30VM for memory cluster

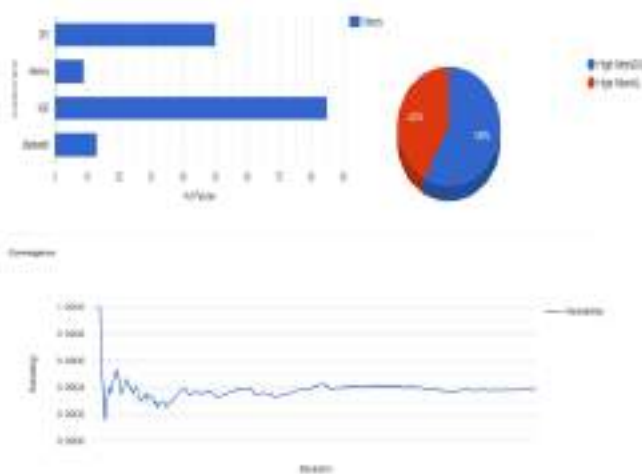


Figure 10 Pictorial representation of result for an instance of 50VM for memory cluster

VI. CONCLUSION

This paper performs a detailed analysis of the reliability of cloud computing systems for their applicability in various domains. We have framed our test cases so that it covers the broad domain where CCS is used. In this broad scenario, our paper reports the failure of its component, i.e., HDD, CPU, Bandwidth and memory, when tested across the various cluster and VM provided by ReliaCloud-NS. We have explored the various VMs available in ReliaCloud-NS and have studied their impact on failure on CCS components.

In future, we would like to explore more on the application of CCS in various domains. Application of CCS in the domain of life sciences, drug discovery, the medical field is the need of the hour. Hence, the future scope of our work is to focus on issues faced by life science researchers on using CCS. Here along with reliability, the sensitivity of data used is of significant concern.

REFERENCES

[1] Costello, K., & Rimol, M. (2020). Gartner Forecasts Worldwide Public Cloud End-User Spending to Grow 18%

in 2021. *Gartner*. Available online: <https://www.gartner.com/en/newsroom/press-releases/2020-11-17-gartner-forecasts-worldwide-public-cloud-enduser-spending-to-grow-18-percent-in-2021> (accessed on 18 February 2021).

[2] Weinman, J. (2012). *Cloudonomics: The business value of cloud computing*. John Wiley & Sons.

[3] Breton, V., Lampe, N., Maigne, L., Sarramia, D., & Quang, B. T. (2016). Clouds in biosciences: A journey to high-throughput computing in life sciences. *Grid and Cloud Computing: Concepts and Practical Applications*, 192, 71.

[4] Garg, V., Arora, S., & Gupta, C. (2011). Cloud computing approaches to accelerate drug discovery value chain. *Combinatorial chemistry & high throughput screening*, 14(10), 861-871.

[5] Snyder, B., Ringenberg, J., Green, R., Devabhaktuni, V., & Alam, M. (2015). Evaluation and design of highly reliable and highly utilized cloud computing systems. *Journal of Cloud Computing*, 4(1), 1-16.

[6] Rashid, L., Pattabiraman, K., & Gopalakrishnan, S. (2012, September). Intermittent hardware errors recovery: Modeling and evaluation. In *2012 Ninth International Conference on Quantitative Evaluation of Systems* (pp. 220-229). IEEE.

[7] Vishwanath, K. V., & Nagappan, N. (2010, June). Characterizing cloud computing hardware reliability. In *Proceedings of the 1st ACM symposium on Cloud computing* (pp. 193-204).

[8] Nightingale, E. B., Douceur, J. R., & Orgovan, V. (2011, April). Cycles, cells and platters: an empirical analysis of hardware failures on a million consumer PCs. In *Proceedings of the sixth conference on Computer systems* (pp. 343-356).

[9] Pham, C., Cao, P., Kalbarczyk, Z., & Iyer, R. K. (2012, June). Toward a high availability cloud: Techniques and challenges. In *IEEE/IFIP International Conference on Dependable Systems and Networks Workshops (DSN 2012)* (pp. 1-6). IEEE.

[10] Sharma, R., & Singh, R. (2021). A Highly Reliable and Cost-effective Service Model for Finite Population Clouds: Analysis and Implementation. *Arabian Journal for Science and Engineering*, 1-16.

[11] Ramos, R. M., Martinello, M., & Rothenberg, C. E. (2013, October). Slickflow: Resilient source routing in data center networks unlocked by openflow. In *38Th annual IEEE conference on local computer networks* (pp. 606-613). IEEE.

[12] Gill, P., Jain, N., & Nagappan, N. (2011, August). Understanding network failures in data centers: measurement, analysis, and implications. In *Proceedings of the ACM SIGCOMM 2011 Conference* (pp. 350-361).

[13] Birke, R., Chen, L. Y., Smirni, E., Birke, R., Chen, L. Y., & Smirni, E. (2012). Data centers in the wild: A large performance study. *IBM Research, Zurich, Switzerland*.

[14] Buyya, R., & Murshed, M. (2002). Gridsim: A toolkit for the modeling and simulation of distributed resource management and scheduling for grid computing. *Concurrency and computation: practice and experience*, 14(13-15), 1175-1220.

[15] Sulistio, A., Cibej, U., Venugopal, S., Robic, B., & Buyya, R. (2008). A toolkit for modelling and simulating data Grids: an extension to GridSim. *Concurrency and Computation: Practice and Experience*, 20(13), 1591-1609.

- [16] Casanova, H. (2001, May). Simgrid: A toolkit for the simulation of application scheduling. In *Proceedings First IEEE/ACM International Symposium on Cluster Computing and the Grid* (pp. 430-437). IEEE.
- [17] Casanova, H., Legrand, A., & Quinson, M. (2008, April). Simgrid: A generic framework for large-scale distributed experiments. In *Tenth International Conference on Computer Modeling and Simulation (uksim 2008)* (pp. 126-131). IEEE.
- [18] Buyya, R., Ranjan, R., & Calheiros, R. N. (2009, June). Modeling and simulation of scalable Cloud computing environments and the CloudSim toolkit: Challenges and opportunities. In *2009 international conference on high performance computing & simulation* (pp. 1-11). IEEE.
- [19] Calheiros, R. N., Ranjan, R., Beloglazov, A., De Rose, C. A., & Buyya, R. (2011). CloudSim: a toolkit for modeling and simulation of cloud computing environments and evaluation of resource provisioning algorithms. *Software: Practice and experience*, 41(1), 23-50.
- [20] Wickremasinghe, B., Calheiros, R. N., & Buyya, R. (2010, April). Cloudanalyst: A cloudsim-based visual modeller for analysing cloud computing environments and applications. In *2010 24th IEEE international conference on advanced information networking and applications* (pp. 446-452). IEEE.
- [21] Buyya, R., Pandey, S., & Vecchiola, C. (2009, December). Cloudbus toolkit for market-oriented cloud computing. In *IEEE International Conference on Cloud Computing* (pp. 24-44). Springer, Berlin, Heidelberg.
- [22] Garg, S. K., & Buyya, R. (2011, December). Networkcloudsim: Modelling parallel applications in cloud simulations. In *2011 Fourth IEEE International Conference on Utility and Cloud Computing* (pp. 105-113). IEEE.
- [23] Calheiros, R. N., Netto, M. A., De Rose, C. A., & Buyya, R. (2013). EMUSIM: an integrated emulation and simulation environment for modeling, evaluation, and validation of performance of cloud computing applications. *Software: Practice and Experience*, 43(5), 595-612.
- [24] Nunez, A., Vazquez-Poletti, J. L., Caminero, A. C., Carretero, J., & Llorente, I. M. (2011, June). Design of a new cloud computing simulation platform. In *International Conference on Computational Science and Its Applications* (pp. 582-593). Springer, Berlin, Heidelberg.
- [25] Núñez, A., Vázquez-Poletti, J. L., Caminero, A. C., Castañé, G. G., Carretero, J., & Llorente, I. M. (2012). iCanCloud: A flexible and scalable cloud infrastructure simulator. *Journal of Grid Computing*, 10(1), 185-209.
- [26] Núñez, A., Andrés, C., & Merayo, M. G. (2012, November). Mascloud: a framework based on multi-agent systems for optimizing cost in cloud computing. In *International Conference on Computational Collective Intelligence* (pp. 436-445). Springer, Berlin, Heidelberg.
- [27] Kliazovich, D., Bouvry, P., & Khan, S. U. (2012). GreenCloud: a packet-level simulator of energy-aware cloud computing data centers. *The Journal of Supercomputing*, 62(3), 1263-1283.
- [28] Snyder, B., Green, R. C., Devabhaktuni, V., & Alam, M. (2018). ReliaCloud-NS: A scalable web-based simulation platform for evaluating the reliability of cloud computing systems. *Software: Practice and Experience*, 48(3), 665-680.

Analytical Study of A Two-Phase Model For Steady Flow of Blood in A Circular Tube

S.R. Verma and Anuj Srivastava

Department of Mathematics, D.A-V. College, Kanpur (U.P.), India

Abstract:

The present paper deals with a mathematical model of blood flow through narrow circular tube. The model consists of a core region of suspension of all the erythrocytes assumed to be a power law fluid and a peripheral cell-depleted layer of plasma as a Newtonian fluid. The system of differential equations has been solved analytically. The expressions for velocity profile, Bluntness parameter, flow rate, the ratio of core hematocrit to discharge hematocrit (H_c/H_D), apparent viscosity (μ_{app}), and the ratio of tube hematocrit to discharge hematocrit (H_T/H_D) and shear stress at the wall have obtained. Some of them have been discussed through graphs.

Key words: Two-phase blood flow, cell-depleted layer, Bluntness, Hematocrit, apparent viscosity.

I. Introduction:

Blood is composed of two major components; the cellular component and the plasma component. In an average adult, the blood volume is approximately 5 litre of which approximately 55% to 60% is plasma and the remaining portion is cellular. More than 99% of the cellular component is composed of red blood cells. The most common way to quantify the percent of blood that is cellular is by quantifying the packed red blood cell volume, which is termed the hematocrit. Hematocrit or red blood cell (RBC) concentration and the shear rate are the principal independent variables for describing the apparent viscosity of blood and other RBC suspension. The formation of RBC aggregates at low shear rates may affect blood flow in the microcirculation. The experimental evidence suggests that hematocrit distribution in the microvasculature is not uniform: RBCs tend to concentrate near the center of the vessel, thus forming and RBC-depleted plasma layer near the wall. RBCs are non-uniformly distributed not only within, but also among the micro vessels. The heterogeneous distribution of RBCs and other blood cells has important implications for microvascular hemodynamic and molecular transport.

The two important mechanisms that cause non-proportional distribution of RBCs and plasma in the microcirculation are "cell screening and "plasma skimming". The cell screening mechanism (Cokelet, 1976 [1]; Pries *et al.*, 1981 [2]), involves direct cell-cell and cell wall-fluid mechanical interactions near the orifice of a side branch.

These interactions cause the RBC trajectories to deviate from the fluid stream lines; which would exist in the absence of the cells. The plasma skimming mechanism is related to the non uniform

distribution of RBCs at the inlet cross-section of arteriolar bifurcations, in particular the formation of a cell-depleted layer near the vascular wall (Tateishi *et al.*, 1994 [3]; Yamaguchi *et al.*, 1992 [4]). For the "ideal" plasma skimming case, when the flow fraction in the branch is less than 0.5 the discharge hematocrit in the branch becomes lower than in the parent vessel.

When blood flows through tubes, the two-phase nature of blood as a suspension becomes important as the diameter of the red blood cell (RBC) becomes comparable to the tube diameter. The following are some of the effects observed in vitro and in vivo:

- (i) Fahraeus - Lindqvist effect: dependence of apparent viscosity on tube diameter;
- (ii) Fahraeus effect: dependence of tube or vessel hematocrit on tube diameter;
- (iii) Existence of a cell-free or cell-depleted layer near the wall;
- (iv) Blunt velocity profile;
- (v) Phase separation effect: disproportionate distribution of red blood cells and plasma at vessel bifurcation.

Fournier [5] have been developed several models to interpret these effects. Pries *et al.* [6] reviewed biophysical aspects of micro-vascular blood flow in vivo as well as in vitro.

Nair *et al.* [7] used a two-phase model for the blood in modeling transport of oxygen in arterioles. They considered a cell-rich cone surrounded by a cell-free plasma layer.

In the cell-rich core, the radial hematocrit distribution was expressed as a power law profile with maximum at the center of the tube. The thickness of the cell-free layer was chosen on the basis of geometrical consideration in terms of RBC size and radius of the tube. However, the

dependence of the thickness on the cell free layer on hematocrit was not taken into account. **Seshadri and Jaffrin [8]** modeled the outer layer as cell-depleted having a lower hematocrit than in the core. The apparent viscosity and the mean tube hematocrit were taken from the measurements obtained in glass tubes. The concentration of RBCs in the cell-depleted layer was assumed to be 50% of that in the core. **Gupta et al., [9]** divided the outer layer into a cell-free plasma layer and cell-depleted layer. In both these studies, the velocity profile in the core was assumed to follow a power law. **Pries et al. [10,11,12]** derived empirical relationship of the relative apparent viscosity and mean tube hematocrit as parametric functions of tube diameter and discharge hematocrit from in vitro **Pries et al. [10,12]** and in vivo **Pries et al. [11]** data.

Numerical modeling can provide information for various hematocrits. Hematocrit is known to affect the viscous properties of blood (**Merril, E.W. [13]** and **Chien, S. et. al. [14]**) and physiological abnormalities in hematocrit are associated with diseases which alter the blood composition (**Chien, S. et. al. [14]**; **Halvorsen, S.[15]**; **Skovborg, R. [16]** and **Leblond, P.F. et. al. [17]**). For example, over production of red blood cells (polycythemia) increases whole blood viscosity, while iron deficiency (anemia) decreases blood viscosity. Changes in blood composition may influence wall shear stress patterns in the arterial system, which may in turn play a role in the sequence of arterial diseases. Effect of hematocrit on wall shear rate in oscillatory flow has been studied by **Kathleen and John [18]** and found that increase in hematocrit produced a decrease in the peak wall shear rate in both the straight and curved artery models and a corresponding decrease in wall shear rate reversal on the inside wall of the curved artery model.

Das et al., [19] considered the effect of nonaxisymmetric hematocrit distribution on non-Newtonian blood flow in small tubes. Eccentric hematocrit distribution is considered such that the axis of the cylindrical core region of red cell suspension is parallel to the axis of the blood vessel but not coincident. Human blood is described by Quemada's rheological model and cat blood is

described by Casson's model. Velocity distribution, shear stress, apparent viscosity and Fahraeus effect have been calculated numerically. These are strongly influenced by the eccentricity factor, the core radius and the tube hematocrit. **Maithili Sharan and Popel [20]** proposed a two-phase model for flow of blood in narrow tubes with increased effective viscosity near the wall. The model consists of a central core of suspended erythrocytes and a cell-free layer surrounding the core. A system of nonlinear equation is solved numerically to estimate bluntness, core radius and core hematocrit. Variation of apparent viscosity and tube hematocrit with the tube diameter and the discharge hematocrit in vitro have been discussed. **Davod Alizadehard et al., [21]** investigated the deformation of RBCs in micro vessels for a variety of vessel diameter (8-50 μ m), Hematocrit (20-45%) and shear rates (20-150 S^{-1}) and comparing the apparent viscosity with experimental results.

The aim of the present investigation is to study the flow of blood as a two-phase model. The behavior of blood is considered as power law in core region and cell-depleted layer as Newtonian fluid. Analytical expressions for velocity profile, bluntness parameter, flow rate, ratio of core hematocrit to discharge hematocrit (H_c/H_D), apparent viscosity and ratio of tube hematocrit to discharge hematocrit (H_T/H_D), shear stress at the wall have obtained. The results are discussed graphically.

II. Mathematical Analysis:

The geometry of the model is shown in Fig.1. The steady laminar two layer model for the blood flow within a cylindrical tube of radius R consisting a central core of radius r_h and effective viscosity μ_c which contains an erythrocyte suspension of uniform hematocrit H_c and a cell-free layer outside the core containing plasma with an effective viscosity μ_0 . The blood is considered as non-Newtonian power law fluid in core region and plasma is Newtonian fluid in cell free layer.

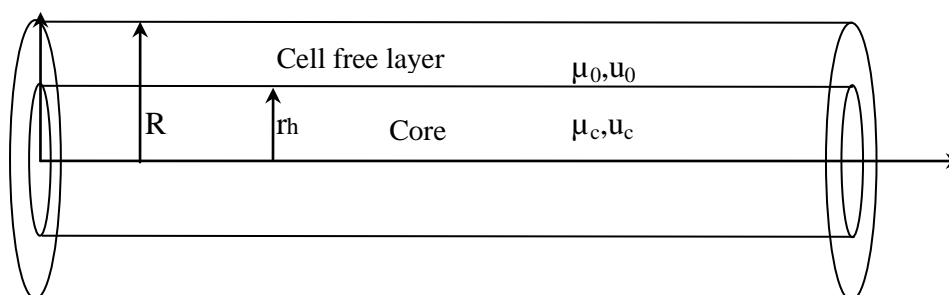


Fig.1. Geometry of the flow model

2.1 Governing equation and boundary conditions:-

The constitutive equation of motion for incompressible steady fully developed flow in a tube reduces to:

$$-\frac{\partial p}{\partial z} + \frac{\mu_c}{r} \frac{\partial}{\partial r} \left[r \left(\frac{\partial u_c}{\partial r} \right)^n \right] = 0, \quad 0 \leq r < r_h \quad (1)$$

for the central core with red blood cells and

$$-\frac{\partial p}{\partial z} + \frac{\mu_0}{r} \frac{\partial}{\partial r} \left[r \left(\frac{\partial u_0}{\partial r} \right) \right] = 0, \quad r_h < r < R \quad (2)$$

for the cell-free layer, where u_c and u_0 are the velocities in the cone and plasma layer respectively, p is the hydraulic pressure and r and z represent the radial and axial direction in the tube.

The boundary conditions are:

- (a) the velocity gradient vanishes along the axis of the tube:

$$\frac{\partial u_c}{\partial r} = 0 \quad \text{at } r = 0 \quad (3)$$

- (b) No slip condition is assumed at the wall;

$$u_0 = 0 \quad \text{at } r = R \quad (4)$$

- (c) The velocity and shear stress are continuous at the interface of plasma and the core:

$$(i) \quad u_c = u_0 \quad \text{at } r = r_h \quad (5)$$

$$(ii) \quad \mu_c \frac{\partial u_c}{\partial r} = \mu_0 \frac{\partial u_0}{\partial r} \quad \text{at } r = r_h \quad (6)$$

2.2 Solution of the problem

The solution of equation (1) and (2), subject to the boundary conditions (3) - (6) is given by

$$u_c(\xi) = -\frac{R^2}{4\mu_0} \frac{\partial p}{\partial z} \left[1 - \lambda^2 + \frac{\mu_0}{\mu_c} \alpha \lambda^{\frac{n+1}{n}} \right] \left[1 - \frac{\frac{\mu_0}{\mu_c} \alpha}{1 - \lambda^2 + \frac{\mu_0}{\mu_c} \alpha \lambda^{\frac{n+1}{n}}} \xi^{\frac{n+1}{n}} \right]; \quad 0 \leq \xi \leq \lambda, \quad (7)$$

$$u_0(\xi) = -\frac{R^2}{4\mu_0} \frac{\partial p}{\partial z} [1 - \xi^2]; \quad \lambda \leq \xi \leq 1 \quad (8)$$

where

$$\xi = \frac{r}{R}, \quad \lambda = \frac{r_h}{R}, \quad \alpha = 2^{\frac{2n-1}{n}} \left(\frac{n}{n+1} \right) \left(\frac{R}{\mu_c} \frac{\partial p}{\partial z} \right)^{\frac{1-n}{n}}$$

$\alpha=1$ for $n = 1$ (Newtonian fluid) and $\frac{\partial p}{\partial z}$ is pressure gradient along the length of the tube.

Velocity in the core $u_c(\xi)$ can be expressed as

$$u_c(\xi) = u_{\max} \left(1 - B \xi^{\frac{n+1}{n}} \right) \quad (9)$$

where,

$$u_{\max} = -\frac{R^2}{4\mu_0} \frac{\partial p}{\partial z} \left[1 - \lambda^2 + \frac{\mu_0}{\mu_c} \alpha \lambda^{\frac{n+1}{n}} \right] \quad (10)$$

$$B = \frac{\frac{\mu_0}{\mu_c} \alpha}{1 - \lambda^2 + \frac{\mu_0}{\mu_c} \alpha \lambda^{\frac{n+1}{n}}} \quad (11)$$

The parameter B is the bluntness of the velocity profile. When $n = 1$ and $\mu_c \rightarrow \mu_0$ then $B \rightarrow 1$ which give the velocity profile becomes parabolic throughout the entire cross-section of the tube and fluid in both layer in Newtonian.

The volumetric flow rate of the blood is given by

$$Q = 2\pi R^2 \int_0^\lambda u_c(\xi) \xi d\xi + 2\pi R^2 \int_\lambda^1 u_0(\xi) \xi d\xi \quad (12)$$

The expression for the flow rate Q is obtained as the evaluation of integrals in (12) with the velocity equations (7) and (8) as:

$$Q = -\frac{\pi R^4}{8\mu_0} \frac{\partial p}{\partial z} \left[1 - \lambda^4 + \frac{2(n+1)}{3n+1} \left(\frac{\mu_0}{\mu_c} \alpha \right) \lambda^{\frac{3n+1}{n}} \right] \quad (13)$$

Mass balance of the cells in the tube is defined as:

$$QH_D = 2\pi \int_0^1 \xi u(\xi) h(\xi) d\xi \quad (14)$$

Where H_D is the discharge hematocrit and $h(\xi)$ is hematocrit function related to core hematocrit H_C as:

$$h(\xi) = \begin{cases} H_c & 0 \leq \xi < \lambda \\ 0 & \lambda < \xi \leq 1 \end{cases} \quad (15)$$

Using (7) and (8) in (14) with (15) we obtain

$$QH_D = -\frac{\pi R^4 H_c}{8\mu_0} \frac{\partial p}{\partial z} \left[2\lambda^2 (1 - \lambda^2) + \frac{2(n+1)}{3n+1} \frac{\mu_0}{\mu_c} \alpha \lambda^{\frac{3n+1}{n}} \right] \quad (16)$$

The ratio H_C/H_D can be obtain from equations (13) and 16) as:

$$\frac{H_C}{H_D} = \frac{1 - \lambda^4 + \frac{2(n+1)}{3n+1} \frac{\mu_0}{\mu_c} \alpha \lambda^{\frac{3n+1}{n}}}{2\lambda^2 (1 - \lambda^2) + \frac{2(n+1)}{3n+1} \frac{\mu_0}{\mu_c} \alpha \lambda^{\frac{3n+1}{n}}} \quad (17)$$

Equation (13) can be written as:

$$Q = -\frac{\pi R^4}{8\mu_{app}} \frac{\partial p}{\partial z} \quad (18)$$

Where μ_{app} is the apparent viscosity of total tube flow given by

$$\mu_{app} = \frac{\mu_0}{\left[1 - \lambda^4 + \frac{2(n+1)}{3n+1} \frac{\mu_0}{\mu_c} \alpha \lambda^{\frac{3n+1}{n}} \right]} \quad (19)$$

The tube hematocrit H_T is defined as:

$$H_T = 2 \int_0^1 h(\xi) \xi d\xi \quad (20)$$

Using equation (15) in (20), we get

$$H_T = \lambda^2 H_C \quad (21)$$

The average velocity of the blood $\left(\bar{U}\right)$ is given as

$$\bar{U} = \frac{Q}{\pi R^2} \quad (22)$$

From equation (10) and (22) the maximum velocity U_{\max} can be expressed as:

$$\frac{u_{\max}}{\bar{U}} = \frac{2\mu_{app}}{\mu_0} \left[1 - \lambda^2 + \frac{\mu_0}{\mu_C} \alpha \lambda^{\frac{n+1}{n}} \right] \quad (23)$$

The shear stress at the wall is defined as

$$\tau_w = -\frac{1}{2} \frac{\partial p}{\partial z} R \quad (24)$$

Using equation (18), and (22) in (24), the expression for the shear stress at the wall is obtained as

$$\tau_w = \frac{4 \mu_{app} \bar{U}}{R} \quad (25)$$

Equation (17), (19) and (21) express H_C , μ_{app} and H_T in terms of λ , H_D , μ_0 and μ_C .

III. Results and Discussion:-

In order to discuss the results of the theoretical model proposed in the study, the analytical expression for velocity profile, Bluntness parameter, flow rate, the ratio of core hematocrit to discharge hematocrit (H_C/H_D), apparent viscosity, the tube hematocrit to discharge hematocrit (H_T/H_D) and shear stress at the wall have been obtained. It may be noted that if we put $n=1$ in present model the results are obtained for both layer is Newtonian.

To discuss the problem, the Bluntness, B; ratio H_C/H_D , apparent viscosity, μ_{app} and ratio H_T/H_D obtained analytically in equation (11), (17), (19) and (21) respectively have been plotted in Figures 2 to 8. For numerical calculations we take $R = 100 \mu m$, $\frac{\partial p}{\partial z} = -75 \times 10^3 \text{ dyne/cm}^3$, $\mu_C = 3.8 \text{ cP}$, $\mu_0 = 1.2 \text{ cP}$.

The parameters B in equation (11) is the bluntness of the velocity profile in core. The parameter depends on the thickness of the cell-free layer. Figure 2 show the variation of bluntness parameter with tub radius R for $n = 3/4$ and $n = 5/4$. It is observe that the numerical values of B for $n=5/4$ are less than that for $n = 3/4$. Bluntness parameter B is plotted in Figure 3 with λ for different values of non-Newtonian parameter. For $n = 3/4$ bluntness parameter B first decreases upto $\lambda=0.2$ and then increases upto $\lambda = 0.6$ and again decreases upto $\lambda = 1$.

Bluntness parameters profile is near about similar for $n = 1$, and $n = 5/4$ but the values for $n = 1$ in greater than that of $n = 5/4$.

Figures 4 and 5 show are variation of ratio H_C/H_D with λ and with R for different values of n. H_C/H_D decreases with λ fastly upto $\lambda=0.4$ and then decreases slowly for $n = 1$ and $n = 5/4$ but increase upto $\lambda=0.5$ then decrease fastly upto $\lambda = 0.6$ and again increase. From figure 4 it is observe that when $n < 1$ the character in very different. Figure 5 shown that H_C/H_D increases fastly upto $R=125 \mu m$ and then slow effect is obtained for $n = 3/4$ whereas H_C/H_D decreases very slowly for $n = 5/4$. Numerical values for $n = 5/4$ of H_C/H_D are greater than that for $n = 3/4$.

The variation of apparent viscosity (μ_{app}) with λ for different value of non-Newtonian parameter n is shown in figure 6. μ_{app} increase slowly with λ upto 0.6 and fastly for $n = 1$ and $n = 5/4$ but the character is very different for $n = 3/4$. The trend of figure are same for $n = 1$ and $n = 5/4$ but numerical values for $n = 5/4$ for different λ are greater than that of $n = 1$.

From figure 7, it is observed that the ratio H_T / H_D increase with λ for $n = 1$ and $n = 5/4$ in similar trend but increases fastly upto $\lambda = 0.4$ then decreases upto $\lambda = 0.7$ and again increases.

Effect of tube radius R on H_T / H_D is plotted in Figure 8 for $n = 3/4, 5/4$. H_T / H_D increase with R for $n = 3/4$ and decreases with R for $n = 5/4$. Numerical values for $n = 5/4$ of H_T / H_D are greater than that for $n = 5/4$.

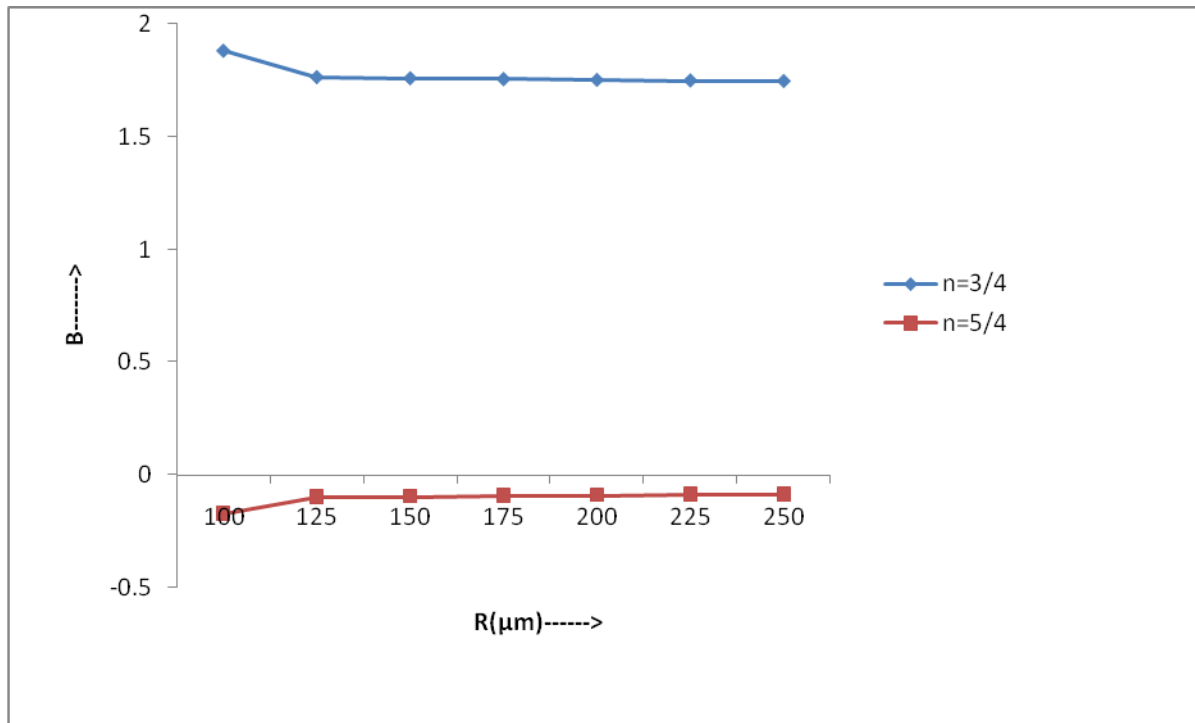


Fig. 2: Variation of Bluntness parameter (B) with R

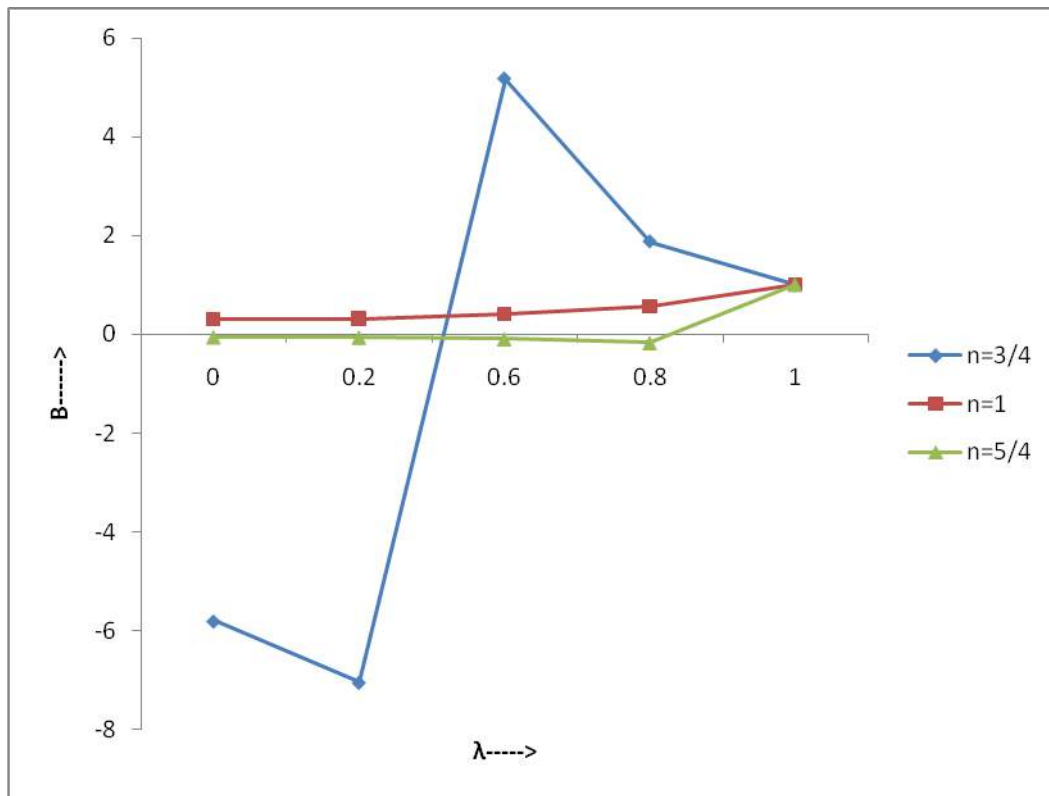


Fig.3: Variation of Bluntness parameter (B) with λ

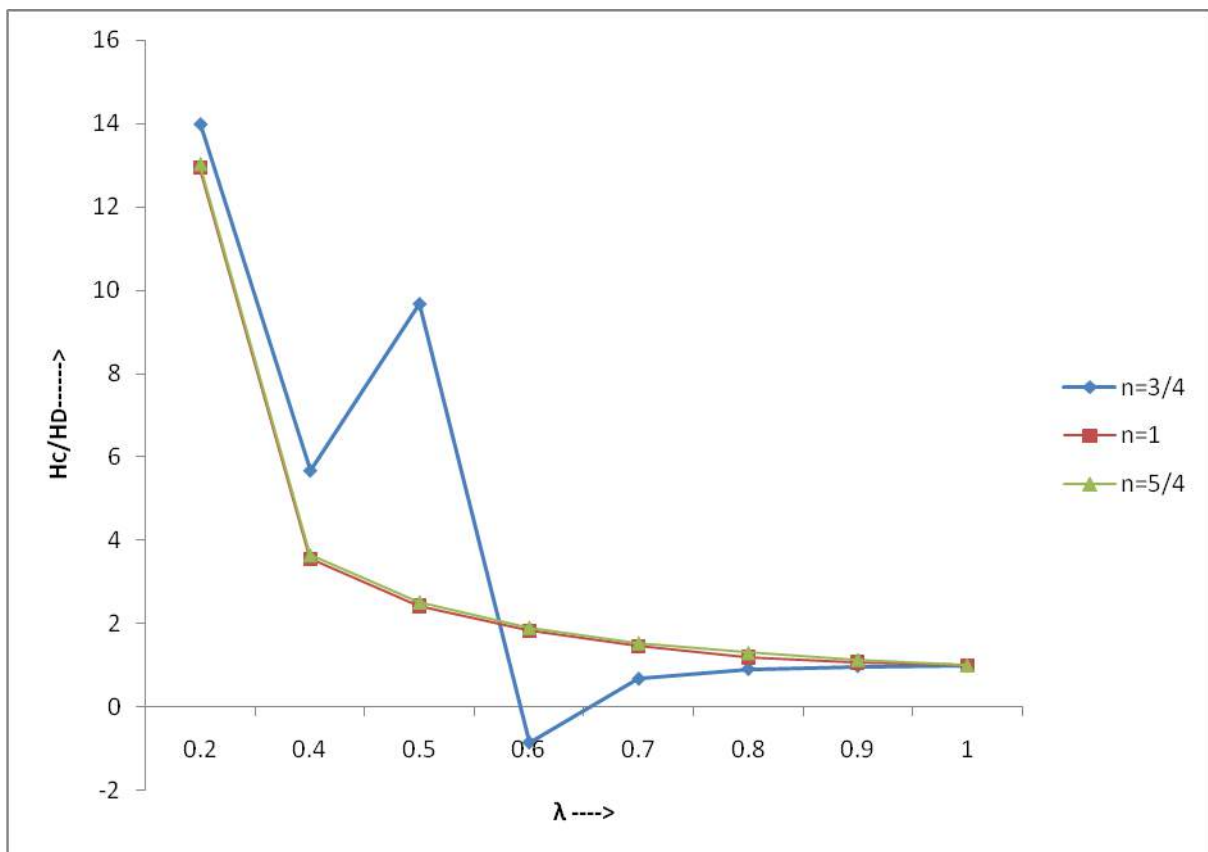


Fig.4: Variation of HC/HD with λ

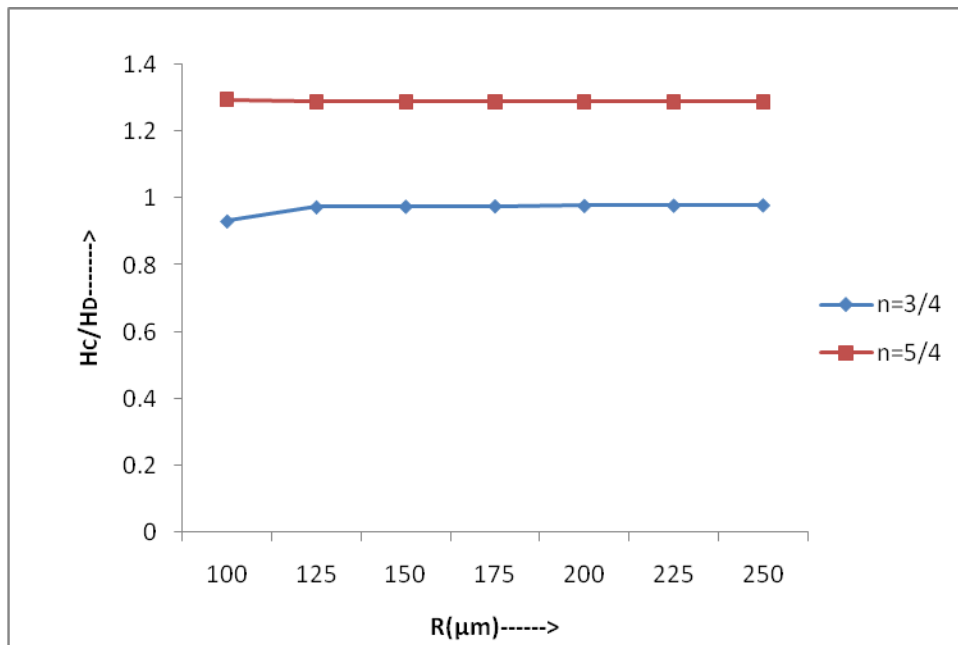


Fig. 5: Variation of HC/HD with R

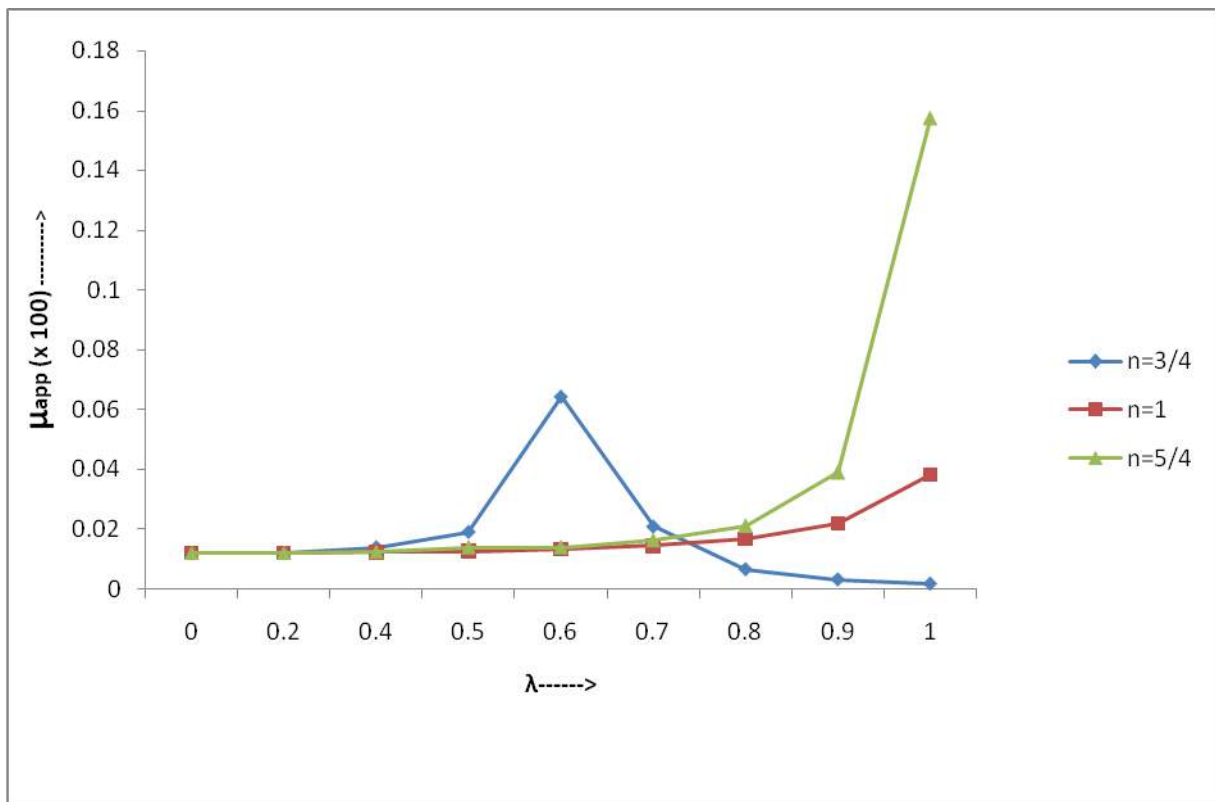


Fig. 6: Variation of apparent viscosity (μapp) with λ

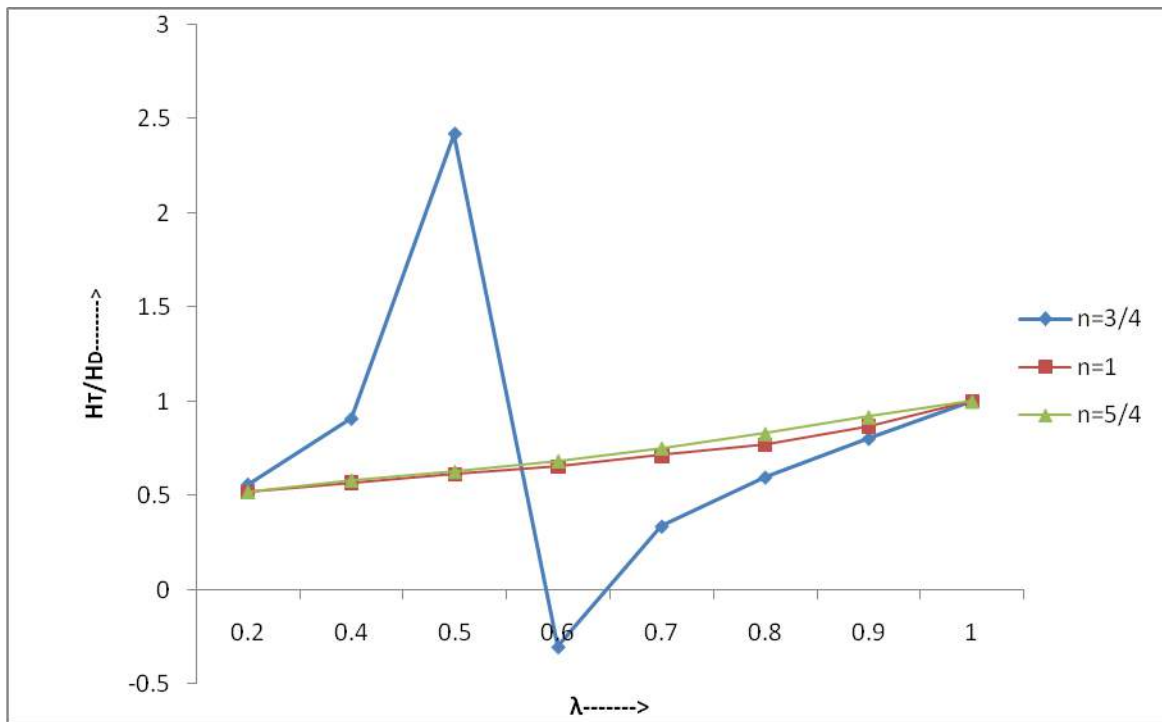


Fig.7: Variation of HT/HD with λ

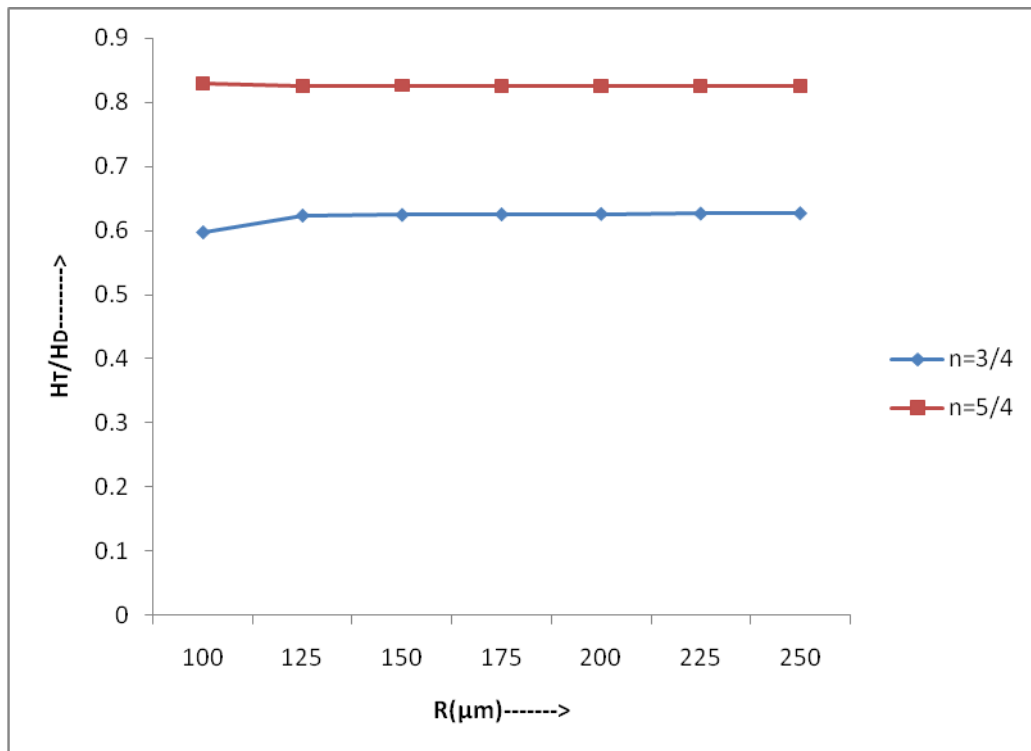


Fig. 8: Variation of HT/HD with R

References

- [1.] Cokelet, G.R. Macroscopic rheology and tube flow of human blood. In: *Microcirculation. Volume 1. Grayson J, Zingg W, Eds; New York: Plenum; pp. 9-31, 1976.*
- [2.] Pries, A.R., Albrecht, K.H. and Gachtgens, P. Model studies on phase separation at a capillary orifice. *Biorheology, 18; pp. 355-367, 1981.*
- [3.] Tateish, N., Suzuki, Y., Soutani, M. and Maeda, N. Flow dynamics of erythrocytes in microvessels of isolated rabbit mesentery: Cell free layer and flow resistance. *Journal of Biomechanics, 27, pp. 1119-1125, 1994.*
- [4.] Yamaguchi, S., Yamakura, T. and Niimi, H. Cell free layer in cerebral microvessels. *Biorheology, 29, pp. 251-260, 1992.*
- [5.] Fournier, R.L. Basic Transport Phenomena in Biomedical Engineering, Taylor and Francis, *Philadelphia, pp. 312, 1999.*
- [6.] Pries, A.R., Secomb, T.W. and Gaehtgens, P. Biophysical aspects of blood flow in the microvasculature, *Cardiovasc. Res. 32, pp. 654-667, 1996.*
- [7.] Nair, P.K., Hellums, J.D. and Olson, J.S. Prediction of oxygen transport rates in blood flowing in large capillaries. *Microvasc. Res. 38, pp. 269-285, 1989.*
- [8.] Seshadri, V. and Jaffrin, M.Y. Anomalous effects in blood flow through narrow tubes: a model. IN *SERM - Euromech. 92, 71, pp. 265-282, 1977.*
- [9.] Gupta B.B., Nigam, K.M. and Jaffrin, M.Y. A three- layer semi-empirical model for flow of blood and other particulate suspensions through narrow tubes. *J. Biomech. Eng. 104, pp. 129-135; 1982.*
- [10.] Pries, A.R., Neuhaus, D. and Gaehtgens, P. Blood viscosity in tube flow: dependence on diameter and hematocrit. *Am.J. Physiol. 263, H1770-H1778, 1992.*
- [11.] Pries, A.R., Secomb, T.W., Gaehtgens, P. and Gross J.F. Blood flow in microvascular networks: experiments and simulation. *Circ. Res. 67, pp. 826-834, 1990.*
- [12.] Pries, A.R., Secomb, T.W., Gesser, T., Sperandio, M.B., Gachtgens, P. and Gorss, J.F. Resistance to blood flow in microvessels in vivo. *Circ. Res. 75, pp. 904-915, 1994.*
- [13.] Merrill, E.W. Rheology of blood, *Physiol. Rews. 49, pp. 863-888, 1969.*
- [14.] Chien, S., Dormandy, J., Ernst, E., and Matrai A. eds., *Clinical Hemorheology, Martinus Nijhoff publishers, Dordrecht, 1987.*
- [15.] Halvorsen, S. Regulation of Erythropoiesis. In. *J. Microcir. Clin. Exp., pp. 109-114, 1984.*
- [16.] Skovborg, R., Nielsen, A.V., Schlichtkrull, J., and Ditzel, J. Blood viscosity in Diabetic Patients *Lancet, 1. pp. 129-131, 1966.*
- [17.] Leblond, P.F., Lacelle, P.L. and Weed, R.I., Cellular Deformability: A possible determination of the normal release of maturing erythrocytes from the bone marrow. *Blood, 7, pp. 40-46, 1971.*
- [18.] Kathleen K. Brookshier and John M. Tarbell, Effect of hematocrit on well shear rate in oscillatory flow: Do the elastic properties of blood play a role? *Biorheology, 28, pp.569-587, 1991*
- [19.] Das, B., Johnson, P.C. and Popel, A.S., Effect of non axisymmetric hematocrit distribution on non-Newtonian blood flow in small tubes. *Biorheology 35: 1, pp. 69-87, 1998*
- [20.] Maithili Sharan and Aleksander S. Popel, A two-phase model for flow of blood in narrow tubes with increased effective viscosity near the wall. *Biorheology 38, pp. 415-428, 2001.*
- [21.] Davod Alizadehrad, Yohsuke Imai, Keita Nakaaki, Takuji Ishikwa and Takami Yamaguchi, Quantification of red blood cell deformation at high-hematocrit blood flow in microvessels. *J. of Bio mechanism 45, pp. 2684-2689, 2012.*